DROPLET FREEZING AND SIGNS OF SMALL SCALE PARTICLE CLUSTERING IN MOUNTAIN WAVE CLOUDS

Darrel Baumgardner[1] and Gregory L. Kok[2]
Centro de Ciencias de la Atmósfera, Universidad Nacional Autónoma de México, Mexico
[2]Droplet Measurement Technologies, Boulder, Colorado

Background

Ice formation processes are enigmatic because of the multiple pathways through which ice crystals form, i.e. via homogeneous freezing or heterogeneous nucleation, as well as from ice multiplication processes. Most of these processes have been studied theoretically (with various levels of sophistication), in the laboratory and in cloud chambers, but there are few, definitive in situ studies, partially because of the lack of instrumentation but also because of the complexity of the clouds.

Orographic wave clouds provide a natural microphysical laboratory that is optimal for studying a subset of the ice formation processes. They have a relatively long lifetime with well defined cloud bases, vertical structure and easily recognizable air mass trajectories through the cloud. These qualities are also optimal for studies by cloud models with explicit microphysics that can be validated by measurements.

The Ice in Cloud Experiment – Layers (ICE-L) was designed to address the question of how ice evolves using wave clouds as the targets for in situ and remote measurements to characterize the aerosol and cloud particles and evaluate them with respect to current hypotheses on ice formation. Two aircraft, the NCAR/NSF C130 and University of Wyoming/NSF King Air were deployed to make in situ and remote measurements, respectively, using an extensive suite of aerosol and cloud particle instruments and cloud lidar and radar.

The objective of the present study is to identify regions where water changes to ice, evaluate the relative fraction of spherical particles and locate regions of inhomogeneity in the cloud particle population that can be related to turbulent mixing or regions of high supersaturation.

The measurements were made in wave clouds that formed over the region of the Rocky Mountains between New Mexico and Wyoming in November and December, 2007. The instrument was the Cloud, Aerosol and Precipitation Spectrometer (CAPS). In the present study, measurements from a single flight are used to illustrate how the unique capabilities of the CAPS can provide information on ice formation processes and the importance of small scale fluctuations as they relate to microphysical processes.

Measurement and Analysis Methodology

The integrated sensors on the CAPS, the Cloud Aerosol Spectrometer (CAS), Cloud Imaging Probe (CIP) (both shown in the photograph in Fig. 1) provide the means to study the small scale structure of these clouds because the scattering and imaging sections measure the angular scattering characteristics of individual droplets and ice crystals in the size range from 0.5 to 50 um and record the gray scale images of particles from 15 um and larger, respectively. In addition, the hotwire liquid water content (LWC) sensor (also shown in Fig. 1), measures principally the liquid phase and excludes the solid phase (Baumgardner et al., 2001).

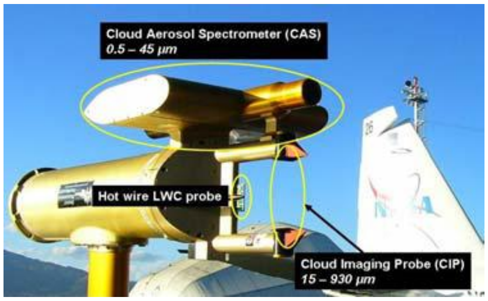

Figure 1

As shown by the block diagram for the optical configuration of the CAS in Fig. 2, individual particles pass through a focused laser beam, with a wavelength of 680 nm, where they scatter light in all directions but the optical collection system only collects light scattered into solid angles of 4º-12º and 168º-176º. The light intensity is converted to an electrical pulse whose peak amplitude is digitized by separate electronics for the forward and backward scattering components.

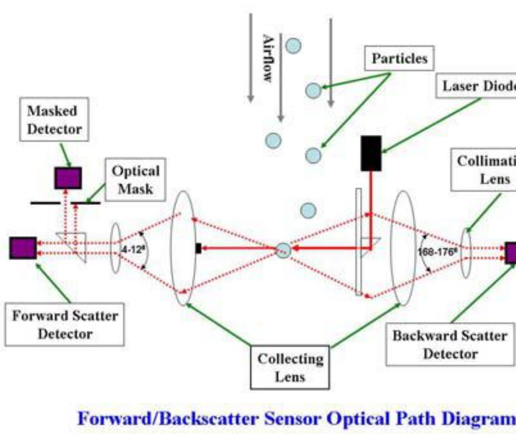

Figure 2

Fig. 3 shows that the intensity of light scattering is not isotropic because of the relative contributions of reflection, refraction and diffraction that depend on size, refractive index, shape and wavelength. For aspherical particles in the size range of the CAS, the near forward scattering is the least and the near backward scattering the most sensitive to deviations from spherical. T-matrix calculations for the collection angles of the CAS (Flores, 2007) show how the ratio of the forward to backward scattering is sensitive to aspect ratio. These calculations were done for the simple case of oblate and prolate spheroids but are approximate surrogates for plate-like and column-like crystals, respectively.

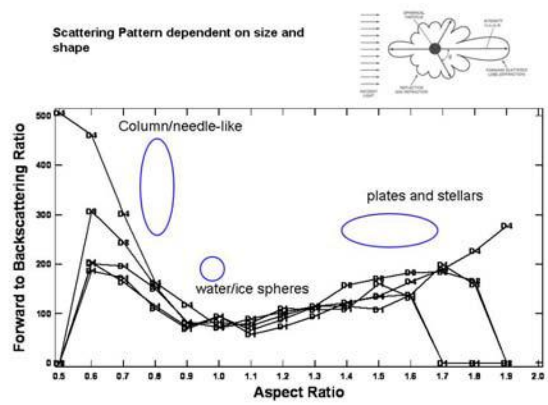

Figure 3

The ratios of the individual forward and backward scattering amplitudes, stored by the CAS, were compared to those theoretically predicted for spherical water droplets in the size range of the CAS. Each forward to backward ratio measured was normalized by the predicted ratio for a water drop with the same forward scattering amplitude. These are referred to in the discussion below as the sphericity factor.

The time between individual particles is also measured and stored by the CAS as an interarrival time in microseconds. These times are an indication of the physical spacing of particle and have been used to evaluate small scale processed in clouds (Baumgardner, 1986; Paluch and Baumgardner, 1989; Baumgardner et al., 1993; Brenguier et al., 1994; Malinowski et al., 1994). Figure 4 illustrates the difference between regions of cloud when the droplets are randomly and uniformly distributed and when in the same region there exist smaller volumes of air where the droplets are clustered with higher concentrations than the average. The graph shows a frequency distribution of the interarrival times measured (solid line) and predicted (dashed). The predicted is derived from the concentration measured by summing all particle events detected over this region and dividing by the sample volume. The dashed curve is the expected frequency distribution of arrival times assuming Poisson statistics for a randomly uniform distribution. The observed deviation indicate fluctuations at smaller scales.

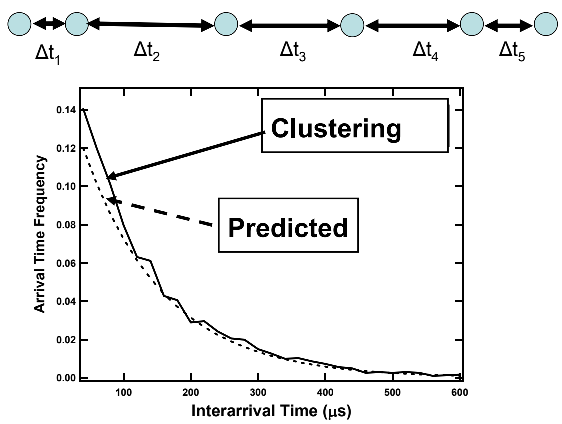

Figure 4

The liquid water content is derived in two ways: i) from integration of the CAS size distribution and assuming spherical particles with density of water or ice (Fig. 5) and ii) from measurements with the hot-wire LWC sensor (Fig. 6).

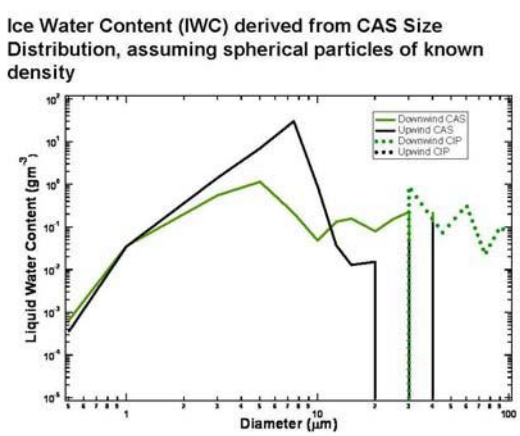

Figure 5

The LWC is derived with the hot-wire technique (King et al., 1978) by measuring the amount of power that is required to maintain a heated, wire-wound cylinder at a constant temperature. The wire is cooled by the air flowing past it and, in clouds, by water droplets that impinge and evaporate.

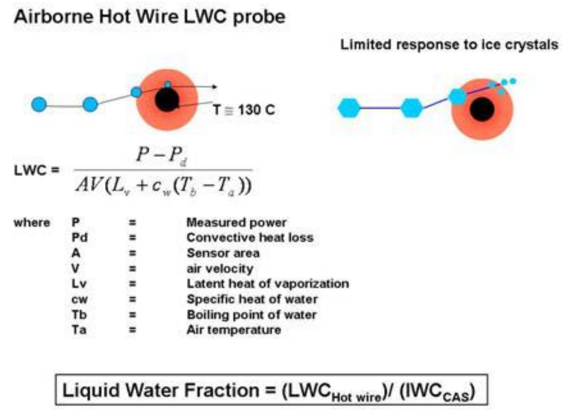

Figure 6

The cooling by convection has been characterized in great detail in wind tunnel studies and can be parameterized by the non-dimensional Reynold's and Prandtl's number. The remaining cooling is due almost entirely to evaporation of hydrometeors. The hot-wire responds primarily to droplets smaller than 30 µm with a very limited response to ice crystals because they shatter or bounce from the wire with very little heat transfer, although there is some evidence that the hotwire will be slightly cooled.

We use the assumption that the hotwire is insensitive to frozen water to derive a parameter we call the LWC fraction that is the ratio of the hotwire derived LWC to the ice water content (IWC) derived from the CAS. We call it IWC since we cannot distinguish between water and ice.

Results and Discussion

The C-130 made 12 research flights between November 13 and December 16, 2007 at different locations over the Central Rocky Mountainss, from southern Colorado to Northern Wyoming. The aircraft was instrumented with multiple sensors to measure aerosol size distributions, cloud condensation and ice nuclei, and chemical composition. The cloud microphysical structure was measured with many optical spectrometers in addition to the CAPS. Total water content was measured with a counterflow virtual impactor. A detailed list of investigators and instruments is available on the project web page.

The measurements discussed in the remainder of this paper were made during the last flight on December 16 in a wave cloud formed over the Wind River Range located in northwestern Wyoming (Fig. 7 – courtesy A. Heymsfield and the Research Aviation Facility).

The top panel in Fig 8 shows the time series of altitude and temperature during the time period that four transects were made through this cloud. The average temperature was -24ºC ± 2º and average altitude 5000 m ± 200. The lower panel displays the concentrations from the CAS and CIP. The average concentration measured with the CAS remained nearly constant at 350 cm^{-3} ± 50 during the 40 minutes of measurements.

Figure 7

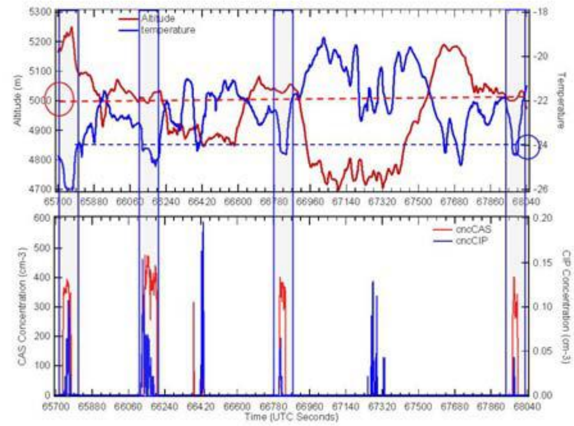

Figure 8

Figures 9 and 10 are more detailed time series of the particle concentrations, LWC, IWC and median volume diameter (MVD) from the third cloud pass (upwind to downwind is from left to right). The MVD is derived only from the CAS measurements. Figure 9 shows that the concentration is quite constant with very little fluctuation at the 1 Hz sample rate shown here. The curve marked FSSP is the concentration measured with a Forward Scattering Spectrometer Probe (FSSP) an instrument with the same fundamental measurement principles as the CAS and one that has been used for more than 30 years for cloud measurements. It is shown here only to validate the measurements from the CAS, a much newer instrument. The higher concentrations from the CAS are a result of the 0.5 µm size threshold compared to the lower size threshold of the FSSP of 2 µm.

The blue curve in Figure 9 is the concentration from the CIP, showing that there are no cloud particles in its size range (> 15 µm) until in the latter half of the cloud pass. This was a persistent feature in all four cloud penetrations.

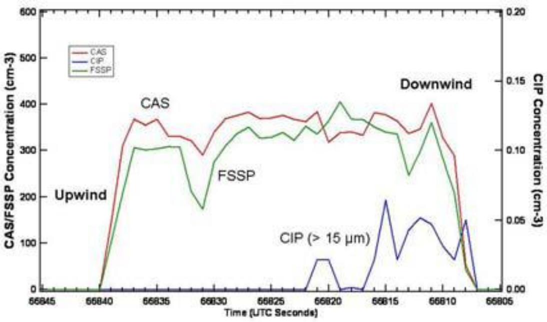

Figure 9

The LWC, IWC and MVD traces in Fig. 10 illustrate the large variation in the size distribution. Although the total number was nearly constant, the LWC and IWC are highly variable. This is a result in the fluctuations in water mass distribution by size, as seen in the MVD that represents the diameter below which 50% of the water mass is found and varies by 50% between 7 and 10.5 µm.

Figure 10 also illustrates that only about 25% of the IWC is liquid water, as seen in a comparison of the IWC from the CAS and LWC from the hotwire.

The fluctuations in water and ice are further identified in Figure 11 that shows the LWC fraction and the spherical fraction. The spherical fraction is defined as the number of individual particles identified as sphere-like, based upon their normalized forward to backward scattering ratio (described above), to the total number of particles measured by the CAS each second.

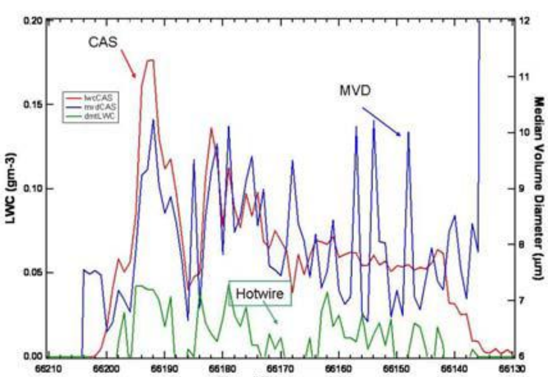

Figure 10

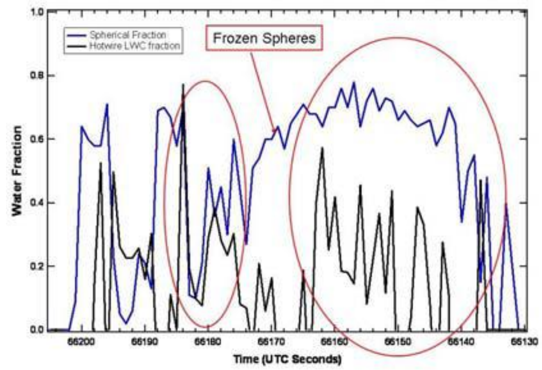

Figure 11

As seen in this figure, the trends in spherical and LWC fraction are similar but the spherical fraction is usually larger than the LWC fraction.

Table I summarizes for the four cloud passes the microphysical properties derived from the CAP's sensors, stratifying by updraft and downdraft region.

Table I

Cloud PASS	Concentration (cm^{-3}) Updraft Downdraft	IWC (gm^{-3})	LWC Fraction	Spherical Fraction
#1	347	0.06	0.9	0.6
	378	0.08	0.9	0.5
#2 +370 s	380	0.09	0.3	0.4
	302	0.04	0.3	0.6
#3 +1075s	350	0.04	0.5	0.7
	357	0.04	0.7	0.7
#4 +2235s	314	0.03	0.3	0.6
	360	0.01	0.5	0.5

The large fraction of spherical hydrometeors in the absence of LWC suggests frozen spheres. Given that homogeneous freezing is thought to only occur when temperatures are lower than -38ºC, this suggests that ice is forming either from contact or immersion freezing. Laboratory studies (Gonda and Takahashi, 1984) and field studies (Korolev and Isaacs) have shown that water droplets will retain an approximately spherical shape for up to 20 minutes after freezing. The air was passing through these clouds at an average velocity of 20 ms^{-1} and the horizontal extent was approximately four kilometers. Hence, the lifetime of the cloud particles was not much more than 200 seconds.

Figure 12 illustrates interarrival time frequencies for two sections of the cloud pass shown in Figs. 9-11 and illustrates the presence of fluctuations at length scales smaller than the 130 meters represented by a one second sample from the CAS. The interarrival time distribution to the left of the figure comes from a region showing little variation at the 1 Hz sample rate. The predicted and measured distributions (dashed and solid lines, respectively), are in very good agreement above 100 μs (13 mm), but deviate at shorter arrival times. This suggests regions of higher concentration where particle spacing is closer.

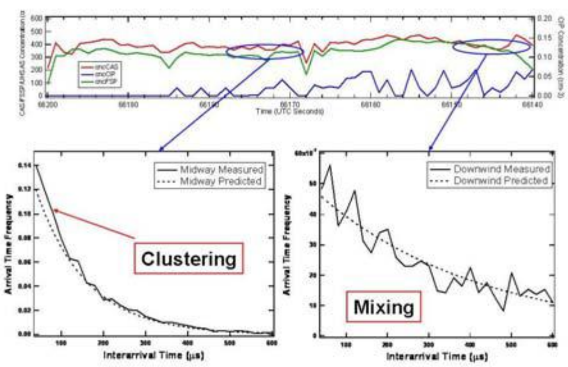

Figure 12

The frequency distribution on the right side of Fig. 12 is also from a section of cloud where the concentration appears relatively constant yet the measured distribution is highly irregular and non-Poissonian with respect to what is predicted. Inhomogeneities of this type can be a result of entrainment and mixing (Paluch and Baumgardner, 1989; Malinowski et al., 1994) or could also be evidence for filaments of higher supersaturations that activate new droplets.

Summary

Particle by particle measurements of the size, shape and spatial distribution of cloud particles, accompanied by measurements of cloud liquid water content, suggest that the transition from water to ice is chaotic even in clouds that are considered smooth compared to other types of clouds. A large fraction of the water droplets that transition to ice maintain their sphericity suggesting that the non-spherical particles are ice that has formed heterogeneously directly from water vapor deposition to ice nuclei.

These results will be combined with those from other measurements of CCN, IN and chemical composition to unravel the complexities of the cloud processes that produce such structure in these clouds.

Acknowledgements
The authors would like to thank the National Science Foundation for supporting their participation in ICE-L, Jeff Stith and the flight crew of the Research Aviation Facility, National Center for Atmospheric Research, for their support of the aircraft and instrumentation, and to Andrew Heymsfield for the nice wavecloud photo and discussions related to our measurements.

References

Baumgardner, D., **1986**: A new technique for the study of cloud microstructure. *J. Oceanic and Atmos. Tech.*, 3, 340-343

Paluch, I. and D. Baumgardner, **1989**: Entrainment and fine scale mixing in a continental convective cloud. *J. Atmos. Sci.*, 46, 261-278.

Baumgardner, D., B. Baker, and K. Weaver **1993**: A technique for the measurement of cloud structure on centimeter scales, *J. Atmos. Oceanic Tech.*, 10, 557-565.

Brenguier, J.L., D. Baumgardner, B. Baker, **1994**: A review and discussion of processing algorithms for FSSP concentration measurements, *J. Atmos. Ocean. Tech.*,11, 1409-1414.

Baumgardner, D., H. Jonsson, W. Dawson, D. O'Connor and R. Newton, **2001**: The cloud, aerosol and precipitation spectrometer (CAPS): A new instrument for cloud investigations, *Atmos. Res.*, 59-60, 251-264.

Flores, M.J., 2007: Caracterización Microfísica e Implicaciones Radiativas de Cirrus Invisibles y Estelas de Avión en la Tropopausa Tropical, Master's Thesis, UNAM, 93 pp.

Gonda and T. Takahashi, 1984: Initial growth forms of snow crystals growing from frozen droplets, *J. Meteor. Soc. Japan*, 62, 190-192.King, W.D., D.A. Parkin, and R.J. Handsworth (1978) A hot wire water device having fully calculable response characteristics, *J. Appl. Meteor.*, 17, 1809-1813.

Korolev, A. and G. Isaacs, 2003: Roundness and aspect ratio of particles in ice clouds. *J. atmos. Sci.*, 60, 1795-1808.

Malinowski, S.P., M.Y. Leclerc and D. Baumgardner, **1994**: Fractal analysis of high resolution cloud droplet measurements, *J. Atmos. Sci.*, 51, 397-413.

DESIGN AND IMPLEMENT OF OROGRAPHIC CLOUDS FIELD OBSERVATION IN A CHINA NSFC KEY PROGRAM

Yue CHEN[1], Tian-Yu CHEN[2], An-Ping SUN[3]
[1] Weather Modification Center of China Meteorological Administration
[2] Weather Modification Office of Gansu Province, China
[3] Weather Modification Office of Qinghai Province, China

1. INTRODUCTION

"Research on Orographic Clouds Structure and Precipitation Mechanism in Northwest China" is a NSFC (Natural Science Foundation of China) key program (2007-2009) which had two years field observation in 2006 and 2007. The advanced detect techniques and theoretical analyses are used in the comprehensive field observation on orographic clouds dynamical and micro-physical structures in Mt. Qi-Lian, improve- ment of the model, climatological analysis and researches on the orographic clouds precipitation mechanism, trying to find the answerers about how the mountain affect the cloud structures and how the orographic clouds precipitation development. The orographic PE concept model and other results from this program will benefit PE operation and improve its scientific levels.

This program consists of different parts as following:

- Research on the synoptic and climatic background of orographic clouds features in Northwest China.
- Comprehensive field observation on orographic clouds dynamical, thermo-dynamic and micro-physical structures.
- Develop and improve orographic clouds modeling.
- Research on precipitation mechanism in Mt. Qi-Lian.
- Find the physical concept model of precipitation in Mt. Qi-Lian.

The rainfall in Mt. Qi-Lian reaches 200-800mm while as the annual mean rainfall is 242.1mm in Northwest China which is only 37.3% that of China.

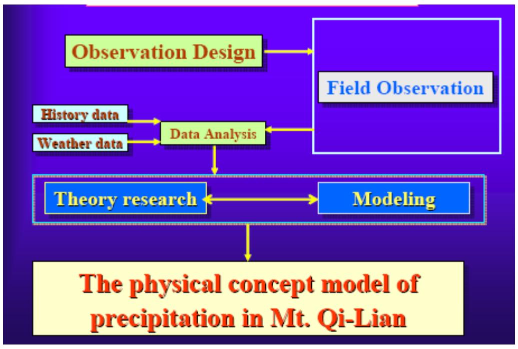

Fig 1 The research scheme

The Chinese Academy of Meteorological Sciences (CAMS), Weather Modification Office of Gansu province and Weather Modification Office of Qinghai province, joint this program.

2. DESIGN OBSERVATION

The primary observation region selected is the strong annual rainfall region, see Fig 2. The observation sites are finally decided in site by features of terrains and the instrumentation to meet the program goal, see Fig 3 and Fig 4. The observation season is chosen in the months in which most low level cloud occurs, see Fig 5.

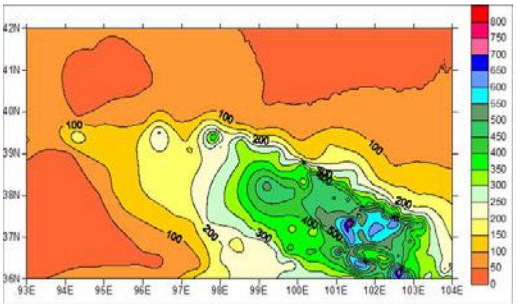

Fig 2 Annual rainfalls in Mt. Qi-Lian.

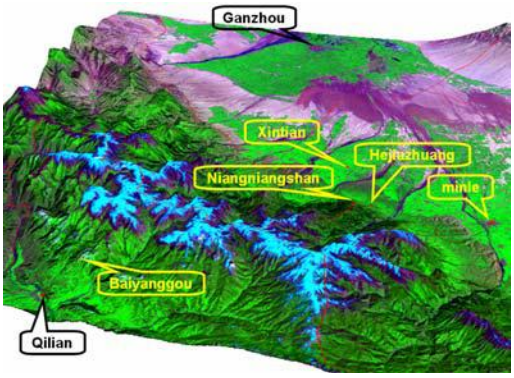

Fig 3 The terrains around the research area.

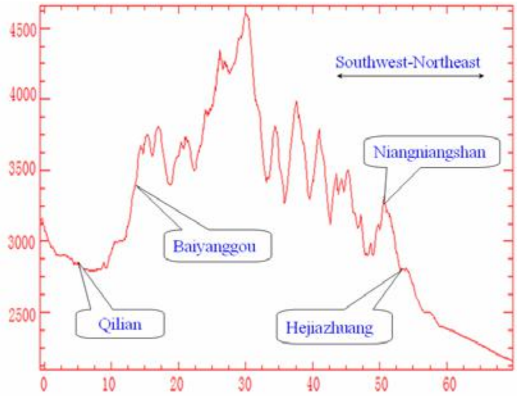

Fig 4 The cross-section (west-westsouthly—east-eastnorthly) of Mt. Qi-Lian.

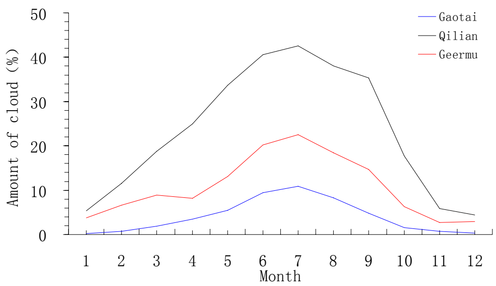

Fig 5 The low level cloud in Mt. Qi-Lian.

The instrumentation is chosen according to the program goals, instrument availability and the fund. The observation methods then set up. Take some changes in 2007 based on the 2006 results.

The instrumentation: Auto Weather Station, Soundings, Rain Drop Distribution, Radar, Profiling Radiometers, Three Dimensional Sonic Anemometer, GPS/MET, CCN counter, FSSP, PCASP, Tethered Balloon and UAV.

3. THE PRIMARILY RESULT

Primarily concept model:

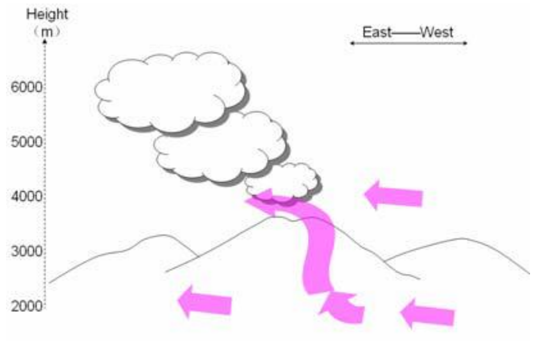

Fig 6a the concept model of orographic cloud development t(east-west) in Mt. Qi-Lian.

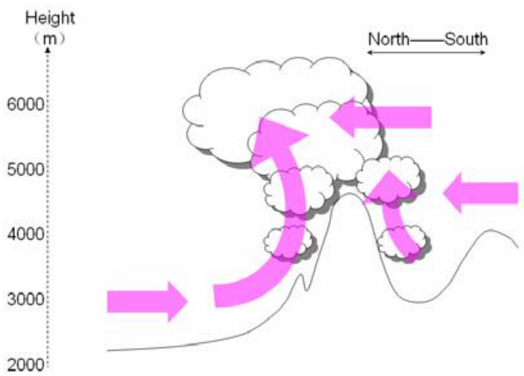

Fig 6b the concept model of orographic cloud development t(south-north) in Mt. Qi-Lian.

RESPONSES OF MIXED-PHASE MICROPHYSICAL PROCESSES TO CLOUD CONDENSATION NUCLEI CHANGES IN A CONVECTION SYSTEM

Chao-Tzuen Cheng[1], Wei-Chyung Wang[1], and Jen-Ping Chen[2]

[1]Atmospheric Sciences Research Center, State University of New York, Albany, NY 12203, USA
[2]Department of Atmospheric Sciences, National Taiwan University, Taipei, Taiwan, ROC

1. INTRODUCTION

Aerosols serving as cloud condensation nuclei (CCN) can initiate liquid drops and regulate cloud properties and precipitation formation. More CCN can result in more but smaller cloud drops, leading to the increases in cloud albedo (Twomey, 1977; Coakley et al., 1987). Meanwhile, the smaller cloud drops would cause weaker autoconversion of cloud drops and prolong the cloud lifetime (Albrecht, 1989; Rosenfeld, 2000). Moreover, decreased raindrops from autoconversion would further result in weaker accretion between cloud drops and raindrops. Therefore, increasing CCN (except giant CCN) usually results in rainfall decrease in warm cloud simulations.

However, the aerosol effect on precipitation process becomes more complicated when ice-phase microphysics participates. In mixed-phase clouds, more cloud drops along with increasing CCN allows more supercooled liquid drops to freeze and enhance accretion and diffusion growths of snow and graupel. Because diffusion growths are important sources of ice-phase precipitations, Bergeron-Findeisen process plays a critical role to show the CCN effect on ice-phase precipitation. Stronger Bergeron-Findeisen process may result in more snow and graupel and the increased melting of more snow and graupel can mitigate the decreases in rainwater production and ease the sensitivity of surface rainfall to CCN changes.

Corresponding author's address: Chao-Tzuen Cheng, Atmospheric Sciences Research Center, State University of New York at Albany, Albany, NY 12203, USA; E-Mail: ctcheng@climate.cestm.albany.edu

Here, we use MM5 coupled with a two-moment mixed-phase cloud scheme to examine the responses of precipitation and microphysical processes to CCN increases in a convection system. The tendencies of microphysical processes are analyzed to distinguish the contributions of "*warm-rain formation"* (rainwater from raindrop deposition growths, cloud drop autoconversion, and rain-cloud accretion), "*cold-rain formation"* (from snow and graupel melting), and "*warm-to-cold-rain conversion"* (raindrops collide with ice-phase hydrometeors and turn into snow/graupel) to rainwater production. The combination of warm-rain formation and warm-to-cold-rain conversion defines the "*corrected warm-rain formation"*.

2. MODEL AND EXPERIMENTS

MM5 incorporated with the two-moment bulk water warm cloud scheme of Chen and Liu (2004), the "CL-scheme", was used in Cheng et al. (2007) to simulate aerosol effect on warm stratiform clouds and is extended to a mixed-phase cloud scheme in this study. The mixed-phase cloud scheme is developed by combining the ice-involved processes from the mixed-phase cloud microphysical processes of Reisner-2 scheme (Reisner et al., 1998) used in MM5 and the warm cloud processes of CL scheme. Hereafter, the new mixed-phase cloud scheme is called the "CLR-scheme". Variables of prognostic hydrometeors include mass mixing ratios of liquid cloud, rain, ice, snow, and graupel and numbers of liquid cloud drops, raindrops and cloud ice. Some modified processes are described as follows.

The equation of Roger and DeMott (1990) is used to calculate homogeneous-freezing nucleation rate in temperature warmer than -40°C. Parameters of Fletcher's formula (1962) were replaced with 5 m^{-3} and 0.304 K^{-1} and a minimum temperature 246 K was set. The initial ice crystal mass per particle is changed to be 5 μm in diameter with a density of 500 kg/m^3. For the Marshall-Palmer (MP) size distribution of raindrops, the intercept and slope of its size distribution is calculated based on its number and mass mixing ratios. Shedding process contributes to raindrops with radius with averaged radius of 1.166 mm. To ensure the size of snowflake and raindrops near melting point would not be too small, the empirical formula of Ryan (2000) to calculate the slope of snowflake MP distribution is adopted.

Following Cheng et al. (2007), aerosols are assumed as ammonia sulfate to serve as CCN and maintain a tri-modal lognormal size distribution. Number of CCN to be activated is decided by the Köhler-curve critical radius (depending on the super-saturation) and the earlier critical radius (retrieved from prognostic dry aerosol and total aerosol masses). Prognostic masses of aerosols inside cloud drops and raindrops are used to account for aerosol recycled from drop evaporations. Parameters for clean continental conditions of Whitby (1978), with a total number concentration of 1800 cm^{-3}, are used to initialize aerosol size distribution at the surface in the control run. These aerosol size distributions contain limited giant CCN, avoiding the opposite giant effects on precipitation. Factors of 0.1 and 10 are applied to the initial aerosol concentrations in different simulations to present "low-CCN" and "high-CCN" cases for the sensitivity test. Changes in high-/low- CCN environment then refer to differences of factor of 0.1 and 10 from the control run.

The radiation model of NCAR-CCM3 is incorporated and fully coupled with cloud microphysical properties where the effective radii are calculated based on mass and number of droplets. The case of a front associated with convection passing through the northern Taiwan during 16-17 May 2003 was simulated. To conduct sensitivity test, lateral boundary conditions are created from results of a MM5 simulation driven by NCEP FNL data with 1°x1° resolution. The inner-most domain is with 3-km horizontal resolution and its 81×72 horizontal grids cover northern Taiwan area, within 120.25-122.75°E and 23.25-21.25°N.

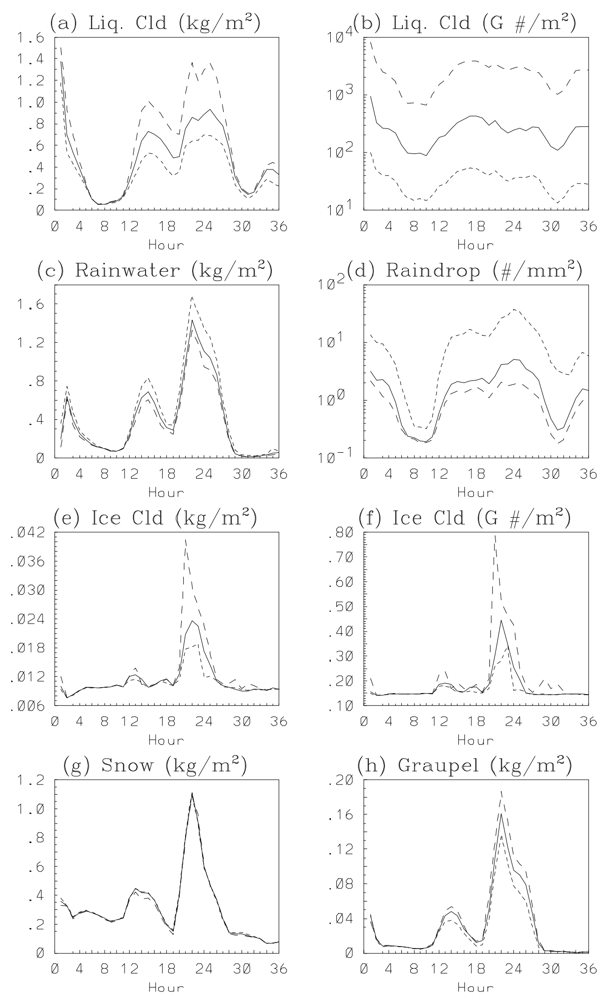

Figure 1. Time series of inner domain averages of column integrated (a) cloud water, (c) rainwater, (e) cloud ice, (g) snow, and (h) graupel water contents and (b) cloud drop, (d) raindrop, (f) ice crystal numbers. Thin dashed, solid, and broken lines indicate results simulated by multiplying a factor of 0.1, 1, and 10 to initial condition of aerosol concentrations, respectively. Hour in horizontal axis starts at 00 GMT, 16 May 2003.

3. SIMULATION RESULTS

Figure 1 shows the time series of inner-domain averaged and column integrated mass and numbers of hydrometeors. Convection started at hour 12, and deep convection occurred during hours 21-28. It is shown that increasing CCN results in more liquid cloud water and cloud drops, less rainwater, and fewer raindrops. Mean cloud drop radius inside the convection zone is about 24, 12, and 6 μm respectively for low-, control and high-CCN cases. Due to the increases in CCN, cloud ice and graupel increase significantly, especially during the convection active period.

More CCN does contribute to stronger growth in ice water content because more cloud water is simulated to sustain a stronger Bergeron-Findeisen process, which converts cloud water to ice. This happens because more and smaller cloud drops evaporate faster to supply water vapor for deposition growth of ice. Thus, cloud drops were depleted much faster through evaporation instead of through freezing. The deposition growths of snow and graupel are also benefited from the enhanced Bergeron-Findeisen process and will contribute to more rainwater when melting occurs. The accumulative rainfall decreased by ~7.2% (from 36.5 to 33.8 mm) in high-CCN environment and nearly unchanged at 36.5 mm in low-CCN environment. Compare with similar simulations using the CL-scheme (no ice phase is considered), where the accumulative surface rainfall is reduced by ~8.7% (from 20.1 to 18.4 mm) in high-CCN environment and increased by ~40 % (from 20.1 to 28.3 mm) in low-CCN environment, rainfall produced by the CLR-scheme is less sensitive to CCN changes.

Although the changes in snow in Fig. 1g seem not noticeable, increasing CCN does affect the amount of snow melting and contribute to significant changes in cold-rain formation. Figure 2 shows the domain-averaged rainfall rates and the differences (from control run) of surface rainfall rates and rainwater production rates. The combination of Fig 2e and 2f actually is very close to Fig. 2b, indicating that the responses of surface precipitation rates can be explained by the changes in the tendencies of microphysical processes. In general, CCN effects do not drastically change surface rainfall (Fig. 2a) and the surface rainfall decreases before hour 12 (Fig. 2b) are mostly dominated by the decreases in warm-rain formation (Fig. 2c and 2e). When CCN increases, less warm rain is produced and the resultant weaker snow-rain accretion above melting level leads to less warm-to-cold-rain conversion to mitigate the rainfall reduction from warm-rain formation (Fig. 2d). After hour 12, convection becomes more active and the changes in cold-rain formation (Fig. 2f) are able to compensate (enhance) the changes in warm-rain formation in low-CCN (high-CCN) case. The changes in warm-rain formation are even offset in low-CCN condition.

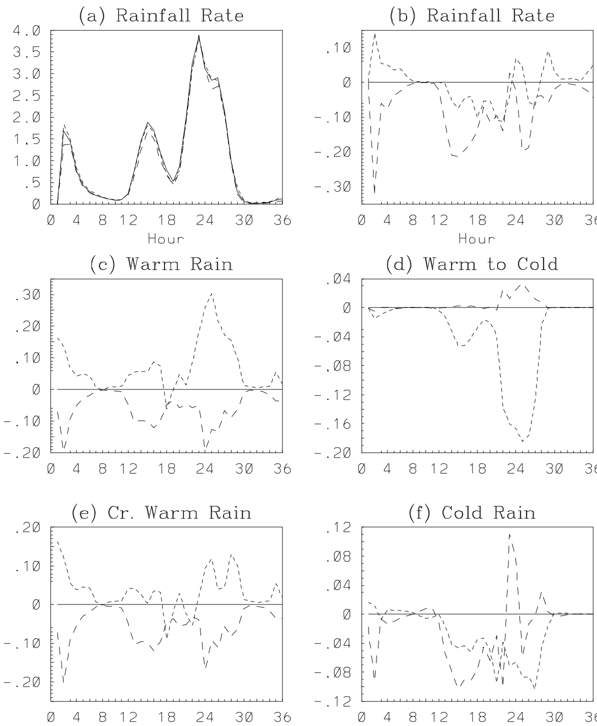

Figure 2. Time series of the inner domain averaged (a) surface rainfall rates; and the differences (from control run) of (b) surface rainfall. Also shown are differences of column integrated rainwater production rates from (c) warm-rain formation, (d) warm-to-cold-rain conversion, (e) corrected warm-rain formation, and (f) cold-rain formation. Unit is mm/hr in each panel with the same line indication as in Fig. 1.

Overall, CCN increases result in increases in graupel and more graupel melting, which contribute to cold-rain formation in Fig. 2f, to counteract the rainfall reduction by warm-rain formation. However, the changes in snow melting reverse and overpower graupel melting in high-CCN environment. Therefore, for most of time in high-CCN environment, the decreased snow melting would enhance the rainfall reduction caused by warm-rain formation.

4. SUMMARY AND DISCUSSION

This study demonstrates that increasing CCN concentration in a convection system not only leads to more cloud drops but also more cloud ice with smaller particle sizes. When CCN increase, freezing of more cloud drops leads to higher ice number production, which will enhance the vapor deposition onto ice and lead to increase ice-phase precipitation. In addition, snow and graupel are three times more efficient than cloud ice in condensing vapor and are able to collect a large amount of liquid-phase hydrometeors, and their melting contribute noticeable amount to the rainwater below. Note that in the current CLR scheme, the snow (and graupel) category does not preserve number information, so their diffusion growth calculations are independent from CCN and cloud drop numbers. Moreover, due to its effective influence on liquid-phase condensates, changes in CCN can also affect the amount and the melting of ice-phase precipitations by influencing their accretions with liquid-phase particles, making the precipitation sensitivity to CCN more complicated.

In this study, the responses of cold-rain formation can offset (enhance) the changes in rainwater from corrected warm-rain formation in low-CCN (high-CCN) cases. The CCN increases lead to increases in graupel melting and decreases in snow melting. The increase in graupel melting dominates cold-rain formation in low-CCN environments while the decrease in snow melting dominates in high-CCN environments. The weaker snow riming process due to smaller cloud drop sizes may be responsible for the reduced snow melting in high-CCN case.

Acknowledgements

The research is sponsored by grants (to SUNYA) from Climate Dynamics and Atmospheric Chemistry of the U.S. National Science Foundation, and the Office of Biological and Environmental Sciences, U. S. Department of Energy and grant (to NTU) by the National Science Council of the Republic of China under Grant NSC 94-2752-M-002-012-PAE.

References

Albrecht, B. A., Aerosols, cloud microphysics, and fractional cloudiness, *Science*, **245**, 1227–1230, 1989.

Chen, J.-P., and S.-T. Liu (2004), Physically based two-moment bulkwater parameterization for Warm Cloud Microphysics, *Quart. J. Roy. Meteor. Soc*., **130**, 51–78, 1989.

Cheng, C.-T., W.-C. Wang, J.-P. Chen, A modelling study of aerosol impacts on cloud microphysics and radiative properties, *Quart. J. Roy. Meteor. Soc*., **133**, 283-297, 2007.

Coakley, J. A., Jr., R. L. Bernstein, and P. A. Durkee, Effect of ship-stack effluents on cloud reflectivity, *Science*, **237**, 1020–1022, 1987.

DeMott, P. J., and D. C. Roger, Freezing nucleation rates of dilute solution droplets measured between -30°C and -40°C in laboratory simulations of natural clouds, *J. Atmos. Sci*., **47**, 1056-1064, 1990.

Rosenfeld, D., Suppression of rain and snow by urban and industrial air pollution, *Science*, **287**, 1793-1796, 2000.

Ryan, Brian, F., A bulk parameterization of the ice particle size distribution and the optical properties in ice clouds, *J. Atmos. Sci*., **57**, 1436–1451, 2000.

Twomey, S., The influence of pollution on the shortwave albedo of clouds, *J. Atmos. Sci*., **34**, 1149–1152, 1977.

Whitby, K. T., The physical characteristics of sulfur aerosols, *Atmos. Environ*.,**12**, 135–159, 1978.

PARTITIONING OF AEROSOL PARTICLES IN MIXED-PHASE CLOUDS

J. Cozic[1,#], B. Verheggen[1,*], E. Weingartner[1], U. Baltensperger[1], S. Mertes[2], D. J. Cziczo[3,+], S. J. Gallavardin[3], K.N. Bower[4], I. Crawford[4], M. Flynn[4], P. Connolly[4], M. Gallagher[4], S. Walter[5], J. Schneider[5], J. Curtius[6], A. Petzold[7]

[1] Laboratory of Atmospheric Chemistry, PSI, CH-5232, Villigen PSI, Switzerland
[2] Leibniz-Institute for Tropospheric Research, D-04318, Leipzig, Germany
[3] Institute for Atmospheric and Climate Science, ETH Zürich, CH-8092 Zürich, Switzerland
[4] University of Manchester, M60 1QD, Manchester, United Kingdom
[5] Max Planck Institute for Chemistry, D-55128, Mainz, Germany
[6] Johannes Gutenberg University, D-55099, Mainz, Germany
[7] German Aerospace Centre, D-82234, Wessling, Germany
[#] Now at: NOAA, Earth System Research Laboratory, Boulder, CO 80305-3337, USA
[*] Now at: Department of Air Quality and Climate Change, Energy research Centre of the Netherlands ECN, 1755 ZG Petten, the Netherlands
[+] Now at: PNNL, Atmospheric Science and Global Change Division, Richland, WA, 99352 USA

1. INTRODUCTION

A series of international field campaigns were carried out at the Jungfraujoch station (3580 m asl) in Switzerland under the name CLACE (Cloud and Aerosol Characterization Experiment). A main focus of CLACE is the investigation of aerosol-cloud interactions in mixed-phase clouds. The Jungfraujoch station is well suited to study these processes since it is situated in the free troposphere with only minor boundary layer influence and is within clouds about 40% of the year. Studying the partitioning of particles into cloud hydrometeors (i.e. droplets and ice crystals) is important because the microphysical and optical properties of the cloud can be altered (indirect aerosol effect). This aerosol indirect effect has been recognized as the greatest source of uncertainty in assessing human impact on climate[1].

2. MATERIAL AND METHODS

The aerosol was sampled by three well characterized inlets: A total inlet (tot) heated to 25°C) designed to evaporate cloud constituents at an early stage of sampling (i.e. sampling both cloud residuals and interstitial particles), an interstitial inlet (int) using a PM2 cyclone and collecting only unactivated aerosol particles (d_p > 2 µm) and an Ice-Counterflow Virtual Impactor (Ice-CVI)[2] designed to sample residual particles of small ice crystals (i.e. particles that served as ice nuclei). Differencing the response downstream of the different inlets provides insight into the partitioning of the aerosol particles into cloud droplets and ice crystals.

A wide variety of physical and chemical parameters was determined downstream of these inlets and were complemented by in-situ measurements of cloud microphysical parameters. Two Scanning Mobility Particle Sizers (SMPS, TSI 3934) were used to measure the particle size distribution between 17 and 900 nm (dry) diameter (one switching between the total and interstitial inlet and another one behind the Ice-CVI inlet). Two Aerosol Mass Spectrometers (AMS, Aerodyne) were operated in parallel to the two SMPS and enabled the determination of the size segregated mass loading of non-refractory chemical components (e.g. sulfate, nitrate, ammonium and organic components) in the size range of 50 – 1000 nm. Two optical particle counters (OPC, Grimm Dustmonitor 1.108) measured the size distribution in the diameter range *dp* = 0.3-20 µm. Three different instrument types measured the aerosol light absorption from which the black carbon (BC) mass concentration was deduced: a multiwavelength Aethalometer (AE31, Magee Scientific), two Multi-Angle Absorption Photometers (MAAP 5012, Thermo Electron Cooperation) and two Particle Soot Absorption Photometers (PSAP, Radiance Research, USA). Cloud droplet size distributions were measured in situ by means of a Forward Scattering Spectrometer Probe (FSSP; modified Model SPP100). A Cloud Particle Imager (CPI; SPEC Inc. Model 230X) was deployed to observe and record real-time CCD images of the ice particles and supercooled droplets with d_p = 10 - 2300 µm present in the clouds. From these images the ice crystal number and mass concentration was determined. The cloud liquid water content (LWC) was continuously measured with two particulate volume monitors (PVM-100, Gerber Scientific).

3. RESULTS

3.1. Partitioning of Aerosol Particles and BC

A result from the latest CLACE campaigns is that the partitioning of aerosol particles to the cloud phase is strongly dependent on the relative fraction of ice in the cloud. Figure 1a shows that the scavenged volume fraction (derived from the size distribution measurements downstream of the total and interstitial inlets and defined as $(V_{tot}-V_{int})/V_{tot}$) is about 60% in liquid clouds. The fraction of scavenged particles decreases with increasing cloud ice mass fraction (IMF)[3] to reach F_{Scav}<10% in mixed-phase clouds with IMF > 0.2. This can be explained by the Wegener-Bergeron-Findeisen process, which describes the effect of a water vapour flux from liquid droplets to ice crystals. The formation of ice during the early stages of cloud development could have prevented additional particles from activating by quickly lowering the supersaturation. This is also due to the difference in vapour pressure over ice and liquid. Figure 1b shows that black carbon (BC) mass is scavenged into the cloud phase to the same extent as the bulk aerosol. Such behaviour is not expected for freshly emitted soot particles because they are hydrophobic[4]. Most soot particles on the Jungfraujoch experienced aging processes which transformed them into an internally mixed hygroscopic aerosol[5]. The scavenged fraction was increased in liquid cloud with increasing liquid water content (LWC) up to a plateau of 60% and decreased with increasing particle (or BC) concentration since there is an increased competition for the available water vapour.

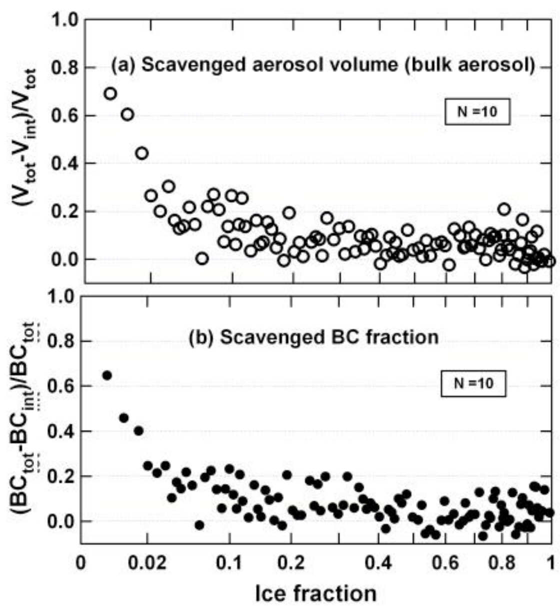

Figure 1. Scavenged fraction of aerosol volume (a) and black carbon mass (b) vs. the ice mass fraction of mixed phase clouds. Each point represents an average of 100 min of measurement.

3.2. Enrichment of Black Carbon in Ice Residuals

The Ice-CVI allowed for the sampling and subsequent analysis of residual particles in small ice crystals (ice residuals). The chemical composition of ice residuals was remarkably different from the total aerosol (Figure 2). Comparison of SMPS and AMS data confirms the findings of Krivacsy et al.[6] that this aerosol is composed to about 95% of non-refractory material (vaporized at 600°C). Ice residuals show a significantly different signature: Ice crystal residuals sampled by the Ice-CVI show a negligible mass concentration of non-refractory material as measured by the aerosol mass spectrometer compared to the SMPS derived mass, indicating that preferably refractory (i.e. non-volatile, such as BC or mineral dust) particles act as ice nuclei. An analysis of the size resolved mass size distributions shows that the ice residuals experience a relatively larger mass contribution from particles larger than 300 nm, suggesting that larger particles (e.g. mineral dust) preferentially act as ice nuclei.

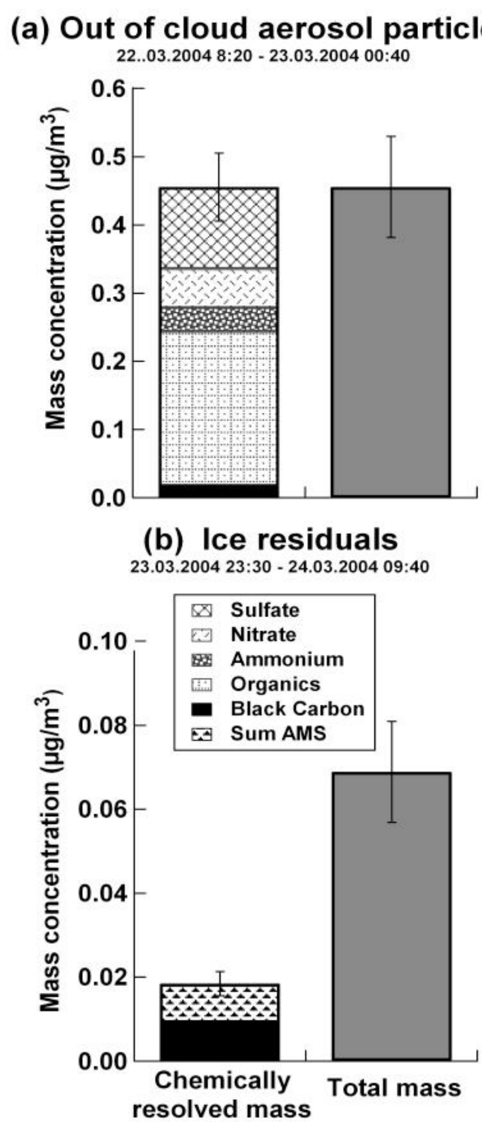

Figure 2. Example of submicrometer chemical composition of (a) the out-of-cloud aerosol and (b) ice residuals.

The BC mass fraction behind the total inlet ($BC_{tot}/(V_{tot} \cdot \rho)$, assuming an aerosol density of ρ =1.5 g/cm^3) was compared to the BC mass fraction behind the Ice-CVI ($BC_{cvi}/(V_{cvi} \cdot \rho)$, assuming an aerosol density of ρ = 2 g/cm^3). It can be observed that BC behind the total inlet represents between 3 to 10% of the total aerosol mass whereas in ice residuals it represents from 4 up to 60% of the aerosol mass. Points above the 1:1 line have a larger BC fraction in the ice residuals than in the total aerosol, while below it is the reverse is true. Figure 3 thus shows that most of the time, BC is enriched in the ice residuals compared to the bulk aerosol. On average 20% of the ice residuals is composed of BC[7].

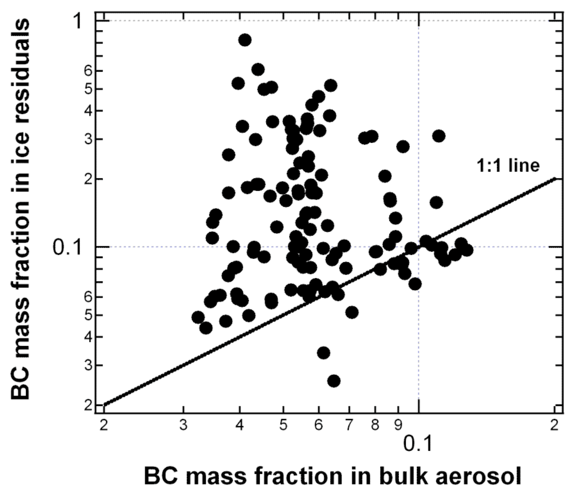

Figure 3. Comparison of the BC mass fraction in the ice residual phase with the corresponding fraction in the bulk aerosol phase in-cloud. Each point represents an average of 30 min of measurement. Note that the scales are logarithmic.

Besides dust, BC also acts as potential ice nuclei. If generally true, this means that in addition to an indirect effect on liquid cloud formation, there is an indirect aerosol effect via glaciation of clouds. This result is highly important for climate since BC has a predominately anthropogenic origin.

4. REFERENCES

1. Intergovernmental Panel on Climate Change (IPCC) (2001).
2. Mertes, S., et al., Aerosol *Sci. Technol.,* 41, 848-864 (2007).
3. Verheggen, B., et al., *J. Geoph. Res., 112, D23202,* doi:10.1029/2007JD008714 (2007).
4. Weingartner, E., et al., *Environ. Sci. Technol.*, 36, 55-62 (2002).
5. Cozic, J., et al., *Atmos. Chem. Phys.*, *7*, 1797-1807 (2007).
6. Krivacsy, Z., et al., *J. Atmos. Chem.,* 39, 235-259 (2001).
7. Cozic, J., et al., *J. Geoph. Res.,* submitted (2007).

5. ACKNOWLEDGMENTS

This work was supported by MeteoSwiss in the framework of the Global Atmosphere Watch program, the German Research Foundation DFG, and the U.K. Natural Environment Research Council NERC. Thanks as well to the Swiss National Science Foundation (grant PBBE2--119260).

CLOUD RESOLVING MODEL WITH BIN- RESOLVED MIXED- PHASE MICROPHYSICS

Zhiqiang Cui, Kenneth S. Carslaw, and Alan M. Blyth
Institute for Climate and Atmospheric Science
School of Earth and Environment, University of Leeds, UK

1. INTRODUCTION

Aerosol-cloud-climate interactions remain a dominant uncertainty in radiative forcing [IPCC, 2007]. Modelling studies play an important role in understanding the interactions. Models for aerosol-cloud interactions need to have better representations of aerosol particles and cloud microphysics. During recent years, bin-resolved schemes have been employed because the schemes directly compute the size distributions of aerosol and hydrometeors without prescribed functions. One such model is MAC3 (Model of Aerosols and Chemistry in Convective Clouds) developed at the University of Leeds, UK. MAC3 has been used to study aerosol cycling (Yin et al., 2005), aerosol effect on mixed phase clouds (Cui et al., 2006), and aerosol transport (Cui and Carslaw, 2006). One limitation of MAC3 is its axisymmetry, which restricts the clouds being studied in an environment of relatively weak wind shear. To improve the model capability, we develop a new model by combining MAC3 with a cloud resolving model.

The United Kingdom Meteorological Office (UKMO) large eddy model (LEM) is a 3-dimensional atmospheric model designed for use at high resolution over a limited spatial domain. A full description of the model equations can be found in Derbyshire *et al.* (1994) and Gray *et al.* (2001). A three-phase microphysics parameterization is present in the LEM. It is a bulk-water scheme dividing all types of water particles into discrete categories, namely, rain, snow, graupel, and liquid water cloud. Recently, Hill (2006) incorporated a bin resolved cloud microphysics package into the LEM. The resulting model (BR-LEM) provides a detailed binned representation of both cloud condensation nuclei and cloud droplet number and mass concentration. This model has been used for evaluation of the semi-direct effect. However, BR-LEM only contains warm rain processes. This presentation will show the new development of the BR-LEM to incorporate cold cloud processes. The new model builds on three existing models:

- LEM: the UK Meteorological Office large eddy model,
- BR-LEM: LEM with bin resolved warm cloud microphysics, and
- MAC3: an axisymmetric dynamic cloud model with bin-resolved microphysics and aqueous-phase chemistry developed by Yin et al. (2005).

2. APPROACH

An adequate representation of both cloud dynamics and microphysics is a very important requirement in aerosol-cloud interaction models.

MAC3 is a cloud model with bin-resolved microphysics (Tzivioin et al., 1987), which exactly conserves total mass, independent of the number of bins, time step, initial conditions, or kernel used. This model has been successfully applied to the processes of aerosol-cloud interactions of a mixed-phase convective cloud (Yin et al., 2005), with the processes of nucleation, vertical transport, aqueous chemistry, resuspension, nucleation scavenging, and impaction scavenging.

The Met Office LEM is the model of choice for cloud dynamics and entrainment studies. The aim of this work is to incorporate the MAC3 aerosol and cloud microphysics in the LEM, thereby producing an advanced dynamical and microphysical coupled model for aerosol-cloud interaction research. Using sensitivity tests the most important processes will be given priority and an improved LEM with explicit ice and liquid microphysics including explicit treatment of the existing aerosol will be developed. The resultant model will be compared to the results of mixed-phase clouds with aerosol and cloud measurements.

3. FEATURES OF THE NEW MODEL

3.1 Aerosol activation

In this study aerosol particles of a certain size are activated when the supersaturation calculated by the model at each grid point exceeds the critical value determined by the Köhler equation. Aerosol particles begin to grow by absorption of water vapour long before they enter the cloud. These wetted particles provide the initial sizes for subsequent activation and condensational growth.

It is assumed the condensation growth of aerosol particles with radii smaller than 0.12 μm to be according to the Köhler equation. After reaching the critical sizes, these particles are then transferred to the cloud droplet bins where their subsequent growth is calculated based on the kinetic condensation equation. For particles with radii larger than 0.12 μm, a factor k_{r0} was used to calculate the initial sizes of the droplets at 100% RH ($k_{r0} = 5.8w^{-0.12}a^{-0.214}$, with vertical velocity w in ms^{-1} and the particle radius a in μm). The formulation of k indicates that the relative growth of a particle decreases with both increasing particle size and increasing updraught, with w representing a proxy for time available for growth.

3.2 Cloud microphysics

The liquid-phase microphysical processes included are drop nucleation, condensation and evaporation, collision–coalescence, and binary break-up. The ice-phase processes considered are ice nucleation (deposition, condensation–freezing, contact nucleation, and immersion freezing), ice multiplication, deposition and sublimation of ice particles, ice–ice and ice–drop interactions (coagulation, accretion, or riming), melting of ice particles, and sedimentation of drops and ice particles. All these microphysical processes are formulated for the first two moments (number and mass) of the distribution functions of each hydrometeor species and are solved using moment-conserving techniques (Tzivion *et al.* 1987).

The present model also includes prognostic equations for the number and specific mass of aerosols in the air and in hydrometeors, and equations to describe impaction scavenging of aerosol particles by hydrometeors, aerosol regeneration following complete evaporation/ sublimation of hydrometeors.

3.3 Impaction scavenging of aerosols

Impaction scavenging of aerosol particles by hydrometeors leads to a decrease in the number concentration and mass of the aerosol particles in the air and to an increase in the corresponding values in the hydrometeors. This process also changes the distribution functions of the hydrometeors involved.

The equations (the number concentration and specific mass for each aerosol bin, and the number concentration and specific mass for each hydrometeor bin) are solved numerically using the moment-conserving method of Tzivion *et al.* (1987). In the scavenging calculations, the efficiencies for collision of hydrometeors with aerosol particles are described in Yin et al. (2005).

4. PRELIMINARY RESULTS

To examine the model performance, we tested the model for a setting of a mixed-phase convective cloud. The initial conditions are same as in Yin et al. (2005).

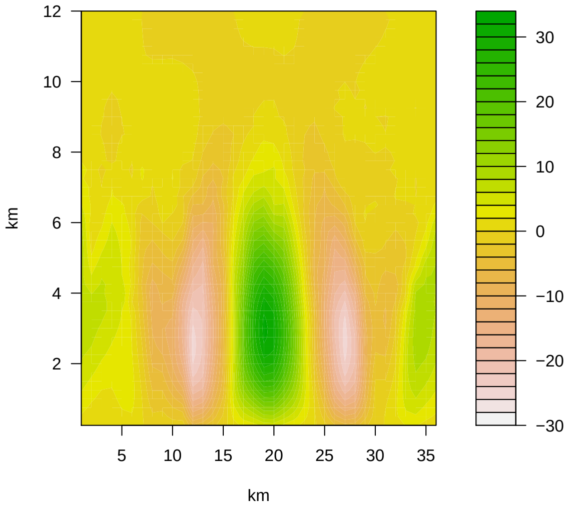

Figure 1. The simulated vertical velocity (unit: ms^{-1}) at 6000 sec.

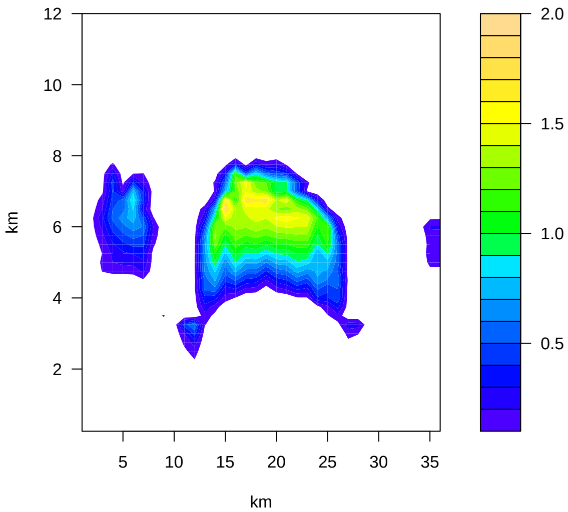

Figure 2. The simulated cloud drop mass (unit: g kg^{-1}) at 6000 sec.

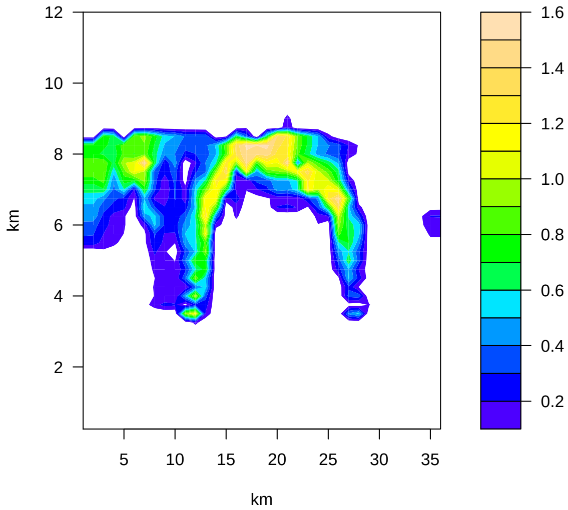

Figure 3. The simulated ice crystal mass (unit: g kg^{-1}) at 6000 sec.

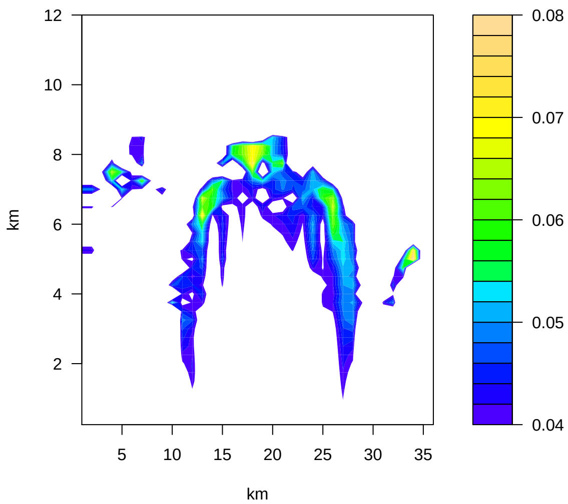

Figure 4. The simulated graupel mass (unit: g kg^{-1}) at 6000 sec.

The figures show the preliminary results. The new model produces cloud drop (Fig. 3), ice crystal (Fig. 4), and graupel (Fig. 5) masses similar to the previous cloud model results. We will make further comparison in the future and examine the effect of aerosol on cloud properties.

5. SUMMARY

In this presentation, we describe the development of a CRM with bin-resolved aerosol and microphysics schemes. We show the preliminary results. How the model does?

In the future, we will simulate more cases in various environments and make inter-model comparisons to examine the performance of the model and model specific cases in APPRAISE (The Aerosol Properties, PRocesses And Influences on the Earth's climate) in conjunction with field observations to examine the nucleation of ice in mixed-phase clouds.

REFERENCES

Cui, Z., K. S. Carslaw, Y. Yin, and S. Davies, 2006: A numerical study of aerosol effects on the dynamics and microphysics of a deep convective cloud in a continental environment, *J. Geophys. Res.*, **111,** D05201, doi:10.1029/2005JD005981.

Cui Z. and K.S. Carslaw, 2006: Enhanced vertical transport efficiency of aerosol in convective clouds due to increases in tropospheric aerosol abundance, *J. Geophys. Res.*, **111**, D15212. doi:10.1029/2005JD006781

Derbyshire, S. H., A. R. Brown, and A. P. Lock, 1994: The Met Office Large-Eddy Simulation Model. *Met Office (APR) Turbulence and Diffusion Note*, **213**.

Gray, M. E. B., J. Petch, S. H. Derbyshire, A. R. Brown, A. P. Lock, H. A. Swann, and P. R. A. Brown, 2001: Version 2.3 of the Met Office Large Eddy Model: Part II. Scientific documentation. *Met Office, (APR) Turbulence and Diffusion*, **276**.

Hill, A, 2006: Assessment of the semi-direct effect in marine stratocumulus using a newly developed bin-resolved LES model, PhD thesis, University of Leeds, UK.

IPCC, 2007: Climate Change 2007: The Physical Science Basis. Contribution of Working Group I to the Fourth Assessment Report of the Intergovernmental Panel on Climate Change, Solomon, S., D. Qin, M. Manning, Z. Chen, M. Marquis, K.B. Averyt, M. Tignor and H.L. Miller (eds.)]. Cambridge University Press, Cambridge, United Kingdom and New York, NY, USA, 996 pp.

Reisin, T., Z. Levin, and S. Tzivion, 1996: Rain production in convective clouds as simulated in as axisymmetric model with detailed microphysics. Part I: Description of the model. *J. Atmos. Sci*., **53,** 479-519.

Tzivion, S., G. Feingold, and Z. Levin, 1987: An efficient numerical solution to the stochastic collection equation. *J. Atmos. Sci.*, **44,** 3139–3149.

Yin, Y., K. S. Carslaw, and G. Feingold, 2005: Vertical transport and processing of aerosols in a mixed-phase convective cloud and the feedback on cloud development, *Q. J. R. Meteorol. Soc.*, **131,** 221-246.

Acknowledgement

This work is funded by UK NERC APPRAISE project.

ON IMMERSION FREEZING AS A NUCLEATION MECHANISM IN MIXED-PHASE STRATUS

Gijs de Boer[1], Tempei Hashino[1], Gregory J. Tripoli[1], Edwin W. Eloranta[1]
[1]The University of Wisconsin - Madison

1. INTRODUCTION

The persistence of mixed-phase stratus clouds at high latitudes remains as an unexplained phenomenon in both theoretical and observational circles. These very common thin cloud layers are observed to persist for several days at a time at both Arctic and mid-latitude locations, exhibiting both a continuous liquid layer and precipitating ice throughout this period. This cohabitation of liquid and frozen phases contrasts with common theory, which would dictate that presence of ice would rapidly deplete the layer of it's liquid, and a complete glaciation would occur. This glaciation of cloud layer and an under prediction of liquid water has been shown to exist in numerical simulations of these structures. Another interesting observation is that these layers have been observed in areas where very few ice forming nuclei (IN) have been detected, leading to the assumption that this ice is not being formed through traditional contact or depositional freezing.

A lack of IN measurements have led some researchers to hypothesize that immersion freezing may play a major role in explaining how ice and liquid persist over extended time periods. Since immersed IN are very difficult to detect with current instruments, these aerosols may have gone undetected. This paper will introduce a conceptual model for the life-cycle of ice and liquid within these clouds. We will evaluate the likelihood of immersion freezing playing a major role in the life-cycle of these cloud structures through a combination of observational and numerical studies.

Observations utilized include those from long-term deployments to two Arctic locations. Instruments used in these deployments include a suite of ground-based remote sensors, such as a Millimeter Cloud Radar (MMCR), Arctic High Spectral Resolution Lidar (AHSRL), Atmospheric Emitted Radiance Interferometer (AERI) and Microwave Radiometer (MWR). In addition to information gathered from observations, sensitivity experiments completed at the Large-Eddy simulation (LES) scale using a size-resolving microphysical scheme are also reviewed for evidence pertaining to the role of immersion freezing. A combination of observational and theoretical work will result in an improved understanding of the likelihood of immersion freezing being a controlling nucleation mechanism within these cloud structures.

Historically, five primary ice nucleation modes have been discussed in the literature (Pruppacher and Klett, 1997). The first of these is homogeneous freezing, in which liquid droplets freeze without influence of IN at low temperatures. Secondly, there is condensation nucleation, in which liquid condenses upon an aerosol particle and freezes during the condensation process. Also included is contact nucleation, in which a liquid droplet comes in contact with an IN and freezes, and depositional nucleation, in which water vapor deposits upon an IN and freezes to form an ice particle. Finally, there is the immersion freezing process, in which an IN is immersed within a liquid droplet, and some alteration of the temperature or concentration of soluble material in the drop allows it to freeze.

When viewed in the context of low-level mixed-phase stratus clouds, several of these ice production mechanisms appear to have issues that would prevent them from producing the amount of ice observed in these clouds. Homogeneous freezing, for example, has been shown to be insignificant at temperatures >238 K (e.g. Hagen et al., 1981; Sassen and Dodd, 1988; Jensen et al., 1998). Figure 1 illustrates that mixed-phase stratus observed at high latitudes often occur at significantly warmer temperatures. Also, measurements of ice particle concentrations often significantly exceed the measured IN concentrations in these cloud structures (Mossop, 1970; Fridlind et al., 2007). This would appear to imply that contact and depo-

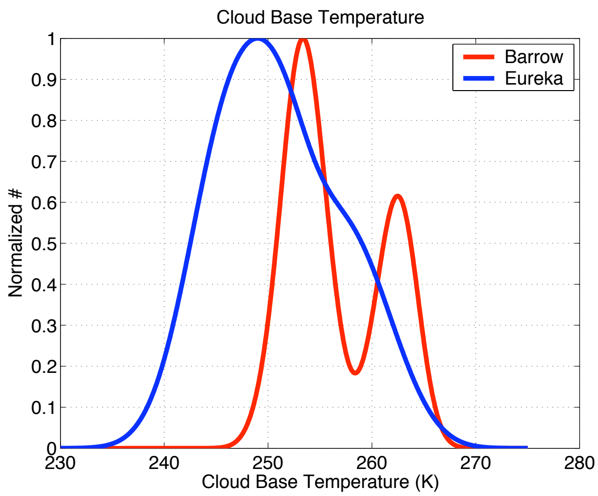

Figure 1: A distribution of cloud base temperatures for observations from Eureka (08/2005-present) and Barrow (09/2004-11/2004).

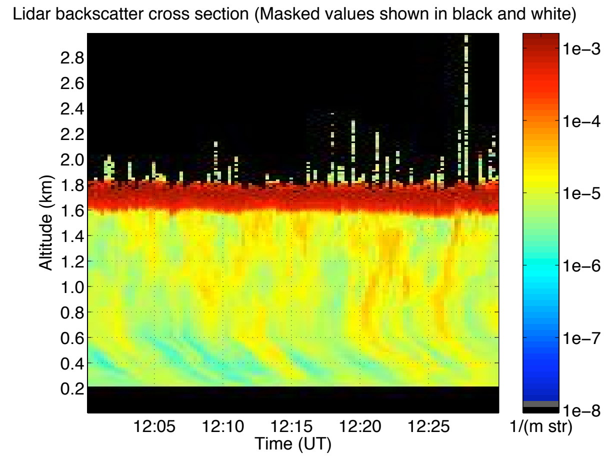

Figure 2: A typical mixed-phase stratus layer as observed by the AHSRL in Eureka. Note the distinct bursts of ice (orange/yellow) precipitating from the mixed-phase layer (red).

sitional nucleation are unlikely to be the drivingnucleation mechanism in these clouds. Finally, IN involved in the condensation nucleation process are likely to be measured by traditional tools such as the Continuous Flow Diffusion Chamber (CFDC).

2. A CONCEPTUAL MODEL FOR IMMERSION FREEZING IN MIXED-PHASE STRATUS

Figure 2 shows an example of a mixed-phase stratus layer as seen by the University of Wisconsin Arctic High-Spectral Resolution Lidar, stationed at Eureka (79.99 N, 85.94 W). The large backscatter cross-section is the result of liquid present in the mixed-phase layer, while higher regions of backscatter below the cloud layer are precipitating ice falling in distinct bursts. Herman and Goody (1976) describe the formation of liquid stratus layers in the Arctic. By their theory, a moist layer advected into the Arctic is cooled radiatively to saturation, at which point a liquid cloud layer is formed. Liquid droplets in this layer are formed on particles that have a significant amount of soluble mass, such as soot coated in sulfuric acid, initially preventing ice formation. At the formation of the cloud layer, radiative cooling to space from cloud-top is initiated, driving internal circulations inside the cloud, and the liquid layer may be maintained. The mystery of these clouds involves the presence and formation of ice within this layer, and the maintenance of the layer once ice is produced.

In the conceptual model presented here, liquid particles cool in the updrafts through expansion and condensational growth increases the size of these drops. Additionally, this increase in size reduces the soluble mass fraction of the resulting solution. After a sufficient decrease in soluble mass fraction, the particle is able to freeze. After formation of a significant number of ice particles, excess vapor is used to grow the ice, and liquid growth (and thereby new ice formation) is halted. The ice particles now grow until they are large enough to precipitate out of the cloud, forming the ice bursts shown in figure 2.

3. OBSERVATIONAL EVIDENCE SUPPORTING THIS MODEL

Discussion of observations start with the aerosol particles upon which these droplets may be formed. Bigg (1980) observed sulfuric acid coating on aerosol particles during winter. Blanchet (2007) hypothesized that this coating results from anthropogenic emissions from Siberia, and that these sulfur coated aerosols are transported throughout the Arctic. This sulfur coating changes a formerly insoluble potential IN into an apparently soluble CCN particle, inhibiting ice formation. This inhibition of ice formation has been confirmed in the laboratory by Möhler et al. (2005) and others.

Of course, the question as to how these aerosols are not observed comes in to play. The reason behind this may lie in the instrument design of the CFDC. At the inlet of the instrument, there is an impactor, removing particles larger than 1 μm. This impactor prevents liquid droplets formed on the coated aerosol from entering the CFDC chamber to be measured as an active IN. Given the highly saturated environment in the cloud layer, it is likely that many of these particles will have nucleated water droplets. Particles that have not yet formed liquid droplets would be able to enter the CFDC chamber. However they would still need to grow to the size necessary for sufficient dilution of the soluble mass in the droplet in order for them to form an ice particle. Whether this would or would not happen is under investigation. Should the critical size not be reached, however, these particles too would be missed as possible IN, as the liquid droplet formed in the chamber would be evaporated, and the aerosol particle removed before IN counting occurs.

In addition to studies on the aerosols involved, several microphysical studies have also taken place which seem to support the presented theory. In-situ measurements by Rangno and Hobbs (2001) revealed that ice crystal concentrations were highly proportional to the concentration of drops larger than 20 μm. This would point to ice and liquid growth occuring in the same regions, and a possible connection between ice nucleation and larger liquid particles. Additionally, Shupe (2008) illustrated that ice formation in Arctic stratus layers is linked to areas of upward vertical motion (figure 3 a,b,c), and that the bursts shown in figure 2 occur in regions of ascent within the cloud layer. Not only does this link ice formation to the dynamics of the cloud, but it also connects ice formation to a likely growth of the liquid particles within the updraft. This is further confirmed in the same work, when liquid and ice water paths

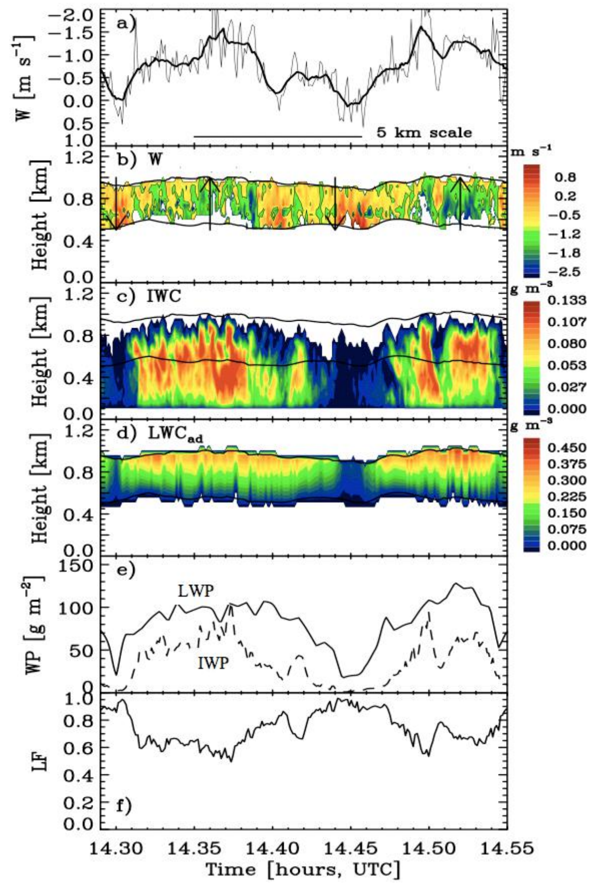

Figure 3: Vertical motion derived from the MMCR spectra (a, b) plotted with retrieved IWC (c), LWC (d), cloud mean IWP and LWP (e), and liquid fraction (f) (from Shupe et al., 2006).

as estimated from an MMCR are shown to change in phase with each other, with IWP lagging slightly behind the LWP.

4. SECONDARY ICE FORMATION

In addition to the primary nucleation modes, there are several secondary processes for ice formation (Pruppacher and Klett, 1997). Included in this group are things such as drop shattering, ice-ice collisions, splinter ejection during riming (Hallett-Mossop process), and evaporation freezing.

Although it is likely that some of these processes are active in mixed-phase cloud layers, there are reservations about their efficiency in these environments. Drop shattering has been shown to produce about 15 ice fragments/drop but only in about 10% of drops larger than 50 μm, increasing total ice by a factor of 2, and rarely (if ever) by more than a factor of 10 (Pruppacher and Klett, 1997). Splinter ejection produces even less particles, with ice multiplication estimated at one splinter per 250 drops larger than 12 μm rimed onto one crystal, and has been shown to be limited to air temperatures of 265-270 K. (Koenig, 1977; Beheng, 1982,1987; Cotton et al. 1986). Neither of these production amounts would make up for observed discrepancies between IN and ice concentrations, and these clouds occur at significantly lower temperatures than the range given. Finally, a process like ice-ice collision requires the presence of many ice particles to begin with, which have to be nucleated through a process other than these collisions. A further review of multiplication processes is given in Fridlind et al. (2007). Although some of these and other processes are likely active, it remains unproven that any one of these mechanisms would serve as the dominant source of ice nucleation.

5. SIMULATION AND MODEL ADVANCEMENT

Efforts are currently underway to investigate the connections discussed above through high resolution simulation of mixed-phase cloud layers. Participation in both the Atmospheric Radiation Measurement (ARM) and GCSS/WMO cloud modeling intercomparisons on these clouds provides ideal cases for implementation and testing of new microphysical schemes. Results from the ARM intercomparison show overproduction of ice by most models in simulating single-layer mixed-phase stratus. This agressive ice production leads to depletion of liquid in the cloud layer (Klein et al., 2008). Although not yet completed at the time of writing of this manuscript, implementation of a new immersion freezing scheme including both temperature and soluble mass fraction as deciding factors in the freezing of drops is sure to provide interesting results, and should be completed within the next few months.

6. SUMMARY

A theory on ice nucleation in mixed-phase clouds through the immersion freezing process has been presented. Observational evidence appears to support this theory as a possible explanation for the ice observed in these mixed-phase cloud layers. Future work will involve further observational investigation along with numerical simulation of these cloud types to search for further evidence of the immersion freezing process within these cloud layers, as well as the testing of new numerical schemes designed to capture this process more accurately.

7. BIBLIOGRAPHY

Beheng, K., 1982: A Numerical Study of the Combined Action of Droplet Coagulation, Ice Particle Riming, and the Splintering Process in Maritime Cumuli, *Contrib. Atmos. Phys.*, **55**, 201-214.

---, 1987: Microphysical Properties of Glaciating Cumulus Clouds: Comparison of Measurements with a Numerical Simulation, *Q.J.R. Meteorol. Soc.*, **113**, 1377-1382.

Bigg, E.K., 1980: Comparison of Aerosol at Four Baseline Atmospheric Monitoring Stations, *J. Appl. Met.*, **19**, 521-533.

Blanchet, J-P, E. Girard, C. Jones, P. Grenier, R. Munoz-Alpizar, P. Du, C. Stefanof, A. Stefanof, and D. Simjanovski, 2007: Arctic Regional Climate Modelling: GEM-Arctic, the DGF Process and CloudSat-CALIPSO New Perspective, Polar Snow Hydrology Mission Workshop, Montreal, Canada.

Cotton, W.R., 1986: Numerical Simulation of the Effects of Varying Ice Crystal Nucleation Rates and Aggregation Processes on Orographic Snowfall, *J. Clim. Appl. Meteorol.*, **25**, 1658-1680.

Fridlind, A.M., A.S. Ackerman, G. McFarquhar, G. Zhang, M.R. Poellot, P.J. DeMott, A.J. Prenni and A.J. Heymsfield, 2007: Ice Properties of Single-Layer Stratocumulus during the Mixed-Phase Arctic Cloud Experiment (M-PACE): Part II, Model Results, J. Geophys. Res., **112**, D24202, doi:10.1029/2007JD008646.

Hagen, D.E., R.J. Anderson, and J.L. Kassner, 1981: Homogeneous Condensation

Freezing Nucleation Rate Measurements for Small Water Droplets in an Expansion Cloud Chamber. *J. Atmos. Sci.*, **38**, 1236-1243.

Herman, G., and R. Goody, 1976: Formation and Persistence of Summertime Arctic Clouds. *J. Atmos. Sci.*, **33**, 1537-1553.

Jensen, E.J., and Coauthors, 1998: Ice Nucleating Processes in Upper Tropospheric Wave-Clouds Observed During SUCCESS. *Geophys. Res. Lett.*, **25**, 1363-1366.

Klein, S.A., R. McCoy, H. Morrison, A. Ackerman, A. Avramov, G. de Boer, M. Chen, J. Cole, A.D. DelGenio, M. Falk, M. Foster, A. Fridlind, J.-C. Golaz, T. Hashino, J. Harrington, C. Hoose, M. Khairoutdinov, V. Larson, X. Liu, Y. Luo, G. McFarquhar, S. Menon, R. Neggers, S. Park, K. von Salzen, J.M. Schmidt, I. Sednev, B. Shipway, M. Shupe, D. Spangenberg, Y. Sud, D. Turner, D. Veron, G. Walker, Z. Wang, A. Wolf, S. Xie, K.-M. Xu, F. Yang, and G. Zhang, Intercomparison of model simulations of mixed-phase clouds observed during the ARM Mixed-Phase Arctic Cloud Experiment. Part I: Single layer cloud., *Q.J.R. Meteorol. Soc.*, in preparation.

Koenig, L.R., 1977: Rime-Splintering Hypothesis of Cumulus Glaciation Examined Using a Field-of Flow Cloud Model, *Q.J.R. Meteorol. Soc*., **103**, 585-606.

Möhler, O., S. Büttner, C. Linke, M. Schnaiter, H. Saathoff, O. Stetzer, R. Wagner, M. Krämer, A. Mangold, V. Ebert, U. Schurath, 2005: Effect of Sulfuric Acid Coating on Heterogeneous Icen Nucleation by Soot Aerosol Particles, *J. Geophys. Res.*, **110**, D11210.

Mossop, S.C., 1970: Concentrations of ice crystals in clouds. *Bull. Amer. Meteorol. Soc*., **51**, 474-479.

Pruppacher, H.R., and J.D. Klett, 1997: Microphysics of Clouds and Precipitation,Springer.

Rangno, A.L., and P.V. Hobbs, 2001: Ice Particles in Stratiform Clouds in the Arctic and Possible Mechanisms for the Production of High Ice Concentrations, *J. Geophys. Res.*, **106**, 15065-15075.

Sassen, K., and G.C. Dodd, 1988: Homogeneous Nucleation Rate for Highly Supercooled Cirrus Cloud Droplets. *J. Atmos. Sci.*, **45**, 1357-1369.

Shupe, M.D., P. Kollias, P.O.G. Persson, and G.M. McFarquhar, 2007: Vertical motions in Arctic mixed-phase straturs. *J. Atmos. Sci.*, in press.

MODELING PHYSICOCHEMICAL PROCESSES INVOLVED IN CLOUD FORMATION TO STUDY THEIR IMPACTS ON THE EVOLUTION OF ATMOSPHERIC CHEMICAL COMPOSITION

L. Deguillaume[1], M. Leriche[2], M. Monier[1], F. Champeau[1] and N. Chaumerliac[1]

[1]LaMP/CNRS, Université Blaise Pascal, Aubière, France

[2]LA/CNRS, Université Paul Sabatier, Toulouse, France

1. INTRODUCTION

This work deals with the development of mixed phase cloud microphysics in the frame of a multiphase cloud chemistry model (Leriche et al., 2007). The coupled model is then applied to evaluate the role of this type of clouds on atmospheric species concentrations. Clouds are good transport vectors for pollutants, they scavenge them through precipitation and they also host complex chemical reactions. Through the parameterization of pollutants partition among the various cloud phases via riming, crystal growth by vapour deposition, melting and collection processes, the importance of ice phase and of crystal habit for the cloud chemical composition is demonstrated.

Various air masses are simulated to form the clouds to assess the influence of cloud precipitation efficiency on their chemical composition. Tests on the ice retention and the burial during riming and crystal growth by vapour deposition respectively are realized to conclude in favour of the major role of ice phase in the trace compounds budget.

2. THE M2C2 MODEL

The M2C2 (*Model of Multiphase Cloud Chemistry*) model results of the coupling (Leriche et al., 2007) between a multiphase chemistry model described in Leriche et al. (2000) and a two-moment warm microphysical scheme module predicting the number concentration and the mixing ratio of cloud water and rainwater categories (Caro et al., 2004). The dynamical framework of the model is an air parcel (Gérémy et al., 2000).

The chemistry included in the chemical module is explicit. The exchange of chemical species between the gas phase and the aqueous phase is parameterised with the mass transfer kinetic formulation developed by Schwartz (1986). The aqueous phase chemistry includes the detailed chemistry of HO_x, chlorine, carbonates, NO_y, sulphur, the oxidation of organic volatile compounds (VOCs) with one carbon atom (Leriche et al., 2003), the chemistry of transition metal ions for iron, manganese and copper (Deguillaume et al., 2004). The model considers calculations of photolysis frequencies both in the gas phase and in cloud droplets. The pH is calculated at each time step by solving the electroneutrality equation.

The activation of aerosol particles is considered following the parameterization of Abdul-Razzak et al. (1998) and Abdul-Razzak and Ghan (2000). Aerosol particles are represented by the sum of three log-normal distributions as:

$$\frac{dN_{ap}}{d\ln a_{ap}} = \sum_{i=1}^{3} \frac{N_{api}}{\ln\sigma_i \sqrt{2\pi}} \exp\left[-\frac{\ln^2(a_{ap}/a_{mi})}{2\ln^2\sigma_i}\right]$$

Where N_{ap} is the total number concentrations of aerosol particles, N_{api} is the number concentrations of aerosol particles for each mode; a_{mi} is the median radius of the log-normal distribution for each mode; σ_i is the geometric standard deviation of the log-normal distribution of each mode and a_{ap} is the radius of aerosol particles.

The parameterization used for computing nucleation of cloud droplets comes down to find an expression for the maximum of the supersaturation on each model time step (Abdul-Razzak et al., 1998 and Abdul-Razzak and Ghan, 2000). Then, the proportion of each mode which is activated can be calculated leading to the number of new droplets formed by nucleation.

The introduction of cloud droplets nucleation in the model allows following the evolution of aerosol particles spectrum. The microphysical scheme for aerosol particles is a two-moment scheme in which the prognostic variables are the number concentration of aerosol particles and the corresponding volumetric concentration (Caro et al., 2004). At each time step, the evolution of aerosol particles spectrum is computed from the number of nucleated droplets and the activated aerosol mass associated.

The impact of aerosol particles on cloud chemistry is considered in the model via the activated mass of aerosol particles and the fraction of soluble chemical species in aerosol particles which are used to compute the chemical concentrations in cloud droplets of species coming from the activated particles.

Mixed-phase cloud processes have been introduced with prognostic variables for both mixing ratios of cloud water, rain, cloud ice, snow and graupel and corresponding hydrometeor number concentrations. The size distribution of the hydrometeors (except cloud water) is assumed to follow a generalized gamma distribution and suitable power laws are taken for the mass-size or for the velocity size relationships to perform analytical integrations in microphysical rates calculations. Also, size parameters can be adjusted to better characterize the shape of ice particles or raindrops. Mixed phase processes are parameterized based upon the work of Reisner et al. (1998), updated with Thompson et al. (2004) and describe pristine formation, vapor deposition and collision/coalescence growth, evaporation, sedimentation and all complex conversions between hydrometeor categories, such as aggregation, accretion, riming, freezing, melting and sublimation.

Then chemistry is coupled with mixed phase microphysics through mass transfer exchanges between gas and aqueous phase and microphysical transfer from one hydrometeor category to another one.
At last ice retention and the burial during riming and crystal growth by vapour deposition respectively are considered to conclude in favour of the major role of ice phase in the trace compounds budget.

3. MIXED PHASE SIMULATIONS

The model simulates the ascent of an air parcel along a predefined trajectory during one hour with a vertical velocity of 0.4 m/s.

Various air masses (continental, maritime) with different chemical composition (polluted, background respectively) are simulated to form the clouds to assess the influence of cloud precipitation efficiency on their chemical composition.

Chemical Species	Maritime Concentrations (ppbv) Williams et al. (2002)	Continental Concentrations (ppbv) Leriche et al. (2000)
O_3	30	37
NO	0	0,9
NO_2	0,1	6,2
CO	140	100
HNO_2	0	0,054
H_2O_2	1	0,07
CH_2O	0,5	6
SO_2	0,1	0,45
HCOOH	0,25	0,28
CH_3OOH	1	0
CH_3OH	0,5	2,25
NH_3	0,5	0,13
HCl	0,5	0,07

Table1: Initial gas phase contents.

Gas concentrations are presented in Table 1 with much higher contents in nitrogen oxides, formaldehyde and sulphur dioxide in the continental polluted case than in the maritime one.

Aerosol particles also have different characteristics depending on the nature of the air mass: maritime aerosol particles are supposed to be made out of salt while continental ones out of ammonium sulphate. Their number size distributions are taken from Jaenicke (1988,1993) as the sum of three log-normal distributions.

Fig. 1 presents the time evolutions of hydrometeors mixing ratios for the two scenario cases. The feature of the continental air mass is a greater number of aerosol particles which leads to a higher number of cloud droplets created through nucleation which is about 20 times higher compared to the maritime case (not shown). This large number of cloud droplets inhibits autoconversion of cloud droplets in rain and delays heterogeneous freezing of cloud droplets and subsequent primary ice formation in the continental case.

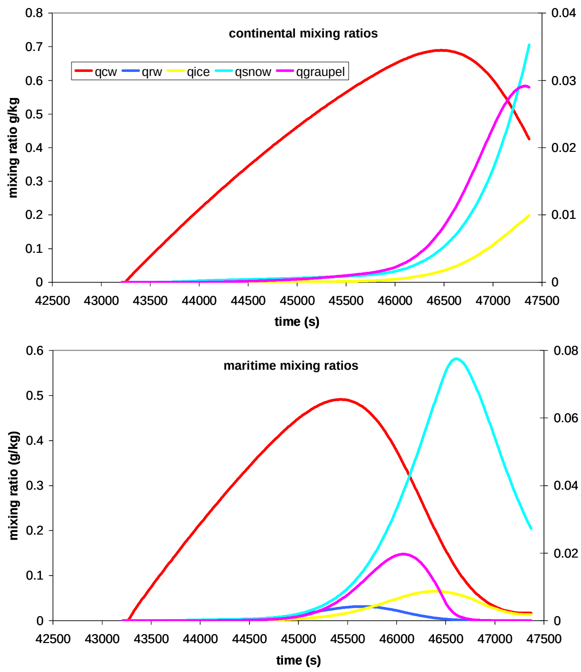

Figure1 : Mixing ratios calculated for cloud water, rain water, cloud ice, snow and graupel in the continental vs maritime scenarios.

4. CHEMICAL EFFECTS OF MIXED-PHASE CLOUDS

Figure 2 illustrates the time evolution of the cloud pH as a function of the mean cloud droplet (or raindrop) diameter for the maritime (in blue) and continental (in red) clouds that form, grow and dissipate following the arrows drawn on the plots.

At the beginning (during cloud formation), the smallest continental cloud droplets are more acidic than the maritime ones. Moreover, higher contents in nitrogen oxides and sulfur dioxide in the more polluted continental cloud also favour acidity.

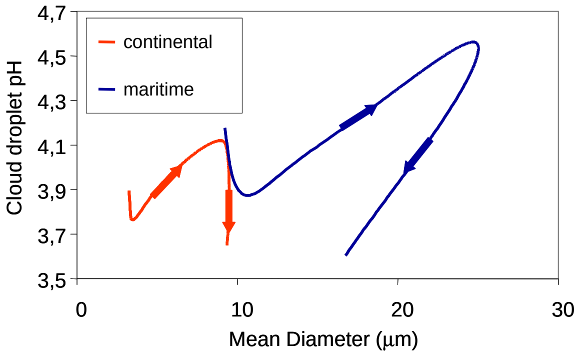

Figure 2 : Cloud droplet pH evolution for maritime vs continental cases.

Then, cloud droplets grow and acidity is transferred to the rain or decreases due to dilution effect. Later on during the simulation, when the cloud droplets are riming, acidification is observed again due to degassing of volatile gases during riming. In the maritime case, the mean cloud droplet diameter tends to decrease because cloud droplets are evaporating through Bergeron process.

Sulfuric acid is a strong acid found in clouds since it is very soluble. It has a retention coefficient temperature dependent as given by Lamb and Blumenstein (1987).

In Figure 3, the top graph shows the time evolution of gas phase concentration of sulfuric acid (in molec/cm^3) during the maritime case simulation (blue curve) and during a sensitivity run where ice phase processes are artificially suppressed in the model.

The bottom graph represents the degassing rate (in molec/cm^3/s) associated to riming of cloud droplets into snow (full line) and graupel (dotted line).

As soon as the cloud appears, sulphuric acid is efficiently transported to aqueous phase and its gas phase concentration regularly depletes for the run considering liquid phase only. When ice processes are considered, same is observed except when riming of cloud droplets into snow starts (at 12:14) and to a less extent riming into graupel (at 12:41) create a sudden increase in sulphuric acid concentration. This result illustrates the strong impact of ice retention on soluble chemical species.

Very preliminary results are shown here but they already demonstrate that ice phase has a major role in the trace compounds budget and should be considered in cloud chemistry models.

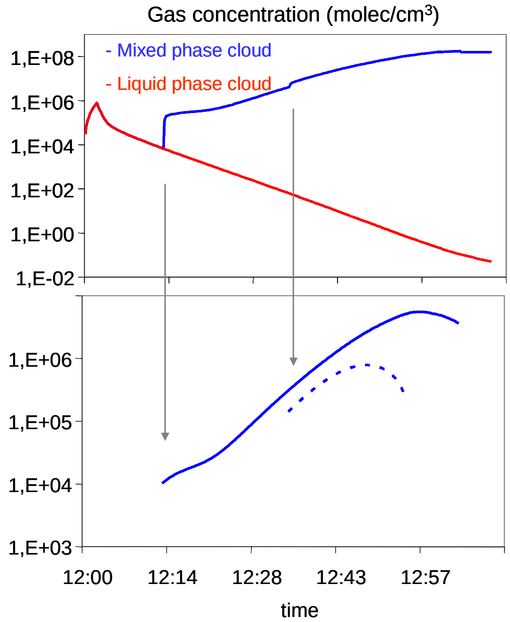

Figure 3: Effect of ice phase on sulphuric acid.

5. BIBLIOGRAPHY

Abdul-Razzak, H., and S. J.Ghan, 2000: A parametrization of aerosol activation, II. Multiple aerosol types, *J. Geophys. Res.*, 105, 6837-6844.

Abdul-Razzak, H., S. J. Ghan and C. Rivera-Carpio, 1998: A parametrization of aerosol activation, I. Single aerosol type, *J. Geophys. Res.*, 103, 6123-6132.

Caro, D., W. Wobrock, A.I. Flossmann, and N. Chaumerliac, 2004: A two-moment parameterization of aerosol nucleation and impaction scavenging for a warm cloud microphysics: description and results from a 2D simulation, *Atmos. Res.,* 70, 3-4, 171-208.

Deguillaume, L., M. Leriche, A. Monod and N. Chaumerliac, 2004: The role of transition metal ions on HO_x radicals in clouds: a numerical evaluation of its impact on multiphase chemistry, *Atmos. Chem. Phys.*, 4, 1, 95-110.

Gear, C.W., 1971: Numerical initial value problems in ordinary differential equation, Prentice-Hall, Englewod Cliffs, NJ, pp. 158-166.

Gérémy, G., W. Wobrock, A.I. Flossmann, A. Schwarzenböck and S. Mertes, 2000: A modelling study on the activation of small Aitken-mode aerosol particles during CIME 97, *Tellus B*, 52, 3, 959-979.

Jaenicke, R., 1988 : Chap 9, In : Aerosols physics and chemistry, Landolt-Börnstein, New Series, Vol. V, Springer, Berlin.

Jaenicke, R., 1993: Tropospheric aerosols, in: Aerosol-cloud-climate interactions, (Ed) Hobbs, P., Academic Press, San Diego, CA, pp. 1–31.

Lamb, D., and R. Blumenstein, 1987: Measurements of the entrapment of sulphur dioxide by rime ice, *Atmos. Environ*., 21, 1765-1772.

Leriche, M., N. Chaumerliac and A. Monod, 2001: Coupling quasi-spectral microphysics with multiphase chemistry : case study of a polluted air mass at the top of the Puy de Dôme mountain (France), *Atmos. Environ.*, 35, 5411-5423.

Leriche, M, D. Voisin, N. Chaumerliac, A. Monod, and B. Aumont 2000: A model for tropospheric multiphase chemistry: application to one cloudy event during the CIME experiment, *Atmos. Environ.,* 34, 5015-5036.

Leriche, M., L. Deguillaume and N. Chaumerliac, 2003: Modeling study of strong acids formation and partitioning in a polluted cloud durin wintertime, *J. Geophys. Res.,* 108, 4433-4444.

Leriche, M., R.L. Curier, L. Deguillaume, D. Caro, K. Sellegri, N. Chaumerliac, 2007: Numerical quantification of sources and phase partitioning of chemical species in cloud: Application to wintertime anthropogenic air masses at the Puy de Dôme station, *J. Atmos. Chem., 57, 3, 281-297.*

Reisner, J., R. M.Rasmussen, and R. T. Bruintjes, 1998: Explicit forecasting of supercooled liquid water in winter storms using the MM5 mesoscale model, *Q.J.R.Meteorol.Soc*.,124, 1071-1107

Schwartz, S.E.: Mass-Transport considerations pertinent to aqueous phase reactions of gases in liquid water cloud, in: Chemistry of Multiphase Atmospheric Systems, Jaeschke, W; Eds., NATO ASI Series, G6, Springer-Verlag, pp. 415-471, 1986.

Thompson, G., P. Field, B. Hall, and R. Rasmussen, 2006: A New Bulk Microphysical Parameterization in WRF. 7th WRF Users' Workshop, Boulder CO, June 2006.

Williams, J.E., F.J. Dentener and A.R. van den Berg, 2002: The influence of cloud chemistry on HOx and NOx in the moderately polluted marine boundary layer: a 1-D modelling study, *Atmos. Chem. Phys.*, 2, 277-302.

ICE NUCLEI MEASUREMENTS IN CLEAN THROUGH PERTURBED AEROSOL CONDITIONS: RESULTS FROM PACDEX AND ICE-L

P. J. DeMott[1], A. Prenni[1], C. Twohy[2], J. Stith[3], D. Rogers[3], A. Heymsfield[3], M.D. Petters[1], T. Eidhammer[1], S. Kreidenweis[1], T. Campos[3], R. Subramanian[4], G. Kok[4], Z. Wang[5], J. French[5], S. Haimov[5] and T. Lersch[6]

[1]Department of Atmospheric Science, Colorado State University, Fort Collins, CO, USA
[2]College of Oceanic and Atmospheric Sciences, Oregon State University, Corvallis, OR USA
[3] National Center for Atmospheric Research, Boulder, CO USA
[4]Droplet Measurement Technologies, Boulder, CO USA
[5]Department of Atmospheric Sciences, University of Wyoming, Laramie, WY USA
[6]R.J. Lee Inc., Monroeville, PA USA

1. INTRODUCTION

Understanding and quantifying the potential effects of changes in natural and anthropogenic aerosol particles on clouds and climate must include consideration of impacts on supercooled clouds. Therefore, it is important to document the number concentrations, compositions and sources of ice nuclei (IN) in the atmosphere and to validate the relation between ice nuclei and ice formation in clouds. Two recent airborne studies add to this knowledge data base. In the Pacific Dust Experiment (PACDEX, see Stith et al. 2008), the ice nucleation behavior of aerosols in dust and pollution plumes exiting the Asian continent were studied during transport across the Pacific Ocean in spring 2007. This permitted sampling a wide range of ice nuclei number concentrations, their transformations, and their interactions with clouds. The second study, the Ice in Clouds Experiment – Layer clouds (ICE-L) (Heymsfield et al. 2008) focused on ice initiation in cloud scenarios (wave clouds and upslope clouds) that permit direct comparison of IN and cloud ice number concentrations. Periods of very low aerosol and IN number concentrations were often encountered during the late fall 2007 sampling period of ICE-L over the Western United States.

This paper examines the relation of IN to other aerosol properties, including aerosol size distribution and single particle compositions. Comparisons of IN and ice number concentrations in clouds are described in the paper of Eidhammer et al. (2008).

2. MEASUREMENT METHODS

The Colorado State University continuous flow diffusion chamber (CFDC) was used to measure IN by exposing aerosol particles to controlled temperature and water vapor saturation ratios between two ice surfaces in a cylindrical, vertically-oriented laminar flow field for several seconds, as described by Rogers et al. (2001). CFDC conditions were controlled whenever possible to be appropriate to nearby clouds. Ice nuclei were sampled directly from the atmosphere or as residual nuclei of cloud particles from a counterflow virtual impactor inlet (Twohy et al. 1997) in both studies. IN were collected as CFDC-activated ice crystals in PACDEX using a jet impactor (Kreidenweis et al., 1997) with 2 micron cut-size and examined for morphology and composition using transmission electron microscopy with energy dispersive x-ray analysis. In ICE-L, parallel measurements of cloud residual composition were made using aerosol mass spectrometry techniques, but are not described here.

Both studies included a suite of instrumentation sampling off of external inlets to measure aerosol particle size, cloud condensation nuclei (CCN) number concentrations, single soot particle concentrations, and gas phase composition. A suite of wing- and airframe-mounted aerosol and cloud particle measuring instruments were also flown in each study. Remote sensing measurements were a part of each study, including cloud radar and lidar in ICE-L.

PACDEX was held during April to May 2007 and utilized the NSF/NCAR Gulfstream V (G-V) aircraft. The CSU airborne continuous flow diffusion chamber was refurbished for FAA-certified flight on the G-V (formerly known as HIAPER) and named the CFDC-1H (for HIAPER version 1). Besides electronic and mechanical safety upgrades, the instrument package size was significantly reduced and the diffusion chamber and its refrigeration system were reconstructed. In comparison to the instrument described by Rogers et al. (2001), the CFDC-1H uses a separate refrigeration system for each ice-coated wall, employs a faster response inner cold wall cooling system, and uses an outer (warm) wall with a continuous ice surface and differential thermal control of the ice surface in the lower one-third of the wall to achieve ice saturation conditions in this region of the chamber. The reduction toward ice saturation at the cold wall temperature is achieved by transitioning the warm wall to equal the cold wall temperature. The purpose of this procedure is to evaporate activated liquid particles so that differentiation of nucleated ice crystals can be achieved by optical sizing at the chamber outlet. This evaporation region was previously designed with passive control through the use of a hydrophobic and non-cooled outer warm wall, but there were concerns that under-saturation with respect to ice could occur if the aircraft cabin was too warm.

The ICE-L experiment utilized flights of the NSF/NCAR C-130 during November to December 2007 over the Western United States region between the borders of northern New Mexico and northern Wyoming, along the eastern spine of the Rocky Mountains. The new CFDC-1H instrument was also used for this study. The aerosol particle sampling strategy in ICE-L wave clouds included upstream sampling in air of the same equivalent potential temperature as the target clouds so that similar in- and out-of-cloud samples were obtained. In addition to CFDC-1H processing of aerosol particles (ambient or from the CVI inlet) at the expected cloud pass temperature, an attempt was made to operate the CFDC-1H for one cloud pass at a temperature 4 to 6ºC colder than cloud top temperature and in the water supersaturated regime. This was done assuming that the activated IN at these conditions might reflect the number of available contact freezing ice nuclei on the basis of the laboratory experiments of Durant and Shaw (2005).

3. MEASUREMENTS IN A PERTURBED DUST AND POLLUTION ENVIRONMENT IN THE MIDDLE TROPOSPHERE - THE PACIFIC DUST EXPERIMENT (PACDEX)

Previous studies have pointed out the role of Asian emissions on impacting ice nuclei populations in the Western United States in springtime (Richardson et al. 2007). This study suggested that large parts of the upper troposphere in Northern Mid-latitudes may be impacted by elevated concentrations of Asian dust in spring. Further, this dust may sometimes be accompanied by pollution particles and be chemically processed during transport. It was expected therefore that PACDEX would present chances to sample strong gradients in ice nuclei number concentrations as well as the impacts of their interaction with pollution. Finally, the project planned for measurements in clouds being impacted by dust and pollution.

Figures 1 and 2 show a visual image and measurements within a dust layer located east of Japan (from 143 to 148 E longitude at 35.3 N latitude) at an altitude of 9.1 km on May 23, 2007. Ice nuclei concentrations exceeding 100 per liter are rare in our atmospheric measurement experience, especially at high altitudes. If in response to the dust particles, we expect a relation to larger aerosol concentrations. Plotted in Figure 2 are number concentrations of aerosol particles measured by the UHSAS (Ultra-high Sensitivity Aerosol Spectrometer) between 500 and 1000 nm (upper limit). A trend between these aerosols and IN number concentrations is evident although discerning this is made difficult by aerosol variations and by the variation of CFDC supersaturation and IN response to this parameter. A relation with black carbon particle concentrations, measured by the single particle soot photometer (SP2; Droplet Measurement Technologies, Boulder, CO), is not obvious, although the numbers of these particles also show a modest upward trend during this time.

Figure 1. Photograph of high altitude Asian dust layer for which measurements are given in Figure 2.

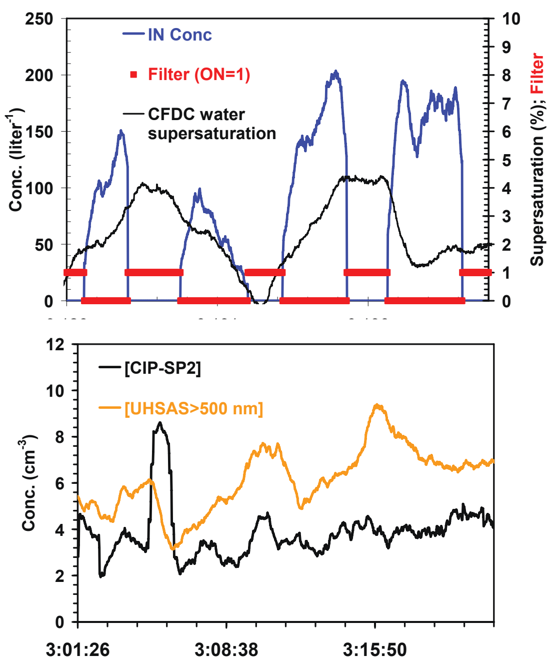

Figure 2. May 23, 2007 constant altitude (9.1 km) measurements of 60 s running mean ambient number concentrations of IN at -32ºC (-35ºC ambient temperature) and indicated water supersaturation, black carbon (SP-2), CCN, and aerosol particles in the 500 to 1000 nm size range (UHSAS).

A relation between IN and larger aerosol number concentrations is expected due to the size characteristics of ice nuclei. In Figure 3 are summarized the size distribution of ice nuclei activated in the CFDC and collected for post-analysis by TEM during PACDEX versus 3 other selected projects. Ice nuclei are favored at sizes above 0.1 μm and have number median sizes that range from 0.35 μm to 0.65 μm depending on location. The upper value applies to PACDEX and is characteristic of size distributions of airborne dust particles. We also note that the median size would be larger if not for the need to purposely limit the entry of particles larger than 2 μm into the CFDC so that the present optical sizing method of IN detection (of activated crystals) can be used. Very high number concentrations of supermicron particles over the Pacific Basin during PACDEX proved difficult to remove, even by a two-stage impactor between the aircraft inlet line and the IN chamber, probably due to particle bounce. Still, these sizes represented nearly 20% of IN. This means that this many particles may have been mis-categorized as IN by size alone, or alternately, just as many or more particles of these sizes were not characterized as IN by the present methods. This result motivates the need to develop phase discrimination detection capabilities.

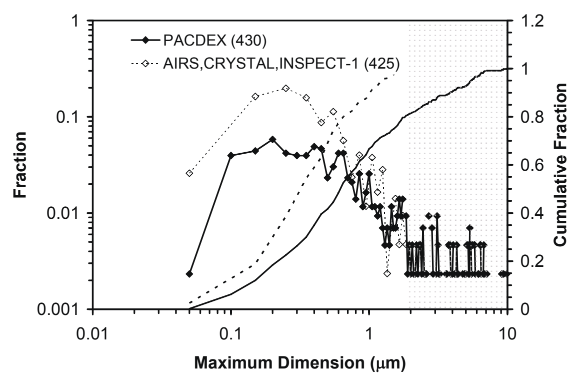

Figure 3. Size distribution of ice nuclei activated in the CFDC-1H during PACDEX versus a compilation from three other field projects. Differential (data points) and cumulative fractional distributions (lines only) are shown. The shaded region indicates the range of aerosol sizes that the inlet impactors are supposed to remove (see text).

Figure 4 shows a vertical descent profile, also for May 23, and for the same processing conditions, but at a location further east toward Hawaii. Of interest in this profile are the correlations of IN number concentrations with those of both larger particles and black carbon at some levels, but anti-correlation with black carbon in regions of elevated carbon monoxide, a likely tracer for pollution. It is also apparent that the relation between ice nuclei and larger aerosol number concentrations is quantitatively different for the entire profile compared to the higher altitude dust layer nearer to Asia; only modestly lower concentrations of aerosols are present in the descent profile, yet ice nuclei concentrations are lower by factors of 3 to 10 times. This may reflect the impact of chemical and/or cloud processing. Aerosol composition measurements of ambient aerosols are under analyses for the profile period on May 23. Collected ice nuclei were examined for composition during the measurement period shown in Figure 2. Elemental compositions reflecting mineral dust and metal oxide compounds comprised two-thirds of all IN in this case. This is the same fraction noted for the composite results of all IN analyzed for composition during PACDEX (Figure 5). Nevertheless, only 20% of the IN during the early

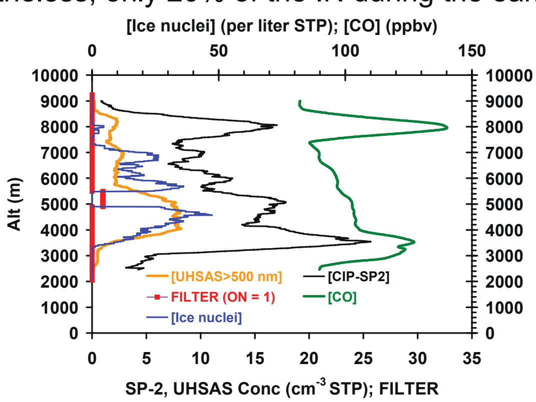

Figure 4. Aerosol, ice nuclei, and CO concentrations during a vertical profile over the mid-Pacific between Japan and Hawaii (approximately 171 W longitude, 28 N latitude). CFDC temperature was constant at -32ºC and CFDC relative humidity was 102±1% for the entire region below about 7700 m MSL. Sample air is filtered at the noted point as a check on background frost counts.

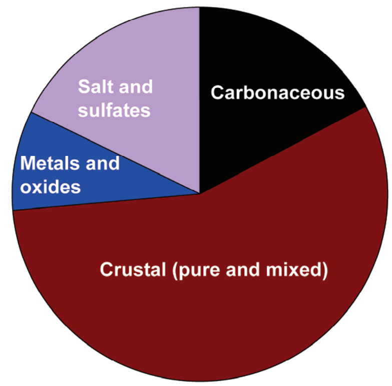

Figure 5. Basic composition of ice nuclei (by number) attributed on the basis of the major elemental composition of particles analyzed from all TEM grids collected during PACDEX (500 particles represented).

flight segment on May 23 indicated the presence of associated salts or sulfates, suggesting that the dusts were relatively unprocessed or interacted only minimally with pollution. IN composition was not assessed for the period of measurements in Figure 3.

The PACDEX data set contains a number of excellent cases for studying aerosol interactions with clouds. Figure 6 shows a pass through the warm frontal region of a weather system described separately by Stith et al. (2008). Ice nuclei were sampled from the CVI inlet in this case. CFDC processing temperature was initially several degrees colder than the cloud level temperature, then was quite similar to that in the cloud region sampled later in the period after the G-V ascended to a higher flight level. The cloud was nearly all ice phase. IN number concentrations trended with ice crystal concentrations larger than 50 μm, but exceeded ice concentrations by 2 to 5 in some areas. Agreement was very good in the higher cloud region where the processing and ambient temperatures were nearly equivalent. These results indicate a strong likelihood that ice nuclei controlled the ice crystal number concentration in the sampled cloud. Nevertheless, IN exceeding ice crystal concentrations is not expected when the cloud residual particle concentrations should be dominated by ice crystals. It is possible that higher concentrations of smaller ice crystals were present or it is possible that the >200 μm average diameter ice crystals were shattering at the inlet and also dislodging aerosol particles from the inner surface of the inlet. This will require further analysis.

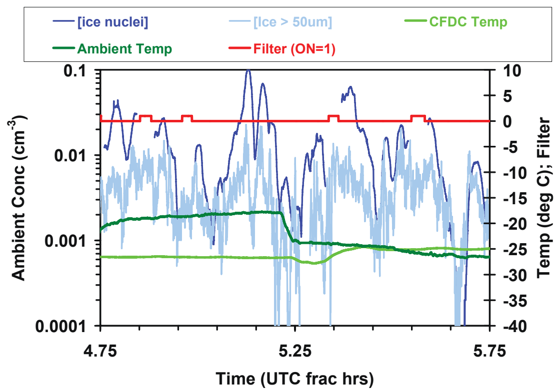

Figure 6. Ice nuclei versus 2Dc ice crystal (>50 μm) number concentrations (60 s running averages) in warm frontal region (see Stith et al., 2008) from 152 to 155 E longitude, 35 to 37 N latitude on May 17, 2007. Processing RH varied from 99 to 102%.

4. MEASUREMENTS OF ICE INITIATION IN RELATIVELY CLEAN AIR – THE ICE IN CLOUDS LAYER (ICE-L) STUDY

The ICE-L sampling period was typified by generally low IN concentrations. In the example shown in Figure 7, the C-130 passed through two levels of a deeper orographic wave cloud that extended at times up to 2 km above the highest flight level. Temperature was adjusted in the CFDC-1H to match the ambient temperature quite well. The coldest ambient temperature reached at flight level was slightly warmer than those favoring homogeneous freezing, but the cloud clearly resided in this regime at higher levels and the aircraft likely crossed streamlines or encountered precipitation from upper levels based on radar and lidar data. Ice nuclei concentrations measured via the CVI inlet ranged from below 1 per liter, consistent with most isolated thin wave cloud passes, to 10 per liter, typical of the highest value measured from the ambient inlet in clear air regions on this day. Ice crystal concentrations larger than 50 μm exceeded IN number concentrations by factors ranging from 2 to 8 times. Thus, while IN activating near water saturation at between -30 to -34ºC can explain between 15 and 50% of larger ice crystal numbers, most were nucleating somewhat colder as heterogeneous ice nuclei or via homogeneous freezing. Inference that even higher number concentrations of smaller ice crystals were present may be seen from the FSSP (Forward Scattering Spectrometer Probe) number concentrations (3 to 45 μm), which agreed within a factor of 2 with cloud residual particle concentrations larger than 500 nm measured by the CFDC-1H optical particle counter (OPC).

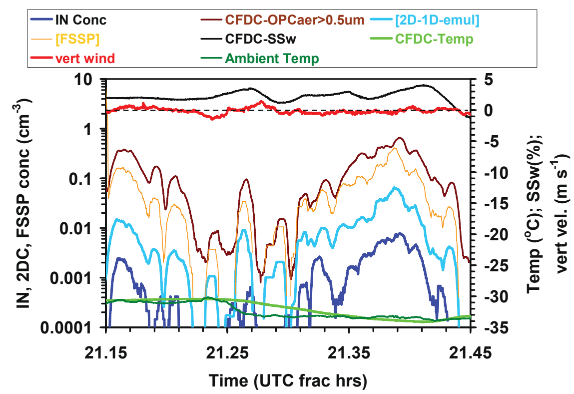

Figure 7. Data from penetration of glaciated high altitude wave cloud at near the homogeneous freezing limit on November 7, 2007 (ICE-L Research flight 1) while sampling IN from the CVI. Number concentrations of IN, ice crystals larger than 50 μm, particles in the 3-45 μm range (FSSP), and cloud residual nuclei larger than 0.5 μm are shown.

A general result of IN measurements during other thin wave cloud cases during ICE-L, highlighted by Eidhammer et al., 2008), is that ice nuclei number concentrations often agreed with the number concentrations of ice crystals present in the mixed-phase and liquid droplet-dominated regions of wave clouds. Figure 8 shows this result, but also indicates the difficulty in resolving the action of other ice formation processes. The CFDC-1H was set to process aerosols at near water saturation at -33ºC, 6ºC colder than the cloud temperature, to focus on ice nucleation under conditions present in colder cloud tops and for estimating potential numbers of contact freezing nuclei.

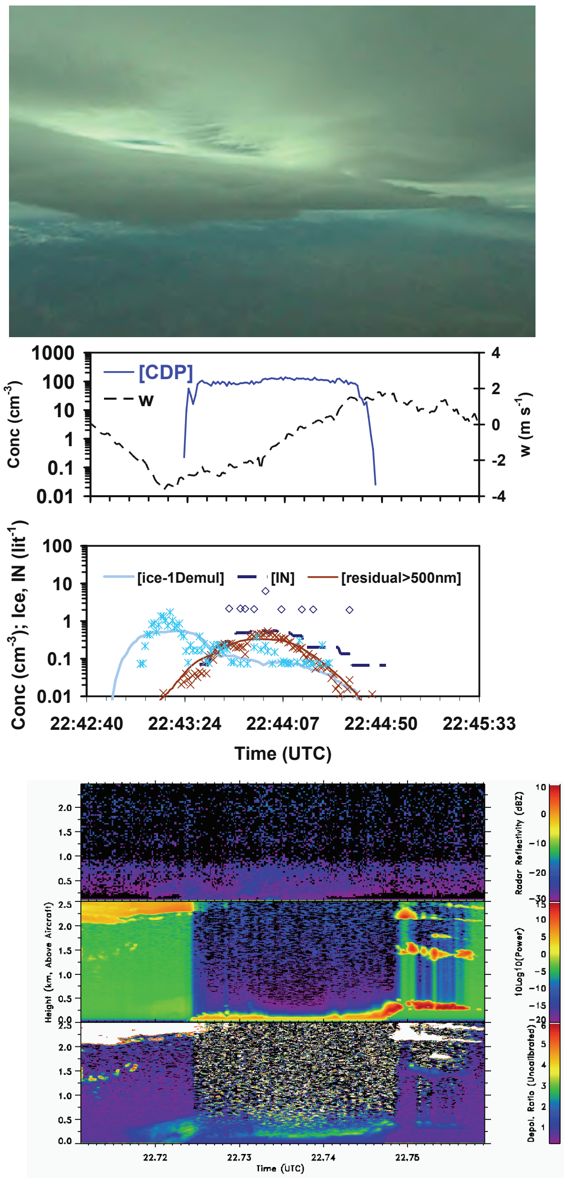

Figure 8. View from forward looking video (top) before entering cloud, and data (middle and bottom) from the cloud pass on November 18, 2007. Flight was from the downstream to upstream sides of the cloud while sampling particles from the CVI inlet. The cloud was at -27ºC minimum temperature at flight level. Smooth curves in the concentration plot are 30 s running averages, while the data points show 1 Hz data. Upward pointing radar and lidar data (bottom) show multiple cloud layers and the ice "tail" (left side) of the sampled cloud.

Radar and lidar data in Figure 7 indicate the isolated character of this cloud compared to higher clouds visible in the video image. Ice precipitation from aloft does not appear to be occurring. Cloud penetration was within about 800 m of cloud top. Ice nuclei number concentrations exceed the ice number concentrations by a factor of two within the mixed-phase cloud region, as might be expected based on the colder CFDC processing temperature. However, modest ice enhancement is indicated in the ice tail of the cloud and is not picked up as ice nuclei. The lidar data suggest that the source of this ice is from the upper regions of the wave cloud. Small numbers of cloud residual aerosols were detected from ice residuals in this region, but if ice nuclei at -33ºC, they should have activated in the CFDC. Crystal sizes were only modestly smaller in this cloud region, but certainly at sizes usually sampled without issue by the CVI. The ice in this region either represents the action of a different ice nucleation process (unknown or homogeneous freezing – not expected) or is the remnants of ice precipitated (at an upstream location) from much higher clouds where homogeneous freezing was occurring.

Another result from initial analyses of the ICE-L data set that will bear careful analysis is that ice nuclei were not enhanced within fresh urban pollution layers.

5. SUMMARY DISCUSSION

Ice nuclei number concentrations varied over a wide range for the temperature and supersaturation conditions examined in these studies; strongly and in general proportion with the number concentrations of larger aerosol particles, and somewhat less strongly with temperature, consistent with results from prior studies. The dominance of mineral dust-like compositions of IN with sizes larger than about 0.4 microns appears to provide the primary explanation for the relation of IN to larger aerosol particle number concentrations, even absent a more detailed consideration of chemical composition. This is emphasized in Figure 9, where three PACDEX flight periods and three ICE-L sampling periods are shown together. For the most direct comparison, the processing temperature was between -25 and -32ºC and relative humidity within 102±2% for the data shown. Ice nuclei and aerosol number concentrations have been normalized to standard temperature and pressure (STP) conditions. These new data from very different locations in the free troposphere confirm a relationship between larger aerosols and ice nuclei that was inferred over 40 years ago by Georgii and Kleinjung (1967). Data from that study, using a >0.3 μm aerosol criteria compared to our 0.5 μm value, is also shown in Figure 9. That these data from a surface site in Germany at 850 m fall to the right side of the present data is fully consistent with the increased concentrations of 0.3 μm particles.

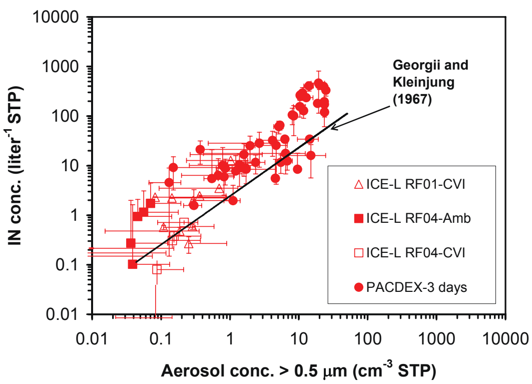

Figure 9. Relationship between number concentrations of aerosols larger than 0.5 microns and ice nuclei using periods from 3 days in PACDEX and two days in ICE-L. These data are selected for a processing temperature regime of -25 to -32ºC. Also shown is the relation between larger aerosols (~>0.3 microns) at -21ºC and ice nuclei in Georgii and Kleinjung (1967).

Significant variability in IN concentrations versus large aerosol concentrations is still evident in Figure 9, even for a narrow range of CFDC processing conditions. Aerosol processing, physically, chemically and by clouds, is likely responsible for some of the variability in the relation between IN and larger aerosols. This remains to be explored via various data sets, including the aerosol and cloud residual compositions not largely discussed here. In this regard, the presence of pollution appears associated with no discernable to negative impacts on IN number concentrations based on preliminary analyses.

Finally, we have noted instances where ice nuclei appear to explain the concentrations of ice in clouds and note specific experiments in wave clouds indicating good correspondence between IN and ice crystal number concentrations initially nucleated. Nevertheless, discrepancies remain that are not always clearly attributable to the action of other known ice nucleation processes such as homogeneous freezing.

The PACDEX and ICE-L data sets include some of the most detailed information ever collected on ice initiation processes and the relation to a large range of aerosol properties representative of both clean and highly polluted air masses. Analyses will be ongoing.

6. ACKNOWLEDGEMENTS

The lead author wishes to acknowledge the U.S. National Science Foundation (Grant ATM-0611936) for support of these projects. Special thanks to V. Ramanathan and W. A. Cooper for their coordinating efforts and guidance on PACDEX research flights. Special thanks to J. Jensen for similar planning and coordination of ICE-L research flights. Thanks to all investigators and the NCAR RAF support staff for their tremendous help during the installations and conduct of these studies. The National Center for Atmospheric Research is sponsored by the National Science Foundation

7. REFERENCES

Durant, A. J., and R. A. Shaw, 2005: Evaporation freezing by contact nucleation inside-out. *Geophys. Res. Lett.*, **32**, L20814, doi:10.1029/2005GL024175,

Eidhammer, T., P. J. DeMott, D. C. Rogers, A. J. Prenni, M. D. Petters, C. H. Twohy, J. G. Hudson and S. M. Kreidenweis, 2008: Ice initiation by aerosol particles: comparing model parameterizations and observations in a parcel framework. 15th International Conference on Clouds and

Precipitation, July 7-11, Cancun, Mexico (in this Proceedings).

Georgii H. W. and E. Kleinjung, 1967: Relations between the chemical composition of atmospheric particles and the concentration of natural ice nuclei. *J. Rech. Atmos.*, 145-155.

Heymsfield, A. H., P. R. Field, D. C. Rogers, J. Stith, Z. Wang, J. French, S. Haimov, P. J. DeMott, and C. Twohy, 2008: Ice initiation in mixed-phase orographic wave clouds. 15th International Conference on Clouds and Precipitation, July 7-11, Cancun, Mexico (in this Proceedings).

Kreidenweis, S.M., Y. Chen, P.J. DeMott, and D.C. Rogers, 1998: Isolating and identifying atmospheric ice-nucleating aerosols: A new technique. *Atmospheric Research*, **46**, 263-278.

Richardson, M. S., P. J. DeMott, S. M. Kreidenweis, D. J. Cziczo, E. Dunlea, J. L. Jimenez, D. S. Thompson, L. L. Ashbaugh, R. D. Borys, D. S. Westphal, G. S. Cassucio and T. L. Lersch, 2007: Measurements of heterogeneous ice nuclei in the Western U.S. in springtime and their relation to aerosol characteristics. J. Geophys. Res., 112, D02209, doi:10.1029/2006JD007500.

Rogers, D.C., P.J. DeMott, S.M. Kreidenweis, and Y.L. Chen, 2001: A continuous-flow diffusion chamber for airborne measurements of ice nuclei, Journal of Atmospheric and Oceanic Technology, 18, 725-741

Stith, J. W. A. Cooper, V. Ramanathan, D. C. Rogers, P. DeMott, T. Campos, B. Adhikary, 2008: Interactions of asian emissions with storms in the pacific ocean: early results from the Pacific Dust Experiment (PACDEX). 15th International Conference on Clouds and Precipitation, July 7-11, Cancun, Mexico (in this Proceedings).

Twohy, C.H., A.J. Schanot, and W.A. Cooper, 1997: Measurement of condensed water content in liquid and ice clouds using an airborne counterflow virtual impactor, *Journal of Atmospheric and Oceanic Technology*, **14**, 197-202.

EVALUATION OF FOUR BULK MICROPHYSICS SCHEMES FOR THE SIMULATION OF ARCTIC MIXED-PHASE CLOUDS OBSERVED DURING M-PACE

Johanne Dorais, Eric Girard, and Ping Du
Department of Earth and Atmospheric Sciences, UQAM
Montréal, Qc., Canada

1. INTRODUCTION

According to Wyser et al. (2006), state-of-the-art regional climate models are currently unable to properly simulate cloud-radiation interactions over the Arctic. Global climate models have been even less successful to simulate these interactions (Walsh et al., 2002). One of the main challenges is to properly simulate cloud microphysical properties. Cloud thermodynamic phase seems to be particularly important in the magnitude of the radiative forcing of clouds (CRF). For instance, Shupe et al. (2006) have shown that CRF can reach 40 W m^{-2} when liquid is present as opposed to 10 W m^{-2} for ice clouds.

Mixed-phase clouds are very common over the Arctic during winter and spring. Observations taken during the Surface Heat Budget of the Arctic Ocean (SHEBA) experiment have shown that cloud cover ranges from a minimum of about 0.4 during winter and a maximum of 0.8 during summer over the Arctic Ocean. Mixed-phase clouds dominate over ice and liquid clouds despite very cold temperatures characterizing the winter season (Shupe et al., 2006). Boundary layer shallow stratus clouds are frequent during winter and often characterized by a very thin liquid layer below which ice crystals dominate. In the summer, multiple thin layers of clouds are common.

Girard and Curry (2001) and Morrison et al. (2006) have shown that the Ice Forming Nuclei (IFN; defined as the aerosols able to nucleate ice) concentration plays a critical role and determine the thermodynamic phase of the cloud. The sensitivity of cloud phase to IFN concentration may also be a function of the surface (ocean vs continental) (Morrison et al., 2007). In addition, the cloud thermodynamic instability characterizing the presence of liquid and ice not only depends on the ratio of liquid and ice mixing ratios but also on the absolute number of ice crystals as shown by Morrison et al. (2008).

Several bulk microphysics schemes of various complexities have been developed for climate models (e.g. Kong and Yau, 1997, Morrison et al., 2005). In this research, we evaluate 4 bulk microphysics schemes with the limited-area version of the Canadian Global Environmental Multiscale Model (GEM-LAM). The main objective is to test the ability of the model to simulate Arctic mixed-phase clouds. The paper is organized as follows. A brief description of the microphysics schemes is done in the next section followed by the design of the experiment. Results using 4 microphysics schemes for the simulation of single layer and multi-layers stratus clouds observed during the Mixed-Phase Arctic Cloud Experiment (M-PACE) are shown in section 4.

2. BULK MICROPHYSICS SCHEMES

For the present study, we choose to evaluate four schemes with different levels of complexity. These microphysics schemes are from: Sundqvist (1981) (hereafter **SUN**), Kong and Yau (1997) (hereafter **KY**), Morrison et al. (2005) (hereafter **MO**) and Milbrandt and Yau (2005) (hereafter **MY**). SUN has one prognostic variable, the total cloud water mixing ratio, which includes both the liquid and ice mixing ratios. SUN assumes a subgrid-scale cloud fraction, which implies that condensed phase can be present before the saturation is reached within the grid tile. This scheme does not have an explicit parameterization for the ice phase. An empirical relationship relates the precipitation to the total cloud mixing ratio as follow:

$$G_p = C_{0F} q_c \left(1 - \exp\left\{ -\left(\frac{q_c}{b m_{rF}} \right)^2 \right\} \right) \quad (1)$$

where q_c is cloud water/ice mixing ratio and b is the cloud fraction. C_{0F} is the inverse of the characteristic time for autoconversion of cloud particles to precipitating hydrometeors and m_{rF} is a threshold value for cloud mixing ratio at which autoconversion starts to be efficient. These parameters include the growth by coalescence and Bergeron-Findeisen process and depend on a freezing function $f_{mr\pm}$, which is a function of temperature:

For 250 K < T < 273 K :

$$f_{mr+} = 1.33 \exp\left\{ -\left(0.066\left(T - T_0\right)\right)^2 \right\} \quad (2)$$

For T < 250 K :

$$f_{mr-} = \max\left(0.03, 0.075\left(1.07 \pm \frac{y}{y+1} \right) \right) \quad (3)$$

where y is a function of the temperature. The generation of precipitation could be viewed like a parameterized relationship between cloud mass and precipitation that considers effects of ice phase through a temperature function.

The scheme developed by KY is a single-moment scheme with four prognostic variables, the liquid, rain, graupel and ice mixing ratios. Ice crystals and snow are treated together in one variable. KY scheme distinguishes itself from SUN by a more elaborated treatment of the ice phase. Eight processes related to ice phase are parameterized in the KY scheme: nucleation by deposition-condensation freezing on active nuclei, contact freezing of cloud water droplets, homogeneous freezing of cloud droplets and raindrops when T<-40°C, deposition and sublimation of vapour on existing ice particles, ice particles growth by riming of supercooled cloud water, accretion and finally, melting of ice. The number concentration of deposition-condensation and contact ice nuclei is given by the empirical relationship of Meyers et al. (1992), which depends only on ice supersaturation.

The third scheme, developed by Morrison et al. (2005), is a double-moment bulk scheme predicting total number concentration and mixing ratio for cloud water, cloud ice, rain and snow. There are two versions of this scheme: one for high-resolution cloud models and one for large-scale models; we use this second version for our study. The two versions are different by there treatments of the supersaturation field and the droplet activation. New parameterizations are included in this scheme for the droplet activation, heterogeneous and homogenous ice nucleation and for the spectral index (width) of the droplet size distribution.

The most complex scheme in this study is from Milbrandt and Yau. It uses a three-moment method where mixing ratio, total number concentration and the shape parameter (α) of the size distributions are predicted for six hydrometeors categories (cloud water, cloud ice, rain, snow, graupel and hail). MY represents the size spectra of each precipitating hydrometeors category by a three-parameter gamma size distribution function:

$$N(D) = N_0 D^{\alpha} e^{-\lambda D} \quad (5)$$

where the shape parameter α gives a measure of the spectral width. Primary ice nucleation includes deposition-condensation freezing (Meyers et al., 1992) and contact freezing (Young, 1974). Homogeneous freezing of cloud water droplets is allowed below -30^{0}C. This scheme can also be used in a 1-moment and 2-moment version. The 2-moment version has been used in this study. The 3-moment version will also be tested in the near future.

3. DESIGN OF THE EXPERIMENT

The Mixed-Phase Cloud Experiment (M-PACE) took place over the North Slope of Alaska during September and October 2004. In-situ and ground-based measurements of cloud microphysical parameters and radiation fluxes were taken during M-PACE. In-situ measurements were taken by the University of North Dakota Citation aircraft, which has made ascents and descents between Barrow and Oliktok. More information about instruments on board the aircraft and methodology used to collect the data can be found in Mc-Farquhar et al. (2007).

Microphysics schemes are run with the version 3.3.0 of GEM-LAM. The physics package of the model includes the following parameterizations: Kain-Fritsch deep convection, Li-Barker Correlated-K radiation, ISBA Land Surface Scheme, McFarlane (1987) gravity wave drag and Lott and Miller low-level blocking. Data for the geophysical field are from the U.S geological Survey (USGS). There are fifty-three vertical hybrid levels with the top of atmosphere at 10 hPa. GEM is first run at 10 km resolution over a domain of 3590 km by 2590 km centered over the MPACE site at 65°N and -174°E. This simulation is driven by the ECMWF ERA 40 reanalysis at lateral boundaries and by GEM mesoglobal for surface conditions. A second simulation at 2,5 km horizontal resolution is then performed driven by the previous lower resolution simulation over a small domain of 447.5 km by 137.5 km. This small domain is centered at 70.5°N and -153°E. A series of 36-hour simulations at 10km resolution were performed from September 27th to October 22nd. Based on qualitative comparisons of results with satellite images, six days were selected: October 5th, 6th, 8th, 9th, 10th and 12th, 2004. These days were simulated using the four microphysics schemes on the little domain with a resolution of 2.5 km. Results are compared with ground observations (liquid water path, LWP) taken at Barrow (71.29 N, 203.21 W), Oliktok (70.51 N, 210.14 W) and Atqasuk (70.47 N, 202.54 W) and flight in-situ measurements (liquid and ice water content , LWC and IWC) between Barrow and Oliktok.

4. RESULTS

In-situ measurements taken during October 5, 6, 8, 9, 10 and 12 are used to evaluate the ability of the microphysics schemes implemented in GEM-LAM to simulate the observed liquid and ice cloud water content. The first 4 days were characterized by relatively warm in-cloud temperatures ranging from -2 to -11^{0}C while the last 2 days were colder with temperatures down to -17^{0}C. Flights were conducted between Barrow and Oliktok for these days and lasted approximately 4 hours. To compare with the model simulation, in-situ observations have been time averaged to get a single vertical profile for both IWC and LWC. The modeled vertical profiles are obtained by averaging the Barrow and Oliktok simulated vertical profiles over 4 hours. Therefore, these vertical profiles represent a temporal and spatial average of LWC and IWC.

Figure 1 shows the simulated and observed vertical profiles of IWC and LWC for

October 5th. A low pressure was centered just south of Alaska that day. Satellite pictures (not shown) show that the mixed-phase cloud was relatively thin and low over Barrow and got thicker eastward toward Oliktok where a ice cloud was also present at 3000 m. Observations show a multilayer stratus mixed-phase cloud at 750 m and 1250 m), which extends from Barrow to Oliktok. An ice cloud was also present over Oliktok at 3000 m. All schemes capture the mixed-phase stratus cloud and its persistence. However, they miss the ice cloud at 3000 m over Oliktok and generally underestimate the IWC and overestimate the LWC of the multilayer cloud. Furthermore, they miss the double maximum of LWC. On the other hand, SUN simulates reasonably well the LWC but does not capture either the double maximum of LWC. IWC is also well simulated by SUN for the stratus but the maximum is a bit too high. The predicted number concentration of cloud water droplets by MY and MO is generally good for the multilayer stratus with concentrations varying between 10 and 20 cm^{-3} (not shown). However, the number concentration of ice crystals is strongly underestimated.

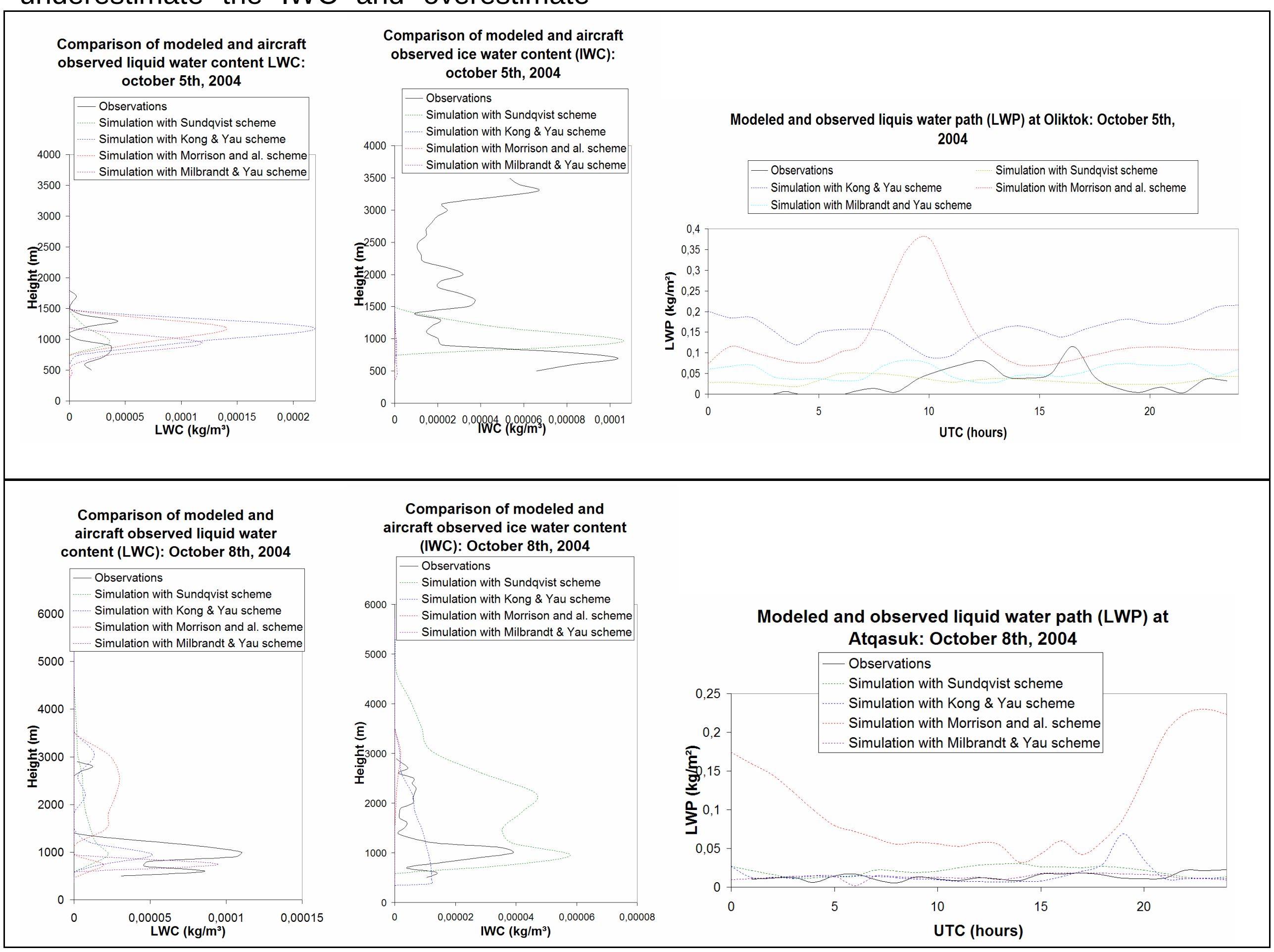

Figure 1: Vertical profiles of LWC and IWC and LWP time series at Oliktok (modelled vs observed) on October 5th and 8th.

The low-pressure system present on October 5th moved southeastward by October 8th. The area between Barrow and Oliktok was under the influence of a high-pressure ridge on October 8th. Clouds were thinner and the upper cloud was almost entirely dissipated with a small amount of LWC at 3000 m and small concentration of ice between 1000 m and 3000 m. The maximum of LWC at 1000 m is reproduced by all schemes although its magnitude is generally underestimated except for the MY scheme, which captures reasonably well its magnitude. On the other hand, MY does not capture the LWC at 3000 m while the other 3 schemes overestimate the magnitude and the vertical extension of this liquid layer. IWC is overestimated by SUN for the whole cloud layer whereas MO and MY strongly underestimate IWC. KY is the best at reproducing this 3000 m IWC layer.

Figure 2 shows modeled vs. observed LWC and IWC following the aircraft for all the flights considered in this study (October 5, 6, 8, 9, 10, 12). Results show that SUN has a negative LWC bias and a positive IWC bias. This is in agreement with the 2 cases shown above. Clearly, the phase partitioning between ice and liquid, which depends on temperature in SUN, does not seem to be appropriate for the cases examined in this study. This LWC negative bias has also been obtained with GEM using SUN for the simulation of the SHEBA field experiment (Wyser et al., 2007).

MO overestimates LWC and underestimates IWC. This is particularly true for thin clouds with low values of LWC. KY and MY do not seem to have any biases. Instead, several 0 values are present for both IWC and LWC suggesting that the model simply often misses the cloud. This is particularly true over Barrow. Indeed, satellite pictures show that Barrow is often either at the edge of the cloud deck northwest of the low-pressure system or below a small area of clear sky. Flights over Barrow often occurred during short period of time where clouds were present. As a result, simulated IWC and LWC are substantially underestimated over this area due to the fact that the model does not always reproduce the small period of times clouds were present.

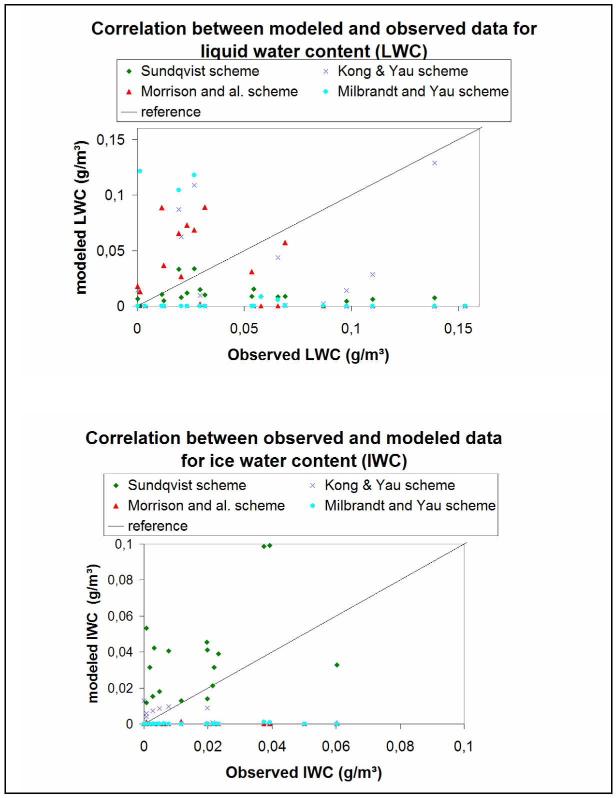

Figure 2: Scattered plot of the modelled vs observed liquid water path (left) and ice water path (right) during the the M-PACE in-situ flights from October 5 to October 12 between Barrow and Oliktok.

The liquid water path was measured at 2 other stations (Oliktok and Atqasuk) with a microwave radiometer. These stations were mostly covered by clouds on October 5th, 6th, 8th and 9th and were located far from the cloud deck northern edges. Therefore, they represent better locations for comparison with the model. Figure 1 shows an example of modeled vs observed LWP time series for Oliktok on October 5th and 8th. Results confirm that SUN and MY underestimate LWP for both stations (see Table 1). This is in agreement with SUN and MY results comparison with in-situ flight measurements showing an underestimation of LWC and overestimation of IWC. On the other hand, KY and MO strongly overestimates the LWP for these 2 stations and possibly underestimates IWP as suggested by in-situ measurements and vertical profiles of IWC for October 5th and 8th shown above. In the KY scheme, ice nucleation is allowed only at temperatures below -5^{0}C. This could contribute to the underestimation of IWC and the overestimation of LWC for warmer days such as October 5th, 6th, 8th and 9th.

Table 1: Average LWP (g m^{-2}) for Oliktok and Atqasuk for October 5th, 6th, 8th and 9th (warm regime)

Observations	56.0
SUN	23.2
MY	20.8
KY	82.5
MO	130.7

Table 2: Average LWP (g m^{-2}) for Atqasuk for October 10th, 12th (cold regime)

Observations	14.0
SUN	3.7
MY	14.8
KY	17.2
MO	16.1

Starting on October 10th, the low pressure center further retreats to the southeast as a strong high pressure was building over the pack ice north of Alaska. Northeast winds brought colder air over Northern Alaska. As a result, in-cloud temperature for October 10th and 12th was colder than the previous days with temperatures down to -17^{0}C. Clouds over Barrow and Oliktok were thin and confined at 900 hPa. Satellite pictures also show a partial cloudiness over the pack ice. The model does not reproduce these very thin clouds over the North Slope of Alaska and over the pack ice. However, clouds observed a few km inland were captured by GEM. Therefore, only the Atqasuk station, which is inland and south of Barrow, was considered for comparison of model results with observations.

Table 2 shows that the simulated LWP by KY, MY and MO is much better for these 2 colder days when compared to the previous warmer days. Finally, SUN LWP negative bias is amplified and the scheme underestimates the LWP by a factor 3 in the cold regime as compared to a factor 2 in the warm regime.

Preliminary analysis of the substantial overestimation of the LWP for the first period (warm regime) simulated by MO has been done. Results indicates that the limitation originally imposed on the nucleation rate of ice crystals by water vapor deposition could explain the strong overestimation of LWC in the MO scheme. Indeed, in its original version, the MO scheme limits the number of new nucleated ice crystals in the deposition mode by the concentration of preexisting ice crystals in the clouds. Thus, if the preexisting ice crystal number concentration is above the active deposition IN concentration, no contribution of ice nucleation by deposition is possible in the original formulation of the scheme. Such a condition would be justified only for cases with no advection of aerosols. In fact, it is possible that aerosols from clear regions be advected in the cloud. In such a situation, the limitation imposed on ice nucleation by deposition is not appropriate. Figure 3 shows the October 6th vertical profile of LWC and IWC as simulated with the original MO scheme and with a modified version of the MO scheme in which the limit on ice nucleation by deposition has been removed. Results show that the LWC of the modified version of the MO scheme is substantially lower than the LWC simulated by the original version of the scheme and much closer to observations. The IWC is also closer to the observations using the modified version of the scheme.

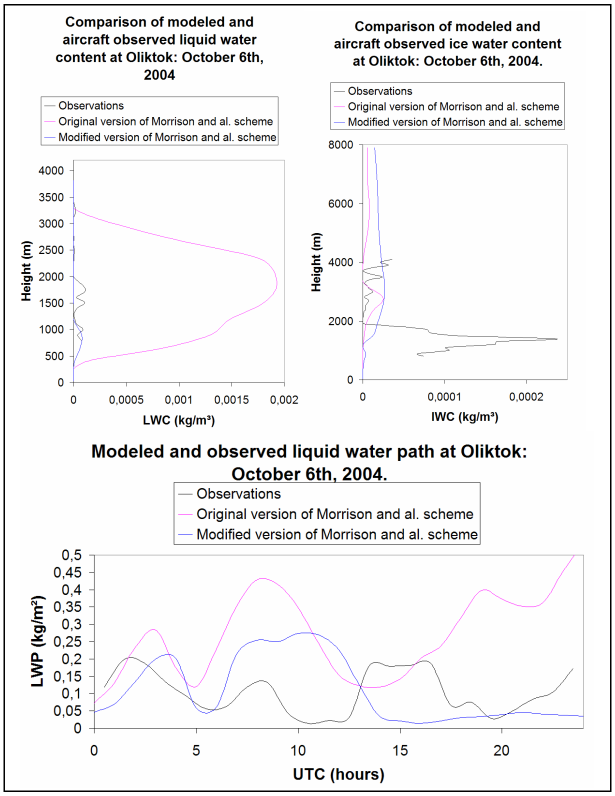

Figure 3: Vertical profiles of LWC and IWC and LWP time series on October 6^{th} at Oliktok as simulated by the original and modified versions of MO.

5. SUMMARY

The Global Multiscale Environmental Limited Area Model (GEM-LAM) is used to evaluate 4 bulk microphysics schemes over the North Slope of Alaska. The main objective of this research is to evaluate the ability of the schemes to reproduce the amount and phase of cloud water for Arctic mixed-phase clouds. The first microphysics scheme (SUN) has a simple formulation with the total cloud water content as the only prognostic variable. It uses a function of temperature to discriminate between ice and liquid cloud water. The second microphysics scheme (KY) has 4 prognostic variables and a more elaborate treatment of the processes related to the nucleation and growth of ice crystals. The third scheme (MO) predicts the number concentrations and mixing ratios of four species (cloud ice, water, snow and rain). Finally, the fourth microphysics scheme (MY) is also a 2-moment scheme that considers the following species: cloud ice and water, rain, snow, graupel and hail.

Results show that all schemes capture the vertical structure of clouds for the 2 investigated days. They are also able to reproduce the persistence of the mixed-phase clouds and their intrinsic thermodynamics instability. Although the mixed-phase is captured by the schemes, the partitioning between liquid and ice differs significantly when compared to observations. SUN has a systematic negative cloud liquid water bias and a positive cloud water ice bias for all cases examined. It seems that the phase partitioning function (which depends on temperature) of SUN is not appropriate for these Arctic stratus clouds. KY behaves differently depending on temperature. Indeed, for warmer in-cloud cases, it has a positive cloud liquid water bias and a negative cloud ice water bias. On the other hand, KY biases are substantially reduced for colder clouds. This bias could be related to the formulation of the scheme, which restricts the ice nucleation at temperatures below -5^{0}C. MY underestimates the cloud liquid water for warmer clouds (October 5^{th}, 6^{th}, 8^{th}, 9^{th}) while it reproduces quite well the concentration of liquid water in colder clouds. MO has a large LWC positive bias for warmer clouds. Preliminary analysis indicate that the LWC overestimation is due to the fact that the number of ice crystal nucleated by water vapor deposition depends on the number concentration of preexisting ice crystals in the cloud. Therefore, the concentration of new nucleated ice crystals by deposition added to the preexisting ice crystals cannot be greater than the concentration of active deposition IN. When this limitation is removed (October 6th simulation), results are much closer to LWC and IWC observations.

6. Aknowledgements

The authors would like to thank the National Science and Engineering Research Council of Canada (NSERC) and the Canadian Foundation for Climate and Atmospheric Sciences (CFCAS) for funding support.

7. References

Curry, Judith A. and al., 1996. *Overview of Arctic Cloud and Radiation Characteristics.* J. Climate, vol. 9, pp.1731-1764.

Curry, Judith A, and al., 2000. *FIRE Arctic Clouds Experiment.* Bulletin of the American Meteorological Society, vol. 81, No 1, pp. 5-29.

Dong, Xiquan and al. 2002. *Comparison of Stratus Cloud Properties Deduced from Surface, GOES, and Aircraft Date during the March 2000 ARM Cloud IOP.* J. Atm. Sci., vol 59. pp. 3265-3284.

Girard, Éric and Judith A. Curry. 2001. *Simulation of arctic low-level clouds observed during the FIRE Arctic Clouds Experiment using a new bulk microphysics scheme.* Journal of Geophysical Research, vol. 106, no. D14, pp. 15139-15154.

Harrington, Jerry and Johannes Verlinde. *Mixed-Phase Arctic Clouds Experiment (M-PACE), Scientific Overview Document.* Pennsylvania State University, Department of Meteorology.

Jiang, Hongli and al., 2000. *Cloud Resolving Simulations of Mixed-Phase Arctic Stratus Observed during BASE: Sensitivity to Concentration of Ice Crystals and Large-Scale Heat and Moisture Advection.* J. Atm. Sci., vol 57, pp. 2105-2117.

Khvorostyanov, Vitaly I. and Judith A. Curry. 2000. *A New Theory of Heterogeneous Ice Nucleation for Application in Cloud and Climate Models.* Geophysical research letters, vol. 27, no. 24, pp. 4081-4084.

Klein, Stephen and al.. *ARM Cloud Parameterization and Modeling Working Group GCSS Polar Cloud Working Group Model Intercomparison.*

Kong, Fanyou and M.K. Yau.1997 *An Explicit Approach to Microphysics in MC2.* Atmosphere-Ocean, vol 35, pp. 257-291.

Lohmann, U. and K. Diehl. 2006. *Sensitivity Studies of the Importance of Dust Ice Nuclei for the Indirect Aerosol Effect on Stratiform Mixed-Phase Clouds.* J. Atm. Sci., vol. 63, pp. 968-982.

Mailhot, Jocelyn and al.. 1998. *Scientific Description of RPN Physics Library, version 3.6*. Recherche en prévision numérique, Atmospheric Environment Service, Dorval, Québec, Canada.

McFarquhar, Greg M., G. Zhang, M. R. Poellot, G. L. Kok, R. McCoy, T. Tooman, A. Fridlind and A. J. Heymsfield. 2007. *Ice properties of single-layer stratocumulus during the Mixed-Phase Arctic Cloud Experiment. 1.Observations.* Journal of Geophysical Research, vol. 112, D24201.

Milbrandt, J.A. and M.K. Yau, 2005. *A Multimoment Bulk Microphysics Parameterization. Part I: Analysis of the Role of the Spectral Shape Parameter.* J. Atm. Sci., vol. 62, pp. 3051-3064

Milbrandt, J.A. and M.K. Yau, 2005. *A Multimoment Bulk Microphysics Parameterization. Part II: A Proposed Three-Moment Closure and Scheme Description.* J. Atm. Sci., vol. 62, pp. 3065-3081

Morrison, H., J.A. Curry and V.I. Khvorostyanov. 2005. *A New Double-Moment Microphysics Parameterization for Application in Cloud and*

Climate Models. Part I: Description. J. Atm. Sci, vol. 62, pp. 1665-1677

Morrison, H. and al.. 2005. *A New Double-Moment Microphysics Parameterization for Application in Cloud and Climate Models. Part II: Single-Column Modeling of Arctic Clouds.* J. Atm Sci., vol. 62, pp. 1678-1692.

Morrison, H. And J. O. Pinto. 2006. *Intercomparison of Bulk Cloud Microphysics Schemes in Mesoscale Simulations of Spingtime Arctic Mixed-Phase Stratiform Clouds.* Monthly Weather Review, vol. 134, pp. 1880-1900.

Morrison, H. and al.. 2007. *Sensitivity of M-PACE Mixed-Phase Stratocumulus to Cloud Condensation and Ice Nuclei in a Mesoscale Model with Two-moment bulk Cloud Microphysics.* Submitted to Journal of Geophysical Research – Atmosphere.

Pinto, James, 1998. *Autumnal Mixed-Phase Cloudy Boundary Layers in the Arctic.* J. Atm. Sci., vol55, pp. 2016-2038.

Shupe, Matthew D., Sergey Y. Matrosov and Taneil Uttal. 2006. *Arctic Mixed-Phase Cloud Properties Derived from Surface-Based Sensors at SHEBA.* Journal of Atmospheric Sciences, vol. 63, pp. 697-711.

Spangenberg, D. A. and al.. 2006. *Characterization of Mixed-Phase Clouds During Mixed-Phase Arctic Cloud Experiment from Satellite, Ground-Based, and In-Situ Data.* Sixteenth ARM Science Team Meeting Proceedings.

Sundqvist, Hilding. 1978. *A Parameterization scheme for non-convective condensation including prediction of cloud water content.* Quart. J. R. Met. Soc., vol. 104, pp. 677-690.

Sundqvist, Hilding. 1981. *Prediction of stratiform clouds: Results from a 5-day forecast with a global model.* Tellus, vol. 33, pp. 242-253.

Sundqvist, Hilding and al.. 1989. *Condensation and Cloud Parameterization Studies with a Mesoscale Numerical Weather Prediction Model.* Monthly Weather Review, vol. 117, pp. 1641-1657.

Pudykiewicz, J. and al.. 1992. *Inclusion and Verification of a Predictive Cloud-Water scheme in a Regional Numerical Weather Prediction Model.* Monthly Weather Review, vol. 120, pp. 612-626.

Verlinde, J. and al.. 2007. *The mixed-phase arctic cloud experiment.* Bull. of American meteorological society, février 2007, pp. 205-221.

Walsh, John E., Vladimir M. Kattsov, William L. Chapman, Veronika Govorkova and Tatyana Pavlova. 2002. *Comparison of Arctic Climate Simulations by Uncoupled and Coupled Global Models.* Journal of Climate, vol. 15, pp. 1429-1446.

Wyser, K. and Colin G. Jones. 2005. *Modeled and observed clouds during Surface Heat Budget of the Arctic Ocean (SHEBA).* Journal of geophysical research, vol. 110, D09207

Wyser, K., C. G. Jones, P. Du, E. Girard, U. Willén, J. Cassano, J. H. Christensen, J. A. Curry, K. Dethloff, J.-E. Haugen, D. Jacob, M. Koltzow, R. Laprise, A. Lynch, S. Pfeifer, A. Rinke, M. Serreze, M. J. Shaw, M. Tjernström and M. Zagar. 2007. *An evaluation of Arctic cloud and radiation processes during the SHEBA year: simulation result from eight Arctic regional climate models.* Climate Dynamics, vol. 30, pp. 203-223.

Zhang, G. and al., 2006. *Contrasting Properties of Single-Layer and Multi-Layer Arctic Stratus Sampled During the Mixed-Phase Cloud Experiment.* Sixtenth ARM Science Team Meeting Proceeding, Albuquerque.

TOWARDS THE RETRIEVAL OF ICE CRYSTALS PROPERTIES WITHIN MIXED-PHASE CLOUDS USING DUAL POLARIZATION SPECTRAL RADAR MEASUREMENTS

Y.Dufournet, C. M. H. Unal, H. W. J. Russchenberg

International Research Centre for Telecommunication-transmission and Radar (IRCTR), Delft University of Technology, the Netherlands.

1. INTRODUCTION:

Among mid-level clouds, the coexistence of ice particles with tiny but dense water droplets are easily observed when the temperature goes down 0°C [3]. They can occur in the form of layers of few hundreds thick either above or embedded within thicker ice clouds [6].

Because of their notable presence as well as their microphysical specifications, mixed-phase clouds (and mainly the water phase) are potentially considered of great importance on the earth radiative budget [2] and cloud evolution. Nowadays such clouds are still poorly represented in Global Climate Models (GCMs) and Forecast Models. Therefore, in order to evaluate and develop cloud parameterization schemes, observation of particles size distribution (PSD), shapes, orientations, size-mass relation and phase distributions are required.

Up to now observational datasets are mainly available from aircraft in-situ measurements [4],[5],[8],[9]. To be able to get a wider time and spatial scale, remote sensing retrieval schemes are also under development [6]. Among them a new technique is built in the university of Delft for remotely determining the properties of the ice particles within mixed-phase clouds from measurements taken by the S band Doppler Polarimetric radar TARA and combining it with a microphysical model which characterizes the bulk of atmosphere being probed [11].

Corresponding author: y.dufournet@tudelft.nl

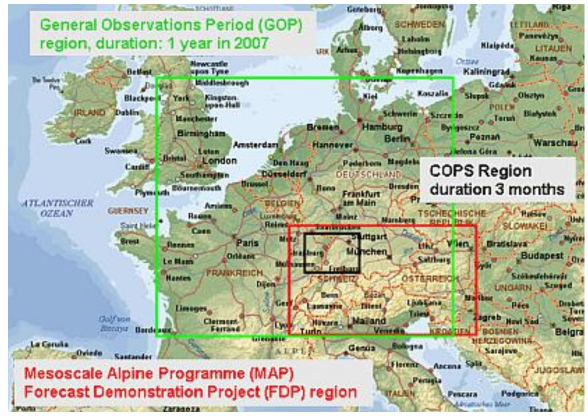

Figure 1 COPS area (black box)

This constitute a first step in the retrieval of ice water content (IWC) and liquid water content (LWC) from a radar / lidar synergy since radars and lidars are sensitive to different type of particles.

This extended abstract will be mainly dedicated to show the possibilities of developing and evaluating the remote sensing retrieval technique explained above using collocated aircraft in-situ and ground-based measurements which have been taken during the COPS campaign (Convective and Orographically-induced Precipitation Study) last summer (2007). During this period a complete set of sensors were deployed in an area located in the border of France and Germany, and in a scale large enough to study mesoscale processes (figure 1). In this abstract only TARA data will be shown as ground-based measurements.

The abstract is structured as follow. Section 2 gives an overview of the retrieval technique from both radar and model point of view. Section 3 will focus on the aircraft measurements obtained from an accepted EUFAR proposal (European Fleet for Airborne Research), and their combination with the radar data. Finally section 4 is going to account for the different ways to improve and assess the retrieval technique using the full panel of instruments available. Since data are still under process up to now, no results will be introduced in this last section.

2. OVERVIEW OF THE RETRIEVAL TECHNIQUE:

The retrieval technique was first meant to characterize the microphysical properties of ice particles above the melting layer [11]. This idea is going to be further developed and extended to mixed-phase layer studies. The retrieval is based on an iterative comparison of expected scattering properties from ice crystals (obtained with a microphysical model) and spectral dual-polarization measurements from radar observations (Transportable Atmospheric Radar - TARA). This method uses the possibility to differentiate several types of hydrometeors by combining polarimetric and Doppler measurements [10]. Thus, for comparison purposes both the radar and the model can provide the polarimetric parameters spectral horizontal reflectivity (sZHH) and spectral differential reflectivity (sZ_{DR}) which gives the axial ratio (from dual polarization) versus the size (from Doppler velocities) of the ice particles, assuming they can be modeled as oblate or prolate spheroids (figure 2):

$$sZ_{HH}(v)dv = \sum_{i=1}^{n} N_i\left(D_i\{v\}\right)\sigma_{HH,i}\left(D_i\{v\}\right)\left|\frac{dD_i}{dv}\right|dv$$

$$sZ_{DR}(v)dv = \frac{\sum_{i=1}^{n} N_i\left(D_i\{v\}\right)\sigma_{HH,i}\left(D_i\{v\}\right)\left|\frac{dD_i}{dv}\right|dv}{\sum_{i=1}^{n} N_i\left(D_i\{v\}\right)\sigma_{VV,i}\left(D_i\{v\}\right)\left|\frac{dD_i}{dv}\right|dv}$$

where the subscripts HH and VV denote respectively horizontal and vertical transmitting and receiving polarization modes of the radar, i represents the particle type, N(D) is the particle size distribution, the Doppler velocity v is related to the terminal fall velocity and σ is the radar cross section.

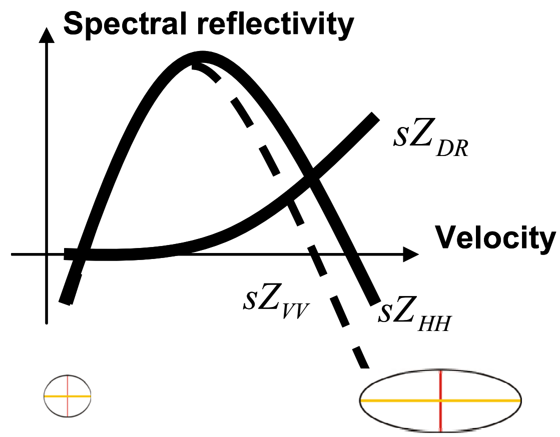

Figure 2 -relation polarimetric spectral parameters (sZHH, sZVV and sZ_{DR}) with shape of the particles being probed.

a- *the microphysical model:*

Ice crystals within mixed-phase clouds consist of many different types of particles. Previous research came up with more than 60 different types (Mogano and Lee, 1966). By using the velocity and shape dependency of the radar cross section, differentiation between several types of spheroidal particles can be performed in the model. Figure 3 summarizes the modelization procedure to get the Doppler spectrum. This model is well explained in Spek et al., 2008 [11].

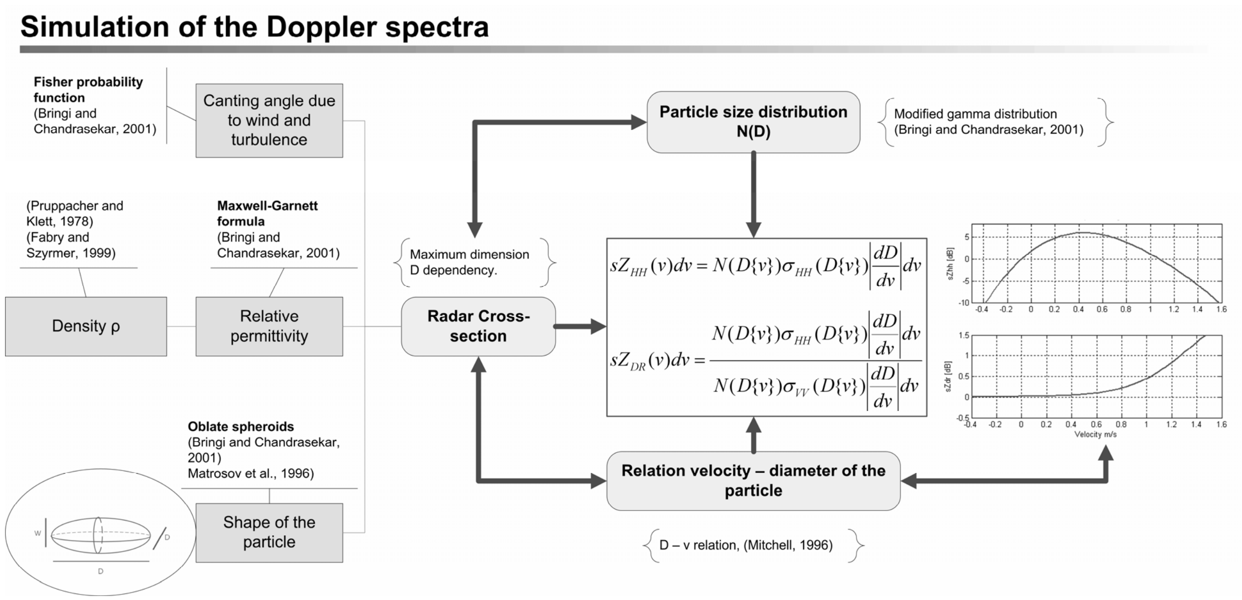

Figure 3 overview of the microphysical model

b- *Tara: microphysical mode*

Measurements are performed with the Transportable Atmospheric S band RAdar TARA. This radar has the advantage to get a direct measurement of the ice phase of mixed-phase clouds since supercooled water droplets are small enough (~ few µm) to be not detectable at this working frequency (3.3 GHz - ~ 10 cm wavelength). The specifications used for optimum microphysical measurements are featured in table 1.

Table 1 TARA specifications

Signal generation		
Frequency excursion	10 MHz	Range resolution: 15m
Sweep time	1 ms	Max unambiguous range= 7680 m (altitude: 6650 m)
Polarization sequence	VV,VH,HH	
Doppler		
Max Doppler velocity	7.5 m.s^{-1}	
Other		
Radar elevation angle	θ = 45°	

The spectral differential reflectivity is easily affected by noise and clutter due to its low value (~ 1 dB). Spectral polarimetric tools have been used to suppress clutter and remove spectral aliasing [12], [13].

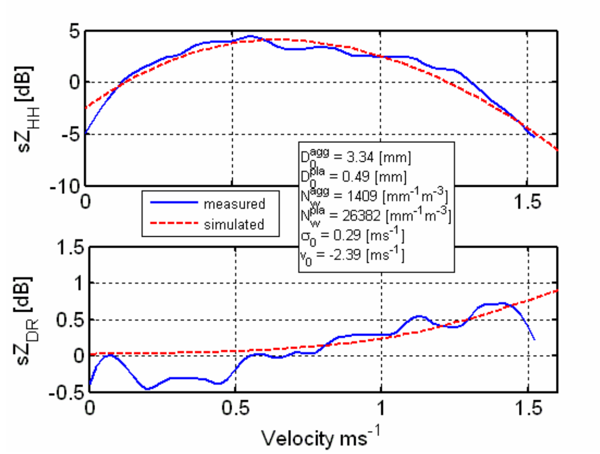

Figure 4 – fitting of the two radar observables with the ones retrieved from the microphysical model assuming plates and aggregates in the cloud

c- *fitting process:*

The retrieval procedure is based on a least square optimization that simultaneously minimizes fit residuals in a Doppler power spectrum and spectral differential reflectivity.

As shown in figure 4 the algorithm obtains the following six parameters by fitting modeled spectra to the measured ones: four particle size distribution parameters for two different types of ice crystals, the spectral broadening parameter and the ambient wind velocity.

From this result time series of the microphysical properties of the clouds can be retrieved. Figure 5 gives an example of time series obtained for the median volume diameter as well as the particle concentration assuming the presence of plates and aggregates within the cloud being probed.

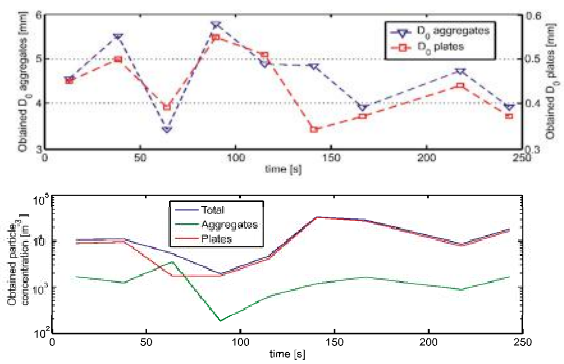

Figure 5 - retrieved time series of median volume diameter and concentration

3. SETTLEMENT OF THE CAMPAIGN – CASE OF THE 21/07/07:

In order to assess and improve the retrieval technique, a measurement campaign has been performed last summer taking advantage of, in one hand, a full set of ground-based sensors provided for the campaign COPS and, in the other hand, 10 flight hours obtained from the accepted EUFAR proposal OSMOC (Observation Strategy for Mixed-phase Orographic Clouds).
The case of the 21/07/07 is exposed in this section since it represents the only day where TARA data used for the retrieval was combined with EUFAR activities. The meteorological situation was mainly driven by a quite intense mesoscale convective system triggered with orographical activities over the black forest mountains and moving northeastwards over the eastern half of the COPS area in the course of the day. This situation lead to widespread mid-level clouds overcast.

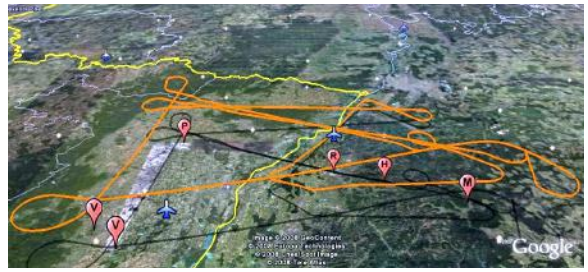

Figure 6 - Flight pattern within the COPS area

a- *radar TARA during COPS*
The radar was located on the supersite H on the very top of a plateau (see figure 6) besides other ground-based devices (lidars, other radars, radiometer, meteorological station…) giving the possibility to perform inter-comparison studies.
Antennas were directed towards the M supersite. About 6 days have been performed with the microphysical radar measurement mode as described in the previous section. Among them the 21/07 and 29/08 could be combined with aircraft measurements (using the ATR42 aircraft within the EUFAR proposal and the BAE146 aircraft respectively). Figure 7 shows the reflectivity profiles obtained the 21/07 together with the aircraft path.

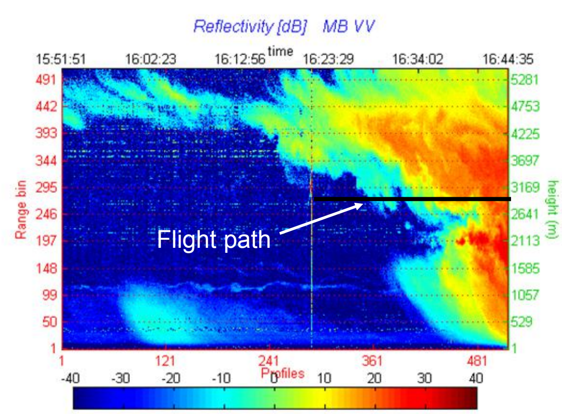

Figure 7 - Reflectivity profiles from the 21/07

Melting layer formation can be observed at about 2200m, leading to rainfall over the site H. The flight path is located just above this melting layer within the altostratus layer for temperature close to the freezing level.

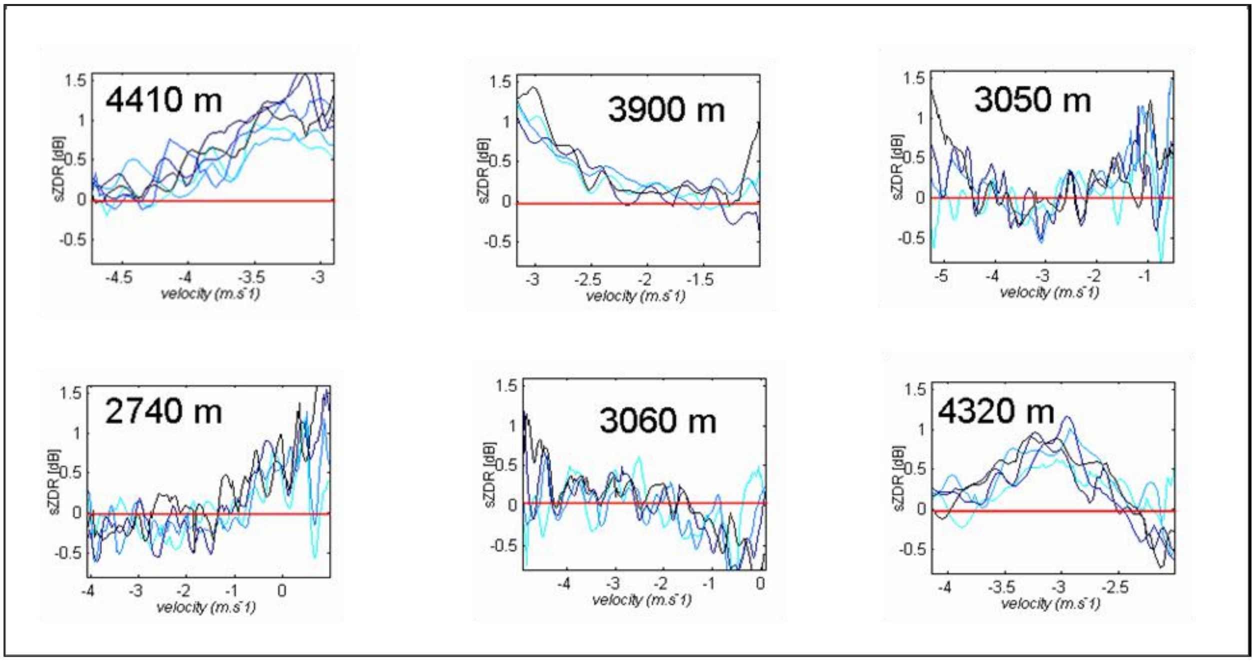

Figure 8 - sZDR behavior - (21/07) – several sZ_{DR} curves are display per figures corresponding to different altitudes around the one mentioned in each box.

During this measurement different sZ_{DR} behaviors have been noticed (figure 8). As previously mentioned this parameter is directly linked to the microphysical property of the observed bulk of atmosphere which means that every configuration can be considered as a variation in the microphysics within the cloud. The ones close to 3000 m are in the same order of altitude than the flight level and thus can be compared with the in-situ data when flying over the sites.

b- Air*craft in-situ measurements during COPS:*

From 20/07 to the 29/07 4 flights measurements through mixed-phase clouds have been performed with the French aircraft ATR42 from the Company Safire. Figure 6 exposes the flight pattern carried out the 21/07 which has also been used the following three flights. It mainly consists of a first gradual ascent from site P to site M in order to detect mixed-phase region within the cloud height. Some horizontal legs with triangular shape were following at the specific flight levels previously determined during the ascent. These legs were meant to sample the heterogeneity of the clouds as well as optimizing the inter-comparison with the different sites P, R, H, M and V (figure 6).

The aircraft was equipped with the following instrumentation:

- Basic avionic sensors: to get time series of pressure, temperature and humidity along the flight path.
- 2 LWC probes (king and Gerber): to get time series of the Liquid Water Content along the flight path.
- A PMS FSSP100 located below the aircraft wing: to measure the PSD from 1 to 50 µm.
- 2 PMS 2D-C probes located below the aircraft wing: measuring the PSD, shape and orientation of the particles from 100 to 800 µm with 25 µm resolutions. Unfortunately one of them didn’t work during the campaign.

The two last ones are needed to derive the PSD for a wide range of particles sizes.

This will be possible for a size range going from 1 to 50 µm and from 100 to 800 µm. The rest of the spectra will have to be interpolated. Furthermore it has to be noticed that when dealing with mixed-phase cloud regions, assumptions have to be taken into account in order to interpret the in-situ data:

- Water droplet and ice particle distributions are assumed to be not overlapped in size.
- Following Heymsfield et al., 2007 [4] particles with size below D_t will be assumed spherical:

$$D_t = \left(\frac{6a}{0.91\pi}\right)\exp\left(\frac{1}{3-b}\right)$$

Where *a* and *b* are two parameters describing the mass dimension relationship and 0.91 account for the threshold density where the non-sphericity of the particle appears.

Figure 9 shows some ice particles which were probed during the flight of the 21/07 with the PMS 2D-C probe. These images constitute the output of a linear array (oriented perpendicularly to the airflow) which is recorded as a function of time, such that 2D images of individual cloud particles can be constructed.

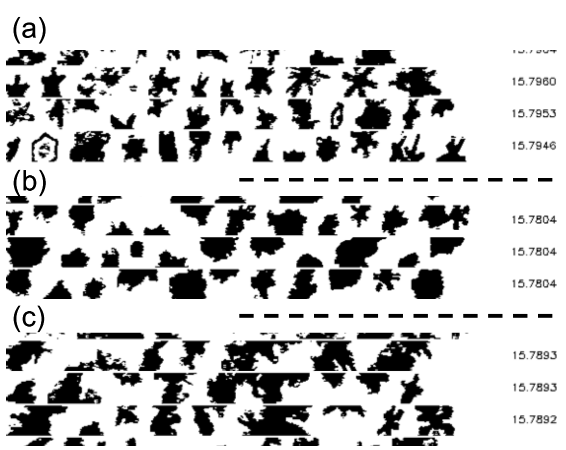

Figure 9 -time series of particles shadows derived from the PMS 2D-C probe

Plates and dendrites were the predominant pristine ice which could be found. The region (a) is mainly composed of different pristine ice particles (plates and dendrites). This has been probed at a temperature level below -12°C. Region (b) depicts some rimed aggregates (graupel) and dendrites. A liquid phase has been determined in parallel with both the King and Gerber probes. Finally region (c) consists of low rimed aggregates and dendrites. Both (b) and (c) were probed above -4°C and are typical of mixed-phase layers.

d- *determination of the spatial scale for inter-comparison between devices:*

When dealing with different instruments, scale issue is often encountered due to different space resolution for each device. For inter-comparison purpose, horizontal and vertical spatial scales will be determined such that microphysical homogeneity within a bulk of cloud can be assumed.

Horizontal scale is going to be evaluated using the combination of the 2D-C data from the horizontal legs of the flight pattern and time series of the radar measurements. Same products are going to be employed for the vertical scale but this time using the ascents and spirals performed during the flights as well as the range information of the radar. This work is not achieved yet and will be done as long as all data are processed and calibrated.

More information on the instrumentation and flights performed can be found on the Eufar website (www.eufar.net) under the project name OSMOC.

4. POSSIBLE IMPROVEMENTS OF THE RETRIEVAL TECHNIQUE:

Because most of the data are still under investigation, no final retrieved results are available yet. But the intended directions to improve the retrieval technique are given below.

a- sZ_{DR} behavior as input for the microphysical model:

As shown in section 3 (figure 8) a set of different sZ_{DR} behaviors could be found when measuring with TARA. Two main parameters can be responsible of such differences by directly affecting the signal backscattered in the vertical and horizontal polarization. This is the shape and the orientation of the particles.

During the experiment various shapes could be discerned from pristine ice crystals to more complex forms (aggregates). Level of rimming could also be considered as a driven parameter in the final shape of the crystal. For instance graupels (quite spherical) could be observed when strong rimming occurred.

Measurements showed also specific orientations. Figure 10 gives an example taken the 23/07 where orientation could be easily checked within columns event.

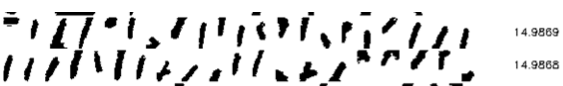

Figure 10 -columns preferred orientation during flight of the 23/07

In the microphysical model used for the retrieval, particles are assumed to be horizontally oriented following a Fisher probability distribution (see Spek et al., 2008 [11]) and only a few shapes-particle size relationships are available. Those assumptions turn to be often incorrect when looking at the 2D images. Then, because of the lack of parameterizations for pristine shapes (columns and rimming level not implemented yet), for sizes and for orientations, only a few measured sZ_{DR} behaviors can be retrieved.

New Shape-size relationships and their integration within the radar cross-section calculation (related to the orientation of the particles) should be implemented in order to model every kind of sZ_{DR} behaviors encountered during the measurements.

b- Improvement of the PSD – implementation of gamma distribution:

For the microphysical model a form of particle size distribution has to be selected. The gamma distribution and the exponential distribution are commonly used in the literature. The general form of the gamma distribution is given by

$$N(D) = N_w f(\mu)\left(\frac{D}{D_0}\right)^{\mu} \exp\left(-(3.67+\mu)\frac{D}{D_0}\right)$$

$$f(\mu) = \frac{6}{3.67^4}\frac{(3.67+\mu)^{\mu+4}}{\Gamma(\mu+4)}$$

with N_w the intercept parameter ($mm^{-1}\ m^{-3}$), D_0 the median volume diameter (mm) and μ the shape parameter. This equation can be reduce to an exponential distribution for μ=0.

In the microphysical model, only the exponential PSD is currently employed. However a sensitivity analysis of the shape parameter revealed that sZ_{DR} is quite affected by this parameter. Figure 11 exposes a sensitivity analysis of the model for sZ_{DR} assuming presence of plates (dendrites) and aggregates within the bulk of cloud.

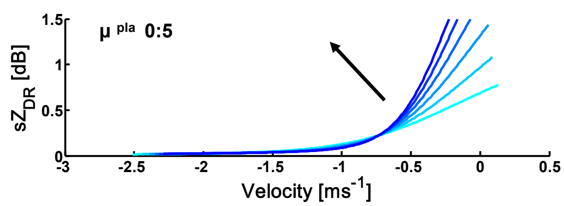

Figure 11 -PSD dependency on shape parameter μ within the microphysical model. The value of sZ_{DR} increase with μ.

In order to include the shape factor in the model some relations 'shape factor μ – slope coefficient Λ' can be drawn as shown in Brandes et al., 2006 [1] with the gamma distribution described as

$$N(D) = N_0 D^{\mu} \exp(-\Lambda D)$$

Where N_0 is now a number concentration parameter ($mm^{-\mu-1}$ m^{-3}) and Λ is the slope term.

c- *Improvement of some other relations:*

Numerous particle area and mass dimension relationships exist in the literature [4,9]. They both come in the computation of the particle fall velocity. As explained in Spek et al., 2008 [11] a change in one of this relation has a significant effect on the spectral differential reflectivity.

Using PSD obtained from in-situ measurements the optimum relationships can be assessed by fitting sZ_{DR} modeled with the ones measured.

5. CONCLUSION

A technique to retrieve the microphysical properties of the ice phase within mixed-phase clouds has been presented in this abstract. First observations (sZ_{DR} behavior and 2D images of the ice crystals) revealed that the retrieval technique is not suitable for every cloud conditions and need to be extended. A specific attention is given to show how to assess and improve this technique by using a synergy of ground-based and in-situ measurements. After calibration of all the data, new parameterizations will be implemented following section 4. First results are going to be presented during the poster presentation.

Acknowledgements. The authors wish to thanks the crew of the ATR42 aircraft as well as the EUFAR organization to make the collection of in-situ data possible. The authors also wish to thanks the COPS organization committee for the help in achieving the collocated measurements during the campaign.

REFERENCES

[1] Brandes et al., 2006: A statistical and Physical Description of Hydrometeor Distribution in Colorado Snowstorms Using a Video Disdrometer. *J. Appl. Meteorol. Clim.*, 46, 634-650

[2] Dong X. and G. G. Mace, 2003: Arctic stratus cloud properties and radiative forcing derived from ground-based data collected at Barrow, Alaska. *J. Clim.*, 16, 445-461

[3] Fleishauer et al., 2001: Observed Microphysical Structure of Mid-level, Mixed-phase Clouds. *J. Atmos. Sci.*, 59, 1779-1804

[4] Heymsfield A.J. et al., 2007: Refinement to Ice Particle Mass Dimensional and Terminal Velocity Relationships for Ice Clouds. Part I: temperature dependence. *J. Atmos. Sci.*, 64, 1047-1067

[5] ________, 2007: Refinement to Ice Particle Mass Dimensional and Terminal Velocity Relationships for Ice Clouds. Part II: Evaluation and Parametrization of Ensemble Ice Particle Sedimentation Velocities. *J. Atmos. Sci.*, 64, 1068-1088

[6] Hogan et al., 2002: Characteristics of mixed-phase clouds. Part I: Lidar, radar, and aircraft observation from CLARE'98. *Q. J. R. Meteorol. Soc.*, 129, pp. 1-999

[7] ________, 2006: The retrieval of Ice Water Content from radar reflectivity factor and temperature and its use in evaluating a mesoscale model. *J. Appl. Meorol. Clim.*, 45, 301-317

[8] Korolev et al., 2003: Roundness and aspect ratio of particles in ice clouds. *J. Atmos. Sci.*, 60, 1795-1808

[9] McFarquhar et al., 2007: Ice properties of single-layer stratocumulus during the Mixed-Phase Arctic Cloud Experiment: 1. Observations. *J. Geophys. Res.*, 112, 10 1029-10 1048

[10] Russchenberg et al., 1992: Ground-based Remote Sensing of Precipitation Using Multi-Polarized FM-CW Doppler Radar. *Delft university press*, 206 pp

[11] Spek et al., 2008: A New Technique to Categorize and Retrieve the Microphysical Properties of Ice Particles above the Melting Layer using Radar Dual-Polarization Spectral analysis. *J. Atmos. Sci*., 25, 482-497

[12] Unal C. M. H. and D.N. Moisseev, 2003: Combined Doppler and Polarimetric Radar Measurements: Correction for Spectrum Aliasing and Nonsimultaneous Polarimetric Measurements. *J. Atmos. Oceanic Technol.*, 21, 443-456

[13] Unal C. M. H., 2008, A new Doppler polarimetric radar clutter reduction technique to enhance atmospheric echoes. *Preprints, Fifth European conf. on radar in Meteorology and Hydrology (ERAD), Helsinki*

CLOUD PHASE IDENTIFICATION OVER ARCTIC MIXED-PHASE CLOUDS FROM AIRBORNE SPECTRAL CLOUD TOP REFLECTANCE MEASUREMENTS

A. Ehrlich[1], E. Bierwirth[1], M. Wendisch[1], J.-F. Gayet[2], G. Mioche[2], A. Richter[3],

[1] Johannes Gutenberg-University Mainz, Institute for Atmospheric Physics, Becherweg 21, 55099, Mainz, Germany

[2] Laboratoire de Météorologie Physique (LAMP), Université Blaise Pascal, Avenue des Landais 24, 63177 Aubière Cedex, France

[3] Alfred Wegener Institute for Polar and Marine Research, Telegrafenberg A43, D-14473 Potsdam, Germany

1. INTRODUCTION

Boundary layer clouds play a crucial role in the radiation budget of Arctic regions. Their impact depends on surface albedo, aerosol, cloud water content, cloud drop size and cloud thermodynamic phase (Curry et al., 1996). Especially the cloud phase influences the cloud radiative properties and cloud live cycle (Sun and Shine, 1994; Harrington et al., 1999; Yoshida and Asano, 2005).

Therefore in situ measurements and/or remote sensing of the thermodynamic cloud phase is required. Recent studies from Knap et al. (2002) and Chylek et al. (2006) show the potential of satellite remote sensing of cloud phase. In this study we present similar methods of cloud phase identification using airborne solar radiation measurements and radiative transfer simulations. Three different approaches to identify cloud phase are applied and discussed. The measurements were performed during the Arctic Study of Tropospheric Aerosol, Clouds and Radiation (ASTAR) 2007 campaign. Additional information on cloud phase is obtained from in situ cloud microphysical and lidar measurements.

2. INSTRUMENTATION

During ASTAR 2007 two aircraft were employed. We report on data from the Polar 2 aircraft, operated by the Alfred Wegener Institute for Polar and Marine Research (AWI). The airborne instrumentation included the SMART-Albedometer (Spectral Modular Airborne Radiation measurement sysTem), in situ instruments as the Polar Nephelometer, CPI (Cloud Particle Imager), and PMS-FSSP (Particle Measuring System, Forward Scattering Spectrometer Probe), and the Airborne Mobile Aerosol Lidar (AMALi).

The SMART-Albedometer measures downwelling and upwelling irradiances $F_\lambda^\downarrow$, $F_\lambda^\uparrow$ simultaneously with upwelling nadir radiance $L_\lambda^\uparrow$. It is actively leveled to compensate deviations of the aircraft attitude to the horizontal plane (Wendisch et al., 2001). Two spectrometer systems are available for $F_\lambda^\downarrow$ and $L_\lambda^\uparrow$ covering the visible (350-1000 nm) and near-infrared wavelength range (1000-2100 nm) with a spectral resolution of 2-3 nm and 9-16 nm, respectively. $F_\lambda^\uparrow$ is measured only in the visible part of the spectrum. The optical inlet for $L_\lambda^\uparrow$ has an angle of view of $1.5°$.

The different in situ instruments provided independent measurements of particle number size distribution, extinction coefficient, ice and liquid water content, effective diameter, scattering phase function and asymmetry parameter. The instruments and data retrieval are described in Gayet et al. (2007).

The AMALi is a 2-wavelength (532 nm and 355 nm) backscatter lidar with depolarization measurements at 532 nm wavelength. AMALi was installed in nadir looking configuration. The vertical resolution amounts to 7.5 m. The minimum horizontal resolution was around 900 m. Further details of AMALi can be found in Stachlewska et al. (2004).

3. OBSERVATIONS OF MIXED-PHASE CLOUDS

During ASTAR 2007 (7th-9th April) a cold air outbreak with northerly winds produced boundary layer clouds over the open Greenland Sea as shown by the MODIS satellite image in Figure 1. Convection over the relatively warm open sea maintained the coexistence of ice and water in these clouds. Observations showed a typical liquid cloud top layer with precipitating ice below (Figure 2). The FSSP measured high particle concentrations between 1000-1700 m altitude. In the same layers the asymmetry parameter obtained by the Polar Nephelometer is about 0.85 which corresponds to spherical water droplets. A narrow ice layer was found between 800-1100 m indicated by lower asymmetry parameters and high particle concentrations measured by the CPI. Below this, precipitating large ice particles were observed down to 500 m.

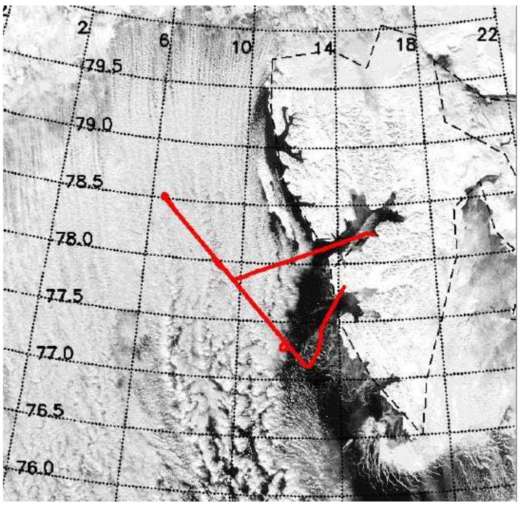

Fig. 1: Flight track of Polar 2 aircraft on 7th April.

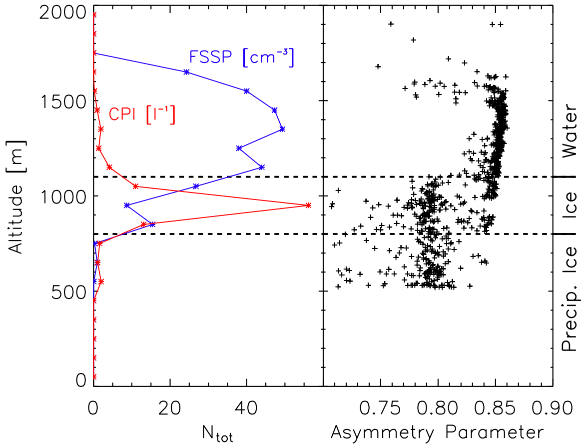

Fig. 2: Profile of microphysical measurements from 7th April. Total particle concentration N_{tot} measured by FSSP and CPI are given in the left panel. The asymmetry parameter g obtained from the Polar Nephelometer is shown on the right panel.

Lidar observations could not penetrate the optically thick clouds, but also identified a liquid cloud top layer from the low values in the depolarization signal. Additionally, precipitating ice could be observed with AMALi in several cloud gaps showing higher depolarization.

4. SPECTRAL CLOUD TOP REFLECTANCE

Simulations of spectral cloud top reflectance $R_\lambda = \pi \cdot L_\lambda^\uparrow / F_\lambda^\downarrow$ for pure ice, pure water and mixed-phase boundary layer clouds ($\tau = 12$) are shown in Figure 3 a. The simulations indicate that the spectral pattern of R_λ in the wavelength range 1450-1750 nm differs for the three cloud types. Of all clouds pure water clouds show the highest values at 1500 nm where the difference of ice and water absorption is maximum. The slope of the reflectance between 1500 nm and 1750 nm is small for water clouds and maximal for pure ice clouds. In the visible part of the spectrum it is noticeable that R_λ is higher for ice clouds than for water clouds of the same optical depth.

With the SMART-Albedometer pure water, pure ice and mixed-phase clouds were observed during ASTAR. The measurements of R_λ show similar spectral pattern in the wavelength range 1450-1750 nm compared

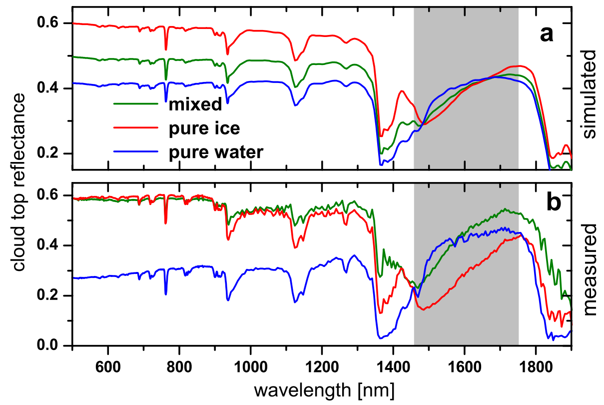

Fig. 3: Examples for cloud top reflectance. Panel a shows simulations for pure ice, pure water and mixed-phase clouds ($\tau = 12$). Measured reflectances (7th April) over a pure ice cloud ($\tau = 12$), pure water cloud ($\tau = 4$) and mixed-phase cloud ($\tau = 15$) are given in panel b.

to the simulations for the three cloud types (Figure 3 b). This information was used in the following to retrieve the cloud phase from the measurements with a common two wavelengths approach and the application of a principle component analysis. A third approach used the combined albedo and reflectance measurements to obtain information on the cloud phase.

Two Wavelengths Approach: The spectral slope of the cloud reflectance between 1640 and 1700 nm is used as ice index in satellite retrievals of the cloud phase (Knap et al., 2002). The ice index $I_S = (R_{1700nm} - R_{1640nm})/R_{1640nm} \cdot 100$ is found to be zero for pure water clouds and up to 30 for pure ice clouds. For our measurements we extended the ice index I_S to the wavelength range 1550 - 1700 nm. To reduce the impact of noise from the single wavelength channels the slope of R_λ was calculated by linear regression and normalized with R_{1640nm} afterwards. The typical values for pure water clouds range around 10. Pure ice clouds show I_S values of 50-60.

Principle Component Analysis: Principle component analysis (PCA) provides a powerful tool to understand the physical meaning of variations in a multivariate data set (Pearson, 1901). The transformation of the original data set into a set of principle components (PC) reduces the information given by the multivariate data to a few PCs. Analyzing spectral atmospheric radiation measurements the obtained PC are correlated to physical processes like molecular scattering, trace gas absorption or aerosol interaction (Rabbette and Pilewskie, 2001). We utilized the PCA to extract the ice and water absorption signature in the spectral cloud top reflectance. First the PCA was applied separately on simulated pure ice and pure water boundary layer clouds of various optical depth ($\tau = 4 - 72$) and effective diameter (4-54 μm for water and 4-180 μm for ice clouds). Therefore the cloud reflectance was normalized with R_{860nm} to eliminate the impact of cloud optical depth. The first principle component derived from the pure water cloud simulations PC_W was found to be related to water absorption. The contribution of R_λ at single wavelength to PC_W is given by the coefficients shown in Figure 4. The maximum weight results from the wavelength close to 1500 nm. In the same way the first PC from the pure ice cloud simulations PC_I is correlated with ice absorption and has the maximum contribution from wavelength around 1750 nm. To utilize PC_W and PC_I for cloud phase identification we calculated the ratio $I_P = (PC_I/PC_W - 2.2) \cdot 100$ as indicator for the cloud phase. Typical values of water clouds are about 2.5. Pure ice clouds are indicated by $I_P > 8$.

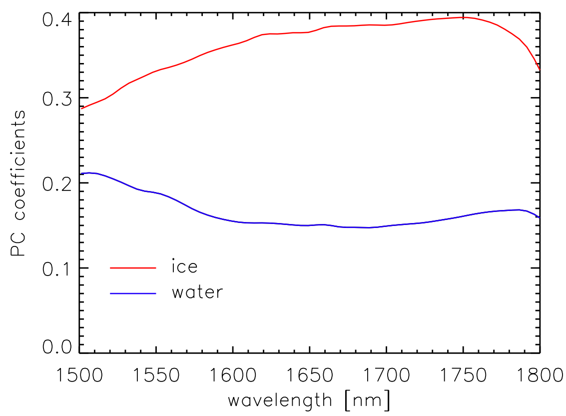

Fig. 4: Coefficients for the calculation of the principle components PC_I and PC_W.

Albedo - Reflectance: As shown in Figure 3 a simulated R_λ in the visible wavelength is higher for ice clouds than for water clouds of same optical depth. This is caused by differences in the scattering phase function of spherical water droplets and nonspherical ice crystals. For large solar zenith angles the enhanced sideways scattering of nonspherical ice crystals results in a more isotropic bidirectional reflectance distribution function (BRDF) of the cloud top. For the same simulations, the calculated cloud top albedo $\alpha_\lambda = F_\lambda^\uparrow / F_\lambda^\downarrow$ exhibit no differences for different cloud phase (not shown here). Therefore the ratio of cloud top reflectance to albedo $\beta_I = R_{645nm}/\alpha_{645nm}$ serves as an indicator of the anisotropy of the cloud BRDF. For solar zenith angles larger than $70°$ nonspherical particles give a higher β_I than spherical particles. The comparison of measured β_I to β_I values for pure water clouds using the ratio $I_A = \beta_I(meas)/\beta_I(water)$ is used as an indicator for the cloud phase.

For remote sensing of mixed-phase clouds the vertical distribution of ice and water has to be considered (Yoshida and Asano, 2005). We investigated the sensitivity of each approach to the vertical layering of the mixed-phase clouds. Therefore, radiative transfer simulation were performed based on the microphysical measurements on 7th April as shown in Figure 2. The cloud was divided into 10 sublayers with a homogeneous water mode of $\tau_w = 1.5$ for each layer. One ice layer ($\tau_I = 1.5$) was added and shifted from cloud top to cloud bottom. For each simulation the ice indices were calculated. The results are given in Table 1.

The results show that all three indices are most sensitive to the upper cloud layer if no water is above the ice layer ($\tau_W^{top} = 0$). Here τ_W^{top} gives the total optical depth of the water layers located above the single ice layer. I_S and I_P decrease slowly with increasing τ_W^{top}. Nevertheless typical boundary layer mixed-phase clouds with a liquid cloud top layer are detectable with these approaches. The I_A deviates from values of pure water clouds only if the ice layer is at cloud top. This suggests that I_A is suitable only for pure ice clouds. Typical boundary layer mixed-phase clouds will be identified as pure water clouds.

Table 1: I_S, I_P and I_A of mixed-phase clouds ($\tau_W = 15$, $\tau_I = 1.5$) for different positions of the ice layer (not all 10 simulations shown here). The position is given by the optical depth of the water layer above τ_W^{top}.

τ_W^{top}	I_S	I_P	I_A
0.0	20.5	4.3	1.12
1.5	18.9	4.0	1.02
3.0	17.2	3.7	1.01
6.0	14.8	3.2	1.00
9.0	13.4	3.0	1.00
15.0	12.0	2.8	1.00

5. CASE STUDY OF 7TH APRIL 2007

On 7th April combined radiation and microphysical measurements were conducted along the path of CALIPSO over the Greenland sea. The flight track shown in Figure 1 included a sampling of the cloud edge in the south eastern part. The in situ microphysical measurements taken on the first passage showed that the cloud edge consisted of ice particles only (Figure 5 a, $77.5°$ N). On the second passage flying above the cloud top the radiation measurements could be used to remotely identify the cloud phase.

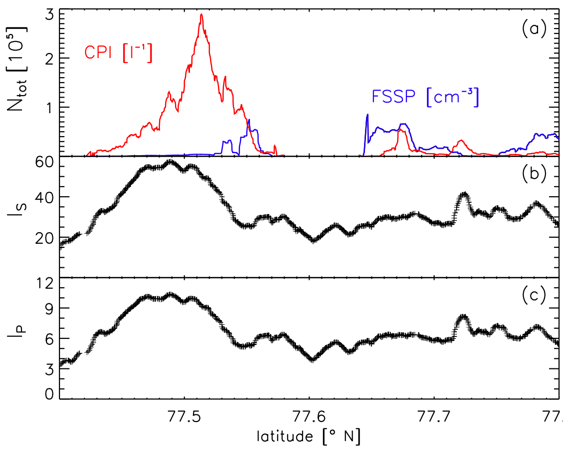

Fig. 5: Ice and water particle concentration measured by CPI and FSSP along the flight track on 7th April (a). The ice indices I_S and I_P for the same positions are given in panel (b) and (c).

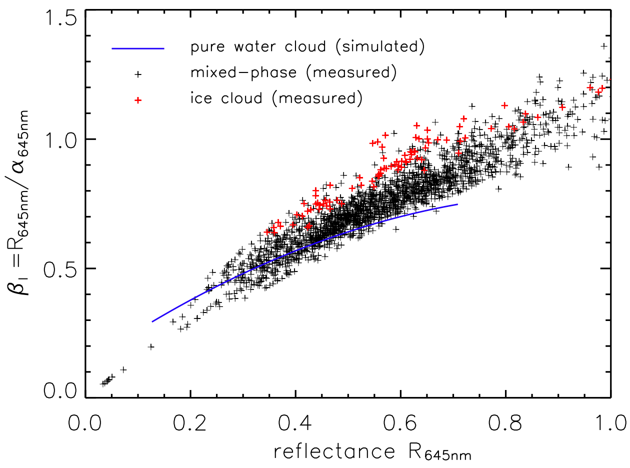

Fig. 6: Measured β_I as function of R_{645nm}. Black crosses show measurements over mixed-phase clouds, red crosses over the ice cloud observed on the cloud edge. Simulation for pure water clouds are shown as blue line.

Figure 5 shows the measured ice indices I_S and I_P along the flight track of 7th April (panel b and c). The particle concentrations measured by CPI and FSSP are given in panel a. Both ice indices show high values around $77.5°$ N correlated with the high ice particle concentration. The mean values $I_S = 55$ and $I_P = 10$ indicate pure ice clouds. Lower values ($I_S = 36$ and $I_P = 6$) corresponding to mixed-phase clouds were measured afterwards when the FSSP measured significant water particle concentrations.

The analysis of the reflectance-albedo ratio β_I also reveals the presence of an ice cloud at the cloud edge. Figure 6 shows all measurement points made on 7th April above clouds. Generally the measured β_I deviate from the theoretical curve of pure water clouds (1D simulations) which is not expected for mixed-phase clouds with a thick liquid layer at cloud top. Further investigations will show whether the deviation is related to measurement uncertainties or 3D effects in radiative transfer. Nevertheless the measurements above the cloud edge (labeled by red crosses) tend to range in higher values of β_I. This shows that at the cloud edge nonspherical ice crystals were present at cloud top.

6. CONCLUSIONS

Three different methods to derive the cloud thermodynamic phase from airborne spectral solar radiation measurements were presented. The ice index I_S analyzing the slope of the spectral reflectance and the ice index I_P obtained from PCA are capable to identify the mixed-phase clouds observed during the ASTAR 2007. A pure ice cloud at the edge of a mixed-phase cloud field also observed by in situ microphysical probes showed significant higher values of I_S and I_P. Both indices are well correlated which suggest to apply I_S in further investigations due to the lower computational effort of calculating I_S. The third approach based on combined albedo and reflectance measurements is not able to detect the mixed-phase cloud with liquid cloud top layer. Only pure ice clouds could be distinguished from the mixed-phase clouds. Further investigations with the combined radiation, lidar and in situ microphysical measurements presented here will help to verify algorithms for cloud phase identification of satellites (CALIPSO, CLOUDSAT, MODIS).

ACKNOWLEDGMENTS

The authors gratefully acknowledge the financial support provided by ICCP, IAMAS, IUGG and WMO which helped us to attend the ICCP conference.

7. BIBLIOGRAPHY

Chylek, P., Robinson, S., Dubey, M. K., King, M. D., Fu, Q., and Clodius, W. B.: Comparison of near-infrared and thermal infrared cloud phase detections, J. Geophys. Res-Atmos., 111, D20 203, 2006.

Curry, J. A., Rossow, W. B., Randall, D., and Schramm, J. L.: Overview of Arctic cloud and radiation characteristics, J. Climate, 9, 1.731–1.764, 1996.

Gayet, J.-F., Stachlewska, I. S., Jourdan, O., Shcherbakov, V., Schwarzenboeck, A., and Neuber, R.: Microphysical and optical properties of precipitating drizzle and ice particles obtained from alternated Lidar and in situ measurements, Annales Geophys, 25, 1487–1497, 2007.

Harrington, J. Y., Reisin, T., Cotton, W. R., and Kreidenweis, S. M.: Cloud resolving simulations of Arctic stratus - Part II: Transition-season clouds, Atmospheric Research, 51, 45–75, 1999.

Knap, W., Stammes, P., and Koelemeijer, R.: Cloud thermodynamic-phase determination from near-infrared spectra of reflected sunlight, J. Atmos. Sci., 59, 83–96, 2002.
Pearson, K.: On lines and planes of closest fit to systems of points in space, Philos. Mag., 2, 559–572, 1901.
Rabbette, M. and Pilewskie, P.: Multivariate analysis of solar spectral irradiance measurements, J. Geophys. Res-Atmos., 106, 9685–9696, 2001.
Stachlewska, I., Wehrle, G., Stein, B., and Neuber, R.: Airborne Mobile Aerosol Lidar for measurements of Arctic aerosols, Proceedings of 22nd International Laser Radar Conference (ILRC2004), ESA SP-561, 1, 87–89, 2004.
Sun, Z. and Shine, K. P.: Studies of the Radiative Properties of Ice and Mixed-Phase Clouds, Quart. J. Roy. Meteor. Soc., 120, 111–137, 1994.
Wendisch, M., Müller, D., Schell, D., and Heintzenberg, J.: An airborne spectral albedometer with active horizontal stabilization, J. Atmos. Oceanic Technol., 18, 1856–1866, 2001.
Yoshida, Y. and Asano, S.: Effects of the vertical profiles of cloud droplets and ice particles on the visible and near-infrared radiative properties of mixed-phase stratocumulus clouds, J. Meteor. Soc. Japan, 83, 471–480, 2005.

MODELING ARCTIC MIXED-PHASE CLOUDS AND ASSOCIATED ICE FORMATION

Jiwen Fan[1,*], Mikhail Ovtchinnikov[1], Jennifer Comstock[1], Sally McFarlane[1], and Alexander Khain[2]

[1] Climate Physics Group, Pacific Northwest National Laboratory, Richland, WA 99352

[2] Department of the Atmospheric Sciences, The Hebrew University of Jerusalem, Jerusalem, Israel.

1. INTRODUCTION

The Arctic is a highly variable and sensitive region in the global climate system [Walsh et al, 2002]. Clouds play an important role in the Arctic climate since they determine the net longwave radiation at the surface and also regulate the incoming solar radiation. Mixed-phase clouds, which are often characterized by liquid water droplets topping over precipitating ice, tend to dominate in the Arctic [Pinto, 1998; Prenni et al., 2007]. The major difficulty in modeling these mixed-phase clouds stems from the uncertainty of ice formation mechanisms including low concentrations of ice nuclei (IN) active at temperatures warmer than –15 ^{0}C. Recently, two enhanced ice nucleation mechanisms: IN formation from drop evaporation residuals and drop freezing during evaporation, were shown to be strong enough to account for the observed ice particle concentrations in Arctic mixed-phase clouds (AMPC) [Fridlind et al. 2007]. The current study attempts to address two interesting aspects of AMPC: the enhanced nucleation mechanisms and the locations of ice initiation.

A cloud-resolving model referred to as the System for Atmospheric Modeling (SAM [Khairoutdinov and Randall, 2003] coupled with an explicit bin microphysics model based on Khain et al. [2004], is employed to simulate the single-layer stratocumulus clouds observed during the Mixed-Phase Arctic Cloud Experiment_(MPACE) from October 9 to 10, 2004. The treatment of the primary ice nucleation is based on a heterogeneous ice nucleation theory that describes the IN-dependent, and the temperature and supersaturation dependent ice nucleation [Khvrostyanov and Curry, 2000; hereafter referred to as HIC_KC]. Two enhanced nucleation mechanisms: IN formation from residues of evaporated droplets active in the condensation-followed-by-freezing mode [Rosinski and Morgan, 1991] and drop evaporation freezing by contact nucleation inside-out [Durant and Shaw, 2005] are applied to simulate the observed liquid and ice clouds. The simulations are evaluated by extensively comparing with in-situ aircraft and remote sensing measurements taken during MPACE. The locations of ice initiation in the model are examined and sensitivity studies are performed to look into the contributions of both enhanced nucleation mechanisms to the ice formation, the significance of IN source from ice evaporation, and the influences of high initial IN concentration.

2. DESIGN OF SIMULATIONS

First, two simulations are run for the enhanced ice nucleation mechanisms: (a) IN formation from residues of evaporated droplets active by condensation-followed-by-freezing [Rosinski and Morgan, 1991], and (b) drop evaporation freezing by contact nucleation inside-out [Durant and Shaw, 2005]. They are referred to as EVAP_RM and EVAP_DS, respectively, hereafter. The primary ice nucleation in these two immersion modes, which are included in HIC_KC. IN is treated as an additional prognostic variable with 33 mass-doubling bins. The initial concentration of IN is set to the observed average value of 0.2 L^{-1} and the shape of the size distribution is the same as that of the aerosol. The ice nuclei recycled from ice evaporation are assumed to be "preactivated", i.e., they are set back to the largest size bin of IN. An additional run referred to as BASE is performed without either of the enhanced nucleation mechanisms to explore the contributions of both enhanced nucleation mechanisms. The significance of IN recycled from ice evaporation is illustrated through a simulation without the IN recycling, which is referred to as NOIN. A high ice nucleus concentration case (HIGH_IN) is run based on BASE, but IN concentrations are boosted by 100 times.

3. RESULTS

Comparisons with Observations

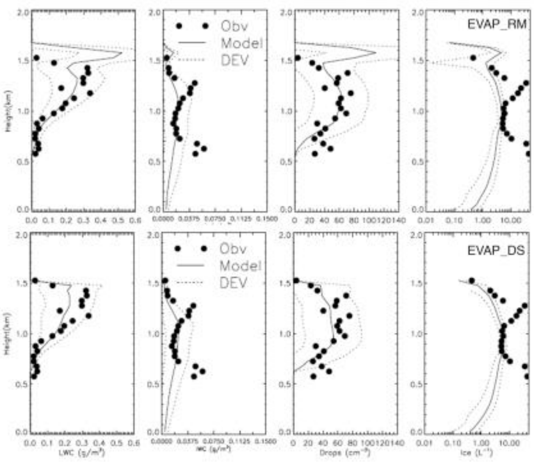

Figure 1. Comparisons of LWC, IWC, droplet number and ice number from EVAP_RM (top) and EVAP_DS (bottom) with the aircraft spiral measurements at Barrow (dot points). Both EVAP_RM and EVAP_DS agree well with the observations. Ice number concentrations are a little underestimated by both simulations.

EVAP_RM has higher liquid and ice water content at the cloud top than EVAP_DS.

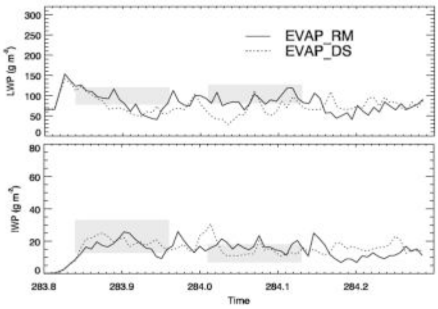

Figure 2. Comparisons of liquid water path (LWP) and ice water path (IWP) from EVAP_RM and EVAP_DS with the interquartile range derived from aircraft measurements at Barrow (shaded area). Good agreements with the observed LWP and IWP are indicated.

Locations of Ice Initiation

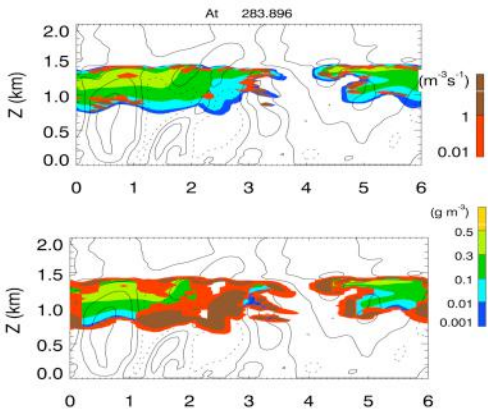

Figure 3. Contours of nucleation rates from primary nucleation mechanisms (top) and evaporation freezing (bottom). Contours with red and green colors represent nucleation rates and condensed water content (CWC), respectively. Solid and dotted lines refer to updrafts and downdrafts, respectively. Nucleation from the enhanced nucleation mechanism (evaporation freezing) is much stronger and occurs with much higher rates. The location of ice initiation is mainly where evaporation occurs and the downdrafts originate, i,e,, near cloud edge and cloud base.

Contributions of Enhanced Nucleation Mechanisms and IN Recycled from Ice Evaporation

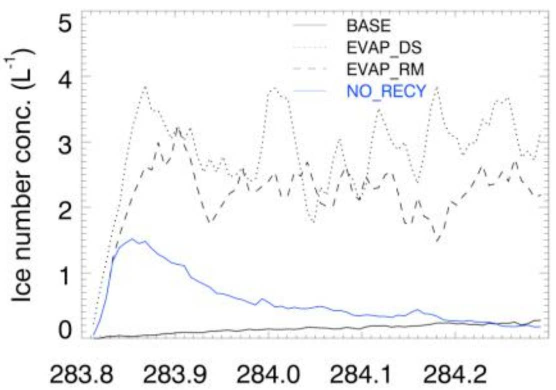

Figure 4. Comparisons of time-dependent ice number concentrations from BASE, EVAP_RM, EVAP_DS, and NO_RECY. Both enhanced ice nucleation mechanisms dramatically contribute to the ice formation. Surprisingly, the contribution of IN recycled from ice evaporation is as significant as the enhanced nucleation mechanisms after about 6-hr of simulation.

4. SUMMARY

The observed mixed-phase clouds are well reproduced by the enhanced ice nucleation mechanisms of drop evaporation residuals and drop freezing during evaporation. The location of ice initiation is mainly where evaporation occurs and the downdrafts originate. The contribution of IN recycled from ice evaporation is very significant to ice formation and the recycle is critical to maintain the steady ice clouds.

5. BIBLIOGRAPHY

Durant, A. J., and R. A. Shaw (2005), Geophys. Res. Lett., 32, L20814, doi:10.1029/2005GL024175.

Fridlind A. M., et al. (2007), J. Geophys. Res., 112, D24202, doi:10.1029/2007JD008646.

Khain, A. P., A. Pokrovsky, M. Pinsky, A. Seifert, and V. Phillips (2004), J. Atmos. Sci., 61, 2963–2982.

Khairoutdinov, M.F., and Y.L. Kogan (1999), J. Atmos. Sci., 56, 2115–2131.

Khairoutdinov, M. F., and D. A. Randall (2003), J. Atmos. Sci., 60, 607-625.

Khvorostyanov, V., and J. Curry (2000), Geophys. Res. Lett., 27(24), 4081-4084.

Pinto, J. O. (1998), J. Atmos. Sci., 55, 2016–2038.

Prenni, A. et al. (2007), Bull. Am. Meteorol. Soc., 88, 541–550, doi:10.1175/BAMS-88-4-541.

Rosinski, J., and G. Morgan (1991), J. Aerosol Sci., 22, 123–133.

Walsh, J.E., et al. (2002), J. Climate, 15, 1429–1446.

ACKOWLEDGEMENTS

This study was supported by the Pacific Nortwest National Laboratory (PNNL) Directed Research and Development (LDRD) program as part of the Aerosol Climate Initiative. This research used resources of the National Energy Research Scientific Computing Center, which is supported by the Office of Science of the U.S. Department of Energy under Contract No. DE-AC02-05CH11231. PNNL is operated by Battelle for the U.S. Department of Energy.

CONTRASTING THE ICE NUCLEATION IN TWO LEE WAVE CLOUDS OBSERVED DURING THE ICE-L CAMPAIGN

Field P.R.[1], Heymsfield A.J.[2], Rogers D.C.[2], Stith J.[2],
DeMott P.J.[3], Haimov S.[4], Murphy S.J.[5], Pratt K.[6], Twohy C.[7], K. Prather[6], Seinfeld J.H.[5]
1. Met Office, paul.field@metoffice.gov.uk
2. National Center for Atmospheric Research
3. Colorado State University
4. University of Wyoming
5. California Institute of Technology
6. University of California, San Diego
7. Oregon State University

1. Introduction

We present some early observations from the recent NSF funded ICE-L (Ice in Clouds Experiment - Layer clouds) field campaign over Wyoming and Colorado in fall 2007. The long term goal of the project is to show that the number of ice particles formed by nucleation mechanisms can be predicted if the aerosol feeding into the cloud is adequately characterised both physically and chemically.

Airborne observations made with the NCAR C-130 in two isolated lee wave clouds on separate days are compared and contrasted. While both clouds were sampled between -20C and -30C, one cloud contained relatively large amounts of ice while the other was relatively devoid of ice.

The data presented are from flights RF03 and RF04 made on the 16 November 2007 and the 18 November 2007, respectively. Over this period the synoptic situation was characterised by a low pressure system in the Pacific to the northwest of the operating area. This system drifted slowly north over three days but spawned a smaller shorter wavelength low pressure system that remained further south. This situation maintained a slight ridging over the operating region and advected moisture at midlevels into Wyoming on strong westerlies.

2. Instrumentation

Instrumentation for the ICE-L campaign aboard the C-130 for hydrometeor characterisation included a new NCAR developed fast 2D-C (64 elements, 25 micron pixel size), Cloud Droplet Probe (CDP 3-50 μm), Small Ice Detector (SID2H, $\sim$3-50 μm), Cloud Particle Imager (CPI 10-2000 μm). Aerosol characterisation intrumentation included a Condensation Nuclei counter (CN D$>$50nm), Ultra High Sensitivity Aerosol Spectrometer (UHSAS 50nm - 1 μm), Counter Flow Virtual Impactor (CVI), Aerosol Time Of Flight Mass Spectrometer (ATOFMS), Aerodyne compact Time of Flight Aerosol Mass Spectrometer (AMS), Ice Nuclei Counter (INC). Bulk and environmental probes included the Rosemount Icing Detector (RICE), and Buck hygrometer. Other core measurements of winds and temperature were also measured.

3. Cloud passes

We present one straight and level leg through a wave cloud for each of the days considered. Figure 1 shows the data for RF03. The flow of air through the cloud is from right to left (i.e. the aircraft was flying into the wind). For RF03, the aircraft encountered (410 s) an updraft of 2 m s^{-1} close to the leading edge of the cloud (390 s). The CDP and SID2H then show concentrations of $\sim$100 cm^{-3} between 390 and 240s (LWC $\sim$0.15 g m^{-3}). Within the liquid cloud the 2DC registers particles with sizes greater than 100 μm and the CPI imagery shows heavily rimed particles. The radar indicates relatively high reflectivities and cloud extending to between 1000 and 1500 m above the sampling altitude. Downstream (time$<$240s) of the liquid cloud there is an ice tail exhibiting ice concentrations of $\sim$50 L^{-1} on the 2DC (D$>$100μm) and $\sim$0.5 cm^{-3} on the CDP and SID2H. The CPI imagery shows ice crystals less or not affected by riming, perhaps representing aseparatee population to the rimed particles seen within the liquid cloud. The minimum temperature encountered by the aircraft

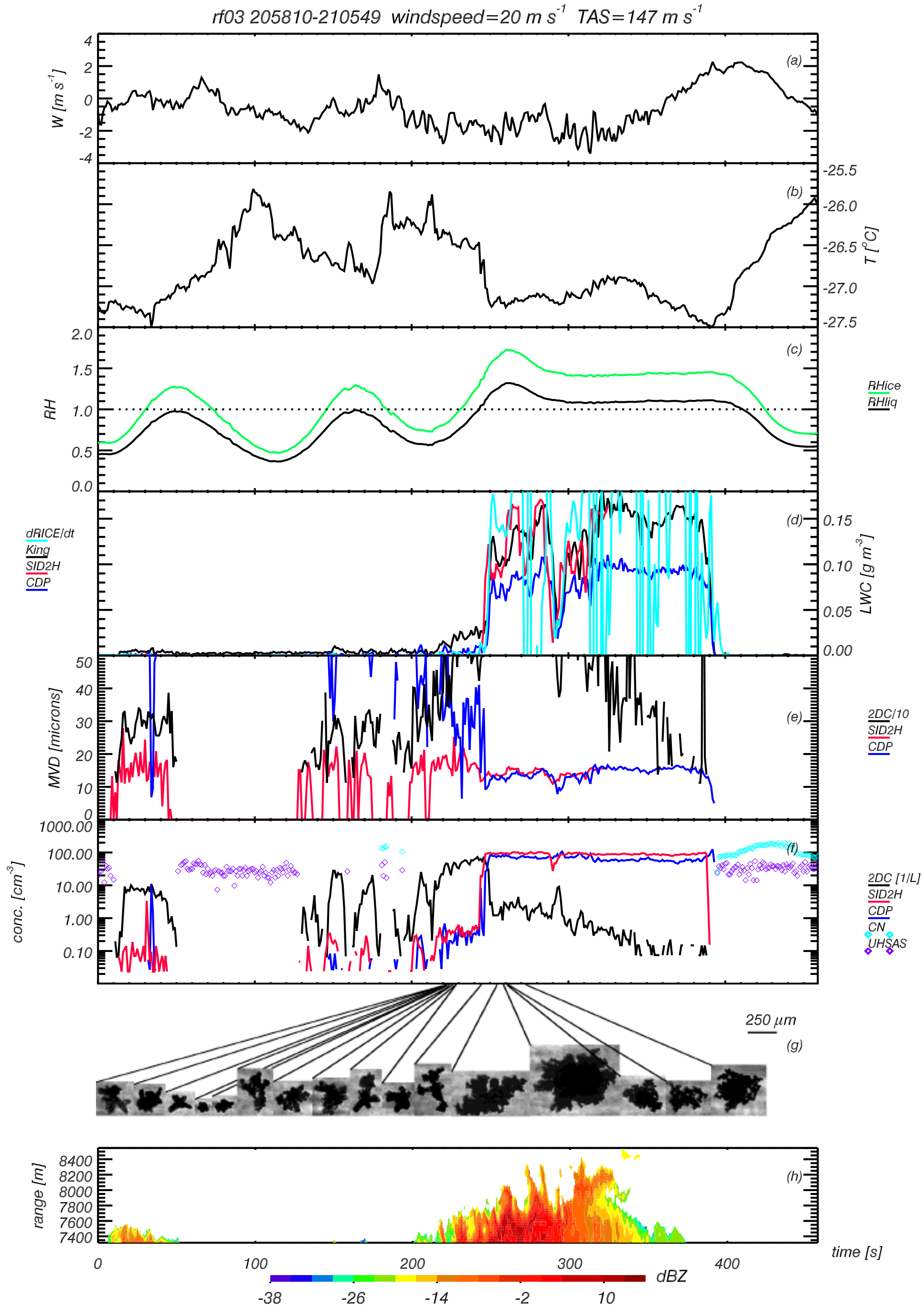

Figure 1: RF03. Various data (1 Hz) versus time along a straight and level run for a) vertical air velocity. b) Air temperature. c) Relative humidity with respect to ice and liquid obtained using the Buck hygrometer. d) Liquid water content (LWC) estimates from the CDP, SID2-H, King hot wire and the time derivative (mV/s) of the Rosemount icing probe (proportional to LWC). e) Mean volume diameter from the CDP, SID2 and ratio of 3rd and 2nd moment of the PSD for the 2DC (D>100μm) - for the 2DC the size has been divided by 10 for plotting purposes. f) Concentrations for the CDP, SID2H, 2DC (D>100μm), also shown are CN (D>50nm) and UHSAS (D>0.1μm) concentrations. g) Example CPI imagery with lines linking to location along the run (250 micron scale bar is shown). h) Radar reflectivity (zenith view) from the Wyoming Cloud Radar.

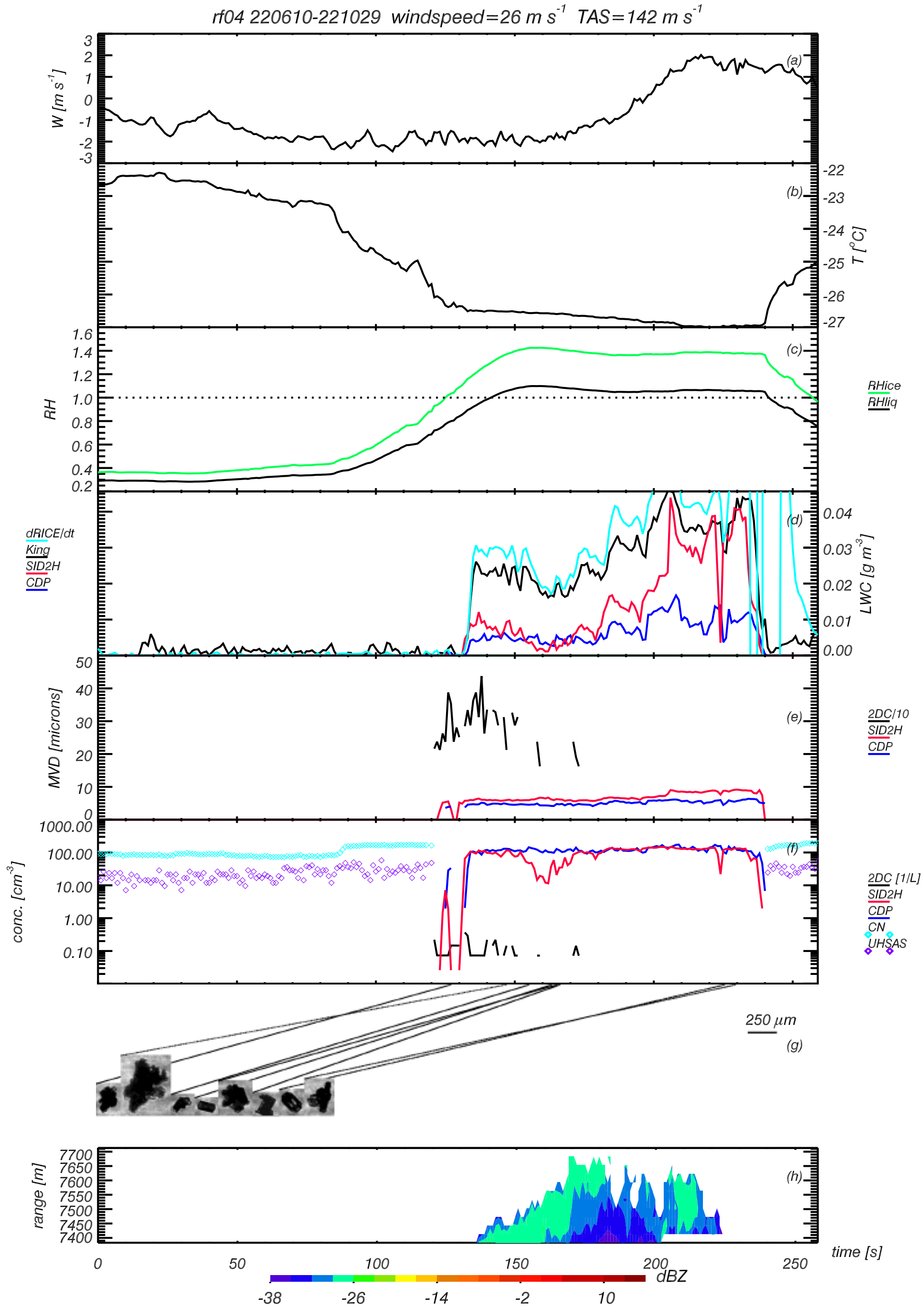

Figure 2: Same as fig. 1, but for RF04

during the run is -27.5C. Figure 2 shows a similar plot for RF04. Again the air flow through the cloud is from right to left. The maximum updraft of 2 m s^{-1} is encountered near the beginning of the liquid cloud and the minimum temperature along the run (-27C). This time the LWC on the King probe is only up to 0.04 g m^{-3} and the liquid cloud is shorter in horizontal extent (240-130s). Again, the CDP and SID2H show droplet concentrations around 100 cm^{-3} but the lower LWC means that the mean droplet size in RF04 is smaller. There is little evidence of an ice tail downwind of the liquid cloud. Ice is present and can be seen on the CPI images as well as the 2DC, but this time the concentrations of particles larger than 100 μm are $\sim$0.1 L^{-1}. The radar image reveals a much thinner cloud than on the previous flight with another thin layer above (500-1000m) that does not appear to be precipitating.

4. Aerosol

Analysis of the UHSAS size distributions on these days at the potential temperatures where clouds were found (fig. 3) indicates that there is a difference in the aerosol concentrations greater than 300 nm in size: there are more larger particles on the day with more ice (RF03). Additionally, X-ray chemical analysis of the CVI residuals larger than 0.5 μm indicate they are composed primarily of salts and show increased industrial, crustal and biomass fractions of the total number analysed in RF03 when compared to RF04, but a reduced fraction of sulphate. The ATOFMS analysis of CVI residuals (larger than 300 nm) showed that salts were the dominant residual in ice and liquid. Residuals collected in ice during RF03 showed increased fractions of silicate material associated with the salts and these salts appeared fresher (decreased presence of nitrate/sulphate) in the ice residuals in comparison to the residuals obtained in the liquid cloud. The AMS showed that ice residuals correlate well with the presence of Chlorine and organic material. The aerosol do appear to exhibit different size distributions and chemical characteristics between the two flights. However, the IN counter operating at water saturation and temperatures close to those measured during the sampling runs only shows concentrations of up to 1 L^{-1} (30s average) for both flights. While this is adequate for explaining the ice concentrations on RF04 (see Eidhammer et al. 2008) and to some extent the concentrations seen in the mixed phase region of the cloud, it is not enough to explain the concentrations seen in the outflow regions downwind of the liquid cloud in RF03.

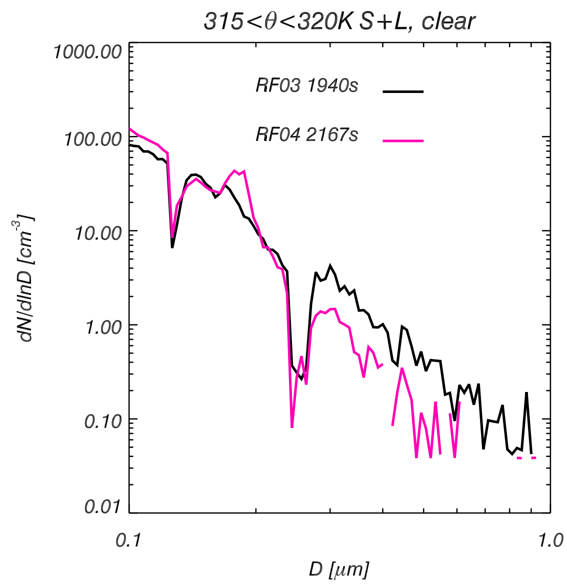

Figure 3: UHSAS aerosol size distributions for RF03 and RF04 averaged over periods when the potential temperature was between 315K and 320K, the range in which the clouds sampled formed.

5. Discussion

The greater concentrations of ice in RF03 when compared to RF04 for similar sampling temperatures, and updraft speeds indicate that the production of ice was different. There are two possibilities: i) A difference in the nature of the aerosol ingested into these wave clouds allowed more condensation/immersion freezing to occur during RF03. ii) The droplets at the top of the cloud in RF03 were exposed to cold enough temperatures (T<-35C) to allow homogeneous freezing to occur (or potentially deposition nucleation at these cold temperatures).

Because the difference in aerosol physical and chemical characteristics is not matched by a difference in IN counter measurements, this casts some doubt on the explanation of the difference in ice concentrations between the two flights being due solely to the nature of the aerosol. The second possibility is ice being formed higher up at colder temperatures through homogeneous freezing and then being sampled as the aircraft intercepts trajectories from higher altitudes. Simply assuming a sinusoidal fit to the wave vertical velocity suggests a maximum vertical displacement of 700m from the sampling level allowing parcels to experience temperatures down to perhaps -34C at the coldest along a trajectory. The aircraft would then intercept these trajectories in the ice tail of the run shown for RF03. The cloud does extend higher than 700 m above the sampling level and this higher cloud could be the source of the rimed particles seen in the liquid cloud. We interpret the proposed existence of two populations of ice crystals (rimed and unrimed) as indicating that some homogeneously frozen ice could have become rimed early on and crossed parcel streamlines becoming increasingly rimed as they fell to the aircraft sampling altitude. The character of the ice crystal images in the ice tail of the RF03 run are less affected by riming and may represent crystals formed on parcel trajectories that only reached -34C. This temperature is not cold enough for homogeneous freezing and so these crystals may have formed through heterogeneous freezing.

RF03 is more complex story than RF04, and it will require multi-trajectory parcel model runs to build up a more comprehensive picture of the history of the cloud intercepted by the aircraft at the sampling level. This approach will be required to rule out the hypothesis that the differences seen between RF03 and RF04 are largely due to aerosol differences.

Acknowledgements

NSF sponsored of the ICE-L project and the National Center for Atmospheric Research is supported by the National Science Foundation. (NSF grants: ATM0611936)

References

Eidhammer, T., P. J. DeMott, D. C. Rogers, A. J. Prenni, M. D. Petters, C. H. Twohy, J. G. Hudson and S. M. Kreidenweis, 2008: Ice initiation by aerosol particles: comparing model parameterizations and observations in a parcel framework. 15th International Conference on Clouds and Precipitation, July 7-11, Cancun, Mexico (this Proceedings).

THE STORM STUDIES IN THE ARCTIC (STAR) PROJECT

John Hanesiak[1], Ronald Stewart[1], Kent Moore[2], Peter Taylor[3], Walter Strapp[4], Mengistu Wolde[5]

(1) Centre for Earth Observation Science, University of Manitoba, Winnipeg, Canada
(2) Dept of Physics, University of Toronto, Toronto, Canada
(3) Dept. of Earth and Space Science, York University, Toronto, Canada
(4) Cloud Physics and Severe Weather Division, Environment Canada, Toronto, Canada
(5) Flight Research Laboratory, National Research Council of Canada, Ottawa, Canada

1. INTRODUCTION

Storms and their related hazards over the Arctic can have profound effects including loss of life and impacts on all life forms, industry, transportation, hunting, recreation, as well as on the landscape (terrestrial, sea ice and ocean). Over the past few decades, there is some evidence that the occurrence of extreme storms have increased (Stone et al. 2000; McCabe et al. 2001; Zhang et al. 2004) and further changes, including over the Arctic, are expected with anticipated climate change.

Storms and associated hazards are common in the Arctic and some of the most intense storms occur in the eastern Arctic. As low-pressure systems naturally progress from the west and south, they often intensify as they track east and north (e.g. Hudson et al. 2001; Hoskins and Hodges, 2002; Intihar and Stewart, 2005). The interaction of these low-pressure systems with local significant topography can result in high wind speed (gap flow) and precipitation events (e.g. Nawri and Stewart, 2006; Martin and Moore, 2005). The fall season is the stormiest when cold air from the north crosses relatively warm surfaces and warm air from southern latitudes, acquiring a great deal of energy, allowing extreme storms to form and evolve.

The Storm Studies in the Arctic (STAR) project (www.starnetwork.ca) focuses on these hazardous Arctic storms over the southern Baffin Island region, primarily due to existing observational infrastructure and greater population density. Iqaluit, the capital of Nunavut and located on southern Baffin Island, is a thriving city with an increasing population and industrial, tourism and recreation developments.

The overall objective of this 4-year (2007-2010) STAR project is to better understand severe Arctic storms and their associated hazardous conditions, and contributing to their better prediction. The objective will be realized through a focus on four themes:

1. Hazardous weather-related conditions in the Iqaluit area
2. Regional hazardous weather-related conditions and sea ice impacts
3. Prediction capabilities and improvements
4. User community interactions

More specifically, the main hazards being investigated are:

1. Blizzards, blowing snow, and reduced visibility
2. Storms producing snow and mixed phase precipitation with significant accumulation
3. Storms, strong winds and their impact on sea ice

STAR will provide, through its major field project and post-analysis, a better understanding of the physical features of Arctic storms and their hazards, the processes controlling them, and our predictive capabilities for them. All of the enhanced detailed field measurements were made in the vicinity of Iqaluit, NU, although storms affecting other communities on southern Baffin Island and CloudSat validation were also of interest.

2. PROJECT AREA AND INSTRUMENTS

2.1 STAR Geography

STAR is geographically focused on the southern Baffin Island region, Nunavut, Canada. The area around Frobisher Bay on Southern Baffin Island is dominated by two mountain ranges (Fig 1). Meta Incognita Peninsula is characterized by low mountain ranges with a typical elevation of the higher ridges of 600 m, with peaks to about 750 m within 50 km to the west-southwest of Iqaluit. On Hall Peninsula, to the north and north-west of Iqaluit, the mountains are generally higher, reaching about 1,000 m within 100 km of the city, with a maximum elevation of 1,295 m close to the southwest coast of Cumberland Sound. These mountains have a strong impact on the surface weather near coastal communities such as Iqaluit. The highest topography, elevations in excess of 2000 m, on southern Baffin Island is associated with the Penny Ice Cap on the Cumberland Peninsula north of Pangnirtung. Available operational meteorological data on Southern Baffin Island are hourly surface observations at the locations shown in Figure 1, and twelve-hourly soundings at Iqaluit. Iqaluit is located at 63°45’N, 68°31’W.

Fig 1: STAR geographic area.

2.2 STAR Instrumentation

Arctic storms and severe weather were sampled using standard meteorological field measurements and remotely sensed observations. Field measurements were collected during two field campaigns in fall 2007 (Oct 10 – Nov 30) and winter 2008 (Feb 1 – 29). The base for the surface observations was at the Environment Canada Weather Office in Iqaluit. Meteorological instruments were installed in the last week of September and remained operational throughout the fall field campaign. Certain instrumentation remained in the field for both the fall storms project and the winter blowing snow project.

The National Research Council of Canada’s (NRC) Convair-580 research aircraft was instrumented by Environment Canada and NRC to collect internal storm measurements of cloud microphysics, thermodynamics, wind and the 4-D dynamic and precipitation structures of storms within a 500 km radius of Iqaluit, Nov 5 - 30, 2007. The aircraft enabled STAR to probe storm events as they approached the area, during their passage and departure over the study area. The aircraft also provided the only sensor validation flights for CloudSAT overpasses in the Arctic. The aircraft was equipped with meteorological instruments that measured temperature, humidity, 3-D winds and gusts, cloud microphysics fields (i.e. liquid & total water probes, icing probes, cloud particle spectrometers, dropsondes, radiometers), Ka band upward/downward looking radar and an NRC dual wavelength (W and X-band) polarimetric up/down/sideways Doppler radar providing remotely sensed measurements of clouds and precipitation. The NRC aircraft flew approximately 48 hours during the project. This time was divided over 14 missions, with variable objectives. A total of 56 dropsondes were deployed from nine of the aircraft flights. Nine flights were performed during CloudSat overpasses.

During storm and interesting weather events, the standard upper air releases were supplemented with additional radiosondes, released at three-hourly or six-hourly intervals in Iqaluit. From the period of Oct 10 – Nov 30, 2007, a total of 51 special radiosondes were released. A portable rawinsonde unit was taken to the community of Pangnirtung to conduct simultaneous launches with Iqaluit during selected severe weather events. A total of 18 radiosondes were released in Pangnirtung between the dates of Nov 2 –18, 2007.

A potable X-band Doppler radar was deployed at the Environment Canada Weather Office in Iqaluit (Oct 10 - Nov 30, 2007) since no operational radars exist in northern Canada. This instrument was used in real-time to map precipitation and wind fields within a radius of approximately 50 km of Iqaluit. It will also be used to validate satellite (CloudSAT, ASTER, MERIS, and MODIS) and surface based precipitation measurements. A passive microwave radiometer (Radiometrics WVR-1100) provided time-series measurements of column-integrated water vapor and liquid water content and an acoustic Doppler sodar (Remtech PA1-NT) was also used to assess the three component winds between 0 – 1.2 km AGL. Both instruments operated between Oct 10 – Nov 30, 2007.

A small mesonet of 10 automatic weather stations, within a 100 km radius of Iqaluit where installed at the end of September (Fig 2). Nine of these stations measured 3 m wind velocity, pressure, 2 m temperature, and 2 m humidity every 10-minutes. The weather stations were positioned over various forms of topography to assess storm influences on surface weather. One of the ten stations was a standard 10-m tower installation in Iqaluit. This 10-m tower was equipped with similar instrumentation as the other mesonet stations, but also had anemometers sampling at 10 m, 4 m, 3 m, 2 m and 1 m and a visibility sensor. In addition to the ten southern Baffin Island weather station sites, an additional automatic weather station was setup in the community of Pangnirtung, Oct 13 – Nov 18, 2007.

Special instruments set up at the Iqaluit weather office site augmented the other instrumentation. This included (1) a double fence facility with a Genore snow measurement system, (2) Thies Clima laser precipitation sensor (precipitation type, size distribution), (3) high resolution digital microphotography camera for precipitation particles.

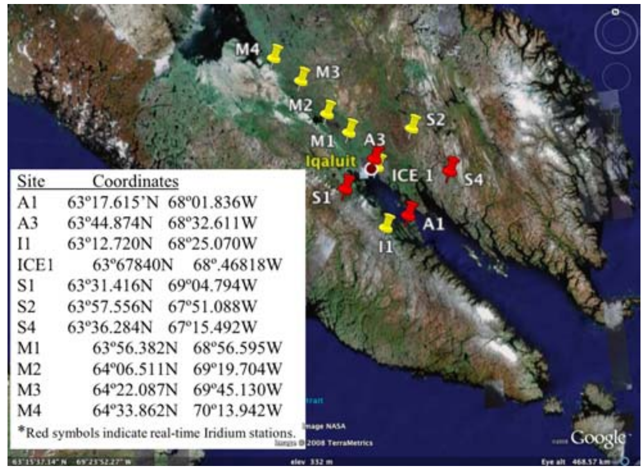

Fig 2: STAR mesonet locations. Red markers indicate real-time iridium data access.

3. ATMOSPHERIC MODELING

Besides the operational GEM (Global Environmental Multi-scale) 15 km horizontal resolution model operated by Environment Canada, STAR had real-time 2.5 km horizontal resolution GEM-LAM (GEM Limited Area Model) simulations available over the STAR domain once a day. The University of Toronto also made real-time MM5 forecast model products available online each day over a similar domain as GEM-LAM. Standard model output fields were provided over the limited domain as well as specialized cross sections through Iqaluit, along and perpendicular to the terrain, along Cumberland Sound and special cross sections where required for flight planning. The model initial fields and output has been archived and special model runs will be performed in the future for further analysis and experiments.

4. STORM CASES AND THEIR FEATURES

Sixteen IOPs (Intensive Observation Periods) took place between Oct 10 – Nov 30, 2007. Table 1 shows the start/end dates/times, number of special rawinsondes (not including regular operational), and aircraft flight and dropsonde status. Table 2 shows the types of phenomena that were sampled during the course of the project. Note that multiple types of phenomena may have been sampled on any given IOP. It can be seen that a wide variety of weather/phenomena were observed, and two IOPs with multiple aircraft flights. Some example case studies are provided in this article.

IOP	Start (UTC)	End (UTC)	# YFB sondes	Aircraft Flight	# Dropsondes
1	15 Oct 2100	17 Oct 1800	8		
2	20 Oct 1800	21 Oct 0000	2		
3	26 Oct 0600	27 Oct 0600	7		
4	29 Oct 1200	30 Oct 1800	3		
5	3 Nov 1200	4 Nov 1200	4 (2 in XYP)		
6	5 Nov 1600	6 Nov 0000	7 (4 in XYP)	yes	4
7	6 Nov 0000	7 Nov 0000	1	yes	
8	7 Nov 2100	8 Nov 0700	3	yes	13
9	9 Nov 2100	10 Nov 0200	1	yes	6
10	11 Nov 2100	12 Nov 1600	5	yes	6
11	16 Nov 1900	19 Nov 0000	23 (12 at XYP)	yes (3 flights)	16
12	20 Nov 1530	20 Nov 2230		yes (2 flights)	
13	22 Nov 1600	22 Nov 1900		yes	
14	23 Nov 1600	23 Nov 2000		yes	4
15	28 Nov 1500	28 Nov 1830		yes	5
16	28 Nov 1500	29 Nov 0000	3	yes	1

Table 1: IOP, rawinsonde, aircraft and dropsonde details. YFB = Iqaluit, XVP = Pangnirtung.

Phenomena / Purpose	**Observations**
Low Pressure System	7
Trough	3
Precipitation in YFB	9
Precipitation in XYP	3
Strong Winds/BS	2
Upslope Precipitation	5
Convergence Zone	2
Convection over Ocean	1
Rain/Snow Boundary	1
CloudSat	8

Table 2: Weather phenomena and/or purpose of IOPs during STAR

Six closed surface low pressure systems crossed southern Baffin Island with two of them being major systems (central surface pressures < 990 hPa). One of the major systems (IOP 11) had three flights devoted to it, with dropsondes in the first flight through the warm front that contained a rain/snow boundary in northern Quebec.

A significant storm that was sampled solely by aircraft was the remnants of Hurricane Noel, the most severe hurricane in 2007 in terms of casualties. The storm tracked northward into Davis Strait between Nov 4 - 5, 2007 as a powerful high latitude system (central pressures estimated to be 960 hPa). The STAR team had its first flight on Nov 5 into this major storm system (IOP 6) (Fig 3), reaching into its northern edge, flying at low altitudes (< 300 m - 1km ASL) inbound and higher altitudes (5 km ASL) outbound, with multiple dropsondes, full radar coverage and cloud microphysical measurements. Minimum pressures and maximum wind speeds measured at 300 m ASL were 962 hPa and >100 km h^{-1}, respectively.

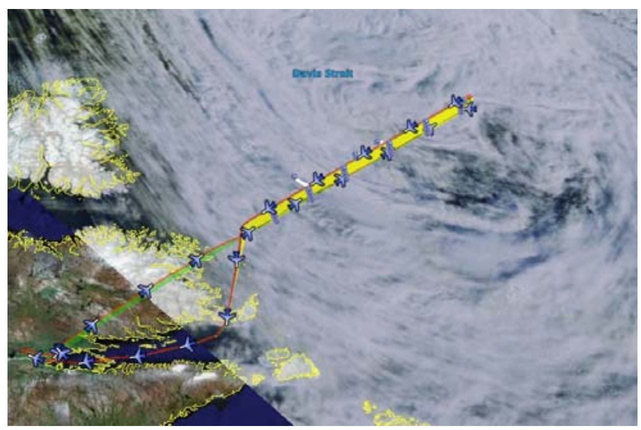

Fig 3: IOP 6 flight track on a MODIS satellite image.

One low-level convection case was sampled via aircraft over Hudson Strait. This system produced unexpected accumulations of snow in Iqaluit between 1900 UTC Nov 9 – 0200 UTC Nov 10. One special rawinsonde was released in Iqaluit at 2100 UTC Nov 9 to sample the thermodynamic state of the atmosphere during the event as well as microphotography. Sample data from the aircraft Ka-band radar returns are shown in Fig 4, highlighting the structure of the convective towers that were flown through. Cloud tops were >3 km with significant

SBCAPE (350-400 J kg^{-1}), based upon radar and dropsonde data. Moderate turbulence was observed. It is hypothesized that the depth of the convection/instability along with moderate 850-700 hPa westerly winds (60-70 km h^{-1}) caused the unexpected snowfall in Iqaluit, however, more extensive analysis is required.

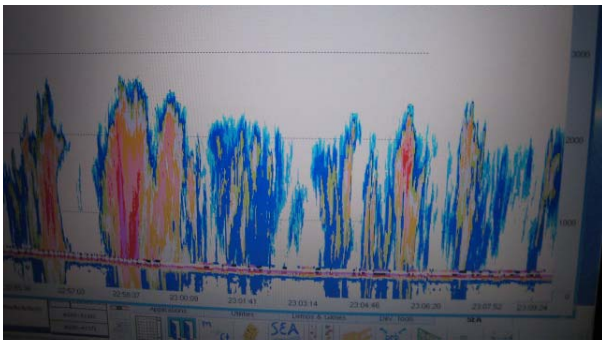

Fig 4: Ka-band downward looking aircraft radar during IOP 9, showing convective tower structure.

A sample CloudSat mission is depicted in Figs 5-7 that took place 1648-1651 UTC Nov 17 in the STAR region (IOP 11). The CloudSat pass was coincident with a major storm system that affected a large area, with cloud top temperatures as cold as -60°C (Fig 5). The CloudSat radar shows significant widespread precipitation along its track with interesting internal precipitation structures and radar returns as high as 10 km (Fig 6). CloudSat ice effective radii reached up to 170 μm in the lower sections of the main precipitation region. A research aircraft flight took place between 1145-1320 UTC Nov 17 directly along part the CloudSat track. Aircraft cloud microphysical and radar measurements will be used to validate CloudSat data on this mission as well as others for the first time in high latitudes.

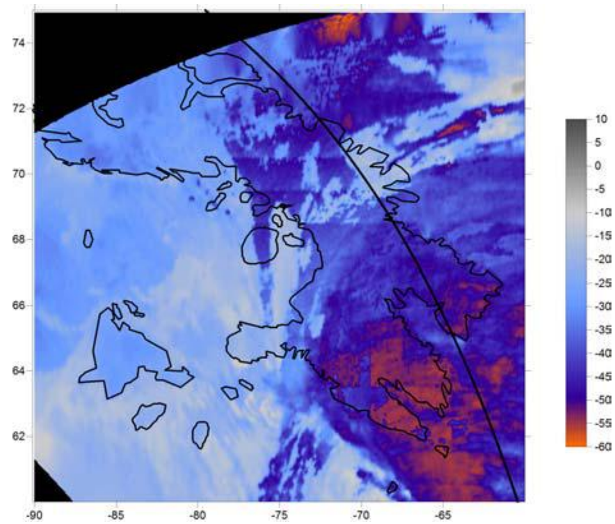

Fig 5: One of the IOP 11 CloudSat passes (black curved line) overlain on an IR satellite image. Cloud top temperatures are color coded in °C.

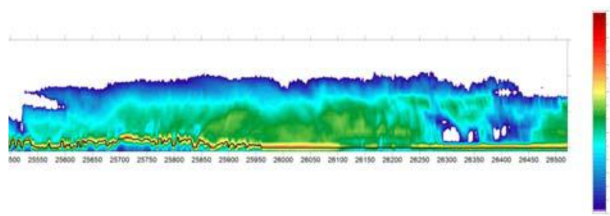

Fig 6: CloudSat radar reflectivity (dBz) from part of the track in Fig 5. The y-axis is in km, the x-axis represents horizontal distance along the satellite track.

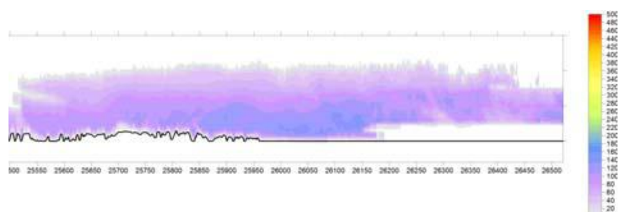

Fig 7: same as Fig 6 but for effective ice radius (μm).

5. CONCLUDING REMARKS

The STAR field project is the first of its kind in the eastern Canadian Arctic, providing a unique dataset for better understanding severe Arctic storms, weather hazards and their processes. It is also the first and only high latitude CloudSat validation dataset in the world, thus far. The field phase was conducted between Oct 10 – Nov 30, 2007 and Feb 2008. Sixteen IOPs were sampled, exhibiting a variety of weather situations and mesoscale phenomena over the region. The results of the project are expected to improve our current understanding of Arctic weather and to contribute to its improved prediction. Although STAR occurred over a limited region of the Arctic, the location is typical of many physiographic features in other parts of the Arctic, and hence, the physical understandings that are gained during STAR, will be applicable to many locations in the Arctic. The STAR dataset will also be a legacy for future projects in the Arctic region, including future IPY projects.

6. REFERENCES

Hoskins, B. J. and K. I. Hodges, 2002: New perspectives on the Northern Hemisphere winter storm tracks. Journal of the Atmospheric Sciences, 59, 1041-1061.

Hudson, E., D. Aihoshi, T. Gaines, G. Simard, and J. Mullock, 2001: Weather of Nunavut and the Arctic. NAV Canada, Ottawa, Ontario, 246 pp.

Intihar, M.R. and R.E. Stewart, 2005: Extratropical cyclones and precipitation within the Canadian Archipelago during the cold season. Arctic, 58, no. 2, 162–174.

Martin, R. E. and G. W. K. Moore, 2006: Transition of a synoptic system to a polar low via interaction with the orography of Greenland, Tellus, 58A, 236–253.

McCabe, G.J., M.P. Clark and M.C. Serreze, 2001: Trends in northern hemisphere surface cyclone frequency and intensity, J. Climate, 14, 2763-2768.

Nawri, N. and R.E. Stewart, 2006: Climatological features of orographic low-level jets over Frobisher Bay. Atmos.-Ocean, 44, 397-413.

Stone, D.A., A.J. Weaver and F.W. Zwiers, 2000: Trends in Canadian precipitation intensity, Atmos-Ocean, 38, 321-347.

Zhang, X., J.E. Walsh, J. Zhang, U.S. Bhatt and M. Ikeda, 2004: Climatology and inter-annual variability of arctic cyclone activity: 1948-2002, J. Climate, 17, 2300-2317.

Acknowledgements

This research and network is primarily funded through a network grant from the Canadian Foundation for Climate and Atmospheric Sciences (CFCAS). We also acknowledge the financial and equipment infrastructure support from the National Science and Engineering Research Council (NSERC), Canada Foundation for Innovation (CFI), and the Northern Studies Training Program (NSTP). The authors also wish to thank its many collaborators who provided significant contributions: from Environment Canada - Meteorological Research Division (MRD), Climate Research Division (CRD), Hydrometeorological and Arctic Lab (HAL), Prairie and Arctic Storm Prediction Centre (PASPC), and the Weather and Environmental Monitoring Section; from the National Research Council – Flight Research Lab; Nunavut Research Institute (NRI); Qulliq Energy Corp.; Indian and Northern Affairs Canada (INAC). A special thank you to George Liu (STAR data manager), Justin Gilligan (STAR Network Manager), Shannon Fargey and Alex Laplante for providing imagery and assistance with this article as well as all of the other STAR students who participated in the field project.

SIMULATIONS OF RADAR BRIGHT BAND FOR X AND W-BAND RADARS

Liang Liao[1], Robert Meneghini[2], Lin Tian[1] and Gerald M. Heymsfield[2]
[1]Goddard Earth Sciences & Technology/UMBC, NASA/GSFC, Greenbelt, MD 20771
NASA/Goddard Space Flight Center, Greenbelt, MD 20771

1. INTRODUCTION

The bright band, a layer of enhanced radar echo associated with melting hydrometeors, is often observed in stratiform rain. Understanding the microphysical properties of melting hydrometeors and their electric scattering and propagation effects is of great importance in accurately estimating parameters of the precipitation from spaceborne radar and radiometers, such as TRMM PR and TMI and future GPM DPR and GMI (Bringi et al. 1986; Fabry and Szymer 1999; Olsen et al., 2001a and 2001b; Meneghi and Liao 2000; Liao and Meneghini 2005). However, one of the most difficult problems in the study of the radar signature of the melting layer is the determination of the effective dielectric constants of melting hydrometeors. Although a number of mixing formulas are available to compute the effective dielectric constants, their results vary to a great extent when water is involved in the mixture, such as in the case of melting snow. It is physically unclear as to how to select among these various formulas (Meneghini and Liao 1996).

Although some success was achieved in simulating the radar bright-band signatures from the TRMM Precipitation Radar (Ku band) and airborne dual-wavelength radar (X and Ka bands) by modeling melting snow as a stratified sphere, a sphere composed of multiple layers (Liao and Meneghini 2005), the accuracy of the formulation needs to be examined in greater detail by means of radar measurements at other frequencies. Simultaneous measurements of the bright band made by the EDOP (X-band) and CRS (W-band) airborne Doppler radars during the CRYSTAL-FACE campaign in 2002 provide an excellent opportunity to check the validity of the stratified-sphere scattering model. Measurements of both radar reflectivities and Doppler velocities at two frequencies with the higher frequency at W-band are particularly useful for testing the model. In the stratified-sphere model the water fraction is constant in each layer of the stratified sphere but is allowed to vary from layer to layer. As such, the stratified-sphere scattering model can be used to compute scattering parameters for non-uniformly melting hydrometeors whose fractional water content is prescribed as a function of radius of sphere. In conjunction with a melting layer model that describes the melting fractions and fall velocities of hydrometeors as a function of the distance below the 0 ^{0}C isotherm, the radar bright-band profiles can be simulated for airborne radars.

The paper is organized as follows. In Section 2 we derive the effective dielectric constants of uniformly mixed snow and water particles from their internal electric fields by using the computational model in which the particles are described by a collection of 128x128x128 cubic cells of identical size and the CGFFT (Conjugate Gradient Fast Fourier Transform) numerical method. Procedures to simulate the radar bright-band signatures by use of the stratified-sphere model are described in Section 3. Comparisons of the simulated radar profiles in the melting layer of the EDOP and CRS airborne measurements are given in Section 4 followed by the summary in Section 5.

2. EFFECTIVE DIELECTRIC CONSTANT

Let **E**(r,λ) and **D**(r,λ) be the local electric and dielectric displacement fields at free-space wavelength λ, satisfying

$$\boldsymbol{D}(\boldsymbol{r},\lambda) = \varepsilon(\boldsymbol{r},\lambda)\boldsymbol{E}(\boldsymbol{r},\lambda)\,, \qquad (1)$$

where ε is the dielectric constant. In view of the local constitutive law described by the above equation, the bulk effective dielectric constant, ε_{eff}, at sufficiently long wavelength is defined as (Stroud and Pan 1978)

$$\varepsilon_{eff} \iiint_V \boldsymbol{E}(\boldsymbol{r},\lambda) d\boldsymbol{v} = \iiint_V \boldsymbol{D}(\boldsymbol{r},\lambda) d\boldsymbol{v} \qquad (2)$$

If the particle, composed of two materials, ε_1 and ε_2, is approximated by N small equal-volume elements, then the ε_{eff} can be written as

$$\varepsilon_{eff} = \frac{\varepsilon_1 \sum_{j \in M_1} \boldsymbol{E}_j + \varepsilon_2 \sum_{j \in M_2} \boldsymbol{E}_j}{\sum_{j \in M_1} \boldsymbol{E}_j + \sum_{j \in M_2} \boldsymbol{E}_j} \qquad (3)$$

The notations $\sum_{j \in M_1}$ and $\sum_{j \in M2}$ denote summations over all volume elements comprising materials 1 and 2, respectively. In this study, the internal fields appearing on the right-hand sides of (3) are computed by the CGFFT numerical procedure in which the volume enclosing the total particle is divided into 128×128×128 identical cells. Validation of the computational procedures for ε_{eff} has been extensively carried out for uniform and non-uniform snow-water mixtures (Meneghini and Liao, 1996 and 2000; Liao and Meneghini, 2005). This is done by comparing the scattering parameters, such as backscattering and extinction cross sections, and phase function, from realizations of the mixed-phase particle models with those from a uniform particle with dielectric constant ε_{eff}. It has been shown that ε_{eff} as derived from (3) is sufficiently accurate to compute the effective dielectric constant of snow and water mixtures in the microwave range.

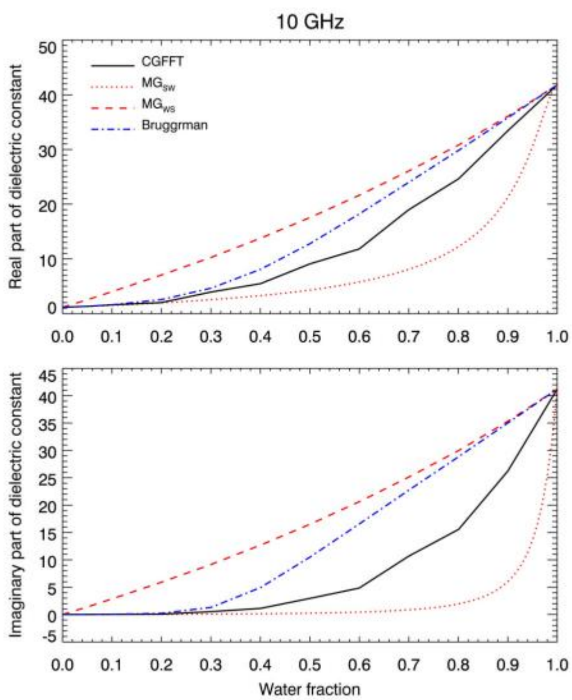

Fig.1 Comparisons of real (top) and imaginary (bottom) parts of ε_{eff} of snow-water mixed spheres as derived from the CGFFT and the mixing formulas at X band.

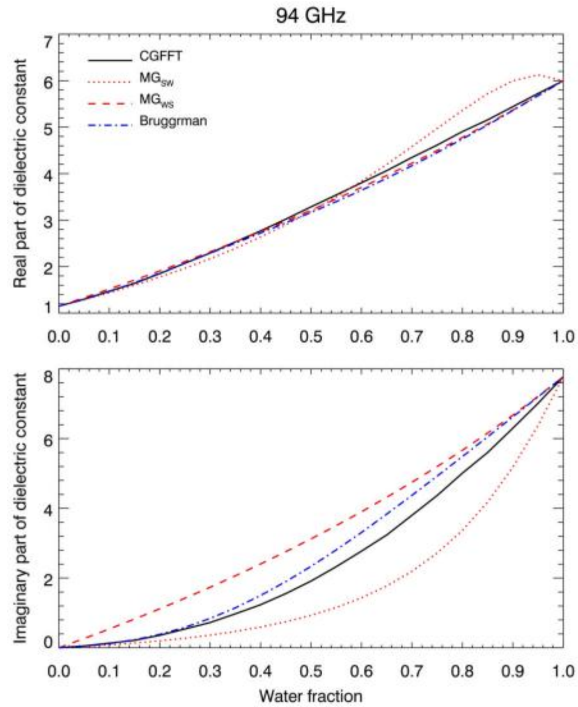

Fig.2 Comparisons of real (top) and imaginary (bottom) parts of ε_{eff} of snow-water mixed spheres as derived from the CGFFT and the mixing formulas at W band.

Figures 1 and 2 display the real and imaginary parts of ε_{eff} of homogeneous snow-water mixtures versus water fractions at X and W bands as computed from (3) by the CGFFT. The computations are made for a snow density of 0.1 g/cm^3. For comparisons, the results from the Maxwell Garnett (1904) and the Bruggeman (1935) mixing formulas are also given in the plots. An example of a realization of a uniformly mixed snow-water particle is shown in Fig.3 for a water fraction of 0.3. The dark and light gray areas

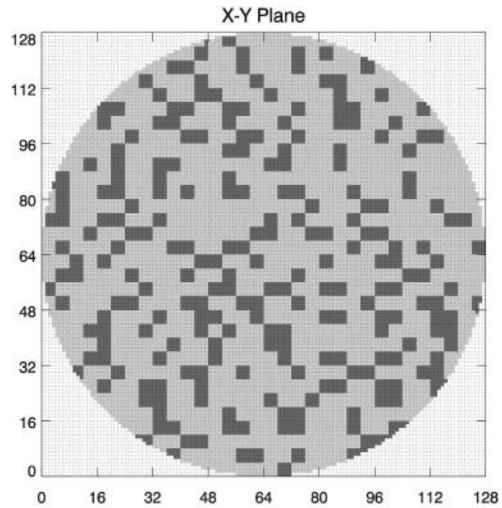

Fig.3 Realization of snow-water spherical particle at a water fraction of 0.3.

represent water and snow, respectively. The minimum size of any snow or water region is chosen to be at least 4×4×4 cells to better satisfy the boundary conditions at the snow-water interfaces. As can be seen in Figs. 1 and 2, the results of ε_{eff} derived from the CGFFT lie between the two results derived from the Maxwell Garnett mixing formula, one in which water is treated as the matrix with snow inclusions (MG_{WS}), and the other in which the roles of water and snow are reversed, i.e., snow as matrix and water as inclusion (MG_{SW}). The results of the Bruggeman's mixing formula are also bounded within the results of MG_{WS} and MG_{SW}, but tend to yield larger real and imaginary parts of ε_{eff} than the CGFFT.

3. BRIGHT-BAND SIMULATIONS

To simulate the radar signatures in the melting layer, two models are required: One is the melting layer model that provides microphysical properties of the mixed-phase hydrometeors, such as melting fractions and fall velocities of individual hydrometeors over their size spectra, as a function of the distance from 0 ^{0}C isotherm; the other is the particle scattering model that is used to compute the scattering properties of melting hydrometeors. Using the information provided by the melting layer model along with the particle scattering model, snow mass density

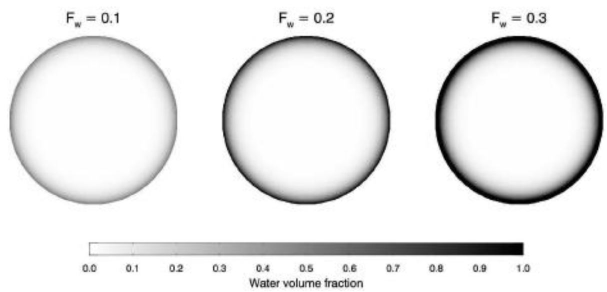

Fig.4 Stratified-sphere models of melting snow for volume-averaged water fraction F_W from 0.1 to 0.3.

and particle size distribution, the backscattering intensities and attenuation coefficients can be computed from any location within the melting region. In this study, the snow falls and melts in accordance with the model described by Yokoyama and Tanaka (1984). Aggregation and drop breakup are not included in the model. To model the fact that melting usually starts at the particle surface and then progresses toward the center, we employ the stratified-sphere particle model, which consists of 100 concentric equal-thickness layers. The melting water distribution or fractional water content inside the particle can be expressed as a function of radius. Within each layer of the stratified sphere the effective dielectric constant is fixed and determined from the results of Figs.1 and 2 (X and W bands, respectively) based on the fractional water content specified at the layer of interest. An exponential function is adopted to describe the fractional water content f_W in terms of radius r

$$f_W(r) = \begin{cases} f_W(0)e^{\frac{\beta r}{r_0}}, & r < r' \\ 1, & r_0 \geq r > r' \end{cases} \tag{4}$$

where r_0 is the radius of the particle, and r' is the radius at which f_W is equal to 1, i.e., $f_W(r')=1$. The coefficient β specifies the radial gradient of the water fraction so that a larger β results in a more rapid transition from snow to water. Its value was found to be 4.5 from the simulation study reported by Liao and Meneghini (2005). Shown in Fig.5 are the simulated results of the X- and W-band radar

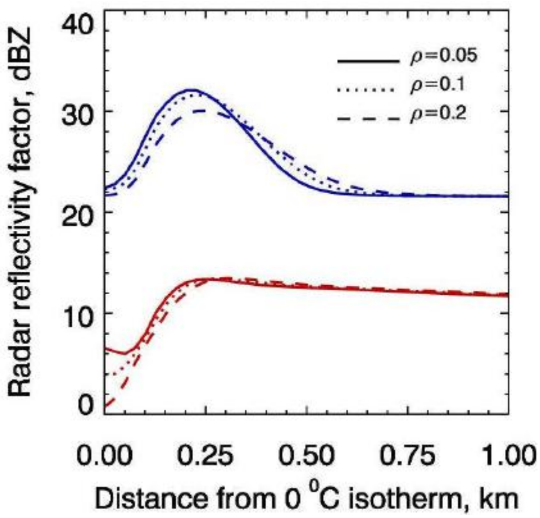

Fig.5 Results of simulated radar profiles at X (blue) and W (red) bands in the melting layer for snow densities of 0.05, 0.1 and 0.2 g/cm^3.

profiles in the melting layer for the snow densities of 0.05, 0.1 and 0.2 g/cm^3 as computed from the melting layer model and stratified-sphere scattering model described above. In these simulations the Marshall-Palmer raindrop size distribution (1948) is assumed for a rain rate of 1.5 mm/h. The attenuation due to hydrometeors is also taken into account in the results. A change in the snow density has different impact on the results of the simulated bright-band profiles at X and W bands. The smallest snow density (ρ=0.05 g/cm^3) gives the biggest enhancement of the reflectivity at X band but yields the narrowest bright-band width. At W band no clear radar bright bands are seen in Fig.5, even though a strong enhancement in the radar reflectivity is apparent in the early stages of melting. In contrast to the results at X band, the biggest change in the radar reflectivity at W band from snow to the bright-band peak occurs at ρ=0.2 g/cm^3, the highest snow density among those used in the plot. After reaching the maximum, the radar reflectivities computed from all the values of the snow density tend to converge, and their intensities remain nearly constant up to the rain region. It should be noted that the primary difference in the bright-band signatures at these frequencies arises from the differences between Rayleigh (X-band) and non-Rayleigh scattering.

4. COMPARISONS TO MEASUREMENTS

Comparisons of the simulated radar bright-band profiles to the measured ones offer a direct check of the models as to their validity and accuracy. Illustrated in Figs.6 and 7 are the measurements of the radar reflectivity factors and mean Doppler velocities by EDOP and CRS on 7 July 2002 from 20:15:00 UTC to 20:25:00 UTC during CRYSTAL-FACE. The EDOP and CRS are the nadir-looking airborne Doppler radars operating at X and W bands respectively, mounted on NASA ER-2 aircraft during the CRYSTAL-FACE field campaign. A detailed description of the EDOP and CRS can be found in the literatures (Heymsfield et al. 1996; Li et al. 2004). The vertical profiles are also plotted in Figs.6 and 7 at selected locations along the flight line to provide examples of the vertical profiles. With a range resolution of 37.5 m, the signatures of the bright band are clearly detected by both radars at an altitude of around 4 km throughout the flight line. To make the measured profiles stable and less noisy, a smoothing procedure is used. This is done by first finding all the pairs of the X- and W-band profiles based on the criteria that the peaks of X-band are in the range of Z_{peak} to Z_{peak}+1 (dB), and then averaging the selected profiles separately for X and W bands. It is worth noting that with such procedure, the stability of the measured radar mean profiles is dramatically improved. Shown in Fig.8 are the 4 EDOP (blue heavy-dotted lines) and CRS (red heavy-dotted lines) mean profiles that corresponding to the Z_{peak} of 30, 32, 34 and 37 dB from top-left panel to bottom-right panel, respectively. Using the stratified-sphere melting particle model described earlier and assuming the Marshall-Palmer size distribution in rain, the simulated radar profiles (solid lines) are plotted and compared with the measured ones, as shown in Fig.8. The snow density used in our simulations is chosen as 0.1 g/cm^3, which is consistent with the findings of the study for the retrieval of the

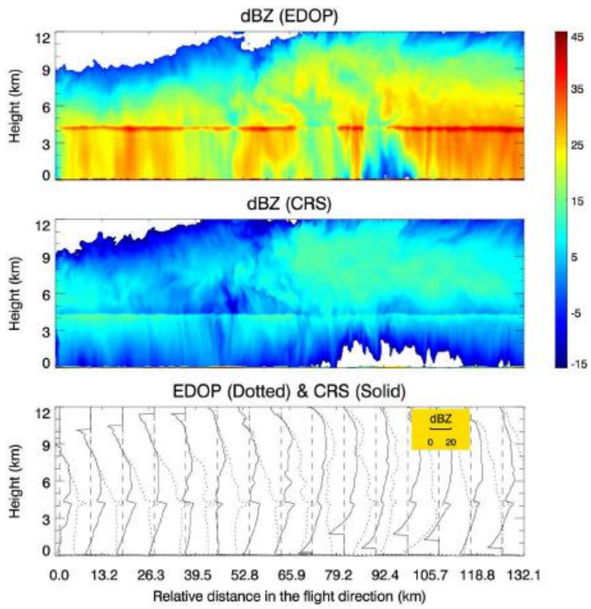

Fig.6 Measured radar reflectivity factors (top and middle panels) from EDOP and CRS nadir-looking airborne radar over a 130-km flight line over stratiform rain. The selected radar reflectivity profiles in the locations given by the dashed lines are shown in the bottom panel where the red and blue curves represent the EDOP and CRS radar reflectivity profiles, respectively.

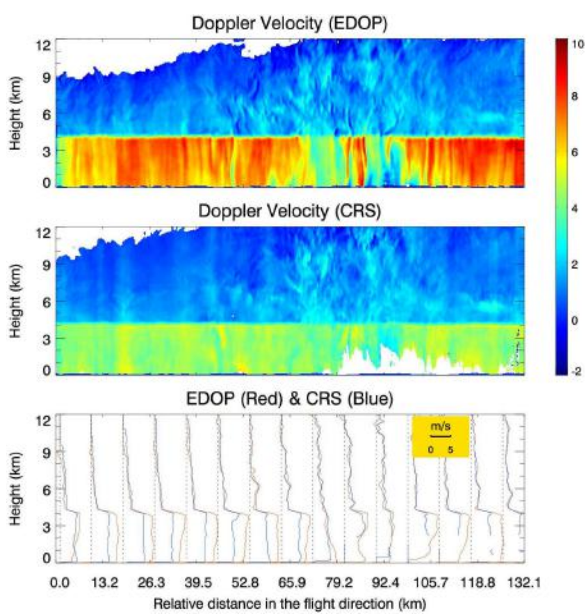

Fig.7 Measured mean Doppler velocities (top and middle panels) from EDOP and CRS for the same storm shown in Fig.6. The selected mean Doppler velocity profiles are shown in the bottom panel where the red and blue curves represent the EDOP and CRS, respectively.

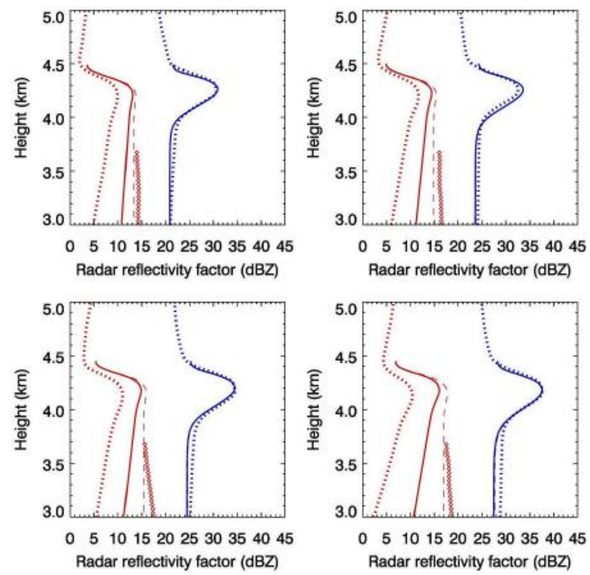

Fig.8 Comparisons of simulated (solid) and measured (dotted) bright-band profiles at X (blue) and W (red) bands. The dashed lines are the simulated results without taking into account of attenuation, and the diamond-shaped data are the constructed un-attenuated W-band profiles based on the Doppler measurements.

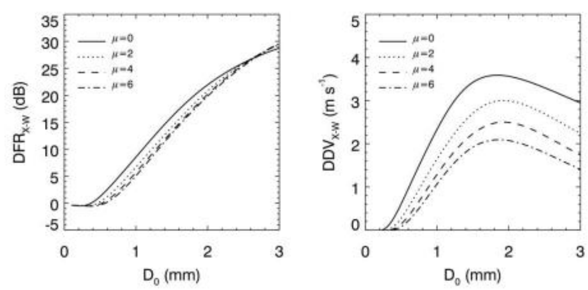

Fig.9 Plots of DFR vs. D_0 (left) and DDV vs. D_0 (right) for X- and W-band radars for rain as the shape factor (μ) of the gamma particle distribution varies from 0 to 6.

snow size distribution by use of dual-wavelength techniques for the same data (Liao et al., 2008). Because there is no particle breakup or aggregation assumed in the melting layer model, and also because the mass flux is constant within the melting layer, the particle size distribution (PSD) specified in rain can be uniquely converted to PSDs in the snow and melting layer regions. With the models being initialized in the way described earlier, the rain rate, which the Marshall-Palmer size distribution solely relies on, is the only free parameter in the simulation. In the comparisons depicted in Fig.8, the rain rates that give the best agreement between the simulated and measured profiles are 1.44, 1.71, 1.83 and 2.38 mm/h, respectively. As can be seen, the simulated radar bright bands are in excellent agreement with the measured ones at X band. They are not only matched well in the peaks of the bright band but also in the widths. However, the comparisons at W band are not as straightforward as those at X band in which the attenuation is negligibly small. This is because difficulties arise in the correction of attenuation caused by cloud water and water vapor. Although attenuation by hydrometeors (snow, melting snow and rain) is taken into account in our simulations, the attenuations from cloud water and water vapor are not included. Since neither cloud water nor water vapor is detectable, they are largely unknown. This introduces uncertainties in the higher-frequency radar retrieval. As illustrated in Fig.8, the simulated profiles (solid) at W band tend to agree with the measured ones (dotted) in shape but offsets in the magnitudes are clearly seen. To see if these offsets can be attributed to cloud water and water vapor attenuations at W band, we will conduct comparisons of non-attenuated radar profiles in rain between the model simulations and the reconstructed W-band profiles by use of the Doppler measurements.

By taking an advantage of simultaneous measurements of the Doppler velocities at X and W bands, we can derive the un-attenuated or true W-band radar profiles in rain. The differential Doppler velocity (DDV), which is defined as the difference of the Doppler velocities between X and W bands, depends only on the particle median volume diameter (D_0). This is also true of the radar dual-frequency ratio (DFR) in dB, which is equal to the difference of the radar reflectivity at X and W bands. Figure 9 depicts the relationships between DFR-D_0 (left) and DDV-D_0 (right) when the rain droplet size distribution is given by the gamma distribution. The μ in the plots is the shape factor of the gamma distribution, which is zero for the Marshall-Palmer size distribution (1948). Since the DDV is independent of the radar attenuation and also unaffected by air motion, D_0 can be estimated from the measured DDV (Tian et al., 2007; Liao et al., 2008). This in turn leads to a value of DFR from the differential Doppler-estimated D_0. The true radar reflectivity at W band is, by definition, the difference between the X-band reflectivity and the DFR, based on the assumption that attenuation at X band is negligible. This should be true for stratiform rain, particularly for the cases shown in Fig.8 where only light rain is present. The diamond-shaped data points in Fig.8 represent the non-attenuated radar profiles of rain at W band, derived from the DDV. The dashed curves refer to the non-attenuated W-band radar profiles generated from the models. There is a fairly good agreement between the non-attenuated radar rain profiles generated from the model on one hand and the estimated results on the other, implying good accuracy in simulating the W-band bright-band profiles. The differences of the W-band radar reflectivity profiles between the simulations (accounting for attenuation) and measurements can be explained by the W-band attenuation that results from cloud water and water vapor.

5. SUMMARY

To describe the snowflake-melting process in the transition of particles from snow to water, a stratified-sphere model is used to characterize the melting particles and compute the radar profiles at X and W bands in the melting layer. The effective dielectric constants, used at each layer of the stratified sphere, are derived from the realizations of the uniform snow-water mixtures by using CGFFT numerical method. As the fractional water content within the melting snow is expressed as an exponential equation, the simulations of the radar bright-band profiles are made at X and W bands under assumption that the rain follows the Marshall-Palmer size distribution. The simulated radar profiles are then compared to the X- and W-band Doppler radar measurements. While excellent agreement is found at X band, there are persistent offsets between the model and measured results at W-band. However, these offsets can be explained by the attenuation caused by cloud water and water vapor at W band. This is confirmed by the comparisons of the radar profiles made in the rain regions where the un-attenuated W-band reflectivity profiles can be estimated through the X- and W-band Doppler velocity measurements. In particular, good agreement is shown for the un-attenuated profiles derived from the model-simulated results and the Doppler-derived results. Despite the difficulty in describing microphysical properties of hydrometeors in the melting layer, our simulations of the radar bright band made at X and W bands appear to be fairly accurate and suggest the usefulness of the stratified-sphere scattering model as well as the effective dielectric constants derived from mixed-phase particle realizations. The bright-band model described in this paper has potential to be used effectively for both radar and radiometer algorithms relevant to the TRMM and GPM satellite missions.

ACKNOWLEDGEMENTS

We wish to thank Dr. Lihua Li, Mr. Ed Zenker, Dr. Steven Bidwell and Dr. Paul Racette for EDOP and CRS data processing and engineering support.

REFERENCES

Bringi, V. N., R. M. Rasmussen, and J. Vivekanandan, 1986: Multiparameter radar measurements in Colorado convective storms. Part I: Graupel melting studies. *J. Atmos. Sci.*, **43**, 2545-2563.

Bruggeman, D. A. G., 1935: Berechnung verschiedener physikalischer Konstanten von heterogenen Substanzen: I. Dielectrizitatskonstanten und Leitfahigkeiten der Mischkorper aus isotropen Substanzen. *Ann. Phys.*, **24**, 636-679.

Fabry, F. and W. Szymer, 1999: Modeling of the melting layer. Part II: Electromagnetics. *J. Atmos. Sci.*, **56**, 3596-3600.

Gunn, K. L. S., and J.S. Marshall, 1958: The distribution with size of aggregate snowflakes. *J. Meteor.*, **15**, 452-461.

Heymsfield, G. M., S. W. Bidwell, I. J. Caylor, S. Ameen, S. Nicholson, W. Boncyk, L. Miller, D. Vandemark, P. E. Racette, and L. R. Dodd, 1996: The EDOP radar system on the high-altitude NASA ER-2 aircraft. . *J. Atmos. Oceanic Technol.*, **13**, 795-809.

Li, L, G. M, Heymsfield, P. E. Racette, L. Tian and E. Zenker, 2004: A 94-GHz cloud radar system on a NASA high-altitude ER-2 aircraft. *J. Atmos. Oceanic Technol.*, **21**, 1378-1488.

Liao, L. and R. Meneghini, 2005: On modeling air/spaceborne radar returns in the melting layer. IEEE Trans. Geosci. Remote Sens., 43, 2799-2809.

Liao, Li., R. Meneghini, L. Tian, and G. M. Heymsfield, 2008: Retrieval of snow and rain from combined X- and W-band airborne radar measurements. IEEE Trans. Geosci. Remote Sens., in press.

Marshall, J. S., and W.M. Palmer, 1948: The distribution of raindrops with size. *J. Appl. Meteor.*, **5**, 165-166.

Maxwell Garnett, J. C., 1904: Colors in metal glasses and in metallic films. *Philos. Trans. R. Soc. London A*, **203**, 385-420.

Meneghini, R. and L. Liao, 1996: Comparisons of cross sections for melting hydrometeors as derived from dielectric mixing formulas and a numerical method. *J. Appl. Meteorol.*, **35**, 1658-1670.

Meneghini, R. and L. Liao, 2000: Effective dielectric constants of mixed-phase hydrometers. *J. Atmos. Oceanic Technol.*, **17**, 628-640.

Olson, W. S., P. Bauer, N. F. Viltard, D. E. Johnson, W.-K. Tao, R. Meneghini, and L. Liao, 2001: A melting-layer model for passive/active microwave remote sensing applications. Part I: Model formulation and comparison with observations. *J. Appl. Meteorol.*, **40**, 1145-1163.

Olson, W. S., P. Bauer, C. D. Kummerow, Y. Hong, and W.-K. Tao, 2001: A melting-layer model for passive/active microwave remote sensing applications. Part II: Simulations of TRMM observations. *J. Appl. Meteorol.*, **40**, 1164-1179.

Stroud, D. and F. P. Pan, 1978: Self-consistent approach to electromagnetic wave propagation in composite media: Application to model granular metals. *Phys. Rev. B.*, **17**, 1602-1610.

Tian, L., G. M. Heymsfield, L. Li, and R. Srivastava, 2007: Properties of light stratiform rain derived from 10 and 94 GHz airborne Doppler radars. *J. Geophys. Res.*, **112**, D11211, doi:10.1029/2006JD008144.

Yokoyama, T. and H. Tanaka, 1984: Microphysical process of melting snowflakes detected by two-wavelength radar. *J. Meteorol. Soc. Jpn.*, **62**, 650-666.

DOPPLER RADAR ECHO ANALYSIS ON A TYPICAL STRATIFORM AND CONVECTIVE MIXED PRECIPITATION SYSTEM IN GUIZHOU

LUO Ning[1] , WEN Jifen[2] MIN Ailian [3]and NIU Shengjie[3]

1:Guizhou Weather Modification Office, Guiyang,550002,China

2: Guizhou Meteorological Bureau, Guiyang,550002,China

3.Key Laboratory of Atmospheric Physics and atmospheric Environment(LAPE), NUIST, Nanjing, China

1. INTRODUCTION

With the population and building of China new generation Doppler weather radar, the increasing of Doppler radar's data production not only provides timely and abundant observation information for precipitation nowcasting and disaster weather warning, but also provides abroad and scientific information for artificial precipitation stimulation. Many radar productions have been thoroughly and widely used to command weather modification operation ,especially radial velocity of Doppler radar in the recent years.

Precipitation of mixed stratiform and convective clouds is the main type of rainfall over Guizhou area, and mixed stratiform and convective clouds system is the major object of artificial precipitation enhancement in Guizhou. Therefore studying precipitation radar echo characteristics of mixed stratiform and convective clouds and analyzing the dynamic structure of it is propitious to accurately operating precipitation enhancement in time in order to well use the water resource in the sky. This precipitation of mixed stratiform and convective clouds taking place on September 7, 2006 in Guizhou province was analyzed by using radar data supplied by CINRAD/CD of Guiyang and rainfall data provided by rainfall stations. The results show that owing to Doppler radar with high spatial and temporal resolution, continuum observation and plenty of echo products, the evolvement from cumulus to mixed stratiform and convective clouds can be seen clearly in this precipitation of mixed stratiform and convective clouds. And by analyzing radial velocity images, the occurrence and evolvement of precipitation can be well grasped, which plays a pivotal role in operating artificial precipitation accurately and in time.

2. CONCURRENT MEASUREMENTS OF THE HOURLY RAIN ACCUMULATION

Between September 7and 8, a precipitation of mixed stratiform and convective cloud occurred in Guizhou region in 2006, which covered a large range, lasted for a long time and the rainfall was very uneven. Figure 1 shows the rainfall intensity recorded by the automatic rainfall station of this precipitation. In this case, total rainfall of Anshun which lies in the southwest of radar station reached 100.6mm, while that of Xifeng lying in the north was just 25.2mm. From the figure we can see that this case was not only very uneven and fluctuant in rainfall but also the peak value of rainfall at each station was asynchronous. Besides, from the variation of rainfall in Douyun we can also see that all of the rainfall intensity before 07:00 on 8th was zero, but at 8:00 it was suddenly increased to 24.4mm, while it suddenly decreased to 9.4mm at 09:00, and in the next two hours it went on decreasing and the rainfall intensity at 11:00 was just 0.5mm. These data indicate that sudden increase and sudden decrease of rainfall intensity is the characteristic of this precipitation. In addition, it can be seen that cloud system of this precipitation moved towards the east as a whole from the starting time of precipitation in those five places and geographical positions of them.

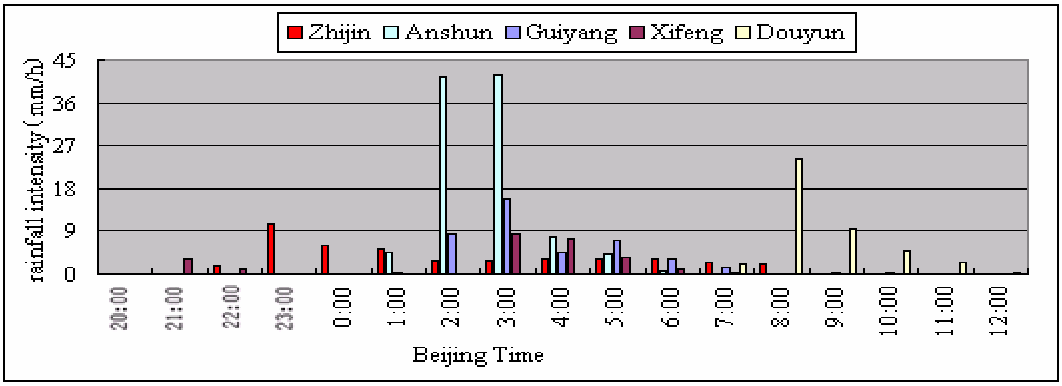

Figure 1. Rainfall intensity recorded by automatic rainfall stations from20:00 on the 7th to 12:00 on the 8th of September 2006 in Zhijin, Anshun, Guiyang, Xifeng and.Douyun.

3. ANALYSIS OF DOPPLER RADAR DATA

According to all the intensity images of this precipitation supplied by Guiyang Doppler radar, it suggests that it was a precipitation of mixed stratiform and convective clouds, that is, stratus was best with convection cells and the distribution of those convection cells was tanglesome.

3.1 RADAR ECHO INTENSITY IMAGE

This precipitation started at 20:00 on September 7, 2006. At that time, many cumulus cells appeared in the area which is about 60 to 150km far away from radar station (Fig 2A). These convection cells growed incessantly when they were moving towards northeast by north., and formed convection short zone by merging with newborn cells. At the same time, a newborn convection cell C appeared between echo flocks A and B (Fig 2B).And then ,When the front of convection short zone A moved away from radar detectable range, cell flocks B spreaded northeastward, and there were stratus echoes appearing around. At that moment (Fig 2C), this precipitation case had changed to a precipitation of mixed convection and stratiform clouds. Until 23:56:56（Fig 2D), three pieces of cloud cluster had integrated together and went on growing and moving towards the northeast. And convective clouds were mainly distributed in the southeast edge of the large sheet precipitation echo. While there were still many newborn convection cells in the southwest by west, about 120km far away from radar station and they merged with the main precipitation echo very soon after upper shifting towards the northeast quickly. So the area covered with this precipitation was enlarged and the rainfall became heavier ceaselessly, and maximal value of echo intensity reached 49dBZ at this moment. By 4:36:20 on September 8, radar echoes had distributed in a rather large area with blurry boundary, and several cumulus cell echo strips, collecting in the lower edge of the large sheet of stratus echo, ranged along the direction of NE-SW parallelly, and in the south many scattered newborn convective bubbles. Now echoes had evolved into typical echoes of precipitation of mixed stratiform and convective clouds. Strong rainfall mostly taken place during this period, and from 3:00 to 5:00, strong precipitation occurred in the area of Guiyang, -Anshun. Due to southeastward move of convective clouds lying in the southeast of the whole echoes, and northeastward move of stratus lying in the northwest, the whole mixed clouds mainly moved towards the east. At this moment, the echo intensity image of Doppler radar at higher elevation shows that there was an obvious echo bright band around 3.5km height, but the bright band was discontinuous and the intensity and thickness of it was unequal, which is the typical feature of precipitation of mixed stratiform and convective clouds. Then the precipitation of mixed stratiform and convective clouds started evolving to a steady stratus precipitation. After this, stratus lying in the tail of precipitation echoes had began to weaken stage by stage, and inanition had also began to emerge in the sheet echoes (Fig 2F). By 11:07:34, stratus echoes of this precipitation had strewn here and there (Fig 2G), and the intensity of frontal convective clouds had greatly weakened, and yet there were still a small quantity of strong echoes about 40dBZ around the southeast and about 100km far away from radar station. This convection agglomerate survived for a long time, nearly 11 hours, which mainly owed to lots of water vapor for convective clouds provided by precipitation air current of steady stratus. After that, the remainder echoes kept on moving towards the southeast and weakened unceasingly. Accordingly, this precipitation process waken and ended gradually.

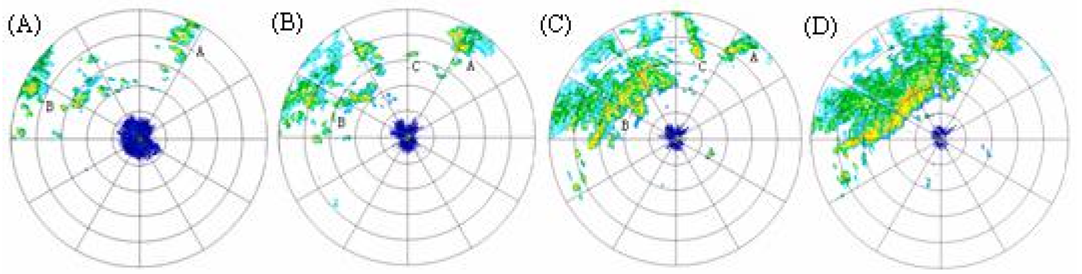

20:00:14,2006-09-07 21:14:12,2006-09-07 22:47:59,2006-09-07 23:56:56,2006-09-07

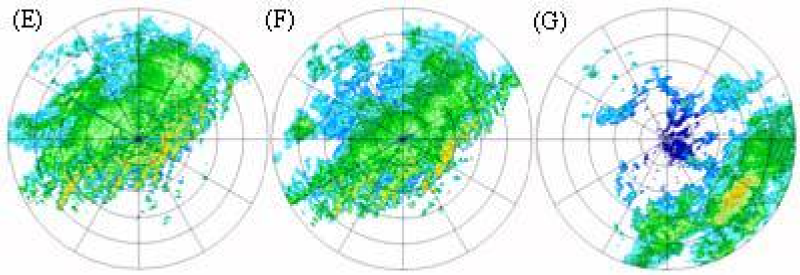

4:36:20,2006-09-08 5:29:47,2006-09-08 11:07:34,2006-09-08

Figure 2 Echo intensity images of Guiyang Doppler radar during the 7th and 8th of September 2006 (elevation: 1.5°, detecting horizontal distance: 150km)

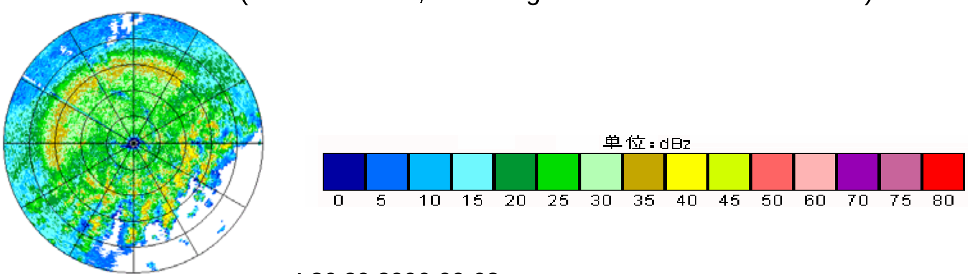

4:36:20,2006-09-08

Figure 3 Echo intensity image of Guiyang Doppler radar (elevation: 4.3°, detecting horizontal distance: 75km)

3.2 RADIAL VELOCITY IMAGE

Average radial velocity can reflect wind field structure among clouds, especially for mesoscale and microscale severe convective systems with obvious velocity structure features. In the process of seeding cumulus and stratocumulus, analysis of radial velocity structure can play an important and indicative role in selecting position of operation.

At the beginning of this rainfall, there was an obvious cyclonic flow field structure around azimuth 106.09°-106.26° in the northwest and 90km far away from radar station (Fig3A).With the ceaseless appearance and mergence of newborn convection cells, radial convergence occurred around azimuth 297.24°-310°and 120km far away from radar station, which is the structure feature of cumulus velocity field (Fig3B). And then with the gradual emergence of stratus, positive and negative velocity echoes began to distribute homogeneously in the northwest (Fig3C). Zero velocity line was presented in the form of a beeline along NW-SE, that is, wind direction was southwest. Echoes of this precipitation moved towards the northeast wholly, according with the moving direction reflected in the intensity images. With the echoes moving to the northeast, parts of the echoes strip of convection cells moved to Anshun, and strong rainfall took place here. In the figure 3D, there was an obvious couple of velocity center with max value about 13m/s in the low level. Distribution of zero velocity line within 30km was changed along NE-SW, and convective clouds in the echoes moved southeastward. While outside of 30km, wind direction contrarotated with height, but as a whole, the echoes of stratus still moved northeastward. With the evolution of this precipitation, the velocity structure feature of steady precipitation was more and more obvious. At 4:36:20(Fig3E), the range of echoes was rather large and echoes distributed homogeneously and closely. In the low level two velocity centers still lasted, and slippery and regular zero velocity line presented in the type of ‘S’ within 20km. Wind direction clockwise rotated with height, so there was a warm advection. While wind direction contra rotated with height within 20-60km and there was a cold advection. Outside of 60km in the north, zero velocity line presented in the form of a beeline in NE-SW, and wind direction shifted from southwest to northwest. While around the height of 800m, wind direction changed too, from northwest by north to southwest. This moment was the golden age of this precipitation. Later, when echoes went on moving eastward, northern stratus took the lead to weaken and radial velocity started to evanesce at a distance, which suggested that cold air mass had made incursions in high level and the whole precipitation process had entered in the stage of weakening (Fig3F). At 8:30:55(Fig3G), remnant echoes had basically moved to the southeast and went on moving northeastward and weakening. By 11:07:34 (Fig3H), radial velocity in the northwest had became very scattered, while in the southeast velocity value and zero velocity line outside of 60km were still whole. According to the distribution of positive and negative velocity fields along zero velocity line, it suggested that echoes still moved towards the northeast and this precipitation tended to end.

4. CONCLUSIONS

According to the analysis, we can clearly see that:

1) This case is a typical precipitation of mixed stratiform and convective clouds. This precipitation took place in a wide range and

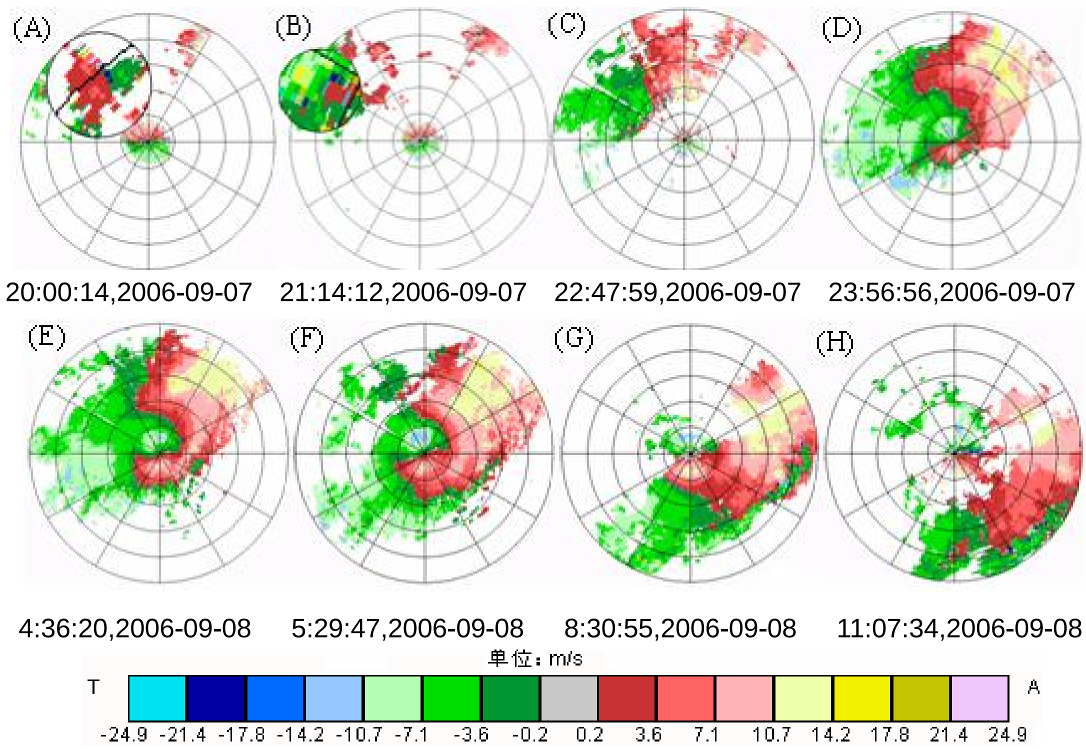

Figure 4 Radial velocity images of Guiyang Doppler radar during the 7th and 8th of September 2006 (elevation:1.5°, detecting horizontal distance: 150km)

it lasted for a long time, but the rainfall is very uneven. At the beginning, clouds were all cumulus cells and almost every cell had zone of convergence. But with the emergence of stratus, the whole echo reveals obvious structure features of steady precipitation, and owing to a mass of water vapor provided by stratus, convective cloud agglomerate sustained for quite some time.

2) Distribution features of Doppler radial velocity have indicatory meanings to deducing the occurrence of rainfall. Through analyzing features of radial velocity image, we can forecast the evolution trend of the occurrence of precipitation of mixed stratiform and convective clouds. This can play a guiding role in a certain extent for precipitation forecast, and meanwhile it can increase the ability of estimating the opportunity of artificial precipitation and guiding the real-time operation availability, that is to say, it is of certain guidance effect for the scientific operation of precipitation enhancement.

5. REFERENCES

Armijo L. A theory for the determination of wind and precipitation velocities with Doppler radar, J. Atmos. Sci. 1969, 26, 3.

Zhang Peichang, Du Binyu, Dai Tiepi. Radar Meteorology. Beijing: China Meteorological Press. 2001:356-383.

Hu Mingbao, Gao Taichang, Tang Dazhang. Analysis and application of the Doppler weather radar. Beijing: Chinese People's Liberty Army Publishing, 2000: 42-51.

Huang Meiyuan, Xu Huanbin. Cloud and Precipitation Physics (in Chinese). Beijing: Science Press. 1999: 157-166.

Chen Jinqing, Yang Lianying. Application of Doppler weather radar in weather modification. Meteor Sci & Tec, 2004, 30, 2.

Gong Fujiu, Wang Jihong, Mu Xiyu, et al. Echo characteristics of precipitation during July and August in Liaoning Province. Meteor Sci, 2006, 4.

A Comparative Analysis of the Rain predicted in the Northern South America Using Two Moment Ice and Rain Microphysical scheme

GERARDO DE J. MONTOYA G.

National University of Colombia, Bogotá, Colombia

1. Introduction

Although significant advances in the Quantitative Precipitation Forecast (QPF) have been achieved through the implementation of explicit microphysical techniques, these schemes still over predict the precipitation in some situations and they underestimate in other cases (Colle et al- 2001, Grubisic et al. 2005, Serafin and Ferreti, 2007). To improve the convective parameterization through explicit microphysics treatment, multi moment microphysical schemes have been implemented.

The development of multi-moment microphysical schemes begun about 3 decades ago (e.g., Clark 1976; Srivastava 1978; Nickerson 1986; Montoya 1986), nevertheless, its implementation in mesoscale models is a current research area. The double-moment microphysical schemes not only predict the rain mixing ratio but the particle number concentration for one or more species in a mixed-phase cloud as well. Except the microphysical scheme used in RAMS, the other two moment schemes have prognostic equations for the concentration of ice particles only ((e.g., Meyers 1997; Ferrier 1994; Reisner et al. 1998; Morrison et al. 2005; Phillips et al. 2007). For this reason we refer to them as two-moment in ice schemes. Although these schemes may [1] be useful for prediction of cold cloud systems, for the tropics where the liquid phase plays an important role, a double-moment in ice and liquid phase is highly convenient.

Our goal in this study is to implement the double-moment in ice and liquid phase schemes over the Northern South America region, which has not been done yet. To do so, the explicit microphysical scheme Reisner2, used in the high-resolution fifth-generation Pennsylvania State University-NCAR Mesoscale Model (MM5) is improved by including an additional prognostic equation to account for the rate of change in the total raindrop number concentration. Thus, this improved scheme is referred as double-moment in ice and rain microphysical scheme. The improved Reisner2 scheme and the original Reisner2 scheme are then compared against observations over a mountain region located in the Northern South America.

2. The improved scheme

The original Reisner2 scheme contains prognostic equations for the mixing ratio of six species or categories; water vapor, cloud water, cloud ice, rain water, snow and graupel and the number concentration of the cloud ice particles. Here, an additional prediction equation for the raindrop number concentration is added to this set of equations. Other additional changes to the original Reisner2 scheme are the following:

[1] Corresponding autor address: Gerardo Montoya Universidad Nacional de Colombia, depto Geociencias, Cra 30 No 45-03, Bogota, Colombia E mail: gdmontoyag@unal.edu.co

A Gamma distribution for the raindrop is assumed

$$f(D) = \frac{N_r \lambda_r^{\alpha} D_{mr}^{\alpha-1} \exp(-D_{mr}\lambda_r)}{\Gamma(\alpha_r)}, \qquad (1)$$

where, N_r is the total raindrop number concentration, D_{mr} is the mean rain drop diameter, $\Gamma(\alpha_r)$ is de gamma function α_r =1 and λ_r =1/ D_{mr}.

The parameter λ_r, which is defined as the inverse of the mean drop diameter is computed diagnostically at each time step by Eq (2).

$$\lambda_r = (\frac{\pi \rho_r N_r}{\rho q_r})^{1/3} \qquad (2)$$

The prognostic equation for the raindrop concentration is written following Reisner et al. (1998)

$$\frac{\partial p^* N_r}{\partial t} = -ADV(p^* N_r) + DIV(p^* N_r) + D(N_r) - N_{rprc} + p^* \{N_{ccnr} - N_{revp}) \qquad (3)$$

where, p^* is the difference between the surface pressure and the pressure at the top. The *ADV*, *DIV* and *D* terms represent the 3D advection, the divergence and diffusion respectively (see the referred paper for details). N_{rprc} is the effect on raindrop number concentration due to the fallout of the precipitation. The last two terms in Eq. (3) are autoconversion of cloud drops into raindrops and evaporation of raindrops respectively.

The change on the the raindrop number concentration due to autoconversion of cloud drops to raindrops is writing according to Berry and Reinhardt (1974)

$$N_{ccnr} = 3.5x10^6 \frac{q_c'}{\tau} \qquad (4)$$

where,

$$q_c' = 2.7x10^{-2}(\frac{1x10^{20}}{16} D_m^4 2^{-1/2} - 0.4) q_c$$

and,

$$\tau = \frac{3.7}{\rho q_c}(0.5x10^6 D_m 2^{-1/2} - 0.75)^{-1}$$

Here, q_c is the cloud mixing ratio. Following the methodology of Ferrier (1994), the change in the raindrop concentration, due to evaporation of raindrops is computed.

Figure 1 shows the interactions between water species according to Reisner et al. (1998). In some cases, the computation of these interactions depends upon the rate of change of the raindrop concentration and the parameter λ_r.

The terms describing these interactions (remarked with bold letter in Fig.1) are written following Reisner et al. (1998) but using the gamma function, instead of the Marshall Palmer distribution.

3. The comparison of the modeling results against observations

The version of MM5 used in this study (MM5V3.7) has been well documented and used in a wide variety of applications. The simulations reported here use three domains (Figure 2): an outer mesh with a grid length of 45km and two inner meshes having grid length of 15km and 5km. The first mesh is centered at 74ºW, 4ºN, covering Northern South America (the outer mesh), Colombia (the middle mesh) and the Bogotá plateau and neighbors (the inner mesh).

To initialize a 36h forecast, the National Center for Environmental Prediction (NCEP) reanalysis at 00Z October 1 2006 was used. Only the two outer-most meshes are used for the first 12h. After

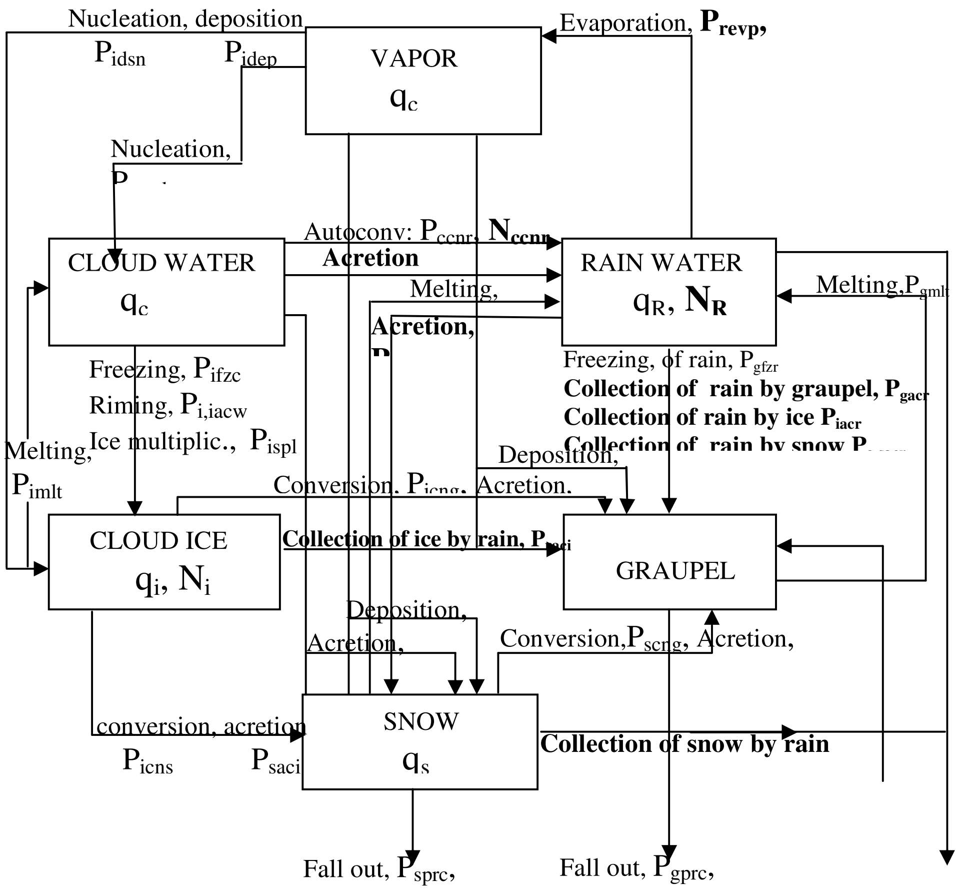

Fig. 1. Interaction between water species according to Reisner et al. (1998). The processes afected by new computation of the rain concentration and the parameter λ_r are outlined in bold.

12h the third mesh (5km) is initialized from the 15km mesh. After 24h of total simulation time, both the improved Reisner2 (Figure 4) and the original Reisner2 (Figure 5B) schemes were compared against the Colombian daily gauge precipitation (Figure 5A), which has been interpolated to the model grid using Kriging.

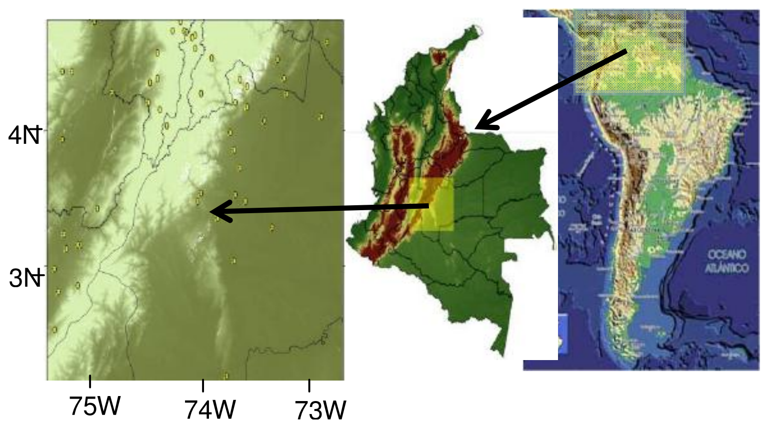

Figure 2. The three nested domains used in the simulation. The points in the inner domain (left figure) indicate the precipitation network.

4. Results

On October 1st, the weather was characterized by traveling easterly wave over the Colombian territory as it can be seen in the infrared image at 23:45Z (Figure3)

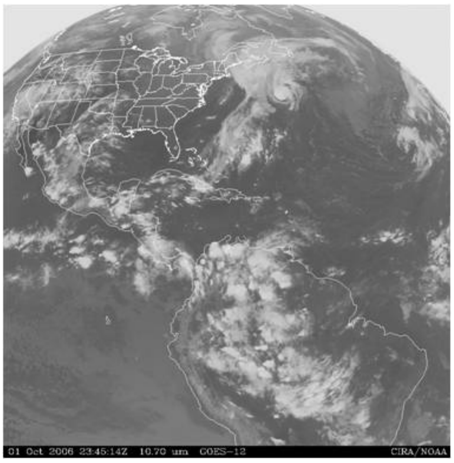

Figure 3 The Infrared image observed in 2006-10-01at 23:45Z

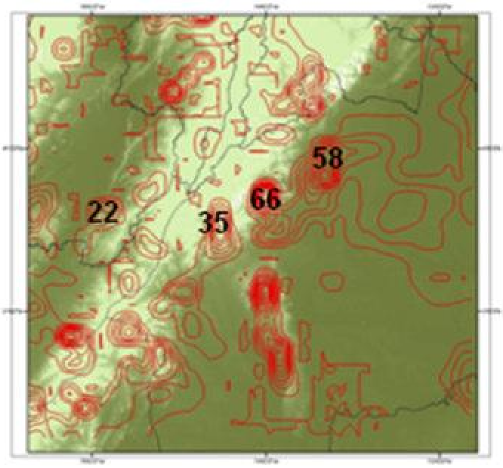

Figure 4. Accumulated convective rain as it was simulated by the improved scheme. Numbers over the figure are maximum rain values in mm.

Figure 4 shows the 24h accumulated convective precipitation simulated by the improved scheme, figure 5A shows the 24h precipitation registered in the third domain and figure 5B shows the precipitation simulated by the original Reisner2.

According to figure 5A, the maximum rain (114mm) occurred approximately at (73.4ºW, 4.1ºN) in the city of Villavicencio. Other maxima (35 and 23 mm) were also registered in the Eastern slope of the Eastern Colombian Andes mountain range and at the south west corner of the domain.

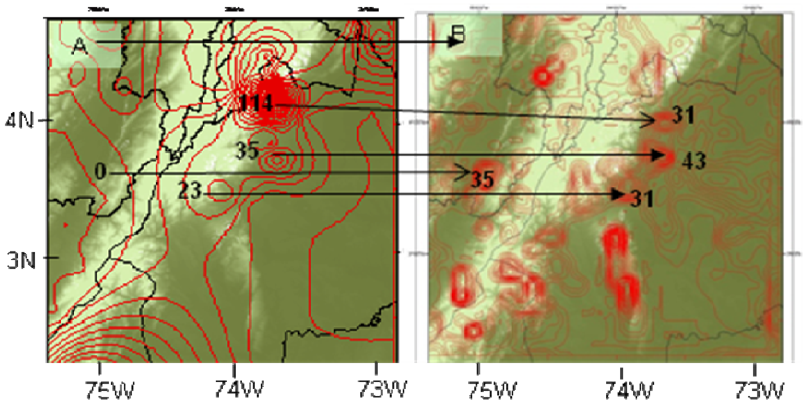

Figure 5: A the accumulated rain as it was registered by the gauge station network. B accumulated convective rain simulated by the Reisner2 scheme. The arrows connect some centers with maximum registered and simulated precipitation.

By comparing figures 5A, 5B and 4 it can be seen that the maxima in precipitation over the eastern slope of the Colombian Andes are reproduced fairly well by both the explicit microphysical Reisner2 and the improved scheme. Although both schemes under predict the observed precipitation in the city of Villavicencio and over predict the precipitation over other points in the eastern slope of the Colombian Andes, the improved scheme indicates a much better performance compared to the original Reisner2 scheme.

Figures 4 and 5B also indicates the presence of heavy precipitation over La Macarena Hill (74ºW, 3ºN). Due to the lack of gauge data over the region it is difficult to conclude if this precipitation is real or spuriously generated by the model.

Over the Western slope of the Eastern Colombian Andes ("cordillera oriental") no significant rain was observed, except the one over the upper left corner of the domain (see figure 5A). Both the Reisner2 and the improved schemes show spurious precipitation at 75.1ºW,3.6ºN (35mm in figure 5B and 22mm in figure 4). Again the improved scheme indicates a better performance over this side of the mountain range.

5. Conclusions

An improvement of the Reisner2 microphysical scheme used in the MM5 model was developed and tested over the Northern South America. This improvement consists in the inclusion of an additional prognostic equation to account for the change with time of the raindrop number concentration.

The results show that over the area under examination; a region of the Andes Mountain Range in the Northern South America, the explicit microphysical schemes reproduce fairly well the centers where the maximum precipitation is observed. However, the schemes under predict heavy rains and over predict the precipitation in both; the windward and lee sides

According to these preliminary results, the improved Reisner2 scheme seems to diminish the under estimation of heavy precipitation and the overestimation in the lee side. However, it is necessary a more rigorously validation before a final conclusion about the precipitation bias over the Colombian territory

References.

Berry, E. X. and R. L. Reinhardt, 1974: An Analysis of Cloud Drop Growth by Collection: Part III. Accretion and Self-collection. J. Atmos. Sci., 31,2118-2126

Clark, T. L., 1976: Use of Log-normal distributions for numerical calculations of condensation and collection. J. Atmos Sci. 33, 810-821.

Colle B. A., M.F. Garvert, J.B. Wolfe, C.F. Mass and C. P. Woods 2005: The 13–14 December 2001 IMPROVE-2 Event. Part III: Simulated Microphysical Budgets and Sensitivity Studies. J. of Atmos. Sci., 62, 3535-3558

Ferrier, B. S. 1994: A double-moment multi phase four-class bulk ice scheme. Part I: Description. J. Atmos. Sci., V 51, 249-280.

Grubisic, V. R. K. Vellore and A.W. Huggins 2005: Quantitative Precipitation Forecasting of Wintertime Storms in the Sierra Nevada: Sensitivity to the Microphysical Parameterization and Horizontal Resolution. Mon. Wea. Rev. 133, 2834-2859.

Meyers, M.P., R.L. Walko, J.Y. Harrington & W. R. Cotton1997: New RAMS cloud microphysics parameterization. Part II: The two moment scheme., J. Atmos Res. 45, 3-39.

Montoya G. G. de J. 1986: An Improved bulk warm rain parameterization of the microphysical processes. Proc. Int. Workshop on Rain Producing system in the tropics and extra tropics. San Jose de Costa Rica 21- 25 July 1986. WMO, TMP Report Series No 2 p. 23-27.

Morrison, H, J. A. Curry, M. D. Shupe & P. Zuidema 2005: A New double-moment microphysics parameterization for application in clouds and climate models. Part II: single column modeling of artic clouds. J. Atmos. Sci. 62, 1678-1693

Nickerson, E. C., E. Richard, R. Rosset and D. R. Smith. 1986: The Numerical Simulation of Clouds, Rains and Airflow over the Vosges and Black Forest Mountains: A Meso-β Model with Parameterized Microphysics. Monthly Weather Review: Vol. 114, No. 2, pp. 398–414.

Phillips, V.T.J., L.J. Donner and S.T. Gardner (2007): Nucleation process in deep convection simulated by a cloud system resolving model with double moment bulk microphysics. J. Atmos, Sci 64, 738-761.

Reisner, J, R.M. Rasmussen and T.T. Bruntjes 1998: Explicit forecasting of supercooled liquid water in winter storms using the MM5 mesoscale model. Q. J. Roy. Meteor. Soc. 124, p.1071-1107

Serafin S. and R. Ferreti 2007: Sensitivity of a Mesoscale Model to Microphysical Parameterizations in the MAP SOP Events IOP2b and IOP8. J. of Appl. Meteor. and Climatol. 46, 1438-1454.

Srivastava, R. C., 1978: Parameterization of the raindrop size distribution. J. Atmos. Sci., 35, 108-117.

SOME PECULIARITIES OF FREEZING OF METASTABLE WATER, INFLUENCING CLOUD ICE DEVELOPMENT

Anatoly N. Nevzorov

Central Aerological Observatory
Dolgoprudny town, Moscow Reg., 141700 Russian Federation.
E-mail: *an.nevzorov@mtu-net.ru*

1. INTRODUCTION

In the present-day knowledge of ice-forming microphysical processes in cold clouds, elements of uncertainty remain as yet. It becomes more and more clear that to understand physical mechanisms of formation of the disperse structure of cloud ice, special physicochemical properties of liquid water associated with its phase states and transitions must be investigated and taken into account. At the same time, to-day possibilities of experimental studying of fine details of these properties are essentially bounded.

Some important peculiarities of the frontal mechanism of freezing (crystallization) of metastable liquid water, supercooled ordinary water and A-water, are here considered basing on established features of interior intermolecular structure of different phase states of water as well as on some empirical facts associated with the freezing process. Specific factors of the impact of cloud droplet freezing process on the formation of parameters of ice disperse phase are discussed.

2. ON A TIME HISTORY OF CLOUD GLACIATION

The measurements performed in stratiform clouds with the cloud microphysical aircraft instrumentation of the Central Aerological Observatory revealed that a fine-dispersed ice fraction with particle sizes smaller than 20 μm is already present in clouds traditionally regarded as pure water ones (Nevzorov, Shugaev, 1992a, 1992b). The concentrations of ice particles in these clouds are comparable with the concentrations of their droplets and, on the whole, by several orders of magnitude exceed the known concentrations of ice-forming nuclei. Their long-time coexistence with the liquid water (ρ = 1 g·cm^{-3}) disperse phase can be explained in terms of very slow mass exchange by molecular diffusion in quiet (relative to a particle) air. In this connection, the question arises about a role of droplet freezing in cloud glaciation process.

As is known, the water freezing nuclei (FN) form the overwhelming part of natural ice-forming nuclei; hence their mean concentration should closely follow the Fletcher's empirical formula for the concentration of ice-forming nuclei against the cloud temperature. However, the cloud droplets freeze on these nuclei far not simultaneously. The time dependence of concentration of freezing droplets can be estimated with taking into consideration the increase of the freezing probability, i.e. of concentration N_{FN} of active FN, along with droplet sizes. The mean concentration of FN active at given temperature, T, and droplet diameter, a, has been deduced (Nevzorov, 2006a) using Bigg's experimental data on their dependence on droplet size (Franks, 1985):

$$N_{FN}(T,a) = N_0 \cdot (a/a_0)^{1.7} \exp(-0{,}6T), \quad (1)$$

where N_0 and a_0 are for T = 0°C. For simplified model of monodisperse droplet cloud in the developmental stage (da/dt > 0), the rate of droplet freezing per a unit volume will follow the expression:

$$N'_{FT} = \frac{\partial N_{FN}}{\partial a}\frac{da}{dt} = 1{,}7 N_0 \frac{a^{0{,}7}}{a_0^{1{,}7}}\frac{da}{dt}\exp(-0{,}6T). \quad (2)$$

In the process, ice crystals grow faster than water droplets owing to higher supersaturation relative to them. With time, the value of da/dt comes to zero and remaining droplets begin evaporating without freezing insomuch as their active FN are spent. As might seem, the added ice portion proves too little to make appreciable contribution to the existing ice fraction and especially to its evolution. However the latter is not so; as will be shown further, a factor accompanies the droplet freezing process that promotes acceleration of ice particle growth in formation of their size spectra.

3. UNIQUE PROPERTIES OF LIQUID WATER AT $T < 0^{o}C$

A number of special properties of water at negative temperatures are caused by the participation of intermolecular hydrogen bonds (HB) in organization of its internal structure. As against a rigid spatial lattice in crystalline ice, in ordinary liquid water (with density ~1 g·cm^{-3}), named here water-1, HB are partly disrupt chaotically in space and time. The higher density of the water-1 specifies that HB hold larger distance between molecules than usual oscillatory bonds (an effect hereinafter called repulsive effect of HB). Even much higher density, somewhat more than 2 g·cm^{-3} (Delsemme, Wenger, 1970; Nevzorov, 2006b), belongs to amorphous water deprived of HB at all to all attributes.

The specific concentration of HB in water-1 experiences an inverse relation with the energy of thermal vibrations of molecules. As a result, with the temperature rising, the water-1 density ρ_w should decrease due to an increase of the amplitude of thermal vibrations of molecules; at the same time, ρ_w should increase due to a decrease of HB concentration. The known maximum of ρ_w value at 4°C is caused by the prevalence of the former tendency at higher temperatures and of the latter one at lower temperatures.

The experimental dependence $\rho_w(T)$ for water-1 in the range from 0°C to –34°C reveals a progressive decrease of its density when the temperature lowers (Franks, 1985). This dependence is shown in Figure 1 for the difference between of the density of liquid water and ice, $\Delta\rho = \rho_w - \rho_i$ where ρ_i = 0,917 g·cm^{-3}, with its extrapolation to the region of lower temperatures, based on the following considerations. The decrease of the water-1 density means that its structure approach to crystalline ice in the specific concentration of HB and therefore in the relative total volume of instant ice-like clusters. Hence the probability increases of the stochastic formation of homogeneous ice nuclei with a zero threshold of nucleation energy. At a critical temperature of water-1 existence, defined as a temperature of its wholly homogeneous freezing and equal to –39°C (Franks, 1985), the water-1 comes up with crystalline ice in density. In turn, the equality of their densities means in principle that the internal energy of water-1 becomes equal to the internal energy of ice at –39°C, and the latent energy of its freezing vanishes.

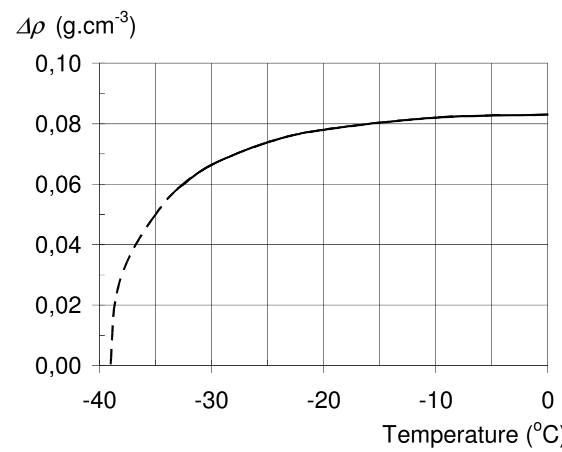

Fig.1. The temperature dependence of the difference between the densities of liquid water-1 and ice I. The solid curve is by (Franks, 1985); the dashed segment is an extrapolation.

Assuming that as a first approximation, the $L_f(T)$ value is proportional to the difference $\rho_w(T) - \rho_i$, the proportionality factor $L_0 \approx 316$ J·g^{-1} is chosen so that the corresponding relation

$$L_f(T) = L_0 \frac{\rho_w(T) - \rho_i}{\rho_w(0) - \rho_i} \quad (3)$$

to be as possible close to the reference dependence at T > –30°C. The ice density is assumed to be temperature-independent. Figure 2 shows the dependence (3) in comparison with the reference curve $L_f(T)$ (e.g. Mazin, Khrgian, 1989).

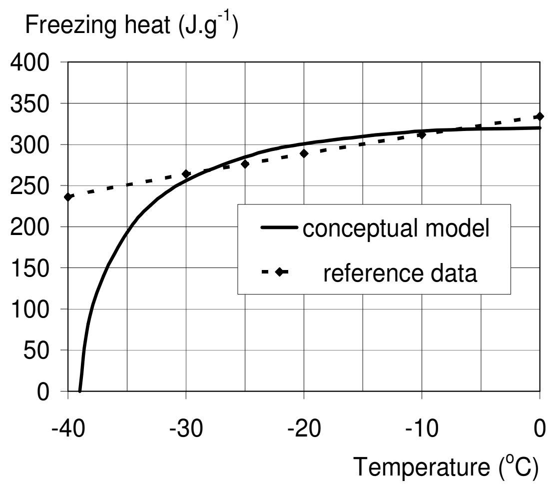

Fig. 2. Conceptual and reference models of the temperature dependence of the specific latent energy of water-1 freezing.

In turn, A-water, as being deprived HB (Nevzorov, 2006b), has not the specified temperature dependences of its properties and behaves as a usual simple liquid.

4. PARADOXES AND PECULIARITIES OF FRONTAL FREEZING MECHANISM

Both the metastable liquid phases of water, ordinary water-1 and amorphous A-water, when freezing (crystallizing) transform into the same phase, ice I with the density ~0.92 g·cm^{-3}. The first-order phase transition takes place in the both cases, which requires the discrete separation of the phase spaces by reason of the absence of intermediate state. The process of freezing of a continual water volume consists in propagation of the phase interface, or the freezing front, in the liquid medium from the nucleation center, leaving behind a continuous medium of crystalline ice.

With different densities of substances before and behind the freezing front, especially in the case of A-water, a freezing droplet should apparently change its shape or be destructed by the internal stress. In fact, a lot of observations and experiments demonstrate that the frozen water droplets of various sizes remain spherical. For A-water, this is pronounced in spherical shape of frozen droplets in a pattern of crystals riming in ICC (Pruppacher, Klett, 1978). The assumptions on the initial formation of an ice crust on the droplet surface or on plicated surface of the freezing front (Franks, 1985) appear devoid of physical basis.

Another apparent paradox of the frontal freezing mechanism follows from the conventional statement that the latent energy of the phase transition is released in purely thermal form. If the heat is released immediately during ice phase formation, just formed ice should be subjected to the initial temperature increment

$$\Delta T_0 = \frac{L_f}{c_{pi}}, \quad (4)$$

where c_{pi} ≈ 2,0 J·g^{-1} K^{-1} is the specific heat capacity of ice. For water-1 at temperatures between –35°C and 0°C, taking L_f according to (4), the ΔT_0 values are from 100K to 160K.

More impressive result is demonstrated by A-water, for which $L_f = L_i - L_e$ ≈ 2300 J·g^{-1}, where L_i is the evaporation heat of ice; here (4) yields ΔT_0 = 1150 K. Thus, at the instant of its formation and during a finite time of temperature relaxation, just formed ice should be at the temperature being much higher than its melting temperature, which in principle rules out the possibility of its existence. As far as we know, this paradox inherent namely to the frontal freezing has yet no physically founded explanation.

Within the current knowledge of the intermolecular structure of various water phases, both paradoxes meet the same explanation (Nevzorov, 2006a).

The continuous motion of the interphase surface is caused by the consecutive attachment of molecules of liquid to the ice lattice. The retained and newly formed HB serve as connecting links between both phases, providing their continuous cohesion. This excludes any possibility of tangential slip of a liquid layer adjacent to the frontal surface. For this reason and due to its internal viscosity, the liquid trapped by the moving front is not deformed with respect to the base of solid ice with the result that the newly formed ice phase retains the initial volume of the liquid phase. However, since the ice density is smaller than the liquid one, an excess in mass of liquid water with respect to ice occurs at the freezing front and is thereby rejected in the form of unbound molecules. The energy released at the front is transferred to these liberated molecules, converting into their kinetic energy.

If these molecules remain in the liquid medium they would totally transfer to it both their mass and energy. At that, the mass excess would distort the initially spherical shape of a frozen droplet. As for the energy, it is known that supercooled water can immediately freeze at temperatures arbitrarily close to 0°C, which implies that the molecules rejected from the freezing front leave the liquid with carrying away all the gained energy. Thus the freezing process remains isothermal in itself, except produced by it molecular flow carrying away all released energy and equivalent to hot vapor.

That these unbound molecules leave the condensed medium through the liquid space can be certified by a behavior of water freezing in a vessel which low part, being the closed volume for liquid, is subjected to deformation or destruction under the internal pressure, rather than the part of ice formation. Using an analogy with quite (film) boiling, the flow of free molecules in liquid can be likened to molecular vapor outflow from a hot surface. Details of this phenomenon, still poorly studied, possibly include a chain energy transfer from molecule to molecule.

As an indirect experimental confirmation of the stated vapor outflow from freezing water, occurrence of "an unidentified gas" (Franks, 1985) in the process can serve.

It follows from all above that the water portion transforming into outside vapor during the freezing is

$$m_v / m_w = (\rho_w - \rho_i) / \rho_w \,, \qquad (5)$$

where m_w and m_v are the liquid and vapor masses, respectively. For water-1, assuming the dependence $\rho_w(T)$ by Fig.1, this fraction is 8.3% at –1°C, 5.2% at –35°C, and rapidly vanishes when the temperature tends to –39°C. In freezing of A-water with the density of ~2.1 g·cm^{-3}, approximately 56% of its mass transforms into vapor independently of temperature. According to estimations (Nevzorov, 2006a), in both cases effective velocity of molecules while crossing the liquid-to-air interface is 60 to 80 m·s^{-1}.

The considered peculiarities of supercooled water freezing mechanism offer a simple alternative explanation of two-stage effect of droplet freezing (Pruppacher, Klett, 1978). The first stage is the isothermal freezing properly, and the second one is the result of condensation of ice supersaturated vapor (including just liberated) on the ice replacing water.

5. MICRO TURBULENCE EFFECT

In the process of freezing of a droplet suspended in air, the motion of water molecules emitted by this droplet is transferred to the surrounding air, thereby causing its forced outflow from the droplet surface and the appearance of compensating eddy motions. As a result, a zone of microscopic (comparable with cloud particle sizes) scale turbulence develops around the droplet. In the light of cloud microstructure evolution, the influence of these disturbances on the rate of growth or evaporation of cloud particles through the mechanism of convective diffusion of water vapor is of interest to us.

Let the zone of disturbances generated by the freezing of an individual droplet with the diameter a occupy a certain effective volume

V. Under the assumption that the time of dissipation of the disturbance energy is much greater than the time of complete freezing of the droplet, the initial turbulent energy, $E_0(a)$, of the disturbance zone can be expressed both in terms of the turbulent kinetic energy of air particles and in terms of the total kinetic energy of liberated molecules directly at their outlet from the droplet:

$$E_0(a) = V\rho_a \frac{\Delta u_a^2}{2} = \frac{\pi}{6} a^3 (\rho_w - \rho_i) \frac{u_{m2}^2}{2}, \qquad (6)$$

whence

$$V = \frac{\pi}{6} a^3 \frac{\rho_w - \rho_i}{\rho_a} \frac{u_{m2}^2}{\Delta u_a^2}. \qquad (7)$$

Here, ρ_a is the air density; u_{m2} and Δu_a are the rms velocities of the molecules and of air pulsations, respectively. Since the velocities of turbulent motions decrease with distance from the droplet increasing, then, as follows from (7), the determination of the disturbance-zone scale depends on the choice of an effective value of Δu_a to answer a required criterion.

Let a crystal with the effective size b, large enough to retain its rest inertia, be located within such disturbance volume. Following and taking into account the anisotropy of turbulent air blow-off, we will assume the inequality

$$\mathrm{Re}_b = \frac{b \cdot \Delta u_a}{\mu} > 1 \qquad (8)$$

(where μ is the kinematic viscosity of air) as a tentative criterion of accelerated convective-diffusion mode of particle growth. It follows from (7) and (8) that the "active" volume V increases with increasing sizes of both the freezing droplet and the particle falling into its disturbance zone. In real clouds, the probability as estimated of this event is rather low compared to unity but increases with the particle size. Hence in the process of collective freezing of droplets a small fraction of cloud particles will experience a progressive acceleration of growth; i.e., the right-hand wing of ice particle size spectrum will increase most rapidly.

Upon the completion of the freezing process of a droplet, the excited turbulent energy attenuates rapidly, thereby converting into heat energy. Owing to the acquired buoyancy, the heated volume of air around the frozen droplet arises. In the process of the cloud glaciation, these scattered zones of buoyancy form spatiotemporal inhomogeneities, or turbulent pulsations of the resulting updraft. Such "secondary" microturbulence additionally accelerates the mass exchange process in a cloud.

The irreversible microscale turbulence is settled in the cloud when the particles of ice and accompanying A-water reach sufficient sizes for the gravitational fall causing appreciable adjacent vortex. The phase transformation of a cloud is concluded with its avalanche transition into mixed state with A-water serving as its liquid disperse phase.

6. CONCLUSION

In the process of development of a water cloud, the freezing of its droplets occurs not at once but is lasting in time owing to increase in probability of freezing of droplets of ordinary water and A-water with their rising. An important specific feature of the frontal mechanism of freezing of an individual droplet is that during freezing, the droplet emits molecular vapor carrying the released energy of the phase transition. As a result, a zone of short-living microscale turbulence arises around each freezing droplet. The ice crystal which falls into this zone experiences much more rapid growth in convective diffusion mode than in molecular diffusion one. Such chance for the acceleration of growth of an individual crystal occurs with very small probability but rising with the crystal becoming larger. By this reason, ice crystals grow far not equally and only their little part reach precipitation sizes. With sufficient collective enlargement of crystals, their gravitational sedimentation becomes a source of the irrevocable microscale turbulence, which results in convective diffusion mode of the Bergeron mass exchange. The phase transformation of a cloud is concluded with its avalanche transition into the mixed state, where A-water becomes the only liquid disperse phase.

REFERENCES

Borovikov, A.M., E.G. Zak, et al., 1961: Physics of clouds. Leningrad, Gidrometeoizdat [in Russian].

Delsemme, A.H., and A. Wenger, 1970: Superdense water ice. Science, 167, 44-45.

Franks, F. (Ed.), 1985: Water and Water Solutions at temperatures below 0°C. Kiev, Naukova dumka [in Russian].

Mazin, I.P., and A.Kh. Khrgian (Eds.), 1989: Clouds and cloudy atmosphere. Handbook. Leningrad, Gidrometeoizdat [in Russian].

Nevzorov, A.N., 2006a: Glory phenomenon informs of presence and phase state of liquid water in cold clouds. Atmos. Res., 82, Nos 1-2, 367-378.

Nevzorov, A.N., 2006b: Some properties of metastable states of water. Phys. of Wave Phenomena, № 1, 45-57.

Nevzorov, A.N., and V.F. Shugaev, 1992à: Observations of the initial stage of evolution of ice phase in supercooled clouds. Soviet Meteorology and Hydrology, No 1, 69-76.

Nevzorov, A.N., and V.F. Shugaev, 1992b: Experimental studies of phase-dispersion structure of stratiform clouds at negative temperatures. Soviet Meteorology and Hydrology, No 8, 41-51.

Pruppacher H.R., and J.D. Klett, 1978: Microphysics of clouds and precipitation. D. Reidel.

MICROPHYSICAL CHARACTERISTICS OF OROGRAPHIC MIXED-PHASE CLOUDS DURING JCSEPA FIELD CAMPAIGNS

Narihiro Orikasa, Masataka Murakami, and Atsushi Saito
Meteorological Research Institute, Tsukuba, Ibaraki, Japan

1. INTRODUCTION

Microphysical parameters on cloud phase composition are important for remote-sensing retrievals and radiative transfer calculations, and numerical forecasting and climate modeling. However, such observational studies have been limited by the lack of suitable instruments for segregating between ice and liquid hydrometeors over wide size ranges. Recently, detailed studies have been conducted with airborne instruments of Nevzorov hot-wire probe (both total-water and liquid-water sensors) and Rosemount Icing Detector (RICE) (Cober et al. 2001; Korolev et al. 2003) or Small Ice Detector, Nevzorov total-water sensor and Lyman-α evaporative probe (Field et al. 2004).

In order to investigate microphysical structures of wintertime orographic snow clouds in Japan and to evaluate seeding effects in the seedable clouds, two field campaigns were conducted in 2007 during a JCSEPA (Japanese Cloud Seeding Experiment for Precipitation Augmentation) project. In-situ microphysical measurements are intended and used to improve monitoring technique of clouds by various remote sensors and to validate numerical simulation results.

The purpose of this study is to examine microphysical parameters segregating liquid, glaciated (or ice), and mixed cloud phase regions in our dataset utilizing the common airborne instruments including the Nevzorov probe. Statistics of mean cloud-particle sizes, number concentration, and ratio of ice water content (IWC) to total water content (TWC) are presented as a function of temperature.

2. DATA AND INSTRUMENTATION

The aircraft data were obtained during the First and Second JCSEPA field campaigns (hereafter JCSEPA I and JCSEPA II, respectively). An instrumented aircraft (MU-2B; Diamond Air Service Co., Ltd.) was used for both campaigns, each of which consisted of about ten flights during three weeks in the intensive observation period. JCSEPA I was conducted in March of 2007, while JCSEPA II was conducted in December of 2007. The study area is located near the Mikuni Mountains in central Japan. During the winter monsoon season, northwesterly or westerly airflows predominantly occur, often accompanied by heavy snowfall on the Sea of Japan side.

The microphysical instruments used in this study include PMS FSSP, 2DC, 2DP, King LWC probe, DMT CAPS, and Nevzorov LWC/TWC probe. The Nevzorov probe is a hot-wire instrument at constant temperature, consisting of two sensors (Korolev et al. 1998). The IWC is basically obtained from the difference of two measurements (TWC – LWC). Summary statistics for each flight are given in Table 1. Care must be taken regarding the CAPS data as the original probe was switched to another one after the second flight in JCSEPA II.

Table 1. Summary of each flight data for JCSEPA I (upper) and JCSEPA II (lower) campaigns. No data or erroneous data are shown as a horizontal bar.

Date	Time [JST]	[℃] Tmax	[℃] Tmin	[g/m3] KLWCmax	[g/m3] NevLWCmax	[g/m3] NevTWCmax	[#/cc] FSSPave	[#/L] 2DCave	[#/L] 2DPave	[#/cc] CASave	[#/L] CIPave
2007/3/5	12:42:13 – 14:18:24	0.4	−21.3	0.30	0.23	0.43	11	20	3.7	12	900
2007/3/6	10:46:03 – 12:32:18	−1.5	−15.1	1.19	1.02	1.24	143	11	1.5	91	7,616
2007/3/7	13:03:18 – 15:24:27	−5.9	−22.9	0.49	0.46	0.79	10	15	2.6	16	403
2007/3/8	14:58:55 – 17:17:23	−6.5	−21.2	0.70	0.62	0.86	93	24	3.4	103	694
2007/3/11	14:46:34 – 16:49:58	−8.4	−24.3	1.20	0.86	1.13	111	32	4.3	126	5,669
2007/3/12	09:48:37 – 11:54:10	−9.7	−25.7	0.57	0.49	1.07	46	52	8.3	62	1,179
2007/3/12	14:45:33 – 17:05:06	−8.5	−24.2	0.76	0.67	1.08	80	41	6.5	85	1,657
2007/3/13	08:20:21 – 10:45:05	−8.6	−19.3	0.78	0.71	1.03	—	43	5.6	201	1,233
2007/3/13	14:40:42 – 16:57:25	−8.6	−20.4	0.99	0.83	1.03	129	24	3.0	152	720
2007/12/4	13:56:39 – 16:10:12	−4.2	−29.1	0.24	0.16	0.51	4	11	1.8	—	—
2007/12/5	10:38:18 – 13:03:46	−3.0	−21.9	0.61	0.43	1.20	25	19	2.1	—	—
2007/12/9	08:54:42 – 10:43:09	−2.3	−16.6	0.94	0.74	1.40	95	11	0.9	166	126
2007/12/9	13:55:24 – 15:31:41	−2.8	−16.7	1.05	0.84	1.20	169	19	0.5	420	64
2007/12/10	08:22:05 – 10:36:55	−1.0	−13.9	0.69	0.49	0.88	67	6	0.4	254	53
2007/12/14	13:56:30 – 16:17:11	−2.8	−22.5	0.67	—	1.05	50	17	1.9	239	13
2007/12/16	08:26:44 – 10:46:42	−4.7	−24.9	0.89	0.91	1.38	82	44	5.1	377	38
2007/12/17	15:36:48 – 16:40:10	−0.5	−27.2	0.71	—	0.94	81	12	1.1	320	19
2007/12/18	14:29:20 – 16:28:13	−9.8	−28.7	0.66	0.71	1.87	48	54	5.3	260	30
2007/12/19	08:15:02 – 08:28:01	−10.1	−13.7	0.39	0.28	0.48	78	5	0.3	302	8
2007/12/20	14:38:33 – 16:04:28	−3.5	−21.5	0.96	0.33	2.06	60	54	4.7	335	27

3. CLOUD PHASE DETERMINATION

Based on the methodology from Korolev et al. (2003) study, the cloud phase (liquid, ice, or mixed) were determined in our dataset. The definition of phase composition is mainly characterized by the ratio (μ_3) of IWC to TWC measured with the Nevzorov probe for each 1 s interval data. Clouds with $\mu_3 < 0.1$ will be defined as liquid, clouds with $0.1 \le \mu_3 \le 0.9$ defined as mixed, and clouds with $\mu_3 > 0.9$ defined as ice. For this work, the same threshold value of water content was set at 0.01 g m^{-3} for identifying cloud regions. Although additional criterion, either cloud droplet concentrations > 0.1 cm^{-3} or those of ice crystal > 0.1 L^{-1}, was applied, the impact was found to be negligible.

Since we have no data on the RICE probe, it might be difficult to evaluate residual effect in pure ice clouds on the Nevzorov LWC sensor (see Korolev et al. 2003). The effect of difference in collection efficiency between two sensors over size ranges of cloud droplet, drizzle or large droplet (Strapp et al. 2003) should be taken into account when improving analysis. For simplicity, if TWC < LWC, then the phase is determined as liquid (TWC = LWC) in this work.

4. RESULTS

Figure 1 shows the dependence of statistics of IWC, LWC, and TWC on temperature during both campaigns for all cloud phase compositions. TWC markedly increases with increasing temperature in both campaigns. In contrast, IWC in JCSEPA I tends to remain nearly constant, while LWC in JCSEPA II does not change as much as LWC in JCSEPA I.

Figure 2 shows average cloud particle concentrations measured with FSSP and 2DC probes as a function of μ_3 in JCSEPA I. Both campaign dataset had the same trend: average FSSP concentration decreased with

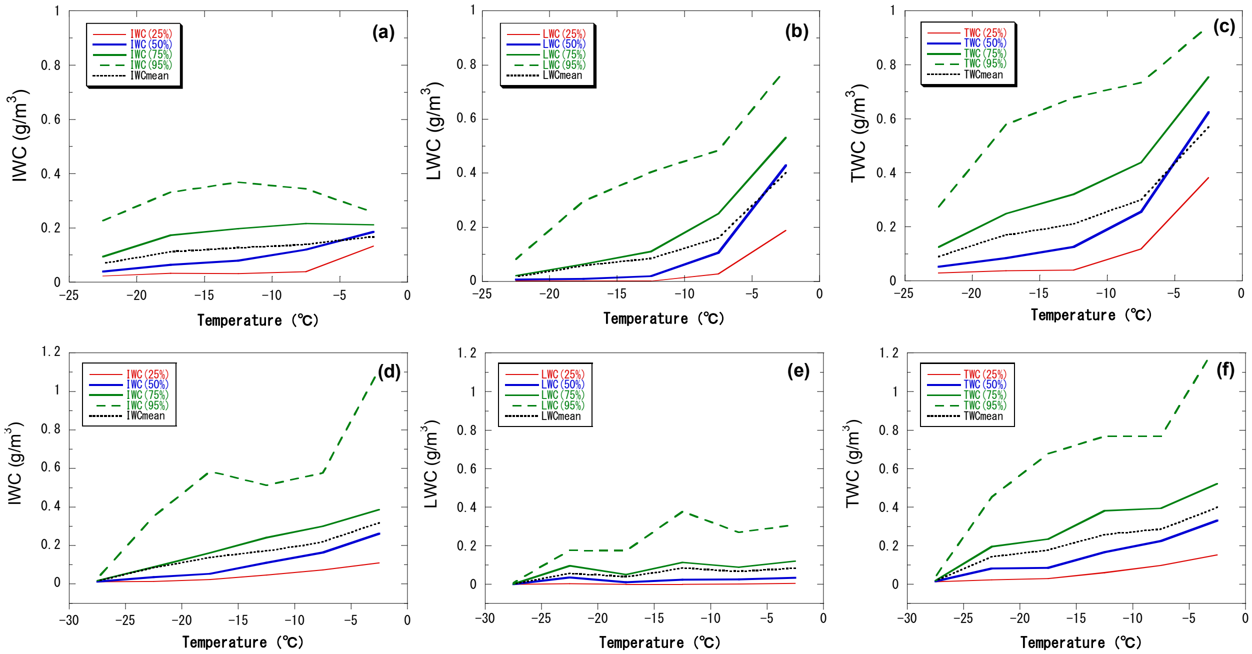

Fig. 1 Water content measured with Nevzorov probe versus temperature during both JCSEPA I (upper panels) and JCSEPA II (lower panels) campaigns: (a),(d) IWC; (b),(e) LWC; (c),(f) TWC.

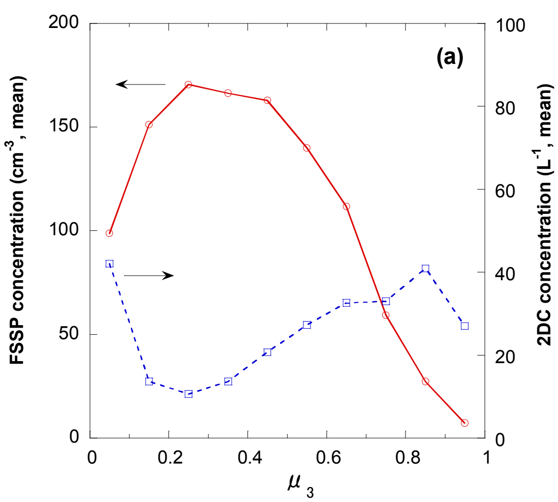

Fig. 2 Average concentrations of cloud particles derived from FSSP and 2DC measurements versus μ_3 for all phase compositions in JCSEPA I.

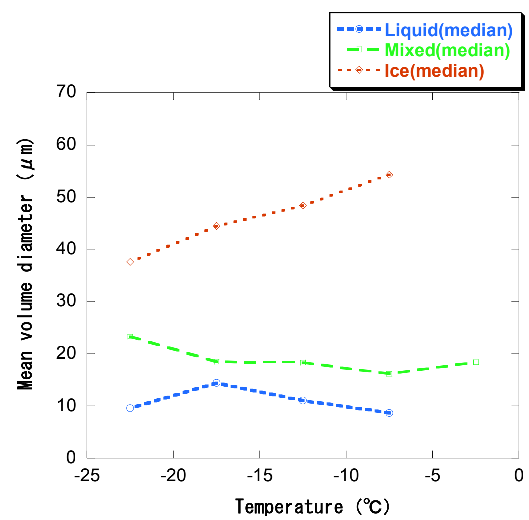

Fig. 3 Average mean volume diameter of cloud particles versus temperature for three phase compositions, derived from Nevzorov TWC and FSSP concentration in JCSEPA I.

μ_3 over its ranges $\mu_3 > 0.2$, while average 2DC concentration had the opposite feature.

Similar to Korolev et al. (2003) study, mean volume diameter of cloud particles were estimated by using data of water content and FSSP concentration. Figure 3 shows the dependence of mean volume diameter on temperature for three cloud phase compositions in JCSEPA I. The particle size in ice clouds increases with temperature, while that in liquid or mixed phase clouds relatively stays nearly constant.

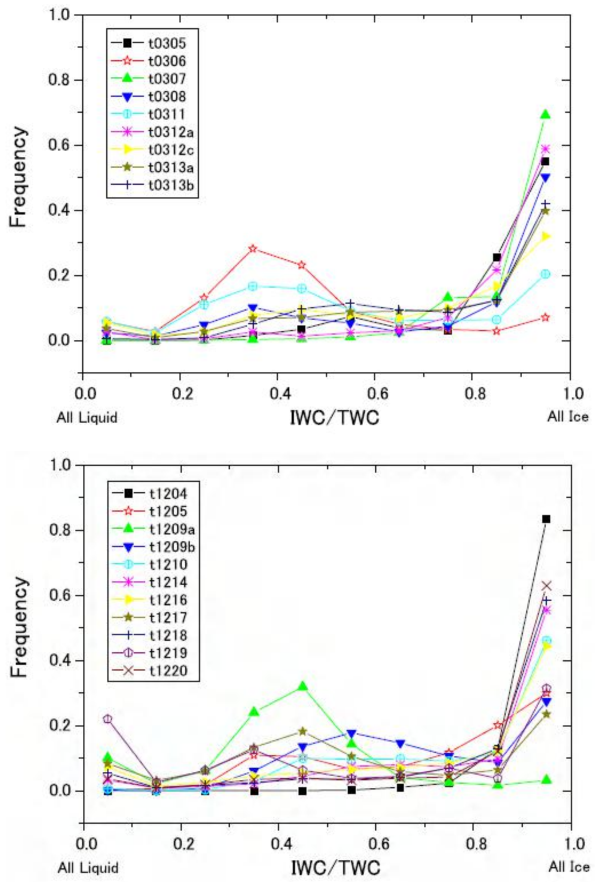

Fig. 4 Relative distribution of μ_3 in each flight. The legend indicates the flight date (tMMDD) (upper panel: JCSEPA I; lower panel: JCSEPA II).

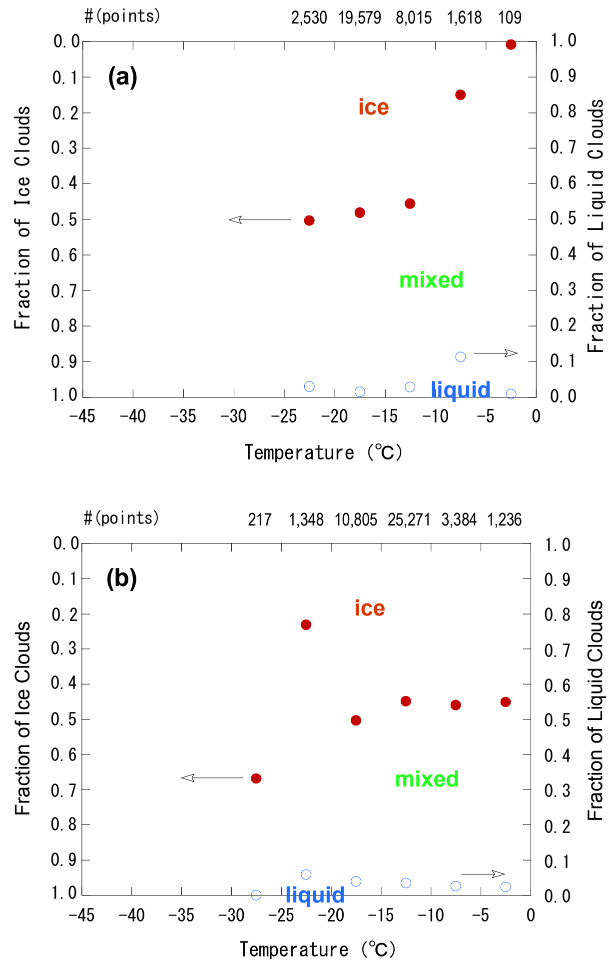

Fig. 5 Fraction of ice, mixed, and liquid clouds versus temperature from the dataset in this study: (a) JCSEPA I, (b) JCSEPA II.

In order to examine the difference of cloud phase composition in each case, Fig. 4 shows the relative distribution of μ_3 in each flight. The case of "t0306" or "t0311" in JCSEPA I and that of "t1209a" or "t1217" in JCSEPA II had a tendency to be relatively small values of μ_3 compared to other cases. Such cases have more supercooled liquid water content, which means more favorable case to the cloud seeding.

Figure 5 shows the fraction of ice, mixed, and liquid clouds in this study. The general trend is similar to other studies (cf. Fig. 14 in Korolev et al.), although our dataset has relatively small fraction of liquid clouds and large fraction of mixed or ice clouds even at warmer temperature.

5. SUMMARY

A study of mixed phase clouds during two JCSEPA campaigns in central Japan is presented. The cloud phase composition is determined from measurements with the Nevzorov LWC/TWC probe based on a study by Korolev et al. (2003). The cloud particle concentration, mean volume diameter, and water content are shown as a function of temperature. In general, those characteristics are quite similar to previous studies. The plot of phase composition distribution in each case helps to quantitatively identify the conditions favorable to the cloud seeding.

The results of this study will be used to improve the monitoring technique of seedable clouds through various remote sensors and to validate the numerical modeling results in JCSEPA research project.

Acknowledgments

This study was supported by the Japanese Cloud Seeding Experiment for Precipitation Augmentation (JCSEPA) project, sponsored by the Ministry of Education, Culture, Sports, Science and Technology of Japan.

REFERENCES

Cober, S. G., G. A. Isaac, A. V. Korolev, and J. W. Strapp, 2001: Assessing cloud-phase conditions. *J. Appl. Meteor.*, **40**, 1967-1983.

Field, P. R., R. J. Hogan, P. R. A. Brown, A. J. Illingworth, T. W. Choularton, P. H. Kaye, E. Hirst, and R. Greenaway, 2004: Simultaneous radar and aircraft observations of mixed-phase cloud at the 100 m scale. *Quart. J. Roy. Meteor. Soc.*, **130**, 1877-1904.

Korolev, A. V., J. W. Strapp, G. A. Isaac, and A. N. Nevzorov, 1998: The Nevzorov airborne hot-wire LWC-TWC probe: Principles of operation and performance characteristics. *J. Atmos. Oceanic Technol.*, **15**, 1495-1510.

Korolev, A. V., G. A. Isaac, S.G. Cober, J. W. Strapp, and J. Hallett, 2003: Microphysical characterization of mixed-phase clouds. *Quart. J. Roy. Meteor. Soc.*, **129**, 39-65.

Strapp, J. W., and Coauthors, 2003: Wind tunnel measurements of the response of hot-wire liquid water content instruments to large droplets. *J. Atmos. Oceanic Technol.*, **20**, 791-806.

AIRBORNE MEASUREMENTS OF ICE CONCENTRATIONS IN WAVE CLOUDS

David C. Rogers[1], Paul J. DeMott[2], Andy Heymsfield[1], Jeff Stith[1]
[1]NCAR, Boulder, Colorado USA
[2]Colorado State University, Fort Collins, Colorado

1. INTRODUCTION

This paper presents an overview of recent airborne measurements of ice crystal concentrations in winter wave clouds in the U.S. Rocky Mountains, such as the example in Figure 1. Wave clouds (altocumulus standing lenticular clouds) provide an ideal natural laboratory for helping to improve our understanding of primary ice formation in the atmosphere. They have relatively simple air flow, are stably stratified, and the air is constantly replaced as air flows through them. Parcel theory can be used to describe the thermodynamic history as air travels through these clouds because there is little mixing and the parcel transit time is typically 1-2 minutes. This is usually sufficient time for ice crystals growing at water saturation to reach detectable size (~50-100 µm).

The initial formation of ice is a long-standing problem in cloud physics. Ice particle numbers, sizes, and growth habits determine a cloud's microphysical and radiative properties. For many mid-latitude clouds, ice is crucial for precipitation. Processes involved in the initial formation of ice are not well understood because there are a number of primary and secondary production processes (Cooper 1991; Rasmussen 1995; Baker 1997).

Past field studies of wave clouds also used instrumented aircraft to examine ice formation. The present work builds on that

Figure 1. Wave cloud 13-Dec-2007 airflow is from right-to-left and into the picture. Lower cloud ~4.2-4.8 km, -13 to -18°C, upper cloud cloud ~5.6 km, -24°C. The C-130 penetrated these clouds 28 times in 90 minutes.

by adding simultaneous measurements of cloud microphysics, CCN, ice nuclei, and (for ICE-L) aircraft-based remote sensing. The focus of research for these projects is improved understanding of fundamental processes and the role of aerosol particles in natural ice formation. The interested reader is referred to several related papers from ICE-L in this conference.

2. FIELD PROJECTS

The measurements described here were made in two airborne field projects. The aircraft were equipped with a variety of instruments to detect cloud particles, state parameters, kinematics and aerosols. Flight decisions favored days with wave clouds in the middle troposphere and dry air above in order to avoid the chance of ice falling from higher altitude cirrus clouds. Forecasts had the expert assistance of John Brown (NOAA). This paper presents a few selected observations and a summary of all cases.

2.1 Wave-Ice (2000)

The **Wave-Ice** project occurred during March 2000 with University of Wyoming King Air aircraft. Instruments were provided by the University of Wyoming and Colorado State University. Ten flights were made in wave clouds with temperatures from -5 to -40℃. The flights occurred in southern Wyoming and northern Colorado, USA.

2.2 ICE-L (2007)

The Ice in Clouds Experiment – Layer clouds **ICE-L** occurred in November and December 2007 using the NSF/NCAR C-130 aircraft, based out of Broomfield, Colorado. Eight of the total twelve flights were in wave clouds in Wyoming. Cloud temperatures were -4 to -38℃. More information is on web page, *http://catalog.eol.ucar.edu/ice_l/*

2.3 Sampling Procedure

After a cloud was selected for study, a number of cloud penetrations were made in vertical steps of ~150 m. Penetrations were generally along the upwind and downwind directions. Sampling was also done in the on the upwind (updraft) region below water cloud base to characterize the inflow aerosol. Each penetration of a cloud was at approximately constant altitude, although the aircraft ascended and descended slightly (~65 m) in response to the vertical wind. The aircraft did not follow air parcel trajectories. Successive penetrations were generally within ~2 minutes, long enough for the aircraft to reverse course and change altitude. Because this re-sample interval is approximately the same as the time for an air parcel to pass through the cloud, we can consider each cloud pass as an independent sample of a “new” cloud.

3. INSTRUMENTATION

Primary measurements included thermodynamics, kinematics, position keeping, water and ice cloud particles. For the research described in this paper, the primary microphysics instruments are listed in Table 1. In both projects, there were additional instruments that generated rich and diverse data sets. These included aerosol sensors for CN, CCN, ice nuclei, size distributions ~10-1000 nm, aerosol mass spectrometers, trace gas sensors (O_3 and CO), and more. In ICE-L, the C-130 was equipped with millimeter cloud radar and polarization lidar from the University of Wyoming.

The ice particle probes are of particular interest for this study. Both projects used the OAP-2DC, although the ICE-L probe was modernized with a diode laser, a fast response 64-diode array and USB2 interface. Both 2DC’s have 25 µm resolution and cover the size range ~50-800 µm (Wave-Ice) and ~50-1600 µm (ICE-L). The OAP-200X probe size range is ~25-200 µm in 15 bins. Only a fraction of the smallest particles are detected by these optical array probes (Korolev et al., 1998; Jensen and Granek, 2002). Data from SID2H and CPI are not included in the present analysis.

	Wave-ICE UWyo K/A	ICE-L NSF/NCAR C130
cloud droplets	FSSP-100 FSSP-300	FSSP-100 (SPP-100) DMT-CDP
ice particles	OAP-200X OAP-2D-C	fast 2D-C, SID2H & CPI
cloud water content	DMT hot-wire	King hot-wire & CVI
cloud water phase	Rosemount icing sensor	Rosemount icing sensor
water vapor	chilled mirror & Licor	chilled mirror & TDL hygo
kinematics	IRS, GPS, & gust probe	IRS, GPS, & gust probe

Table 1. Microphysics instrumentation

4. ANALYSIS

In general, the wave clouds in this study were stationary with respect to the ground, and they occurred when horizontal wind speeds at mountain ridge level were ~20 m s^{-1}. For both projects, the microphysical data were examined at 1-second intervals to determine periods when the aircraft was in cloud. "Clouds" were identified as:

continuous regions > 5 s (ICE-L) or 6 s (Wave-Ice) with concentrations of droplets > 1 cm^{-3} or ice > 0 L^{-1}

This definition is somewhat arbitrary but necessary since the two aircraft did not carry identical instruments, and they flew at different speeds (K/A ~115 m s^{-1} and C-130 ~130 m s^{-1}). Furthermore, this definition does not account for the difference in cloud penetration time of the aircraft, which could be ~30% greater when flying upwind, compared to flying downwind. Future analysis will adjust for these differences, but the general results are likely to be very similar to those described here. In total, there were 428 cloud penetrations in Wave-Ice and 541 in ICE-L.

5. RESULTS

Selected observations from two flight days are shown to illustrate the kind of data that were obtained.

5.1 Wave-Ice case March 14

A series of stationary wave clouds formed downwind of the mountain ridge on this day. The aircraft made 56 cloud penetrations, and the first 19 of these cover a period of 77 minutes, as shown in Figure 2. The measurements are plotted

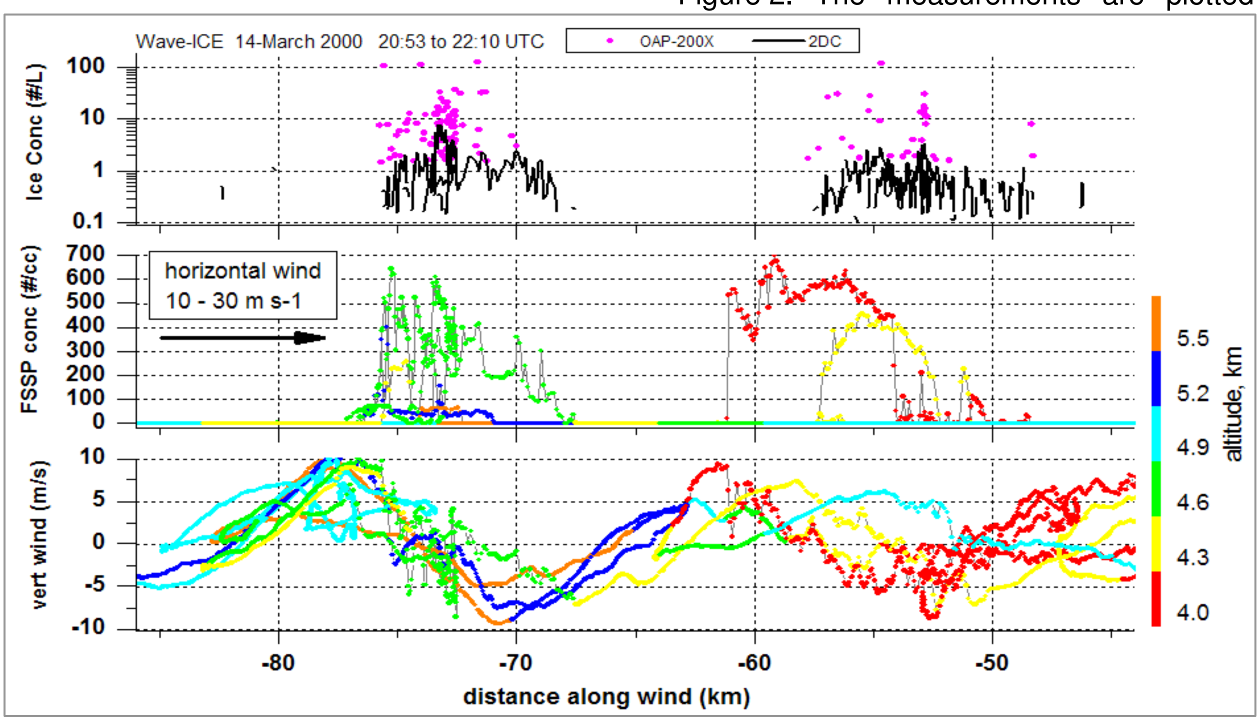

Figure 2. Measurements during 77 minutes of study during which 19 penetrations were made through wave clouds. See discussion in section 5.1.

relative to distance on the ground, oriented along the mean wind direction. The top panel shows estimates of ice concentration from two probes. The middle panel is droplet concentration, and the bottom panel is vertical wind. For the middle and bottom panels, colors identify the aircraft altitude.

Ice crystal concentrations measured by the 2DC were ~0.1-3 L^{-1}, whereas the OAP-200X probe (magenta dots) measured ~1-100 L^{-1}. This discrepancy of a factor 30X is due to the 2DC's low detection efficiency for particles smaller than ~100 µm, compared to the OAP-200X. We assume the detected particles are small ice crystals and not large droplets, although there is some uncertainty about this. Typical droplet size distribution (FSSP) means were ~15-25 µm diameter and dispersion (σ/mean) ~0.3, but there were a few drops > 40 µm.

Average droplet concentrations (middle panel) were ~300 to 600 cm^{-3} with peaks > 700 cm^{-3}. The higher concentrations were preferentially at lower altitudes. Maximum vertical wind speeds were +10 to –10 m s^{-1}. It's interesting that the peak updrafts occurred in the clear air just upwind of the cloud, whereas the strongest downdrafts were in-cloud at the trailing edges of outflow.

A summary of crystal concentrations for all 56 cloud penetrations on this day is shown versus temperature in Figure 3. The number label of each point identifies the cloud pass and is plotted at the mean value. Error bars show ranges. As expected, the general trend shows higher concentrations at colder temperatures. On average, concentrations increase ~10X for 10℃ cooling. These data also show wide variations between cloud passes, and they show a spread of concentration ~10X at any one temperature. These large variations may result from several factors, such as natural or statistical uncertainties and the size detection sensitivity of the OAP-200X probe. Either the ice is not uniformly distributed in these clouds, or we have a limited ability to measure the ice concentration precisely. Indeed, if data from the 2DC probe were plotted, then concentrations for these same clouds are smaller by a factor ~40X, as shown in Figure 4.

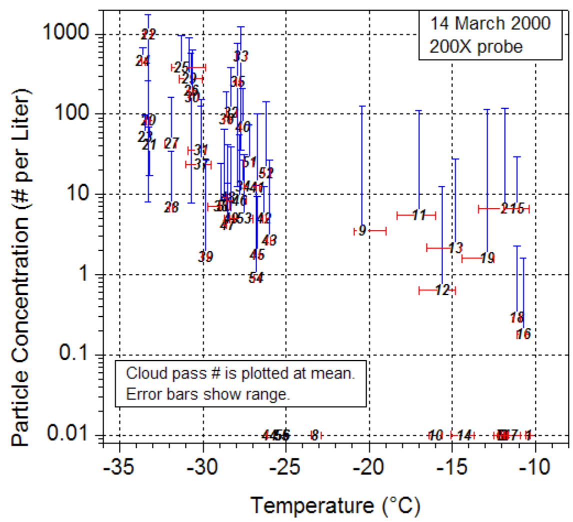

Figure 3. Summary crystal concentrations from 200X probe for 56 cloud penetrations. Concentrations of zero are plotted at 0.01/L.

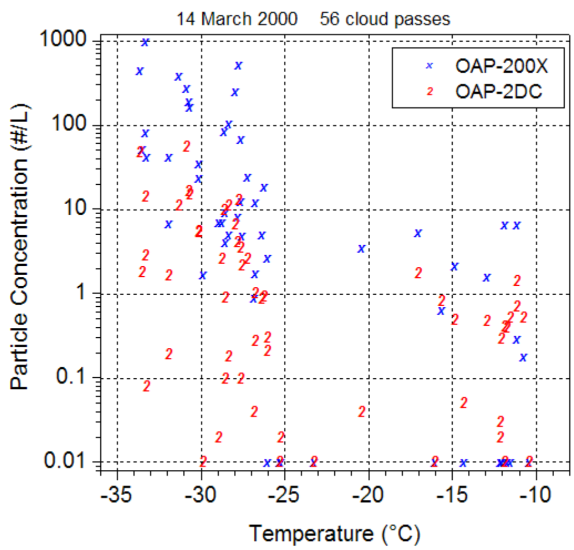

Figure 4. Same data as Figure 3, but showing ice particle concentrations from both the OAP-200X and 2DC probes during the same cloud passes.

From this view of OAP-200X and 2DC data, we conclude that it is preferable to use the same type instruments when comparing data from successive cloud passes or from different projects. Both Wave-Ice and ICE-L had 2DC probes, and so in subsequent sections of this paper, we use data from the 2DC, although it may underestimate the actual ice concentration because its detection threshold size is larger.

5.2 ICE-L case December 13

The C-130 made 92 passes through wave clouds on December 13, 2007. Figure 1 was one of the study clouds and was penetrated 28 times in 90 minutes. Ice concentrations from the fast 2DC probe for the 92 cloud passes are shown in Figure 5, plotted versus cloud temperature. These data appear to be consistent with those from Wave-Ice (Figure 4, OAP-2DC). The ICE-L data show the same wide variation, but there is no obvious trend of ice concentration with temperature.

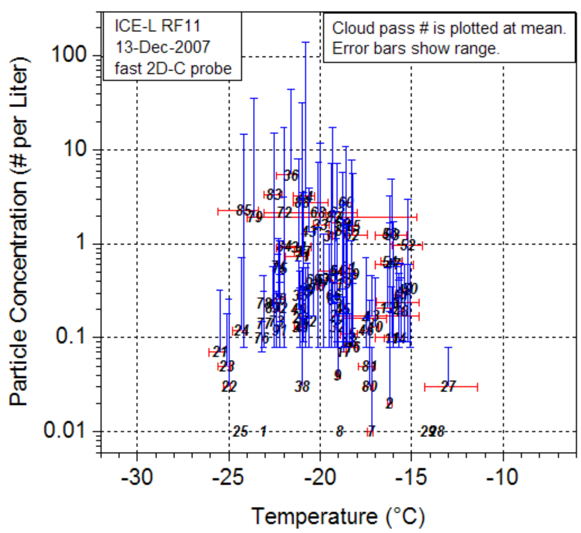

Figure 5. Snow crystal concentrations from OAP-2DC probe on one flight in ICE-L.

6. DISCUSSION

The wave clouds in these two projects covered the temperature range -4 to -40°C. Overall, there were 969 cloud penetrations, and the average cloud pass temperature was between -10 and -35°C for 95% of these. Hence, most of the data are descriptive of heterogeneous freezing mechanisms that produce ice crystals through primary nucleation processes.

Data from both projects were combined by using measurements from 2DC probes. The concentration values are plotted versus average in-cloud temperatures in Figure 6, with concentrations of zero plotted at 0.01 /L. The plot shows considerable overlap of these data sets and reinforces our expectation that the clouds in these two projects were quite similar. Other impressions from this plot include:

- The spread of concentrations is comparable for each project and for the combined set and for individual days (cf., Figures 4 and 5).
- The variability of ice concentrations is ~factor 100X from -10 to -35°C.
- It is difficult to see a clear temperature dependence in this scatter plot, although it is possible that stratifications of the data may reduce the variance.

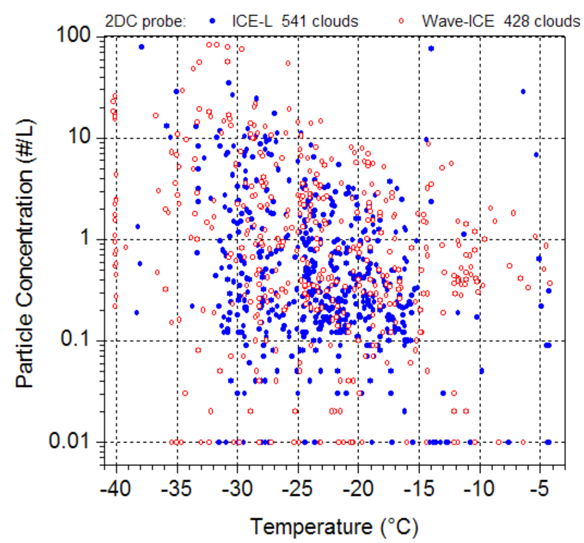

Figure 6. Measurements of temperature and 2DC ice concentrations from both projects. Each point represents cloud-average values

Additional analyses are underway. They focus on attempting to explain the large variance in ice concentrations by examining measurements of ice nucleating aerosols, by stratifying the data according to factors that affect thermodynamic forcing (updraft speed and droplet concentration), and by restricting the identification of cloud passes to more rigorous criteria (for example, to ensure there were no crystals falling in from higher altitude clouds).

Other instruments were used in ICE-L. The analysis of those data is underway, but they did not contribute to this overview paper. They offer great potential for helping to improve our understanding of the initial formation of ice. In particular, the Small Ice Detector (SID2H) covers the size range ~2-60 µm and discriminates ice from water. The SPEC Cloud Particle Imager (CPI) data offer potential similar to SID2H, and some flights had data from a SPEC fast-FSSP and 2D-S. Up/Down viewing cloud radar data and up-looking polarization lidar imagery are also available and will be especially valuable for establishing the vertical structure of clouds. Forward-looking video will help place the meteorological scene.

7. ACKNOWLEDGEMENTS

This research was supported by NSF grants ATM97-14177, ATM06-11936, NASA grant NASA NRA-01-OES-02 and by NCAR. The National Center for Atmospheric Research is operated by the University Corporation for Atmospheric Research under sponsorship of the National Science Foundation. Any opinions, findings, conclusions, or recommendations expressed in this publication are those of the author(s) and do not necessarily reflect the views of the National Science Foundation.

We are grateful for technical support from the Research Aviation Facility at NCAR and the University of Wyoming for helping install the instruments and conducting the flights. John Brown (NOAA Forecast Systems Laboratory) provided outstanding forecasting of wave cloud conditions for flight planning in both projects.

8. REFERENCES

Cooper, W.A., 1991: Research in cloud and precipitation physics: Review of the U.S. theoretical and observational studies, 1987-1990. Rev. Geophys., Suppl., 69-79.

Baker, M.B., 1997: Cloud microphysics and climate. Science, 276, 1072-1078.

Jensen, J.B., and H. Granek, 2002: Optoelectronic simulation of the PMS 260X optical array probe and application to drizzle in a marine stratocumulus. J. Atmos. Oceanic Technol., 19, 568–585.

Korolev, A.V., J.W. Strapp, and G.A. Isaac, 1998: Evaluation of the accuracy of PMS optical array probes. J. Atmos. Oceanic Technol., 15, 708–720.

Rasmussen, R. M., 1995: A review of theoretical and observational studies in cloud and precipitation physics: 1991-1994. Rev. Geophys., Suppl., 795-809.

A REVISED CLOUD MICROPHYSICAL PARAMETERIZATION FOR OPERATIONAL NUMERICAL WEATHER PREDICTION USING THE COSMO MODEL

Axel Seifert[1] and Susanne Crewell[2]

[1] German Weather Service, Offenbach, Germany

[2] University of Cologne, Cologne, Germany

1. INTRODUCTION

Quantitative precipitation forecasting (QPF) is one of the major applications of limited-area numerical weather prediction (NWP) models. With a limited-area NWP model, like the 7-km COSMO-EU at DWD, the detailed orography and the explicit simulation of mesoscale dynamical structures should lead to an increased forecasting skill compared to global models with coarser horizontal resolution.

Unfortunately, the last years have shown some problems with the precipitation forecasts of COSMO-EU. For example, an overestimation of orographic precipitation, a too frequent occurrence of very light precipitation (drizzle) and a general overestimation of the wintertime precipitation amounts.

Together with a model evaluation against cloud radar measurements which revealed that the model often predicted too low values of liquid and ice water content (Illingworth et al. 2007), these deficiencies point towards problems in the microphysical parameterization. Therefore a revised version of the COSMO-EU microphysics scheme has been developed and brought into operations.

2. MICROPHYSICS OF COSMO-EU

The grid-scale microphysics parameterization of COSMO-EU predicts the four hydrometeor species cloud droplets, raindrops, cloud ice and snowflakes using the mixing ratio of each hydrometeor type as prognostic variable and includes horizontal and vertical advection for all species. Rimed particles like graupel are not taken into account, since a convection scheme is used in the COSMO-EU at 7 km grid spacing. For most cloud microphysical processes the scheme follows the work of Rutledge and Hobbs (1983) and a detailed description is given in Doms and Schättler (2004). At DWD this scheme has been operational since 16 September 2003.

To improve the mesoscale precipitation structures predicted by COSMO-EU several modification have been made to the scheme:

Autoconversion/accretion

The Kessler-type autoconversion/accretion scheme has been replaced by the parameterization of Seifert and Beheng (2001) reading

$$\left.\frac{\partial L_r}{\partial t}\right|_{au} = \frac{k_{cc}}{20\,x^*}\frac{(\nu+2)(\nu+4)}{(\nu+1)^2} \times L_c^4\,N_c^{-2}\left[1+\frac{\Phi_{au}(\tau)}{(1-\tau)^2}\right]$$

with $L_{c/r}$ cloud/rain water content, N_c cloud droplet number concentration, ν shape parameter, $k_{cc} = 9.44\times10^9\ \mathrm{s^{-1}\,kg^{-2}\,m^3}$, $x^* = 2.6\times10^{-10}\ \mathrm{kg\,m^{-3}}$. The function $\Phi_{au}(\tau)$ describes the aging (broadening) of the cloud droplet distribution as a function of the dimensionless internal time scale

$$\tau = 1 - \frac{L_c}{L_c+L_r}$$

(for details see Seifert and Beheng 2001). In the one-moment scheme of COSMO-EU we simplify the scheme by assuming a constant cloud droplet number concentration of $N_c = 5\times10^8\ \mathrm{m^{-3}}$ and a constant shape parameter $\nu = 2$.

Corresponding author's address: Dr. Axel Seifert, Deutscher Wetterdienst, GB Forschung und Entwicklung, Kaiserleistr. 42, 63067 Offenbach, Germany. E-mail: axel.seifert@dwd.de

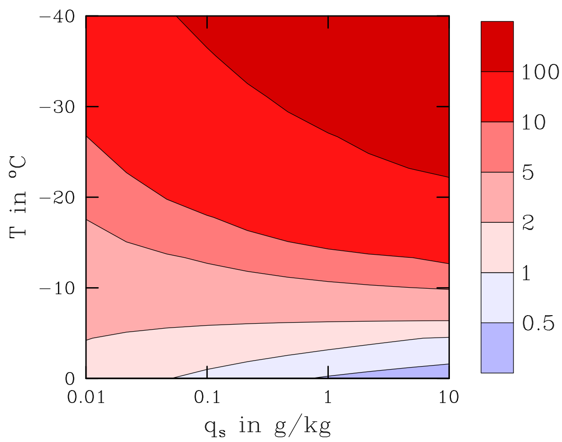

Figure 1: Snow intercept parameter $N_{0,s}$ normalized by $\mathcal{N}_{0,s} = 8\times10^5$ m^{-4} as a function of snow mixing ratio q_s and temperature T in °C.

Size distribution of snow

Based on measurements of Field et al. (2005) a new parameterization of the intercept parameter $N_{0,s}$ of the exponential snow size distribution

$$f(D) = N_{0,s}\exp(-\lambda D),$$

is introduced. In the revised scheme the intercept parameter is parameterized as a function of temperature T and snow mixing ratio q_s by:

$$N_{0,s} = \frac{27}{2}a(3,T)\left(\frac{q_s}{\alpha}\right)^{4-3b(3,T)}$$

with $\alpha = 0.069$. The functions $a(3,T)$ and $b(3,T)$ are given by Table 2 of Field et al. (2005). This parameterization is used instead of the constant $\mathcal{N}_{0,s} = 8\times10^5$ m^{-4} which was used in the old version of the scheme. Especially at cold temperatures this leads to a much higher intercept parameter (see Fig. 1), this corresponds to smaller snowflakes at high levels which fall out much slower.

Sticking efficiency of ice and snow

For the autoconversion of cloud ice and the aggregation of cloud ice by snow a temperature dependent sticking efficiency has been introduced similar to Lin et al. (1983):

$$e_i(T) = \max(0.2, \min(\exp(0.09(T-T_0)), 1.0))$$

with $T_0 = 273.15$ K.

Geometry and fall speeds of snow

The geometry of snow has been changed to more dendrite-like habit with a mass-diameter relation of $m = \alpha\ D^2$ with $\alpha = 0.069$ and a terminal fall velocity of $v = 15\ D^{1/2}$ with D in m, m in kg and v in m/s.

Overall these changes lead to a slower formation of rain and snow as well as a reduced sedimentation velocity of snow. The terminal fall velocity of snow of $v = 15\ D^{1/2}$ is somewhat lower than usually assumed based on observations or laboratory measurements. This 'tuning' can be justified by the fact that a 7-km model cannot yet fully resolve the updraft structures of mesoscale orography, as e.g. shown by Garvert et al. (2005) who compare simulations with 4 km and 1.3 km resolution with observations.

3. RESULTS

Results for surface precipitation

The revised version of the microphysical scheme of COSMO-EU has been tested in an operational setup including full data assimilation over several weeks from 20 Dec 2006 to 8 Feb 2007. Using consistent data assimilation is especially important, since the change of the model physics alters all microphysical variables. Not using separate data assimilation would lead to inconsistent initial conditions and therefore to spurious results by introducing a large model spin-up.
Figure 2 shows two examples of the 24-hour accumulated precipitation for 11 January 2007 and 22 December 2006. For 11 Jan COSMO-EU overestimates the orographic precipitation in the mountainous regions of Germany. This effect is reduced with the new version of the cloud microphysics scheme (LMEp). The COSMO-EU forecast of 22 Dec 06 shows widespread light precipitation in Brandenburg and Sachsen (East Germany) which was not observed. The model using the new microphysics (LMEp) does not show this problem.

1) Accumulated precipitation 06-06 UTC from 00 UTC forecasts of 11 Jan 2007

a) Observations

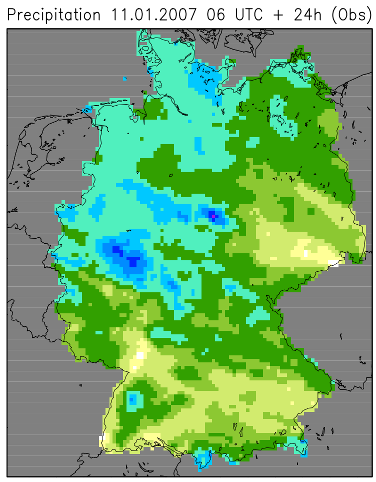

b) Old microphysics

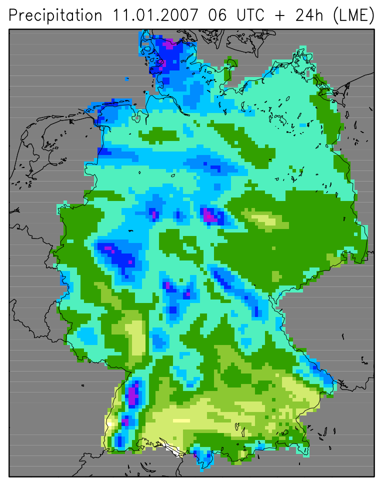

c) Revised microphysics

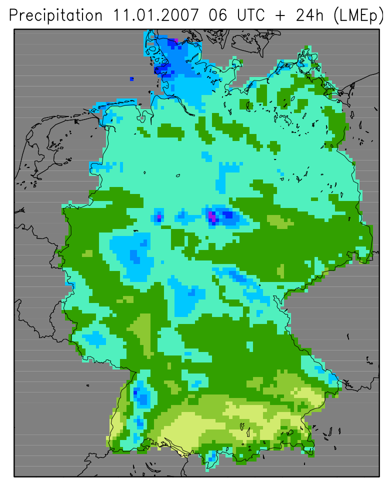

2) Accumulated precipitation 06-06 UTC from 00 UTC forecasts of 22 Dec 2006

d) Observations

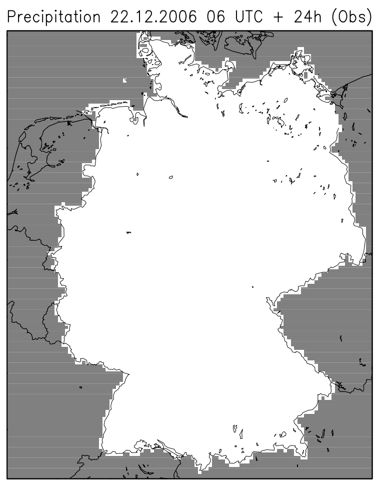

e) Old microphysics

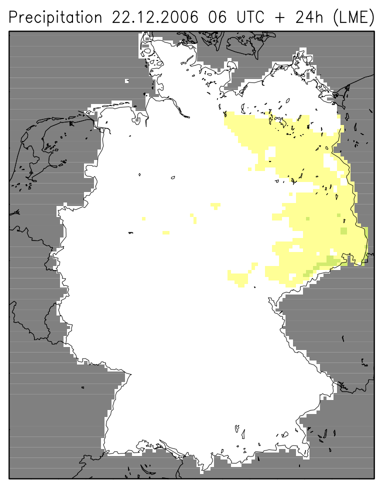

f) Revised microphysics

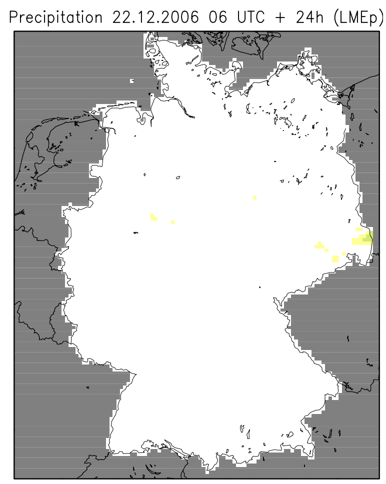

Accumulated precipitation in mm

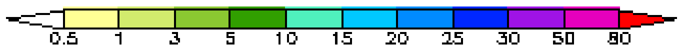

Figure 2: Accumulated precipitation 06-06 UTC from 00 UTC forecasts of 11 Jan 07 and 22 Dec 06 (LME: old microphysics, LMEp: revised microphysics) and surface observations (Obs).

a) Frequency Bias b) Equitable Threat Score

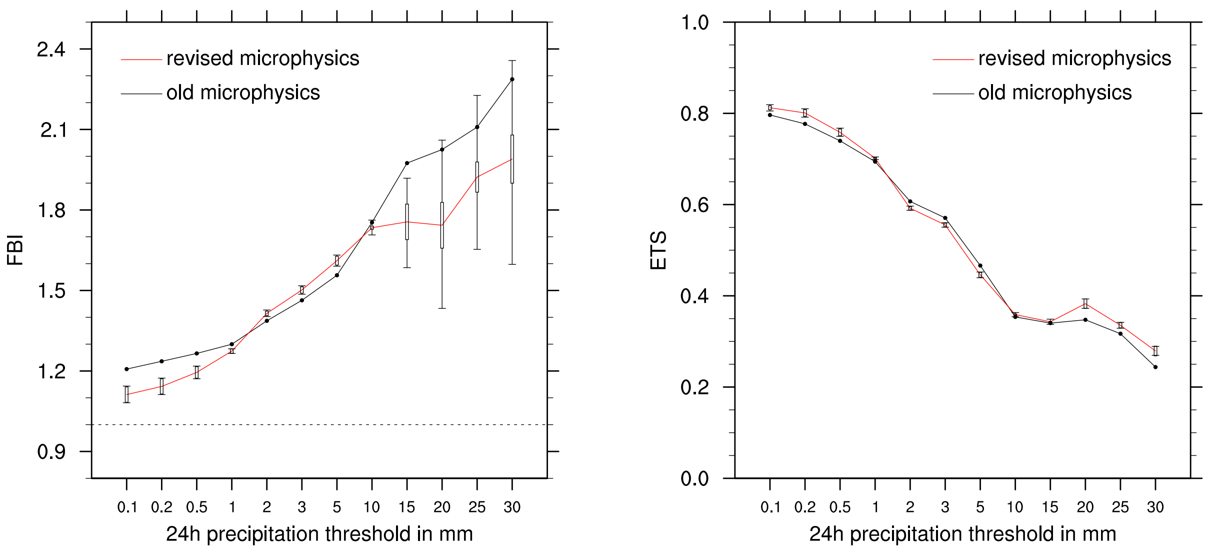

Figure 3: Frequency bias (left) and equitable threat score (right) for 24h precipitation accumulations for various thresholds. Error bars indicate statistical significance at 5 % level of a difference between the two model versions using a bootstrap hypothesis test (outer bars: resampling over model and days, inner bars/boxes: resampling over models only).

Table 1: QPF scores of the 6 week forecasting experiments of COSMO-EU with old vs revised microphysical scheme for 3 different precipitation thresholds (FBI frequency bias, POD probability of detection, FAR false alarm rate, TSS true skill statistics, ETS equitable thread score).

	> 0.5 mm / 24 h		> 2.0 mm / 24 h		> 20 mm / 24 h	
Score	old	revised	old	revised	old	revised
FBI	1.265	1.195	1.387	1.415	2.025	1.743
POD	0.963	0.950	0.907	0.906	0.794	0.771
FAR	0.239	0.204	0.346	0.360	0.608	0.558
TSS	0.597	0.655	0.661	0.645	0.776	0.756
ETS	0.740	0.758	0.607	0.592	0.348	0.384

In the test period of 6 weeks the new version shows an improvement in many QPF scores (see Table 1). Especially the scores for weak precipitation (> 0.5 mm / 24 h) and heavy precipitation (> 20 mm / 24 h) are improved, while the forecasts for intermediate thresholds (e.g. > 2.0 mm / 24 h) are neutral or slightly worse. FBI and ETS are also shown for various thresholds in Figure 3 which supports the data of Table 1. The reduction of the FBI for weak events can be mainly attributed to the new autoconversion scheme as seen in the example of 20 Dec 2006. The improved FBI and ETS for heavy precipitation are due to improved orographic precipitation structures, like in the example of 11 Jan 2007.

In addition, Fig. 3 shows the results of a statistical test with the null hypothesis that differences of the scores of both model versions are zero. Using the resampling (bootstrap) procedure of Hamill (1999) suggests that all scores are significant at a 5% level (indicated by the inner error bars/boxes) when the resampling is performed over models only (as suggested by Hamill (1999)). If the resampled distribution is constructed by randomly choosing models and days (outer error bars), i.e. the finite length of the time series is taken into account, the difference in FBI for large thresholds is no longer statistically significant. This suggests that a longer test period would have been necessary to prove that the results on the better orographic precipitation structures are robust.

The total amount of precipitation, e.g. the accumulated sum over the period from 20 Dec 2006 to 8 Feb 2007, is hardly sensitive to the changes in the microphysical scheme. Compared the the observed precipitation amount of 121 mm averaged over Germany, both model versions show a strong overestimation of 181 mm in case of the old scheme and 177 mm for the revised scheme. The precipitation amounts are obviously more constrained by the synoptic-scale dynamics, e.g. the intensity of low pressures systems and fronts, rather than being sensitive to the details of the microphysical parameterizations.

Validation of IWC using cloud radar

The modification of the cloud microphysical scheme does not only change the surface precipitation, but also the clouds aloft. Due to the slower formation of precipitation sized particles and the reduced fall speeds of snow, an increase of the mixing ratios of cloud water and snow is evident in the new model. Here we compare the ice water content (IWC) predicted by COSMO-EU with an estimation from cloud radar measurements. Figure 4 shows time-height cross sections of the ice water content of 4 May 2007 as measured by the ARM Mobile Facility (AMF) which was, during 2007, located in the Murg Valley in the Black Forest (Southwest Germany). The IWC retrieval used here is based on the radar reflectivity and temperature only (see Illingworth et al. 2007, and the references therein). On this day a weak warm front passed the AMF site. The clouds extend up to 10 km height and were completely glaciated, resulting in weak precipitation during the late evening hours. We have simulated this event with a slightly smaller domain compared to the operational COSMO-EU, but again using full data assimilation which was initialized from the operational global model on 1 May 2007. The model using the old microphysical scheme (Exp6372) shows only thin ice clouds and a frontal structure is hardly visible. Using the revised cloud scheme (Exp6369), the predicted IWC is about an order in magnitude higher and compares well with the observations.

4. Summary and Conclusions

We have presented a revised version of the cloud microphysical scheme of the COSMO model for mesoscale NWP. The new version includes a more sophisticated and physically-based autoconversion scheme, an improved empirical parameterization of the particle size distribution of snow and other modifications of the ice/snow microphysics.
The results show a better representation of orographic precipitation, e.g. reducing the common overestimation over the Black Forest mountains, and a reduction of drizzle events. Both effects lead to an improved QPF skill during wintertime and demonstrates the importance of cloud microphysics for precipitation patterns on the mesoscale. Unfortunately, but not unexpected, the general overestimation of wintertime precipitation cannot be cured by this change of the microphysical parameterization. The revised microphysics scheme is in operation in the 7-km COSMO-EU at DWD since 31 January 2007. A similar microphysics scheme using the same warm rain and snow microphysics, but with an additional graupel category, is operational in the 2.8-km COSMO-DE of DWD.

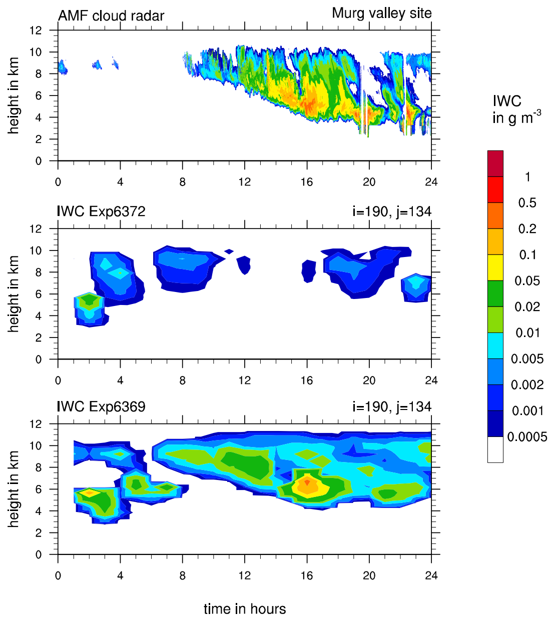

Figure 4: Time-height cross section of ice water content (IWC) measured by cloud radar (top), predicted by the old microphysical scheme (middle) and the revised scheme (bottom).

Acknowledgments: We thank Ewan O'Connor for providing the IWC retrievals of the ARM Mobile Facility as well as the whole AMF team.

References

Doms, G. and U. Schättler, 2004: A description of the nonhydrostatic regional model LM. Part II: Physical parameterization. Technical report, Deutscher Wetterdienst, Offenbach, (available from http://www.cosmo-model.org/public/documentation.htm).

Field, P., R. Hogan, P. Brown, A. Illingworth, T. Choulartona, and R. Cotton, 2005: Parametrization of ice-particle size distributions for mid-latitude stratiform cloud. *Quart. J. Roy. Met. Soc.*, **131**, 1997–2017.

Garvert, M., B. Colle, and C. Mass, 2005: The 13-14 december 2001 IMPROVE-2 event. Part I: Synoptic and mesoscale evolution and comparison with a mesoscale model simulation. *J. Atmos. Sci.*, **62**, 3474–3492.

Hamill, T., 1999: Hypthesis tests for evaluating numerical precipitation forecasts. *Weather and Forecasting*, **14**, 155–167.

Illingworth, A. J., R. J. Hogan, E. J. O. D. Bouniol, M. E. Brooks, J. Delano353, D. P. Donovan, J. D. Eastment, N. Gaussiat, J. W. F. Goddard, M. Haeffelin, H. K. Baltink, O. A. Krasnov, J. Pelon, J.-M. Piriou, A. Protat, H. W. J. Russchenberg, A. Seifert, A. M. Tompkins, G.-J. van Zadelhoff, F. Vinit, U. Will351n, D. R. Wilson, and C. L. Wrench, 2007: Cloudnet. *Bull. Am. Met. Soc.*, **88**, 883–898.

Lin, Y.-L., R. D. Farley, and H. Orville, 1983: Bulk parameterization of the snow field in a cloud model. *J. Clim. Appl. Meteorol.*, **22**, 1065–1092.

Rutledge, S. and P. Hobbs, 1983: The mesoscale and microscale structure and organization of clouds and precipitation in midlatitude cyclones. VIII: A model for the 'seeder-feeder' process in warm-frontal rainbands. *J. Atmos. Sci.*, **40**, 1185–1206.

Seifert, A. and K. D. Beheng, 2001: A double-moment parameterization for simulating autoconversion, accretion and selfcollection. *Atmos. Res.*, **59-60**, 265–281.

10 YEARS OF LIDAR OBSERVATIONS OF MIXED–PHASE CLOUDS WITH FOCUS ON TEMPERATURE AND AEROSOL PROPERTIES

P. Seifert, A. Ansmann, I. Mattis, U. Wandinger, and D. Müller

Leibniz Institute for Tropospheric Research, Permoserstr. 15, 04318 Leipzig, Germany

1. ABSTRACT

Based on more than 10 years of regular observations of aerosols and clouds with a three-wavelength depolarization Raman lidar at the Leibniz Institute for Tropospheric Research (IfT) Leipzig, studies on heterogeneous ice formation in free tropospheric clouds are performed. The focus is set on clouds showing cloud top temperatures between -40 °C and 0 °C. Cloud top height and temperature, respectively, are taken as the primary parameters determining the initiation of cloud glaciation. The cloud phase is determined from the depolarization ratio measured with the lidar. Until the end of 2006, 400 cloud cases were found in the defined range of temperature. The primary goal of the study is to establish a statistic regarding the relationship between cloud top temperature and the percentage of ice–containing clouds with respect to all observed clouds. First results of the data analysis indicate that at temperatures below -15 °C already 50% of the observed clouds contain ice. With decreasing temperature the fraction of ice-containing clouds increases, reaching 80% at -25 °C and almost 100% at -35 °C. Besides temperature, the properties of aerosol particles acting as ice nuclei are an important parameter for heterogeneous freezing processes. Thus a further goal is to extend the study by including information about the presence or absence of aerosol layers and the type of aerosol in the vicinity of the clouds observed with the lidar.

2. INTRODUCTION

The process of heterogeneous ice formation in the free troposphere currently is an important topic of atmospheric science. Heterogeneous ice formation plays a major role for an accurate precipitation forecast in meteorological models and influences optical properties of clouds because ice and water have different radiative properties (*Yoshida and Asano*, 2005).

This proceeding describes the approach to setup a lidar–based study of the temperature– and aerosol–type dependence of heterogeneous ice formation in free–tropospheric clouds. The work is done in the scope of the project DRIFT (Dust related ice formation in the troposphere). The description of the applied instrumentation is given in Section 3. Section 4 presents the methodology. First, preliminary results are Shown in Sec. 5.

3. INSTRUMENTATION

The described study is based on data acquired with the zenith–pointing three–wavelength Raman depolarization lidar of the Leibniz Institute for Tropospheric Research Leipzig, Germany. Aerosol and cloud optical properties can be retrieved at 355, 532 and 1064 nm. The depolarization ratio, indicating cloud phase, is measured at 532 nm.

Since 1997 regular lidar measurements have been performed in the scope of GERLIN (German Lidar Network; 1997–2000) and EARLINET (European Aerosol Research Lidar Network, since 2000). In addition to the regular measurements observations have been performed during Saharan dust outbreaks and episodes with long–range transport of forest fire smoke, Arctic haze, and urban pollution from North America to Central Europe. Since the beginning of 2006 additional measurements have been performed with special emphasis on thin mid–tropospheric clouds (mostly altocumulus clouds). Currently, the database contains more than 1000 measurements.

4. METHODOLOGY

In the first step of the statistical analysis, all available lidar measurements performed since 1997 were examined for the occurrence of suitable cloud cases. For each cloud case the following information was compiled:

(a) Geometrical cloud properties (Cloud top and base height and time of occurrence)
(b) Cloud phase
(c) Meteorological cloud properties (Temperature, humidity, and wind at the cloud boundaries)
(d) Aerosol properties (10 day backward trajectories, backscatter coefficient at 532 nm)

A. Geometrical Cloud Properties

Heterogeneous ice formation is known to occur at temperatures between approximately -40 °C and -10 °C. Therefore, as a first step in the data analysis process a database was created containing the geometrical properties, i.e. cloud top height and cloud base height, and the time of occurrence of all clouds observed during the measurements performed since 1997 that had top heights of below 10 km height ($>$-40 °C).

In the case of opaque clouds with optical depths larger than approx. 3 the cloud top can not be determined directly from the averaged signal because no information is returned from altitudes above the cloud. Instead, the cloud top is retrieved from measurements in cloud holes or from the cloud and aerosol structures after the passage of the cloud field. If also this approach gives no information about the cloud top, the cloud is removed from the database. For less than 3% of all clouds no cloud top could be determined.

B. Cloud Phase

The determination of the phase of the observed clouds is based on the depolarization ratio at 532 nm wavelength. The laser emits parallel polarized light. The receiver detects the parallel and cross–polarized components of the backscattered light separately. The volume depolarization ratio is now defined as the ratio of the volume backscatter coefficient measured with the cross–polarized channel to the respective backscatter coefficient measured with the parallel polarized channel.

During scattering events at aerosol and cloud particles the polarization of a fraction of the scattered light is modified. The strength of this depolarization primarily depends on the deviation of the shape of the scattering particle from a sphere. Thus, liquid water droplets cause no depolarization whereas ice crystals cause significant depolarization to the returned laser light.

Besides particle shape two masking effects alter the depolarization of the detected signal. Multiple scattering of light in optically thick water clouds causes additional depolarization that increases linearly with cloud penetration depth of the laser beam. Many clouds show depolarization ratios of up to 10% at cloud top. This behavior is in agreement with modelling results. The second effect is caused when measurements are performed with a zenith–pointing lidar and horizontally oriented ice crystals are present and produce specular reflections which result in the detection of strong lidar signals and low depolarization ratios close to those of water clouds.

Extensive lidar observations with Doppler, Raman, and depolarization lidar have been done to study the relationship between the depolarization ratio and the dynamical behavior of ice crystals (*Seifert et al.*, 2008). In conclusion, we found clear signatures of water, mixed-phase and ice cloud layers in terms of depolarization ratio, so that an unambiguous separation of cloud layers containing liquid drops

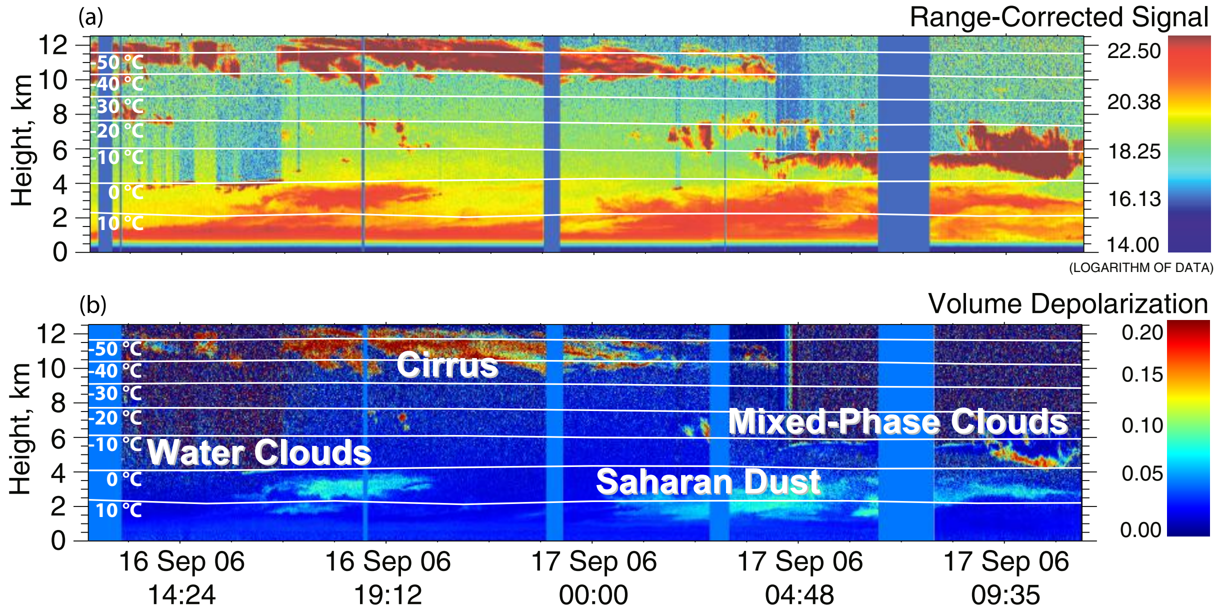

1: Observation of Saharan dust, mixed–phase and water clouds, and cirrus over Leipzig on 16 Sep and 17 Sep 2006. Shown are the range–corrected signal (a), volume depolarization ratio (b) and isothermes (white horizontal lines in both figures) based on model reanalyses.

only or a mixture of drops and ice crystals or ice crystals only became possible.

A water cloud always shows no depolarization at cloud base and a weak to considerable multiple scattering effect in the depolarization ratio at cloud top. Layers containing ice crystals always cause a non–monotonic, inhomogeneous vertical profile of the depolarization ratio. By applying these features, we were able to group the cloud cases found during the last 10 years into two different cloud classes (liquid, ice, mixed–phase).

C. Meteorological Cloud Properties

Between September of 2000 and September 2006 two radiosondes were launched per day (00 UTC, 12 UTC) at Oppin, 40 km west of Leipzig, by the German Meteorological Service. The sondes measured temperature, humidity, and wind speed and direction. During special events additional radiosondes were launched at the lidar station. For times not covered by the radiosonde data the meteorological properties are obtained from model reanalyses based on the Global Data Assimilation System (GDAS) of the U.S. National Weather Service's National Center for Environmental Prediction (NCEP) that can be accessed via http://www.arl.noaa.gov/NOAAServer/.

D. Aerosol Properties

Laboratory and modeling studies show that besides temperature the efficiency of heterogeneous freezing strongly depends on the type of aerosol that acts as an ice nuclei (*Diehl et al.*, 2006). Thus as a final step of the presented study it is planned to investigate the impact of the aerosol type on cloud glaciation. We use the backscatter coefficient calculated at 532 nm wavelength to determine if there was aerosol observed at cloud level. To obtain the type of aerosol that was present during the observation of a cloud we use, if available, the analyzed aerosol optical data of the multiwavelength Raman lidar (*Müller et al.*, 2007) and 10 day backward trajectory calculations. The focus is basically set on the discrimination between scenarios with and without Saharan dust. However, it is also possible to identify anthropogenic haze and forest fire smoke but cases with mid–tropospheric clouds in such aerosol layers are rare.

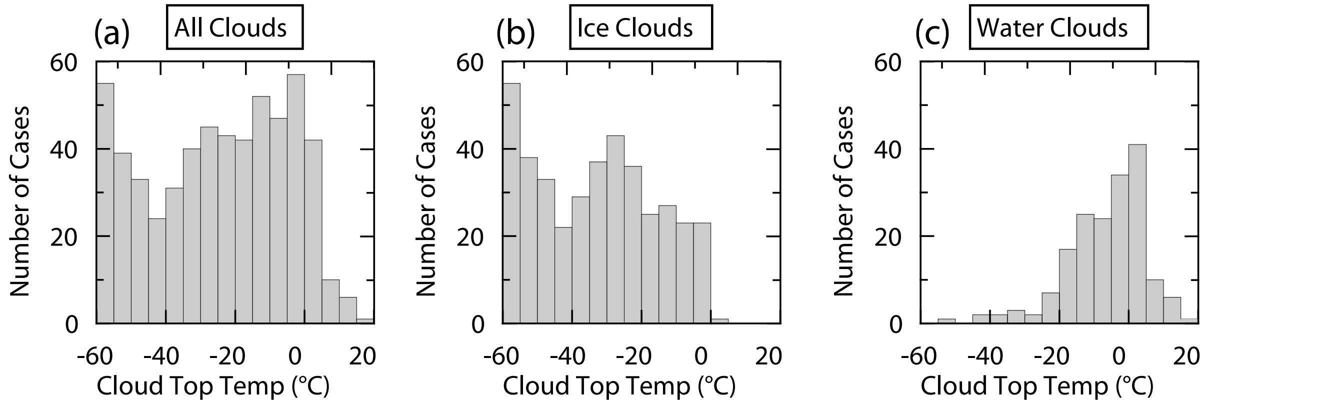

3: Number of all observed clouds (a), ice–containing clouds (b) and water cloud layers (c) versus cloud top height. GERLIN, EARLINET and DRIFT observations (1997–2006) are analyzed.

5. RESULTS

A. Case Study

Figure 1 presents height–time plots of range–corrected lidar signal and depolarization ratio measured on 16 September and 17 September 2006. The 120–hour backward trajectories shown in Fig. 2 all passed the Sahara before they arrived at Leipzig at altitudes of 3000, 5000, and 7000 m. Thus the aerosol type that was present during the time of the measurement is classified as Saharan dust.

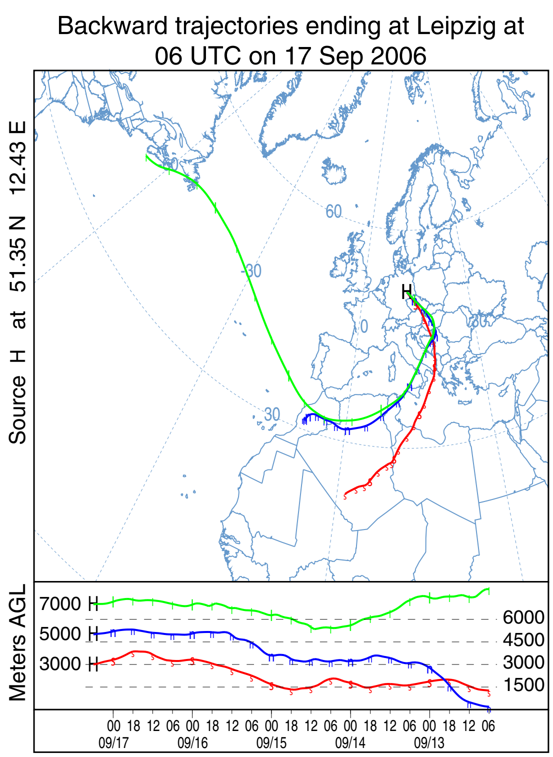

2: 5–day backward trajectories computed with HYSPLIT (*Draxler and Rolph*, 2003) ending at heights of 3000, 5000, and 7000 m at Leipzig at 06 UTC on 17 Sep 2006.

The dust plume is clearly visible up to heights of 4 km in the range corrected signal in Fig. 1. Traces of dust are found up to 8 km height. The volume depolarization ratio also identifies the dust at lower heights. However, the volume depolarization ratio depends on Rayleigh and particle depolarization. Rayleigh scattering at air molecules produces very low depolarization ratios so that the volume depolarization ratio is low if the particle signal is low and Rayleigh scattering dominates.

Above heights of about 4 km several cloud layers are visible extending up to heights of 12 km. They were separated into different cloud cases according to Sec. 4-A and Sec. 4-B.

B. Statistics

In the scope of the presented study more than 600 cloud cases were found in the height range between the ground and 10 km. 400 cloud cases could be classified in the temperature range between -40 °C and 0 °C.

Figure 3 shows the number of analyzed cloud cases as a function of cloud top temperature binned into intervals of 5 K. The three histograms show the data separately for all clouds(a), ice–containing clouds(b) and water clouds(c).

The dataset is well distributed over the temperature range with approximately 40 cases per 5 K temperature interval. Only around -40 °C less cloud cases were found, suggesting that the region of around -40 °C separates the temperature range dominated by homogeneous freezing (Cirrus; T<-40 °C) from the temperature range dominated by heterogeneous freezing (Altocumulus; T>-40 °C).

Figure 3(b) shows that ice–containing clouds spread homogeneously over a wide vertical range, probably caused by the concurrence of homogeneous and heterogeneous freezing, falling ice crystals and cloud seeding effects.

An interesting feature of Fig. 3(c) is that pure water clouds with cloud top temperatures ≤-25 °C are rare. This is further illustrated in Fig. 4 that shows the fraction of ice–containing clouds with respect to all observed clouds as a function of cloud top temperature. The relative amount of ice-containing clouds is a strong function of temperature in the range from about -12 °C to about -27 °C. This is the range of temperatures where the efficiencies of the different heterogeneous ice formation mechanisms rapidly increase with decreasing temperature. Whereas heterogeneous ice formation is comparably inefficient at temperatures above -15 °C, heterogeneous ice formation has almost a 100% probability at temperatures lower than -30 °C. This finding was recently confirmed by lidar measurements in southern Morocco during the SAMUM (Saharan Mineral Dust Experiment) campaign (*Ansmann et al.*, 2008). At temperatures <-35 °C homogeneous ice formation is initiated and dominates ice production. At temperatures below -40 °C cirrus is the only remaining cloud type.

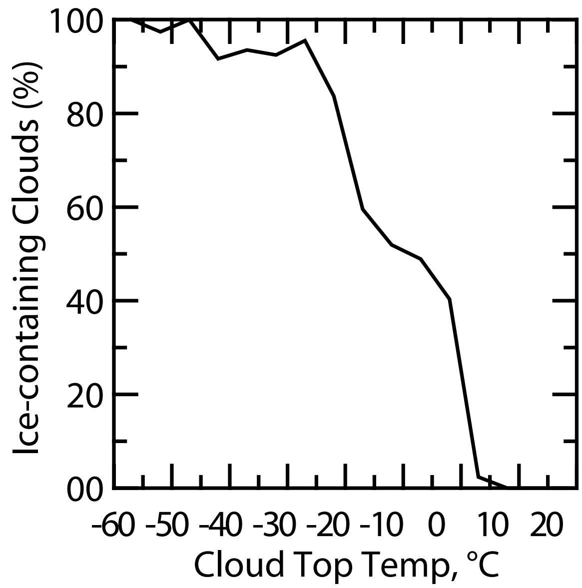

4: Fraction of observed ice–containing clouds (related to the totally observed number of clouds) as a function of cloud top temperature.

6. BIBLIOGRAPHY

Ansmann, A., M. Tesche, D. Althausen, D. Müller, P. Seifert, V. Freudenthaler, B. Heese, M. Wiegner, G. Pisani, P. Knippertz, and O. Dubovik, Influence of Saharan dust on cloud glaciation in southern Morocco during the Saharan Mineral Dust Experiment, *Journal of Geophysical Research (Atmospheres)*, *113*, 4210, doi:10.1029/2007JD008785, 2008.

Diehl, K., M. Simmel, and S. Wurzler, Numerical sensitivity studies on the impact of aerosol properties and drop freezing modes on the glaciation, microphysics, and dynamics of clouds, *Journal of Geophysical Research (Atmospheres)*, *111*, 7202, doi: 10.1029/2005JD005884, 2006.

Draxler, R., and G. Rolph, HYSPLIT (HYbrid Single-Particle Lagrangian Integrated Trajectory). Model access via NOAA ARL READY Website (http://www.arl.noaa.gov/ready/hysplit4.html), *NOAA Air Resources Laboratory, Silver Spring, MD*, 2003.

Müller, D., A. Ansmann, I. Mattis, M. Tesche, U. Wandinger, D. Althausen, and G. Pisani, Aerosol-type-dependent lidar ratios observed with Raman lidar, *Journal of Geophysical Research (Atmospheres)*, *112*, 16,202, doi:10.1029/2006JD008292, 2007.

Seifert, P., R. Engelmann, A. Ansmann, U. Wandinger, I. Mattis, D. Althausen, and J. Fruntke, Characterization of specular reflections in mixed–phase and ice clouds based on scanning, polarization, and Raman lidar, in *Proceedings of the 24th ILRC, Boulder, CO*, 2008.

Yoshida, J., and S. Asano, Effects of the vertical profiles of cloud droplets and ice particles on the visible and near-infrared radiative properties of mixed-phase stratocumulus clouds, *Journal of the Meteorological Society of Japan*, *83*, 471–480, 2005.

MESOSCALE AND MICROSCALE SIMULATIONS OF COLD FRONT CLOUDS IN CHINA

Yue Qin SHI[1,2], Xiao Feng LOU[2], Xue Jiao DENG[3]
[1]Department of Atmospheric Sciences, School of Physics, Peking University, Beijing 100871, China
[2]Chinese Academy of Meteorological Sciences, Beijing 100081, China
[3]Guangzhou Institute of Tropical and Marine Meteorology of Chinese Meteorological Administration, Guangzhou 510080, China
Corresponding author:Yue Q. SHI , Tel.: 0086-10-68409042
Email: shiyq@cams.cma.gov.cn

1. INTRODUCTION

Effected by high trough and surface weaker cold air, storm rainfall occurred during 31st Mar. ~1st Apr., 2004 in South China. The rainfall case was studied with a meso-scale dual-moment cloud resolving model, which was revised in Chinese Academy of Meteorological Sciences based on MM5v3. The cloud resolving model uses quasi-implicit calculating scheme, includes 11 prognostic microphysical variables, which are the mass content of water vapor, cloud droplets, raindrops, ice crystals, snow and graupels, the number concentration of raindrops, ice crystals, snow and graupels and the broadness of cloud droplets size distribution and 31 microphysical processes.

The central point was at (23°N, 113°E), two-way nested, horizontal resolution was 30 km and 10 km, respectively, the nest domain basically covered south China. 23 layers in vertical, the top pressure was 100 hPa. Grell convective scheme, Blackadar high boundary layer scheme, cloud-radiation scheme and the coupled cloud scheme were chosen. The model was initialed with NCEP re-analysis data at 00:00 UTC March 31, 2004, and run 36-h.

2. ANALYSIS OF CLOUDS AND RAINFALL

At 2100 UTC 31 March, 2004 there was southwest-northeast cloud band over north of Guangdong Province in GOES-9 infrared imagine. Cloud band gradually intensified during moving southward, at 0000 UTC 1 April, cloud developed to mature stage, which were about 200 km in width. Then, cloud continued to move southward, about 0300 UTC the front of cloud band was over South Sea, decayed away. The occurring time, location, shape and orientation of simulated cloud bands and their evolution were consistent with GOES-9 infrared imagine.

The distribution and amount of simulated surface rainfall during the main precipitating period were coincided with the observation. The mesoscale southwest-northeast rain band moved southeasterly with cold front moving. There were 4 strong precipitating centers in the rain band, whose lifetimes were beyond 3 hours, and moved mostly eastward, which agreed with the moving of radar echoes.

3. ANALYSIS OF SIMULATED AND OBSERVED RADAR ECHOES

Known from CAPPI Radar echo of 3 km height in HongKong, stronger radar echoes mainly moved eastward with time, however the main cloud bands moved gradually southeastward. Fig. 1a was CAPPI of 3 km height at 0100 UTC 1 April in Hongkong. In the cloud bands there were some stronger radar echoes, which was about 50 km in horizontal scale and whose rainfall rate was about 20 mm/h.

Known from fig. 1b, the southwest-northeast band echoes mainly occurred at surface frontal line and post-frontal part. The maximum radar echoes reached 45 dBZ.

Seen from fig. 1c, the cold front clouds were not homogeneous, where lain convective cells. In the AA segment, the stronger echoes in lower layer linked up each other, which reached 200 km in horizontal scale, but in the upper layer could been resolved into 3 cells.

Seen from fig. 1d, the horizontal width of radar echoes is about 90 km. Near to the surface cold frontal line, the horizontal gradient of echoes is great, and the intensity changed sharply, which was characteristic of narrow cold front rainbands[1-3].

Seen from fig. 1e, there was another weak echo band in post-frontal cold air area, whose top was about 9 km high, horizontal width was about 40 km. There were 2 strong centre in the upper range and lower range of the cell. This belonged to wide cold front rainbands.

Seen from fig. 1f, the echoes in the warm areas was weaker, whose top was about 5 km. The distribution of these echoes was separated, which was different from those in fig. 1d.

In brief, the distribution of simulated radar echoes was agreement with radar observation. The southwest-northeast band echoes mainly occurred at surface frontal line and post-frontal part. The difference of individual echo in the different part of cold front was great.

4. ANALYSIS OF MICROPHYSICAL CONVERSION RATE

Conversion of hydrometers was the important microphysical process. So we should analyze the main precipitating process of cold front. We chose two points B1(24.33 ºN,113.83 ºE) and B2(24.85ºN, 113.465ºE) , which was located in different part of cold front (specified sites seen in fig.1b).

The maximum updraft of B1 reached 0.9 m/s, located during k=7~13. However, below k=12, there were downdrafts for B2, its maximum updraft was only 0.3 m/s, located in upper layer. Temperature profile of the two points was almost the same.

Seen from fig. 2a, for B1 the main growth process of raindrops was the collection of cloud droplets by raindrops in warm layer (Ccr). Warm rain process was clear. The melting of graupels (Mgr) was another main process for the growth of raindrops. But for B2, seen from fig.2b, the main process for the growth of raindrops was the melting of graupels (Mgr). And evaporation of raindrops (Svr) was a little big for there was no cloud water in lower layer. The main growth process of raindrops of the two points is different.

For B1 (fig. 2c), the main newborn processes of graupel are the collection of raindrops by ice (Ncri) and by snow (Ncrs). For there was little snow, the process of autoconversion of snow to graupel (Nasg) wasn't the main process for B1. The mechanism is different from that of narrow cold front rainband[4]. But for B2 (fig.2d), during k=12~16, Ncrs was the main process of newborn graupel, next was Nasg and Ncri. During k=17~20, only Nasg could produce newborn graupel.

Seen from fig.2e, the collection of cloud by graupel (Ccg) was the main process of graupel for B1, for there were full of supercooled cloud water. The mechanism is the same as the study of Rutledge and

Hobbs [4]. Snow was another source term for the growth of graupel. But for B2 (fig.2f), the collection of snow by graupel (Csg) was the main growth process of graupel.

In all, near the surface line, the updrafts was a little great, and the mass content of cloud water was great, then the processes of ice particles riming and collection of cloud droplets by raindrops were the main microphysical processes. However, in the wide rain band areas, updrafts only lay in upper layers, downdrafts were in lower layers, and there were mainly supercooled cloud water, graupels and snow crystals. Snow crystals was the main source term for graupel growing, precipitation was mainly formed by graupels melting, cold rain process was more important.

Acknowledgements

This work was sponsored jointly by National Natural Science Foundation of China (40705002, 40305001) and National Key Technology R&D Program in China (2006BAC12B01).

REFERENCE

[1] Hobbs P V, Locatelli J D. Rainbands, precipitation cores, and generating cells in a cyclonic storm. *J. Atmos. Sci.*, 1978, **35:** 230~241

[2] Huang Meiyuan, Xu Huaying. *Cloud and Precipitation Physics* (in Chinese). Beijing: Science Press, 1999. 251~268

[3] Evans A G., Locatelli J D, Stoelinga M T, et al. The IMPROVE-1 Storm of 1-2 February 2001. Part II: Cloud Structures and the Growth of Precipitation. *J. Atmos. Sci.*, 2005, **62:** 3456~3473

[4] Rutledge S A, Hobbs P V. The mesoscale and microscale structure and organization of clouds and precipitation in midlatitute cyclones. XII: a diagnostic modeling study of precipitation development. *J. Atmos. Sci.*, 1984, **41:** 2949~2972

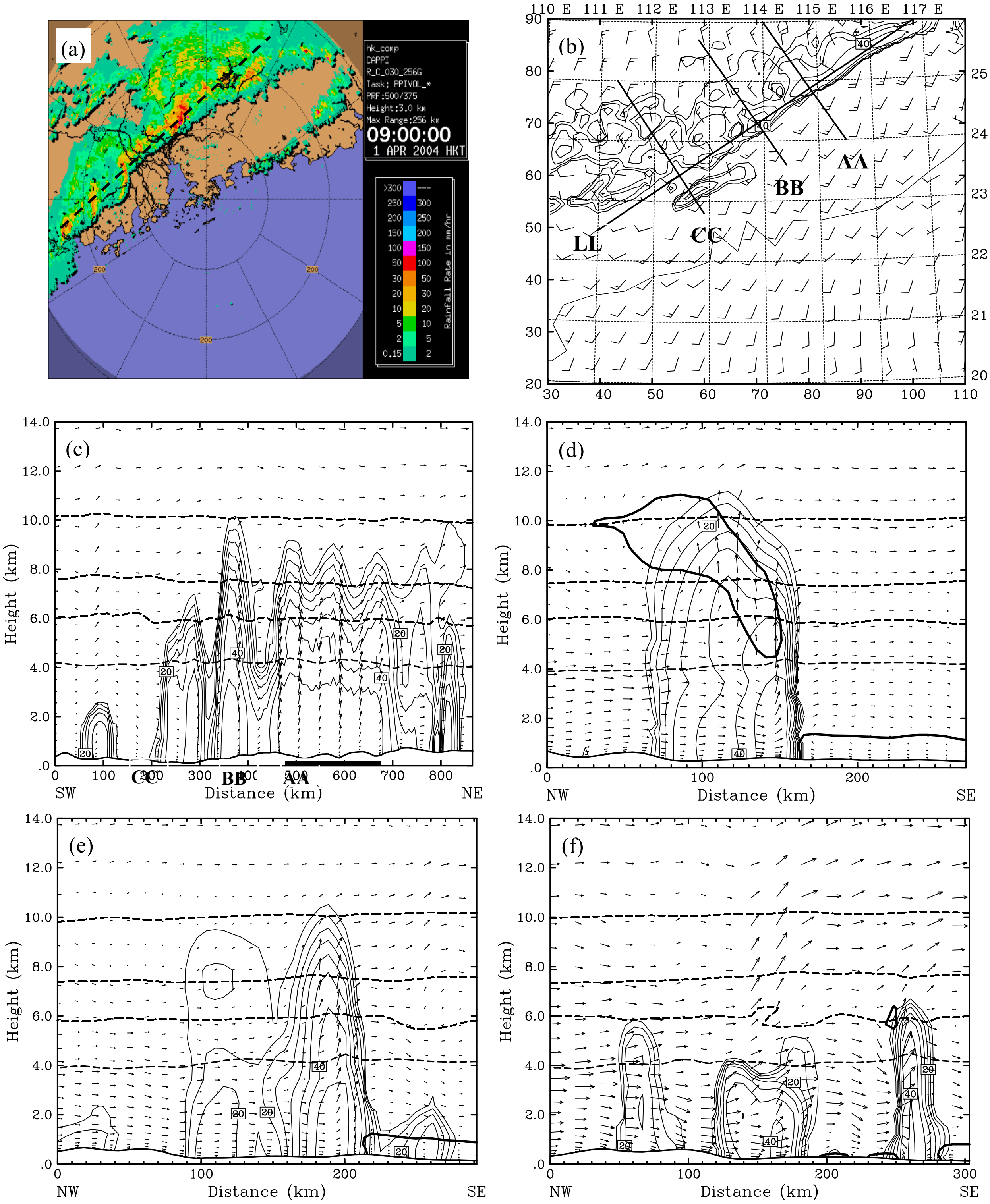

Fig. 1 Radar reflectivity of simulation and observation at 0100 UTC 1 April, (a) CAPPI of 3 km height at Hongkong (rainfall rate，mm/h, scan radius is 300 km); (b) simulated CAPPI of 3 km height (contour interval is 10 dBZ) and surface wind fields; simulated vertical cross section of radar reflectivity and wind fields along line LL(c), AA(d), BB(e), CC(f) in fig. 4b (contour interval is 5 dBZ), short dash line is 0℃，-10℃，-20℃ and -40℃ from bottom to up, respectively, thicker solid line is zero horizontal wind component parallel to the cross section

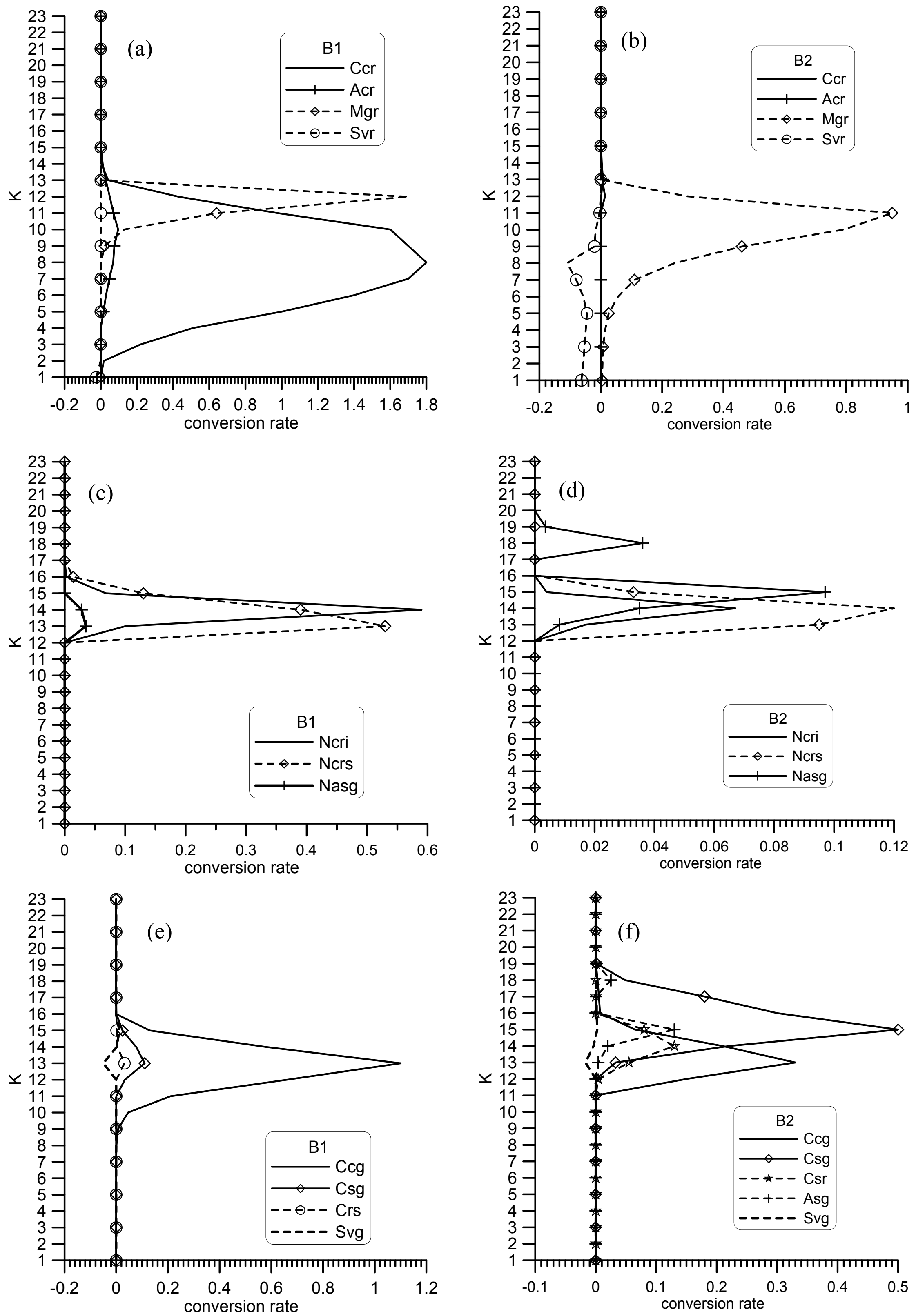

Fig. 2 Instantaneous microphysical conversion rate of rain drops (a, b), graupel (e, f) mixing ratio(10^{-3} $g \cdot kg^{-1} \cdot s^{-1}$) and number concentration of graupel (c, d, $kg^{-1} \cdot s^{-1}$) at 0100 UTC 1 April, (a, c, e) B1, (b, d, f) B2, vertical coordinate is grid

MODELLING OF THE WEGENER-BERGERON-FINDEISEN PROCESS - IMPLICATIONS FOR AEROSOL INDIRECT EFFECTS

T Storelvmo[1] J E Kristjansson[2], U Lohmann[1], T Iversen[23], A Kirkevag[3] and O Seland[3]

[1]Institute for Atmospheric and Climate Science, ETH Zurich, 8092 Zurich, Switzerland

[2]Department of Geosciences, University of Oslo, Oslo, Norway

[3]Norwegian Meteorological Office, Oslo, Norway

1 INTRODUCTION

Anthropogenic aerosols influence clouds differently depending on the thermodynamic state of the cloud, i.e. whether it consists of liquid only (warm clouds), both ice crystals and cloud droplets (mixed-phase clouds) or ice only (cirrus clouds). For warm clouds, anthropogenic aerosols increase the cloud albedo by acting as cloud condensation nuclei (CCN), thereby decreasing cloud droplet sizes (Twomey, 1977) and/or increasing cloud lifetime (Albrecht, 1989). Aerosol effects on mixed-phase clouds are less well understood, and it is still not clear if anthropogenic aerosols affect them. Ice formation in these clouds always occurs by the aid of so called ice nuclei (IN). Such IN are typically insoluble particles, often with crystalline structure, candidates being mineral dust, biological particles and soot (Pruppacher and Klett, 1997). Soot particles are largely of anthropogenic origin, so if they are in fact efficient IN, anthropogenic activity has introduced additional IN into the atmosphere. Such an increase in IN would lead to an anthropogenic increase in freezing and cloud glaciation. This effect has been referred to as the *cloud glaciation effect* (Lohmann, 2002). Conversely, anthropogenic sulfur coatings can potentially deactivate the IN (Girard et al., 2004), or alternatively make them less efficient in relatively warm mixed-phase clouds (Storelvmo et al. (2008); Hoose et al. (2008)). This complete or partial de-activation will hereafter be referred to as the *deactivation effect*. Additionally, as large droplets freeze more readily than small droplets (Pruppacher and Klett, 1997), the anthropogenic decrease in cloud droplet radius would be expected to counteract freezing. This effect has been termed the *thermodynamic effect*, and has been discussed by e.g. Rosenfeld and Woodley (2000). All in all, it is far from obvious what the net anthropogenic aerosol effect on mixed-phase clouds is.

In this paper we focus on the Wegener-Bergeron-Findeisen process and its importance for aerosol indirect effects associated with stratiform mixed-phase clouds. We study these effects in the CAM-Oslo general circulation model (GCM) with an extended mixed-phase cloud microphysics scheme taking the three mechanisms mentioned above (the *glaciation, deactivation* and *thermodynamic* effects) into account. In this microphysics scheme, we recently implemented a new parameterization of the Wegener-Bergeron-Findeisen (WBF) process, based on a derivation presented in Korolev (2007). The WBF process refers to the rapid growth of ice crystals at the expense of cloud droplets (at temperatures below 0°C and above approximately -35 °C) due to the difference in saturation vapor pressure over water compared to that over ice. So far, this process has typically not been accounted for in general circulation models (GCMs), as various forms of interpolation have been used to specify the liquid fraction of a cloud at temperatures below freezing (Rasch and Kristjánsson (1998);Lohmann and Roeckner (1996)). In recent years, some GCM studies have accounted for the WBF process in a simplistic manner, by assuming that when a critical cloud ice mixing ratio is reached the entire cloud glaciates (Lohmann and Diehl (2006);

2 DESCRIPTION OF CAM-OSLO AND THE NEW WBF PARAMETERIZATION

2.1 CAM-Oslo

The CAM-Oslo GCM is an extended version of the National Center for Atmospheric Research (NCAR) Community Atmosphere Model Version 3 (CAM3) (Collins et al., 2006). For this study the simulations were carried out with an Eulerian dynamical core at T42 spectral truncation, which corresponds to a horizontal gridspacing of 2.8° x 2.8° on a Gaussian grid. There are 26 levels in the vertical. The stratiform cloud microphysics scheme used in CAM3 was developed by Rasch and Kristjánsson (1998). To form CAM-Oslo, CAM3 has been extended with a framework for calculations of aerosol direct and indirect effects on climate. The framework is developed by the aerosol and cloud researchers at the University of Oslo and the Norwegian Meteorological Institute, and consists of the following components:

- **An aerosol life cycle scheme** treating the life cycle of 5 aerosol components and 2 aerosol precursor gases in the atmosphere. The components treated are: i) Sea-salt, ii) Mineral soil dust iii) Black Carbon (BC), iv) Particulate Organic Matter, v) Particulate sulphate, vi) Di-methylsuphide (DMS) and vii) Sulphur dioxide (Seland et al., 2008).

- **A scheme calculating aerosol size distribution and optical properties** treating internal and external aerosol mixing.

- **A scheme calculating aerosol effects on warm clouds** based on a double moment liquid cloud microphysics scheme (Storelvmo et al., 2000). Cloud droplet activation is calculated based on a subgrid distribution of vertical velocity and hence supersaturation, employing the scheme of Abdul-Razzak and Ghan (2000).

- **A scheme calculating aerosol effects on mixed-phase clouds** based on a double moment ice microphysics scheme. The scheme accounts for heterogeneous freezing via the contact and immersion/condensation freezing modes, precipitation release through the ice phase, ice multiplication processes, melting and sublimation. Mineral dust and BC are the two ice nucleating aerosol species in the model. The BC number concentrations are significantly higher than the mineral dust number concentrations, but initiate freezing at substantially lower temperatures. Heterogeneous freezing processes are calculated based on the parameterization presented in Lohmann and Diehl (2006) and described in detail in Storelvmo et al. (2008).

2.2 The mixed-phase cloud microphysics scheme with the new treatment of the WBF process

In this section we present the novel treatment of the WBF process in the model, which employs the equations presented by Korolev and Mazin (2003). In Korolev (2007) it is pointed out that the WBF process can only occur in a limited range of conditions, and that one can not automatically apply it to all mixed-phase clouds, which is currently a common modeling approach. The relationship between i) the in-cloud vapor pressure (e), ii) the saturation vapor pressure over liquid water (e_s) and iii) the saturation vapor pressure over ice (e_i) determines the growth/evaporation of cloud droplets and ice crystals. For mixed-phase clouds, there are three possible regimes:

- **Regime 1** – Both droplets and ice crystals grow simultaneously:
  For a given cloud or cloud fraction, this occurs when the following is true:

  $$e > e_s > e_i \tag{1}$$

  It was shown by Korolev and Mazin (2003) that this may occur if the updraft velocity u_z is higher than a critical updraft velocity, u_z^* given by

  $$u_z^* = \frac{e_s - e_i}{e_i} N_i \overline{r_i} \eta \tag{2}$$

  where η is a coefficient dependent on temperature (T) and pressure (p), N_i is the ice crystal number concentration and $\overline{r_i}$ is the mean volume radius of the ice particles ($\overline{r_i} = (\frac{3IWC}{4\pi N_i \rho_i})^{\frac{1}{3}}$, where IWC is the cloud ice water content and ρ_i is the density of ice.). For Regime 1 conditions, the mixed phase is maintained for an indefinite period, as long as (1) holds.

- **Regime 2** – Ice crystals grow at the expense of cloud droplets (WBF process):
  The WBF process takes place if the following requirement is fulfilled:

  $$e_s > e > e_i \tag{3}$$

  If (3) is true, cloud droplets will inevitably evaporate, providing a source of water vapor for depositional growth of ice crystals. A cloud or cloud fraction in Regime 2 will eventually glaciate, the glaciation time scale being dependent on ice crystal number, ice water content (IWC) and liquid water content (LWC), among others. From Korolev and Mazin (2003), (3) is fulfilled if

  $$u_z^0 < u_z < u_z^* \tag{4}$$

  where u_z^0 is the negative vertical velocity below which ice crystals will sublimate rather than grow:

  $$u_z^0 = \frac{e_i - e_s}{e_s} N_w \overline{r_w} \chi \tag{5}$$

  where χ is a coefficient dependent on p and T, and N_w and $\overline{r_w}$ are the cloud droplet number concentration and cloud droplet mean volume radius, respectively ($\overline{r_w} = (\frac{3LWC}{4\pi N_w \rho_w})^{\frac{1}{3}}$, where ρ_w is the density of water.) .

- **Regime 3** – Both ice crystals and droplets evaporate simultaneously:
  A cloud or cloud fraction falls in Regime 3 in case of

  $$e_s > e_i > e \tag{6}$$

  According to Korolev and Mazin (2003), (6) is true in downdrafts when $u_z < u_z^0$.

In CAM-Oslo, a subgrid distribution of vertical velocity is already implemented for calculations of cloud droplet activation. The same distribution is now used to determine the fractions of a given cloud dominated by each of the three regimes outlined above. The subgrid vertical velocity distribution is described by a Gaussian normal distribution centered around the mean grid box vertical velocity $\overline{u_z}$, following the parameterization of Ghan et al. (1997). The width of the distribution is given by the standard deviation (σ_{u_z}), calculated as follows:

$$\sigma_{u_z} = \frac{\sqrt{2\pi K}}{\Delta z} \tag{7}$$

where K is the vertical eddy diffusivity and Δz is the model layer thickness. As the relatively coarse resolution of the model may lead to an underestimation of σ_w, a lower limit of 0.30 ms^{-1} is necessary. Figure 1 gives an illustration of the subgrid vertical velocity distribution, indicating typical but idealized grid box fractions dominated by regimes 1, 2 and 3, respectively.

3 DISCUSSION AND CONCLUSION

The new WBF treatment yields smoother transitions from liquid to ice in clouds with cloud temperatures from -35°C to 0°C than the earlier treatment. Previously, glaciation occured abruptly when a critical ice mixing ratio was obtained (Storelvmo et al., 2008). Applying such a sudden glaciation to a cloud extending horizontally over hundreds of square kilometers is not physically realistic. Furthermore, as no observational guidance exists as to what such a critical ice mixing ratio should be, the previous approach added a free parameter and therefore uncertainty to climate simulations. The new approach allows gradual cloud glaciation with increasing ice formation, as evident from Figure 2. Preliminary results indicate that the implementation of the new WBF scheme reduces the aerosol indirect effect. An explanation for this reduction is that the cloud ice fraction is significantly increased with the new approach. Consequently, the influence of the aerosol indirect effects on warm clouds, which are practically always increasing cloud albedo, are reduced. Instead, the aerosol effects on freezing processes may dominate the anthropogenic effect on cloud radiative properties. As discussed in Section 1, these processes can both increase and decrease cloud albedo.

The modelling of heterogeneous freezing processes currently suffers from large uncertainties in laboratory and in-situ measurements of IN efficiencies for different aerosol species in the various heterogeneous freezing modes. While more reliable IN measurements would allow modellers to be more confident about the realism of their results, we believe that the improved treatment of mixed-phase cloud evolution presented here is a step towards more realistic simulations of mixed-phase clouds.

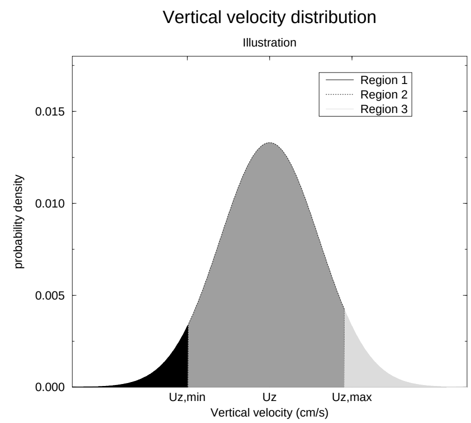

Fig. 1: Illustration of the subgrid vertical velocity distribution, with shadings indicating typical but fictive grid box fractions dominated by Regime 1 (black shading), Regime 2 (dark gray shading) and Regime 3 (light gray shading), respectively

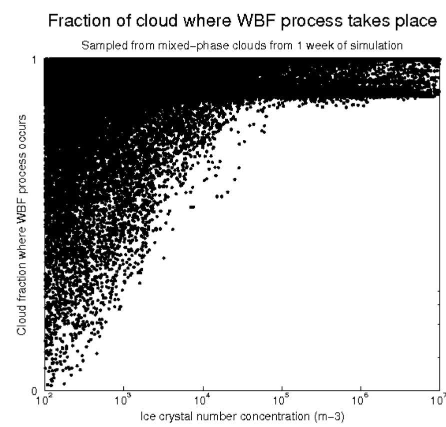

Fig. 2: Fraction of the cloud where the WBF process takes place as a function of ice crystal number concentration

References

Abdul-Razzak, H. and S. J. Ghan, 2000: A parameterization of aerosol activation, 2. multiple aerosol type. *J. Geophys. Res., 105, 6837-6844*.

Albrecht, B., 1989: Aerosols, cloud microphysics, and fractional cloudiness. *Science, 245, 1227-1230*.

Collins, W. D., P. J. Rasch, B. A. Boville, J. J. H. J. R. McCaa, D. L. Williamson, J. T. Kiehl, B. P. Briegleb, C. M. Bitz, S.-J. Lin, M. Zhang, and Y. Dai, 2006: The formulation and atmospheric simulation of the community atmosphere model version 3 (cam3). *J. Climate, 19, 2144-2162*.

Ghan, S. J., L. R. Leung, R. C. Easter, and H. Abdul-Razzak, 1997: Prediction of cloud droplet number in a general circulation model. *J. Geophys. Res., 102, 21777-21794*.

Girard, E., J.-P. Blanchet, and Y. Dubois, 2004: Effects of arctic sulphuric acid aerosols on wintertime low-level atmospheric ice crystals, humidity and temperature at alert, nunavut. *Atm. Res. 73, 131-148*.

Hoose, C., U. Lohmann, R. Erdin, and I. Tegen, 2008: Global influence of dust mineralogical composition on heterogeneous ice nucleation. *Env. Res. Lett., Accepted for publication*.

Korolev, A., 2007: Limitations of the wegener-bergeron-findeisen mechanism in the evolution of mixed-phase clouds. *J. Atmos. Sci., 64, 3372-3375*.

Korolev, A. and I. P. Mazin, 2003: Supersaturation of water vapor in clouds. *J. Atmos. Sci., 60, 2957-2974*.

Lohmann, U., 2002: Possible aerosol effects on ice clouds via contact nucleation. *J. Atmos. Sci., 59, 647-656*.

Lohmann, U. and K. Diehl, 2006: Sensitivity studies of the importance of dust ice nuclei for the indirect aerosol effect on stratiform mixed-phase clouds. *J. Atmos. Sci., 63, 968-982*.

Lohmann, U. and E. Roeckner, 1996: Design and performance of a new cloud microphysics scheme developed for the echam general circulation model. *Clim. Dyn., 12, 557-572*.

Pruppacher, H. R. and J. D. Klett, 1997: Microphysics of clouds and precipitation. *2nd edn, Kluwer Academic, Norwell, Massachusetts*.

Rasch, P. J. and J. E. Kristjánsson, 1998: A comparison of the ccm3 model climate using diagnosed and predicted condensate parameterizations. *J. Clim., 11, 1587-1614*.

Rosenfeld, D. and W. L. Woodley, 2000: Deep convective clouds with sustained supercooled liquid water down to -37.5°c. *Nature, 405, 440-442*.

Rotstayn, L., 1997: A physically based scheme for the treatment of startiform clouds and precipitation in large-scale models. i: Description and evaluation of the microphysical processes. *Q. J. R. Meteorol. Soc, 123, 1227-1282*.

Seland, O., T. Iversen, A. Kirkevåg, and T. Storelvmo, 2008: Aerosol-climate interactions in the cam-oslo atmospheric gcm and investigation of associated basic shortcomings. *Tellus 60A*.

Storelvmo, T., J. E. Kristjánsson, A. K. S. J. Ghan, Ø.. Seland, and T. Iversen, 2000: A parameterization of aerosol activation, 2. multiple aerosol type. *J. Geophys. Res., 105, 6837-6844*.

Storelvmo, T., J. E. Kristjánsson, and L. U, 2008: Aerosol influence on mixed-phase clouds in cam-oslo. *J. Atmos. Sci., Accepted for publication*.

Twomey, S., 1977: The influence of pollution on shortwave albedo of clouds. *J. Atmos. Sci., 34, 1149-1152*.

PARAMETERIZATION OF THUNDERSTORM CHARGING INCLUDING THE CLOUD SATURATION EFFECT

B. Tsenova[1], R. Mitzeva[2], C. Saunders[3]

[1]National Institute of Meteorology and Hydrology, Bulgarian Academy of Sciences, Bulgaria

[2]Department of Meteorology, Faculty of Physics, University of Sofia, Bulgaria

[3]School of Earth, Atmospheric and Environmental Science, Manchester University, England

1. ABSTRACT

Empirical equations of the influence of cloud water vapour saturation on the sign of charging of riming graupel during collisions with ice crystals are proposed based on numerical simulations. The new equations are incorporated into existing parameterizations of charging obtained from laboratory studies. Two cloud cases are simulated with a 1-D model to evaluate the impact of the cloud water vapour saturation on the charge structure in the updraft. Results show that including supersaturation in the model affects the net charge sign in the updraft regions of some thunderstorms.

2. INTRODUCTION

The electrification of thunderclouds is considered during numerical modeling of such clouds. Laboratory and theoretical studies in recent years have shown that charge transfer between colliding ice crystals and graupel pellets is a viable mechanism of thunderstorm electrification. It is well established that the sign of charge transfer is influenced by the cloud temperature and effective liquid water content, EW, where E is the graupel/ droplet collection efficiency and W is the liquid water content. Empirical equations for the separated charge as a function of these parameters are used as parameterization of the charging in numerical cloud models. More recently (Saunders et al., 2003, Mitzeva et al., 2005), have shown that cloud supersaturation, via the effect it has on the diffusional growth rates of the interacting ice surfaces, also affects the sign of the charge transfer. Based on the hypothesis for the crystal/graupel charging mechanism proposed by Baker et al., (1987), that the ice surface growing faster by diffusion of water vapour charges positively while the slower growing surface charges negatively, Mitzeva et al., (2005) determined that increasing the cloud supersaturation favours the negative charging of graupel. Furthermore, this theory involving the Relative diffusional Growth Rate (RGR) of the interacting particles was able to account for a range of experimental observations of charging under different supersaturation conditions (Saunders et al., 2006). In the present study, a new parameterization of the impact of cloud saturation on the charge sign is proposed based on theoretical numerical simulations and regression analysis. This parameterization is incorporated into the published empirical equations for ice crystal/graupel charging as a function of cloud liquid water content and temperature. Two thunderclouds are simulated using the new parameterization and results are compared with those obtained without the inclusion of the cloud saturation effect on charging in the updraft.

3. PARAMETERIZATION OF THE SATURATION EFFECT ON THE SIGN OF CHARGE TRANSFER

To consider the effect of saturation on the charge sign, the same model as in Mitzeva et al., (2005) is used. Fig.1 shows different charge sign reversal lines depending on the cloud water vapour saturation with respect to water with equations based on the RGR hypothesis.

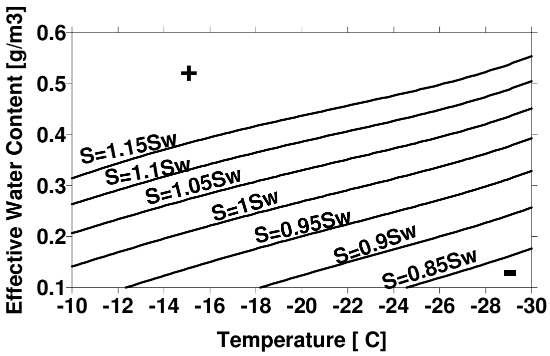

Fig.1. Charge sign reversal lines at different values of cloud water vapour saturation.

Furthermore, based on regression analysis, equations describing these reversal lines are obtained with the general form:

$$EW_{cr}(s) = A_s(s).T_a + B_s(s) \tag{1}$$

where EW_{cr} is the critical value of the effective water content [g m^{-3}], s - the sub/super/saturation with respect to water, T_a – the air temperature [^{o}C] and the constants A_s and B_s are given in Table 1.

Table1. Values for the constants A_s and B_s in eq.(1) for different sub/super/saturations s; A_n and B_n are their normalized values (assuming that at s=1, A_n = 1 and B_n = 1)

s	A_s	A_n	B_s	B_n
0.85	-0.018462	1.27	-0.367692	10.64
0.9	-0.015077	1.03	-0.184462	5.34
0.95	-0.013299	0.91	-0.070876	2.05
1	-0.014592	1	-0.034549	1
1.05	-0.012209	0.84	0.078065	-2.26
1.1	-0.011499	0.79	0.151885	-4.40
1.15	-0.011142	0.76	0.208524	-6.04

Using multiple regression analysis, equations for the coefficients A_n and B_n as a function of s:

For s ≤1 :

$$\begin{aligned} A_n(s) &= 11.5705s^3 - 31.5944s + 21.01938 \\ B_n(s) &= 153.246s^3 - 458.581s + 306.3294 \end{aligned} \tag{2}$$

For s > 1:

$$\begin{aligned} A_n(s) &= 13.8843s^2 - 31.3672s + 18.4783 \\ B_n(s) &= 162.016s^2 - 394.822s + 233.774 \end{aligned} \tag{3}$$

Thus, eq.(1) takes the form:

$$EW_{cr} = A_1 A_n(s).T_a + B_1 B_n(s) \tag{4}$$

where A_1 and B_1 are the coefficients at s=1. In this manner,

- if s ≤ 1:

$$\begin{aligned} &EW_{cr} = A_1 T_a \times \\ &(11.5705s^3 - 31.5944s + 21.0194) + \\ &+ B_1 \times \\ &(153.246s^3 - 458.581s + 306.3294) \end{aligned} \tag{5}$$

- if s > 1:

$$\begin{aligned} &EW_{cr} = A_1 T_a \times \\ &(13.8843s^2 - 31.3672s + 18.4783) + \\ &+ B_1 \times \\ &(162.016s^2 - 394.822s + 233.774) \end{aligned} \tag{6}$$

Thus, to include the effect of cloud saturation, one can take the equations for the reversal line based on laboratory experiments carried out at saturations with respect to water and incorporate the impact of the saturation following eqs.(5) and (6). Below is shown the inclusion of the saturation effect in the parameterizations of Saunders et al., (1991) – hereafter called SKM. In SKM, the equation for the reversal line is given by:

$$EW_{cr} = -0.0664.T_a - 0.49 \qquad (7)$$

Assuming that the experiment-based equation (7) is obtained in conditions at water vapour saturation then (7) is valid for s=1. Thus, it is accepted that A_1 = -0.0664 and B_1 = -0.49; and with the impact of the saturation proposed above included, the charge sign reversal line equations become:

- if s ≤ 1:

$$EW_{cr} = -0.0664.T_a \times (11.5705 \cdot s^3 - 31.5944 \cdot s + 21.01938) - -0.49 \times (153.246 \cdot s^3 - 458.581 \cdot s + 306.3294) \qquad (8)$$

- if s > 1:

$$EW_{cr} = -0.0664.T_a \times (13.8843 s^2 - 31.3672 s + 18.4783) - -0.49 \times (162.016 s^2 - 394.822 s + 233.774) \qquad (9)$$

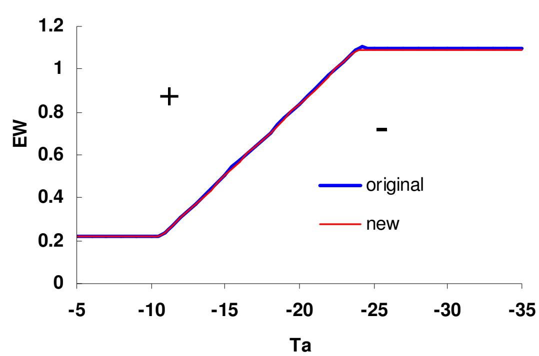

Fig.2. Reversal line in Saunders et al., 1991: original is obtained from eq.(7), new – from eq.(8) with s=1

Figure 2 shows that the proposed parameterization of the impact of the saturation on the charge sign reversal line works correctly in the case of the SKM parameterization.

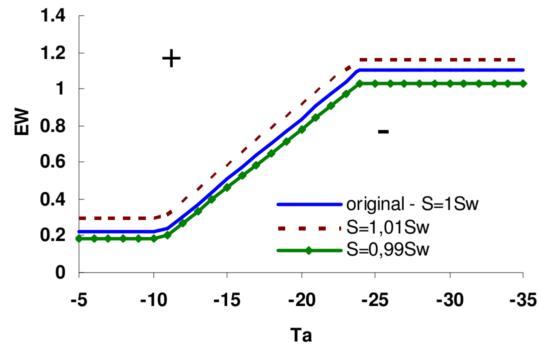

Fig.3. Reversal lines for different cases of water vapour saturation

Figure 3 shows how the reversal line shifts depending on cloud sub- and super-saturation, obtained using eqs.(8) and (9). These results are in agreement with the previously determined result that increasing saturation with respect to water favours negative graupel charging.

4. NUMERICAL SIMULATIONS

Numerical simulations are performed with the same model of cloud microphysics and dynamics as in Brooks et al., (1997), and Mitzeva et al., (2003). According to the model, convective clouds are composed of active (formed by successive ascending spherical thermals) and non-active cloud masses (formed by previously risen and stopped thermals). For the present simulations, the cloud saturation effect on charge transfer is included only in the cloud updraft. Different thunderstorm cases were simulated with the new parameterizations involving the effect of cloud saturation on the updraft charging. Results show that the supersaturation effect is significant in more dynamically intensive thunderclouds. Presented here are results for two of the simulated cases (C1 and C2).

The C1 cloud case has a maximum updraft velocity of 16.15 m s^{-1} at 2335 m (-10°C), while the maximum updraft velocity in C2 is 27.33 m s^{-1} at 8866 m (-58°C).

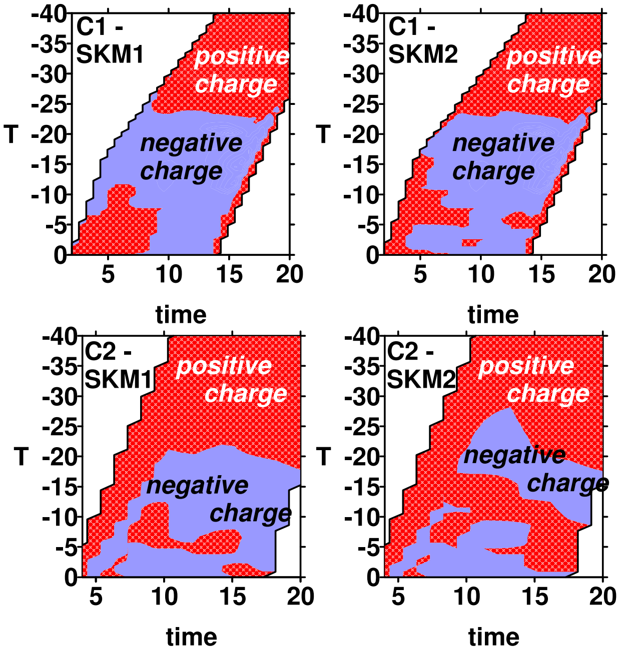

Fig.4. Total charge density in the updrafts of C1 and C2 simulated thunderstorms. SKM1 – parameterizations of charge transfer at water saturation; SKM2 – with variable water vapour saturation.

Figure 4 shows the updraft charging in the temperature interval [0, -40^{o}C] for the cases SKM1 and SKM2 with and without the saturation effect included. In C1, the two parameterizations give similar updraft charging at cloud temperatures between -5 and -25^{o}C, although there are some differences in the evolution of the lower region with small positive charge density. In C2 the impact of the saturation effect is more discernible, leading to a reduction of the lower negatively charged region; it also ascends in altitude (in C2-SKM1 it reaches -20^{o}C, while in C2-SKM2 – about -29^{o}C).

5. CONCLUSIONS

A new parameterization of the impact of cloud saturation on the charge sign reversal line is proposed based on theoretical numerical simulations and regression analysis. The inclusion of this parameterization in a model with empirical equations for ice crystal/graupel charging as a function of cloud liquid water content and temperature, shows that the cloud saturation effect on charging is stronger in more intense updrafts. To determine the importance of this effect on thundercloud charge structure, numerical simulations of charging in other cloud regions will be made.

6. REFERENCES

Baker, B., Baker, M. B., Jayaratne, E. R., Latham, J., Saunders, C. P. R., 1987. The influence of diffusional growth rates on the charge transfer accompanying rebounding collisions between ice crystals and soft hailstones. Quart. J. R. Met. Soc. 113, 1193-1215.

Brooks, I. M., Saunders, C. P. R., Mitzeva, R. P., Peck, S. L., 1997. The effect on thunderstorm charging of the rate of rime accretion by graupel. Atmos. Res. 43, 277-295.

Mitzeva R., N. Samarjiev and C.Saunders, 2003: Charge density in the updraughts of thunderstorms: a numerical study in the frame of a Lagrangian model, Atmospheric Research, v. 69, p.51-71

Mitzeva, R., Saunders, C., Tsenova, B., 2005. A modeling study of the effect of cloud saturation and particle growth rates on charge transfer in thunderstorm electrification. Atmos. Res., 76, 206 – 221.

Saunders, C. P. R., Bax-Norman, H., Emersic, C., Avila, E. E., Castellano, N. E., 2006. Laboratory studies of the effect of cloud conditions on graupel/crystal charge transfer in thunderstorm electrification. Quart. J. Roy. Met. Soc. 132, 2655-2676.

Saunders, C. P. R., Keith, W. D., Mitzeva, R. P., 1991. The effect of liquid water on thunderstorm charging. J. Geophys. Res. 96, 110007 – 11017.

Saunders, C. P. R., H. Bax-Norman, R. P. Mitzeva, B. Tsenova, E. E. Avila and N. E. Castellano, 2003. The effect of cloud conditions on charge transfer in thunderstorm electrification, Proceedings of the International Conference of Lightning and Static Electricity

THE MICROPHYSICAL CHARACTERISTICS OF FOG IN THE RIME AND GLAZE

Wen Ji-fen[1] Luo Ning[2] Meng lei[3]
1:Guizhou Weather Modification Office, Guiyang,550002,China
2: Guizhou Meteorological Bureau, Guiyang,550002,China
3：Key Laboratory of Atmospheric Physics &Atmospheric Environment(LAPE),NUIST. Nanjing, 210044,China

1.INTRODUCTION

Because of different kinds of climate characteristics, the fluence of rime and glaze are very high in Guizhou, China. Rime and glaze are not only the winter scenery, but also the natural disaster. In order to prohibit the transmission line from the disaster and do some research on the microphysical characteristics of this kind of weather phenomenon. Through analizing the data of microphysical characteristic of fog during the lasting of rime or glaze in the winter of 1990,1991 in Guizhou province Lou Hill and Maluojing area.Based on the theory of fog ,make clear that the relationship among the elements in the rime and glaze.We can find out that the fluent of the foggy evolution in the rime and glaze is less obvious than that in the fog. The relationship between the fluent and micro -physical characteristics of droplet spectrμm is very tight.

Overhead wires ice accretion by glaze and rime ice is harmful to electric power,tr -ansportation,communication,industrical ang agricultural production,conduct ice accretion is a common meteorological disastar in YUNGUI Plateau and other mountain areas.Each year the economical loss of GUIZHOU Province by this disastar is very great.,the loss of 2008 year is greatest during 80 years.

According to (Person et al,1988),the main factors affecting wire ice accretion are:liguid water content,distribution of drop -let spectrum,wind direction velocity and temperature.Because of the transmission line being through very complex geographi -cal environment,and the complexity of meteorological factors in different areas as wellas their temperal and spacial difference, study of ice accretion is very difficult.. ice accretionobservatory station hanve been established in CHINA and some developed countries ,depended on the data aggrandiz -ed for long time, ice accretion diameter changed as the height above sea level was summarized.The studies above are significa -nt to the selection of overhead conductor direction road,however,they only reflected the climatic characteristics of ice accretion,and did not involve the mechanis -m of icing formation..It is short of reality observation data.This paper is studing liguid water content and distribution of droplet spectrum during ice accretion.

2. INVESTIGATED DATA

In order to reveal the law and mechanism of wire ice accretion in GUIZHOU plateau, micro-characteristics of fog and cloud were obseverved while investigating and collect -ing the micro-meteorological and macro -meteorological conditions in heavy ice acc -retion areas.

Accidents of wire ice accretion usually take place in heavy ice accretion areas . M ore fog is a typical climate characteristic of heavy ice accretion areas.Three heavy ice accretion areas of GUIZHOU Province were selected as field investigation areas in the project,they are MALUOQIN in the west LOUSHAN Mountain in north and YUNWU Mountain in the centre ,and their heights above sea level are 2128,1780 and 1659 meters respectively.The typical characteris -tic includes ice accretion data and routine meteological data: :liguid water content,dis -tribution of droplet spectrum,wind direction velocity , temperature and ice increasing .

3.THE MICROPHYSICAL CHARACTER -ISTICS OF FOG IN THE RIME AND GLAZE

Liguid water content and distribution of droplet spectrum during ice accretion are very important to research micro-physical characteristics of ice accretion.

3.1 CHARACTERISTICS OF DROPLET SPECTRUM

According to the cloud droplet spectrum data of west part and north part in GUOZHOU,the calculated value are show -ed in table 1.

Table1 Physical characteristics of supercooled cloud droplet spectrum

parameter		west 1988	1989	1991	north 1990 Lee side	1990 windwardside	total average
Arithmetic mean	range	4.3-13.3	3.7-7.0	5.4-14.3	4.1-15.8	4.1-19.8	
diameter(μm)	average	7.0	6.1	9.3	7.8	7.4	7.52
Cobe root	range	7.3-14.4	4-12.3	8.0-19.1	5.8-26.2	4.4-26.7	
diameter(μm)	average	11.8	8.4	14.4	11.6	10.4	11.32
Peak diameter(μm)		4.0	4.3	4.2	4.2	4.0	4.1
The rate of peak concentration to Total concentration		62%	73%	51%	63%	64%	63%
Cloud droplet	range	37-546	41-1178	26-384	45-1000	39-1539	
Concentration(/cm^3)	average	235	259	140	227	312	234
samples		16	21	13	52	53	

The cloud droplet spectrums have slight difference in different years in the west of GUIZHOU Province.The characteristic values of cloud in the north and west have the same order.

The elementary characteristic of cloud droplet spectrum distribution is that the cloud droplet concentration is small,the characteristic diameter of droplet spectrum is relatively great,for example in 1991. the cloud droplet concentration is great,and the characteristic diameter of droplet spectrums is small.Most distribution of the cloud droplet spectrum is single peak type.Under most peak diameter, the greater the diameter,the greater the droplet concentration.Above the peak diameters, the greater the diameter, the smallerer the droplet concentration.This rule meets the droplet spectrum formula of Khrgian –Mazin:

$$n^{'}(r)dr = cr^2 e^{-br} dr$$

Table2 droplet spectrum fofmula per year

year	place	droplet spectrum fofmula
1988	MALUOQIN	$n(d) = 7.28 d^2 e^{-0.25 d}$
1989	MALUOQIN	$n(d) = 7.55 d^2 e^{-0.235 d}$
1991	MALUOQIN	$n(d) = 5.38 d^2 e^{-0.235 d}$
1990	LOUSHAN1	$n(d) = 6.8 d^2 e^{-0.235 d}$
1990	LOUSHAN2	$n(d) = 7.45 d^2 e^{-0.25 d}$

Where,n’(r) the droplet concentration as radius between r+dr.c and b are constants. Different cloud droplet spectrum can be distinguished with different c and b.From the actual data of table1,the average droplet spectrum fofmula of glaze and rime ice per year in GUIZHOU Province can be obtained. Fog droplet spectrum shown in fig1,cloud and fog droplet spectrum shown in fig2.

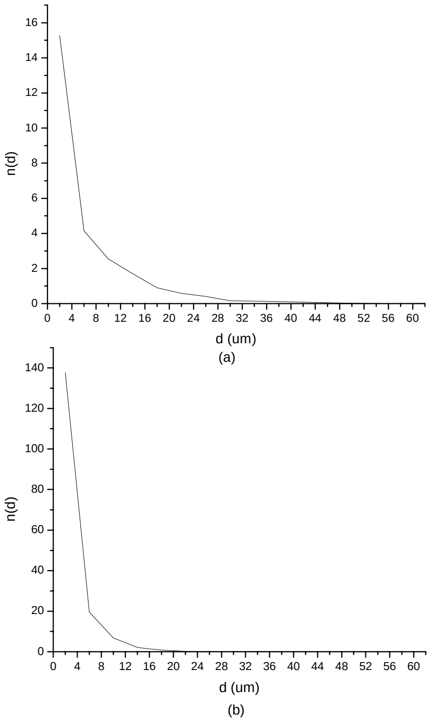

FIG.1. The Fog droplet spectrum distribution

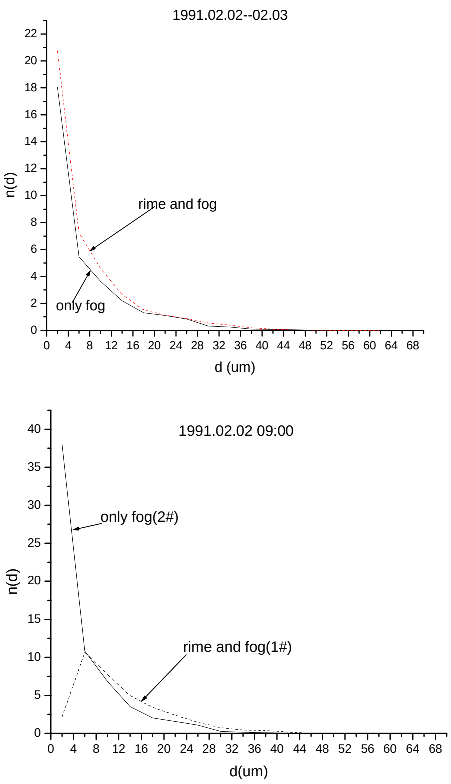

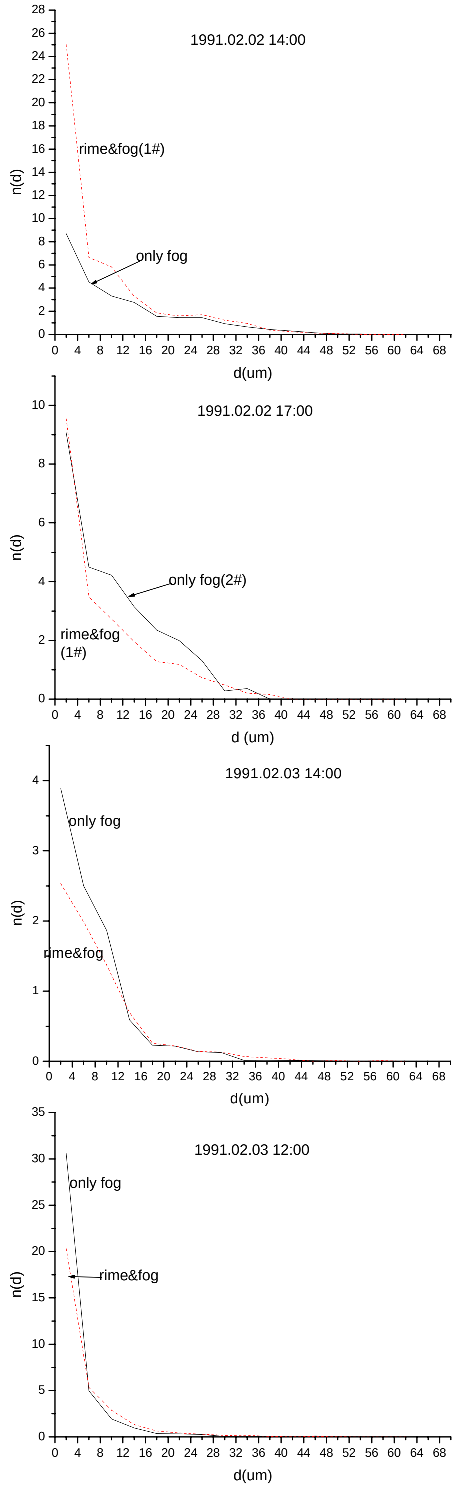

FIG.2. The Fog and cloud droplet spectrum distribution

According to calculating of reality obser -vation data, the average formula of cloud and fog droplet spectrum is follow:

$$n(d) = 6.88\, d^{2} e^{-0.24\, d}$$

3.2 THE BIG DROPLET CHARACTERIST -IC ITS CONTRIBUTION TO LIQUID WATER CONTENT(LWC)

Some experiments of collection efficiency show:collection efficiency has direct ratio with the radius of fluid particles (Makkonen et al,1987).The greater the droplet in cloud and fog,the higher the collision frequency with circular wires, the more the amount of wire ice accretion .Therefore the study of ice accretion especially concerns droplet spect -rum width and big droplet .The minimum of median volume diameter caculated with actual cloud droplet data of GUIZHOU is 14 μm.The droplet above 14μm is regarded as big droplet in cloud in this paper.Counting the rate of cloud droplet above 14μm. among total cloud droplet concentration,the rate is 15% in 1988,6.3% in1989,12% in 1990,18.6% in 1991.Statistics shows:the m -aximal droplet diameter of cloud droplet is between 35 and 50μm,and the concentrati -on only makes up about 1% of the total concentration.The total contribution of cloud droplet of the two areas in the West and the North to the liquid water content is showed in fig.3.

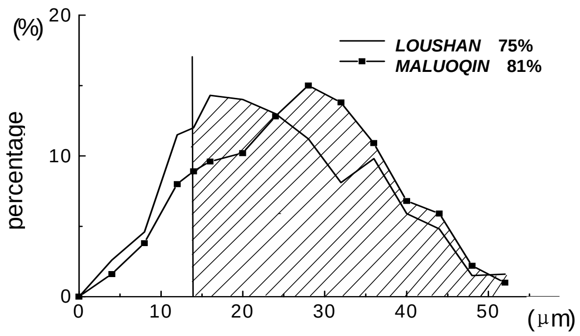

Fig.3 Percentage of the cotribution of different colud –fog droplet size to LWC,Shade areas is the integration of cloud droplet about 14μm to LWC.

Fig.3 show that:.the big droplet above 14 μm only makes up about 15% of total cloud droplet,but the contribution to liquid water content is up to 75%～81%.Therefore,the studies of cloud droplet spectrum shoud emphasize mean cube root diameter and median volume diameter whose characteris -tic diameter could represent big droplet and have the most contribution to liquid water content.

3.3 LIQUID WATER CONTENT(LWC)

Liquid water content is a key factor of studing ice accretion.394 LWC data in several years are showed in the table 3:

In the West of GUIZHOU,the heights above sea level are the maximum,the average LWC is the minimal. The heights above sea level are minimal.among the three areas,because of the very low temperature during observation, LWC is not very high. LWC is related not only with height above sea level of topography but also with the distribution of temperature.The actual average LWC in different scope in three areas of the west,north and centre of GUIZHOU are showed in table 4.

A relationship of LWC and temperature is obtained:between 0℃ ～-6℃,LWC tends to decrease as the temperature decreases, and in the same temperature scope,the heigher the height above sea level,the lower the LWC,and vice versa. This phenomenon is mainly related with the environment,geo -graphic position of three observatory spots and the height of cloud layer of winter stationary front in GUIZHOU-YUNNAN Plateau.Because the temperature scope was only between -4℃ ～-6℃ during observation in the centra areas,the relationship of temperature and LWC can not be determined easily.

4.CONCLUSIONS

The study of liguid water content and droplet spectrum by observation data during ice accretion indicates the following:

a.The cloud-fog droplet concentration and average diameter characteristic observed in

Table 3 Characteristic value of LWC

Geographic position	Height above sea level（m）	Year	**LWC**$_{min}$ （g/m^3）	**LWC**$_{max}$ （g/m^3）	**LWC** (g/m^3）	Samples	Days	Temperature (℃)
West	2128	1988	0.030	0.438	0.160	64	5	4.6～-2.6
	2128	1989	0.040	0.318	0.148	64	4	-1.1～-4.2
	2128	1991	0.017	0.473	0.180	23	3	0.0～-2.2
North	1736	1990	0.082	0.564	0.247	121	13	0.0～-5.6
	1780	1990	0.023	0.412	0.261	112	12	0.0～-5.5
Centre	1659	1994	0.114	0.382	0.216	10	2	-4.0～-6.0

Table 4 LWC distribution of temperature range of different height

Geographic position	Height above sea level（m）	Temperature（℃）						Average
		0～-1	-1～-2	-2～-3	-3～-4	-4～-5	-5～-6	
West	2128	0.223	0.164	0.151	0.128	0.103		0.154
North	1780	0.291	0.305	0.240	0.178	0.140	0.121	0.213
Centre	1659					0.219	0.215	0.217

The west and north of GUIZHOU Province in several years,don't have obvious regional difference.Tdifference of each value should be the natural diffience of cloud-fog.The main Characteristics are: cloud-fog. Droplet average concenration is between 140 and 312 per cm^3.Arithmetic mean diameter and cube root diameter of cloud-fog droplet are 7.4 and 13.2 respretively.The average rate of maximal concentration to total concentra -tion is 62%.

b.The cloud droplet concentration and droplet value meet the formula of Khrgian –Mazin:$n(d)=cd^2e^{-bd}$.After c,b were calcula -ted with the actual cloud-fog droplet spec -trum formual is: $n(d)=6.88d^2e^{-0.24d}$.

c. Summing up several years cloud-fog droplet spectrum data,the cloud-fog droplet concentration above 14μm makes up 12.5% of the total cloud-fog droplet concen -tration ,but its contribution to LWC is up to 78%.Since big droplet contributes greatly to LWC ,and collision efficiency with wire is high,the characteristic of big droplet is agreat problem concerning ice accretion.

d.LWC of cloud-fog is between0.03 and 0.56 g/m^3 ,the average is 0.20 g/m^3.LWC is obviously related with temperature and height above sea level. Within 0℃ ～-6℃, LWC descends as temperature descends, the higher the Height above sea level,the less the average LWC.

REFERENCE

Person,P.and Gaget,J.F.,1988:IceAccretion on Wires and Anti-Icing Induced by Joule Effect.*J.Appl.Metor.,27,101-114.*

Makkonen,L. et al., 1987:Experiments on Cloud Droplet Colision Efficiency of Cylind -ers.*J.Climate Appl.METOR.,26,1406-1411.*

COMPARISON BETWEEN RADAR AND DISTROMETER MEASUREMENTS AND PRECIPITATION FIELDS SIMULATED BY A 3D CLOUD MODEL WITH DETAILED MICROPHYSICS FOR A MEDIUM CONVECTIVE CASE IN THE CÉVENNES REGION

Wolfram Wobrock, Céline Planche, Delphine Leroy, Andrea I. Flossmann

Laboratoire de Météorologie Physique, Université Blaise Pascal-CNRS-OPGC,
24, avenue des Landais, F-63177 Aubière Cedex, France
E-mail : W.Wobrock@opgc.univ-bpclermont.fr

1. ABSTRACT

The results of a numerical model with detailed microphysics is compared with distrometer measurements (rain rates and size distribution at the ground) and with radar reflectivities for the case of the 27/28 Oct 2004 over the Cevennes mountains in southern France.

The cloud and rain drop field simulated with DESCAM 3-D considering cold microphysical processes show good agreement with the radar and disdrometer observations for the period between midnight and 4 o'clock in the morning. In the model the vertical profiles of the size distribution prove the importance of the ice phase for the formation of the precipitation. However, the simulated reflectivities in the bright band are clearly underestimated.

In the case of a polluted air mass, the model produces a precipitation field which is horizontally reduced and has cumulated rain rates lower than the ones resulting from the simulation with a cleaner air mass. The onset of rain is delayed if the concentration of aerosol particles is increased.

2. INTRODUCTION

The goal of the present study is to test the performance of the cloud model with spectral (bin) resolved microphysics - *DESCAM 3D*- for the precipitation at the ground. To forecast in mountainous regions the location and the rate of precipitation is in fact essential in order to study the response of the catchment basins and to predict possible flooding.

The volumetric radar of Bollène, installed since 2002 in southern France in the region of the Cevennes Mountains allows obtaining a horizontal and vertical distribution of the reflectivity and thus the rain field in an area with is often subject to devastating flash floods.

During autumn 2004 a disdrometer was added in Alès in order to obtain an additional characterisation of the size distribution of these precipitation events. In order to test the capacity of *DESCAM 3D* to simulated these rain fields, the event of 27/28 Oct 2004 was selected where a cumulative rain rate of 80mm was measured. The top of the clouds stayed below 6km, thus, we will call this situation "medium convection".

3. OBSERVATION WITH THE VOLUMETRIC RADAR AT BOLLÈNE AND THE DISDROMETER

The disdrometer installed at Alès was run between September and December 2004 (Chapon, 2006). It classified the rain drops as a function of their size and their terminal velocity. Each of these parameters is distributed in a grid of 32 classes (from 62 µm to 24.5 mm). During the night of 27 / 28 October, the rain event deposited at the ground more than 80 mm (Fig. 1). The maximum intensity was about 65 mm h^{-1}.

The volumetric scan of the radar of Météo France at Bollène allows the reconstruction of the vertical profiles of reflectivity. Between 18.00 and midnight the radar reflectivities were stronger than 40 dBZ

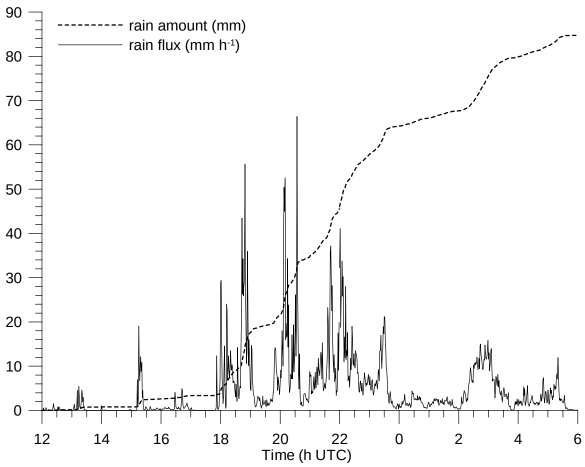

Figure 1 : Cumulated rain on the ground (mm) and intensity (mm h^{-1}) measured by the disdrometer at Alès on 27 and 28 October 2004.

between the surface and 3 km. After midnight, the reflectivities decreased (around 35 dBZ at most) and reached less high altitudes: between midnight and 2 o'clock, 30 dBZ were found above 3 km while the same value was found around 2.5 km between 2 and 4 o'clock in the morning (Fig.2). The simulation was limited to the second phase of precipitation at Alès as only the initialisation with the sounding of Nimes at midnight allowed the formation of precipitation. Using the noon sounding of the 27 October 2004 or the analysis of the ECMWF model remained also without success.

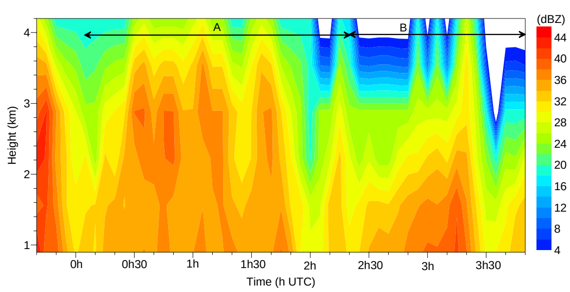

Figure 2 : Time evolution of the vertical profile of radar reflectivity above Alès. The letters A and B correspond to the structure in Fig. 5.

4. CLOUD MODEL WITH DETAILED MICROPHYSICS AND INITIALISATION OF THE MODEL

The 3D model with detailed (bin) microphysics used herein couples the 3D non-hydrostatic model of Clark and Hall (1991) with the Detailed Scavenging Model DESCAM (Flossmann et al., 1985) A detailed description of the microphysical package, including sensitivity studies of DESCAM under mixed phase conditions can be found in Leroy et al. (2007).

Below only a brief summary of the essential features is given. The microphysical model employs five distribution functions: three number density distributions functions respectively for the wet aerosol particles (AP), the drops and the ice crystals and two mass density distributions of aerosol particles inside drops and ice particles. The five functions are discretized over 39 bins that cover a range of radius from 1 nm to 6 µm for the wet AP and from 1 µm to 6 mm for the liquid or solid hydrometeors. All together, the detailed microphysics introduces 195 supplementary prognostic variables to the initial code.

The microphysical processes that are considered in the model are: condensational growth and activation/deactivation of AP, condensation and evaporation of droplets, coalescence, homogeneous and heterogeneous nucleation, vapor deposition on ice crystals and riming. Droplet nucleation relies on the calculation of the activation radius derived from the Köhler equation (Pruppacher and Klett, 1997), but is also dependent on temperature as described in Leroy et al. (2007). Growth rate of drops and ice crystals are given by Pruppacher and Klett (1997). Homogeneous and heterogeneous nucleation follows respectively the works of Koop et al. (2000) and Meyers et al. (1992). Ice crystals are assumed to be spherical and the density of ice is 0.9 g m^{-3}. Coalescence and riming are treated with the numerical scheme of Bott (1998). The collection kernels for coalescence of drops are calculated with the collection efficiencies of Hall (1980) and the terminal velocities of Pruppacher and Klett (1997). Riming description includes collection of droplets by large ice crystals as well as collection of small ice particles by large drops. The collection kernels for riming are set to be the same as those for coalescence of drops, i.e. we assume that the collection efficiency of a spherical ice crystal is equal to the one of a water drop of the same mass.

Aggregation and secondary production of ice particles during riming is also neglected in the model for the moment.

For the simulations presented in this paper, the model domain is 128 km x 128 km in the horizontal (Δx, Δy= 1km) and 62 vertical level with a vertical resolution of 250 m. The dynamical time step is 4 second.

Three simulations will presented below. The first simulation with cold and warm microphysics will be considered as the reference simulation. In the second simulation the cold microphysics processes are turned off in order to study the impact if the ice phase on the formation of rain for the given situation. These two simulations will use the same initial aerosol particle size distribution of Jaenicke (continental case, 1988). The total number of aerosol particles close to the ground is 700 cm^{-3} and decreases exponentially between the surface up to 3km and stays constant above. For the third simulation the total number of initial aerosol particles is multiplied by a factor of three and the cold microphysical processes are again active, in order to study the impact of a polluted air mass on the ice phase and rain formation.

5. RESULTS

5.1.SIMULATION WITH COLD MICRO-PHYSICS

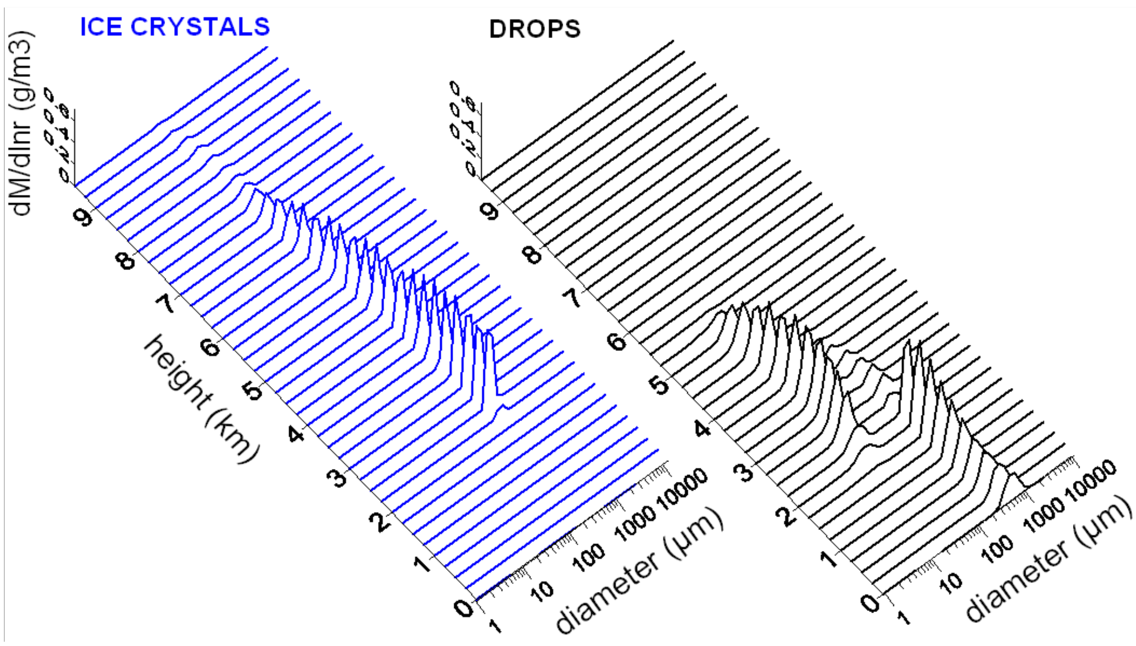

Figure 3 :Vertical profile of the mass spectra of crystals (left in blue) and drops (right in black) at a grid point next to Alès.

Due to the *spin-up* time of the simulation the first precipitation over Alès formed after 2h. The cloud field reached up to 6km altitude, rain water was only present below 3.5km. The ice phase is confined to regions above 2.5km.

Fig.3 presents the size distributions of crystals and drops between the ground and 9.5km altitude in a vertical column of a grid point close to Alès.

In Fig. 3 on the left, the distribution of the mass of ice crystals stays mono-modal irrespective of altitude. The size of the crystals varies between 200 µm in high altitudes to 800 µm around 3 km. On the right hand side, the size distribution of the drops shows a bi-model character at some places: cloud drops between 20 and 40 µm of diameter and rain drops around 1mm of diameter.

We can deduce from Fig.3 the principal microphysical processes responsible for rain formation in this case study. Between 2.5 and 4km, rain drops form by collision/coalescence inside the cloud. As at these altitudes the cloud is in mixte phase, the riming process transforms large drops into crystals. The total mass of crystals increases, thus, with decreasing altitude. Then, between 2.5 and 2.25km the crystals pass the 0°C isotherm and melt. This process is assumed instantaneous in the model, and, thus, the total mass of crystals can now be found in the drop reservoir. This can be seen in Fig. 3 by a brutal increase in drop mass in this altitude. The formation of rain passes, thus, by the processes of collision/coalescence of drops, riming and then melting.

Fig. 4 shows the distribution of rain on the ground after 4h of integration time. The maximum rates can be found on the slopes of the mountains, where the rain starts. As the time passes, the rain extends to the plains and later until the sea.

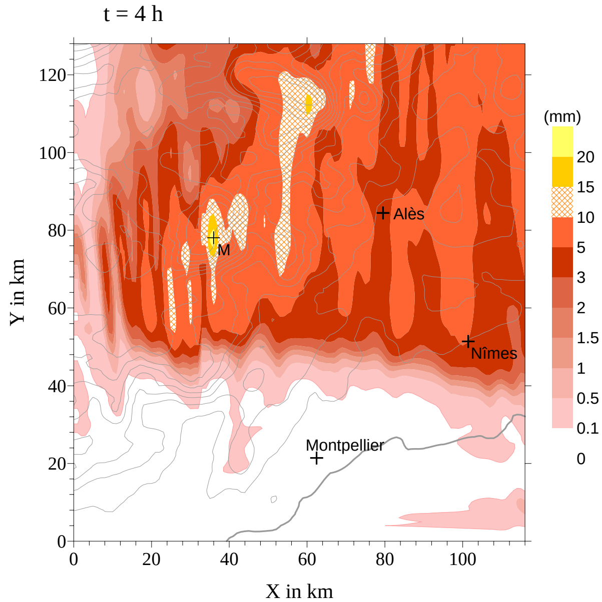

Figure 4: Cumulative rain on the ground in mm after 4 h of integration time

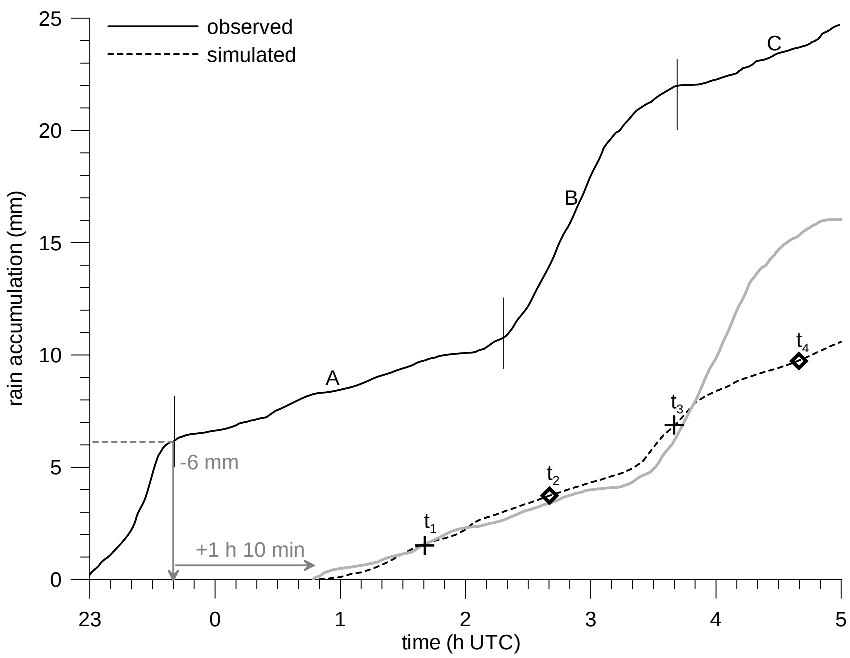

Figure 5 : Cumulative rain of the ground recalculated from the disdrometer data (continuous lines) and simulated for Alès (X=79 km, Y=85 km, dotted line). The grey line corresponds to the observations with a temporal delay of +1 h 10 in order to take into account the spin-up of the model.

Fig.5 gives the evolution of the cumulative rain on the ground measured by the disdrometer and simulated for a point close to Alès. One can note a strong increase of observed rain between 23h and 23h 40 UTC which can be attributed to the end of the convective period which began before midnight and which the model cannot reproduce as it is initialised with the sounding of 23 UTC. In the following we restrict ourselves to the observations after 23h 40. Due to the spin-up time of the model we will consider a time shift of 1h30 when comparing the model output with the observations.

The evolution of the cumulative rain can be divided in three phases A, B, and C in Fig. 5, as a function of the slope of the curve. The first phase A lasts about 2h 30 and the slope is 2 mm h^{-1}. The slope is more important during phase B, around 9 mm h^{-1}, for about 1 h 20 min. Afterwards, the precipitation becomes stronger and a situation resembling phase A reappears. This is phase C with a slope of 2 mm h^{-1}.

Between 1h and 1h 30 the simulated cumulative rain for Alès increases linearly and the simulated and observed slope are coherent for phase A (Fig.5). The same applies around 3h 30 integration time when the slope increases (about 7 mm h^{-1}) and the cumulated rain increases more strongly. Finally, at 4h in the morning, the model results show also a return to a situation similar to the one between 1 h and 3 h 30 in the morning. Thus, considering the slopes of the three phases the model results agree with the observations of the disdrometer. The main difference lies in the duration of the phase B which is only 30 min in the model but only lasts 1h 20 in the observations.

Fig. 6 compares the measured and simulated drop spectra for four different times t_1 to t_4 marked in Fig 5. As in Fig 4 and 5 the simulations are not averaged over a domain but represent the grid point representing Alès in the model.

The distributions in Fig. 6a represent phase A (compare Fig.5) where the rain drops are smaller in the simulation than actually observed. This is surprising as the rain rates showed a very good agreement (Fig.5) during this phase.

Fig.6b shows the results for phase B. Here, we find a very good agreement between observed and modelled spectra. Finally, the spectra with the diamonds in the Fig. 6b correspond to the end of phase B or the beginning of phase C for the observations, but belong clearly to phase C regarding the model results. Here, the model produces a smaller drops mass, but the agreement for the large drops (diameter larger than 1.1 mm) is good.

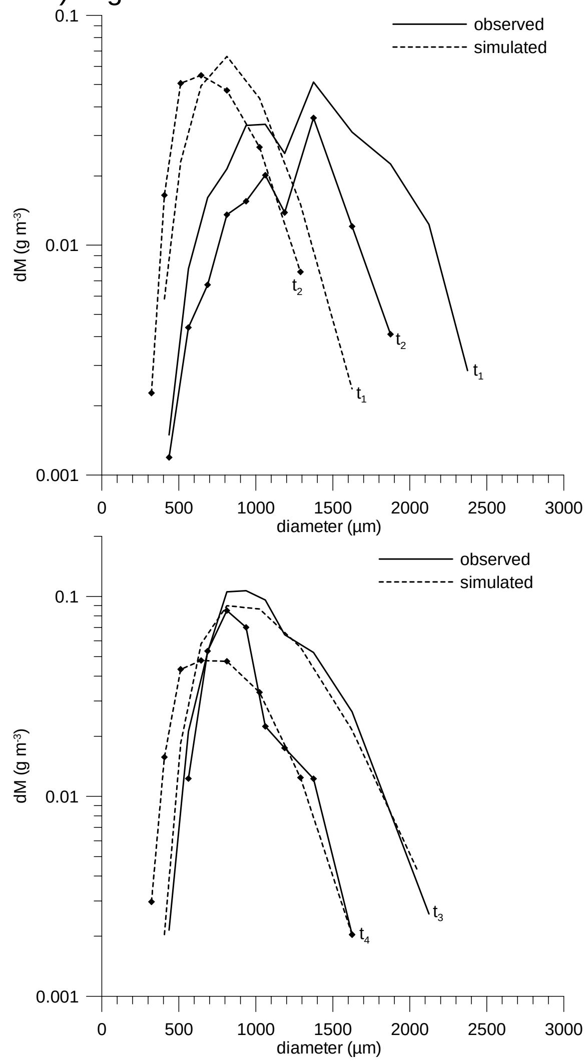

Figure 6 a (top) and b (bottom): Mass distributions of measured rain drops (continuous lines) and simulated rain drops (dotted lines) for 4 times t_1 to t_4 given in Fig. 5.

The microphysical processes responsible for the formation of drops in phase A and B are certainly different. In order to find an explanation for the behaviour, an analysis of the radar reflectivities (Fig. 2) is attempted.

Fig. 2 shows that the maxima of the reflectivities are not at the same altitude for phase A and phase B. During phase A, the maxima can be found between 2.5 and 3 km altitude. The isotherm 0°C is located in this case study around 2.5 km. During phase A the reflectivites show, thus, a bright band. This bright band can be associated to the fact that the radar attributes the melting crystals to large rain drops and an increase in the radar reflectivity results. The large observed drops result, thus, directly from the melting of large ice crystals.

During phase B, however, the maxima of the radar reflectivites are observed close to the ground. This a related to the growth of large drops by collision/coalescence during the sedimentation.

The formation of the large drops on the ground is, thus, different in phase A and B which explains the differences noted in the size distribution at the ground.

The vertical profile of the radar reflectivities above Alès displays also a different vertical extension of the convection in phase A and B. During phase A the radar reflectivities at 4km are around 30 dBZ while those during phase B have values below 4 dBZ. Convection is, thus, weaker during phase B which explains a smaller contribution of the ice phase to the precipitation.

For phase A the simulated radar reflectivities stay 10-15 dBZ below the observations and do not show the bright band at 2.5 km. This is due to the hypothesis of an instantaneous melting of tall ice particles at temperatures above 0°C. During phase B the simulated reflectivities are closer to the observed ones as the drops grow by collision/coalescence in temperatures warmer than 0°C.

5.2. SIMULATION WITHOUT COLD MICROPHYSICS

Without cold microphysics, the liquid water can reach altitudes of 7km instead 4.4 km for the cloud water and 6km instead of 3.5 km for the rain water.

When the ice phase is active, the crystals consume the water vapour present in high altitudes. The corresponding layers become sub-saturated with respect to liquid, however, stay supersaturated with respect to ice. The Bergeron effect makes the water vapour condense on the ice at the expense of the liquid drops. Consequently, in the case without ice, the air stays supersaturated with respect to liquid up to 7km. The maximum values of RH reach 103.5% in the mixte case as compared to 105.5% in the "all liquid" case.

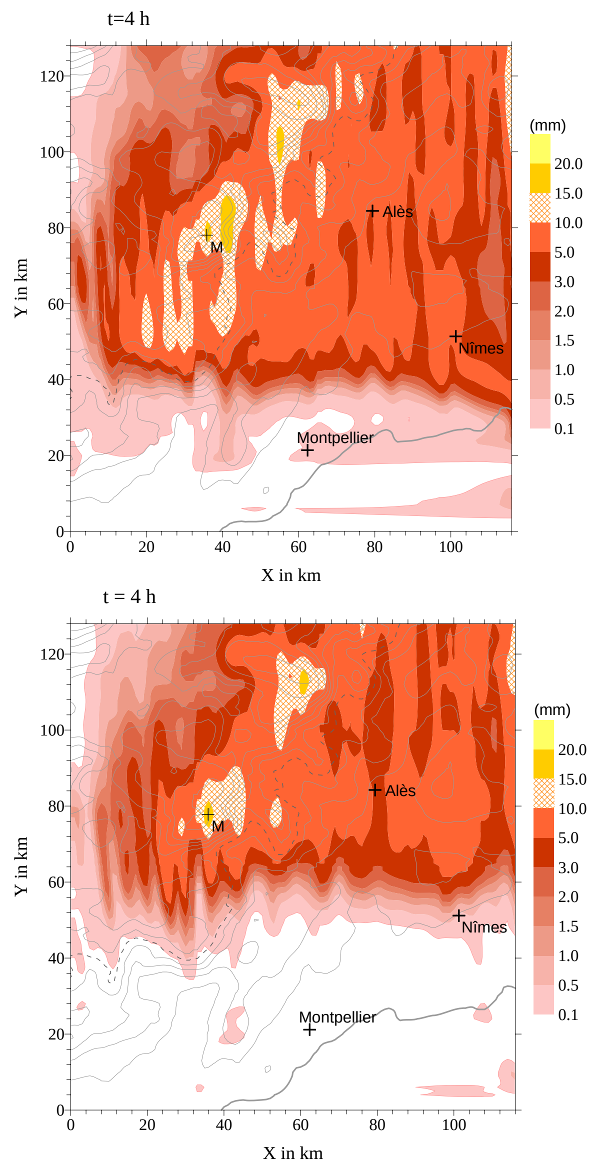

Figure 7: Cumulative rain at the ground after 4 h of integration a) (top) without ice and b) (bottom) for the polluted case

Fig.7a shows the cumulative rain on the ground after 4h of integration time. The region with rates exceeding 5mm is larger in the "all liquid" case than in the reference

case (Fig.4). This increase is most pronounced in the south around y=50km.
Table 1 compares the total mass of rain in megatons integrated over the entire domain for three different times for the mixte and the “all liquid” case. The simulation without ice always gives more rain, even if the difference in percentage decreases with time. We can, thus, conclude that the absence of ice in this case of medium convection increases the rain over the domain studied and extends the region of the rain towards the south.

Table 1: Total mass of rain on the ground in megatons for three different times for the reference case, the “all liquid case” and the polluted case. The columns “difference” give the variation in percentage with respect to the reference case.

time	Ref case	“All liquid” case	Difference (%)	Polluted case	Difference (%)
2 h	7.1	16.3	+130	5.7	-20
3 h	30.9	43.7	+41	26.4	-15
4 h	62.3	77.3	+24	54.3	-13

Table 2 : Time evolution of the cumulative rain on the ground for the entire domain for the reference case, the “all liquid” case and the polluted case.

Accumulation on the ground larger than	“All liquid” case	Reference case	Polluted case
1 mm	45 min	65 min	75 min
5 mm	90 min	110 min	120 min
10 mm	130 min	140 min	170 min
15 mm	180 min	180 min	225 min

Table 2 gives the integration times necessary to reach certain values for the cumulative rain on the ground (1, 5, 10 and 15 mm), for the simulations with and without the ice phase. In the absence of the ice phase the first rain appears 10 min earlier and the threshold of 1 and 5 mm are equally reached about 20 min earlier. Then, the time difference decreases, and the threshold of 15 mm is reached at the same moment for the two simulations.
After 4h of integration time the maximum accumulation for point M (compare Figs. 4 and 7) is even larger in the mixte phase case (25 mm) than in the “all liquid” case (16 mm).

5.3 SIMULATION IN A POLLUTED AIR MASS

In order to represent polluted air, the number of aerosol particles initially present (700 cm^{-3} in the first two simulations of sections 5.1 and 5.2) were multiplied by a factor of 3, which results in a particle concentration of 2400 cm^{-3}. The shape of the distribution stays unchanged.
Some differences can be noted. For the liquid phase, the cloud water content exceeds 0.5 g m^{-3} more often in the polluted case. The presence of rain water contents larger than 0.5 g m^{-3}, however, is less frequent.
We find here that with increasing number of particles the cloud water content increases at the expense of the rain water content. Concerning the ice water content, however, we note practically no change with respect to the reference case. This is a consequence of the parameterisation of Koop et al. (2000) and Meyers et al. (1992) for homogeneous and heterogeneous nucleation used in the model. There, the number of crystals formed is only dependant on super-saturation with respect to ice and temperature but stays independent of the number of aerosol particles present.
Fig. 7b shows the accumulated rain after 4h of integration time for the polluted case. As

before, the main differences can be observed in the south east around Y=55 km. The results concerning the total mass of rain on the ground, as well as the temporal evolution of the accumulation in the model domain are included in Table 1 and 2.

Table 1 shows that the cumulative rain on the ground in the polluted case is 10 to 20% less than in the reference case. Table 2 indicates that the precipitations start later in the polluted case and the time shift increases with integration time. This time shift is certain responsible for the different rain accumulation around Y=55 km (Figs. 4 and 7b): the precipitation in the polluted case started later and is less wide spread, especially in direction to the sea.

6. CONCLUSION

The cloud water and rain water fields simulated with DESCAM 3D including cold microphysics show a satisfactory agreement with the observation of the radar and the disdrometer for the episode from midnight to 4 o'clock in the morning for the 27/28 Oct 2004 in the Cevennes region in southern France.

During phase A the radar shows for the region above Alès the presence of a bright band. The drops collected by the disdrometer resulted, thus, from the melting of ice crystals with size above 1mm aloft.

During phase B the maxima of radar reflectivities were observed close to the ground. Convection is now weaker and the collision/coalescence of drops can explain the increase of the radar reflectivities close to the ground.

In the model, the vertical variation of the size distributions show that the ice phase contributes significantly to rain formation. However, the simulated reflectivities are clearly underestimated when melting is present.

The convection in the initial phase is less developed in the model and the drops on the ground are smaller than observed.

In the following phase with weaker convection, the model reproduces well the maxima of reflectivity close to the ground and the measurements of the disdrometer.

In a polluted air mass the model produces less precipitation, in area as well as in accumulation. Also, this precipitation starts later. Analysing the content of liquid and ice, is seems that in a medium convective situation the warm microphysical processes are more affected by an increase of the aerosol particle number. This can certainly be attributed to the parameterization of the ice nucleation used in the model. This aspect will be studied in the future, taking into account other nucleation ways.

7. LITTERATURE

Bott A., 1998 : A flux method for the numerical solution of the stochastic collection equation. *J. Atmos. Sci.*, **55**, 2284-2293.

Clark, T. L., and W. D. Hall, 1991 : Multi-domain simulations of the time dependent Navier-Stokes equations : benchmark error analysis of some nesting procedure, *J. Comp. Phys.*, **92**, 456-481.

Chapon B., 2006 : Etude des pluies intenses dans la région des Cévennes-Vivarais à l'aide du radar météorologique. Régionalisation des traitements radar et analyse granulométrique des pluies au sol. Thèse de l'Université Joseph Fourier, Grenoble. 187 p.

Flossmann, A. I. and. H. R. Pruppacher, 1988 : A theoretical study of the wet removal of atmospheric pollutants. Part III : The uptake, redistribution, and deposition of (NH4)2SO4 particles by a convective cloud using a two-dimensional cloud dynamics model. J. Atmos. Sci., 45, 1857-1871.

Hall W. D., 1980 : A detailed microphysical model within a two-dimensional dynamic framework : Model description and preliminary results. *J. Atmos. Sci.*, **37**, 2486-2506.

Jaenicke, R., 1988 : Aerosol physics and chemistry. In Landolt-Boernstein : Zahlenwerte und Funktionen aus Naturwissenschaften und Technik, V 4b, G. Fischer Editor, Springer, 391-457.

Koop, T., B. Luo, A. Tsias and T. Peter, 2000 : Water activity as the determinant for homogeneous ice nucleation in aqueous solutions. Nature, **406**, 611-615.

Leroy, D., W. Wobrock, and A. I. Flossmann, 2007 : On the influence of the treatment of aerosol particles in different bin microphysical models : a comparison between two different schemes. *Atmos. Res.* In print. doi: 10.1016/j.atmosres.2007.01.003

Meyers, M.P., P. J. Demott and W. R. Cotton, 1992 : New primary ice nucleation parameterizations in an explicit cloud model. *J. Appl. Met.*, **31**, 708-721.

Pruppacher H. R. and J.D. Klett, 1997 : Microphysics of clouds and precipitation. 2nd ed. Kluwer Academic, 954pp.

8. ACKNOWLEDGEMENTS:

The calculations for this paper have been done on computer facilities of the “Institut du Développement et des Ressources en Informatique Scientifique” (IDRIS, CNRS) in Orsay (France) and the “Centre Informatique National de l’Enseignement Supérieur” (CINES) in Montpellier (France), under project no.940180. The authors acknowledge with gratitude the hours of computer time and the support provided. The authors also acknowledge this gratitude the support received from the French CNRS/INSU program *OHMCV/Lefe.*
.

Properties of arctic mixed-phase stratus and their impacts on longwave surface radiation

Gong Zhang and Greg M. McFarquhar

University of Illinois at Urbana-Champaign, Urbana, IL

1. INTRODUCTION*

The arctic region is of great interest for future climate change projections as higher surface temperature increases compared to mid-latitude regions are occurring here. In the doubling CO_2 scenario it is commonly recognized that the surface temperature increase in the mid-latitude region would be in the range of 2~4 ^oC while in the arctic region the surface temperature increase could reach 10 ^oC (Walsh and Crane 1992). This phenomenon is known as 'the polar amplification effect', which is mainly caused by the snow/ice-albedo positive feedback (Vavrus 2004). Unlike mid-latitudes, the arctic is generally covered with either snow or ice on the ground, which has high surface solar albedo and reflects much of the incoming solar radiation back to the space. With the external radiative forcing associated with doubling CO_2, the surface temperature increases and the snow or ice on the ground melts accordingly. This reduces the overall surface albedo, so that the ground absorbs more incoming solar radiation and further increases the surface temperature. This forms a positive feedback loop as the initial temperature increase introduced by the external radiative forcing is amplified through the feedback process. This positive feedback is what causes the 'polar amplification effect'.

This feedback process was initially (IPCC 1990) introduced without considering cloud effects on the radiation budget (Walsh and Crane 1992). In the arctic region, boundary level mixed-phase stratus especially has a profound effect on the surface radiation budget (Dong et al. 2001, Dong and Mace 2003, Shupe and Intrieri 2004). A boundary level cloud coverage of 70% is not uncommon in the transition seasons of spring and fall. Further, the radiative forcing introduced by arctic boundary level clouds is highly sensitive to their macrophysical and microphysical properties. For example, a change in liquid r_e or cloud fraction can change the surface energy budget by 40 W m^{-2} (Curry et al. 1993) and a change in ice cloud r_e can change the surface energy by 80 W m^{-2} (Harrington and Olson 2001).

As ice crystals and water droplets have different radiative properties (Downing and Williams 1975, Warren 1984), ice and liquid components have different impacts on the radiative properties of mixed-phase clouds. Past studies have explored the cloud phase effect on the radiative properties of mixed-phase clouds in the visible channel (McFarquhar et al. 2004, Sun and Shine 1994). This work focuses on how the vertical location, LWP, r_e and mixture of phase of mixed-phase clouds affects the surface radiation budget in the infrared channel.

This extended abstract is organized as follows. Part 2 discusses the Mixed-Phase Arctic Cloud Experiment (M-PACE) during which the data analyzed in this abstract were collected. Part 3 describes the radiative transfer model used to simulate the surface longwave radiance. Part 3 also illustrates how the cloud microphysical data are used in the radiative transfer model as inputs. Part 4 compares the simulated surface longwave radiance with the surface longwave radiance observation. Part 5 explores how the mixed-phase cloud properties affect the longwave surface radiance.

2. Mixed-Phase Arctic Cloud Experiment (MPACE)

To collect a comprehensive dataset to study arctic boundary level mixed-phase stratus, MPACE was conducted over the North Slope of Alaska in the fall of 2004 (Verlinde et al. 2007). The data used in this work include aircraft in-situ cloud observations, continuous ground-based radiation observations and soundings released over Barrow and Oliktok Point. This dataset provides the necessary information needed to simulate radiative transfer in arctic stratus and estimate surface longwave radiation observation. In particular, in-situ microphysical data collected when the aircraft was spiraling over Oliktok Point (shown in Fig 1) were used to construct vertical profiles that describe how the number concentrations and the effective radii of liquid droplets and ice crystals varied as a function of altitude for inputs to the radiative transfer model (McFarquhar et al. 2007).

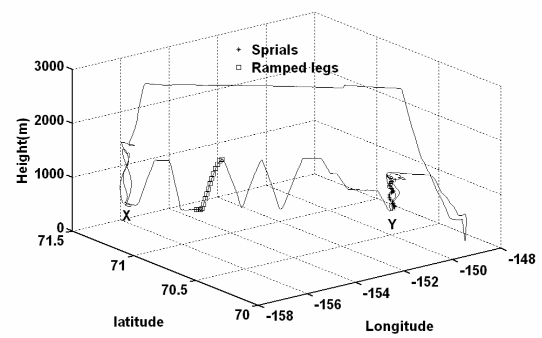

Fig 1: Flight track flown by the University of North Dakota (UND) Citation on 9 October 2004 between 2010 and 2250 UTC. Locations of ground-based remote sensing sites at Barrow and Oliktok Point are indicated by X and Y, where soundings were released. Surface longwave radiation was measured by Atmospheric Emitted Radiance Interferometer (AERI) at Oliktok Point.

3. Simulations of Cloud Radiative Effects

Atmospheric state variables, such as temperature and dewpoint temperature, and cloud properties derived from aircraft in-situ data are used as inputs to line by line radiative transfer model (LBLRTM), which simulates the radiance at the surface that is compared against that measured by the AERI at the surface.

Fig 2 shows the structure of a single-layer cloud observed on Oct 10, 2004 over Oliktok Point. The radar reflectivity in the top panel shows that the stratus extended from 300 m to 1.2 km above ground. The lidar backscatter in the middle panel saturates before reaching the radar cloud top at 1200 m. The lidar depolarization ratio in the bottom panel gives information about particle shape. Large depolarization ratios at the bottom of the cloud indicate ice whereas

* Corresponding Author: Gong Zhang, University of Illinois, Dept. of Atmospheric Science, 105 S. Gregory Street, Urbana, IL, 61801. gzhang2@atmos.uiuc.edu

smaller depolarization ratios at height from 700 to 800 m indicate supercooled water. From this and other radar and lidar observations during MPACE, a general structure of stratus clouds with supercooled water droplets on top and precipitating ice underneath can be seen. Because the stratus was single-layered, a normalized height within cloud can be defined (McFarquhar et al. 2007) as $Z_n = (Z-Z_b)/(Z_t-Z_b)$, where Z_t is the cloud top height and Z_b is the cloud base height. This permits an examination of how the microphysical properties varied with height without the complication of considering how Z_b and Z_t vary during a single day or between days.

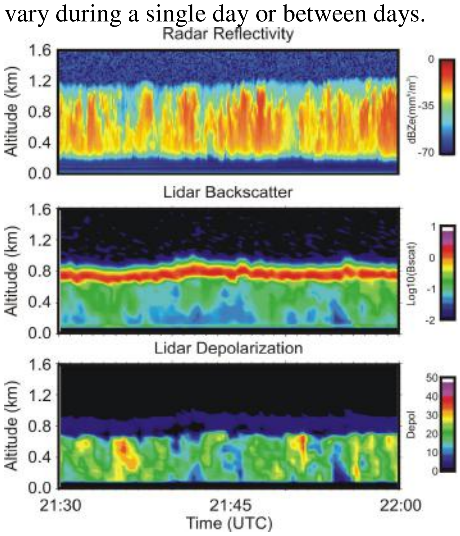

Fig 2: Ground-base cloud radar and lidar observation of a single-layer mixed-phase stratus observed on 10 Oct. 2004.

The LBLRTM requires inputs of number concentration and effective radius of water droplets (N_w and r_{ew}) and the number concentration and effective radius of ice crystals (N_i and r_{ei}), which are derived from in-situ aircraft data. For a given height and a time period when the aircraft was spiraling over Oliktok Point, the microphysical properties were calculated by averaging over the relevant time period with 100m vertical resolution. Fig 3 and Fig 4 (McFarquhar et al. 2007) show how r_{ei}, r_{ew}, N_w and N_i varied with Z_n for the single-layer mixed-phase clouds for the three days during MPACE when the clouds were sampled.

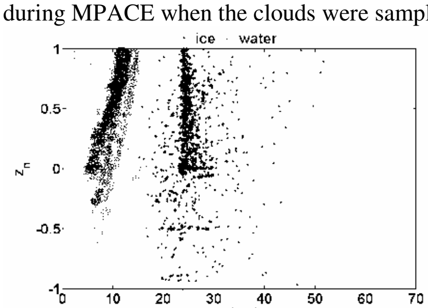

Fig 3: Variation of r_{ew} and r_{ei} as function of Z_n derived from all spirals flown through single-layer mixed-phase clouds sampled on 9 October, 10 October and 12 October.

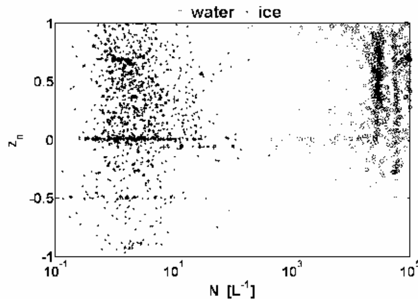

Fig 4: Variation of N_w and N_i for all spirals flown through single-layer mixed-phase clouds on 9 October, 10 October and 12 October.

The atmospheric temperature and dewpoint profiles needed as model inputs are obtained from the closest soundings in time released from Oliktok Point during that day when the aircraft was spiraling over the site.

4. Comparison of simulated and observed radiance

Using inputs described in Section 3 the surface longwave radiance was simulated by LBLRTM and compared against surface radiance observations by AERI between 21:30 and 22:45 UTC on Oct 10, 2004, when spirals were executed over Oliktok Point (Fig. 5). The observed and simulated radiances over the range of 400-1800 cm^{-1} differed by 3.09 $Wm^{-2}str^{-1}$, which is less than 5% of the total integrated radiance. The discrepancy is mainly caused by disagreement in the range of 700-1200 cm^{-1}. The surface longwave radiance was simulated for all the single-layer stratus cases observed by aircraft during MPACE and the results are summarized in Fig 6.

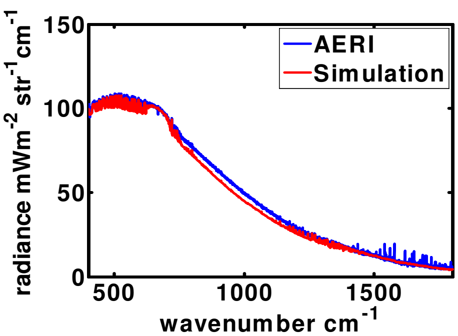

Fig 5: Simulated and observed surface longwave radiance as function of wavenumber; AERI observations and in-situ data averaged between 2130 and 2245 UTC on 10 Oct. 2004

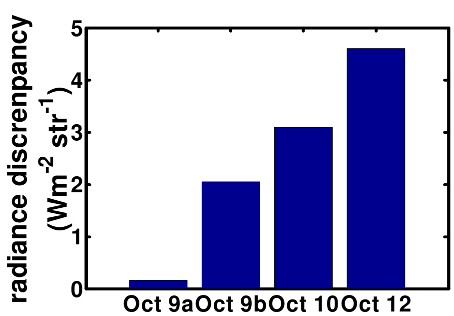

Fig 6: Summary of difference between observed AERI radiance integrated over wavenumber and that simulated by LBLRTM for 4 flights through single-layer boundary layer stratus.

In general, there is good agreement between the simulations and observations as the discrepancy is less than 5% (Vogelman and Ackerman 1995) of the total integrated radiance and the simulated radiance is biased low compared to AERI observations.

5. Sensitivity tests

The discrepancy between observations and simulations could be caused by inaccuracies of either microphysical properties or macrophysical properties (the cloud altitude). Sensitivity tests varying N_w, r_{ew}, and the location of clouds were performed in an attempt to explain discrepancies between simulated and observed longwave radiances, and to examine the importance of cloud microphysical and macrophysical quantities in determining the longwave surface radiation. First, a base simulation, where the cloud is modeled as a single-layer mixed-phase stratus extending from 400m to 1.4 km, with constant r_{ew}, r_{ei}, N_w and N_i throughout the whole cloud layer, was conducted. Then, the location of the clouds were varied by shifting the single-layer stratus up or down by 100 or 200 meters to test the change of surface radiance. For microphysical properties, two important properties, N_w and r_{ew} were varied to test the change of surface longwave radiance.

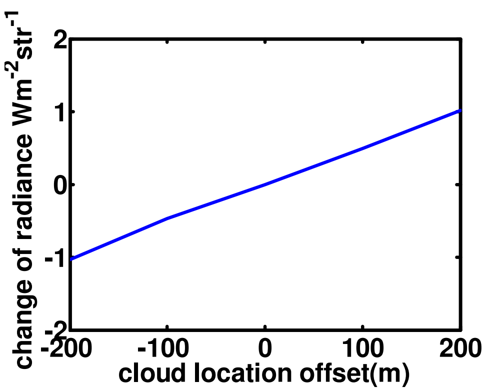

FIG 7 Change of radiance compared to the simulated radiance in the base run as function of cloud location offset. In the LBLRTM simulation, the location of clouds was shifted up or down compared to observed value.

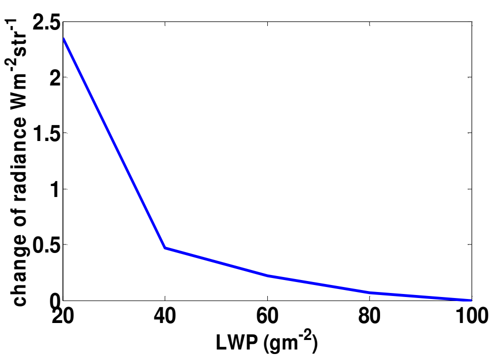

FIG 8 Change of radiance as function of LWP compared to the simulated radiance in the base run

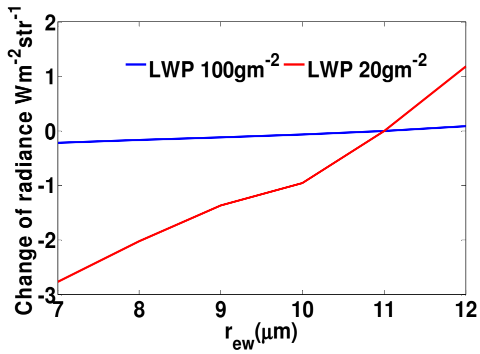

FIG 9 Change of radiance as function of r_{ew} compared to the simulated radiance in the base run (keeping LWP constant)

For optically thick clouds (LWP=100 gm^{-2}) the longwave surface radiance changed by 0.5 Wm^{-2}str^{-1} when the location of the cloud was shifted 100 m higher or 100 m lower. On the other hand, changing LWP from 100 gm^{-2} to 80 gm^{-2} by adjusting the N_w input to the LBLRTM only introduced a 0.08 W m^{-2} str^{-1} change in surface radiance. But, changing LWP from 40 gm^{-2} to 20 gm^{-2} by again adjusting the N_w input to the LBLRTM introduced a 1.88 Wm^{-2}str^{-1} change in surface radiance.

The sensitivity of the surface longwave radiance to the variation of r_{ew} depended on the LWP. Changing r_{ew} from 7 µm to 12 µm introduced a 3.96 Wm^{-2}str^{-1} radiance difference when the LWP was 20 gm^{-2} but only a 0.31 Wm^{-2}str^{-1} difference when the LWP was 100 gm^{-2}.

In summary, the sensitivity tests show that the longwave radiance on the surface was not sensitive to r_{ew} when the LWP value was 100 gm^{-2}. Instead, it was more related to the cloud position. The reason may be that single-layer stratus with LWPs of 100 gm^{-2} are optically-thick enough to act like a black body. The microphysical properties of the clouds have a smaller effect on the surface longwave radiance for these higher LWPs.

To further explore how the microphysical properties of stratus impact the surface longwave radiance, more sensitivity tests were run where the vertical position, r_{ew} and the phase of small particles were adjusted for varying LWPs. The results are presented in Fig 10. The simulation shifting the cloud position up by 100 m reduced the simulated surface longwave radiance. The reduction increased with LWP and reached a maximum value of 0.50 Wm^{-2} str^{-1}at a LWP of 100 g m^{-2}. Contrastingly, reducing the r_{ew} to half of the original observed value increased the simulated surface longwave radiance. The amount of the change decreased with increasing LWP with a maximum reduction of 3.50 Wm^{-2} str^{-1} at a LWP of 20 g m^{-2}. The third sensitivity test explored the effect of varying the phase of small cloud particles (D<50 µm). In the base simulation it was assumed that all small particles were water droplets as suggested by prior works (e.g., McFarquhar and Cober 2004). However, recent work (Zhang and McFarquhar 2008) suggests that some fraction of small particles may be ice phase. This sensitivity test assumed that 20 % of the small cloud particles were ice crystals with the same effective radius (r_{ei}) as that of the water droplets (r_{ew}). This change was introduced by adding an ice cloud component, with N_i given as 20% of the original N_w. The N_w was set to 80% of the original N_w while r_{ew} is kept as the original r_{ew}. This change only introduced a minimal change of surface longwave radiance of 0.17 Wm^{-2} str^{-1}.

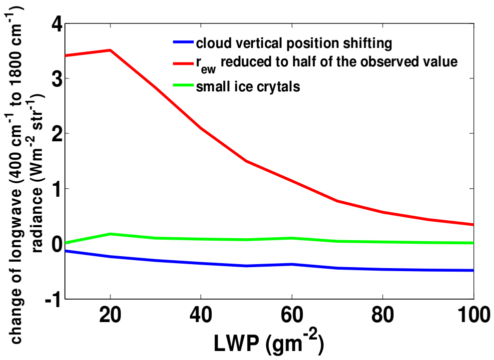

FIG 10 impacts of cloud properties variation with LWP

6. Summary

The longwave radiances simulated by the LBLRTM using in-situ observations and soundings obtained over the North slope of Alaska in optically-thick boundary layer stratus averaged 2.4 $Wm^{-2}str^{-1}$ lower than AERI observations. For optically thick clouds the longwave surface radiance was more sensitive to the cloud base position while for optically thin clouds the surface longwave radiance was more sensitive to the cloud droplet effective radius. However, the results were not sensitive to assumptions about the small particle (D< 50μm) phase.

7. ACKNOWLEDGMENTS

This research was supported by DOE ARM under contract number DE-FG02-00ER62913.The findings of this study do not necessarily reflect the views of DOE ARM.

8. REFERENCES

Curry J. A., J. L. Schramm, and E. E. Ebert, 1993: Impact of clouds on the surface radiation balance of the Arctic Ocean. *Meteor. Atmos. Phys.*, **51**, 197–217.

Dong X., and G. G. Mace, 2003: Arctic stratus cloud properties and radiative forcing at the ARM NSA site. *J. Climate*, **16**, 445–461.

Dong X., G. G. Mace, P. Minnis, and D. F. Young, 2001: Arctic stratus cloud properties and their effect on the surface radiation budget: Selected cases from FIRE ACE. *J. Geophys. Res.*, **106**, 15297–15312.

Downing H. D., and D. Williams, 1975: Optical constants of water in the infrared. *J. Geophys. Res.*, **80**, 1656–1661.

Harrington, J. Y., and P. Q. Olsson (2001): On the potential influence of ice nuclei on surface-forced marine stratocumulus cloud dynamics, *J. Geophys.Res*., 106, 27,473–27,484.

McFarquhar, G. M., and S. G. Cober (2004), Single-scattering properties of mixed-phase Arctic clouds at solar wavelengths: Impacts on radiative transfer, *J. Climate*., **17**, 3799– 3813.

McFarquhar, G., G. Zhang, M. Poellot, G. Kok, R. McCoy, T. Tooman, A. Fridlind and A. Heymsfield, 2007: Ice properties of single layer stratocumulus during the Mixed-Phase Arctic Cloud Experiment (M-PACE): Part I. Observations. *J. Geophys. Res*. **112**, D24201

IPCC, 1990: Climate Change: The IPCC Scientific Assessment. J.T. Houghton, G.J. Jenkins, and J.J. Ephraums, EDs., Cambridge University Press, **365** pp.

Shupe M. D., and J. M. Intrieri, 2004: Cloud radiative forcing of the Arctic surface: The influence of cloud properties, surface albedo, and solar zenith angle. *J. Climate*, **17**, 616–628.

Sun, Z., and K. P. Shine, 1994: Studies of the radiative properties of ice and mixed-phase clouds. *Quart. J. Roy. Meteor. Soc*., **120**,111–137.

Vavrus, S., 2004: The impact of cloud feedbacks on Arctic climate under greenhouse forcing. *J. Climate*, **17**, 603–615.

Verlinde and Coauthors, 2007: The Mixed-Phase Arctic Cloud Experiment. *BAMS*, **88**, 205–221.

Vogelman, A. M., and T. P. Ackerman, 1995: Relating cirrus cloud properties to observed fluxes: A critical assessment. *J. Atmos. Sci.*, **52**, 4285–4301.

Walsh J., and C. Crane, 1992: A comparison of GCM simulations of Arctic climate. *Geophys. Res. Lett*, **19**, 29–32.

Warren S., 1984: Optical constants of ice from the ultraviolet to the microwave. *Appl. Opt.*, **23**, 1206–1225.

Zhang G,. and McFarquhar, G, 2008: Small cloud particle shape in mixed-phase clouds, in preparing

In-situ and remote observations of Arctic July ice and mixed-phase clouds during SHEBA

Paquita Zuidema[1], Paul Lawon[2], Brad Baker[2], Bryan Pilson[2], Qixu Mo[2]

[1]U of Miami (RSMAS), Miami, FL
[2]SPEC, Inc. Boulder, CO

Microphysical data collected in Arctic clouds by a research aircraft during the Surface Heat Budget of the Arctic (SHEBA) are discussed and compared with surface-based millimeter Doppler radar products. Three days in 1998 are analyzed: a mid-level all-ice cloud on July 8, a deep mixed-phase stratus cloud on July 18, and a deep cloud with embedded convection on July 28. A feature of this study is that for the first time, 2D particle probe imagery is being used in the microphysical analysis of these data. Previous studies reported in the literature used 1D probe and cloud particle imager (CPI) data, but these probes do not adequately capture the large portion of the particle size distribution (> ~ 600 microns). The new observations include measured ice water contents exceeding 2 g m^{-3} on July 18 and 28, and particle dimensions up to 3 cm on 28 July. The exceptionally high ice water contents observed in the mixed-phase clouds, and the very large aggregates of July 28, are unexpected in Arctic clouds. There was even incidence of 3 to 5 mm graupel particles on July 28. Supercooled liquid water was observed throughout much of the mixed-phase clouds, even at -27^0 C on 28 July, the highest altitude reached by the C-130. On 18 July, 1 to 3 km pockets with high concentrations (2 to 4 cm^{-3}) of small ice particles were observed embedded within the deep stratus cloud. One instance of these high ice concentrations was observed at -12^0 C, a temperature where there is no known ice multiplication mechanism. The inhomogeneous structure of these mixed-phase Arctic clouds, with layers of ice overlying layers of water, pockets of high ice concentrations at temperatures from – 4 to – 12^0 C, supercooled drizzle at -19^0 C, supercooled cloud drops at -27^0 C, large ice particles and ice water contents present formidable challenges for remote retrievals, radiative transfer and climate models, but interesting opportunities for mixed-phase cloud process modeling studies.

A manuscript on this work is currently under preparation and will placed at the URL site http://www.rsmas.miami.edu/users/pzuidema/publications.html when it is sumitted. The title is subject to change.

ONE DIMENSION CLOUD MODEL WITH ELECTRIFICATION SCHEME: THE DEPENDENCE OF THE CCNS ON THE DEVELOPMENT OF THE ELECTRICAL CHARGE CENTERS

Rachel I. Albrecht[1], Carlos A. Morales[1] and Maria Assunção F. Silva Dias[1,2]

[1]University of São Paulo, Department of Atmospheric Science, São Paulo, Brazil

[2]Center for Weather and Climate Prediction (CPTEC-INPE), Cachoeira Paulista, Brazil

1. INTRODUCTION

Determining how a thunderstorm become electrified has been a goal of laboratory experiments and field observations for several decades (MacGorman and Rust, 1998). Investigators had made substantial progress evaluating various electrification processes, and have found that non-inductive charging mechanism appears capable of producing maximum electric filed magnitudes comparable of those observed in nature (Takahashi, 1978; Saunders et al., 1991; Williams et al. 1994; Avila and Pereyra, 2000). The non-inductive charging mechanism do not require a previous polarization of hydrometeors by an electric field, and is also known as the graupel-ice mechanism: during a rebounding collision between graupel and ice crystals electrical charges are transferred according to the growth stage of the particles (Williams et al., 1994), and many laboratory studies agree that the magnitude and sign of the charge transferred depends onto the environment supercooled droplets liquid water content, temperature, particle sizes, and cloud vertical velocity (Takahashi, 1978; Saunders et al., 1991; Williams et al. 1994; Avila and Pereyra, 2000). Pereyra and Avila (2002) also found that sign and magnitude of charge transferred can also be related to the size distribution of the supercooled cloud droplets, being more positive as the cloud spectra has smaller droplets.

However, observations of myriad electrical properties of thunderstorms remain unexplained. The reason for this is that it is nearly impossible to sample adequately all processes important to thunderstorm electrification because (MacGorman and Rust, 1998): i) relevant scales range from properties of ions and water particles to wind patterns and particle trajectories; ii) storms are complex and can change drastically in a few minutes, so differences in the time and location of which various properties are measured often interfere with analysis of causality; and iii) access for measurements is limited because clouds are remote from ground and many regions inside the cloud are hostile to instrumentation, aircraft and balloons.

Therefore, one powerful and possible instrument to test laboratory and theoretical hypothesis of thunderstorm electrification is also the simulation of electrified clouds using numerical weather prediction models. At this framework, we present here numerical simulations of a one-dimensional cloud model implemented with a electric charge transfer scheme, based on the cloud droplet size distribution dependency of Pereyra and Avila (2002). We try to investigate influence of an enhancement in the number of cloud condensation nuclei on the cloud electrification based on the aerosol effect of Rosenfeld 1999 and Williams et al. (2002): "Air taken from clean (pollued) boundary layer will have a small (large) number of large (small) droplets. The coalescence and precipitation take place in the warm portion of the cloud, diminishing or not growing into the cold (ice) phase. The vapor diffusion growth and the suppression of the coalescence dominate in clouds rich in cloud condensation nuclei, preventing the precipitation and allowing liquid water to ascend into the mixed phase, where it can contribute to the development of graupel and catalyze the electrical charge transfer separation by graupel-ice crystal collisions."`

2. THE ONE-DIMENSIONAL MODEL

The cloud model used in this work is based on a cumulonimbus convection of the dynamic model of Ferrier and Houze (1989), coupled with a four ice category representation of bulk cloud microphysics Ferrier (1994) and a parametrization of charge transfer between classes of hydrometers (Petersen, 1997) The four ice category scheme includes prognostic equations for cloud ice, snow, graupel and hail mixing ratios. In order to use the model for examining the microphysical and electrical evolution of convection, the addition of parameterizations for non-inductive collision charging of the precipitation, and lightning discharges. The model dynamics was not modified.

The cloud microphysics is based on exponential (rain, snow, graupel and hail) and monodisperse (cloud water and ice) distributions of the hydrometeons. The mixing ratio (q_x) of these particles (x) are governed by the continuity equation of mass, which can be expressed as a balance of the advection, turbulence, sources and sinks of the hydrometers. The sources (SOUR) and sinks (SINK) of x are the microphysical processes of formation, development and vanishment of cloud particles, such as condensation, evaporation, autoconversion, coalescence, breakup, rimming, acreation, etc. From all these processes, those that involve the interaction by collision-rebounds between ice particles accounts for the electrification of the cloud and charge transferred (Q_x). Per unit time, the volume in which a particle x=1 of diameter D_1 collides with a particle x=2 of diameter D_2 is given by the *collision kernel* K_{12}, and number densities (N_1, N_2) of diameters D_1 and D_2, that is

$$SOUR_1 = \iint K_{12} N_1(D_1) N_2(D_2) \delta\mu \, dD_1 \, dD_2 = SINK_2$$
$$K_{12} = \frac{\pi}{4}(D_1 + D_2)^2 |v_1 - v_2| \varepsilon_{12} \qquad (1)$$

where v_1 and v_2 are particles 1 and 2 terminal fall velocities. The collision kernel is the effective cylindric volume for collision of particles 1 and 2 times the fraction of particles 1 in this volume that collides with particles 2 and separate from it (collision-separation efficiency, ε_{12}). δm is the magnitude of charge transferred during the collision based on laboratory measurements. From these laboratory works (Takahashi, 1978; Saunders et al., 1991; Williams et al. 1994; Avila and Pereyra, 2000), only the work done at the *National University of Cordoba* by Pereyra and Avila (2002) have not been tested at numerical models. Therefore, here we summarize their laboratory measurements in the following equations, which were also incorporated in the 1D cloud model. The mean charge transferred per collision of a graupel and an ice crystal $\delta\mu$ is:

$$\delta\mu = 1.5(T - T_0)\alpha$$
$$\alpha = \frac{\delta v}{8.5}\left(\frac{D_{0i}}{24.4}\right) \qquad (2)$$

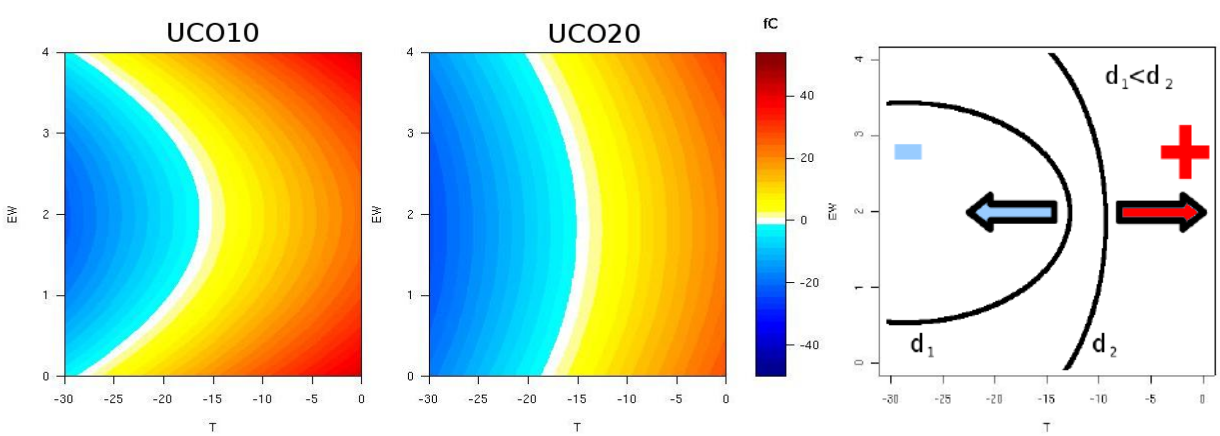

Figure 1 *– Charge gained by graupel colliding with ice particles as a function of temperature and liquid water content from Pereyra and Avila (2002), for cloud droplets of 10 (UCO10) and 20 (UCO20) μm, and a scheme of how the charge gained by graupel change with mean volumetric cloud droplet size distribution diameter (d in Equation 3).*

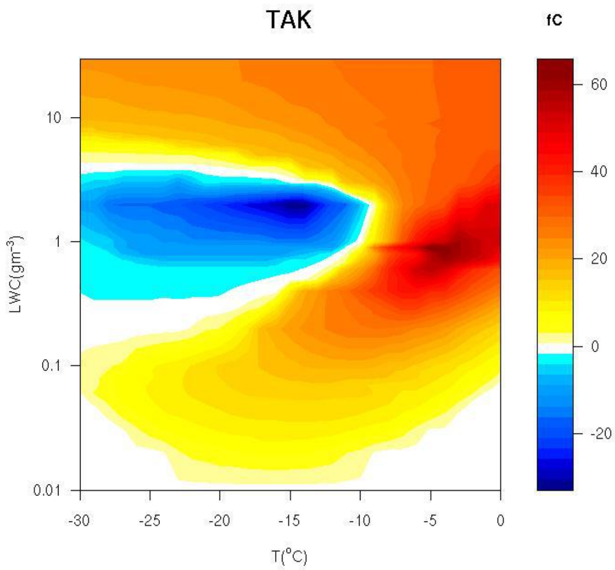

Figure 2 *– Charge gained by graupel colliding with ice particles as a function of temperature and liquid water content from Takahashi (1978, 1984).*

$$\begin{aligned} &T_0=[A(EW)^2+B(EW)+C]\beta \\ &A=min(0;0.41\text{d}-9.3) \\ &B=max(0;-1.7\text{d}+38) \\ &C=2\text{d}-58 \\ &\beta=1.6=0.07\delta v \end{aligned} \quad (3)$$

where T is the environment temperature, EW is the effective liquid water content, Δv is the relative vertical velocity between the graupel and the ice crystal, and d is the mean volumetric cloud droplet size distribution diameter. The term a is a scale correction for all range of graupel and ice crystal sizes (same as Takahashi, 1984), once their measurements where taken with a ice crystal distributions of mean volumetric diameter D_{0i} of 24.4 μm. and a relative vertical velocity Δv of 8.5 ms-1. The concept of equations (2) and (3) is illustrated in Figure 1.

Takahashi (1978, 1984) charge transferred parametrization is a function *f(LWC,T)* of the liquid water content (*LWC*) and temperature (*T*), as shown in Figure 2 and mathematically expressed as

$$\delta\mu=f(LWC,T)\times\alpha, \qquad \alpha=5\left(\frac{D_1}{D_0}\right)^2\frac{|v_1-v_2|}{v_0} \quad (4)$$

where *a* is a correction factor for the laboratory measurements conditions, which varies from 0 to a maximum of 10, D_0=100 μm and v_0=8 ms^{-1}.

The lightning channel parameterization is adapted from the work of MacGorman et al. (2001). After found the grid point that exceeded the E_{even}, given as:

$$E_{even}=\pm167\left(1.208\exp\left(-\frac{z}{8.4}\right)\right) \quad (5)$$

the leader is propagated bi-directionally towards the top and bottom of the storm, in all consecutive grid points where *E* is higher than E_{stop}=15 kVm^{-1}. Having the upper and bottom ends of the lightning, the leader is extended four more grid points up and down to guarantee that fact that lightning can also propagate into regions of very electric charges. The charge density added to the grid point for the neutralization is:

$$\begin{aligned} &\delta Q_{net}=0, && if\ \ |Q_{net}|\le Q_{th} \\ &\delta Q_{net}=(|Q_{net}|-Q_{th})f_p-\delta Q_{cor}, && if\ \ Q_{net}<-Q_{th} \\ &\delta Q_{net}=-(Q_{net}-Q_{th})f_p-\delta Q_{cor}, && if\ \ Q_{net}>-Q_{th} \end{aligned} \quad (6)$$

where δQ_{net} is the net charge density before the lightning, Q_{th} is a threshold equal to 0.5 nCm-3, f_p is the fraction to be neutralized and equal to 0.33, and δQ_{cor} is a correction to guarantee that same amount of negative and positive charges are neutralized:

$$\delta Q_{cor}=\frac{\left[\sum(|Q_{net}|-\delta Q_{th})f_p\right]_- -\left[\sum(\delta_{net}-\delta_{th})f_p\right]_+}{N_{dis}} \quad (7)$$

with N_{dis} as the number of points where $|Q_{net}|$ $>Q_{th}$, and the subscripts + and - indicate summation over the grid point with excess of positive and negative charges, respectively. Finally, the distribution of neutralized charge densities for each *x* type of hydrometeor (dQ_x) is calculated based on its relative surface area σ_x:

$$\delta Q_x=\frac{\sigma_x}{\sum\sigma_x}\delta Q_{net} \quad (8)$$

The relative surface areas are considered as spheres of median radius r_x, that is $s_x=2\pi\, r_x^2$. Graupel, snow and hail mean radius are obtained by adjusting their mixing ratios int an exponential distribution, while ice crystal has a fixed diameter of 10 μm.

3. RESULTS

It is presented here a case study of one simulation using the 1D model with initial thermodynamic conditions (vertical profiles of temperature T and dew point temperature T_d) given by a radiosonde launched at Ouro Preto d'Oeste, RO, Brazil on 0600 UTC 24 September 2002 (Figure 3). The 1D model was initiated with a low level profile of vertical velocity w (Ferrier and Houze, 1989), which lifts the air to higher levels and initiate the cloud. The vertical profile of w increases parabolically from 0 ms^{-1} at the surface to 2 ms^{-1} at z=1 km, during the first 30 minutes of simulation. The simulation was conducted for two hours with a time step of approximately 5 s (Ferrier and Houze, 1989), and the vertical resolution of the model is Δz=200 m. Three different simulations were done: (*i*) one taking into account the Takahashi (1978, 1984) parameterization (TAK), and two taking into account the Pereyra

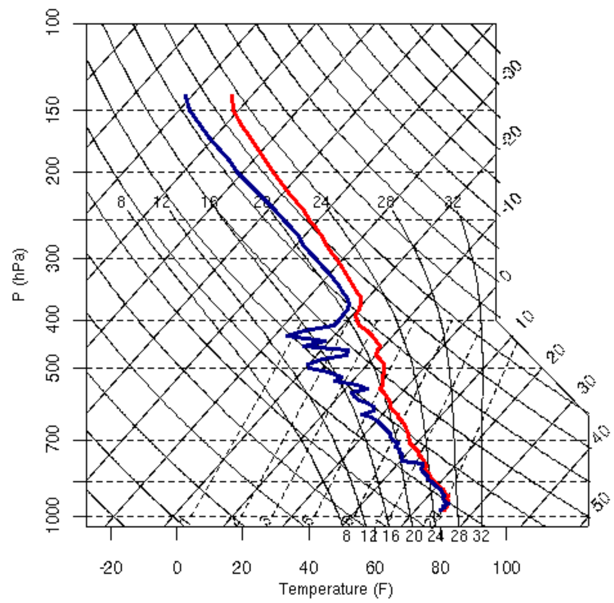

Figure 3 *– SkewT-logP radiosonde diagram for the model initial conditions. Temperature and dew point temperature are denoted by blue and red lines, respectively, and gray dashed lines are moist adiabats. Ouro Preto d'Oeste, RO, Brazil 0600 UTC 24 September 2002.*

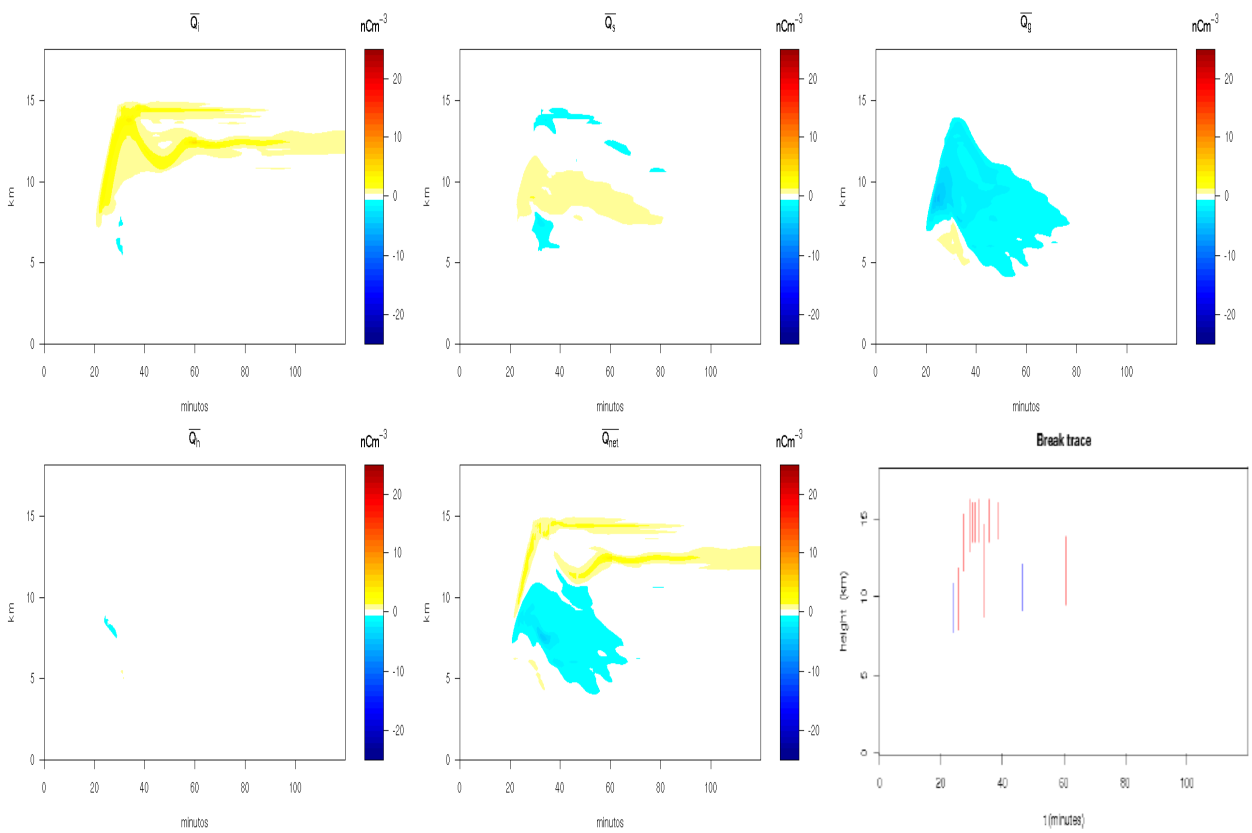

Figure 4 *- Temporal evolution of the charge densities of the four iced hydrometeors considered in this model Q_x (nCm^{-3}) (ice crystals (i), snowflakes (s), graupel (g), and hail (h)), as well as the net charge density (Q_{net}), and the lightnings occurred (Brake trace - red for positive polarity, and blue for negative polarity). Results from the simulation using the Takahashi parameterization – TAK.*

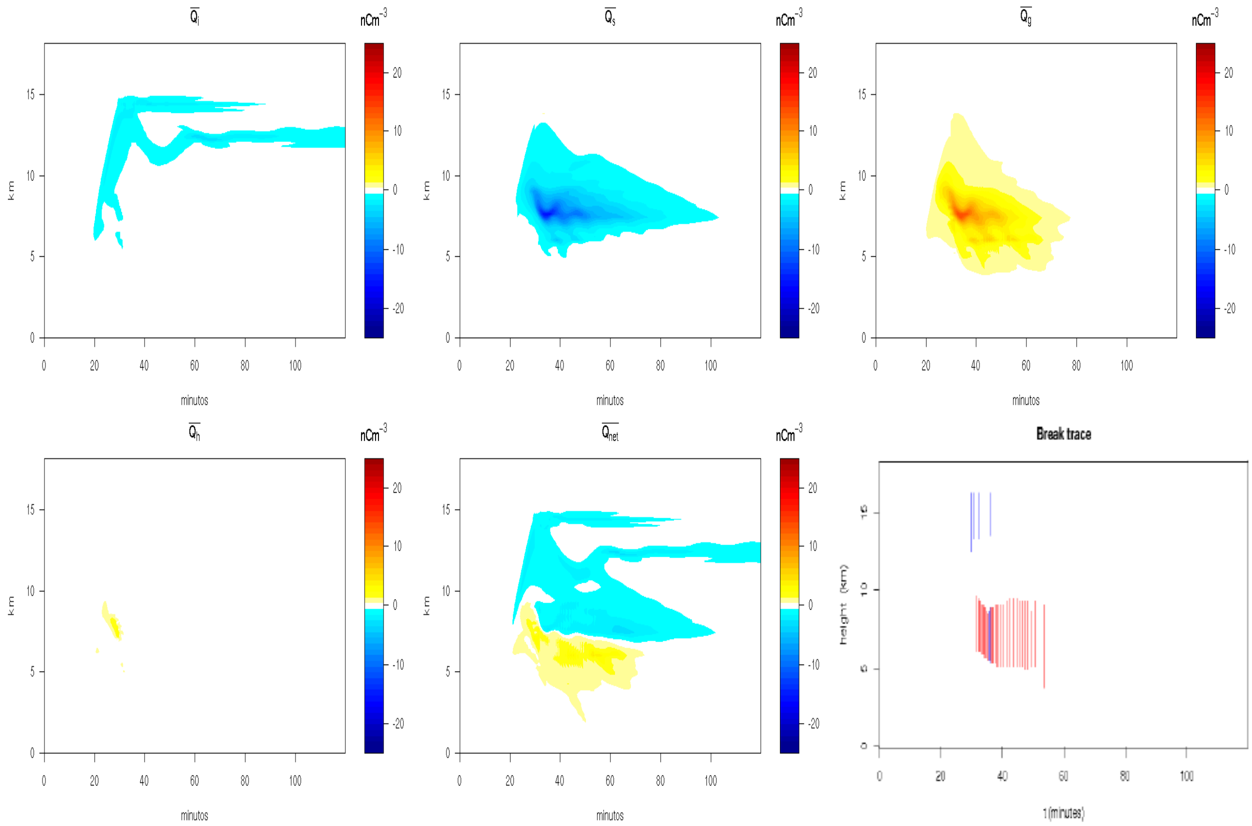

Figure 5 – Same as Figure 3, except for results from the simulation using Pereyra and Avila parametrization with mean volumetric cloud droplets size of 10 μm– UCO10.

and Avila (2002) parametrization (UCO), presented here in the equations 2 and 3: one considering the mean volumetric droplet size distribution set to (*ii*) 10 µm (UCO10), and (*iii*) other to 20 µm (UCO20). The total number concentration of the cloud droplet spectra was set to 8000 cm^{-3} in all three simulations.

The charge electrification of hydrometeors in ice phase occurred in a rapid and intense way for TAK, UCO10 and UCO20 as shown in Figures 4, 5, and 6 respectively. Charge transfer was confined to the mixed cloud phase (where there is the presence of ice particles and supercooled cloud droplets, ~4.8 km of height) due to the collision-rebounding mechanism between ice particles presented at these levels. All the schemes were able to charge the particles in an amount that that the electric field was high enough to breakdown the air rigidity, represented by the breakeven electric field in equation (5). TAK and UCO20 presented a similar structure of sign charging for all particles, with UCO20 having a higher magnitude of charge transferred for the same amount of graupel +hail and ice crystals+snow mixing ratios. However, this difference the magnitude lead to a more complicated charge distribution structure (seen from Q_{net}). The UCO20 simulation (Figure 6) had a dipolar structure during the begging of the thunderstorm life cycle, turning into a tripolar from ~35 to 43 minutes of simulation, and finally became a quadripolar thunderstorm until the complete evaporation of graupel. This behavior is mainly a reflection of the more intense charging of snowflakes in the UCO20 scheme than in TAK. The TAK simulation (Figure 4) had a tripolar just a tripolar structure in the first minutes of the thunderstorm life. These different structures also induced a difference in the number of lightnings: TAK scheme produced 12 lightnings while UCO20 produced a much higher number, 67, all of them being cloud-to-cloud lightnings. The percentage of negative lightnings where higher for UCO20 scheme (70% - 47 negatives and 20 positives) than for TAK scheme (17% - 2 negatives and 10 positives). This difference is due to the higher number of lightnings that occurred during the dissipation of the storm, where the lightnings were mainly negatives. It can be seen from Figures 6 and 4 that the magnitude of negative charging is much higher for UCO20 than for TAK, which explain the higher number of lightnings and mainly of negative polarity.

The scheme of UCO10 also presented more number of lightnings than TAK, but less than UCO20. However, the consideration of a smaller cloud droplet size decreased the temperature of negative charging and also the magnitude, and then graupel and hail were just charged positively as we can see in Figure 5. This reversion in the charging polarity created an inverted polarity charge structure, a dipolar with a thicker positive layer below an also thicker negative layer. This inversion in the polarity, produced more positive lightnings, decreasing the percentage of negative lightnings into 14%.

The similarities in the TAK and UCO20 simulations are explain by the similarities of Takahashi and University of Cordoba work. Both works presented an approximated equal experiment apparatus, but their method of creating cloud droplets (liquid water content - LWC) were different. TAK used a boiler to create a cloud of small droplets and also a low LWC, and an spray to create high LWC by having cloud droplets of very large sizes (a mean size of 90 μm and sizes up to 140 μm of diameter – Takahashi, 1978, Figure 5). The UCO work, however, created high LWC cloud environments maintaining the mean droplet size distributions (~15 and 21 μm of mean volumetric cloud droplet sizes). This difference and the analyses of the charge transferred to the graupel when colliding with ice crystals of the same size permitted these authors (Pereyra and Avila, 2002) to verify and distinguish the dependence of cloud droplet size, while TAK did the charge analyses of all droplet spectra just in one chart (Figure 1). Probably, Takahashi (1978) work would have a similar cloud droplet dependence if there was an controlling of the spectra.

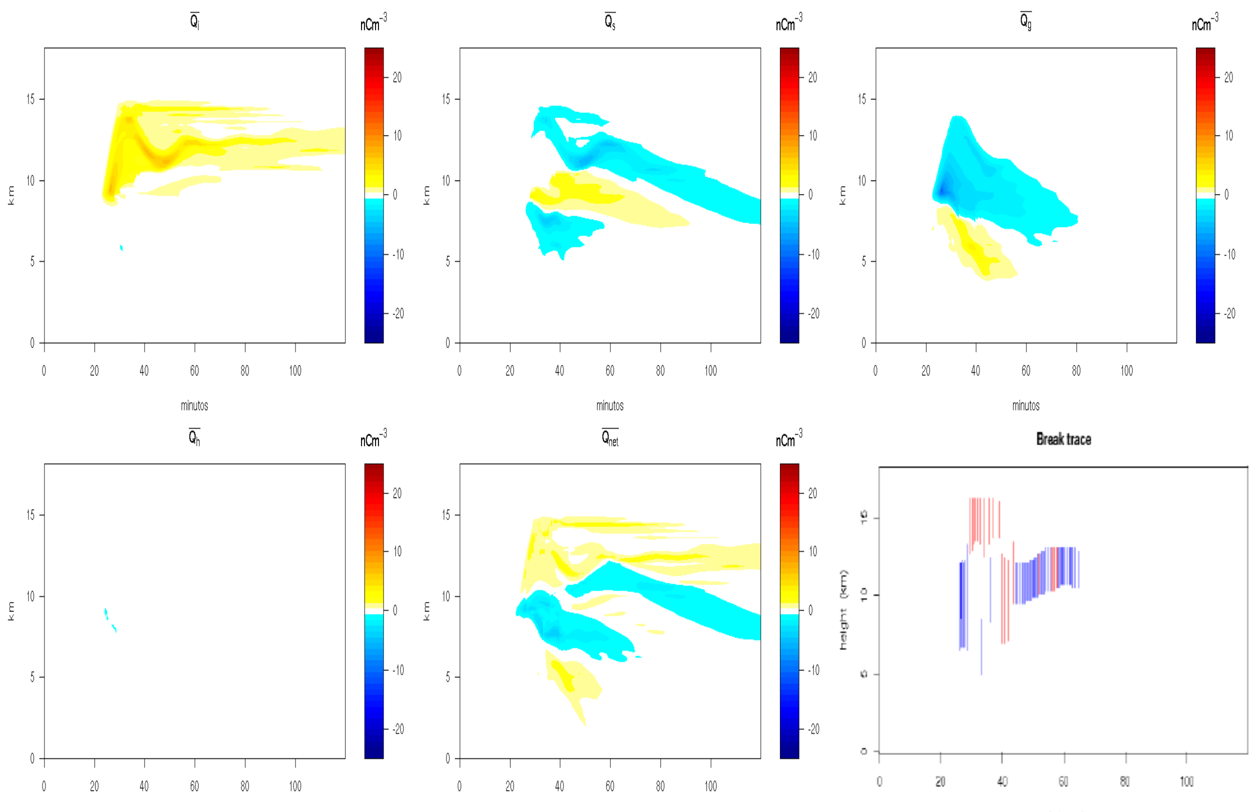

Figure 6 – Same as Figure 3, except for results from the simulation using Pereyra and Avila parametrization with mean volumetric cloud droplets size of 20 μm– UCO20.

4. CONCLUSIONS

The new charge transfer parameterization based on Pereyra and Avila (2002) produced an inverted dipole for a droplet size distribution with smaller diameter, and a normal tripole similar to the simulation using Takahashi parametrization. Therefore, the aerosol effect (Rosenfel 1999; Williams et al. 2002) could influence on the electric charge of the clouds producing more positive cloud-to-ground lightning, as observed during the dry-to-wet season over the Amazon Basin by Albrecht and Morales (2008).

Acknowledgments
This work was supported by FAPESP (Fundação de Amparo a Pesquisa de São Paulo) on the grant number 04/09049-3.

REFERENCES

Albrecht, R. I., and C. A. Morales, 2008: Effects of the biomass burning in the thunderstorm development: An analysis in the Amazon Basin, *this Conference Proceedings*.

Avila, E. E., and R. G. Pereyra, 2000: Charge transfer during crystal-graupel collisions for two different cloud droplet size distribution, *Geophys. Res. Lett.*, 27, 3837-3840.

Ferrier, B. S. and R. A. Houze, 1989: One-Dimensional time-dependent cumulonimbus convection. *J. Atmos. Sci.*, 43, 330-352.

Ferrier, B. S., 1994: A double-moment multiple-phase four-class bulk ice scheme. Pat I: Description. *J. Atmos. Sci.*, 51, 249-280.

MacGorman, D. R., and W.D. Rust,1998: *The electrical nature of storms*, New York, Oxford University Press.

MacGorman, D. R., J. M. Straka, and C. L. Ziegler, 2001: A Lightning Parameterization for Numerical Cloud Models, *Journal of Applied Meteorology*, 40, 459-478, 2001.

Pereyra, R. G., and E. E. Avila, 2002: Charge transfer measurements during single ice crystal collisions with a target growing by rimming, *J. Geophys. Res.*, 107, 4735.

Petersen, W., 1997: *Multi-scale processes studies in the tropics: Results from lightning observations*, Ph. D. dissertation, Colorado State University, Paper No 632, April, pp. 354.

Rosenfeld, D, 1999: TRMM observed first direct evidence of smoke from forest fires inhibiting rainfall, *Geophys. Res. Lett.*, 26, 3105-3108.

Saunders, P. R. , W. D. Keith, and R. P. Mitzeva, 1991: The effect of liquid water on thunderstorm charging, *J. Geophys. Res.*, 96, 11007-1101.

Takahashi, T., 1978: Rimming electrification as a charge generation mechanism in thunderstorms, *J. Atmos. Sci.*, 35, 1536-1548.

Takahashi, T., 1984: Thunderstorm electrification – A numerical study, *J. Atmos. Sci.*, 41, 777-1794.

Williams, E. R., R. Zhang, D. Boccippio, 1994: Microphysical growth state of ice particles and large-scale electrical structure of clouds, *J. Geophys. Res.*, 99, 10787-10792.

Williams, E., and co-authors, 2002: Contrasting convective regimes over the Amazon: Implications for cloud electrification, *J. Geophys. Res.*, 107, 8082.

TOWARDS A BETTER REPRESENTATION OF HIGH DENSITY ICE PARTICLES IN A STATE-OF-THE-ART TWO-MOMENT BULK MICROPHYSICAL SCHEME

Ulrich Blahak*
Institut für Meteorologie und Klimaforschung, Universität Karlsruhe / Forschungszentrum Karlsruhe

1 INTRODUCTION

One of the upcoming topics in cloud microphysics is to investigate the influence of increased air pollution by anthropogenic aerosols on the evolution of convective clouds and formation of hail in midlatitude storms. In this context, it is of importance that the cloud microphysical scheme is able to predict the evolution of hail with a certain degree of confidence. Hail particles may influence the microphysical-dynamical feedback and the simulated precipitation efficiency due to their ability for efficient collision and riming growth and high sedimentation velocity.

Originally, the 2-moment bulk microphysical scheme by Seifert and Beheng (2006) with the modifications given in Seifert et al. (2006), henceforth called "bulk scheme", comprised the 5 hydrometeor categories cloud water, rain water, cloud ice, snow and graupel. It predicts the first 2 moments of the underlying particle size distribution with respect to particle mass, namely the number- and mass density, for each of the hydrometeor classes. In principal, this enables a more realistic simulation of most cloud microphysical processes (e.g., collision/coalescence, accretion, sedimentation, evaporation) compared to conventional 1-moment schemes. In contrast to other 2-moment schemes, a new detailed parameterization of warm rain processes (autoconversion, accretion, selfcollection) is applied as well as a very careful treatment of all other collision processes (solid-solid and liquid-solid). E.g., collision processes between ice species take into account a variation of the fallspeed for particles of a given size. Moreover, the scheme is able to take into account different aerosol regimes (high-CCN versus low-CCN conditions).

Recently, the Seifert-Beheng-scheme (referred to as two-moment scheme in the following) has been revised with respect to a better representation of high density ice particles like hail. These revisions are motivated (sections 2 and 3) and described (section 5) in the following.

2 FORMATION OF HAIL PARTICLES

According to the WMO definition, a hailstone is a high-density ice particle with a diameter larger than 5 mm. It is known that such particles originate preferably in the updraft regions of convective clouds. Here, freezing raindrops or other dense ice hydrometeors might serve as initial "hail embryos" which subsequently grow by accretion of supercooled water droplets (riming) and maintain a rather high particle bulk density ρ_b during their growth, accompanied by a comparatively high particle fall speed. However, usually such particles cannot grow to large dense hailstones with sizes of up to several cm through riming alone. An important mechanism leading to large hail is the recirculation of falling and probably partially melting hailstones into an adjacent strong updraft with subsequent refreezing and further growth by riming, leading to the often observed concentrically layered structure of hail stones.

A further mechanism to create larger sized dense ice particles is the conversion of large graupel into a high density particle by the so called "wet growth" process. If the graupel particle under consideration is located in an environment with large concentration of supercooled liquid water, it exhibits a high riming rate and a large release of latent heat of freezing. Initially this latent heat is stored within the growing graupel particle, increases its heat content and temperature and is transported away from the particle by turbulent heat transfer. In a steady state environment the growing particle would reach a steady temperature as equilibrium between latent heat release on and heat flux away from the particle. If this temperature T_S reaches 0°C, no more freezing of supercooled water can occur (Schumann-Ludlam limit, e.g., Young, 1993). Instead, liquid water accumulates on the particle and/or gets soaked into pores and air inclusions of the growing particle. Moreover, excess heat now is used to melt the ice core. It is said that the particle has reached the "wet growth regime" and transforms into a higher density particle, which eventually may refreeze completely later. Theoretical considerations show (e.g., Dennis and Musil, 1973) that, at given environmental supercooled water content and temperature, particles are in wet growth mode if their diameter D exceeds a certain threshold diameter D_{wg}. Particles having $D > D_{wg}$ are in wet growth mode, smaller particles are not. Besides the increased bulk density, a particle in wet growth mode more efficiently grows by accretion of ice particles since its sticking efficiency is near unity in contrast to lower values for dry particles.

3 PREVIOUS REPRESENTATION OF HIGH DENSITY ICE PARTICLES

As mentioned above, the two-moment scheme in its initial version comprised 5 classes of hydrometeors, namely cloud drops, rain, cloud ice, snow and graupel. It did not contain a hail-like class of high density particles with a distinctively large fall speed. There was only the abovementioned class of graupel particles which exhibited an "intermediate" bulk density and fallspeed. The corresponding size-mass and fallspeed-mass relations are specified in the bulk scheme in the usual form of simple two-parametric power laws

$$D = a_g x^{b_g} \qquad , \qquad v = a_v x^{b_v} \tag{1}$$

with parameters a_g, b_g, a_v and b_v and particle mass x. The above original graupel class was specified in a way that $\rho(D)$ increased from rather small values of 300 kg m^{-3} for $D = 1$ mm to about 600 kg m^{-3} at $D = 8$ mm. Fallspeed increased from about 1 m s^{-1} for $D = 1$ mm to about 8 m s^{-1} at $D = 8$ mm. Graupel was initiated by riming of snow and cloud ice as well as by freezing of raindrops. This seems inappropriate to realistically represent hail.

*Corresponding author address: Ulrich Blahak, Institut für Meteorologie und Klimaforschung, Universität Karlsruhe / Forschungszentrum Karlsruhe, Postfach 3640, D-76021 Karlsruhe, Germany;
e-mail: ulrich.blahak@imk.fzk.de.

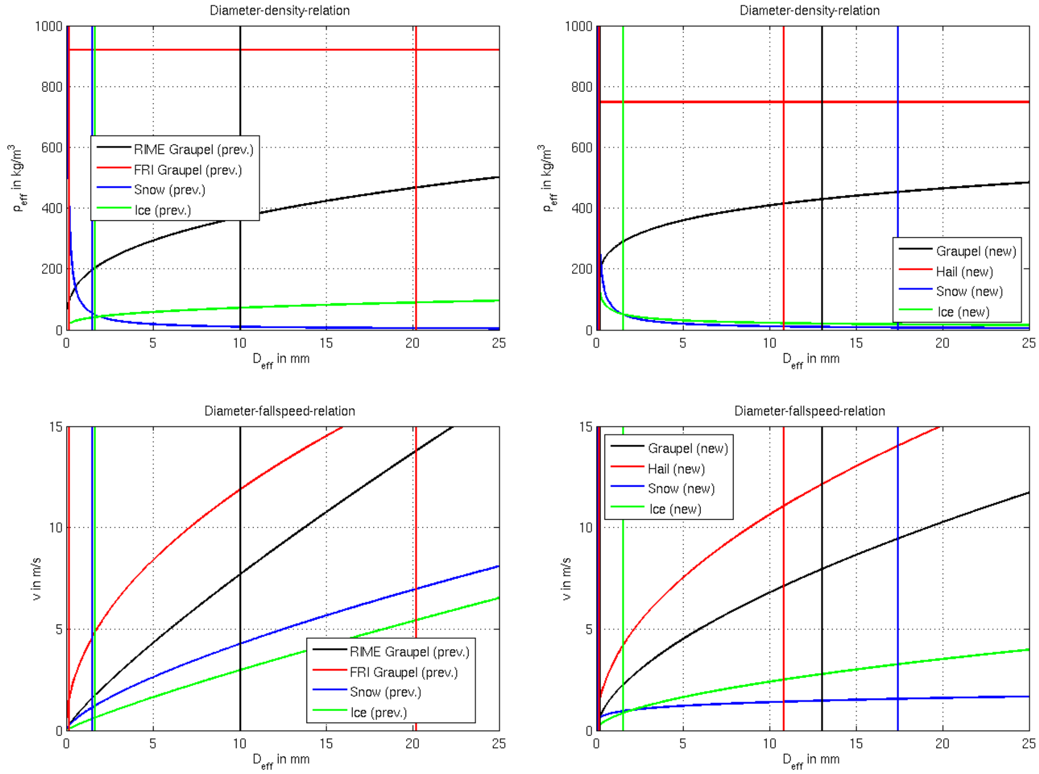

Fig. 1: Diameter-density- and diameter-fallspeed-relations for the ice hydrometeor types of the previous version of the bulk scheme (left column) and the new version (right column). Spherical equivalent particle diameter D (denoted by D_{eff} in the figures) is in mm, bulk density ρ in $\mathrm{kg\,m^{-3}}$ and fallspeed v in $\mathrm{m\,s^{-1}}$. Vertical lines denote minimum and maximum allowed mean mass diameters D_M (if D_M is outside this range at a certain grid box, number density is changed in a way to clip D_M to this allowed range).

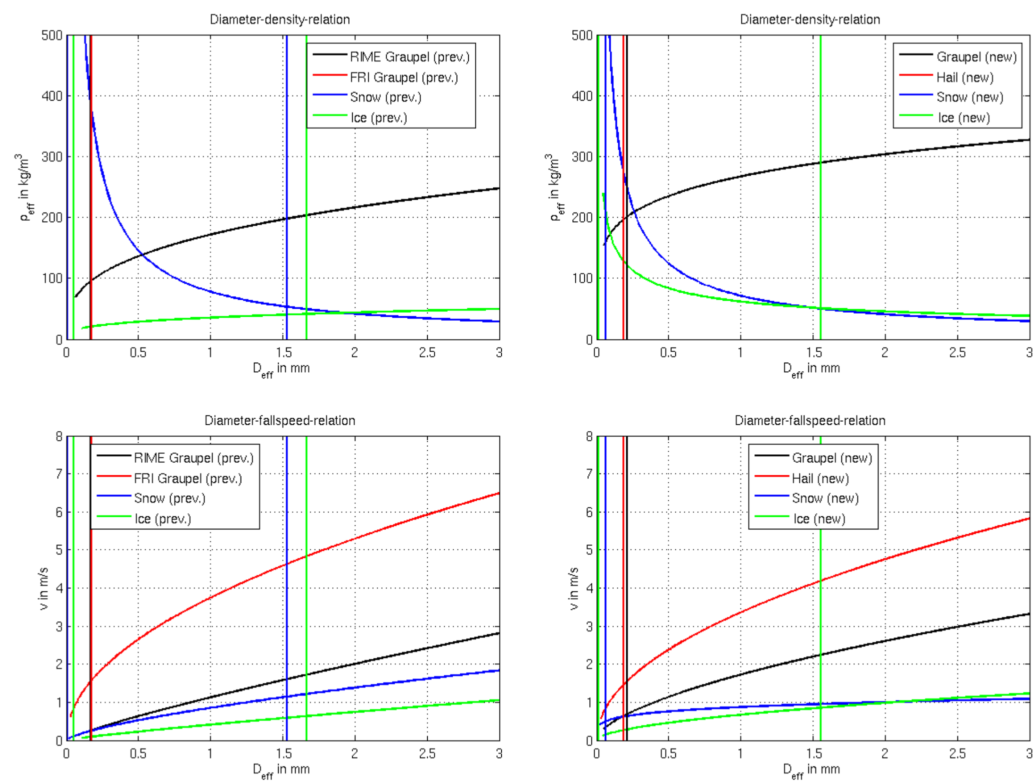

Fig. 2: Same as Figure 1, but diameter range zoomed in to values smaller than 3 mm.

As a first step, the graupel class has been split into two classes according to its formation process. Graupel particles originating from riming of snow and ice were retained in a class of rather low bulk density and fallspeed (RIME Graupel), and those particles initiated by freezing of raindrops have been put into a graupel class with bulk density and fallspeed resembling solid ice spheres (FRI Graupel). The bulk density and fall speed of these two graupel classes as well as those of snow and cloud ice are depicted in Figure 1, left column (full size range up to $D = 25$ mm) and Figure 2, left column (zoomed in to small sizes up to $D = 3$ mm). Vertical lines represent the minimum and maximum allowed mean mass diameters D_M,

$$D_M = a_g \left(\frac{Q}{N}\right)^{b_g} = \left(\frac{6}{\pi \rho_b} \frac{L}{N}\right)^{\frac{1}{3}} \quad . \qquad (2)$$

ρ_b denotes bulk density, Q and N are mass- and number densities of the corresponding hydrometeor species. FRI-graupel is allowed to interact with other hydrometeors exactly in the same way as the previous single graupel class, except collisions between the two graupel classes are not considered (collision efficiency of 0 assumed). More details can be found in Noppel et al. (2006).

With the implementation of the FRI-graupel class it was hoped to be able to simulate more realistically the commonly higher sedimentation velocity and accretional growth of high density ice particles, which enables them to grow bigger and "survive" a larger fall distance at temperature above freezing. More of these high density particles are expected to "make it" to the ground as compared to the original version of the scheme.

However, due to the lack or imperfection of certain process parameterizations like melting, shedding of melt water, refreezing of a wet particle and wet growth, it was not expected to reflect the processes of wet growth and recirculation in a realistic way. Note that the added higher density FRI-graupel class has not yet been termed "hail". With this scheme (henceforth "previous" or "old" scheme), a test case has been simulated using the COSMO model of the German Weather service (DWD), which will be presented in the next section.

4 RESULTS OF THE PREVIOUS TWO-MOMENT-SCHEME VERSION — IDENTIFIED FEATURES AND DEFICIENCIES

The above two-moment-scheme-version with the two splitted graupel classes has been tested using different idealized test cases. One of these test cases will be presented here. Simulations have been carried out with a test version of the nonhydrostatic, fully compressible COSMO model of the German Weather Service (DWD). The characteristics of the simulations are:

- COSMO model version 3.19
- Two-dimensional setup (X-Z-plane)
- $\Delta X = 350$ m, $\Delta Z = 125$ m, 485 grid points in X-direction, 176 vertical levels
- Timestep of 3 s, simulation up to 3 h

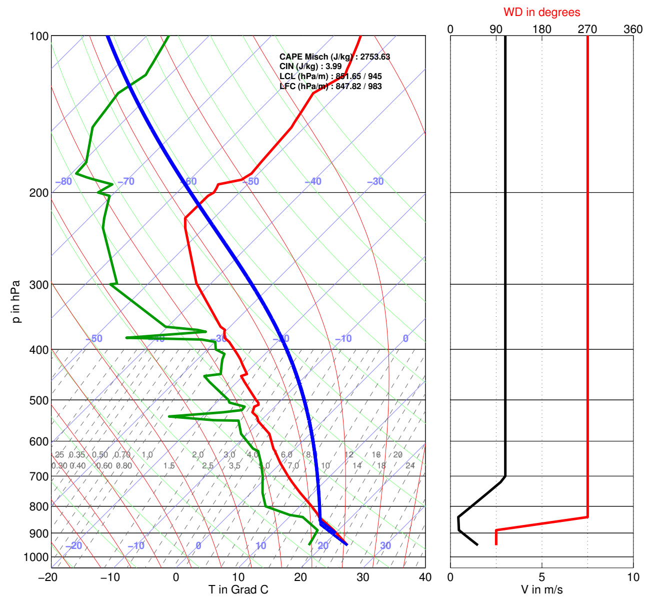

Fig. 3: Skew-T / log-p diagram of the initial profiles of temperature T in °C (red, left plate), dewpoint T_d in °C (green, left plate), wind direction in degrees (red, right plate) and windspeed in m s-1 (black, right plate) as function of pressure in hPa. Blue lines in the left figure: T of moist adiabatically lifted air parcels, one lifted from ground level, and one composed of mixed boundary layer air (lowest 100 hPa).

- Idealized initial and (fixed) lateral boundary conditions: profiles of temperature, moisture and wind speed as depicted in Figure 3. For these profiles, CAPE is about 2800 J kg^{-1}. These profiles have been synthesized from a sounding of 28/06/2006 near the city of Stuttgart, Germany (occurence of a strong hail storm) and nearby surface observations of temperature and dewpoint at the ground. Wind profile idealized adapted to the two-dimensional setup (i.e., $v = 0$)
- Initiation of a convective cell by constantly heating a bubble-like volume in the boundary layer during 15 min, leading to formation of a multicellular type storm system, beginning after about 25 min into the simulation.
- Nucleation of cloud droplets: look-up table for the initial cloud number concentration as a function of vertical velocity and aerosol properties by Segal and Khain (2006)
- Concerning ambient aerosol conditions, two cases: 1) low initial cloud droplet number concentration of about 100 cm^{-3} ("low CCN" case) and 2) large number concentration of about 1100 cm^{-3} ("high CCN" case).

In this paper, our studies on the properties of the two-moment scheme in the context of convective cloud simulations solely relie on the comparison of simulated radar reflectivity fields with commonly observed properties of the reflectivity profile for convective storms in a qualitative way. Radar reflectivity has been calculated from the modeled hydrometeor fields by methods described in Blahak (2007).

Referring to the simulations described above, Figure 4 depicts X-Z-cuts of simulated radar reflectivity along with isolines of temperature in °C after 50 min (upper row) and 100 min (lower row). For now, it is referred only to the left column which contains results obtained with the previous two-

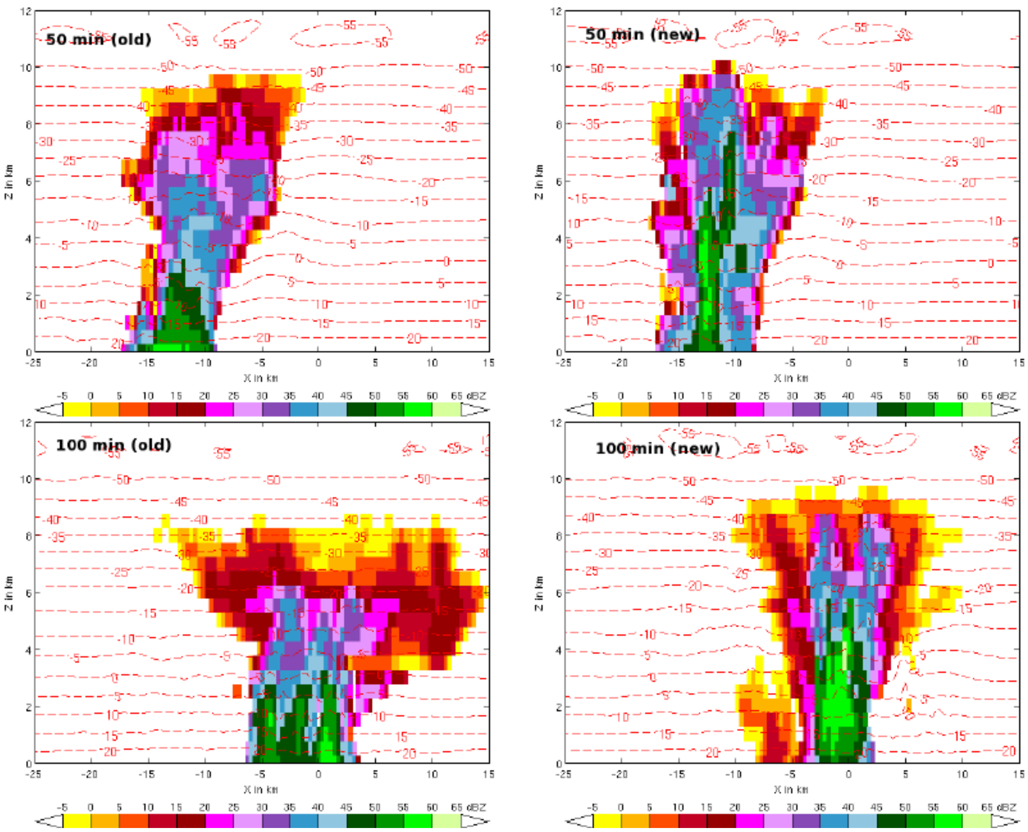

Fig. 4: X-Z-cuts of simulated radar reflectivity in dBZ for the high CCN case, after 50 min (top row) and 100 min (bottom row) simulation time, for the old updated version of the two-moment scheme (left column) and the newly updated version (right column).

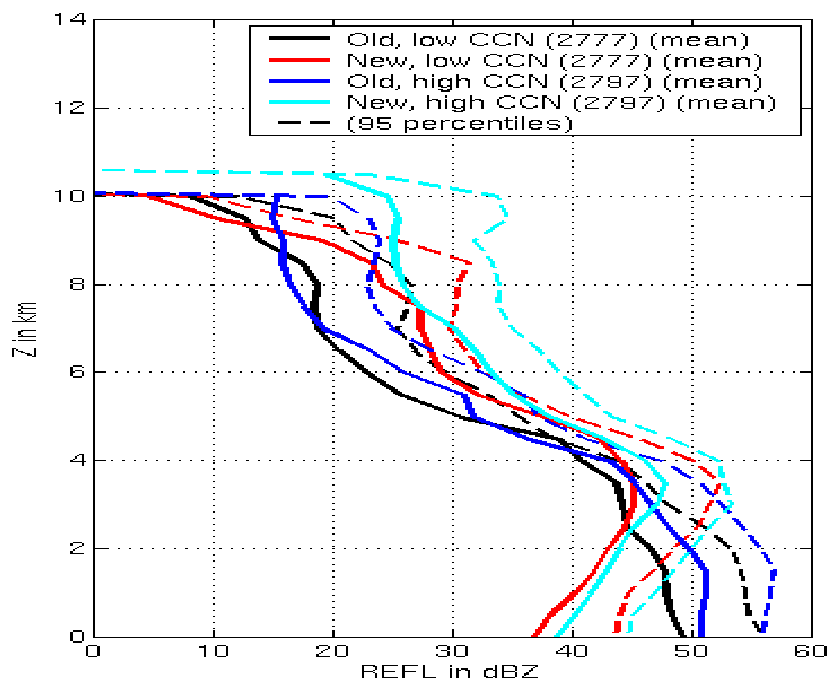

Fig. 5: Space-time-average profiles of reflectivity in dBZ as function of height in km. Averaging has been done in linear space and only gridbox values with a total Q exceeding 1×10^{-6} kg m^{-3} have been included in the average profile. Solid lines represent the actual average profiles, dashed lines show the corresponding 95-%-percentiles. "Old" denotes the previous version of the two-moment scheme, "New" the updated version. The 4-digit numbers in the legend are internal book-keeping codes denoting different settings of the scheme.

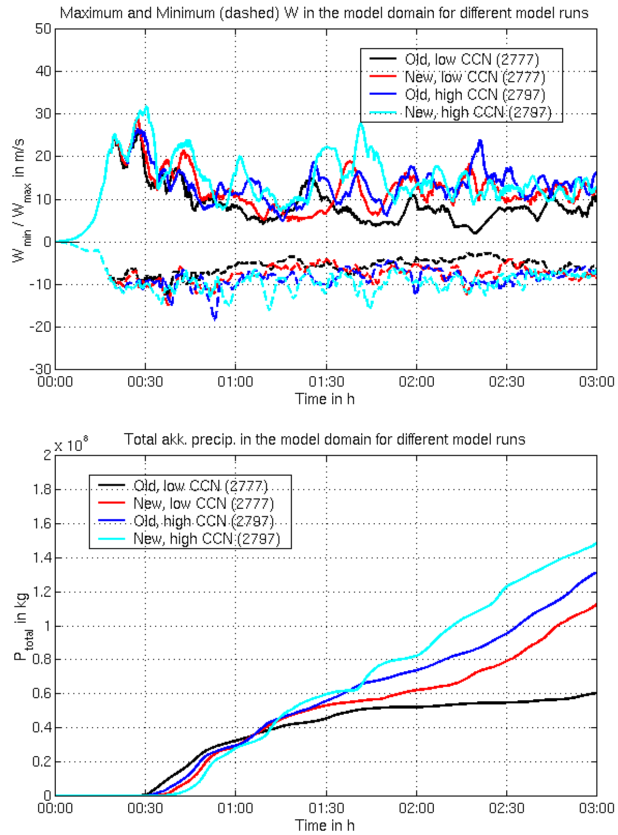

Fig. 6: Time series in h of maximum and minimum vertical velocity W_{max}/W_{min} within the model domain in m s^{-1} (top) and timeseries of total accumulated precipitation P_{tot} in kg (bottom). ***Note the factor 10^8 for $\mathbf{P_{tot}}$*** *values.*

moment model version (n the right side, results are shown after the further changes mentioned in the introduction (”new”), which will be described later). These reflectivity cuts (”old”) show a very typical feature which was observed in all simulations performed with the ”old” updated version: a very abrupt jump in reflectivity from very high values below the melting level (> 50 dBZ) to rather low values above (< 40 dBZ at $Z =$ 8 km). But radar observations of storms often show zones of high reflectivity (typically $>$ 50 dBZ and more) which reach up to heights of 10 km and above in midlatitude regions. These are commonly called ”reflectivity cores” and are probably connected to the presence of large ice particles (graupel and hail). This reflectivity deficit above the freezing level is consistently observed in all our other studies and is considered as a systematic behaviour of the 2-moment scheme.

To investigate the reflectivity profile in an average sense, conditional space-time-average profiles of reflectivity have been computed for the above simulations, i.e., horizontal averages over all grid boxes with Q exceeding a threshold of 1×10^{-6} kg m^{-3}. This reflects the average reflectivity where hydrometeors are present and rules out the influence of horizontal cloud extension as compared to horizontal domain averages. Figure 5 shows these profiles (blue and black solid lines for the ”old” version), along with 95-%-percentiles to indicate also the extremes of the space-time distribution of gridpoint values. It is obvious that the abovementioned jump in reflectivity (see blue and black solid line) at the melting level is observed not only for single timesteps but on average for the entire simulations.

It has to be mentioned that updraft speeds are rather low for the presented simulations and barely reach up to 15 m s^{-1} at later times of the simulation (see the upper part of Figure 6, blue curve for the high CCN case). The maximum updraft speed may be viewed as an indication of the overall vigorousness of vertical air motions within the storm, and may be a proxy for the amount of supercooled water and hail embryos present in the ice region, which initiate and support the growth of large particles. However, the apparently too low reflectivity in the ice region has been consistently obtained also for other simulations with higher updraft speeds.

As deeper analyses show, the explanation is, that just too many small particles are present so that riming growth of individual particles is limited by competition for the available supercooled water. To illustrate this, mass densities Q, number densities N and mean diameters D_M of the different hydrometeor classes are presented in the following. Again, conditional space-time-averaged vertical profiles of Q and D_M are utilized, i.e., horizontal averages over all grid boxes with Q and N exceeding thresholds of 1×10^{-6} kg m^{-3} and 1 m^{-3}, which shows the average mass density and size of hydrometeors where hydrometeors are present. These profiles for the above simulations are depicted in Figure 7 (Q) and 8 (D_M) for all 6 hydrometeor categories. Again, for now the focus is on the curves with label ”old” (black and blue). Solid lines are the space-time-average profiles and dashed lines show the corresponding 95-%-percentiles.

The following observations are drawn from these profiles:

- RIME-graupel and FRI-graupel particles (labeled as ”hail”) may be too small, and, since Q seems realistic, number concentrations may be too large.

- Strong increase of D_M of evaporating rain towards the ground, contributing to the sharp reflectivity jump near the melting layer.

- Strong increase of D_M of melting ice particles towards the ground, also contributing to the reflectivity jump.

These observations lead to major changes to the two-moment scheme which are discussed in the next section.

5 IMPROVING REPRESENTATION OF ICE PHASE PROCESSES

Motivated by the results presented in the last section, several modifications and extentions to the two-moment scheme have been made. These may be summarized as follows:

1) Particles of the same as well as of different ice species compete for available supercooled water, therefore, measures have been taken to decrease number concentration and (hopefully) increase particle size. These have been mainly changes to the mass-size- and mass-velocity- relations of ice, snow, and RIME-graupel. The previously discussed Figures 1 and 2 show a comparison of the previous (left column) and new (right column) bulk-density-size-relations (upper figures) and fallspeed-size-relations (lower figures) for all hydrometeor types. Main changes are:
(a) increased (spherical equivalent) bulk density of small cloud ice particles causing a decreased collision cross section and riming (decreased ice-to-graupel conversion)

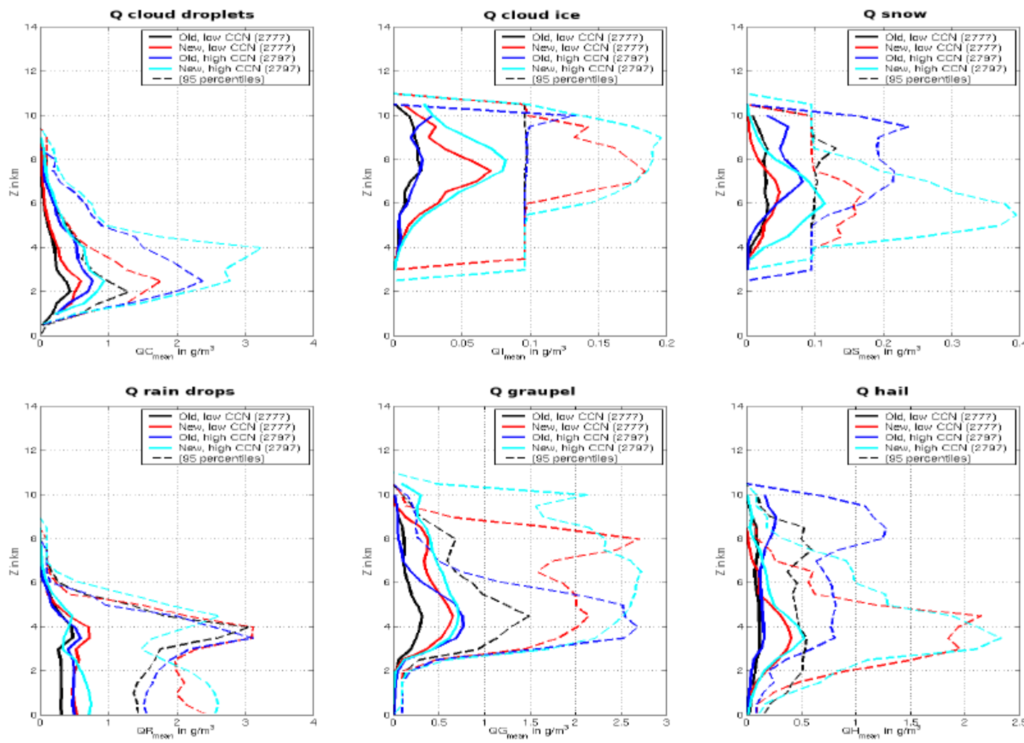

Fig. 7: Space-time-average vertical profiles of hydrometeor mass contents Q_x in $g\,m^{-3}$ of the 6 hydrometeor categories ($x \in \{c, r, i, s, g, h\}$, one plot for each category) as function of height in km. Averaged profiles include only those grid points with Q_x exceeding 1×10^{-6} $kg\,m^{-3}$. Different colors denote the different model runs (see legends of the plots). Solid lines are the actual mean profiles and dashed lines denote the 95-%-percentiles.

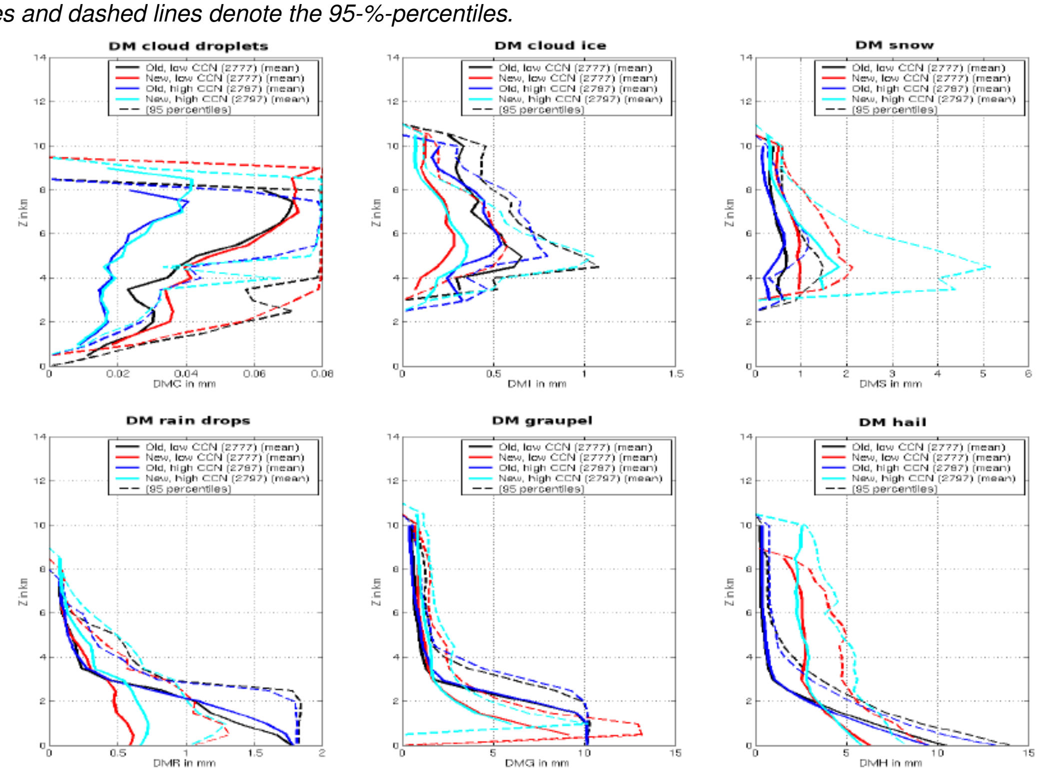

Fig. 8: Same as Figure 7 but for the mean mass diameter D_M. Only grid box values with $Q_x > 1 \times 10^{-6}$ $kg\,m^{-3}$ and $N_x >$ 1 m^{-3} included in the mean profiles and the percentiles.

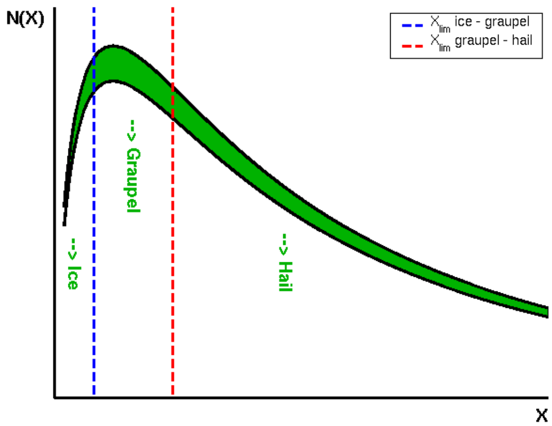

Fig. 9: Schematic diagram of spectral partitioning of freezing raindrops. See text for explanation.

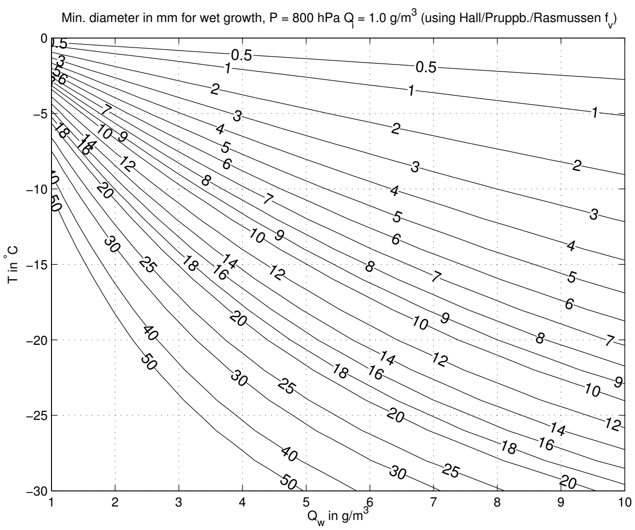

Fig. 10: Dividing diameter D_{wg} for wet growth regime in mm for the updated graupel category, as function of T in $^\circ$C, supercooled liquid water content Q_w in $g\,m^{-3}$ and for an ice particle content $Q_i = 1\ g\,m^{-3}$. Graupel particles having $D > D_{wg}$ are in wet growth mode. A pressure of 800ăhPa has been assumed here.

(b) Increased bulk density and fall speed of small graupel (increased riming of single particles)

2) Change with respect to the unrealistic behavior of D_M of rain: time rate of change of rain number concentration during evaporation now diagnosed based on the assumption of mean size conservation during evaporation, as is done in other schemes (e.g, Khairoutdinov and Kogan, 2000). The previously used parameterization of evaporative number concentration tendency had proven to be inappropriate.

3) Moreover, thoughts about the outcome of freezing rain have been stimulated. Does every freezing raindrop, "small" or "large", serve as an embryo for a high density ice particle? Considering that in a convective updraft ice hydrometeors also grow quite efficiently by depositional growth, mostly on the expense of supercooled cloud droplets (Bergeron-Findeisen-process), and if the conceptual model holds true that a very small initial ice particle may grow by deposition into a branched shape with lots of air inclusions inbetween (lower bulk density and fall speed), then it does seem inappropriate to treat every freezing raindrop as a solid ice sphere. Rather, the idea is now to split the outcome of freezing rain into ice, to lower- and to higher density graupel, according to raindrop size. This is now parameterized by a spectral partitioning approach: the rate of change of mass- and number concentration of raindrops is computed as before by integration of a mass (or size) dependent stochastic freezing probability over the (diagnosed) gamma-type raindrop mass distribution. Since the freezing probability is mass dependent, it is possible to split this integration into different parts according to threshold masses/sizes. Then, number and mass concentration of freezing raindrops in the size range from 0 to a first threshold size (say, $D = 0.5$ mm) are assigned to cloud ice particles. From there to a second threshold size, freezing drops are transferred to RIME graupel (larger initial ice particles do not attain as much air inclusions by depositional growth and retain a larger bulk density). Only those droplets with a size larger than this second threshold freeze into the FRI graupel category. A simple schematic sketch of this approach can be found in Figure 9: the sketched graph depicts the initial rain mass distribution at a certain gridpoint, diagnosed from rain N_r and Q_r. The green area is the part of it which freezes during one timestep. The part of the green area with mass smaller than the blue dashed threshold is converted to cloud ice, the part between blue and red to RIME graupel and the remainder to FRI graupel ("hail").

This technique seems to be beneficial in that it leads to larger mean size of FRI graupel, which resembles better the size aspect of the WMO definition of hail. Therefore the name "FRI graupel" is changed to "hail" in the following to indicate the now included size aspect. Consequently, "RIME graupel" looses its "RIME" suffix. This new freezing approach proofed to be beneficial in considerably increasing hail and graupel sizes aloft and in a better resemblance of the frequently observed reflectivity cores.

4) To further increase the hail-likeness of the hail category, the mechanism of conversion of graupel to hail by wetgrowth of graupel has been implemented (see section 2 for a description of the physical mechanism). The implementation is based on the calculation of D_{wg} (Schumann-Ludlam-limit) by means of the heat budget equation of individual high density ice particles, written as equation for the particle's core temperature T_s, as given by, e.g., Dennis and Musil (1973) and Nelson (1983), as well as on ventilation coefficients by Rasmussen, Pruppacher and Hall (Pruppacher and Klett, 1997). This equation predicts the time evolution of TS under the influence of latent heat release by riming, collection of other ice particles and turbulent heat exchange with the surrounding air. Important parameters are ambient temperature T, particle diameter, mass and fallspeed, as well as surrounding (supercooled) liquid water content and "accretable" ice content. Solving for a steady state and setting $T_s = 0^\circ$C leads to an equation for the dividing diameter D_{wg} for wet growth (see section 2). D_{wg} depends on T and pressure p (because of the fallspeed dependence of the accretion rate), on supercooled liquid water content and to a minor extent on the "accretable" ice- and snow content. Figure 10 shows isolines of D_{wg} for the updated graupel class as function of T and environmental supercooled water content Q_w. It is valid for $p = 800$ hPa

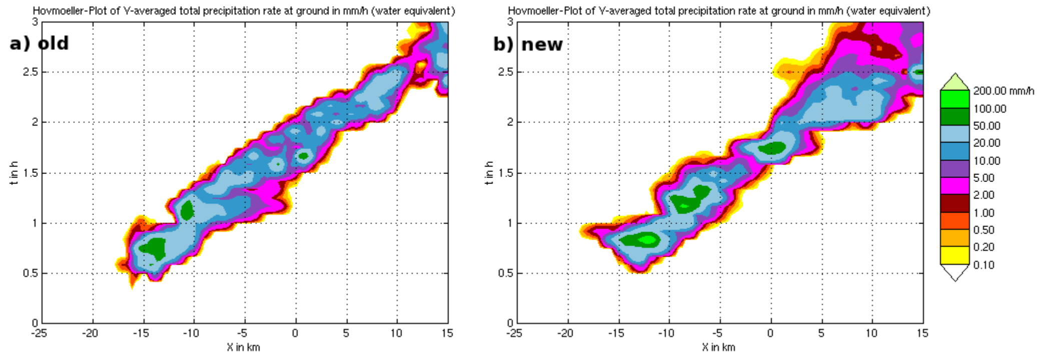

Fig. 11: Hovmoeller-diagram of total precipitation intensity at ground in mm h^{-1} as function of X in km and time in h, for the high CCN case. Previous verson of the two-moment scheme (left plate) and new version (right plate). Time runs from bottom to top.

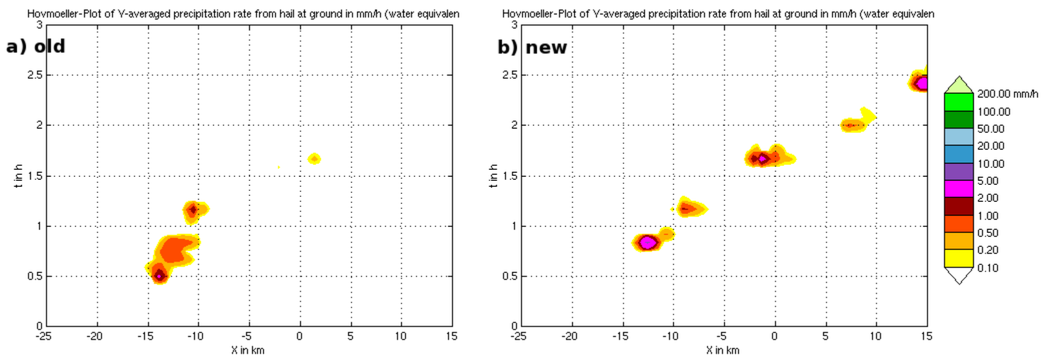

Fig. 12: Same as Figure 11, but for the hail only intensity at ground in mm h^{-1}.

and an ice content $Q_i = 1$ g m^{-3}. It can be seen that D_{wg} increases with decreasing Q_w and T. For $Q_w = 4$ g m^{-3} and $T =$ -10°C, D_{wg} equals 7 mm. D_{wg} as a function of the abovementioned 4 parameters is stored in a lookup table which covers the relevant range of atmospheric conditions.

Parameterization of wet growth conversion from graupel to hail is again based on a spectral partitioning approach, as for the abovementioned partitioning of freezing rain drops. For each grid box and at each time step, DWG is diagnosed using a precalculated lookup table, and based on this threshold and if graupel is present, the part of the (diagnosed) graupel size distribution exceeding the threshold, or more specifically, mass and number concentration contained therein, are converted into hail. This constitutes a further source for large hail particles.

5) To address the issue of strongly increasing mean diameters of melting ice particles towards the ground, the time rate of change of number concentration during melting is now diagnosed also in a way that mean size of the ice species is preserved. Similar parameterization issues as compared to treatment rain number concentration during evaporation have been responsible for the apparently wrong behaviour. The above solution, however, is only regarded as an intermediate practical solution, until a better way has been found, probably based on the explicit prediction of the melted fraction in conjunction with a proper shedding parameterization for large graupel and hail particles.

The version of the bulk scheme which comprises all abovementioned changes will be called the "updated version". The overall effect of these changes is depicted in Figures 4 to 8, 11 and 12: Figure 4 shows X-Z-cuts of simulated radar reflectivity after 50 min and 100 min (high CCN case) for the previous ("old") and updated version ("new") of the two-moment scheme. Figure 6 compares timeseries of maximum and minimum vertical velocity in the model domain and total accumulated precipitation. Also shown are conditional space-time-averaged vertical profiles of simulated reflectivity (Figure 5), of hydrometeor mass densities (Figure 7) and mean mass diameters (Figure 8). Finally, precipitation rate at the surface as function of time is presented as Hovmoeller-Plots in Figure 11 (overall precipitation rate) and Figure 12 (hail only).

Observations and results can be summarized as follows:

- After changes to the scheme: now we get bigger hail particles aloft. The main effect is caused by introduction of spectral partitioning in raindrop freezing parameterization. The graupel mean size is only marginally larger.
- Parameterization of graupel-to-hail conversion due to implementation of wet growth acts as further source for large hail particles.
- More hail reaches the ground due to increased size and fallspeed.
- Due to the presence of larger hail aloft, now reflectivity cores are simulated more realistically.
- Vertical profiles of mean particle size D_M are more plausible since now D_M of rain, graupel and hail does not increase as much towards the ground as before.
- Increased precipitation in both the low-CCN and high-CCN cases. Interestingly, the high-CCN clouds overall produce more precipitation in this case due to longer cloud lifetime.

The reason for the longer lifetime has yet to be determined and may either be due to stronger secondary cell generation by stronger coldpools (stronger evaporation of smaller raindrops) or due to enhanced latent-heat-of-freezing-release due to less active warm rain processes.

For an even more realistic parameterization of hail, one would need to incorporate a parameterization of shedding along with the prediction of the liquid water fraction for the hail category. This would enable a better parameterization of melting and refreezing, important for the recirculation process, and also would improve the calculation of radar reflectivity.

6 CONCLUSIONS

The two-moment bulk microphysical scheme of Seifert and Beheng (2006) including an additional particle category of high density (FRI-)graupel particles (Noppel et al., 2006) has been qualitatively assessed concerning the simulated reflectivity structure in convective clouds. It has been found that especially the often observed high reflectivity values in the upper central part of active convecitve clouds, forming the socalled reflectivity cores, cannot be adequately simulated by this version of the scheme. Rather, a systematic feature of the simulated reflectivity field is a distinct jumplike drop from reflectivites below to above the freezing region. As analyses of the mean particle sizes (defined as the ratio Q/N transferred to an equivalent diameter) show, this is behaviour is due to very small particles in both graupel categories (dominating particles in convective updrafts), associated by very high number concentration. In this case, particle size is the dominating factor contributing to reflectivity.

Therefore, the parameters of size-mass- and velocity-mass-relations of all ice categories have been changed in a way that less RIME-graupel particles initiate by riming, which then can grow bigger by further riming because there is less competition for the available supercooled water. In addition, the initiation of high density FRI-Graupel by freezing of raindrops has been changed. Before, all freezing raindrops were converted to FRI-graupel. Now only particles exceeding a certain size threshold initiate to FRI-graupel, all others are converted either to cloud ice (very small raindrops) or to RIME-graupel. Again, this leads to fewer but larger particles. Further, to render the FRI-graupel more "hail-like", the conversion of RIME- to FRI-graupel by the socalled wet-growth process has been implemented. RIME-graupel will be called "hail" from now on. However, for a realistic simulation of certain hail formation processes (e.g., melting $\rightarrow$ recirculation $\rightarrow$ refreezing), better treatment of melting and shedding is needed, probably including the prediction of the water fraction of melting particles.

All these measures lead to a more realistic simulation of high reflectivity values in the upper part of convective clouds, and there is also an increase of the precipitation efficiency due to stronger sedimentation of the now larger graupel and hail. However, the arguments leading to the model changes are mostly based on qualitative and sometimes intuitive "backwards guessing" from common radar observations, due to lack of proper in situ observations of particle properties within strong convective updrafts. Further verification by real case studies and comparison to a detailed bin microphysics model (Hebrew University Cloud Model) is currently under way.

REFERENCES

Blahak, U., 2007: RADAR_MIE_LM and RADAR_MIELIB — calculation of radar reflectivity from model output, *Internal report, Inst. f. Meteor. and Climate research, University/ Research Center Karlsruhe*, available on request.

Dennis, A. S. and D. J. Musil, 1973: Calculations of hailstone growth and trajectories in a simple cloud model, *J. Atmos. Sci.*, **30**, 278–288.

Khairoutdinov, M. and Y. Kogan, 2000: A new cloud physics parameterization in a large-eddy simulation model of marine stratocumulus, *Mon. Wea. Rev.*, **128**, 229–243.

Nelson, S. P., 1983: The influence of storm flow structure on hail growth, *J. Atmos. Sci.*, (40).

Noppel, H., U. Blahak, K. D. Beheng and A. Seifert, A two-moment cloud microphysics scheme with two process-separated modes of graupel, 12. AMS Conference on Cloud Physics, 10. – 14.7.2006, Madison, Wisconsin, available online: http://ams.confex.com/ams/pdfpapers/113532.pdf, 2006.

Pruppacher, H. R. and J. D. Klett, *Microphysics of Clouds and Precipitation*, Kluwer Academic Publishers, Dordrecht, Boston, London, 1997, 2. edition.

Segal, Y. and A. Khain, 2006: Dependence of droplet concentration on aerosol conditions in different cloud types: Application to droplet concentration parameterization of aerosol conditions, *J. Geophys. Res.*, **111**, D15204, doi:10.1029/2005JD006561.

Seifert, A. and K. D. Beheng, 2006: A two-moment cloud microphysics parameterization for mixed-phase clouds. part I: Model description, *Meteorol. Atmos. Phys.*, **92**, 45–66.

Seifert, A., A. Khain, A. Pokrovsky and K. D. Beheng, 2006: A comparison of spectral bin and two-moment bulk mixed-phase cloud microphysics, *Atmos. Res.*, **80**, 46–66.

Young, K. C., *Microphysical Processes in Clouds*, Oxford University Press, 1993.

NEW INSIGHTS INTO Q VECTOR ANALYSIS AND ITS APPLICATIONS IN TORRENTIAL RAIN EVENTS

Jie Cao[1,2,3], Shouting Gao[1]

[1] Institute of Atmospheric Physics, Chinese Academy of Sciences, Beijing 100029

[2] Graduate University of Chinese Academy of Sciences, Beijing 100049

[3] Cooperative Institute of Mesoscale Meteorological Studies, Oklahoma University, USA 73072

1. INTRODUCTION

The concept of Q-vector was invented when *Hoskins et al.* [1978] gave a new look at the ω equation. The right hand side for their quasigeostrophic ω equation, the geostrophic forcing term, becomes a simple divergence form of this new vector. Since the Q-vector form for ω equation can be easily applied in synoptic diagnoses with observed temperature and wind fields, and can avoid some drawbacks in the Sutcliffe development theory [*Sutcliffe*, 1947], it has been used ever since then. From the last two decades of last century, studies using the Q-vector concept to understand and analyze the synoptic scale vertical motions and frontal vertical circulations were quite popular [*Hoskins and Pedder*, 1980; *Barnes*, 1985; *Branick et al*, 1988; *Gyakum and Barker*, 1988; *Keyser et al*, 1988; *Schwartz et al*, 1990; *Xu*, 1990; *Davies-Jones*, 1991; *Zhang*, 1995; *Doswell III*, 1998; *Morgan*, 1999; *Yue*, 1999; *Wetzel and Martin*, 2001]. Recently, researchers also take the moisture term into consideration and derived other forms of Q-vector [*Yao et al.*, 2004; *Yang et al.*, 2007], while these applications still stayed on the relationship between the divergence of Q-vector and vertical motions.

Xu [1992] added the vertical ageostrophic vorticity equation into the originally used quasigeostrophic diagnostic equations. This is the first attempt in finding other relationship between Q-vector and ageostrophic motions and an encouraging result was reached theoretically. *Cao and Gao* [2007] re-derived the mathematical relation and put the set of two equations, i.e., the curl and the divergence of Q-vector equations, into the usage of diagnosing a torrential rain event. Compared to the merely adoption of the curl of Q-vector, advantages are quite obvious when the divergence of Q-vector is added into the consideration in determining the location of rainbelt as well as strengths of its maximum centers. This result inspired us to perform further researches and experiments on this useful concept and its applications in severe weather analysis.

Helmholtz principle in separating two-dimensional wind into its nondivergent and irrotational parts is common long time ago. This separation and the deduced the streamfunction and velocity potential are quite effective in getting more information of weather systems. But few researches have touched the separation of other vectors as far as we know, except a gradient of the equivalent isobaric geopotential height in σ coordinate takes some consideration of the separation in the paper of *Chen and Bromwich* [1999]. Since the Q-vector has the good quality to represent ageostrophic motion from the respect of its divergence and vorticity which is similar to the wind field, why don’t we separate this vector into its nondivergent and irrotational parts and test its applications? As we all known, severe storms systems are hard to seize, more ways to identify their dynamic structures more accuracy we may reach in prediction level. So the main point of this paper is to combine the usage of Q-vector vorticity, Q-vector components and its streamfunction and velocity potential into the traditional mere use of Q-vector divergence to see whether or not it will provide more information hidden.

Next section focuses on the description of specific steps in this approach. Section 3 performs some applications of the new usage in Q-vector analysis in real torrential rain events. Last section is discussions and conclusions.

2. APPROACH

First of all, the Q-vector expression in our research is specified as

$$Q_x = \frac{1}{2}\left[f\left(\frac{\partial v}{\partial p}\frac{\partial u}{\partial x} - \frac{\partial v}{\partial x}\frac{\partial u}{\partial p} \right) - h\frac{\partial \mathbf{V_h}}{\partial x}\cdot\nabla\theta - \frac{\partial F}{\partial x} \right] = \frac{1}{2}\left(f^2\frac{\partial u_a}{\partial p} - \sigma\frac{\partial \omega}{\partial x} \right) \quad (1)$$

$$Q_y = \frac{1}{2}\left[f\left(\frac{\partial v}{\partial p}\frac{\partial u}{\partial y} - \frac{\partial v}{\partial y}\frac{\partial u}{\partial p} \right) - h\frac{\partial \mathbf{V_h}}{\partial y}\cdot\nabla\theta - \frac{\partial F}{\partial y} \right] = \frac{1}{2}\left(f^2\frac{\partial v_a}{\partial p} - \sigma\frac{\partial \omega}{\partial y} \right) \quad (2)$$

Here, only the latent heat is considered. The non-uniformly saturation for real atmosphere is described in the introduction of the adiabatic heating effects function F. The specific form used in this paper, $F = \frac{LR}{C_p P}\frac{d}{dt}(q_s(\frac{q}{q_s})^k)$, adopts the one put forward by *Gao et al.* [2004] and got satisfactory results in the paper by *Yang et al.* [2007]. In expressions (1) and (2), $\sigma = -\alpha\frac{\partial ln\theta}{\partial p}$ ($h = \frac{R}{p}\left(\frac{p}{1000}\right)^{R/C_p}$) is a static stability parameter. Other variables follow ordinarily used designations.

The basic motivation for the following studies is to separate the two dimensional Q-vector into its nondivergent and irrotational components, $\mathbf{Q_2}$ and $\mathbf{Q_3}$ separately.

According to Helmholtz principle, the two vectors can be expressed by two scalars as

$$\mathbf{Q_2} = \mathbf{k} \times \nabla H_2 \quad (3)$$

$$\mathbf{Q_3} = \nabla H_3 \quad (4)$$

Here H_2 and H_3 are the streamfunction and velocity potential for Q-vector separately. Physical and mathematical senses for these two scalars are the same as the stramfunction and velocity potential in wind partitioning and reconstruction.

Applying the curl and divergent operations of Q-vector yield to

$$W_2 = \nabla^2 H_2 \quad (5)$$

$$W_3 = \nabla^2 H_3 \quad (6)$$

where $W_2 = \nabla \times \mathbf{Q} = \nabla \times \mathbf{Q_2}$ and $W_3 = \nabla \cdot \mathbf{Q} = \nabla \cdot \mathbf{Q_3}$ are the curl and divergence of Q-vector.

In order to obtain $\mathbf{Q_2}$ and $\mathbf{Q_3}$ in the limited regions, we need to construct such a differential problem with a coupled boundary conditions to solve H_2 and H_3 first. The special boundary conditions with similar forms as those used in wind separation and reconstruction problem are listed as

$$\mathbf{Q_2} = \frac{\partial H_2}{\partial x}\mathbf{i} + \frac{\partial H_2}{\partial y}\mathbf{j} \quad (7)$$

$$\mathbf{Q_3} = \frac{\partial H_3}{\partial x}\mathbf{i} + \frac{\partial H_3}{\partial y}\mathbf{j} \quad (8)$$

Only one step to make sure that the computing process is consistent is added at the beginning of that harmonic-cosine series expansion approach by *Chen and Kuo* [1992] to solve Poisson equations (5) and (6) under the boundary values (7) and (8). A flow chart to solve Q-vector is outlined concisely in Table 1. Detailed information can be inferred in Chen's paper.

Table 1 Schematic flow chart for solving the problem (5)-(8) with harmonic-cosine series expansion approach to compute the distribution of Q-vector both inside the rectangular target region R and its enclosed boundary Σ, together with W_2 and W_3.

$\Downarrow$

to obtain the inner parts of H_2 and H_3, i.e., H_{2i} and H_{3i}, from the Poisson equations $\begin{array}{l}\nabla^2 H_{2i} = W_2 \\ \nabla^2 H_{3i} = W_3\end{array}$ with simultaneous boundary conditions like $\begin{array}{l} -\frac{\partial H_{2i}}{\partial y} + \frac{\partial H_{3i}}{\partial x} = 0 \\ \frac{\partial H_{2i}}{\partial x} + \frac{\partial H_{3i}}{\partial y} = 0 \end{array}$

$\Downarrow$

to compute the inner part components of Q-vector, Q_{xi} and Q_{yi}, from

$$Q_{xi} = -\frac{\partial H_{2i}}{\partial y} + \frac{\partial H_{3i}}{\partial x}$$

$$Q_{yi} = \frac{\partial H_{2i}}{\partial x} + \frac{\partial H_{3i}}{\partial y}$$

to obtain the boundary values for the harmonic part of Q-vector which is the difference between the total Q-vector and its inner part along Σ as $Q_{xe}|_{\Sigma} = (Q_x - Q_{xi})|_{\Sigma}$, $Q_{ye}|_{\Sigma} = (Q_y - Q_{yi})|_{\Sigma}$.

$\Downarrow$

to solve the Laplace equations for the harmonic parts, H_{2h} and H_{3h}, under the prescribed boundary conditions

$\Downarrow$

to obtain streamfunction and velocity potential of Q-vector as $H_2 = H_{2i} + H_{2h}$ and $H_3 = H_{3i} + H_{3h}$

$\Downarrow$

to obtain $\mathbf{Q}_2$ and $\mathbf{Q}_3$ from expressions (7) and (8)

The advantage of this computing method is that the boundary conditions are well handled, and thus the two components of Q-vector and the derived streamfunction and velocity potential can be obtained with high accuracy. The following section will focus on comparing the traditional usage of Q-vector divergence in diagnosing heavy rain events with new attempts with $\mathbf{Q}_2$ and $\mathbf{Q}_3$, H_2 and H_3.

3. APPLICATIONS IN REAL CASES

Since location and intensity of rain centers are important in diagnosing and forecasting torrential rains operationally, we perform the following analyses on these emphases. Two torrential rain events are simulated. One happened from 00UTC August 12th to 00UTC August 13th 2004, and the other one happened from 00UTC July 22nd to 00UTC July 23rd 2005. A numerical model (Version 3 of the PSU/NCAR mesoscale model, known as MM5V3) was used. The detailed information about modeling parameters and synoptic descriptions can be referred in the paper by *Li et al.* [2007] and *Cao et al.* [2008]. Figure 1a shows the divergence of Q-vector above the heavy rain area (Figure 2). The southwestern location of the rain belt can be seen more clearly in the convergent belt of $\mathbf{Q}_3$ (Figure 1d), while $\mathbf{Q}_2$ (Figure 1c) give good correspondence to the two main heavy rain centers. The interesting thing we find is that the horizontal distribution of Q-vector streamfunction above the rain area (Figure 1b) shows two closure centers near heavy rain centers. It is due to the fact that they carry on some flow information as the streamfunction of wind field do in synoptic analysis. Figure 3 takes a look at a latitude-height cross section along 116°E. There are two large centers in the north-south rainbelt in Figure 4. Correspondence of negative centers in longitudinal distributions of Q-vector divergence (Figure 3a) to heavy rain centers as in traditional usage is not as clear as that of high value areas of Q-vector vorticity (Figure 3b). Values for $\mathbf{Q}_2$ and $\mathbf{Q}_3$ have been calculated as shown in Figure 3c and 3d separately. They both hold two centers in lower layer near rain centers. In a short conclusion, both horizontal and vertical distributions of Q-vector vorticity and its two components show advantages in identifying the heavy rain centers and locations over those of divergence of Q-vector. Studies on other times have been performed and similar conclusion can be reached.

Figure 1 Horizontal distributions of (a) Q-vector divergence (unit in 1e-16 m s kg^{-1}), (b) Q-vector streamfunction (unit in 1e-7 m^3 s kg^{-1}), (c) nondivergent part of Q-vector, and (d) irrotational part of Q-vector on 03UTC August 11^{th} 2004 near the 925hPa layer.

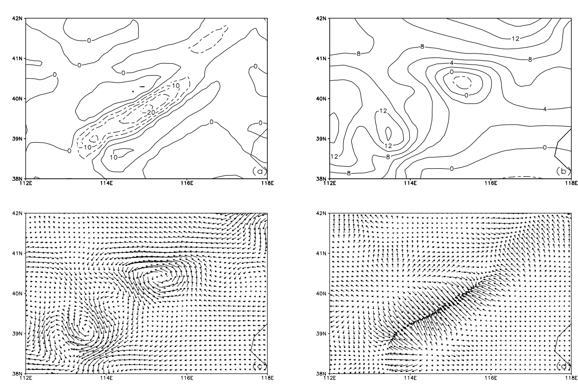

Figure 2 Horizontal distribution of one hour

accumulative surface precipitation on 22UTC July 22nd 2005 (unit in mm).

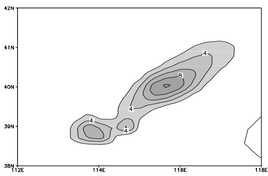

Figure 3 Longitudinal distribution of (a) Q-vector divergence (unit in 1e-16 m s kg^{-1}), (b) Q-vector vorticity (unit in 1e-16 m s kg^{-1}), (c) absolute value of nondivergent component of Q-vector (unit in 1e-12 kg s^{-3}), and (d) Q-vector velocity potential (unit in 1e-7 m^3 s kg^{-1}) at 116°E on 22UTC July 22nd 2005.

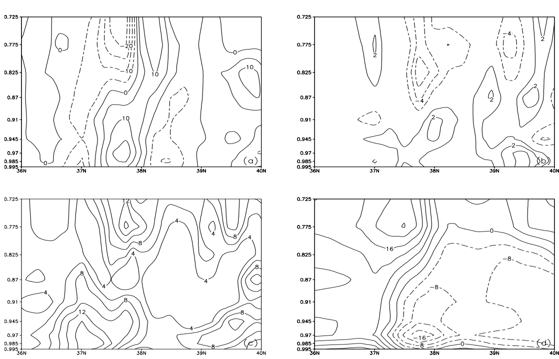

Figure 4 Horizontal distribution of one hour accumulative surface precipitation on 03UTC August 11th 2004 (unit in mm).

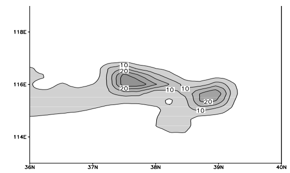

Now we move on to check the ability of these variables in identifying heavy rain centers during a time span. Figure 5 present time evolutions of Q-vector divergence, Q-vector vorticity and value of $\mathbf{Q}_2$ at 114°E. Compared to the time evolution of precipitation in Figure 6, negative centers for Q-vector divergence (Figure 5a) are always accompanied with positive ones. They show some similarities in the tendency but always south to the heavy rain centers and do not give good signals at the beginning. Distributions of Q-vector vorticity (Figure 5b) resemble much more likely to precipitation, especially at the beginning and ending time of the period. Figure 5c gives a picture of time evolution of $\mathbf{Q}_2$. It also shows good correspondence in both layout and large centers locations with precipitation almost all the time. Therefore, advantages of the derived Q-vector streamfunction and its separated components over the traditionally usage of Q divergence merely are easy to be seen.

Figure 5 Time evolutions of (a) Q-vector divergence (unit in 1e-16 m s kg^{-1}), (b) Q-vector vorticity (unit in 1e-16 m s kg^{-1}), and (c) absolute value of nondivergent component of Q-vector (unit in 1e-12 m^2 s kg^{-1}) from 02UTC to 20UTC August 11th 2004 near the 925hPa layer.

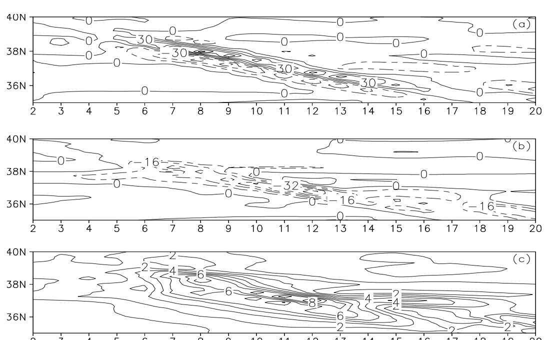

Figure 6 Time evolution of one hour accumulative surface precipitation from 02UTC to 20UTC August 11th 2004.

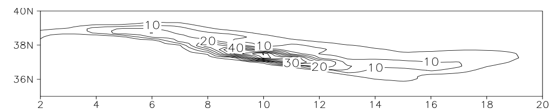

One thing to mention is that two cases were presented here and three more are studied. Since the purpose of the development of Q-vector analysis is to provide a more effective way to diagnose torrential rain events, the statistical analysis of this method may play a less important role. However we will perform more cases studies and finally and hopefully to present a statistical index to score this approach in the future.

4. CONCLUSIONS

Q-vector always shows benefits in severe weather analysis with the usage of its divergence. Recently its vorticity has been studied theoretically and used in real case studies. Based on the finding that both divergence and vorticity of Q-vector relates to ageostrophic motions, Q-vector streamfunction and Q-vector velocity potential have been calculated in the same way used in flow fields. The separation of Q-vector into its nondivergent and irrotational parts has been completed with the approach of harmonic-cosine series expansion. Both the two components and the vorticity of Q-vector are been put into torrential rain events analyses of two real cases, instead of merely usage of Q-vector divergence in traditional way. Comparing studies between traditional usages and new insights into Q-vector have been performed to test their ability in identifying precipitation. Horizontal distributions can lead to a convincing result that Q-vector vorticity and the associated streamfunction, nondivergent and irrotational components of Q-vector present more resemblances to the location of rainbelt than Q-vector divergence does. In other words, heavy rain centers are always accompanied with large value centers or closures of these variables rather than negative centers of Q-vector divergence. Time evolution of precipitations during a period gives similar results. Therefore, a conclusion can be reached that new insights into Q-vector may give more means in identifying heavy rain systems with higher accuracy. More cases are needed and then a systematic approach can be summed up for Q-vector analysis.

5. BIBLIOGRAPHY

1) Barnes, S. L. (1985), Omega diagnosis as a supplement to LFM/MOS guidance in weakly forced convective situations, *Mon. Wea. Rev.*, *113*, 2122-2141.

2) Branick, M. L., F. Vitale, C. C. Lai, and L. F. Bosart (1988), The synoptic and subsynoptic structure of a long-lived severe

convective system, *Mon. Wea. Rev.*, *116*, 1335-1370.

3) Cao, J., and S. T. Gao (2007), Physical basis of generalized potential temperature and its application to cyclone tracks in nonuniformly saturated atmosphere, *J.* Geophys*. Res.*, *112*, D18101, doi: 10.1029/2007JD008701.

4) Cao, J., S. T. Gao, and Y. S. Zhou (2008), Improved Q vector analysis from the perspective of field separation and its application in a torrential rain event, to be pressed in *Acta Phys. Sin.*

5) Chen, Q. S., and Y. H. Kuo (1992), A harmonic-sine series expansion and its application to partitioning and reconstruction problems in a limited area, *Mon. Wea. Rev.*, *120*, 91-112.

6) Chen, Q. S., and D. H. Bromwich (1999), An equivalent isobaric geopotential height and its application to synoptic analysis and a generalized ω equation in σ coordinates, *Mon. Wea. Rev.*, *127*, 145-172.

7) Davis-Jones, R. P. (1991), The frontogenetical forcing of secondary circulations. *J. Atmos. Sci.*, *48*,497-509.

8) Doswell III, C. A., C. Ramis, R. Romero, and S. Alonso (1998), A diagnostic study of three heavy precipitation episodes in the western Mediterranean region, *Wea. Forecasting*, *13*, 102-124.

9) Gao, S. T., X. R. Wang, and Y. S. Zhou (2004), Generation of generalized moist potential vorticity in a frictionless and moist adiabatic flow, *Geophy. Res. Lett.*, *31*, L12113, doi:10.1029/2003GL019152.

10) Gyakum, J. R., E. S. Barker (1988), A case study of explosive subsynoptic-scale cyclogenesis, *Mon. Wea. Rev.*, *116*, 2225-2253.

11) Hoskins, B. J., I. Draghici, and H. C. Davies (1978), A new look at the ω-equation. *Quart. J. Roy. Meteor. Soc.*, *104*, 31-38.

12) Hoskins, B. J., and M. A. Pedder (1980), The Diagnosis of Middle Latitude Synoptic Development, *Quart. J. Roy. Mer. Soc., 106*, 707-719.

13) Keyser, D., M. J. Reeder, and R. J. Reed (1988), A generalization of Petterssen's frontognesis function and its relation to the forcing of vertical motion, *Mon. Wea. Rev.*, *116*, 762-780.

14) Li, B., Y. S. Zhou Y, and P. Y. Zhang (2007), Application of the China New Generation Weather Radar data to the torrential rain simulation over the Jianghuai Basin in 2003: Validation of precipitation and wind. *Chinese J. Atmos. Sci.*, in press.

15) Morgan, M. C. (1999), Using piecewise potential vorticity inversion to diagnose frontogenesis. Part I: A partitioning of the Q vector applied to diagnosing surface frontogenesis and vertical motion. *Mon. Wea. Rev.*, *127*, 2796-2821.

16) Schwartz, B. E., C. F. Chappell, W. E. Togstad, and X. P. Zhong (1990), The Minneapolis flash flood: meteorological analysis and operational response, *Wea. Forecasting*, *5*, 3-21.

17) Sutcliffe, R. C. (1947), A contribution to the problem of development, *Quart. J. Roy. Meteor. Soc.*, *73*, 370-383.

18) Wetzel S. W., J. E. Martin (2001), An operational ingredients-based methodology for forecasting midlatitude winter season precipitation, *Wea. Forecasting*, *16*, 156-167.

19) Xu, Q. (1990), Cold and warm frontal circulations in an idealized moist semigeostrophic baroclinic wave, *J. Atmos. Sci.*, *47*, 2337-2352.

20) Xu, Q. (1992), Ageostrophic pseudovorticity and geostrophic C-vector forcing-a new look at the Q vector in three dimensions. *J. Atmos. Sci.*, *49*, 981-990.

21) Yang, S., S. T. Gao, and D. H. Wang (2007), Diagnostic analysis of the ageostrophic Q vector in the non-uniformly saturated, frictionless and moist adiabatic flow, *J. Geophys. Res., 112,* D09114, doi: 10.1029/2006JD008142.

22) Yao, X. P., Y. B. Yu, and S. W. Shou (2004), Diagnostic analyses and application of the moist ageostrophic vector Q. *Adv. Atmos. Sci.*, *21*, 96-102.

23) Yue, C. J. (1999), Q vector and advance in studies on its applications in weather diagnostic analyses, *Chinese Meteor.*, *25*, 3-8.

24) Zhang, X. W. (1995), Modified Q vector and its applications, Chinese Jour. Trop. *Meteor.*, *15*, 162-167.

Acknowledgements

This work was supported by the National Key Basic Research and Development Project of China 2004CB418301, the National Natural Sciences Foundation of China under the Grants No. 40433007, and “Outstanding Oversea Scholars” Project No. 2005-1-19. And Jie Cao wants to thank for the financial support given by the conference.

A NEW MULTI-MOMENT, MULTI-HYDROMETEOR CLASS, BULK MICROPHYSICS PARAMETERIZATION SCHEME. PART II: PRELIMINARY RESULTS

Matthew S. Gilmore[1] and Jerry M. Straka[2]

[1]Dept. of Atmos. Sciences, University of Illinois, Urbana, IL, 61801, USA, gilmore1@ uiuc.edu
[2]School of Meteorology, University of Oklahoma, Norman, OK, 73019, USA, jstraka@ou.edu

I. INTRODUCTION

The purpose of this manuscript is to present a new method for evaluating how well a bulk microphysics scheme reproduces storms observed with polarimetric radar. We illustrate this with a new 24-class multi-moment microphysics scheme by comparing the classes of precipitation of the simulated storms to hydrometeor classes retrieved from polarimetric radar observations (using a hydrometeor classification algorithm - HCA). Although we illustrate using a 24-class microphysics scheme, any scheme could be used following a similar methodology.

The usual way that simulations have been compared with observations in the past is to transform the simulations into radar products for direct comparison. Numerous papers in the last 30 years have computed standard radar reflectivity using the Rayleigh approximation (i.e., Smith et al., 1975) when doing comparisons. In addition, a few papers have demonstrated how to compute polarimetric radar variables from the model microphysics data (e.g., Huang et al. 2005), which could also be used for a direct comparison. Both types of computations involve numerous assumptions, as does the method proposed herein. In Fig. 1, such a comparison is made between the observations and simulations for the Z_h field using the storm complex to be described.

Instead of transforming the model output into simulated radar data, our novel approach is to transform the radar data into products that can be directly compared with the model. This is made possible by using a hydrometeor identification algorithm (HCA) whereby the most likely microphysics species in each radar volume are retrieved. These retrievals then can be compared directly with the model.

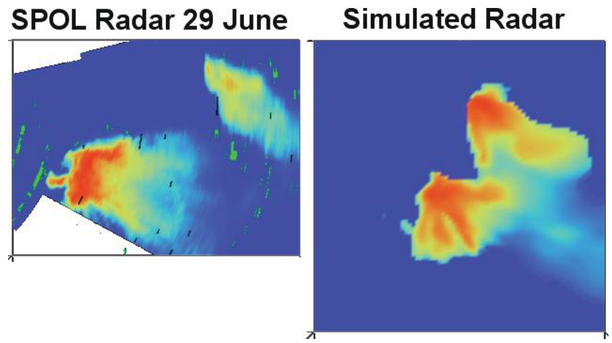

FIG. 1: Z_h CAPPI (2.4 km AGL) as observed by NCAR's SPOL radar at 2343 UTC on 29 June 2000 in comparison to that computed at approximately the same time in storm evolution within the simulation using the 24-class scheme. Values of Z_h < 0 dBZ were thresholded to insure the same color scale (ranging 0 to 70 dBZ) in both images.

II. CLOUD MODEL SETUP

The supercell case study considered here for evaluation is the 29 June 2000 STEPS storm. The storm was simulated with a representative proximity sounding at relatively coarse resolution (dx=1km) using the Straka Atmospheric Model. All model settings were chosen to precisely follow those used by Kuhlman et al. (2006) except that the 24-class multi-moment scheme was used (Straka and Gilmore 2009a,b) instead of the 13-class single-moment scheme (Straka and Mansell 2005).

III. HYDROMETEOR CLASSIFICATION ALGORITM

The hydrometeor classification algorithm (HCA) used herein is that belonging to NCAR (see description in Vivekanandan et al. 1999). There are several HCA's available. NCAR and NOAA/NSSL use similar versions (Straka et al. 2000; Vivekanandan et al. 1999) whereas Colorado State has a slightly different version (Lim and Chandrasekar

2003; Lim et al. 2005). In brief, these algorithms assign likelihood for the presence of about 14 different microphysics species (or species combinations) via the particular values of the polarimetric variables for each radar volume.

Although the second and third most likely species can be output from such algorithms, for simplicity, we only use the *first most likely* species herein.

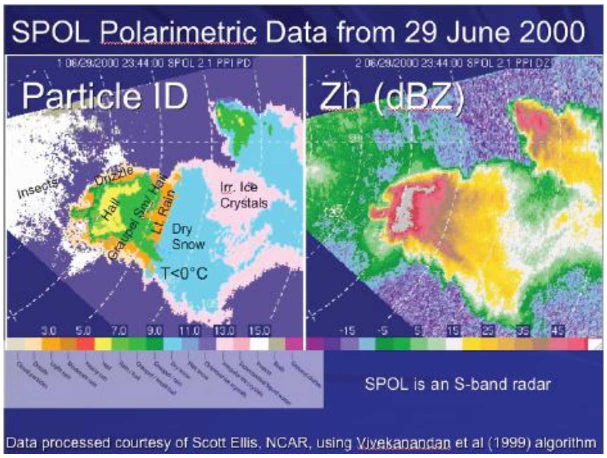

FIG. 2: Example PPI at 2.1° elevation angle of Particle ID output (left) and Zh (right) at 2344 UTC.

IV. METHODOLOGY FOR COMPARING HCA SPECIES TO CLOUD MODEL SPECIES

As a first step in comparing the simulation to the observations, the radar data was gridded and interpolated to a similar grid spacing using CEDRIC and SPRINT. For the HCA output, a flag was assigned depending upon the species presence. A separate three-dimensional field was created for each species to enable toggling on/off using the *Vis-5d* visualization software.

Then the 24-class cloud model output (which has 24 individual species) had to be transformed into groups of species for two main reasons: 1) to match the HCA output which provided some "species" as a mixed-phase group; 2) there were more model microphysics species than could be discriminated in the HCA output. Table 1 below shows how the model species were grouped to better mimic the HCA output. Different microphysics routines may require different grouping strategies. In our scheme, rime storage on ice crystals helps in judging crystal shape irregularity for the mimicking procedure.

Table 1: Suggested flags to apply to the 24-class (Straka and Gilmore 2009a,b) cloud model output which mimic the "species" as output by the HCA. Below, "hail" refers to any of the several hail species; "graupel" refers to any of the graupel species; "rain" refers to any of the rain species but not cloud or drizzle. QT refers to mixing ratio threshold value of 0.1 g/kg, which was chosen *ad hoc*. The rime storage threshold was also chosen *ad hoc*. The model reflectivity thresholds for light, moderate, and heavy rain come from those used in actual radar classification (Straka et al. 2000).

Dominant species from the HCA	How to group the 24-class model output at a grid cell to "match" the HCA	
	Main Criteria	Additional Criteria
Cloud particles	cloud > QT	T > 0°C
Drizzle	drizzle > QT	
Light rain	Zrain[1]< 28 dBZ	
Moderate rain	28 dBZ ≤ Zrain < 44 dBZ	
Heavy rain	Zrain > 44 dBZ	
Hail	hail > 0.1 g/kg	rain < QT
Hail/rain mix	hail > 0.1 g/kg	rain > QT
Graupel/small hail	Any of graupel; small hail ; frozen drops > QT	rain < QT
Graupel/rain mix	Any of graupel; small hail ; frozen drops > QT	rain > QT
Dry snow	snow > QT	T < 0°C
Wet snow	snow > QT	T > 0°C
Oriented ice crystals	Any ice crystal habit > QT	<10% mass of rime storage
Irregular ice crystals	Any ice crystal habit > QT	≥10% mass of rime storage
Super-cooled cloud	cloud > QT	T < 0°C

[1]Zrain is the radar reflectivity computed using only the liquid species.

V. PRELIMINARY RESULTS

As a typical example, we show a simple comparison between the radar reflectivity of the actual storm and the model simulation (Fig. 1). Standard radar reflectivity can be used to show that the northern-most storm was stronger in the simulation than in the observations for the same time in storm evolution (Fig. 1) – approximately 2 hours after storm initiation. Among other things, this could likely be due to a lack of capturing stabilization within the environment further E.

The remainder of the comparisons between the HCA and other model output will be presented at the conference.

VI. FUTURE WORK

The precise percentage of rime mass that gives a good discrimination between "irregular ice" and "oriented ice crystals" compared to HCA retrievals has yet to be determined. Also, the mixing ratio thresholds to be used for declaring the presence of certain species (Table 1) are *ad hoc* and likely need to be tuned. Although this is somewhat undesirable, it seems unavoidable in the current methodology.

Overall scoring is another issue that is needs further work. If a species (or species combination) that is assigned by HCA matches at least one of the modeled species at that same time and location, then a success should probably be declared. How the scoring should be applied in all directions in time and space is something that needs to be carefully considered. A best-fit correlation algorithm should probably be applied to sync the two analyses in time/space prior to scoring.

VII. ACKNOWLEDGMENTS

This research was funded by the following U.S. National Science Foundation grants: ATM–0340693, ATM–0449753, and ATM–0339519. This work was partially supported by the U.S. National Center for Supercomputing Applications under TG-MCA94T023 and utilized Tungsten (Dell Xeon IA-32 Cluster). We thank Kristin Kuhlman (OU) who provided the modified MGLASS sounding and model parameters, Jon Siwek (UIUC Atmospheric Sciences Dept.) who helped grid the radar data and process the model output, and Scott Ellis (NCAR) who ran and provided output from NCAR's hydrometeor ID algorithm.

VIII. REFERENCES

Huang, G.-J., V. N. Bringi, S. van den Heever, and W. Cotton, 2005: Polarimetric radar signatures from RAMS microphysics. *32nd Conf. on Radar Meteorology, Albuquerque, New Mexico, Amer. Meteor. Soc.,* Paper P11R.6

Kuhlman, K. M., C. L. Ziegler, E. R. Mansell, D. R. MacGorman, J. M. Straka, 2006: Numerically simulated electrification and lightning of the 29 June 2000 STEPS Supercell Storm. *Mon. Wea. Rev.,* **134**, 2734–2757.

Lim, S., V. Chandrasekar, and V. N. Bringi, 2005: Hydrometeor classification system using dual-polarization radar measurements: model improvements and in situ verification. *IEEE Transactions on Geoscience and Remote Sensing,* **43**, 792–801. Doi = 10.1109/ TGRS.2004.843077

Lim, S. and V. Chandrasekar, 2003: Hydrometeor classification system using dual-polarization radar measurements. *IEEE Workshop on Advances in Techniques for Analysis of Remotely Sensed Data,* 227 – 236. Doi =10.1109/WARSD.2003.1295197

Smith, P. L., C. G. Myers, and H. D. Orville, 1975: Radar reflectivity factor calculations in numerical cloud models using bulk parameterization of precipitation, *J. Appl. Meteor.*, **14**, 1156–1165.

Straka, J. M., D. S. Zrnic, and A. V. Ryzhkov, 2000: Bulk hydrometeor classification and quantification using polarimetric radar data: Synthesis of relations. *J. Appl. Meteor.,* **39**, 1341–1372.

Straka, J. M. and M. S. Gilmore, 2009a,b: A multi-moment, multi-hydrometeor species, bulk microphysics scheme: Part I. Foundations and liquid water parameterization. Part II. Ice water parameterization *To be submitted to J. Appl. Meteor. Clim.*

Straka J. M. and Mansell E. R., 2005: A bulk microphysics parameterization with multiple ice precipitation categories. *J. Appl. Meteor.*, **44**, 445–466.

Vivekanandan, J., S. M. Ellis, R. Oye, D. S. Zrnic, A. V. Ryzhkov, and J. Straka, 1999: Cloud microphysics retrieval using S-band dual-polarization radar measurements. *Bull. Amer. Meteor. Soc.,* **80**, 381–388.

EMBRYO DIFFERENCES BETWEEN SIMULATED HIGH AND LOW PLAINS HAILSTORMS

Matthew S. Gilmore[1], Lee M. Cronce[1], Jerry M. Straka[2], and Robert B. Wilhelmson[1]

[1] *Department of Atmos. Sciences, Univ. of Illinois, Urbana, IL, 61801, USA, gilmore1@uiuc.edu*
[2] *School of Meteorology, University of Oklahoma, Norman, OK, 73019, USA, jstraka@ou.edu*

I. INTRODUCTION

Previous observational studies have shown that marked differences exist in the embryo composition of hailstones collected at the ground between hailstorms of the High Plains of Colorado and Lower Plains of Oklahoma. Knight (1981) found a strong relationship between the temperature at cloud base and the collected hail embryo type at the surface. The colder (warmer) cloud bases of the High Plains (Oklahoma) were associated with more hail reaching ground with graupel (frozen drop) embryos. Although Knight postulated why, our study attempts to provide insights to this behavior using a three-dimensional non-hydrostatic cloud model with sophisticated two-moment microphysics.

II. MODEL SETUP

A 10-class two-moment microphysics scheme was used (an early/simple version of the Straka and Gilmore 2009a,b scheme) that includes two distinct classes of the most common embryo types (frozen drops & graupel) as well as a single hail category. A flow chart of the process rates is included herein (Fig. A1). Frozen drops or graupel become hail for sufficiently large riming of cloud water (following formulas in Straka and Mansell 2005, in bulk form) or when the mass-weighted density of ice riming one of the three rain categories exceeds a threshold density (following Ferrier et al. 1994).

The NCOMMAS model domain was initialized and run with soundings that were taken in close proximity to hailstorms from the High Plains & Oklahoma (see, e.g., Fig. 1). All soundings (1946-2004 High Plains and 1946-1995 Oklahoma) with hail reports occurring within ±1 hour of 0000 UTC and within 160 km of the sounding site were collected. Cases with unrepresentative or missing sounding data were discarded. This resulted in 101 (29) Oklahoma (High Plains) cases for possible simulation and the statistics of these environments are shown in Table 1. The very low *p*-values strongly suggest differences in mean sounding values between regions for all but the convective inhibition (CIN). The simple thermal bubble method was used for triggering the storm in each case. A total of 41 Oklahoma and 18 High Plains cases were successfully simulated for 2 hours of cloud time.

TABLE 1: Means proximity sounding parameters and the probability of falsely declaring the means of the distributions as distinctly different.

Parameter	Mean of 29 High Plains cases	Mean of 101 Low Plains cases	*p*-value for difference in means
CAPE (J kg^{-1})	656	1319	<.0001
CIN (J kg^{-1})	62	55	0.2
LCL (m)	1930	1319	<.0001
LCL T (°C)	5	15	<.0001
WCD (m)	1044	3133	<.0001

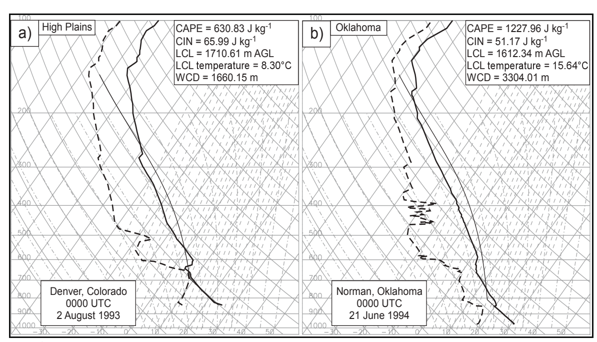

FIG. 1: Example skew-T log-P sounding diagrams representing each region. Warm cloud depth (WCD) is that layer between the LCL and freezing.

III. ANALYSIS

In order to determine differences in the mean simulated hail growth behavior between environments, Student's test statistics and *p*-values were generated for important model and environmental sounding variables. Linear regression was also used to test the presence of and the degree of relationship between model and sounding variables within a single environment and between environments. Transformations were required to normalize some of the data distributions prior to calculating the test statistics.

IV. RESULTS USING ONE HAIL CATEGORY

The depth of the cloud layer between the cloud's base and freezing level (the WCD) is directly correlated to the total production of warm rain mass by the storm (Fig. 2). It is more physically meaningful than using the LCL temperature. Interestingly, warm cloud depths ranging 1000-2000m (where the distributions overlap), the High Plains storms are more effective at producing rain via collision-coalescence processes (see best-fit curves in Fig. 2). The total mass flux of rain upward through the freezing level is proportional to both the total warm mass rain produced (not shown), and the environmental CAPE (Fig. 3a). A larger flux of rain corresponds to more frozen drops produced (not shown) and consequently more hail with frozen drop embryos (Fig. 3b). Because the rain mass flux values are generally higher in Oklahoma (owing to larger CAPE and warm rain production), this likely explains why more hail from frozen drops are produced in Oklahoma storms compared to High Plains storms.

One drawback of these initial experiments is that the embryo history is lost due to only having a single hail category. That is, we cannot tell whether the greater hail production from frozen drop embryos in the simulated Oklahoma storms actually reach ground in similar proportion. In the next section, we attempt to remedy this problem by repeating some of the experiments using a microphysics scheme with one additional hail category so that the embryo type can be tracked: hail with frozen drop embryos (qhf) and hail with graupel embryos (qhg).

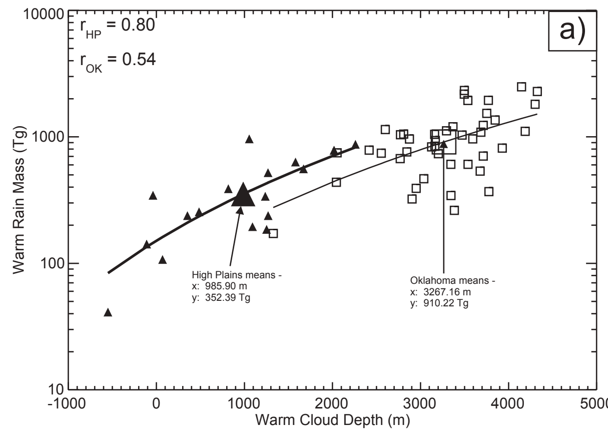

FIG. 2: Scatter plot of sounding-derived warm cloud depth (WCD) versus total warm rain mass that was produced by each simulation for both High Plains (triangles) and Oklahoma (open squares) storms. The large symbols signify distribution means. Linear regression lines are curved due to the chosen plotting method and due to a required data transformation. Correlation coefficients are also given.

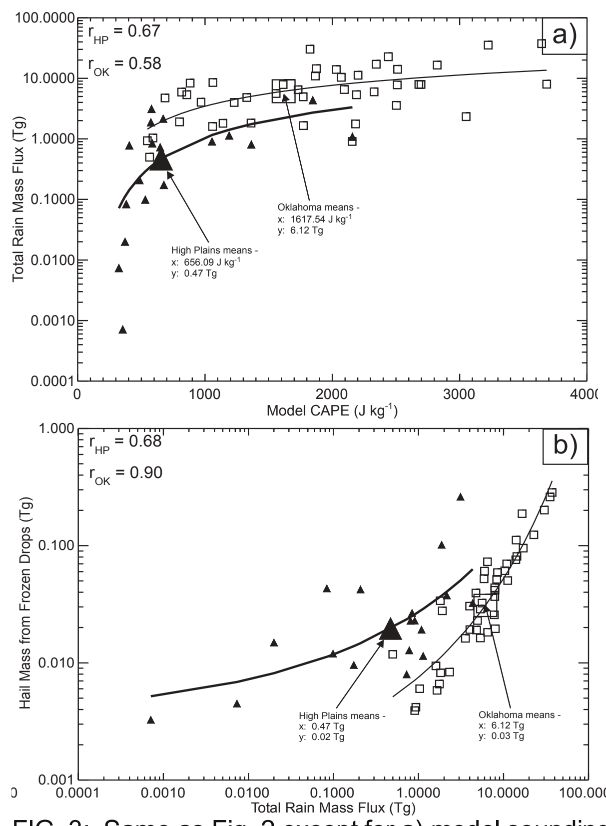

FIG. 3: Same as Fig. 2 except for a) model sounding CAPE versus simulation total rain mass flux through the freezing level and b) simulation total rain mass flux through the freezing level versus simulation total hail mass production with frozen drop embryos.

V. RESULTS USING TWO HAIL CATEGORIES

In the second part of this research, two representative cases were repeated with a 11-class version of the scheme having two distinct hail classes, which allows tracking of embryo type within the hailstones all the way to the ground. The flow chart of this two-hail scheme is similar to Fig A1 except that the graupel (frozen drops) that convert to hail are put entirely into the qhg (qhf) species.

Representative cases were chosen from each environment by ranking each of the 41 Low Plains and 18 High Plains simulations by how close each of 26 different output parameters came to the respective group mean. These output parameters included microphysical descriptions of the storm such as domain total mass production and surface mass accumulations of various species. An overall normalized mean rank was computed, which resulted in the following cases being chosen as overall representative mean cases: DEN 17 July 1983 and OUN 29 June 1992.

These two cases were re-run with the improved microphysics scheme with a separate hailstone categories for each dominant embryo type so that the amount and size of those hailstones could be followed to the ground. To summarize, it was found that compared to the Low Plains case, the High Plains case produced...

- a more vigorous and larger-scale convective storm (not shown);
- a greater amount qhf accumulating on the ground (Fig. 4);
- more qhg production aloft and less qhg melting (not shown);
- a greater fraction of qhg/(qhf+qhg) accumulating on the ground (Fig. 4).

The greater amount of qhf reaching ground in the High Plains storm seems inconsistent with observations, however, the larger fraction of hail with graupel embryos seems consistent. Part of the inconsistency may arise from only investigating two "mean storms" rather than all of the storms. Also, given the relatively simple conversion rules used in this version of the microphysics model with somewhat arbitrary conversion thresholds, it would not be surprising if the thesholds for conversion of frozen drops to hailstones was set too low.

Figures corresponding to these and other points will be shown at the conference.

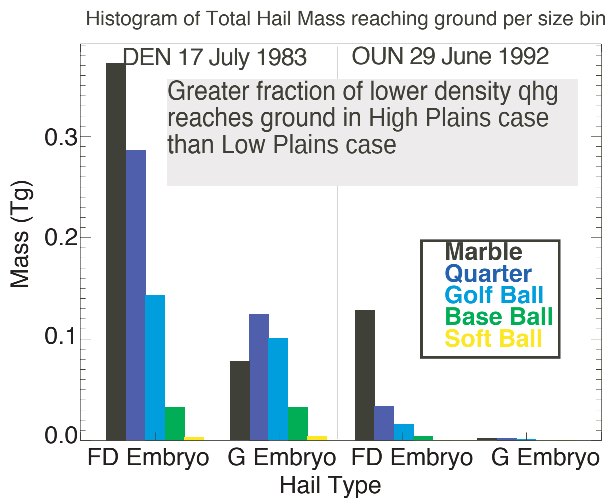

FIG. 4: Comparison of the total hail mass reaching ground for five discrete hail sizes and each hail embryo type in a) DEN 17 July 1983 and b) OUN 29 Jun 1992. Tg is the abbreviation for teragrams.

VI. ACKNOWLEDGMENTS

This research was funded by the following US National Science Foundation grants: ATM–0340693, ATM–0449753, and ATM–0339519. Part of this research was conducted by the second author in partial fulfillment of a M. S. degree at the Univ. of Illinois. This work was partially supported by the National Center for Supercomputing Applications under TG-MCA94T023 and utilized Copper (IBM P-690) resources.

VII. REFERENCES

Cronce, L. M., M. S. Gilmore, R. B. Wilhelmson, and J. M. Straka, 2009: Hail embryo differences between simulated High Plains and Oklahoma storms. Part I: Results ensemble using a 5ICE/4LIQ double-moment microphysics scheme. *In preparation for Atmos. Res.*

Ferrier B., 1994: A double-moment multiple-phase four-class bulk ice scheme. Part I: Description. *J. Atmos. Sci.,* **51** 249–280.

Gilmore M. S., Straka J. M., and Rasmussen E. N., 2004: Precipitation uncertainty due to variations in precipitation particle parameters within a simple microphysics scheme. *Mon. Wea. Rev.,* **132** 2610–2627.

Knight N. C., 1981: The climatology of hailstone embryos. *J. Appl. Meteor.,* **20** 750-755.

Straka J. M. and Gilmore M. S., 2009a: A multi-moment, multi-hydrometeor species, bulk microphysics scheme: Part I. Foundations and liquid water parameterization. In preparation for *Appl. Meteor. Clim.*

Straka J. M. and Gilmore M. S., 2009b: A multi-moment, multi-hydrometeor species, bulk microphysics scheme: Part II. Ice water parameterization. In preparation for *Appl. Meteor. Clim.*

Straka J. M. and Mansell E. R., 2005: A bulk microphysics parameterization with multiple ice precipitation categories. *J. Appl. Meteor.*, **44**, 445–466.

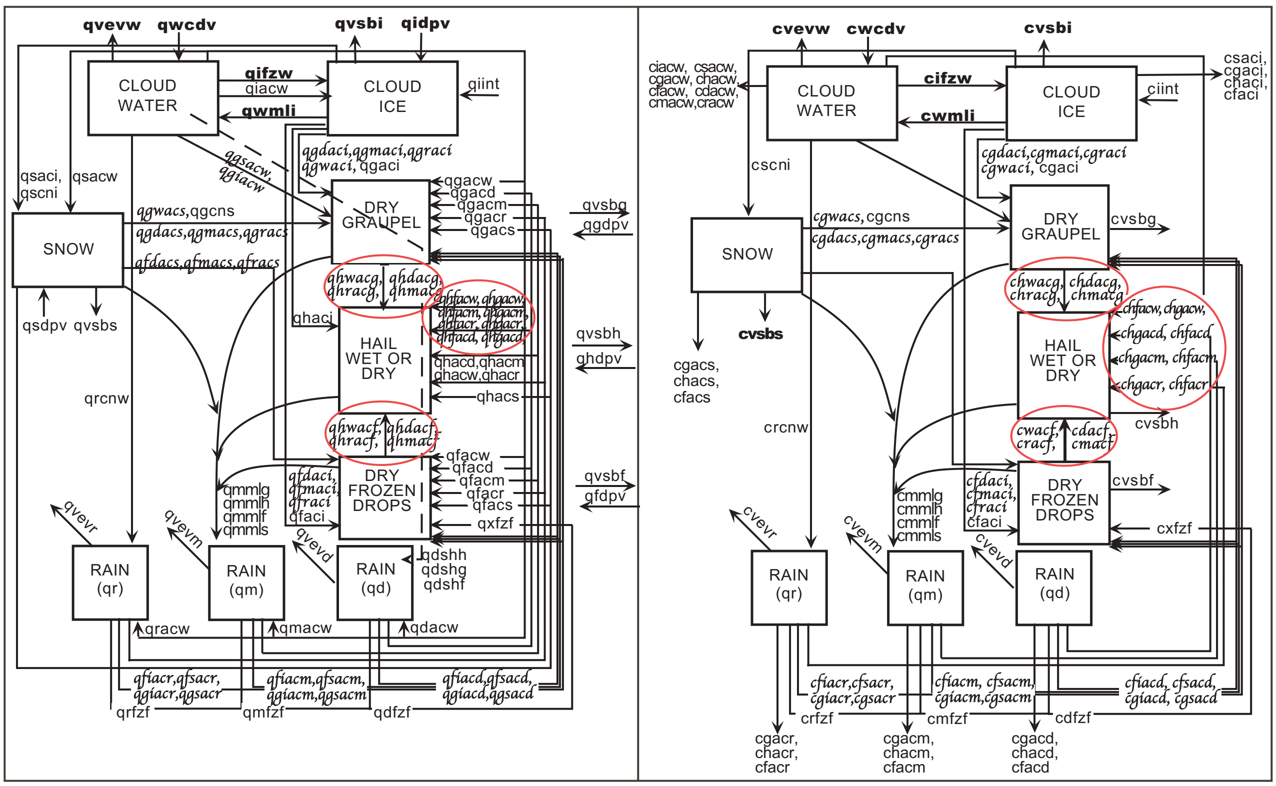

FIG A1: Flow chart of mixing ratio transfers (left panel) and number concentration transfers (right panel) between the 10 different microphysics species used in this study. There are five ice categories: cloud ice (i), snow (s), graupel (g), frozen drops (f), and hail (h). There are three rain categories: warm rain (r) melt water (m) and shed water (d). Sinks in number concentration do not necessarily have a corresponding source term. The rate naming convention is such that the second letter in the name always represents the gaining species and the last letter represents the loss species. Italicized 6-letter rates indicate three-body interactions whereby certain riming criteria are satisfied such that mass is transferred from two different categories to a third species; circled in red are those rates where riming graupel or frozen drop embryos become hail. See the appendix of Gilmore et al. (2004) for more on the naming convention.

TRENDS IN HYDROMETEOR FREQUENCY IN SPAIN

Miguel González-Colino, Elisabeth Alonso-Blanco, María Fernández-Raga, Ana I. Calvo, Covadonga Palencia, Roberto Fraile

Department of Physics, University of León, 24071 León, Spain.
roberto.fraile@unileon.es

1. INTRODUCTION

Climate change is today one of the natural phenomena that causes great concern among the general public. Extreme weather events in particular cause important damages in many parts of the world and are therefore the focus of a large number of research projects (Diaz et al., 2002).

There seems to be a generalized belief that there is an increase in the number of extreme weather phenomena such as heat waves, droughts or flash floods. However, this fact needs to be verified with empirical data. One way to do this is by studying trends in the frequency of certain weather events.

The importance of these trends in the case of hydrometeors when analyzing climate change has been evident for several years now in studies on the evolution of precipitation (Díaz, 1996; González-Rouco et al., 2000).

The main parameters of climate change are the same as the parameters of climate itself: precipitation and temperature. Brunetti et al., (2000) have analyzed the evolution of these parameters in Italy over a period of more than 100 years. According to IPCC (2007), climate change will not affect the amount of precipitation, but rather the precipitation regime. The number of days with hydrometeors will change, as well as the return period of the precipitations. In other words, droughts will become more frequent and will be followed by torrential rain periods, thus causing a strong impact in society.

This study analyzes trends in the frequency of hydrometeors and in their return periods between 1950 a 2005 in the Iberian Peninsula. The main aim is to detect any possible trends and determine their relationship with climate change.

2. STUDY ZONE

Spain comprises four clearly distinct territories: the mainland in the Iberian Peninsula, the Balearic Islands, the Canary Islands and the cities of Ceuta and Melilla in the north of Africa. The total area is approximately 506,000 km^2.

Spain lies between 36º and 46º N in the west of Europe. The climate is mostly Mediterranean, but the northwest is clearly affected by the maritime climate of the western Atlantic coast. The south-east has a subtropical dry climate (Almería and Murcia).

Precipitation varies in the different regions of the Iberian Peninsula with two clearly distinct regimes: the Mediterranean regime, characterized by its irregularity, with annual average values between 400 and 500 liters per square meter, and the Atlantic or Oceanic regime, with regular and abundant precipitation the whole year round and annual average values of about 1,000 liters per square meter (Font, 1983).

The study was carried out with the data provided by the weather stations on mainland Spain (Fig.1).

3. METHODOLOGY

The data for this study were provided by the weather stations run by the Spanish National Institute for Meteorology (INM in its Spanish acronym). Data series for the period 1950-2005 have been analyzed. In cases of weather stations that did not have at least 70% of full annual series for the 56 years of the study period, those series were not used.

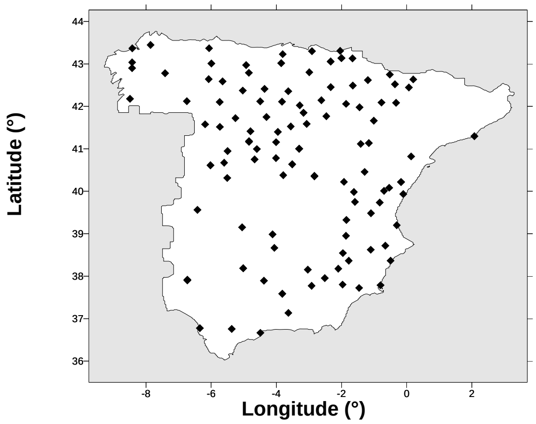

Fig.1. Weather stations with at least 70% of full annual series since 1950.

Initially, there were several thousand weather stations in the database, but the limiting criterion reduced that number to 119. Fig. 1 shows that the stations that fulfill the requirement are not distributed homogeneously over the whole of the Iberian Peninsula. The INM network has a homogeneous distribution, but not all the stations had enough full series, so the weather stations that provided the data are not distributed homogeneously.

This study focuses on extreme weather events, so no attempt was made at filling gaps in the data series because this would greatly influence the results.

The number of days with one of the following hydrometeors was studied: rain, snow, hail and thunderstorm (as a source of hydrometeors).

Two variables were analyzed in the case of each hydrometeor representing its evolution in time: the number of days and the return periods. In addition, statistical tests were applied to check the significance of the trends.

The final aim of the study is to follow the frequencies of the two variables through the whole of the study period. The focus lies on relatively infrequent meteorological events, so it is assumed that they fit the Gumbel distribution, which is the one generally recommended for extreme values (Reiss and Thomas, 2007). The return periods (time it takes for a phenomenon to occur again) were calculated this way. The events that have been followed are the ones that have a return period of 20 years in the first series (the first value of all the return period series is 20 years).

In each year the return period was calculated with the 20 years immediately before. The Mann-Kendall test was used to reveal the trends. This test provides two parameters known as U(t) and U'(t). The graphic representation may indicate the approximate year the trend began (Sneyers, 1990).

The areas with significant trends have been represented on a map of the Iberian Peninsula. The Kriging method was used to represent the results. This is a geostatistical interpolation method that has proved to be useful in various fields (Burgess and Webster, 1980). The results are shown in Figures.

4. RESULTS

4.1 Rain days

Figure 2a shows that approximately 70% of the Iberian Peninsula has a positive trend, i.e., the number of annual rain days tends to grow. However, there is a negative trend in two stations. In the southern half of the Peninsula the trend is not as clear as in the north, as approximately 50% of the south does not have any trend at all. The program used for building the figures assigns an average value to the territories with no data (areas with no station), so the areas with a trend may appear in the figures larger than they really are if there are no other stations close by.

It can be seen in Fig. 2a that in the northern half of the Peninsula there is an area without a trend with a small spot with a negative trend in the middle. In Fig. 2b there is an area with a positive trend for return periods which coincides with the area with no trend in Fig. 2a. A positive trend in the return period means that certain rain days are becoming less frequent every year. Even though there is this area with a trend, it seems that in the long term the trend in Fig. 2a weakens.

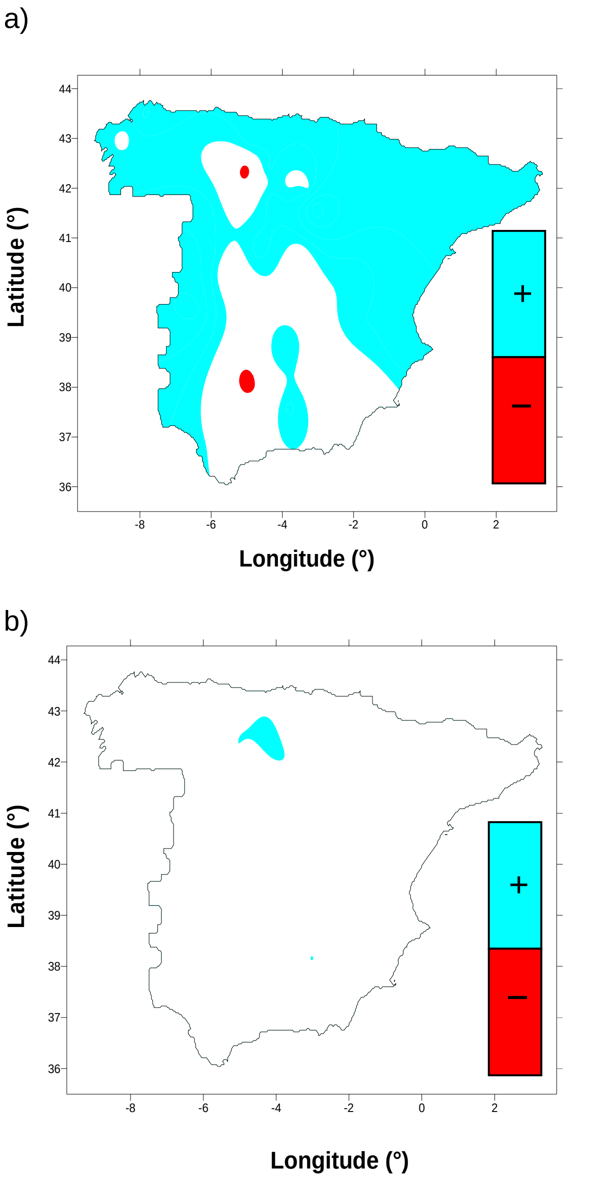

Fig. 2. a) Trends in annual number of rain days. b) Trends in return periods for rain days.

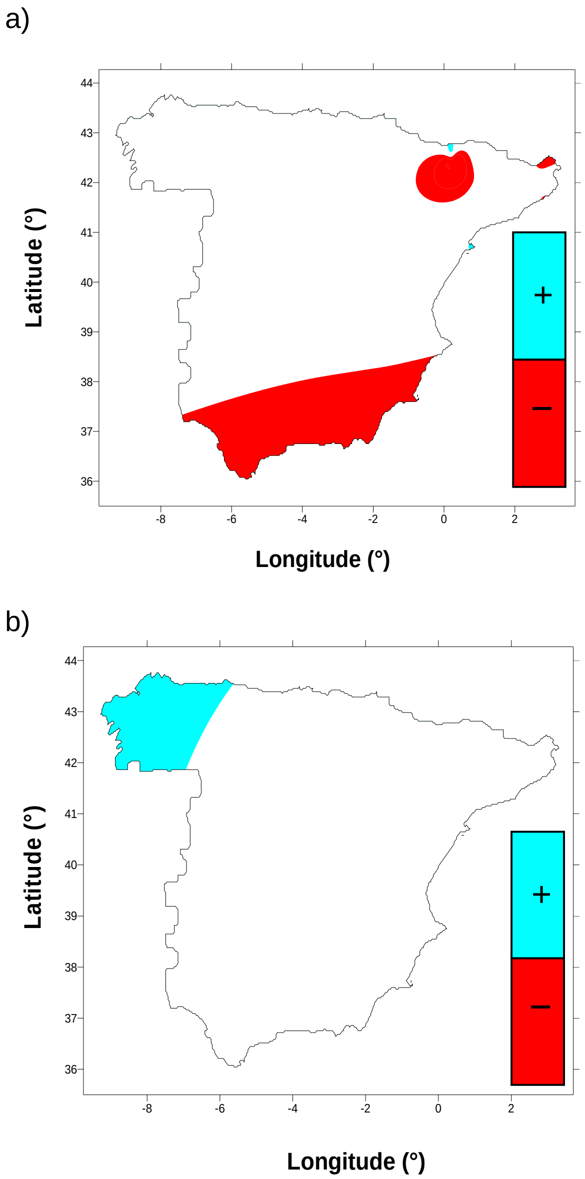

Fig. 3 a) Trends in annual number of snow days. b) Trends in return periods for snow days.

4.2 Snow days

Figure 3a shows that in most of the Iberian Peninsula there is no trend. Only two stations had a positive trend, i.e., an increase in the number of snow days. Two areas show a negative trend in the south and in the north-east. Fig. 3b shows that there is no uniform trend in most of the study zone, with only one area in the north-west with a trend towards longer return periods.

The most important conclusion that may be drawn from the frequencies of snow days is that there simply is no trend in most of the study zone, as shown in Fig. 3.

a)

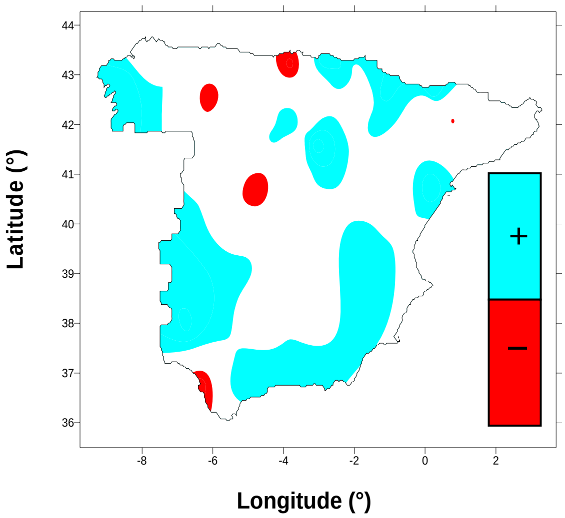

b)

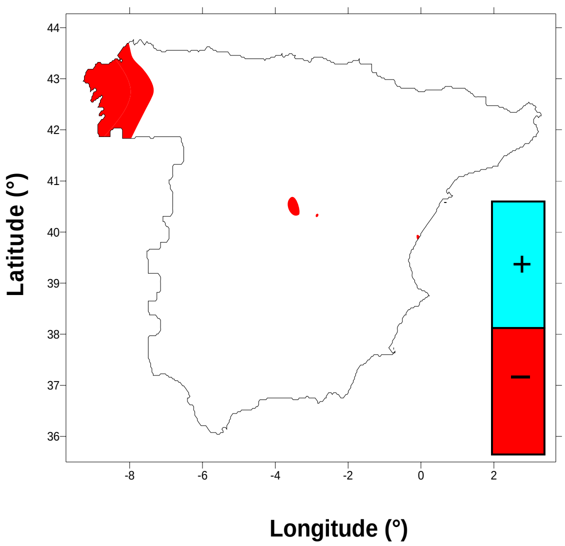

Fig. 4. a) Trends in annual number of hail days. b) Trends in return periods for hail days.

4.3 Hail days

Figure 4a on the spatial distribution of trends for hail day in the Iberian Peninsula shows that there are 5 stations with a negative trend. The remaining stations that have a trend all have a positive one. It may be concluded that the regime of hail days is changing in most of the study zone. No topographic pattern seems to control this change, so no geographic model may be used to determine the way in which the hail regime changes.

When comparing Fig. 3b) and 4b) it can be seen that in the north-west there is a positive trend in return periods for snow (the frequency of snow days decreases), and a negative trend in return periods for hail (a phenomenon that occurs mostly in summer). So hail is becoming more frequent to the detriment of snow, a phenomenon that occurs in winter. However, no significant variations have been detected in the past few years in the precipitation volume registered in the northwest of Spain (Mossmann et al., 2004).

4.4 Storm days

Fig. 5a shows the trend in the number of storm days per year. As in Fig. 4a, the many small areas with a trend are distributed irregularly in isolated spots.

In the case of storms, 66% of the stations have a trend, so there seems to be a movement towards changes in the storm regime. The high percentage of stations with a trend indicates that the frequency in the number of storm days has changed, although no clear pattern appears that could explain the distribution in small isolated spots all over the Peninsula illustrated in Fig. 5a, as in the case of hail days. Fig. 5b shows no relevant circumstance, except for two small areas with a positive trend in the northwest and one single station with a negative trend in the northeast. Comparing Fig. 5a and 5b it may be seen that the trends tend to weaken in the long term.

5. CONCLUSIONS

The results found have led to the following conclusions:

- The study has focused on the analysis of trends in the number of days with hydrometeors and in the return periods of these same hydrometeors in mainland Spain. The following variables have been used: annual number of days with rain, snow, hail and storm.

a)

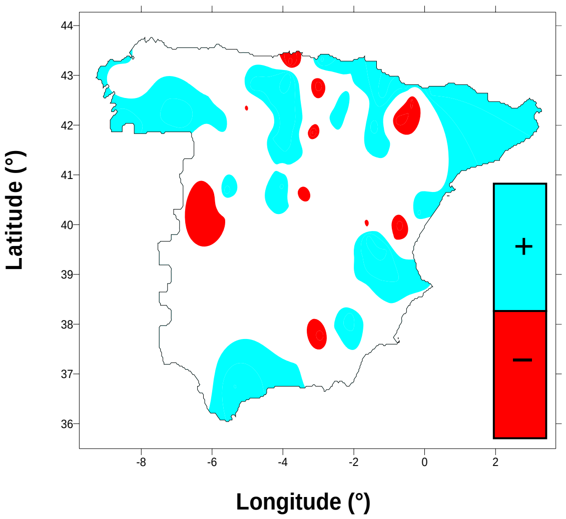

b)

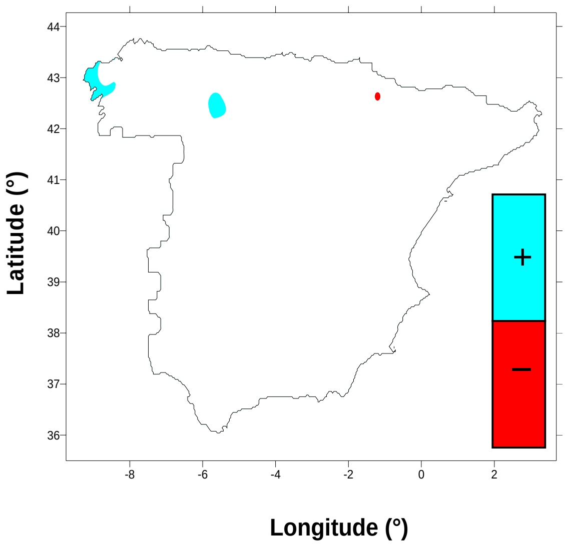

Fig. 5. a) Trends in annual number of storm days. b) Trends in return periods for storm days.

- In the case of the number of days with hydrometeors, a trend towards changes in the regimes is detected, but following no clearly defined pattern. In general, there are positive trends (trends towards an increase in the annual number of days) in rain, hail and storm. No geographic pattern is observed, so the different trends cannot be explained on the basis of topographic features.

- The return periods show trends in fewer stations than in the case of the number of days, so the trends seem to weaken in the long term.

- Considering the whole of mainland Spain, no general trend can be said to exist for the number of days with hydrometeors or for the return periods. However, the data found for the number of days seem to point towards a change in the regime.

If different data series are used, even with shorter chronological series, the results may show a greater homogeneity, but this will be the aim of future research.

BIBLIOGRAPHY

Brunetti, M., M. Maugeri, T. Nanni, 2000. Variations of temperature and precipitation in Italy from 1866 to 1995. Theor. Appl. Climatol. 65, 165-174

Burgess, T.M; R. Webster, 1980. Optimal interpolation and isarithmic mapping of soil properties. I the semi-variogram and punctual kriging. Journal of Soil Sciense. 31, 315-331.

Díaz, H.F, 1996. Precipitation monitoring for climate change detection. Meteorol. Atmos. Phys. 60,179-190

Díaz, J., A. Jordán, R. García, J.C. Alverdi, E. Hernández, A. Otero, 2002. Heat waves in Madrid 1986-1997: effects on the health of elderly. Int. Arch. Occup. Environ. Health 75. 163-170

Font, I., 1983. Climatología de España y Portugal. INM, Madrid, 226 pp.

González-Rouco, J.F, H. Heyen, E. Zorita, F. Valero, 2000. Agreement between observed rainfall trenes and climate change simulations in the southwest of Europe. Journal of climate, 13, 3057-3065.

IPCC. 2007. The physical Basis of Climate Change 2007: Contribution of Working Group I to the Four Assessment Report of the Intergovernmental Pannel on Climate Change [Houghton, J.T., et al.]. Cambridge University Press, Cambridge, United Kingdom and New York, NY, USA.

Mossmann, V, A. Castro, R. Fraile, J. Dessens, J.L. Sánchez, 2004. Detection of statistically significant trends in the summer precipitation of mainland Spain. Atmos Res, 70, 43–53.

Reiss, R.D. and M. Thomas, 2007. Statistical analysis of extreme values. Third ed., Birkhäuser, Basel, 511 pp.

Sneyers, R., 1990. On the statistical analysis of series of observations. WMO, Tech. Note 143, Geneva, 192 pp.

Acknowledgements

The authors are grateful to Dr. Noelia Ramón for translating the paper into English. This study was supported by the Junta de Castilla y León (Grant LE014A07).

ANALYSES ON OBSERVED CHARACTERISTIC OF A STRONG STORM WITH DOPPLER RADAR DATA

Li Bin
The Meteorological Bureau of Xinjiang Production and Construction Group, Urumqi, Xinjiang, P.R.China, 830002, btlibin@126.com

1. INTRODUCTION

A strong storm weather occurred from 21:00 to 24:00 on July 22 2003 at Kuitun River and Manas River area at the north of Tianshan Mt., which made disasters by hail shooting and high wind at Shihezi cultivated area, Manas County, Xinhu Farm and Fangcaohu Farm. The biggest diameter of hailstone is 5 cm, and the moment wind velocity at Fangcaohu Farm is $35ms^{-1}$. Over $2500hm^2$ cotton crops, equal to 90 million RMB was lost by the strong storm.

In this paper, with the data of weather, sounding and C band Doppler radar in Wujiaqu of Xinjiang, the features of the strong storm have been analyzed,including the synoptic background, radar echo evolution and Doppler velocity characteristics. The results are significant for monitoring strong storms in north-west Chinese area with C band Doppler radar.

2. SYNOPTIC BACKGROUND

With weather maps of hail fallout zone at that day, there was a over $38ms^{-1}$ upper air jet at 300hPa level, which made a divergence at that high level. At 500hPa map, there was a developing trough, and a warm-moist air flow providing vapors for the strong storm at the south. There was a convergence zone at 850hPa level.

With the data of radiosouding observation, the K index was 37, and the Si index was -2.7. These indicated a huge latent instable energy existing.

So the structure of the divergence at high level, the convergence warm-moist air flow at lower level, and unstable stratification were advantages of trigging the strong storm.

3. EVOLUTION OF THE STRONG STORM

The initial radar echoes of the strong storm with the moving path from northwest to southeast formed at the desert and dune area near Kelamayi., and it had hail shooting at the range from No.121 Farm to No.105 Farm(Fig.1). Finally, the strong storm was extinct near No.222 Farm at 00:35. The moving distance of the strong storm with the longer life cycle about 4h was 220km, and the average moving speed of it was more fast with $61km.h^{-1}$.

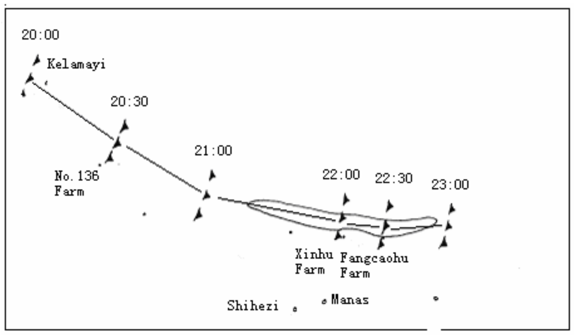

Fig.1 Moving path of strong storm and hail shooting areas.

4. CHARACTERISTICS OF INTENSITY ECHOES STRUCTURE

In PPI map, the intensity echoes are compact, with the strong gradient of echo intensity. The echoes' scale is about 40km^2.

In RHI map, it can be seen that the strong storm successively undergoes forming, developing, gestating, hail shooting and extinct phases. The period of hail shooting is 1 hour and 57 minutes, which is 51% of whole life period of strong storm. According to Fig.2, the top altitudes of different intensity echoes rise quickly at forming, developing and gestating phases, and fluctuate but descent in general at hail shooting phase, descent quickly at extinct phase finally. It indicates that there is a strong updraft in the cloud at forming, developing and gestating phases, leading to the cloud developing vigorously. There is a downdraft in the cloud at extinct phase, because of precipitation trail, leading to the cloud extinct quickly. The updraft and downdraft are organized in the cloud at hail shooting phase, so the strong storm can be maintained. But the top altitudes of different intensity echoes are descent in general with continuous precipitation leading energy consuming in the cloud.

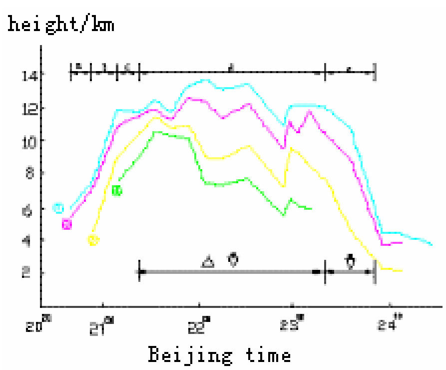

Fig.2 Evolution of top altitudes of different intensity echoes (20:39—00：27).
Letters a, b, c, d, e differently stand for forming, developing, gestating, hail shooting(raining) and extinct phases of the strong storm.
Numbers ① ② ③ ④ differently stand for the echo intensity of 10、30、50、60dBz.

5. CHARACTERISTICS OF DOPPLER VELOCITY OF THE STRONG STORM

The echoes of the strong storm showed compact lump with 56dBz maximum intensity, obviously the inflow zone in front of moving direction when the strong storm moved at the place 145km away from Radar Station at 21:43(Fig.3). Corresponding to the velocity echoes map, there is a cyclone structure with a pair of positive velocity center and negative velocity center symmetry by orientation. After velocity fuzziness process, the maximum positive velocity is 5.4ms^{-1} (away), and the maximum negative maximum is -19ms^{-1} (toward). The rotation velocity of the cyclone with 10km diameter is (|-19|+|5.4|) /2 = 12.2 ms^{-1}. The value at the positive center is less than that at the negative center because the environmental wind is WNW toward Radar Station.

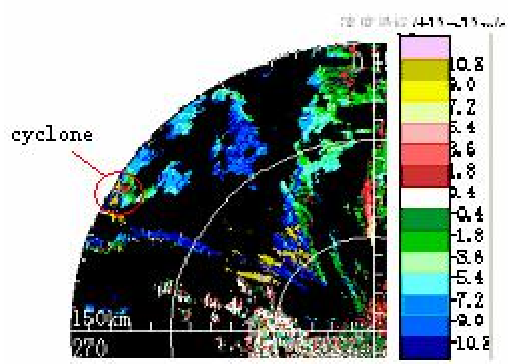

Fig.3 The radial velocity map of PPI along elevation angle 0.5° at 21:43.

According to different VPPI maps at 22:08(Fig.4), there is a pair of positive velocity center with 8 ms^{-1} and negative velocity center with -12.5 ms^{-1} at 0.5°VPPI map (about 2km high), and the positive velocity center is right below the negative velocity center. At 1.5°VPPI map (about 5km high), there is a pair of positive velocity center and negative velocity center symmetry by orientation. At 4°VPPI map (about 9km high), there is also a pair of positive velocity center and negative velocity center at the same area, but the former is right over the latter.

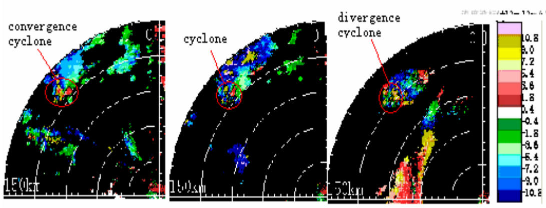

Fig.4 The radial velocity maps of VPPI along elevation angles 0.5^{o},1.5^{o},4.0^{o} respectively at 22:08.

According to some research results(Hu Mingbao, 2000), the velocity structure is respectively a convergence cyclone at 0.5°VPPI map, a cyclone at 1.5°VPPI map and a divergence cyclone at 4°VPPI map. So it indicates that the structure of the strong storm is convergence cyclone at lower level, a cyclone at middle level and a divergence cyclone at high level. This kind of high-lower level allocation is benefit of maintaining updraft, transporting instability energy at lower up, further maintaining the strong storm.

At RHI map, the strong storm developed vigorously at 22:06, with 10dBz top height 13.6km. At the radial velocity RHI map, there is positive velocity at the combined area of forward overhang echoes and main unit. It shows an inflow area there. There is a negative velocity indicating an outflow at the plume. There is a very small positive velocity at middle of the cloud, it is not indicated a real small velocity, but a strong updraft vertical to radar orientation there. There is negative velocity indicating an inflow area behind middle cloud. According to the velocity continuity principle, the stream field of the strong storm is described as Fig9. At Fig.6, the strong storm is composed with a pair of updraft and downdraft which they are organization, and not interference each other. It is convergence at lower level and divergence at higher level in line with the analyses result at PPI map. This kind of stream structure provides the vapour transfer and dynamical condition, which the development and maintenance of the strong storm need.

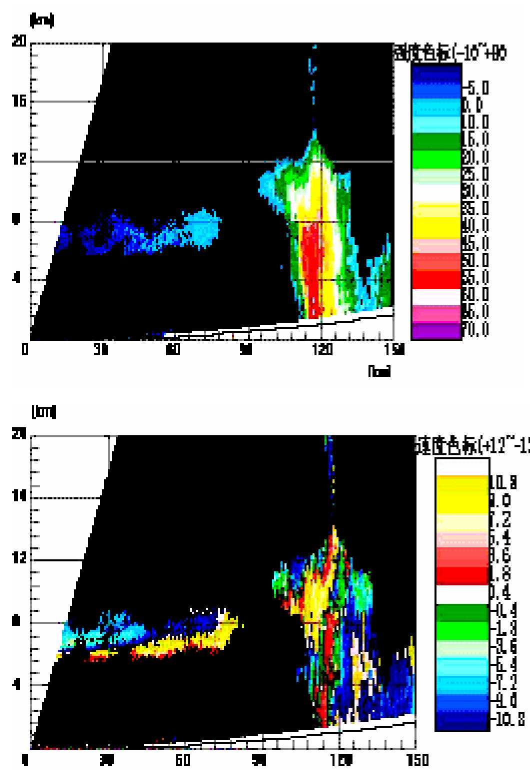

Fig.5 Intensity echoes and velocity echoes of RHI map along azimuth 302.2° at 22:06.

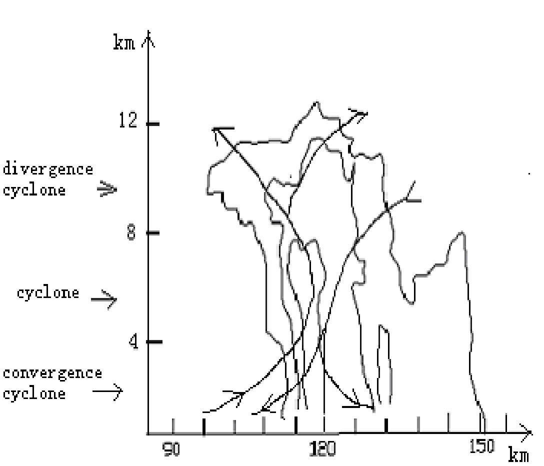

Fig.6 Stream field of the strong storm.

6. CONCLUSIONS

According to above analyses, we can get main results as follow:

6.1 The advantages of triggering the strong storm are that the weather situations such as the upper air jet, match lower convergence warm-wet air flow and unstable stratification.

6.2 The strong storm with 220km long path and 4h duration and 61km.h^{-1} average moving speed may cause great damage and loss at the range from No.121 Farm to No.105 Farm.

6.3 The echoes' scale of the strong storm is about 40km^2. The intensity echoes of the strong storm obviously have structure features of dense structure、big intensity gradient etc., and shape features of forward overhang、echo wall、vault echo etc., as the strong convective units should have. At RHI map, the top altitudes of different intensity echoes rise quickly at forming, developing and gestating phases, and fluctuate but descent in general at hail shooting phase, descent quickly at extinct phase finally.

6.4 According to the analyses of the Doppler velocity echoes, the stream field characteristics of the strong storm are that there are the convergence cyclone at the low-level, the divergence cyclone at the high-level and a pair of organized updraft and downdraft flow existing inside the storm. This kind of high-lower level allocation is benefit of maintaining updraft, transporting instability energy at lower up, further maintaining the strong storm. These analysis results are in line with some theory research results(Zhang Peichang, 1992).

REFERENCES

Hu Mingbao, etc. 2000: Analyses and application of Doppler weather radar data. PLA Press, Beijing, China, 129-133. (in Chinese)

Zhang Peichang, etc. 1992: Radar meteorology. Meteor. Press, Beijing, China, 236-237. (in Chinese)

NUMERICAL STUDY OF CONVECTIVE SUPERCELL EVENTS OBSERVED IN CRIMEA

Ganna Pirnach and Vitalii Shpyg
Ukrainian Hydrometeorological Research Institute

1. INTRODUCTION

A recent work continued many years of theoretical investigation of the dynamic and microphysics of cloud and precipitation on the mesoscale of atmospheric fronts and fulfilled in UHRI and other scientist community. Numerical models of the frontal cloud systems passing over Crimea have been used for theoretical interpretation of the field measurements in cumulus clouds that were carried out on the Hail Suppression Proving Ground. Field investigation has been conducted in the eastern Crimea. System "Antigrad" was used for radar measurements. Cases with a severe storm on July 22, 2002 and a super cell on September 27, 2002 will be presented.

2. METHODOLOGY

Formation and development in space and time of atmospheric front and its cloud system are simulated by integration of the set of the full equations for dynamic and thermodynamic and kinetic equations for the cloud particle sizes distribution functions:

The 3-D nowcasting and forecasting models that have been developed in UHRI for modeling of the winter and summer frontal cloud systems were modified by orography and carried out for numerical simulation of warm-season frontal clouds (see Pirmach, 1998, Pirnach, 2004, Pirnach and Shpyg, 2007, etc.). Cartesian coordinates and terrain-following sigma coordinates have been used. Coordinates named as (x, y, z) for all cases directed in east, north and vertical directions.

Features of the vortex movement in cumulus clouds and their nearest environment were basically investigated. A process of spout formation has been investigated by means of analyses of the vorticity and components its equation.

Cyclonic and anticyclonic whirls that developed in investigated spout-dangerous region were modeled for different frontal cumulonimbus.

3. NUMERICAL RESULTS

Numerical models of the frontal cloud systems passing over the Crimea were used for theoretical interpretation of the field measurements in cumulus clouds that were carried out on the Hail Suppression Proving Ground (HSPG). For modeling of the supercell evolution the calculated scheme developed in (Pirnach and Shpyg, 2007) was used. This scheme sometime increase updraft, and downdrafts and precipitation but that let more clearly found the location, and formation, and development of deep convective cell features and heavy precipitation. The prognostic models were used in recent runs for founding of key parameters and processes leading to formation deep convective cell, and supercell, and heavy rainfall events, and damaging event observed in Crimea.

Case of September 27. Numerical modeling of cloud evolution with initial stage t = 0 at 1100 GMT depicted that most strong vertical motion, clouds and precipitation were in region of observed supercell centred at point (x, y)=(75, 40 km). Synoptical situation and details of the field experiment observations see in (Pirnach and Shpyg, 2007). Location of the real supercells and their vertical sizes is shown in Fig.1. During field measurements the supercell was fixed nearby the proving ground area in north-east about 10-20 km farther it in moment of field experiment starting and move in named direction.

Mesoscale convective systems with heavy precipitation were identified by strong updraft and downdraft columns, intensive rotor movement of both signs, heterogeneous distribution of equivalent potential temperatures, positive kinetic energy, cell structure of pressure, etc.

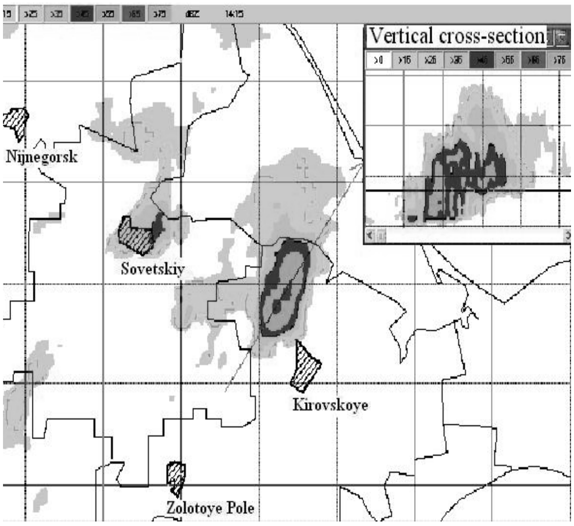

Figure 1. Horizontal (5 km height) and vertical cross-sections of the convective cloud reflectivity (1115 GMT). Sizes of grid cell are 10 km and 5 km in horizontal and vertical section respectively.

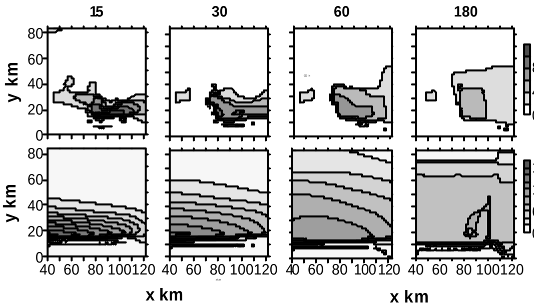

Figure 2. Spatial and temporal distribution of z-maximum updrafts. Numbers on top are t min. First row presented a run with orography, second row presents the run without including relief.

Fig.2 presented calculating of cloud cells for complex relief with and without topography. Comparison between both rows on fig.2 is clearly confirming a key role of relief on development of cloudiness in mountain region.

Disturbance zones promoted formation of cells and bands of frontal ascending movement and were responsible for transportation mechanism of moisture. High updraft columns caused appearance of deep *Cb* clouds with crystal tops (seeder zones) and mixed layers under (feeder zones) (see Figs. 2, 3).

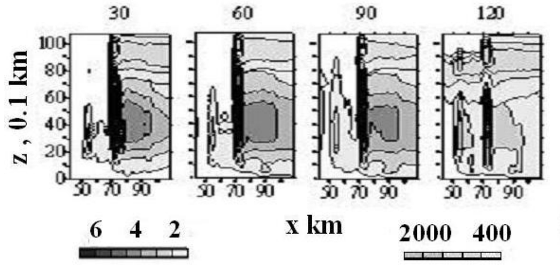

Figure 3. Vertical cross-sections of cloudiness at different calculated time, t, min; numbers on tops). First scale presents water content, q_{w}, g/kg; numbers near second scale are ice concentration, N_i, 1/g.

Number falling crystals seeded the feeder zones, grown to size of precipitation particles and resulted in heavy precipitation. Vortical features in cumulus clouds and nearest environment were investigated basically. Theoretical interpretation of field experiments by numerical modeling has shown that appearance of new cyclonic cells predicted a new convective cells formation. Cyclonic vortical cells correspond to the initial stage and stage of maximal development of convective cells. An existence of the coupled cyclonic and anticyclonic vortexes is possible at the stage of maximal development of convective cloud. Decomposition of convective cells was followed by reduction of angular rotation and anticyclonic vortex.

Case of July 22. In this case the possible reasons of formation such interesting and dangerous atmospheric phenomenon as a convective severe storm is considered. Time t = 0 corresponds to 1100 GMT. Inspection of an operative range of spouts in village Vypasne has shown, that in a zone of villages Tomashivka-Vypasne operated four spouts, in a zone of village Lobanove one spout operated (see Fig.4). Here it has not been genetically connected to the others. It has been connected to other cloudy system and moved it toward. The exact times of spouts action (1250 GMT). In more detail, description of this phenomena see in Leskov at al., 2008.

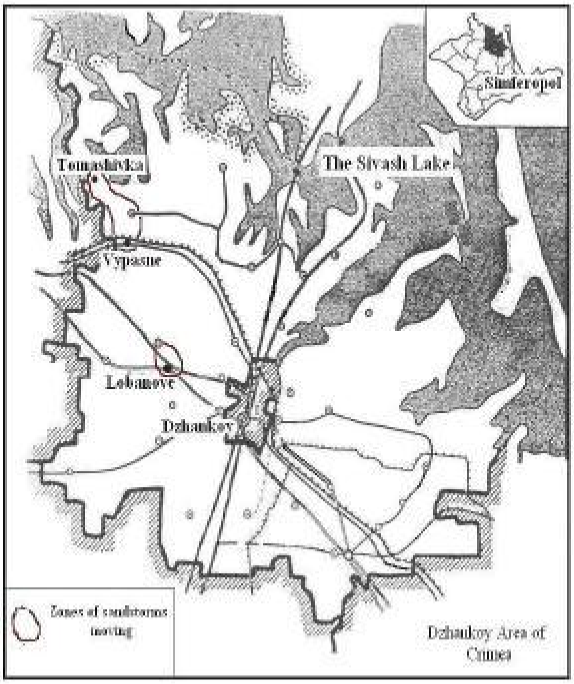

***Figure 4*. T**he scheme of Dzhankoy Area and zones of spout moving.
Coordinates (x; y): Simferopol(0; 0 km), Dgankoy (19; 113 km), Lobanove(9; 120 km), Vypasne (3; 132 km), Tomashivka (-1; 139 km).

Spout was formed under powerful Cb which tops have reached to tropopause. Passage of spout was accompanied by thunder-storms and showers, and the area occupied with these phenomena, there were more than zones with spouts. Numerical simulation were conducted with aim to determine key parameters and processes leading to formation deep convective cells and observed damaging events. Three series of numerical runs have been conducted with aim of investigation of key parameters of spout development: (Case 1) runs with clouds for complex relief; (Case 2) runs without clouds; (Case 3) runs for flat terrain. In Fig.5 presented those cases for pressure, temperature and vertical component of vorticity as named as rotor (rot) at 12 45 GMT.

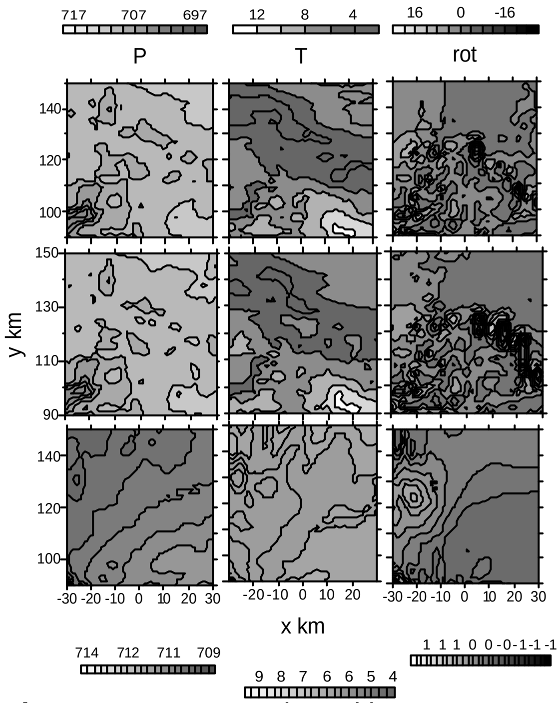

Figure 5. Pressure (p, mb), temperature (T^o, C), rotor (rot, 10^{-3}/s) at t=105 min (1245 GMT) and z = 3 km. First row shows results of run with clouds for complex relief; second row presents the run without including cloudiness; third row shows a case with clouds and flat relief.

Cell structure of pressure, and rotor, and band of cold air mass has place in investigated regions for first and second cases and directed from north-west to south-east. In first case cyclonic rotor cells dominate in north-west and anticyclonic cells dominate in east part area in second case. Those cells surrounded the area with anticyclonic movement. In Case 3 presented features have more regular structure and cyclonic rotor was clearly depicted in north-west part of the picture.
Vertical motions in spout-dangerous region were very strong and reached 15m/s and more sometime. Calculated updraft z-maximums (see Fig.6) for first and third cases corroborate the physical mechanism explaining the development of those storms. Prevalence of the topography is explained. It is intended also to corroborate the hypothesis that the storm can be classified

as a supercell from the point of view of the simulation.

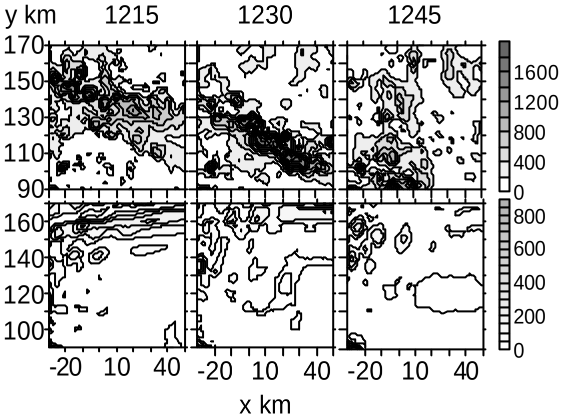

Figure 6. Space and time distribution of updraft z-maximums, w_{max}, during the spout activity. Digits near scale are w_{max}, cm/s. Digits in the picture tops note the time, GMT. First row: runs by terrain-following sigma coordinates. Second row: Cartesian coordinates were used.

Table 1 presented the highest w_{max} and mean w_{max} for target area included place of spout activity. At t=1h 30 min (1230 GMT) w_{max} reached 18 m/s for Case1.
It is time approached to time of dangerous spout described.

Table 1.
Time development of updraft z-maximum, w_{max} [cm/s] and mean updrafts, w_{mean} [cm/s] in area -20<x<30 km, 100<y<150 km

t, h	1	2	3	4
		w_{max}		
1.0	629	614	204	201
1.5	1773	1682	73	86
2.0	500	628	63	79
2.5	609	456	30	29
3.0	400	490	69	51
4.0	644	537	801	588
		w_{mean}		
1.0	184	190	63	64
1.5	386	355	15	16
2.0	138	159	17	23
2.5	135	109	7	7
3.0	108	114	10	11
4.0	127	112	97	162

In Case 1 and Case 2 vertical motions have difference distribution but convective values of updrafts and downdrafts maintained. Runs for flat relief decreased those motions fundamentally. Super cells disappeared.

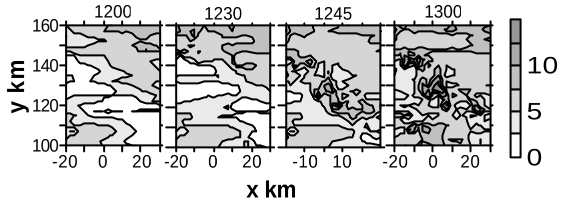

Figure 7. Space and time distribution of clouds, during the spout activity. Digits near scale are the total water content z-integral, s, mm.

During investigated time in cloud cover appeared convective cells with highest s exceeded 20 mm (see fig. 7).

4. CONCLUSION

Highiest gradient of pressure, and temperature, and rotor forced by orography caused development of cold stream of air, bands of strong updraft and downdraft, chain cyclonic and anticyclonic rotors and strong convective cells with updraft reached tens m/s.
Supercells disappeared if relief is flat.
Clouds modified the rotor and convective cells distribution but keep their power and existence.

5. BIBLIOGRAPHY

1. Leskov, B.N, Pirnach, A.M., Sirota, M.V., Shpyg, V.M., 2008: Spouts in Crimea of 2002, July 22. Trudy UHRI, **256**.
2. Pirnach, A.M., 1998: Construction and application of the various numerical models for study the cloud dynamics and structure of the frontal rainbands. J. Atmos. Res., **45-47**, 356- 376.
3. Pirnach, A.M., 2004: Numerical simulation of frontal clouds with heavy precipitation for flat and mountain relief. Trudy UHRI **251,** 31-50.
4. Pirnach, A.M., Shpyg V.M., 2007: Simulation the deep convective clouds. Geoinformatic, **4,** 86-94**.**

Acknowledgements
We would like to express our gratitude to organizers of the 15th Conference on Clouds and Precipitation for the help in representation of this abstract at the conference.

HAILSTONE SIZE: RELATIONSHIP TO METEOROLOGICAL VARIABLES

Fidel Rodríguez-Wüthrich[1], Covadonga Palencia[1], Dario Giaiotti[2], Fulvio Stel[2], Roberto Fraile[1],

[1]Department of Physics, University of León, 24071 León, Spain
[2]ARPA FVG Palmanova, Italy

1. INTRODUCTION

Hail may be defined as a form of precipitation which consists of small balls of ice with a diameter of 5 mm or more. These balls of ice fall to the ground individually or grouped in irregular ways. Hail causes important damages of various types. Detecting and forecasting hail and hailstone sizes is essential to alert the areas that may be affected with the aim of minimizing losses.

Several different techniques have been developed to forecast the occurrence of hail and to predict hailstone sizes. The latter will be the focus of this paper.

One of the best known methods for forecasting hail is the one put forward by Farnbush and Miller (1953). The success of this technique is firmly based on the theory that strong updrafts allow the formation and growth of hailstones. These authors highlight the importance of a dry layer over a warm and moist layer close to the ground. This situation is required to dissipate the latent fusion heat through the evaporation of liquid water in dry air. The vertical thermal gradient of the saturated air parcels is then steeper than the moist adiabatic gradient. The presence of cool air over a moist layer also increases potential instability.

The problem becomes more complex with vertical movements from topographic or other sources. Most hailstorms producing hailstones of sizes large enough to cause considerable damages come with instability lines.

Particularly interesting is the study by Moore and Pino (1990), which estimates the maximum diameter of hailstones on the basis of the positive areas (parcels) over the convective condensation level (CCL) and the level of free condensation (LFC).

2. STUDY ZONE

The study zone lies in the Friuli-Venezia-Giulia plain, just under 500 m above sea level, in the northeast of Italy (Fig. 1). The area is geographically surrounded by the Alps to the north, the Adriatic Sea to the south and the Po Valley to the southwest. These features determine the meteorology of the region (Giaiotti et al., 2001).

In this region the Italo-Slovenian Thunderstorm and Hail Prevention Research Project runs a polystyrene hailpad network (Giaiotti et al., 2001) for detecting and monitoring the frequency and intensity of hail. Fig. 1 shows in red the area where the hailpad network is installed.

This study covers 11 annual data-gathering campaigns. Campaigns typically run from April to September. The data used cover from 01/04/1988 until 31/12/1998 and include approximately 600 hail days.

Fig. 1. Study zone in red.

3. DATA BASE AND METHODOLOGY

For the present study we used data from the hailpad network mentioned above and from the Udine/Campoformido weather station (LIPD 16044).

The hailpad network is formed by 362 plates distributed in grid form over an area of 5790 km^2. The polystyrene plates are 30 x 42 cm. The network's main features, the procedures followed for the study of the plates and the measurement of the dents are all explained in Giaiotti et al. (2001). Once the dented hailpads are processed, the maximum diameter (DMAX) in each day is selected provided the plate presents more than 10 dents.

The weather stations supply information on various parameters at surface level and at different altitudes by means of radio soundings (Brooks and Craven, 2002). The data provided by the soundings carried out at 0000 and 1200 UTC (the 0000 UTC sounding is only used to calculate the difference in pressure between 0000 and 1200 UTC), and the data provided by the weather station at surface level are used to calculate the physical variables. The sounding data are stored by the University of Wyoming (http://www.weather.uwyo.edu/upperir/sounding).

The following are the physical variables computed directly in the data provided by the University of Wyoming (the definition and computing procedures of each variable are available at www.weather.uwyo.edu/upperir/indices):

Showalter index (ºC) (SHOW) (Showalter, 1953); Lifted index (ºC) (LIFT) (Galway 1956); LIFT computed by using virtual temperature (LFTV); SWEAT index (SWET) (Miller, 1975) developed specifically to forecast storms in ºC; K index (ºC) (KINX) (Marcos, 2001); Cross Totals index (CTOT) (Sturtevant, 1995); Vertical Totals index (VTOT) (Sturtevant, 1995); Total Totals index (TOTL) (Miller, 1975); Convective Available Potential Energy (J/kg) (CAPE) and CAPE computed by using virtual temperature (CAPV) (Moncrieff and Miller,1976); Convective Inhibition (J/kg) (CINS) and CINS computed by using virtual temperature (CINV) (Blanchard, 1998); Equilibrium level (hPa) (EQLV) and EQLV computed by using virtual temperature (EQTV), on a sounding, the level above the level of free convection (LFCT) at which the temperature of a rising air parcel again equals the temperature of the environment (López, 2003); Level of Free Convection (hPa) (LFCT) by comparing temperature between a parcel and the environment and LFCT computed by using virtual temperature (LFCV) (Doswell, 1987); Bulk Richardson number (BRCH) and BRCH computed by using CAPV (BRCV) combining CAPE and wind shear (Weisman and Klemp, 1982; Hart and Korotky, 1991). It is interpreted as the ration between CAPE derived from thermodynamic instability and the kinetic energy available due to the vertical wind shear, both leading to convection (López, 2003); Temperature (K) at the lifted condensation level (LCL), from an average of the lowest 500 meters (LCLT) (Inman, 1969); Pressure (hPa) at the LCL, lifted condensation level, from an average of the lowest 500 meters (LCLP) (Nicholas et al., 1985); Potential temperature of the Mean mixed layer (K) (MLTH); Mixing ratio of the Mean mixed layer MIXR (g/kg) (MLMR); 1000 mb to 500 mb thickness (m) (THTK); and finally the Precipitable water (mm) for the entire sounding (PWAT).

Stability indices are useful for predicting storms, tornados or intense precipitation. They are based on the association of thermal gradients and humidity in the lower and middle layers of the troposphere.

The second group of variables listed above is extracted from the data provided by the soundings, skew-T and the weather station at surface level: the difference of pressure at surface level between 1200 and 0000 UTC (PRES12-00); at surface level are measured the temperature (TSUP) and the dew point temperature (TdSUP) as predictors of the possible occurrence of storms (Angus et al. 1988); TdSUP also indicates the likelihood of a storm during the day (Fuelberg and Biggar 1994); Relative humidity at surface level (RHSUP) and the Mixing Ration at surface level (g/kg) (MRSUP) (Giaiotti et al., 2006); Angle shear between 850-500 hPa and Module shear between 850-500 hPa (Johns and Doswell, 1992); Tropopause height (m) (HTROP) and Temperature at the tropopause height (TTrop) (Molenat, 1974); Height of zero (H0ºC) and Height of the dew zero (Hd0ºC) refer to the likelihood that hailstones, eventually formed in convective processes, may reach the ground later. Some authors provide the final size of hailstones according to the height of 0ºC (Marcos, 2001), but Molenat (1974) predicts it according to the height of the dew point temperature; the minimum temperature (TMIN) in the night before the sounding strongly correlates with the occurrence of hail (Dessens, 1995).

To sum up, all these variables and indices represent an essential tool for forecasting hail and the diameter of hailstones. The problem lies in how to use and properly correlate the most significant and adequate of these parameters.

The 618 hail days recorded were reduced to 313 days for which all of the variables were available. A statistical analysis of the physical variables and the maximum diameter was carried out. Pearson’s correlation was used to compute the value r between the variables and the maximum diameter.

To determine which variables are the most closely linked to the prediction of hailstone sizes we carried out a Principal Components Analysis and a Varimax rotation with Kaiser normalization (all the variables except DMAX). The relationships among the different variables are thus studied in detail. The analysis attempts to explain to what extent these variables account for the hail formation mechanisms and it enables us to interpret the results. To know which variables make up each of the principal components, the variables with saturations over 0.5 are associated to each of the principal components. A simpler solution is reached this way and the number of factors is minimized (López, 2003). Next, the variance that explains each component is determined. Finally, the maximum diameter is computed by means of a linear estimation of the principal components.

4 RESULTS AND DISCUSSION

The results obtained for r in Pearson’s correlation between the physical variables and the maximum diameter is shown in Table 1. It can be seen that the variables significant for 0.01 are p12-p00, LFTV and LIFT, and for 0.05 SHOW, MLTH, CAPV, CAPE, EQTV, SWET, EQLV, H0ºC, HD0ºC, MLMR, TTROP. In general, it may be argued that the maximum diameter is more closely related to the stability indices (if we include the evolution of pressure), followed by the height of 0ºC and the height of the dew point at 0ºC and the potential temperature of the mixing layer. It may be said that nearly all the variables that correlate well are already well-known as predictors of instability. However, the innovative variable in this paper (the only one that accounts for evolution in time) is the one that correlates best with the maximum hailstone size registered.

Could this variable be used as a predictor of hailstone size? The most basic model (the linear one) was used to build the graph shown in Fig. 2. As expected, an opposite relationship may be noted between the difference in pressure and the hailstone size: if the pressure drops suddenly, the instability and the updraft force are high and larger hailstones may grow.

The variables were also used in a principal components analysis. Table 2 represents the matrix of rotated components, the result of the principal components analysis with a Varimax rotation with Kaiser normalization. The variables that make up each component are the ones that have their value represented. The variables were selected by means of the procedure described above in the methods section: 8 components were obtained with all their details. The explained variance is represented in Table 3.

Table 2 shows how the variables group together in principal components: the first component contains some variables indicating mainly altitudes and temperatures; the second component includes few and very different variables; in the third and fourth components dominate the stability indices, etc. It catches the eye that the variable that

Table 1. Pearson r between the physical variables and the maximum diameter using 313 daily data sets.

Variables	Pearson **r**
PRES12-00	-0.179(**)
LFTV	-0.167(**)
LIFT	-0.166(**)
SHOW	-0.137(*)
MLTH	0.134(*)
CAPV	0.129(*)
CAPE	0.128(*)
EQTV	-0.126(*)
SWET	0.126(*)
EQLV	-0.123(*)
H0ºC	0.120(*)
HD0ºC	0.115(*)
MLMR	0.111(*)
TTROP	0.111(*)
KINX	0.110
TSUP	0.108
LCLT	0.102
PWAT	0.102
TdSUP	0.095
MRSUP	0.085
TMIN	0.080
VTOT	0.076
Shear Angle	0.067
TOTL	0.061
HTROP	0.058
Shear Module	0.052
CTOT	0.027
CINV	-0.006
THTK	-0.008
CINS	-0.022
LFCV	-0.025
BRCH	-0.033
BRCV	-0.036
LCLP	-0.038
RHSUP	-0.046
LFCT	-0.078

**. Correlation significant for 0.01 (bilateral).

*. Correlation significant for 0.05 (bilateral).

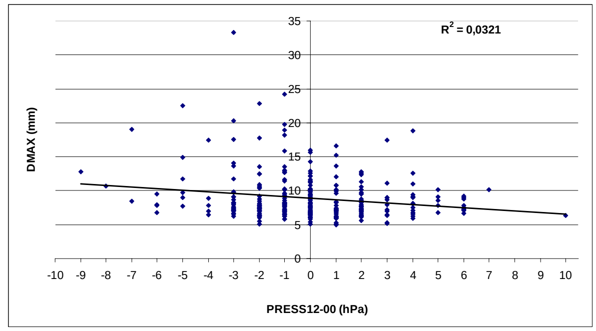

Fig. 2. Relationship between the maximum diameter and PRESS12-00.

announced above as the one that correlates best with hailstone size is left out of these 8 principal components because it supplies a different type of information which is independent of all the other variables. This fact has consequences in the next stage of our study.

First, the maximum diameter was estimated using exclusively a linear relation between the three first principal components. The result is shown in Fig. 3, relating the estimated size to the actual size registered. The first three components explain only 63.40% of the accumulated variance, so the linear estimation model was rebuilt using the first 8 principal components, which explain 87.83% of the variance. It was not considered necessary to continue extracting any further components. The relationship between the estimated and the measured sizes is represented in Fig. 4. For the 313 data considered the correlation with three components (Fig. 3) is r = 0.146; with eight components it improves until r = 0.201.

From the results found it may be concluded that the variables selected explain a high percentage of the variance, thus suggesting that from a mathematical perspective the choice of the variables was adequate. From the perspective of atmospheric physics, it could be argued that for setting up a forecast model it is necessary to take into account instability, a sufficiently deep and moist layer in the mid or low troposphere, and an updraft to trigger convection (Johns and Doswell, 1992).

Table 2. Matrix of rotated components.

Variables	Component 1	2	3	4	5	6	7	8
SHOW				-0.800				
LIFT			-0.837					
LFTV			-0.839					
SWET				0.692				
KINX	0.545			0.639				
CTOT				0.872				
VTOT			0.619					
TOTL				0.802				
CAPE						0.759		
CAPV						0.744		
CINS					0.947			
CINV					0.950			
EQLV			-0.748					
EQTV			-0.749					
LFCT		0.508			0.777			
LFCV					0.801			
BRCH						0.961		
BRCV						0.950		
LCLT	0.867							
LCLP		0.929						
MLTH	0.687							
MLMR	0.890							
THTK								0.750
PWAT	0.945							
PRES12-00								
TSUP	0.626	-0.671						
TdSUP	0.908							
RHSUP		0.948						
MRSUP	0.886							
Shear Angle		-0.949						
Shear Module								0.692
HTROP	0.533						0.692	
TTROP							-0.887	
H0ºC	0.835							
HD0ºC	0.899							
TMIN	0.837							

Table 3. Variance explained by the principal components.

Component	Initial autovalues		
	Total	% variance	% accumulated
1	11.580	32.17	32.17
2	6.254	17.37	49.54
3	4.991	13.86	63.40
4	2.966	8.24	71.64
5	2.188	6.08	77.72
6	1.454	4.04	81.76
7	1.150	3.19	84.95
8	1.037	2.88	87.83

However, none of the principal components used in Fig. 3 and 4 includes variable PRES12-00, which is the one that best describes the maximum hailstone size.

Therefore, the results presented above need to be discussed further. These results may be summarized as follows:

- The difference in pressure between midnight before the hail fall and noon on the hail day is a variable that correlates with the largest hailstone size registered.
- The present study has taken the data on hailstone size directly from hailpads. The result would certainly improve if other corrections were applied to the hailpad (Palencia et al., 2007) or to the spatial representativeness of the data from the hailpad network (Smith and Waldvogel, 1989). Hailstones larger than the ones registered by the hailpads may have hit the network: a statistical model may help correct these types of errors.
- In addition, the hailpad network has a limited range, so there may have been hail falls that have not directly fallen on the network or only partially so. And many hailstones may lie on the border of the area. In this second case the best solution would have been to consider in the sample only the hail falls that have fallen entirely within the sampling area.
- This model for estimating the maximum hailstone size may be improved simply with the inclusion of the variable PRES12-00, which is the one that best estimates the maximum size. This research line will be the focus of further studies.

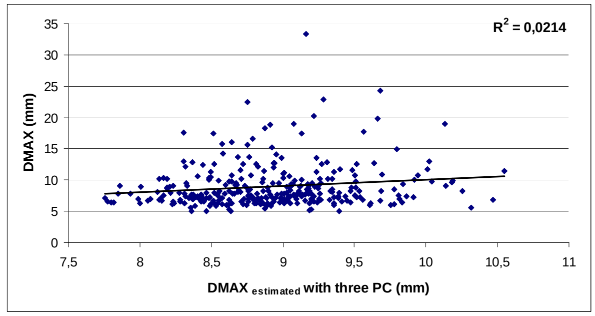

Fig. 3. Relationship between the maximum diameter and the estimated diameter with the first three principal components.

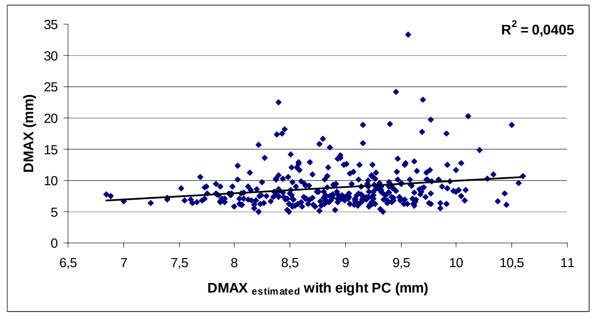

Fig. 4. Relationship between the maximum diameter and the estimated diameter with the first eight first principal components.

6 BIBLIOGRAPHY

Angus, P.J., S. Rasmussen and K. Seiter, 1988: Short-Term prediction of thunderstorm probability and intensity by screening observational and derived predictors. *15th Conference on Severe Local Storm,* AMS, Baltimore, 368-371.

Blanchard, D.O., 1998: Assessing the Vertical Distribution of Convective Available Potential Energy. *Weather and Forecasting,* **13** (3), 870–877

Brooks and Craven, 2002 H.E. Brooks and J.P. Craven, A database of proximity soundings for significant severe thunderstorms, 1957–1993, *Preprints, 21st Conference on Severe Local Storms*, American Meteorological Society, San Antonio, Texas, 639–642.

Dessens, J., 1995: Severe convective weather in the context of nighttime global warning. *Geophys. Res. Lett*., **22**, 1241-1244.

Doswell, C.A., 1987: The distinction between large-scale and mesoscale contribution to severe convection: A case study example. *Wea. Forecasting*, **2**, 3-16.

Farnbush, E.F., Miller, R.C., 1953 :A method for forecasting hailstone size at the earth's surface*. Bull. Amer. Meteor. Soc.*, **34**, 235-244.

Fuelberg, H.E. and Biggar, D.G., 1994: The preconvective environement of summer thunderstorms over the Florida panhandle. *Wea. Forecasting*, **9**, 316-326.

Galway, J.G.,1956. The Lifted Index as a predictor of latent inestability. *Bull. Amer. Meteor. Soc.,* **37**, 528-529.

Giaiotti, D., and F. Stel, 2006: The effects of environmental water vapor on hailstone size distributions. *Atmos. Res.,* **82**, 455-462.

Giaiotti, D., E. Gianesini, and F. Stel, 2001: Heuristic considerations pertaining to hailstone size distributions in the plain of Friuli-Venezia Giulia. *Atmos. Res.,* **57**, 269-288.

Hart, J.A. and W.D. Korotky, 1991: The SHARP workstation v 1.50. A skew T/hodograph analysis and research program for the IBM and compatible PC: User's manual. NOAA/NWS Forecast Office, Charleston, WV, 62 p.

Inman, R. L., 1969: Computation of Temperature at the Lifted Condensation Level. *J. Appl. Meteor.*, **8**, 155-159.

Johns, R.H. y C.A. Doswell III., 1992: Severe local Storms Forecasting. *Wea. Forecasting*, **7**, 588-612.

López, L., 2003: *Convección atmosférica severa: pronóstico e identificación de tormentas con granizo.*Tesis doctoral. Universidad de León.

Marcos, J. L., 2001: *Ampliación de modelos estadísticos de decisión dicotómica para la predicción a corto plazo de tormentas y caída de granizo.* Tesis doctoral. Universidad de Salamanca. 160 pp.

Miller, R.C., 1975: Notes on analysis and severe storm forecasting procedures of the military weather warning center. Technical Report nº 200, AWS, USAF.

Molenat, J., 1974: *Technique de la prévisiondes risques de grêle dans* le *sud-ouest de la France au bénéfice de l'Association Nationale de Lutte contre les Fléaux Atmosphériques.*

Moncrieff, M.W., and M.J. Miller, 1976: A theory of organised steady convection and its transport properties. *Quart. J. Roy. Meteor*. Soc., **102**, 373-394.

Moore, J.T., Pino, J.P., 1990: An interactive method for estimating maximum hailstone size from forecast soundings. *Weather and forecasting*, **5**, 508-525.

Nicholas P. Wilde, Roland B. Stull, and Edwin W. Eloranta, 1985: The LCL Zone and Cumulus Onset. *J Appl. Meteor.,* 640–657.

Palencia, C., C. Berthet, M. Massot, A. Castro, J. Dessens, and R. Fraile, 2007: On the individual calibration of hailpads. *Atmos. Res.*, **83**, 493-504.

Showalter, A.K., 1953: A stability indices for thunderstorm forecasting. *Bull. Amer. Meteor. Soc.*, **34**, 250-252.

Smith, P.L. and A. Waldvogel, 1989: On Determinations of Maximum Hailstone Sizes from Hailpad Observations. *J. Appl. Meteor*., **28**, 71-76.

Sturtevant, J. S., 1995. *The Severe Local Storm Forecasting Primer*, 197 pp.

Weisman, M.L., and J.B. Klemp, 1982: The dependence of numerically simulated convective on vertical win shear and buoyancy. *Mon. Wea. Rev*., **110,** 504-520.

Acknowledgments

The authors are grateful to Dr. Noelia Ramón for translating the paper into English. We would also like to thank all the volunteers who contribute to the Italian hailpad network maintenance. We are in debt with Elena Gianesini for her work on hailpad data reduction.

FLASH FLOOD EVENT OVER CENTRAL ARGENTINA: A CASE STUDY

Paola Salio [(1)], Yanina Garcia Skabar[(2)] and Matilde Nicolini [(1)]

[(1)] Departamento de Ciencias de la Atmósfera y los Océanos. UBA.
Centro de Investigaciones del Mar y la Atmósfera. CONICET – UBA.
Buenos Aires. Argentina.

[(2)] Servicio Meteorológico Nacional
Cátedra de Climatología y Fenología Agrícolas. FA - UBA
Buenos Aires. Argentina.

1. INTRODUCTION

Flash flood events occur within minutes or hours of excessive rainfall, this kind of events can destroy buildings and triggers catastrophic situations due to sudden water stream. The central region of Argentina presents a flat terrain with a weak slope to the Atlantic Ocean. March 26 to April 1, 2007 was a week characterized by the presence of successive convective systems over central Argentina that generate strong rain rates, flooding large areas and producing important damages and lost of lives.

A primary goal of the present work is to describe the synoptic and mesoscale characteristics of the environment associated to a flash flood case over the central region of Argentina, with a special emphasis in the relationship between the behaviour of convective precipitation and the evolution of the low level jet. In order to achieve this objective a numerical simulation is performed considering a version of the Brazilian Regional Atmospheric Modeling System (BRAMS), that include a microphysics scheme and explicit convection in the finest resolution grid and estimations of precipitation are considered in order to detect convective and stratiform precipitation areas.

Corresponding Author Address: Dr. Paola Salio. salio@cima.fcen.uba.ar
Departamento de Ciencias de la Atmósfera y los Océanos. UBA. Bs. As. Argentina.

2. METHODOLOGY

The evolution of the successive mesoscale convective systems (MCSs) that affect the area of interest and their impact on precipitation rain rates have been studied considering satellite images every half hour and 4km-resolution and satellite estimation every one hour (CMORPH), it is important to consider this kind of information due to the lack of hourly rain rate over the area. 24 hour accumulated precipitation is used to validate CMORPH data. A clusterization and tracking technique called ForTraCC (Vila et al 2008) are employed to determine the life-cycle of each system considering two temperature thresholds 235 and 218 K. 235 K was considered to determine the contour of the rain area and 218 K was considered in order to follow areas associated with deep convection.

CMORPH performance in this extreme precipitation event is evaluated in figure 1, extreme values are well detected specially at El Trébol, Rosario, Paraná and Gualeguaychú. Although stations in Buenos Aires province (last 10 stations from the right on the figure) present an overestimation where observed values were higher than 100 mm, the region associated with the flooded area is well represented.

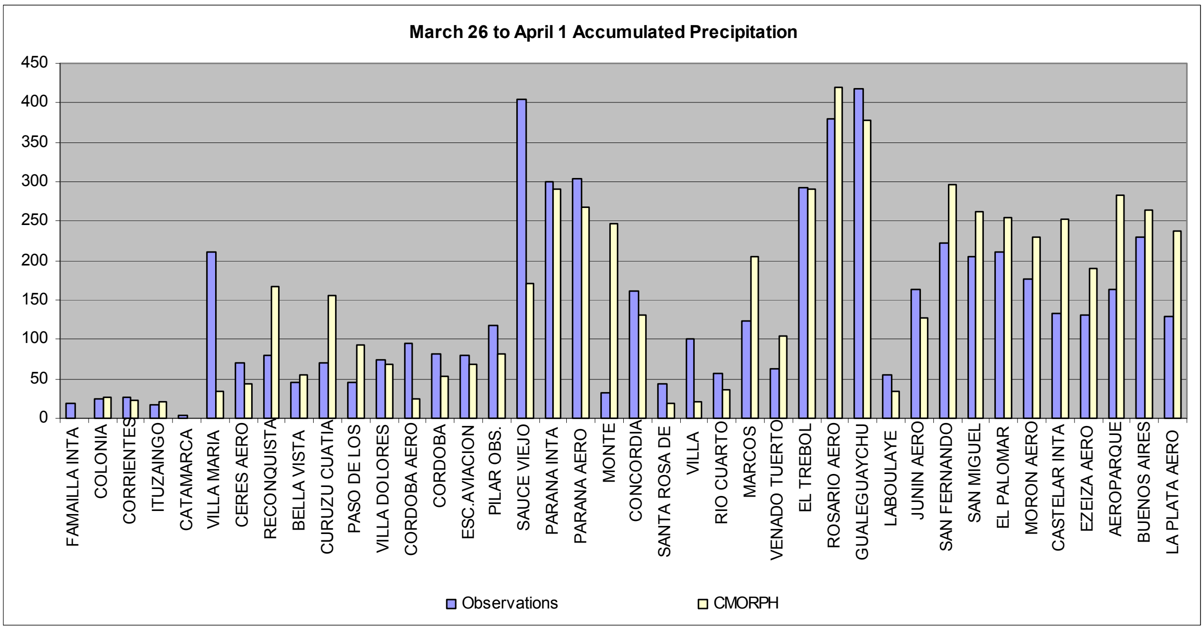

Figure 1: 24-hour accumulated precipitation observed over central Argentina (violet) and CMORPH estimations (yellow) accumulated between March 26 to April 1, 2007.

In order to determine areas that present different internal structure in the MCS, CMORPH information is applied in order to determine stratiform and convective precipitation regions, this estimation is considered due to the lack of radar observations and hourly precipitation information over the area. 235 K contour in IR images is used as a threshold to identify the precipitation areas associated with each system. Then stratiform and convective areas are differentiated considering the threshold of 7.5 mm hour^{-1} suggested by Mc Annelly and Cotton (1989) using CMORPH. Areas with values higher than 7.5 mm hour^{-1} are considered as convective and areas with values lower than this threshold are denoted as stratiform, all precipitation regions must be contained by a 235 K contour. Different thresholds were tested over radar area coverage closely located to the flooded region and the selected threshold is close to 40 dBz contour.

This case study was simulated with BRAMS. It is a regional non-hydrostatic, primitive equation model, formulated with an interactive multi-scale grids nesting capability. A complete and general description of the model can be found at Cotton et al (2003). Version used in this experiment includes several improvements from the original one. It includes a shaved ETA vertical coordinate, making it suitable to use in steep topographies as the Andes Mountains (Tremback and Walko, 2004). It also includes a shallow cumulus parameterization (Souza and Silva 2002) that complements the Grell cumulus scheme for deep convection (Grell and Devenyi, 2002). BRAMS model was applied in the region to simulated different mesoscale phenomena and results shows that it satisfactorily represents the observed conditions (Salio et al, 2006; Ruiz et al, 2006; Nicolini et al, 2005a and Nicolini et al, 2005b).

To simulate this case study a 156 hours simulation was performed starting at 12 UTC of 2007 March 25. Results were analyzed each 3 hours. Global Data Assimilation System (GDAS) analyses from National Oceanic and Atmospheric Administration/ National Center of Enviromental Prediction (NOAA/NCEP) were used as initial and boundary conditions. Numerical experiment was configured with three nested domains, with an increasing horizontal resolution of 50, 12.5 and 3.125 km. Geographical location of nested domains is shown in figure 2. Grell cumulus parameterization and shallow convection scheme were only activated in the lower resolution grid. It was used the “bulk water” scheme for the microphysical representation in all grids. Shaved eta vertical coordinate was applied and the model was configured with 30 atmospheric and 9 soil vertical levels, including topography data (1km resolution), terrain land use (1km resolution), soil types (50km resolution) and weekly sea surface temperatures.

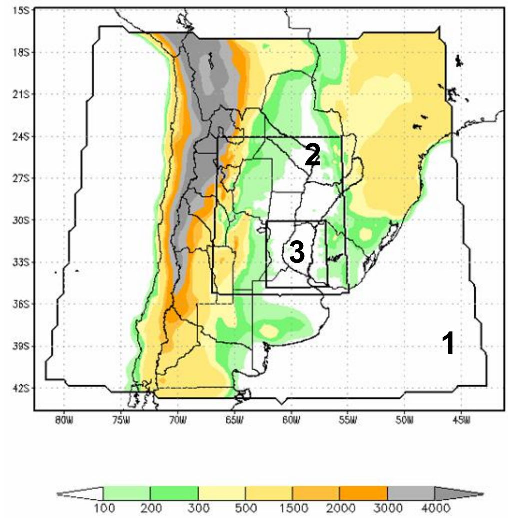

Figure 2: BRAMS nested domains considered in the simulation.

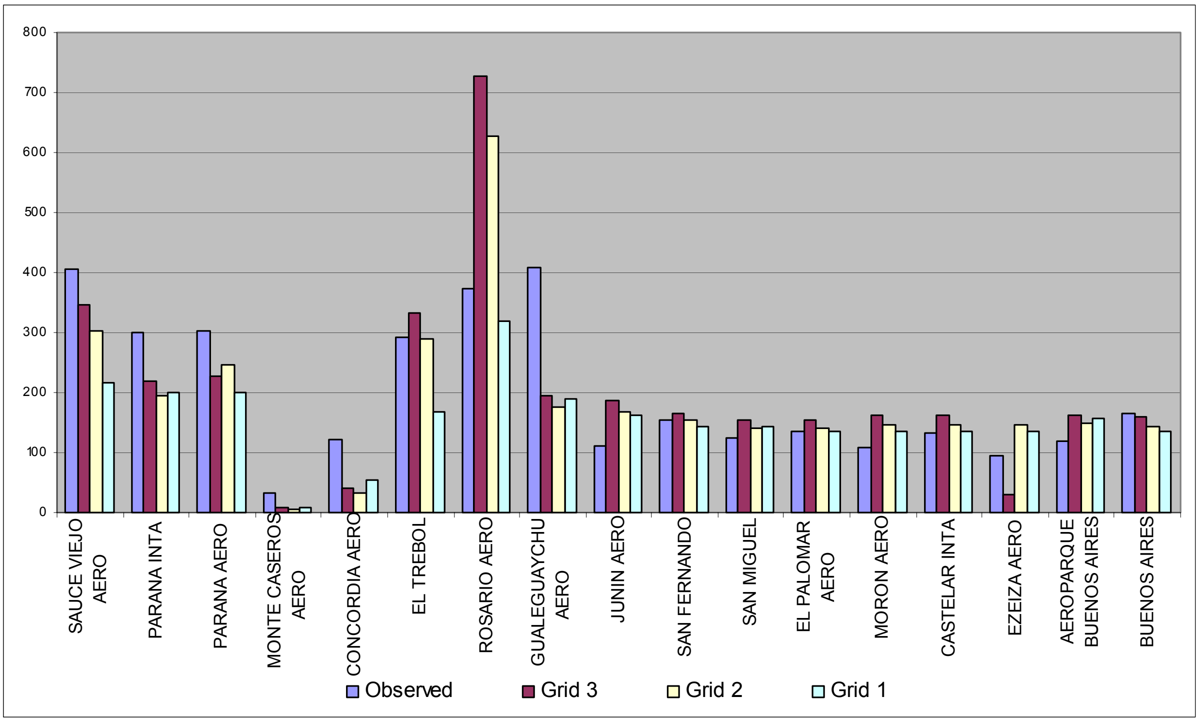

Figure 3: 24-hour accumulated precipitation observed over central Argentina (violet) and models forecast by different grids accumulated between March 26 to April 1, 2007. Grid 1 (light blue) represent the precipitation forecast for 50 km resolution, Grid 2 (yellow) for 12.5 km and Grid 3 (bordeaux) for 3.125 km respectively.

Accumulated precipitation over the entire study period observed and estimated by different models grids is showed in Figure 3 for all meteorological stations available in the region covered by the higher resolution grid, where maximum values of accumulated precipitation were registered. The accumulated precipitation simulated by the model results in most locations very close to the observed values, but in some locations as in Rosario rain simulated is significantly overestimated, reaching nearly twice the observed value in the higher resolution grid.

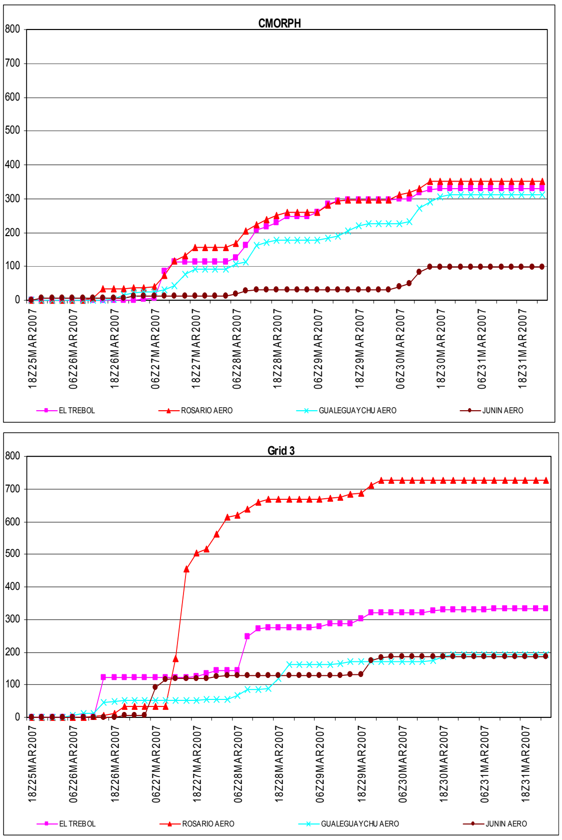

Figure 4: Accumulated precipitation every 3 hours in Rosario (red), el Trébol (pink), Gualeguaychú (light blue) y Junín (bordeaux) estimated by CMORPH data (left) and simulated for the 3.125 km - model resolution grid (right).

Figures 4 presents accumulated precipitation every 3 hours in Rosario, el Trébol, Gualeguaychú y Junín estimated by CMORPH data and simulated by the higher resolution grid. Figure 4.b shows a good representation of the rain initiation time in Rosario. Accumulated precipitation is overestimated only between 12 and 15 UTC March 27 whereas the 3 hours accumulated values for the rest of the period are correctly represented. In Gualeguaychú rain evolution adjusts to observed values, except at the end of the period when accumulated precipitation is underestimated. In El Trébol the initiation of precipitation is anticipated in 12 hours, but time of maximum intensity during March 28 was satisfactory simulated. While in Junín, temporal evolution of phenomena is correctly simulated, accumulated precipitation is overestimated at the beginning of the period (March 27). Although the model evidences some spatial and temporal misplacements in maximum precipitation respect to CMORPH estimation, systems evolution and accumulated precipitation during the whole period are properly represented by the model.

3. RESULTS

3.1 LARGE SCALE CONDITIONS

The role of the large scale processes are essential in the development of deep moist convection, this situation is characterized by the presence of a strong trough centered on 75°W, Associated with this system an important advection of cyclonic vorticity affects the central part of the country. This system remains stationary over the whole studied period and develops in a cut-off low over the coast of Chile favouring large scale rising motions over central Argentina.

The availability of moisture is favoured by the presence of a low over northwestern Argentina that deepens over the period and intensifies the northerly flow over the region. A low-level jet profile (LLJ) within this northerly flow attains speeds stronger than 20 ms^{-1} at 850 hPa over northern Argentina. The presence of this characteristic feature in the circulation is closely related with the occurrence of convection downstream of the maximum in wind speed (Salio et al, 2007, Siqueira and Machado 2004, among others). A cold front advances to the north-east from 42°S remaining stationary up to April 1st when it eventually crosses the studied area.

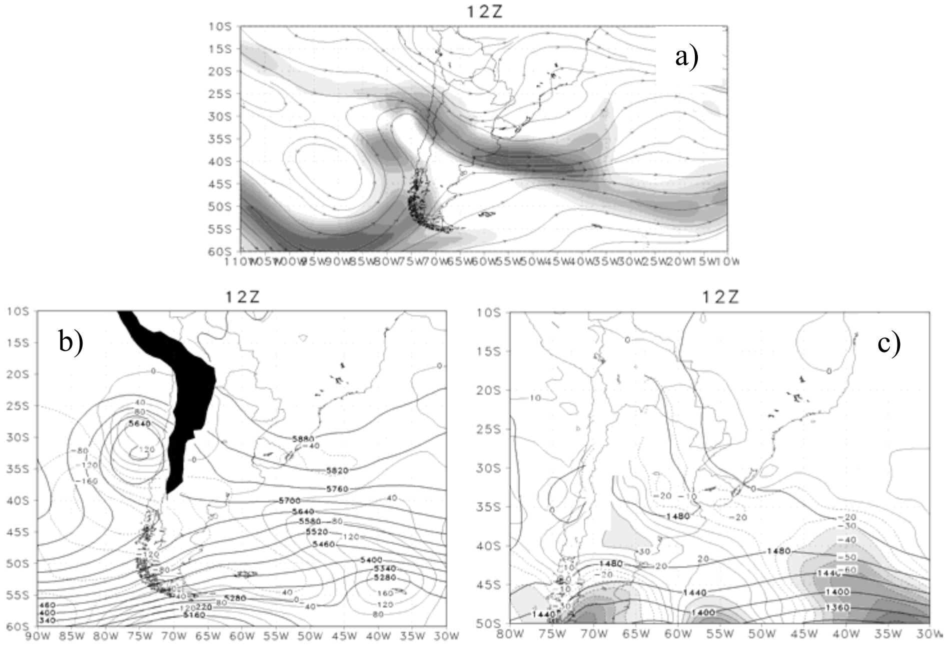

Figure 5: a) Streamlines and wind intensity higher than 30 m s-1 at 200 hPa on March 27 12UTC. b) Geopotential and 24-hour tendency at 500 hPa on March 27 12UTC. c) idem b) for 850 hPa.

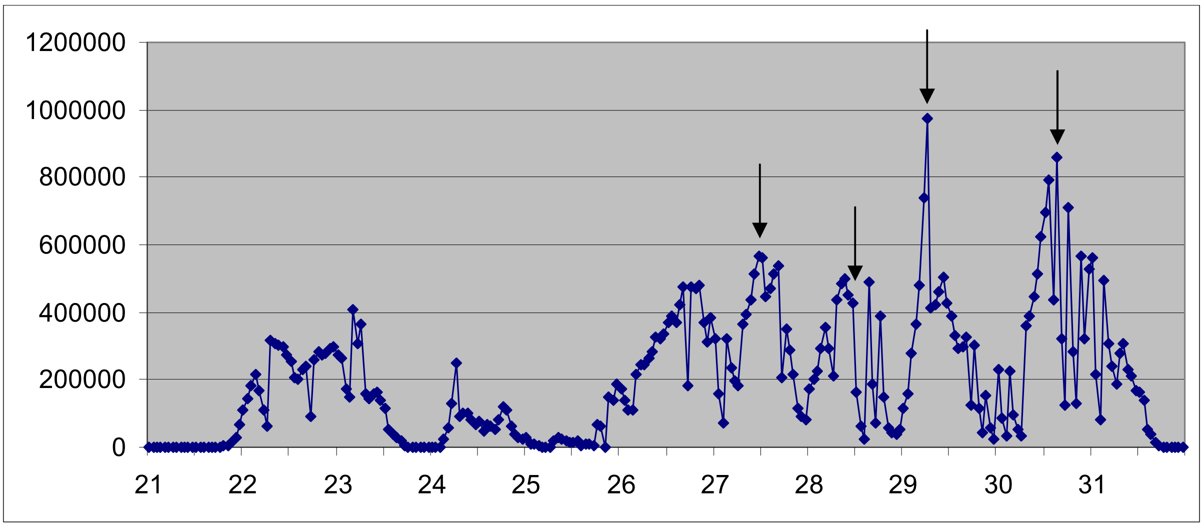

Figure 6: 218 K covered area in km^2 by the mesoscale convective systems every half hour that affect the central and northern region of Argentina between March 21 to April 1, 2007. Arrows indicate different extreme moments showed in figure 7.

3.2 MESOSCALE CONVECTIVE ACTIVITY

The convection activity over central Argentina is characterized by the presence of numerous mesoscale convective systems that develop ahead of the cold front. Figure 6 shows the temporal evolution of the size of the whole area covered by the convective systems considering 218 K IR brightness temperature as the threshold to define this area. The evolution of convection before the study situation is also included. IR brightness temperature images at significant times associated with the development of the convection are shown in figure 7 and denoted by an arrow in figure 6. Convective, stratiform and total precipitation for the overlapping period and the same systems are showed in figure 8.

Convection generated before March 26 area principally associated with stratiform precipitation over the whole area, but this situation evidences potential conditions of soil saturation over the flat terrain of central Argentina.

Mesoscale convective activity from March 26 shows that all systems tend to generate during the beginning of the night and decay during the day. The maximum extension of the systems varies from small systems to the bigger one on March 29 at 8Z that cover all area, and shows also developments over northwestern Argentina. Most extreme rainfall producer systems area detected on March 26 and 31 with maximum rates close to 12 UTC. Strong convective rates are

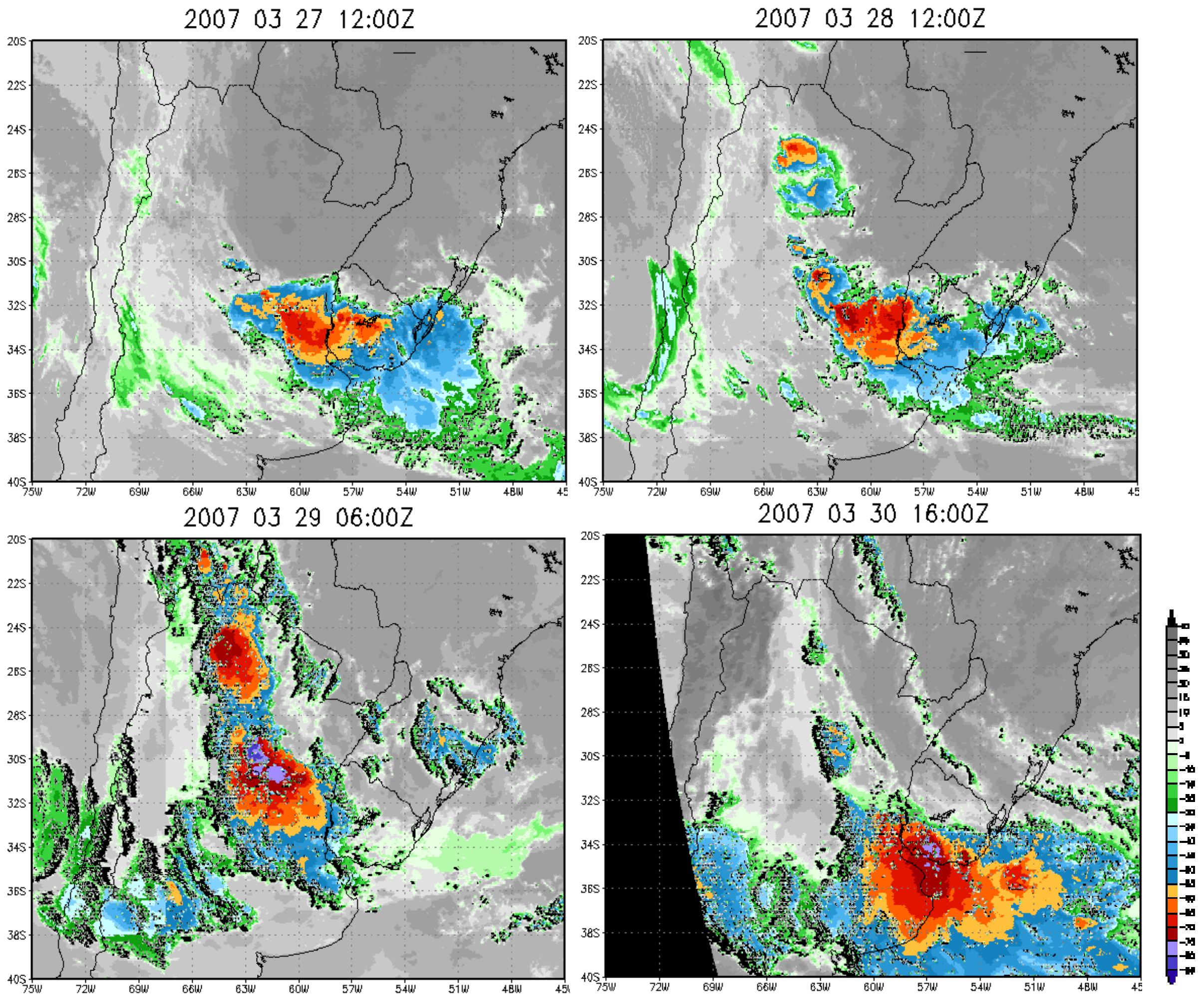

Figure 7: IR brightness temperature for the most important moments associated to the development of the mesoscale convective systems indicated in figure 6 by an arrow. Black areas represent regions with undefined values.

detected at these times, these rates overpass by three times the total stratiform precipitation generated by the systems. Systems during the rest of the period present an equivalent total stratiform and convective precipitation but, in general, convective maximum precipitation occurs before the stratiform precipitation.

Convection generated before March 26 are principally associated with stratiform precipitation over the whole area, but this situation evidences potential conditions of soil saturation over the flat terrain of central Argentina.

Mesoscale convective activity from March 26 shows that all systems tend to generate during the beginning of the night and decay during the day. The maximum extension of the systems varies from small systems to the bigger on March 29 at 8Z that cover all area, and shows also developments over northwestern Argentina. Most extreme rainfall producer systems area detected on March 26 and 31 with maximum rates close to 12 UTC. Strong convective rates are detected in these moments, these rates overpass by three times the total stratiform precipitation generated by the systems. Systems during the rest of the period present a equivalent total stratiform and convective precipitation but, in general, convective maximum precipitation occurs before than stratiform precipitation.

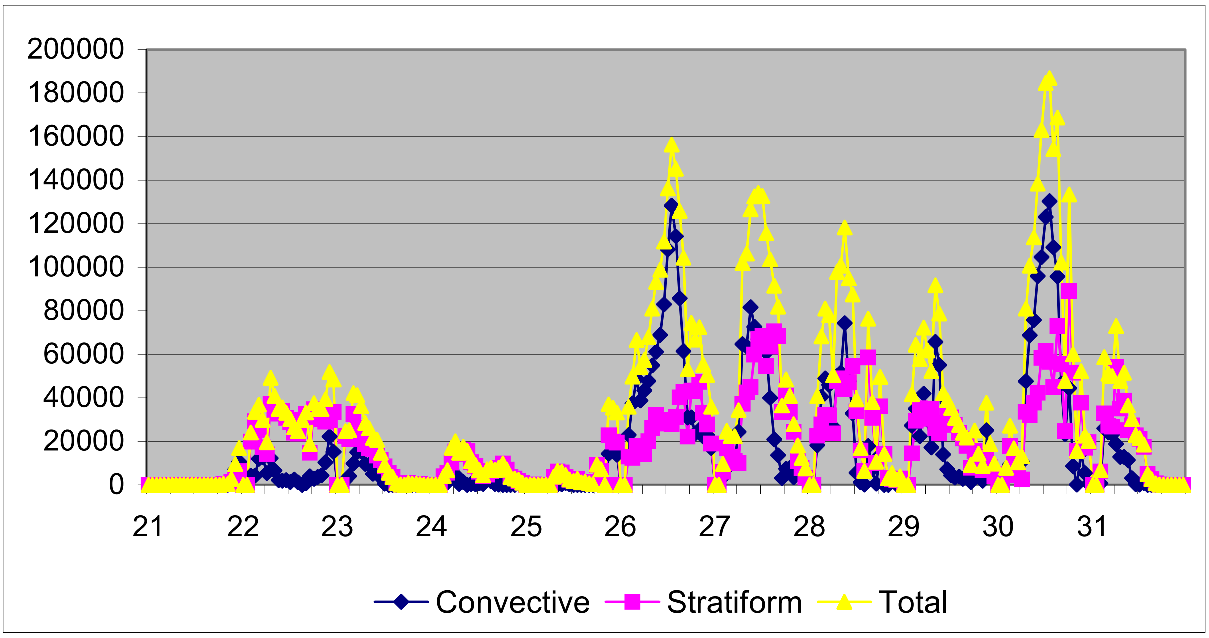

Figure 8: Stratiform (pink, boxes), convective (blue, diamond) and total (yellow, triangle) volumetric precipitation estimated for all systems that affect the central and northern region of Argentina between March 21 to April 1, 2007.

3.3 ENVIRONMENT ASSOCIATED TO CONVECTION

The thermodynamic environment is characterized by strong CAPE, low CINE and the presence of a deep flow from the north that shows a LLJ profile. These environmental features present the ideal conditions to the formation of convection, because they establish a favorable situation associated with large-scale vertical ascent and potential instability over the area.

In order to advance in the knowledge of the relationship between the LLJ and the development of convection, BRAMS simulation was performed and the interaction between LLJ and convective precipitation is investigated.

Figure 9 shows two groups of variables, on one side the estimations of convective and stratiform precipitations by CMORPH and on the other side the evolution of the northerly flux that transport moisture into the region where the convective systems develop from the BRAMS finest grid (3.125 km). A wind average is performed at 32 S between 58 and 60W, and also the northerly geostrophic and ageostrophic component of the wind are calculated at 850 hPa.

The northerly component of the wind is clearly generated by an ageostrophic circulation of the wind due to the fact in this area the pressure gradient generates southerly winds that increasing with time. Preceding the clear development of convective precipitation rates the northerly ageostrophic wind tends to increase denoting an interaction between the incipient development of convection and the intensification of the circulation directed toward the storm.

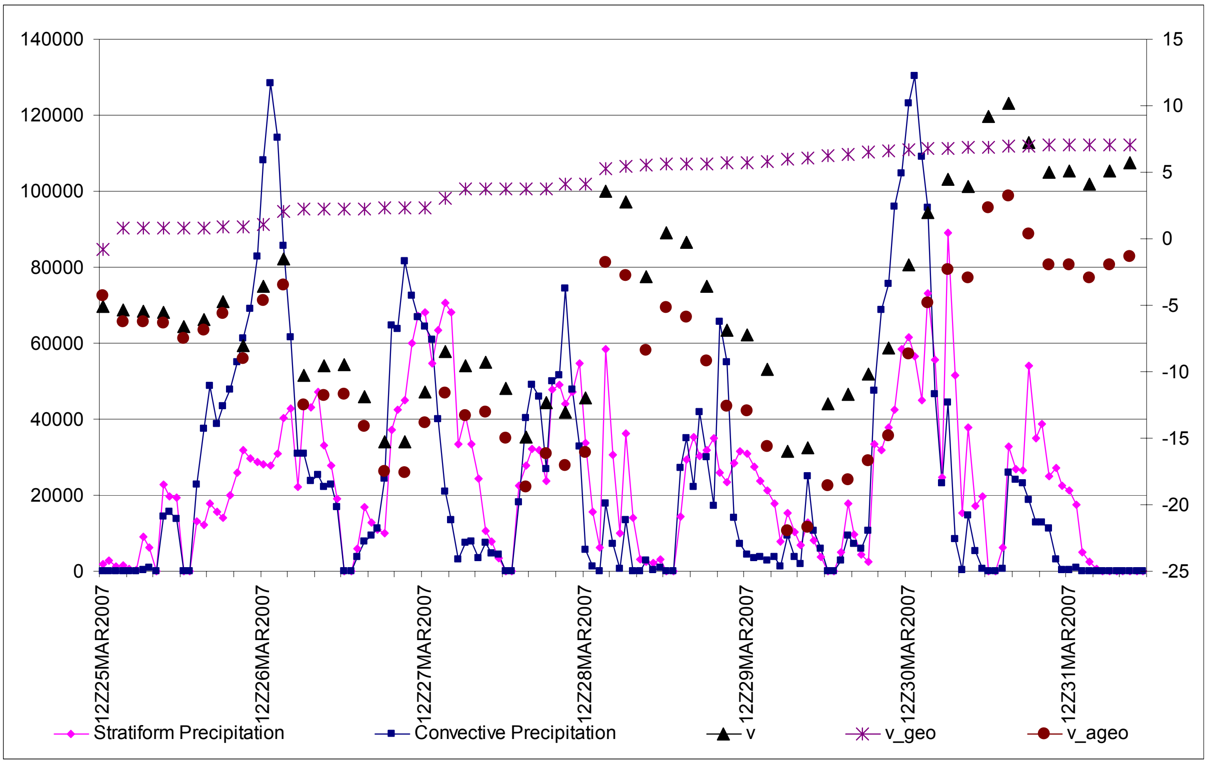

Figure 9: Convective (blue line) and stratiform (pink line) precipitation estimation from CMORPH left y axis, total meridional wind (triangle), meridional geostrophic wind (asterix) and meridional ageostrophic wind (circle) averaged at 32S and between 58 and 60W at 850 hPa on right y axis.

ACKNOWLEDGMENTS

This research was supported by UBA grant X266, ANPCyT grant Nº PICT 07 – 14420, PIP 5582.

ANEXO

Latitude and longitude of the stations mentioned in the text.

Lat	LON	Station
-27.05	-65.42	FAMAILLA INTA
-27.42	-58.93	COLONIA BENITEZ INTA
-27.45	-58.77	CORRIENTES AERO
-27.58	-56.67	ITUZAINGO
-28.60	-65.77	CATAMARCA AERO
-29.90	-63.68	VILLA MARIA DEL RIO SECO
-29.88	-61.95	CERES AERO
-29.18	-59.70	RECONQUISTA AERO
-28.43	-58.92	BELLA VISTA INTA
-29.78	-57.98	CURUZU CUATIA AERO
-29.68	-57.15	PASO DE LOS LIBRES AERO
-31.95	-65.13	VILLA DOLORES AERO
-31.32	-64.22	CORDOBA AERO
-31.40	-64.18	CORDOBA OBSERVATORIO
-31.45	-64.27	ESC.AVIACION MILITAR AERO
-31.67	-63.88	PILAR OBS.
-31.70	-60.82	SAUCE VIEJO AERO
-31.83	-60.52	PARANA INTA
-31.78	-60.48	PARANA AERO
-30.27	-57.65	MONTE CASEROS AERO
-31.30	-58.02	CONCORDIA AERO
-32.67	-65.32	SANTA ROSA DE CONLARA AERO
-33.73	-65.38	VILLA REYNOLDS AERO
-33.12	-64.23	RIO CUARTO AERO
-32.70	-62.15	MARCOS JUAREZ AERO
-33.67	-61.97	VENADO TUERTO
-32.20	-61.67	EL TREBOL
-32.92	-60.78	ROSARIO AERO
-33.00	-58.62	GUALEGUAYCHU AERO
-34.13	-63.37	LABOULAYE AERO
-34.55	-60.92	JUNIN AERO
-34.45	-58.58	SAN FERNANDO
-34.55	-58.73	SAN MIGUEL
-34.60	-58.60	EL PALOMAR AERO
-34.67	-58.63	MORON AERO
-34.67	-58.65	CASTELAR INTA
-34.82	-58.53	EZEIZA AERO
-34.57	-58.42	AEROPARQUE BUENOS AIRES
-34.58	-58.48	BUENOS AIRES
-34.97	-57.90	LA PLATA AERO

REFERENCES

Cotton, W.R., R.A. Pielke, Sr., R.L. Walko, G.E.Liston, C.J. Tremback, H. Jiang, R.L. McAnelly, J.Y. Harrington, M.E. Nicholls, G.G. Carrió, J.P. McFadden, 2003: RAMS 2001: Current status and future directions. Meteor. Atmos Physics, Vol. 82, 5-29.

Grell, G.A. y D. Devenyi, 2002: A generalized approach to parameterizing convection combining ensemble and data assimilation techniques. Geophysical Research Letters, Vol.29, nº14, 1963.

McAnelly R. and W. R. Cotton, 1989: The Precipitation Life Cycle of Mesoscale Convective Complexes over the Central United States Monthly Weather Review, 117, 4, 784–808.

Nicolini M., Y. García Skabar, A. G. Ulke, and P. Salio, 2005a: A hailstorm simulation in Mendoza. Proc. IX Congreso Argentino de Meteorología., Buenos Aires, Argentina, Centro Argentino de Meteorólogos, CDROM. Published in Spanish.

Nicolini M., M. Torres Brizuela, and Y. García Skabar, 2005b: Numerical simulation of a tornadic storm using a mesoscale model of high resolution. Proc. IX Congreso Argentino de Meteorología., Buenos Aires, Argentina, Centro Argentino de Meteorólogos, CDROM. Published in Spanish.

Ruiz, J.J., A. C. Saulo, Y. García Skabar, and P. V. Salio, 2006: The representation of a mesoscale convective system using RAMS model. Meteorológica. Vol. 31, Nº 1y 2, pp.13-35,ISSN: 0325-187X. Published in Spanish.

Salio, P., M. Nicolini, and A. C. Saulo, 2002: Chaco low level jet events characterization during the austral summer season by ERA reanalysis. J. Geophys. Res., 107, 4816.

Salio, P., C. Campetella, J. Ruiz, Y. García Skabar, and M. Nicolini, 2006: Snow-fall over Southeast of Buenos Aires province:

Synoptic climatology and a case study. Meteorológica, Vol. 31, Nº 1y 2, pp. 67-84. ISSN: 0325-187X. Published in Spanish.

Salio, P., M. Nicolini, and E. J. Zipser, 2007: Mesoscale Convective Systems Over Southeastern South America and Their Relationship with the South American Low-Level Jet. Mon. Wea. Rev., 135, 1290-1309.

Siqueira J.R. and L:A:T: Machado 2004: Influence of the Frontal Systems on the Day-to-Day Convection Variability over South America. J. of Climate, vol 17, Nº 9, 1754–1766.

Souza, E. P. y E. M. Silva, 2002: Impacto da Implementaçao de uma Parametrizaçao de Convecçao Rasa em um Modelo de Mesoscala. Descriçao e Testeo de Sensibilidade do Esquema. Revista Brasileira de meteorologia, Vol.18, Nº1, 33-42.

Tremback, C.J. y R.L. Walko, 2004: Implementing Very-high Resolution Capabilities into a mesoscale Atmospheric model: New Capabilities for the Regional Atmospheric Modeling System (RAMS). Extended abstract in Mesoscale and CFD modeling for military applications, Jackson State University.

Vila D., L.A.T. Machado, H. Laurent, I. Velasco, 2008: Forecast and Tracking the Evolution of Cloud Clusters (ForTraCC) Using Satellite Infrared Imagery: Methodology and Validation. Wea.and Forecasting, vol. 23, Nº 2, 233–245.

A NEW MULTI-MOMENT, MULTI-HYDROMETEOR CLASS, BULK MICROPHYSICS PARAMETERIZATION SCHEME. PART I: DESCRIPTION

Jerry M. Straka[1], Matthew S. Gilmore[2], and Katharine M. Kanak[1]

[1] *School of Meteorology, University of Oklahoma, Norman, Oklahoma, 73019, USA,* *jstraka@ou.edu, and kkanak@ou.edu*

[2] *Department of Atmospheric Sciences, University of Illinois, Urbana, Illinois, 61801, USA,* *gilmore1@ uiuc.edu*

SECTION 1. INTRODUCTION

The purpose of this paper is to describe a new highly comprehensive bulk microphysics parameterization scheme. The scheme uses three-moments for prediction of microphysical field evolution including number concentration, mixing ratio, and if desired, reflectivity. In all, 17 ice habits are used and seven liquid habits are used. The model represents seven main categories cloud water, raindrops, ice crystals, snow aggregates, graupel, frozen raindrops, and hail. Sub-categories are designed to complement these main categories for three reasons: for various physical bases, to obtain more realistic radar signatures, and to help track particle history. For example, there are columns, plates, dendrites, needles, sectors, bullet rosettes, and side planes, which physically form at different temperatures and start to rime at different sizes. These may aggregate into snow aggregates. As the ice crystal habits, frozen drizzle, and snow aggregates rime, their shapes and fall speeds change as they grow into graupel particles. Prediction of graupel particle density permits covering three smaller ranges in density from 100 to 900 kg m^{-3} in the same volume. These different graupel density categories affords a better possible match against *in situ* aircraft observations, which show co-existing densities – presumably all experiencing different accretional and diffusional growth rates. Only the frozen drops and higher-density graupel, which rime to a size larger than D=5 mm, become hail. Including more sub-categories should improve how well the model might simulate an observed event and to avoid the modeler's uncertainty in choosing a single representative class/ habit. In the model, hail has sub-categories of small hail (5<D<20 mm) and large hail (D>20mm). In order to better track hailstone history, the small hail is further sub-categorized by its source: 1) hail from melted large hail, 2) hail with frozen drop embryos, and 3) hail with graupel embryos. Finally the history, growth, and radar signatures of liquid precipitation are better represented by allowing for six separate liquid categories: 1) cloud drops, 2) drizzle drops, 3) big rain drops from melting of small hail, 4) small rain drops from melt water shed from larger hail, 5) medium sized rain drops from melting of graupel and snow, and 6) a rain drops from warm processes. Through prediction of mixing ratio, number density, and reflectivity, the shape of the gamma distribution can be diagnosed. In addition, as larger ice particles change categories, artificial "jumps" in particle density and fall speed are prevented because the rime mass and particle density are predicted. Results will be shown in part II. In section 2 of this paper the initiation of cloud and ice particles is discussed. In section 3 the vapor diffusion is described. This followed in section 4 by collection, section 5 melting and freezing, and section 6 autoconversion and conversion.

SECTION 2. NUCLEATION

The spectral number density function is given by a variant of the gamma distribution,

$$\boxed{n(D)=\frac{N_T\alpha^{\nu}\mu}{\Gamma(\nu)}\left(\frac{D}{D_n}\right)^{\nu\mu-1}\frac{1}{D_n}\exp\left(-\alpha\left[\frac{D}{D_n}\right]^{\mu}\right)}$$

The model uses power laws for mass, terminal velocity and ice crystal densities, $m(D) = aD^{b}$; $V_T(D) = cD^{d}$; $r(D) = eD^{f}$

Nucleation of ice is without a prognostic ice nuclei number concentration at present. Instead Meyers et al. (1992) parmeterization is used. Cotton et al.'s (1986) formulation for rime splintering is also employed. After nucleation they are grown by explicit vapor diffusion. As this is a very sensitive calculation to time step length a small step approach is used to progress forward from t to t+dt. Typically, a small time step of 0.1 to 0.5 sec long is employed.

Nucleation of cloud drops follows that of Cohard and Pinty (2000), where number concentrations of aerosols are explicitly predicted. Again, after nucleation particles are grown by explicit vapor diffusion. As this is a very sensitive calculation to time step a small step approach is used to progress forward from t to t+dt. This approach allows super-saturations with respect to liquid water and ice water as well as mixtures of the two.

SECTION 3. DIFFUSION

Particles increase/decrease mass by vapor diffusion using standard formulas (Lin et al. 1983; and Rogers and Yau 1989), with the prescribed number spectral density function given in section 2. Particles are lost by assuming ventilation is one, solving for the largest sizes that evaporates or sublimes and removing this number using an equation presented in Rogers and Yau (1989).

SECTION 4. COLLECTION

Collection is one of the more difficult processes to handle properly I the model. General collection growth follows Murakami (1990), where the absolute value of the mass/number weighted terminal velocity is pulled out of the integrands. The equation is modified by writing the difference as the following for terminal velocity difference for mass

$$\Delta\overline{V}_{TQxy}=\left|\overline{V}_{TQx}-\overline{V}_{TQy}\right|=\left(\left\{\overline{V}_{TQx}-\overline{V}_{tyQ}\right\}^{2}+0.04\overline{V}_{TQx}\overline{V}_{TQy}\right)^{1/2}$$

For self-collection the Verlinde et al. (1990) and Verlinde and Cotton (1993) method and is employed with the various crystals to generate aggregates.

SECTION 5. MELTING AND FREEZING

Melting follows the standard equations used by for example Lin et al. (1983) and Straka and Mansell (2005). The change in number concentration is similar to tat done for vapor diffusion loss. Bigg freezing is the primary means of cloud droplets, drizzle, and raindrop, freezing. Care also must be taken to freeze melt water still on ice particles that get recycled into an updraft. Contact freezing also plays an appropriate roll in freezing raindrops.

SECTION 6. CONVERSION

There are many autoconversions and especially conversions in the model. These include autoconversion of cloud water to drizzle following Berry and Reinhardt (1974) and Gilmore and Straka (2008). Also, frozen drizzle and ice crystals rime to become low-density graupel. Eventually with high density riming of low-density graupel, hail from graupel forms. The various graupel density categories and frozen drop category are transferred from one category to another owing to changes in density by higher or lower density riming. High-density frozen drops are converted into hail from frozen drops. These types of hail can become giant hail.

A VERY-SHORT-RANGE INTERACTIVE PREDICTION SYSTEM FOR REGIONAL SEVERE WEATHER WARNING SERVICE

Debin Su[1,2] Daren Lu[2]
Chengyun Sun[1] Daoru Zhu[1]
1 Beijing Meteorological Bureau
2 Institute of Atmospheric Physics, Chinese Academy of Sciences

ABSTRACT

Weather warning is one of the key issues for the public and government decision maker. For the purpose of providing high temporal and spatial forecast for the 2008 Olympic weather service in Beijing, a new interactive prediction system was developed according to the requirement from Olympic and also from public weather warning service. Based on the concept of layered composite display and using mesoscale observation network data, mesoscale NWP product with the GIS information at the same time, this Very-short-range Interactive Prediction System (VIPS) can help forecasters to review realtime weather information quickly and interactively modify the forecasting from product generation system and then issue the warning efficiently. In this paper, we will introduce the system structure and emphasizing the networked Doppler radar composite analysis with lightning locating network data as well as dense network Automatic Weather Station surface data. Also we will introduce the interactive process of warning generation and issuing.

KEYWORDS: weather warning, nowcasting, VIPS, OpenMap

1. INTRODUCTION

With the rapid progress of meteorological modernization in recent years, more observational facilities have been established in Beijing area. Weather service need to focus more on the severe weather locally developed and high resolution observation should be integrated to nowcasting to support the warning making procedure. Also, government departments related to emergency management need to have weather products integrated with GIS information. VIPS is the result of this requirement and will be used in 2008 weather service.

2. CONCEPTS

For nowcasting and severe weather warning operation, the most important thing is how to issue the warning just in time (as earlier as possible) and as accurate in temporal and spatial aspects (higher resolution) as possible for the public and government to take effective steps to avoid lost in people and properties. So to provide a good very-short-range severe weather service, we need:

- Selected Multi-Sensor Realtime Observations
- Nowcasting Products (0-2 hours)
- High resolution NWP products (2-6 hours)

• GIS information

• Effective interactive warning making platform

3. SYSTEM STRUCTURE

VIPS is the key steps to connect the forecasting operation to the end-user like public, government and specified users. And the structure for the system is as Figure 1

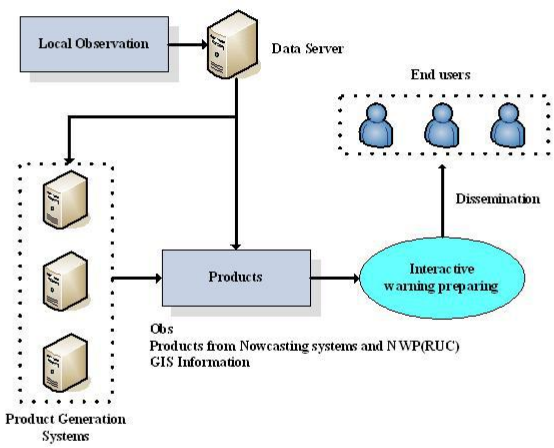

Figure 1

4. METHODOLOGY

Based on the concept of layered composite display and using mesoscale observation network data, mesoscale NWP products with GIS information at the same time, this Very-short-range Interactive Prediction System (VIPS) can help forecasters to review realtime weather information quickly and interactively modify the forecasting from product generation system and then issue the warning efficiently.

This system is emphasizing the networked Doppler radar composite analysis with lightning locating network data as well as dense surface data of Automatic Weather Station network.

The methodology for this very-short-range interactive prediction system is as follows:

- System developed using Java language, and it's platform (operational system) independent;
- GIS support from Open Source resource of OpenMap;
- Different kinds of data or products be ingested and displayed in separate Layers of OpenMap;
- Using standard data interface (NetCDF and XML format) for regional data sharing;
- System can easily be maintained and updated later with open source support and structured design;
- Nowcasting analysis based on integration of selected real time weather observation (regional Doppler Radar network data, lightning detection system data, AWS data, wind profiler data and other nowcasting-related observation products) , nowcasting products from Product Generation Systems like ANC, and gridded forecasting products from regional Numeric Weather Prediction system;
- When observation data or nowcasting products are enough to support a severe weather warning issue, forecasters can easily make and modify warning information interactively;
- Warning making is easy and quick with mouse drawing of areas affected by severe weather, then warning information can be

automatically generated accordingly;

- Warnings issued with several kinds of formats according to template definitions, and those definition can easily modified or adjusted by requirement;
- Observation products with GIS support can be used separately in other specified weather service.

OPERATIONAL FLOW CHART

For operational work, the flow chart related to use the system to issue the warning is showed below as Figure 2.

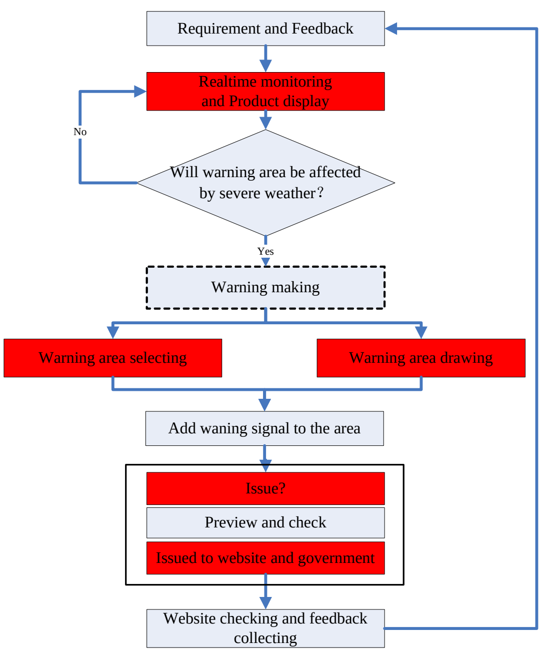

Figure 2

5. SUMMARY

VIPS provides and easy-to-use platform with GIS support for weather warning making and issuing. With the help of this tool, severe weather warning can be quickly prepared according to available products analysis and then be disseminated in different formats to specified end-users. Developed with Open Source resources of Java and OpenMap, and using standard interface for different data source, this system can easily be extended and used in other area of weather service in the future.

ACKNOWLEDGEMENTS

The authors would like to acknowledge people in WWRP B08FDP group in the development. This work was supported under a project of National Key Science and Technology, No.2005BA904B05, and supported by the project of 2007 Olympic High Resolution Forecasting System from CMA (China Meteorological Bureau).

NUMERICAL SIMULATION ON HAIL FORMATION IN THE MOUNTAINOUS REGION OF GUIZHOU

ZHANG Fang-jun, HUANG Huao-juan , WEN Ji-fen and ZHOU Li-na
Guizhou Weather Modification Office, Guiyang, 550002,China

1. INSTRUCTION

In the mountainous of Guizhou, hail da -mage occurred is largely due to the local hailstorm. In this paper, put the hailstorm formed in the 3D hail cloud model develope -d by IAP into the model involved orographic influence, and simulate to analyze change of hail formation. It is shown that orographic influence is mainly factor to local hailstorm, suppression by AgI seeding. Experiments have been done to seek for optimal seeding scheme. Through the simulations of differe -nt seeding schemes including seeding time, location and amount of seeding agents. So -me implications for operational hail supper -ssion projects are suggested.

2. STRUCTURE OF MODELS

2.1 MODEL01:THREE-DIMENSIONAL DY -NAMICAL MODEL

2.1.1 BASIC EQUATION GROUP

The equation group of this model is :

$$\frac{du}{dt} = -\theta\frac{\partial\pi}{\partial x} + fv + g\frac{\overline{Z}-H}{H}\cdot\frac{\partial Z_g}{\partial x} + Fu \qquad (2.1.1)$$

$$\frac{dv}{dt} = -\theta\frac{\partial\pi}{\partial y} - fu + g\frac{\overline{Z}-H}{H}\cdot\frac{\partial Z_g}{\partial y} + Fv \qquad (2.1.2)$$

$$\frac{\partial u}{\partial x} + \frac{\partial v}{\partial y} + \frac{\partial\overline{w}}{\partial\overline{z}} - \frac{1}{H-Z_g}\left(u\frac{\partial Z_g}{\partial x} + v\frac{\partial Z_g}{\partial y}\right) = 0 \qquad (2.1.3)$$

$$\frac{\partial\pi}{\partial\overline{z}} = -\frac{H-Z_g}{H}\cdot\frac{g}{\theta} \qquad (2.1.4)$$

$$\frac{d\theta}{dt} = F_{\Phi} \qquad (2.1.5)$$

here, $Z_g = Z_g$ (x, y), is topographic height. $\pi = C_p$ (P/1000) $^{R/C_p}$,is Exner function of atmospheric pressure.

F is turbulence diffusion item, Φ represent u, v, w and θ .

2.1.2 INITIAL CONDITION AND BOUN -DARY CONDITION

(1) Initial condition

The wind field is directly input by the num -erical integral result of basic equation (2.1.1)-(2.1.4), their initial condition is given by meteorological data.

(2) Boundary condition

The inflow boundary condition calculate -ed by wind field is given by meteorological data.

2.1.3. NUMERICAL METHOD

The time step and integral step are decided by the stability of calculation. Generally, in stable condition, time step is 10s, calculate 360 steps (1 hour), in neutral or unstable condition, time step is 3-5s, calculate 720-1200 steps (1 hour).

2.2 MODEL02:THREE-DIMENSIONAL HA -IL CLOUD MODEL

The model include 18 predictands, they are velocity component u, v, and w, non-dimen -sional atmospheric pressure π , potential temperature θ , specific water content of vapour, cloud water, rain, ice, snow, graupel and hail Q_v, Q_c, Q_r, Q_i, Q_s, Q_g, Q_h, specific content of AgI X_S, specific density of rain, ice, snow, graupel and hail N_r, N_i, N_s, N_g, and N_h.

2.2.1 CONTROL EQUATION GROUP

The control equation group of this model is

$$\frac{du}{dt}+C_p\overline{\theta}_v\frac{\partial\pi}{\partial x}=D_u \tag{2.2.1}$$

$$\frac{dv}{dt}+C_p\overline{\theta}_v\frac{\partial\pi}{\partial y}=D_v \tag{2.2.2}$$

$$\frac{dw}{dt}+C_p\overline{\theta}_v\frac{\partial\pi}{\partial z}=g\left(\frac{\theta'}{\overline{\theta}}+0.608Q_v-Q_t\right)+D_w \tag{2.2.3}$$

$$\frac{d\pi'}{dt}+\frac{\overline{C}^2}{C_p\overline{\rho}\overline{\theta}_v^2}\frac{\partial\overline{\rho}\overline{\theta}_v u_j}{\partial x_j}=-\frac{R_d}{C_v}\pi'\frac{\partial u_j}{\partial x_j}+\frac{C^2}{C_p\theta_v^2}\frac{d\theta_v}{dt}+D_{\pi'} \tag{2.2.4}$$

$$\frac{dQ_x}{dt}=S_{Qx}+D_{Qx}+\frac{1}{\overline{\rho}}\frac{\partial}{\partial z}\left(\overline{\rho}Q_xV_x\right) \tag{2.2.5}$$

$$\frac{dN_x}{dt}=S_{Nx}+D_{Nx}+\frac{1}{\overline{\rho}}\frac{\partial}{\partial z}\left(\overline{\rho}N_xV_x\right) \tag{2.2.6}$$

$$\frac{dX_s}{dt}=S_{Xs}+I_{Xs}+D_{Xs} \tag{2.2.7}$$

$$\frac{d\theta}{dt}=Q_{lv}+Q_{il}+Q_{iv}+D_\theta \tag{2.2.8}$$

2.2.2 INITIAL CONDITION AND BOUND -ARY CONDITION

(1) Boundary condition

The lateral, up and down boundary condition are considered in the model.

(2) Initial condition

Initial environment field $\overline{u}$, $\overline{v}$, $\overline{\theta}$, $\overline{\pi}$, $\overline{Q}_V$ can be determined by sounding data. The initial disturbance field of potential temperature is related to convection start mode.

2.2.3 NUMERICAL EVALUATION TECHNI -QUE

In the model, the numerical evaluation technique of the standard spatial staggered mesh system and the time step separation is adopted, the technique of smooth operation, absorbing layer on top boundary and parallel moving of simulation field is applied.

3. NUMERICAL STUDY

The numerical study of hail suppression by AgI shows that the principle of hail formation and growth conforms to the theory of accumulation zone. The basic theory of hail suppression by seeding is “competitive principle”. A series of seeding experiments are done to seek optimal seeding methods.

3.1 SIMULATION OF HAIL CLOUD

The seeding and natural (no seeding) experiment is a simulation of moist convection initiated by a warm, moist bubble. The integration domain is 40 km in both horizontal directions and 14.0 km in vertical, with grid intervals△x=△y=1000m and △z=500m.The sounding data is used as the initial fields of temperature, moisture and velocity. To initiate disturbance, a warm moist bubble is inserted in the center of the domain at a height of 2 km. The initial impulse is 12km wide and 4km deep, with a maximum disturbance temperature of 2.5℃. Fig.1(omitted) shows Vertical cross section of total water content in natural simulation through the center of hail cloud at t = 2, 7,10,16 min. The hail cloud derived from simulation is similar to that measured by radar (radar map omitted). From Fig.1 (omitted), it can be seen that the center of water content of hail cloud is located 2km high at two minutes from the beginning of the developing hail cloud and it is becoming higher with the developing hail cloud. Seven minutes later, it is 3.5km high, ten minutes, 4 km. Then sixteen minutes later, the hail cloud becomes weaker. In addition, during the period of hail cloud developing, the total water content is always located in the maximum updraft area. In simulation, the top of hail cloud reach 12.0 km high, the body of hail cloud leans southwest, hail shooting begin on surface at ten minutes, the total hailfall on surface is 163.24 ton, and the maximum radium of hailstone is 6.24mm.

3.2 SIMULATION OF HAIL SUPPRESSION

On the basis of the simulation of hail cloud case, A series of experiments simulate -ed seeding by AgI for this hail cloud has been done. In this paper, the seeding effect (E) is defined by the percentage of decreas -ing of hail fall on surface.

The simulation of hail suppression are shown in Fig.2(omitted), from which it can be seen the seeding effect at second minute at height 2km, 3km, 4km, 5km and 6km separately (shadow area denotes E>50%). Shown as Figure 2(omitted), seeding active -ties with different height, or different site, or different amount of agents can all get the effect more than 50%. For the same seeding agents, the shadow area increases with height from 2km to 4km, while decreases from 4km to 6km. But it is possible for the total hailfall to increase at height 6km. The shadow area extends to southwest; it has the consistency with the hail cloud southwest leaning. At the same height, the shadow area by 300g AgI seeding is larger than that by 50g. The hail suppression can be taken with the best effect of 88%. Beca -use AgI taken by cannon only reach 3-5km high, it can be obtained that the seeding activities for hail suppression with cannon have certainly reached good effects in Weining, Guizhou province of China.

$$\frac{AgI}{\text{催化}}\left\{\begin{matrix} 4.33\% & 17.7\% \\ TQ_i\downarrow & TQ_s\downarrow \\ TN_i\downarrow & TN_s\uparrow \\ 1\% & 48.8\% \end{matrix}\right\}-\left\{\begin{matrix} 92\% \\ TNCL_{rig}\uparrow \\ TNCL_{srg}\uparrow \\ 11.9\% \end{matrix}\right\}-\left\{\begin{matrix} 12.5\% \\ TQ_g\uparrow \\ TN_g\uparrow \\ 63.17\% \end{matrix}\right\}-\begin{matrix} 76\% \\ P_{gh}\downarrow \end{matrix}-\left\{\begin{matrix} 69.7\% \\ TQ_h\downarrow \\ TN_h\downarrow \\ 69.5\% \end{matrix}\right\}\Rightarrow E\ 68.33\%$$

The hail suppression may be concluding like this:

a.Because of seeding by AgI for the hail cloud, in the 24 minute, the quantity and the quality of ice in the simulation cloud have a little change. The ice changes to graupel become more and more weak and to snow become more and more strong.

b.The number of the snow is increasing, and the quality of the snow is decreasing.

c.The quantity and quality of the graupel increase obviously. The collision of the super-cooled water with ice and the super-cooled water with the snow is more than the ice and the snow change to graupel; this is the reason of the increasing quantity and quality of the graupel.

d.By the reason of the quantity increasing more than the quality increasing of the graupel, the graupel change to hail is weak, so the precipitation is decreasing.

4. NUMERICAL EXPERIMENT

From March to September every year, these two numerical models were used to forecast the hail weather in the numerical region. The sounding data on 08h is used to simulate the initial disturbance resulting from the thermodynamic and dynamic nonuniformity of underlying surface by mod -el01 every day. If the initial disturbance exists, model02 starts to simulate the deve -lopment of cloud and forecast hail weather.

It can be seen that the prediction accur -acy of hail is high. The models can not only forecast hail but also determine total hail shooting amount, direction of hail shooting and maximum hail diameter. The production process of hail cloud on March to Septemb -er are analyzed in detail.For verifying the numerical method, meteorological data in 1997 and 2007 were used to calculate the rate of failure to forecast. Several forecast methods such as the numerical model, Emagram and scatter diagram are compare -ed in the end.It can be proved that the numerical forecast method is the best way.

5. CONCLUSION

a. The simulation results of hail suppressi -on by AgI seeding with cannon are as follows: 1)It explains effect of hail suppressi

-on with cannon. 2) The seeding is made at 5-8 minutes before hail shooting, the optimal seeding position is located at 3-4km height in the updraft area. 3) Other things being equal, the effect of hail suppression increas -es with amount of AgI.

b. By simulating initial disturbance accord -ing to topographic condition and developme -nt of hail cloud according to microstructure of cloud, the total hail shooting amount, direction of hail shooting and maximum hail diameter over a hill can be forecasted.

c. Compared with the methods of Emagr -am and scatter diagram, the accuracy of numerical model is high.

ACKNOWLEDGEMENTS

The author thanks Guizhou Weather Mo -dification Office for supplying sounding infor -mation.

RERERENCES

1.Hong Yanchao, 1999: Study on mechan -ism of hail formation and hail suppression with seeding, ACTA METEOROLOGICA SINICA, Vol.57, No.1, 30-44.

2.Farley, R. D and H. D. Orville, 1986: Num -erical modeling of hailstorms and hailstone growth. Part I: Preliminary model verification and sensitivity tests. *J. Clima. Appl. Meteor*., 25, 2014-2036.

3.Farley, R. D, 1987: Numerical modeling of hailstorms and hailstone growth. Part II: The role of low-density riming growth in hail prod -uction. *J. Clima. Appl. Meteor.*, 26,234-254.

4.Farley, R. D, 1987: Numerical modeling of hailstorms and hailstone growth. Part III: Si -mulation of an Alberta hailstorm-Natural and seeded cases. *J*. *Clima*. *Appl*. *Meteor*., 26,789-912.

5.Farley,R.D.,P.Nguyen and H. D. Orville.,19 -94: Numerical simulation of cloud seeding using a three-dimensional cloud model. *J. Wea. Mon*., 26, 113-124.

6.Kong Fanyou, Huang Meiyuan，Xu Huay -ing，1990：Three-dimensional numerical si -mulation of ice phrase microphysics in cum -ulus cloud （I）：model build and cold cloud parameterization. Chinese Journal of Atmos -pheric Sciences. 14（4）：441-453.

7.Hong Yanchao，1998: A 3-D hail cloud numerical seeding model. Acta. Meteoro logica. Sinca.，56(6)：641-651.

Arbitrary-Moment Internally-Mixed Dynamic Equation

B.Y. Grits[1] and A.S. Wexler[1,2,3]
[1]Departments of Mechanical and Aeronautical Engineering,
[2]Civil and Environmental Engineering,
[3]Land, Air and Water Resources,
University of California, Davis

1. INTRODUCTION

Aerosols influence atmospheric radiative properties. The increase of atmospheric reflectance due to the presence of aerosols is referred to as direct radiative aerosol forcing. In parallel to this effect, aerosols are known to cause indirect radiative forcing, whereby aerosol particles serve as nuclei upon which cloud droplets form (cloud condensation nuclei or CCN). The consequent increase in cloud droplet number concentrations leads to brighter clouds with longer lifetimes. The Intergovernmental Panel on Climate Change (IPCC) has estimated that the global and annual average indirect aerosol radiative forcing is somewhere between 0 and 2.0 W m^{-2}, as compared with 2.5 W m^{-2} imposed by changes in greenhouse gases [IPCC, 2001]. Moreover, this estimate neglects potential changes in cloud lifetime, including only the effect of aerosols on cloud brightness.

Recent studies have shown an association between ultrafine particles and adverse health effects: Studies on rodents demonstrate that ultrafine particles administered to the lung cause a greater inflammatory response than do larger particles, per unit mass (Oberdorster, 2001); the health effects of the 5-day mean of the number of ultrafine particles were found to be larger than those of the mass of the fine particles and its effects on the peak expiratory flow were stronger than those of PM_{10} (Peters et al., 1997).

The aforementioned scenarios and others illustrate the importance of accurately simulating multiple moments of the size distribution of aerosol particles. State-of-the-art aerosol models are far from satisfactory. In the so called one-moment models, one of the particle distribution moments (usually mass or number) is numerically estimated. Other moments may be then calculated from it, but this approach suffers from substantial uncertainties that are introduced when moving from one moment to another.

For example, the internally mixed mass distribution evolution due to condensation and evaporation may be estimated using the following equation (Dhaniyala and Wexler, 1996):

$$\frac{\partial p_i}{\partial t} = H_i p - \frac{1}{3}\frac{\partial\left(Hp_i\right)}{\partial \mu}. \qquad (1)$$

where p_i is the mass distribution of the *i*-th species, such that $p_i \cdot d\mu$ is the mass in the size range μ to $\mu + d\mu$, μ is the natural logarithm of the particle diameter, *D*. $H_i = \frac{1}{m}\frac{dm_i}{dt}$ and $H = \sum_i H_i = \frac{1}{m}\frac{dm}{dt}$ are the *i*-th species and total condensation/evaporation rates, respectively. The number distribution may be calculated from the mass distribution by assuming the particles are spherical, but uncertainties in the diameter necessitated by the finite diameter bin width are amplified because the number is inversely proportional to the cube of the particle diameter.

To solve this problem the two-moment aerosol sectional (TOMAS) model was proposed recently by Adams and Seinfeld (2002). The essence of this approach is that

Corresponding author:
A.S.Wexler aswexler@ucdavis.edu

two moments (mass and number) are estimated simultaneously. This results in significant improvement in prediction of both number and mass distributions but necessitates simulating two equations and storing two distributions, one for each desired moment. This inevitably results in additional computation burdens, which may become crucial when incorporated into large scale climate models.

In this study we offer an alternative approach to this problem. Rather then concentrating on improving the model for some concrete distribution moment, we change the modeled function itself to solve the aforementioned task or in general any moment of the size distribution, which may have application in a wide range of aerosol applications.

2. ARBITRARY-MOMENT DYNAMIC EQUATION

Our goal is to obtain a general equation that describes an arbitrary moment of the internally-mixed, multi-component aerosol size distribution as well as arbitrary linear combination of such moments. We define new functions $q_i \equiv p_i \cdot f(\mu,t)$ and $q \equiv p \cdot f(\mu,t)$, where *f* is an arbitrary function of particle diameter and time. After substituting into (1) and rearrangement one gets:

$$\frac{\partial q_i}{\partial t} = H_i q + H_f q_i - \frac{1}{3}\frac{\partial (H q_i)}{\partial \mu} \tag{2a}$$

$$H_f \equiv \frac{1}{f}\left[\frac{\partial f}{\partial t} + \frac{H}{3}\frac{\partial f}{\partial \mu}\right], \tag{2b}$$

These are the equations we were looking for. They allow one to follow the evolution of arbitrary distribution functions $\{q_i\}$ using known condensation rates $\{H_i\}$ and function *f*. We call therefore equation (2a) the Arbitrary-Moment Dynamic Equation (AMDE). Throughout this paper we restrict our attention to functions *f* that are time independent, so their partial derivative with respect to time falls out everywhere.

3. ANALYTICAL SOLUTION

For constant $\{H_i\}$ equation (2a) has the following solution:

$$\begin{aligned} q_i(\mu,t) = \Big\{ & q_{0,i}\left(\mu - \frac{H}{3}t\right) + \frac{H_i}{H}\cdot \\ & q_0\left(\mu - \frac{H}{3}t\right)\cdot\left[e^{H\cdot t} - 1\right]\Big\}\cdot \exp\left(\int_0^t H_f\,dt\right) \end{aligned}. \tag{3}$$

for $H \neq 0$. Essentially, $\left\{q_{0,i}\left(\mu - \frac{H}{3}t\right)\right\}$ are initial profiles shifted by $-\frac{H}{3}t$.

4. NUMERICAL SOLUTION

To solve numerically equation (2a) one has to estimate the advection term $\frac{1}{3}\frac{\partial (H q_i)}{\partial \mu}$. We employed Bott's positive definite advection scheme (Bott, 1989) to shift initial profiles:

$$\begin{aligned} \left[q_i\right]_j^{n+1} = \Big\{ & \left[q_{0,i}^B\right]_j^n + \frac{H_i}{H}\left[q_0^B\right]_j^n\cdot \\ & \left[e^{H\cdot\Delta t} - 1\right]\Big\}\cdot \exp\left(\int_{t-\Delta t}^t H_f(\mu_j)\,dt\right) \end{aligned}. \tag{4a}$$

$\left[q_{0,i}^B\right]_j^n$ is the solution at time step (n-1)Δ*t* advected using Bott's scheme to the next time step *n* Δ*t*:

$$\left[q_{0,i}^B\right]_j^n = \left[q_{0,i}^B\right]_j^{n-1} - \frac{\Delta t}{\Delta \mu}\left(F_{j+1/2}^n - F_{j-1/2}^n\right). \tag{4b}$$

where $\exp\left(\int_{t-\Delta t}^t H_f(\mu_j)\,dt\right)$ was estimated analytically and $\{\mu_j\}$ are section centers. The values of mass and number distributions at the end of simulation were obtained with the relations (the density of all species was set to unity for simplicity):

$$\left[p_i\right]_j = \frac{\left[q_i\right]_j}{f(\mu_j)}. \tag{5a}$$

$$[n_i]_j = \frac{6[p_i]_j}{\pi \exp(3\mu_j)} . \quad (5b)$$

5. AMDE TESTS

To test our approach two scenarios were run. Aerosol particles in both the scenarios consisted of two components with identical initial lognormal profiles. Median diameter and standard deviation were chosen typical of atmospheric conditions: $\overline{\mu_n} = \ln \overline{D_n}(\mu m) = -2.27$ (for number distribution); $\ln\sigma = 1.33$ (Seinfeld and Pandis, 2006). In the first scenario both the components evaporate: $H_1 = -3$ and $H_2 = -2$ ($H = -5$). In the second case – condense: $H_1 = 3$ and $H_2 = 5$ ($H = 8$). The Courant number, defined as $c = \frac{1}{3}\frac{H\cdot\Delta t}{\Delta\mu}$, was set 0.1 in all runs, determining the time step. Three versions of the function *f* were tested:

$$\begin{aligned} f_1 &= 1 + \left(\frac{D_0}{D}\right)^3 = 1 + \exp(3\mu_0 - 3\mu) \\ f_2 &= \frac{1}{D^{1.5}} = \exp(-1.5\mu) \\ f_3 &= 1 + \left(\frac{D_0}{D}\right)^3 + \frac{1}{D^{1.5}} = 1 + \\ &\exp(3\mu_0 - 3\mu) + \exp(-1.5\mu) \end{aligned} . \quad (6)$$

corresponding to function q_i in the first case representing the sum of the 3rd (mass) moment and 0th (number) moment; in the second case, an intermediate 1.5th moment; and in the last case, the sum of all the three moments. We tested the last variant to check if the smoothing provided by the intermediate moment helps reducing numerical error.

The simulations were performed for two grid resolutions: fine ($\Delta\mu = 0.1$) and coarse ($\Delta\mu = 2.0$). The resolution of the latter was chosen to represent the typical resolution of regional or global climate models.

The error was estimated according to:

$$\text{r.m.s. error} = \frac{\sqrt{\sum_{j=1}^{N}\left([p]_j^n - [p]_j^{an}\right)^2}}{\sum_{j=1}^{N}[p]_j^{an}} , \quad (7)$$

$[p]_j^{an}$ being the analytical solution. The error for the number distribution was estimated in the same way. Thus we used the total mass and number distributions to evaluate the errors.

6. RESULTS

First we calculate the error for one-moment algorithm, estimating the mass distribution using (4a) with $f = 1$ and obtaining the number distribution using (5b). Error as a function of time for the fine grid evaporation scenario is shown in fig. 1

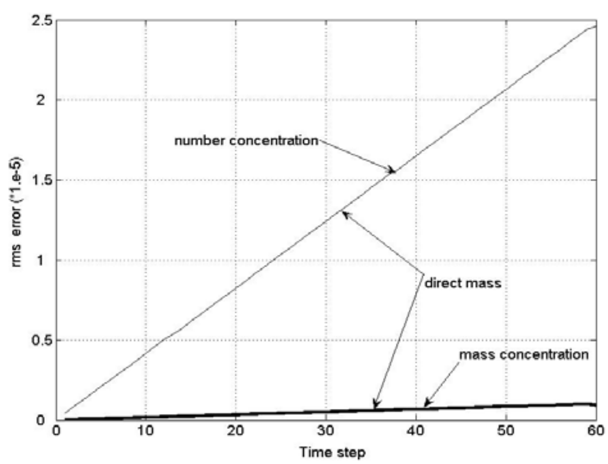

Fig. 1 Mass and number r.m.s. errors in the "direct mass" algorithm for evaporation scenario on the fine grid.

As expected the error for the number distribution calculated from the mass distribution (thin line) is much higher than that for mass distribution (bold line). To emphasize that number is recalculated from mass we designate these curves everywhere as "direct mass". The analogous results when using functions f_1 through f_3 from equations 6 are presented in fig. 2.

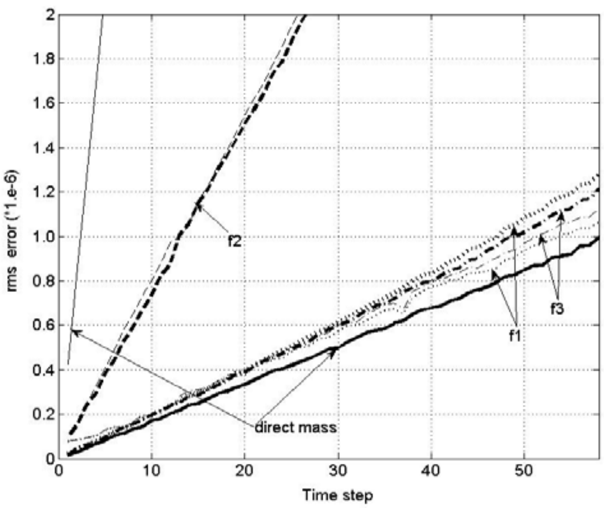

Fig. 2 Mass and number r.m.s. errors when using functions f_1 through f_3 for evaporation scenario on the fine grid.

Bold lines represent mass distribution errors and thin lines number distribution errors. One can see that functions f_1 (dotted lines) and f_3 (dashed-dotted lines) improve the result dramatically, reducing the number error to that of mass error in the "direct" method (~20 times). Function f_2 did not perform as well but was still better than the one-moment algorithm.

The analogous results for coarse grid are shown in fig. 3.

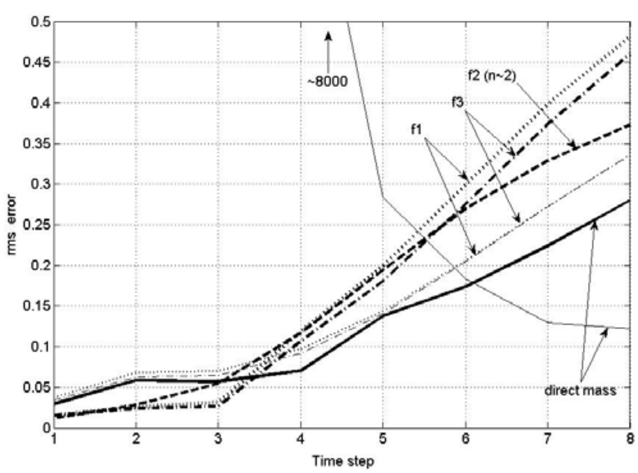

Fig. 3 Mass and number r.m.s. errors when using functions f_1 through f_3 for evaporation scenario on the coarse grid.

The "direct" method in this case actually failed: number error blew up (to ~8000) within several time steps. In contrast, the errors when using functions f_1 and f_3 are again similar to mass error for the "direct" method and f_2 again does not perform as well: number error (not shown) lies near 2.0.

Next we investigate condensation. The fine grid results (not shown) are quite close to those for evaporation: functions f_1 and f_3 reduce number error approximately 20 times comparing with "direct" method; again function f_2 does not perform as well but still better than "direct" method.

Figures 4 and 5 present analogous results for the coarse grid.

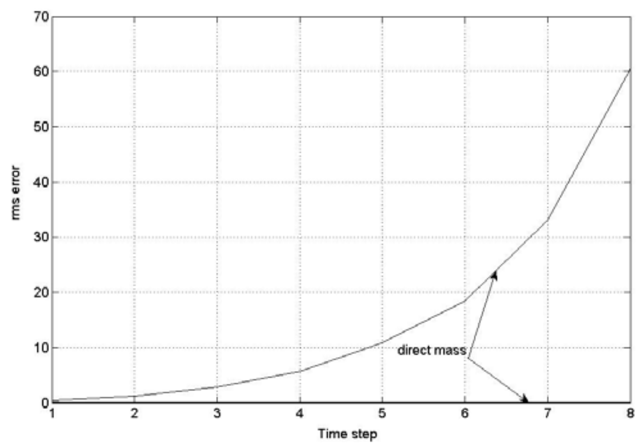

Fig. 4 The same as in fig. 1 for condensation scenario on the coarse grid.

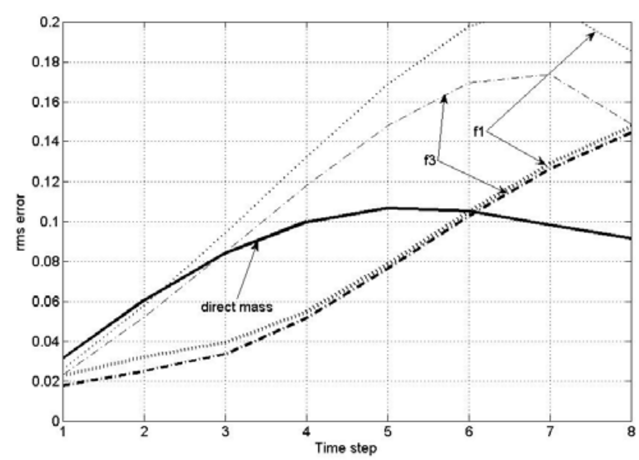

Fig. 5 The same as in fig. 3 for condensation scenario.

This time the "direct" method is stable but still the number error is several hundred times larger than that for mass and f_1 and f_3 reduce number error several hundred times.

We want to emphasize that function f_3 everywhere provided slightly better result than f_1 illustrating that the *smoothing by means of an intermediate moment reduces numerical error*.

7. SUMMARY

Most atmospheric particle dynamic models simulate one moment, typically mass or number. Substantial errors are introduced in these models moving from mass to number or vice versa since these moments are related by the cube of the particle diameter. Analogous problems may emerge when an application requires prediction of non-integer or intermediate moments. Under the existing practice of working with mass or number distributions, calculating the non-integer moment from available integer ones introduces again significant errors.

An alternative two-moment aerosol sectional (TOMAS) model was proposed by Adams and Seinfeld (2002) that solves the aforementioned problem by estimating both the mass and number distributions simultaneously. This method provides good accuracy for both moments but requires the solution of two equations and storage of both moments.

In this paper we propose the Arbitrary-Moment Dynamic Equation that simulates an evolution of the internally-mixed multicomponent aerosol population distribution due to condensation/evaporation. This equation predicts an arbitrary function of aerosol particle diameter. In other words, it may describe arbitrary distribution moments (both integer and non-integer), as well as an arbitrary linear combination of such moments. For example, it may consist of number and mass distributions, which allows obtaining both these distributions at the end of simulation from a single function while minimizing moment transformation errors. Another useful application may be found when the non-integer moments are necessary, such as may be encountered when dealing with radiative properties of aerosols.

To test our approach we simulated two scenarios for the two component case: evaporation scenario (both components evaporate) and condensation (both components condense). These simulations were performed on fine and coarse grids. Three *f* functions, determining three different distribution functions q_i, were tested.

For all cases we compared the accuracy (normalized difference between numerical and analytical results) in the number distribution from both the mass distribution and from q_i functions. We also compared accuracy for mass distribution when calculated directly and from q_i. Mass errors were found to be similar in all the cases. However, tremendous error reductions was observed for number distribution when using distribution functions the represent the sum of moments proportional to mass and number or when an intermediate smoothing function is added to these. Both these functions reduced the error approximately **20 times** (fine grid) and **several hundreds times** (coarse grid) compared to number distributions estimated from mass distributions.

In summary, when multiple moments (such as mass and number) are needed, their sum provides better accuracy then an intermediate moment. Also the use of an intermediate moment as a smoothing component reduces error additionally. Thus the best results were obtained when all three moments were summed.

Important feature of the AMDE is that it may be solved by arbitrary advection numerical schemes. In this work Bott's positive-definite scheme was employed, but other schemes, like accurate space derivatives (Wexler *et al*., 1994) or finite elements (Pilinis, 1990) could be used as well.

REFERENCES

Adams, P. J. and Seinfeld, J. H. (2002). Predicting global aerosol size distributions in general circulation models. *Jour. Geophys. Resear.*, 107, D19.

Bott, A. (1989). A positive definite advection scheme obtained by nonlinear renormalization of the advective fluxes. *Monthly Weath. Rev.*, **117**, p. 1006.

Dhaniyala, S. and Wexler, A. S. (1996). Numerical schemes to model condensation and evaporation of aerosols. *Atmos. Envir.*, **30**, 6, pp 919-928.

Gelbard, F. and Seinfeld, J. H. (1980). Simulation of multicomponent aerosol dynamics. *J. Colloid Interface Sci.*, **78**, 485-501.

Intergovernmental Panel on Climate Change (IPCC), Third Assessment Report, Cambridge Univ. Press, New York, 2001.

Oberdorster, G. (2001). Pulmonary, effects of inhaled ultrafine particles. *International Archives of Occupational and Environmental Health*, **74** (1), 1–8.

Peters, A., Wichmann, H. E., Tuch, T., Heinrich, J. and Heyder, J. (1997). Respiratory effects are associated with the number of ultrafine particles. *American Journal of Respiratory and Critical Care Medicine*, **155** (4), pp. 1376–1383.

Pilinis, C. (1990). Derivation and numerical solution of the species mass distribution equations for multicomponent particulate systems. *Atmos. Envir.*, **24A**, 7, pp. 1923-1928.

Seinfeld, J. H. and Pandis, S. N. (2006). Atmospheric chemistry and physics. Wiley & Sons, Inc, *Second Ed.*

Yanenko, N. N. (1971). The Method of Fractional Steps. Springer, Berlin.

Zhang, K. M. and Wexler, A. S. (2002). Modeling the number distributions of urban and regional aerosols: theoretical foundations. *Atmos. Envir.*, **36**, pp 1863-1874.

Wexler, A. S., Lurmann, F. W. and Seinfeld, J. H. (1994). Modelling urban and regional aerosols-I. Model development. *Atmos. Envir.*, **28**, 3, pp. 531-546.

ACKNOWLEDGEMENTS

This work was supported by the California Air Resources Board.

ANALYSIS OF LUNAR VARIATION OF PRECIPITATION ON VARIOUS TIME SCALES

L. Hejkrlík
Czech Hydrometeorological Institute, 400 11, Ústí nad Labem, Czech Republic

1. MOTIVATION

The phenomenon of association of precipitation amounts with lunar phase was discovered simultaneously by *Bradley et al. (1962)* in the USA and by *Adderley and Bowen (1962)* in Australia. It was demonstrated that extreme precipitation events occur more frequently on the third to fifth day after syzygies ("Bowen's signal") and variation of ice nuclei of meteoric origin was suggested as possible mechanism. The hypothesis was supported by observed frequency of radar meteor rates and by links of precipitation singularities with peaks of activity of specific meteor streams. The idea was not generally accepted and awareness of scientific community of the effect slowly died away, even though similar variation was later observed also by other authors, as seen in Fig. 1.

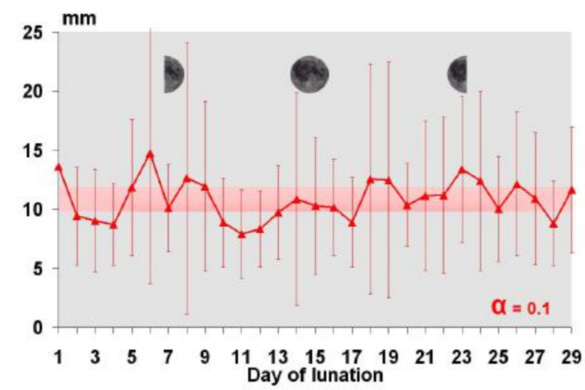

Figure 1. Bowen's signal at meteorological station Ústí n. L., North-western Bohemia in period 1980-1992. Hejkrlík (2001)

2. DATA

We took advantage of existence of an extremely long daily precipitation data series at Prague-Klementinum (PRGK) since 1804 to present time. Daily series of observations at 13 other meteorological stations in 1900-2000 throughout Europe, presented at the website of European Climate Assessment & Dataset Project were also used.

3. METHOD

The data were analysed by superposed epoch technique. The zero day was the day

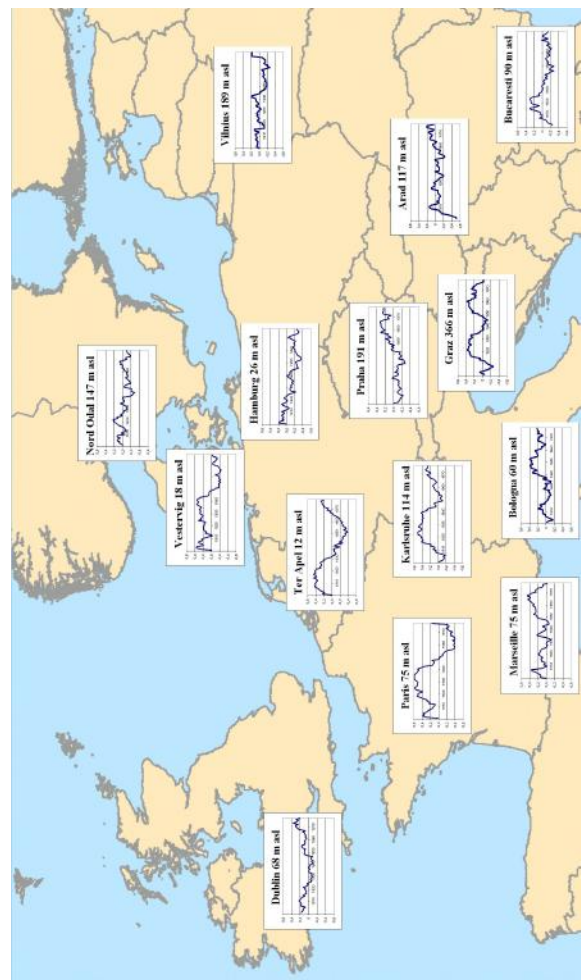

Figure 2. Secular development of ψ(250) at selected European stations in period 1900 to 2000. Hejkrlík and Novák (2006)

of new moon and the number of superposed synodic epochs *N* varied from *N*≈250 (20 years) to *N*≈62 (5 years) or *N*=12-13 (1 year). In order to evaluate similarity of real signal with model Bowen's signal (cosine with maximum at 4th day) we computed for every single year i and for various numbers of superposed synodic months N factor ψ_i, defined as $\psi_i(N)=Corr\{signal_i(N,x);\ cos(4\pi(x-4)/29{,}53)\}$ where $x=0..28$. The greater was the ψ the more was synodic variation of precipitation expressed.

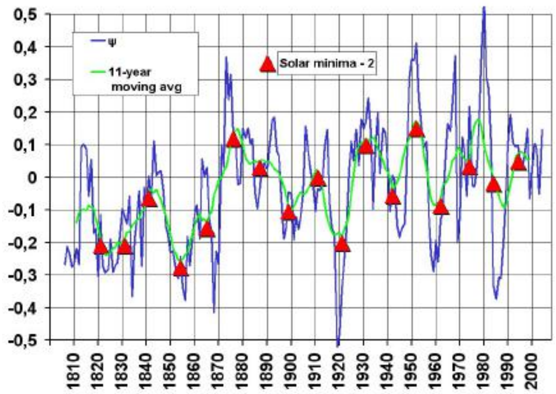

Figure 3. Secular development of ψ(62) at PRGK in 1804-2006. Hejkrlík (2007)

4. RESULTS

The analysis of heavy rainfalls (≥10 mm) for the longest period of superposition of 20 years (Fig. 2) indicates spatial development of the presence of Bowen's signal across Europe. Preliminary results suggest probable spatial and/or temporal consequences. The stations in Western Europe demonstrate nearly parallel behaviour with positive *ψ(250)* in the first half of the 20th century and negative *ψ(250)* for the rest of the period while peripheral stations exhibit nearly no correlation at any moment of the century.

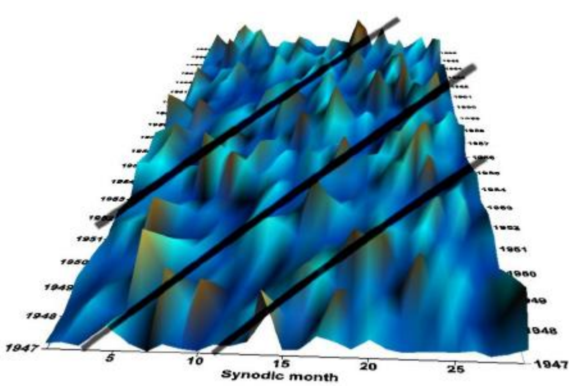

Figure 4. Development of annual synodic variation of precipitation amounts (N=12 to 13) at PRGK in period 1947-1966

We analysed also every day with precipitation amount greater than zero at PRGK since 1804. Calculation of *ψ(62),* smoothed by 11 years, demonstrated quasi-periodical variations with the largest changes occurring at most cases two years before solar activity minima, Fig. 3. The data suggest that the sign of the changes alternates in 22-year rhythm what may imply the role of solar magnetic (Hale) cycle. Similar periods seem to be superposed on general long-term course at some stations in Fig. 2 (e. g. Dublin, Nord Odal or Hamburg) what clearly implies the need to repeat the analysis from this paragraph in the European datasets.

Recently we tried to verify the hypothesis from the 1960's about possible regular displacement of the Bowen's signal according draconic period of 8,85 years. Repeating the study of *Andrlík and Brůžek (1967)* on a longer dataset by superposing synodic series for only one year actually revealed some shifts of the peaks. The diagonal displacement of the extremes in the signal takes about the whole analysed period 1947-1966, what is very near to double draconic period.

5. CONCLUSION

Originally we intended to draw attention of scientists to this multidisciplinary phenomenon (it includes climatology, meteorology, geophysics and astronomy) and to explain why the effect disappears in some periods what probably leads to its disregarding. We used different tresholds of daily precipitation amounts, various numbers of superposed epochs and several data series. Because it was found that different "temporal focusing" exposed diverse effects in long-term behaviour of Bowen's signal with probable involvement of Sun we dared to propose a "starting point explanation". According to current ideas about modulation of galactic cosmic rays by solar polar field reversals, *Havromichalaki et al. (1997),* and about the role of galactic cosmic rays in cloud microphysical processes, *Tinsley and Yu (2004),* we suggested a hypothesis about possible physical chain: *changes in orientation of solar magnetic field – different types of interaction with Earth's magnetosphere during even or odd* *solar cycles – modulation of the magnetosphere by the Moon – semilunar variation of cosmic rays – changes in CCN formation – lunar variation of precipitation, Hejkrlík (2007, 2007*).

Some links of this chain are speculative, some of them are based on ambiguous results, but we feel that especially results from Fig. 3 demand explanation.

6. BIBLIOGRAPHY

Adderley, E. E. - Bowen, E. G.: Lunar component in precipitation data. Sci., 137, 1962, p. 749-750

Andrlík, L. - Brůžek, V.: Effect of the Moon on the rainfall course (in Czech). Meteorol. Zpr., 20, 1967, No 3-4, p. 102-103

Bradley, D. A. et al.: Lunar synodic period and widespread precipitation. Sci., 137, 1962, p. 748-749

Havromichalaki et al.: Hale-cycle effects in cosmic-ray intensity during the last four cycles. Astrophysics and Space Science, 246, 1997, p. 7-14

Hejkrlík L.: Lunar influence on rainfall: a case for doubting Thomas? In: Geophysical Research Abstracts, Volume 3, OA28.01 Study of past climates: Climate of the past millennium. 26th General Assembly of European Geophysical Society, 2001, CD

Hejkrlík L. – Novák M.: Long-term changes in lunar variation of precipitation over Europe. EGU General Assembly 2006. Vienna, Austria, 2 - 7 April 2006, In: Geophysical Research Abstracts, Volume 8, 2006, on CD

Hejkrlík L.: New clues for explanation of lunar variation of precipitation. EGU General Assembly 2007. Vienna, Austria, 15 - 20 April 2007, In: Geophysical Research Abstracts, Volume 9, 2007, on CD

Hejkrlík L.: Lunar variation of precipitation. XXIV IUGG General Assembly. Perugia, Italy, 2 - 13 July 2007. On http://www.iugg2007perugia.it/abstractDetails.asp?inObj=6214

Hejkrlík L.: Lunar variation of precipitation supports links between solar activity and atmospheric ionization. European Aerosol Conference 2007. Salzburg, Austria, 9 - 14 September 2007. In Program and abstracts, on CD

Tinsley, B. A., - Yu F.: Atmospheric Ionization and Clouds as Links between Solar Activity and Climat. In Solar Variability and its Effect on Climate, editors: J. M. Pap and P. Fox, Geoph. Monograph Series Vol. 141, 2004, p. 321-340

THE SIMULATION OF ARCTIC CLOUDS AND THEIR RADIATIVE PROPERTIES FOR PRESENT-DAY CLIMATE IN THE CMIP3 MULTI-MODEL DATASET

J. Karlsson[1] and G. Svensson[1]
[1]Department of Meteorology, Stockholm University

1 INTRODUCTION

It is well known that the simulation of clouds in global climate models is a brain-teaser for the the modeling community. This is manifested in the fact that the main uncertainty of future projections is associated with clouds and how a change in cloudiness feeds back on the Earth's climate system (IPCC, Solomon et al., 2007).

It is also known that the Arctic region, due to positive feedbacks, is one of the most sensitive regions to global climate change (ACIA, 2005). The Arctic region is a very cloudy region and clouds play a crucial role for the Arctic surface energy budget and thus for the surface temperature (Shupe and Intrieri, 2004). This is especially true wintertime, when low clouds substantially decrease the surface energy loss by re-emitting longwave radiation to the surface. A study by Walsh and Chapman (1998) showed that clear sky conditions during wintertime are associated with 6°-9°C colder temperatures than for cloudy sky conditions. Cloud characteristics relevant for the magnitude of the cloud forcing are the cloud fraction, temperature, condensate amount and phase.

In our study, we analyze the simulation of present-day Arctic cloudiness and its effect on the radiative fluxes both at the surface and at the top of the atmosphere (TOA) in coupled general circulation models (GCMs). The model results are evaluated towards satellite observations. The focus of the analysis is on the Arctic climatological macroscopic cloud features and radiative fluxes at the surface and at the top of the atmosphere. We define the Arctic as the region north of the Arctic circle (66.6°N). During the winter large part of the region experience polar night while summertime the sun is over the horizon constantly. As a consequence of this contrast in radiative conditions, the Arctic experience extreme seasonal variations. With respect to this, the evaluation have been on seasonal averages rather than annual. In the analysis we have also distinguished between open-ocean and sea-ice covered regions because we expect significant differences in the surface energy budget between these surfaces.

2 MODELS AND OBSERVATIONS

The model data we have utilized are from the World Climate Research Programme's (WCRP's) Coupled Model Intercomparison Project phase 3 (CMIP3) multi-model dataset. Table 1 lists the GCMs included in our study. The simulation studied is the climate of the 20th Century experiment (20C3M) and climatologies of the relevant parameters have been calculated over the period 1980-1999 from monthly-mean data. The model data is compared to each other and with data from the extended AVHRR Polar Pathfinder (APP-x) product (Wang and Key 2003; Wang and Key 2005a,b). The APP-x retrievals have been optimized for high latitude conditions and the data has shown reasonable agreement with data from the Surface Heat Budget of the Arctic Ocean (SHEBA) campaign. To distinguish between open ocean and sea-ice for the observations we have used data from the NIMBUS satellites (Cavalieri et al., 1996, updated 2006)

Table 1: For more model information see http://www-pcmdi.llnl.gov/

CMIP3 ID	ATM. Resolution
CCSM3	T85, L28
CGCM3.1	T47, L31
ECHAM5	T63, L31
GFDL-CM2.0	2.0°x2.5°, L24
INM-CM3.0	4°x5°, L21
IPSL-CM4	2.5°x3.75°, L19
MIROC3.2(hires)	T106, L56
UKMO-HadCM3	2.5°x3.75°, L19
UKMO-HadGEM1	1.25°x1.875°, L38

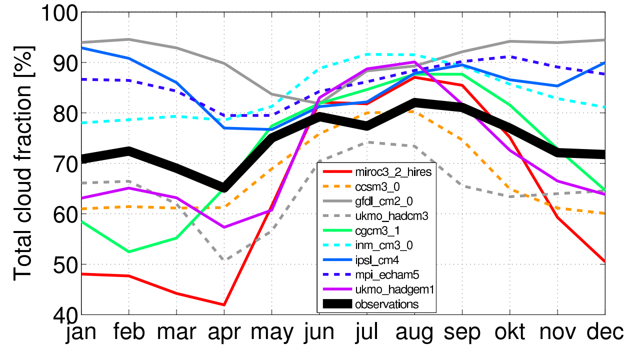

Figure 1: The climatological annual cycle of total cloudiness for the Arctic ocean north of 66.6°N. Black solid line represent the APP-x observations. The periods considered for the models and for the observations are 1980-1999 and 1982-1999 respectively.

3 RESULTS AND DISCUSSION

Figure 1 shows the 20 years climatological annual cycle in total cloud fraction according to the models and the observations. The satellite data show a rather week but cloudy annual cycle which peak during summer and early fall. The annual mean cloudiness is 74% according to the observations. Approximately half of the models have an annual cycle in phase with the observations. The other half have the cloudiness peak wintertime, out of phase with the observations. Most models which manage to describe the phase, have a more pronounced annual amplitude in cloudiness than observations indicate. On the other hand, models which fail with the phase, in general have a more realistic annual amplitude. The simulation of cloud fraction in the models is more consistent during the summer than during the winter. This seems reasonable since the surface temperature during the summer is constrained by the melting.

The discrepancy in total cloud fraction between the models mainly originates from how the low cloudiness is simulated (not shown). The large across-model spread in wintertime cloudiness indicate a ditto spread in surface cloud forcing.

In Figure 2 the mean winter cloud fraction (DJF) is plotted against the surface cloud forcing. Since most of the region north of 66.6°N experience polar night during the winter months, there is only a small contribution from the shortwave cloud forcing. Except for two model outliers (IPSL and GFDL) there seems to be a rather solid linear relationship between the total cloud fraction in the models and their cloud forcing at the surface (r=0.60, 0.84 with and without outliers included, respectively). Models with relatively high cloud fractions are associated with higher surface cloud forcing and vice versa. The across model variability for both quantities is rather large. For the sea ice coverd ocean the winter model mean cloud fraction range between 35% and 95% and the surface cloud forcing range between 15 and 45 Wm^{-2}. Models in general underestimate the surface cloud heating over the sea ice (mean model bias -10 Wm^{-2}). In Figure 2 we also see that all models and the observations have open ocean regions associated with higher cloud amounts and also higher surface cloud forcing.

The mean model and mean observation surface skin temperature for the sea ice covered region is plotted against the total cloud fraction in Figure 3 (upper panel). As in total cloud fraction and surface cloud forcing there is also a large spread in the model's winter surface temperature (range between 239 and 251°K). In general models are too cold compared to the observations (model mean bias is -3.5°K), simi-

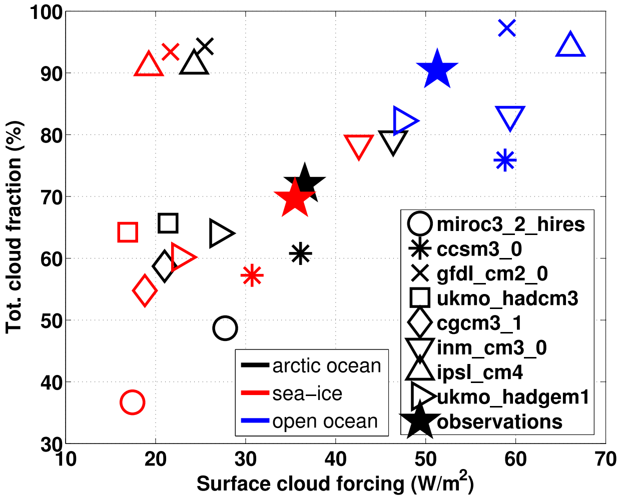

Figure 2: Scatter plot of the climatological winter mean (DJF) total cloud fraction and surface cloud forcing. The fields have been regionally averaged north of 66.6°N for the arctic ocean (black markers), sea-ice covered ocean (red) and the open ocean (blue).

lar mean model bias for the arctic in comparison with ERA40 data was reported by Chapman and Walsh (2007). There is no apparent across model relationship between differences in cloud cover and surface temperature. This indicate, not surprisingly, that other processes play a role in the across model spread in winter time surface temperature. The spread could partly be due to model differences in other cloud properties (e.g. the phase and amount of cloud condensate or the cloud base temperature), but is also be due to non-cloud processes (e.g. differences in the amount of heat and moistured transported to the Arctic). In the lower panel of Figure 3 the winter mean surface cloud forcing is plotted against the mean surface temperature for the models and the observations. The fact that six models have the same magnitude of cloud forcing but a spread in surface mean temperature of more than 10°, indicate that non-cloud processes are important for the temperature spread. On the other hand, it is interesting that all but one model which underestimate the surface cloud forcing also underestimate the surface temperature.

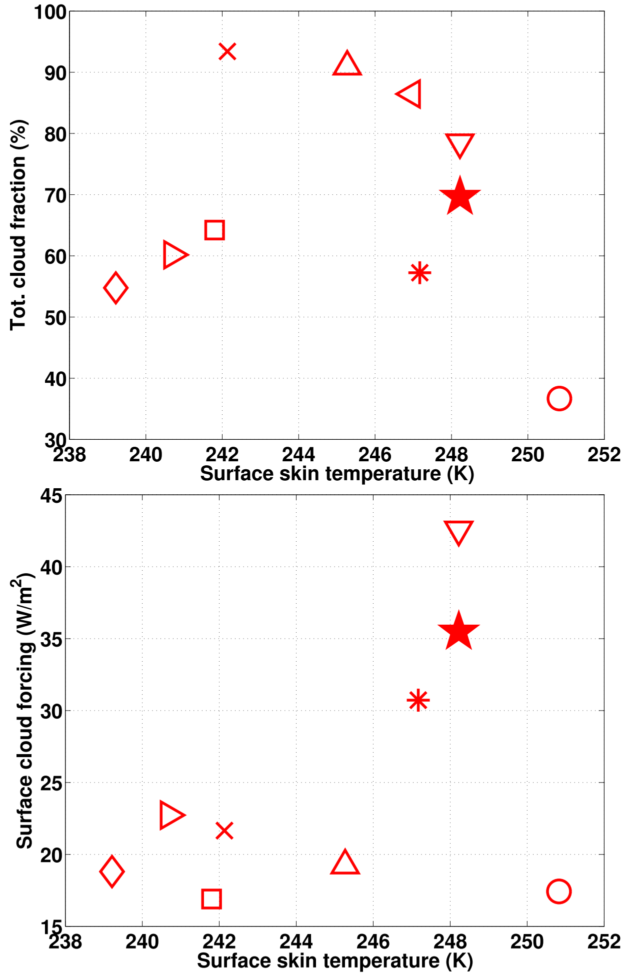

Figure 3: Scatter plot of the sea-ice climatological winter mean (DJF) total cloud fraction and surface cloud forcing vs. surface skin temperature north of 66.6°N. For marker labels see Figure 2

References

ACIA, 2005: Impacts of a warming arctic. arctic climate impact assessment (acia). Technical report, Cambridge University Press, Cambridge, United Kingdom and New York, NY, USA, 140 pp.

Cavalieri, D., C. Parkinson, P. Gloersen, and H. J. Zwally, 1996, updated 2006: Sea ice concentrations from nimbus-7 smmr and dmsp ssm/i passive microwave data, [1982-1999]. Technical report, National Snow and Ice Data Center, Boulder, Colorado USA. Digital media.

Chapman, W. L. and J. E. Walsh, 2007: Simulations of Arctic Temperature and Pressure by Global Coupled Models. *Journal of Climate*, **20**, 609–+, doi:10.1175/JCLI4026.1.

IPCC, Solomon, S., D. Qin, M. Manning, Z. Chen, M. Marquis, K. Averyt, M. Tignor, and H. M. (Eds.), 2007: IPCC: Climate Change 2007: The Scientific Basis. Contribution of Working Group I to the Fourth Assessment Report of the Intergovernmental Panel on Climate Change. Technical report, Cambridge University Press, Cambridge, United Kingdom and New York, NY, USA, 996 pp.

Shupe, M. and J. Intrieri, 2004: Cloud radiative forcing of the arctic surface: The influence of cloud properties, surface albedo, and solar zenith angle. *J. Climate*, **17**, 616–628.

Walsh, J. E. and W. L. Chapman, 1998: Arctic Cloud-Radiation-Temperature Associations in Observational Data and Atmospheric Reanalyses. *Journal of Climate*, **11**, 3030–3045.

Wang, X. and J. Key, 2003: Recent trends in arctic surface, cloud, and radiation properties from space. *Science*, **299**, 1725–1728.

— 2005a: Arctic surface, cloud, and radiation properties based on the avhrr polar pathfinder data set. part i: Spatial and temporal characteristics. *J. Climate*, **18**, 2558–2574.

— 2005b: Arctic surface, cloud, and radiation properties based on the avhrr polar pathfinder data set. part ii: Recent trends. *J. Climate*, **18**, 2575–2593.

USE OF MICROPHYSICAL RELATIONSHIPS TO DISCERN GROWTH/DECAY MECHANISMS OF CLOUD DROPLETS WITH FOCUS ON Z-LWC RELATIONSHIPS

Yangang Liu[1], Huan Guo[1], Seong Soo Yum[2], Peter H. Daum[1], and Jian Wang[1]
[1] Brookhaven National Laboratory, Bldg. 815E, Upton, NY 11973, USA
[2] Yunsei University, Atmospheric Sciences Department, Seoul, South Korea
(Corresponding Author: Yangang Liu, lyg@bnl.gov)

1. INTRODUCTION

Cloud droplet size distributions ---- hence the key microphysical quantities (e.g., radar reflectivity, droplet concentration, liquid water content, relative dispersion, and mean-volume radius) are determined by different physical mechanisms, including pre-cloud aerosols as CCNs, cloud updraft, and various turbulent entrainment-mixing processes. Therefore, different relationships among these microphysical properties are expected in response to these various mechanisms. The effect of turbulent entrainment-mixing processes is particularly vexing, with different entrainment-mixing processes likely leading to different microphysical relationships.

Cloud radar has been widely used to infer the cloud liquid water content (L) from the measurement of radar reflectivity (Z) using a Z-L relationship. Existing Z-L expressions have been often obtained empirically, and differ substantially (Khain et al. 2008). The discrepancy among Z-L relations, which has been hindering the application of cloud radar in measuring cloud properties, likely stems from the different relationships between the relevant microphysical properties caused by different physical processes.

This study first analyzes the Z-L relationship theoretically, and identify the key microphysical properties that affect this relationship, and then address the effects of various processes on the Z-L relationship by discerning the characteristics of the relationships between the relative dispersion, droplet concentration, liquid water content, and mean-volume radius calculated from in-situ measurements of cloud droplet size distributions. Effort is also made to further relate the microphysical relationships to physical processes such as turbulent entrainmen-mixing.

2. THEORETICAL ANALYSIS

Define the p-th mean radius r_p as

$$r_p^p = \left[\frac{\int r^p n(r)dr}{N}\right]^{1/p}, \qquad (1)$$

where r is the droplet radius, n(r) the droplet concentration per unit r interval, and N the total droplet concentration. Radar reflectivity Z can be expressed as

$$Z = 64\int r^6 n(r)dr = 64 N r_6^6 \qquad (2a)$$

Equation (2a) can be rewritten in two different forms:

$$Z = \frac{36}{\pi^2}\frac{\beta_6^6}{N}L^2, \qquad (2b)$$

$$Z = \frac{3\times 64}{4\pi\rho_w}\beta_6^6 r_3^3 L, \qquad (2c)$$

The following two results are expected from Eqs. (2b) and (2c) respectively:

1) For adiabatic clouds with constant N and β_6 as commonly assumed (Atlas, 1954)

$$Z \propto \frac{\beta_6^6}{N} L^2 = BL^2 \propto L^2 . \qquad (3a)$$

2) For extreme inhomogeneous mixing with constant r_3 and β_6 as commonly assumed in studies of entrainment-mixing mechanisms (Paluch et al., 1996),

$$Z \propto \beta_6^6 r_3^3 L = AL \qquad (3b)$$

Equations (3a) and (3b) cover only two ideal scenarios; there exist many different mechanisms in reality that likely lead to different microphysical relationships among β_6, r_3, N, and L, and hence different Z-L relationships. Accordingly, if Z and L follow a power-law relationship given by

$$Z = \alpha L^{\gamma} , \qquad (4)$$

scenarios with γ differing from 1 or 2 can not be ruled out, and moreover, the specific value of γ is expected to depend on the acting physical mechanisms. This simple analysis reveals the potentially important roles of β_6, r_3, N and their relationships to L in determining the specific Z-L relation and its relevance to the physical processes at work. It is noteworthy that β_6 actually measures the relative width of the cloud droplet size distribution because it generally is an increasing function of the relative dispersion (e.g., Liu and Daum, 2000, 2004). As will become evident, β_6 is very useful in identifying the different entrainment-mixing mechanisms, although its role has been ignored in the common assumption of a constant β_6.

3. Observational Results

To examine the effects of aerosol particles on cloud microphysics, the DOE Atmospheric Sciences Program (ASP), the DOE Atmospheric Radiation Measurements Program (ARM), and the Naval Research Laboratory's Center for Remotely Piloted Vehicles for Atmospheric Studies (CIRPAS) conducted a joint field campaign in the 2005 summer, The Marine Stratus/Stratocumulus Experiment (MASE), to investigate the marine stratus/stratocumulus clouds that commonly occur off the coast of Northern California (ARM deployed its mobile facility at Pt Reyes National Seashore just North of San Francisco as part of the Marine Stratus Radiation, Aerosol and Drizzle experiment (MASRAD). The DOE G-1 aircraft carried a suite of instrumentation to measure aerosol composition and microphysical properties of aerosols and clouds, state parameters, winds, and radiation fields. Here we report results derived from the cloud droplet size distributions from 0.5 to 25 μm in radius measured with a Cloud Aerosol and Precipitation Spectrometer (CAPS) (Droplet Measurement Technologies, Boulder, CO). This two-section instrument measures droplets in the 0.5 – 25 μm diameter range using a light scattering technique, and droplets in the 25 – 1550 μm diameter range using an imaging technique (see Daum et al. 2008; Lu et al, 2007 for details about MASE). A segment of data from a horizontal flight during ACE1 is also analyzed in view of its long sampling period, wide range of variability, and features of homogeneous mixing processes.

3.1. Horizontal-Vertical Contrast

Cloud microphysics is affected by different mechanisms in horizontal and vertical directions, and these differences are expected to manifest themselves in the Z-L relationship. This general expectation should hold for horizontal legs at different altitudes and in different clouds as well. To confirm this, we partition the data into horizontal legs and vertical profiles (averages of all the horizontal legs at different altitudes), and then compare them. As expected, substantial differences are found. The contrasts between horizontal and vertical results are especially striking, generally with $\gamma < 1$ for the vertical profiles but $\gamma > 1$ for the corresponding horizontal legs. Figure 1 shows an example derived from flight 20 July 2005a. It is clear that generally the slopes of the horizontal legs are steeper than that of the vertical profile. This result reinforces the need to distinguish between horizontal and vertical variations in studies of cloud properties. See next for more discussions on the physics underlying this striking difference.

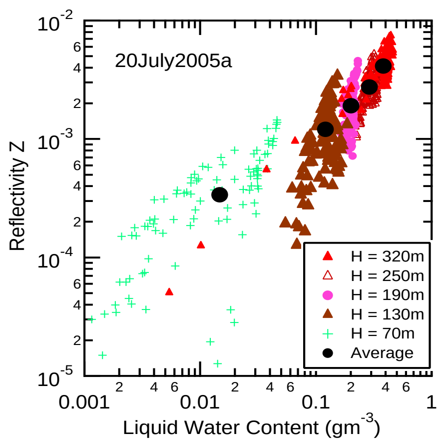

Figure 1. Z-L relationship for horizontal legs at different altitudes and the vertical profile.

3.2. Occurrence Frequency of γ

A total of 35 horizontal cases and 12 vertical profiles are analyzed for the Z-L power-law fit given by Eq. (4) for the MASE data. Figure 2 depicts the occurrence frequency of different values of γ for the 47 cases. It is evident that γ ranges from less than 1 to larger than 2, although it peaks between 1 and 2. It is noteworthy that many cases with $\gamma < 1$ are for the vertical profiles, a surprising result in view of the conventional wisdom that in vertical direction, adiabatic condensational growth dominates and γ should be close to 2 according to Eq. (3a).

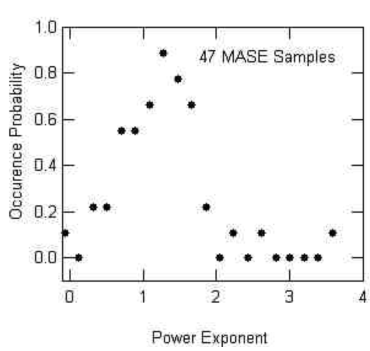

Figure 2. Occurrence frequency of different values of γ.

3.3. Case Studies

Here three special cases that span the typical range of γ values are examined in details. First, according to Eq. (3b), $\gamma < 1$ requires a negatively correlated relation between the parameter A and L. This can happen when some inhomogeneous mixing is in action whereby both β_6 and r_3 decrease with increasing L, i.e., spectral broadens toward large droplets, in expense of evaporation of small droplets (Daum et al., 2008). This scenario can also happen with a proper combination of changes of β_6^6 and r_3^3 with L. Figure 3 shows an example of the latter with $\gamma = 0.73$. Evidently, the parameter A decreases with increasing L when L is small, and this decrease is caused by a relatively faster decreasing rate of β_6^6 compared to the increasing rate of r_3^3.

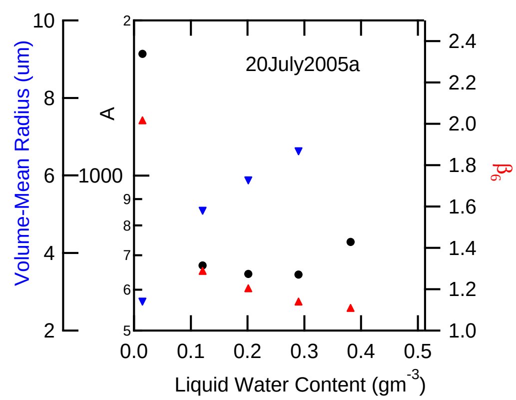

Figure 3. An example of $\gamma = 0.73$

It is expected that the other cases of the vertical profiles with $\gamma < 1$ are due to the same reason because of condensational growth (positive r_v-L correlation) and narrowing spectra (negative β_6-L correlation) with increasing altitudes above cloud bases.

Figure 4a shows an example of Z-L relationship with $\gamma = 1.31$, along with the corresponding A and B parameter. Unlike the case with $\gamma < 1$ shown in Fig. 3, which is due primarily to condensational growth and spectral narrowing with increasing heights, this case is likely associated with the homogeneous entrainment-mixing process. The value γ is larger than 1 because of the increase of A but the decrease of B with increasing L.

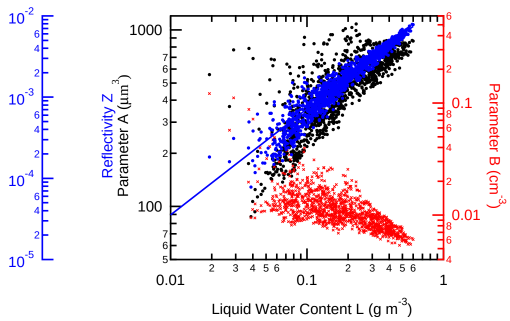

Figure 4a. An example of Z-L relation with γ = 1.31. The colors of the symbols correspond to those of the axes.

As further shown in Fig. 4b, the behavior of A occurs because, although the changes of β_6 and r_3 with L are similar to the first case, the increase of r_3^3 with L is steeper than the decrease of β_6^6, resulting a positive dependence of A but a negative dependence of B on L and $1 < \gamma < 2$. Note that A is proportional to BL; a slope of A less than 1 guarantees a negative slope of B. This is why the B curve is omitted in Fig. 3.

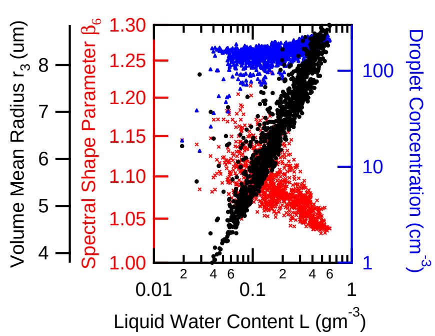

Figure 4b. Variation of β_6, N and r_3 with L. The colors of the symbols correspond to those of the axes.

Figure 5a depicts an example with $\gamma > 2$ derived from the flight leg at altitude of 260 m, 15 July 2005, during the MASE experiment. In contrast to the previous two scenarios, the striking feature of this case is that the parameter B increases with increasing L, inducing a $\gamma > 2$ according to Eq. (2b). Again the A curve is omitted because a positive B-L correlation guarantees a positive A-L correlation.

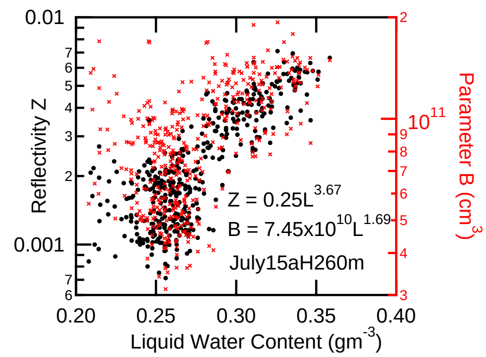

Figure 5a. An example of Z-L relation with γ = 3.67. The colors of the symbols correspond to those of the axes.

Figure 5b shows the relationships of r_v, β_6, and N to L. Strikingly, β_6 increases with increasing L but N decreases with increasing L for most large values of L. This behavior is unexpected from the traditional views of homogeneous or inhomogeneous or ETEM mixing mechanisms because the opposite is expected from all of them. There are two plausible mechanisms for this. First, when L is large, collection process kicks in, leading to larger dispersion and smaller N. However, the small value of r_3 seems contradictory to this hypothesis. The second possibility is that the mixed parcel with reduced N and enhanced dispersion further mixes with parcels with large L. Clearly, more needs to be done about this scenario.

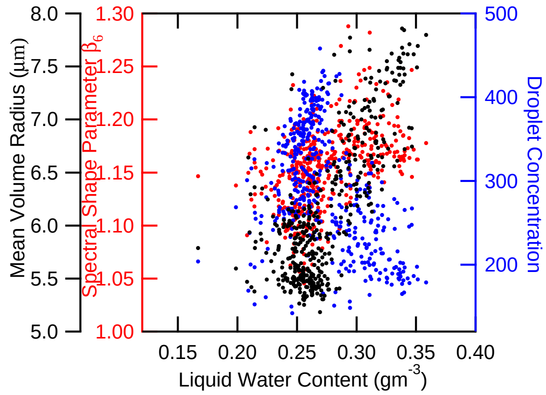

Figure 5b. Relationships of r_v, β_6, and N to L. The colors of the symbols correspond to those of the axes.

4. Concluding Remarks

Theoretical analysis reveals that the commonly assumed two scenarios about the Z-L relationship only represent two ideal cases, and that the real scenario depends on combined dependences of r_v, β_6, and N on L. Empirical examination of the data derived from measured droplet size distributions further shows the possibility for the power exponent γ in the Z-L relation to range from less than 1 to larger than 2. Three examples with γ = 0.73, 1.31, and 3.67 are analyzed in detail from the perspective of the relationships of r_v, β_6, and N to L. The results indicate that the three examples likely arise from condensational growth together with narrowing with increasing heights, homogenous mixing, and inhomogeneous/ITEM mixing/collection processes, respectively.

Although the results are preliminary and much remains to be explored, this work does point to the close link between the Z-L relations and the relationships of r_v, β_6, and N to L that have been long overlooked. The important role of the spectral shape needs to be re-emphasized as it has been largely ignored in remote sensing studies of cloud properties. This work also suggests a potential remote sensing approach to address the outstanding problem of entrainment-mixing mechanisms, which are mainly limited to using aircraft measurements so far. Of course, more analyses are necessary to establish a solid basis for the link between the Z-L relationship and various turbulent entrainment-mixing processes. Such kind of research is underway.

References

Atlas, D., 1954: The estimation of cloud content by radar. J. Meteor., 11, 309-317.

Daum, P. H., Y. Liu, R. L. McGraw, Y. Lee, J. Wang, G. Senum, M. Miller, and J. G. Hudson, 2008: Microphysical Properties of Stratus/stratocumulus Clouds During the 2005 Marine Stratus/Stratocumulus Experiment (MASE). J. Geophys. Res.

Khain, A., M. Pinsky, L. Magaritz, O. Krasnov, and H. W. J. Russchenberg, 2008: Combined observational and model investigations of the Z-LWC relationship in stratocumulus clouds.

Liu, Y. and P. H. Daum, 2000: Spectral dispersion of cloud droplet size distributions and the parameterization of cloud droplet effective radius. Geophy. Res. Lett. 27, 1903-1906.

Liu, Y. and P. H. Daum, 2004: Parameterization of the autoconversion process. Part I: Analytical formulation of the Kessler-type parameterizations. J. Atmos. Sci, 61, 1539-1548.

Lu, M-L, W. C. Conant, H. H. Jonsson, V. Varutbangkul, R. C. Flagan, and J. H. Seinfeld, The Marine Stratus/Stratocumulus Experiment (MASE): Aerosol-cloud relationships in marine stratocumulus(2007), *J. Geophys. Res., 112,* D10209, doi:10.1029/2006JD007985.

Paluch, I. R., C. A., Knight, and L. J. Miller, 1996: Cloud liquid water and radar reflectivity of nonprecipitating cumulus clouds. J. Atmos. Sci., 53, 1587-1602.

Acknowledgement: This research is supported by the DOE ARM program and ASP program.

A SATELLITE AND MODEL STUDY OF RAINFALL ASSOCIATED WITH THE WEST AFRICAN MONSOON

Samantha. Melani [1,2], Andrea Antonini [2,3] , Massimiliano Pasqui [1,2], Alberto Ortolani [1,2] , Vincenzo Levizzani [4], Roberto Ginnetti [4]

[1] National research Council, Institute of Biometeorology (IBIMET-CNR), Firenze, Italy
[2] LaMMA, Laboratory for Meteorology and Environmental Modelling, Firenze, Italy
[3] Hydrological Service of the Tuscany Region, Firenze, Italy
[4] National Research Council, Institute of Atmospheric Sciences and Climate (ISAC-CNR), Bologna, Italy

1. INTRODUCTION

The West African Monsoon (WAM) shows the evidence of large and coherent fluctuations in the rainfall and wind fields at intra-seasonal (10-60-day period) as well as interannual and interdecadal (Janicot and Sultan 2001) time scales.

The knowledge of WAM's complex phenomenology is to date still far from a full understanding of its driving multiple mechanisms, and consequently its spatial and temporal precipitation distribution remains a great challenge to unveil.

Many global circulation models (e.g., Kalnay et al. 1996) have been applied for reproducing the WAM dynamics but their capability to correctly represent deep convection is still very limited. The synergic use of satellite observations and regional models may result crucial in understanding and reconstructing the monsoon fine dynamics.

The last generation of geostationary satellites (METEOSAT Second Generation, MSG) has opened up great possibilities to study and analyze the complexity of the monsoon dynamics, due both to the numerous spectral channels, and to the higher temporal sampling (every 15 min) with respect to the old generation of satellites.

A four-year climatology (2004-2007) of half-hourly rainfall intensities retrieved using a multi-sensor precipitation estimation method involving geostationary infrared (IR) and polar microwave (MW) (Special Sensor Microwave Imager, SSM/I) satellite data is used to investigate the dynamics and phenomenology associated with the African monsoon characteristics, the intraseasonal variability and the diurnal cycle of the rainfall episodes.

In addition, the Regional Atmospheric Modelling System (RAMS) forced by the reanalysis of the National Centers for Environmental Prediction/National Center for Atmospheric Research (NCEP/NCAR) was used to reproduce the African monsoon variability in terms of periodicity and phase of the organized convective systems, taking advantage of its higher spatial resolution (50 km) and better physical description with respect to the reanalysis dataset.

2. DATA AND METHODOLOGY

2.1 Satellite data

Four years (2004-2007) of MSG-based half-hourly instantaneous rainfall maps were retrieved from an automatic real time operational chain, which processes MSG IR (10.8 µm) and SSM/I MW data (Antonini et al. 2007); http://www.lamma.rete.toscana.it/previ/eng/rain_msg_eng.html). The procedure is a blended-technique based on the rapid update technique from Turk et al. (2000), and adapted to the MSG data processing.

Propagation characteristics of rainfall episodes were determined using a methodology similar to that of Carbone et al. (2002), Wang et al. (2004) and Laing et al. (2004), even if some modifications have been introduced on the identification of the convective cloud episodes.

Corresponding author address: Samantha Melani, CNR-IBIMet, via Madonna del Piano 10, Edificio D, I-50019 Sesto Fiorentino (FI), Italy, e-mail: melani@lamma.rete.toscana.it

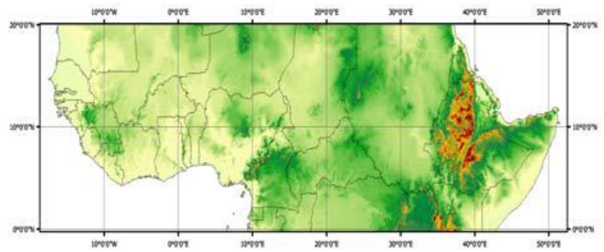

FIGURE 1. *Computational domain for rainfall estimates Hovmöller diagrams.*

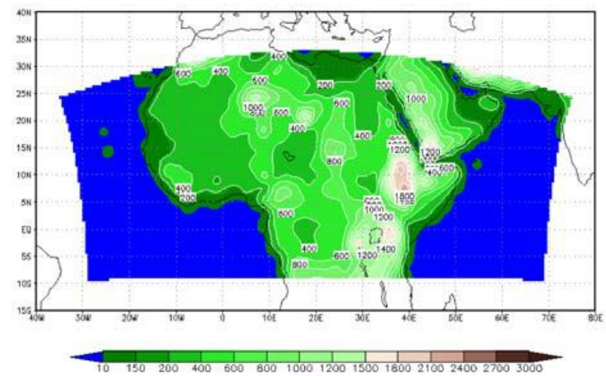

FIGURE 2. *RAMS model domain and topography.*

The instantaneous rainfall maps (every 30 min.), projected onto a regular Lat/Lon grid (~0.04°) represented the database for generating the Hovmöller diagrams. The domain of interest (see Fig. 1), centered on the prevailing African monsoon flow area, is divided into 1650 narrow strips, each 0.04° wide in longitude and running from 3° to 20° in the N-S direction.

Basically, the analysis algorithm identifies all the precipitation cloud sequences (longer than 15 pixels) which are associated to a rain rate higher than a chosen threshold along a certain latitude and then calculates the average value. Finally, the longitude-time Hovmöller diagrams are produced considering only the coldest sequences.

A quantitative analysis on the rainfall streaks was also conducted to quantify their coherency, longevity, and span. A two-dimensional (2D) autocorrelation function, uniform in one direction and cosine weighted in the other, was superimposed to the instantaneous rainfall estimate strips in the Hovmöller space to find their angle, duration and span. For a more detailed description of the mathematical aspects see Carbone et al. (2002).

2.2 Model data

The latest version of RAMS (Pielke et al. 1992, http://www.atmet.com) was used for this study as a powerful instrument for a regional reanalysis simulation (e.g., Pasqui et al. 2004).

Due to the specific physical mechanisms acting in the tropics and the geomorphology of sub–Sahelian Africa, in particular the Ethiopian high plains, the low resolution global reanalysis datasets cannot resolve many characteristics of the atmospheric regional dynamics. The convective triggering mechanisms, produced by the interaction between large scale atmospheric dynamics, such as the African Easterly Jet (AEJ), and the Ethiopian mountains are not well represented at that resolution. Thus, it is important to define a “downscaling technique” for catching local interactions and increasing the quality of the description of the atmospheric state. We adopted a dynamic downscaling strategy using RAMS nested into the NCAR/NCEP atmospheric fields, along with a weekly high resolution sea surface temperature dataset, for two long period simulation runs.

These long simulation periods started on April up to October for both 2004 and 2005, and were structured in two single long RAMS runs without any model restart. Initial and boundary conditions are those of the reanalysis global fields updated every 6 h while the SST fields were updated only every 8 days (PODAAC–MODIS SST fields, http://podaac.jpl.nasa. gov). One single RAMS grid was used with 50 km grid spacing as reported in Fig. 2 where the model domain is shown along with its topography. Numerical stability was ensured by typical RAMS configuration as regards to a proper lateral nudging parameters set, following previous seasonal simulations experience (Baldi et al. 2003).

Since one of the key features for describing convection in the sub-Sahelian area is the interaction between AEJ and Ethiopian high plains, the final domain (see Fig. 2) was set with the eastern boundary far away from the

African coast. Furthermore, the reflected envelope topography scheme in RAMS (see model documentation) has been adopted to obtain a reasonable representation of the mountains.

3. PROPAGATION CHARACTERISTICS OF CONVECTIVE EPISODES

In order to investigate the coherent behaviour of precipitation episodes, a set of Hovmöller diagrams was created for the whole 2004-2007 period. Figure 3 shows an example of such diagrams for JJA 2007, the last year chosen for its particular long-lived and strong monsoon characteristics.

The scale represents the latitudinal-average rainfall estimates with a rain rate threshold value greater than 1 mm h^{-1}. In this domain the well-organized precipitating systems appear as streaks of estimated rainfall rate showing coherent eastward propagation characteristics.

The propagating convection occurs daily and it frequently originates west of the Ethiopian highlands (west of 35°E).

Secondary maxima are also evident, influenced by the Darfur mountains (west of 20°E), the Jos Plateau and the Cameroon mountains (west of 10°E). The non-propagating convection mainly occurs east of 30°E. It is in phase with the diurnal heating and represents the dominant way of convection east of the Ethiopian highlands. The development of convection is also linked to the lower levels of the African Easterly Jet, which becomes more stable when progressing into the rainy season. Indeed, from June to August, we assist to a strengthening of the monsoon intensity, both in terms of a more marked organization and coherency of the Mesoscale Convective Systems (MCS), and also in terms of rainfall intensities and higher phase speed.

3.1 Statistics of rainfall streaks

The mean zonal span, duration and zonal propagation speed for all the precipitation episodes with a duration greater than 3 h, identified in June-August 2004-2007, were found to be 471 km, 9.4 h, 13.6 m s^{-1} (see Table 1).

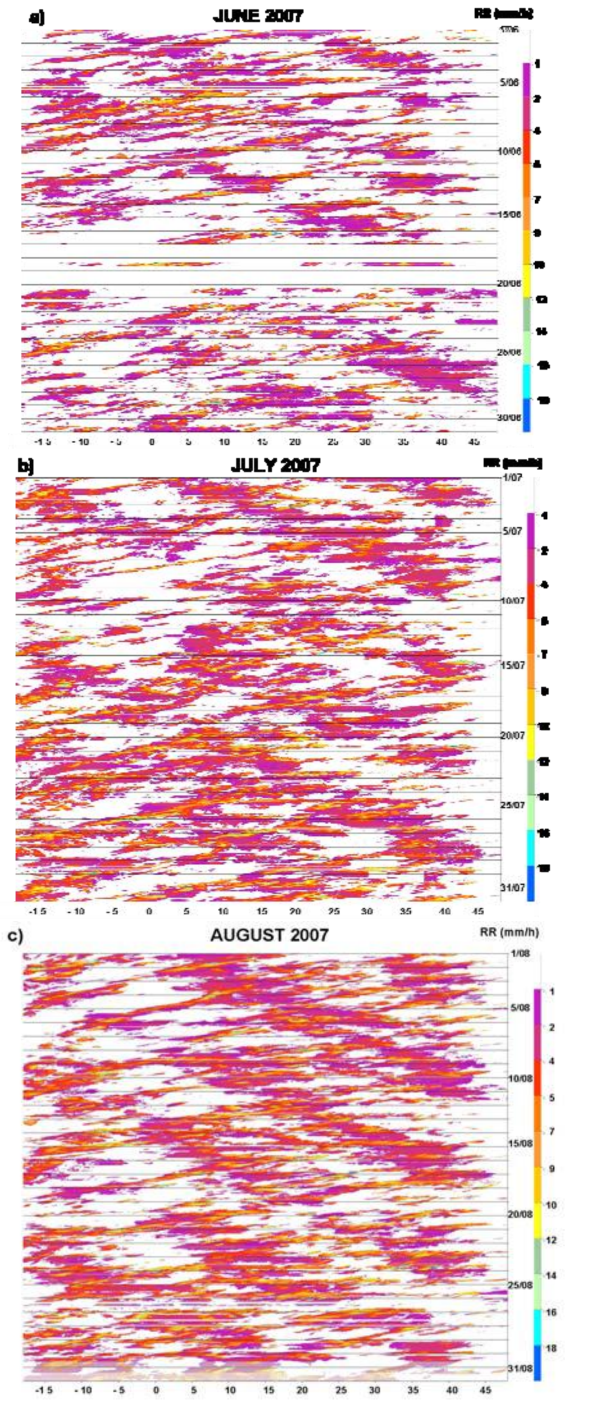

FIGURE 3. *Hovmöller diagrams (longitude-time) of instantaneous rainfall estimates > 1 mm h^{-1} for a) June, b) July, and c) August 2007. The white horizontal strips are due to missing data.*

We point out the strength of the African monsoon in 2007, in terms of both a larger size of the rainfall events and a higher phase speed.

TABLE 1. *Averaged cloud streak zonal span, duration and zonal propagation speed for all rainfall events with a duration longer than 3 h identified in June-August 2004-2007. The same quantities are shown for those events (i.e., the longest in space and time and the fastest) that belong to the top 50%.*

Rain streaks (no. samples)	2004 (819)	2005 (834)	2006 (837)	2007 (886)	mean (3376)
All events					
span (km)	461	471	465	487	471
duration (h)	9.4	9.7	9.2	9.5	9.4
speed (m/s)	13.1	12.9	13.3	14.3	13.6
Top half					
span (km)	735	756	750	790	758
duration (h)	13.9	14.7	13.7	14.3	14.2
speed (m/s)	14.1	16.8	17.6	20.1	17.9

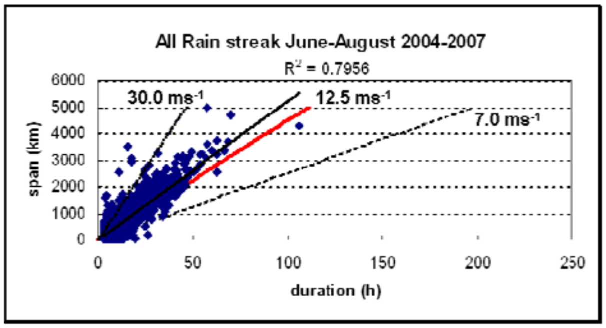

FIGURE 4. *Scatter plot of zonal span vs duration of all rain streaks June to August 2004-2007. The solid red line shows the median phase speed (12.5 m s^{-1}) for all the identified rain events. Black dotted and solid lines represent the zonal phase speed values of 7 and 30 m s^{-1}, respectively.*

When considering only the streaks longest in space and time, and the fastest 50% among them, the mean values become 758 km, 14.2 h, 17.9 m s^{-1}, respectively. Only few rainfall episodes spanned more than 4000 km and last more than 40 h, as shown in Fig. 4.

The majority of rainfall events have a zonal propagation speed between 7 and 30 m s^{-1}, coherently with the results of Carbone et al. (2002), Wang et al. (2004) and Laing et al. (2004). The median phase speed for all the events is 12.5 m s^{-1}. Note that our analysis was conducted using rainfall estimates derived by a blended technique rather than IR brightness temperatures used by the other authors, and that temporal periods and domains of calculation differ.

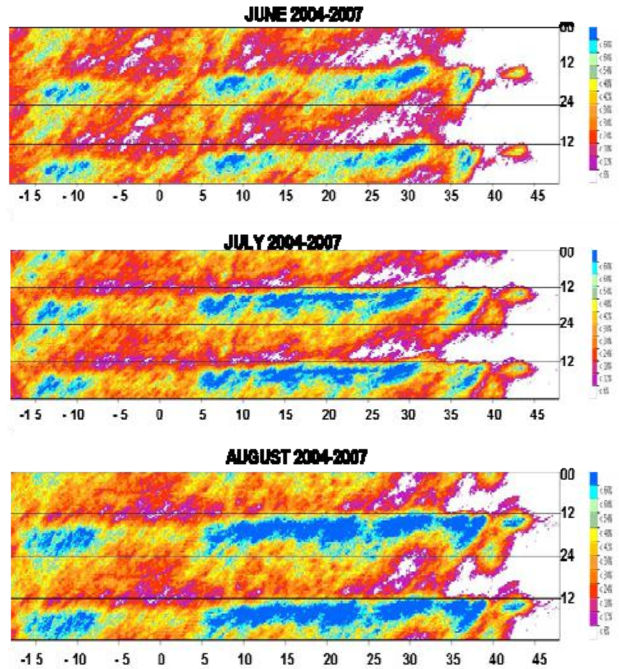

FIGURE 5. *Mean diurnal cycle of pixels with an instantaneous rainfall rate > 1 mm h^{-1} in the Hovmöller (longitude-time) space for June, July and August 2004-2007. The diagrams are repeated twice on top of each other for more clarity.*

4. DIURNAL CYCLE

The periodicity and phase of rainfall have been examined through coherent structures associated with average MSG-based rainfall estimates and RAMS vertical velocity at 300 hPa, considered as a major signal for the occurrence of modelled convection.

4.1 MSG-based rainfall estimates

The mean diurnal cycle of rainfall patterns during the warm seasons (JJA) for the entire period, coupled with the zonal displacement of precipitation, were examined in order to get basic information regarding periodicities at time scales of 1 day or more. The number of days during which precipitation intensity was higher than 1 mm h^{-1} constitutes an event, for each longitude-time coordinate, with a temporal sampling of 30 min and spatial resolution of 0.04°. Figure 5 shows the mean diurnal cycle for the June, July, August averages over the four-years (2004-2007) at a given longitude-UTC hour coordinate.

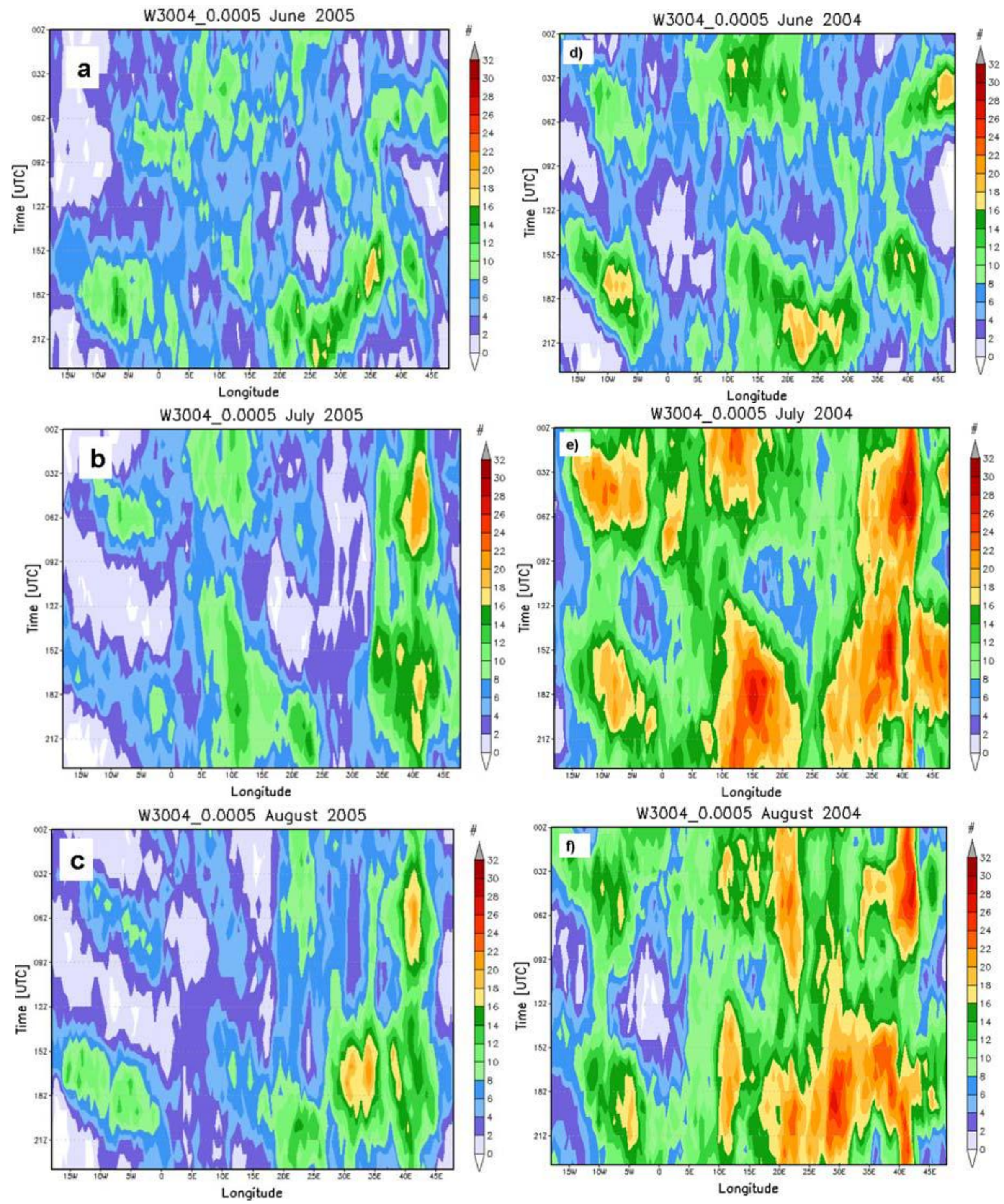

FIGURE 6: *Mean diurnal cycle for a) June, b) July, c) August 2005, and for d) June, e) July, f) August 2004. The scale corresponds to the number of days during which the vertical velocity at 300 hPa is registered (with a threshold value of 0.0005 m s^{-1}) at a given longitude-UTC hour coordinate.*

In general, the persistency of the precipitation systems decreases toward the west, while the signal due to the diurnal variations is generally evident across all longitudes between 0° and 40°E but becomes less evident westward.

The convection in the eastern part of the domain shows a daily oscillation across the African continent (maxima near 1500-1600 UTC) and mainly initiates in the lee of steep topography (maxima in correspondence to the Ethiopian highlands, the Darfur mountains, the Jos Plateau and the mountains of Cameroon) and it is consistent with the thermal heating due to the terrain elevation and the results in literature (Tetzlaff and Peters 1988; Laing and Fritsch 1993). Farther west, maxima can be found in correspondence to the late evening or night time hours.

The westward propagation of precipitation patterns was even more evident in the average diurnal cycle when moving from June to August and signals could travel longest distances.

In June, the convection exhibits diurnal maxima in the early afternoon, located mainly around 5°, 30°, and 35°E. With the strengthening of the monsoon, especially in August, there was a marked widespread distribution of rainfall and the diurnal cycle presents a major intensity, maxima in correspondence to the early afternoon in the eastern part of domain, while in the western part the convection originated in the late evening hours. In this case the precipitation maxima are located around 10°W, 15°E, 25°E, and 38°E.

In these diagrams, the coherent rainfall patterns represent a phase-locked occurrence of the precipitation events.

4.2 RAMS modelled vertical velocity

As a first step in setting RAMS simulations, we verified that the AEJ pattern in RAMS resembles closely the one in the NCEP/NCAR reanalyses (not shown). This must not be considered obvious, even if RAMS was forced (i.e. boundary conditioned) by the reanalyses.

AEJ fine representation is in turn crucial for a correct simulation of WAM phenomena, as AEJ drives the occurrence and pulsation features of the WAM precipitation. The RAMS added value with respect to NCEP/NCAR reanalyses is apparent on orography driven instabilities (as for the Ethiopian highlands, the Darfur and the Jos Plateau). The advantages of finer scale simulations are to be found first in the enhanced description of mountain relieves: as a consequence precipitation becomes more reliable and diurnal cycle recognisable.

Convective precipitation is however accounted by convection schemes also at our RAMS simulation resolutions, and it is affected by significant physical approximations. Vertical velocity at 300 hPa is on the contrary a “cleaner” tracer of convection and it was preferred in the comparison with the precipitation estimations at higher resolution retrieved from satellite observations. Figure 6a-f shows the mean diurnal cycle of RAMS modelled vertical velocity at 300hPa for the months of June, July and August 2004-2005,at a given longitude-UTC coordinate.

A stronger convective activity can be observed for the last two months (Fig. b-c, e-f), with precipitation peaks near 1600-1700 UTC and a maximum amplitude corresponding to the Ethiopian highlands (33°E-38°E). In 2005 less defined but still visible peaks are observable at longitudes corresponding to the other main relieves while in 2004 a more marked convective activity is observed (Fig. 6e-f) with maximum amplitudes corresponding to the Ethiopian highlands (33°E-38°E) and the Darfur mountains (20°E). Unrealistic precipitation peaks are however visible during morning time in the easterly part of the domain, especially in July and August 2004. Probably this is due to the incorrect representation of the dynamical interactions between the African Easterly Jet (AEJ) and the Ethiopian orography by the regional model, producing a physically unrealistic dynamical signal. Further investigations are needed to increase the quality of the representation of such dynamical interactions.

5. CONCLUSIONS

A climatology of 4-year (2004-2007) warm season (June-August) precipitating convection in Africa was presented. The proposed satellite rainfall estimation method, based on a multispectral blended technique, show its capability of capturing all major precipitation types over Africa and a clear evidence of coherent rainfall patterns, associated with the monsoon regime.

The methodology has correctly detected and followed the evolution of the intense convection dynamics in terms of organized rainfall events with coherent propagation in the longitude-time space, characteristics of those tropical areas (Melani et al. 2007). In this sense, the coherency characteristics allowed to study the intraseasonal variability of the monsoon regime, the diurnal cycle and the zonal component of motion. These results are relevant in the overall understanding of the dynamics of monsoon precipitation genesis and evolution, and their impacts in the long-term forecasting and climatic changes.

The reconstruction of the monsoon dynamics with a regional model has shown good capacity in the detection of some phase-locked behaviours, typical of those precipitation patterns, in the perspective of a better comprehension and forecasting of the considered phenomenology.

In order to represent the African climate variability at small scales we need regional high resolution modelling. This is why we have to tune small scale dynamics simulated by the regional models: diurnal cycle analysis can highlight problems arising from the simulations and thus numerical modelling should be able to correctly represent such cycle.

The investigation of these very peculiar dynamic issues is a promising way for improving numerical modelling description at all dynamical scales. Thus, for example, any positive tuning at small scale that improves the representation of the diurnal cycle has a large positive impact on the spatial and temporal precipitation distribution analysis.

Further investigations have to be carried out, but some interesting suggestions come out from this first study. Among them, we aim at investigating the various components of the monsoon through sensitivity tests to various factors (aerosol, SST, etc.), which could influence its complex dynamics.

6. BIBLIOGRAPHY

Antonini, A., S. Melani, A. Ortolani, A. Orlandi, and G. Maracchi, 2007: Stime di precipitazione mediante dati da piattaforme satellitari. In: *Clima e Cambiamenti Climatici - Le attività di ricerca del CNR.* B. Carli, G. Cavarretta, M. Colacino, and S. Fuzzi, Eds., CNR, ISBN 978-88-8080-075-0, 381-384.

Baldi M., F. Meneguzzo, M. Pasqui, A. Crisci. G. A. Dalu, and G. Maracchi, 2003: Numerical analysis of the teleconnection of the west african monsoon to the mediterranean summer climate. *Proc. 5th EGS Plinius Conf. on Mediterranean Storms*, Ajaccio, Corsica, France.

Carbone, R. E., J. D. Tuttle, D. Ahijevych, and S. B. Trier, 2002: Inferences of predictability associated with warm season precipitation episodes. *J. Atmos. Sci*., 59, 2033-2056.

Janicot, S., and B. Sultan, 2001: Intra-seasonal modulation of convection in the West African monsoon*. Geophys. Res. Lett.*, 28, 523-526.

Kalnay, E., M. Kanamitsu, R. Kistler, W. Collins, D. Deaven, L. Gandin, M. Iredell, S. Saha, G. White, J. Woollen, Y. Zhu, A. Leetmaa, B. Reynolds, M. Chelliah, W. Ebisuzaki, W. Higgins, J. Janowiak, K.C. Mo, C. Ropelewski, J. Wang, R. Jenne, and D. Joseph, 1996: The NMC/NCAR 40-Year Reanalysis Project. *Bull. Amer. Meteor. Soc*., 77, 437-471.

Laing, A. G., and J. M. Fritsch, 1993: Mesoscale convective complexes in Africa. *Mon. Wea. Rev*., 121, 2254-2263.

Laing, A. G., R. E Carbone, and V. Levizzani, 2004: Developing a warm season climatology of precipitating systems in Africa. *Proc. 14th Int. Conf. on Clouds and Precipitation*, Bologna, 18-23 July, 1806-1807.

Melani, S., M. Pasqui, B. Gozzini, F. Guarnieri, A. Ortolani, A. Antonini, V. Levizzani, R. Ginnetti, 2007: Observed and model-simulated intraseasonal wam variability for the 2005 rainy season. *Proc. 2007 EUMETSAT Meteorological Satellite Conf. & 15th AMS Conf. on Satellite Meteorology and Oceanography*, Amsterdam, 24-28 September.

Pasqui, M., C. J. Tremback, F. Meneguzzo, G. Giuliani, and B. Gozzini, 2004: A soil moisture initialization method, based on antecedent precipitation approach, for regional atmospheric modelling system: a sensitivity study on precipitation and temperature*. Proc. 18th Conf. on Hydrology*, AMS, Seattle.

Pielke R. A, W. R Cotton, R. L Walko, C. J Tremback, W. A Lyons, L. D Grasso, M. E Nicholls, M. D Moran, D. A Wesley, T. J Lee, and J. H Copeland, 1992: A comprehensive meteorological modeling system-RAMS. *Meteorol. Atmos. Phys*, 49, 69-91.

Tetzlaff, G., and M. Peters, 1988: A composite study of early summer squall lines and their environment over West Africa. *Meteorol. Atmos. Phys*., 38, 153-163.

Turk, J. F., G. Rohaly, J. Hawkins, E. A. Smith, F. S. Marzano, A. Mugnai, and V. Levizzani, 2000: Meteorological applications of precipitation estimation from combined SSM/I, TRMM and geostationary satellite data. In: *Microwave Radiometry and Remote Sensing of the Earth's Surface and Atmosphere*, P. Pampaloni and S. Paloscia Eds., VSP Int. Sci. Publisher, Utrecht (The Netherlands), 353-363.

Wang, C.-C., G. T.-J. Chen, R. E. Carbone, 2004: A climatology of warm season cloud patterns over East Asia based on GMS Infrared Brightness Temperature Observations. *Mon. Wea. Rev*., 132, 1606-1629.

ACKNOWLEDGEMENTS

MSG-1 imagery is copyright of EUMETSAT and was made available by the EUMETSAT on-line Archive.

EVALUATION OF A GENERAL-CIRCULATION MODEL PROGNOSTIC CLOUD SCHEME USING CLOUD-RESOLVING MODEL DATA.

Cyril Morcrette* and Damian Wilson
Met Office, United Kingdom

1 INTRODUCTION

The purpose of a general circulation model (GCM) cloud scheme is to determine what fraction of the grid box is covered by cloud, and what the condensed water content is in those clouds, given the grid-box mean values of temperature, pressure and humidity, These values of cloud fraction and condensate amount are then used by the GCM radiation and precipitation schemes.

A new prognostic cloud fraction and prognostic condensate scheme (PC2) is being developed at the Met Office for use in its GCM: the Met Office Unified Model (MetUM). Each of the physical processes in the GCM, such as large-scale ascent, radiation, convection and boundary-layer processes, will affect the cloud fraction and condensate amounts and these are then advected by the dynamics.

After a brief overview of the theoretical framework that underlies the PC2 cloud scheme, we present cloud-resolving model (CRM) simulations of tropical deep convection which have been analysed using this theoretical framework.

The CRM temperature and humidity data is averaged horizontally to mimic the gridbox-mean values which are the inputs to the scheme. The PC2 scheme then calculates cloud fraction and condensate tendencies in the same way that it would when used in a GCM. These parametrized tendencies for cloud fraction and condensate amount from the scheme can then be compared to the evolution of the fraction of cloudy pixels and mean condensate amount at each level found in the CRM data.

This analysis of the behaviour of the scheme will allow to gain confidence that it is behaving sensibly when used in a GCM.

2 THEORETICAL OVERVIEW

A brief summary of the PC2 cloud scheme is given here for convenience. Further details are given by Wilson *et al.* (2008a). The performance of the PC2 scheme in a climate model is described by Wilson *et al.* (2008b).

2.1 THE 's' FRAMEWORK

The amount of cloud fraction and condensate depends on:

$$Q_c = a_L(\overline{q_T} - q_{sat}(\overline{T_L}, \overline{p})) \qquad (1)$$

(the difference between the grid-box mean specific total water content and the saturation specific humidity (Smith, 1990)) and

$$s = a_L(q'_T - \alpha T'_L - \beta p') \qquad (2)$$

(the local deviation from the mean (Mellor, 1977)). Where q_T is the total (vapour plus liquid) specific humidity, T_L is the "liquid temperature", and p is the pressure. We use the notation $\phi = \overline{\phi} + \phi'$, where $\overline{\phi}$ represents the gridbox-mean value and ϕ' represents the difference of ϕ from its mean. Additionally L is the latent heat of condensation, c_p the specific

*Author address: Dr C. J. Morcrette, Met Office, FitzRoy Road, Exeter, EX1 3PB, United Kingdom. Email: cyril.morcrette@metoffice.gov.uk

heat capacity at constant pressure, q_{cl} the liquid water content, $\alpha = \partial q_{sat}/\partial T$ at constant pressure, $\beta = \partial q_{sat}/\partial p$ at constant temperature and $a_L = (1 + \alpha \frac{L}{c_p})^{-1}$.

Within each gridbox, there is a distribution G, of s, and cloud water content will be present whenever $s > -Q_c$. So the liquid cloud fraction, C_l, and grid-box mean liquid condensate amount, $\overline{q_{cl}}$, are given by

$$C_l = \int_{s=-Q_c}^{\infty} G(s)ds \qquad (3)$$

and

$$\overline{q_{cl}} = \int_{s=-Q_c}^{\infty} (Q_c + s)G(s)ds \qquad (4)$$

2.2 HOMOGENEOUS FORCING

Certain physical processes, such as large-scale ascent and adiabatic cooling, can be assumed to act uniformally over the whole GCM gridbox. As a result, the underlying distribution of G is unchanged (Gregory *et al.*, 2002). By calculating the new position of Q_c, which representing the grid box mean values, and knowing the values of $G(-Q_c)$, then, following Wilson and Gregory (2003), the effects of the cooling on cloud fraction and liquid water content can be quantified using:

$$\frac{\partial \overline{q_{cl}}}{\partial t} = C \frac{\partial Q_c}{\partial t} \qquad (5)$$

and

$$\frac{\partial C_l}{\partial t} = G(-Q_c) \frac{\partial Q_c}{\partial t} \qquad (6)$$

This procedure is illustrated in Fig. 1. By taking temperature and humidity increments from say, the boundary-layer scheme, or the radiation scheme, the change in Q_c can be foud using Eq. 1. The changes to $\overline{q_{cl}}$ and C_l can then be found from Eqns. 5 and 6.

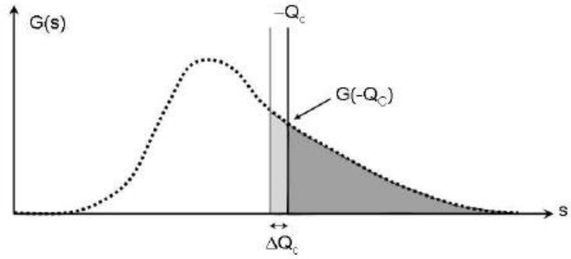

Figure 1: Homogeneous forcing. The change in cloud fraction, C, which is proportional to the area under the G curve, can be estimated, by knowing the change in grid-box mean properties (ΔQ_c), the value of the PDF at the saturated/unsaturated boundary $G(-Q_c)$, and assuming that G is linear over the small interval ΔQ_c.

2.3 PRODUCTION OF CONVECTIVE CLOUD

Building on the work of Tiedtke (1993), Jakob (2000) and Bushell *et al.* (2003) show how the evolution of cloud fraction as a result of convection can be written as:

$$\frac{\partial C_l}{\partial t} = D(1 - C_l) + M \frac{\partial C_l}{\partial z} \qquad (7)$$

where D is the detrainment rate and M the mass-flux. The first term on the righ-hand side represents the detrainment of cloudy air out of the convective plume and into the large-scale environment, while the second term represents the vertical advection of pre-existing cloud by the compensating subsidence. A similar form:

$$\frac{\partial \overline{q_{cl}}}{\partial t} = D(q_{cl,plume} - \overline{q_{cl}}) + M \frac{\partial \overline{q_{cl}}}{\partial z} \qquad (8)$$

is used to represent the detrainment of condensate from the convective plume, as well as the vertical advection. Two similar equations are used to represent the detrainment and vertical advection of ice cloud fraction and frozen condensate. The effects of adiabatic warming from compensating subsidence may lead to the sublimation of some ice. This is calculated within the large-scale precipitation scheme, while the effects of evaporation of liquid water by the same process are modelled using the homogeneous forcing framework.

2.4 LARGE-SCALE PRECIPITATION

The changes to q_{cl} and q_{cf} due to large-scale microphysics, are taken from the Wilson and Ballard (1999) large-scale precipitation scheme which is used by the Met Office GCM. This calculates the microphysical transfer rates between water vapour, cloud ice water content, snow and rain. In addition to the cloud condensate tendencies provided by the large-scale precipitation scheme, it is necessary to represent the effects of large-scale precipitation on the evolution of the cloud fractions.

2.4.1 DEPOSITION AND SUBLIMATION

The change in cloud fraction due to deposition and sublimation assume that there is a uniform distribution of moisture in the part of the gridbox in which the process is acting. By knowing the change in condensate amount, it is possible to work out what the change in cloud cover should be. Figure 2 shows the

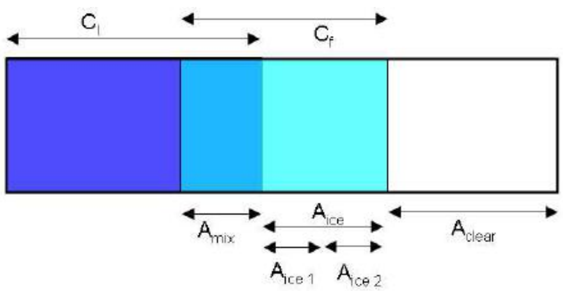

Figure 2: Regions to consider, when calculating where sublimation can occur.

relevant areas when working out the effects of sublimation on ice cloud fraction. (Sublimation does not change the liquid cloud fraction). C_l is the liquid cloud fraction, C_f, the ice cloud fraction. Sublimation can only occur in the part of the grid box, where there is ice, but no liquid, so somewhere within A_{ice}. Additionally, A_{ice}, is further divided into the part above saturation, A_{ice1}, and below saturation, A_{ice2}. Sublimation actually occurs only in A_{ice2}. Let $C_2 = C_1 + dC$ and $q_2 = q_1 + dq$ be the end states, defined in terms of the initial states C_1 and q_1 and difference dC and dq. The total amount of ice is $q_1 = 0.5C_1Q_1$ initially and $q_2 = 0.5C_2Q_2$ at the end. Using similar triangles: $Q_2/Q_1 = C_2/C_1$. By rearranging and using $C_1 = A_{ice2}$ we find that

$$dC_{f,sublime} = A_{ice2}\sqrt{1 + \frac{\Delta q}{q_1}} - A_{ice2}. \quad (9)$$

Deposition only occurs when there is some ice already present, and leaves C_f unchanged. A similar derivation, shows that for deposition the change in liquid cloud fraction is given by

$$dC_{l,deposition} = C_l\sqrt{1 - \frac{\Delta q}{q_1}} - C_l. \quad (10)$$

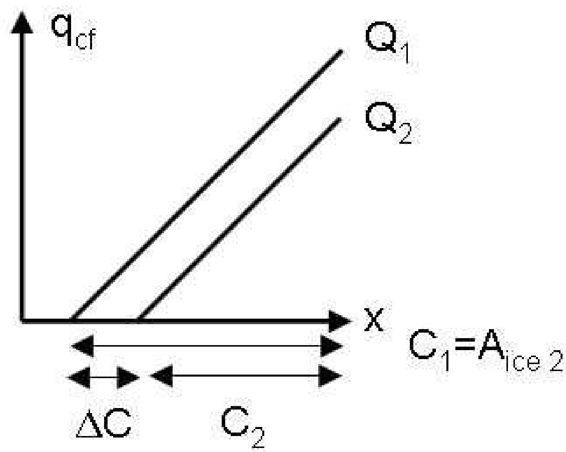

Figure 3: The amount of ice present in the subliming region, when assuming a "top hat" distribution of ice water content across the grid-box.

2.4.2 FALL OF ICE

Consider two layers with ice cloud fractions of $C_f(k)$ and $C_f(k+1)$ (Fig. 4(a)). The "overhang" between the two layers is defined as $\mathcal{O} = Max(C_f(k+1) - C_f(k), 0)$, which ensures that the overhang cannot be negative. Ice is assumed to fall out of the base of the top layer, with the velocity, v, calculated by the large-scale microphysical scheme. In time Δt, the ice has fallen a distance $\Delta h = v\Delta t$ (Fig. 4(b)), which corresponds to a fraction $v\Delta t/\Delta z$ of the layer depth. The volume of ice that falls into the *cloud-free* region in the layer below is then *assumed* to completely fill the grid-box in the vertical and is redistributed, leading to an increase in cloud fraction of $\Delta C_f = \mathcal{O}\text{Min}(v\Delta t/\Delta z, 1)$ (Fig. 4(c)). The minimum check being to limit the increase in cloud fraction if the ice falls further than one layer depth per timestep.

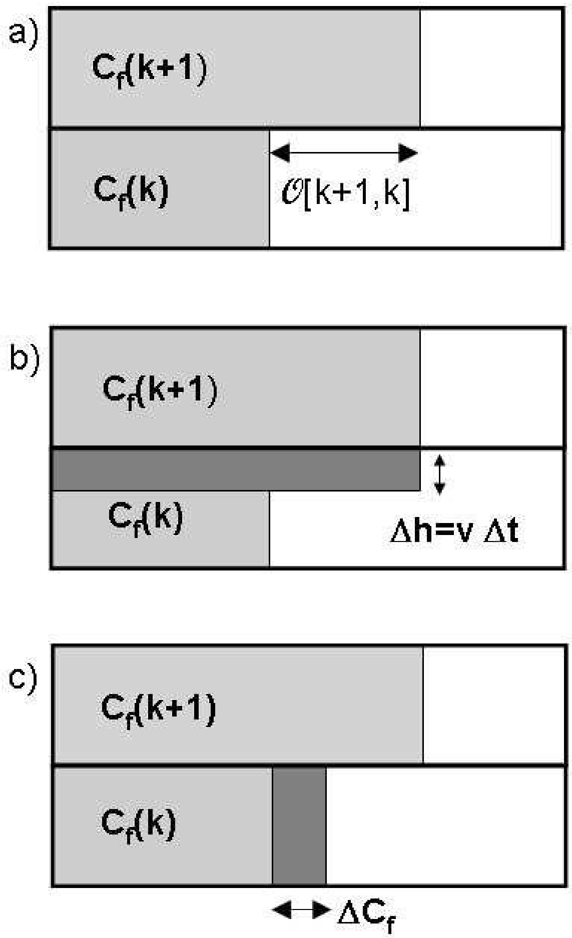

Figure 4: Schematic of how ice falling from one layer increases the ice cloud fraction in the layer below.

2.4.3 MELTING

The melting of ice and evaporation of melting snow are both assumed to reduce the ice cloud fraction in proportion to how much of the ice condensate has been removed.

2.4.4 OTHER MICROPHYSICAL PROCESSES

The remaining microphysical processes (i.e. riming, capture, evaporation of rain, accretion and autoconversion) are all assumed to have no effect on the cloud fractions.

3 RESULTS

Results are presented from a CRM simulation using the Met Office Large-Eddy Model (LEM). The case studied is from TOGA-COARE between 20-26 December 1992 (Petch and Gray, 2001). The CRM was run in two-dimensions over a 256 km wide domain with a horizontal gridlength of 500m. The model top was at 20 km and a stretched grid was used with 120 levels, giving a vertical gridlength of around 165 m between 2 and 14 km in the region where clouds formed.

Figure 5 shows the evolution of the liquid and ice cloud fraction and of the liquid and ice water contents averaged over the large-scale environment. The "large-scale environment" is the part of the domain that is not part of the convective plume (i.e. not a bouyant cloudy updraught).

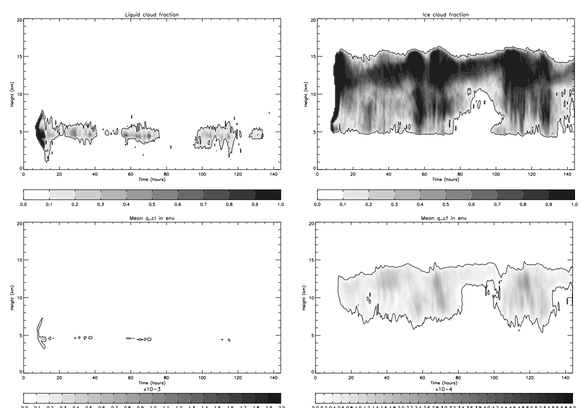

Figure 5: a) Liquid cloud fraction and b) ice cloud fraction. c) Liquid water content and d) ice water content, averaged over the environement.

Following Arakawa and Schubert (1974) the mass-flux can be defined as $M = \rho\sigma w$, where ρ is the density, σ is the fraction of the GCM gridbox occupied by the convection and w is the vertical velocity in the convective plume.

The mass-flux from the CRM is shown in Fig.6(a). In order to calculate the rate of transport of condensate and cloud fraction from the convective plume into the environment we need to have an estimate of the detrainment rate. A height-dependent passive tracer is inserted into the CRM. We then compare the mean profiles of the tracer averaged over the convective points and averaged over the environment. As the tracer is passive any difference between these two profiles is due to transport from the environment into the convective plume (entrainment) or from the convective plume into the environment (detrainment) (Swann, 2001). Figure 6(b) shows the detrainment rate calculated from the CRM data.

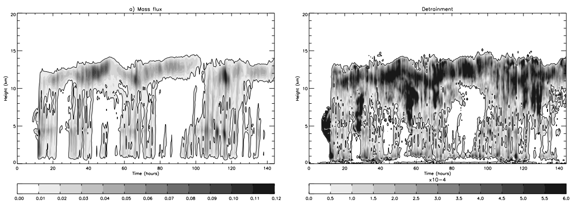

Figure 6: a) Mass flux, b) detrainment calculated using passive tracers and the equation from Swann (2001).

3.1 THE "TRUTH"

Figure 7 shows the time-derivative of Fig. 5. These are the "true" rates of change of liquid and ice condensate and cloud fraction, as modelled in the CRM. These are the fields that we want the PC2 scheme to be able to parametrize.

Although all the mechanisms that can modify the cloud fields have been considered, for this case, it turn out that processes such as large-scale forcing, boundary-layer mixing and radiation all have minor impacts (not shown). Perhaps unsurpringly sine we are looking at a case of tropical deep convection, the dominant terms turn out to be due to the detrainment from convection and the large-scale precipitation. We will look at the two areas of convection and microphysics in more detail.

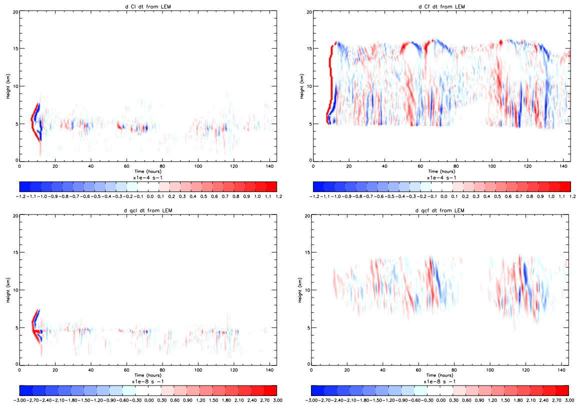

Figure 7: Rate of change of a) liquid cloud fraction, b) ice cloud fraction, c) environmental liquid water content and d) environment ice water content, calculated from the LEM fields. These tendencies can be considered to be the "truth" and are what we would want a cloud scheme to be able to predict.

3.2 CONVECTION

Figure 8 shows the liquid cloud fraction tendencies, $\partial C_l/\partial t$, due to convection. These consist of terms due to detrainment and vertical advection from compensating subsidence (see Eqn. 7) as well as a term representing evaporation of cloud following adiabatic warming by compensating subsidence which is modelled using the homogeneous forcing framework (see Eqn. 6).

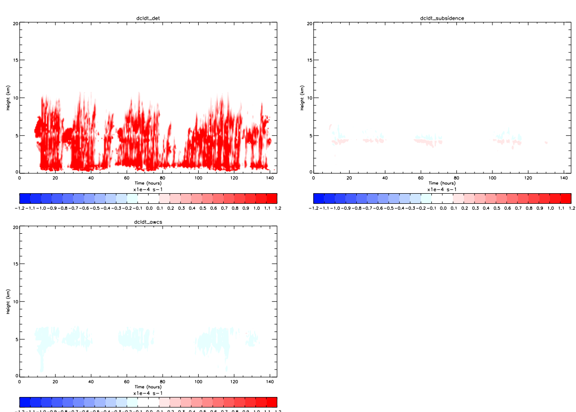

Figure 8: Liquid cloud fraction tendencies due to convection: a) detrainment of liquid cloud fraction from convective plume into the large-scale environment, b) advection of liquid cloud fraction by the compensating subsidence, c) evaporation following adiabatic warming from compensating subsidence.

Figure 9 shows the liquid water tendencies, $\partial\overline{q_{cl}}/\partial t$, due to convection. As for cloud fraction, these consist of terms due to detrainment and vertical advection from compensating subsidence (see Eqn. 8) and evaporation following adiabatic warming by compensating subsidence (see Eqn. 6).

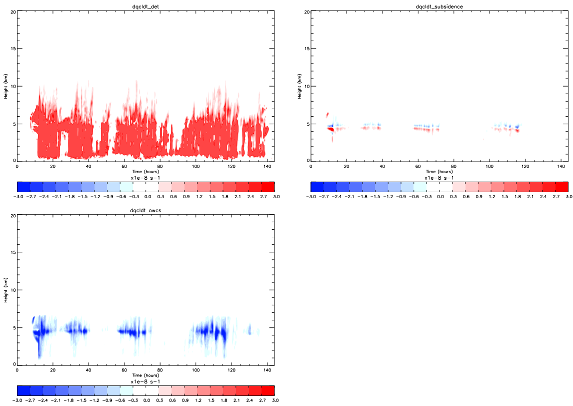

Figure 9: Liquid water tendencies due to convection: a) detrainment of liquid water from convective plume into the large-scale environment, b) advection of liquid water by the compensating subsidence, c) evaporation following adiabatic warming from compensating subsidence.

Figures 10 and 11 show the ice cloud fraction, and ice water content tendencies ($\partial C_f/\partial t$ and $\partial\overline{q_{cf}}/\partial t$), due to convection. As for the liquid phase, these consist of terms due to detrainment and vertical advection from compensating subsidence, however, the effects of adiabatic warming from compensating subsidence on the C_f and q_{cf} are included in the sublimation terms calculated by the large-scale precipitation scheme (see Section 3.3).

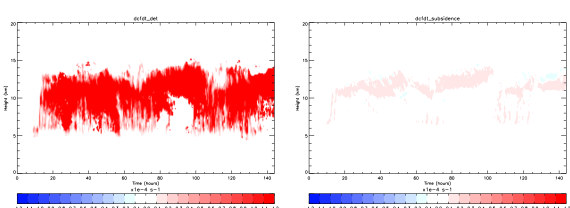

Figure 10: Ice cloud fraction tendencies due to convection: a) detrainment of ice cloud fraction from convective plume into the large-scale environment, b) advection of ice cloud fraction by the compensating subsidence.

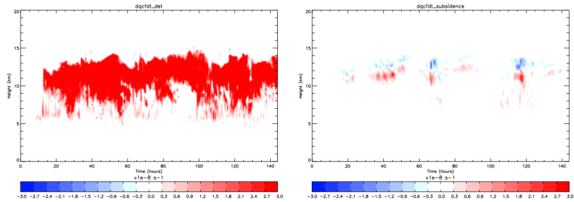

Figure 11: Ice water tendencies due to convection: a) detrainment of ice from convective plume into the large-scale environment, b) advection of ice water by the compensating subsidence.

3.3 MICROPHYSICS

Figure 12 shows the tendencies associated with the CRM microphysical transfers which occur in the large-scale environment (as opposed to within the convective plume) and which we assume would be represented by the GCM large-scale precipitation scheme. Although microphysical processes have a direct effect on the ice cloud fraction (the dominant processes being sublimation, deposition and the fall of ice all), the warm-rain microphysical processes (such as autoconversion, accretion and evaporation) are *assumed* to have no effect on the liquid cloud fraction. These processes do however effect the liquid water content, so changes to the liquid cloud fraction occur indirectly.

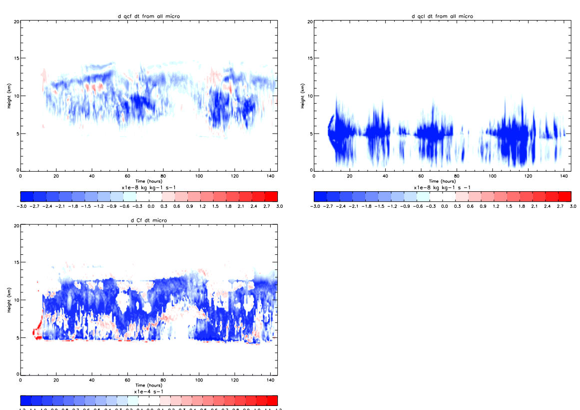

Figure 12: The tendencies from the large-scale precipitation scheme for a) ice water content, b) liquid water content and c) ice cloud fraction. The large-scale precipitation is *assumed* to have no effect on the liquid cloud fraction.

3.4 PC2 PARAMETRIZATION

After having calculated the tendencies from all the physical processes we can add them up to create the parametrized tendencies that the PC2 scheme would produce (Fig. 13). These are what the PC2 cloud scheme would predict given the horizontally averaged CRM data as input. These should be compared to the "truth" shown in Fig. 7.

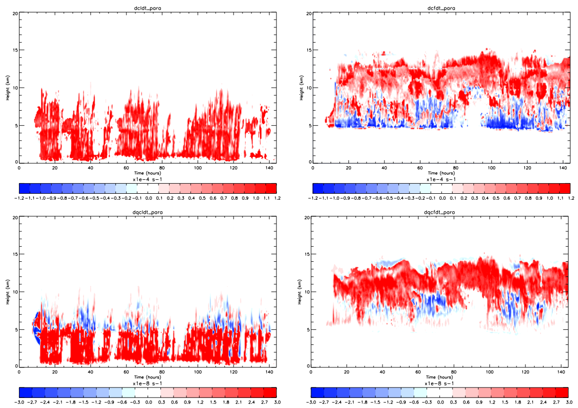

Figure 13: Rate of change of a) liquid cloud fraction, b) ice cloud fraction, c) environment liquid water content and d) environment ice water content, calculated by adding all the PC2 process rates calculated from the LEM fields.

4 DISCUSSION

Although Figs. 13 and 7 do not look very similar, the analysis has been useful at it has highlighted the dominant terms that may require further attention. The main source term is the detrainment from convection, while the main sink term comes from large-scale microphysics.

The resolution and number of dimensions in the domain will have an effect on the mass-flux profiles and the representation of turbulent mixing due to radiative cooling near cloud top (Petch and Gray, 2001). Further CRM simulations, with smaller gridlengths and a some coarse resolution 3D tests are being planned in order to quantify the uncertainty in the mass-flux and detrainment profiles which are then used to estimate the truth for subsequent comparison with the PC2 parametrization.

The other possible reason for differences between Figs. 13 and 7 is because some important process has not so far been included in the PC2 framework or because the processes that are included could be represented more realistically. This is an area for further research.

The current analysis suggests that there is no significant sink of liquid cloud fraction. A mechanism known as "cloud erosion" (Tiedtke, 1993) has been included in other GCM prognostic cloud schemes. This process aims to represent the removal of liquid cloud condensate and liquid cloud fraction as a result of sub-grid motions within the GCM gridbox mixing clear and cloudy air and leading to evaporation of the cloud. A parametrization of this effect has been included in PC2, however, in this case it does not appear to produce sink terms which are large enough to be significant.

4.1 FUTURE WORK

4.1.1 EROSION TRACERS

The process of "cloud erosion" is not well understood. Following Stiller and Gregory (2003), PC2 represents sub-grid mixing as a narrowing of the moisture PDF. Figure 14 illustrates how a narrowing of the moisture PDF (darker grey lines) leads to a reduction in cloud fraction and liquid cloud condensate (assuming that the peak of the PDF is to the left of $-Q_c$). Some CRM simulations are planned, where an age tracer is used to measure the time since a parcel of air was inside the convective plume. By studying the evolution of the moisture probability density function we hope to gain insight into how to better parametrize the effects of "cloud erosion" in our GCM.

4.1.2 SINGLE COLUMN MODEL

It is hoped that this work will be combined with some simulations using the PC2 code within a Single Column Model (SCM) version of the GCM. The various PC2 tendencies from the SCM can then be compared to their analogues from the CRM.

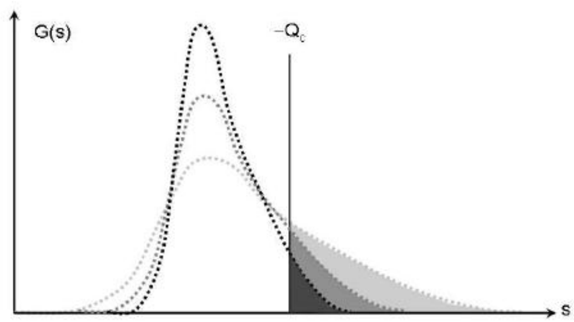

Figure 14: Schematic of how reducing the width of the moisture PDF will reduce the amount of cloud fraction and condensate.

References

Arakawa, A. and Schubert, W. H. (1974). Interaction of a cumulus ensemble with the large-scale environment, Part I. *J. Atmos. Sci.*, **31**, 674–701.

Bushell, A. C., Wilson, D. R., and Gregory, D. (2003). A description of cloud production by non-uniformly distributed processes. *Q. J. R. Meteorol. Soc.*, **129**, 1435–1455.

Gregory, D., Bushell, A. C., and Wilson, D. R. (2002). Insights into cloud parametrization provided by a prognotic approach. *Q. J. R. Meteorol. Soc.*, **128**, 1485–1504.

Jakob, C. (2000). The representation of cloud cover in atmospheric general circulation models. Ph.D. thesis, Ludwig-Maximilians-Universität.

Mellor, G. (1977). The Gaussian cloud model relations. *J. Atmos. Sci.*, **34**, 356–358.

Petch, J. C. and Gray, M. E. B. (2001). Sensitivity studies using a cloud-resolving model simulation of the tropical west Pacific. *Q. J. R. Meteorol. Soc.*, **127**, 2287–2306.

Smith, R. N. B. (1990). A scheme for predicting layer cloud and their water content ina general circulation model. *Q. J. R. Meteorol. Soc.*, **116**, 435–460.

Stiller, O. and Gregory, D. (2003). The evolution of subgrid-scale humidity fluctuations in the presence of homogeneous cooling. *Q. J. R. Meteorol. Soc.*, **129**, 1149–1168.

Swann, H. (2001). Evaluation of the mass-flux approach to parametrizing deep convection. *Q. J. R. Meteorol. Soc.*, **127**, 1239–1260.

Tiedtke, M. (1993). Representation of clouds in large-scale models. *Mon. Weather Rev.*, **121**, 3040–3061.

Wilson, D. and Gregory, D. (2003). The behaviour of large-scale model cloud schemes under idealised forcing scenarios. *Q. J. R. Meteorol. Soc.*, **129**, 967–986.

Wilson, D., Bushell, A., Kerr-Munslow, A., Price, J., and Morcrette, C. (2008a). PC2: A prognostic cloud fraction and condensation scheme. I: Scheme description. *Q. J. R. Meteorol. Soc.* submitted.

Wilson, D., Bushell, A., Kerr-Munslow, A., Price, J., Morcrette, C., and Bodas-Salcedo, A. (2008b). PC2: A prognostic cloud fraction and condensation scheme. II: Results of climate model simulations. *Q. J. R. Meteorol. Soc.* submitted.

Wilson, D. R. and Ballard, S. P. (1999). A microphysically based precipitation scheme for the UK Meteorological Office Unified Model. *Q. J. R. Meteorol. Soc.*, **125**, 1607–1636.

EFFECTS OF THE BIOMASS BURNING IN THE THUNDERSTORM DEVELOPMENT: AN ANALYSIS IN THE AMAZON BASIN

Rachel I. Albrecht and Carlos A. Morales

University of São Paulo, Department of Atmospheric Science, São Paulo, Brazil

1. INTRODUCTION

Cloud-to-ground lightning activity in thunderstorms are related to several environmental features that accounts to their development: microphysics (changes in droplet size distributions due to pollution, which consequently changes the life cycle and ice particles formation), thermodynamics (local convection) and large-scale forcings (seasonal humidity conditions and motions configurations, such as the South Atlantic Convergence Zone, squall lines that propagate through the Amazon, Bolivian high), as studied by Rosenfeld (1999), Petersen et al. (2001, 2002), Cifelli et al. (2002), Williams et al. (2002), among others. These features modify the development of thunderstorms that is observed in its life cycle and lightning flash density. This study investigates the impact of such dependencies on the development of the thunderstorms in the Amazon region based on four 4 years of cloud-to-ground lightning measurements over the state of Rondonia, Brazil. A special attention will be given between the dry and wet season (September to November), where biomass burning take place, and can contribute or not to the development of thunderstorms or even modify the electrical charge center.

2. DATA AND METHODOLOGY

Cloud-to-ground lightning (CG) data from 2000 to 2004 were collected by four Advanced Lightning Direction Finder (ALDF) sensors installed by the Marshall Space Flight Center/ NASA (MSFC/NASA) at the state of Rondonia as part of the Tropical Measuring Mission Ground Validation (TRMM/GV). During the RaCCI (Radiation, Clouds and Climate Interactions) and SMOCC (Smoke Clouds, and Climate – Andreae et al., 2004) campaigns at the state of Rondonia, Brazil, an unique set of data were collected representing the transition season from dry to wet conditions in the southwest Amazon, from September to November of 2002. The RaCCI campaign was part of the LBA (Large-Scale Biosphere-Atmosphere Experiment) project (Silva Dias et al., 2002). The campaigns instrumentation used in this work are presented in Figure 1, and they are:

- CAPPIs (Constant Altitude Plan Indicator) of 2 km horizontal and 1 km vertical resolutions, with a radius of 150km, from a Brazilian S-band Doppler radar, manufactured by the TECTELCOM company, installed just for the campaings (62.42W, 10.9S).
- Measurements of aerosol optical thickness (AOT) are taken by the AERONET (Aerosol Robotic Network)[1] at the pasture site (Fazenda Nossa Senhora), since 1999 to nowadays. The AOT is defined as the extinction coefficient (partial radiance per wavelength, also called attenuation) integrated in a vertical column of unit section from the direct radiation beam in each wavelength (340, 380. 440, 500, 670, 870 e 1020 nm) based on the Beer-Bouguer's law (Procopio et al., 2004). Therefore, AOT gives the degree in which the aerosol blocks the sunlight transmission: higher the aerosol concentration in the atmospheric column, higher will be the blocking and higher will be the AOT value, indicating the degree of atmospheric pollution.
- Measurements of aerosol size distribution and cloud condensation nuclei (CCN) concentrations were taken at the pasture

1 http://aeronet.gsfc.nasa.gov/

site, by the Max Planck Institute for Chemistry.

- Radiosondes were launched every 3 hours at pasture site, measuring vertical profiles of temperature, humidity and wind velocity. CAPE (Convective Potential Available Energy), CINE (Convective Inhibition Energy) were calculated using these profiles of temperature and humidity (Bolton, 1980), as well as the warm cloud depth (WCD – the difference between the height of 0ºC isotherm and the cloud base height).

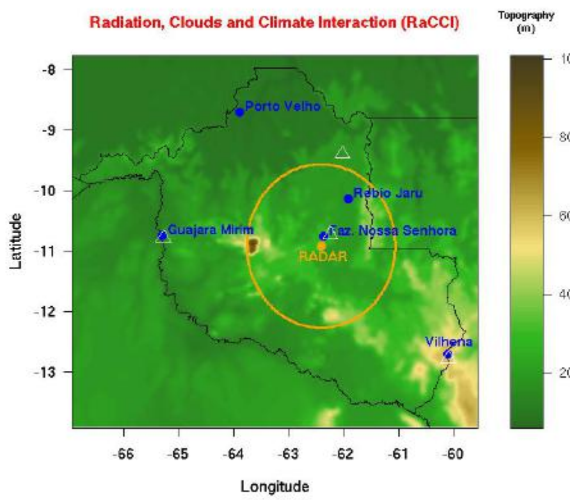

Figure 1 *– RaCCI field campaign instrumentation at Rodonia state, Brazil: TECTELCOM radar (orange), radiosonde sites (blue), and BLDN sensors (white).*

3. RESULTS

Figure 2 shows the CG lightning detected over the state of Rondonia and the aerosol optical thickness from 2000 to 2004. It can be seen that the lightning activity has a major increase from September to November, that is, from the dry to the wet seasons. The AOT started to increase in the dry season, and continued high until the transition season. These high values of AOT are due to forest and pasture fires. Specially during the transition season, the local farmers burn their pastures to prepare them for cattle with the first rains of the wet season. Another interesting feature is the increase in the percentage of CGs with positive polarity (+CGs) during August and September for all 4 years studied (Figure 2a). We can see that the fact is that, coincidentally or not, this same modulation of precipitation and lightning activity (with an increase in the number of +CGs) regulates the period of fires, releasing high concentrations of aerosols into the atmosphere. Many authors have suggested the aerosols from biomass burning can be associated to changes in the polarity of CG lightnings (Lyons et al. 1998, Murray et al. 2000, Smith et al. 2003, Fernandes et al., 2006).

From September to November the aerosol pollution and number of fires decreases, which simulates conditions that vary from very polluted to clean environments. In order to study also the effect of the biomass burning over the precipitating systems, we divided the RaCCI campaign into three distinct periods of pollution and humidity, considering the period of the radar functionality (September 16 though 07 November):

- 16/Sep to 04/Oct: end of the dry season *(DRY)*;
- 05/Sep to 25/Oct: transition between the dry and the wet seasons *(TRANS)*;
- 26/Oct to 07/Nov: begging of the wet season *(WET).*

The thunderstorms that passed by the radar were divided into classes of lifetime duration (30-60 min, 60-120 min, and >120 min) and then normalized by their total time duration in a scale of 0 to 1. Therefore it is possible to compare different thunderstorms in the same life cycle stage, such as initiation, maturation, and decaying stages. This procedure was done using the a satellite cloud tracking algorithm called FORTRACC (Mathon and Laurent, 2001), modified to use radar reflectivity fields. To track the rain storms, a threshold of 20 dBZ is established to define the rain area clusters (clouds). The CG lightning measurements were navigated in the radar reflectivity maps and the thunderstorms were identified. Finally for each storm, the lightning rate was evaluated.

The panels in Figure 3 show the mean number of lightnings per system per time during the life cycle of the systems, represented by the normalized lifetime. We can see from Figure 3 that during the DRY periods the thunderstorms had more lightning of

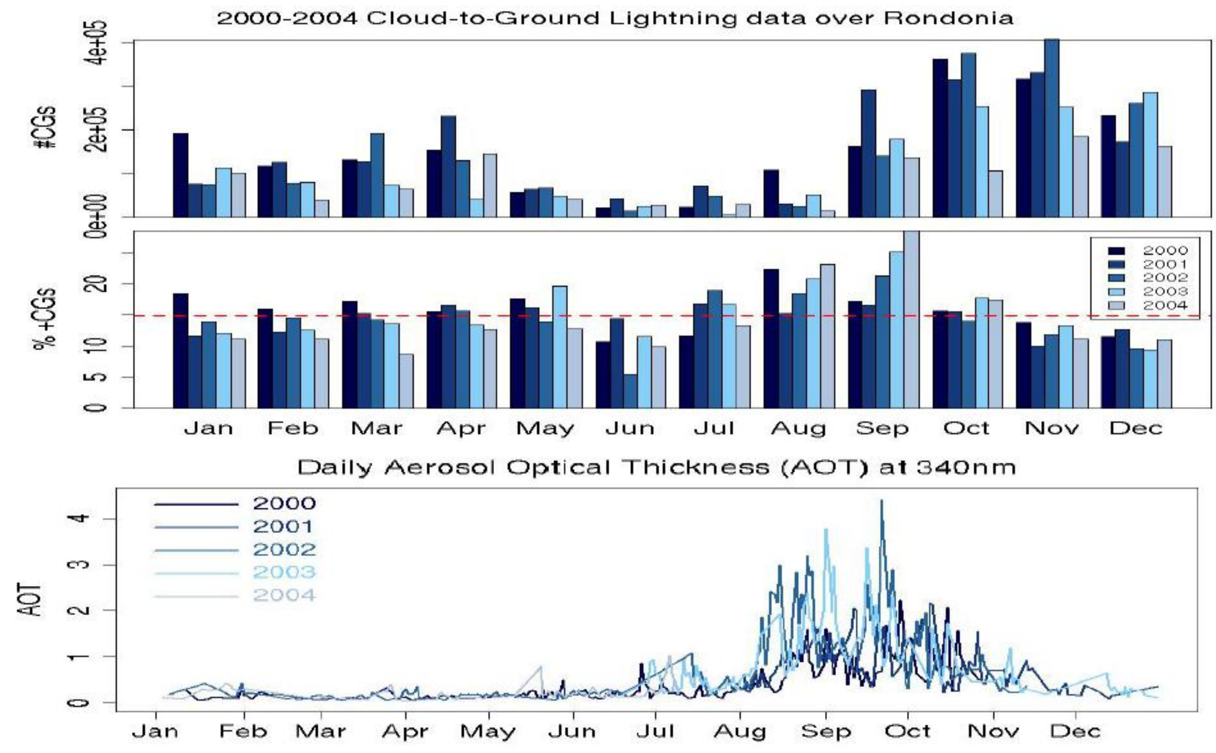

(a)

(b)

***Figure 2** – **(a)** CG strokes detected over Rondonia and the percentage of CGs with positve polarity (+CGs) (the dashed red line indicates the mean percentage) and **(b)** Aerosol Optical Thickness (AOT) measured over the Fazenda Nossa Senhora, from 2000 to 2004.*

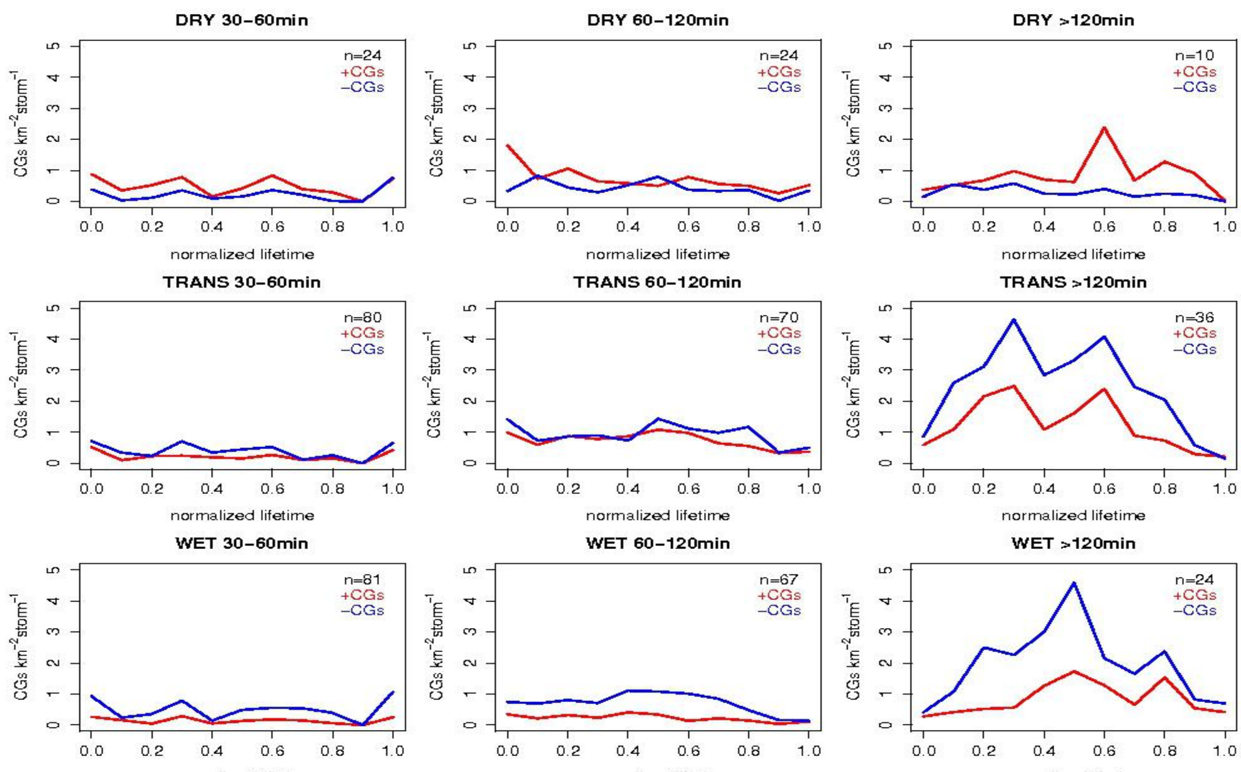

***Figure 3** –Life cycle of the thunderstorms detected by the radar, divided into total time duration(30-60, 60-120, >120 minutes) and humidity/pollution period. Negative CGs are the blue lines, positive CGs are the red lines, and 'n=' are the number of cases studied.*

positive polarity during all their life cycle for all total time duration families. In the thunderstorms that occurred during the other two periods (TRANS and WET), the number of negative CGs (-CGs) overcame the number of positive (+CGs), being this characteristic more strong during the clean period. This result indicates that the very dry and polluted environments could influenced not only in the number of CGs per thunderstorm, but also in their polarity.

More specific studies of how the thermodynamic can affect the CG polarity were conducted by Williams et al. (2005) and Cary and Buffalo (2007). Both studies found out that high cloud base heights may provide larger cloud water in the mixed phase, which is favorable for the positive charging of large ice particles that may result in storms with reversed polarity of its main dipole. Carey and Buffalo (2007) also found that positive storms occurred in environments associates with a drier low level mid-troposphere, higher cloud base, smaller warm cloud depth, and stronger conditional instability. They also pointed out that the differences in the warm cloud depth from negative to positive storm were the most dramatic one.

Following the above studies, we calculated the Lifting Condensation Level (LCL) - which is a measure of the cloud base height, the height of the 0°C isotherm and the Warm Cloud Depth (WCD), which corresponds to the depth between the height of the cloud base to the height of the 0°C isotherm. Figure 4 shows these variables from the pasture site radiosondes. It can be seen from this figure that there was a clear tendency of higher LCL during the dry period, while the T= 0°C height did not follow this tendency. This feature lead also to a tendency of lower WCD during the dry period. Considering that we had mainly

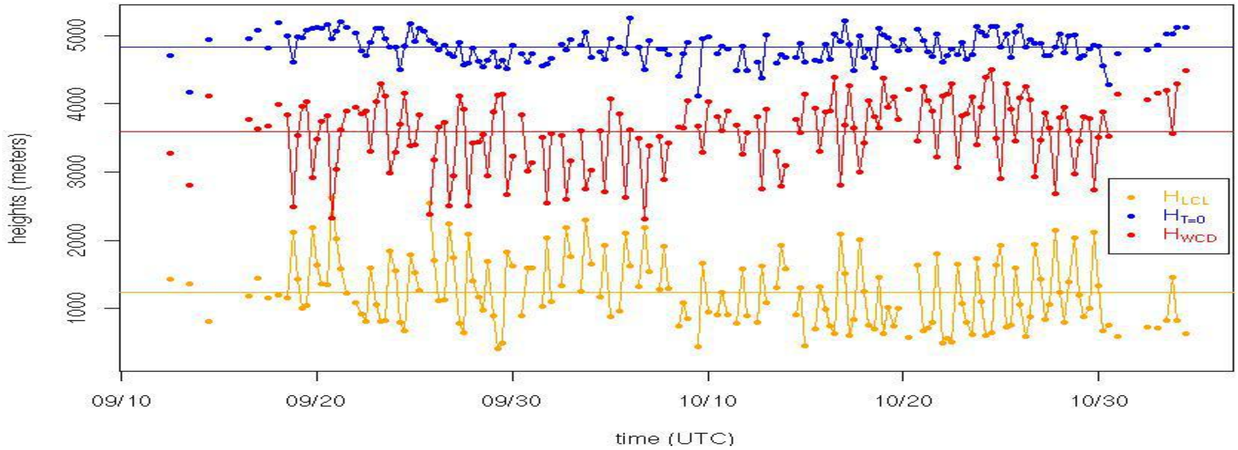

Figure 4 *– Lifting condensation level (LCL) height, height of 0oC isotherm, and Warm Cloud Depth (WCD). The horizontal lines correspond to the mean values.*

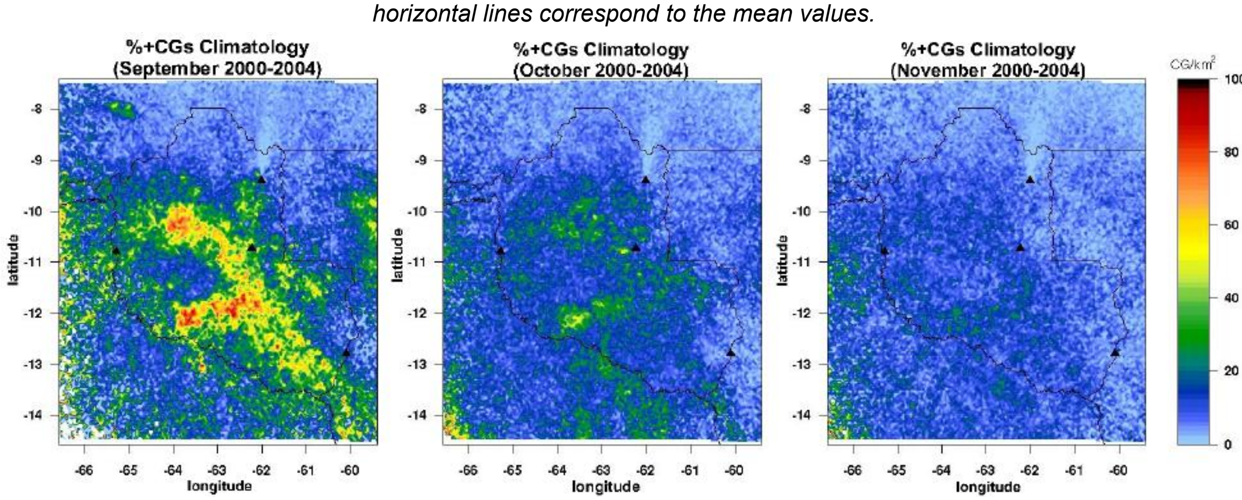

Figure 5 *– Climatological percentage of +CGs from 2000-2004 during September, October and November.*

positive storms at the dry season (Figures 2 and 3), our results agree with Williams et al. (2005), and specially with Carey and Buffalo (2007).

Figure 5 shows the spatial distribution +CGs percentages. As expected from the other results shown above, September shows an enhancement, followed by degrading decrease from October to November. However, the spatial configuration observed in September follows the map of deforestation. As seen in Figure 6, the changes in land cover that follow the construction of paved roads typically result in a so-called fishbone pattern of land-use: the construction of the main road, which is often followed by the development of numerous perpendicular secondary roads accompanied by intensive deforestation along the main axis and successive stripes of forested and deforested areas, depending on the distance from the secondary roads. Figure 7 shows the climatology of percentages of +CGs stratified by the land cover use of Figure 6. We can see that from August to October, +CGs occurs predominantly over deforested areas, and during September more than 30% of this type of lightning occurs over deforestation. This feature can be linked to changes in the thermodynamics of the atmospheric boundary layer (BL), such as more sensible heat and turbulence that elevates the top of the BL and consequently the cloud base heights, as discussed in Figure 4.

Figure 8 shows the mean aerosol size distributions measured at the pasture site (Fazenda Nossa Senhora) during events of clouds that were detected by the radar of RaCCI campaign. These clouds were divided by their electrification activity: those that did not produce lightning (Non-Thunderstorms), those that did produce lightning in general (Thunderstorms), and the storms that produced mainly +CGs (Positive Thunderstorms) and mainly -CGs (Negative Thunderstorms). It can be seen that during the DRY and more polluted period, there is no major differences in the size distributions of the aerosols, except at the size range of 0.005-0.02 μm: there was ~2000cm^{-3} more aerosols during thunderstorms that produced more +CGs, and the negative and non-thunderstorms spectra are the same. Again, no major differences could be identified between

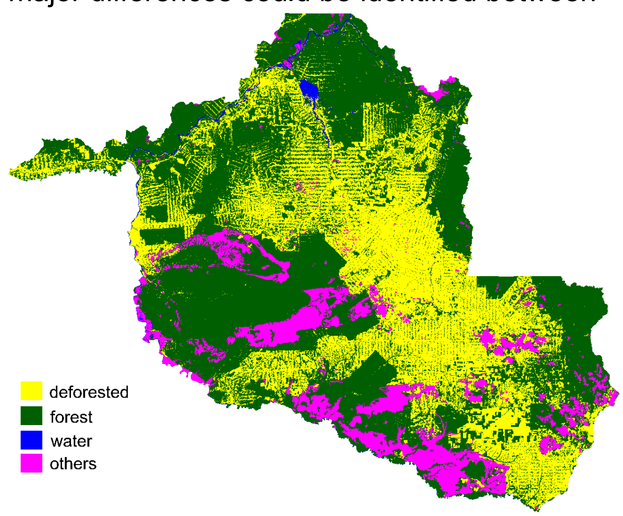

Figure 6 *- Deforestation status at Brazilian State of Rondonia, in southwestern Amazon, based on LANDSAT images (NPE, 2008).*

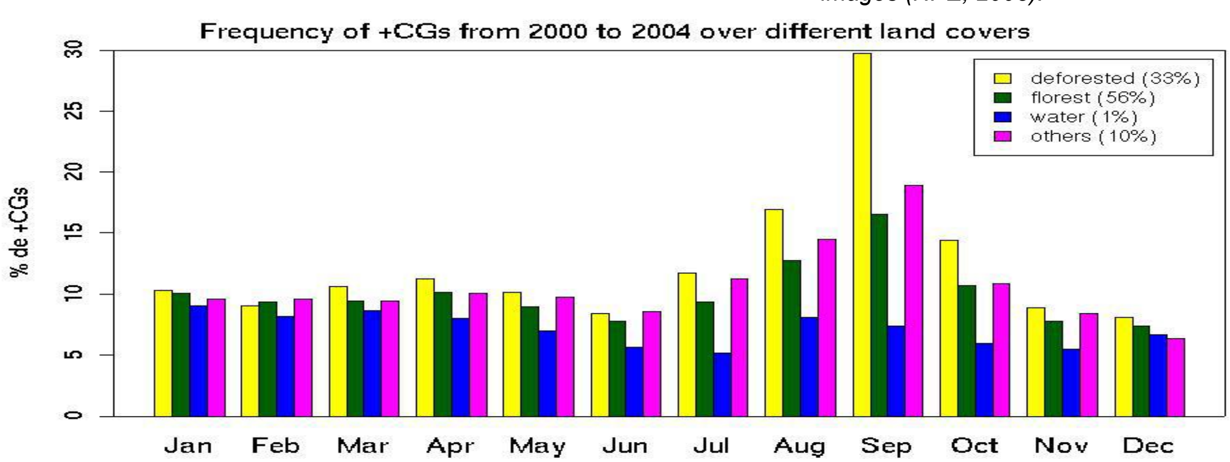

Figure 7 – Percentage of the 2000-2004 +CGs that occurred over deforested, forest, water and other areas over the state of Rondonia, Brazil.

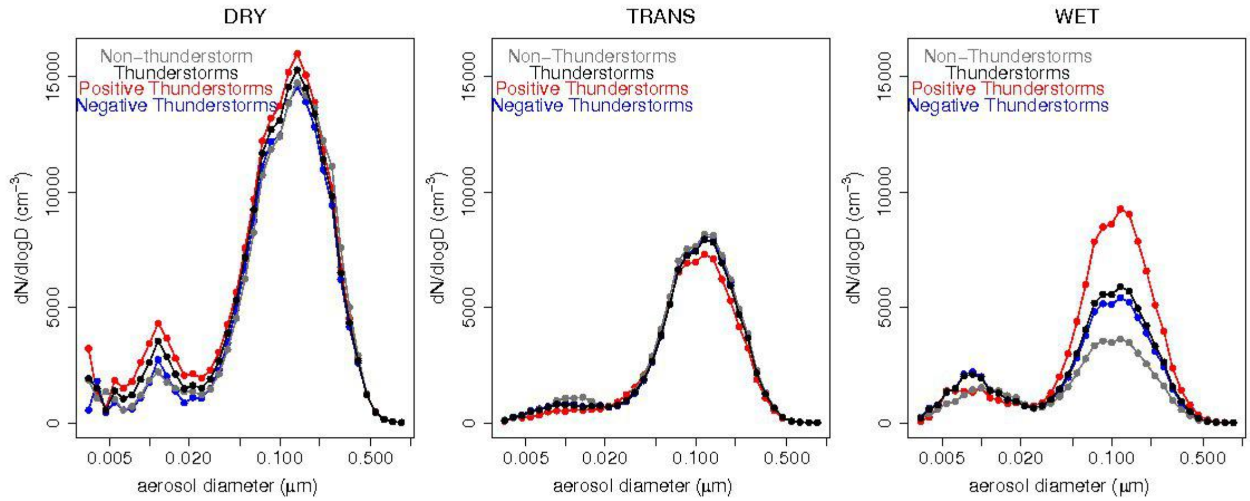

Figure 8 *– Aerosol size distributions during events that did not produce lightning (Non-Thunderstorms), storms that produced mainly +CGs (Positive Thunderstorms), mainly -CGs (Negative Thunderstorms), and clouds that produced lightning regardless the polarity (Thunderstorms=Positive Thunderstorms+Negative Thunderstorms).*

non-thunderstorms and thunderstorms of either polarity. However, the aerosol size spectra during the WET and clean period presented interesting features: non-thunderstorm clouds were formed in more clean environments (with ~6500cm^{-3} less total aerosols), while negative and positive thunderstorms presented ~2500 and ~6500 cm^{-3} more total aerosols, respectively. Therefore, the aeorosol may not affect the clouds electrification during the DRY and TRANS, but can be an import key during the clean and WET period.

4. CONCLUSIONS

Amazonian convective systems have unique microphysical characteristics, varying from a maritime convective behavior (rainy season) to a continental behavior (wet-dry transition season). These characteristics modulate the electrification of these systems, however it is not well understood which are the dominant processes that intensify the number of lightning from one season to another. The fact is that coincidentally or not the same modulation of the Amazonian precipitation regulates the period of farmer fires to prepare the pasture for cattle, releasing high concentrations of aerosols into the atmosphere.

The weather radar and lightning measurements at Southwest Amazon showed that convective storms of different sizes happened to have more positive CG lightning during the very polluted period of biomass burning, while this tendency was decreased with the establishment of the wet season and consequently less pollution.

The thermodynamic analysis of the environment showed a smaller warm cloud depth, which is favorable for the positive charging of large ice particles that may result in storms with reversed polarity of its main dipole (Carey and Buffalo, 2007). This analysis also showed that the dry period had also more conditional instability, which could eventually produce deep convective systems if a low level forcing acts. The thermodynamic variability could also be associated to the land cover over Rondonia. We showed that +CGs occurred mainly over the deforested areas, where the top of the boundary layer can be higher and decrease the warm-cloud-depth, which have been reported as a condition for inverted polarity storms (Carey and Buffalo, 2007).

The aerosol effect on cloud formation and electrification is still not well established. We showed that the aerosol size distributions during thunderstorms and non-thunderstorms events do not differ during the DRY and TRANS periods. However, a major difference was found during the WET period, suggesting that thunderstorms only occur around a more polluted environment. Another aerosol effect that was not explored here is their composition. Jungwirth et al. (2005) found that biomass burning aerosols can change the molecular structure of the cloud ice crystals exposing more positive ions at their surface. More work is needed to be done in this field.

Acknowledgments

This work was supported by FAPESP (Fundação de Amparo a Pesquisa de São Paulo) on the grant number 04/09049-3.

REFERENCES

Andreae, M. O., D. Rosenfeld, P. Artaxo, A. Costa, G. Frank, K. Longo, M. Silva Dias, 2004: Smoking rain clouds over the Amazon, *Science*, **303**, 1337-1342.

Bolton, 1980: The computation of equivalent potential temperature, *Mon. Wea. Rev.*, **108**, 1046-1053.

Carey, L., and K. Buffalo, 2007: Environmental control of cloud-to-ground lighting polarity in severe storms, *Mon. Wea. Rev.*, **135**, 1327-1353.

Cifelli, R. W.A. Petersen, L.D. Carey, and S.A. Rutledge, 2002: Radar Observations of the Kinematic, Microphysical, and Precipitation Characteristics of Two MCSs in TRMM-LBA. *J. Geophys. Res*, **29**, 8077.

Fernandes, W., I. Pinto, O. Pinto, K. Longo, S. Freitas, 2006: New findings about the influence of smoke from fires on the cloud-to-ground lightning characteristics in the Amazon region, Geophys. Res. Lett., 33, L20810, doi:10.1029/2006GL027744.

INPE, 2008: Satellite monitoring of the Amazon Forest – Porject PRODES (availabel on-line through the INPE website: http://www.obt.inpe.br/prodes/indes.html. In Portuguese). S. J. dos Campos, Brazil.

Jungwirth, P., D. Rosenfeld and V. Buch, 2005: A possible new molecular mechanism of thundercloud electrification, *Atmos. Res.*, **76**, 190-205.

Lyons, W.A., T.E. Nelson, E.R. Williams, J. A. Cramer, and T.R. Turner, 1998: Enhanced Positive Cloud-to-Ground Lightning in Thunderstorms Ingesting Smoke from Fires, *Science*, **2**, 77-80, 1998.

Mathon, V. and H. Laurent, 2001: Life Cycle of the Sahelian convective cloud systems, *Quart. Royal. Meteor. Soc.*, **127**, 377-406.

Murray, N. D., R. E. Orville, and G. R. Huffines, 2000: Effect of pollution from Central American fires on cloud-to-ground lightning in May 1998, *Geophys. Res. Lett.*, **27**, 2249-2252.

Petersen, W.A., and S.A. Rutledge, 2001: Regional Variability in Tropical Convection: Observations from TRMM. *J. Climate,* , **14**, 3566-3585

Petersen, W.A., S.W. Nesbitt, R.J. Blakeslee, R. Cifelli, P. Hein, and S.A. Rutledge, 2002: TRMM Observations of Intraseasonal Variability in Convective Regimes Over the Amazon. *J. Climate,* **15**, 1278-1294.

Procopio, A.S., Artaxo, P., Kaufman, Y.J., Remer, L.A., Schafer, J.S., Holben, B.N., 2004: Multiyear analysis of amazonian biomass burning smoke radiative forcing of climate, *Geophys. Res. Lett.*, **31**, 3108-3112.

Rosenfeld, D, 1999: TRMM observed first direct evidence of smoke from forest fires inhibiting rainfall, *Geophys. Res. Lett.*, **26**, 3105-3108.

Silva Dias,and co-authors, 2002: Clouds and rain processes in a biosphere-atmosphere interaction context in the Amazon region, *J. Geophy.l Res.*, **107**, 8072.

Smith, J. A., M. B. Baker, and J. A. Weiman, 2003: Do forest fires affect lightning?, *Quart. J. Royal Meteor. Soc.*, **129**, 2651-2670.

Williams, E., and co-authors, 2002: Contrasting convective regimes over the Amazon: Implications for cloud electrification, *J. Geophys. Res.*, **107**, 8082.

Williams, E., V. Mushtak, D. Rosenfeld, S. Goodman, and D. Boccippio, 2005: Thermodynamic conditions favorable to superlative thunderstorm updraft, mixed phase microphysics and lightning flash rate, *Atm. Res.*, **76**, 288-306.

AEROSOL SIZE DISTRIBUTION IN PRECIPITATION EVENTS IN LEÓN, SPAIN

Elisabeth Alonso-Blanco, Miguel González-Colino, Ana I. Calvo, María Fernández-Raga, Amaya Castro*, Roberto Fraile

Department of Physics, University of León, 24071 León, Spain
*acasi@unileon.es

1. INTRODUCTION

One of the consequences of climate change is an alteration in precipitation regimes, hence making it necessary to study the mechanisms that may cause these alterations. Aerosol concentration is among the main factors triggering rain because aerosols function as condensation nuclei (CCN) inside clouds. On the other hand, in aerosol-precipitation interaction the elimination of aerosols through precipitation must also be taken into account. Thus, variations in aerosol concentration may be seen as one of the causes of precipitation or as one of its consequences. This balance has prompted the present study, which is an attempt to relate the air masses causing precipitation in León to aerosol size distribution and aerosol concentration. Changes in aerosol size distributions during rain events will also be studied because aerosol size distribution influences the dynamics of aerosol population (Vakeva et al., 2001), their production and removal processes, size transformation, lifetime, optical properties and radiative effects (Huebert et al., 1996). The size distribution of atmospheric aerosols strongly depends on the sources and sinks as well as on the meteorological processes prevailing during their lifetime (Suzuki and Tsunogai, 1988; Ito, 1993).

Authors such as Slinn (1971) or Dana and Hales (1976) established theoretically the linear relationships between the scavenging coefficient and rain intensity for different aerosol types and this can also be used to describe the time variation of mass/number concentration of pollutants in the atmosphere in other areas. Other authors such as Mircea et al. (2000), Dana (1971) and Dana (1972) obtained experimental data showing that below-cloud scavenging is much more efficient for the polydisperse aerosol than might be expected for particles with a specified mean size.

2. STUDY ZONE

The measurements were performed in León, Spain, a city in the northwest of the Iberian Peninsula (42º 36’ N, 05º 35’ W and 838 m above sea level) shown in Fig.1. Because of the lack of large emitting industries, the main source of particulate emissions is considered to be vehicular traffic. León has a population of about 135,000 inhabitants.

3. MATERIALS AND METHODS

Continuous particle number/size distributions were measured using a passive cavity aerosol spectrometer probe:

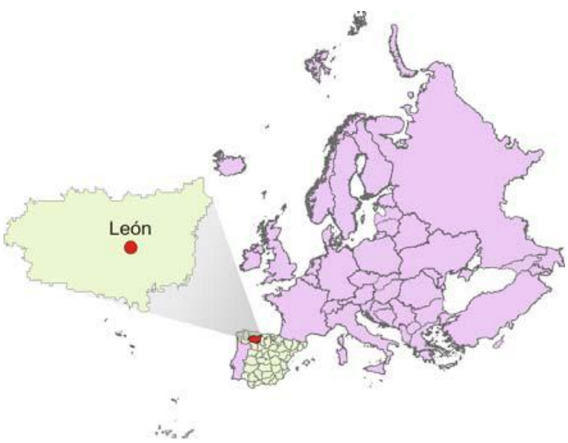

Fig. 1. Geographic location of the city of León, Spain.

PCASP-X. This instrument measures aerosol size distribution from diameters ranging between 0.1 and 10µm in 31 channels on the basis of the light-scattering properties of the particles at a wavelength of 633 nm between angles of 35º and 135º. The probe was calibrated by the manufacturer using polystyrene latex particles of a known size. The refractive index of latex beads (1.59 − 0i) is different from that of atmospheric particles, resulting in an aerosol size distribution that is “latex equivalent”. Here, we are presenting PCASP size distributions corrected for an average refractive index of 1.56-0.087i typical of urban aerosols (Lide, 1993). During each study day, two sets of measurements were taken every hour. Each set lasted 15 minutes and the data registered were saved every minute.

The precipitation was collected by a rain gauge in a Davis weather station. The data were registered every 15 minutes and the minimum volume was 0.25 liters per square meter. The weather station and the aerosol probe were installed in the same site to the southwest of the city of León, Spain.

Back trajectories for three different altitudes (500, 1,500 and 3,000 m) were calculated with the HYSPLIT model in order to interpret the different source regions of the air masses reaching the study zone. Back trajectories for the 5 previous days are considered up until the time the rain event began. This study will be complemented by a description of these air masses.

The surface-level synoptic maps that have been used were those published in the official bulletins issued by the Spanish National Institute for Meteorology.

In order to identify the type of weather associated to a particular synoptic situation a Circulation Weather Type classification (CWTs) was carried out based on Jenkinson and Collison (1977) and Jones *et al.* (1993). These procedures were developed to define objectively Lamb Weather Types (LWTs) (Lamb, 1972) for the British Isles. The daily circulation affecting the Iberian Peninsula is described using a set of Indices associated to the direction and vorticity of the geostrophic flow. The Indices used were the following: southerly flow (SF), westerly flow (WF), total flow (F), southerly shear vorticity (ZS), westerly shear vorticity (ZW) and total shear vorticity (Z). These Indices were computed using sea level pressure (SLP) values obtained for the 16 grid points, distributed around the Iberian Peninsula. This method allows for a maximum of 26 different CWTs. Like Trigo and Cámara (2000) in their study for Portugal, this study did not use an unclassified class, but rather opted for disseminating the fairly few cases (<2%) with possible unclassified situations among the retained classes.

The study period comprises the 59 days of the months of February and March 2005. For each day the aerosol size distributions are analyzed, as well as the Count Mean Diameter (CMD) and the Geometric Deviation.

In addition, the distributions corresponding to the five most intense precipitation events in these two months are studied in depth. In these five cases the Circulation Weather Type and the corresponding air masses are also described.

4. RESULTS AND DISCUSSION

4.1 Meteorological study

A total of 59 days were analyzed and the meteorological study of the two months is shown in Table 1. The average temperatures (3.8ºC in February and 8.1º C in March) were typical of winter months and the humidity was about 60%. The rainiest month was March with 31.9 mm of precipitation: it rained on 8 days. In contrast, in February rain was registered only on 3 days and the total precipitation registered was 15.9 mm.

Table 1. Meteorological study of the months of February and March with data on maximum, minimum and average temperatures, relative humidity, and total precipitation registered and wind intensity.

	February	March
Tmin(ºC)	-5.6	-8.5
Tmax(ºC)	17.9	21.9
Tav(ºC)	3.8	8.1
Relative Humidity (%)	60.2	56.1
Total Precipitation (mm)	15.9	31.9
Wind (m/s)	1.0	1.7

The 5 most intense rain events in those two months were studied (Table 2) by analyzing several meteorological parameters such as the duration of the event, the total precipitation registered and the rain intensity. The relative humidity is remarkably high on these days, between 80% and 90%, and the wind intensity can be classified according to the Beaufort scale as between calm and moderate breeze for the most intense event with 5.9 m/s. The precipitation registered varied between 2.5 mm and 14.7 mm.

The events studied on those days lasted between 2h 30m and 11h 30m. The maximum rain intensity was 2.4 mm/h and was registered on March 26.

4.2 Circulation Weather Type and Air masses

The Circulation Weather Type classification (CWTs) shows that during the months of February and March, (Figure 2), the CWTs were mainly of two types controlled by geostrophic vorticity: cyclonic (C) and anti-cyclonic (A), with 11 and 9 days, respectively. The next most frequent types were two purely directional types, southwesterly (SW) and westerly (W), followed by the NW, ASW and CSW types. In other words, westerly flows seem to have a strong influence on the Iberian Peninsula in the months of February and March.

Table 2. Meteorological values of the days where a rain event was analyzed: maximum, minimum and average temperature, relative humidity, wind intensity, and total precipitation of the day. For the rain events studied the following data are added: time interval (Δt), precipitation (P) and rain intensity (R).

DAY	T_{max} (ºC)	T_{min} (ºC)	$T_{av.}$ (ºC)	HR (%)	Wind (m/s)	P_{total} (mm)
06/02/2005	5.2	1.4	2.8	80.1	0.0	10.9
22/02/2005	3.9	1.6	2.4	84.0	5.9	2.5
20-21/3/2005	15.3	10.6	11.7	83.6	1.2	9.3
25/03/2005	12.3	8.0	9.3	82.6	3.9	3.8
26/03/2005	7.3	6.6	6.9	90.4	2.7	14.7

EVENT	Δt (UTC)	P (mm)	R (mm/h)
06/02/2005	1130-2300	10.6	0.9
22/02/2005	0645-0915	2.5	1.1
20-21/3/2005	1815-0530	7.5	0.7
25/03/2005	1100-1330	2.8	1.2
26/03/2005	0100-0600	12.2	2.4

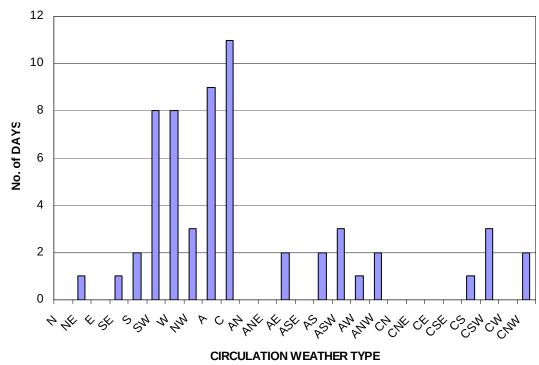

Fig. 2. Circulation Weather Type classification in the months of February and March (59 days) on the days with precipitation events and surface-level synoptic map

Back trajectories for three different altitudes (500, 1,500 and 3,000 m) were analyzed to determine the air masses present in the city of León during the days with rain events (Figure 3) . On February 6 and 22 the air masses have been identified as of the maritime Polar (mP) type with low temperatures and a high relative humidity. On March 21 and 25 the air masses were of the maritime Tropical (mT) type and on March 26 of the mP type, with a considerable drop in the temperatures and a remarkable increase in the relative humidity.

4.3 Aerosol size distributions

Fig. 4 shows a comparative study of the average distributions of the days with rain events with reference to the month in which they occurred. The situation varies from one day to another.

In each event the evolution of the number of aerosols has been analyzed, as well as the Count Mean Diameter and its Geometric Deviation. This was done to detect the variations occurring and their development before the actual precipitation was registered, during the precipitation, and after the event, in intervals of 15 minutes (Fig 5, 6 and 7).

Fig. 5 shows the number of particles and the precipitation registered in each 15-minute interval. For each of these intervals the rain intensity was calculated to assess how the two parameters vary simultaneously. In the days analyzed it was found that during the rain event, if the rain intensity is over 2 mm/h, a drop in the number of aerosols is immediately detected due to the washout effect. However, if the rain intensity is about 0.4 mm/h or lower, the result is an increase in the number of aerosols measured. It may be the case that during weak rain events the probe does not discriminate adequately between aerosols and very small droplets or the extremely small droplets that remain in suspension in the atmosphere.

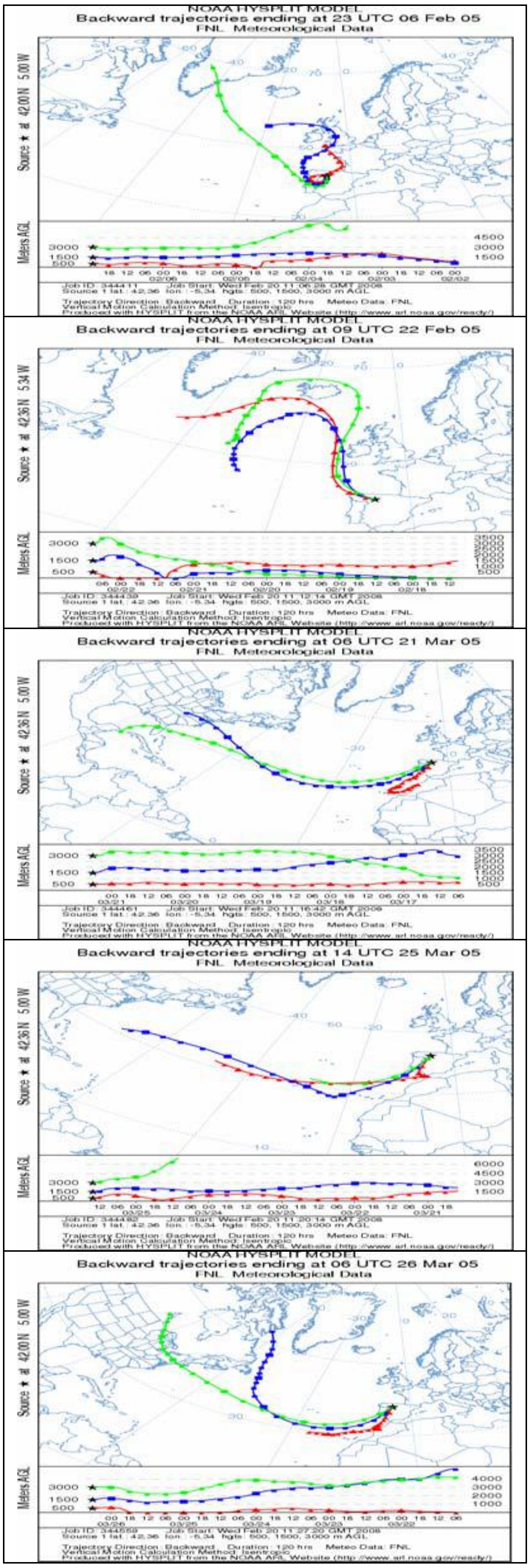

Fig. 3. Back trajectories for three different altitudes (500, 1,500 and 3,000 m) using the HYSPLIT model.

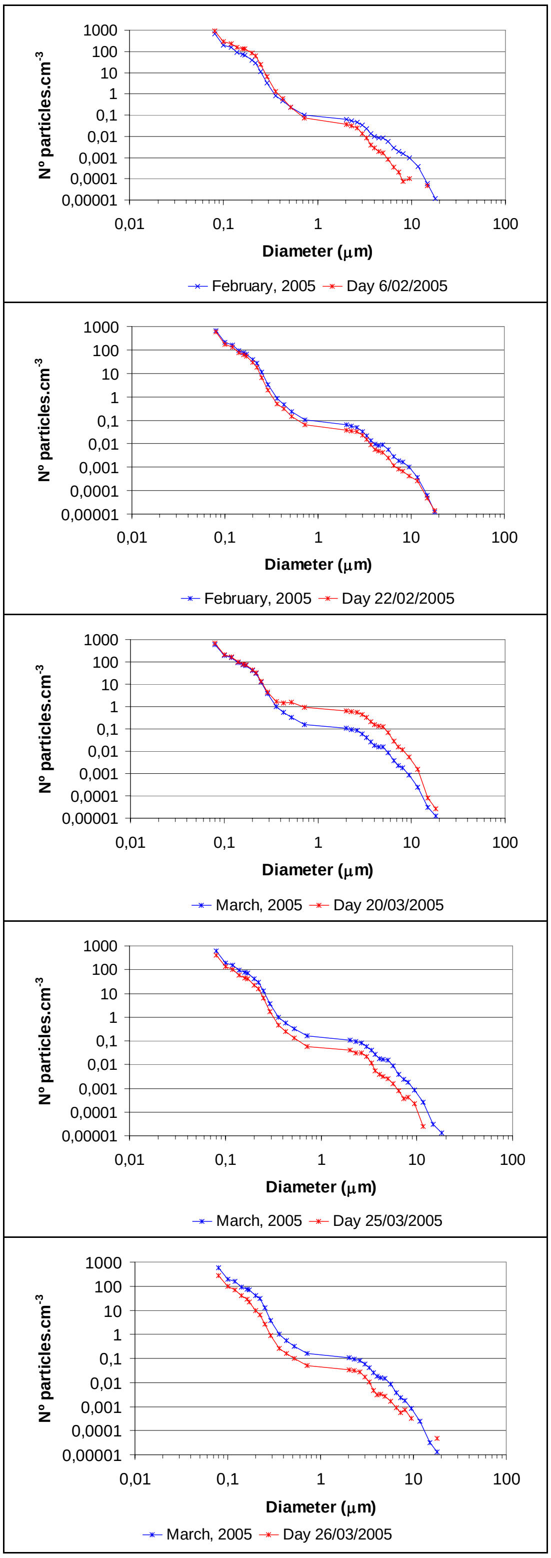

Fig. 4. Average aerosol size distributions in the day with the rain event and in the corresponding month.

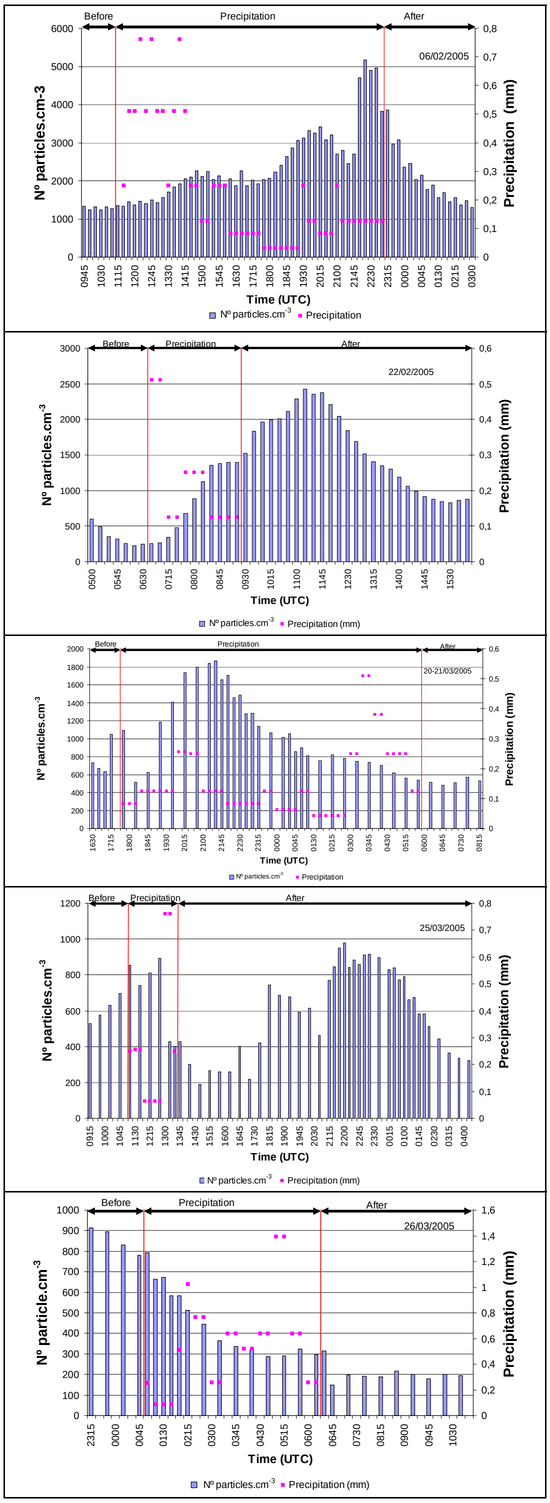

Fig. 5. Time variation of the number of aerosols and the precipitation in the 5 days with intense rain events. Three stages are distinguished: before, during and after the rain event.

Because of this fact, the measurements carried out by an aerosol probe like the one employed for this study must be treated separately in the case of rain days and in the case of days with no rain. At least during the rain event, and even for several hours after it, there may be difficulties in the measurements that might make them less reliable.

The reason is that when assessing the size distributions before and after the rain event, there are cases where the total number of particle increases and other cases where it decreases. Count Mean Diameter was between 0.37-0.38 μm before precipitation and its Geometric Deviation was between 1.14-1.18 μm. It was found that after the rain event, if the intensity of the precipitation has been very low, it took several hours for the number of particles to regain values similar to or lower than the initial number registered before the rain event. The removal of the smallest droplets left in suspension is not immediate, but takes some time. However, when the precipitation intensity was over 2 mm/h, after the rain event the number of particles was smaller than before the event in a much shorter span of time.

This is related to the washout effect. If there is an intense washout, the number of particles decreases significantly, large and small particles alike. However, the average size of the particles after the precipitation and their geometric deviation is quite similar. This means that a short time after the precipitation the air mass recovers the same type of lognormal distribution it had before the rain event.

If no washout takes place, it is observed that immediately after the rain event the number of particles is higher, sometimes even considerably so, than before the rain event. In the event on February 22, before the rain there were 355 particles/cm^3 and after there were 2,019 particles/cm^3, and on February 6 there was an increase from

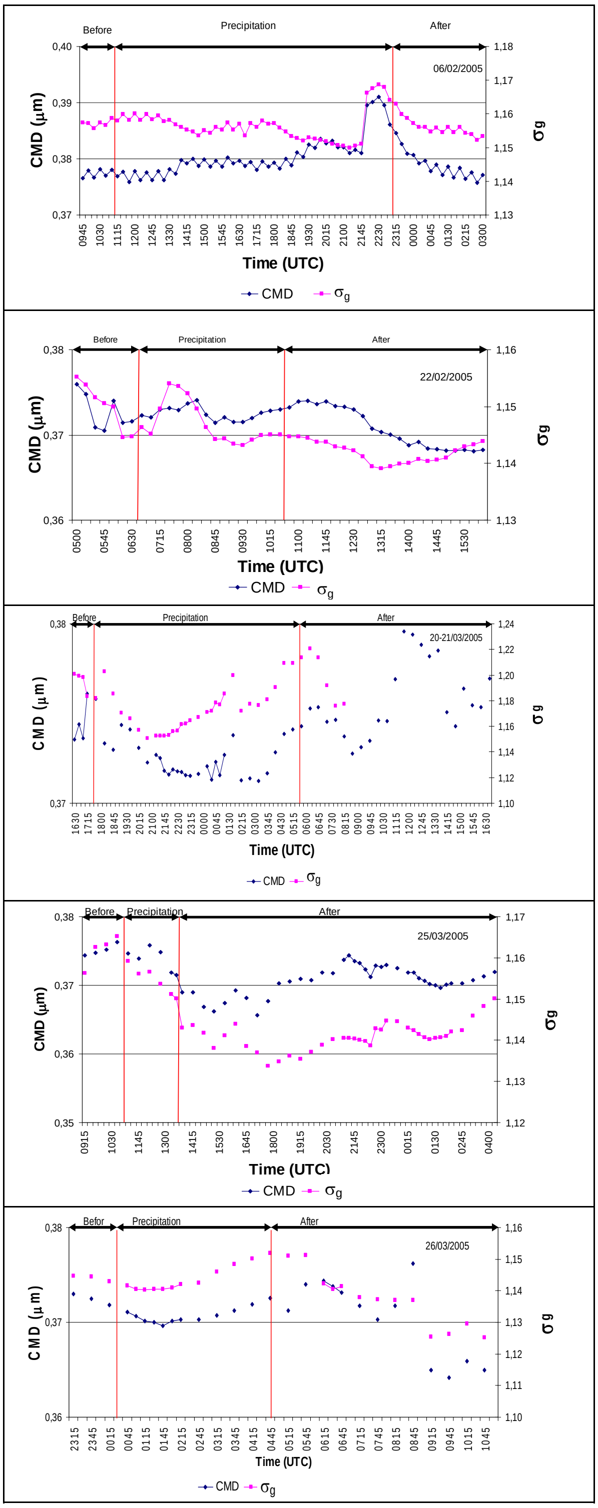

Fig. 6. Time variation of the Count Mean Diameter and its Geometric Deviation in the in the 5 days with intense rain events. Three stages are distinguished: before, during and after the rain event.

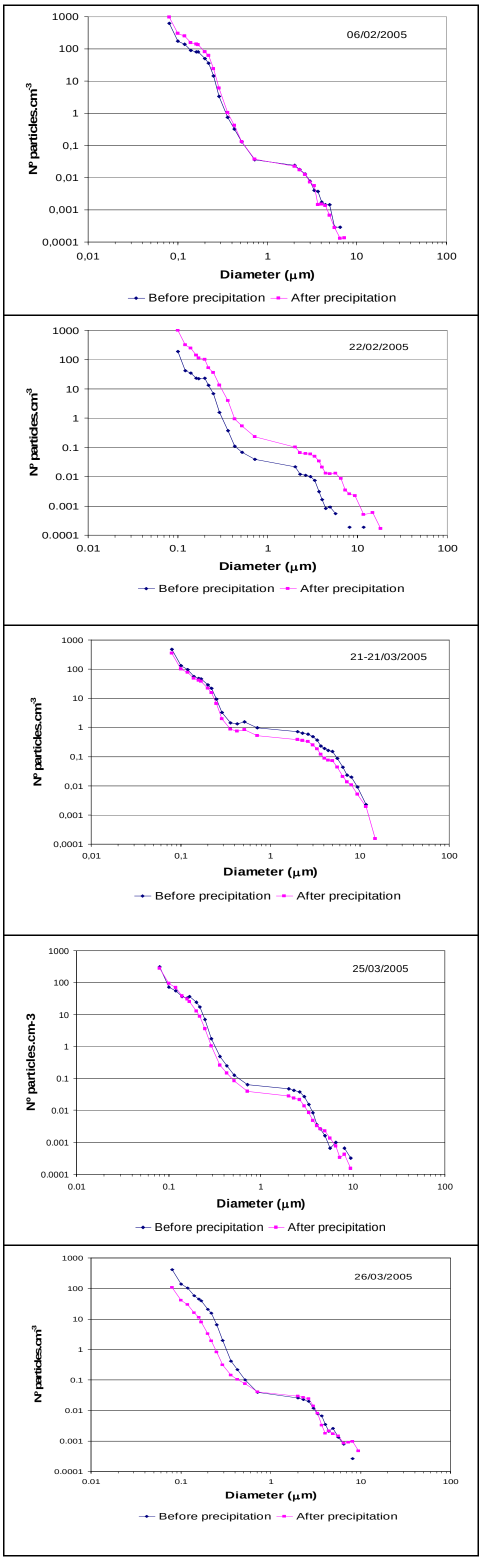

Fig. 7. Aerosol size distributions of each day with a rain event before and after the precipitation.

1,297 to 2,117 particles/cm^3, with average sizes and geometric deviations lower than the ones registered before the beginning of the rain event. In other words, the lognormal distributions varied greatly. Consequently, the number of small particles must not vary a lot, but the number of large particles must have decreased. In conclusion, the number of large particles decreases irrespective of the intensity of the precipitation, but the smaller particles are only washed out by the raindrops if the intensity of the precipitation is higher than 2 mm/h.

These preliminary results must still be confirmed in further studies.

5. CONCLUSIONS

When the precipitation intensity exceeds 2 mm/h the washout is obvious and quick, whereas in the case of weak precipitation of 0.4 mm/h or less, the number of particles increases. This may be due to the fact that the probe does not discriminate between aerosols and very small precipitating droplets or the smallest droplets that are left in suspension in the atmosphere.

The authors think that the measurements carried out using the aerosol probe employed in this study must be treated separately for the case of rain days and for the case of days with no rain. At least during the rain event, and even for several hours after it, there may be difficulties in the measurements that might make them less reliable.

When it rains the number of large particles decreases irrespective of the intensity of the precipitation, but the smaller particles are only washed out by the raindrops if the intensity of the precipitation exceeds 2 mm/h.

6. BIBLIOGRAPHY

Dana, M.T., 1971. Washout of soluble dye particles. In: Simpson et al. (Eds.), Pacific Northwest Laboratory Annual Report for

1970 to the USAEC Division of Biology and Medicine. Vol. II. Physical Science. Part I. Atmospheric Sciences, USAEC Report BNWL-1551, Battelle Pacific Northwest Laboratories, pp. 63–67.

Dana, M.T., 1972. Washout of Rhodamine dye particles. In: David, H.S. (Ed.), Meteorology and Atomic Energy – 1968. USAEC Report TID-24190, Environmental Science Services Administration, NTIS, pp. 36–44.

Dana, M.T. and Hales, J.M., 1976. Statistical aspects of the washout of polydisperse aerosols. *Atmospheric Environment* 10, pp. 45–50.

Huebert, L. Zhuang, S. Howell, K. Noone and B. Noone, 1996. Sulphate, nitrate, methanesulfonate, chloride, ammonium and sodium measurements from ship, island and aircraft during the Atlantic stratocumulus transition experiment/marine aerosol gas exchange, Journal of Geophysical Research, 101, pp. 4413-4423.

Ito, T. 1993. Size distribution of Antarctic submicron aerosols, Tellus 45, pp. 145-159.

Jenkinson AF, Collison FP. 1977. An initial Climatology of gales over the North sea. Synoptic Climatology Branch Memorándum, 62, Meteorological Office, London.

Jons P.D., Hulme M., Briffa K.R., 1993. A comparison of Lamb circulation types with an objective classification scheme. International Journal of Climatology., 13, 655-663.

Lamb HH. 1972. British Isles weather types and a register of daily sequence of circulation patterns, 1861-1971. Geophysical Memoir 116, HMSO, London.

Lide D.R., 1993. *Handbook of Chemistry and Physics*, CRC, Boca Raton, (74th Edn. ed.), pp. 6–193.

Mircea M., Stefan S.and Fuzzi S. 2000. Precipitation scavenging coefficient: influence of measured aerosol and raindrop size distributions Atmospheric Environment. Volume 34, Issues 29-30, , Pages 5169-5174.

Slinn, W.G.N., 1971. Numerical explorations of washout of aerosol particles. In: Simpson et al. (Eds.), Pacific Northwest Laboratory Annual Report for 1070 to the USAEC Division of Biology and Medicine, Vol. II. Physical Sciences, C.L. USAEC Report BNWL-1751 (Part. 1), Battelle Pacific Northwest Laboratory, pp. 75–81.

Suzuki, T. and S. Tsunogai,1988. Daily variation of aerosols of marine and continental origin in the surface air over a small island Okushin in Japan sea, Tellus 40, pp. 42-49.

Trigo R.M. and DaCamara C. C. 2000. Circulation Weather Types and their Influence on the Precipitación Regime IN Portugal. Int. J. Climatol. 20: 1559-1581.

Vakeva, M. , K. Hameri, T. Puhakka, E.D. Nilsson, H. Holiti and J.M. Makela, 2001, Effects of meteorological processes on aerosol particle size distribution in an urban background area, Journal of Geophysical Research 105 pp. 98079821.

Acknowledgements

The authors are grateful to Antonio Ortín and Toyi del Canto for their cooperation and to Dr. Noelia Ramón for translating the paper into English.

ROBUSTNESS ANALYSIS OF ATMOSPHERIC AEROSOL REMOVAL BY PRECIPITATION

C. Andronache[1] and V. T. J. Phillips[2]

[1]Boston College, Chestnut Hill, MA 02467, USA
[2]University of Hawaii, Honolulu, HI 96822, USA

1. INTRODUCTION

The wet removal by precipitation is the most efficient atmospheric aerosol sink and the detailed mechanism of this process involves microphysical interactions between aerosols and hydrometeors (Flossmann et al., 1985, 1987;Jennings, 1998; Pruppacher and Klett, 1998). Aerosol wet removal is represented in current numerical models by scavenging coefficients in aerosol mass continuity equations. These scavenging coefficients are often expressed as a function of bulk quantities such as the precipitation rate.

Aerosol particles can be removed from atmosphere by precipitation as a result of two main processes. The first process involves nucleation scavenging of the aerosol particles which serve as cloud condensation nuclei (CCN) or ice nuclei (IN) in the initial stage of cloud formation (Phillips et al., 2005; 2008). As a result of the nucleation scavenging, some aerosol particles become cloud droplets and can be removed from atmosphere after in-cloud collection by falling raindrops. This process is often called in-cloud scavenging and depends strongly on rainfall intensity. The second process is represented by the collection of aerosol particles present in the boundary layer (BL) by falling raindrops. This process depends on the net action of various forces influencing the relative motion of aerosol particles and hydro-meteors. It is strongly dependent on aerosol size, and rainfall intensity.

Corresponding author's address: Constantin Andronache, Boston College, 140 Common -wealth Ave., Chestnut Hill, Massachusetts, 02467, USA; E-Mail: andronac@bc.edu

2. SCAVENGING RATE

The scavenging rate of aerosols, or the scavenging coefficient, is evaluated based on the efficiency of collision between an aerosol particle and a falling raindrop (Slinn, 1983; Pruppacher and Klett, 1998; Seinfeld and Pandis, 1998). The rate of mass concentration change of all particles of diameter *d* is

$$\frac{dn_M(d)}{dt} = -l(d)n_M(d) \qquad (1)$$

where: $n_M(d)$ is the mass size distribution of aerosol, and the scavenging rate $l(d)$ has expression

$$l(d) = \int_0^\infty \frac{p}{4} D^2 U(D) E(d,D) N(D) dD \qquad (2)$$

where, *U(D)* is the raindrop terminal velocity, *N(D)* is the raindrop size distribution (DSD), and *E(d,D)* is the collection efficiency. The parameters involved in scavenging rate estimation change in time and space, and cause significant variability in l. We describe the main characteristics of *N(D), U(D),* and *E(d,D)* needed to estimate the scavenging rate and investigate how their uncertainty might impact the scavenging rates by liquid precipitation.

2.1 Raindrop size distribution

Typical raindrops are oblate spheroids, and in the description of DSD it is assumed that *D* is the equivalent diameter, or the diameter of a sphere with the volume equal with that of the deformed drop. The DSD is linked to the rainfall rate, *R* expressed in mm h^{-1}

$$R = 6p \times 10^{-4} \int_0^{\infty} N(D)U(D)D^3 dD \qquad (3)$$

where, *U(D)* is in ms^{-1} units. Marshall and Palmer (1948) introduced an exponential fit of measured DSD, representative for averaged widespread precipitation events. Generally, the Marshall - Palmer DSD overestimates the number of very small raindrops as well as the number of large raindrops. Other DSD have been proposed, and the three-parameter gamma distribution is the preferred function when fitting observations, especially since the rapid advances in rain measurements by radar (Ulbrich and Atlas, 1998). This DSD is represented as

$$N(D) = N_0 D^m \exp(-\Lambda D) \qquad (4)$$

where *N(D*) is in m^{-3} mm^{-1}, *D* is in mm, N_0 $m^{-3}mm^{(-1-\mu)}$, and L is in mm^{-1}. The three-parameter gamma distribution is general enough to describe fluctuations in the DSD observed on small space and timescale, and includes the exponential distribution as a special case. For rain DSD retrieval, the problem is how to determine the three parameters (N_0, m, L) from radar measurements. Zhang et al. (2001) showed that the three parameters can be determined from radar measurements of: reflectivity (Z_{HH}), differential reflectivity (Z_{DR}), and a constrained relation between shape (μ) and slope (L) derived from video disdrometer observations (Figure 1).

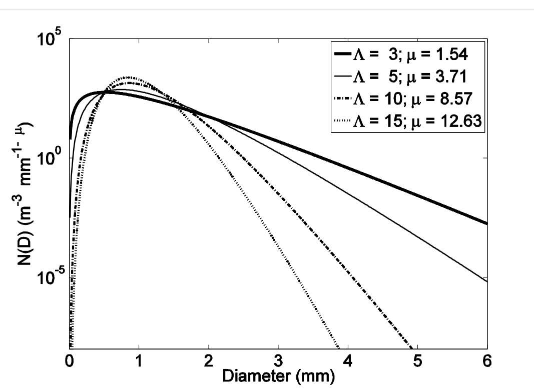

Figure 1. Example of variations in the raindrop size distribution.

We note that parameters of the gamma DSD have significant variability, and are not universal. Recent advances in radar technology and its wide use in precipitation measurements and air pollution studies, make the gamma type DSD an appropriate choice for aerosol scavenging studies. We found that: 1) DSD variability can significantly impact the calculated λ; 2) it is desirable to consider DSD from radar observations, and 3) if model evaluations of DSD are used, they should be represented as a function of precipitation type and intensity.

2.2 Raindrop terminal velocity

Experimental determination of the raindrop terminal velocity was reported by Gunn and Kinzer (1949), and their data was fitted with various functions and used in scavenging studies. Model computations of the terminal velocity are based on solving the problem of raindrop equilibrium in air at various Reynolds numbers. The raindrop falls under the forces of gravity (F_g) and drag (F_d). These forces change the shape of the raindrop, leading to shape distortion which in turn, changes the drag force. For small raindrops (*D* < 0.05 mm), the surface tension is strong enough to keep the drop shape close to spherical. The flow around the drop is considered to be laminar, and in this case, the Stokes law applies. For drops larger than about 0.1 mm, the flow around the raindrop becomes turbulent and Stokes law does not apply. The transition to a turbulent flow regime is characterized by the Reynolds number *Re(D)*. For large raindrops, the aerodynamic differences around the drop will distort the drop shape, such that the vertical dimension will decrease and the horizontal dimension will increase (producing an oblate spheroid).

We found several aspects of the raindrop fall velocity that can impact the scavenging rate: 1) raindrops do not fall in still air, and their trajectories are impacted by advection and turbulent flow; 2) for solid precipitation (snow and ice crystals), the fall velocity has large variability due to wide range of particle shapes and drag force; 3) the raindrop terminal velocity varies with altitude. U(D) can be expressed as a function of atmospheric density and temperature. Figure 2 illustrates the increase of the terminal velocity of raindrops with altitude, shown as atmospheric pressure level. For larger raindrops, the terminal velocity increases significantly with altitude, and this impacts the scavenging kernel in equation (2).

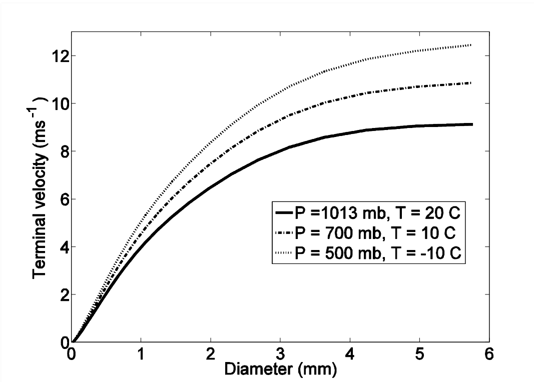

Figure 2. Variation of terminal velocity with raindrop diameter and altitude.

2.3 Collection efficiency

The general formulation of the collection efficiency allows its application both in-cloud and below-cloud scavenging processes, with special attention to the dominant factors. The collection efficiency is given by $E=E_b+E_{int}+E_{imp}$, where E_b is the Brownian diffusion contribution, E_{int} is the contribution of interception term, and E_{imp} is the contribution of inertial impaction (Slinn, 1977, 1983; also summarized by Seinfeld and Pandis, 1998). In addition to these terms, it has been shown that E is significantly enhanced for aerosol particles with diameters d in the range [0.1 - 2] μm by phoretic forces, and turbulence (Slinn and Hales, 1971; Grover et al., 1977; Wang et al., 1977; 1978; Tinsley et al., 2000; Andronache et al., 2006). The effects of phoretic and electric forces are not well known in part because of lack of measurements of electric charge, and the temperature difference between falling raindrop and ambient air.

We found that the main uncertainties in the collection efficiency are caused by: 1) phoretic effects; 2) electric charge; 3) deviation of the air flow around real raindrop, in turbulent flow, versus the simplified airflow around a perfect sphere. For nonspherical solid hydrometeors, the airflow around these particles has a complex nature and experimental data are expected to provide improvements in understanding collection of aerosols by snowflakes and ice crystals.

3. ESTIMATIONS AND OBSERVATIONS

3.1 Below-cloud scavenging

Studies have been performed to measure and estimate the below-cloud scavenging coefficient. This is mainly justified by the following: a) Interest in understanding how small aerosol particles emitted from Earth's surface or from the BL, are removed by precipitation (Andronache, 2003, 2004, 2006; Laakso et al., 2003; Sportisse, 2007); b) In laboratory studies it is possible to control the falling water drop diameter D, the aerosol particle size d, and the ambient conditions such as air temperature, pressure, and relative humidity; c) In many experiments, it was possible to control the aerosol properties (such as diameter and physical properties), during precipitation events; d) It is more affordable to study the below-cloud scavenging than to conduct experiments of in-cloud scavenging. Reported data show that l varies between 10^{-6} and 10^{-3} (s^{-1}) for variations of R in the range [0 – 50] mm h^{-1}. The variation of the below-cloud scavenging coefficient of particles of diameter d, given by our model captures the range of values reported, as is illustrated in Figure 3 as a function of particle size and rainfall rate, R.

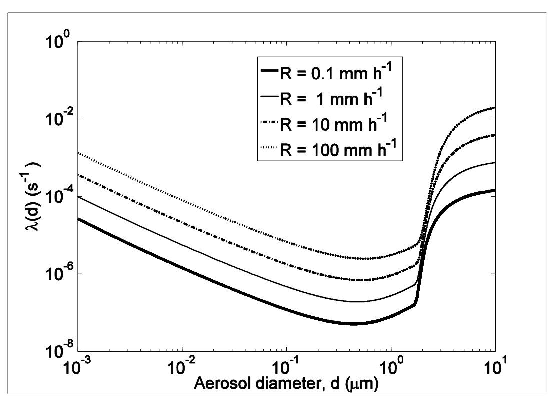

Figure 3. Variation of the scavenging rate with aerosol diameter and rainfall intensity.

For a given aerosol size, we note a variation of about 2 orders of magnitude as R varies between 0.1 and 100 mm h^{-1}, which is a range that covers most of the observed precipitation rates. Sensitivity calculations show that phoretic and electric effects can enhance the scavenging in the range of accumulation mode.

3.2 In-cloud scavenging

In-cloud scavenging is the main process of wet removal and is the result of nucleation scavenging of CCN, followed by rapid growth of cloud droplets and collection by falling raindrops. Contributions to in-cloud scavenging are made by collection of falling raindrops with cloud droplets (typical diameter of about 10 μm, and with interstitial aerosol (with typical d less than on micrometer). Cloud droplets collect also interstitial aerosols by coagulation. From all these processes, the collection of cloud droplets by falling raindrops is the dominant contributor to in-cloud scavenging rate, and the other processes are often neglected due to lack of information about interstitial aerosol and cloud micro-structure. In this sense, for the in-cloud scavenging, λ, the dependence on aerosol particle diameter is neglected. The efficiency of collision E_{IC} is in the range 0.5 - 0.8 for soluble aerosol scavenged by liquid drops. For snow, the collection efficiency, E_{IC} ~ 0.2 - 0.3 (Scott, 1982). Both experimental data and model data show that in-cloud scavenging rate (in s^{-1}) can be expressed as $l = aR^b$, where a is in the range [10^{-5} – 10^{-3}] and b is in the range [0.67 – 0.93], and R is in mm h^{-1}. Such variability was attributed to changes in aerosol solubility, precipitation type, vertical distribution of the precipitating system and raindrop size distribution. For air quality studies, it is useful to have a simple expression for the in-cloud scavenging, and have the rainfall intensity R prescribed from observations or from forecast with a weather model. The challenge remains to validate the models against detailed surface deposition data such as those available from the National Atmospheric Deposition Program/National Trends Network (NADP/NTN). Additional work is needed to characterize in-cloud scavenging dependence on aerosol chemical composition and precipitation type, variation with altitude and dependence on other microphysical parameters.

4. CONCLUSION

We investigated the main factors affecting the below-cloud and in-cloud scavenging coefficients of aerosols by rainfall, useful in air quality studies, and aerosol-cloud interaction models. Results show that below-cloud scavenging coefficient depends mainly on the aerosol size distribution parameters and on rainfall intensity. For a given aerosol size, the below-cloud scavenging coefficient varies about two orders of magnitude for a variation of rainfall rate between 0.01 and 100 mm h^{-1}. For a given rainfall rate, below-cloud scavenging coefficient varies significantly with aerosol diameter. In-cloud scavenging dominates the removal or aerosol particles and can be expressed as $l = aR^b$, where a, and b are parameters that show significant variability. Some of the outstanding issues which require further evaluation are: 1) determine the role of phoretic, electric forces and turbulence on the collection efficiency between raindrop and aerosols; 2) extend aerosol scavenging studies to snow and ice particles and provide robust parameterizations of these processes;3) evaluate scavenging schemes in comprehensive laboratory studies, for a wide range of conditions as encountered in real atmosphere;4) evaluate the scavenging schemes in field experiments; 5) evaluate wet scavenging schemes in air quality models using surface measurements as those available form acid deposition programs.

Acknowledgements

The authors acknowledge the use of data from the National Climatic Data Center (NCDC), from the Interagency Monitoring of Protected Visibility Environments IMPROVE and from the Atmospheric Integrated Research Monitoring Network (AIRMoN). The AIRMoN program is part of the NADP/NTN.

References

Andronache, C., Estimated variability of below-cloud aerosol removal by rainfall for observed aerosol size distributions, Atmos. Chem. Phys., 3, 131-143, 2003.

Andronache, C., Estimates of sulfate aerosol wet scavenging coefficient for locations in the Eastern United States, Atmos. Environ. 38, 795 - 804, 2004.

Andronache, C., T. Gronholm, L. Laakso, V. Phillips, and A. Venalainen, Scavenging of ultrafine particles by rainfall at a boreal site: observations and model estimations, Atmos. Chem. Phys., 6, 4739 - 4754, 2006.

Flossmann, A. I., W. D. Hall, and H. R. Pruppacher, A theoretical study of the wet removal of atmospheric pollutants. Part I: The redistribution of aerosol particles captured through nucleation and impaction scavenging by growing cloud drops, J. Atmos. Sci., Vol. 42, No. 4, 583 - 606, 1985.

Flossmann, A. I., H. R. Pruppacher, and J. H. Topalian, A theoretical study of the wet removal of atmospheric pollutants. Part II: The uptake and redistribution of (NH4)2SO4 particles and SO2 gas simultaneously scavenged by growing cloud drops, J. Atmos. Sci., Vol. 44, No. 20, 2912 - 2923, 1987.

Grover, S. N., Pruppacher, H. R., and Hamielec, A. E., A numerical determination of the efficiency with which spherical aerosol particles collide with spherical water drops due to inertial impaction and phoretic and electric forces, J. Atmos. Sci., 34, 1655 - 1663, 1977.

Gunn, R., and G. D. Kinzer, The terminal velocity of fall for water droplets in stagnant air. J. Meteor., 8, 249 - 253, 1949.

Jennings, S. G., Wet processes affecting atmospheric aerosols, in Atmospheric Particles, Edited by R. M. Harrison and R. Van Grieken, John Wiley and Sons Ltd., pp. 601, 1998.

Laakso, L., Gronholm, T., Rannik, U., Kosmale, M., Fiedler, V., Vehkamaki, H., and Kulmala, M., Ultrafine particle scavenging coefficients calculated from 6 years field measurements, Atmos. Environ., 37, 3605 - 3613, 2003.

Marshall, J. S. and Palmer, W. M., The distribution of raindrop with size, J. Meteorol., 5, 165 - 166, 1948.

Phillips, V.T.J., Sherwood, S., Andronache, C., Bansemer, A. Conant, W.C., DeMott, P.J., Flagan, R.C., Heymsfield, A., Jonsson, H., Poellot, M., Rissman, T.A., Seinfeld, J.H., Vanreken, T., Varutbangkul, V. and J.C. Wilson. Anvil glaciation in a deep cumulus updraft over Florida simulated with an Explicit Microphysics Model I: The impact of various nucleation processes. Quarterly Journal of the Royal Meteorological Society, 131(609), 2019 - 2046, 2005.

Phillips, V.T.J., P.J. DeMott, and C. Andronache, Empirical Parameterization of Heterogeneous Ice Nucleation for Multiple Chemical Species of Aerosol, J. Atmos. Sci., (in press), 2008.

Pruppacher, H. R. and Klett, J. D., Microphysics of clouds and precipitation, Kluwer Academic Publishers, Dordrecht, Boston, London, pp. 954, 1998.

Scott, B. C., Theoretical estimates of the scavenging coefficient for soluble aerosol particles as a function of precipitation type, rate, and altitude, Atmos. Environ., 16, 7, 1753 - 1762, 1982.

Seinfeld, J. H. and Pandis, S. N., Atmospheric Chemistry and Physics, Wiley, New York, 1326 pp., 1998.

Slinn, W. G. N. and Hales, J. M., A reevaluation of the role of thermophoresis as a mechanism of in- and below-cloud scavenging, J. Atmos. Sci., 28, 1465 - 1471, 1971.

Slinn, W. G. N., Some approximations for the wet and dry removal of particles and gases from the atmosphere, Water, Air, and Soil Pollut., 7, 513 - 543, 1977.

Slinn, W. G. N., Precipitation scavenging, in: Atmospheric Sciences and Power Production -- 1979, chap.11, Division of Biomedical Environmental Research, U.S. Department of Energy, Washington, D.C., 1983.

Sportisse, B., A review of parameterizations for modelling dry deposition and scavenging of radionuclides, Atmos. Environ., 41, 2683 - 2698, 2007.

Tinsley, B. A., Rohrbaugh, R. P., Hei, M., and Beard, K. V., Effects of image charges on scavenging of aerosol particles by cloud droplets and on droplet charging and possible ice nucleation processes, J. Atmos. Sci., 57, 2118 - 2134, 2000.

Ulbrich C. W., and D. Atlas, Rainfall microphysics and radar properties: analysis method for drop size spectra, J. Appl. Meteo., Vol. 37, 912 - 923, 1998.

Wang, P. K. and Pruppacher, H. R., An experimental determination of the efficiency with which aerosol particles are collected by water drops in subsaturated air, J. Atmos. Sci., 34, 1664 - 1669, 1977.

Wang, P. K., Grover, S. N., and Pruppacher, H. R., On the effect of electric charges on the scavenging of aerosol particles by clouds and small raindrops, J. Atmos. Sci., 35, 1735 - 1743, 1978.

Zhang, G., J. Vivekanandan, and E. Brandes, A method for estimating rain rate and drop size distribution from polarimetric radar measurements, IEEE Transactions in Geosciences and Remote Sensing, 39, 830 - 841, 2001.

WINTER PRECIPITATION CHEMISTRY IN THE BACKGROUND EMEP STATION IN VÍZNAR (GRANADA, SPAIN) (2002-2006)

A. I. Calvo[1*], F. J. Olmo[2,3], H. Lyamani[2,3], L. Alados-Arboledas[2,3], A. Castro[1], R. Fraile[1], M. Fernández-Raga[1]

[1]Department of Physics, University of León, 24071 León, Spain
[2]Group for Atmospheric Physics. CEAMA. University of Granada. Av. del Mediterráneo s/n. 18071 Granada, Spain
[3]Departament of Applied Physics. University of Granada. 18071 Granada, Spain.
*aicalg@unileon.es

1. INTRODUCTION

The removal of gases and aerosols from the atmosphere has an important role in inter-reservoir transfers. Airborne particulate matter released by natural and anthropogenic sources is transported and scavenged by wet removal or deposited by other mechanisms. The removal of airborne particulate matter through wet deposition, also called scavenging, is achieved through a series of steps that lead eventually to the incorporation of trace particulate into falling raindrops or cloud droplets.

The chemical composition of rain and cloud water is a particularly sensitive indicator of pollution emissions. Determining the chemical composition of rainwater provides an understanding of the source types that contribute to rainwater chemistry and enhances the understanding of the local and regional dispersion of pollutants and their potential impacts on ecosystems through deposition processes (Zunckel et al., 2003).

The aim of this study is to detect variations in the chemical composition of the rainwater samples collected during five winters (2001/02-2005/06) in a rural EMEP station near Granada. The levels of ions, their variability, and a description of the mean chemistry for the main transport routes reaching this EMEP station are provided.

2. STUDY ZONE

The measurements were carried out at the EMEP station (Cooperative Programme for the Monitoring and Evaluation of Long Range Transmission of Air Pollutants in Europe) of Víznar, in the province of Granada, Spain, (37º 14’ N, 03º 28’ W and 1,260 m above sea level) (Fig.1). Víznar is a rural area located 6 km NE of the city of Granada in one of the surrounding mountains. Because of this location, Víznar is influenced by various factors: North Africa (200 km to the south) is the main source of natural dust; Europe is the main source of anthropogenic pollutants; the Mediterranean Sea lies 50 km to the east; and/or smoke from forest fires may also reach this site. Moreover, the chemical composition of rainwater may vary due to the influence of local sources.

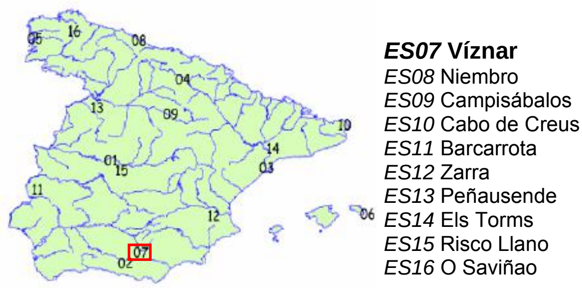

Fig.1 Spanish EMEP stations. Only stations in operation (ES07-ES16) are mentioned.

3. MATERIALS AND METHODS

The precipitation for the analysis was collected daily in Víznar during five winters (from 2001/02 to 2005/06). Since the station is an EMEP station (ES07), site selection criteria, sampling, analysis and data quality

control protocols are pre-established (EMEP, 2001).
Samples were collected daily at 7:00 UTC using an ERNY ARS721 sampler, and were then stored in the refrigerator until they were sent - once a week - to the laboratory at the Carlos III Health Institute (Madrid, Spain). In the samples Cl^-, NO_3^-, SO_4^{2-} concentrations were measured by means of ion chromatography. Ca^{2+}, Mg^{2+}, Na^+, K^+ concentrations were measured using an Atomic Absorption or Emission Spectrophotometer and NH_4^+ concentrations were measured by means of the Spectrophotometric Indophenol method.
Back trajectories (120 h, 00 and 12 UTC; FNL) for three different altitudes (500 m, 1,500 m and 3,000 m agl) were calculated with the HYSPLIT model in order to interpret the different source regions of the air masses reaching the study zone.
Data relationships and source types for precipitation constituents were explored by means of the Principal Components Factor Analysis (PCA).

4. RESULTS AND DISCUSSION

4.1 Chemical composition

A total of 108 samples were collected during the winters 2001/02 - 2005/06. All the events occurring between December 22 and March 30 have been included in this study (2001/02, n=21; 2002/03, n=32; 2003/04, n=20; 2004/05, n=11; 2005/06, n=24).
Winter rainfall ranged between 38.4 mm in 2004/05 and 226 mm in 2002/03, and an average of 145 mm has been calculated for the entire studied period. The most important rain events took place in March 2002 and January 2003 when about 110 mm month^{-1} were registered.
The following parameters were determined in the precipitation samples: pH, electrical conductivity and the concentrations of SO_4^{2-} (S), NO_3^-(N), NH_4^+ (N), Cl^-, Na^+, K^+, Ca^{+2}, Mg^{+2} and H^+. Statistical information, minimum and maximum concentration (μeq L^{-1}) of the measured anions and cations are summarized in Table 1.
The pH of rain is considered neutral at 5.6. Below this value precipitation is considered acid rain. This station did not have an acid rain problem: the rainwater collected had a typical pH in the 5.8–7.4 range (the average pH was 6.4±0.3). Extensive conductivity range values (between 5 μS cm^{-1} and 84.0 μS cm^{-1}) were registered. If mean concentration values of the complete study period are observed, wet-only precipitation chemistry is dominated by Ca^{2+}, SO_4^{-2} and Cl^-. These elements contributed over 20%, 18% and 17%, respectively, of the total ion concentrations analyzed. NO_3^-, NH_4^+ and Na^+ constitute about 12% of the total concentration each. The winter 2004/05 can be considered as a relatively dry winter when compared with the rest, with only 38.4 mm of precipitation. Particularly high Ca^{+2} concentrations were registered in this winter with a mean value of 110 $\pm$ 100 μeq L^{-1}. The maximum Ca^{+2} concentration of the study period was registered on 16 March 2005 with a value of 299.4 μeq L^{-1} during a Sahara episode. High concentrations of Ca^{2+} often found in the Mediterranean area are usually attributed to the intrusion of carbonate-rich air masses arriving from the Sahara (Alastuey et al., 1999). In addition to Ca^{+2}, the highest pH and conductivity, Mg^{+2}, K^+, NH_4^+, NO_3^- and SO_4^{2-} mean concentrations were also registered during this winter 2004/05.
The highest precipitation was registered in the winter 2002/03 with 225.6 μeq L^{-1} and the winter 2003/04 is characterized by its high Cl^- concentration.

4.2 Trajectory analysis

Many studies have pointed out the fundamental role of meteorological factors in determining the chemical features of precipitation. Using back-trajectory analysis with the aim of studying the influence of different air masses on the chemical winter precipitations in our study zone, the precipitation events were classified into six groups: (1) Mediterranean (2) Tropical Maritime (3) Polar Maritime (4) Local (5) Continental (6) Arctic. Three additional groups were defined to describe the influence of the frequent Sahara intrusions on the chemical composition of the precipitation in Víznar and in particular to reveal the influence of Sahara air masses at high levels on this chemical composition: (7) Sahara 500 m (8) Sahara 1,500 m and (9) Sahara 3,000 m. To carry out this classification, the Sahara 500 m air masses input days were selected. With the rest of the events, and without taking into account the 500 m classification, the Sahara 1,500 m air masses input days were selected. The same process was carried out with the 3,000 m classification. The rest of the events were classified in the other groups on the basis of 500 m back-trajectories. The geometric mean has been calculated (as a better descriptor of the central tendency in log-normal distributions, as is the case here) for each meteorological group (Fig. 2 and 3).

Sahara rain event chemistry is characterized by high pH and Ca^{2+} concentration levels (Ávila and Alarcón, 1999). They present high cation and marine ion concentrations. The high cation load and alkalinity of Sahara events have been attributed to the calcareous dust dissolution in the precipitation originated in the North of Africa. According to Ávila and Alarcón (1999), the high SO_4^{2-}, Na^+, and Cl^- concentrations are probably due to gypsum ($CaSO_4$) and halite (NaCl) dissolution in Sahara dust. Sahara rain events at different heights (500, 1,500 and 3,000 m) present a high mean conductivity (15.9, 15.7 and 14.6 μS cm^{-1}, respectively) and the highest Ca^{+2} and Mg^{+2} concentrations of the nine groups studied (Fig. 2 and 3). Sahara 500 m (n=22) and Sahara 1,500 m (n=15) rain events show similar mean concentrations for the different elements (except for Cl^-).

Sahara 500 m registers the highest Ca^{+2} (43.9 μeq L^{-1}) concentrations and the highest conductivity means. During Sahara 1,500 m (n=15) rain events, the highest pH (6.6), Mg^{2+} (15.2 μeq L^{-1}) and K^+ (4.1 μeq L^{-1}) mean concentrations were registered.

Table 1. Minimum, maximum and mean concentrations for ions, conductivity and pH in rain water samples collected at Víznar during the winter study campaign (December 2001-Mars 2006) with the standard deviation. Number of events (N) and precipitation (P) in mm have been included. Concentrations are reported in μeq L^{-1} units except pH and Conductivity (μS cm^{-1})

Winter	N	P		Conduc.	pH	H^+	Cl^-	NO_3^-	SO_4^{2-}	Na^+	NH_4^+	K^+	Mg^{2+}	Ca^{2+}
2001/02	21	192.0	min	5.1	6.1	0.2	16.1	10.7	17.5	4.8	5.7	1.5	5.8	18.5
			max	45.4	7.0	0.6	39.8	128.5	116.0	30.0	73.5	7.4	57.6	168.7
			mean	15.4	6.6	0.3	26.0	30.4	39.5	17.8	18.3	3.5	16.5	51.3
			σ	9.2	0.2	0.1	7.1	26.5	23.7	7.0	18.5	1.4	12.3	34.2
2002/03	32	225.6	min	5.2	5.9	0.1	13.3	10.0	19.3	4.3	5.7	1.5	4.1	7.5
			max	39.3	7.0	1.2	135.4	57.8	69.2	87.0	64.2	5.1	23.0	90.8
			mean	16.2	6.2	0.7	40.8	20.3	35.9	30.0	18.1	3.2	12.4	28.4
			σ	8.9	0.2	0.3	31.7	10.2	12.7	21.5	14.1	1.0	6.3	21.4
2003/04	20	112.6	min	5.2	5.9	0.2	15.5	6.4	11.9	10.0	5.7	2.8	6.6	24.0
			max	50.1	6.7	1.2	209.0	102.1	111.7	40.4	74.2	8.7	38.7	116.3
			mean	19.6	6.4	0.5	58.6	33.3	50.5	26.5	28.7	5.6	17.8	46.1
			σ	11.2	0.2	0.2	59.3	22.0	26.6	8.9	16.1	1.6	9.4	23.3
2004/05	11	38.4	min	11.0	6.4	0.1	5.1	9.3	15.6	10.4	8.6	3.6	10.7	33.4
			max	84.1	7.0	0.4	28.8	82.1	117.3	47.0	82.8	9.0	65.8	299.4
			mean	32.1	6.7	0.2	15.3	37.2	49.7	27.8	45.7	5.8	31.2	111.3
			σ	22.6	0.2	0.1	8.2	24.4	34.8	14.2	52.5	2.1	21.5	99.4
2005/06	24	155.6	min	5.0	5.8	0.2	10.2	5.7	8.1	5.2	5.0	1.5	5.8	14.0
			max	33.9	6.7	1.5	65.4	57.1	85.5	63.9	77.1	7.2	19.8	49.4
			mean	13.6	6.5	0.4	22.9	16.2	23.8	22.0	29.3	3.2	10.1	25.2
			σ	7.3	0.2	0.3	14.5	11.3	17.6	15.7	17.8	1.6	4.0	9.8
2001/06	109	144.8	mean	17.8	6.4	0.5	35.3	25.2	37.7	24.6	24.1	3.9	15.1	42.1
			σ	12.2	0.3	0.3	33.9	19.4	22.7	15.5	18.4	1.8	11.1	41.4

Sahara 3,000 m (n=3) rain events present different characteristics. The highest load of pollutant species (SO_4^{2-}, NO_3^- and NH_4^+) was registered in this group. The pH mean value is the lowest observed in the nine groups studied with a value of 6.1. Although the minimum pH value in this group was 6.0, this is not a low value for Sahara events, as minimum 4.2 pH values have been registered for this type of events by Ávila and Alarcón (1999). In order to explain this fact we have to consider that, on the one hand, anthropogenic species (NO_3^- and nss-SO_4^{2-}) are usually transported with mineral dust (Savoie et al., 1992, Prospero et al, 1995). Concentrations of Particulate Matter (PM) of non-sea-salt sulphate between 2 and 6 $\mu g\ m^{-3}$ have been registered in the Canary Islands during Sahara events (Prospero et al., 1995). On the other hand, it is necessary to consider that we have a Sahara air mass at high levels, but the characteristics of air masses at low levels (500 m and 1,500 m) influence rain chemistry too. The events included in the Sahara 3,000 m group have mainly a continental and tropical maritime origin at low levels (500 m and 1,500 m). If Sahara 3,000 m events are compared with the continental or tropical maritime group, no real similarities are founded. Ca^{+2} concentrations at 3,000 m are similar to the mean Sahara 500 m and 1,500 m concentrations for this element. It is remarkable that the third highest Ca^{+2} concentration of the study period was registered in one of the three events included in this class (168.7 $\mu eq\ L^{-1}$), only preceded by two Sahara 500 m events. Thus, the Sahara 3,000 m group seems to have an important influence on chemical rain composition.

Tropical and Polar Maritime groups present similar mean values (except for NH_4^+ and Ca^{+2}). These marine groups present high concentrations for ions of marine origin (Na^+ and Cl^-).

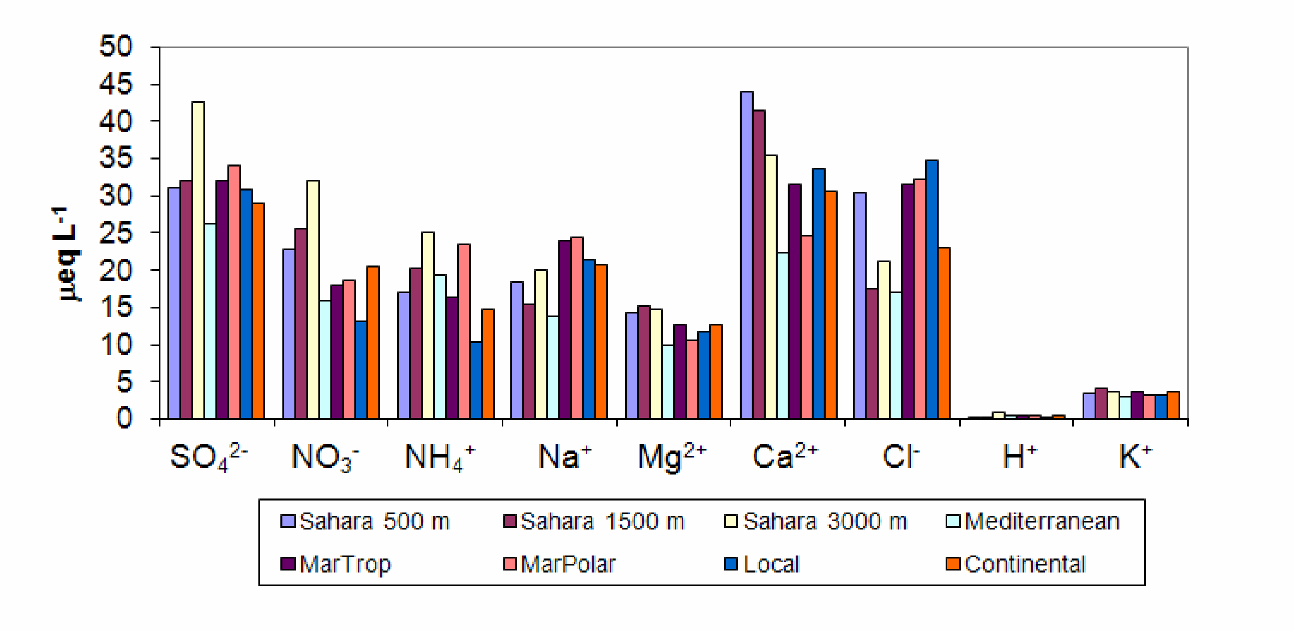

Fig. 2. Geometric ion concentrations for the different air masses.

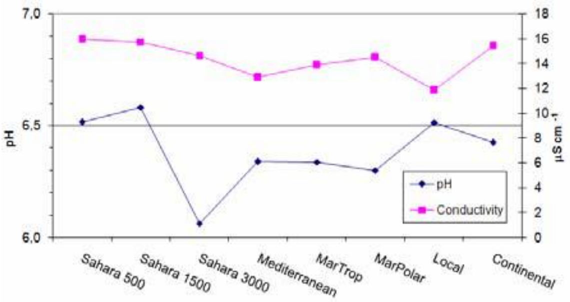

Fig. 3. Conductivity (μS cm^{-1}) and pH geometric mean for air masses.

Mediterranean rain events (n=4) can be considered as one of the lowest pollution rains. They have the lower mean concentration of SO_4^{2-}, Mg^{+2}, Na^+ Ca^{+2}, Cl^- and K^+ of the nine groups studied.

As for continental rains (n=17), they present intermediate characteristics when compared with the rest of air masses. There are studies that have demonstrated the influence of European pollutants in the precipitation chemistry in north-eastern Spain (Carratalá and Bellot, 1998; Ávila and Alarcón, 1999). In these studies, very high SO_4^{2-}, NO_3^- and NH_4^+ concentrations have been registered. In our study the concentrations of these elements are moderate. The Sahara groups (at the three levels) show higher concentrations of these three elements than the continental group. Escudero et al. (2007) study the origin of the exceedances of European daily PM limit in regional background areas of Spain (Víznar is included). These authors question the fact that these exceedances are caused by European transport only, and argue that the common scenario giving rise to European PM transport also favors the formation of typical local and regional winter pollution episodes at urban and industrial sites due to the anticyclone over the Bay of Biscay. It is therefore difficult to say whether the proportion of high PM levels measured under this scenario should be attributed to long-range transport from Europe or to local/regional emissions (Viana et al., 2003). On the other hand, these high PM level episodes only refer to regional background sites, which should not be strongly influenced by anthropogenic sources. PM exceedances associated with European episodes were only registered in the northern Iberian flank. The pollutants in the European air masses suffer less dilution/dispersion reaching the northern Iberian Peninsula than the center or the south owing to the shorter transect from central Europe (Escudero et al., 2007). This fact could support the influence of Sahara air masses on SO_4^{2-}, NO_3^- and NH_4^+ concentrations.

Local rain events (n=3) register the lowest NO_3^-, NH_4^+, H^+ concentrations and conductivity. They present a pH of 6.5. Nevertheless, they register the highest Cl^- mean concentration (with a concentration similar to Polar and Tropical Maritime groups).

Only one arctic event was registered, so no sufficient data are available to draw any conclusion.

4.3 Statistical approach

Multivariate techniques have generally been employed to determine the sources of data variability. These techniques are particularly useful for the identification of pollution sources in studies of air quality and will be applied here for a comparison with the meteorological classification. The principal component analysis extracted three factors explaining 80.0 % of the total variance (Table 3). Component one, with the highest variance of 48.0%, was positively correlated to most ions SO_4^{2-}, NO_3^-, NH_4^+, K^+, Mg^{+2}, Ca^{+2}) and conductivity. This ion grouping may be interpreted as a size factor. For the second component, which explains 18.1 % of the total variance of the investigated data set, high loadings negatively correlated –as expected- for pH and H^+ were obtained. The third component represents 13.9% of the total variance and has high loadings of Cl^- and Na^+, therefore representing the marine contribution. Similar results in the interpretation of the principal components have been reported for the precipitation chemistry in the Iberian

Table 3. Principal component analysis of elemental composition pattern in wet-only winter precipitation in Víznar.

	Components		
	1	2	3
Conductivity	0,97	0,09	0,04
NO_3^-	0,91	0,18	-0,11
SO_4^{2-}	0,91	0,19	-0,04
Mg^{2+}	0,90	0,02	-0,05
Ca^{2+}	0,86	-0,16	-0,12
K^+	0,72	0,05	0,26
NH_4^+	0,71	0,01	-0,18
pH	0,22	-0,97	0,03
H^+	-0,17	0,96	-0,11
Cl^-	0,02	-0,03	0,87
Na^+	0,18	0,19	0,79

Peninsula (Escarré et al., 1998; Ávila and Alarcon, 1999).

5. CONCLUSIONS

- The winters 2001/2006 present different characteristics as regards wet-only precipitation chemistry and height precipitation according to the data registered at the Viznar EMEP station.
- In the total study, wet-only precipitation chemistry was dominated by Ca^{2+}, SO_4^{-2} and Cl^-.
- Rain events were classified into nine groups on the basis of back-trajectories. They present different characteristics.
- The Sahara 1,500 m and 3,000 m classes seem to have an important influence in chemical rain composition.
- ACP extracted three components that explained 80.0 % of the total variance, interpreted as size, acidity and marine factors.

6. BIBLIOGRAPHY

Alastuey, A., Querol, X., Chaves, A., Ruiz, C.R., Carratalá, A., and López-Soler, A. 1999. Bulk deposition in a rural area located around a large coal-fired power station, northeast Spain. Environmental. Pollution. 106, 359-367.

Avila, A., Alarcón M. 1999. Relationship between precipitation chemistry and meteorological situations at a rural site in northeastern Spain. Atmospheric Environment 33, 1663-1677.

Carratalá, A., Bellot, J., 1998. Neutralization of nitrate and sulphate in precipitation on the eastern Mediterranean coast of Spain. Implications for acidification risk. Water, Air and Soil Pollution 104, 237–257.

EMEP, 2001. EMEP Manual for sampling and chemical analysis. EMEP/CCC-Report 1/95, Revision 1/2001, NILU, Norge.

Escarré, A., Carratalá, A., Avila, A., Bellot, J., Piñol, J., Millán, M. 1998. Precipitation chemistry anda ir pollution. In: Rodà, F., Retana, J., Gracia, C., Bellot, J. (Eds.), Ecology of Mediterranean Evergreen Oak Forest. Berlin. Ed. Springer-Verlag, Series Ecological Studies, pp. 195-206.

Escudero, M., Querol, X., Ávila, A., Cuevas, E. 2007. Origin of the exceedances of the European daily PM limit value in regional background areas of Spain. Atmospheric Environment, 41, 4, 730-744.

Prospero, J.M., Schmitt, R., Cuevas, E., Savoie, D.L., Graustein, W.C., Turekian, K.K., Volz-Thomas, A., Díaz, A., Oltmans, S.J., Levy II, H., 1995. Temporal variability of summer-time ozone and aerosols in the free troposphere over the eastern North Atlantic. Geophysical Research Letters 22, pp. 2925–2928.

Savoie, D.L., Prospero, J.M., Oltmans, S.J., Graustein, W.C., Turekian, K.K., Merril, J.T. and Levy II, H., 1992. Sources of nitrate and ozone in the marine boundary layer of the Tropical North Atlantic. Journal of Geophysical Research 97 11, pp. 575–589.

Viana, M., Querol, X., Alastuey, A., Gangoiti, G., Menendez, M., 2003. PM levels in the Basque Country (Northern Spain): analysis of a 5 yr data record and interpretation of seasonal variations.

Atmospheric Environment 37 (21), 2879–2891.
Zunckel, M., Saizar, C. and Zarauz, J., 2003. Rainwater composition in northeast Uruguay, Atmospheric Environment, 37, 1601–1611.

Acknowledgements

The authors would like to thank Alberto Gonzalez Ortíz (MMA) and Jaume Almera Institut (CSIC) for the information provided about Viznar station. Borja Ruíz Reverter is gratefully acknowledged for the back-trajectories classification. This work was supported by the Spanish Ministry of Education CGL2004-05984-C07-03 and by Andalusian Regional Government P06-RNM-01503
.

INFLUENCE OF CLOUD CONDENSATION NUCLEI AND GIANT CONDENSATION NUCLEI ON THE DEVELOPMENT OF PRECIPITATING TRADE WIND CUMULI IN A LARGE EDDY SIMULATION

William Y.Y. Cheng[1], Gustavo G. Carrió, and William R. Cotton

Department of Atmospheric Science, Colorado State University, Fort Collins, CO 80523

1. INTRODUCTION

Trade wind cumulus clouds have been receiving more attention lately due to their important impact in the Earth's climate. These clouds are ubiquitous over the subtropical oceans, forming under the trade wind inversion that corresponds to the descending branch of the Hadley circulation. Convection associated with these clouds enhances air-sea surface exchange of momentum, moisture, and heat. In addition, their extensive coverage impact climate's radiational budget.

Recently, the impact of aerosols on cloud systems and their effects on climate is one of the most important questions researchers are trying to address. Besides scattering and absorbing incoming shortwave radiation and absorbing outgoing longwave radiation (the aerosol direct effect), aerosols act as cloud condensation nuclei (CCN), causing changes in the cloud droplet concentration (Twomey's first indirect effect, Twomey 1974) and are hypothesized to cause clouds to persist longer (Albrecht's second indirect effect, Albrecht 1989). While there have been many studies focusing on the effects of cloud condensation nuclei (CCN) on cloud systems, there are fewer studies focusing on the effects of the more rare giant CCN (GCCN) on cloud systems. GCCN can come from a variety of sources including sea salt from air-sea exchange and dust, as well as from anthropogenic activities.

Corresponding author address: William Y.Y. Cheng, Department of Atmospheric Science, Colorado State University, Fort Collins, CO 80512. Email: cheng@atmos.colostate.edu

2. METHODLOGY

To investigate the effects of both CCN and GCCN, the Regional Atmospheric Modeling System (RAMS) was used to investigate the effects of various CCN and GCCN concentrations on the development of precipitating trade wind cumuli in a large eddy simulation (LES) framework.

The LES domain contained 101 X 101 X 101 grid points in the x, y, and z direction, respectively with $\Delta x = \Delta y = 100$ m and $\Delta z = 40$ m. The LES model used the two-moment microphysics with new features with explicit nucleation of small cloud droplets (cloud1 mode with diameter of 2-65 μm) and larger cloud droplets (cloud2 mode with diameter of 65-120 μm) via activation of cloud condensation nuclei (CCN) and giant CCN (GCCN), respectively (Saleeby and Cotton 2004). Compared to cloud1 mode only simulations, the use of the additional cloud2 mode slows down the collision-coalescence process by requiring cloud1 to be converted to cloud2 before conversion to rain or drizzle. Note that the range of diameters of cloud1 and cloud2 has been modified in this version of the microphysics by Steven Saleeby to improve the performance of the scheme.

The sounding to initialize the LES was taken from the Rain in Cumulus over the Ocean Experiment (RICO) archive for 11 January 2005. Several sensitivity experiments were performed in which two levels of CCN (GCCN) concentrations were used: 100 (0.01) and 1000 (0.1) cm^{-3} corresponding to low and high values. The numerical experiments began at 0000 UTC 11 January 2005 and were run for 24 h. The model results will be used to evaluate how various combinations of high/low CCN and GCCN concentrations affected the physics, dynamics, precipitation and radiational properties of the trade wind cumuli in the LES.

The model u, v, θ_{il}, q_t fields were nudged from soundings obtained from the RICO archive as in the formulation of Cheng et al. (2001). Note that θ and q_v from the RICO sounding archive were used to nudge θ_{il} and q_t, respectively, as a reasonable approximation. The nudging time scale was 3600 s. The vertical profiles in this study were obtained by averaging temporally and horizontally.

3. RESULTS

3.1. Precipitation

For both low CCN concentration (hereafter referred to as [CCN]) and GCCN concentration (hereafter referred to as [GCCN]) as in exp. C100G0.01, the relatively high precipitation rate occurred throughout the integration period with values exceeding 0.1 mm h^{-1} (Fig. 1). With the introduction of higher [GCCN] in C100G0.1, the precipitation rate was generally small until after hour 6. After hour 6, the precipitation rate had peaks that exceeded 0.05 mm h^{-1} in C100G0.1 and even exceeded the precipitation rate of C100G0.01 at the end of the integration period at 0.15 mm h^{-1}. The initial low precipitation rate in C100G0.1 may be attributed to the slightly lower cloud droplet concentration (Table 1).

With high [CCN] but low [GCCN] as in C1000G0.01, the precipitation rate was lower than that of C100G0.01 and its value rarely exceeded 0.05 mm h^{-1} (Fig. 1). This is due to the fact the there are many more small cloud droplets, making them inefficient in forming rain drops from collision coalescence processes. This is the result that most researchers found when they increased the [CCN] without representation of GCCN in most LES of cloud systems.

However, the largest sensitivity in the precipitation rate and accumulated precipitation occurred when both [CCN] and [GCCN] were increased as in C1000G0.1. With the high [CCN] already present, the conversion from cloud1 to cloud2 to drizzle occurred rapidly. In fact, in C1000G0.1, the precipitation rate reached its maximum in the first 6 hours (more than 0.3 mm h^{-1}, Fig. 1). This maximum exceeded all of the other maxima and occurred earlier than the other experiments. Although the accumulated precipitation in C1000G0.1 did not reach as high as C100G0.01 or C100G0.1 due to the high [CCN], its final accumulated precipitation (0.16 mm) was more than twice that of C1000G0.01 (0.07 mm) due to the high [GCCN] (Table 1).

The 24-h accumulated precipitation for the various experiments were as follows: 0.28 mm (C100G0.01), 0.31 mm (C100G0.1), 0.07 mm (C1000G0.01), and 0.16 mm (C1000G0.1). This shows that in general, increasing the [GCCN] will increase the accumulated precipitation. However, the timing of the high precipitation rates differed depending on the [CCN]. Having a small (large) [CCN], the high precipitation rate occurred (early) later in the cloud development when the [GCCN] was increased.

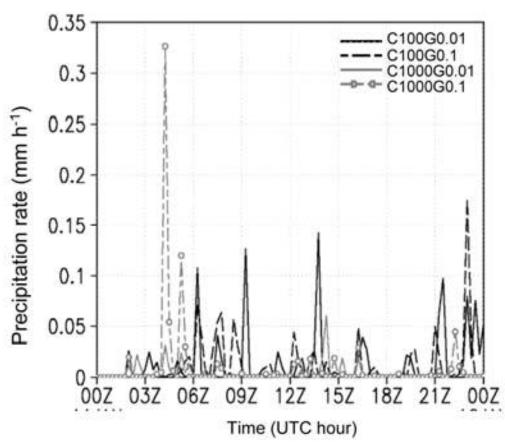

Figure 1 Time series of domain averaged precipitation rate (mm h-1) from 0000 UTC 11 Jan to 0000 UTC 12 Jan 2005.

3.2. Cloud properties

Figure 2 shows the vertical profile of liquid water mixing ratio (q_l) (cloud1, cloud2, and drizzle mixing ratios). Liquid water mixing ratio is the sum of cloud1, cloud2, and drizzle mixing ratios. Qualitatively, the vertical profiles from the different experiments were similar. In particular, q_l was maximized between 900 m and 1600 m AGL for all of the experiments, with values ~0.01 g kg^{-1}. However, there were quantitative differences amongst the vertical profiles. Increasing the [CCN] led to a decrease in q_l below 1900 m AGL. Also, increasing [GCCN] led to an increase in q_l. Increasing both [CCN] and [GCCN] resulted in the highest q_l below 1800 AGL. The results can be explained by cloud-top entrainment instability (CTEI).

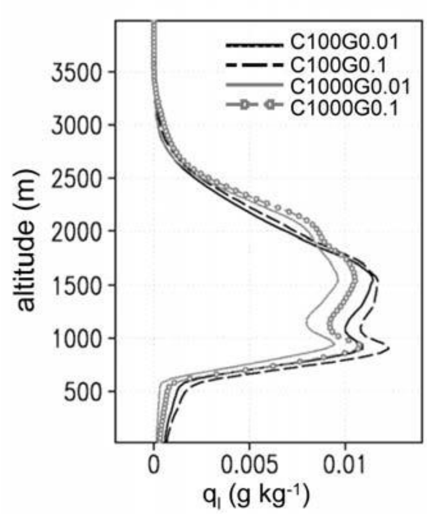

Figure 2 Horizontally and time averaged liquid water mixing ratio (g kg^{-1}) from 0000 UTC 11 Jan to 0000 UTC 12 Jan 2005.

For higher [CCN] experiments, we would expect CTEI to be more active (Xue et al. 2008). Essentially, smaller droplets would evaporate faster when the cloud entrains drier environmental air at the cloud top, generating negative buoyancy (Xue et al. 2008). Hence, the overall q_l was lower in the higher [CCN] experiments below 1900 m AGL (Fig. 2). The slightly higher q_l above 1900 m AGL for higher [CCN] experiments can be explained by the fact that some small evaporated droplets lingered at these levels.

Higher [GCCN] had the effect of increasing q_l at all levels (Fig. 2). This was due to the fact that the presence of [GCCN] allowed cloud water to form more rapidly.

Figure 3 shows the vertical profile cloud fraction for the various experiments. Cloud fraction for each level was defined as the number of cloudy grid cells at each level versus the total number of grid points at that level. Cloudy grid cells were defined as any grid cells with cloud mixing ratio ≥ 0.01 g kg^{-1}. It is clear that qualitatively the shape of the profile is the same for all of the experiments. The cloud fraction is maximized just below 1000 m AGL. Below 1000 m AGL, increasing [CCN] increased the cloud fraction. This is likely due to the fact that smaller droplets in the larger [CCN] experiments resulted in precipitation being more difficult to form in accordance to Albrecht's hypothesis. However, above 1000 m AGL, the cloud fraction for the higher [CCN] experiments was lower than their lower [CCN] counterparts due to CTEI as explained previously. Increasing [GCCN] increased the cloud fraction at all levels. Again, this was due to the fact that the presence of [GCCN] allowed cloud water to form more rapidly.

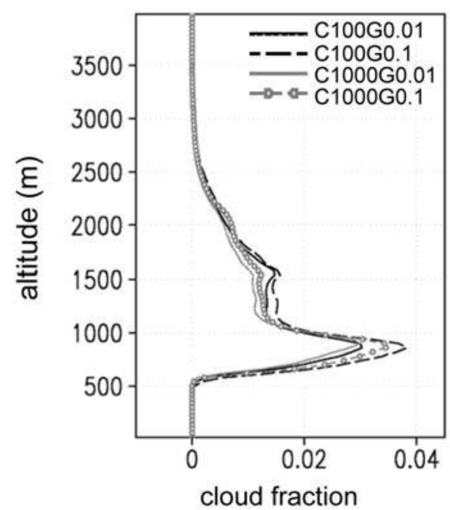

Figure 3 Horizontally and time averaged cloud fraction from 0000 UTC 11 Jan to 0000 UTC 12 Jan 2005.

It is generally thought that cloud albedo should increase with increasing cloud droplet concentration (with all factors being equal) due to the higher optical depth from the more numerous smaller cloud droplets present (Twomey's (1974) first indirect effect). Albrecht (1989) hypothesized that an increase in the cloud droplet number concentration decreases the size of the cloud droplets.

Thus, it is more difficult for clouds with smaller cloud droplets to form precipitation by collision and coalescence, leading to a lower precipitation efficiency, longer cloud lifetime, and a higher cloud fraction (Albrecht's (1989) second indirect effect).

We computed the time and domain averaged albedo (ratio of upwelling versus downwelling shortwave radiative fluxes) and we found that the albedo decreased only slightly with increasing [CCN] and/or [GCCN]. The albedos for the various experiments were as follows: 11.84% (C100G0.01), 11.80% (C100G0.l), 11.77% (C1000G0.01), and 11.72% (C1000G0.1) (Table 1). The result of negligible change in albedo with increase in [CNN] is contrary to Twomey's first indirect. Similar results were observed in a LES simulation of a case of marine cumuli (Zuidema et al. 2008). Even though the optical depth increased with increasing [CCN] in individual cumuli, CTEI decreased the liquid water path (LWP) and total cloud coverage (tcc, fraction of columns with LWP $\geq$ 10 g m^{-2} as in Xue et al. 2008) with increasing [CCN] (Table 1), compensating for the increase in cloud droplet concentration. Again, the decrease in LWP and tcc with increase in [CCN] is contrary to Albrecht's second indirect effect. However, neither Twomey nor Albrecht took into account entrainment processes.

With the increase in [GCCN], there were slight increases in optical depth, LWP, and total cloud coverage compensated by a decrease in cloud droplet concentration, leading to negligible decrease in albedo (Table 1).

Table 1 Time and domain averaged optical depth (σ), albedo (α, %), liquid water path (LWP, g m^{-2}), total cloud coverage (tcc, %), and cloud droplet concentration (cm^{-3}).

	α (%)	σ	LWP (g m^{-2})	tcc (%)	N_c (cm^{-3})
C100G0.01	11.84	0.42	16.8	8.39	22.8
C100G0.1	11.80	0.51	18.5	9.20	20.9
C1000G0.01	11.77	0.58	14.7	7.80	173.4
C1000G0.1	11.72	0.70	17.0	8.62	158.2

4. DISCUSSION AND CONCLUSION

Both [CCN] and [GCCN] can affect the timing of the precipitation and the magnitude. The lowest accumulated precipitation and precipitation rate occurred in the experiment with high [CCN] but low [GCCN] (exp. C1000G0.01). However, with both high [CCN] and [GCCN], the maximum precipitation rate was higher than any other experiment and was achieved the most quickly due to the vigorous collection and coalescence processes between the smaller and larger cloud droplets.

Cloud fraction in the upper (lower) part of the cloud was lower (higher) for experiments with higher [CCN]. This is likely due to entrainment of drier environmental air from the cloud top. As the higher [CCN] experiments had smaller cloud droplets, they evaporated more easily. Hence, the lower cloud fraction in the upper part of the cloud for higher [CCN] experiments.

For this case, the time- and domain-averaged albedo decreased very slightly with increased [CCN] and/or [GCCN]. This result can be explained by a compensating increase/decrease amongst the optical depth, LWP, cloud coverage, and cloud droplet concentration. Increase in either [CCN] or [GCCN] can increase the optical depth. However, *increase* in [CCN] ([GCCN]) can lead to *lower* (*higher*) LWP and total cloud coverage and *higher* (*lower*) cloud droplet concentration. Thus, CCN and GCCN play different roles in affecting cloud properties.

5. ACKNOWLEDGMENT

This research was funded by the National Science Foundation under grant ATM-0526600 (amd 002). We thank Steve Saleeby for modifying the cloud1 and cloud2 modes in the RAMS microphysics code.

6. REFERENCES

Albrecht, B. A., 1989: Aerosols, cloud microphysics and fractional cloudiness. *Science*, **245**, 1227–1230.

Cheng, W.Y.Y., T. Wu, and W.R. Cotton, 2001: Large-eddy simulations of the 26 November 1991 FIRE II cirrus case. *J. Atmos. Sci.*, **58**, 1017-1034.

Saleeby, S. M., and W. R. Cotton, 2004: A large droplet mode and prognostic number concentration of cloud droplets in the Colorado State University Regional Atmospheric Modeling System (RAMS). Part I: Module descriptions and supercell test simulations. *J. Appl. Meteor.*, **43**, 182-195.

Twomey, S. A. ,1974: Pollution and the planetary albedo. *Atmos. Env.*, **8**, 1251–1256.

Xue, H., G. Feingold, and B. Stevens, 2008: Aerosol effects on clouds, precipitation, and the organization of shallow cumulus convection. *J. Atmos. Sci.*, **65**, 392-406.

Zuidema, P., H. Xue, and G. Feingold, 2008: Shortwave radiative impacts from aerosol effects on shallow marine cumuli. *J. Atmos. Sci.*, In press.

INFLUENCE OF CLOUD CONDENSATION NUCLEI AND GIANT CONDENSATION NUCLEI ON THE DEVELOPMENT OF PRECIPITATING TRADE WIND CUMULI IN A LARGE EDDY SIMULATION

William Y.Y. Cheng[1], Gustavo G. Carrió, and William R. Cotton

Department of Atmospheric Science, Colorado State University, Fort Collins, CO 80523

1. INTRODUCTION

Trade wind cumulus clouds have been receiving more attention lately due to their important impact in the Earth's climate. These clouds are ubiquitous over the subtropical oceans, forming under the trade wind inversion that corresponds to the descending branch of the Hadley circulation. Convection associated with these clouds enhances air-sea surface exchange of momentum, moisture, and heat. In addition, their extensive coverage impact climate's radiational budget.

Recently, the impact of aerosols on cloud systems and their effects on climate is one of the most important questions researchers are trying to address. Besides scattering and absorbing incoming shortwave radiation and absorbing outgoing longwave radiation (the aerosol direct effect), aerosols act as cloud condensation nuclei (CCN), causing changes in the cloud droplet concentration (Twomey's first indirect effect, Twomey 1974) and are hypothesized to cause clouds to persist longer (Albrecht's second indirect effect, Albrecht 1989). While there have been many studies focusing on the effects of cloud condensation nuclei (CCN) on cloud systems, there are fewer studies focusing on the effects of the more rare giant CCN (GCCN) on cloud systems. GCCN can come from a variety of sources including sea salt from air-sea exchange and dust, as well as from anthropogenic activities.

Corresponding author address: William Y.Y. Cheng, Department of Atmospheric Science, Colorado State University, Fort Collins, CO 80512. Email: cheng@atmos.colostate.edu

2. METHODLOGY

To investigate the effects of both CCN and GCCN, the Regional Atmospheric Modeling System (RAMS) was used to investigate the effects of various CCN and GCCN concentrations on the development of precipitating trade wind cumuli in a large eddy simulation (LES) framework.

The LES domain contained 101 X 101 X 101 grid points in the x, y, and z direction, respectively with $\Delta x = \Delta y = 100$ m and $\Delta z = 40$ m. The LES model used the two-moment microphysics with new features with explicit nucleation of small cloud droplets (cloud1 mode with diameter of 2-65 μm) and larger cloud droplets (cloud2 mode with diameter of 65-120 μm) via activation of cloud condensation nuclei (CCN) and giant CCN (GCCN), respectively (Saleeby and Cotton 2004). Compared to cloud1 mode only simulations, the use of the additional cloud2 mode slows down the collision-coalescence process by requiring cloud1 to be converted to cloud2 before conversion to rain or drizzle. Note that the range of diameters of cloud1 and cloud2 has been modified in this version of the microphysics by Steven Saleeby to improve the performance of the scheme.

The sounding to initialize the LES was taken from the Rain in Cumulus over the Ocean Experiment (RICO) archive for 11 January 2005. Several sensitivity experiments were performed in which two levels of CCN (GCCN) concentrations were used: 100 (0.01) and 1000 (0.1) cm^{-3} corresponding to low and high values. The numerical experiments began at 0000 UTC 11 January 2005 and were run for 24 h. The model results will be used to evaluate how various combinations of high/low CCN and GCCN concentrations affected the physics, dynamics, precipitation and radiational properties of the trade wind cumuli in the LES.

The model u, v, θ_{il}, q_t fields were nudged from soundings obtained from the RICO archive as in the formulation of Cheng et al. (2001). Note that θ and q_v from the RICO sounding archive were used to nudge θ_{il} and q_t, respectively, as a reasonable approximation. The nudging time scale was 3600 s. The vertical profiles in this study were obtained by averaging temporally and horizontally.

3. RESULTS

3.1. Precipitation

For both low CCN concentration (hereafter referred to as [CCN]) and GCCN concentration (hereafter referred to as [GCCN]) as in exp. C100G0.01, the relatively high precipitation rate occurred throughout the integration period with values exceeding 0.1 mm h^{-1} (Fig. 1). With the introduction of higher [GCCN] in C100G0.1, the precipitation rate was generally small until after hour 6. After hour 6, the precipitation rate had peaks that exceeded 0.05 mm h^{-1} in C100G0.1 and even exceeded the precipitation rate of C100G0.01 at the end of the integration period at 0.15 mm h^{-1}. The initial low precipitation rate in C100G0.1 may be attributed to the slightly lower cloud droplet concentration (Table 1).

With high [CCN] but low [GCCN] as in C1000G0.01, the precipitation rate was lower than that of C100G0.01 and its value rarely exceeded 0.05 mm h^{-1} (Fig. 1). This is due to the fact the there are many more small cloud droplets, making them inefficient in forming rain drops from collision coalescence processes. This is the result that most researchers found when they increased the [CCN] without representation of GCCN in most LES of cloud systems.

However, the largest sensitivity in the precipitation rate and accumulated precipitation occurred when both [CCN] and [GCCN] were increased as in C1000G0.1. With the high [CCN] already present, the conversion from cloud1 to cloud2 to drizzle occurred rapidly. In fact, in C1000G0.1, the precipitation rate reached its maximum in the first 6 hours (more than 0.3 mm h^{-1}, Fig. 1). This maximum exceeded all of the other maxima and occurred earlier than the other experiments. Although the accumulated precipitation in C1000G0.1 did not reach as high as C100G0.01 or C100G0.1 due to the high [CCN], its final accumulated precipitation (0.16 mm) was more than twice that of C1000G0.01 (0.07 mm) due to the high [GCCN] (Table 1).

The 24-h accumulated precipitation for the various experiments were as follows: 0.28 mm (C100G0.01), 0.31 mm (C100G0.1), 0.07 mm (C1000G0.01), and 0.16 mm (C1000G0.1). This shows that in general, increasing the [GCCN] will increase the accumulated precipitation. However, the timing of the high precipitation rates differed depending on the [CCN]. Having a small (large) [CCN], the high precipitation rate occurred (early) later in the cloud development when the [GCCN] was increased.

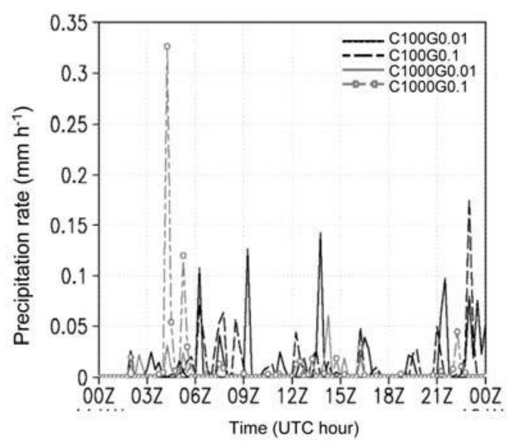

Figure 1 Time series of domain averaged precipitation rate (mm h-1) from 0000 UTC 11 Jan to 0000 UTC 12 Jan 2005.

3.2. Cloud properties

Figure 2 shows the vertical profile of liquid water mixing ratio (q_l) (cloud1, cloud2, and drizzle mixing ratios). Liquid water mixing ratio is the sum of cloud1, cloud2, and drizzle mixing ratios. Qualitatively, the vertical profiles from the different experiments were similar. In particular, q_l was maximized between 900 m and 1600 m AGL for all of the experiments, with values ~0.01 g kg^{-1}. However, there were quantitative differences amongst the vertical profiles. Increasing the [CCN] led to a decrease in q_l below 1900 m AGL. Also, increasing [GCCN] led to an increase in q_l. Increasing both [CCN] and [GCCN] resulted in the highest q_l below 1800 AGL. The results can be explained by cloud-top entrainment instability (CTEI).

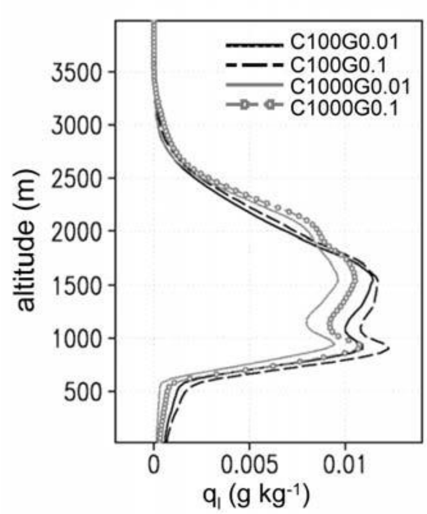

Figure 2 Horizontally and time averaged liquid water mixing ratio (g kg^{-1}) from 0000 UTC 11 Jan to 0000 UTC 12 Jan 2005.

For higher [CCN] experiments, we would expect CTEI to be more active (Xue et al. 2008). Essentially, smaller droplets would evaporate faster when the cloud entrains drier environmental air at the cloud top, generating negative buoyancy (Xue et al. 2008). Hence, the overall q_l was lower in the higher [CCN] experiments below 1900 m AGL (Fig. 2). The slightly higher q_l above 1900 m AGL for higher [CCN] experiments can be explained by the fact that some small evaporated droplets lingered at these levels.

Higher [GCCN] had the effect of increasing q_l at all levels (Fig. 2). This was due to the fact that the presence of [GCCN] allowed cloud water to form more rapidly.

Figure 3 shows the vertical profile cloud fraction for the various experiments. Cloud fraction for each level was defined as the number of cloudy grid cells at each level versus the total number of grid points at that level. Cloudy grid cells were defined as any grid cells with cloud mixing ratio $\geq$ 0.01 g kg^{-1}. It is clear that qualitatively the shape of the profile is the same for all of the experiments. The cloud fraction is maximized just below 1000 m AGL. Below 1000 m AGL, increasing [CCN] increased the cloud fraction. This is likely due to the fact that smaller droplets in the larger [CCN] experiments resulted in precipitation being more difficult to form in accordance to Albrecht's hypothesis. However, above 1000 m AGL, the cloud fraction for the higher [CCN] experiments was lower than their lower [CCN] counterparts due to CTEI as explained previously. Increasing [GCCN] increased the cloud fraction at all levels. Again, this was due to the fact that the presence of [GCCN] allowed cloud water to form more rapidly.

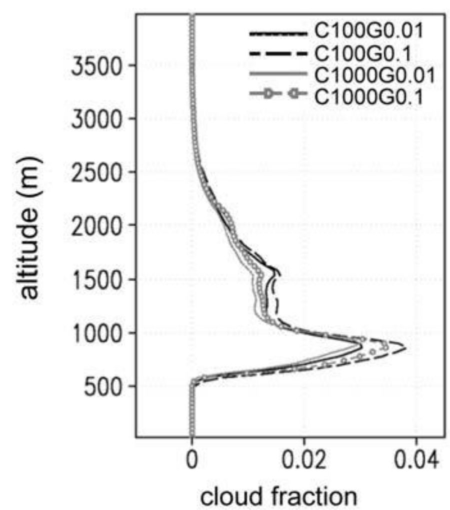

Figure 3 Horizontally and time averaged cloud fraction from 0000 UTC 11 Jan to 0000 UTC 12 Jan 2005.

It is generally thought that cloud albedo should increase with increasing cloud droplet concentration (with all factors being equal) due to the higher optical depth from the more numerous smaller cloud droplets present (Twomey's (1974) first indirect effect). Albrecht (1989) hypothesized that an increase in the cloud droplet number concentration decreases the size of the cloud droplets.

Thus, it is more difficult for clouds with smaller cloud droplets to form precipitation by collision and coalescence, leading to a lower precipitation efficiency, longer cloud lifetime, and a higher cloud fraction (Albrecht's (1989) second indirect effect).

We computed the time and domain averaged albedo (ratio of upwelling versus downwelling shortwave radiative fluxes) and we found that the albedo decreased only slightly with increasing [CCN] and/or [GCCN]. The albedos for the various experiments were as follows: 11.84% (C100G0.01), 11.80% (C100G0.I), 11.77% (C1000G0.01), and 11.72% (C1000G0.1) (Table 1). The result of negligible change in albedo with increase in [CNN] is contrary to Twomey's first indirect. Similar results were observed in a LES simulation of a case of marine cumuli (Zuidema et al. 2008). Even though the optical depth increased with increasing [CCN] in individual cumuli, CTEI decreased the liquid water path (LWP) and total cloud coverage (tcc, fraction of columns with LWP $\geq$ 10 g m^{-2} as in Xue et al. 2008) with increasing [CCN] (Table 1), compensating for the increase in cloud droplet concentration. Again, the decrease in LWP and tcc with increase in [CCN] is contrary to Albrecht's second indirect effect. However, neither Twomey nor Albrecht took into account entrainment processes.

With the increase in [GCCN], there were slight increases in optical depth, LWP, and total cloud coverage compensated by a decrease in cloud droplet concentration, leading to negligible decrease in albedo (Table 1).

Table 1 Time and domain averaged optical depth (σ), albedo (α, %), liquid water path (LWP, g m^{-2}), total cloud coverage (tcc, %), and cloud droplet concentration (cm^{-3}).

	α (%)	σ	LWP (g m^{-2})	tcc (%)	N_c (cm^{-3})
C100G0.01	11.84	0.42	16.8	8.39	22.8
C100G0.1	11.80	0.51	18.5	9.20	20.9
C1000G0.01	11.77	0.58	14.7	7.80	173.4
C1000G0.1	11.72	0.70	17.0	8.62	158.2

4. DISCUSSION AND CONCLUSION

Both [CCN] and [GCCN] can affect the timing of the precipitation and the magnitude. The lowest accumulated precipitation and precipitation rate occurred in the experiment with high [CCN] but low [GCCN] (exp. C1000G0.01). However, with both high [CCN] and [GCCN], the maximum precipitation rate was higher than any other experiment and was achieved the most quickly due to the vigorous collection and coalescence processes between the smaller and larger cloud droplets.

Cloud fraction in the upper (lower) part of the cloud was lower (higher) for experiments with higher [CCN]. This is likely due to entrainment of drier environmental air from the cloud top. As the higher [CCN] experiments had smaller cloud droplets, they evaporated more easily. Hence, the lower cloud fraction in the upper part of the cloud for higher [CCN] experiments.

For this case, the time- and domain-averaged albedo decreased very slightly with increased [CCN] and/or [GCCN]. This result can be explained by a compensating increase/decrease amongst the optical depth, LWP, cloud coverage, and cloud droplet concentration. Increase in either [CCN] or [GCCN] can increase the optical depth. However, *increase* in [CCN] ([GCCN]) can lead to *lower* (*higher*) LWP and total cloud coverage and *higher* (*lower*) cloud droplet concentration. Thus, CCN and GCCN play different roles in affecting cloud properties.

5. ACKNOWLEDGMENT

This research was funded by the National Science Foundation under grant ATM-0526600 (amd 002). We thank Steve Saleeby for modifying the cloud1 and cloud2 modes in the RAMS microphysics code.

6. REFERENCES

Albrecht, B. A., 1989: Aerosols, cloud microphysics and fractional cloudiness. *Science*, **245**, 1227–1230.

Cheng, W.Y.Y., T. Wu, and W.R. Cotton, 2001: Large-eddy simulations of the 26 November 1991 FIRE II cirrus case. *J. Atmos. Sci.*, **58**, 1017-1034.

Saleeby, S. M., and W. R. Cotton, 2004: A large droplet mode and prognostic number concentration of cloud droplets in the Colorado State University Regional Atmospheric Modeling System (RAMS). Part I: Module descriptions and supercell test simulations. *J. Appl. Meteor.*, **43**, 182-195.

Twomey, S. A. ,1974: Pollution and the planetary albedo. *Atmos. Env.*, **8**, 1251–1256.

Xue, H., G. Feingold, and B. Stevens, 2008: Aerosol effects on clouds, precipitation, and the organization of shallow cumulus convection. *J. Atmos. Sci.*, **65**, 392-406.

Zuidema, P., H. Xue, and G. Feingold, 2008: Shortwave radiative impacts from aerosol effects on shallow marine cumuli. *J. Atmos. Sci.*, In press.

STUDY OF DUST EFFORTS ON CLOUDS AND PRECIPITATION DURING NAMMA

D. Allen Chu[1], Chung-Lin Shie[1], Sergio DeSouza-Machado[2],Gao Chen[3], H.-C. Liu[4], Bruce Anderson[3]

[1]GEST, NASA Goddard Space Flight Center, Greenbelt, MD 20771
[2]JCET, University of Maryland Baltimore County, Baltimore, MD 21250
[3]Science Directorate, NASA Langley Research Center, Hampton, VA 23681
[4]SAIC/NASA Goddard Space Flight Center, Greenbelt, MD 20771

Abstract

Active easterly waves are clearly observed by satellites over the western Africa and tropical Atlantic Ocean in the summertime. Tropical depressions and tropical storms are frequently seen as a result of wave breaking and cyclogenesis. Under the prevailing easterlies, dust outbreaks from the Sahara Desert appear to coincide with storm development along the western and southern boundaries of Saharan air layer (SAL). An integrated month-long field experiment, NAMMA (NASA African Monsoon Multidisciplinary Analysis), was thus conducted from August 15 to September 15, 2006 using a suite of remote sensing and in-situ sensors onboard DC-8 and B-200 airplanes together with ground networks and EOS A-train satellites to derive dust and cloud properties. In this paper, case studies of dust outbreaks coincident with DC-8 flights and satellite measurements are focused. Simulated cloud hydrometeors and surface precipitation will be presented, along with available in situ and TRMM (Tropical Rainfall Measuring Mission) counterparts, during the conference presentation.

In-situe and Satellite Measurements

The DC-8 airborne in-situ observations of dust size distribution, scattering/absorption profiles, and associated meteorological parameters [*Chen et al.,* 2007] provide unique measurements at limited locations while satellite observations cover a large space routinely. The use of in-situ data to validate satellite retrievals and subsequently using satellite data to evaluate spatial variabilities of dust parameters over the model domain is essential for the comparison with model assimilation. In this study, the uniquely derived dust heights from MODIS (Moderate Resolution Imaging Radiometer) and AIRS are comparied with in-situ dust profiles to characterize dust vertical extent of SAL (Saharan Air Layer) in addition to dust loading and effective radius (size) obtained from MODIS standard aerosol products. Shown in **Figure 1** are the linear regressions of AIRS- and MODIS-derived aerosol optical depth (AOD) assuming dust layers at 700-800 and 800-900 mb, respectively. The corresponding correlation to the linear regression indirectly indicates the likelihood of the position of dust layer [*DeSouda-Machado et al*., 2006]. To achieve the best estimate of dust layer height, we restrict the correlation coefficient to be greater than 0.8 [Chu et al., 2007].

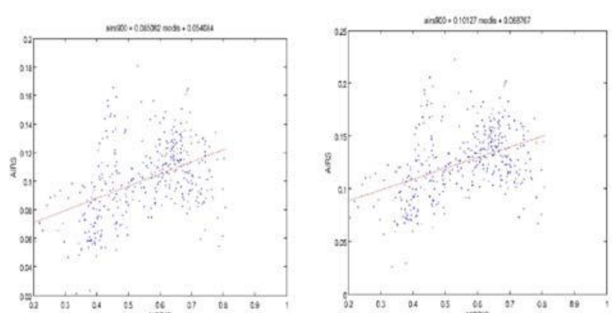

Figure 1. Linear regression of AIRS and MODIS-derived dust optical depths on August 19, 2006. Results are derived assuming the top/bottom layer dust height (mb): 700/800 (left), and 800/900 (right), respectively.

An optimal estimation method is undergone testing for retrieving both dust and temperature from AIRS as opposed to the use of ECMWF temperature profile as background in the retrievals shown in Figure

1. Detailed results will be illustrated in the conference presentation.

GEOS-5 Assimilated Meteorological Fields

NASA GEOS-5 (Goddard Earth Observing System Model, Version 5) products assimilated meteorological fields provide large-scale forcing to the cloud-resolving model. During NAMMA, three tropical storms were developed into hurricanes while dust outbreaks were frequently seen throughout the NAMMA field campaign. The GEOS-5 6-hourly meteorological and large-scale temperature and moisture forcing data were averaged over a selected box region between 10^0W-32^0W and 8^0N-20^0N. The reason we selected the region because several legs of DC-8 flights were conducted during NAMMA field campaign.

GCE (Goddard Cloud Ensemble) Model Bulk Scheme Simulations

The period of "point-source" (the box-area averaged) GEOS-5 data from August 18 to 31, 2006 has then been applied to perform the cloud simulations for a horizontal domain of 512x512 km (with a resolution of 2x2 km) and a height of about 20 km (with 34 vertical levels of resolutions ranging from 80 m to 1000 m). The series of 14-day simulations mainly include 12 atmospheric 3D parameters (temperature, water vapor, horizontal and vertical velocity, pressure, long-wave and short-wave radiation rates, and five different cloud species, cloud water, rain, cloud ice, snow and graupel), along with the upward/downward short-wave and long-wave radiation fluxes at both top and bottom boundaries, which are generated at a 12-second time step, and saved with an hourly sample rate. Shown in Figure 2 are the results of cloud water, rainwater, cloud ice, snow, and graupel simulated by the 2-D GCE bulk scheme.

(a)

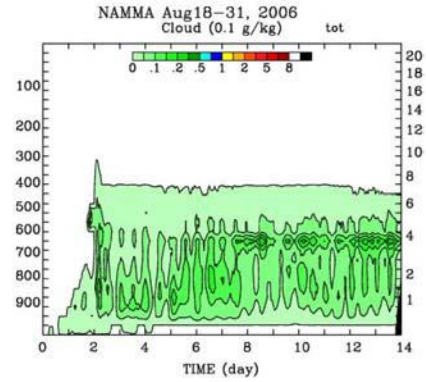

(b)

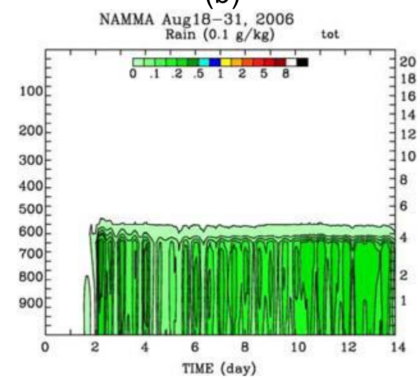

(c)

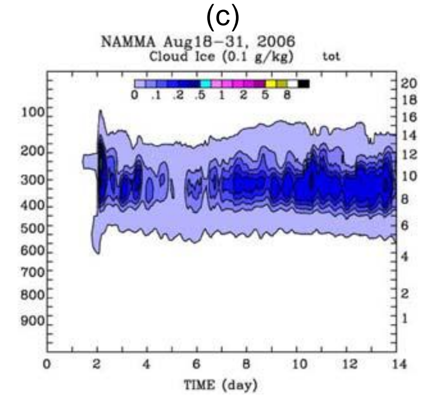

(d)

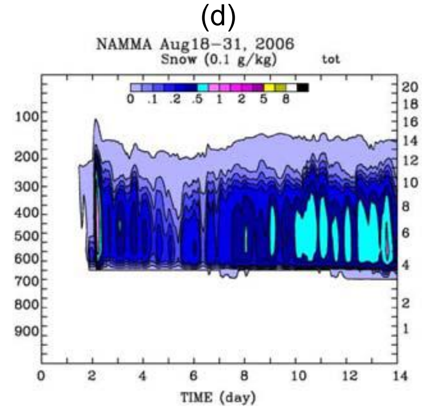

(e)

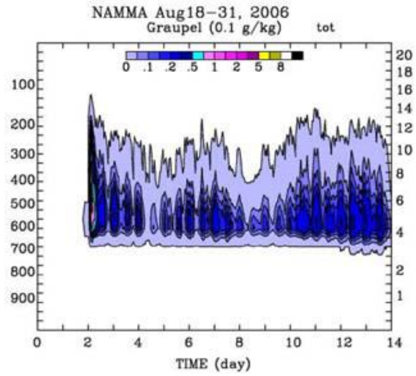

Figure 2. Evolution of the domain-averaged (a) cloud water, (b) rainwater, (c) cloud ice, (d) snow, and (e) graupel (g kg $^{-1}$) for the period of August 18-31, 2006. The vertical coordinates are in mbar (left) and kilometer (right), respectively.

Concluding Remarks

Though the magnitudes of the hydrometeors vary slightly from day to day, cloud water and rainwater are largely concentrated below 600 mb whereas cloud ice, snow, and graupel are generally above 700 mb. Figure 3 demonstrates the time-averaged vertical profiles of the hydrometeors over the 14-day period. The results clearly show a physically consistent scenario that convections are prevail under a cold/moist environment, yet are suppressed under a warm/dry condition.

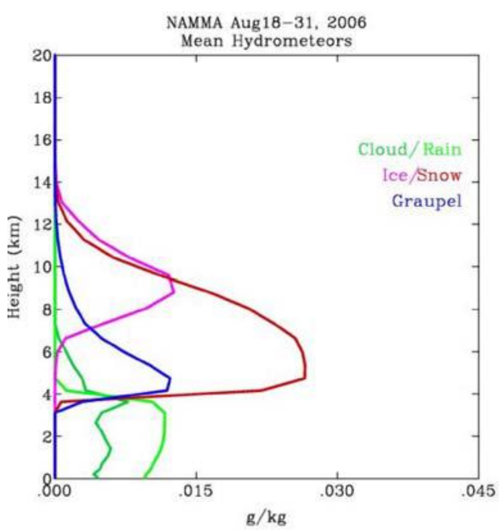

Figure 3. Vertical profiles of time- and domain-averaged simulated hydrometeors for the period of August 18-31, 2006. Cloud water, rainwater, cloud ice, snow and graupel are shown in green, light green, pink, red, and blue, respectively.

Numerical simulations using a WRF model with a two-moment scheme will soon conducted for investigating the dust impact on the targeted convective systems, for which satellite-derived dust height will be used to the impact of spatial variability on the model simulations.

References

Chen Gao, K. L. Thomhill, C. Kittaka, K. Gleicher, E. Winstead, G. Diskin, Bruce Anderson et al., The microphysical and optical properties of Saharan dust as observed during NAMMA. AAAR, Austin, Texas, September 2007.

Chu D. A., S. DeSousa-Machado, Chung-Lin Shie, Xiao-Wen Li, Study of the effects of dust radiative and microphysical properties on precipitation and energy budget using A-Train satellite measurements and cloud-resolving model, NAMMA Science Team Meeting Workshop, Baltimore, May 2007.

DeSouza-Machado, S., D. A. Chu, N. R. Nalli, L. L. Strow, S. E. Hannon, H. E. Motteler, P. J. Minnett, Estimation of dust loading and height using MODIS, AIRS, and MAERI data, *Proc. of SPIE, Vol. 6299*, 62990D, SPIE Annual Meeting, San Diego, California, August 13 – 17, 2006.

EFFECTS OF AEROSOLS ON LIGHTNING AND INTENSITY OF HURRICANES

N. Cohen and A. Khain

Department of Atmospheric Sciences, The Hebrew University of Jerusalem, Israel
Emails: khain@vms.huji.ac.il; naftalic@gmail.com

ABSTRACT

According to the observations of hurricanes located at comparatively low distances from the land, intense and persistent lightning takes place within the 250-300 km-radius ring around the hurricane center, while the lightning activity in the eye wall takes place only during comparatively short periods usually attributed to the eyewall replacement. The mechanism responsible for the formation of the maximum flash density at the TC periphery is not well understood as yet. In this study we hypothesize that lightning at the TC periphery arises under the influence of small continental aerosol particles (AP), which affect the microphysics and the dynamics of clouds at the TC periphery. To show that aerosols change the cloud microstructure and the dynamics in the way to foster lightning formation we use a 2-D mixed phase cloud model with spectral microphysics. It is shown that aerosols which penetrate cloud base of maritime clouds, dramatically increase the amount of supercooled water, as well as the ice contents and vertical velocities. As a result, in clouds developing in the air with high AP concentration ice crystals, graupel, frozen drop/hail and supercooled water can coexist within one and the same cloud zone which allows collisions and charge separation. The simulation of possible aerosol effects on the landfalling tropical cyclone has been carried out using a 3-km resolution WRF mesoscale model. It is shown that aerosols change the cloud microstructure in a way that allows us to attribute the observed lightning structure to the effects of continental aerosols. It is also shown that aerosols, invigorating clouds at 250-300 km from the TC center decrease the convection intensity in the TC center leading to some TC weakening. The results suggest that aerosols change the intensity and the spatial distribution of precipitation in landfalling TCs and can possibly contribute to the weekly cycle of the intensity and precipitation of landfalling TCs.

1. INTRODUCTION

Tropical cyclones (TCs) are known for their destructive power, particularly as they make landfall. TCs are often accompanied by extreme winds, storm surges and torrential rainfall. The TC wind fields, the area of heavy rain, and the rain rate are determined by cloud microphysical processes. At the same time, both experimental and numerical investigations of cloud microphysics in TCs are quite limited. Microphysical observations are usually limited by the zones of the melting level (McFarquhar and Black 2004). Lightning is one of the factors, which can shed light on the microphysical cloud structure and the TC evolution. For instance, increasing lightning rate indicates invigoration of convection, accompanying increasingly larger volumes of graupel or small hail/frozen drop aloft, strengthening updrafts and increasing the probability of heavier rainfall (e.g. Lhermitte and Krehbiel, 1979; Wiens et al, 2005; Fierro et al 2007). The presence of lightning activity in storms crossing the West African coast can be used as a precursor to TC formation (Chronis et al 2007). The appearance and intensification of lightning in the eyewall can be a predictor of TC intensification (Orville and Coyne 1999, Molinari et al 1999; Shao et al 2005; Demetriades and Holle, 2006; Fierro et al 2007). Rodgers et al (2000) found that the closer the lightning is to the storm center, the more likely the TC is to intensify. The latter makes lightning and its distribution in TCs to be an important characteristic that can serve as the predictor of TCs intensity and precipitation changes.

Molinari et al (1994, 1999) analyzed the radial distribution of lightning in hurricanes approaching the US coast using the National Lightning Detection Network data. This system detects only the cloud-to-ground (CG) flashes that occur over the water. They found three zones of distinct electrical characteristics: a) the inner core, which contains a weak maximum of flash density; b) the region with a well –defined minimum in flash density extending 80-100 km outside this maximum; and c) the outer band region, which contains a strong maximum of the flash density within the 200-300 km-radius ring around the hurricane center. Further investigations of lightning in tropical cyclones over the Atlantic and Eastern Pacific Oceans (e.g., Cecil at al, 2002a,b; Demetriades and Holle, 2006) reinforced many findings of Molinari et al (1999) as regards the radial distribution of the flash density. An example of the lightning activity in hurricane Katrina (2005) at several successive time instances is presented in **Figure 1** adopted from the study by Shao et al (2005). Shao et al (2005) applied the LASA data that detect lightning using "very low" and "low" radio frequency (VLF/LF) signals and used time-of-arrival techniques to locate the lightning sources.

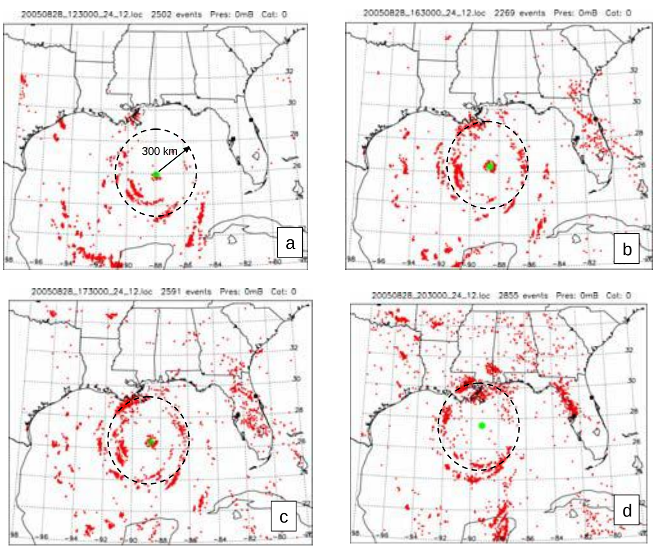

Figure 1. *Lightning in Katrina (2005) at different time instances (after Shao et al, 2005). Zones of lightning are marked by red dots; the TC eye is marked green. Dashed circles have radius of about 300 km around the TC center. One can see the high lightning intensity (which even exceeds that over the land) within the 250-300 km radii rings.*

According to the current concept the charging of hydrometeors in clouds takes place in a mixed-phase region at temperatures less than about -13^{o}C, when collisions of ice crystals and graupel take place in the presence of supercooled droplets [e.g., Takahashi, 1978; Saunders 1993, Cecil et al 2002b; Sherwood et al (2006)]. The latter means that a significant mass of supercooled drops must ascend in clouds above ~5-6 km to trigger flash formation. Actually, the lightning onset indicates significant changes in the cloud dynamics and in the microphysics of maritime clouds: an increase in updrafts and in ice content and the appearance of supercooled water at high levels. Numerical investigations of lightning formation in clouds can be found, for instance, in studies by Solomon and Baker (1994, 1998), (Solomon et al, 2002), Mansell et al (2002) and Mitzeva et al (2006).

Molinari et al (1999) see the reasons causing the rarity of ground flashes in the vicinity of eyewall in the absence of supercooled water in the eyewall (Black and Hallet 1986), which makes a significant charge separation unlikely according to the current theories of noninductive charge transfer between ice particles in the presence of supercooled liquid water (Saunders 1993). The lack of supercooled water in the eyewall can be attributed to a) low updrafts hardly exceeding 5 ms^{-1} (Black et al 1996; Szoke et al 1996; Jorgensen et al 1985); and b) to low aerosol concentrations making the eyewall clouds microphysically extremely maritime. Both reasons lead to the formation of raindrops below the freezing level, which fall efficiently collecting remaining droplets. Low updrafts also do not allow the suspension of graupel, either, which is the key ingredient for electrification. Black and Hallet (1986) also suppose that supercooled water can be eliminated by the efficient seeding of eyewall clouds by ice in the rapidly rotating storm core. The eyewall lightning outbreaks (which tend to occur within relatively small time periods of several hours) are attributed by Molinari et al (1999) to the replacement of the inner eyewall by a new one, which usually precedes TC intensification. Such eyewall lightning outbreaks were also observed by Demetriades and Holle (2006) in many TC over the Northern Atlantic and the Pacific using the Long-Range Lightning Detection Network. In more details the eyewall replacement has been recently investigated in studies by Houze et al (2006, 2007).

Molinari et al (1999) attribute the well-defined minimum in the lightning flash density extending 80 to 100 km outside the eyewall to lower-tropospheric downdrafts and suppressed convection.

Finally, Molinari et al (1999) attribute the well-defined maximum of the flash density at the TC periphery to the higher instability of environmental air flows around the storm as compared to that in the eyewall. They suppose that the environmental air is convectively unstable, as it follows from the Jordan's (1958) mean West Indies sounding. Williams (1995), Williams and Satori (2004) and Williams et al. (2004, 2005) stressed the dominating role of the atmospheric instability as regards the land-ocean lightning flash density difference. The question arises: Is Jordan's (1958) sounding unstable enough to be fully responsible for the high flash density at the TCs periphery? Emanuel (1994) argued, for instance, that the buoyancy of oceanic convection dramatically decreases by the condensate loading, so that in fact Jordan's (1958) sounding turned out to be close to the neutral one. Molinari et al (1999) also mentioned that the difference in the atmospheric instability between the eyewall and the TC periphery "*cannot be a complete explanation. Tropical oceanic convection often has convective available potential energy values as larger as over the land (Zipser and LeMone 1980), but it does not realize as high a fraction of the pseudoadiabatic ascent rate (Jorgensen and LeMone 1989) and contains much smaller ground flash rates than over the land (see, e.g., Lucas and Orville 1996). The reason for larger flash density in outer bands remains somewhat uncertain".* Note in this connection that simulations of evolution of an idealized hurricane by Fierro et al (2007) using a mesoscale 2-km resolution model with a bulk parameterization scheme describing 12 distinct hydrometeor habits (Straka and Mansell, 2005) and a lightning scheme (Mansell et al 2002) showed much more intense convection and lightning within a TC ~ 50-km radius central convective zone rather than within outer rain bands. This result was obtained under the environmental conditions typical of the TC formation.

In case the atmospheric instability would be the only mechanism affecting lightning formation, one could expect an increase in the lightning frequency in the zones of high sea surface temperature (SST). To check whether lightning at the TC periphery is related to the SST we compared the SST fields in the area of hurricane Katrina calculated using the TC-ocean coupled model of Graduate School of Oceanography, the University of Rhode Island (I. Ginis, personal communication, 2007) and the lightning intensity. The comparison of the SST fields and the lightning frequency indicates no obvious correlation between the SST and the lightning rate. For instance, according to Fig.1 (panel a) at 12:30 UTC intense lightning takes place to the south from the Katrina center, where the SST is relatively low. At the same time the lightning frequency is very weak to the north of the center, where the SST is maximum. During the 20:30 UTC -24 UTC period intense lightning takes place both to the south and to the north of the TC center, while the SST is significantly higher to the north of the TC center. Besides, there is no clear dependence of the lightning rate within the lightning ring in the south-north direction (see, e.g, Fig 1c), while the SST increases northward. Note that the characteristic scales of the SST changes are much larger than the depth of the lightning ring. Thus, the comparison does not reveal any relationship between the variations of the SST and those of lightning activity at the TC periphery.

Therefore, the first question we address in the paper is: *under what microphysical conditions the instability corresponding to Jordan's (1958) sounding (typical of TC development, Molinari et al, 1999) is able to provide the conditions favorable for negative ground flashes observed at the TC periphery?* In a wider context, the first question can be formulated as follows: *" Can the high instability of the atmosphere, which can take place, say,* *over the zones of especially high sea surface temperature (SST) be considered and <u>necessary and</u> <u>sufficient</u> condition for the intense lightning formation?".*

Getting ahead, numerical simulations with a high resolution cloud model with spectral bin microphysics indicate that the instability is necessary, but, supposedly, not sufficient for lightning formation.

In this study we check the hypothesis to the effect that continental aerosols penetrating TC clouds at the TC periphery (taken together with a higher instability at the TC periphery) create conditions favorable for lightning formation. Some support of the idea concerning the possible aerosol effects can be found in **Figures 2a,b.**

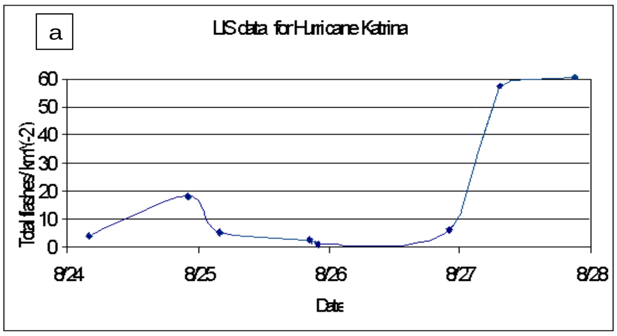

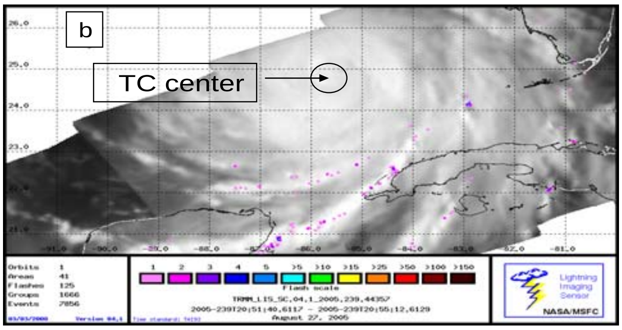

***Figure 2**. a) The time dependence of total flashes in Hurricane Katrina from 24 Aug. to 28 Aug, 2005. (b) Flash number in Katrina, August 27, 20.51-20.55. The figures are plotted using the Lightning Imaging Sensor (LIS) data. The data above is the total flashes for 6°x 6° area composite to hurricane Katrina best track center (http://thunder.nsstc.nasa.gov/data/#LIS_DATA*

Figure 2a shows that intense lightning begins when the TC approach the land at a comparatively low distance (intense lightning starts on 27-27 Aug. (see also Figure 1a corresponding to the period of the lightning ring formation). Figure 3b shows that lightning arises within the airmass downwind from the land. This air mass can contain a significant amount of aerosols that can affect the microstructure of the convective clouds.

(Note that at present it is impossible to determine the spatial structure of lightning activity in hurricanes far from the land, E. Williams and C. Price, personal communications 2008). The view of Hurricane Rita on September 23, 2005 at 12:52 pm EDT observed by the NASA's TRMM spacecraft is shown in **Figure 3**.

***Figure 3.** The view of Hurricane Rita on September 23, 2005 at 12:52 pm EDT observed by NASA's TRMM spacecraft. The cloud cover is evaluated by TRMM's Visible and Infrared Scanner and the GOES spacecraft (http://www.nasa.gov/vision/earth/lookingatearth/h2005_rita.html).*

One can see that TC circulation penetrates far into the land even when the TC center is located several hundred kilometers from the cost line. The latter means that the TCs approaching the land involve a lot of continental aerosols into their circulation. This assumption will be tested using a numerical model. We will also show that these aerosols can lead to the formation of a narrow ring with the radii of 250-300 km and a high lightning flash density. Finally, we evaluate the possible effect of continental aerosols on the intensity, the structure of cloudiness and precipitation of landfalling TC.

The effects of aerosols on individual convective clouds under conditions typical of the TC periphery are investigated using the 250 m resolution 2-D mixed phase Hebrew University cloud model (HUCM) with spectral bin microphysics (Khain et al 2004, 2005). The aerosol effects on the cloudiness structure of a TC approaching and penetrating the land is investigated using a two nested grid Weather Research Model (WRF) (Skamarock et al., 2005). In the latter case the WRF was used to simulate the evolution of a TC moving along the track close to that of Hurricane Katrina from August 28 12z to August 30 00 z.

The combination of the two models for the investigation is natural: the high resolution HUCM can describe fine microphysical processes to evaluate the aerosol effects on the vertical profiles of liquid water and ice particles contents in individual clouds. These simulations will represent the main justification that an increase in the aerosol concentration can create conditions favorable for lightning in maritime clouds. The 3-D simulations with the WRF model cannot be carried out with so high resolution and with the microphysical scheme used in the HUCM. These simulations do not resolve small clouds and underestimate vertical velocities. Thus, the TC simulations provide less exact but useful evidence concerning aerosol effects on individual clouds. At the same time the 3D model illustrates the effects of aerosols on the structure of TC cloudiness and precipitation over large areas.

Taking into account the factors affecting the lightning rate (Fierro et al 2007) the lightning probability will be characterized by the product of the total ice content, the supercooled content and the vertical velocity above the 5-km level.

2. AEROSOL EFFECTS ON THE INDIVIDUAL TROPICAL MARITIME CLOUDS

2.1 DESCRIPTION OF THE CLOUD MODEL

A 2-D mixed phase Hebrew University cloud model (HUCM) with spectral bin microphysics has been used (Khain and Sednev 1996; Khain et al 2004, 2005) to investigate whether an increase in aerosol concentration in the zone of maritime tropical convection can change the cloud microphysical structure of individual clouds to make it favorable for lightning formation. The HUCM model microphysics is based on solving a kinetic equations system for size distribution functions for water drops, ice crystals (plate-, columnar- and branch types), aggregates, graupel and hail/frozen drops, as well as atmospheric aerosol particles (AP). Each size distribution is described using 43 doubling mass bins, allowing simulation of graupel and hail with the sizes up to 4 cm in diameter. The model is specially designed to take into account the AP effects on the cloud microphysics, dynamics, and precipitation. *The initial* (at t=0) CCN size distribution is calculated using the empirical dependence

$$N = N_o S_1^k , \qquad (1)$$

and applying the procedure described by Khain et al (2000). In (1) N is the concentration of activated AP (nucleated droplets) at supersaturation S_1 (in %) is with respect to water, N_o and k are the measured constants. The values of the constants used in the simulations are presented in Table 1. At t>0 the prognostic equation for the size distribution of non-activated AP is solved. Using the value of S_1 calculated at each time step, the critical AP radius is calculated according to the Kohler theory. The APs with the radii exceeding the critical value are activated and new droplets are nucleated. The corresponding bins of the CCN size distributions become empty.

Primary nucleation of each type of ice crystals is performed within its own temperature range following Takahashi et al (1991). The dependence of the ice nuclei concentration on supersaturation with respect to ice is described using an empirical expression suggested by Meyers et al. (1992) and applied using a semi-lagrangian approach (Khain et al 2000) allowing the utilization of the diagnostic relationship in the time dependent framework. The secondary ice generation is described according to Hallett and Mossop (1974). The rate of drop freezing is described following the observations of immersion nuclei by Vali (1974, 1975), and homogeneous freezing according to Pruppacher (1995). The homogeneous freezing takes place at temperature about -38C. The diffusional growth/evaporation of droplets and the deposition/sublimation of ice particles are calculated using analytical solutions for supersaturation with respect to water and ice. An efficient and accurate method of solving the stochastic kinetic equation for collisions (Bott, 1998) was extended to a system of stochastic kinetic equations calculating water-ice and ice-ice collisions. The model uses height dependent drop-drop and drop-graupel collision kernels following Khain et al, (2001a) and Pinsky et al (2001). Ice-ice collection rates are assumed to be temperature dependent (Pruppacher and Klett, 1997). An increase in the water-water and water-ice collision kernels caused by the turbulent/inertia mechanism was taken into account according to Pinsky and Khain (1998) and Pinsky et al. (1999, 2000). Advection of scalar values is performed using the positively defined conservative scheme proposed by Bott (1989). The computational domain is 178 km x 16 km with the resolution of 250 m and 125 m in the horizontal and vertical directions, respectively.

2.2. DESIGN OF SIMULATIONS WITH THE CLOUD MODEL

Simulations of individual maritime deep convective clouds under the conditions typical of tropical oceans during the hurricane season (Jordan 1958) have been performed. The sounding used is quite close to that observed during the GATE-74 Experiment, 261 day used for cloud simulations in many studies (e.g. Ferrier and Houze 1989; Khain et al 2004, 2005). The sounding used indicates high about 90 %. humidity near the surface. The sea surface temperature is $27^{o}C$. The averaged wind shear was 15 m/s per the atmospheric layer of 14 km depth. The zero temperature level is at 4.2 km. The reasons of the choice of the Jordan (1958) sounding in our simulations are as follows. The Jordan (1958) sounding was used by a great number of scientists simulating TC genesis and evolution (e.g, Khain et al 1983, 1984). This sounding was mentioned by Molinari et al (1999) in their attempt to explain, why the lightning at the TC periphery is stronger than in the eyewall. The main reason why this sounding has been used in our 2-D simulations is that it is quite unstable and leads to the formation of deep convective clouds with the vertical velocity maximum of 18-20 m/s (see below). Such vertical velocities are unusually high for maritime convection (with typical updrafts of 5-10 m/s). We used this sounding to check the "thermal" or "instability" hypothesis, namely, *is the atmospheric instability the sufficient condition for lightning formation, i.e., are the conditions favorable for lightning formation if vertical updrafts are high, but aerosol concentration is very low?*

Note that we have no data concerning the possible aerosol flux from the land to the sea area. Hence, we assume that the aerosol particle (AP) size distributions over the sea can be represented as the sum of the distributions typical of maritime and continental conditions. The aerosol particles in all simulations were assumed soluble. Under high winds aerosol size distribution can contain a significant amount of large cloud condensational nuclei (CCN) arising because of the sea spray formation. Hence, the penetration of continental aerosol must create aerosol size distributions containing a significant concentration of both small continental aerosols and tails of large aerosols. To investigate the effects of a high concentration of small continental aerosols on cloud microphysics and dynamics in the presence of a significant amount of large maritime CCN, the following simulations have been performed (see table 1): a) the "M-case" corresponding to the typical maritime distribution outside the area of strong winds. In this case the maximum radius of dry AP was set equal to 2-μm. The CCN number (at S=1%) was set equal to 60 cm^{-3}. The activation of the largest APs leads to the formation of 10 μm-radius droplets. b) the "M_c case", in which the AP distribution represents the sum of a continental AP distribution (with the maximum AP radius of 0.6 μm) and the maritime distribution similar to the M-case described previously. We suppose that this case represents the AP size distribution over the sea when continental aerosol intrusion under weak and moderate winds occurs. c) In the "M_tail-case" the AP distribution is similar to that in the M-case within the dry AP radii range below 0.6 μm, but with a 100 times higher AP concentration with radii exceeding 0.6 μm. As a result, the concentration of dry CCN (at S=1%) with the radii exceeding 0.6 μm is 60 cm^{-3}, which includes the concentration of 2 μm-radius CCN of 3.5 cm^{-3}. We suppose that this case may represent the AP distribution under hurricane winds in the central TC zone. d) In the "M_c_tail case" the AP is the same as in M_c, but with a large CCN tail of the size distribution as in the M-tail case. We suppose that this case represents the AP size distribution under the intrusion of continental aerosols and very strong wind.

Parameters N_o and k assumed in these simulations and the corresponding references are presented in **Table 1**.

We have not included the CCN with the dry radius above 2 μm into the simulations. In all simulations clouds were triggered by the initial heating within the zone centered at x=54 km, to allow the cloud hydrometeors be located in the computational zone during a longer time period. The maximum heating rate was set equal to 0.01 $^oC/s$ in the center of the 4.9 km x 2 km heating area and decreased linearly to the periphery of the zones. The duration of initial heating was 600 s in all experiments.

Table 1. List of simulations and parameters characterizing aerosol distributions

Type of cloud	Short title	$N_0(cm^{-3})$	k	references
Maritime cloud	M	60	0.308	Khain et al 2005
Sum of maritime and continental	M-c	2500 60	0.921 0.308	Khain et al 2001b; 2004; 2005; Khain and Pokrovsky, 2004
Maritime cloud with increased fraction of large CCN	M_tail cloud	60 tail: 60 CCN with the radii exceeding 0.6 μm	0.308	Sensitivity study
Sum of maritime and continental but with the increased fraction of large CCN	M_c_tail	2500 cm^{-3} 60 cm^{-3} tail: 60 particles with the radii exceeding 0.6 μm	0.92 0.308	Sensitivity study.

The maximum value of the dynamical time step was 5 s. Most simulations were conducted for 3 to 4 hours.

2.3 RESULTS OF SIMULATIONS

The first important result was the following: the tail of large CCN (within the 0.6 μm to 2 μm radii range) actually does not influence cloud microstructure and precipitation in the presence of a high concentration of small CCN. For instance, horizontally averaged accumulated rain amounts in the M_c and M_c_tail simulations are just similar (**Figure 4**).

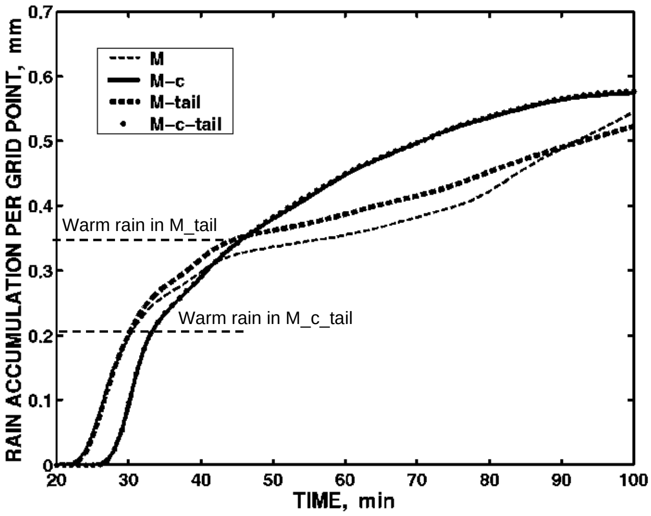

Figure 4. *Time dependence of accumulated precipitation at the surface in the simulations with different concentrations and size distributions of aerosols (see Table 1). The horizontal dashed lines denote the approximate amount of warm rain in the simulations. The remaining accumulated rain is mostly cold (melted) precipitation. The warm rain from the clouds developing in the polluted air is smaller than that in the cloud developing in clean air. At the same time, the total accumulated rain is larger in clouds developing in polluted air.*

This result can be explained as follows: the rate of the diffusion growth is determined by supersaturation. In the case when about 1000 cm^{-3} droplets are nucleated (as in the M_c and the M_c_tail cases), the supersaturated water vapor is shared between a great number of droplets and the supersaturation is small. Moreover, the droplets growing on large CCN also contribute to the decrease in the supersaturation. As a result, the largest nucleated droplets with the initial radius of about 8 μm grow relatively slowly and reach the size necessary to collect smaller droplets at the heights of about 5.5-6 km. It is necessary to recall that smaller droplets increase their size by diffusional growth faster than the largest ones (Rogers and Yau 1989), so that at the 6 km level the contribution of the CCN tail to the concentration of raindrops is not substantial. A stronger effect of the large tail takes place in the case of low droplet concentration, when supersaturation is higher than in the case of high droplet concentration. Hence, raindrops in the M_tail form at about 3 km and not at 4 km as in the M-case. The accumulated rain in the M_tail run is larger than that in the M-run during the first 1.5 h. However, the difference between the rain amounts is not substantial in this case either. The low sensitivity of clouds developing under tropical maritime environmental conditions to the amount of large CCN allows us to discuss the effects of continental aerosols on TC clouds under a high uncertainty as regards the concentration of large CCN. Since we expect the existence of the tail of large CCN in the TC clouds, we will discuss the effects of continental aerosols on the cloud structure in the M_tail and the M_c_tail simulations below. Note that no giant CCN with the radii above 15-20 μm, which are able to trigger drop collisions immediately after their penetration into a cloud, were assumed in the simulations.

Figure 5 shows the fields of cloud water contents CWC (droplets with the radii below 50 μm) in the M_tail and M_c_tail simulations at t=25 min. One can see that while the CWC in clouds with a low AP concentration decreases dramatically above 3.5-4 km because of rapid raindrop formation, the CWC in clouds with a high AP concentration remains significant till

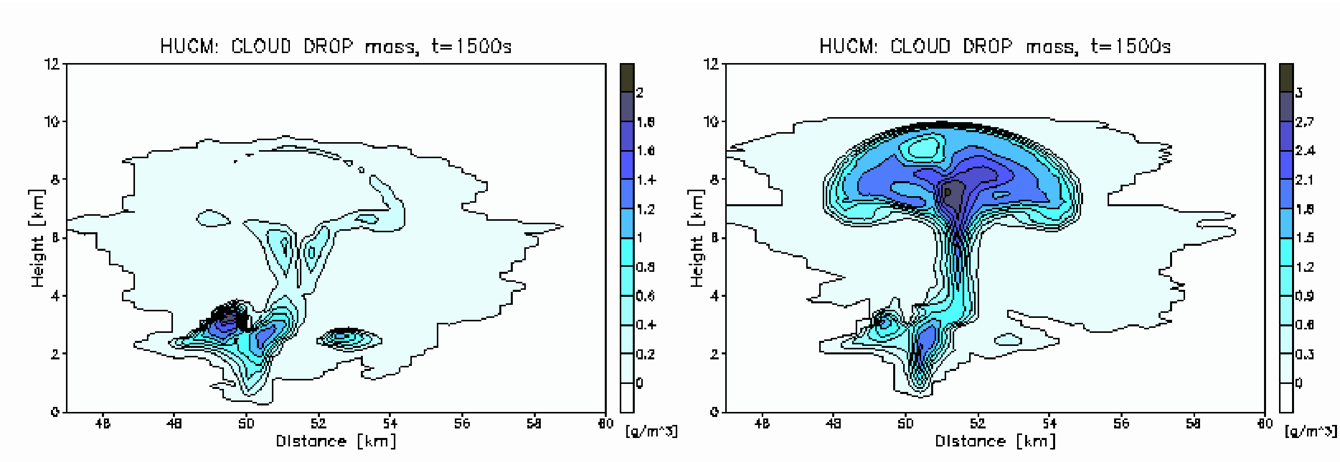

Figure 5. Fields of the cloud water content CWC (droplets with the radii below 50 μm) in the M_tail (left) and M_c_tail (right) simulations at t=25 min. The CWC is significantly higher and reaches higher levels in the clouds developing in polluted air.

the upper atmosphere. The latter is a typical feature of the clouds developing in highly polluted air (e.g., Andreae et al 2004; Ramanathan et al, 2001; Khain et al 2004, 2005). The specific feature of the present results is that high CWC forms in the polluted air in the presence of a high concentration of large CCN.

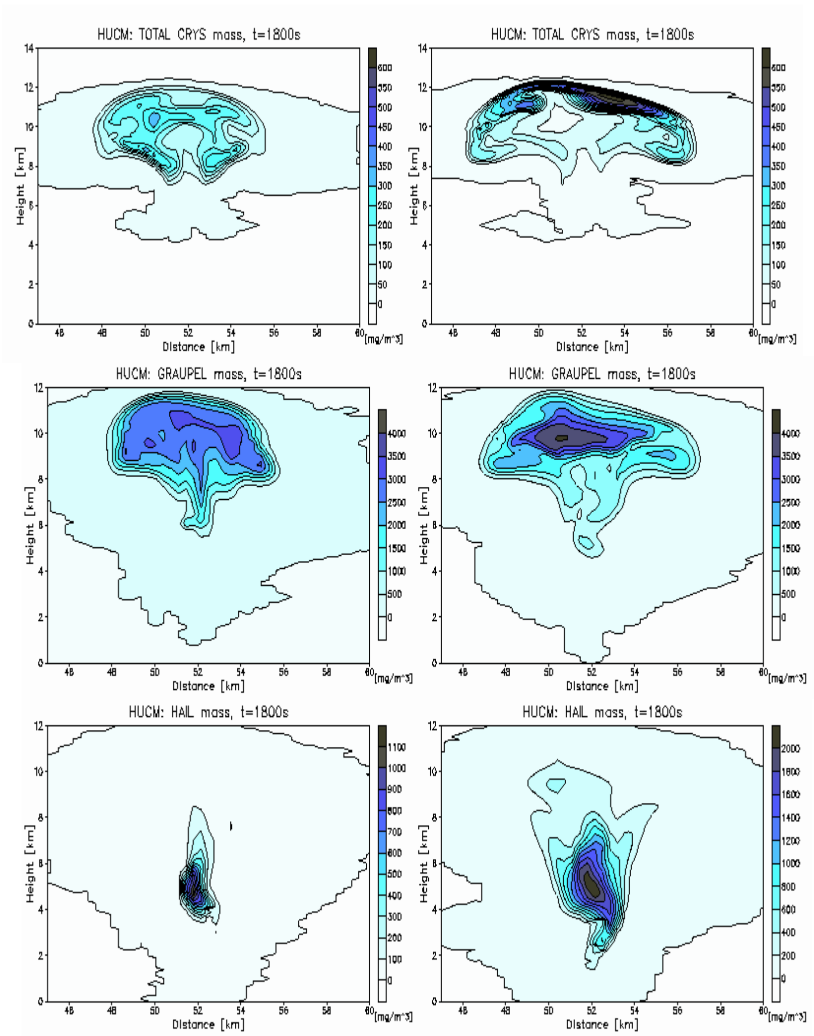

Figure 6. *The fields of crystal (upper panels), graupel (middle) and hail/frozen drops contents in the M_tail (left) and the M_c_tail (right) simulations. One can see that these contents are higher in the clouds developing under high aerosol concentration.*

Figure 6 shows the fields of crystal (upper panels), graupel (middle) and hail/frozen drops contents in the M_tail (left) and the M_c_tail (right) simulations. One can see that these contents are higher in the clouds developing in continental air, which can be attributed to a larger amount of the CWC penetrating above the freezing level in this case. On the average the total mass of graupel under high aerosol concentration is about 1.5 times higher than in case of low aerosol concentration.

Comparison of the fields of the vertical velocity in the M_tail and in the M_c_tail runs indicates (not shown) that the vertical velocities in the clouds developing within high AP concentration air are higher by a few ms^{-1} than in the clouds developing under low aerosol concentration cases. This aerosol effect on cloud dynamics was simulated and discussed in detail by Khain et al (2005) and then simulated in many studies (e.g. Lynn et al 2005 a,b). The increase in the vertical updrafts in tropical clouds developing in microphysically continental air can be attributed to an extra latent heat release caused by an extra condensational droplet growth (larger CWC) and an extra freezing (higher ice contents) (see Figures 5 and 6). Note that the difference between the vertical velocities (a few meters per second) is much smaller than the maximum updrafts of 15-18 ms^{-1}. Thus, the effect of aerosols on the maximum velocities is comparatively small. The vertical velocities are determined mainly by the CAPE in agreement with the results reported by Williams (1995) and Williams et al. (2004, 2005). The cloud base tops were actually similar in both clean and polluted air cases. This result agrees well with those reported by Khain et al (2005). The comparatively small effect of aerosols on the dynamical characteristics of clouds can be attributed to the following. On the one hand, the latent heat release in the clouds developing in the high CCN concentration case is larger, which can be seen by the generation of larger condensate mass. On the other hand, the mass loading in clouds developing in the microphysically continental air is larger. These two factors have opposite effects on the buoyancy and largely compensate each other. Thus, the dramatic difference between the microstructure of clouds seen in Figures 5 and 6 can be attributed mainly to aerosol effects. The comparison of the mass contents fields shown in Figures 5 and 6 indicates that favorable conditions for the charge separation (the coexistence of a significant amount of supercooled water, ice crystals and graupel at the temperatures below -13 ^{o}C) exists only in the case of high aerosol concentration. Hence, *the second conclusion that can be derived from the results is that the instability of the atmosphere at the TC periphery corresponding to the Jordan's (1958) sounding is necessary, but the condition it is not sufficient to create the microphysical structure favorable for intense electrification.*

So, it appears that aerosols represent an important component as regards production of a significant amount of supercooled water at the upper levels even under unstable atmospheric conditions, and in particular under maritime conditions. Of course, we mean the results of the numerical cloud model with the parameters of the aerosol distributions chosen as mentioned in Table 1.

Figure 7 (upper panels) shows the radar reflectivity fields in the M_tail (left), and in the M_c_tail (right) simulations probably representing the clouds in the eye wall (clean air) and at the periphery cloud bands in case of continental aerosol intrusion, respectively.

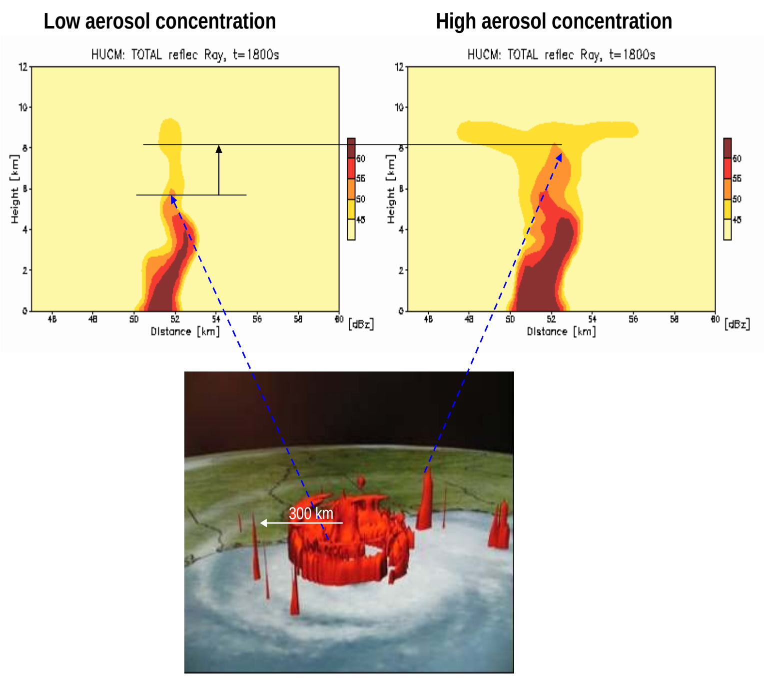

***Figure 7.** .The upper row: Radar reflectivity fields in the M_tail (left), the M_c_tail (right) simulations. Low panel: The rain structure of hurricane Rita.*

The comparison shows that the high values of the radar reflectivity in the clouds forming in the case of high AP concentration reach (better to say, start) at higher levels as compared to the clouds developing in clean air (one can expect that the air in the TC eyewall can be regarded as clear, see below). In the low panel the rain structure of hurricane Rita measured by the TRMM's Tropical Microwave Imager (TMI) on September 23, 2005 at 12:52 pm EDT is shown. At this time the storm was the category 4 hurricane with the minimum pressure of 924 mb, and sustained winds of 60 ms^{-1}. The zones with the precipitation rate at least 2.0 inches (58 mm/h) of rain per hour are marked. One can see that the model reveals some similar features, namely: precipitation particles start forming at higher levels at the TC periphery than in the eyewall.

We interpret all these results as some justification of the hypothesis *that aerosols penetrating into the maritime convective clouds are able to change dramatically the cloud microphysics and dynamics. These effects plus the atmospheric instability make possible the coexistence of cloud ice and supercooled water at high levels with the temperatures below-13^{o}C, i.e, the formation of thunderstorms over the ocean.*

Figure 4 shows the time dependence of accumulated precipitation at the surface in the simulations with different concentrations of small and large CCN (see Table 1). Horizontal dashed lines denote the transition from the warm rain regime to the cold (melted) rain. This transition is seen by the change in the slopes of the curves. Cold (melted) rain is less intense and the slope is lower. The ratio of the accumulated rain amount toward the end of warm rain and beginning of cold (melted) rain to the total accumulated rain represents the fraction of the warm rain within the cumulative precipitation. One can see that a) the accumulated precipitation from clouds developing in microphysically continental air is higher, which corresponds to a higher convective heating of the atmosphere. As it was discussed in Khain et al (2004, 2005, 2008), a higher accumulated rain is related to the generation of larger condensate mass in clouds developing in polluted air. At the same time the precipitation loss in the wet air by evaporation is low. There was no secondary cloud formation in these simulations.
b) The warm rain amount decreases in clouds developing in microphysically continental air, so that most precipitation in dirty clouds is cold rain formed by melting graupel and hail. On the contrary, precipitation from clouds developing in clean air is mainly warm rain.

It is reasonable to assume that the concentration of aerosols decreases from the TC periphery toward the TC center. This decrease can be caused by the wash out of aerosols in TC rain bands, as well as by a significant time required by the aerosols to reach the TC center in the TC boundary layer (see below). Hence, the conditions at the TC periphery where the concentration of continental CCN is higher remain favorable for flash formation during the whole time period when the TCs are in the vicinity of the land.

The conclusions derived in this section help us to carry out the simulations using a 3-D mesoscale model.

3. AEROSOL EFFECTS ON THE TCs APPROACHING THE LAND

A two nested grid Weather Research Model (WRF) was used to simulate landfall of a hurricane in the Gulf of Mexico. The resolution of the finest and the outer grid was 3 km and 9 km, respectively. The number of the vertical levels was 31, with the distances between the levels increasing with the height. The Thompson et al. (2006) bulk-parameterization was applied. Hurricane Katrina (August 2005) has been TC chosen as the case study. The initial fields were taken from the Global Forecast System Reanalysis data. The lateral boundary conditions were updated every six hours using the data as well. The Gulf of Mexico surface water temperatures were initialized on 28 August 12 Z, and were not updated during the experiments described below.

Note that the WRF used was not a TC forecast model, so that no specific adjustment procedures were used to adopt the TC structure derived from the crude resolution Reanalysis data to the intensity of the real TC at t=0. Hence, some relaxation period was required to get the model TC intensity close to the observed one. Note, however, that the accurate prediction of the Katrina's intensity was not the primary purpose of the study. The main purpose of the simulations was to compare the lightning spatial distributions in the simulations with and without aerosol effects on the clouds at the TC periphery in a strong hurricane, which would be able to involve aerosols from the continent. Because of the computer limitations, the simulations were performed in two stages.

At the first stage the TC was simulated on 27 August 00 Z (when it was located to the south of Florida) up to August 30, 00Z. The purpose of the simulation was to check whether continental aerosols, which were assumed to be located initially over the land (with zero concentration over the sea) may be involved into the TC circulation and penetrate into the TC to the distances up to about 300 km to the TC center toward the beginning of lightning in the Mexican Gulf (Fig 1). Aerosols were considered to be a passive scalar in the run.

Figure 8 (left panels) shows time dependence of the minimum pressure and tracks of TC simulated. The minimum pressure and track of TC Katrina is shown as well. One can see that the model TC (after some spin up period) reaches the intensity of hurricane Katrina. The errors in the location of TC center are small and hardly can affect significantly the formation of the spatial aerosol distribution. We believe that these results indicate that the model TC creates the field of the continental aerosol concentration quite similar to that could be expected around hurricane Katrina.

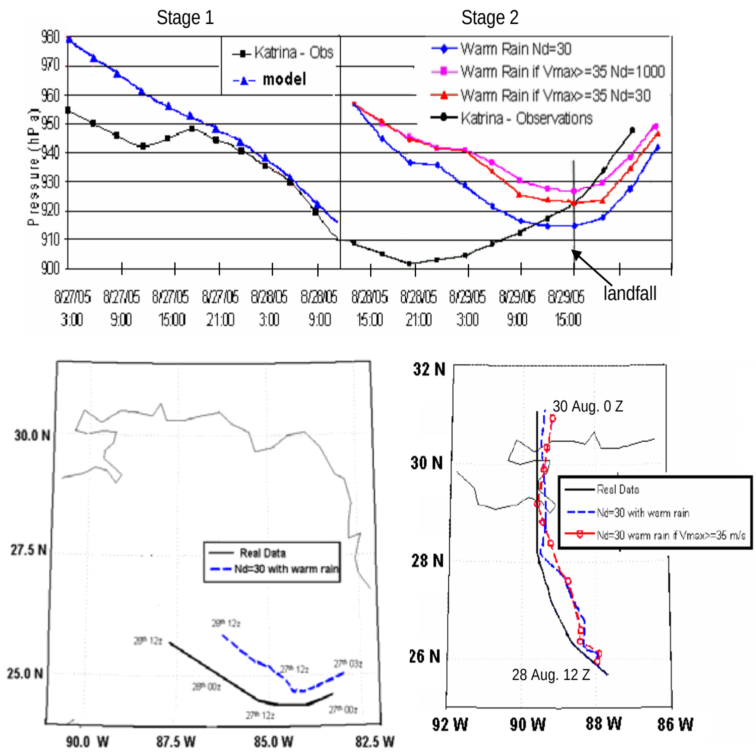

Figure 8. *Time dependencies of the minimum pressure and tracks of the model TC and of Katrina in two simulation stages: Aug. 27-Aug.28 (left panes) and Aug. 28- Aug 29 (right panels). The right upper panel shows that the warm rain prevention at the TC periphery increases the pressure by 7-12 mb, i.e., decreases the TC intensity.*

Figure 9 shows the field of aerosol concentration toward the end of the first stage of simulations. One can see that aerosols do penetrate the lower troposphere of the TC "in time". Towards August 28 , 12 Z aerosols form a front with the radius of about 250-300 km and a quite sharp gradient of aerosol concentration: while at the radii $r \geq 250km$ the concentration in the lower atmosphere was actually similar to that over the land, the central TC zone with the radius below 250 km was free from the continental aerosols. These results indicate that while lightning at the distances of a few hundred km from the TC center may be related to aerosols as it is hypothesized in the present study, the lightning in the TC eye wall seen in Fig 1 is not related to the continental aerosol effects. Note that developed rain bands form in the TC within zone of about 300 km radius. We suppose that the concentric lightning ring seen in Figure 1 forms in the zone of the aerosol “front”, which transforms the maritime clouds into thunderstorms with more continental characteristics.

Figure 9 (left) shows that the aerosols penetrate closer toward the TC center on the south side. This effect can be attributed to the fact that aerosols are advected along spirals by the TC wind speed. Aerosols starting their motion at the continent (to the north of the TC) should approach the TC center during their motion along the spirals because of the radial wind directed inward. Thus, aerosols should be closer to the TC center on the southern and the eastern sides of TCs then in the west side. However, the AP concentration decreases along the stream limes. Hence, the concentration on the south side turns out to be higher than on the east side. It is interesting to note that the spatial distribution of the AP concentration obtained in the simulation resembles the locations of negative ground flashes observed during hurricane stage in the nine storms in the Western Atlantic (see Figure 9 (right) adopted from Molinari et al 1999), composited with respect to the hourly center position of each hurricane. One can see a good correlation between the distribution of aerosols and the lightning density. The similarity of the fields may be interpreted as some evidence of the validity of the aerosol hypothesis (at

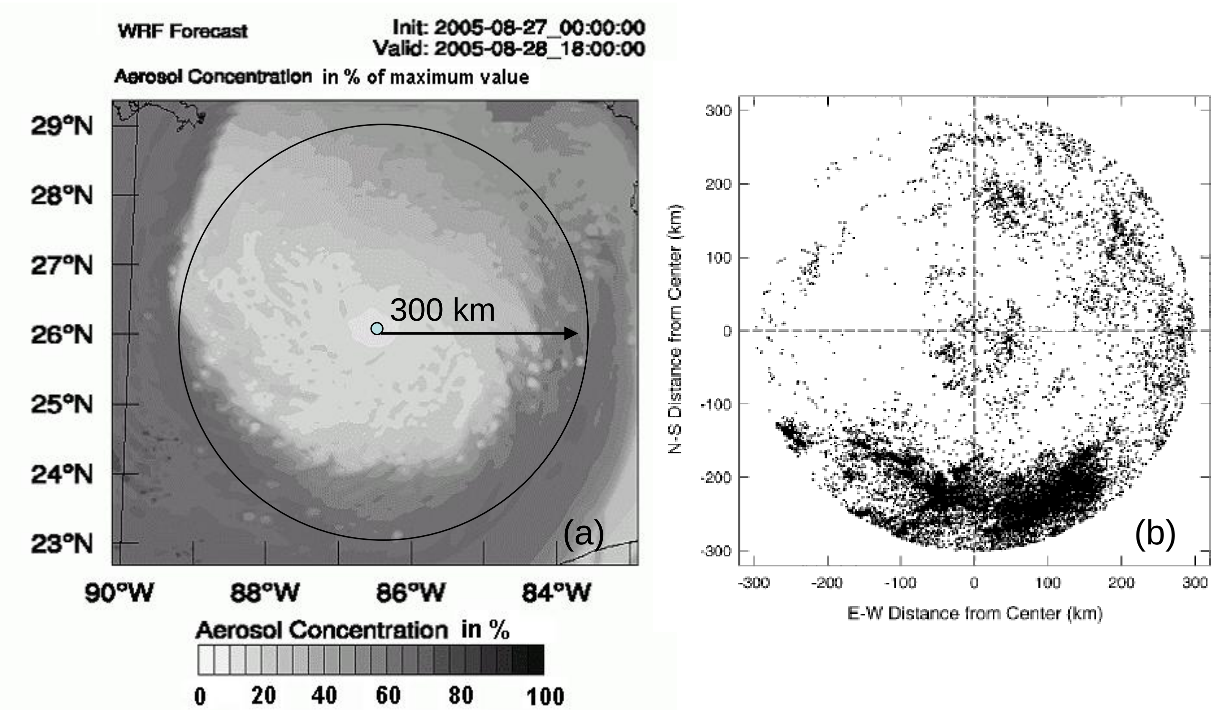

Figure 9. The field of the aerosol concentration simulated in the TC zone on 28 August, 12 00Z in % to the maximum value assumed to be over the continent (left panel). The right panel adopted from Molinari et al (1999) is composited with respect to the hourly center position of each hurricane. One can see a good correlation between the distribution of aerosols and the lightning density.

least, it does not contradict the hypothesis).

In the simulation, in which aerosols are treated as a passive scalar the aerosol front approaches the TC center in the inflow layer quite slowly, with the velocity close to the radial velocity of the flow. Passive aerosols reach the central TC towards the time, when Katrina was quite close to the land and the lightning in its eye wall had already terminated (Fig. 1, right panel). In the case cloud-aerosol interaction is taken into account, the concentration of continental aerosols must decrease from the TC periphery toward the TC center even more intensely because of the wash out of aerosols in the TC rain bands.

The results indicate the following:

a) The lightning in the TC eye wall is not related to aerosols involved into the TC circulation from the continent. To attain a significant concentration of supercooled droplets above the -13^{o}C level in the TC eye wall the vertical velocities must be especially high (or some still unknown mechanisms should be involved). At the same time the conditions at the TC periphery where the concentration of continental CCN is high remain favorable for flash formation during the whole time period when the TC approaches or penetrates the land. This result agrees with the observations that the lightning in the TC eye wall takes place only during eyewall replacements, while the lightning is a permanent feature at the TC periphery of TCs approaching the land (see .e.g. Fig 1).

b) The problem whether giant CCN arise in the zone of the maximum winds or not is not very important for our purpose because continental aerosols do not reach the TC center (at least, in the TC simulated in the study).

At the second stage the calculations of the TC were performed for the cases when the aerosol effects on TC clouds were taken into account. The calculation was performed within the period Aug. 28, 12 00Z to 30 Aug. 00 Z. The way how the aerosol effects were accounted for requires some preliminary comments. The 3-km resolution and the relatively crude vertical resolution do not allow one to reproduce the fine microphysical cloud features discussed in Section 2.3. It is well known that crude resolution decreases vertical velocities, whose values are of crucial importance for the simulation of cloud dynamics, microphysics and precipitation. As it was shown by Khain et al (2004), the increase in the distance between the neighbouring grids in the 2-D HUCM from 250 m to 1 km has resulted in a decrease in the maximum vertical velocities from 25 ms^{-1} to 10 ms^{-1}. Since the fall velocities of different hydrometeors do not depend on the grid resolution, the cloud microphysical structure turns out to be quite different under different grid resolutions. For instance, the terminal velocity of raindrops is about 10 ms^{-1}. In case the vertical updraft velocity is less than 10 ms^{-1} raindrops will rapidly fall out. Thus, the utilization of the crude resolution artificially makes the clouds “maritime” by their character, even if the concentration of AP is high. Besides, most bulk-parameterization schemes are, as a rule, less sensitive to aerosols than the spectral bin microphysical scheme (Lynn et al 2005b). To "sidestep" this problem, we simulated the effects of continental aerosols in the simulations by preventing warm rain in the scheme altogether. As seen in Figure 4, it is hardly possible to prevent warm rain in maritime deep clouds by an increase in aerosol concentration up to the magnitudes typical of continental conditions. However, small aerosols significantly decrease the warm rain amount, and even more relevantly, the prevention of warm rain in the 3-D model allows the reproduction of aerosol effects qualitatively similar to those obtained in the 2-D 250 m resolution cloud model, namely, a substantial transport of large CWC upward and an increase in the ice content.

The following simulations have been performed with the 3-D WRF model at the second stage. The control run allowed warm rain (WR) formation by drop-drop collisions (the WR run). In this run droplet concentration at the cloud base N_d was set equal to 30 cm^{-3}. This case corresponds to the M-run with the 2D model, where CCN concentration (at S=1%) was assumed to be 60 cm^{-3} (usually about half of the available CCN are activated). In the second run referred to as No Warm Rain at the Periphery (NWRP-30), aerosol effects were parameterized by shutting off the drop-drop collisions only at the hurricane periphery, where the surface wind was smaller than 35 m s^{-1}. This threshold was chosen because the continental aerosol concentration in the TC central zone where wind speed exceeds 35 m s^{-1} should be negligibly small, as it was discussed above. Besides, very high wind speed supposedly is able to produce a significant amount of giant CCN in the eye wall which most likely renders any effects of small aerosols ineffective. Hence, warm rain is shut off only in that part of the hurricane that has winds speeds less than the threshold value. A similar approach has been used by Rosenfeld et al (2007b). The third simulation, referred to as NWRP-1000, is similar to NWRP-30, but the droplet concentration at the cloud base was set 1000 cm^{-3}. This is a supplemental run, whose purpose was to illustrate the difficulties connected with simulation of the continental aerosol effects on maritime convection using the model with crude horizontal and vertical resolution and changing only the droplet concentration.

Figure 8 (right lower panel) shows the tracks of the simulated storms in the WR and NWRP-30 runs (The TC track in the NWRP-1000 was actually similar to that in NWRP-30) as well as the track of hurricane Katrina. One can see that the model reproduces Karina's track well enough. The deviation of the model TC track from that of the real TC can be attributed to the errors in the initial TC intensity derived from the Reanalysis data, rather than to aerosol effects. The simulated minimum pressures of the storm with time are shown in **Figure 8** (right upper panel). After a relatively short spin up period, the simulated TC reaches the super hurricane intensity with the minimum pressure of about 915-920 hPa, also observed in Katrina. In spite of the differences between the intensity of the simulated TC and that of Karina during the spin up period, the intensity of the simulated storm was quite close to that of Katrina when the intense lightning at the Katrina's periphery was observed (Fig. 1). The main result that follows from Figure 11 and those presented below is that aerosols affecting the hurricane clouds affect both TC structure and the intensity. One can see that the TC moving within polluted air at its periphery has a smaller intensity than that moving in clean air during the course of the entire simulation. This effect (see below) can be attributed to the convection invigoration at TC periphery, which was caused by turning off the warm rain (representative of the potential impacts of high concentrations of aerosols on the formation of droplets). As a result, some fraction of the air moving within the inflow layer ascends at the periphery instead of reaching the TC eye wall. Hence, the rate of the latent heat release within the eye wall decreases, which results in some increase in the central pressure.

Figure 10 shows the maximum values of the super cooled CWC above 5 km in simulations WR (with warm rain permitted) (left) and NWRP-30 (right) with no warm rain at the TC periphery. One can see a good qualitative correspondence of values obtained in

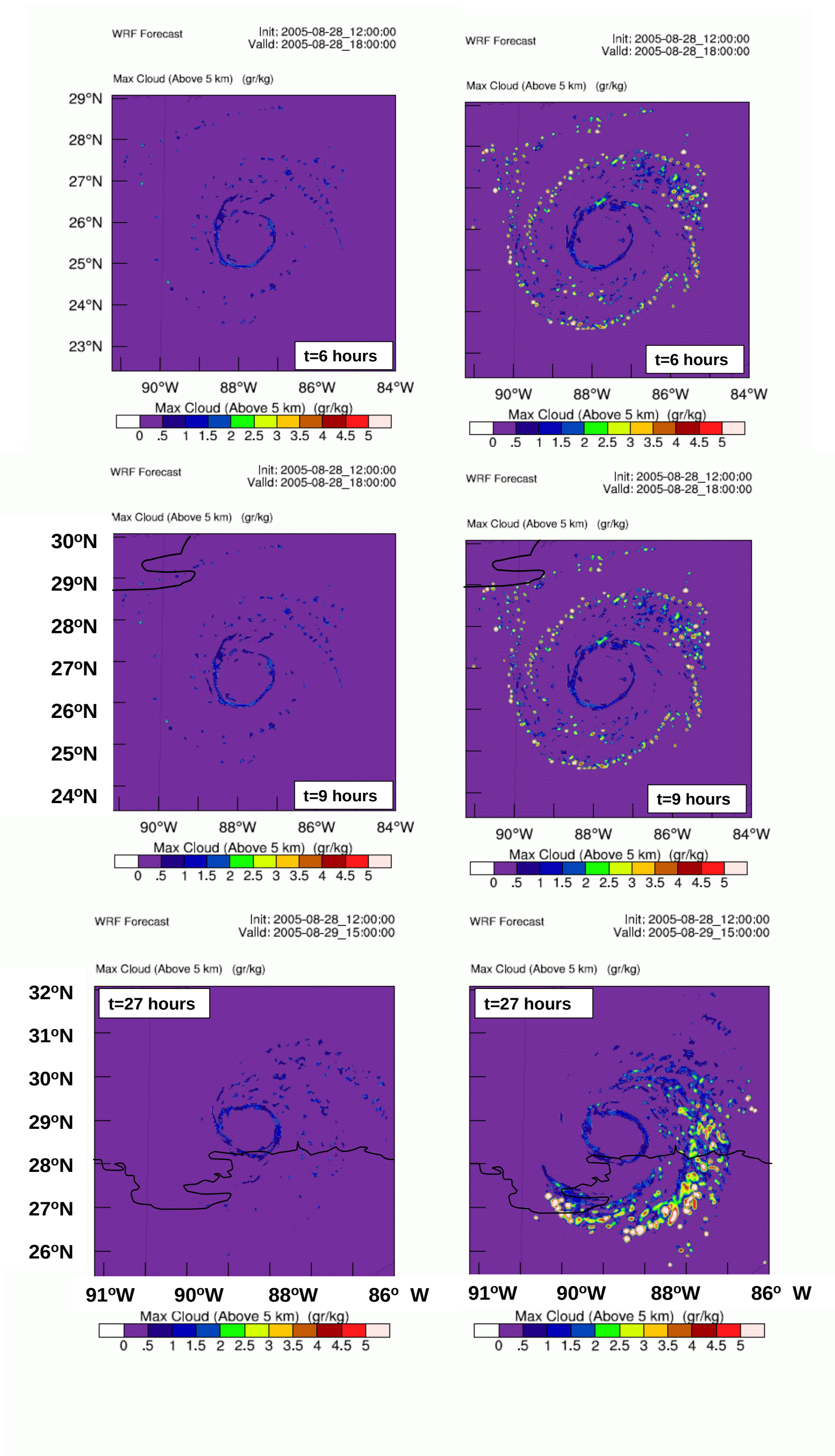

Figure 10. The maximum values of the super cooled CWC above the 5 km-level in the simulations with warm rain permitted (left) and no warm rain at the surface wind speeds exceeding 35 ms^{-1} *at different time instances.*

the 3-D simulation and those found in the 2-D individual cloud simulations: the CWC maximum in microphysically continental air is about 5 g/kg, while in the clean air it does not exceed 2 g/kg.

The amount of ice in the high AP concentration air is also larger than that in the clean air (not shown). The aerosol-induced increase in the total ice content at the TC periphery in agreement with the results of the 2D model with the spectral microphysics. The maximum values of the total ice content are also in good agreement with the 2-D results.

The difference between the condensate mass contents in the WR and NWRP-30 indicates the differences in the latent heat release and the vertical updrafts. The maximum vertical velocity in many small clouds arising in polluted air exceeds 10 ms^{-1}, while in the TC central zone the typical maximum vertical velocity ranges mainly from 4 to 10 ms^{-1}. Thus, aerosols increase the intensity of convection within the cloud bands located at the distance of 250-300 km from the TC center. This radius corresponds to the TC most remote cloud bands.

As it was discussed above, an increase of the CWC and the ice content in the zones of high vertical velocity should foster the lightning formation. **Figure 11** shows the fields representing the maximum values of products of updrafts, the CWC and the total ice content calculated in each grid point in a column. The maximum values of the products will be referred to as the lightning probability (LP). The two upper panels correspond to the time periods of the lightning rate depicted in Figure 1. One can see that the LP fields calculated in NWRP-30 resemble quite well the structure of the lightning observed: a) the maximum lightning in both cases takes place within a comparatively narrow ring of the 250-300 km radius; b) lightning (in the calculations

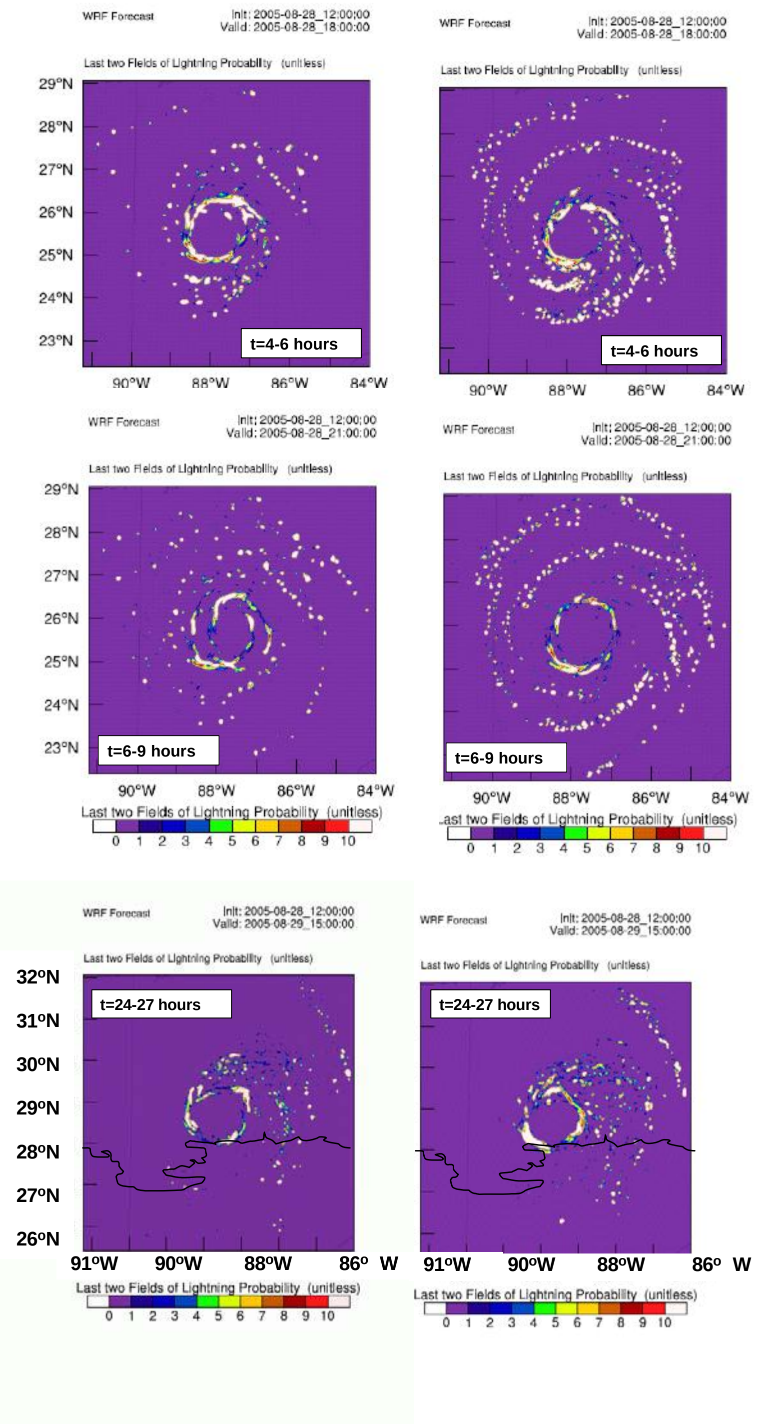

Figure 11. Lightning probability (LP) at different time periods in the case of clouds developing in clean air (left) and continental air (right). The LP is calculated as the maximum product of updrafts, CWC and total ice contents. The LP plotted represents a sum of the LP fields calculated within the time ranges shown in the panels.

LP) at the TC central zone is as a rule weaker than in the rain bands at the TC periphery. Contrary to it, in the WR simulation lightning is much weaker and is concentrated in the eye wall (similarly to Fierro's et al 2007 results), which does not agree with the observations.The lower panels correspond to the time when the entire TC has penetrated into the land and rapidly decays. **Figure 11** indicates that while in clean air the lightning probability decreases over the land, it remains high in polluted air. Moreover, the lightning rate increases in the TC central zone. These figures show that aerosols significantly affect the spatial distribution of intense convection in TCs.

The results also indicate that aerosols affect the cloud structure, the intensity and spatial distribution of the precipitation of TCs approaching and penetrating the land (**Figure 12**).

4. DISCUSSION AND CONCLUSIONS

The potential effects of continental aerosols penetrating into the clouds (via the cloud bases) at the periphery of a TC approaching the land on the cloud structure and the lightning rate has been investigated using a 2-D cloud model with spectral bin microphysics and a 3D mesoscale WRF model with the bulk microphysics. Numerical experiments with the 2D cloud model with the resolution of 250 m and 125 m in the horizontal and vertical directions, respectively, show that the continental aerosols with the CCN concentrations of about 1000 cm^{-3} significantly increase the amount of supercooled cloud water, as well as ice (mainly ice crystals, graupel and hail) even under the high concentration of large CCN. In addition, the vertical updrafts were several m/s higher in the polluted clouds. All these factors taken together lead to the coexistence of ice and cloud water within a suppercooled cloud zone, which

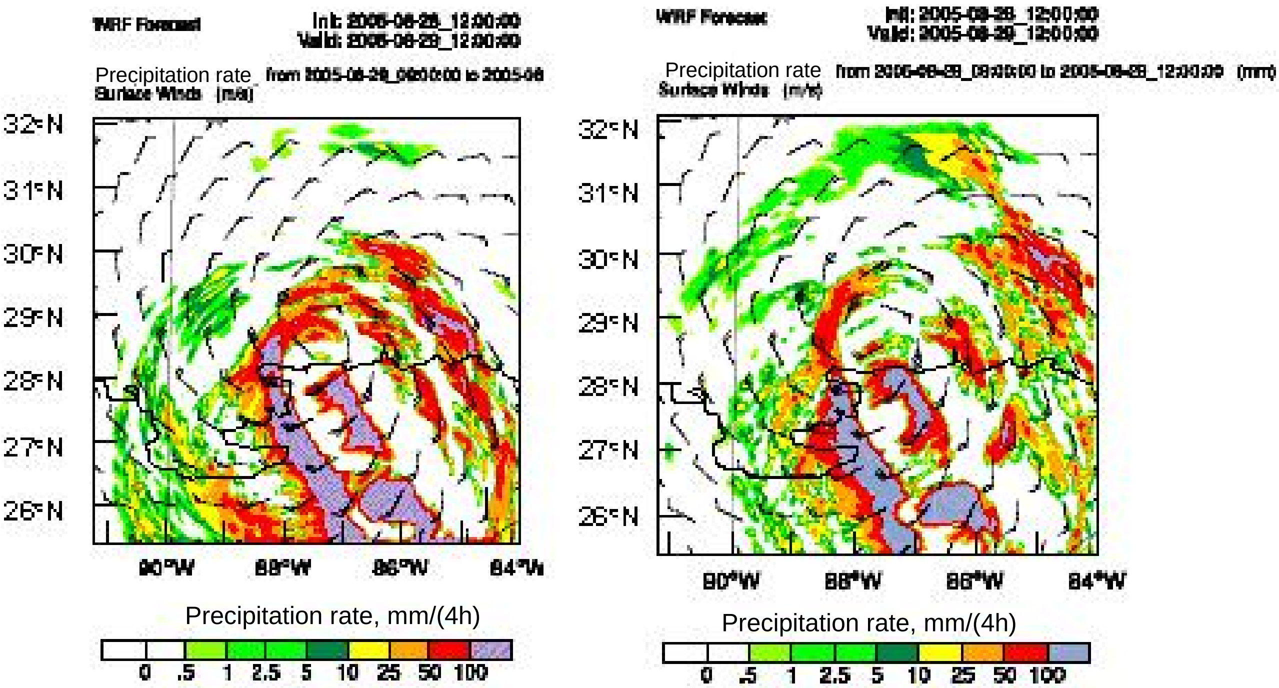

Figure 12. *The field of the precipitation rate in the run with warm rain allowed over the entire computational area (WR-simulation)(left) and in the case when warm rain has been turned off at the TC periphery (NWRP-30) (right) during the TC landfall.*

is considered to be favorable for charge separation and lightning formation.

The purpose of the simulations using a mesoscale 3-km resolution model was to investigate the possible effects of aerosols on lightning at periphery of hurricanes approaching the land as well as, on the cloud structure, precipitation and the TC intensity. The utilization of the 3-km resolution and crude vertical resolution, as well as the bulk-parameterization scheme used do not allow one to reproduce aerosol effects related to the fine balance between the fall velocity of growing droplets and the vertical velocity. For instance, although the results of the supplemental simulation with the droplet concentration N_d of 1000 cm^{-3} indicate some increase in central pressure and an increase in the supercooled CWC, but in general the results were quite similar to those obtained in the case when the droplet concentration was set equal to $30\,cm^{-3}$.

As a result, the aerosol effects were parameterized by "switching off" droplet collisions, and preventing warm rain at the TC periphery, where the surface wind speed was under 35 ms^{-1}. This simple parameterization of the aerosol effects leads to the results, which agree better with those, obtained using a spectral microphysical model with the 100-250 m grid resolution.

The product of the ice content, the supercooled cloud water content and the updraft velocity was chosen as the measure of the lightning activity (lightning probability, LP). It was shown that the LP field calculated in the model resembles quite well the structure of lightning observed: a) the maximum lightning takes place within a comparatively narrow ring with the radius 250-300 km; b) lightning in the TC central zone is, as a rule, weaker than that in the rain bands at the TC periphery. The LP minimum was found to be related to the suppression of the deep convection within the ring of the 50-150 km radius range. This minimum becomes more pronounced when the outermost rain bands are invigorated. In the simulation, where no aerosol effects were taken into account, the magnitude of the LP parameter was smaller and concentrated in the eye wall, which does not agree with the observations.

The analysis of the intensity variations of simulated TCs, as well as the observed variation of the intensity of hurricanes Katrina (2005) and Rita (2005) (Fierro et al 2007), shows that the disappearance of lightning in the TC central zone and its intensification at the TC periphery can be a good indicator of the TC decaying. Such behavior of the TC lightning may be useful for a short range TC intensity forecast. Note that the simulations of TC lightning in an idealized TC performed by Fierro et al (2007) showed a negligible lightning activity at the TC periphery as compared to that in the TC eye wall. The instability of the atmosphere at the TC periphery was higher than in the TC center in those simulations. However, it did not lead to convective invigoration and lightning at the TC periphery. Thus, the comment of Molinari et al (1999) that the higher instability of the atmosphere at the TC periphery "*cannot be a complete explanation"* of the lightning maximum at the TC periphery seems to be correct. We attribute the result obtained by Fierro et al (2007) to the fact that no aerosol effects have been taken into account in their simulations. Their results indicate that the changes of the instability of the atmosphere can lead to the variability of the lightning in the TC eye wall, but not within a narrow ring at the TC periphery. Hence, the comparison of the results obtained by Fierro et al (2007) and those in this study supports the assumption that lightning at the TC periphery is caused by the synergetic effect of continental aerosols and higher atmospheric instability.

The results also indicate that aerosols affect the cloud structure, the intensity and the spatial distribution of precipitation of TCs approaching and penetrating the land, or the TCs located in the air of continental nature containing a significant amount of aerosols. According to the results obtained, aerosol-induced convection invigoration at TC periphery leads to a TC weakening. From observations (e.g., Dvorak, 1984) and numerical results (e.g., Khain et al, 1984) it follows that TC formation and intensification takes place when the convection is concentrated in the TC center leading to latent heat release and the pressure fall there. According to the results of a great number of simulations with a TC model (Khain 1984) the intensification of convection at TC periphery decreases the TC intensity. This decrease can be attributed to the fact that the convection invigoration at the TC periphery leads to a) a decrease in the air mass penetrating to the TC eyewall and to a decrease the mass flux there. Correspondingly, the latent heat release also decreases in the eyewall. The second mechanism is as follows. Any deep cloud induces compensating downdrafts in its surrounding. As a result, deep clouds are usually surrounded by quite small ones, because of the competition. This competition between clouds was studied in several studies. The convection at the TC periphery affects the convection in the TC center in the similar way.

The mechanism of the TC weakening discussed in our paper resembles the hypothesis of the field experiment Storm Fury (Simpson and Malkus, 1964, Willoughby et al., 1985) according to which intensification of convection at the periphery of the eyewall should decrease air mass penetrating further toward the TC axis and weaken the wind speed maximum. However, in Storm Fury it was hypothesized that there is a significant amount of supercooled water at high levels in the eyewall. More detailed analysis (Willoughby et al., 1985) showed that there was too little supercooled water and too much hail in these clouds. Correspondingly, the cloud microphysical structure did not match the Storm Fury hypothesis. In our study the convection invigoration is caused by small aerosols. Such invigoration agrees both with the observations (e.g., Koren et al 2005) and the results of numerical cloud models with detailed microphysics

(Khain et al, 2005, 2008). A possible application of such finding to the TC mitigation by seeding is discussed by Rosenfeld et al. (2007b).

Zhang et al (2007) simulated the evolution of the idealized TC beginning with a weak initial vortex and found that the maximum TC intensity decreases when the aerosol concentration increases. We suppose that the reason of the TC weakening was similar to that found in this study: Zhang et al (2007) took aerosol scavenging into account, so the aerosol concentration was, supposedly, larger at the TC periphery as it was simulated in the present study.

Precipitation in the TC zone of the 350-400 km radius range decreases in the high AP concentration air mainly due to the convection weakening in the central zone of the TCs. At the same time precipitation at the TC periphery, as well as the precipitation area increase. More detailed simulations are required to conclude, whether continental aerosols increase or decrease precipitation from landfalling TCs over the land. We speculate that a weekly variation of the anthropogenic aerosols concentration can lead to a weekly cycle of intensity and precipitation of landfalling TCs. Note that the weekly cycle of the intensity and precipitation of landfalling TCs was reported first by Cerveny and Balling (1998). They attributed the variations to the weekly variations of the anthropogenic aerosol production. According to the hypothesis by Cerveny and Balling (1998), the aerosol loading increase leads to the increase in the solar heating in the boundary layer around a cyclone. In the present study we considered another mechanism that potentially can contribute to the weekly cycle of precipitation and the wind speed. Cerveny and Balling (1998) reported an increase in the precipitation under aerosol effects. Figure 12 indicates some possibility that such increase is caused by effects of aerosols on microphysical cloud structure. Note that the radiative effects of aerosols have not been taken into account in the present study. Thus, we cannot conclude what mechanism is dominating. More investigations are required to make a definite conclusion.

A decrease in the TC intensity under the influence of the Saharan air was also reported by Dunion and Velden (2004). They attributed the decrease in the intensity to thermodynamical effects. We suspect that microphysical effect of the Saharan dust on TC convection may be also significant (see e.g. Zhang et al, 2007). Further investigations are required.

According to the results obtained using the 2-D cloud model, aerosols lead to an more significant increase of the CWC at higher levels than that it has been simulated using the WRF mesoscale model. We suppose, therefore, that the aerosol effect on cloudiness, precipitation and intensity of TCs may be more pronounced than that demonstrated in the study using the model with the 3-km resolution.

Note in conclusion that in spite of the encouraging and consistent results, this study must be considered as a plausible hypothesis as to how continental aerosols might affect hurricanes. Much more work must be done in the area of aerosol mapping and the trajectory analysis to formulate a consistent picture of TC/aerosol interactions. The utilization of high resolution models with spectral bin microphysics is desirable to make the results quantitative. More observational studies are required to investigate the microphysical structure (e.g., supercooled water, cloud ice contents) of clouds in TCs. Observational and numerical studies are also needed to determine aerosol properties (e.g., size distributions), as well as aerosol fluxes from the land to tropical cyclones.

Acknowledgements We express a deep gratitude to I. Ginis for providing results of the SST simulations in the zone of hurricane Katrina, as well as to E. Williams and C. Price for useful observation data and advice. The study was supported by the Israel Science Foundation (grant 140/07).

References:

Andreae, M.O., D. Rosenfeld, P. Artaxo, A.A. Costa. G.P. Frank, K.M. Longlo, and M.A.F. Silva-Dias, 2004: Smoking rain clouds over the Amazon. *Science*, **303**, 1337-1342.

Black , M.L , R. W. Burpee, and F.D. Marks, Jr.1996: Vertical motion characteristics of tropical cyclones determined with airborne Doppler radar velocities. *J. Atmos. Sci*. **53**, 1887-1909.

Black R. A. and Hallett J., 1986: Observations of the distribution of ice in hurricanes. *J. Atmos. Sci*. 43, 802-822.

Black R. A. and Hallett J. 1999: Electrification of the hurricane. *J. Atmos. Sci.*, **56**, 2004-2028

Cecil D.J., E.J. Zipser, and S.W. Nebitt 2002a: Reflectivity, ice scattering, and lightning characteristics of hurricane eyewalls and rainbands. Part 1: Quantitative description. Mon Wea. Rev. 130, 769-784.

Cecil D.J., E.J. Zipser, and S.W. Nebitt, 2002a: Reflectivity, ice scattering, and lightning characteristics of hurricane eyewalls and rainbands. Part 2: Intercomparison of observations. *Mon Wea. Rev*., **130**, 785-801.

Cerveny R. S. and R. C. Balling (1998). Weekly cycles of air pollutants, precipitation and tropical cyclones in the coastal NW Atlantic region. *Nature* **394** (6693) 561-563.

Chronis T, E. Williams, E. Anagnostou, and W. Petersen, 2007: African Lightning: indicator of tropical Atlantic cyclone formation. *EOS*, **88**, 40, 2 October 2007.

Demetriades N.W.S and R.L Holle, 2006: Long-range lightning nowcasting applications for tropical cyclones. *Preprints, Conf. Meteorology Application of Lightning Data, Atlanta*, AMS, 9 pp.

Dunion J. P. and C. S. Velden, 2004: The impact of the Saharan air layer on Atlantic Cyclone activity. *Bull Amer Met. Soc*., 353-365.

Dvorak, V.F., 1984: "Tropical cyclone intensity analysis using satellite data" NOAA Tech. Rep. NESDIS 11, 47pp

Emanuel K. A. 1994. *Atmospheric convection*. *Oxford University Press.* 580pp.

Fierro A.O. , L. Leslie, E. Mansell, J. Straka, D. MacGorman, and C. Ziegler, 2007: A high-resolution simulation of microphysics and electrification in an idealized hurricane-like vortex*. Meteorol. Atmos. Phys*. Doi: 10.1007/s00703-006-0237-0.

Ferrier, B.S. and R.A. Houze 1989: One-dimensional time dependent modeling of GATE cumulonimbus convection. *J. Atmos. Sci.,* 46, 330-352.

Houze R.A., Jr., S.S. Chen, B.F. Smull, W.-C Lee, Rogers R.F., J.A. Moore, G. J. Stossmeister, M.M. Bell, J.Ceetrone, W. Zhao and S.R. Brodzik, 2006: The Hurricane rainband and intensity change experiment. Observations and modeling of hurricanes Katrina, Ophelia, and Rita: *Bull. Amer. Meteor. Soc*. , 87, 1503-1521.

Houze. R.A., Jr., S.S. Chen, B.F. Smull, W.-C Lee, M.M. Bell, 2007: Hurricane intensity and eyewall replacement. *Science*, **315**, 1235-1239.

Jordan, C.L., Mean soundings for the West Indies area. *J. Meteor.,* 15, 91-97, 1958.

Jorgensen, D.P., and M.A. LeMone 1989: Vertical velocity characteristics of oceanic convection. *J. Atmos. Sci*., **46**, 621-640.

Jorgensen , D. P., E.J. Zipser, and. M.A. LeMone, 1985: Vertical motions in intense hurricanes. *J. Atmos. Sci.,* 42, 839-856.

Khain, A.P. and G.G. Sutyrin, 1983: *Tropical cyclones and their interaction with the ocean*, Gidrometeoizdat, Leningrad (St. Petersburg), 241p.

Khain, A. P., 1984: *Mathematical modeling of tropical cyclones*, Gidrometeoizdat, St.Petersburg, 247p.

Khain, A.P. and E. A. Agrenich, 1987: Possible effect of atmospheric humidity and radiation heating of dusty air on tropical cyclone development. *Proc. Institute Experim. Meteorol*., 42(127), 77-80.

Khain A., A. Pokrovsky and M. Pinsky, A. Seifert, and V. Phillips, 2004: Effects of atmospheric aerosols on deep convective clouds as seen from simulations using a spectral microphysics mixed-phase cumulus cloud model Part 1: Model description. *J. Atmos. Sci 61, 2963-2982.*

Khain A. and A. Pokrovsky, 2004: Effects of atmospheric aerosols on deep convective clouds as seen from simulations using a spectral microphysics mixed-phase cumulus cloud model Part 2: Sensitivity study, *J. Atmos. Sci. 61, 2983-3001*

Khain, A., D. Rosenfeld and A. Pokrovsky, 2005: Aerosol impact on the dynamics and microphysics of convective clouds. *Quart. J. Roy. Meteor. Soc.* 131, 2639-2663.

Khain A.P., N. BenMoshe, A. Pokrovsky, 2008: Aerosol effects on microphysics and precipitation in convective clouds with a warm cloud base: an attempt of classification. J. Atmos. Sci. (in press).

Koren I., Y. J. Kaufman, D. Rosenfeld, L. A. Remer, Y. Rudich, 2005: Aerosol invigoration and restructuring of Atlantic convective clouds, *Geophys. Res. Lett.,* **32**, L14828, doi:10.1029/2005GL023187.

Lhermitte R.M., and P. Krehbiel, 1979: Doppler radar and radio observations of thunderstorms. *IEEE Trans Geosci Electron* **17**, 162-171

Li,G., Y. Wang and and R. Zhang 2008: Incorporation of a two-moment bulk microphysics scheme to the WRF model to investigate aerosol-cloud interaction. *J. Geophys. Res.* (in press)

Lucas, C. and R.E. Orville, 1996: TOGA COARE: Oceanic lightning. *Mon. Wea. Rev*. **124**, 2077-2082.

Lynn *B*., A. Khain, J. Dudhia, D. Rosenfeld, A. Pokrovsky, and A. Seifert 2005: Spectral (bin) microphysics coupled with a mesoscale model (MM5). Part 1. Model description and first results. *Mon. Wea. Rev.* **133**, 44-58.

Lynn *B*., A. Khain, J. Dudhia, D. Rosenfeld, A. Pokrovsky, and A. Seifert, 2005: Spectral (bin) microphysics coupled with a mesoscale model (MM5). Part 2: Simulation of a CaPe rain event with squall line *Mon. Wea. Rev.* , **133**, 59-71.

Mansell E.R. , D.R. Mac.Gorman and J.M. Straka, 2002: Simulated three-dimensional branched lightning in a numerical thunderstorm model. *J. Geophys. Res*. **107**, D9, doi: 10.1029/2000JD000244.

McFarquhar G., and R.A. Black, 2004: Observations of particle size and phase in tropical cyclones: implications for mesoscale modeling of microphysical processes, *J. Atmos. Sci*., **61**, 422-439

Mitzeva,R.P.,J.Latham,and S.Petrova,2006:A comparative modeling study of the early electrical development of maritime and continental thunderstorms. *Atmos. Res.,* 82,26,doi:10.1016/j.atmosres.2005.01.006.

Molinari J., P.K. Moore, V.P. Idone, R.W. Henderson and A.B. Saljoughy, 1994: Cloud-to-ground lightning in hurricane Andrew. *J. Geophys. Res*., **99**, 16665-16676.

Molinari J., Moore P., and V. Idone, 1998: Convective structure of hurricanes as revealed by lightning locations, *Mon. Wea. Rev*., **127**, 520-534

Orville R.E. and J.M. Coyne, 1999: Cloud-to-ground lightning in tropical cyclones (1986-1996). *Preprints, 23-rd Conf. on Hurricanes and tropical meteorology, Dallas, Amer. Meteor. Soc.* , 194pp.

Pinsky, M. and A. P. Khain, 2002: Effects of in-cloud nucleation and turbulence on droplet spectrum formation in cumulus clouds. *Quart. J. Roy. Meteorol. Soc*., 128, 1–33.

Ramanathan, V., P. J. Crutzen, J. T. Kiehl and D. Rosenfeld, 2001: Aerosols, climate, and the hydrological cycle, *Science,* **294**, 2119-2124

Rogers, R. R. and Yau, M. K., 1989: *A short course of cloud physics*. Pregamon, Oxford, 293 pp.

Rodgers E., J. Weinman, H. Pierce, W. Olson , 2000: Tropoical cyclone lightning distribution and its relationship to convection and intensity change. *Preprints, 24th Conf. on Hurricanes and Tropical meteorology, Ft. Lauderdale, Amer. Meteor. Soc*. Pp. 537-541.

Rosenfeld D, R. Lahav, A. Khain, and M. Pinsky, 2002: The role of sea spray in cleaning air pollution over ocean via cloud processes. *Science*, **297**, 1667-1670.

Rosenfeld D., M. Fromm, J. Trentmann, G. Luderer, M. O. Andreae, and R. Servranckx, 2007: The Chisholm firestorm: observed microstructure, precipitation and lightning activity of a pyro-Cb. *Atmos. Chem. Phys.*, **7**, 645-659.

Rosenfeld D., A. Khain, B. Lynn, W.L. Woodley 2007b: Simulation of hurricane response to suppression of warm rain by sub-micron aerosols. *Atmos. Chem. Phys. Discuss*., **7**, 5647-5674.

Saunders, C.P.R., 1993: A review of thunderstorm electrification processes, J. Appl. Meteor., 32, 642-655.

Simpson, R.H., and Malkus J.S.: Experiments in hurricane modification. Sci. Amer., 211, 27-37, 1964.

Sherwood S.C., V. Phillips and J. S. Wettlaufer (2006). Small ice crystals and the climatology of lightning. *Geophys. Res. Letters*, 33, L058804, doi. 10.1029/2005GL.

Shao X.M., Harlin J., Stock M., Stanley M., Regan A., Wiens K., Hamlin T., Pongratz M., Suszcynsky D. and Light T., Los Alamos National Laboratory, Los Alamos, N.M, 18 October 2005, Katrina and Rita were lit up with lightning, *EOS*, Vol. 86, No.42, page 398-399.

Skamarock, W.C., Klemp J.B., Dudhia J., Gill D.O., Barker D.M., Wang W., and Powers J.G., 2005: A description of the Advanced Research WRF Version 2. NCAR Tech Notes-468+STR.

Solomon, R. and M.B. Baker, 1996. A one-dimensional lightning parameterization, J. Geophys. Res., 101, 14, 983-90.

Solomon, R. and M.B. Baker, 1998. Lightning flash rate and type in convective storms. *J. Geophys. Res.*, 103, D12, 14, 041-14,057.

Solomon R., C. Adamo, and M. Baker, 2002: A lightning initiation mechanism: application to a thunderstorm electrification model*, C.R. Physique3,* 1325-1333.

Straka J.M. and E.R. Mansell, 2005: A bulk microphysics parameterization with multiple ice precipitation categories. *J. Appl. Meteorol*. **44**, 445-466.

Szoke, E.J., E.J. Zipser, and D.P. Jorgensen, 1986: A radar study of convective cells in mesoscale systems in GATE. Part 1: Vertical profile statistics and comparision with hurricanes. *J. Atmos. Sci*., **43**, 182-197.

Takahashi, T., 1978: Riming electrification as a charge generation mechanism in thunderstorms. *J. Atmos. Sci*., **35**, 1536-1548.

Thompson, G., R. R. Rasmussen, and K. Manning, 2004: Explicit forecasts of winter precipitation using an improved bulk microphysics scheme. Part 1: Description and sensitivity analysis, *Mon. Wea. Rev.*, **132**, 519-542.

Wang C. A modeling study of the response of tropical deep convection to the increase of cloud condensational nuclei concentration: 1. Dynamics and microphysics. *J. Geophys. Res*., **110**; D21211, doi:10.1029/2004JD005720.

Williams E., Meteorological aspects of thunderstorms 1995. *Handbook of Atmospheric Electrodynamics.* Hans Volland, Ed. CRC, 27-60.

Williams E., T. Chan and D. Boccippio, 2004: Islands as miniature continents: Another look at the land-ocean lightning contrast. *J. Geophys. Res*., **109**, D16206, doi:10.1029/2003JD003833

Williams E, G., Satori, 2004: Lightning, thermodynamic and hydrological comparison of the two tropical continental chimneys. *J. Atmos. And Solar-terristical Phys*. **66**, 1213-1231.

Williams E., V. Mushtak, D. Rosenfeld, S. Goodman and D. Boccippio, 2005: Thermodynamic conditions favorable to superlative thunderstorm updraft, mixed phase microphysics and lightning flash rate. *Atmos. Res.*, **76**, 288-306**.**

Wiens K.C., S.A. Rutledge, and S.A. Tessendorf , 2005: The 29 June 2000 supercell observed during steps. Pt 2: Lightning and charge structure. *J. Atmos. Sci.* **62**, 4151-4177.

Willoughby, H.E., Jorgensen D.P., Black R.A., and Rosenthal S.L.: Project STORMFURY, A Scientific Chronicle, 1962-1983, Bull. Amer. Meteor. Soc., 66, 505-514, 1985.

Zhang H., G.M. McFarquhar, S.M. Saleeby and W.R. Cotton, 2007: Impacts of Saharan dust as CCN on the evolution of an idealized tropical cyclone. Geophys. Res. Lett., 34, L14812, doi: 10.2029/2007GL029876.

Zipser, E.J. and M.A. LeMone, 1980: Cumulonimbus vertical velocity events in GATE. Part II: Synthesis and model core structure. *J. Atmos. Sci*., **37**, 2458-2469.

RESEARCH ON INFLUENCE OF AEROSOL ON REGION PRECIPITATION IN NORTH CHINA USING GROUND OBSERVATION DATA

DUAN Jing，MAO Jietai
(Department of Atmospheric Sciences，School of Physics，Peking University，Beijing 100871)

1. INTRODUCTION

The Aerosol change the microphysical characterizes of cloud though influence the microphysical process, then effect on precipitation processes [Ramanathan et al., 2001].

China's National Assessment Report on Climate Change [2007] point out that North China is the region in which the precipitation was reduced and the temperature was increased obviously after 1960’s, sulfate aerosol increased faster and also was one of black carbon aerosol higher place in recent twenty years. In this study, the North China as the research region, the surface observation data of precipitation and visibility of station in this region were used to try to find Vn in order to analyze region precipitation amount influenced by the anthropogenic aerosol finally.

2. DATA AND METHOD

In this study, the main aim is to determine how many the precipitation amount influenced by anthropogenic aerosol is in total precipitation amount. The analyzed data include observation precipitation and visibility of station which can stand for AOD. The relative humidity (RH) was used to correct the visibility data in order to reduce the effect of RH on visibility, RH values greater than 40 and less than 99% were converted to the equivalent visibility [Rosenfeld et al., 2007].

The North China (including Hebei province, Beijing and Tianjin) is the research region in which there are large AOD and faster aerosol increasing speed [Qiu et al., 2000; Li et al., 2003]. The 89 stations (Appendix 1) average precipitation data of ten days from 1960 to 2005 and the 28 stations (involved in the 89 stations) average visibility data of ten days from 1990-2005 in summer were used in this study. Because of accelerated development of society and industrial economy after 1980 in China, the aerosol concentration appears the different trend in before and after 1980. Since the time from 1960 to 2005 was divided into three stages: the first stage is from 1960 to 1979 (less aerosol change, less precipitation influenced by aerosol), the second period is from 1980 to 1990 (the accelerated effect precipitation stage by aerosol, the transition period of calculation), the last stage is from 1990 to 2005 (calculated precipitation amount effected by aerosol in this stage, the objective stage). The study has the following methodological steps.

1) The first stage data (1960-1979): The 13 kinds of different precipitation characters regions were apart in the whole year by the method adding significance test to cluster analysis.

2) The third stage data (1990-2005): obtain the visibility trend of different

stations and four seasons.

3) The first stage data (1960-1979): analyze the natural precipitation regular of each station in different seasons.

4) The third stage data (1990-2005): estimate the precipitation amount effected by anthropogenic aerosol in each sample station, different seasons.

5) Statistical test about results: rule out the effects by natural variation on results.

The nonparameter test was analyzed to the possible effecting by natural variation in order to make sure the results which were really influenced by anthropogenic aerosol but not natural precipitation variation.

3. THE PRECIPITATION CHANGE EFFECTED BY AEROSOL

3.1 Clustering Method Analyzed the Natural Precipitation

For the purpose of making good use of the big range and so many stations data, the cluster analysis were applied to obtain the different region in which there was the different precipitation regular.

In order to distinguish the precipitation effected by aerosol and effected by the other factor, based on the above-mentioned cluster method and precipitation data of twenty years from 1960 to 1979, the cluster analysis results is shown in Figure 1. The detail step as follows. The cluster chooses division method. The neatest neighbor method is applied to solve the comparability question. The measure distance between two individual samples depends on the Euclidean distance. The 13 sorts are the most reasonable clustering sorts. Figure 1 presents the locations of each sort.

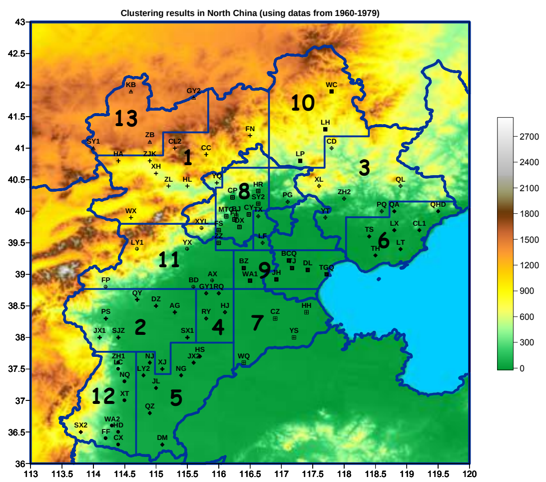

Figure 1. The clustering results (13 sorts)

Because of the first time stage (1960-1979) chosen in here in which less precipitation influenced by anthropogenic aerosol, in the individual cluster region, the stations have the similar precipitation characterizes influenced by all the possible factors except for anthropogenic aerosol.

3.2 The Variation Regular Of Natural Precipitation

Reliable precipitation sorts by clustering help to study the precipitation regular of different station. The trend analysis of visibility though linear regress can obtain the visibility trend of each station in the third stage (1990-2005) and make sure the standard station that is the minimum absolute value of visibility trend in each sort. These standard stations in each sort are the station in which there is the minimum effect on precipitation aroused by anthropogenic aerosol. Figure 2 shows the visibility trend and the clustering sorts came from precipitation data. There are visibility data of 28 stations matching with the precipitation data in the all 89 stations. Black means decrease of visibility (increase of aerosol), red means increase of visibility (decrease of aerosol), the scale of solid circle and the visibility trend value are direct proportion (larger solid circle, more increase of aerosol). The standard station of each sort is signed by blue hollow circle in Figure 2.

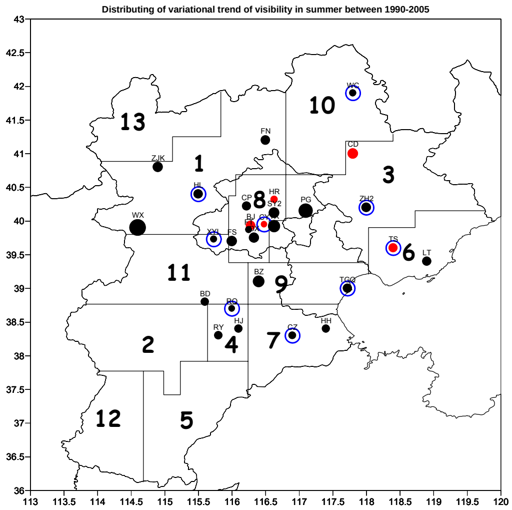

Figure 2 the trend of visibility adding with clustering results

On second thoughts of Figure 2, the absolute value of visibility trend (VVIS) of some standard station is the minimum in its own sort, but if compare with the standard station in the other sorts, VVIS also larger then them. Since the threshold of 0.1 (km/year) is set in order to choose the better standard stations. It means that VVIS change 0.1 kilometer every ten years and this value is so small enough that this change can be omitted. Figure 3 displays the VVIS of different sorts in summer. Only if VVIS of the standard station in some sort is less then 0.1, this standard station can be used in the next step, otherwise this sorts will be overleaped and do not continue to study next. According to this critical value, the VVIS of standard station in the 4th sort, the 8th sort, the 11th sort is suitable in summer. The 10th sort is not considered because there is only one station in this sort.

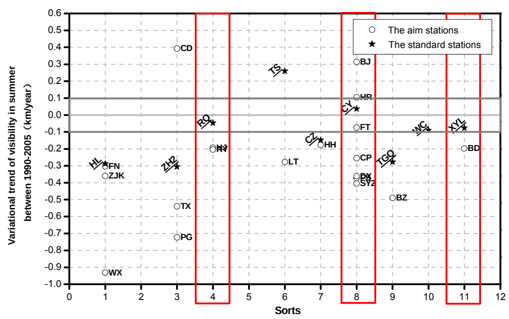

Figure 3. Compare with the trend of visibility of selected stations in summer

In three chosen sorts, except for the standard station, A and B of each sample station which is the natural precipitation regular of the related station is calculated though linear regression (y=Ax+B). The precipitation regulars of 10 stations in three sorts were omitted here.

3.3 Estimated the Natural Precipitation in Summer

Appling the precipitation regulars of sample stations and precipitation data in the third stage (after 1990) of standard station, the natural precipitation (Rm) were calculated in each sample. Rm minus the real precipitation (R) is the precipitation effected by anthropogenic aerosols (Table1).

Table 1. The compare of precipitation between real rainfall and estimated rainfall in summer in 1990-2005

station	The variational trend of visibility (km/year)	Amount of Real precipitation R (mm)	Amount of Natural precipitation Rm (mm)	(R-Rm)/Rm %	The percent of precipitation change affected by aerosol ((R-Rm)/R %)
HJ (HeJian)	-0.19368	481.11	565.775	-14.98	-17.60
BD (BaoDing)	-0.19764	522.12	521.3549	0.15	0.15
RY (RaoYang)	-0.20412	508.05	519.8606	-2.27	-2.33
SY2(ShunYi)	-0.405	759.52	776.1995	-2.15	-2.20
HR (HuaiRou)	0.104184	815.09	863.0995	-5.56	-5.89
CP(ChangPing)	-0.25452	715.56	746.2013	-4.11	-4.28
FT (FengTai)	-0.0738	666.95	766.3737	-12.97	-14.91
FS(FangShan)	-0.37188	652.19	769.0475	-15.20	-17.92
DX (DaXing)	-0.36144	586.79	741.6972	-20.89	-26.40
BJ (BeiJing)	0.313308	648.94	751.9154	-13.70	-15.87

Table 1 gives the comparison among Rm, R and visibility trend from 1990 to 2005 in summer. The decrease of precipitation because of anthropogenic aerosols increase leads to the 26.4%. These results included the effect of all possible mechanism that anthropogenic aerosols can bring to the precipitation. They are the synthetical results.

3.4 The Significance Test Of Results In Summer

In fact, the natural variation of precipitation took no account of aerosol is remarkable. It should make sure that the results in Table 1 (R-Rm) were not lead by natural variation of precipitation. A kind of nonparameter test and is used to analyze the significance of precipitation effected by anthropogenic aerosol in this research.

The results of significance test in summer shows that except for SY2 (ShunYi) and BD (BaoDing), the other eight stations all pass the significance test (α=0.05), and make sure it is the different amount effected by anthropogenic aerosol in summer.

The variation of visibility reflects on the variation of aerosol. Figure 4 displays the compare of aerosol variation trend and precipitation amount influenced by anthropogenic aerosol in summer. Aerosol increase on the left of x=0, aerosol decrease on the other side. Except for BJ (BeiJing) and HR (HuaiRou), the stations locate in the third quadrant in the Figure 4. The points in third quadrant means the increasing aerosol suppress the precipitation. This is the observation evidence of Albrecht effect [Albrecht, 1989] and coincides with the results of Rosenfeld [2000, 2007].

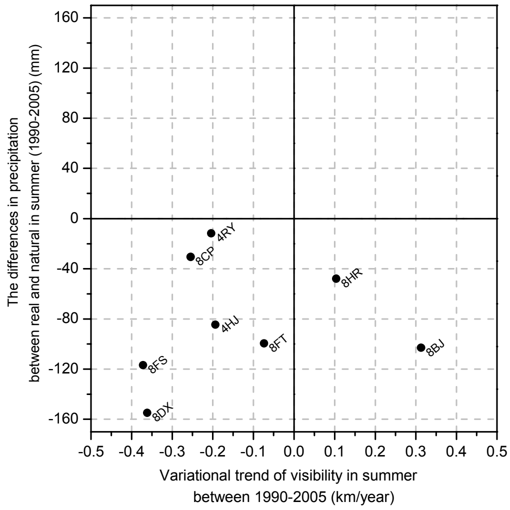

Figure4. Compare the variation of precipitation effected by aerosol with trend of visibility in summer from 1990 to 2005

The variation trend of aerosol is given in x-coordinate of Figure 4. The aerosols in BJ and HR increase from 1990 to 2005 in summer. This indicates the pollution control in BJ is useful. HR locates on the northernmost of 8th sort stations and it is suburb near the mountain area. The background level of aerosol is clean and there is no the big source of pollution around HR, so the variation trend of aerosol is decreased in HR. The opposite trend of aerosol is in HJ, RY, CP, FT, FS and DX. They all lie in the small city or the area in that there is no the big source of pollution. The background level of aerosol is lower then clean station such as HR. After 1980's, along with the quick development of economy in circumjacent areas and in itself, emission enhance gradually and transmit to the surrounding stations. Action of the lower background level of aerosol and larger emission or transmission from surrounding areas, the trend of aerosol is increased.

4. CONCLUSION

Being one of many factors influenced the precipitation, aerosol effect many different processes on precipitation. The effect on precipitation by anthropogenic aerosol is studied in this paper using the observation data. The research results prove the suppression of precipitation by anthropogenic aerosol in region areas that is remarkable in summer. The decrease of precipitation because of anthropogenic aerosols increase leads to the 26.4% at most.

Because of the special characteristic of precipitation in summer, the results in summer are analyzed in detail. The mechanism of interaction between aerosol and convective precipitation, the influence extent on the suppression effect of precipitation by background level of aerosol they need the deeply research and more evidences to proved.

Acknowledgements: This research was supported by National Natural Science Foundation of China (No.40475003) and a grant from the Major State Basic Research Development Program of China (973 Program) (No. 2006CB403706)

BIBLIOGRAPHY

Albrecht B. A. Aerosols, cloud microphysics, and fractional cloudiness [J]. Science, 1989, 245, 1227–1230.

D. Rosenfeld, Suppression of Rain and Snow by Urban and Industrial Air Pollution [J]. Science, 2000, 287, 1793.

D.Rosenfeld, Jin Dai, Xing Yu, Et Al..Inverse Relations between Amounts of Air Pollution and Orographic Precipitation [J].Science.2007, 315(9):1396-1398.

Li chengcai, Mao Jietai, Liu Qihan et al.Characteristics of distribution and seasonal variation of aerosol optical depth in Eastern China with MODIS products. Chinese Sci Bull (in Chinese), 2003, 48(22): 2488-2495

Qiu Jinhuan,Yang Liquan,Variation characteristics of atmospheric aerosol optical depths and visibility in North China during 1980-1994[J]. Atmospheric Environment, 2000, 34(4), 603-609.

Ramanathan, V., Crutzen, P. J., Kiehl, J. T., and Rosenfeld, D.: Aerosols, climate and the hydrological cycle, Science, 294, 2119–2124, 2001

RESEARCH ON INFLUENCE OF AEROSOL ON REGION PRECIPITATION IN NORTH CHINA USING GROUND OBSERVATION DATA

DUAN Jing，MAO Jietai
(Department of Atmospheric Sciences，School of Physics，Peking University，Beijing 100871)

1. INTRODUCTION

The Aerosol change the microphysical characterizes of cloud though influence the microphysical process, then effect on precipitation processes [Ramanathan et al., 2001].

China's National Assessment Report on Climate Change [2007] point out that North China is the region in which the precipitation was reduced and the temperature was increased obviously after 1960's, sulfate aerosol increased faster and also was one of black carbon aerosol higher place in recent twenty years. In this study, the North China as the research region, the surface observation data of precipitation and visibility of station in this region were used to try to find Vn in order to analyze region precipitation amount influenced by the anthropogenic aerosol finally.

2. DATA AND METHOD

In this study, the main aim is to determine how many the precipitation amount influenced by anthropogenic aerosol is in total precipitation amount. The analyzed data include observation precipitation and visibility of station which can stand for AOD. The relative humidity (RH) was used to correct the visibility data in order to reduce the effect of RH on visibility, RH values greater than 40 and less than 99% were converted to the equivalent visibility [Rosenfeld et al., 2007].

The North China (including Hebei province, Beijing and Tianjin) is the research region in which there are large AOD and faster aerosol increasing speed [Qiu et al., 2000; Li et al., 2003]. The 89 stations (Appendix 1) average precipitation data of ten days from 1960 to 2005 and the 28 stations (involved in the 89 stations) average visibility data of ten days from 1990-2005 in summer were used in this study. Because of accelerated development of society and industrial economy after 1980 in China, the aerosol concentration appears the different trend in before and after 1980. Since the time from 1960 to 2005 was divided into three stages: the first stage is from 1960 to 1979 (less aerosol change, less precipitation influenced by aerosol), the second period is from 1980 to 1990 (the accelerated effect precipitation stage by aerosol, the transition period of calculation), the last stage is from 1990 to 2005 (calculated precipitation amount effected by aerosol in this stage, the objective stage). The study has the following methodological steps.

1) The first stage data (1960-1979): The 13 kinds of different precipitation characters regions were apart in the whole year by the method adding significance test to cluster analysis.

2) The third stage data (1990-2005): obtain the visibility trend of different

stations and four seasons.

3) The first stage data (1960-1979): analyze the natural precipitation regular of each station in different seasons.

4) The third stage data (1990-2005): estimate the precipitation amount effected by anthropogenic aerosol in each sample station, different seasons.

5) Statistical test about results: rule out the effects by natural variation on results.

The nonparameter test was analyzed to the possible effecting by natural variation in order to make sure the results which were really influenced by anthropogenic aerosol but not natural precipitation variation.

3. THE PRECIPITATION CHANGE EFFECTED BY AEROSOL

3.1 Clustering Method Analyzed the Natural Precipitation

For the purpose of making good use of the big range and so many stations data, the cluster analysis were applied to obtain the different region in which there was the different precipitation regular.

In order to distinguish the precipitation effected by aerosol and effected by the other factor, based on the above-mentioned cluster method and precipitation data of twenty years from 1960 to 1979, the cluster analysis results is shown in Figure 1. The detail step as follows. The cluster chooses division method. The neatest neighbor method is applied to solve the comparability question. The measure distance between two individual samples depends on the Euclidean distance. The 13 sorts are the most reasonable clustering sorts. Figure 1 presents the locations of each sort.

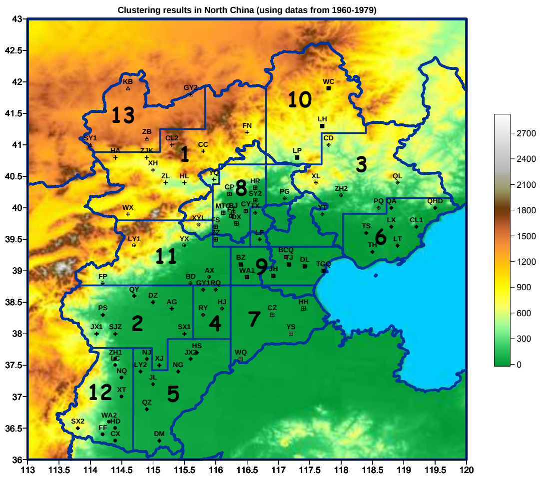

Figure 1. The clustering results (13 sorts)

Because of the first time stage (1960-1979) chosen in here in which less precipitation influenced by anthropogenic aerosol, in the individual cluster region, the stations have the similar precipitation characterizes influenced by all the possible factors except for anthropogenic aerosol.

3.2 The Variation Regular Of Natural Precipitation

Reliable precipitation sorts by clustering help to study the precipitation regular of different station. The trend analysis of visibility though linear regress can obtain the visibility trend of each station in the third stage (1990-2005) and make sure the standard station that is the minimum absolute value of visibility trend in each sort. These standard stations in each sort are the station in which there is the minimum effect on precipitation aroused by anthropogenic aerosol. Figure 2 shows the visibility trend and the clustering sorts came from precipitation data. There are visibility data of 28 stations matching with the precipitation data in the all 89 stations. Black means decrease of visibility (increase of aerosol), red means increase of visibility (decrease of aerosol), the scale of solid circle and the visibility trend value are direct proportion (larger solid circle, more increase of aerosol). The standard station of each sort is signed by blue hollow circle in Figure 2.

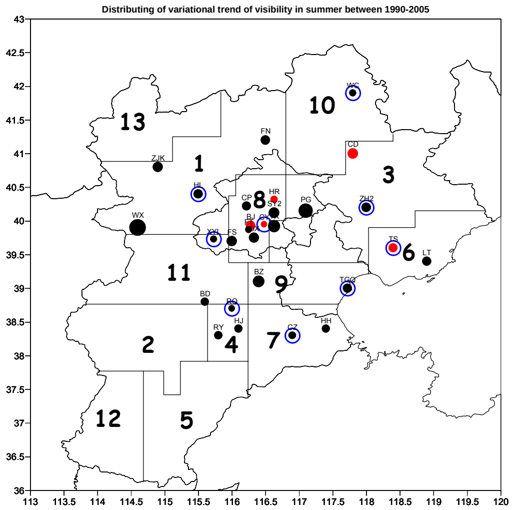

Figure 2 the trend of visibility adding with clustering results

On second thoughts of Figure 2, the absolute value of visibility trend (VVIS) of some standard station is the minimum in its own sort, but if compare with the standard station in the other sorts, VVIS also larger then them. Since the threshold of 0.1 (km/year) is set in order to choose the better standard stations. It means that VVIS change 0.1 kilometer every ten years and this value is so small enough that this change can be omitted. Figure 3 displays the VVIS of different sorts in summer. Only if VVIS of the standard station in some sort is less then 0.1, this standard station can be used in the next step, otherwise this sorts will be overleaped and do not continue to study next. According to this critical value, the VVIS of standard station in the 4th sort, the 8th sort, the 11th sort is suitable in summer. The 10th sort is not considered because there is only one station in this sort.

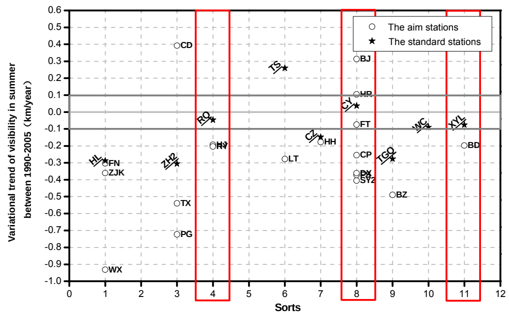

Figure 3. Compare with the trend of visibility of selected stations in summer

In three chosen sorts, except for the standard station, A and B of each sample station which is the natural precipitation regular of the related station is calculated though linear regression (y=Ax+B). The precipitation regulars of 10 stations in three sorts were omitted here.

3.3 Estimated the Natural Precipitation in Summer

Appling the precipitation regulars of sample stations and precipitation data in the third stage (after 1990) of standard station, the natural precipitation (Rm) were calculated in each sample. Rm minus the real precipitation (R) is the precipitation effected by anthropogenic aerosols (Table1).

Table 1. The compare of precipitation between real rainfall and estimated rainfall in summer in 1990-2005

station	The variational trend of visibility (km/year)	Amount of Real precipitation R (mm)	Amount of Natural precipitation Rm (mm)	(R-Rm) /Rm %	The percent of precipitation change affected by aerosol ((R-Rm) /R %)
HJ (HeJian)	-0.19368	481.11	565.775	-14.98	-17.60
BD (BaoDing)	-0.19764	522.12	521.3549	0.15	0.15
RY (RaoYang)	-0.20412	508.05	519.8606	-2.27	-2.33
SY2(ShunYi)	-0.405	759.52	776.1995	-2.15	-2.20
HR (HuaiRou)	0.104184	815.09	863.0995	-5.56	-5.89
CP(ChangPing)	-0.25452	715.56	746.2013	-4.11	-4.28
FT (FengTai)	-0.0738	666.95	766.3737	-12.97	-14.91
FS(FangShan)	-0.37188	652.19	769.0475	-15.20	-17.92
DX (DaXing)	-0.36144	586.79	741.6972	-20.89	-26.40
BJ (BeiJing)	0.313308	648.94	751.9154	-13.70	-15.87

Table 1 gives the comparison among Rm, R and visibility trend from 1990 to 2005 in summer. The decrease of precipitation because of anthropogenic aerosols increase leads to the 26.4%. These results included the effect of all possible mechanism that anthropogenic aerosols can bring to the precipitation. They are the synthetical results.

3.4 The Significance Test Of Results In Summer

In fact, the natural variation of precipitation took no account of aerosol is remarkable. It should make sure that the results in Table 1 (R-Rm) were not lead by natural variation of precipitation. A kind of nonparameter test and is used to analyze the significance of precipitation effected by anthropogenic aerosol in this research.

The results of significance test in summer shows that except for SY2 (ShunYi) and BD (BaoDing), the other eight stations all pass the significance test (α=0.05), and make sure it is the different amount effected by anthropogenic aerosol in summer.

The variation of visibility reflects on the variation of aerosol. Figure 4 displays the compare of aerosol variation trend and precipitation amount influenced by anthropogenic aerosol in summer. Aerosol increase on the left of x=0, aerosol decrease on the other side. Except for BJ (BeiJing) and HR (HuaiRou), the stations locate in the third quadrant in the Figure 4. The points in third quadrant means the increasing aerosol suppress the precipitation. This is the observation evidence of Albrecht effect [Albrecht, 1989] and coincides with the results of Rosenfeld [2000, 2007].

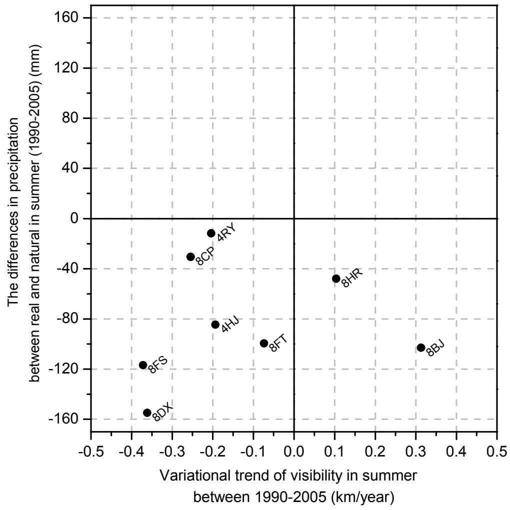

Figure4. Compare the variation of precipitation effected by aerosol with trend of visibility in summer from 1990 to 2005

The variation trend of aerosol is given in x-coordinate of Figure 4. The aerosols in BJ and HR increase from 1990 to 2005 in summer. This indicates the pollution control in BJ is useful. HR locates on the northernmost of 8th sort stations and it is suburb near the mountain area. The background level of aerosol is clean and there is no the big source of pollution around HR, so the variation trend of aerosol is decreased in HR. The opposite trend of aerosol is in HJ, RY, CP, FT, FS and DX. They all lie in the small city or the area in that there is no the big source of pollution. The background level of aerosol is lower then clean station such as HR. After 1980’s, along with the quick development of economy in circumjacent areas and in itself, emission enhance gradually and transmit to the surrounding stations. Action of the lower background level of aerosol and larger emission or transmission from surrounding areas, the trend of aerosol is increased.

4. CONCLUSION

Being one of many factors influenced the precipitation, aerosol effect many different processes on precipitation. The effect on precipitation by anthropogenic aerosol is studied in this paper using the observation data. The research results prove the suppression of precipitation by anthropogenic aerosol in region areas that is remarkable in summer. The decrease of precipitation because of anthropogenic aerosols increase leads to the 26.4% at most.

Because of the special characteristic of precipitation in summer, the results in summer are analyzed in detail. The mechanism of interaction between aerosol and convective precipitation, the influence extent on the suppression effect of precipitation by background level of aerosol they need the deeply research and more evidences to proved.

Acknowledgements: This research was supported by National Natural Science Foundation of China (No.40475003) and a grant from the Major State Basic Research Development Program of China (973 Program) (No. 2006CB403706)

BIBLIOGRAPHY

Albrecht B. A. Aerosols, cloud microphysics, and fractional cloudiness [J]. Science, 1989, 245, 1227–1230.

D. Rosenfeld, Suppression of Rain and Snow by Urban and Industrial Air Pollution [J]. Science, 2000, 287, 1793.

D.Rosenfeld, Jin Dai, Xing Yu, Et Al..Inverse Relations between Amounts of Air Pollution and Orographic Precipitation [J].Science.2007, 315(9):1396-1398.

Li chengcai, Mao Jietai, Liu Qihan et al.Characteristics of distribution and seasonal variation of aerosol optical depth in Eastern China with MODIS products. Chinese Sci Bull (in Chinese), 2003, 48(22): 2488-2495

Qiu Jinhuan,Yang Liquan,Variation characteristics of atmospheric aerosol optical depths and visibility in North China during 1980-1994[J]. Atmospheric Environment, 2000, 34(4), 603-609.

Ramanathan, V., Crutzen, P. J., Kiehl, J. T., and Rosenfeld, D.: Aerosols, climate and the hydrological cycle, Science, 294, 2119–2124, 2001

SIMULATED ANTHROPOGENIC AEROSOL EFFECTS ON MIDLATITUDE CYCLONES

Paul R. Field[1], A. Gettelman[2]
1. Met Office, Exeter, UK, paul.field@metoffice.gov.uk
2. National Center for Atmospheric Research , Boulder, Colorado

1. Introduction

There is currently uncertainty in the magnitude of so called indirect effects in which aerosols change the microphysical properties of clouds and feed back onto the radiative budget. Highest aerosol loading occurs in the Northern Hemisphere mid-latitude storm tracks. It is reasonable to ask if increases in global aerosol loading due to anthropogenic effects modify midlatitude cyclones. In this study we used the NCAR Community Atmosphere Model (version 3) with a new microphysics implementation (Morrison and Gettelman, 2008) that can react to differences in background aerosol to investigate this question.

The new stratiform microphysics scheme in CAM predicts the number concentrations and mixing ratios of cloud droplets and cloud ice. This allows the effective radius of these cloud particles to evolve freely in the model, which is critical for cloud radiative forcing. The scheme includes a number of microphysical processes that transfer water between vapour, clouds, and precipitation that were not present in the original CAM3 microphysics formulation, representing processes such as the Bergeron effect, and removing the requirement for a temperature dependent phase determination.

One way to focus model intercomparisons is to use compositing. Here we present composites of model midlatitude cyclones from 1870 (pre-industrial conditions) and 1990 (present conditions) following the method of Field and Wood (2007). In that work it was asserted that *i) On average a cyclone will exhibit similar precipitation and cloud structure to another cyclone if the thermodynamic and mesoscale dynamical environments are comparable. ii) The thermodynamic and mesoscale dynamical environment for each cyclone can be categorized by two metrics that represent the mean atmospheric moisture and the mean cyclone strength.* By compositing cyclones based on their strength and moisture we believe we are able to compare like-with-like and examine differences within cyclones caused by different aerosol loadings.

2. Model runs

The model runs presented here have been made using the CAM3 finite volume dynamical core at a horizontal grid spacing of 1.9 degrees $\times$ 2.5 degrees, 26 vertical levels (surface to 3 mb) and a timestep of 30 minutes. The new microphysics described above was implemented and used a slowly varying 3d aerosol climatology as input. The aerosol climatology was produced using an off line version of CAM run with the MOZART3 aerosol. model. This model has simulated emissions for preindustrial (1870) and present day (1990) conditions and produces a climatology of externally mixed aerosol masses of dust, sea-salt, black and organic carbon.

Model runs were carried out for three years using the same sea surface temperature and atmospheric greenhouse gas climatology but different aerosol climatologies appropriate for a pre-industrial period (1870) and the present day industrial period (1990). For these runs only the liquid phase was allowed to be modulated by variations in aerosol interactions with the clouds. The ice phase was unaffected directly, but will be influenced by changes to process rates controlling the conversion of water between the three phases. It is also important to note that no scavenging of the aerosol by cloud takes place. Preliminary analyses indicate that allowing aerosol to be scavenged reduces the indirect effect of aerosols by 10%.

3. Cyclone Compositing

From three years of the runs, daily averaged output was obtained. For compositing the model cyclones we followed the same method used for the satellite and reanalysis data described in Field

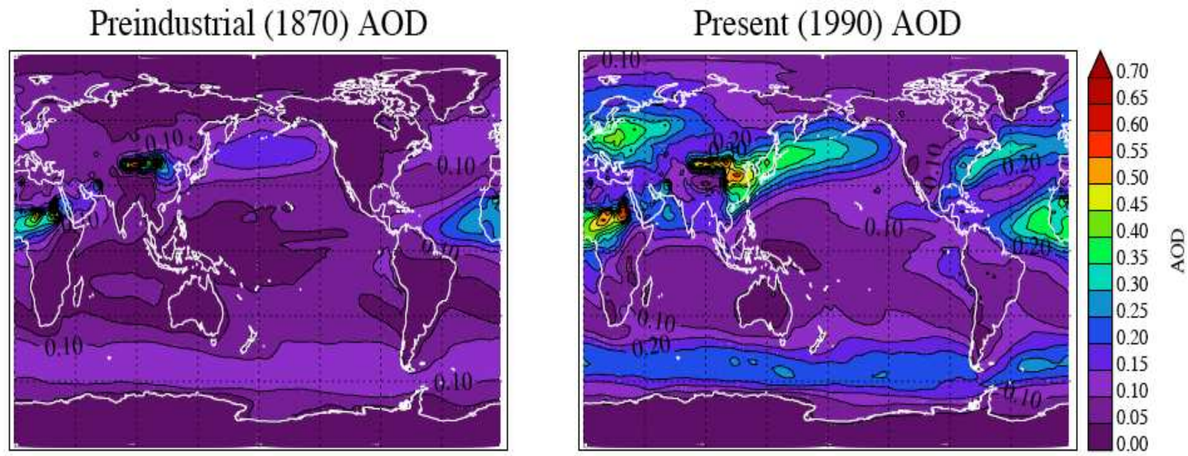

Figure 1: Annual mean aerosol optical depth (AOD) for pre-industrial (1870) and present day (1990) conditions.

and Wood (2007). To locate the cyclones we used surface pressure and derived first and second order derivatives that were thresholded to obtain candidate gridpoints to represent the cyclone center These candidates were then filtered to locate the maximum negative anomaly within a 1900 km radius. Therefore a single cyclone throughout its evolution could be identified as separate systems on consecutive days. From the global analysis of cyclone locations we focus the analysis in this paper upon two subregions: North Pacific (30-55°N, 145°E-165°W); North Atlantic (30-60°N, 10-50°W). Cyclone centres must be located within these domains to be considered for analysis.

For each cyclone the model output fields are translated and regridded using bilinear interpolation onto a 4000 km by 4000 km domain with 100 km grid spacing and the cyclone located centrally. Statistics are then derived from the resulting ensemble of cyclones.

We examine cyclone properties as a function of cyclone strength and atmospheric moisture metrics that are defined as follows. *Cyclone strength*, $\langle V \rangle$, is determined as the mean 10 m wind speed, within a circle of radius 2000 km centred on the cyclone. Our atmospheric *cyclone moisture* metric, $\langle WVP \rangle$, is similarly defined as the mean water vapour path within a circle of radius 2000 km centred on the cyclone. We choose a measure of the atmospheric moisture content as a metric because it determines the availability of moisture for the development of cloud and precipitation.

Cyclone-wide composite means (within 2000 km radius of center) of a number of parameters have been generated. We will use error bars to represent the standard error in the mean due to variability from cyclone to cyclone. These errors are obtained by calculating the weighted mean of the standard error of the means at each point in the composite, and then dividing by the square root of the degrees of freedom in the composite field (typically 5–20).

4. Results

The mean annual aerosol optical depth (AOD) is shown in fig. 1 and it is a combination of aerosol number and relative humidity. It is clear that the main increase (up to ~ 0.2) in AOD between 1870 and 1990 is in the northern hemisphere midlatitudes associated with industrialisation. Over oceans this is a doubling of AOD in 1990 from 1870.

Figure 2. shows cyclone-wide composite mean values of various model data as a function of cyclone strength for the pre-industrial run (1870, red) and the present day run (1990, blue) for nine strength and moisture categories (see fig. 3 for legend). As expected, the mean aerosol optical depth shows a distinct difference between the 1870 and 1990 runs (fig. 2a). The difference is smaller (~ 0.06) for the stronger and/or drier storms which we interpret as being related to storms located towards the pole where conditions are less polluted or eastward and away from the pollution sources where the cyclones are more

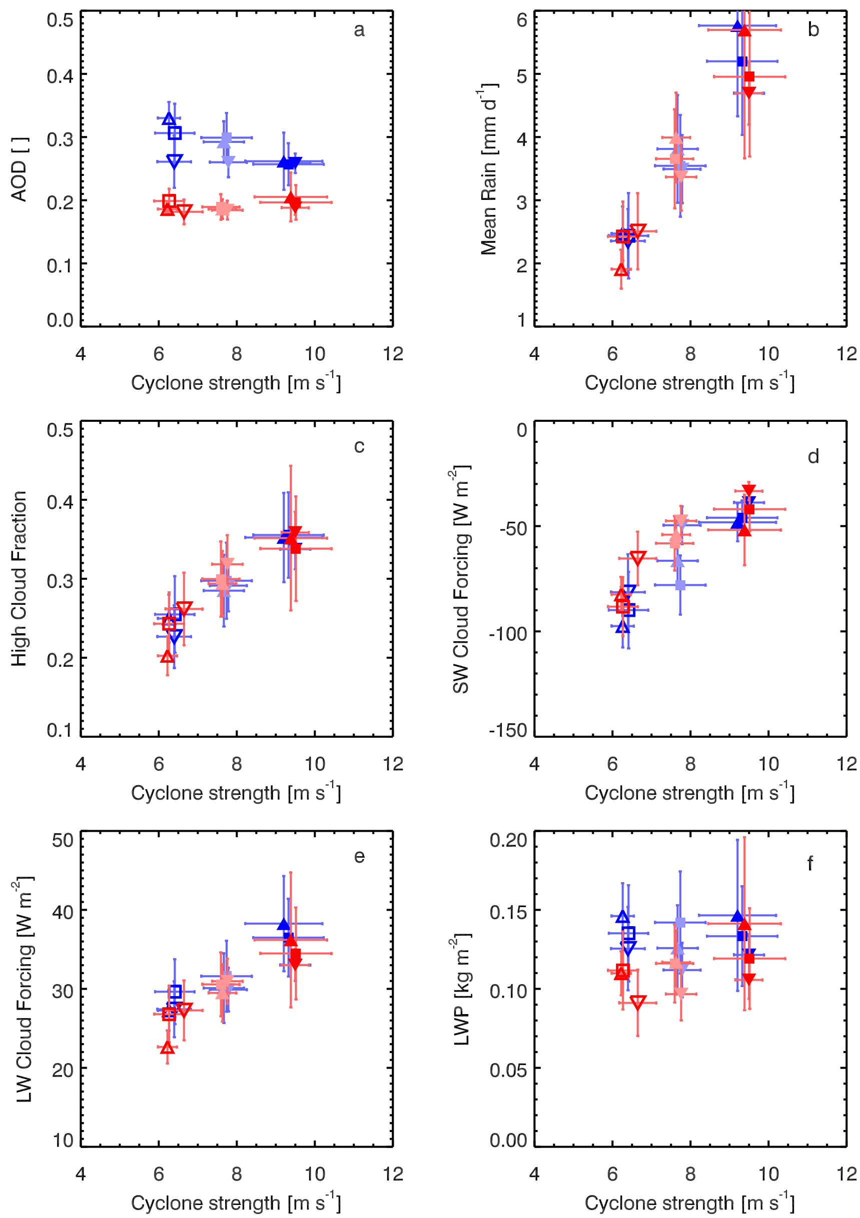

Figure 2: Cyclone-wide composite mean values as a function of cyclone strength. Red symbols represent results from 1870 and blue symbols represent 1990. Error bars indicate 2× the standard error in the mean due to variability contained in the composite. a) aerosol optical depth (aod), b) mean rain, c) high topped cloud fraction, d) Shortwave cloud forcing, e) Long wave cloud forcing, f) liquid water path. The different symbols represent 9 strength and moisture categories that cyclones were conditionally sampled into ($\langle WVP \rangle$: 10-18,18-21,21-33 kg m^{-2}) and three strength categories ($\langle V \rangle$: 4.9-6.95, 6.95-8.14, 8.14-12.3 m s^{-1}, see fig. 3 for legend)

mature and potentially stronger. The maximum difference in AOD is seen for the weak moist storms (~ 0.15). Mean rainrates (fig. 2b) and mean high topped (tops above 440 mb) cloud (fig. 2c) show no change related to the change in aerosol loading. However, the short wave cloud forcing, of up to -20 W m^{-2}, (fig. 2d) does exhibit some differences as opposed to the long wave cloud forcing (fig. 2e) that exhibits little difference between the present and pre-industrial periods. Finally, the liquid water path (fig. 2f) does show an increase of ~ 0.02 kg m^{-2} between the results for

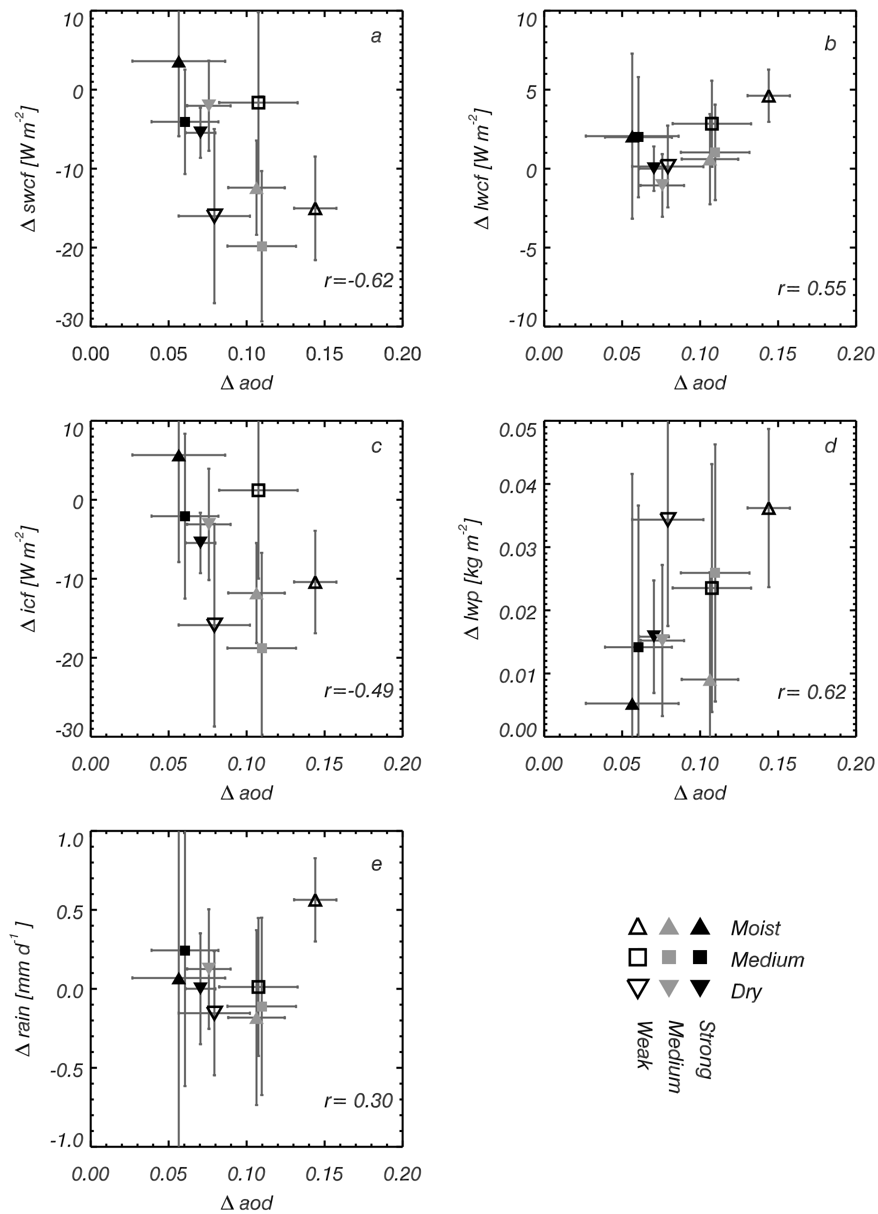

Figure 3: Changes in cyclone-wide composite mean values as a function of the change seen in aerosol optical depth (Δaod) between 1870 and 1990 (1990 values - 1870 values). Error bars indicate 1 standard error in the mean due to variability contained in the composite. Changes in a) short wave cloud forcing (swcf), b) longwave cloud forcing (lwcf), c) indirect cloud forcing (icf=swcf+lwcf), d) liquid water path (lwp), e) rainrate (rain). The legend for the 9 strength and moisture categories used in fig. 2-3 is also given.

present and pre-industrial conditions.

It is helpful to look again at these variables by considering the change between 1870 and 1990 as a function of the change in AOD for those two periods (there is no change seen in the relative humidity and so the difference in AOD is due to aerosol number). Figure 3a-c shows the change in shortwave cloud forcing, longwave cloud forcing and their sum: the indirect cloud forcing as a function of change in aod. It can be seen that the indirect cloud forcing is mainly a function of the change in shortwave cloud forcing only and exhibits values up to -20 W m^{-2} (i.e. cyclones are more reflective to space) with increased change in AOD (~ 0.15). Changes in liquid water path exhibits a consistent increase with increasing difference in AOD (fig. 3d), but the cyclone-wide mean rain (fig. 3e) appears unaffected as suggested by fig. 2b.

5. Summary

This analysis shows a like-for-like comparison based on thermodynamic and dynamic metrics (strength and moisture). The increased aerosol loading does not significantly affect the cyclone mean rain or cloud amounts in these simulations, although there is noise in the statistics for these short term runs. Cyclones, do however, become more reflective under increasing aerosol loading, and there may be enhancements to the liquid water path. However, we note that this simulation does not include the effects of aerosol scavenging by cloud particles and so represents the maximum effect possible. These runs have low pre-industrial sulfate emissions, so we believe they may represent and upper bound on potential effects

6. References

Field, PR, Wood, R. 2007. Precipitation and cloud structure in midlatitude cyclones. J. Climate 20 (2): 233-254.

Morrison, H., and A. Gettelman, 2007: A new two-moment bulk stratiform cloud microphysics scheme in the NCAR Community Atmosphere Model (CAM3), Part I: Description and numerical tests. J. Climate. (submitted)

MEASUREMENT OF TRACE METALS AND INORGANIC IONS IN RAIN FROM RANCHO VIEJO A RURAL WOODED AREA AND FROM SOUTHWEST SITE OF MEXICO CITY.

García R[1*], Torres Ma. del C[1], Padilla H[1], Belmont R[1], Báez A[1].

[1]Centro de Ciencias de la Atmósfera. Universidad Nacional Autónoma de México. 04510 México D.F.

*Corresponding author: gmrocio@atmosfera.unam.mx

ABSTRACT

In the large cities, industrialization and population growth have adverse effects on the chemical composition of the rain precipitation, the study of the rain chemistry in contaminated zones is an useful tool, because is important to consider the degree environment deterioration of pollute regions, besides permitting to determine the impact of anthropogenic and natural sources on the chemical composition of rain. With the aid of meteorological parameters, the studies of the chemical composition of the precipitation in urban, rural and remote areas, allow the identification of important sources of contaminants and understand the processes of chemical transformation, transports, advection and sedimentation of these pollutants.

This work is aimed to study for the first time the chemical composition of the soluble and insoluble fraction of the rainwater in an urban area that was Mexico City (MC), the rain collected on the Universidad Nacional Autónoma de México (UNAM) and Rancho Viejo (RV), a rural forest region in the Mexico State.

In this studied the heavy metals (Al, Cd, Cr, Fe, Mn, Ni, Pb and V), were analyzed in the rainwater, in both soluble and insoluble fractions, and in the soluble fractions the inorganic ions (SO_4^{2-}, NO_3^-, Cl^-, Ca^{2+}, Mg^{2+}, Na^+, K^+, NH_4^+ and H^+), were determinated. The heavy metals were analyzed by atomic absorption spectroscopy with a graphite furnace accessory and for ion analysis a Perkin Elmer liquid chromatograph was used.

The statistical analysis was made using the nonparametric test of "Mann Whitney" to know if significant differences between the concentrations of the soluble and insoluble fraction of analyzed heavy metals exist. These tests demonstrated that there was significant difference between both sampling sites. The average of weighed concentrations (VWMC) of Al were highest of all followed by Fe, Mn, Pb, Ni, V, Cr and

Cd, in both fractions, soluble and insoluble. With respect to ions SO_4^{2-}, NO_3^- they presented the highest concentrations (VWMC), followed by NH_4^+, Na^+, Cl^-, Ca^{2+}, Mg^{2+} and K^+. The Rho Spearman correlation analysis, allowed to found that the acidity was giving by SO_4^{-2} and NO_3^- and the most important neutralizing ion was NH_4^+. The calculated enrichment factors (EFc) showed that the Cd, Cr, Mn, Pb and V, were more enriched in MC than in RV. The high EFc values suggested that the metals had an anthropogenic origin. The deposition for each analyzed metal was determined, in both periods of rain (2003-2004).

1. INTRODUCTION

In the last decades, the study of heavy metals has increased, not only in the atmosphere, but also in the pluvial precipitation, due to its effects in the atmosphere. The metals like Pb, Cd, As, Hg, etc., are known to accumulate in the biosphere and be toxic for living organisms, even at low levels (Lighty et al., 2000).

Human activities obviously have a major impact on the global and regional cycles of most trace elements (Duce, 1983; Britton et al., 1980; Nriagu, 1990, 1996; Duce et al., 1991; Bertan et al., 2004). These biogeochemical perturbations are a matter of crucial interest since many trace metals are potentially toxic for marine and terrestrial life above certain concentration levels (Nriagu and Pacyna, 1988).

The magnitude of atmospheric input of metals exhibits a strong temporal and spatial variability due to both their short atmospheric residence times and meteorological factors (Scudlank, 1994). Thus, the impact of atmospheric deposition of trace metal on oceanic chemistry cannot be obtained by a simple consideration of global mass balance, accurate data on the net air-to-sea fluxes for any oceanic region are needed (Ramirez-Marcial, 2001).

The presence of particulate matter in urban areas represents after tropospheric ozone, the second most significant atmospheric pollution problem, which is responsible for a decrease in visibility and other effects on public health when their dimensions are below 10 µm, as they can penetrate deeply into human respiratory tract (Wood and Goldberg, 1988; Miranda et al., 2000). The atmospheric metal particle presence is primarily related to the inorganic fraction, in where the inorganic fraction is the one that causes to the toxic damage and the organic fraction is of fast excretion (GDF, 2002, 2004).

The natural sources of aerosols are those which include terrestrial dust, marine aerosol, volcanic emissions and forest fires. In contrast, anthropogenic emissions have their origin in industrial processes, fossil fuel combustion, processes of incomplete combustion of hydrocarbons, automobile mufflers, worn parts from components of engines and corrosion of metallic parts (Collinson and Thompson, 1989; Díaz-Báez et al., 2000).

The thermal power stations are a potential center of gas discharges. The chimneys of some industrial furnaces also contribute to the presence of heavy metals in the atmosphere. These gases are generated at high temperatures in energy generating plants and combustion processes.

2. EXPERIMENTAL

2.1. SAMPLING

Rancho Viejo (RV) sampling site was selected at a rural forested region. RV is located at 19.10 N and 99.91 W, about 80 km southwest of Mexico City, in the state of Mexico, with no nearby air pollution sources but downwind from the city. It is located at 2700 m above sea level with a mean rainfall of 1400 mm. During the rainy season, most of the time easterly winds at 700-600 mb transport air pollutants emitted in Mexico City and in the industrial zone of Toluca City, capital of the State of Mexico, to Rancho Viejo.

Mexico City (MC) sampling site was on the roof of the Atmospheric Sciences building at UNAM campus, located in southern Mexico City at 2200 meters above sea level (masl) at 19°19.57’ N latitude and 99°10.55’ W longitude, with mean rainfall of 800 mm. Buildings surrounded by green areas with moderate to high traffic density characterize the UNAM campus (Figure 1).

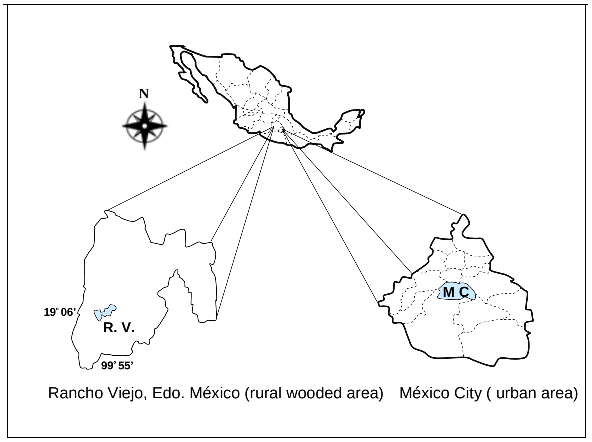

Figure 1 Mexico City (MC) and Rancho Viejo (RV) sampling sites locations

Wet precipitation samples were collected at RV site per event and MC site was collected daily, from mid May to the end October in 2003 and 2004.

Sampling was made two automatic wet/dry precipitation collectors were used. (Andersen, General Metal Works, Inc.). One collector was used to collect samples for the analysis of trace metals in soluble and insoluble fractions, and the other one for the analysis of pH (H^+), and the major ions SO_4^{-2}, $NO_3^-Cl^-$, Ca^{2+}, Mg^{2+}, Na^+, K^+, NH_4^+, in soluble fractions only. The lid arms of both collectors were coated with Teflon and the original aluminum cover and plastic–covered pad was replaced with an aluminum lid covered with Teflon and Teflon pad, and the buckets were tightly sealed with polyethylene covers. All samples were sent to the analytical chemical laboratory of the Centro de Ciencias de la Atmósfera, Universidad Nacional Autónoma de México (UNAM); precipitation samples from the two rain collectors were filtered through a 0.4 µm polycarbonate membrane filter. Samples were preserved at 4°C until analysis.

2.2. ANALYTICAL PROCEDURES

Chloride, NO_3^- and SO_4^{2-} were analyzed by non-suppressed ion chromatography with a Perkin Elmer liquid chromatograph, equipped with an LC isocratic pump and a Conductivity Detector LDC Analytical monitor III and a Hamilton PRPX-100 analytical strong- anion column. The injection volume was 100 µl. Flow rate 2 ml min^{-1} (Metrohm method). Ammonium was analyzed by a suppressed chromatography. The analytical conditions were as follows: Hamilton PRPX-200 analytical column, Alltech 335PCS suppressor module; Alltech cation suppressor cartridge; and flow rate 2 ml min^{-1} (Hamilton method).

Sodium, K^+, Ca^{2+} and Mg^{2+} were analyzed by flame atomic absorption spectroscopy with a GBC 932A a double beam atomic absorption spectrophotometer: Deuterium and hollow cathode lamps (Photron Super lamp) for background correction and analysis were used.

The detection limits in mg l^{-1} were: 0.22, 0.04, 0.31, 0.002, 0.006, 0.01, 0.002, and 0.05 for SO_4^{2-}, Cl^-, NO_3^-, Na^+ K^+, Ca^{2+}, Mg^{2+} and NH_4^+, respectively.

The pH (H^+) was measured by a combination electrode using an Orion 960 auto chemistry system. Calibration was performed by means of buffer solutions at pH 4 and 7.

Samples for heavy metal analyzed using an atomic absorption spectrophotometer, model GBC double beam 932AA, coupled with a System 3000 graphite furnace accessory. Calibration standards were prepared with the same acid concentration that the samples, using certified standards for each metal. High-Purity Standards traceable to National Institute of Standards and Technology (NIST). Cross check methods of standard additions were used. The detection limits, in µg l^{-1}, were: Al=6.03, Cd=0.07, Cr=0.38, Fe=2.04, Mn=0.46, Ni=0.78, Pb=1.14 and V=3.12.

3. RESULTS AND DISCUSSION

3.1. STATISTICS

The Spearman Rank Order correlation was applied to the total trace metal concentration as well to all major inorganic ions. The matrix correlations are shown in tables 1a and 1b, in bold letters are marked the significant correlations. The table 1a shows that in general, positive and good correlations occurred among all the elements; as an example Al correlated with Cd, Cr, Mn, Ni, Pb and V at RV. MC sampling site (table 1b), shows the correlation of Al with Cr, Fe, Mn, Ni, Pb and V.

	Al	Cd	Cr	Fe	Mn	Ni	Pb	V	SO_4^{2-}	Cl^-	NO_3^-	NH_4^+	Na^+	K^+	Ca^{2+}	Mg^{2+}
Al	1.00															
Cd	**0.74**	1.00														
Cr	**0.79**	**0.70**	1.00													
Fe	0.28	0.15	0.28	1.00												
Mn	**0.63**	**0.62**	**0.61**	0.34	1.00											
Ni	**0.71**	**0.62**	**0.82**	0.28	0.56	1.00										
Pb	**0.75**	**0.69**	**0.64**	0.39	**0.62**	**0.58**	1.00									
V	**0.76**	**0.62**	**0.73**	0.37	**0.70**	**0.64**	**0.80**	1.00								
SO_4^{2-}	0.19	0.28	0.19	0.16	0.19	0.23	0.21	0.21	1.00							
Cl^-	-0.09	0.13	0.08	0.05	0.004	0.08	0.06	0.03	0.49	1.00						
NO_3^-	0.27	0.36	0.24	0.39	0.31	0.24	0.25	0.18	**0.60**	0.29	1.00					
NH_4^+	0.09	-0.12	0.13	**0.56**	0.13	0.18	0.11	0.12	**0.53**	0.17	**0.77**	1.00				
Na^+	0.29	-0.07	0.22	0.16	**0.64**	0.22	0.23	0.16	0.38	0.38	**0.63**	**0.72**	1.00			
K^+	0.16	0.29	0.25	0.40	0.13	0.33	0.14	0.14	0.20	0.22	0.30	0.23	0.33	1.00		
Ca^{2+}	0.22	0.15	0.14	**0.69**	0.25	0.17	0.18	0.11	0.32	0.03	**0.71**	**0.72**	**0.79**	0.43	1.00	
Mg^+	0.09	0.06	0.13	**0.56**	0.13	0.18	0.25	0.25	0.49	0.19	**0.63**	**0.54**	**0.63**	**0.75**	**0.75**	1.00

Table 1a. Spearman Rank Order correlation between the different trace metal and ions (insoluble fraction) in rainwater at Rancho Viejo, 2003-2004. Bold numbers are significant at $p<0.05$, N= 51.

	Al	Cd	Cr	Fe	Mn	Ni	Pb	V	SO_4^{2-}	Cl^-	NO_3^-	NH_4^+	Na^+	K^+	Ca^{2+}	Mg^{2+}
Al	1.00															
Cd	-0.09	1.00														
Cr	**0.69**	-0.13	1.00													
Fe	**0.61**	-0.09	**0.62**	1.00												
Mn	**0.52**	0.12	**0.53**	**0.60**	1.00											
Ni	**0.64**	-0.07	**0.55**	**0.55**	**0.57**	1.00										
Pb	**0.74**	-0.17	**0.67**	**0.67**	**0.50**	0.46	1.00									
V	**0.66**	-0.23	**0.60**	**0.63**	0.47	0.39	**0.68**	1.00								
SO_4^{2-}	0.25	0.08	0.15	0.22	0.03	0.13	0.19	0.07	1.00							
Cl^-	0.12	0.008	0.04	0.14	0.06	0.17	0.14	0.02	0.43	1.00						
NO_3^-	0.27	0.11	0.19	0.28	0.11	0.20	0.20	0.13	**0.69**	**0.54**	1.00					
NH_4^+	0.37	0.17	0.23	0.28	0.17	0.26	0.28	0.13	**0.75**	0.49	**0.78**	1.00				
Na^+	0.35	0.11	0.23	0.27	0.29	0.37	0.32	0.13	**0.54**	0.45	0.48	**0.89**	1.00			
K^+	0.39	0.13	0.28	0.31	0.27	0.34	0.37	0.17	**0.57**	0.44	0.47	**0.68**	**0.89**	1.00		
Ca^{2+}	0.34	0.12	0.15	0.29	0.18	0.30	0.32	0.14	**0.69**	0.48	**0.64**	**0.81**	**0.84**	**0.79**	1.00	
Mg^+	0.32	0.12	0.16	0.30	0.18	0.28	0.32	0.16	**0.71**	**0.50**	**0.64**	0.79	**0.86**	**0.83**	**0.97**	1.00

Table 1b. Spearman Rank Order correlation between the different trace metal and ions (insoluble fraction) in rainwater at Mexico City, 2003-2004. Bold numbers are significant at $p<0.05$, N=107.

These correlations suggest a common anthropogenic origin, though Al and Mn have also a significant contribution from crustal material, as have been pointed out by some authors (Kim, et al, 2000; Kaya and Tuncel, 1997). Halstead et al, 2000, found that Cd, Cu, Pb and Zn were enriched in rainwater relative to crustal material and significant anthropogenic contribution of this element was suggested. Although correlation between species are frequently used to know about the sources of pollutants, it is necessary to be cautious in the interpretation of correlation coefficients in rainwater data because the concentration may vary by scavenging of particles from the atmosphere. Scavenging of elements from the atmosphere by rain depends on sizes and hydroscopic properties of particles in which elements are associated (Galloway et al, 1996).

3.2. FACTOR STATISTICAL 6.4 ANALYSIS

To have a better knowledge of the origin of the heavy metals in rainwater, a StatSoft, Inc. (2003) Factor Statistical 6.4 Analysis was used. The results of the concentrations from 158 samples with 8 elements (Al, Cd, Cr, Fe, Mn, Ni, Pb and V) obtained with the 6.4 statistical method are shown in table 2a and 2b. Three factor groups were obtained. The first factor can be considered of anthropogenic origin, since Al, Fe, Mn and Pb that mostly originated from anthropogenic sources is the major component of this group. This factor group accounted by 54.28% (RV) and 46.27% (MC) of the total variance in the factor analysis. Cr and V were included in this first factor group suggesting that these metals were emitted from anthropogenic sources such as combustion processes, industrial metallurgical emission, smelters etc. (Nriagu et al, 1988; Nriagu, J.O., 1996).

The high concentrations of Al present in the rainwater may be attributed to two sources: (a) the relative abundance of Al in crustal material (Duce et al, 1982; Al-Momani, 2003) and (b) at present, most of the vehicle motors are made out of aluminum, then the wear of such motors emit substantial amounts of this metal to the atmosphere. There are also several industries that process Al, so emissions of this metal are expected, Mn is of crustal origin, as well it is emitted by high temperature processes such as smelters, (Nriagu et al, 1988; Nriagu, J.O., 1996).

3.3. ENRICHMENT OF METALS

Crustal enrichment factors (EF_{crust}), of an element compared with relative abundance of that element in crustal material, were calculated to evaluate the contribution of non-crustal sources to elements concentrations in rainwater. EF_c's were

Variable	Factor 1	Factor 2	Factor 3
Al insol	**0.84**	0.02	0.17
Cd insol	0.40	-0.23	**0.53**
Cr insol	**0.91**	0.09	0.06
Fe insol	**0.69**	-0.11	-0.18
Mn insol	**0.88**	0.12	-0.02
Ni insol	**0.78**	0.03	0.09
Pb insol	**0.75**	-0.14	0.31
V insol	**0.94**	0.12	-0.03
% total variance	32.97	11.22	10.09

Table 2a Factor loading normal varimax extraction to Rancho Viejo, 2003-2004. Principal components (bold numbers are significant at>0.5).

Variable	Factor 1	Factor 2	Factor 3
Al insol	**0.84**	-0.08	0.11
Cd insol	-0.10	-0.75	0.16
Cr insol	**0.75**	-0.01	-0.27
Fe insol	**0.82**	-0.002	-0.24
Mn insol	**0.77**	-0.03	0.14
Ni insol	**0.72**	-0.03	0.22
Pb insol	**0.76**	-0.002	-0.29
V insol	**0.64**	-0.09	-0.12
% total variance	27.70	9.93	8.64

Table 2b Factor loading normal varimax extraction to Mexico City, 2003-2004. Principal components (bold numbers are significant at>0.5).

calculated using the following equation (Miranda et al., 2000):

$$EF_{crust} = (C_x / C_{Al})_{sample} / (C_x / C_{Al})_{crust}$$

Where:

$(C_x/C_{Al})_{sample}$ is the ratio of the concentrations of an element X and Al in the rainwater sample and $(C_x C_{Al})_{crust}$ is the concentration of the same element with respect to crustal material. The EF_c's were calculated by using average concentrations from crustal elements and the average EF_c's of elements from rainwater For trace metals, the soluble plus insoluble rainwater fractions were considered.

By convention, an arbitrary average EF_{crust} value < 10 was chosen to indicate that an element in rainwater has a significant crustal source, this element is referred to as a non-enriched element (NEE). If an average EF_{crust} value is >10, it is considered that a significant proportion of an element has a non-crustal source, this element is referred to as an anomalously enriched element (AEE).

Using the VWM concentrations of each trace metal in Rancho Viejo and Mexico City, the EF_c´ values were calculated using the individual concentration of Al (as a chemical tracer of anthropogenic pollution) and trace metals; and Ca^{2+} (as chemical tracer of crustal particles) (Table 3).

Element	Rancho Viejo	Mexico City	Rancho Viejo	Mexico City
	VWMC ppm		VWMC EFcrustal ppm	
Cd	$1x10^{-3}$	$8x10^{-4}$	5,612	4,263
Cr	$1x10^{-3}$	$1x10^{-3}$	11.37	12.01
Fe	0.086	0.077	1.31	1.49
Mn	$7x10^{-3}$	0.014	6.11	14.38
Ni	$3x10^{-3}$	$3x10^{-3}$	30.35	41.36
Pb	$2x10^{-3}$	$5x10^{-3}$	142.6	404.8
V	$6x10^{-3}$	$9x10^{-3}$	36.14	66.7
Na^+	0.099	0.315	0.79	1.99
K^+	0.257	0.094	2.25	0.64
Mg^{2+}	0.074	0.040	0.80	0.34

Table 3 VWMC and enrichment factors calculated to Rancho Viejo and Mexico City, 2003-2004.

The high values of EF_c found for Cd and Pb show that these metals in rainwater are non crustal, because Pb and Cd are associated with fine particles (<1 µm), which are generated as high temperature combustion condensates and infected by smoke-stacks into the boundary layer. However the low values of Mn close to unity and a slightly higher for Cr indicated a crustal origin, although Cr and Mn can also have a significant contribution from anthropogenic sources.

Whit respect to MC, Al, K^+ and Ca^{2+} were the only elements with a crustal source being considered as NEE. Cadmium, Pb, V, Ni, Mn and Cr, in decreasing order, presented EF_{crust} values > 10 and are considered as AEEs indicating a non-crustal source. In general, Pb, V, Ni, Mn and Cr are associated with fine particles (<1 µm), which are generated as high–temperature combustion condensates and injected into the boundary layer by smoke-stacks (Scudlark et al., 1994)

The high enrichment factor of Na^+ is difficult to explain in terms of anthropogenic sources. Enrichment factors are based on a "standard crust composition", thus they must be interpreted with caution in areas where the chemical composition of dust particles differs from that of the standard crust. In the case of this study, as far as we know, there are not anthropogenic sources in the Mexico City capable of raising the enriching factor of sodium ion to the high value. Obviously, sea spray is ruled out as a source because of the distance to the seashore and the high mountains that surround the Mexico City. Al-Momani et al. (2002) have also stated that there is uncertainty in defining the composition of the crustal source material.

Kaya and Tuncel (1997). Halstead et al. (2000) and Kim et al. (2000) found that Cd, Cu, Pb and Zn were enriched in rainwater relative to crustal material, thus a significant anthropogenic contribution.

3.4. BACK TRAJECTORY ANALYSIS

Some examples of the VWMC of the elements analyzed in relation to wind directions obtained by air mass back trajectory analysis are presented in figures 2 and 3 from RV and MC, respectively. The individual concentrations of SO_4^{2-} (as a chemical tracer of anthropogenic pollution), of Al and Ca^{2+} (as chemical tracers of crustal particles) and trace metals, were associated with the corresponding air mass back trajectories calculated by the NOAA HYSPLIT model (Hybrid Single-Particle Lagrangian Integrated Trajectory Model) (Draxler and Rolph, 2003). Air mass back trajectories were calculated for 1000 and 3000 meters above ground level (MAGL). NOAA trajectories were calculated for 2003 and 2004. Since the MC is surrounded by

Figure 2 Some air-mass back trajectories observed during the rainy season in 2003 and 2004 for RV corresponding to 1000 and 3000 MAGL.

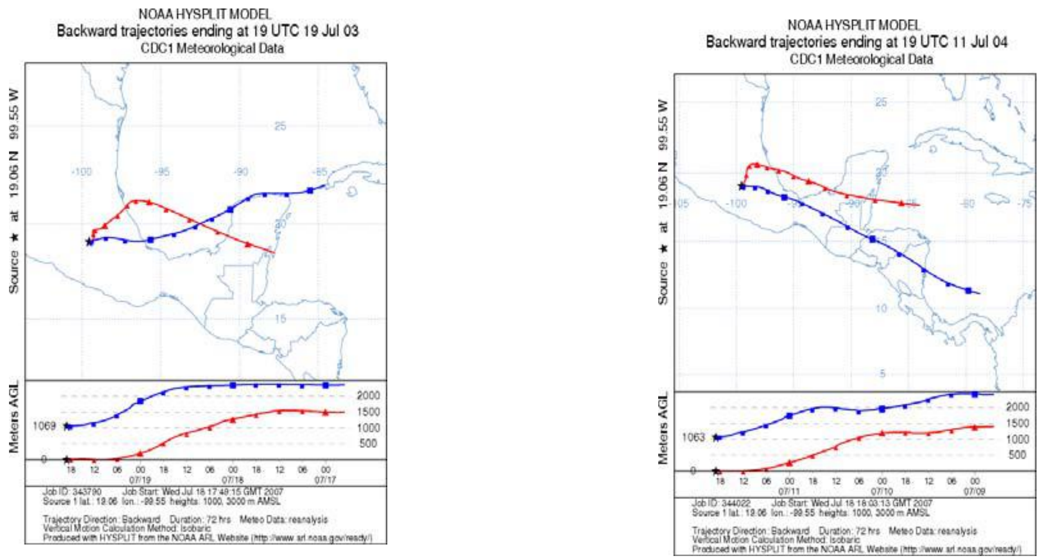

Figure 3 Some air-mass back trajectories observed during the rainy season in 2003 and 2004 for MC corresponding to 1000 and 3000 MAGL.

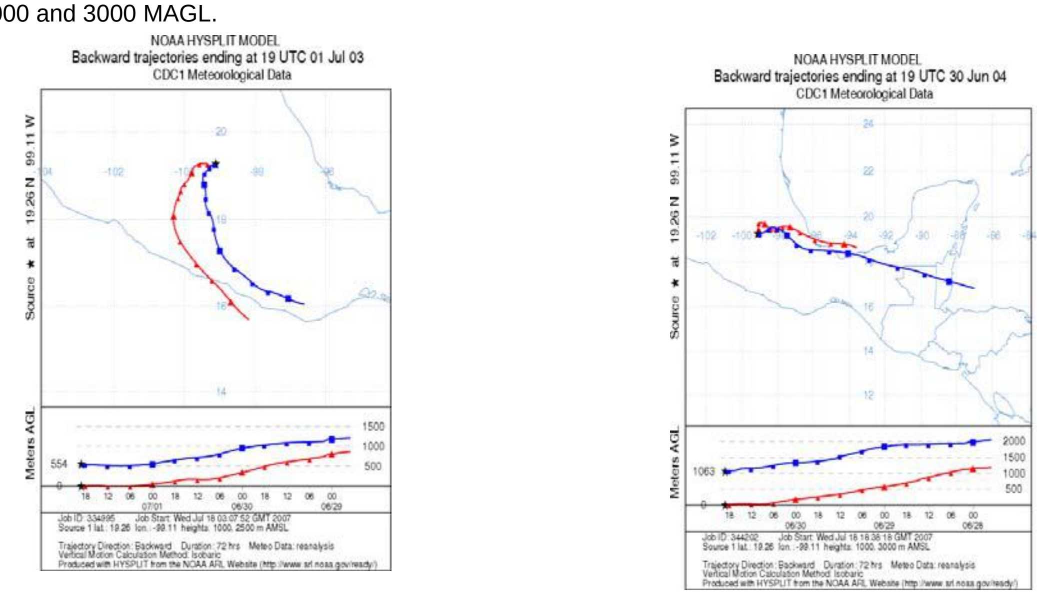

intense anthropogenic emission sources, figure 3 shows some examples of air mass the rainy season in period 2003-2004.The concentration of major trace metals and ions observed in rainwater when winds back trajectories indicated winds north and southeast. This is agree with the synoptic meteorological conditions that prevail in Central Mexico during the rainy season; trade winds have a consistent component from the east, that is winds blow between north and southeast most of the time during this season. There was also a reasonably well correspondence with the physical characteristics of the sampling site. The highest concentrations of Al were observed for both sites, the analysis at 3000 MAGL where large extensions of barren soils lie. An attempt was made to associate trace metals and major ions concentrations with surface wind. However, the results suggest that these trace metals different anthropogenic or natural sources.

4. CONCLUSIONS

Rancho Viejo is located in a complicated orographic area; frequent turbulences are present at several times of day, and at intervals of one or two hours. With no nearer industrial source emissions, as it was expected the transport of air pollutants from the industrial zones of Toluca and Mexico Cities contributed to the contents of trace metals in rainwater.

The elemental concentrations found at the UNAM are in many cases highest than those found in other areas of Mexico City. Due to the heavy polluted atmosphere of Mexico City higher mean concentrations of trace metals and inorganic ions, were found in rains from Mexico City, when the high concentration of trace metals in rainwater; with air mass back trajectory analysis, occurred due to the complex topography of Mexico Valley and surrounding areas. Therefore, also a detailed analysis of wind flow patterns by means of reliable soundings at various altitudes above ground level at various zones of Mexico Valley.

ACKNOWLEDGEMENTS

The authors want to thank Alfredo Rodríguez, Miguel Angel Meneses, David Mendoza, Manuel García, Jorge Escalante and Wilfrido Gutiérrez for their technical support and also to Delibes Flores and Carlos Contreras for their support in computation.

REFERENCES

Al-Momani I.F., Ya'qoub, A-R A., Al-Bataineh B.M. 2002 Atmospheric deposition of major ions and trace metals near and industrial area, Jordan. Journal Environment Monitoring. 4: 985-989.

Al-Momani I.F., 2003. Trace elements in atmospheric precipitation at Northern Jordan measured by ICP-MS: acidity and possible sources. Atmospheric Environment. 37: 4507–4515

Bertan, B., Alagha, O., 2004. The chemical composition of rainwater over Büyükçekmece Lake, Istambul. Atmospheric Resarch. 71:275-288.

Britton, L. G., Clarke, A.G. 1980. Heteterogeneous reactions of sulfur dioxide and SO_2/NO_2 mixtures with a carbon soot aerosol. Atmospheric Environment. 14: 829-839.

Collison, J.D and Thompson, D.B. 1989. Sedimentary structures. Unwin & Hyman. 207.

Díaz-Báez, M.C., Cruz, L.E., Rodríguez, D., Pérez, J. & Vargas, C.M., 2000, Evaluation of Three Water Concentration Techniques as a Prior Step to Test Acute Toxicity, Environ. Toxicol., 15 (4): 345-351.

Draxler, R.R. Rolph, G.D. 2003. HYSPLIT (Hybrid Single-Particle Lagrangian Integrated Trajectory Model) 4.0 (http://www.arl.noaa.gov/ready.html). NOAA Air Resources Laboratory, Silver Spring, MD.

Duce, A.R., Hoffman, G.L., Zoller, W.H., 1982. Atmospheric trace metals at remote northern and southern hemisphere sites: Pollution or natural? Science 187, 339-342.

Duce A.R., Mohnen V.A., Zimmerman P.R., Grosjean D., Cautreels W., Chatfield R., Jaenicke R., Ogree J.A., Pellizari E.D. y Wallace G.T. 1983. Organic material in the global troposphere. Rev. Geophys. Space Phys. 21: 921-952.

Duce A.R., P. Liss, J. Merrill, E. Atlas, P. Buat-Menard, B. Hicks, J. Miller, J. Prospero, R. Arimoto, T. Church, W. Ellis, J. Galloway, L. Hansen, T. Jickells, A. Knap, K. Reinhardt, B. Schneider, A. Soudine, J. Tokos, S. Tsunogai, R. Wollast and M. Zhou. 1991. The atmospheric input of trace species to the world ocean. Global Biogeochemical Cycles 5:193–259

Galloway, J.N., Keene, W.C., Likens, G.E. 1996. Processes controlling the composition of precipitation at a remote southern hemisphere location: Torres de Paine National Park, Chile. Journal of Geophysical Research, 101: 6383-6897.

GDF, 2002. Inventario de emisiones Zona Metropolitana del Valle de México, 2002. Gobierno del Distrito Federal, Secretaría del Medio Ambiente, Dirección General de Gestión Ambiental del Aire (www.sma.df.gob.mx).

GDF, 2004. Inventario de emisiones Zona Metropolitana del Valle de México, 2004. Gobierno del Distrito Federal, Secretaría del Medio Ambiente, Dirección General de Gestión Ambiental del Aire (www.sma.df.gob.mx).

Halstead, H.J.R., Cunninguhame, R.G. Hunter, K.A. 2000. Wet depositation of trace metal to a remote site in Fiordland. New Zeland. Atmospheric Environment. 34: 665-676.

Kaya, G., Tuncel, G. 1997. Trace element and major ion composition of wet and dry deposition in Ankara, Turkey. Atmospheric Environment. 31: 3985-3998.

Kim Guebuem, Joseph R., Scurdlark, Thomas M. Church. 2000. Atmospheric wet depositation of trace elements to Chesapeake and Delaware Bays. Atmospheric Environment., 34, 3437-3444.

Lighty J.S., Veranth J.M., Sarofi A.F. 2000. Combustion aerosols: factors governing their size and composition and implications to human health, J. Air Waste Manage., 50, 1565–1618.

Miranda, J., Crespo, I., Morales M.A. 2000. Absolute principal component analysis of atmospheric aerosols in México City. Environmental Science and Pullution Research. 7(1): 14-18.

Nriagu, J.O., Pacyna, J.M. 1988. Quantitative assessment of worldwide contamination of air water and soils by trace metals. Nature. 333: 134-139.

Nriagu, J.O. 1990. Global metal pollution. Poisoning the biosphere? Environment 32: 7-11 and 28-33.

Nriagu, J.O. 1996. A history of global metal pollution. Science. 272: 223-224.

Ramirez-Marcial N., Gonzalez-Espinosa M., Williams-Linera G. 2001. Antropoghenic disturbance and tree diversity in montane rain forest in México. Management, 116. 311-326.

Scudlark, J.R., Conko, K.M., Church, T.M., 1994. Atmospheric wet deposition of trace elements to Chesapeake Bay: CBAD study year 1 results. Atmos. Environ. 28, 1487-1498.

StatSoft, Inc. (2003). STATISTICA (data analysis software system) version 6. www.statsoft.com.

Wood, J.M. and Goldberg, E.D. 1988. Impact of metals on the biosphere in: Global Chemical Cycles and Their Alteration by Man: Dahlem Workshop. 137-153.

INFLUENCE OF AEROSOL PARTICLES ON CONVECTIVE CLOUDS MODELLED BY COSMO-SPECS

Verena Grützun, Oswald Knoth, Martin Simmel
Leibniz Institute for Tropospheric Research, Leipzig

1. INTRODUCTION

Aerosol particles play an important role for the entire cloud microphysics, ranging from the initial formation of cloud droplets and ice particles to the point of precipitation. The number, size and composition of the cloud droplets depend on the number, size and composition of the aerosol particles serving as cloud condensation nuclei. Further growth of the droplets occurs through condensation and coalescence, until they are finally large enough to produce rain. At temperatures below 0 °C, droplet freezing can take place also, being dependent on the availability of suitable ice nuclei. This cloud ice can further influence the precipitation formation, by (a) enhancing precipitation through quick ice particle growth at the expense of droplets, and (b) by delaying or reducing precipitation through the release of latent heat [e.g. Altaratz et al., 2008]. To better comprehend the mechanisms leading to precipitation and to understand the influence of atmospheric aerosols on the amount of precipitation, we combined a spectral bin cloud microphysics considering the aerosol particles explicitly with the mesoscale weather model COSMO [formerly “Lokalmodell” (LM), *Steppeler et al.*, 2003] resulting in the model system COSMO-SPECS [Grützun et al., 2008]. First Results from a realistic case study of a deep convective cloud, which was observed in Texas in 1999, are presented in this study.

2. COSMO-SPECS

COSMO is the non-hydrostatic mesoscale weather forecast model of the German Weather Service (“Deutscher Wetterdienst” DWD). The spectral bin microphysics model by *Simmel and Wurzler* [2006] and *Diehl et al.* [2007] explicitly describes partly soluble and completely insoluble aerosol particles, liquid hydrometeors and mixed phase hydrometeors consisting of an ice core and a liquid shell in size resolved spectra. Each spectrum consists of 66 size bins ranging from a radius of 10^{-3} µm up to 4.2×10^{3} µm. The warm cloud microphysics processes in the model are condensation and evaporation, collision and coalescence, and spontaneous break-up. The nucleation of cloud droplets is included implicitly as condensational growth of aerosol particles beyond their activation radius. For primary ice formation, immersion freezing after Diehl and Wurzler, [2004], contact freezing after Diehl et al., [2006], and deposition freezing is implemented. The latter is not considered in this study, though, since it occurs at much lower temperatures than immersion and contact freezing. At sufficiently cold temperatures, the liquid shell can freeze further, while at sufficiently warm temperatures the ice core melts. Both processes result in a feedback to the dynamics through the release or consumption of latent heat.
Since the microphysics operates on much smaller scales than the dynamics, it is calculated with a smaller time step. The performance of the model system has been tested on idealized test cases such as a heat bubble over flat terrain and an idealized mountain overflow. Now, aiming at realistic case studies in the future, COSMO-SPECS is applied to first realistic cases.

3. CASE SETUP

A deep convective mixed phase cloud having been observed over Midland/Texas in August 1999, [*Rosenfeld and Woodley*, 2000] was modeled in a two-dimensional framework.

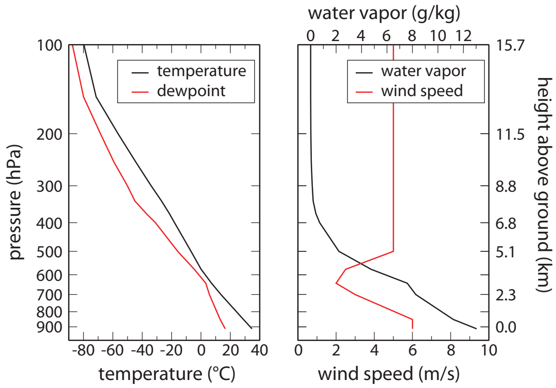

Fig. 1: *Idealized sounding data, Texas, August 13th, 1999.*

The model domain is 125 km in horizontal direction with a resolution of 250 m. The model top was at 22 km, the vertical resolution was 125 m. The atmosphere was initialized with an idealized vertical sounding [*Khain et al.*, 2001; edited by *Blahak*, 2007]. The temperature, dewpoint, wind speed and water vapor mixing ratio (MR) of this sounding are illustrated in Figure 1. The dynamics was calculated with a time step of 2 s. For the microphysics as well as the dynamical tendencies of the moist quantities, a time step of 1 s was used. Convection was initialized by a differential heating of the boundary layer with a heating rate of 0.0042 K/s for 10 min. A uni-modal lognormal distribution was used to initialize the internally mixed aerosol spectra. The standard deviation of the distribution was 2, the median radius 0.04 µm. A sensitivity study with respect to the initial number concentration of the aerosol particles was performed. No ice was present at the beginning of the runs, kaolinite was assumed as heterogeneous ice nuclei for immersion and contact freezing.

4. RESULTS

The model setup results in deep convective mixed phase clouds drifting eastward, as were observed. Figure 2 shows the development of the cloud for an aerosol number concentration of 566 cm^{-3} [*Kreidenweis et al.*, 2003]. The total water MR, which is a sum of the water in the liquid and in the mixed phase particle spectrum, is illustrated by the colored contours. Black contours (same levels) only represent the water from the liquid particle spectrum including rain. After 30 min, a purely liquid cloud has formed. The cloud base is located at a height of about 4 km. After 35 min, ice has formed, yet in all parts of the cloud the liquid phase is still present. The rather symmetric structure of the cloud starts dissolving due to the westerly wind. In the following, water is transported further up, the cloud top is found at about 14 km. In the upper part, only mixed phase particles are present after 40 min. At 45 min, in a region of strong updraft in the cloud centre, much liquid water is formed. This water partly freezes and is transported further upward as ice, and partly falls out as precipitation. At 55 min, a glaciated anvil has formed, characterized by a wider horizontal spread of the water. These results compare well with other model studies of the Texas cloud by, e.g., *Seifert et al.* [2006], which indicates that COSMO-SPECS is performing reasonably well under realistic conditions.

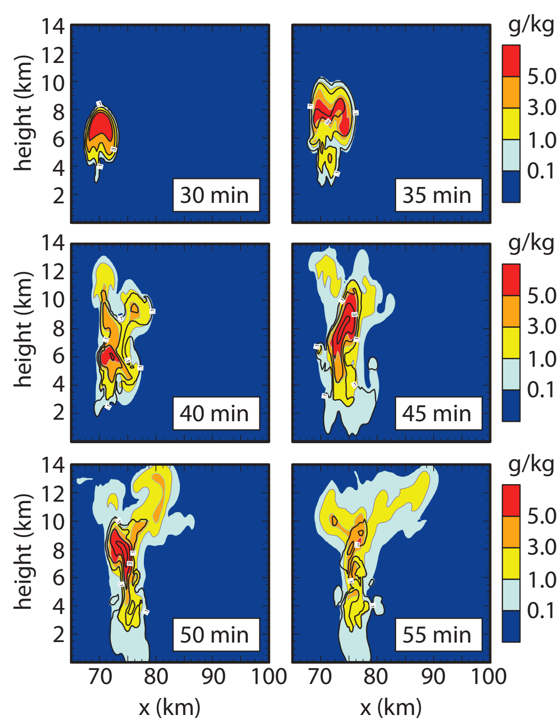

Fig. 2: *Time evolution of the Texas cloud. Colours: total condensed water MR; black: liquid water MR (same levels).*

Figure 3 shows a comparison of the accumulated precipitation for the cloud presented above ("clean case", red) in comparison with a "polluted case", (black, N_{init} = 5000 cm^{-3}) for the times 50 min, 60 min and 120 min. In the clean case, precipitation

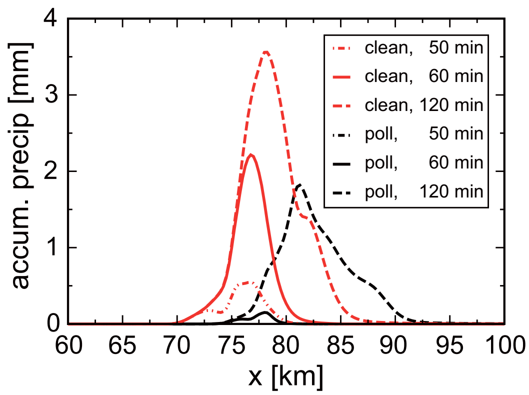

Fig. 3: *Accumulated precipitation for the clean (red) and the polluted case (black) at 50, 60 and 120 min.*

has already started after 50 min, where in the polluted case no precipitation has reached the ground yet. After 60 min, the polluted case also starts precipitating. Due to the westerly wind, the precipitation peak is shifted further to the East. At 120 min, the peak resulting from the clean case is almost twice as high as the one from the polluted case and is located about 3 km to the West. Also, the distribution is narrower. In both cases, a secondary maximum has developed downwind of the peak, being due to the formation of a secondary cloud at later stages of the cloud. The differences of the precipitation patterns result from smaller cloud droplets evolving from a larger number of aerosol particles in the polluted case. Since the available water is distributed to this larger number of droplets, they remain smaller. Thus, coalescence is less efficient. The onset of precipitation is therefore delayed and its amount is reduced.

5. CONCLUSIONS AND OUTLOOK

We present first results from a realistic case study with the model system COSMO-SPECS. The study based on observations of a deep convective cloud over Texas in August 1999. COSMO-SPECS reproduces the basic characteristics of the cloud. Also, a strong increase of the initial aerosol particle number density led to a decrease of the resulting accumulated rain, which points to the importance of including a proper description of aerosols for the correct prediction of precipitation. Though the model initialization with regard to the aerosol particle spectrum was rather simple, the results already compare well with results from other modeling groups [*Seifert et al.*, 2006]

Further improvements of the model system are planned. This includes an extension of the mixed phase particle spectrum to larger particles and also the association of differing ice particle characteristics with different parts of the mixed phase spectrum to represent a wider range of ice particle types. Further case studies are planned. Finally, COSMO-SPECS will serve to investigate in detail the influence of aerosol particles on the formation of precipitation. The knowledge gained here may serve to improve the currently used one- and two-moment bulk parameterizations with regard to a more appropriate consideration of aerosol particles.

6. BIBLIOGRAPHY

Altaratz, O., I. Koren, T. Reisin, A. Kostinski, G. Feingold, Z. Levin, Y. Yin (2008), Aerosols' influence on the interplay between condensation, evaporation and rain in warm cumulus cloud. *Atmospheric Chemistry and Physics 8*(1), 15-24.

Blahak, U. (2007), personal communication.

Diehl, K. and S. Wurzler (2004), Heterogeneous drop freezing in the immersion mode: Model calculations considering soluble and insoluble particles in the drops. *Journal of the Atmospheric Sciences 61*(16): 2063-2072.

Diehl, K., M. Simmel, and S. Wurzler (2007), Effects of drop freezing on microphysics of an ascending cloud parcel under biomass burning conditions, *Atmos. Environ.*, *41*(2), 303-314.

Grützun, V., O. Knoth, and M. Simmel (2008), Simulation of the influence of aerosol particle characteristics on clouds and precipitation with LM-SPECS: Model description and first results. *Atmospheric Research*, in print.

Khain, A. P., D. Rosenfeld, and A. Pokrovsky (2001), Simulating convective clouds with sustained supercooled liquid water down to -37.5 degrees C using a spectral microphysics model, *Geophys. Res. Lett.*, *28*(20), 3887-3890.

Kreidenweis, S. M., C. J. Walcek, G. Feingold, W. M. Gong, M. Z. Jacobson, C. H. Kim, X. H. Liu, J. E. Penner, A. Nenes, and J. H. Seinfeld (2003), Modification of aerosol mass and size distribution due to aqueous-phase SO2 oxidation in clouds: Comparisons of several models, *J. Geophys. Res.-Atmos.*, *108*(D7).

Rosenfeld, D., and W. L. Woodley (2000), Deep convective clouds with sustained supercooled liquid water down to-37.5 degrees C, *Nature*, *405*(6785), 440-442.

Seifert, A., A. Khain, A. Pokrovsky, and K. D. Beheng (2006), A comparison of spectral bin and two-moment bulk mixed-phase cloud microphysics, *Atmos. Res.*, *80*(1), 46-66.

Simmel, M., and S. Wurzler (2006), Condensation and activation in sectional cloud microphysical models, *Atmos. Res.*, *80*(2-3), 218-236.

Steppeler, J., G. Doms, U. Schattler, H. W. Bitzer, A. Gassmann, U. Damrath, and G. Gregoric (2003), Meso-gamma scale forecasts using the nonhydrostatic model LM, *Meteor. Atmos. Phys.*, *82*(1-4), 75-96.

Acknowledgements

This project was funded by the German Research Foundation (DFG), Bonn, Germany. It was part of the Priority Program 1167, “Quantitative Precipitation Forecast”.

AEROSOL-CLOUD INTERACTION DERIVED FROM AIRCRAFT OBSERVATIONS OVER URBAN REGION OF NORTHERN CHINA

Xueliang Guo[1,2], Danhong Fu[2], Guoguang Zheng[1], Hongyu Li[3] and Qiang Zhang[3]
[1]Chinese Academy of Meteorological Science, Beijing, China
[2]Institute of Atmospheric Physics, Chinese Academy of Sciences, Beijing, China
[3]Beijing Weather Modification Office, Beijing, China

1. INTRODUCTION

Aerosol is not only directly scattering and absorbing the radiation but also acting as Cloud Condensation Nuclei (CCN) to change the microphysical properties of clouds. The aerosol-cloud interactions over eastern Asian region are very complex due to the uncertainties of source of pollutant emissions. Lack of enough observational data, physical and chemical properties of human-made aerosols, it is extremely difficult for cloud and climate modeling in this region. The spectrum properties and vertical structure of aerosol and cloud particles are thought to be fundamental parameters in understanding precipitation formation and climate change.

The indirect effect of aerosol is more closely linked to aerosol number with diameter between 0.05μm and 1μm, thus by their interactions with atmospheric radiation and clouds, aerosols are able to influence global and local climate (e.g., Charlson et al., 1992; Clarke and Kapustin, 2002). Most of remote sensing instruments used in aerosol measurements are passive using the either thermal radiation from the Earth or reflected solar radiation, and generally have little ability to discriminate altitudinal information.

The effect of man-made emissions on cloud formation has been paid great attention in 21th century. It was found that cloud reflectivity at 0.63 μm measured by satellite to be significantly higher for clouds contaminated by ship-track exhaust emission than neighboring uncontaminated clouds (Coakley et al. 1987). Aircraft measurements near St. Louis, Missouri and have found that the cloud condensation nuclei (CCN) concentrations active at any supersaturation are higher downwind than upwind of the city. Furthermore, the droplet size distributions are narrower in clouds formed downwind than upwind of the city. Anthropogenically produced CCN can result in marked variations in cloud microphysics (e.g., Radke et al.,1989; Graf,2004). Thus, the better understanding of cloud physical properties, and the interactions between aerosol and cloud has profound meanings in improving weather forecast ability, understanding variations of hydrological cycle and climate, and also some environmental issues related to interactions between cloud and air pollutants.

The northern China has experienced a substantial increase in population over past several decades. In particular, the Beijing metropolitan area population has grown by nearly 50% within the last several decades. Associated with this population increase are increases in emissions of anthropogenic pollutants from a variety of stationary and mobile sources. These pollutants include particulate matter, which is directly emitted (e.g., soot and trace metals) as well as formed in the atmosphere from the reactions of gaseous precursors (such as NO_x, SO_2, and

VOCs).

This article reports on aerosol, cloud and precipitation particle size distribution measurements made in stratiform clouds over Beijing metropolitan region where an urban plume and rural air interacted with the clouds at different locations with the cloud volume. The data presented here were collected as part of a program designed for rain enhancement operation in spring clouds.

2. MEASUREMENTS

Aircraft observational experiments have been conducted over and surrounding regions of Beijing metropolitan in northern China in 2004. Aircraft location was determined using an onboard global positioning system (GPS). The altitudes given in this paper are measured from AGL. Ambient pressure was measured onboard with a Rosemount 830BA barometer (range: 1100-150 hPa). Ambient temperature was measured with a UW-manufactured reverse-flow thermometer (range:-60 to 40 ℃), and in-flight relative humidity (RH) was measured

The experiment was carried out using a research aircraft Y-12 instrumented to measure aerosol and cloud physics, and meteorological parameters. Aerosol particle size distributions are measured with an airborne Passive Cavity Aerosol Spectrometer Probe, model 100X (PCASP-100X, PMS Inc., Boulder, Colorado). The PCASP classifies aerosol particles into 15 size channels in the diameter range between 0.1 and 3 μm. Its measurement principle is on basis of light scattering of individual particles and calibration was conducted in the laboratory using latex spheres and particles sizing needs to be adjusted based on the actual aerosol composition estimated from filter sampling. The PCASP uses inherent heating within it, and thus, the measured particle size distributions are considered dehydrated and this will make the particles smaller than in their ambient atmospheric state.

The cloud-droplet-size distributions were measured using forward-scattering spectrometer probe, model 100(FSSP-100). The FSSP-100 is capable of measuring droplets in the diameter range of 2-32 μm with a sampling time of 0.25 s. Ice-crystal concentrations were measured using the PMS 2-DC probe, which has a minimum detection limit of 30 μm particle size. Both probes were mounted on instrument pylons under the wings of the aircraft.

The precipitation probes of an airborne PMS were also used to precipitating particles properties.

3. RESULTS

The atmospheric condition in experimental days was given in Table 1, and the statistical results of number concentration and diameter of aerosol and small cloud particles was shown in Table 2. It was shown that due to the important effect of fog and haze near the surface, the maximum number concentration of aerosol changed from $10^2 – 10^4$ cm^{-3}. The maximum number concentration could reach as high as 12169.9 cm^{-3} in the cloudy condition while in the clean condition it could only be 783.4 cm^{-3}. The order of the mean number concentration was $10^2 – 10^3$ cm^{-3}. The maximum diameter of aerosol particles was primarily distributed around 0.29 – 0.47 μm and the mean diameter was around 0.21–0.31 μm. The number concentration of aerosol particles could be high in both clean and cloudy condition when wind was week. In the temperature inversion condition, the distinct accumulation zone could be found under the inversion layers. The size distribution of aerosol follows unimodal distribution.

The cloud properties on the day of September 14, 2004 in the warm frontal stratocumulus presented the maximum number concentration of 318.97 cm^{-3}, 0.03 cm^{-3}, and 0.0065 cm^{-3} measured by FSSP-100, GA2 and GB2, respectively. On the other two days

Table 1 Atmospheric condition in experimental days

Flight number	Horizontal visibility (m)	Vertical Visibility (m)	Ground layer situation	Synoptic type	Wind direction	Wind speed ($m\ s^{-1}$)
2004–08–27	5000	2	Fog, haze	Cloudy, weak instability	300	2
2004–08–29	4000	4	light fog	Fair	310	5
2004–09–04	6000	3	light fog, haze	Fair, partly cloudy, weak inversion	190	1
2004–09–05	4500	3	light fog	Cloudy, light rain	220	1
2004–09–07	4000	4	light fog, haze	Fair	340	6
2004–09–12	5000	3	light fog, haze	Fair, stronger inversion	310	2
2004–09–14	2500	3	light fog, haze	Cloudy, weak instability	220	2
2004–09–16	3000	3	light fog	Cloudy, strong inversion	330	2

Table 2 Statistical results of number concentration and diameter of aerosol and small cloud particles

Date	PCASP Concentration (cm^{-3})		PCASP Diameter (μm)		FSSP-100 Concentration (cm^{-3})		FSSP-100 Diameter (μm)	
	Max	Mean	Max	Mean	Max	Mean	Max	Mean
2004–08–27	12169.9	2894.2	0.47	0.31	297.6	16.2	7.2	3.7
2004–08–29	783.4	356.0	0.33	0.22	1.7	0.1	17.0	3.3
2004–09–04	6128.0	1428.2	0.29	0.23	0.8	0.1	17.0	3.4
2004–09–05	5240.3	1254.3	0.40	0.25	1.6	0.2	25.6	3.7
2004–09–07	2437.0	452.9	0.38	0.21	8.3	0.1	27.0	1.7
2004–09–12	8760.6	1258.7	0.34	0.24	1.5	0.1	9.5	0.8
2004–09–14	10630.0	1224.0	1.26	0.25	298.0	3.4	31.0	6.0
2004–09–16	8657.0	2622.4	0.33	0.25	8.7	1.1	11.0	3.8

controlled by cold frontal system, several dry layers were observed. The supercooled cloud and rain water, graupel, columnar and needle crystal have the same order of number concentration above 0℃ layer in the cold frontal clouds. The peak content of supercooled water was 0.26 g/m^3.

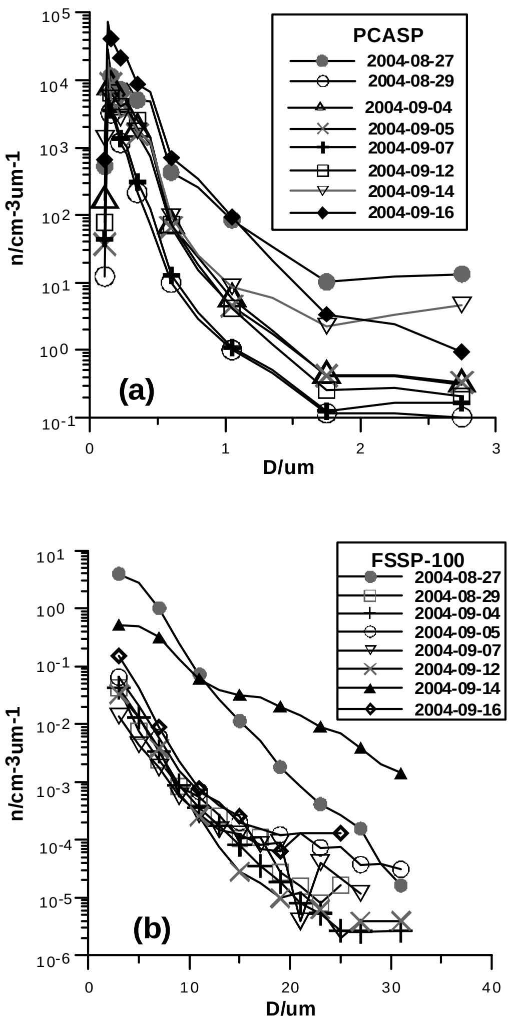

Fig.1 Mean size distributions of aerosol for each flight during ascending: (a) PCASP; (b) FSSP-100. *n*: number concentration; *D*: diameter

It was shown in Fig.1 that the size distribution of aerosol follows unimodal distribution. The minimum number concentration was 4734 cm^{-3}μm^{-1}, and occurs on August 29 under clear and strong wind condition. The peak was 72607 cm^{-3}μm^{-1} presented on September 16 under strong inversion and foggy condition. The size distribution of cloud particles by FSSP-100 decrease with increase of diameter, its peak value occurred on September 7 under light foggy and strong wind condition. The maximum of 3.9 cm^{-3}μm^{-1} occurred on August 27 was under cloudy condition. The size distribution of cloud particles was also unimodal.

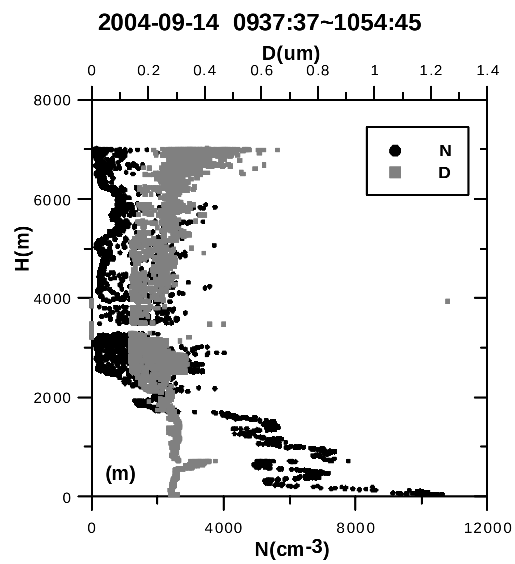

Fig 2 Vertical distribution of aerosol number concentration and diameter during ascending flights derived from PCASP on September 14, 2004. *N,* number concentration (black dot), and *D*, diameter (gray rectangle).

An observation on vertical distribution of aerosol for a relatively deeper stratiform cloud was displayed in Fig.2. The vertical temperature range of flight is 21.32 ~ –17.94 ℃, and observation was conducted over the northwestern area of Beijing City. Due to weaker surface wind, the aerosol number concentration was over 6000 ~ 8000 cm^{-3}.

There was an obvious accumulation zone of haze aerosol at boundary layer. Cloud could be divided into two layers, one was low-cloud layer between 1000~3000 m, the layer between 3000~3800 m was a dry layer, that above the dry layer was altstratiform clouds. The aerosol number concentration was around 1500 cm^{-3} in low-cloud layer, and only around 150 cm^{-3} in dry layer, and around 1400 cm^{-3} in high-layer clouds.

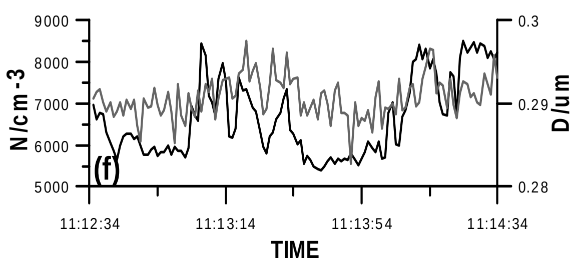

Fig.3 Horizontal distributions of aerosol particles at 637 m (18.83 ℃) on September 12, 2004.

The horizontal distribution of aerosol particles near surface was shown in Fig.3. Under cloudy and inversion condition, the horizontal distribution of aerosol showed a bigger inhomogeneity and high value. In particular, aerosol number concentration was much higher over urban region.

4. CONCLUSSION

The aircraft observation campaign in the northeastern China provided an opportunity to investigate physical property of haze aerosol related to the anthropogenic activities. The haze aerosol data sampled with the airborne optical array probe (Passive Cavity Aerosol Spectrometer Probe, model PCASP-100X, for measuring particles with diameter of 0.1-3 μm) under different atmospheric conditions during August to September in 2004 over Beijing City and its surrounding areas in northern China were analyzed. The results show that due to the important effect of fog and haze near the surface, the maximum number concentration of haze aerosol could reach as high as 12169.9 cm^{-3} in the polluted and cloudy condition, and only 783.4 cm^{-3} in pristine and clean condition. The mean number concentration was in order of 10^2 –10^3 cm^{-3}. The maximum diameter of aerosol particles was primarily distributed around 0.29 – 0.47 μm, and the mean diameter was around 0.21–0.31μm. The number concentration of aerosol particles could be high in both clean and cloudy condition when wind was weak. Under the temperature inversion condition, the distinct accumulation zone could be found under the inversion layers. The size distribution of aerosol follows unimodal distribution.

ACKNOWLEDGEMENTS

This research was jointly sponsored by the Key Sci & Tech Supporting Project of the Ministry of Science and Technology of China (Grant No. 2006BAC12B03), and the Chinese Natural Science Foundation (Grant No. 40575003 and 40333033).

REFERENCES

Charlson et al., 1992: Climate forcing by anthropogenic aerosols. *Science,* 255, 423-430.

Clarke, A.D. and V. N., Kapustin, 2002: A pacific aerosol survey. Part I: A decade of data on particle production, transport, evolution, and mixing in the troposphere, *J. Atmos. Sci.,* 59, 363-382.

Graf, H. -F, 2004: The complex interaction of aerosols and clouds, *Science,* 303, 1309-1311.

Radke et al., 1989: Direct and remote sending observations of the effects of ships on clouds. *Science*, 246,1146-1149.

CLOUD SEEDING EXPERIMENT WITH THREE-DIMENSIONNAL CLOUD RESOLVING MODEL FOR WINTER OROGRAPHIC CLOUD IN JAPAN

Akihiro Hashimoto, Teruyuki Kato, Syugo Hayashi, and Masataka Murakami

Meteorological Research Institute, Japan Meteorological Agency

1. INTRODUCTION

From 2006, the five-year project, Japanese Cloud Seeding Experiment for Precipitation Augmentation (JCSEPA) was started by the research group composed of the Meteorological Research Institute (MRI) of Japan Meteorological Agency (JMA) and others, funded by the Ministry of Education, Culture, Sports, Science and Technology, Japan under the program of Special Coordination Funds for Promoting Science and Technology. The aim of the project is to sophisticate cloud seeding techniques and to establish the method of evaluation of seeding effect on surface precipitation and its impact on the drainage rate of targeted dam catchment. Airborne cloud seeding experiments have been conducted using dry ice pellets for winter seasons in the orographic snow clouds that form upwind and over the Echigo mountains behind which the dams, the main water reservoirs of metropolitan area vicinity of Tokyo, are located. Since, in the present stage, the scale of cloud seeding still is small in time, just for several minutes in an experiment, the seeding effect is possible to be detected in the atmosphere as a spike in the number concentration of ice crystals but is hard to be found at the surface in the target area (dam catchment) several tens km distant from seeding position. For that reason as well as the scarcity of surface measurement in the mountainous area and difficulty to newly set up enough number of measuring sites, a numerical model is applied to evaluate the seeding effect on seasonal precipitation amount.

In the present study, numerical simulations of cloud seeding were successively performed, as well as control ones, through the winter season of 2006/07 (December 1, 2006 to March 31, 2007) for the cases which are found to have favorable super-cooled clouds in a pre-analysis. Based on the simulation results, we evaluated the additional precipitation amount that the dam catchments potentially have and the influences on the environment.

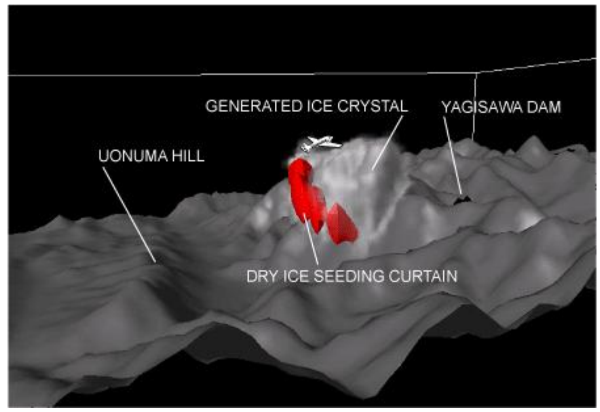

Fig. 1 Example of simulation using the module to represent the airborne cloud seeding with dry ice pellets. Red polygon indicates the distribution of dry ice pellets. White cloud-like area indicates the distribution of generated ice crystals. Cloud water, snow and graupel are not displayed. Winter monsoon directs from the left to the right in the figure.

2. MODEL

The nonhydrostatic model of JMA (JMA-NHM; Saito *et al.*, 2006) is applied in the present study. For cloud and precipitation processes, the JMA-NHM has five categories of liquid and solid water substances: cloud water, rain, cloud ice, snow, and graupel as described in Ikawa and Saito (1991). New module has been implemented in the NHM so as to explicitly simulate the airborne seeding

Table 1. Individual score assigned to each meteorological parameter.

Score	0	1	2	3	4
WD	the others	N to W			
WS (m s^{-1})	< 8	8 - 13	13 - 18	18 - 23	> 23
LWP (mm)	< 0.05	0.05-0.10	0.10-0.15	0.15-0.20	> 0.20
T_{Q_c}(°C)	> 0	-6 - 0	-6 - -11	-11 - -16	< -16
Q_c/Q_t	< 0.01	0.01 - 0.1	0.1 - 0.3	0.3 - 0.5	> 0.5

as a moving-point source of dry ice pellets, as well as their deposition and fall, and generation of ice crystals (Fig. 1).

3. SEEDABILITY ASSESSMENT

In advance of seeding experiment, we analyzed a data set provided from the winter season numerical prediction experiments with the JMA-NHM, in order to select the cases favorable to the cloud seeding (seedability assessment). The data set completely covers the focused geographical region with a horizontal resolution of 1 km and the period from December 1, 2006 to March 31, 2007 with a time interval of 1 hour. The setup for the seasonal numerical experiment is described in the Appendix A in detail. For the analysis, the data set was divided into 6-hour subsets. The meteorological situation for the 6 hours is defined as one case in the present study. The meteorological parameters: direction (*WD*), wind speed (*WS*), liquid water path (*LWP*), cloud-water-weighted temperature (T_{QC}), and the mass ratio of cloud water to total condensate water (Q_c/Q_t), were averaged within the 6 hours and over the analysis area (Fig. A1) to represent the meteorological situation. The *WS*, *WD* and Q_c/Q_t were further averaged between the heights of 1 and 3 km.

For the seedability assessment, we defined a seedability score, which represent how the meteorological situation is adequate for cloud seeding, as follows.

$$S = S_{WS} + S_{LWP} + S_{T_{QC}} + S_{Q_c/Q_T} \qquad (1)$$

where S_{WS} , $S_{LWP,}$ S_{TQC} , and $S_{QC/QT}$ are individual scores assigned to each meteorological parameter, as shown in Table 1. If one of those scores is zero, the seedability score *S* is set zero. On that definition, the seedability score *S* can be an integer between 4 and 16 or zero.

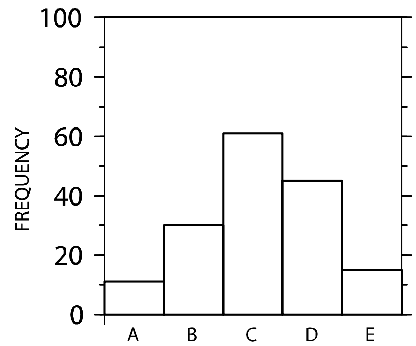

Fig. 2 (a) Frequency of each rank of priority in 2006/07 winter season (December 1, 2006 to March 31, 2007).

In a field experiment, the fund and man-power which can be injected are limited, compared to the requested scientific fruits. It is necessary to select preferable cases from those appear through a season to make seeding experiment more effecient. In order to provide instructive information for the planner of field experiment, we define the rank of priority based on the seedability score as follows: A[*S*;12,16], B[*S*;10,12), C[*S*;8,10), D[*S*;6,8), E[*S*;4,6). Those cases with priority A are assumed to be most adequate for a seeding experiment and expected the best efficiency to have seeding effect. Figure 2 shows the frequency of priority ranks through the winter season. In 2006/07 winter, the ranks A to E have 11, 30, 61, 45, and 15 cases, respectively.

The numerical seeding experiments were conducted for the cases with A to E. The number of simulated cases is 162 in all cases of 484.

4. NUMERICAL EXPERIMENT

The model domain covers the area of 320 km × 320 km centered at the dam catchment with a horizontal resolution of 1 km (1km-NHM), as shown in Fig. 3. This domain is nested into the outer model which has the area of 1000 km × 1000 km centered at the offing of Niigata prefecture with a horizontal

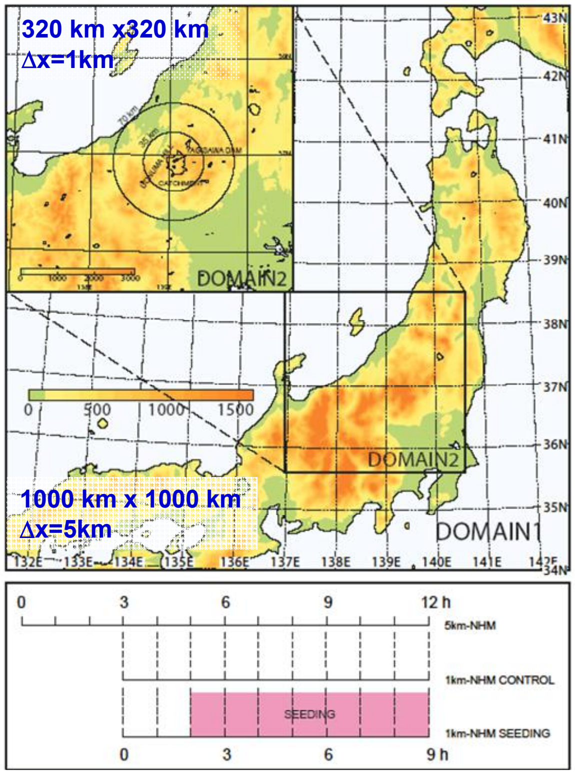

Fig. 3 Calculation domains for 1km-NHM and 5km-NHM, and sequence of time integration.

resolution of 5 km. The top height of the model domains is about 22 km. Fifty variable vertical layers are employed for both models. The regional analysis data (RANAL) provided by JMA were used as initial and boundary conditions for the outer model.

The initial time in 1km-NHM was set 3 hours after the initiation of outer model and the last 6-hour data in 9-hour integration time were adopted for analysis to avoid a spin-up effect. Control and seeding runs are conducted with the 1km-NHM. Cloud seeding is started at 2 hours after the beginning of seeding run, as shown in Fig. 3. This sequence of simulations is repeated for the cases in the winter season of 2006/07, which were specified according to the seedability assessment described in the previous section.

Seeding rate is set to 3 kg min^{-1} in the present study. Seeding position is determined in each simulation, following the manner to define optimal seeding position after Hashimoto *et al.* (2008). Most of the

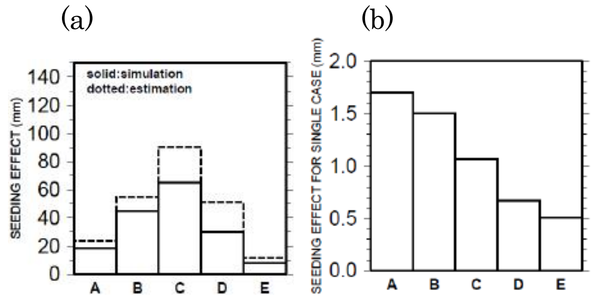

Fig. 4 (a) Seeding effect of each rank of priority on surface precipitation in target area simulated in seeding experiments (solid column) and statistically estimated (dotted column). (b) Seeding effect for single case averaged for each rank.

determined positions were located in several tens km north-west of the dam catchment.

5. RESULTS

5.1 Seeding effect

As a result of numerical experiment of cloud seeding through the winter, it is found that the potential precipitation of 166 mm for the dam catchment is possible to be stored as a form of non-precipitating cloud water in the atmosphere.

Figure 4a (solid column) shows the enhancement of surface precipitation in the target area due to the cloud seeding for each rank of priority. The rank C most contributes for the increase in surface precipitation through the winter (65 mm), scince this rank appears most frequently (Fig. 2). The contribution of rank A is 19 mm, which is about one-third of that of rank C, while the frequency of rank A is about one-sixth of that of rank C. Looking into the increase in surface precipitation for single case in Fig. 4b, the rank A has the increase of 1.7 mm on average, which is 1.54 times larger than the rank C (1.1 mm). It is clear that the rank A has the best efficiency to obtain seeding effect and the others have better ones in turns of B to E. Those results of analysis indicate that it will be effective means of planning an efficient seeding experiment in a field to stratify the meteorological conditions according to the priority.

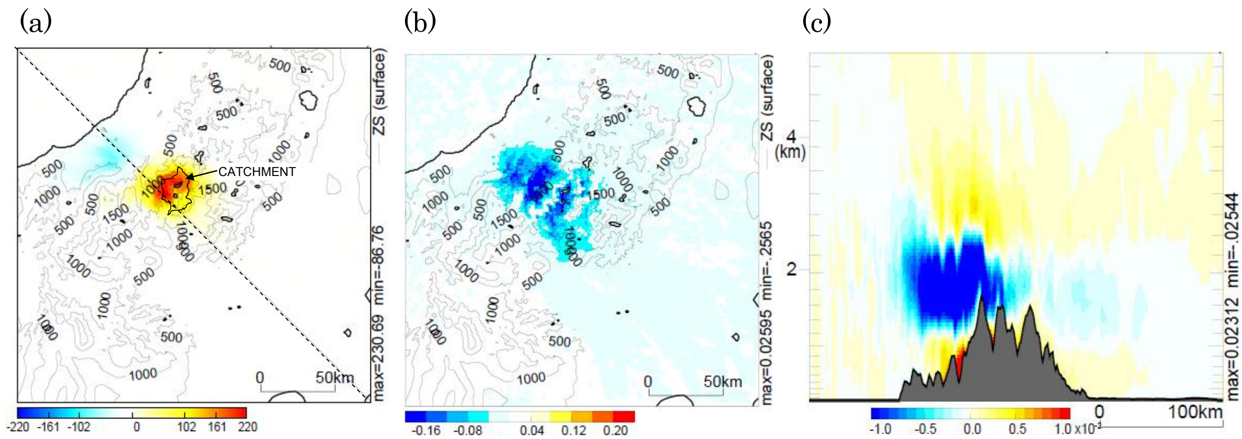

Fig. 5 (a) Distribution of seeding effect on surface precipitation through the winter season of 2006/07. (b) Influence on surface temperature. (c) Influence on relative humidity in vertical cross section along the dotted line in (a). The values in (b) and (c) are those averaged for all 162 simulated cases.

Figure 5a shows the distribution of seeding effect on surface precipitation through the winter season. It is found that the area of seeding effect covers the target area, which means that the optimal method to determine seeding position (Hashimoto *et al*., 2008) well work in the simulations.

5.2 Influences on the environment

Figure 5b shows the influence of cloud seeding on surface temperature. The surface temperature became slightly lower upwind and downwind the divide. This is because the night time radiative cooling is enhanced due to consumption of cloud water by depositional growth of the generated ice crystals. According to Fig. 5c, the relative humidity, on average, decreases by two or three % at most in the super-cooled cloud layer of seeding area. The decrease extends downwind the divide, but its magnitude is one order less than upwind the divide. In both sides of divide, the influence of cloud seeding on relative humidity is found to be limited, compared to the natural fluctuation.

6. DISCUSSIONS AND SUMMARY

Cloud seeding experiment was conducted using the three-dimensional cloud resolving model in order to evaluate the potential seeding effect on seasonal precipitation amount in target area. In the present study, the basis of evaluation fundamentally consists of the seedability assessment and optimal seeding method. The function of seedability assessment is demonstrated in Fig. 4b, since the efficiency of each rank of priority to have seeding effect resulted from the seeding experiment is better in turns of A to E, which is the same to that expected in the seedability assessment.

The dotted columns in Fig. 4a show the possible maximums of seeding effects, which are statistically estimated based on the 14 cases of Hashimoto *et al.* (2008), as described in Appendix B. The seeding effects simulated in the present study are found to be short to reach the possible maximums. The result means that the optimal seeding method still has room of improvement for an application to many and unspecified cases, although the optimal seeding position well work to target the seeding effect on the dam catchment, as mentioned previously. The dependence of seeding effect on seeding rate should be taken into account as well in order to improve the seeding effect.

Evaluation of seeding effect with numerical simulation indicates that the dam catchment potentially has the additional precipitation amount of 166 mm in the 2006/07 winter. This amount would be a great contribution to water resource management in the same winter with record little snow, where the seasonal precipitation amounts observed at nearby

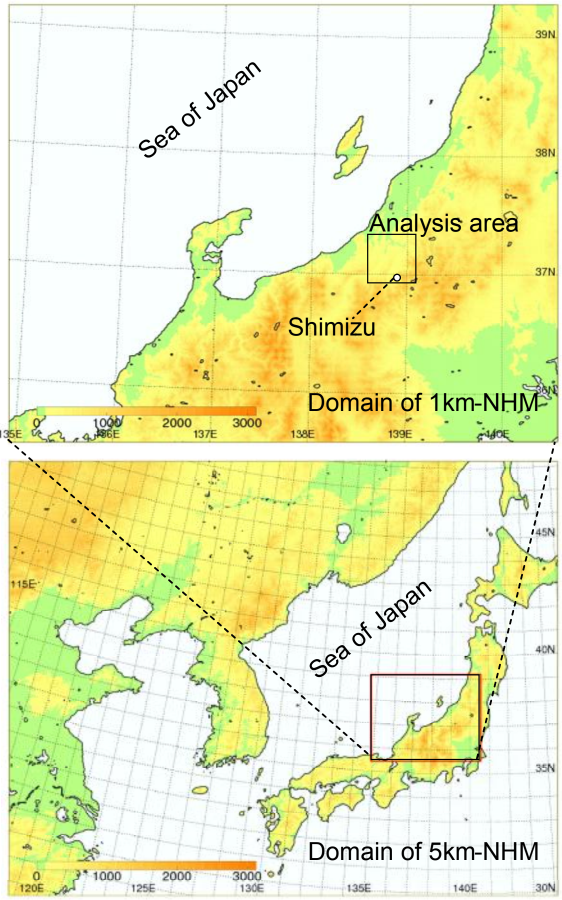

Fig. A1 Calculation domains for 1km-NHM and 5km-NHM in the winter season numerical prediction experiment. The rectangle in the 1km-NHM domain corresponds to the analysis area where the meteorological parameters are averaged.

routine measuring points were only several hundreds mm. Also, it is to be noted that the amount of 166 mm will be revised upward, when the optimal seeding method is improved in a future.

The cloud seeding was found to have an influence to lower the surface temperature through cloud radiation process. Quantitative evaluation is out of focus of the present study, since the radiative cooling rate at the surface should be dependent on the parameterization scheme of cloud radiation process in a model. This is the subject of the future study.

APPENDIX

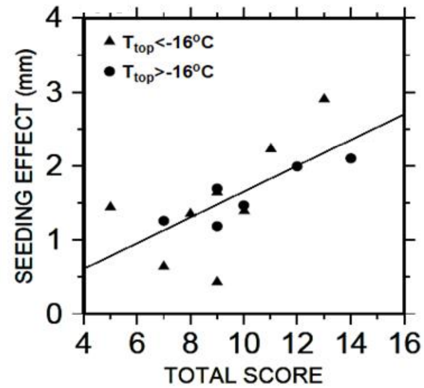

Fig. B1 The relationship between the seedability score and seeding effect on snowfall amount in the target area (dam catchment).

A. WINTER SEASON NUMERICAL PREDICTION EXPERIMENTS

The calculation domain of outer model (5km-NHM) has the area of 2500 km × 2000 km covering East Asia, with a horizontal resolution of 5 km (Fig. A1). The top height of the model domain is about 22 km. Fifty variable vertical layers are employed. The time integration up to 12 hours was conducted with a time step of 12 sec for the outer model. The RANAL data provided by JMA were used as initial and boundary conditions. As shown in Fig. A1, the inner model (1km-NHM), whose domain has the area of 500 km × 400 km with a horizontal resolution of 1 km, was nested into the outer model in a one-way interaction manner. The vertical grid spacing was the same as that of outer model. For the inner model, the initial time was set 3 hours after the initiation of outer model. Time integration was conducted for 9 hours. The data were stored at one-hour interval. This sequence of simulations was performed successively through the two winter seasons from December 1, 2005 to March 31, 2006 and from December 1, 2006 to March 31, 2007. The latter season was focused in this study. Data for the first 3 hours were discarded in each simulation with inner model, in order to avoid a spin-up effect, and the last 6-hour data were adopted for analysis.

B. RELATIONSHIP BETWEEN THE SEEDABILITY SCORE AND SEEDING EFFECT

Figure B1 shows a relationship between the meteorological condition and the seeding effect in target area. The meteorological condition is represented by the seedability score. The seeding effect corresponds to that found as the maximum by the sensitivity experiment to seeding position for the 14 cases in Hashimoto *et al.* (2008). It is clear that the seedability score has a good correlation with the seeding effect. The solid line in Fig. B1 is obtained with a regression analysis, as follows.

$$E = -0.089 + 0.174 \times S \qquad \text{(B1)}$$

where E and S are the seeding effect and the seedability score, respectively.

REFERENCES

Hashimoto, A., T. Kato, S. Hayashi, and M. Murakami, 2008: Numerical experiment on the sensitivity of precipitation enhancement to cloud seeding position for the winter orographic cloud in Japan. *CAS/JSC WGNE Research Activities in Atmospheric and Oceanic Modelling*, **37**, submitted.

Ikawa, M. and K. Saito, 1991: Description of a nonhydrostatic model developed at the Forecast Research Department of the MRI. *Tech. Rep. MRI*, **28**, 238pp.

Saito, K., T. Fujita, Y. Yamada, J. Ishida, Y. Kumagai, K. Aranami, S. Ohmori, R. Nagasawa, S. Kumagai, C. Muroi, T. Kato, H. Eito, Y. Yamazaki, 2006: The operational JMA nonhydrostatic mesoscale model. *Mon. Wea. Rev.*, **134**, 1266–1298.

IMPORTANCE OF BIOLOGICAL AEROSOLS ON CLOUD FORMATION AND PRECIPITATION: A MODELING STUDY

Anupam Hazra, Jen -Ping Chen* and Pei -Yun Tang
Department of Atmospheric sciences, National Taiwan University, Taipei, Taiwan.

1. INTRODUCTION

Aerosols are one of the key components of the climate system and the hydrological cycle (Ramanathan et al., 2001). The aerosol effect on precipitation processes, also known as the second type of aerosol indirect effect (Albrecht, 1989), is even more complex, especially for mixed-phase convective clouds because of the intricate roles of certain aerosols that acting as ice nuclei. The origin of atmospheric ice nuclei (IN) has been of scientific interest for decades. Originally, this interest was due to the discovery in the 1940s that precipitation could be induced via the seeding of clouds with ice nuclei. More recently, it has been suggested that ice nuclei may have an important climatological effect due to their role in cloud microstructure and radiative properties. When ice-phase microphysics is considered, aerosol effect on clouds and rains becomes more complex; for example, ice crystal can be initialized either from vapor deposition onto ice nuclei or from freezing of liquid drops, which are initialized from cloud condensation nuclei (CCN) activation.

Primary biogenic organic aerosols (hereafter called bio-aerosols) include whole organisms (e.g. bacteria, fungi, and phytoplankton), reproductive materials (e.g. pollen) and fragments (e.g. plant wax). Matthias-Maser et al., (2000) suggest that the proportion by volume of atmospheric particles made up by biological material in remote continental, polluted continental and remote maritime environments is respectively 28%, 22% and 10%. These bio-aerosols may lead to the formation of ice crystal by serving as ice nuclei (IN) (Schnell & Vali, 1973). Bacteria are considered a major type of ice-nucleating bio-aerosols because of their large quantities. Worldwide availability of such nuclei was established by finding ice-forming nuclei in plant litters collected in different climatic zones. The subsequent studies of Vali et al., (1976), Yankofsky et al., (1981), Levin et al., (1987), Hazra et al., (2004) showed that it might be released from earth's surface to the atmosphere and to be active in initiating ice formation at relatively warm temperature as high as -2 ºC. Because of their strong ice nucleation activity and large abundance, bio-aerosols may play an important role in exerting control over cloud development and precipitation.

Different IN has different nucleation efficiency and their ice nucleation rate is also being different. In most cloud models the number of ice nuclei which are available to initiate the formation of primary ice particles in supercooled liquid clouds is calculated with simple equations mainly as function of the temperature and/or the ice supersaturation that serve as surrogates for explicitly resolving deposition and freezing mechanisms. Earlier work partially based on measurements of atmospheric ice nuclei using a static filter approach (Fletcher, 1962; Huffman, 1973). It is one of the major challenges of cloud physics to improve these equations and to formulate the formation of ice in cloud models. The main objective of this paper is to apply the

*Corresponding author: Prof. Jen-Ping Chen, Department of Atmospheric Sciences, National Taiwan University, Taipei, Taiwan. E-mail: jpchen@as.ntu.edu.tw

nucleation rate equation for bacteria that includes temperature and ice supersaturation in a cloud resolving model (modified MM5) to evaluate the cloud microphysical processes. The case of a front passed through the northern Taiwan during 16-18 May 2003, which resulted in deep convection and heavy precipitation was chosen to test the sensitivity of clouds and precipitation to bacterial aerosols.

2. MODEL FRAMEWORK

2.1. GENERAL DESCRIPTION

THe model we used is a non-hydrostatic mesoscale cloud model (MM5) modified with a two-moment warm-cloud microphysical scheme (Chen and Liu, 2004) and coupled with ice-phase processes (Cheng et al., 2007) is applied to examine the importance of biological aerosols on precipitation formation. The two-moment C&L scheme consists of a series of empirical bulk formulas for masses (the third moment) and number concentrations (the zero-th moment) of liquid water condensates. These formulas are derived based on the statistical analyses of a parcel model simulation using the detailed cloud microphysics of Chen and Lamb (1994). In addition, C&L scheme also provides diagnostic equations to calculate the terminal velocities and the effective radius of condensates, which are critical to precipitation process and radiation heating/cooling, respectively. It assumes the CCNs to maintain a tri-modal lognormal size distribution and keep track of the Köhler-curve critical radius of the last time step retrieved from prognostic dry aerosol and total aerosol masses. When the Köhler-curve critical radius of the present time step, which depends on the supersaturation, is smaller than that of the previous time step, CCNs with radius values in between are activated. In addition, the masses of aerosols inside clouds and inside precipitation are two new prognostic variables to account for the aerosols recycled from the evaporation of cloud drops. The ice-phase scheme adopts that from Reisner et al., (1998) used in MM5 but modified to couple with the two-moment warm cloud scheme (Cheng et al., 2007), which is called the CLR scheme here. Processes considered including ice nucleation, ice multiplication, deposition/sublimation and melting of ice crystal, snow, graupel, cloud ice riming, freezing of rain drops, homogeneous and heterogeneous freezing of cloud drops, collection between condensates with modifications on some processes. Prognostic hydrometeor variables include mass mixing ratios of liquid cloud, rain, ice, snow, graupel and number mixing ratios of liquid drops, raindrops, and cloud ice. Besides the CCN activation/deactivation and cloud microphysics, other considered tendencies of prognostic hydrometeor and aerosol variables are those of advection, diffusion and vertical mixing. Furthermore, the heterogeneous ice nucleation formula of the Reisner scheme is replaced with new rate formulas to allow the inclusion of different ice nuclei, such as biological aerosols and their conversion into ice particles. Here we put the shades on a very common leaf bacteria *Pseudomonas syringae* and its ice nucleation rate equation has been derived from laboratory experiments (Yankofsky et al. 1981). Huffman's empirical formula (Huffman, 1973) has been taken to represent the condition of general natural IN concentration, which we called the empirical IN scheme. The number concentration of general IN increases with supersaturation over ice s_i, according to the relationship

$$N_{IN} = Cs_i^{\,k}$$

Where, C and k are constants. C = 1007.08, k = 4.5 (Huffman, 1973).

The model (MM5) is run with four nested grids with resolutions of having 81 km X 27 km X 9 km X 3km, and the 4th domain covers the northern Taiwan in the area within 120.25 to 122.75ºE and 23.25 to 21.25ºN (Fig. 1). Each simulation was integrated for 48 hours. Lateral boundary condition is driven by NCEP FNL data with 1° X 1° horizontal resolution. Grell cumulus parameterization is used for the two outer domains without both the explicit moisture scheme and aerosol-cloud interaction that are used for the two inner domains only. Other model options selected include the MRF scheme for planetary boundary layer processes, five layer soil model scheme for land surface process, and cloud radiation that provides surface radiation fluxes for radiation scheme.

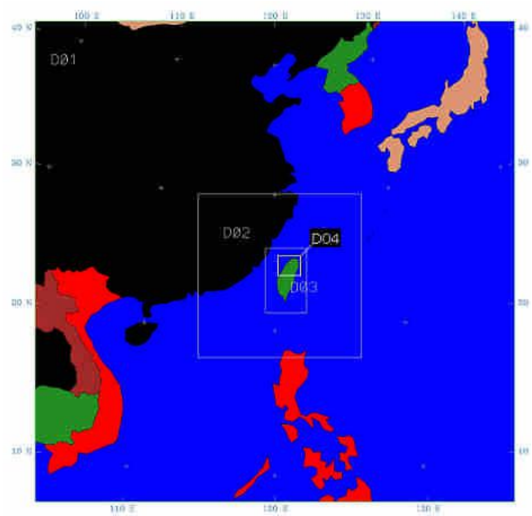

Figure 1: The domain used for simulating cold cloud system with detailed microphysics

2.2. ICE NUCLEATION RATE

Classical theory expresses the rate of heterogeneous nucleation per particle as (Fletcher 1958),

$$J = C \cdot \exp\left(-\frac{\Delta g_g}{kT}\right) \text{ ------------ (1)}$$

here, C is a kinetic coefficient. Δg_g is the energy of critical embryo (germ) formation, k is the Boltzman constant and T is the temperature. The energy of germ formation for heterogeneous freezing from classical theory is given by (Pruppacher and Klett 1997),

$$\Delta g_g = \frac{16\pi v_w^{\ 2} \sigma_{i/w}^{\ \ 3}}{3[kT \ln S_i]^2} . f \text{ ------------ (2)}$$

Where, S_i is the saturation ratio, $\sigma_{i/w}$ is the surface tension between ice and liquid water interface and v_w is volume of water molecules. For our present study the air properties namely temperature and super saturation have been separated out from equation (2) and the equation (1) will simplified as,

$$J = A.\exp\left[-B.T^{-3}(\ln S_i)^{-2}\right] \text{ ----------- (3)}$$

For the biological IN (*P. syringae*), the rate of heterogeneous freezing is obtained from laboratory experiment (Yankofsky et al. 1981). We have obtained the coefficients A (=1.072 #/sec) and B (121658 K^3) by exponential fitting of the ice nucleation rate for *P. syringae*, for which the coefficient of determination is r^2 = 0.9964. For the case of general IN, the empirical nucleation rate depends only on supersaturation with respect to ice (Huffman, 1973). Aerosols at the surface are initialized with average type (total number concentration of 6.4×10^9 m^{-3}, Whitby, 1978).

3. SIMULATION RESULTS

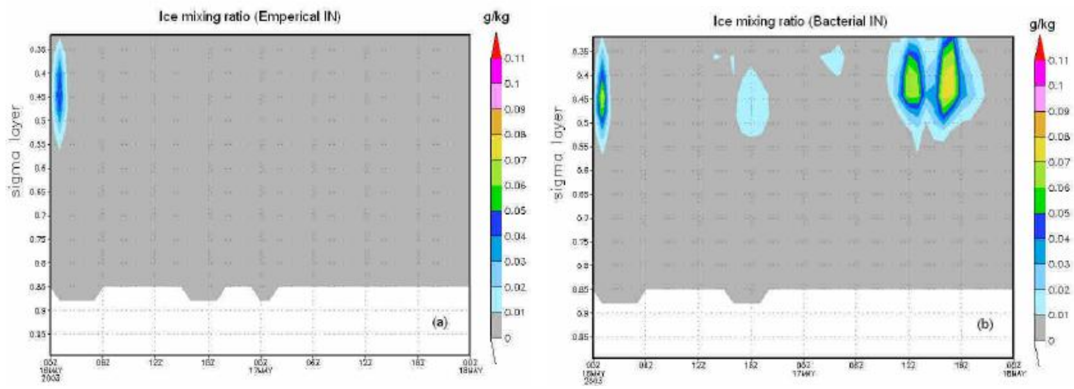

Figure 2: Time-height profiles of ice mixing ratio for empirical IN (left) and bacteria IN (right).

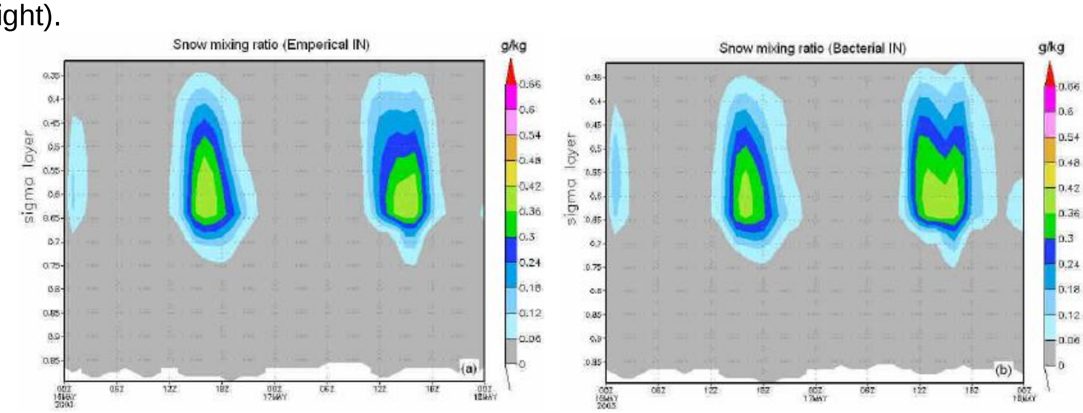

Figure 3: Time-height profiles of snow mixing ratio for empirical IN (left) and bacteria IN (right).

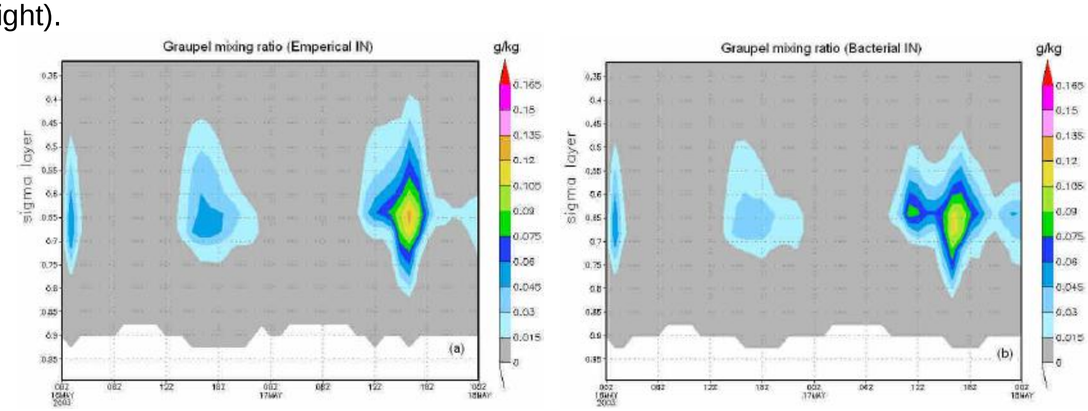

Figure 4: Time-height profiles of graupel mixing ratio for empirical IN (left) and bacteria IN (right).

The model results presented here are the averages over the inner-most domain (3 km resolution). We first compare results of precipitation formation from using empirical IN and bacterial IN. Ice mixing ratio, snow mixing ratio and graupel mixing ratio for empirical IN and biological IN are presented in Figs. 2, 3 and 4 respectively. The simulation with bacteria as IN produced more cloud ice due to stronger heterogeneous nucleation ability of bacteria, particularly during the second (12-24Z May 16) and third (09-20Z May 17) convection events. However, snow and graupel mixing ratio is somewhat lower during the second convection event for the

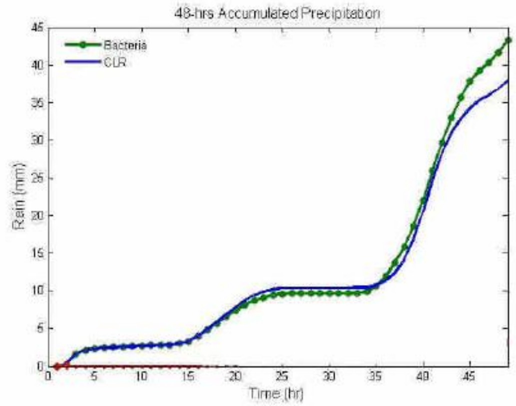

Figure 5: Total accumulated surface precipitation. Line with dots is for bacteria IN and without dots is for empirical IN.

bacteria case. This is because when there is more cloud ice, the growth of each ice particle is slower due to competition in acquiring vapor (deposition growth) and cloud water (accretion growth), hence the production of snow and graupel is delayed. In addition, the convections of the second and third events are quite strong so that ample of ice crystals may also be formed by homogeneous freezing. Thus, putting in more numerous or more effective IN might not be favorable to ice-phase precipitation formation. Note that for the bacteria case, the snow and graupel fields at the third convection period lasted longer, most likely due to the slower growth of more ice particles. So, given longer lifetime, those “excess” ice particles may still be able to develop into precipitation at a later time. Therefore, after 40 hours of simulation, clouds with bacteria IN produced more precipitation on the ground (Fig. 5).

To further clarify the role of bacteria IN, the next part of our work is to apply three different IN concentrations (2×10^4 m^{-3}, 2×10^5 m^{-3}, and 2×10^6 m^{-3}) and see the effect of IN population on cloud microphysics and precipitation. The final results are shown in Fig. 6, from which one can see that the amount of precipitation at the surface differs very little with varying IN concentration during the first two events. If looks closely, one may notice that the one with the most bacteria produced slightly less precipitation than the others.

For the second event, heterogeneous nucleation has less impact on precipitation because this time homogeneous process dominates. Actually convection started at hour 12, and was deeper during hours 21-28. In these periods, abundant cloud drops brought up to the upper troposphere were frozen and contributes to cloud ice formation. If the total water content is sufficiently high within the admixture of these particles, ice crystal gain mass by vapor deposition at the expense of the still unfrozen cloud drops via the Bergeron-Findeisen process. This is in accordance with earlier assertion that IN is relatively unimportant and may even have negative effects to precipitation formation when there is strong ice production through homogeneous freezing.

For the third event, when the cloud lifetime is longer (or with larger area of stratiform precipitation), more bacteria indeed produced more precipitation, and the effect is somewhat limited when the concentration exceeds 2×10^5 per cubic meter.

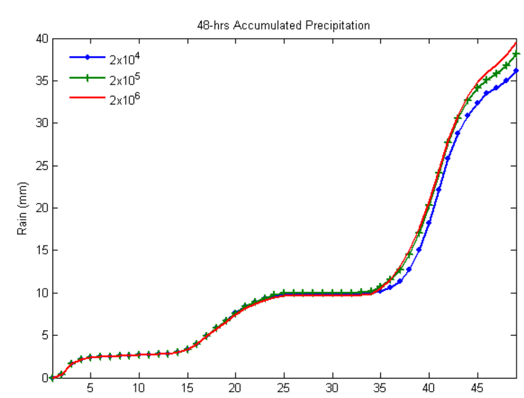

Figure 6: Time series of total accumulated precipitation for bacterial IN at three different concentrations.

4. CONCLUSIONS

This study demonstrates the importance of biological IN on the cloud microphysical processes and then formation of surface precipitation using a regional cloud model with two-moment warm-cloud bulkwater scheme coupled with a three-class ice-phase bulkwater scheme. Bio-aerosol like bacteria can be nucleated at higher temperature and lower supersaturation value that may helps to initiate cloud glaciation more quickly in terms of precipitation. When temperature decreases below 0 ºC the formation of large ice crystals in the mixed phase region depends on ice nuclei concentration, its property in terms of nucleation rate and also the size and concentration of cloud drops that where formed at lower altitudes. So, increase concentration can result in more frequent glaciations of supercooled clouds and may alter the formation of precipitation via ice phase processes.

However, during strong convection, cloud ice may also form effectively by homogeneous freezing. In our particular case, homogeneous freezing may be sufficient to intiate ice-phase precipitation, and the presence of IN is less important and may even cause “overseeding” effect to reduce precipitation. Only when there is enough time for the excess ice to grow further can more precipitation be produced on the surface. So the lifetime and the extent of the stratiform region of a convective cloud are also important factors that determines the role of IN.

As a whole, increasing of activated IN can notably modify cloud microphysics and precipitation formation processes. Biological aerosol (e.g. Bacteria, *P, syringae*) is more efficient than empirical IN to produce more precipitation.

A threshold response to increasing biological IN concentration in vigorous deep convection was found by Phillips et al. 2008 that also support our current results. Nevertheless, these results show that emissions on biological aerosols into the atmosphere, if sufficiently intense, can affect the microphysical and meteorological conditions. Future work may focus on simulation of clouds that are less vigorous.

The fraction of crystals nucleated heterogeneously by biological IN has not yet been observed directly that limits the validation of this study. In view of these biases of the cloud model, the results documented here may be viewed qualitatively.

Field measurements of biological IN and coincident meteorological observations may provide in future better cases for simulation with our advanced cloud model. So it is worthy of further investigation on the role of different kind of aerosols on the microphysics and precipitation processes. Finally, a novel framework has been proposed for modeling not only bacteria but also dust, soot ice nucleation and the biosphere-atmosphere interaction.

REFERENCES

Albrecht, D. J.: Aerosols, cloud microphysics, and fractional cloudiness, Science, 245, 1227-1230, 1989.

Chen, J. –P.: Numerical Simulations of the redistribution of atmospheric trace chemicals through cloud processes, Ph.D Thesis, Department of Meteorology, The Pennsylvania State University, December 1992.

Chen, J.-P., and Lamb, D.: Simulation of cloud microphysical and chemical processes using multicomponent framework, Part I: Description of the microphysical model, J. Atmos. Sci., 51, 2613-2630, 1994.

Chen, J.-P., Liu, and S.-T.: Physically based two-momment bulk water parameterization for warm cloud microphysics, Quart. J. Roy. Meteor. Soc., 123, 51-78, 2004.

Cheng, C.-T., Wang, W.-C., and Chen, J.-P.: A modeling study of aerosol impacts on cloud microphysics and radiative properties, Quart. J. Roy. Meteor. Soc., 133**,** 283-297, 2007.

Fletcher, N. H.: Size effect in heterogeneous nucleation, J. Chem. Phys., 29, 572-576, 1958.

Hazra, A., Saha, M., De, U. K., Mukherjee, J., and Goswami, K.: Study of ice nucleating characteristics of *Pseudomonas aeruginosa*, J. Aeros. Sci., 35, 1405-1414, 2004.

Huffman, P. J.: Supersaturation spectra of AgI and Natural ice nuclei, J. Appl. Meteor.,12, 1080-1083, 1973.

Levin, Z., Yankofsky, S. A., Pardes, D. And Magal, N.: Possible application of bacterial condensation freezing to artificial rainfall enhancement, J. Clim. Appl. Meteor., 26, 1188-1197, 1987.

Matthias-Maser S., Bogs, B., Jaenicke R.: The size distribution of primary biological aerosol particles in cloud water on the mountain Kleiner Feldbergr/Taunus (FRG), Atmos. Res. 54, 1-13, 2000.

Phillips, V. T. J., Andronache, C., Morris, C. E., and Sands, D. C.: Impacts from ice-nucleating bacteria on deep convection: implications for the biosphere-atmosphere interaction in climate change, Biogeosciences Discuss., 5, 1035–1067, 2008

Pruppacher, H. R., and Klett, J. D.: Microphysics of clouds and precipitation. Kluwer Acad., 300 p, 1997.

Ramanathan, V., Curtzen, P.J., Kiehl, J. T., and Rosenfeld, D.: Aerosols, climate and hydrological cycle, Science, 294, 2119-2124, 2001.

Reisner, J., Rasmussen, R.M., and Bruintjes, R.T.: Explicit forecasting of supercooledliquid water in winter storms using the MM5 mesoscale model, Quart. J. Roy. Meteor. Soc., 124**,** 1071-1107, 1998.

Schnell, R.C., and Vali, G.: World wide source of leaf derived freezing nuclei, Nature, 246, 212-213, 1973.

Vali, G., Christensen, M., Fresh, R. W., Galyan, E. L., Maki, L. R., and Schnell, R. C. : Biogenic ice nuclei, Part I : Bacterial sources, J. Atmos. Sci., 33, 1565-1570, 1976.

Yankofsky, S. A., Levin, Z., Bertold, T., and Sandlerman, N., Some basic characteristics of bacterial nuclei, J. Appl., Meteor., 20, 1013-1019, 1981.

Acknowledgements

The authors acknowledge National Science Council (NSC), Taiwan for the sanction of the research project and the work forms a part of it. One of the authors (A. Hazra) thanks WMO, IUGG, IAMAS and ICCP for their financial support to attend the ICCP 2008 conference. Thanks are also due to NSC and college of science, NTU, Taiwan for their financial help to attend the conference.

GLOBAL SIMULATIONS OF AEROSOL PROCESSING IN CLOUDS

Corinna Hoose[1*], **Ulrike Lohmann**[1] **and Glen Lesins**[2]

[1] ETH Zurich, Institute for Atmospheric and Climate Science, Switzerland
[2] Department of Physics and Atmospheric Science, Dalhousie University, Halifax, Canada

1 INTRODUCTION

Pruppacher and Jaenicke (1995) estimated that globally averaged an atmospheric aerosol particle, sampled at a distance from a specific source, has been cycled three times through a cloud. Uptake into cloud droplets, collision-coalescence, chemical processing inside hydrometeors and release back into the atmosphere has important implications for the physical and chemical properties of the aerosol.

In detail, a cycle of an aerosol particle through a liquid cloud can involve the following processes: Preferably the bigger and hygroscopic aerosol particles act as the cloud condensation nuclei on which cloud droplets form. Cloud droplets can collect more aerosol particles and other cloud droplets by collisions. The soluble part of the aerosol particles (e. g. sulfate, salts) dissolves in the water. Additionally, atmospheric gases can also transfer into droplets and undergo chemical reactions in the aqueous phase. E. g., the major part of atmospheric sulfate mass is formed from reactions inside cloud droplets (Barth et al., 2000). If precipitation is formed, all material collected in the precipitating droplets is removed (scavenged) from the atmosphere. However, a large fraction of clouds does not form precipitation, but evaporates (Lin and Rossow, 1996). In this case the dissolved material concentrates in the liquid phase again or crystallizes, and together with the possible insoluble material contained inside the droplet forms one new, internally mixed aerosol particle (Pruppacher and Klett, 1997). These reemitted particles are larger than prior to cloud processing.

Effects of cloud processing on the aerosol size distribution have been observed by Hoppel et al. (1986) and Hoppel et al. (1990). Marine boundary layer aerosol size distributions were found to exhibit a distinct bimodal shape. The second (larger) peak is attributed to activated particles which have grown through cloud processing, while freshly nucleated, not activated particles constitute the smaller mode. Bower et al. (1997) observed significant modifications of the aerosol size distribution and hygroscopic properties by the passage through a hill cap cloud. Addition of sulfate mass often increased the number of cloud condensation nuclei available for subsequent cloud formation.

In this chapter we apply the extended aerosol-climate model, as introduced by Hoose et al. (2008b), to global simulations of aerosol processing in clouds. The model includes prognostic equations for in-droplet and in-crystal aerosol mass.

2 MODEL DESCRIPTION

ECHAM5-HAM (Stier et al., 2005) is a global aerosol-climate model with a prognostic treatment of cloud droplets and ice crystals (Lohmann et al., 2007). Both the cloud droplet activation and the ice crystal formation through

[*] corinna.hoose@env.ethz.ch

homogeneous and heterogeneous freezing depend on the simulated aerosol number concentration, size distribution and composition.

The aerosol module HAM represents the atmospheric aerosol in seven internally and externally mixed modes, consisting of the five components sulfate, black carbon, organic carbon, sea salt and mineral dust. We have extended HAM by two additional modes which include in-droplet and in-crystal particles, respectively. A detailed model description of this aerosol processing can be found in Hoose et al. (2008b). The aerosol processing is now applied globally. Contrary to the single column model studies by Hoose et al. (2008b), aerosol, cloud droplet and ice crystal vertical and horizontal transport, vertical diffusion and aerosol and ice crystal sedimentation are now included. Transport and diffusion of in-droplet and in-crystal aerosol mass and the corresponding droplet and crystal numbers can be inconsistent if different gradients exist, and can lead to unrealistic sizes of the cloudborne particles. Cloudborne particles with a dry radius smaller than 5 nm or larger than 50 μm are removed. It was carefully examined that the global aerosol mass budgets are closed and no significant aerosol mass losses occurred.

Simulation CTL (table 1) is similar to the reference simulation described by Lohmann et al. (2007), with minor updates and corrections (Lohmann, 2007). For autoconversion, the process of transformation of cloud droplets to rain droplets, a different parameterization is used in this study. Lohmann et al. (2007) used Khairoutdinov and Kogan's (2000) scheme. This parameterization has the disadvantage that it does not provide a term for selfcollection, i. e. cloud droplet growth which does not lead to precipitation yet. As previous studies (Flossmann et al., 1985; Ivanova and Leighton, 2008) have shown that droplet collision-coalescence leads to important redistributions of the in-droplet aerosol, we revert to the parameterization by Beheng (1994) in order to include this process. Beheng's (1994) scheme was previously used in the ECHAM4 GCM (Lohmann and Roeckner, 1996). The autoconversion tuning parameter γ is used to scale the conversion of cloud liquid water to rain in such a way that a balanced radiation budget at the top of the atmosphere is achieved. A higher value of γ increases precipitation formation and lowers the global mean droplet number concentration and liquid water path, therefore decreasing the reflected shortwave radiation. This tuning is necessary and justified because subgrid-scale variations in the cloud droplet number concentration can not be resolved in global models, but can have a strong impact on the nonlinear process of rain formation. For the simulations in this study, γ ranges between 15 and 400.

Simulation AP includes the new explicit treatment of aerosol processing. Through the processes discussed below, aerosol particle and droplet number concentrations are considerably higher in this simulation. Consequently clouds are more reflective, leading to an imbalance of the net radiation at the top of the atmosphere. In simulation AP, this has been corrected for with an increased γ. Both simulations have been integrated for 1 year in T42 horizontal resolution, with 19 vertical levels after a 3-months spin-up.

3 COMPARISON TO THE STANDARD MODEL

3.1 GLOBAL AND ZONAL MEAN CLOUD AND AEROSOL PARAMETERS

Table 2 gives an overview over global annual mean values of cloud-related variables. The global mean liquid water path is 67 g m^{-2} in simulation CTL, and 38 g m^{-2} in simulation AP. As can be seen in figure 1, CTL lies in the upper range of values retrieved from satellite data (Greenwald et al., 1993; Wentz, 1997) except for the tropics, while AP follows more closely the retrieval by Weng and Grody (1994). The ice water path is similar in both simulations ($\approx$ 22 g m^{-2}), which is somewhat lower than an estimate from ISCCP data by Storelvmo et al. (2008) of 29 g m^{-2}. The shortwave cloud forcing (SCF) is $-$55.8 W m^{-2} in simulation CTL and $-$50.1 W m^{-2} in simulation AP, compared

Tab. 1: Sensitivity simulations. γ is the autoconversion tuning parameter.

Simulation	Description	γ
CTL	Control simulation, similar to simulation ECHAM5-RH by Lohmann et al. (2007), but with a different autoconversion parameterization (Beheng, 1994)	15
AP	as CTL, but with explicit representation of aerosol processing	400

to ERBE retrievals (Kiehl and Trenberth, 1997) of -50 W m^{-2}. Figure 1 (b) illustrates that the zonal distribution of the SCF is well captured in both simulations. The longwave cloud forcing, which depends mainly on ice clouds, is similar in all simulations and close to the observed value of approximately 30 W m^{-2}.

Figure 1 (c) reveals that the aerosol optical depth (AOD) is significantly higher in simulation AP (global mean 0.35) than in simulation CTL (0.19) and as obtained from observations (0.15$-$0.19). CTL agrees generally well with the observations, but overestimates the AOD at southern latitudes. Overestimation of aerosol optical depth can be due to several reasons: a too high aerosol mass burden, mispredicted aerosol size distributions or an incorrect parameterization of aerosol optical properties. The aerosol burden and size distribution are significantly different with the new treatment of aerosol processing, as discussed below. Resulting from the differences in the atmospheric aerosol, the droplet number burden N_l^{B} is also higher in simulation AP than in simulation CTL (with a grid-mean value of 2.7$\times 10^{10}$ m^{-2}), although tuning of the autoconversion rate has reduced it from 4.6 to 2.8$\times 10^{10}$ m^{-2}. In a previous publication (Lohmann et al., 2007), this value has been compared to a retrieval by Han et al. (1998). Han et al. (1998) obtain a global mean droplet burden of 4$\times 10^{10}$ m^{-2}, but this value refers to an average over cloudy pixels with liquid cloud tops only ($N_{l,\mathrm{cloudy}}^{\mathrm{B}}$). The analogous calculation for the simulations yields high values of 7.9$\times 10^{10}$ m^{-2} (CTL) and 8.5$\times 10^{10}$ m^{-2} (AP).

3.2 SCAVENGED AEROSOL MASS

Differences in the aerosol lifetime, burden, the aerosol optical depth, and consequently in the cloud droplet concentrations and further cloud parameters are caused by the different treatment of in-cloud aerosol in simulations CTL and AP. Of highest impact are differences in the wet removal of particles from the atmosphere.

The scavenged fraction, i. e. the fraction of aerosol mass and number which is incorporated in hydrometeors and is removed from the atmosphere when precipitation forms, is prescribed to fixed values for the seven modes and for three temperature ranges in the ECHAM5-HAM standard version (Stier et al., 2005). For stratiform liquid clouds, these parameters range from 0.1 for the nucleation mode to 0.99 for the mixed coarse mode (see table 3). With the prognostic treatment of in-cloud particles, the scavenged mass depends on the history of the cloud (vertical velocities at cloud base, time available for collision scavenging, Bergeron-Findeisen process).

Figure 2 compares the scavenged aerosol mass simulation CTL, diagnosed with the fixed scavenging parameters, to the prognostic in-droplet and in-crystal mass in simulation AP. The scavenged aerosol masses are in general smaller in simulation AP than in CTL, except at high altitudes. In the ice-cloud levels above approximately 400 hPa, most of the available aerosol mass is in-cloud in simulation AP, because the large soluble aerosol particles are assumed to freeze homogeneously (Hoose et al., 2008b; Kärcher and Lohmann, 2002). In contrast, in CTL, the scavenged mass fraction in ice clouds is assumed to be only 0.1 for all modes.

At lower levels, the scavenged mass is simi-

Tab. 2: Global mean liquid water path LWP, ice water path IWP, shortwave cloud forcing SCF, longwave cloud forcing LCF, net top-of-the-atmosphere radiation F_{net}, grid-mean cloud droplet burden N_l^{B}, the cloud droplet burden $N_{l,\mathrm{cloudy}}^{\mathrm{B}}$ from cloudy areas only, and aerosol optical depth AOD for the sensitivity simulations described in Table 1. Observational estimates are from Wentz (1997), Greenwald et al. (1993) and Weng and Grody (1994) (LWP), Storelvmo et al. (2008) (IWP), Kiehl and Trenberth (1997) (SCF and LCF), Han et al. (1998) ($N_{l,\mathrm{cloudy}}^{\mathrm{B}}$) and S. Kinne, personal communication (AOD).

Simulation	LWP in gm^{-2}	IWP in gm^{-2}	SCF in Wm^{-2}	LCF in Wm^{-2}	F_{net} in Wm^{-2}	N_l^{B} in $10^{10}\mathrm{m}^{-2}$	$N_{l,\mathrm{cloudy}}^{\mathrm{B}}$ in $10^{10}\mathrm{m}^{-2}$	AOD
Observations	48−83	29	−50	30	0[a]		4	0.15−0.19
CTL	67.0	22.1	−55.8	31.7	−1.23	2.7	7.9	0.19
AP	37.8	21.9	−50.1	31.0	+0.15	2.8	8.5	0.35

[a]The radiation budget at the top of the atmosphere has to be balanced, otherwise the climate would rapidly drift to a warmer/colder state.

Tab. 3: Scavenging coefficients R_j for stratiform clouds, applied to both mass and number, of the seven modes in standard ECHAM5-HAM (simulation CTL). Adapted from Stier et al. (2005). The abbreviation of the modes are: NS = nucleation soluble, KS = Aitken soluble, AS = accumulation soluble, CS = coarse soluble, KI = Aitken insoluble, AI = accumulation insoluble, CI = coarse insoluble.

	R_{NS}	R_{KS}	R_{AS}	R_{CS}	R_{KI}	R_{AI}	R_{CI}
$0°\mathrm{C} < T$	0.10	0.25	0.85	0.99	0.20	0.40	0.40
$-35 < T < 0°\mathrm{C}$	0.10	0.40	0.75	0.75	0.10	0.40	0.40
$T < -35°\mathrm{C}$	0.10	0.10	0.10	0.10	0.10	0.10	0.10

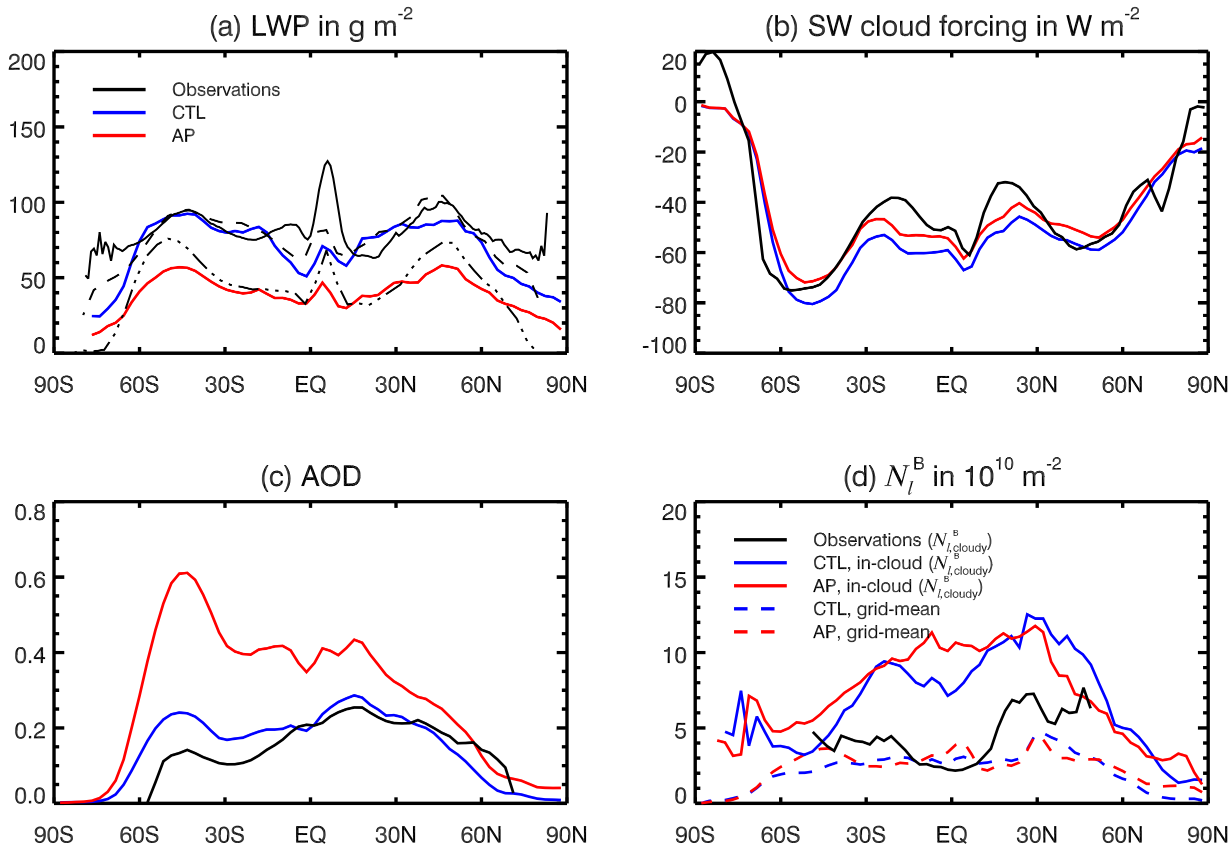

Fig. 1: Annual zonal mean (a) liquid water path over ocean, (b) shortwave cloud forcing, (c) aerosol optical thickness, and (d) cloud droplet number burden in simulations AP and CTL. Black lines are different satellite observations: (a) SSM/I retrievals by Wentz (1997) (continuous line), Greenwald et al. (1993) (dashed line) and Weng and Grody (1994) (dash-dotted line), (b) ERBE measurements (Kiehl and Trenberth, 1997), (c) a combined MODIS/MISR retrieval (S. Kinne, personal communication), and (d) a retrieval based on ISCCP data (Han et al., 1998).

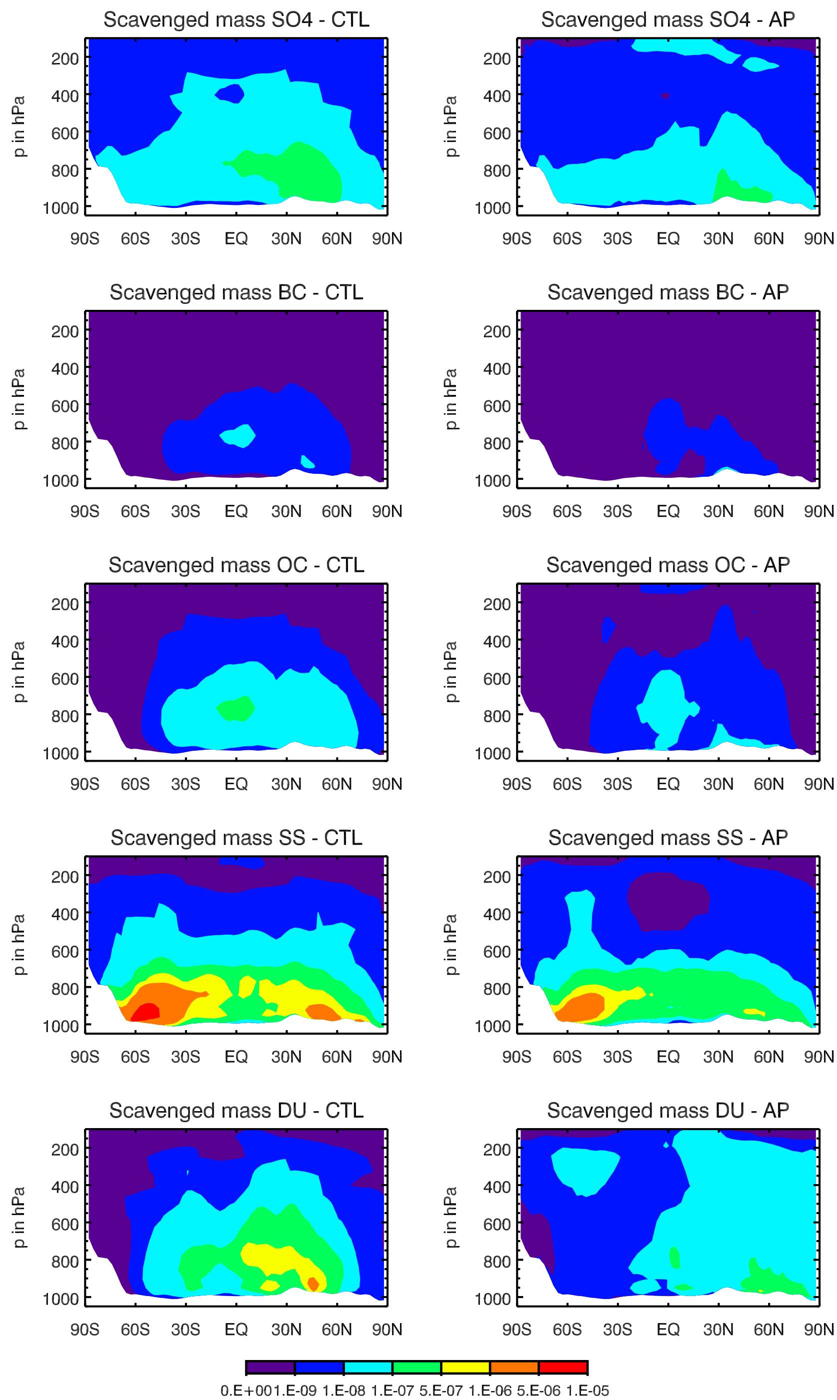

Fig. 2: Zonal and annual mean scavenged aerosol mass, diagnosed from simulation CTL (left), and simulated in simulation AP (right), in μg m^{-3}.

lar between the two simulations for sulfate. For black carbon and organic carbon, the scavenged mass is considerably smaller in simulation AP, because the carbon particles are generally small and therefore rarely activate to cloud droplets. Collision scavenging, though of some importance at these particle sizes, can not compensate for the low nucleation scavenging. For mineral dust, about half of the mass is in the insoluble modes, which are not assumed to activate to cloud droplets at all (Hoose et al., 2008b; Lohmann, 2007), and collision scavenging is negligible for the coarse modes. In simulation CTL, on the other hand, 40% of the insoluble dust is assumed to be scavenged in clouds at temperatures warmer than $-35°$C. Therefore the scavenged mass is lower approximately by a factor of 5 with the prognostic treatment in simulation AP. This results in an increase of more than 50% the insoluble accumulation and coarse mode particle number burdens.

4 COMPARISON WITH OBSERVATIONS

Comparisons between global climate model simulations and observations are hampered by the different scales in space and time for which simulated and observed values are representative. If a GCM is not nudged to the synoptic conditions at the observation time, the model results can only be compared as climatological mean values to long timeseries of observations. Furthermore, many observations reflect local conditions, which can vary within a few kilometers, while a GCM gridbox size in T42 resolution is over 300 km x 300 km at the equator. Here we have chosen several observations of aerosol or cloud microphysical parameters, which cover either large parts of the globe (sections 4.1–4.2) or are based on the statistical analysis of clouds sampled under different conditions at one location (section 4.3).

4.1 MARINE BOUNDARY LAYER AEROSOL

Heintzenberg et al. (2000) provide a compilation of aerosol concentration and size distribution measurements in the marine boundary layer (MBL). A multimodal lognormal size distribution was fitted to the original data, and from this the number concentrations and dry mean diameters of the Aitken and accumulation modes are given as zonal mean values. These observations are compared to the ECHAM5-HAM simulations CTL and AP in figure 3. The model data were averaged over the surface level at all ocean gridpoints.

While the Aitken mode zonal mean number concentrations are slightly lower in AP than in CTL, the accumulation mode number concentrations are significantly higher. The Aitken mode concentrations in both simulations are reasonably close to observations on the Northern Hemisphere, but too low between 15 and 60°S. The accumulation mode numbers in simulation AP agree better with the observations. Both the Aitken and the accumulation mode zonal mean diameters are similar in CTL and AP, but smaller in AP. For the Aitken mode CTL agrees slightly better with the observations on the Southern Hemisphere. The accumulation mode diameter is overestimated up to 100% by both simulations, especially at higher latitudes. Furthermore, an increase towards the south is simulated, while the observations are relatively constant or decrease slightly. The diameter overestimation is probably due to the size of the emitted sea salt particles in ECHAM5-HAM. The windspeed-dependent mass median radii of accumulation mode sea salt particles ranges between 271 and 284 nm (Stier et al., 2005). Conversion to number mean diameters gives 317 to 332 nm. As sea salt is expected to be the dominant aerosol type in remote ocean regions, the average number mean diameter in the model is probably dominated by this prescribed value. In the light of the observed diameters (Heintzenberg et al., 2000), which are on average 140 nm at high Southern latitudes, the emitted particle size might be to large.

4.2 AERONET SIZE DISTRIBUTIONS

The Aerosol Robotic Network (AERONET) provides ground-based remote sensing observa-

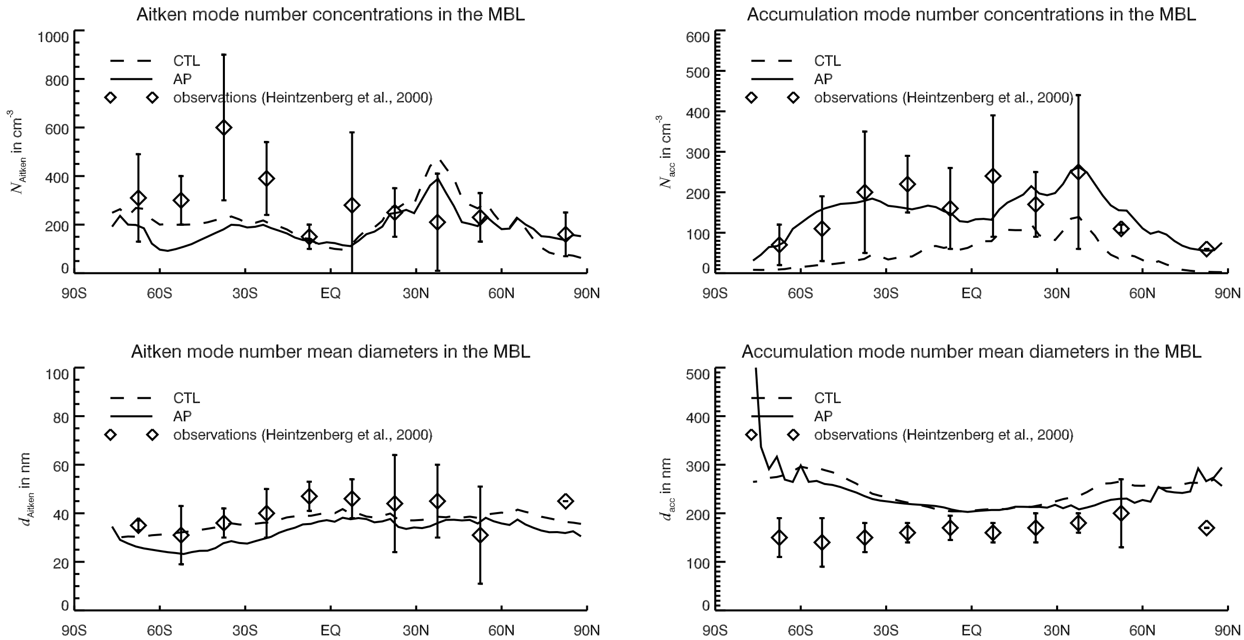

Fig. 3: Aitken and accumulation mode number concentrations and number mean diameters over the oceans, averaged over zonal bands, in simulations CTL and AP, compared to observations compiled by Heintzenberg et al. (2000).

tions of aerosol optical parameters from a large world-wide network of automated sun photometers (Holben et al., 1998). AERONET results from 1993–2003 have been used to derive column mean aerosol size distributions and aerosol volume burdens for 103 stations (G. Lesins, personal communication). The same dataset has been used by Ma and von Salzen (2006) to evaluate simulations of sulfate aerosol size distributions.

The column integrated aerosol volume size distribution ($\mathrm{d}V(d)/\mathrm{d}\ln d$) has been calculated for simulations CTL and AP as follows, as a function of the particle diameter d.

$$\frac{\mathrm{d}V(d)}{\mathrm{d}\ln d} = \sum_k \left(\sum_{j=1}^{7} \frac{\pi}{6} d^3 \frac{N_{j,k}}{\sqrt{2\pi}\ln\sigma_j} \times \exp\left(-\frac{(d-2r_{\mathrm{wet},j,k})^2}{2\ln^2\sigma_j} \right) \right) \times \frac{\Delta p_k}{g\rho_{\mathrm{air},k}} \quad (1)$$

The index k runs over all vertical levels. $N_{j,k}$ is the aerosol number concentration of mode j in level k, and $r_{\mathrm{wet},j,k}$ the median aerosol wet radius of mode j in level k. The standard deviation σ_j is fixed to the value of 2.0 for the coarse modes and to 1.59 for all other modes. The vertical integral is weighted with the geometrical layer thicknesses, calculated from the pressure difference Δp_k between adjacent layer interfaces, the acceleration of gravity g and the air density $\rho_{\mathrm{air},k}$. As the sun photometers only measure during cloud-free conditions, the simulated data are filtered to include only points with a cloud fraction smaller than 15% (similar to the analysis by Ma and von Salzen (2006)). The AERONET size distributions are provided for the radius range of 50 nm to 15 μm, i. e. the accumulation, coarse and supercoarse modes.

In figure 4, the size distributions for all stations calculated by equation (1) and the total volume, integrated over the size distribution, from simulations CTL and AP are compared to the AERONET retrievals. The simulated size distributions have a higher variance than the AERONET size distributions. The accumula-

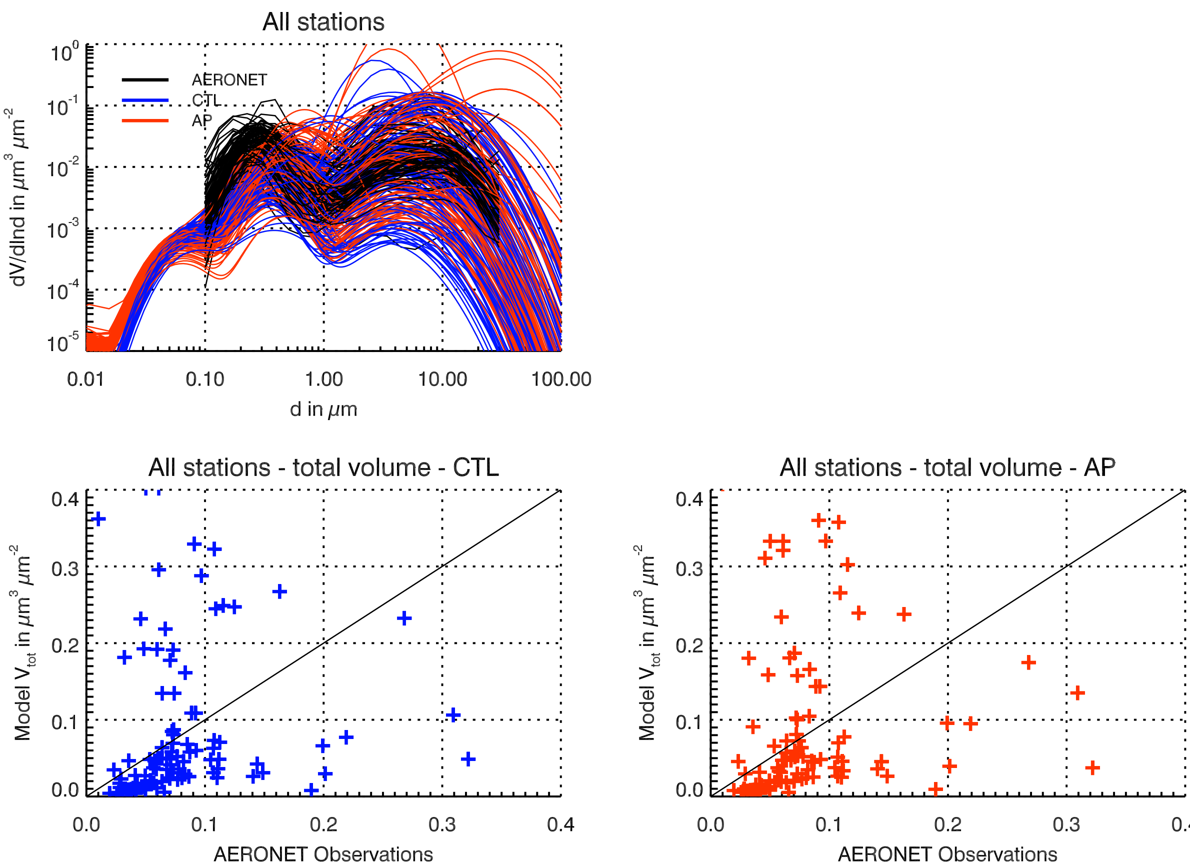

Fig. 4: Vertically integrated size distributions and volume burden for all analyzed AERONET stations (G. Lesins, personal communication) compared to simulations CTL and AP.

tion mode wet diameter is frequently overestimated in both simulations. Simulation AP exhibits higher particle numbers in the nucleation and Aitken modes ($d < 0.1\mu$m), where no observations are available. This is consistent with the higher nucleation and Aitken mode global number burdens. The total vertically integrated aerosol volume correlates poorly between both simulations and the observations. In all continental regions, the total volume is generally underestimated except for some European and South American stations. On all ocean stations, on the other hand, ECHAM5-HAM overestimates the total volume by up to an order of magnitude (not shown). Consistent with figure 3 and the conclusion of section 4.1 that the emitted size of sea salt particles in ECHAM5-HAM might be too large, the missmatch in the accumulation mode diameter is also worst for the ocean stations. A second reason for the overestimation of the volume can also be the aerosol water uptake, as here aerosol size distributions at ambient relative humidity are compared. The AeroCom model intercomparison (Textor et al., 2006) has revealed that except for one outlier, ECHAM5-HAM has the highest global water uptake by aerosols relative to the aerosol dry mass. This is related to the fact that unlike in most other models, the sea salt burden in ECHAM5-HAM is higher than the dust burden, and the hygroscopic salt particles take up more water.

On a number of stations, AERONET measured annual mean volume burdens of more than 0.15 μm$^3\mu$m^{-2}. These are mainly stations in arid regions, especially in West Africa and at the Persian Gulf. The high values can possibly be influenced by severe dust events, and thus are not reproduced by the model.

4.3 SCAVENGED FRACTION AT THE JUNGFRAUJOCH

Henning et al. (2004) and Verheggen et al. (2007) have analyzed a large set of observations of interstitial and in-cloud aerosol in mixed-phase clouds at the high-altitude research site Jungfraujoch (Swiss Alps). Aerosol size distributions were measured by a Scanning Mobility Particle Sizer (SMPS) behind two different inlets, one sampling interstitial aerosol and one sampling total aerosol (interstitial plus residuals from hydrometeors). From these measurements, a “scavenged particle number fraction” can be defined as follows.

$$F_N = \frac{N_{\rm tot}(r > 50\text{nm}) - N_{\rm int}(r > 50\text{nm})}{N_{\rm tot}(r > 50\text{nm})} \quad (2)$$

$N_{\rm tot}$ is the measured total aerosol concentration, and $N_{\rm int}$ the interstitial aerosol concentration. The cut-off of 50 nm is chosen because it is the typical dry radius of the smallest activated particles under the orographic conditions of the Jungfraujoch research station (Baltensperger et al., 1998). The studies by Henning et al. (2004) and Verheggen et al. (2007) have shown that the fraction of scavenged particles decreases with decreasing temperatures in the temperature range $-25°$ to 0°C. The Wegener-Bergeron-Findeisen process is the most likely explanation for this finding. The lower the temperature, the higher is the probability of cloud glaciation and with that the evaporation of cloud droplets, releasing formerly scavenged particles back into the interstitial phase. For temperatures above $-5°$C, Verheggen et al. (2007) found a decrease of the scavenged fraction with increasing total aerosol number.

In figure 5, the simulation AP is compared to Verheggen et al.’s (2007) and Henning et al.’s (2004) observations. The data are sampled over a whole year of instantaneous data which were saved every 12 hours, from the four gridpoints which are closest to the Jungfraujoch, throughout the lowest 9 model layers (approximately five kilometers). This was required in order to obtain a sample which was large enough for the subsequent statistical analyses. Note that the Alpine topography is not well represented on the coarse model grid. The in-cloud values of the cloud droplet concentration N_l and the ice crystal concentration N_i have been used.

The scavenged fraction in simulation AP is calculated similar to the measurements.

$$F_{\mathrm{AP}} = \frac{N_l + N_i}{N_l + N_i + N_{\mathrm{int}}(r > 50\mathrm{nm})} \qquad (3)$$

By definition, F_{AP} is always smaller than 1 in clouds. Figure 5 shows that we observe a clustering of values from pure ice clouds below 0.1, and clouds containing liquid with higher scavenged fractions. For AP the median is around 0.5. As the fraction of liquid clouds decreases with decreasing temperature, the scavenged fraction exhibits a decreasing trend, similar to but weaker than the observations. The mean scavenged fraction is lower than observed at temperatures above $-5°$C and higher than observed at temperatures below $-10°$C.

Verheggen et al. (2007) furthermore report that F_N decreases monotonically as a function of the total aerosol number concentration $N_{\mathrm{tot}}(r > 50\mathrm{nm})$ for $T > -5°$C, but is rather insensitive to $N_{\mathrm{tot}}(r > 50\mathrm{nm})$ in the mixed-phase clouds below $-5°$C. Above $-5°$C, they find the mean scavenged fraction to decrease from 0.8 to 0.3, while below $-5°$C, the mean scavenged fraction is approximately 0.1 except at low aerosol concentrations. Verheggen et al.'s (2007) study is based on a very large dataset with over 900h of in-cloud measurements. In other observational studies, based on fewer data, this effect is less pronounced. Gillani et al. (1995) find higher scavenged fractions (with a median of 85-90%) for total aerosol number concentrations up to 600 cm^{-3} in continental stratiform clouds, and a decrease only for concentrations above this value. Their values are based on measurements of unactivated accumulation mode particles ($0.1 - 1\mu$m in radius) and cloud droplets. In a previous campaign at the Jungfraujoch, no dependence of the activated fraction on the aerosol particle concentration was found (Baltensperger et al., 1998), and the average activated fraction for $r > 50$nm from four events during a campaign in October/November 1993 was 0.48.

The dependency of F_N on the total aerosol concentration has been analyzed for simulation AP in figure 6. In figures 6(a) and (b), we distinguish between clouds containing liquid droplets and pure ice clouds. As the minimum cloud droplet number concentration in ECHAM5 is prescribed to 40 cm^{-3}, the scavenged fraction is constrained in the range of low aerosol concentrations. For simulation AP, values of $(N_l + N_i + N_{\mathrm{int}}(r > 50\mathrm{nm}))$ below 40 cm^{-3} are impossible in liquid/mixed-phase clouds. Above 40 cm^{-3} the scavenged fraction for liquid/mixed clouds is enveloped by a function of the form $1/(1 + x)$. Pure ice clouds have in general low values of F_N in both simulations except at total aerosol concentrations below 20 cm^{-3}. Liquid clouds often exhibit the maximum scavenged fraction of 1 in simulation CTL, but tend to spread broadly between the minimum envelope and 1 in simulation AP. As not enough data were available for higher total aerosol concentrations, the 10th, 25th, 50th, 75th and 90th percentiles and the median for x-axis-intervals of 20 cm^{-3} are limited to $N_{\mathrm{tot}}(r > 50\mathrm{nm})$ and $(N_l + N_i + N_{\mathrm{int}}(r > 50\mathrm{nm}))$, respectively, below 200 cm^{-3}. Verheggen et al.'s (2007) data for this range are also included in figures 6(c) and (d). In simulation AP, F_N is underestimated for $T > -5°$C for $(N_l + N_i + N_{\mathrm{int}}(r > 50\mathrm{nm}))$ below 40 cm^{-3}, because these values only include ice clouds. Above 40 cm^{-3}, the mean of the scavenged fraction is in good accordance with the measurements. For $T < -5°$C, F_N is overestimated in intervals which include many liquid/mixed-phase clouds. No clear dependence of the scavenged fraction on the total aerosol concentration can be found. In the observations, this dependency becomes more obvious at higher total aerosol concentrations (Verheggen et al., 2007), which could not be analyzed here.

5 CONCLUSIONS

An explicit treatment of in-cloud aerosol particles in the global aerosol-climate model ECHAM5-HAM has allowed a global assessment of the turnover of aerosol particles in stratiform clouds. Compared to previous estimates (Pruppacher and Jaenicke, 1995), ECHAM5-HAM simulates a lower number of cycles

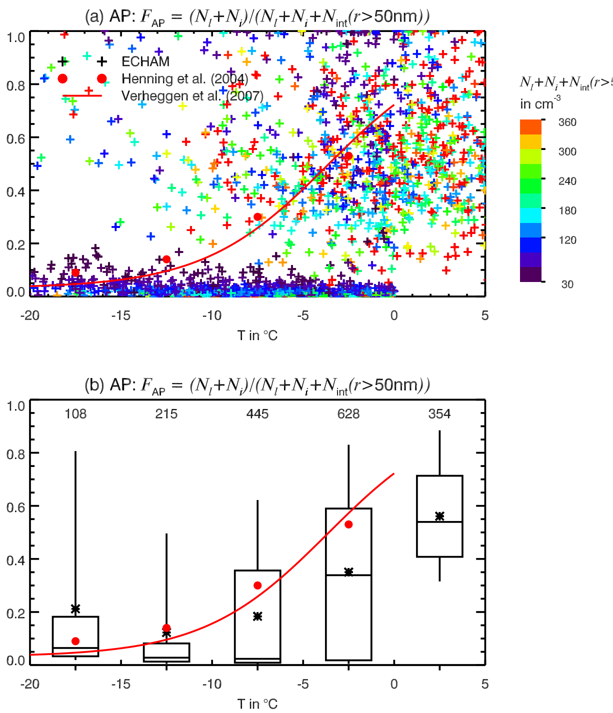

Fig. 5: Scavenged fraction F_{AP} versus temperature for simulation AP. The boxplot (b) is based on the same data as (a). The boxes and whiskers indicate the 10th, 25th, 50th, 75th and 90th percentiles. The mean per temperature interval is marked with an asterisk. The number of data points per temperature interval is given above each box. Observations by Henning et al. (2004) and Verheggen et al. (2007) are included for comparison.

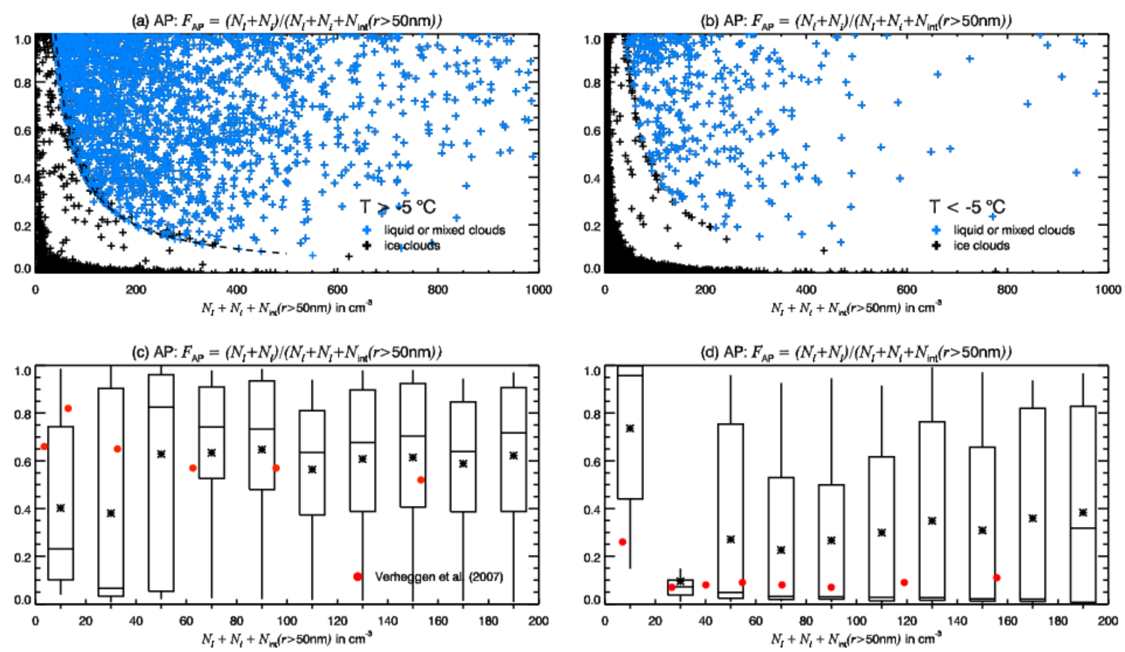

Fig. 6: Scavenged fraction F_{AP} versus aerosol concentration for simulation AP, for temperatures above ((a) and (c)) and below ((b) and (d)) $-5°$C. The dashed line gives the scavenged fraction for the minimum droplet concentration of 40 cm^{-3}. The boxplots (c) and (d) are based on the same data as the plots above, but are displayed only for $N_{\text{tot}}(r > 50\text{nm}) \leq 200$ cm^{-3}. The boxes and whiskers indicate the 10th, 25th, 50th, 75th and 90th percentiles. The mean per concentration interval is marked with an asterisk. Observations by Verheggen et al. (2007) are included for comparison.

through clouds (0.43 compared to 3) (Hoose, 2008; Hoose et al., 2008a). As in the simulation with explicit aerosol processing (AP) in general fewer particles are scavenged into the cloud phase than in the control simulation CTL, more particles are available for activation, resulting in higher cloud droplet concentrations. An enhancement of the autoconversion rate is necessary in order to achieve an equilibrated radiation balance, and this in turn reduces the liquid water path.

Comparison to different observations reveals several inconsistencies. While the marine boundary layer accumulation mode number concentrations are better reproduced in simulation AP than in simulation CTL, the wet and dry diameter of the accumulation mode is overestimated especially over ocean, resulting also in an overestimation of cloud droplet concentrations (Hoose, 2008; Hoose et al., 2008a). Total volume burden at a large number of AERONET stations is not well simulated. The scavenged particle number fraction at the Jungfraujoch is satisfactorily simulated in both simulation CTL and AP, with a general overestimation at low temperatures in CTL and an underestimation at warm temperatures in AP. While for CTL this is analyzed only diagnostically and the scavenged fraction for wet deposition is fixed to excessively high values at low temperatures, the scavenged fraction in AP is actually directly applied for wet deposition calculations.

ACKNOWLEDGEMENTS

This study was conducted within the Swiss climate research program NCCR Climate. The authors thank Betty Croft, Hans Feichter, Bernd Kärcher and Philip Stier for helpful discussions, and Bart Verheggen and Ernest Weingartner for providing data.

REFERENCES

Baltensperger, U., Schwikowski, M., Jost, D. T., Nyeki, S., Gäggeler, H. W., Poulida, O., 1998. Scavenging of atmospheric constituents in mixed phase clouds at the high-alpine site Jungfraujoch Part I: Basic concept and aerosol scavenging by clouds. Atmos. Environ. 32 (23), 3975–3983.

Barth, M. C., Rasch, P. J., Kiehl, J. T., Benkovitz, C. M., Schwartz, S. E., 2000. Sulfur chemistry in the National Center for Atmospheric Research Community Climate Model: Description, evaluation, features, and sensitivity to aqueous chemistry. J. Geophys. Res. 105 (D1), 1387–1416.

Beheng, K. D., 1994. A parameterization of warm cloud microphysical conversion processes. Atmos. Res. 33 (1-4), 193–206.

Bower, K., Choularton, T., Gallagher, M., Colvile, R., Wells, M., Beswick, K., Wiedensohler, A., Hansson, H., Svenningsson, B., Swietlicki, E., Wendisch, M., Berner, A., Kruisz, C., Laj, P., Facchini, M., Fuzzi, S., Bizjak, M., Dollard, G., Jones, B., Acker, K., Wieprecht, W., Preiss, M., Sutton, M., Hargreaves, K., Storeton-West, R., Cape, J., Arends, B., 1997. Observations and modelling of the processing of aerosol by a hill cap cloud. Atmos. Environ. 31 (16), 2527–2543.

Flossmann, A., Hall, W. D., Pruppacher, H., 1985. A theoretical study of the wet removal of atmospheric pollutants. Part I: The redistribution of aerosol-particles captured through nucleation and impaction scavenging by growing cloud drops. J. Atmos. Sci. 42 (6), 583–606.

Gillani, N. V., Schwartz, S. E., Leaitch, W. R., Strapp, J. W., Isaac, G. A., 1995. Field observations in continental stratiform clouds: Partitioning of cloud particles between droplets and unactivated interstitial aerosols. J. Geophys. Res. 100 (D9), 18687–18706.

Greenwald, T. J., Stephens, G. L., Vonder Haar, T. H., Jackson, D. L., 1993. A physical retrieval of cloud liquid water over the global oceans using Special Sensor Microwave/Imager (SSM/I) observations. J. Geophys. Res. 98, 18471–18488.

Han, Q., Rossow, W. B., Chou, J., Welch, R. M., 1998. Global variation of column droplet concentration in low-level clouds. Geophys. Res. Lett. 25 (9), 1419–1422.

Heintzenberg, J., Covert, D. C., van Dingenen, R., 2000. Size distributions and chemical composition of marine aerosols: a compilation and review. Tellus 52B (4), 1104–1122.

Henning, S., Bojinski, S., Diehl, K., Ghan, S., Nyeki, S., Weingartner, E., Wurzler, S., Baltensperger, U., 2004. Aerosol partitioning in natural mixed-phase clouds. Geophys. Res. Lett. 31 (L06101), doi:10.1029/2003GL019025.

Holben, B., Eck, T., Slutsker, I., Tanré, D., Buis, J., Setzer, A., Vermote, E., Reagan, J., Kaufman, Y. J., Nakajima, T., Lavenu, F., Jankowiak, I., Smirnov, A., 1998. AERONET - A federated instrument network and data archive for aerosol characterization. Remote Sens. Environ. 66 (1), 1–16.

Hoose, C., 2008. Aerosol processing and its effect on mixed-phase clouds in a global climate model. Ph.D. thesis, ETH Zurich, Switzerland, diss. ETH No. 17648.

Hoose, C., Lohmann, U., Bennartz, R., Lesins, G., 2008a. Global simulations of aerosol processing in clouds, in prep.

Hoose, C., Lohmann, U., Stier, P., Verheggen, B., Weingartner, E., 2008b. Aerosol processing in mixed-phase clouds in ECHAM5-HAM: Model description and comparison to observations. J. Geophys. Res., doi:10.1029/2007JD009251 in press.

Hoppel, W. A., Fitzgerald, J, W., Frick, G. M., Larson, R. E., Mack, E. J., 1990. Aerosol size distributions and optical properties found in the marine boundary layer over the Atlantic Ocean. J. Geophys. Res. 95 (D4), 3659–3686.

Hoppel, W. A., Frick, G. M., Larson, R. E., 1986. Effect of nonprecipitating clouds on the aerosol size distribution in the marine boundary layer. Geophys. Res. Lett. 13 (1), 125–128.

Ivanova, I. T., Leighton, H. G., 2008. Aerosol-cloud interactions in a mesoscale model. Part I: Sensitivity to activation and collision-coalescence. J. Atmos. Sci. 65 (2), 289–308.

Kärcher, B., Lohmann, U., 2002. A parameterization of cirrus cloud formation: Homogeneous freezing including effects of aerosol size. J. Geophys. Res. 107 (D23), doi:10.1029/2001JD001429.

Khairoutdinov, M., Kogan, Y., 2000. A new cloud physics parameterization in a large-eddy simulation model of marine stratocumulus. Mon. Weather Rev. 128 (1), 229–243.

Kiehl, J. T., Trenberth, K., 1997. Earth's annual global mean energy budget. B. Am. Meteorol. Soc. 78 (2), 197–208.

Lin, B., Rossow, W. B., 1996. Seasonal variation of liquid and ice water path in nonprecipitating clouds over oceans. J. Clim. 9 (11), 2890–2902.

Lohmann, U., 2007. Global anthropogenic aerosol effects on convective clouds in ECHAM5-HAM. Atmos. Chem. Phys. Discussions 7 (5), 14639–14674.
URL http://www.atmos-chem-phys-discuss.net/7/14639/2007/

Lohmann, U., Roeckner, E., 1996. Design and performance of a new cloud microphysics scheme developed for the ECHAM general circulation model. Clim. Dynam. 12, 557–572.

Lohmann, U., Stier, P., Hoose, C., Ferrachat, S., Kloster, S., Roeckner, E., Zhang, J., 2007. Cloud microphysics and aerosol indirect effects in the global climate model ECHAM5-HAM. Atmos. Chem. Phys. 7, 3425–3446.

Ma, X., von Salzen, K., 2006. Dynamics of the sulphate aerosol size distribution on a global scale. J. Geophys. Res. 111 (D08206), doi:10.1029/2005JD006620.

Pruppacher, H. R., Jaenicke, R., 1995. The processing of water vapor and aerosols by atmospheric clouds, a global estimate. Atmos. Res. 38, 283–295.

Pruppacher, H. R., Klett, J. D., 1997. Microphysics of Clouds and Precipitation. Atmospheric and Oceanographic Sciences Library. Kluwer Academic Publishers, Dordrecht, The Netherlands.

Stier, P., Feichter, J., Kinne, S., Kloster, S., Vignati, E., Wilson, J., Ganzeveld, L., Tegen, I., Werner, M., Balkanski, Y., Schulz, M., Boucher, O., 2005. The aerosol-climate model ECHAM5-HAM. Atmos. Chem. Phys. 5, 1125–1156.
URL http://www.atmos-chem-phys.net/5/1125/2005/

Storelvmo, T., Kristjánsson, J. E., Lohmann, U., 2008. Aerosol influence on mixed-phase clouds in CAM-Oslo. J. Atmos. Sci., in press.

Textor, C., Schulz, M., Guibert, S., Kinne, S., Balkanski, Y., Bauer, S., Berntsen, T., Berglen, T., Boucher, O., Chin, M., Dentener, F., Diehl, T., Easter, R., Feichter, H., Fillmore, D., Ghan, S., Ginoux, P., Gong, S., Grini, A., Hendricks, J., Horowitz, L., Huang, P., Isaksen, I., Iversen, I., Kloster, S., Koch, D., Kirkevåg, A., Kristjánsson, J. E., Krol, M., Lauer, A., Lamarque, J. F., Liu, X., Montanaro, V., Myhre, G., Penner, J., Pitari, G., Reddy, S., Seland, Ø., Stier, P., Takemura, T., Tie, X., 2006. Analysis and quantification of the diversities of aerosol life cycles within aerocom. Atmos. Chem. Phys. 6 (7), 1777–1813.
URL http://www.atmos-chem-phys.net/6/1777/2006/

Verheggen, B., Cozic, J., Weingartner, E., Bower, K., Mertes, S., Connolly, P., Gallagher, M., Flynn, M., Choularton, T., Baltensperger, U., 2007. Aerosol partitioning between the interstitial and the condensed phase in mixed-phase clouds. J. Geophys. Res. 112 (D23202), doi:10.1029/2007JD008714.

Weng, F., Grody, N. C., 1994. Retrieval of cloud liquid water using the special sensor microwave imager (SSM/I). J. Geophys. Res. 99, 25535–25551.

Wentz, F. J., 1997. A well-calibrated ocean algorithm for SSM/I. J. Geophys. Res. 102, 8703–8718.

MODIFICATION OF PRECIPITATION LOCATION BY NATURAL AND ARTIFICIAL CLOUD SEEDING

A. Khain[1], H. Noppel[2], K. Beheng[2] and A. Pokrovsky[1]
[1]The Hebrew University of Jerusalem, Israel
[2] The University of Karlsruhe, Germany

ABSTRACT

The rate of precipitation formation depends of the droplet concentration and the width of droplet spectrum. An increase of the concentration of small aerosols (with radii below 0.1 μm) leads to a delay (sometimes by several tens of minutes) in the precipitation formation and often fosters the formation of low density ice with small fall velocity. In the presence of a background wind, the delay in the precipitation formation means the spatial shift of precipitation. This spatial redistribution can be used for the purposes of rain enhancement. In the study we simulate cloud and precipitation distribution in the Eastearn Mediterranean region during the cold season under different aerosol concentrations.

1. INTRODUCTION

During the rain season in the Eastern Mediterranean (from November to April) the sea surface temperature (SST) is several degrees higher than the land temperature. The typical SST in December is 19-20^{o}C, while the mean surface temperature in Tel Aviv is 13^{o}C. The difference in the temperatures induces the local circulation of the land-breeze type. The interaction of this local circulation with the background westerlies leads to a convergence zone formation over sea 10-20 km off the coastal line (Khain and Sednev, 1996). This convergence results in the formation of new convective clouds or to invigoration of existent clouds (within cyclones approaching the coast). Most of these clouds precipitate rapidly over sea, not reaching the land, or reaching the coastline creating floods in such cities as Tel Aviv, Haifa located at the coastline. An example of the cloud and precipitation propagation in the region is shown in **Figure 1**, where radar reflectivity fields during the rain event on 20.01.07 at three time instances are presented. This specific feature of the region leads to the climatologic rain distribution, according to which precipitation over the sea ~10-20 km off the coast line exceeds precipitation maximum over the land more than three times.

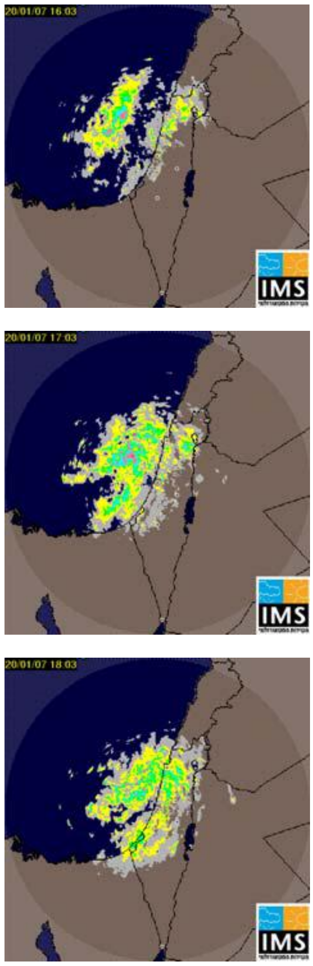

Figure 1. Radar reflectivity fields during the rain event on 20/01/0 7in one hour intervals . One can see that a significant fraction of precipitation falls over the sea not reaching the land.

The rate of precipitation formation depends of droplet concentration and width of droplet size spectrum. An increase in the concentration of small aerosols (with radii below 0.1 μm) leads to a delay of precipitation formation and often fosters the formation of low density ice with small fall velocity. In the presence of a background wind, the acceleration or the delay in precipitation formation means a spatial shift of precipitation. The conceptual scheme of such precipitation shift downwind with an increase in the aerosol concentration is presented in **Figure 2**.

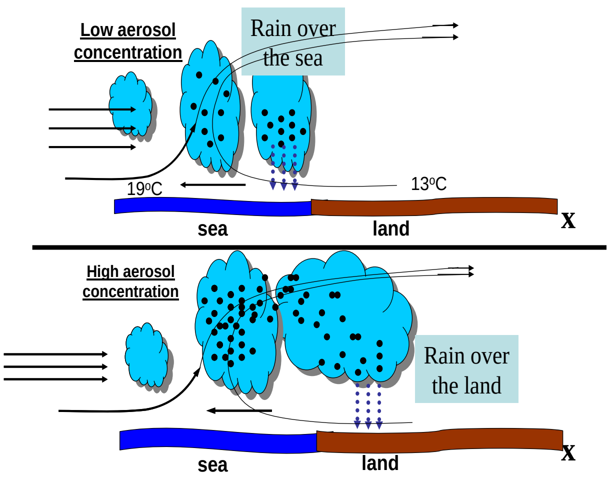

Figure 2. The conceptual scheme of the precipitation shift from sea to land by an increase in the concentration of small aerosols.

Simple computations indicate that the time delay of the surface precipitation beginning at 20 min corresponds to a precipitation shift downwind by ~15-20 km. However, this estimate does not take into account the formation of light ice particles in case of high aerosol concentration. These particles have a low sedimentation velocity, which increases the residential time of the particles in clouds and increases a possible spatial shift of precipitation. We hypothesize that the ability of small aerosols to decelerate precipitation formation and to shift precipitation can be used for the purposes of rain enhancement over land at the expense of the decrease precipitation over sea.

In this study we simulate cloud and precipitation distribution in the Eastearn Mediterranean region during the cold season under different aerosol concentrations and discuss the possibility to use this effect for purposes of precipitation enhancement.

2. RESULTS OF SIMULATIONS

2.1 THE 2-D SIMULATIONS

The simulations have been performed using a 2D spectral bin microphysics Hebrew University cloud model (HUCM) with 350 m x 125 m horizontal spatial resolution. A detailed description of the model can be found in Khain et al (2004; 2005 and 2008) and other extended abstracts of the authors in this issue. The model microphysics is based on solving the equation system for size distribution functions of water, three types of ice crystals, as well as of snow, graupel and hail. Aerosols are described using a aerosol size distribution function with maximum aerosol radius of 2 μm. Aerosols are advected by the air velocity. In case of supersaturation takes place, aerosols with sizes exceeding the critical value are transferred to drops. The corresponding aerosol mass bins become empty. In this model version all size distributions are described using mass grids containing 33 doubled mass bins. Simulations with HUCM have been performed with two concentrations of cloud condensational nuclei (CCN) (at supersaturation of 1%): 100 cm^{-3} and 2000 cm^{-3}. The first simulation will be referred to as L(ow)-run; the second as to H(igh)-run. In both cases the maximum aerosol radius was 2 μm. These aerosols produce cloud droplets of the 8-10 μm radius at cloud base. The existence of aerosols of such size is assumed to take into account a possible effect of sea spray on precipitation.

Figure 3 shows fields of droplet concentration (t=1800s), and fields of cloud water content (CWC) at t=1800s, 3600s and 7200s obtained in the H-run and L-run simulations. One can see that CWC in the H-run is larger than in the L-run. The physical reason of this result is clear: in the H-run droplets are smaller and their

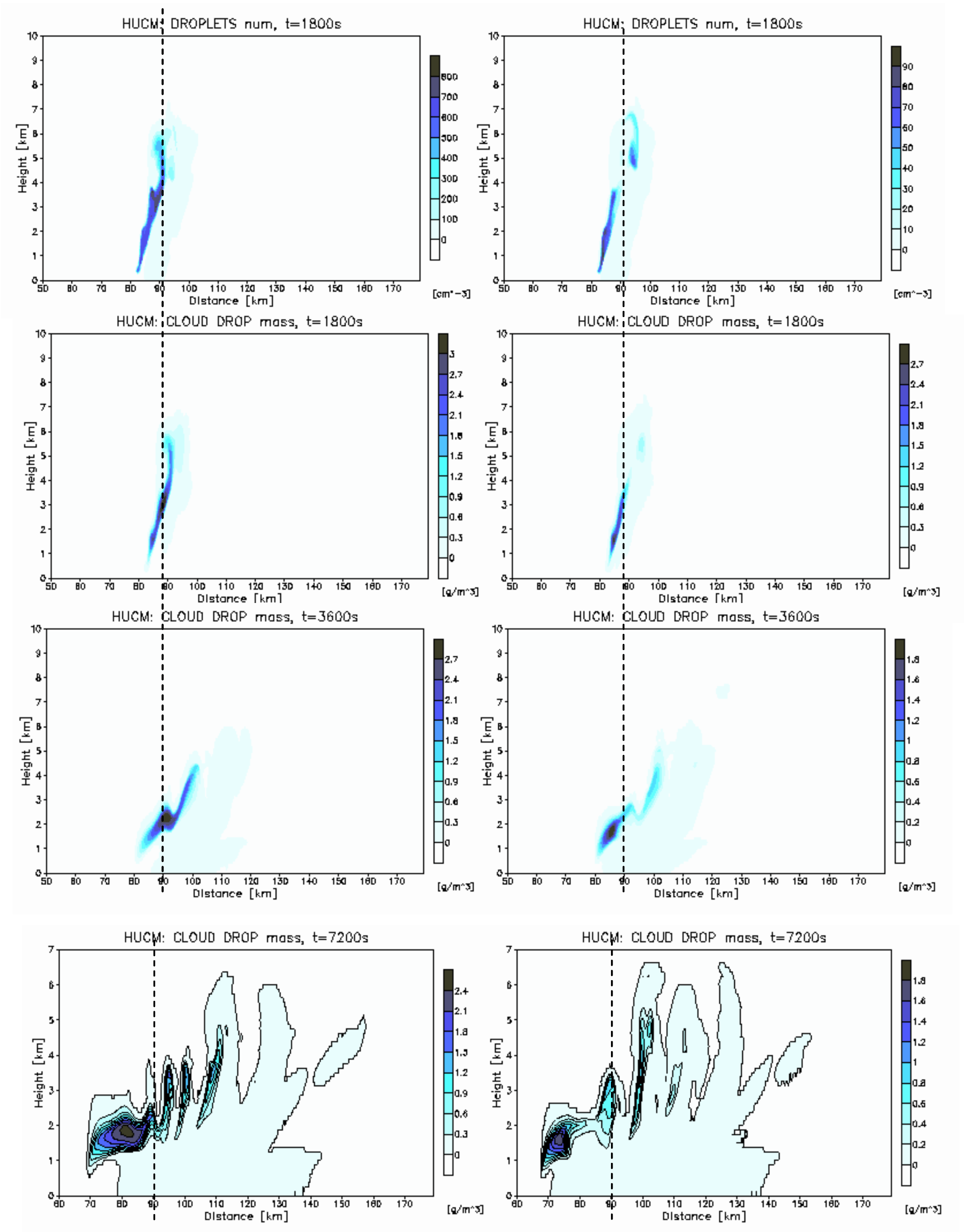

Figure 3. *Fields of droplet concentration (t=1800s), as well as fields of CWC (units indicated by the color bars) at t=1800s, 3600s and 7200 in sea breeze simulations with high (left panels) and low (right panels) aerosol concentrations. The dashed line indicates the coastal line.*

collisions are much less intense as compared to those in the L-run. As a result, in the L-run raindrops form faster and fall out. At the same time, smaller droplets in the H-run continue ascending growing by diffusion growth (condensation). This feature was observed and simulated in many studies (see references in Khain et al 2008).

The clouds forming under the effect of sea-land temperature difference arise in the convergence zone about 10 km off the coastal line. Having their roots in the boundary layer, these clouds within the sheared background flow break up into several clouds as it is seen in the lower panel in Fig. 3. These secondary clouds have higher cloud base, lower cloud base velocity and respectively, lower droplet concentration. The high humidity in the boundary layer diminishes the height of the cloud base over the sea to 700 m (lower panel of Figure 3). As a result, warm rain dominates in the vicinity of the coastal line (**Figure 6**).

Farther inland precipitation is determined by rain formed by melting of graupel and snow. Fields of graupel mass contents at 3600s and 7200 in the sea breeze simulations with high (left panel) and low (middle panel) aerosol concentrations are shown in **Figure 4**. The H-L-run difference of these fields is shown on the right panels.

From the difference of the fields it can be seen that in the H-run graupel is transported farther inland because their size is smaller than in the L-run, i.e. they have smaller fall velocity.

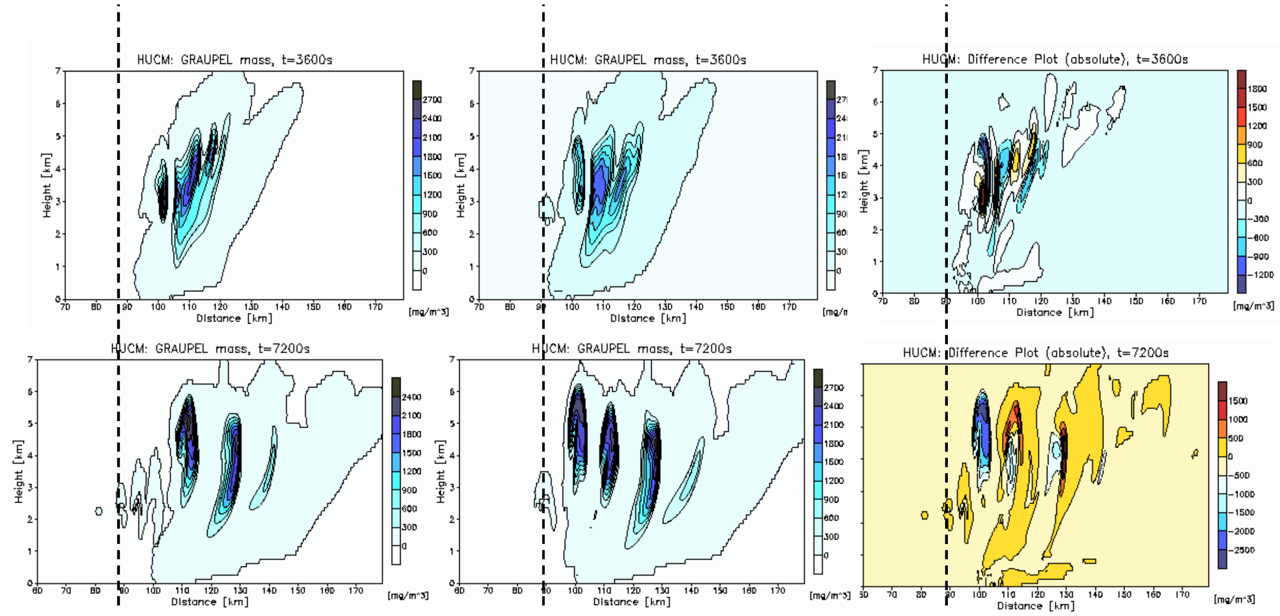

Figure 4. Fields of graupel mass contents at 3600s and 7200s in simulations with high (left panel) and low (middle panel) aerosol concentrations. The difference of these fields is shown on right panels.

An even larger difference between cloud microphysical structures in the H-run and the L-run is seen in the snow mass content (**Figure 5**). The amount of snow is substantially larger in the H-run, which agrees well with results of single clouds, discussed above. The higher production of snow in the H-run can be attributed to the fact that small droplets reach higher levels in this case and freeze producing small ice particles which are assigned to ice crystals. Their collisions produce snow. Since snow particles have a low sedimentation velocity and form in zones of strong background wind snow can be advected inland by several tens of kilometers. At such distances from the coast line snow is the major contributor to the precipitation.

As a result, an increase in aerosol concentration leads to a significant shift in precipitation from the sea to the land as it is seen in **Figure 6**. While the rainwater content (RWC) over sea is larger in the low aerosol concentration case, the RWC over land is larger in the large AP concentration case. The same conclusion can be derived from **Figure 7** showing the radar reflectivity fields in the H- and the L-runs.

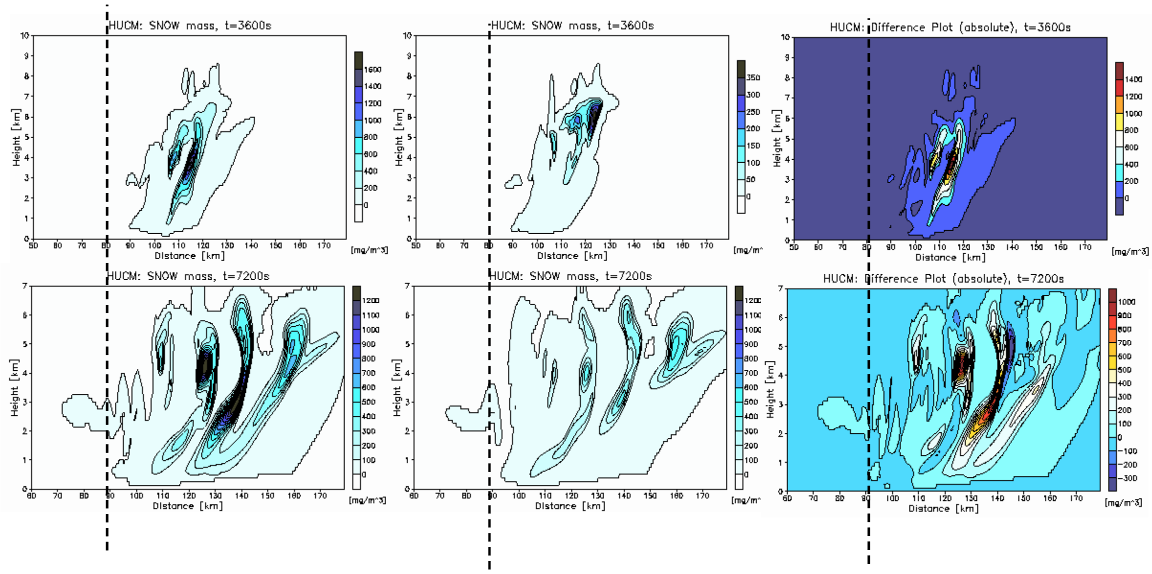

Figure 5. Fields of snow mass contents at 3600s and 7200 in simulations with high (left panel) and low (middle panel) aerosol concentrations. The difference of these fields is shown on right panels.

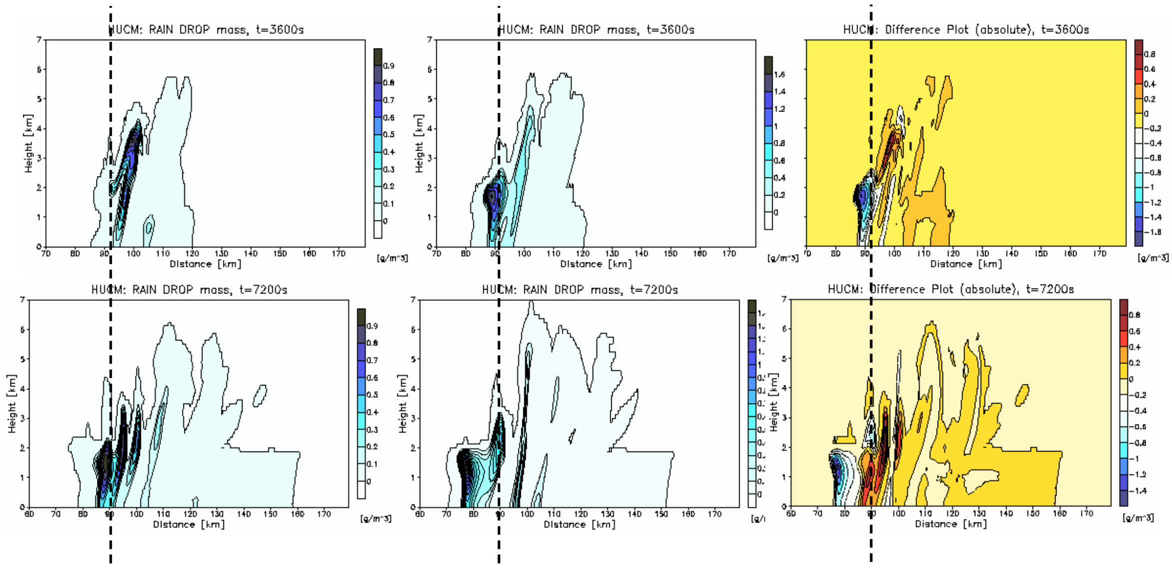

***Figure 6**. Fields of rain water content at 3600 and 7200 s in simulations with high (left panels)*

and low (middle panels) aerosol concentrations. The differences between these fields are shown in the right panels. While RWC over the sea is larger in low aerosol concentration case, the RWC over the land is significantly larger in the large AP concentration case.

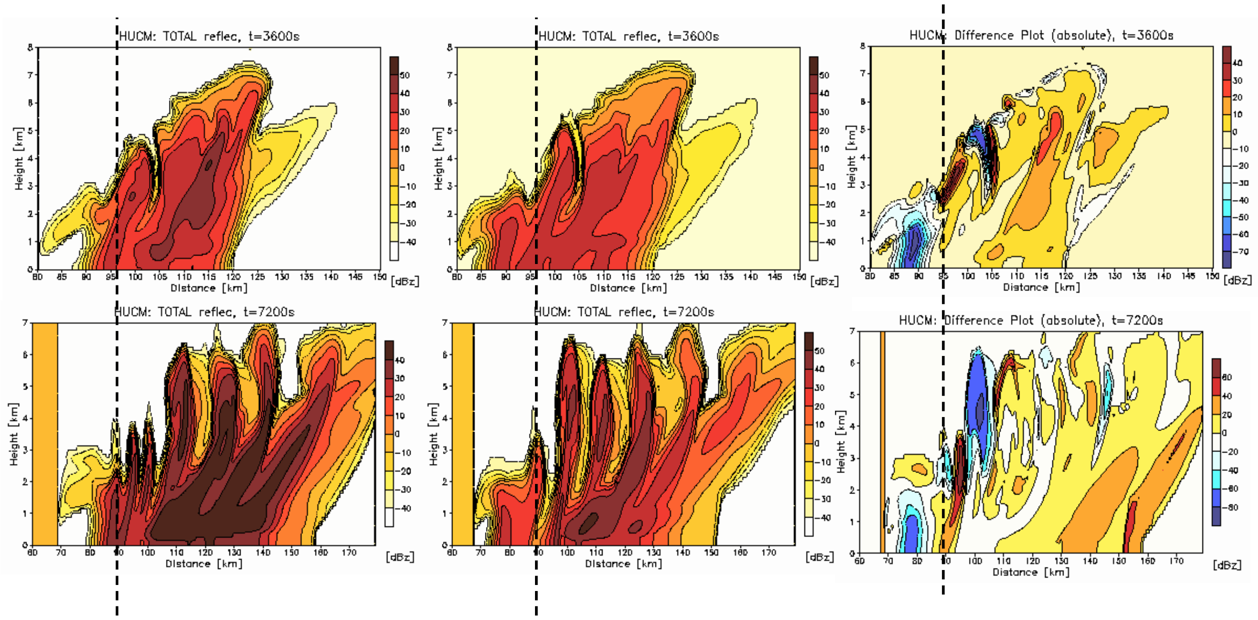

***Figure 7**. Fields of radar reflectivity at 3600 and 7200 s in simulations with high (left panels) and low (middle panels) aerosol concentrations. The differences between these fields are shown in the right panels. While radar reflectivity over the sea is larger in the low aerosol concentration case, the radar reflectivity over the land is significantly larger in the high AP concentration case.*

Accumulated rain amount as a function of time in the simulations with high and low aerosol concentrations are shown in Figure 8 (left panel). Figure 8 (right panel) shows accumulated rain over the land only. One can see that precipitation starts earlier (i.e., more westward) in the low AP concentration case.

Over the whole computational area precipitation in the low aerosol concentration case dominates. At the same time, the increase in the aerosol concentration redistributes precipitation in such a way that precipitation over the land increases and exceeds that in the low aerosol concentration case.

3.2 3-D SIMULATIONS

In order to investigate the possible 3-D effects and include effects of topography two 3-D models have been used: a) Weather Research

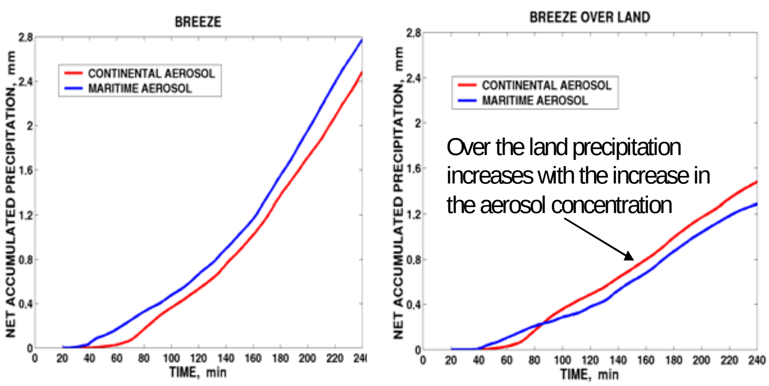

***Figure 8**. Accumulated rain amount as the function of time in the simulations with high and low aerosol concentrations over the whole computational area (left panel) and over the land only (right panel).*

Forecast model (WRF) (developed in NCAR) (Skamarock et al 2005) with the 1 km-resolution and the COSMO (Weather prediction model of the German Meteorological Service) with 2 km resolution and an advanced two-moment bulk microphysics parameterization.
Two rain events have been simulated: on 5 January 2007 and on 20-21 January 2007. Each rain event was simulated for low (maritime) and high (seeded) concentrations of small aerosol particles.

In the simulations using WRF the microphysics module of Thompson et al (2004) was used. The input of this scheme is the droplet concentration. In the low and high aerosol concentrations the droplet concentrations were set equal to 50 and 500 cm^{-3}, respectively.

Fields of accumulated rain calculated for rain event on 5 January 2007 in cases of low aerosol concentration (left panel) and high aerosol concentration (right panel) are shown in Figure 9.

Accumulated precipitation: rain event 5 January 2007, t=15.00

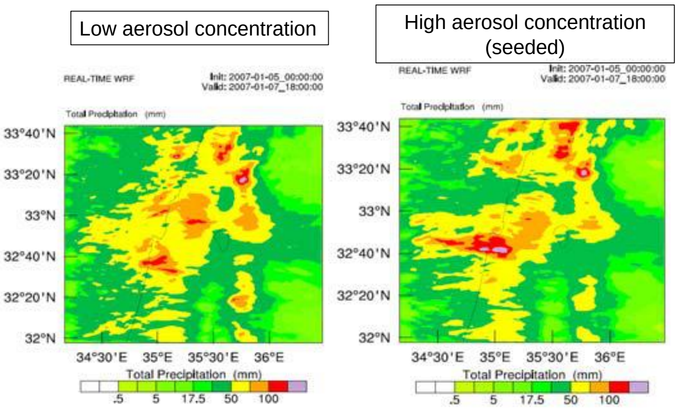

Figure 9. Fields of accumulated rain calculated for the rrain event on 5 January 2007 in cases of low aerosol concentration (left panel) and high aerosol concentration (right panel).

One can see that an increase in the aerosol concentration leads to a significant increase precipitation over land; b) this increase takes place both in Northern Israel, and in the southern part of Israel. Similar results are obtained in simulation of the rain event on 20 January 2007 (**Figure 10**).

Accumulated precipitation: rain event 20-21 January 2007

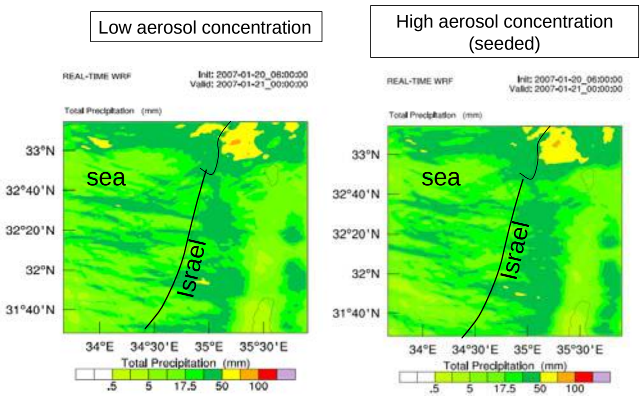

Figure 10. Fields of the accumulated rain calculated for the rain event on 20-21 January 2007 in cases of low aerosol concentration (left panel) and high aerosol concentration (right panel).

Figure 11 shows the time series of the accumulated rain over the land in simulations with low and high aerosol concentrations (rain event on 20 January).

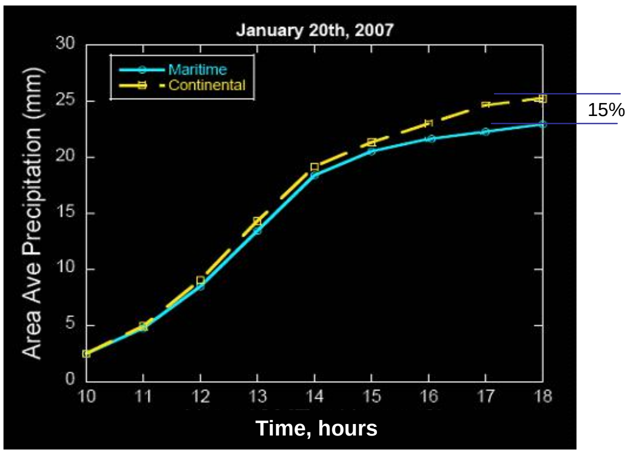

Figure 11. Time series of the accumulated rain over the land in the simulations with low and high aerosol concentrations (the rain event on 20 January 2007).

One can see that the increase in the aerosol concentration led to the increase in the accumulated rain by 15%. Similar results were obtained for the rain event on 5 January 2007.

Another set of 3-D simulations was performed using the COSMO model which is an operational weather forecast model of the Germany Weather Service. This model uses an advanced two-moment bulk parameterization scheme developed in the Karlsruhe University (Seifert and Beheng 2006). In this parameterization the size distribution functions of hydrometeors are given in the form of generalized Gama-distributions. The parameters of this distribution allow one to vary the concentrations and widths of drop size distributions. **Figure 12** shows the size distributions used in the simulations. The first distribution is characterized by smaller droplet concentration and higher width and is referred to as low AP concentration case. The second distribution has higher drop concentration, but smaller width. This distribution can be assigned to the high AP concentration case but is called here intermediate

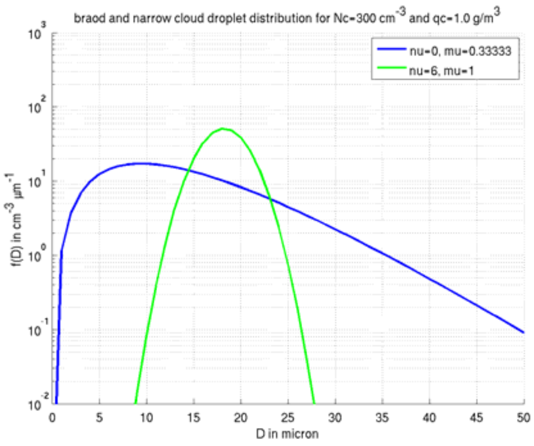

Figure 12. *Droplet size distributions used in simulations with the model COSMO of the Germany Weather Forecast Service in cases of clean air (blue) and polluted air (green).*

In this case idealized initial and boundary conditions were assumed and the simulations performed with a SST-land temperature difference equal to $6\,^{o}C$. Figure 13 shows the fields of accumulated rain in case of low (left) and high (right) aerosol concentrations.

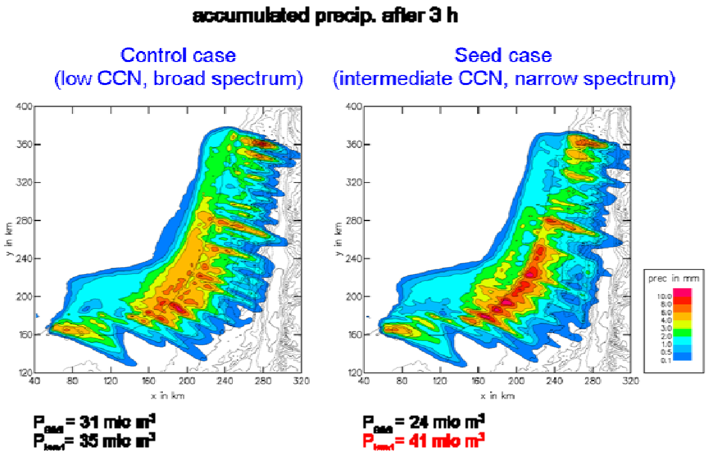

Figure 13. Fields of accumulated rain calculated using the COSMO model in case of low (left) and high (right) aerosol concentrations. The numbers denote amount of precipitation over the sea and over the land in these two cases. One can see that increase in the aerosol concentration leads to increase in precipitation over the land

One can see that that the increase in the aerosol concentration led to an increase of the precipitation over land and to decrease in the precipitation over sea in a good agreement with the results obtained using HUCM and WRF models. According to the results of the COSMO model the increase in precipitation caused by the increase in the aerosol concentration is about 18-20%.

The good agreement in the results obtained by different models increases the reliability of the results obtained. We attribute this good agreement to the fact that the effect of aerosols on the shift of precipitation is reproduced well by most models with advanced microphysics.

4. DISCUSSION AND CONCLUSION

Numerical simulations of sea breeze-affected cloud systems under the conditions typical of Mediterranean area have been carried out using the spectral bin microphysics model HUCM and two high resolution 3D mesoscale models (WRF and COSMO) with different bulk microphysical schemes. It was found that an increase in the small aerosol particles concentration leads to a delay in the precipitation formation and to a significant increase of the snow amount. Snow has smaller fall velocity and advected downwind for larger distances. Hence, the increase in the aerosol concentration leads to a shift of precipitation from sea to land sometimes up to 100 km, so that precipitation over land increases and exceeds that it was under low aerosol concentration.

According to the results obtained, an increase in the small aerosol production in Europe should lead to an increase in precipitation at the coastal zone of Israel. Such an increase has been indeed reported by Alpert et al (2007), who analyzed precipitation at coastal stations during several past decades.

Note that this result was obtained in case when large aerosols with 4 μm in diameter presented in the initial AP size distribution. The reason of a comparatively low effect of large CCN on precipitation from deep convective clouds in case of high drop concentration is discussed by Khain et al (2008b) in detail. The main reason is that if the droplet concentration is high supersaturation is low and large drops forming on largest CCN grow slowly. One of the reasons is that in course of the diffusional growth, the radii of smaller droplets grow faster than those of large ones (Rogers and Yau, 1989) and the sizes of the initially small droplets tend to those of the largest ones. Besides, in the presence of a comparatively high vertical velocity and comparatively low freezing level, all droplets ascend above the freezing level being of nearly the same size and participate in cold processes. Thus, large aerosols that potentially can exist at strong winds, do not affect significantly the spatial shift of precipitation downwind in case the concentration of small aerosols is significant and the concentration of droplets exceeds about 600- 700 cm^{-3}.

The fact that all models indicate comparable results shows that the effect can be attributed to quite strong mechanism, clear from the physical point of view and relatively simple for simulations. To get an increase in the precipitation over land, it is not necessary to get total precipitation enhancement (which simulation requires very fine description of all microphysical processes).

We consider our results as potentially important for the rain enhancement activities in the regions when such synergetic interaction of local (sea breeze) and synoptic circulation can take place. In addition to Israel, such conditions supposedly take place in Italy, Egypt, Lebanon, Bulgaria, Portugal and some other countries.

We propose to seed clouds arising over the sea in the vicinity of the coastal zone by small aerosol particles near cloud base. Such seeding would affect the entire cloud, but not only its upper cold part (as it takes place by glaciogenic seeding). The seeding with small aerosols will lead to the formation of larger amount of ice crystals and snow via effects crystal-water and crystal-crystal collisions at the expense of large graupel falling over the sea of over the coastal line (and melted within the boundary layer).

The size of seed aerosol particles may be around 0.1 μm. The mass of such particle is ~10^7 times smaller than the size of "optimum" size of soluble particle in hygroscopic seeding (Segal et al 2004). Thus, the mass of a seed material to provide a significant increase in the droplet concentration may be of the same order as the mass usually used for the hygroscopic seeding.

It is possible to combine this method of hygroscopic seeding with that of glaciogenic seeding. In this case seeding particles should represent small soluble aerosol particles with some insoluble fraction (which replaces the role of ice nuclei). Small aerosols will increase the mass of supercooled water which can be transferred into snow by glaciogenic component of the seed particles. This can lead to an increase of the formation of larger mass of snow and to shift precipitation downwind because of lower sedimentation velocity of snow as compared to that of graupel.

The advantages of the method proposed are: a) the cloud development can be predicted with a high precision by the high resolution weather forecast models, so that the zones of the potential seeding will be known well before the seeding operation. b) The radar observations allow us to choose clouds for the seeding; c) the radar will also be used to follow both seeded and non seeded clouds. It will allow one to distinguish between seeded and non seeded clouds. The effects of seeding must be seen by a longer penetration of seeded clouds inland. We propose such a seeding experiment which will be the first one, where seeding effects could be evaluated and controlled with high accuracy.

A significant advantage of the method is that it does not require obtaining the total precipitation enhancement. Many uncertainties in cloud microphysics, which are of crucial importance for simulation of precipitation enhancement, are of the secondary importance when the spatial shift of precipitation is simulated.

Acknowledgements

The study has supported by the Ministry of Science, Culture and Sport of Israel (Joint German-Israel research projects) and Bundesministerium für Bildung und Forschung (BMBF, Germany) (grants WT403 and 02WT0536), and the Israel Water Company, grant 162/03.

References

Alpert, P., N. Halfon and Z. Levin, Does air pollution really suppress precipitation in Israel?, J. Appl. Meteoro. And Climatolo., 2007 (accepted)

Khain, A.P. and I. Sednev, 1996: Simulation of precipitation formation in the Eastern Mediterranean coastal zone using a spectral microphysics cloud ensemble model. *Atmospheric Research*, 43: 77-110.

Khain A., A. Pokrovsky and M. Pinsky, A. Seifert, and V. Phillips, 2004: Effects of atmospheric aerosols on deep convective clouds as seen from simulations using a spectral microphysics mixed-phase cumulus cloud model Part 1: Model description. *J. Atmos. Sci 61, 2963-2982.*

Khain, A. D. Rosenfeld and A. Pokrovsky 2005: Aerosol impact on the dynamics and microphysics of convective clouds. *Q. J. Roy. Meteor. Soc.* 131, 2639-2663.

Khain, A. P., N. BenMoshe, A. Pokrovsky, 2008a. Factors determining the impact of aerosols on surface precipitation from clouds: attempt of classification. J. Atmos. Sci. (in press)

Khain, A. N. Cohen, B. Lynn and A. Pokrovsky, 2008b: Possible aerosol effects on lightning activity and structure of hurricanes. J. Atmos. Sci. (in press).

Rogers, RR., and Yau, M.K., 1989: A short course of cloud physics. Pregamon, Oxford, 293 pp.

Segal Y., A. Khain, and M. Pinsky, and D. Rosenfeld, 2004: Effects of hygroscopic seeding on raindrop formation as seen from simulations using a 2000-bin spectral cloud parcel model. *Atmos. Res.* 71, 3-34.

Seifert, A, and K. Beheng, 2006: A two-moment cloud microphysics parameterization for mixed-phase clouds. Part II: Maritime vs. continental deep convective storms. *Meteorol. Atmos. Phys.*, **92**, 67-88.

Skamarock, W., J.B. Klemp, J. Dudhia, D. O. Gill, D. M. Barker, W. Wang, J.G. Powers, 2005: A description of the Advanced Research WRF Version 2, NCAR Technical Note, June 2005, Mesoscale and Microscale Meteorology Division, NCAR, Boulder, Colorado, USA.

Thompson, G., R. R. Rasmussen, and K. Manning, 2004: Explicit forecasts of winter precipitation using an improved bulk microphysics scheme. Part 1: Description and sensitivity analysis, *Mon. Wea. Rev.*, **132**, 519-542.

Is the dependence of warm and ice precipitation on the aerosol concentration monotonic?

A. Khain, A. Pokrovsky, U. Blahak and D. Rosenfeld
Department of Atmospheric Science, The Hebrew University of Jerusalem, Israel

ABSTRACT

Effects of aerosols on microphysics and precipitation of deep convective clouds was simulated in many numerical studies. Most of them were related to clouds with warm cloud base and high (~4 km) freezing level. Only a few studies investigated aerosol effects on precipitation from convective clouds developing in the atmosphere with a comparatively low (~2-3 km) freezing level. The difference between these cases is quite significant: while clouds with high freezing level produce warm rain at low aerosol concentration, and melted (cold) precipitation at high aerosol concentration, in case of low freezing level precipitation is formed by melted ice at any aerosol concentrations.
Effects of aerosols on ice microphysics and especially on hail formation are not well known. In this presentation we perform preliminary results of simulations of deep convective clouds under different thermodynamic and aerosol conditions. The main focus of the study is investigation of aerosol effects on hail formation process, hail content and size. The investigation is performed using a modified version of the Hebrew University Cloud model (HUCM) with spectral (bin) microphysics.

1. INTRODUCTION

Effects of aerosols on microphysics and precipitation of deep convective clouds was simulated in many numerical studies (Khain et al, 2004; 2005, 2008; Khain and Pokrovsky 2004; Lynn et al 2005a,b; Wang 2005; Teller and Levin 2006; Van Heever et al 2006, Iguchi et al 2008, Fan et al 2007; Tao et al, 2007, Lee et al 2008, etc.) In most studies the environmental conditions were characterized by high (~4 km) freezing level, so that the cloud base temperatures were above 10-15^{o}C. Only a few studies investigated aerosol effects on precipitation from convective clouds developing in the atmosphere with a comparatively low (~2 km) freezing level (e.g. Teller and Levin 2006). The simulations have been performed for the time period of 1 hour. The difference between these cases is quite significant: while clouds with high freezing level produce warm rain at low aerosol concentrations and melted (cold) precipitation at high aerosol concentrations, in case the freezing level is low melted precipitation dominates at any aerosol concentrations. Hence, in the latter case there is no simple separation between warm and cold rain regimes. In this cases the effects of aerosols on ice microphysics becomes of major importance. At the same time effects of aerosols on ice microphysics and especially on hail formation are not well understood. This problem is also of a significant practical importance, because the high damage caused by hail.
In this study we address the following questions:
- How do aerosols affect hail formation and hail size?
- How do aerosols affect precipitation from deep convective clouds forming at a comparatively low freezing level (relatively low cloud base temperature)?

One of the main objectives is to simulate hail formation in a deep convective cloud under conditions close to those observed during hailstorm on 28 June 2006 in southwest Germany. In this storm the radar reflectivity exceeded 60 dBz within the layer from the surface to 12 km, and the largest size of hailstones at the surface was a few centimeters with a lot of hail and graupel particles with diameters of ~0.5-1 cm.

The investigation is performed using a modified version of the Hebrew University Cloud model (HUCM) with spectral (bin) microphysics.

2. THE CLOUD MODEL

Different aspects of the 2-D mixed phase Hebrew University cloud model (HUCM) with spectral bin microphysics can be found in studies by Khain and Sednev (1996); Khain et al (2004, 2005; 2008). The HUCM model microphysics is based on solving a kinetic equations system for size distribution functions for water drops, ice crystals (plate-, columnar- and branch types), aggregates, graupel and hail/frozen drops, as well as atmospheric aerosol particles (AP). Each size distribution is described using 43 doubling mass bins, allowing simulation of graupel and hail with the sizes up to 5 cm in diameter. The model is specially designed to take into account the AP effects on the cloud microphysics, dynamics, and precipitation. *The initial* (at t=0) CCN size distribution is calculated using the empirical dependence

$$N = N_o S_1^k , \qquad (1)$$

and applying the procedure described by Khain et al (2000). In (1) N is the concentration of activated AP (nucleated droplets) at supersaturation S_1 (in %) is with respect to water, N_o and k are the measured constants. At t>0 the prognostic equation for the size distribution of non-activated AP is solved. Using the value of S_1 calculated at each time step, the critical AP radius is calculated according to the Kohler theory. The APs with the radii exceeding the critical value are activated and new droplets are nucleated. The corresponding bins of the CCN size distributions become empty.

Primary nucleation of each type of ice crystals is performed within its own temperature range following Takahashi et al (1991). The dependence of the ice nuclei concentration on supersaturation with respect to ice is described using an empirical expression suggested by Meyers et al. (1992) and applied using a semi-lagrangian approach (Khain et al 2000) allowing the utilization of the diagnostic relationship in the time dependent framework. The secondary ice generation is described according to Hallett and Mossop (1974). The rate of drop freezing is described following the observations of immersion nuclei by Vali (1994, 1975), and homogeneous freezing according to Pruppacher (1995). The homogeneous freezing takes place at temperature about -38^oC. The diffusion growth/evaporation of droplets and the deposition/sublimation of ice particles are calculated using analytical solutions for supersaturation with respect to water and ice. An efficient and accurate method of solving the stochastic kinetic equation for collisions (Bott, 1998) was extended to a system of stochastic kinetic equations calculating water-ice and ice-ice collisions. The model uses height dependent drop-drop and drop-graupel collision kernels following Khain et al, (2001a) and Pinsky et al (2001). Ice-ice collection rates are assumed to be temperature dependent (Pruppacher and Klett, 1997). An increase in the water-water and water-ice collision kernels caused by the turbulent/inertia mechanism was taken into account following Pinsky and Khain (1998) and Pinsky et al. (2008). The collision enhancement factors are assumed independent on time and location within a cloud. Advection of scalar values is performed using the positively defined conservative scheme proposed by Bott (1989).

To simulate formation of large hail and to calculate the sizes of ice particles falling to the surface properly the following main modifications of the model version described by Khain et al (2008a) have been made:

a) Shedding of water from melting hail and graupel has been implemented following Phillips et al (2007).

b) Collisions of all hydrometeors (including melting particles) were included and the new liquid water fractions within hail, graupel and snow were calculated as a result of the collisions in each bin at each time step.

c) The calculation of the rimed fraction of snow (additional size distribution) has been implemented, and new snow bulk density is recalculated at each time step and in each bin.

d) Snow is transferred to graupel, if its bulk density exceeds 0.2 gm^{-3}.

e) Graupel is transferred to hail in three cases: if the wet growth begins; if its radius exceeds 1 cm and, if graupel collides water drops at positive temperatures. The condition of the wet growth beginning is calculated using the scheme developed by U. Blahak. The condition depends on the graupel size, temperature and the contents of liquid water and ice in its surrounding.

f) Dependencies of the collision kernels on height are included for all hydrometeors.

The computational domain is 178 km x 16 km with the resolution of 350 m and 125 m in the horizontal and vertical directions, respectively.

3. DESIGN OF SIMULATIONS AND RESULTS

The rain event on 28 June 2006 in the area of Stuttgart accompanied by falling down of hail stones of a few cm in diameter has been simulated. We performed simulations for several aerosol (CCN) concentrations within the range 100 cm^{-3} to 6000 cm^{-3} covering the whole range of possible CCN variations in this region. The slope parameter k in (1) was assumed equal to 0.5.

The convection has been triggered by a cold pool of 20 min duration. The sounding of Stuttgart chosen for simulations is shown in **Figure 1**. Note that the surface temperature has been increased as compared to the sounding data by 2-3 C. As a result, two sets of simulation with the surface temperatures of 23C and 24 C have been performed.

Figure 1. Sounding used in the 2-D simulations of the 28 June 2006 hail event.

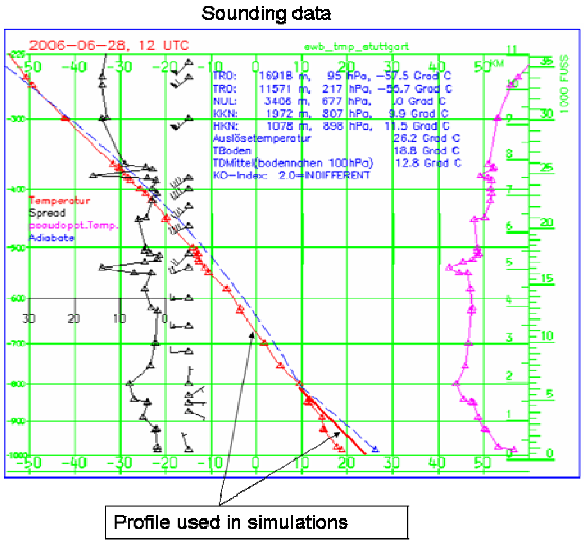

To trigger convection in the model the temperature gradient in the boundary layer has been increased as it is shown by red line.

Figure 2 shows time dependence of maximum and minimum vertical velocities in the simulations of hail storm under different aerosol concentrations. One can see that after t=80 min a quasi-stationary state is reached. One can see that the velocities vary within the range 15-35 ms^{-1}. Peaks of maximal positive vertical velocity indicate the intensification of cloud cells. No significant effects of aerosol concentration on the values of the vertical velocity are seen. The absence of the aerosol effect on the vertical velocity can be attributed to low warm rain in these simulations. As a result, independently on the aerosol concentration droplets freeze (mainly by collisions with ice) and contribute to the increase in the latent heat release.

Figure 3 shows time dependence of the hail and graupel kinetic energies at the surface (left panels) and corresponding hail and graupel accumulated precipitation (right panels) for different CCN concentrations in case the surface temperature of $24^{o}C$.

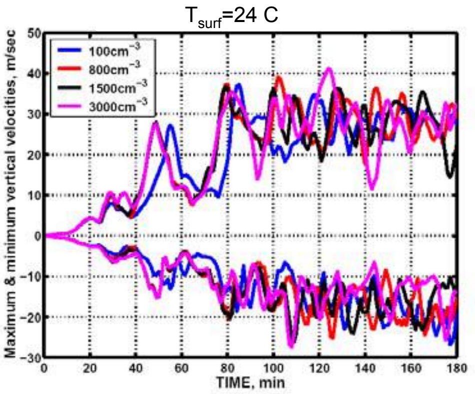

***Figure 2**. Time dependence of maximum and minimum vertical velocities in the simulations of hail storm at different aerosol concentrations.*

One can see that the kinetic energies of hail and graupel depend significantly on the aerosol concentration. Within a wide range of aerosol concentrations the hail and graupel kinetic energies at the surface increase with the increase in the aerosol concentration. In simulation with the CCN concentration as high as 6000 cm^{-3} the kinetic energies of hail and graupel turn out to be smaller than in the 3000 cm^{-3} case. The latter indicates the existence of a particular aerosol concentration N_{hail_max}, at which the hail kinetic energy at the surface reaches its maximum. According to the results obtained N_{hail_max} is about 3000 cm^{-3} for the meteorological conditions analyzed.

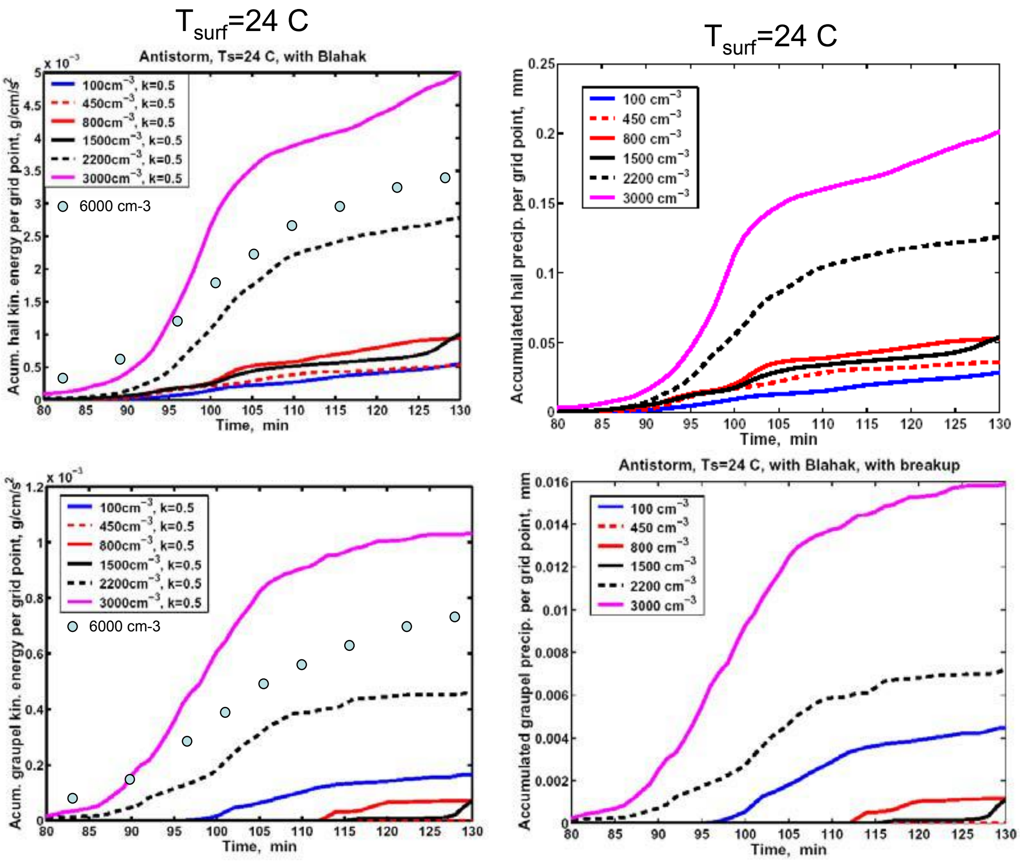

Figure 3 Time dependence of the hail and graupel kinetic energy (left panels) and hail and graupel accumulated precipitation (right panels) at the surface for different CCN concentration

In spite of significant similarity in the behavior of hail and graupel kinetic energy on aerosol concentration, there are some differences. For instance, kinetic energy of

graupel in the 100 cm^{-3} case turned out to be higher than those in the 800 cm^{-3} and 1500 cm^{-3} cases.
The accumulated precipitation of hail and graupel behaves similarly to the corresponding kinetic energies. Graupel precipitation is lower than that of hail, supposedly, because the faster melting of graupel, which has as a rule smaller size.

Figure 4 shows time dependence of the domain average total precipitation (upper panel) and liquid rain (lower panel) at the ground for different CCN concentrations in the simulations with the surface temperature of 24 ^oC.

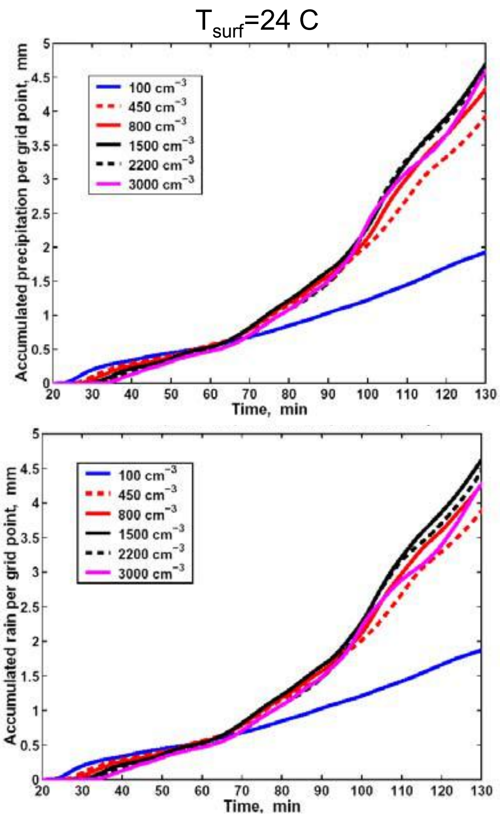

Figure 4. Time dependence of the total accumulated precipitation and accumulated rain at the surface for different CCN concentrations in the simulations of the 28 June hail storm in Germany.

Figure 4 shows that:
a) Precipitation at low CCN concentrations (especially 100 cm^{-3}) begins earlier and exceeds that in clouds with higher CCN concentration during the first hour (this result agrees well with that reported by Teller and Levin, 2007). Later on precipitation in the 100 cm^{-3} case turns out to be significantly lower as compared to the cases with higher CCN concentrations. At CCN concentration exceeding 450 cm^{-3}, the accumulated rain amount depends on the aerosol concentration only slightly. The maximum accumulated precipitation is reached in the 1500 cm^{-3} case. We would like to mention that the maximum hail precipitation was in the 3000 cm^{-3} case.
b) Rain precipitation is only slightly lower than the total precipitation. The latter indicates that graupel and hail contribute to precipitation largely via melting. The solid precipitation is a small fraction of the total precipitation in our simulations.

The question arises: why is the hail content low under low CCN concentration and increases with the concentration of small CCN ?
It is reasonable to assume that if the supercooled water content is high, hail particles can grow to large sizes by collecting small water drops. The increase in the supercooled water content can be achieved under two main conditions: a) high vertical velocity when drops of any size ascend, and b) in case of high aerosol concentration (see section of Discussion for more detail). In the latter case droplet concentration is large, droplet size is small, the efficiency of droplet collisions between themselves and with ice particles is low. In this case these small droplets can ascend to higher levels under comparatively low vertical velocities. We suppose that in reality both mechanisms work often together, i.e. high vertical velocities are often accompanied by high aerosol concentration.

In order to figure out the possible role of aerosols we compare microstructure of clouds in simulations with CCN concentrations 100 cm^{-3} and 3000 cm^{-3} during time periods with nearly similar vertical velocities.

Figure 5 shows the fields of vertical velocity W at time instances 5100 and 5400 s (the surface temperature is equal to 24C). Maximum values of W are about 25 m/s in both cases. Note that the simulations indicate the formation of long lasting convection with formation of secondary convective cells, and quasi-periodic intensification of clouds (see fig. 2).

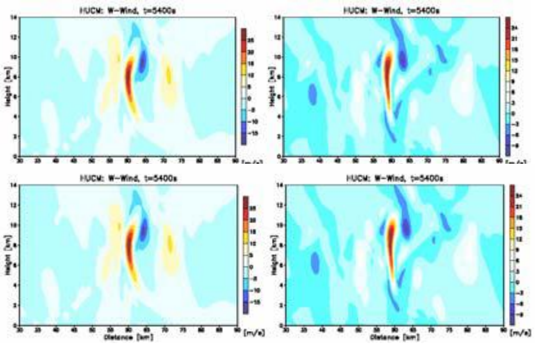

***Figure 5** The vertical velocity W fields at time instances 5100 and 5400 s in simulations with CCN concentrations of 100 cm-3 (left panels) and 3000 cm-3 (right panels) (the surface temperature is equal to 24C). Maximum values of W are about 25 m/s in both cases.*

Figure 6 shows fields of CWC and RWC in the simulations with concentration of 100 cm^{-3} (left panels) and 3000 cm^{-3} (right panels). One can see that a) in the 3000 cm^{-3} run CWC is higher and penetrates to higher levels; and b) there is a warm rain formation in the 100 cm^{-3} CCN case (above 3 km)**,** while the rain is negligible in simulations with high CCN concentration in (3000 cm^{-3}).

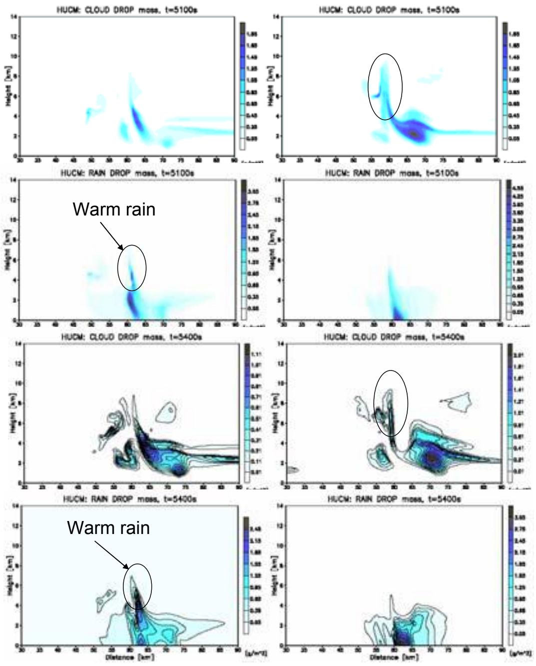

***Figure 6** The fields of CWC and RWC in the simulations with concentration of 100 cm-3 (left panels) and 3000 cm-3 (right panels)*

Figure 7 compares hail mass contents at 5400 s (at 5100 s the difference in the hail mass is similar) and radar reflectivities from hail in these simulations.

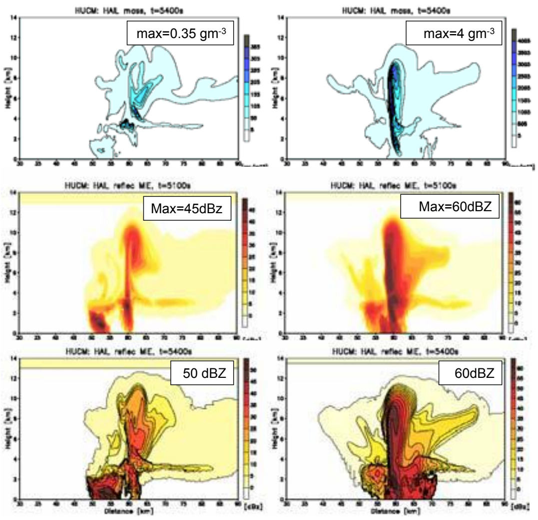

***Figure 7** Hail mass contents at 5400 s and radar reflectivities from hail in the simulations at 5100 s and 5400 s under low (left panels) and high (right) aerosol concentrations.*

One can see a) hail arises in zones of large CWC; b) In case of high aerosol concentration the hail mass is much larger than in the case of low aerosol concentration; c) Radar reflectivities from hail reaches 60 dBZ in case of high CCN concentration, which is 10-15 dBZ larger than in case of the low CCN concentration.

Figure 8 shows the fields of radar reflectivity from snow and graupel in these simulations. One can see that**:** a) the maximum radar reflectivities are 40 dBZ to 50 dBZ, i.e. lower than the maximum hail reflectivity. We conclude therefore, that the high radar reflectivity in observations comes from hail; b) the maximum values of radar reflectivities from graupel and snow in case of the low CCN concentrations is close to those with high CCN concentration.

Figure 9 shows the fields of water radar reflectivity in simulations with low (left) and high (right) aerosol concentrations. One can see that reflectivity is significantly larger in case of high CCN concentration. These values agree well with the observations, according to which radar reflectivity exceeded was equal or larger than 60 dBZ within the layer from the surface to ~12 km.

Figure 10 shows size distribution functions of hail and water at different levels in simulations with low (left) and high (middle and right panels). One can see that a) hail mass distributions are significantly wider in case of high AP concentration. In case of 100 cm-3 concentration maximum size of hail is 0.6 cm in diameter. Besides, the amount of the hail is negligible.

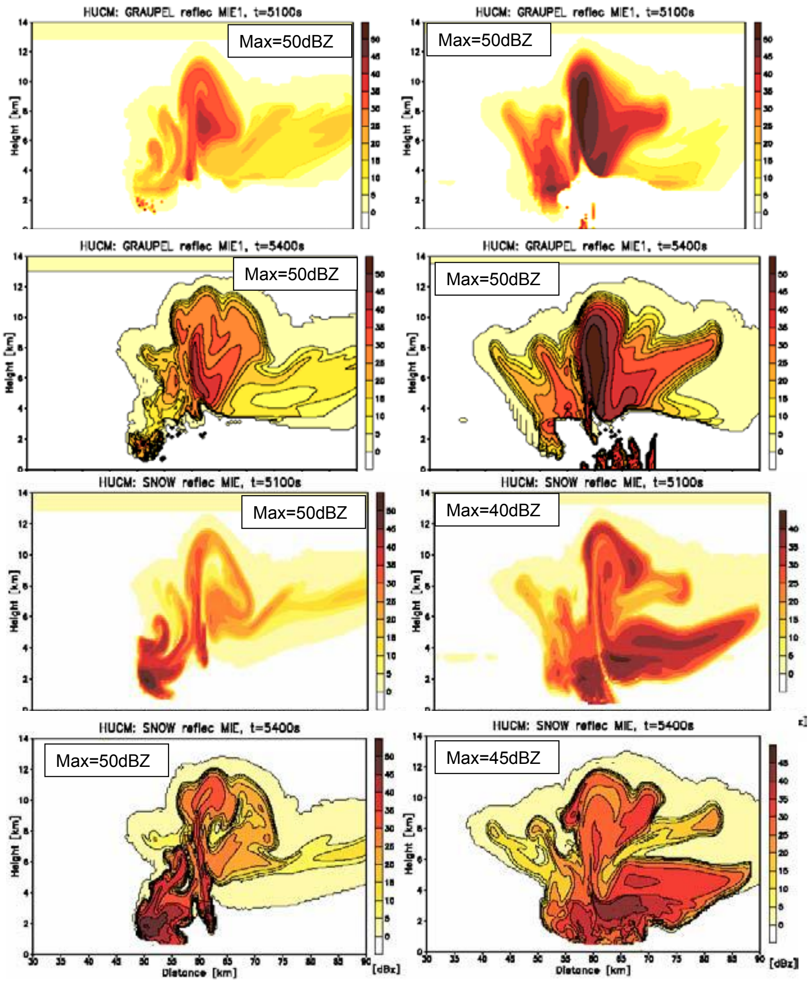

Figure 8*. Fields of radar reflectivity from snow and graupel in simulations with low (left) and high (right) aerosol concentrations.*

Mass distribution of hail in case of high CCN concentration is bimodal. The maximum diameter in the first mode is 1.2 cm. The mode is centered at diameter of 0.8-1 cm, which is quite close to observations.

The second mode contains a small amount of giant hailstones with diameters of a few cm. The hail stones of these sizes were also observed during the hail storm simulated.

The maximum raindrop diameter is 0.4 cm.

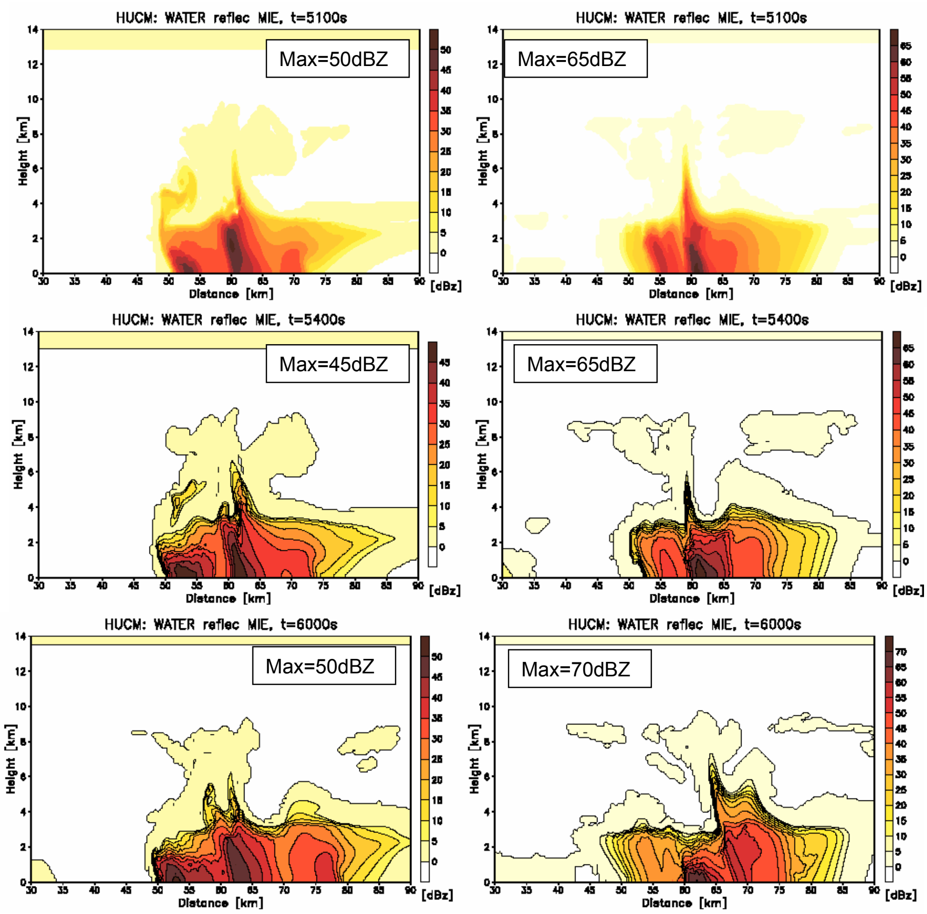

***Figure 9**. Fields of water radar reflectivity in simulations with low (left) and high (right) aerosol concentrations.*

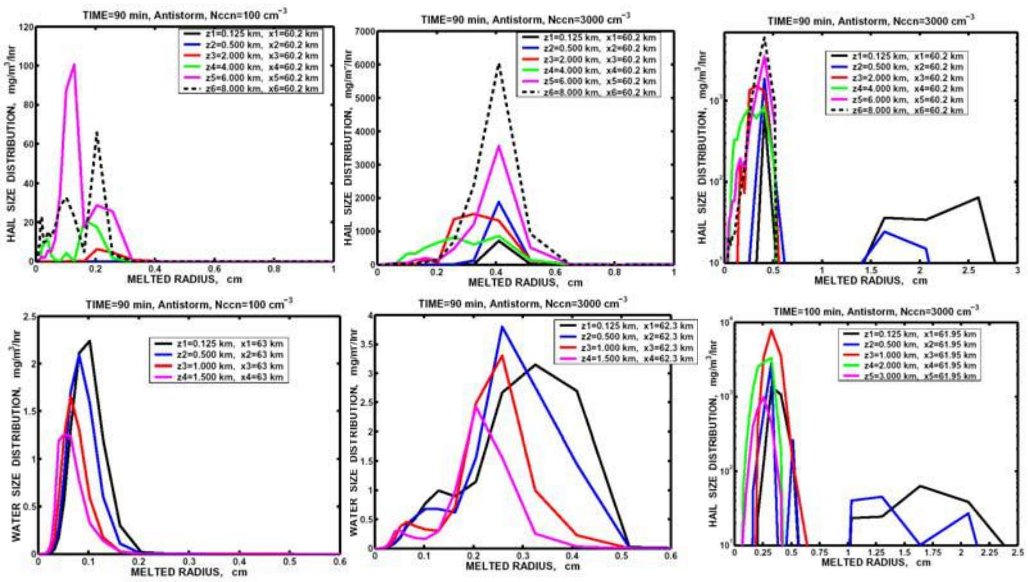

***Figure 10** Mass distribution functions of hail and water at different levels in simulations with low (left) and high (middle and right panels).*

In case of 3000 cm^{-3} CCN concentration maximum hail mass distribution is two modal. Maximum raindrop diameters in case of low and high CCN concentrations are 0.4 cm and 1 cm, respectively.

Comparison of snow contents in cases of low and high aerosol concentrations (**Figure 11**) indicates that amount of snow is larger in case of low CCN concentration. We attribute this result to comparatively low amount supercooled water in this case. As a result, the process of intense riming is suppressed, and snow grows as a result of ice crystal and snow-crystal collisions. When snow penetrates the layer with positive temperature, it intensively melts and is transferred in graupel if the liquid water fraction exceeds 0.6.

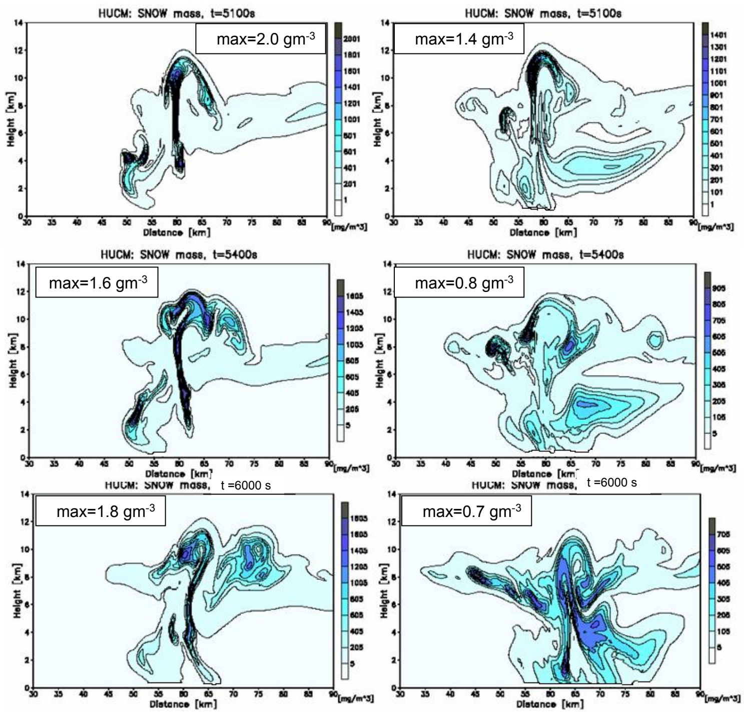

Figure 11. Snow contents in cases of low (left) and high (right) aerosol concentrations at different time instances. One can see that the snow mass content is larger in cases of low aerosol concentration, supposedly because of lower supercooled water content.

We suppose that the intense snow production, as well as the rapid production of large amount of comparably small graupel by collisions of raindrops with crystals and snow are the main microphysical processes in the clouds with low aerosol concentration (instead of hail production by riming in clouds developing under high aerosol concentration).

Note that the formation of hail or graupel and snow depends on many microphysical and theromodynamical conditions. In the model hail forms by freezing of drops with radius larger than ~60 μm. Homogeneous freezing of droplets of smaller size leads in the model to the formation of ice crystals (plates). In case small hail falls within cloud regions with large supercooled water content, it reaches large sizes. In case when droplet spectrum is very narrow (which can be if aerosol concentration or vertical velocities are very high) freezing of droplets takes place above the homogeneous freezing level, where supercooled water is absent. In this case many ice crystals form. These crystals can fall along the cloud periphery where the CWC is low producing snow by collisions. This snow will transfer to graupel by riming below.

Thus, formation of large hail requires a) large supercooled water content to high levels (it means that the droplet spectrum should be narrow to high levels) and on the width of droplet spectrum just below the level of the homogeneous freezing. To form hail, the spectrum must contain enough drops which freeze within the zone of high CWC.

The considerations presented indicate the existence of the regime optimum for hail formation. At low aerosol concentrations and low vertical velocities drops grow fast and freeze at low levels producing graupel and small hail (because of low supercooled water content). At very high W and aerosol concentrations a lot of ice crystals will form in cloud anvil without producing hail.

Figure 12 shows the hail kinetic energy in simulations with surface temperature 23C (only one degree less than in case analyzed above). The figure for the accumulated kinetic energy of hail at T=24C is presented for comparison.

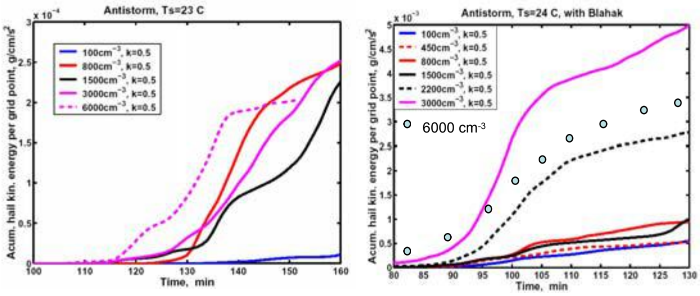

Figure 12. The hail kinetic energy in simulations with surface temperature 23C (only one degree less than in case analyzed above). The figure for the accumulated kinetic energy of hail at T=24C is presented for comparison.

One can see that the hail falls to the surface later than in case T=24^oC, and the hail kinetic energy decreases with the decrease in the surface temperature. Hail first form and falls at high CCN concentration (6000 cm^{-3}). However, 15 min later the hail kinetic energy turns out to be maximal at the CCN concentration of 800 cm^{-3}. We attribute this result to the mechanisms discussed above: decrease in the surface temperature leads to decrease in the cloud base. In this case drops large enough to freeze form within the region of high CWC at the CCN concentration of 800 cm^{-3}. At higher CCN concentrations droplets freeze by homogeneous freezing.

Figure 13 shows time dependence of the accumulated rain amount in cases T=23^oC (left) and T=24 ^oC (right).

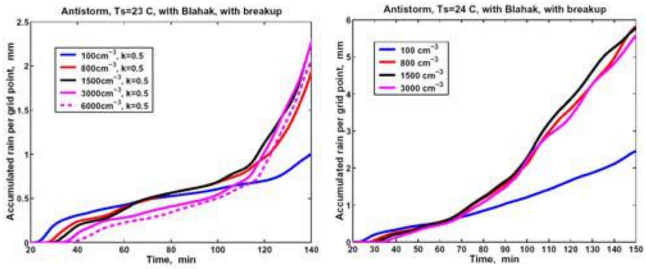

***Figure 13** shows time dependence of the accumulated rain amount in cases T=23^oC (left) and T=24 ^oC (right panel).*

One can see that decrease in the surface temperature by one degree leads to a significant decrease in precipitation at the surface. Similarly to the 24^oC case, precipitation at low (100 cm^{-3}) CCN concentration begins first and remains maximal during first one hour. Later on secondary cells turn out to be stronger in case of higher CCN concentration. It is possible that process of recycling start to be efficient, so that comparatively large particles formed within the primary cloud penetrate to the secondary one. In this case precipitation process starts to be efficient even in case of high concentration of small CCN. In 1.5-2 h precipitation turns out to be dependent on CCN concentration only slightly (except the case of very low CCN concentration, when precipitation turns out to be minimal).

4. DISCUSSION AND CONCLUSIONS

Response of cloud precipitation and microphysical structure of clouds with comparatively low freezing level remains a one of most difficult problems in the Cloud Physics. The same concerns hail formation. Simulations of the hailstorm in Germany using the 2-D Hebrew University cloud model (HUCM) with the spectral bin microphysics indicated non-monotonic dependence of hail kinetic energy and precipitation on concentration of small aerosols (small CCN).

According to the simulations, the maximum hail kinetic energy, maximum hail size take place at CCN concentrations higher than 800 cm-3. The "optimum" CCN concentration producing maximum hail kinetic energy increases with the increase in the surface temperature in agreement with the "Antistorm concept" presented in this issue in the paper by Rosenfeld and Khain. The radar reflectivity and hail size agree well with observations.

The existence of such "optimum" follows from simple considerations: at a very small CCN concentration and low vertical velocity drops reach significant size at low heights and give rise to the formation of a significant concentration of graupel, which, however, have a comparatively low size. At very high aerosol concentrations droplets are small and their collisions between each other and with ice are inefficient. In case of very high vertical updrafts, the droplets freeze homogeneously producing high amount of ice crystals which spread in cloud anvils. These crystals produce snow and graupel by riming.

At the same time the magnitude of the optimum size depends on air vertical velocities in clouds (CAPE) (see Antistorm concept), wind shear and the rate of turbulence in clouds and some other factors.

These conclusions are supported by supplemental simulations of Texas summertime clouds (and other types of clouds). In case of very high vertical velocities (high CAPE or large temperature forcing) drops are transported to high levels. In case of *low aerosol concentration* ($\sim 100\,cm^{-3}$) and *no turbulent effects on collisions taken into account* droplets become large and freeze below the level of the homogeneous freezing producing large hail. In case of high aerosol concentration and high vertical velocity (*no turbulent effects on collisions taken into account)* droplets remain small and cross the level of homogeneous freezing giving rise to crystal and snow formation. Amount of hail is small in this case.

In case turbulent effects on collisions are taken into account, the situation changes dramatically: a) in case of low aerosol concentration droplets become large at comparatively low levels and freeze producing a large amount of small graupel. Amount of supercooled water at upper levels is small in this case. At the same time in case of high aerosol concentrations and if the effects of strong turbulence on collisions are taken into account, droplets reach comparatively large size just below the level of the homogeneous freezing. In this case the frozen drops collect a great amount of supercooled water leading to formation of large hail.

These examples indicate the necessity of accurate description of both dynamical and fine microphysical mechanisms to simulate aerosol effects of cloud microphysics, precipitation, and hail formation, in particular.

Acknowledgements

The study has been performed under support of the European project "ANTISTORM", as well under support of Binational US-Israel Science Foundation (grant 2006437).

REFERENCES

Bott A., 1989: A positive definite advection scheme obtained by nonlinear renormalization of the advective fluxes. *Mon. Wea. Rev*., 117, 1006-1015.

Bott, A., 1998: A flux method for the numerical solution of the stochastic collection equation *J. Atmos. Sci.,* 55, 2284-2293.

Braham, R.R., Jr. 1981, urban precipitation processes, in METROMEX; A REVIEW AND SUMMARY. METEOROL. Monogr. Ser.v 40 75-116, AMS, Boston

Cerveny, R.S. and Balling R.C.J r 1998: Weekly cycles of air pollutants and tropical cyclones in the coastal NW Atlantic region. Nature, 394, 561-563.

Fan, J., R. Zhang, G. Li, W-K Tao and X. Li, 2007: Simulations of cumulus clouds using a spectral microphysics cloud resolving model. J. Geophys. Res. 112, D 04201, doi:10.1029/2006JD007688.

Feingold, G., H. Jiang, and J.Y. Harrington, 2005: On smoke suppression of clouds in

Amazonia. Geophys. Res. Lett. 32, L02804, doi:1029/2004GL021369.

Ferrier, B.S., J. Simpson, and W-K Tao, 1996: Factors responsible for precipitation efficiencies in midlatitute and tropical squall simulations. Mon. Wea.Rev., 124, 21000-2125.

Changnon Jr., S.A., F.A. Huff and R.G. Semonin, 1971: METROMEX: an investigation of inadvertent weather modification. Bull. Amer. Meteor. Soc., **5**2, 958-968.

Cheng, C-T, W-C Wang, and J.-P. Chen, 2006: A modeling study of aerosol impacts on cloud microphysics and radiative properties. Quart. J. Roy. Meteorol. Soc. (in press).

Cohen, N. and A. Khain, 2008 Aerosol effects on lightning and intensity of landfalling hurricanes. Chapter in the book: Hurricanes and Climate Change**.**

Givati A. and D. Rosenfeld , 2004: Quantifying precipitation suppression due to air pollution. *J. Appl. Meteorol.* 43, 1038-1056.

Hallett, J. and Mossop, S. C., Production of secondary ice crystals during the riming process. *Natur*e, 249, 26-28, 1974.

Hobbs, P.V., T.J. Matejka, P.H. Herzegh, J.D. Locatelli, and R.A. Houze, 1980: The mesoscale and microscale structure and organization of clouds and precipitation in midlatitude cycles. I: A case of a cold front, *J. Atmos. Sci.,* **37***,* **3**7,568–596,1980.

Iguchi T., T. Nakajima, A. Khain, K. Saito, T. Takemura, and K. Suzuki (2008); A study of the cloud microphysical properties in an East Asian region by a bin microphysics coupled with a meso-scale model. J. Geophys. Res. (in press)

Jirak I. L. and W. R. Cotton. 2006: Effect of Air Pollution on Precipitation along the Front Range of the Rocky Mountains. *J. Appl. Meteorol. and Climatol*, 45, No. 1, pp. 236–245

Khain, A.P. and I. Sednev, 1996: Simulation of precipitation formation in the Eastern Mediterranean coastal zone using a spectral microphysics cloud ensemble model. *Atmospheric Research*, 43: 77-110.

Khain, A. P., M. Ovtchinnikov, M. Pinsky, A. Pokrovsky, and H. Krugliak, 2000: Notes on the state-of-the-art numerical modeling of cloud microphysics. *Atmosph. Res.* 55, 159-224.

Khain A.P., Pinsky, M.B., M. Shapiro and A. Pokrovsky, 2001a: Graupel-drop collision efficiencies. *J. Atmos. Sci.,* 58, 2571-2595.

Khain A. P., D. Rosenfeld and A. Pokrovsky, 2001b: Simulation of deep convective clouds with sustained supercooled liquid water down to –37.5 C using a spectral microphysics model. *Geophys. Res. Lett.*, 3887-3890.

Khain, A., D. Rosenfeld and A. Pokrovsky, 2003: Simulations of aerosol effects on convective clouds developed under continental and maritime conditions. *Nice, Assembly of WMO, April 6-11, 2003.*

Khain A., A. Pokrovsky and M. Pinsky, A. Seifert, and V. Phillips, 2004: Effects of atmospheric aerosols on deep convective clouds as seen from simulations using a spectral microphysics mixed-phase cumulus cloud model Part 1: Model description. *J. Atmos. Sci 61, 2963-2982.*

Khain A. and A. Pokrovsky, 2004: “Effects of atmospheric aerosols on deep convective clouds as seen from simulations using a spectral microphysics mixed-phase cumulus cloud model Part 2: Sensitivity study”, *J. Atmos. Sci. 61, 2983-3001*

Khain, A. D. Rosenfeld and A. Pokrovsky 2005: Aerosol impact on the dynamics and microphysics of convective clouds. *Q. J. Roy. Meteor. Soc.* 131, 2639-2663.

Khain, A. P., N. BenMoshe, A. Pokrovsky, 2008a. Factors determining the impact of aerosols on surface precipitation from clouds: attempt of classification. J. Atmos. Sci. (in press)

Khain, A. N. Cohen, B. Lynn and A. Pokrovsky, 2008b: Possible aerosol effects on lightning activity and structure of hurricanes. J. Atmos. Sci. (in press)

Khain A. and B. Lynn (2008) Simulation of a supercell storm under different aerosol conditions. J. Geophys. Res. (in press).

Khvorostyanov, V.I., Khain A.P., and Kogteva E. L., 1989: A two-dimensional non stationary microphysical model of a three-phase convective cloud and evaluation of the effects of seeding by a crystallizing agent. *Soviet Meteorology and Hydrology*, No. 5, 33-45.

Kogan E.L A 3-D warm rain cloud model with a detailed description of microphysical processes, 1978: Atmospheric and Oceanic Physics, v 14, 8, 876-886.

Lee S., L. Donner and V. Phillips and Yi Ming, 2008: Impact of aerosols on precipitation in deep convection, J. Geophys. Res. (in press).

Levin Z., and W.R. Cotton, 2007: Aerosol pollution impact on precipitation: A scientific Review, WMO/IUGG report.

Li X, W-K. Tao, A. P. Khain, J. Simpson and D.E. Johnson, 2008: Sensitivity of a cloud-resolving model to bulk and explicit bin microphysical schemes. Part 2: Cloud microphysics and storm dynamics interaction. J. Atmos. Sci. (in revision).

Li G., Y. Wang and R. Zhang, 2008b: Implementation of a two-moment bulk microphysics scheme to the WRF model to investigate aerosol-cloud interaction. J. Geophys. Res. 2008.

Lin, J.C., T Matsui, R. A. Pielke Sr., and C. Kummerow, 2006: Effects of biomass-burning-derived aerosols on precipitation and clouds in the Amazon Basin: a stallite-based empirical study. J. Geophys. Res. 111, D19204, doi: 10.1029/2005JD006884.

Lynn *B*., A. Khain, J. Dudhia, D. Rosenfeld, A. Pokrovsky, and A. Seifert *2005a:* Spectral (bin) microphysics coupled with a mesoscale model (MM5). Part 1. Model description and first results. *Mon. Wea. Rev.* 133, 44-58.

Lynn *B*., A. Khain, J. Dudhia, D. Rosenfeld, A. Pokrovsky, and A. Seifert *2005b:* Spectral (bin) microphysics coupled with a mesoscale model (MM5). Part 2: Simulation of a CaPe rain event with squall line *Mon. Wea. Rev.* , 133, 59-71.

Lynn B., A. Khain, D. Rosenfeld**,** William L. Woodley, 2007: Effects of aerosols on precipitation from orographic clouds. *Journal of Geophysical Research*, **112**, D10225, doi:10.1029/2006JD007537

Lynn B. and A. Khain, 2007: Utilization of spectral bin microphysics and bulk parameterization schemes to simulate the cloud structure and precipitation in a mesoscale rain event. J. Geophys. Research 112, D22205, http://dx.doi.org/10.1029/2007JD008475, November 2007

Magaritz, L., M. Pinsky and A. Khain, 2007: Drizzle formation in stratocumulus clouds. Abstracts of IUGG, Italy, Perugia, July, 2007.

Meyers, M. P., P. J. DeMott, and W. R. Cotton, 1992: New primary ice-nucleation parameterizations in an explicit cloud model. *J. Appl. Meteor.*, **31**, 708-721.

Ohashi Y. and H. Kida, 2002: Local Circulations Developed in the Vicinity of Both Coastal and Inland Urban Areas: A Numerical Study with a Mesoscale Atmospheric Model, *J. Appl. Meteorol,41,.30-45*

Phillips V., A. Khain, and A. Pokrovsky 2007: The Influence of Melting on the Dynamics and Precipitation Production in Maritime and Continental Storm-Clouds. *J. Atmos. Sci.*, 64, no. 2, 338-359

Pinsky, M., and A. Khain, 1998: Some effects of cloud turbulence on water-ice and ice-ice collisions, *Atmos. Res.,* 47-48, 69-86

Pinsky, M., A. Khain, and M. Shapiro, Collisions of small drops in a turbulent flow. Pt.1: Collision efficiency: problem formulation and preliminary results. *J. Atmos. Sci.*, 56, 2585-2600, 1999.

Pinsky, M., A. P. Khain, and M. Shapiro 2001: Collision efficiency of drops in a wide range of Reynolds numbers: Effects of pressure on spectrum evolution. *J. Atmos. Sci.* 58, 742-764.

Pinsky M. B., A. P. Khain , and M. Shapiro, 2007, Collisions of cloud droplets in a turbulent flow. Part 4. Droplet hydrodynamic interaction. *J. Atmos. Sci , 64, 2462-2482.*

Pinsky, M., A. Khain , L. Magaritz and A. Sterkin, 2008a: Simulation of droplet size distributions and drizzle formation using a new trajectory ensemble model of cloud topped boundary layer. Part 1: model description and first results in non-mixing limit. J. Atmos. Sci. (in press).

Pinsky M., A. Khain and H. Krugliak, 2008b: Collisions of cloud droplets in a turbulent flow. Part 5: Application of detailed tables of turbulent collision rate enhancement to simulation of droplet spectra evolution. J. Atmos. Sci. (in press).

Pruppacher, H. R., A new look at homogeneous ice nucleation in supercooled water drops. *J. Atmos. Sci.,* 52, 1924-1933, 1995.

Pruppacher, H. R., and J. D. Klett, 1997: *Microphysics of clouds and precipitation.* 2-nd edition, Oxford Press, 1997, 963p.

Ramanathan, V., P.J. Crutzen, J. T. Kiehl, D. Rosenfeld, 2001: Aerosols, climate and the hydrological cycle. Science, 294, 2119-2124.

Rosenfeld D. (1999): TRMM observed first direct evidence of smoke from forest fires inhibiting rainfall. *Geophys. Res. Lett.* 26, (20), 3105-3108.

Rosenfeld, D. and W. L. Woodley, 1999: Satellite-inferred impact of aerosols on the microstructure of Thai convective clouds. Proceedings, *Seventh WMO Scientific Conference on Weather Modification***.** Chiang Mai, Thailand, 17-22 February 1999, p. 17-20

Rosenfeld, D, 2000: Suppression of rain and snow by urban and industrial air pollution. *Science*, 287 (5459), 1793-1796.

Rosenfeld, D., W.L. Woodley, 2000: Deep convective clouds with sustained highly supercooled liquid water until - 37.5 o C. *Nature,* 405, 440-442.

Rosenfeld D. and A. Khain 2008: Anthropogenic aerosol invigorating hail (this issue)

Segal Y. and A. Khain, 2006: Dependence of droplet concentration on aerosol conditions in different cloud types: application to droplet concentration parameterization of aerosol conditions, J. Geophys. Res. 111, doi:10.1029/2005JD006561

Shepherd, J.M., and S.J. Burian, 2003: Detection of urban-induced rainfall anomalies in a major coastal city. *Earth Interactions,* **7**, 1-17.

Sui, C.-S., X.Li, and M.-J. Yang 2008: On the definition of the precipitation efficiency. J. Atmos. Sci. (in press).

Takahashi, T., Endoh, T., and G. Wakahama, 1991: Vapor diffusional growth of free-falling snow crystals between –3 and -23 C. *J. Meteor. Soc. Japan*, **69**, 15-30.

Tao, W-K, X. Li, A. Khain, T. Matsui, S. Lang and J. Simpson, 2007: The role of atmospheric aerosol concentration on deep convective precipitation: cloud-resolving model simulations. J. Geophys. Res. VOL. 112, D24S18, doi:10.1029/2007JD008728.

Teller A., and Z. Levin, 2006: The effects of aerosols on precipitation and dimensions of subtropical clouds: a sensitivity study using a numerical cloud model. Atmos. Chem. Phys. 6, 67-80.

Wang C. 2005: A modelling study of the response of tropical deep convection to the increase of cloud condensational nuclei concentration: 1. Dynamics and microphysics. *J. Geophys. Res.,* v. 110; D21211, doi:10.1029/2004JD005720.

Wang, L-P, O. Ayala, S.E. Kasprzak, and W.W. Grabowski, 2005: Theoretical formulation of collision rate and collision efficiency of hydrodynamically interacting cloud droplets in turbulent atmosphere. *J. Atmos. Sci*. **62**, 2433-2450.

Van den Heever, S. C.; G.G. Carrió, .; W.R. Cotton, .; P. J. Demott, .; A. J Prenni, 2006: Impacts of Nucleating Aerosol on Florida Storms. Part I: Mesoscale Simulations. J. Atmos. Sci., 63, Issue 7, pp.1752-1775

Vali, G., Freezing rate due to heterogeneous nucleation. *J. Atmos. Sci.,* 51, 1843-1856, 1994.

Vali, G., Remarks on the mechanism of atmospheric ice nucleation. Proc. 8th Int. Conf. on Nucleation, Leningrad, 23-29 Sept., Gidrometeoizdat, 265-269, 1975.

EFFECT OF HYGROSCOPIC SEEDING ON WARM RAIN
- NUMERICAL SIMULATION WITH A HYBRID CLOUD-MICROPHYSICAL MODEL –

Naomi Kuba
kuba@jamstec.go.jp
Frontier Research Center for Global Change, Japan Agency for Marin-Earth Science and Technology
(FRCGC / JAMSTEC), Yokohama, Japan

1. INTRODUCTION

To estimate the effect of hygroscopic seeding on precipitation accurately, numerical study needs cloud microphysical model that can estimate nucleation process of cloud condensation nuclei (CCN) accurately. The number concentration of cloud droplets, which influences significantly the precipitation efficiency of clouds, depends on CCN spectrum and the maximum value of supersaturation which the air mass has experienced. This maximum value can not be estimated by values on the grid points with a interval larger than tens meters. In addition, the supersaturation is affected not only by the updraft velocity but also by the number of activated nuclei. Therefore it is desired to calculate the condensation growth of CCN in the Lagrangian framework accurately in order to find out if each nucleus can be activated.

To accurately estimate the number concentration of cloud droplets and the effect of CCN on the microstructure of clouds, the hybrid microphysical cloud model was developed.

2. CLOUD-MICROPHYSICAL MODEL

Our cloud-microphysical model estimates the maximum values of supersaturation and the number concentration of cloud droplets by using the parcel model with Lagrangian framework. And our model estimates condensation, coalescence, breakup, sedimentation, and advection of cloud droplets and raindrops by using bin model on the grid points with semi-Lagrangian or Eurelian framework. This hybrid cloud-microphysical model is described in Kuba and Fujiyoshi (2006) in detail.

2.1 Lagrangian framework

In our hybrid microphysical cloud model, each grid point has a parcel model to estimate the activation of nuclei. In the case that the relative humidity of the grid point reaches 100% for the first time, or the case that relative humidity of the grid point is larger than 100% and cloud water on the windward side of the point does not exist, air parcel including CCN and vapor starts to rise from the windward side of the point. In each parcel, the condensation growth of CCN is estimated in Lagrangian framework using the microphysical model described in Takeda and Kuba (1982). When droplets condensed on CCN grow enough to be distinguished from embryo, which can not become cloud droplets, the cloud droplets size distribution, the mixing ratio of vapor and potential temperature in the parcel are given to the grid points.

2.2 *Semi-Lagrangian framework*

Time changes due to growth by condensation and coalescence on grid points are calculated in the semi-Lagrangian framework by using the two-moment bin method developed by Chen and Lamb (1994) to minimize numerical diffusion of cloud droplet size distribution. There are 71 bins for radii between 1 μm and 3.25 mm. Coalescence efficiency developed by Seifert et al. (2005) is used to estimate coalescence and breakup.

The time steps for growth by condensation and coalescence are 0.5 seconds. To estimate multi-coalescence in one time step properly, two kinds of scheme are used. One is general stochastic coalescence for rare lucky coalescence with a large droplet, the other is continuous coalescence for frequent coalescence with small droplets following to Chen's doctoral thesis. If only general stochastic coalescence scheme is used, very short time step (0,01 s) is needed to avoid the underestimation of coalescence growth caused by the underestimation of multi-coalescence.

Sedimentation and advection of droplets are estimated in the Eulerian framework among grid points.

3. CLOUD-DYNAMICAL MODEL

The dynamical framework of this study was based on the model designed to test the warm rain microphysical model in Case 1 of the fifth WMO Cloud Modeling Workshop (Szumowski et al. 1998). The dynamical cloud model predicts an evolving flow and performs a two-dimensional advection of the temperature and water variables (domain: 9 km x 3 km, dx and dz: 50 m, dt: 3 seconds). The flow pattern shows low level convergence, upper level divergence, and an updraft located in the center of the domain. The magnitude, vertical structure, width and tilt of the flow through the central updraft are all prescribed using simple analytical functions. The updraft intensifies to a peak value (0.8, 4.0, or 8.0 m s^{-1} in this study) at 25 min and subsequently decays.

4. NUMERICAL EXPERIMENTS

Seeding particles are assumed to be NaCl that consist of similar size particles (0.25, 1.0, 2.5, or 5.0 μm in radius). Cloud seeding was simulated by adding seeding particles to the background CCN size distribution for 10 minutes under the cloud base. Several kinds of the timing of seeding and total mass of seeding particles were tested to find out the optimum seeding condition.

5. RESULTS

In cases of 50-minute-simulation for shallow convective clouds (updraft: 1 – 8 ms^{-1}), clouds rises at 5min. Accumulated rainfall at surface in domain is shown in Figs. 1 and 2. It is assumed that seeding is carried out between 10 and 20 min. (Fig.1) or between 20 and 30 min. (Fig.2) under the cloud base. In Fig. 1 or 2, black line shows the case of background CCN (polluted maritime in this study). Other lines show the seeding cases. Radius of seeding particles in each case is 0.25 μm (red line), 1.0 μm (green line), 2.5 μm (blue line), 5.0 μm (purple line). In atmosphere, seeding particles are assumed to be 2000 cm^{-3} for 0.25 μm-particle-seeding, 31.25 cm^{-3} for 1.0 μm-particle-seeding, 2.0 cm^{-3} for 2.5 μm-particle-seeding, or 0.25 cm^{-3} for 5.0 μm-particle-seeding, respectively. Total mass of seeding particles is same for all cases. This values are corresponds to the total mass of micro-powder-seeding. Other total masses (10 times or 0.1 times) are also tested in this study to find out the optimum seeding condition.

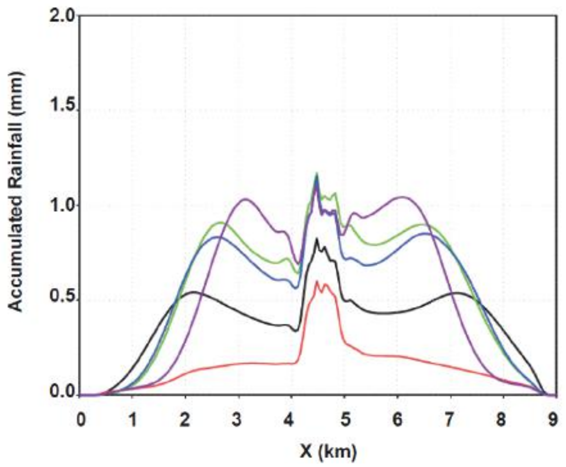

Fig.1 Accumulated rainfall for cases in which seeding is carried out after 5 min. after clouds rises.

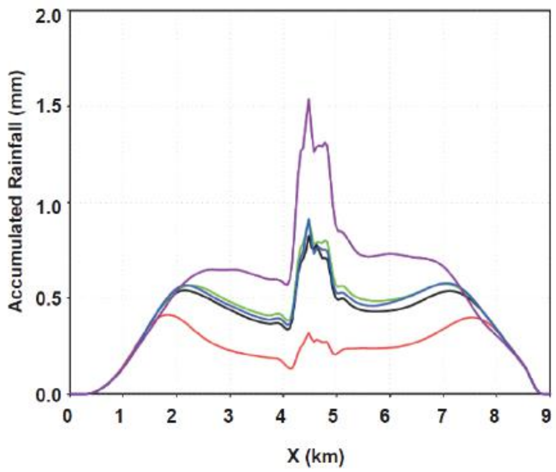

Fig.2 Accumulated rainfall for cases in which seeding is carried out after 15 min. after clouds rises.

It is shown that seeding particles larger than 1 μm in radius are effective in case of seeding at 5 min. after cloud rises. In case of seeding at 15 min. after cloud rises, only 5.0 μm-particle-seeding is effective. Small seeding particles seem to need longer time to grow to rain drops.

Table1 shows the results for shallow convective clouds (updraft: 1 – 8 ms^{-1}) including cases in which total mass of seeding particles are changed. Table 2 and 3 are same as Table 1, but for shallow convective clouds (updraft: 0.5 – 4ms^{-1}) and for layer clouds (updraft: 0.1 – 0.8 ms^{-1}), respectively.

From Tables 1 (updraft: 1 – 8 ms^{-1}), it is shown that seeding particles larger than 1 μm in radius with total mass larger than some value is effective. In addition, very large total mass of seeding of particles larger than 2.5 μm is more effective. Seeding at 5 min. after cloud rises is more effective than seeding at 15 min. after cloud rises.

Comparison between Table 1 (updraft: 1 – 8 ms^{-1}), Table 2 (updraft: 0.5 – 4 ms^{-1}) and Table 3 (updraft: 0.1 – 0.8 ms^{-1}) shows that increasing precipitation by hygroscopic seeding is difficult in case of layer clouds with small updraft velocity.

6. SUMMARIES

Using the hybrid cloud-microphysical model, the effect of hygroscopic seeding on warm rain was studied. The following conclusions were reached:

1. In case of shallow convective clouds (updraft: 1 – 8 ms^{-1} or 0.5 – 4 ms^{-1}), hygroscopic seeding with particles larger than 1μm in radius is effective in increasing precipitation. Especially, seeding particles larger than 2.5 μm in radius with large total mass is more effective in increasing precipitation.

2. In case of layer clouds (updraft: 0.1 – 0.8 ms^{-1}), increasing precipitation by hygroscopic seeding is difficult.

3. Seeding at 5 min. after cloud rises is more effective than seeding at 15 min. after cloud rises.

Table1 Ratio of mean accumulated rainfall in domain at surface for 50-min.-simulation in case of shallow convective clouds (updraft: 1 – 8 ms^{-1})

Radius of seeding particles	Tseed - Tcloud	Total mass of seeding particles	Ratio of mean accumulated rainfall
No seeding		0	1.0
0.25 μm	5 min.	1	0.4
1.0 μm	5 min.	1	1.5
2.5 μm	5 min.	1	1.4
5.0 μm	5 min.	1	1.4
0.25 μm	5 min.	0.1	1.0
1.0 μm	5 min.	0.1	1.0
2.5 μm	5 min.	0.1	1.0
5.0 μm	5 min.	0.1	1.0
1.0 μm	5 min.	10	1.5
2.5 μm	5 min.	10	2.3
5.0 μm	5 min.	10	2.0
0.25 μm	15 min.	1	0.6
1.0 μm	15 min.	1	1.1
2.5 μm	15 min.	1	1.0
5.0 μm	15 min.	1	1.4

Tseed: Time to start seeding
Tcloud: Time when cloud rises

Table2 Same as Table 1 but in case of shallow convective clouds (updraft: 0.5 – 4 ms^{-1})

Radius of seeding particles	Tseed - Tcloud	Total mass of seeding particles	Ratio of mean accumulated rainfall
No seeding		0	1.0
0.25 μm	5 min.	1.0	0.3
1.0 μm	5 min.	1.0	1.6
2.5 μm	5 min.	1.0	1.5
5.0 μm	5 min.	1.0	1.5
0.25 μm	5 min.	0.1	1.1
1.0 μm	5 min.	0.1	1.1
2.5 μm	5 min.	0.1	1.1
5.0 μm	5 min.	0.1	1.1
0.25 μm	15 min.	1.0	0.8
1.0 μm	15 min.	1.0	1.1
2.5 μm	15 min.	1.0	1.0
5.0 μm	15 min.	1.0	1.0

Table3 Same as Table 1 but for 150-min.-simulation in case of layer clouds (updraft: 0.1 – 0.8 ms^{-1})

Radius of seeding particles	Tseed - Tcloud	Total mass of seeding particles	Ratio of mean accumulated rainfall
No seeding		0	1.0
0.25 μm	5 min.	1.0	0.9
1.0 μm	5 min.	1.0	1.0
2.5 μm	5 min.	1.0	1.0
5.0 μm	5 min.	1.0	1.1
0.25 μm	5 min.	0.1	1.0
1.0 μm	5 min.	0.1	1.0
2.5 μm	5 min.	0.1	1.0
5.0 μm	5 min.	0.1	1.0
0.25 μm	15 min.	1.0	1.0
1.0 μm	15 min.	1.0	1.0
2.5 μm	15 min.	1.0	1.0
5.0 μm	15 min.	1.0	1.0

ACKOWLEDGMENTS

This study was supported by Special Funds for Promoting Science and Technology (Japanese Cloud Seeding Experiment for Precipitation Augmentation).

REFERECES

Chen, J. -P. and Lamb, D.1994: Simulation of cloud microphysics and chemical processes using a multicomponent framework. Part I Description of the microphysical model. *J. Atmos. Sci.* **51**, 2613-2630.

Kuba, N. and Y. Fujiyoshi, 2006: Development of a cloud microphysical model and parameterizations to describe the effect of CCN on warm cloud. *Atmos. Chem. Phys.*, **6**, 2793-2810. http://www.copernicus.org/EGU/acp/acp/6/2793/acp-6-2793.pdf

Seifert, A., A. Khain, U. Blahak, and K. D. Beheng, 2005: Possible effect of collisional breakup on mixed-phase deep convection simulated by a spectral (bin) cloud model. *J. Atmos. Sci.,* **62**, .1917-1931.

Szumowski, M. J., W. W. Grabowski and H. T. Ochs III, 1998: Simple two-dimensional kinematic framework designed to test warm rain microphysical models. *Atmos. Res.,* **45**, 299-326.

Takeda, T. and N. Kuba, 1982: Numerical Study of the effect of CCN on the size distribution of cloud droplets. Part I. Cloud droplets in the stage of condensation growth. *J. Meteor. Soc. Japan,* **60**, 4, 978-993.

EVALUATION OF THE INFLUENCE OF POLLUTION ON THE INITIATION AND DEVELOPMENT OF WARM RAIN PROCESSES IN MEXICO CITY

Beata Kucieńska [1], F. García-García [1,2] and G. Montero-Martínez [1,2]

[1] *Centro de Ciencias de la Atmósfera, Universidad Nacional Autónoma de México*
[2] *Posgrado en Ciencias de la Tierra, Universidad Nacional Autónoma de México*

1. INTRODUCTION*

It is well known that the production of aerosol particles from anthropogenic sources modifies cloud droplet distributions, thus affecting cloud radiative and precipitation properties. For example, the effects on cloud droplet concentration and on the subsequent production of rain due to the emission of smoke from sugar-cane fires, has been investigated by Warner and Twomey (1967) and Warner (1968). The influence of urban and industrial air pollution on precipitation has been postulated to both inhibit (Gunn and Phillips, 1957) and enhance (Eagen *et al.*, 1974) rainfall at local and regional scales, but the issue remains in controversy. Later on, tracks of enhanced cloud reflectivity over the ocean became widely recognized as the impact of ship-stack effluents on cloud drop size distribution and water content (Coakley *et al.*, 1987; Radke *et al.*, 1989). More recently, Rosenfeld and Lenski (1998) and Rosenfeld (1999) have shown that smoke from biomass burning acts to suppress coalescence processes in clouds ingesting it. Nevertheless, the detailed understanding of the chain of events leading to those particular conditions is still limited.

The purpose of the present work consists in investigating the effects of aerosols produced by urban pollution on the initiation and development of warm-rain processes. This was accomplished making use of a one-dimensional numerical model with detailed microphysics (Cooper *et al*. 1997), thus representing the growth of a cloud droplet population during adiabatic ascent of a closed parcel in a cloud. The results presented here correspond to representative cases occurring during severe urban pollution episodes. Data including cloud condensation nuclei (CCN) and total particle concentrations were gathered from field projects carried out near the ground in Mexico City.

*Corresponding author's address:
Fernando García-García.
Centro de Ciencias de la Atmósfera,
Universidad Nacional Autónoma de México.
Circuito de la Investigación Científica,
Ciudad Universitaria.
Del. Coyoacán. 04510 México, D.F. México.
e-mail: ffgg@atmosfera.unam.mx

2. METHODOLOGY AND DATA

In what follows, a brief description of the model is presented, whereas the details on the numerical procedures can be found in Cooper *et al*. (1997). Simulated warm microphysical processes included the activation of a CCN population and the simultaneous growth via condensation and collision-coalescence. Drop breakup and sedimentation are not included in the calculations. The model uses a variable bin location scheme that concentrates size categories where resolution is needed. Droplets are assigned to one of up to 256 logarithmically spaced bins, ranging from 0.02 μm to 2 cm particle diameter, *D*.

For modeling purposes, it has been found convenient to describe the initial aerosol spectra through the superposition of several analytical forms. In the present investigation Aitken nuclei ($D \lesssim 0.2$ μm) were represented by an activation equation, with a power-law functional form for the cumulative number concentration of cloud condensation nuclei, $N(S)$, active at or below the supersaturation S, as follows:

$$\boldsymbol{N(S) = C\,(S/S_o)^k}, \qquad (1)$$

where k is the slope parameter of the fit and S_o is the reference supersaturation at which $N(S)$ equals C. For large ($0.2 \lesssim D \lesssim 2$ μm) and giant ($D \gtrsim 2$ μm) nuclei, Junge power laws for the cumulative number concentration, $N(D)$, of CCN with diameters larger than D, were used:

$$\frac{dN\,(D)}{d\,(\log D)} = A_{\beta} \left(\frac{D}{D_o}\right)^{\beta}, \qquad (2)$$

where β is the slope parameter of the fit and D_o is the reference diameter at which the particle concentration per logarithmic size interval equals A_{β}.

The CCN distributions that served as input data for the simulations were taken from measurements reported by Herrera and Castro (1988) and Montañez and García (1993). These distributions are considered to be representative of severe pollution episodes in Mexico City. In order to analyze the influence of contaminants on the initiation and development of warm-rain processes, three basic scenarios were simulated by considering different amounts of Aitken nuclei (AN) concentrations, as follows:

1. *Scenario H*: High AN concentration. Average aerosol particle concentrations measured near the ground and reduced to CCN concentrations according to the scheme proposed by Montañez and García (1993), were used.
2. *Scenario M*: Medium AN concentration. CCN concentrations measured near the ground during the morning (1100 LST) and parameterized by Herrera and Castro (1988) with a functional form given by Equation 1 were used. This function attains a similar slope parameter k as the curve in *Scenario H*, but with smaller (by almost one order of magnitude) CCN concentrations.
3. *Scenario L*: Low AN concentration. CCN data presented by Herrera and Castro (1988) for evening measurements were used. Average CCN concentrations near the ground during evenings are reported to be about five times smaller than those before mid-day.

In each of these "basic" scenarios, large and giant ($D \gtrsim 0.2$ μm) nuclei were parameterized using functional forms given by Equation 2. Following the trend on the aerosol particle distribution shown by Montañez and García (1993), a slope parameter of $\beta = -3$ was used (*Scenarios H1*, *M1* and *L1*). Simulations were also performed assuming the absence of giant particles. In this latter case, particles with diameters larger than about 0.8 μm were also parameterized with a Junge power law, but with a slope parameter $\beta = -9$, thus minimizing the concentration of giant particles (*Scenarios H2*, *M2* and *L2*). An additional *Scenario HL* was built to test the influence of high concentrations of Aitken nuclei in the presence of very few larger particles. The characteristics of each of these scenarios are shown in Table 1.

The particle distribution parameterizations for each of the scenarios described above (Figures 1, 2 and 3) were fed as initial conditions into the model. As it can be observed in these figures, particle spectra in each of the "basic" scenarios are almost parallel, the only difference being the number concentration in each size-range. It should be mentioned that, for CCN activation purposes, it was assumed that all particles chemical composition was ammonium sulfate [$(NH_4)_2SO_4$].

For the simulation of the thermodynamic vertical profile, a local temperature sounding (29 May 1984 at 1800 LST) was used. This profile was selected due to the significant relative humidity (93% - 97%) it shows in mid-tropospheric levels. The cloud base pressure and temperature were 732 mb and 9.3°C, respectively. During simulations, the parcel was allowed to rise as driven by buoyancy, with an initial updraft of 2.8 m/s, from cloud base until reaching zero vertical velocity at about 587 mb (1,800 m above cloud base). Above this level, any further ascent was inhibited by the introduction of an artificial, stable layer of 20ºC, thus arbitrarily holding the parcel at the 0ºC temperature level and providing "at will" simulation time (typically up to 30 minutes) under warm-rain conditions.

Table 1. Summary of simulated scenarios and modeling results in terms of raindrop production. Initial Aitken nuclei distributions were parameterized with an activation equation (Equation 1, S_o = 1%); whereas for large and giant particles, Junge power laws (Equation 2, D_o = 1 cm) were used. Notice that raindrops form only when giant particles are present, independently of smaller ($D \lesssim$ 2 μm) nuclei concentrations.

Scenario	**Aitken Nuclei** ($D \lesssim$ 0.2 μm) [Equation 1]	**Large Nuclei** (0.2 $\lesssim D \lesssim$ 0.8 μm) [Equation 2]	**Giant Nuclei** (D $\gtrsim$ 0.8 μm) [Equation 2]	**Raindrop Production**
H1	C = 40,566 cm $^{-3}$ k = 0.76	A_β = 3.7 X 10 $^{-10}$ cm $^{-3}$ $\beta = -3$	A_β = 3.7 X 10 $^{-10}$ cm $^{-3}$ $\beta = -3$	Yes
H2	C = 40,566 cm $^{-3}$ k = 0.76	A_β = 3.7 X 10 $^{-10}$ cm $^{-3}$ $\beta = -3$	A_β = 3.0 X 10 $^{-35}$ cm $^{-3}$ $\beta = -9$	No
M1	C = 5,339 cm $^{-3}$ k = 0.78	A_β = 4.7 X 10 $^{-11}$ cm $^{-3}$ $\beta = -3$	A_β = 4.7 X 10 $^{-11}$ cm $^{-3}$ $\beta = -3$	Yes
M2	C = 5,339 cm $^{-3}$ k = 0.78	A_β = 4.7 X 10 $^{-11}$ cm $^{-3}$ $\beta = -3$	A_β = 3.9 X 10 $^{-36}$ cm $^{-3}$ $\beta = -9$	No
L1	C = 1,068 cm $^{-3}$ k = 0.78	A_β = 9.4 X 10 $^{-12}$ cm $^{-3}$ $\beta = -3$	A_β = 9.4 X 10 $^{-12}$ cm $^{-3}$ $\beta = -3$	Yes
L2	C = 1,068 cm $^{-3}$ k = 0.78	A_β = 9.4 X 10 $^{-12}$ cm $^{-3}$ $\beta = -3$	A_β = 7.8 X 10 $^{-37}$ cm $^{-3}$ $\beta = -9$	No
HL	C = 40,566 cm $^{-3}$ k = 0.76	A_β = 6.6 X 10 $^{-19}$ cm $^{-3}$ $\beta = -4.9$	A_β = 9.4 X 10 $^{-12}$ cm $^{-3}$ $\beta = -3$	Yes

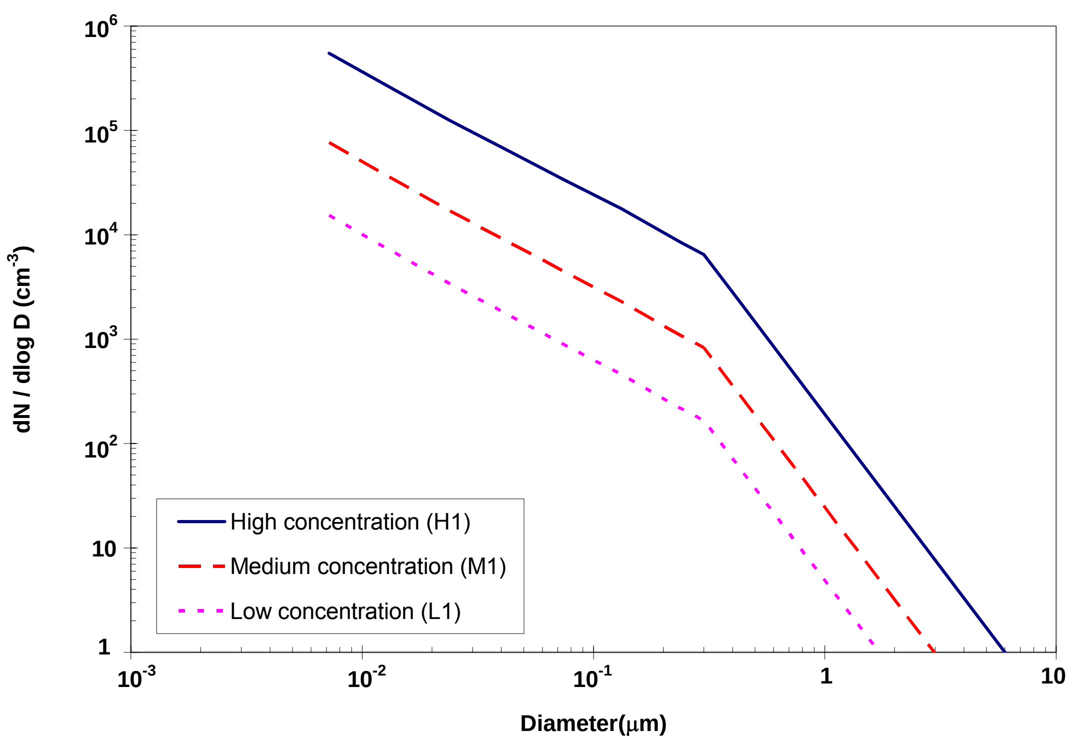

Figure 1. Initial particle distribution parameterizations for *Scenarios H1*, *M1* and *L1*, which include all particle size-ranges. Aitken nuclei were parameterized with Equation 1, whereas large and giant particles were parameterized using Equation 2 with a slope parameter $\beta = -3$.

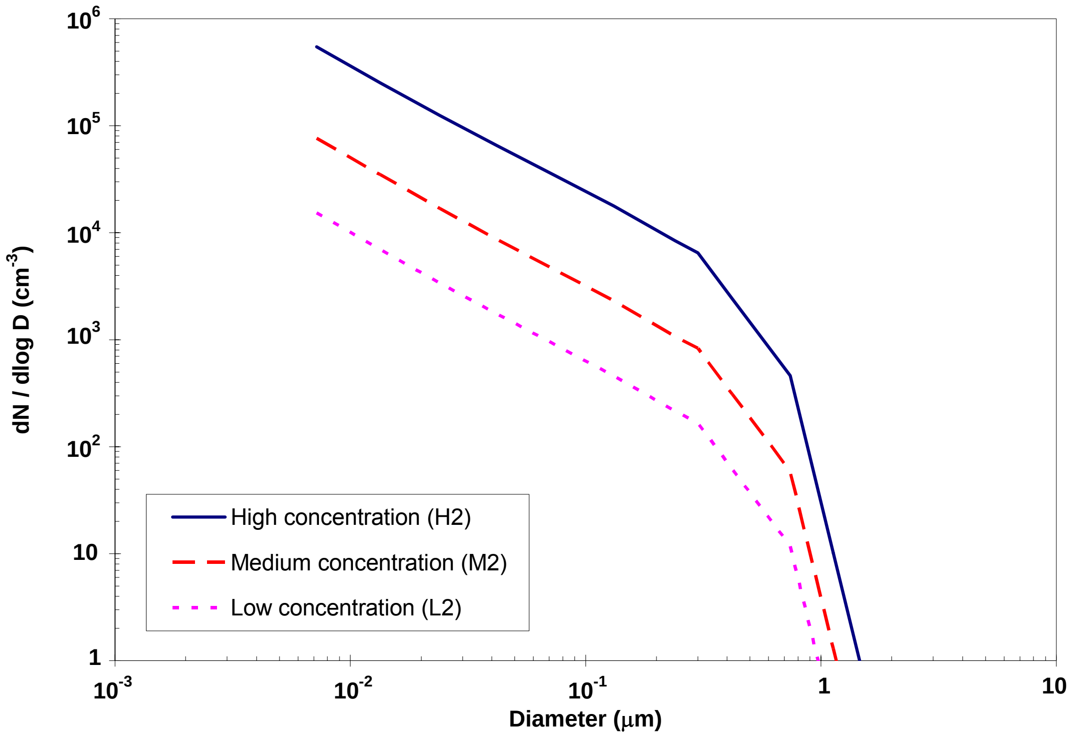

Figure 2. As in Figure 1, but for *Scenarios H2*, *M2* and *L2*. Nuclei larger than $D \gtrsim 0.8$ μm were suppressed using a slope parameter of $\beta = -9$ in the corresponding Junge power law.

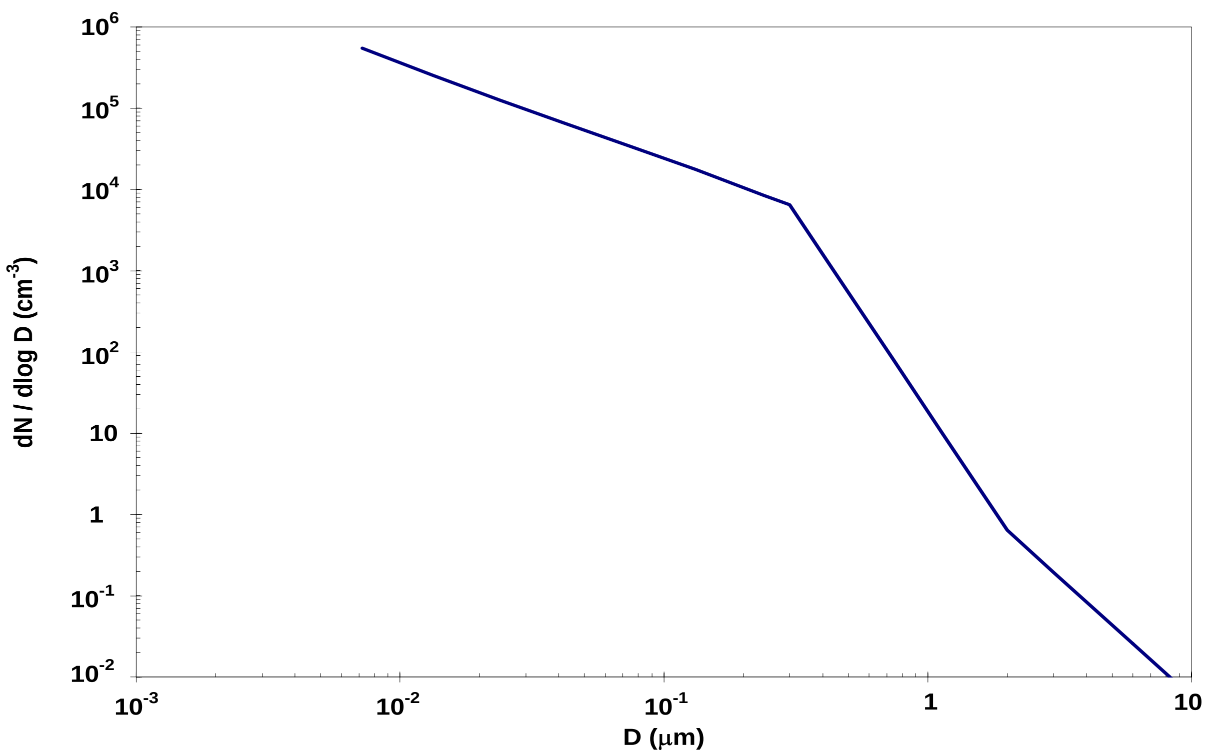

Figure 3. As in Figure 1, but for *Scenario HL*. See Table 1 for details on the parameterizations for the different particle size-ranges.

3. RESULTS AND DISCUSSION

A summary of the modeling results for all simulated scenarios in terms of the production or not of rain-sized particles is shown in Table 1. As it can be appreciated, raindrops (D > 200 μm) form only if giant particles are included in the initial CCN spectra, and this result is independent of Aitken nuclei concentration. The presence of large nuclei is not sufficient to initiate rain, but even a very small number of giant particles can start warm-rain process. For example, in the case of *Scenario L1*, there is a concentration of approximately one giant particle ($D \gtrsim 0.2$ μm) per cubic centimeter.

Figures 4 and 5 show the calculated mass distributions for *Scenarios H1* and *M1*, respectively, corresponding to selected growth times of up to 30 minutes after passage through cloud base. It can be appreciated that raindrops form earlier in *Scenario H1*. After 15 minutes of simulation time, *Scenario H1* produces a significant amount of raindrops, whereas at that time rain starts to form in *Scenario M1*, accounting for a mass about one order of magnitude smaller than in case *H1*. This behavior could have been expected, as in *Scenario H1* there is a larger concentration of giant particles that can initiate the collision-coalescence process following a quick activation. Also there are different timings for the development of precipitation between *Scenarios H1*, *M1* and *L1*. For example, at 15 minutes of simulation time, the differences between the values of total mass of raindrops in these three basic scenarios are quite large. This can be appreciated in Table 2, which shows the total mass of raindrops that form 15 and 30 minutes after passage through cloud base for all scenarios that include giant particles in the initial spectrum. It can be concluded that if parallel CCN spectra are introduced as input data into the simulations, the differences in concentrations of giant nuclei influence the initiation and development of warm-rain process. In particular, a higher initial concentration of giant particles results in an earlier initiation of rain.

The simulations of *Scenarios H1*, *M1* and *L1* show the influence of the presence of giant nuclei on the initiation and development of warm-rain process, but they do not give information on the particular role played by the smaller particles. *Scenario HL* was designed to reduce the presence of large nuclei, using a large concentration of small particles (taken from *Scenario H1*) and a low concentration of giant nuclei (taken from *Scenario L1*). The number concentration of large nuclei is intermediate between those of *Scenarios H1* and *L1*, with a slope parameter $\beta \approx -5$ typical of "clean" atmospheres. The results of the simulations for all scenarios with giant nuclei presence (see Table 2), show that the "combined" *Scenario HL* produces a smaller amount of rainwater than *Scenarios H1*, *M1* and *L1*. When comparing the resulting raindrop spectra of *Scenarios H1* and *M1* with that of *Scenario HL*, this effect seems rather evident, as a smaller concentration of giant particles in *Scenario HL* results in a delayed formation of raindrops. However, the combined scenario produces less rainwater mass than *Scenario L1* (25% less after 15 minutes and 47% less after 30 minutes). Here, both scenarios have the same amounts of giant nuclei, but the combined scenario has a much higher (two orders of magnitude) concentration of Aitken particles.

The combined scenario can be interpreted as a polluted situation with an extremely large number of small particles. (Note that all scenarios were based on field data collected in 1984 and 1985, when Mexico City was extremely polluted.) The observed delay (as compared with *Scenario L1*) in the rain-sized drop formation can be attributed to an exaggerated competition for the available water vapor among the numerous small droplets present in the combined scenario. Actually, this effect seems to be occurring in all scenarios simulated in this study and explains the necessity of introducing giant nuclei in order to initiate warm-rain formation through collision and coalescence.

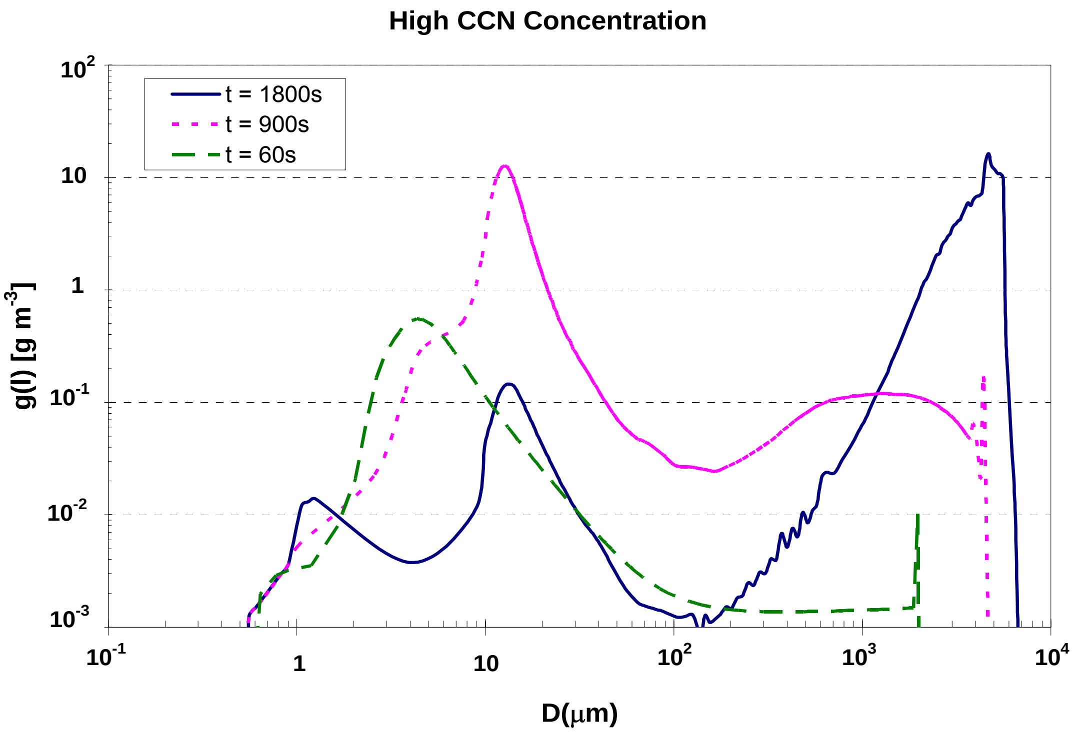

Figure 4. Mass distribution functions for different times after passage through cloud base for *Scenario H1*. Notice the clearly defined bimodal cloud droplet spectrum at 30 minutes, due to growth by condensation.

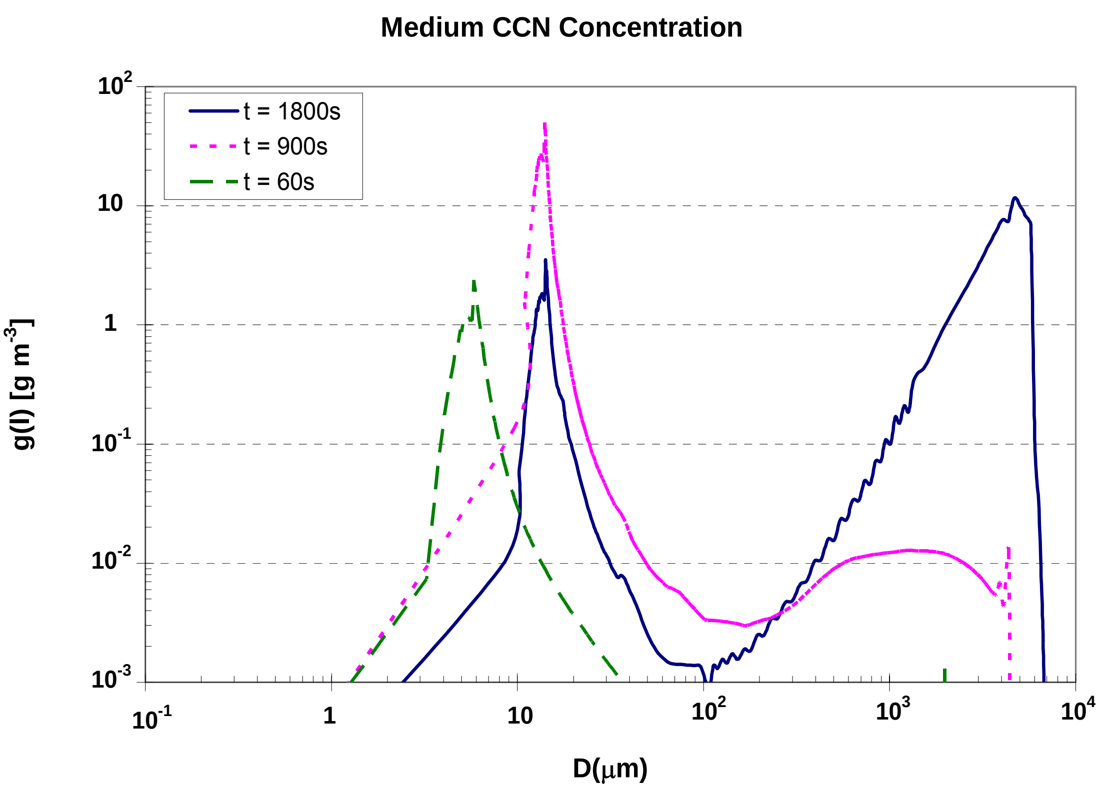

Figure 5. As in Figure 4, but for *Scenario M1*.

Table 2. Total mass concentration of raindrops (D > 200 μm), in g m^{-3}, formed 15 and 30 minutes after passage through cloud base, for all scenarios including giant nuclei.

Time	H1	M1	L1	HL
15 min	1.12×10^{-1}	1.21×10^{-2}	1.97×10^{-3}	1.48×10^{-3}
30 min	2.72	2.53	2.34	1.24

4. CONCLUSIONS

The simulations performed in this study show that pollution can initiate or delay rain-sized drop formation, depending on the size of pollutants. Small, numerous particles may delay the production of raindrops due to the effect of competition. Giant nuclei, which initiate coalescence, accelerate warm-rain processes. These topics deserve further research, and studies are required to verify these initial results on a larger set of data.

Because the objective of the investigation is to determine if warm-rain processes can be accelerated, delayed or even suppressed by modified natural aerosol spectra, conclusions drawn from these calculations must be interpreted in a comparative and qualitative manner. In other words, the modeling results require careful interpretation to compensate for the inherent weaknesses of closed parcel models. In any case, the current results provide some evidence that urban pollution modify the precipitation efficiency of warm clouds.

Acknowledgments. The authors are indebted to Roelof T. Bruintjes for providing the original computational code of the numerical model.

References

Coakley, J.A., R.L. Bernstein and P.R. Durkee, 1987: Effects of ship-stack effluents on cloud reflectivity. *Science*, **237**, 1020-1022.

Cooper, W.A., R.T. Bruintjes and G.K. Mather, 1997. Calculations pertaining to hygroscopic seeding with flares. *J. Appl. Meteor.*, **36**, 1449-1469.

Eagen, R.C., P.V. Hobbs and L.F. Radke, 1974: Particle emissions from a large Kraft paper mill and its effects on the microstructure of warm clouds. *J. Appl. Meteor.*, **13**, 535-552.

Gunn, R., and B.B. Phillips, 1957: An experimental investigation of the effect of air pollution on the initiation of rain. *J. Meteor.*, **14**, 272-280.

Herrera, J.R., and J.J. Castro, 1988: Production of cloud condensation nuclei in Mexico City. *J. Appl. Meteor.*, **27**, 1189-1192.

Montañez, R.A., and F. García-García, 1993: Some urban and meteorological effects on the production of cloud condensation nuclei in Mexico City. *Atmósfera*, **6**, 39-49.

Radke, L.F., J.A. Coakley and M.D. King, 1989: Direct and remote sensing observations of the effects of ships on clouds. *Science*, **246**, 1146-1149.

Rosenfeld, D., 1999: TRMM observed first direct evidence of smoke from forest fires inhibiting rainfall. *Geophys. Res. Lett.*, **26**, 3105-3108.

Rosenfeld, D., and I.M. Lenski, 1998: Satellite-based insights into precipitation formation processes in continental and maritime convective clouds. *Bull. Amer. Meteor. Soc.*, **79**, 2457-2476.

Warner, J., 1968: A reduction in rainfall associated with smoke from sugar-cane fires. An inadvertent weather modification? *J. Appl. Meteor.*, **7**, 247-251.

Warner, J., and S. Twomey, 1967: The production of cloud nuclei by cane fires and the effect on cloud droplet concentration. *J. Atmos. Sci.*, **24**, 704-706.

THE SENSITIVITY OF LOCAL AND SYNOPTIC SCALE PRECIPITATION SYSTEMS TO THE CLOUD CONDENSATION NUCLEI CONCENTRATION: A NUMERICAL MODELING EVALUATION

Jorge A. Martins[1,2], Leila D. Martins[2], Edmilson D. Freitas[2], Caroline R. Mazzoli da Rocha[2], Ricardo Hallak[2], Fabio L. T. Gonçalves[2], Maria A. F. Silva Dias[2,3]

[1] Universidade Tecnológica Federal do Paraná, C. Procópio, PR, Brazil

[2] Universidade de São Paulo, São Paulo, SP, Brazil

[3] Centro de Previsão de Tempo e Estudos Climáticos, Cachoeira Paulista, SP, Brazil

E-mail: jmartins@utfpr.edu.br

1. INTRODUCTION

The atmospheric aerosol particles have long been recognized as an important agent of climate change. Firstly, the particles are thought to act directly, absorbing or reflecting sunlight back to the space. Indirectly, the aerosols alter the Earth-atmosphere radiation balance by modifying cloud albedo (first indirect effect) and cloudiness (second indirect effect). The later effect cause modification in the cloud spatial structure with consequences on surface accumulated precipitation (Lohmann and Feichter, 2005). Local and synoptic scales precipitation systems might be very sensible to the second aerosol indirect effect. The South Atlantic Convergence Zone (SACZ) is an important example of synoptic scale precipitation system, consisting of an elongated convective band covering a large area of tropical South America, extending from the western Amazon to the Atlantic Ocean. The characteristics of intensity, geographical location, and persistence of the SACZ during the austral summer were investigated by Carvalho et al. (2004), where a more detailed description can be found. The system predominated during a few days between January and February of 2003. A number of local storms triggered by topography were also observed in the border of this band. The phenomenon enabled a great opportunity to study the effects of aerosols on precipitation development by simulating simultaneously the local and synoptic precipitation systems. At this time of the year, parts of the region show a pristine atmosphere with very low cloud condensation nuclei (CCN) while in the most industrialized areas and to the north of the SACZ, CCN concentration may be quite high. Using the Brazilian Regional Atmospheric Modeling System (BRAMS), the possible impacts of CCN in modify the precipitation structure and intensity associated to SACZ were investigated.

2. METHODOLOGY

In an attempt to study the impacts of CCN in modify the precipitation structure associated to SACZ, a set of numerical experiments was performed using BRAMS model. The numerical simulations were performed in a similar configuration as described by Martins et al. (2008) for the Amazonian Region, since measurements of CCN for Southwestern South America are not available. Two simulations were run for 48 hours, starting on February 01 2003. The first simulation involved running the model with a low CCN concentration (300 cm^{-3}) in order to represent clean atmospheric conditions. In this case, the shape parameter for the distribution of cloud droplets and pristine ice was 2, whereas the distribution of the other hydrometeor types was specified with a shape parameter of 1. This numerical simulation is hereafter referred to as CLEAN scenario. In the second numerical simulation, designated as POLLUTED scenario, the CCN concentration was set equal to 1200 cm^{-3}, the shape parameter for cloud droplets/pristine ice was 5, and the remaining parameters were the same as those used in the CLEAN scenario. The additional datasets such as atmospheric fields, soil humidity, topography; sea surface temperature, soil and surface features and physical parameterizations of radiation, turbulence, and convection were equally specified in both scenarios. Additional specifications are summarized in Table 1. The two-moment cloud model (Meyers et al., 1997) was applied to microphysical parameterization.

Table 1 Grid specifications for the numerical simulations.

	Grid 1	Grid 2	Grid 3
# grid points (x, y, z)	(62, 62, 43)	(62, 62, 43)	(82, 82, 43)
Hor. grid resolution (x, y)	(64 km, 64 km)	(16 km, 16km)	(4 km, 4 km)
Time step (s)	120	30	7.5
Start time – end time	00 UTC, September 23 2002 – 00 UTC, September 24 2002		
Vertical grid spacing	43 levels with variable stretching factor starting from 70 m		
Grid center	23.59°S; 43.66°W (São Paulo city)		

3. RESULTS AND DISCUSSION

According to the numerical results of this study, different aspects referring to the precipitation structure were observed. The mean value of the vertically integrated water content (total water path) did not show a clear pattern as the CCN concentration increases. However, the fraction of area covered by water categories suffered a reduction of about 11% in the POLLUTED scenario. Otherwise, the maximum values of the total water path increased about 24% when compared to the CLEAN scenario. In terms of vertically integrated water content, the results suggest that an increase in CCN concentration has the potential to concentrate the spatial distribution of condensed water.

The total accumulated precipitation decreased in most of the area covered by precipitation systems associated to the SACZ in response to the increase in CCN concentration. The systems predominating over almost flat continental areas of South America showed different behavior when compared to orographic storms occurring near coastal zones. While some areas of the synoptic system experienced an increase in accumulated precipitation of about 7%, the mean value was decreased in 9% for the polluted scenario. Figure 1 compares the two simulated scenarios in terms of total accumulated precipitation. The fraction of the area associated to each predominating structure is clearly different. Values lower than 10 mm predominate in the CLEAN scenario in a grid fraction larger than the POLLUTED scenario (Fig. 1).

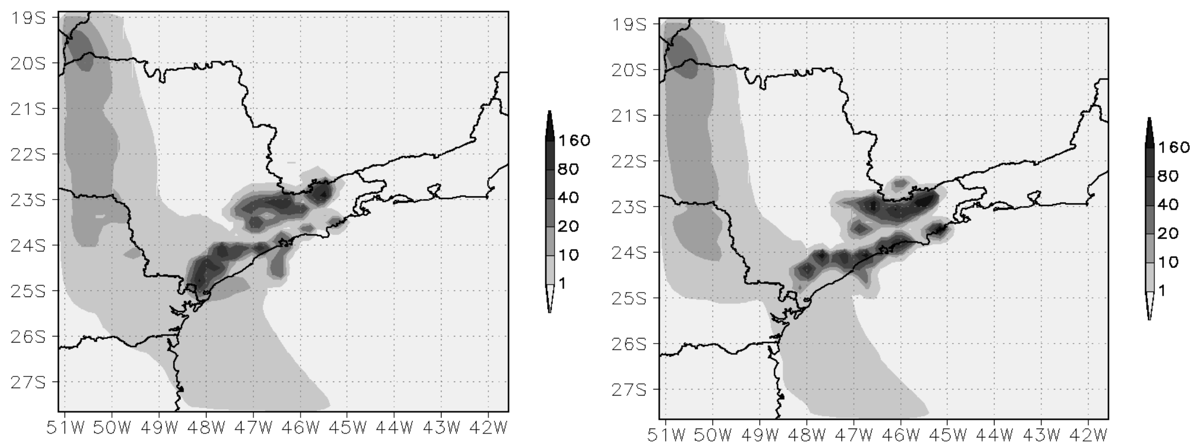

Figure 1: Spatial distribution of accumulated precipitation (mm) in the CLEAN (left) and the POLLUTED (right) simulated scenarios.

The observed accumulated precipitation suggests that warm rain process dominating the periphery of precipitating systems was suppressed by the increase in CCN concentration. Otherwise, orographic storms showed an increase up to 30% in precipitation. The fraction of the area dominated by increase in precipitation represents 28% of the synoptic system while this value increased to more than 43% in the orographic convective cells. Both precipitation types showed increase in cloud and ice water with the increase in CCN concentration.

This study also indicates the predominating pattern associated to glaciated phase in response to the increases in CCN concentration. Figure 2 shows horizontal distribution of ice water mixing ratio at 300 mb level during the early evening of the first day of simulation. There is a substantial difference between the spatial distributions of ice for each scenario. The results showed that higher CCN concentrations increase ice cover. The intensification of the ice phase can be responsible for the increasing precipitation in the core of the main orographically-induced cells. This intensification might have also implications on the energy balance in the Earth-atmosphere system.

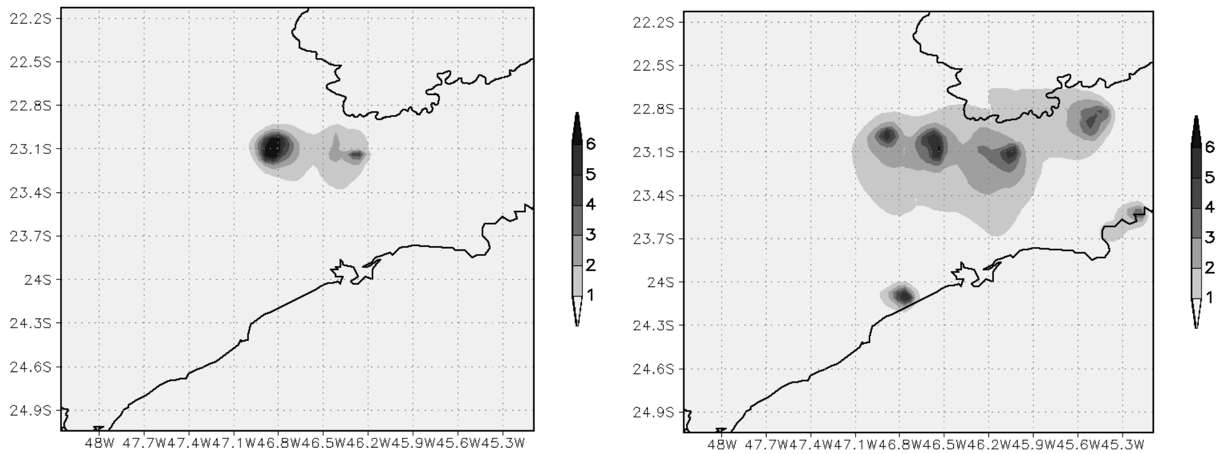

Figure 2: Simulated ice water mixing ratio (in g kg^{-1}) at 300 mb for the CLEAN (left) and the POLLUTED (right) scenarios.

Clouds with more numerous smaller droplets have a low efficiency in producing warm rain precipitation. The smaller water droplets in the cloud fall more slowly, thereby prolonging the lifespan of the cloud and potentially strengthening its cooling effect as indicated by Figure 2. As a consequence the cloud system in the POLLUTED scenario occupy a larger surface area in high level than the CLEAN scenario and therefore could potentially reflect more sunlight as predicted by the second aerosol indirect effect. Otherwise the downdraft movements can overwhelm the development in warm rain areas in the vicinity of deep cells. Analyzing the central part of the simulated area, where local convective structures predominate, the results show up to 20 % more sunlight in the POLLUTED scenario than in the CLEAN one, which corroborates the inhibiting role of the downdrafts. In addition, considering the overall domain, which covers a great part of South America and Atlantic Ocean, there is no predominating sign in the solar radiation flux reaching the surface. This result might be seen as a compensating effect caused by large warm rain regions that occur in most of continental and maritime areas. In these areas the above-mentioned prolonging effect on cloudiness may be dominating.

The results suggest that the mechanisms by which the core of the precipitation systems are more efficient in rainfall production, simultaneously suppresses warm rain in peripheral areas where ice is almost absent. In addition, a different behavior can be expected on local convective structures or synoptic ones. This is an important result and contributes to improve our understanding of the aerosol impact on global precipitation. Note that aerosol size distributions obtained in Amazonian Region and in Metropolitan Area of São Paulo have shown different properties. Then, the present results should be seen as preliminary. However, they can be used to help determine future study needs and the aerosol/CCN study location to be used during numerical simulations.

BIBLIOGRAPHY

Carvalho, L.M.V., C. Jones, and B. Liebmann (2004): The South Atlantic Convergence Zone: Intensity, Form, Persistence, and Relationships with Intraseasonal to Interannual Activity and Extreme Rainfall. *J. Climate*, 17, 88–108.

Lohmann, U., and J. Feichter (2005): Global indirect aerosol effects: A review, *Atmos. Chem. Phys., 5*, 715-737.

Martins, J. A., M. A. F. Silva Dias, and , F. L. T. Gonçalves (2008): Impact of biomass burning aerosols on precipitation in the Amazon: A modeling case study*, J. Geophys. Res.*, in press.

Meyers, M. P., R. L. Walko, J. Y Harrington, W. R. Cotton (1997): New RAMS cloud microphysics parameterization. Part II: the two moment scheme. *Atmos. Res*., 45, 3-39.

COMPARATIVE MODELING STUDY OF THE IMPACT OF AEROSOLS AND GLOBAL WARMING ON MICROPHYSICS AND DYNAMICS OF MIXED-PHASE CONVECTIVE CLOUDS

R. Mitzeva[1], B. Tsenova [2], A.Todorova [1]and J.Latham[3,4]

[1] Faculty of Physics, University of Sofia
[2] National Institute of Meteorology and Hydrology
[3] MMM Division, NCAR, Boulder, CO, USA,
[4] SEAES, University of Manchester, Manchester, UK

1. INTRODUCTION

As stated in the Report of the Intergovernmental Panel on Climate Change (IPCC, 2007) , it is expected that global warming will give rise to a greater frequency and severity of extreme weather events. Also, recent studies reveal that air pollution influences the development of convective clouds (Levin and Cotton,2007). Preliminary numerical simulations indicate that in a polluted environment the updraft velocity and cloud top height increase in some of the simulated clouds, while in others - they decrease.

The aim of the present work is to compare the influence of global warming and pollution, (represented by CCN concentration) on convective cloud dynamics and microphysics. A mixed-phase convective cloud is simulated using a numerical model with bulk water parameterization. Comparison between simulated in-cloud characteristics for different CCN concentrations (clean and polluted air) reveal the impact of aerosols on cloud development. The comparison between simulated in-cloud characteristics for given CCN using different temperature profiles (in the range of expected increase) give an indication of the impact of global warming on cloud development.

2. MODEL DESCRIPTION

The model (Mitzeva et al., (2003), is based on the assumption that convective clouds are composed of active and non-active cloud masses (Andreev et al,1979). The active mass is modelled by successive ascending spherical thermals, while the non-active cloud region is formed by thermals that have previously risen and stopped at the level where their velocity is zero. One can speculate that the ascending thermals represent the updraught region of convective clouds, while non-active masses represent the environment surrounding the updraughts. The thermals are driven by the buoyancy force reduced by entrainment and the weight of the hydrometeors present. They entrain air from a cloudless environment or from a non-active cloud region depending on their position. Parameterization of the merging of thermals during their ascent is included in the model. As the thermals ascend, the temperature in the rising thermals changes due to cooling, entrainment of environmental air and heat released by the microphysical processes. The model uses bulk microphysical parameterizations with five classes of water substance - water vapor, cloud water S_c, rain S_p, cloud ice S_{cf}, and precipitating ice (graupel) S_{pf}. The cloud droplets and ice crystals are assumed to be monodisperse, with negligible fall velocities, and so move upward with the air in the ascending thermals. A Marshall-Palmer type size distribution is assumed for raindrops and graupel.

In the model cloud, droplets are formed by condensation. Raindrops form by autoconversion of the cloud droplets and grow by collision and coalescence with cloud drops. Below $0^{o}C$, ice crystals originate by heterogeneous freezing at the expense of cloud droplets. Homogeneous freezing occurs below $-40^{o}C$. Graupel forms by the freezing of raindrops, contact nucleation of ice crystals and rain drops and conversion of ice crystals. Ice crystals grow by deposition of water vapor; graupel grows by coalescence with cloud and rain drops. Precipitation fallout is calculated in the same manner as Cotton,1972, and comprises that portion of the raindrops and graupel having terminal velocities greater than the updraft speed. Evaporation of raindrops and melting of graupel during their descent as well as recycling of precipitating particles is included in the model. The model takes account of the changes of the mass of drops and crystals due to the entrainment of environmental air and by the incorporation of the mass of rain drops and graupel falling out from the upper ascending successive thermals. The non-active cloud mass also expands, and the temperature excess, water vapor, cloud droplets and ice crystals in this region vary in time because of turbulent diffusion and evaporation.

The differential equations describing the dynamical and microphysical processes in the ascending thermals are integrated numerically by the Runge-Kutta method. The calculations are carried out for thermals ascending from cloud base to the height of zero velocity. The numerical integration of the equations, describing the changes with time of the characteristics of the non-active cloud region, begins after one of the ascending thermals stops. The calculated temperature, vapour mixing ratio, and cloud liquid and ice mixing ratio of the diffusing thermals are used in the estimation of the environmental conditions of the ascending thermals. The mass of raindrops and graupel falling out of the ascending thermals are calculated at each integration step.

3. NUMERICAL SIMULATIONS AND RESULTS

To reveal the impact of aerosols through their role as CCN on cloud development the simulated in-cloud characteristics for given environmental conditions using different CCN (for clean and polluted air) are analyzed and compared. Comparison between simulated in-cloud characteristics for prescribed CCN (clean and polluted air) using a modified temperature profile (in the range of expected increase) give an indication of the impact of global warming on cloud development.

In studying the impact of CCN input we emphasize that the transformation of cloud water - composed of. small droplets, S_c (gm^{-3}) - to rainwater - composed of. large drops, S_p (gm^{-3}) - is parameterized by autoconversion, following Kessler (1969), namely,

$$\frac{dS_p}{dt} = -\frac{dS_c}{dt} = k_1\left(S_c - S_0\right)$$

where S_0 is the autoconversion threshold and k_1 the autoconversion rate. If $S_c<S_0$ there is no autoconversion. When $S_c \geq S_0$ part of the cloud water S_c transforms to rainwater S_p with a rate k_1. It is assumed that the conversion of cloud droplets to raindrops is accelerated when the CCN are fewer and bigger and decelerated when the CCN are numerous and small, so the pollution of the air leads to the reduction of conversion of cloud to rain water. Thus, larger/smaller values of S_0/k_1 have to be used for the simulation of large number of small CCN (typical for the polluted continental airmass), and smaller/larger values of S_0/k_1 for the simulation of fewer and bigger CCN (typical for clean maritime airmass). The values of S_o and k_1 used for the simulations of different CCN inputs are given in Table 1.

Table1. Autoconversion threshold S_o and autoconversion rate k_1 used to simulate different types of CCN input in the model simulations

S_0	k_1	Type of CCN input
0,01	0,02	Maritime (***M***)
0,5	0,005	Continental (***C***)
1	0,001	Poluted Continental (***PC***)

The impact of global warming on cloud development is examined by comparison between simulated in-cloud characteristics for three different temperature soundings: one shown on Fig.1 (further denoted with dT=0) and two modified soundings in accordance with the expected climate changes. The modifications of the temperature profile used in the present study (Fig. 2) are based on IPCC, 2007 and Santer et al., 2003. IPCC climate projections predict an increase of global mean surface temperature from 2 to 6 degrees C per 100 years. The change over the continents in summer is expected to be twice as large as the global mean. The investigations of Santer et al.,2003 reveal that temperature changes with height depend on latitude and the temperature increase in the upper troposphere for the midlatitudes is about 1,5 times greater than the surface temperature with maximum around 400 mb. In our further analyses we denote with dT=3s and dT=5s the modification of temperature profile according to Fig.2 following bold and dash line respectively. Due to the very limited studies and no clear trend in relative humidity (Elliot and Angell, 1997) in our simulations the dew-point temperature profile was modified in such a way to keep the relative humidity in accordance to the original sounding (dT=0), i.e. the relative humidity was not modified. In order to reveal the impact of both CCN type input and climate warming, the detailed analyses of the evolution of dynamical and microphysical profiles is needed. Here only the maximum values of in-cloud characteristics will be presented as a preliminary analysis of the results.

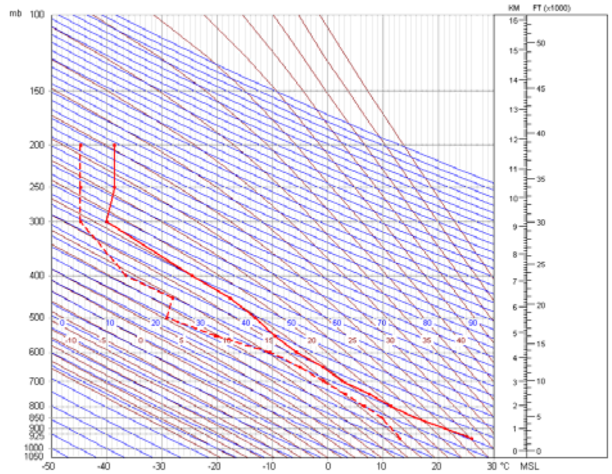

Fig.1 Aerological sounding used for model simulations with dT=0.

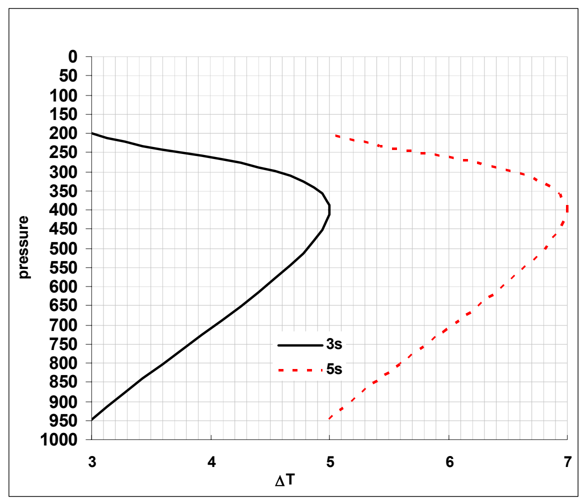

Fig.2 Temperature change ΔT (^oC) as a function of pressure used for the simulation of climate warming.

The analyses show that with global warming the cloud depth increases at all types of CCN input (top panel of Fig.3) The increase is most significant when the cloud has formed in airmass with maritime CCN (green color), and less pronounced when the cloud is formed in the polluted continental airmass (brown color). There is also significant increase in the maximum updraft velocity (bottom panel in Fig.3) at the warming following the profile dT=5s independent of CCN input. However when environmental temperature increases following profile dT=3s there are no significant changes in Wmax and it even decreases when the simulated cloud has formed in the airmass with ***M*** (blue color) and ***PC*** (brown) CCN. These results indicate that the impact of assumed climate warming on cloud dynamics varies depending on the CCN input and this relation is not linear. The results also indicate that the impact of CCN on cloud dynamics depends on the profile of environmental temperature.

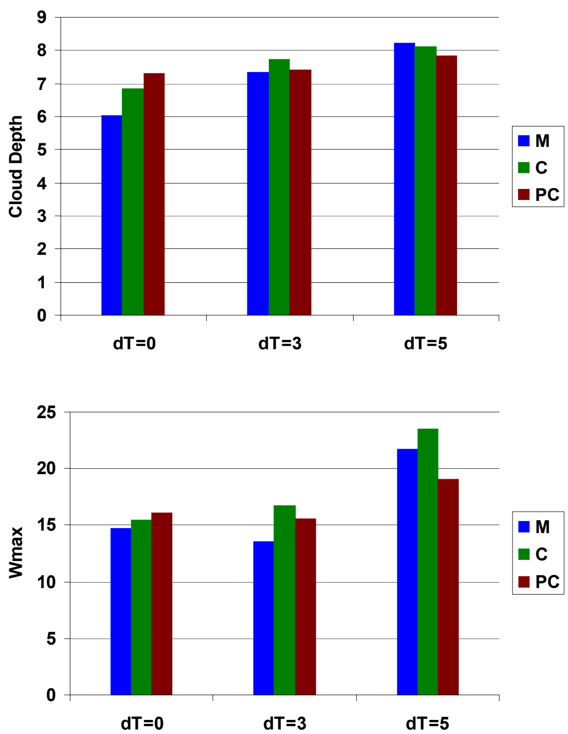

Fig.3 Cloud depth (top panel) and maximum updraft velocity Wmax (bottom panel) for different aerological soundings (dT=0, dT=3s and dT=5s) and different CCN input- ***M*** – blue colors, ***C***- green colors and ***PC*** – brown colors

Fig.4 (top panel) shows that maximum cloud water content S_{cmax} does not change noticeably with the increase of environmental temperature independent of the type of CCN input and decreases significantly in clouds with a few and big CCN (***M***) due to the acceleration of conversion of cloud to rain water. Maximum rain water content S_{pmax} (bottom panel of Fig,4) increases as a result of climate warming at the three CCN inputs, with the biggest values in clouds formed in maritime airmass. It is clear that for given environmental conditions the decrease of cloud water and increase of rain water for maritime CCN in comparison with continental and polluted continental CCN input is due to the acceleration of the conversion of cloud to rain water. However, to identify the reasons for the evolution of cloud and rain water in changing climate, more detailed analysis is needed.

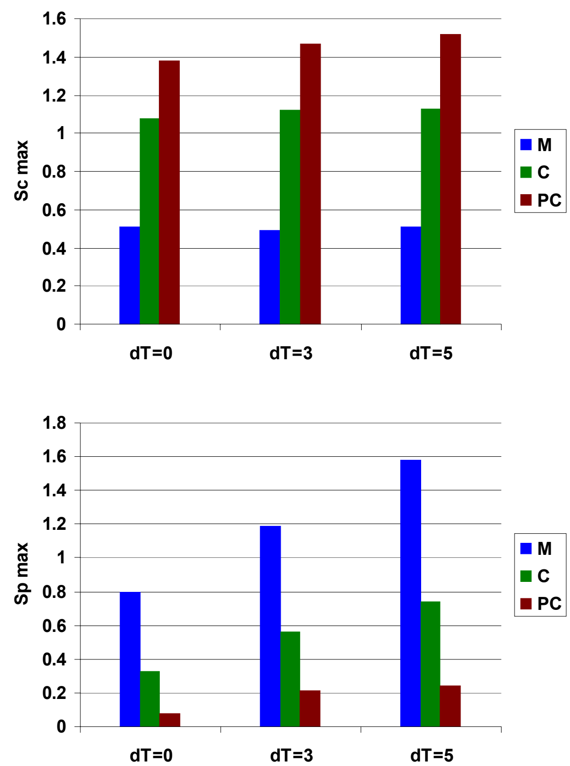

Fig 4. Maximum cloud water content $S_{c\ max}$ (top panel) and rain water content S_{pmax} (bottom panel) for different aerological soundings (dT=0, dT=3s and dT=5s) and different CCN input- ***M*** – blue colors, ***C***- green colors and ***PC*** – brown colors

Fig. 5 shows that the maximum ice crystal and graupel content increase with the deceleration of the conversion of cloud to rain water, i.e. their values are biggest when the clouds developed in the polluted environment. This tendency is pronounced independent of climate warming. The impact of climate warming on maximum ice and graupel content is not well defined. There is a significant increase of maximum ice crystals content S_{cfmax} at climate warming when maritime CCN input is used for the simulation. The main tendency is to the increase of maximum ice crystal content S_{cfmax} and to the decrease of maximum graupel content S_{pfmax} with climate warming. However this impact is not linear and depends on CCN input. For example S_{cfmax} is smaller at dT=3s in comparison with dT=0 when the simulated cloud is developed in the polluted environment (see top panel of Fig. 5 -brown color). The maximum values of graupel content S_{pfmax} are smaller for climate warming, however there is a bigger decrease in these values at dT=3s in comparison with dT=5s (see bottom panel of Fig.5)

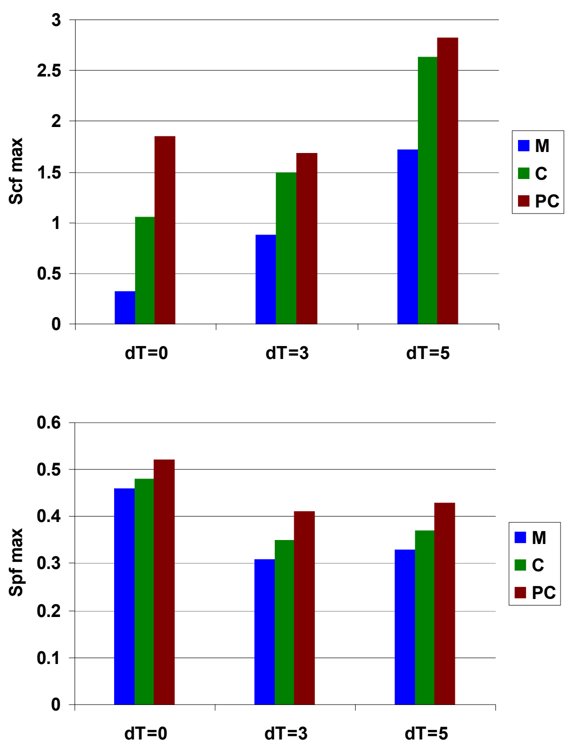

Fig.5. Maximum ice content S_{cf} (top panel) and graupel content S_{pf} (bottom panel) at a prescribed aerological sounding (dT=0, dT=3s and dT=5s) for different CCN inputs- ***M*** – blue colors, ***C***- green colors and ***PC*** – brown colors

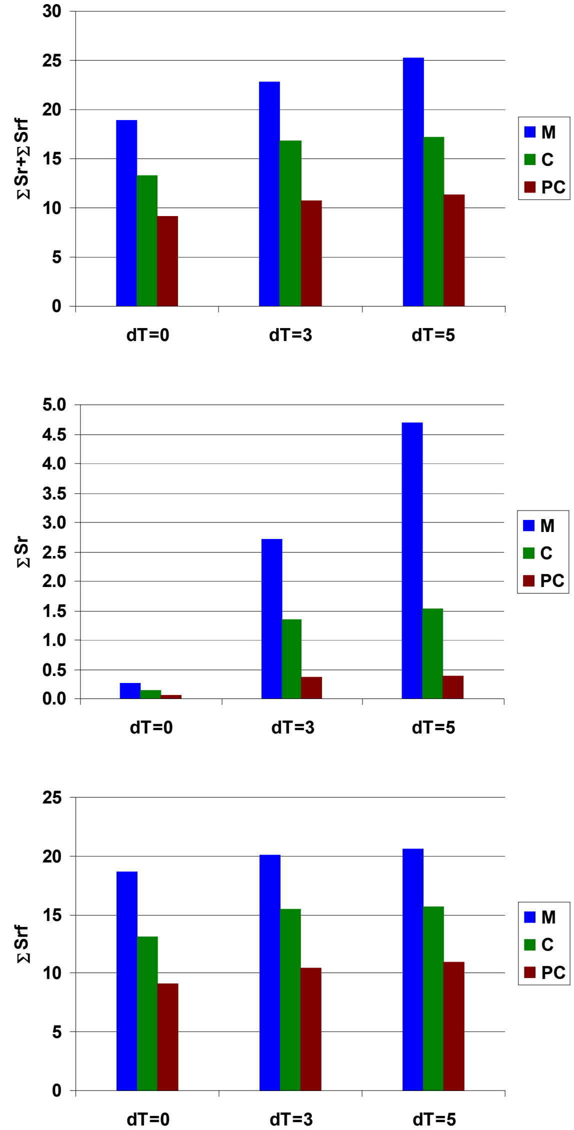

Fig.6. Total fallout ∑Sr+∑Srf (top panel), sum of liquid ∑Sr (middle panel) and solid ∑Srf (bottom panel) fallout for a prescribed aerological sounding (dT=0, dT=3s and dT=5s) for different CCN input- ***M*** – blue colors, ***C***- green colors and ***PC*** – brown colors

Since the model simulations are carried out from the cloud base height to the height of zero updraft velocity it is obvious that the model does not give information about precipitation at the ground. That is why, in our study the impact of type of CCN and climate warming on the precipitation is evaluated indirectly and is based on the estimations of the amounts of liquid and solid fallout from the ascending thermals. We assume that there will be a positive correlation between these amounts and those reaching the ground when the temperature below cloud base is not changed. Part of (probably all) the solid fallout may melt during descent to the ground.

Results presented in Fig. 6 (top panel) show that total fallout (∑Sr+∑Srf) increases when the conversion of cloud to rain water is accelerated (compare different colors) and with global warming. Based on this one can conclude that in the frame of our model the pollution of the air leads to decrease of precipitation on the ground. The increase of temperature as a result of global warming leads to an increase of evaporation below cloud base. That is why we cannot make a conclusion whether the precipitation on the ground will increase at global warming although the total fallout increases. The impact of global warming is more pronounced in clouds developed in maritime air mass (blue color) and rather small in a polluted air (brown color). The more detailed analyses reveal that the increase of total fallout (∑Sr+∑Srf) is due to the increase of both liquid ∑Sr (middle panel of Fig.6) and solid ∑Srf (bottom panel of Fig.6) fallout. The warming has significant impact on liquid fallout and relatively smaller impact on solid fallout.

4. CONCLUSIONS

The results indicate that the simulated climate warming leads to the formation of clouds with larger vertical dimension and to the increase of “precipitation” (total fallout in the cloud) for all types of CCN input. At a fixed environmental sounding the amount of precipitation increases when the conversion of cloud water to rain water is accelerated, although less dynamically active clouds have formed. Thus, the pollution of the air leads to the increase of cloud depth and decrease of precipitation. Our preliminary analyses reveal that the increase of cloud depth due to climate warming and different CCN input is a result of the increase of instability in higher levels and latent heat released at the formation of ice particles. It is clear that the distribution of solid particles depends on the distribution of cloud and rain water, which depends on CCN input and on cloud dynamics. A more detailed analysis is needed for the explanation of the combined impact of climate warming and CCN input on microphysical and dynamical properties of the simulated clouds. The non-linear impact is a result of the interactions between cloud dynamics and microphysics.

We stress that the current work is based only on one case study, and that different conclusions might emanate from further modeling runs encompassing wide ranges of meteorological conditions. To evaluate the impact of global warming on precipitation, the calculations have to be carried out below cloud base down to ground level.

Taking into account the recent study of Pierce et al, 2006, who argue that the real increase in water vapor is not large enough to maintain the relative humidity constant, it is deemed worthwhile to study the impact of relative humidity change due to climate warming.

5. ACKNOWLEDGEMENTS

The present work is partially supported by EC through 6FP projects ACCENT (GOCE-CT-2002-500337).

6. REFERENCES

Andreev, V., D. Syrakov, and R. Mitzeva., 1979, Modelling of convective cloud formation as successive ascending thermals, Bulg. Geophys. J., 5, 3-9.

Cotton W., Numerical simulation of precipitation development in super-cooled cumuli - Part II. Mon. Wea. Rev., 100, 764 - 784, 1972

Elliot, W.P. and J.K. Angell, 1997. Variations of cloudness, precipitable water, and relative humidity over the United

States;1973-1993, Geophysical research letters, vo.24, N1, p.41-44.

IPCC, 2007, Climate Change 2007: Report of the Intergovernmental Panel on Climate Change, Cambridge University Press, pp.921.

Kessler, E., 1969, On the distribution and continuity of water substance in atmospheric circulations, Meteorol. Monogr., Boston, 10, No 32.

Marshall, J. S., and W. McK. Palmer, 1948, The distribution of raindrops with size, J. Met., 5, 165-166.

Pierce et al, 2006, Three-dimensional tropospheric water vapor in coupled climate models compared with observations from the AIRS satellite system, Geophysical Research, vol. 33, L21701, doi:10.1029/2006GL027060, 2006

Santer B.D, R. Sausen et al., 2003, Behaviour of tropopause height and atmospheric temperature in models, reanalyses and observations. Decadal changes., Journal of Geophysical Research, vol.108, N D1,4001, doi: 10.1029/2002JD002258

Zev Levin and W.Cotton,2007 The WMO/IUGG International aerosol precipitation science assessment group, 2007 Aerosol Pollution Impact on Precipitation: A Scientific Review

AN ASSESSMENT OF CLOUD-POLLUTION-PRECIPITATION INTERACTIONS AND VARIATIONS OVER AN URBAN AREA USING VERTICALLY-POINTING MICRO-RAIN RADARS, SATELLITE REMOTE SENSING AND CHEMICAL ANALYSES

Catherin L. Muller[1] and Chris Kidd[1]
[1]*School of Geography, Earth and Environmental Sciences, The University of Birmingham, Edgbaston, Birmingham, B15 2TT*

1. INTRODUCTION

Aerosols, especially water-soluble aerosols, play important roles in the atmosphere. They act as cloud condensation nuclei (CCN), changing the equilibrium size to which a droplet may grow at a given relative humidity and are therefore important in cloud and precipitation processes. This has prompted atmospheric scientists to explore the impact of urban environments and increasing anthropogenic activities on cloud and precipitation processes. Satellites provide an excellent platform to examine cloud microphysics. The Cloud-Aerosol-Precipitation Satellite Analysis Tool (CAPSAT), developed by Lensky and Rosenfeld (2008), is used in this work.

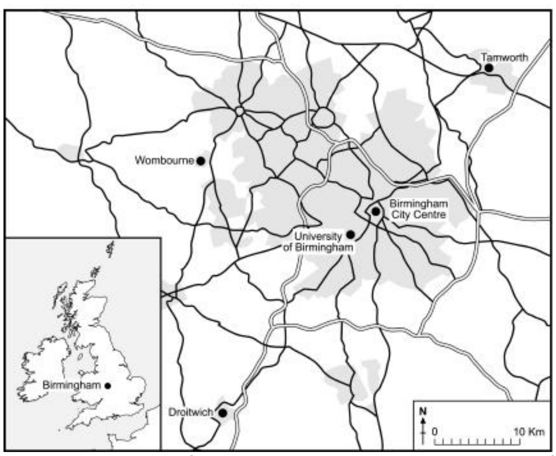

Figure 1: Location of MRRs and sampling site: University of Birmingham (UoB, urban sampling site), Droitwich (DTW); Tamworth (TMW); Wombourne (WMB). Inset: Location of Birmingham within the UK

This presentation will show the initial results from 3 years of data collected in Birmingham, United Kingdom (Figure 1). Using a selection of events, it will describe a) how precipitation samples were collected for chemical analyses, b) how CAPSAT was used to assess cloud-top microphysics and spatial variations, and c) how an array of vertically-pointing micro-rain radars (MRRs) were used to assess the spatial variations in precipitation parameters.

2. METHODOLOGY

Sequential samples from individual precipitation events were collected in Birmingham, United Kingdom between April 2005 and January 2008, using an automatic sampler. These were analysed using a pioneering fluorescence technique in order to assess the dissolved organic carbon (DOC) content. This technique provides a non-invasive, rapid method to examine the content of precipitation samples. This chemical data, along with other meteorological variables - including particulate matter concentrations, wind speed, wind direction, back trajectory analysis, and synoptic charts - were used to categorise and highlight precipitation events of interest.

Cloud top microphysical data was derived from the EUMETSAT Meteosat Second Generation (MSG) satellite, every 15 minutes covering the duration of the individual precipitation events. CAPSAT was used to examine cloud microphysics over Birmingham. It uses red-green-blue (RGB) composites of the computed physical values of picture elements to represent much of the physical information retrieved by MSG (Lensky and Rosenfeld, 2008). Physical quantities can be displayed: reflectance (%) in the solar channels and brightness temperature (BT) (K) in the thermal channels. Meaningful RGB combinations can be used for qualitative analysis of cloud microphysics. CAPSAT uses pre-defined colour schemes which have been officially adopted by the EUMETSAT MSG interpretation guide. Satellite observations were extracted along transects across the city, and for pixels corresponding to the location of the MRRs. This allowed microphysical parameters, such as cloud droplet effective radius (r_e) and cloud-top temperatures (T) along the transects to be investigated more quantitatively.

Reflectivity (Z), drop size distribution (DSD), liquid water content (LWC), fall speed (W) and rain rate (R) parameters were collected every minute over heights of 6,000m, by an array of four MRRs located within and surrounding the city. These were located at urban, upwind and downwind locations (Figure 1). Additional meteorological data such as backward trajectories, synoptic charts and secondary meteorological data was also used in order to assess the interactions, and spatial and temporal variations, occurring during individual precipitation events over Birmingham.

3. RESULTS

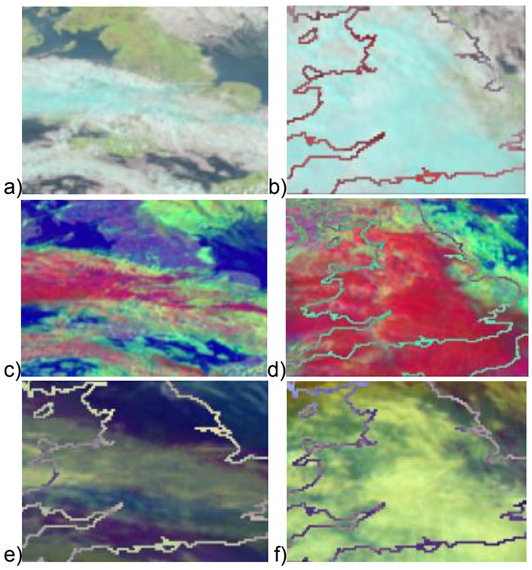

Figure 2: CAPSAT images: a) ”Day natural colours enhanced”: 23/04/05, water clouds with small droplets; b) “Day natural colours enhanced”: 05/07/07, snow and ice clouds; c) ”Day Microphysical”: 23/04/05, precipitating cloud, supercooled water clouds in places; d) ”Day Microphysical”: 05/07/07, cold thick clouds with tops containing large ice particles; e) ”Air Mass”: 23/04/05, rich ozone polar air mass/’polluted’ case; f) “Air Mass”: 05/07/07, low ozone tropical air mass/’clean case’. Coastline displayed on some images for clarity.

Results include a selection of images generated using CAPSAT for a number of ‘polluted’ and ‘clean’ events - the term ‘polluted’ and ‘clean’ used herein refer to precipitation events containing high/low DOC, and high/low pollution days, respectively - to qualitatively show how cloud microphysics vary under certain conditions. For example, cloud-top radii appear to be smaller for ‘polluted’ cases, and for cases which are continentally sourced, when compared to ‘clean’ and maritime cases (Figure 2).

Graphs showing variations in solar reflectance differences (RD) and brightness temperature differences (BTD) are presented using extracted data for transects over Birmingham for the contrasting events. This provides further information on spatial variations in the microphysical characteristics. T-r_e graphs (Figure 3) are used to assess the variation in the shape of curves for different precipitation events, including one in which a tornado occurred over Birmingham (28/07/2005).

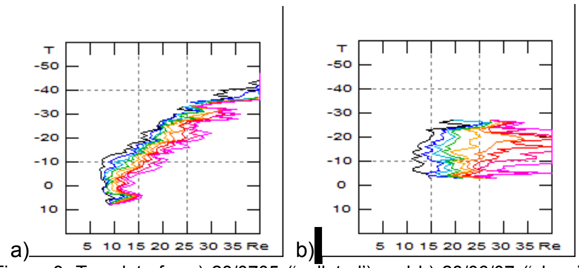

Figure 3: T-r_e plots for a) 28/0705 (‘polluted’) and b) 28/06/07 (‘clean’). Plotted are every 10th percentiles of the r_e for each 1°C interval. The median is indicated by the thick red line.

Finally, MRR images show how rainfall parameters vary spatially for selected events. Extracted data is used to quantitatively assess the relationships between the data sets, and variations in parameters, such as DSD, for different events.

4. BIBLIOGRAPHY

Dinar, E., Taraniuk, I., Graber, E. R., Katsman, S., Moise, T., Anttila, T., Mentel, T. F., Rudich, Y. (2006). Cloud condensation nuclei properties of model and atmospheric HULIS, *Atmospheric Chemistry and Physics Discussions,* 6, 1073–1120

Kieber, R.J., Whitehead, R. F., Reid, S. N., Willey, J. D., Seaton, P. J. (2006). Chromophoric Dissolve Organic Matter (CDOM) in rainwater, Southeast North Carolina, USA, *Journal of Atmospheric Chemistry*, 54, 21-41

Lensky, I. M. and Rosenfeld, D. (2008) Clouds-Aerosols-Precipitation Satellite Analysis Tool (CAPSAT), *Atmospheric Chemistry and Physics Discussions*, 8, 4765-4809

Muller, C.L. and Kidd, C. (2006) Quantitative rainfall measurements: A comparison of micro rain radars (MRRs) and rain gauges, *EGU General Assembly, Vienna,* 2nd-7th April 2006

Peters, G., Fischer, B. and Andersson, T. (2002) Rain Observations with a vertically looking Micro Rain Radar (MRR), *Boreal Environment Research*, 7, 353-362

Acknowledgements

The Authors would like to thank the ICCP, the British Hydrological Society, the Royal Meteorological Society and the University of Birmingham for their financial support.

TRAJECTORIES AND MICROPHYSICS WITHIN WINTERTIME MOUNTAIN WAVE CLOUDS: IMPLICATIONS FOR THE AEROSOL SIZE DISTRIBUTION

Binod Pokharel, Jefferson R. Snider and David Leon
Department of Atmospheric Science, University of Wyoming, Laramie, Wyoming, USA

1. INTRODUCTION

Removal of the atmospheric aerosol via their interaction with hydrometeors (i.e., droplets, rain and snow) is the main process by which the atmosphere is cleansed of particulate. Aerosol particles and hydrometeors interact by impaction, by diffusive processes and when particles function as condensation or ice nuclei. These processes influence the aerosol and can also indirectly impact the microphysical and macrophysical structure of clouds. This interaction arises because aerosol number concentration influences hydrometeor concentration; in particular cloud droplet number concentration. The latter is a key determinant of the propensity of both cold and warm clouds to produce precipitation (Ramanathan et al., 2001).

Most previous studies of aerosol removal by hydrometeors are either based on laboratory (e.g., Vittori and Prodi, 1967) or theoretical studies (e.g., Martin et al., 1980). Analysis of the former requires the assumption that observed aerosol changes are solely due to removal and not due to airmass advection (Laakso et al., 2003). All of these previous studies investigated the removal of relatively large aerosol particles (diameter > 0.01 µm) and did not consider the ultrafine nuclei (UFN); the latter are commonly defined as particles with diameter less than ~0.01 µm (Clarke, 1993). Similar to Clarke's definition, we define the UFN as particles with diameters between 0.003 to 0.015 µm. In general, the UFN are not activated to cloud droplets but they are viewed as an important precursor for the cloud condensation nuclei (CCN), provided they can grow to CCN size (D>0.1 µm) by either coagulation or by condensing vapors other than water. To become activated as cloud droplets, the UFN need sufficient time to grow by condensation and coagulation (Petters et al., 2006; Andronache et al., 2006). Formation and growth of the UFN can increase the concentration of CCN by a factor more than two over the course of 1 day (Kulmala et al., 2004). Since the removal of the UFN represents a short-circuiting of CCN production, it is important to improve understanding of the UFN removal processes. This work focuses on field studies of the attachment of UFN to both liquid and ice hydrometeors in mountain wave clouds formed over the Rocky Mountains in southeastern Wyoming.

2. MEASUREMENTS

2a - Aerosols

Aerosol particles were measured on the Wyoming King Air with an ultrafine condensation particle counter (UCPC, Model 3025, TSI Inc.) and a condensation particle counter (CPC, Model 3010, TSI Inc.) during the winter of 2006. The UCPC and CPC concentrations were made upwind and downwind of mountain wave clouds formed over the Medicine Bow Mountain Range (~50 km west of Laramie, WY). Our laboratory tests show that the UCPC and CPC measure particles of diameter larger than 0.003 µm and 0.015 µm, respectively. The UCPC and CPC concentration measurements were used to formulae the ultrafine nuclei concentration defined as: UFN = UCPC – CPC.

Figure 1 shows the position of the research aircraft (Wyoming King Air) and UFN measurements on January 18, 2006. The left panel shows the aircraft during the sampling conducted upwind and downwind of a mountain wave cloud; the center panel shows the height of the aircraft during the horizontal flight legs and during spiral soundings conducted upwind and downwind of the cloud; i.e., during the upwind and downwind soundings. The upper right panel shows the upwind and downwind vertical profiles of the UFN and the lower right panel shows the horizontal UFN measurements as frequency distributions. Wind vectors derived by averaging horizontal wind components, acquired during the upwind and and alongwind flight legs, are shown in the upper-left panel and demonstrate that air was flowing perpendicular to the barrier at low altitude (3000 m) and was also nearly perpendicular to the barrier at the level of the alongwind leg (4300 m). The UFN decrease, seen in the comparison of the downwind to upwind data, and the wind data, is suggesting that the UFN was removed during its passage through the mountain wave cloud.

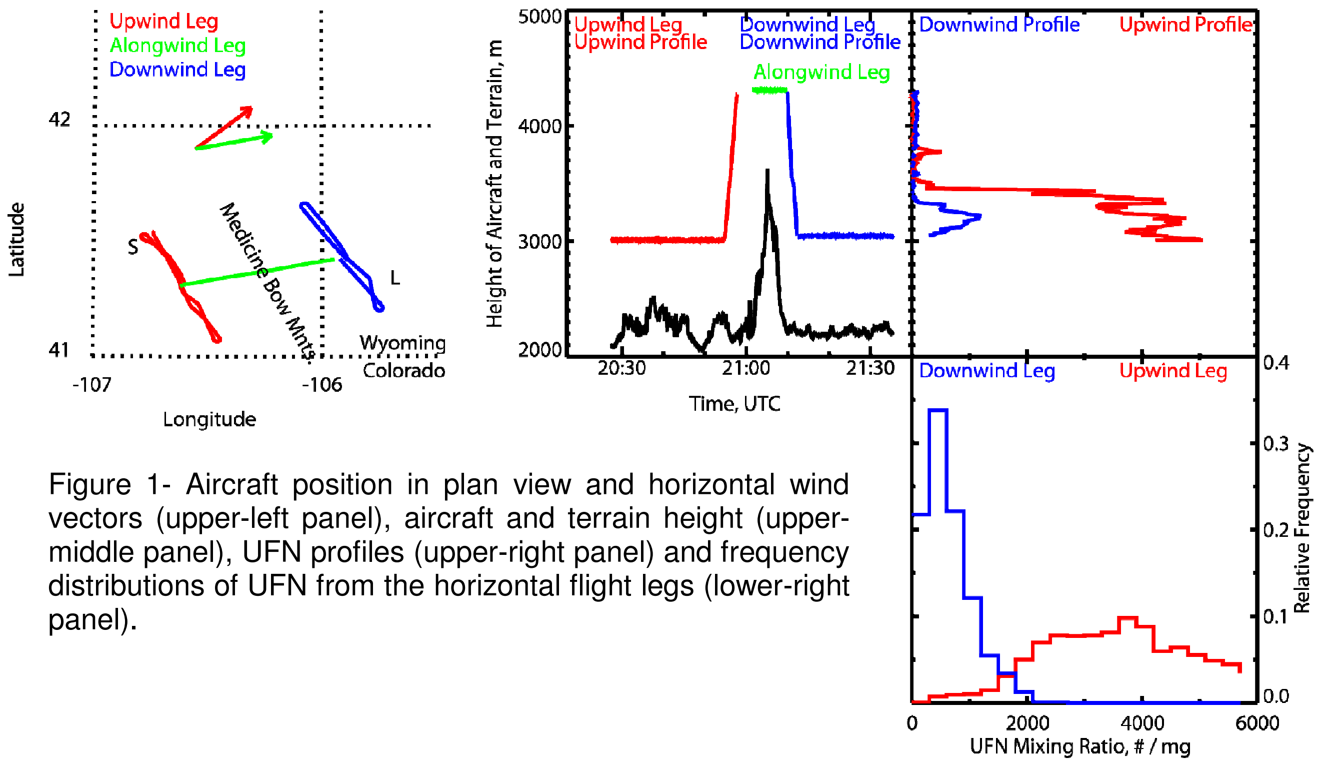

Figure 1- Aircraft position in plan view and horizontal wind vectors (upper-left panel), aircraft and terrain height (upper-middle panel), UFN profiles (upper-right panel) and frequency distributions of UFN from the horizontal flight legs (lower-right panel).

2b - Kinematics

The Wyoming Cloud Radar (WCR, Leon et al., 2006) was operated on the King Air during these studies. The top two panels of Figure 2 present two WCR-measured quantities, the radar reflectivity at a wavelength of 3 mm and the vertical-component Doppler velocity. Also shown in these two panels is the flight track of the King Air (dashed horizontal line). The reflectivity and vertical-component Doppler velocity data is available both above and below the aircraft. The bottom panel of Figure 2 presents the along-track horizontal wind velocity component; derived by combining Doppler velocities obtained from the nadir and forward-slant antennas of the WCR (Leon et al., 2006). The black line shown in the three panels is an air parcel trajectory which starts at the altitude of the upwind flight leg and ends at approximately the altitude of the downwind flight leg. We present a description of the trajectory calculation in the following section. The time interval needed to conduct the upwind to downwind flight plan is 50 minutes and sampling progressed in the direction of the wind. Data from four days have been analyzed and the results from 20080118 are showcased here.

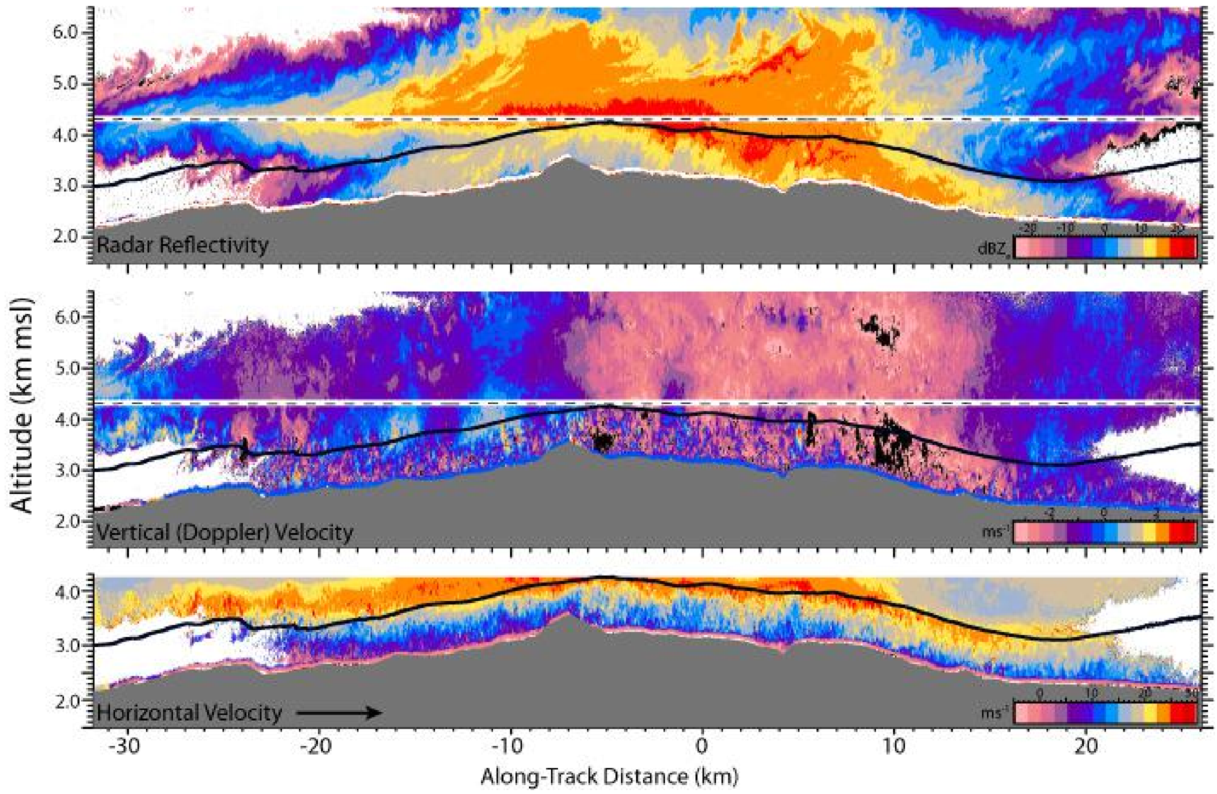

Figure 2 – WCR reflectivity (top panel), WCR vertical-component Doppler velocity (middle panel) and the derived along-track horizontal wind velocity (bottom panel) from January 18, 2006. The black line is a derived air parcel trajectory. The top two panels show the flight track of the King Air at 4300 m.

3. TRAJECTORY CALCULATIONS

Air parcel trajectories derived in this work are based on measurements of the wind field derived from measurements made by the Wyoming Cloud Radar. Since we use wind velocities acquired while flying along the direction of the mean wind, our air parcel trajectories lie in the plane defined by an alongtrack dimension (x) and the vertical dimension (z). The trajectory of the air parcel is obtained by numerical integration of the following equations.

$$x - x_o = \sum u_{i,j} \cdot \Delta t \quad (1a)$$

$$z - z_o = \sum w_{i,j} \cdot \Delta t \quad (1b)$$

Here the coordinates x and z define the position of the parcel (relative to an initial location), $u_{i,j}$ and $w_{i,j}$ are the velocities derived from Doppler velocity measurements obtained from the WCR (Leon et al., 2006), and Δt is the time step. The latter is taken to be 0.1 s; a value which is compatible with the time step of a parcel model which we use to simulate the microphysical properties of the cloud along the trajectory (Section 4).

The rest of this section provides detail on how we correct the vertical component of Doppler velocity to account for the sedimentation of hydrometeors. Also examined is a trajectory derived using an alternate approach and how that compares to the trajectory derived from the WCR wind measurement.

Since the WCR Doppler velocity is the vector sum of the vertical wind and the particle fall speed, a retrieval of the vertical wind speed requires an estimation of the particle fall speed. Our estimate requires the vertical component Doppler velocity measurements obtained from the radar range gates immediately above and below the altitude of the aircraft and the vertical wind velocity from the King Air gustprobe. Figure 3 shows the end result of the calculation, i.e. the above and below Doppler velocities are averaged, summed with a constant, and plotted versus the gustprobe velocity. Here the constant is 1.35 m/s, a value which minimizes the intercept of the best-fit line. We interpret this number as the average fall speed of the ice particles detected by the WCR. Alternatively, the value can be thought of a correction which accounts for both particle fall speed and bias in the WCR Doppler velocity (Vali et al., 1998).

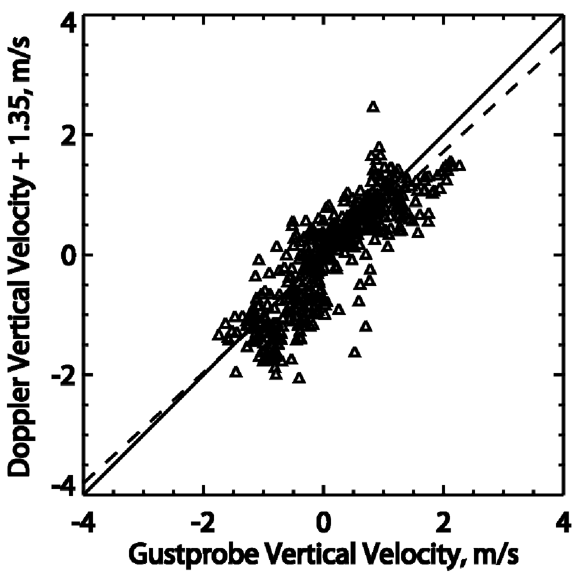

Figure 3 – Comparison of gustprobe and radar measured vertical velocity. The constant value, 1.35 m/s, is added to the Doppler vertical velocity and this minimizes the y-axis intercept of the best-fit line.

Figure 4 shows the trajectories derived from both the gustprobe and radar wind measurements. The gustprobe of the King Air measured the velocities at the flight level (4300 m) and the trajectory was derived assuming the horizontal wind is uniform below the aircraft, similar to the approach of Cotton and Field (2002). Since the wind field derived from WCR reveals a sheared layer close to the mountain surface (middle panel of Figure 2), the uniformity assumption does not appear to be justified. One consequence of this assumption is that the time for a parcel to transit through the cloud is overestimated when synthesizing trajectories using the gustprobe wind and the uniformity assumption. Another consequence is that the strong vertical velocities seen below the aircraft (middle panel Figure 2, e.g. at -12 km) are not seen by the gustprobe, consequently the gustprobe trajectory is flatter than the WCR trajectory. This is evident in Figure 4 and has consequence for both cloud droplet activation, which is sensitive to vertical speed, and condensate production. To first order, the latter quantity increases with the altitude change from cloud base to the top of the trajectory.

One disadvantage of our approach is its dependence on the presence of hydrometeors who are sufficiently large, and sufficiently numerous, to backscatter a signal which is detectable by the receiver of the WCR (approximately -20 dBZ at 1 km range). The absence of such scatters is evident at the starting point of the trajectory shown in Figure 2. We account for this data gap by using the wind speed measured along the upwind flight track, and the terrain slope below the aircraft, to calculate the initial section of the trajectory.

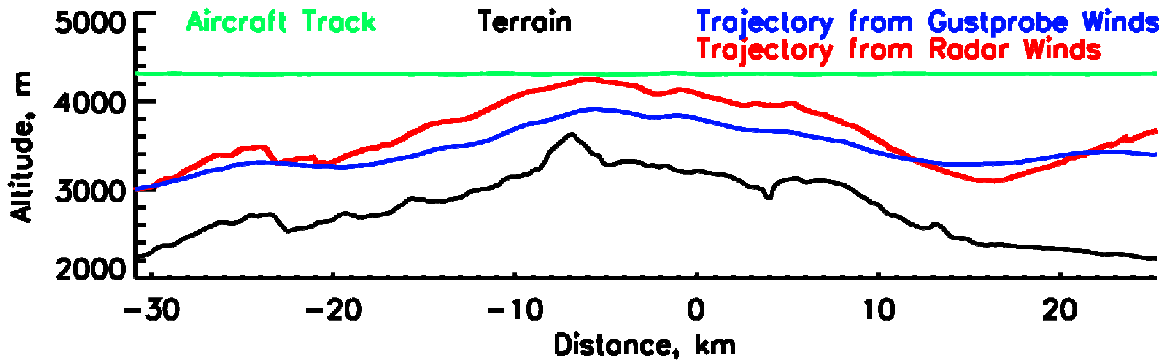

Figure 4 – Air parcel trajectories derived using gustpobe wind measurements and using WCR-derived winds. The vertical component of the latter is the vertical component derived from the dual-Doppler analysis (Leon et al., 2006) plus the 1.35 m/s correction discussed in the text. The height of the aircraft track and the terrain are also illustrated.

4. PARCEL MODEL

Our trajectory calculation initializes at the altitude and location of the measurements made upwind of the Medicine Bow Mountains (Figure 1). At this upwind location we sampled the properties of the airmass entering the cloud, including the thermodynamic state (i.e., pressure, temperature and humidity), the aerosol size distribution ($0.12 \le D \le 3$ µm with Passive Cavity Aerosol Spectrometer Probe (PCASP)), the cumulative concentration of particles larger than 0.015 µm (CPC, Section 2a) and the cumulative concentration of particles larger than 0.003 µm (UCPC, Section 2a). Averages of these properties were used to initialize our parcel model (Snider et al., 2003). The model simulates cloud droplet activation, ice particle formation, and the attachment of interstitial aerosol to liquid and solid hydrometeors. For the latter process we assume a single UFN size (D=0.01 µm) and assume that the UFN are non-hygroscopic. We employ the assumptions because they give the best agreement between the observed and predicted removal of the UFN. Assuming larger UFN size or that the UFN particles grow in response to the increased relative humidity of the cloud results is smaller predictions of UFN removal. This dependence is explained below. The enhancement of UFN removal by phoretic processes is not considered because Brownian diffusion dominates at these particle sizes (Martin et al., 1980).

The CCN activity spectrum used to initialize the parcel model was derived from the average of the upwind PCASP size distribution. We fit that average to a single-mode lognormal size distribution, discriminate the distribution into 30 bins extending from 0.02 to 0.267 µm (each dry diameter is a factor 1.2 larger than the adjacent smaller bin), and assume that the particles are composed of ammonium sulfate.

4a. UFN Removal

The model-calculated UFN removal is based on the following equation

$$dN_a = -4\pi \cdot D_a \cdot N_a \cdot r_h \cdot N_h \cdot \Delta t \qquad (2a)$$

Here dN_a is the change in UFN concentration in the time step Δt, D_a is diffusivity of the UFN (base a formulation given in Seinfeld and Pandis (1998)), r_a is the radius of hydrometeors, and N_h and N_a are hydrometeor and aerosol concentrations. Equation 2a is used to describe the UFN removal by both cloud droplets and ice crystals. The latter are initialized at a small size (1 µm) and with a concentration equal to the average ice crystal concentration observed during the alongwind flight leg.

In addition to Equation 2a, we evaluated the UFN removal in terms of an water content (IWC). This quantity was calculated at each point in the x/z plane using the WCR measurements of radar reflectivity and the reflectivity-to-IWC parameterization of Liu and Illingworth (2000). This process was considered because the top panel of Figure 2 suggests that ice particles originating from either above or below the trajectory can cross the parcel trajectory. The UFN removal by this alternate ice pathway is described by the following equation.

$$dN_a = -\frac{1}{3} \cdot D_a \cdot N_a \cdot IWC \cdot \Omega^2 \cdot \rho_e \cdot \Delta t \qquad (2b)$$

Here Ω is the surface area of snowflakes specific to a unit mass (100 m^2/kg, Huffman and Snider, 2004), and ρ_e is the effective density of the snowflake, which we take to be 200 kg/m^3. In the next section we label UFN removal predicted by Equation 2a as either "Droplet" or "Ice" and UFN removal predicted by Equation 2b as "IWC."

4b. Model Output

Model output from the trajectory-parcel model simulation is shown in Figure 5. Results are presented as a function of time along the air parcel trajectory. The left panel reveal that the ice-to-water mass ratio is small – a result which is at odds with the airborne observations made during the alongwind flight leg and pointing to an inadequacy of the model. Mitigating against this conclusion is the fact that the aircraft observations were made at 4300 m and that the trajectory is at altitudes between 3000 and 4000 m (Figure 1). Not only is it warmer along the trajectory, which may translate into smaller ice nucleation rates, but there is evidence enhanced vertical motion at horizontal scales ~0.5 km which may reestablish liquid condensate depleted by riming (middle panel Figure 2). Also evident is the much larger size of the ice hydrometeors compared to the liquid cloud droplets. This results because of the larger population of the latter (100 cm^{-3} versus 0.01 cm^{-3}) and the fact that the ice hydrometers grow faster because of the larger maximum saturation ratio for ice relative to liquid water (S_i=1.2 versus S_w=1.01, right panel Figure 5).

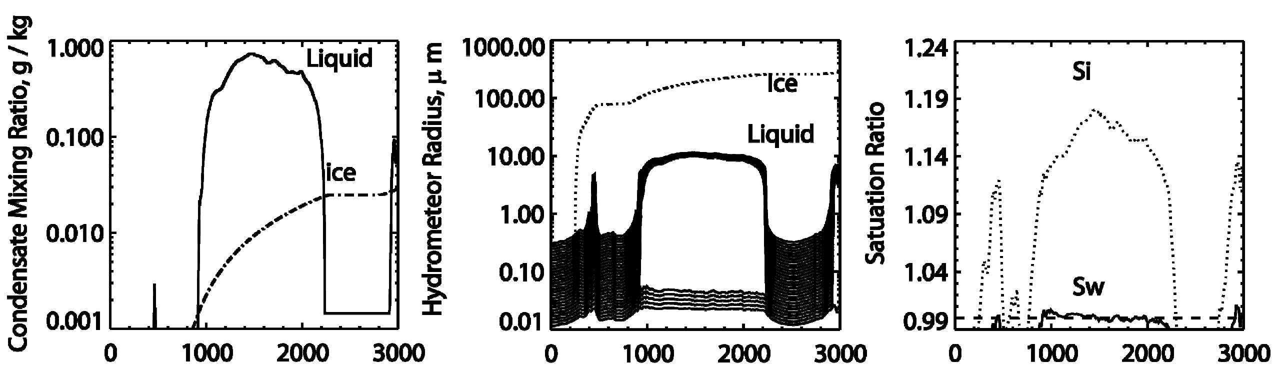

Figure 5 – Model output for January 18, 2006. Condensate mixing ratio (left panel), hydrometeor radius (center panel), and saturation ratio with respect to water (solid lines) and with respect to ice (dotted lines) (right panel).

Figure 6 shows the UFN removal by the three pathways described in Section 4b (Droplet, Ice and IWC). The "Droplet" pathway is dominating and the overall UFN removal (combined effect of all three pathways) is consistent with the change seen from upwind to downwind of the mountain wave cloud observed on 18 January 2006.

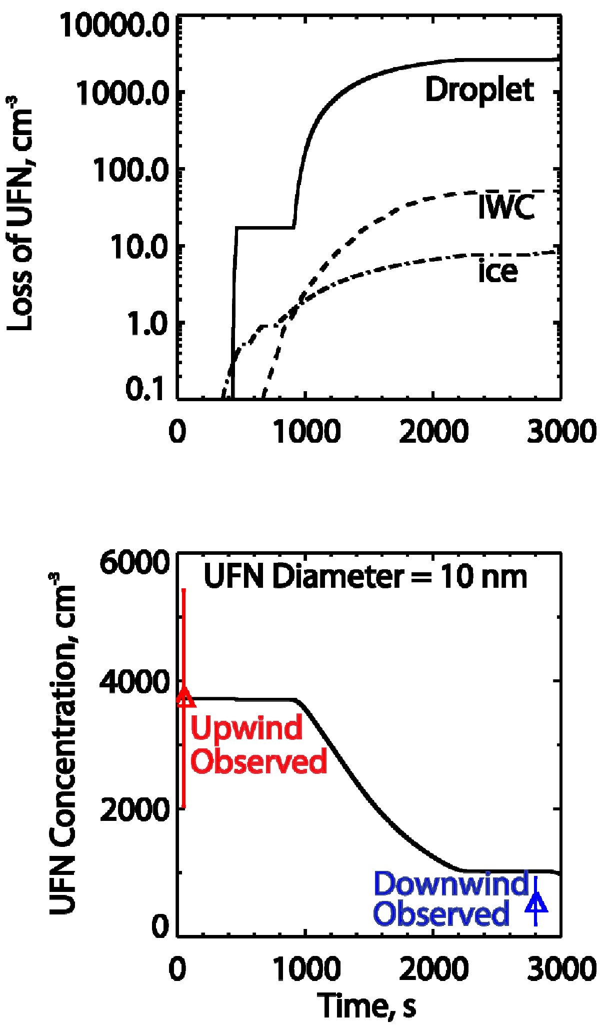

Figure 6 – Removal of UFN predicted by the model and comparison to observations. The upper panel shows the modeled UFN removal via the "Droplet", "Ice" and "IWC" pathways. The lower panel compares the model-predicted UFN concentration (effect of all three removal pathways) to measurements made upwind and downwind of the mountain wave cloud on January 18, 2006.

5. SUMMARY OF OTHER CASES

In addition to case examined in the previous sections (20060118), airborne measurements from three additional days have been analyzed and modeled. Results from these additional cases help to reinforce our assertion that the UFN decrease from upwind to downwind occurs in association with the passage of the aerosol through the mountain wave cloud. Those cases also support the conjecture that the UFN decrease is predominately due to their attachment to cloud droplets. The three additional cases were conducted on 20060126, 20060131 and 20060202.

In this summary we consider how particles larger than 0.003 µm were vertically distributed during the four cases. Next we examine the horizontal wind vectors observed upwind, alongwind and downwind to see if the winds are indicative of flow over the barrier, as opposed to flow around it. Next we consider measurements of water vapor mixing ratio and equivalent potential temperature. How these properties change from upwind to downwind also helps to address the question of flow continuity over the barrier. Finally, we examine if the condensate amount predicted by the model, at the top of the trajectory, is consistent with airborne measurements made at nearly the same altitude.

Measurements made during the upwind sounding during three of the four case studies revealed substantially larger aerosol concentrations ($D>0.003$ µm) below 3500 m. The one exception to this was the case from 20060126 which exhibited larger concentrations above 3500 m. Curiously, the UFN measurements ($0.003<D<0.015$ µm) from this day suggest that these particles were formed during transit through the mountain wave cloud. This observation is reminiscent of the model of Kazil et al. (2007).

Wind vectors derived by averaging the constant-altitude measurements (upwind, alongwind and downwind) show a consistent result for all four cases. Specifically, the horizontal wind speed is observed to increase from the upwind flight leg (2500 to 3000 m) to the along wind flight leg (4300 to 5200 m). In addition, the wind direction was nearly perpendicular to the barrier, veering by 10^{o} to 30^{o} between the upwind and alongwind flight legs. In none of the cases was there evidence for barrier-parallel flow.

Vertical profiles of water vapor mixing ratio, from the upwind and downwind soundings, were also analyzed. This quantity is expected to decrease between the upwind and downwind flight legs in response to precipitation formation that occurred over the Medicine Bow Mountians. Estimates of the decrease (0.5 g kg^{-1}) were based on the assumptions that the air is lifted 1 km, that the lapse rate of condensate mixing ratio is 1 g kg^{-1} km^{-1}, and that 60% of the condensate is precipitated (Dirks, 1973). All of the cases exhibited a vapor mixing ratio decrease (upwind-to-downwind) that was consistent with the 0.5 g kg^{-1} estimate.

The downwind soundings of equivalent potential temperature (θ_e) are erect, and the value obtained by averaging through a layer is in reasonable agreement with the average from the upwind wind sounding. The height interval for these averages was from 3000 to 4200 m.

For the two cases that had cloud extending to the altitude of the alongwind aircraft track, where the trajectory altitude is comparable to the flight altitude (20060118 and 20060131), comparisons can be made between condensate amount, predicted by the model, and observed. In both cases the model-calculated total water content (i.e., ice water content + plus liquid water content) was consistent with the observations. For the latter we derive the IWC using particle size distribution measurements data from the 2DC probe, assuming the size-to-mass relationship for dendrites of Locatelli and Hobbs (1974). The model and the observations diverge when the LWC/IWC ratio is compared. For the observations this ratio is 0.4 and 0.1 on 20060118 and 20060131, respectively, while for the model this ratio is 70 and 20.

The model/observation comparisons discussed in the previous paragraph demonstrate that the model is underestimating the abundance of ice relative to liquid. We presume that this occurs because the model simulates a closed parcel while in the actual cloud ice particles are moving across the parcel trajectories. In our simulation of UFN removal we address this issue by using the radar reflectivity to derive an ice water content and by using that ice water content to calculate an UFN removal. The prediction shown in Figure 6 indicates that even when employing the IWC derived from the radar reflectivity the UFN removal process is weak in comparison to the pathway mediated by cloud droplets.

6. CONCLUSIONS

We have analyzed field measurements of UFN particle removal associated with the passage of an aerosol through a mountain wave cloud. The horizontal wind speeds are relatively large in these clouds (~20 m/s), the in-cloud transport times are relatively short (~1000 s) and the temperatures (~-20 °C) do not prohibit the coexistence of liquid with ice hydrometeors. Conditions along the trajectory connecting air upwind of the cloud to air downwind are described using a hybrid trajectory-parcel model initialized with airborne measurements of the wind field. We report UFN removals which are consistent with model prediction, but this consistency rests on the assumptions made about the size and chemical composition of the UFN. The model shows that UFN removal is dominated by the liquid water phase, a result which is consistent with the much larger first moment of the cloud droplet size distribution in comparison with the first moment of the ice particle size distribution. Our documentation of this efficient and rapid UFN removal process serves as a reminder of the complex interplay between clouds and aerosols.

7. REFERENCES

Andronache, C., T. Gronholm, L. Laakso, V. Phillips, and A. Venalainen, 2006: Scavenging of ultrafine particles by rainfall at boreal site: observations and model estimations. *Atmos. Chem. Phys.,* **6,** 4739-4754.

Clarke, A. D., 1993: Atmospheric Nuclei in the Pacific Midtroposphere: Their Nature, Concentration, and Evolution. *J. Geophys. Res.,* **98,** 20,633-20,647.
Cotton, R. J. and P. R. Field, 2002: Ice nucleation of an isolated wave cloud. *Q. J. R. Meteorol. Soc.,* **128,** 2417-2437.
Dirks, R., 1973. The precipitation efficiency of orographic clouds, *J.Res.Atmos.*, **7,** 177-184
Huffman, W. A., J. R. Snider, 2004: Ice-oxyhydrocarbon Interactions in the Troposphere. *J. Geophys. Res.,* **109,** 1-15.
Kazil, J., E.R.Lovejoy, E.J.Jensen and D.R.Hanson, 2007: Is aerosol formation in cirrus clouds possible?, *Atmos. Chem. Phys.,* **7,** 1407-1413.
Kulamala, M., H. Vehkamaki, T. Petaja, M. D. Maso, A. Lauri, V.-M. Kerminen, W. Birmili, and P. H. McMurry, 2004: Formation and growth rates of ultrafine atmospheric particles: a review of observations. *J. Aerosol Sci.,* **35,** 143-176.
Laakso, L., T. Gronholm, Ullar Rannik, M. Kosmale, V. Fiedler, H. Vehkamaki, and M. Kulmala, 2003: Ultrafine particle scavenging coefficient calculated from 6 years field measurements. *Atmos. Environ.,* **37,** 3605-3613.
Leon, D., G. Vali, and M. Lothon, 2006: Dual-Doppler Analysis in a Single Plane from an Airborne Platform. *J. Atmos. and Oceanic Technol.,* **23**, 3-22.
Liu, C. L. and A. J. Illingworth, 1999: Towards More Accurate Retrievals of Ice Water Content from Radar Measurements of Clouds. *J. Appl. Meteor.,* **39,** 1130-1146.
Locatelli, J. D. and P. V. Hobbs, 1974: Fall Speeds and Masses of Solid Precipitation Particles. *J. Geophys. Res.,* **79,** 2185-2197.
Martin, J. J., P. K. Wang, and H. R. Pruppacher, 1980: A Theoretical Determination of the Efficiency with which Aerosol Particles are Collected by simple Ice Crystal Plates. *J. Atmos. Sci.,* **37,** 1628-1638.
Petters, M. D., A. J. Prenni, S. M. Kreidenweis, P. J. DeMott, A. Matsunaga, Y. B. Lim, and P. J. Ziemann, 2006: Chemical aging and the hydrophobic-to-hydrophilic conversion of carbonaceous aerosol. *Geophys. Res. Lett.,* **33,** 1-5.
Ramanathan, V., P. J. Crutzen, J. T. Kiehl, and D. Rosenfeld, 2001: Aerosols, Climate, and the Hydrological cycle. *Science,* **294,** 2119-2124.
Seinfeld, J. H. and S. N. Pandis, 1998: Atmospheric Chemistry and Physics: From Air Pollution to Climate Change. Wiley, New York.
Snider, J.R., and, S.Guibert, J.-L. Brenguier, and J.-P.Putaud, 3003: Aerosol activation in marine stratocumulus clouds: Part – II Köhler and parcel theory closure studies, *J.Geophy. Res.,* **108,** 8629, doi:10.1029/2002JD002692
TSI Inc., St. Paul, Minnesota, 1999, Model 3010 Condensation Particle Counter. *Product Information*.
TSI Inc., St. Paul, Minnesota, 2002, Model 3025A Ultrafine Condensation Particle Counter. *Instruction Manual*.
Vali, G., R. D. Kelly, J. French, S. Haimov, D. Leon, R. E. McIntosh, and A. Pazmany, 1998: Finescale Structure and Microphysics of Coastal Stratus. *J. Atmos. Sci.,* **55,** 3540-3564.
Vittori, O. A., and V. Prodi, 1967: Scavenging of Atmospheric Particles by Ice Crystals. *J. Atmos. Sci.,* **24,** 533-538.

INFLUENCE OF GIANT CCN ON WARM RAIN PROCESSES IN THE ECHAM5 GCM

Rebekka Posselt and Ulrike Lohmann

Institute for Atmospheric and Climate Science, ETH Zurich, 8092 Zurich, Switzerland

1 INTRODUCTION

Clouds play an important role in the energy budget of the earth. Anthropogenic influences change the radiative properties of clouds. Aerosol particles emitted from the earth's surface are thought to change the physical and optical properties of clouds. Cloud droplet size decrease and cloud albedo increase as the concentration of (anthropogenic) aerosols increases for a constant liquid water content (Twomey, 1974; Denman et al., 2007). Furthermore, cloud droplets will less likely grow to precipitation sized drops which presumably results in a prolonged lifetime of clouds within the atmosphere (Albrecht, 1989; Denman et al., 2007).

The impact of GCCN on the formation of precipitation is the subject of various studies Johnson (1982); Feingold et al. (1999); Rosenfeld et al. (2002). Main outcome of these modeling studies was that the incorporation of GCCN in an otherwise non-precipitating cloud (e.g., continental with high CCN amounts) could initiate precipitation and enhance drizzle production. This effect becomes larger the more background CCN are present (i.e., with increasing pollution). Nevertheless, polluted clouds (high CCN concentrations) with GCCN do not produce the same amount of drizzle as clean clouds (low CCN concentration) without GCCN. Furthermore, it was found that a cloud in the presence of GCCN has a lower optical thickness and, therefore, a lower albedo. Hence, GCCN might be able to moderate the effects of anthropogenic CCN on clouds and climate. However, the effect of GCCN is not yet incorporated in GCMs. Thus, the estimates of the aerosol indirect effect might be too high.

2 MODEL DESCRIPTION AND SETUP

The ECHAM5-GCM is based on the ECMWF model and has been further developed at the Max-Planck-Institute for Meteorology in Hamburg. Within ECHAM5 the prognostic equations for temperature, surface pressure, divergence and vorticity are solved on a spectral grid with a triangular truncation (Roeckner et al., 2003). Prognostic equations for cloud water and cloud drop number concentration, for cloud ice and the ice crystal number concentration as well as detailed cloud microphysics are used according to Lohmann et al. (2007).

In order to incorporate the GCCN and their effect on precipitation properly, prognostic equations for rain water mass mixing ratio and rain drop number concentration were introduced into the ECHAM5 (Posselt and Lohmann, 2007). The sedimentation of the rain drops is treated as a vertical one dimensional advection with an explicit fall speed for mass and number, respectively. The fall speed is a function of rain water mass and number and is limited by the grid velocity (layer height/model time step). Furthermore, all processes involved in rain formation are evaluated repeatedly on smaller sub-time steps within one model time step. Atmospheric aerosol distributions are represented by the aerosol module HAM (Stier et al., 2005). GCCN are not explicitly included in the HAM thus soluble coarse mode particles with $r > 10\mu$m (GCCN$_{10}$) or $r > 5\mu$m (GCCN$_5$) are regarded as GCCN in this study. Activation of GCCN is represented by a transfer of condensed water to rain water based on the number of GCCN and a initial rain drop size of $r = 25\mu$m. The schematic in Fig. 1 summarizes the changes within the large-scale cloud microphysics scheme due to the GCCN.

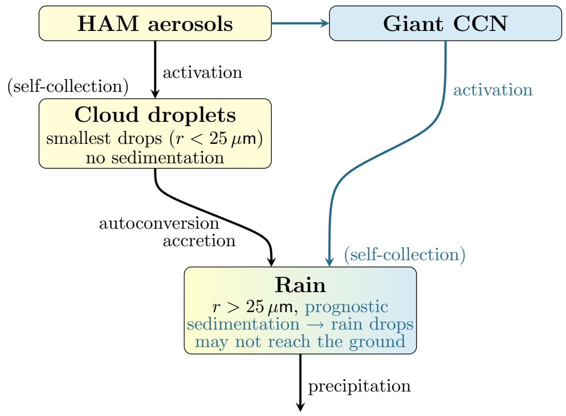

Fig. 1: Schematic of the coupling of the GCCN to the large-scale cloud microphysics scheme. Parts in blue represent changes or additions to the standard large-scale cloud microphysics scheme

The global simulations are conducted at a T42 horizontal resolution (corresponds to $2.8125^\circ \times 2.8125^\circ$) with 19 vertical model levels (uppermost layer at $10\,\text{hPa}$) and a time step of 30 minutes. The simulations are integrated for 10 years after a 3 month spin-up using climatological sea-surface temperatures and sea-ice extend. For the simulations in this study the relative humidity based cloud cover scheme of Sundqvist et al. (1989) is used. The conducted global simulations are summarized in Tab. 1. The control runs are tuned so that the radiative balance at top-of-the-atmosphere (TOA) is within $\pm 1\,\text{W}\,\text{m}^{-2}$. The aerosol indirect effect (AIE) is estimated by comparing present-day (PD) to pre-industrial (PI) simulations. For the PI simulation, aerosol emission representative of the year 1750 are used (Dentener et al., 2006).

3 RESULTS AND DISCUSSION

3.1 Validation of GCCN concentrations

A realistic estimate of the effect of GCCN on clouds, precipitation and the global radiative budget is based on a realistic representation of the GCCN within the ECHAM5. Validation of the giant sea salt concentration is done by a point-to-point comparison of observed and simulated concentrations as shown in Fig. 2. Therefore, the number distributions reported by Lewis and Schwartz (2004) are integrated with respect to the chosen cutoff radius of 5 or $10\,\mu$m.

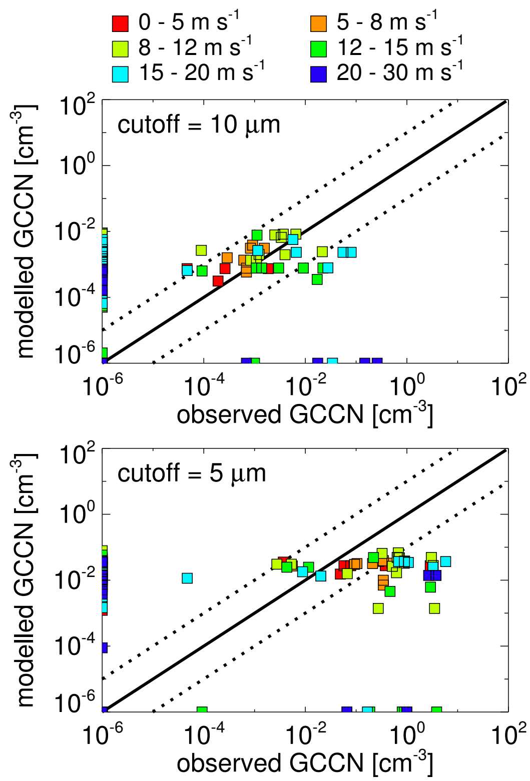

Fig. 2: Scatter plot of simulated and measured giant sea salt concentrations [cm^{-3}] for a cut-off radius of $10\,\mu$m (upper panel) and $5\,\mu$m (lower panel) for different wind speed ranges

The obtained concentrations are then compared to the simulated GCCN concentration at the same location in the lowest model level. First of all it can be seen that the natural variability of the GCCN concentration is much larger than the simulated one because the modeled concentrations depend mainly on the wind speed whereas the observed concentration are also influenced by various other factors which might be underestimated in ECHAM5.

Tab. 1: Summary of presented global simulations

Simulation	Description
CTL30	Control simulation; Simulation with ECHAM5-HAM (Lohmann et al., 2007) and the prognostic rain scheme by (Posselt and Lohmann, 2007) with 30 sub-time steps
CTL10	Same as CTL30 but with 10 sub-time steps in the prognostic rain scheme
$GCCN_{10}$	Same as CTL30 but with included GCCN at a cutoff radius of 10μm
$GCCN_5$	Same as $GCCN_{10}$ but with a cutoff radius of 5μm

The comparison for the 5μm cutoff (Fig. 2, lower panel) shows that the ECHAM5 underestimates the GCCN concentrations. A large portion of the data points are more than a factor of 10 smaller than the observed values. Using a cutoff radius of 10μm (Fig. 2, upper panel) improves the agreement between simulated and observed GCCN concentrations. Most model data fall within a factor of 10 of the observations. Furthermore, the obtained GCCN concentrations for the 10μm cutoff agree much better with the GCCN concentrations of $10^{-2} - 10^{-4}\,\text{cm}^{-3}$ reported by Feingold et al. (1999).

3.1.1 Effect of GCCN on cloud parameters and precipitation

The results of the global simulations with present-day emissions are summarized as annual global means in Tab. 2 for the CTL30, $GCCN_{10}$, $GCCN_5$ simulations and additionally for the CTL10 simulation. The results show that some of the considered variables are quite susceptible to the incorporation of the GCCN whereas others do not depend on them at all. Further insight into the impact of the GCCN on the global scale are obtained by looking into the global difference distributions of precipitation (large scale and convective) and of TWP and conversion rate (autoconversion+accretion) which are shown in Fig. 3 and 4, respectively. All shown variables are vertically integrated annual means. The difference distributions are calculated between the GCCN-simulations and the control run.

The incorporation of the GCCN hardly affects the global precipitation amount. Compared to CTL30 (Tab. 2), the total precipitation amount is hardly affected by the incorporation of the GCCN or by the number of sub-time steps within the prognostic rain scheme (CTL30 vs CTL10). Compared to the monthly averaged precipitation fields from the Global Precipitation Climatology Project (GPCP) dataset (Huffman et al., 1997; Adler et al., 2003) ECHAM5 generally produces too much precipitation. Fig. 3 shows the global difference distributions of stratiform and convective precipitation. Changes in the stratiform precipitation are mainly located in the midlatitudes along the storm tracks. It can be seen that regions of increased and decreased precipitation rates alternate along the zonal band so that the changes cancel each other in the zonal mean. The differences in stratiform precipitation show similar patterns for both GCCN simulations with a slightly higher magnitude for the $GCCN_{10}$-CTL30 case. This implies that the formation of stratiform precipitation itself depends mainly on whether GCCN are considered and less on the concentration and the associated transfer of condensed water to the rain class.

Convective precipitation is not directly influenced by GCCN (and aerosols, in general). Nevertheless, the incorporation of GCCN changes the amount and location of convection significantly (Fig. 3, lower row). Differences in convective precipitation between the GCCN simulations and the control run have a higher magnitude than those for the stratiform precipitation. In both considered cases the magnitude of the difference is similar but the pat-

Tab. 2: Annual global mean cloud properties and TOA energy budget

		CTL30	$GCCN_{10}$	$GCCN_5$	CTL10	OBS
P_{tot}	$[\mathrm{mm\,d^{-1}}]$	2.89	2.89	2.88	2.88	2.74
TWP	$[\mathrm{g\,m^{-2}}]$	74.6	72.9	67.7	63.3	50 – 4
LWP	$[\mathrm{g\,m^{-2}}]$	66.7	65.0	59.6	57.3	–
RWP	$[\mathrm{g\,m^{-2}}]$	7.9	7.9	8.1	6.0	–
N_l	$[10^{10}\,\mathrm{m^{-2}}]$	2.2	2.1	1.9	1.9	4
R_{eff}	$[\mu\mathrm{m}]$	11.0	11.0	11.0	10.5	11.4

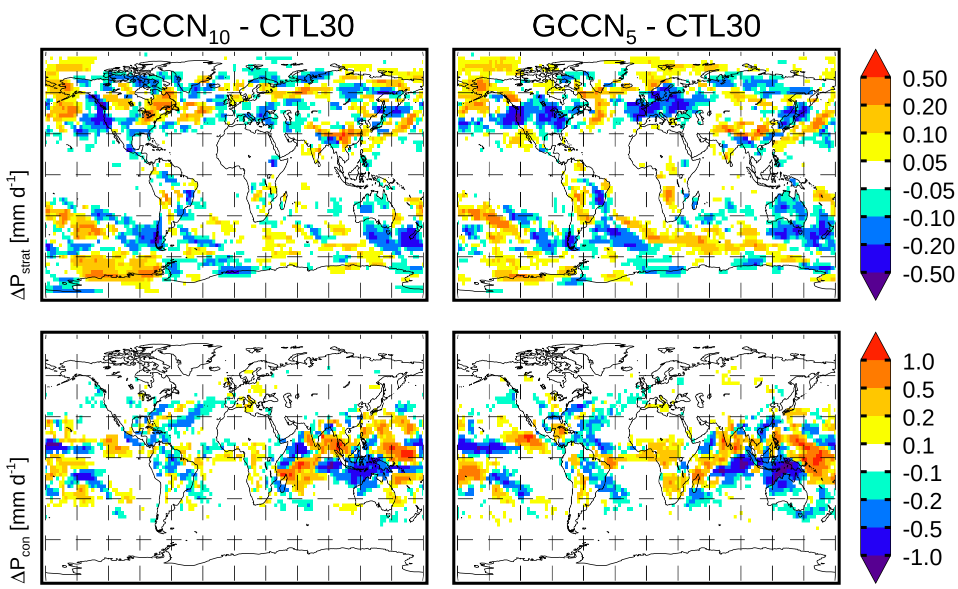

Fig. 3: Differences in the global distribution of stratiform (upper row) and convective (lower row) precipitation between the $GCCN_{10}$ (left column) and $GCCN_5$ (right column) simulations and CTL30 (please note the different scales)

terns differ substantially. As there is no direct influence of the GCCN the changes must be caused by feedbacks of the convection scheme to the changes in the hydrological state (moisture field, CAPE, ...) of the model.

The observed LWP by satellite (SSM/I) retrievals of the LWP (Greenwald et al. (1993); Weng and Grody (1994); Wentz (1997) is compared to the TWP (over the oceans) of the simulations because the model artificially distinguishes between the smaller cloud drops and the larger rain drops that the satellites do not make. The TWP produced by all simulations falls within the range given by the observations. The incorporation of the GCCN leads to a decrease in the TWP. The main decrease appears in the midlatitudes and subtropics where the precipitation formation is mainly done via the large-scale cloud scheme (see Fig. 4). The TWP shows a strong dependence on the amount of GCCN which is closely connected to the amount of GCCN and the transfer of condensed water. The higher the GCCN concentration the higher is the transfer of condensed water to rain. Thus, cloud water (i.e., the LWP) is reduced as large amounts of condensed water are transfered to rain water. The RWP stays fairly constant throughout all simulations (with

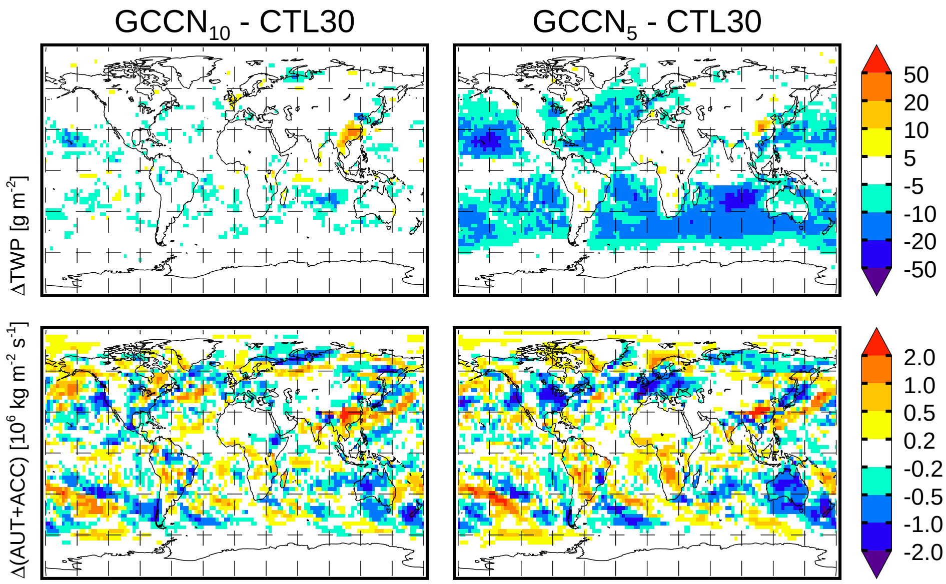

Fig. 4: Differences in the global distribution of TWP (upper row) and total conversion rate (autoconversion+accretion, lower row) between the $GCCN_{10}$ (left column) and $GCCN_5$ (right column) simulations and CTL30

the same number of sub-time steps) because all "excessive" rain water is removed from the atmosphere by sedimentation.

Although TWP is reduced quite significantly, autoconversion and accretion rate are hardly affected by the presence of GCCN (see Fig. 4, lower row). These results imply that the reduction in TWP due to the GCCN is not large enough to change the autoconversion and accretion rates significantly. One important process missing here is the competition effect of GCCN and CCN during activation. As GCCN would activate preferentially, less of the smaller CCN would activate which result in a lower number of cloud droplets. This in turn could cause an increase in the autoconversion rate and could lead to higher precipitation rates. But, with the current activation scheme by Lin and Leaitch (1997) it is not possible to consider that process. However, the incorporation of GCCN does not cause an increase in precipitation (as shown above) but rather an acceleration of the hydrological cycle with shorter residence times and less accumulation of liquid water in the atmosphere.

Observations of vertically integrated cloud drop number N_l and effective radius R_{eff} at cloud top for warm clouds ($T > 0°C$) are retrieved from the ISCCP dataset by Han et al. (1994, 1998) for an area between $-50°$ and $50°$ based on four months of 1987. The annual global means show that the ECHAM5 simulations of N_l underestimate the observations by a factor of two. Similar to the TWP, N_l is decreasing with higher amounts of GCCN. This results in a quite constant R_{eff} for all simulations but compared to the observations R_{eff} is underestimated.

3.1.2 Present-day vs. Pre-industrial

The difference between present-day and pre-industrial simulations gives an estimate of the effect of anthropogenic aerosols on climate.

Total aerosol concentration is increasing vastly especially over the northern hemisphere. This increase is mainly attributed to human activity and industrial development. Hence, the GCCN ratio which is defined as the ratio between GCCN to total aerosol concentration is decreasing because the total aerosol increase is much larger than the increase in GCCN concentrations due to changes in the wind speed. Hence, the influence of the GCCN is larger in the present-day climate with high aerosol concentrations than it is in the pre-industrial climate.

In Tab. 3 and Fig. 5 the differences in the annual global and zonal means due to anthropogenic aerosols for the ECHAM5 simulations are summarized, respectively. The changes in global precipitation due to anthropogenic activity are rather faint which is due to the application of fixed sea-surface temperatures within the simulations and, thus, fixed evaporation from the oceans no matter how many GCCN are present or how many sub-time steps are used in the prognostic rain scheme.

The anthropogenic changes in total global cloud cover (TCC) are also very small and have no clear tendency to more or less cloud cover with higher amounts of GCCN.

The incorporation of GCCN reduces the difference between present-day and pre-industrial TWP. Thus, the increase in TWP due to enhanced, anthropogenic aerosol numbers is partly compensated by the presence of GCCN. Cloud drop number and cloud drop effective radius are almost constant for all considered simulations and thus, do not show any significant tendency like the TWP in the global mean differences. The annual zonal mean differences give a more detailed insight into the anthropogenic changes of TWP and cloud drop number and radius. The TWP and cloud drop number differences are largest in the northern hemisphere. Industrialization in Europe, North America and, recently, Asia result in enhanced aerosol number that act as CCN and influence cloud and precipitation formation. As Lohmann et al. (2007) stated the TWP increase is mainly due to a retardation of drizzle formation in clouds over the ocean. Hence, clouds (and cloud water) stay longer in the atmosphere. The presence of GCCN causes a reduction of the TWP and cloud drop number difference. Thus, the GCCN counteract the CCN increase and therefore reduce the aerosol indirect effects. Nevertheless, there are also regions (like the tropics, the subtropics and the high latitudes) where the incorporation of GCCN lead to an increase in TWP and N_l from PI to PD.

Closely connected to cloud cover and TWP is the TOA radiative budget. The prognostic rain scheme lowers the effect of aerosols on the short-wave radiation. The obtained values of $-1.05\,\mathrm{Wm^{-2}}$ for CTL30 and $-1.18\,\mathrm{Wm^{-2}}$ for CTL10 are almost reduced by a factor of two compared to a value of $-2.0\,\mathrm{Wm^{-2}}$ reported by Lohmann et al. (2007) for the standard ECHAM5. This is caused by the much smaller increase in TWP from PI to PD in these simulations. While TWP increased by $6.9\,\mathrm{g\,m^{-2}}$ from PI to PD in Lohmann et al. (2007), here the increase in TWP amounts to $1.8-2.4\,\mathrm{g\,m^{-2}}$ in much better agreement to observations (e.g., Nakajima et al., 2001). The incorporation of the GCCN does not lead to a further systematic decrease of the short-wave radiation. For the $\mathrm{GCCN_{10}}$-simulation the short-wave radiation increases to $-1.19\,\mathrm{Wm^{-2}}$ whereas for the $\mathrm{GCCN_{10}}$-simulation the short-wave radiation decreases to $-1.03\,\mathrm{Wm^{-2}}$. The annual zonal mean differences show that the SW radiation difference is mainly increased in the northern midlatitudes because of the reduction of TWP in that region. Within the tropics and the higher latitudes the SW radiation is decreasing which is most likely due to changes in the convection patterns.

The long-wave (LW) radiation budget, which is closely connected to high clouds, shows much smaller differences between PI and PD. The prognostic rain scheme and the GCCN does not influence the long-wave radiation radiation very much. The obtained values of $0.08\,\mathrm{Wm^{-2}}$ for the CTL30 simulation and of $0.12\,\mathrm{Wm^{-2}}$ for the CTL10 simulation are similar to the value of $0.1\,\mathrm{Wm^{-2}}$ reported by Lohmann et al. (2007) for the standard ECHAM5-HAM.

The difference in the net radiation between present-day and pre-industrial climate is referred to as the anthropogenic aerosol effect including the direct and indirect effects. The net radiative effect of anthropogenic aerosols is $-0.97\,\mathrm{Wm^{-2}}$ for CTL30 and $-1.06\,\mathrm{Wm^{-2}}$ for CTL10. Similar to the SW radiation, these

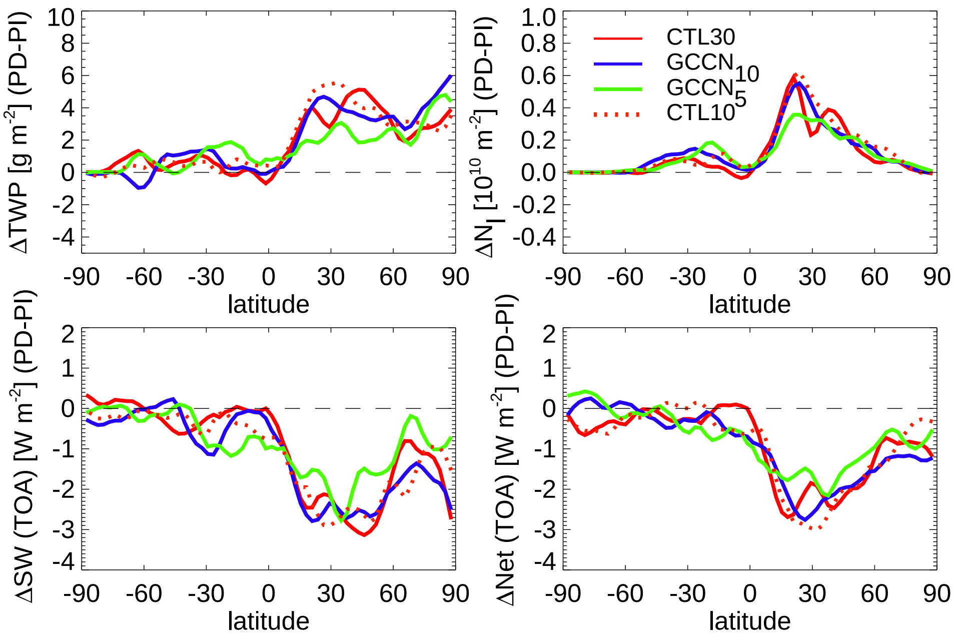

Fig. 5: Annual zonal means differences between the present-day and pre-industrial simulations of precipitation, total cloud cover, total water path, column integrated cloud droplet number, effective cloud droplet radius at cloud top (T > 273.15K) as well as short-wave and net radiation at TOA from CTL30, $GCCN_{10}$, $GCCN_5$, and CTL10 simulations

Tab. 3: Annual global mean changes and interannual standard deviations of cloud properties and TOA energy budget from PD to PI

		CTL30		$GCCN_{10}$		$GCCN_5$		CTL10	
P_{tot}	[mm d^{-1}]	0.001	±0.011	−0.001	±0.008	0.004	±0.007	0.001	±0.006
TCC	[%]	0.12	±0.18	0.18	±0.18	0.11	±0.14	0.12	±0.18
TWP	[g m^{-2}]	2.2	±0.74	2.1	±0.6	1.8	±0.51	2.4	±0.52
N_l	[10^{10} m^{-2}]	0.17	±0.4	0.19	±0.5	0.16	±0.3	0.19	±0.4
R_{eff}	[μm]	−0.16	±0.02	−0.16	±0.03	−0.17	±0.03	−0.14	±0.02
SW	[W m^{-2}]	−1.05	±0.24	−1.19	±0.31	−1.03	±0.23	−1.18	±0.26
LW	[W m^{-2}]	0.08	±0.14	0.15	±0.11	0.12	±0.22	0.12	±0.23
Net	[W m^{-2}]	−0.97	±0.19	−1.04	±0.29	−0.91	±0.27	−1.06	±0.35

values are almost a factor of two smaller than the net radiation value of $-1.9\,\mathrm{Wm^{-2}}$ of the standard ECHAM5 (Lohmann et al., 2007). Incorporation of the GCCN do not have much influence on the net radiation budget and thus, on the aerosol indirect effect. For the $GCCN_{10}$-simulation the short-wave radiation increases to $-1.04\,\mathrm{Wm^{-2}}$ whereas for the $GCCN_{10}$-simulation the short-wave radiation decreases to $-0.91\,\mathrm{Wm^{-2}}$. Again, no clear tendency of the net radiation with increasing amount of GCCN is given. However, the changes in the net radiation are small compared to the interannual variability. Thus, it can be concluded that the AIE hardly changes due to the incorporation of the GCCN. The discussion of the annual zonal means of the net radiation follows mainly the one for the SW radiation.

4 CONCLUSION

The effect of GCCN on the global climate, specifically on clouds and precipitation within a GCM, is investigated.

The introduction of the prognostic rain scheme leads to a strong decrease in the AIE compared to the standard ECHAM5-HAM presented by Lohmann et al. (2007) resulting mainly from a decreasing importance of the autoconversion in the rain formation process. The size on the AIE does hardly depend on the number of sub-time steps within the prognostic rain scheme for the shown simulations with 30 and 10 sub-time steps. Further differences due to the number of sub-time steps arise only for in-cloud properties like TWP, N_l and R_{eff} which are also directly affected by the changes in the conversion rates. This leads also to changes in cloud cover and consequently the short-wave cloud forcing. Other variables like precipitation, and long-wave cloud forcing do not show any dependence on the sub-time step number.

The incorporation of the GCCN results in rather faint changes in the precipitation. In the global and zonal averages hardly any differences are detectable. The global patterns are zonally redistributed meaning that regions with increasing precipitation rates alternate with regions with decreasing precipitation rates so that the zonal average does not change. Interestingly, the rather small changes in the large-scale precipitation patterns feed back to the convective precipitation scheme due to changes in the global moisture field. The subsequent changes in the convective precipitation rates are larger than the changes in the large-scale precipitation rates. Nevertheless, the GCCN change cloud properties such as TWP and N_l. This is mainly due to the transfer of condensed water to rain water and only to a very small part to the changes in the conversion rates. For the simulations with the 10μm cutoff the changes are rather small because small GCCN concentration result in a low transfer of water to the rain phase.

Main differences between present-day and pre-industrial simulations are found for TWP and N_l in the midlatitudes of the northern hemisphere where the strongest increase in anthropogenic aerosols is observed. The changes in cloud properties lead to subsequent changes in the radiative budget of the earth. Zonal means show that the SW budget becomes less negative in the regions where TWP and N_l decrease. The same is true for the net radiation budget, but changes in the LW budget partly compensate changes in the SW-budget. Thus, in that regions the GCCN are able to counteract the effects of increased aerosol loads in the present-day climate. In the tropics the incorporation of the GCCN leads to the opposite effect so that the net radiation budget become more negative. In the annual global mean this leads to a nearly constant net radiation difference between PD and PI. That means, that on a global scale the GCCN do not influence the radiation budget and therefore do not compensate for the effects of increased aerosol loads in PD.

5 BIBLIOGRAPHY

Adler, R. F., G. J. Huffman, A. Chang, R. Ferraro, P. P. Xie, J. Janowiak, B. Rudolf, U. Schneider, S. Curtis, D. Bolvin, A. Gruber, J. Susskind, P. Arkin, and E. Nelkin, 2003: The version-2 Global Precipitation Climatology Project (GPCP) monthly precipitation analysis (1979-present). *J. Hydrometeorol.*, **4**, 1147–1167.

Albrecht, B. A., 1989: Aerosols, cloud microphysics, and fractional cloudiness. *Science*, **245**, 1227–1230.

Denman, K. L., G. Brasseur, A. Chidthaisong, P. Ciais, P. M. Cox, R. E. Dickinson, D. Hauglustaine, C. Heinze, E. Holland, D. Jacob, U. Lohmann, S. Ramachandran, P. L. da Silva Dias, S. C. Wofsy, and X. Zhang, 2007: Couplings Between Changes in the Climate System Biogeochemistry. *Climate*

Change 2007: The Physical Science Basis. Contribution of Working Group I to the Fourth Assessment Report of the Intergovernmental Panel on Climate Change, S. Solomon, D. Qin, M. Manning, Z. Chen, M. Marquis, K. Averyt, M.Tignor, and H. Miller, eds., Cambridge University Press, Cambridge, United Kingdom and New York, NY, USA, chapter 7, 499 – 588.

Dentener, F., S. Kinne, T. Bond, O. Boucher, J. Cofala, S. Generoso, P. Ginoux, S. Gong, J. J. Hoelzemann, A. Ito, L. Marelli, J. E. Penner, J. P. Putaud, C. Textor, M. Schulz, G. R. van der Werf, and J. Wilson, 2006: Emissions of primary aerosol and precursor gases in the years 2000 and 1750 prescribed data-sets for aerocom. *Atmos. Chem. Phys.*, **6**, 4321–4344.

Feingold, G., W. R. Cotton, S. M. Kreidenweis, and J. T. Davis, 1999: The impact of giant cloud condensation nuclei on drizzle formation in stratocumulus: Implications for cloud radiative properties. *J. Atmos. Sci.*, **56**, 4100–4117.

Greenwald, T. J., G. L. Stephens, T. H. Vonderhaar, and D. L. Jackson, 1993: A physical retrieval of cloud liquid water over the global oceans using special sensor microwave imager (SSM/I) observations. *J. Geophys. Res.-Atmos.*, **98**, 18471–18488.

Han, Q. Y., W. B. Rossow, J. Chou, and R. M. Welch, 1998: Global variation of column droplet concentration in low-level clouds. *Geophys. Res. Lett.*, **25**, 1419–1422.

Han, Q. Y., W. B. Rossow, and A. A. Lacis, 1994: Near-global survey of effective droplet radii in liquid water clouds using ISCCP data. *J. Clim.*, **7**, 465–497.

Huffman, G. J., R. F. Adler, P. Arkin, A. Chang, R. Ferraro, A. Gruber, J. Janowiak, A. McNab, B. Rudolf, and U. Schneider, 1997: The Global Precipitation Climatology Project (GPCP) Combined Precipitation Dataset. *Bull. Amer. Meteorol. Soc.*, **78**, 5–20.

Johnson, D. B., 1982: The Role of Giant and Ultragiant Aerosol Particles in Warm Rain Initiation. *J. Atmos. Sci.*, **39**, 448–460.

Lewis, E. R. and S. E. Schwartz, 2004: *Sea Salt Aerosol Production - Mechanisms, Methods, Measurements, and Models*, volume 152 of *Geophysical Monograph*. American Geopysical Union.

Lin, H. and R. Leaitch, 1997: Development of an In-Cloud Aerosol Activation Parameterization for Climate Modelling. *WMO Workshop on Measurements of Cloud Properties for Forecasts of Weather and Climate, Mexico City, June 1997*.

Lohmann, U., P. Stier, C. Hoose, S. Ferrachat, S. Kloster, E. Roeckner, and J. Zhang, 2007: Cloud microphysics and aerosol indirect effects in the global climate model ECHAM5-HAM. *Atmos. Chem. Phys.*, **7**, 3425–3446.

Nakajima, T., A. Higurashi, K. Kawamoto, and J. E. Penner, 2001: A possible correlation between satellite-derived cloud and aerosol microphysical parameters. *Geophys. Res. Lett.*, **28**, 1171–1174.

Posselt, R. and U. Lohmann, 2007: Introduction of prognostic rain in ECHAM5: Design and Single Column Model simulations. *Atmos. Chem. Phys. Discuss.*, **7**, 14675–14706.

Roeckner, E., G. Bäuml, L. Bonaventura, R. Brokopf, M. Esch, M. Giorgetta, S. Hagemann, I. Kirchner, L. Kornblueh, E. Manzini, A. Rhodin, U. Schlese, U. Schulzweida, and Tompkins, 2003: The atmospheric general circulation modell ECHAM5, Part I: Model description. Technical Report 349, Max-Planck-Institute for Meteorology, Hamburg, Germany.

Rosenfeld, D., R. Lahav, A. Khain, and M. Pinsky, 2002: The role of sea spray in cleansing air pollution over ocean via cloud processes. *Science*, **297**, 1667–1670.

Stier, P., J. Feichter, S. Kinne, S. Kloster, E. Vignati, J. Wilson, L. Ganzeveld, I. Tegen,

M. Werner, Y. Balkanski, M. Schulz, and O. Boucher, 2005: The aerosol-climate model ECHAM5-HAM. *Atmos. Chem. Phys.*, **5**, 1125–1156.

Sundqvist, H., E. Berge, and J. E. Kristjansson, 1989: Condensation and cloud parameterization studies with a mesoscale numerical weather prediction model. *Mon. Weather Rev.*, **117**, 1641–1657.

Twomey, S., 1974: Pollution and planetary albedo. *Atmos. Environ.*, **8**, 1251–1256.

Weng, F. Z. and N. C. Grody, 1994: Retrieval of cloud liquid water using the Special Sensor Microwave Imager (SSM/I). *J. Geophys. Res.-Atmos.*, **99**, 25535–25551.

Wentz, F. J., 1997: A well-calibrated ocean algorithm for SSM/I. *J. Geophys. Res.-Oceans*, **102**, 8703–8718.

THE ROLE OF THE INFLOW OF ANTHROPOGENIC AEROSOLS ON PRECIPITATION IN THE TROPICAL EAST PACIFIC

Pozo, D.*, G.B. Raga and D. Baumgardner
Centro de Ciencias de la Atmósfera, Universidad Nacional Autónoma de México, Ciudad Universitaria, México DF, CP 04510, México
dpozo@atmosfera.unam.mx

INTRODUCTION

Several observational studies (Petersen et al. 2003; Pereira et al. 2006) have shown that deep convection in the tropical East Pacific is modulated by the passage of easterly waves. Larger CAPE, convective rain fraction and conditional mean rain rate, smaller convective inhibition, weaker tropospheric shear and more robust convective vertical structure occur in northerly flow regimes compared with southerly ones. In addition, pollution increases in the region when northerly winds predominate.

Baumgardner and Raga (2007) also observed larger aerosol concentration when wind came from the North, bringing air masses from pollution sources in the continent. The numerical study by Pozo et al. (2006) indicated that precipitation development in this region was suppressed by the presence of more anthropogenic aerosols. Nevertheless, further analysis of aircraft data by Raga and Baumgardner (2008), indicate that the frequency of large drops and the derived rain rates and reflectivities at lower levels in the clouds are similar, even though the background aerosol population and cloud droplet concentrations are quite different.

In the present study the influence of polluted northerly winds on convection and precipitation over the tropical East Pacific is investigated. A number of simulations with the Weather Research and Forecasting (WRF) model were performed and compared with TRMM observations.

SIMULATIONS

Twenty days during the EPIC2001 project (Raymond et al. 2004) were chosen for the study. They were divided into two groups: polluted and clean, depending whether the wind was predominantly flowing from the North or South, respectively.

The WRF model was initiated with Final (FNL) tropospheric analyses, which also provided the lateral boundary conditions every 6 hours. Clean and polluted days were simulated using the microphysics scheme by Thompson et al.

(2004), the autoconversion parametrization of Walko et al. (1995), which uses a cloud droplet concentration Nc=100 cm^{-3}, and the Cooper (1986) parametrization for ice initiation. Hereafter, these simulations will be referred to as CONTROL.

For each polluted day, however, two additional simulations were made: one with Nc=650 cm^{-3} (650CO) (similar values were observed by Baumgardner and Raga (2007) in polluted clouds), and the other with Nc=650 cm^{-3}, but using the Meyers et al. (1992) microphysics scheme (650ME). The rest of parametrizations were kept unchanged.

All simulations were run for 24 h, starting at 00 UTC on each day. A 400 x 400 domain with 4 km of horizontal resolution and 31 vertical levels were employed. Simulations were compared with observations from the TRMM (Tropical Rainfall Measurement Mission) TMI sensor.

RESULTS

Mean reflectivity profiles from TRMM, calculated for clean and polluted days, show larger values in the latter (blue and black solid lines in Fig. 1). According to Petersen et al. (2003), Pereira et al. (2006) and Cifelli et al. (2007), the increase in reflectivity is explained by the different thermodynamic and convective characteristics inherent to both wind regimes. Both reflectivity profiles, however, show similar behaviors with height, with maximum values located between 6 and 8 km, associated with maximum graupel concentrations (Fig. 2d).

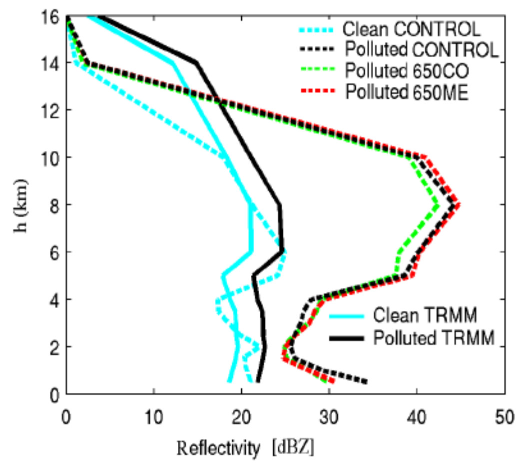

Fig. 1 Mean reflectivity profiles for clean and polluted days. See legend.

CONTROL simulations (blue and black dashed lines in Fig. 1) also show larger reflectivity values in polluted days. However, reflectivity is largely overestimated at all heights below 13 km and it is underestimated above it in polluted days. Clean days show a reasonable agreement below 8 km, but reflectivity is underestimated at higher levels. The large differences shown from 5 to 9 km between observed and modeled polluted profiles are related to the overestimation of precipitable ice (graupel and snow) in the simulations, due to an inappropriate representation of microphysical processes. This is also observed in clean days, to a lesser extent.

Fig. 2 shows mean vertical profiles of the different water categories for clean and polluted days from TRMM and model results. Simulations reproduce reasonably well the observed behavior in all water categories, although large differences in magnitude exist. The worst agreement is shown in polluted days since all simulated profiles are largely overestimated, except in cloud ice where it is underestimated. Clean simulated days, however, show good agreement in rain water and precipitable ice profiles (Figs. 2b,d), but the agreement is not as good in cloud water and cloud ice profiles (Figs. 2a,c).

An increasing aerosol concentration in the atmosphere, would lead to the formation of more small cloud droplets, which would be carried away by the updraft to higher levels. Once these drops cross the freezing level (FL), a large number of them would become small ice particles, and transform into snow or graupel through the accretion process.

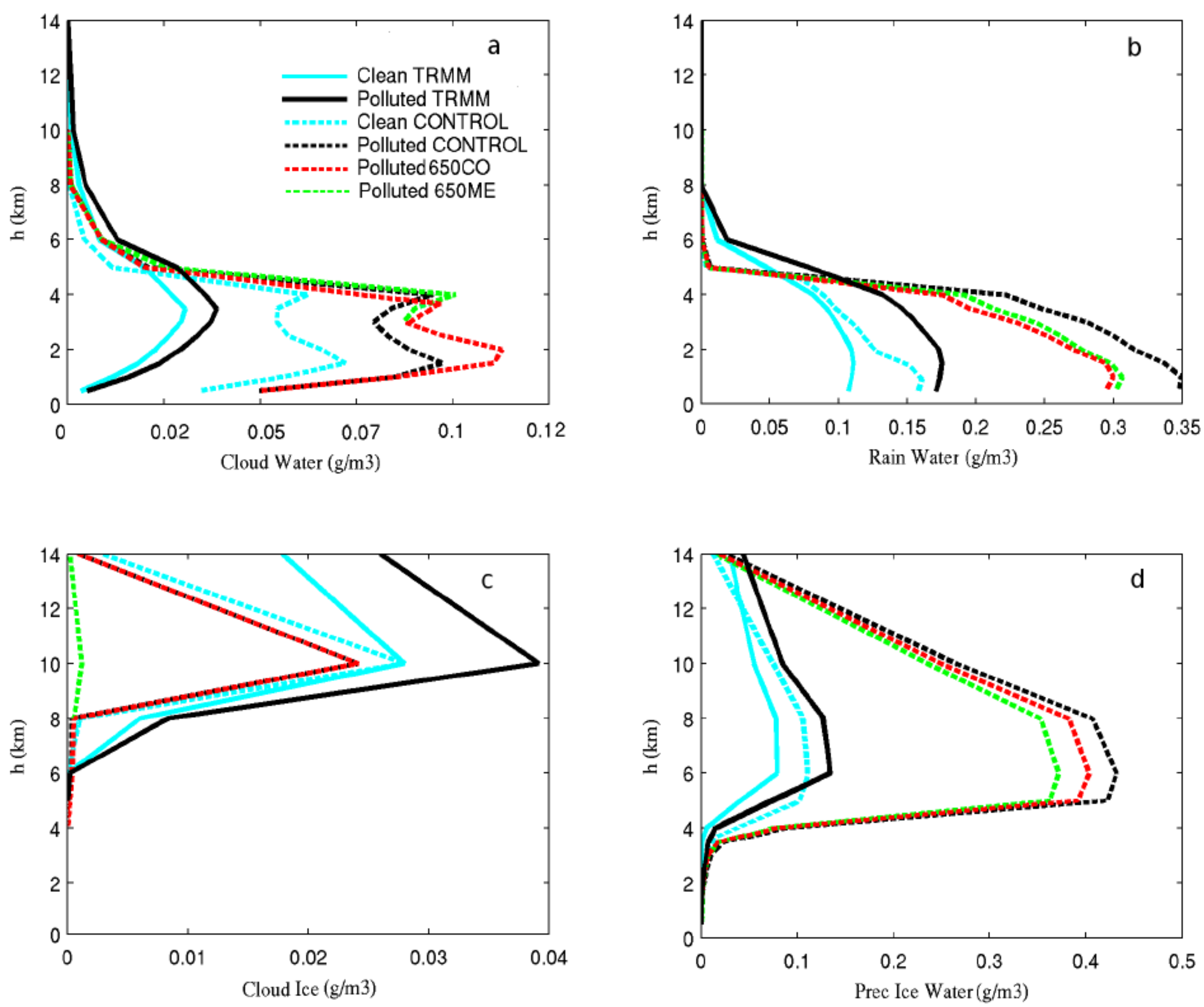

Fig. 2 Mean profiles of a) cloud water (g m^{-3}), b) rain water (g m^{-3}), c) cloud ice (g m^{-3}) and d) Precipitable ice (g m^{-3}) for clean and polluted days. See legend.

All simulations overestimate cloud water, being larger in 650CO and 650ME. This large cloud water, however, is not transformed into more cloud ice, maybe suggesting a poor representation in the parametrization that converts cloud water into ice or that ice formed is depleted into precipitable ice through accretion processes.

Fig. 3 shows the time evolution of simulated water categories shown in Fig. 2, at the heights were they reach their maximum values, averaged for all days. Clean CONTROL shows a more rapid increase and larger values in cloud, rain and ice water and precipitable ice in the first hours of simulations. After that, it shows much smaller values than polluted simulations. 650CO and 650ME show larger cloud water values than polluted CONTROL during the 24 h. However, rain water, cloud ice and precipitable ice show similar values, except the much smaller cloud ice shown by 650ME at all times.

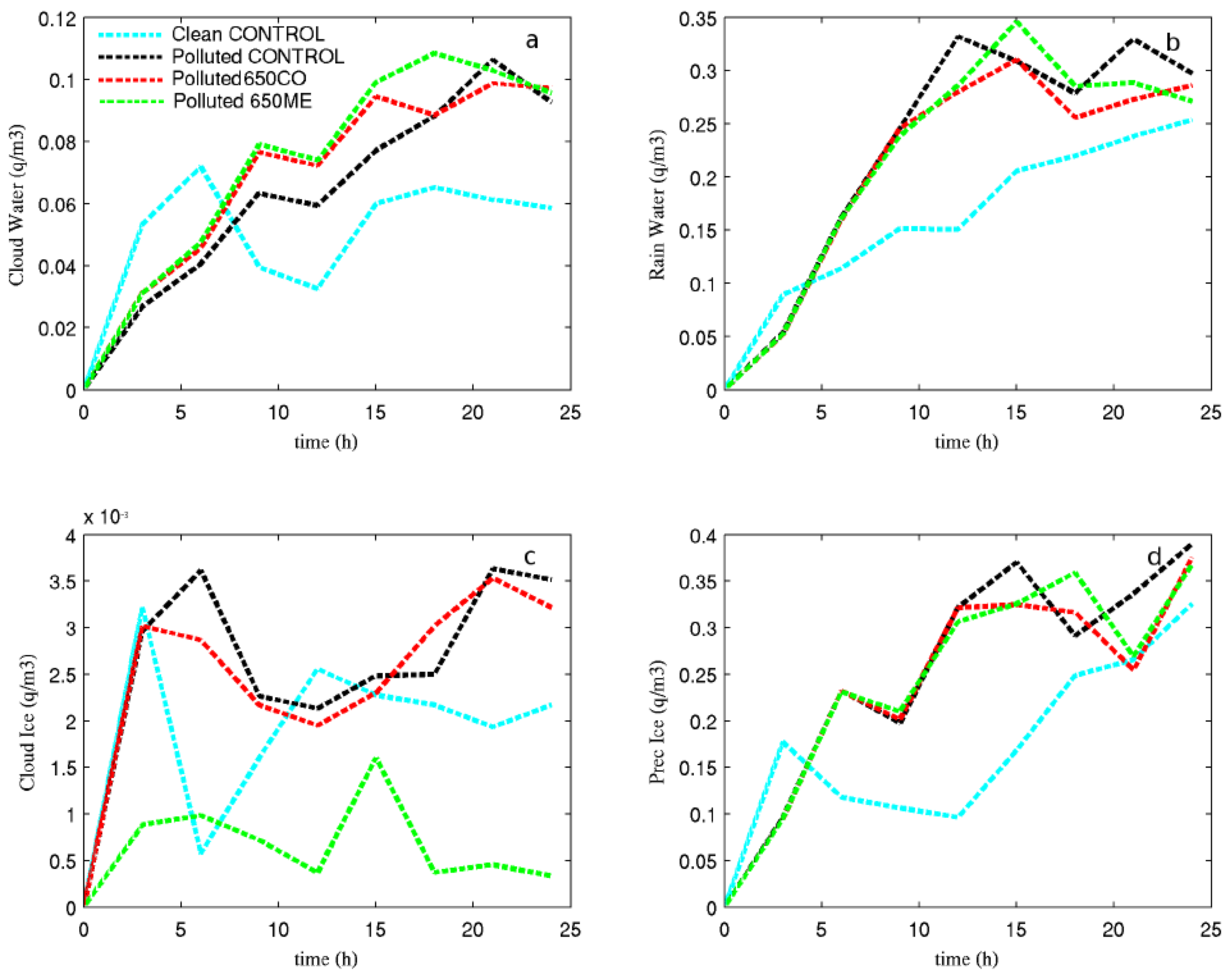

Fig. 3 Temporal distributions of mean a) cloud water (g m^{-3}) at 2 km, b) rain water (g m^{-3}) at the surface, c) cloud ice (g m^{-3}) at 10 km and d) Precipitable ice (g m^{-3}) at 6 km for clean and polluted days during the whole simulation period (24 h). See legend.

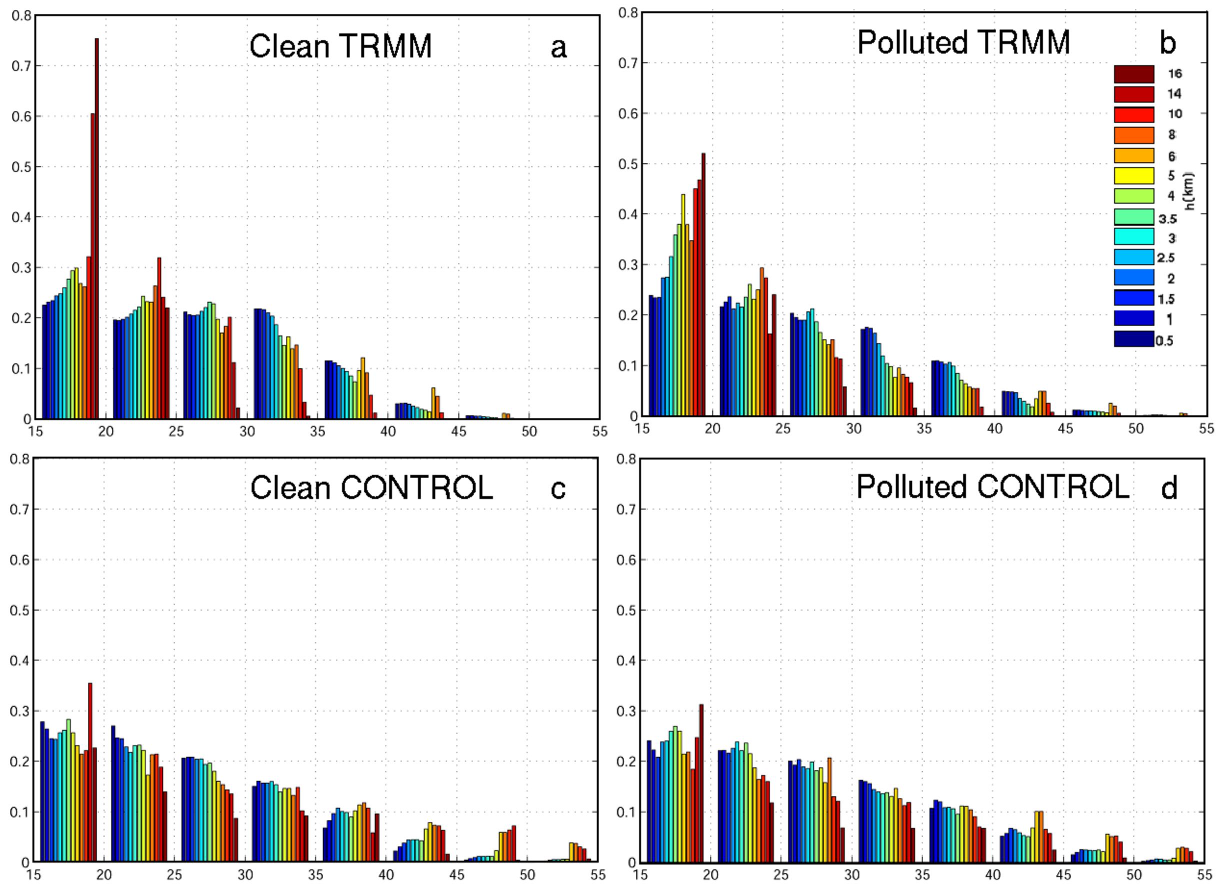

Fig. 4 Probability density functions (PDF) of the reflectivity at different heights, see legend, for a) clean days from TRMM, b) polluted days from TRM, c) Clean days from CONTROL simulations and d) polluted days from CONTROL simulations.

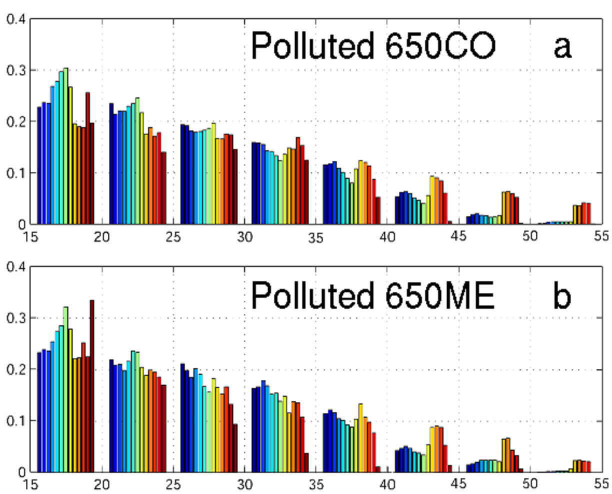

Fig. 5 Same as Fig. 4 but for a) 650CO and b) 650 ME.

The parametrization for ice initiation of Meyers et al. (1992), produces a larger ice number concentration than that in Cooper (1986) for temperatures greater than -30ºC, likely found between 5 and 8 km. However, at these heights the maximum values of precipitable ice are observed, resulting in a large depletion of cloud ice through accretion (Figs. 2c,d). Maximum values of cloud ice are located at 10 km, coincident with the fact that ice number concentration in Cooper parametrization is larger than that in Meyers between -30ºC and -45ºC (approximately between 8 and 11 km).

Reflectivity profiles from the simulations 650CO and 650ME (red and green dashed lines in Fig. 1) do not show an appreciable improvement compared to the CONTROL polluted profile. This indicates that increasing the number of aerosols in polluted days does not affect precipitation, suggesting that the observed differences between clean and polluted days are mainly the result of the changing thermodynamic conditions of the environment.

Probability density functions (PDF) for reflectivity show that TRMM values larger than 40 dBZ are slightly more frequent at all heights in polluted days (Figs. 4a,b), while clean days show a larger frequency between 30 and 35 dBZ. Values lower than 25 dBZ are more frequent at higher levels in clean days and at mid and low-levels in polluted ones. This is associated with larger convective development, the presence of hail at higher levels and larger amount of precipitation at lower heights in polluted days.

CONTROL simulations show a larger frequency of reflectivities > 40 dBZ than observations at all heights and they underestimate the observed reflectivities smaller than 25 dBZ above 8km (Figs. 4c,d). CONTROL polluted simulations show a larger frequency of reflectivities > 35 dBZ at low and mid-levels than clean ones. At other heights and reflectivity ranges, they are similar.

PDF for 650CO (Fig. 5a) show that reflectivies larger than 45 dBZ are more frequent above 6km than those in CONTROL, increasing the difference with observations. 650CO presents the same underestimation of reflectivities < 25 observed in CONTROL, although differences at low and mid-levels decreases. PDF for 650ME (Fig. 5b) show a small decrease in the frequency of reflectivities larger than 45 dBZ at all heights. While some differences are discussed among PDFs for polluted simulations, such differences are small, resulting in similar distributions.

CONCLUSIONS

A number of numerical simulations were performed with the WRF model in the East Pacific region for several days during the EPIC2001 experiment. Days were divided into polluted or clean, depending whether the wind was predominantly flowing from northern pollution sources in the continent or from the open ocean at the South, respectively.

Results show that there is a larger convective development in polluted days, as observed from TRMM measurements.

Mean simulated vertical profiles of cloud water, rain water and precipitable ice are overestimated in simulations, while cloud ice is underestimated. The largest differences are observed in polluted days. Simulated profiles suggest problems in representing the conversion of cloud water to cloud ice and problems in the formation and generation of precipitable ice, specially in polluted days.

Simulations for polluted days were performed with larger CCN concentrations and a new parametrization for ice initiation to investigate whether polluted profiles were better represented in the model. No significant differences with CONTROL simulations were obtained, suggesting that aerosol inflow into the East Pacific region does not affect convection and the increase in precipitation observed in polluted days is likely the result of more favorable environmental conditions.

REFERENCES

Baumgardner and Raga, 2007: 2D Optical Array Probe Analysis of Precipitating Cumulonimbus Clouds during EPIC 2001. Annual Spring Meeting, American Geophysical Union, Acapulco, May.

Cifelli, R., S. W. Nesbitt, S. A. Rutledge, W. A. Petersen, and S. Yuter, 2007: Radar characteristics of precipitation features in the EPIC and TEPPS regions of the east Pacific. *Mon. Wea. Rev*., **135**, 1576-1595.

Cooper, W. A., 1986: Ice initiation in natural clouds. Precipitation Enhancement. A Scientific Challenge, *Meteor. Monogr.*, **43**, Amer. Meteor. Soc., 29 –32.

Meyers, M. P., P. J. DeMott, and W. R. Cotton, 1992: New primar y ice-nu-cleation parameterizations in an explicit cloud model. *J. Appl. Meteor.*, **31**, 708–721.

Petersen, W. A., R. Cifelli, D. J. Boccippio, S. A. Rutledge, and C. Fairall, 2003: Convection and easterly wave structures observed in the eastern Pacific warm pool during EPIC-2001. *J. Atmos. Sci*., **60**, 1754–1773.

Pereira, L.G., and S.A. Rutledge, 2006: Diurnal cycle of shallow and deep convection for a tropical land and an ocean environment and its relationship to synoptic wind regimes. *Mon. Wea. Rev*., **134**, 2688-2701.

Pozo, D., G.B. Raga, D. Baumgardner, 2006: A theoretical study of the impact of anthropogenic CCN on the dynamics of deep convective clouds in the EPIC region, 12th Conference on Cloud Physics, July, 2006, Madison Wisconsin. CD-Rom, 2pp.

Raga and Baumgardner, 2008: Precipitation from tropical clouds sampled during EPIC2001. 15th International Conference on Clouds and Precipitation, Cancun, Jul.

Raymond, D., and Coauthors, 2004: EPIC 2001 and the coupled ocean–atmosphere system of the tropical east Pacific. *Bull. Amer. Meteor. Soc*., **85**, 1341–1354.

Thompson, G., R. M. Rasmussen, and K. Manning, 2004: Explicit forecasts of winter precipitation using an improved bulk microphysics scheme. Part I: Description and sensitivity analysis. *Mon. Wea. Rev.*, **132**, 519–542.

Walko, R. L., W. R. Cotton, M. P. Meyers, and J. Y. Harrington, 1995: New RAMS cloud microphysics parameterization. Part I: The single-moment scheme. *Atmos. Res.*, **38**, 29 –62.

NUMERICAL SIMULATIONS OF MICROPHYSICAL PROCESSES IN PYRO-CONVECTIVE CLOUDS: ACTIVATION OF AEROSOL PARTICLES AS CLOUD CONDENSATION NUCLEI

P. Reutter[1,2], J. Trentmann[2], M. Simmel[3],
H. Wernli[2], M.O. Andreae[1], U. Pöschl[1]

[1]Dept. of Biogeochemistry,
Max Planck Institute for Chemistry, Mainz, Germany
[2]Institute for Atmospheric Physics, Johannes Gutenberg
University Mainz, Germany
[3]Leibniz Institute for Tropospheric Research, Leipzig, Germany

1. INTRODUCTION

A crucial factor for the dynamical and microphysical evolution of clouds is the activation of aerosol particles (AP) to cloud droplets. The rain forming processes are enhanced when a cloud contains only few but large cloud droplets. In contrast rain formation is suppressed when a cloud holds a high number of small cloud droplets (e.g. Andreae et al., 2004). To correctly simulate clouds, it is important to accurately determine the number concentration of cloud droplets and therefore the activation of aerosol particles at the cloud base.

The activation of aerosol particles is determined by several parameters like the available supersaturation, the aerosol number and size distribution and the hygroscopic properties of the aerosol.

In most previous studies investigating aerosol activation and aerosol-cloud-interaction the number concentration of aerosol particles did not include values larger than $5000\,\mathrm{cm}^{-3}$ (e.g. Segal and Khain, 2006). This is a rather low threshold and does not apply for more polluted areas like megacities (e.g. Beijing) with number concentrations of more than $20,000\,\mathrm{cm}^{-3}$ (Rose, *private communication*). In the extreme case of young smoke from biomass burning aerosol number concentrations can reach values of more than $100,000\,\mathrm{cm}^{-3}$ (Andreae et al., 2004). The size distribution of the aerosol particles also has a strong impact on their ability to activate. An aerosol distribution with a large fraction of small particles will lead to fewer activated aerosol particles than a distribution with many large particles.

Another important aerosol particle property is their hygroscopic behavior. Commonly in modeling studies it is assumed that the aerosol consists of a soluble fraction (mostly assumed to be $NaCl$ or $(NH_4)_2SO_4$) and an insoluble fraction. The soluble fraction and the assumed model salt determine the hygroscopic properties. In reality, the aerosol composition can be arbitrarily complex.

For studies of pyro-convection, it has to be taken into account that the updraft velocity at the cloud base can be ten times larger than in regular clouds (Trentmann et al., 2006). This fact is also not considered in most model studies.

The issues described above are motivating the following studies that are presented now in detail.

The remainder of this extended abstract is organized as follows: in Section 2 the parcel model is described; in Section 3 the Köhler theory including the hygroscopicity parameter κ is introduced; in Section 4 we compare our

[1]Corresponding author's address: Philipp Reutter, Institute for Atmospheric Physics, Johannes Gutenberg University Mainz, Becherweg 21, 55099 Mainz, Germany, preutter@uni-mainz.de

results with the findings of a previous study and discuss results from sensitivity studies with different aerosol distributions and different values for κ for pyro-convective conditions.

2. MODEL DESCRIPTION

The model used for this study is a cloud parcel model with a spectral description of cloud microphysics (Simmel et al., 2002; Simmel and Wurzler, 2005; Diehl et al., 2006). As the air parcel rises growth of aerosol particles by water uptake, activation of aerosol particles to form cloud droplets, condensational growth and collision-coalescence of cloud droplets are simulated. The model also includes a full description of ice phase processes. The solution of the different equations is obtained using the Linear Discrete Method (LDM) which is presented in detail in Simmel et al. (2002).

The model does not distinguish between unactivated aerosol particles and cloud droplets. A particle is considered as a cloud droplet, when its diameter is larger than $1\,\mu$m. The prognostic parameters include liquid water mass, soluble and insoluble particulate matter as well as particle number for each size bin.

The simulations presented here are carried out using 264 bins between 1 nm and 3.5 mm and a time step of 0.01 s. For every model simulation, the parcel starts with a relative humidity of 95 % and is lifted with a constant vertical velocity until a liquid water content of $0.2\,\mathrm{g\,kg^{-1}}$ is reached. Only condensation is taken into account and no entrainment is considered.

3. κ-KÖHLER THEORY

The parcel model has been extended to describe the hygroscopicity of the aerosol particles with the newly derived single parameter representation of hygroscopic growth (Petters and Kreidenweis, 2007). The parameter κ is included into the drop growth equation through the Köhler equation.

The drop growth equation with respect to mass x is defined by Pruppacher and Klett (1997):

$$\frac{dx}{dt} = \frac{4\pi r(S_\infty - S_{eq})}{(\frac{L_V}{R_V T} - 1)\frac{L_V}{K^* T} + \frac{R_V T}{e_{s,w}(T) D^*}} \qquad (1)$$

with L_V the latent heat of condensation, K^* the modified thermal conductivity of air, $e_{s,w}$ the saturation water vapor pressure, D^* the modified diffusion coefficient for water vapor in air, S_∞ the saturation ratio of the surrounding air and S_{eq} the equilibrium water vapor saturation ratio at the particle/air interface.

The equilibrium water vapor saturation ratio S_{eq} is given by the Köhler equation and depends on the thermodynamical and chemical properties of the aerosol:

$$S_{eq} = a_w \cdot \mathrm{Ke} \qquad (2)$$

where a_w denotes the water activity, also known as the Raoult term, and Ke the Kelvin term.

The Raoult term takes the hygroscopical aerosol properties into account and can be written in the form (Rose et al., 2007):

$$a_w = \exp(-\nu_s \Phi_s \mu_s M_w) \qquad (3)$$

with ν_s the van t'Hoff factor, Φ_s the osmotic coefficient, μ_s the molality (i.e. the concentration of the model salt) and M_w the molar mass of water. ν_s, Φ and μ_s are specific properties of the model salt that represents the soluble fraction of the aerosol. An alternative description of the Raoult term uses the κ-formulation (Petters and Kreidenweis, 2007):

$$a_w = \frac{1}{1 + \kappa \frac{V_s}{V_w}} \qquad (4)$$

with κ the hygroscopicity parameter, V_s the volume of the dry particulate matter and V_w the volume of the water. This formulation allows to describe the hygroscopic properties of the aerosol in the model based on atmospheric measurements. This makes the assumptions of model salts dispensable.

The Kelvin term in the parcel model is represented by

$$\mathrm{Ke} = \exp\left(\frac{2\sigma}{R_w T \rho_w r_{wet}}\right) \qquad (5)$$

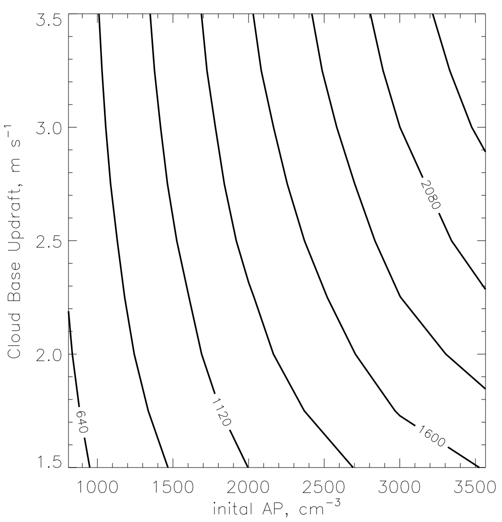

Figure 1: Simulated cloud droplet number concentration for a range of cloud base updraft velocities and initial aerosol particle concentrations. Sodium chloride is used as model salt.

with σ the surface tension of the droplet, R_w the specific gas constant for water, T the temperature, ρ_w the density of water and r_{wet} the radius of the droplet. When using the κ-formulation, the surface tension is set to $\sigma = 0.072\ J/m^2$. Combined with Equation (4) to the so-called "κ-Köhler theory", the equilibrium water vapor saturation ratio over an aqueous droplet including a multi-component aerosol particle can be calculated.
In the following we will compare model results obtained using the two different descriptions of Raoult terms. When Equation (3) is used it will be referred as the Φ-formulation. When Equation (4) is used it will be called the κ-formulation.

4. RESULTS AND DISCUSSION

In a recent study, the activation of aerosol particles to form cloud droplets for typical atmospheric conditions has been investigated using an air parcel model with a 2000-bin spectral description of warm microphysics (Segal and Khain, 2006). The parameters that mainly determine the cloud droplet concentration are the number of aerosol particles and the updraft velocity at cloud base. The resulting number of cloud droplets was investigated for aerosol number concentrations ranging from 100 to $6,400\,\mathrm{cm}^{-3}$ and for cloud base updraft velocities between 0.5 to $3.75\,\mathrm{m\,s}^{-1}$. Here, as a first step, we want to reproduce these results using our parcel model. In a second step, after a comparison of the two different descriptions of the Raoult terms for two typical profiles, we extend the range of aerosol number concentrations and cloud base updraft velocities to values that are more relevant for pyro-convection with the new κ-formulation.

	r_m , [nm]	σ	n
Reference aerosol (Segal and Khain, 2006)			
Mode 1	30	1.35	
Haze aerosol (Reid et al., 1998)			
Mode 1	80	1.65	
Young biomass burning aerosol (Helsper et al., 1980)			
Mode 1	10	1.4	0.7
Mode 2	50	1.6	0.3

Table 1: Parameters of the aerosol size distributions used in this study. r_m is the mean diameter and σ the width of the distribution. n denotes the ratio of each mode on the whole distribution.

4.1 Comparison with reference study

In Fig. 1, the dependency of droplet concentration on cloud base updraft and initial aerosol particle concentration is shown. The calculations were conducted assuming a log-normal aerosol size distribution of pure sodium chloride with a mean radius of 30 nm and a width of 1.35 (Table 1). The result shown in Fig. 1 is in good agreement with Fig. 6 f of the reference study by Segal and Khain (2006), especially for aerosol concentrations below $2,000\,\mathrm{cm}^{-3}$. For larger numbers of initial aerosol particles, our model results in slightly less nucleated drops than the reference study.

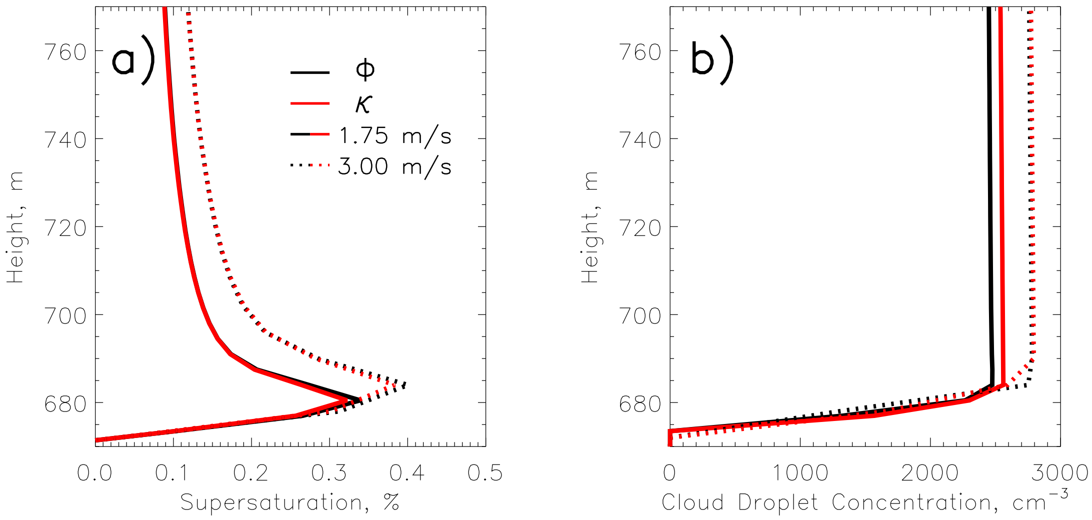

Figure 2: Vertical profile of a) the supersaturation and b) the cloud number concentration for the ϕ- (black) and the κ-formulation (red). Solid lines denote simulations with a constant vertical velocity of $1.75\,\mathrm{m\,s^{-1}}$ and dashed lines of $3\,\mathrm{m\,s^{-1}}$. The initial AP number concentration is set to $3,000\,\mathrm{cm^{-3}}$, and pure sodium chloride is taken as model salt.

Fig. 1 shows that the cloud droplet concentration is mainly determined by the initial number of aerosol particles. The influence of the cloud base updraft is increasing with increasing number of initial aerosol particles. Therefore we are interested in this dependence for more polluted areas like megacities or regions of intense biomass burning.

In the following section we compare the results obtained using the two descriptions of the Raoult term in the Köhler equation.

4.2 Comparison between different Köhler schemes

To evaluate the κ-formulation of the Köhler equation, we compare model simulations using sodium chloride as model salt in the Φ-formulation. A κ value of 1.28 corresponds to sodium chloride (Petters and Kreidenweis, 2007).

The influence of the two Köhler schemes on the activation of cloud droplets is shown in Fig. 2. The calculations were conducted for two constant cloud base updraft velocities, namely $1.75\,\mathrm{m\,s^{-1}}$ and $3.0\,\mathrm{m\,s^{-1}}$, and were started with an aerosol number concentration of $3,000\,\mathrm{cm^{-3}}$. The same log-normal aerosol size distribution as in Section 4.1 was used (Table 1). For an updraft velocity of $1.75\,\mathrm{m\,s^{-1}}$, the κ-formulation results in a slightly higher number of cloud droplets than the traditional Φ-formulation. According to the higher number of cloud droplets in the κ case, the supersaturation is slightly lower than in the Φ case. This difference results from differences in the critical supersaturation for the two Köhler schemes shown in Fig. 3. For the κ case, the value for the critical supersaturation is lower than for the Φ-formulation. Therefore, the particles in the κ-formulation are activated sooner, which leads to a higher number of cloud droplets.

In the case of the high updraft velocity ($3.0\,\mathrm{m\,s^{-1}}$) the differences between the two formulations arise only in the evolution of the cloud droplet number concentration below the cloud base. Above the cloud base both formulations result in almost identical cloud droplet number concentrations. In this case, the high vertical velocity results in enough supersaturation to activate almost all initial aerosol par-

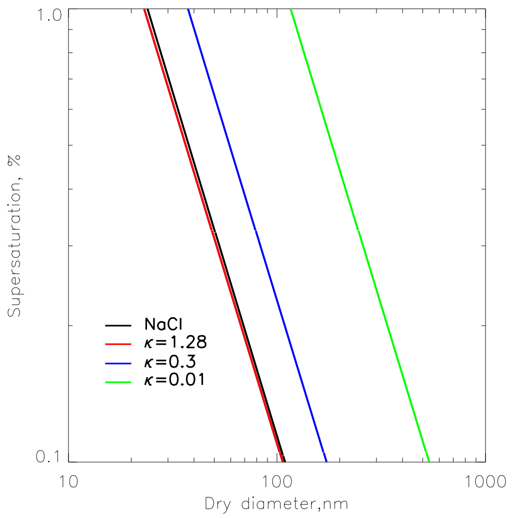

Figure 3: Critical supersaturation and dry diameter for the Φ-formulation (black) using sodium chloride as model salt and the κ-formulation with κ values of 1.28 (red), 0.3 (blue) and 0.01 (green).

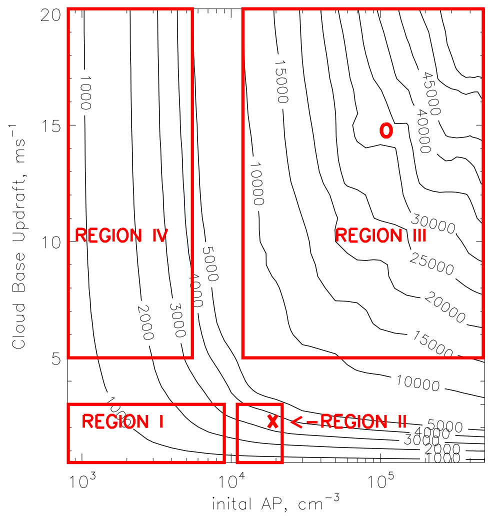

Figure 4: Dependency of droplet concentration on cloud base updraft velocity and initial aerosol particle concentration with the parcel model with a hygroscopicity of $\kappa = 0.3$. Red boxes indicate different atmospheric conditions.

ticles. Therefore, in this situation with high supersaturation, the difference in the descriptions of the Köhler equation is neglectable for the number of cloud droplets.

The good agreement between the Φ- and the κ-formulations allows us to use the κ-formulation to simulate the hygroscopic properties, which are obtained from observations and therefore, to reduce the uncertainties in the activation of atmospheric aerosol particles to cloud droplets.

4.3 Cloud droplet dependency

To investigate the influence of the cloud base updraft velocity and the initial number of aerosol particles for polluted and pyro-convective conditions, the simulations from Section 4.1 were expanded. In Fig. 4 the results are shown for an updraft velocity up to $20\,\mathrm{m\,s^{-1}}$ and an initial aerosol concentration up to $500,000\,\mathrm{cm^{-3}}$. In contrast to Fig. 1, the calculations were performed with the κ-formulation of the Köhler theory using a κ of 0.3, which represents continental aerosol (Andreae and Rosenfeld, 2007). The reference aerosol size distribution (Table 1) was used.

The red boxes in Fig. 4 represent different atmospheric conditions.

- Region I: *Polluted*
  This region with moderate aerosol number concentrations and updraft velocities corresponds to continental and urban conditions. The updraft velocity at the cloud base does not exceed values of $3\,\mathrm{m\,s^{-1}}$.

- Region II: *Highly Polluted*
  This category represents highly polluted regions (e.g. megacities or smoky regions) with a high number concentration of aerosol particles. The cloud base updraft velocity is comparable to the values of the urban region.

- Region III: *Pyro-convection*
  This region with a high number concentration and high updraft velocities at cloud base corresponds to conditions in pyro-convective clouds.

- Region IV: *"Clean pyro-convection"*
  There is no atmospheric regime that corresponds to conditions with a low aerosol number concentration and high updraft

velocities at the cloud base. It is included here for completeness.

This four regions in Fig. 4 show different regimes of dependency. In region II, i.e., with a high number of initial aerosol particles ($> 10,000\,\mathrm{cm}^{-3}$) and a low updraft velocity ($< 3\,\mathrm{m\,s}^{-1}$), a small increase in the updraft velocity can lead to a significant increase of the cloud droplet concentration. The number of initial aerosol particles has almost no effect on the droplet concentration. In this case, the supersaturation remains low ($< 0.1\,\%$), because of the low updraft velocity and high number of aerosol particles. The supersaturation is limiting the aerosol activation and therefore, an increased updraft velocity has a larger impact on the number of cloud droplets than an increased initial aerosol number concentration.
In region IV, i.e., low initial aerosol concentrations ($< 5,000\,\mathrm{cm}^{-3}$) and high updraft velocities ($> 5\,\mathrm{m\,s}^{-1}$), the number of cloud droplets strongly depends on the number of aerosol particles. A small change in the aerosol concentration leads to a strong modification of the droplet concentration. On the other hand, a change in the updraft velocity has almost no effect on the droplet concentration. The reason for this behavior is that the high supersaturation at high updraft velocities activates almost all available aerosol particles.
Also, for very high aerosol number concentrations in region III ($> 200,000\,\mathrm{cm}^{-3}$) the number of cloud droplets strongly depend on the updraft velocity. The reason for this behavior is the same as described above for region II.
In between these regimes, especially in region I, the cloud droplet number concentration is sensitive to both the aerosol number concentration and the updraft velocity.

4.4 Sensitivity studies for polluted and pyro-convective conditions

In this section we investigate in detail aerosol activation under polluted and pyro-convective conditions and its sensitivity to the hygroscopicity of the aerosol particles. Therefore we use realistic aerosol size distributions for both conditions and vary the value of κ within the range found in the atmosphere.
Fig. 5 shows the number of cloud droplets as a function of the hygroscopicity parameter κ. Calculations were conducted with a constant vertical velocity of $2.5\,\mathrm{m\,s}^{-1}$ and an initial aerosol concentration of $18,000\,\mathrm{cm}^{-3}$ (see red cross in region II, Fig. 4) using an aerosol size distribution for typical biomass burning haze conditions (see Table 1). The figure shows that with increasing κ (corresponding to a more hygroscopic aerosol), the cloud droplet concentration increases. When κ is increased, the critical supersaturation and radius is reduced and therefore smaller aerosol particles can be activated. This effect results in a higher cloud droplet concentration for an increased κ.
In Fig. 6, the dependency of the droplet concentration on the hygroscopicity parameter κ for pyro-convective conditions ($15\,\mathrm{m\,s}^{-1}$ and $100,000\,\mathrm{cm}^{-3}$, see red circle in region III, Fig. 4) is shown. A young biomass burning aerosol size distribution was used (Table 1). Typical values of κ for young biomass burning aerosol range from 0.01 for fresh smoke containing mostly soot particles to 0.55 for aerosol particles from grass burning (Andreae and Rosenfeld, 2007). Fig. 6 shows a high sensitivity of the droplet concentration for $\kappa < 0.2$. Hence, in pyro-convective clouds the number of activated aerosol particles depends on the hygroscopic properties of the emitted aerosol particles and the updraft velocity at the cloud base (see section 4.3).

5. Conclusions

In this study we investigated the influence of the updraft velocity, the number of initial aerosol particles and the hygroscopicity on the cloud droplet concentration at cloud base. The results of our cloud parcel model have been compared with a study by Segal

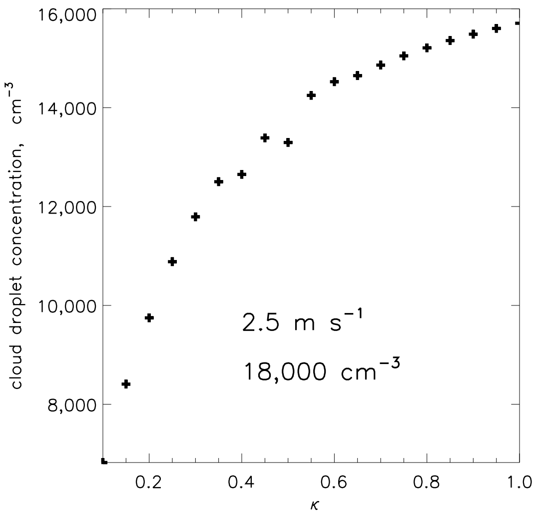

Figure 5: Dependency of droplet concentration on the hygroscopicity parameter κ for a constant vertical updraft of $2.5\,\mathrm{m\,s^{-1}}$ and a young biomass burning haze aerosol concentration of $18,000\,\mathrm{cm^{-3}}$.

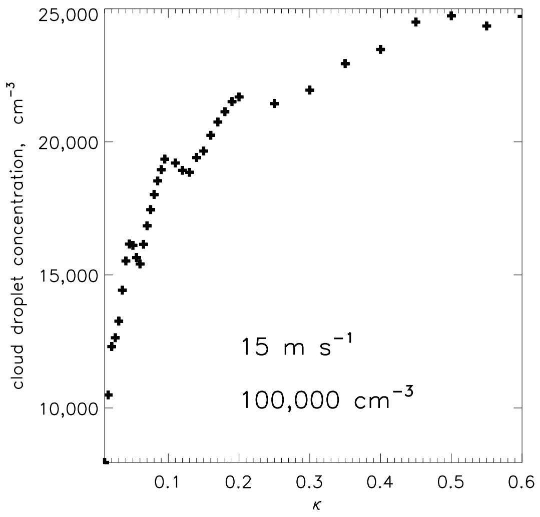

Figure 6: Dependency of droplet concentration on the hygroscopicity parameter κ for a constant vertical updraft of $15\,\mathrm{m\,s^{-1}}$ and an initial young biomass burning aerosol concentration of $100,000\,\mathrm{cm^{-3}}$.

and Khain (2006) and a good agreement has been found. It was shown, that for updraft velocities between 1.5 and $3.5\,\mathrm{m\,s^{-1}}$, and for initial aerosol concentrations between 800 and $3,500\,\mathrm{cm^{-3}}$, the number of aerosol particles is the governing factor that to determines the cloud droplet concentration.

When expanding the range of vertical velocities up to $20\,\mathrm{m\,s^{-1}}$ and the initial aerosol number concentration up to $500,000\,\mathrm{cm^{-3}}$ different regimes can be found. For low initial aerosol concentration ($< 5,000\,\mathrm{cm^{-3}}$) and high updraft velocities ($> 5\,\mathrm{m\,s^{-1}}$) at the cloud base, the number of cloud droplets is most sensitive to the number of initial aerosol particles. In contrast, for a high number of initial aerosol concentrations ($> 10,000\,\mathrm{cm^{-3}}$) and a low updraft velocity ($< 1\,\mathrm{m\,s^{-1}}$), the number of cloud droplets is very sensitive to the updraft velocity. In between these regimes, the cloud droplet concentration depends on both parameters.

The cloud parcel model was extended to include a formulation of the Raoult term in the Köhler equation based on a single parameter representation of the aerosol hygroscopicity. The parameter κ can be derived from atmospheric measurements and allows the description of the hygroscopic aerosol properties. Differences resulting from the use of the traditional description of the Köhler equation and the newly derived hygroscopicity parameter κ have been investigated. The difference between the Φ- and κ-formulation is most distinct for low supersaturations. In this case, the κ-formulation produces slightly more cloud droplets than the Φ-formulation. Nevertheless, for atmospheric aerosol, the composition is typically not known in such detail that the soluble part can be described by inorganic salt, and the application of κ directly from observations reduces the uncertainties for the activation of atmospheric aerosol.

Finally, the sensitivity of the cloud droplet concentration on the value of κ was investigated. Calculations were conducted for polluted and pyro-convective conditions with an appropriate aerosol size distribution for each case. In the polluted case, κ was varied between 0.1 and 1.0. The results show a strong dependence of the cloud droplet number on the hygroscopicity of the aerosol. For the pyro-convective case, κ was varied between

0.01 and 0.6. For κ values below 0.2, the cloud droplet concentration strongly depends on the hygroscopicity. This dependency is weaker for values > 0.2.
For microphysical investigations of polluted and pyro-convective clouds, the aerosol number concentration, their hygroscopic properties and the dynamical feature of such clouds have to be taken into account.

6. ACKNOWLEDGMENT

This work has been funded by an International Max Planck Research School fellowship.
We thank D. Rose for helpful discussions.

7. REFERENCES

Andreae, M. O., Rosenfeld, D., Artaxo, P., Costa, A. A., Frank, G. P., Longo, K. M., and Silva-Dias, M. A. F.: Smoking Rain Clouds over the Amazon, *Science*, 303, 1337-1342, 2004.

Andreae, M. O., Rosenfeld, D.: Aerosol-cloud-precipitation interactions. Part 1: The nature and sources of cloud-active aerosols, submitted to *Earth Science Review*, 2007.

Diehl, K., Simmel, M., and Wurzler, S.: Numerical sensitivity studies on the impact of aerosol properties and drop freezing modes on the glaciation, microphysics, and dynamics of clouds, *J. Geophys. Res.*, 111, D07202, doi:10.1029/2005JD005884, 2006.

Helsper, C., Fissan, H. J., Muggli, J., and Scheidweiler, A.: Particle number distribution of aerosols from test fires, *J. Atmos. Sci.,* 11, 439-446,1980.

Petters, M. D. and Kreidenweis, S. M.: A single parameter representation of hygroscopic growth and cloud condensation nucleus activity, *Atmos. Chem. Phys.*, 7, 1961-1971, 2007.

Pruppacher, H. R. and Klett, J. D.: Microphysics of Clouds and Precipitation, *Kluwer Academics Publishers*,511 pp. 1997.

Reid, J. S., and P. V. Hobbs, Physical and optical properties of young smoke from individual biomass fires in Brazil, *J. Geophys. Res.*, 103,32,013-32,030,1998.

Rose, D., Gunthe, S. S., Mikhailov, E., Frank, G. P., Dusek, U., Andreae, M. O., and Pöschl, U.: Calibration and measurement of a continuous-flow cloud condensation nuclei counter (DMT-CCNC): CCN activation of ammonium sulfate and sodium chloride aerosol particles in theory and experiment, *Atmos. Chem. Phys. Discuss.*, 7, 8193-8260, 2007.

Segal, Y. and Khain, A.: Dependence of droplet concentration on aerosol conditions in different cloud types: Application to droplet concentration parameterization of aerosol conditions, *J. Geophys. Res.*, 111, D15204, doi:10.1029/2005JD006561, 2006.

Simmel, M. and Wurzler, S.: Condensation and activation in sectional cloud microphysical models, *Atmos. Res.*, 80, 218-236, 2006.

Simmel, M., Trautmann, T., and Tetzlaff, G.: Numerical solution of the stochastic collection equation - comparison of the Linear Discrete Method with other methods, *Atmos. Res.*, 61, 135-148, 2002.

Trentmann, J., Luderer, G., Winterrath, T., Fromm, M., Servranckx, R., Textor, C., Herzog, M., and Andreae, M.O.: Modelling of biomass smoke injection into lower stratosphere by a large forest fire (Part I): Reference study, *Atmos. Chem. Phys.*, 6, 5247-5260, 2006

AIRCRAFT MEASUREMENTS OF THE IMPACTS OF POLLUTION AEROSOLS ON CLOUDS AND PRECIPITATION OVER THE SIERRA NEVADA

D. Rosenfeld[1], W. L. Woodley[2], D. Axisa[3], E. Freud[1], J. G. Hudson, A. Givati[1]

1. Institute of Earth Sciences, The Hebrew University of Jerusalem, Israel .
2. Woodley Weather Consultants, 11 White Fir Court, Littleton CO 80127 .
3. Seeding Operation & Atmospheric Research, POB 130, Plains TX 79355
4. Desert Research Institute, University of Nevada, Reno, Nevada .

ABSTRACT

Recent publications suggest that anthropogenic aerosols suppress orographic precipitation in California and elsewhere. A field campaign (SUPRECIP: Suppression of Precipitation) was conducted to investigate this hypothesized aerosol effect. The campaign consisted of in situ aircraft measurements of the polluting aerosols, the composition of the clouds ingesting them, and the way the precipitation-forming processes are affected. SUPRECIP was conducted during February and March of 2005 and February and March of 2006. The flights documented the aerosols and orographic clouds flowing into the central Sierra Nevada from the upwind densely populated industrialized/urbanized areas and contrasted them with the aerosols and clouds downwind of the sparsely-populated areas in the northern Sierra Nevada.

SUPRECIP found that the aerosols transported from the coastal regions are augmented greatly by local sources in the Central Valley resulting in high concentrations of aerosols in the eastern parts of the Central Valley and the Sierra foothills. This pattern is consistent with the detected patterns of suppressed orographic precipitation, occurring primarily in the southern and central Sierra Nevada, but not in the north. The precipitation suppression occurs mainly in the orographic clouds that are triggered from the boundary layer over the foothills and propagate over the mountains. The elevated orographic clouds that form at the crest are minimally affected. The clouds are affected mainly during the second half of the day and the subsequent evening, when solar heating mixes the boundary layer up to cloud bases. Local, yet unidentified non-urban sources are suspected to play a major role.

Corresponding author's address: Daniel Rosenfeld, Institute of Earth Sciences, The Hebrew University of Jerusalem, Jerusalem 91904, Israel.
E-Mail: daniel.rosenfeld@huji.ac.il

1. INTRODUCTION

Anthropogenic aerosols from major coastal urban areas pollute the pristine maritime air masses that flow inland from the sea and bring much of the precipitation, especially over the mountain ranges. Satellite observations indicated that urban aerosols reduce cloud drop effective radii (r_e) and suppress both warm and mixed phase precipitation in the clouds downwind of the urban areas (Rosenfeld, 2000). This prompted studies that quantified the precipitation losses over topographical barriers downwind of major coastal urban areas in the western U.S (particularly in California) and in Israel. These results suggested losses of 15 – 25% of the annual precipitation over the western slopes of the hills (Givati and Rosenfeld, 2004, 2005; Rosenfeld and Givati, 2006, Givati and Rosenfeld, 2007, Rosenfeld et al., 2007). The suppression occurs mainly in the relatively shallow orographic clouds within the cold air mass of cyclones. The suppression that occurs over the upslope side is coupled with similar percentage enhancement on the much drier down slope side of the hills.

These results are consistent with other studies that have shown that higher cloud condensation nuclei (CCN) concentrations increase cloud droplet concentrations, decrease cloud droplet sizes, reduce droplet coalescence and thus precipitation (e.g., Hudson and Yum 2001; McFarquhar and Heymsfield 2001;Yum and Hudson 2002; Hudson and Mishra 2007). Therefore CCN from air pollution could be incorporated into orographic clouds, slowing down cloud-drop coalescence and riming on ice precipitation, hence delaying the conversion of cloud water into precipitation. The evidence includes significant decreasing trends of the ratio of hill / plains precipitation during the 20th century in polluted areas. Aerosol measurements from the IMPROVE aerosol monitoring network in the western U.S showed that the negative trends in the orographic precipitation are associated with elevated concentrations of fine aerosols (PM2.5). No trends are observed in similar nearby pristine areas (Givati and Rosenfeld, 2004).

In Central California the main precipitation suppression is postulated to occur during westerly flow that ingests anthropogenic CCN, which are incorporated into orographic clouds that form over the Sierra Nevada and are so shallow that their tops do not fully glaciate before crossing the mountain crest. This means that at least some of the water in these clouds remains in the form of cloud droplets that are not converted to precipitation (or at least ice hydrometeors) before crossing the divide, and hence re-evaporate after producing some precipitation on the downwind side of the crest. Recent model simulations support this hypothesis (Lynn et al., 2007; Woodley Weather Consultants, 2007).

Clouds with very cold base, near 0°C, already form as supercooled clouds with little room for rainout. In such clouds only quite pristine conditions would produce excess of precipitation embryos that would compete on the available cloud water and prevent the formation of hail. Already moderate concentrations of aerosols can suppress the formation of ice precipitation embryos to the extent that hail is substantially reduced.

2. THE SUPRECIP PROGRAM

Following the publication of many of the recent findings cited above a research effort called the Suppression of Precipitation (SUPRECIP) Program was conducted to make in situ aircraft measurements of the polluting aerosols, the composition of the clouds ingesting them, and the way the precipitation-forming processes are affected. The SUPRECIP field campaigns were aimed at making the measurements necessary for the validation of the above hypothesis that urban air pollution suppresses orographic precipitation.

SUPRECIP was conducted during February and March of 2005 (SUPRECIP 1) and February and March of 2006 (SUPRECIP 2). The Seeding Operations and Atmospheric Research (SOAR) Cheyenne II, turbo-prop, cloud physics research aircraft was used in SUPRECIP-1; the Cheyenne and an additional (SOAR) Cessna 340 aerosol aircraft were flown in SUPRECIP-2. These aircraft were used to measure atmospheric aerosols in pristine and polluted clouds and the impact of the aerosols on cloud-base microphysics, on the evolution with height of the cloud drop-size distribution and on the development of precipitation under warm and mixed-phase processes. They were used also to validate the multi-spectral satellite inferences of cloud structure and the effect of pollutants on cloud processes, especially the suppression of precipitation. This research effort is funded by the PIER (Public Interest Energy Research) Program of the California Energy Commission.

The Cheyenne II cloud physics aircraft that was used in SUPRECIP. The instruments and respective data sets taken by the aerosol and cloud physics airplanes included measurements of cloud microstructure, CN and CCN aerosols. The flights of these aircraft documented the aerosols and orographic clouds downwind of the densely populated areas in the north-central Sierra Nevada and contrasted them with the aerosols and clouds downwind of the sparsely-populated areas in the far northern Sierra Nevada.

3. A CASE STUDY

The linkage between ingested sub-cloud aerosols and cloud microphysics is best illustrated by a case study on the afternoon of February 28, 2006. A cold front had passed through the area the previous night and a post-frontal cold air mass moved from the west southwest over all of Central California by the following afternoon. Post-frontal instability caused convective clouds over the ocean, and triggered convective clouds over the coastal hills and over the Sierra Nevada. Although the instability decreased gradually during the day, rain showers from shallow clouds were still occurring over the ocean and the coastal ranges at 00Z on 1 March 2006. Figure 1 shows the Oakland radiosonde at that time.

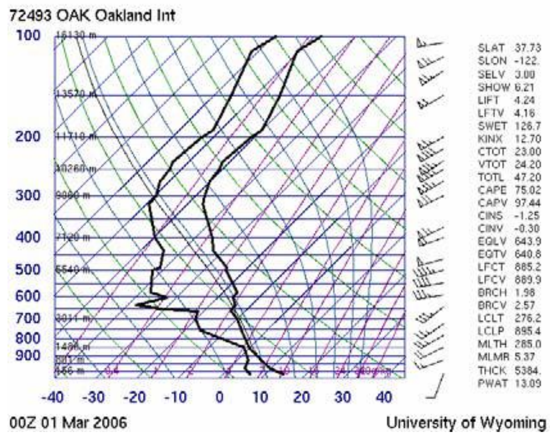

Figure 1: The Oakland radiosonde of 1 March 2006 at 00Z, which is near the time that the aircraft flew near Oakland.

A coordinated mission of the Cloud and Aerosol airplanes originated from the Sacramento Executive Airport to document the gradient in aerosols and cloud properties by doing cross sections from the Sierra Nevada to and from the Pacific Ocean. The aircraft departed Sacramento at 23:05Z and flew due east to the foothills and measured the convection generated there by the mountains. The next destination was the clouds that formed over the hills bounding the Central Valley to its west, about 60 km to the NE of Monterey. Next the aircraft sampled the clouds forming over the hills just at the Pacific coast at Big Sur. There the aircraft continued 35 km westward over the ocean and then turned north to measure convective clouds that were triggered by the ocean shoreline of San Francisco. Then the aircraft turned east over the north part of San Francisco Bay and measured a cloud just inland over Richmond, and then another cloud over Sacramento before finally landing. The tracks of the two aircraft and the locations of the measured clouds are provided in Figure 2.

The aerosol aircraft measurements are summarized in Figure 2. Because the supersaturation (or the temperature difference between the plates, dT) in the Cloud Condensation Nuclei Counter cycles every ~7 minutes, there was a need to correct the CCN data measured at low supersaturations to a common SS. Without correction or adjustment there would be too few data points measured at the same SS. In order to do this, it was necessary to find the relation between dT (instead of SS) and the CCN concentration for each flight separately, because this relation might be affected by the chemical composition of the aerosols, their sizes and their concentrations. After determining and applying the correction, the CCN concentrations were plotted for an entire flight to a common 0.85% SS for measurements in the boundary layer. On average, the ratio of CCN counts at super saturations of 0.85% and 0.5% was 1.89 with a standard deviation of 0.4.

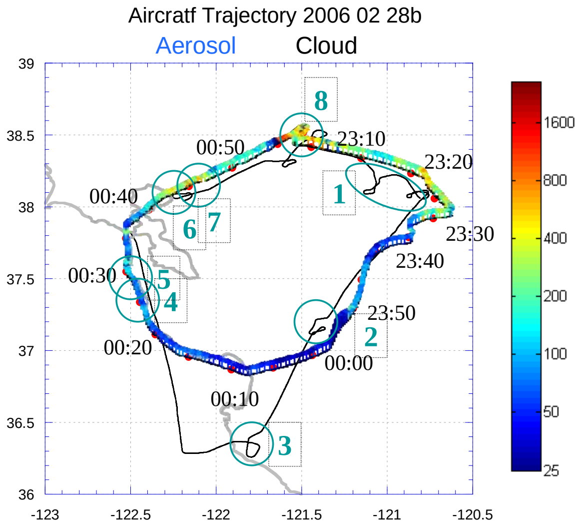

Figure 2: The tracks of the Cloud (black) and Aerosol (colored) airplanes. The time marks every 5 minutes are posted on the aerosol aircraft tracks, and labelled every 10 minutes. The CCN concentrations adjusted to supersaturation of 0.9% are shown in the color scale. The relative height of the aerosol aircraft above sea level is shown by the vertical displacement of the track. The measured clouds by the cloud physics aircraft are marked with green circles and numbered sequentially.

The aircraft aerosol measurements show CCN concentrations varying between 300 and 800 cm-3 over the first section to the SE at the western slopes of the Sierra Nevada. The CCN concentrations fell to about 100 cm^{-3} over the hills 60 km NE of Monterey, and continued falling to less than 40 cm^{-3} over Monterey Bay and likely also over Big Sur. The CCN increased again gradually to the north along the coastline and reached about 70 cm^{-3} there. They kept rising to about 100 cm^{-3} over the peninsula of San Francisco airport, and jumped locally to 800 cm^{-3} just to the north of the airport, but recovered back to less than 80 cm^{-3} to the north of the Golden Gate Bridge. The aircraft turned to the east and experienced a sharp increase of the CCN to more than 700 cm^{-3} over Richmond. The condensation nuclei (CN) then shot up > 10,000 cm^{-3}. This suggests an ample source of fresh small aerosols. The CCN remained generally above 500 cm-3 within the boundary layer all the way to landing in Sacramento.

The cloud- and precipitation particle size distributions are given in Figures 3-7. Cloud 1 was sampled stepping upward from base through its upshear towers, whereas its more mature portions glaciated and precipitated. Due to air traffic control limitations it was necessary to use different clouds in the same area for the lower and upper portions of the cross sections. The modal liquid water cloud drop diameter (D_L, defined as the drop diameter having the greatest

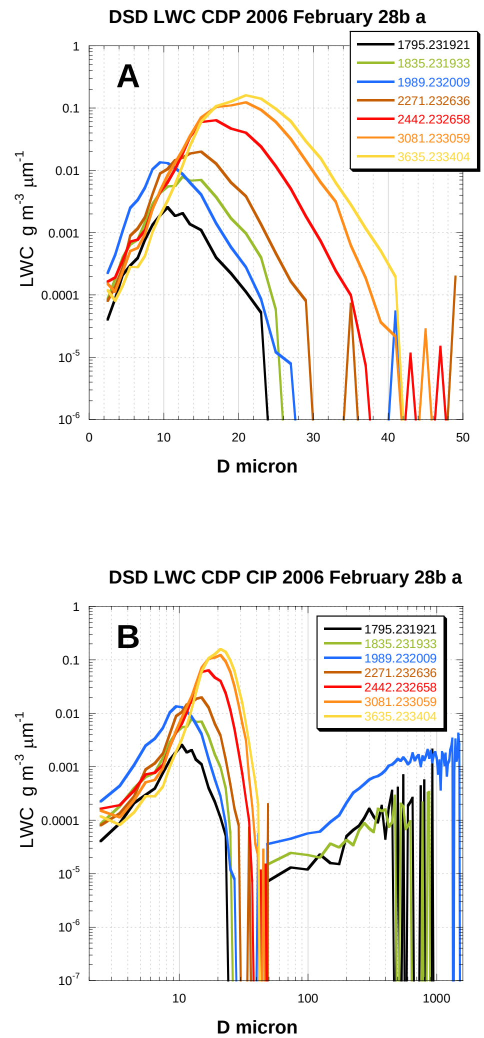

Figure 3: Plot of cloud droplet diameters as a function of liquid water content (LWC) for Cloud 1 over the western slopes of the Sierra Nevada (see location in Figure 2). The modal liquid water drop diameter occurs at the droplet size having the greatest water content. Cloud 1 developed in an air mass that had 300-800 CCN cm^{-3}. Panel A shows the Cloud Droplet Probe (CDP) measured LWC distribution. Each line represents the gross cloud drop size distribution of a whole cloud pass. The legend of the lines is composed of the pass height [m] to the left of the decimal point, and the pass starting GMT time [hhmmss] to the right of the point. The passes are ordered in altitude ascending order. Note the increase in cloud drop volume modal size with increasing cloud depth. Panel B shows the combined distributions of the CDP and the cloud imaging probe (CIP). According to the figure the large precipitation particles were well separated from the cloud drop size distribution, indicating lack of appreciable coalescence.

LWC) increased with height above cloud base. It reached 21 μm at the altitude of 3635 m, which is about 1900 m above cloud base. The temperature there was -8°C. This size is below the D_L threshold for the development of warm rain that was documented elsewhere as 24 μm (Andreae et al., 2004). In agreement with that, the D_L did not expand to drizzle size. Large precipitation particles occurred as graupel and formed a well separated distribution at the 1-mm size range (Figure 3).

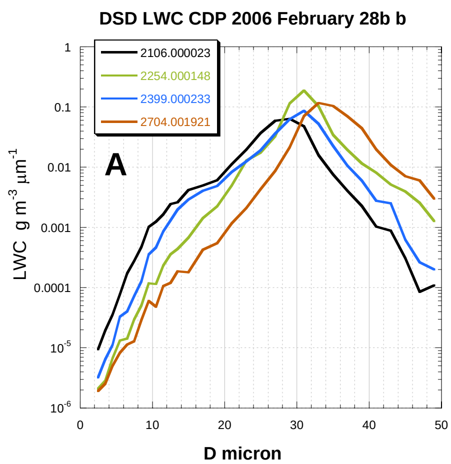

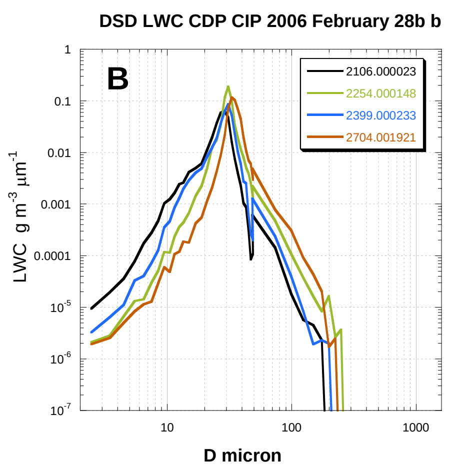

Figure 4: Same as Figure 3, but for Cloud 2 over the hills 60 km NE of Monterey (see location in Figure 2). It developed in an air mass that had 100 CCN cm^{-3}. The cloud drops are quite large and the distribution continues smoothly into the rain drop sizes. This indicates active warm rain processes.

From the location of Cloud 1 the aircraft was flown diagonally to the southwest and across the Central Valley. The valley was mostly cloud-free, except for some mid-level layer clouds. The next area of clouds was triggered by the ridge that bounds the Central Valley on its west. The cloud tops had a convective appearance and were sampled at the lowest allowed altitude - (2100 m, to provide safe-ground clearance over the highest terrain) up to the cloud tops at 2700 m. The temperature there was -3°C, but the maturing clouds were visibly turning into a diffused fibrillation texture, indicating the conversion of the cloud water to precipitation and/or ice crystals. Glaciation would be in such case produced probably by a mechanism of ice multiplication. The modal LWC drop size was 28 μm at 2100 m and reached 33 μm at the cloud top at 2700 m. This is clearly beyond the threshold (D_L = 24 μm) for warm rain (Gerber 1996; Yum and Hudson 2002). In agreement with that, the cloud droplet size distribution (DSD) was extended smoothly to the drizzle and small rain drop sizes, as measured by the CIP and presented in the panel B of Figure 4. The appearance of the warm rain is consistent with the decrease of the CCN concentrations to about 100 cm^{-3}.

The aircraft continued flying to the SW to the next area of clouds (cloud 3). These were triggered by the coastal hills near Big Sur. The aircraft stepped vertically through the convective- looking cloud tops from the lowest safe height of 1880 m to their tops at a height of 2250 m at temperature of -3°C. The CCN concentrations as measured by the aerosol aircraft in Monterey Bay varied between 20 and 50 cm^{-3}. These low CCN concentrations produced large cloud drops ranging from a modal LWC drop diameter of 30 μm at 1880 m to 43 μm at the cloud tops. The DSD extended smoothly into drizzle and small rain drops (see Figure 5). Large hydrometeors were nearly absent. The cloud drops were so large so that the solar radiation reflected from the particles near the cloud top formed a cloud bow. These clouds had clearly created active warm rain.

From Big Sur the flight continued over the ocean and then turned north and flew at a constant altitude across Monterey Bay to the Golden Gate and then eastward back to Sacramento. This flight path took the aircraft along an aerosol gradient that increased from pristine over the ocean to polluted air just to the east of San Francisco Bay. Convective clouds grew along that flight path and reflected the impact of the changing CCN concentrations at that fixed altitude. Clouds 4 to 8 were penetrated along this gradient flight (Figure 6).

Cloud 4 was penetrated at the coastline of the peninsula to the west of San Francisco. The CCN concentration there was about 70 cm-3 and the cloud had a DL of 31 μm and created warm rain. A faint cloud bow was barely visible. Cloud 5 was penetrated a short distance to the north, where the CCN increased to 100 cm^{-3}. Cloud 5 still had warm rain, but to a lesser extent than Cloud 4. Shortly after passing directly over San Francisco International airport, over the Golden Gate Bridge, a short jump in the CCN occurred to about 600 cm^{-3} and recovered to the background of < 70 cm^{-3}.

The aircraft turned east and crossed the northern arm of San Francisco Bay. The CCN concentrations increased to about 300 cm^{-3} shortly after crossing the coast line. Cloud 6 formed over the eastern part of Richmond. Its modal LWC DSD decreased to 17 μm, well below the warm rain threshold of 24 μm. The CIP confirmed that this cloud had no precipitation particles. This occurred less than an hour after the time of the Oakland sounding at 00Z, which represented pretty well the local conditions and showed light southwesterly winds near the surface that veered to stronger west-southwest winds at the higher levels.

Cloud 7 occurred a few km farther east of cloud 6, where the CCN concentrations increased to 600 cm^{-3}. Its DL decreased further to 15 µm. Cloud 8 developed farther east over Sacramento, where the CCN concentration varied between 600 and 1000 cm^{-3}. The cloud had a similar microphysics to cloud 7. A vertical stepping through cloud 8 showed little widening of the DSD with height (Figure 7), which serves as an additional indication of the scarcity of coalescence in that cloud.

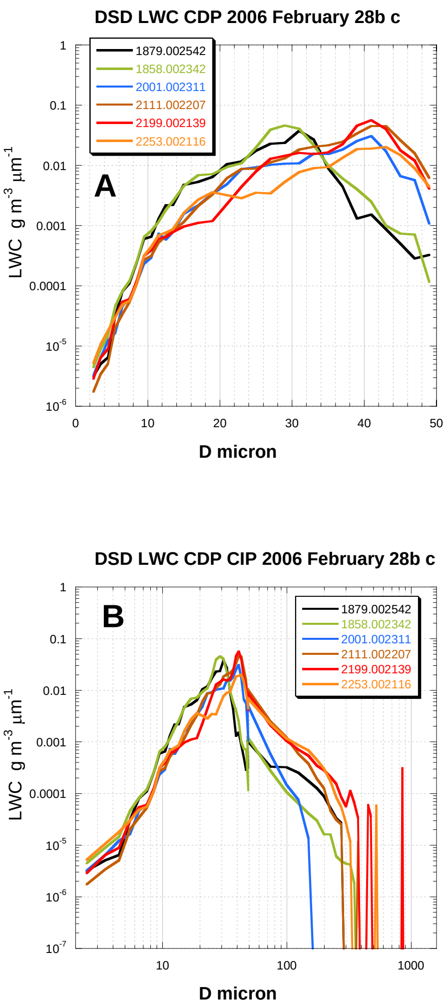

Figure 5: Same as Figure 3, but for Cloud 3 over the hills near Big Sur (see location in Figure 2). It developed in an air mass that had about 40 CCN cm^{-3}. The cloud drops are very large and the distribution continues smoothly into the rain drop sizes. This indicates very active warm rain processes.

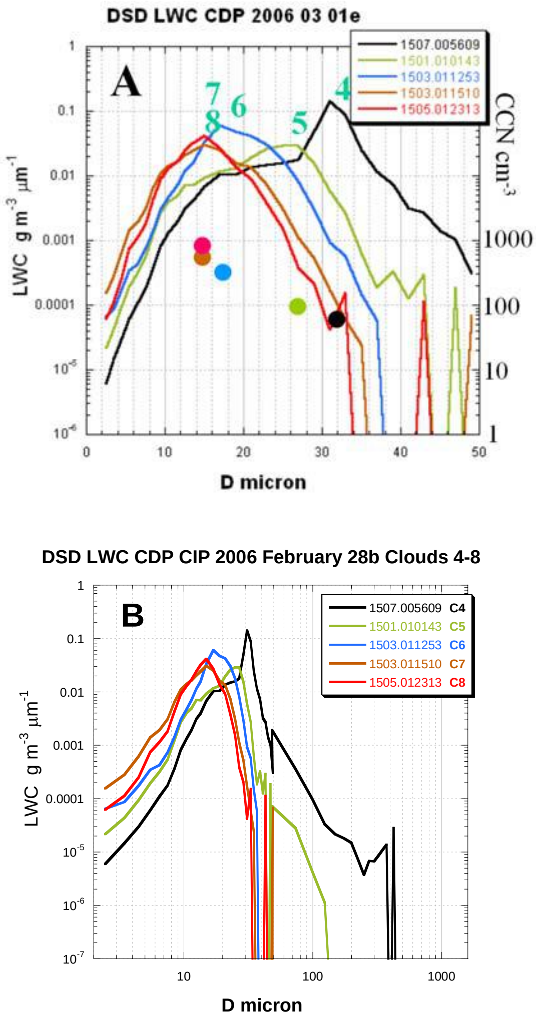

Figure 6: Same as Figure 3, but for single heights in clouds 4 – 8 in a cross-section from the Pacific Ocean to Sacramento, marked by C4, C5, C6, C7, and C8 respectively. The respective approximated CCN concentrations from the measurements made by the aerosol aircraft are denoted by the circles and are located under the peaks of the D_L plots having the same color. The CCN values are to be read from the right ordinate. The CCN concentrations are: C4: 70, C5: 100, C6: 300, C7: 600, C8: 800 cm^{-3}. The drops become markedly smaller with increasing CCN concentrations. Warm rain ceases at cloud 3 where 300 CCN cm^{-3} were present.

A satellite analysis shows that the satellite retrieved microphysics of the cloud field is in agreement with the in situ measurements. In summary, a detailed analysis of a single flight of SUPRECIP 2 showed a clear relationship between CCN concentrations, cloud microphysics and precipitation forming processes. The distribution of the CCN showed an unambiguous urban source, at least in the San Francisco Bay area. The role of the anthropogenic aerosols is demonstrated by the contrast between Cloud 2 some 50 km inland in a relatively sparsely populated area, compared with clouds 6 and 7 only several km inland over the heavily populated and industrialized Bay area. While Cloud 2 was quite pristine and produced ample coalescence and warm rain, coalescence in cloud 7 was highly suppressed and it produced no precipitation.

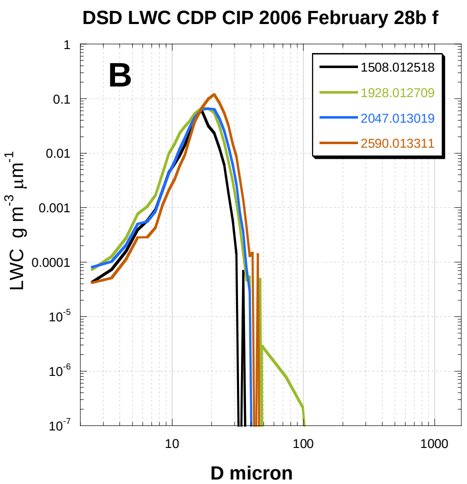

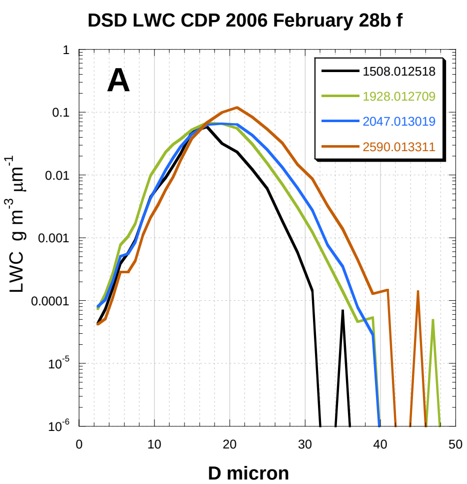

Figure 7: Same as Figure 3, but for the vertical cross section in Cloud 8 over Sacramento (see location in Figure 2). It developed in an air mass that had about 800 CCN cm^{-3}. The cloud drops are very small and do not expand much with height into raindrops, again as in Cloud 1.

The differences in the anthropogenic CCN likely explain the observed differences. Cloud base temperature over the coast (San Francisco) was warmer by about 2ºC than the cloud base inland (Sacramento). This cannot explain the observed differences in the clouds microstructure for the same height above cloud base, because it incurs a difference of less than 10% in the amount of adiabatic water for the same height above cloud base for the heights of interest. The fastest growth of D_L in near the cost line cannot be explained by the probable greater abundance of sea-spray generated giant CCN, because they would act to enlarge the tail of the cloud DSD and not its mode. Furthermore, both cloud base temperature and sea salt CCN should change at the same rate with distance from the coast over the urban and rural areas. Differences in land use would, if anything, contribute to the opposite effects with respect to the actually observed. The mountains at the coast line near Big Sur should enhance the updraft and cause smaller cloud drops and less coalescence, but in fact the largest drops and strongest warm rain were observed there. The urbanized area should have provided more sensible heat for greater updrafts, but this should play a minimal role with the weak winter solar heating. Therefore, there is no probable mechanisms that can explain the observed differences in the cloud microstructure and precipitation properties to which the authors are aware of, except for the differences in the anthropogenic CCN.

The satellite image, taken 3 to 4 hours before the flight, supports the aircraft observations and shows that an even greater source than the urban San Francisco Bay area for aerosols occurred in the central and southern Central Valley. A flight earlier in the day measured CN concentrations exceeding 20,000 cm^{-3} and CCN concentrations reaching 1000 cm^{-3} over the southern Central Valley.

The pristine clouds with large drops and warm rain processes produced a continuum of drop sizes from the cloud drops through the drizzle sizes to the small rain drops. In contrast, clouds with suppressed coalescence due to large CCN concentrations that grew to heights with cold temperatures still produced mixed phase precipitation mainly in the form of graupel. They produced distinctly different size distribution of the hydrometeors, which was separated from the cloud drop DSD. It is known from theoretical considerations and simulation studies that the decreased cloud drop sizes reduce also the mixed phase precipitation (Khain et al., 2001; Rosenfeld and Ulbrich, 2003, but the extent of this possible effect from the cloud physics measurements remains to be documented.

Similar response of clouds and precipitation forming processes to aerosols is apparent also in all the other research flights of SUPRECIP-2 as shown in the next subsection. The continued analyses and evaluation of the aircraft measurements provides compelling evidence for the detrimental role of anthropogenic aerosols on orographic precipitation in California, and explains how a climatological trend of increased CCN aerosols would cause the climatologically observed trends of the reduction in the orographic precipitation component in the southern and central Sierra Nevada.

4. ENSEMBLE RESULTS

The next step was the analysis of all of the cloud passes on all the flights of SUPRECIP 2 to determine the cloud depth necessary for each cloud to develop particles of precipitation size as a function of the measured sub-cloud CCN concentrations. This was done by determining the D_L for each measurement. The dependence of D_L on the CCN for all the measured clouds is provided in Fig. 8. This parameter has been used elsewhere (Andreae et al., 2004; Rosenfeld et al., 2006) as shown in Figure 9 that gives the drop size for the modal LWC as a function of height for several regions and weather regimes around the world. The precipitation threshold was found to be D(LWC) = 24 µm (Andreae et al., 2004) or D_{L24}. From this diagram one can determine the typical cloud depths necessary for clouds to reach this precipitation threshold.

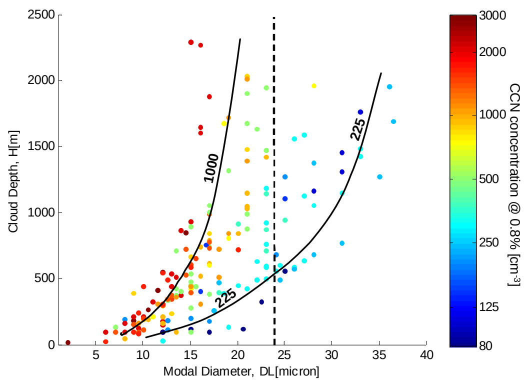

Figure 8. Scatter plot of the modal liquid water drop diameter (D_L) vs. the distance above cloud-base height. Each plotted point has been colorized according to the scale on the right where browns, reds and yellows indicate cloud passes with high sub-cloud CCN concentrations and blue points indicate cloud passes having low sub-cloud CCN concentrations. The vertical line marks the threshold for formation of precipitation-sized drops is when D_L = 24 µm. The two lines are the approximated contours of 225 and 1000 CCN cm^{-3}, as done by the contouring routine of MATLAB. The contouring was done after transferring the individual data points to a surface by linear interpolation and initial smoothing.

The results of the analysis of the SUPRECIP 2 cloud passes are presented in Figure 8. Each dot on the figure represents the D_L and its height above cloud base (H) for one cloud penetration. A cloud penetration was defined as a sequence of at least 3 seconds of CDP droplet concentration larger than 20 cm^{-3} and CDP LWC larger than 0.001 g/m^3. For each such penetration the average number of droplets in every size bin was calculated, and this gave the average size distribution for that penetration. Plotting the LWC density (for each bin normalized to the bin width) made it possible to derive the D_L for each penetration manually. Only convective or cloud elements (mostly embedded) entered this analysis. Embedded small convective elements constituted much of the orographic clouds that formed at the foothills of the Sierra Nevada. Layer cap clouds dominated near the crest, but even they were mostly composed of embedded convection with elevated bases. Due to the uncertainty of cloud base height of these clouds, the clouds that were included in Figure 8 were formed mostly at the foothills and lower to mid-level western slopes of the Sierra Nevada.

In order to be able to compare penetrations from different clouds and from different days, the cloud base height was subtracted from the penetration altitude to get the distance of the penetration from the cloud's base. The determination of the cloud's base is not always simple and straightforward because cloud base height can vary significantly even during a flight. Therefore, in some cases the cloud base height needed to be adjusted so that the D_L vs. Cloud Depth (on a logarithmic scale) would fall approximately on a straight line (because the droplets grow very fast near cloud base and then at a decreasing rate thereafter (only when coalescence is not playing an important role). This uncertainty in the exact cloud base height leads to some uncertainty in the lowest parts of Figure 8.

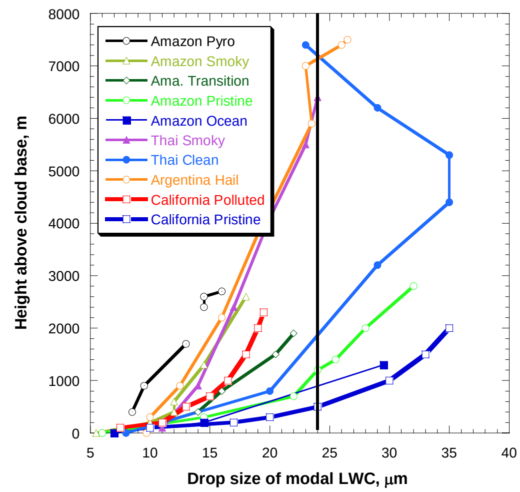

Figure 9. The global context of the dependence of the drop size modal LWC D_L on height above cloud base and temperature. The lines, according to their order in the legend, are: Amazon pyro-Cb, smoky, transition, pristine over land and pristine over ocean clouds (Andreae et al., 2004); Thailand pre-monsoon smoky and monsoon relatively clean clouds (Andreae et al., 2004); Argentina microphysically continental hail storms (Rosenfeld et al., 2006); California polluted and pristine clouds (Fig. 8 of this study). The vertical line at D_L=24 µm represents the warm rain threshold.

Lastly, the color of each small circle is determined by the measured (by the aerosol aircraft) CCN concentration in the vicinity and below the bases of the penetrated clouds at the maximum supersaturation of ~0.85%. The scale of the coloring is logarithmic in order to increase the definition/resolution at low CCN concentrations.

Figure 8 shows that the difference in D_L between clouds developing in polluted air (high CCN concentrations) and clouds developing in clean air becomes more and more pronounced with height. The D_L of polluted clouds having high CCN concentrations is significantly smaller higher in the clouds, because it increases more slowly with cloud depth than in clouds with low CCN concentrations. The clouds need to be deep enough and the D_L needs to reach ~24 µm before significant warm rain can occur. Therefore, the differences in the (warm) precipitation processes become larger higher in the clouds, at least up to 2-2.5 km above their bases, which was reached by the cloud physics aircraft. Because deeper clouds have a greater potential to precipitate large amounts of water, this figure indicates that the aerosols influence the precipitation amounts from these clouds. This serves as evidence of the direct connection between pollution aerosols and the suppression of precipitation at least in the winter shallow convective and orographic clouds in Central California.

Again, Figure 9 shows the global context of the height-D_L relations found for pristine and polluted clouds in the study area. According to Figure 9, the pristine clouds in California precipitated at heights starting at 0.5 km, shallower than in the pristine tropical clouds. The polluted clouds in California had larger drops than the respective smoky clouds in the Amazon and Thailand, reflecting the much greater concentration of smoke CCN there than exist currently in the California air pollution during rainy days. This means that the precipitation in these California clouds could be suppressed further if the air pollution concentrations become even greater.

5. DISCUSSION

The pieces of the research puzzle are slowly falling into place with respect to the trend of decreasing orographic precipitation over many areas of the globe and attendant losses in runoff (Woodley Weather Consultants, 2007) and spring flows (Rosenfeld et al., 2007. With respect to California it was determined also that the Pacific decadal oscillation (PDO) and the Southern Oscillation index (SOI) (Allan et al., 1991; Dettinger et al., 2004), cannot explain the observed declining trends in the orographic enhancement factor (Ro) (Rosenfeld and Givati, 2006).

These apparent losses in orographic precipitation are not limited to California. Rosenfeld and Givati (2006) expanded their study to the whole western USA, where they showed that Ro remained stable over hills in the more pristine areas in northern California and Oregon, but decreased again to the east of the densely populated and industrialized Seattle area. Similar effects were observed not only in the Pacific coastal areas, but also well inland. Precipitation was decreased by 18% over the mountains to the east of Salk Lake City, Utah, but remained unchanged at the southern extension of the same mountain range (Rosenfeld and Givati, 2006; Griffith et al., 2005). Similar effects were found during easterly winds over the eastern slope of the Rocky Mountains downwind (i.e., to the west) of Denver and Colorado Springs (Jirak and Cotton, 2006).

The common denominator for the regions suffering losses in orographic precipitation has been found in the multi-spectral satellite imagery that shows decreased cloud-particle (r_e) for the affected regions. In California this was addressed using multi-spectral satellite images from polar-orbiting satellites (Woodley Weather Consultants, 2007). On each day with a satellite overpass, the multi-spectral imagery was processed to infer the re of cloud particles for the clouds within selected areas within the field of view. This was done because previous studies had shown that areas with small re are slow to develop precipitation. After the satellite inferences had been made they were composited geographically. It was found that re increases more slowly with decreasing T in the central and southern Sierra compared to the northern Sierra. The slower increase of re with elevation is the most robust indicator for the slower development with height of precipitation in the clouds. This finding is consistent with the gauge and stream-flow analyses that show that the greatest losses of water occur in the central and southern Sierra (Woodley Weather Consultants, 2007). This suggested a major role of CCN pollutants that are ingested by the orographic clouds with consequent suppression of coalescence along the lines of the hypothesis put forth at the outset of this paper.

SUPRECIP was designed to address the potential linkages between pollution aerosols and the loss of orographic precipitation and subsequent runoff. SUPRECIP 1 showed a strong positive correlation between the satellite-inferred cloud microphysics and the aircraft-measured cloud microphysics. Thus, the areas in the central and southern Sierra that were shown by satellite to have smaller re than over the northern Sierra likely really do have suppressed precipitation forming processes.

It took SUPRECIP 2 to make this direct connection between the pollution aerosols and suppressed precipitation-forming processes. The scatter plot of the modal liquid water drop diameter (D_L) vs. the depth above cloud-base height (Figure 8) as a function of the ingested CCN shows that clouds growing in a polluted environment must reach greater depths to develop precipitation than clouds growing in a more pristine environment where the CCN concentrations are lower.

In looking at the temporal and spatial patterning of the pollution aerosols in California, it was determined that they typically exhibit a strong diurnal oscillation with the strongest upward transport during the late afternoon. Thus, the sampled clouds are more continental in character with smaller droplet sizes and diminished coalescence at this time of day. The aerosol concentrations were minimal over the sea and increased after traversing the shoreline, where urban and industrial development has taken place. The aerosols found over the Central Valley were not simply transported from the coastal areas, because on most days the CN and CCN concentrations in the Valley to the Sierra foothills exceeded what was found in the coastal urbanized areas. This is true especially in the central and southern Valley well to the east of sparsely populated coastal regions. This is consistent with slow gas to particle conversion and aging by coagulation of aerosol to form CCN. It appears, therefore, that the large aerosol concentrations that are likely suppressing the Sierra orographic precipitation are generated locally in the Valley itself having unknown specific origins and chemistry. This is consistent with the findings of Chow et al (2006) from an extensive aerosol measurement program in the San Joaquin Valley. Although transport of pollution aerosols from the sea and from coastal regions may play a role in the suppression of Sierra orographic precipitation, it would appear to be secondary to the role being played by the local generation of aerosols in regions of highest concentrations. Understanding this role would appear to be the next logical step in this research effort.

A component of this research effort was model simulation of the effects of aerosols (Lynn et al., 2007). The simulation with clean air produced more precipitation on the upwind mountain slope than the simulation with continental aerosols. After 3 hours of simulation time, the simulation with maritime aerosols produced about 30% more precipitation over the length of the mountain slope than the simulation with continental aerosols. Greater differences in precipitation amounts between simulations with clean and dirty air were obtained when ice microphysical processes were included in the model simulations.

Thus, the totality of the evidence from the research effort, involving precipitation and stream flow analyses, quantitative satellite measurements, numerical modeling and extensive aircraft measurements of cloud properties and aerosols, makes a strong case for the loss of precipitation and stream flows in the California Sierra Nevada due to the generation of anthropogenic pollutants and their ingestion into Sierra clouds.

6. CONCLUSIONS

SUPRECIP 2 met its primary objective of documenting the effects of pollution aerosols on clouds and their precipitation over the California Sierra Nevada. The aircraft measurements of cloud properties validated the satellite inferences of cloud microphysics. Those regions over which the processed multi-spectral imagery indicated the clouds had small droplet sizes and suppressed coalescence vs. those areas where the satellite inferences indicated the clouds had large droplet sizes and coalescence were verified by the aircraft measurements. This makes the satellite inferences of altered cloud properties in the central and southern Sierra all the more credible.

The key uncertainty at the outset of SUPRECIP was whether the altered cloud properties were due to the ingestion of pollution aerosols. Although SUPRECIP 1 gave the first indications of a link between the pollution aerosols and the suppression of precipitation-forming processes, it took SUPRECIP 2 utilizing two cloud physics aircraft to demonstrate the direct linkage between these aerosols and the regions in the central and southern Sierra Nevada that have suffered losses of orographic precipitation and stream flows. The analysis of several hundred cloud passes shows that in regions where high concentrations of CCN were measured by the base aerosol aircraft the clouds had to grow to greater depths to develop precipitation than clouds growing in regions of low CCN concentrations.

The spatial and temporal documentation of the CCN and CN aerosols was highly informative. Although the initial source of the pollution aerosols was clearly the urbanized coastal regions, the pollution aerosols in the Central Valley to the Sierra foothills cannot be explained readily by simple advection of the pollutants from the coastal urban areas. There is probably a major source of pollution aerosols in the Central Valley itself and these CCN and total (CN) aerosols are concentrated primarily over the Central Valley from just to the north of Sacramento southward along the foothills to south of Fresno. This is the same region that has been shown through statistical analysis of precipitation and stream-flow records to suffer the greatest loss of winter orographic precipitation and subsequent stream flows.

The pollution aerosols show a strong diurnal oscillation. In the morning these aerosols are concentrated at low levels, but by late afternoon they have been transported upward due to the afternoon heating. Thus, the regional clouds are most affected by the pollutants late in the day. The aircraft measurements indicate that the ratio of CCN to CN (total) aerosols is typically 0.10 to 0.20 whereas the measurements at the ground-based (Blodgett) site indicate that the ratios are higher.

Because the local generation of the pollution aerosols in the Central Valley appears to be a greater problem than the transport of pollution from the urbanized/industrialized coastal regions or inland from the Pacific, the next step in the research progression is to document the sources and chemical constituency of the aerosols in the Central Valley. The evidence amassed from SUPRECIP and the ancillary precursor research conducted by the authors indicates that the precipitation and stream flow losses are real and due primarily to the ingestion of pollutants by orographic clouds over the Sierra Nevada. Further, the results of model simulations demonstrating the detrimental effects of pollutants on Sierra orographic precipitation give additional weight to the hypothesis put forth at the outset of this paper.

7. ACKNOWLEDGEMNTS

The authors gratefully acknowledge the major contributions that the pilots made to the success of the SUPRECIP field effort. Dr. David Prentice piloted the Cheyenne II cloud physics aircraft during SUPRECIP 1 and Mr. Gary Walker, Manager of the SOAR program of the Sandyland Underground Water Conservation District piloted this aircraft in SUPRECIP 2. Mr. Kevin McLaughlin piloted the Cessna 340 aerosol aircraft. The authors also acknowledge Dr. Don Collins and Ms. Crystal Reed of Texas A&M University for their support with the DMA/TDMA system and Ing. Grazio Axisa for maintaining the aircraft instruments in SUPRECIP 2.

The research was supported by the Public Interest Energy Research (PIER) program of the California Energy Commission (CEC). We especially appreciate the enthusiastic encouragement of Mr. Guido Franco of PIER/CEC throughout the research effort.

REFERENCES

Allan, R.J., Nicholls, N., Jones, P.D. and Butterworth, I.J., 1991: A further extension of the Tahiti-Darwin SOI, early SOI results and Darwin pressure. J. Climate ,4, 743-749.

Andreae M.O., D. Rosenfeld, P. Artaxo, A.A. Costa, G.P. Frank, K.M. Longo, and M.A.F. Silva-Dias, 2004: Smoking rain clouds over the Amazon. Science, 303, 1337-1342.

Chow, J.S., L.-W. A. Chen, J.G. Watson, D. H. Lowenthal, K.A. Magliano, K.T. Turkiewicz, and D.E.

Dettinger, M., K. Redmond, and D. Cayan, 2004: Winter Orographic Precipitation Ratios in the Sierra Nevada – Large-Scale Atmospheric Circluations and Hydrologic Consequences. J. Hydromet., 5, 1102-1116

Gerber, H, 1996: Microphysics of marine stratocumulus clouds with two drizzle modes. J. Atmos. Sci. 53, 1649-1662

Givati A. and D. Rosenfeld, 2004: Quantifying precipitation suppression due to air Pollution. Journal of Applied meteorology 43, 1038-1056.

Givati A. and D. Rosenfeld, 2005: Separation between Cloud Seeding and Air Pollution Effects. Journal of Applied Meteorology, 44, 1298-1314.

Givati A. and D. Rosenfeld, 2007: Possible impacts of anthropogenic aerosols on water resources of the Jordan River and the Sea of Galilee. Water Resources Research, In press.

Griffith, D. A., M. E. Solak, and D. P. Yorty, 2005: Is air pollution impacting winter orograhic precipitation in Utah? Weather Modification Association. J. Wea. Modif., 37, 14–20.

Heymsfield, A. J., McFarquhar, G. M., 2002: Microphyics in INDOEX clean and polluted trade cumulus clouds. *Journal of Geophysical Research*, **106**, 28,653-28,676.

Hudson, J. G., and S. Mishra, 2007: Relationships between CCN and cloud microphysics variations in clean maritime air, Geophys. Res. Lett., 34, L16804, doi:10.1029/2007GL030044.

Hudson, J.G., and S.S. Yum, 2001: Maritime-continental drizzle contrasts in small cumuli. J. Atmos. Sci., 58, 915-926.

Jirak, I. L., and W. R. Cotton, 2006: Effect of air pollution on precipitation along the Front Range of the Rocky Mountains. J. Appl. Meteor., 45, 236–245.

Khain A. P., D. Rosenfeld and A. Pokrovsky, 2001: Simulating convective clouds with sustained supercooled liquid water down to -37.5oC using a spectral microphysics model. Geophysical Research Letters, 28, 3887-3890.

Lynn B., A. Khain, **D. Rosenfeld**, W. L. Woodley, 2007: Effects of aerosols on precipitation from orographic clouds. J. Geophys. Res., **112**, D10225, doi:10.1029/2006JD007537, 2007.

McFarquhar, G. M., Heymsfield, A. J., 2001: Parameterizations of INDOEX microphysical measurements and calculations of cloud susceptibility: applications for climate studies. J. Geophys. Res., 106, 28,675-28,698.

Rosenfeld D., 2000: Suppression of Rain and Snow by Urban and Industrial Air Pollution. Science, 287 (5459), 1793-1796.

Rosenfeld D. and C. W. Ulbrich, 2003: Cloud microphysical properties, processes, and rainfall estimation opportunities. Chapter 10 of " Radar and Atmospheric Science: A Collection of Essays in Honor of David Atlas". Edited by Roger M. Wakimoto and Ramesh Srivastava. Meteorological Monographs 52, 237-258, AMS.

Rosenfeld, D. and A. Givati, 2006: Evidence of orographic precipitation suppression by air pollution induced aerosols in the western U.S. J. Applied Meteorology and Climatology, 45, 893-911.

Rosenfeld D., W. L. Woodley, T. W. Krauss, V. Makitov, 2006: Aircraft Microphysical Documentation from Cloud Base to Anvils of Hailstorm Feeder Clouds in Argentina. J. Appl. Meteor., 45, 1261–1281, September 2006.

Rosenfeld, D., J. Dai, X. Yu, Z. Yao, X. Xu, X. Yang, C. Du, 2007: Inverse relations between amounts of air pollution and orographic precipitation. *Science*, **315**, 9 March 2007, 1396-1398.

Woodley Weather Consultants, 2005: The Use of a Cloud Physics Aircraft for the Mapping of Pollution Aerosols Detrimental to Winter Orographic Precipitation over the California Sierra Nevada. California Energy Commission, PIER Energy-Related Environmental Research. CEC-500-2005-205

Woodley Weather Consultants. 2007. Physical/Statistical and Modeling Documentation of the Effects of Urban and Industrial Air Pollution in California on Precipitation and Stream Flows. California Energy Commission, PIER Energy-Related Environmental Research Program. CEC-500-2007-019.

Yum, S.S., and J.G. Hudson, 2002: Maritime/continental microphysical contrasts in stratus. Tellus, 54B., 61-73.

Does Aerosol Concentration Affect Whether Mixing Occurs Inhomogeneously or Homogeneously in Warm Cumulus?

Jennifer D. Small[1], Patrick Y. Chuang[1], Graham Feingold[2], and Hongli Jiang[2]
[1]Cloud and Aerosol Lab, University of California, Santa Cruz
[2]NOAA Earth System Research Laboratory, Boulder, Colorado, USA

We analyze the affect of aerosol on mixing processes in warm cumulus clouds observed during the GoMACCS field campaign near Houston, TX in summer 2006. Cloud drop size distributions and cloud liquid water contents from the Artium flight phase Doppler interferometer in conjunction with clouds simulated with LES model will be used to investigate whether inhomogeneous verses homogenous mixing is preferred for different aerosol regimes.

1. INTRODUCTION

Clouds are important for transporting both moisture and energy in the atmosphere. Small warm continental cumulus clouds are of particular interest due to their extensive coverage. Indirect effects of aerosol on clouds such as a reduction of cloud drop size and increased drop number (N_d) with increasing aerosol concentration (N_a) have been related to a reduction in precipitation (Warner, 1968; Rosenfeld and Lensky, 1998) and increased cloud albedo. There have been few studies looking specifically at the effects of aerosol concentration on mixing processes in warm cumulus.

Previous investigators have described how evaporation, via inhomogeneous and/or homogenous entrainment mixing can alter drop size distributions and thus other processes such as precipitation initiation. If we consider the process of homogeneous mixing we see that as unsaturated air is entrained into cloudy air the size distribution would have the same number of drops as prior to mixing but with decreased diameters shifting the distribution to smaller sizes. If we consider the process of inhomogeneous mixing we see that for each size drop some of them fully evaporate. Thus, after a cloudy parcel is inhomogeneously mixed the total number of drops in each size class decreases without shifting the distribution to a new size range (Latham and Reed, 1977) also known as 'extreme' inhomogeneous mixing (Blyth and Latham, 1990).

Mixing and entrainment are intimately related to drop size and drop number. As we decrease drop size and increase drop number evaporation becomes easier (Wang et al, 2003). Increased evaporation is also related to increased entrainment that can lead to more extreme horizontal buoyancy gradients (Xue and Feingold, 2006) and increased vortical circulation (Zhao and Austin, 2005). Jiang et al (2006) show evidence of increased horizontal buoyancy gradients with increasing aerosol concentrations. Small and Chuang (2008, in prep) show similar results (Figure 1) with observations made during the Gulf of Mexico Atmospheric Composition and Climate Study (GoMACCS) in 2006.

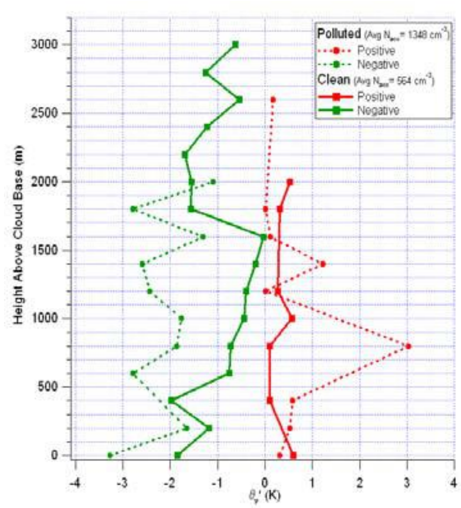

Figure 1. Positive and negative virtual potential temperature perturbations in clean and polluted clouds.

The goal of this work is to explore if aerosol effects whether mixing occurs homogeneously or inhomogeneously in continental cumulus clouds sampled during the GoMACCS.

2. DATA

The GoMACCS project took place during August and September 2006. Data used in this study were obtained with a flight phase Doppler interferometer (f-PDI) and cabin instrumentation on the Center for Interdisciplinary Remotely-Piloted Aircraft Studies (CIRPAS) Twin Otter. Data from two flights, one clean case and one polluted are the focus of this study. During each flight an individual cloud was penetrated multiple times. From each cloud pass f-PDI cloud drop number concentrations (CDNC) and cloud liquid water content (LWC) were obtained.

3. METHODS

Following Small and Chuang (2008), conditional sampling was used to look for signs of inhomogeneous or homogeneous mixing at all sampled levels. CDNC and spectral width of observed distributions are then correlated to out of cloud aerosol concentrations observed at each level. Continental cumulus clouds simulated with an LES model for both a polluted case and a clean case. They are then compared to observed clouds o the clean and polluted days.

For both observed and modeled clouds clean and polluted cases will be compared by producing 2-D PDFs of the density function for each aerosol regime to evaluate the mixing process represented in LES when viewed from this perspective. In depth analysis will be conducted using data from multiple passes (at many altitude levels) through individual well developed warm cumulus clouds for both a clean case and a polluted case.

4. REFERENCES

Jiang, H., H. Xue, A. Teller, G. Geingold, and Z. Levin, (2006), Aerosol effects on the lifetime of shallow cumulus, *Geo. Res. Letters*, 33, L14806, doi:10.1029/2006GL026024.

Rosenfeld, D., and I. M. Lensky (1998), Satellite-based insights into precipitation formation processes in continental and maritime convective clouds, *Bull. Amer. Meteorol. Soc,* **79**, 2457-2476.

Small, J. D., and P. Y. Chuang, (2008), New observations of precipitation initiation in warm cumulus clouds, *J. Atmos. Sci.*, in press.

Warner, J. (1968), A reduction in rainfall associated with smoke from sugar-cane fires—An inadvertent weather modification? *J. Appl. Meteorol.*, **7**, 247-251.

Xue, H., and G. Feingold (2006), Large eddy simulations of trade-wind cumuli: Investigation of aerosol indirect effects, *J. Atmos Sci.*, **63**, 1605-1622.

Zhao, M., and P. H. Austin, (2005), Life cycle of numerically simulated shallow cumulus clouds.part II: Mixing dynamics, *J. Atmos. Sci.*, **62**, 1291-1310.

PRELIMINARY ASSESSMENT OF CLOUD-AEROSOL INTERACTION AND RELATED MICROCLIMATOLOGICAL STUDIES IN URBAN ENVIRONMENT

Steinberga I.
University of Latvia, Faculty of Geography and Earth Sciences

ABSTRACT

This study describes a set of studies which has attempted to make a first estimate of the contribution and role of aerosols in cloud formation processes in urban environment and changes in related microclimatological parameters in urban environment. Clouds strongly interact with climate by regulating the temperature and moisture stucture of the atmosphere. They modify the Earth`s energy budget, are an esential part of the hydrological cycle, play an important role in processing and cycling atmospheric pollutants, and are responsible for many optical effects as well. Some of the physical and chemical processes are involved in clouds formation processes including aerosol activation, aqueous-phase chemistry, and wet deposition, and they also act as trace gas and aerosol redistributors. Vertical mixing transports trace gases from the other more polluted areas to less polluted areas. It is estimated that up to 80 % of the total production of sulphate globally is contributed by aqueous-phase oxidation in the clouds. Precipitation formed in clouds is one of the most efficient sinks for aerosols and other soluble tracers, which is known as wet deposition. On the other hand, it`s well known that the large anthropogenic releases of sulphur dioxide into the atmosphere obvious lead to sulphate aerosols which cool the climate at least in two ways - directly by scattering solar radiation, and indirectly by increasing the number of cloud condensation nuclei and the concentration of cloud droplets (greater concentration of aerosol particles increased cloud cover and decreased near-surface temperatures resulting lowering of near-surface wind speeds).

Keywords: aerosols, microclimatology, urban environment

1. INTRODUCTION

In general clouds form by condensation of water vapour onto atmospheric aerosol particles in the air which has become supersaturated. About 60 % of the Earth`s surface is covered by clouds. Clouds constitute a multiphase atmospheric system, insofar as gaseous species, atmospheric water vapor onto atmospheric aerosol particles. The environmental impact of aerosols is dependent on their chemical and physical properties, lifetime and abundancy as well. Clouds are efficient reaction media for chemical transformations, which the atmospheric sulphur cycle being particularly affected by their presence, since the different oxidation pathways for the conversion of SO_2 to sulphate are all characterized by much faster reaction rates in the aqueous phase than in the gas phase (Calvert et al., 1986).

Clouds produce precipitation which is a quite efficient mechanism for removing trace species from atmosphere. However, most clouds do not lead to precipitation and evaporate. Upon cloud evaporation, gas and particles are released back into the atmosphere.

2. CLOUD FORMATION PROCESS

Cloud droplets are formed in the atmosphere by the condensation of water vapor onto aerosol particles when the relative humidity exceeds the saturation level. Cloud particles may grow or merge in various mechanisms, to become larger precipitation particles leading to rain or snow. Most slouds do not produce precipitation and usually cloudiness and rainfall are observed seperately. Raindrop sizes may range from 0.5 mm to greater than 5 mm in diameter and they most often fall from nimbostatus and cumulonimbus clouds.

3. SITE DESCRIPTION

Riga city (Latvia) has been selected for investigations. Riga is a city in Eastern Europe with 1 million inhabitants located close to the Baltic Sea. Industrial point sources (sulphur dioxide and nitrogen oxides emitters) are located mainly in central part and close to the river Daugava which is dividing city in two parts. Air quality data were obtained from traffic monitoring station located in Riga sea port (economicly active urban territory).

The meteorological data set (56.91 N and 23.96 E) used was from station located at central part of Riga.

4. METHODS AND INSTRUMENTS

Used monitoring methods for major inorganic ion measurements were described in Table 1. Particulates PM_{10} and $PM_{2.5}$ were measured by PM monitoring device (SM200, beta gauge method) with uncertainty 1.05 $\mu g/m^3$. Other gas measurements were performed by UV DOAS (Ultraviolet Absorption Spectroscopy) technique. Challenging the UV DOAS systems with a known concentration of span gasess accuracy and precision for specific gas measurements performance of qualitu control measures were acording with OPSIS *Analyzer Software User`s Guide*. The measurement uncertainty is 2 $\mu g/m^3$, sensitivity – 1 ppb.

Meteorological measurements were done with Vaisala (Finland) equipment.

5. RESULTS AND DISCUSSION

Daily mean concentrations of aerosols (PM_{10} and $PM_{2.5}$) and weekly mean concentrations of major ions have been obtained from more that 8 month sampling period (April 2007 to December 2007), are presented in Fig. 1 and their variations are detailed in this section.

Particulate matter PM_{10}:
The most frequenty used indicator for suspended particles in the air has been PM_{10} which reffers to particles with an aerodynamic diameter less than 100 μm. Annual average concentrations in Asian cities range from 35 $\mu g/m^3$ to 129 $\mu g/m^3$, while in Europe and North America it typically ranges from 15-60 $\mu g/m^3$. About 70 % of the cities had annual average concentrations above 50 $\mu g/m^3$ (WHO, 2005). According to long term mesurements in Riga city yearly average concentrations are high and very stable for last 5 years. Detected PM_{10} concentrations in similar monitoring site were about 48 μ/m^3.

In Europe in urban areas the average concentrations were 26.3 $\mu g/m^3$ in urban background and 32.2 $\mu g/m^3$ in streets. In rural areas the concentrations are lower and were 21.7 $\mu g/m^3$ (WHO, 2005).

Particulate matter $PM_{2.5}$:
$PM_{2.5}$ is an important indicator of antropogenic PM_{10} pollution indicator in many areas. The ratio of $PM_{2.5}$ to PM_{10} has been reported form many cities worldwide: in USA ratio varies between 0.44 and 0.71, in Central Europe cities it could be about 0.71, but in intensive traffic sites in Europe about 0.6-0.7. This ratio for Riga city based on 8-month monitoring results exceed 0.87 level in average what indicates quite high relative level of $PM_{2.5}$ pollution. $PM_{2.5}$ pollution levels depend on type of source, distance from the source and wind speed as well.

The rural background concentrations of $PM_{2.5}$ in Europe in general is quite uniform at between 11-13 $\mu g/m^3$, and substantially lower than urban background levels what is about 15-20 $\mu g/m^3$. The highest annual average concentrations have been observed at traffic sites and it typically ranges from 20-30 $\mu g/m^3$ (WHO, 2005).

Fine particles often are responsible for visibility problems, but it`s often connected with quite high $PM_{2.5}$ pollutions levels exceeding over 100 $\mu g/m^3$ which are never achieved in Latvia.

Chloride:

No any substantial changes in chloride concentrations were detected. Concentrations were quite stable all period of observations and weekly concentrations varies between 0.05 to 0.13 μg/m^3 (average concentration 0.09 μg/m^3). This stable concentration level could be explained by substantial pollution input from sea.

Sulphate and nitrate:

No clear seasonal or weekly variation trends were observed for these two compounds. But it seems that, in summer a decrease of fosil fuel emissions might be balanced by an increase of the photochemical production of theese species (Khoder, 2002). Sulphate was found in much higher concentrations comparing to nitrate (approximately 0.87 and 0.29 μg/m^3 respectively).

Meteorology and variations:

Statistics of the wind directions for the Baltic Sea region show that a stedy wind from a constant direction very seldom observed for more than one or half day (Vana, 2002). Analyzed aerosol pollution levels and microclimatolocial parameters show some substantial consequences. Theese relationships between parameters included in correlation matrix (Table 2). For some correlation pairs (aerosol ratio and ozone, aerosol ratio and sulphur dioxide) seems to be a week or no correlation at all. After linearization process relationships become although week, but statistically significant (correlation coefficient for aerosol ratio and ozone become 0.23, but for aerosol ratio and sulphur dioxide 0.17). Minor changes in PM_{10} concentrations were observed during summer season and during this season variability of concentrations are not so high as in winter season. Comparing aerosol concentrations during working days and weekend days detected difference were about 10 μg/m^3 in case of PM_{10}.

Weak but statisticaly significant positive linear correlation was detected between temperature and $PM_{2.5}$ pollution level. Weak but statisticaly significant negatvive linear correlation was detected between precipitation and PM_{10} pollution level.

Analyzing $PM_{2.5}$ and PM_{10} pollution levels in context with relative humidity it seems no any consequencies, but there are several episodes with higher PM soncentrations and lower relative humidity. Some unexplained cases are established in witer season, but it could be explained by local seasonally working sources.

More clear situation were detected for $PM_{2.5}$ and PM_{10} pollution levels in context with precipitation. Several episodes (beginning of may, end of july, end of september, beginning of october, end of november and december) were detected when after dry periods (periods without precipitation) concentrations of $PM_{2.5}$ and PM_{10} growing rapidly. This fact could be explained by tendency of particulate accumulation tendency.

Table 1.

Parameter	*Method*	*Accurancy, %*
SO4	LVS EN ISO10304-1:2004	3.2
NO3	LVS EN ISO10304-1:2004	2.7
Cl	LVS EN ISO10304-1:2004	5.0

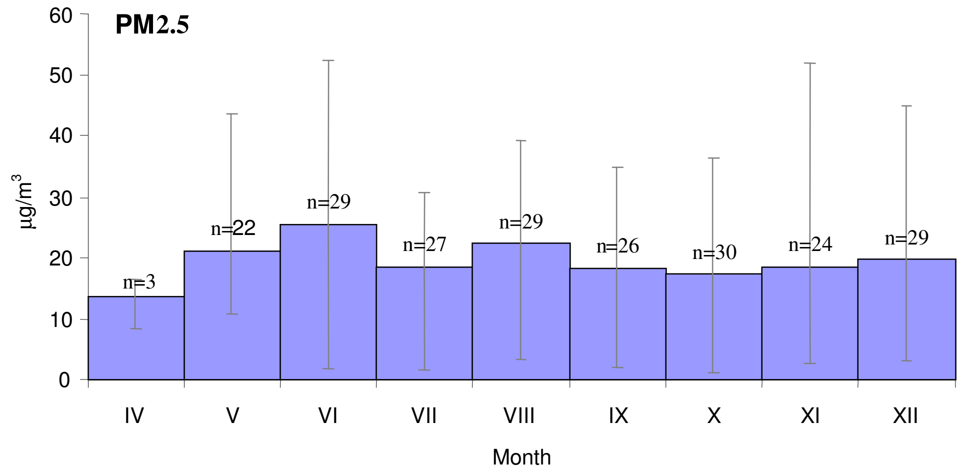

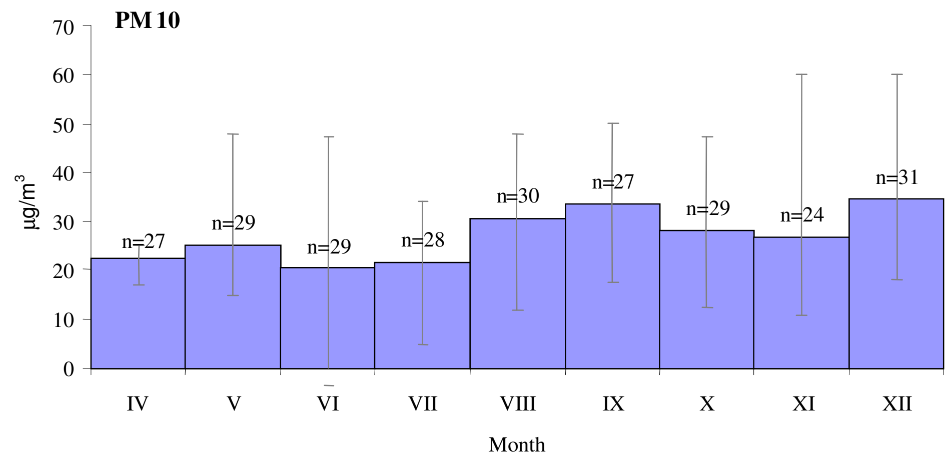

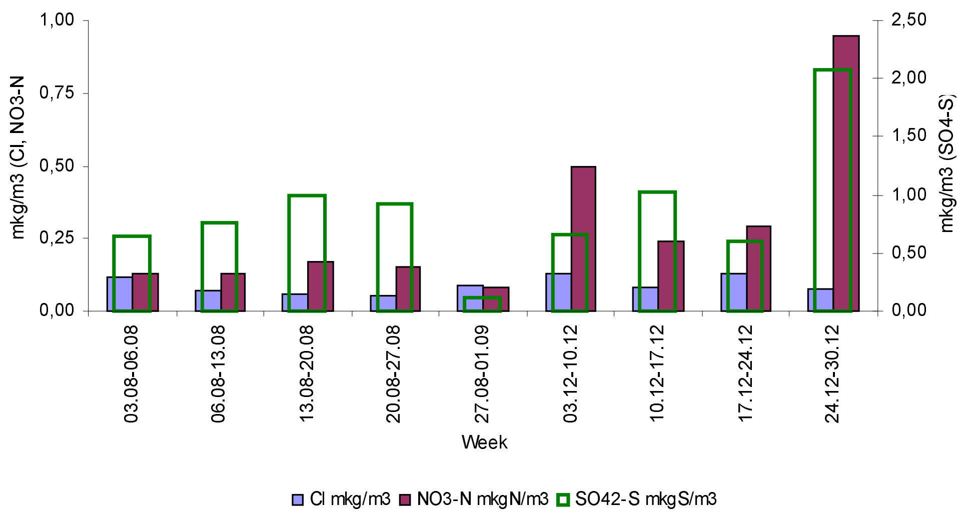

Fig.1. Mean concentrations of $PM_{2.5}$, PM_{10} and major inorganic ions from April 2007 to December 2007 (n represents number of samples)

Table 2

	$PM_{2,5}$	PM_{10}	$PM_{10}/PM_{2,5}$	O_3	SO_2	NO_2	*Precip.*	*Temp.*	*WS*	*RH*
$PM_{2,5}$	1									
PM_{10}	**0.63**	1								
$PM_{10}/PM_{2,5}$	**-0.39**	0.066	1							
O_3	0.09	**-0.24**	-0.07	1						
SO_2	0.05	0.166	-0.03	-0.089	1					
NO_2	0.07	0.065	-0.08	**-0.344**	**0.352**	1				
Precip.	-0.16	**-0.27**	0.05	0.0764	-0.082	0.074	1			
Temp.	**0.28**	0.008	-0.10	**0.4902**	-0.168	**-0.251**	0.16156	1		
WS	-0.03	-0.07	0.06	-0.141	-0.008	-0.162	0.02691	-0.257	1	
RH	-0.13	0.122	0.04	**-0.662**	0.175	**0.289**	0.22735	**-0.559**	0.171	1

Explanation: (1) Precip. – precipitation; (2) Temp. – atmospheric temperature; (3) WS – wind speed; (4) RH – relative humidity; (5) substantial relationships were indicated in bold).

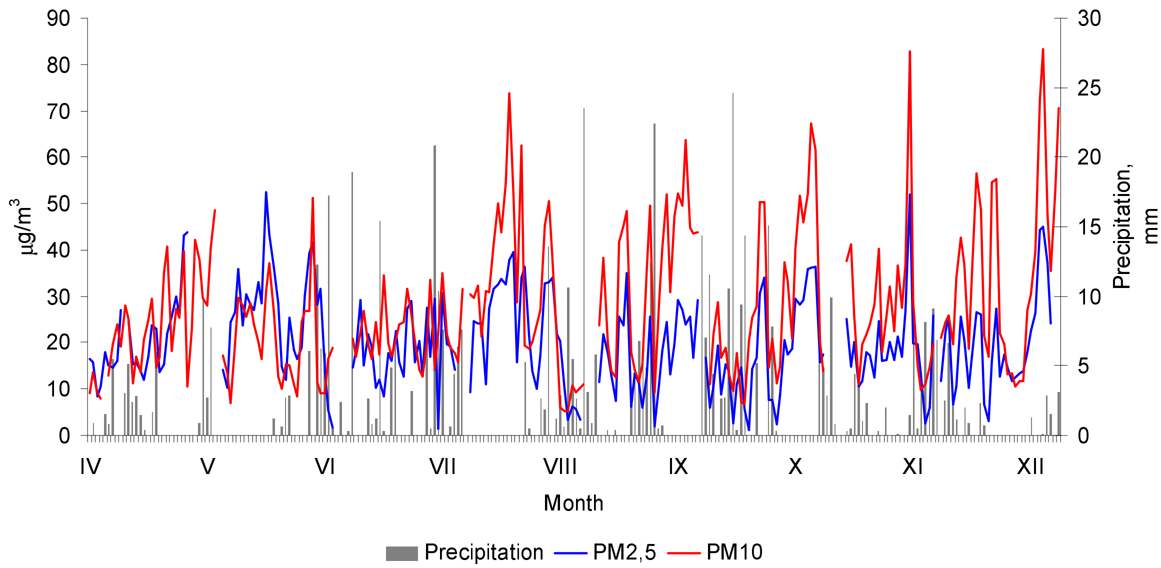

Fig.2. Precipitation and aerosol concentration measurements from April 2007 to December 2007

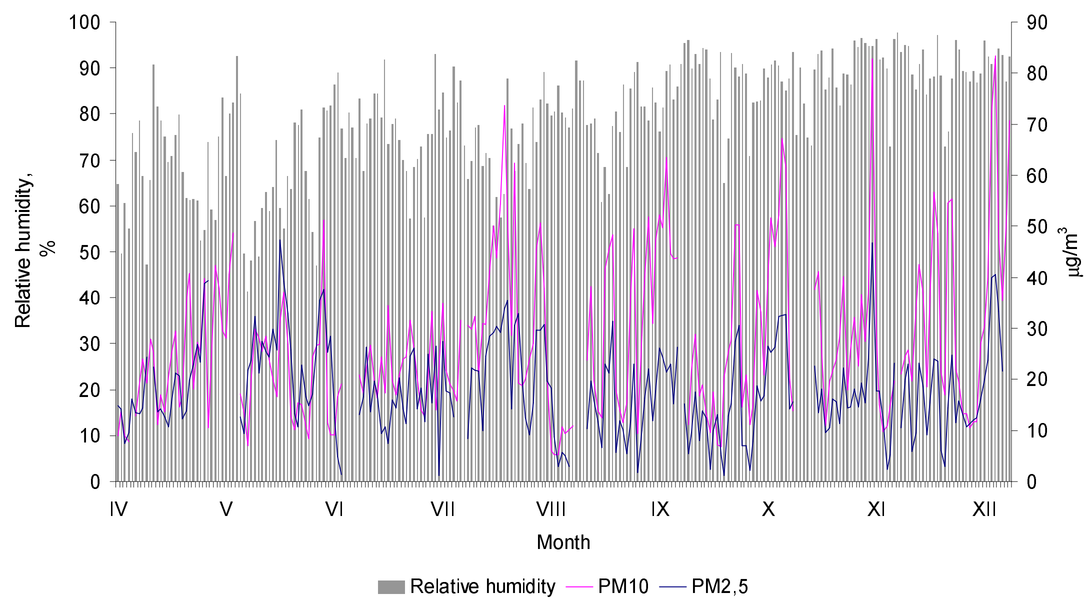

Fig.3. Relative humidity and aerosol concentration measurements from April 2007 to December 2007

CONCLUSIONS

(1) Due to low aerosol pollution levels no changes in visibility were detected on local level.
(2) Quite stable $PM_{2.5}$ pollution level coulde be exolained by dominatind background pollution level which is very afected by local sources.
(3) During analysis were established positive close relationship between $PM_{2.5}$ and PM_{10}.
(4) There are identified several episodes with higher PM soncentrations and lower relative humidity. Some unexplained cases are established in witer season, but it could be explained by local seasonally working sources.
(5) Several episodes were detected when after dry periods (periods without precipitation) concentrations of $PM_{2.5}$ and PM_{10} growing rapidly. This fact could be explained by tendency of particulate accumulation tendency.
(6) No any relationships between cloudiness and PM pollution levels were detected. It could be due geographical location of Riga city what is connected to changing weather conditions.

BIBLIOGRAPHY

Air quality guidelines (2005). WHO.

Khoder M. I. (2002). Atmospheric conversion of sulphur dioxide to particulate sulfate and nitrogen dioxide to particulate nitrate and gaseous nitric acid in an urban area. Chemosphere 49, 675-684.

Calvert J. G., Heikes B. G., Stockwell W. R., Mohnen V. A. and Kerr J. A. (1986). Some considerations of the important chemical processes in acid deposition. Chemistry of Multiphase Atmospheric Systems, Corfu 26 September – 8 October 1983, W. Jaeschke Ed. (Springer Verlag, Berlin) pp. 615-647.

Vana M., Tamm E. (2002). Propagation of atmospheric aerosol and the area of representiveness of its measurements in the Baltic Sea region. Atmospheric Environment 36, 391-401.

Acknowledgements

This work was supported by European Social Fund (ESF). The air quality and meteorological dataa were obtained from Latvian Environment, Geology and Meteorology agency.

THE IMPACT OF AEROSOLS ON CLOUD AND PRECIPITATION PROCESSES: CLOUD-RESOLVING MODEL SIMULATIONS

Wei-Kuo Tao[1], Xiaowen Li[1,2], Alexander Khain[3], Toshihisa Matsui[1,2], Stephen Lang[4], and Joanne Simpson[1]

[1]Laboratory for Atmospheres, NASA/Goddard Space Flight Center, Greenbelt, MD, 20771, USA

[2]Goddard Earth Sciences and Technology Center, University of Maryland, Baltimore County, Baltimore, MD

[3]Department of Atmospheric Science, Hebrew University of Jerusalem, Jerusalem, Israel

1. INTRODUCTION

Aerosols and especially their effect on clouds are one of the key components of the climate system and the hydrological cycle [Ramanathan et al., 2001]. Yet, the aerosol effect on clouds remains largely unknown and the processes involved not well understood. A recent report published by the National Academy of Science states "*The greatest uncertainty about the aerosol climate forcing - indeed, the largest of all the uncertainties about global climate forcing - is probably the indirect effect of aerosols on clouds [NRC, 2001].*" The aerosol effect on clouds is often categorized into the traditional "first indirect (i.e., Twomey)" effect on the cloud droplet sizes for a constant liquid water path [Twomey, 1977] and the "semi-direct" effect on cloud coverage [e.g., Ackerman et al., 2000]. Enhanced aerosol concentrations can also suppress warm rain processes by producing a narrow droplet spectrum that inhibits collision and coalescence processes [e.g., Squires and Twomey, 1961; Warner and Twomey, 1967; Warner, 1968; Rosenfeld, 1999].

The aerosol effect on precipitation processes, also known as the second type of aerosol indirect effect [Albrecht, 1989], is even more complex, especially for mixed-phase convective clouds. Table 1 summarizes the key observational studies identifying the microphysical properties, cloud characteristics, thermodynamics and dynamics associated with cloud systems from high-aerosol continental environments. For example, atmospheric aerosol concentrations can influence cloud droplet size distributions, warm-rain process, cold-rain process, cloud-top height, the depth of the mixed phase region, and occurrence of lightning. In addition, high aerosol concentrations in urban environments could affect precipitation variability by providing an enhanced source of cloud condensation nuclei (CCN). Hypotheses have been developed to explain the effect of urban regions on convection and precipitation [*van den Heever and Cotton*, 2007 and S*hepherd*, 2005]. Please see Tao *et al.* (2007) for more detailed description on aerosol impact on precipitation.

Recently, a detailed spectral-bin microphysical scheme was implemented into the Goddard Cumulus Ensemble (GCE) model. Atmospheric aerosols are also described using number density size-distribution functions. A spectral-bin microphysical model is very expensive from a computational point of view and has only been implemented into the 2D version of the GCE at the present time. The model is tested by studying the evolution of deep tropical clouds in the west Pacific warm pool region and summertime convection over a mid-latitude continent with different concentrations of CCN: a low "clean" concentration and a high "dirty" concentration. The impact of atmospheric aerosol concentration on cloud and precipitation will be investigated.

Corresponding author's address: W.-K. Tao, Code 912, NASA GSFC, Greenbelt, MD 20771, USA; E-Mail: Wei-Kuo Tao <Wei-Kuo.Tao-1@nasa.gov>

Properties	High CCN (Dirty)	Low CCN (Clean)	References (Observations)
Cloud droplet size distribution	Narrower	Broader	*Rosenfeld and Lensky* [1998], *Rosenfeld* [1999 & 2000], *Rosenfeld et al.* [2001], *Rosenfeld and Woodley* [2000], *Andreae et al.* [2004], *Koren et al.* [2006],
Warm-rain process	Suppressed	Enhanced	*Rosenfeld* [1999 & 2000], *Rosenfeld and Woodley* [2000], *Rosenfeld and Ulbrich* [2003], *Andreae et al.* [2004], *Lin et al.* [2006]
Cold-rain process	Enhanced	Suppressed	*Rosenfeld and Woodley* [2000], Orville et al. [2001], Williams *et al.* [2002], *Andreae et al.* [2004], *Lin et al.* [2006], *Bell et al.* [2007]
Mixed phase region	Deeper	Shallower	*Rosenfeld and Lensky* [1998], Williams *et al.* [2002], *Lin et al.* [2006]
Cloud-top height	Higher	Lower	*Andreae et al.* [2004], *Koren et al.* [2006], *Lin et al.* [2006]
Lightning	Enhanced (downwind side)/higher max flash	Less and lower max flash	*Williams et al.* [2002], *Orville et al.* [2001]

Table 1 Key observational studies identifying the differences in the microphysical properties, cloud characteristics, thermodynamics, and dynamics associated with clouds and cloud systems developed in dirty and clean environments. References of papers can be found in Tao et al. (2007).

2. MODEL DESCRIPTION AND CASE STUDIES

2.1 GCE Model

The model used in this study is the 2D version of the GCE model. Modeled flow is anelastic. Second- or higher-order advection schemes can produce negative values in the solution. Thus, a Multi-dimensional Positive Definite Advection Transport Algorithm (MPDATA) has been implemented into the model. All scalar variables (potential temperature, water vapor, turbulent coefficient and all five hydrometeor classes) use forward time differencing and the MPDATA for advection. Dynamic variables, u, v and w, use a second-order accurate advection scheme and a leapfrog time integration (kinetic energy semi-conserving method). Short-wave (solar) and long-wave radiation as well as a subgrid-scale TKE turbulence scheme are also included in the model. Details of the model can be found in Tao and Simpson (1993) and Tao *et al.* (2003).

2.2 Microphysics (Bin Model)

The formulation of the explicit spectral-bin microphysical processes is based on solving stochastic kinetic equations for the size distribution functions of water droplets (cloud droplets and raindrops), and six types of ice particles: pristine ice crystals (columnar and plate-like), snow (dendrites and aggregates), graupel and frozen drops/hail. Each type is described by a special size distribution function containing 33 categories (bins). Atmospheric aerosols are also described using number density size-distribution functions (containing 33 bins). Droplet nucleation (activation) is derived from the analytical calculation of super-saturation, which is used to determine the sizes of aerosol particles to be activated and the corresponding sizes of nucleated droplets. Primary nucleation of each type of ice crystal takes place within certain temperature ranges. A detailed description of these explicitly parameterized processes can be found in Khain and Sednev (1996) and Khain *et al*. (1999, 2001).

2.3 Case Studies

Three cases, a tropical oceanic squall system observed during TOGA COARE *(Tropical Ocean and Global Atmosphere Coupled Ocean-Atmosphere Response Experiment,* which occurred over the Pacific Ocean warm pool from November 1992 to February 1993), a midlatitude continental squall system observed during PRESTORM (*Preliminary Regional Experiment for STORM-Central,* which occurred in Kansas and Oklahoma during May-June 1985), and mid-afternoon convection observed during CRYSTAL-FACE (Cirrus Regional Study of Tropical Anvils and Cirrus Layers – Florida Area Cumulus Experiment, which occurred in Florida during July 2002), will be used to examine the impact of aerosols on deep, precipitating systems.

The June 10-11, 1985 PRESTORM case has been well studied (e.g., Johnson and Hamilton 1988; Rutledge *et al.* 1988; Tao *et al.* 1996; Lang *et al.* 2003). The PRESTORM environment was fairly unstable but relatively dry with a lifted index of -5.37 and a Convective Available Potential Energy (CAPE) of 2300 J/kg. The February 22, 1993 TOGA COARE squall line has also been well studied (Jorgensen *et al.* 1997; Trier *et al*. 1996, 1997; Wang et al. 1996). The CAPE and lifted index are moderately unstable, 1776 J/kg and -3.2, respectively. The CRYSTAL-FACE July 16, 2002 case is a sea breeze convection case that developed over South Florida [*Ridley et al.*, 2004; *Heymsfiedl et al.*, 2004]. It originated near the coast and propagated inland and dissipated within a couple of hours. The CAPE, total precipitable water and lifting index, are 2027 J/kg, 4.753 g/cm^2 and -4.23, respectively,

A stretched vertical coordinate was used in the model with 31 grid points. There were 1024 horizontal grid points; the central 872 had a fixed 750, 750 and 1000 m resolution for TOGA COARE, CRYSTAL and PRESTROM, respectively. The outer grids were stretched. Radiation was included, and a low-level cold pool was used to start the system.

3. RESULTS

3.1 Rainfall and Its Characteristics

Table 2 shows the domain-averaged surface rainfall amounts, and stratiform percentages for the TOGA COARE, PRESTORM and CRYSTAL-FACE cases under clean and dirty conditions. The precipitation is divided into convective and stratiform components [*Tao et al.,* 1993; *Lang et al.,* 2003]. The convective region includes areas with strong vertical velocities (over 3-5 m s^{-1}) and/or heavy surface rainfall. The stratiform region is simply non-convective. For the PRESTORM case, the dirty scenario produces more stratiform (light) precipitation than does the clean case. It is expected that a high CCN concentration allows for more small cloud droplets and ice particles to form. The lower collection coefficient for smaller cloud and ice particles allows for a larger amount of ice phase particles to be transported into the trailing stratiform region, producing a higher stratiform rain percentage in the dirty case. Aerosols do not have much impact on the straiform percentage for the CRYSTAL-FACE case because of its short life span. The reduction in stratiform rain (or light rain) in the dirty environment for the TOGA COARE case is due to its enhanced convective activity (stronger updrafts).

	TOGA COARE Clean	***TOGA COARE Dirty***	***PRESTORM Clean***	***PRESTORM Dirty***	***CRYSTAL Clean***	***CRYSTAL Dirty***
Averaged Rain	**18.0**	**28.4**	**38.3**	**29.1**	**12.6**	**11.0**
Stratiform (%)	**50**	**17**	**43**	**70**	**43**	**40**

Table 2 *Domain-averaged surface rainfall amount (in mm day^{-1}), stratiform percentage (in %) for the TOGA COARE, PRESTORM and CRYSTAL-FACE case under dirty and clean conditions. Note there are 9 hours in the PRESTORM and TOGA COARE simulations, and 5 hours in the CRYSTAL-FACE simulation*

Figure 1 shows time sequences of the GCE model-estimated domain mean surface rainfall rate for the PRESTORM, TOGA COARE and CRYSTAL cases. Rain suppression in the high CCN concentration (i.e., dirty environment) runs is evident in all three case studies but only during the first hour of the simulations. Rain reaches the ground early in all the clean cases. This is in good agreement with observations [e.g., *Rosenfeld,* 1999, 2000]. During the mature stage of the simulations, the effect of increasing the CCN concentration ranges from rain suppression in the PRESTORM case to little effect in the CRYSTAL-FACE case to rain enhancement in the TOGA COARE case. These results suggest that model simulations of the whole life cycle of convective system are needed in order to assess the impact of aerosols on precipitation processes associated with mesoscale convective systems and thunderstorms. These results also show the complexity of aerosol-cloud-precipitation interaction within deep convection.

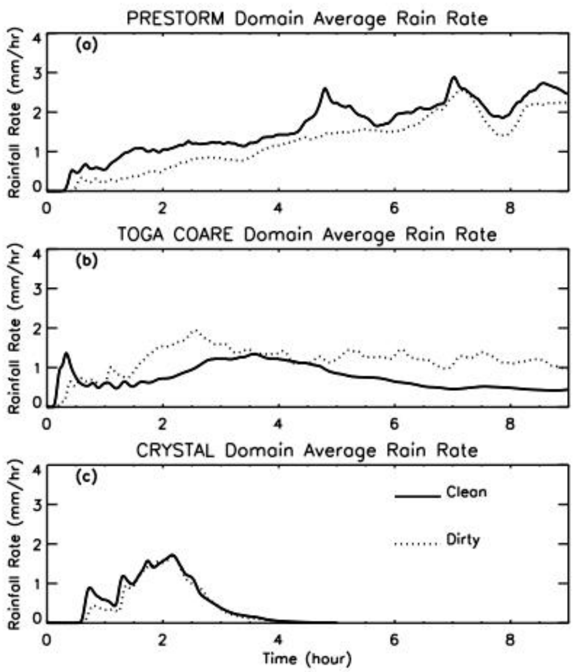

*Fig. 1 Time series of GCE model-estimated domain mean surface rainfall rate (mm h^{-1}) for the **(a)** PRESTORM, **(b)** TOGA COARE, and **(c)** CRYSTAL case. The solid/dashed line represents clean/dirty conditions.*

Figure 2 shows a schematic diagram of the physical processes that cause either enhancement (TOGA COARE) or suppression (PRESTORM) of precipitation in a dirty environment. In the early developing stages, small cloud droplets are produced in both the TOGA COARE and the PRESTORM cases with high CCN. Both cases also show narrower cloud drop size spectra for high CCN (not shown). This result is in good agreement with observations [i. e., *Twomey et al.,* 1984; *Albrecht,* 1989; *Rosenfeld,* 1999]. In this early stage, rain is suppressed for both cases with high CCN, which is also in good agreement with observations [*e.g., Rosenfeld,* 1999, 2000]. The suppression of precipitation in dirty conditions is mainly due to microphysical processes only. Smaller cloud droplets collide/coalesce less efficiently, delaying raindrop formation. These microphysical processes are very important especially in the early/developing stage of a cloud system.

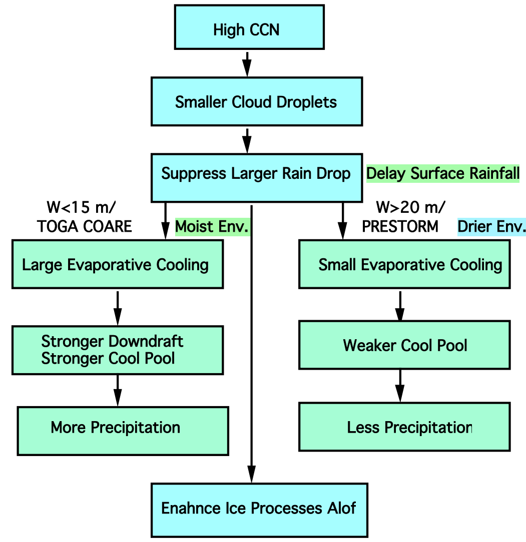

Fig. 2 Schematic diagram showing the physical processes that lead to either enhancement (TOGA COARE case) or suppression (PRESTORM case) of precipitation in a dirty environment. Adapted from Tao et al. (2007).

The model results also indicated that the low-level evaporative cooling is quite different between the clean and dirty case (Fig. 3). Stronger evaporative cooling could enhance the near surface cold-pool strength. When the cold pool interacts with the lower level wind shear, the convergence could become stronger, producing stronger convection for the dirty cases. This can lead to more vigorous precipitation processes and therefore enhanced surface precipitation (positive feedback)[1]. These processes seem to be occurring in the TOGA COARE case. In this case, evaporative cooling is more than twice as strong in the lower troposphere for the dirty scenario compared to the clean scenario. More rain reaches the surface after 30 minutes of model integration in the dirty case as compared to the clean case. During this period, more evaporative cooling in the dirty case is already evident from the model results.

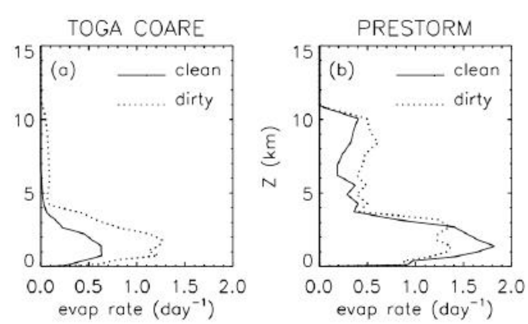

*Fig. 3 Domain average evaporation rate (day^{-1}) profiles during the first two hour of simulation for the **(a)***

[1] Note that the enhanced precipitation can cause enhanced evaporation that in turn has a positive feedback on the rainfall amounts by triggering additional convection.

*TOGA COARE and (**b**) PRESTORM case. The solid/dashed line represents the dirty/clean scenario.*

4. COMPARISON WITH PREVIOUS MODELING STUDIES

Most previous modeling results found that high CCN concentrations could suppress precipitation processes [i.e., *Khain et al.,* 2004, 2005; *Cheng et al.,* 2007, *Lynn et al.,* 2005b; *Van den Heever et al.,* 2006; *Teller and Levin,* 2006; *van den Heever and Cotton,* 2007]. However, high CCN concentrations could also enhance precipitation processes [*Wang 2005*; *Khain et al.* 2005]. These results show the complexity of aerosol interactions with convection. More case studies are required to further investigate the aerosol impact on rain events. In almost all previous cloud-resolving modeling studies (including the present study), idealized or composite [i.e., *van den Heever et al.,* 2006] CCN concentrations were used in the model simulations. In addition to IN and GCCN, the chemistry of CCN needs to be considered in future modeling of aerosol-precipitation interactions. In addition, many previous CRM studies did not compare model results with observed cloud structures, organization, radar reflectivity and rainfall. Some of the CRM domains were too small to resolve the observed clouds or precipitation systems (the domain size has to be at least twice as large as the simulated features). It may require major field campaigns to gather the data necessary to both initialize (with meteorological and aerosol) and validate (i.e., in situ cloud property observations, radar, lidar, and microwave remote sensing) the models. Although CRM-simulated results can provide valuable quantitative estimates of the indirect effects of aerosols, CRMs are neither regional nor global models and can only simulate clouds and cloud systems over a relatively small domain. Close collaboration between the global and CRM communities is needed in order to expand the CRM results to a regional and global perspective.

5. SUMMARY

- For all three cases, higher CCN produces smaller cloud droplets and a narrower spectrum. Dirty conditions delay rain formation, increase latent heat release above the freezing level, and enhance vertical velocities at higher altitude for all cases. Stronger updrafts, deeper mixed-phase regions, and more ice particles are simulated with higher CCN in good agreement with observations.
- In all cases, rain reaches the ground early with lower CCN. Rain suppression is also evident in all three cases with high CCN in good agreement with observations (*Rosenfeld,* 1999, 2000 and others). Rain suppression, however, only occurs during the first hour of simulation. This result suggests that microphysical processes dominate the impact of aerosols on precipitation in the early stage of precipitation development.
- During the mature stage of the simulations, the effect of increasing aerosol concentration ranges from rain suppression in the PRESTORM case to little effect on surface rainfall in the CRYSTAL-FACE case to rain enhancement in the TOGA COARE case.
- The model results suggest that evaporative cooling is a key process in determining whether higher CCN reduces or enhances precipitation. Cold pool strength can be enhanced by stronger evaporation. When cold pool interacts with the near surface wind shear, the low-level convergence can be stronger, facilitating secondary cloud formation and more vigorous precipitation processes. Evaporative cooling is more than two times stronger at low levels with higher CCN for the TOGA COARE case during the early stages of precipitation development. However, evaporative cooling is slightly stronger at lower levels with lower CCN for the PRESTORM case. The early formation of rain in the clean environment could allow for the formation of an earlier and stronger cold pool compared to a dirty environment. PRESTORM has a very dry environment and both large and small rain droplets can evaporate. Consequently, the cold pool is relatively weaker, and the system is relatively less intense with higher CCN.
- Sensitivity tests are conducted to determine the impact of ice processes on aerosol-precipitation interaction. The results suggested that ice processes are crucial for suppressing precipitation due to high CCN for the PRESTORM case. More and smaller ice particles are generated in the dirty case and transported to the trailing stratiform region. This reduces the heavy convective rain and contributes to the weakening of the cold pool. Warm rain processes dominate the TOGA COARE case. Therefore, ice processes only play a secondary role in terms of aerosol-precipitation interaction.
- Two of the three cloud systems presented in this paper formed a line structure (squall system). A 2D simulation, therefore, gives a good approximation to such a line of convective clouds. Since the real atmosphere is 3D, further 3D cloud-resolving simulations are needed to address aerosol-precipitation interactions.

6. REFERENCES

Tao, W.-K., X. Li, A. Khain, T. Matsui, S. Lang, and J. Simpson, 2007: The role of atmospheric aerosol concentration on deep convective precipitation: Cloud-resolving model simulations. *J. Geophy. Res.,* **112**, D24S18, doi:10.1029/2007JD008728.

All other references can be found in above paper.

7. Acknowledgements

The GCE model is mainly supported by the NASA Headquarters Atmospheric Dynamics and Thermodynamics Program and the NASA Tropical Rainfall Measuring Mission (TRMM). The authors are grateful to Dr. R. Kakar at NASA headquarters for his support of this research. The research was also supported by the Office of Science (BER), U. S. Department of Energy/Atmospheric Radiation Measurement (DOE/ARM) Interagency The authors are grateful to Dr. Kiran Alapaty at DOE/ARM for his support of this research. The authors acknowledge NASA Goddard Space Flight Center for computer time used in this research.

AEROSOL EFFECTS ON PRECIPITATION PATHWAYS IN POPULATIONS OF SIMULATED DEEP CONVECTIVE CLOUDS

Sarah Tessendorf[1*] and Graham Feingold[2]

[1]National Center for Atmospheric Research, Boulder, CO
[2]NOAA Earth Systems Research Laboratory, Boulder, CO

1. INTRODUCTION

Aerosol particles have long been associated with modifications to cloud microphysics and precipitation (e.g., Gunn and Phillips 1957, Warner 1968). When more cloud condensation nuclei (CCN) are present, the warm rain process is suppressed as a result of a reduction in drop size and reduced collection efficiencies. The evidence for precipitation reduction beyond the effect on individual clouds is scarce, and mostly derives from observations and simulations of warm stratiform clouds (WMO/IUGG IAPSAG 2008).

Recently, however, more attention has been paid to aerosol effects on deep convection, and a variety of results have been found. In general, modeling results suggest that clouds that form in polluted conditions, i.e., higher CCN concentrations, tend to yield less accumulated precipitation (Reisin et al. 1996, Saleeby and Cotton 2004). In contrast, studies by Khain et al. (2005) and Lynn et al. (2005) have indicated that for cloud *systems* precipitation may be enhanced in polluted conditions, by invigoration of secondary convection. Tao et al. (2007) showed similar results, but that the longer-term effect of increased aerosol varied depending on the geographic region of the cloud system. Furthermore, Yin et al. (2005) and Seifert et al. (2006) have shown that tracking aerosol processing in clouds (scavenging and evaporation) also has a marked effect on how aerosol affects the evolution of cloud systems and their precipitation production.

In this paper we use a numerical model to explore aerosol effects on populations of deep convective clouds over several hours, to study the collective effect on rainfall.

2. SIMULATION DESIGN

The Regional Atmospheric Modeling System (RAMS, version 4.3) model was used to simulate deep convective cloud systems. The simulations employ the two-moment bulk microphysics scheme (Meyers et al. 1997) utilizing seven hydrometeor categories: cloud drops, rain, pristine ice crystals, snow, aggregates, graupel, and hail. The bulk riming scheme was used to represent riming processes between cloud drops and precipitation ice. The microphysical pathways that are considered in this model are illustrated in Figure 1.

Two-dimensional idealized simulations were run for 9 hours (time step of 5 seconds) on a grid with a horizontal domain of 150 km (dx =500 m) and a stretched vertical grid up to 16 km (dz = 100 m near surface stretched to no greater than 750 m aloft, with a stretch ratio of 1.1). The simulations were initialized with a modified version of the sounding taken at 2028 UTC 29 June 1997 from the Atmospheric Radiation Measurement (ARM) program central facility (Fig. 2). Modifications included a reduction in the 700 mb inversion and no initial horizontal winds. Random temperature perturbations of +/- a maximum of 1 °C were added to the lowest vertical grid level at time = 0 to help initiate a field of convective clouds. Radiation and surface models were turned off in these simulations,

* *Corresponding Author:* Sarah Tessendorf, NCAR/RAL, P.O. Box 3000, Boulder, CO 80307, email: saraht@ucar.edu

in order to keep the output simple and focused on microphysical effects.

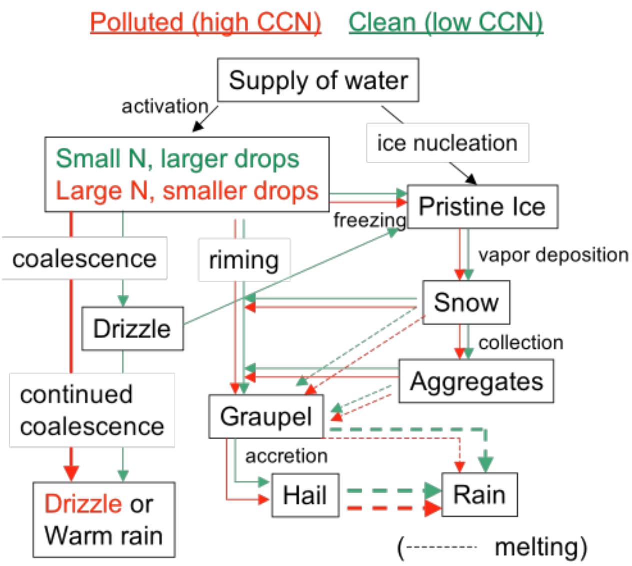

Figure 1. Illustration of the microphysical pathways in the RAMS model, and how they could differ for clean versus polluted conditions.

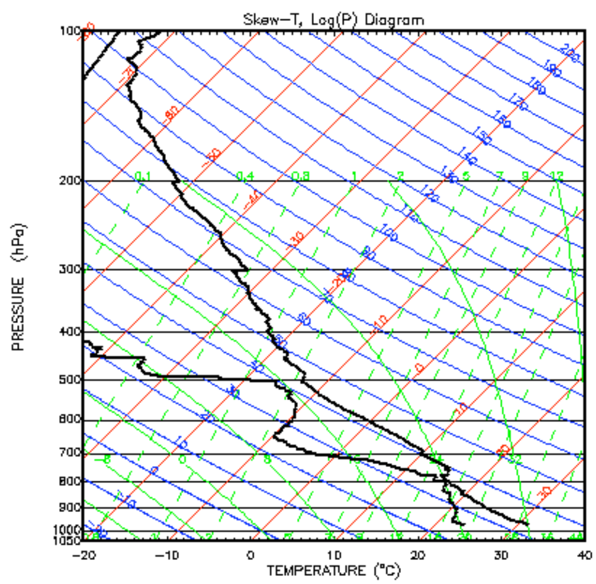

Figure 2. Sounding used to initialize model simulations. The temperature profile has been modified (reducing the inversion at 750 mb) from the original ARM sounding taken at 2028 UTC 29 June 1997.

Three cases with varying CCN concentration profiles were used: "clean" (100/cc), "intermediate" (500/cc), and "polluted" (1000/cc). All CCN profiles exhibited a linear decrease in CCN from the surface (maximum CCN concentration) up to 4 km, above which they all had a baseline concentration of 100/cc. These simulations did not utilize any CCN tracking methods, to either scavenge CCN in fallen precipitation or generate CCN from evaporation of drops. This feature is an option in the version of RAMS used for this study, however, and may be used in future simulations to test the response of these processes, as other modeling studies have elucidated their importance (Yin et al. 2005, Seifert et al. 2006).

3. RESULTS

In all the simulations, low-level cloud (~2 km altitude) formed within 40 min into the simulation (not shown). By 60 min, this cloud was more horizontally extensive in the clean case, whereas in the polluted case very little cloud had extended horizontally from the initial cloud. During the next hour, all cases showed a low-level (fair weather) non-precipitating cumulus field across most of the horizontal domain. During this phase, maximum vertical velocities for all cases were approximately 4 m s^{-1} (Fig. 3). Only in the clean case did a small amount of rain developed, although it did not reach the surface (Figs. 4-5).

By 140 min, the fair weather cumulus field had dissipated and in the clean case three midlevel clouds formed (not shown). The cloud bases were approximately at 5 km altitude (or –7 °C) and thus were cold-based clouds. They produced rain in the cloud after 150 min (Fig. 4). At least six similar midlevel clouds formed in the intermediate case but not until 155 min, and only two midlevel clouds formed initially in the polluted case (one by 160 min, and the other by 175 min). Thus, the midlevel clouds formed sooner in the clean case, which also led to earlier precipitation development and surface rainfall onset, while the intermediate and polluted cases had later surface rainfall onset (Figs. 4-5). During this phase, the dominant pathways to rain in all cases were ice (hail and graupel) melt processes (Figs. 6-8). The intermediate case tended to produce more of these midlevel clouds though, so by the time they were all precipitating (after 200 min), the intermediate case accumulated surface rainfall was similar to that of the clean case (Fig. 5).

Shortly after 200 min, the intermediate case also developed the first warm-based deep convective cloud, with cloud tops reaching 15 km by 240 min (Fig. 9). Maximum vertical velocities in this convective surge were as high as 50 m s^{-1}. The warm rain contribution to rain production during this period is evident by the increase in the cloud drop collection source to rain shown in Figure 7. Soon thereafter (near 240 min), the clean case

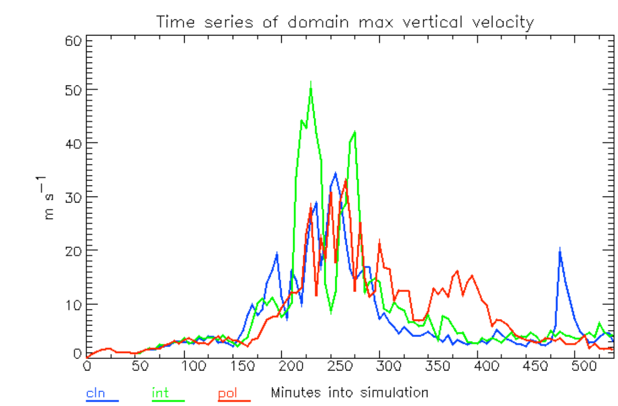

Figure 3. Time series of total domain maximum updraft velocity in all three cases: clean (blue), intermediate (green), and polluted (red).

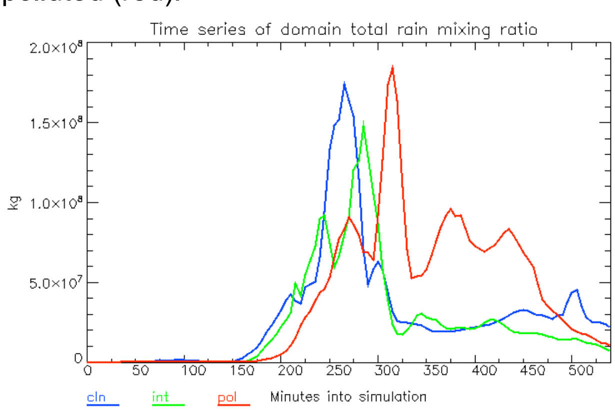

Figure 4. Same as Fig. 3, except for domain total rain mass.

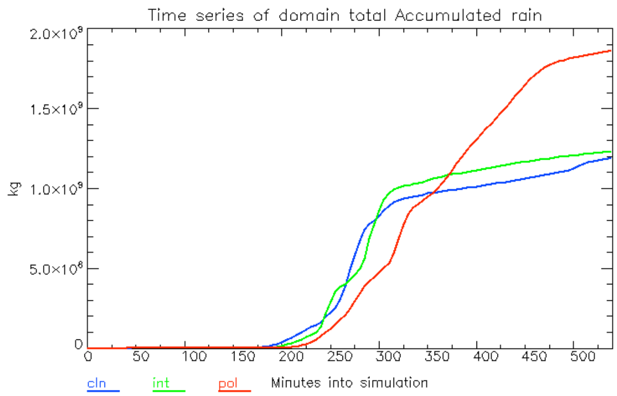

Figure 5. Same as Fig. 3, except for total accumulated surface rainfall.

also developed deep warm-based convection, though tops only reached 14 km (Fig. 10). The warm rain contribution during the growth of this deep convective cloud is also evident in Figure 6. The intermediate case also had a second surge of deep convection around 280 min, again with tops near 15 km (not shown). Maximum updrafts in this surge were only near 40 m s^{-1}, but the warm rain contribution to rain is again evident (Figs. 3, 7).

The polluted case never had quite the convective surge that either the clean or intermediate cases had, but warm-based deep convection was initiated shortly after 200 min, although tops were generally less than 10 km. By 260-300 min, however, the polluted case exhibited some cloud tops close to 12 km, and a large area of warm-based deep convection was developing in the center of the domain (Fig. 11). This convection appeared to be forced by convergence of low-level winds that emanated as outflow from the two primary convective cells shown in Figure 11. A brief period where collection of cloud drops became the dominant rain source can be seen at this time in Figure 8.

After this slight surge at 300 min, the precipitation in the polluted case became very widespread and the convection was less isolated. After this time in the clean and intermediate cases, precipitation had diminished and primarily non-precipitating midlevel and upper-level cloud was left in the domain. The exception was that a late convective cell formed by 500 min in the clean simulation.

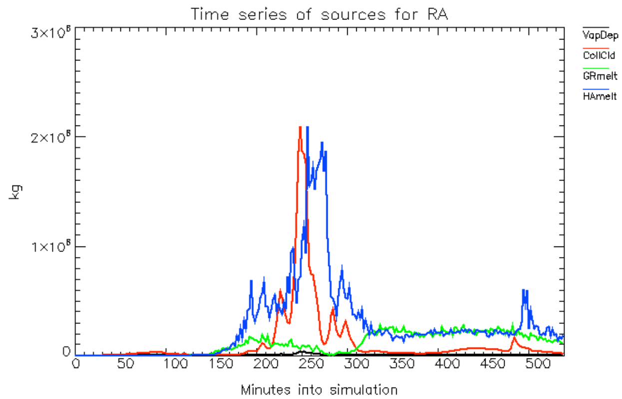

Figure 6. Time series of domain total rain mass sources for the clean case. Sources include vapor deposition (black), collection of cloud drops (red), graupel melt (green), and hail melt (blue).

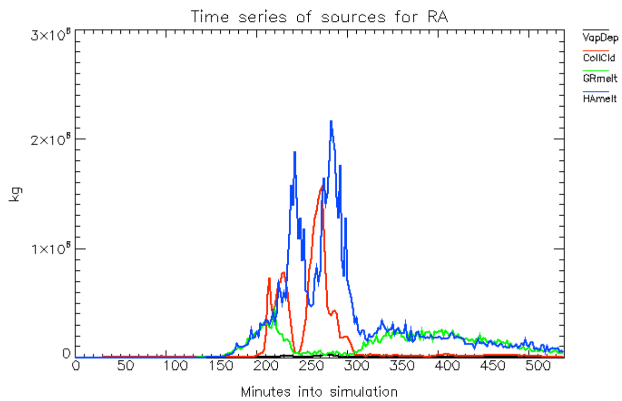

Figure 7. Same as Fig. 6, except for intermediate case.

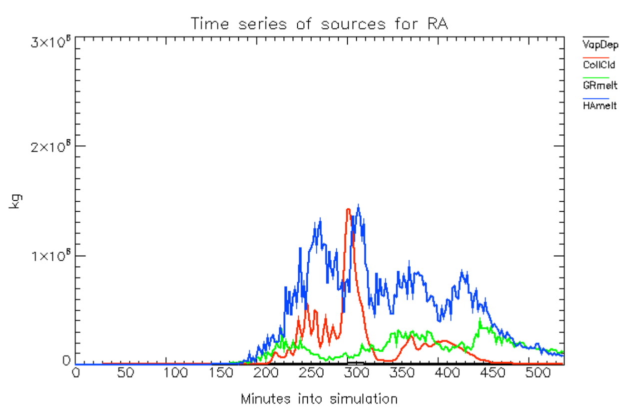

Figure 8. Same as Fig. 6, except for polluted case.

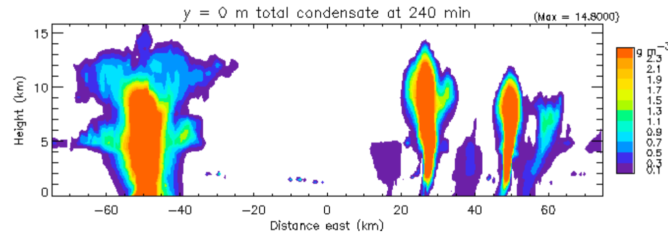

Figure 9. Cross-section of total condensate at 240 min from the intermediate case simulation.

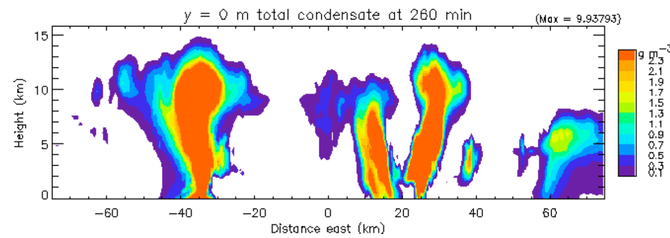

Figure 10. Same as Fig. 9, except at 260 min from the clean case simulation.

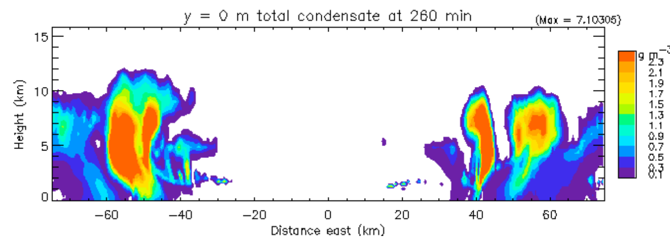

Figure 11. Same as Fig. 10, except from the polluted case simulation.

4. SUMMARY

Three simulations were run using the RAMS model, each with a different CCN profile: clean, intermediate, and polluted. The clean case produced rain the soonest, but did not produce the most rain overall. The intermediate case had the most intense and deepest convection, but didn't produce much more accumulated rain than the clean case. The polluted case was the last to produce surface rainfall, and although the convection in this scenario was not as deep or as strong as in the clean and intermediate cases, it produced large scale areas of moderate rainfall, which yielded the most accumulated surface rainfall of all three simulations. The sources of rain were dominated by ice melt processes in all three cases, especially initially since early cloud bases were high and above the freezing level. The clean case only had one major convective surge (between 240-260 min), while the intermediate case had two surges of deep and strong convection (~220 min and 280 min). The polluted case had its greatest “surge” around 300 min, though again it was not as strong or deep as the other two cases. There appears to be a relationship between warm rain dominance in the early growth of the warm-based deep convection and then a shift back to ice melt dominated rain production during the later stages of the convective surges.

It is clear that results of this kind defy simple categorization into “warm rain dominated precipitation”, or “pollution-induced cloud invigoration” and that thermodynamic and dynamic feedbacks in these simulations played an important role in the differences in the evolution of these cloud ensembles. Establishing the predictability of cloud systems, and the extent to which aerosol increases or decreases the level of predictability is a topic of great interest. This will be studied in greater detail and presented at the conference.

Acknowledgements: The authors thank Steve Saleeby, Hongli Jiang, Bill Cotton, Adrian Hill, Hailong Wang, and Louis Grasso for sharing model expertise and offering scientific guidance. This work was partially supported by a CIRES postdoctoral fellowship.

REFERENCES

Gunn, R., and B.B. Phillips, 1957: An experimental investigation of the effect of air pollution on the initiation of rain. *J. Meteor.,* **14**, 272-280.

WMO/IUGG International Aerosol Precipitation Science Assessment Group (IAPSAG), 2008: Aerosol pollution impact on precipitation: A scientific review. 482 pp.

Khain, A., and A. Pokrovsky, 2004: Simulation of Effects of Atmospheric Aerosols on Deep Turbulent Convective Clouds Using a Spectral Microphysics Mixed-Phase Cumulus Cloud Model. Part I: Model Description and Possible Applications, *J. Atmos.Sci.,* **24**, 2983-3001.

Khain, A., D. Rosenfeld, and A. Pokrovsky, 2005: Aerosol impact on the dynamics and microphysics of deep convective clouds, *Quart. J. Roy. Meteor. Soc*., **131**, 2639-2663.

Lynn, B. H., A. P. Khain, J. Dudhia, D. Rosenfeld, A. Pokrovsky, and A. Seifert, 2005: Spectral (bin) microphysics coupled with a mesoscale model (MM5). Part I: Model description and first results. *Mon. Wea. Rev.*, 133, 44-58.

Meyers, M.P., R.L. Walko, J.Y Harrington, and W.R. Cotton, 1997: New RAMS cloud microphysics parameterization. Part II. The two-moment scheme. *Atmos. Res*., **45**, 3-39.

Reisin, T., Z. Levin, and S. Tzivion, 1996: Rain production in convective clouds as simulated in an asisymmetric model with detailed microphysics. Part II. Effects of varying drops and ice initiation. *J. Atmos. Sci*., **53**, 1815-1837.

Saleeby, S.M., and W.R. Cotton, 2004: A large-droplet mode and prognostic number concentration of cloud droplets in the Colorado State University Regional Atmopsheric Modeling System (RAMS). Part I. Module descriptions and supercell test simulations. *J. Appl. Meteor*., **43**, 182-195.

Seifert, A., A. Khain, A.Pokrovsky, an dK. Beheng, 2006: A comparison of spectral bin and two-moment bulk mixed phase microphysics. *Atmos. Res*., **80**, 44-66.

Warner, J., 1968: A reduction of rain associated with smoke from sugar-cane fires—An inadvertent weather modification. *J. Appl. Meteor.*, **7**, 247-251.

Yin, Y., K.S. Carslaw, and G. Feingold, 2005: Vertical transport and processing of aerosols in a mixed-phase convective cloud and the feedback on the cloud development. *Quart. J. Roy. Meteor. Soc.*, **131**, 221-245.

PRELIMINARY OBSERVATIONS OF CLOUD AND PRECIPITATION CHARACTERISTICS IN THE BRISBANE REGION

Sarah Tessendorf[1*], Roelof Bruintjes[1], Jim Wilson[1], Rita Roberts[1], Ed Brandes[1], Peter May[2], Justin Peter[3], Steve Siems[3], Michael Manton[3], Mike Dixon[1], Matt Pocernich[1], Duncan Axisa[1], Ian Craig[4], and Roger Stone[4]

[1]National Center for Atmospheric Research, Boulder, Colorado
[2]Bureau of Meteorology, Melbourne, Australia
[3]Monash University, Melbourne, Australia
[4]University of Southern Queensland, Toowoomba, Australia

1. INTRODUCTION

The region of Southeast Queensland, Australia, has been experiencing a severe drought over the past few years, and in response to this drought the Queensland government called for a cloud seeding feasibility program. The aims of this program are to conduct preliminary studies of the atmospheric aerosols, pollution levels, and cloud microphysics and dynamics to determine if cloud seeding is a viable and cost-effective option for enhancing rainfall in the southeast Queensland region. Of particular importance, is assessing if clouds in the region are amenable to seeding, and if so, if these suitable clouds occur frequently enough to warrant a cloud seeding program.

Randomized experiments using hygroscopic flares in South Africa and Mexico showed statistical enhancement in the radar reflectivity estimated rainfall from seeded clouds versus non-seeded clouds (Bigg 1997, Mather et al. 1997, Silverman 2000, WMO 2000. Bruintjes et al. 2001). In particular, they found that seeded clouds produced precipitation over a longer period than the unseeded cases, rather than producing more intense rainfall. The results of hygroscopic seeding are highly dependent on several thermodynamic and microphysical characteristics that vary by region, however, such as the natural background aerosol in the region and their chemical and size characteristics. Some modeling studies have shown that the size of the cloud condensation nuclei (CCN) introduced into a cloud by the hygroscopic flares influences the impact of seeding, such that if the CCN are large (> 10 micron), precipitation growth may occur too rapidly depleting the cloud of drizzle-sized drops for further rainfall formation, thus leading to less overall precipitation production (Cooper et al. 1997, Reisin et al. 1996, Yin et al. 2000a-b). It has been suggested by Rosenfeld et al. (2002), however, that hygroscopic seeding could offset the inhibition of rainfall in polluted conditions. Other issues that affect the results of hygroscopic seeding are the challenge of spreading the seeding material throughout the cloud and the use of radar to estimate rainfall in the randomized experiments could show a false enhancement due to seeding-induced drop size changes that affect the estimation of rainfall using radar reflectivity.

The Queensland program offers a unique opportunity to characterize the microphysical properties, as well as to study the effectiveness of hygroscopic seeding, of clouds in the Brisbane, Australia area. This paper will present an overview of the experimental design of the cloud seeding research program (CSRP) in southeast Queensland, and provide some preliminary observations collected during the field project. Additional analyses will be completed over the next few months and will be presented at the conference.

* *Corresponding Author:* Sarah Tessendorf, NCAR/RAL, P.O. Box 3000, Boulder, CO 80307, email: saraht@ucar.edu

2. OVERVIEW OF FIELD CAMPAIGN

The Queensland CSRP took place between 15 December 2007 and 31 March 2008 (with a break between 21 December-13 January), and was based in the Brisbane, Australia region.

2.1 Objectives

The primary objectives of the Queensland CSRP was to make preliminary assessments of: 1) the climatological characteristics of precipitation, in particular, frequency of clouds suitable for seeding, 2) the approaches necessary to make robust estimates of precipitation amount and retrieve microphysical properties of clouds, 3) the effect of cloud seeding on storm microphysics and dynamics, 4) evidence from cloud seeding of increased secondary convection initiation, and 5) evidence of precipitation enhancement from cloud seeding.

The target area for the project primarily focused on the two major water catchments that serve Brisbane, namely the Wivenhoe and Somerset dam catchment areas (Fig. 1). A secondary target area was designated over the water catchments south of Brisbane. This secondary target area happened to include our areas for dual-Doppler radar coverage (see section 2.2.1).

2.2 Facilities

2.2.1 Radar

The primary research radar for the project was the CP2 dual-polarization and dual-wavelength (S- and X-band) Doppler radar. This radar was located at Redbank Plains, southwest of Brisbane (Figs. 1-2). The Operations center was also located at the CP2 radar facility. Several other Bureau of Meteorology (BoM) radars were also available during the project, such as the Marburg (S-band) and Mt. Stapylton (S-band Doppler) radars (Figs. 1-2). The CP2 and Mt. Stapylton radars create a dual-Doppler network, within which we can estimate the three-dimensional winds. Though the north dual-Dpopler lobe was located mostly over the city of Brisbane, in a high air traffic area, so we primarily had to rely on the southern lobe for our seeding operations and research aircraft missions to coincide with the dual-Doppler domain (Fig. 2). While the BoM radars operated continuously in surveillance mode, the CP2 radar scanning strategies were dictated by the mission conditions. Thus, PPI (plan position indicator) and RHI (range height indicator) sector scans were often run during operations, and surveillance volume scans run at all other times. A complete low elevation angle (~0.5°) PPI scan was

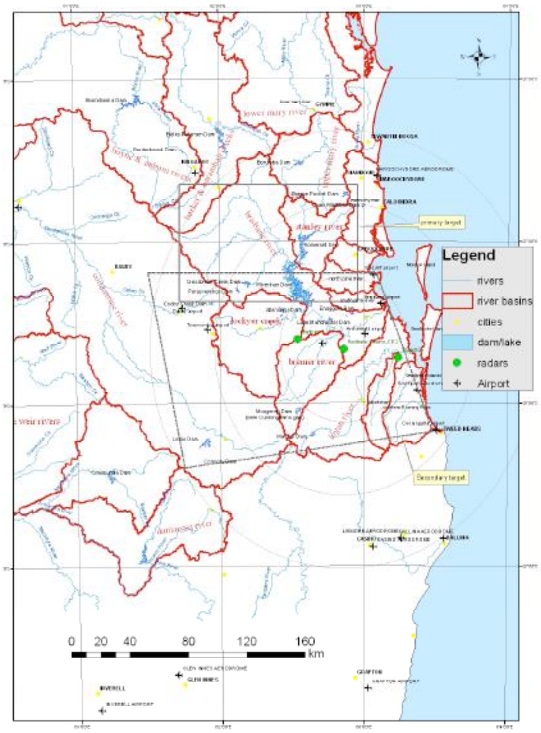

Figure 1. River basin and water catchment areas of Southeast Queensland, with operational target areas marked by black boxes. The Marburg, CP2, and Mt. Stapylton radars are indicated by green dots (respectively from west to east).

conducted roughly every 6 minutes, even during sector scanning sequences.

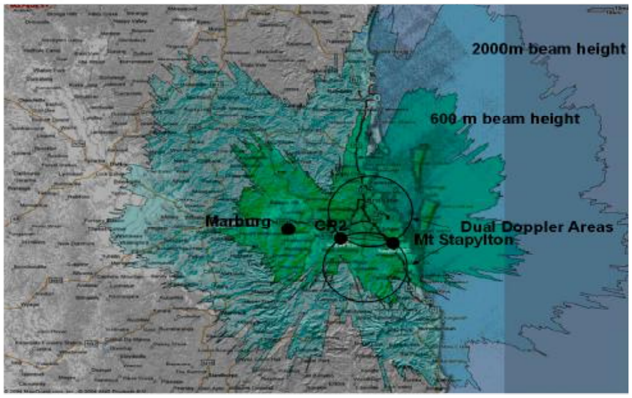

Figure 2. Map of southeast Queensland with radar locations and the CP2-Mt. Stapylton dual-Doppler lobes.

2.2.2 Aircraft

There were two aircraft deployed during the project: a research (and secondary seeding) aircraft, and a primary seeding aircraft. The research aircraft, the South African Weather Service (SAWS) Aerocommander, was equipped with a broad suite of instrumentation (see Table 1), as well as wing-mounted flare racks (20 total flares). It could also serve as a secondary seeding aircraft if needed. The primary seeding aircraft, the Weather Modification Inc (WMI) Piper Cheyenne II (operated by WMI and MIPD), had wing-mounted flare racks (24 total flares) and could carry 306 ejectable flares in its undercarriage flare rack. The Archerfield airport, located in southwest Brisbane, served as the base for aircraft operations.

2.2.3 Raindrop Disdrometer

The NCAR video distdrometer was deployed to take ground-based measurements of drop size distributions (DSDs) in rainfall. It was located roughly 17 km from the CP2 radar, and used to provide supplemental calibration for the radar and to develop techniques for estimating DSDs in precipitation using the CP2 polarimetric measurements.

2.3 Observational goals and strategies

The goals of the aircraft measurements fell roughly into five data collection categories to study: 1) aerosol and CCN characterization, 2) cloud droplet characterization, 3) development of drizzle-sized drops, 4) ice phase processes, and 5) DSDs in rain shafts. To meet these goals several flight plan strategies were employed. First of all, regular surveys of the ambient aerosol were conducted in the boundary layer below cloud base, to build up a dataset of the aerosol and CCN characteristics in the region. Cloud and aerosol microphysical flights were also conducted, in which the research aircraft sampled the subcloud layer and then penetrated clouds at several heights to assess the initial DSD characteristics just above cloud base and as droplet growth occurred higher in the cloud up to cloud tops.

Experimental seeding process studies, primarily with hygroscopic flares, were also conducted. In these cases, the research aircraft profiled a cloud prior to seeding, and then during and after seeding, to collect detailed in situ measurements to help assess possible seeding effects.

An integral part of the research project was the randomized seeding experiment. These cases were declared by the pilots of the seeding aircraft if rain-free cloud bases with at least 200 ft/min updrafts were encountered. These cases were always coordinated with the CP2 radar, and thus only cases within 100 km from CP2 were declared. Often, the randomized cases were coordinated with the research aircraft, so as to obtain in situ measurements in these cases also.

Table 1. Instrumentation on the SAWS Aerocommander.

we	Purpose/Comment	Range
	State Variables	
Rosemount Temperature, Static and Dynamic Pressure, and GPS parameters	Temperature, pressure, altitude, TAS, and location – recorded on telemetry box and on the data system (SAWS)	*multiple*
Vaisala Temperature and Relative Humidity	Secondary temperature and moisture content (SAWS)	-50 to 50C, 0-100%
	Cloud Physics	
PMS FSSP	Cloud droplet spectra (SAWS)	.5-47 µm
DMT SPP-100 FSSP	Cloud droplet spectra	.5-47 µm
PMS 2D-C	Small precipitation particle size, concentration and shape (SAWS)	25-800 µm
PMS 2D-P	Large precipitation particle size, concentration and shape (SAWS)	200 -6400 µm
PMS Hot-wire (King) Liquid Water Content Probe	Liquid water content (SAWS)	0.01 – 3 g m^{-3}
DMT CAPS probe	Aerosol through precipitation size spectrometer; LWC; cloud imaging probe; static and dynamic pressure; temperature (NCAR)	*multiple*
	Aerosols	
DMT CCN Counter	Cloud condensation nuclei concentration and spectra (WITS)	Depends on Supersaturation
Texas A&M DMA	Fine mode aerosol spectra and concentration (NCAR)	0.01 to 1 µm
PCASP	Aerosol concentration and spectra (WITS)	0.1 to 3 µm
	Trace Gases	
TECO SO_2 (43c)	Sulphur dioxide (WITS)	0-100 ppm
TECO CO (48c)	Carbon monoxide (WITS)	0-10,000 ppm
TECO O_3 (49i)	Ozone (WITS)	0-200 ppm
TECO NO_y (42c)	Nitrogen oxides (NCAR)	0-100 ppm
	Cloud and Situation Imagery	
Digital still camera	To show development of clouds and treatment situations for historical purposes	N/A
Video camera	To film cloud penetrations and flight conditions	N/A

3. CLIMATOLOGY

Establishing the characteristics of weather patterns, common cloud systems, the typical distribution of rainfall and what types of cloud systems the majority of rainfall is attributed to are all components to understanding the precipitation climatology of the Brisbane region and is a primary objective of this research project. Our analysis will include radar-based climatologies of rainfall and precipitating systems, to help understand which types of cloud systems are more frequent and which produce the most rainfall. Additionally, synoptic analysis to determine what dynamic and thermodynamic conditions are common to the region and if they produce clouds that are amenable to seeding will be conducted.

To date, our analysis has focused on historical rainfall data, and it is clear that the annual distribution of rainfall in the Brisbane region peaks in the summer months of January and February (Fig. 3).

Furthermore, Figure 4 puts into perspective the 2008 season, during which time the CSRP was operational. It was an anomalously wet summer season for the region, and there were several weeks of intense flooding in some parts of the area. This flooding restricted our seeding operations, however, we were still able to conduct cloud microphysical studies with the aircraft.

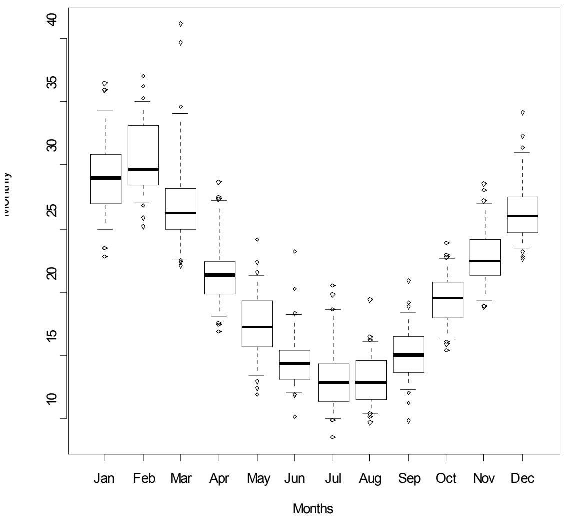

Figure 3. Monthly precipitable water (kg/m^2) over the Brisbane/Toowoomba area from 1948-2008. (Figure courtesy Erin Towler, NCAR).

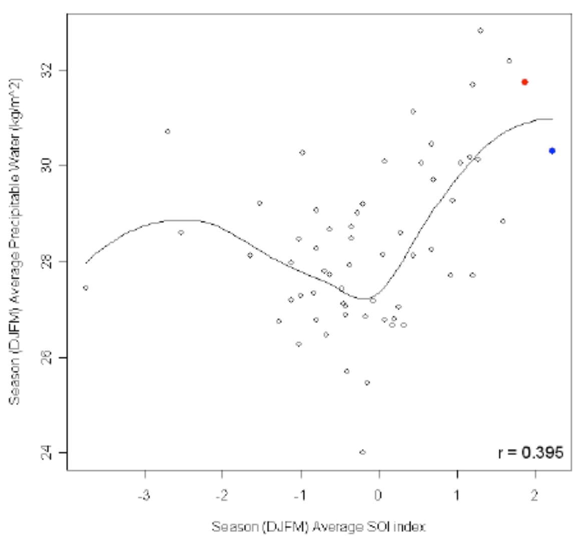

Figure 4. Scatterplot of seasonal average DJFM precipitable water versus DJFM Southern Oscillation Index (SOI) from 1948-2008. The 2008 DJFM season is highlighted with a red dot, and the 1974 DJFM season is highlighted with a blue dot. (Figure courtesy Erin Towler, NCAR)

4. OBSERVATIONAL HIGHLIGHTS

We had a total of 47 days during the project where we conducted flight operations with at least one of our aircraft. The majority of clouds observed during the project (based on our flight days) were shallow convective clouds, with tops well below the freezing level (Table 2). Deep convective clouds occurred most often in January and February, and typically brought heavy rainfalls that led to severe flooding in some areas of Queensland (Table 2). We ceased seeding operations during the flooding periods, but were still able to conduct cloud microphysical flights on those days in the less severe deep convective systems that did not create safety concerns for our pilots. The least common cloud systems observed during this field project were deep stratiform systems (Table 2). These systems tended to last longer than one day, however, but we typically only conducted one day of flight operations for each of these systems. Nonetheless, we have continuous dual-polarization radar measurements of all of these cloud systems.

4.1 Shallow convection

Shallow convection, with cloud tops warmer than freezing, were fairly common on days with a strong southeasterly trade wind regime. On these days, it was common to have a temperature inversion around 700 mb, sometimes as low as 850 mb, and often could be several degrees strong. This inversion essentially capped any convection that developed, and kept cloud depths to around 1-2 km.

Table 2. Summary of flight days per month that each cloud type was observed. Shallow convection refers to clouds with tops warmer than freezing. Note that only one week of flight operations occurred in December, and flight operations didn't include the beginning of January, so the lower frequency of days in those months may be somewhat artificial given the operations time period. The percentage each cloud type was observed out of all the flight days is listed in the bottom row, noting that the remaining (2%) of flight days were used for aerosol surveys on days with little cloud activity.

	Shallow convection	**Deep convection**	**Deep stratiform systems**
December	2	0	0
January	6	6	1
February	10	4	2
March	12	3	0
% of flight days	64	28	6

An example of a day with such shallow convection was 6 March 2008. On this day, several shallow convective cells moved through the southern dual-Doppler lobe, three of which were targeted for randomized cases. The research aircraft took subcloud aerosol measurements on this day, and then made several penetrations of these warm clouds, including a few of the randomized cases.

The preliminary DMA data shows a slight bimodal aerosol distribution, though the dominant mode is near 0.2 microns, in the accumulation mode. Further analysis is needed to determine how representative this aerosol distribution is of the area, and how it relates to the CCN and cloud DSDs on this day. Preliminary FSSP measurements from the cloud penetrations of one cloud on this day indicate a somewhat clean environment, with typical droplet concentrations less than 600/cc, and mean droplet diameters that increase with increasing cloud depth (Fig. 6). The aerosol size distributions characteristic of various locations upwind and downwind of the Brisbane area will also be studied in our upcoming analysis. After more detailed analysis, we will be able to determine if these distributions on 6 March were common, and what may have influenced the observed aerosol and droplet spectra.

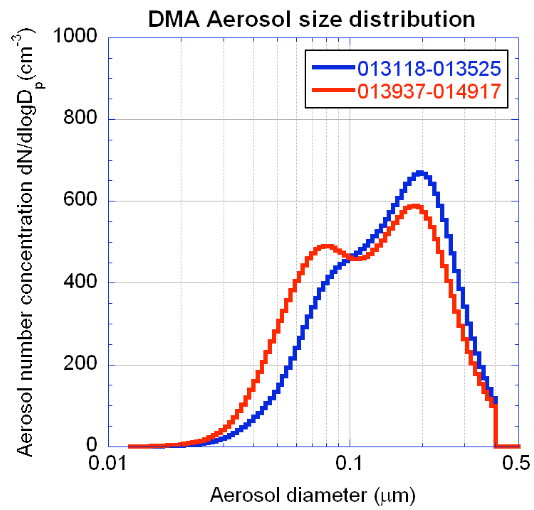

Figure 5. DMA aerosol size distribution during two time segments on 6 March 2008 when the research aircraft was flying just below cloud base. The dominant mode in these distributions is near 0.2 microns, or in the accumulation mode.

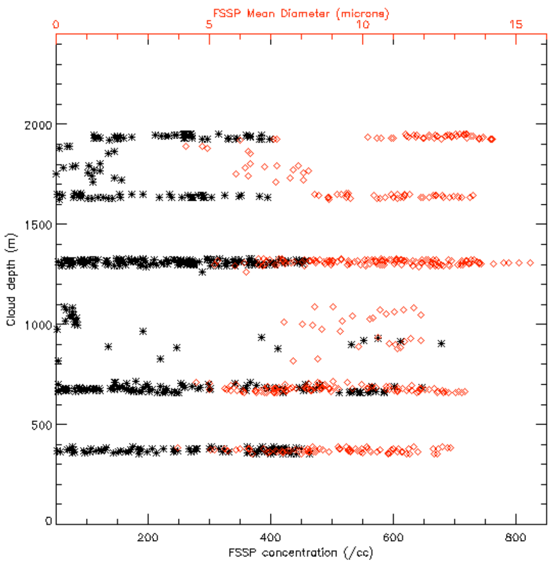

Figure 6. FSSP measurements of total droplet concentration and mean diameter versus cloud depth on 6 March 2008.

4.2 Deep convection

Deep convective storms were usually associated with approaching toughs, which helped destabilize the atmosphere, especially by cooling aloft. Some of these deep convective storms were quite strong, producing cloud-to-ground lightning and hail. An example of a strong deep convective storm occurred on 8 February 2008 in the evening after our flight operations had ended. Figure 7 shows this strong hailstorm exhibiting a flare echo (indicative of hail) and reflectivity wrapping up into the low-reflectivity overhang, a sign of hydrometeors recirculating back into the updraft.

4.3 Deep stratiform systems

Deep stratiform cloud systems were the least common cloud system observed during the project. They often occurred when the monsoon trough was nearby and exhibited nearly moist adiabatic sounding profiles. The first deep stratiform case was observed on 15 January 2008, and signs of liquid water at the -5 °C level were observed, however the latter two cases did not appear to have supercooled liquid water. This of course has implications for the use of glaciogenic (silver iodide) seeding techniques, and will be analyzed further to understand why there was an apparent lack of supercooled liquid water in the later season deep stratiform events.

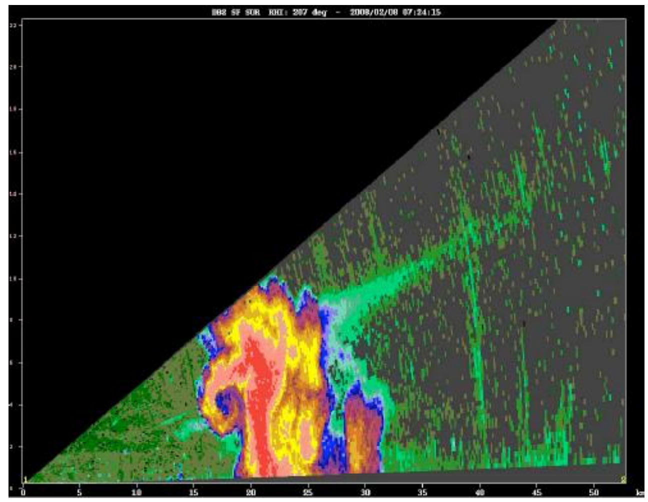

Figure 7. Radar reflectivity (dBZ) RHI (207°) from the CP2 radar on the evening of 8 February 2008 (0724 UTC).

5. RANDOMIZED EXPERIMENT

A total of 62 randomized cases were declared during this project. Of those, 52 (84%) were in convection with tops warmer than 0 °C. Furthermore, hygroscopic burn-in-place flares were used in all cases, often burning 3-4 sets of flares per case (if the updraft sustained itself that long). This usually took 10-15 minutes for the seeding time. CP2 scans were set up to follow these clouds for at least 30 minutes after the end of seeding. Several of the randomized cases were also located within the dual-Doppler lobes of the CP2 and Mt. Stapylton radars, and thus in those cases we can estimate the three-dimensional winds, and perhaps estimate the trajectory of the flare material into the cloud. Another unique aspect of this randomized study is the availability of polarimetric radar data, which can provide better estimations of precipitation rates and estimates of DSDs, however traditional analysis using the radar reflectivity estimates of rainfall will also be performed.

6. SUMMARY

The Queensland CSRP provides a good dataset to characterize the background aerosol conditions and to relate it to the cloud microphysics in the Brisbane region. During the program we collected an extensive dataset of shallow convection, as well as some deep convection, with both in situ aircraft observations and dual-polarization and dual-Doppler radar measurements. Furthermore, we took measurements in a few deep stratiform systems that impacted the area.

The data collected in this field program will allow us to study the effects of hygroscopic seeding through both experimental seeding process case studies, as well as via traditional randomized methods. However, the randomized component in this project is unique since it can utilize the dual-polarization rainfall estimates, which should be superior to traditional estimates based on radar reflectivity alone. Furthermore, the polarimetric radar measurements can also be used in the case study analyses, alongside in situ aircraft observations, to build a more complete picture of the microphysics in these clouds than we have been able to do in past experiments.

Acknowledgements: This field effort was a collaboration of many universities and institutions, including the Queensland Government, the Bureau of Meteorology, Weather Modification Inc., MIPD, University of Southern Queensland, Monash University, CSIRO, South African Weather Service, and NCAR, with funding from the Queensland Government. The authors thank Nancy Rehak (NCAR), Ken Glasson (BoM), and Shelly Knight (NCAR) for engineering support with the CP2 radar display software and operations. Thanks to David Yates and Erin Towler (NCAR) for contributing to the historical climatological analysis. We also acknowledge the efforts of our aircraft crews (SAWS, WMI/MIPD) for their contribution to our in situ data collection.

REFERENCES

Bigg, E.K., 1997: An independent evaluation of a South African hygroscopic cloud seeding experiment, 1991-1995. *Atmos. Res*., **43**, 111-127.

Bruintjes, R.T., D.W. Breed, V. Salazar, MJ. Dixon, T. Kane, B.G. Foote, and B.G Brown, 2001: Overview and results from the Mexican hygroscopic seeding experiment. Preprints, *15th Conf. on Planned and Inadvertent Weather Modification*, Albuquerque, NM, Amer. Meteor. Soc., 45-68.

Cooper, W.A., R.T. Bruintjes, and G.K. Mather, 1997: Some calculations pertaining to hygroscopic seeding with flares. *J. Appl. Meteor*., **36**, 1449-1469.

Mather, G.K., D.E. Terblanche, F.E. Steffens, and L. Fletcher, 1997: Results of the South African cloud seeding experiments using hygroscopic flares. *J. Appl. Meteor*., **36**, 1433-1447.

Reisin, T., Z. Levin, and S. Tzivion, 1996: Rain production in convective clouds as simulated in an asisymmetric model with detailed microphysics. Part II. Effects of varying drops and ice initiation. *J. Atmos. Sci*., **53**, 1815-1837.

Rosenfeld, D., R. Lahav, A. Khain, and M. Pinsky, 2002: The role of sea spray in cleansing air pollution over ocean via cloud processes. S*cience*, **297**, 1667-1670.

Silverman, B.A., 2000: An independent statistical reevaluation of the South African hygroscopic flare seeding experiment. *J. Appl. Meteor*., **39**, 1373-1378.

World Meteorological Organization (WMO), 2000: Report of the WMo workshop on hygroscopic seeding: Experimental results, physical processes, and research needs. WMP Report No. 35, G.B. Foote and R.T. Bruintjes (Ed's), World Meteorological Organization, WMO/TD No. 1006, Geneva, Switzerland, 68 pp.

Yin, Y. Z. Levin, T.G. Reisin, and S. Tzivion, 2000a: The effects of giant condensation nuclei on the development of precipitation in convective clouds –a numerical study. *Atmos. Res.*, **53**, 91-116.

Yin, Y., Z. Levin, T.G. Reisin, and S. Tzivion, 2000b: Seeding convective clouds with hygroscopic flares: Numerical simulations using a cloud model with detailed microphysics. *J. Appl. Meteor.,* **39**, 1460-1472.

Mixing of dust aerosols into a mesoscale convective system. An examination of the relative importance of downdraft generation and removal scavenging processes observed during the AMMA field campaign

P. Tulet[1], K. Crahan-Kaku[1], S. Crumeyrolle[1], L. Gomes[1]

[1] GAME/CNRM, METEO-FRANCE - CNRS, FRANCE

1 Introduction

Mineral dust contributes significantly to the global radiative budget calculations through absorption and scattering of longwave and shortwave radiation (Houghton et al., 2001). On a local level, high dust concentrations are shown to impact the vertical structures of storms (Lohmann and Diehl, 2006) and local energy budgets (Grini et al., 2006).

The AMMA field campaign coupled with the French mesoscale model, the MesoNH, provides an excellent opportunity to compare modeled dust concentrations to field observations in order to improve the knowledge of dust generation, transport and scavenging associated with mesoscale convective systems. Because of its large range in size, with diameters ranging from below 0.2 to 40 μm, both wet and dry deposition are essential to successfully simulate dust transport. Dry deposition includes turbulent transfer to the surface and gravitational settling, and wet deposition includes activation of dust aerosols into cloud droplets and subsequent growth to drizzle, and collection of the aerosols by rain drops through Brownian motion, interception and impaction in and below the cloud layer. Global models have estimated that wet deposition only accounts for 10% of the total dust loss globally (Ginoux et al., 2001; Tegen and Lacis, 1996). Locally, wet deposition can be expected to play a larger role in dust removal processes, especially in areas of intense convection, as observed during the monsoon season in West Africa. Observations have reported strong winds during the gust front and in the convective areas of MCS are accompanied by the lofting of local dust. However, the high dust concentration rapidly subsides after the passage of a storm. This study modeled an observed MCS during the AMMA field campaign. During the passage of this MCS, the dust concentrations will be examined and the relative importance of the wet deposition of dust aerosols versus that of updrafts, downdrafts and advection on the local concentration of dust aerosols will be explored.

2 Model Description

The mesoscale-scale, non hydrostatic atmospheric model MesoNH was used in this study. This model has been jointly developed by CNRM (Meteo France) and the Laboratoire d'Aérologie (CNRS) (Lafore et al., 1998). Within this application, three nested grids with domains of 36 km, 12 km and 3 km are use to model the West African monson. The 3 km resolution grid is used to simulate explicitly several MCSs observed over Niger during the episode of 2006, 1-2 of July. Simulation was initiated using ECMWF data, commenced on midnight 29 July 2006 and finished on midnight 02 July 2006. The model includes deep and shallow convective transport and precipitation (Bechtold and Bazile, 2001) including five categories of hydrometeors based on the ICE3 microphysical scheme (Pinty and Jabouille, 1998). MesoNH is coupled with a surface model that allows the dust generation to take into account four different surfaces: vegetation, town, oceans and lakes, as well as the humidity of the soil (Masson et al., 2003). The dust aerosols are parameterized following Grini et al. (2006). This parameterization uses the three dust aerosol modes of Alfaro and Gomes (2001) which evolve through the ORILAM lognomal aerosol scheme (Tulet et al., 2005). For emission processes, dust is mobilized using the Dust Entrainment And Deposition model (DEAD) (Zender et al., 2003). Dust generation is determined by wind speed, (Alfaro and Gomes, 2001), such that the fine, accumulation and coarse mode each have their own friction velocity saltation threshold. The initial dust size distribution contains three modes with mean radius of 0.32, 1.73 and 4.33 μm and standard deviations of 1.7, 1.6 and 1.5, respectively. For the purpose of this study, rainout (wet deposition caused by the activation of aerosol particles and subsequent growth to a rain drop) and washout (wet deposition caused by the collision between a falling rain drop and an aerosol particle) have been added to the model. Washout is calculated in the MesoNH based upon first order principals. In- and below-cloud impaction scavenging by cloud droplets and raindrops uses a kinetic approach to calculate the aerosol mass transfer as defined by Seinfeld and Pandis (1997); Pruppacher and Klett (2000); Tost et al. (2006). The in-cloud mass aerosol tranfer into rain droplets by autoconversion and accretion processes have been introduced as described by (Pinty and Jabouille, 1998). The sedimentation of aerosol mass included in raindrops as been solved using a time splitting technique with an upstream differencing scheme of the vertical sedimentation raindrops flux. The rerelease of aerosols into the air due to rain evaporation is assumed to be proportional to the water evaporated (Chin et al., 2000).

3 Analysis of an MCS vertical profile

West of Banizoumbou (Niger), the model successfully reproduced one of observed MCS on the 1st of July, 2006. The vertical cross section of the cloud water of the MCS is represented on Figure 1. More than 3 $g.kg^{-1}$ of water has been simulated within the convective core of the system. Detrainment of the system has been modeled at the tropopause located at 16000 meters in altitude. The convective overshoot reaches 19000 meters and transports to the lower stratosphere more than 1 $g.kg^{-1}$ of water. Above 6000 meters in altitude, precipitation of raindrops appear with a maximum of 4 $g.kg^{-1}$ at 2000 meters under the convective core.

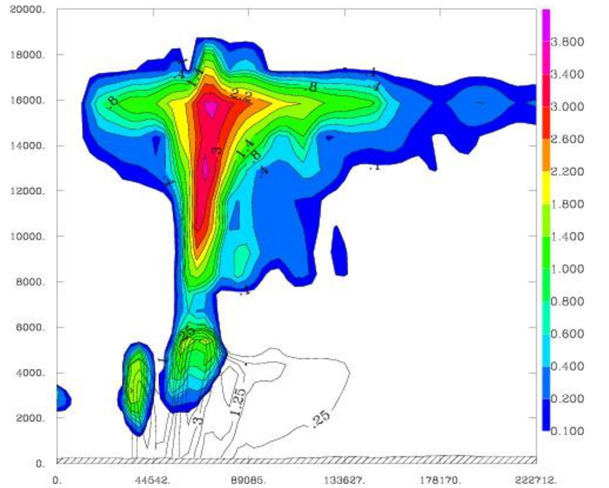

Figure 1: The vertical cross section of cloud water concentration (liquid and ice) ($g.kg^{-1}$) on July, 1th at 20 UTC. Isolines correspond to the mixing ratio of rain water ($g.kg^{-1}$)

This intense precipitation creates downdrafts and a gust front at the surface. High surface wind associated with the gust front (more than 12 $m.s^{-1}$ at 10 m in altitude) generates sandblasting and a saltation flux of dust particles under the convective core (Figure 2). Without any dust scavenging (simulation NOSCAV), more than 3000 $\mu g.m^{-3}$ of dust concentration has been modeled in the gust front near the surface. Convection lifts respectively more than 300 $\mu g.m^{-3}$, 100 $\mu g.m^{-3}$ and 50 $\mu g.m^{-3}$ of these new particles to 5000 meters, 1000 meters, and 16000 meters in altitude. At the tropopause, these particles have been detrained far from the convective core in the anvil.

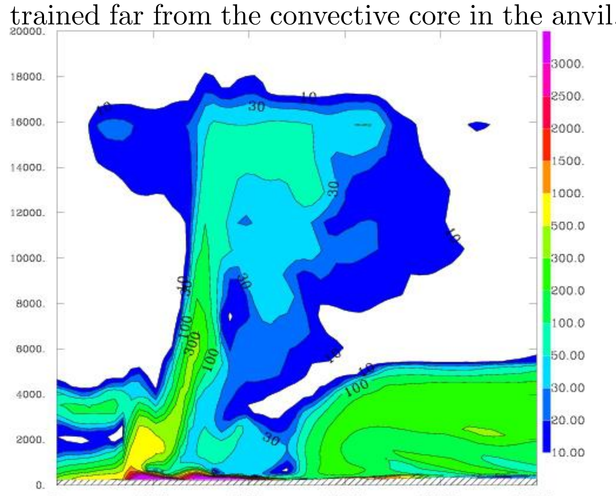

Figure 2: The vertical cross section of dust mass concentration by the NOSCAV simulation

($\mu g.m^{-3}$) on July 1st at 20 UTC.

When introducing aqueous mass transfer as described in section 2 (simulation SCAV), most of the dust concentration produced by the gust front has been scavenged. There are significant differences modeled in the dust concentration between the simulation NOSCAV and SCAV, where all dynamical and cloud microphysics are same (Figure 3). In-cloud, the differences of dust concentration between the two simulations are in the same order of magnitude with simulation NOSCAV, showing that the major mass of dust has been scavenged by raindrops. In fact, with dust scavenging, less than 1500 $\mu g.m^{-3}$ of dust is modeled in the gust front and a few mass (10 $\mu g.m^{-3}$) is able to reach 10000 meters (not shown here). Furthermore, some notable differences have been modeled in the rain and cloud evaporation zone areas. Dust particles collected by cloud droplets and raindrops have been rereleased in the SCAV simulation with more than 200 $\mu g.m^{-3}$ near the surface due to precipitation evaporating.

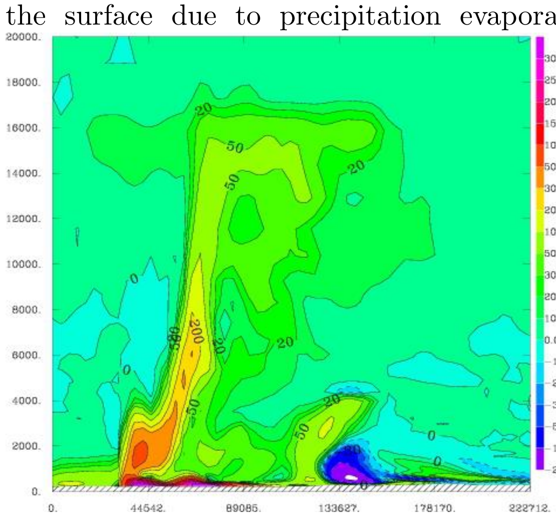

Figure 3: The vertical cross section of the difference of dust mass concentration between NOSCAV and SCAV simulations ($\mu g.m^{-3}$) on July 1st at 20 UTC.

Even though most of the aerosol mass has been scavenged, the number of small particles reaching higher altitudes is important in the SCAV simulation (Figure 4). The collection efficiency factor is less than 0.5 % for smallest particles (mode at 0.32 μm) whereas for the two biggers ones, the efficiency factor are more significant (between 30 and 99 %). As a consequence, the majority of the dust concentration of two larger modes has been scavenged and 99 % of the mass of smallest mode has not been collected by raindrops and is able to be transported upwards in the convective core. Simulation SCAV show that 20 particles by cm^{-3} have been transported to 7000 meters in altitude and more than 6 particles cm^{-3} reach the tropopause. This represents 1 to 2 % of the number concentration modeled at the surface in the gust front whereas only 0.3 % of the mass concentration in the gust front reaches the upper troposphere. This number reaching the upper troposphere may influence the ice number concentration observed, as these small particles can served as ice nuclei. In this assumption, these particles could have a strong impact on the cloud ice concentration, modifying the type of ice cristals, which is known to have a strong impact on the convective precipitation (Gilmore et al., 2004).

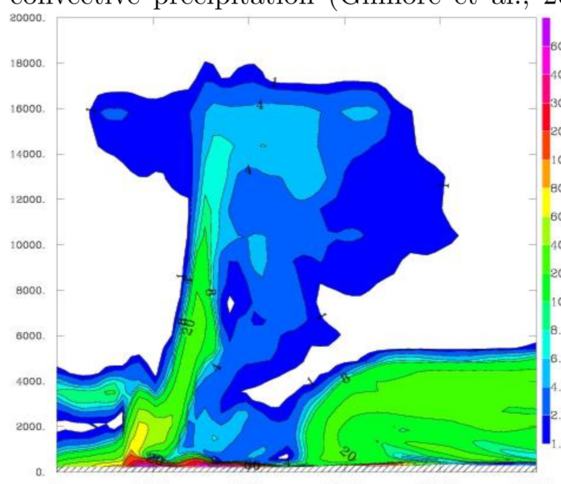

Figure 4: The vertical cross section of dust concentration of the mode centered at 0.32 μm during the SCAV simulation (in particles by cm^{-3}) on July 1st at 20 UTC.

This study emphasizes the particularity of MCS in desert areas that can generate their own emission of dust aerosols that are transported upwards in the convective core. Precipitation influenced the dust concentration with radius larger than 1.5 μm while the smaller mode is preserved, with the MCS transporting high concentrations of the smallest mode particles to the upper troposphere.

References

Alfaro, S. C. and Gomes, L. (2001). Modeling mineral aerosol production by wind erosion: Emission intensities and aerosol size distributions in source areas. *J. Geophys. Res.*, 106(D16):18075–18084.

Bechtold, P. and Bazile, E. (2001). The 12-13 November flux flood in southern France. *Atmospheric Research*, 56(3):173–191.

Chin, M., Rood, R., Lin, S. J., Müller, J. F., and Thompson, A. (2000). Atmospheric sulfur cycle simulated in the global model GOCARD : Model description and global properties. *J. Geophys. Res.*, 105:24,671–24,687.

Gilmore, M., Straka, J. M., and Rasmussen, E. N. (2004). Precipitation uncertainty due to variations in precipitation particle parameters within a simple microphysics scheme. *Mon. Wea. Rev.*, 132:2610–2627.

Ginoux, P., Chin, M., Tegen, I., Prospero, J., Holben, B., Dubovik, O., and Lin, S.-J. (2001). Sources and distributions of dust aerosols simulated with the GOCART model. *J. Geophys. Res.*, 106:20255.

Grini, A., Tulet, P., and Gomes, L. (2006). Dusty weather forecast using the MesoNH atmospheric model. *J. Geophys. Res.*, 111. doi:10.1029/2005JD007007.

Houghton, J., Ding, Y., Griggs, D. J., Noguer, M., van der Linden, P. J., Dai, X., Maskell, K., and Johnson, C. A., editors (2001). *IPCC 2001:* Climate Change 2001. Cambridge University Press, Cambridge, England.

Lafore, J., Stein, J., Asencio, N., Bougeault, P., Ducrocq, V., Duron, J., Fischer, C., Hereil, P., Mascart, P., Pinty, V. M. J., Redelsperger, J., Richard, E., and de Arellano, J. V.-G. (1998). The MesoNH atmospheric simulation system. part I: adiabatic formulation and control simulations. *Ann. Geophys.*, 16:90–109.

Lohmann, U. and Diehl, D. (2006). Sensitivity studies of the importance of dust ice nuclei for the indirect aerosol effect on stratiform mixed-phase clouds. *J. Atmos. Sci.*, 63:968–982.

Masson, V., Champeaux, J., Chauvin, F., Meriguet, C., and Lacaze, R. (2003). A global database of land surface parameters at 1-km resolution in meteorological and climate models. *J. Climate*, 16(9):1261–1282.

Pinty, J. and Jabouille, P. (1998). A mixed-phase cloud parameterization for use in mesoscale non hydrostatic model: simulations of a squall line and of orographic precipitations. *Conference of Cloud Physics*, Everett, WA, USA:217–220.

Pruppacher, H. and Klett, J. (2000). *Microphysics of clouds and precipitation*. Kluwer academic publishers.

Seinfeld, J. and Pandis, S. (1997). Atmospheric Chemistry and Physics. *Wiley interscience pub.*

Tegen, I. and Lacis, A. A. (1996). Modeling of particle size distribution and its influence on the radiative properties of mineral dust aerosol. *J. Geophys. Res.*, 101:19237–19244.

Tost, H., Jockel, P., Kerkweg, A., Sander, R., and Lelieveld, J. (2006). Technical note: A new comprehensive scavenging submodel for global atmospheric chemistry modelling. *Aerosol Chem. Phys.*, 6:565–574.

Tulet, P., Crassier, V., Cousin, F., Shure, K., and Rosset, R. (2005). Orilam, a three moment lognormal aerosol scheme for mesoscale atmospheric model. on-line coupling into the MesoNH-c model and validation on the Escompte campaign. *J. Geophys. Res.*, 110. doi:10.1029/2004JD005716.

Zender, C., Bian, H., and Newman, D. (2003). The mineral dust entrainment and deposition (DEAD) model: Description and global dust distribution. *J. Geophys. Res.*, 108(D14):4416. http://dust.ess.uci.edu/dead/.

OZONE VERTICAL AND DIURNAL VARIABILITY INFLUENCED BY SHALLOW CUMULUS: LARGE-EDDY SIMULATION STUDY

Jordi Vilà-Guerau de Arellano and Kees van den Dries
Meteorology and Air Quality Section, Wageningen University, The Netherlands
e-mail: jordi.vila@wur.nl

1. Introduction

The presence of shallow cumulus in the atmospheric boundary layer (ABL) modifies the transport, turbulent mixing and reactivity of chemical species. Vertical transport is enhanced in the cloud layer by the buoyant convection associated to cloud formation. As a result, reactants emitted at the surface reach higher altitudes (up to 3 to 4 km depending on surface forcing and free troposphere conditions) compare to the vertical distribution on clear boundary layer (limited by the ABL growth). While in the sub-cloud layer, reactants are well mixed, in the cloud layer the variability quantified by the reactant co-variances indicates the difference in the turbulent characteristics between clouds (highly turbulent) and their environment (minimum levels of turbulence). Finally, scattering of radiation by cloud droplets perturb the photolysis rates enhancing the values at cloud top and decreasing them below cloud compare to the clear sky situation.

In this research, we present numerical experiments carry out using the Dutch Atmospheric Large-Eddy Simulation (DALES) (Dosio et al.(2003)) to investigate the interaction of these processes on the ozone production. By including a semi complex chemical mechanism for the $O_3 - HO_x - NO_x - CO$ system, we are able to reproduce the vertical and diurnal variation of ozone and related species. Emphasis is placed on studying: (a) the effect of the dilution and enhanced vertical transport by shallow cumulus convection, (b) the evolution of the reactants in the sub-cloud layer and in the cloud layer and the net transport and (c) the study of potential departures of chemical equilibrium due to the presence of clouds. This research extends the previous simulation of the influence of shallow cumuli over land on a the simple chemical mechanism composed by the triad $NO - O_3 - NO_2$ (Vilà-Guerau de Arellano et al.(2005)).

2. Dynamics

The study is based on the meteorological situation described by Brown et al.(2002). A cloudy boundary layer characterized by the presence of clouds was observed on 21 June 1997 at the Southern Great Plains site of the Atmosphere Radiation Measurement (ARM). Based on the surface and the upper air observations, Brown et al.(2002) proposed an idealized experiment to study the dynamics of shallow cumulus over land. Our simulation is based on exactly the same domain size and discretization and the same surface forcing. The diurnal variation of the surface turbulent fluxes yields the formation of unsteady shallow cumulus. The vertical initial profiles for liquid water potential temperature and specific moisture are the same as the one prescribed by Brown et al.(2002) with the only difference to have a less stable profile (γ_θ=1.7 K/km) between 1300 and 2500 m (see figure 10a at Brown et al.(2002)). By so doing, we are able to enhance the vertical growth rate of the cloud layer. Moreover, the only surface forcing prescribe is a westerly wind equal to 10 ms^{-1}. The small external tendencies representing the advection of heat and moisture are not included. The initial vertical profiles for the wind component U, potential temperature and specific humidity are shown at figure 1a 1b and 1c.

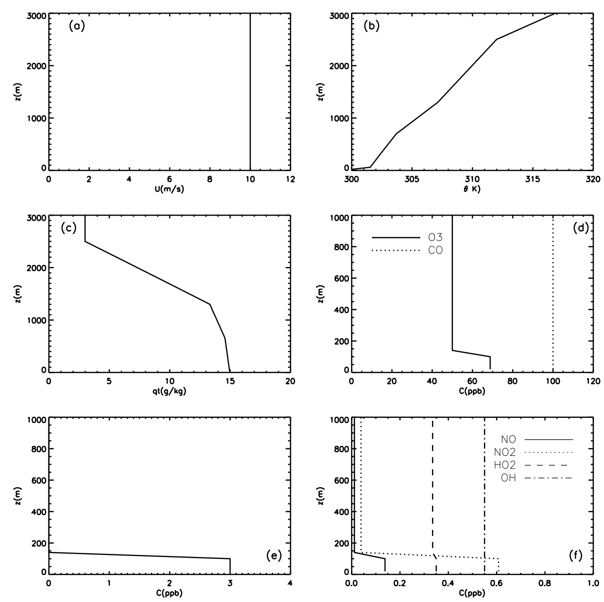

FIG. 1: Initial vertical profiles of (a) wind speed (U-component), (b) liquid water potential temperature, (c) specific humidity, (d) O_3 and CO, (e) RH and (f) NO, NO_2, 10*HO_2 and 1000*OH.

3. Chemistry

The semi-complex chemistry which reproduces the diurnal variability of ozone is based on Krol et al.(2000). The chemical mechanism includes the following reactions:

$$O_3 \overset{H_2O}{\rightarrow} 2OH + O_2 \qquad j_1\ varies \qquad (1)$$

$$NO_2 \overset{O_2}{\rightarrow} NO + O_3 \qquad j_2\ varies \qquad (2)$$

$$NO\ +\ O_3 \rightarrow NO_2 + O_2 \qquad k_1 = 4.75\ 10^{-4} \qquad (3)$$

$$OH\ +\ CO \overset{O_2}{\rightarrow} HO_2 + CO_2 \qquad k_2 = 6.00\ 10^{-3} \qquad (4)$$

$$OH\ +\ RH \rightarrow HO_2 + Prd \qquad k_3 = fx6.00\ 10^{-3} \qquad (5)$$

$$HO_2\ +\ NO \rightarrow OH + NO_2 \qquad k_4 = 2.10\ 10^{-1} \qquad (6)$$

$$HO_2 \ + \ O_3 \rightarrow OH + 2O_2 \qquad k_5 = 5.00\ 10^{-5} \qquad (7)$$

$$2HO_2 \qquad \rightarrow H_2O_2 + O_2 \qquad k_6 = 7.25\ 10^{-2} \qquad (8)$$

$$OH \ + \ NO_2 \rightarrow HNO_3 \qquad k_7 = 2.75\ 10^{-1} \qquad (9)$$

$$OH \ + \ O_3 \rightarrow HO_2 + O_2 \qquad k_8 = 1.75\ 10^{-3} \qquad (10)$$

$$OH \ + \ HO_2 \rightarrow H_2O + O_2 \qquad k_9 = 2.75. \qquad (11)$$

By using this chemical scheme, we aim at reproducing the essential reactions in the ozone diurnal variability without increasing the computer burden. The units of the photolysis frequencies are in s^{-1}. For this control run we have assumed that the photolysis rates j_1 and j_2 are constant on time with values equal to $2.7\ 10^{-6}\ s^{-1}$ and $8.9\ 10^{-3}\ s^{-1}$ (maximum values 21st at a latitude 45N). The second-order reaction are in $ppb^{-1}s^{-1}$. The factor f of reaction (5) is variable and it ranges from 100 to 300. In the case understudy, we have taken the value equal to 300. In the numerical experiment, we have assumed that the mixing ratio of CO is fixed at 100 ppb uniformly in the whole domain. Furthermore, we have also prescribed the following emission fluxes constant on time: NO flux (0.1 $ppbms^{-1}$) and RH flux (1.0 $ppbms^{-1}$). In the simulations, the dry deposition of species is neglected. Figures 1d, 1e and 1f also show the initial profiles of the reactant species.

An important aspect of this study is to investigate the modification of the photolysis rates by the presence of clouds. Because clouds alter the different proportions of direct and diffuse ultraviolet radiation, the actinic flux (and therefore the photolysis rates) has different values below, in, and above the clouds (Madronich(1987)). We have implemented this effect by calculating at every time step a factor below and above the clouds and by applying this factor to the clear sky value of the photolysis rate j_{clear} following Chang et al.(1987):

$$j_{clouds} = F\ j_{clear} \qquad (12)$$

Above the cloud, the factor (F) is defined as:

$$F = 1 + \alpha\ (1 - t_r)\ cos(\chi_o). \qquad (13)$$

While, below the cloud, F is defined as:

$$F = 1.6\ t_r\ cos(\chi_o). \qquad (14)$$

Here, t_r is the energy transmission coefficient for normally incident light, χ_o is the solar zenith angle, and α is a reaction dependent coefficient (for nitrogen dioxide α=1.2). To simplify the calculation, a linear interpolation is assumed inside the cloud scaled with the value of the liquid water content (q_l). Based on measurements of j$_2$ (Früh et al.(2000)), the linear interpolation assumption likely overestimates the photolysis rate in the middle to lower regions of the cloud while underestimates the photolysis rate near cloud top.

The energy transmission coefficient t_r depends on the cloud optical depth and a scattering phase function asymmetry factor (f) equal to 0.86 for the typical cloud particle size ranges under study (Joseph et al.(1976)). The expression reads:

$$t_r = \frac{5\ -\ e^{-\tau}}{[4\ +\ 3\tau(1-f)]}. \qquad (15)$$

The cloud optical depth (τ) is calculated according to the expression given by Stephens(1984)

$$\tau = \frac{3}{2}\frac{W}{\rho_l}\ r_e^{-1}, \qquad (16)$$

where W is the vertically integrated liquid water ($kg\ m^{-2}$), ρ_l is the water density ($kg\ m^{-3}$) and r_e is the effective radius. Here, we have used a constant value of $r_e = 10\ \mu m$. For clouds characterized by values of $\tau < 5$ and for regions between clouds, we have assumed the photolysis rate of clear sky conditions. Regions between clouds may actually have enhanced photolysis rates due to cloud scattering. Here, we are simply investigating the importance of cloud scattering in the cloud column as a first step in our research. Our control simulation includes the modification of photolysis rates due to cloud scattering, while a sensitivity simulation excludes this effect on the chemistry.

Notice that reaction (1) does not take into account possible spatial and temporal variations of specific moisture in the cloudy boundary layer. A possible solution to account this variation is allowing water vapour to be "active" in the chemical system. In short, reaction (1) represents the following three reactions:

$$O_3\ + h\nu \rightarrow O_2 + O(^1D) \quad j_3\ varies \qquad (17)$$

$$O(^1D)\ +\ M \rightarrow O(^3P) + M \quad k_{10} = 7.13\ 10^{-1} \qquad (18)$$

$$O(^1D)\ +\ H_2O \rightarrow 2OH \quad k_{11} = 5.41, \qquad (19)$$

where M is a molecule of air.

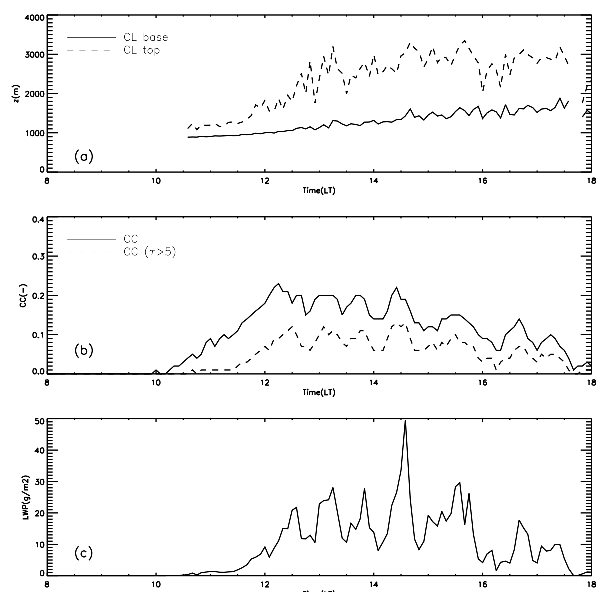

FIG. 2: Time evolution of (a) cloud base and cloud top, (b) cloud cover for the whole cloud population and the dense clouds defined with a cloud optical depth larger than 5 and (c) integrated liquid water path.

In our study, the value of the specific humidity in the sub-cloud layer is around 15 g/Kg (approximately a relative humidity at the surface of RH=50% (T=305 K) at 12 LT) and at the top of the sub-cloud layer around

81%. Future numerical experiments will be addresses to determine the sensitivity of the results to the spatial distribution of water vapour in cloudy boundary layers by including explicitely reactions (17)-(19) instead of reaction (1).

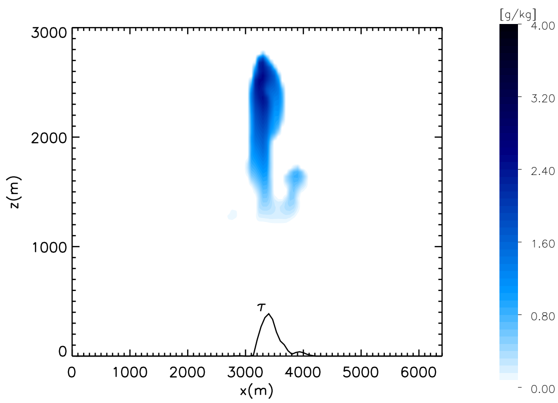

FIG. 3: Instantaneous cross section of the liquid water content at 15.45 LT. The cloud optical depth calculated according expression 16 is also included.

4. Results

4.1 *Cloud evolution and vertical structure*

The main dynamic characteristics of the evolution of shallow cumulus are shown at figures 2. The results agree very well with the previous simulations summarized by Brown et al.(2002) and Vilà-Guerau de Arellano et al.(2005). In short, shallow cumulus are formed around 10 LT with a cloud base increasing linearly on time from 800 m to 1200 m. Cloud depth fluctuates on time with maximum values around 2000 m between 13 and 16 LT. Notice that from a thermodynamic perspective cloud top height defines the boundary layer top. The values of cloud cover (figure 2b) and liquid water path (figure 2c) are characteristic of shallow cumuli over land. In the figure of cloud cover (figure 2b), we have also included the cloud cover of clouds characterized by a $\tau > 5$ since these thick clouds are the ones which perturb the photolysis rate.

In order to illustrate the shallow cumulus simulated by DALES, we show at figure 3 an instantaneous vertical cross section of the liquid water content and the corresponding instantaneous cloud optical depth (expression (16)). The characteristic horizontal and vertical length scales are around 500 m and between 1000-2000 m. However, during the simulation not all the clouds fully developed vertically and therefore they can be characterized as forced clouds (see the difference in the cloud covers ar figure figure 2b). Notices that DALES is able to represent the spatial distribution of the liquid water content (q_l) with a high degree of detail which is fundamental to determine the perturbation of the photolysis rate due to the presence of clouds. As a result, we obtain very large values for τ which can have a large impact on the photolysis rate.

Figure 4 show the evolution of the vertical profiles of the thermodynamic variables spatially averaged over the whole domain. The time averaged is 1 hour. In the sub-cloud layer, all the variables are well mixed. At figure 4b, the liquid water potential temperature profile after 12 LT is conditionally unstable ifrom 1000 m up to the the limit of convection located approximately at around 2700 m. Above this level, there is an absolutely stable boundary layer. In figure 4d, the liquid water content profile shows the transition from a clear maximum near cloud base in the early stages of cloud development to a more homogeneous distribution with height once the clouds are fully vertically developed.

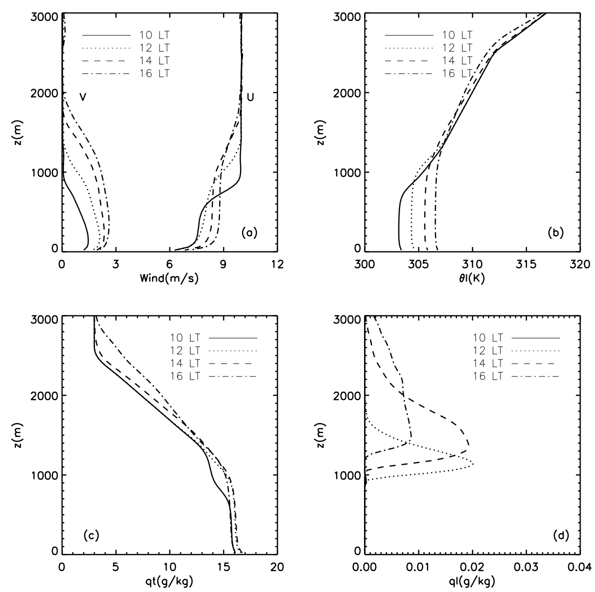

FIG. 4: Vertical profiles of (a) wind speed (U- and V-component), (b) liquid water potential temperture, (c) specific humidity and (d) liquid water (one-hour averaged)

4.2 *Spatial patterns*

The modification of the photolysis rate by the parameterization (12) is shown in the instantaneous cross section of the ratio j_{cloud}/j_{clear} (Figure 5). As expressed by the factors (13) and (14), there is an enhancement above the cloud, a linear decrease in the cloud and a decrease in the photolysis values below cloud. Notice that the parameterization gives perhaps very low photolysis values because of the large *local and instantaneous* values of the cloud optical depth, *i.e.* $\tau > 300$. In consequence, below thick cloud, photolysis rate can be closer to zero. A possible future improvement is a better characterization of the effective radius (see expression (16) for shallow cumuli over land. This characterization will require the validation, in future work, of these values with in-situ observations. Furthermore, the parameterization is only 1-dimensional and consequently neglects the possible contributions of the reflection at the lateral side by neighbour clouds. In spite of these shortcomings, the main goal of the study is to have a reliable numerical tool which allow us to study simultaneously the role of dynamics, mixing, radiation and chemical transformations in turbulent reacting flows driven by the presence of clouds.

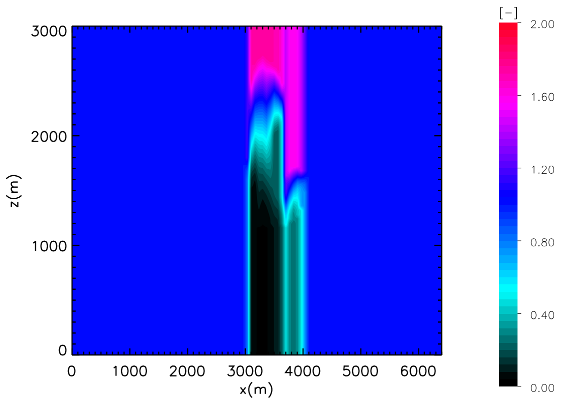

FIG. 5: Instantaneous cross section of the j_{cloud}/j_{clear} ratio for the photolysis rate of reactions (1) and (2) at 15.45 LT

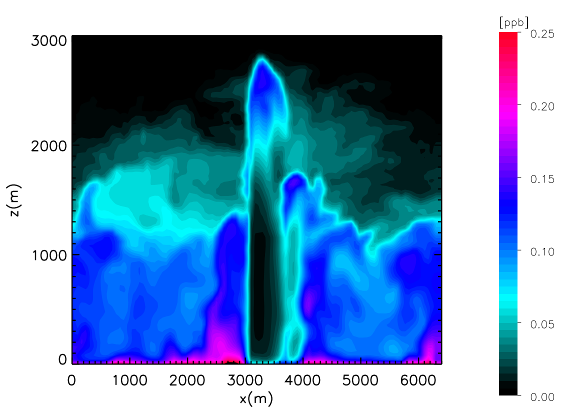

FIG. 6: Instantaneous cross section of the nitric oxide (NO) mixing ratio at 15.45 LT

Figures 6 and 7 show the spatial distribution of the NO and O_3 mixing ratio. The intrusion of the polluted

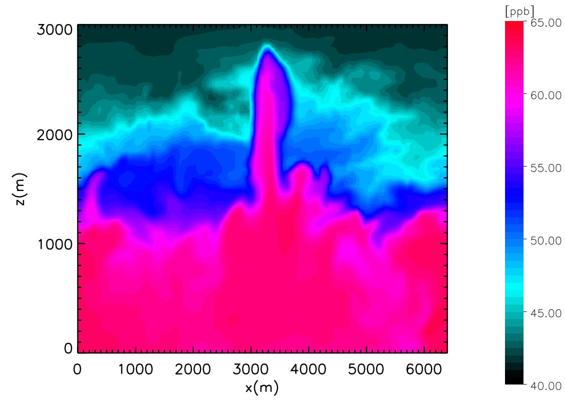

FIG. 7: Instantaneous cross section of the ozone (O_3) mixing ratio at 15.45 LT

air masses into the free troposphere due to the extension of the atmospheric boundary layer until cloud top is well reproduced by DALES. Notice that the cloud top defines now the boundary layer height. The less abundant species (NO) is largely influenced by the photolysis perturbation. In consequence, very small values of the nitric oxide mixing ratio are found below the cloud due to the large decrease of the photolysis rate at reaction (2). In turn, a NO maximum is found near cloud top related to the increase of the UV-actinic flux due to the combined contributions of direct and diffuse ultraviolet radiation at this region and the largest mixing ratio of NO_2 available originated and ventilated from the sub-cloud layer. Once again, it will be important to contrast these numerical results with aircraft observations taken in polluted areas influenced by shallow cumulus. At figure 7, one can distinguish the large difference in ozone values within the cloud ($\approx$ 65 ppb) and around the cloud ($\approx$ 50 ppb). Furthermore, as shown by the figure, the environment around the cloud is characterized by a rather stratified layering indicating low activity of turbulence and therefore of mixing.

4.3 *Vertical characteristic of the mean and flux profiles of the reactants*

The results corresponding to the evolution and distribution of the chemical reactants are shown at figures 8-9. Similarly to the thermodynamic vertical profiles, we found well-mixed values within the sub-cloud layer. The enhancement of the vertical transport within the cloud layer is noticeable for the inert compounds and the NO, NO_2 and HNO_3 reactants (see the profiles above 1000 m) whereas the generic hydrocarbon RH is totally depleted of the sub-cloud layer. In that respect, it is worth to mention the dependence of the $RH-$profile on the factor f which controls the reaction speed of re-

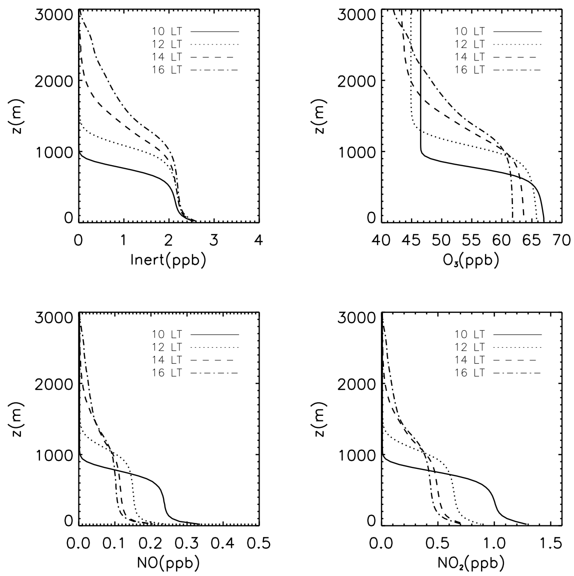

FIG. 8: Vertical profiles of the (a) inert, (b) ozone, (c) NO and (d) NO_2 (one-hour averaged)

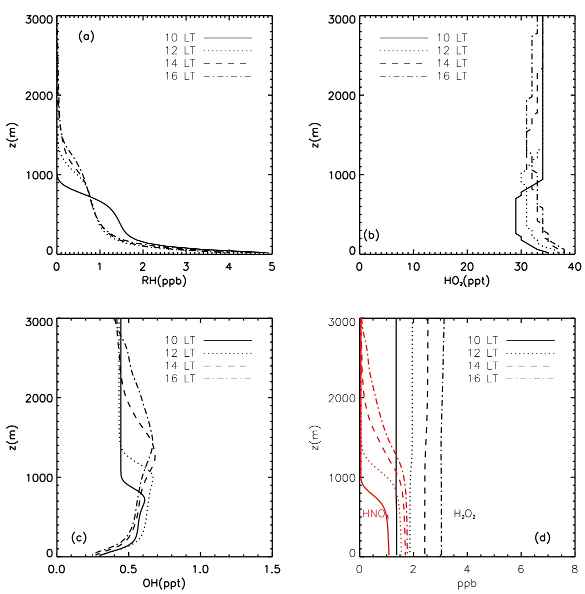

FIG. 9: Vertical profiles of the (a) generic hydrocarbon RH, (b) HO_2, (c) OH and (d) H_2O_2 and HNO_3 (one-hour averaged)

action 5. Notice that these profiles are averaged vertical profiles over the whole domain including cloud and environment regions. As such, and in spite the relative small cloud cover shown at figure 2b, the vertical profiles show the active role of clouds in diluting and transporting reactants from the sub-cloud layer to the cloud top. However, the cloud ventilation occurs within the boundary layer since cloud top is now defining the boundary layer height (Cotton et al.(1995)). The OH profile (figure 9c) shows an almost constant on height value, with a characteristic minimum near the surface due to reaction 5 and the maximum value located at cloud base. End product species, HNO_3 and H_2O_2 (figure 9d) show a clear difference in their vertical pattern. HNO_3 is mainly produced at the sub-cloud layer and trnsported upwards by the cloud whereas H_2O_2 is locally produced through out the atmospheric boundary layer.

Figures 10 and 11 show the vertical flux profiles for the inert and reactive species. Focusing first on the inert species, one can observed a flux profiles almost constant on height in the sub-cloud layer similar to the ones observed in dry convective boundary layers. Within the cloud layer, the flux decrease with height through out the cloud depth. This flux is entirely driven by the buoyancy flux due to the latent heat release.

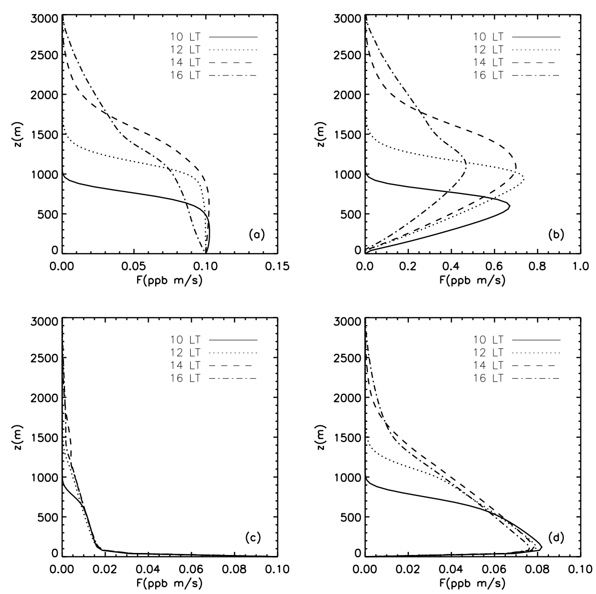

FIG. 10: Vertical flux profiles of the (a) inert, (b) ozone, (c) NO and (d) NO_2 (one-hour averaged)

Reactant emitted at the surface (NO and RH) are clearly modified due to chemical reactions departing from the linear profiles characteristic of inert species and with the following values of the flux divergence: for NO and RH the values are 0.05 ppb/hour and 3.6 ppb/hour, respectively. The latter value shows that the flux divergence largely contributes to the budget of RH and therefore it has to be taken into account.

In absence of deposition fluxes, the maximum flux for ozone (figure 10b) and nitric acid (figure 11d) is situated near the cloud base height where species are introduced in the cloud layer. This indicates the importance of estimated and represent adequately this region in large atmospheric scale models. In a previous study (Vilà-Guerau de Arellano et al.(2005)) have shown that the parameterization of shallow cumulus convection using the mass flux represents well the transport flux within the cloud, but it tends to underestimate the flux value at cloud base.

Our last comment is related to the importance of the flux divergence in all the reactant profiles. Com-

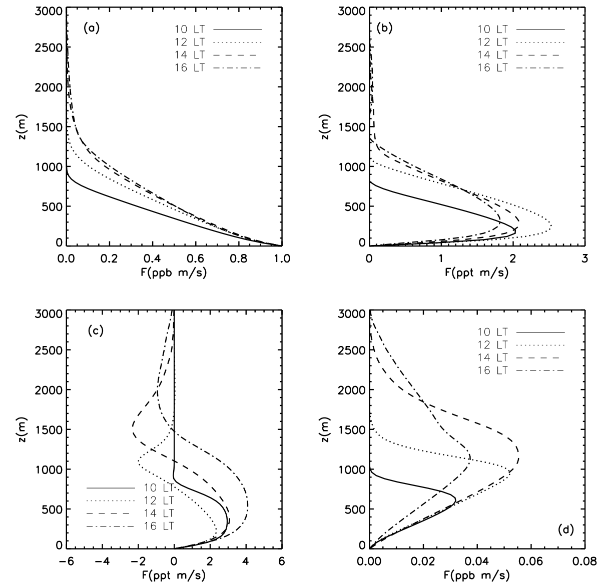

FIG. 11: Vertical flux profiles of the (a) generic hydrocarbon RH, (b) HO_2, (c) OH and (d) HNO_3 (one-hour averaged)

pared to the flux profile of the inert species, all the fluxes vary with height. For reactants like O_3 and HNO_3 the flux divergence changes sign between the sub-cloud layer and the cloud layer which could lead to large errors in the inferring of flux profiles from observations taken from airborne platforms.

4.4 ***Conclusions***

The spatial distribution and evolution of the system $O_3 - HO_x - NO_x - CO$ influenced by the dynamic and radiative processes associated to shallow cumuli field is simulated by using the large-eddy simulation DALES. These first results show the capacity of reproducing the dynamic, radiation and chemical transformation with a high degree of accuracy. Therefore, we are confidentthat the DALES-chemistry will allow us to carry out process study and support data interpretation of the turbulent-radiative reacting flows influenced by the presence of clouds.

The presence of clouds increases the volume in which species are transported, which leads to a dilution of reactant mixing ratio within the boundary layer. Mixing ratios of tracers below cloud decrease by up to 12% while mixing ratios averaged in the volume defined from the surface to the maximum elevation where tracers are vertically transported decrease by up to 50% compared to the clear sky situation. Furthermore, reactants transported to elevated regions remain at those levels following the clouds dissipation, which should have an effect on simulating nocturnal chemistry of the residual layer. The vertical flux profile show a large variation with height due to the chemical transformations and the cloud dynamics. In consequence, flux divergence should be taken into account in inferring flux estimation from upper air observations.

The perturbation of photodissociation rates due to the presence of clouds is discussed comparing a simulation that uses a photodissociation rate perturbed by the cloud with one that uses clear sky values. By analyzing the instantaneous fields of the mixing ratio, we find differences up to a 40% below the cloud base height and up to 20% close to cloud top, which indicates a large variability in the reactant distribution, an important aspect in the interpretation of the chemical processes in and around clouds.

REFERENCES

Brown, A. R., R. T. Cederwall, A. Chlond, P. G. Duynkerke, J. Golaz, J. M. Khairoutdinov, D. Lewellen, A. Lock, M. K. Macveen, C. Moeng, R. A. J. Neggers, A. P. Siebesma and B. Stevens, 2002: Large-eddy simulation of the diurnal cycle of shallow cumulus convection over land. *Quart. J. Roy. Meteorol. Soc.*, **128(B)**, 1075–1094.

Chang, J., R. Brost, I. Isaksen, S. Madronich, P. Middleton, W. Stockwell and C.J.Walcek, 1987: A three-dimensional eulerian acid deposition model: physical concepts and formulation. *J. Geophys. Res.-Atmosphere*, **92**, 14681–14700.

Cotton, W. R., G. Alexander, R. Hertenstein, R. Walko, R. McAnelly and M. Nicholls, 1995: Cloud venting-a review and some new global annual estimates. *Earth Science Reviews*, **39**, 169–206.

Dosio, A., J. Vilà-Guerau de Arellano, A. A. M. Holtslag and P. J. H. Builtjes, 2003: Dispersion of a passive tracer in buoyancy- and shear-driven boundary layers. *J. Appl. Meteorol.*, **42**, 1116–1130.

Früh, B., T. Trautmann, M. Wendisch and A. Keil, 2000: Comparison of observed and simulated NO_2 photodissociation frequencies in a cloudless atmosphere and in continental boundary layer clouds. *J. Geophys. Res.-Atmosphere*, **105**, 9843–9857.

Joseph, J. H., W. J. Wiscombe and J. A. Weinman, 1976: The delta-Eddington approximation for radiative transfer flux. *J. Atmos. Sci.*, **33**, 2452–2458.

Krol, M. C., M. J. Molemaker and J. Vilà-Guerau de Arellano, 2000: Effects of turbulence and heterogeneous emissions on photochemically active species in the convective boundary layer. *J. Geophys. Res.-Atmosphere*, **105**, 6871–6884.

Madronich, S., 1987: Photodissociation in the atmosphere: 1. Actinic fluxes and the effects of ground reflections and clouds. *J. Geophys. Res.-Atmosphere*, **92**, 9740–9752.

Stephens, G., 1984: The parameterization of radiation for numerical weather prediction and climate models. *Mon. Wea. Rev.*, **112**, 826–867.

Vilà-Guerau de Arellano, J., S. Kim, M. C. Barth and E. G. Patton, 2005: Transport and chemical transformations influenced by shallow cumulus over land. *Atmos. Chem. Phys.*, **5**, 3219–3231.

VERTICAL AND SPECTRAL DISTRIBUTIONS OF AEROSOL PARTICLES OVER SHIJIAZHUANG AREA, NORTHERN CHINA

Yan Yin[1], Yu Zhang[1], Ying Duan[2], Lixin Shi[2], Zhihui Wu[2], Yunchuan Li[2]
[1]Nanjing University of Information Science & Technology, Nanjing 210044 China
[2]Hebei Provincial Office of Weather Modification, Shijiazhuang 050021 China

1. INTRODUCTION

Aerosol particles play an important role in regional and global climate change (IPCC, 2007). However, large uncertainties exist in current estimates of aerosol forcing because of incomplete knowledge concerning the spatial and temporal distributions of aerosol loading, the physical and chemical properties of aerosol particles, as well as their interactions with clouds and climate.

In this study, the vertical and spectral distributions of aerosol particles over Shijiazhuang area, northern China, are analyzed based on airborne measurements obtained in autumn 2005.

2. INSTRUMENTATION AND METHODS

A passive cavity aerosol spectrometer probe (PCASP-100X, PMS Inc., Boulder, CO, USA) was mounted under the wing of an aircraft (Cheyenne IIIA) to measure the spectra and concentrations of aerosol particles. Particles ranging from 0.1 to 3.0 μm in diameter with 15 unequally sized bins were recorded at 1-s intervals. The in-situ meteorological parameters such as ambient air temperature (T), dew point (Td), and air pressure (P) are measured during flights.

The PCASP instrument is calibrated using polystyrene latex spheres by Droplet Measurement Technologies Inc. in the United States. The calibration is performed every year before the field measurements. In this study, the data obtained in October, 2005, are analyzed, including the number concentration, size distribution, and mean diameter of aerosol particles.

The mean diameter $\overline{D}$ which is weighted by the number concentrations is calculated using the following equation:

$$\overline{D} = \sum_{i=1}^{15} n_i D_i / \sum_{i=1}^{15} n_i \ , \qquad (1)$$

where D_i is the middle diameter of *i*th bin, n_i is the particle number of *i*th bin.

3. THE VERTICAL DISTRIBUTION OF PARTICLE CONCENTRATION AND SIZE

Four flights were conducted on October 7, 17, 21, and 29, 2005, to measure aerosol properties over Shijiazhaung area. In the following section we are concentrated on the results measured on the 17th and 21st of October, to represent a typical clear and a cloudy weather conditions, respectively.

Figure 1 shows the vertical distribution of concentration and mean diameter of aerosol particles (both are averaged over a vertical distance of 100 meters) measured on 17th October, 2005, and the vertical profiles of ambient temperature and relative humidity. It can be seen from Fig. 1(a) that the boundary layer was heavily polluted in this area with the concentration of aerosol particles ranging from 7000 cm^{-3} to more than 9000 cm^{-3} below 500 m. It should be kept in mind that the aerosol particles presented here only refer to those ranging from 0.1 to 3.0 μm in diameter, that is, the accumulation mode and the smaller particles in the coarse mode. The concentrations can be orders of magnitude higher if particles in the nucleation mode (smaller than 0.1μm in radius) are also included. The particle concentration decreases sharply with height from 8000 cm^{-3} at 500 m to about 2500 cm^{-3} at 750 m level, and then fluctuates around 3500 cm^{-3}. The peak concentration of about 5500 cm^{-3} appeared between 1000 and 1250 m is closely related to a local inverse layer at the same altitude (Fig. 1(b)).

The mean diameter of the particles is 0.143 μm near the surface and decreases to 0.125 μm at 760 m level. It is interesting to note that there are several secondary peak values in the profile of the mean diameter. A close comparison of this profile with that of relative humidity in Fig. 1 (b) indicates that the peak values are closely correlated with the local maximal values of relative humidity, implying that the humidity of the air to a large extent determines the aerosol size distribution, and in turn, the optical properties of the aerosol particles. This is consistent with measurements from other places (e.g., Pruppacher and Klett, 1997).

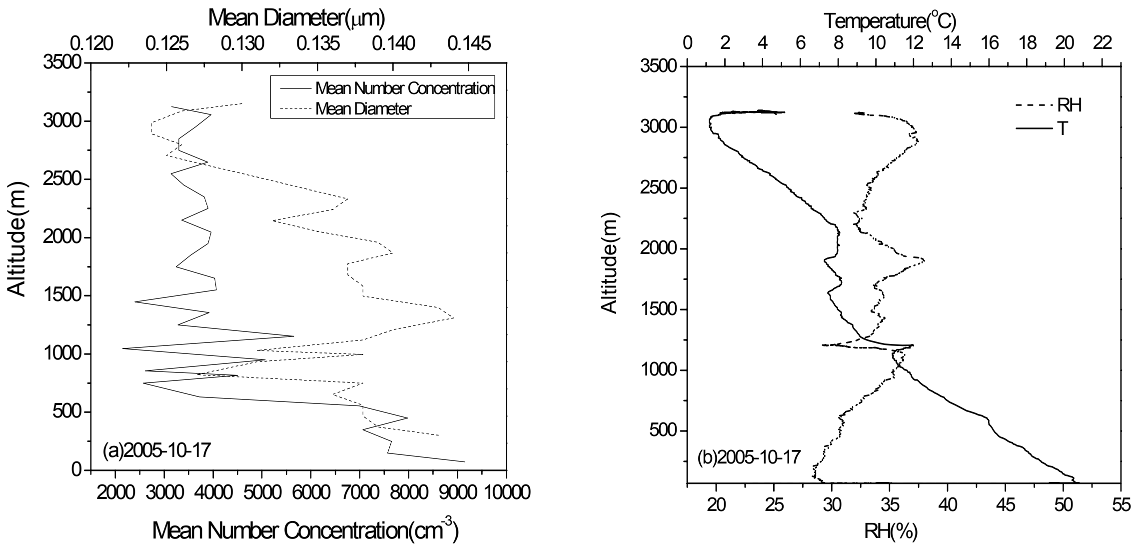

Fig. 1 Vertical profiles of (a) mean number concentration (solid line) and diameter (dashed line) of aerosol particles, and (b) ambient air temperature (solid line) and relative humidity (dashed line), measured on October 17, 2005.

Figure 2 shows the vertical distribution of concentration and mean diameter of aerosol particles, and the ambient temperature and relative humidity, measured on October 21, 2005, a typical cloudy day in this region. Similar to the previous case, the concentration of aerosol particles is the largest near the Earth's surface, but the absolute value is smaller than the previous case (about 5700 cm^{-3}). This value sharply decreases to ~3100 cm^{-3} at 150 m. Thereafter, the concentration decreases gradually to about 1700 cm^{-3} at 2000 m and ~1500 cm^{-3} above 3000 m. The secondary peaks appeared in the profiles of concentration and diameter between 2000 and 3000 m, are correlated with the maximum value of relative humidity (Fig. 2 (b)), and may resulted from the wet aerosols or from drop shattering when the aircraft entered the cloud. Particle concentration remains about 1500 cm^{-3} above 3000 m with size of about 0.12 μm until the highest level the aircraft climbed.

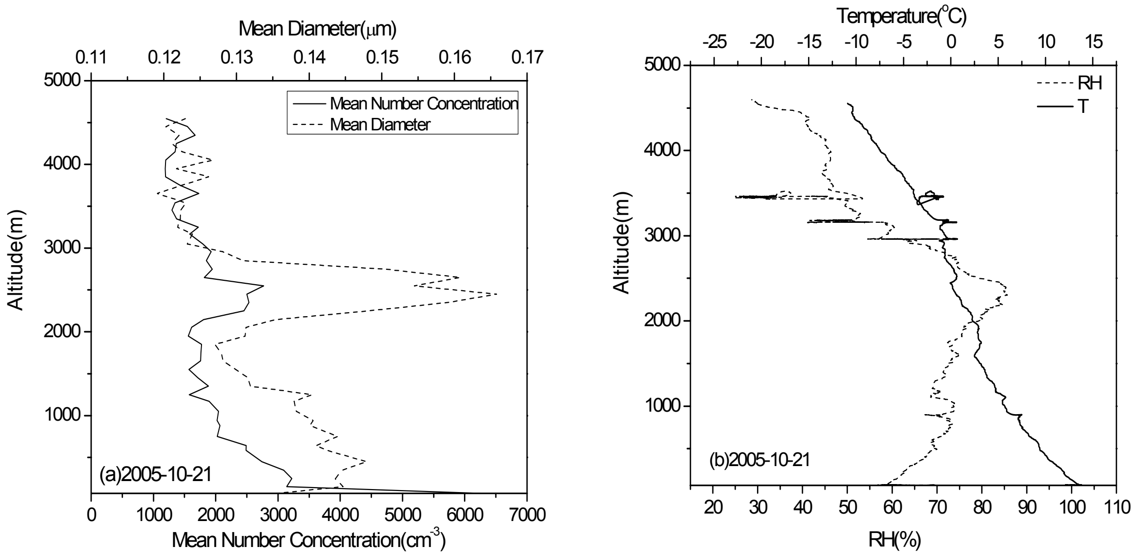

Fig. 2 Vertical profiles of (a) mean number concentration (solid line) and diameter (dashed line) of aerosol particles, and (b) ambient air temperature (solid line) and relative humidity (dashed line), on October 21, 2005.

4. THE SIZE DISTRIBUTIONS OF AEROSOL PARTICLES

Figure 3(a) and (b) show the particle size distributions at selected altitudes measured during the two flights described in the previous section, while Fig. 4 presents the mean size distributions obtained from the four flights. It can be seen from Fig. 3 that the particle spectra are broader near the surface and become narrower with increasing height. This is related to the fact that coarse mode aerosol particles are mainly produced by bulk to particle conversion from the Earth's surface.

From Fig. 4 one may find that the mean size distributions from all the flights are quite similar with respect to the peak concentrations, the number of modes, and the positions of the modes. In general, the mean size distributions from these measurements can be fitted with three or four lognormal distribution functions with similar parameters, except for that obtained on October 21. The concentration of coarse mode particles on October 21 is slightly higher than that from other flights, and is caused by higher relative humidity as compared to other days (Fig. 3(b)) and resulted in hazy weather on the ground.

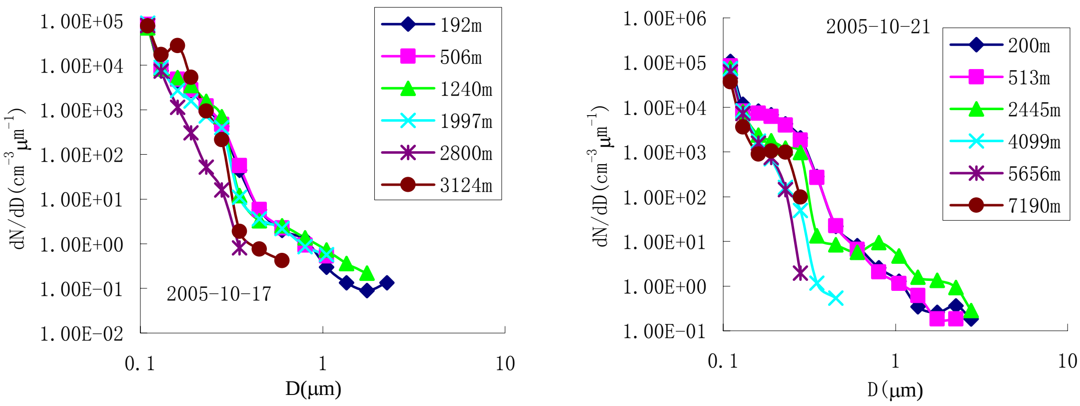

Fig. 3 The aerosol size distributions at selected altitudes on October 17 (a) and 21 (b), 2005.

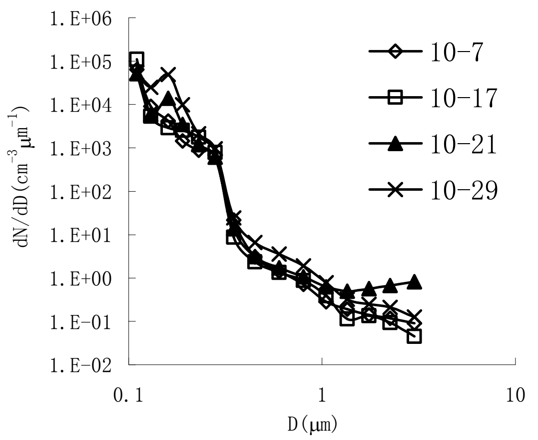

Fig. 4 The mean size distributions of aerosol particles measured during different flights.

5. SUMMARY

Airborne measurements of the concentration and size distribution of aerosol particles with diameter ranging from 0.1 to 3.0 µm over Shijiazhuang area, northern China, are analyzed. The preliminary results show that maximum mean number concentration of aerosol particles ranges from 6000 to more than 9000 cm^{-3} near the ground and decreases sharply to 1500-3500 cm^{-3} above the boundary layer. It is also found that particle size distributions are the broadest close to the surface and become narrower with increasing height, but the general feature of the particle distributions obtained from all the four flights are quite similar and can be fitted with three or four lognormal distribution functions. The results also indicate that aerosol particle size is to a large extent very dependent on the meteorological conditions such as humidity, and the presence of inversion layers.

BIBLIOGRAPHY

Intergovernmental Panel on Climate Change (2007), The Physical Science Basis –Contribution of Working Group I to the Fourth Assessment Report of the Intergovernmental Panel on Climate Change, edited by S. Solomon et al., 996 pp., Cambridge Univ. Press, New York.

Pruppacher, H. R., and J. D. Klett (1997), Microphysics of Clouds and Precipitation, 1954 pp., Kluwer Acad., Norwell, Mass.

Acknoledgements

This study was partially funded by the 973 Program of China through Grant No. 2006CB403706, the National Natural Sciences Foundation of China through Grant No.

40475003, and Jiangsu Key Laboratory of Meteorological Disaster (Nanjing University of Information Science & Technology), China, through Grant No. KLME060209.

IMPACT OF METEOROLOGICAL MODEL IN PREDICTING CLOUD MICROPHYSICS ON SULPHATE PRODUCTION SIMULATED IN A CANADIAN AIR QUALITY MODEL

Junhua Zhang, Wanmin Gong, W. Richard Leaitch, Anne Marie Macdonald, and Kurt Anlauf
Science and Technology Branch, Environment Canada, Toronto, Canada

1. INTRODUCTION

Clouds play a significant role in processing and cycling of chemicals in atmosphere. Cloud processes have been parameterized in chemical transport models at varying levels of sophistication (e.g., Lohmann et al., 1999; Barth et al., 2000; von Salzen et al., 2000; Gong et al., 2006). Previous air quality model evaluations indicate that the modeled cloud processing of gases and aerosols depends critically on the meteorological driver's ability to predict cloud microphysics fields (Gong et al., 2006). However, validation of the model performance in representing the cloud processes remains a great challenge partly due to the lack of suitable observations.

During the summer of 2004, a large field study was conducted under the coordination of the International Consortium for Atmospheric Research on Transport and Transformation (ICARTT). As a component of the ICARTT campaign, Environment Canada in collaboration with the National Research Council of Canada (NRCC) and Canadian Universities, conducted airborne measurements using the NRC-IAR (National Research Council Canada - Institute for Aerospace Research) Convair 580 aircraft. The study focused on the interactions among trace gases, aerosols and clouds, as well as the transport of pollution into the Canadian Maritimes. One of the study objectives was to provide a dataset for evaluating air quality models particularly on the representation of cloud processes. Various trace gas and aerosol measurements and cloud microphysics measurements were conducted onboard.

As a first step in an effort to evaluate cloud processing in a Canadian air quality model –AURAMS (A Unified Regional Air-quality Modeling System), Zhang et al. (2007) examined the performance of the meteorological driver model - GEM (Global Environmental Multiscale model) in predicting summertime cloud liquid water contents (LWC) against aircraft observations at two horizontal resolutions (15- and 2.5-km). Results show that the model reproduced the observed variation of LWC from flight to flight. However, the "in-cloud" LWC values were generally over-predicted by 99% and 45% for the 15- and 2.5-km resolution simulations, respectively. When the model-observation comparison is done at grid scales for the Stratocumulus cases, the model at 2.5km resolution still significantly overpredicted the mean LWC by 120% while the model at 15-km resolution agrees better with observation with smaller overprediction (46%).

Zhang et al. (2007) also pointed out the uncertainties that are associated with the model predicted LWC. For example, at 2.5km model resolution, clouds are assumed to be fully resolved. The inability of the microphysics scheme to represent clouds at a scale smaller than that resolution (2.5 km) led to the underprediction of the occurrence of low LWC (<0.1 g m^{-3}). On the other hand, the "in-cloud" LWC for GEM at 15-km resolution is obtained by dividing the modeled grid-scale LWC by the modeled cloud fraction. Although the parameterization of condensation in the model takes fractional cloudiness into account at 15-km model resolution, cloud fraction is determined solely from relative humidity and a predefined threshold relative humidity above which clouds are assumed to form within a grid box. Therefore, significant uncertainty exists in the modelled cloud fraction which will in turn affect the calculated "in-cloud" LWC. Due to the division (by modelled cloud fraction), the level of uncertainty in the diagnosed "in-cloud" LWCs will increase as the cloud fraction gets smaller. These are cases where the modeled mean "in-cloud" LWC is strongly influenced by a few data points with unrealistically large LWC values, which in turn are often driven by the small modelled cloud fractions at some grid points.

The overestimation of LWC by meteorological model (the GEM model) will have subsequent impact on the cloud processing of gases and aerosols in the air quality model –AURAMS, which is driven by GEM model. AURAMS considers fractional cloud cover for the cloud processing of gases and aerosols (Gong et al., 2006). For a given cloudy grid the cloud processing (scavenging of aerosol particles, condensation of soluble gases on cloud droplets, and aqueous-phase oxidation) is carried out for the cloudy portion of the grid only. For model at high resolution, such as 2.5km, cloud is assumed to be resolved and the grid can be either cloudy (cloud fraction is equal to 1) or clear. However, for model at low resolution (eg. 15km), the grid can be partially cloudy (cloud fraction is less than 1), the "in-cloud" LWC is derived from the modelled grid-scale LWC and modelled cloud fraction in much the same way as in the study conducted by Zhang et al. (2007), i.e., grid-scale LWC divided by cloud fraction. The gas and aerosol concentrations at model grid scale are then updated by a weighted average between the cloud-processed and the clear-air gas and aerosol concentrations according to the cloud fraction.

In this study, sulphate production simulated by AURAMS is examined at two horizontal resolutions (15- and 2.5-km). Impact of model-predicted cloud microphysics on air-quality predictions will be discussed. Selected aircraft flights for this study are described in Section 2. Section 3 describes the model setup. Difference between AURAMS predictions at two resolutions (15- and 2.5-km) will be analyzed and discussed in Section 4, and Section 5 summarizes the preliminary findings.

2. SELECTED AIRCRAFT FLIGHTS

Three flights (Flight 16, 17 and 18) measured stratocumulus are chosen for this study. They consist several relatively long level flight legs, usually one below cloud base in the clear air and other one or two in cloud. In this study, comparisons are only done at cloud level.

Flight 16 and 17 were conducted the same day on Aug. 10, 2004 to study the cloud processing of plumes from the Chicago area. Flight 16 (16:24-20:15 UTC) was mainly to sample a north-south line east of the south end of Lake Michigan both below and in cloud. Figure 1a shows the track of this flight and Figure 1b illustrates the time series of flight altitude and observed LWC. Focus of this flight is on the south-north leg conducted between 17:50-19:54. According to the aircraft sampling level, comparisons are done at one model level at 1235m for this flight. Flight 17 (21:22 -00:53) was conducted two hours later. It sampled a north-south line further downwind of Chicago plumes just west of Toledo. The flight track and time series of flight altitude and observed LWC are shown in Fig. 2a and 2b (Fig. 1a and 2a are copied from ftp://ftp.tor.ec.gc.ca/Measurement_Data/Data_Summaries/aug11_e.html). For this flight, the focus is on the south-north flight leg sampled between 21:44-24:10. Two model levels are chosen for this flight: one at 1235m and another at 1810m. The weather over this region was mainly associated with a cold front system with southwestly flow. Fig. 3 is the satellite visible channel image at 19:15UTC on that day showing dense cloud cover over the flight region.

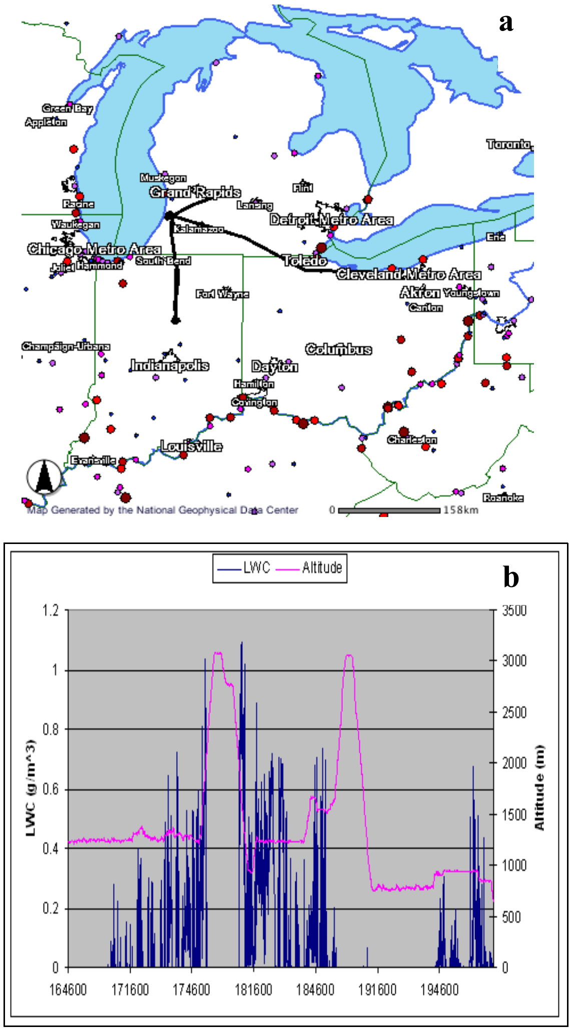

Fig. 1 The flight track of Flight 16 (a) and the observed LWC with corresponding aircraft altitude(b)

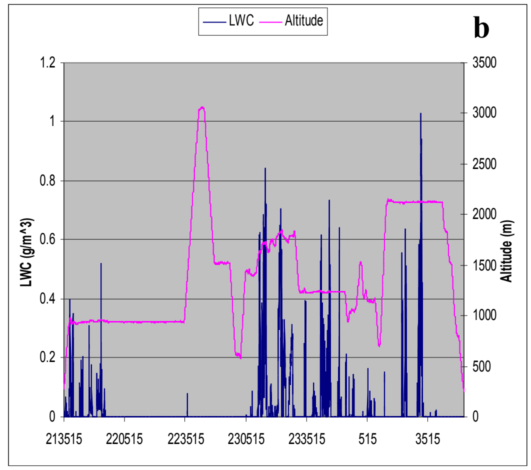

Fig. 2 The same as Fig.1, but for Flight 17.

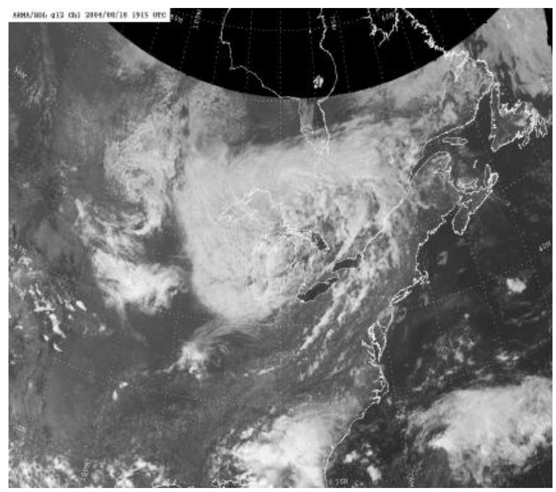

Fig. 3 Visible channel image (ch1) of GOES satellite at 19:15 UTC on Aug. 10, 2004

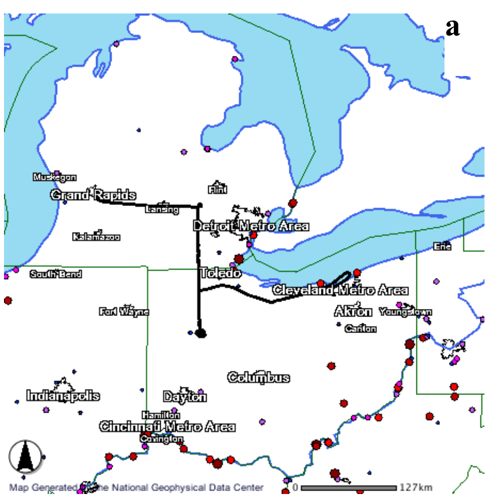

Flight 18 was conducted the next day on Aug. 11, 2004 (18:29 – 21:43 UTC) to study the downwind of the Detroit-Windsor plumes along two cross plume-centre lines both below and in cloud. Figure 4a shows the track of this flight (see ftp://ftp.tor.ec.gc.ca/Measurement_Data/Data_Summaries/aug11_e.html) and Figure 4b illustrates the time series of flight altitude and observed LWC. Two model levels are selected: one at 1500m and another at 1810m. During the observation period, the flow is still from west-south-west with patchy cloud cover associated with post front system as shown in the 20:15 UTC satellite visible channel image (Figure 5)

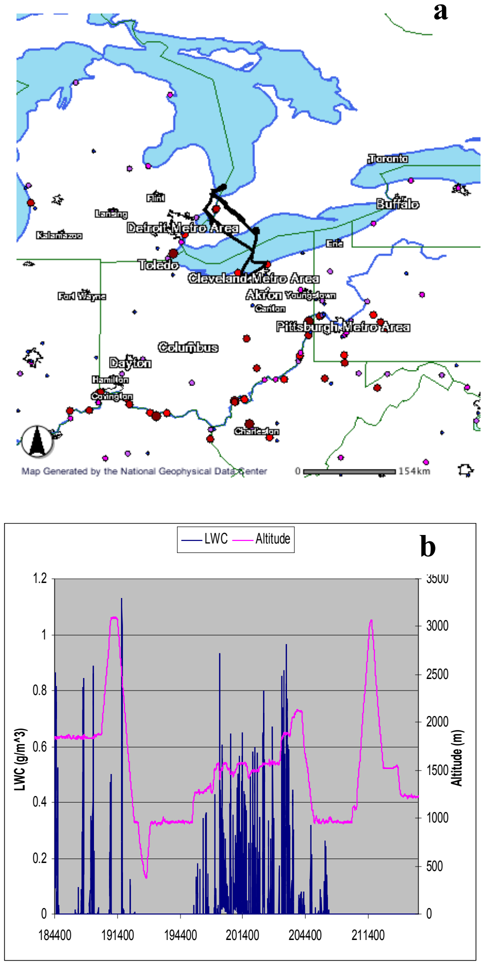

Fig. 4 The same as Fig. 1, but for Flight 18

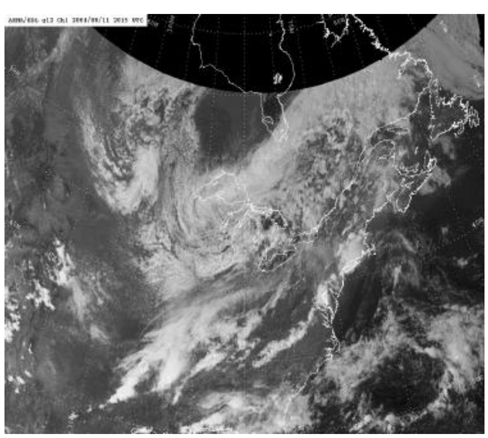

Fig. 5 Visible channel image (ch1) of GEOS satellite at 20:15 UTC on Aug. 11, 2004

3. MODEL DESCRIPTION

AURAMS (A Unified Regional Air-quality Modelling System) is a multi-pollutant, regional air-quality modelling system with size segregated and chemically speciated representation of aerosols (Gong et al., 2006). It has a polar-stereographic grid projection with 28 vertical levels up to 25 km and is driven offline by the Canadian weather forecast model – GEM model (Global Environment Multiscale model, Côté et al., 1998).

The GEM model with a latitude-longitude grid projection can be configured to run either globally at uniform resolution or with a variable resolution over the global domain and a uniform (core) mesh over an area of interest, and can be arbitrarily rotated (Côté et al., 1998). GEM model can also be configured to run with a Limited Area Modeling (LAM) setup with the boundary conditions provided by either the objective analysis or a coarser resolution forecast model. In this study, GEM with LAM configuration at 15- and 2.5-km horizontal resolutions with 58 vertical levels is used to provide the meteorological fields for AURAMS. The GEM runs are conducted in a cascade fashion: the initial and boundary conditions for the 15-km resolution runs are obtained from the best available objective analysis datasets from the Canadian Meteorological Centre, and the model simulation is run for 36 hours starting from 12 UTC of the previous day with the first 12 hours as spin-up. Boundary conditions from the objective analysis are available every 6 hours. The time step is 450 s for the 15-km GEM simulation. While the initial and boundary condition for the 2.5-km resolution runs are provided by the 15-km LAM forecast and the model is run for 24 hours starting from 00 UTC with the boundary conditions provided every hour. The time step is 60 s for the 2.5-km simulation. Discussions regarding the microphysical schemes used at the two resolutions can be found in Zhang et al. (2007). Figure 6 shows the 15- and 2.5-km horizontal resolution model domains. The GEM meteorological fields on a latitude-longitude grid are interpolated vertically and horizontally onto the AURAMS polar stereographic grid to drive AURAMS.

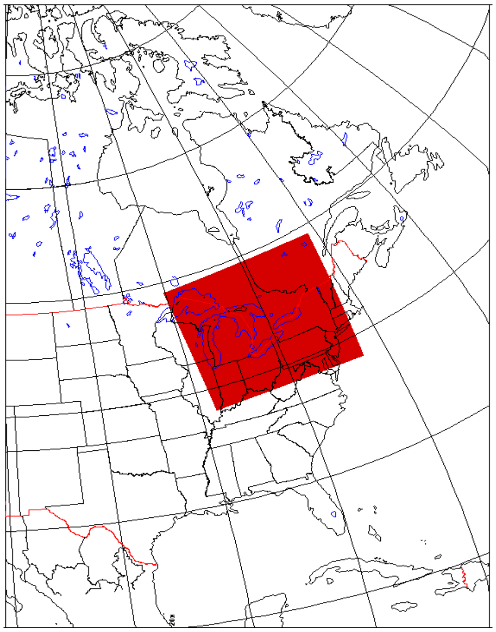

Fig. 6 The GEM LAM domains for the 15- and 2.5-km (red area) resolutions.

AURAMS simulations were conducted in a cascaded fashion as well. First, simulation was carried out on a polar-stereographic grid over eastern North America with a horizontal resolution of 42 km (true at 60°N) and a time interval of 900 s. It is driven by the GEM 15-km LAM predictions. The simulation period is July 7 – August 19, 2004. See Gong et al. (2007) for detailed description for the 42-km resolution AURAMS run.

Then a 15-km resolution simulation at a time step of 900 s is conducted with the initial and boundary conditions interpolated from the 42-km resolution simulations. The simulation is still driven by GEM 15-km LAM predictions and the simulation period is the same as the 42-km resolution with the boundary conditions provided every hour. Finally, a 2.5-km resolution simulation driven by GEM 2.5-km LAM predictions over domain cover individual flight at a time step of 120 s is conducted with the initial and boundary conditions interpolated from the 15-km simulations. The simulation period is 24 hours starting from 00 UTC. The boundary conditions are provided every hour as well. Figure 7 shows the cascaded AURAMS domains. In the figure, the domain at 2.5km resolution is for the Flights 16 and 17. The two flight tracks are also shown in the figure.

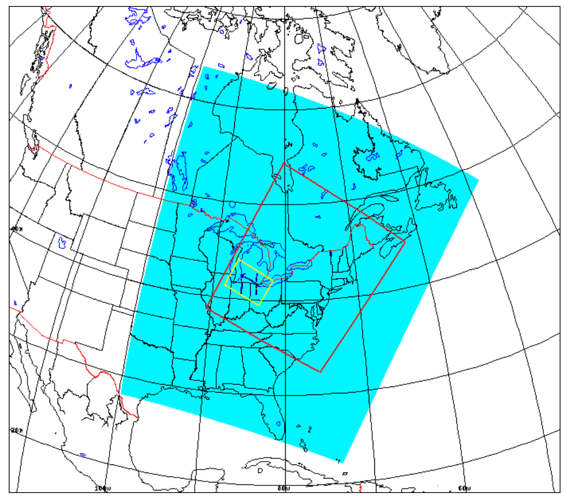

Fig. 7 AURAMS domains for the 42- (shaded aqua), 15- (red box) and 2.5-km (for F16 and 17, yellow box) resolutions, and the two flight tracks for Flights 16 and 17 (blue lines in the 2.5km domain).

The anthropogenic emissions for AURAMS at 42- and 15km resolutions are prepared from the 2000 Canadian, 2001 U.S., and 1999 Mexican national emissions inventories with version 2.2 of the SMOKE emissions processing system (http://www.smoke-model.org/index.cfm). State-specific adjustments to the NO_x emission from major point sources are also incorporated to account for the emission changes due to the NO_x State Implementation Plan (SIP) Call by the U.S. EPA (U.S. EPA, 2004) which came into effect in 2003. The biogenic emission fields were processed in-line using BEIS v3.09. To keep the difference between AURAMS at 15- and 2.5-km resolutions as little as possible, the emissions for the 2.5km resolution are extracted from the emissions processed for 15km resolution.

4. COMPARISON OF AURAMS SIMULATIONS AT 15 AND 2.5-KM RESOLUTIONS

Results from AURAMS simulations are outputted at each model time step interval, i.e., every 15 minutes for 15-km resolution and every 2 minutes for 2.5-km resolution. Several approaches are used to compare AURAMS simulations at 15- and 2.5-km resolutions.

4.1 Compare AURAMS simulation along flight track

Zhang et al. (2007) stated that comparison of model simulation with aircraft observation point by point along flight track is not a proper way to evaluate model performance, especially for the fields associated with clouds, due to the temporal and spatial mismatch between model simulation and aircraft observation. However, it is still interesting to see how well the model is able to capture the plume. Therefore, model simulated CO and SO2 are extracted to the aircraft flight time and location to enable a strict point to point comparison between aircraft observation and model simulation. Because temporal resolution for model at 15-km resolution is too low (15 minutes) to conduct a meaningful comparison with aircraft observation along flight track, the comparison is only done for AURAMS at 2.5-km resolution.

Figure 8 is the comparison of CO and SO2 for Flight 16. It shows that model is able to capture the main plume well for this flight, especially as indicated from the CO comparison. Good agreement is also seen for Flight 17, but to a less degree. The flight pattern of Flight 18 is a little complicated, model and observation agreement is not as good as for Flight 16 and 17. However, it still shows that model is able to capture the plumes from major sources in the area (results for Flight 17 and 18 are not shown).

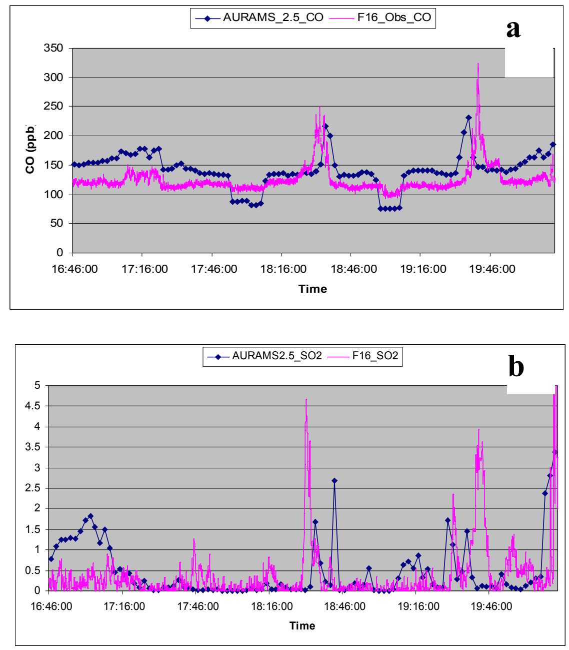

Fig. 8 Comparison of model simulated CO (a) and SO2 (b) at 2.5-km resolution with aircraft observations along flight track for Flight 16.

4.2 Comparison of AURAMS simulation over a sub-domain

This study focuses on investigation of the impact of meteorological model predicted cloud microphysics on sulphate production simulated in air quality model. Therefore, only sulphate aqueous production at cloud levels (see Section 2 for selected cloud levels) is examined here.

Similar to the method used by Zhang et al. (2007), model predicted cloud cover, cloud liquid water content, SO2 and H2O2 concentration, and aqueous sulphate production rate at two resolutions (2.5- and 15-km) are compared within a subdomains which cover individual flight track. Average of these fields over the selected subdomains are compared in table 1a for cloud cover (CF), grid mean LWC (kg/kg), and in-cloud LWC (kg/kg, for model at 15-

km resolution) and in table 1b for SO2 (ppb) concentration, aqueous sulphate production rate (DS4=, ug/kg/minute).

Table 1a sudomain averaged CF, LWC (*e-4, kg/kg) and in-cloud LWC (*e-4, kg/kg, for model at 15-km resolution) at different cloud levels

	Cloud Level (m)	2.5km CF	15km CF	2.5km LWC	15km LWC	15km In-cld LWC
F16	1235	0.79	0.41	1.85	1.55	3.76
F17	1235	0.19	0.12	0.218	0.197	1.66
	1810	0.66	0.47	1.81	2.97	6.12
F18	1500	0.14	0.13	0.203	0.185	1.20
	1810	0.24	0.30	0.420	0.724	3.69

Table 1b sudomain average of SO2 (ppb) concentration and aqueous sulphate production rate DS4= (*e-2 ug/kg/minute)

	Cloud Level (m)	2.5km SO2	15km SO2	2.5km DS4=	15km DS4=
F16	1235	0.331	0.336	2.72	2.87
F17	1235	0.217	0.25	0.110	0.127
	1810	0.132	0.133	0.558	0.730
F18	1500	0.433	0.587	0.978	1.01
	1810	0.279	0.263	0.866	1.42

Table 1a shows that at lower cloud levels (1235 and 1500m), the model at 2.5-km resolution usually predicted higher mean LWC and CF, while at higher level (1810m), the model at 15-km resolution predicted higher LWC. It agrees with one of the conclusions made by Zhang et al. (2007) that the model at 15-km resolution tends to predict higher cloud base. The altitudes where the highest LWC occurs for Flight 17 and 18 are, therefore, higher in the lower model resolution. On the other hand, the in-cloud LWC for model at 15-km resolution is always much higher than model at 2.5-km resolution.

Comparison of subdomain mean SO2 concentration shows good agreement between the two resolutions (Table 1b). However, the simulated aqueous production rate is in general higher for the model at 15-km resolution than at 2.5-km resolution, with the largest difference at highest level where model at 15-km resolution predicted higher LWC.

In addition to the cloud water and SO2 concentration, oxidants (such as O3 and H2O2) also play an important role in aqueous sulphate production. Liquid-phase oxidation of SO2 by O3 is only significant at PH>5 (Seinfeld and Pandis, 1998). Over the studied region, with abundant SO2 available, cloud-water PH is expected to be low. Examination of model predicted cloud water PH shows that it is usually lower than 5. Therefore, aqueous oxidation of SO2 is expected to be dominated by the H2O2 pathway for the cases studied here. Table 2 shows the subdomain averaged H2O2 simulated by the model at both resolutions.

Table 2 sudomain average of H2O2 concentration (ppb), SO2 concentration (ppb) is also included.

	Cloud Level (m)	2.5km SO2	15km SO2	2.5km H2O2	15km H2O2
F16	1235	0.331	0.336	2.41	3.16
F17	1235	0.217	0.25	2.03	3.00
	1810	0.132	0.133	1.87	2.88
F18	1500	0.433	0.587	2.45	2.63
	1810	0.279	0.263	2.24	2.36

The model at 15-km resolution predicted higher concentration of H2O2, especially for Flight 16 and 17. Higher H2O2 simulated by model at 15-km resolution can be a reason for the higher aqueous production rate simulated at this resolution if the system is oxidant-limited. However, if we compare LWC, SO2, H2O2 and DS4= at different cloud level for Flight 17 and 18, we can see that SO2 and H2O2 concentration are lower at higher level and the LWC is higher at higher level, and the model simulated aqueous production rate is usually higher at higher level, especially for Flight 17. Table 1a shows that cloud fraction at higher level is higher than at lower level for model at both resolutions. This is one reason for the higher subdomain averaged sulpate production rate at higher cloud level. For flight 17, however, the difference between two cloud levels can only be explained by the higher LWC predicted by the model. For this flight, SO2 and H2O2 concentration at 1810m is lower than at 1235m. Cloud fraction at 1810m is about 3 and 4 times larger than at 1235m for model at 2.5- and 15-km resolutions, respectively. While the aqueous sulphate production rate at higher cloud level (1810m) is around 5 and 6 times larger than at lower cloud level (1235m) for the two resolutions. The relatively larger aqueous production rate, therefore, is contributed by the larger LWC at higher level, which are 8 and 15 times larger than at lower cloud level for the two model resolution, respectively.

4.3 Comparison of AURAMS simulation at 15-km scale over 2.5-km model domain

Similar to Zhang et al. (2007), it is interesting to look at the comparison of model simulation at the same scale. Because the same rotation is used for both AURAMS domains at 15- and 2.5-km resolutions, it is straightforward to scale the 2.5km simulation to the 15-km resolution for the comparison, i.e., every 15-km grid includes thirty-six 2.5-km grids. Therefore, thirty-six 2.5-km grid values within a 15-km grid are averaged to compare with the corresponding 15-km grid value except for cloud fraction. At 15k-m scale, the 2.5k-m cloud cover is calculated as total grid points with LWC larger than 1.0e-5 kg/kg (to be consistent with the aircraft observation limit) divided by total grid points in a 15km scale (i.e. 36) to compare with CF simulated at 15-km resolution.

This comparison is done over the whole 2.5km domain. Table 3a shows the comparison of cloud cover (CF) and LWC. SO2 concentration and aqueous sulfate production rate are compared in Table 3b.

Table 3a Averaged CF and LWC (*e-4, kg/kg) over the 2.5km model domain at 15-km scale for different cloud levels

	Cloud Level (m)	2.5km CF	15km CF	2.5km LWC	15km LWC
F16	1235	0.59	0.31	1.39	0.966
F17	1235	0.25	0.09	0.187	0.168
	1810	0.50	0.38	1.34	1.89
F18	1500	0.20	0.19	0.275	0.345
	1810	0.29	0.27	0.609	0.723

Table 3b Averaged SO2 (ppb) and aqueous sulphate production rate (*DS4=, *e-2, ug/kg/minute) over the 2.5km model domain at 15-k scale for different cloud levels

	Cloud Level (m)	2.5km SO2	15km SO2	2.5km DS4=	15km DS4=
F16	1235	0.535	0.647	3.00	2.37
F17	1235	0.263	0.492	0.262	0.286
	1810	0.151	0.229	0.620	0.935
F18	1500	0.175	0.363	0.517	0.899
	1810	0.098	0.213	0.398	0.845

At 15-km scale, model at 2.5km resolution predicted higher cloud fraction than model at 15-km resolution. However, the mean LWC predicted by the model at 15-km resolution is higher than the model at 2.5-km resolution for Flight 17 at 1810-m level and for Flight 18 at both levels, indicating higher in-cloud LWC is predicted by model at 15-km resolution.

The model at 15-km resolution simulated higher domain average SO2 at all of the cloud levels and also simulated higher aqueous production rate except for Flight 16 at 1235m cloud level where much higher LWC was predicted by model at 2.5km resolution. This is similar to the findings from Section 4.2.

Comparison between the two model resolutions at 15-km scale has also been done for individual 15-km grid point. Figure 9a and 9b show the model simulated SO2 field for Flight 16 at the two resolutions. Red box is the area we chose for this comparison. Comparison is done line by line (red arrow line along Y direction) along X direction (green arrow line) so that we can see the plume occurs periodically in Figure 10a and 10b for the comparison of SO2 and sulphate particles smaller than 2.5um (SU2.5).

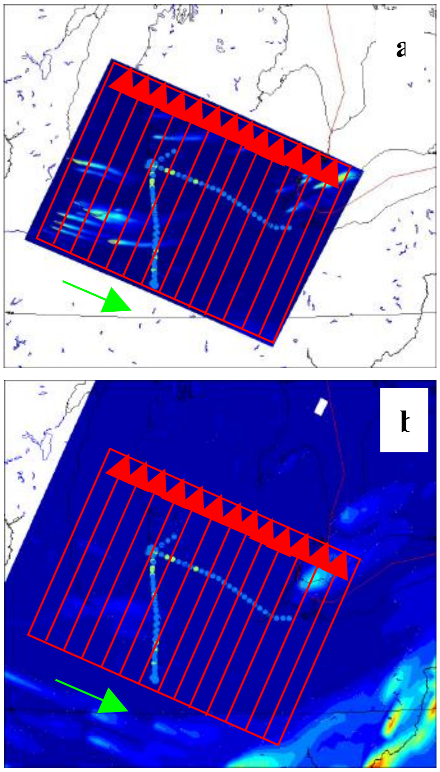

Fig. 9 Area selected to compare model simulation at 15-km scale for model at 2.5km resolution (a) and 15km resolution (b)

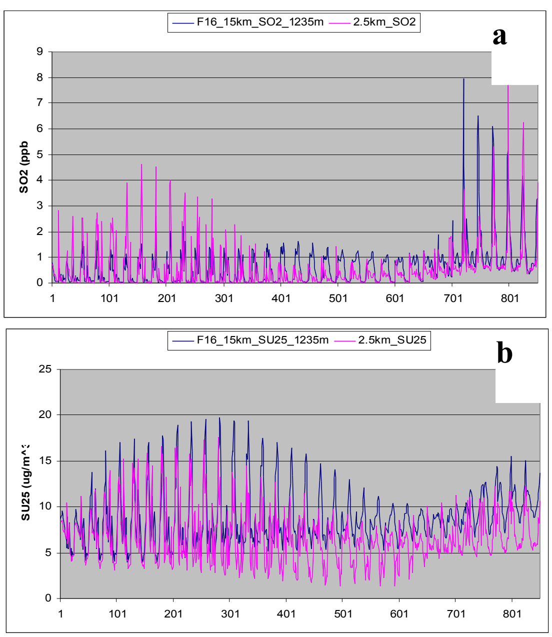

Fig. 10 Comparison of model simulated SO2 (a) and SU2.5 (b) at 15-km scale for Flight 16.

Although the model at 2.5-km resolution resolves the plumes better than at 15-km resolution as shown in Fig. 9, Fig. 10 shows that the locations of the plumes predicted by the model at both resolutions agree well. The model at 15-km resolution simulated higher SU2.5 especially towards the downwind side of the domain. This coincides with the higher sulphate production at this resolution discussed earlier. Similar results are also seen for other flights at different cloud levels (results not shown)

5. CONCLUSIONS

The comparison of air quality model simulations with aircraft observations shows that the model is able to capture the plumes observed by the aircraft.

Aqueous sulphate production rate simulated by the model at 15-km resolution is in general larger than simulated at 2.5-km resolution at the cloud levels studied here. Many possible reasons could contribute to the larger sulphate production rate, such as the higher H2O2 concentration predicted at 15-km resolution. However, results indicate that larger LWC predicted by model at 15-km resolution is one of the main reasons.

At 15-km resolution, the ability of model to correctly predict cloud fraction also has an impact on the model simulation of aqueous-phase sulphate production because the in-cloud LWC, which is calculated by dividing the grid LWC by cloud fraction, is used to calculate the aqueous production rate. The uncertainty in predicting cloud fraction will eventually lead to an uncertainty in simulating sulphate production.

The analysis so far indicates that the meteorological model predicted cloud microphysics does have a significant impact on the aqueous-phase sulfate production. Further analysis is underway to evaluate modelled aqueous-phase production at the two resolutions against the available aircraft observations.

ACKNOLEDGEMENT:

One of the authors, Junhua Zhang, is supported by Environment Canada contract No. KM062-07-0446 and is grateful for the computer facilities provided by MSC.

REFERENCES:

Barth, M.C., P.J. Rasch, J.T. Kiehl, C.M. Benkovitz, and S.E. Schwartz, 2000: Sulfur chemistry in the National Center for Atmospheric Research Community Climate Model: description, evaluation, features, and sensitivity to aqueous chemistry. *J. Geophys. Res*., 105, 1387-1415.

Gong, W., A.P. Dastoor, V.S. Bouchet, S. Gong, P.A. Makar, M.D. Moran, B. Pabla, S. Ménard, L-P. Crevier, S. Cousineau, and S. Venkatesh, 2006, Cloud processing of gases and aerosols in a regional air quality model (AURAMS), *Atmos. Res*., 82, 248-275.

Gong, W. et al., 2007, Modelling regional aerosols: impact of cloud processing on gases and particles over eastern North America and in its outflow during CARTT 2004. To appear in 'Air Pollution Modeling and Its Application XIX', edit. C. Borrego and A.I. Miranda, Springer, New York.

Côté, J., J.-G. Desmarais, S. Gravel, A. Méthot , A. Patoine, M. Roch and A. Staniforth, 1998, The operational CMC/MRB Global Environmental Multiscale (GEM) model. Part 1: Design considerations and formulation, *Mon. Wea. Rev*., 126, 1373-1395.

Lohmann, U., K. von Salzen, N. McFarlane, H.G. Leighton and J. Feichter, 1999, Tropospheric sulfur cycle in the Canadian general circulation model. *J. Geophys. Res.*, 104, 26,833- 26,858.

Seinfeld, J.H., and Pandis, S.N., 1998, Atmospheric Chemistry and Physics, Wiley, New York, pp. 363-380.

U.S. EPA, 2004, NOx Budget Trading Program: 2003 Progress and Compliance Report, Clean Air Markets Program, Office of Air and Radiation, U.S. Environmental Protection Agency, Washington, D.C., August, 28 pp. + App. [Available from http://www.epa.gov/airmarkets/progress/progress-reports.html: viewed 11 June 2007]

von Salzen, K., H.G. Leighton, P.A. Ariya, L.A. Barrie, S.L. Gong, J.-P. Blanchet, L. Spacek, U. Lohmann and L.I. Kleinman, 2000: Sensitivity of sulphate aerosol size distributions and CCN concentrations over North America to SOx emission and H2O2 concentrations, *J. Geophys. Res.*, 105, 9741-9765.

Zhang, J., W. Gong, W. R. Leaitch, and J. W. Strapp, 2007, Evaluation of modeled cloud properties against aircraft observations for air quality applications, *J. Geophys. Res.*, 112, D10S16, doi:10.1029/2006JD007596

A STATISTICAL EVALUATION OF THE AEROSOL EFFECT ON OROGRAPHIC PRECIPITATION

Elias M. Zubler[1], A. Muhlbauer[1] and U. Lohmann[1]
[1]Institute for Atmospheric and Climate Science, IACETH, Zurich

Since aerosols act as cloud condensation nuclei (CCN) they alter the microphysical properties of clouds. Increasing the aerosol load in a cloud with constant liquid water content (LWC) leads to more numerous but smaller cloud droplets. These do not convert into rain as efficiently as larger droplets. With respect to orographic flow, the resulting effect may be a suppression of precipitation on the windward side of the orographic barrier and possibly an enhancement of spillover precipitation on the drier lee side.
A statistical analysis of 178 2-dimensional simulations with the non-hydrostatic limited-area model COSMO is provided. The model uses a 2-moment warm-phase cloud microphysics scheme which is coupled to aerosol microphysics. Two groups of simulations (clean and polluted cases) with different dynamical initializations are compared. Both groups are represented by one typical aerosol size distribution.
The study shows that on average the spillover precipitation is increased by approximately 3% in the polluted cases. The total domain precipitation is reduced by more than 50% in some polluted cases, the average loss being 13%. The reduction in precipitation is smaller for more humid simulations which suggests that the relative difference in total precipitation is subject to interseasonal variability due to temperature and moisture changes throughout the annual cycle.

1. INTRODUCTION

Aerosol particles act as cloud condensation nuclei (CCN). Therefore, they influence the microphysical properties and the formation of clouds and precipitation. According to several studies by e.g. Twomey et al. (1984) and Peng et al. (2002), increasing aerosol loads in a cloud with constant liquid water content (LWC) result in more numerous but smaller cloud droplets. Since smaller droplets in warm-phase clouds have a lower collision efficiency than larger droplets (Pruppacher and Klett 1997), it is suggested that an increase in aerosol concentrations could lead to a deceleration of hydrometeor growth and therefore to a change of precipitation in time and space. This phenomenon is known as the cloud lifetime effect or the second indirect effect of aerosols (Albrecht 1989).
Statistical approaches based on annual rain rates by Givati and Rosenfeld (2004), Rosenfeld and Givati (2006) and Jirak and Cotton (2006) indicate that the cloud lifetime effect presumably leads to a significant change in the measured amounts of orographic precipitation. Givati and Rosenfeld (2004) found precipitation losses of 15-25% downwind over topographic barriers in California and Israel that were attributed to the second indirect aerosol effect.
Knowledge of the impact of aerosols on precipitation formation may be crucial to the understanding of the water cycle in alpine terrain. Thus, we investigate the aerosol effect on warm-phase orographic precipitation triggered by stable upslope ascent.
First modelling approaches in this area of research by Muhlbauer and Lohmann (2008) and Lynn et al. (2007) observed such an effect in both idealized experiments and cases based on observational data. Lynn et al. (2007), for example, obtained a decrease in precipitation of 30% due to continental polluted aerosols in comparison with maritime clean air.

In our study, we conducted a series of idealized 2D model simulations with altered aerosol configurations. The statistical perspective allows us to give an estimate of the changes in the precipitation pattern due to an increase of the aerosol load for the area of the Jungfraujoch, a high mountain ridge in the Swiss Alps. Since we are using different sets of initial conditions, we can estimate the possible range of the aerosol effect on orographic precipitation and its sensitivity to changes in ambient temperature and humidity.

2. METHODS

In order to simulate orographic flow the mesoscale weather prediction model COSMO (Steppeler et al. 2003) is applied. The development of the COSMO is advanced within the Consortium for Small-Scale Modeling (http://www.cosmo-model.org). Aerosol-cloud microphysical processes are treated with a 2-moment bulk-microphysics scheme (Seifert and Beheng 2006), which is coupled to the 2-moment aerosol microphysical module M7 (Vignati et al. 2004) via parameterized activation of aerosols following Lin and Leaitch (1997).
The domain is 2-dimensional along a meridional cross-section through the Jungfraujoch in the Swiss Alps (grid spacing 2.2 km, 50 vertical levels). A series of model simulations over 12 hours was performed. The initial state of all simulations is given by horizontally homogeneous fields of temperature, pressure, relative humidity, wind speed and an aerosol size distribution. These are derived from soundings in the proximity of the Jungfraujoch.
178 initial soundings from all seasons of the years 2002-2006 were simulated separately using one clean and one polluted aerosol setup following Muhlbauer and Lohmann (2008).

3. RESULTS

The longer cloud lifetime that is suggested to result from an increased aerosol load may lead to a shift in the precipitation pattern such that the windward precipitation is reduced and the leeward precipitation is enhanced (Rosenfeld and Givati 2006; Givati and Rosenfeld 2004). A common way to study the relationship between lee and total precipitation is the spillover factor (SP). It corresponds to the ratio of lee precipitation to total precipitation. According to Jiang and Smith (2003) the precipitation efficiency is increased with mountain height (stronger orographic barrier). Hence, higher mountains are expected to produce intensive luff precipitation while the dry-adiabatic downdrafts on their lee are too strong to yield much lee precipitation. Consequently, an inverse relationship is found between the spillover factor and the mountain height (Colle 2004). The SP values found in our study are in good agreement with the ARPS findings from Jiang and Smith (2003). The comparison of clean and polluted cases in figure 1 yields a higher SP by up to 3.7% in the polluted cases due to the advection of rain water to the lee side of each ridge.

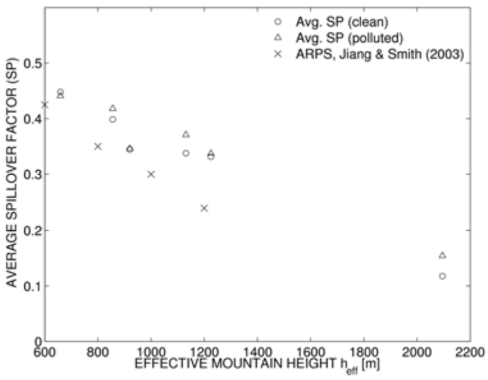

Fig 1. Spillover factor as a function of mountain height.

In absolute terms the loss of precipitation in the polluted case is strongest at the Jungfraujoch as shown in figure 2. On its luff side 5% of the cases show losses of more than 30 mm/12h. Contrarily, an enhancement on the lee side of more than 15 mm/12h is found for the upper 5-percentile. Note that the cases with a reduction of more than 30 mm/12h on the windward side of the JFJ are not necessarily the same as those 5% of the cases with the strongest lee precipitation enhancement. This analysis shows that the variability of the precipitation amounts is very strong, depending on the large variety of initial conditions.

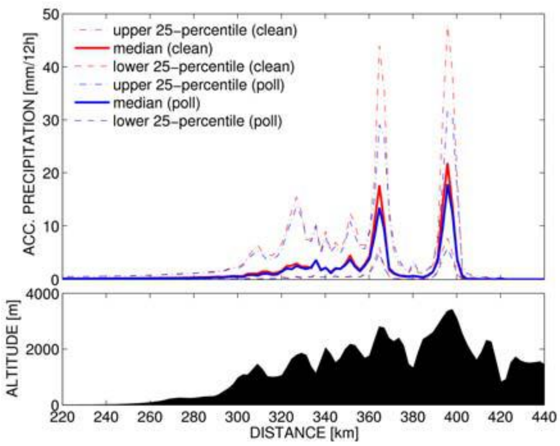

Fig 2. 12h accumulated precipitation pattern and model topography.

If the lee side precipitation in the polluted case is not enhanced enough to compensate the loss of precipitation on the windward side the accumulated total domain precipitation (ATDP) is decreased as compared to the clean case. In order to compare our results with those from Givati and Rosenfeld (2004), Jirak and Cotton (2006), Rosenfeld and Givati (2006) and Lynn et al. (2007), we use the relative differences in total domain precipitation between clean and polluted cases (RPD = P_{PC}/P_{CC} - 1).

Figure 3 shows that RPD clearly tends toward negative values. On average the polluted cases produce about 13% less precipitation than the clean simulations with the same initial sounding but the winter aerosol configuration. The standard deviation for RPD is 10%. The Wilcoxon signed-rank test, which was performed because RPD is not normally distributed, indicates that the median of the distribution of RPD differs significantly from zero.

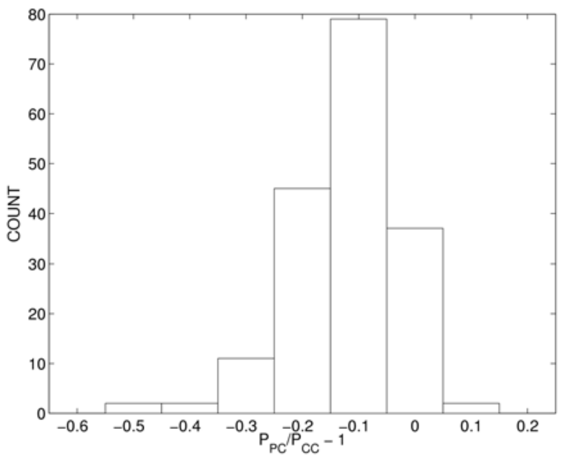

Fig 3. Distribution of the relative differences in total domain precipitation.

It is found that RPD is strongest for cases with very little precipitation in the domain. These correspond to the coldest and driest simulations. On the other hand, very warm (and humid) simulations show smaller differences or even a slight increase in precipitation in the polluted simulation. A warm atmosphere generally contains more water vapor than a colder atmosphere. Hence, as condensation is triggered due to orographic lifting, larger cloud droplets can form in the warmer simulations. Consequently, these cases show higher cloud- to rain drop transformation rates which makes hydrometeor growth more efficient in some of the polluted cases.

Figure 4 shows that RPD varies particularly between the colder winter season and the warmer late-summer and autumn period. The summer soundings used to initialize the model yield smaller differences in total domain precipitation than the colder winter and spring soundings.

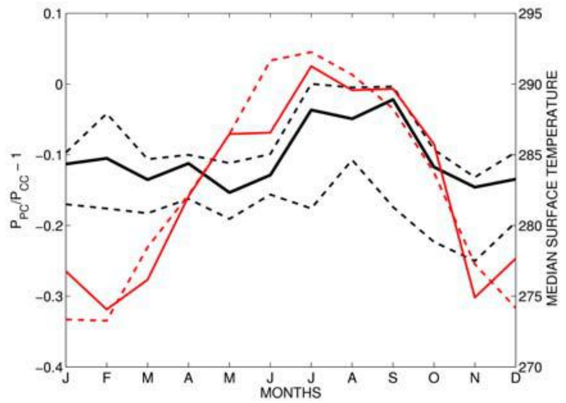

Fig 4. Annual cycle of relative differences in total domain precipitation (black) and monthly median temperatures (red) of the applied soundings (red solid) and nearby station (dashed).

4. DISCUSSION & CONCLUSIONS

A statistical evaluation of 2-dimensional model forecasts was conducted in order to quantify the indirect aerosol effect on orographic precipitation. Primarily, it was shown in terms of relative differences in total domain precipitation that the polluted cases generally produce less rainfall due to the deceleration of hydrometeor growth. Applying a Wilcoxon signed-rank test for paired differences, we could show that the effect of an increased aerosol load on total domain precipitation is highly significant. However, we have reason to believe that the aerosol effect on precipitation has been overestimated in previous studies. Particularly, the simulations with warmer and therefore more humid conditions show a weak relative difference in the accumulated precipitation.

With respect to spillover precipitation, the change due to an increased aerosol load was found to be positive for most of the ridges located on the windward side of the Jungfraujoch. The effect is significant but rather small.

We quantified the indirect aerosol effect on stratiform warm-phase precipitation with respect to a high-resolution 2-dimensional flow over complex topography in Switzerland. Since the formation of orographic precipitation depends on many different aspects (Roe 2005), a modeling approach is probably the best way to quantify the aerosol effect on precipitation, because it allows to keep all other important variables constant. Nonetheless, the limitations of this work arise from the constraint of the simulations to (1) 2-dimensionality and (2) to warm-phase cloud microphysics. 3D model simulations with mixed-phase cloud microphysics that allow for a flow around an elevation could yield a different result of the aerosol effect.

Above all, it can be concluded that the indirect aerosol effect on precipitation may be strongly dependent on the model setup and parameterization of the aerosol-cloud-precipitation interaction. Huang et al. (2007) used a coupled climate-chemistry model to show that the precipitation loss due to the cloud lifetime effect varies between 3-20%, dependent in particular on the autoconversion function.

For future work, we suggest to consider the climatological perspective as well. There may be a significant impact of aerosols on the global hydrological cycle (Ramanathan et al. 2001). The climatological perspective may also provide a better basis to compare the results with Givati and Rosenfeld (2004), Jirak and Cotton (2006) and Rosenfeld and Givati (2006), since these studies focus on the change in annual rain rates over several decades.

5. BIBLIOGRAPHY

Albrecht, B., 1989: Aerosols, cloud microphysics, and fractional cloudiness. *Science*, **245**, 1227–1230.

Colle, B. A., 2004: Sensitivity of orographic precipitation to changing ambient conditions and terrain geometries: An idealized modeling perspective. *J. Atmos. Sci.*, **61**, 588–606.

Givati, A. and D. Rosenfeld, 2004: Quantifying precipitation suppression due to air pollution. *J. Appl. Meteor.*, **43**, 1038–1056.

Huang, Y., W. L. Chameides, and R. E. Dickinson, 2007: Direct and indirect effects of anthropogenic aerosols on regional

precipitation over east asia. *J. Geophys. Res.*, **112**, doi:10.1029/ 2006J D007 114.
Jiang, Q. and R. Smith, 2003: Cloud timescales and orographic precipitation. *J. Atmos. Sci.*, **60**, 1543–1559.
Jirak, I. L. andW. R. Cotton, 2006: Effect of air pollution on precipitation along the front range of the Rocky Mountains. *J. Appl. Meteor.*, **45**, 236–245.
Lynn, B., A. Khain, D. Rosenfeld, andW. L.Woodley, 2007: Effects of aerosols on precipitation from orographic clouds. *J. Geophys. Res.*, **112** (D10225), doi:10. 1029/2006JD007 537.
Muhlbauer, A. and U. Lohmann, 2008: The role of aerosols in warm-phase orographic precipitation in different dynamical flow regimes. *Accepted for publication in the J. Atmos. Sci.*
Peng, Y., U. Lohmann, R. Leaitch, C. Banic, and M. Couture, 2002: The cloud albedocloud droplet effective radius relationship for clean and polluted clouds from RACE and FIRE.ACE. *J. Geophys. Res.*, **107** (D11), doi:10.1029/2000JD000 281.
Pruppacher, H. and J. Klett, 1997: Microphysics of Clouds and Precipitation. 2nd ed., *Kluwer Academic Publishers*, 954 pp.
Ramanathan, V., P. J. Crutzen, J. T. Kiehl, and D. Rosenfeld, 2001: Aerosol, climate and the hydrological cycle. *Science*, **294**, 2119–2124.
Roe, G. H., 2005: Orographic precipitation. *Annu. Rev. Earth Planet. Sci.*, **33**, 645–671.
Rosenfeld, D. and A. Givati, 2006: Evidence of orographic precipitation suppression by air pollution-induced aerosols in the western united states. *J. Appl. Meteor.*, **45 (7)**, 893–911.
Seifert, A. and K. D. Beheng, 2006: A two-moment cloud microphysics parameterization for mixed-phase clouds. Part I: Model description. *Meteorol. Atmos. Phys.*, **92**, 45–66.
Steppeler, J., G. Doms, U. Sch¨attler, H. Bitzer, A. Gassmann, U. Damrath, and G. Gregoric, 2003: Meso-gamma scale forecasts using the nonhydrostatic model LM. *Meteorol. Atmos. Phys.*, **82**, 75–96.
Twomey, S., M. Piepgrass, and T. Wolfe, 1984: An assessment of the impact of pollution on global cloud albedo. *Tellus, Ser. B*, **36**, 356–366.
Vignati, E., J. Wilson, and P. Stier, 2004: M7: An efficient size-resolved aerosol microphysics module for large-scale aerosol transport models. *J. Geophys. Res.*, **109**, D22 202.

Acknowledgements

Above all, the authors thank Christoph Schär, ETH Zurich, for his helpful comments and suggestions. Kassiem Jacobs and Sylvaine Ferrachat deserve many thanks for technical support.

CLOUD EFFECTS ON UV RADIATION AT TWO OPPOSING HEMISPHERIC SITES

Josep Calbó[1], Jeff Sabburg[2], Jordi Badosa[1], Josep-Abel González[1]
[1]Group of Environmental Physics, Universitat de Girona, Spain
[2]Australian Centre for Sustainable Catchments, University of Southern Queensland, Australia

1. ABSTRACT

The effect of clouds on modifying the ultraviolet (UV) radiation that reaches the Earth's surface is quantitatively assessed through Cloud Modification Factors (CMF), defined as the ratio between measured UV irradiance in cloudy skies and an estimated cloudless UV irradiance. Behavior of CMF derived from measurements taken at two sites placed in Girona, Spain and Toowoomba, Australia, is presented. In both sites, there have been sky cameras and UV radiometers taking images and measurements during the last 5 years. Combining information about the sky conditions with the UV data, CMF have been computed depending on cloud fraction and for different cloud types. Effects of the solar zenith angle have also been analyzed. Results obtained support the previous knowledge about CMF: cloud effects are in general significant for cloud fraction larger than 0.7; similar cloud fractions produce a large range of CMF values, partly due to different cloud types; cloud effects result sometimes in an enhancement of UV radiation.

2. INTRODUCTION

The interest in solar ultraviolet (UV) radiation from the scientific community and the general population has augmented significantly in recent years due to the link between increased UV levels at the Earth's surface and depletion of ozone in the stratosphere (Parisi et al., 2004). There are well established relationships between, for example, total ozone column and UV radiation levels at the Earth's surface. Effects of clouds, however, are not so well described, given the intrinsic difficulties in properly describing cloud characteristics. Nevertheless, the effect of clouds cannot be neglected, and the variability that clouds induce on UV radiation is particularly significant when short time scales are involved. Several studies have addressed this issue in the past; a complete review of such studies is found in Calbó et al. (2005).

In general, works that deal with the effect of clouds on UV radiation approach the issue from the empirical point of view, providing some relationship between measured UV radiation in cloudy conditions and cloud related information. In particular, most works calculate Cloud Modification Factors (CMF) defined as the ratio between measured UV radiation in a cloudy sky and estimated radiation for a cloudless sky, and relate CMF with cloud fraction derived from observations of cloudiness (either from human observers or by using devices such as sky cameras).

In the already mentioned review (Calbó et al., 2005) some recommendations were given for future research. In the present study, some of those recommendations are followed. In particular, the time basis of our analyses is 15 minutes; the databases used cover 5 years of measurements and observations; a limitation is set on solar zenith angle, SZA (SZA ≤ 80º); data from two very different sites are included; effect of different cloud types is studied. Other aspects, however, are not fully considered here. For example, the cloudless model does not compare perfectly with the measured values (and this is addressed by using correction factors on the measurements), and the variability of sky conditions in the 15 min interval is not investigated.

The goal of this paper is to show preliminary results about the behavior of CMF (i.e., of the cloud effect on UV radiation), at two sites on both hemispheres. We do not intend to suggest here a new formula to compute CMF; but CMF behavior respect to cloud fraction will be analyzed on the basis of previous formulae.

3. DATA AND METHODOLOGY

In this study, we use data derived from UV irradiance measurements taken at two sites placed in geographically and climatically different areas: Girona, Spain; and Toowoomba, Australia. Girona is in the Northern Hemisphere (41.97°N, 2.82°E, 100 m asl), 30 km inland from the Mediterranean Sea and has a typical Mediterranean climate. Toowoomba is in the Southern Hemisphere (27.5°S, 151.9°E, 693 m asl), 100 km from the Pacific Ocean and enjoys a subtropical/temperate climate with no dry season, except for recent drought conditions.

There have been sky cameras and UV radiometers taking images and measurements simultaneously during the last 5 years at both sites. Specifically, a UV meter model 501, from Solar Light Co. and a Total Sky Imager (TSI), manufactured by Yankee Environmental Systems, Inc. were installed at Toowoomba; while a UV meter model UV-S-E-T, from Kipp & Zonen, and a self-manufactured whole sky camera (WSC) system were used at Girona. Both UV radiometers approximate the erythemal response of the human skin; their output signal is converted to UV index (UVI) using the adequate calibration constants. Details on the UV instruments, the sky cameras and the digital processing of their images are given in Parisi et al. (2003), Badosa et al. (2005), Long et al. (2006a), and Calbó and Sabburg (2008).

UV measurements were averaged in 15 min intervals. Although there are some gaps in the data (due for example to periods when the radiometers were sent out for calibration), the number of available records is large enough (more than 50% of possible records at both sites) and cover all seasons. UVI values for cloudless conditions were compared with the UVI estimation made by means of the Madronich (2007) parameterization. From this comparison, an annual correction factor was derived to account for trends in the sensitivity of instruments. By applying these factors, measured UVI and estimated UVI, for cloudless skies, agreed within a ±8% (one sigma) for SZA < 70º. However, for the current analyses all data with SZA up to 80º were included.

Whole sky images were used to derive cloud fraction and an assessment of cloud type (classified into 5 different categories, namely clear, cumuliform, layered, cirriform, mottled). Cloud fraction is estimated with 10% accuracy in comparison with visual evaluation (Long et al. (2006a); while cloud type, when compared with visual assessments of the images, is correct about 75% of times. Cloud fraction used in our analyses is the average from all the available images within the 15 min interval. Therefore, a variability of cloud fraction within the time interval was also estimated, but it is not used in the further analyses presented here. In Girona, due to optical and electronic problems, most recent images (2005-2006) suffered a degradation that increased cloud fraction estimate uncertainty. Therefore, for Girona we also used the algorithm by Long et al. (2006b) to estimate cloud fraction from solar radiation (global, direct, and diffuse) measurements.

At both sites, CMF was calculated by dividing the corrected UVI measurements (explained above) by the estimated UVI for cloudless (and aerosol free) sky under the same conditions of SZA and ozone column. This estimation was obtained from the already mentioned Madronich (2007) paper, and the ozone column was taken from the TOMS/OMI archives (overpass files for Toowoomba and global gridded files for Girona).

4. RESULTS AND DISCUSSION

Figure 1 shows the CMF values obtained at Toowoomba, as function of cloud fraction. All records have been organized in bins of cloud fraction that have a width of 10%, except for the first bin, (i.e., cloudless cases, cloud fraction less than 5%) and the last bin (i.e., overcast, cloud fraction greater than 95%). In order to show the dispersion of the values, the boxes for the percentiles 25-75 and for percentiles 5-95 are also plotted in Fig. 1.

Note that the typical (median) CMF for cloud fractions as large as 70% is still above 0.8, meaning that cloud typically reduce less than 20% of UV radiation even under this large cloud cover. There is of course big dispersion, that produces CMF greater than 1 (i.e., enhancements) for cloud fractions as large as 80%. The greatest dispersion is found for overcast skies, with a median CMF of 0.47, but including values of CMF in the range 0.12-0.89. CMF values follow qualitatively the behavior found at many other sites, but the fit to previously suggested formulae, such us a second order polynomial (Lubin and Frederick, 1991) or a simplified third order expression (Thiel et al., 1997) is not perfect (not shown).

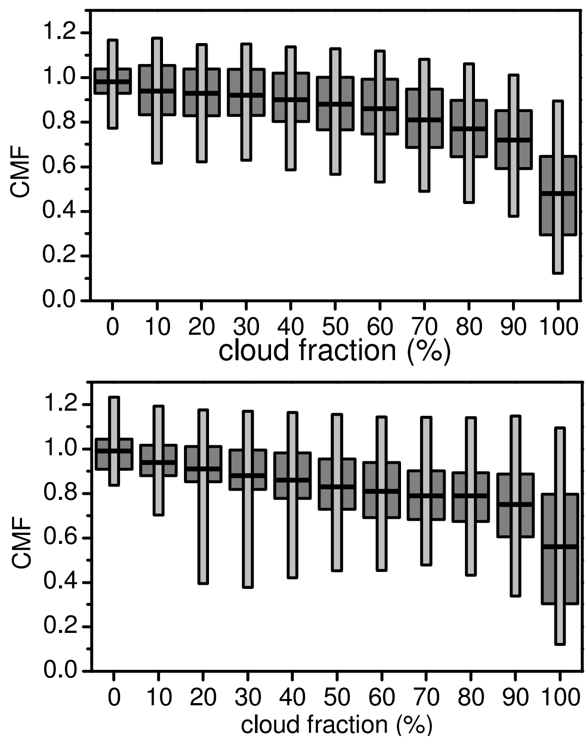

Fig. 1. CMF with respect to cloud fraction. The median (bold black lines), and the percentiles 5, 25, 75, and 95 are shown. For Toowoomba (top), cloud fraction from sky images. For Girona (bottom), cloud fraction from solar radiation.

Also in Fig. 1, CMF for Girona is presented as a function of cloud fraction. In this case, however, cloud fraction has been estimated from solar radiation measurements, as commented above. Again, CMF for cloud fraction less than 80% are greater than 0.8. The median CMF for overcast skies is 0.54. The most remarkable fact, however, is the great dispersion of CMF values, particularly for cloud fraction between 20-50%.

There might be many reasons for the different behavior at these two sites, one of them being the different cloud climatology. Table 1 shows the frequency of some selected cloud type combinations, at both sites, with the corresponding mean CMF. It is obvious that Girona is cloudier than Toowoomba, and that the dominant types are also different. In some cases, the CMF are similar, in particular for Cirrus (the expected high CMF of 0.96-0.97); but in other cases, they are quite different, as for example for the Layered (stratiform) clouds (CMF = 0.38 at Toowoomba and CMF = 0.67 at Girona). This latter result must be due to the different optical depth of such stratiform clouds.

Table 1. Selected cloud type frequencies (% with respect to all records in the databases) and corresponding mean CMF.

Cloud type	Toowoomba		Girona	
	Freq.	CMF	Freq.	CMF
La	4.6	0.38	0.5	0.67
LaCu	9.5	0.46	8.9	0.54
Cu	2.2	0.77	4.8	0.74
CuLa	2.5	0.74	11.4	0.56
CuMo	1.8	0.77	4.2	0.56
CuMoLa	9.7	0.69	6.9	0.47
Ci, CiCl	2.2	0.97	11.7	0.96

However, the main reason for the different behavior is probably related to the different cosine response of both UV instruments. In Figure 2 we show the CMF respect to SZA, at both sites and grouping the data according with cloud fraction intervals. While CMF slightly decrease with SZA at Toowoomba, it clearly increases at Girona. Although CMF dependency on SZA has been described by other authors, we do not find physical explanation for these two opposite patterns, other than different cosine responses of the instruments that affect the CMF calculation. The clear sky estimation, however, also affects CMF values, so it could partially contribute to the differences.

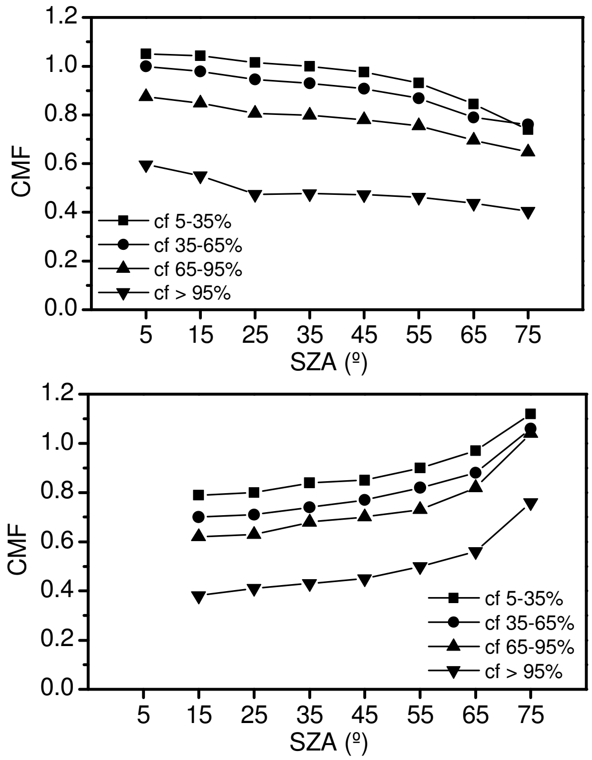

Fig. 2. CMF with respect to SZA, for different categories of cloud fraction. For Toowoomba (top); for Girona (bottom).

5. CONCLUSIONS AND FURTHER WORK

We have confirmed that the average effect of clouds on UV radiation is notable (reduction of more than 20%) only for quite high cloud fraction (greater than 70%) independently of the location analyzed. However, in particular cases and depending on cloud type and SZA, the radiation reduction may be large even for cloud fractions as low as 20%. Cirrus clouds clearly attenuate less UV radiation than other cloud types. Enhancements have also been detected in our data. Investigation on the causes of the very different (in Toowoomba compared to Girona) behavior of CMF with respect to SZA is required.

ACKNOWLEDGEMENTS

Dr. Sabburg acknowledges financial support from the University of Southern Queensland and the University of Girona for his sabbatical to undertake this research, and financial support from the Australian Centre for Sustainable Catchments involvement in the South East Queensland Cloud Seeding Program for attendance at this conference. Associate Professor Alfio Parisi provided the Biometer data. TOMS/OMI ozone and aerosol index data were provided by NASA/Goddard Space Flight Center. Dr. Calbó acknowledges the support of the Spanish Ministry of Science and Education project NUCLIEREX (CGL 2007-62664/CLI).

REFERENCES

Badosa, J., González, J.-A., Calbó, J., Van Weele, M., McKenzie, R.L. (2005). Using a Parameterization of a Radiative Transfer Model to Build High-Resolution Maps of Typical Clear-Sky UV Index in Catalonia, Spain, *J. Appl. Meteorol*. 44, 789-803.

Calbó J., Pages D., Gonzalez J.A. (2005). Empirical studies of cloud effects on UV radiation: A review, *Rev. Geophys*., 43 (2): Art. No. RG2002, 1-28.

Calbó, J. and Sabburg, J. (2008), Feature extraction from whole-sky ground based images for cloud type recognition, *J. Atmos. Oceanic Technol.* 25, 3-14.

Long, C. N., Sabburg, J.M., Calbó, J. and Pagès, D. (2006a). Retrieving Cloud Characteristics from Ground-based Daytime Color All-sky Images, *J. Atmos. Oceanic Technol*., 23, 633-652.

Long, C. N., Ackerman, T. P., Gaustad, K. L. and Cole, J. N. S. (2006b). Estimation of fractional sky cover from broadband shortwave radiometer measurements, *J. Geophys. Res*., 111, D11204.

Lubin, D. and J.E. Frederick (1991). The Ultraviolet Radiation Environment of the Antarctic Peninsula: The roles of Ozone and Cloud Cover, *J. Appl. Meteorol*., 30, 478-493.

Madronich, S. (2007). Analytic Formula for the Clear-sky UV Index, Photochem. Photobiol., 83, 1537-1538.

Parisi, A.V., Sabburg, J., Kimlin, M.G. & Downs, N. (2003). Measured and modelled contributions to UV exposures by the albedo of surfaces in an urban environment, *Theor. Appl. Climatol.*, doi 10.1007/s00704-003-0012-9.

Parisi, A.V., Sabburg, J., Kimlin, M.G. (2004). *Scattered and filtered solar UV measurements*, The Advances in Global Change Research Series. Kluwer Academic Publishers, Dordrecht.

Thiel, S., K. Steiner, and H.K. Seidlitz (1997), Modification of Global Erythemally Effective Irradiance by Clouds, Photochem. Photobiol., 65, 969-973.

USE OF SATELLITE OBSERVATION FOR CONSTRAINING CLOUD PARAMETERIZATION

Jean-Pierre Chaboureau and Jean-Pierre Pinty
Laboratoire d'Aerologie, University of Toulouse and CNRS, France

1. INTRODUCTION

Clouds are critical regulators of the earth's weather and climate. They affect the earth's radiation budget, they control the latent-heat release and soil-water availability, and they are important sites where chemistry takes place. Clouds are also a convenient signature of atmospheric vertical motions, at least at synoptic and mesoscale scales. Yet, because of their complexity and the vast range of space and time scales over which they operate, it is difficult to validate cloud predictions by atmospheric models and, even more, to assess the cloud parameterization assumptions.

This extended abstract presents several evaluations of cloud predictions simulated by the Meso-NH mesoscale model. Indeed, mesoscale models are an ideal modeling tool to perform detailed and explicit simulations of cloud. First these models are able to follow the time evolution of the cloud amounts in the context of real meteorological conditions. Second the horizontal resolution of cloud fields in mesoscale models is comparable to satellite pixels in the infra-red so facilitating a direct comparison of observed scenes. Here we adopt the model-to-satellite approach, in which satellite brightness temperature (BT) images are directly compared to BTs computed from predicted model outputs. The approach is especially powerful in identifying discrepancies of cloud cover forecasts with BTs at 10.8 µm (Chaboureau et al. 2000). The model-to-satellite approach associated with the BT Difference (BTD) technique is also useful to verify specific forecasts such as cirrus cover, dust occurrence, and convective overshoots.

Recent applications of the approach to MSG observations are shown here. In particular, the BTD technique leads us to improve objectively the cloud scheme of the Meso-NH model by tuning a critical parameter in a cirrus parameterization. This improvement yields a better predicted diurnal cycle of upper-tropospheric humidity in the Tropics. The BTD technique highlights the diurnal cycle of Saharan dust that is correctly predicted by Meso-NH. The model-to-satellite approach is further combined with the calculation of meteorological scores for an objective and long-term evaluation of the model forecasts. These recent applications of the approach to the MSG observations and the Meso-NH forecasts are shown in the context of AMMA and TROCCINOX experiments over West Africa and Brazil, respectively.

2. TUNING A CLOUD SCHEME

A first example of the use of satellite observation for constraining a microphysical scheme is taken from Chaboureau et al. (2002). Figure 1 shows a comparison between observed and simulated BTs for an Atlantic extra tropical storm. The cloud cover in the control run (Fig. 1 middle) is clearly overestimated compared to the observation (Fig. 1 left). In the microphysical scheme, the ice content is controlled by a critical parameter, a threshold above which the ice is converted into snow. A wind range of values for this threshold can be found in the literature. In the modified run (Fig. 1 right), the threshold was reduced in order to minimize the bias between the observed and simulated BTs. As a result, a much better agreement is obtained when focusing to the storm area.

Another deficiency in representing cloud cover can be seen in the southeastern part of the domain with BTs overestimated for both the simulations. However, shallow clouds are effectively produced by the convection scheme, but with not enough of condensed water in the model grid. Indeed the model considers either clear or cloudy grid points. As a consequence, a statistical

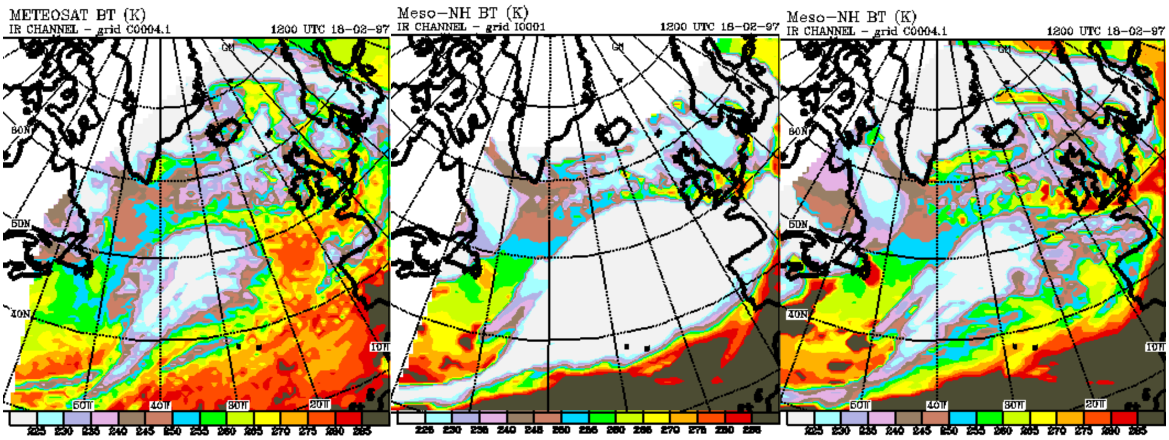

Fig. 1. BT in the infrared (left) observed by METEOSAT and simulated after 60-h by Meso-NH (middle) before and (right) after tuning of the cloud scheme (Chaboureau et al. 2002).

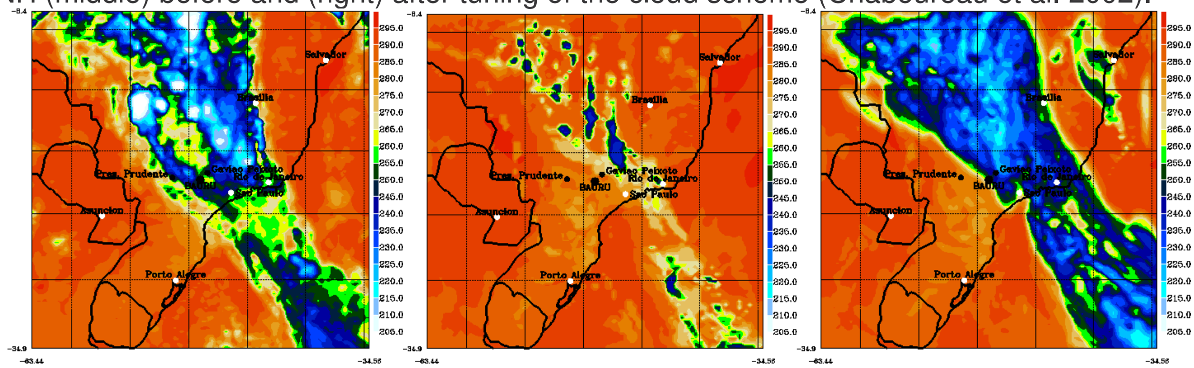

Fig. 2. IR BTs (left) observed by GOES-E, and simulated by Meso-NH (middle) without and (left) with the cloud fraction scheme (Chaboureau and Bechtold 2005).

cloud scheme was developed. Subgrid cloud cover and condensed content are parameterized as a function of the normalized saturation deficit by taking into account both turbulent and convective contributions (Chaboureau and Bechtold 2002, 2005).

Figure 2 shows the results of the model-to-satellite approach at 0000 UTC 24 February 2004 obtained in the context of the TROCCINOX campaign. The observed convection associated with the South Atlantic Convergence Zone, is clearly seen with patchy BTs lower than 220 K (Fig. 2 left). In the resulting CTRL image, several convective cells appear at the right location (Fig. 2 middle). However, the cloud patterns have a smaller spatial extent and significantly higher BTs than the observed ones. The differences between the observation and the simulation are significantly reduced with the aid of the subgrid cloud parameterization (Fig. 2 right). The areas with BTs less than 240 K exhibit a spatial extent comparable to the observations, and the overall cloud pattern associated to the SACZ is fairly well reproduced. With the aid of the diagnostic cloud parameterization the domain averaged bias is reduced. Furthermore, the subgrid cloud parameterization has a persistent positive impact on the simulations as shown by the 30-day time evolution of the BTs averaged over the whole domain (Fig. not shown). It also reduces both the biases and phase between the observed and simulated precipitation intensities, resulting in an improved representation of the diurnal cycle of convection over land, mainly as a consequence of reduced surface fluxes due to cloud shading and a change in tropospheric stability due to condensation.

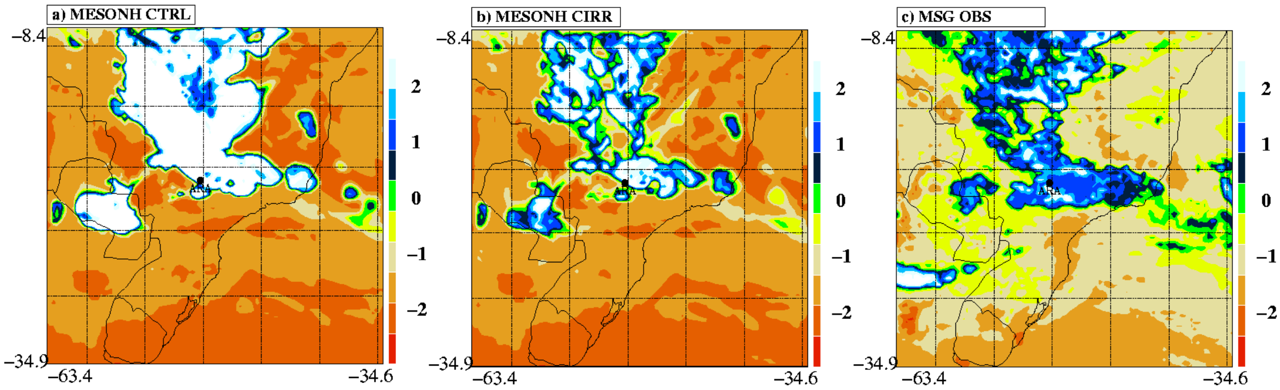

Fig. 3. BTD (K) between 8.7 and 10.8 µm bands obtained from (left) the MSG observations and the simulations (middle, CTRL) before and (right, CIRR) after changing of the cirrus parameterization (Chaboureau and Pinty 2006).

Meteosat Second Generation (MSG) observations in the 8.7- and 10.8-µm bands are helpful to check the cirrus cover. The technique is based on a contrasted absorption property of ice crystals at two wavelengths within the atmospheric infrared window. More specifically, BT difference (BTD) between the 8.7- and 10.8-mm bands tends to be positive for ice clouds that have infrared optical thickness greater than 0.5. Observed BTD larger than 1 K found at borders of deep convective systems are interpreted as anvils of convective outflows (Fig. 3c). BTD from the CTRL image after 21 h of model run are clearly excessive (Fig. 3a). In contrast, BTD from the CIRR simulation shows a better agreement with the observation. The CIRR simulation differs from the CTRL simulation by a further change of the ice to snow autoconversion threshold that increases as a function of the air temperature. This parameterization is believed to be better for controlling thin very cold cirrus sheets, in which the critical ice content decreases with temperature.

The BTD technique applied to the MSG observations allowed us to monitor the cirrus cover in near real time during the 2005 TROCCINOX campaign (Fig. 4a). Observed BTD averaged over the domain presents a diurnal cycle superimposed on a lower frequency variability. The simulations mimic this low-frequency variability reasonably well. However, the CTRL simulation presents a BTD increasing dramatically with the forecast time. In contrast, the diurnal amplitude of the BTD in the CIRR simulations is much lower, without noticeably increasing with the forecast time. The cirrus cover over the domain is deduced from the BTD fields by taking an arbitrary threshold of 1 K (Fig. 4b). The cirrus cover oscillates between 5 and 25% in the observations. The CTRL simulations greatly overestimate this value with a maximum greater than 60%. The CIRR simulations find the cirrus cover less ubiquitous with good matches for both first-day (thin-solid) and second-day (thick-solid) forecasts. The improved diurnal cycle furthermore better captures the observed upper-tropospheric humidity (UTH) maximum that lags the cirrus cover by 12 hours (Fig. not shown)

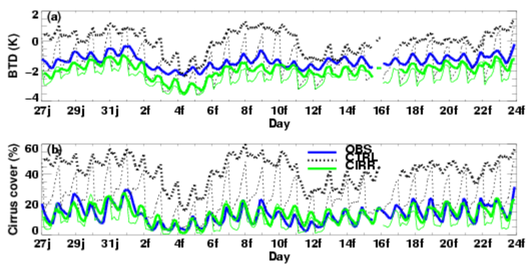

Fig. 4. Time evolution of the cirrus cover (BTD 8.7-10.8 µm > 1 K) from the MSG observations (blue line), the CTRL (dotted line), and the CIRR (green line) simulations. Results from the 3–24 h (27–48 h) forecasts are displayed with thin (thick) lines. The diurnal cycle of water vapor in the upper troposphere is captured using the new cirrus parameterization (Chaboureau and Pinty 2006).

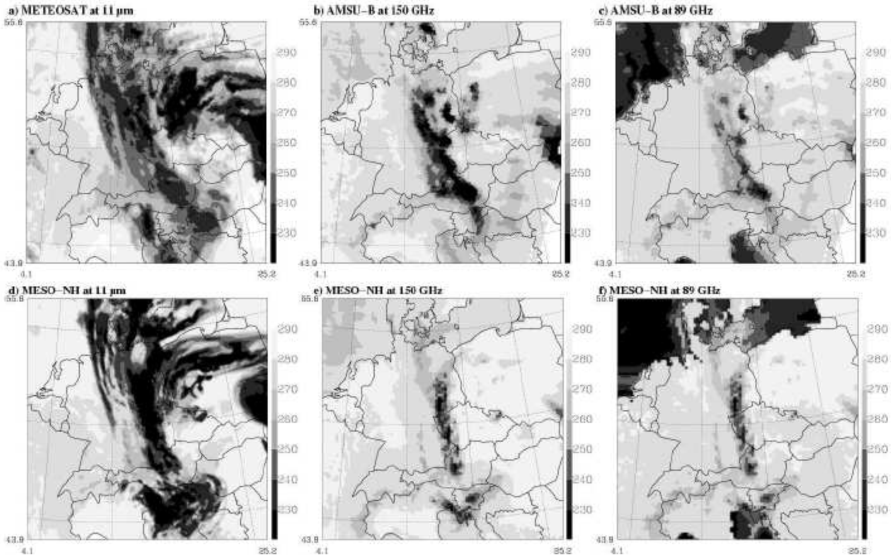

Fig. 5. From left to right, (top) observed and (bottom) simulated BT (K) for the 11-µm, 150-GHz and 89-GHz channels at 07 UTC 12 August 2002 (Chaboureau et al. 2008).

3. VERIFICATION OF FORECASTS

Comparison between observed and simulated BTs was also achieved in the microwaves both for tropical (Wiedner et al. 2004) and extratropical (Meirold-Mautner et al. 2007) cases. A good agreement was reached. As an example, the observed and simulated BTs maps for a case taken from Chaboureau et al. (2008) are shown in Fig. 5. Observations from the 11-µm METEOSAT channel show the high- and middle-level cloud cover with BTs of less than 260 K that rolls around the low centred over central Europe, from Slovakia to Croatia. Elsewhere BTs greater than 260 K mostly result in low-level clouds and clear sky. At 89 and 150 GHz, BTs from AMSU-B of less than 250 K are found over eastern Slovakia and on a line going from eastern Germany to Croatia. These depressed BTs result from significant scattering by large rimed ice particles embedded in the clouds. The Meso-NH simulation coupled with the radiative transfer codes captures the overall situation as seen in the 11-µm channel well, with high- and middle-level clouds at the right locations. This indicates that the model captures the overall atmospheric circulation. Depressed BTs for the 89-GHz and 150-GHz channels are also simulated correctly over central Europe, but with a smaller extent. The system over eastern Slovakia is almost missing. At 89 and 150 GHz, the surface signature of the cloud-free areas is correctly estimated by the surface climatology over snow and correctly modeled over sea. For several midlatitude cases, a Relative Operating Characteristic (ROC) diagram plots the POD against the POFD using a set of increasing probability thresholds (for BTD 89-150 GHz decreasing from 4 K to -4 K; Fig. 6). The comparison is made here pixel by pixel. The diagonal line means no skill at all, while the better the classifier, the closer the curve moves to the upper-left corner (high POD with a low POFD). Almost all the points are in the top-left quadrant. This demonstrates the skill of all the simulations to detect BTD events, which by extension means the occurrence of rain events.

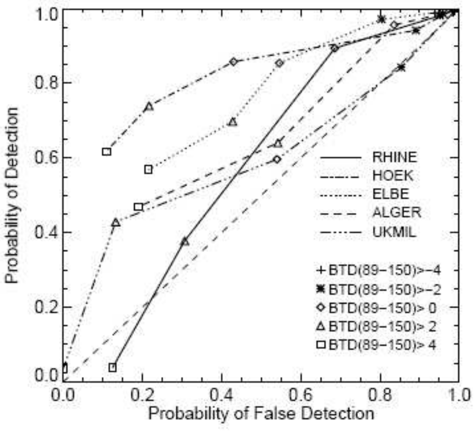

Fig. 6. ROC diagram for BTD between the 90- and 150-GHz channels over land (Chaboureau et al. 2008).

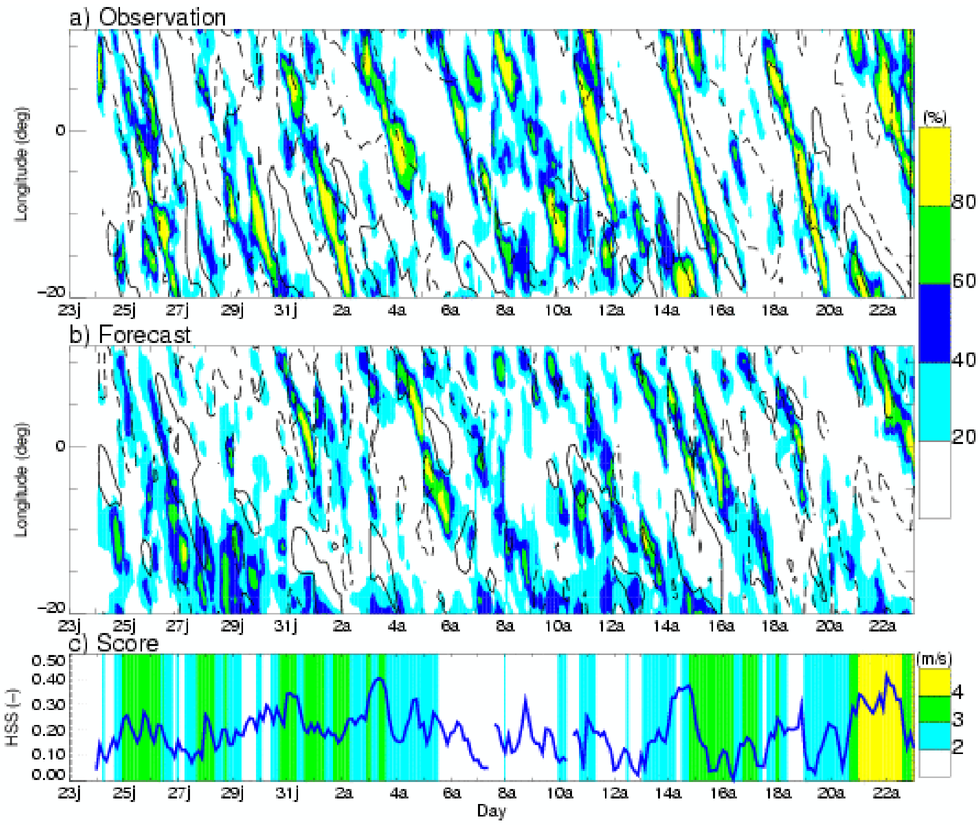

Fig. 7. (a, b) Time-longitude diagram of wind and cloud fraction averaged between 10°N and 15°N from 23 July to 22 August 2006: MSG cloud fraction (shading, %) and 700-hPa meridional wind contours at –3 m s–1 (dashed) and at 3 m s–1 (solid). Fields are taken from (a) MSG observations and ECMWF analyses and (b) Meso-NH forecasts at D+1. c) time evolution of the HSS calculated point-by-point (line) and absolute meridional wind intensity from the analyses (shading, m s–1) averaged over 10-15°N (Söhne et al. 2008).

The model-to-satellite allows us to examine the variability of the skill in forecasting high-cloud cover during a one-month period in the context of AMMA (Söhne et al. 2008). A large part of the variability during summer is due to travelling African Easterly Waves (AEW) of 3-5 day periods. Figure 7a, b presents a Hovmoller diagram of the high-cloud cover and the 700-hPa meridional winds between 10 and 15°N taken from MSG observation and ECMWF analyses and forecasted by the Meso-NH model at D+1 for the whole period. As illustrated in Fig. 7a, the cloud cover and meridional wind both display coherent and strong synoptic signatures, pointing out the significance of synoptic dynamics in shaping the cloud cover over West Africa. On one hand, the presence of strong synoptic features can be thought as a constraint that may benefit the forecast of cloud cover, at least at the larger synoptic scales. On the other hand, these features involve interactions across synoptic and meso scales. In the observations, several cloud systems propagate westward ahead of an AEW trough. The term trough refers to the travelling coherent zero 700-hPa meridional wind. Many studies have shown that the region ahead of the AEW trough, where northerly flow both advects dry air equatorward and increases vertical shear, promotes the mesoscale organization of convective systems. In the forecasts, as the cloud cover is patchier than observed, the organization of cloud systems as propagating lines appears less dramatic, albeit present. Another source of difference is the simulated dynamics: the meridional wind intensity in the forecasts shows weaker AEW activity than the analysis does. The outlines of the AEW activity over the one-month period are shown with the time evolution of the absolute meridional wind intensity from the analyses (Fig. 7c). It can be defined by two periods of enhanced

AEW activity (the last week of July and the last two weeks of August) separated by an inactive week-long period around mid-August. Overall, the Heidke Skill Score (HSS) tends to show higher skill forecasts during the active periods, particularly on 25-26 July, 31 July, and 21-22 August. On 16 August, the poor skill is due to failure to forecast a cloud system observed ahead of a trough.

4. CONCLUSION

Several systematic evaluations of cloud and precipitation forecasts by the Meso-NH mesoscale model by comparison with satellite observation are presented. First, the model-to-satellite approach gives a specific constraint to the ice to snow autoconversion threshold of the microphysical scheme in the mesoscale model Meso-NH. Combined with the calculation of scores, the approach is also shown to be worthwhile, especially over data-sparse regions such as the Tropics, in giving an objective evaluation of the representation of clouds in the model and in measuring the skill of cloud forecasts.

5. REFERENCES

Chaboureau, J.-P. and P. Bechtold, 2002: A simple cloud parameterization derived from cloud resolving model data: diagnostic and prognostic applications. J. Atmos. Sci., 59, 2362-2372

Chaboureau, J.-P., and P. Bechtold, 2005: Statistical representation of clouds in a regional model and the impact on the diurnal cycle of convection during Tropical Convection, Cirrus and Nitrogen Oxides (TROCCINOX), J. Geophys. Res., 110, D17103, doi:10.1029/2004JD005645.

Chaboureau, J.-P., J.-P. Cammas, P. Mascart, J.-P. Pinty, C. Claud, R. Roca, and J.-J. Morcrette, 2000: Evaluation of a cloud system life-cycle simulated by Meso-NH during FASTEX using METEOSAT radiances and TOVS-3I cloud retrievals. Q. J. R. Meteorol. Soc., 126, 1735-1750

Chaboureau, J.-P., J.-P. Cammas, P. Mascart, J.-P. Pinty, and J.-P. Lafore, 2002: Mesoscale model cloud scheme assessment using satellite observations, J. Geophys. Res., 107(D17), 4301, doi:10.1029/2001JD000714

Chaboureau, J.-P., N. Söhne, J.-P. Pinty, I. Meirold-Mautner, E. Defer, C. Prigent, J. R. Pardo, M. Mech, and S. Crewell, 2008: A midlatitude precipitating cloud database validated with satellite observations. J. App. Meteorol. Clim., in press

Chaboureau, J.-P., J.-P. Cammas, J. Duron, P. J. Mascart, N. M. Sitnikov, and H.-J. Voessing, 2007: A numerical study of cross-tropopause transport by convective overshoots. Atmos. Chem. Phys., 7, 1731-1740

Chaboureau, J.-P., P. Tulet, and C. Mari, 2007: Diurnal cycle of dust and cirrus over West Africa as seen from Meteosat Second Generation satellite and a regional forecast model. Geophys. Res. Lett., 33, L03815, doi:10.1029/2006GL027771

Chaboureau, J.-P. and J.-P. Pinty, 2006: Evaluation of a cirrus parameterization with Meteosat Second Generation observations. Geophys. Res. Let., 33, L03815, doi:10.1029/2005GL024725

Meirold-Mautner, I., C. Prigent, E. Defer, J. R. Pardo, J.-P. Chaboureau, J.-P. Pinty, M. Mech, and S. Crewell, 2007: Radiative transfer simulations using mesoscale cloud model outputs and comparisons with passive microwave and infrared satellite observations for mid-latitude situations. J. Atmos. Sci., 64, 1550-1568

Söhne, N., J.-P. Chaboureau, and F. Guichard, 2008, Verification of cloud cover forecast with satellite observation over West Africa, Mon. Weather Rev., in revision

Wiedner, M., C. Prigent, J. R. Pardo, O. Nuissier, J.-P. Chaboureau, J.-P. Pinty and P. Mascart, 2004: Modeling of passive microwave responses in convective situations using outputs from mesoscale models: comparison with TRMM/TMI satellite observations. J. Geophys. Res., 109, D06214, doi:10.1029/2003JD004280

CIRRUS THERMAL INFRARED SOURCE FUNCTION FROM AIRCRAFT AND SPACEBORNE MEASUREMENTS

William D. Hart*[1], Dennis L. Hlavka[1], and Matthew McGill [2]
[1]Science Systems and Applications Inc., Lanham, MD
[2]NASA Goddard Space Flight Center/613.1, Greenbelt, MD

1. INTRODUCTION

The effect of clouds upon the terrestrial radiation balance is strongly influenced by the vertical distribution of particle density relative to the temperature profile. The thermal infrared emission by the cloud into space is a convolution of the vertical emissivity of the cloud, which is related to particle density, and the Planck black body function, which is a function of temperature only. The emission to space from a point in the cloud is modulated by the optical depth of the cloud above that point. A vertical profile of the combination of these effects is referred as the thermal source function.

In the remote sensing of clouds, much effort has been given to determining the altitude of clouds in order to deduce their thermal emission characteristics. Oxygen A-band , CO2 slicing, thermal infrared brightness temperature are some techniques that use passive measurements to get cloud boundary heights. Lidars alone give cloud boundaries and particle density without providing thermal information. Techniques have been described to combine observations from these two types of instruments to derive thermal source profiles. Simultaneous active and passive observations are therefore valuable for finding the radiative effects of clouds.

The A-train satellite suite has a nadir looking lidar, CALIOP aboard CALIPSO, and a scanning spectroradiometer, MODIS aboard AQUA. A similar pair of instruments, Cloud Physics Lidar (CPL) and MODIS Airborne Simulator (MAS) or MODIS/ASTER (MASTER), was flown on the ER-2 during the TC-4 campaign in 2007. These instruments pairs provide an opportunity to determine the thermal vertical source function. Results from these instruments are best for layers of cirrus with small optical depths.

In this presentation, we will show results of computation of the thermal source function derived from these instrument pairs. For the airborne instrumentation, case studies from flight tracks over thin cirrus will be analyzed and discussed. Case studies from the spaceborne pair will be analyzed. Repeat passes over particular locations will provide opportunity for initiating a climatology of such analysis. Nearly simultaneous airborne and spaceborne observations will allow comparisons between the two techniques to be made. These studies will provide information on the feasibility of doing such analysis on a large scale and the effectiveness of remote sensing analysis done by multiple instruments on separate platforms.

2. ALGORITHM

The analysis presented here is based on one described by Platt et al. 1998 where ground based instruments were used. LIRAD is the acronym used to identify this technique where ground based lidars and radiometers view upward to sense downwelling backscattered lidar and emitted infrared energy. Our analysis uses airborne and spaceborne instrumentation, which gives an alternative perspective in that the highest clouds are closest to the sensors. As a result, cirrus is the primary cloud type for this analysis. The cloud community has a strong

*Corresponding author address: William D. Hart, Code 613.1, NASA/GSFC, 8800 Greenbelt Rd. Greenbelt, MD 20771
Email William.D.Hart@gsfc.nasa.gov

interest in the often subtle influence cirrus clouds have on the radiative balance of the atmosphere. This downward looking technique was used in an analysis described by Spinhirne et al. (1996).

The technique employed in this study relies on the energy balance described by the equation for a single cloud layer

$$\mathbf{I_r} = \mathbf{I_B}\mathbf{T}_{lw} + \mathbf{g}\eta\mathbf{S_p}\int_{\mathbf{z_b}}^{\mathbf{z_t}}\mathbf{I_{BB}}(\mathbf{z})\mathbf{T}_{lw}(\mathbf{z})\beta_{\mathbf{c}}(\mathbf{z})\mathbf{dz} \qquad (1)$$

where $\mathbf{I_r}$ is upwelling thermal long wave infrared radiation detected by the radiometer, $\mathbf{I_B}$ is upwelling background radiation at the bottom of the cloud, $\mathbf{T}_{lw} = \mathbf{e}^{-\mathbf{g}\tau_{sw}}$ is the long wave infrared transmission of the layer, $\mathbf{g} = \sigma_{\mathbf{lw}} / \sigma_{\mathbf{sw}}$ is the ratio of the long wave extinction coefficient to the shortwave, τ_{sw} **is** the short wave optical depth of the layer, η is a multiple scattering factor which is assume to be 1 for this analysis, S_p is the shortwave extinction to backscatter ratio determined with lidar analysis, $\mathbf{I_{BB}}(\mathbf{z})$ is the Planck black body radiation as a function of altitude, $\mathbf{T_{lw}}(\mathbf{z})$ is the long wave transmission from **z** to the top of the cloud, $\beta_c($ z) is the lidar-determined backscatter coefficient, z is the vertical coordinate, and z_b and z_t are the bottom and top altitude of the cloud layer. We define the term

$$\mathbf{F_{lw}}(\mathbf{z}) = \mathbf{T}_{lw}(\mathbf{z})\beta_{\mathbf{c}}(\mathbf{z})\Delta\mathbf{z} \qquad (2)$$

where Δz is the vertical bin depth of the lidar, as the source function. It represents, when multiplied by the constants preceding the integral, the contribution of a cloud vertical element to the total long wave energy detected by the radiometer. In the analysis, the integral is evaluated by a summation $\mathbf{F_{lw}(z)}$ through the cloud layer.

In order to compute $\mathbf{F_{lw}(z)}$ **of** a cloud layer, an estimate of $\mathbf{I_B}$, the upwelling long wave energy must be made. If homogeneous conditions are assumed beneath the cloud, an estimate of the background radiance can be made by using the upwelling radiance from a clear area. Another method is to assume a typical value of $\mathbf{g}$ and computing

$$\mathbf{I_B} = \mathbf{I_{BB}}(\mathbf{z_m}) + (\mathbf{I_r} - \mathbf{I_{BB}}(\mathbf{z_m})) / \mathbf{T_{lwg}} \qquad (3)$$

where $\mathbf{I_{BB}}(\mathbf{z_m})$ is the Planck radiance at the cloud mid-point and $\mathbf{T_{lwg}}$ is the long wave transmission of the cloud found by using $\mathbf{g}$ and the cloud short wave optical depth. The maximum $\mathbf{I_B}$ found under the cloud layer would be used for the entire layer for homogeneous conditions.

The parameter $\mathbf{g}$, the ratio of long wave extinction to short wave extinction must be determined for each profile. This parameter appears both as a factor in the integral term in equation 1 and in the computation of $\mathbf{T}_{lw}$. The technique employed for this analysis uses an iterative algorithm which the computes the energy balance of equation 1 to within a certain tolerance.

3. DATA AND RESULTS

A case study was selected from the 2007 field campaign Tropical Compostion, Cloud and Climate Coupling (TC-4) which was a NASA project based in Costa Rica. The ER-2 was based at San Jose, Costa Rica. The CPL and MAS/MASTER were installed on the ER-2. TC-4 results were chosen since the CPL's data quality was good in this campaign and MAS Level-1 and Level-2 data sets were readily available. Figure 1 shows CPL and MAS products from this segment. The prevalence of multiple cloud layers throughout the campaign limited the number a cases that could be chosen. A four minute segment was selected from

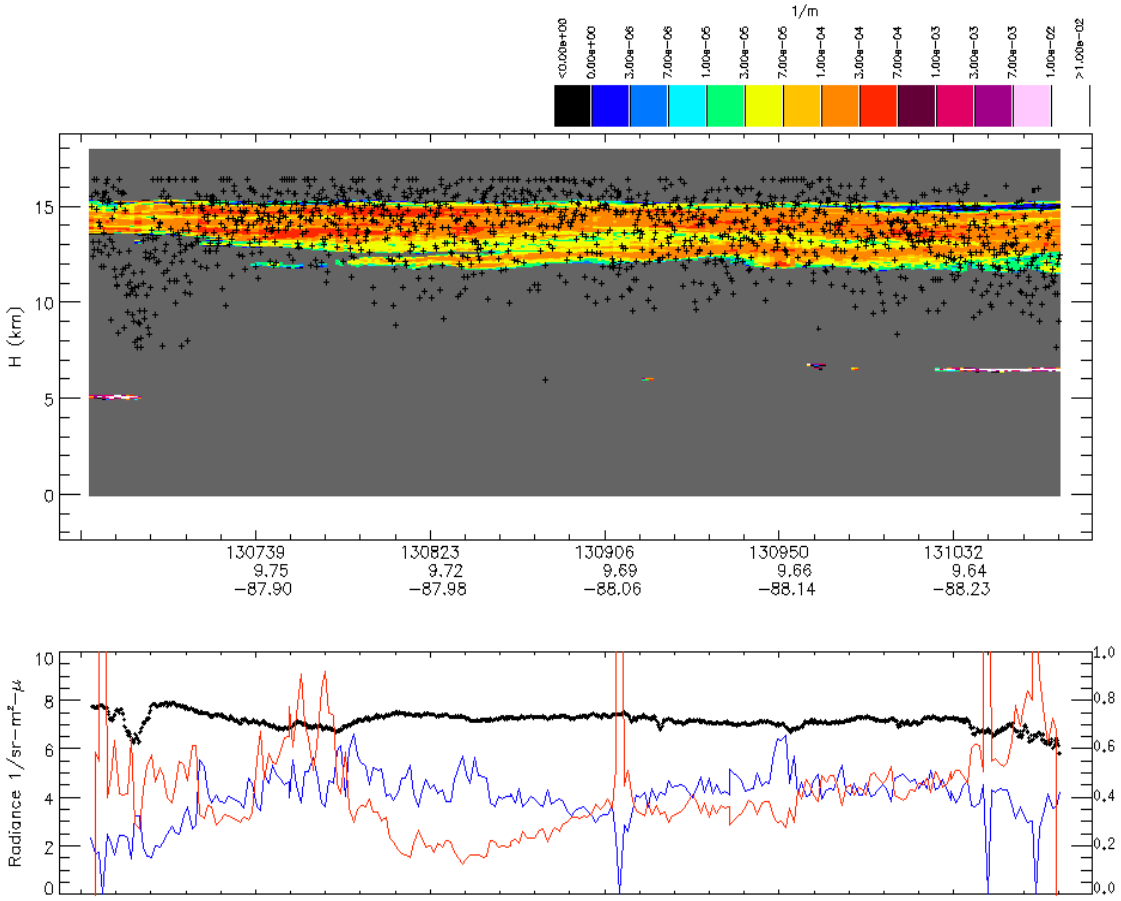

Figure 1: July 19, 2007 CPL/MAS case from TC-4. The top image shows the CPL derived extinction coefficient at 532 nm with MAS CO_2 cloud top heights superimposed in black symbols. The bottom plot shows coincident MAS long wave radiance at 10.5 μm in black along with CPL derived layer optical depth at 532 nm in blue and g in red. The right axis scale is for both optical depth and g. The axis values universal time in hhmmss format, latitude, and longitude.

19 July, 2007. This segment was chosen since it is generally a single layer of cirrus overlying the ocean.

The upper segment of Fig. 1 shows a layer of cirrus over generally clear skies with an intervening dense middle layer at the beginning and end of the segment. The CPL parameter displayed is the extinction coefficient at 532 nm. The magnitude of the extinction coefficient implies that this is a moderately dense cirrus cloud with typical midrange extinction values. The layer is transmissive to the laser for its entire length. The superimposed MAS cloud top heights, based upon CO_2 –slicing algorithm illustrate typical results of radiometer analysis of a optically thin cirrus layer. The scatter indicates that the algorithm is sensitive to other factors that are not conspicuous in the figure. An indication of the influence of lower layers on the CO_2 slicing analysis is seen where the MAS cloud tops trend toward the middle cloud at the segment's begining and end. The lower figure segment shows the MAS observed radiance at 10.5 μm which is used in the source function computation, but not in CO_2 slicing. The MAS radiance shows a decreasing trend in the single-layer left half of the plot as the CPL optical thickness, shown in blue, shows an increase. This is an expected result. The red line in the lower plot shows the value of the ratio of long-wave extinction to the short wave extinction, $\mathbf{g}$, determined by the iterative method mentioned under equation 3. It shows an increasing value as the optical depth increases. Its range of values in the clear area from 0.25 to 0.55 is in the expected range. The values before 13:08:05 range from high to low, possibly because of multiple layer issues.

Fig. 2 shows the source function $\mathbf{F}_{\mathbf{lw}}(\mathbf{z})$ given by equation 2. The black markers indicate the altitude where the maximum is for each profile. The maximum for this case tends to be in the middle region of the cloud. In the time region near 13:09:50 the maximum is near the bottom of the cloud where there is a dense cloud element. At 13:08:23, the maximum is at the top of the cloud where is a denser cloud element exists as indicated by the extinction image in Fig. 1. The level of the maximum may be considered an median center from which the long wave energy originates and influence where long wave radiometer algorithms find cloud tops. The results clearly show the advantage of combining the lidar with radiometer data to derive the vertical thermal structure of the cirrus cloud.

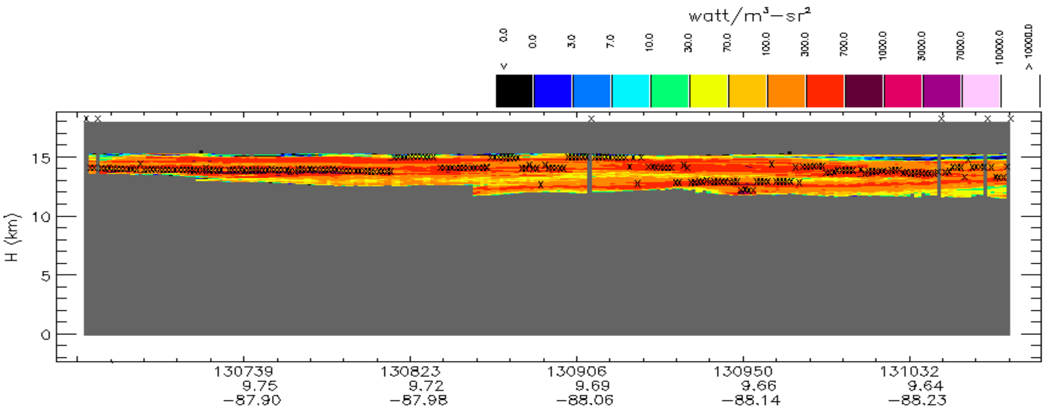

Figure 2: Thermal source function derived from CPL and MAS products for the TC-4 case study segment. The black markers indicate the level of the maximum for each profile.

4. SUMMARY AND CONCLUSIONS

This presentation provides an analysis that shows a method to determine the vertical structure of cirrus clouds using airborne and spaceborne combination of lidar and radiometer observations. A parameter termed thermal source function is used to show the structure. Equations of an algorithm are presented and results from a case study from the NASA campaign TC-4, 2007 are shown. The case demonstrates the potential for the analysis to reveal the influence that cirrus cloud have on the radiative balance at long wave infrared wavelengths. Routine use of such an algorithm in appropriate circumstances would enhance the overall measurement of the radiative effects of cirrus clouds.

At the time of submission of this abstract, analysis of similar cases from MODIS and CALIOP were still in progress. Also, additional airborne cases and possibly simultaneous airborne and spaceborne cases will be found and analyzed. These will be presented as a poster at the ICCP conference.

5. ACKNOWLEDGEMENTS

MODIS Airborne Simulator

MAS products for the case study were provided by T. Arnold of NASA/GSFC. Also see
King, Menzel, Grant, Myers, Arnold, Platnick, Gumley, Tsay, Moeller, Fitzgerald, Brown, and Osterwisch, 1996: Airborne scanning spectrometer for remote sensing of cloud, aerosol, water vapor and surface properties. Journal of Atmospheric and Oceanic Technology, 13, 777-794.

Cloud Physics Lidar

CPL data products are publicly available at http://cpl.gsfc.nasa.gov

6 REFERENCES

Platt, C.M.R., S.A. Young, P.J. Manson, G.R. Patterson, S.C. Marsden, R.T. Austin, and J.H. Churnside, 1998: The Optical Properties of Equatorial Cirrus from Observations in the ARM Pilot Radiation Observation Experiment. *J. Atmos. Sci.*, **55**, 1977–1996.

Spinhirne, J.D., W.D. Hart, and D.L. Hlavka, 1996: Cirrus Infrared Parameters and Shortwave Reflectance Relations from Observations. *J. Atmos. Sci.*, **53**, 1438–1458.

THE IMPACT OF VARYING METEOROLOGICAL CONDITIONS ON AEROSOL INDIRECT EFFECTS OVER THE INDIAN OCEAN

Greg M. McFarquhar and Hailong Wang*

University of Illinois at Urbana-Champaign, Urbana, IL
*Current Affiliation: CIREIS/NOAA Earth System Research Laboratory, Boulder, CO

1. INTRODUCTION

The impact of aerosols on climate remains a complex and unsolved problem. In the fourth assessment report of the Intergovernmental Panel on Climate Change (IPCC 2007), the aerosol effect on enhancing cloud albedo, which is often called the first aerosol indirect effect (Twomey 1977), had the largest uncertainty in the calculation of the radiative forcing of the climate system among all processes listed. The level of scientific understanding on the second indirect effect of increasing cloud lifetime (e.g., Albrecht 1989) and the semi-direct effect of altering cloud properties due to soot heating (e.g., Ackerman et al. 2000) is also very low.

Shallow cumuli not only affect the Earth's radiation budget, but also impact the heat, moisture and momentum budget in the atmosphere. Because of the low altitude and small size of shallow cumuli, the influence of aerosols on them has the potential to be large, making them a good choice for studying aerosol-cloud interactions. However, it is often difficult to separate the impact of aerosols on the properties of shallow cumuli from the impact of meteorological factors that also have a big influence on the cloud properties.

In this study, the sensitivity of shallow convection and cloudiness to aerosol properties is examined under a wide range of meteorological conditions using a LES model and observations obtained during the Indian Ocean Experiment. The northern Indian Ocean is an ideal environment for studying aerosol effects on clouds in varying meteorological conditions because anthropogenic aerosols are transported from the Indian subcontinent and southeast Asia to the trade-wind boundary layer over the northern Indian Ocean during the winter monsoon, interacting with shallow cumuli (McFarquhar and Heymsfield 2001) and producing large regional climate forcing (Ramanathan et al. 2001). Aerosols in both clean and polluted environments were sampled during INDOEX under a range of meteorological conditions, ideal for initializing and evaluating modeling studies of aerosol effects on shallow cumuli.

2. OBSERVATIONS FROM INDOEX

Radiosonde data collected during INDOEX were used to define a range of thermodynamic profiles and the height, depth and strength of stable layers over the northern Indian Ocean. From January to March of 1999, 183 radiosondes were launched from the Kaashidoo Climate Observatory (KCO), Republic of Maldives. All used Väisälä RS-80 sondes which utilized Global Positioning System (GPS) tracking to determine winds and were averaged to 80 m resolution. On each sounding inversions and absolutely stable layers (SLs) were identified using an objective method, where the environmental temperature lapse rate $\Gamma(z)$ was used to describe the stability of a layer from

$$\begin{cases} \Gamma(z) < 0 \ , \ \textit{inversion} \\ \Gamma(z) < \Gamma_m(z) \ , \ \textit{absolutely stable} \end{cases} \quad (1),$$

where z is the height and $\Gamma_m(z)$ the moist adiabatic lapse rate. By this definition, some of the absolutely stable layers are also inversions.

The soundings followed the structure of a typical trade-wind boundary layer that consists of a surface layer, a mixed layer (ML), a transition layer (TL), and a cloud layer topped by an inversion layer (IL). To provide context for the modeling studies, the distributions of the height, depth and strength of the TL and IL were obtained as described below.

Any absolutely stable layer lower than 1 km was defined as a TL. The frequency of occurrence of 50.9% for the TL and 58% for the IL between the surface and 3 km are comparable to those of 44.8% (TL) and 60% (IL) for the trade-wind regime over the eastern equatorial Pacific (Yin and Albrecht 2000). Because cooling and moistening associated with convection in the boundary layer would erode these stable layers, their frequent presence shows that some physical forcing is maintaining them. The median depth of both the TL and the IL was 0.16 km whereas the maximum depths were 0.48 km and 0.32 km, respectively. The median TL base was 0.64 km with a standard deviation of 0.15 km, and the median IL base between 1 and 2 km was 1.52 km with a standard deviation of 0.26 km. For all inversions below 3 km, median strengths of 12 K km^{-1} and 18.4 g kg^{-1} km^{-1} and a median base of 1.6 km are close to those of inversions located between 1 and 2 km. The inversion strength is comparable to that of 11.6 K km^{-1} used by Siebesma et al. (2003) for a cumulus case study over Barbados, in which the depth of the inversion, 0.52 km, was much bigger than the median value of 0.16 km observed during INDOEX, while the strength is much weaker than that of 36 K km^{-1} used by Stevens et al. (2001) for a stratocumulus case study over the Atlantic Ocean.

Figure 1 shows mean profiles of θ, q_v, and wind speeds u and v that were derived from the soundings. The dotted lines indicate the mean of the profile and the shaded bands represent one standard deviation from the mean. Above the ML top of about 0.52 km, the mean

· Corresponding Author: Prof. McFarquhar, University of Illinois, Dept. of Atmospheric Science, 105 S. Gregory Street, Urbana, IL, 61801.

lapse rate of θ is at 4.7±0.6 K km^{-1}. To initialize some of the model simulations, the profiles of θ and q_v were modified to alternately include a TL or an IL characterized by the properties derived from these observations as discussed in the following section.

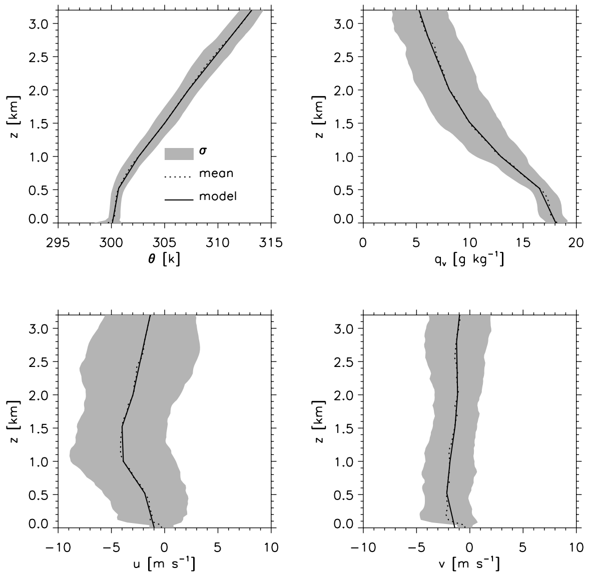

Figure 1: Profiles of θ, q_v, u and v. Dotted lines in the middle indicate the mean of all nocturnal soundings and the shaded bands represent one standard deviation from the mean on each side. The solid lines are fits to the means.

3. SIMULATION STRATEGY/EXPERIMENT SETUP

Sensitivity studies were setup using the EULAG model (Smolarkiewicz and Margolin 1997) with warm-rain bulk microphysics (Grabowski 1998) to examine how changes in RH and the TL/IL, within the range of INDOEX observations, affect the convective, cloud and radiative properties. The model setup followed that of McFarquhar and Wang (2006) who used EULAG model for LES studies over the northern Indian Ocean.

The numerical experiments were sorted into six groups according to the initial profiles of θ and q_v which were selected from $(\overline{\theta}, \overline{\theta}-\sigma_\theta, \overline{\theta}+\sigma_\theta)$ and $(\overline{q_v}, \overline{q_v}-\sigma_q, \overline{q_v}+\sigma_q)$, where the mean profiles ($\overline{\theta}$ and $\overline{q_v}$) and one standard deviation (σ_θ and σ_q) away from the mean profile were shown in Fig. 1. The six groups were chosen to give a wide range of θ, q_v and RH in the trade-wind boundary layer that encompassed conditions observed during INDOEX.

Figure 2 shows the initial profiles of $\overline{\theta}$ and $\overline{q_v}$ with or without the TL/IL. The median derived depths of the TL and IL of 0.16 km were assumed. Although the median strength of the TL (i.e., $d\theta/dz$=6.3 K km^{-1}, dq_v/dz=12.5 g kg^{-1} km^{-1}) was used for the sensitivity studies, the maximum observed strength of the IL ($d\theta/dz$=19.5 K km^{-1}, dq_v/dz=42.2 g kg^{-1} km^{-1}) was used because a test simulation with an IL of median strength showed less than 5% changes in cloud properties compared to the base case without an IL. Another test simulation showed that convection did not develop during the typical 6-hour spin-up time when a TL with the maximum observed strength was added to the $\overline{\theta}$ and $\overline{q_v}$ initial profiles and maintained by large-scale forcing.

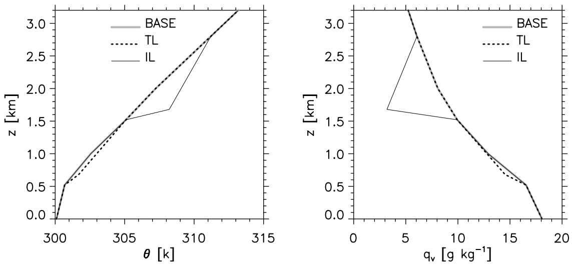

Figure 2: The $\overline{\theta}$ and $\overline{q_v}$ profiles with no stable layer (BASE), with the TL or with the IL.

Following Wang and McFarquhar (2008), the surface sensible and latent heat fluxes in the model were fixed at 8 and 122 W m^{-2}, the average values obtained from the ECMWF meteorological analysis for the same time period, in order to exclude the feedbacks of varying surface fluxes on turbulent dynamics and cloud properties from the impact of other factors. Aerosol optical properties at solar and infrared wavelengths were calculated from measurements made during INDOEX as described by McFarquhar and Wang (2006). For clean (polluted) conditions, the characteristic aerosol extinction profile (Welton et al. 2002) with an optical depth of 0.05 (0.38) and single scattering albedo of 0.998 (0.889) at 0.55 μm was assumed. Cloud droplet number concentration for clean (polluted) clouds in the single-moment bulk microphysics scheme was prescribed as 89 (316) cm^{-3}, the median value measured during INDOEX.

A domain of 6.4×6.4 km^2 by 3.2 km with a uniform grid spacing of 100 m in the horizontal and 40 m in the vertical was used for the numerical simulations. The simulations were started near the local sunset (6 pm) and run for 36 h to provide sufficient spin-up time and to cover one complete diurnal cycle. Simulation results in the last 24 hours were analyzed.

The initial profiles of temperature and moisture can only be sustained if there is a forcing that counteracts the adiabatic cooling due to the expansion of rising air parcels and longwave radiative cooling near cloud top and moistening from evaporation from the ocean surface. Sensitivity tests with a TL, with an IL and without any stable layer showed that in the absence of such a forcing shallow convection became deeper with time, causing a continuous increase in cloud bases and tops, and a rapid erosion of the TL and IL inconsistent with observations. Large-scale forcing most likely causes drying and warming through subsidence that balances the cooling and moistening of convection.

However, because there were no reliable data that can be used to describe forcing on scales larger than the model domain in the region of interest, a relaxation scheme (Wang and McFarquhar 2008) was used to nudge the domain-average vertical profiles of θ, q_v, u and v towards their initial states that were assumed to represent the daily mean profiles.

Overall, the forcing produced by the relaxation scheme gave a warming and drying tendency to the mean states which was a local maximum near the TL or IL when present. In cases without a SL, the increase of forcing with height in the cloud layer (between 0.5 and 1.5 km) produced by the relaxation scheme is consistent with the trend in large-scale subsidence estimated from the ECMWF analysis for the INDOEX domain (Wang and McFarquhar 2008) and from budget analysis in other trade-wind regimes (e.g., Stevens et al. 2001; Siebesma et al. 2003).

4. NUMERICAL SIMULATIONS

Figure 3 shows how the daily mean LWP, cloud fraction, cloud top height and vertically averaged relative humidity, hereafter RH, changed with the vertically averaged initial relative humidity, hereafter RH_0, for simulations without a TL or IL. Vertical error bars represent one standard deviation about the mean value over the last 24 hours of simulated time. Horizontal error bars indicate the spread of RH_0 between the surface and model top. Both the mean LWP and cloud fraction consistently increased with increasing RH_0. The average cloud top also increased with RH_0 except for the two driest cases. The variation of LWP, cloud fraction and cloud top in the diurnal cycle, as indicated by the standard deviations, also increased with RH_0.

The mean LWP and cloud fraction were less in the polluted environment compared to the clean environment for all cases. This suggests that the semi-direct effect, which typically reduces LWP and cloud fraction, dominated the first and second indirect effects, which increase LWP and cloud fraction. Further, the average cloud top heights were higher in the presence of anthropogenic aerosols because precipitation is reduced in the presence of aerosols (second indirect effect) and cloud droplets remain in the updrafts to reach higher altitudes above cloud base. At the same time, heating induced by absorbing aerosols below cloud elevated the cloud bases by about 0.2 km. The mean RH in polluted environment was smaller than in clean environment even though the RH_0 was the same, likely due to the heating induced by the absorbing aerosols.

Figure 4 shows the daily means of cloud fraction, LWP, cloud top height and RH as a function of RH_0 with and without the impact of the TL. Compared to cases without a TL, the cloud fraction, LWP and cloud top were reduced for all simulations with a TL. The reduction in cloud fraction ranged from 23% to 70%, with greater reduction in drier and cleaner environments. The reduction in LWP and cloud top ranged from 38% to 89% and from 5% to 32%, respectively, with again more reduction in drier and cleaner environments. When the TL was present, anthropogenic aerosols either decreased or increased cloud fraction and LWP depending upon the RH_0 but they increased cloud top height consistently for all RH_0. Moreover, increase in cloud tops in the presence of anthropogenic aerosols was 29% to 7% more than that in cases with no stable layer for RH_0 varying between 49 and 76%.

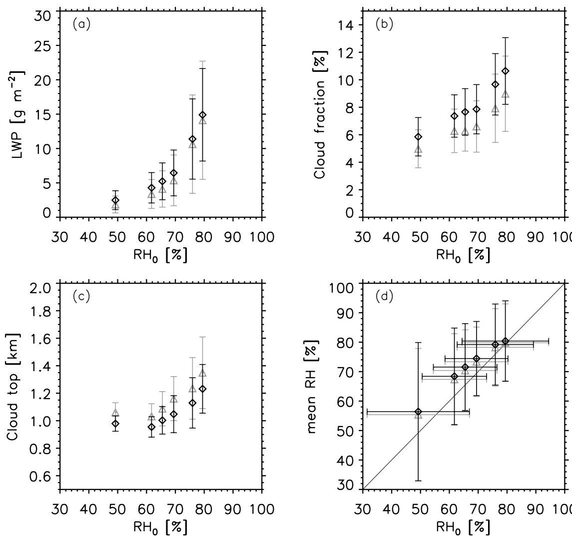

Figure 3: Daily mean LWP, cloud fraction, cloud top and RH vary with RH_0 for experiments with no stable layer in the sounding. Triangles (diamonds) indicate experiments in polluted (clean) environments. Error bars represent one standard deviation about the mean.

The results demonstrated the importance of a TL of median strength in affecting shallow cumuli properties. This conclusion is significant because TLs occurred 50.9% of the time over the northern Indian Ocean during INDOEX. The results differ from those of Stevens et al. (2001) who showed that a thinner (0.05 km thick) but stronger ($d\theta/dz$=7.5 K km^{-1}, dq_v/dz=20 g kg^{-1} km^{-1}) TL had a minor impact on the cloud fields generated by their LES. However, their TL was lost before the analysis period started since there was not a sufficiently strong forcing to maintain it. In this study, the role of persistent transition layer maintained by a large-scale forcing induced by the relaxation scheme was examined.

As previously mentioned a strong IL was used in the sensitivity tests instead of the median-strength IL. Although this strong IL is weaker than inversions observed in other trade-wind regimes (e.g., Stevens et al. 2001), its impact on cloud properties should not be interpreted as typical during INDOEX.

Figure 4 shows that the impact of the IL on cloud properties was dependent on RH_0. In a clean environment, the IL reduced or enhanced the total cloud fraction by less than 5% compared to cases with no stable layer when RH_0 ranged from 49% to 76%. However, the IL reduced cloud fraction by 12% when RH_0 was 80%. Reductions in mean LWP caused by the IL were less than 5% for the three driest cases, but were 15% and 35% for RH_0 of 69% and 80% respectively. Because the IL suppressed the vertical development of clouds in cases with high RH_0, the increase in average cloud top height of 0.25 km for increases in RH_0 from 49% to 80% for cases without an IL was reduced to 0.1 km for cases with an IL. The presence of the IL did not change the direction of the response of cloud properties to the anthropogenic aerosols. The LWP and cloud fraction were consistently reduced while the average cloud top was increased in the polluted environment.

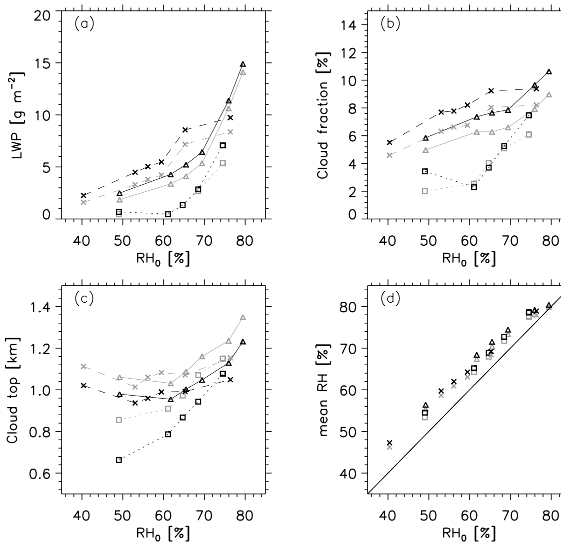

Figure 4. Same as in Fig. 3 but for experiments without stable layer (triangles on solid line), with the TL (squares on dotted line) and with the IL (crosses on dashed line) in polluted (gray) and clean (black) environment.

Figure 5 shows the daytime mean net indirect forcing at the surface and TOA as a function of the difference in cloud fraction between the clean and polluted simulation (ΔCF). Here the net indirect forcing refers to the summation of indirect forcings due to the first and the second indirect effect and the semi-direct effect that were calculated following McFarquhar and Wang (2006). Shortwave (SW), longwave (LW) and SW+LW net indirect forcings at the surface and TOA are plotted separately. The daytime mean cloud fraction was reduced in the polluted environment for each of the 17 cases. This resulted in a positive SW net indirect forcing at the surface (TOA) ranging between 0.7 (0.7) and 5.8 (4.6) W m^{-2}. The LW net indirect forcing at the surface was negative in all cases ranging between –1.5 and –0.3 W m^{-2}. Except for 3 cases with a TL, the LW net indirect forcing at the TOA was negative and reached down to –0.7 W m^{-2}. The SW+LW net indirect forcing was positive in all cases, ranging from 0.2 to 4.5 W m^{-2}, indicating that the semi-direct effect dominated the indirect effects regardless of the meteorological conditions.

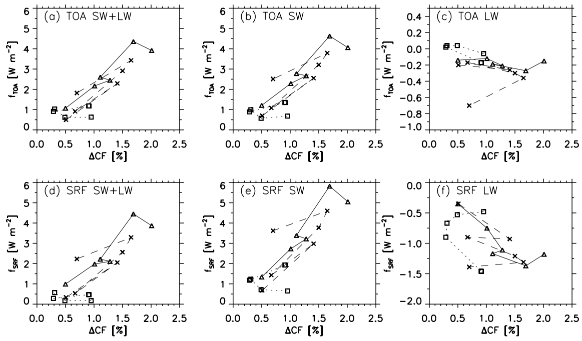

Figure 5: Daytime mean shortwave (SW), longwave (LW) and total (SW+LW) net indirect forcing at surface/TOA change with difference in cloud fraction caused by the anthropogenic aerosols for experiments without stable layer (triangles on solid line), with a transition layer (square on dotted line) or inversion layer (cross on dashed line) in the initial sounding.

This finding is consistent with the calculations based on cloud covers and optical depths retrieved from a multi-channel radiometer over the Indian Ocean (McFarquhar et al. 2004). Overall, the magnitude of the SW+LW net indirect forcing increased with increasing ΔCF. The correlation coefficient between ΔCF and SW+LW net indirect forcing at the surface (TOA) is 0.86 (0.9), indicating that change in cloud fraction that occurred in polluted conditions was an important indicator of indirect forcing. Because the surface and TOA SW net indirect forcing were both related to ΔCF, they were affected by changes in RH and the presence of the TL/IL as documented earlier.

For simulations with a TL or IL, the SW and LW forcing increased with RH_0 but the trend was modified by the presence of a stable layer. With a TL, the SW forcing increased slower with increasing RH_0 and was mostly cancelled out by the LW forcing, resulting in a small net forcing. The IL had a more complex impact on the indirect forcing. It enhanced the forcing for some RH_0 but reduced it for others.

5. SUMMARY

Shallow convection and cumuli in the trade-wind boundary layer during the winter monsoon over the northern Indian Ocean were simulated using the EULAG model. Using sounding data obtained during the Indian Ocean Experiment (INDOEX), a total of 18 meteorological scenarios were constructed using 6 different temperature and humidity profiles with a transition layer (TL), an inversion layer (IL) or no stable layer added. Separate simulations for each scenario assuming clean and polluted conditions examined how absorbing anthropogenic aerosols impact shallow cumuli in a variety of meteorological scenarios.

In the absence of any forcing to counteract the cooling and moistening effects of shallow convection, the stable layer in the initial sounding eroded quickly. Because these stable layers persist in nature, some forcing must provide the warming and drying needed to maintain the stable layer. To quantify the impact of the TL and IL on shallow cumuli, a large-scale forcing needing to maintain them was assumed, something lacking in some previous studies.

Cloud fraction, LWP, and cloud top height were reduced in simulations with a TL. This differs from Stevens et al.'s (2001) finding that the TL had a minor impact on simulated cloud properties, the difference occurring because the TL was not maintained during their study. Moreover, a persistent strong TL can shut off the convection all together. Simulations assuming an IL with the median observed strength had minimal impacts on simulation results. Additional sensitivity studies using the maximum observed strength of $d\theta/dz$=19.5 K km^{-1}, still weaker than that observed in other trade-wind regimes (e.g., Stevens et al. 2001), showed varying impacts depending on whether clouds reached the inversion base. For cases with higher RH_0 that produced stronger convection, the presence of the IL decreased cloud tops by up to 0.2 km, cloud fraction by 12% and LWP by 35%. For cases with smaller RH_0, where convection did not penetrate through the inversion, the IL reduced or enhanced cloud fraction and LWP by less than 5%, showing that even an IL stronger than typically observed over the Indian Ocean did not impact simulated cloud properties significantly.

Compared to pristine simulations, polluted simulations had lower cloud fractions and LWPs. However, cloud bases and tops were higher due to the heating induced by absorbing soot. This led to a positive daytime mean SW net indirect forcing varying between 0.7 (0.7) and 5.8 (4.6) W m^{-2} at the surface (TOA). The daytime mean LW net indirect forcing at the surface varied between –0.3 and –1.5 W m^{-2}. Except for 3 cases with a TL, the LW net indirect forcing at the TOA was negative and reached down to –0.7 W m^{-2}. The SW+LW net indirect forcing was positive in all cases, ranging from 0.2 to 4.5 W m^{-2}. This shows that the semi-direct effect was larger than the indirect effects for the range of conditions observed over the Indian Ocean. Overall, the magnitude of both the SW and LW net indirect forcing increased with increasing RH_0. The TL reduced the SW+LW net indirect forcing by up to 4.0 W m^{-2} while the effect of the IL was RH_0 dependent. In the absence of a TL or an IL, mean turbulent fluxes of buoyancy, heat, moisture and cloud mass were all reduced in polluted conditions compared to pristine conditions.

In summary, using observed ranges of meteorological factors and aerosol properties, it was seen that the simulated cloud cover and LWP were more sensitive to meteorological conditions than to aerosol properties. This indicates large uncertainties can be introduced when solely using observations of aerosols and clouds made under different meteorological conditions to quantify aerosol indirect effects.

6. ACKNOWLEDGMENTS

W. Grabowski provided help with EULAG. This work was supported by the National Aeronautics and Space Administration (NASA) grants *NASA NAG 5-11756* and *NNG06GB92G*, and the National Oceanic and Atmospheric Administration (NOAA) grant *COM NA06OAR4310003*. The observations over KCO made during INDOEX were provided by NCAR's Earth Observing Laboratory data sever.

7. REFERENCES

Ackerman, A. S., O. B. Toon, D. E. Stevens, A. J. Heymsfield, V. Ramanathan, and E. J. Welton, 2000: Reduction of tropical cloudiness by soot. *Science*, **288**, 1042-1047.

Albrecht, B. A., 1989: Aerosols, cloud microphysics, and fractional cloudiness. *Science*, **245**, 1227-1230.

Grabowski, W. W., 1998: Toward cloud resolving modeling of large-scale tropical circulations: A simple cloud microphysics parameterization. *J. Atmos. Sci.,* **55,** 3283–3298.

IPCC, 2007: *Climate Change 2007: The physical science basis.* Contribution of Working Group I to the fourth assessment report of the Intergovernmental Panel on Climate Change, Cambridge Univ. Press., Cambridge, United Kingdom and New York, NY, USA.

McFarquhar, G.M., and A.J. Heymsfield, 2001: Parameterizations of INDOEX microphysical measurements and calculations of cloud susceptibility: applications for climate studies. *J. Geophys. Res.*, **106**, 28 675-28 698.

McFarquhar, G.M., S. Platnick, L. Di Girolamo, H. Wang, G. Wind, and G. Zhao, 2004: Trade wind cumuli statistics in clean and polluted air over the Indian Ocean from in situ and remote sensing measurements. *Geophys. Res. Lett.*, **31**, L21105, doi:10.1029/2004GL020412.

McFarquhar, G. M., and H. Wang, 2006: Effects of aerosols on trade wind cumuli over the Indian Ocean: model simulations. *Quart. J. Roy. Meteor. Soc.*, **132**, 821–843.

Ramanathan, V., and 39 co-authors 2001: Indian Ocean Experiment: An integrated analysis of the climate forcing and effects of the great Indo-Asian haze. *J. Geophys. Res.,* **106**, 28371-28398.

Siebesma, A.P., C.S. Bretherton, A. Brown, A. Chlond, J. Cuxart, P.G. Duynkerke, H. Jiang, M. Khairoutdinov, D. Lewellen, C.-H. Moeng, E. Sanchez, B. Stevens and D. E. Stevens, 2003: A large eddy simulation intercomparison study of shallow cumulus convection**.** *J. Atmos. Sci.* **60**, 1201–1219.

Smolarkiewicz, P.K., and L.G. Margolin, 1997: On forward-in-time differencing in fluids: an Eulerian/semi-Lagrangian nonhydrostatic model for stratified flows. *Atmosphere-Ocean*, **35**, 127-152.

Stevens, B., A.S. Ackerman, B.A. Albrecht, A.R. Brown, A. Chlond, J. Cuxart, P.J. Duynkerke, D.C. Lewellen, M.K. Macvean, R.A.J. Neggers, E. Sánchez, A.P. Siebesma, and D.E. Stevens, 2001: Simulations of trade wind cumuli under a strong inversion. *J. of Atmos. Sci.*, **58**, 1870-1891.

Twomey, S., 1977: The influence of pollution on the shortwave albedo of clouds. *J. Atmos. Sci.*, **34**, 1149-1152.

Wang, H., and G. M. McFarquhar, 2008: Large-eddy simulations of the diurnal cycle of shallow convection and cloudiness over the tropical Indian Ocean. Submitted to *Quart. J. Roy. Meteor. Soc.*, under review.

Welton, E.J., K.J. Voss, P.K. Quinn, P.J. Flatau, K. Markowicz, J. R. Campbell, J.D. Spinhirne, H.R. Gordon, and J.E. Johnson, 2002: Measurement of aerosol vertical profiles and optical properties during INDOEX 1999 using micropulse lidars. *J. Geophys. Res.*, **107**, 8019, doi:10.1029/2000JD000038.

Yin, B., and B. A. Albrecht, 2000: Spatial variability of atmospheric boundary layer structure over the eastern equatorial Pacific. *J. Climate.*, **13**, 1574–1592.

RADIATIVE EFFECTS OF GLOBAL CLOUD RESOLVING MODEL
IN THE FRAMEWORK OF
1-MOMENT BULK SCHEME COUPLED WITH AEROSOL TRANSPORT MODEL

Tatsuya Mitsui[1], Kentaroh Suzuki[2],
Hirohumi Tomita[3], Akira Noda[3], Masaki Satoh[1, 3] and Teruyuki Nakajima[1]
[1]Center for Climate System Research, University of Tokyo, Japan
[2]Department of Atmospheric Science, Colorado State University, USA
[3]Frontier Research Center for Global Change, JAMSTEC, Japan

1. INTRODUCTION

Our group has developed Global Cloud Resolving Model (GCRM) named NICAM (Satoh et al., 2008) to overcome limitations of conventional AGCMs such as horizontal grid resolution or parameterization schemes characterized by locality of phenomena and so on. By using NICAM we can calculate Cloud Radiative Forcing (CRF) on the basis of cloud microphysics with less assumption. And it is well known that cloud number concentration has a great impact for CRF and highly depends on aerosols (Lohmann and Feichter, 2005). So our framework, 1-moment bulk scheme coupled with Aerosol Transport Model named SPRINTARS (Takemura et al. 2005), have advantages of both Cloud Resolving Model and AGCM to study climate and could fill the gap among phenomena.

There are still many discussions to determine which resolution would better to represent cloud formation. Iga et al. (2007) reported that 14 km seemed to be enough to represent global-scale climatology without cumulus parameterization so here we used 14km resolution and performed control experiment to understand CRF.

2. EXPERIMENTAL DESIGN

We used the 1-moment bulk scheme of Grabowski (1998) (G98) which is extension of warm cloud process. We also used different Auto-conversion scheme (Seifert and Beheng, 2006) (G98-SB06) to confirm aerosol Lifetime effects as control experiments. SPRINTARS predicts aerosol mass and treats species as a category of Black Carbon(BC), Organic Carbon(OC), Sulfate, Dust and Sea Salt. In SPRINTARS we can choose aerosol nucleation scheme between empirical formula (Suzuki et al., 2004) and theoretical formula (Abdul-Razzak et al., 1998). Cloud optical parameters are calculated in cloud microphysics assuming cloud droplet size distribution as modified Gamma distribution following Berry and Reinhardt (1974b),

$$\overline{x_c} = \frac{L_c}{N_c},$$

$$f_c(x) = \frac{\lambda_c^{\,\nu_c+1}}{\Gamma(\nu_c+1)}\left(\frac{x_c}{\overline{\overline{x_c}}}\right)^{\nu_c} \exp\left(-\lambda_c \frac{x_c}{\overline{\overline{x_c}}}\right),$$

$$r_{effc} = \frac{\int_0^\infty r_c^3 f(r_c)dr}{\int_0^\infty r_c^2 f(r_c)dr}$$

$$= \left(\frac{3}{4\pi\rho_w}\overline{x_c}\right)^{1/3} \frac{\Gamma(\nu+2)}{\Gamma(\nu+5/3)}(\nu+1)^{-1/3}.$$

We calculated CRF with Effective Radius of hydrometeors and pre-calculated Look-Up-Table of extinction coefficient and absorption coefficient.

The Initial conditions of experiments was made by using SPRINTARS(T42L20) with nudging to NCEP. Initial time was 00:00UTC on 1 July 2006 and we calculated 30 days to compare with satellite products.

3. OVERVIEW OF CTL-RUN

At first we show several comparisons with satellite observational data to confirm reproducibility of our model before discussing CRF and aerosol indirect effects.

Fig.1 shows zonal mean of OLR and OSR derived by control run (G98) compared with climatology derived by SRB.

Fig.2 shows monthly mean of low level cloud fraction defined by ISCCP-D series (Rossow and Schiffer, 1999) and climatology of ISCCP-D2 products. Lower "Warm Cloud" is directly influenced by aerosols through activation process. Reproducibility of shallow clouds over the west coast of California or Peru seems to be insufficient. This may owe to role of turbulence transport therefore higher horizontal resolution could solve this problem.

Fig.3 shows monthly mean of Aerosol Optical Thickness (AOT) derived by control run and MODIS level3 products. Satellite observed high AOT over Siberia and Canada. These high AOT were originated by forest fire but our model cannot diagnose fire map. So we should focus on the range from -60S to 45N. We can also recognize smaller AOT over desert such as Taklamakan, Saharan and Saudi Arabia. This may be caused by threshold of cloud masking of retrieval algorithm and MODIS products maybe recognize higher AOT as cloud. Especially retrieval of AOT over land has much uncertainty because of variability of surface albedo and aerosol species.

Although zonal mean or synoptic spatial structures of above variables highly depend on initial condition, we can see the impacts of cloud microphysics on CRF within a month because of its timescale.

In the presentation, we will discuss further about radiative effects of aerosols and cloud microphysics, limitation of our framework and future work to refine on GCRMs.

4. BIBLIOGRAPHY

Abdul-Razzak et al. (1998), J. Geophys. Res., 103, doi:10.1029/97JD03735.

Berry and Reinhardt (1974b), J. Atmos. Sci., 31, p.1825-1831.

Grabowski (1998), J. Atmos. Sci., 55, p3283-3298.

Iga et al. (2007), Geophys. Res. Lett., 34, doi:10.1029/2007GL031038.

Lohmann and Feichter, (2005), Atmos. Chem. Phys., 5, p.715-737.

Rossow and Schiffer (1999), Bull. Atmos. Meteor. Soc., 80, p.2261-2287.

Satoh et al. (2008), J. Comput. Phys., 227, p.3486-3514.

Seifert and Beheng (2006a), Meteorol. Atmos. Phys., 98, 45-66.

Suzuki et al. (2004), J. Atmos. Sci., 61, p.179-194.

Takemura et al. (2005), J. Geophys.

Res., 110, doi:10.1029/2004JD005029.

5. ACKNOWLEDGEMENTS

Numerical experiments of NICAM were done by using the Earth Simulator. This research was supported by Innovative Program of Climate Change Projection for the 21st. Century (KAKUSHIN Program).

6. FIGURES

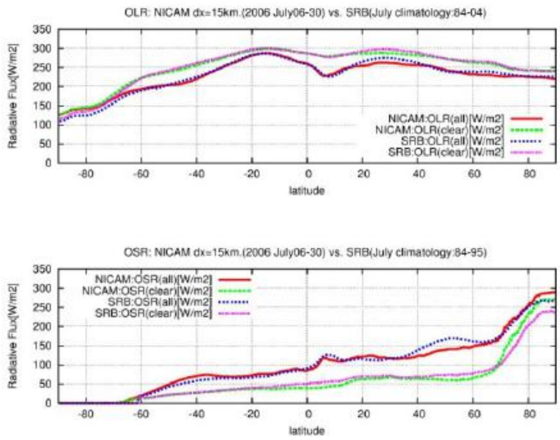

Fig.1. Zonal mean of OLR(all sky and clear sky)[w/m2](top) and OSR(all sky and clear sky)(bottom)[w/m2].Red and green lines are derived by NICAM and blue and purple lines are derived by SRB July climatology data during 1984-2004 for LW and 1984-1995 for SW.

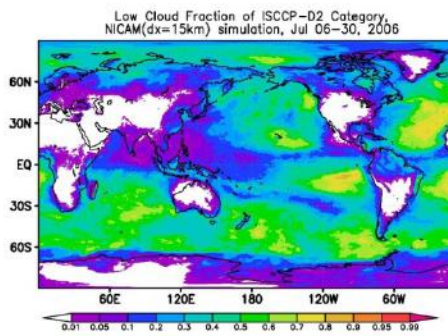

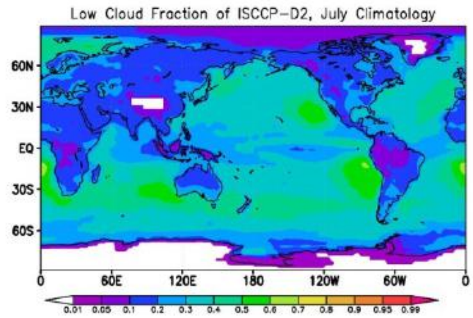

Fig.2. Lower cloud distribution categorized by ISCCP-D series. Top figure is derived by NICAM and bottom one is derived by ISCCP-D2 July climatology data during 1983-2005.

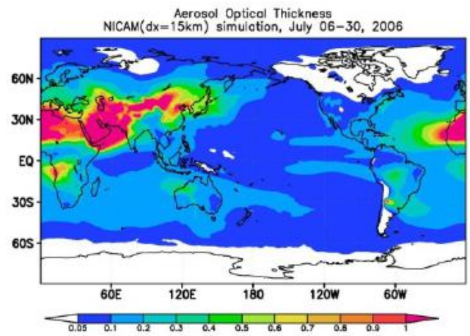

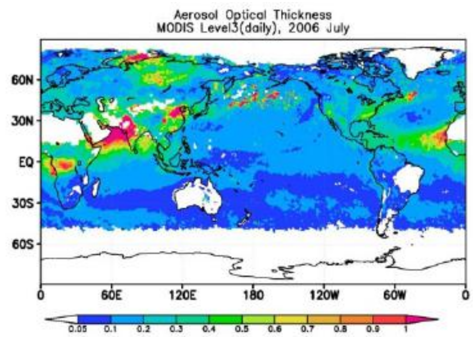

Fig.3. Monthly mean of Aerosol Optical Thickness distribution on 2006 July. Top figure is derived by NICAM and bottom one is derived by MODIS level3 daily products of Terra and Aqua.

NUMERICAL SIMULATIONS OF HESITANT CLOUDS IN THE TWILIGHT ZONE

Tamir G. Reisin[1], Ilan Koren[2], Orit Altaratz[2] and Sabine Wurzler[3]
[1]Soreq Nuclear Research Center, Yavne, Israel
[2]Department of Environmental Sciences, Weizmann Institute, Rehovot, Israel
[3]Nort Rhine, Westphalia State Agency for Nature, Environment and Consumer Protection (LANUV), Recklinghausen, Germany

1. INTRODUCTION

Clouds and aerosol interact and form a complex system leading to high uncertainty in understanding climate processes. To study this non-linear system pixels are commonly distinguished between "cloudy" and “cloud free” and each class is analyzed separately. However, it was found that clouds are surrounded by a ‘‘twilight zone’’ – a transition zone with forming and evaporating cloud fragments and hydrated aerosols (Koren et al., 2007). Among the twilight zone components there are pockets of high humidity that are close to the critical supersaturation (as defined by the Kohler equation). Such pockets are sensitive to small changes in the environmental conditions and can oscillate between growing droplets that form a clear visible cloud to haze (Koren et al., 2008). We define such pockets as hesitant clouds (Fig 1).

In this study we focus on these hesitant clouds. A box model will be used to simulate the transition between the "cloudy" and "cloud free" areas. The model simulates the growth of aerosols through the haze mode to droplets for fluctuating saturation conditions. Since these hesitant clouds can cover big areas and for long times their optical properties are of a great importance. Estimation of the optical properties will be made based on the microphysical box model results.

Figure 1 - Enhanced contrast of forward scattering view of a scatter cumulus cloud reveals the presence of many high humidity pockets with hesitant clouds within the cloud field.

2. MODEL DESCRIPTION

A box model based on the numerical solution of the condensation/evaporation equation was developed.

The change in time of the distribution function *n(m,t)* is of the form (since it is a box model there is no spatial dependence),

$$\left.\frac{\partial n(m,t)}{\partial t}\right|_{cond,evap} = -\frac{\partial}{\partial t}\left[n(m,t)\left(\frac{dm}{dt}\right)_{cond,evap}\right] \quad (1),$$

where the rate of change of drop mass is given by:

$$\left(\frac{dm}{dt}\right)_{cond,evap} = \frac{C(T)}{\rho^{1/3}}\left[m^{1/3}S_{vw} - A\rho^{1/3} + \frac{m^{1/3}Bm_{AP}}{(m-m_{AP})}\right] \quad (2)$$

The haze/drop mass is m, ρ its density and t represents time. S_{vw} is the supersaturation (or subsaturation) defined as e/e_s-1, where e is the vapor pressure and e_s is the saturation vapor pressure ($S_{vw}>0$ – condensation, $S_{vw}<0$ - evaporation). The second term in the square parentheses is the curvature term and the third one is the solute term (for their definitions see e.g. Pruppacher and Klett, 1997). Since we are considering the growth of submicron particles as well, we cannot discard these two terms. m_{AP} is the mass of the aerosol particle in the drop. The function $C(T)$, where T is temperature, is given by (see e.g. Pruppacher and Klett, 1997)

$$C(T) = \left(\frac{48\pi^2}{\rho}\right)^{1/3} \frac{1}{\frac{R_v T}{e_s(T)D_v} + \frac{L}{K_a T}\left(\frac{L}{R_v T} - 1\right)} \quad (3)$$

where R_v is the gas constant for water vapor, L the latent heat for vaporization, D_v the coefficient of diffusion of water vapor in air and K_a the coefficient of thermal conductivity of air.

A drop with mass m_{ki} at time t will have a mass of m_k at time $t+\tau$ (τ the time step), as given by the solution of Eq. (2):

$$m_k = \left\{m_{ki}^{2/3} + \frac{2}{3}\frac{C(T)}{\rho^{1/3}}\left[\int_t^{t+\tau} S_{vw}dt - \tau\left(\frac{A\rho^{1/3}}{m^{1/3}} + \frac{Bm_{AP}}{(m-m_{AP})}\right)\right]\right\}^{3/2} \quad (4)$$

In this solution we assume that τ is short enough so we can neglect the changes of $C(T)$ and of the curvature and solute terms in the time integration.

The calculation of $\int_t^{t+\tau} S_{vw}dt$ follows the approach presented by Tzivion et al. (1989) adapted to include the solute and curvature terms.

$$\int_{t_0}^{t_0+\tau} S_{vw}dt = \frac{(\mathrm{X}(t_0)S_{vw}(t_0) - \mathrm{Y}(t_0))}{\mathrm{X}^2(t_0)}\left[1 - \exp(-\mathrm{X}(t_0)\tau)\right] + \frac{\mathrm{Y}(t_0)}{\mathrm{X}(t_0)}\tau \quad (5)$$

where

$$X(t_0) = D(T)C(T)\int_0^\infty \frac{m^{1/3}n(m,t_0)}{\rho^{1/3}}dm \quad (6)$$

and

$$\mathrm{Y}(t_0) = -D(T)C(T)\left[\int_0^\infty An(m,t_0)dm + \int_0^\infty \frac{Bm^{1/3}m_{AP}}{\rho^{1/3}(m - m_{AP})}n(m,t_0)dm\right] \quad (7)$$

with:

$$D(T) = \frac{1}{q_s(T)}\left[1 + \frac{q_v}{e_s(T)}\frac{\partial e_s(T)}{\partial T}\frac{L}{c_p}\right] \quad (8)$$

where q_v and q_s are the specific humidity and the saturation specific humidity, respectively, and c_p the specific heat at constant pressure.

The haze/drop spectrum is divided into 55 spectral bins with a minimum radius of 0.005 µm, a maximum radius of 330 µm and mass doubling every bin. The integrals in

Eqs. (7) and (8) can now be written as:

$$X(t_0) = D(T)C(T)\bar{\xi}_{1/3}\sum_{i=1}^{I}\frac{\overline{m_i}^{-1/3}N_i(t_0)}{\rho_i^{1/3}} \tag{9}$$

and

$$\mathrm{Y}(t_0) = -D(T)C(T)\left[A\sum_{i=1}^{I}N_i(t_0) + \right. \\ \left. +\bar{\xi}_{1/3}\sum_{i=1}^{I}\frac{B\overline{m_i}^{-1/3}m_{AP}N_i(t_0)}{\rho_i^{1/3}\left(\overline{m_i}-m_{AP}\right)}\right] \tag{10}$$

where $\bar{\xi}_{1/3}$ is a non-dimensional parameter used to represent nonintegral moments of the distribution function with the aid of integral moments (for details see Tzivion et al., 1989), $\overline{m_i}$ represents the average mass in bin *i*, N_i is the number concentration of drops/haze particles in bin *i* and *I* is the total number of bins (55).

A reference time step τ is defined, representing the frequency at which the environmental conditions change (specific humidity in this case). Two additional characteristic time steps are considered, they are calculated as:

$$\tau_{k,ch} = \int_{r_k}^{r_k^*}\frac{dt}{dr}dr \\ = C^*(T)\int_{r_k}^{r_k^*}\frac{\rho}{\dfrac{S_{vw}}{r}-\dfrac{A^*}{r^2}+\dfrac{Br_{AP}^3}{r(r^3-r_{AP}^3)}}dr \tag{11}$$

The expression dr/dt represents the rate of change of drop radius, similar to Eq. (2) ($C^*(T)$ and A^* are proportional to $C(T)$ and A, respectively). Two characteristic times are calculated:

τ_1 - In this case $r_k^* = r_k^{eq.}$; the time required for a drop with radius r_k to reach its radius of equilibrium (calculated from Kholer equation) according to the environmental conditions (temperature and specific humidity).

τ_2 - In this case $r_k^* = r_{k+2}$; we assume that during this time step the changes in the curvature and solute terms can be neglected and Eq. (4) (the solution of Eq. (2)) is valid.

The input parameters required for initializing the calculations are temperature, pressure, relative humidity and a dry aerosol spectrum. This last one was fitted by superimposing three log-normal distributions with different parameters to characterize marine and rural conditions, as in Wurzler (1995). We assume that at the beginning of the simulation the aerosol/haze/drops distribution is at equilibrium, namely, it follows Kholer equation for the given initial relative humidity and temperature. To simulate the fluctuating saturation conditions we modify the specific humidity every time step τ by a random perturbation of a few percentage of its value (both supersaturation and subsaturation conditions can be achieved).

The evolution of the haze/drops spectra is calculated as follows:

1) Calculate S_{vw} from T and q_v.

2) For those bins for which $r_k^{eq.}$ exists

calculate τ_1; if $\tau_1 < \tau$ move the drops in those bins to their corresponding equilibrium radius.

3) For those bins that $\tau_1 > \tau$ or $r_k^{eq.}$ does not exists calculate the shortest τ_2. Using τ_2 calculate the integral of the supersaturation (or subsaturation) (Eq. (5)) and then move the drops in the bins according to Eq. (4).

4) Update T and q_v and S_{vw} due to phase transition (not changes in ambient conditions yet).

5) Repeat steps 3 and 4 until the reference time step τ is reached. Update T and q_v and S_{vw} due to changes in ambient conditions.

6) Repeat from step 2 until the final simulation time is achieved.

3. SUMMARY

A box model was developed that describes the time evolution of aerosol spectra into haze and drops particles due to condensation and evaporation for fluctuating conditions close to saturation.

The haze/drops spectra will be used to infer optical properties of hesitant clouds. A radiation transfer model will be used to estimate changes in fluxes above and below the hesitant cloud based on the haze and drops size distributions.

Sensitivity to the aerosols concentrations and size distributions and their impact on the optical properties of the twilight zone will be presented.

The calculations in this box model will be the base for a future treatment of hesitant clouds in three dimensional models including detailed dynamics.

4. BIBLIOGRAPHY

Koren, I., L.A. Remer, Y.J. Kaufman, and Y. Rudich, 2007: On the twilight zone between clouds and aerosols. *Geophys. Rev. Lett.*, **34**, L08805, doi: 10.1029/2007GL029253.

Koren, I., O. Altaratz, G. Feingold, L.A. Remer, T.G. Reisin, and L. Oreopoulos, 2008: On the contribution of hesitant and small clouds to the twilight zone in a sparse cumulus field. *Proceedings of the 15th Int. Conf. on Clouds and Precip., Cancun, Mexico, ICCP2008.*

Pruppacher, H.R., and J.D. Klett, 1997: Microphysics of Clouds and Precipitation. *Kluwer Acad.*, Norwell, Mass, 1954pp.

Tzivion, S., G. Feingold, and Z. Levin, 1989: The evolution of raindrop spectra: Part II: Collisional Collection/Breakup and Evaporation in a Rainshaft. *J. Atmos. Sci.*, **46**, 3312-3327.

Wurzler, S., 1995: The scavenging and wet deposition of nitrogen compounds by warm convective cloud using two cloud dynamic models. *Ph.D. Thesis*, 160pp. Shaker Verlag Aachen, Berichte aus der Physik, Phys. Dep., Johaness Gutenberg – Univ. Mainz, Mainz, Germany.

Acknowledgments – This research was supported in part by the Israel Science Foundation (grant 1355/06)

THE SHORTWAVE RADIATIVE PROPERTIES OF CLOUD FIELDS DURING GOMACCS AND TC4

S. Schmidt[1], P. Pilewskie[1], G. Feingold[2], H. Jiang[2], S. Platnick[3], G. Wind[3,4]

[1] University of Colorado, Laboratory for Atmospheric and Space Physics, 392 Campus Box, Boulder, CO, 80309, USA

[2] NOAA Earth System Research Laboratory, Chemical Sciences Division, 325 Broadway, Boulder, CO, 80305, USA

[3] NASA Goddard Space Flight Center, Greenbelt, MD, 20771, USA

[4] SSAI, Inc., Lanham, MD, 20706, USA

1. INTRODUCTION

Clouds and aerosols represent a factor of uncertainty in energy budget calculations – not only because their microphysical properties cannot be determined with sufficient accuracy, but also because the radiative transfer calculations may be offset due to spatial inhomogeneities or spectral effects that are not resolved when applying 1-dimensional broadband models. Large inconsistencies between measured and modeled cloud absorption have been extensively discussed in literature. They have broad consequences for the cloud energy budget and the related radiative forcing on the one hand, and remote sensing applications on the other. Among possible explanations for the observed mismatch between measurement and model (still not resolved) are

- cloud spatial variability which increases photon path length and thus the effectiveness of atmospheric absorbers,
- water vapor or other absorbers not properly accounted for, and
- microphysical measurements.

Most of those studies were based on solar broadband measurements and one-dimensional broadband models (for example, Cess et al., 1995).

Since then, considerable progress has been made on the modeling side: various 3D radiative transfer models have been developed, and the spectral resolution was increased. At the same time, 3D dynamic or stochastic cloud models have been established. Also, solar spectral irradiance measurements were introduced (Pilewskie et al., 2003; Wendisch et al., 2001). Only with the spectral information, it is possible to identify reasons for gaps by isolating effects such as water vapor absorption or aerosol effects by wavelength. However, with the ubiquitous cloud spatial variability, consistency of measured and modeled radiation can mostly only be achieved when accounting for 3D structure. Absorption is particularly hard to measure because it requires simultaneous above- and below cloud measurements and is even difficult to obtain when two aircraft are perfectly coordinated (Marshak et al., 1999). Our suggested path to reliable cloud budget or forcing calculations goes through 3D radiative transfer calculations, based on cloud fields from remote sensing or dynamic cloud models, and a validation of the modeled irradiance fields with spectral measurements of the cloud scene.

2. CLOUD RADIATIVE PROPERTIES

The quantities examined here are cloud radiative forcing and cloud absorption and albedo. Albedo is the ratio of upward to downward irradiance, $\alpha = F^{\uparrow}/F^{\downarrow}$. Radiative forcing is generally described as the difference in net irradiance $F_{\text{net}} = F^{\downarrow} - F^{\uparrow}$ which is caused by a perturbation to the atmosphere. For example, cloud radiative forcing is the difference in net irradiance under presence of clouds to clear sky. Forcing can be defined at any level of the atmosphere, but is most often needed at the surface and at the top of the atmosphere (provided by satellites). To relate those two, it is necessary to know atmospheric absorption (including clouds and aerosols). Absorption is defined as the difference between net irradiance on top and at the bottom of an atmospheric layer. Finally, cloud absorption in the near-infrared part of the solar spectrum is related to cloud effective drop (crystal) radius, which is used for remote sensing applications.

3. EXPERIMENTAL SETUP – GOMACCS AND TC4

Recently, the Solar Spectral Flux Radiometer (SSFR) was flown in two missions under completely different premises: the Gulf of Mexico Atmospheric Composition and Climate Study (GoMACCS, August/September 2006), and the Tropical Composition, Cloud and Climate Coupling experiment (TC4, July/August 2007). GoMACCS was conducted in the heavily polluted industrial Houston area, specifically designed to study the transformations that boundary layer clouds may undergo when influenced by aerosol. TC4, in contrast, was dedicated to ice clouds: it was held in Costa Rica to characterize tropical convective cloud systems and their outflow.

A. GOMACCS

During GoMACCS, the SSFR was mounted on a single aircraft, the CIRPAS Twin-Otter, which also carried various instruments for probing cloud and aerosol microphysical and chemical composition. For a number of atmospheric conditions, large eddy simulations (LES) with detailed microphysics and aerosol processing were performed to study polluted boundary layer clouds. They were initialized with an atmospheric profile from Houston University and run until full convection had developed. The cloud microphysical composition was validated with measurements onboard the Twin-Otter.

These cloud fields were used as input to 3D radiative transfer calculations, along with spectral surface albedo, obtained from SSFR measurements (Coddington et al., 2008). Calculations were performed for a number of scenes for 50 wavelengths throughout the spectral range of SSFR (350-2150 nm), and separate runs were made with and without aerosol. Sensitivity studies were performed with respect to surface albedo, aerosol radiative properties, and cloud cover. The combined LES and 3D RT model are compared with up- and downward measured irradiance above and below cloud fields through histograms. Subsequently, absorption and forcing can be derived, supported by the measurements.

B. TC4

During TC4, the SSFR was mounted on two aircraft: the NASA ER-2 and DC-8. The ER-2 served as an A-Train simulator, carrying ample active and passive remote sensing instrumentation, and overflew cloud systems at 20 km altitude. The DC-8 was used to probe clouds in-situ and underfly them for radiation as well as aerosol and trace gas measurements. By means of a ground-based operation center, coordination between the two aircraft could be achieved with a temporal separation of two minutes or less, over legs of two hundred kilometers or more. Using SSFR measurements from both platforms and the MODIS Airborne Simulator (MAS) observations from the ER-2, it is possible to connect MAS retrievals of cloud optical thickness, effective ice crystal radius, and cloud top height with the resulting above- and below-cloud irradiance fields through 3D radiative transfer calculations, as presented by Schmidt et al. (2007) for the CRYSTAL-FACE experiment. In this case, absorption could also be derived directly from measurements of flux divergence.

4. RESULTS

A. GOMACCS

In a first step, the microphysical cloud properties of the LES cloud fields were compared with the Twin-Otter aircraft measurements through histograms of measured and modeled liquid water content (LWC), effective radius (R_{eff}), and cloud drop number (N_d) for each flight. In a second step, those fields were used as input to the 3D Monte-Carlo model MYSTIC (Monte Carlo code for the physically correct tracing of photons in cloudy atmospheres; Mayer, 1999), with 50 wavelengths ranging from 400 to 2120 nm (on a cluster with 10^8 to 10^9 photons per wavelength). Optionally, horizontal photon transport was switched off (i.e. running the model in independent column mode). This showed immediately the need of full 3D calculations because for overcast sky, slightly oblique sun (solar zenith angle 28 degrees), and absorbing aerosols, independent columns do not reproduce the observed irradiance field. Aerosol extinction was also obtained through the LES model, as 3D field. Aerosol single scattering albedo and asymmetry parameter were taken from retrievals of the Houston station of AERONET (Aerosol Robotic Network), and from in-situ measurements at the same location.

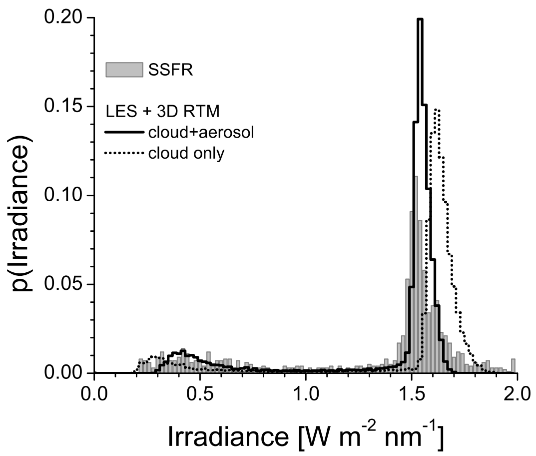

Fig. 1. Histogram of modeled and measured downward irradiance below clouds for September 15, 2006, at 500 nm.

Figure 1 shows the modeled and measured downward irradiance below a cloud layer with 10-15% cloud cover at 500 m altitude and 500 nm wavelength, for a flight on September 15, 2006. The gray bars indicate the measurements; the wide peak at 0.4 W m^{-2} nm^{-1} is related to below-cloud measurements where the direct beam is blocked by the cloud and only diffuse radiation is measured. The second peak at 1.5 W m^{-2} nm^{-1} originates from measurements below cloud gaps where direct and diffuse radiation are measured, sometimes enhanced by extra diffuse radiation from cloud edge scattering. The relative height of the two peaks reflects the magnitude of fractional cloud cover, which can be derived from the area under the below-cloud peak, divided by the total area. The cloud cover thus derived from the calculations (solid line: cloud and aerosol, dotted line: cloud only) is in good agreement with the cloud cover calculated directly from the LES field. The measured cloud cover is sometimes above the LES counterpart, especially later in the day, when processes on synoptic scale have an increasing impact on the Houston weather. With the histogram approach, it is still possible to compare irradiance under the individual peaks even though the mean values would differ due to differing cloud cover. Naturally, the presence of aerosol decreases the downward irradiance. At the same time, the diffuse irradiance below clouds is increased, because more radiation is scattered from the direction of the directly transmitted irradiance into multiple downward directions below clouds. With increasing aerosol absorption (decreasing aerosol single scattering albedo), both peaks are shifted to lower positions. Agreement between model and measurement is only obtained if aerosol is included in the calculations and best agreement occurred using aerosol optical properties from AERONET, rather than the in-situ measurements, probably because they are representative of the whole atmospheric column.

Figure 2 shows the location of the two peaks from Fig. 1; the lower spectrum (gray line) shows the measured downward irradiance below clouds, the upper one (black line) the same under cloud gaps. A comparison with model runs confirms the results from Fig. 1 for other wavelengths as well, in so far as the best measurement-model agreement is achieved only when including the aerosols. The

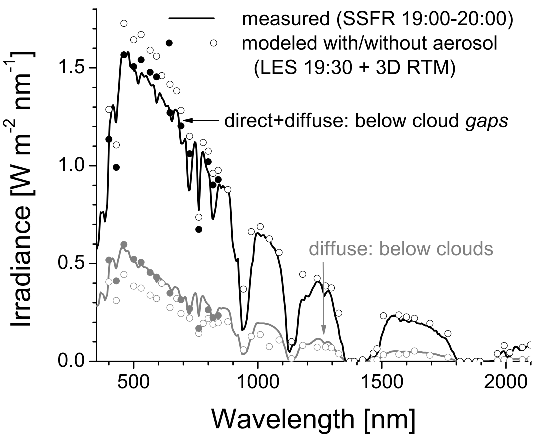

Fig. 2. Mean measured and modeled downward irradiance below clouds (lower spectrum) and below cloud gaps (upper spectrum), including and excluding the aerosol.

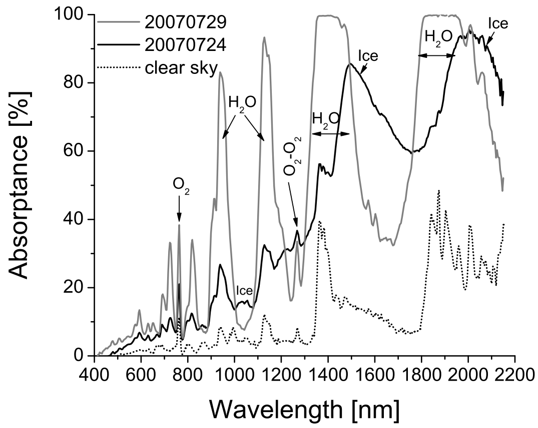

Fig. 3. Spectral absorptance for a water cloud (grey line), an ice cloud (black line), and clear sky (dotted line).

model-based spectral absorption (not shown) is 5-10% in the visible range, mostly caused by aerosols. The total absorption within the SSFR wavelength range is 158 W m^{-2}) for the aerosol-cloud field ; clouds without aerosol absorb 129 W m^{-2}. Thus aerosols increase the total absorption by about 20%.

B. TC4

The TC4 experiment provided the unique opportunity of coordinated irradiance measurements onboard the NASA ER-2 and DC-8, enabling a direct measurement of spectral absorption. Figure 3 shows the percentage of spectral absorption for a water cloud, an ice cloud, and a clear sky column, where the absorbed irradiance has been divided by the incident irradiance at ER-2 level (representing top of the atmosphere). Highest relative absorption occurs in the near-infrared with contributions from water vapor, ice, and liquid water. For the shown water cloud, 50% of the absolute absorption (266 W m^{-2}) occurs at wavelengths below 1100 nm; for the ice cloud (absolute absorption: 188 W m^{-2}) the 50% demarcation is at 1400 nm, indicating that for the ice clouds, much more radiation is absorbed by condensed water and at higher altitude. The non-zero absorption in the visible range is caused by 3D effects (see explanations for Fig. 5).

For TC4, the input cloud fields are created from MAS retrievals (2D fields of optical thickness and effective radius). Since they only provide cloud top height, the geometrical thickness was assumed to be constant (1 km). In the future, radar and lidar soundings will complement this information. Since the MAS observations occurred simultaneously with the SSFR measurements on both ER-2 and DC-8,

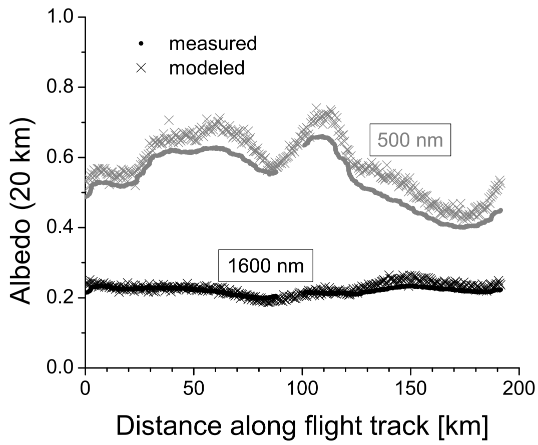

Fig. 4. Measured and modeled albedo at ER-2 altitude (20 km), for 500 and 1600 nm wavelength.

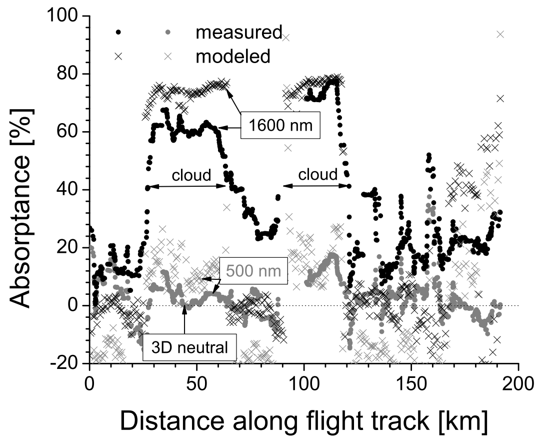

Fig. 5. Measured and modeled absorptance along a flight

the results of the concurring radiative transfer calculations can be compared directly with the measurements (not through histograms), which has been done for albedo in Fig. 4: Shown are the measured and modeled cloud albedo for a leg on July 17, 2007, at 20 km altitude, for 500 nm and 1600 nm wavelength. The SSFR measurements from the ER-2 are thus consistent with the MAS retrievals. A more difficult problem is to derive cloud absorption, from the net irradiance difference between the collocated ER-2 and DC-8 (flight altitude about 10 km).

Figure 5 shows this difference along the coordinated flight leg, for 500 and 1600 nm. Measured values are full symbols, modeled are crosses. Around 50 and 100 km flight distance, a thick cloud was present between the DC-8 and the ER-2. At 500 nm, no cloud absorption occurs. However, both measured and modeled absorption deviate from zero in both directions, which is caused by horizontal photon transport. Strictly speaking, absorption is obtained from flux convergence; the difference of net irradiance on cloud top and bottom is only the vertical component. If it is below-zero this simply means that the horizontal component of flux divergence is non-zero. A region where the 500 nm flux convergence is near-zero is ”3D neutral”, i.e. there is no horizontal photon transport. If aerosols are present (not during most TC4 cases), this definition (Ackerman and Cox, 1981) cannot be applied. In the flight segments with thick clouds present, both modeled and measured absorption at 500 nm follow the same pattern; in the other flight segments with thinner clouds (e.g., after 120 km), vertical cloud structure becomes more important, and the model-measurement agreement deteriorates. At 1600 nm, ice absorbs; for this case, the modeled cloud absorption is above the measurements. The reason is that for large parts of this case, the DC-8 was actually still within the cloud, not below – therefore, ER-2 and DC-8 did not comprise the whole cloud column and thus not the full absorption. In the future, cloud radar images from ER-2 and DC-8 may help improving the vertical cloud structure.

5. CONCLUSIONS

We have shown for two different cloud experiments how spectral irradiance measurements, an LES model, 2D cloud retrievals, and 3D radiative transfer calculations can work together to obtain measurement-supported radiative cloud properties such as spectral absorption. With this technique, it is possible to distinguish the contribution of, e.g., aerosols, water vapor, ice, to the measured and modeled energy budget, and to identify and correct for 3D radiative effects. As cloud input, an LES model and MAS retrievals have been used, and validated with the irradiance measurements. For GoMACCS, we found that the measurements can only be reproduced when including aerosol in the radiative transfer calculations. In this way, the model-based radiative properties are supported by the measurements, and can be extrapolated to, e.g., other solar zenith angles, later on.

6. REFERENCES

Ackerman, S. A., Cox, S. K., 1981: Aircraft observations of the shortwave fractional absorptance of nonhomogeneous clouds. *J. Appl. Meteor.*, **20**, 1510–1515.

Cess, R. D., Zhang, M. H., Minnis, P., Corsetti, L., Dutton, E. G., Forgan, B. W., Garber, D. P., Gates, W. L., Hack, J. J., Harrison, E. F., Jing, X., Kiehi, J. T., Long, C. N., Morcrette, J.-J., Potter ,G. L., Ramanathan, V., Subasilar, B., Whitlock, C. H., Young, D. F. and Zhou, Y., 1995: Absorption of Solar Radiation by Clouds: Observations Versus Models. *Science,* **267,** 496–499.

Coddington, O. Schmidt, K. S., Pilewskie, P., Gore, W., Bergstrom, R. W., Roman, M., Redemann, J., Russell, P. B., Liu, J., and Schaaf, C. C., 2008: Aircraft measurements of spectral surface albedo and its consistency with ground-based and space-borne observations. *Submitted to J. Geophys. Res.*

Marshak, A., Wiscombe, W., Davis, A., Oreopoulos, L., Cahalan, R., 1999: On the removal of the effect of horizontal fluxes in two-aircraft measurements of cloud absorption. *Quart. J. Roy. Meteor. Soc.*, **125**, 2153–2170.

Mayer, B., 1999: 'I3RC phase 1 results from the MYSTIC Monte Carlo model'. Proceedings of the I3RC workshop, Tucson, Arizona, USA

Pilewskie, P., Pommier, J., Bergstrom, R., Gore, W., Howard, S., Rabbette, M. Schmid, B. Hobbs, P. V., Tsay, S. C., 2003: Solar spectral radiative forcing during the Southern African Regional Science Initiative, *J. Geophys. Res.*, **108**(D13), 8486.

Schmidt, K. S., Pilewskie, P., Platnick, S., Wind, G., Yang, P.,and Wendisch, M., 2007: Comparing irradiance fields derived from Moderate Resolution Imaging Spectroradiometer airborne simulator cirrus cloud retrievals with solar spectral flux radiometer measurements, *J. Geophys. Res.,* **112**, D24206.

Wendisch, M., Müller, D., and Schell, D., 2001: An airborne spectral albedometer with active horizontal stabilization. *J. Atmos. Oceanic Technol.,* **18,** 1856–1866.

THE ROLE OF THE GLOBAL ELECTRIC CIRCUIT
IN FORCING OF CLOUDS AND CLIMATE

Brian A. Tinsley, Tinsley@UTDallas.edu
University of Texas at Dallas

1. OBSERVED ATMOSPHERIC RESPONSES TO Jz CHANGES

When winter cyclonic storms (and hurricanes) intensify they concentrate vorticity by drawing in low levels of vorticity from the surrounding regions. In the case of winter cyclones, the low level vorticity is present in the baroclinic winter circulation, which is concentrated by the baroclinic instability, with a reduction of surface pressure near the storm center. The vorticity area index (VAI) was defined by Roberts and Olsen (1973) and is an objective measure of storm intensity in terms of the area (in units of 10^5 km^2) of the atmosphere at a defined pressure level (typically 500 hPa) where the absolute vorticity is above a certain threshold. The area of increased vorticity near storm center is thus isolated by the threshold vorticity from the surrounding areas where there was little change or a decrease.

Wilcox et al. (1973) found reductions in the VAI (reduced intensities of cyclones) for a few days at times of solar wind magnetic sector boundary crossings, in the northern hemisphere in winters 1964-1970, following the Agung volcanic eruption. (The events are now called HCS crossings, for heliospheric current sheet crossings). The effect was subsequently confirmed with new crossings by Hines and Halevy (1977) and with an especially sensitive analysis by Larson and Kelly (1977). Tinsley et al. (1994) and Kirkland et al. (1996) related these VAI decreases to decreases of the precipitation of relativistic electrons into the stratosphere, affecting the current flow in the global electric circuit, for periods of a few days that included the times of the crossings. However, they showed that the effect was present only during years of high stratospheric aerosol loading, and was strong again (1983-86) after the El Chicon eruption, and (1992-96) after the Pinatubo eruption. The effect on the global circuit was a reduction in the downward ionosphere – surface (ocean and land) current density, (J_z), observed in balloon and ground–based atmospheric electricity observations (Tinsley et al., 1994), consistent with a global circuit model (Tinsley and Zhou 2006). The figure below is a compilation of data on these events for the three epochs of stratospheric volcanic aerosols and the relation to solar wind speed and relativistic electron flux.

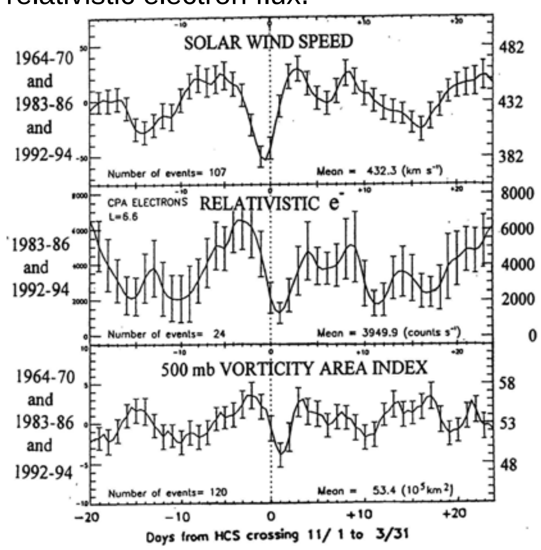

VAI response to solar wind, relativistic electron flux, and J_z decreases (Kirkland, et al., 1996).

Other responses to these events include changes in cloud cover (Kniveton and Tinsley, 2004) for the Pinatubo stratospheric aerosol era; changes in atmospheric transmission (Roldugin and Tinsley, 2004) for the El Chicon volcanic era; and changes in 500 hPa temperature (Misumi, 1983) for the Agung volcanic era. For each of these eras, winter vorticity decreases associated with relativistic electron flux changes or sector boundary crossings were found (Kirkland et al., 1996).

Similar VAI responses to short-term decreases in the galactic cosmic ray (GCR) flux, called Forbush decreases, were first apparent as correlations of surface pressure in winter storms with magnetic storms, since data on these was available since the beginning of the 20th century (see Duell and Duell, 1948, McDonald and Roberts, 1960 and their references to earlier work). Objections that magnetic storms might be influenced by the dynamics of winter storms led to the suggestion that solar wind sector boundary crossings be used as totally independent markers for solar wind changes (Markson, 1971). Also, responses of winter storm intensity were made more objective by being characterized by the VAI, first defined by Roberts and Olson (1973), which led to the discovery of the stronger but intermittent Wilcox effect (Wilcox et al., 1973), but this unfortunately distracted attention from the more reliable correlations with magnetic activity, which in turn generated skepticism about the reality of all sun-weather effects when the Wilcox effect disappeared (Williams and Gerety, 1978).

Time series of the VAI were published (Olson et al., 1977, 1979) and enabled Padgoankar and Arora (1981) to re-examine the winter VAI response to magnetic storms. They found that the VAI response persisted in eras when the Wilcox effect at sector boundary crossings was not present. Magnetic storms usually follow solar flares and are usually accompany by Forbush decreases, and work by Tinsley et al. (1989) and Tinsley and Deen (1991) showed that the clearest VAI response for winter storms was that associated with Forbush decreases. These produce J_z decreases at middle and high latitudes by changes in tropospheric ionization, and thus the J_z change is independent of stratospheric volcanic aerosols, as shown by theory (Tzur et al., 1983; Sapkota and Varshneya, 1990) and observations (Märcz, 1990). We now call this association the Roberts effect, as illustrated below, for (a) a set of larger Forbush decreases, and (b) a set of smaller Forbush decreases. Other responses to Forbush decreases have been observed at high latitudes and in the polar caps in the form of changes in high altitude cloud cover (Pudovkin and Veretenenko, 1995; Todd and Kniveton, 2001) and changes in atmospheric temperature and pressure (Egorova et al., 2000).

Vorticity Area Index Decreases with Forbush Decreases and Jz Decreases

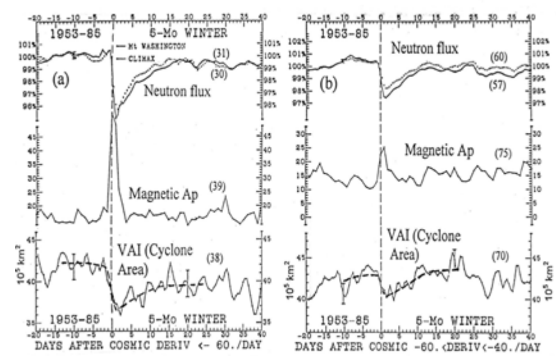

Superposed epoch variations of GCR flux, Ap index, and 500 hPa northern hemisphere Vorticity Area Index, with key days onsets of Forbush decreases (and Jz decreases), November through March (Tinsley and Deen, 1991)

Responses to solar proton events (also known as SEP events) that are associated with J_z increases at high latitudes have been found in terms of pressure increases at 500 hPa centered on the north magnetic pole by Schuurmans (1965), and vorticity increases near Greenland by Veretenenko and Thejll (2004, 2005), as illustrated below. The pressure and vorticity increases were for about a day. Theory (Tzur et al., 1983) and observation (Kokorowski et al. 2006) show J_z increases at these times at high magnetic latitudes. The vorticity increase with the J_z increase makes a consistent pattern with the vorticity decreases associated with the J_z decreases of the Wilcox and Roberts effects.

Vorticity Increases with Solar Energetic Particles and Jz

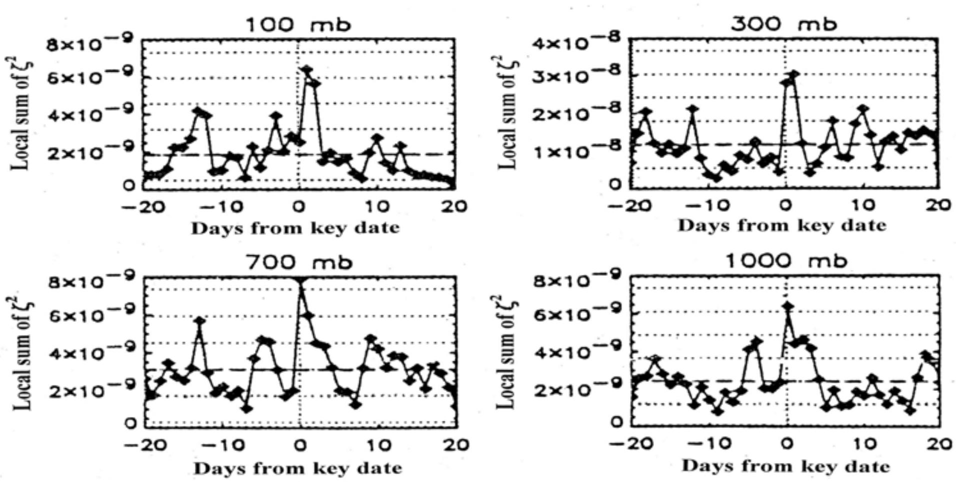

Variation of the squared vorticity (in s^{-2}) in North Atlantic region 50°-70° N, 0°-40°W, associated with the energetic SEP events. Dashed line is the mean level, and dotted lines are 1, 2, 3 etc. standard deviations from it.

From Veretenenko and Thejll, *J. Atmos. Solar Terr. Phys., 66*, 393, 2004

Responses to the north-south component of the solar wind electric field in the Antarctic and Arctic polar caps have been found in terms of surface pressure changes, which are evidently due to changes in the strength of the polar vortices in each case. (Mansurov et al., 1974; Tinsley and Heelis, 1993; Burns et al., 2007, 2008). The north-south solar wind electric field is generated by the cross product of the solar wind speed and the east-west solar wind magnetic field (V_x **×** B_y), which produces opposite changes in the vertically downward electric field in the northern as compared to the southern magnetic polar caps. These produce opposite changes in the vertical current density, J_z, and in the measured vertical electric fields at the surface. Burns et al. (2007, 2008) analyzed five years of surface pressure variations from seven Arctic stations and eleven Antarctic stations with respect to the solar wind B_y parameter, and found pressure changes in both hemispheres proportional to the B_y change, that were opposite in the two hemispheres, consistent with the opposite Jz changes. These are illustrated below.

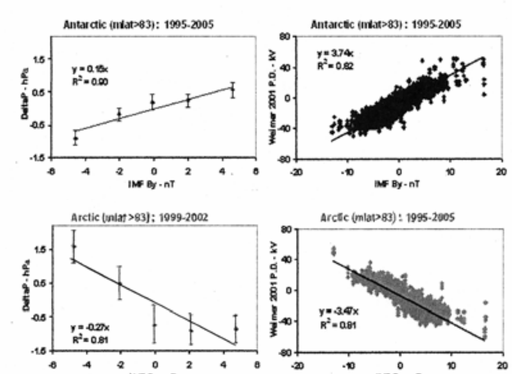

Left: pressure responses to B_y for the Antarctic and Arctic; Right: changes in overhead ionospheric potential from the Weimer (2001) empirical fit to satellite observations. (Burns et al (2008)

Responses to day-to-day changes in the output of the internal convective cloud generators in the global circuit have been found in terms of changes in surface pressure, at the same stations in the Arctic and Antarctic as for the external forcing. Measurements of the surface electric field, E_z, at Vostok in Antarctica, corrected for the external input (which is several times smaller in amplitude and which changes on a time scale several times longer) are used as a proxy for the internal changes, reflected in J_z changes worldwide. The figure on the right compares responses for 7 coastal Antarctic stations and 7 Arctic stations. The abscissa is the change in E_z from a 27-day running mean, and the ordinate is the change in surface pressure from a 27-day running mean. The similarity of the responses in the two hemispheres (both positive correlations, as compared to the opposite correlations of the external forcing) justifies the use of the 'constructed' Vostok E_z as representing

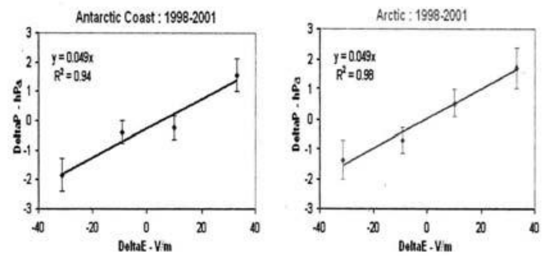

the day-to-day changes in the internal generators, the ionospheric potential V_i, and J_z worldwide. The figure below compares the pressure responses to external and internal V_i forcing. The values of B_y for the external input are converted to V_i values using the empirical relationship between B_y and V_i at Vostok from Weimer (2001), and the changes in 'constructed' E_z are converted to V_i changes using the globally representative average value of the ionospheric potential V_i of 250 kV.

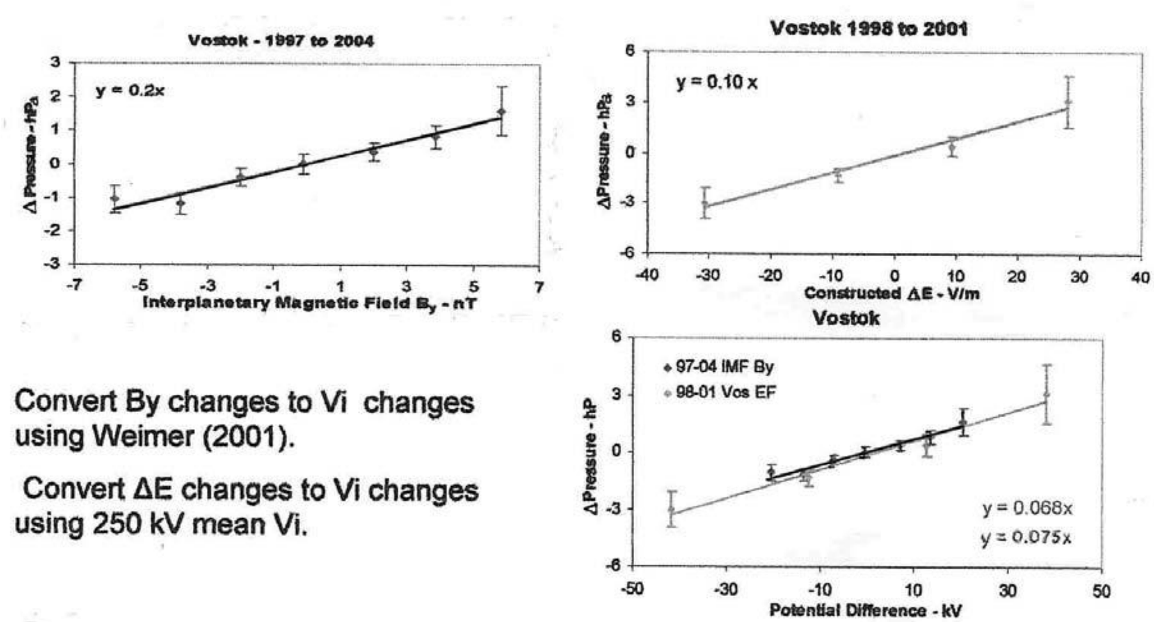

The lower right panel shows that the pressure sensitivity (hPa/kV) is essentially the same for both the internal and external forcing in the polar caps, consistent with a single mechanism being responsible for both.

2. CONCEPTUAL MODEL

All the above observations of atmospheric dynamics, temperature, and cloud cover correlating with the downward current density J_z can be understood in terms of a conceptual model in which the flow of J_z through layer clouds deposits charge in the conductivity gradients at the tops and bases of layer clouds, with positive charge at cloud tops and negative charge at cloud base, in accordance with Gauss's Law. The conductivity gradients are due to the gradients in droplet concentration and in absolute humidity. The deposition of such charge on aerosol particles, including ice forming nuclei (IFN) and cloud condensation nuclei (CCN) has been modeled by Zhou and Tinsley (2007), in agreement with the measurements of Beard et al., (2004). The charge affects the rate at which these and other aerosol particles are scavenged by cloud droplets (Tinsley et al. 2000, 2001, 2006). For cold clouds the result is an increase in contact ice nucleation and precipitation rates. For warm and cold clouds the result is increased scavenging of large CCN and IFN and decreases in the phoretic and Brownian scavenging of small CCN, with a narrowing of the size distribution and increase in small CCN concentration, with similar effects on the droplet size distribution and concentration in later cloud formation. This is likely to reduce precipitation and increase cloud lifetime (Albrecht effect) as discussed by Tinsley (2004) and Tinsley et al. (2006). The main uncertainty in the conceptual model is whether these changes are large enough to produce the observed effects.

The figure on the next page summarizes the model in which the four external (B, C, D, E) and one internal input (A) all change J_z which changes the amount of charge at cloud boundaries, with further consequences depending on the cloud thickness and whether the cloud tops are colder than freezing. In the latter case contact ice nucleation and precipitation are initiated. For thin clouds, changes in the concentration of CCN and IFN can affect droplet size distributions and cloud lifetime and cloud cover.

Our conceptual model suggests that for winter cyclones the vorticity increases (decreases) with increased (decreased) J_z are due to enhanced (decreased) contact ice nucleation and precipitation in the layer clouds in the warm front sector, at the time when the wedge of warm front air lifts the layer clouds to just above the 0ºC level. In the temperature range 0ºC to -15ºC contact ice nucleation appears to be more effective than other ice nucleation processes in initiating precipitation (Tinsley et al. 2001). So the latent heat redistribution, due to enhanced precipitation, increases the vertical motions that lead to enhanced vorticity extracted from the baroclinic instability in the storm. This can also be amplified

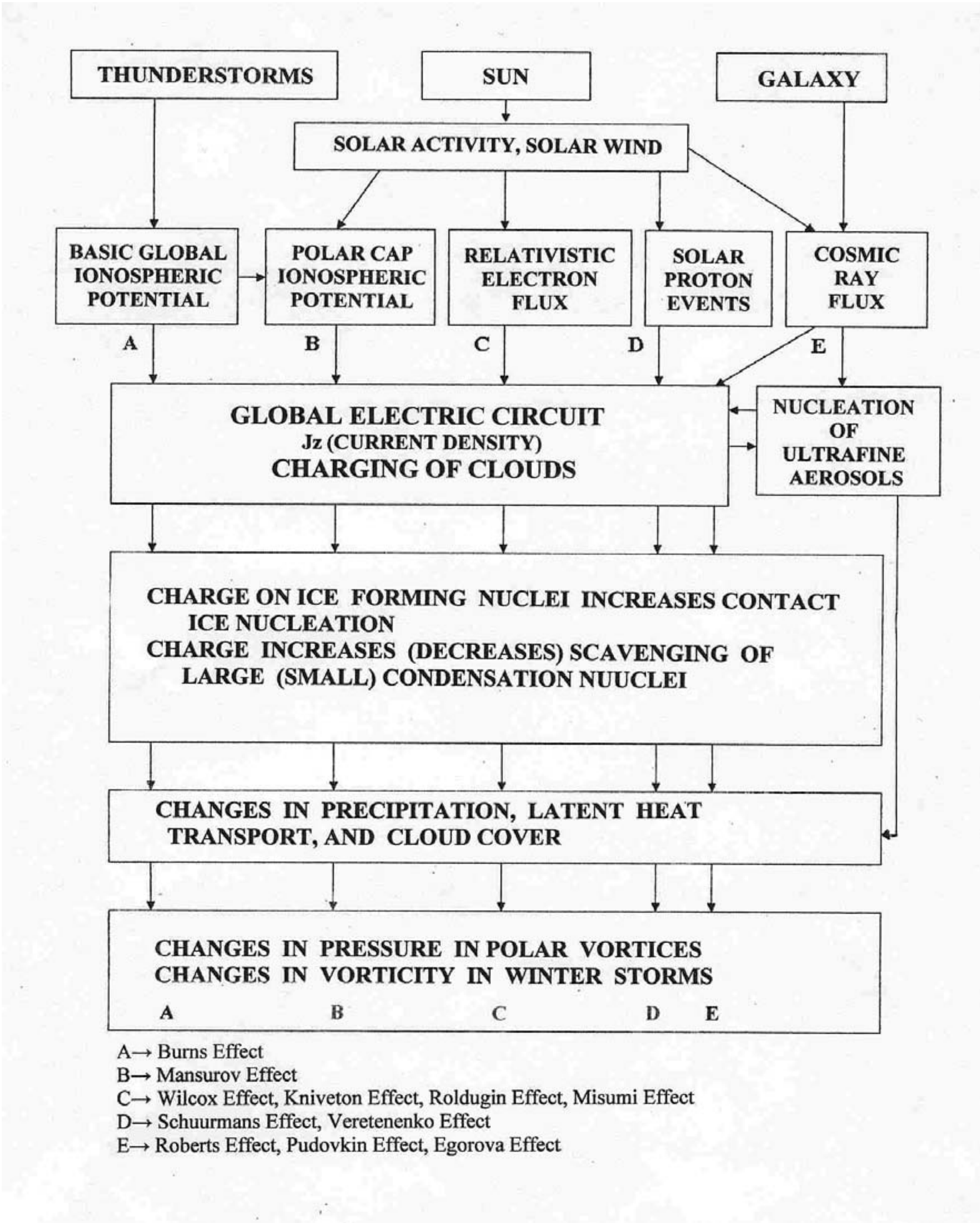

by positive feedback. An alternative explanation for vorticity changes (Veretenenko and Thejll, 2004, 2005) is that latitude gradients in the forcing by relativistic electrons, Forbush decreases of cosmic rays, and solar protons extend over the cyclogenesis regions, and that latitude-dependent gradients in cloud cover and atmospheric radiative effects appear across the polar fronts, changing the baroclinic gradients and thus the resulting cyclone vorticity. It should be possible to investigate the relative contributions from both the latent heat mechanism and the radiative mechanism with suitable adjustments to cloud cover and precipitation efficiency in winter cyclone models.

For the observed pressure changes in the polar regions, the role of thin, high clouds, where the optical thickness to visible and infrared absorption depends sensitively on droplet size distribution, cloud lifetime and cloud cover, may be relevant. Direct observations noted earlier show changes in cloud cover associated with J_z changes. The change in the amounts of incoming shortwave radiation, and longwave radiation radiated back to the surface will have consequences for tropospheric heating and cooling that causes changes in atmospheric dynamics that are reflected in surface pressure changes associated with change in the polar vortices.

The cosmic ray flux variations produce tropospheric ionization and J_z changes on time scales from decades to millennia, as well as on the day-to-day timescales discussed above. The solar irradiance mechanisms cannot explain the day-to-day correlations. The J_z/cloud processes are all applicable to the longer time scales, and it has not yet been demonstrated that the irradiance mechanisms are required for the longer term climate changes that correlate with changes in cosmic ray flux and solar activity. Mechanisms involving J_z are sufficient as an explanation for these.

3. BIBLIOGRAPHY

Beard, K. V., H. T. Ochs III, and C. H. Twohy (2004), Aircraft measurements of high average charges on cloud drops in layer clouds, *Geophys. Res. Lett., 31*, L14111.

Burns, G. B., B. A. Tinsley, A. V. Frank-Kamenetsky and E. A. Bering (2007), Interplanetary magnetic field and atmospheric electric circuit influences on ground-level pressure at Vostok, *J. Geophys. Res., 112*, D04103, 1-10.

Burns, G. B., B. A. Tinsley, W. J. R. French, O.A. Troshichev and A. V. Frank-Kamenetsky (2008), Atmospheric circuit influences on ground-level pressure in the Antarctic and Arctic, in press, *J. Geophys. Res.*

Duell, B., and G. Duell, The behavior of barometric pressure during and after solar particle invasions and solar ultraviolet invasions, *Smithsonian Miscellaneous Collections, 110*, no. 8, Smithsonian Institution, Washington, DC.

Egorova, L. V., V.Ya. Vovk, O.A. Troshichev (2000), Influence of variations of the cosmic rays on atmospheric pressure and temperature in the Southern geomagnetic pole region, *J. Atmos. Solar Terr. Phys., 62*, 955-966.

Hines, J. R., and I. Halevy (1977), On the reality and nature of a certain sun-weather correlation, *J. Atmos. Sci., 34,* 382-404.

Kirkland, M. W., B. A. Tinsley and J. T. Hoeksema (1996), Are stratospheric aerosols the missing link between tropospheric vorticity and Earth transits of the heliospheric current sheet?, *J. Geophys. Res., 101*(D23), 29,689-29699.

Kniveton, D. R., and B. A. Tinsley (2004), Daily changes in global cloud cover and Earth transits of the heliospheric current sheet, *J. Geophys. Res., 109*, D11201.

Kokorowski, M. et al. (2006), Rapid fluctuations s of stratospheric electric field following a solar energetic particle event, *Geophys. Res. Lett., 33*, L20105.

Larsen, M. F., and M. C. Kelley (1977), A study of an observed and forecasted meteorological index and its relation to the interplanetary magnetic field, *Geophys. Res. Lett., 4*, 337-340.

Macdonald, N. J., and W. O. Roberts (1960), Further evidence of a solar corpuscular influence on large-scale circulation at 300 mb., *J. Geophys. Res., 65*, 529-534.
Mansurov, S. M., L. G. Mansurova, G. S. Mansurov, V. V. Mikhenvich, A.M. Visotsky (1974), North-south asymmetry of geomagnetic and tropospheric events, *J. Atmos. Terr. Phys., 36*, 1957-1962.
Märcz, F. (1997), Short term changes in atmospheric electricity associated with Forbush decreases, *J. Atmos. Solar Terr. Phys., 59*, 975-982.
Markson, R., (1971), Considerations regarding solar and lunar modulation of geophysical parameters, atmospheric electricity, and thunderstorms, *Pure and Appl. Geophys., 84*, 161-200.
Misumi, Y. (1983), The tropospheric response to the passage of solar sector boundaries, *J. Meteorol. Soc. Japan, 61*, 686-694, 1983.
Olson, R. H., W. O. Roberts and E. Gerety (1977), Vorticity area index 1946 -1976, p. 83 -114, in *Solar Terrestrial Physics and Meteorology*, Working Document - II, Report by World Data Center A, NOAA, ed. A. H. Shapley and H. W. Kroel, SCOSTEP, Nat. Acad. Sci., Washington, DC.
Olson R. H., W. O. Roberts and E. Gerety, (1979), Vorticity area index 1976-1978, p. 86 -88, in *Solar Terrestrial Physics and Meteorology*: Working Document - III, Report by World Data Center A, NOAA, ed. A. H. Shapley, C. D. Ellyett and H. W. Kroel, SCOSTEP, Nat. Acad. Sci., Washington, DC.
Padgoankar, A. D., and B. R. Arora, (1981), Tropospheric vorticity responses to the solar magnetic sector structure and geomagnetic disturbances, *Pure and Appl. Geophys., 119*, 893-900.
Pudovkin, M. I., and S. V. Veretenenko (1995), Cloudiness decreases associated with Forbush-decreases of galactic cosmic rays, *J. Atmos. Solar Terr. Phys., 57*, 1349-1355.
Roberts, W. O., and R. H. Olson (1973)Geomagnetic storms and wintertime 300-mb trough development in the North Pacific – North America area, *J. Atmos. Sci., 30*, 135-140.
Roldugin, V. C., and B. A. Tinsley (2004), Atmospheric transparency changes associated with solar wind-induced atmospheric electricity variations, *J. Atmos. Solar Terr. Phys., 66*, 1143-1149.
Sapkota, B. K., and N. C. Varshneya (1990), On the global atmospheric electric circuit, *J. Atmos. Sol. Terr. Phys., 50*, 1-20.
Schuurmans, C. J. E. (1965), Influence of solar flare particles on the general circulation of the atmosphere, *Nature, 205*, 167-168.
Tinsley, B. A., (2004), Scavenging of condensation nuclei in clouds: Dependence of sign of electroscavenging effects on droplet and CCN sizes, presented at the 14th ICCP, Bologna, Italy,18-23July, 2004.
Tinsley, B. A., and G. W. Deen (1991), Apparent tropospheric response to MeV-GeV particle flux variations, a connection via electrofreezing of supercooled water in high level clouds?, *J. Geophys. Res., 96*, 2283-2296.
Tinsley, B. A., and R. A. Heelis (1993), Correlations of atmospheric dynamics with solar activity; evidence for a connection via the solar wind, atmospheric electricity, and cloud microphysics, *J. Geophys. Res., 98*(D6), 10375-10384.
Tinsley, B. A., and L. Zhou (2006), Initial results of a global circuit model with stratospheric and tropospheric aerosols, *J. Geophys. Res. 111*, D16205.
Tinsley, B. A., G. M. Brown and P. H. Scherrer (1989), Solar variability influences on weather and climate: possible connections through cosmic

ray fluxes and storm intensification, *J. Geophys. Res., 94*(D12), 14,783-14,792.

Tinsley, B. A., J. T. Hoeksema and D. N. Baker (1994), Stratospheric volcanic aerosols and changes in air-earth current density at solar wind magnetic sector boundaries as conditions for the Wilcox tropospheric vorticity effect, *J. Geophys. Res., 99*, 16,805 – 16,813.

Tinsley, B. A., R. P. Rohrbaugh, M. Hei and K. V. Beard (2000), Effects of image charges on the scavenging of aerosol particles by cloud droplets and on droplet charging and possible ice nucleation processes, *J. Atmos. Sci., 57*, 2118-2134.

Tinsley, B. A., R. P. Rohrbaugh, and M. Hei (2001), Electroscavenging in clouds with broad droplet size distributions and weak electrification, *Atmos. Res., 59-60*, 115-136.

Tinsley, B. A., L. Zhou, and A. Plemmons (2006), Changes in scavenging of particles by droplets due to weak electrification in clouds, *Atmospheric Res., 79*, 266-295.

Todd, M. C., and D. R. Kniveton (2001), Changes in cloud cover associated with Forbush decreases of galactic cosmic rays, *J. Geophys. Res., 106*, 32,031 - 32,042.

Tzur, I., R. G. Roble, H. C. Zhuang and G. C. Reid (1983), The response of the Earth's global electric circuit to a solar proton event, p. 427-435 in *Weather and Climate Responses to Solar Variations,* ed. B. M. McCormac, Colo. Assoc. Univ. Press, Boulder, USA.

Veretenenko, S., and P. Thejll (2004), Effects of energetic solar protons events on the cyclone development in the North Atlantic, *J. Atmos. Solar Terr. Phys., 66*, 393-405.

Veretenenko, S., and P. Thejll (2005), Cyclone regeneration in the North Atlantic intensified by energetic solar proton events, *Adv. Space Res., 35*, 470-475.

Weimer, D. R. (2001), An improved model of ionospheric electric potentials including substorm perturbations and application to the Geospace Environment Modeling November 24, 1996, event, *J. Geophys. Res., 106*(A1), 407-416.

Wilcox, J. M., P. H. Scherrer, L. Svalgaard, W. O. Roberts and R. H. Olson (1973), Solar magnetic structure: relation to circulation of the Earth's atmosphere, *Science, 180*, 185-186.

Williams, R. G. and E. J. Gerety (1978), Does the troposphere respond to day-to-day changes in solar magnetic field? *Nature, 275*, 200-201.

Zhou, L., and B. A. Tinsley (2007), The production of space charge at the boundaries of layer clouds, *J. Geophys. Res.,112*, D11203.

Acknowledgements. This work has been supported by the US National Science Foundation grant ATM0242827 to the University of Texas at Dallas.

FREEZING OF SUPERCOOLED SULPHURIC ACID PARTICLES IN THE AEROSOL CHAMBER AIDA

S. Benz, H. Bunz, T. Leisner, O. Möhler, H. Saathoff, M. Schnaiter, and R. Wagner

Forschungszentrum Karlsruhe, Institute for Meteorology and Climate Research,
POB 3640, D-76021 Karlsruhe

1. INTRODUCTION

Cirrus clouds in the upper troposphere can be formed by homogeneous freezing of supercooled liquid aerosol particles, by heterogeneous processes involving solid particles or by a combination of both. Homogeneous freezing is expected to occur in increasingly concentrated solution particles as temperature decreases. It can be parameterised by the approach of Koop et al. [2000] which assumes that the homogeneous freezing rate only depends on water activity and temperature of the solution. Thereby, the homogeneous nucleation of ice from an aqueous solution can be expressed as a function of temperature and relative humidity independently of the nature of the solute. Alternatively, the temperature in an expression for the homogeneous freezing of pure water [e.g. Jeffery and Austin, 1997] can be replaced by the effective freezing temperature T_{eff}. This approach was first proposed by Sassen and Dodd [1988]. T_{eff} can be calculated from the molality and a specific constant of the solution. Recent experiments in the AIDA (Aerosol Interaction and Dynamics in the Atmosphere) cloud chamber of Forschungszentrum Karlsruhe have indicated that in particular at temperatures below 220 K both the water activity parameterisation and the effective temperature approach seem to overestimate homogeneous freezing rates of solution particles. In this contribution we compare the experimental findings with model output from our comprehensive process model MAID. We focus on onset relative humidity and ice number density. The different approaches to parameterise the homogeneous ice nucleation rate are assessed.

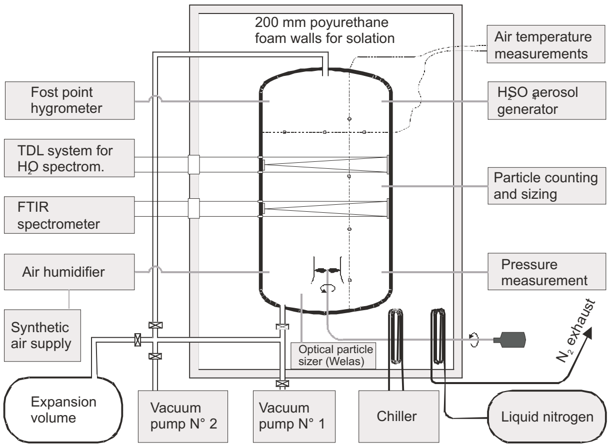

Figure 1: Schematic view of AIDA facility with key instrumentation

2. EXPERIMENTAL

The technical setup of the aerosol chamber and the experimental methods are described in our recent publications [Wagner et al., 2007, Möhler et al., 2006] and will be described here only briefly. Figure 1 depicts the AIDA setup including the key instrumentation. AIDA enables the investigation of ice clouds in the laboratory at realistic conditions with regard to temperature and cooling rate. It consists in substance of a large aerosol vessel (Volume 84 m^3) which is placed inside a coolable containment. At static conditions (with respect to temperature and ice saturation ratio) sulphuric acid particles were injected into the vessel at concentrations between 10^3 and $6\times10^4\,cm^{-3}$. Ice supersaturated conditions in the aerosol vessel were achieved by expansion cooling with a mechanical pump at different pumping speeds corresponding to cooling rates between 1.7 and 0.5 K/min. In particular at the lowest temperatures we pumped very slowly to allow the aerosol taking up water from the gas phase. Thereby, a thermodynamic equilibrium between aerosol and gas phase is assured. Figure 2 depicts time series of AIDA experiment IN11-48 starting at –62 °C. The pressure was reduced from 1000 hPa to 750 hPa within 17 min. The water vapour concentration was measured in situ by a tunable diode laser absorption spectrometer (TDL). A frost point hygrometer measured ex situ total water concentration (gas + condensed phase). The ice saturation increased from a slightly subsaturated value to a maximum value $S_{ice}^{max} = 1.70$. After about 725 s (indicated by the blue vertical line) the threshold relative humidity for homogeneous freezing was exceeded. Due to water uptake of the growing ice particles the saturation ratio decreased shortly after onset of ice formation. An optical particle counter (WELAS) was used to monitor simultaneously the number concentration of ice and aerosol particles. Ice particles get visible in the WELAS record as they grow quickly to large sizes, clearly beyond the size range of the remaining aerosol particles. The light scattering device SIMONE was used to observe growth of solution particles by hygroscopic uptake of water as well as the onset of freezing. Onset of freezing is indicated by the sharp increase of depolarization ratio. Hygroscopic growth of aerosol particles causes the ratio of forward-to-backward scattered light to increase. By means of a FTIR-spectrometer the composition of the sulphuric acid/water particles was deduced (not shown here).

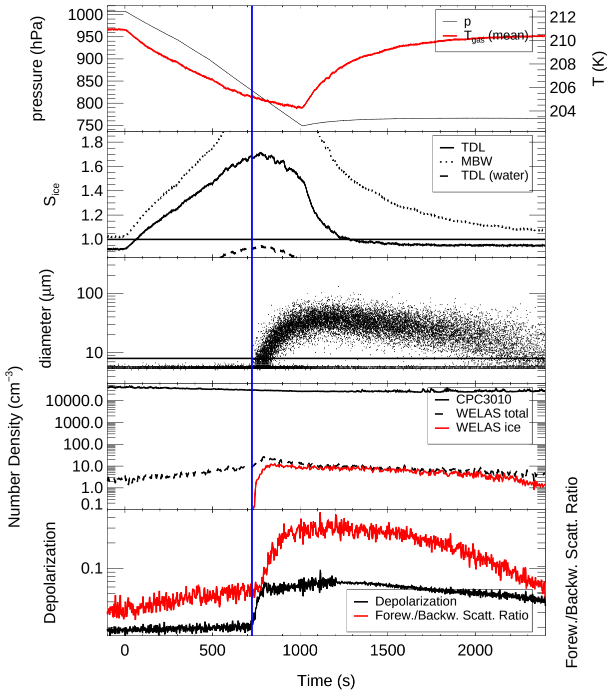

Figure 2: AIDA Experiment IN11-48: Experimental course of pressure and temperature (*Panel 1*); ice and water saturation ratio (gas-phase water, TDL) and ice saturation ratio (gas-phase + condensed phase, MBW) (*Panel 2*); optical particle counter WELAS (each dots represents an individual particle as function of experimental time and size based on Mie-calculations for spherical particles with refractive index 1.33, horizontal line separates aerosol particles from ice particles) (*Panel 3*); aerosol number concentration (CPC 3010), WELAS ice and total number concentration (*Panel 4*); backscattering depolarization ratio and ratio of forward to backward scattered laser light intensity (SIMONE) (*Panel 5*). Vertical blue line denotes onset time of freezing.

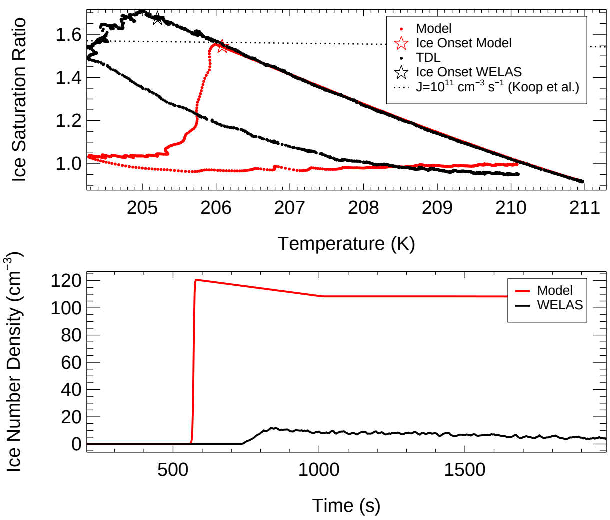

Figure 3: *Upper Panel:* Evolution of the ice saturation ratio (modelled and measured) as function of temperature. Dashed line indicates constant homogeneous ice nucleation rate $J = 10^{11}\,\mathrm{cm}^{-3}\,\mathrm{s}^{-1}$ according to Koop et al. [2000]. Open asterisk indicate onset of freezing. *Lower Panel:* Development of calculated and measured ice number density

3. MODELLING

The detailed process model MAID (**M**odel for **A**erosol and **I**ce **D**ynamics, Bunz et al. [2008]) was applied to analyze the experimental findings. It simulates the growth and freezing of the solution droplets by taking into consideration the thermodynamic conditions in the aerosol vessel. The aerosol ensemble is simulated by a log-normal density function. The size distribution keeps its shape with distribution parameters varying as function of time. The temporal courses of pressure and temperature were prescribed to the model. The course of ice saturation ratio is calculated by the model taking into account the fluxes of water vapour from the ice covered chamber wall into the volume and the partitioning of water vapour to the condensed and gas phase. By model calculations we could show that 98 % of the aerosol volume exhibited a composition which did not deviate more than 1 % from the equilibrium composition given by the temperature and humidity during the expansion cycle. We tested both approaches to parameterise the homogeneous ice nucleation rate by comparing model and experimental results.

4. RESULTS

At the lowest temperature investigated we observed the freezing onset of the aerosol at a considerably higher ice saturation ratio than expected from literature data: At $T = 204$ K we measured a freezing onset threshold of 1.73 ($\pm$ 0.06) while according to the activity based parameterisation for homogeneous ice nucleation [Koop et al., 2000] an ice saturation ratio of 1.57 is expected to freeze the solution particles during the AIDA experiment. Furthermore, the process model significantly overestimated the measured ice particle number concentration. The effective-temperature approach [Sassen and Dodd, 1988] revealed somewhat smaller deviations between modelled and measured values. At higher temperature a much better accordance was found by using the parameterisation of Koop et al. [2000]: at $T = -42.5$ we found experimentally an onset value of $S_{ice} = 1.41$ ($\pm$ 0.05) while the model run revealed $S_{ice} = 1.46$ at $T = -42.8\,^{\circ}$. The approach of Sassen and Dodd [1988] revealed a similar ice saturation ratio while the number density of ice particles formed was notably larger than observed.

REFERENCES

H. Bunz, S. Benz, I. Gensch, and M. Krämer. MAID: a model to simulate UT/LS aerosols and ice clouds. *submitted to Environ. Res. Lett.*, 2008.

C. Jeffery and P. Austin. Homogeneous nucleation of supercooled water: results from a new equation of state. *J. Geophys. Res.*, 102: 25269–25279, 1997.

T. Koop, B. Luo, A. Tsias, and T. Peter. Water activity as the determinant for homogeneous ice nucleation in aqueous solutions. *Nature*, 406:611–614, 2000.

O. Möhler, P. Field, P. Connolly, S. Benz, H. Saathoff, M. Schnaiter, R. Wagner, R. Cotton, M. Krämer, and A. Heymsfield. Efficiency of the deposition mode ice nucleation on mineral dust particles. *Atmos. Chem. Phys.*, 6: 3007–3021, 2006.

K. Sassen and G. Dodd. Homogeneous nucleation rate for highly supercooled cirrus cloud droplets. *J. Atmos. Sci.*, 45:1357–1369, 1988.

R. Wagner, S. Benz, O. Möhler, H. Saathoff, M. Schnaiter, and T. Leisner. Influence of particle aspect ratio on the midinfrared extinction spectra of wavelength-sized ice crystals. *J. Phys. Chem. A*, 111:13003–13022, 2007.

RESULTS OF ICE NUCLEATING ABILITY OF VARIOUS AEROSOLS SAMPLED AT THE INTERNATIONAL WORKSHOP ON COMPARING ICE NUCLEATION MEASURING SYSTEMS (ICIS 2007) USING A CONTINUOUS FLOW DIFFUSION CHAMBER.

Richard J. Cotton[1]
1. Met Office, Exeter, UK, richard.cotton@metoffice.gov.uk

ABSTRACT

A continuous-flow diffusion chamber for measurements of ice nuclei has been developed for airborne measurements on the UK Met Office/NERC BAe-146 atmospheric research aircraft. In order to validate the operation and gain operating experience the instrument took part in the International Workshop on Comparing Ice Nucleation Measuring Systems (ISIS 2007) based at the AIDA aerosol and cloud chamber facility during September 2007. Various aerosol samples were tested for their ice nucleating ability. These included Arizona test dust, soot, Saharan desert dust, Isreali desert dust, Canary island dust, SnowMax and bacteria used in artificial snow generation. The results are generally in agreement with the other instruments. However, in order to operate in an aircraft environment, some technical issues with the instrument must first be addressed.

1. INTRODUCTION

In cold clouds, with temperatures below -35℃, the dominant ice nucleation mode is homogeneous freezing of the supercooled water droplets with the nucleation rate increasing very rapidly for colder temperatures. At temperatures much warmer than -35℃, homogeneous freezing is negligible and ice nucleation must take place heterogeneously. Heterogeneous ice nucleation requires ice forming nuclei (IN) which are a special subset of atmospheric aerosols. Laboratory experiments have categorised various ice nucleation mechanisms into four main modes: deposition nucleation, condensation-freezing, contact-freezing and immersion freezing nucleation. In-situ aircraft based observations of IN and ice crystals have also enabled the nucleation mode to be inferred, subject to experimental uncertainty. There are however, many questions including what properties of the IN determine their ice nucleation ability, what are the spatial and temporal distribution, what are the sources and how IN age.

There are a variety of instrument types for ice nuclei measurements. These include mixing chambers, diffusion chambers and filters. Continuous-flow diffusion chambers (CFDC) have been used in many airborne and ground-based field campaigns. Because of the short residence time, a CFDC instrument cannot detect all nucleation modes, in particular contact-freezing.

A number of ice nucleation instruments took part in the International Workshop on Comparing Ice Nucleation Measuring Systems (ISIS 2007) based at the AIDA aerosol and cloud chamber facility during September 2007. As well as comparing the ice nucleation results from each instrument, the AIDA chamber was used to activate the IN. There were additional instrumentation measuring from the AIDA chamber, including humidity, aerosol and cloud particle probes. A summary paper describing all the instruments, the experimental setup and preliminary results has been submitted to this conference (DeMott et. el. 2008)

Results of the ice nucleating ability of various aerosol samples using a CFDC are shown. Further improvements to the instrument which are required for aircraft operation are then described.

2. INC DESIGN AND OPERATION

The ice nucleation instrument was originally developed by Manchester University for airborne measurements on the old UK Met Office C-130 atmospheric research aircraft. This has been extensively refurbished and upgraded ready for installation on the UK Met Office/NERC BAe-146 atmospheric research aircraft.

The basic design is identical to that described in Rogers et. al. 2001. It is a continuous-flow diffusion chamber built from two concentric vertical cylinders, made from copper except for the lower third of the inner cylinder which is plastic. The copper surfaces are coated in ice, so that by when they are at different temperatures ice supersaturation is created near the centre of the annular gap. An inertial impactor removes aerosol particles larger than 1.5 – 2 microns and the remaining aerosols are injected into the centre of the annular gap. The aerosol laden laminar is kept away from the CFDC walls by two laminar of particle free sheath air.

By varying the difference in temperature between the two cylinders, the CFDC can be operated over a range of humidity. The sample temperature is the near the average of the two wall temperatures (buoyancy forces due to the different wall temperatures moves the sample laminar slightly towards the cold wall). By varying the sample temperature and humidity, the IN activity as a function of humidity and temperature can be determined. Water saturation is reached when the temperature difference is around 20°C. Then both IN and CCN activate. The lower plastic section of the inner wall creates a region below water saturation, forcing drops to evaporate. This evaporation section enables condensation-freezing in addition to deposition ice nucleation to be measured. Particles leaving the CFDC are counted and sized by an optical particle counter (OPC). Particles larger than 3 microns indicate ice crystals, since the inertial impactor has already removed aerosols large than this.

3. ICIS-07 DATA

Four mineral dust and two bacteria aerosol samples were measured:

- Arizona Test Dust (ATD): a milled mineral sample representative of Southwestern U.S. desert dust.
- Saharan dust (SD4): a surface dust sample collected from the Sahara.
- Canary Islands dust (CI01): a surface dust sample from the Canary Islands (Saharan dust is transported here).
- Israel dust (ID1): dust collected as sedimented particles from a dust storm in Israel.
- Snowmax: manufactured for artificial snow generation.
- Live bacteria: cells of pseudomonas syringae.

Because of refrigeration issues (power and control), the ice nucleation instrument was only able to operate over a narrow range of temperature and therefore sampled from the smaller aerosol preparation and characterisation chamber (NAUA) rather than from the main expansion cloud chamber at AIDA (which was operated over a wide range of temperatures). The aerosol concentrations in NAUA were typically thousands per cm^3, much higher than in the atmosphere. The refrigeration control problems and large thermal mass led to only one humidity scan for each aerosol sample. An initial temperature was chosen, and each ice coated cylinder wall was at this temperature (the aerosol laminar is there at ice saturation). The outer cylinder temperature was then increased slowly, typically 10–20°C over one hour.

Fig. 1 shows the temperature, humidity and OPC count rate for one humidity scan using Canary Island dust. Over the humidity scan from ice saturation to 115% water saturation, the sample temperature ranged -34°C to -28°C. At near water saturation, the OPC large particle count rate started to increase, indication a threshold for IN activation has been passed. Above 110% relative humidity wrt. water, droplets activated on CCN do not fully evaporate in the lower section of the CFDC and the small-particle count rate increases. This makes a good check for humidity and therefore temperature calibrations and also as an estimate for any particle losses.

During the humidity scan, the aerosols within the NAUA chamber were continuously counted and sized (the concentration steadily decreased as each instrument sampled the aerosol). Fig. 2 shows the fraction of the NUAU aerosols activated as IN within the CFDC for each of the six aerosol samples. The ice nucleation onset, shown by the light-grey band, is just when the OPC detects an increase in large particles.

4. DISCUSSION AND UPGRADES

While the instrument measured ice nuclei at AIDA, there are some major issues that need addressing before it is capable of proper scientific measurements in an aircraft environment. These include: an underpowered refrigeration system with non-intuitive control system, the OPC and readout electronics signal to noise limit the detection of small ice particles from ambient background aerosols, significant particle loss–probably in the inlet injector assembly, and a suspect structural integrity of the CFDC and inlet injectors.

The instrument is now being completely rebuilt to address these issues and to have further improvements. The main improvement is to lengthen the CFDC cylinders . This enables a much longer residence time and therefore larger ice particles. The cylinders will be made from aluminium rather than copper for weight reasons.

5. SUMMARY AND CONCLUSIONS

For the four dust aerosol samples, the ice nucleation onset was always around water saturation indicating immersion freezing. This agrees with observations from other CFDCs and from expansions in the AIDA cloud chamber.

The instrument is now in the process of being upgraded ready for future airborne measurements on the UK Met Office/NERC BAe-146 atmospheric research aircraft.

6. ACKNOWLEDGEMENTS

The author thanks Paul DeMott, Olaf Stetzer and Ottmar Mohler for organising the ICIS 2007 workshop. Acknowledged are all the AIDA staff for their support and the Forschungszentrum Karlsruhe which provided funding for the facility infrastructure. Also, the European Science Foundations INTROP program supported a data workshop soon after the measurement campaign.

7. REFERENCES

DeMott P. J. et. al. The Fourth International Ice Nucleation Workshop (ICIS-2007): Objectives and Preliminary Results, submitted ICCP 2008.

Rogers, D. C., 1988: Development of a Continuous Flow Thermal Gradient Diffusion Chamber for Ice Nucleation Studies. *Atmos. Res.,* **22,** 149–181

Rogers, D. C., DeMott, P. J., Kreidenweis S. M. and Chen Y. 2001: A Continuous-Flow Diffusion Chamber for Airborne Measurement of Ice Nuclei. *J. Atmos. Oceanic Tecnol.,* **18,** 725–741

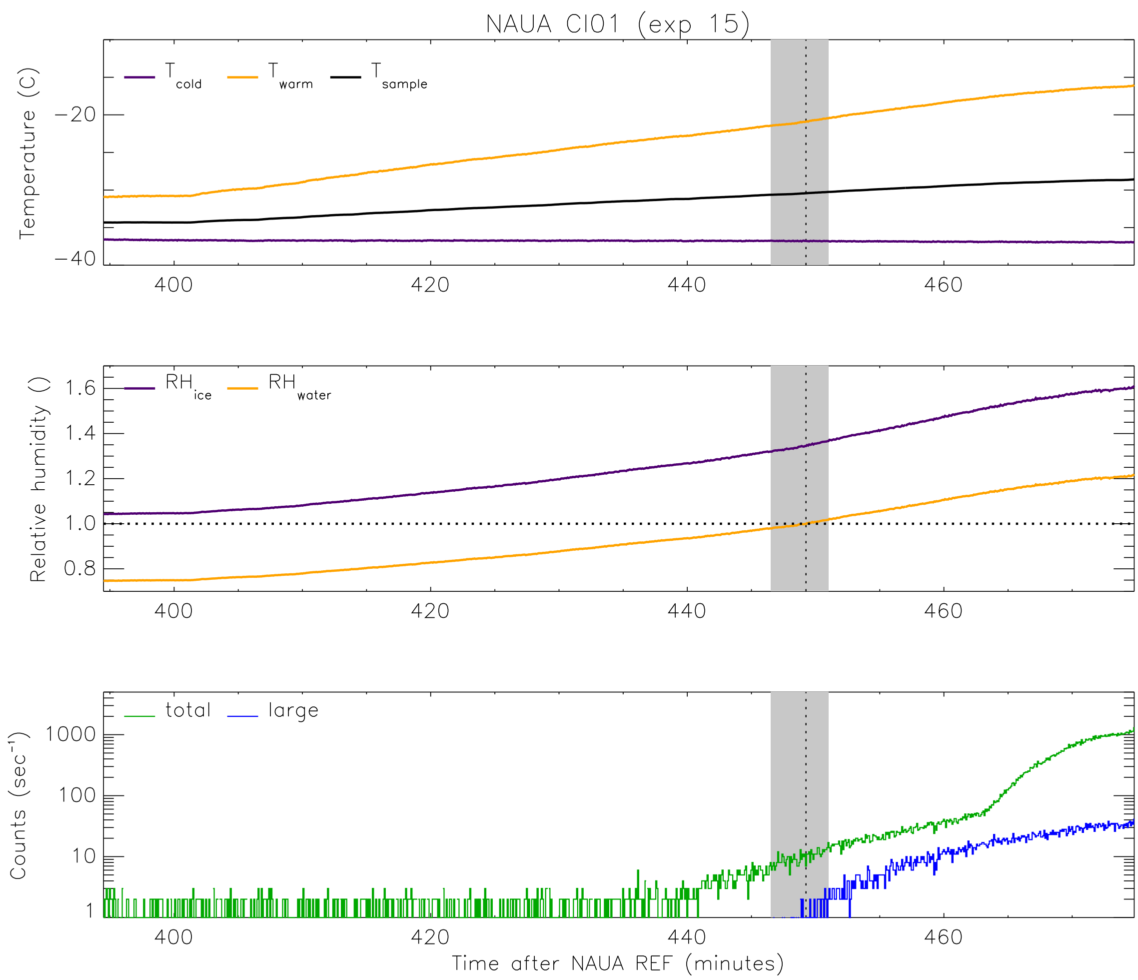

Figure 1: Humidity scan for Canary Island dust CI01. The light-grey band covers the time during the onset of ice nucleation (when the OPC large particle count in blue increases). The vertical dotted line is water-saturation. Within experimental errors water saturation is required for ice nucleation.

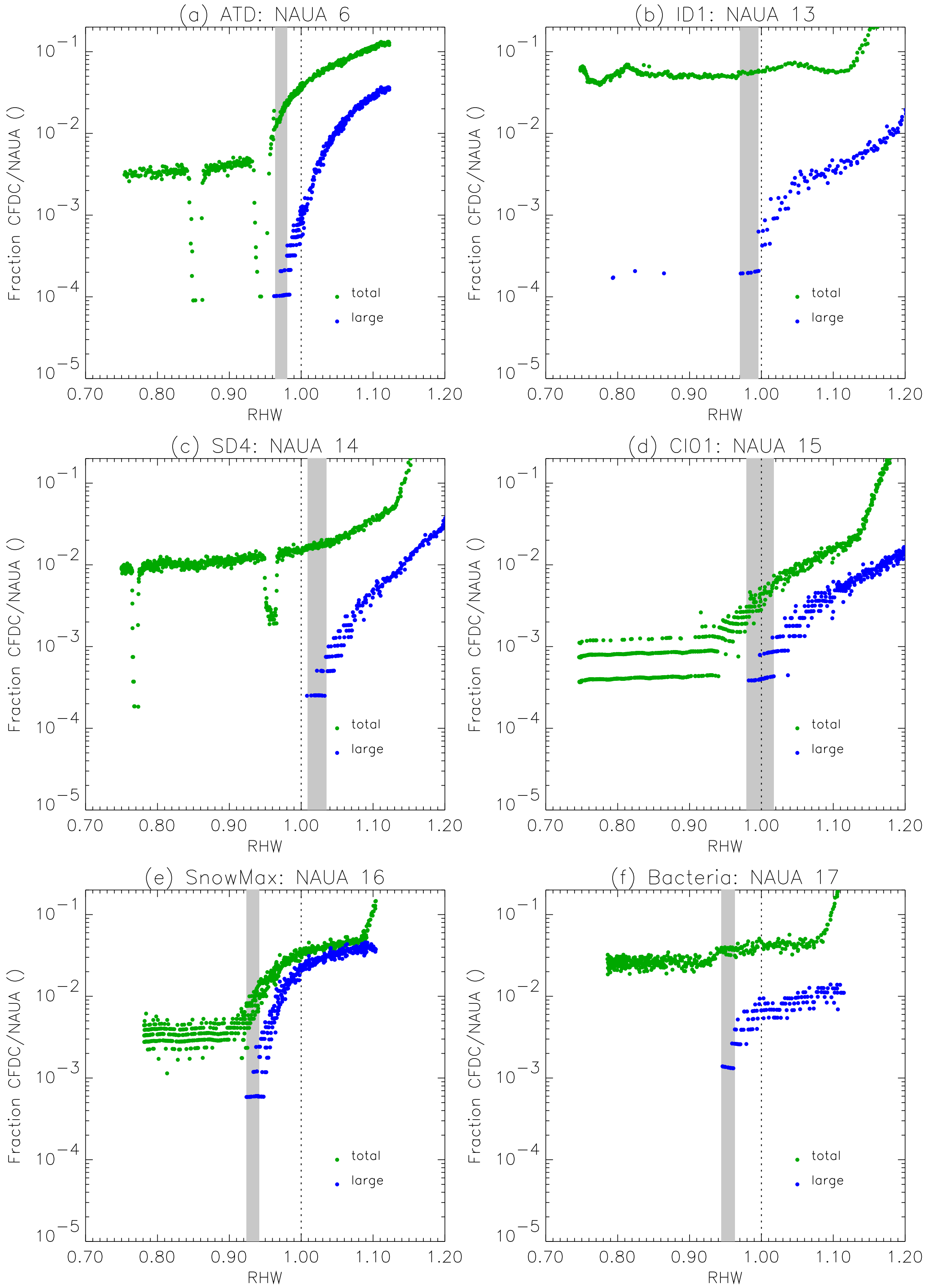

Figure 2: The green symbols are the all OPC particle count (including small signal background counts) and the blue are the OPC large particle count (expected ice crystals from IN activation). The light-grey band covers the time during the onset of ice nucleation (the spread of the blue symbols).

RELATIONSHIP BETWEEN HYGROSCOPICITY / CCN EFFICIENCY AND ICE NUCLEATION POTENTIAL OF COATED AND UNCOATED SOOT – RESULTS FROM THE AIDA CAMPAIGN IN11

S. Henning[1], M.Ziese[1], K. Mildenberger[1], A. Kiselev[1], F. Stratmann[1], O. Möhler[2], S. Benz[2], V. Michaud[3], P. Laj[3], A. Buchholz[4], Ch. Spindler[4], Th. F. Mentel[4] and the AIDA IN11-team

[1]Leibniz Institute for Tropospheric Research, Permoserstr. 15, 04318 Leipzig, Germany
[2]Forschungszentrum Karlsruhe, Postfach 3640, 76021 Karlsruhe, Germany;
[3]LaMP Université Blaise Pascal, 24, Avenue des Landais, 63177 Aubière Cedex, France.
[4]Research Centre Jülich, ICG-II: Troposphere, Leo-Brandt-Str., 52425 Jülich, Germany

1. EXPERIMENTAL

The main objective of the AIDA [*Möhler, et al.*, 2005] IN11 campaign was the investigation of a possible relationship between the hygroscopic / CCN properties and the ice nucleation potential of different soot types - pure and coated with inorganic / organic substances. Soot particles were generated on one hand by a spark generator (GFG-1000, PALAS, Germany) either with Argon or Nitrogen as carrier gas. On the other hand flame soot with high, medium and low organic carbon content was synthesized by a flame generator (CAST, Jing Ltd., Switzerland). Either sulfuric acid or succinic acid coatings were applied by means of a tube furnace followed by a condensation section. The synthesized particles were then fed into a reservoir chamber (NAUA) that supplied particles for the freezing experiments to the AIDA chamber and for the hygroscopicity / activation measurements to a Hygroscopicity Tandem Differential Mobility Analyzer (HTDMA), a Volatility HTDMA, two DMT continuous flow CCN instruments [*Roberts and Nenes*, 2005] and LACIS-field [*Stratmann, et al.*, 2004]. The aerosol compositions were monitored with two aerosol mass spectrometers and an SP-2 instrument. In this abstract we will focus on the CCN instrument data.

2. RESULTS

Activation was observed for GFG-soot with Argon as carrier gas (see Fig. 1). Particles of 150 nm electrical mobility diameter exhibited 50% activation at about 1% supersaturation, 200 nm particles at about 0.85%. Almost complete activation was observed for the three particles sizes at the instruments maximum supersaturation (1.2%).

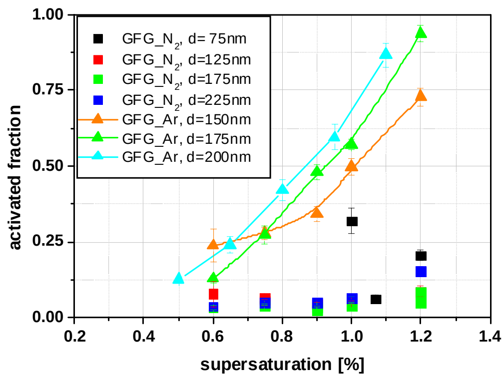

Figure 1 Activated particle fraction for GFG-soot with argon or nitrogen as carrier gas (error bars give one standard deviation).

For GFG-soot with nitrogen as carrier gas no activation was observed in the investigated supersaturation range (0.6% up to 1.2%). In addition to the data presented in Fig. 1, size scans for 225 - 350nm were taken, but also for the larger dry diameters no activation was observed.

For pure CAST-soot of all three organic carbon contents no activation was detected with the CCN instrument.

Sulfuric acid coating increased the hygroscopicity of the CAST-soot. Figure 2 shows the critical diameter versus supersaturation of CAST-soot / H_2SO_4 coated with three different organic carbon contents. The activation properties were found to be similar for all soot core types. This might be due to the sulfuric acid coating which seems to overrule the effect of the organic carbon content.

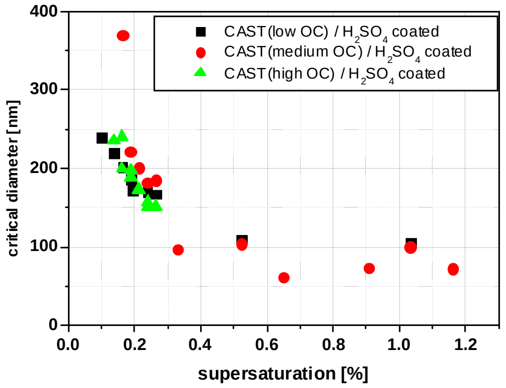

Figure 2 Critical diameter versus supersaturation for CAST soot / H_2SO_4 coated with different OC levels.

Both, CAST-soot and GFG-soot particles coated with succinic acid seem to be rather hydrophobic. However, these data are still under evaluation.
The AIDA measurements showed that GFG-soot particles with argon are also more efficient ice nuclei than the GFG-soot with nitrogen as carrier gas.
The ice nucleation efficiency of pure CAST-soot with low organic carbon content was similar to the GFG-soot with nitrogen as carrier gas. The ice forming potential for CAST-soot with medium and high organic carbon content is rather low.

3. Summary

The data set clearly revealed the hydrophobic nature of the GFG and in particular of CAST flame soot. A transition to more hygroscopic and more CCN active particles with increasing acid coating was observed.
At first view the CCN properties and ice nucleation potential seems to be related in a way that soot particles which are good CCN exhibit also a higher ice forming potential.
The relations between the chemical composition of the aerosol particles and their cloud formation properties will be further analyzed and discussed.

3. BIBLOGRAPHY

Möhler, O., et al. (2005), Effect of sulfuric acid coating on heterogeneous ice nucleation by soot aerosol particles, *Journal of Geophysical Research-Atmospheres*, *110*.

Roberts, G. C., and A. Nenes (2005), A continuous-flow streamwise thermal-gradient CCN chamber for atmospheric measurements, *Aerosol Sci. Technol.*, *39*, 206-221.

Stratmann, F., et al. (2004), Laboratory studies and numerical simulations of cloud droplet formation under realistic supersaturation conditions, *J. Atmos. Oceanic Technol.*, *21*, 876-887.

Acknowledgments

We thank the Helmholtz Virtual Institute VI-ACI for their financial assistance. The AIDA-team we thank for their on-the-spot support.

INITIAL RESULTS FROM THE MANCHESTER ICE NUCLEATION COUNTER TAKEN DURING ICIS2007

Hazel Jones[1], Jonathan Abbatt[2], James Bowles[3], Richard Cotton[3], Paul DeMott[4], Zamin Kanji[2], Ottmar Möhler[5], Marcus Petters[4], Clive Saunders[1], Bierko Sierau[6], Olaf Stetzer[6]

[1] University of Manchester, Centre for Atmospheric Science, Manchester, UK
[2] University of Toronto, Department of Chemistry, Toronto, Canada
[3] UK Met Office, Exeter, UK
[4] Colorado State University, Department of Atmospheric Science, Fort Collins, CO, 80523, USA
[5] Institute for Meteorology and Climate Research (IMK-AAF), Forschungszentrum Karlsruhe, Germany,
[6] ETH Zurich, Institute for Atmospheric and Climate Science, Switzerland

1. INTRODUCTION

Heterogeneous ice formation in the atmosphere is an important process as it leads to the glaciation of clouds at temperatures >-40°C. The current understanding of the various formation pathways is such that these processes cannot be predicted well in cloud models, which are important for weather prediction and ultimately global climate prediction. It is therefore important to be able to study these processes in detail to obtain the important information required to produce parameterisations for ice nucleation.

There are many difficulties regarding the identification and measurement of Ice Nuclei (IN). IN may act in supercooled water or supersaturated vapour or at the interface of the two. Typical atmospheric concentrations of IN are ~1l^{-1} (around 8 orders of magnitude less than the total aerosol concentration), and almost any physical or chemical process may alter the effectiveness of IN.

It is also important to note that IN can only be discerned from non-ice nucleating aerosol particles if they activate: IN must nucleate ice first so that the ice crystal formed may be detected. The multitude of possible processes within the atmosphere makes realistic simulations of natural atmospheric conditions within measuring techniques difficult and most measurement techniques are insensitive to one or more mode of activation.

The *International Workshop on Comparing Ice Nucleation Measuring Systems* (ICIS) 2007 was held at the Forschungszentrum Karlsruhe AIDA facility, Germany, 10 - 28 September. The objective of this workshop was to compare all currently existing instruments which measure ice nucleation with a common aerosol generation system, with the overall purpose of assessing present measurement capabilities.

2. INSTRUMENTATION

The *University of Manchester Ice Nucleus Chamber* (MINC) was still in the development stages when it took part in the ICIS2007 workshop (see Table 2.1 for chamber participants). The MINC is of similar design to several of the other instruments, mainly those owned by Colorado State University (CSU), the UK Met Office and MRI Japan. These are all based on the 1988 design by Rogers, [Rogers, 1988]. Below is a schematic showing the five main sections of the instrument: the chamber, the refrigeration system, the airflow system, the detection system (optical particle counter, OPC) and the sample inlet section.

[1] Correspondence author
Email: Hazel.Jones@Manchester.ac.uk
Telephone: 00-44-161-306-????

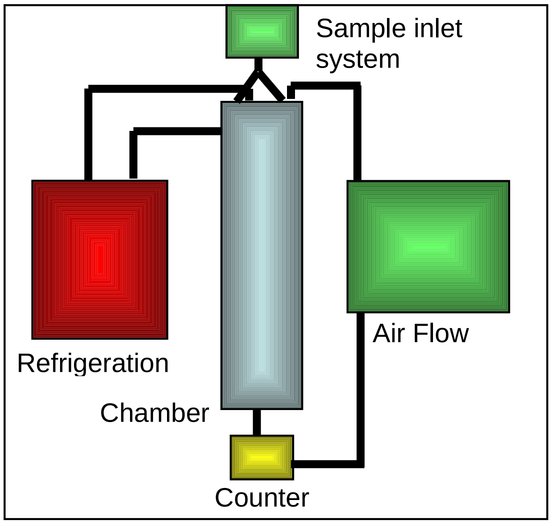

Figure 2.1: Schematic of the Manchester Ice Nucleation Chamber (MINC)

Continuous flow IN chambers work on the principle that an air sample passes between two ice-coated plates each at its own temperature. The temperature profile across the flow is assumed to be linear so that the vapour pressure profile is also linear. Equilibrium vapour pressure is not a linear function of temperature, therefore the region between the plates is supersaturated. Sample air is injected into the peak supersaturation region as a laminar flow sandwiched between layers of dry, filtered air. Ice crystals grow up to 10µm in size during an approximate passage time of 10 seconds. Exhaust air from the chamber is drawn through an OPC to detect and size any crystals. The airflow through the chamber is a combination of Poiseuille and buoyant flow [Sinnarwalla and Alofs, 1973] and the aerosol lamina is deflected towards the cold wall by an amount depending on the total flow and temperature gradient [Rogers, 1988].

Test samples were chosen for their suspected/known ice nucleability [e.g. DeMott et al. 2003, Mohler et al. 2006] in the hope that the instruments would record similar results (see Table 3.1). Samples were prepared such that the vast majority of the particles in the sample were <1µm, allowing instruments without impactors to detect IN more easily. Instruments sampled from the small aerosol chamber (NAUA) once aerosol number concentrations were sufficient (~10^5/cm^3). After aerosol characterisation (number, size distribution, composition) a minor part of the aerosol (resulting in ~500/cm^3) was transferred to the larger AIDA chamber for IN activation in expansion experiments. For ~1hour prior to an expansion run, instrument could sample directly from the AIDA chamber at atmospheric pressure.

Group	Instrument	Impactor	Detection
University of Manchester (UMAN)	MINC (VC CFDC)	~1µm cut	OPC (>3µm)
Colorado State University (CSU)	CFDC-1H (VC CFDC)	~1µm cut	OPC (>2µm)
ETH Zurich	ZINC (V FP CFDC)	N/A	Phase Discrimination [Stetzer et al. 2008]
MRI Japan	MRI CFDC (VC CFDC)	~2µm cut	OPC (>3.5um)
UK Met Office	MOINC (VC CFDC)	~1µm cut	OPC (>3µm)
University of Frankfurt	FINCH (Mixing chamber)	N/A	OPC [Bundke et al. 2006]
University of Toronto	UTCFDC (H FP CFDC)	N/A	OPC (>0.5, >5µm)

Table 2.1: Participants at ICIS2007. (IN chamber participants only, for full participant list please contact the first author.) [V = vertical, H = horizontal, FP = flat plate, C = concentric]

During ICIS2007 the MINC performed relative humidity (RH) scans whilst holding the sample temperature steady. Sample conditions in the sample laminar were brought from ice saturation to ~5% supersaturation with respect to water[2]. This method was mirrored by CSU and MRI Japan. Due to technical difficulties, the UK Met Office were not able to hold sample temperature steady.

[2] Due to time constraints, some calibrations were performed post-workshop. The wall temperature calibration was carried out upon return to Manchester and revealed the inner wall temperature to be significantly warmer than first thought; this consequently affected the recorded sample temperature and supersaturation.

3. RESULTS

The MINC successfully recorded data for five out of seven samples tested. Below is a table outlining the details of the RH scans performed:

Sample	Source	Scan Temp
Arizona Test Dust (ATD)	Powder Technology Inc (PTI)	-28°C -25°C -26°C -26°C -32°C -31°C -31°C
Israeli Dust	Zev Levin, Tel Aviv University	-32°C -26°C -32°C
Saharan Dust	Ottmar Mohler, IMK-AAF	-25°C -29°C
Canary Island Dust	Paul DeMott CSU	-25°C -29°C
Snomax ®		-26°C -18°C

Table 3.1: Details of RH-scans taken with the MINC at ICIS2007 workshop.

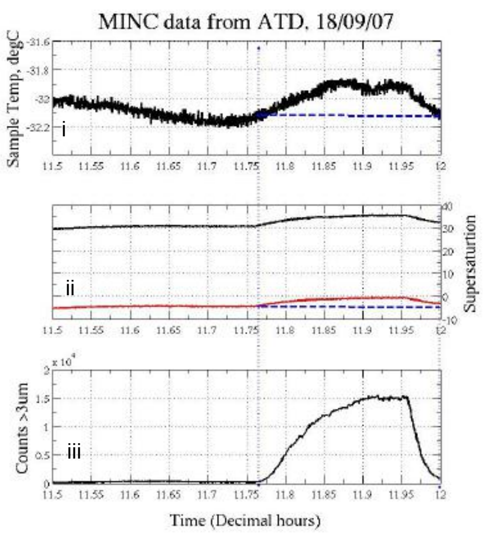

Figure 3.1: a, A time series of MINC data for ATD sample (18/09/07), i, shows the temperature of the sample lamina, ii, shows supersaturation with respect to ice (black line) and water (red line), iii, shows particle counts over the threshold level.

Figure 3.1a. Shows a typical time series of data from the MINC during ICIS2007. Both walls were bought to the intended sample temperature, then separated in such a way as to retain a continual sample temperature while increasing the supersaturation. In this plot, RH does not exceed supersaturation with respect to water, so this shows ATD acting as a deposition ice nuclei, activating ~$10^4 l^{-1}$, a small fraction of the total aerosol passing through the MINC. An easier way to look at the data is shown in Figure 3b,c. Activated fraction, AF (No. particles >3µm at outlet divided by total at inlet), plotted against RH_{water}.

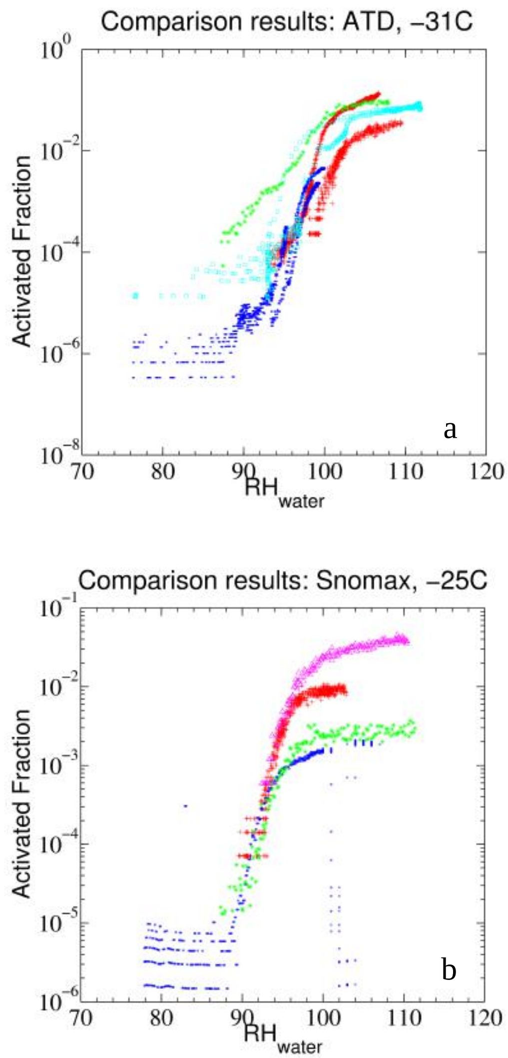

Figure 3.2: a, Activated Fraction (AF) comparison results for ATD sample at -31ºC. b, AF comparison results for Snomax sample at -25ºC.
[MINC data = blue circle, CSU data = red cross, MOINC data = pink triangle, ZINC data = green star, UTCFDC = cyan squares]

4. DISCUSSION AND CONCLUSION

Overall, the MINC performed well at the workshop with results obtained for the majority of samples tested. Of the results obtained, many of them are compared to other groups as shown in Figure 3.2. These results show that some instruments compare better than others. An obvious problem with the MINC data is the extent of the RH scans, the reason for this has already been outlined – wall temperatures were uncorrected at the time of the workshop. Despite this factor, sometimes the MINC detects fewer IN than CSU-CFDC-1H and other instruments. This is probably a combined result of the amount of available growth time inside the different chambers, the use of passive (potentially allowing ice crystals to evaporate when the instrument is in a very warm environment) or active water droplet evaporation sections, and the cut-size chosen for the threshold of IN detection.

In addition to the above potential issues, the MINC detection system employed at ICIS2007 experienced counting efficiency problems across its channels, a problem which is not readily correctable. Even though the MINC detection system experienced problems, the design and set up have proven to be capable of successfully detecting ice nucleation over a range of atmospherically relevant temperatures.

5. FUTURE WORK

The results obtained from the ICIS2007 workshop show that several improvements are needed to the current MINC set-up. It is hoped that future funding can be secured to allow these upgrades so that the MINC can be used in future field projects for the University of Manchester.

6. ACKNOWLEDGEMENTS

The first author would like to thank Paul DeMott and Tony Prenni from CSU for their support. All authors gratefully acknowledge the support of AIDA staff members. The University of Manchester contribution to the ICIS2007 workshop was funded by the UK Natural Environment Research Council (NERC). Attendance at the AIDA ICIS2007 workshop was funded by the ACCENT Access to Infrastructures Program. Attendance to the Pontresina ICIS2007 results workshop was funded by ESF/INTROP. Collaboration between the University of Manchester and the UK Met Office was funded by the DIAC UKAAN Aerosol Knowledge Transfer Visit program.

7. REFERENCES

Bundke, U., Bingemer, H., Wetter, T., Nilius, B., and Jaenicke, R., The FINCH (Frankfurt Ice Nuclei Chamber) Counter – new developments and first measurements. *7th International Aerosol Conference*, St. Paul, MN, USA, 2006.

DeMott, P. J., Sassen, K., Poellot, M. R., Baumgardner, D.,Rogers, D. C., Brooks, S. D., Prenni, A. J., and Kreidenweis, S. M., African Dust Aerosols as atmospheric ice nuclei, *Geophys. Res. Lett.*, **30**, 1732, 2003.

Mohler, O., Field, P. R., Connolly, P., Benz, S., Saathoff, H., Schnaiter, M., Wagner, R., Cotton, R., Kramer, M., Mangold, A., Heymesfield, A. J., Efficiency of the deposition mode ice nucleation on mineral dust particles, *ACPD*, **6**, 1539-1577, 2006.

Rogers, D. C., Developments of a continuous flow thermal gradient diffusion chamber for ice nucleation studies, *Atmos. Res.*, **22**, 149-181, 1988.

Sinerwalla, A. M. and Alofs, A. J., A cloud nucleus counter with long available growth time, *J. Appl. Meteorol.,* **12**, 831-835, 1973.

Stetzer, O., Baschek, B., Lüönd, Felix., and Lohmann, U., The Zurich Ice Nucleation Chamber (ZINC) - A New Instrument to Investigate Atmospheric Ice Formation, *Aerosol Science and Technology,* **42 ,** 64 - 74 , 2008.

HOW COATING LAYERS INFLUENCE THE DEPOSITION MODE ICE NUCLEATION ON MINERAL PARTICLES

O. Möhler[1], J. Schneider[2], S. Walter[2], A. J. Heymsfield[3], C. Schmitt[3], Z. J. Ulanowski[4], and the AIDA team

[1] Forschungszentrum Karlsruhe, Germany.
[2] Max Planck Institute for Chemistry, Mainz, Germany.
[3] National Centre for Atmospheric Research, Boulder, CO, USA.
[4] University of Hertfordshire, UK.

1. INTRODUCTION

Mineral particles are known to be efficient ice nuclei at cirrus cloud temperatures (Möhler et al., 2006). Single particle mass spectrometry revealed the abundance of mineral particles in the upper troposphere which often contained significant amount of nitrate, sulphate and other substances probably originating from photochemical production and (Murphy et al., 2006). Here we investigate the effect of coating with secondary organic substances and sulphuric acid on the efficiency of mineral particles to act as heterogeneous ice nuclei.

2. EXPERIMENTAL METHODS

The experiments were carried out at cirrus temperatures between 205 and 210 K in the AIDA facility (Möhler et al., 2006). The cloud chamber was equipped with instrumentation for aerosol and ice particle characterisation which included external partner instruments like an Aerosol Mass Spectrometer (Q-AMS) from the Max Planck Institute for Chemistry in Mainz, Germany, the Small Ice Detector (SID-2) from the University of Hertfordshire, and two ice imaging instruments, a Cloud Particle Imager (CPI) and a Video Imaging Particle Spectrometer (VIPS), from NCAR in Boulder, Colorado.

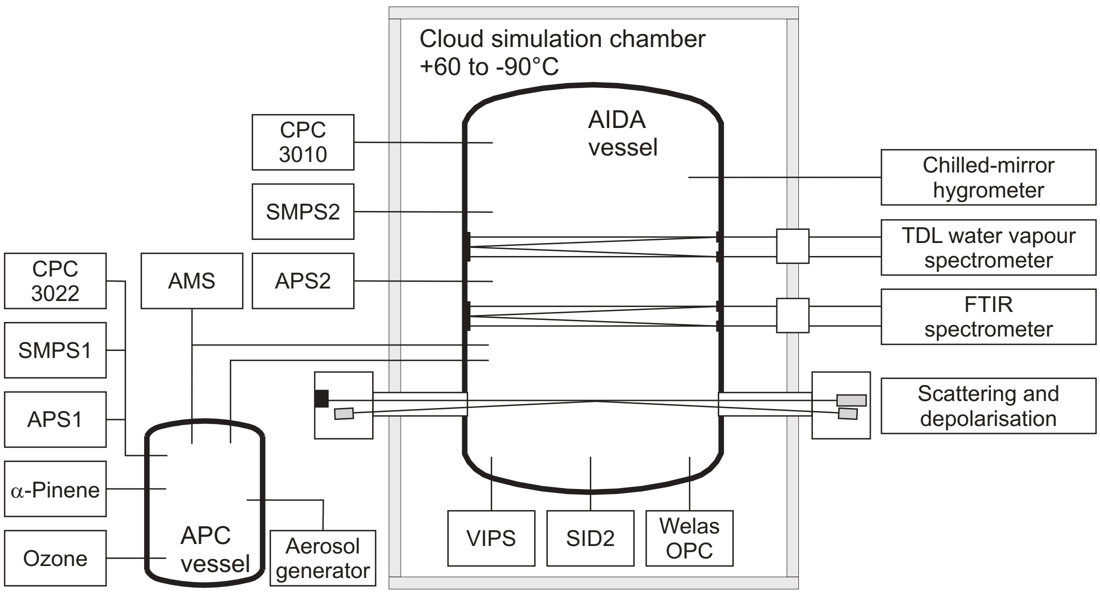

Figure 1: Schematic of the AIDA facility with aerosol and cloud instrumentation.

Corresponding author's address:
Ottmar Möhler, IMK-AAF, Forschungszentrum Karlsruhe, Postfach 3640, 76021 Karlsruhe, Germany; Ottmar.Moehler@imk.fzk.de

3. AEROSOL PREPARATION

The effect of organic and inorganic coating on the heterogeneous ice nucleation efficiency of mineral dust particles was investigated for Arizona Test Dust (ATD) and illite particles as surrogates for atmospheric dust aerosol mainly originating from desert areas. The ATD sample is the same as the one already used for previous AIDA experiments (Möhler et al. 2006). The illite sample is a commercial clay mineral product from Arginotec.

The dry ATD and illite samples were roughly dispersed with a rotating brush disperser (RBG-1000, Palas), further deagglomerated in a dispersion nozzle, and then passed through a cyclone impactor to remove particles larger than about 1 μm in diameter. The resulting aerosol was then added to the APC (aerosol preparation and characterisation) chamber and uniformly distributed with a mixing fan.

Coating with secondary organic aerosol (SOA) mass was achieved by first adding ozone to the dust aerosol in the APC chamber, and then a certain amount of α-pinene. The initial volume mixing ratios ranged from 0.5 to 1.5 ppmv for ozone and from 0.3 to 1.0 ppmv for α-pinene. Ozone was added in excess to ensure complete conversion of the α-pinene. The semi-volatile reaction products condensed on the mineral dust particle surface.

For coating with sulphuric acid the dust aerosol flow from the aerosol generator was mixed at a temperature of about 150℃ with a flow of synthetic air saturated with sulphuric acid vapour. The sulphuric acid condensed to the dust particles upon slow cooling of the mixture. The coat amount was varied by selecting different flow rates and saturation temperatures of the synthetic air flow. The coated dust aerosol was then added to the APC chamber.

The particle size distribution (PSD) was measured with a scanning mobility particle spectrometer SMPS and an aerodynamic particle spectrometer APS (both from TSI Inc.). For comparing the results of the two instruments, the mobility-equivalent particle diameter of the SMPS and the aerodynamic diameter of the APS were converted into a volume-equivalent sphere diameter d_p.

Figure 2 depicts an example of a PSD measured after coating of illite aerosol with SOA. The illite aerosol shows a bimodal PSD with a major mode of particles with diameters between 0.15 and 1.0 μm and a minor fraction of smaller particles around 0.1 μm. This bimodal PSD results from the nature of the dust sample and is not a measurement artifact. We were not able to further analyse the chemical or mineralogical nature of the both modes. The solid line represents a bimodal lognormal fit to the measured PSD.

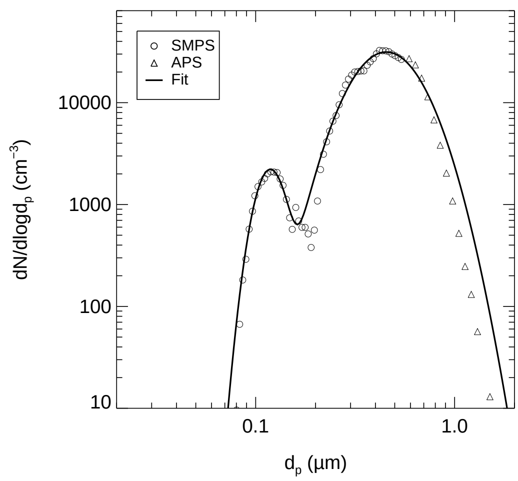

Fig. 2: Number size distribution of illite aerosol after coating with typical secondary organic aerosol (SOA) compounds from the reaction of α-pinene with ozone.

An estimate of the SOA mass fraction after the coating step was obtained from the amount of α-pinene added to the APC chamber and the aerosol yield for the reaction with ozone, which is about 35 % at a temperature of about 300 K. A density of 1.25 g cm^{-3} was used for the SOA material. The SOA mass fraction was 17% for the coated ATD aerosol and 41% for the coated illite aerosol.

A minor fraction of the uncoated or coated aerosol was transferred into the large AIDA chamber for investigating the ice nucleation efficiency in cloud expansion experiments. The SOA mass fraction of the aerosol in the AIDA chamber was also measured with an Aerodyne Quadrupole Aerosol Mass Spectrometer, Q-AMS (Canagaratna et al. 2007). This instrument quantitatively analyses the non-refractory components of submicron aerosol particles (organics, nitrate, sulfate, and ammonium). The Q-AMS is not sensitive to mineral dust, but to the SOA and sulphuric acid coating on the surface of the dust particles. The aerodynamic inlet lens transmits particles with 100% efficiency in the size range (vacuum-aerodynamic diameter) between 0.06 and 0.6 μm, which corresponds to an upper cut-off volume-equivalent diameter of about 0.3 μm for ATD and illite particles. Therefore, we were not able to measure the full size distribution of the SOA coating. The Q-AMS measured only a lower limit of the total SOA coat mass which was consistent with the mass fraction obtained from the yield calculation

4. CLOUD EXPANSION EXPERIMENTS

After the aerosol was added to the AIDA chamber and characterised as described above, the cloud simulation experiments were started by pumping to the AIDA chamber at a constant rate, which induced an expansion cooling in the well-mixed volume and thereby a steadily increasing humidity RHi with respect to ice. The nucleation of ice crystals by the different aerosols was thereby measured as a function of RHi. All cloud expansion experiments discussed here were started at almost ice saturated conditions, a pressure of about 1000 hPa, and a homogeneous temperature of about 210 K with temporal and spatial temperature variability of less than ±0.3 K throughout the cloud chamber.

In all experiments, the number concentration of ice crystals steadily increased as long as RHi continued to rise, but stayed almost constant as soon as RHi approached or reached its peak value. Such a relationship between the ice-active number fraction of dust particles and RHi was already observed in previous AIDA experiments on the deposition ice nucleation to mineral dust particles and interpreted as the result of a distribution of surface sites which are rapidly activated as soon as the respective RHi thresholds are reached (Möhler et al. 2006).

5. EFFECT OF SOA COATING

Figure 3 shows the relation of the ice active aerosol number fraction f_{ice} and RHi for untreated (black) and SOA coated (blue) ATD particles, with f_{ice} determined as the ratio of the ice and aerosol number concentrations. During the expansion experiment with uncoated ATD almost all aerosol particles are active as deposition mode ice nuclei at RHi between 105 and 115 %, in agreement with previous AIDA experiments (Möhler et al. 2006). The heterogeneous ice nucleation efficiency of the SOA coated ATD particles is significantly reduced. These particles are ice-active only at RHi larger than 115 %. At the peak RHi of 130 % only about 20 % of the aerosol particles were ice-active.

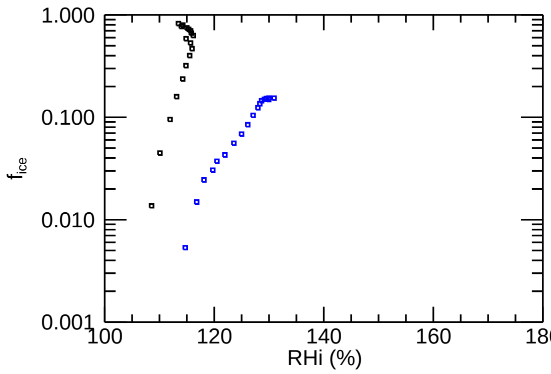

Fig 3: Ice active aerosol fraction f_{ice} as a function of RHi for untreated (black symbols) and SOA coated (blue symbols) ATD particles. The SOA mass fraction of the coated aerosol was about 17%.

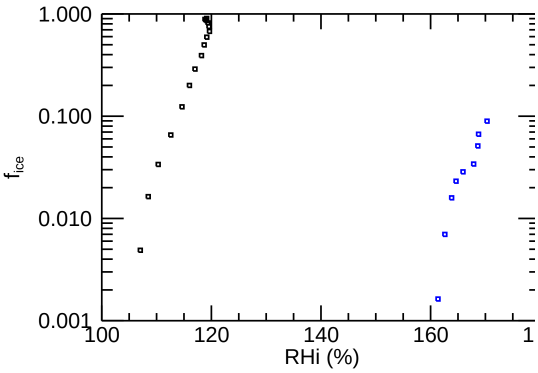

Fig 4: Ice active aerosol fraction f_{ice} as a fun tion of RHi for untreated (black symbols) a SOA coated (blue symbols) illite particles. T SOA mass fraction of the coated aerosol w about 41%.

The uncoated illite particles are also very efficient ice nuclei in the deposition mode (see Figure 4, black symbols). The RHi is limited to a peak value of 120%, and almost all illite particles nucleate ice in the RHi range between 105 and 120%. The ice nucleation of the SOA coated illite particles (Figure 4, blue symbols) is even more suppressed than that of the SOA coated ATD particles. Only 10% of the SOA coated illite particles nucleate ice between 160 and 170%, which is above the threshold for homogeneous freezing of solution particles at the same temperature. The more pronounced suppression of ice nucleation is probably due to the larger SOA mass fraction of about 41% compared to about 17% for the ATD case. We assume that the suppression of deposition mode ice nucleation by SOA coating mainly depends on the fractional surface coverage.

6. EFFECT OF H_2SO_4 COATING

Coating with sulphuric acid also markedly reduced the ice nucleation efficiency of illite particles (Figure 5, blue symbols). A significant fraction of the coated dust particles nucleated ice only at RHi above 145 %. This is close to the threshold of homogeneous freezing which is about 160 % at the given temperature of about

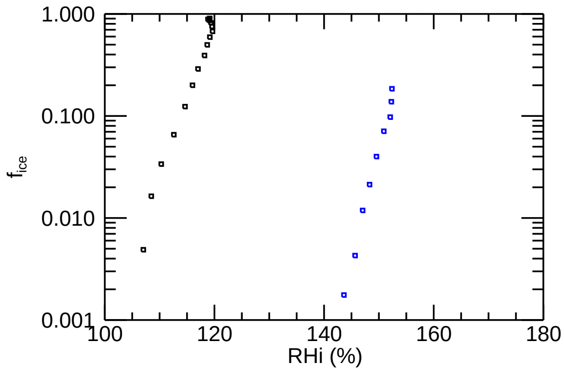

Fig 5: Ice active aerosol fraction f_{ice} as a function of RHi for untreated (black symbols) and sulphuric acid coated (blue symbols) illite particles. The H_2SO_4 mass fraction of the coated aerosol was about 30%.

With increasing relative humidity at the beginning of the pumping experiments the coated illite started to grow by water uptake of the sulphuric acid coat, indicated by sensitive forward scattering of the aerosol inside the AIDA chamber. The ice nucleation at RHi above 145% can therefore interpreted as immersion freezing induced by the illite particles.

6. CONCLUSIONS

The present work demonstrates the marked changes of heterogeneous ice nucleation efficiency of dust particles due to coating with secondary organic aerosol compounds and with sulphuric acid. Because atmospheric dust particles have been found to often contain organic compounds as well as nitrate and sulphate (Hinz et al., 2005; Murphy et al. 2006) we can assume that the heterogeneous ice nucleation potential of atmospheric dust particles is lowered by organic and inorganic coatings.

BIBLIOGRAPHY

Canagaratna, M. R., J. T. Jayne, J. L. Jimenez, J. D. Allan, M. R. Alfarra, Q. Zhang, T. B. Onasch, F. Drewnick, H. Coe, A. Middlebrook, A. Delia, L. R. Williams, A. M. Trimborn, M. J. Northway, P. F. DeCarlo, C. E. Kolb, P. Davidovits, and D. R. Worsnop (2007), Chemical and microphysical characterization of ambient aerosols with the Aerodyne aerosol mass spectrometer, *Mass Spectrom. Rev. 26*, 185-222.

Hinz, K. P., A. Trimborn, E. Wingartner, S. Henning, U. Baltensperger, and B. Spengler (2005), Aerosol single particle composition at the Jungfraujoch, *J. Aerosol Sci.*, *36*, 123-145.

Möhler, O., P. R. Field, P. Connolly, S. Benz, H. Saathoff, M. Schnaiter, R. Wagner, R. Cotton, M. Krämer, A. Mangold, and A. J. Heymsfield (2006), Efficiency of the deposition mode ice nucleation on mineral dust particles, *Atmos. Chem. Phys. 6*, 3007-3021.

Murphy, D. M., D. J. Cziczo, K. D. Froyd, P. K. Hudson, B. M. Matthew, A. M. Middlebrook, R. E. Peltier, A. Sullivan, D. S. Thomson, and R. J. Weber (2006), Single-particle mass spectrometry of tropospheric aerosol particles, *J. Geophys. Res. 111*, D23S32, doi:10.1029/2006JD007340.

THE EFFECT OF AIR POLLUTION ON ICE NUCLEI CONCENTRATION IN ISRAEL

Karin Ardon[1], Zev Levin[1], Eli Ganor[1], Holger Klein[2] and Heinz Bingemer[2]

[1] Department of Geophysics and Planetary Science, Tel Aviv University
[2] Institute of Atmospheric and Environmental Science, University of Frankfurt

1. INTRODUCTION AND BACKGROUND:

Air pollution aerosols as well as aerosols from natural sources affect our health, our environment and our climate on both local and global scales. The effects of aerosols from air pollution on the formation of clouds containing only water drops are fairly well understood. On the other hand the effects of air pollution aerosols on the formation and growth of ice crystals in clouds is still not clear. Some papers claim that air pollution can enhance ice crystal concentration (DeMott et al., 2003) while others like Braham and Spyers-Duran (1974) claim that the air pollution can de-activate them.

Ice crystals play an important part in the generation of precipitation in many types of clouds and greatly affect the global climate by influencing the global radiation balance (IPCC, 2001, 2007). They are formed in clouds by nucleation on very special particles called Ice Nuclei (IN). The ice nuclei are airborne, aerosol particles that vary from place to place and from season to season. Their sources and composition are still being debated. In addition, according to Levin and Cotton (2007) the ice formation in clouds is not well understood, there is a great deal of uncertainty in measurements of their concentrations and even in their characterization. The connection between ice crystal concentration in clouds, temperature and supersaturation is not clear. Therefore, it is not yet possible to forecast correctly the role of ice in clouds and in precipitation, and to estimate its effect on climate.

In this research we investigate the role of air pollution in modifying the concentrations of ice nuclei in Israel. We collected aerosols on filter samples from three locations (Fig 1) 1) near the shores of Tel Aviv, up wind of pollution sources; 2) on the campus of Tel Aviv University, inside the polluted area about 3 km from the sea shore, 3) east of the city of Tel Aviv and downwind of the pollution centers. For this purpose we used Nitrocellulose filters with a diameter of 47 mm and 0.45 pore sizes, 300L (for deposition and condensation freezing) and 400L (for immersion freezing) of air were sampled on each filter. During the sampling, an aerosol concentration was measured using the TSI Condensation Particle Counter Model 3010.

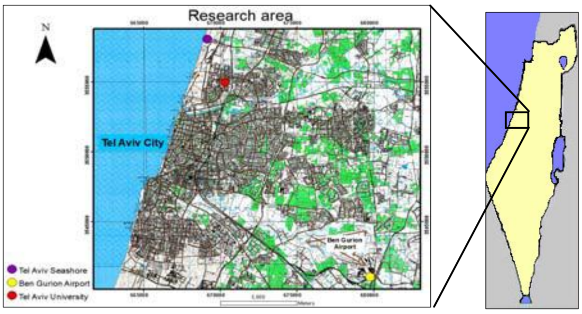

Figure 1: Research area.

2. METHODS AND EXPERIMENTAL SET UP

Three modes of heterogeneous nucleation have been investigated: immersion, deposition and condensation freezing. The analysis has been made in the newly designed IN-Counter called FRIDGE-TAU (Frankfurt Ice-nuclei Deposition freezing Experiment - the Tel Aviv University version), see Fig 2a-b.

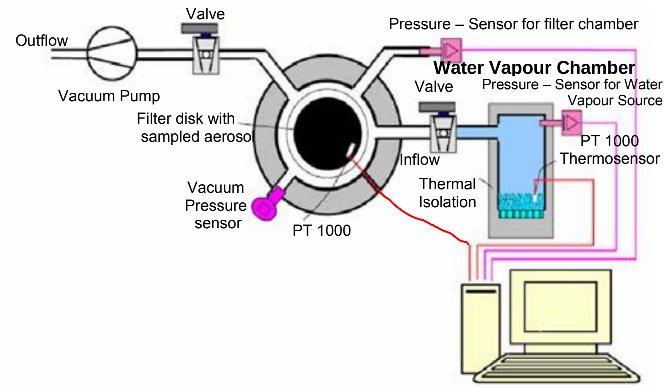

Figure 2a: Schematic diagrams of the FRIDGE-TAU instrument top view.

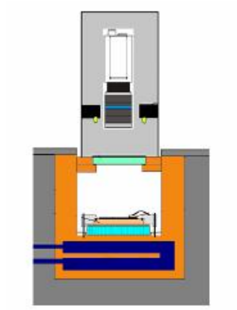

Figure 2b: Schematic diagram of the FRIDGE-TAU ice nucleation chamber, side view.

The procedure for operating this chamber can be found in (Nillius et al, 2008). In brief, the filters are exposed to the desired and known vapour pressures at each temperature, thus allowing for determination of the ice nuclei concentrations active at these temperatures. Measurements were performed from around 0°C down to -30°C, with a number of different values of vapour pressure at each temperature, from ice saturation to just above water saturation. The ice crystals that are formed are recorded with a computer controlled CCD camera.

In addition to the samples collected on the filters for the analysis described above, we also collected aerosols on filters for evaluating the immersion freezing properties, using the drop freezing method (e.g. Vali, 1985; Levin et al, 1987). The filters with the collected aerosols were washed with 10 ml of double distilled water. From the mixture of water and aerosols, about 100 small drops (2 µl) were placed on the substrate of the chamber in the FRIDGE-TAU. As the chamber is cooled, the number of frozen drops at each temperature is recorded with the CCD camera.

3. PRELIMINARY RESULTS

3.1 IMMERSION FREEZING:

We compared the average temperatures at which the drops froze at each of the three locations on the same day (about 1 hour apart between samples). As can be seen from Fig 3, the freezing temperature (average of three samples) at which 50% of the drops froze varies by about 3 degrees between samples collected at the three sites. The freezing temperatures of the drops containing aerosols collected downwind of the polluted area are the highest (about -22°C), suggesting that the pollution sources of Tel Aviv may contain some efficient IN. The drops containing particles from TAU (inside the polluted area) exhibit an intermediate freezing spectrum with a modal freezing temperature of -23˚C. It can be concluded that air which comes from the Mediterranean and is up wind of the pollution of Tel Aviv contains less efficient IN.

Our results are similar to those reported by Hobbs and Locatelli (1970), but in contradiction to Borys and Duce (1979) who found no detectable effects of the urban atmosphere on the IN concentration.

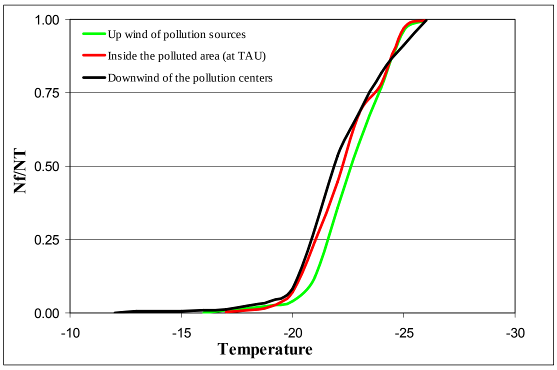

Figure 3: immersion freezing result for comparison of freezing spectrum as a function of air pollution concentration.

Comparing immersion freezing efficiency between two days with dust (090308 & 170308) reveals differences in the IN activity spectrum of the dust particles (Fig 4). Dust particles collected on 090308 are more effective as freezing nuclei (freezing occurs at higher temperatures) than those collected on 170308. The difference in the freezing temperatures of the drops could possibly be explained by the different source and composition of the dust particles.

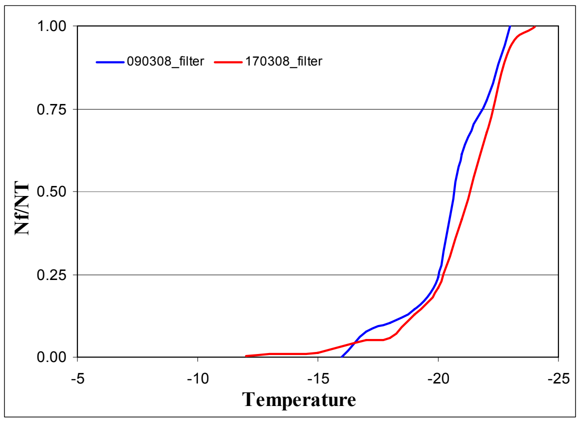

Figure 4: comparison immersion freezing between two days with dust.

3.2 DEPOSITION AND COCDENSATION FREEZING RESULT:

Using the FRIDGE-TAU we also compared the deposition and condensation freezing of filter samples taken during the same two days with dust, 090308 and 170308 (Fig 5). It can be seen that at the same supersaturation with respect to water, the colder the temperature the higher the number of ice crystals that appear on the filter. The highest concentrations of ice crystals appear close to, or at water saturation. It is interesting to point out that the slope of the curves (although only a few measurements are available) is smoothly approaching water saturation. This is a puzzling observation, since at low water saturation ratio one would expect deposition. At water saturation, or close to it, immersion freezing is expected. The fact that in most cases the slope is smooth as water saturation is approached, may imply that condensation freezing occurs already below water saturation. Such conditions could occur if the particles contain some soluble material on them. Levin et al (2005) reported that dust passing over the Mediterranean contains high concentrations of dust coated with sea salt. One cautionary note is in order; the FRIDGE experiments for deposition and immersion freezing in the setup described above seem to undercount the ice nucleation by about two orders of magnitude as compared with the measurements with a number of Continuous Flow Diffusion Chambers, as illustrated in the AIDA workshop in October 2007. The reasons for the undercount may have to do with the petroleum jelly that is used to improve the contact between the filter and the cold substrate. Apparently, some of the petroleum jelly penetrates through the filter holes, coats some of the particles and deactivates the ice nuclei. An attempt to collect the aerosols on metal substrate by electrical deposition is now underway.

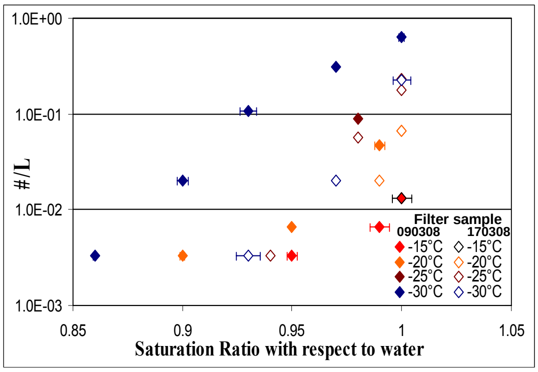

Figure 5: Comparing the Deposition and Condensation freezing for two days with dust.

Elemental composition of suspended mineral dust (d<100µm) using the EM-EDS method described by Levin et al (1996), showed that the dust particles from 090308 contained more soluble material, probably sea salt, then the dust particles collected on the 170308 (Fig 6). This would support the hypothesis that many of the dust particles passing over the Mediterranean Sea are coated with sea salt. Thus these are good condensation freezing nuclei, which form ice more efficiently than pure dust particles that require higher water saturation ratio before ice nucleation can occur.

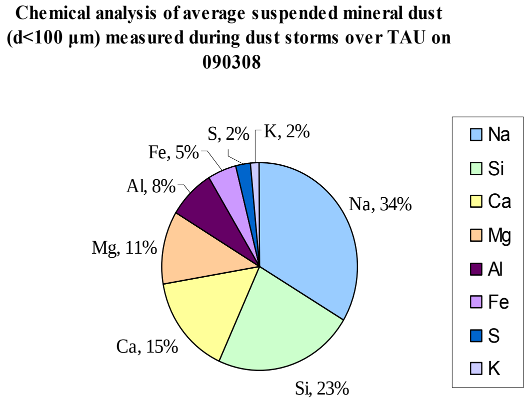

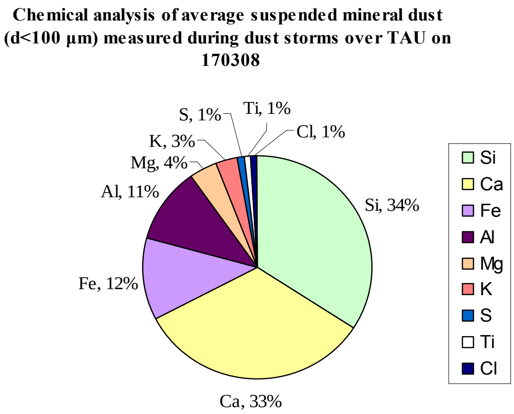

Figure 6: Elemental composition of suspended mineral dust (d<100µm) for the two days with dust.

Back trajectory analysis (Fig. 7) of these two days confirms that the air reaching Tel Aviv at the low levels on the 090308 passed over the sea, probably picking up some of the sea salt. In contrast, the air reaching Tel Aviv at the low levels on the 170308 came directly from the east, without passing over the Sea.

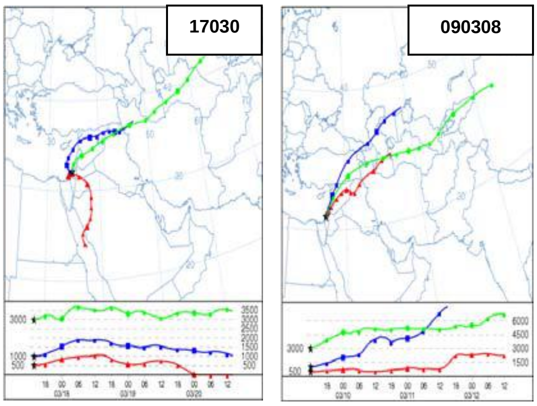

Figure number 7: Back trajectory analysis for the two days with dust, Source: http://www.arl.noaa.gov.

4. CONCLUSIONS

In this study we are trying to measure the ice nuclei upwind and down wind of urban areas in Israel in order to determine the effects of pollution on ice nucleation in Israel. The results will then be compared with similar measurements carried out in Europe, in order to determine the geographical distribution of these particles. The present preliminary results show some effects of the city of Tel Aviv on enhancement of effective IN. Furthermore, immersion freezing of drops seems to be a much more effective ice nucleation process than deposition nucleation. The filter method, in which deposition could be separated from immersion freezing, indicates that condensation freezing on dust particles starts at water sub-saturation due to the presence of soluble material on the dust particles. Elemental analysis and back trajectory calculations confirm the presence of soluble material on the dust particles.

5. BIBLIOGRAPHY

Borys, R. D. and Duce, R. D: Relationships among lead, iodine, trace metals and ice nuclei in a coastal urban atmosphere, *J. Appl. Meteor.,* 18, 1490–1494, 1979.

Braham, R.R. and Spyers-Duran, P: Ice nucleus measurements in an urban atmosphere, *J. Appl. Meteo.,* 13, 940-945, 1974.

DeMott, P.J., Sassen, K., Poellet, M.R., Baumgardner, D., Rogers, D.C., Brooks, S.D., Prenni, A.J. and Kreidenweis, S.M: African dust aerosols as atmospheric ice nuclei, *Geophys. Res. Lett.,* 30, 1732, doi:10.1029/2003GL017410, 2003.

Hobbs, P.V. and Locatelli, J: Ice Nucleus Measurements at Three Sites in Western Washington, *J. Appl. Meteor*., 27, 90–100, 1970

IPCC, Climate Change 2001: The Scientific Basis, Contribution of working Group I to the Third Assessment Report of the Intergovernmental Panel on Climate Change, Cambridge University Press, 2001.

IPCC, Climate Change 2007: The Physical Science Basis, Contribution of Working Group I to the Fourth Assessment Report of the Intergovernmental Panel on Climate Change, Paris, 2007.

Levin, Z. and Cotton, W.R: Aerosol Pollution Impact on Precipitation: A Scientific Review, Report of the International Aerosol Science Assessment Group to the WMO and the IUGG, 2007.

Levin, Z., Yankofsky, S.A., Pardess D. and Magal, N: Possible Application of bacterial condensation freezing to artificial rainfall enhancement, *J. Climate and Appl. Meteor.*, 26, 1188-1197, 1987.

Levin, Z., Ganor, E. and Gladstein, V: The effects of desert particles coated with sulfate on rain formation in the eastern Mediterranean, *J. Appl. Meteor.*, 35, 1511-1523, 1996.

Levin, Z., Teller, A., Ganor E. and Yin, Y: On the interactions of mineral dust, sea salt particles and clouds – A Measurement and modeling study from the MEIDEX campaign, *J. Geophys. Res.,* 110, D20202, doi:10.1029/2005JD005810, 2005.

Nillius, B., Bingemer,H., Bundke, U., Jaenicke, R. and Wetter, T: First Measurement Results of the Fast Ice Nucleus Counter FINCH, *Geophysical Research Abstracts*, 9, 08681, 2008

Vali, G:. Atmospheric ice nucleation —a review. *J. Rech. Atmos*., 19, 105–115, 1985.

Acknowledgement:

The authors would like to thank the German Israeli Foundation (GIF) and the Virtual Institute on Aerosol-Cloud Interactions, supported by the Helmholtz-Gemeinschaft (HGF) for their partial support of this project. Karin Ardon would like to thank the Porter School of Environmental Studies at Tel Aviv University for its financial support during this work, to the ESF MedCLIVAR Program for providing a fellowship to attend the AIDA workshop and to the ICCP and WMO for covering the registration fee of the present conference.

SOURCES OF ATMOSPHERIC AEROSOLS DURING WINTERTIME STORMS IN THE SNOWY MOUNTAINS

Thomas Chubb[1], Steven Siems[1], Michael Manton[1]

[1]Monash University, Melbourne, Australia

May 1, 2008

Abstract

Wintertime storms in the Snowy Mountains of south-eastern Australia provide an interesting circumstance to investigate the effect of atmospheric aerosols on clouds and precipitation. This alpine region forms the catchment for the Snowy Mountains Scheme, which in addition to energy generation, is responsible for the redirection of water to the Murray river for irrigation. Severe droughts in the past decade have put significant pressure on this river system, motivating a cloud seeding research project currently being conducted by Snowy Hydro Ltd, the operators of the Scheme.

As a precursor to performing high resolution numerical modelling to investigate the sensitivity of precipitation processes in wintertime storms in the Snowy Mountains region, a climatology of the atmospheric aerosol content is performed. A back-trajectory model, in conjunction with mesoscale meteorological data is used to identify potential aerosol sources for wintertime precipitation events in the Snowy Mountains. The results of this study are to be verified by comparison with microphysical and meteorological data gathered by Snowy Hydro during cloud seeding operations since 2005.

1 INTRODUCTION

The Snowy Mountains Scheme is a hydroelectricity and irrigation complex in south-east Australia. Eastward flowing waters from the Snowy River are diverted inland through a complex of underground tunnels beneath the Snowy Mountains to the Murray and Murrumbidgee Rivers, and are used to generate hydroelectricity during national peak-load periods. Diverted waters from the Snowy Mountains region make up about five to ten percent of total inflows into the Murray River basin, and the hydroelectricity generated in the process provides about 3.5 per cent of Australia's electricity.

The most significant precipitation in the Snowy Mountains region falls in the winter months between May and September. Wintertime precipitation events in the region are generally characterised by the passage of a cold front, where a 'pristine' airmass originating from the Southern Ocean passes over south-eastern Australia. Precipitation during these events is enhanced by orographic uplift over the western slopes of the mountains. Increased lifting in these regions results in the availability of additional condensate for scavenging by precipitation at higher levels within the cloud (Reinking et al., 2000).

The amount of precipitation from these events is highly variable and depends principally on the dynamics of individual storms. It has been suggested that precipitation is being suppressed in the Snowy Mountains due to the influence of atmospheric aerosols emitted from anthropogenic sources. Rosenfeld (2000) uses observations from the Tropical Rainfall Measuring Mission satellite to deduce reduced cloud particle size in 'pollution plumes' originating from sources in south-eastern Australia. Rosenfeld infers that cloud droplet coalescence and ice particle formation have been inhibited as a result, and that this leads to suppression of precipitation in water catchments, including the catchments of the Snowy Mountains (Rosenfeld et al., 2006).

Supporting Rosenfeld's claims of precipitation suppression in orographic clouds is a modelling study (Lynn et al., 2007), in which a two-dimensional simulations performed by the Weather Research and Forecast (WRF) model were coupled to a spectral microphysics module. The study compared the effects of "clean-air" maritime and "dirty-air" continental aerosol loadings on precipitation from orographic cloud in the Sierra Nevada, and found that the increased aerosol concentration led to a downwind shift of precipitation particles compared to the "clean-air" case. Lower precipitation was accumulated in the "dirty-air" case, especially on the lower slopes of the terrain. Importantly, it was noted in particular that anthropogenic aerosols had been shown to decrease precipitation in comparatively dry environmental conditions.

Attempts have been made to correlate mountain-top cloud microphysical observations with precipitation accumulation during wintertime storms. For example, Borys et al. (2003) compare observations of two storms in the Rocky Mountains considered to be similar except for differences in cloud particle number concentration and size distribution. Dramatically different precipitation rates are attributed to inhibition of snow particle riming growth. However, a systematic correlation between aerosol concentration and precipitation was not confirmed in a statistical analysis (Hindman et al., 2006) of microphysical and precipitation records for the same site over the twenty year period between 1984 and 2004. If a subset of wintertime storm conditions susceptible to precipitation suppression by increased aerosol concentration is to be identified, Hindman et al. conclude that continuous monitoring of the chemistry and physics of cloud, snow and aerosol must be done in concert with fine-grid, meso-scale modelling to ascertain the seasonal role of aerosols on precipitation rates.

To date, suggestions of precipitation suppression in the Snowy Mountains are yet to be supported by measurement based evidence (Ayers, 2005). Substantial differences in orography and meteorology, as well as the extent of aerosol pollution between south-eastern Australian and the US south-west must be considered. As discussed by Ayers, supporting precipitation observations are required to verify a decline in rain and snowfall, and further that the anthropogenic aerosol dispersion patterns require validation. Although an intensive measurement campaign has yet to be conducted, a cloud seeding research project is being conducted by Snowy Hydro, during which a variety of microphysical and meteorological data are being collected.

2 CLIMATOLOGY OF PRECIPITATION EVENTS

2.1 Ten year climatology

A ten year climatology of wintertime precipitation events in the Snowy Mountains region was performed in order to identify some of the key features of winter storms currently affecting the region. Daily precipitation records were obtained from the Australian Bureau of Meteorology for four sites within the Snowy Mountains alpine region for the winter months (May-September) during the period 1997-2007. An automated method was used to objectively identify and distinguish between precipitation events, which were defined as a set of monotonically increasing daily precipitation readings to a peak value followed by a set of decreasing values. This was considered to be an appropriate criteria for precipitation events associated with a dominant synoptic feature, such as a cold front or extra-tropical cyclone, that typically influence a region for two to five consecutive days.

	Frequency; Rel. Contribution			
Year	Type-1	Type-2	Type-3	Other
2005	6; 41.3%	13; 42.6%	2; 4.3%	14; 11.5%
2006	7; 31.8%	10; 42.4%	3; 8.8%	7; 12.6%
2007	12; 17.5%	12; 35.3%	4; 2.4%	22; 3.1%
3-yr	8.3; 35.6%	11.6; 49.0%	3; 5.5%	14.3; 9.9%

Table 1: Wintertime precipitation statistics for 2005-2007

The one hundred most significant precipitation events, ranked by mean total precipitation accumulated over the duration of the event, were then classified subjectively by inspection of Mean Sea Level Pressure (MSLP) analyses. Precipitation events fell into three dominant categories:

- Type-1: Cold frontal passage associated with cut-off extra-tropical cyclone in Great Australian Bight and Bass Strait region.
- Type-2: Cold frontal passage associated with extra-tropical cyclone or trough in the Southern Ocean.
- Type-3: Moist flow associated with cut-off low pressure centre in Tasman Sea.

2.2 Three year climatology

Further attention was paid to the three years between 2005 to 2007, as these years coincide with the first three years of cloud seeding operations in the Snowy Mountains, marking the availability of in-situ microphysical observations during precipitation events.

Table 1 summarises the frequency of occurrence and relative importance of each of the three categories of precipitation events in terms of precipitation accumulated during the course of the event for the three years. These result show that cold frontal passages are by far the dominant precipitation producing weather systems in the Snowy mountains region in the most recent three years. This is somewhat at odds with the findings of the ten year climatology of major precipitation events, where cut-off Tasman depressions contributed a more significant proportion of the total precipitation. The most intense of these depressions, the so-called meteorological ‘bombs’, produce significant precipitation and regional flooding, but occur relatively infrequently (Leslie et al., 2005).

3 CLIMATOLOGY OF AIR PARCEL HISTORIES

Central to developing an atmospheric aerosol climatology is an understanding of air parcel histories during precipitation events. In order to present an overview of air parcel histories during the different types of precipitation events discussed in section 2.1, parcel back trajectories during the events were computed at three hourly intervals with the use of the NOAA Air Resources Laboratory Hybrid Single-Particle Lagrangian Integrated Trajectory (HYSPLIT) model. Back trajectories were computed using two different data sets. For the three years between 2005 and 2007, all precipitation events were analysed using three hourly Global Data Assimilation System (GDAS) analyses, over a one degree latitude-longitude grid, produced by the National Centre for Environmental Prediction (NCEP). For several selected case studies, 0.125 degree resolution Mesoscale Limited Area Prediction System (MLAPS) analyses produced by the BoM were used in order to resolve mesoscale features.

3.1 Preliminary Climatological Features

Subjective analysis of MSLP analyses and time series of back trajectories was used to identify the approximate time of frontal passages in the Snowy Mountains region for the type-1 and type-2 precipitation events. Back trajectories from each event were classified as pre-frontal or post- frontal according to their arrival time. In order to identify general features of air parcel histories, trajectories arriving six and twelve hours before and after the frontal passage were considered statistically. Figures 1 and 2 show mean trajectories and probabilistic envelopes of one standard deviation in position and height respectively, for 35 type-2 precipitation events between 2005 and 2007. Parcel histories are shown to an age of 36 hours.

3.1.1 General features of trajectory envelopes

General patterns of the frontal passage are captured by the statistical approach used here. A change in the orientation of the lower level back trajectory envelope of approximately 90° between pre-frontal and post-frontal trajectories at 500 m is evident. Less marked shifts are also apparent for 1000 m and 2000 m arrival trajectories. An increase in wind speed following the frontal passage is shown by the significantly longer post-frontal mean trajectories for the 36 hour duration considered here.

Significant variability within both the pre-frontal and post-frontal trajectory sets is displayed by the width of the envelopes. The lower level trajectories are particularly variable, with correlations of histories longer than 36 hours becoming very poor. The correlation between the post-frontal histories is better for the 1000 m and 2000 m, where the 500 m histories show increasing divergence before about 18 hours prior to arrival. This feature indicates that lower level parcels are 'caught' by the front as it approaches. By twelve hours prior to arrival the correlation between the lower level parcels is similar to that of the upper level parcels.

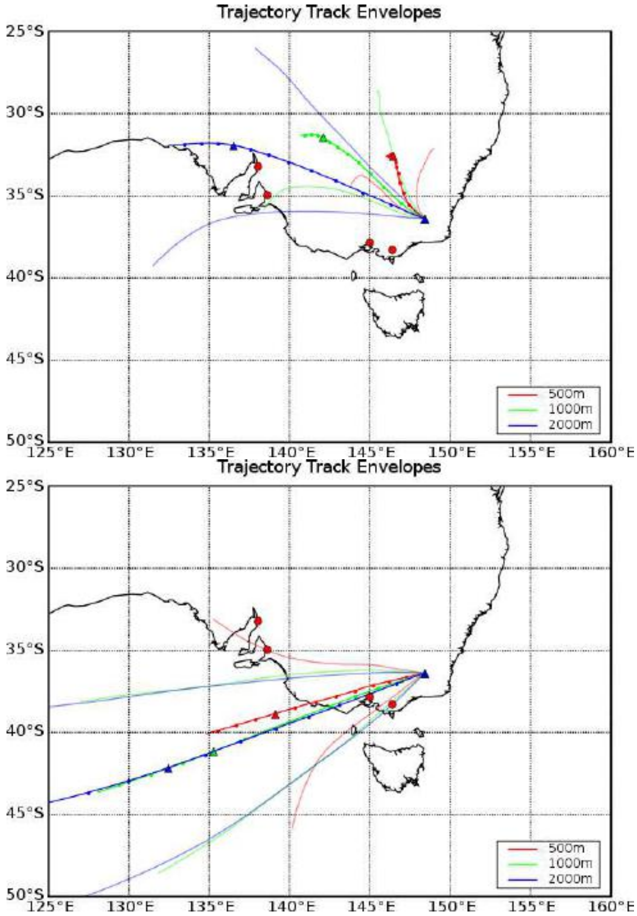

Figure 1: Mean trajectories and 1-σ envelopes for trajectories arriving six hours pre-frontally (upper) and post-frontally (lower). The trajectories are timestamped with 3-hourly (dot) and 24-hourly (triangle) markers.

On average, trajectories arriving before the passage of a cold front pass closer to ground level than those arriving post-frontally. Vertical profiles of pre-frontal trajectories show consistent ascent for each of the three levels as they reach their endpoint in the Snowy Mountains region. This may in part be due to orographic influence, but as this feature is not apparent in the post-frontal trajectories it is also attributed to surface level convergence ahead of the cold front. In particular for upper-level post-frontal arrivals, the parcels spend the entire duration of the 96 hour

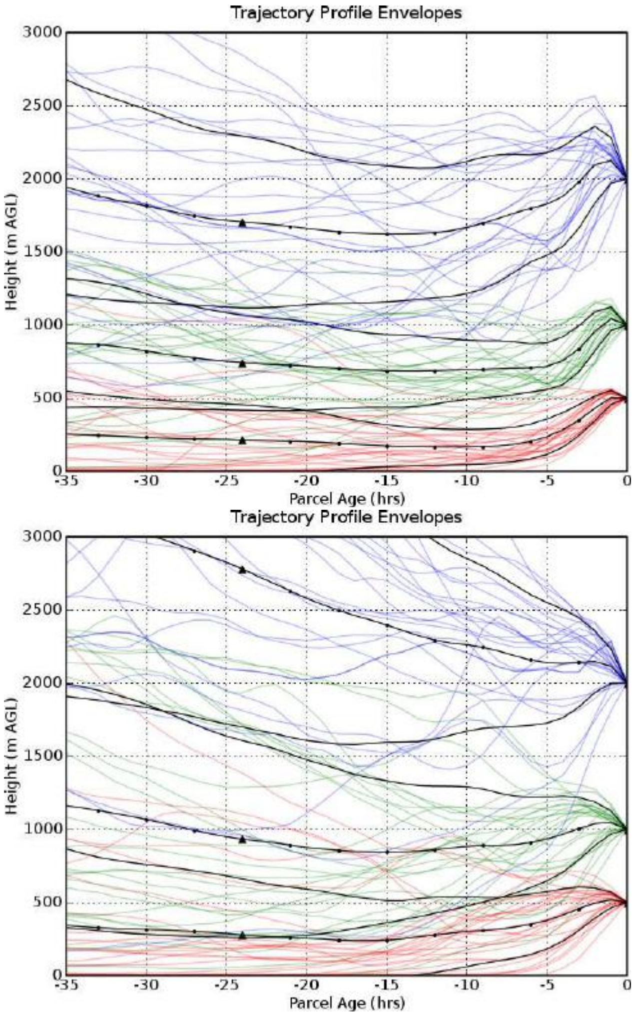

Figure 2: Same as Figure 1 but for vertical profiles of trajectories.

trajectories in the cold airmass, and a general subsiding trend can clearly be seen for these parcels.

There is significant spread within the profiles of the post-frontal trajectories in particular. Initial analyses of these have indicated that this is primarily due to the existence of some outlying trajectories that deviate far from the probabilistic envelope. There is also evidence of trends within these sets of post-frontal trajectories, with the 1000 m arrivals showing a sets of ‘ascending’ and ‘descending’ trajectories. The spreads may be significantly reduced if particular synoptic scale features can be identified to influence this characteristic.

As shown by the narrower envelopes, the spreads of the pre-frontal trajectory profiles are somewhat smaller. There are fewer outliers than in the post-frontal trajectories, and there do not appear to be any systematic trends within the trajectories displayed.

3.1.2 Implication for aerosol loading

The air parcel history climatology of this set of precipitation events illustrates an important point about cold frontal passages in south-eastern Australia. During the passage of the front, there is a significant change in the origin of air parcels arriving at the Snowy Mountains region, with parcel histories changing from continental to maritime over the course of about twelve hours. The exposure that these air parcels have had to different types of terrain and proximity to urban or industrial centres will have significant bearing on the atmospheric aerosol content of the airmass in the region. Results obtained to date suggest that lower level parcels arriving pre-frontally are most likely to have been isolated from major industry and in general the mid and upper level trajectories are stratified and thus unlikely to have been significantly influenced by emissions in lower levels.

During and following the frontal passage, there is potential for pollution of an otherwise pristine airmass from urban and industrial centres in the region. Emissions from several urban and industrial sites in particular have been implicated as possible sources for aerosol pollution resulting in precipitation suppression (Rosenfeld, 2000), and are plotted as red dots in Figure 1. Of these, only the Melbourne urban centre falls clearly within the envelope of influence of the lower-level trajectories for type-2 precipitation events for trajectories arriving six hours post-frontally. Further analysis will yield more information about the potential for significant impact by these sources on the aerosol loading during wintertime precipitation events under these conditions

REFERENCES

Ayers, G.: 2005, *Clean Air and Environmental Quality* **39(2)**, 51

Borys, R. D., Lowenthal, D. H., Cohn, S. A., and Brown, W. O. J.: 2003, *Geophysical Research Letters* 30(10)

Hindman, E. E., Borys, R. D., Lowenthal, D. H., and Phillip, N.: 2006, *Atmospheric Research* **82(1-2)**, 194, Hindman, Edward E. Borys, Randolph D. Lowenthal, Douglas H. Phillip, Neal Sp. Iss. SI

Leslie, L. M., Leplastrier, M., Buckley, B. W., and Qi, L.: 2005, *Meteorology and Atmospheric Physics* **89(1-4)**, 207

Lynn, B., Khain, A., Rosenfeld, D., and William, W. L.: 2007, *Journal of Geophysical Research* 112

Reinking, R. F., Snider, J. B., and Coen, J. L.: 2000, *Journal of Applied Meteorology* **39**, 733

Rosenfeld, D.: 2000, *Science* **287(5459)**, 1793

Rosenfeld, D., Lensky, I. M., Peterson, J., and Gingis, A.: 2006, *Clean Air and Environmental Quality* **40(2)**, 43

IN-SITU CHARACTERISATION OF SUBMICRON AEROSOL PHYSICAL, CHEMICAL AND HYGROSCOPIC PROPERTIES AT THE SUPERSITE HORNISGRINDE DURING THE COPS FIELD CAMPAIGN

J. Crosier, M. Irwin, P. Williams, G. McFiggans, H. Coe, T. Choularton

Centre for Atmospheric Science, SEAES, University of Manchester, UK

INTRODUCTION

Aerosols have both a direct and indirect effect on climate. They alter the Earths radiation balance by direct scattering and absorption of solar and terrestrial radiation [*Haywood and Boucher*, 2000]. Aerosol properties also have a large impact on cloud properties, as particles around 100nm diameter and larger are potential Cloud Condensation Nuclei [*McFiggans, et al.*, 2006]. The impact of aerosol properties on clouds includes alterations in cloud optical thickness, cloud lifetime, cloud top height and precipitation suppression (Lohmann et al 2007).

The uncertainty associated with the influence of particles on cloud properties was identified as one of the largest sources of uncertainty in global radiative forcing [*Forster, et al.*, 2007].

FIELD STUDY

The Convective and Orgographically-induced Precipitation Study (COPS) is an international field campaign initiated within the Quantitative Precipitation Forecast (QPF) program funded by the German Research Foundation (DFG). The study aims to improve the accuracy of precipitation forecasts through the use of in-situ and remote sensing instrumentation, advanced high resolution models optimised for use in complex terrain, and data assimilation/ensemble prediction systems.

The region under observation during COPS was in Southwest Germany/Eastern France. This area is prone to frequent thunderstorms in summer, with the skill of numerical weather forecasts in the area being low. The main observation period within COPS was conducted from 1st June until 30th August 2007.

Figure 1: COPS Study Region

Instrument	Measured property
CPC (TSI 3010)	Total particle number concentration (10nm > D > 1000nm)
DMPS	Number size distribution (20nm > D > 600nm)
GRIMM OPC	Number size distribution (250nm > D > 4000nm)
HTDMA	Hygroscopic growth factor @ 90% RH (43,85,127,169,211 and 254nm)
CCNC	Activated particle number concentration
HR-ToF-AMS	Size resolved non-refrectory chemical composition (40nm > D > 700 nm)
MAAP	Equivalent total black carbon mass concentration

Table 1: Aerosol instrumentation deployed and properties measured in-situ at the Hornisgrinde hilltop site during COPS-UK.

A contribution to COPS from the United Kingdom (COPS-UK) was made in the form of the deployment of various in-situ and remote sensing instrumentation from the ground and an aircraft platform (the UK Facility for Airborne Atmospheric Research, FAAM BAE-146). Results from the in-situ aerosol sampling instrumentation situated on top of the Hornisgrinde (1164m asl) hill top site are presented here. The in-situ aerosol measurements made at this site by COPS-UK are listed in Table 1.

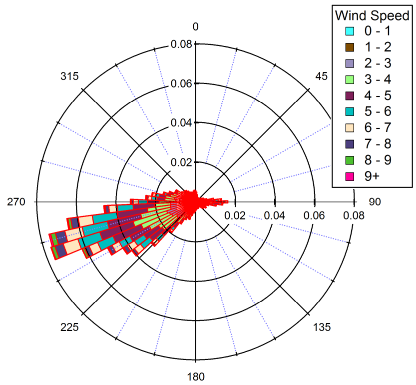

Figure 2: Wind rose from the Horninsgrinde measured during COPS

Measurements were taken from 23rd June and 27th July 2007. Instruments were sampling through an inlet 3m above ground level through a cyclone impactor which removed all particle above 4µm diameter. This impactor was used to remove water droplets to prevent instrument damage during in cloud events which occurred frequently throughout the experiment. The correct operation of the impactor was confirmed by the GRIMM OPC which saw no particles above 4 microns diameter. The data presented here are for out of cloud conditions only. Figure 2 show the wind rose measured at the Hornisgrinde during COPS. The wind was nearly always from the South West with typical wind speeds averaging around 5 m/s.

AEROSOL COMPOSITION

The aerosol composition was measured online using a High-Resolution Time-of-Flight Aerosol Mass Spectrometer (HR-ToF-AMS, [*DeCarlo, et al.*, 2006]) which provides mass loadings of Organic, Nitrate, Sulphate and Ammonium submicron aerosol, and a Multi-Angle Absoprtion Photometer (MAAP, [*Petzold, et al.*, 2005]) to provide a measure of the Black Carbon (BC) mass concentration. The Organic, Nitrate, Sulphate and Ammonium mass concentrations shown here have not been corrected for collection efficiency which would result in a predicted doubling of mass loadings [*Drewnick, et al.*, 2003].

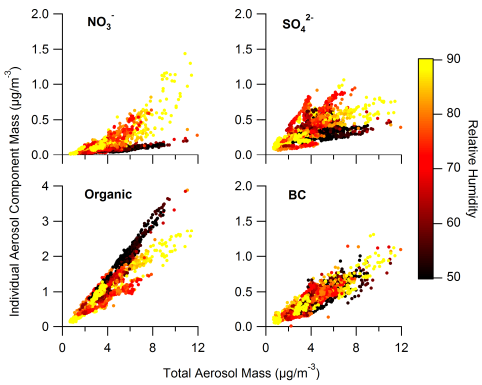

Figure 3: Uncorrected submicron aerosol mass loadings derived from the HR-ToF-AMS (Organic, Sulphate and Nitrate) and MAAP equivalent Black Carbon. Data are coloured according to relative humidity.

The mass loadings of each aerosol component against the total aerosol mass are shown in Figure 3. Organic aerosol contributes the largest amount of material to the total aerosol mass. The relative amount of organic material also seems to be relatively constant. The amount of nitrate in the aerosol, while small in magnitude, exhibits a considerable amount of variability. The highest loadings of nitrate appear during times of high relative humidity. The black carbon and sulphate mass contributions vary in response to these changes and probably for other reasons including air mass trajectory.

The average organic mass spectrum measured during COPS-UK can be seen in Figure 4. The major mass fragments seen in the spectrum are from *m/z*'s 18 and 44, both of which are from poly-acidic organics. This suggests the organic aerosol is of a highly aged secondary nature. The mass spectrum compares well with that seen by Alfarra et al [2004] in a clean rural environment. The hygroscopic growth factor of the aerosol measured using the Hygroscopicity Tandem Differential Mobility Analyser was low (typically 1.3) which agrees with the high organic aerosol content. The HTDMA also suggests the presence of a single internally mixed accumulation mode in the aerosol population.

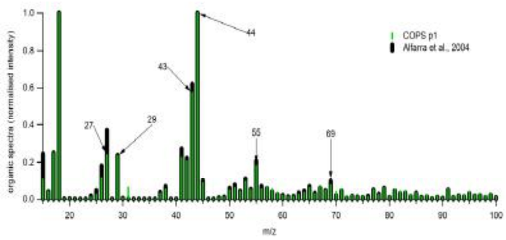

Figure 4: Average organic mass spectrum from COPS and from a rural location [*Alfarra, et al.*, 2004].

CCN MEASUREMENTS

Measurements of CCN concentrations were made using a DMT CCNC which was ran cycling at 5 different super saturation ratios. The instrument measured total and mono-disperse CCN concentrations at alternate hours. The CCNC measured through a DMPS system to measure mono-disperse aerosol. The data presented here are uncorrected for multiple charge effects which may alter the measured CCN spectra. Comparing the measured CCN concentrations with the measured CN concentrations throughout the particle size distribution allow the determination of the critical diameter (D_{50}, the diameter at which 50% of the particles activate at a given supersaturation). A time series of aerosol composition from the HR-ToF-AMS shown in Figure 5 shows 2 highlighted areas. One is dominated by organics and the other which has significantly more inorganics relative to the organics.

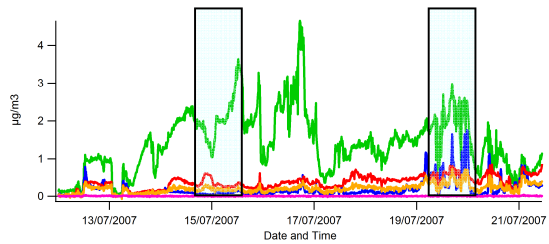

Figure 5: Time series of uncorrected mass loadings of organic (green), nitrate (blue) sulphate (red) and ammonium (orange) aerosol components.

Figures 6 and 7 show the uncorrected CN and CCN concentrations, as well as the particle size being sampled as a function of time. The CCNC was exposing the sample to a supersaturation of 0.07% during these scans. The highly organic aerosol seen on the 15th July and shown in Figure 6 appears to have a D_{50} of around 256nm, with the corresponding D_{50} of the more inorganic influenced aerosol being around 210nm.

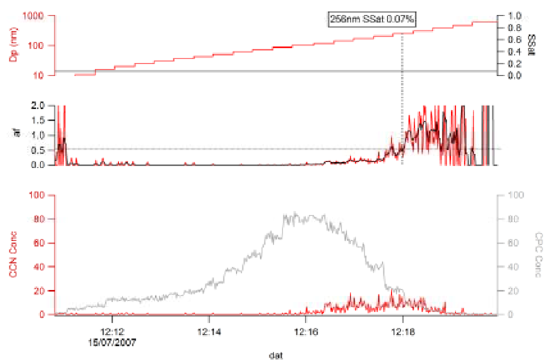

Figure 6: Time series of uncorrected CN and CCN number concentration during mono-disperse sampling in high organic mass fraction aerosol. Also shown are activated fraction and particle size.

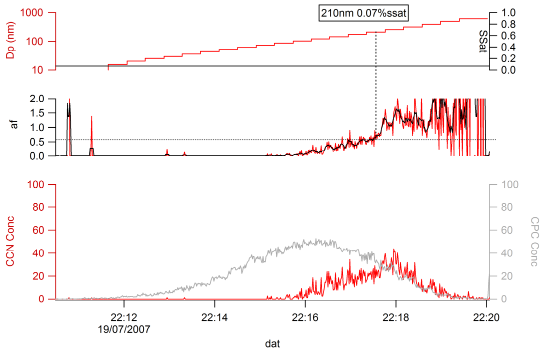

Figure 7: Time series of uncorrected CN and CCN number concentration during mono-disperse sampling in high nitrate mass fraction aerosol. Also shown are activated fraction and particle size.

CONCLUSIONS

Aerosol composition on the Hornisgrinde hill top site during COPS-UK was found to be highly organic in nature. The organic aerosol was also seen to be highly oxidised. The lack of variability in these properties could be due to the central European location and due to the altitude of the field site. Ammonium nitrate was enhanced during periods of high relative humidity. The aerosol measured by the HR-ToF-AMS was found to be pH neutral at all times.

Aerosol particles exhibited low sub-saturated growth at 85% humidity due to the high organic content. The measured D_{50} which dictates the number of CCN formed from a particle size distribution was seen to be large in a period of very of organic to inorganic aerosol mass.

ACKNOWLEDGMENTS

We would like to acknowledge the University of Innsbruck for the data from the Automated Weather Station on the Hornisgrinde. Funding for this work was provided by the UK National Centre for Atmospheric Science (NCAS).

REFERENCES

Alfarra, M. R., et al. (2004), Characterization of urban and rural organic particulate in the lower Fraser valley using two aerodyne aerosol mass spectrometers, *Atmospheric Environment*, *38*, 5745-5758.

DeCarlo, P. F., et al. (2006), Field-deployable, high-resolution, time-of-flight aerosol mass spectrometer, *Analytical Chemistry*, *78*, 8281-8289.

Drewnick, F., et al. (2003), Intercomparison and evaluation of four semi-continuous PM2.5 sulfate instruments, *Atmospheric Environment*, *37*, 3335-3350.

Forster, P., et al. (2007), Changes in Atmospheric Constituents and Radiative Forcing, in *Climate Change 2007: The Physical Science Basis. Contribution of Working Group I to the Fourth Assessment Report of the Intergovernmental Panel on Climate Change*, edited by S. Solomon, et al., Cambridge University Press.

Haywood, J., and O. Boucher (2000), Estimates of the direct and indirect radiative forcing due to tropospheric aerosols: A review, *Reviews of Geophysics*, *38*, 513-543.

McFiggans, G., et al. (2006), The effect of physical and chemical aerosol properties on warm cloud droplet activation, *Atmospheric Chemistry and Physics*, *6*, 2593-2649.

Petzold, A., et al. (2005), Evaluation of multiangle absorption photometry for measuring aerosol light absorption, *Aerosol Science and Technology*, *39*, 40-51.

THE PRIMARY STUDY ON DISTRIBUTION CHARACTERISTICS OF AEROSOLS AND CCN UNDER CLEAR SKY WEATHER CONDITION IN SUMMER USING AIRCRAFT DETECTION OVER THE BOHAI SEA GULF AREA ,CHINA

Ying Duan[1], Zhihui Wu[1], Lixin Shi[1] and Yan Jiang[1]

[1] Weather Modification Office of Hebei Province, Shijiazhuang, China 050021

1. INTRODUCTION

Since 2005 year, in order to study the distribution characteristics of aerosol and CCN in atmosphere over the Bohai sea gulf area of north China, aircraft observations were carried out using PMS (Particle measuring Systems) and the CCN counter. In this paper, based on the summer data over the Bohai sea gulf area of north China on 21June 2005, which obtained by PMS PCASP-100X probe (Passive Cavity Aerosol Spectrometer Probe) and CCN counter, the distribution characteristics of aerosol and CCN were primarily analyzed.

2. INSTRUMENT, FLYING DESINE AND WEATHER

On 21 June 2005, weather was dominated by northwestern flow at upper air level over North China and the sky mostly was clear with surface temperature was more than 35℃ all the area at LST 1400. The detected area was clear during aircraft observation but shower occurred after observation in the evening.

A Cheyenne ⅢA aircraft with airborne PMS and other instruments was use for the observation. Measurements were made by aerosol probe PCASP-100X (size range 0.1-3.0 μm), cloud droplet probe FSSP-100ER (1-95μm), OAP 2D-GA2 (25-1550 μm) , OAP 2D-GB2 (150-9300 μm), thermometer, King LWC meter, M300 dada system, GPS and a CCN counter. The aircraft took off at 16:00 and landed at 19:26 at

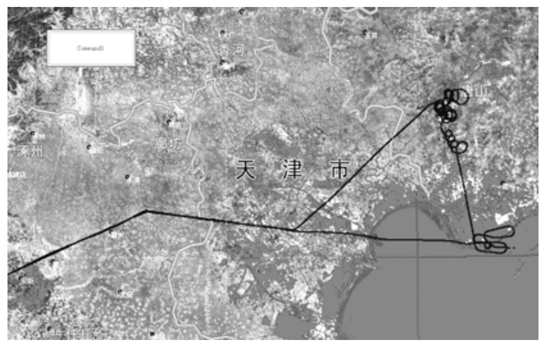

(a) Flight path

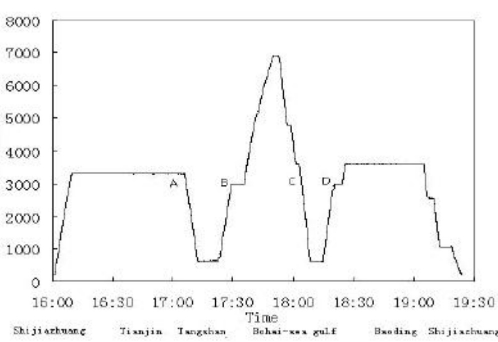

(b) Flight pattern

Fig.1 Flight path and pattern

Shijiazhuang Airport. Flight path was Shijizhuang, Tianjin, Tangshan, Bohai sea gulf, Tianjin and Shijiazhuang. The flight altitude was from 600-7000 m. The flight path, altitude and position are shown in Fig.1.

3. PRIMARY ANALYSIS ON DISTRIBUTION

CHARACTERISTICS OF AEROSOLS AND CCN

3.1 The distribution of aerosols

The number concentration, average diameter, volume concentration, and aerosol particle rapid with height increasing at 1600-3500 m, and the average number concentration is 130-940 cm^{-3}. Average diameter is approximately 0.12μm, average volume concentration is 4.2-5.5 $\mu m^3 cm^{-3}$ in boundary layer, which decreased with height increasing.

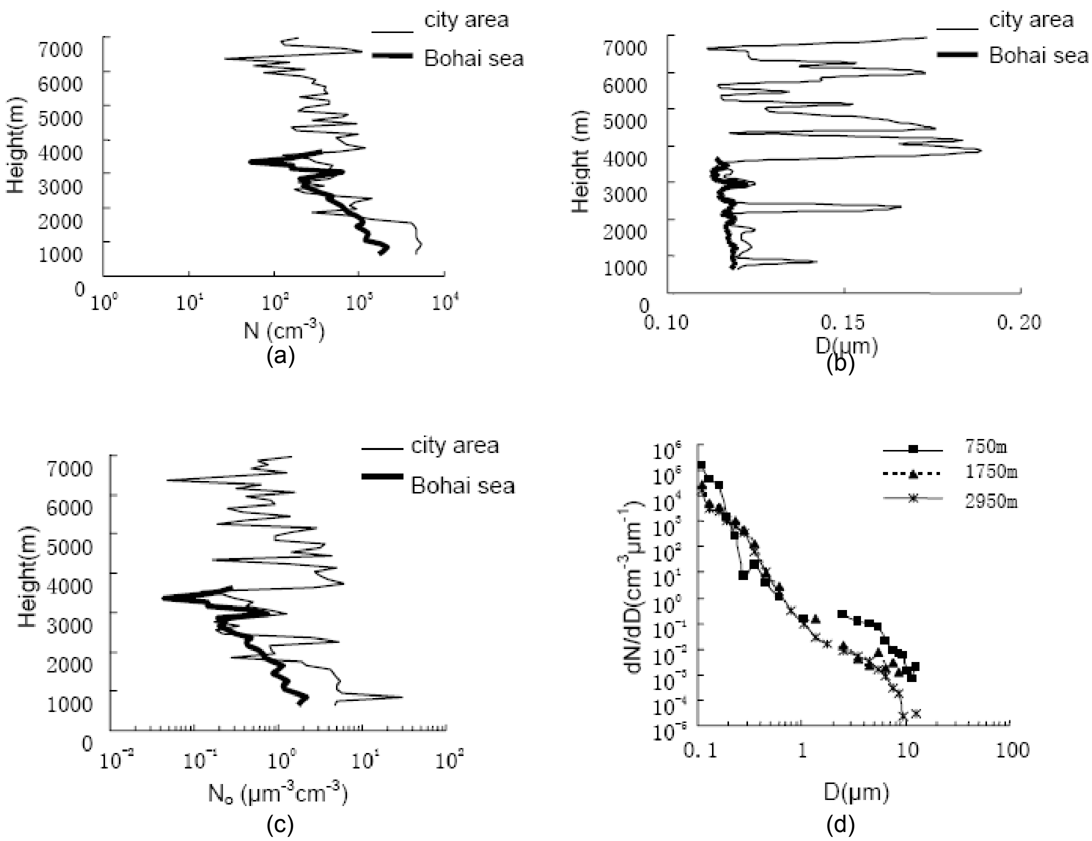

Fig.2 Vertical distribution of (a) aerosol concentration, (b) average diameter, (c) volume concentration and (d)spectra.

size spectrum distribution with height over Tangshan city and Bohai sea gulf are given in Fig.2. The results show that aerosol average number concentration range is 4200-5500 cm^{-3} at 1600 m level over the city. Below 1600m, the value changed little with height increasing. It indicates turbulence mixing is symmetrical in boundary layer. Average aerosol number concentration decreased very From 600 to 3500 m over Bohai sea gulf area, average concentration is 1700-2200 cm^{-3}. From 3000 to 3600 m, average aerosol concentration decreased from 150 to 370 cm^{-3}. Compared with Tangshan, average aerosol concentration over Tangshan city is two to five times than that over Bohai sea gulf. Average diameter over Bohai sea gulf is less than that over Tangshan from 600 to 3500 m. The

volume concentration decreased with height increasing. Average volume concentration over Tangshan is two to five times than that over Bohai sea gulf (see Fig.2(a),(b) and (c)).
Aerosol particle size spectrum distribution at different level over Tangshan city is given in Fig.2(d). It can be seen that size spectrum range is 1.05 μm, 1.35 μm and 1.75 μm at 750 m, 1750 m and 2950 m, respectively. Comparatively, size spectrum distribution character is basal consistent over different area.

3.2 The distribution of CCN

The distribution of CCN concentration with

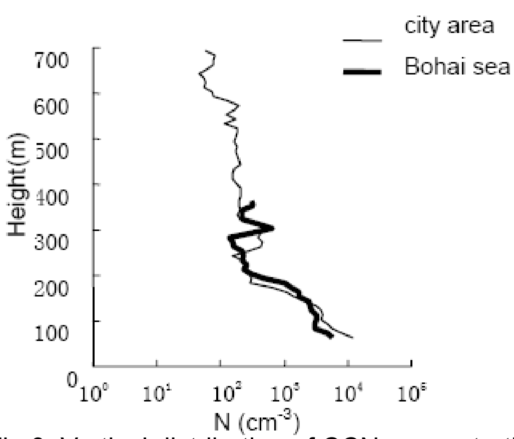

Fig.3. Vertical distribution of CCN concentration

height is shown in Fig.3, which the supersaturation was set at 0.3%. The result shows that CCN concentration reduced with height increasing over Tang Shan city and also Bohai sea gulf. From 600 to 2500 m in boundary layer, CCN concentration decreased rapidly. At 600 m level over Tangshan city, CCN concentration was 11770 cm^{-3}, at same level of Bohai sea gulf, CCN concentration was 5790 cm^{-3}, the latter is less than one half than that over city area. At 2000m, CCN concentration reduced to about one tenth, it was about 300 cm^{-3}. From the measurements, it can be seen that the variety trend of CCN concentration is consistent with that of aerosol concentration with height increasing.

REFERENCES

1. Duan Ying, Wu Zhihui et al., An Analysis on Aerosol Variable Tendency and Clouds Physical Effect for Decrease of Natural Precipitation over Hebei Area. C. D. O'Dowd and P. E. Wagner (Eds.), Nucleation and Atmospheric Aerosols. Springer, Germary, P507–511, 2007.
2. Duan Ying, Wu Zhihui, Yang Baodong et al., A Primary Study on the Variable Tendency of the Aerosol with Low Cloud Days and Drizzle days over the Bohai Sea Gulf Area in North China. The Scientific Assembly of the International Association of Meteorology and Atmospheric Sciences (IAMAS), P33-34, August 2-11, 2005, Beijing, China.
3. Shi Guangyu et al, Atmospheric Sounding of the vertical distribution of atmospheric ozone and aerosol by air-balloon. Atmospheric Science, 20(4), P401-407 (In Chinese), 1996.
4. An Yuegai, Guo Jinping et al., An Analysis of the Evolution Characteristics and Physical Cause of Formation about Forty Years Natural Rainfall in Hebei Province. Proceeding of 13th International Conference on Clouds and Precipitation, Reno, Nevada, USA, P395-397. 2000.

Acknowledgment

This research is supported by the project 40475003 of National Natural Science Foundation of China and the project D2005000593 of Natural Science Foundation Hebei Province.

ICE INITIATION BY AEROSOL PARTICLES: COMPARING MODEL PARAMETERIZATIONS AND OBSERVATIONS IN A PARCEL FRAMEWORK

T. Eidhammer[1], P. J. DeMott[1], D. C. Rogers[2], A. J. Prenni[1], M. D. Petters[1], C. H. Twohy[3], J. G. Hudson[4] and S. M. Kreidenweis[1]

[1]Department of Atmospheric Science, Colorado State University, Fort Collins, Colorado, USA
[2]National Center for Atmospheric Research, Boulder, Colorado, USA
[3]Department of Atmospheric and Oceanic Sciences, Oregon State University, Corvallis, OR, USA
[4]Atmospheric Science Division, Deserts Research Institute, Reno, NV, USA

1. INTRODUCTION

In parameterizing ice formation in numerical models, it is clearly desirable to account for the contributions of different aerosol types and their variable concentrations in the atmosphere. However, the link between aerosol and ice nucleation is still poorly understood. The ICE-L campaign (Ice in Cloud Experiment-Layer clouds) was designed to study the initiation of ice via heterogeneous nucleation in clouds by linking them to measurements of aerosol characteristics. The target was wave clouds, which offer the opportunity to separate heterogeneous ice nucleation from secondary ice formation processes. Airborne microphysical, thermodynamic and remote sensing measurements, in and around these clouds were conducted during ICE-L.

In idealized wave clouds, the air flow is laminar. Parcels follow the streamlines and spend only a few hundred seconds in the cloud. Thus precipitation and mixing are expected to be minimal. Parcel models are therefore suitable for modeling ice initiation in these clouds [*Cotton and Field*, 2002].

We have implemented three heterogeneous ice nucleation parameterizations that account for different aerosol types and concentrations into a Lagrangian parcel model. These parameterizations are tested for a selected case during ICE-L, and compared with the measurements.

2. PARCEL MODEL

The parcel model used in this study is an extended version of the Lagrangian parcel model developed by *Feingold and Heymsfield* [1992]. The original parcel model calculates droplet growth by condensation in an adiabatic updraft, or along trajectories, with prescribed atmospheric parameters. Some of the changes to the original parcel model are the inclusion of ice nucleation and crystal growth, and modification of the parameterization of water activity and hygroscopic growth for solution drops.

The calculation of water activity of a solution drop follows *Petters and Kreidenweis* [2007] where hygroscopicity is expressed with a single parameter κ. Kappa can be understood as the “unit volume of water that is associated with the unit volume of the dry aerosol” [*Petters and Kreidenweis*, 2007]. Further, internally mixed aerosols follow the simple mixing rule where κ is the sum of volume weighted κ_i of each individual component in the aerosol. Fairly complex aerosol types can therefore be assumed without having to determine the physiochemical properties, and the use of κ allows for straightforward implementation of internally, as well as externally mixed aerosols.

Three heterogeneous ice nucleation parameterizations developed by *Khvorostyanov and Curry* [2004], *Diehl and Wurzler* [2004] and *Phillips et al.* [2008] are implemented. The scheme by *Khvorostyanov and Curry* [2004], hereafter called KC04, is based on classical heterogeneous nucleation theory. Freezing rate is mainly dependent on temperature, water activity, and ice nuclei (IN) size and surface properties. The various aerosol types that can serve as IN are accounted for through the surface properties from choice of contact angle, relative area of

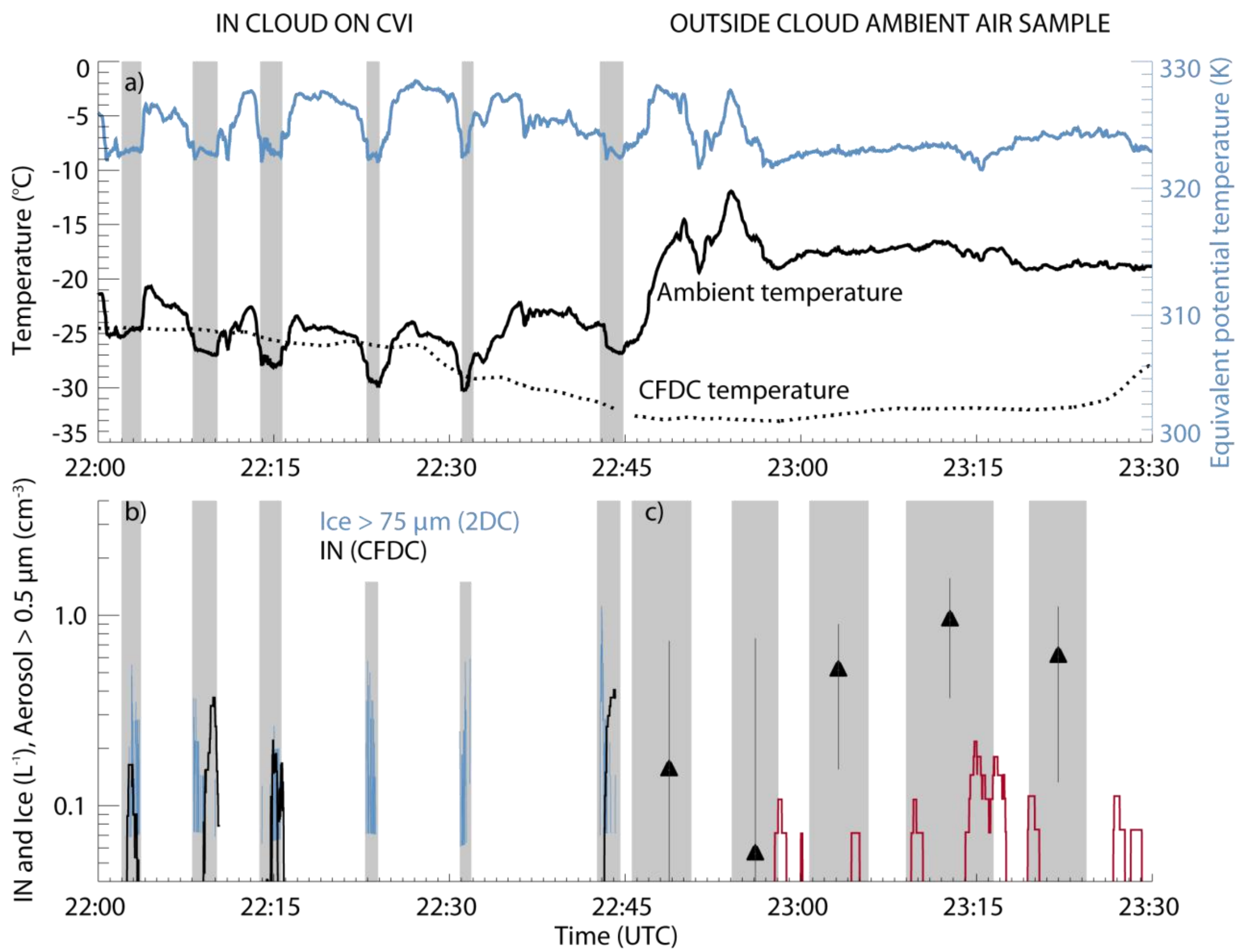

Figure 1 a) Ambient (black solid curve) and equivalent potential temperature (blue curve). Also shown are CFDC processing temperature (dotted curve). Grey areas indicate cloud passes. Note that a) spans over the entire time period. b) Ice > 75 µm (blue) and IN concentrations (black) in the cloud passes (up to about 22:45 UTC). The CFDC was on the CVI in this time period. c) Measured (triangles) interval-averaged IN concentrations from the ambient air sample inlet. The bars indicate the 90% confidence interval of the mean IN concentration. Grey areas here are measurement periods and white areas are CFDC filter periods. Also shown are aerosol concentration for particles > 0.5 µm in diameter (red lines).

active sites and misfit strain. The parameterization by *Diehl and Wurzler* [2004], hereafter called DW04, is based on laboratory measurements of freezing droplets, and include seven different aerosol types that can serve as IN (three types of mineral, three types of bacteria and soot). The freezing in this parameterization is mainly dependent on temperature and droplet volume. The *Phillips et al.* [2008] parameterization, hereafter called PDA08, is based on field measurements and constrained by laboratory measurements. Three different groups of aerosols are included (dust or metallic compounds, black carbon and insoluble organics). The number of IN from an aerosol population with these components is mainly related to the surface area of the aerosol population, temperature and saturation ratio.

While growth by droplets follow a Lagrangian framework in the parcel model, ice crystal growth follows a hybrid Eulerian/Lagrangian framework based on *Cooper et al.*, [1997].

3. CASE STUDY, NOVEMBER 18

3.1. Measurements

The NSF/NCAR C-130 aircraft served as the airborne measurement platform for ICE-L. Measurements were obtained over Colorado and Wyoming in November and December 2007. Due to the recent time frame of this experiment, all data used in this paper must be considered preliminary. We focus here on a wave-cloud mission on November 18. During this flight, two wave clouds were targeted. Here we consider the second cloud since aerosol measurements downwind of this cloud were obtained and can be used as initial conditions for the model.

In cloud

There were six passes through the cloud, at different altitudes. The passes were along, or in opposite direction to the horizontal component of the wind. Cloud level was between 7 and 7.5 km and temperatures were between -25 and -30°C as seen in Figure 1a, black solid curve. The grey shaded areas indicate the cloud passes. A clear sinusoidal wave structure, in some of the cloud passes, was evident from updrafts and temperature (not shown here) and vertical velocities in the wave were up to ± 3 m/s but with some variation in each pass.

Measured concentrations of ice > 75 µm and IN are shown in Figure 1b. The ice concentrations were measured with the NCAR "fast" 2DC probe which has a 64-diode array with 25 µm resolution and fast response electronics. The 2DC concentrations were between 0.05 and 0.6 L^{-1} for particles ≥ 75 µm (blue curve). IN measurements were conducted with an aircraft version of the Colorado State University Continuous Flow Diffusion Chamber (CFDC). This instrument is similar to the one described by *Rogers et al.* [2001], but with several modifications that will be described in a publication in preparation. Sample air within cloud was taken from a Counterflow Virtual Impactor (CVI) [*Twohy et al.*, 1997] and IN concentration was therefore only measured from cloud residual particles. The CFDC exposes sampled aerosols to a narrow range of processing temperature and relative humidity for a period of several seconds. Processing temperature was here close to the ambient temperature (dotted black curve in Figure 1a) and processing relative humidity ranged from 101 to 103% with respect to water to ensure that all aerosol particles are activated into cloud droplets, allowing them to freeze if an IN is present. The measurements indicate that 60 s average IN concentrations were up to 0.4 L^{-1} (black curve in Figure 1b). This is in agreement with the measured ice crystal concentration from the 2DC except for one cloud pass (22:23 UTC) where no IN were detected. This is expected due to the very low IN concentrations. No IN were measured during the 22:31 UTC cloud pass because the CDFC measured filtered air. There was a cloud layer above the target cloud, but University of Wyoming 85 Ghz cloudradar and lidar data indicate that the upper cloud maintained a separation of about 800 m (Zhien Wang, personal communication) and so there was probably no seeding of ice into the lower sampled cloud.

Cloud droplet concentrations (not shown here), which was measured with the Droplet Measurement Systems (Boulder, CO) Cloud Droplet Probe (CDP), were between 100 and 150 cm^{-3}.

Out of cloud

Aerosol measurements were obtained downwind of the cloud at the same equivalent potential temperature as in the cloud (~ 322 K, blue curve in Figure 1a).

In the region downwind of the cloud, IN measurements were conducted with an ambient air sample collected from an inlet that was separate from the CVI [*Rogers and DeMott*, 2002]. The inlet flow rate was adjusted to be isokinetic at the tip. The tip was heated to +7°C to avoid blocking from rime ice accumulating in regions of supercooled water. Measurement results are shown in Figure 1c. Here the grey areas indicate sampling periods while the white areas indicated filter periods to determine background counts in the CFDC method. Average IN concentrations are found for the intervals between the filter periods (triangles) and range from 0.05 to 1 L^{-1}. These concentrations compare well to the IN measurements in cloud. Error bars represent the 90% confidence interval of mean IN concentration. Also shown are aerosol concentrations measured with a PMI Ultra-High Sensitivity Aerosol Spectrometer (UHSAS) of particles > 0.5 µm in diameter (red lines) since IN concentrations have shown positive correlations with aerosol concentrations in this size range [*Richardson et al.*, 2007].

3.2 Parcel Model Simulation

We performed a simple parcel modeling study, assuming a sinusoidal wave structure of ± 2.5 m/s. We used a combination of measurements of potential temperature and the vertical wind component to estimate the wavelength, which was about 2.7 km. With an average horizontal wind speed of 23 m/s, the wave parcel transit time is about 1100 s. The initial temperature is -23°C and initial relative humidity is 70%.

For aerosol input parameters, we used fitted size distributions from UHSAS measurements downwind of the cloud, where the equivalent potential temperature was 322 K. The aerosol measurements were obtained from 22:54 to 23:24 UTC. Since the initial aerosol distribution for the simulations is from downwind of the cloud, we assume that any potential cloud processing does not affect the aerosols. We performed simulations with an average input distribution form the entire period, and with four different input distributions, taken from the same time periods when the CFDC was sampling.

Three lognormal modes were fit to the 30 minute average distribution measured with UHSAS (Figure 2). The smallest mode is assumed to be ammonium sulfate and is allowed to act only as CCN, with κ_{as} = 0.6. The largest mode is assumed to be an internal mixture with 0.9 volume fraction dust (κ_d = 0.04) and 0.1 volume fraction ammonium sulfate (total κ_{d+as} = $0.9\kappa_d+0.1\kappa_{as}$= 0.1). The second mode is assumed to not contribute to ice nucleation, and due to the low concentration compared to the first mode, for simplicity, this mode is not included in the simulations. Thus, only the largest mode contributes to ice crystal generation.

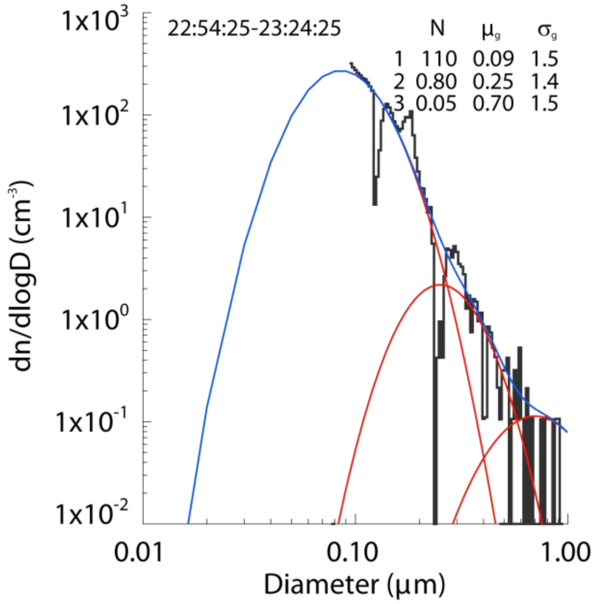

Figure 2 Measured 30 min average aerosol distributions (black lines) and fitted size distributions for the time period 22:54:25 – 23:24:25 UTC. Individual distributions are shown in red and total distribution is shown in blue.

Clearly the measured concentration of coarser mode particles is low, and the uncertainties of the fitted distributions are large. Further, the sizes measured with UHSAS are limited to > 0.1 µm and information of the distribution for smaller particles is not available at present. However, the integrated size distributions are comparable with measured CN concentrations.

For heterogeneous ice nucleation we used the three above-mentioned parameterizations.

3.3 Results

Figure 3 shows modeled ice concentrations using the average aerosol size distribution from the time period 22:54:25-23:24:25 UTC. Also shown are average ice crystal diameter, cloud droplet concentration, temperature, updraft and supersaturation. Different line styles represent different heterogeneous ice nucleation parameterizations. The solid line is the result using the PDA08 parameterization, and the ice crystal concentration is predicted to be about 0.9 L^{-1}, which is in reasonable agreement with measured IN concentrations (see Figure 1). All aerosols > 20 nm in the distribution activate cloud droplets and the modeled cloud droplet concentration is ~ 110 cm^{-3}. This compares well with measured cloud droplet concentration with the CDP (between 100 and 150 cm^{-3}). Further, CCN measurements were conducted with a DRI CCN spectrometer [*Hudson*, 1989]. Measurements in the ambient sampling region indicate an average CCN concentration of 70 cm^{-3} at supersaturation s = 0.5% and about 100 cm^{-3} at s = 1.05 %. The maximum supersaturation modeled in the parcel was 1.68%. This indicates that the assumption that all aerosols from the aerosol population can serve as CCN is adequate to model the droplet activation. Model temperatures range from -23 to -30°C and are in agreement with measurements. The droplets evaporate immediately (< 1 s) after reaching a relative humidity of 98%. The ice crystals, however, are too large to completely evaporate in the wave valley when relative humidity with respect to ice is less than 100%. Nevertheless, the simulated mean ice crystal diameter (~140 μm) is in reasonable agreement with 2DC ice crystal diameters that had a mode size near 180 μm.

The dotted lines in Figure 3 represent the DW04 parameterization. We assumed that the large particles are montmorillonite, which is one of the mineral types that can serve as IN in the DW04 parameterization. The predicted ice crystal concentration is close to 30 L^{-1}, which is in poor agreement with measurement. However, the droplet concentration is the same as measured and predicted with the Phillips parameterization.

The dashed lines represent the KC04 scheme. For this simulation we assumed that the contact angle was 50° (typical for quartz). All dust particles contribute to the modeled ice crystals with this parameterization. Since the ice crystal concentration is high, the ice crystal grows on expense of the droplets (Bergeron-Findeisen process), and water subsaturation is reached in the updraft. The droplets evaporate earlier than with the other parameterizations, and the mixed phased part of the cloud is therefore slightly smaller. To assume that all dust par-

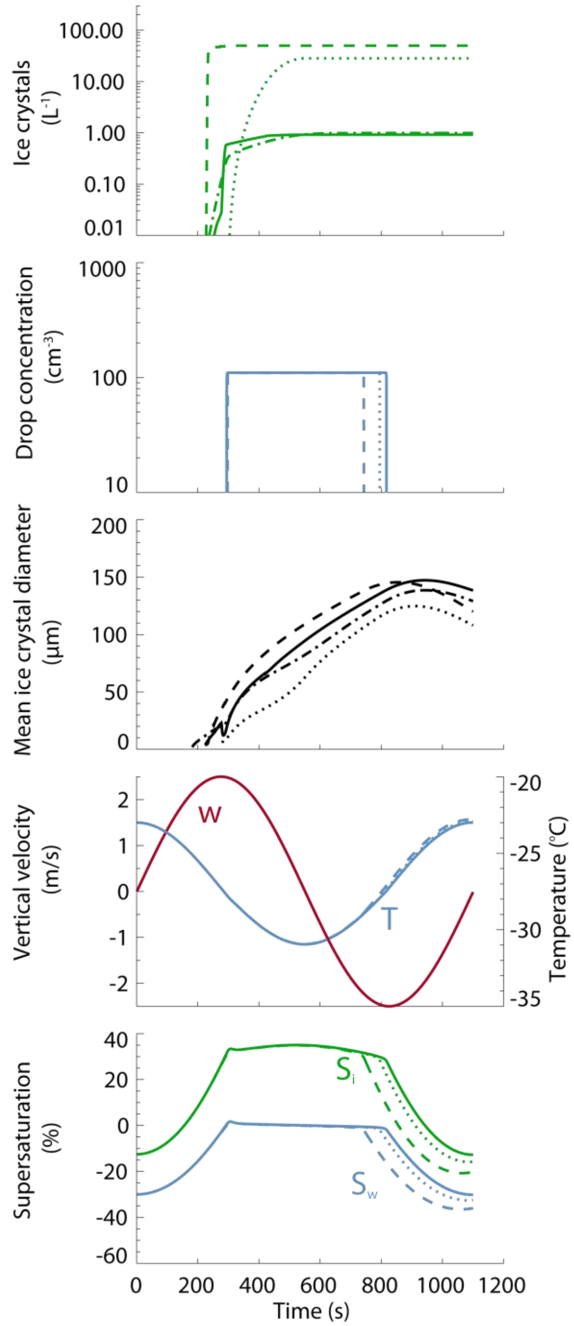

Figure 3 Modeled ice crystal and droplet concentrations in an idealized wave cloud. Also included are mean ice crystal diameter, temperature, updraft, and water and ice supersaturations along the trajectories. The different line styles are represented as follow: PDA08, solid curves; DW04, dotted curves; KC04, dashed curves; KC04 with contact angle probability function, dot dashed curves.

ticles have the same contact angle, however, is probably not realistic. For example, freezing measurements of emulsified aqueous suspensions of dust can be modeled with

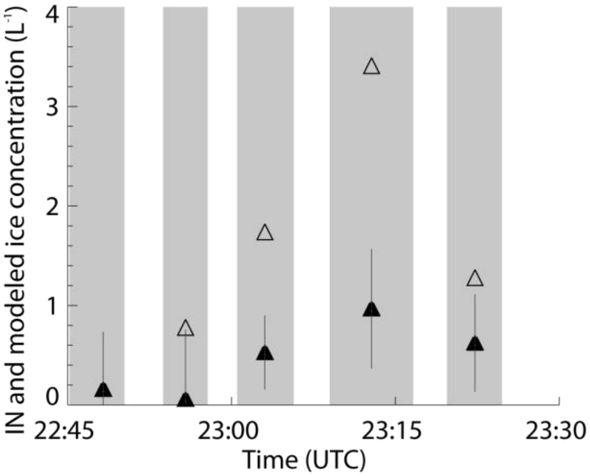

Figure 4 Modeled ice concentrations using the PDA08 parameterization (open triangles). Fitted size distributions from the same time periods as CFDC sampling periods (grey shaded areas) are used as initial size distributions for the simulations. Filled triangles are measured IN concentrations and are the same as in Figure 1c.

classical ice nucleation theory when assuming that each individual dust particle has a distribution of contact angles [*Marcolli et al.*, 2007]. If we assume that dust in each size class in our model has a contact angle distribution of

$$P(\theta) = 2 \cdot \mathrm{N}(\mu,\sigma),$$

where N is the normal distribution, $\mu = 180^{\circ}$, $\sigma = 37$ and $0^{\circ} < \theta < 180^{\circ}$, then an ice crystal concentration of about 1 L^{-1} can be obtained with the KC04 parameterization (dot dashed curve in Figure 3). Note that this probability function is not based on measurements, but was constructed to reduce the freezing rate so KC04 model results could be reasonably comparable with measurements.

4. DISCUSSION AND CONCLUSION

The modeled ice crystal concentrations with the individual four size distributions from CFDC sampling period (measured size distributions not shown here), using the PDA08 parameterization are shown in Figure 4 as open triangles. Filled triangles are the measured IN concentrations from the same time period (also as shown in Figure 1c). All simulations are with same prescribed updrafts and temperatures as for Figure 3. The individual modeled ice crystal concentrations are up to a factor of 3.5 larger than the measured IN concentrations. The concentration of coarse mode aerosols was low, and the statistics in the individual size distributions have relatively larger uncertainties than the average distribution. Thus there are also larger uncertainties in the fitted individual distributions. However, the modeled ice crystal concentrations for each sample period follow the trend as seen for measured IN; higher concentration of aerosols above 0.5 µm relates to higher concentrations of IN (shown in Figure 1c).

We acknowledge that the thermodynamic path of particles through activation is different in the CFDC (rapid cooling from aircraft cabin temperature to a steady-state supercooled temperature and water supersaturation) compared to the wave cloud simulation, so a direct comparison between measured IN concentration and simulated ice crystal concentration must be viewed critically. However, both measurements and simulations reflect ice activation at similar peak water supersaturation conditions and comparable temperatures, Thus it is expected that the modeled ice crystal concentration should be in reasonable agreement with the measurements if the connection between aerosol properties and IN activation is specified correctly.

The PDA08 parameterization seems to predict ice crystal concentrations in closest agreement with IN measurements compared to the two other parameterizations considered. On the other hand, by assuming a contact angle distribution, the KC04 scheme can also predict ice crystal concentrations comparable with measurements. However, more information supporting typical contact angle distributions for dust are needed from many more atmospheric cases in varied regions.

For future work we plan to look at more cases from ICE-L along with cases from Wave-Ice [*Rogers and DeMott*, 2002]. Further, with more detailed information about the particle composition measured during ICE-L, additional aerosol types that can serve as IN can be included in the model, such as carbonaceous and biologically derived particles. For now, only dust particles were assumed. However, the predicted ice crystal concentration with PDA08 scheme compares reasonably well with measurements by assuming that only dust particles are ice nuclei. Further, we also plan to constrain the simulations by using a combination of CCN data and composition from single particle aerosol mass spectrometry for the composition and mixing state of CCN.

5. BIBLIOGRAPHY

Cooper, W.A., R.T. Bruintjes, and G.K. Mather (1997), Calculations pertaining to hygroscopic seeding with flares, *J. Appl. Meteorol.*, *36*, 1449-1469

Cotton, R.J., and P.R. Field (2002), Ice nucleation characteristics of an isolated wave cloud, *Q. J. Royal Met. Soc.*, *128*, 2417-2437

Diehl, K., and S. Wurzler (2004), Heterogeneous drop freezing in the immersion mode: Model calculations considering soluble and insoluble particles in the drops, *J. Atmos. Sci.*, *61*, 2063-2072

Feingold, G., and A.J. Heymsfield (1992), Parameterizations of Condensational Growth of Droplets for Use in General-Circulation Models, *J. Atmos. Sci.*, *49*, 2325-2342

Hudson, J.G. (1989), An Instantaneous CCN Spectrometer, *J. Atmos. Ocean. Tech.*, *6*, 1055-1065

Khvorostyanov, V.I., and J.A. Curry (2004), The theory of ice nucleation by heterogeneous freezing of deliquescent mixed CCN. Part I: Critical radius, energy, and nucleation rate, *J. Atmos. Sci.*, *61*, 2676-2691

Marcolli, C., S. Gedamke, T. Peter, and B. Zobrist (2007), Efficiency of immersion mode ice nucleation on surrogates of mineral dust, *Atmos. Chem. Phys.*, *7*, 5081-5091

Petters, M.D., and S.M. Kreidenweis (2007), A single parameter representation of hygroscopic growth and cloud condensation nucleus activity, *Atmos. Chem. Phys.*, *7*, 1961-1971

Phillips, V.T.J., P.J. DeMott, and C. Andronache (2008), An empirical parameterization of heterogeneous ice nucleation for multiple chemical species of aerosol, *J. Atmos. Science*, *In press*

Richardson, M.S., P.J. DeMott, S.M. Kreidenweis, D.J. Cziczo, E.J. Dunlea, J.L. Jimenez, D.S. Thomson, L.L. Ashbaugh, R.D. Borys, D.L. Westphal, G.S. Casuccio, and T.L. Lersch (2007), Measurements of heterogeneous ice nuclei in the western United States in springtime and their relation to aerosol characteristics, *J. Geophys. Res*, *112*, D02209 doi:10.1029/2006JD007500

Rogers, D.C., and P.J. DeMott (2002), Ice crystal formation in wave clouds, airborn studies -10 to -35˚C., in *American Meterological Society Conference on Cloud Physics*, Ogden, UT

Rogers, D.C., P.J. DeMott, S.M. Kreidenweis, and Y.L. Chen (2001), A continuous-flow diffusion chamber for airborne measurements of ice nuclei, *J. Atmos. Ocean. Tech.*, *18*, 725-741

Twohy, C.H., A.J. Schanot, and W.A. Cooper (1997), Measurement of condensed water content in liquid and ice clouds using an airborne counterflow virtual impactor, *J. Atmos. Ocean. Tech.*, *14*, 197-202

6. ACKNOWLEDGEMENTS

This work has been supported by the National Science Foundation (NSF) Science and Technology Center for Multi-Scale Modeling of Atmospheric Processes, managed by Colorado State University under cooperative agreement No. ATM-0425247, NSF grant ATM-0611936, and by the NASA MAP (Modeling and Analysis Program) No. NNG06GB60G.

THE CCN PROPERTIES OF 2-METHYLTETROLS AND C3-C6 POLYOLS

S. Ekström[1], B. Nozière[1], and H. - C. Hansson[1]

[1]Department of Applied Environmental Science, Stockholm University, Stockholm, Sweden

1. INTRODUCTION

The contribution of atmospheric aerosols to the climate and their control of cloud droplet activation and cloud optical properties is poorly understood [*Forster et al.,* 2007]. Atmospheric observations have previously shown that organic matter are involved in cloud activation [*Novakov and Penner*, 1993; *Liu et al*., 1996; *Rivera-Carpio*, 1996; *Matsumoto et al*., 1997; *Ishizaka and Adhikari*, 2003; *Moshida et al*, 2006; *Chang et al*., 2007]. Organic compounds seem especially important in clean environments and were found to have a large contribution to the Cloud Condensation Nuclei (CCN) numbers in marine regions and at a continental semi-rural site [*Novakov and Penner*, 1993; *Rivera-Carpio*, 1996; *Matsumoto et al*., 1997, *Chang et al*., 2007]. The presence of organic compounds was also necessary to account for the CCN numbers observed in the Amazon basin [*Mircea et al.*, 2005]. A contribution of organic material to CCN could be especially critical in pristine regions where CCN numbers are limited by very low aerosol concentrations [e.g. *Fitzgerald*, 1991; *Roberts et al*., 2001].

A large number of investigations have tried to identify the organic compounds that would take part in cloud droplet activation. A property that seems essential in these processes is their solubility in water, which has been shown to affect, if not CCN numbers, particles growth factors [e.g. *Mircea et al*., 2005]. It has been shown that a significant fraction of biogenic aerosols consists of compounds of solubility comparable or even larger than those of inorganic salts such as polyols and the 2-methyltetrols, methylerythritol and methylthreitol [*Claeys et* al., 2004; *Ion et* al., 2005; *Kourtchev et* al., 2005; *Böge et* al., 2006]. These compounds were found in clean environments [*Claeys et* al., 2004] and fine aerosols [e.g. *Kourtchev et* al., 2005; *Böge et* al., 2006], which makes them good candidates for CCN in the natural atmosphere. This role could important for both the 2-methyltetrols and the polyols at global scale. The methyltetrols are thought to be produced by the oxidation of isoprene, one of the organic gases the most emitted globally and the polyols are mainly emitted by fungi. Although the CCN properties of polyols and 2-methyltetrols are central to the understanding of cloud formation in clean environments, they have not been investigated until now. This work presents the first investigation of the CCN properties of C3 to C6 polyols and of the tetrols, methylerythritol and methylthreitol.

2. EXPERIMENTAL

The experimental approach used in this work was recently described by Kiss and Hansson, [*2004*] and Varga et al., [*2007*]. For each compound or mixture studied solutions of different concentrations up to 2 M were prepared. The particle radius, r, corresponding to each concentration was calculated from the density of the pure material (CRC [*1970*], except for arabitol and the methyltetrols assumed to be 1480 kgm^{-3} and 1460 kgm^{-3}, respectively), and adding up the volumes of aqueous solution and organic material. The osmolality of these solutions (reduction of water vapor pressure due to the solute), C_{osmol} (kg^{-1}), was measured with a KNAUER K – 7000 vapor pressure osmometer. The surface tension of each solution, σ_{sol} (mN m^{-1}), was measured with a FTÅ 125 tensiometer. The water activity, a_w, was determined from the osmolality [*Kiss and Hansson*, 2004].

The experimental values for a_w and σ_{sol} were then used to calculate the supersaturation, S, the excess vapor pressure necessary to activate the aerosol particle into a droplet, using the original (i.e. non-simplified) Köhler equation. The Köhler curves were thus built point by point for the different organic compounds and salt solutions. As discussed previously [Kiss and Hansson, *2004*], this method is experimentally simple, accurate and has the advantage of eliminating the uncertainties contained in the simplified Köhler equation, in particular in the Van't Hoff factors. Finally, this method can be applied to particles of almost any size, the range accessible to measurements being only limited by the solubility of the compounds in the solutions of interest.

A first series of experiments determined the CCN properties of the polyols, glycerol (C3), erythritol (C4), arabitol (C5), and mannitol (C6), and the two 2-methyltetrols in water, as well as those of their analogue di-acids, malonic acid (C3), succinic acid (C4), and adipic acid (C6). Because previous studies have shown that the presence of inorganic salts could dramatically affect CCN efficiency of partly soluble organic compounds [*Bilde and Svenningsson*, 2004], a second series of experiments focused on the CCN properties of the polyols and 2-methyltetrols in sodium chloride and ammonium sulfate solutions.

3. RESULTS AND DISCUSSION

In order to present the measurements made in this work Köhler curves were determined by the method explained in the previous section for the various organic compounds and a dry particle radius of 30 nm. For the polyols and di-acids in water these curves are shown in Figure 1, and for the 2-methyltetrols in water in Figure 2. The results obtained in this work for the organic acids, in particular the critical supersaturation (maxima of the curves), are in good agreement with earlier studies [*Bilde et al*., 2004, *Hori et al*., 2003, *Giebl et al*., 2002,

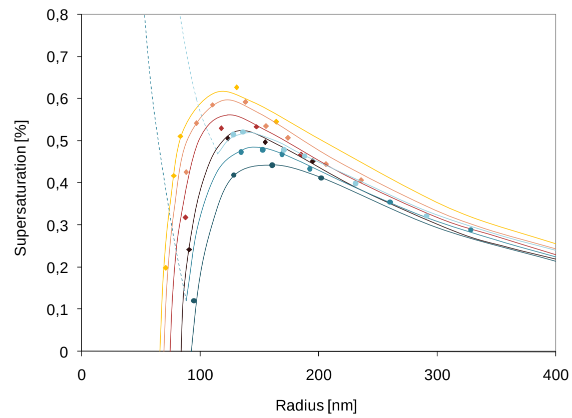

Figure 1: Köhler curves for polyol and dicarboxylic acid particles. Diamonds Polyols (glycerol: black, erythritol: red, arabitol: orange, mannitol: yellow); Circles: dicarboxylic acids (malonic acid: dark blue, succinic acid: medium blue, adipic acid: light blue).

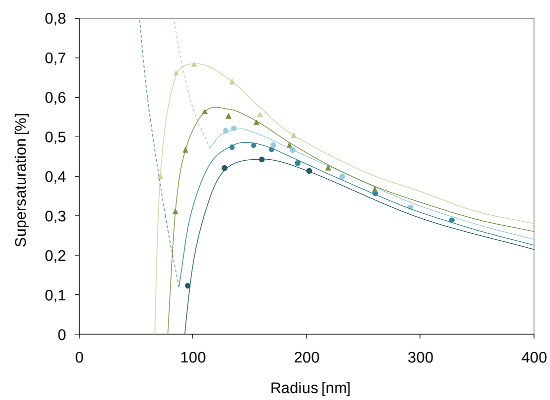

Figure 2: Köhler curves for 2-methyltetrol and dicarboxylic acid particles. Triangles: Methyltetrols (2-methylthreitol: light green, 2-methylerythritol: dark green). Other compounds as in figure 1.

Prenni et al., 2001, *Corrigan et al*., 1998, *Cruz and Pandis*, 1997], which confirms the validity of the technique and of the measurements.

Figures 1 and 2 show that the critical supersaturation for the polyols (Sc = 0.52 – 0.62 ± 0.02 %) and 2-methyltetrols (Sc = 0.57 – 0.68 ± 0.02 %) are slightly higher than those of the analogue di-acids (Sc = 0.44 – 0.52

%), but lower than for mono- and disaccharides (Sc = 0.55 – 0.85 %) [*Rosenørn et al*., 2005]. Thus, in contrast to what expected, high solubility does not necessarily correspond to high CCN efficiency. It is well established that the high CCN efficiencies of sodium chloride and ammonium sulfate result from their Raoult effect, corresponding to high osmolalities. The organic compounds studied in this work had significantly lower osmolalities than the inorganic salts, especially the 2- methyltetrols. This difference reflects mostly the degree of dissociation of each compound and the corresponding concentration of solute.

The organic acids are known to have some surface tension effects that partly compensate for their low water activities and improve their CCN efficiencies [*Facchini* et al., 1999]. In this work, the surface tension of all compounds were measured and none of the polyols displayed any significant surface tension effect, but the 2-methyltetrols displayed a small effect. These effects contributed to lower their critical supersaturation, but not enough to compete with the inorganic salts or even the organic acids.

Experiments salt solutions showed that sodium chloride strongly reduces the critical supersaturation for adipic acid compared to pure water. However, ammonium sulfate were found to have a smaller effect. For mannitol, the critical supersaturation was reduced by both salts, which suggests that mannitol is only partly soluble in water, in agreement with the moderate solubility [*Saxena and Hildemann*, 1996]. As with adipic acid, a smaller reduction of the critical supersaturation was observed with ammonium sulfate than with sodium chloride. By contrast, the critical supersaturation of methylthreitol was hardly affected by the presence of either salt. Assuming a solubility for this compound similar to the one of threitol [*Cohen*, 1983] suggests that it should be completely soluble in water, in which case no effect of salt on the Köhler curve is expected [*Bilde and Svenningsson*, 2004]. Interestingly, the critical supersaturation for methylerythritol was increased by both salts. Assuming a solubility for this compound similar to the one of erythritol [*Cohen*, 1983] suggests that this compound should be only partly insoluble in water. However, unlike the di-acids and other polyols, the non-soluble part would be liquid, not a solid, which could form a film at the surface of the droplets and de-activate the uptake of water.

Although the results of this work show that the polyols and 2-methyltetrols would not activate cloud formation at lower supersaturation than inorganic salts or organic acids, their high solubility gives them one advantage: to activate smaller particles than less soluble compounds. For organic compounds of limited solubility, the very high critical supersaturation of the non-soluble part of the Köhler curves (dashed lines in the Figures) is an efficient barrier against the activation of small particles [*Bilde and Svenningsson*, 2004]. The presence of highly soluble biogenic material such as polyols, 2-methyltetrols, or sugars in aerosols could thus increase CCN numbers compared to aerosols containing only partly soluble compounds. This effect could be especially critical in pristine environments where aerosol concentrations are very low [*Fitzgerald*, 1991; *Roberts et al*., 2001], which are precisely the environments where this highly soluble biogenic material is present.

4. REFERENCES

Bilde, M., and B. Svenningsson (2004), CCN activation of slightly soluble organics: the importance of small amounts of inorganic salt and particle phase, *Tellus, 56B*, 128 – 134.

Böge, O., Y. Miao, A. Plewka A, and H. Herrmann H (2006), Formation of secondary organic particle phase compounds from isoprene gas-phase oxidation products: An aerosol chamber and field study, *Atmos. Environ*., *40*, 2501 – 2509.

Chang, R.Y.-W., P.S.K. Liu, W.R. Leaitch, and J.P.D. Abbatt (2007), Comparison between measured and predicted CCN concentrations at Edberg, Ontario: focus on the organic aerosol fraction at a semi-rural site, *Atmos. Environ*., *41*, 8172 – 8182.

Claeys, M., B. Graham, G. Vas, W. Wang, R. Vermeylen, V. Pashynska, J. Cafmeyer, P. Guyon, M.O. Andreae, P. Artaxo and W. Maenhaut (2004), Formation of secondary organic aerosols through photooxidation of isoprene, *Science 303,* 1173 – 1176.

Cohen, S., Y. Marcus, Y. Migron, S. Dikstein, A. Shafran (1993), Water sorption, binding and solubility of polyols, *J. Chem. Soc. Faraday Trans. 89*, 3271.

Corrigan, C. E., and T. Novakov (1998), Cloud condensation nucleus activity of organic compounds: a laboratory study, *Atmos. Environ. 33*, 2661–2668.

Cruz, C.N., and S.N. Pandis, (1997) A study of the ability of pure secondary organic aerosol to act as cloud condensation nuclei, *Atmos. Environ. 31,* 2205-2214.

Facchini, M.C., M. Mircea, S. Fuzzi, and R.J. Charlson (1999) Cloud albedo enhancement by surface active organic solutes in growing droplets, *Nature, 401,* 257 – 259.

Fitzgerald, J.W. (1991), Marine aerosols: a review, *Atmos. Environ. A, 25*, 533 – 545.

Forster, P, Ramaswamy, V, Artaxo, P, Berntsen, T, Betts, R, Fahey, DW, Haywood, J, Lean, J, Lowe, DC & Myhre, G, *et al*. (2007) in Changes in Atmospheric Constituents and in Radiative Forcing in: Climate Change 2007: The Physical Science Basis. Contribution of Working Group I to the Fourth Assessment Report of the Intergovernmental Panel on Climate Change eds. Solomon, S, Qin, D, Manning, M, Chen, Z, Marquis, M, Averyt, KB, Tignor, M& Miller, HL. (Cambridge Univ Press, Cambridge, UK), 129–234.

Giebl, H., A. Bernera, G. Reischla, H. Puxbaumb, A. Kasper-Gieblb, R. Hitzenberger (2002), CCN activation of oxalic and malonic acid test aerosols with the university of Vienna cloud condensation nuclei counter, *J. of Aerosol Science 33*, 1623-1634.

Hori, M., S. Ohta, N. Murao, S.Yamagata (2003), Activation capability of water soluble organic substances as CCN, *J. of Aerosol Science 34*, 419-448.

Ion, A.C., R. Vermeylen, I. Kourtchev, J. Cafmeyer, X. Chi, A. Gelencser, W. Maenhaut and M. Claeys (2005), Polar organic compounds in rural $PM_{2.5}$ aerosols from K-puszta, Hungary, during a summer 2003 field campaign: sources and diel variations, *Atmos. Chem. Phys., 5*, 1805 – 1814.

Ishizaka, Y., and M. Adhikari (2003), Composition of cloud condensation nuclei, *J. Geophys. Res*., *108*, 4138, doi:10.1029/2002JD002085.

Kiss, G., and H.-C. Hansson (2004), Appli cation of osmolality for the determination of water activity and the modelling of cloud formation, *Atmos. Chem. Phys*. Discuss., *4*, 7667 – 7689.

Kourtchev, I., T. Ruuskanen, W. Maenhaut, M. Kulmala and M. Claeys, (2005) Observation of 2-methyltetrols and related photo-oxidation products of isoprene in boreal forest aerosols from Hyytiälä, Finland, *Atmos. Chem Phys., 5*, 2761 –2770.

Liu, P.S.K., W.R. Leaitch, C.M. Banic, S.-M. Li, D. Ngo, and W.J., Megaw (1996), Aerosol observations at Chebogue Point during the 1993 North Atlantic Regional Experiment: Relationships among cloud condensation nuclei, size distribution, and chemistry, *J. Geophys. Res.*, *101*, 28971 – 28990.

Matsumoto, K., H. Tanaka, I. Nagao, and Y. Ishizaka (1997), Contribution of particulate sulfate and organic carbon to cloud condensation nuclei in the marine atmosphere, *Geophys. Res. Lett.*, *24*, 655 – 658.

Mircea, M., Facchini, M. C., Decesari, S., Cavalli, F., Emblico, L., Fuzzi, S., Vestin, A., Rissler, J., Swietlicki, E., Frank, G., Andreae, M. O., Maenhaut, W., Rudich, Y., and Artaxo, P. (2005), Importance of the organic aerosol fraction for modeling aerosol hygroscopic growth and activation: a case study in the Amazon Basin, *Atmos. Chem. Phys., 5*, 3111-3126.

Moshida, M., M. Kuwata, T. Miyakawa, N. Takegawa, K. Kawamura, and Y. Kondo (2006), Relationship between hygroscopicity and cloud condensation nuclei activity for urban aerosols in Tokyo, *J. Geophys. Res.*, *111*, D23204, doi:10.1029/2005JD006980.

Novakov, T., and J.E Penner (1993), Large contribution of organic aerosols to cloud-condensation-nuclei concentrations, *Nature*, *365*, 823 – 826.

Prenni, A.J., P.J. DeMott, S.M. Kreidenweis, D.E. Sherman, L.M. Russell, and Y. Ming (2001), The effects of low molecular weight dicarboxylic acids on cloud formation, *J. Phys. Chem. A 105*, 11240 – 11248.

Rivera-Carpio, C.A., C.E. Corrigan, T. No vakov, J.E. Penner, C.F. Rogers, and J.C. Chow (1996), Derivation of contribution of sulfate and carbonaceous aerosols to cloud condensation nuclei from mass size distributions, *J. Geophys. Res.*, *101*, 19483 – 19493.

Roberts, G. C., M. O. Andreae, J. Zhou, and P. Artaxo (2001), Cloud Condensation Nuclei in the Amazon Basin: “Marine” Conditions over a Continent?, *J. Geophys. Res. Lett.*, *28*, 2807–2810.

Rosenørn, T., G. Kiss, and M. Bilde (2006), Cloud droplet activation of saccharides and levoglucosan particles, *Atmos. Environ., 40*, 1794-1802.

Saxena, P., and L. Hildemann (1996), Water-soluble organics in atmosperic particles: a critical review of the literature and application of thermodynamics to identify candidate compounds, *J. of Atmospheric Chemistry 24*. 57-109.

Varga, Z., G. Kiss, and H.-C. Hansson (2007), Modelling the cloud condensation nucleus activity of organic acids on the basis of surface tension and osmolality measurements, *Atmos. Chem. Phys.*, *7*, 4601 – 4611.

Weast, R.C. (Ed) (1970), CRC handbook of chemistry and physics, 51th edn, CRC Press, Cleveland, USA.

Acknowledgements

Erik Swietlicki, Lund University, Sweden, and Greg Roberts, CNRM, France, are gratefully acknowledged for their useful discussions. Ulla Widequist, Stockholm University, is thanked for her help with the instruments. B. N. acknowledges support from the European Commission, Marie Curie Chair EXC2005-025026, and International Reintegration Grant IRG2006-036547, and from the Swedish Research Council (research grant NT-2006-5066).

FUNGI SPORES AS ICE NUCLEI AND THEIR IMPACTS ON RAINFALL AMOUNT OVER SÃO PAULO CITY

Gonçalves, F. L.T.[1]; Martins, J. A.[2]; Silva Dias, M. A. F.[1,3], Cardoso, M.R.A.[4]
Bauer, H.[5]
[1]Dept. of Atmospheric Sciences, IAG/USP/Brazil
[2] Universidade Tecnológica Federal do Paraná, 86300-000, Cornélio Procópio, Paraná,
[3] Center for Weather Forecasting and Climate Studies – CPTEC/INPE – Cachoeira Paulista, 12630-000, SP, Brazil
[4]Faculty of Public Health, USP/Brazil.
[5] Institute for Analytical Chemistry, Vienna University of Technology, Vienna, Austria

Abstract

Airborne bacteria can act as cloud condensation nuclei and some airborne bacterial and fungal species are able to act as ice nuclei and therefore induce rainfall in moderate climates. Preliminary results show that São Paulo City area presents high number of atmospheric fungi, reaching values over 30,000 spores per cubic meter. São Paulo City presents an increase in number of thunderstorms during last few decades, which is associated primarily with the heat island. However, there are indications that air pollutants, such as Vanadium, may contribute to this storm enhancements through ice nuclei increase, releasing latent heat. Fungal spores could also play a role in that enhancement, as well, acting as ice nuclei. Numerical modeling may help the understanding of how ice nuclei affect rainfall amounts. Therefore, the impact of these high scores is under investigation, in order to evaluate their effect on cloud microphysics through numerical modeling, using, BRAMS, Brazilian version of RAMS. The first modeling results show that modified ice nuclei distribution can increase the maximum condensed water by a factor of 2%, comparing with normal distribution. However, the results also present smaller average concentration, indicating a non-linear effect on microphysics variables. That means an interesting impact on rainfall distribution which must be better investigation.

1. Introduction

Airborne microorganisms have been found in the atmosphere for the first time at the end of XIX century. Since then, many studies on airborne fungi have been carried out to investigate atmospheric concentrations and compositions and their impact on the environment which cloud physic processes are involved. Airborne bacteria can act as cloud condensation nuclei and some airborne bacterial and fungal species are able to act as ice nuclei and therefore induce rainfall in moderate climates.

Microbiology as well as atmosphere physicists have been shown that certain types of plant-associated bacteria and fungi, in the atmosphere, could be important to rainfall formation (Morris, C.E. et al. 2004; Bauer, H. et al. 2003; Szyrmer, W. and Zawadzki, I., 1997). The physicists came to this conclusion because these bacteria produce a protein on their outer membrane that is one of the most active of the naturally-occurring ice nuclei (compounds capable of catalyzing the freezing of water- Jaenicke, R. 2005), and because freezing of cloud water is a critical step for rainfall over major parts of the earth (Sattler, B. et al. 2002; Ariya

P.A. and Amyot M. 2004; Diehl, K. et al. 2000 and, Hamilton, W.D. and Lenton, T.M. 1998). These bacteria are widely distributed across the planet, multiply readily, survive airborne dissemination up to the clouds and fall out with precipitation. If these fungi and bacteria play a catalyzing role in the formation of precipitation, is under investigation toward applications as drought mitigation. Fungi as IN is reported in Pouler et al. (1992), where the species *Fusarium* can behave as IN around -1.0^{o}C and -2.5^{o}C.

To understand the ice nuclei formation processes could also give important insight into the role of other biological ice nuclei, such as pollen and fungi, in atmospheric processes.

Many of those cited authors agree that, in spite of its critical importance, research on this question has been on the back burner for several decades. The forum for the needed intersection of competence does not exist. For example, the impact of aerosol particles, in general, on clouds and climate is a poorly quantified forcing process (Morris, C.E. et al., 2004). The global climate models are presently being improved to ingest such details and predict the impacts on clouds and precipitation. Furthermore, the impact of biological particles on clouds extends beyond potentially affecting precipitation alone. Impacts on the phase of clouds and on precipitation feed into the global energy and water cycle. This alone is motivation for understanding the role of biological aerosols(Morris et al., 2007).

To understand how biological materials contribute to climate forcing will require knowledge of source and dispersal functions, dependence on meteorological conditions, differences among the types of bacteria produced in different areas, and implementing such knowledge into regional and global climate models that are presently being improved to ingest such details and predict the impacts on clouds and precipitation. Much of the groundwork being done for other aerosol types can be utilized for describing biological aerosol impacts. Furthermore, the impact of biological particles on clouds extends beyond potentially affecting precipitation alone. Impacts on the phase of clouds and on precipitation feed into the global energy and water cycle. This alone is motivation for understanding the role of biological aerosols (Hamilton, W.D., Lenton, T.M. 1998; Ariya P.A. and Amyot M. 2004 and Morris et al., 2007). Therefore, numerical modeling seems to play an important role in order to understanding these processes.

In this investigation, we used a high-resolution configuration of the Brazilian Regional Atmospheric Modeling System (BRAMS). The RAMS model utilizes the full set of non-hydrostatic, Reynolds-averaged primitive equations (Tripoli and Cotton, 1982). The model solution is advanced in time by using a hybrid time-stepping scheme in which the momentum and scalar fields are integrated using a second-order accurate leapfrog scheme and a forward scheme, respectively. The RAMS uses a terrain-following coordinate designated sigma-z in the vertical scheme, and numerous options are available for the boundary conditions, turbulence parameterization, radiation schemes, microphysical parameterizations and surface schemes. The present study addresses only cloud microphysical parameterization. For a more general discussion of the numerous options available in the model, readers are referred to Pielke et al. (1992) and Cotton et al. (2003). The Brazilian version of the model (BRAMS) is the result of changes incorporated by Brazilian users in recent years, which include a simple photochemical and a soil moisture scheme. Validation of the BRAMS for use in Amazon region simulations was presented by Freitas et al. (2007).

2. Methodology

The methodology is divided in 2.1 Input data; 2.2 Fungi concentration calculus and 2.3 Numerical modeling through BRAMS.

2.1 Input data

The data were obtained as it follows:

It was sampled *Coffea arabica* leaves from the trees, mature leaves. The leaves were cut and placed at agar-agar media with two kinds of medium: with meat for bacteria and with potato for fungi. The fungi, resulting from the media growing, were analyzed and some species were identified as it follows with *Penicillium sp*. the chosen species.

The fungi of spores from above species were submitted to freezing as it follows: 30 droplets of 20 μl with fungi spores and suspended bacteria were submitted to a lyophylizator and the frezzing point was observed for each droplet. Two tests were performed, totalizing around 60 droplets with 60 freezing points; b- A curve of droplet freezing distribution was calculated from each fungi and bacteria species and c) Salt and bi-distilled water tests were also performed in order to have a blank freezing point distribution. Salty droplets were saturated. The result is shown in Figure 1.

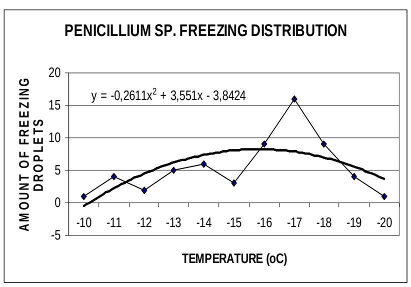

Figure 1. Freezing points of sterilized water with *Penicillium sp*. *suspension*.

2.2 Fungi spores air concentration

The air concentration of spores was developed according to Gonçalves et al. (2008). The samplings were performed indoors and outdoors of different homes scattered through the São Paulo City. The obtained concentrations were from 3000 spores per cubic meter up to 36000 spores. Around 10% were viable spores. Therefore, viable spores present an average of 300 spores per cubic meter.

These were the input data, freezing points as well as total concentrations, as ice nuclei to BRAMS, according to the following section.

2.3 RAMS modeling

The numerical simulations were developed in order to investigate the effect on the total amount of rainwater intergrated on column and raifnall amount as function of IN concentrations. Homogeneous initializations were performed and simulations carried for a time interval of 3 hrs. Heating and wetting at the central area were introduced after 10 minutes in order to develop a convective cell. The chosen radiosonde data is the day March 3 of 2003, typical summertime, at São Paulo City (43.66 long and -23.59 lat)

With the purpose of testing the sensitivity of microphysical parameters, the wet and hot bubble was activated without topography, wind and surface characteristics, emphasizing the cloud microphysical aspects.

The objective of the simulations is to analyze effect of the IN concentrations on the RAMS modeled cloud properties and precipitation. The model setup was:

- Horizontal grid spacing (x, y): 100 km × 100 km; Vertical grid spacing: 43 levels with variable stretching factor (70 m for the finest resolution in the lowest levels) and sponge upper boundary condition;
- Shape parameter 2 and CCN is set as 300 cm^{-3}
- ice nuclei concentrations are: IN-0 (default), IN-1 (305 cm^{-3}), IN-2 (3050 cm^{-3}) and IN-3 (30500 cm^{-3}).

[a1] Comentário: O espaçamento é esse mesmo??? Sera que não é 1km??

The simulation was a simple running with a moist and heat bubble based on Walko et al. (1995), using one single sounding as cited above and with no topography and wind.

2. Results

Preliminarly numerical modeling results are shown in Table 1, using BRAMS with different fungi concentrations as explained in Section 2.2.

Table 1 Total water integrated on column and rainfall amount at the surface using different IN concentrations.

	IN-0	IN-1	IN-2	IN-3
M_{cloud}	2.42	2.42	2.42	2.42
$M_{pristine}$	0.58	0.96	1.36	2.11
M_{snow}	0.57	0.10	0.00	0.00
$M_{aggregates}$	1.16	2.54	3.28	2.93
$M_{graupel}$	0.84	0.13	0.04	0.01
M_{hail}	9.19	11.76	11.66	11.65
M_{cond}	54.15	55.22	54.82	54.36
Av_{cond}	0.70	0.73	0.73	0.73
M_{pcp}	19.50	17.02	16.28	15.89
Av_{pcp}	0.42	0.35	0.33	0.32
Ice_{200mb}	4.51	6.36	6.53	6.47

M_{cloud} is maximum cloud water (g.kg^{-1}); $M_{pristine}$ is maximum pristine ice (g.kg^{-1}); M_{snow} is maximum snow crystals (g.kg^{-1}); $M_{aggregates}$ is maximum aggregates ice (g.kg^{-1}); $M_{graupel}$ is maximum graupel (g.kg^{-1}); M_{hail} is maximum hail (g.kg^{-1}); M_{cond} is maximum column integrated condensed water (mm); Av_{cond} is average column integrated condensed water (mm); M_{pcp} is maximum accumulated precipitation (mm); Av_{pcp} is average precipitation (mm.grid^{-1}); Ice_{200mb} is maximum ice at 200 mb level.

Table 1 shows modeling results with all kind of hydrometeors with differen secnario from no modification (IN-0) to IN concentration of 30500 cm^{-3} (IN-3). comparing with normal distribution.

The first modeling results show that modified ice nuclei distribution have a non-linear response in the average total rainfall and other microphysics variables, comparing with the normal distribution. The maximum condensed water, for example, presents the smallest amount at IN-0, increasing by a factor of 2% with IN-1 and decreasing with the other two forcing factors. However, they present values still higher than the IN-0 simulation.

On the other hand, Av_{pcp}, the average precipitation (mm.grid^{-1}) as well as M_{pcp} (maximum accumalated precipitation) present an steady decrease along the simulations, with the highest at IN-0 and the lowest at IN-3.

For their turn, ice parameters (aggregates, snow, pristine, graupel and hail) present each particular variability where pristine shows increasing values, according to the fungi spores concentrations (from IN-0 to IN-3). Aggregates present similar result. On the other hand, graupel and snow present the opposite behavior, probably because the higher temperature during freezing processes for these variables.

3. Conclusions

Therefore, previous works presents results where São Paulo City area shows high number of atmospheric fungi, reaching values over 30,000 spores per cubic meter. However, there are indications that air pollutants, such as Vanadium, may contribute to the ice nuclei formation, releasing latent heat and enhacing thunderstorms. Fungal spores could also play a role in that enhancement, as well, acting as ice nuclei around -10 and -15^{o}C , such as *Penicillium sp*. .As a possible consequence, São Paulo City presents an increase in number of thunderstorms during last few decades, which is associated primarily with the heat island, but it could be also indicated to the ice nuclei amount.

Anyway, it is quite clear that different patterns are presented when we change the IN concentrations based on fungi spores concentrations and freezing distributions. That means an interesting impact on rainfall and other variables which must be better investigation.

4. References

Ariya P.A., Amyot M. 2004. New directions: The role of bioaerosols in atmospheric chemistry and physics. Atmospheric Environment 38: 1231–1232.

Bauer H. et al. 2003. Airborne bacteria as cloud condensation nuclei. J. Geophys. Res. 108: (D21), 4658, doi:10.1029/2003JD003545, 2003.

Cotton, W. R., R. A. Sr. Pielke, R. L. Walko, G. E. Liston, C. J. Tremback, H. Jiang, R. L. McAnelly, J. Y. Harrington, M. E. Nicholls, G. G. Carrio, and J. P. McFadden (2003), RAMS 2001: Current satus and future directions, *Meteor. Atmos. Phys., 82*, 5–29.

Diehl, K. et al. 2000. Laboratory studies on the ice nucleating ability of biological aerosol particles in condensation freezing, immersion freezing and contact freezing modes. J. Aerosol Sci. 31: S70-S71.

Freitas, S. R., K. M. Longo, M. A. Silva Dias, R. Chatfield, P. L. Silva Dias, P. Artaxo, M. Andreae, G. Grell, L. F. Rodrigues, A. L. Fazenda, and J. Panetta (2007), The coupled aerosol and tracer transport model to the Brazilian developments on the Regional Atmospheric Modeling System (CATT-BRAMS). Part 1: Model description and evaluation, *Atmos. Chem. Phys. Disc., 7*, 8525-8569.

Gonçalves F.L.T., H. Bauer, Cardoso, M.R.A., Matos, D., Melhem, M., H. Puxbaum (2008). Atmospheric fungi spore variability at São Paulo Metropolitan Area. Submitted to Aerobiology.

Hamilton, W.D., Lenton, T.M. 1998. Spora and Gaia: how microbes fly with their clouds. Ethology, Ecology and Evolution 10 :1-16.

Jaenicke, R. 2005. Abundance of cellular material and proteins in the atmosphere. Science 308:73.

Morris C.E. et al. 2004. Ice nucleation active bacteria and their potential role in precipitation. J. Physiques IV 121:87-103.

Morris, C.E., Sands, D.C. and Ariya, P. A. , 2007. Microbiology and atmospheric processes: airborne micro-organisms on the atmosphere and climate, Biogeosciences.

Pielke, R. E., W. R. Cotton, R. L. Walko, C. J. Tremback, W. A. Lyons, L. D Grasso, M. E. Nicholls, M. D. Moran, D. A. Wesley, T. J. Lee, and J. H. Copeland (1992), A comprehensive meteorological modeling system – RAMS, *Meteor. Atmos. Phys., 49*, 69-91.

Pouleur, S., Richard, C., Martin, JG., Antoun, H., 1992. Ice Nucleation Activity in *Fusarium acuminatum* and *Fusarium avenaceum* App. Environ. Microbiol. 58:2960-2964.

Sattler, B. et al. 2002. Clouds as habitat and seeders of active bacteria. Proc. SPIE-The International Society for Optical Engineering 4495 (Instruments, Methods, and Missions for Astrobiology IV): 211-222.

Sattler, B. et al. 2001. Bacterial growth in supercooled cloud droplets. Geophys. Res. Lett. 28/2: 239-242.

Szyrmer, W., Zawadzki, I. 1997. Biogenic and anthropogenic sources of ice-forming nuclei: A review. Bull. Am. Meteorol. Soc. 78, 209-228.

Tripoli, G. J., and W. R. Cotton (1982), The Colorado State University three-dimensional cloud mesoscale model, 1982: Part I: General theoretical framework and sensitivity experiments*, J. Rech. Atmos*., 16, 185-220.

LABORATORY STUDY ON CCN EFFICIENCY OF AEROSOL PARTICLES SIMULATING WOOD COMBUSTION PARTICLES

S. Henning[1], H. Wex[1], F. Stratmann[1], C. Wennrich[1], D. Rose[2], U. Dusek[2], G. P. Frank[2], U. Pöschl[2], A. Kristensson[3], M. Bilde[3], T. Hennig[1], R. Tillmann[4], A. Kiendler-Scharr[4], Th. F. Mentel[4], A. Kiselev[1], S. Walter[5], J. Schneider[5], J. Snider[6]

[1]Leibniz Institute for Tropospheric Research, Permoserstr. 15, 04318 Leipzig, Germany
[2]Max Planck Institute for Chemistry, Biogeochemistry Department, P.O. Box 3060, 55020 Mainz, Germany
[3]Department of Chemistry, University of Copenhagen, Universitetsparken 5, 2100 Copenhagen, Denmark
[4]Research Centre Jülich, ICG-II: Troposphere, Leo-Brandt-Str., 52425 Jülich, Germany
[5]Max Planck Institute for Chemistry, Particle Chemistry Department, P.O. Box 3060, 55020 Mainz, Germany
[6]University of Wyoming, Department of Atmospheric Science, Dept. 3038, 1000 E. University Ave., Laramie, WY 82071, USA.

1. EXPERIMENTAL

The goal of the LExNo campaign, which was conducted November 2005 at the ACCENT site Leipzig Aerosol Cloud Interaction Simulator (LACIS), was to get further insight in the activation properties of aerosol particles resulting from wood combustion [*Stratmann, et al.*, 2008].

In this laboratory experiment, wood combustion aerosol particles were simulated using spark-generated soot (pure or compacted with propanol) coated with ammonium sulfate (AS, coating temperatures 93°C to 170°C) and/or levoglucosan (LG, coating temperature 80°C to 106°C) using two tube furnaces.

Thermal decomposition of ammonium sulfate is known to take place in this temperature range (e.g. [*Halstead*, 1970; *Kiyoura and Urano*, 1970]). The molar ratio of ammonia to sulfate (resulting for the AMS measurements) leads to the conclusion that the particle coating consisted of ammonium hydrogen sulfate (AHS) independent from the coating temperature (cf. Fig. 1). In addition to AHS an organic substance was detected in the AMS spectra for this coating type, which is most probable propanol. Soot particles passed over AS for coating are therefore considered as soot / ammonium hydrogen sulfate coated including propanol (AHSp).

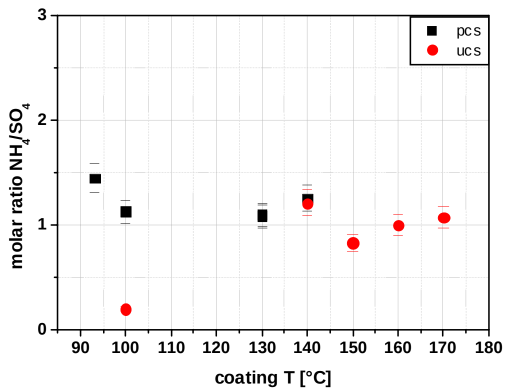

Figure 1 Dependency of coating composition on furnace temperature. The molar ratio of NH4/SO4 should be 2 for AS and 1 for AHS (error bars: 10% error in mass).

For LG decomposition is not expected, because it decomposes above 110°C.

The synthesized particles were analyzed using two aerosol mass spectrometers (AMS), a hygroscopicity tandem differential mobility analyzer (HTDMA), two Wyoming static diffusion cloud condensation nuclei (CCN) instruments, a continuous flow CCN instrument (Droplet Measurement Tech.) and LACIS.

2. RESULTS

Particles were investigated with respect to their critical supersaturation (Sc) and with

respect to their growth factor (GF). Both properties have an impact on the particles cloud-forming potential.
The coating on the soot particles had a clear, hygroscopicity enhancing effect on the particles. The AHSp coating was more efficient in enhancing hygroscopicity than LG. For soot / AHSp coated activation was observed between 0.3% and 0.6% supersaturation for a dry particle diameter of 84.4 nm. For soot / LG coated the critical supersaturation was observed to be between 0.5% and 0.75% for the same particle diameter. Propanol-compacted soot / LG + AHSp coated activated around 0.32%. The range of the critical supersaturation results from the differences in the coating temperature, which influences the coating thickness.
The growth factor (GF) of the particles was clearly related to Sc for all particle types investigated in this humidity range (Fig. 2, RH=98%). The higher the GF was, the more easily the particles were activated. For soot / AHSp coated GFs were found between 1.3 and 2.2. Soot / LG coated particles did not adsorb as much water, and their GF was between 1.25 and 1.5. The soot particles / LG + AHSp coated had a GF of 1.7.

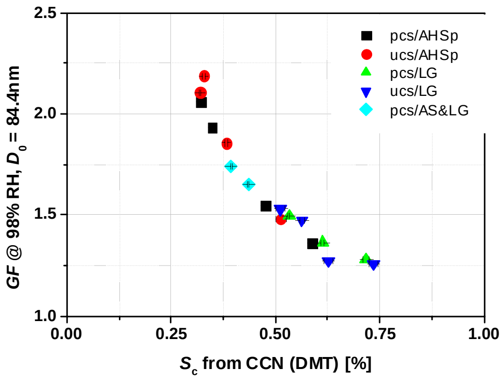

Figure 2 Relationship between growth factor at 98% RH and critical supersaturation of particles (d0=84.4nm).

No influence of propanol-compaction was observed in either growth factor or the critical activation. This is attributed to observed compaction of the particles when coated with AHSp or LG independent from a previous compaction with propanol.
Closure in terms of the prediction of the critical supersaturation was achieved with two different approaches: (1) based on the parameterization of the subsaturated hygroscopicity [*Petters and Kreidenweis*, 2007; *Wex, et al.*, 2007] and (2) based on the chemical composition as determined with the AMS.
Predicted and measured values of the critical supersaturation based on the subsaturated properties were in very good agreement for all investigated particles types (cf. Fig. 3, slope=1.06, R^2=0.98). Growth factors measured at high relative humidities seem to represent the activation properties perfectly for this type of internally mixed particles.

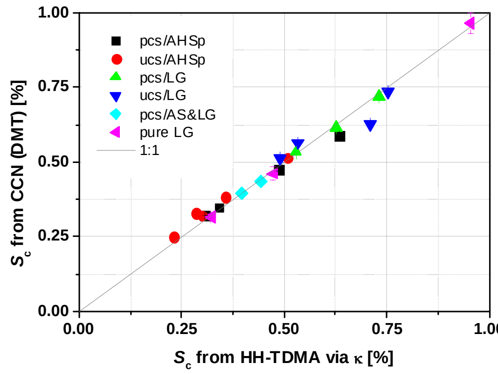

Figure 3 Measured versus predicted critical supersaturation based on subsaturated measurements.

Closure based on the soluble mass as detected with the AMS was not as good, if all particle compositions are taken into account (cf.4, slope=1.26, R2=0.75). However, for soot / AHSp coated predicted and measured Sc are in good agreement (slope=1.13, R2=0.94). Soot particles coated with LG activate at lower Sc than predicted from the measured organic mass from the AMS and scatter more. The reason for this is at this point still under investigation. Possible reasons could be: (1) the high number of doubly charged particles – as observed during the pure LG experiments - could bias mass analysis from AMS (2) a complex reaction might take place between soot and LG and hinder to regain all the organic material for analysis.

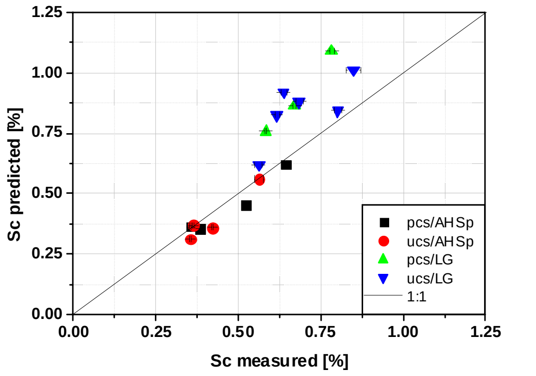

Figure 4 Predicted versus measured critical supersaturation: Prediction is based on soluble particle mass, as detected by the AMS, and Köhler theory (T=20°C, σ(T)=72.8 mN/m).

3. CONCLUSIONS

The particles generated in the laboratory, mimicking biomass-combustion products, were varied in terms of (1) the fractal dimension of the soot core and (2) the applied coating which was either an two component system, levoglucosan or both.
The thermal decomposition of ammonium sulfate in the coating furnace together with a bias from the propanol-compaction unit resulted in a ternary mixed particle, composed of soot / ammonium hydrogen sulfate and propanol (soot / AHSp). The complex coating did not turn out as a disadvantage for the closure experiments, because it could be described explicitly.
Concerning the fractal dimension of the soot particles it was found that initially uncompacted soot particles became compacted when a coating was applied. This effect was more pronounced for the ammonium hydrogen sulfate / propanol coating than for the soot / levoglucosan coated. The differences in the resulting hygroscopic properties were therefore minor between propanol-compacted and initially uncompacted soot cores.
For all particle types a clear correlation between hygroscopic growth at high relative humdities (~98%) and critical supersaturation was observed. This leads to the conclusion, that both of them are dominated by the same particle properties.
Closure between hygroscopicity, activation and soluble mass was achieved by applying two different approaches.
The relationship between hygroscopicity and activation was described via two slightly different one-parameter approaches, which avoid unknown properties (e.g., density, molar mass of mixture) in Köhler theory. The found closure is excellent for all particles types. This might be explained by the fact that the data included in this analysis (HHTDMA and CCN) are measures for the same kind of particles properties.
Closure between soluble mass as measured by the AMS and activation works also very good, although the AMS measures a completely independent particle property.
Between all cumulated data sets closure is achieved and this shows a consistent picture of the activation properties of the investigated particles. It also allows an estimate of the cloud forming potential of combustion particles based on only one of the presented independent measurement data.

4. BIBLOGRAPHY

Halstead, W. D. (1970), Thermal Decomposition of Ammonium Sulphate, *Journal of Applied Chemistry of the USSR*, *20*, 129-&.

Kiyoura, R., and K. Urano (1970), Mechanism, Kinetics, and Equilibrium of Thermal Decomposition of Ammonium Sulfate, *Industrial & Engineering Chemistry Process Design and Development*, *9*, 489-&.

Petters, M. D., and S. M. Kreidenweis (2007), A single parameter representation of hygroscopic growth and cloud condensation nucleus activity, *Atmospheric Chemistry and Physics*, *7*, 1961-1971.

Stratmann, F., et al. (2008), LExNo – Hygroscopic Growth and Activation of

Laboratory-generated Aerosol Particles Imitating Combustion Aerosols.
Wex, H., et al. (2007), Hygroscopic growth and measured and modeled critical super-saturations of an atmospheric HULIS sample, *Geophys. Res. Lett.*, *34*.

Acknowledgments

The authors thank ACCENT for the financial support.

CLOUD FORMING POTENTIAL OF SECONDARY ORGANIC AEROSOL

Zs. Jurányi[1], M. Gysel[1], J. Duplissy[1], E. Weingartner[1], S. Henning[2], F. Stratmann[2], U. Baltensperger[1]

[1]Laboratory of Atmospheric Chemistry, Paul Scherrer Institut, CH-5232, Villigen PSI, Switzerland
[2]Leibniz-Institute for Tropospheric Research, Permoser Strasse 15, 04318, Leipzig, Germany

1. INTRODUCTION

Secondary organic aerosol (SOA) contribute an important fraction of the atmospheric organic aerosol. SOA is formed by oxidation of volatile organic compounds (VOC), which results in complex mixtures of organic species in the particle phase. Their hygroscopic and cloud condensation nuclei (CCN) properties are much less understood than those of inorganic mixtures. Even though SOA is to a great extent water soluble, its contribution to cloud formation is still largely unknown.

2. EXPERIMENT

Experiments were conducted on SOA formed through photooxidation of the gaseous precursor species α-pinene –representative of natural emissions– under controlled conditions in a smog chamber. The precursor concentration was varied between atmospherically relevant (10-20 ppb) and an order of magnitude higher values (180-240 ppb). The hygroscopicity and CCN activity of the SOA particles were investigated at different relative humidities (RH) in the sub- and supersaturated region.

A Hygroscopicity Tandem Differential Mobility Analyzer (HTDMA) and the Leipzig Aerosol Cloud Interaction Simulator (LACIS-field) were used to measure diameter growth factors (GF) at 90–98% RH and 97–99% RH, respectively. The CCN activation behavior of SOA at supersaturated RH was followed by two CCN counters (DMT-CCNC) operated behind a differential mobility analyzer (DMA) selecting the same dry size as the HTDMA.

3. THEORY

A simplified one parameter representation of the concentration dependence of the water activity (a_w) [Petters and Kreidenweis, 2006], which shows up in the Köhler equation was used to compare the results that were measured at different relative humidities:

$$a_w^{-1} = 1 + K\frac{V_s}{V_w}$$

where K is the free parameter, V_s is the volume of the solute and V_w is the volume of the water in the aerosol particle.

4. RESULTS

The HTDMA measurements show that the GF of SOA particles at RH≈97% depends on the initial precursor concentration (green symbols in Figures 1 and 2), confirming the results of an earlier study [Duplissy et al., 2008]. The GFs measured by the HTDMA are systematically lower at high precursor concentrations compared to low precursor concentrations, which is reflected in a decrease of the HTDMA dervied K-values. This can be the consequence of the higher partial vapor pressures of the gas phase components at higher precursor concentration thus driving a larger fraction of species with relatively high vapor pressures into the particle phase. The latter compounds are less oxygenated and less hygroscopic and therefore lowering the measured GFs and thus the HTDMA derived K-values.

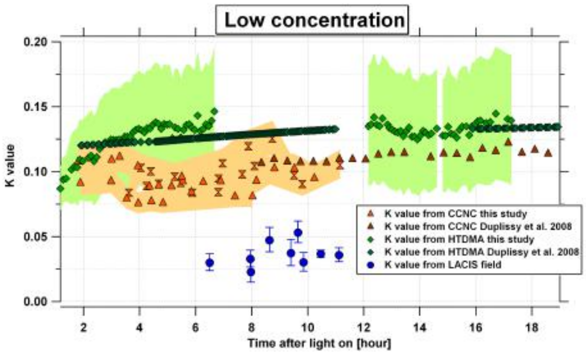

Figure 1: K-values retrieved from CCNC, HT-DMA and LACIS during low concentration experiments

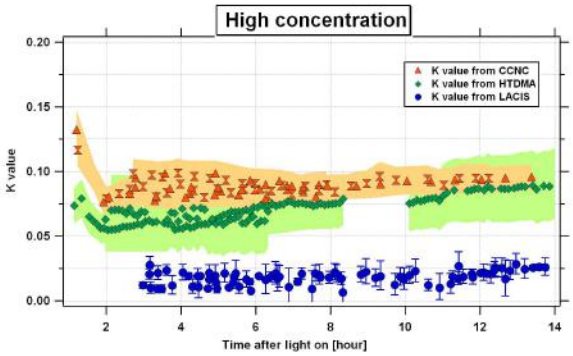

Figure 2: K-values retrieved from CCNC, HT-DMA and LACIS during high concentration experiments

Contrary to the HTDMA data no precursor concentration dependence of the critical supersaturation for CCN activation was measured by the two CCNCs, which is reflected in comparable CCN derived K-values shown in Figures 1 and 2. The reason for these different effects of precursor concentration changes on hygroscopicity and CCN activity is not yet clear. Growth factors at subsaturated RH depend mostly on the concentration dependence of the water activity and on the dissolved fraction of SOA if there are solubility limitations. CCN properties are more sensitive to the surface tension due to the Kelvin term in the Köhler equation (all K-values were calculated assuming surface tension of pure water), though surface partitioning effects may compensate surface tension changes to some extent. More sophisticated modeling efforts will be undertaken, in order to explore possible combinations of effects which might explain the observed behavior. However, HTDMA and CCN derived K-values still overlap within experimental uncertainty (colored bands in the Figures), showing that this simple one-parameter model makes approximate predictions of CCN activity from GF measurements possible. Currently it is unclear why the LACIS measures a significant lower hygroscopicity, which is in good agreement with the results of Prenni et al., 2007.

5. BIBLIOGRAHPY

Duplissy, J., et al. (2008), Cloud forming potential of secondary organic aerosol under near atmospheric conditions, Geophys. Res. Lett., 35, L03818, doi:10.1029/2007GL031075.

Petters, M. D., and S. M. Kreidenweis (2007), A single parameter representation of hygroscopic growth and cloud condensation nucleus activity, Atmos. Chem. Phys. Discuss., 6, 84358456.

Prenni, A. J., M. D. Petters, S. M. Kreidenweis, P. J. DeMott, and P. J. Ziemann (2007), Cloud droplet activation of secondary organic aerosol, J. Geophys. Res., 112, D10223, doi:10.1029/2006JD007963.

Acknowledgements

We thank the IFT and the PSI team for performing the experiments, special thanks to M. Ziese, A. Kiselev and T. Tritscher.

MEASUREMENT OF AEROSOL HYGROSCOPICITY AND CLOUD CONDENSATION NUCLEI AT A REMOTE NORTHEAST ASIAN COASTAL SITE IN GOSAN, KOREA IN SUMMER 2006 AND SPRING 2007

Jong Hwan Kim[1], Seong Soo Yum[1] James G. Hudson[2] and Sungbo Shim[1]
[1]Department of Atmospheric Sciences, Yonsei University, Seoul South 120-749, Korea
[2]Division of Atmospheric Sciences, Desert Research Institute, Reno, Nevada, USA

1. INTRODUCTION

Hygroscopicity of aerosols affect radiation energy reaching the surface both by altering aerosol optical depth in the atmosphere. Aerosols that can experience large hygroscopic growth at a relatively small supersaturation (S) can act as cloud condensation nuclei (CCN), which is a key parameter in the assessment of indirect aerosol effects..

The hygroscopicity of submicron aerosol and CCN concentration (N_{CCN}) were measured at a remote northeast Asian coastal site in Gosan, Korea in summer 2006 and spring 2007. The site is strategically located at the western tip of Jeju Island, south of the Korean Peninsula and provides a unique opportunity to monitor aerosols from Asian continental outflow.

2. EXPERIMENT SETUP

During the Gosan campaign (August 16 ~ September 1, 2006), N_{CCN} at 0.2, 0.4, 0.6, 0.8 and 1.0% S were measured using a DMT CCN counter every 30 minute. Aerosol concentrations for diameter, d, larger than 10 nm (N_{CN10}) were measured every minute using a TSI CPC 3010. Submicron size distribution ranging between 10 and 300nm were measured with 95 size bins using an SMPS every 3 minute.

Hygroscopic growth factors (GF) for aerosols having diameter 50, 100, 150 and 200 nm were measured by a humidified tandem differential mobility analyzer (H-TDMA) at 85~95% relative humidity (RH). With a single SMPS available, this could only be done when the SMPS was not used for aerosol size distribution measurement. H-TDMA measurement produces GF values for controlled relative humidity (RH). Due to the temperature variation within the instrument shelter, the temperature within the DMA also varied from time to time, resulting in RH fluctuation. Therefore, only the samples with small fluctuation (standard deviation less than 0.2% RH, which is one-tenth of instrumental accuracy) during the 2-minute voltage scan were used for analysis.

Similar instruments were used in the 2006 autumn campaign in Seoul.

During April 16 ~ May 15, 2007, as a part of Pacific Dust Experiment (PACDEX), N_{CCN} and GF were measured at Gosan using the same instruments mentioned above, except that the measurement was continuously done this time and 250 nm instead of 50 nm was selected along with the other three diameters. N_{CN10} and submicron size distribution were measured by other research groups but effort has not been made to incorporate all the data yet.

3. OVERALL HYGROSCOPICITY

Fig. 1 illustrates the relationship between measured GF and RH for 150 nm aerosols during the whole 2007 spring campaign. The embedded black curve represents the GF of $(NH_4)_2SO_4$. It is clearly shown that most of the aerosols were hygroscopic but not as hygroscopic as $(NH_4)_2SO_4$. There were also some hydrophobic aerosols having GF less than 1.1. The results for 100, 200 and 250 nm aerosols were also similar (not shown).

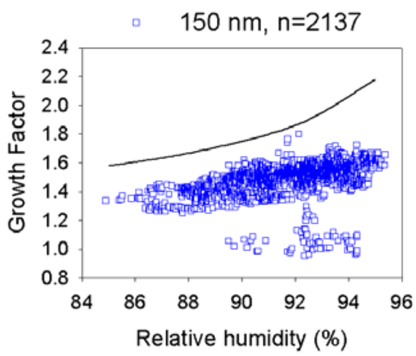

Fig. 1. GF as a function of RH during the 2007 spring campaign.

These GF values are similar to Massling et al.'s (2007) GF measurement at 90% RH in the marine region between Korea and Japan during ACE-Asia in spring 2001. The authors have attributed the reason for such aerosol hygroscopicities as pollution from Korea and Japan. They also found that the aerosols as hygroscopic as $(NH_4)_2SO_4$ were always present. Surprisingly, such aerosol was seldom measured throughout the whole PACDEX campaign.

Maria et al. (2003) reported that there were virtually no sea salts in the submicron sizes in this region based on filter measurement. Massling et al. (2007) also did not found any sea salts except for the case when the air mass had traveled over the ocean for 6 days with no contact with the land. These results agree well with the fact that the aerosols with growth factors significantly exceeding that of $(NH_4)_2SO_4$ were measured only in two occasions throughout the whole measurement period: one at 200 nm and another at 250 nm.

4. SOLUBLE FRACTION

GF can be converted to soluble fraction (ε), assuming that the soluble part of the aerosol volume consists of $(NH_4)_2SO_4$ by simple relation (Pitchford and McMurry, 1994):

$$\epsilon = \frac{GF_a^3 - 1}{GF_{ref}^3 - 1}$$

where GF_a and GF_{ref} stand for measured GF and the reference GF for $(NH_4)_2SO_4$, respectively. Although the exact chemical composition of aerosols may not be $(NH_4)_2SO_4$, such an assumption provides a convenient measure of comparing GFs.

The frequency distributions of soluble fraction are shown in Fig. 2. The soluble fraction of about three-fourth of the samples fall in the range 0.3~0.5. For the smallest diameter, 100 nm, the soluble fraction is almost normally distributed, with a distinct peak at 0.4, while more evenly distributed shape is shown for the largest diameter, 250 nm. This suggests changes in aerosol chemical composition with size.

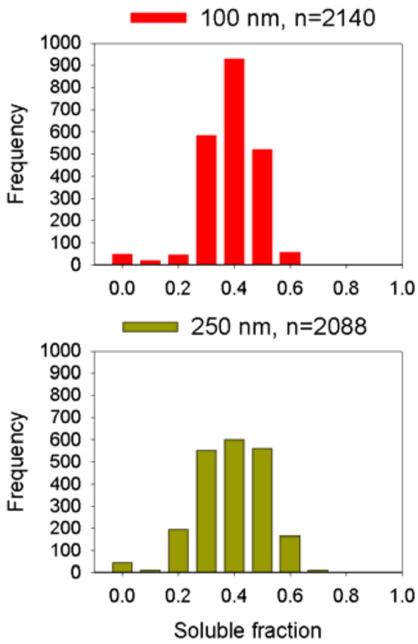

Fig. 2. Frequency of soluble fractions for two different dry sizes for 2007 spring campaign.

Daily variation of solubility frequency ratio is shown for the two diameter, 100 and 250 nm in Fig. 3. Here soluble fraction, <0.3, 0.3-0.6, and >0.6 are termed as hydrophobic, less hygroscopic and more hygroscopic, respectively. The frequency ratio varied much from day to day and from size to size. The wind was very strong on April 21 when the long tongue of more hygroscopic aerosols is found at sizes 150 nm and above, although there was no sign of sea salt. Heavily polluted air mass was reported on April 25~27, when there was a tendency to show greater hygroscopicity in all size ranges. It is not clear what caused a large increase in hydrophobic aerosols on May 10 for 100 nm and May 10~13 for 250 nm.

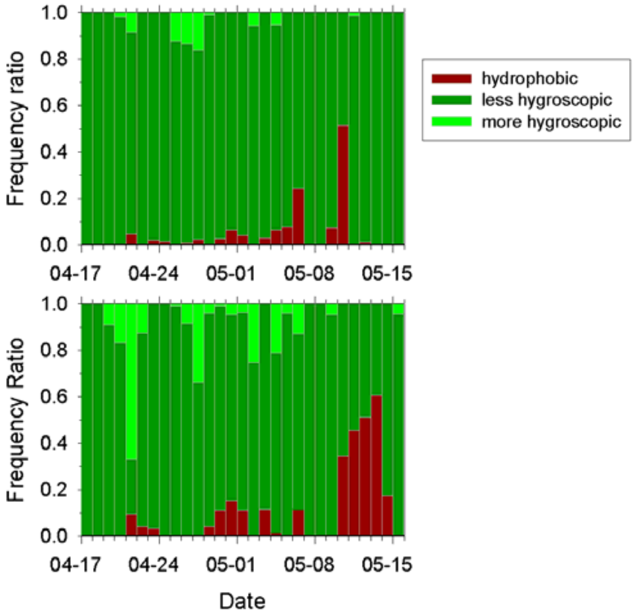

Fig. 3. Daily variation of solubility frequency ratio for (top) 100 nm and (bottom) 250 nm during 2007 spring campaign.

Similar analysis is made for the diurnal variation for 200 nm (Fig. 4). It is noted that hydrophobic aerosols were reduced in the afternoon hours.. Other sizes showed similar diurnal trend but with less significance.

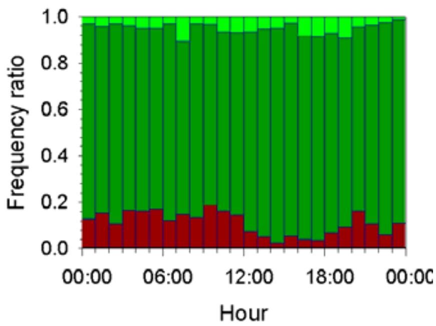

Fig. 4. Average diurnal variation of soluble fraction for 200 nm during 2007 spring campaign.

The aerosol nucleation and growth event

was frequently observed at Gosan. Fig. 5 is an example of such event during the 2006 summer campaign. The GF measurement was made before and after the event, during which the mode diameter grew from 10 nm to about 70 nm, with the average growth rate of 3.3 nm hr^{-1}. To note is that the soluble fraction for 50 nm increased from less than 0.4 before the event to greater than 0.6 after the event, suggesting that condensation of gaseous species during the growth enhanced the hygroscopicity. Similar hehavior was observed for 100 nm.

These results are consistent with Buzorius et al. (2004) who measured GF during aerosol growth events at Gosan during ACE-ASIA for 25 nm aerosol and found that its growth was similar to that of $(NH_4)_2SO_4$. Hameri et al. (2001) also reported growth in GF during the growth event in Finland boreal forest.

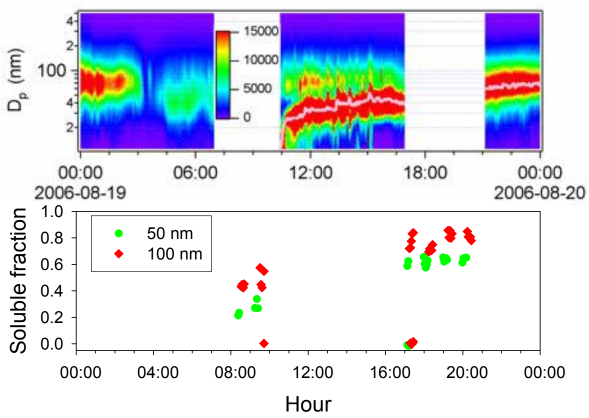

Fig. 5. Aerosol growth event and soluble fraction during 2006 summer campaign: (Top) Temporal variation of aerosol size distribution showing growth event with mode diameter marked as tracer, (Bottom) Temporal variation soluble fraction.

5. HYGROSCOPIC MEASUREMENT IN SEOUL

Shown in Fig. 6 is the measurement in Seoul, highly populated city wih many local sources. Seoul aerosols are comprised of two distinct types: one with extreme hydrophobicity (GF=1) and the other as soluble as, or even more hydroscopic than $(NH_4)_2SO_4$. Consistently, soluble fraction of zero has the highest frequency (Fig. 6)..

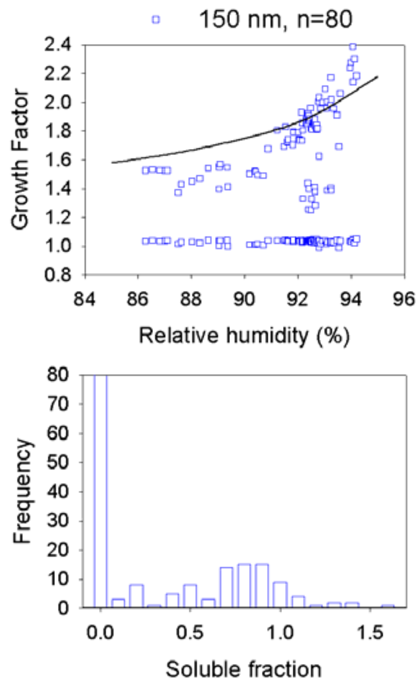

Fig. 6. (Top) GF as a function of RH, (Bottom) Frequency of soluble fractions for Seoul during the 2007 autumn.

6. HYGROSCOPICITY AND CCN

To investigate the effect of hygroscopicity on CCN activity, soluble fraction was compared with CCN number ratio (N_{CCN}/N_{CN}) on daily basis (Fig. 7). In order to account the fact that aerosols with larger diameter tends to act as CCN more easily under same S, samples with soluble fraction larger than 0.4

was selected for 200 and 250 nm while soluble fraction larger than 0.6 was selected for 100 and 150 nm.

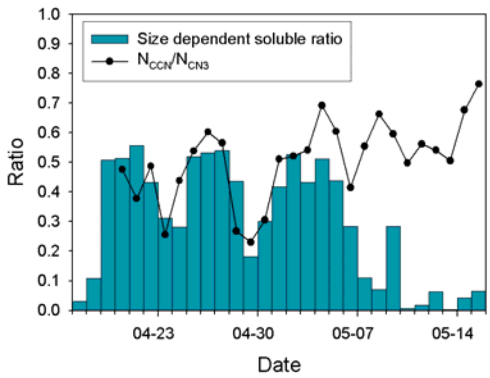

Fig. 7. Daily variations of N_{CCN}/N_{CN} and size-dependent soluble ratio during 2007 spring campaign. CCN was measured under 0.6% S.

The result shows that the two patterns tend to share their local maximum and local minimum until May 5th. The soluble fraction stayed low compared to CCN fraction, indicating that particles with less solubility also acted as CCN. Since May 6th, the CCN number ratio increases but the soluble fraction stays very low. Aerosols with diameter larger than 250 nm must have contributed during that period.

Yum et al. (2007) have reported that Gosan aerosols act almost like $(NH_4)_2SO_4$ as far as CCN activity is concerned. Their cut-off size was 300 nm which is comparable to 250 nm. However, this study shows that particles less soluble than $(NH_4)_2SO_4$ can also act as CCN.

7. BIBLIOGRAPHY

Buzorius et al., 2001: *J. Geophys. Res.*, **109**, D24203, doi:10.1029/2004JD004749, 2004.

Hameri et al., *Tellus*, **53B**, 359-379.

Maria et al., 2003: *J. Geophys. Res.*, **108**, D23, 8637, doi:10.1029/2003JD003703.

Massling et al., 2007: *Atmos. Chem. Phys.*, **7**, 3249-3259.

Pitchford and McMurry, 1994: *Atmos. Environ.*, **28**, 827-839.

Yum et al., 2007: *J. Geophys. Res.*, **112**, D22S32, doi:10.1029/2006JD008212.

Acknowledgement

This subject is supported by Ministry of Environment as "The Eco-technopia 21 project". The authors would also like to acknowledge WMO, IUGG, IAMAS and ICCP's financial support for attending ICCP-2008 conference.

THE VARIABILITY OF ICE NUCLEATING AEROSOLS OVER CENTRAL EUROPE

Holger Klein[1],Ulrich Bundke[1], Björn Nillius[2], Lothar Schütz[2] ,Thomas Wetter[1]and Heinz Bingemer[1]

[1] Institute for Atmosphere and Environment, J.W.Goethe-University, Frankfurt/M , Germany
[2] Institute for Atmospheric Physics, J. Gutenberg-University, Mainz, Germany

1. Introduction

The role of ice nuclei (IN) in the development of clouds and precipitation is poorly understood. Understanding the growth of hydrometeors and development of precipitation from mixed-phase clouds in a given situation requires knowledge of the generation of primary ice. Therefore, the number concentration of ice nuclei and their activation behavior have to be known. We attempt to characterize the natural variability of ice nucleus concentration as a function of airmass history and degree of pollution. This may serve as a basis to further study the sensitivity of cloud microphysical development on the conditions of primary ice initiation.

We report measurements of ice nuclei concentration on a diurnal basis at the Taunus Observatory on Mt. Kleiner Feldberg (825 m above sea level), about 25 km north of Frankfurt/M, Germany.
Sampling conditions includes airmasses of continental, marine, subpolar or subtropical character, and various degrees of pollution. Interpretation is based on trajectories, local meteorological and air pollution data and aerosol physical spectra in the 5 -1000 nm size range.

2. Experimental Method and Results

Aerosol has been sampled on substrates. Samples were analyzed in a static vapor diffusion processing chamber. Substrates are exposed to temperatures of between -5°C and -25°C and to supersaturation with respect to ice of 0 to 40%. Ice crystals grow by deposition and condensation freezing. They are viewed by a CCD camera, and are counted automatically. The experimental setup of the processing chamber FRIDGE (Frankfurt Ice Nuclei Deposition freezinG Experiment) is described by Bundke et al. (2008) and by Ardon et al. (2008) in the proceedings of this conference.

The sampling of aerosol on filters and subsequent processing and detection of ice nuclei is a well established technique and has been applied since several decades, using chambers of various designs (Bigg, 1963, Gravenhorst and Meyer, 1976). In the past, intercomparisons (Vali, 1975) had shown large differences of deposition mode freezing IN concentrations measured by various methods. However it appears that continuous-flow-device measurements (e.g. Rogers et al., 1982; Al-Naimi and Saunders, 1985) exhibit roughly a factor of 10 higher concentrations of IN at warmer temperatures than filter processing systems (Levin and Cotton, 2007). A recent intercomparison of techniques for the measurement of ice nuclei (Moehler et al., 2008) again revealed a large underestimate of IN number concentration by the technique of filter sampling and subsequent processing and detection in a vacuum diffusion chamber. While the processing chamber and detection system successfully reproduce the nucleation characteristics (temperatures and supersaturations at the onset of icing) of various test substances like silver iodide, kaolinite and Arizona test dust ATD (see Figure 1) it obviously underestimates the number of natural ice nuclei present in an aerosol sample on a filter substrate. We currently believe that this may be caused by the recondensation of Vaseline ® organic vapour onto the active ice nucleating sites of aerosol particles during filter processing. During filter processing under vacuum a small amount of Vaseline ® is applied to improve the heat conduction from the filters to the cooling plate underneath and to inhibit condensation and freezing at the metal surface of the filter support.

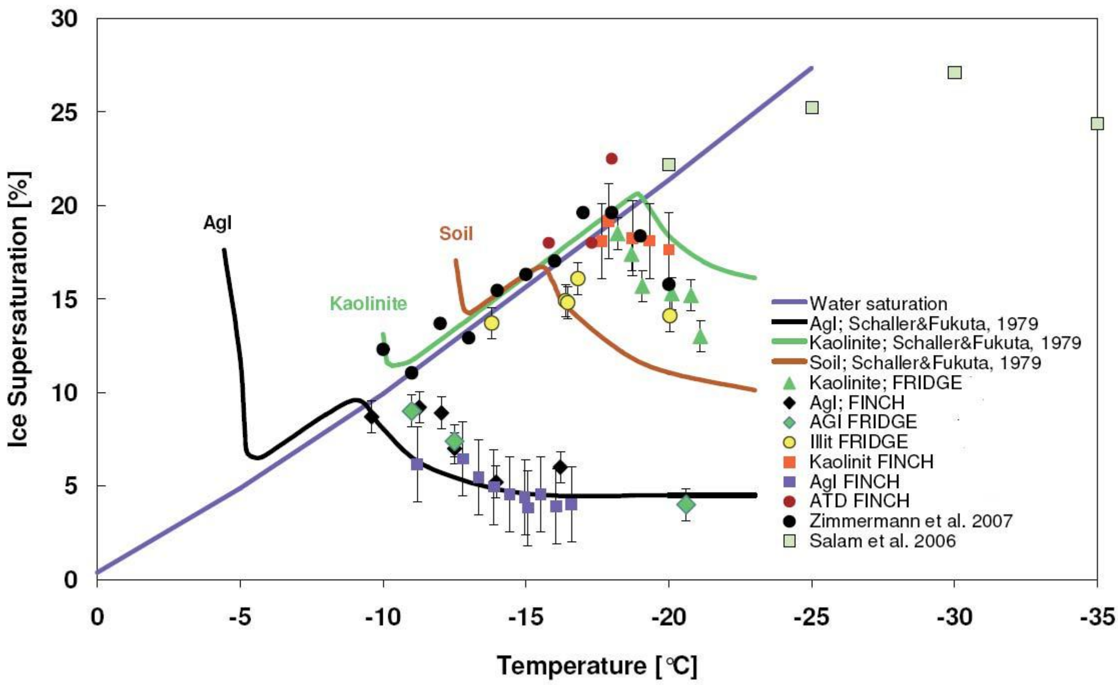

Figure 1. Ice onset temperatures of Silver iodide (AgI), Kaolinite, Illite measured by FRIDGE and FINCH and Arizona Test Dust (ATD) measured with FINCH in comparison with data published by Schaller and Fukuta (1979), Salam et al. (2006), Zimmermann et al. (2007). Adapted from Bundke et al., (2008)

As a new approach to the quantitative sampling of ice nuclei on substrates we have recently set up a device for the charging of aerosol in a sample air flow and its subsequent electrostatic precipitation onto the surface of 47 mm diameter circular silicon wafers (yet unpublished). The design of the Electrostatic Aerosol Collector (EAC) is shown in Figure 2.

These substrates are then processed in the chamber. In atmospheric samples (urban air) collected in parallel on filters and on wafer substrates the IN concentration on the wafers on average was higher by a factor of 45 (Figure 3). This finding is supported by the relatively good agreement (Figure 4) between atmospheric IN concentrations (urban air) sampled with this new technique and those measured by the continuous–flow IN instrument FINCH (Bundke et al., 2008) during parallel measurements in our laboratory. In contrast, our previous intercomparisons pointed to a serious underestimate of the ice nuclei concentration by the filter method.

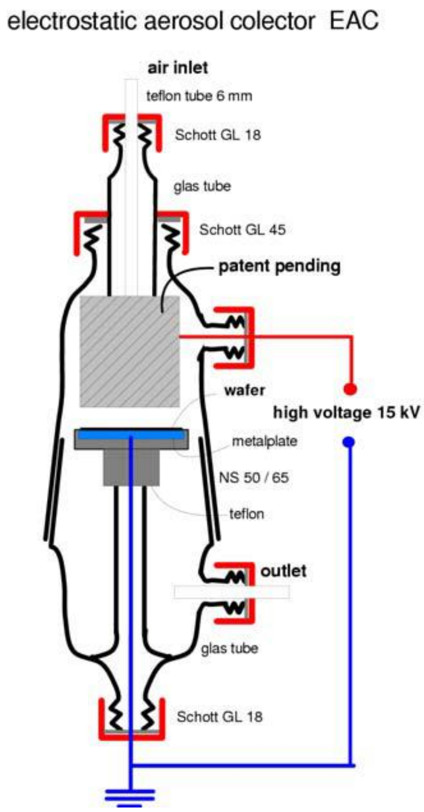

Figure 2. Design of the Electrostatic Aerosol Collector developed at the University Frankfurt. Particles are precipitated in a field of corona-discharge.

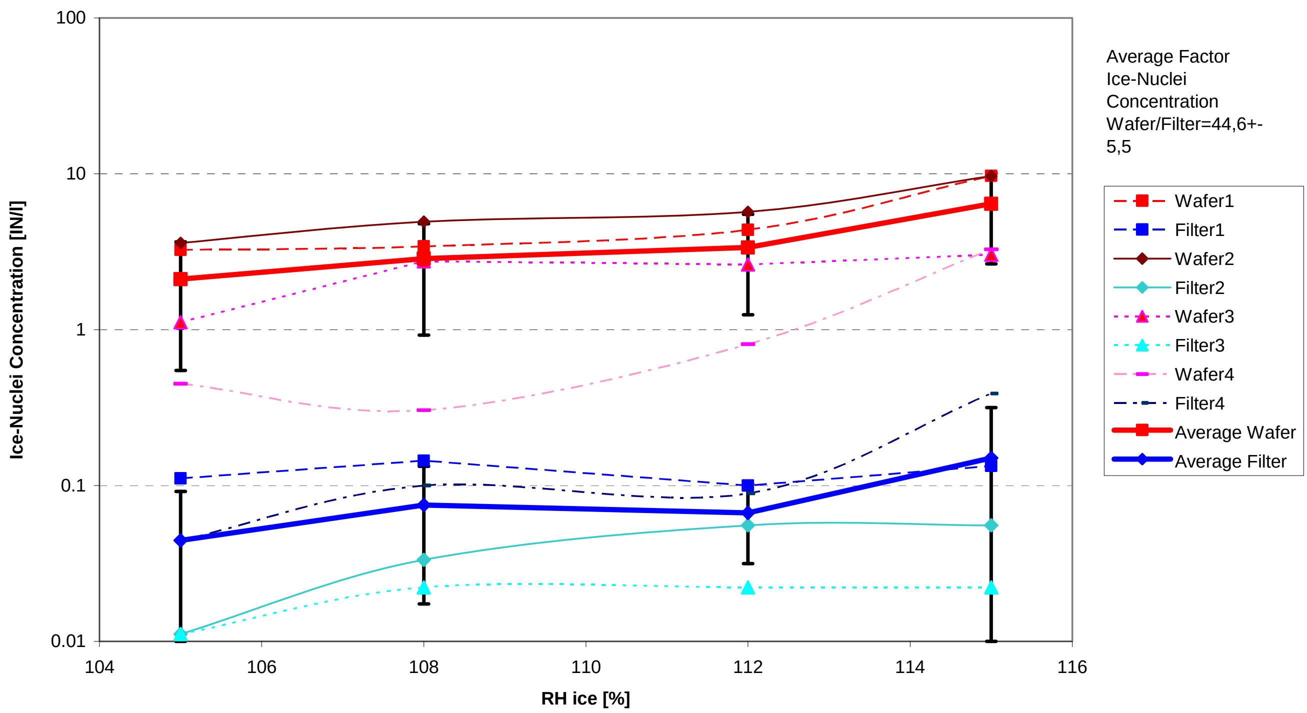

Figure 3: Analysis of parallel samples on wafer/filter (30 l) at -14°C. Results of the filter analysis are shown in blue, while results of the wafer analysis shown in red. Thick lines represent average values, with standard deviation (black bars). The sampled aerosol is ambient aerosol from Frankfurt.

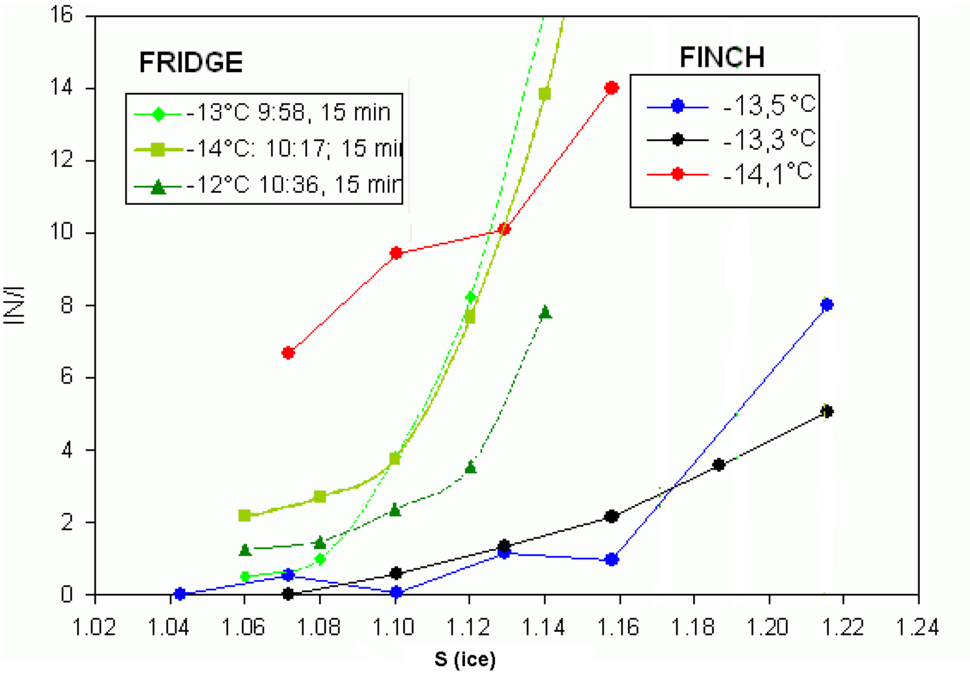

Figure 4: Comparison between the FRIDGE –Chamber (sampled of wafers, green lines) and the Fast Ice Nucleus Chamber FINCH (described in Bundke et al., 2008).

Furthermore, for Arizona test dust sampled with the new technique at our laboratory the nucleating conditions for activation of a 0.1% fraction of ATD matches the envelope of data obtained from other instruments during the ICIS campaign reasonably well (Figure 5).

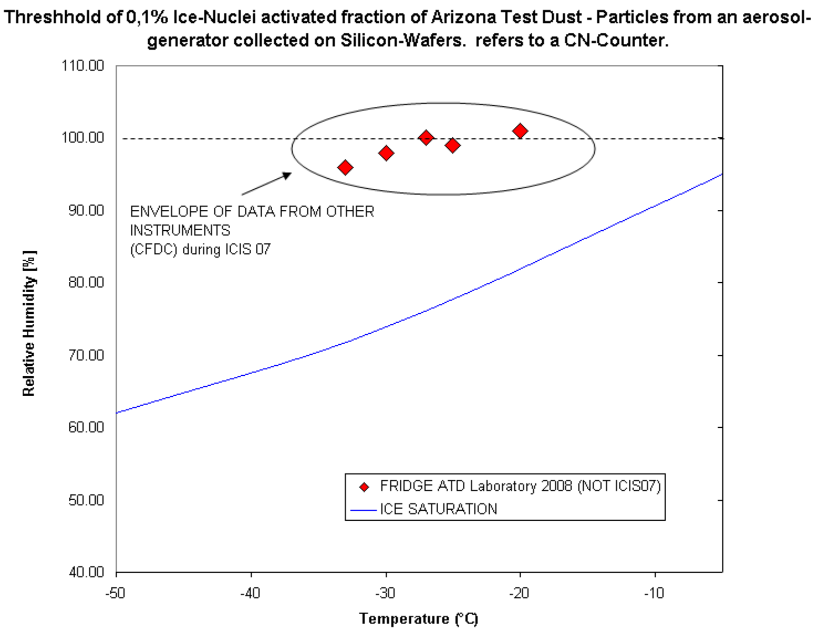

Figure 5: Threshold of 0,1% Ice-Nuclei activated fraction of Arizona Test Dust – Particles. Dust from an aerosol- generator was dispersed in a clean air flow and collected on silicon-wafers. Red diamonds show the FRIDGE-Results. Total Particle Concentrations were measured with a CN-Counter.

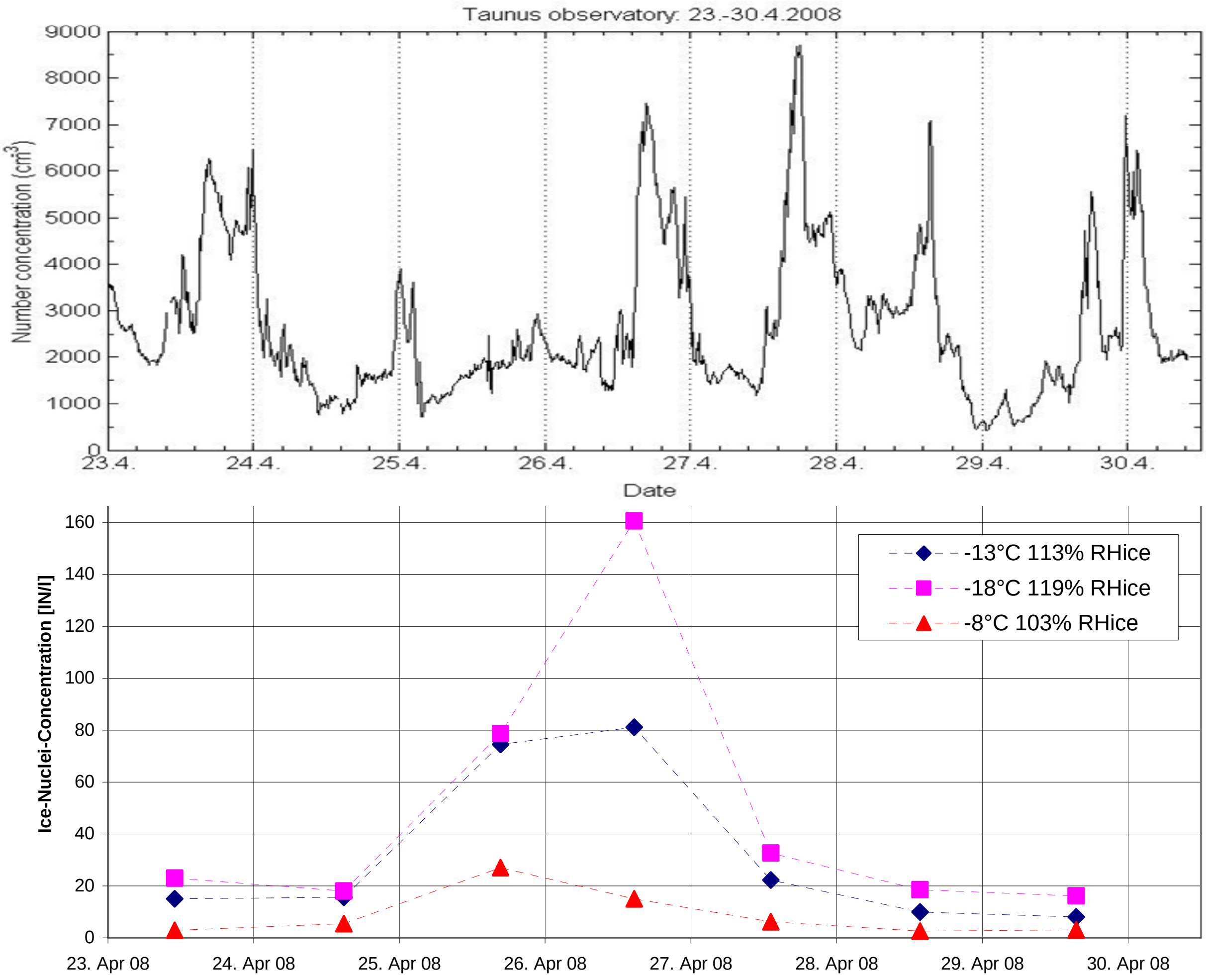

Figure 6: Measurements of particle concentration (TSI WCPC 3785, upper part) and ice nuclei concentrations (lower part) for a sequence of days at the Taunus Observatory Mt. Kleiner Feldberg. Ice nuclei concentrations are shown for -8°C, - 13°C, and -18°C.

Measurements of the concentration of atmospheric ice nuclei using the electrostatic precipitation onto silicon wafers were started at the Taunus Observatory on regular basis. First results (Figure 6) show IN to be highly variable between 10 to 160 IN/L, with their mean of 49 IN/L at -18°C and water-saturation being roughly a factor of 100 higher during that period than the mean of 0.5 /L reported for this location by Stein (1984).

3. References

Al-Naimi, R. and C.P.R. Saunders, Measurements of natural deposition and condensation-freezing ice nuclei with a continuous flow chamber, Atmos. Environ., 19, 1871-1882, 1985

Ardon, K. et al.: The Effect of Air Pollution on Ice Nuclei Concentration in Israel this issue, 2008.

Bigg, E.K. et al.: The measurement of ice nucleus concentrations by means of Millipore filters, J. Appl. Meteor.,2, 266-269, 1963

Bundke, U., Nillius, B., Jaenicke, R., Wetter, T., Klein, H., Bingemer, H., The fast Ice Nucleus chamber FINCH, Atmospheric Research In Press, Corrected Proof, doi:10.1016/j.atmosres.2008.02.008, 2008 (http://www.sciencedirect.com/science/article/B6V95-4RX06WB-1/1/ab3005f247e2dcce43e3f79067eaedc6)

Levin, Z., and Cotton, W., Aerosol pollution impact on precipitation: a scientific review, The WMO/IUGG International Aerosol Precipitation Science Assessment Group (IAPSAG), Geneva, 2007

Meyer, D., Gravenhorst, G., A low pressure diffusion chamber. In: Vali, G. (Ed.), 336 III. International workshop on ice nucleus measurements, Laramie (Wyo) 1975, 337 pp. 128–148, 1976.

Moehler et al., THE FOURTH INTERNATIONAL ICE NUCLEATION WORKSHOP ICIS-2007, this Issue, 2008

Rogers, D.C., Field and laboratory studies of ice nucleation in winter orographic clouds, Ph.D. dissertation, Dept. Of Atmospheric Science, Univ. Of Wyoming, Laramie, 161 pp., 1982

Salam, A. et al., Ice nucleation studies of mineral dust particles with a new continous flow diffusion chamber. Aerosol Science and Technology 40, 134-141, 2006

Schaller, R.C., and Fukuta, N., J. Atmos. Sci. 36, 1788, 1979

Stein, D. : Untersuchung über die Aktivität atmosphärischer Gefrierkerne in Abhängigkeit von Feuchte und Temperatur, PhD Dissertation, University of Frankfurt, 1984.

Vali, G., 1975. Ice Nucleation Workshop. Bull. Amer.Meteorol. Soc. 56, 1180-1184.

Zimmermann, F. et al., Environmental scanning electron microscopy (ESEM) as a new technique to determine the ice nucleation capability of individual atmospheric aerosol particles, Atmospheric Environment, doi:10.1016/j.atmosenv.2007.06.023, 2007

Acknowledgements: We gratefully acknowledge financial support by the German Science Foundation DFG under “SFB 641: The tropospheric ice phase”.

The influence which subsidence inversion in the spring had on aerosol over Beijing regian

Ma XinCheng Zhang Qiang Huang MengYu

Beijing Weather Modification Office，Beijing 100089

1、Introduction

Atmospheric aerosols have large impact on climate forcing by effecting global cloud albedo,radiative forcing,ozone layer,acid rain and visibility. Increasing number of aerosol particales may also cause significant health effects.Through the measurement from 12 aircraft flights over Beijing, China in the spring of 2005 and 2006, we found that the aerosol pollution in the Beijing region was very heavy when the subsidence inversion occurred in the spring. This paper analyzed the vertical distribution of aerosol concentrations of five cases under subsidence inversion in the spring. and discussed the influence which subsidence inversion in the spring had on aerosol concentration.

2、Instrumentation on the aircraft

Several instruments were mounted on the wingtip on an aircraft (Cheyenne IIIA) to measure the spectrum of particles over the Beijing region. Particles rang from 0.1 to 3.0 um in diameter with 15 unequally size bins were recorded at 1-s intervals by a particle measuring systems (PMS Inc., Boulder, CO ,USA).The airplane has multi-engines with flight speeds of about 100 ms^{-1}. Passive cavity aerosol spectrometer probe (PCASP) instrument throughout the flight .The In-site meteorological parameters such as ambient air temperature (T),relative humidity(RH), and air pressure(P) are measured during flights. The instruments(PCASP) is calibrated using polystyrene latex spheres(PSL) by Particle Metrics Inc.(PMI) in the United States. The calibration is conducted every year before the measurements take place.

Fig.1. aircraft (Cheyenne IIIA)

Fig.2. Passive cavity aerosol spectrometer probe (PCASP) instrument (left)

3、Analysis of the result

Table 1 shown summary of five cases about aircraft measurement. We carried out the vertical measurement of aircraft in the spring of 2005 and 2006 over Beijing region. The site、time and maximal altitude of vertical measurement is the same by and large. The aircraft first climb to about 3.6 km, and then gradually descents to the ground with a descending time of about half an hour. During descending, vertical profile of aerosol particles is measured.

Fig.3,The measured vertical profiles of temperature and dew point of five cases during descending period are shown. The character of subsidence inversion In synoptic meteorology is that the different value of temperature and dew point is bigger in some altitudes, and the different value of temperature and dew point increased with altitude increasing. Table 2 showed the summary of character about subsidence inversion for five cases. The Fig.3 and Table 2 shows that there are inversion layer placed between average 0.7 and 1.2 km with a average gradient of 0.7 ℃ /100m, indicating that the PBL height is about 1.2 km.

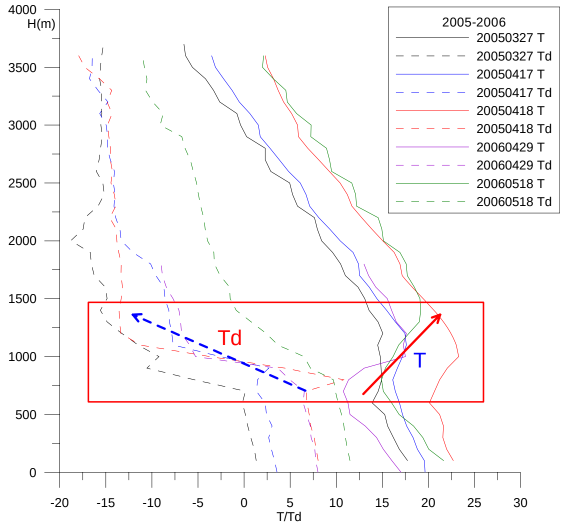

Fig.3. The measured vertical profiles of temperature and dew point of five cases during descending period

Table 1 summary of five cas

Date	Time of vertical measurement (Beijing Time)	Maximal altitude of vertical measurement (m)
2005-03-27	11:53-12:37	3600
2005-04-17	13:35-14:01	3600
2005-04-18	13:10-13:37	3600
2006-04-29	11:40-12:06	1800
2006-05-18	11:35-12:04	3600

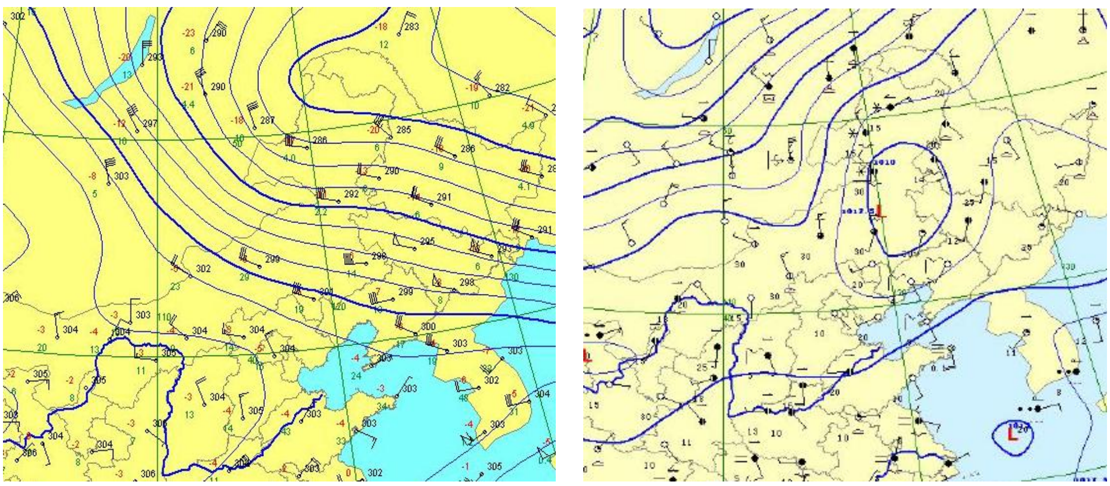

Fig.4. weather map of one cases. 1 March 27,2005, 0800(Beijing Time), 700 pha(left)

and 1100(Beijing Time), ground(right)

Table 2 summary of character about subsidence inversion for five cases

Date	Bottom of subsidence inversion（m）	Top of subsidence inversion（m）	thickness of subsidence inversion(m）	subsidence inversion（△T，℃）	Gradient of subsidence inversion（℃/100m）
2005-03-27	600	1200	600	+1.2	0.2
2005-04-17	800	1100	300	+1.5	0.5
2005-04-18	600	1000	400	+3.2	0.8
2006-04-29	700	1200	500	+6.8	1.4
2006-05-18	800	1400	600	+4.3	0.7
average	700	1180	480	+3.4	0.7

The whole weather situation formed two conditions witch brought about have severe pollute: (1)there is weak barometric depression in the ground , it is disadvantage to diffuse for pollute and advantageous to the accumulation of pollution;(2)atmosphere in the high went down and formed subsidence inversion layer, it is like a "cover", the smoke、dust and so on which suspend in the atmosphere are all hard to diffuse into the upper air by cutting through it, namely, it is disadvantageous for pollution to diffuse vertically.

Fig 5, the measured vertical profile of average number concentrations of aerosol particles during descending period is shown. The subsidence inversion layer has prevented the mixing between the particles below and above 1.2 km. Fig.5 indeed shows the strong separation of the characterization of aerosol particles between the two layers. The measurement from the PCASP instrument shows that above the PBL, the measured aerosol average number concentrations are about 1500 cm^{-3} with 1.2 um. By contrast, below the PBL, the aerosol average number concentrations significantly increase to about 10000 cm^{-3}, and the size of the particles is greatly decreased to about 0.5 um. The striking different characterizations of aerosol particles suggest that aerosol above the PBL and below the PBL form different sources. The PBL maybe plays an important role to prevent the dust particles to be transported onto the surface, and confine the local emitted particles inside the PBL.

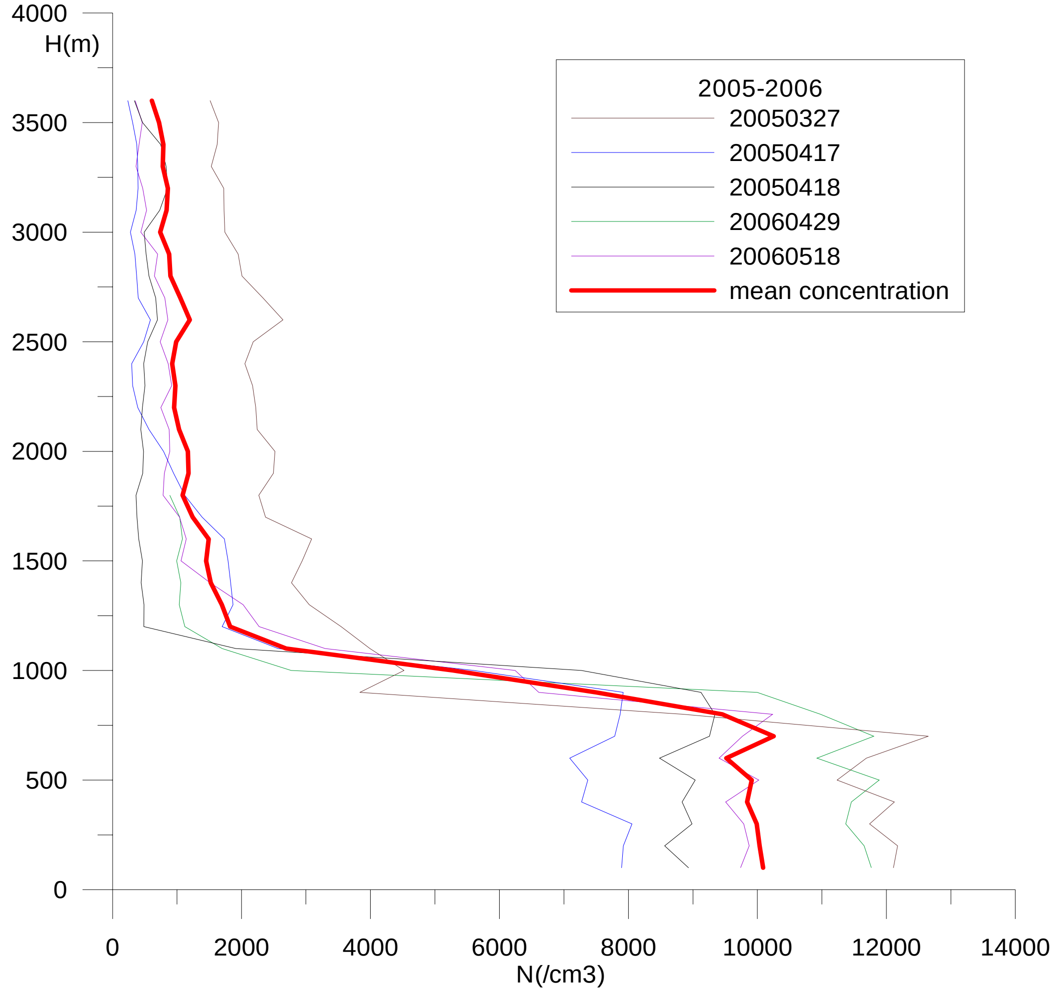

Fig.5.The measured vertical profiles of average number concentrations of aerosol particles during descending period.

Acknowledgements

This work was supported by the Beijing Natural Sciences Foundation Contract 80710002 and the National Key

Research Project of Ministry of Science and Technology of China “Key Technology and Equipment Research and Development on Weather Modification”(2006BAC12B00). We thank the members of the Cheyenne Ⅲ A crew for help in collecting data. The first author greatly thanks and appreciates to the Operating Committee of the International Conference on Clouds and Precipitation(ICCP2008) for accepting this paper and for providing partial financial support to the first author. The first author would also thanks to other donor and sponsor who has given the opportunity to the first author to attend personally in this conference.

References

Kleinman L I,Daun P H。《Vertical distribution of aerosol particles,water vapor,and insoluble trace gases in convectively mixed air》。J Geophys Res,1991,96(D1):991-1005。

Kim Y J,Sievering H,Boatman J F。《Airbone measurement of atmospheric aerosol particles in the lower troposphere over the central United States》。J Geophys Res,1988,93(D10):12631-12644。

Fouquart Y,Bonnel B,Brogniez G,et al。《Observations of Saharian aerosols:Results of ECLATS field experiment, Part I:Broadband radiative characteristics of the aerosols and vertical radiative flux divergence》。J Climate Appl Meteor,1987,26(1):38-52。

Isaac G A,Leaitch W R,Strapp J W,et al。《Summer aerosol profiles over Algonquin Park,Canada》。Atmos Environ,1986,20(1):157-172。

PHYSICO-CHEMICAL CHARACTERISATION OF ICE PARTICLE RESIDUALS IN TROPOSPHERIC MIXED-PHASE CLOUDS BASED ON ICE PARTICLE COLLECTION USING THE COUNTERFLOW VIRTUAL IMPACTOR TECHNIQUE

S. Mertes[1], B. Verheggen[2,8], M. Kamphus[3], S. Walter[4], M. Ebert[5], B. Nilius[3,6], J. Schneider[4], Dan Cziczo[7,9], J. Curtius[3,6], J. Cozic[2,10], A. Worringen[5] and E. Weingartner[2]

[1] Leibniz-Institute for Tropospheric Research, Leipzig, Germany
[2] Paul Scherrer Institute, Villigen, Switzerland
[3] University of Mainz, Germany
[4] Max Planck Institute Mainz, Germany
[5] University of Darmstadt, Germany
[6] University of Frankfurt, Germany
[7] ETH Zürich, Switzerland
[8] present affiliation: ECN Petten, The Netherlands
[9] present affiliation: PNNL, Richland, USA
[10] present affiliation: NOAA, Boulder, USA

1. INTRODUCTION

The nucleation of ice particles in middle and lower tropospheric clouds can initiate precipitation and change cloud optical properties, thus affecting the radiative forcing of supercooled clouds [Lohmann and Feichter, 2005]. In mixed-phase clouds of the lower and middle troposphere heterogeneous nucleation, which is triggered by a subset of atmospheric particles named ice nuclei (IN), is the dominant process initiating primary ice formationat temeratures above -38 °C. The heterogeneous ice formation can proceed via different mechanisms [Cantrell and Heymsfield, 2005] which include the creation of new frozen hydrometeors by deposition and condensation freezing or icing of existing cloud drops via contact, immersion or evaporation freezing.

Closely related to the heterogeneous ice nucleation process is the question of the physico-chemical IN properties. Our knowledge about atmospheric particles that act as ice nuclei in tropospheric mixed-phase clouds is incomplete, because the ice phase develops in between super-cooled drops, which complicates the experimental and theoretical investigation.

For this reason a ground-based sampling device was developed in order to extract small ice particles from tropospheric mixed-phase clouds and to identify the size and chemical composition of their residues by state-of-the-art analysis methods [Mertes et al., 2007]. These measurements have been carried out within the cloud and aerosol characterization experiments (CLACE) at the high alpine research station Jungfraujoch (Swiss Alps, 3580 m asl).

2. EXPERIMENTAL

This sampling system is based on a counterflow virtual impactor (CVI), which cannot distinguish between frozen and liquid hydrometeors of the same aerodynamic size. Large particles are additionally sampled, so that in mixed-phase clouds the residues include cloud condensation nuclei (CCN) and scavenged interstitial particles besides the desired IN. Thus, the novel inlet, called Ice-CVI, is supplemented with further components to avoid the collection of supercooled drops and large ice particles. A vertically oriented inlet horn in combination with a virtual impactor (VI) removes the precipitating ice particles larger than 20 µm. The upper limit of 20 µm assures an aspiration efficiency of nearly one for the sampled small ice particles. Downstream of the VI a pre-impactor (PI) segregates the super-cooled drops by their freezing at contact on cold impaction plates. The remaining ice particles bounce off without significant shattering due to their small size and low velocity and remain in the sample airflow. The CVI itself is located downstream of the PI to reject interstitial particles smaller than 5 µm by a controlled counterflow. Inside the CVI the small ice particles are injected into a particle-free and dry carrier air leading to their complete evaporation, and the released dry residual particles are analyzed.

3. RESULTS

Results will be presented from CLACE 4, 5 and 6 carried out in February/March 2005, 2006 and 2007, respectively.
Background aerosol particles were sampled before, during and after a cloud event by means of a total aerosol inlet and analyzed in the same way as the ice particle residues in order to identify special features of the IN physico-chemical properties.
Mean background aerosol and ice particle residue number size distributions measured with two scanning mobility particle sizers (SMPS) simultaneously during two different cloud events are shown in Fig.1.

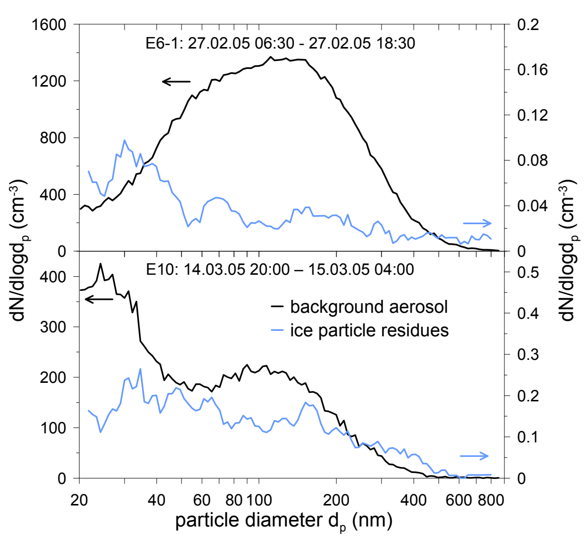

Fig.1: Mean background aerosol (black line) and ice particle residue (blue line) number size distributions measured with two scanning mobility particle sizers (SMPS). The latter is linked to the right y-scale.

Averaging times are several hours due to the very low concentration of the ice particle residues. It is obvious that the background aerosol particle number size distributions have different but distinct modes whereas the residual particle number size distributions show no clear structures. However, a weak minimum around 100 nm is visible with a slight increase of residual particles to smaller sizes. These residues are not considered to have served as ice nuclei but most likely to stem from small secondary ice particles. Those ice particles are expected to be generated by rime splintering, ice-ice collisions and fragmentation during drop freezing in mixed-phase clouds [e.g. McFarquhar et al., 2007]. Part of these secondary ice particles should be smaller than 20 µm [Fridlind et al., 2007] and thus sampled by the Ice-CVI. Since they mainly contain scavenged interstitial particles and/or part of the soluble material of the frozen drop they release rather small residues after their evaporation in the CVI. This consistently explains the occurrence of residual particles below a diameter of about 100 nm. Assuming that only residual particles larger than 100 nm acted as ice nuclei results in IN number concentrations of about 0.17 and 0.08 cm^{-3} for the two cloud events presented in Fig.1.

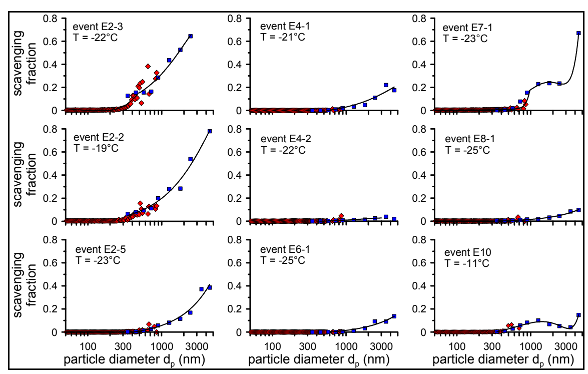

***Fig.2**: Scavenged number fractions of IN as a function of their particle size. Diamonds (red) and squares (blue) present SMPS and OPC measurements, respectively.*

Dividing the ice particle residue distributions by those of the background particles yields the number fraction of IN as a function of particle size. This scavenging fraction is plotted in Fig.2 extended to the super-micrometer size range using data from two optical particle counters (OPC) operated simultaneously at the Ice-CVI and total inlet. It is easily seen that super-micrometer particles preferentially serve as IN but also sub-micrometer particles larger than 300 nm acted as IN.

Beside the size information, findings about the chemical composition of IN were obtained. These studies were analytically restricted to particles larger than 100 nm, i.e. the results can be attributed to residues acting as IN and are hardly influenced by residues from secondary generated ice particles.

Average black carbon (BC) mass concentrations of the ice particle residues were derived from a particle soot absorption photometer (PSAP). They varied between 0.3 and 1.9 ng m^{-3} for the cloud events during CLACE 4 which was only 2 – 3 % of the totally abundant BC in the background aerosol particles (15 – 60 ng m^{-3}). However, when inferring a BC mass fraction in the IN (by relating its mass to the total residual mass inferred from the SMPS results) an enrichment of BC with respect to the background aerosol particles could be found (Fig.3).

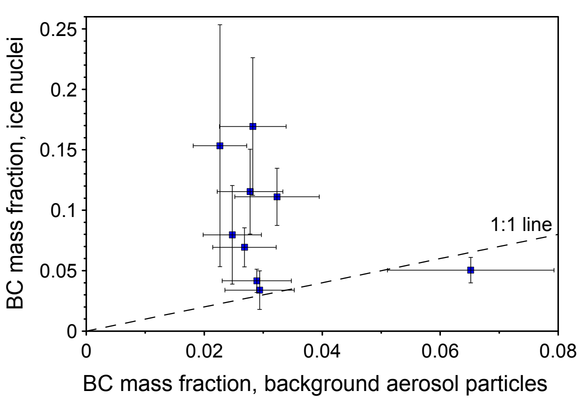

Fig.3: *Scatterplot of BC mass fractions derived for ice nuclei and background particles sampled simultaneously with the Ice-CVI and total inlet, respectively. The dotted line indicates the 1:1 relation.*

This enrichment suggests that BC plays an active role in heterogeneous ice nucleation or is related to another ice forming aerosol compound [Cozic et al., 2008].

Another indication of an anthropogenic influence on heterogeneous ice nucleation in the lower troposphere was observed with a high-resolution, time-of-flight aerosol mass spectrometer (HR-ToF-AMS). In the ice particle residues only the hydrocarbon-like organic compound ($C_3H_7^+$) that has primary anthropogenic sources but hardly any secondary generated oxygenated organic compound ($C_2H_3O^+$) was detected in contrast to the background aerosol particles (Fig. 4).

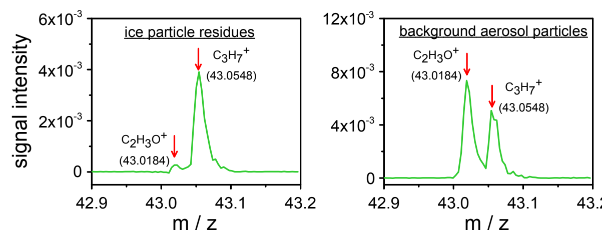

Fig.4: *Relative contributions of hydrocarbon-like and oxygenated organic aerosol particles to the ice particle residues and background particles.*

Since the importance of the particle ice nucleating capability is mainly a number and not a mass related phenomenon one main effort was to couple single particle analyzing techniques to the Ice-CVI to permit the analysis of single ice nuclei. Hence, two in-situ aerosol mass spectrometers, the single particle laser ablation time-of-flight spectrometer (SPLAT) and an aerosol time-of-flight mass spectrometer (ATOFMS) and an impactor for off-line analysis with an environmental scanning electron microscope were connected to the Ice-CVI. Results of the SPLAT measurements are illustrated in Fig.5. The pie charts show the percentage of particles (regardless of the particle size) that belong to different particle groups. It is evident that the IN composition differs strongly from the background aerosol composition. Mineral dust is by far the dominating substance in the ice particle residues. But also organic/carbonaceous particles were present whereas sulfate is depleted compared to the background particles.

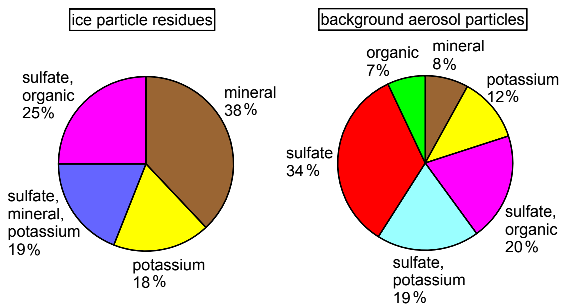

Fig.5: *Relative distribution of different particle classes in background aerosol particles and in ice particle residues obtained from single particle SPLAT measurements.*

These findings were supported by mass size distribution results from the ATOFMS (Fig.6) and by the analysis of ice particle residue impactor samples (Fig.7) with ESEM.

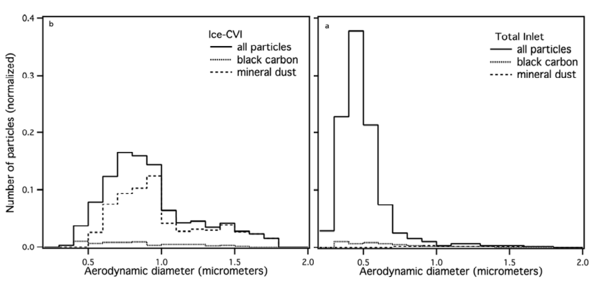

Fig.6: *Comparison of mass size distributions of background aerosol (total inlet) and ice particle residues (Ice-CVI) measured with the ATOFMS.*

The ATOFMS results imply that almost all super-micrometer IN are mineral dust particles whereas in the sub-micrometer size range there are still some unidentified residues. With respect to the background aerosol mineral dust and BC particles are enriched in the ice particle residues, the latter verifying the bulk aerosol results obtained from the PSAP (cf. Fig.3).
Qualitatively the ESEM analysis yields similar results. The large ice nuclei are dominated by mineral dust (Si) but carbonaceous (C) particles are found for the smaller ones above 200 nm.

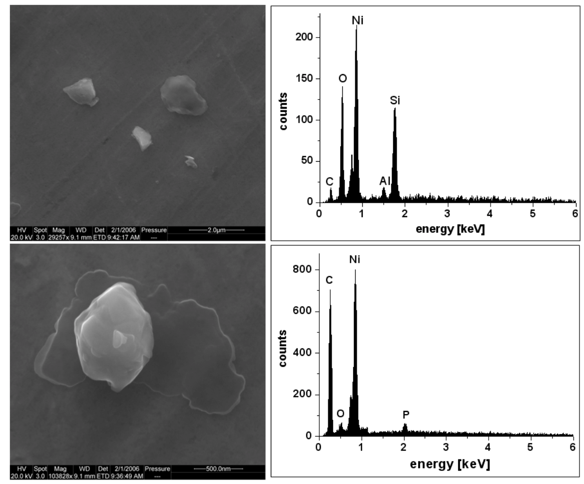

Fig.7: *Secondary electron image and EDX spectrum of ice particle residues. The Ni peak is caused by the substrate.*

During CLACE 6 the IN chamber FINCH was connected to the Ice-CVI in order to activate the ice particle residues by deposition and condensation freezing to which IN counters are generally restricted to. FINCH could activate approximately only 1 of 100 residues implying that drop freezing processes like immersion, contact or evaporation freezing are much more important ice formation mechanism in the investigated lower tropospheric mixed-phase clouds.

5. CONCLUSION

By means of the novel Ice-CVI sampling system is was feasible to separate ice particle residues in scavenged or nucleated particles from secondary ice and true heterogeneously acting ice nuclei by their different size ranges. The latter have been chemically analyzed revealing that they are mainly mineral dust particles. Moreover, carbonaceous particles (organic, black carbon) have been identified in the IN but it needs to be further investigated whether they play an active role in heterogeneous ice nucleation or are at least related to

another ice forming aerosol compound not identified until now.
From the coupling of the Ice-CVI with an IN counter it is assumed that deposition and condensation freezing are not important ice forming processes in lower tropospheric mixed-phase clouds as long as super-cooled drops dominate the number of cloud particles.
It is intended to continue the investigation of ice formation in atmospheric clouds using the IfT CVI technology in cooperation with other research institutions within the German collaborative research centre "The tropospheric ice phase (TROPEIS)", onboard the new German high altitude long range research aircraft HALO, and in lab studies at the Leipzig aerosol and cloud simulator LACIS.

6. ACKNOWLEDGEMENTS

This work is funded by the German Research Foundation (DFG, grants HE 939/8-1 and HE 939/8-2) and is additionally supported by the DFG collaborative research centre SFB-641 (TROPEIS), the Swiss National Science Foundation (No. 200020-108032), and the FP6 network of excellence ACCENT (access to infrastructures, field stations). We thank the International Foundation High Altitude Research Stations Jungfraujoch and Gornergrat (HFSJG) for the opportunity to perform experiments on the high alpine research station Jungfraujoch.

7. REFERENCES

W. Cantrell and A. Heymsfield (2005), Production of ice in tropospheric clouds, *Bull. Amer. Meteor. Soc.*, ***86***, 795-806.

J. Cozic, S. Mertes, B. Verheggen, D.J. Cziczo, S.J. Gallavardin, S. Walter, U. Baltensperger and E. Weingartner (2008), Black carbon enrichment in atmospheric ice particle residuals observed in lower tropospheric mixed-phase clouds, *J. Geophys. Res.*, accepted.

A. Fridlind, A.S. Ackerman, G.M. McFarquhar, G. Zhang, M.R. Poellot, P.J. DeMott, A.J. Prenni and A. Heymsfield (2007), Ice properties of single-layer stratocumulus during the Mixed-Phase Arctic Cloud Experiment: 2. Model results, *J. Geophys. Res.*, ***112***, doi: 10.1029/2007JD008646.

U. Lohmann and J. Feichter (2005), Global indirect aerosol effects: a review, *Atmos. Chem. Phys.*, ***5***, 715-737.

G.M. McFarquhar, G. Zhang, M.R. Poellot, G.L. Kok, R. McCoy, T. Tooman, A. Fridlind and A. Heymsfield (2007), Ice properties of single-layer stratocumulus during the Mixed-Phase Arctic Cloud Experiment: 1. Observations, *J. Geophys. Res.*, ***112***, doi:10.1029/2007JD008633.

S. Mertes, B. Verheggen, S. Walter, P. Connolly, M. Ebert, J. Schneider, K.N. Bower, J. Cozic, S. Weinbruch, U. Baltensperger and E. Weingartner (2007), Counterflow virtual impactor based collection of small ice particles in mixed-phase clouds for the physico-chemical characterization of tropospheric ice nuclei: sampler description and first case study, *Aerosol Sci. Technol.*, ***41***, 848-864.

MIXING STATE, GROWTH KINETICS AND AGING OF AMBIENT POLLUTED CCN

A. Nenes[1, 2], A.Asa-Awuku[2], S.Lance[1], R. Moore[2], J.N. Smith[7], R. Bahreini[3, 6], C.Brock, R.C. Flagan[3, 5], H. Jonsson[4], S. Murphy[5], J.H. Seinfeld[3, 5], A. Sullivan[1], A. Sorooshian[5], V. Varutbangkul[5], R. Weber[1]

[1]Earth and Atmospheric Sciences, Georgia Institute of Technology, Atlanta, GA. [2]Chemical and Biomolecular Engineering, Georgia Institute of Technology, Atlanta, GA. [3]Environmental Science and Engineering, California Institute of Technology, Pasadena, CA. [4]CIRPAS, Naval Postgraduate School, Monterey, CA. [5]Chemical Engineering, California Institute of Technology, Pasadena, CA. [6]National Oceanic and Atmospheric Administration, Boulder, CO. [7]National Center for Atmospheric Research, Boulder, CO

INTRODUCTION

We present an overview of Cloud Condensation Nuclei (CCN) measurements in the vicinity of Houston, TX during the GoMACCS/TEXAQS campaign (August-September, 2006), and in Mexico City during the MILAGRO campaign (March, 2006). Measurements in Houston were obtained aboard the NOAA P3 and the CIRPAS Twin Otter platforms, and polluted air masses in and out of cloudy regions were sampled over a total of 40 flights. Measurements in Mexico City were ground-based, using a DMT Cloud Condensation Nucleus counter (CCNc) that sampled classified aerosol from a Differential Mobility Analyzer (DMA) to obtain the size-resolved activation fraction as a function of water vapor supersaturation (SS).

The wide range of CCN concentration, aerosol composition and aging/mixing state makes these particularly valuable datasets for constraining uncertainties associated with prediction of CCN concentration and cloud droplet number for polluted clouds.

ASPECTS OF THE HOUSTON DATASET

Ambient aerosol in Houston, Texas was sampledonboard the Center for Interdisciplinary Remotely-Piloted Aircraft Studies (CIRPAS) Twin Otter during the Gulf of Mexico Atmospheric Composition and Climate Study (GoMACCS) field campaign (August 25-September 15, 2006). Aersol was also sampled onboard the NOAA WP-P3 during the Texas Air Quality Study (TexAQS). CCN sampled originated from a variety of local sources as petrochemical industries, refineries, power plants, ship yards, and the urban Houston plume. Figure 1 shows the flight tracks for the Twin Otter Research Flights (RF), all of which occurred during the daylight hours.

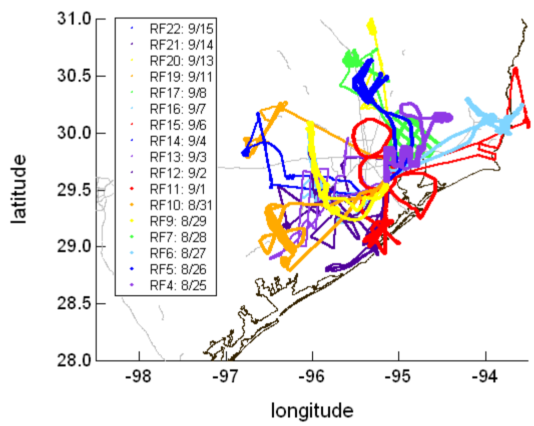

Figure 1. Research flight tacks conducted with the CIRPAS Twin Otter.

The concentration of CCN was measured using a Droplet Measurement Technologies continuous flow streamwise thermal gradient CCN counter (CCNc), operated between 0.1 and 0.4% supersaturation. CCN closure was obtained using the particle size distribution measured by the Dual Automated Classified Aerosol Detector (DACAD) and the aerosol chemical composition measured by an Aerodyne Aerosol Mass Spectrometer (AMS). CCN concentrations ranged from 100 cm^{-3} to more than 10,000 cm^{-3}. The aerosol was typically composed of a mixture of organic and sulfate; organic mass fraction in the aerosol ranged from 10 to 90%.

Figure 2 shows the predicted vs. measured CCN concentrations, assuming that particles are composed purely of ammonium sulfate; data is presented for all the research flights in Figure 1. On average, the CCN closure is remarkably good, given the very simple assumption on particle chemistry; CCN concentrations were on average overpredicted by 20%. Explicit consideration of chemical composition further improves closure (not shown). The same aspects in the CCN closure were also seen in the P3 dataset.

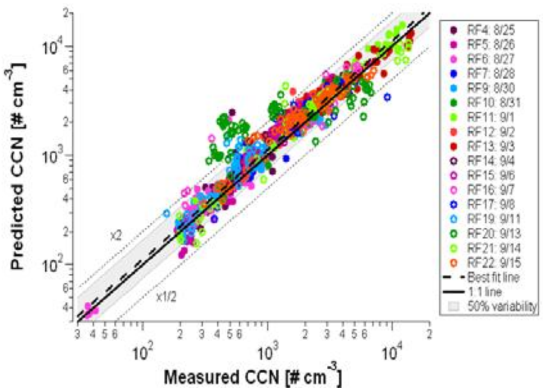

Figure 2. CCN Closure for all research flights conducted with the CIRPAS Twin Otter, where particles are assumed to be composed of ammonium sulfate.

ASPECTS OF MEXICO CITY DATASET

MIRAGE, a part of a larger international study MILAGRO (Megacity Initiative: Local and Global Research Observations), encompassed measurements from several aircraft and ground-based sites. Our measurements focused on the CCN activity of ambient aerosol downwind of Mexico City at the University of Tecámac ground site. The measurements were obtained at the peak of the dry season, from March 16 - April 1, 2006. The aerosol sampled were impacted by strong dust events, heavy rains, local biomass burning, vehicular emissions from a nearby roadway, extremely high ammonium concentrations and the Mexico City plume. On occasion, emissions from the Tula power plant (~40 km away) impacted the aerosol sampled.

Size-resolved CCN activity measurements were used to determine the "activated fraction," or the fraction of particles that activate into cloud droplets as a function of water vapor supersaturation and dry particle size. These measurements, combined with Köhler theory, are used to determine the fraction of particles that act as CCN, and, infer the distribution of soluble volume fraction (SVF) for the CCN-active fraction as a function of time and dry particle size (Lance, 2008). Contours of SVF for 100 nm particles are shown in Figure 3.

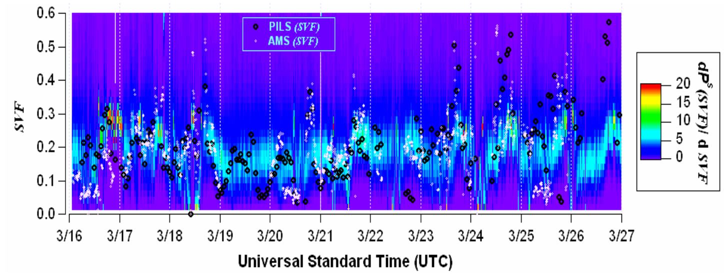

Figure 3. Contours of SVF for the data of this study. Superimposed are SVF obtained from PILS and an aerosol mass spectrometer.

Inferred SVF agrees well with direct measurements of composition (PILS, AMS), (except when the amount of dust is high) and affirms the applicability of the method.

Inferred SVF is relatively insensitive to wind direction, rain, dust, or local biomass burning events; suggesting that the aerosol retain the characteristics of the larger-scale "background" particulate matter. The most obvious trend in SVF is a diurnal pattern, where SVF tends to be maximum (and with a narrow distribution) during the daytime, likely due to condensation of hydrophilic compounds (photochemically generated) onto aerosol particles.

REFERENCES

Lance, S, PhD Thesis, Georgia Institute of Technology, 2008.

ACKNOWLEDGMENTS

We acknowledge support from NOAA, an NSF CAREER award, a GT Presidential Graduate Fellowship, NCAR ASP Graduate Fellowship, a NASA ESS Fellowship, a DOE Graduate Study Fellowship, and the Office of Naval Research.

CCN SCAVENGING AND DRIZZLE

Stephen Noble
and
James G. Hudson
Desert Research Institute
Reno, Nevada

1. INTRODUCTION

The effect of preexisting or precloud aerosol on cloud microphysics is fundamental to cloud physics. Interest is piqued by the wide range of observed aerosol and cloud droplet concentrations, compositions, and size distributions. The fact that a large but as yet unknown component of the aerosol is of anthropogenic origin gives rise to the indirect aerosol effect(IAE), which is the largest climate uncertainty.

IAE consists of at least two components: 1st IAE the effect on cloud radiative properties—i.e., higher cloud droplet concentrations producing brighter clouds, and 2nd IAE precipitation inhibition due to smaller droplets. Both subjects are addressed here in a study that builds upon Hudson and Mishra [2007] (hereafter HM7). That study was from the RICO project (Rauber et al. 2007), which was done in December-January 2004-05 in the northeastern Caribbean. Measurements presented in HM7 and here were all from the NCAR C-130 airplane. HM7 showed both of the expected effects of aerosol, namely cloud condensation nuclei (CCN) concentration variations, on cloud microphysics. However, the analysis of HM7 was limited to only the early stages of cloud development near the bases of the small cumulus clouds that were studied. Although HM7 did find a strong positive correlation of CCN concentrations with cloud droplet concentrations (N_c) [1st IAE] and a strong negative correlation with mean cloud droplet sizes from the FSSP (2nd IAE), the analysis was restricted to cloud parcels with liquid water content (LWC) greater than 0.25 g m^{-3}, updrafts (w) exceeding 0.5 m/s and altitudes of 600-900m. Although that article demonstrated the greater influence of CCN than giant nuclei (GN) on precipitation initiation, the limits placed on that analysis did not really demonstrate the effects of CCN on either cloud radiative properties or precipitation. For instance it has been suggested that dynamical processes could washout initial aerosol effects at cloud base [e.g., Baker et al. 1979]. Thus at higher altitudes where cloud radiative properties are of greater importance and where precipitation is usually initiated the effect of the subcloud CCN effect may be washed out. Entrainment may have more influence on cloud microphysics at higher altitudes and moreover the CCN concentrations in the entraining air may also be different from the subcloud concentrations. To address these issues this analysis broadens all aspects of HM7—LWC, w, droplet/drop sizes, and altitude.

2. RESULTS

Table 1 shows the consideration of three more flights than HM7, RF4, 11 and 17 (D10, J7 and J19). Figure 1 expands Figure 2a of HM7 by including all parcels with LWC > 0.1g m^{-3}. This adds two data points, two more flights. The CCN-cloud droplet concentration (N_c) correlation coefficient (R) is not diminished by this expansion of cloud parcels and flights, but is actually higher (0.85 versus 0.80) than that of the more restricted analysis of HM7. The slope of the linear regression is diminished from

1.08 to 0.60 because these cloud parcels have lower average concentrations while the low magnitude intercept is nearly identical. Restricting this analysis to only the same 14 flights reported by HM7, results in only a further increase of R to 0.88. When the data is further expanded by considering a lower LWC threshold of 0.01 g m^{-3}, R increases to 0.88 for the 16 flights and 0.89 for the 14 flights considered by HM7. This expansion actually allows the inclusion of RF17, so that this R for 17 flights is 0.89. Further expansion of the data under consideration by using an even lower LWC threshold of 0.001 g m^{-3}, results in a further increase of R to 0.90 for 16 flights, 0.91 for 14 flights and 0.92 for 17 flights.

Figure 2 shows that droplet concentrations were roughly similar with altitude. Figures 3 and 4 show that the CCN-N_c correlations diminished only slightly with altitude even as the average N_c concentrations decreased with altitude (smaller regression slopes). Rather than the gross measure of the overall droplet spectra expressed by the mean of the FSSP distribution we now examine CCN correlations with droplet concentrations that exceed various threshold sizes. Figure 5 shows how R reverses for larger droplets. Figures 6 and 7 show how R changes with altitude for the various droplet size thresholds. Figure 6 considers all of the flights that had data at the various altitude bands, but this means different numbers of flights at the different altitudes. The different flights among the different altitudes may bias the data, so Figure 7 considers data from only the same eight flights that had data at the same five altitude bands. The smallest droplet size thresholds have rather similar large positive R values at all levels, whereas the largest cloud droplets have negative R at all levels and similar large negative R at all but the lowest levels. Intermediate droplet size thresholds shift from low positive or high negative values at low altitudes to high positive values at higher altitudes as a result of greater droplet sizes at higher altitudes. This results in greater droplet concentrations for the higher threshold sizes. The lower R for the small droplets (total droplets N_c) in the 1500-1800m altitude band in Fig. 6 is due to the RF9 data. RF9 small droplet concentrations are a significant outlier in this altitude range as they are more than 100 cm^{-3}, whereas N_c is for RF9 is less than 50 cm^{-3} at the lower altitudes. This was probably due to the fact that an especially large CCN concentration "spike" was measured during the 100m altitude circles on RF9. As noted by HM7 these usually small concentration spikes that occurred during most flights were removed from calculation of the averages. Apparently that high CCN concentration air parcel measured on RF9 produced some cloud parcels with high droplet concentrations and those parcels happened to be observed only in this altitude range. This anomalously low R is not displayed in Fig. 7 because RF9 was not one of the eight flights displayed in this figure because it did not have data at all altitudes.

Figure 8 shows the increase in the concentration of large cloud droplets at higher altitudes as the droplets grow in size because of the lower temperatures at the higher altitudes; more water is condensed on the same droplets as the same parcels of air move upward. Figures 9 and 10 display the negative correlations of these large droplet concentrations with the surface CCN concentrations. In these figures the data seems to split along two separate regression lines that have much greater negative R noted in the caption. This split of the flights may be indicative of other influences on cloud microphysics such as dynamics that may have common manifestations for these two sets of flights. Figure 11 shows that the negative R continues to higher altitudes and further out in the tail of the droplet distribution. Figure 12 shows that a higher order regression produces a much higher R suggesting that the effect of CCN on the tail of the droplet distribution may be nonlinear.

Figures 13-16 show the vertical distributions of drizzle drop concentrations measured with the 260X probe. The large differences in drizzle drop concentrations require a log scale. This shows the increase in drizzle with altitude. Figures 17 and 18 show that there is no correlation of drizzle concentrations with CCN concentrations in the lowest cloud layers. On the other hand Figures 19 and 20 show that there is a negative correlation of surface CCN with drizzle at a higher altitude range. These figures show divisions of the flights along the same lines as in Figs. 9 and 10 for cloud droplets. This again may indicate groupings of data from certain flights because of other factors such as dynamics that are common to each group of flights. Figures 21-24 show how the correlations of CCN with drizzle go with altitude. Figures 21 and 22 display all of the data whereas Figures 23 and 24 are restricted to the same eight flights for all levels displayed. All correlations are negative albeit very week for the cloud base layer. R generally increases in magnitude with altitude. R is generally lower in magnitude for the larger drizzle drops except at cloud base. Figure 25 displays the same data shown in Figs. 6, 21 and 22 with R plotted against threshold diameter for each altitude range. Likewise Figure 26 shows the same data as in Figs. 7, 23 and 24.

Figure 27 is like Figs. 25 and 26 except that it shows R as function of threshold cloud droplet diameter for various LWC bins only in the 600-900m altitude range. Similar high positive R is seen for all LWC up to 10 µm threshold droplet diameter. Between 10 and 20 µm diameter R plunges to extreme negative values of 0.7-0.8 and then gradually decreases in magnitude for larger droplets. The only positive R above 20 µm is for the 40 µm droplets in the lowest LWC bin. Figure 28 displays the same data as a function of LWC bins for each cumulative diameter. The similarity of R for most LWC bins is significant. The only exception is the one just mentioned and 15 µm, which transitions from the tail of the distributions in the low LWC bins (negative R) to a greater share of the cloud droplets in higher LWC bins (positive R).

Figures 29 and 30 show the same data as Figs. 27 and 28 for the next higher altitude range (900-1200m). Since there is more condensed water at higher altitudes there are more LWC bins. The positive R for total cloud droplets (N_c) are even greater in magnitude (~0.9) for all but the two extreme LWC bins. Because of the greater droplet sizes, R continues to be uniformly high out to 15 µm. The plunge to negative R then occurs between 15 and 25 µm, again larger than at the 600-900m altitude because the droplets are larger. The size where the plunge takes place is generally higher for higher LWC. The maximum magnitude of the negative R here is 25 rather than 20 µm and it is greater in magnitude than the 600-900m range (0.8-0.9 compared to 0.7-0.8). The gradual decrease in magnitude of R is much less than the 600-900m range and is never anywhere near positive. The least negative R above 25 µm is for the lowest LWC bin. In spite of the low positive R for the two extreme LWC bins for total droplets the negative R for diameter 25 µm is similar to the other LWC bins. The highest LWC bin shows the most negative R above 30 µm. The more extreme R values of this higher altitude range are apparent by comparing Fig. 30 with Fig. 28. Here the transition size is 20 rather than 15 µm. Figure 31 continues to higher LWC but these LWC are observed only for a more limited number of flights as noted in the caption. On the other hand a larger number of flights are available here for the lower LWC bins.

Figures 32-34 are comparable to Figs. 29-31 for the next higher altitude range (1200-1500m). These show mostly the same overall trend of positive R for small sizes and negative R for large sizes. However, the R values are of much lower magnitude indicating that the CCN have less influence at this higher altitude that is further from the CCN measurements. Notable is the negative or lack of correlation for the lowest two LWC bins at the small sizes. However R is positive at least for the 15 and 20 µm sizes for these LWC bins.

Figures 35-37 are comparable to Figs. 32 and 33 for the next higher altitude range (1500-1800m). Here the correlations are of slightly greater magnitude than they were for 1200-1500m but not nearly as great as for the lowest two altitude ranges.

3. CONCLUSIONS

The results presented here show that CCN concentrations exert ubiquitous effects on cloud microphysics. Strong correlations were found not only between CCN concentrations and total cloud droplet concentrations but just as strong negative correlations were found between CCN and large cloud droplets and drizzle droplet concentrations. These strong correlations continued from cloud base for more than 2 km in altitude. The correlations extended to nearly all liquid water content levels in these small cumulus clouds. This study confirms and extends HM7 that CCN are the aerosol that exerts the most influence on cloud microphysics—both on cloud radiation and precipitation properties. Moreover, this was observed in air masses that all were within the traditional maritime regime; i.e., concentrations less than 200 cm^{-3}. These results uphold the basis for both the 1st and 2nd indirect aerosol effects (IAE).

Acknowledgements.

This work was supported by US NSF grant ATM-0342618.

References

Baker, M.B., R.G. Corbin, and J. Latham, 1979: The evolution of droplet spectra and rate of production of embryonic raindrops in small cumulus clouds. *J. Atmos. Sci.*, **36**, 1612-1615.

Hudson, J. G., and S. Mishra (2007), Relationships between CCN and cloud microphysics variations in clean maritime air, *Geophys. Res. Lett.*, **34**, L16804, doi:10.1029/2007GL030044.

Rauber, R.M., et al., 2007: Rain In shallow Cumulus over the Ocean, the RICO campaign. *Bulletin, AMS*, 88, 1912-1928.

flight	date	N_c HM7	N_c LWC>0 .1gm^{-3}	N_c HM7	N_c LWC> 0.1gm^{-3} rank	CCN	CCN rank	Dur LWC> 0.1	Dur LWC >0.01	Dur LWC> 0.001
RF01	D07	201	108	2	1	200	1	601	1011	1293
RF02	D08	123	77	4	3	133	3	30	113	173
RF03	D09	74	39	12	11	98	9	230	629	868
RF04	D10	--	32	--	--	92	11	22	357	663
RF05	D13	71	30	13	13	91	12	92	212	331
RF06	D16	111	64	7	4	131	4	270	924	1308
RF07	D17	46	25	14	14	55	16	73	379	620
RF08	D19	98	48	9	10	79	15	266	875	1299
RF09	D20	74	38	11	12	94	10	128	335	414
RF10	J05	80	52	10	9	108	8	224	666	900
RF11	J07	--	62	--	--	86	14	60	383	601
RF12	J11	135	63	3	5	90	13	181	482	608
RF13	J12	114	61	5	6	119	6	226	842	1375
RF14	J14	207	102	1	2	142	2	211	754	1145
RF15	J16	112	57	6	7	108	7	141	362	528
RF17	J19	--	--	--	--	48	17	--	1	5
RF18	J23	104	55	8	8	126	5	142	331	411
ave		111				106				
sd		46				35				

Table 1. Flight number; date; flight-averaged concentrations of cloud droplets (N_c) (cm^{-3}) from Table 1 HM7 (LWC > 0.25 gm^{-3}; updraft > 0.5 m/s, 600-900m altitude), N_c for LWC > 0.1gm^{-3}, 600-900m altitude; rank order of N_c (HM7) (not the rank shown in in HM7 but the rank of all 14 flights considered by HM7; rank order of N_c(0.1gm^{-3}) CCN concentrations at 1% S (cm^{-3}) at 100m altitude (same as HM7 but 3 extra flights); and rank order of CCN concentrations. Duration (number of seconds) of data in each LWC category. Everything in this table pertains to 600-900m altitude.

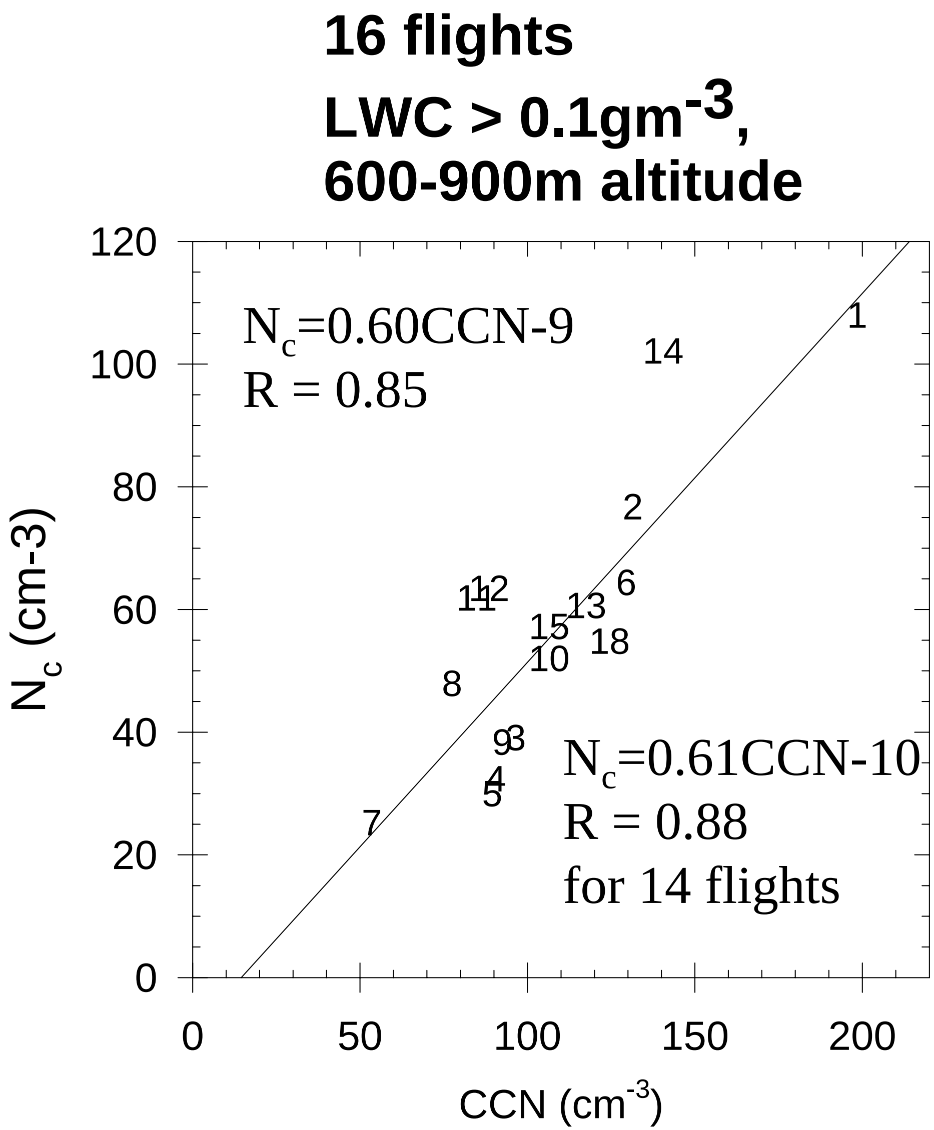

Figure 1. Average total (>2.4 µm) FSSPdroplet concentrations (N_c) measured during each flight within the denoted altitude and LWC range against the average 100m altitude CCN concentrations at 1% S for each flight. Data points are plotted as the flight number (Table 1). All of the 17 flights under consideration here with the exception of RF17 (J19) had clouds within this altitude range. The linear regression line, equation and correlation coefficient (R) are shown as well as the linear regression and R for only the same 14 flights considered by HM7. This excludes RF4 and 11 (D10 and J7).

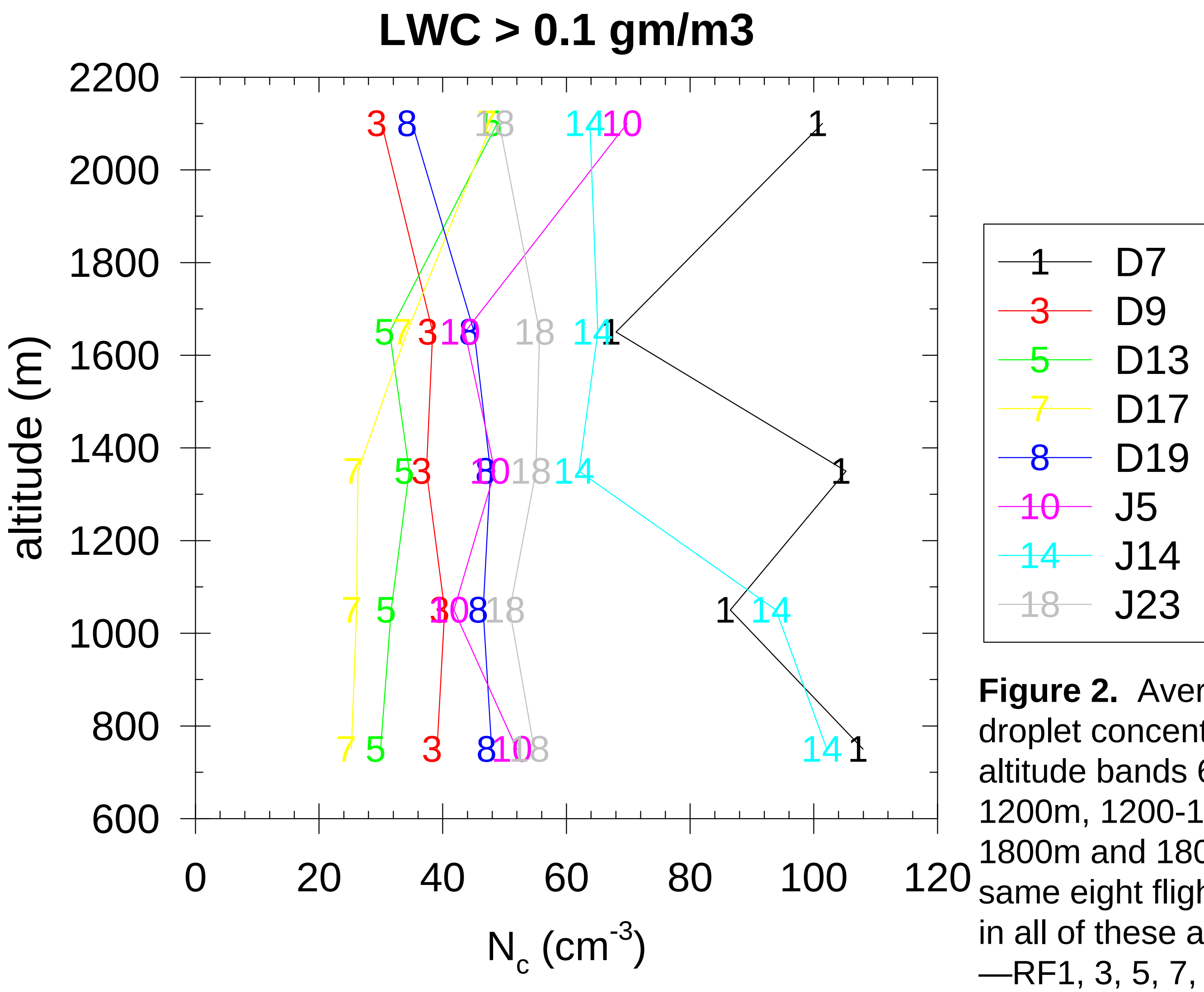

Figure 2. Average total cloud droplet concentrations within altitude bands 600-900m, 900-1200m, 1200-1500m, 1500-1800m and 1800-2400m for the same eight flights with clouds in all of these altitude ranges—RF1, 3, 5, 7, 8, 10, 14 and 18 (D7, D9, D13, D17, D19, J5, J14 and J23).

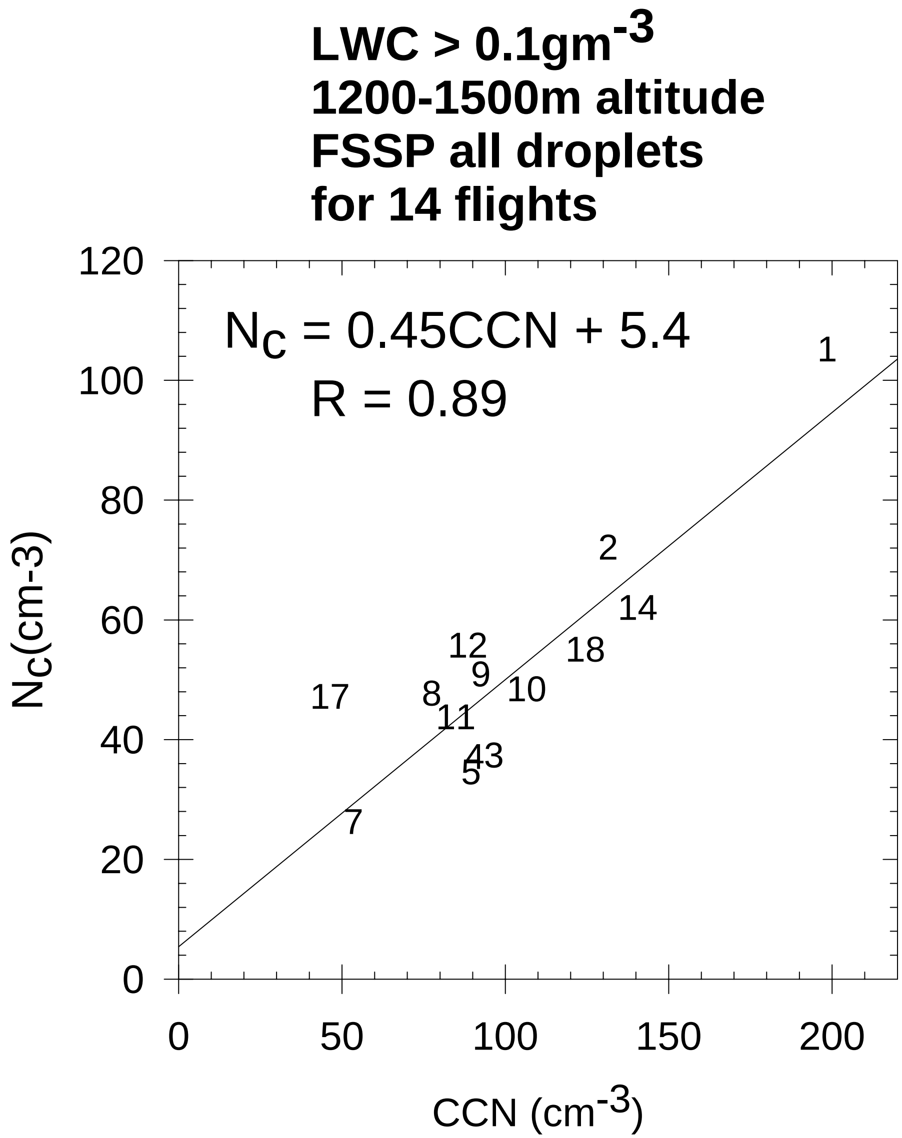

Figure 3. As Fig. 1 but for a higher altitude range and a different missing flight, RF6 (D16) that did not have cloud data in this altitude range. Note the lower N_c range.

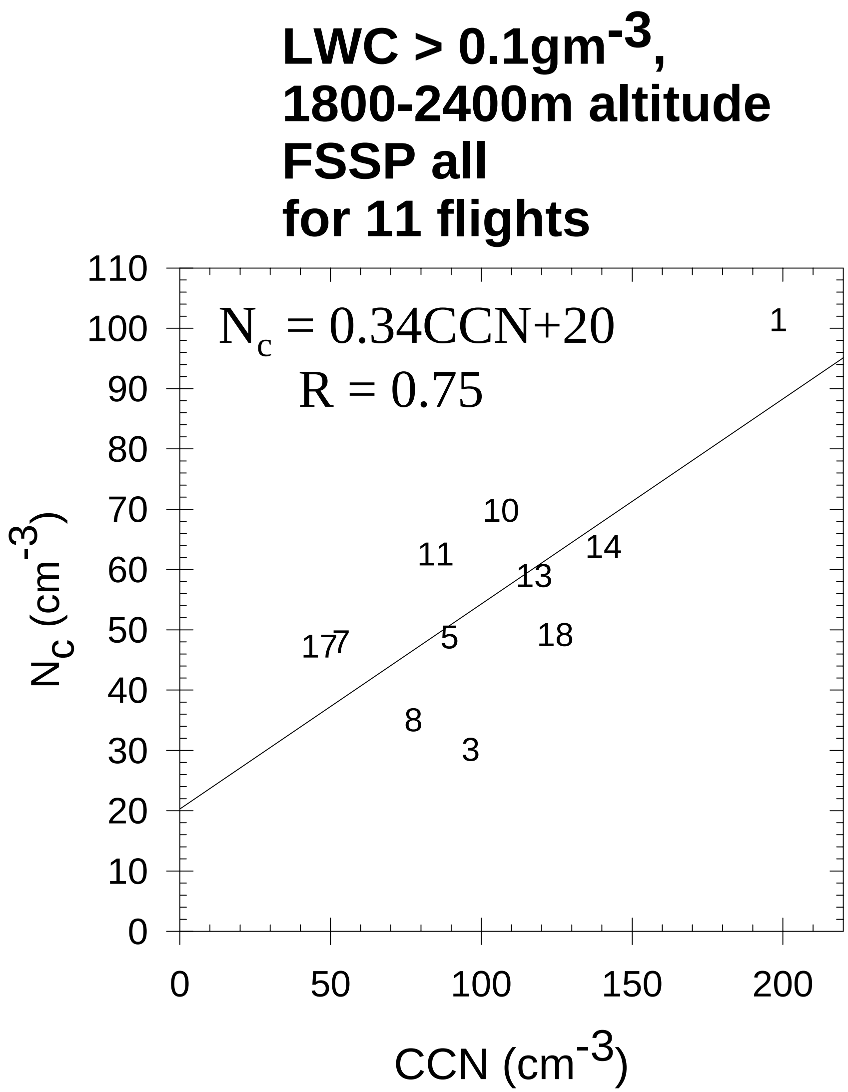

Figure 4. As Fig. 3 but for an even higher altitude range that had fewer flights with cloud data in this altitude range; no data from RF2, 4, 6, 9, 12 or 15 (D8, D10, D16, D20, J11 and J16).

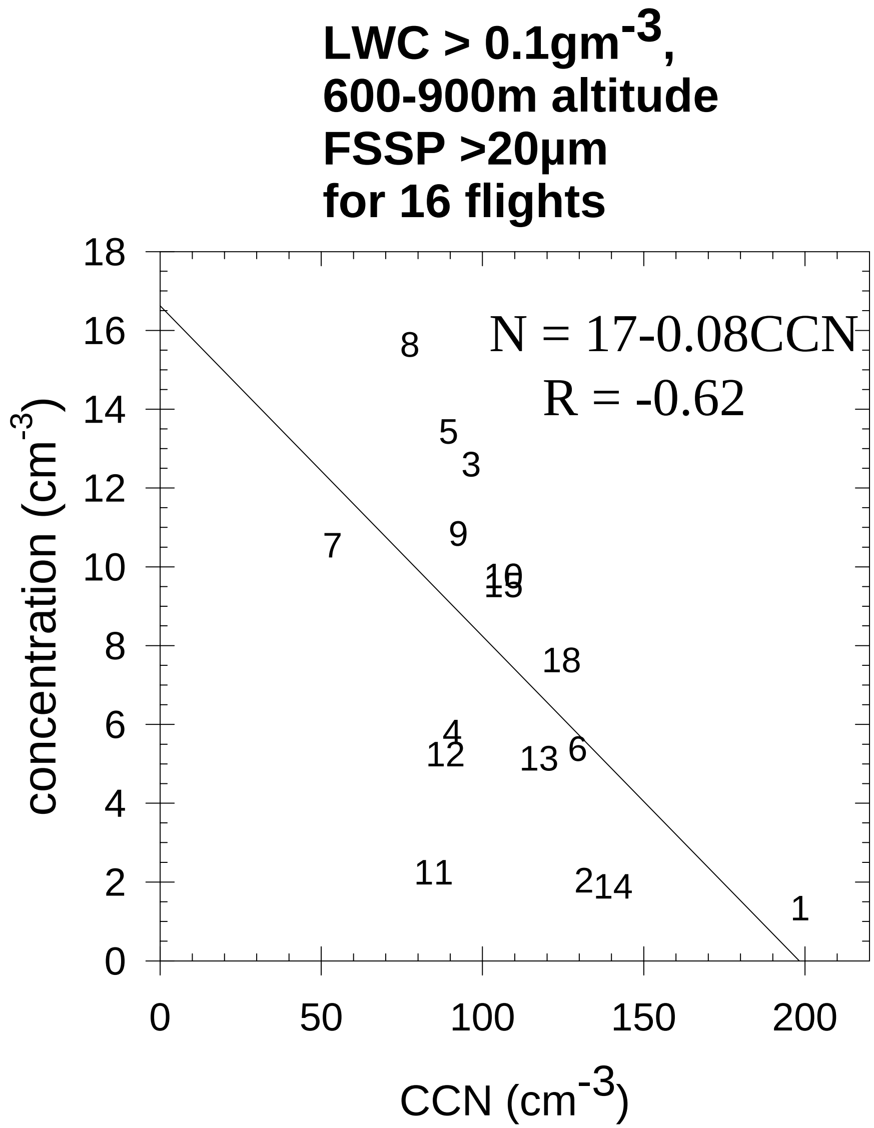

Figure 5. As Fig. 1 but only for larger cloud droplets. Note the much smaller droplet concentration range.

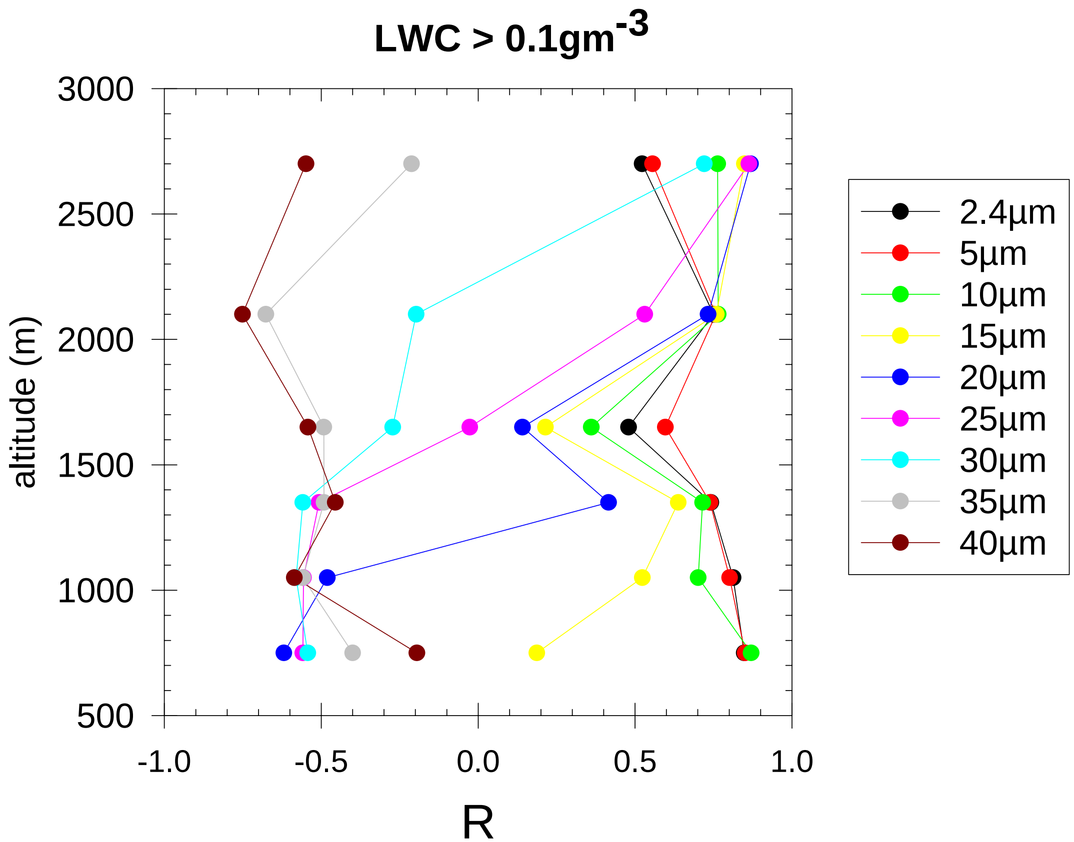

Figure 6. Correlation coefficients (R) as a function of altitude for CCN at 1% S measured during the half hour circles at 100m altitude versus cumulative cloud droplet concentrations measured within various altitude bands. Cloud is defined here as LWC > 0.1 gm-3. The number of flights and the actual flights considered at each altitude here were different because there were not always clouds within some of the altitude bands for some of the flights. 600-900m—16 flights (no RF17); 900-1200m—15 flights (no RF13 or 17); 1200-1500m—16 flights (no RF6); 1500-1800m—13 flights (no RF2, 4, 6 or 11); 1800-2400m—11 flights (no RF2, 4, 6, 9, 12 or 15); 2400-3000m—6 flights (no RF2, 4, 5, 6, 8, 9, 10, 12, 14, 17 or 18).

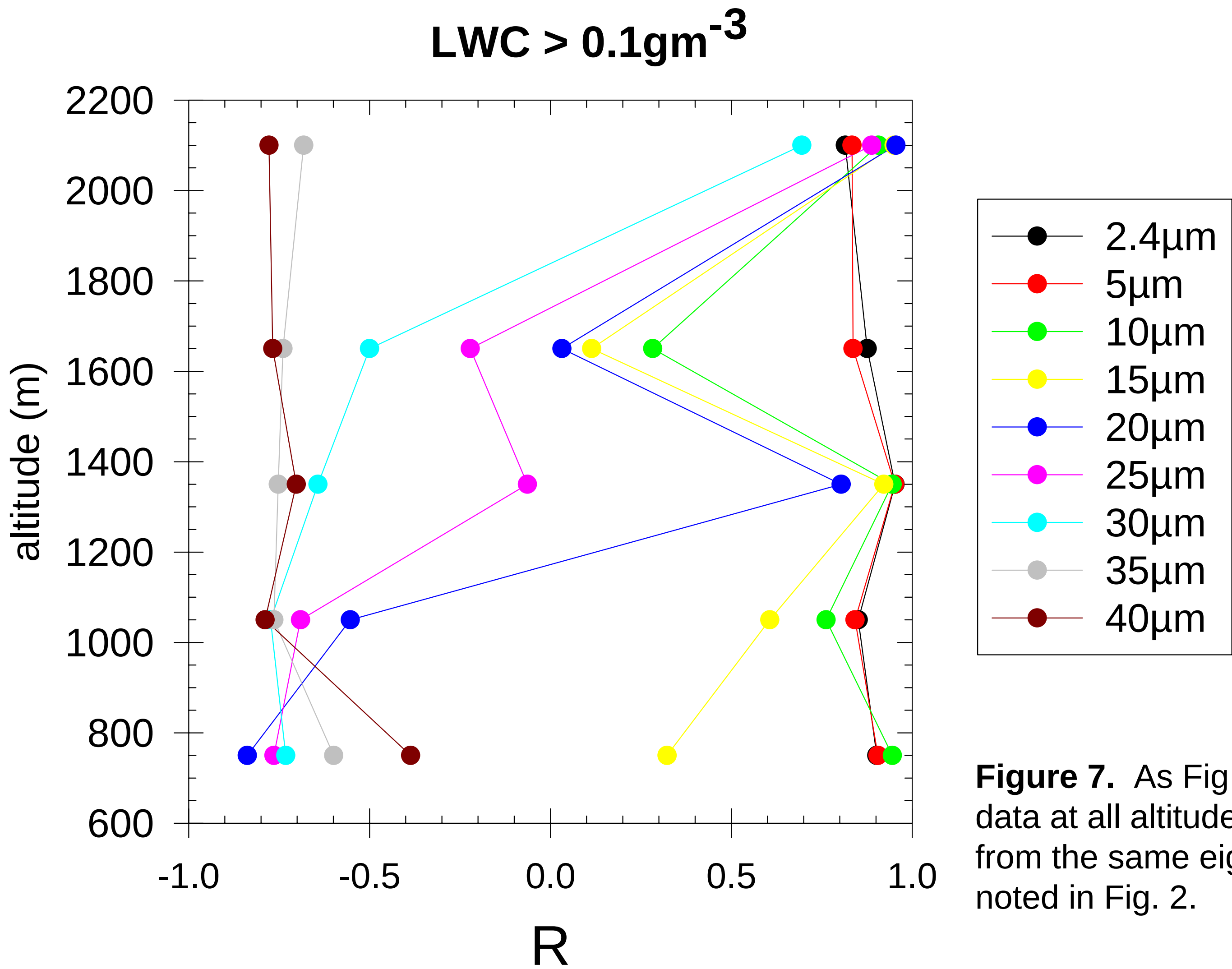

Figure 7. As Fig. 6 but all data at all altitudes are from the same eight flights noted in Fig. 2.

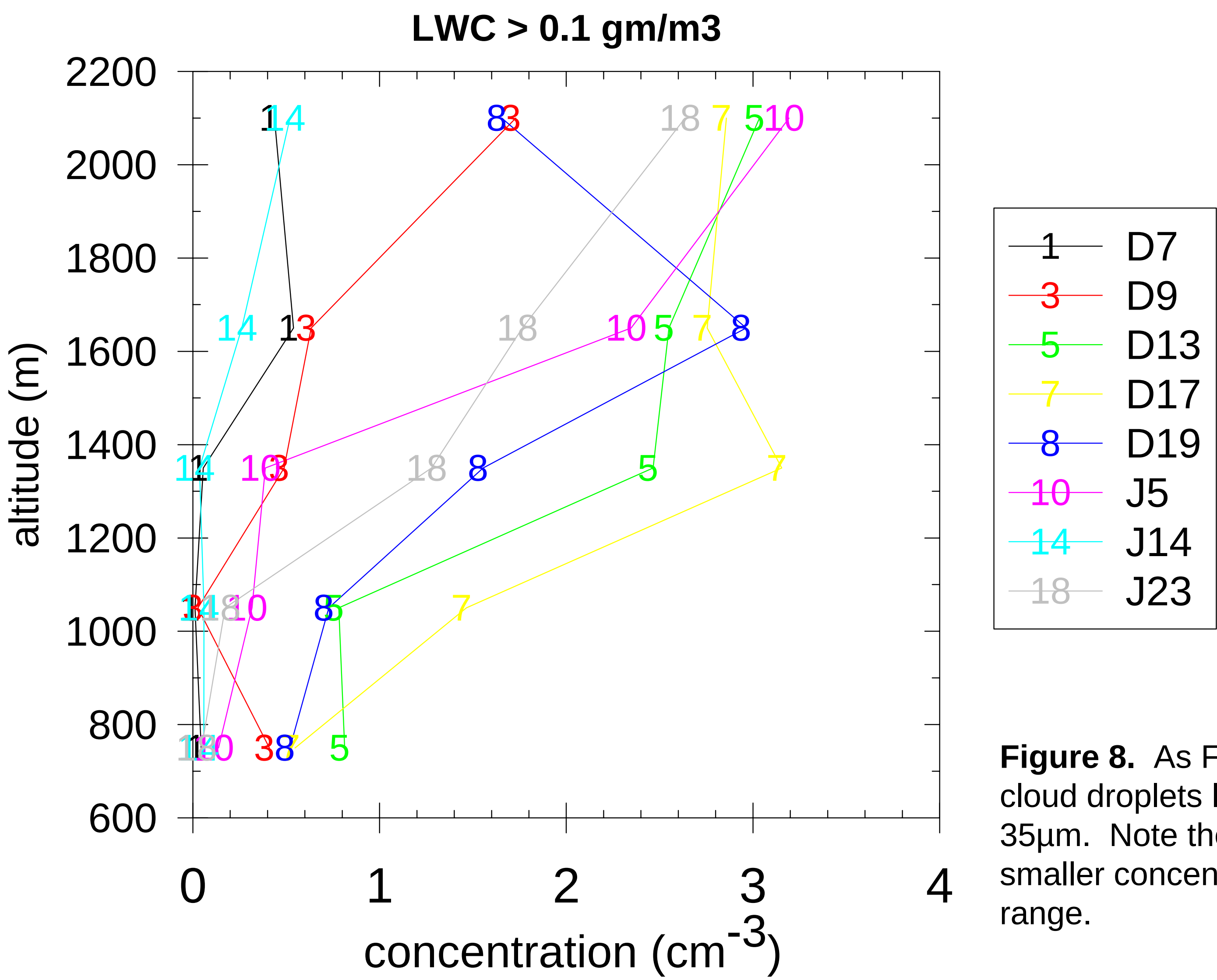

Figure 8. As Fig. 2 but for cloud droplets larger than 35µm. Note the much smaller concentration range.

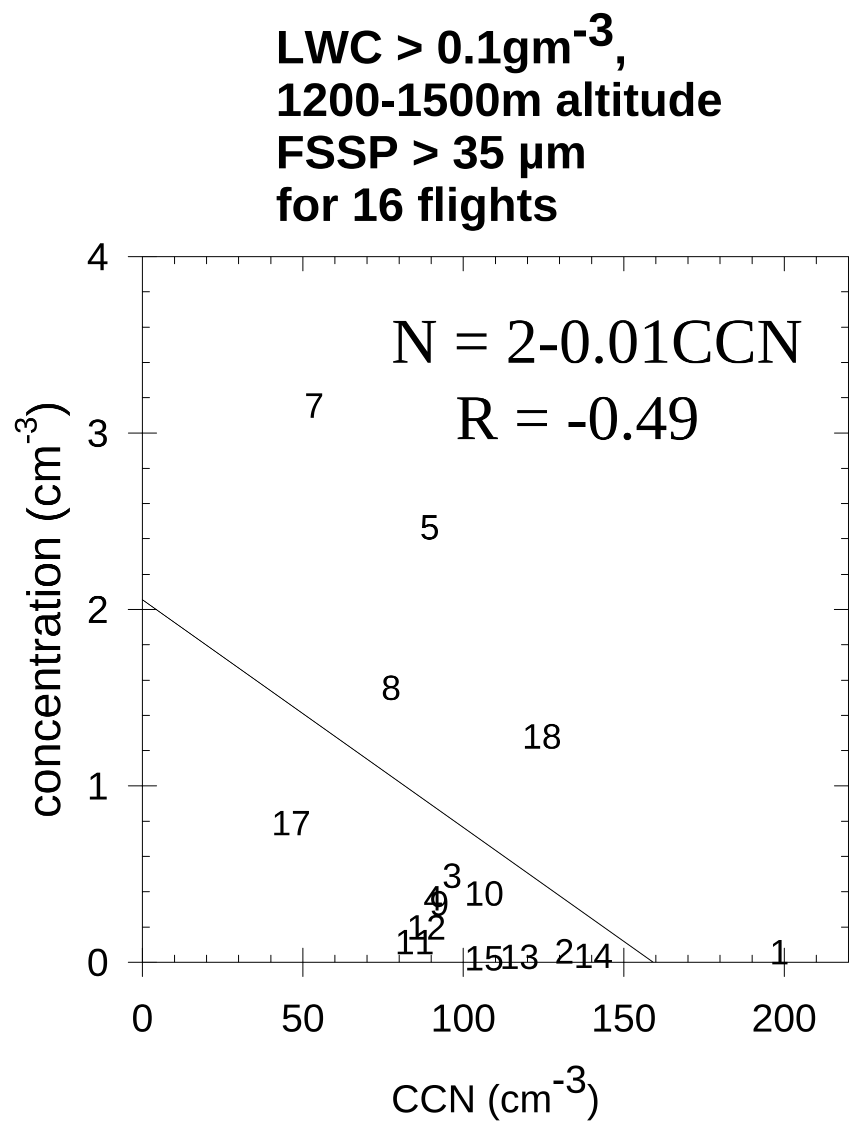

Figure 9. As Fig 5 but for an even larger size range and a higher altitude. Note the smaller droplet concentration range. If only RF1, 5, 8, 7 and 18 are considered R is -0.92. R for the other 11 flights displayed here is -0.77.

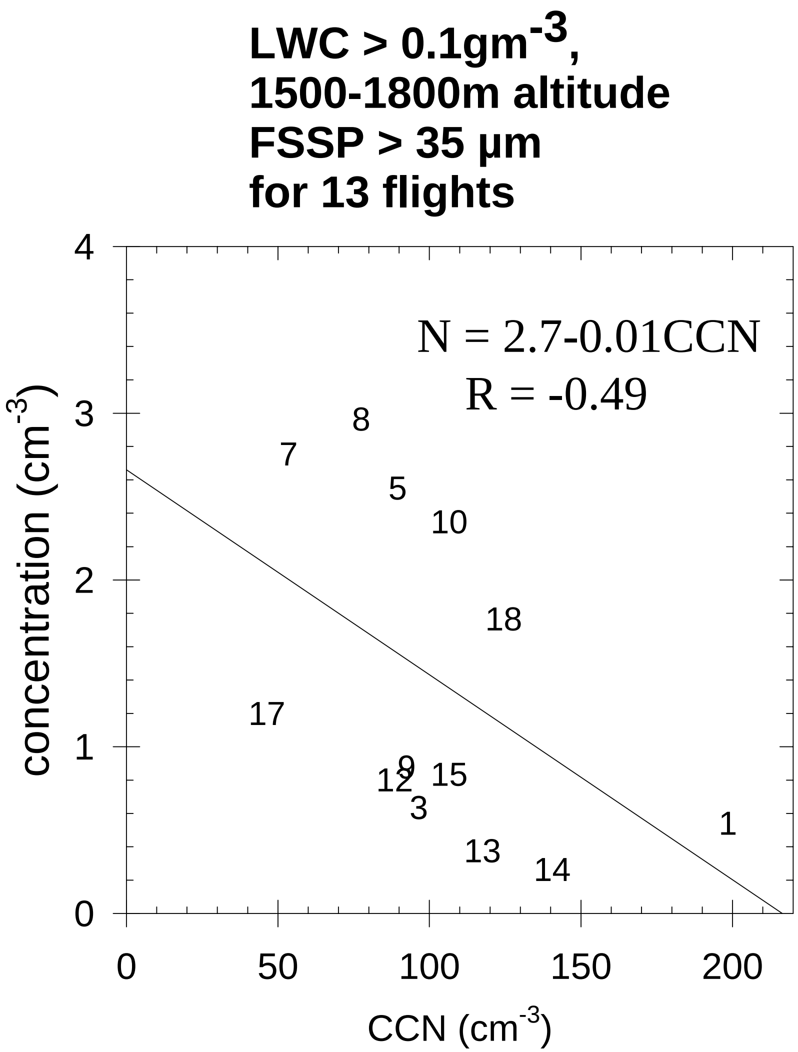

Figure 10. As Fig. 9 but for the next altitude range, which has 3 fewer flights (see Fig. 6 caption). If only RF1, 5, 7, 8, 10 and 18 are considered R is -0.97. This is the same group first separately considered in Fig. 9 except for the addition of RF10. R for the other seven flights in this figure is -0.93.

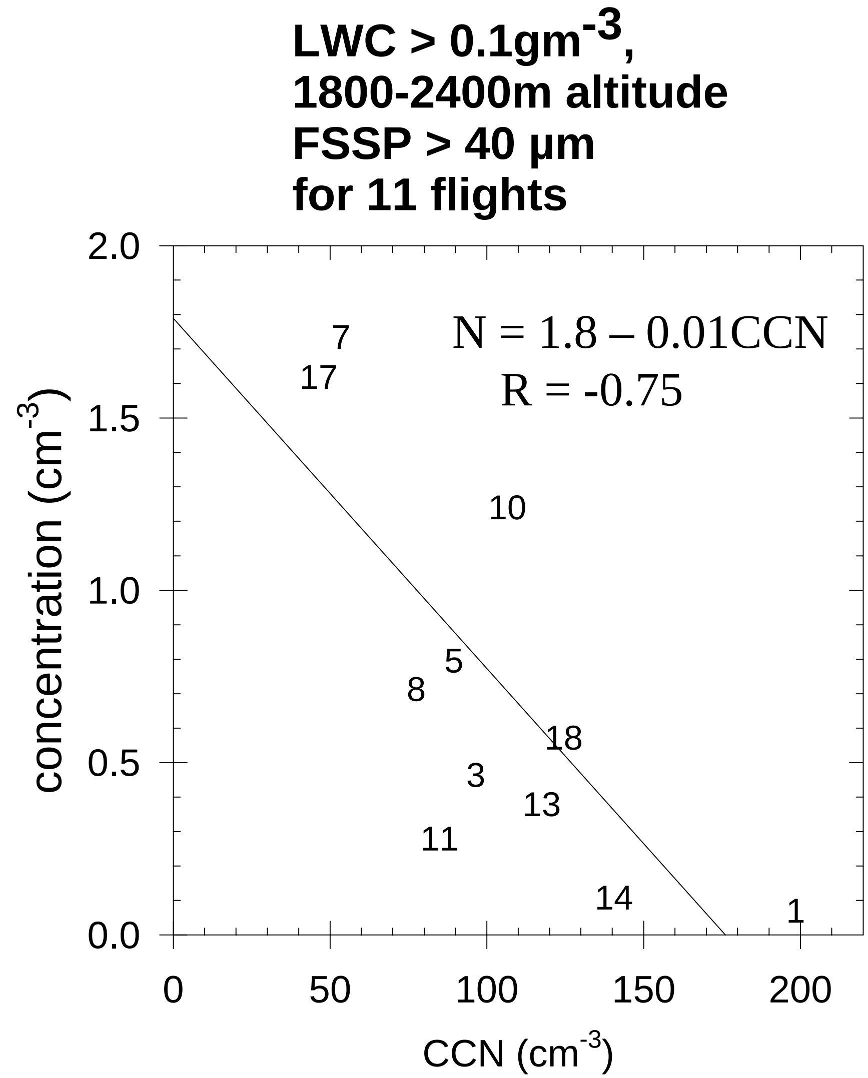

Figure 11. As Fig. 10 but for the next higher altitude range, which has two fewer flights (see Fig. 6 caption) and the next larger droplet size range. Note the even smaller droplet concentration range.

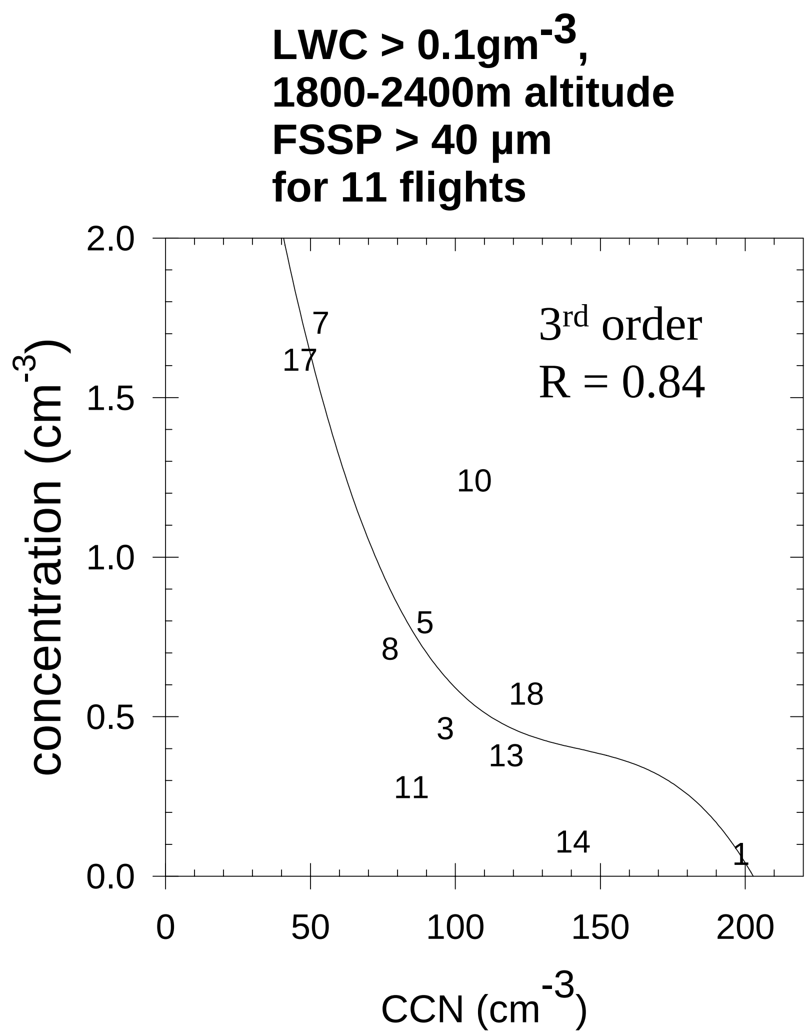

Figure 12. As Fig. 11 but for 2nd order regression.

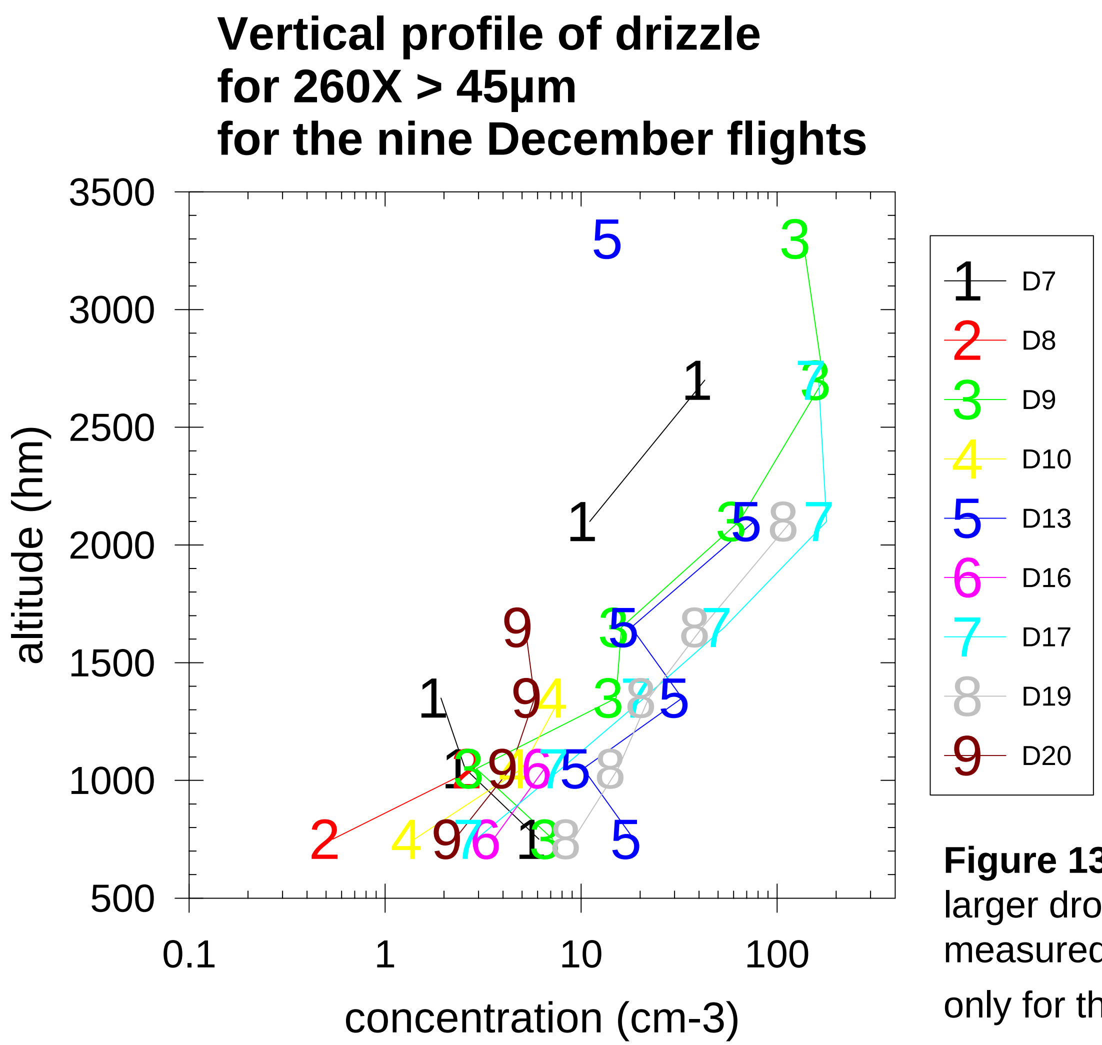

Figure 13. As Fig. 8 but for even larger drops (> 45 µm; drizzle) measured with the 260X probe only for the December RICO flights.

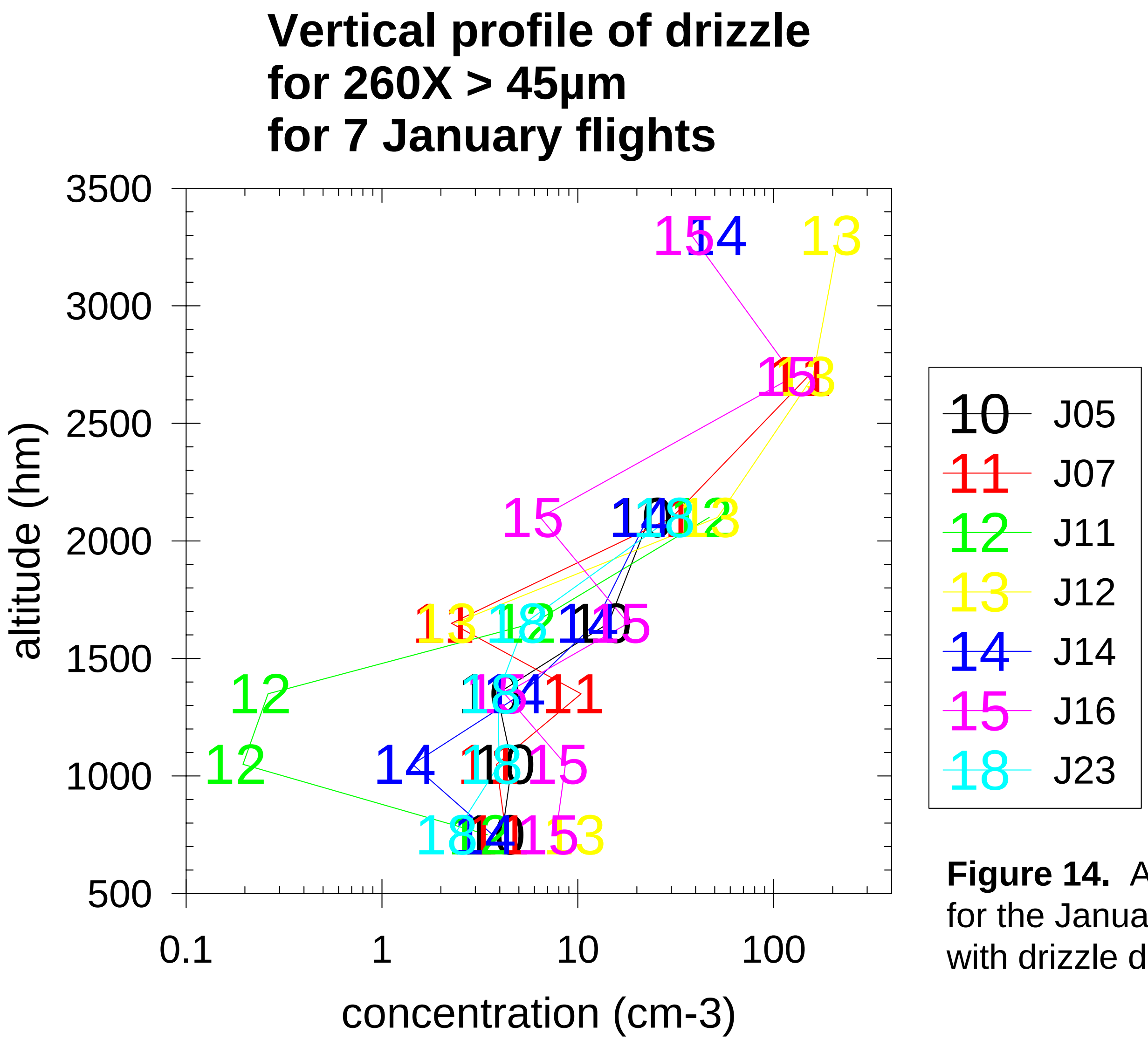

Figure 14. As Fig. 13 but for the January RICO flights with drizzle data.

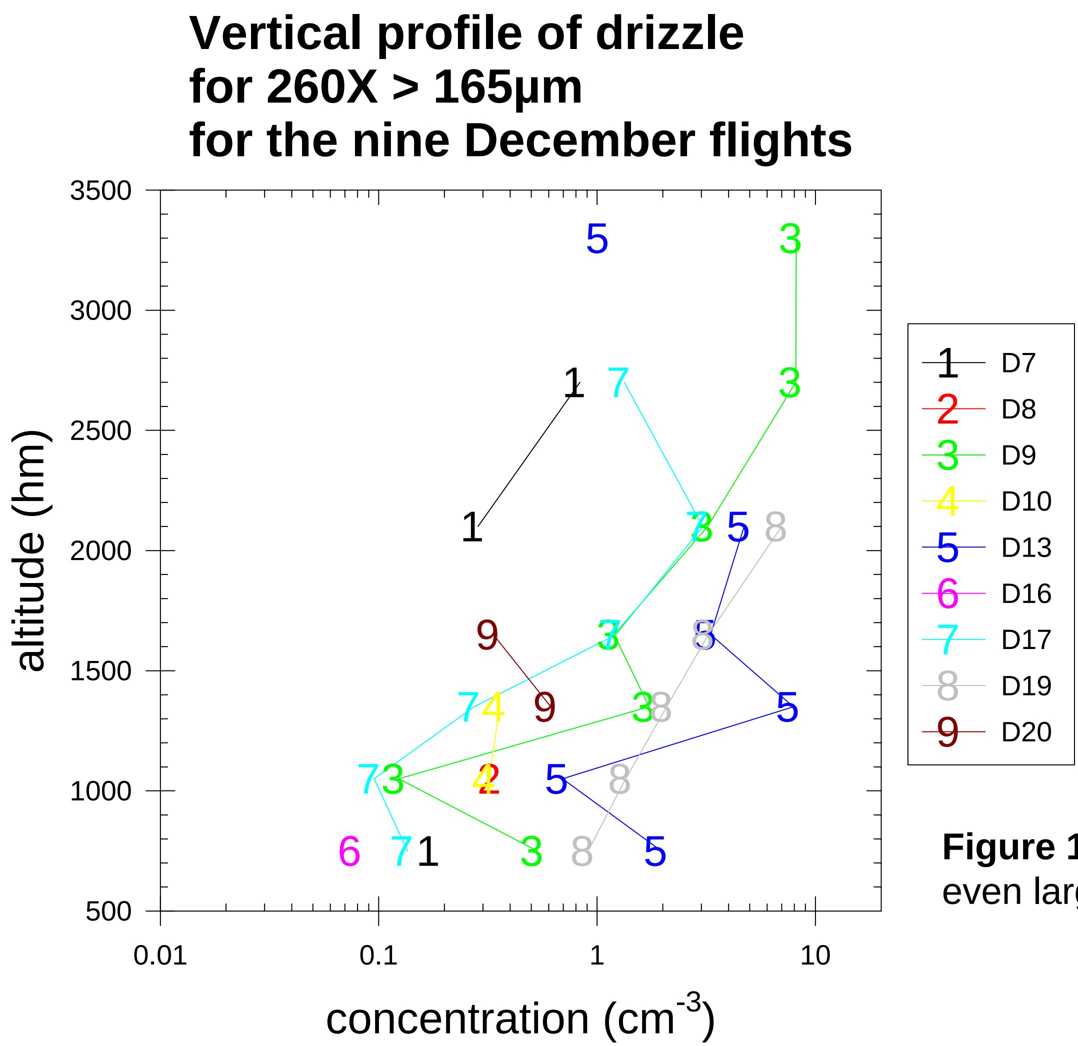

Figure 15. As Fig. 13 but for even larger drops (> 165 µm).

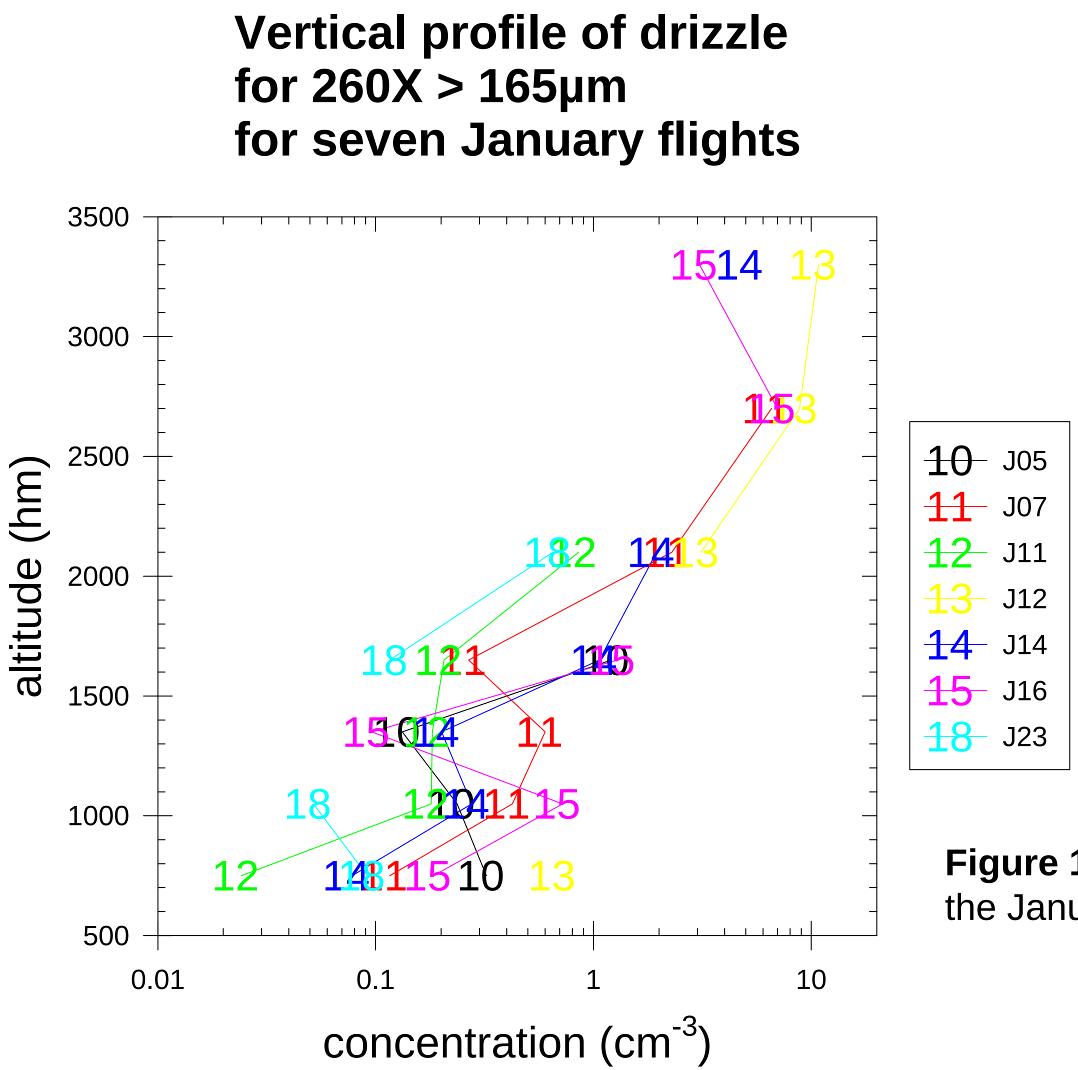

Figure 16. As Fig. 15 for the January flights.

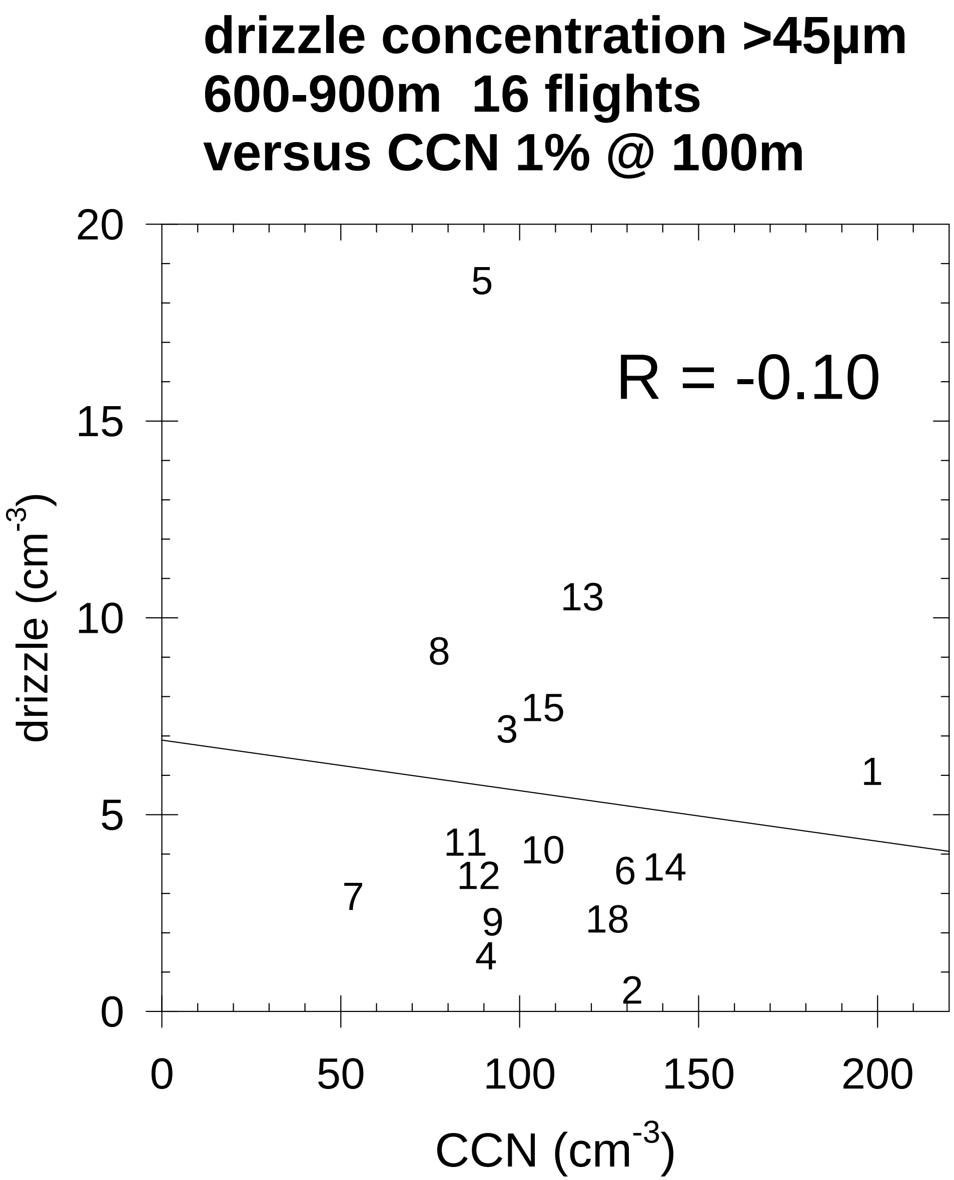

Figure 17. As Fig 1 but for drizzle drops > 45 µm measured by the 260X probe

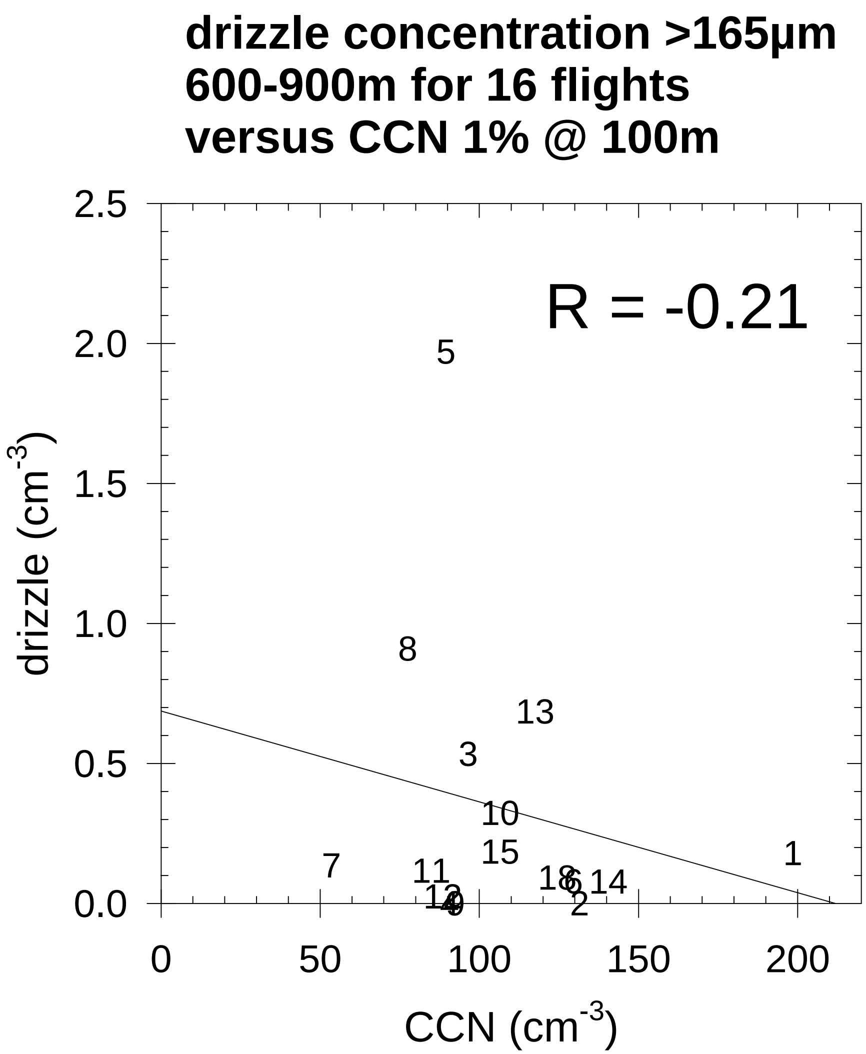

Figure 18. As Fig. 17 but for drops > 165 µm diameter.

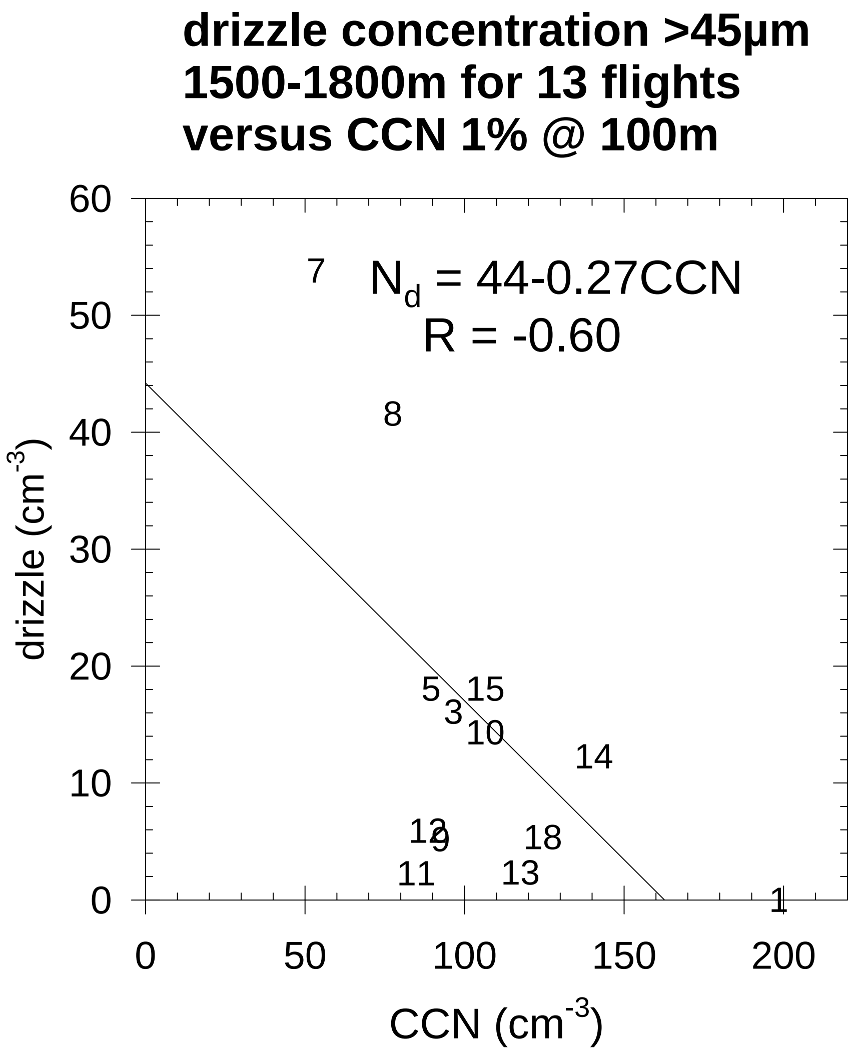

Figure 19. As Fig. 17 but for a higher altitude. Note the higher drop concentration range because of the greater amount of drizzle at higher altitudes (Figs. 13 and 14).

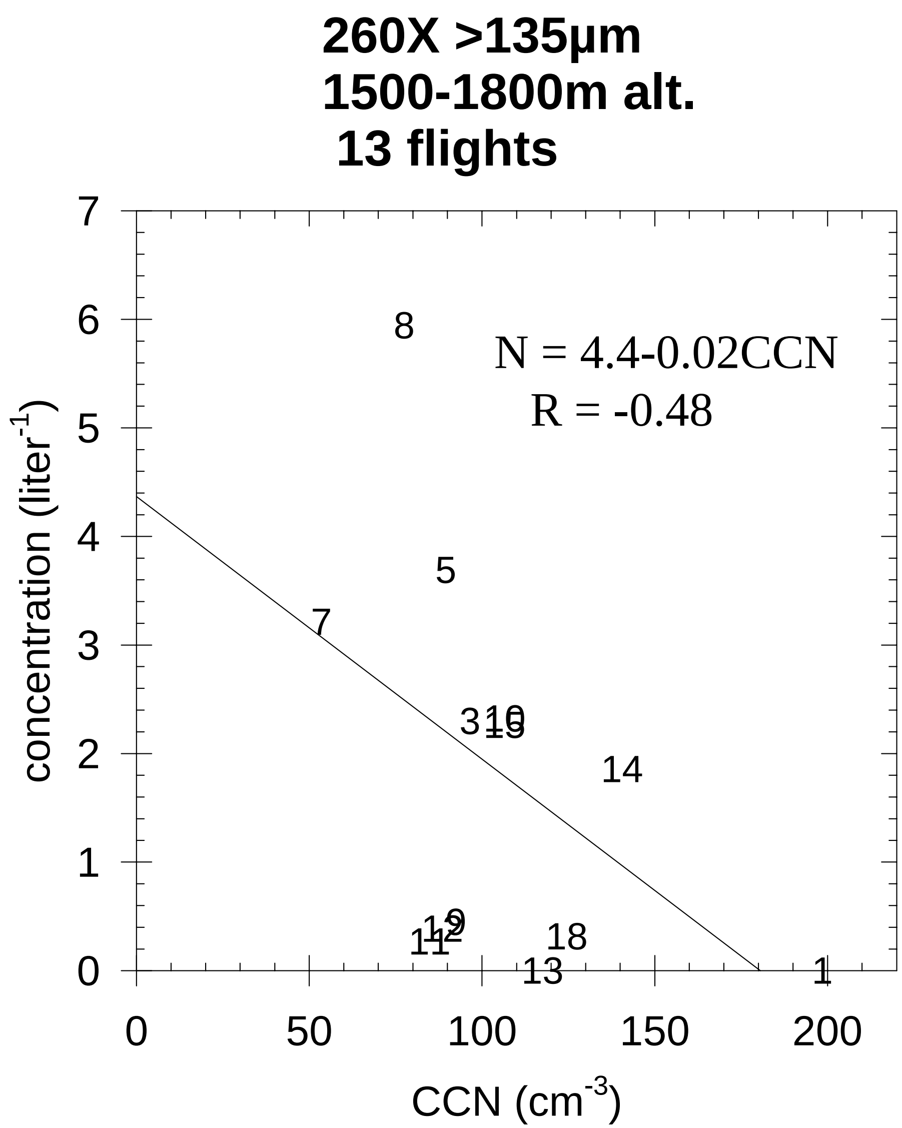

Figure 20. As Fig. 19 but for larger drizzle drops. Note the smaller scale due to the lower drop concentrations at the larger sizes.

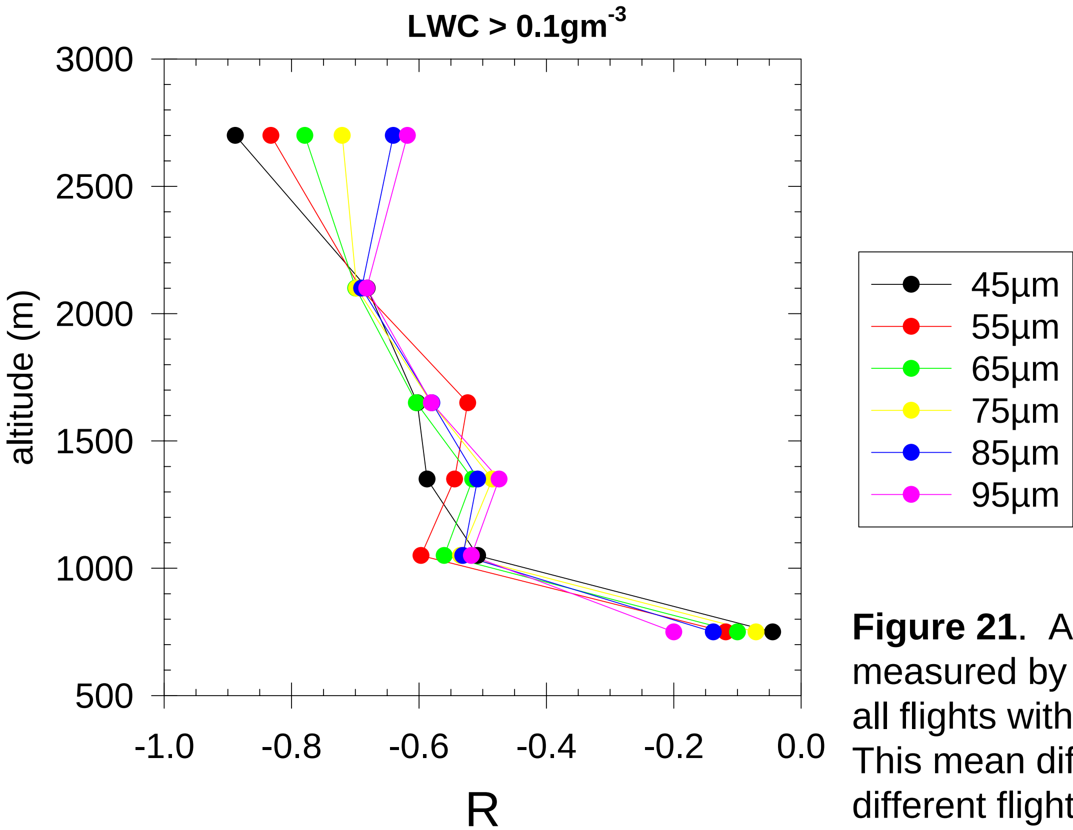

Figure 21. As Fig. 6 but for drizzle drops measured by the 260X probe. This includes all flights with data in each altitude band. This mean different numbers of flights and different flights at the various altitudes. 600-900m—16 flights (no RF17; same flights as the cloud data at this altitude noted in Fig. 6 caption); 900-1200m—15 flights (no RF13 or 17; same as cloud data noted in Fig. 6 caption); 1200-1500m—15 flights (no RF6 or 17; there was one more data point for the cloud data for this altitude as there was cloud data for RF17); 1500-1800m—13 flights (no RF2, 4, 6 or 17; this differs from the cloud data, which did have RF17 data but not RF11); 1800-2400m—12 flights (no RF2, 4, 6, 9, or 15; this is one more than the cloud data because there is drizzle data at this altitude for RF12); 2400-3000m—6 flights (no RF2, 4, 5, 6, 8, 9, 10, 12, 14, 17 or 18; the same flights as the cloud data at this altitude).

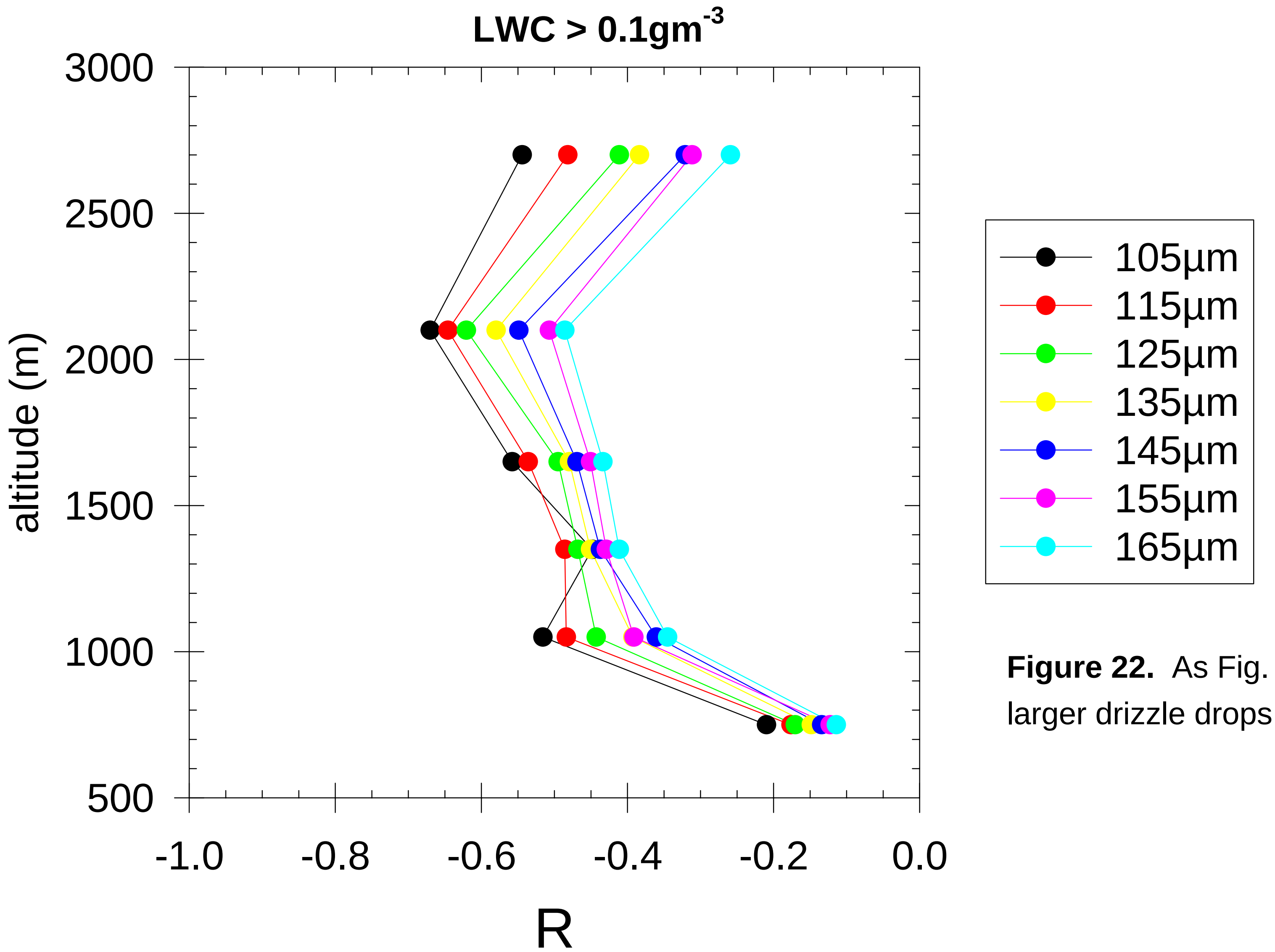

Figure 22. As Fig. 21 for larger drizzle drops.

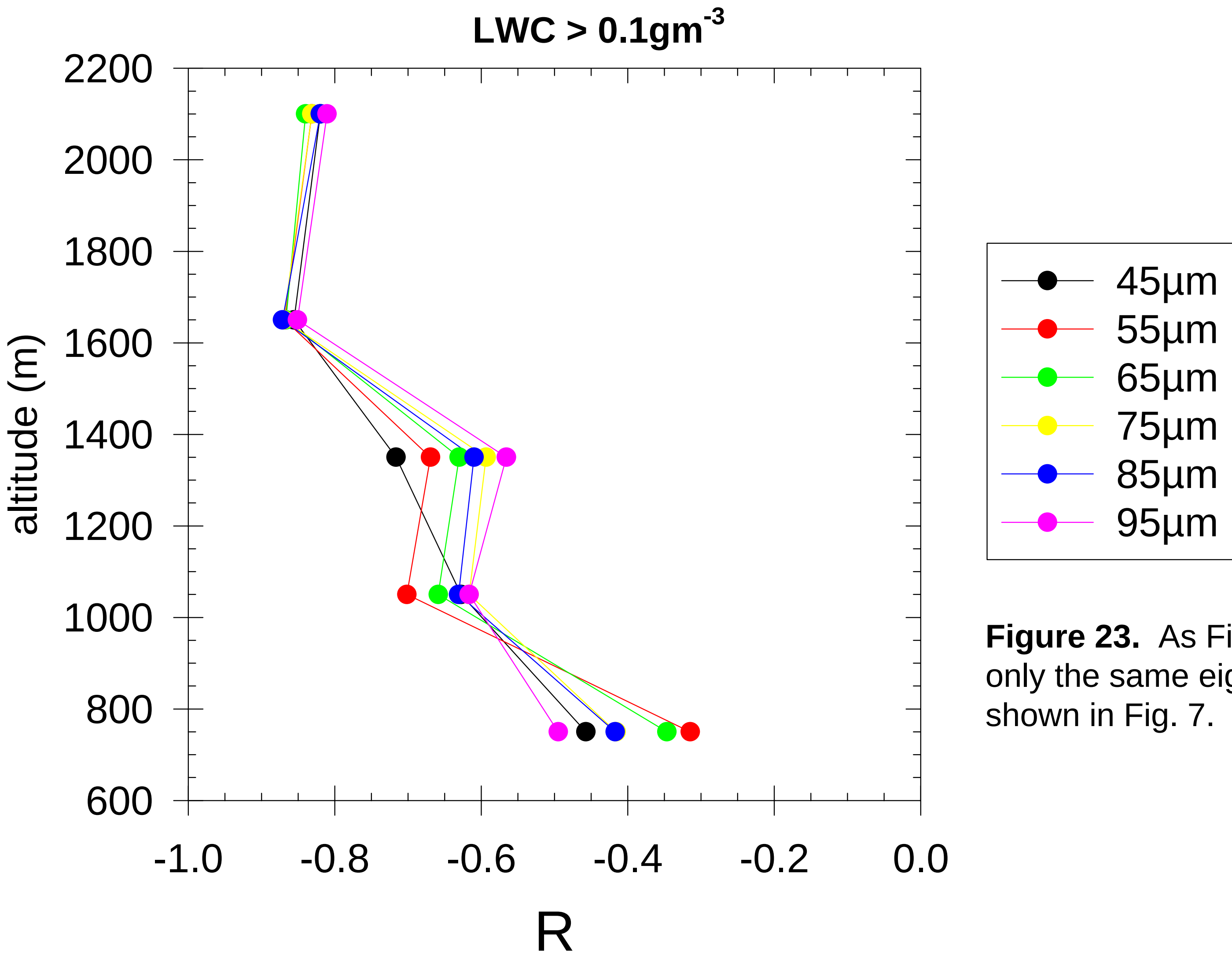

Figure 23. As Fig. 21 but for only the same eight flights shown in Fig. 7.

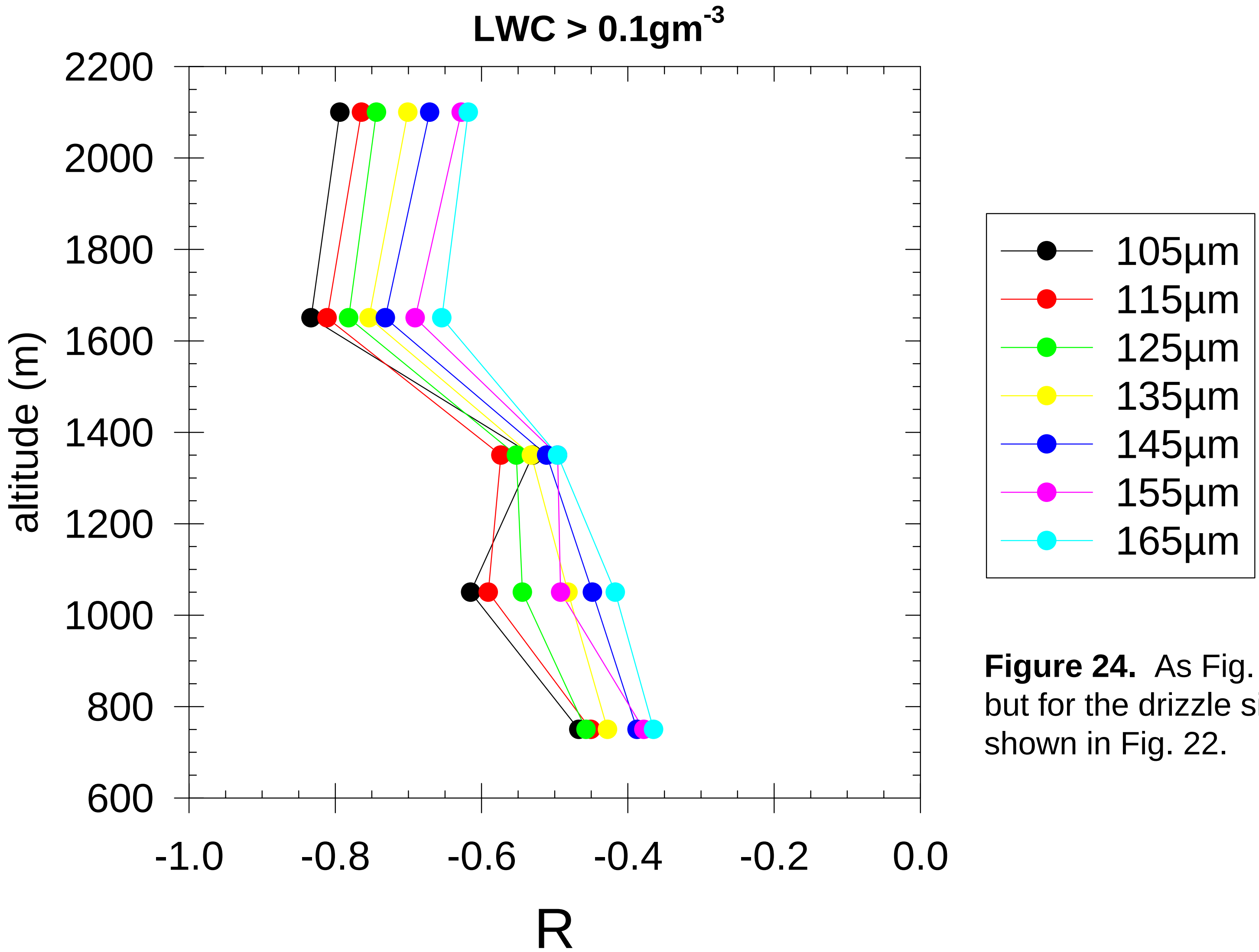

Figure 24. As Fig. 23 but for the drizzle sizes shown in Fig. 22.

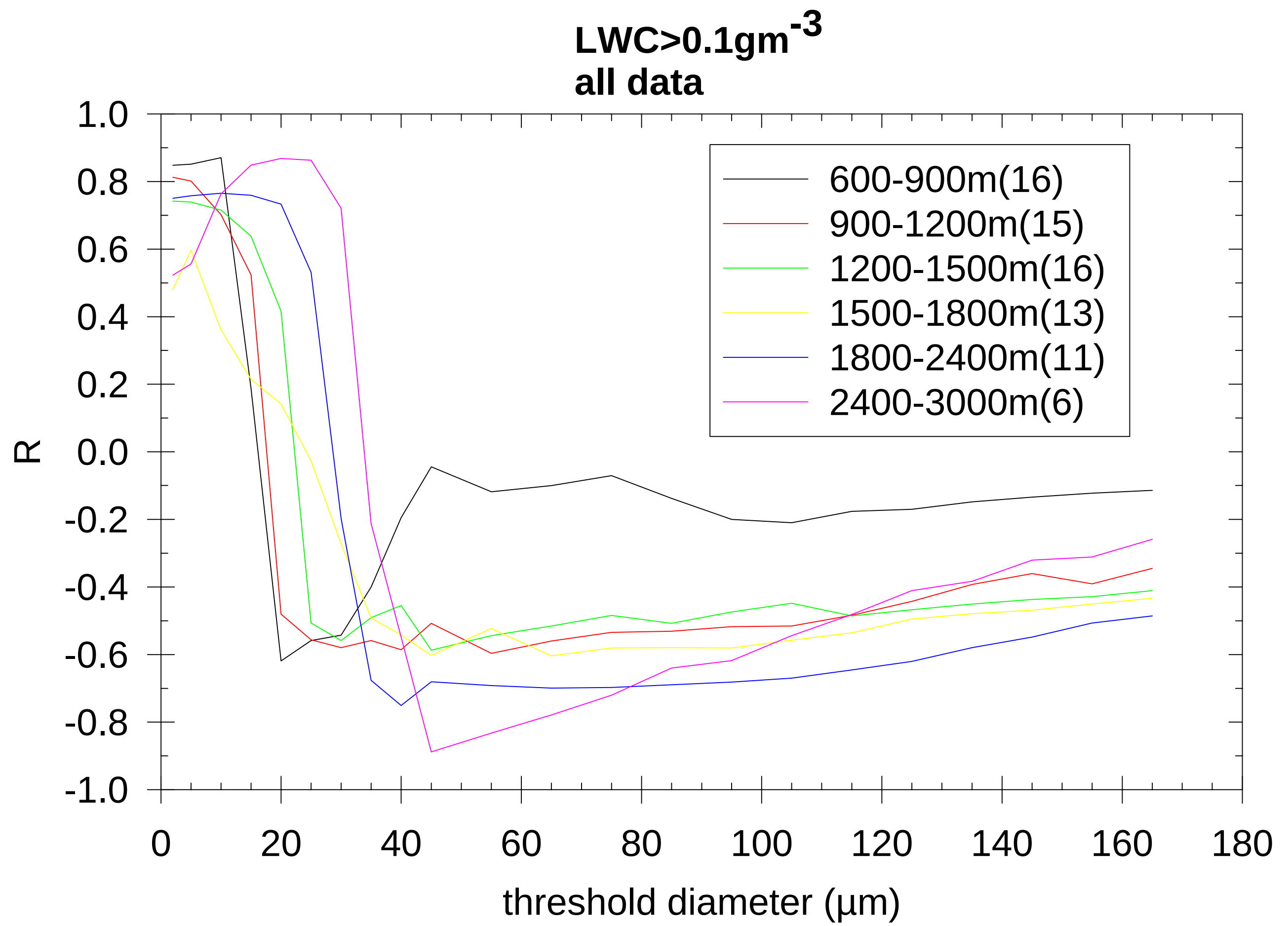

Figure 25. Correlation coefficients (R) displayed in Figs. 6, 21 and 22 displayed for each altitude band as a function of cumulative droplet size. As in those other figures the flights considered varied with altitude range and this may cause biases. The number of flights in each altitude range is shown in parentheses in the legend.

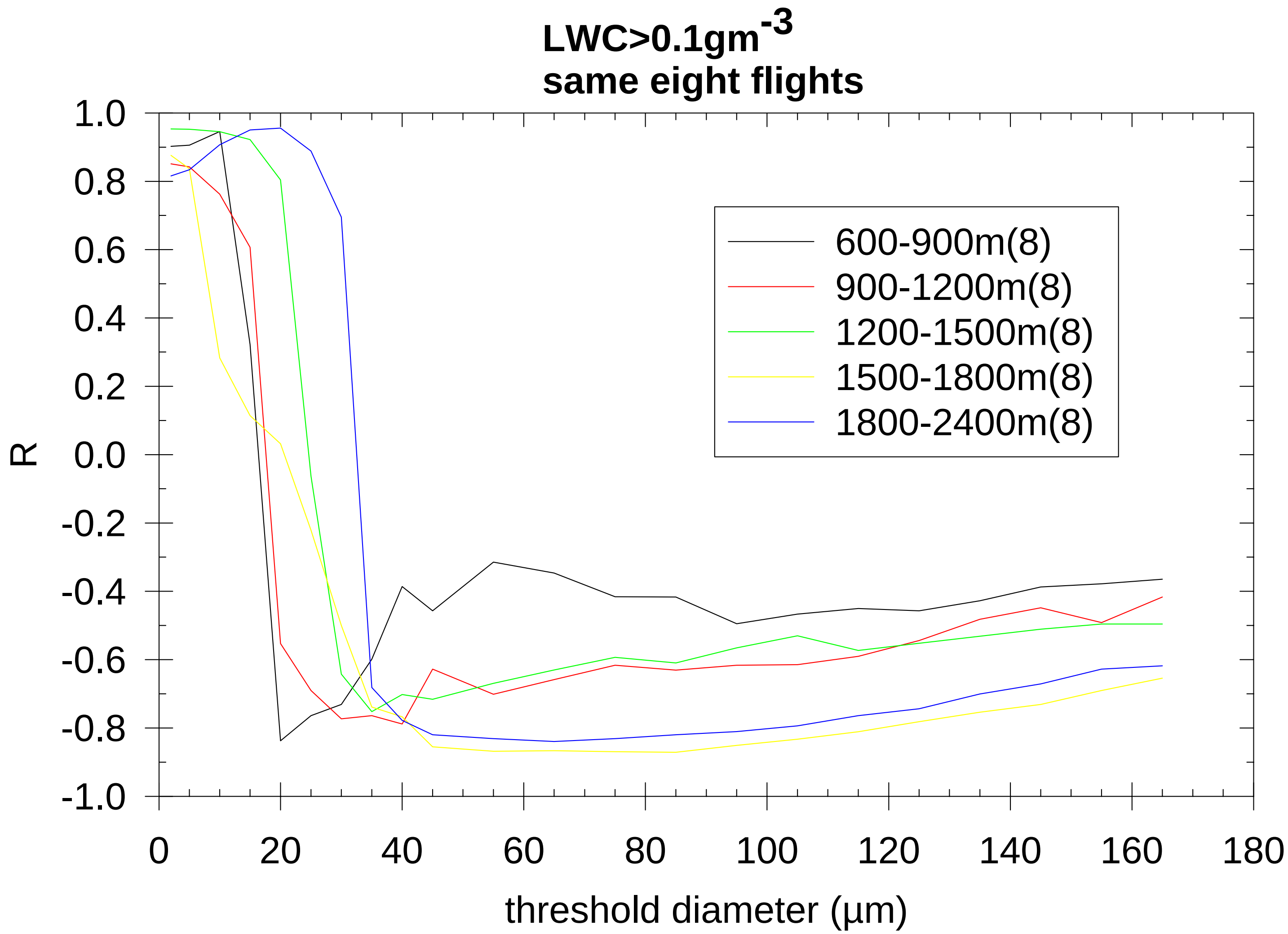

Figure 26. As Fig. 25 but for R displayed in Figs. 7, 23, and 24. The same eight flights are for all altitudes.

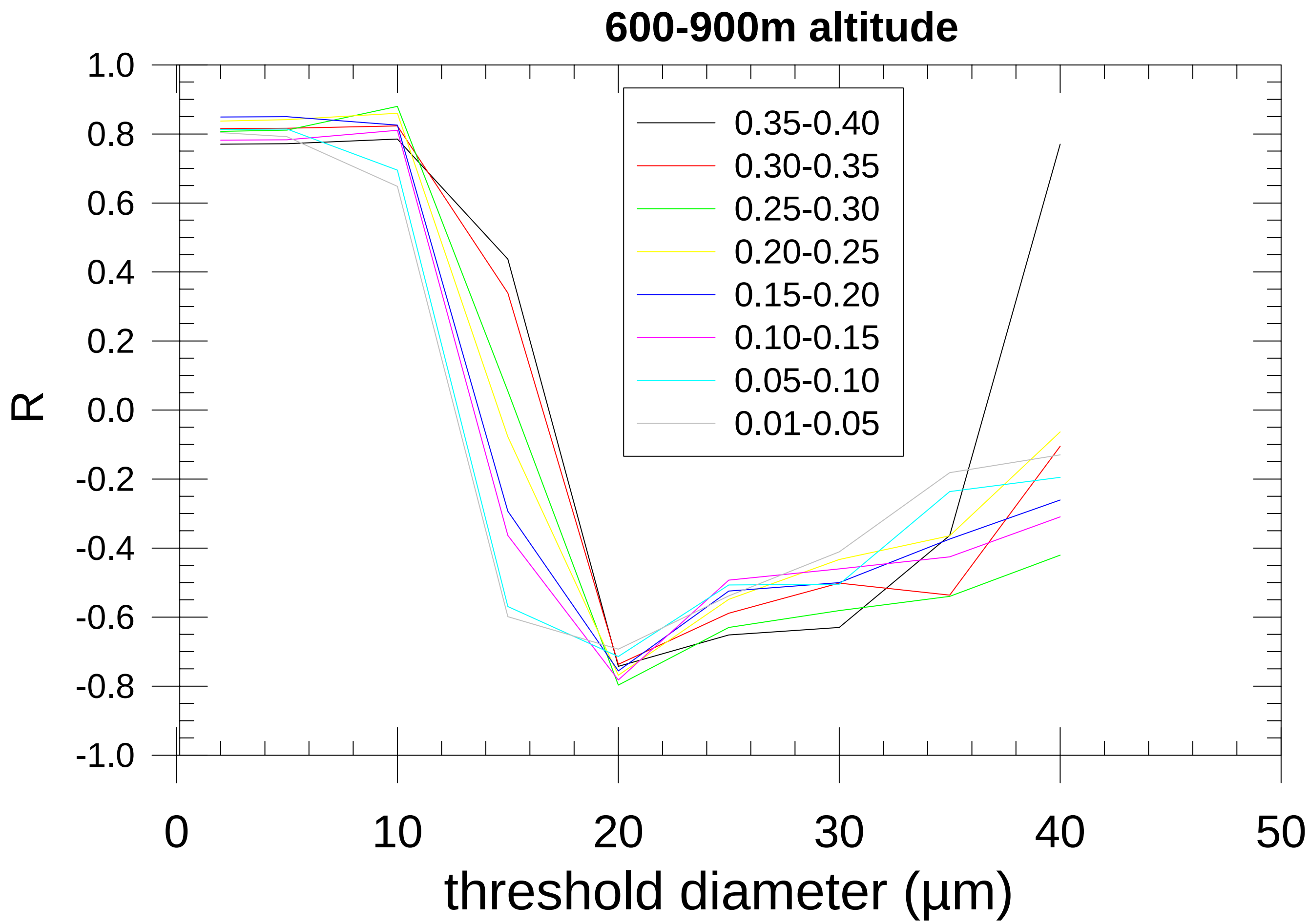

Figure 27. As Fig. 26 except that all data are from the 600-900m altitude range. The different lines are for various LWC ranges denoted in the legend. All data are from the same eleven flights that had data in these LWC intervals. This then excludes RF2, 4, 7, 11, 17 and 18 (D8, D10, D17, J7, J19, J23).

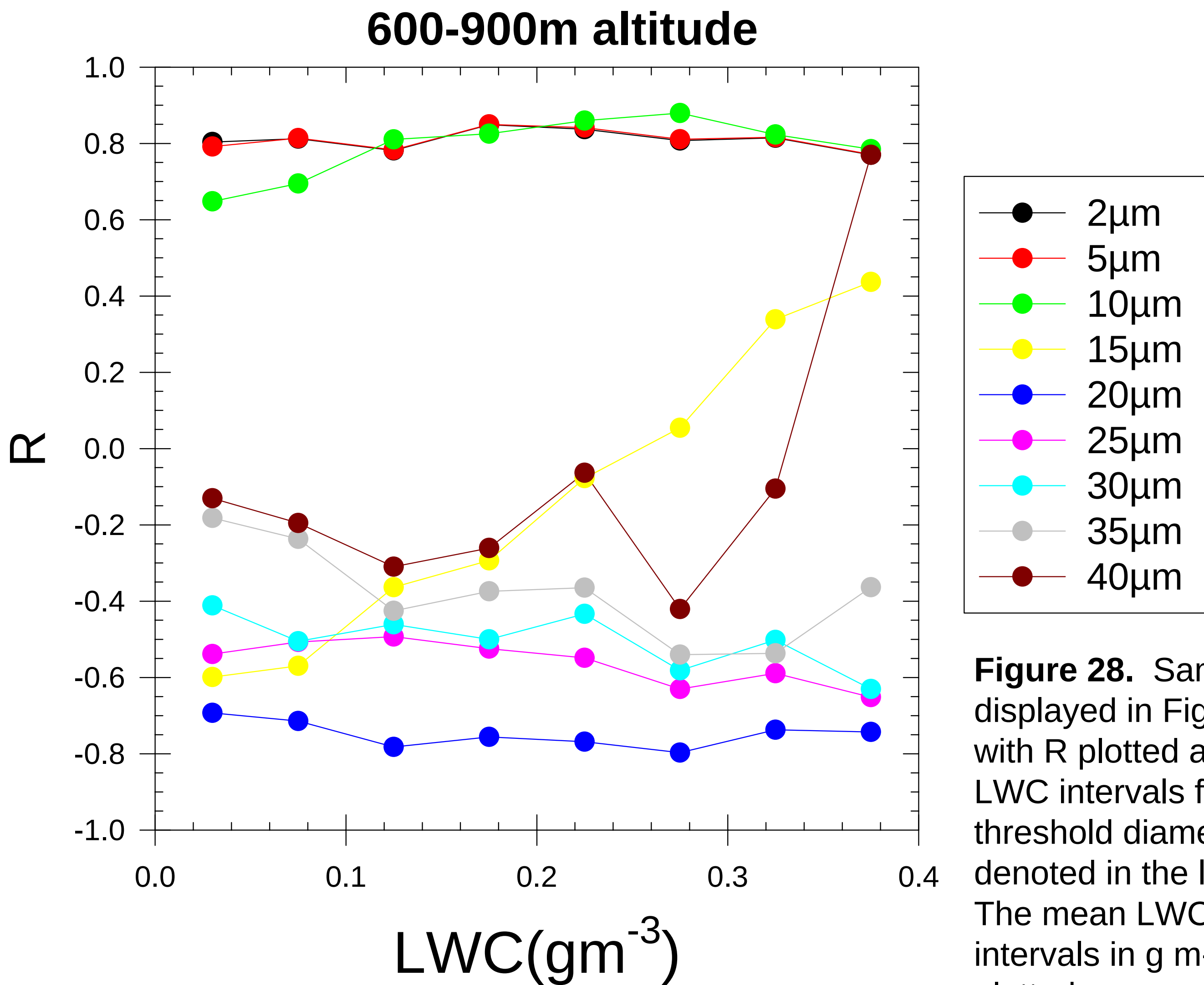

Figure 28. Same data displayed in Fig. 27, but with R plotted against LWC intervals for each threshold diameter denoted in the legend. The mean LWC of the intervals in g m-3 are plotted.

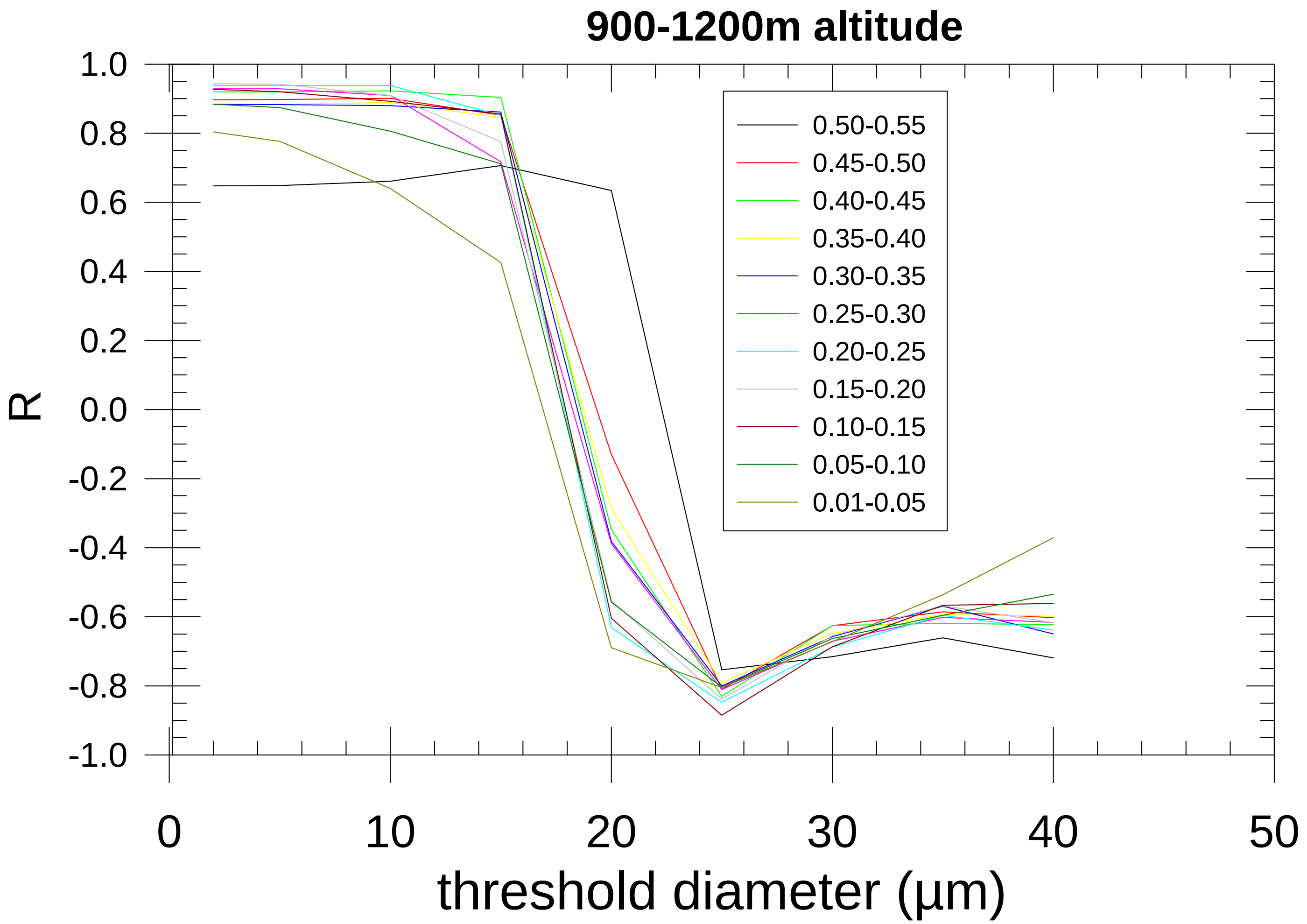

Figure 29. As Fig. 27, but for 900-1200m altitude range. There are also eleven flights with data in these LWC but they are different from the flights in Fig. 27. Here RF2, 3, 11, 13, 14 and 17 (D8, D9, J7, J12, J14 and J19) are excluded.

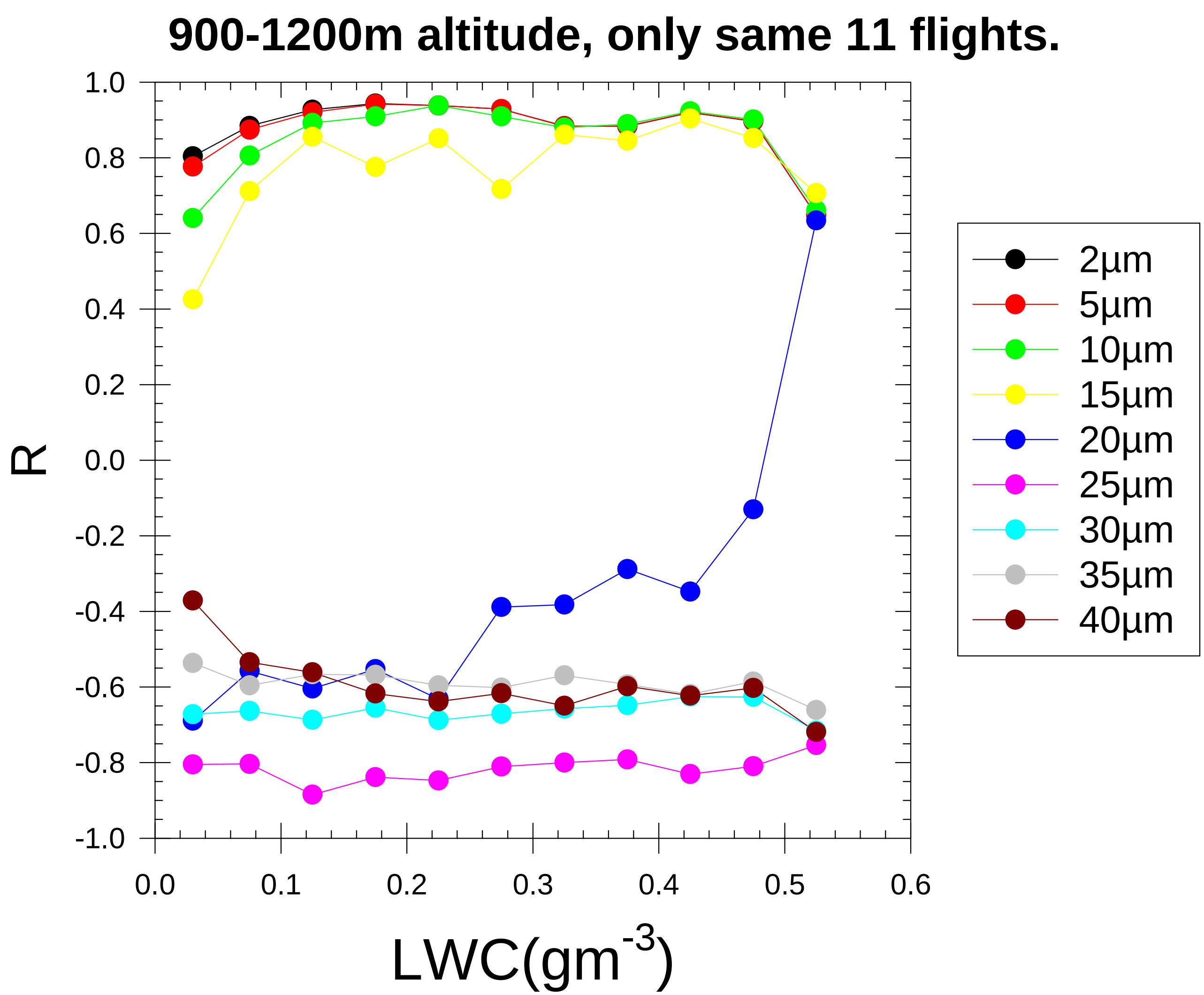

Figure 30. As Fig. 28 except that the data are from 900-1200m altitude range. The same data shown in Fig. 29.

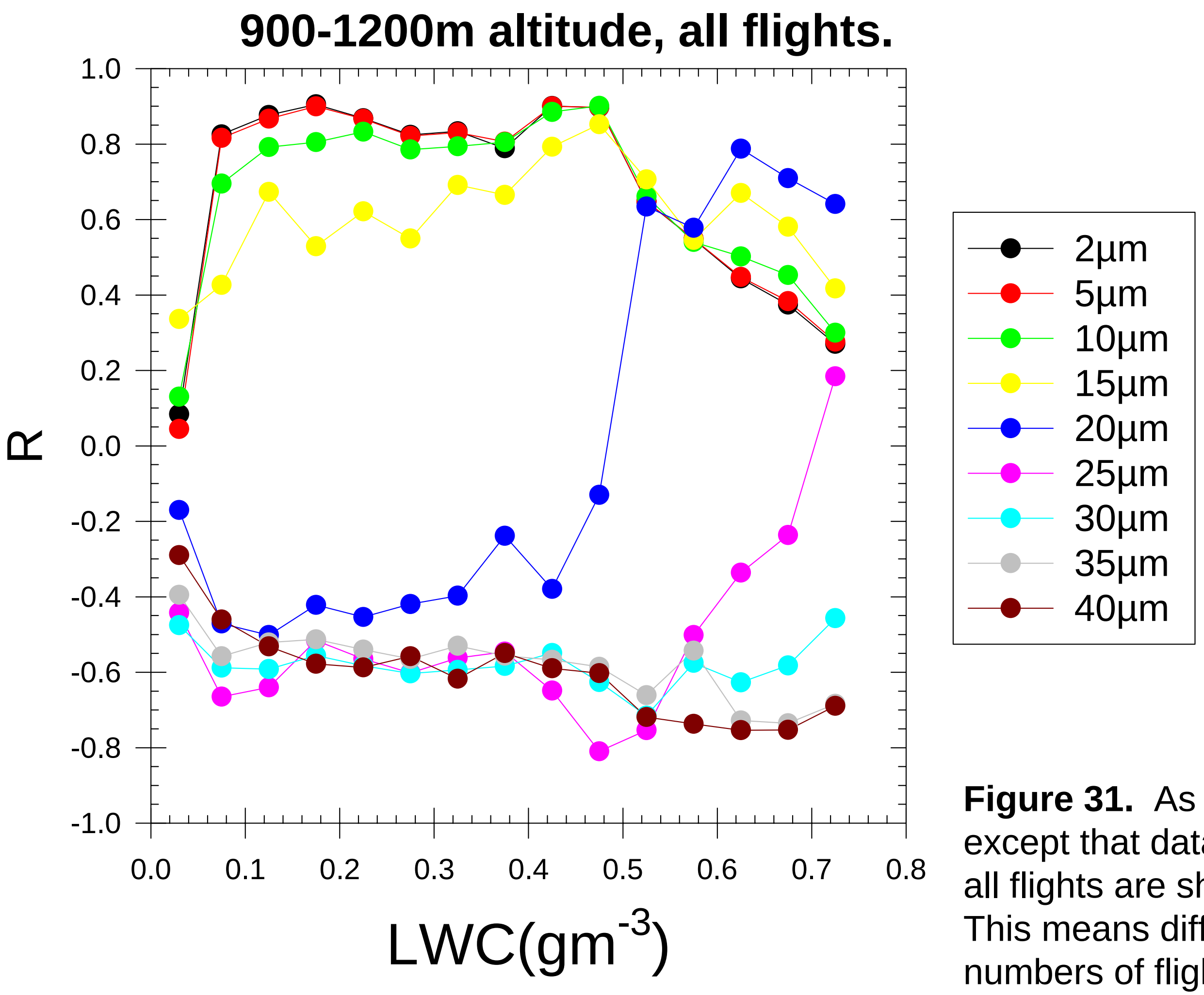

Figure 31. As Fig. 30 except that data from all flights are shown. This means different numbers of flights in the different LWC bands; six flights for 0.70-0.75, seven flights for 0.65-0.70, eight flights for 0.55-0.65, eleven flights for 0.45-0.55, twelve flights for 0.40-0.45, thirteen for 0.35-0.40, fifteen for 0.25-0.35, fourteen for 0.10-0.25 and sixteen for 0.01-0.10 g m-3.

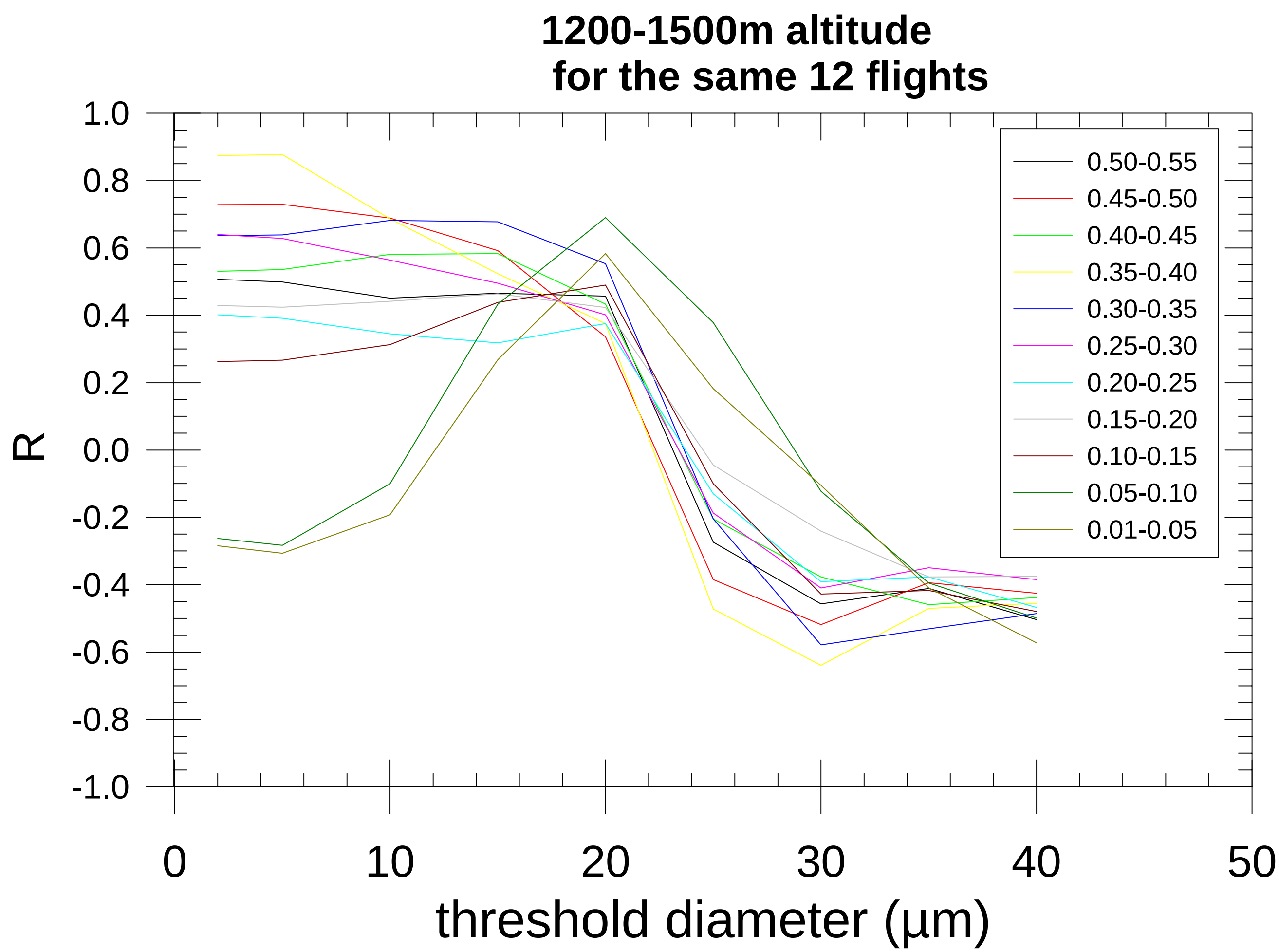

Figure 32. As Fig. 29, but for 1200-1500m altitude range. There are twelve flights with data in all of these LWC bins. Here RF1, 2, 6, 13 and 15 (D7, D8, D16, J12 and J16) are excluded.

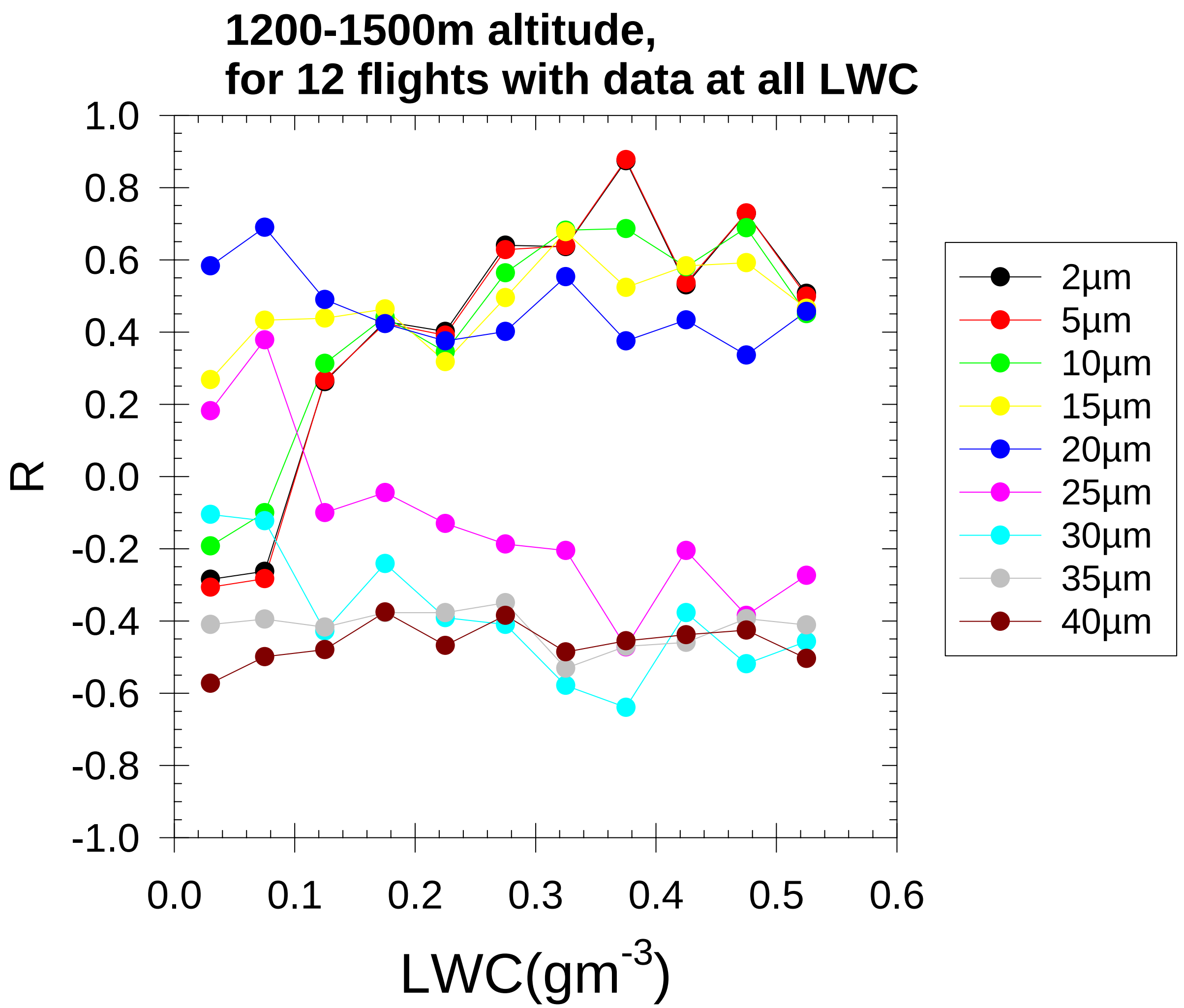

Figure 33. As Fig. 30 except that data are from 1200-1500m altitude range. The same data shown in Fig. 32.

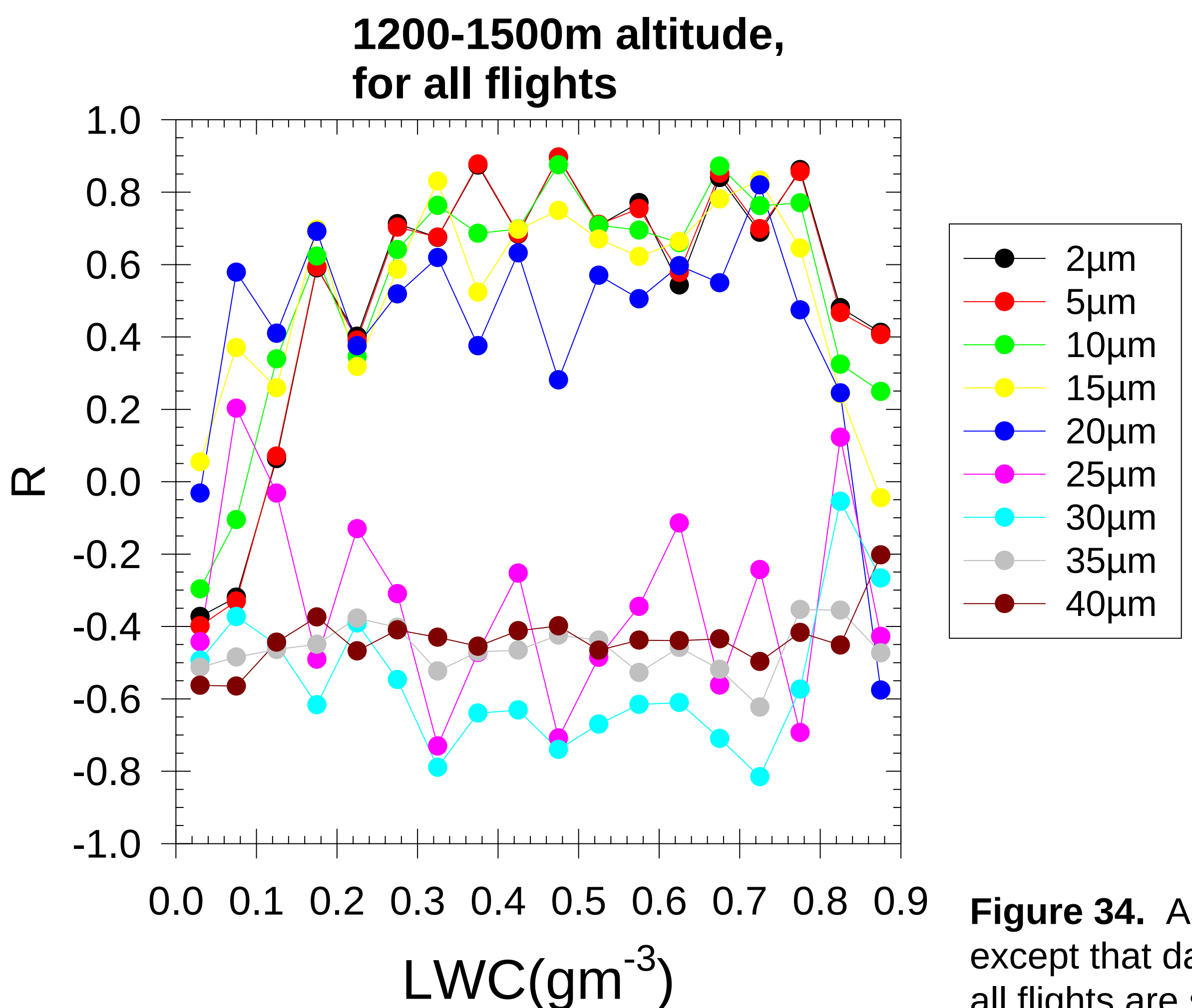

Figure 34. As Fig. 30 except that data from all flights are shown.

Five flights for 0.85-0.90, seven flights for 0.80-0.85, nine for 0.75-0.80, eleven for 0.60-0.75, thirteen for 0.55-0.60, 0.40-0.50 and 0.25-0.35, fourteen for 0.50-0.55 and 0.15-0.20, twelve for 0.35-0.40 and 0.20-0.25, fifteen for 0.05-0.15, and sixteen for 0.01-0.05 g m-3 LWC.

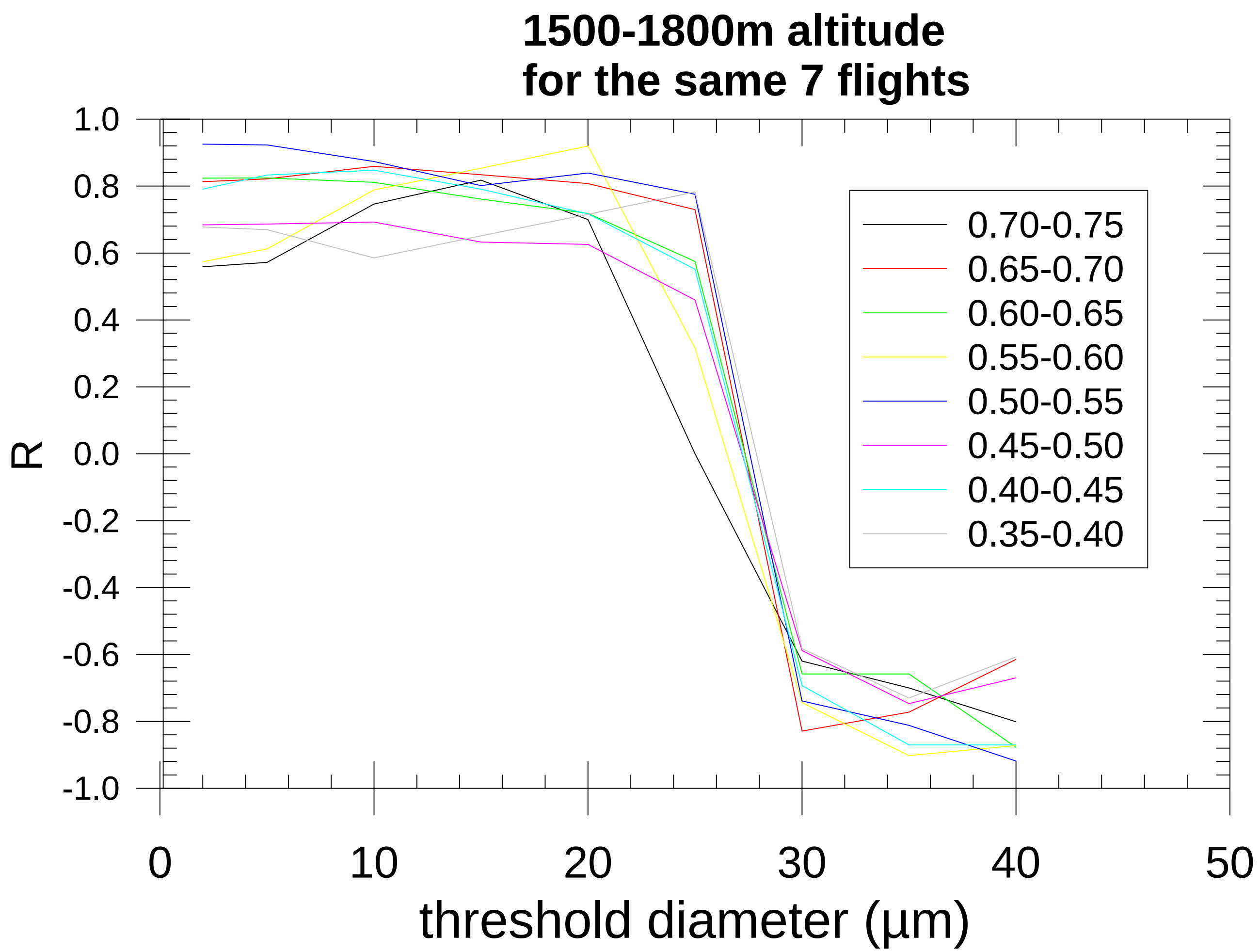

Figure 35. As Fig. 32, but for 1500-1800m altitude range. Here there are only 7 flights with data in all of the LWC bins shown. Here there is no data for RF1, 2, 3, 4, 6, 9, 11, 12, 13 and 17 (D7, D8, D9, D10, D16, D20, J7, J11, J12, J19).

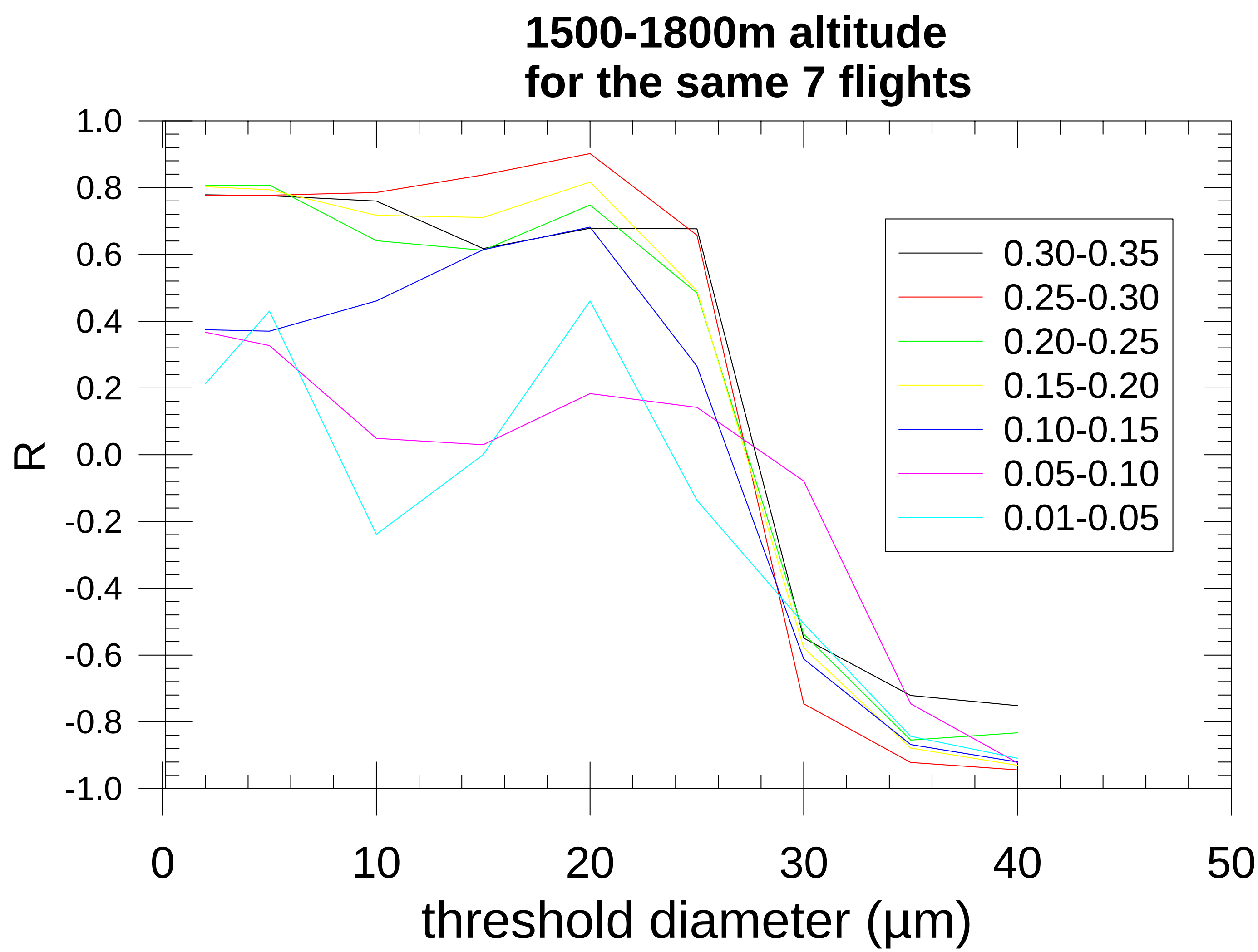

Figure 36. As Fig 35 for lower LWC bins. With so many more bins at this altitude it is necessary to use two figures.

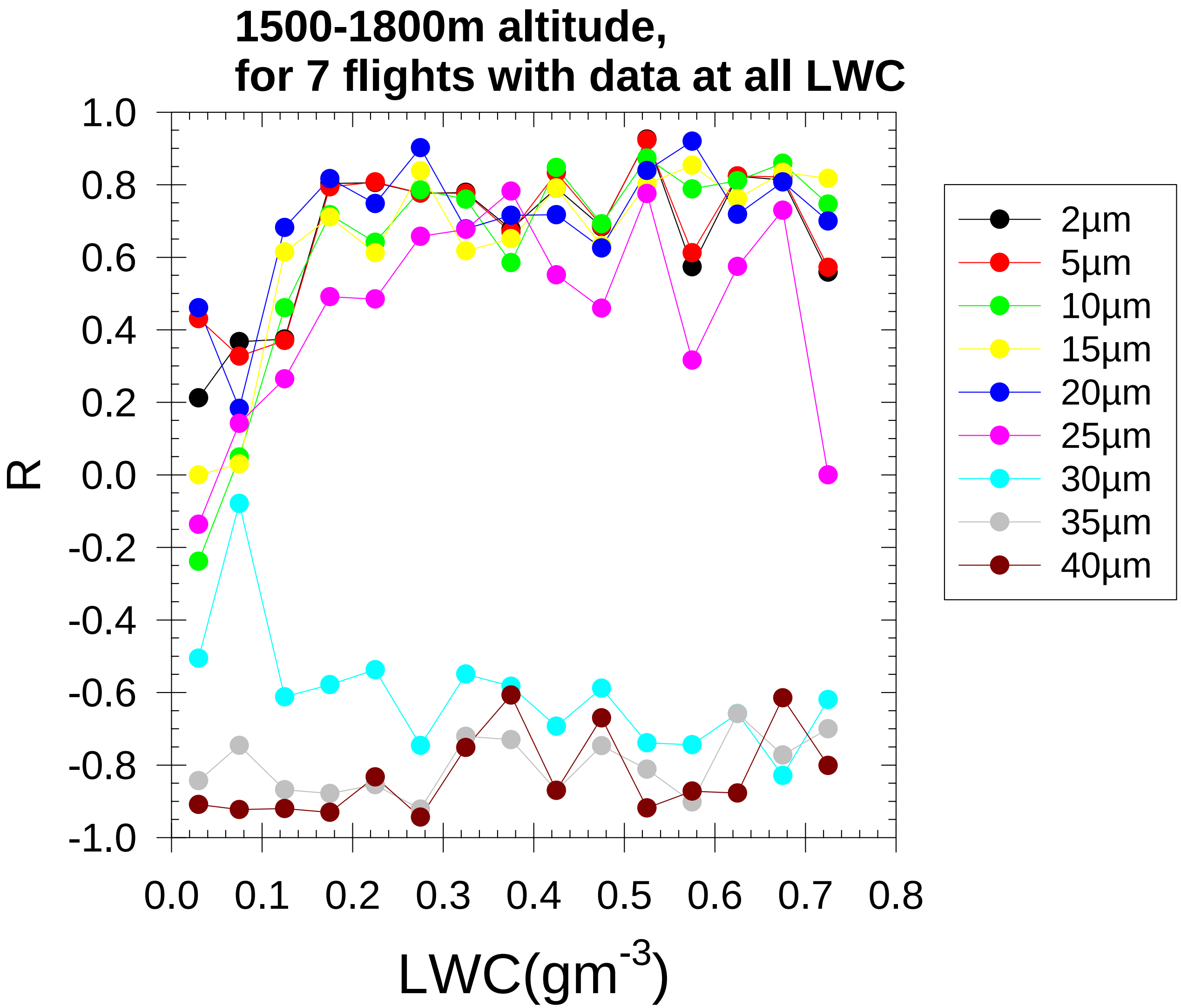

Figure 37. As Fig. 33 except that data are from 1500-1800m altitude range. The same data as shown in Figs. 35 and 36.

MEASUREMENT OF NATURAL ICE NUCLEI BY CONTINUOUS-FLOW THERMAL-DIFFUSION-CHAMBER TYPE ICE NUCLEUS COUNTER

Atsushi SAITO[1], Masataka MURAKAMI[1]

[1]Meteorological Research Institute/ Japan Meteorological Agency, Tsukuba, Japan

1. INTRODUCTION

Ice crystals play an important role in precipitation processes and affect precipitation forecast. Ice crystals also determine microphysical and radiative properties of clouds and affect the earth's climate system through modulations of coverage and life of clouds and precipitation distributions. Therefore, understanding of activation processes of natural ice nuclei and knowledge of spatial and temporal distributions of ice nuclei are very important from the viewpoint of both short range precipitation forecast and climate change prediction.

Studies on ice nuclei have been continued for more than 60 years, However many things remain unsolved.

The cloud physics group of MRI (Meteorological Research Institute) has been studying ice initiation processes through field observation, laboratory experiment and numerical modeling for many years. As a part of the study, we built a Continuous Flow Diffusion Chamber (CFDC) based on the design of Rogers et al. (1988, 2001) at Colorado State University, USA and have improved it to operate automatically.

This paper describes the performance of MRI-CFDC through examples of measurements on activation spectrum of ice nuclei in the atmosphere and test aerosol particles prepared during the International Workshop on Comparing Ice Nucleation Measurement Systems (ICIS-2007).

Rack A: front view

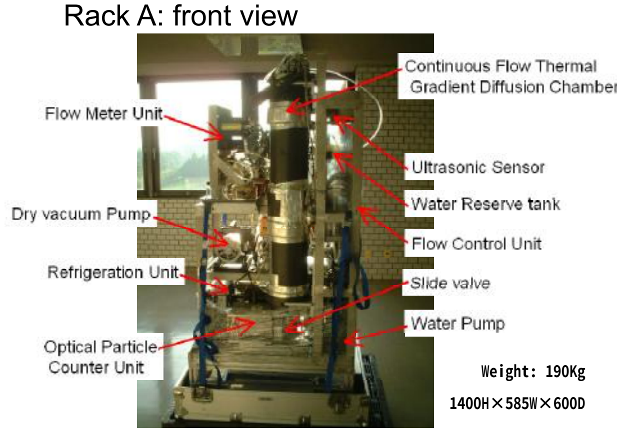

Rack B: front view

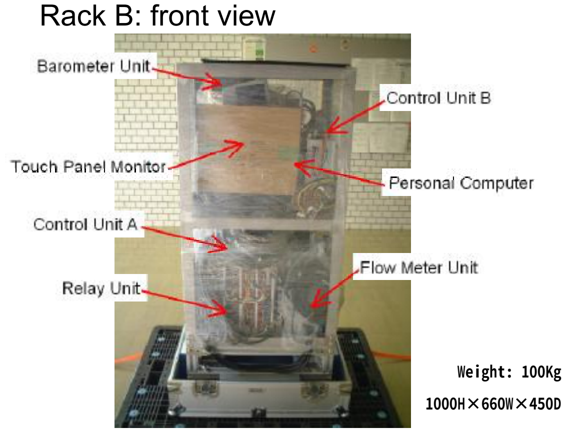

Figure 1.Rack mount arrangement for MRI-CFDC instrument.

[1] *Corresponding author's address:*
Atsushi SAITO, Meteorological Research Institute/ Japan Meteorological Agency, 1-1 Nagamine, Tsukuba, Ibaraki, 305-0052 Japan; E-mail: asaito@mri-jma.go.jp

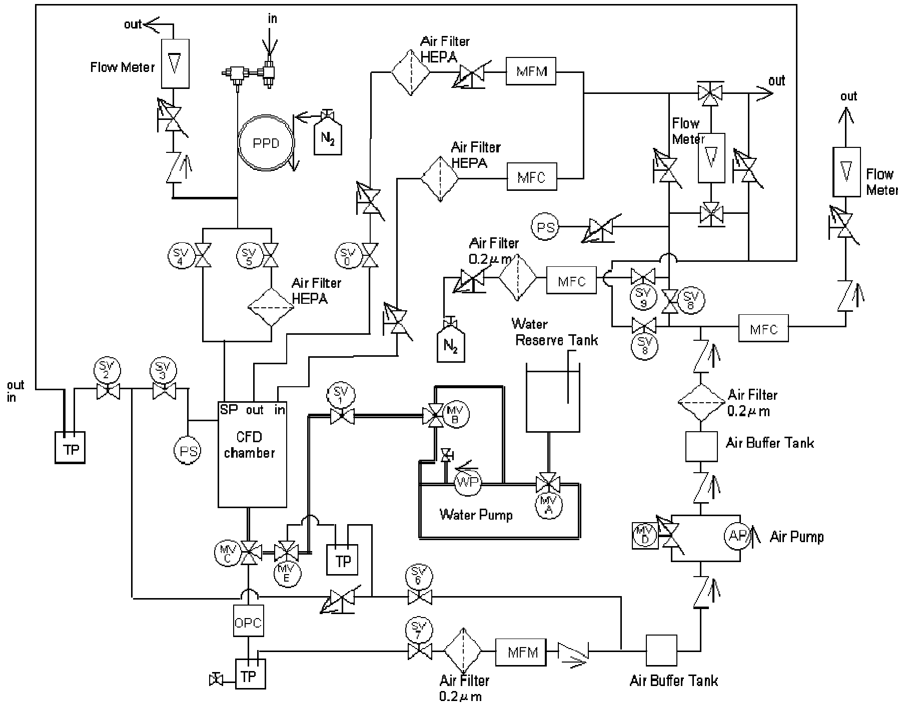

Figure 2. Airflow and waterflow diagram of MRI-CFDC

2. APPARATUS DESCRIPTION

We built a Continuous Flow Diffusion Chamber (CFDC) based on the design of Rogers et al. (1988, 2001) at Colorado State University, USA and have improved it to operate automatically. Main improvements are

1) decreasing heat inertia of inner cylinder so as to control wall temperatures more quickly.
2) automatic measurement of temperature and supersaturation spectrum of ice nuclei activation for a fully-automated operation and efficient measurement of activation spectrum.
3) automatic procedure to ice cylinder walls for a fully-automated operation.

Figure 1 shows the rack mount arrangement for MRI-CFDC instrument.

Airflow and waterflow diagram of MRI-CFDC is shown in Figure 2. Specifications of MRI-CFDC are as follows.

- Sample flow rate is 1.0L/min.
- Temperature range is -10℃ ~ -35℃.
- Humidity range is from RHi = 100% to RHw = 110%.
- Particle detector is OPC (0.5~8 μm).
- Inlet impactors remove particles > 1 μm or > 2 μm.
- Nucleated ice particles are determined by size > 2.5 μm or > 3 μm, respectively.

It is possible to control temperature and humidity of the sample air by controlling ice-coated wall temperatures of inner and outer cylinders. Figure 3 shows the time series of temperatures of warm and cold wall and temperature, SSi and SSw of sample air

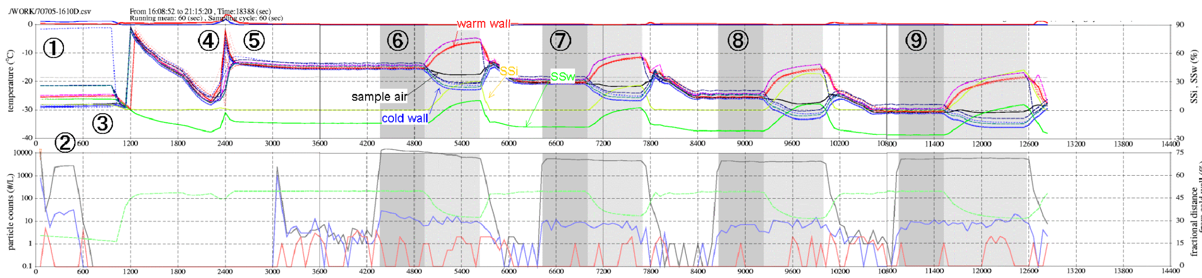

Figure 3. Time series of temperatures of warm wall, cold wall and sample air, SSi, SSw (upper panel), number concentrations of particles with d < 3 μm, 3 μm < d < 8 μm, d > 8 μm, and fractional distance of sample air from cold wall (lower panel).

(upper panel), number concentrations of particles with d < 3 μm, 3 μm < d < 8 μm, d > 8 μm, and fractional distance of sample air from cold wall (lower panel). Measurements of ice nuclei activation spectrum at 4-5 different temperatures and in the humidity range of RHi=100% to RHw=110% were automatically made within 2-3 hours.

The numbers in Figure 3 indicate the automated procedures for the measurements of ice nucleus activation spectrum:

① Initialization of airflow rate and valve setting
② Introduction of the sample (1L/min) and sheath air (9L/min)
③ Measurement of the background noise
④ Icing walls
⑤ Preparation for the measurement
⑥ Target temperature: -15°C
⑦ Target temperature: -20°C
⑧ Target temperature: -25°C
⑨ Target temperature: -30°C

3. MEASUREMENTS

Example of ground-based measurements of aerosol particles and ice nuclei in the summer of 2007 in Japan is shown in Figures

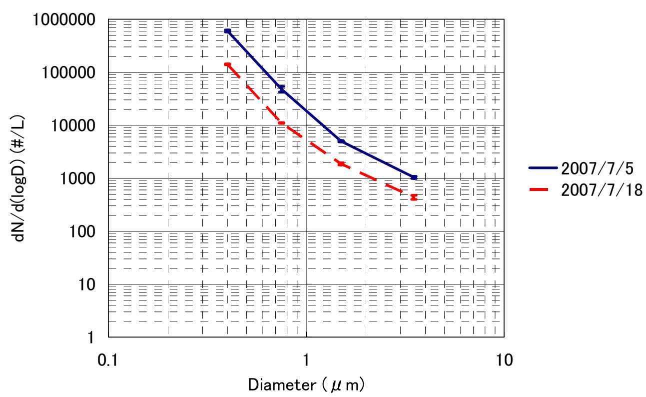

Figure 4. Aerosol size distributions on July 5th and July 18th.

4 and 5. Figure 4 shows size distributions of aerosol particles ranging from 0.3 to 5 μm on 5th and 18th July 2007. Figure 5 shows the number concentrations of activated ice nuclei as a function of temperature and supersaturation with respect to water. Although ice nuclei tend to increase with decreasing temperature and increasing relative humidity in general, the temperature dependency of ice nuclei on 18th July is stronger than that on 5th July. Figure 6 shows that the relationship between the concentrations of ice nuclei activated at water saturation and the total number concentrations of aerosol particles in July 2007. The difference in the temperature dependency of activated ice nuclei concentra-

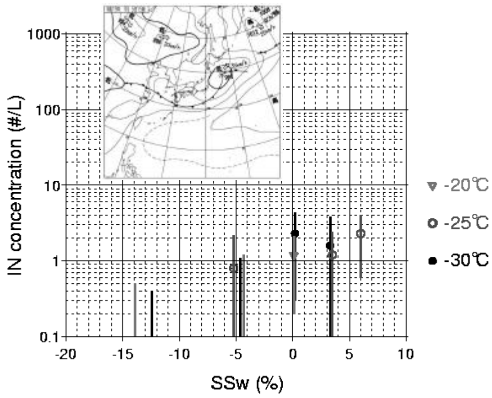

Figure 5. Ice nuclei activation spectrum and weather chart (left: July 5th, right: July 18th).

tions on 5th and 18th July is clearly shown in Figure 6. The remarkable changes in aerosol concentrations and ice nuclei activation spectrum occurred on July 15th. Before July 15th, the observation site was located on the north side of the seasonal rain front, and a tropical cyclone passed through the observation area on July 15th and brought maritime air mass to the area (Figure 5).

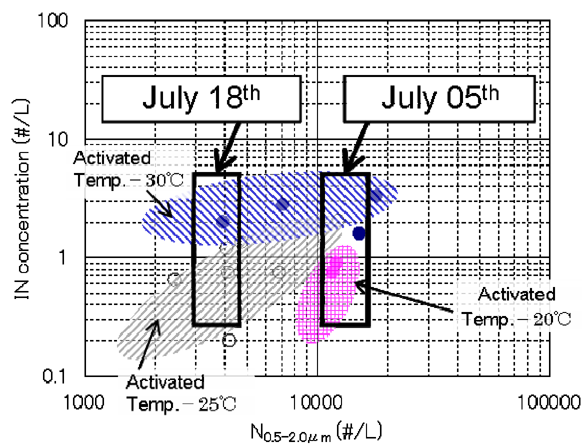

Figure 6. The relationship between the concentration of ice nuclei with water saturation and the total number of aerosol particles in July 2007.

We attended ICIS-2007, which was held at the AIDA facility of the Institute for Meteorology and Climate Research (IMK-AAF) at Forschungszentrum Karlsruhe, Germany in September 2007, for the purpose of comparison among our automated CFDC ice nucleus counter and other group's ice nucleus counters. During the ICIS-2007 workshop, we measured high concentrations of aerosol particles from aerosol chamber (NAUA) and aerosol particles with much less concentrations from cloud simulation chamber (AIDA). Their physical and chemical properties were well characterized. Figure 7 shows the activated fraction of sub-micron Arizona Test Dust (ATD) particles. ATD particles began to be activated at -25 ℃ through condensation-freezing nucleation mode. At -35℃ they began to be activated at 93% of relative humidity with respect to water through deposition nucleation mode, and showed a rapid increase in concentrations of activated ice nuclei beyond water saturation, which is probably due to the transition from deposition to condensation-freezing mode. Figure 8 shows the conditions (temperatures and RHi) for which 0.01% (0.0001 fractions) of aerosol particles was activated for ATD and bacteria

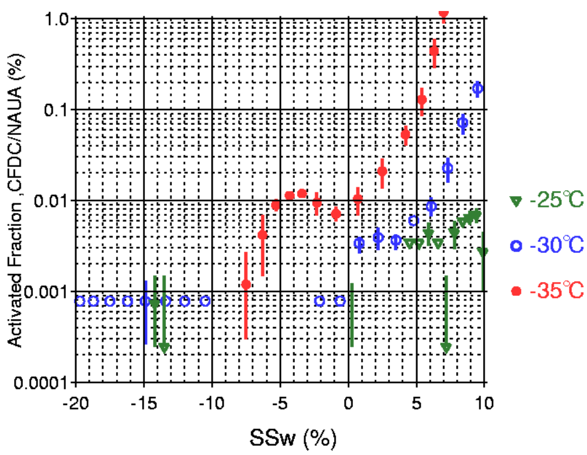

Figure 7. Activated fractions of ATD as a function of temperature and supersaturation with respect to water.

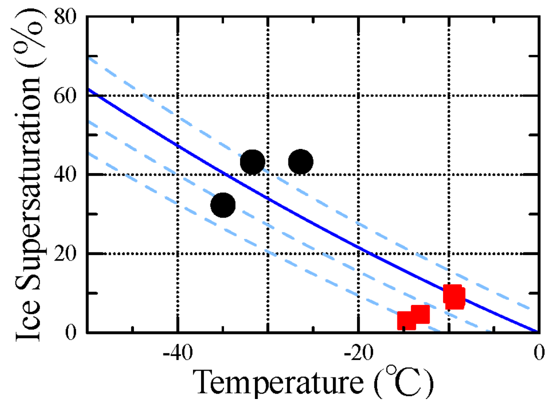

Figure 8. Conditions (temperature and ice supersaturation) for which 0.01% activation of particles was activated for ATD (black dots) and Snomax® (red squares).

(Snomax®). Snomax® particles were easily activated through condensation-freezing mode at temperatures as warm as -9℃ and started to be activated through deposition mode at temperatures colder than -12℃.

4. CONCLUSIONS

Ground-based measurements in summer time in Japan showed that the concentration of natural ice nuclei activated under the condition of water saturation was about one particle per liter at -20℃, and ten particles per liter at -30℃. The concentrations of activated ice nuclei increase with decreasing temperature and with increasing relative humidity.

On the other hand, laboratory measurements during ICIS-2007 workshop showed aerosol type dependency of activation spectrum and a rapid increase in concentrations of activated ice nuclei beyond water saturation, which is probably due to the transition from deposition to condensation-freezing mode.

Thus it appears that MRI-CFDC can measure ice nuclei for identifying and quantifying the mechanism of the ice initiation. And our future plan includes the followings.

1) Calibrating the relative humidity that MRI-CFDC produced in sampling air flow.
2) Discriminating ice particles from water droplets.
3) Enhancing refrigeration ability.
4) Using it for continuous ground-based measurements and aircraft measurement and for simultaneous measurements with MRI dynamic cloud chamber.

ACKNOWLEGEMENTS

This study is supported by the Ministry of Education, Culture, Sports, Science and Technology of the Japanese Government under the program of Special Coordination Funds for Promoting Science and Technology, “Japanese Cloud Seeding Experiments for Precipitation Augmentation (JCSEPA)”. The European Network of Excellence ACCENT financially supported for the attendance of ICIS-2007.

BIBLIOGRAPHY

Rogers, D. C., 1988: Development of a continuous flow thermal gradient diffusion chamber for ice nucleation studies. Atmos. Res., 22, 149-181.

Rogers, D. C., and et al., 2001: A continuous-flow diffusion chamber for airborne measurements of ice nuclei. J. Atmos. Ocean. Technol., 18, 725-741.

ATMOSPHERIC PARTICLES ACTING AS ICE FORMING NUCLEI IN DIFFERENT SIZE RANGES

G.Santachiara[1], L. Di Matteo[1] , F.Prodi[1,2] and F.Belosi[1]

[1]Institute ISAC-CNR, Clouds and Precipitation Group, Bologna, Italy
[2]Department of Physics, University of Ferrara, Dept. of Physics, Ferrara, Italy

1- INTRODUCTION

Aerosol particles that catalyze the formation of ice crystals in cloud are called Ice Forming Nuclei (IFN or IN) and can form ice through different thermodynamic mechanisms or modes: deposition (or sorption), condensation-freezing, immersion and contact.
A wide variety of measurement techniques have been developed over the past 50 years for detecting IN and measuring their characteristics. These techniques include drop freezing, particle capture on supercooled droplets, particle sampling on filters followed by processing in static or dynamic chambers, continuous flow ice thermal diffusion chamber, and others.
It is generally agreed that ice will form on nuclei in response to different kinds of thermodynamic forcing, the primary variables being temperature and supersaturation with respect to ice and water (S_{ice} and S_w, respectively).
Even after 50 years of ice nuclei studies, a calibration ice nucleating material does not exist, and there is no general agreement on a standard technique for measuring IN.
Ice nucleation measurement comparison workshops were held in the United States in 1970 and 1975. Measurements from the various instruments did not produce tight quantitative agreement, but important factors for IN activation were identified, including sensitivity to vapour supersaturation, competition for vapour in filter processing, increasing activity with particle size.
Another important conclusion was the need to study with deeper insight the nucleation mechanisms.
The main goals of our experimental campaign can be summarized as follow:
a) Comparison of IN concentration in different size ranges, supersaturations and temperatures. b) Check a diurnal trend in the IN concentrations. c) Investigate the relationship between IN and condensation nuclei (CN).

2- EXPERIMENTAL

An experimental campaign was performed at a rural site (S.Pietro Capofiume, near Bologna) covering the period 09 -12 July 2007.
Simultaneous samplings of various aerosol fraction were taken on nitrocellulose membrane (Millipore HABG04700, nominal porosity 0.45 µm) of various aerosol fraction, i.e. PM1, PM2.5, PM10 and total suspended particles (PTS), four times a day (period 06 -22 h), at 3 m above ground level. The mean flow rate was 38.3 lpm with a sampling time of 10 min.
In addition the aerosol was sampled by means of an inertial spectrometer (INSPEC), which separates the particles on the basis of their aerodynamic size (Prodi et al., 1979). The flow rate was 20 l per hour and the sampling time was usually 12h, representing day-time and nigh-time samples.
Simultaneous measurements of particle number concentrations (CNC-TSI–Mod.3020, with 50% detection at ~10nm) and particle concentration in 15 different size classes starting from 0.3 µm (Optical Spectrometer Grimm, Mod.1.108) were also performed.
Meteorological data (air temperature, wind speed, pressure) were recorded and the range of temperature, relative humidity (r.h.) and wind speed is reported in Table 1. The atmospheric pressure was about 1010 mbar.

Table 1 – Details of the sampling campaign

Date of sampling	T, °C	r.h., %	v, m s^{-1}
09/07	25.4 -32	31-39	1.3-3.5
10/07	18.5 – 27.6	30-59	1.9-3.2
11/07	13.3-22.7	43-87	0.3-2.4
12/07	14.1-26.2	36-71	0.9-1.9

Concentrations of IN were detected by the membrane filter technique, using a continuous diffusion chamber, which allows the control of the filter and of the air temperature, the latter saturated with respect to ice, thus obtaining different supersaturations. With this device the problem of competition among the nuclei on the filter for the vapour supply is minimized.
For each sampling, PM1, PM2.5, PM10 and PTS filters were cut into four pieces, and one piece for each fraction was inserted into the same metal plate in the diffusion camber and simultaneously developed.
The nucleation event was detected by counting on a monitor the number of ice crystal growing on the sampled filter, lighted with a grazing light.
Fig. 1 shows an example of ice crystals grown on different aerosol size range in the diffusion chamber.

Fig.1 – Picture of ice crystals grown on different aerosol size range

Measurements were made also at high supersaturation (Table 2), even through the common understanding is that the maximum supersaturation rarely exceeds 1% or 2% in natural clouds.

Table 2 – Operating conditions

T_{air} ,°C	T_{filter} , °C	S_{ice} , %	S_w , %
-15	-17	20	2
-15	-18	32	10
-17	-19	21	0

As a matter of fact the discrepancy between the concentration of ice nuclei and of ice crystals observed in clouds (Mossop et al., 1972) could be attributed to an occasional occurrence of very high supersaturations in clouds. During the entire freezing process the temperature of drop is 0°C , heat and water vapour are released into the surrounding air, whose temperature is lower than 0°C, and a region of supersaturated water vapour surrounds a freezing drop. Within this region of high supersaturation aerosol particles can act as CN or even IN (Rosinski, 1979).

3 - RESULTS AND DISCUSSION

Figs. 2, 3 and 4 show the time series of concentrations of aerosol particles active as IN in conditions reported in Table 2.
Measurements below water saturation should allow to detecte deposition (sorption) nuclei, while those above water saturation allow the detection of deposition and condensation-freezing nuclei.

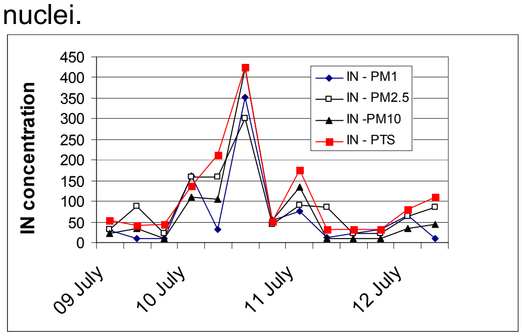

Fig.2 - Time series of concentrations of IFN (m^{-3}) active at T_{air} = -15°C, T_{filter}=-17°C

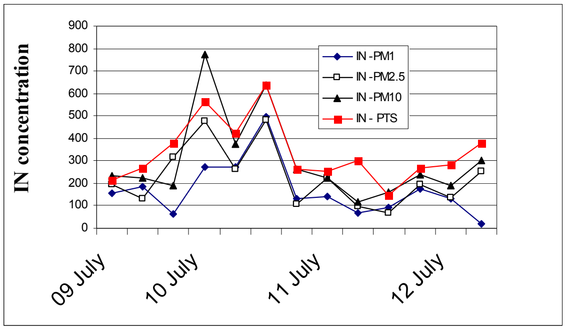

Fig.3 - Time series of concentrations of IN (m^{-3}) active at Tair = -15°C, Tfilter= -18°C

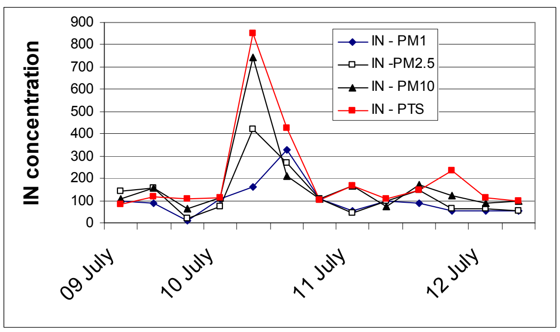

Fig.4 - Time series of concentrations of IN (m^{-3}) active at T_{air} = -17°C, T_{filter}=-19°C

From Table 3 it can be observed that PM1 fraction of the aerosol contributes to about 50% of the total measured IN for the atmospheric air sampled. Since the concentration of aerosol particles in the fine fraction is much higher than in the coarse one, it can be inferred that the nucleation efficiency, i.e. the fraction of natural aerosol particles nucleating ice at some given temperature and supersaturation, increases with increasing particle size. The increased ability of larger particles to act as freezing nuclei is counteracted in nature by the decrease in the concentration aerosol particles with increasing size.
This is in agreement also with the measurements performed with the INSPEC.

Table 3 –Percentage of IN obtained in PM1, PM2.5, PM10 fraction with respect to IN measured in the total suspended aerosol

	IN_{PM1} / IN_{PTS}, %	**$IN_{PM2.}$ / IN_{PTS}, %**	**IN_{PM10} / IN_{PTS}, %**
S_{ice}=20%; S_w =2%	61	82	70
S_{ice}=32%;S_w =10%	50	67	90
S_{ice}=21%;S_w =0%	49	62	83

The ratio between IN measured in the PM10 fraction and those in the PTS ranges from 70 to 90%, i.e. the dominant fraction of aerosol that can be activated concerns particles with aerodynamic diameter less than 10 µm.
It is observed a positive correlation between higher S_w and S_{ice} values and IN concentration numbers. As a matter of fact the variation of filter temperature from -17°C to -18°C (T_{air} = -15°C) determines an increase of about three times (from 110 to 337 m^{-3}) in the IN average number concentration.
Experiments with S_{ice} =21% and S_w= 0% (prevalently deposition nuclei) gives an IN concentration (about 200 m^{-3}) between values obtained at S_{ice}=20%; S_w =2% and S_{ice}=32%;S_w =10% (110 and 337 m^{-3} , respectively).
For comparison, Castro et al. (1998) in a rural area, far away from any potential source of pollution, measured at ground level a background concentration of IN active at -15°C, -19°C and -23°C at water saturation, of 7, 35 and 95 l^{-1}. There is not correlation between IN measured in the different size range and number particle concentration measured with the counter spectrometer (D>0.3 µm) and CNC, even if we can observe that the highest IN concentrations, measured when air masses came from west (10/07/2007), are coupled with high values of CN (Fig.5). Lower IN concentration values were measured when air masses came from N-NE.

The ratio of IN to CN concentration, depending on T, Sice and Sw , in our measurements ranges from about 1:108 to 1:10^7. IN constitutes a very small fraction of the aerosol population.

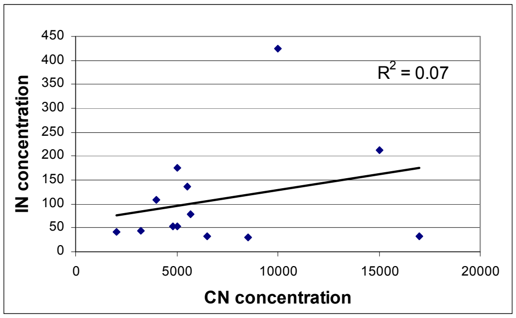

Fig. 5 – Correlation between IN measured (T_{air} = -15°C ; T_{filter} = -17°C) in total suspended aerosol (m^{-3}) and CN concentration (cm^{-3})

There is no correlation between particle number measured with the optical counter and CN concentration (Fig.6). Therefore, it can be concluded that the variation in the particle concentration during the experimental campaign is mainly due to particles smaller than 0.3 µm.

A few filters sampled with INSPEC during day (6 -18h) and night time (18-06 h) do not allow to evidence a diurnal trend in the IN concentration.

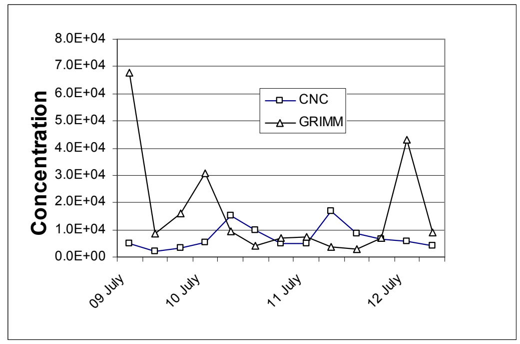

Fig.6 - Time series of particle concentration measured with optical (l^{-1}) and CN counters (cm^{-3}) .

BIBLIOGRAPHY

Mossop, S.C., R.E. Cottis and B.M. Bartlett, 1972: Ice crystal concentration in cumulus clouds. Quart.J. Royal Meteor. Soc., 98, 105-123.

Prodi, V., Melandri, C., De Zaiacomo, T., Formignani, M., Tarroni, G., 1979: An Inertial Spectrometer for Aerosol Particles. J. Aerosol Sci. 101, 411-419.

Rosinski, J. , 1979: The role of natural and man-made ice-forming nuclei in the atmosphere. Advances in Colloid and Interface Science, 10, 1979, 315-367.

ORGANIC COMPOUNDS AS DEPOSITION NUCLEI BEFORE AND AFTER OXIDATION

Ashley Shackelford and Will Cantrell
Department of Physics
Michigan Technological University
Houghton MI 49931 USA

1. INTRODUCTION

Biomass burning contributes to overall atmospheric aerosol and ozone concentrations. Although at times natural, the majority of this activity (such as burning land for clearing) is anthropogenic. Biomass burning, in conjunction with deep convection, has the potential to quickly transport high molecular weight organic compounds into the upper troposphere, which could affect cirrus cloud formation through heterogeneous nucleation processes. Enhancing the concentration of these aerosol, which could increase cirrus cloud development, could affect earth's radiation budget and, thus, temperature distribution.

Not only is the concentration of atmospheric organic aerosol increased during biomass burning, but the properties of the constituent compounds can also be altered through oxidation by (for example) ozone or OH radicals. Frequently such oxidation results in the formation of polar head groups, which interact more strongly with water. The relatively slow dissolution of high molecular weight organics, coupled with the cold temperatures and low water content of the upper troposphere create prime environmental conditions for deposition nucleation.

In order to better understand this process, we initially gather a general understanding of the nucleation rates for various compounds affiliated with biomass burning. Determining the rates at which these compounds act as deposition ice nuclei will enable a better understanding of the contribution that biomass burning has on the formation of cirrus clouds. Following this analysis we expose the system to an oxidizing agent such as ozone or OH radicals and once again analyze the nucleation rates of the compound.

2. STUDY OF ICE NUCLEATION IN THE DEPOSITION MODE BY HIGH MOLECULAR WEIGHT ORGANIC COMPOUNDS.

Infrared spectroscopy is the principal tool for the investigation. It is uniquely suited to this topic since both organic compounds and water have characteristic absorption bands in the infrared. The positions of the symmetric and anti-symmetric stretch can be used to gage the degree of order within the organic film (Dluhy and Cornell, 1985). For instance, using the position and integrated absorbance of those two features, Ochshorn and Cantrell (2006) showed that the structure of films of heptadecanol changes in response to the changes in the structure of the water sub-phase as a function of temperature. Infrared spectroscopy not only determines the characteristics of organics, it also enables the presence of water vapor and ice to be quantified.

Careful control and measurement of the relative humidity (with respect to ice) is critical. As noted above, FTIR enables monitoring of

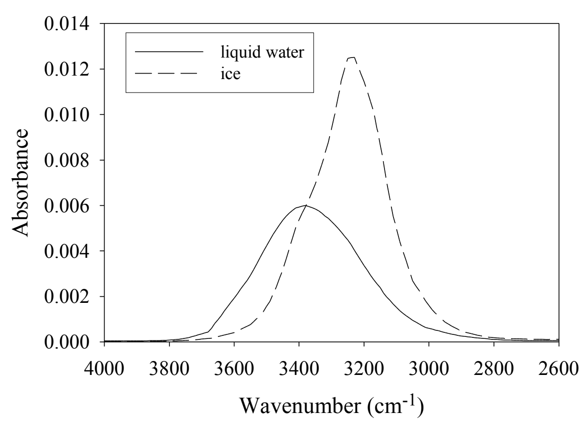

Figure 1: Calculated absorbances for films of water on an attenuated total reflection prism for both liquid (solid line) and ice (dashed line). Notice that the peak in the liquid water absorbance is approximately 3400 cm^{-1}, while the peak absorbance of ice is approximately 3200 cm^{-1}. In both cases, the thickness of the film is 15 nm.

the amount of water absorbed to the organic at any point during the study. Figure 1 is an illustration of the sensitivity. The magnitude of the absorption band of the condensed phase (liquid or ice) indicates the amount of water interacting with the organic, while the band position and shape provides information on the phase. The peak absorbance for liquid water is ~ 3400 cm^{-1} while peak absorbance for ice is ~ 3200 cm^{-1}. Because the optical cross sections are known in both phases, the area under the curve can be inverted to determine the amount of water in the condensed phase.

Representative compounds for study include octadecene, octadecanol, and oleic acid (cis-9 octadecenoic acid). The compounds are chosen not only because of their affiliation with biomass burning, but also because they have a wide range of characteristics such as functional groups (alcohols and acids), conformation, linearity, and saturation. Each functional group exemplifies unique characteristics when exposed to water vapor.

The presence of a functional group such as alcohol or acid should affect the way in which an organic compounds interacts with water, which has an intrinsic dipole moment. As a consequence, we expect that, octadecanol (for instance) would be associated with more water than octadecene at a given relative humidity. However, it is not clear whether more water will necessarily lead to a higher nucleation rate.

Once emitted to the atmosphere, organic compounds are oxidized, for example by O_3 a product of biomass burning, and OH radicals. Hearn and Smith (2004) have predicted that oxidation has the ability to increase the number of polar head groups in certain organic compounds. This could increase the organics' ability to act as deposition nuclei. For example, when 1-octadecene is oxidized by ozone the products include formaldehyde, formic acid, heptadecanal, and heptadecanoic acid (Hearn and Smith, 2004). In this case, a relatively poor deposition nucleator with a carbon-carbon double bond is cleaved during oxidation to form acid groups and aldehydes, both of which are hydrophilic. The new mixture of compounds will interact with water vapor in a different manner, which may lead to a higher nucleation rate (in the deposition mode).

3. REFERENCES

Dluhy, R., D.G. Cornell (1985), In-situ measurement of the infrared spectra of insoluble monolayers at the air-water interface. *Journal of Physical* Chemistry 89(15) DOI:10.1021/j10026/a006

Hearn, J. and G. Smith (2004). Kinetic and product studies for ozonolysis reactions of organic particles using aerosol CIMS. *Journal of Physical Chemistry* 108(45) DOI: 10.1021/jp0404145

Ochshorn, E. and W. Cantrell (2006). Towards understanding ice nucleation by long chain alcohols, J. Chem Phys., 124(5): Art. No. 054714.

Acknowledgments

Funding from the National Science Foundation (CHE-04100007) and NASA's New Investigator program is appreciated.

MEASUREMENT OF CLOUD CONDENSATION NUCLEI OVER NORTH CHINA

Lixin Shi[1], Yupeng Deng[1], Yan Jiang[1], Zhijun Zhao[1], Xiaobo Dong[1] and Zuohui Qi[1]

[1]Weather Modification Office of Hebei Province, China, 050021

1. INTRODUCTION

Cloud condensation nuclei (CCN) have close relation with cloud. With the increasing of global climate studies, the interest of cloud physics has shifted emphasis away from precipitation toward radiative properties (Hudson, 1993). CCN are the aerosol particles that can form cloud droplets. There is indirect effect arises from the possible influence of anthropogenic CCN. The first is Twomey effect that the increase in cloud droplets number concentration could increase the multiple scattering within clouds thereby increasing cloud-top albedo (Twomey et al., 1984; Platnick et al., 1994). The second is Albrecht effect that the increase in cloud droplet concentration may also inhibit precipitation development, enhancing cloud lifetime and resulting in an increase in planetary shortwave albedo (Albrecht, 1989) and possibly also in the atmospheric absorption of longwave radiation by the resultant increased atmospheric loading of liquid water and water vapour (Schwartz, 1996).

Observations of CCN in North China were made by Lixin and Ying (2007). The paper is to present the measurement of CCN and preliminary analysis of the relation of CCN and cloud droplet over North China.

2. INSTRUMENTATION

A Piper Cheyenne ⅢA twin turbo-prop aircraft was used for the observations. The cloud droplet was measured by a PMI (Particle Metrics Inc, USA) Forward Scattering Spectrum Probe FSSP-100ER. CCN were measured by a DMT (Droplet Measurement Technologies, USA) continuous flow streamwise thermal gradient CCN counter (Roberts et al., 2005). It has a cylindrical continuous flow thermal gradient diffusion chamber employing a novel technique by establishing a constant streamwise temperature gradient so that the difference in water vapor and thermal diffusivity yielding a quasi-uniform centerline supersaturation (S). An optical particle counter at the outlet of the chamber counts droplets with diameters larger than 0.75 μm. Those particles larger than 0.75 μm are considered activated CCN and comprise the CCN concentration. The temperature gradient and the flow though the column control the S and may be modified to retrieve CCN spectra. The instrument can operate between S = 0.1% and S = 2% at sampling rate of 1 Hz. CCN spectra can be derived by different supersaturation cycling measurements.

3. CASE ANALYSIS

The flight was performed on 21 May 2007. The non-precipitating stratiform cloud was observed with cloud top temperature more than 0°C. Cloud droplets were measured in traverse within 150m of cloud base. Sub-cloud CCN concentration was obtained at 0.1%, 0.2%, 0.3% and 0.5% saturation cycling measurements.

Fig.1 shows the flight track during cloud traverse and sub-cloud observation. The measurements of CCN and cloud droplet are given in Table 1. N_{CCN} is the averaged concentration, and N_{cd} is the averaged concentration of cloud droplet. It can be seen that the relation between N_{cd} and N_{CCN} is close at S=0.1%.

CCN spectrum can be fitted by the expression $N = CS^k$ (Twomey, 1959), where

N is the number of CCN activated at supersaturation S, C is the number activated at S=1%, and k is a constant.

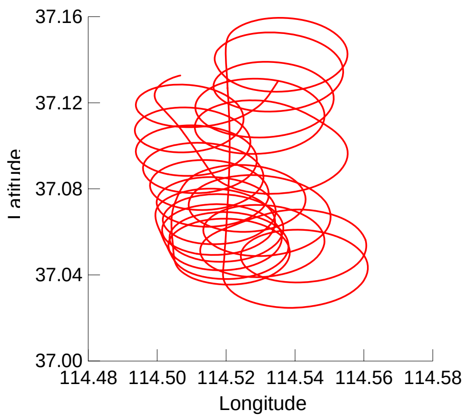

Fig.1 Flight track on 21 May, 2007

Fig.2 shows the sub-cloud CCN spectrum fitted by Twomey expression. The high values of C and k represent the polluted continental type of cloud.

Table 1 Sub-cloud CCN and cloud measurements

N_{CCN} (cm^{-3})				N_{cd} (cm^{-3})	N_{cd}/N_{ccn}
S=0.1%	S=0.2%	S=0.3%	S=0.5%	102	S=0.1%
207.89	1120.22	1962.91	2354.53		0.49

Twomey (1959) also derived a simple analytical approximation to obtain cloud droplet concentration from updraft velocity and a two-parameter fit to the CCN spectrum,

$$N_{cd} = C^{2/(k+2)}\left[\frac{0.069w^{3/2}}{kB(k/2,3/2)}\right]^{k/(k+2)}$$

where w is updraft velocity, B is the beta function, C and k are the fitted parameters from CCN spectrum.

Because there is no way to derive the updraft velocity (w) during the observation, the different w is assumed for calculating the N_{cd} by Twomey equation.

Table 2 Calculated N_{cd} at different w

W(cm s^{-1})	10	35	50
Predicted N_{cd} (cm^{-3})	213	483	609

Table 2 shows the predicted N_{cd} from Twomey equation at w=10, 35 and 50 cm s^{-1}. If Twomey equation could properly describe the relation between cloud droplet and updraft velocity, the lower velocity is suitable for the stratiform cloud in the case.

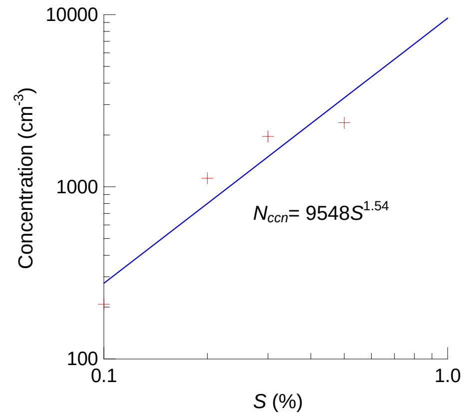

Fig.2 CCN spectrum below cloud base

4. DICUSSION

Twomey and Warner (1967) compared the cloud droplet concentrations with that computed from below cloud CCN spectrum with an updraft of 3 m s^{-1} in cumulus clouds. They found the high degree of agreement. Chuang et al. (2000) compared CCN data (S=0.1%) obtained during ACE-2 with cloud droplet data acquired by FSSP-100 in summer marine stratocumulus clouds. They found N_{cd} was closely related with sub-cloud CCN as N_{cd}~0.71N_{CCN} (R=0.9) or N_{cd}~$N_{CCN}^{0.31}$ (R=0.88). There is a relation of N_{cd}~0.49 N_{CCN} here, but it was derived only from one flight measurement, more observations need to be made.

REFERENCES

Albrecht B. A., Aerosols, cloud microphysics, and fractional cloudiness. Science, 245, 1227-1230, 1989

Chuang P. Y., D. R. Collins, H. Pawlowska, J. R. Snider,H. H. Josson, J. L. Brenguier, R. C. Flagan and J. H. Seinfeld, CCN measurements during ACE-2 and their relationship to cloud microphysical properties. Tellus, 52B, 843-867, 2000

Hudson J. G., Cloud condensation nuclei. J. Appl. Meteor., 32, 596-607, 1993

Lixin S. and Ying D., Observations of cloud condensation nuclei in North China. Acta Meteor Sinica, 65(4), 644-652, 2007. (in Chinese)

Platnick S. E. and S. Twomey, Determining the susceptibility of cloud albedo to changes in droplet concentration with the advanced very high resolution radiometer. J. Appl. Meteor., 33, 334-347, 1994

Roberts G. C. and A. Nenes, A continuous-flow streamwise thermal-gradient CCN chamber for atmospheric measurements. Aeros. Sci. Tech., 39, 206-221, 2005

Schwartz, S. E., Cloud droplet nucleation and its connection to aerosol properties, In Nucleation and Atmospheric Aerosols 1996. Edited by M. Kulmala et al., Oxford, Elsevier Science Ltd, 770-779, 1996

Twomey, S., The supersaturation in natural clouds and the variation of cloud droplet concentration. Geofis. Pura Appl., 43, 243-249, 1959

Twomey, S. and J. Warner, Comparison of measurements of cloud droplets and cloud nuclei. J. Atmos. Sci. 24, 702-703, 1967

Twomey S., M. Piepgrass, and T. L. Wolfe, An assessment of the impact of pollution on global cloud albedo. Tellus, 36B, 356-366, 1984

Acknowledgments

This work was supported by the National Natural Science Foundation of China under Contract 40475003 and the Natural Sciences Foundation of Hebei Province under Contract D2005000593.

CAPRAM MODELLING OF THE PHYSICO-CHEMICAL CLOUD PROCESSING OF TROPOSPHERIC AEROSOLS

A. Tilgner[1]*, R. Wolke[1] and H. Herrmann[1]

[1]*Leibniz-Institut für Troposphärenforschung, Permoserstr. 15, D-04318 Leipzig, Germany*

Keywords: CAPRAM, aqueous phase chemistry, aerosol-cloud-processing aerosol–cloud-interaction modelling

ABSTRACT Clouds and deliquescent particles are a complex multiphase and multicomponent environment with simultaneously occurring gas and aqueous phase as well as heterogeneous chemical transformations which potentially alter the physico-chemical composition of tropospheric aerosols. Moreover, chemical cloud interactions contribute significantly to the physico-chemical aerosol processing together with significant effects on the whole multiphase oxidation budget. In order to improve the still limited understanding of the cloud chemistry processing, detailed model studies using the SPectral Aerosol Cloud Chemistry Interaction Model (SPACCIM) have been performed.

The parcel model SPACCIM includes a complex microphysical and multiphase chemistry model. In chemistry model, the multiphase mechanism RACM-MIM2ext/ CAPRAM 3.0i with about 1100 processes was applied incorporating a detailed description of the tropospheric multiphase processes. Simulations were carried out for different environmental conditions using a non-permanent meteorological scenario. Furthermore, simulations were performed with and without aqueous phase chemistry to study the effects of aerosol-cloud interaction. The model results have been analysed including time-resolved source and sinks studies particularly focused on multiphase phase radical as well as non-radical oxidants and multiphase oxidations of C_2–C_4 organic compounds.

The model studies shows significant effects of multiphase cloud droplet and aqueous aerosol interactions on the tropospheric oxidation budget for polluted and remote environmental conditions as well as influenced VOC's oxidation due to the changed oxidation budget within the clouds. Furthermore, the simulations implicate the potential role of deliquescent particles to act as a reactive chemical medium due to the in-situ aqueous phase oxidant productions. Moreover, the model study shows the importance of the aqueous phase for the formation of higher oxidised organic compounds such as substituted mono- and diacids. In particular, the aqueous phase oxidations of methylglyoxal and 1,4-butenedial were newly identified as important OH radical sinks under polluted environmental conditions contributing to the production of less volatile organic compounds and thus the organic aerosol particle mass. Furthermore, the in-cloud oxidation of methylglyoxal and its oxidation products represents an efficient sink for NO_3 radicals in the aqueous phase. Additionally, the model studies have shown in-cloud organic mass productions up to about 1 µg m^{-3} preferably under polluted day time cloud conditions mainly due to OH initiated multiphase oxidation processes. Finally, the sum of the results implicates the importance of the aqueous phase processes to be considered in future higher scale multiphase chemistry transport models. Consequently, also a reduced CAPRAM mechanism describing the main inorganic and organic aqueous phase chemistry issues have been developed.

*Corresponding author. Tel.: +49341 235 2406;
fax: +49341 235 2325.
E-mail address: tilgner@tropos.de

1 INTRODUCTION

Clouds and deliquescent particles play a crucial role in the entire tropospheric multiphase system. Tropospheric clouds fill about 15% of the lower half of the troposphere [Pruppacher and Jaenicke, 1995] and are a complex multiphase and multi-component environment with simultaneously occurring gas and aqueous phase as well as heterogeneous chemical proceses. Even if the volume of clouds is relative small, multiphase processes can potentially alter the physico-chemical composition of the tropospheric aerosol on global scale [Ravishankara, 1997]. Moreover, chemical aqueous phase interactions contribute significantly to the physico-chemical aerosol processing together with effects on the whole multiphase oxidation budget.

Chemical aqueous phase components of deliquescent particles and cloud droplets are originated from the soluble fraction of the aerosol particles which can act also as cloud condensation nuclei (CCN) and from the dissolution of soluble trace gases as well as from scavenging processes. The multiphase processing of chemical components in the aqueous phase can influence both the chemical composition of the aerosol and the physical particle properties such as solubility, size and mass distribution. However, the understanding of physico-chemical modifications of the aerosol properties is currently still restricted chiefly because of the high complexity of multiphase interactions. While significant amount of work has been done regarding the in-cloud chemistry of inorganic species such as sulphur [Warneck, 1999], the aqueous phase chemistry of organic aqueous phase constituents and their oxidative effects are investigated to a much smaller extend.

In order to enhance the understanding of the system, a proper knowledge and description of both microphysical and multiphase chemistry processes are therefore crucial to appraise the role of the tropospheric aerosol processing. In this context, tropospheric multiphase models provide a very convenient instrument for investigating individual physico-chemical processes in detail. Consequently, models can help to improve the understanding of the aerosol cloud processing and to assess the relevance of tropospheric chemistry processes in a multiphase context. Recently developed as well as applied multiphase mechanisms [Herrmann et al., 2000, 2003, 2005; Ervens et al. 2003; Tilgner et al., 2005] and multiphase models [Wolke et al., 2005; Knoth, 2005] describe the physico-chemical processes occurring in the tropospheric multiphase environment predominantly in clouds. These more recent mechanisms and model studies have introduced also the importance of the in-cloud processing of soluble organic compounds by aqueous phase chemical processes. In context of an inorganic and organic multiphase environment, the Chemical Aqueous Phase RAdical Mechanism (CAPRAM) was developed for the application in multiphase models. The model studies in the past have been carried out mostly considering permanent cloud conditions which is expedient to investigate in-cloud aerosol modifications. However for more realistic studies of the physico-chemical aerosol cloud interactions as well as processing, model studies are necessary considering non-permanent cloud conditions. For this reason, the SPectral Aerosol Cloud Chemistry Interaction Model (SPACCIM; Wolke et al. [2005]) has been developed and applied to investigate the effects of the multiphase aerosol-cloud-interaction on tropospheric aerosol particle and trace gas constituents.

2 MULIPHASE CHEMICAL MECHANISM AND MODELLING

2.1 AQUEOUS PHASE CHEMISTRY MECHANISM CAPRAM

The chemical aqueous phase mechanism CAPRAM in its version 3.0 [Herrmann et al., 2005] is the most recent development of the CAPRAM series with a total of 777 reactions. CAPRAM 3.0 incorporates the former version CAPRAM 2.4 [Ervens et al., 2003] and an extended reaction mechanism for atmospherically relevant organic compounds containing more than two and up six carbon atoms. The chemistry of organic compounds containing one to four carbon atoms as well as different functional groups is described in detail with more than 400 reactions. Furthermore, CAPRAM 3.0 includes reactions involving OH, HO_2, NO_3, SO_4^-, Cl_2^-, Br_2^- and CO_3^- radicals with inorganics (transition metal ions (TMI), NO_3^-, Cl^-, Br^-). Both radical and redox reaction pathways are integrated in the N(III) and S(IV) oxidation. In fact, CAPRAM considers an explicit description of the S(IV) oxidation by radicals, iron (Fe^{3+}), peroxides, ozone and peroxy nitric acid as well. CAPRAM 3.0 is currently the most detailed aqueous phase mechanism and an adequate tool for studies of multiphase aerosol processing. Further specific details regarding the CAPRAM mechanism including mechanism tables, references, corrections, revisions and the corresponding CAPRAM 3.0 mechanism data base are available at the CAPRAM homepage[2].

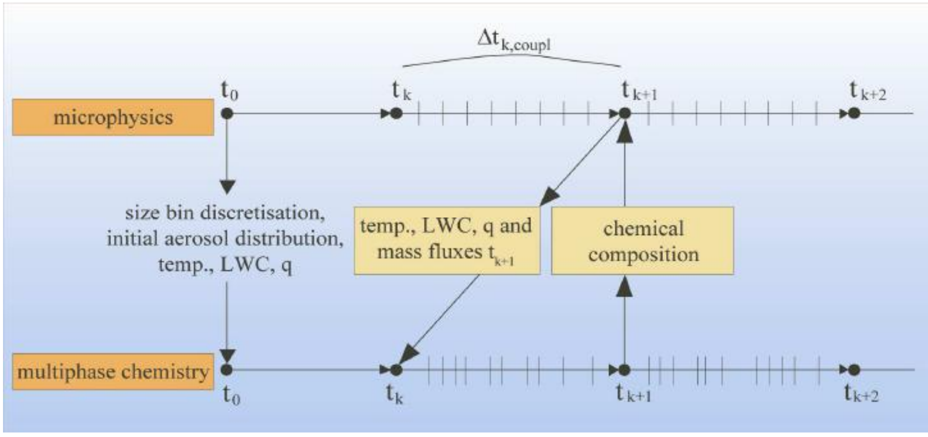

Figure 1. Schematic depiction of the SPACCIM model coupling of microphysics and chemistry.

2.2 ATMOSPHERIC MULTIPHASE MODEL SPACCIM

The air parcel model SPACCIM (Wolke et al. [2005]) was developed for the description of multiphase processes combining a complex multiphase chemistry mechanism and a detailed microphysical model. In SPACCIM the description of both separate processes is performed for a highly size-resolved particle and droplet spectrum. The model allows a detailed description of the processing of gases and deliquescent particles before the cloud formation, under cloud conditions and after cloud evaporation. The adiabatic air parcel model includes a description of microphysical processes of deliquescent particles and cloud droplets. All microphysical parameters required by the multiphase chemistry model are taken over from the microphysical model after a coupling time step (see **Figure 1**). In the performed model studies the coupling time step has been fixed at 10 seconds and the moving bin SPACCIM version has been used.

2.3 ACTUALISATION OF THE SPACCIM MODEL SIMULATIONS

In SPACCIM the complex aqueous phase mechanism CAPRAM 3.0 with 777 reactions was coupled to an updated and revised RACM mechanism (lumped gas phase mechanism with 281 reactions). The uptake processes of 52 soluble compounds are included in the mechanism following the resistance model approach by Schwartz [1986] considering Henry solubility, gas phase diffusion and mass accommodation coefficients.

The original gas phase mechanism RACM (Stockwell et al., 1997) was updated and revised. Particularly, the important iso-

[2] CAPRAM homepage: http://projects.tropos.de/capram/

prene oxidation has been updated with about 25 new reactions mainly based on the work Karl et al. [2006] including a detailed description of important oxidation products such as metacrolein and methylvinylketone. The further oxidation of methylvinylketone has been additionally implemented with 4 reactions after Zimmermann and Poppe [1996]. This oxidation chain leads to the formation of glycolaldehyde an important precursor for the formation of oxalic acid in the aqueous phase. To this end, the chemistry of glycolaldehyde is treated now separately using the oxidation scheme of the Master Chemical Mechanism (MCM; Saunders et al. [2003]). Moreover, the gas phase oxidation of ethene and ethylene glycol has been updated and implemented, respectively. Additionally, the inorganic gas phase chemistry has been updated according to available revised reaction rates (see Karl et. al. [2006]). In conclusion, the applied new gas phase mechanism contains 25 new reactions and 10 new species compared to the formerly used RACM mechanism.

The SPACCIM model was initialised with physical and chemical data from the EUROTRAC-2 project CMD (cp. Poppe et al. [2001] and references therein) for 2 different atmospheric scenarios urban (polluted case) and remote (continental background case). For the simulations a finely resolved particle spectrum is considered. The particle number initialisation is based on 3 particle modes which were discretised with 64 size bins within the microphysical model. The corresponding chemically homogeneous initial particle compositions has been derived from the aerosol distributions given by Poppe et al. [2001] and the chemical mass ratios of the different aerosol modes. The chemical initialisation of the gas phase has been used from the previous studies. Moreover, gas emissions and deposition were considered throughout the simulation time.

The simulations have been carried out using a meteorological scenario which is based on the global calculations of Pruppacher and Jaenicke [1995] with an in-cloud residence time about 15% (global average).In the scenario, an air parcel moves along a predefined trajectory including 8 cloud passages (4 day and 4 night clouds) of about 2 hours within 108 hours modelling time and an intermediate aerosol state at a 90% relative humidity level (see **Figure 2**) by neglecting the effects of non-ideal solutions. This means, the deliquescent particles are treated as well dissolved. Simulations have been performed for the two different atmospheric scenarios beginning at 0:00 on the 19th of June (45°N). Simulations have been carried out with and without (used acronym: woCloud) aqueous phase chemistry to investigate the effect of multiphase aerosol-cloud chemistry interaction on the tropospheric multiphase system. Finally, this non-permanent cloud meteorological scenario including more realistic in-cloud and cloud free time periods allows improved investigations of the aerosol cloud interaction compared to the former permanent cloud model studies.

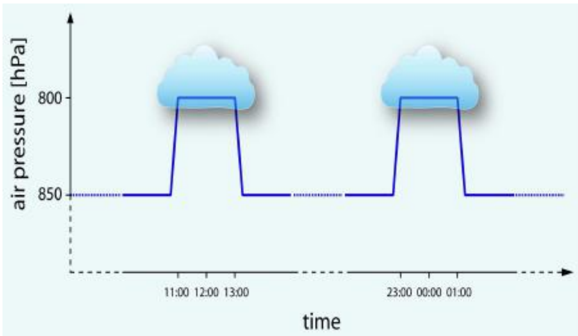

Figure 2. Schematic illustration of the used SPACCIM model scenario.

3 RESULTS AND DISCUSSION

3.1 GAS PHASE OH RADICAL OXIDATION BUDGET

The most important radical oxidant in the tropospheric multiphase system is the OH-radical. In **Figure 3**, the gas phase radical concentrations in molecules per cm^{-3} vs. time are presented for the urban and remote scenario both with and without aqueous phase chemistry interaction. According to the importance of the photochemistry for the OH-radical, the concentration profiles shows a day-time profile which is significantly influenced by the cloud occurrence. This fact can be seen directly in the difference between the case with cloud and without cloud interaction.

Under cloud conditions the radical concentration of OH is decreased by about 90% and 75% in the urban and remote scenario (2. day cloud event), respectively. This reduction is mainly caused by the uptake of very soluble HO_2 and not only by the direct phase transfer into the droplets. The efficient HO_2 uptake leads to an OH precursor separation between the two phases and a remarkable formation flux decrease. As can be seen from **Figure 3**, the reduction in the cloud is more substantial under urban conditions. This is caused by the relevance of the different sources for the OH formation. In contrast to the remote case, the OH formation pathway based on the reaction of HO_2 and NO is more important in the urban case. Therefore, the decrease is more recognisable in the urban case. In conclusion, the in-cloud reduction of the OH gas phase budget is mainly an indirect cloud effect regarding the OH based on a direct effect on HO_2.

The fluctuations which occur for the case without cloud interaction are caused by the relatively fast air pressure change during the air parcel lifting along the trajectory which leads to different fluxes of the pressure depended reactions. Therefore, the OH profile is characterised by chemical balancing effects.

Another interesting observation under remote conditions is the higher OH concentration after the day-time cloud evaporation. This effect is caused by a significant production of H_2O_2 in the remote day-time clouds leading to an increase of H_2O_2 in the gas phase and finally to a changed NO_X/HO_X budget and a short-time OH increase after the cloud evaporation. Furthermore, for the urban case a difference between the two cases can be recognised under wet aerosol conditions. The reduction there is caused also by the interaction of OH itself and it's precursors with the deliquescent particles.

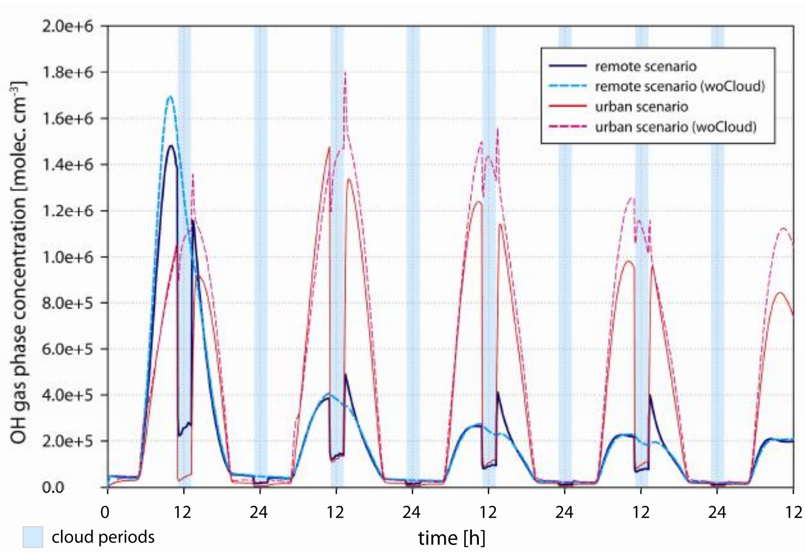

Figure 3. Modelled OH gas phase concentrations in molecules per cm^{-3} vs. modelling time for the urban and remote scenario both with and without (woCloud) aqueous phase chemistry interaction, respectively.

3.2 AQUEOUS PHASE OH RADICAL OXIDATION BUDGET

The OH day profile is also reflected in the aqueous phase. In **Figure 4** the aqueous concentration of OH is plotted for the urban and remote scenario in mol l^{-1}. The aqueous phase concentration itself depends on both the available water this means on the microphysical conditions and on the chemical sinks as well as sources of the species itself. The day-time concentrations of OH reach values of about $6.0\cdot10^{-14}$ and $1.0\cdot10^{-14}$ mol l^{-1} in the cloud droplets for the remote and urban scenario, respectively. The lower concentrations in the urban case result from the larger possible sink fluxes under polluted conditions. The corresponding night-time cloud concentrations are about 1 order of magnitude lower.

For both scenarios, a reduced OH budget in the aqueous phase can be mostly observed after the cloud evaporation. This reflects the effective oxidation within the cloud. As can be seen form the **Figure 4** the difference between deliquescent particle and cloud droplet concentration is only in the range of about two orders of magnitude and not only in the range of the LWC variation of about 5 order of magnitude. Therefore, other sources of OH in the aqueous phase have to be important for the concentration of the aqueous phase OH. The solution effect is more dominant in the night-time clouds. For this reason in-situ sources of OH act more effectively under day-time conditions. This also results from the flux diagnosis of the most important sinks and sources of the OH radical in the aqueous phase.

In **Figure 5**, the total sinks and sources of OH in the aqueous phase are plotted vs. a selected time interval of the modelling time. The positive reaction fluxes are sources for OH in the aqueous phase; the negative fluxes represent the sinks of OH. The mass fluxes are given in mol m^{-3} s^{-1} for the corresponding OH sink and source reactions. This kind of time resolved sink and source analysis leads to the determination of the most important chemical processes and interactions. Finally this leads to a more comprehensive understanding of the physico-chemical aerosol processing.

As can be seen from the total fluxes, the OH fluxes show also a characteristic day-profile as expected for the gas phase. The colours show significant differences in the sinks and sources between deliquescent aerosol conditions and cloud conditions. This is caused by the phase transfer of soluble compounds into the droplets which can act there as additional sink and sources.

Integrated over all cloud periods, the most important source of OH in the aqueous phase under cloud conditions is the direct transfer from the gas phase with about 73% in the urban case (64% in the remote case). But also the aqueous NO_3^- photolysis, $FeOH^{2+}$ photolysis and the HO_3 decomposition contribute with about 7%, 14% and 4%, respectively, to the OH formation in the aqueous phase under urban cloud conditions. In the remote case, mainly the Fenton type reactions of Cu(I) and Fe(II), the HO_3 decomposition as well as the photolytic decay of H_2O_2 and $FeOH^{2+}$ act with about 3%, 16%, 7%, 7% and 2%, respectively, as important in-cloud sources of the OH radical among the direct uptake from the gas phase.

In contrast to the cloud conditions, the OH formation is dominated by the Fenton reaction of Fe(II) with H_2O_2 in the deliquescent particles. Interestingly, the total source fluxes in the particles are fully comparable with that in the cloud droplets under urban conditions. The model results implicate that the in-situ OH production under wet aerosol particle condition strongly depends on the TMI concentration and especially on the H_2O_2 concentration. Contrary to the almost comparable OH production fluxes in the urban case, the remote case shows mostly somewhat smaller OH formations under particle conditions depending mainly on the availability of H_2O_2.

The above mentioned results are a good agreement with measurements of Arakaki et al. [2006]. They have analysed aqueous extracts of aerosol particles regarding to the photochemical formation of OH in deliquescent particles. They found a direct correlation between the OH formation and the dissolved iron concentration. But more experimental work has to be done to point out the importance of the different formation pathways including the Fenton reaction.

A much more complex picture can be obtained for the OH sinks. The most important sinks under cloud conditions (urban case) are the reaction with hydrated glyoxal (13%), methylglyoxal (5%), formaldehyde (29%), ethylene glycol (11%), and 1,4-butenedial (31%) which lead to the production of less volatile organic compounds. In a good agreement with the results of simple conceptual model studies of Gelencser and Varga [2005], predominantly organic compounds with effective Henry constants above 10^{-3} M atm^{-1} (mostly bifunctional compounds) acts as important OH sinks under cloud conditions. In contrast to the cloud conditions, the reactions with the various less volatile oxidation products of the mentioned before organics such as pyruvic acid (6%) and glyoxylic acid (12%) act as sinks for OH in the urban scenario in the deliquescent particles. The reaction of these species is less important under cloud conditions because of the competitive reactants which are effectively taken up into the cloud droplets like formaldehyde.

The integrated percentage contributions of the most important OH sources and sinks for the urban case are summarised in **Table 1** and grouped into 4 classes regarding to the different microphysical conditions.

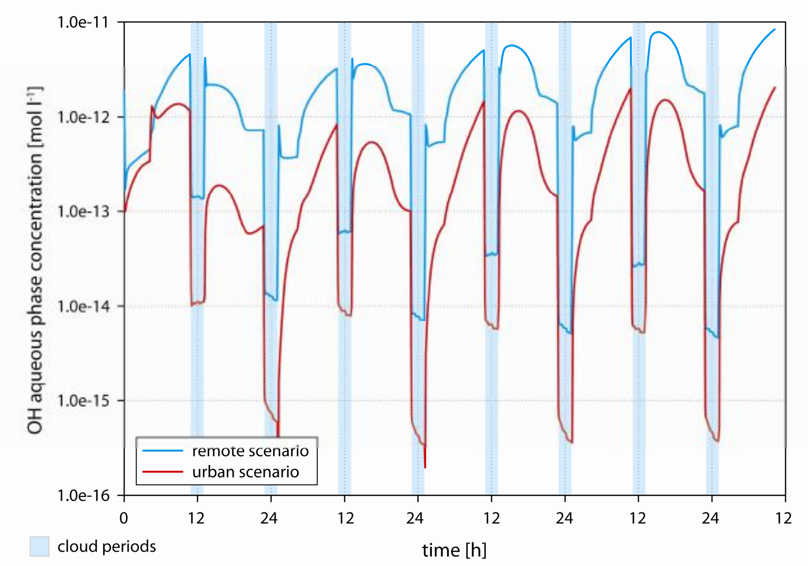

Figure 4. Modelled OH aqueous phase concentrations in mol l^{-1} vs. modelling time for the urban and remote scenario, respectively.

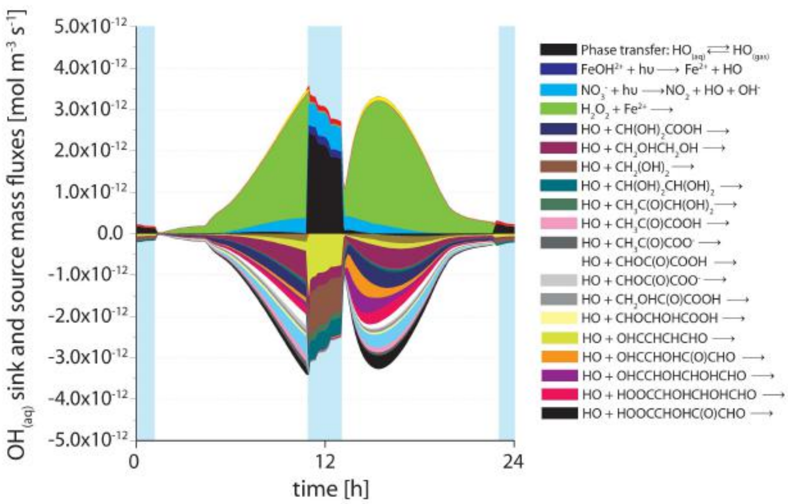

Figure 5. Modelled chemical sinks and sources mass fluxes of OH in aqueous phase mol m^{-3} s^{-1} for the third day of modelling time for the urban.

Table 1. Integrated percentage contributions of the most important $OH_{(aq)}$ radical sources and sink reactions for the urban case classified regarding to the different microphysical conditions during the simulation time (total = total contributions throughout the simulation time, total clouds = contributions throughout all cloud events, day-/nighttime clouds = contributions throughout all day and night cloud events, aqueous particles = contribution throughout the deliquescent particle conditions) (only sinks and sources with contributions larger than ±1 % presented).

reaction	total	Total clouds	Daytime clouds	Nighttime clouds	Aqueous particles
phase transfer: $OH \rightleftarrows OH_{(aq)}$	18%	73%	73%	76%	1%
$Cl^- + OH \rightleftarrows ClOH^-$	-2%	0%	0%	2%	-3%
$Br^- + OH \rightleftarrows BrOH^-$	-1%	0%	0%	0%	-2%
$FeOH^{2+} + h\nu \longrightarrow Fe^{2+} + OH$	2%	7%	7%	0%	0%
$NO_3^- + h\nu \xrightarrow{H_2O} NO_2 + OH + OH^-$	10%	14%	15%	0%	9%
$H_2O_2 + Fe^{2+} \longrightarrow Fe^{3+} + OH + OH^-$	67%	1%	1%	2%	87%
$H_2O_2 + Cu^+ \longrightarrow Cu^{2+} + OH + OH^-$	2%	0%	0%	0%	2%
$Cu^+ + O_3 \xrightarrow{H^+} Cu^{2+} + OH + O_2$	0%	1%	1%	4%	0%
$HO_3 \longrightarrow OH + O_2$	1%	4%	3%	14%	0%
$SO_4^- + H_2O \longrightarrow SO_4^{2-} + OH + H^+$	0%	0%	0%	2%	0%
$OH + HSO_4^- \longrightarrow$	-3.1%	0.0%	0.0%	0.0%	-4.1%
$OH + Fe^{2+} \longrightarrow$	-8.4%	-0.3%	-0.3%	-0.2%	-10.9%
$OH + CH_2(OH)_2 \longrightarrow$	-7.7%	-28.6%	-28.6%	-29.6%	-1.3%
$OH + HCOO^- \longrightarrow$	-0.4%	-1.6%	-1.6%	-1.5%	0.0%
$OH + CH_2OHCH_2OH \longrightarrow$	-14.1%	-10.8%	-10.7%	-12.3%	-15.1%
$OH + CH_3CH_2OH \longrightarrow$	-0.9%	-3.4%	-3.3%	-3.8%	-0.1%
$OH + CH(OH)_2CH(OH)_2 \longrightarrow$	-4.5%	-13.1%	-13.0%	-13.8%	-1.8%
$OH + CH(OH)_2COOH \longrightarrow$	-9.4%	-0.3%	-0.3%	-0.4%	-12.2%
$OH + CH_3C(O)CH(OH)_2 \longrightarrow$	-1.2%	-4.6%	-4.6%	-5.5%	-0.2%
$OH + CH_3C(O)COOH \longrightarrow$	-2.8%	0.0%	0.0%	0.0%	-3.6%
$OH + CH_3C(O)COO^- \longrightarrow$	-2.1%	-0.2%	-0.2%	-0.3%	-2.7%
$OH + CH_2(OH)C(O)COOH \longrightarrow$	-1.9%	0.0%	0.0%	-0.1%	-2.5%
$OH + CHOC(O)COOH \longrightarrow$	-3.6%	0.0%	0.0%	0.0%	-4.7%
$OH + CHOC(O)COO^- \longrightarrow$	-1.3%	0.0%	0.0%	0.0%	-1.7%
$OH + OHCCHCHCHO \longrightarrow$	-10.5%	-31.1%	-31.3%	-28.1%	-4.2%
$OH + OHCCH(OH)C(O)CHO \longrightarrow$	-5.1%	-0.6%	-0.7%	-0.2%	-6.4%
$OH + OHOCCH(OH)C(O)CHO \longrightarrow$	-5.0%	-0.1%	-0.1%	-0.2%	-6.4%
$OH + OHCCH(OH)CH(OH)CHO \longrightarrow$	-5.1%	-0.6%	-0.7%	-0.2%	-6.4%
$OH + OHOCCH(OH)CH(OH)CHO \longrightarrow$	-4.8%	-0.1%	-0.1%	-0.1%	-6.2%
$OH + CHOCH(OH)COOH \longrightarrow$	-1.7%	0.0%	0.0%	-0.1%	-2.2%

Finally, it has to be noted that all these results imply the potential relevance of deliquescent particles to act as a reactive medium within the tropospheric multiphase system. Moreover, the availability of OH radical sources in deliquescent particles may also be important for the formation of atmospheric secondary organic matter. Particularly, the entrainment and detrainment areas of tropospheric clouds may be also quite reactive media for the chemical aerosol processing. These so-called “twilight zones” with forming and evaporation cloud fragments as well as hydrated aerosols can extend up to tens of kilometres from the clouds in the free troposphere [see Koren et al., 2007] and can thereby fill large volume of the free troposphere. Therefore, the free troposphere provides conditions in which aqueous phase reactions also in deliquescent particles are conceivable and maybe potentially important.

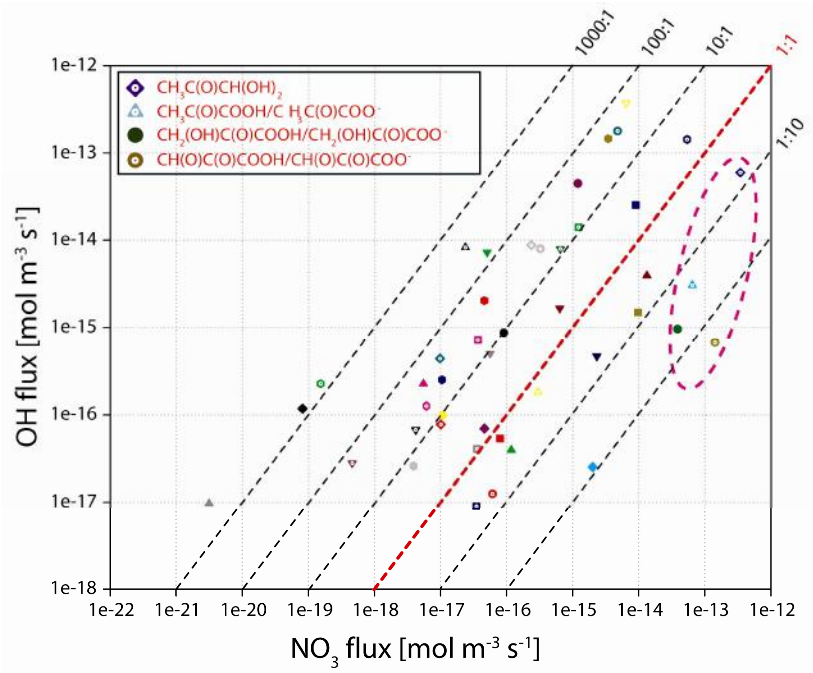

Figure 6. Comparison of the modelled mean in-cloud NO_3 and OH degradation fluxes of organic compounds under urban conditions.

3.3 IMPORTANCE OF THE NO_3 AND OH RADICAL FOR THE IN-CLOUD OXIDATION OF ORGANIC SPECIES

Moreover, the last paragraph has been pointed out the importance of organic compounds for the aqueous phase budget of the main radical oxidant OH. However, among the OH radical, other radical oxidants such as the NO_3 radical can contribute significantly to the oxidation of organic compounds under cloud conditions particularly during the night. Their competitive reactivity for the in-cloud oxidation of organic compounds is shown in **Figure 6**. For the actualisation of this comparison, the aqueous phase OH and NO_3 organic oxidation fluxes have been analysed classified according to the different microphysical conditions during the simulation time. In **Figure 6**, a comparison is shown of the importance of the two main tropospheric radical oxidants for the in-cloud degradation of organic compounds under polluted in-cloud conditions. The red line in **Figure 6** marks the 1:1 ratio. The results point out that for some organic compounds the NO_3 radical oxidation can be potentially more important than the OH pendant. However, for the majority of the species, the OH reaction is the main sink in the aqueous phase also under highly polluted environmental conditions. Moreover, the in-cloud oxidation of methylglyoxal and its oxidation products like pyruvic acid seems to be an efficient sink for NO_3 radicals in the aqueous phase particularly under both urban and remote conditions. Furthermore, the results reveal a dominating OH chemistry under deliquescent particle conditions due to the in-situ sources of OH radical.

3.4 AQUEOUS PHASE IMPACT ON ORGANIC GAS PHASE TRACE GAS BUDGETS

Further investigations following the studies on the tropospheric oxidants were related to the influence of the changed gas phase oxidation budget on the oxidation of organic trace gases. For emitted less soluble gas phase species like xylene, a significant reduction of the degradation rate can be observed if aqueous phase chemistry interactions are considered (see **Figure 7**). In particular, the changed oxidation budget in the day-time clouds leads to the reduction of the gas phase degradation for this kind of compounds. The concentrations of the model run including aqueous phase chemistry are about 20% higher compared to the model run with gas phase consideration only. Moreover, trace gas concentrations of less soluble organics can also be altered by a modified NO_3 radical budget as well as modified O_3 levels.

A much more complex concentration patterns can be obtained for oxidation products which are soluble enough to be taken up into the aqueous phase. For this kind of compounds additionally to the gas phase, the aqueous phase can act as a significant sink as well as source.

For instance in the case of ethylene glycol, the chemical interaction with deliquescent particles as well as droplet leads to decreasing concentrations in comparison to the case without consideration of aqueous phase chemistry. Because of the high Henry-solubility ethylene glycol is transferred efficiently into wet aerosol particles and cloud droplets. It's effectively oxidised there particularly during the high OH day time conditions. As **Figure 7** shows, the aqueous phase oxidation can compensate also the reduced gas phase oxidation budget and leads finally to a lower concentration of ethylene glycol in the gas phase.

Among the species which are well degraded in the aqueous phase, species exist which are efficiently produced and transferred to the gas phase like acetic acid (see **Figure 7**). Without considering multiphase interactions, the productions of the acetic acid are significantly underestimated. Under remote environmental conditions about $^{2}/_{3}$ of acetic acid is produced in the cloud droplets and largely degassed to the gas phase with the cloud evaporation.

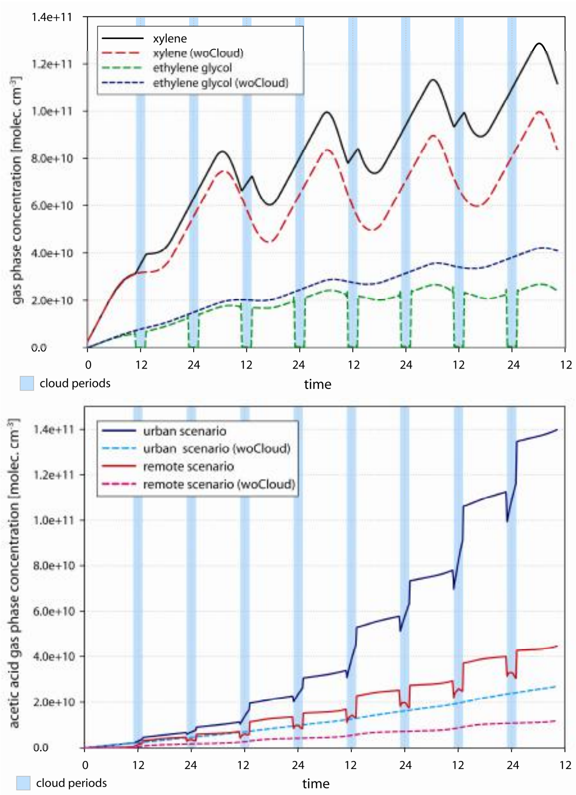

Figure 7. Modelled gas phase concentrations of xylene and ethylene glycol under urban conditions (top) as well as acetic acid under remote and urban conditions (down) both with and without (woCloud) aqueous phase chemistry interaction, respectively.

In conclusion, without reflection of aqueous phase chemical processes organic trace gas concentrations can be significantly under- and overestimated by pure gas phase chemistry models.

3.5 ORGANIC PROCESSING IN THE AQUEOUS PHASE

Based on the studies on oxidation budget, the most important aqueous phase oxidation pathways have been determined by comprehensive flux analyses. In **Figure 8**, the modelled mean sink and source fluxes for the most important multiphase oxidation processes contributing to organic particle mass formation are presented for the remote scenario.

Figure 8 shows the chief aqueous organic oxidations leading to the formation substituted mono- and diacids as well as substituted dialdehydes. The main identified precursors for the organic mass production in the gas phase are 1,4-butenedial, methylglyoxal, glyoxal, glycolaldehyde and ethylene glycol. The aqueous phase contributes with about 36%, 7%, 31%, 47% and 93% to their total multiphase degradation. Under continental background conditions, in particular the oxidation of glycolaldehyde can contribute to the in-cloud C_2 organic particle mass formation. The most important source for glycolaldehyde in the gas phase represents the oxidation of methylvinylketone which is one of the main isoprene oxidation products. As similar shown by Lim et al. [2005], this pathway links the emitted isoprene and oxalic acid which is one of the main identified single organic particle mass components. The oxidation of methylglyoxal has been identified as the most important C_3 oxidation pathway which is moreover able to influence significantly the aqueous phase NO_3 and OH radical budget.

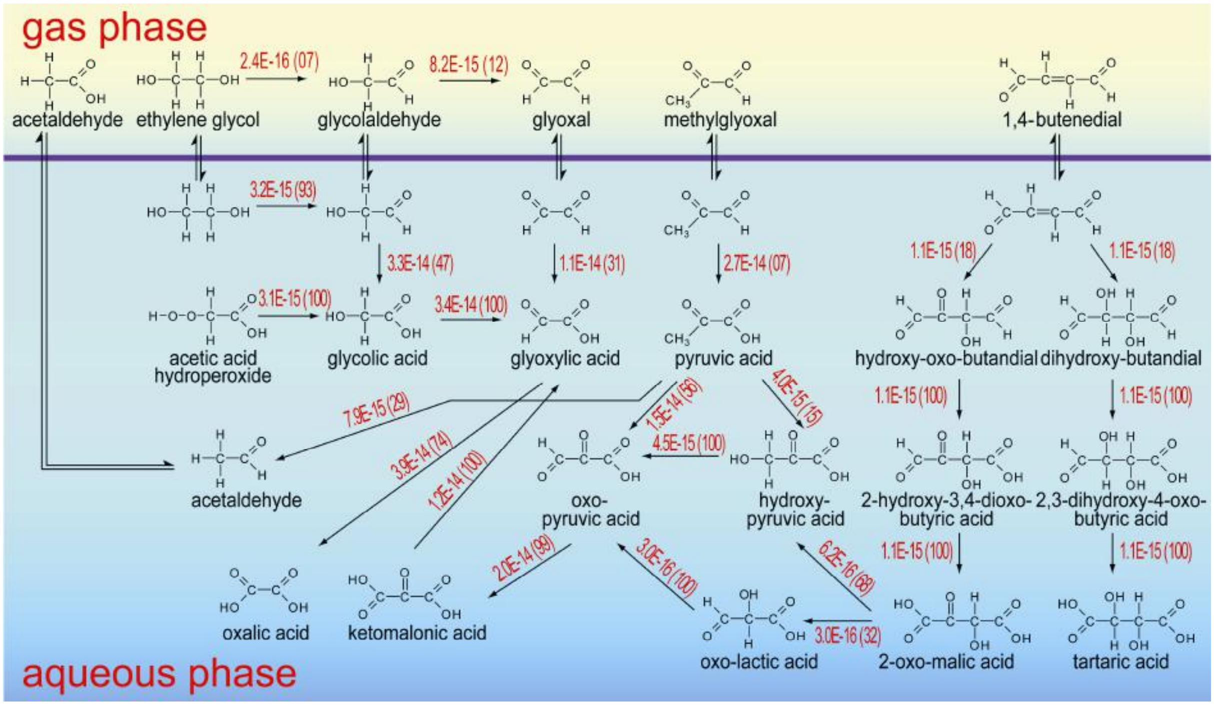

Figure 8. Schematic presentation of the most important aqueous phase C_2-C_4 organic oxidation paths and contributing to the particulate organic matter (remote scenario). The integrated mean oxidation fluxes are given in mol m^{-3} s^{-1} and the corresponding percentages in brackets.

Among the total mass production the spectral processing of the organics has been investigated exemplary shown in **Figure 9** for the pyruvic acid. In **Figure 9,** the spectral pyruvic acid mass concentration in mol m^{-3} is depicted vs. modelling time and the corresponding particle and droplet spectra, respectively.

Figure 9 shows that the aqueous phase pyruvic acid production is mainly restricted to the size interval between the activation radius and about 800 nm. This pattern has been observed quite a lot of the organic compounds and is also reflected in the spectral distribution of the total organic mass, which can be increased after the daytime cloud evaporation by about 1 µg m^{-3} under urban conditions.

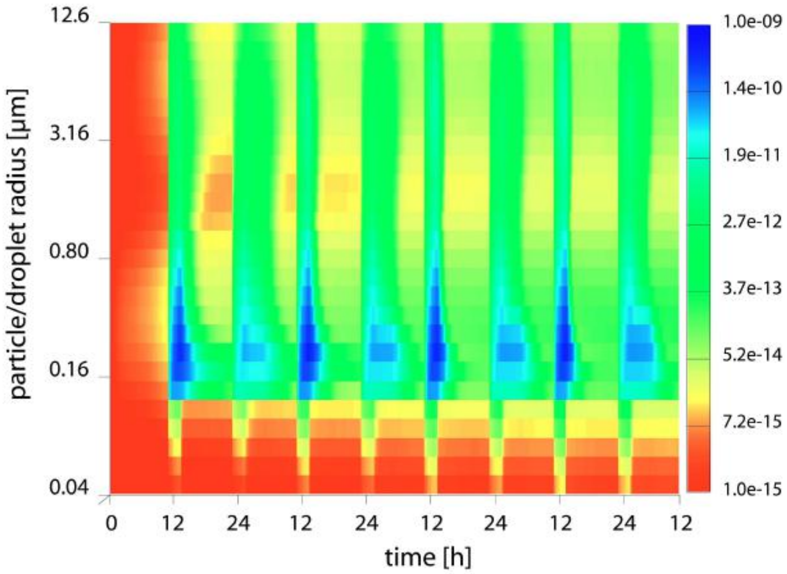

Figure 9. Depiction of the modelled spectral pyruvic acid mass concentration in mol m^{-3} as function of time and the corresponding dry particle/droplet radius.

4 SUMMARY AND OUTLOOK

Simulations with the parcel model SPACCIM have been performed for different atmospheric conditions considering detailed microphysics and multiphase chemistry (RACM-MIM2ext/CAPRAM 3.0i) to investigate the effect of multiphase processing of tropospheric aerosol particles and trace gases using a more realistic meteorological non-permanent cloud model scheme. The model studies show considerable effects of multiphase cloud droplet and deliquescent aerosol particle interactions on the tropospheric oxidation budget for polluted and remote environmental conditions as well as affected VOC's oxidation due to the influenced oxidation budget. Moreover, the simulations implicate the potential role of deliquescent particles to act as a reactive chemical tropospheric medium due to the in-situ aqueous phase production of radical oxidants such as OH and non-radical oxidants such as H_2O_2. Additionally, the model study have revealed the importance of the aqueous phase for the formation of higher oxidised organic compounds such as substituted mono- and dicarboxylic acids such as pyruvic acid and tartaric acid. In particular, the aqueous phase oxidations of methylglyoxal and 1,4-butenedial have been identified as important OH radical sinks under polluted environmental conditions contributing to the production of less volatile organic compounds and thus the organic aerosol particle mass. Further, the in-cloud oxidation of methylglyoxal and its oxidation products have been shown to be an efficient sink for NO_3 radicals in the aqueous phase particularly under urban and remote conditions. Finally, the sum of the results implicates the necessity of the aqueous phase processes to be considered in future higher scale chemistry transport models. Moreover, important cloud effects are mainly not yet considered or less represented in presently available regional scale chemistry transport models (CTM's) because of both the restricted knowledge in the past and the high computational costs of detailed aqueous phase chemistry mechanisms such as CAPRAM 3.0.

To this end, a reduced aqueous phase mechanism with less than 250 reactions has been already developed. This mechanism is able to reproduce the most important aqueous phase chemistry processes for key compounds including reasonable computational costs. Finally, the application of this reduced mechanism will allow further investigations of the multiphase chemical processing on regional scale in the future CTM's.

5 ACKNOWLEDGEMENTS

This study was supported by the scholarship programme of the German Federal Environmental Foundation (DBU).

6 REFERENCES

Arakaki, T., Kuroki, Y., Okada, K., Nakama, Y., Ikota, H., Kinjo, M., Higuchi, T., Uehara, M., Tanahara, A., 2006, Chemical composition and photochemical formation of hydroxyl radicals in aqueous extracts of aerosol particles collected in Okinawa, Japan, *Atm. Env.* **40**: 4764–4774.

Charlson, R.J., Schwartz, S.E., Hales, J.M., Cess, R.D., Coakley, J.A., Jr., Hansen, J.E., and Hoffman, D.J., 1992,: Climate forcing by anthropogenic aerosols, *Science* **255**: 423-430.

Ervens, B., George, C., Williams, J. E., Boxton, G. V., Salmon, G. A., Bydder, M., Wilkinsons, F., Dentener, F., Mirabel, P., Wolke, R., and Herrmann, H., 2003, CAPRAM 2.4 (MODAC mechanism): An extended and condensed tropospheric aqueous phase mechanism and its application, *J. Geophys. Res.* **108**, doi:10.1029/2002JD002202.

Gelencsér, A., and Varga, Z., 2005, Evaluation of the atmospheric significance of multiphase reactions in atmospheric secondary organic aerosol formation, *Atmos. Chem. Phys.*, ***5***, 2823-2831.

Herrmann, H., Majdik, Z., Ervens, B., and Weise D., 2003, Halogen production from aqueous tropospheric particles, *Chemosphere* **52**: 485-502.

Herrmann, H., Ervens, B., Jacobi, H.-W., Wolke, R., Nowacki P. and Zellner, R., 2000, CAPRAM 2.3: A Chemical Aqueous Phase Radical Mechanism for Tropospheric Chemistry, *J. Atm. Chem.* **36**: 231-284.

Herrmann, H., Tilgner, A., Barzaghi, P., Majdik, Z., Gligorovski, S., Poulain, L., and Monod, A., 2005, Towards a more detailed description of tropospheric aqueous phase organic chemistry: CAPRAM 3.0, *Atm. Env.* **39** (23-24): 4351-4363.

Knoth, O., 2005, SPACCIM: A parcel model for the combined treatment of microphysical and multiphase chemistry processes, *Atm. Env.* **39** (23-24): 4331-4340.

Koren, I., Remer, L. A., Kaufman, Y. J., Rudich, Y., and Martins, J. V., 2007, On the twilight zone between clouds and aerosols, *Geophys. Res. Lett.*, **34**, L08805, doi:10.1029/2007GL029253.

Lim, H.-J., Carlton, A., and Turpin, B.J., 2005, Isoprene forms secondary organic aerosol through cloud processing: Model simulations, *Environ. Sci. Technol.* **39**: 4441-4446.

Poppe, D., Aumont, B., Ervens, B., Geiger, H., Herrmann, H., Roth, E.-P., Seidl, W., Stockwell, W. R., Vogel, B., Wagner, S., and D. Weise, 2001, Scenarios for modeling tropospheric chemistry, *J. Atm. Chem.* **40**: 77-86.

Pruppacher, H.R., and Jaenicke, R., 1995, The processing of water vapor and aerosols by atmospheric clouds: A global estimate, *Atm. Res.* **38**: 283 - 295.

Ravishankara A.R., 1997, Heterogeneous and multiphase chemistry in the troposphere, *Science* **276**: 1058–1065.

TERNARY MIXTURE OF SODIUM CHLORIDE, SUCCINIC ACID AND WATER; SURFACE TENSION AND ITS INFLUENCE ON CLOUD DROPLET ACTIVATION

J. Vanhanen[1], A.-P. Hyvärinen[1], T. Anttila[1], Y. Viisanen[1] and H. Lihavainen[1]

[1]Finnish Meteorological Institute, Erik Palmènin aukio 1, 00560, Helsinki, Finland

Keywords: Aerosol thermodynamics, surface tension, CCN.

1. INTRODUCTION

Indirect effect of aerosol particles to the atmosphere (the cloud albedo effect) is currently the most uncertain piece in the climate change puzzle (IPCC 2007). In order to understand quantitatively how aerosols and clouds interact, the physico-chemical properties of aerosols have to be known. As the atmospheric aerosols have highly heterogeneous properties and there are only limited set of measurements characterizing them, these properties have to be treated in approximative manner in climate models. For example surface tension of pure water is often used (Anttila *et al.* 2002).

It is known that a large fraction of aerosol particles is inorganic salts (Dusek *et al.* 2006; McFiggans *et al.* 2005). Owing to their hygroscopicity, salt particles act as efficient cloud condensation nuclei (CCN). In addition of inorganic salts, an extensive number of both water-soluble and water-insoluble organic acids are present in the aerosol phase (Legrand *et al.* 2007). Organic acids are often surface active. According to Köhler theory (Köhler 1936), a decrease in surface tension induces a decrease in the critical supersaturation of a droplet. This means that organic acids can enhance the cloud droplet activation of mixed particles by decreasing the surface tension of the droplet (Cruz and Pandis, 1997, 1998; Li *et al.* 1998).

There are only a few extensive data sets on surface tensions of ternary mixtures of atmospheric relevance. To this end, we studied the surface tension of ternary solution of sodium chloride, succinic acid and water as a function of both concentration and temperature. The measured surface tensions were used as an input to an adiabatic air parcel model (Anttila *et al.* 2002) to study the effect of the surface tension on cloud droplet activation.

2. MATERIALS AND METHODS

The surface tension was measured using a capillary rise technique (figure 1). The sample was placed in a small glass in the bottom of a double-walled glass. The temperature of the glass was controlled by circulating thermostatically controlled liquid between the walls (Lauda RC6 CS).

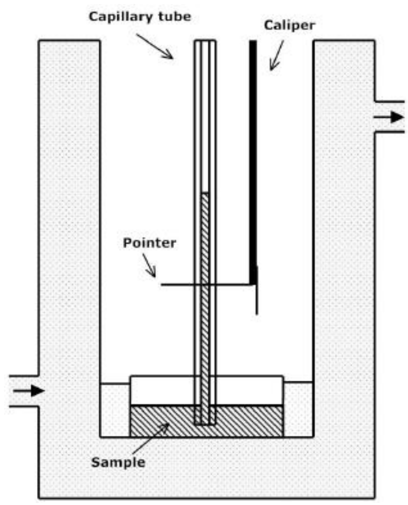

Figure 1. Experimental setup

The samples were made of pure substances with purity of 99 % or better. Both sodium chloride and succinic acid were dried before weighing in an oven at temperature of about 100 ^{o}C to evaporate all the volatile impurities. Before every measurement the capillary tubes were cleaned using 96% sulfuric acid and purified water (Milli-Q).

The height of the liquid in the capillary tube was measured using a slide caliper modified to this purpose. Accuracy of the caliper is ±0.02 mm. The measurements were performed inside temperature range 283.15 K to 303.15 K. The meniscus was allowed to both rise and descent by altering the pressure in the tube. Uncertainty of the surface tension measurement was estimated to be less than 1 %.

3. SURFACE TENSION

Surface tension of the ternary solution of sodium chloride, succinic acid and water was measured as a function of mixture composition and temperature. The range of concentrations covered by measurements was limited by their solubilities. The maximum mole fractions used were 0.0075 and 0.06 for succinic acid and sodium chloride respectively.

In figure 2 the surface tension measurements of aqueous succinic acid is presented and compared to the previous measurements made with the Wilhelmy-plate method by Hyvärinen *et al.* 2006. It can be seen that succinic acid decreases the surface tension of the solution already at quite small mole fractions. Results agree well with the previous measurements done using a different method. Sodium chloride was found to increase surface tension linearly as a function of concentration.

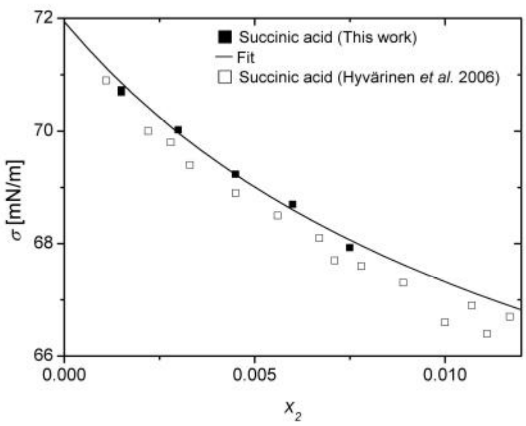

Figure 2. Surface tensions of aqueous succinic acid as a function of the mole fraction of succinic acid (x_2) at 25°C.

In figure 3 the surface tension of the ternary solution is presented as a function of temperature for four different mole fractions of succinic acid. The sodium chloride mole fraction is 0.02. Surface tension of the solution decreased with increasing temperature as expected. The behaviour is similar also with other concentrations of sodium chloride. The gradient of surface tension with respect to the temperature gets lower with increasing concentrations of both solvents.

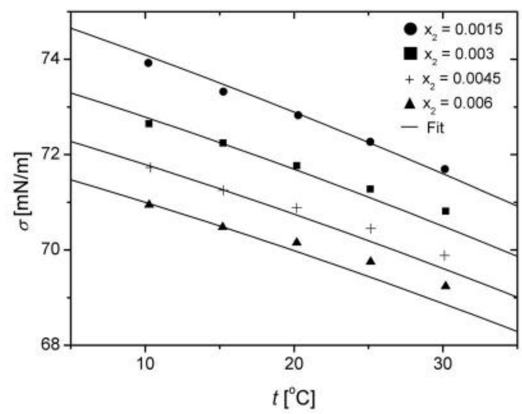

Figure 3. Surface tension of ternary solution of sodium chloride, succinic acid and water as a function of temperature. Mole fraction of sodium chloride is kept constant (x_3 = 0.02).

In figure 4 the surface tension of the ternary solution is presented as a function of mole fractions of succinic acid and sodium chloride at 25°C. The decrease of the surface tension as a function of succinic acid mole fraction is steeper for solutions with larger amount of the salt. This indicates that succinic acid, as a surface active compound, tends to fill the surface of the ternary solution. It has been found in previous studies that in some cases inorganic salts can even enhance the surface tension lowering of organic acids (Tuckermann 2007; Kiss *et al.* 2005).

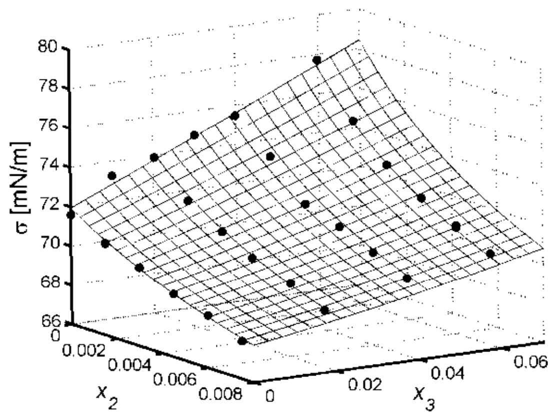

Figure 4. Surface tension of the ternary mixture as a function of mole fractions of succinic (x_2) acid and sodium chloride (x_3) at 25°C.

To make the measurement results useful for numerical models, they need to be extrapolated to a larger concentration and temperature range. To this end, a function by Chunxi *et al.* (2000) was fitted to the data. This way we got a surface tension parameterization which can be used beyond solubility limits. Fit can be seen in the figures as a solid line.

5. CLOUD DROPLET ACTIVATION

To see if surface tension has an effect on cloud droplet activation, we compared results from cloud model simulations that used two different surface tensions in *S*: that of pure water and that predicted by the developed surface tension parameterization.

The aerosol size distribution used in the simulations represents a typical aerosol size distribution measured in marine environment (Heintzenberg *et al.* 2000). Succinic acid is treated as a completely soluble compound despite of its solubility limit (88 g/l; Saxena *et al.* 1996). Previous studies have shown that the solubility of a slightly soluble compound has an effect only when there is no or very little of sodium chloride in the particle (Bilde *et al.* 2004). Also, particles have usually undergone different kinds of humidity conditions in the atmosphere. This means that the solution can be supersaturated with respect to succinic acid, and the assumption of complete solubility is sensible.

Cloud model simulations were made using three different updraft velocities; 0.1, 0.5 and 1.0 m/s. In figure 5 the ratio of the number of cloud droplets (N_a) to the total number of particles (N_i) (activated fraction) is presented as a function of the initial mass fraction of succinic acid in the aerosols. The activated fraction decreases as the mass fraction of succinic acid increases. This is because succinic acid has higher molar volume than sodium chloride and because sodium chloride is able to dissociate in water.

In figure 5, it can be seen that there is a difference in the number of cloud droplets arising from the choice of the surface tension. The difference increases with increasing mass fraction of succinic acid and with increasing updraft velocity. By using the surface tension of pure water in the cloud model the amount of activated particles is underestimated up to 8 % for aerosol size distributions containing succinic acid and overestimated up to 8 % for size distributions containing only sodium chloride. This is because succinic acid decreases the surface tension of the solution while sodium chloride increases it. When the updraft velocity of the air parcel is 1.0 m/s, the effect of surface tension can clearly be seen with particles having mass fraction of succinic acid over 40%. Mass fractions of organic compounds in atmospheric aerosol particles can easily exceed this value (Dusek *et al.* 2006). The effect of updraft velocity can be explained by a larger dry diameter of activated particles, which is due to the lower updraft velocity, and thereby lower supersaturation. This decreases the Kelvin effect, which takes into account the surface tension of the solution. This was also observed for marine aerosol size distribution previously by Nenes *et al.* (2002).

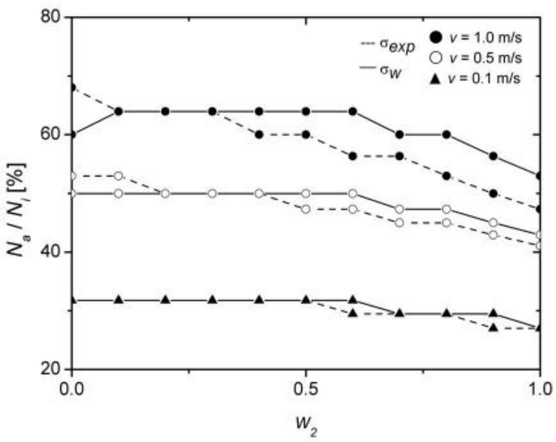

Figure 5. Activated fraction as a function of mass fraction of succinic acid (w_2). v is the updraft velocity, σ_w is the surface tension of pure water and σ_{exp} is the surface tension parameterization.

4. CONCLUSIONS

In this study the surface tension of ternary solution of sodium chloride, succinic acid and water was measured using the capillary rise technique. Measured surface tensions of binary solutions agreed well with literature values, confirming that the method is applicable to these solutions. Measurements were performed within the concentration range defined by the solubility limits of the solvents. To estimate the surface tension beyond these limits, an equation developed by Chunxi *et al.* (2000) was fitted to the data. As a result a parameterization of surface tension of the ternary solution was obtained over the whole concentration range. The parameterization is applicable inside temperature range of 10 to 30 ^{o}C, but it can be extrapolated beyond these limits. There are many benefits with these kinds of parameterizations. First, it gives the surface tension of ternary system as a function of both composition and temperature. Second, the parameterization is based on thermodynamics having fit parameters which can be, for example modelled. This gives many options for future research. Because the parameterization can be used beyond solubility limits, it can be also applied, for example, in numerical calculations regarding nucleation or cloud droplet formation.

To estimate the atmospheric relevance of the surface tension data, cloud droplet activation simulations were performed with particles of different composition. Three different updraft velocities (0.1, 0.5 and 1.0 m/s) were used. It was found that while sodium chloride particles act as efficient cloud condensation nuclei, succinic acid can enhance the activation further by decreasing the surface tension of the aqueous solution. By using the surface tension of pure water in the cloud model the amount of activated particles was underestimated up to 8% if the initial particles contained succinic acid. For pure sodium chloride particles it was overestimated up to 8%. Although the changes are small percent-wise, they still may have significance to the cloud radiative properties, in particular over the oceans. The marine clouds are usually clean clouds having lower number concentration of cloud droplets, which makes them especially sensitive to changes in the cloud droplet concentration (Platnic and Twomey 1994).

REFERENCES

IPCC (Intergovermental panel on climate change), Climate change 2007: The physical science basis, eds. Solomon, S., Qin, D., Manning, M., Marquis, M., Averyt, K., Tignor, M. M. B., Miller, H. LR. Jr., and Chen, Z.

Anttila, T., Kerminen, V.-M. *J. Geophys. Res.*, 107, D22, 4662, 2002.

Dusek U., Frank, G. P., Hildebrandt, L., Curtius, J., Scheider, J., Walter, S., Chand, D., Drewnick, F., Hings, S., Jung, D., Borrmann, S., Andreae, M. O. *Science*, 312, 5778, 1375-1378, 2006.

McFiggans, G., Artaxo, P., Baltensperger, U., Coe, H., Facchini, M. C., Feingold, G., Fuzzi, S., Gysel, M., Laaksonen, A., Lohmann, U., Mentel, D. M., O`Dowd, C. D., Snider, J. R. and Weingartner, E. *Atmos. Chem. Phys.*, 6, 2593-2649, 2006.

Legrand, M., Preunkert, S., Oliveira, T., Pio, C. A., Hammer, S., Gelencsér, A., Kasper-Giebl, A., Laj, P. *J. Geophys. Res.*, 112, D23S07, doi:10.1029/2006JD008019, 2007.

Köhler, H. T. Faraday Soc., 32, 1152-1161, 1936.

Cruz, C. N. and Pandis, S. N. *Atmos. Environ.*, 31(15), 2205–2214, 1997.

Li, Z., Williams, A. L., Rood, M. J. *J. Atmos. Sci.*, 55, 1859-1866, 1998.

Hyvärinen, A.-P., Lihavainen H., Gaman, A., Vairila, L., Ojala, H., Kulmala, M., Viisanen, Y. *J. Chem. Eng. Data*, 51, 255-260, 2006.

Tuckermann, R. *Atmos. Environ.*, 41, 6265-6275, 2007.

Kiss, G., Tombácz, E., Hansson, H.-C. *J. Atmos. Chem.*, 50, 279-294, 2005.

Chunxi, L., Wenchuan, W., & Zihao W. *Fluid Phase Equilibr.*, 175, 185-196, 2000.

Heintzenberg, J., Covert, D. C., van Dingenen R.: *Tellus*, 52B, 1104-1122, 2000.

Saxena, P., Hildemann, L. M. *J. Atmos. Chem.*, 24, 1, 1996.

Bilde M., Svenningsson, B. *Tellus B*, 56, 2, 128-134, 2004.

Nenes, A., Charlson, R. J., Facchini, M. C., Kulmala, M., Laaksonen, A., Seinfeld, J. H. *Geophys. Res. Lett.*, 29, 17, 1848, doi:10.1029/2002GL015295, 2002.

Platnic, S., and Twomey, S. *J. Appl. Meteorol.*, 33, 334-347, 1994.

TOWARDS CLOSING THE GAP BETWEEN HYGROSCOPIC GROWTH AND ACTIVATION FOR SECONDARY ORGANIC AEROSOL (SOA)

H. Wex[1], M. D. Petters[2], S. M. Kreidenweis[2], E. Hallbauer[1], and F. Stratmann[1]

[1]*Leibniz-Institute for Tropospheric Research, Leipzig, Germany*
[2]*Colorado State University, Fort Collins, Colorado, USA*

1. INTRODUCTION

Atmospheric aerosol particles consist of both, inorganic and organic substances, with varying mass fractions. One way to form particulate matter is by oxidation of precursor gases. When organic compounds are formed by this process, the different products of this reaction are called SOA (Secondary Organic Aerosol). Among biogenic volatile organic compounds, monoterpenes appear to be the major precursors of SOA particulate matter [*Sun and Ariya*, 2006]. Many studies have examined SOA particles generated by the oxidation of α-pinene, which belongs to the group of monoterpenes.

For SOA particles generated from different precursor gases, in general a slight hygroscopic growth with growth factors of about 1.1 at 90% RH is observed [e.g. *Virkkula et al.*, 1999; *Varutbangkul et al.*, 2006]. Contrary to this, SOA particles are commonly found to be more CCN active than their hygroscopic growth factors would suggest [e.g. *VanReken et al.*, 2005, *Prenni et al.*, 2007, *Duplissy et al.*, 2008,]. Assuming a constant hygroscopicity derived from measured hygroscopic growth at RHs below 95% implies, that a very low surface tension of about 30 mN/m is needed to explain the measured CCN activity [e.g. *Prenni et al.*, 2007]. This is lower than values that have been measured for atmospheric rain and fog water samples [*Facchini et al.*, 2000], HULIS (HUmic LIke Substances) extracts from atmospheric samples [*Kiss et al.*, 2005; *Salma et al.*, 2006] and for different organic substances that are thought to contribute to SOA [*Huff Hartz et al.*, 2006].

Here we report measurements of hygroscopic growth at RH < 99.5% and cloud condensation nucleus activity for SOA generated via dark ozonolysis of α-pinene. Using these data we explore the potential role of surface tension for cloud droplet activation.

2. MEASUREMENTS

The SOA particles were generated via gas-phase oxidation of α-pinene and ozone. The generation was performed in a reaction vessel with a volume of about 12 dm^3. Inside the reactor the following air flows were mixed: synthetic hydrocarbon free air (hereafter synthetic air) carrying α-pinene vapor, synthetic air with ozone concentrations of 100 to 1000 ppbv, and additional pure synthetic air. The residence time in the tank was several minutes, and the generated SOA particles were directly fed to the different instruments.

For all measurements, different dry particle sizes were selected with a DMA (Differential Mobility Analyzer). LACIS (Leipzig Aerosol Cloud Interaction Simulator, [*Stratmann et al.*, 2004] and an HH-TDMA (High Humidity Tandem Differential Mobility Analyzer, [*Hennig et al.*, 2005]) measured the hygroscopic growth at high relative humidities (RHs) above 80%, with the HH-TDMA measuring up to 98% and LACIS up to 99.5% RH [*Wex et al.*, 2005]. A continuous-flow streamwise thermal-gradient CCNc (Cloud Condensation Nucleus counter [*Roberts and Nenes*, 2005]) was used for measurements of the particle activation.

3. MODELING

The modeling was based on the approach of a single parameter representation of the hygroscopicity, which is described e.g. in *Petters and Kreidenweis* [2007] and in *Wex et al.* [2007], using κ or ρ_{ion} as this single parameter, respectively. The basic assumption of these approaches is, that the number of ions/molecules in the particle/ droplet solution does not change, once the particle has deliquesced. In these approaches, this single parameter, be it κ or ρ_{ion} (both differ only by a constant), models the properties of the particle substance(s) in the Raoult (or solubility) term of the Köhler equation. Then the only other unknown in the Köhler equation is the surface tension (σ) in the Kelvin term.

For evaluating the data measured for the SOA particles in our study, hygroscopicity (i.e., κ and ρ_{ion}) was derived based on the measured hygroscopic growth and cloud droplet activation. For this, a value was ascribed to σ, and the value for the hygroscopicity was obtained, that, together with this σ, reproduced the measured values.

4. RESULTS

Figure 1 shows values of κ (and ρ_{ion}) derived from hygroscopic growth and activation measured with LACIS and with the CCNc, respectively. For the measured hygroscopic growth, the values were derived for σ of 30 and 72.8 mN/m (the latter being the value for water). The results are depicted as filled symbols. The measured activation (open symbols) was modeled assuming σ of 30, 50, 55, 60, 65, and 72.8 mN/m. Three things can be seen from Figure 1:

1) The hygroscopicity increases as the particles become more dilute, i.e. the values obtained for κ (and ρ_{ion}) are not constant but vary with the SOA concentration in the particle. This change in hygroscopicity becomes clearly obvious only at RHs above 98% and thus could not be observed in the past. This explains the low values of σ that had to be assumed in the past, when a constant hygroscopicity was assumed.

2) Looking at the grey area, it becomes obvious that a value for σ of 30 mN/m is too low to get a consistent transition from hygroscopic growth to activation data, and σ of water likely is too high. It can reasonably be assumed that σ is not lower than 50mN/m. The upper limit of σ is unclear, since it depends on the nature of the volume fraction versus hygroscopicity relationship. This will be discussed in a future publication.

3) The change in hygroscopicity can not be counteracted by a concentration dependent σ. Would the hygroscopicity be constant (a horizontal line in Figure 1), the measured activation could only be reproduced if σ was decreasing towards more diluted particle/ droplet solutions, instead of increasing towards the value of water, which usually is observed for organic solutions.

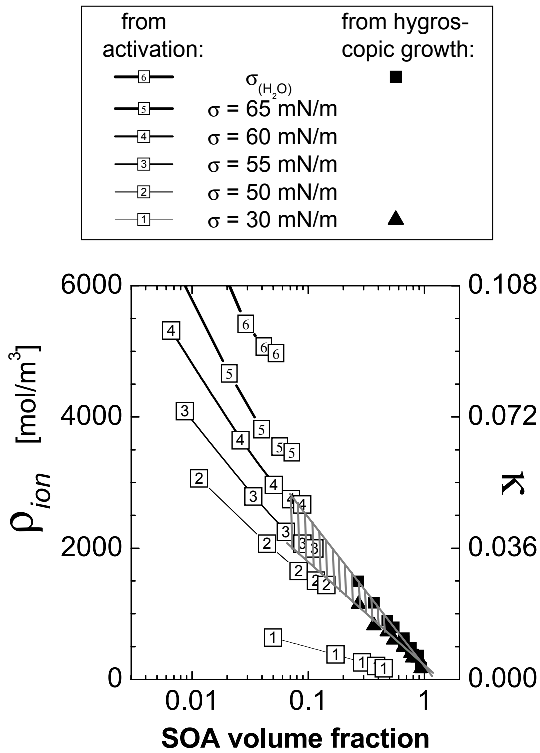

Fig. 1: *Hygroscopicity of SOA particles derived from LACIS and CCNc measurements assuming different values for σ, expressed as ρ_{ion} (and κ) as a function of the SOA volume fraction.*

ACKNOWLEDGEMENTS

This work was funded in part by the National Science Foundation under grant ATM-0436196. Logistical support was provided from the Atmospheric Composition Change, the European Network of Excellence (ACCENT) program Access to Infrastructures.

BIBLIOGRAPHY

Duplissy, J., M. Gysel, M. R. Alfarra, J. Dommen, A. Metzger, A. S. H. Prevot, E. Weingartner, A. Laaksonen, T. Raatikainen, N. Good, S. F. Turner, G. McFiggans, and U. Baltensperger (2008), Cloud forming potential of secondary organic aerosol under near atmospheric conditions, *Geophys. Res. Lett.*, *35*, doi:10.1029/2007GL031075.

Facchini, M. C., S. Decesari, M. Mircea, S. Fuzzi, and G. Loglio (2000), Surface tension of atmospheric wet aerosol and cloud/fog droplets in relation to their organic carbon content and chemical composition, *Atmos. Environ.*, *34*, 4853-4857.

Hennig, T., A. Massling, F. J. Brechtel, and A. Wiedensohler (2005), A tandem DMA for highly temperature-stabilized hygroscopic particle growth measurements between 90% and 98% relative humidity, *J. Aerosol Sci.*, *36*, 1210-1223.

Huff Hartz, K. E., J. E. Tischuk, M. N. Chan, C. K. Chan, N. M. Donnahue, and S. N. Pandis (2006), Cloud condensation nuclei activation of limited solubility organic aerosol, *Atmos. Environ.*, *40*, 605-617.

Kiss, G., E. Tombacz, and H.-C. Hansson (2005), Surface tension effects of humic-like substances in the aqueous extract of tropospheric fine aerosol, *J. Atmos. Chem.*, *50*, 279-294.

Petters, M. D., and S. M. Kreidenweis (2007), A single parameter representation of hygroscopic growth and cloud condensation nucleus activity, *Atmos. Chem. Phys.*, *7*, 1961-1971.

Prenni, A. J., M. D. Petters, S. M. Kreidenweis, P. DeMott, and P. J. Ziemann (2007), Cloud droplet activation of secondary organic aerosol, *J. Geophys. Res.*, *112*, doi:10.1029/2006JD007963.

Roberts, G., and A. Nenes (2005), A continuous-flow streamwise thermal- gradient CCN chamber for atmospheric measurements, *Aerosol Sci. Technol.*, *39*, 206-221.

Salma, I., R. Ocskay, I. Varga, and W. Maenhaut (2006), Surface tension of atmospheric humic-like substances in connection with relaxation, dilution, and solution pH, *J. Geophys. Res.*, *111*, doi:10.1029/2005JD007015.

Stratmann, F., A. Kiselev, S. Wurzler, M. Wendisch, J. Heintzenberg, R. J. Charlson, K. Diehl, H. Wex, and S. Schmidt (2004), Laboratory studies and numerical simulations of cloud droplet formation under realistic super-saturation conditions, *J. Atmos. Oceanic Technol.*, *21*, 876-887.

Sun, J., and P. A. Ariya (2006), Atmospheric organic and bio-aerosol as cloud concensation nuclei (CCN): A review, *Atmos. Environ.*, *40*, 795-820.

VanReken, T. M., N. L. Ng, R. C. Flagan, and J. H. Seinfeld (2005), Cloud condensation nucleus activation properties of biogenic secondary organic aerosol, *J. Geophys. Res.*, *110*, D07206, doi:07210.01029/02004JD005465.

Varutbangkul, V., F. J. Brechtel, R. Bahreini, N. L. Ng, M. D. Keywood, J. H. Kroll, R. C. Flagan, J. H. Seinfeld, A. Lee, and A. H. Goldstein (2006), Hygroscopicity of secondary organic aerosols formed by oxidation of cycloalkenes, monoterpenes, sesquiterpenes, and related compounds, *Atmos. Chem. Phys.*, *6*, 2367-2388.

Virkkula, A., R. van Dingenen, F. Raes, and J. Hjorth (1999), Hygroscopic properties of aerosol formed by oxidation of limonene, α-pinene, and β-pinene, *J. Geophys. Res.*, *104*, 3569-3579.

Wex, H., A. Kiselev, F. Stratmann, J. Zoboki, and F. Brechtel (2005), Measured and modeled equilibrium sizes of NaCl and $(NH_4)_2SO_4$ particles at relative humidities up to 99.1%, *J. Geophys. Res.*, *110*, doi:10.1029/2004JD005507.

Wex, H., T. Hennig, I. Salma, R. Ocskay, A. Kiselev, S. Henning, A. Massling, A. Wiedensohler, and F. Stratmann (2007), Hygroscopic growth and measured and modeled critical super-saturations of an atmospheric HULIS sample, *Geophys. Res. Lett.*, *34*, doi:10.1029/2006GL028260.

NUCLEATION AND GROWTH OF DROPLETS SIMULATED IN THE DYNAMIC CLOUD CHAMBER AND THE MICROPHYSICAL PARCEL MODEL

Katsuya Yamashita, Takuya Tajiri, Akihiro Hashimoto, Masataka Murakami,
Narihiro Orikasa, and Atsushi Saito
Meteorological Research Institute, Tsukuba, Japan

1. INTRODUCTION

Aerosol particles affect characteristics of clouds, namely, their microphysical structures, radiation properties, spatial extent, and lifetime, and consequently surface rainfall as well. Although some of the mechanisms have been investigated with numerical models (e.g., Khain et al., 1999), our knowledge of them is still not sufficient. For a better understanding of the influences of aerosol particles on cloud, it is important to investigate the microphysical properties of various kinds of clouds and physico-chemical properties of CCN and IN.

In order to study the effect of aerosol particles on the initiation of water and ice clouds, we have been developing a new parcel model with detailed cloud microphysics. We have also been conducting the laboratory experiment using the dynamic cloud chamber which simulates the cloud processes in adiabatically ascending air parcel.

The comparison of results from model simulation and laboratory experiment is very useful for understanding the each result. The preliminary comparison of nucleation and condensational growth of the warm cloud was conducted. This result is reported in this paper.

2. NUMERICAL PARCEL MODEL

Our parcel model is based on that originally developed by Chen and Lamb (1994). This model has multi-dimensional bins to express a variety of properties of hydrometeors to investigate the initiation of water and ice cloud. For droplets, the masses of pure water and soluble material are the prognostic variables in two-dimensional bin space.

The liquid-phase microphysical processes included in the model are the activation of soluble aerosol particles and the growth of droplets by condensation, collision, and coalescence.

3. DYNAMIC CLOUD CHAMBER

The dynamic cloud chamber was built in 2005 at Meteorological Research Institute (MRI) of Japan Meteorological Agency (JMA). The detailed description of chamber, equipped instruments, and experimental procedure are available in Tajiri et al. (2006). The chamber consists of a 1.4m^3 test volume (1.8 m high and 1 m in diameter) inside a perforated cylindrical stainless steel chamber. The pressure can be controlled between 30 hPa and 1000 hPa by adjusting the evacuation rate of a vacuum pump. And the temperature can be controlled to any temperature between 30 to –100 °C by circulating the coolant through stainless steel plate coil that is welded to the wall. Our dynamic cloud chamber is able to simulate the cloud processes (adiabatic expansion) in the troposphere by synchronously controlling the temperature and pressure inside the chamber.

To simulate adiabatic ascents, the initial condition of pressure, temperature, dew-point temperature, and ascent rate

Corresponding author: Katsuya Yamashita, Meteorological Research Institute, 1-1 Nagamine, Tsukuba, Ibaraki 305-0052, Japan.
E-mail: kayamash@mri-jma.go.jp

are necessary for calculating the cooling/evacuation rate and LCL.

The chamber is equipped with some instruments for measuring the size distribution and shape of the aerosol and cloud particles from 0.3 µm to 5 mm in diameter. The instruments used in this study are briefly summarized here.

Sizes and concentrations of aerosol particles and cloud droplets are measured with a Cloud Aerosol Spectrometer (CAS, DMT). It is able to detect particles in the size range between 0.3 and 30 µm by measuring the forward and backward scattering intensities of laser. This device is installed directly in a flange on the side wall of the outer chamber. The data that was for particles smaller than 10 µm were used here for CAS data, because sampling efficiency was low for particles larger than 10 µm.

Sizes, concentrations, and shapes of cloud droplets and ice particles larger than 10 µm are measured with a Cloud Particle Imager Probe (CPI, Lawson et al., 2001). It is able to measure cloud and ice particles in the size range between 10 µm and 2 mm by using triggering, illuminating lasers, and high resolution CCD camera. It is installed at the bottom of the chamber.

4. DATA FOR COMPARISON

To compare the model result with that from the cloud chamber experiment, it is necessary to give the thermodynamic data and CCN size distribution as the initial condition of the model. The measurement data immediately before the start of adiabatic expansion in chamber experiment were input into the model as the initial thermodynamic and microphysical conditions.

Figure 1 shows the profiles of temperatures and number concentrations of particles from the chamber experiment. In order to simulate the warm convective cloud, the initial pressure, temperature, dew-point temperature, and ascending speed were set to 1000 hPa, 20 °C, 10 °C, and 3 m/s, respectively. The broken horizontal lines in the Fig. 1 show the lifting condensation level (LCL). In this experiment, the pressure and temperature at the LCL were 840 hPa and 5.9 °C, respectively.

The small NaCl particles (supermicron range) were used as test aerosol for this experiment. Figure 2 shows the size distribution of the small NaCl particles immediately before the start of adiabatic expansion in the experiment. The size range was between 0.3 µm (minimum) and 10 µm (maximum). From the results of the elemental composition analysis using energy dispersion X-ray spectrometer (EDX) equipped with electron microscope, impurities were hardly included in the

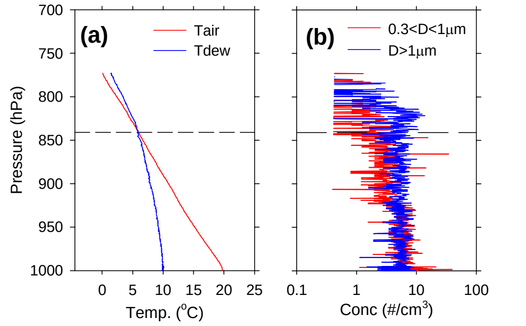

Figure 1 Vertical profiles of (a) temperature (red) and dew-point temperature (blue) and (b) number concentrations of different size range in diameter (red: 0.3<D<1um, blue: D>1um). Broken horizontal line shows the LCL level.

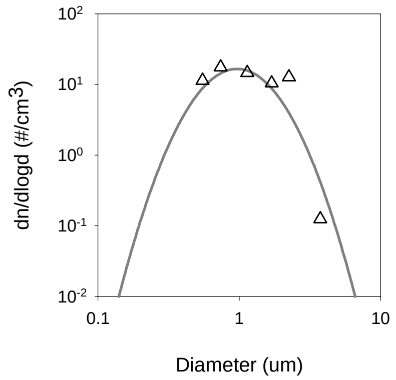

Figure 2 Size distribution of the NaCl particles measured by CAS. Solid curve is the fitted log-normal distribution.

NaCl particles. The log-normal distribution (solid curve), fitted to the measured size distribution, was input into the model as the initial size distribution of CCN. The total number concentration was 9.0 particles cm^{-3}. The mode diameter and standard deviation were 0.97 µm and 0.5, respectively. Note that all aerosol particles are assumed to be composed of sodium chloride and to be able to work as CCN in the model.

In this study, 45 and 32 bins were adapted for water mass and solute mass, respectively. The time step for calculation was 1 s.

5. RESULT AND DISCUSSION

Figure 3 shows time series of hydrometeor variables. Abscissa indicates the relative time from the LCL. The water vapor mixing ratio obtained from the experiment (red line in Fig. 3a) started to decrease before reaching the LCL. It is suspected that condensation of the water vapor occurred on the wall inside the chamber. Although the loss of the water vapor presented here was about 10% at the LCL, it is about 3% now by the improvement.

The liquid water content estimated from droplet size distributions (green line in Fig. 3b) suddenly increases at the LCL. After that, it gradually decreases with time. It is supposed that the larger droplets settle to the bottom of the inner chamber due to gravitational sedimentation. On the other hand, in the model, the liquid water content (blue line in Fig. 3b) increases with time because the sedimentation was not included here.

From Fig. 3c, the number concentrations of cloud droplets with diameter larger than 5 µm obtained from the experiment were almost the same as those from the model simulation until about 50 second after passing the LCL. However, time variations of mean volume diameter (Fig. 3d) were different from each other. This difference means that the growth of droplets is different between the experiment and the model.

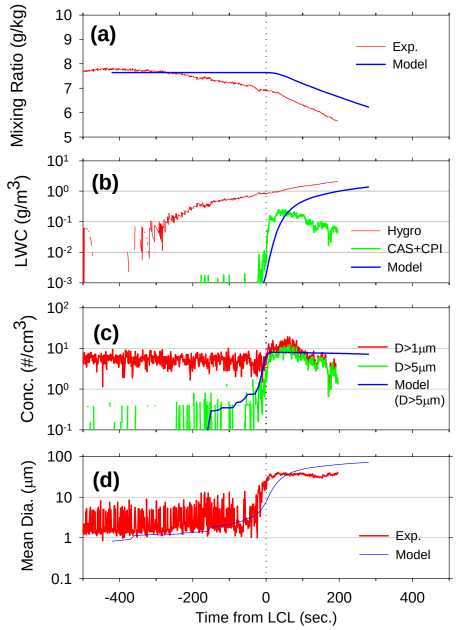

Figure 3 Time series of (a) water vapor mixing ratio, (b) LWC, (c) number concentration, and (d) mean volume diameter in the experiment. Red line shown in (b) is calculated from hygrometer data and blue one is calculated from the size distribution measured by CAS and CPI. Vertical dotted lines show the time at the LCL.

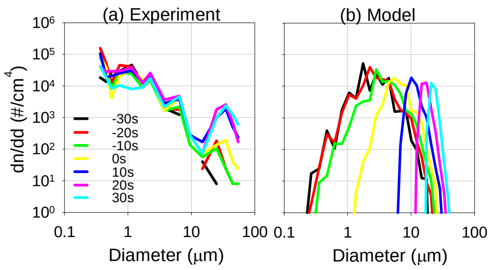

Figure 4 Size distributions around the LCL in (a) the experiment and in (b) the model. The each color indicates the times acquired data.

Figure 4 shows the size distributions before and after the formation of cloud droplets. In the experiment, the concentrations of droplets larger than 10 µm mainly increased with time, but those of droplets smaller than 10 µm did not change so much. On the other hand, in the model, those of droplets smaller than 10 µm decreased with time by condensational growth. Time evolutions of the size distribution, especially droplets smaller than 10 µm, before and after the cloud formation were different. In our model, it is assumed that all the particles grow to equilibrium sizes before attaining their critical supersaturation. Once supersaturation exceeds the critical values for the particles, they are activated and quickly grow by vapor condensation. However, the NaCl particles smaller than 10 µm used in the experiment did not change so much although the NaCl particles were hygroscopic. The cause of the difference in the size distributions between the experiment and the model around the LCL may be the difference in the maximum supersaturation produced. Water vapor condensation onto the wall surface may have decreased the maximum supersaturation in the chamber experiment and prevent smaller salt particles from being activated. In order to clarify the cause, it is needed to investigate the wall effect as water vapor sink and consequent modulation of CCN activation and growth processes.

Figure 5 shows the time series of size distributions. The droplets grown up to 30 µm seemed not to grow up any more in the experiment, while those in the model grew up to 60 µm. Because the droplets larger than 40 µm settled to the bottom of the chamber within 60 seconds, most droplets larger than 40 µm can not be detected easily in the chamber experiment. In the size range of smaller than 40 µm, droplets larger than 10 µm suddenly appeared at the LCL in the experiment. This feature was seen in other adiabatic expansion experiments using the ambient air, though the size of droplets appeared at the LCL was different. On the other hand, droplets in the model gradually grew up. This reason of the difference between the experiment and the model is now being investigated.

6. SUMMARY

The simulation of the warm cloud was conducted by using MRI dynamic cloud chamber and the detailed cloud model.

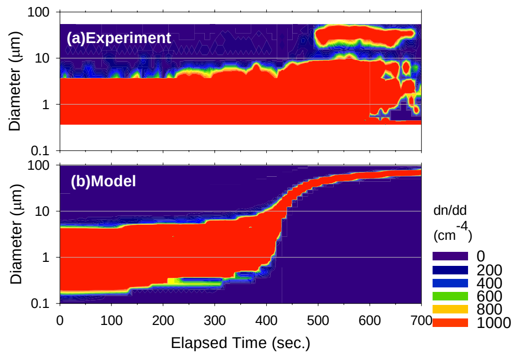

Figure 5 Time series of size distribution obtained from (a) experiment and (b) model. The vertical white line indicates the time reached to the LCL (0 sec.).

The preliminary results of comparison between both the simulations were presented. It was found that there were some differences in the microphysical characteristics, such as LWC, size distribution, and condensation growth rate. From these, it is necessary to investigate some aspects of chamber performance (e.g., larger droplets loss by the gravitational sedimentation, etc.) in order to better understand the results of the chamber experiment.

We will further improve the detailed microphysical model and MRI dynamic cloud chamber through comparisons between them and investigate aerosol-cloud interactions and ice nucleation processes.

REFERENCES

Chen J. –P. and D. Lamb, 1994: Simulation of cloud microphysical and chemical processes using a multicomponent framework. Part 1: Description of the microphysical model. *J. Atmos. Soc.*, 51, 2613-2630.

Khain A., A. Pokrovsky, and I. Sednev, 1999: Some effects of cloud-aerosol interaction on cloud microphysics structure and precipitation formation: Numerical experiments with a spectral microphysics cloud ensemble model. *Atmos. Res.*, 52,

195-220.
Lawson R. P., B. A. Schmitt, and T. L. Jensen, 2001: An overview of microphysical properties of Arctic cloud observed in May and July 1988 during FIRE ACE. *J. Geophys. Res.*, 106, D14, 14989-15014.
Tajiri T., M. Murakami, N. Orikasa, A. Saito, and K. Kusunoki, 2006: Laboratory experiments of ice formation in cloud simulation chamber. *Proceedings of the 12th Conference on Cloud Physics of the American Meteorological Society*, 10-14 July, 2006, Madison WI. P2.53.

A NOVEL RADIOSONDE PAYLOAD TO STUDY UPPER TROPOSPHERIC / LOWER STRATOSPHERIC AEROSOL AND CLOUDS

Martin Brabec, Frank G. Wienhold, Marc Wüest, Ulrich Krieger, Thomas Peter
Institute for Atmospheric and Climate Science, ETH Zurich

1. INTRODUCTION

Dehydration mechanisms driven by the formation of visible and subvisible cirrus clouds determine the atmospheric water vapor budget and thus the chemical and radiative properties of the upper troposphere and the stratosphere. In contrast to previous understanding recent in situ observations have revealed high supersaturation with respect to ice of several 10% occurring not only in clear air surrounding cirrus clouds but also inside the cirrus themselves, and apparently also in large interconnected regions where they cannot be explained easily in terms of local upwelling. It is not well understood how such supersaturations, if not caused by instrumental artifacts, can be maintained within clouds exposing large ice surface areas to the water vapor. Precise and frequent measurements of cirrus properties and relative humidity using independent instrumentation are required to obtain a better understanding of dehydration processes and of their influence on the global atmospheric radiation budget.

To further investigate these findings a radiosonde payload was developed that is launched regularly on meteorological sounding balloons from Zurich and Payerne since early 2008. A pTu sonde along with the «SnowWhite» frost point hygrometer (meteolabor SRS-C34, night type) is supplemented by the new Compact Optical Backscatter AerosoL Detector (COBALD). This lightweight (500 g including power supply) and cost-effective sensor applies high power LEDs to measure optical backscatter at wavelengths centered around 455 and 870 nm. We demonstrate the potential of the new COBALD sonde for the characterization and understanding of cirrus nucleation and growth. The sonde observations provide particle surface area densities vis-à-vis relative humidity in the clouds.

2. INSTRUMENT DESCRIPTION

(a) PRESENT STATUS OF INSTRUMENT. Backscatter sondes are a valuable tool to characterize in-situ aerosol or cloud particles on balloon soundings. The lightweight balloon sonde COBALD (Compact Optical Backscatter AerosoL Detector) was designed and tested at our institute (IACETH) recently. It is based on similar principles as the sonde of Rosen and Kjome [1991] which has been used extensively in field studies. The new sonde development was initiated in close consultation with Jim Rosen and Norm Kjome. Their original design, even in a downscaled version, does not meet the weight restrictions of the operational sounding payloads in many countries including Switzerland. Table 1 lists some technical properties of COBLAD.

(b) OPTICS. COBALD applies two high-power LEDs. Rated to 250 mW optical power each, the total light utilizable on average for the backscatter measurement is comparable in magnitude to that of the flashtube sonde (Rosen and Kjome, 1991). The operation scheme chosen for COBALD is depicted in Figure 1. The emitted light is collimated to cones of less than 4° beam divergence (HWHM). The backscatter is collected by a fast lens (25 mm aperture with 18 mm focal length)

Table 1: The backscatter sonde employed within this package has following properties.

Feature	**Expected specification**	**Remark**
backscatter intensity dynamic range	40dB	covers range from aerosols (0.1 ppb cond.) to thick anvil outflow (100 ppm ice)
detectable RH relative to ice	20 - 200 %	lower and upper limit determined by SnowWhite single Peltier stage
weight of backscatter sonde including power supply	540 g	suited for piggyback in many applications
weight of entire ensemble incl. SnowWhite and pT sonde	< 1700 g	for operational service
time resolution backscatter	1 Hz	digital transmission via pTu-sonde data stream

and focused onto a silicon detector yielding a field of view of ±6° oriented into the same direction as the LED emission. With a geometric separation of 3 cm limited by the optical-apertures a good overlap between the emission and reception fields of view is established at a distance greater than 0.5 m from the sonde.

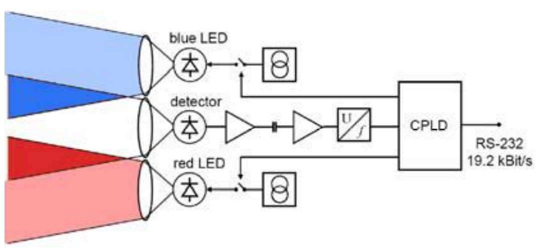

Figure 1: Operation scheme of the backscatter sonde.

In wavelength the emission is confined to $\Delta\lambda_{½}$ = 20 nm around 455 nm in the blue and to $\Delta\lambda_{½}$ = 50 nm around 870 nm in the red optical channel and continuous in time. The wavelength characteristics, together with the high LED current to light conversion efficiency, is advantageous for lowering power consumption and weight. The continuous beam, however, demands special means for data acquisition in order to discern the backscattered light from background and noise sources. In addition, high dynamic range is required in backscatter measurements in order to adequately resolve the molecular Rayleigh scattering which is used as a reference, to provide sufficient headroom for the aerosol scattering on top of the Rayleigh scattering, and to cover the pressure span of an approximate factor 50 encountered during a balloon sounding.

(c) ELECTRONIC CONFIGURATION. To meet these requirements the LED emissions are chopped with a duty cycle of 50 % and a phase sensitive (lock-in) detection scheme is applied to retrieve the backscattered light signal. The modulation of the two LEDs is 90° out of phase so that both optical channels are carried on the same frequency of 300 Hz. Adequate dynamic range and low signal offset are assured by frequency conversion of the detector signal through a highly linear synchronous circuit with subsequent digital implementation of the phase sensitive detection scheme inside a complex programmable logic device (CPLD) that directly communicates to the monitoring computer or the sonde telemetry through a standard RS-232 interface.

The electrical noise of the first amplifier stage following the detector limits the minimum detectable optical power to 200 fW (red channel) at the given 1 Hz bandwidth. This corresponds to a fraction of 10^{-12} of the power emitted by the LED. Daylight saturates the first amplifier stage which has to be DC coupled to the detector photodiode in order to obtain the described signal-to-noise performance. Thus, only nighttime measurements are carried out. This is common for backscatter sondes and no serious limitation since also the SnowWhite sensor is best operated at nighttime to obtain high quality data.

(d) SIGNAL TREATMENT. Backscatter sonde signals obtained at the optical wavelength λ are usually expressed as backscatter ratios T_λ (the ratio of the aerosol to the molecular (Rayleigh) scattering intensity) or as aerosol backscatter ratios B_λ (the ratio of the particle backscatter to the Rayleigh backscatter intensity), where $T_\lambda = B_\lambda - 1$. Particle

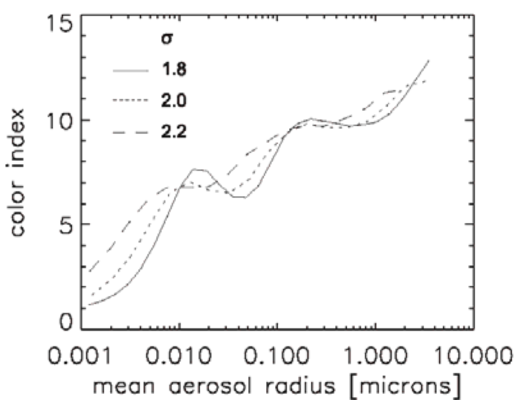

Figure 2: Color index. The color index of a lognormal aerosol distribution as measured by COBALD. The aerosol is assumed to have a refraction index of 1.45. The calculations were carried out for lognormal aerosol distributions with mean radius given on the x-axis and a spread σ indicated by the different lines. All lines will approximate the color index of 15 for larger particles.

size information can be retrieved from the ratio B_{870} / B_{455} which we, following the convention of Rosen and coworkers, refer to as color index *CI*. The *CI* = 1 limit is reached for purely molecular Rayleigh backscatter, whereas for large particles *CI* converges towards 15, since the the aerosol scattering for both probing wavelengths equal and the Rayleigh scattering ratio is 15 (λ^{-4}).

Figure 2 presents the color index dependence on mean radius and spread of lognormal particle distributions. It reveals that a mean aerosol radius of approx. 5 µm can be quantified at maximum with the probing wavelengths used. Above this level it can only be stated that the particle radius must be larger than this limit. For narrow aerosol distributions (σ ≤ 2) radius retrieval may not be unique due to the non monotonic dependence. Still, total particle surface area density can be determined for arbitrarily large particles with the help of the backscatter intensity, provided this measure is robustly characterized and the signal remains within the instrumental dynamic range.

4. FIRST BALLOON FLIGHT OF THE BACKSCATTER SONDE

The COBALD sonde had its premier flight in the late evening of 15 February 2007. The night from 15 to 16 February 2007 was selected because the weather forecast indicated a relatively clear and thus cool night with weak wind. Both parameters were important to have a relaxed premier launch avoid passing through thick low level clouds that could contaminate the sonde optics. The radiative cooling and winterly conditions further let suppose the growth of cirrus clouds.

Two units, orientated to opposite directions were flown hosted by a modified pT-sonde of Meteolabor using GPS data interface to transmit the backscatter sondes' signals. This implied removal of the GPS unit for this flight. At a later stage we intend to use the interface for a combined transmission of the CO-

BALD and GPS telemetry. We chose to fly with two COBALD sondes to be able to intercompare and hence learn about design issues. Figure 3 shows a scatter plot of the two sondes' blue channel

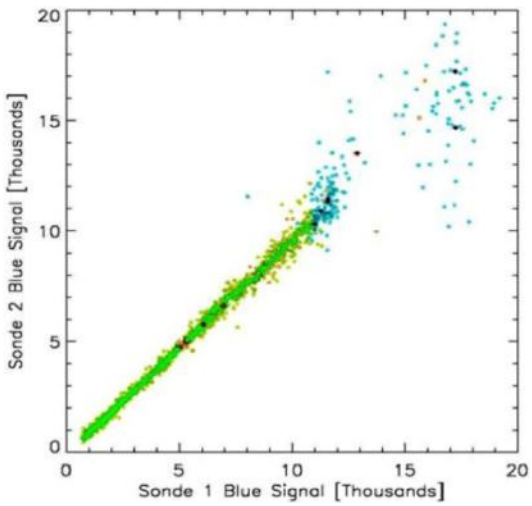

Figure 3: Correlation of the blue channels. Thin light points: unscaled one-second raw data; thick dark points: 100 m altitude averages. Blue colors: planetary boundary layer; red colors: cirrus between 9.2 and 9.8 km altitude; green colors: other altitudes.

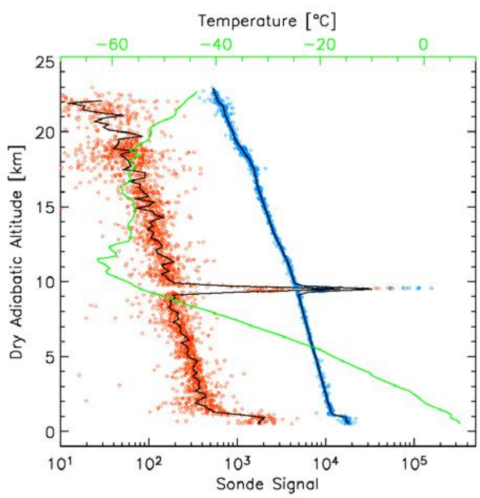

Figure 4: The temperature profile is provided in green. It shows the raw data of the 455 nm (blue) and 870 nm (red) channels. The black lines denote averages over 200 m altitude bins.

data. The correlation is excellent outside the boundary layer (green colors). Due to the higher spatial variability of the aerosol in the planetary boundary layer (blue colors) the correlation is smaller for the two sondes probing opposite directions. The two sondes gave almost identical results.

Figure 4 shows altitude profiles from the first flight. Temperature and pressure data served to calculate the dry adiabatic pressure altitude. Temperature data is superimposed in green on both panels indicating a location of the tropopause near 12 km.

Figure 5 provides estimated aerosol backscatter data together with the deduced color index at expanded altitude scale around the cirrus cloud. A signal increase of more than two orders of magnitude is observed in the 455-nm channel, the maximum cirrus signal at 870 nm exceeds that of the aerosol level by almost three orders of magnitude.

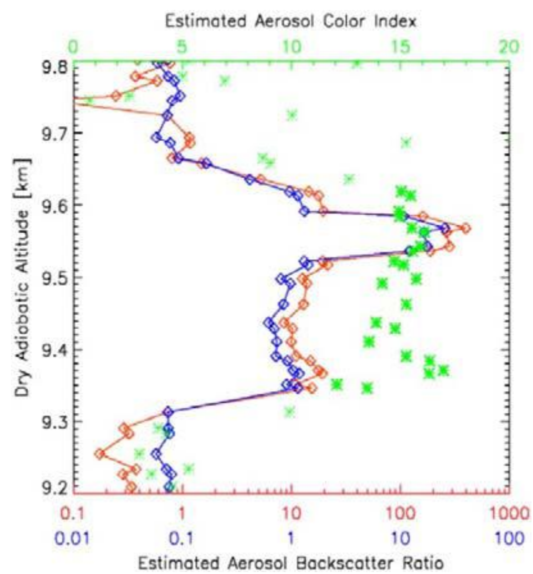

Figure 5: Cirrus cloud. Data integrated over 1 s. The color index (defined as the ratio of the red over blue aerosol backscatter ratios) is given by green symbols. Bold symbols indicate color index values found inside the cloud.

Figure 5 also confirms that both channels are below the saturation limit of 3 x 10^5 signal units. The color index of approximately 15 found inside the cirrus, illustrated as bold symbols, indicates that the particle mean radius exceeds the 5 μm limit that the instrument can resolve according to Figure 2. With the accompanying increase of aerosol backscatter signal, however, cirrus clouds can clearly be discerned from (large) aerosol particles. This is of key importance to examine the occurrence of supersaturation in clear sky or cirrus cloud conditions.

5. CONCLUSION

First observations with COBALD show the new backscatter sonde can robustly provide parameters of the aerosol and hydro particle size distributions in the troposphere (resolving the boundary layer) and stratosphere. Combined with a pTu sonde and an accurate hygrometer (SnowWhite proposed) it will give new insight into the water vapor budget and cloud-physical processes especially in cirrus clouds.

Due to the small weight of the backscatter sonde, the sonde can be launched with ordinary pTu-sondes. It will be possible to use this sonde extensively in future monitoring and research programs or international services (though with the present version only for nighttime measurements). Indeed, a main part of the planned outreach activities will aim at reaching widespread distribution of this new development.

Through an attractive pricing and the widespread deployment a new climatology of cirrus clouds, their cloud particle densities and sizes and the relative humidity in and around midlatitude cirrus clouds can be derived from regular measurements.

References

Rosen JM, Kjome NT, Appl. Opt., 30 (12): 1552-1561, 1991

CHARACTERIZING CLOUD ENVIRONMENTS TO SUPPORT THE DEVELOPMENT OF AIRCRAFT ICING CERTIFICATION STANDARDS FOR THE REGULATORY AUTHORITIES

Stewart G. Cober and George A. Isaac

Cloud Physics and Severe Weather Research Section, Environment Canada
Toronto, Ontario, Canada

1. INTRODUCTION

The Code of Federal Regulations Title 14 Chapter 1 Part 25 Appendix C (FAR 25-C) (Federal Aviation Administration 1999) presents characterizations of aircraft icing environments for continuous maximum (stratiform) and intermittent maximum (convective) clouds. The icing environments are defined as functions of air temperature, maximum liquid water content (LWC), droplet median volume diameter (MVD) and horizontal extent. The FAR 25-C characterizations of stratiform cloud environments only included MVD values up to 40 µm, likely because it was not possible to accurately measure larger MVD values during the 1940's when the observations were collected. The maximum icing envelopes (nominally ≥ 99 percentile for LWC) included in FAR 25-C have been used for the certification of commercial aircraft since the mid 1950s. While an upper MVD limit of 40 µm for stratiform clouds has been used for aircraft certifications, hazards associated with supercooled large drops (SLD) > 100 µm in diameter and icing environments with drop MVD > 40 µm have been demonstrated in numerous reports (Sand et al. 1984, Cooper et al. 1984, Politovich 1989, Pobanz et al. 1994, Cober et al. 1996, Ashenden and Marwitz 1998, and Cober et al. 2001a). Collectively, these reports have demonstrated that the FAR 25-C envelopes do not adequately capture all aircraft icing environments that include SLD conditions. This has led to a series of measurement programs in the past 15 years which were designed in part to adequately characterize icing environments that contained SLD conditions. Following the crash of a turbo-prop commuter aircraft near Roselawn Indiana in 1994, the National Transportation Safety Board report (NTSB 1996) suggested that the aircraft encountered SLD > 100 µm in diameter and that these drops contributed to the development of a ridge of ice that accumulated behind the de-icing boots of the aircraft (Marwitz et al. 1996). Subsequent to the Roselawn accident, the Federal Aviation Administration developed an In-flight Aircraft Icing Plan (FAA, 1997) which contained specific recommendations for preventing accidents caused by in-flight icing. One recommendation of this plan was to consider a comprehensive redefinition of the current aircraft icing certification envelopes when sufficient information was available worldwide on SLD and other icing conditions. The plan also recommended the establishment of an aviation rulemaking advisory committee harmonization working group (HWG) which was to be tasked with the development of certification criteria and advisory material for the safe operation of airplanes in SLD icing conditions. An Ice Protection HWG (IPHWG) was subsequently established with the specific task of "defining an icing environment that includes SLD aloft, near the surface, and in mixed-phase (supercooled liquid drops and ice crystals) conditions if such conditions are determined to be more hazardous than the supercooled liquid-phase icing environment." In support of the IPHWG, a large data base of aircraft icing observations was acquired and analyzed, and the data were used to characterize aircraft icing environments that included SLD. The primary analysis undertaken in support of the IPHWG is presented here. This characterization may eventually be used for aircraft certification purposes.

Corresponding Author: S.G. Cober, Environment Canada, 4905 Dufferin Street, Toronto, Ontario, Canada, M3H 5T4. Stewart.Cober@ec.gc.ca

2. FIELD PROJECTS

Observations of aircraft icing environments that included SLD were made during five field projects conducted by researchers from Environment Canada and the NASA-Glenn Icing Technology Branch during the period from 1995 through 2000. These field projects included the First (CFDE I) and Third (CFDE III) Canadian Freezing Drizzle Experiments (Isaac et al. 2001a, Cober et al. 2001a), the First International Satellite Cloud Climatology Project (ISCCP) Regional Experiment Arctic Cloud Experiment (FIRE.ACE) (Curry et al. 2000), the First Alliance Icing Research Study (AIRS I) (Isaac et al. 2001 a, b) and the SLD Flight Research Study (Miller et al. 1998). With the exception of FIRE.ACE, each of these projects had a specific objective to gather in-situ observations with instrumented research aircraft in winter storm environments where SLD was forecast or observed to exist. In all cases, the instrumentation on the aircraft was specifically oriented to adequately measure SLD environments including the concentrations, sizes and LWC of the entire drop spectrum. In total there were 134 research flights undertaken during these projects including 81 flights with the National Research Council of Canada Convair-580 aircraft and 53 flights with the NASA-Glenn Twin Otter aircraft.

3. INSTRUMENTATION

Common instruments were mounted on the NRC Convair-580 research aircraft during CFDE I, CFDE III, FIRE.ACE, and AIRS I. These included two King hot wire liquid water content (LWC) probes, a Nevzorov hot wire LWC probe, a Nevzorov hot wire total water content (TWC) probe, a Rosemount Icing Detector (RID), two Particle Measuring System (PMS) Forward Scattering Spectrometer Probes (FSSP), two PMS 2D Cloud Particle Imaging Probes (2D-C and 2D-G), a PMS 2D Precipitation Particle Imaging Probe (2D-P), and two Rosemount Temperature Probes. The instruments were mounted on three under-wing pylons including a dedicated pylon for the LWC probes and two pylons that could each hold four PMS type probes. These instruments are described in Cober et al. (2001 a,b,c). The NASA- Glenn Twin Otter research aircraft flew with a similar instrumentation suite for AIRS I and the NASA SLD Study, although there were fewer duplicate instruments. Its instruments included a King LWC Probe, Nevzorov LWC and TWC Probe, FSSP, 2D-G, RID, and Rosemount Temperature Probe. The temperature, LWC, and RID instruments were mounted on the fuselage, while the FSSP and 2D probes were mounted on under wing pylons.

4. DATA BASE OF SLD OBSERVATIONS

The data from each flight were averaged in sequential 30-second intervals, corresponding to a horizontal length scale of 2.9 ± 0.3 km for the Convair-580 data and 2.1 ± 0.2 km for the Twin Otter data. The 30-s averaging scale was chosen because it represented a short averaging scale and a scale that generally allowed sufficient 2D measurements for statistical significance (i.e. > 100 counts). The phase of each 30-second data point was determined following Cober et al. (2001b). The data were also averaged in 60-s, 120-s and 300-s intervals. For each 30-s data point that was assessed to be liquid-phase or mixed-phase with an ice crystal concentration < 1 L^{-1}, the entire FSSP spectrum, 2D-C spectrum ≥ 5 pixels (125 μm for the 2D-C), and 2D-P spectrum ≥ 5 pixels (1000 μm) were used to produce a binned drop spectrum. FSSP and 2D channels were required to have 10 counts before they were used in the analysis. When the number of counts per bin fell below 10, bins were combined until 10 counts were obtained. The spectra were truncated when there were fewer than 10 counts in sizes larger than the last useful bin. The maximum diameter (Dmax) for each spectrum was assessed as the mid point of the last useful bin. Each data point with a temperature ≤ 0 °C and with at least one measurement bin of drops larger than 100 μm in diameter was considered as an SLD environment. For each SLD environment, the drop spectrum was used to compute the LWC, mean, mean volume, median volume, 95 percent, and 99 percent mass diameters. In total, there were 48,301 30-second in-flight data points (approximately 400 hours) collected during the flight campaigns. Of these, 27,497 data points (57%) were assessed as being in-cloud with a TWC > 0.005 g m^{-3}. There were 22,263 in-cloud observations (46% of in-flight) with an average static temperature ≤ 0 °C, and 14,199 observations (29% of in-flight) where supercooled liquid water was assessed to exist. There were 10,128 in-cloud in-icing data points with ice crystal concentrations < 1 L^{-1} where the drop spectra could be accurately determined. Finally, there were 2,444 observations with an average static temperature ≤ 0 °C, an average LWC > 0.005 g m^{-3}, an ice crystal concentration < 1 L^{-1}, an assessment of either liquid or mixed phase, and drops > 100 μm in diameter. The latter data points, which represent 5 percent of the in-flight observations, represent the SLD data base used for the analysis. Only data points with adequate measurements of both LWC and the drop spectrum were included in the SLD data base.

5. CHARACTERIZATION OF SLD DROP SPECTRA

The majority of reports of SLD measurements have simply presented the spectra that were observed (Politovich 1989, Ashenden and Marwitz 1998, Cober et al. 1996), with no attempt to reconcile or average different environments. Icing environment characterizations such as Cober et al. (2001a) have typically followed the analysis methodology of FAR 25-C. Jeck (1996) suggested that reported drop spectra could be averaged together in specific diameter bins (i.e., 50-100 µm, 100-200 µm, etc.). Shah et al. (2000) suggested that in-situ SLD observations could be segregated into distinct subsets by varying only two parameters including the maximum drop diameter (Dmax) and the drop median volume diameter (MVD). They suggested that by varying Dmax and MVD, the SLD environments could be classified into four distinct sub-sets that physically represented environments with freezing drizzle or freezing rain, with high or low MVD values respectively, and that these four environments would be unique from, and supplementary to FAR 25-C because FAR 25-C was assumed to not include SLD conditions. This was recognised as being potentially extremely useful to the aviation community. Following Shah et al. (2000) the SLD data were segregated into four subsets as listed in Table 1.

Environment	MVD (µm)	Dmax (µm)	Data Points
Freezing drizzle	< 40	100-500	1469
Freezing drizzle	> 40	100-500	335
Freezing rain	< 40	> 500	193
Freezing rain	> 40	> 500	447

Table 1. Subsets of the SLD observations

Each SLD data point at 30-second resolution had a drop spectrum that was derived from the combination of FSSP and 2D probes and that spanned the range from 1 µm to the maximum drop diameter observed. Following the methodology described in Cober et al. (2003), for each of the four SLD subsets listed in Table 1, all of the drop spectra concentrations for each subset were averaged together to derive a single drop spectrum that was considered representative of the SLD subset. The average drop spectrum of concentration was then used to derive the mass spectrum, cumulative mass spectrum, mass distribution, and characteristic diameters such as the MVD. Table 2 shows the MVD and Dmax values for each of the four average SLD spectra.

Environment	MVD Range (µm)	Dmax Range (µm)	MVD (µm)	Dmax (µm)
Freezing drizzle	< 40	100-500	20	389
Freezing drizzle	> 40	100-500	110	474
Freezing rain	< 40	> 500	19	1553
Freezing rain	> 40	> 500	526	2229

Table 2. MVD and Dmax for the spectrum of each SLD environment.

The cumulative mass distribution, as a fraction of the LWC, for each of the freezing drizzle and freezing rain spectra appear in Figures 1 and 2 respectively.

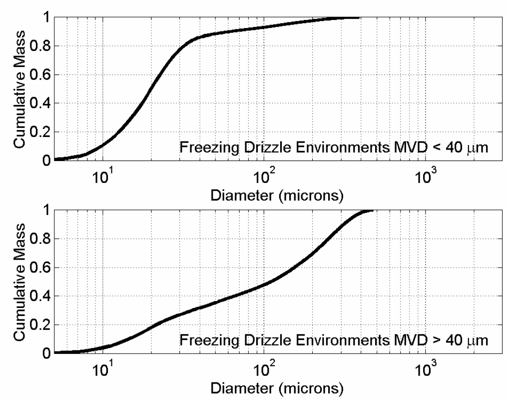

Figure 1. Cumulative mass distributions for SLD environments that include freezing drizzle drops > 100 µm and with MVD < 40 µm (top) and MVD > 40 µm (bottom).

The bimodal natures of the SLD spectra are evident in these plots, and very clearly evident in corresponding plots of mass spectra or of normalized mass spectra (not shown). For freezing drizzle and rain conditions with MVD < 40 µm the cloud drop mass peak around 20 µm is the dominant one. For freezing drizzle conditions with MVD > 40 µm and freezing

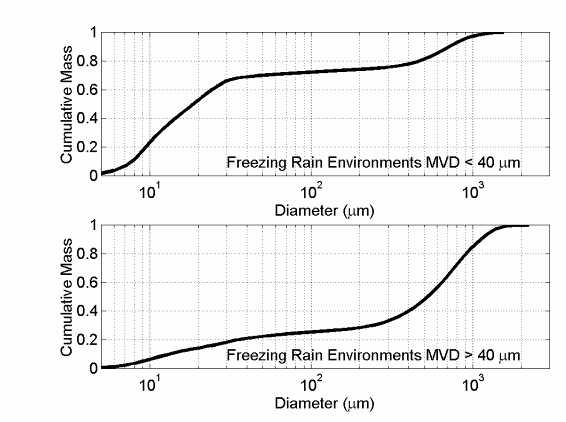

Figure 2. Cumulative mass distributions for SLD environments that include freezing rain drops > 500 μm and with MVD < 40 μm (top) and MVD > 40 μm (bottom).

rain conditions with MVD > 40 μm conditions, the dominate peak for mass is in the peak that occurs in the drizzle (around 200-300 μm) or rain (around 700-800 μm) size ranges. The wide variation in the cumulative mass curves suggests that the four spectra have distinct characteristics, and that they collectively appear to cover a wide range of naturally observed SLD icing conditions. Using the observed vertical temperature profiles, the formation mechanism for each 30-second SLD data point was assessed as either classical implying that it formed through a melting and re-supercooling mechanism, or non-classical implying that it formed through a condensation and collision-coalescence mechanism. For freezing drizzle conditions, 88 percent were observed to have formed through a non-classical process. Conversely, for freezing rain conditions, 92 percent were observed to have formed through a classical process. This highlights that the freezing drizzle and freezing rain conditions observed are relatively distinct in that they primarily formed through fundamentally different mechanisms in the atmosphere.

6. SLD HORIZONTAL SCALE FACTOR

In order to simulate SLD conditions in a wind tunnel or a numerical ice accretion model for aircraft certification, it is necessary to have both a drop spectrum and a maximum LWC where the maximum LWC value is normally associated with a high percentile value such as 99% or 99.9%. The determination of a maximum LWC value predicted for each SLD condition was complicated by the requirement to have a horizontal scale factor that would project the maximum LWC value at one length scale to different length scales. It was also necessary to determine the maximum LWC value as a function of temperature. FAR 25-C includes a horizontal scale factor and a temperature dependency for LWC.

The LWC value for each data point was normalized to a standard temperature of 0^oC following the suggestion of Isaac et al. (2004). The normalization was done by assuming that the liquid water mixing ratio would remain constant for any change in temperature or pressure. Assuming a constant mixing ratio, the pressure was held constant while the temperature was changed to 0^oC. The normalization of the LWC values to 0^oC had a minimal effect on the LWC values used in the analysis. For each averaging interval, including the 30-s, 60-s, 120-s and 300-s averages which corresponded to horizontal extents of 3, 6, 12 and 30 km respectively, the collective SLD LWC observations, normalized to 0^oC, were used to compute the 99% LWC value using an extreme value analysis technique (Cober and Isaac, 2006). The SLD 99% LWC values are plotted against the averaging length in Figure 3. The data in Figure 3 were fit to the following equations:

$$LWC_{dH} = LWC_{32.2}*SF \quad (1)$$
$$SF = 1.322 - 0.213 \log10(dH_{km}) \quad (2)$$

where LWC_{dH} is the 99% LWC at an arbitrary horizontal distance of dH, dH_{km} is the horizontal averaging distance in km, LWC32.2 is the 99% liquid water content at a horizontal scale of 32.2 km, and SF is a dimensionless scale factor that is designed to be 1 at a horizontal scale of 32.2 km. The value of 32.2 km was chosen to be consistent with FAR 25-C which uses 17.4 nautical miles (32.2 km) as a reference horizontal length scale where the scale factor equals 1. The dimensionless scale factor SF was also found to accurately fit the 97% and 99.9% LWC values.

The SF was also found to adequately represent each of the 99% LWC values for the four subsets of SLD environments listed in Table 1. This is shown in Figure 4 which shows the 99% LWC values along with their 95% confidence limits for each SLD subset, along with a fit that uses the SF given in Equation 2. The uncertainty intervals in Figure 4 are larger than those in Figure 3 because there were fewer data points for each fit. For the freezing drizzle with MVD

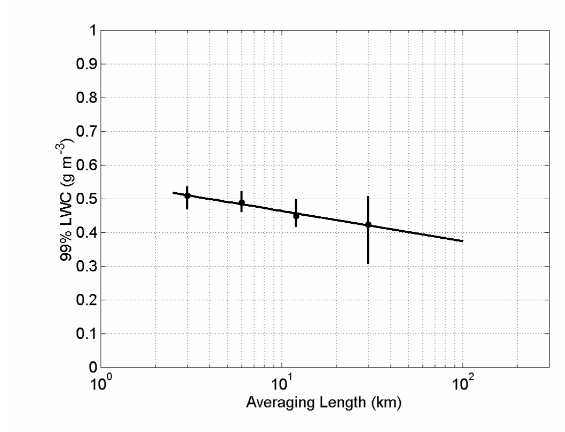

Figure 3. Plot of 99 percent LWC versus averaging distance for SLD conditions. All observed SLD conditions were used for each data point. The solid curve represents the linear best fit. The vertical lines represent the 95% confidence limits.

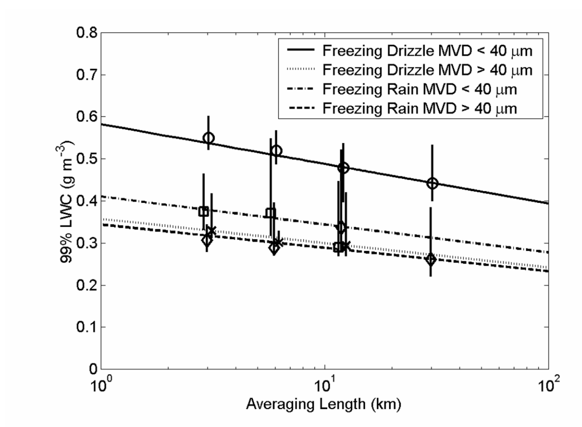

Figure 4. 99% LWC as a function of horizontal extent for each subset of SLD conditions. The vertical lines represent the 95% confidence limits for each data point. The fitted lines use the SF given in Equation 2.

> 40 μm at 30 km resolution and the freezing rain with MVD < 40 μm at 30 km resolution there were insufficient data points to undertake an extreme value analysis. To compute the 99% LWC value for any horizontal distance for any of the four SLD environments, the LWC32.2 value for the SLD environment must be used with the dimensionless scale factor SF given in Equation 2. The LWC32.2 values can be taken from Figure 4 and are given in Table 3. The LWC32.2 values corresponding to the 99.9% LWC are also given in Table 3. These use the same SF.

Environment	MVD (μm)	Dmax (μm)	99% LWC g m^{-3}	99.9% LWC g m^{-3}
Freezing drizzle	< 40	100-500	0.44	0.58
Freezing drizzle	> 40	100-500	0.27	0.31
Freezing rain	< 40	> 500	0.31	0.37
Freezing rain	> 40	> 500	0.26	0.33

Table 3. 99% and 99.9**%** LWC values for each SLD subset for a horizontal distance of 32.2 km.

7. SLD TEMPERTURE CHARACTERIZATION

Using the 99% LWC values in Table 3, a LWC-temperature relationship was developed with the following methodology. The mean temperature and pressure of all of the 30-s SLD data observed were -4.2°C and 865 mb respectively. These values were used to modify the U.S. standard atmosphere, which provides a relationship between temperature and pressure, so that the U.S. standard atmosphere temperature at 865 mb was also equal to -4.2°C. The modification required was a systematic reduction of the temperature profile by 11.0°C which represents a cooler atmosphere than the U.S. standard atmosphere. This is consistent with the winter nature of the SLD observations. The 0°C LWC values from Table 3 were assigned a pressure of 939 mb which is consistent with the pressure at 0°C in the modified U.S. standard atmosphere described above. For each LWC value in Table 3, starting at 0°C and 939 mb, the change in LWC was computed for each temperature between 0 and -25°C following a temperature-pressure curve that was consistent with the modified U.S. standard atmosphere and assuming that the liquid water mixing ratio remained constant for the changes in temperature and pressure from 0°C and 939 mb.

Figure 5 shows a plot of temperature versus LWC for freezing drizzle environments with MVD < 40 μm and MVD > 40 μm. The values of LWC at 0°C are valid for the reference distances of 32.2 km and are taken from Table 3. Figure 6 shows a similar plot for freezing rain environments. The in-situ observations at 300-s (30 km) are shown for comparison. The data are adequately bounded by the temperature-LWC curves.

The curves are truncated at -25°C for freezing drizzle and -13°C for freezing rain because there are no or negligible numbers of observations at colder temperatures. These limits are consistent with climatologies of surface observations for freezing drizzle and freezing rain (Stuart and Isaac, 1999; McKay and Thompson, 1969).

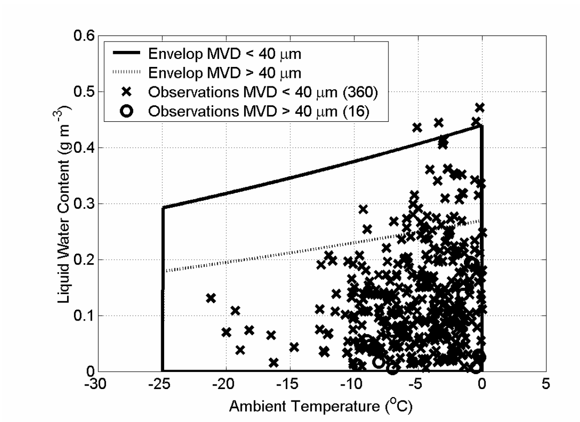

Figure 5. 99% LWC envelopes versus temperature for freezing drizzle environments compared with 300-s data. The number of data points observed for each subset of SLD data are shown in the caption.

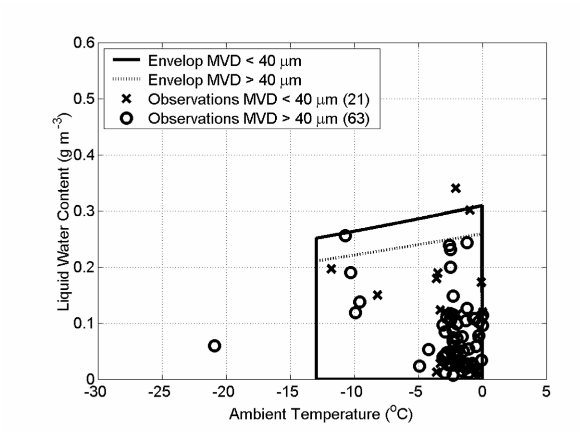

Figure 6. 99% LWC envelopes versus temperature for freezing rain environments compared with 300-s data. The number of data points observed for each subset of SLD data are shown in the caption.

8. SLD ICING ENVELOPES

The FAR 25-C envelopes only include MVD values up to 40 μm, although Jones and Lewis (1949) suggested that extreme freezing rain conditions could be represented by a droplet MVD of 1000 μm, LWC of 0.15 g m^{-3}, and a horizontal extent > 100 km. Newton (1978) described icing accumulation envelopes, which physically represented the sweep out of LWC and the potential accumulations of ice on a 3-inch diameter icing cylinder in g cm^{-2} h^{-1}. The potential accumulation rate would depend on the collision-collection efficiency of the hydrometeor spectra, which is a function of aircraft speed and droplet size. However, for drops greater than approximately 50 μm in diameter the collision efficiency would be essentially 1, and there would be no way to distinguish the accumulation associated with 50 μm drops with that from 500 μm or 1000 μm drops.

The SLD observations for freezing drizzle and freezing rain conditions for horizontal extents of 300-s (30 km) are compared to the FAR 25-C and the potential accumulation envelopes in Figures 7 and 8 respectively. The 99% and 99.9% LWC limits from Table 3 for 32.2 km horizontal extents are also shown for the MVD < 40 μm and MVD > 40 μm conditions. Note that the FAR 25-C envelopes, 99% and 99.9% LWC limits are valid for 32.2 km, while the individual data points are valid for 30 km. The comparison is acceptable because the difference in length scales is quite small. Since the SLD observations are not segregated by temperature and include all observations at temperatures < 0°C, it is only valid to compare the observations and envelopes with the 0°C envelope for FAR 25-C.

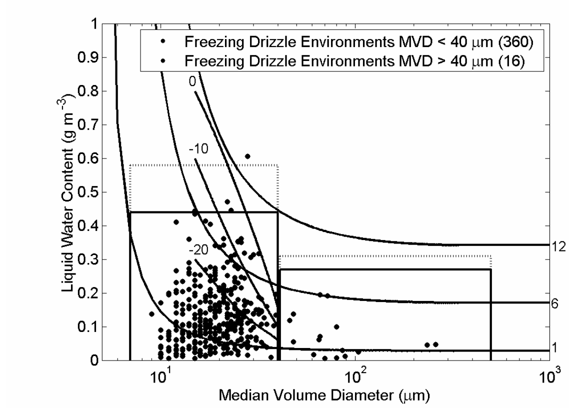

Figure 7. Plot of MVD versus LWC for 300-s (30 km) averaged data for freezing drizzle conditions. The 99 and 99.9% LWC values from Table 3 are shown. The FAR 25-C envelopes for 0, -10 and -20°C and the Newton (1978) potential accumulation envelopes for 1, 6 and 12 g cm^{-2} hr^{-1} are also shown for comparison and labelled accordingly. The LWC limits (envelopes) are

shown as boxes ranging from 7 to 40 μm (for MVD < 40 μm) and from 40 to 500 μm (for MVD > 40 μm). The 99% LWC limits are shown as solid lines while the 99.9% LWC limits are shown as dotted black lines.

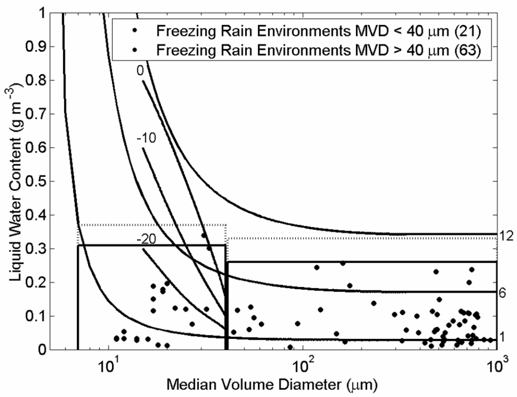

Figure 8. Same as Figure 7 for freezing rain conditions. The upper limit of the LWC envelope/box for MVD > 40 μm is not shown.

For the SLD observations (both drizzle and rain) with MVD < 40 μm the FAR 25-C envelope for 0°C seems to capture the data extremely well. For MVD > 40 μm conditions, the potential accumulation envelope of approximately 10 g cm^{-2} h^{-1} bounds the data very well. Newton (1978) suggested that a potential accumulation of 12 g cm^{-2} h^{-1} could be interpreted as severe icing. The 99% and 99.9% LWC limits derived are smaller than the qualitatively named severe icing potential accumulation envelope. It is interesting to note that a single potential accumulation envelope of 10 g cm^{-2} h^{-1} would have captured all but one of the observed 300-s SLD observations at all MVD values. The potential accumulation envelopes are more physically based than those in FAR 25-C. The consistency of the SLD observations with the potential accumulation envelopes suggests that a maximum potential accumulation envelope could have formed the basis of an alternative SLD environmental characterization.

Because of the limited number of SLD conditions at 300-s or 30 km resolution, it can be difficult to visually reconcile the individual data shown in Figures 7 and 8 with the 99% and/or 99.9% LWC envelopes. Figures 9 and 10 show the MVD versus LWC for 30-s (3-km) averaged data for freezing drizzle and freezing rain conditions respectively. The 99% and 99.9% LWC envelopes were computed using the scale factor in Equation 2 and the 99% and 99.9% LWC values for 32.2 km from Table 3. The 95% confidence limits for the 99% and 99.9% SLD LWC values are shown as solid and dotted vertical bars respectively. Note that the potential accumulation envelopes for 1, 6 and 12 g cm^{-2} h^{-1} are also shown for comparison however, the FAR 25-C envelopes are not shown because they were not valid at 3 km. The applicability of the 99 percent envelopes to the data is much clearer to visualize in these figures. It can be seen that approximately 1% of the SLD observations exceed the 99% LWC envelopes which is consistent with the 99% analysis. There are enough data points to have a higher degree of confidence in the 3-km 99% LWC analysis. This is further demonstrated by the small width of the 95% confidence limits for the 99% LWC analysis. The 99.9% LWC analysis had significantly wider 95% confidence limits and there were no SLD observations that exceeded the upper confidence limit of the 99.9% LWC envelopes. A potential accumulation envelope of 12 g cm^{-2} h^{-1} would bound all of the freezing rain observations and 99.5% of the freezing drizzle observations at 3-km resolution.

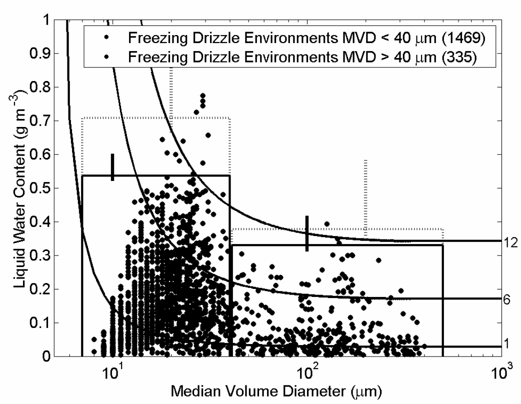

Figure 9. Plot of MVD versus LWC for 30-s (3 km) averaged data for freezing drizzle conditions. The Newton (1978) potential accumulation envelopes for 1, 6 and 12 g cm^{-2} hr^{-1} are also shown for comparison. The LWC limits (envelopes) are shown as boxes ranging from 7 to 40 μm (for MVD < 40 μm) and from 40 to 500 μm (for MVD > 40 μm). The 99% LWC limits are shown as solid lines while the 99.9% LWC limits are shown as dotted black lines. The 95%

confidence limits to the 99 and 99.9%LWC limits are shown as vertical solid and dotted lines respectively.

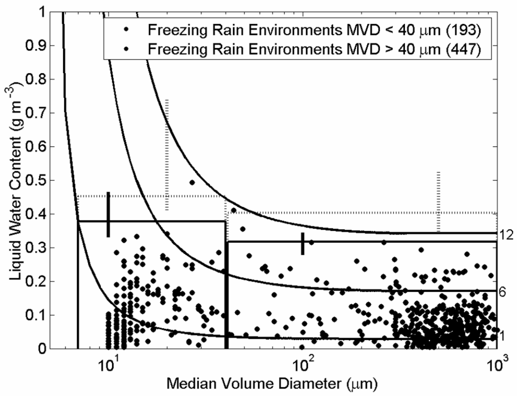

Figure 10. Same as Figure 9 for freezing rain conditions.

9. CONCLUSIONS

Observations of aircraft icing environments that included supercooled large drops greater than 100 μm in diameter have been collected by instrumented research aircraft from 134 flights during five field programs in three different geographic regions of North America. In total 2444 SLD icing environments were observed at 3-km resolution which had an average LWC > 0.005 g m^{-3}, drops > 100 μm in diameter, ice crystal concentrations < 1 L^{-1} and an average static temperature ≤ 0^{o}C.

The research aircraft were highly instrumented in order to accurately measure the microphysics of the icing environments and there was a high degree of consistency observed between the direct measurements of LWC and the spectrum derived LWC. SLD conditions were observed approximately 5% of the in-flight time of the research aircraft. These observations were used to determine potential aircraft icing certification envelopes that would be supplementary to those envelopes currently used for commercial aircraft certification. The data were analysed in order to develop a characterization of aircraft icing environments that included SLD. The analysis has the following conclusions:

1) The observations with SLD > 100 μm were subdivided into four categories including freezing drizzle conditions where the maximum drop sizes were < 500 μm in diameter and freezing rain conditions where the maximum drop sizes were > 500 μm in diameter, each of which had MVD < 40 μm and MVD > 40 μm. These four subsets appear to capture the full range of SLD conditions that were observed, especially the bi-modal drop distributions that are characteristic of SLD environments. In general there is a formation mechanism distinction between freezing drizzle and freezing rain conditions, based on the fact that 88% of the freezing drizzle conditions formed through a condensation and collision-coalescence mechanism while 92% of the freezing rain conditions formed through a melting and supercooling process.

2) The 99% and 99.9% LWC values for four different horizontal length scales were determined using an extreme value analysis methodology. The 99% LWC values were used as the basis for the development of a horizontal scale factor and a LWC-temperature relationship.

3) A horizontal scale factor was developed that allows a maximum (99%) LWC value at one length scale to be translated into another length scale. The scale factor was independent of LWC percentile in the range from 97 to 99.9%.

4) A LWC-temperature relationship was developed that bounded the majority of observations. This allows the translation of a maximum (99%) LWC at 0^{o}C to a lower temperature. It is suggested that freezing drizzle environments do not need to be considered at temperatures < -25^{o}C while freezing rain environments do not need to be considered at temperatures < -13^{o}C.

5) The SLD environments were compared to the original FAR 25-C envelopes and to the potential accumulation envelopes described by Newton (1978). A potential accumulation envelope of 12 g cm^{-2} h^{-1} would bound 99.5% of the SLD observations at 3-km resolution and 99.8% of the SLD observations at 30-km resolution. The FAR 25-C envelops which are valid for 32.2 km and MVD < 40 μm capture all of the 30-km SLD observations with MVD < 40 μm, demonstrating consistency between the two characterizations.

The analysis is sufficient for simulation of SLD environments with either numerical icing accretion models or wind tunnel icing simulations. The characteristic drop spectra can be used to define the desired SLD environment. The maximum LWC values (i.e. either 99% or 99.9%) can be determined for any desired horizontal length scale or temperature. In terms of temperature, LWC, and horizontal length scale, the SLD icing envelopes are similar in structure to the original aircraft icing envelopes described in FAR 25-C, the latter having been used for aircraft certification for the past 50 years.

10. ACKNOWLEDGEMENTS

Funding for this research was provided by Environment Canada (EC), the National Research Council of Canada (NRC), Transport Canada (TC), the Canadian National Search and Rescue Secretariat, NASA-Glenn, the Federal Aviation Administration, and Boeing Commercial Airplane Group. Walter Strapp, Alexei Korolev, Tom Ratvasky, Dave Marcotte and Jim Riley are acknowledged for their assistance in collecting the data and/or their support. Mohammed Wasey and his technical team are thanked for their long term support to the various measurement programs.

11. REFERENCES

Ashenden, R., and J.D. Marwitz, 1998: Characterizing the supercooled large droplet environment with corresponding turboprop aircraft response. *J. Aircraft*, **35**, 912-920.

Cober, S.G., and G.A. Isaac, 2006: Estimating maximum aircraft icing environments using a large data base of in-situ observations. *AIAA 44th Aerospace Sci. Meeting and Exhibit*, Reno Nevada, 9-12 January 2006, AIAA 2006-0266.

Cober, S.G., G.A. Isaac, A.D. Shah, and R. Jeck, 2003: Defining characteristic cloud drop spectra from in-situ measurements. *AIAA 41st Aerospace Sci. Meeting and Exhibit*, Reno Nevada, 6-10 January 2003, AIAA 2003-0561.

Cober, S.G., G.A. Isaac, and J.W. Strapp, 1995: Aircraft icing measurements in east coast winter storms. *J. Appl. Meteor.*, **34**, 88-100.

Cober, S.G., J.W. Strapp, and G.A. Isaac, 1996: An example of supercooled drizzle drops formed through a collision-coalescence process. *J. Appl. Meteor.*, **35**, 2250-2260.

Cober, S.G., G.A. Isaac, and J.W. Strapp, 2001a: Characterizations of aircraft icing environments that include supercooled large drops. *J. Appl. Meteor.*, **40**, 1984-2002.

Cober, S.G., G.A. Isaac, A.V. Korolev, and J.W. Strapp, 2001b: Assessing cloud-phase conditions. *J. Appl. Meteor.*, **40**, 1967-1983.

Cober, S.G., G.A. Isaac, and A.V. Korolev, 2001c: Assessing the Rosemount icing detector with in-situ measurements. *J. Atmos. Oceanic Technol.*, **18**, 515-528.

Cooper, W.A., W.R. Sand, M.K. Politovich, and D.L. Veal, 1984: Effects of icing on performance of a research aircraft. *J. Aircraft*, **21**, 708-715.

Curry, J.A., P.V. Hobbs, M.D. King, D.A. Randall, P. Minnis, G.A. Isaac, J.O. Pinto, T. Uttal, A. Bucholtz, D.G. Cripe, H. Gerber, C.W. Fairall, T.J. Garrett, J. Hudson, J.M. Intrieri, C. Jakob, T. Jensen, P. Lawson, D. Marcotte, L. Nguyen, P. Pilewskie, A. Rangno, D. Rogers, K.B. Strawbridge, F.P.J. Valero, A.G. Williams, and D. Wylie, 2000: FIRE Arctic Clouds Experiment. *Bull. Amer. Meteor. Soc.*, **81**, 5-29.

Federal Aviation Administration, 1999: U.S. Code of Federal Regulations, Title 14 (Aeronautics and Space), Part 25 (Airworthiness Standard: Transport Category Airplanes), Appendix C, Office of the Federal Register, National Archives and Records Administration, U.S. Government Printing Office, Washington D.C., 20402-9328.

Federal Aviation Administration, 1997: FAA Inflight Aircraft Icing Plan, (April, 1997; 35 pp), Federal Aviation Administration, Washington, DC 20591.

Isaac, G.A., S.G. Cober, J.W. Strapp, A.V. Korolev, A. Tremblay, and D.L. Marcotte, 2001a: Recent Canadian research on aircraft in-flight icing. *Canadian Aeronautics and Space Journal*, **47**, 213-221.

Isaac, G.A., S.G. Cober, J.W. Strapp, D. Hudak, T.P. Ratvasky, D.L. Marcotte, and F. Fabry 2001b: Preliminary results from the Alliance Icing Research Study (AIRS). *AIAA 39th Aerospace Sci. Meeting and Exhibit*, Reno Nevada, 8-11 January 2001, AIAA 2001-0393.

Isaac, G.A., I. Gultepe, and S.G. Cober, 2004: Use of mass versus volume units for cloud microphysical parameters. *Proceedings 14th Intl. Conf. on Clouds and Precipitation*, Bologna, 19-23 July 2004, 800-803.

Jeck, R.K., 1996: Representative Values of Icing-Related Variables Aloft in Freezing Rain and Freezing Drizzle, Technical Note DOT/FAA/AR-TN95/119, (March, 1996; 45 pages), Federal Aviation Administration Technical Center, Atlantic City, NJ 08405.

Jones, A.R., & Lewis, W., 1949: Recommended Values of Meteorological Factors to be Considered in the Design of Aircraft Ice-Prevention Equipment, NACA TN-1855 (March, 1949).

McKay, G.A., and H.A. Thompson, 1969: Estimating the hazard of ice accretion in Canada from climatological data. *J. Appl. Meteor.*, **8**, 927-935.

Marwitz, J., M. Politovich, B. Bernstein, F. Ralph, P. Neiman, R. Ashenden, and J. Bresch, 1996: Meteorological conditions associated with the ATR72 aircraft accident near Roselawn, Indiana on 31 October 1994. *Bull. Amer. Meteor. Soc.*, **78**, 41-52.

Miller, D., T. Ratvasky, B. Bernstein, F. McDonough, and J.W. Strapp, 1998: NASA/FAA/NCAR supercooled large droplet icing flight research: Summary of winter 96-97 flight operations. *AIAA 36th Aerospace Sci. Meeting and Exhibit*, Reno, Nevada, 12-15 January 1998, AIAA 98-0577.

Newton, D.W., 1978: An integrated approach to the problem of aircraft icing. *J. Aircraft*, **15**, 374-380.

National Transportation Safety Board, 1996: Aircraft Accident Report, ATR Model 72-212, Roselawn, Indiana, October 31, 1994, NTSB/AAR-96/01, National Transportation Safety Board.

Pobanz, B.M., J.D. Marwitz, and M.K. Politovich, 1994: Conditions associated with large-drop regions. *J. Appl. Meteor.*, **33**, 1366-1372.

Politovich, M.K., 1989: Aircraft Icing Caused by Large Supercooled Droplets, *J. Applied. Meteorology*, **28**, 856-868.

Sand, W.R., W.A. Cooper, M.K. Politovich, and D.L. Veal, 1984: Icing conditions encountered by a research aircraft. *J. Climate Appl. Meteor.*, **23**, 1427-1440.

Shah, A.D., M.W. Patnoe, and E.L. Berg, 2000: Engineering analysis of the atmospheric icing environment including large droplet conditions. *Society of Automotive Engineers,* 2000-01-2115.

Stuart, R.A. and G.A. Isaac, 1999: Freezing Precipitation in Canada. Atmosphere Ocean, 37-1, 87-102.

THE NSF/NCAR GULFSTREAM GV:
A NEW PLATFORM FOR STUDIES OF CLOUDS

William A. Cooper, Jeffrey L. Stith, David C. Rogers, and Jorgen B. Jensen
National Center for Atmospheric Research, Boulder CO USA

1. AIRCRAFT CHARACTERISTICS

A new research aircraft, operated by the National Center for Atmospheric Research for the National Science Foundation, is now in operation (Fig. 1):

Figure 1: The NSF/NCAR GV Research Aircraft (HIAPER) at takeoff.

The aircraft, also called “HIAPER” (High Altitude Instrumented Airborne Platform for Environmental Research), is capable of flight to 15.5 km MSL (51,000 ft), and its range (typically around 8000 km or 5000 n mi) makes studies possible that have global scale. The aircraft was selected for its ability to support research in climate science, atmospheric chemistry, weather and mesoscale studies, global atmospheric cycles, aerosols, clouds, and many other areas of geoscience. It provides special opportunities for research in the upper troposphere and lower stratosphere and for studies that exploit its range to achieve coverage up to global scales.

Figure 2: Modifications to be able to carry instrument canisters under the wings.

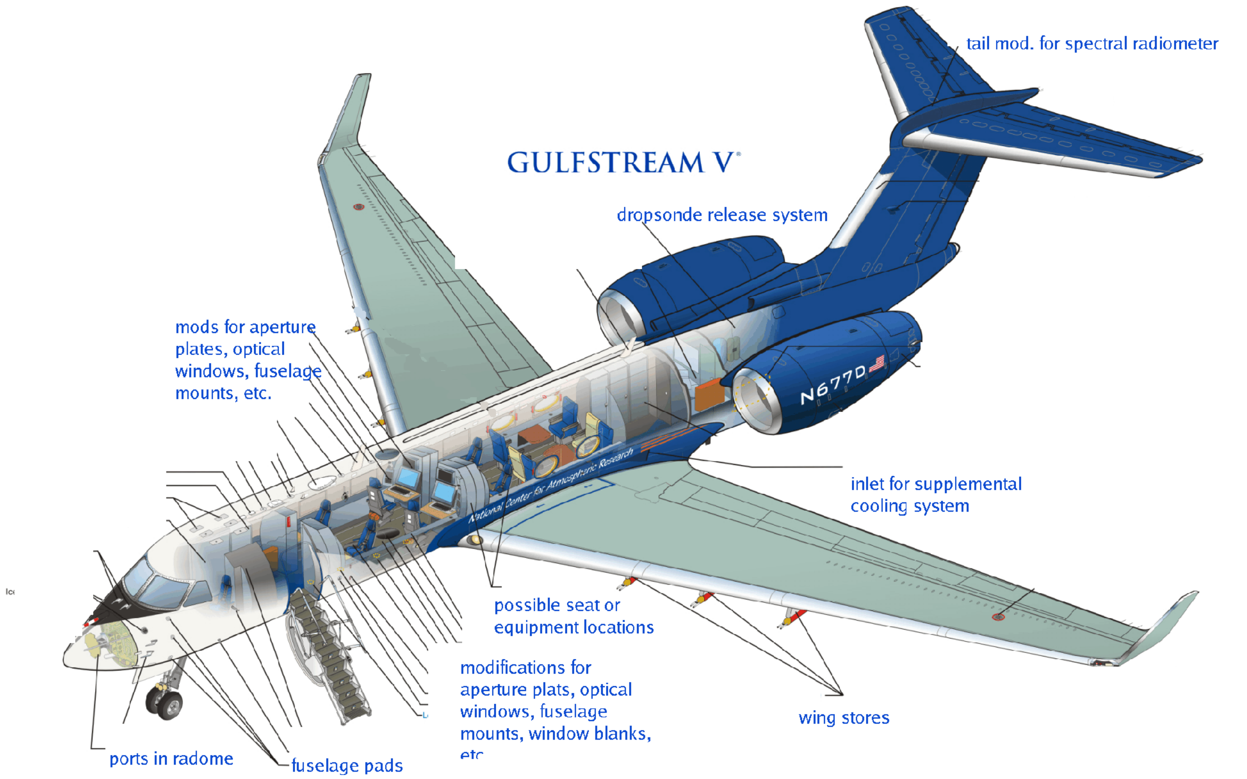

Figure 3: Illustration of some of the mechanical modifications made to the aircraft to accommodate research equipment. In addition, extensive installation of cables and other wire provides for research power distribution to instrument locations, signal routing, and data acquisition and monitoring.

The aircraft has been modified extensively to accommodate research equipment, as illustrated by Figs. 2 and 3. These modifications included the installation of aperture pads (e.g., for inlets), instrument aperture plates, optical view ports, fuselage mounts, and four forward fuselage pads. Cabin pressurization (to a pressure altitude of 6000 ft when flying up to its ceiling) provides a comfortable working environment for instrument operators and other crew members. The payload with maximum fuel is 3400 lb; maximum payload is 8300 lb, but typical payloads are about 4000 lb and are often limited by the available floor space. Substantial power is available for research instrumentation, up to 20 KVA of 115VAC at either 60 or 400 Hz (or split between these). The platform is certified for flight as a standard-category aircraft, and instrumentation provided also meets these certification standards (as must all equipment provided by users).

The aircraft was delivered in 2005 and began flights in support of research in 2006, although infrastructure upgrades have continued and are still continuing (e.g., the addition of wing stores). The acquisition and performance of the aircraft are described by Laursen et al. (2006), and the Investigator's Handbook provides additional detail; the latter and additional documents are available from the NCAR Research Aviation Facility web site: www.eol.ucar.edu/instrumentation/aircraft/G-V.

2. INSTRUMENTATION

Standard instrumentation: For normal missions, there are likely to be three categories of instrumentation in use, standard, special-request, and user-provided. The first is standard for the aircraft and normally operated on all flights; this set includes measurements of position (duplicate Honeywell LASEREF IV inertial systems, Honeywell 12-channel global positioning systems (GPS), and when useful a GPS system with differential capability), state parameters (pressure, temperature, and dewpoint), and wind (using a gust system sensing pressure differences among ports placed in the forward radome). There are also a set of standard inlets to provide air samples to cabin-mounted instruments, and a camera for video recording is mounted under a wing to provide a good view. Most experiments will also use some of the available aerosol instruments and/or hydrometeor spectrometers, including a cabin-mounted CN counter and mobility analyzer and wing-mounted size spectrometers for aerosols, cloud droplets, and ice crystals. The spectrometers have fast electronics to permit measurements at flight speeds up to about 235 m/s, a speed common during high-altitude flight of this aircraft. A tunable-diode laser hygrometer is available for measuring humidity at upper troposphere / lower stratosphere values. These capabilities are all available on request and the instruments are operated and maintained by NCAR.

Table 1, appended to the end of this paper, summarizes the available standard instruments. Some additional instruments for atmospheric chemistry are supported by the Atmospheric Chemistry Division of NCAR and are also requestable.

Special-request instruments. An extensive set of special instruments have been or are being developed for use on the GV. (See Table 2 at the end of this paper.) These instruments are designed specifically to operate on the GV, and so will meet certification requirements for expected deployments. For some, operation of the instrument is best conducted by arrangement and involvement of the developers, although some will be operated by NCAR for the community.

Of special interest to the cloud-physics community will be the instruments for characterizing hydrometeors. A wing-mounted Small Ice Detector (SID-2) has been developed for use on the aircraft, and a new probe called a 3V-CPI is under development by SPEC Corp.; the latter combines two orthogonal 2D-array spectrometers (as in the SPEC 2D-Stereo instrument) with a SPEC Cloud Particle Imager (CPI), using the spectrometers to trigger the CPI. Also of special utility to studies of clouds will be the cloud radar (initially W-band, but envisioned to become dual W/K band), a high spectral resolution lidar (HSRL), and a radiation-sensing package consisting of spectral radiometers as well as measurements of spectrally resolved actinic flux. An aerosol mass spectrometer will provide information on the composition of aerosol particles, and a counterflow virtual impactor is available for measuring total water content in clouds and for providing residue particles from evaporated cloud droplets or ice particles to instruments for analysis.

User-supplied instruments. Most payloads will also include user-supplied instruments for special needs. There is ample power for most such instrumentation, and there are capabilities for incorporating the measurements into the recorded data files or for providing information from the standard data system to these instruments. Some special requirements are associated with certification of such instruments, so early discussion is needed before such planned uses.

3. SATELLITE COMMUNICATIONS

Early operations of the aircraft have shown that the satellite communications system enables a new style of operation, in which a distributed team of investigators can participate in the missions remotely while the aircraft covers continent-spanning distances, perhaps without returning to the originating point for a week or more. The system provides for telemetry of measurements to the ground where they are made available via internet to an extended observing team, some of whom can remain at their home institutions and still participate in missions. It also provides for transmission of images from the ground to the aircraft so that investigators on the ground can construct images representing developing weather situations or other events pertaining to flight objectives and then transmit those to the crew on the aircraft. Communications are via text messages (internet relay chat) that are logged so that they can be dealt with when it is convenient for the air crew. Those on the ground can see the measurements as they are made, see the images from the video camera on the aircraft, and communicate with the scientists on the aircraft. Those in the air can see updated satellite or radar images sent from the ground, receive updated weather information and "nowcasts" and other model output during the flight, and discuss flight procedures with the extended team on the ground. It may laterprove possible and advantageous to transmit measurements from the aircraft for incorporation or assimilation into models. The platform is also attractive to consider for exploiting targeting of observations, because targets could be determined during flight and transmitted for incorporation into the flight plan.

These capabilities were exploited during the PACDEX (Pacific Dust Experiment) campaign by PIs J. Stith and V. Ramanathan. Some results from that experiment are included elsewhere in this conference; cf., e.g., Stith et al., 2008. The flight crew consisted of ten people who flew from Colorado to either Alaska or Hawaii and then on to Japan (cf. Fig. 4) in order to cover large parts of the Pacific Ocean. To conduct repeated flights, a ground-based team monitored the weather and developed tentative flight plans that were communicated to the flight crew during and between flights. The operations center re-

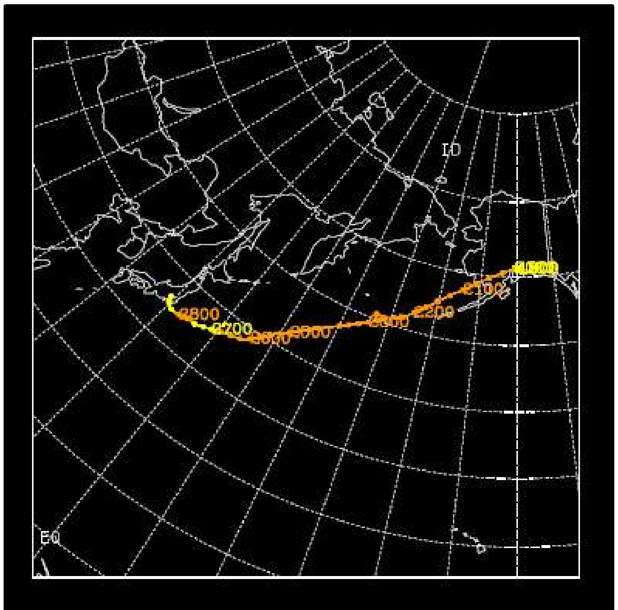

Figure 4: Sample flight track (15 May 2007), showing a flight segment from Anchorage Alaska to Japan during PACDEX, with a low level flight segment (in yellow) enroute to study dust emerging from Asia.

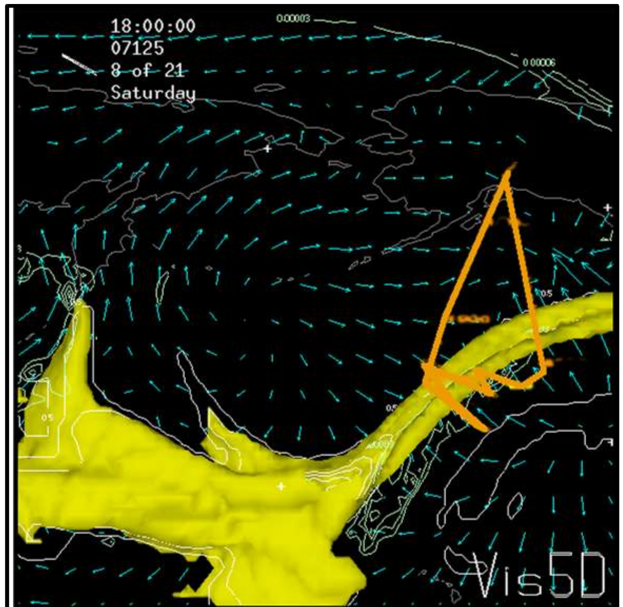

Figure 5: The flight track of the PACDEX flight of 5 May 2007 to study a cold front over the Pacific Ocean. The flight began and ended in Anchorage Alaska; to set the scale, Hawaii is visible at the bottom of the plot and Japan on the left side. The yellow contour is the dust plume predicted by the STEM model of G. Carmichael (Univ. of Iowa) and collaborators for the time of the flight, with a dust plume riding along a jet associated with the cold front. This image was transmitted to the aircraft during the flight to help them design the flight track, shown as the orange line.

mained in Colorado even for the flights conducted from Japan. Investigators at locations including the University of Iowa (G. Carmichael) were able to run chemical transport models while remaining at their home institution, then communicate the results to the operations center for flight planning and for forwarding to the air crew.

Another example was the Terrain-Induced Rotors Experiment (T-REX; cf. Grubišić and Doyle, 2006), which was conducted by PI V. Grubišić and associates from a location in the lee of the Sierra Nevada Mountains of California while the GV remained based in Colorado. Ferry to or from Colorado required less than 2 h, leaving about 6 h for operations in the study area. This allowed the instrument operators to remain based in Colorado and yet be able to respond quickly when the weather was appropriate for flight operations. The speed and range of the aircraft make it possible to conduct flights from a single base and yet cover many flight objectives, perhaps even those of different experiments (as was done in the "Progressive Science" flights of 1996, when four different teams shared use of the aircraft in order to meet their different needs, requiring flight sometimes to near the

Arctic Circle, sometimes to the Pacific Ocean off the coast of Mexico, and sometimes across the latitudinal span of the U.S., all from a single base in Colorado.) The START-08 project recently conducted a flight from Colorado to over the Hudson Bay and back in a single flight, as shown in Fig. 6. This range enables a different experimental model, using the ability of the aircraft to reach distance weather events and conduct experiments with multiple objectives and weather targets.

It is likely that this continent-spanning style of operation will become common in future uses of the aircraft. The speed of the aircraft makes it possible to collect measurements over distances that span regions observed by satellites or modeled by global models, opening new opportunities for validation studies. The communications link also provides opportunities for educational uses of the operations that are only beginning to be developed.

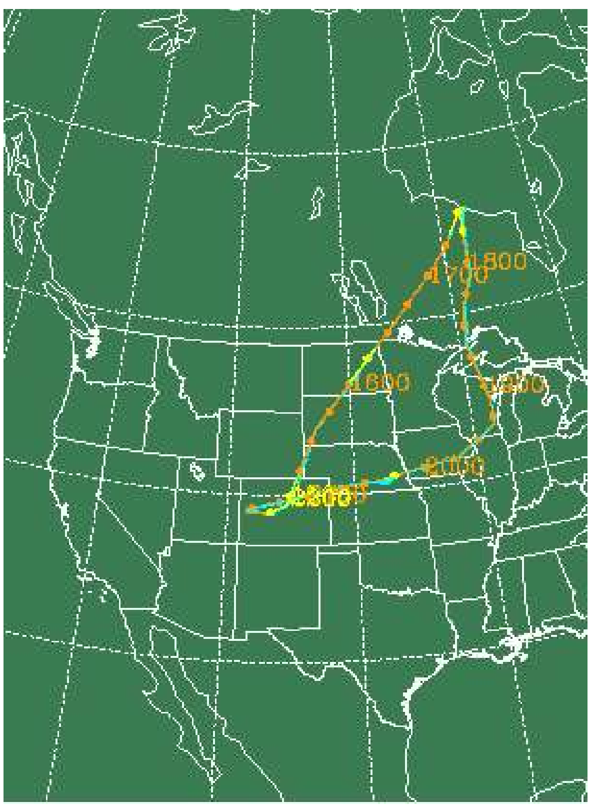

Figure 6: Sample long-range flight (START-08 flight 1, 18 April 2008, 7 h duration).

4. SPECIAL OPPORTUNITIES FOR STUDIES OF CLOUDS

The capabilities of this aircraft and instrumentation provide new opportunities for studies of clouds, many linked to the performance of the aircraft but others also associated with the newly developed or under-development instrumentation. These include:

- The ability to reach most sub-tropical Cirrus clouds and to measure the size distributions, ice-crystal residues after evaporation, and radiative properties of such clouds;
- The ability to climb rapidly, at rates matching ascent rates of most Cumulus clouds, and so to observe the vertical development of Cu via repeated penetration of rising parcels; cf. Fig. 7;
- The ability to cover distances appropriate for climate-scale studies, so that it is possible to characterize clouds over areas comparable to grid sizes in global models or to reach remote mid-ocean locations in order to characterize the clouds in ways that have climatological significance;

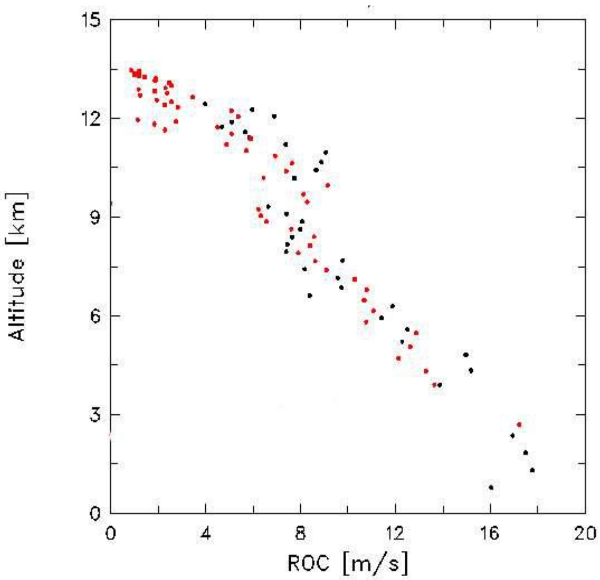

Figure 7: Measured rate of climb (ROC) vs altitude for sample climbs of the GV with normal payload. Red dots show an initial climb with full fuel; black dots show a climb midway through an 8-h flight.

- High-speed response to developing weather, so that clouds can be reached rapidly during their early stages of growth or practical research areas can be covered to target particular cloud or weather conditions;
- Mobility upward and downward, so that observers on the aircraft can benefit from an unobstructed high-altitude view of developing cloud conditions and then reach targets of interest and so that soundings can be measured routinely;
- Linking airborne observations and nowcast modeling during flight so that operations can adapt to evolving weather patterns;
- Downward and upward irradiance measurements associated with clouds, conducted above, below, or within clouds, along with the ability to characterize the hydrometeor and aerosol populations and trace gases affecting those irradiances;
- Coupling of trace-gas measurements with studies of clouds to learn about entrainment and detrainment processes or other processes in clouds and to detect and follow cloud-processed air;
- Use of a Microwave Temperature Profiler and/or dropwinsondes to measure the temperature structure of the atmosphere and so characterize the environment in which clouds develop;
- Use of pressure measurements in combination with the high-resolution differential-GPS measurements to study pressure perturbations associated with clouds and other dynamic effects arising from pressure gradients that have been difficult to study;
- Exploitation of new hydrometeor probes that offer the ability to measure small ice or drizzle-size hydrometeors with increased confidence and so to address questions related to the effective radius of Cirrus ice particles or the development of drizzle in clouds;
- The combination of a W-band radar with a high spectral resolution lidar, which can support high-resolution characterization of cloud structure and motions, cloud boundaries, and early precipitation development.

5. AN EXAMPLE: A POSSIBLE APPROACH TO DETERMINING INDIRECT CLIMATE EFFECTS OF CLOUDS

A key uncertainty in predictions and understanding of global warming remains that associated with the indirect effects of aerosols on climate, especially the effect of increasing concentrations of cloud condensation nuclei on the radiative properties of clouds. If the albedo of low clouds is increased by such increasing concentrations, this may reduce the warming expected in a future climate. The remainder of this paper discusses a possible approach to study of this effect that would exploit the capabilities of this new research aircraft and also the very capable research aircraft available elsewhere, including the BAe-146 of the UK and the German "HALO" aircraft under development at DLR. This is offered here as an example of the ways in which a continent-spanning aircraft can begin to establish links between cloud-scale processes and the global scale needed if studies are to be relevant to climate.

An approach to determining effects on a global scale might be along the following lines:

- Use chemical-transport models (CTMs) to predict where sulfate aerosols are enhanced. Concentrate on areas where models predict that clouds have significant radiative impact, like the Sc regions of the California coast or the Chile coast and elsewhere.
- Test those predictions against observations (of CCN and sulfate) in regard to position and amounts. Aircraft observations are probably needed for these tests; some information can also be gathered from satellite radiances, esp. over the ocean, and from satellite-lidar observations. Ground stations in the aerosol networks are also possible sources of information.
- (if the preceding test is encouraging) Determine if the CTM predictions can be used to predict CCN concentrations. This probably requires CCN measurements from aircraft, perhaps complemented by measurements at ground stations. This step would benefit from the existence of multiple CCN spectrometers, intercompared or identical, for use on different aircraft, because the task probably is best conducted by more than one aircraft in more than one area.
- (if the preceding test is encouraging) Determine how CCN properties relate to cloud characteristics. This is probably best done by correlating sulfate predictions with satellite-measured cloud albedo, bypassing the CCN step -- but the CCN step would be important anyway for developing confidence in the chain of cause-and-effect. Aircraft measurements of radiative properties of clouds, esp. albedo, may play a role here also, especially in studying the fine-scale variations in albedo.
- (if warranted by the preceding steps:) Use predictions of effects on cloud characteristics to generalize globally and so develop an estimate of the indirect effect of aerosols on the global radiation balance.

Components of this study might be:

- A chemical-transport model or a global model with chemistry incorporated. The model would need to represent meteorological fields, sources of various chemicals and aerosols, and scavenging and transport, in order to be able to predict trace-gas and aerosol fields over large areas.
- Aircraft studies in different regions, conducted in coordination and collaboration, to increase the extent to which the coverage can be considered representative of global conditions. The GV is a good candidate for studies in remote areas or requiring long range. The BAe-146 provides superb capabilities for characterizing the aerosol, chemical, and radiative properties. HALO would of course offer capabilities like those of the GV. It may be possible to interest other groups in a coordinated study, because of the obvious importance of this problem.
- Satellite observations of cloud albedo, which would have a key role to play in extrapolating results over broad areas and in developing possible correlations between aerosol-model predictions and satellite observations of albedo. (Indeed, one might think of undertaking the study only with this latter step, but such a correlation would be less convincing without verification of the steps in the cause-and-effect chain.)

Acknowledgment: NCAR is sponsored by the U. S. National Science Foundation, which also provided funds for acquisition and instrumentation of this new platform.

REFERENCES

Grubišić, V., and J. D. Doyle, 2006: Terrain-induced Rotor Experiment. Paper 9.1, 12th Mountain Meteorology Conference, Santa Fe, Amer. Meteor. Soc., http://ams.confex.com/ams/pdfpapers/114664.pdf

Laursen, Krista K., David P. Jorgensen, Guy P. Brasseur, Susan L. Ustin, and James R. Huning, 2006: HIAPER: The Next Generation NSF/NCAR Research Aircraft. *Bulletin American Meteorological Society,* **87,** 896-909.

Stith, J, W. A. Cooper, V. Ramanathan, D. C. Rogers, P. J. DeMott, T. Campos, and B. Adhikary, 2008: Interactions of Asian emissions with storms in the Pacific Ocean: Early results from the Pacific Dust Experiment (PACDEX). This conference.

Table 1: Standard Requestable Instruments

Measurement	***Instrument(s)***
position, attitude, ground speed	inertial reference units and GPS receivers, Honeywell LASEREF III/IV with Garmin GPS-16
pressure	Paroscientific Model 1000 Digiquartz Transducer, separate fuselage static buttons
temperature	HARCO Model 100990-1 De-iced TAT Sensor (2 units/4 outputs); Rosemount Model 102AL TAT Sensor.
dewpoint	Buck Research Model 1011C Hygrometers (dual units)
dynamic pressure	Mensor Model 6100 Digital Pressure Transducer
wind gust sensing	Mensor Model 6100 Digital Pressure Transducers measuring differential pressures between ports on the forward nose radome
aerosol measurements	Condensation nuclei (water based) and differential mobility analyzer, scanning
stratospheric water vapor	tunable diode laser system
cloud water content	heated wire (King) probe, DMT, and Rosemount icing probe
aerosol size distribution	PMI Ultra-High Sensitivity Aerosol Spectrometer
cloud droplet sizes	DMT cloud droplet spectrometer
ice sizes and shapes	2D probe, modified for the high speed of the GV

Table 2: Special-Use Instruments

Measurement	***Instrument / Developer***
hydrometeor sizes	3V-CPI / Lawson, SPEC, Inc.
small ice crystals	small ice detector (SID-2) / Heymsfield, NCAR
aerosol backscatter	high spectral resolution lidar / Eloranta, U. Wisconsin
temperature profile	microwave temperature profiler (MTP) / Mahoney, JPL
spectral irradiance, actinic flux	HIAPER Airborne Radiance Package (HARP) / Shetter, NCAR
full-range humidity	Vertical Cavity Surface Emitting Laser Hydrometer / Zondlo, SW Sciences
nitric acid, SO_2, & others	Chemical Ionization Mass Spectrometer / Huey, Georgia Tech.
CO, CO_2, CH_4, N_2O	Quantum Cascade Laser Spectrometer (QCLS) / Wofsy, Harvard
O_3	ozone photometer / Rawlins, PSI
O_3 (fast response)	chemiluminescence detection / Campos, NCAR
organic trace gases	Trace Organics (TOGA) / Apel, NCAR
occultation sounding	GPS full-spectrum receivers / Garrison, Purdue
aerosol composition	Time-of-Flight Aerosol Mass Spectrometer / Jimenez, U. Colorado
aerosol particles from evaporated hydrometeors, or total water content	Counterflow Virtual Impactor / Twohy, U. Oregon
radar reflectivity and Doppler velocity	HIAPER Cloud Radar (HCR), a pod-mounted Doppler W-band radar / NCAR

RESPONSE OF THE SMALL ICE DETECTOR (SID-2) TO ICE AND WATER CLOUD PARTICLES AND TO AEROSOLS, OBTAINED DURING FLIGHTS OF THE UK MET OFFICE/BAE-146 ATMOSPHERIC RESEARCH AIRCRAFT.

R. J. Cotton[1], Z. Ulanowski[2], E. Hirst[2], P. H. Kaye[2], R. S. Greenaway[2]
1. Met Office, Exeter, UK, richard.cotton@metoffice.gov.uk
2. Science and Technology Research Centre, University of Hertfordshire, Hatfield, UK

ABSTRACT

The Small Ice Detector 2 (SID-2) built by the University of Hertfordshire has been operated by the UK Met Office on the BAe-146 research aircraft during a large number of flights. These flights included runs in Stratocumulus, Cirrus, and mixed phase clouds, clear-sky flights over the sea and over desert surfaces. SID-2 is a laser scattering device which fits into a standard PMS canister to provide in situ data on cloud particle concentration, size and some information on the particle shape. The response of SID-2 to water drops, ice particles and aerosols are presented. Results include the particle size range and concentration capability, the discrimination of liquid and ice phase, and background problems.

1. INTRODUCTION

The in-situ measurement of cloud particle number concentration, size and (liquid/ice) phase are important for the study of cloud microphysics and for radiative properties. Being able to measure these properties of small cloud particles (of the order of a few microns in size) should for example, enable the onset of ice nucleation to be determined in a mixed-phase cloud. The Small Ice Detector 2 (SID-2) was built by the University of Hertfordshire to discriminate between super-cooled liquid drops and small ice particles, and to estimate the size of the ice particles which are generally below the size capability of current cloud particle probes. The SID-2 therefore complements the current ice particle probes (2D-C and CPI). While it is not designed to replace the FSSP for warm liquid drops in Sc, by comparison with the FSSP it can be validated.

2. SID-2 DESIGN AND OPERATION

SID-2 is an improved version of the first SID version, described in Hirst et. al. 2001. There are three important improvements: the probe inlet is open-path to reduce any possible shattering of large cloud particles, the spatial resolution of the photodetector is increased from 6 to 24 segments, and the data acquisition is capable of time-stamping individual particles.

The scattered light is detected by a hybrid photo-diode (HPD) which is a segmented silicon photodiode mounted in a vacuum tube with a photocathode. The HPD has 27 photodiode elements, with 3 central and 24 arranged azimuthally covering a forward scattering angle up to 20 degrees. The spatial scattering onto these outer elements give information about the particle shape. Spherical particles scatter light uniformly giving a uniform response across all 24 elements.

3. FLIGHT DATA

The flight data shown here was taken during a large number of flights which included runs in Stratocumulus, Cirrus, and mixed phase clouds, clear-sky flights over the sea and over desert surfaces. The details of the runs used are shown in Appendix C.

3.1 Behaviour in water only clouds: warm Stratocumulus and super-cooled wave cloud

Two flights are selected where aircraft instrumentation indicated that only liquid water was present: One was mainly in extensive Stratocumulus (flight B256) and the other in orographic lenticular cloud (flight B252) which was supercooled liquid water only.

The SID-2 response during one straight and level run in Stratocumulus is shown in fig. 1.

This was at 1600 ft above MSL with air temperature around 9°C. The SID-2 particle diameter measurement range covers the FFSSP range (which is from 2 to 47μm), so the concentration agreement is expected to be good if the sample volume has been estimated correctly. The SID-2 bulk-water content obtained from integration of the particle size spectrum is compared to the bulk-water probes. For all the runs, each at different altitude in the Stratocumulus, the agreement with the FSSP and bulk-water probes is good.

The cloud particle phase is determined by the scattering asymmetry factor, A_f, defined in Appendix B. A contour plot of frequency of occurance as a function of A_f and calculated particle size for this single run is shown in fig. 2. Most particles have $A_f < 8$, but there are significant numbers with larger A_f. Fig. 3 is a similar plot but for a run in a super-cooled liquid water wave cloud, where other aircraft instruments indicated no ice present. This was at FL250 with air temperature around -32°C. For this run, there are negligible numbers of particles with large A_f, confirming the no ice observation.

3.2 Behaviour in ice only clouds: frontal Cirrus

One flight in frontal Cirrus (B257) is selected. The SID-2 response during one straight and level run near the Cirrus top is shown in fig. 4. This was at FL320 with air temperature around -57°C. At this cold temperature, no liquid water will be present. Near the cloud top, all ice particles are small enough to be measured by the SID-2 without detector saturation. The SID-2 size distribution and calculated bulk-water content can be compared with that from the 2D-C. The number concentration for ice particles around the size overlap region is in good agreement. The under-reading of the Nevzorov total water content in ice cloud is expected. Fig. 5 shows that most particles have $A_f > 5$. This run with very small, more pristine ice particles, is a more difficult test for the SID-2 phase discrimination capability than using larger, possibly aggregated particles.

3.3 Behaviour in mixed-phase clouds: super-cooled Cumulus

One flight in Cumulus (B246) is selected. The SID-2 response during one straight and level runs near the Cumulus top is shown in fig. 6. This was at FL135 with air temperature around -9°C. The A_f values indicate that there are significant amounts of both liquid drops and ice particles present.

3.4 Behaviour in aerosols: industrial pollution and sea-salt

4. DISCUSSION

Data from the wave-cloud flight shows that the SID-2 detection limit for cloud particles (observed at the leading edge of the cloud) is around 3μm radius. This is due to the low laser power and photodetector dark current noise. The detector elements are saturated for cloud particles above 70μm radius (80μm radius for ice particles).

The SID-2 inlet design is open-path to reduce possible large particle shattering. As described in Field et. al. 2003, the distribution of particle inter-arrival times indicates where shattering is occurring.

Surrounding the small trigger volume is an extended sensing volume (60 times larger). The coincidence of particles in this sensing volume while another particle triggers the detector read-out will add to the scattered light intensity of the triggered particle. This will lead to a non-uniform azimuthal detector element response and lead to skewing the particle size distribution towards larger particle sizes. The probability of coincidence can be calculated using Poission statistics and depends on the particle concentration (there is a 5% probability when the concentration is 30cm^3). The coincidences might be displayed in the scattering patterns for the Stratocumulus run shown in fig. 7 typified by the particle 28.

There is extra information relating to the ice particle habit is the detailed scattering pattern rather than just using A_f. Also, the three central detector elements contain information that is not, so far, used.

5. SUMMARY AND CONCLUSIONS

The SID-2 probe is capable of counting, sizing and determining the phase of cloud particles. The laboratory derived sample volume (which determines the particle concentration) and size calibration have been validated against the FSSP and 2D-C probes in Stratocumulus, wave-cloud and Cirrus. SID-2 can discriminate between super-cooled drops and just-nucleation ice particles in mixed-phase cloud.

6. REFERENCES

Hirst E., Kaye P. H., Greenaway R. S., Field. P. and Johnson D. W., 2001: Discrimination of micrometre-sized ice and super-cooled droplets in mixed-phase cloud. *Atmos. Env.,* **35,** 33–47

Field P. R., Wood R., Brown P. R. A., Kaye P. H., Hirst E. and Greenaway R., 2003: Ice particle interarrival times Measured with a fast FSSP. *J. Atmos. Oceanic Tec.,* **20,** 249–261

APPENDIX

A. Laboratory calibrations

The size calibration of SID-2 was carried out in the laboratory using polystyrene latex spheres (PSL) spheres. For larger spheres the scattering cross-section is expected to scale with the projected area of the sphere. The detector response should therefore depend on the square of the particle size. The size calibration is also corrected for the different refractive index of 1.32 (water and ice average) and 1.6 (polystyrene). For spherical particles, the diameter is

$$D = 2.2\overline{S}^{0.5} \tag{1}$$

where $\overline{S}$ is the mean outer detector response. The angular dependence of scattering from ice crystals is expected to be different from spheres. For scattering angles corresponding to the outer detector ring, the ice crystals are undersized by a factor 1.7, ignoring crystal habit details.

The particle number concentration (cm^{-3}) is given by $\frac{f}{AV}$, where f is the count frequency (s^{-1}), A is the area of the triggering zone and V is the average particle velocity (which is equated to the true airspeed in-flight). The trigger is defined by the scattering from an area within the laser beam into two photomultiplier tubes. The trigger area depends on the particle size and phase (laboratory tests indicate $A = 0.88$mm^2 for 25μm ice particles.

B. Data processing

Each detector element has a different gain. The non-uniformity of the detector element response is corrected for by taking a large number of particles and assuming that on average the particle orientation is random. (The gain ranges from 0.58 to 1.88, where 1.0 is the average response).

Each detector element also has a different background noise level. This is temperature dependent and therefore varies during the flight. To determine the noise levels, all detector elements are read every second without the need for a trigger. The background levels are derived from these 'forced-particles' when in clear air.

For each triggered particle, the variation of the scattered light intensity around the azimuthal detector elements is calculated. This asphericity is given by,

$$A_f = \frac{k\sqrt{\sum_{i=1}^{n}\left(\overline{S} - S_i\right)^2}}{\overline{S}} \tag{2}$$

where S_i is the i'th detector element response out of n elements, and k is a scale factor so that $A_f < 100.0$.

The SID-2 data acquisition counts particles that are triggered but not read-out due to electronics dead time. These 'missing particles' are included in the time-series by distributing randomly over the relevant size-spectrum.

C. Flight details

D. Scattering patterns

The scattered light intensity onto each outer detector element for a sample of particles from each of the flight runs are shown in figs. 7–10. For all detector elements the response $2.2S_i^{0.5}$ is given as polar plots. Hence plot area is proportional to particle cross-section area, and for spherical particles (with uniform azimuthal response) plot radius is proportional to particle radius. Each figure uses the same size scale.

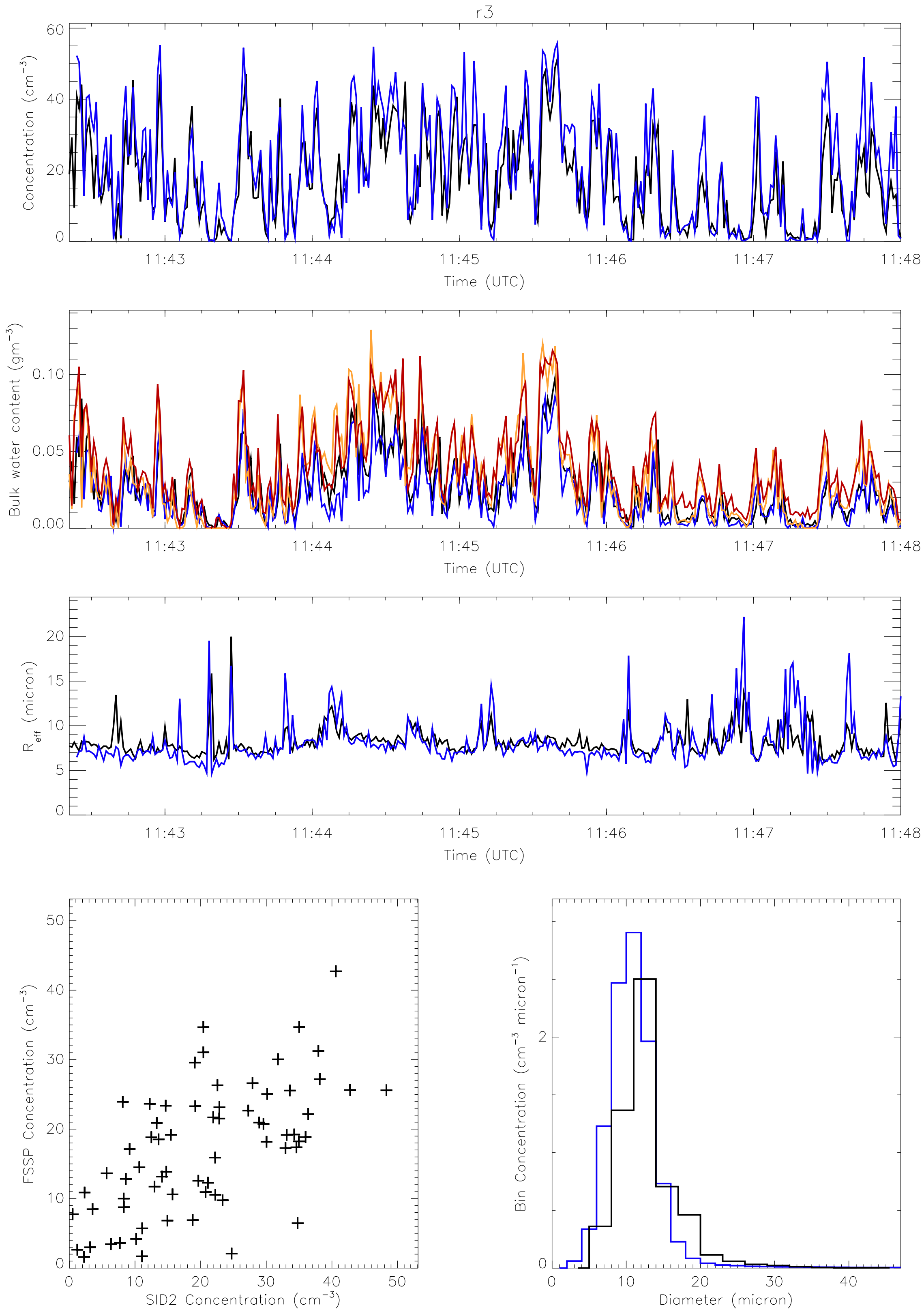

Figure 1: The blue line is SID-2, black is FSSP, red is Johnson-Williams LWC and orange is Nevzorov LWC. The time-series are 1 second data, the scatter-plot is averaged over 5 second intervals.

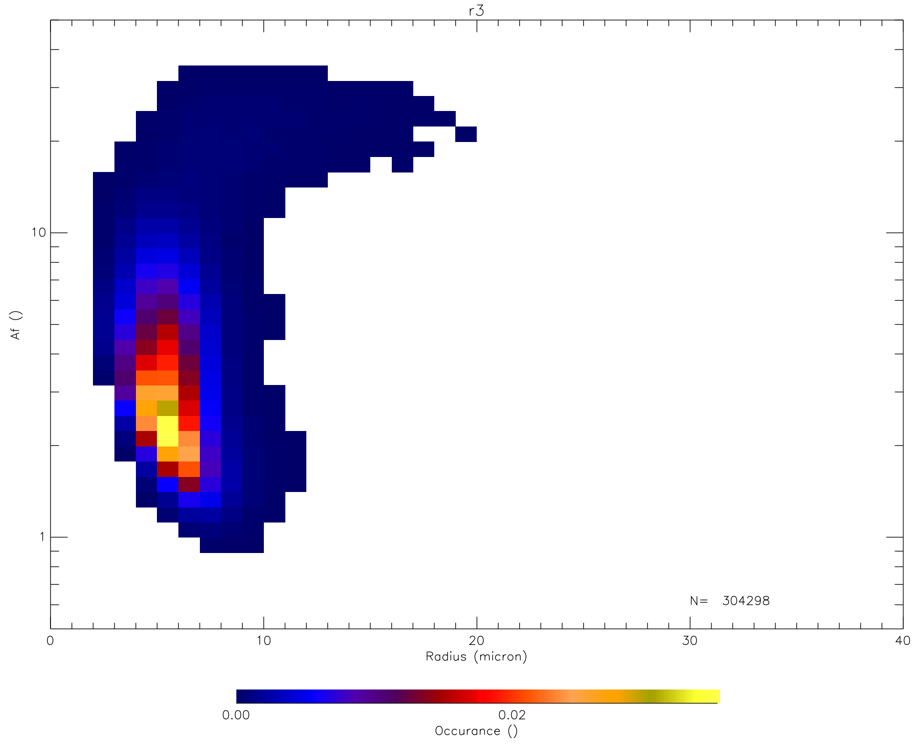

Figure 2: Stratocumulus cloud drops.

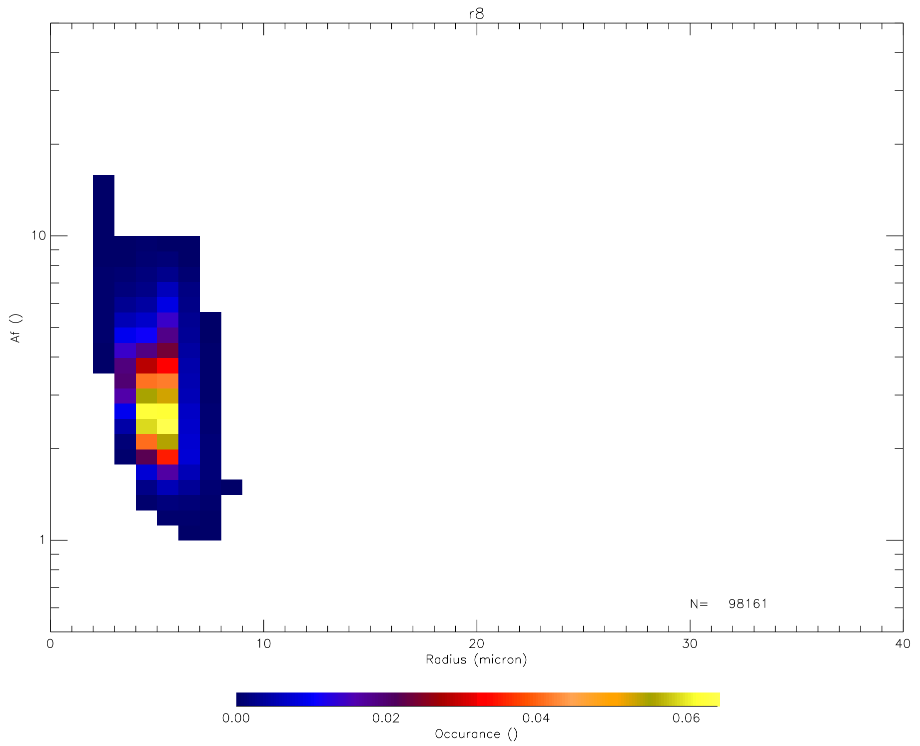

Figure 3: Wave-cloud super-cooled drops.

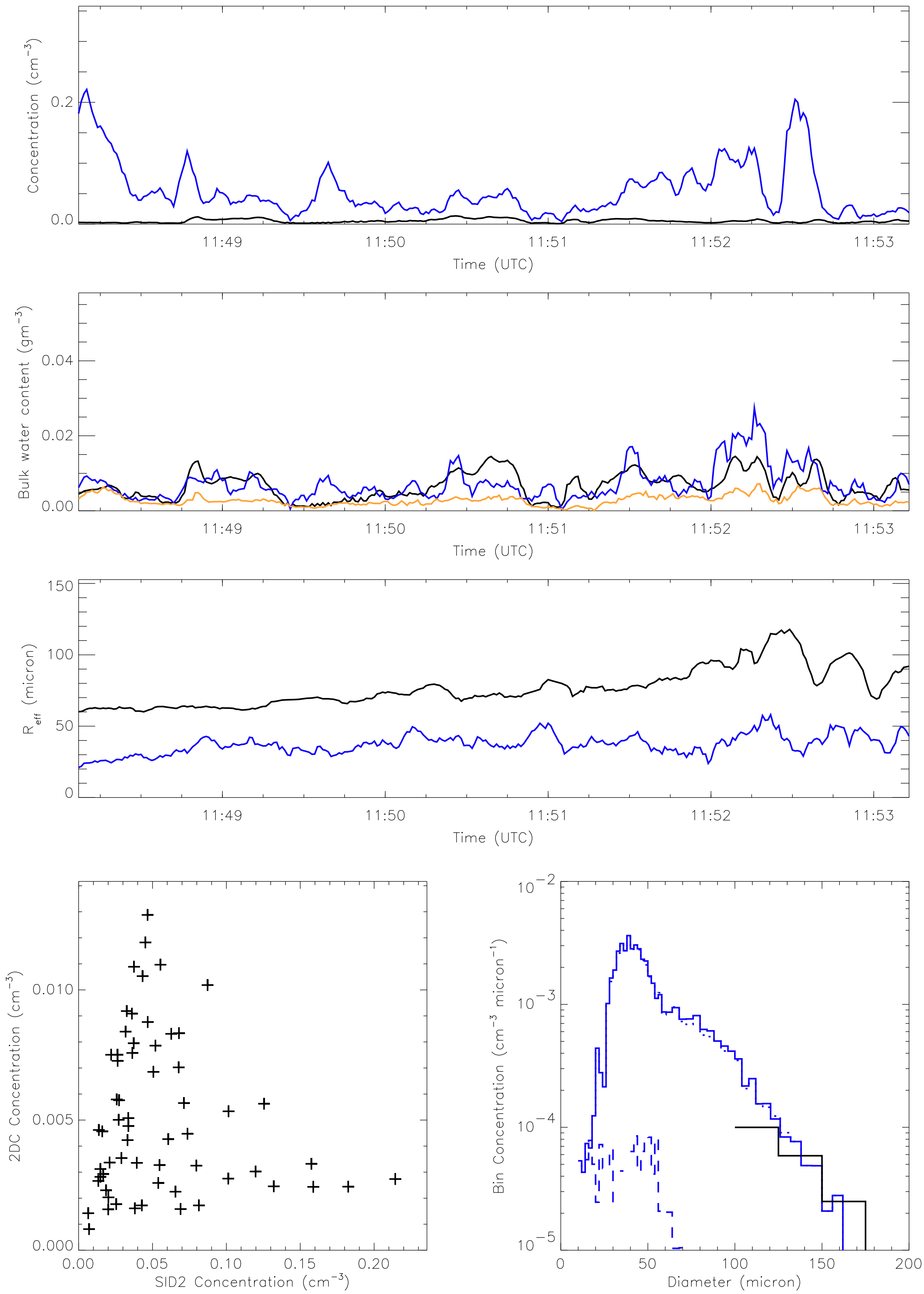

Figure 4: The blue line is SID-2, black is 2D-C, orange is Nevzorov TWC.

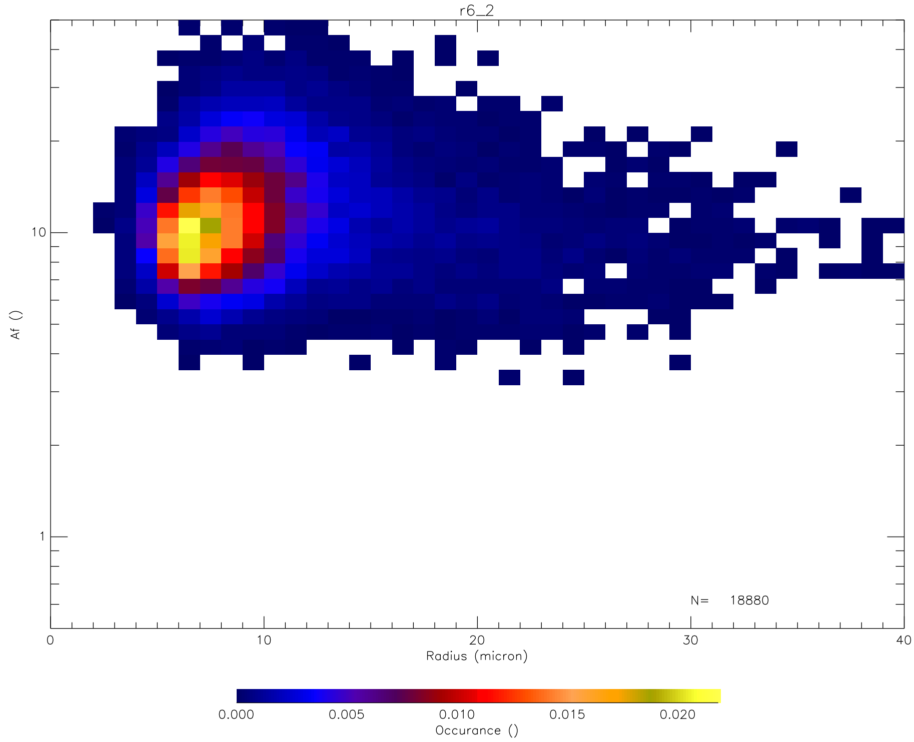

Figure 5: Cirrus pristine ice particles.

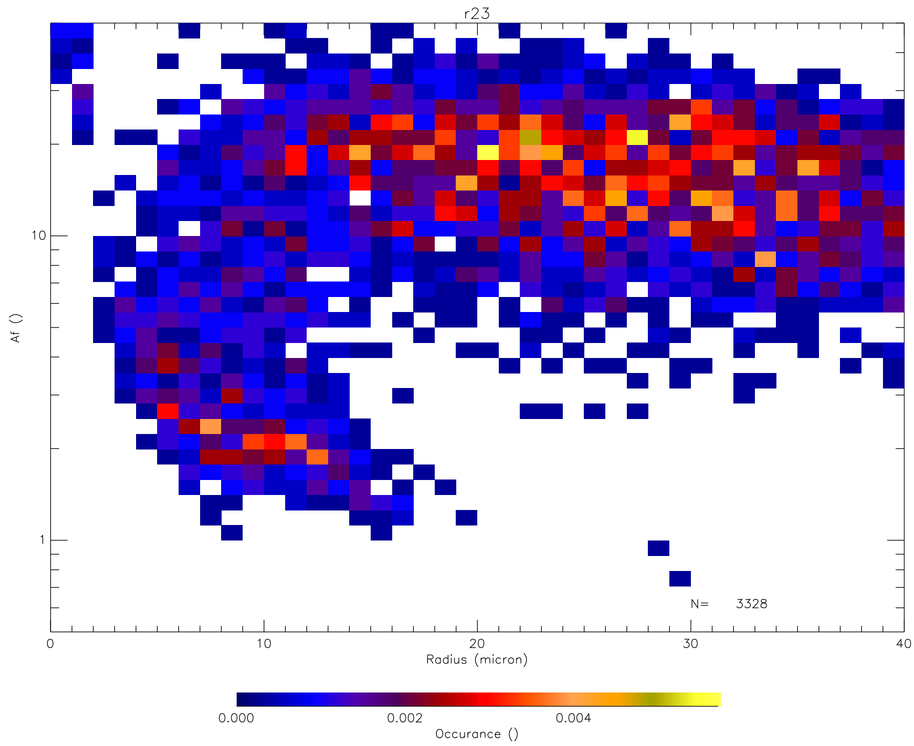

Figure 6: Cumulus mixed-phase.

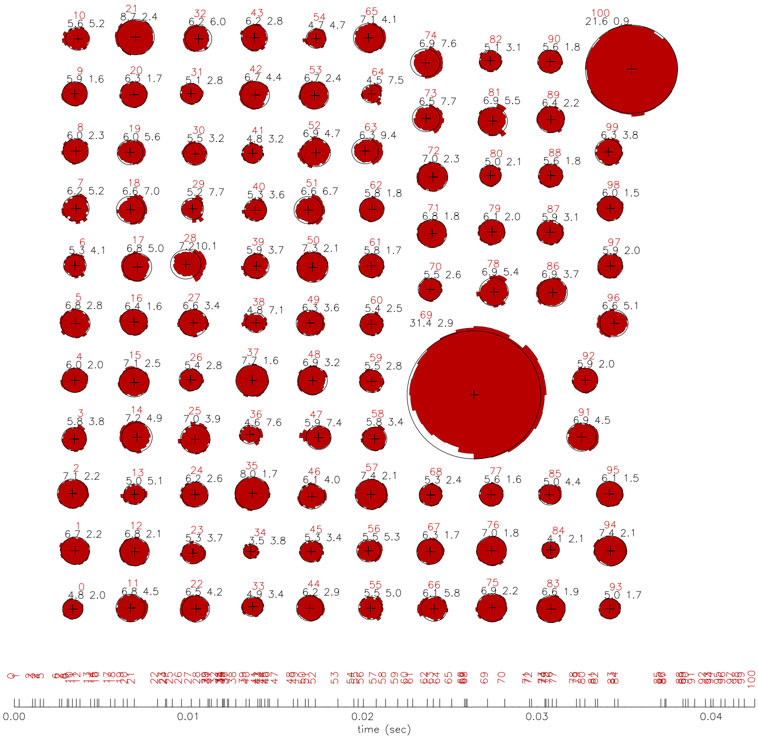

Figure 7: Stratocumulus cloud drops. The red particle number indicates the order of arrival. The two black numbers are the particle radius and A_f value. The black circle represents the calculated particle radius.

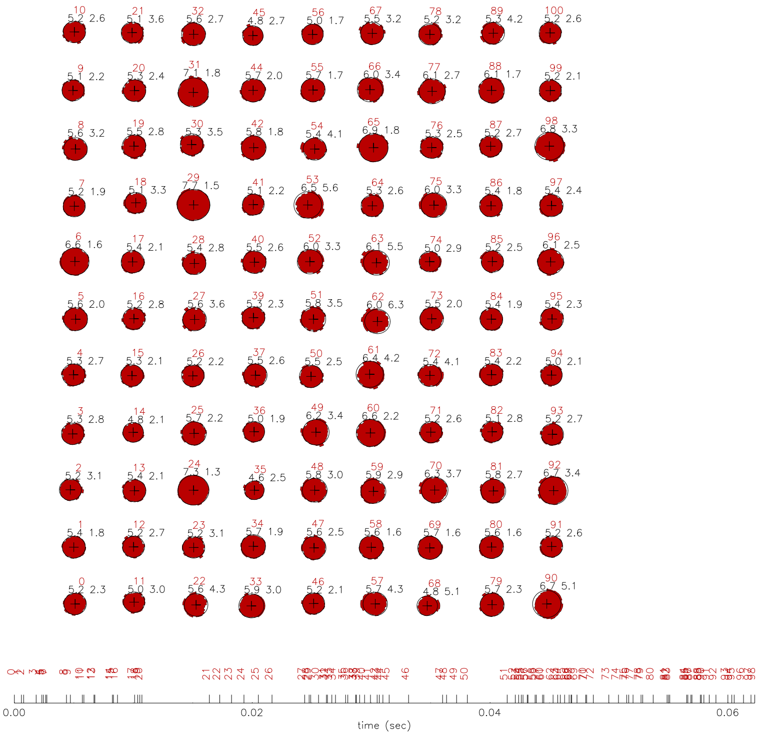

Figure 8: Wave-cloud supercooled drops.

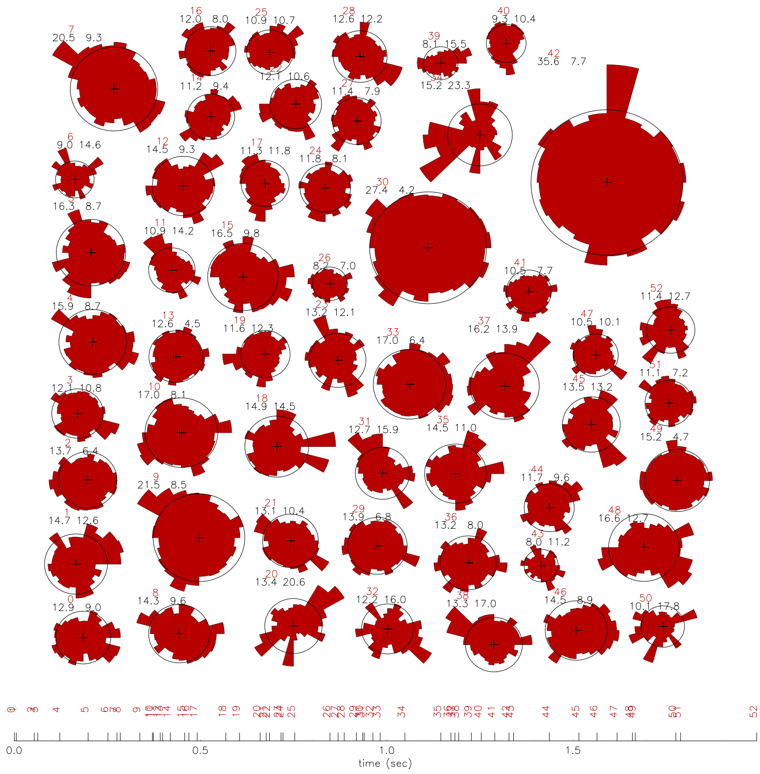

Figure 9: Cirrus pristine ice particles.

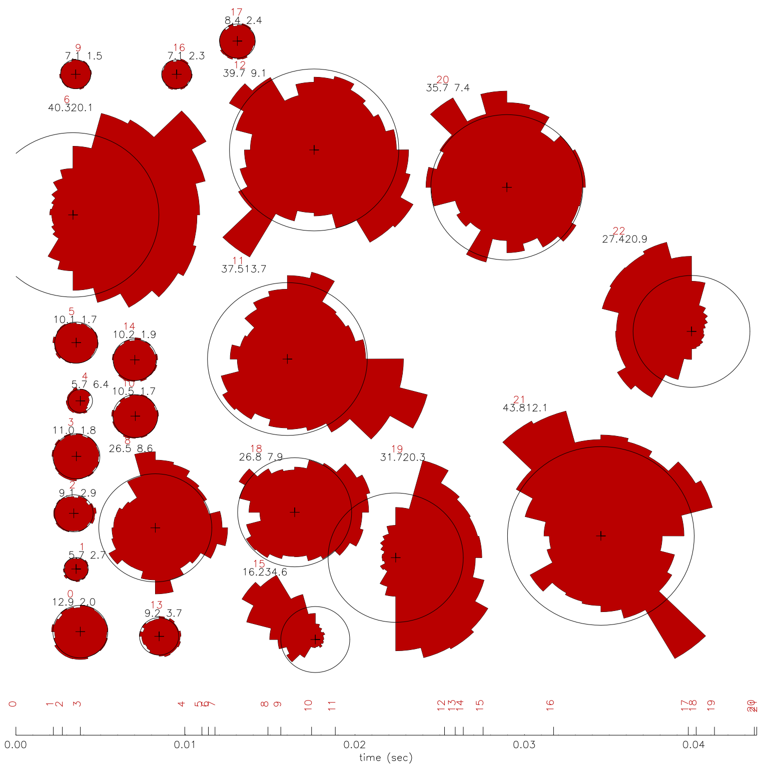

Figure 10: Cumulus mixed-phase.

ON ESTIMATION OF EFFICIENCY OF CLOUD SEEDING BY UNGUIDED ROCKETS

Marat Z. Dosaev, Boris Ya. Lokshin, Yury D. Selyutsky
Institute of Mechanics of Lomonosov Moscow State University, Russia

1. INTRODUCTION

The different antihail rockets (AHR) are used in the some countries (Russia, Moldavia, China, Argentina and others) for protecting of the agricultural crops against the hail hits. In accordance with contemporary method, these rockets deliver the large number of coagulative hailstone embryos (nuclei) to the certain area determined by the specific isotherm. The nuclei collect the atmospheric moisture and thereby prevent the formation of the big hailstones.

These rockets should be cheap enough, so usually they are not supplied with the control system. However, they are used in instrument meteorological conditions. Rough air can essentially deflect the rocket from the required sown area in horizontal and vertical directions.

One of the main problems that should be solved for the seeding process is to ensure the seeding of the required area with the specific probability, taking into account the rocket dispersion along the trajectory. The information about the number of rockets necessary to obtain this probability can be used for estimation of economical efficiency of different types of rockets.

Thus, designers of AHRs need a tool that would allow them optimization of AHR design and estimation of AHR efficiency for cloud processing.

In order to estimate the efficiency of cloud processing by AHRs of a given type and to ensure the accuracy of delivery of the reagent and compliance with requirements of the safe application of AHR, it is necessary to perform preliminary study of rocket external ballistic characteristics. In contrast to the ordinary external ballistic problem, it is necessary to take into account the following features when analyzing AHR flight trajectories:

- The flight is realized in the rough air in the presence of the ground and ballistic winds.
- The altitude echelon is defined. The only “useful” part of the trajectory is the part lying inside of this echelon.
- The number of hailstone embryos is calculated in the defined altitude echelon.
- The AHR flight is controlled by initial orientation only.
- In AHR there are used single-impulse or double-impulse engines.

2. VIRTUAL PROVING GROUND: MATHEMATICAL MODEL

Authors developed the special computer tool – the virtual rocket proving ground. This program is intended for solving of problems concerned with rocket flight modeling, as well as with calculation of probabilistic characteristics of seeding for given initial conditions. The process of reagent propagation inside the cloud is described on the basis of empirical approach.

The mathematical model used in the virtual proving ground describes space motion of the rocket taking into account rocket rotation.

The following algorithm is used for determination of the required number of rockets. First, the directions of rocket launches that ensure complete coverage of the horizontal projection of the specified area are defined. Thus, the nominal (minimal) number of rockets is determined. Then, taking into account the random rocket dispersion along the trajectory, the probability of complete seeding of the vertical section of the cloud in the launching plane for each launch direction is calculated. The probability of seeding of the entire cloud is found as a product of corresponding probabilities. If this product is greater than the required probability, then the necessary number of rockets is equal to the nominal one. If this product is less than the required probability, then the combinatorial problem is solved in order to determine, which launches should be repeated to reach the required value of the probability of seeding.

3. VIRTUAL PROVING GROUND: FEATURES

The user can select rocket type, for which it is necessary to calculate trajectories. It is possible to create a new rocket or open and modify one of the previously created.

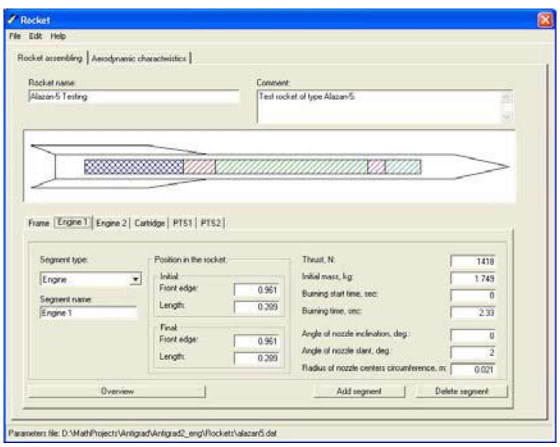

Fig. 1

The program provides possibility to assemble the rocket from a set of different segments. For each segment user defines mass, start position and end position of the segment, thrust produced by the segment, duration of burning and time when the burning starts. Besides, user defines characteristics of the rocket frame (length, mass, moments of inertia, etc.). Then the program automatically calculates all required characteristics of the rocket (mass, moments of inertia, center of mass position, total thrust) as time functions.

Aerodynamic characteristics of the rocket are entered as table functions of the Mach number and the angle of attack. Thus, user can input data obtained during wind tunnel tests.

User can also give the rocket some name and to enter a comment. The information about rocket is then saved on disk as text file. Later these files can be used for calculations.

Besides, the virtual proving ground allows defining of some parameters of the launcher (name, guide rail length, number of rockets).

Before calculation the user must enter launch conditions (initial conditions for the rocket, wind speed and wind direction, cloud size and position with respect to launcher position, echelon boundaries). After these data is input, it is possible to start the simulation.

The program can operate in two modes: *Phase planes* and *Ground*.

The *Phase planes* mode is intended for calculation of single AHR trajectories. It allows user to see all characteristics of rocket trajectory in given conditions (length of the “useful” part of the trajectory, effective distance, probability of 100% seeding of vertical section of the cloud, number of nuclei in the echelon and in the cloud, etc.).

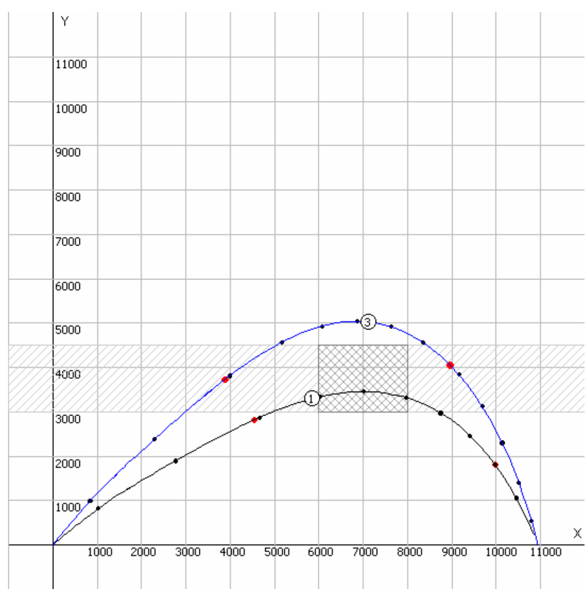

Fig. 2

The typical example of calculation result (altitude vs. distance) is presented in Fig. 2.

The *Ground* mode is intended for estimation of efficiency of different AHR types for seeding of specific area. There are two regimes: automatic and interactive.

In the automatic regime the program determines minimum set of rocket trajectories necessary to seed the whole cloud (Fig. 3) and shows the corresponding launch azimuths in the horizontal plane along with the cloud projection.

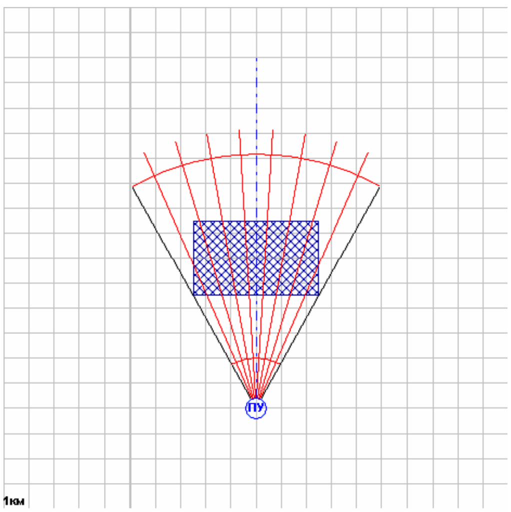

Fig. 3

In the interactive regime the user can simulate seeding of the cloud launching single rockets. The result is visualized as the projection of trajectories and of the cloud to the horizontal plane (top view) (Fig. 4).

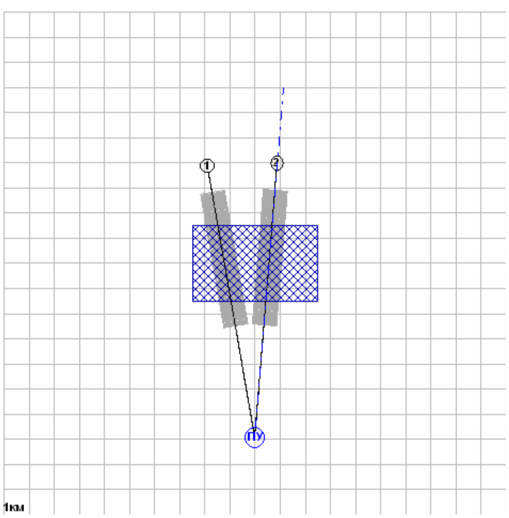

Fig. 4

Simulation results are saved in text files that can be reused in this program or transferred to other programs for following processing.

The graphics along with additional information about calculation can be printed out.

4. COMPARISON WITH EXPERIMENTAL DATA

In order to verify the mathematical model used in the program, telemetric data were used obtained during field tests of AHR "Alazan-5".

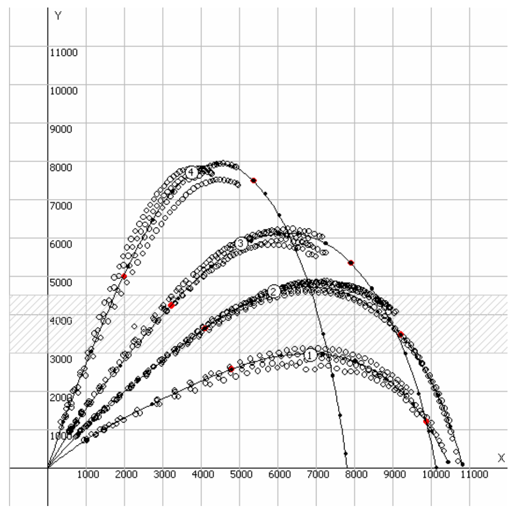

Fig. 4

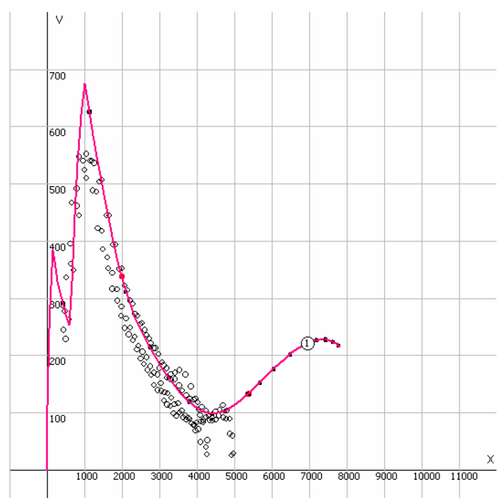

Fig. 5

There were launched several rockets at different initial elevation angles. The results of computation and experimental data are presented in Fig. 4 (altitude vs. distance) and Fig. 5 (speed vs. distance). Evidently, the results of numerical simulation with the virtual proving ground are in good agreement with experimental information.

5. OPTIMIZATION OF ROCKET DESIGN

The virtual proving ground allows designers to optimize the rocket construction changing parameters of segments (for instance, mass, duration of burning, burning start time, thrust produced, etc.).
The example of calculations basing on a certain rocket is shown in Fig. 6.

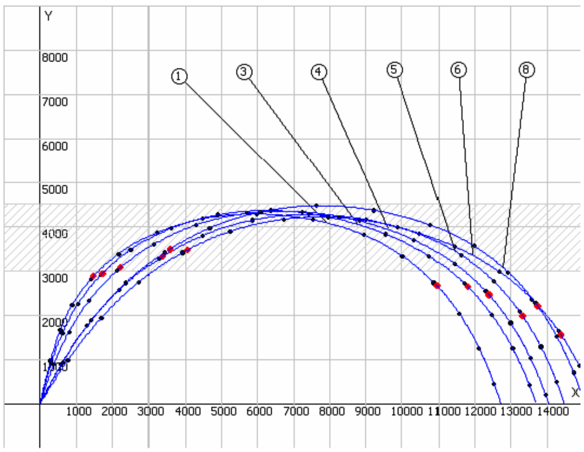

Fig. 6

Different trajectories correspond to different sets of rocket parameters. Evidently, optimization of rocket design allows obtaining rather considerable (up to 20%) improvement of rocket trajectory characteristics (for instance, effective distance).

5. CONCLUSION

The developed computer program (“virtual proving ground”) is an easy-to-use tool for solving of different problems concerning the research, development and usage of anti-hail rockets:

- Estimation of external ballistic characteristics of anti-hail rockets being designed (influence of initial conditions, wind, etc.)
- Optimization of construction parameters of anti-hail rockets
- Comparison of different anti-hail rockets and complexes in identical operating conditions
- Optimization of anti-hail rockets usage

ACKNOWLEGEMENTS

The work is supported by RFBR (grants NN 06-01-00079 and 08-08-00390).

THE KINETIC ENERGY OF RAIN: APPLICATION ON SOIL EROSION

María Fernández-Raga [1*], Roberto Fraile[1], Jan Jacob Keizer[2], Amaya Castro[1], Covadonga Palencia[1], Ana I. Calvo[1], Joost Koenders[2], Renata Liliana Da Costa Marques[2]

[1]Department of Physics, University of León, 24071 León, Spain

[2]Centre for Environmental and Marine Studies (CESAM), Dept. of Ambiente e Ordenamento. University of Aveiro. Portugal.
*mferr@unileon.es

1. INTRODUCTION

Our modern societies are increasingly concerned by the effects of extreme weather events. These phenomena occur more and more often and alarm the general public because of the important damages they may cause. Severe precipitation events in particular cause high economic losses and environmental disasters. Both problems converge in the case of soil erosion. From a meteorological perspective, the study of soil erosion by precipitation requires the knowledge of parameters such as drop size, precipitation volume, rain intensity, and above all the kinetic energy of the drops that hit the ground turning over and dislodging soil aggregates.

The present study is integrated in the EROSFIRE project (POCTI/AGR /60354 /2004), funded by the Portuguese Foundation for Science and Technology (FCT) with co-funding by FEDER through the POCI2010 Programme, which aims at developing a model-based tool for erosion hazard assessment following forest wildfires in Portugal. In this part the aim is determining soil sensitivity to erosion caused by rain after forest fires.

Splashing is considered the main factor in soil erosion because it is the first stage in erosion by water (Ellison, 1944). The impact of raindrops does not only modify the surface (Moss, 1991), but may also dislodge and release soil fragments that will later be carried to even very distant places if additional runoff processes occur at the same time (Moss and Green, 1983).

Splash erosion has often been studied in relation with the characteristics of rain, but less so than in the case of other causes of soil erosion because of the intrinsic difficulties associated to this phenomenon. A study on splash erosion will have to take into account not only the kinetic energy released by each storm, but also the variables type of soil and size of released particles (Sharma et al 1991), as well as the characteristics of the layer of water formed on the ground (Moss and Green, 1983, Kinnell, 1991, Leguédois et al., 2005). Because of these peculiarities, the studies carried out until now have been highly specific and it is difficult to extrapolate the results to larger areas that are not the study zone where the samples have been gathered (Van Dijk et al, 2002). However, there are studies that have attempted comparative analyses of soils with very different degrees of vulnerability (Terry, 1989).

This paper is an attempt to relate the energy released by rain to splash erosion making use of raindrop size and energy measured by means of an optical disdrometer. Raindrop size is used to calculate the volume, the terminal energy and the kinetic energy. Finally, the characteristics of the precipitation were compared with the mass of soil dislodged by splashing in two rain events in 2007.

2. STUDY ZONE

The data were gathered between the 22 May and the 30 September 2007 in Soutelo, Aveiro, Portugal (Fig. 1).

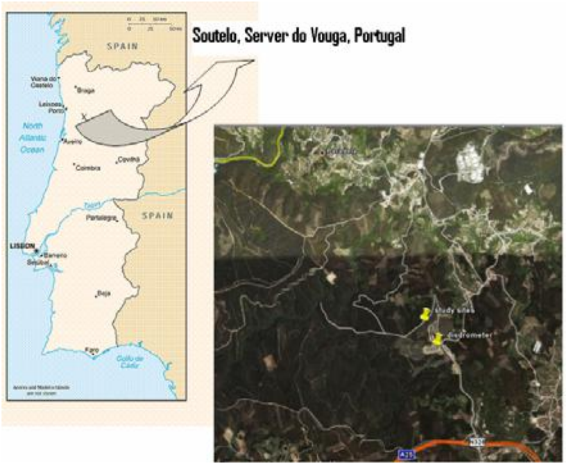

Fig. 1. Study zone close to Aveiro, Portugal.

In the study period occurred 91 rain events with a volume of more than 0.2 mm: 24 in May, 34 in June, 13 in July, 16 in August and 4 in September. All in all, the amount of rain collected was 258.2 mm, which contrasts with the typical climate in the region.

From a climatic perspective, the study zone belongs to an area of transition between the Atlantic and the Mediterranean climate zones, i.e., it is influenced by moist air masses from the Atlantic and also by strong winds. Consequently, very intense precipitation is relatively common in this region, even in inland areas.

The soil type is schist with cambisol and a franco-sandy texture. The vegetation in the area, which should serve as a first defense line against erosion, is formed almost exclusively by forests of *Eucalyptus globulus*, thus explaining the severe abrasions and landslides suffered in the area.

The vulnerability was increased by a moderate wildfire in August 2006 (one year before).

The study zone is part of the Erosfire international Project aiming at developing a GIS tool for surveying erosion in recently burned areas according to the different degrees of the slope.

3. MATERIALS AND METHODS

A Davis station was used to measure precipitation. This weather station lies 410 m above sea level (40º 40´48"N and 8º 20´31"W) and provided data on accumulated precipitation, pressure, wind speed, wind direction and temperature.

Fig. 2. Installing the optical disdrometer in Soutelo, Portugal.

In addition, an optical disdrometer of the Thies model (Fig. 2) was used. This tool is described in Bloemink and Lanzinger (2005) and registers raindrop size spectra every minute.

The range of the disdrometer measures droplets with diameters between 0.125 mm and 8 mm.

The equipment used to carry out this study on erosion is represented in Fig. 3 and 4, including diagrams and pictures of the models that will be called here *Terry* (Fig. 3) and *Cup* (Fig. 4), installed 3 cm above the ground. Both models have simple designs, both are cheap and easy to build, and their main advantage is the fact that once installed the paper filters may be removed without taking the devices apart or altering the surface in any way. So the loss of soil is calculated by measuring these filters, after drying into oven, both before and after the field.

The *Terry* model, based on the design by Terry (1989), is formed by two funnels with some space in between to insert a filter to gather the soil released. The sampling range is of 12 cm. The two-funnel system ensures that the soil particles captured by the device will not be lost again as it protects the filter from washout.

The *Cup* model is based on an original design by Poesen and Torri (1988), later

Fig. 3. Structure of the *Terry* model. Picture of a *Terry* ready to register splashings.

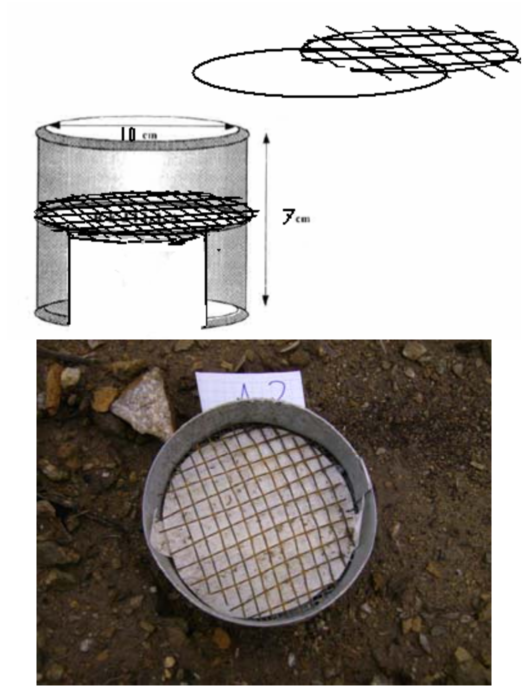

Fig. 4. Structure of the *Cup* model. Picture of a *Cup* ready to register splashings.

modified following Molina and Llinares (1996). It consists of a 7 cm long aluminum cylinder with a diameter of 10 cm. Inside this cylinder is fixed a 0.5 cm opening wire mesh. The filter is secured on top of the mesh, and on top of the filter is fixed another mesh, this time a movable one with a much larger opening. The aim is to reduce the likelihood of the raindrops washing out the filters that have already collected samples of splashed soil particles. The device is fixed to the ground with legs instead of with long cylinders to avoid runoff water swirling down the slope and contaminating the filters with dragged and not splashed soil particles.

4. KINETIC ENERGY OF RAIN

The information provided by the disdrometer was used to calculate the kinetic energy of rain: drop size distribution (DSD). This piece of data is used to calculate the mass of each drop and its fall velocity (Ryzhkov et al 1999). It is necessary to know the shape of the drop in order to calculate its mass.

The shape of raindrops has been the focus of several studies (Brandes, 2002, Sansom, 2004). The main conclusion of these studies is that drops smaller than 1 mm are spherical, whereas drops with diameters larger than 1 mm have more of an ellipsoid shape. Beard et al. (1989) established index α = vertical measurement / horizontal measurement. For raindrops with a diameter d= 1 mm, $\alpha = 0.98$, but for d > 5 mm, $\alpha < 0.7$).

The studies carried out by Jones (1959), Brook and Latham (1968) and Chandrasekar et al. (1988), among others, have contributed to solve the problem, and the studies by Beard and Chuang (1987) and Park, et al (2004) have provided the following criterion: it will be assumed that raindrops are spherical if they are smaller than 1 mm in diameter; in the case of raindrops smaller than 1.075 mm the calculations by Brandes et al. (2002) were applied. From that size on a polynomial equation of degree 12 was calculated. The result is shown in Fig. 5, together with the volume calculated assuming that all drops are spherical.

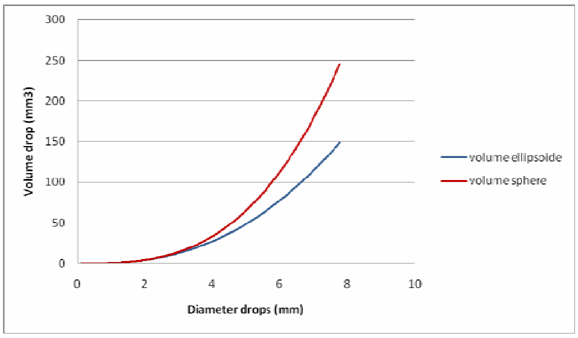

Fig. 5. Relationship between the drop size measured by the disdrometer and its volume. It may be compared with the volume of the supposedly spherical drop.

The mass and the velocity need to be known for calculating the kinetic energy. The dated studies by Gunn and Kinzer (1949) are still useful due to the fact that the results are based on experimental measurements. These are taken into consideration in this paper. The measurements were limited to sizes between 0.125 and 5.8 mm, and do not reach values of 8 mm, which our disdrometer measures. Even though such large drops rarely appear, the need to count on a relationship between the velocity and the diameter in the whole interval led us to extrapolate the results and achieve a good fit for the entire range of measurements by Gunn and Kinzer (1949). The results are listed in Fig. 6.

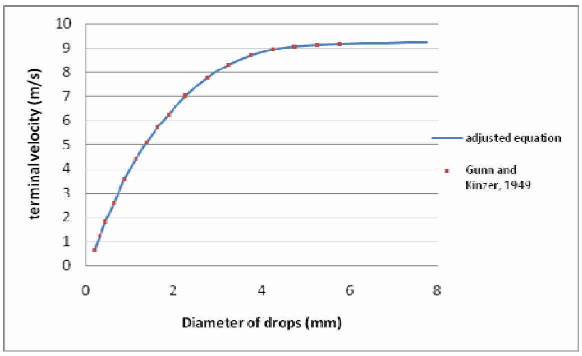

Fig. 6. Relationship between the drop size measured by the disdrometer and their terminal velocity.

In each of the size channels of the disdrometer the kinetic energy was calculated as the mean value of the kinetic energies corresponding to the two extremes of the channel.

5. RESULTS AND CONCLUSIONS

Figure 7 shows the DSD data at Soutelo during the study period. A practically exponential distribution is observed except in the case of large sizes. Fig. 7 also presents the total kinetic energy by unit of area of the rain registered in the study period. The data show that drops in the interval between 2 and 2.5 mm are the greatest contributors to the kinetic energy that hits the ground.

The two devices used for measuring splash erosion were installed in two different periods: one from 23 July to 6 August, and the other from 6 August to 27 August 2007. Figure 8 shows the characteristics of drops in those two periods. Figure 9 presents details (minute by minute) of the energies registered over 4 hours on the first rain day. This provides data on the evolution of energy in time.

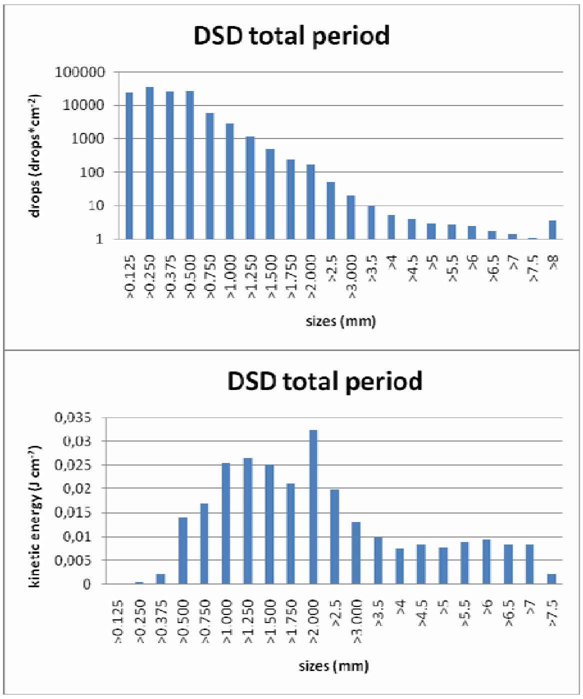

Fig. 7. Drop size distribution and energy distribution by drop size during the sampling period.

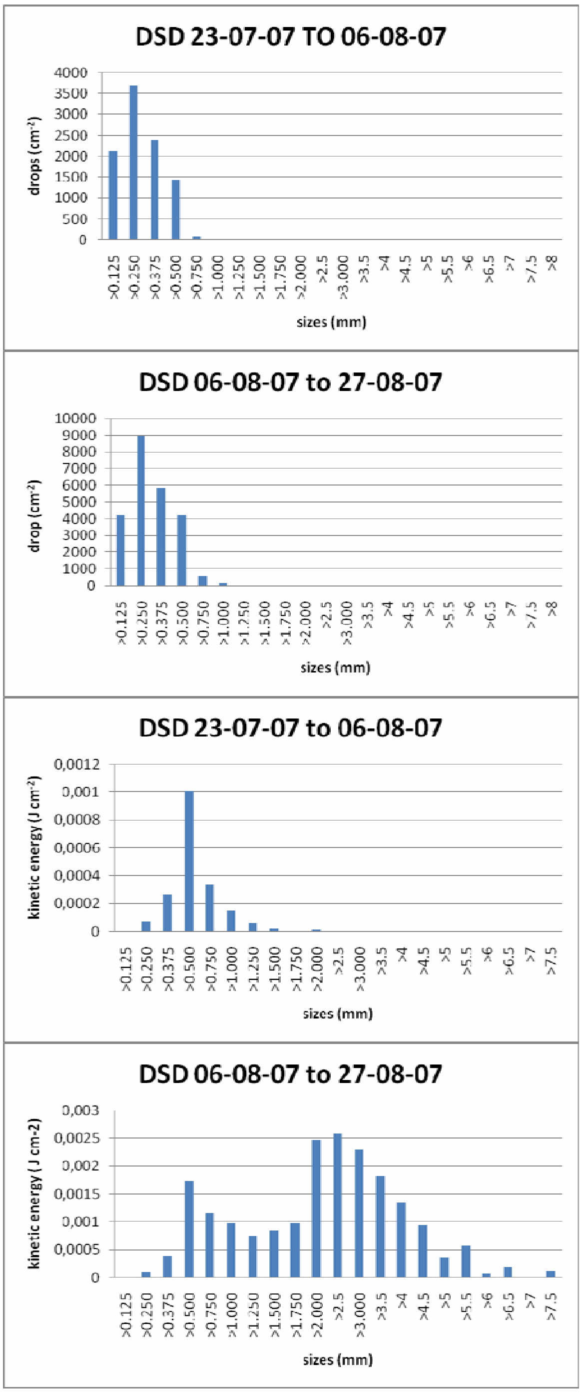

Fig. 8. Drop size distribution and energy distribution by drop size during the two rain periods with splash erosion samplings.

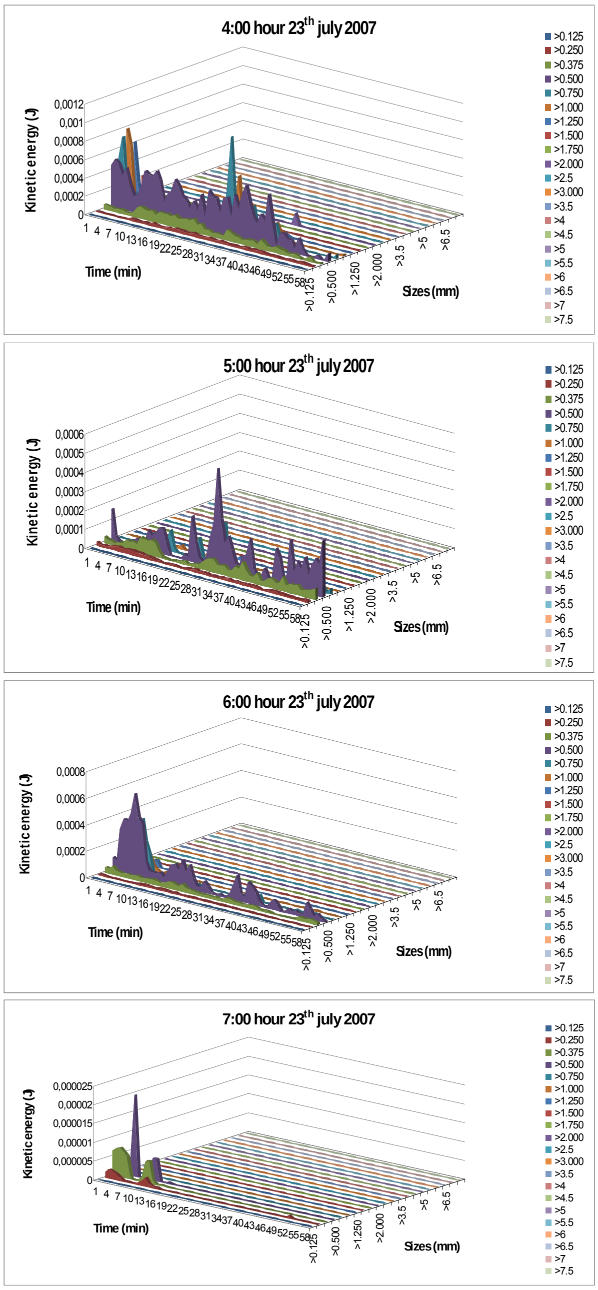

Fig. 9. Energy distribution, minute by minute, by drop size during 4 hours on 23 July 2007.

Figures 7-9 provide the necessary information to calculate the total energy of the rain in the two different sampling periods. The result is 0.0019 J/cm² in the period between 23 July and 6 August and 0.020 J/cm² in the period between 6 and 27 August.

Finally, Fig. 10 shows the amount of soil that was splashed as measured by the two devices, *Terry* and *Cup,* during the two rain periods.

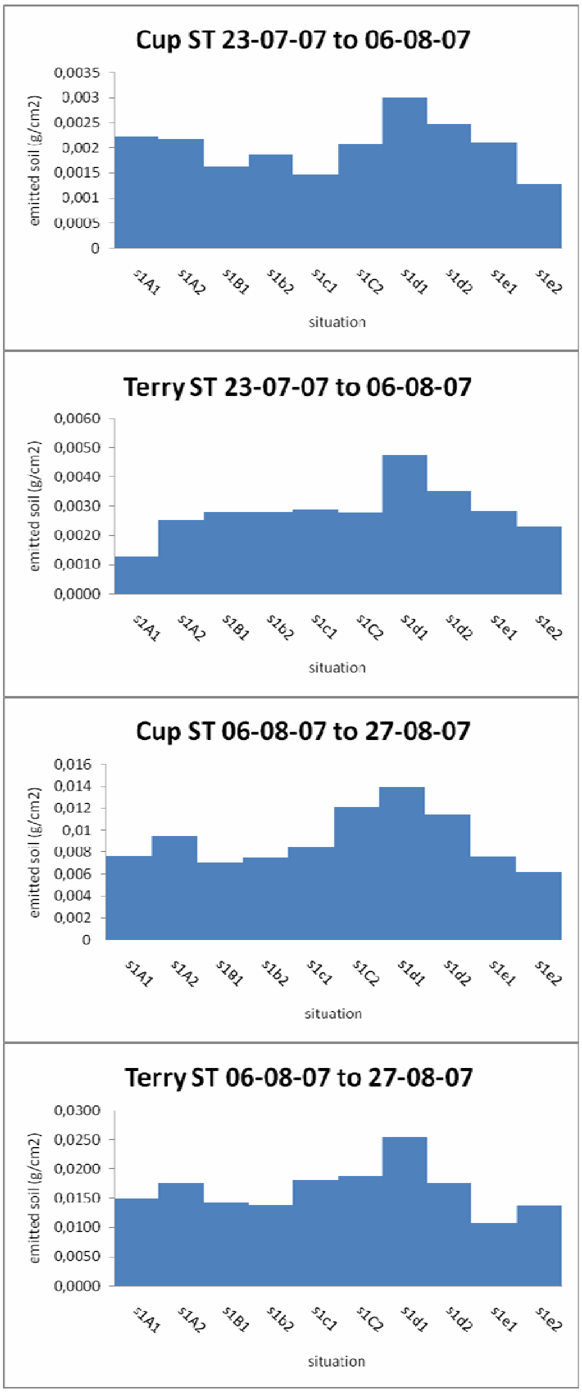

Fig. 10 Mass of soil splashed by rain in the two rain periods as measured by *Cup* and *Terry*. The identifiers of each device appear on the axis of abscissas.

Figure 10 shows that the two measuring devices offer different results. The mean values and the standard deviation are presented in Table 1.

Table 1. Mean value and standard deviation of the mass of soil splashed (in g/cm³) in each rain period.

	23-VII a 6-VIII	6-VIII a 27-VIII
Terry	0.0029 ±0.0009	0.017 ±0.004
Cup	0.0020 ±0.0005	0.009 ±0.003

The Terry gives higher estimates than the cups and this is in line with the fact that the Terry was specifically designed to avoid blow out.

The results pointed out above, together with the comparison of the values in Table 10 with the total kinetic energy in each rain period, enable us to draw the following conclusions:

- The correction of the drop volume because of the fact that they are not spherical represents up to 50% of its value or more, which leads to the same relative error in the kinetic energy calculated. With ordinary drop sizes (smaller than 4 mm), the error may lie under 15%.
- The DSD of the precipitation in Aveiro follows an exponential or gamma distribution. The energy distribution, however, is gamma.
- The *Terry* and *Cup* devices provide different results when measuring the soil splashed by rain, but more data are needed to establish general principles on the goodness of the measurement.
- In any case the two devices point towards the fact that the kinetic energy of rain is an important factor in splash erosion and that erosion increases with an increase in the kinetic energy.
- The mass of soil affected by splash erosion is not directly proportional to the kinetic energy of rain.

6. BIBLIOGRAPHY

Beard and Chuang (1987) A new model for the equilibrium shape of raindrops, *J. Atmos. Sci.* 44 (1987), pp. 1509–1524.

Beard, K.V.,Ochs HT and Kubesh RJ 1989 Natural oscillations of small raindropsraindrop Nature.342.408-410

Bloemink, hi, lanzinger, e., 2005.precipitation type from the thies disdrometer. Wmo technical conference on meteorological and environmental instruments and methods of observations (teco-2005)bucharest, romania, 4-7 may, 3 (11).

Brandes, e. A., g. Zhang, and j. Vivekanandan, 2002: experiments in rainfall estimation with a polarimetric radar in a subtropical environment. J. Appl. Meteor., 41, 674–685.

Brook and Latham (1968)Fluctuating radar echo: modulation by vibrating drops.J. Geophys. Res., 73, 7137-7144.

Chandrasekar, v., w. A. Cooper, and v. N. Bringi, 1988: axis ratios and oscillations of raindrops. J. Atmos. Sci., 45, 1323–1333.

Ellison, W.D. 1944. Studies of raindrop erosion. Agric. Eng. 25:131 136, 181–182.

Gunn, r., and g. D. Kinzer, 1949: the terminal velocity of fall for water droplets in stagnant air. *J. Meteor.,* 6, 243–248.

Jones (1959): The shape of raindrops. J. Meteor., 16, 504-510.

Kinnell, P.I.A. 1991. The effect of flow depth on sediment transport induced by raindrops impacting shallow flows. Trans. ASAE. 34: 161–168.

Leguedois C., S., Malam-Issa O., and Bissonnais Y. L.E. 2005. Splash distance and size distributions for various soils. Geoderma (In press).

Molina M.J., Llinares J.V. 1996. Movilización del suelo por impacto de las gotas de lluvia: ensayo de un nuevo diseño de cápsulas para su determinación en pendientes. *Cuaternario y Geomorfología* 10: 21-31

Moss, A.J., and P. Green. 1983. Movement of solids in air and water- by raindrop impact. Effects of drop-size and water-depth variations. Austr. J. Soil Res. 21:257–269.

Moss, A J. 1991. Rain impact soil crust.I. Formation on a granite derived soil.Austr. J. Soil Res 29:271-289.

Park R., Jacob, D. Field B. and Yantosca, R.,2004. Natural and trans-boundary pollution influences on sulfate–nitrate–ammonium aerosols in the United States: implications for policy, *Journal of Geophysical Research* 109 , p. 15204.

Poesen J, Torri D. 1988. The effect of cup size on splash detachment and transport measurements. Part I: field measurements. *Catena Supplement* **12**: 113–126.

Ryzhkov A., T. Schuur, D. Zrnic, and M. Schönhuber (1999) "Comparison of radar polarimetric measurements of rainfall with 2D-video disdrometer observations" Preprints, National Radio Science Meeting, 1999, Boulder, CO, USA.

Sansom, J., 2004. Rainfall as breakpoints: observations and physically based Markov models. International Precipitation Conference, Quantifying Uncertainties in Precipitation Measurements, Estimates, and Forecasts, Vancouver, Canada.

Sharma, P.P., Gupta, S.C. and Rawls, W.J.. 1991. Soil detachment by single raindrops of varying kinetic energy. Soil Sci. Soc. Am. J. 55: 301–307.

Terry 1989 The development of a new device for measuring rainsplash erosion. Swansea Geographer, 26, 54-63.

Van Dijk A.I.J.M., Meesters, AGCA., Bruijnzeel, L.A. 2002 Exponential distribution theory applied to splash detachment and transports experiments. Journal of Applied Meteorology 18, 654-660.

Acknowledgements

The authors are grateful to Antonio M. Ortín for his essential contribution, and to Dr. Noelia Ramón for translating the paper into English. This study was integrated in the EROSFIRE project (POCTI/AGR /60354 /2004), funded by the Portuguese Foundation for Science and Technology (FCT) with co-funding by FEDER through the POCI2010 Programme, and also supported by the Junta de Castilla y León (Grant LE014A07).

AN INSTRUMENT FOR STUDIES OF THE RELATION BETWEEN CLOUD DROPLET SIZE AND DRY RESIDUAL PARTICLE SIZE – THE DROPLET AEROSOL ANALYSER

Göran P. Frank and Bengt G. Martinsson
Department of Physics, Lund University, Lund, Sweden

1. INTRODUCTION

The Droplet Aerosol Analyser (DAA) is an instrument especially developed for studies of the interaction between aerosol particles, and cloud/fog droplets and interstitial particles. The DAA measures the ambient size of individual droplets and interstitial particles, the size of the dry residual particle after evaporation of the water vapour, and the number concentration of dry residual particles. This gives a unique three-parameter data-set (ambient diameter, dry residual particle diameter and number concentration).

Having access to these parameters, a number of related aerosol/cloud parameters can be determined:

- Number size distribution of ambient droplets/particles
- Number size distribution of dry residual particles
- The relation between ambient diameter and dry (residual) diameter on a single droplet/particle basis
- Characterisation of the droplet activation as defined by the Köhler equation
- The size dependent scavenging of particles due to activation
- Concentration of soluble matter in the individual droplets (solute concentration)
- Liquid water concentration

The DAA is based on a concept where the aerosol is processed in several steps by aerosol charging mechanisms, diffusion drying, and electrostatic aerosol spectrometry (using Differential Mobility Analysers, DMAs). The first version of the instrument (Martinsson, 1996; Cederfelt et al., 1997; Frank, 2001) was developed during the 1990-ies, and used in a number of ground based cloud and fog experiments (Martinsson et al., 1997; Frank et al., 1998; Martinsson et al., 1999; Martinsson et al., 2000). After a period of low activity, a second generation instrument is currently under development. The improved version will be more suited for long term measurements, which are favourable in order to obtain results with high statistical confidence. The time resolution of the instrument will be improved as well.

Here, we will present the features and capabilities of the DAA, by showing examples of previously obtained results. In addition, the technical details of the improved instrument will be described, and the planned scientific projects will be outlined.

2. FEATURES AND CAPABILITIES OF THE DAA

Results from a cloud event during the ground based cloud experiment at the mountain summit of Great Dun Fell in northern England 1995 (Bower et al., 1999; Martinsson et al., 1999) are used as examples. Average values of the event 1995-03-23, 00:00-05:00 (local time) can be seen in the figures. The total droplet number concentration was 1500 cm^{-3}, and the aerosol particle concentration (D_p>0.1 µm) was 2500 cm^{-3}. It must be emphasized that the results presented here are measured with the DAA only, and show the unique capabilities of the instrument.

Contact:
G. Frank: goran.frank@pixe.lth.se
B. Martinsson: bengt.martinsson@pixe.lth.se

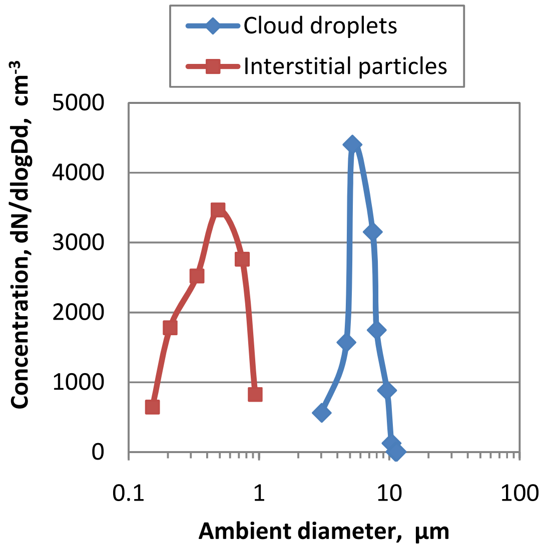

Figure 1. Number concentration of cloud droplets and interstitial particles

Figure 1 presents the ambient number size distribution of cloud droplets and interstitial particles. The separation between the two modes is clear.

In Figure 2, the dry (residual) aerosol particle number size distributions are presented for cloud droplet residuals, interstitial particle residuals and the sum of these (total). The total size distribution can be compared to a size distribution measured by a Differential/Scanning Mobility Particle Sizer, placed for example at an upwind station, in order to validate the results. This was indeed done, showing good agreement (Martinsson et al., 1999).

Figure 3 shows the cloud droplet scavenging ratio as a function of dry particle diameter, calculated from the results presented in Fig. 2, by dividing the cloud droplet residual concentrations by the total concentrations.

Figure 4 shows the relation between the ambient and dry residual diameters. In addition the critical diameter for activation according to the Köhler equation, as a function of dry diameter, is presented for particles consisting of ammonium sulphate and an insoluble core, for three different compositions. Although the particle chemical composition has been assumed, it can be concluded that cloud droplets smaller than 10 µm were activated, and that the largest droplets were possibly not activated.

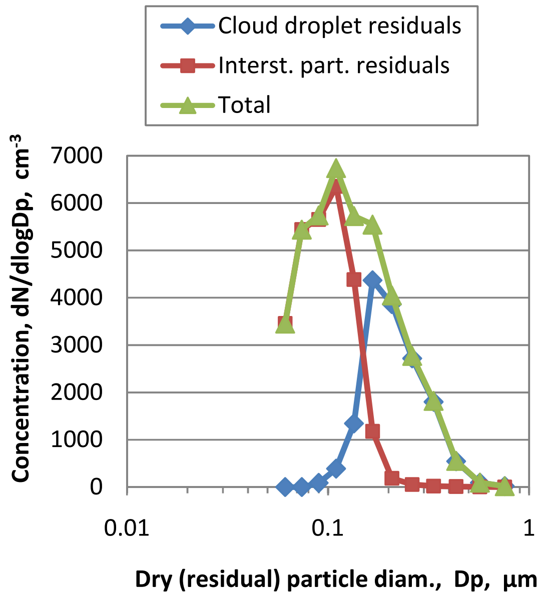

Figure 2. Number concentration of dry (residual) particles

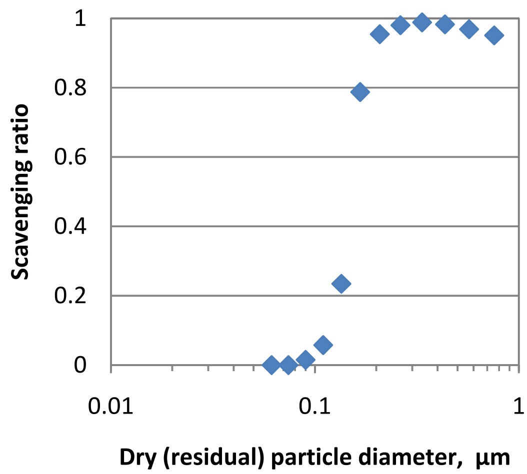

Figure 3. Cloud droplet scavenging ratio as a function of dry particle diameter

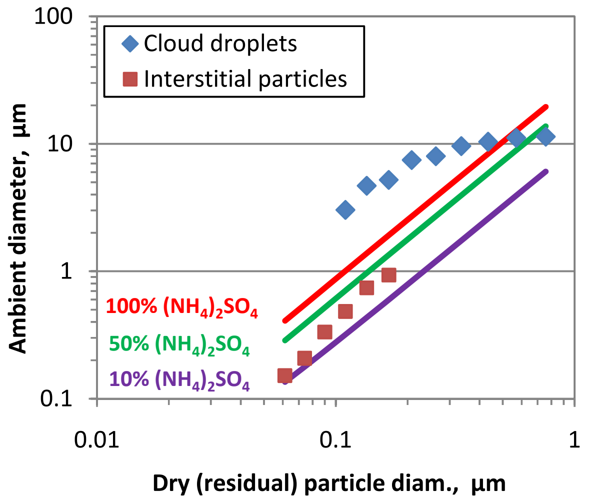

Figure 4. Relation between ambient and dry residual diameter, as well as critical diameter for activation. See details in the text.

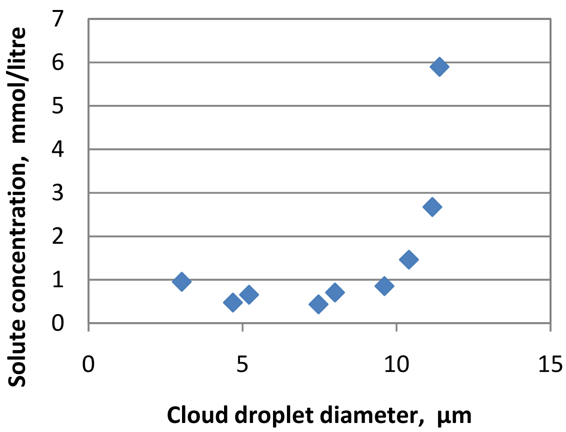

Figure 5. Solute concentration as a function of droplet diameter. See details in the text.

By measuring or estimating a chemical composition of the aerosol particles, the solute concentration of the cloud droplets can be calculated, since both the ambient and the dry diameters are known. In the example here, we have assumed the particles to consist of 50% ammonium sulphate (by volume) and the rest of an insoluble core. Figure 5 shows the solute concentration, and it can be seen that the dependence on ambient diameter is very strong for the largest droplets.

These were some examples of the results that can be obtained from DAA measurements. To summarize, the DAA instrument can give very detailed information about cloud microphysics, and the aerosol-cloud droplet relation. Together with complementary measurements, for example chemical composition of the aerosol particles, unique data-sets can be obtained, which can be used to improve the understanding of the aerosol-cloud relations.

3. INSTRUMENT PRINCIPLE

Below follows a description of the principle of the DAA, see also Figure 6. The theoretical background of the instrument can be found in Martinsson (1996). A detailed description of the first version of the instrument and a field inter-comparison with respect to six aerosol and cloud characteristics can be found in Cederfelt et al. (1997).

1. *Air inlet.* The inlet collects droplets and interstitial particles. A vane directs the inlet into the wind. The DAA can characterise droplets up to 20 µm, possibly 30 µm in diameter (the upper limit has not been exactly determined). To avoid sedimentation losses the instrument employs vertical flows as much as possible, and there is a bend after the inlet.

2. *Bipolar charging unit.* After the bend, the aerosol particles are charged in a bipolar charger, to give a well defined bipolar charge state and a low number of charges on the individual droplets and particles, when they enter the unipolar charger.

3. *Unipolar charging unit*. In the unipolar charger the droplets and particles, still at their original size, are positively charged. The number of charges acquired by the droplets and particles is

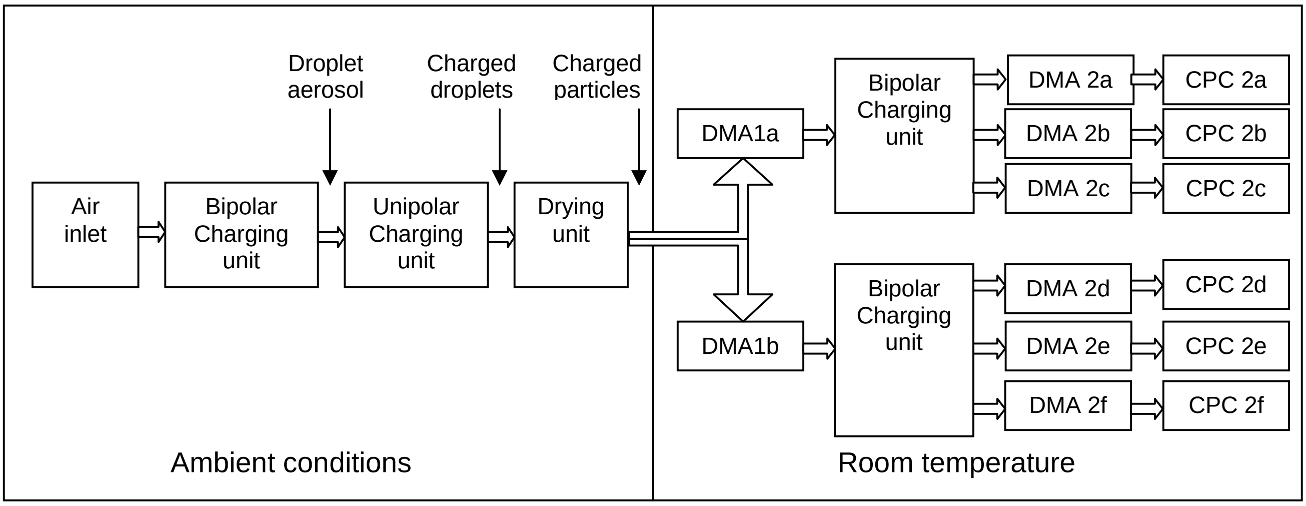

Figure 6. ***The principle of the DAA and the basic units.***

dependent on their size (larger droplets will acquire a higher charge) and the relationship is determined by a calibration. The charging process is a combination of diffusion charging and field charging. Ions are produced with a radioactive α-source and transported to the charging region by an electric field. The development and calibration of the charger used in the DAA are described in Frank et al. (2004).

4. *Drying unit.* The sample flow then passes through a diffusion drier that removes the water. The result is highly charged dry residual particles. Some volatile matter, e.g. HNO_3, may also be removed in the drier.

The aerosol is then transported from the part at ambient conditions (the outdoor part) to the indoor part, where the size, number and charge level of the residue particles are measured. The aerosol is divided into two lines in order to optimize the scanning performance and shorten the time required.

5. *DMA 1.* In the first DMAs, the electrical mobilities of the residual particles are determined. The DMAs are stepping over the interesting ranges.

6. *Bipolar charging unit.* This unit recharges the particles to bipolar charge equilibrium (low number of charges on the individual particles). Bipolar charging is carried out in order to measure the dry size of the residual particles in DMA 2a-f, as in normal electrostatic classification.

7. *DMA 2a-f.* The six DMAs work in parallel, and each of them is set to measure a fixed dry particle diameter. For every voltage step of DMA 1, the number of particles is counted after each DMA 2. By knowing the dry diameter from DMA2, and the electrical mobility from DMA1, the number of charges on each individual cloud droplet can be calculated. The original ambient size can then be obtained via the calibration of the unipolar charger.

8. *CPC 2a-f.* After each DMA2 there are particle counters (CPC = condensation particle counter) to count the number of particles.

The dry particle sizes measured are chosen in order to cover the region where particles are scavenged by droplet formation, i.e. the chosen sizes should be from the smallest particles that do not act as cloud condensation nuclei (CCN), up to particle sizes where the major part of the particles act as CCN. In most cases the number concentration decreases with increasing dry particle size from about 0.2 µm in diameter and the upper dry particle size limit should preferably be where the particle number concentration is negligible.

The six dry particle sizes measured simultaneously can be set to cover the whole region of interest, and one scan with DMA 1 takes ~5 minutes, depending on the particle concentration in the air. The six dry particle sizes are then changed to six new sizes that lie in between the first six, and a new scan is performed with the first DMA, giving a total scan time of 10 minutes. However, the scans can be used independently and the time resolution obtained is thus 5 min.

4. UPCOMING PROJECT

After finishing the instrument development, long-term measurements at the summit of the mountain Brocken (51.80º N, 10.67º E, 1142 m asl) in the Harz region in central Germany will be be performed. The project is in collaboration with the Air chemistry group of the Technical University of Brandenburg (BTU Cottbus), who has a cloud measurement site at mount Brocken since many years. Measurements during a longer time period will provide the possibility for a variety of air masses with different aerosol properties to reach the site, such as more marine type air coming from the west, northwest; relatively freshly polluted air coming from the industrialised regions in Germany and central Europe, and aged polluted air coming from Eastern Europe. Different cloud types with different dynamical properties will immerse at the site, such as orographically induced clouds (high updraught velocity) and stratiform clouds (low updraught velocity). The long-term measurements will lead to many events with several combinations of different aerosol properties, different air masses, and different cloud types. These events will be classified and the results for each main combination can thus be described with high statistical confidence. Focus will be on warm clouds, since the available instrumentation cannot be used for studies of ice or super cooled water clouds.

Descriptions of the aerosol-cloud relation will then be derived, and used for validations of model results, parameterisations, etc. One major goal of the project is to improve existing and/or to develop new aerosol-cloud parameterisations.

5. OUTLOOK

After gaining experience of the improved version of the instrument, and from the first scientific project with the new instrument, the next step would be to study other cloud types at other locations. We have been thinking of both long-term ground based measurements, as well as aircraft measurements. The instrument probably has to be further improved for aircraft measurements, to lower the weight and, if possible, improve the time resolution, but we are confident that this is doable. A DAA version for aircraft measurements would provide an excellent tool for aerosol-cloud interaction studies.

We are interested in future collaborations. Suggestions are most welcome.

REFERENCES

Bower et al., Atmos. Res. 50, 151-184, 1999
Cederfelt et al., Atmos. Environ. 31, 2657-2670, 1997
Frank et al., Contr. Atmos. Phys. 71, 65-85, 1998
Frank, PhD thesis, http://nuclearphysics.pixe.lth.se/theses/gf.asp, 2001
Frank et al., J. Aerosol Sci.,35, 117-134, 2004
Martinsson, J. Aerosol Sci., 27, 997, 1996
Martinsson et al., Atmos. Environ. 31, 2477-2490, 1997
Martinsson et al., Atmos. Res. 50, 289-315, 1999
Martinsson et al., Tellus 52B, 801-814, 2000

AIRCRAFT TOWED SENSOR SHUTTLE (AIRTOSS): A TANDEM MEASUREMENT PLATFORM FOR CLOUD-RADIATION STUDIES

W. Frey[1], M. de Reus[1], H. Eichler[1], R. Maser[2], B. Mey[1], M. Wendisch[1], and S. Borrmann[1,3]

[1] *Institute for Atmospheric Physics, Johannes Gutenberg University Mainz, Germany*
[2] *Enviscope GmbH, Frankfurt, Germany*
[3] *Max-Planck-Institute for Chemistry, Mainz, Germany*

1 INTRODUCTION

Clouds play a significant role in regulating the radiation balance of the Earth-atmosphere system. Therefore, it is important to investigate the influence of cloud particle properties on radiative transfer by in-situ measurements. Cirrus clouds are challenging in particular because they may cool or warm the atmosphere [Solomon et al., 2007]. In order to investigate the radiative impact of (cirrus) clouds simultaneous observations above and below the cloud are required to obtain optical layer properties and radiative budget quantities of the clouds. In this regard the close coordination of the radiation measurements above and below, and the microphysical measurements within the clouds is crucial. Usually this is attempted by using several aircraft in stack as for example in the CRYSTAL-FACE (2002) or TC^4 (2007) experiments. However, the aircraft usually have different speeds which makes it hard to obtain truly simultaneous measurements around and in the clouds. Also there are often series flight safety regulations which additionally complicate aircraft coordination. Moreover, using several aircraft is expensive. Therefore, a new tandem measurement platform has been developed and applied within a measurement campaign funded by the Collaborative Research Center SFB641 *The Tropospheric Ice Phase*. This tandem platform consists of (1) a Learjet 35A aircraft mainly equipped with radiation instruments and (2) the AIRcraft Towed Sensor Shuttle (AIRTOSS) equipped with instrumentation to measure cloud microphysical properties. The AIRTOSS sonde is detached from, towed by, and retracted onto the Learjet. By varying towing-cable length (maximum length is 4 km) and air speed, the horizontal and vertical distance between the AIRTOSS and the research aircraft can be varied, providing possibilities for different vertical profile flight patterns. In this way the measurements conducted on the aircraft and on the AIRTOSS are truly collocated, which has not been possible in earlier coordinated aircraft experiments.

By comparing the microphysical properties

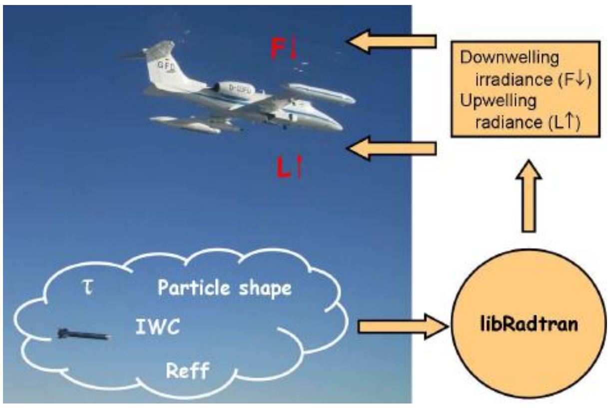

Figure 1. Illustration of AIRTOSS operating mode.

derived from a combination of radiation measurements and radiative transfer modelling (e.g. using the Library for Radiation Transfer calculations (LibRadtran) model [Mayer and Kylling, 2005]), closure studies of the radiative effect of cirrus clouds can be performed. Furthermore, the microphysical cloud properties (such as effective particle radius and/or optical thickness of the cloud) can be retrieved and compared to the simultaneous microphysical measurements conducted with AIRTOSS.

1.1 Campaign

A 'proof-of-concept' campaign was conducted in September 2007 from Hohn, Northern Germany. Three test flights with AIRTOSS have been made, whereof the first flight was accompanied by a second aircraft to closely watch the flight attitude of the AIRTOSS drag-body. The duration of the test flights was about two hours each. Due to safety regulations, flying with the AIRTOSS sonde underlies some flight restrictions when not attached to the winch, as for example, not flying through mixed-phase clouds due to possible icing and flying over restricted military area in a maximum height of 25.000 feet. Beyond testing the flight characteristics of AIRTOSS, first measurements with AIRTOSS were performed within low marine stratus clouds.
For measurements of cirrus inhomogeneities two additional flights without AIRTOSS were made in order to be able to fly at higher altitudes.

2 INSTRUMENTATION

The instrumentation for radiation and cloud microphysics is described in the following section. Figure 2 shows the locations of the instruments within the tandem platform.

2.1 Learjet

Instruments on the Learjet are either installed in the wingpod or on top of the fuselage. Here, the newly developed Stabilized Platform for Airborne Radiation Measurements (SPARM) is used for horizontal stabilization of the downwelling irradiance sensor (Fdw). Downwelling irradiances are measured in a wavelength-range of 350 – 2200 nm. The wingpod contains

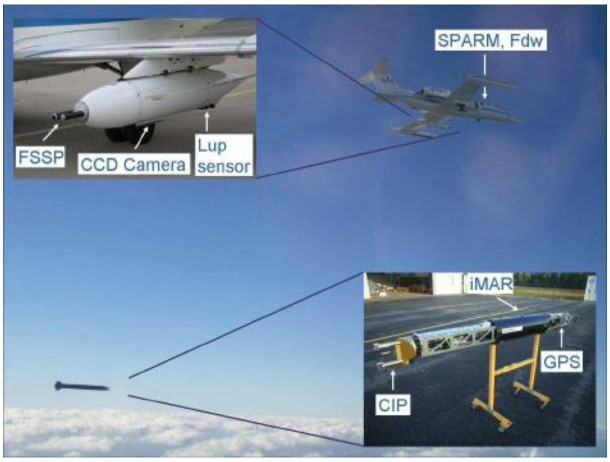

Figure 2. Instrumentation of Learjet/AIRTOSS tandem.

the Forward Scattering Spectrometer Probe (FSSP-100) at the front for measuring size distributions of particles in the size range of 2 – 45 μm [Dye and Baumgardner, 1984]. Also installed in the wingpod are the downward looking sensor for upwelling radiances (Lup) and the multispectral two-dimensional CCD camera [DuncanTech, 2002]. The CCD camera captures pictures at three different wavelengths: green (550 nm), red (660 nm), and near-infrared (880 nm) and has a viewing angle of 58.1°. Upwelling radiances are measured in a wavelength-range of 350 – 2200 nm, the viewing angle of the radiance inlet is 1.5°. The radiation sensors are described in Wendisch et al. [2001].

2.2 AIRTOSS

The AIRTOSS drag-body is equipped with the Cloud Imaging Probe (CIP), a Global Positioning System (GPS) and a System for Inertial Navigation, Guidance, Stabilization and Surveying (iMAR system) for measuring the attitude angles of the AIRTOSS. The CIP generates two dimensional shadow images of cloud particles with diameters between 25 and 1550 μm. From these images information about shape and size distribution of the cloud particles as water droplets or ice crystals can be obtained [Knollenberg, 1970]. For determining the exact position of the AIRTOSS a GPS

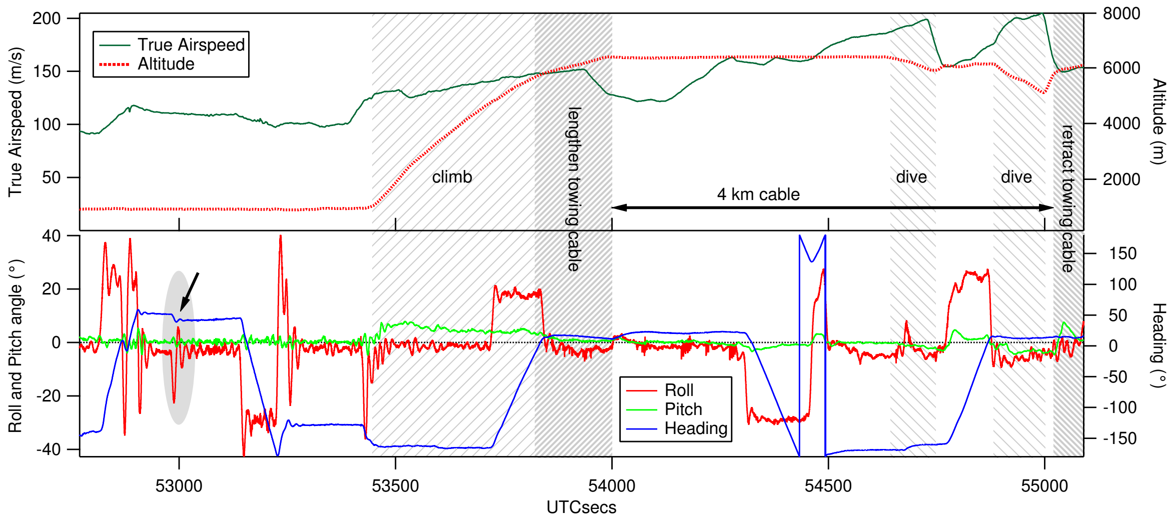

Figure 3. Flight characteristics on 6 of September 2007, shaded areas indicate climbing or diving of Learjet, lengthening and retracting of towing cable. The arrow in the ellipse denotes an example of a slight turn which causes a high amplitude in roll angle.

is used. The iMAR system provides measurements of the flight attitude as roll and pitch angle as well as heading information of the AIRTOSS. Small changes in roll and pitch angle should not affect the accuracy of CIP measurements. Stable flight conditions are more crucial for the planned integration of radiation sensors into the AIRTOSS. The power supply for AIRTOSS is given by batteries.

3 OBSERVATIONS

3.1 AIRTOSS flight characteristics

The Learjet/AIRTOSS platform has been tested for altitudes up to 25.000 feet, aircraft speeds of 180 – 300 knots and a towing-cable length up to 4 km. While AIRTOSS is attached to the Learjet no measurements are carried out, in this time the batteries are disconnected in order to save battery power. The first test flight of AIRTOSS on 4 of September 2007 has been accompanied by a second Learjet to be able to closely watch the flight behaviour of the drag-body and thus to testify the operational capability of the Learjet/AIRTOSS tandem. No data have been collected on this flight. About 90 minutes of continuous data of the GPS, iMAR system, and CIP are available during the AIRTOSS flights on 6 and 7 of September 2007.

During the AIRTOSS flight on 6 of September 2007 tests were made for different flight altitudes and airspeeds as shown in Figure 3. Even slight turns cause high oscillations in roll angle as pointed out by the arrow. During the following straight on flight the oscillation diminishes. The coarse shaded areas denote climbing or diving of the Learjet which can also be seen in the pitch angle of AIRTOSS. Climbing causes a higher air resistance on the 'wings' at the end of AIRTOSS and thus a positive pitch angle as the front section looks up, diving of the Learjet a negative pitch angle, respectively. Narrow shaded areas denote a change in towing cable length which adds some noise to the attitude angles. In Figure 4 the attitude angles of the flight on 7 of September 2007 are displayed. The time segment shows a period with constant airspeed (∼ 100 m/s) and AIRTOSS height (∼ 500 m). After flying a turn the roll angle needs about 35 seconds to diminish its oscillation. Roll and pitch angles show absolute deviations up to 4° and 2°, respectively. The pitch angle is slightly positive at this airspeed.

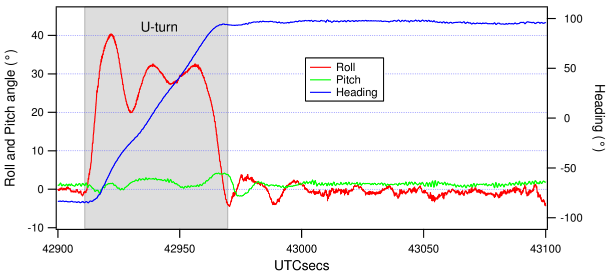

Figure 4. Flight characteristics on 7 of September 2007 in a period with constant aircraft speed and height.

3.2 Microphysics

During several flight legs on test flights on 6 and 7 of September 2007 the AIRTOSS sonde was dropped into marine stratus clouds. In-cloud measurements of size, shape, and size distribution of the cloud water droplets were made by the CIP. As Figure 5 demonstrates mostly small droplets with a size of about 39 μm in diameter were imaged. A mean number concentration of 12.9 particles per litre was observed in the clouds.

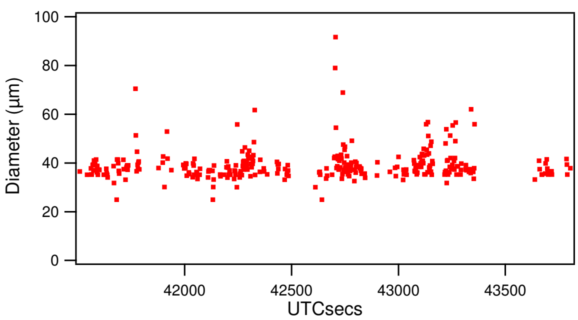

Figure 5. Mean diameter of cloud droplets measured on 7 of September 2007 in marine stratus clouds.

3.3 Radiation

The radiation measurements focused on observations of cirrus clouds. The spectral upwelling radiance (Lup) measured above the clouds on 6 of September 2007 shows cirrus inhomogeneities (Figure 6). In the time series of Lup at 670 nm and 1600 nm wavelength the signal drops by about 50% within about 30 seconds (about 4.5 km flight path). The big differences in the radiances at the two wavelengths result from the fact that ice is almost not absorbing at 670 nm but strongly absorbing at 1600 nm.

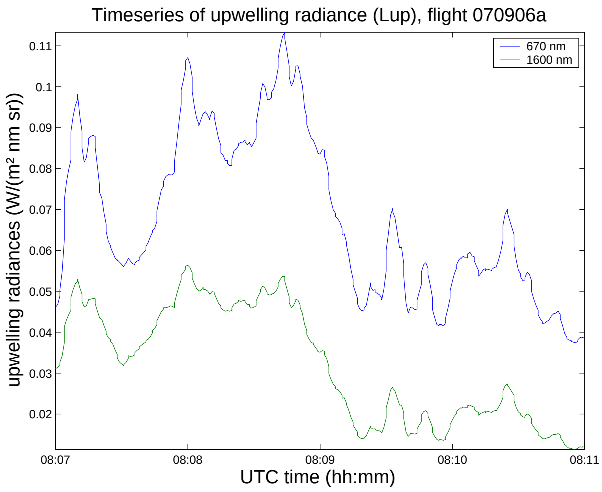

Figure 6. Upwelling radiances illustrating cirrus inhomogeneities measured on 6 of September 2007.

4 CONCLUSIONS AND OUTLOOK

The proof-of-concept campaign has shown that the principle of the tandem measurement platform worked out well. The AIRTOSS sonde was able to stabilize its flight after several flight manoeuvres. Thus, for future studies of the interaction between cloud microphysics and radiation AIRTOSS has proven to be a very useful platform. To achieve a preferably stable flight of the AIRTOSS airspeed, height, and towing cable length should be kept constant in straight on flight.
A wireless local area network (WLAN) connection between AIRTOSS and Learjet shall be made available for the next AIRTOSS mission, to gain inflight information whether the dragbody is in a cloud or not. This is of particular importance for measurements in thin clouds as for example cirrus clouds. For measurements of cloud-radiation interactions of cirrus clouds, the allowed maximum flight altitude has to be extended to 10 – 12 km. This shall be achieved until the next scientific campaign with the AIRTOSS which is planned for October

2008. For this campaign, the integration of instruments for radiation measurements into the AIRTOSS sonde is planned. Here, the same radiation sensors will be used as in the Learjet. These implementations will make the AIRTOSS an even more powerful tool for studies of interactions between cloud radiation and microphysics.

5 ACKNOWLEDGEMENTS

AIRTOSS would not have been flying without *enviscope GmbH* who modified the drag-body to a scientific usable sensor shuttle. We gratefully acknowledge funding of this work by the *Deutsche Forschungsgemeinschaft* (DFG) as part of the Collaborative Research Center *The Tropospheric Ice Phase* (SFB641) - project B5.

6 BIBLIOGRAPHY

References

DuncanTech. *MS4000 and MS4100 High-Resolution Digital Color and Multispectral Camera*. DuncanTech, 11824 Kemper Rd. Auburn, CA 95603, 2002.

James E. Dye and Darrel Baumgardner. Evaluation of the forward scattering spectrometer probe. part i: Electronic and optical studies. *Journal of Atmospheric and Oceanic Technology*, 1(4):329–344, December 1984.

Robert G. Knollenberg. The optical array: An alternative to scattering or extinction for airborne particle size determination. *Journal of Applied Meteorology*, 9(1):86–103, February 1970.

B. Mayer and A. Kylling. Technical note: The libradtran software package for radiative transfer calculations - description and examples of use. *Atmospheric Chemistry and Physics*, 5 (7):1855–1877, 2005. ISSN 1680-7316.

S. Solomon, D. Qin, M. Manning, Z. Chen, M. Marquis, K. B. Averyt, M. Tignor, and H. L. Miller, editors. *Climate Change 2007: The Physical Science Basis. Contribution of Working Group I to the Fourth Assessment Report of the Intergovernmental Panel on Climate Change*. Cambridge University Press, Cambridge, U.K. and New York, USA, 2007.

M. Wendisch, D. Müller, D. Schell, and J. Heintzenberg. An airborne spectral albedometer with active horizontal stabilization. *Journal Of Atmospheric And Oceanic Technology*, 18(11):1856–1866, November 2001.

RAINFALL ALGORITHM INVARIANT TO THE WEATHER RADAR OPERATING FREQUENCY AND IMMUNE TO VARIABILITY IN RAINDROP SHAPE-SIZE MODEL

E. Gorgucci and L. Baldini

Istituto di Scienze dell'Atmosfera e del Clima
Via Fosso del Cavaliere, 100 – 00133 Roma, Italy

1. INTRODUCTION

Polarization diversity radar measurements such as reflectivity factor, differential reflectivity, and differential propagation phase are extensively used in rainfall estimation (Bringi and Chandrasekar 2001). Algorithms to estimate rainfall from polarimetric radar measurements are based on the assumption of a model describing the raindrop shape as a function of drop diameter. Deviation of the prevailing raindrop shape from the assumed model has a direct impact on the accuracy of radar rainfall estimates. Moreover, rainfall algorithms can be only used at the specific radar band frequency for which they have been developed.

A rainfall algorithm for estimating rainfall rate from polarimetric radar data without an a priori assumption about the specific form of mean raindrop shape–size model is presented. This algorithm, obtained from Z_h and Z_{dr}, is invariant in the frequency domain ranging from S- to X-band.

Reconstructed profiles obtained from real radar observations are used to validate the rainfall algorithm. For a comparative analysis, two other algorithms based on Z_h and Z_{dr} have been found assuming fixed drop shape-size relations and r frequency. The comparison shows that, in the presence of raindrops described by the model of Pruppacher and Beard (1970) or Beard and Chuang (1987), the new rain algorithm follows the DSD variability better than the rain algorithm obtained from a fixed non-linear shape-size model.

2. RADAR POLARIMETRIC MEASUREMENTS AND THEIR RELATION TO RAIN MICROPHYSICS

Dual-polarization radar measurements Z_h, Z_{dr} and K_{dp} are influenced by drop size distribution (DSD) and drop shape. The normalized form of the gamma DSD was introduced to compare the probability density function of D in the presence of varying water contents (Willis 1984; Illingworth and Blackman 2002). The corresponding form of the gamma DSD can be expressed as

$$N(D) = N_w f(\mu)\left(\frac{D}{D_0}\right)^{\mu} \exp\left[-(3.67+\mu)\frac{D}{D_0}\right] \quad (1)$$

where $f(\mu)$ is a dimensionless function of μ. One interpretation of N_w is that it is the intercept of an equivalent exponential distribution with the same water content. D_0 is the median volume diameter and μ is the shape factor.

For weather radar applications the shape of raindrops can be approximated by oblate spheroids described by the semimajor axis a and semiminor axis b. Several equations relating the axis ratio $r= b/a$ with drop diameter have been proposed. Gorgucci et al. (2000) proposed an approximation of the form

$$r(D) = 1.03 - \beta D \quad (2)$$

with r=1 for $D \leq 0.03/\beta$. The linear fit to the wind tunnel data of Pruppacher and Beard (1970) corresponds to β=0.062 mm^{-1} (the drop-shape model corresponding to this

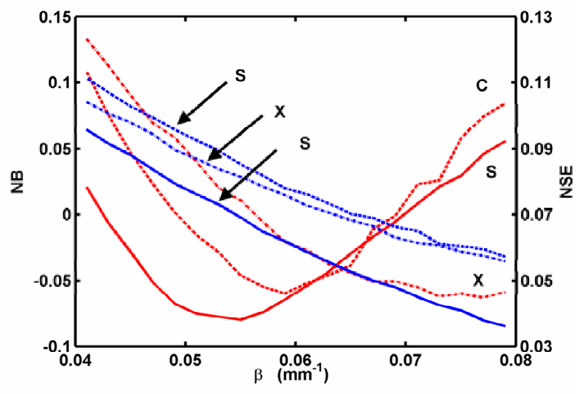

Figure 1: *Error analysis of the performance of the algorithm (22) as a function of β and for the three wavelengths corresponding to S- (solid line), C- (dashed line), and X- band (dashed-dot line) due to the DSD variability. The analysis was obtained by dividing β into classes and computing in each class the average values of NSE (red lines) and NB (blue lines).*

value of β will be henceforth referred to as PB). If the mean axis ratio versus D relation is nonlinear, it is always possible to define a linear relation that results in the same K_{dp} (Bringi et al. 2003).

Investigating the relation among radar polarimetric measurements and rain microphysics, Gorgucci et al. (2006), following Bringi and Chandrasekar (2001) and Jameson (1985), expressed the ratio K_{dp}/Z_h as a function of the parameters D_0 and μ of (1) and the mass-weighted mean axis ratio. Using properties of the gamma function, and assuming (2) this relation can be modified in terms of the drop-shape slope factor β and the reflectivity-weighted mean drop diameter $D_Z = \mathrm{E}\{D\, D^6\} / \mathrm{E}\{D^6\}$ as

$$\frac{K_{dp}}{Z_h} = C\frac{\Gamma(4+\mu)}{\Gamma(7+\mu)}(7+\mu)^2(4+\mu)\frac{\beta}{\lambda D_Z^2} \tag{3}$$

An empirical relationship between Z_{dr} and the reflectivity-weighted axis ratio defined as $r_Z = \mathrm{E}\{r\ D^6\} / \mathrm{E}\{D^6\}$ was proposed by Jameson (1983). An approximate form of that relation can be attained as

$$\xi_{dr} = 1 + p(\beta\, D_Z)^q \tag{4}$$

where $Z_{dr} = \log_{10}(\xi_{dr})$. Parameters p and q can be found using the simulation described in the next section and result equal to 0.687 and 1.184, respectively. Replacing (4) in (3) and using the moment properties of the normalized gamma DSD, it is possible to derive the relation

$$\beta = \left[\frac{1}{C'\cdot g(\mu)}\frac{\lambda K_{dp}}{Z_h}\right]^{1/3}(\xi_{dr}-1)^{2/(3q)} \tag{5}$$

where C' is a constat and g(μ) is a slowly increasing function of μ that can be approximated by its average value 0.92. Eq. (5) states that in a domain defined by the three radar variables Z_h, Z_{dr}, and K_{dp}, these are constrained to take up a limited region of the domain unequivocally defined by the same slope factor.

3. PRACTICAL ISSUES FOR β ESTIMATION

Equation (5) is valid from S- to X-band if resonance effects are not taken into account. In order to consider such effects, for the three more common weather radar frequencies of 3 GHz (S-band), 5.4 GHz (C-band), and 9.3 GHz (X-band), a simulation was built on the following conditions: *i*) the shape size relation is described by (2) with β ranging between 0.04 and 0.08 mm^{-1}; *iii*) gamma DSD parameters vary in the range defined by $0.5 < D_0 < 3.5$ mm; $3<\log_{10} N_w < 5$; $-1 < \mu <5$; *iv*) radar measurements are constrained to $(10\log_{10}Z_h)<55$ dBZ and $R<300$ mm h^{-1}; *v*) drops are assumed to be canted with the mean and standard deviation equal to zero 10°, respectively (Bringi and Chandrasekar 2001). Equation (5) presents some practical problems. In fact, when K_{dp} tends to zero, due to the signal fluctuation, its values can be negative. Moreover, when Z_{dr} approaches zero, the quantity (ξ_{dr}-1) can assume negative values and then (5) becomes meaningless. Therefore, (ξ_{dr} - 1) was replaced by (ξ_{dr} - κ) and the resulting equation is studied as a function of κ. It can be seen that κ does not have a big influence on merit factors since the maximum variation of the NSE is 2%. For this reason, in the following, $\kappa = 0$ is assumed and the following equation will be considered

$$\beta = a\left(\lambda \frac{K_{dp}}{Z_h}\right)^b \xi_{dr}{}^c \tag{6}$$

Figure 1 shows an error analysis of the performance of the algorithm (5) as a function of β due to the DSD variability and for three wavelengths corresponding to S- (solid line), C- (dashed line), and X-band (dash-dot line). The analysis is obtained by dividing β into classes and computing in each class the average values of NSE (black lines) and NB (light grey lines). The NSE accuracy as a function of β shows different profiles varying with the radar operating frequency. In fact, at S-band the minimum value of the NSE in correspondence with $\beta = 0.055$ mm^{-1} moves toward higher values of β as the frequency increase to C- and X-band. Figure shows that, for all frequencies, NSE can be estimated with an accuracy ranging between 4% and 7% when β moves between 0.055 mm^{-1} and 0.07 mm^{-1}. Over the same β interval, the NB presents an overestimation of about 4% at C- and X-band and an underestimation of 6% at S-band.

4. IMPLICATIONS FOR RAIN ESTIMATION

Rainfall algorithms consistent with equation (6) can be built for the operating frequency domain of weather radars. A simple algorithm using Z_h, and Z_{dr} optimized for the three weather radar frequencies may be of the form

$$R_Z = a_Z\, \beta^{b_Z} Z_h^{c_Z}\, \xi_{dr}^{d_Z}\,. \tag{7}$$

The parameters of (7) can be found by a nonlinear regression analysis using the simulation described in the previous section. The coefficients a_Z, b_Z, c_Z, and d_Z are 12.63, 2.57, 0.936, and -4.218, respectively. The NSE of (7) is 20% and the correlation coefficient is 99%.

An algorithm using K_{dp} optimized for the three bands can be expressed using (λK_{dp}) as:

$$R_K = a_K\, \beta^{b_K} \left(\lambda K_{dp}\right)^{c_K}. \tag{8}$$

Coefficients a_K, b_K, and c_K resulting from the simulation described before are 12.63, 1.21, and 0.96, respectively. Eq. (8) presents an NSE of 31.9 % and a correlation coefficient of 97%. From a general point af view, (6), (7), and (8) establish a transform coordinate system that relates the radar parameters Z_h, Z_{dr}, β or K_{dp}, β, and λ to rain rate under the control of a generalized self-consistency relation defined in the domain Z_h, Z_{dr}, β, K_{dp}, and λ.

Due to the lower NSE and to the higher correlation coefficient, (7) shows better ability than (8) to take into account the DSD variations. For this reason, this study focuses only on (7), henceforth indicated as β algorithm. Eq. (7) is compared with standard algorithms obtained assuming nonlinear raindrop shape-size relations. Among the relations available in the literature, those recently proposed by Brandes et al. (2002) and Thurai et al. (2007) (henceforth BZV and THBRS, respectively) are considered in the analysis. Coefficients of standard rain algorithm $R = a_1 \beta^{b_1} Z_h^{c_1}$ were obtained using the same simulation described in Sect 3, except that shape of raindrops follows the BZV and THBRS model. For the latter, accordingly to Thurai et al. (2007), for 0.7 ≤ D ≤ 1.5 mm has been used the relation of Beard and Kubesh (1991), whereas below 0.7 mm drops have been assumed to be spherical. Specific coefficients for S-, C- and X-bands were derived. Both parameterizations are characterized by very high correlation coefficients, negligible bias, and low NSEs. For both BZV and THBRS, NSE is 13%, 17% at C- and X band. At C-band, NSE of

Table 1: *NB and NSE of rainfall estimations obtained using the BZV, THBRS, and β algorithms with respect to the corresponding true value for raindrops following the PB or BC shape-size model and for Z_h, Z_{dr}, and K_{dp} measurements at S- or C- or X-band (with measurement errors)*

Profiles		Rain Algorithms					
		BZV		THBRS		β	
Drop-shape	Band	NB	NSE	NB	NSE	NB	NSE
PB	S	-0.210	0.363	-0.181	0.339	0.111	0.342
	C	-0.158	0.354	-0.134	0.339	0.140	0.332
	X	-0.305	0.438	-0.278	0.411	0.090	0.298
BC	S	-0.085	0.266	-0.046	0.255	-0.025	0.270
	C	-0.064	0.268	-0.036	0.262	-0.023	0.249
	X	-0.152	0.332	-0.116	0.318	-0.057	0.284

BZV is 16% and that of THBRS is 14%. Correlation coefficient is always above 99%. In comparison with the β algorithm, while the correlation coefficients are similar, the NSEs of this algorithm are greater than that of THBRS of about 7%, 3% and 6 % at S-, C- and X-band, respectively. For BZV, increases are 7%, 3%, and 4%.

It must be pointed out that the coefficients of the BZV and THBRS algorithms are specific for each considered frequency, while the the β algorithm have a unique set of coefficients for all three frequency bands. This is because the β shape factor works as a normalizing factor for Z_{dr} with respect to the drop shape, making it independent from the operating radar frequency.

5. VALIDATION

The impossibility of testing the proposed algorithm with respect to all the implications rising from the electromagnetic and microphysical aspects of the problem by directly using real radar polarimetric measurements, forces this study to adopt a simulation. Radar profiles are generated from real profiles collected by the NCAR S-POL radar during the TEFLUN-B campaign following Chandrasekar et al. (2006). The considered rain profiles correspond to a 15 km-long path containing 100 range bins spaced 0.150 m apart over which the differential phase increase is greater than 6 degrees. Gorgucci et al. (2006) observing the mean shape of raindrops resulting from radar measurements in Florida and in Italy, observed that oblateness of raindrops varies between the PB and the BC model. Therefore, for each of the three weather radar bands, two distinct sets of profiles were constructed assuming these two models. To take into account the different error structures of the different radar measurements, random signal fluctuation is generated in such a way that the measurement errors of Z_h, Z_{dr}, and Φ_{dp} correspond to 1 dB, 0.2 dB, and 4 degrees, respectively. The differential phase on backscattering is added to the differential phase profiles.

Fixed a weather radar frequency, for each profile, the path-averaged values Z_h, Z_{dr} and K_{dp} are computed with and without measurement errors, and used to obtain the mean values of β from (6). Then, this β is used to compute the rain rate in each range bin with (7) and with the corresponding relations derived from the BZV and THBRS algorithm for each band.

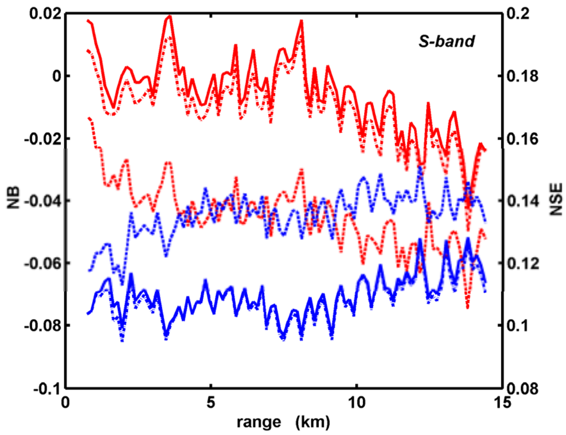

Figure 2: *NSE (red lines) and NB (blue lines) of rainfall estimate obtained using BZV (dash-dot line), THBRS (dashed line), and β algorithm (solid line) due only to the DSD variability. Rain profiles are obtained at S-band with raindrops following the BC model. Measurement errors are not included*

Figure 2 shows the NSE and NB of rain computed with respect to the true rainfall rate as a function of range for BZV, THBRS, and β algorithms, for the case that raindrops follow the BC model and for S-band. Measurement errors are not included in order to compare algorithms with respect to DSD variations only. Given that BC and THBRS shape-size models are quite similar, the THBRS algorithm presents the best performance along the range, with an average NSE of about 14%, pointing out a better ability to describe the variability of the raindrops than BZV and β algorithms, characterized by an average NSE of 17%. Results for PB rain profiles (not shown) indicate again that the β algorithm meets the DSD variability requirements better than the BZV and THBRS algorithms.

Results obtained with measurement errors are summarized in Table 1 that compares the different algorithms in terms of NB and NSE of rainfall estimation for range profiles simulated assuming raindrops following the PB or BC shape-size models, for S- or C- or X-band. It is worth remarking that attenuation effects on Z_h and Z_{dr} measurements at C- and X- band are not considered in this study. When raindrops follow the PB model, the NSE of the β algorithm presents values that are comparable to the THBRS algorithm at S- and C-band and is lower than 10% at X-band. Regarding the NSE of the BZV algorithm, they present values of about 2% more than THBRS. With regard to NB of the β algorithm, it demonstrates better results when compared to the BZV and THBRS algorithms. This performance is because the β algorithm, using the self-consistency principle, produces a kind of tuning for the radar measurements that minimizes the biases. In fact, even though the THBRS algorithm presents values lower than the BZV algorithm, they are 7% and 18% greater than those obtained with the β algorithm for S- and X-band, and are comparable at C-band. Once again, it must be recalled that the lower NB differences at C-band between the different algorithms may be determined by the effects of resonance scattering that may reduce any consistency among Z_h, Z_{dr}, and K_{dp}.

In the presence of raindrop media following the BC model and measurement errors, the NSE of the BZV and THBRS algorithm, due to the closeness of BZV and THBRS to the BC equilibrium shape, is a little better than that of the PB model. In fact, the NSEs of the BZV and THBRS algorithms are lower at 0.4% and 1.5% than the β algorithm at S-band, whereas they are greater than 1.9% and 1.3% at C-band. For the X-band, the NSE of the β algorithm is lower at 3.4% and 4.8% than the THBRS and BZV algorithm, respectively. With regard to the NB, once again, the β algorithm shows the best performance, with values lower than 2% and 6% at S-band, 1.3% and 4% at C-band, 5.9% and 10.5% at X-band for the THBRS and BZV algorithms, respectively.

A general result of the analysis is that, in the presence of the raindrops whose shape is described by the PB or BC models, the β algorithm follows the DSD variability much better than the THBRS and BZV algorithms. Due to the different weight of the measurement errors on the three algorithms, the β algorithm presents a reduction in the ability to take into account the DSD variability even though its performance remains comparable to or better than the other two. Finally, an important result is that the β algorithm presents the lowest NB, both for PB and BC models, at S-, C- and X-band.

REFERENCES

Beard K. V., and C. Chuang, 1987: A new model for the equilibrium shape of raindrops. J. Atmos. Sci., 44, 1509–1524.

Brandes, E. A., G. Zhang, and J. Vivekanandan, 2002: Experiments in rainfall estimation with a polarimetric radar in a subtropical environment. J. Appl. Meteor., 41, 674-685.

Bringi, V. N. and V. Chandrasekar, 2001: Polarimetric Doppler weather radar: Principles and applications. Cambridge University Press, 648 pp.

Bringi, V. N., V. Chandrasekar, J. Hubbert, E. Gorgucci, W. L. Randeu, and M. Schoenhuber, 2003: Raindrop size distribution in different climatic regimes from disdrometer and dual-polarized radar analysis. J. Atmos. Sci., 60, 354–365.

Chandrasekar, V., S. Lim, and E. Gorgucci, 2006: Simulation of X-band rainfall observations from S-band radar data, J. Atmos. Oceanic Technol., 23, 1195–1205.

Gorgucci, E., G. Scarchilli, V. Chandrasekar and V. N. Bringi, 2000: Measurement of mean raindrop shape from polarimetric radar observations. J. Atmos. Sci., 57, 3406–3413.

Gorgucci, E., L. Baldini, and, V. Chandrasekar, 2006: What is the shape of raindrops? An answer from radar measurements. J. Atmos. Sci., 63, 3033-3044.

Jameson, A. R., 1983: Microphysical interpretation of multi-parameter radar measurements in rain. Part I: Interpretation of polarization measurements and estimation of raindrop shapes. J. Atmos. Sci., 40, 1792–1802.

Jameson, A. R., 1985: Microphysical interpretation of multi-parameter radar measurements in rain. Part III: Interpretation and measurement of propagation differential phase shift between orthogonal linear polarizations. J. Atmos. Sci., 42, 607–614.

Beard K. V., and R. J. Kubesh, 1991: Laboratory measurements of small raindrop distortion. Part II: Oscillation frequencies and modes. J. Atmos. Sci., 48, 2245–2264.

Pruppacher, H. R. and K.V. Beard, 1970: A wind tunnel investigation of the internal circulation and shape of water drops falling at terminal velocity in air. Quart. J. Roy. Meteor. Soc., 96, 247-256.

Scarchilli G., E. Gorgucci, V. Chandrasekar, and A. Dobaie, 1996: Self-consistency of polarization diversity measurement of rainfall. IEEE Trans. Geosci. Remote Sens., 34, 22–26.

Thurai, M., G. J. Huang, V. N. Bringi, W. L. Randeu and M. Schönhuber, 2007: Drop shapes, model comparisons, and calculations of polarimetric radar parameters in rain. J. Atmos. Oceanic Technol., 24, 1019-1032.

Willis, P. T., 1984: Functional fits to some observed drop size distributions and parameterization of rain. J. Atmos. Sci., 41, 1648–1661.

Acknowledgements

This research was supported by the Italian Ministry of University and Research through the AEROCLOUDS project and by the Civil Protection Department of the Presidency of the Council of Ministers of Italy.

SIMPLE METHOD OF AEROSOL PARTICLE SIZE DISTRIBUTION RETRIEVING FROM MULTIWAVELENGTH LIDAR SIGNALS

A. K. Jagodnicka[1], T. Stacewicz[1], G. Karasiński[1], M. Posyniak[2]

[1]Institute of Experimental Physics, University of Warsaw
ul. Hoża 69, 00-681 Warsaw, Poland

[2]Institute of Geophysics, University of Warsaw
ul. Pasteura 7, 02-093 Warsaw, Poland

ABSTRACT

An improved lidar retrieval of the aerosol particle size distribution (APSD) is presented. A predefined APSD function with few free parameters is directly substituted into the lidar equations. The minimization technique allows to find the parameters which provide the best fit of APSD comparing theoretically generated signals with the experimental ones. The method does not require former knowledge of the lidar ratio. The approach was tested on typical APSD presented by Seinfeld and Pandis (1997). For our purpose these distributions were approximated with two mode combination of lognormal functions. With a lidar working at five wavelengths in UV – near IR spectral range a satisfactory retrieval of synthetic APSD is possible for the particles within the range 100 – 5000 *nm*.

INTRODUCTION

Among many methods of the aerosol investigation the optical remote studies play very important role. Lidars working simultaneously at several wavelengths are often used for these observations. This technique provide opportunity for remote investigation of aerosol particle size distribution (APSD). Such studies are possible due to different properties of the light scattering by particles of different sizes at various wavelengths (λ). A common approach to the retrieving of APSD from the lidar signals consists in determination of total scattering coefficients α_λ and/or the backscattering coefficient β_λ. Both coefficients can be related to APSD function *n(z,r)* by following equations (Seinfeld and Pandis, 1997):

$$\alpha_\lambda(\mathrm{z}) = \int_0^\infty Q_\lambda^E(r)\pi r^2 n(z,r)dr$$

$$\beta_\lambda(\mathrm{z}) = \int_0^\infty Q_\lambda^B(r)\pi r^2 n(z,r)dr\,, \qquad (1)$$

where z is a distance from the lidar, r - the particle radius, while Q_λ^E and Q_λ^B denote the efficiencies of total extinction and backscattering, respectively. These efficiencies can be calculated using *e.q.* Mie theory (Bohren and Huffman, 1999), when spherical shape of the particles is assumed.

On the other hand α_λ and β_λ can be found from lidar signals $S_\lambda(z)$ described by lidar equations. For each wavelength:

$$S_\lambda(z) = \frac{A_\lambda}{z^2}\beta_\lambda(z)\exp\left(-2\int_{z_0}^{z}\alpha_\lambda(y)dy\right). \qquad (2)$$

where A_λ are the apparatus constants. In each single equation (2) both α_λ and β_λ are unknown, therefore in order to retrieve them an additional information is necessary. The relation - so called *lidar ratio* - is usually used (Klett, 1981). For the white light it takes the form:

$$q_L = \frac{\beta_\lambda}{\alpha_\lambda^k}\,, \qquad (3)$$

where k is a number.

Deriving APSD from the scattering coefficients (1) is a classic example of inverse ill-posed problem, typical in earth sciences. Solution of Fredholm integral equations of 1st kind is required. Various inversion techniques have been proposed for this purpose. Successful approach to this problem needs some additional assumptions about the solution, like a smoothness or/and a positivity. This can be obtained with a predefined form of *n(z,r)* distribution, like histogram or Junge function, log-normal function or linear combination of these functions with different parameters (Seinfeld and Pandis*,* 1997). In such a case the solution is reduced to finding these parameters.

Such approach was presented by Herman *et al* (1971). They fit Junge distribution to signals from bistatic lidar. Rajeev and Parameswaran (1998) have shown two iterative methods of APSD determination: with assumed Junge distribution or without any assumed shape, taking for calculations an arbitrary lidar ratio. Heitzenberg *et al* (1998) proposed randomized minimization search technique (iterative least square algorithm) to derive an assumed histogram distribution. The research group from ITR applied the inversion with regularization for deriving both APSD and the refractive index using the signals registered with their aerosol and Raman lidar (Müller *et al*, 1999). They developed the technique based on Tichonov regularization (Veselovskii *et al*, 2002, 2004). In recent years the eigenvalue analysis was applied for the lidar data inversion (Veselovskii *et al*, 2005). Detailed review of different approaches to APSD retrieval was done by Böckman (2001). Her hybrid method presented in this paper was later applied for experimental data (Böckmann *et al*, 2005). As the result APSD, the refractive index and single scattering albedo was retrieved.

Another solution to the problem of lidar data analysis was proposed by Kusiel and Zolotov (1997, 2003). They developed mean ordinates method. They assumed APSD function as combination of several log-normal functions. Using these distributions, the optical characteristics (like α_λ and β_λ), were calculated and compared with those measured by lidar technique. Then the mean ordinates over those solutions were calculated and model closest to the mean ordinates was taken as the most probable solution. The mean ordinates method was used for inverting the horizontal lidar data.

A different approach was presented by Ligon *et al* (1996, 2000). In order to shorten the calculation time they used the Monte Carlo method of approximation of APSD.

Certainty of retrieving the APSD was experimentally tested by Joshiyama *et al* (1996). They measured optical parameters of artificial aerosol with bistatic lidar and compared the results with mathematical model.

As mentioned above in all these methods APSD is derived from α_λ and/or β_λ coefficients (1), with the use of lidar ratio (3). The lidar ratio was first suggested by Curcio and Knestrick (1966). They have experimentally evaluated k to be equal to *0.66,* while Fenn (1966) reported different values. Then Twomey and Howell (1965) found the linear relation between α_λ and β_λ basing on Mie theory and various size distributions of particles. They also concluded that in general such relation could not be a unique one, and that the linear correlation between the backscattering and the extinction coefficients is evident only for the white light. Good linearity is reported for clouds where a multiple light scattering takes place (O'Connor *et al*, 2004). It is not clear, however, whether the linear lidar ratio can be used for the monochromatic laser radiation. Analysis of large data-set of lidar returns of EARLINET shows about 40 % variability of $\beta_\lambda/\alpha_\lambda$ ratio for aerosols in boundary layer (Pappalardo, 2005). Therefore the value of the lidar ratio is often guessed or assumed (Landulfo *et al*, 2003; Iwasaka *et al*, 2003).

The coefficients α_λ and β_λ that are necessary for APSD inversion can be found using the lidar signal inversion technique by Klett (1981) and Fernald (1984). However in this case the aerosol parameters in the reference point must be known. When the vertical profiling is performed the reference point is usually selected at high altitudes, where the aerosol concentration is negligible and the molecular lidar ratio: $\beta_\lambda/\alpha_\lambda$ = $3/8\pi$ can be used. Then the backward solving of the lidar equation is applied. In case of clear sky the measurement of total optical thickness by sun-photometers allows to deduce the lidar ratio (G. Karasiński *et al*, 2007), which is usually considered constant with height. Such solutions are not applicable in many experimental situations, *e.q.* for aerosol layer under the cloud cover. Some problems can be also overcame when common measurement by aerosol and Raman lidars is performed, however the Raman signal registration is short-distant and is not well applicable for multiwalelength lidars.

In this paper an approach to the problem of APSD determination is proposed. It does not require the lidar ratio knowledge. Predefined functions $n(z,r)$ are substituted directly to equations describing the lidar signals (2). The experimental estimates of α_λ and/or β_λ values are not needed. Application of the minimization technique allows to derive the best fit of APSD by comparison the artificially generated signals with the lidar returns.

DESCRIPTION OF THE METHOD

In a first step equations (2) representing the registered signals $S_\lambda(z)$, should be converted to so called range corrected form:

$$L_\lambda(z) = S_\lambda(z)\cdot z^2 = A_\lambda \beta_\lambda(z)\exp\left[-2\int_{z_0}^{z}\alpha_\lambda(x)dx\right]\cdot \qquad (4)$$

Due to digitization the lidar signals are quantitized *e.q.* in space with the interval of dz. For further analysis the ratio of the signals $L_\lambda(z_l)$ at distance z_l and at its neighbour distance $z_{l+1}=z_l+dz$ is taken:

$$\frac{L_\lambda(z_{l+1})}{L_\lambda(z_l)} = \frac{\beta_\lambda(z_{l+1})}{\beta_\lambda(z_l)}\exp[-2\alpha_\lambda(z_{l+1})dz]\cdot \qquad (5)$$

This form allows to omit the apparatus constants A_λ, which are usually unknown. Left hand side of (5) describe the experimental signals, while the right hand side can be calculated from Mie equations (1) when $n(z,r)$ is assumed. Using a minimization technique with the cost function:

$$\chi^2(z_l) = \sum_\lambda\left\{\frac{L_\lambda(z_{l+1})}{L_\lambda(z_l)} - \frac{\beta_\lambda(z_{l+1})}{\beta_\lambda(z_l)}\exp[-2\alpha_\lambda(z_{l+1})dz]\right\}^2 \qquad (6)$$

allows to find APSD.

In order to fit the size distribution the predefined form is necessary. Sum of modes: $n(r,z) = \sum_{j=1}^{K} n_j(r,z)$ $(K=1,2)$ is usually used. Each mode is described by the log-normal function:

$$n_j(r,z) = \frac{C_j(z)}{\sqrt{2\pi}\cdot\log\sigma_j(z)}\cdot$$

$$\cdot\frac{1}{r}\cdot\exp\left\{-\frac{[\log r - \log R_j(z)]^2}{2\cdot\log^2\sigma_j(z)}\right\}, \qquad (7)$$

where R_j denotes the modal radius, C_j - concentration of aerosol in a given mode, and σ_j - width.

TEST OF THE METHOD

The approach was tested with the synthetic size distributions after Seinfeld and Pandis (1997). They described several typical APSD with three mode lognormal functions. We assumed a uniform spatial distribution of aerosol. Particles are characterized by the refraction coefficients of water. That allowed to find the scattering coefficients (1). In order to simulate a typical experiment with multiwavelength lidar, the synthetic range corrected lidar signals $L_\lambda(z_l)$ for five wavelengths (1064, 800, 532, 375 and 355 *nm*) were calculated by means of formulas (2). Using these signals the reconstruction of the left hand side of (5) was possible.

Our initial test consisted in approximation of APSD by single lognormal function. Such approach is used by some researchers (Hess *et all*, 1998). A matrix of lognormal functions $n_{RC\sigma}(r,z_0)$ was constructed. Each element of the matrix was expressed by equation (7). In order to cover ranges of parameters predicted by Seinfeld and Pandis (1997), the matrices were generated for the modal radiuses R in the range 5 to 650 *nm*, the particle concentrations C changing from 0.01 to 3500 cm^{-3} and widths σ varying from 1.7 to 7. Using these functions and the equation (1) the matrices of coefficients $\alpha_{RC\sigma\lambda}$ and $\beta_{RC\sigma\lambda}$ were calculated for each wavelength. Integration for particle radiuses from 1 *nm* to 10 *μm* was performed. Then with pairs of elements from $\alpha_{RC\sigma\lambda}$ and $\beta_{RC\sigma\lambda}$ matrices the right hand side of (5) were constructed. For each pair the value of $\chi^2_{RC\sigma}$ was determined by minimization technique. Cost function (6) was applied. The optimal distribution $n(r,z_0)$ was found as the arithmetic mean of all analyzed cases of weights $1/\chi^2_{RC\sigma}$.

Results of these investigation are presented in Fig 1. A good approximation of the assumed APSD by single mode lognormal function was found only for *free troposphere* aerosol (Fig. 1a), due to a specific shape of its distribution. In other cases this approximation was not satisfactory. For some particle radius ranges (like *remote continental*, r≈400-700 *nm*) the discrepancies between the assumed and fited distributions reached two orders of magnitude. For *polar* APSD (Fig. 1c), the approximation is quite good for the particles of radius larger than 300 *nm*, but it is not acceptable for smaller ones. In all cases for r<100 *nm* the approximation is poor.

Much better approximation of APSD can be achieved with two mode lognormal distribution. In such case matrices of $\alpha_{RC\sigma\lambda}$ and $\beta_{RC\sigma\lambda}$ coefficients were prepared for each mode separately: for the accumulation mode modal radiuses R were in a range 5 – 200 *nm* and concentrations C changed from 20 to 3500 cm^{-3}; for the coarse mode R from 200 to 2500 *nm* and C from 0.01 to 20 cm^{-3} were used. For both modes the widths of the functions changed from 1.7 to 7.

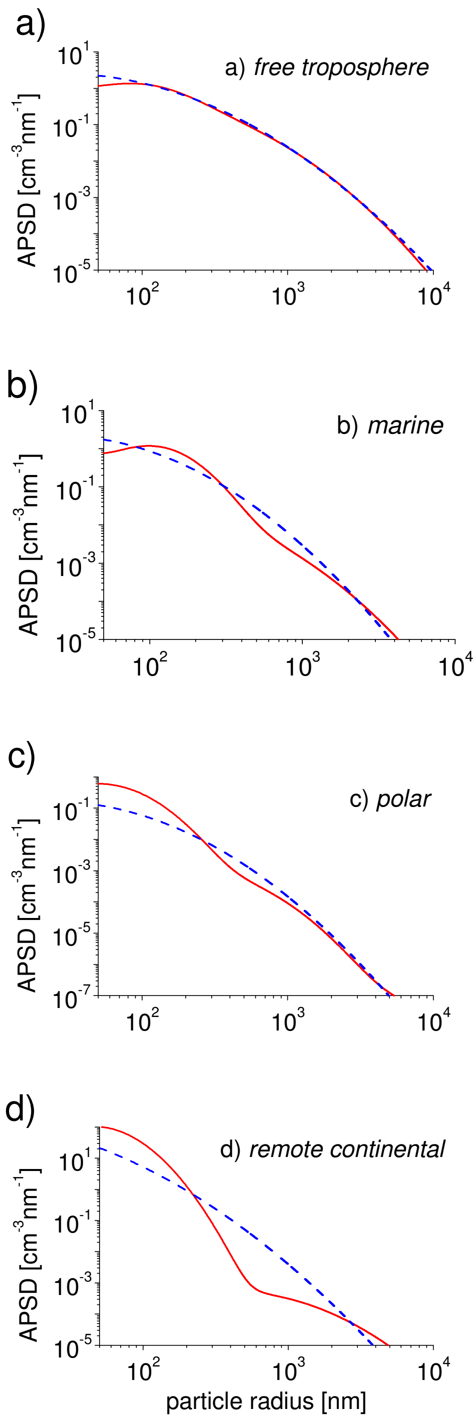

Fig. 1. Reconstruction of APSD with single mode lognormal function. Continuous lines - assumed APSD, dashed lines - their approximation.

When the two mode approximation is applied the systematic search of these matrixes needs the calculation of the cost function (6) for billions of cases. For this reason the Monte Carlo method, probing about 0.1% of all the cases was used.

Similarly to the single mode approximation, the value of $\chi^2_{RC\sigma}$ (6) for each probe was determined and the optimal distribution *n(r,z₀)* was found as the arithmetic mean of the results with weights $1/\chi^2_{RC\sigma}$.

The fits are presented in Fig 2(a-d). In this case the quite good approximation was received for all considered aerosols. For the particle radiuses beginning from 50 *nm* (i.e. within the range larger than for single mode approximation) the discrepancy between assumed and retrieved distribution is smaller than 20 %. For the particle radiuses smaller than 50 *nm* (except for special cases, like *polar* aerosol – Fig. 2c) the fit is poor. We believe that it is due to a weak contribution of small particles to the light scattering.

EVALUATION OF PARTICLE REFRACTION INDEX

Precise fit of two mode log-normal function to the APSD provides the opportunity to evaluate the refraction index of aerosol particles. In order to verify its value a following numerical experiment was performed. *Marine* aerosol at certain distance z_0 *was* considered. The right hand side of equation (5) was generated for the refraction coefficient of water (Segelstein, 1981) as well as for the refraction coefficient of sea salt (Volz, 1972). Then the matrices of $\alpha_{RC\sigma\lambda}$ and $\beta_{RC\sigma\lambda}$ coefficients were calculated.

The fiting procedure was repeated two times: ones within the broad range of parameters (as described in previous chapter) and then in a narrow range of the parameters, around that determined in the previous step. In this case the matrices of $\alpha_{RC\sigma\lambda}$ and $\beta_{RC\sigma\lambda}$ coefficients were calculated again with high

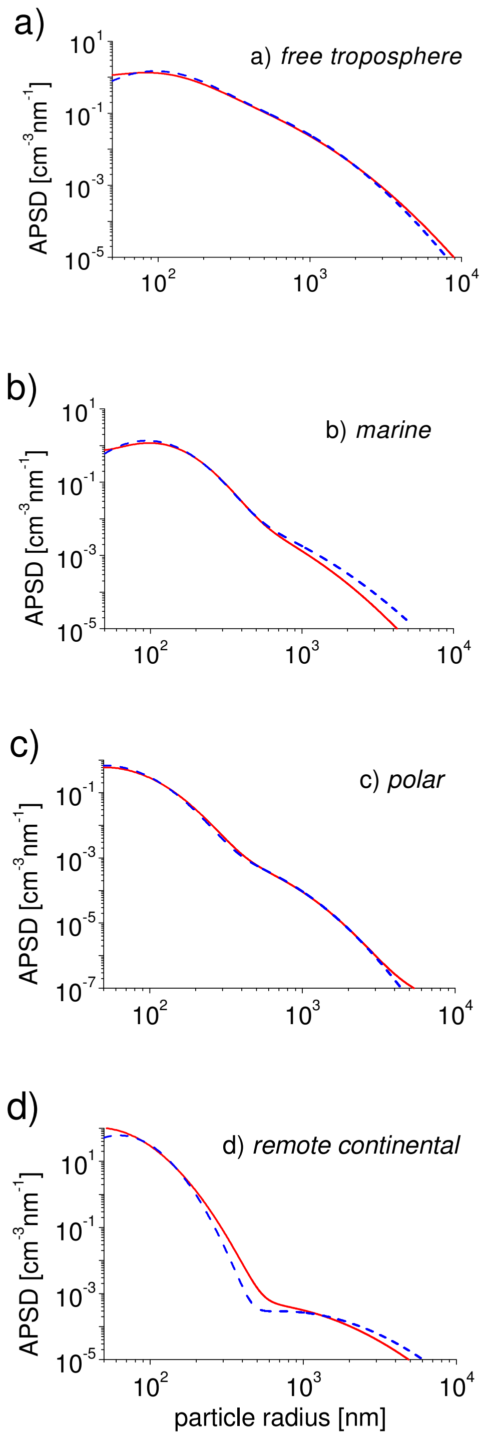

Fig. 2. Reconstruction of APSD with two-mode lognormal function. Continuous lines - assumed APSD, dashed lines - their approximation.

precision for water and for sea salt refraction indexes. Both cases were compared with the lidar signals which also were calculated for the water and for the sea salt. For all considered cases values of the cost function were found. Results of such procedure are shown in Fig. 4(a-d).

The lowest values of χ^2 were obtained for the case when the refractive index assumed for the signal generation coincides with the refractive index that was used in the fit. On the contrary, for the signals with water refractive index and the matrices calculated for the sea salt refractive index the value of χ^2 was about 15 – 20 times larger. This indicates that search for the minimum of χ^2 - parameter versus the refraction index provides the opportunity to determine the optimal refraction index and, in turn, to evaluate the chemical composition of aerosol particles.

EXPERIMET

We applied this method for analysis of measurements performed during the campaign in Warsaw, (Poland) in July 2006. The experiment was done with our multiwavelength lidar (Ernst *et al*, 2003, Chudzyński *et al*, 2006). Its sender generated five wavelength (1064, 782, 532, 391, 355 *nm*).

Example of results, i.e. the effective radius of aerosol particles r_{eff} under the base of cloud as a function of the altitude, is presented in Fig. 4. The registration was done 26th of July 2006 at 11:45 UTC. At this time the sky was covered by sparse cumulus clouds of bases at 1.8 *km* altitude. The effective radius was calculated using the retrieved APSD and the formula:

$$r_{eff}(z) = \frac{\int r^3 n(r,z)dr}{3\int r^2 n(r,z)dr}. \qquad (8)$$

The refraction index of water was assumed. As one can see at low altitudes, up to 1.65 *km*, the effective particle radius r_{eff} is uniform. Its mean value is about 180 *nm.*

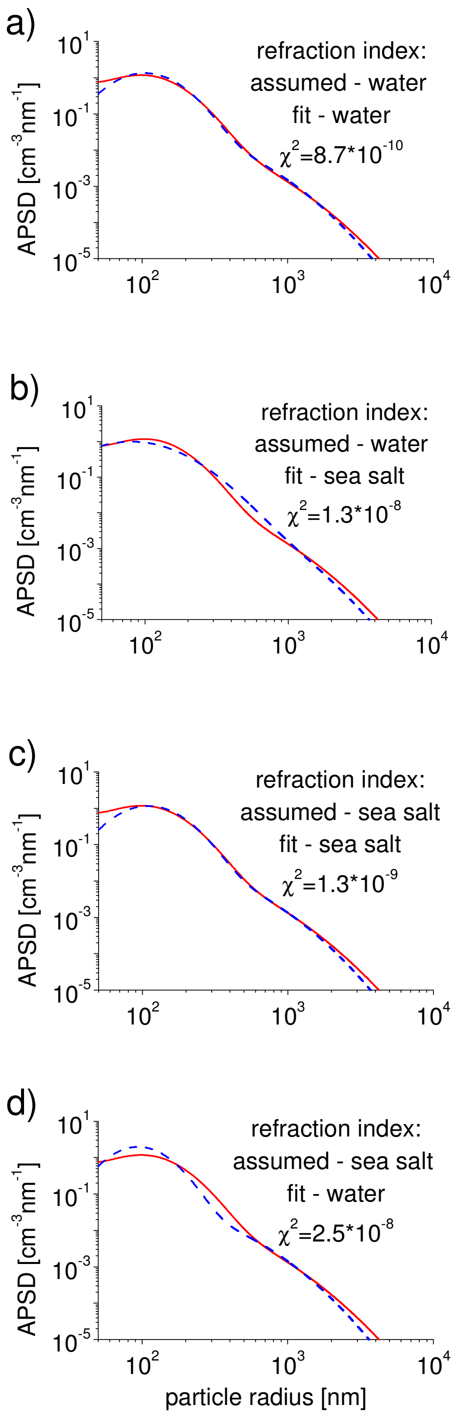

Fig. 3. Illustration of method of the refraction coefficient evaluation (marine aerosol). Continuous lines - assumed APSD, dashed lines - their two - mode approximation.

A fast increase of r_{eff} up to the value of 1200 *nm* is observed starting from about 1.65 *km*, i.e. about 150 *m* below the could base.

More detailed description of investigation of aerosol properties in vicinity of clouds is presented by Jagodnicka *et al* (2008).

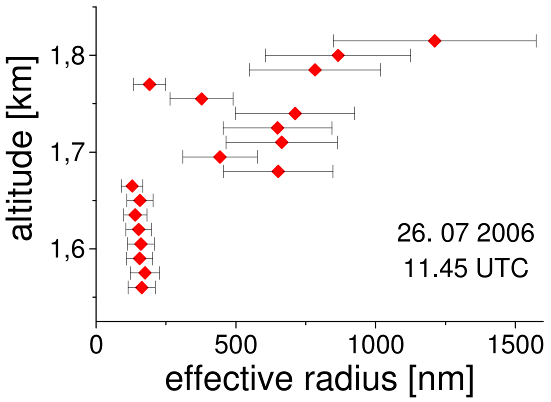

Fig. 4. Effective radius of aerosol particles as a function of the altitude. Measurement done under the base of cumulus (26.06.2006, Warsaw, Poland).

CONCLUSION.

Simple method of aerosol particle size distribution retrieving from lidar signals was presented. Due to application of direct fiting of APSD to the lidar signals this technique does not need knowledge of lidar ratio. Therefore our method can be successfully used when retrieving the aerosol scattering coefficients is difficult, for example under the clouds. To our knowledge this is an unique method providing opportunity to determine the APSD as a function of distance from the lidar.

BIBLIOGRAPHY

Bohren, C.F., D.R. Huffman, 1999: Absorption and Scattering of Light by Small Particles. *John Wiley & Sons*, New York

Böckmann, C., 2001: Hybrid regularization method for the ill-posed inversion of multiwavelength lidar data in the retrieval of aerosol size distribution. *Appl. Opt.*, **40**,1329–1342

Böckmann, C., I. Mironova, D. Müller, L. Schneidenbach, R.Nessler, 2005: Microphysical aerosol parameters from multiwavelength lidar, *J. Opt. Soc. Am.*, **22**, 518-28.

Chudzyński, S., G. Karasiński, W. Skubiszak, T. Stacewicz, 2006: Investigation of atmospheric aerosol with multiwavelenght lidar. *Optica Applicata,* **36**, 621 – 628

Curcio, J.A. , G.L. Knestric, 1958: Correlation of Atmospheric Transmission with Backscattering, *Journal of Optical Society of America*, **48**, 686-689

Ernst, K., S. Chudzyński, G. Karasiński, A. Pietruczuk, T. Stacewicz, 2003: *SPIE Proc.* **5229**, 45 – 50

Fenn, R.W., 1966: Correlation Between Atmospheric Backscattering and Meteorogical Visual Range, Appl. Opt., **5**, 293-295

Fernald, F.G., 1984: Analysis of atmospheric lidar observations: some comments, *Appl. Opt.*, **23**, 652-653.

Heintzenberg, J., H. Müller, H. Quenzel, and E. Thomalla, 1981: Information content of optical data with respect to aerosol properties: numerical studies with a randomized minimizationsearch-technique inversion algorithm*, Appl. Opt.* **20**, 1308–1315

Herman, B.M. ,S.R. Browning, and J.A. Reagan, Determination of Aerosol Size Distributions from Lidar Measurements**.** *J.Atmos.Sci.*, **28,** 763–771

M. Hess, P. Koepke, and I. Schult (1998): Optical Properties of Aerosols and clouds: The software package OPAC, Bull. Am. Met. Soc., **79**, 831-844

Iwasaka, Y., T. Shibata, T. Nagatani, G.-Y. Shi, Y.S. Kim, A. Matsuki, D. Trochkine, D. Zhang, M. Yamada, M. Nagatani, H. Nakata, Z. Shen, G. Li, B. Chen, K. Kawahira, 2003: Large depolarization ratio of free tropospheric aerosols over the Taklamakan Desert revealed by lidar measurements: Possible diffusion and transport of dust particles. *J.Geophys.Res.*, **108**, ACE 20-1-8

Jagodnicka, A.K., T. Stacewicz, M. Posyniak, S. Malinowski, S. Blindheim, M. Gaussa, 2008: Lidar investigation of aerosol particle size distribution in the vicinity of clouds. C*ommunication at 15th International Conference on Clouds and Precipitation ICCP-2008* - Cancun.

Karasiński, G., A.E. Kardaś, K. Markowicz, S.P. Malinowski, T. Stacewicz, K. Stelmaszczyk, S. Chudzyński, W. Skubiszak, M. Posyniak, A.K. Jagodnicka, C. Hochhertz, L. Woeste, 2007: LIDAR investigation of properties of atmospheric aerosol. *Eur. Phys. J.*, **144**, 129 – 140

Klett, J.D., 1981: Stable Analitical Inversion Solution for Processing Lidar Returns. *Appl. Opt.*, **20**, 211-220

Kusiel, S., I. Zolotov, 1997: Determination of the aerosol particle-size distribution from simultaneous data on spectral attenuation and the small-angle phase function. *Appl. Opt.*, **36,** 6047-6056

Kusiel, S., I. Zolotov, 2003: The Use of Direct Observations over the Aerosol Particle Size Distribution for Inverting Lidar Data. *Journal of Atmosheric and Oceanic Technology*, **20**, 1411-1420

Landulfo, E., A. Papayannis, P. Artaxo, A.D.A. Castanho, A.Z. De Freitas, R.F. Souza, N.D. Vieira Junior, M.P. Jorge, O.R. Sanchez-Coyllo, D.S. Moreira, 2003: Synergetic measurements of aerosols over São Paulo, Brazil using LIDAR, sunphotometer and satellite data during the dry season. *Atmos. Chem. Phys.*, **3**, 1523–1539.

Ligon, D. A., J. B. Gillespie and T. W Chen, 1996: Determination of aerosol parameters from light – scattering data using an inverse Monte Carlo technique. *Appl. Opt.*, **35**, 4297 – 4303

Ligon, D.A., J.B. Gillespie and P. Pellegrino, 2000: Aerosol properties from spectral extinction and backscatter estimated by an inverse Monte Carlo method. *Appl. Opt.*, **39**, 4402-4410;

Müller, D., U. Wandinger, and A. Ansmann, 1999: Microphysical particle parameters from extinction and backscatter lidar data by inversion with regularization: Theory. *Appl. Opt.*, ***38,*** 2346–2357

Müller, D., U. Wandinger, and A. Ansmann, 1999: Microphysical particle parameters from extinction and backscatter lidar data by inversion with regularization: Simulation. *Appl. Opt.*, **38,** 2358–2368

O'Connor, E.J., A.J. Illingworth and R.J. Hogan, 2004: A technique for autocalibration of cloud lidar, *J.Atmos. Oceanic Technol.*, **21**, 777-786

Twomey S., H.B. Howell, 1965: The Relative Merit of White and Monochromatic Light for the Determination of Visibility by Backscattering Measurements. *Appl. Opt.*, **4**, 501-506

Pappalardo, G., 2005: Aerosol lidar ratio measurement in the framework of EARLINET, *Geophysical Research Abstracts*, **7**, 08329

Rajeev K and K. Parameswaran, 1998: Iterative method for the inversion of multiwavelength lidar signals to determine aerosol size distribution. *Appl. Opt.* **37**, 4690–4700

Segelstein, D. J., 1981: *Thesis (M.S.).*Department of Physics. University of Missouri-Kansas City

Volz, F. E., 1972: Infrared refractive index of atmospheric aerosol substance, *Appl. Opt.*, **11**, 755-759

Seinfeld J. H., Pandis S.N., 1997*:* Atmospheric Chemistry and Physics, *John Wiley & Sons New York*

Van de Hulst, H. C., 1957: *Light Scattering by Small Particles.* John Wiley & Sons, New York

Veselovskii, I., A. Kolgotin, V. Griaznov, D. Müller, U. Wandinger, D.N. Whiteman, 2002: Inversion with regularization for the retrieval of tropospheric aerosol parameters from multiwavelength lidar sounding, *Appl. Opt.*, **28**, **41**, 3685-3699

Veselovskii, I., A. Kolgotin, V. Griaznov, D. Müller, K. Franke, D.N. Whiteman, 2004: Inversion of Multiwavelength Raman Lidar Data for Retrieval of Bimodal Aerosol Size Distribution. *Appl. Opt.*, **43**, 1180-1195

Veselovskii, I., A. Kolgotin, D. Müller, and D.N. Whiteman, 2005: Information content of multiwavelength lidar data with respect to microphysical particle properties derived from eigenvalue analysis. *Appl.Opt.* **44**, 5292-5303

Yoshiyama H., Ohi A., Kazuyuki Ohta, 1996: Derivation of the aerosol size distribution from a bistatic system of a multiwavelength laser with the singular value decomposition method. *Appl. Opt.,* **35**, 2642-2648

LIDAR INVESTIGATION OF AEROSOL PARTICLE SIZE DISTRIBUTION IN THE VICINITY OF CLOUDS

A. K. Jagodnicka [1], T. Stacewicz [1], M. Posyniak [2], S. Malinowski [2], S. Blindheim [3], M. Gaussa [3]

[1] Institute of Experimental Physics, University of Warsaw, ul. Hoża 69, 00-681 Warsaw, Poland

[2] Institute of Geophysics, University of Warsaw ul. Pasteura 7, 02-093 Warsaw, Poland

[3] Andøya Rocket Range, Andenes, Norway

ABSTRACT

We present Aerosol Particle Size Distribution (APSD) retrieved from multiwavelength lidar profiles in the vicinity of convective clouds. The data were collected in summer 2006 in Warsaw (Poland). For the retrieval of APSD a recent algorithm based on direct fit of this function to the lidar signals was employed.

INTRODUCTION

Remote and nonperturbative investigation with lidars provides information about profiles of atmosphere. In case of muliwavelength lidars aerosol particle size distribution (APSD) can be achieved. In this study we analyzed multiwavelength lidar returns collected in vicinity of boundary layer convective clouds. The data were gathered in July - August 2006 in Warsaw (Poland).

A multiwavelength lidar working at 5 wavelengths described elsewhere (Ernst *et al* 2003a, Chudzyński *et al*, 2006) was used. It consists of the optical sender with pulsed Nd:YAG laser generating at three harmonics (1064, 532 and 355 *nm*) and additional pulsed Ti:Sa laser generating at two harmonics (782 and 391 *nm*). Energies of the light pulses were about 200 *mJ*, while their repetition rate was 10 *Hz*. The laser beams were sent vertically to the atmosphere.

In the optical receiver a Newtonian telescope with the mirror of 40 *cm* in diameter and focal length of 120 *cm* was used. The light, collected by the telescope, was spectrally separated by a polychromator. Acquisition of the lidar echoes was done with a set of photomultipliers and 12 bit 50 *MHz* digitizers. The signals were averaged over 300 pulses.

For retrieval of APSD original method was elaborated (Ernst *et al*, 2003b, Jagodnicka *et al*, 2008). It is based on direct fit of particle size distribution to the lidar signals. APSD was approximated with combination of two lognormal modes with free parameters (Reidmiller *et al*, 2006). Using such function for each lidar wavelength the extinction and backscattering coefficients were calculated and substituted into the lidar equations (Measures, 1992). In this way synthetic lidar signals were achieved. Varying the parameters and using Monte Carlo sampling the best fit of the synthetic signals to experimental ones was found.

In principle, an inversion of the lidar signal is an ill-posed problem and requires many additional assumptions. First, refraction index of the aerosol is taken as this one for water. Second, aerosol particles are assumed spherical. Additionally, activation of CCN and growth of certain classes of particles with height is expected. Signature of this process should be seen in the retrieved particle size spectrum.

AEROSOL AT THE BASE OF CUMULUS

On July 26th at 09:40 UTC scattered *Cumulus* below a weak *Cirrostatus* cover was present. *Cumulus* clouds were developing in a humid marine polar air advecting from north. Noon sounding from Legionowo (~30 *km* north from the measurement site) showed the mixed layer present up to 2000 *m* height. The wind was weak, 3 *m/s* in the boundary layer and 6 *m/s* above. No significant directional shear was observed. The convection period was not long. After some development, the convective clouds disappeared around 14:00 UTC damped by *Cirrostratus*.

In Fig. 1(a - d) determined for single cumulus cloud is shown. Plots were done from below to the base of *Cu* passing through the lidar beam within 2 minutes period. The base (as seen in Figs 1 and 2) oscillated around 1.75 - 1.85 *km* altitude, which is in agreement with the sounding.

The effective radius was calculated according to the formula:

$$r_{eff}(z) = \frac{\int r^3 n(r,z)dr}{3\int r^2 n(r,z)dr}. \qquad (1)$$

Here *n(r,z)* denotes APSD as a function of particle radius *r* and distance from the lidar *z*. The distributions were achieved due to analysis of four consecutive profiles of lidar returns collected every 30 *s*

In all plots of Fig. 1 a rapid increase of effective particle radius is clear. It takes place within a layer of several tens of meters thick. Note that there is no data from the cloud interior. Due to extinction the lidar signals at higher altitudes weaken rapidly and the retrieval of APSD is not possible.

In Fig. 1a a steep increase of r_{eff} from 0.2 up to 1.3 *μm* within 45 *m* deep layer is evident. Vertical resolution of the lidar (~15 *m*) does not allow to see finer details of this layer. Strong gradient corresponds well to the results parcel model of CCN activation (Johnson, 1980).

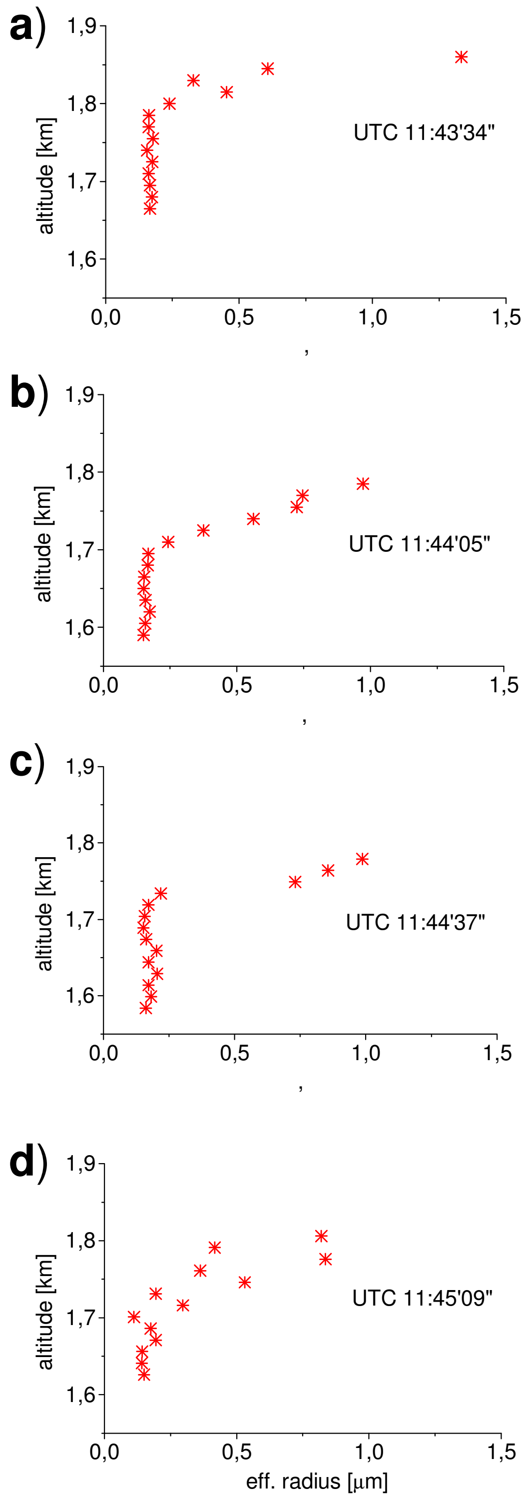

Fig. 1. Effective radius of aerosol particles below the cumulus cloud base (Warsaw, 26.07.2006)

Smaller vertical gradient of r_{eff} (growth from ~0.18 to 1 *µm* within 100 *m* deep layer) can be seen in Fig. 1b. Growth of particles begins at the level of 1.7 *km*, *i.e.* lower than 30 *s* earlier, suggesting spatial inhomogeneity of the updraft. In Fig. 1c, 30 *s* later, the gradient of r_{eff} is also steep what suggests that the growth of particles is similar to this shown in Fig. 1a. In Fig. 1d fluctuations of the effective radius are superimposed on the slower average growth. This may reflect nonuniformity of the APSD below the cloud base within 30 *s* averaging period.

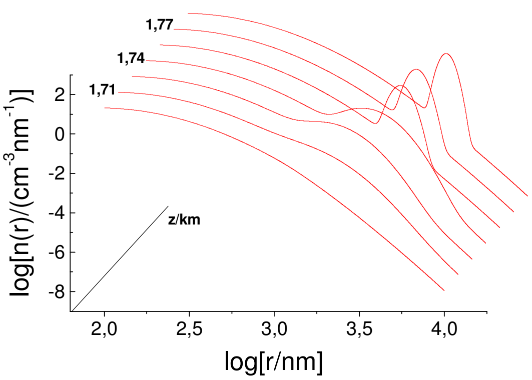

Fig. 2. Aerosol particle size distribution at 11:44'05" UTC (Warsaw, 26. 07. 2006).

In Fig. 2 the APSD taken from lidar profile 11:44'05" UTC (corresponding to r_{eff} in Fig. 1b) is shown. At the 1.7 *km* altitude large particles start to form. The initial modal radius of $r_m = 1$ *µm* grows quickly with height and at 1.8 *km* rises up to 3.2 *µm*. Droplet number concentration in this mode increases through first 50 *m* and then stabilizes. The relative width of the peak decreases with height and at the top of the detection range its value is about 1 *µm*. Such behavior is also consistent with adiabatic model of CCN activation in updraft (Johnson, 1980).

AEROSOL BELOW STRATOCUMULUS BASE

On July 30th, 2006 broken *Cumulus* clouds transformed around 11:00 UTC into stratocumulus. Noon sounding from Legionowo showed mixed layer under capping inversion at 1600 *m* height. Wind was from NW with constant speed of 10 *m/s* in the whole boundary layer and above it. Increased relative humidity in the upper part of the mixed layer corresponds well to the lidar-detected cloud base at the altitudes of 1.2 - 1.3 *km*.

Typical examples of the retrieved effective radius profiles below the cloud base are shown in Fig. 3. In most cases $r_{eff}(z)$ shows some fluctuations and less regular behavior than below *Cu* clouds. There are no evident cases which could be attributed to adiabatic activation of CCN. Note, that at 10 *m/s* wind speed averaging of lidar signal over 30 *s* corresponds to 300 *m* spatial averaging in horizontal. While this value is less than the size of typical convective cell in *Sc*, it is more than the size of large turbulent eddies. It is not surprising, that turbulent mixing, almost certain in stratocumulus topped boundary layer results in the variability of the observed profiles.

SUMMARY AND CONCLUSION

We demonstrated the ability to retrieve effective radius of the aerosol particle size distributions in the vicinity of the clouds from remote sensing with the multivavelength lidar. Presented results seem to confirm presence of process of CCN activation and growth in updraft. First achievements seem encouraging, despite many issues in the measurement technique and retrieval details.

For example there are problems with APSD retrieval close to sharp cloud boundaries. In Fig. 4 we present observation of orographic cloud in ALOMAR lidar observatory in northern Norway. Rapid changes in extinction prevent from retrieval of APSD inside the cloud. The model of aerosol below the cloud is also uncertain because an assumption that it consists of water droplets is doubtful.

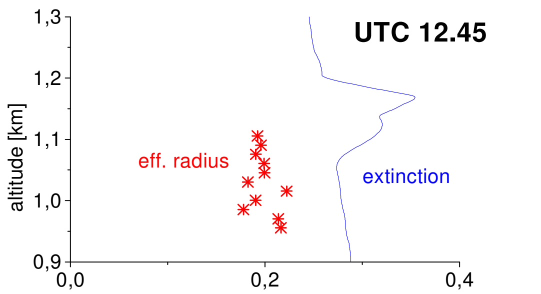

Fig. 4. Effective radius of aerosol particles and the aerosol extinction coefficient in vicinity of thin stratus layer (Andøya, Norway, 3. 07. 2007).

Nevertheless, we believe that further development of presented approach will help to resolve some important problems in cloud physics – e.g. problem of aerosol closure.

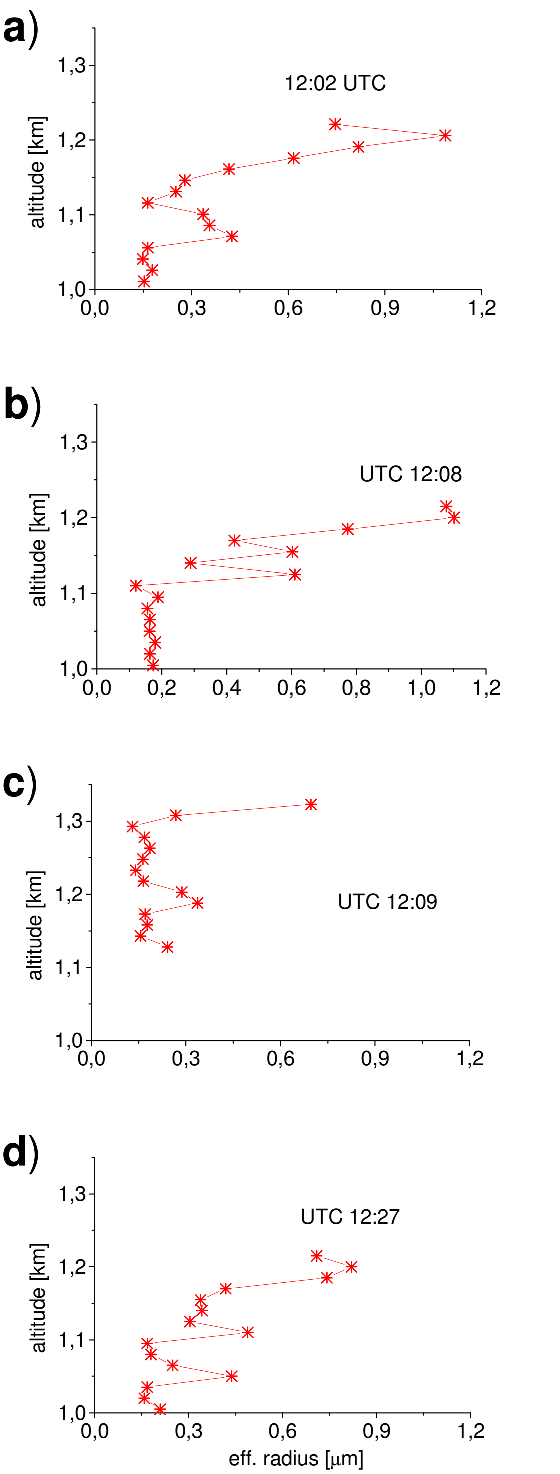

Fig. 3. Profiles of the effective radius of aerosol under stratocumulus deck (Warsaw, 30 of 2006).

BIBLIOGRAPHY

Chudzyński, S., G. Karasiński, W. Skubiszak, T. Stacewicz, 2006: Investigation of atmospheric aerosol with multiwavelength lidar. *Optica Applicata* **36**, 621 – 628

Ernst, K., S. Chudzyński, G. Karasiński, A. Pietruczuk, T. Stacewicz, 2003a: Multiwavelenth lidar for determination of the atmospheric aerosol size distribution. *SPIE Proc.* **5229**, 45 – 50.

Ernst, K., G. Karasiński, A. Pietruczuk, T. Stacewicz, 2003b: Retrieving the atmospheric aerosol size distribution by means of multiwavelength lidar*. SPIE Proc.* **5258**, 156 – 159

Jagodnicka, A.K., T. Stacewicz, G. Karasiński, M. Posyniak, 2008: Simple method of Aerosol Particle Size Distribution retrieving from multiwavelength lidar signals, 15th International Conference on Clouds and Precipitation, Cancun, Mexico

Johnson, D.B., 1980: The influence of cloud base temperature and pressure on droplet concentration. *J. Atmos. Sci.*, **37**, 2079-2085

Measures, R.M., 1992: Laser Remote Sensing: Fundamentals and Applications Malabar, FL: *Krieger Publishing, reprint of 1984 John Wiley ed*.

Reidmiller D.R., Hobbs P.V., Kahn R., 2006: Aerosol Optical Properties and Particle Size Distributions on the East Coast of the United States Derived from Airborne In Situ and Remote Sensing Measurements. *J. Atmos. Sci.*, **63,** 785-814

THE RELATION BETWEEN POWER LINE ICING AND METEOROLOGICAL CONDITIONS IN GUIZHOU, CHINA

Ran JIA[1]，Sheng-Jie NIU[1*]，Ning LUO[2]，Ji-Fen WEN[2]

1. Laboratory for Atmospheric Physics& Environment of China Meteorological Administration, Nanjing University of Information Science & Technology, Nanjing 210044, P.R.China
2. GuiZhou weather Modification Office .Guiyang 550002, P.R.China

1. INTRODUCTION

Power line icing is a serious problem during winters in China and has been studied for many years by individual provincial meteorological bureaus yet there are no systemic studies at the national level. A comprehensive, quantitative study, however, has been stymied because of inconsistencies between the various data sets, lack of quality control and differences in how data are reported. As a result, we initiated a new study to try and provide a higher quality data set that can provide new information useful for relating the power line icing features to the meteorology so that avoidance strategies can be developed through modern weather prediction. Continuous observations were made over 152 hours of temperature, wind direction and speed at a sports stadium and under a television tower midnight on January 3th,1990 to 8:00 on January 9th,in the Lou mountains, Guizhou province. An additional 81 hours of continuous measurements were made of temperature, wind direction and speed, ice diameter and the thickness and icing damage to cables in Liupanshui-Panxian, JiuZun, Shuicheng county and Kaiyang county were also made.

2. THE METEOROLOGICAL CONDITIONS OF THE FORMATION OF POWER LINE ICING

Glaze is a hard ice which is made when the supercooled water drop comes into contact with things on the ground. While rime is an ivory-white ice crystal which is made by condensation of vapor in the air or when the supercooled fog-drop is directly frozen on a solid object. The phenomenon is called power line icing when glaze, rime or snow is frozen on the power line.

Power line icing is formed by some combinational meteorological conditions. According to observations of weather station, power line icing is often appeared when the wind velocity is under 5m/s, the air humidity is between -10℃ and 0℃ and the relative air humidity is over 95%.When the real disaster is caused to the power line, it should meet the following three conditions:

1) the supercooled water drop or cloud droplet exists and there is additional water vapor;
2) the wind velocity is 3~5m/s,and southeaster is better to the increase of ice;
3) it is the most serious when the temperature is -6~-3℃.

3. THE ANALYSIS OF METEOROLOGICAL CHARACTERISTICS DURING POWER LINE ICING

When glaze or rime weather occurs, power line icing does not always appears. The temperature and air humidity should be in a certain scope, the wind velocity should not be too high and the wind direction should be propitious to the formation of icing.

* Correaponding author.
E-mail address: niusj@nuist.edu.cn

1). The influence of temperature to the formation of power line icing

Table 1 Temperature and weather between 1990 and 1994 during the observation of power line icing

Time	fog			Rime&glaze			Power line icing		
	frequency	temperature (℃)	Average temperature (℃)	frequency	temperature (℃)	Average temperature (℃)	frequency	temperature (℃)	Average temperature (℃)
1990y 1#	32	-2.5～5.0	1.40	7	-0.8～-0.2	-0.47	5	-0.6～-0.2（glaze）	-0.42
1990y 2#	35	-1.0～6.7	1.46	5	-0.6～0.5	-0.22	naught		
1994y Lou mountain	naught			non-stat			28	-6.0～-1.8（rime）	-4.49

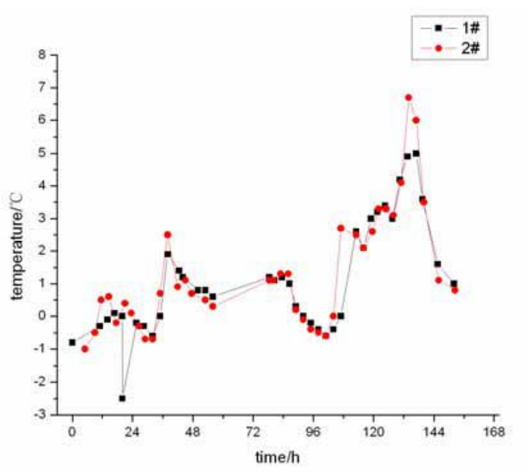

Fig. 1 Temperature changes with time during the observation of power line icing on Lou mountain in Zunyi city (the number of samples of the two observation points respectively is 39,40,totalling 79)

Temperature range is closely related to the type of icing. It influences the type of power line icing by influencing the freezing course of supercooled water drop. The temperature of the formation of icing in Zunyi ranges form -6.0~-1.8℃, got from Table 1.

From figure 1, when the ice crystals and the supercooled water drop coexist, the ice crystals will grow more quickly than the other one. In the progress of the power line icing, the ice increases when the supercooled water droplet diffuses and deposits on the wire. According to the meteorological record, fog sustained during all the observations in 1990.Trends of temperature changes are almost the same, and the overall trend of temperature is upward, with small fluctuations in the middle. When the temperature substantially decreased, fog gradually dissipated.

2) The influence of wind direction and wind speed to power line icing

The growth of supercooled water drop, namely riming，exists during collision and freezing of it ,in the course of the formation of both glaze and rime. The increase of ice can be figured out by continuing coagulation equation：

$$\frac{dm}{dt} = EA_s q_w \left| v_s - v_w \right| ,$$

E is the coagulation coefficient of supercooled water drop and ice crystal. A_s is the section of the ice crystal, q_w is content of water vapor in the cloud, v_s and v_w is respectively the landing speed of ice crystal and water drop. For the power line icing in the practical circumstances, icing on the wire could be regarded as ice crystal, and the icing thickness could be considered as the section of ice crystal. Consequently, the increase of power line icing is related to coagulation coefficient, the content of water vapor in the cloud and the landing velocity of water drop. The influence of the landing velocity of water drop to the increase of icing is mainly considered in this paper. For Non-quiescent air, the landing speed of water drop is also influenced by the direction and velocity of wind.

Table 2 Frequency of wind directions during observations of power line icing in Zunyi city in 1990 and 1994

	Wind direction	N	NNE	NE	ENE	E	ESE	SE	SSE	S	SSW	SW	WSW	W	WNW	NW	NNW	C
1990y	frequency	6	1	9	0	4	0	15	1	18	1	4	0	4	0	7	1	7
1994y	frequency	0	2	5	0	9	1	8	0	1	0	0	0	0	0	0	0	0
add up	frequency	6	3	14	0	13	1	23	1	19	1	4	0	4	0	7	1	7

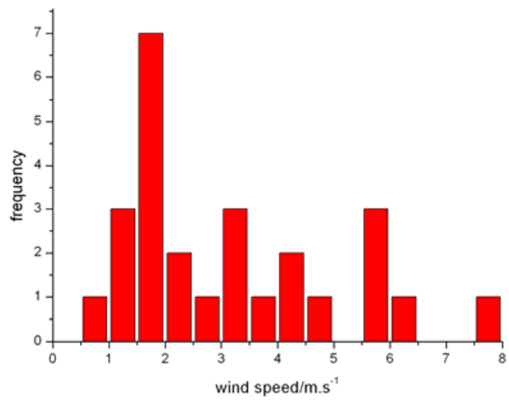

Fig. 2 Frequence of wind speeds during observations of power line icing in Zunyi city in 1994(26 samples)

When power line icing happened on Lou mountain in 1994, east accounted for maximum proportion, with southeaster also for a sizeable one, got from Table 2.

From figure 2, the wind velocity when power line icing appeared was mostly between 1.0~4.5m/s.That is because low wind speed goes against supercooled water drop adhesion to the wire; and when the wind speed is too high, the degree of wire oscillation will increase, which would change the molecular dynamical structure, accordingly the adhesion force of icing would be reduced and thus the ice falls.

4. ANALYSIS OF ICING CHARACTERISITICS

Macro characteristics of power line icing as follow:

We can find from the meteorological records in Shuicheng and Kaiyang that the longer time the ice accretion sustains, the higher the icing accident probability is. Both of their critical icing day is the fourth day of the icing days. After that time, the icing accident probability shows a rising trend.

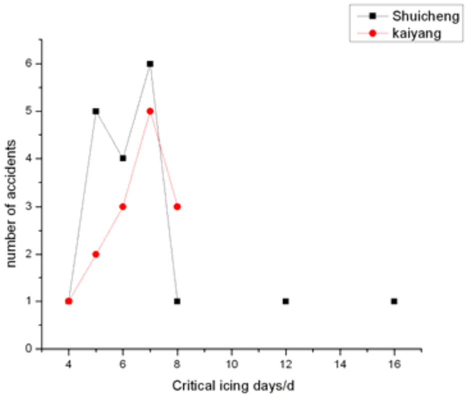

Fig. 3 Critical icing days of icing accidents in Shuicheng city and Kaiyang city(19 samples in Shuicheng city and 11 in Kaiyang)

Table 3. Icing accident probability in Shuicheng county and Kaiyang county during 1967~1989

Icing days	Shuicheng			Kaiyang			Add up		
	Icing times	Accident times	disaster	Icing times	Accident times	disaster	Icing times	Accident times	disaster
3～10	23	9	39%	25	6	24%	48	15	31%
11～20	13	11	85%	19	6	32%	32	17	53%
21～30	2	2	100%	1	1	100%	3	3	100%

5. SUMMARY

1). Power line icing by rime happens most frequently when the temperature ranges from -6.0～-1.8 C, 2) the growth of the ice is proportional to the wind speed, 3) four days of sustained meteorological conditions that produce icing is the critical time period after which the probability of cable damage begins to increase., 4) the changes in the ice diameter and thickness represents different phases of a icing process, i.e. steady increases in the diameter and thickness represents the development phase, no increase represent the maintenance phase and steady decrease is the dissipative stage.

6. BIBLIOGRAPHY

He-yun Liu , Di Zhou, A Simple Model For Pedicting Glaze Loads on Wires. Proceedings of The Chinese Society For Electrical Engineering. 2001.21(4)

Qian-gen Zhu, Synoptic meteorology theory and method. China Meteorological Press.2003.313-318

Hong-ni Zhang, The experience of icing observation. Meteorology of Gansu1999.17 (1) :35-36

Sidi,Frost and Rime. China Meteorological Press.

Ru-rong Wang. Observation Data Analysis Of Nanling Icing Meteorological Station and Exploration Of Ultra-High Voltage Transmission Line Construction.Shanxi Meteorological Quarterly.1997.4:16-18

Pei-xuan Sheng. Atmospheric Physics. Peking University Press.2003.304-343

ACKNOWLEDGEMENT

Key Basic Research Foundation for Natural Science of the Jiangsu Higher Education Institutions of China (Grant No. 06KJA17021), and Special Foundation for Meteorological Vocation from the Ministry of Science and Technology of China(Grand No. GYHY200706026) supported this research.

IMPROVED AIRBORNE HOT-WIRE MEASUREMENTS OF ICE WATER CONTENT IN CLOUDS.

Korolev, A.V.[1], J. W. Strapp[1], G.A. Isaac[1], and E. Emery[2]
[1] *Environment Canada, Toronto, Ontario, Canada*
[2] *NASA, Cleveland, OH, USA*

1. Introduction

Ice water content (IWC) is one of the fundamental microphysical parameters of clouds. Currently, there are three techniques used in the measurement of IWC. The first one involves the calculation of IWC from the measurements of particle size distribution, based on the size-to-mass conversion (e.g. Locatelli and Hobbs, 1974; Brown and Francis 1995). The second technique consists of estimating IWC from the measurements of water vapor density which results from total evaporation of ice particles (e.g. Kyle 1975; Ruskin 1976; Nicholls et al. 1990). The third approach utilizes the hot-wire technique (e.g. Nevzorov 1980, 1983; Korolev et al. 1998).

Despite the substantial efforts invested in the development each of the above techniques, there are still considerable uncertainties in accuracy of the IWC measurements. The existing problems are a result of multiple causes: (1) the large range of ice particle sizes covering a scale of four orders of magnitude. This creates specific problems for in-situ sampling and requirements for geometrical characteristics of the probes' inlets; (2) the variable density of ice particles, which does not allow for unique coefficients for size-to-area parameterization, such as the case of liquid droplets; and (3) the present absence of calibrating standards in wind tunnels. As a result of the latter, only one strategy of assessment of the IWC measurement accuracy is currently possible. It is based on multiple comparisons of measurements of instruments utilizing different IWC techniques. Although this approach may not necessarily provide an ultimate conclusion about the accuracy of the IWC measurements, it may reveal some specific measurement problems and help formulate new directions for future improvement of the IWC instrumentation.

Corresponding Author: Alexei Korolev, Environment Canada, 4905 Dufferin Street, Toronto, Ontario, M3H5T4 Canada, e-mail: alexei.korolev@ec.gc.ca,

Efforts are in fact currently underway to develop absolute IWC calibrations in a wind tunnel usingice shaved from blocks (Strapp et al. 2008), which will hopefully provide a significant new tool for making progressing on this problem.

In the present paper we compare measurements of three IWC probes: (1) the Sky Tech Research hot-wire Nevzorov probe (Korolev et al. 1998) with a modified TWC sensor; (2) the counterflow virtual impactor (Twohy et al 1998) component of the Droplet Measurement Technology (DMT) Cloud Spectrometer and Impactor (CSI),(www.dropletmeasurement.com/product) using the evaporation technique; and (3) Particle Measuring Systems (PMS) OAP-2DC and OAP-2DP (Knollenberg, 1981) for measurements of particle size distributions, which were converted in IWC based on size-to-mass conversion. The first part of the paper is focused on the problems inherent in the sampling of ice particles by the hot-wire sensors. The second part describes the intercomparisons of the IWC measured from in-situ by the Nevzorov probe, DMT CVI and that deduced from particle size spectra.

2. High speed video tests

The concept of the IWC measurements by the hot-wire Nevzorov TWC sensor is based on the assumption that ice particles remain inside the conical capture volume and then melt and evaporate (see Fig. 2b in Korolev et al. 1998). However, despite this assumption, it has now been unclear for some time as to whether ice particles are truly captured, retained, and evaporated,, or simply rebound off the sensor after striking its surface.

A high speed video recording reported by Emery et al. (2004) and Strapp et al. (2005) showed that ice particles may bounce from the surface of the Nevzorov TWC cone sensor and other hot-wire sensor geometries. The tests were conducted in the Cox & Co wind tunnel. The

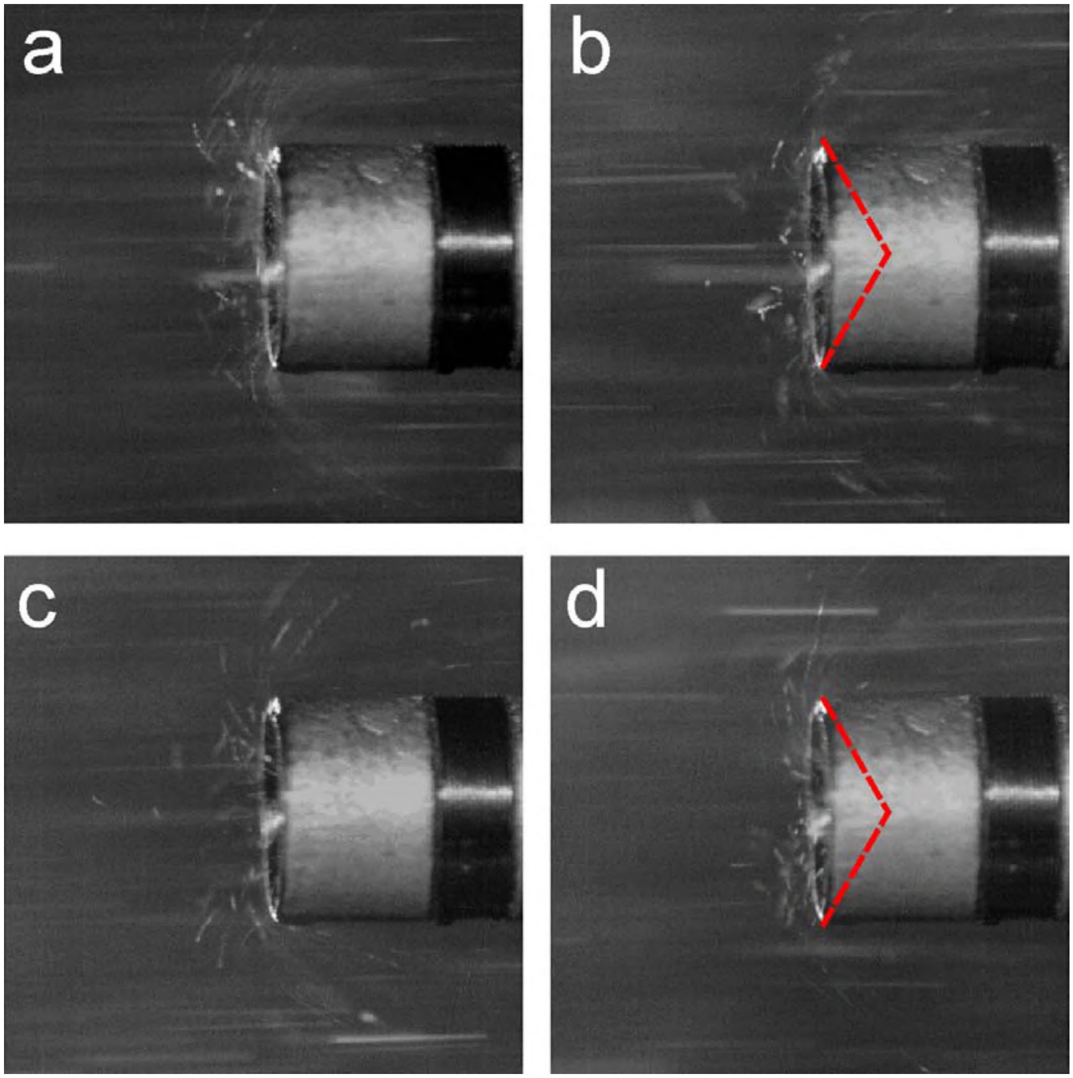

Figure 1. The images of the Nevzorov TWC sensor 120^{o} cone taken with high speed video camera in the flow of ice particles in the Cox & Co wind tunnel. Red dashed lines in (b)&(d) indicate the shape of the hollow cone of the hot-wire sensor. Air speed 70m/s.

Cox wind tunnel has the capability of producing an ice spray by shaving ice blocks. The shaved ice particles had an irregular shape with a characteristic size ranging from 15 μm to 400μm. Fig. 1 shows images of the side view of the Nevzorov TWC sensor in the flow of ice particles. The pictures were taken in the Cox &Co wind tunnel with help of the Phantom V5.0 high frame rate camera manufactured by Vision Research, Inc. As seen from Fig. 1 some of the particles rebound off the TWC cone surface into the air-stream and are swept away. The bouncing of the ice particles results in an underestimate of the measured IWC. However, the efforts to quantify the IWC losses by counting the incoming ice particles, which approach the sensor cone and then rebound off based on high speed video frames, proved unsuccessful.

The ice particles produced in the Cox wind tunnel studies may have a higher density and less fragile structure than most vapor-grown ice crystals. The OAP-2D imagery indicates that the majority of the artificial ice particles produced in the wind tunnel had a quasi-spherical shape (Emery et al. 2004). Such particles may behave like solid balls resulting in elastic bouncing on the impact with the sensor surface (Fig. 3a).

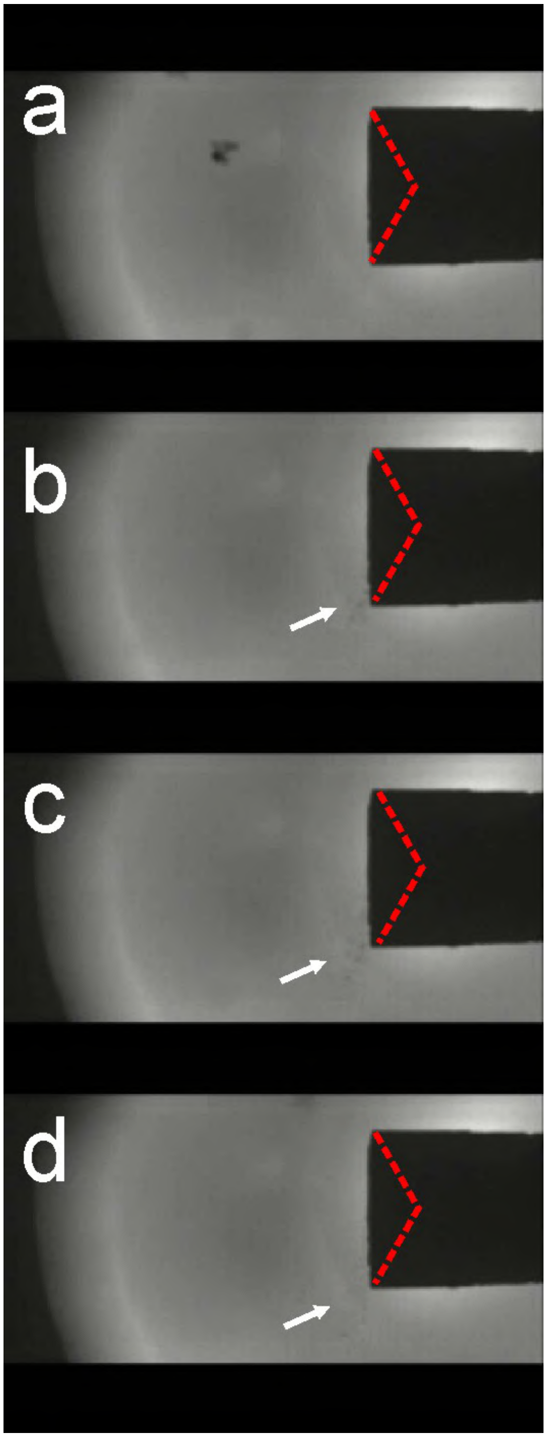

Figure 2. Sequence of video frames captured by the high speed video camera of the impact of the spatial dendrite (a) with the standard (120°) Nevzorov TWC hot-wire sensor cone. Arrows in (b,c,d) indicate the outflow of the powdered ice particles resulted from the shattering of the dendrite shown on (a) after the impact with the cone. The measurements were obtained during the NRC Convair-580 flight in Ns on 18 December 2004. Red dashed lines indicate the shape of the hot-wire sensor cone.

Because of the specific features inherent in the wind tunnel environment, a decision was made to run tests only in natural clouds, where it is known that the turbulence, particle trajectories, and particularly the ice particle properties would be different. A series of tests were conducted using the National Research Council (NRC) Convair-580 in December 2004 using a total of 16 flight hours. The particles striking the TWC sensor of the Nevzorov probe were imaged using a Phantom V5 high speed camera.

Fig. 2 shows a sequence of video frames captured of the impact of the spatial dendrite with the Nevzorov TWC cone. Image analysis of numerous events of impact between ice particles and the sensor cone indicated that the ice particles shattered into a large number of small ice fragments, a fraction of which were visibly swept away from the cone with the airflow. Arrows in Fig.2b, c, d indicate the outflow of the small ice particle fragments which resulted from the shattering of the dendrite shown on Fig. 2a before it entered the TWC cone.

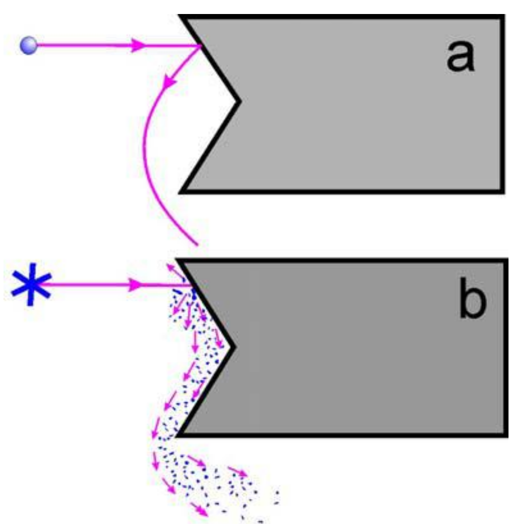

Figure 3. Conceptual diagram of the elastic (a) and inelastic (b) bouncing of ice particles with shallow TWC sensor cone.

The comparisons between the high speed videos recorded in the wind tunnel and the natural cloudy environment revealed differences in the behavior of artificial and natural ice particles after their impact with the TWC cone. On one hand, in a high density case, the artificial ice particles may behave more like solid balls, with elastic bouncing on impact. Whereas, naturally grown ice particles with complex morphology and low densities, such as a spatial dendrite, tend to shatter into a large number of small fragments. Some fraction of this shattered ice may be removed from the cone by airflow, or bounce elastically from the surface. The conceptual diagram in Fig. 3 demonstrates the difference between the behavior of artificial and natural ice particles of this type. It is reasonable to assume that natural ice particles with more compact geometry and higher densities may behave more similarly to the artificial ice produced in tunnels, although no such data were available from the flight tests with the high speed video.

Strapp et al. (2005) compared the response of hot-wire sensors of different geometry to shaved ice particles in the Cox and Co. Icing Wind Tunnel, showing that a 16 mm deep sensor displayed far fewer particles bouncing out of the capture volume than the 2 mm deep Nevzorov shallow sensor. Furthermore, 16 mm deep sensor measured at least 2 times larger IWC than the Nevzorov standard shallow sensor. This work indicated that the efficiency of the capture of ice particles by hot wires could potentially be increased greatly by modifications to the sensor geometry.

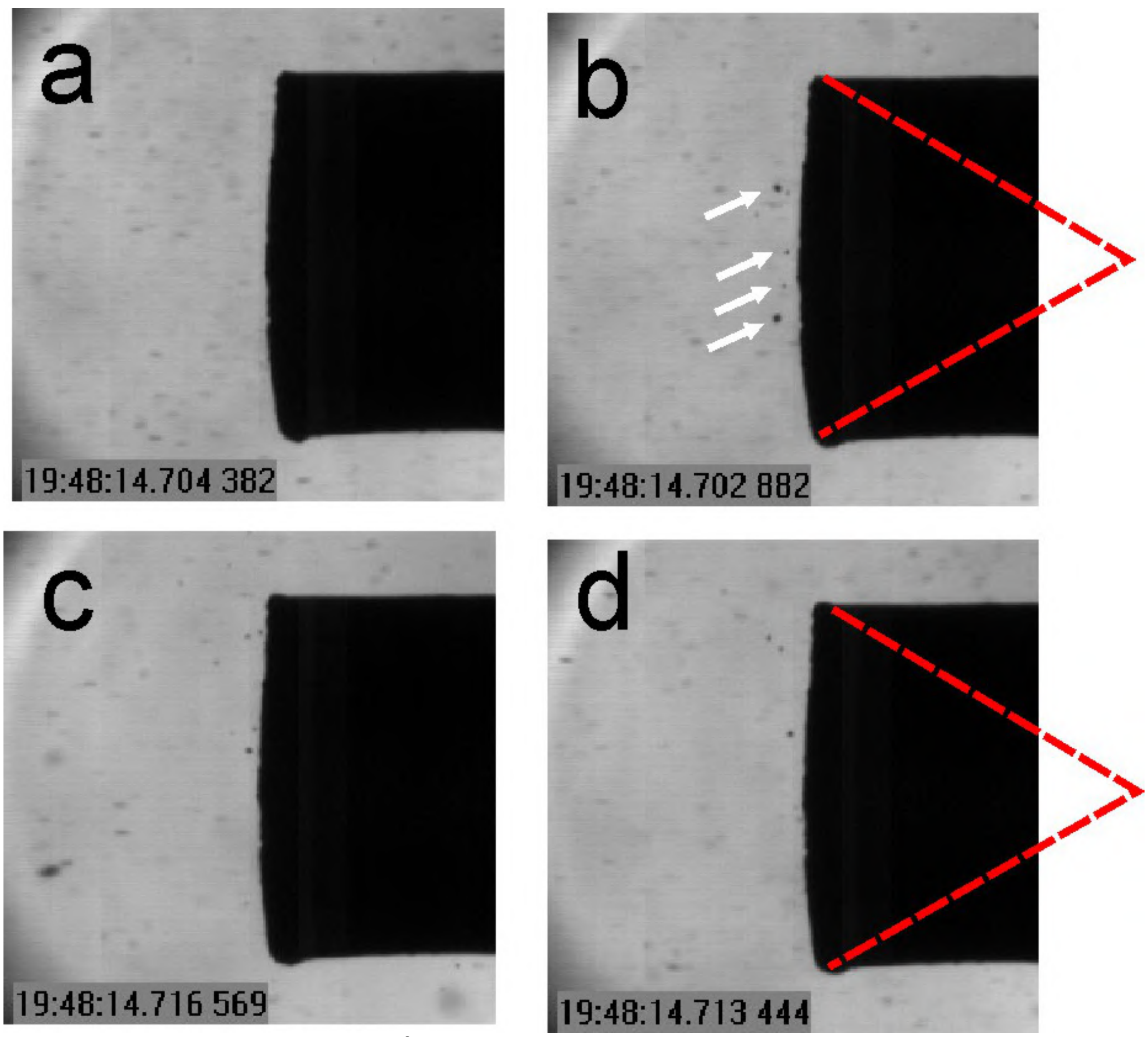

Figure 4. The images of the modified (60^o) Nevzorov TWC sensor cone taken with the high speed camera in the flow of ice particles in the Cox &Co wind tunnel. Arrows in (b) indicate the ice particles rebounded from the cone. The rebounded ice particles in (b,c,d) appear as quasi-circular images. Image frame in (a) does not contain rebounded particles. Red dashed lined in (b)&(d) indicate the shape of the hollow cone of the hot-wire sensor. Air

The fraction of bounced particles is expected to depend on the geometrical characteristics of the sensor. The ice particles striking the shallow cone with the wide angle are expected to experience just one bounce before they leave the sensor (Fig. 3a). However, ice particles entering a cone with sharper angle may bounce several times within the cone's surface, thus reducing the probability of exiting the sensor before their complete evaporation (Fig. 5a). To reduce the ice bouncing efficiency, a special 'deep' TWC sensor cone was constructed with a 60^o angle . This also results in a deeper catch volume requiring particles to bounce further into the airstream to exit the capture volume.

Figure 4 shows video frames of the modified deep TWC cone exposed to the flow if ice particles. The video in this sequence was shot with a different exposure rate that does not result in the particle streaks as in the case of Figs. 1a-d. The bounced particles in this video appear as quasi-spherical sharp images, whereas the ice particles in the undisturbed flow appear as elongated streaks due to their higher velocity. Bouncing ice particles are indicated by the arrows in Fig. 4b. It appeared that most video frames of the deep cone did not contain evidence of particles bouncing out of the capture cone (Fig. 4a).

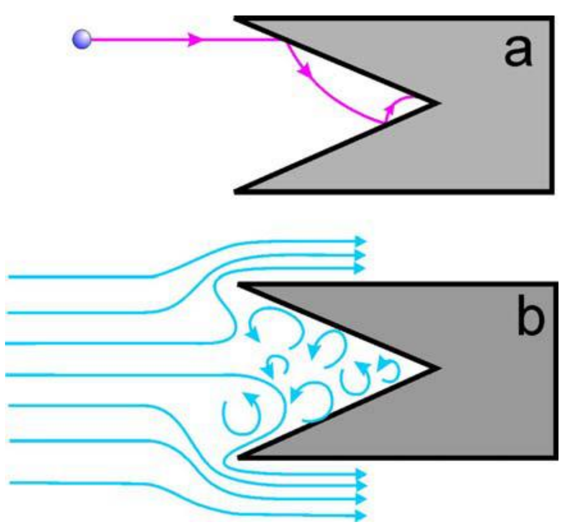

Figure 5. Conceptual diagrams of (a) elastic bouncing of ice particles in the deep TWC sensor cone; (b) vorticity inside the deep cone.

The high speed video gives a general idea whether ice particle bouncing exists or not. Nevertheless, the quantification of the underestimation of IWC due bouncing based on high speed video analysis does not seem plausible. In particular, the shattering of fragile ice particles results in a large number of small ice fragments that may not be visible on the image frames because of coarse pixel resolution and limited depth-of-field, and therefore can not be accounted for in an estimate of mass-loss. Furthermore, an assessment of the bouncing of any original particles smaller than the practical size limit of the camera also cannot be quantified.

3. In-situ comparisons of IWC techniques

In order to characterize the underestimate of IWC due to bouncing, the standard Nevzorov shallow (120^o) and new prototype deep (60^o) TWC sensor cones were mounted on the same sensor vane (Fig. 6a). This configuration allows for simultaneous measurements of IWC to be taken by both sensors. The Nevzorov probe along with a DMT CVI (Fig.6b) (Twohy et al. 1997) and PMS OAP-2DC/2DP were mounted on the NRC Convair 580. The measurements of IWC were obtained from glaciated clouds measured during the Canadian CloudSat Calipso Validation Project (C3VP) in Southern Ontario. The ice clouds were identified based on the measurements Rosemount Icing Detector and suite of cloud particle spectrometers as described in Korolev and Isaac (2006) Mixed phase and liquid clouds were not included in the following analysis.

The calculation of the mass of ice particles from their 2D imagery was performed based on the size-to-mass parameterization $M=aD^b$ (Mason 1957). The coefficients a=7.38 10^{-11} and b=1.9 were provided by Brown and Francis (1995), as originally determined by Locatelli and Hobbs for "aggregates of unrimed bullets, columns, and side planes". IWC was computed by the integrating the mass of ice particles over size distribution measured by the OAP-2DC & 2DP. In order to improve the statistical significance of the particle size distributions the OAP data were averaged over four second time intervals. The measurements of the Nevzorov probe and CVI were averaged over the same

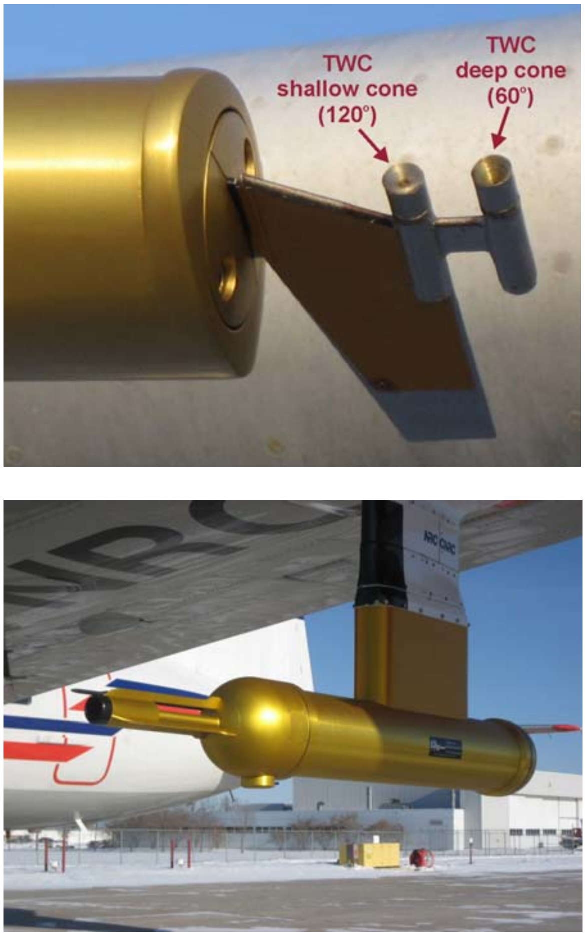

Figure 6. Modified Nevzorov sensor head; both shallow and deep sensors mounted on the same vane (top). DMT CVI probe installed on the NRC Convair-580.

time intervals in order to synchronize all measurements and enable the intercomparisons of all probes

The comparisons reveal that IWC measurements by four the IWC probes, are all linearly related to one another. However, the slope of the linear regression is a function of the size of ice particles. Fig. 7 shows scatterdiagrams of IWC measured by different pairs of instruments for the ice clouds with particle D_{max}<4mm. Fig. 8 shows the scatterdiagrams of IWC measured by the same pairs of probes but particle D_{max}>4mm. As seen from Fig. 7a, the IWC measured by the Nevzorov deep cone sensor is approximately three times higher than that measured by the shallow cone. The rest of the probes – the Nevzorov deep cone, CVI, and size-to-mass conversion – agree relatively well with one

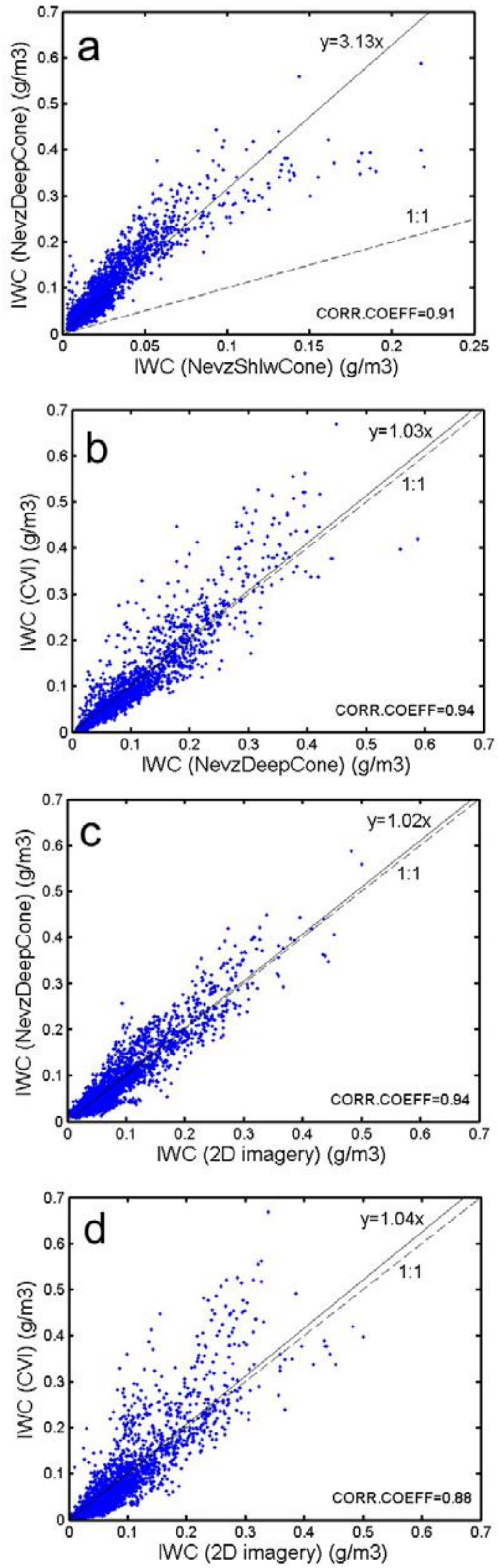

Figure 7. Scatterdiagrams of IWC measured by the Nevzorov deep and shallow TWC sensors, DMT CVI and OAP-2DC&2DP in ice clouds with D_{max}<4mm.

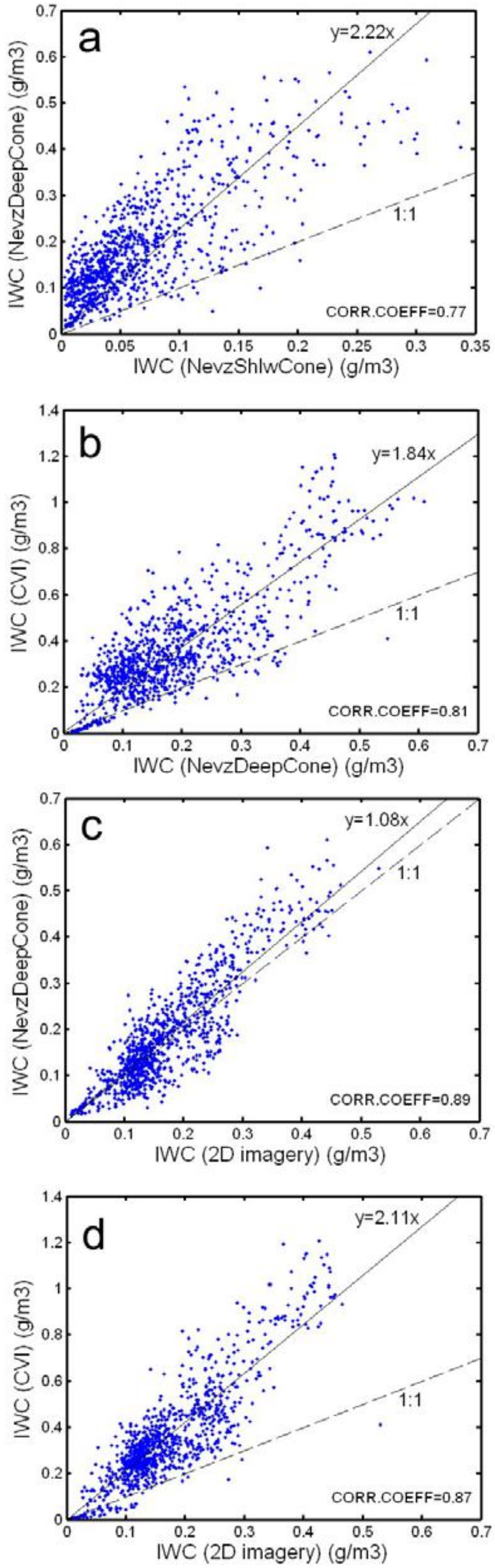

Figure 8. Scatterdiagrams of IWC measured by the Nevzorov deep and shallow TWC sensors, DMT CVI and OAP-2DC&2DP in ice clouds with D_{max}>4mm.

another for ice clouds with particle D_{max}<4mm. For the case of clouds with large ice particles (D_{max}>4mm) the correlation between the IWC measurements is degraded and the slope changes.

Fig. 9 shows the dependence of the slope versus the maximum size of ice particles in the measured size distributions. The obtained results suggest that the proportion between IWC measured by different instruments changes with the particle size. Interestingly, the IWC measured by the Nevzorov deep cone agrees reasonably well with that deduced from the OAP size distributions for the whole size range. Fig. 9 indicates that for small ice particle clouds with D_{max}<3mm, the Nevzorov deep cone gives very similar IWC values to the CVI. For large ice particles (D_{max}>10mm), the IWC measured by the CVI is than two times greater than that measured by the Nevzorov deep cone. At all particle sizes, the Nevzorov shallow cone measures a factor of 1.5 or more lower than the other probes, and is clearly the probe with the lowest readings.

It is worth mentioning that most ice clouds with large ice particles (D_{max}>4mm) were associated with temperatures -15<T<10C (Fig 10a). This temperature range corresponds to the dendrite ice growth regime. Dendrites typically unambiguous conclusion as to which instrument provides the most accurate result in this region

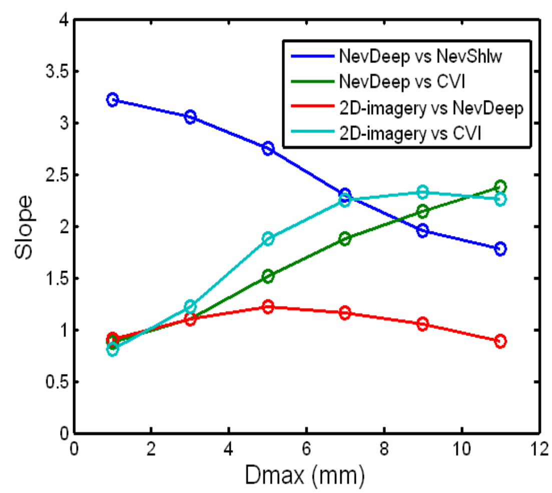

Figure 9. Slope of the linear fit versus D_{max} for pairs of different IWC instruments indicated in the legend. Each data point on the diagram was calculated for 2mm interval of D_{max}.

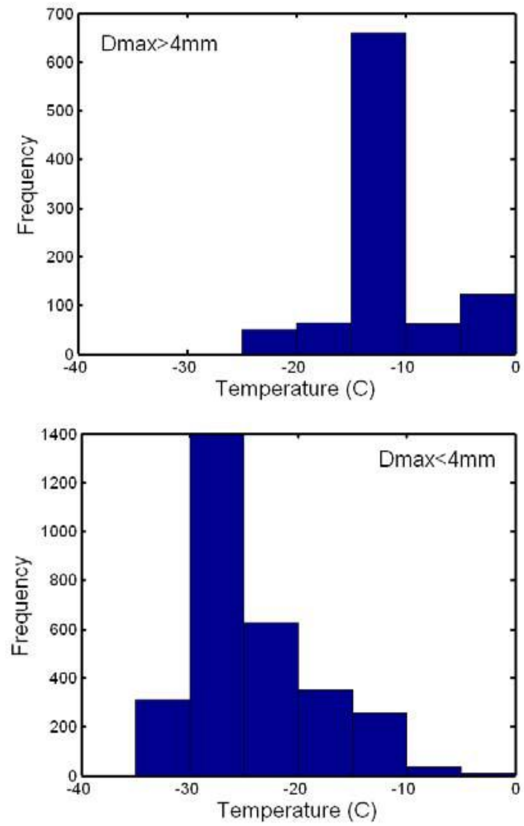

Figure 10. Frequency distribution of temperatures corresponding data presented in Fig.8 (ice particles D>4mm) (top) and that shown in Fig.7 (ice particles D<4mm) (bottom).

form large fluffy low density aggregates. The results of this study do not allow for an of maximum discrepancy. One may speculate that a potential underestimation of IWC by the Nevzorov deep cone sensor is caused by the vorticity in the cone, resulting in the sweeping away of miniscule particles resulting from dendrite shattering (Fig. 5b). On the other hand, one may hypothesize that an overestimation of IWC measured by the CVI may be caused by the shattering of dendrites due to their collision with the shroud, with a subsequent focusing of the inlet tube.

4. Conclusions

The data from this study supports the following conclusions:

1. IWC measurement taken by the new prototype Nevzorov deep cone, DMT CVI and IWC calculated from OAP particle size spectra agree well for ice clouds with ice particles D_{max}<4mm. This agreement suggests that all three techniques may provide reasonably accurate IWC measurements for small ice particles (D_{max}<4mm). When larger ice particles are present, the CVI measures higher IWC values than both the Nevzorov deep cone and OAP. Interestingly, IWC measured by the Nevzorov deep cone and that estimated by applying mass-diameter relationships to OAP imagery are approximately equal throughout the entire range of ice particle sizes.
2. For ice particle spectra with D_{max}<4mm, the IWC measured by the standard Nevzorov shallow cone is approximately 3±0.2 times lower than that measured by the Nevzorov deep cone and CVI. Assuming that the close agreement between the CVI and the deep cone indicates that both are measuring approximately correctly, this allows for corrections of IWC data sets collected with the Nevzorov shallow cone TWC sensor during previous flight campaigns, in cases where large particles are not present. The correction must take into account any liquid fraction in the cloud, which will be measured at a much higher efficiency.
3. The obtained results do not allow for an unambiguous conclusion about the accuracy of the IWC measurement devices when large particles such as large dendrites and aggregated ice particles are present, and when large discrepancies between the different sensors are observed. More studies are required to resolve this problem.

Acknowledgements: Many thanks to Vincent Reich from NASA Glenn for providing the high speed video equipment during the Cox wind tunnel tests and the in-situ sampling using the NRC Convair-580. The aircraft data were obtained using the NRC Convair-580 and the scientific and technical efforts of many NRC and Environment Canada (EC) staff. The Canadian Space Agency (CSA) provided funding for the C3VP aircraft project. Besides their host institutions of Environment Canada and NASA Glenn, the authors would also like to acknowledge the financial contributions of NRC, Transport Canada and the FAA.

References

Brown, P. R. A., 1993: Measurements of the ice water content in cirrus using an evaporative technique. *J. Atmos. Oceanic Technol.,* **2**, 340-352.

Brown, P.R.A., and P.N. Francis, 1995: Improved Measurements of the Ice Water Content in Cirrus Using a Total-Water Probe. *J. Atmos. Oceanic Technol.* **12**, 410–414.

Emery, E., Miller, D., Plaskon, S., Strapp, J.W., And Lilie, L.E., 2004: "Ice particle impact on cloud water content Instrumentation," *42nd AIAA Aerospace Sciences Meeting and Exhibit*, Jan. 2004, AIAA-2004-0731.

Isaac, G.A., A.V. Korolev, J.W. Strapp, S.G. Cober, F.S. Boudala, D. Marcotte and V.L. Reich, 2006: Assessing the collection efficiency of natural cloud particles impacting the Nevzorov total water content probe. AIAA 44th Aerospace Sciences Meeting and Exhibit, Reno, Nevada. 9-12 January 2006. AIAA-2006-1221..

Locatelli, I.D., and P.V. Hobbs, 1974: Fall speed and masses of solid precipitation particles. *J. Geoph. Res.*, **79**, 2185-2179

Mason, B. J., 1957: *The Physics of Clouds*. Oxford University Press, 671 pp.

Nevzorov, A. N., 1980: Aircraft cloud water content meter. *Comm. a la 8eme conf int. sur la phys. des nuages, Clermont-Ferrand, France*, v. II, 701-703.

Nevzorov, A. N., 1983: Aircraft cloud water content meter. *Transactions of Central Aerological Observatory (Trudi TsAO)*, **147**, 19-26 (in Russian).

Nicholls, S., J. Leighton, and R. Barker, 1990: A New Fast Response Instrument for Measuring Total Water Content from Aircraft *J. Atmos. Oceanic Technol.*, **7**, 706–718

Knollenberg, R. G. 1981 Techniques for probing cloud microstructure. In: *Clouds, their formation, Optical properties, and Effects*, P. V Hobbs, A. Deepak, Eds. Academic Press, 495 pp.

Korolev, A.V., Strapp, J.W. Isaac, G.A. and Nevzorov, A.N. 1998: The Nevzorov airborne hot-wire LWC-TWC probe: principle of operation and performance characteristics. *J. Atmos. Oceanic Technol.* **15**, 1495-1510.

Korolev, A. V., and G. A. Isaac, 2006: Relative humidity in liquid, mixed-phase, and ice clouds. *J. Atmos. Sci*., **63,** 2865-2880

Kyle, T.G., 1975: The measurement of of water content by an evaporator, *J. Appl. Meteor*., **14**, 327-332.

Ruskin, A.L., 1976: Liquid water content devices. *Atmospheric Technology*, N.8, 38-42

Strapp, J.W., Lilie, L.E., Emery, E. and D. Miller, 2005: Preliminary Comparison of Ice Water Content as Measured by Hot Wire Instruments of Varying Configuration. *43rd AIAA Aerospace Sciences Meeting*, Reno, NV, 11-13 January 2005**,** AIAA-2005-0860.

Strapp, J.W., J. MacLeod, and L.E. Lilie, 2008: Calibration of Ice Water Content in a Wind Tunnel / Engine Test Cell Facility. 15th Inter. Conf. On Clouds and Precipitation, Cancun, Mexico, 7-11 July 2008.

Twohy, C. H., A. J. Schanot, and W. A. Cooper, 1997: Measurement of condensed water content in liquid and ice clouds using an airborne counterflow virtual impactor. *J. Atmos.Oceanic Technol.*, **14,** 197–202.

NEW AIRBORNE CLOUD EXTINCTION PROBE

Alexei Korolev
Environment Canada, Toronto Canada

1. INTRODUCTION

The extinction coefficient is an important parameter in characterizing bulk microphysics properties of clouds. Knowledge of the extinction coefficient is of crucial importance for radiation transfer calculations in weather predictions and climate models, as well as validation of remote sensing and satellite retrievals (e.g. Barker et al. 2008).

Early attempts to use airborne extinctiometers for measurements of visibility in clouds go back to works of Kampe (1950) and Weickmann and Kampe (1953). The first airborne extinctiometer utilized the transmissiometric method. It consisted of incandescent lamp, collimator and a photocell for measuring the light intensity. The source of light separated by a few meters from the photocell were mounted on the wing. Zabrodsky (1957) built an airborne a double pass transmissiometer where light traveled to a retroreflector and back, and then it was measured by a photodetector. Nevzorov and Shugaev (1972, 1974) built an advanced version of this transmissiometer with improved stability and high sensitivity. This was a successful design which allowed for the collection of a large data set on the extinction coefficient in different types of clouds (Kosarev et al, 1976; Korolev et al. 2001). King and Handsworth (1979) built a single pass transmissiometer with an ultraviolet source of light generated by a germicidal lamp. Zmarzly and Lawson (2000) designed a multi-pass and multi-wavelength Cloud Extinctiometer. Gerber et al (2000) built a Cloud Integrated Nephelometer where the extinction coefficient was calculated from an arrangement of four Lambertian sensors, two of which had a cosine masks.

Author's address: Alexei Korolev, Environment Canada, 4905 Dufferin Street, Toronto, Ontario, M3H5T4 Canada, e-mail: alexei.korolev@ec.gc.ca

In many studies the extinction coefficient of clouds was estimated from composite size distributions measured by several cloud spectrometers. Earlier measurements (Korolev et al. 1999) showed a good agreement between the extinction coefficient measured by a cloud transmissiometer and that derived from the PMS FSSP droplet size spectra. However calculations of the extinction coefficient from particle size distributions in ice and mixed phase clouds is subject to potentially large errors due to uncertainties related to the size-to-area conversion technique, shattering issues and limited accuracy in measurements of concentration and sizes of ice particles smaller than approximately 100μm.

Despite great significance of the extinction coefficient on our knowledge of the radiation transfer in clouds and the Earth's climate in general, probes that are capable of direct measurements of the extinction coefficient have not become a part of conventional airborne microphysical instrumentation. The effort to fill this gap has been undertaken by Cloud Physics Research and the Severe Weather Section of Environment Canada. This paper presents a description of the newly designed Airborne Cloud Extinction Probe. As well, some of the airborne measurement results of the extinction coefficient of clouds are discussed.

2. DESCRIPTION OF THE EXTINCTION PROBE

The Cloud Extinction probe utilizes the transmissiometric method. The principle of operation is based on the measurements of the attenuation of visible light between the emitter and receiver. This method enables the calculation of the extinction coefficient from first principles based on the Beer-Bouguer law. The Extinction Probe consists of an optical unit that combines a transmitter and receiver as well as a retroreflector.

Figure 1 shows a general schematic of the optical unit. A collimated light beam is generated by an optical system consisting from the superbright LED with the wavelength λ=0.635μm (1), diffuser (2), condenser (3), pinhole (4), and objective (5). The beam travels from the optical unit to the retroreflector (6), and then returns the same distance back to the optical unit. Then after passing though the objective and beam-splitter (7) its intensity is measured by a photodetector (8). The optical chopper (9) modulates the light beam and controls turning on and off the LED with the help of the optocouple (10). The optical chopper consists of a sequence of holes, dark areas and mirrors glued on its surface. During the first half of the period when the hole is opened, the LED is on, and the photodetector measures the intensity of transmitted light plus the background intensity (I_{tot}). During the second half of the period, when the hole is opened, the LED is off, and the photodetector measures the intensity of the background light (I_{bkg}). During the first half of the period, when the hole is closed, the LED is on, and the light is reflected from the mirrored surface. After passing though a beam-splitter the reflected light is measured by the photodetector (I_{norm}). This signal characterizes the intensity of the LED, and is used to normalize all other measured signals. During the second half of the period, when the chopper hole is closed, the LED is on and the beam hits the blackened surface of the chopper. In this case, the photodetector measures the signal (I_{int}) related to the light scattered inside the optical unit due to reflection from the optical surfaces and the different parts inside the probe's housing. The advantage of such a scheme is that it allows measurements of the intensities of the LED, background and attenuated light with the same photodetector. Utilizing of the above scheme minimizes the effect of changes of the photodetector sensitivity during flight (e.g. caused by temperature drift) on the measurements of the extinction coefficient.

The optical scheme was designed to produce a highly uniform collimated beam (Fig,2). The inhomogeneity of the light intensity across the beam does not exceed 1%. This minimizes the effect of vibration and mutual motion the optical unit and retroreflector with respect to each other during the flight operation. A similar approach has been used by Nevzorov and Shugaev (1974). The size of the retroreflector was chosen so that its

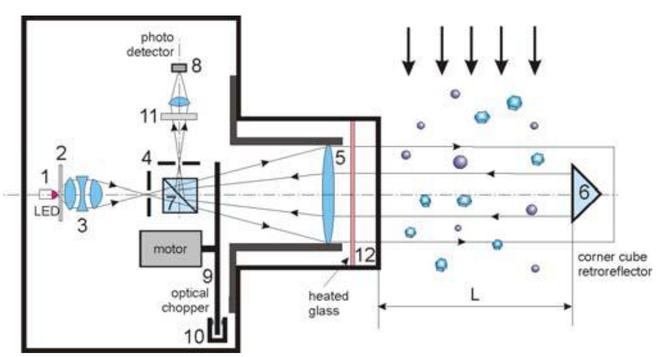

Figure 1. Schematic diagram of the Cloud Extinction Probe: (1) LED 0,635μm; (2) diffuser; (3) condenser; (4) pinhole; (5) objective; (6) cone cube retroreflector; (7) beamsplitter; (8) photodetector; (9) optical chopper; (10) optocouple; (11) filter; (12) front heated glass.

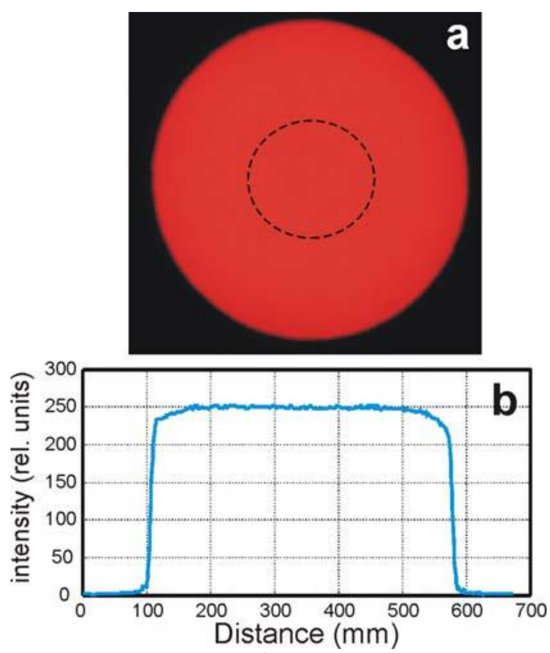

Figure 2. Distribution of the light intensity in the beam in the Cloud Extinction Probe. (a) beam cross-section. The dashed lines show the relative size of the retroreflector; (b) distribution of the intensity along the beam diameter

displacement from the center of the beam in each direction at the distance of approximately 1cm does not affect the output signal. The dashed lines in the center of the beam cross-section in Fig. 2a show the relative size of the retroreflector. During the flight the retroreflector always stayed inside the beam within the light intensity homogeneous area, whereas the reflected beam always stayed within the objective. This provides a stable output signal non-sensitive to the aircraft vibration.

The Extinction Probe was designed to operate in all weather conditions. The optics of the probe are well heated to prevent fogging, on impact with liquid droplets and during rapid aircraft descent at vertical speed higher 5m/s. The environment inside the optical unit is temperature controlled, so that the instrument can operate at air temperatures as low as -60°C. Based on the flight tests described in section 3, the threshold sensitivity of the probe was found to be approximately 0.2 km^{-1}. The upper limit of the measured extinction coefficient is estimated to be no less than 200 km^{-1}. The picture of the Extinction Probe is presented in Fig.3.

The Cloud Extinction Probe was installed on the National Research Council (NRC) Convair 580. The optical unit was mounted inside the wing tip canister and the retroreflector inside a hemispherical cap at the rear side of a PMS probe canister (Fig.4). The distance between the optical unit and the retroreflector was L=2.35m.

Figure 3. Cloud Extinction Probe: optical unit (top); control box (bottom); retroreflector (right).

The sample area of the probe is defined by the length of the beam (L) and the diameter of the reflector (d=25mm) and is calculated as $S=Ld$. For the installation on the Convair-580 $S\approx$0.06m^2. At a typical airspeed of 100m/s, the corresponding cloud volume sampling rate is approximately 6m^3/s. Assuming a decent sensitivity, the above sampling rate allows measurements of a statistically significant extinction coefficient of ice particles with concentration few per cubic meter.

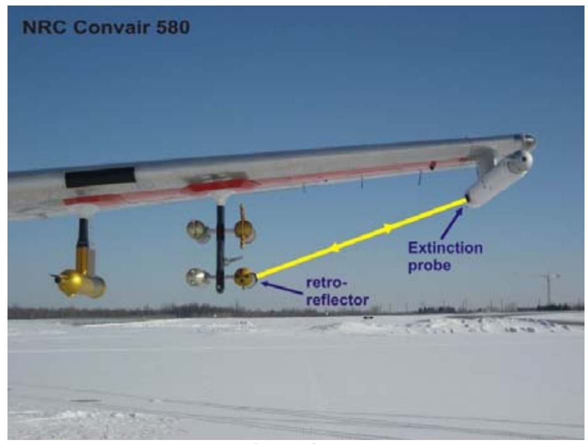

Figure 4. Installation of the Cloud Extinction Probe on the NRC Convair 580. The yellow line indicates the position of the beam under the wing.

3. CALCULATION OF THE EXTINCTION COEFFICIENT

The extinction coefficient measured by the Extinction Probe was calculated based on the Beer-Bouguer law as

$$\beta_{CEP} = -\frac{1}{2L}\ln\frac{I}{I_0} \qquad (1)$$

Here I and I_0 are the output signals which characterize the radiant fluxes transmitted in clouds and in clear sky, respectively. The intensity of the attenuated signal was calculated as $I=I_{tot}-I_{bkg}-I_{int}$; I_0 was determined the same as I but in a cloud free atmosphere. The signals I_{tot}, I_{bkg} and I_{int} were normalized on the current values of I_{norm}.

The Extinction Probe provides measurements of the extinction coefficient in any type of clouds regardless their phase composition, i.e. liquid, ice and mixed phase. Since there are no calibrating standards for the attenuation of light by dispersed media, we attempted to compare the extinction coefficient measured by the Extinction Probe with that deduced from the PMS Forward Scattering Spectrometer Probe (FSSP) cloud droplet spectra in liquid clouds and from the PMS Optical Array Probes (OAP) 2DC and 2DP particle images in ice clouds.

In liquid clouds, the extinction coefficient was calculated from the FSSP droplet size distribution measured in fifteen size bins.

$$\beta_{FSSP} = \frac{\pi Q}{4}\sum_{j=1}^{15} n_j D_j^2 \qquad (2)$$

Here n_i, D_i are the concentration and diameter of droplets in the FSSP i-th size bin; Q is the extinction efficiency. Since the size of the FSSP measured droplets $D>>\lambda$, then to a good accuracy it can be assumed $Q \approx 2$.

In ice clouds the extinction coefficient was calculated from the OAP imagery. Optical Array Probes provide shadowgraphs of cloud particles, which pass though the sample area of the probe (Fig.5a). In general, the OAP can be considered as an extinctiometer, which instead of measuring of the attenuation of light integrated over the whole beam, measures local attenuation associated with the discrete binary images with the shadow areas A_j (Fig.5b). Therefore, the extinction coefficient can be calculated through the integration of the area shadowed by all particles $\sum A_j$ as,

$$\beta_{OAP} = \frac{Q}{LA_0}\sum_j A_j \qquad (3)$$

Here L is the distance between the OAP arms (Fig. 5b); A_0 is the total area covered by the probe's laser beam having the width W and moving at speed U during time Δt, i.e. $A_0=WU\Delta t$. Substituting this expression into Eq.3 yields

$$\beta_{OAP} = \frac{Q}{LWU\Delta t}\sum_j A_j \qquad (4)$$

In this approach the transmittance $T=I/I_0$ in Eq.1 is approximated by the ratio $\sum A_j / A_0$, i.e. $I/I_0 \cong \sum A_j / A_0$.

The direct area calculation (DAC) technique of estimation of the extinction coefficient is based on the following assumptions regarding the OAP imagery: (1) the depth-of-field and the sample area width do not depend on the particle size, i.e. the sample area of the probe stays constant for all particles; (2) the shadow images represent geometrical shadows of cloud particles and the diffraction effects are neglected.

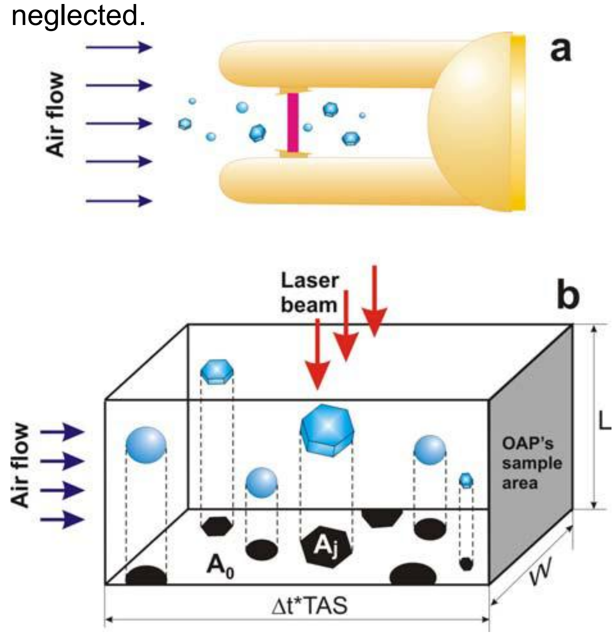

Figure 5. Conceptual diagram of calculation of the extinction coefficient from the OAP-2D imagery.

The assumption (1) is satisfied for particles with $D \geq 125\mu$m for OAP-2DC and for particles with $D \geq 400\mu$m for OAP-2DP, i.e. when the depth-of-field for these particles is larger than the distance between the arms. Korolev et al (1998) showed that the projected image area experiences several oscillations, when a particle moves from the object plane to the edge of the depth-of-field. The effect of the particle distance on the projected area decreases with the increase of particle size. In other words the DAC technique is expected to work better for larger particles than for the small ones. It should be mentioned that calculation of the extinction coefficient from OAP-2DP/2DP imagery in ice clouds with large concentration of ice particles

(D<100μm) may result in significant underestimation of the extinction coefficient.

The DAC method gives more accurate estimation of the extinction coefficient, as compared to the alternative method based on the size-to-area conversion (STAC) $A=aD^b$. The sources inaccuracy for the size-to-area conversion method are related to the uncertainty in the coefficients a and b for different particle habits. The size-to-area conversion also cannot be applied to partial images, which significantly limits the use of STAC method for particles with $D>W$.

4. RESULTS OF MEASUREMENTS

In this section we demonstrate the performance of the Cloud Extinction Probe in liquid, ice and mixed phase clouds and compare the results of its measurements with the extinction coefficient calculated from the size distribution measured by the PMS FSSP, OAP-2DC and 2DP.

Liquid clouds

Figure 6 shows the results of the measurements of the extinction coefficient during flights through strato-stratocumulus. The high frequency of cycling of the Rosemount Ice Detector (RICE) signal (Fig.6c) indicates that the cloud contains supercooled liquid water. As seen from Fig.6a the extinction coefficient measured by Extinction Probe and that calculated from the FSSP varied from approximately 20 to 120km^{-1}. The studied cloud layer also contained some ice particles. However, the estimations from the OAP-2DC/2DP imagery suggest that the extinction coefficient associated with ice is lower than 1km^{-1} for the most of the cloud. This value is much less than the extinction coefficient associated with liquid. Therefore, this cloud layer can be considered as conditionally liquid and the effect of ice particles on the extinction coefficient measured by the Extinction Probe and FSSP can be neglected.

Figure 7 shows the scatter diagram with the comparisons between Extinction Probe and FSSP measurements of the extinction coefficient. As seen from Fig.7 in liquid clouds the extinction coefficients measured by the Extinction Probe and FSSP agree reasonably well with each other.

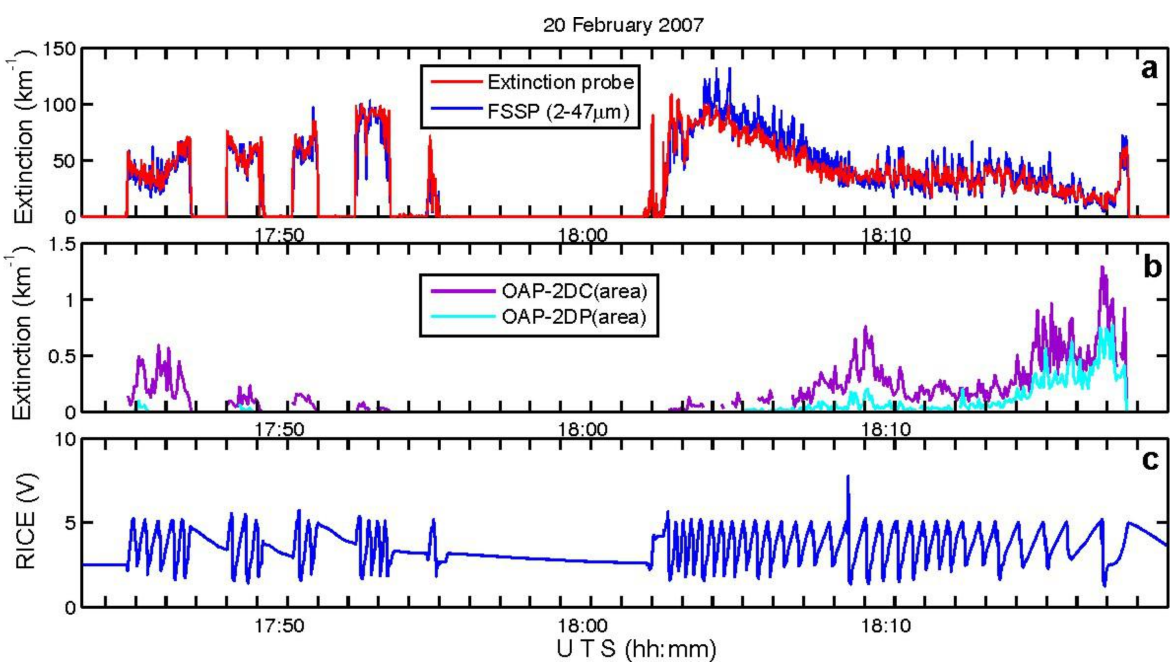

Figure 6. (a) Comparison of the extinction coefficient measured by the Cloud Extinction Probe and FSSP-100 (3-47μm), (b) Extinction coefficient deduced from the measurements of OAP-2DC and 2DP; (c) Rosemount Icing Detector signal. The oscillating RICE signal indicates on presence of supercooled liquid. Measurements were conducted in St-Sc, 1500<H<1800m; T=-10C, Southern Ontario.

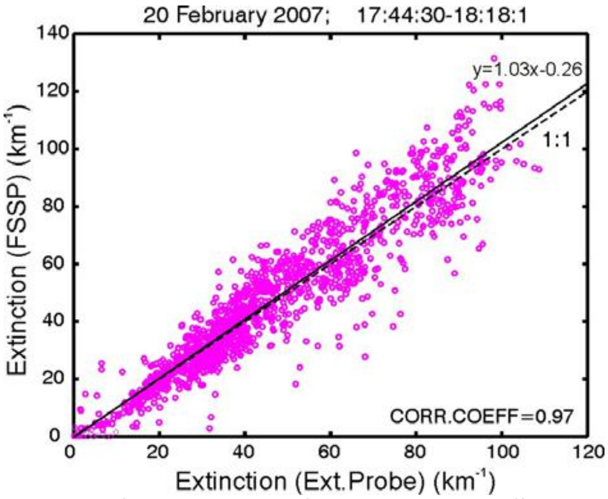

Figure 7. Scatterdiagram of the extinction coefficient measured by the Cloud Extinction Probe and that measured by FSSP-100 for the cloud segment shown in Fig.6a.

Ice clouds

Figure 8 shows spatial variations of the extinction coefficient during a flight beneath a precipitating altocumulus. The continuous decrease of the RICE signal in Fig.8b indicates on the absence of liquid along the flight line (Mazin et al. 2001), which helps identify this cloud as glaciated. The images measured by the OAP-2DC shown in Fig.9 suggests that most ice particles were spatial dendrites having irregular shape with maximum size varied from 6mm at the beginning of cloud and up to 10mm at the end.

The scatterdiagrams in Fig.10 show good agreement between the extinction coefficient measured by the Extinction Probe and that derived from the OAP-2DC/2DP. The OAP extinction coefficient was calculated using Eq.4. The agreement between the Extinction Probe and OAP suggests that the major input to the extinction coefficient is due to particles larger than approximately 200μm. This indicates absence of a high concentration of small ice particles in this cloud, which can noticeably affect the extinction coefficient.

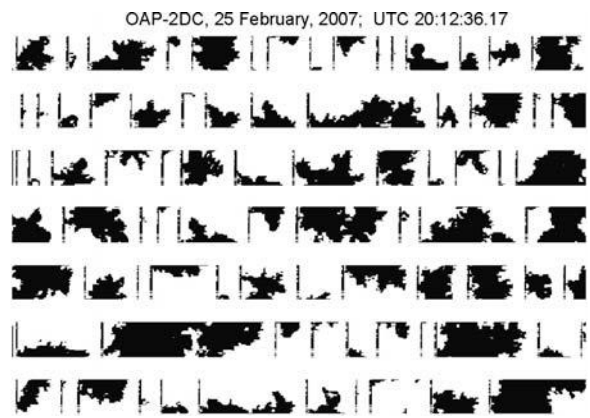

Figure 9. OAP-2DC imagery of ice particles from the cloud shown in Fig.8.

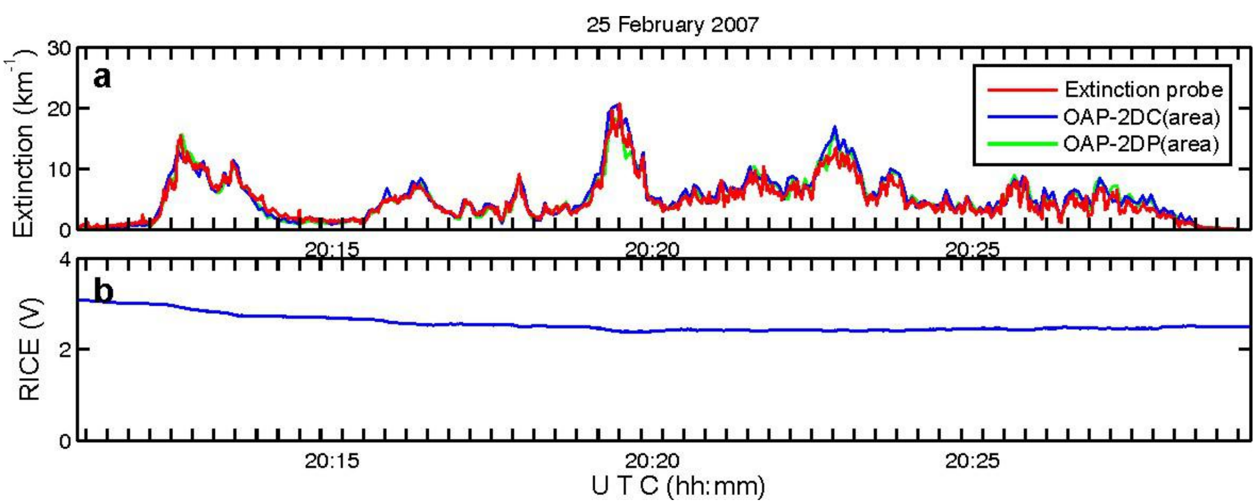

Figure 8. Spatial changes of the extinction coefficient measured by the Cloud Extinction Probe and that deduced from the cloud particle image areas measured by OAP-2DC and OAP-2DP (a). Rosemount Icing Cylinder signal (b) during traverse of precipitating region of altocumulus, 4500<H<5500m, -20<T<-15C, Southern Ontario.

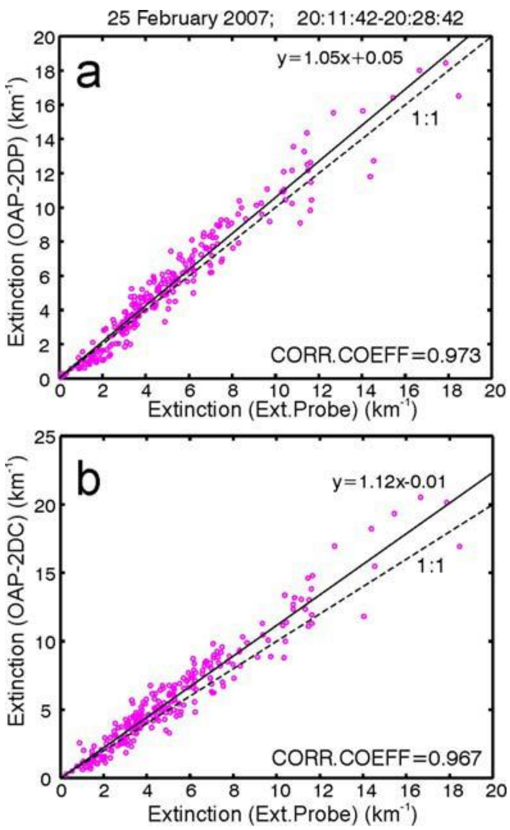

Figure 10. Scatterdiagram of the extinction coefficient measured by the Cloud Extinction Probe and that calculated from cloud particle images areas measured by OAP-2DC (a) and OAP-2DP (b) for the cloud segment shown in Fig.8.

Mixed phase clouds

Joint analysis of the extinction coefficient measured by the Extinction Probe and OAPs, in some cases allows for the separation of the extinction coefficients associated with liquid and ice in mixed phase clouds. Figure 11 shows a spatial variation of the extinction coefficient during descent through a precipitating stratocumulus. The airplane traversed through the topmost cloud layer, which was at 1500m at 13:48 (leftmost side of the Fig.11a) and then leveled flight at 1100m at 13:51. The cloud had liquid top with no ice particles. However, the ice particles began to appear at lower levels and then amount of ice increased during a horizontal flight from approximately 13:52 to 14:00. During the leveled flight, the Convair 580 traversed though three mixed phase zones highlighted in grey in Fig.11. The presence of liquid is indicated by the oscillations (1st zone) or gradual increase (2nd and 3rd zones) of the RICE signal. In mixed phase cloud regions, the extinction coefficient measured by the Extinction Probe is larger than that calculated from the OAPs. Since OAP-2DC is insensitive to cloud droplets with D<30μm, and assuming that cloud particles with D>50μm are all ice, this assumption allows for the estimation of the extinction coefficient of ice particles as $\beta_{ice} \approx \beta_{AOP}$. Therefore, the extinction coefficient for liquid droplets can be estimated as

$$\beta_{liq} = \beta_{CEP} - \beta_{OAP} \qquad (5)$$

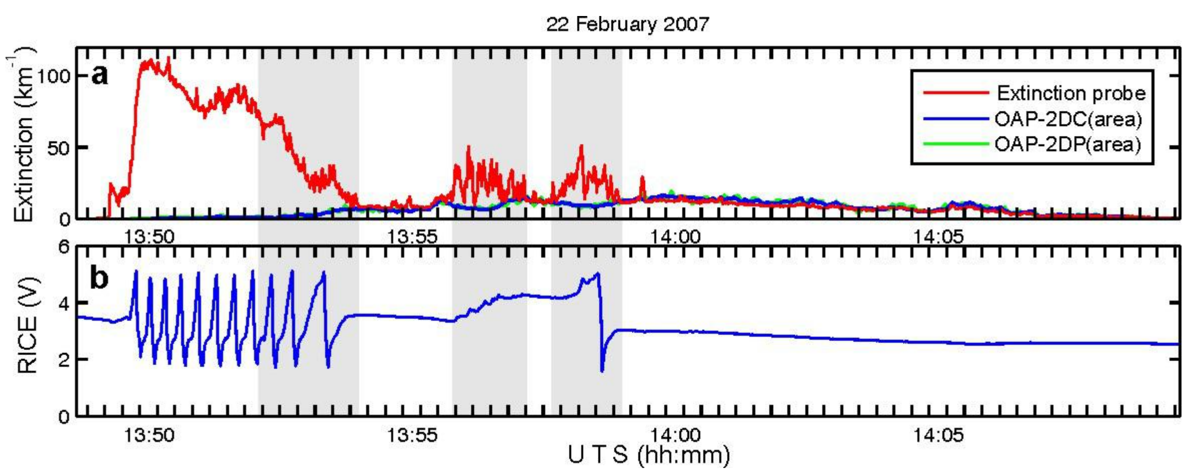

Figure 11. Spatial changes of the extinction coefficient measured by the Cloud Extinction Probe and that deduced from the cloud particle image areas measured by OAP-2DC and OAP-2DP (a) and the Rosemount Icing Cylinder signal (b) during traverse of stratocumulus, 1100m<H<1800m, -6<T<-2C, Southern Ontario. Highlighted grey areas indicate mixed phase cloud regions.

It should be noted that the above approach of separation of the extinction coefficient for liquid and ice can be applied only for mixed phase clouds with a relatively low concentration of small ice particles with D<50μm. Particles of this size are invisible to the OAP-2DC/2DP, and if such particles are present in significant numbers, β_{ice} will be underestimated from β_{AOP}.

5. CONCLUSION

A new airborne Cloud Extinction Probe utilizing the transmissiometric technique has been designed by Environment Canada and tested on the NRC Convair 580 airplane. The Extinction Probe demonstrated the capability to measure the extinction coefficient in ice, liquid and mixed phase clouds. The threshold sensitivity is estimated at 0.2 km^{-1}. The extinction coefficient measured by the Extinction Probe agrees well with that calculated from the FSSP droplet spectra in liquid clouds and that deduced from the OAP-2DC/2DP images in ice clouds.

The advantages of the Extinction Probe are its large sample area (~60cm^2) and its measurements are practically not contaminated by shattered ice particles. Ice shattering and droplet splashing by sampling inlets is a serious problem for most optical cloud microphysical instruments. The Cloud Extinction Probe can be used to identify and characterize shattering and splashing efficiency of different cloud particle size spectrometers.

Acknowledgements: The author expresses gratitude to Vladimir Torgashev for his role in the mechanical design of the Cloud Extinction Probe. Special thanks to Rob Reed of Environment Canada for his support of the electronic functionality of the probe during the C3VP flight campaign, and to the NRC staff for the help for the installation of the Extinction Probe on the Convair 580.

BIBLIOGRAPHY

Barker, H. W., A. V. Korolev, D. R. Hudak, J. W. Strapp, and K. B. Strawbridge A. 2008: Comparison between CloudSat and Aircraft Data for a Multi-layer, Mixed-Phase Cloud System during C3VP. *J. Geophys. Res.* (submitted)

Gerber, H., Y. Takano,T. J. Garrett and P. V. Hobbs, 2000: Nephelometer Measurements of the Asymmetry Parameter, Volume Extinction Coefficient, and Backscatter Ratio in Arctic Clouds. *J. Atmos. Sci.,* **57**, 3021-3034

Kampe, aufm, H.J., 1950: Visibility and Liquid Water in Clouds and in the Free Atmosphere. *J. Atmos. Sci.,* **7**, 54-57

King, W. D., and R. J. Handsworth, Total droplet concentration and average droplet sizes from simultaneous liquid water content and extinction measurements, *J. Appl. Meteorol.*, *18,* 940-944, 1979.

Korolev A. V., J. W. Strapp, and G. A. Isaac, 1998: Evaluation of accuracy of PMS Optical Array Probes. *J. Atmos. Oceanic Techn.*, **15**, 708-720.

Korolev A. V., J. W. Strapp, and G. A. Isaac, A. N. Nevzorov, 1999: In situ measurements of effective diameter and effective droplet number concentration. *J.Geoph.Res.*, **27**, 3993-4003.

Korolev, A.V., G. Isaac, I. Mazin and H. Barker, 2001: Microphysical properties of continental stratiform clouds. *Quart. J. Roy. Meteor. Soc.,* **127**, 2117-2151

Kosarev, A. L., I. P. Mazin, A. N. Nevzorov, and V. F. Shugaev, 1976: Optical density of clouds. *Trans. Cent. Aerol. Obs.*, *124,* 44-110.

Mazin, I.P., A.V. Korolev, A. Heymsfield, G.A. Isaac, S.G. Cober, 2001: Thermodynamics of Icing Cylinder for Measurements of Liquid Water Content in Supercooled Clouds. *J. Atmos. Oceanic Techn.,* **18**, 543–558

Nevzorov A. N., and V. F. Shugaev, 1974: Aircraft cloud extinction meter. *Trans. of Cent. Aerol. Obs.*, **106,** 3-10.

Nevzorov A. N., and V. F. Shugaev, 1972: The use of integral parameters for study of cloud microstructure (in Russian), *Trans. Cent. Aerol. Obs.*, *101***,** 32-47.

Ruskin, R.R., 1974: The measurements of cloud elements: the use of transmission and scattering techniques to measure ice and water. *Proc. Symp. Measuremen of Cloud Elements*, W.D. Scott, Ed. NOAA, Tech Memo ERL WMPO-19, 117

Zabrodsky, G.M., 1957: Measurements and some results of study of visibility in clouds. in "*Study of clouds, precipitation and cloud electrification*" Gidrometeizdat, 131-134.

Zmarzly, P.M. and R.P. Lawson, 2000: An Optical Extinctiometer for Cloud Radiation Measurements and Planetary Exploration. Final Report submitted to NASA Goddard Space Flight Center in fulfillment of Contract NAS5-98032, September, 2000, 131 pp. (available from http://www.specinc.com/publications/Extinctiometer_Report.pdf)

Weickmann, H. K. and H. J. aufm Kampe, 1953: Physical properties of cumulus clouds. *J. Atmos. Sci.,* **10**, 204-211

RAIN RATE RETRIEVAL USING THE 183-WSL ALGORITHM

Sante Laviola[1] and Vincenzo Levizzani[1]

[1] National Research Council – Institute of Atmospheric Sciences and Climate, Bologna, Italy

1. INTRODUCTION

One of the main open scientific challenges lasting since a few decades is the compelling need for a substantial improvement of techniques adopted to retrieve precipitation intensities and their duration in time. This is particularly pressing for those precipitation episodes that interest very small areas, where also light rains are often trigger disastrous flooding events. Note that an accurate knowledge of the terrain features such as morphological and orographic aspects is crucial.

In this context, satellite sensors with their large number of spectral bands and their wide spatial coverage can be easily employed for a global research and monitoring strategy. In particular, the increasing spatial resolutions of the new passive microwave (PMW) sensors and the constantly increasing number of orbiting platforms are providing data at an unprecedented temporal frequency.

Usually, PMW estimation algorithms for the retrieval of rain rates or of other atmospheric parameters (e.g., Grody et al. 2000, Ferraro et al. 2005) are based on two different approaches: scattering and absorption. Scattering methods infer rain intensities by exploiting the brightness temperature depression due to the frozen hydrometeors located in the upper part of the cloud. The scattering signal (or index) is strictly linked to the probability of melting ice crystals into the clouds and their conversion into rain droplets. As demonstrated by Bennartz et al. (2002) the measure of the scattering signature can be efficiently used to select and classify rain rate intensities distinguishing conditions ranging from no-rain to heavy rain. The quantitative comparison with co-located radar data shows the robustness of the technique in classifying heavier precipitation characteristic of a convective system, where the amount of scatterers is relatively large.

The second approach is founded on the water vapor properties to absorb and successively emit the radiation centered on specific absorption bands (Grody 1991, Staelin et al. 1999, 2000). As to this method, the retrieval at low and high frequencies must be considered differently. If the retrieval is carried out at low frequencies, i.e. around the water vapor band at 22.235 GHz, the scattering is weak and the absorption dominates the extinction. Nevertheless, Wang et al. (1989) note that this absorption band provides only enough sensitivity to measure the total column water vapor and the high emissivity background masks the atmospheric contribution over land. On the other hand, at higher frequencies the scattering effect increases also into the strong absorption bands such as at 183.31 GHz. The presence of cold clouds can depress the brightness temperature particularly for the frequencies located farther from the center of the absorption line (Greenwald et al. 2002, Burns et al. 1997).

In this work, we report the results of two new fast algorithms over land and ocean to estimate rain rates using PMW opaque frequencies of the Advanced Microwave Sounding Unit module B (AMSU-B) of the National Oceanic and Atmospheric Administration (NOAA). Our choice of using these frequencies is mainly founded on considerations reported in section 2 and other studies not reported here. In section 3

Corresponding author address: Sante Laviola, CNR-ISAC, via Gobetti 101, I-40129 Bologna, Italy, e-mail: s.laviola@isac.cnr.it

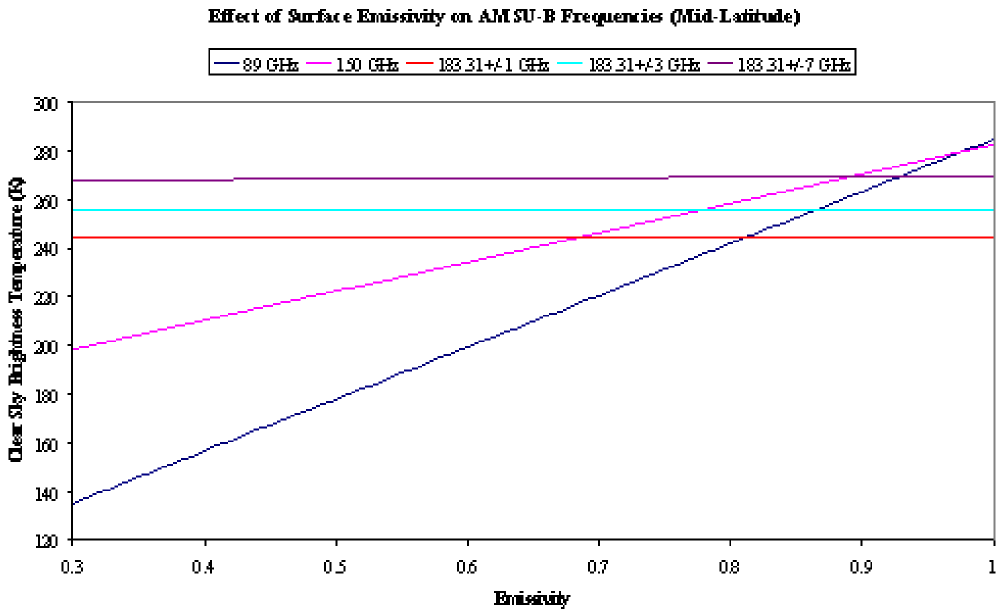

FIGURE 1. *Emissivity effects on the AMSU-B channels. The two window channels are strongly dependent on the surface emissivity showing an increasing value up to 280 K from the simulated sea surface (ε = 0.50) to dry land (ε = 1.00). At moisture frequencies, where the weighting functions are higher than window, the surface emissivity effect is low.*

a few case studies are presented where the new algorithm at 183 GHz (called hereafter 183-WSL) is compared with a precipitation index (hereafter called MSG-PI) initially proposed for AVHRR by Thoss et al. (2001) but here modified to fit the channels of Meteosat Second Generation (MSG) Spinning Enhanced Visible and InfraRed Imager (SEVIRI, Schmetz et al. 2002). In the same section, we discuss the method for validating the precipitation type classification by comparing the 183-WSL results (mm h^{-1}) with the co-located Scattering Index (SI) values.

2. 183.31 GHZ SENSITIVITY TO SURFACE EMISSIVITY AND RAINY CLOUD ALTITUDES

Since the 183.31 GHz bands are mainly dedicated to the sounding of the atmospheric water vapor amount (Kakar 1983, Wang et al. 1989), several studies have demonstrated the effects of clouds on these frequencies and their possible application into retrieval schemes. Note that the use of PMW information is necessary to detect rainy systems or correct and integrate infrared (IR) measurements, for instance in the blended techniques. However, their use is limited because of the variability of surface emissivity (ε). Grody et al. (2000) proposed a few algorithms based on different land type studies to evaluate surface emissivity using AMSU data.

Here we chose radiative transfer results with different values of surface emissivity, which refers to land if ε is typically > 0.6 and to water in the other cases, to quantify the effect of surface on AMSU-B channels.

Figure 1 shows the simulated brightness temperatures for all AMSU-B frequencies as a function of surface emissivity in clear sky conditions. The results are obtained by a adding/doubling radiative transfer model (Evans et al., 1995a,b) running with mid-latitude profiles and coupled to Rosenkranz (2001) for the computation of the absorption at selected frequencies.

As we can expected, the signal around 89 and 150 GHz has strong surface contributions showing a deep depression near low emissivity values and converging about to same brightness temperature when ε=1 (dry-land). Therefore, the decreasing surface emissivity from dry-land value to water bodies enhances the influence of atmospheric moisture on these channels. Another significant aspects of Fig. 1 is that, since their weighting functions are peaked beyond 2 km altitude, the three moisture channels are little or not affected by different emissivities thus suggesting their application both over land and over sea.

Other sensitivity studies not reported here have emphasized that, when moving towards higher latitudes where the atmosphere is less optically thick, the contribution of surface emissivity affects more and more the measurement particularly at 190 GHz where also thinner ice clouds can modify then signal.

Precipitating cloud altitude is another important variable affecting the AMSU-B brightness temperatures. We studied the behavior of AMSU-B moisture channels as a function of the position of a rainy cloud in the troposphere. All simulations have been carried out using radiosonde temperature and humidity profiles screening out the possible cloud formations along balloon trajectory with the threshold suggested by Karstens et al. (1994). The cloud structure is built adopting a Marshall-Palmer's water drop size distribution (Marshall et al. 1948) and the Mie theory to solve the scattering equations.

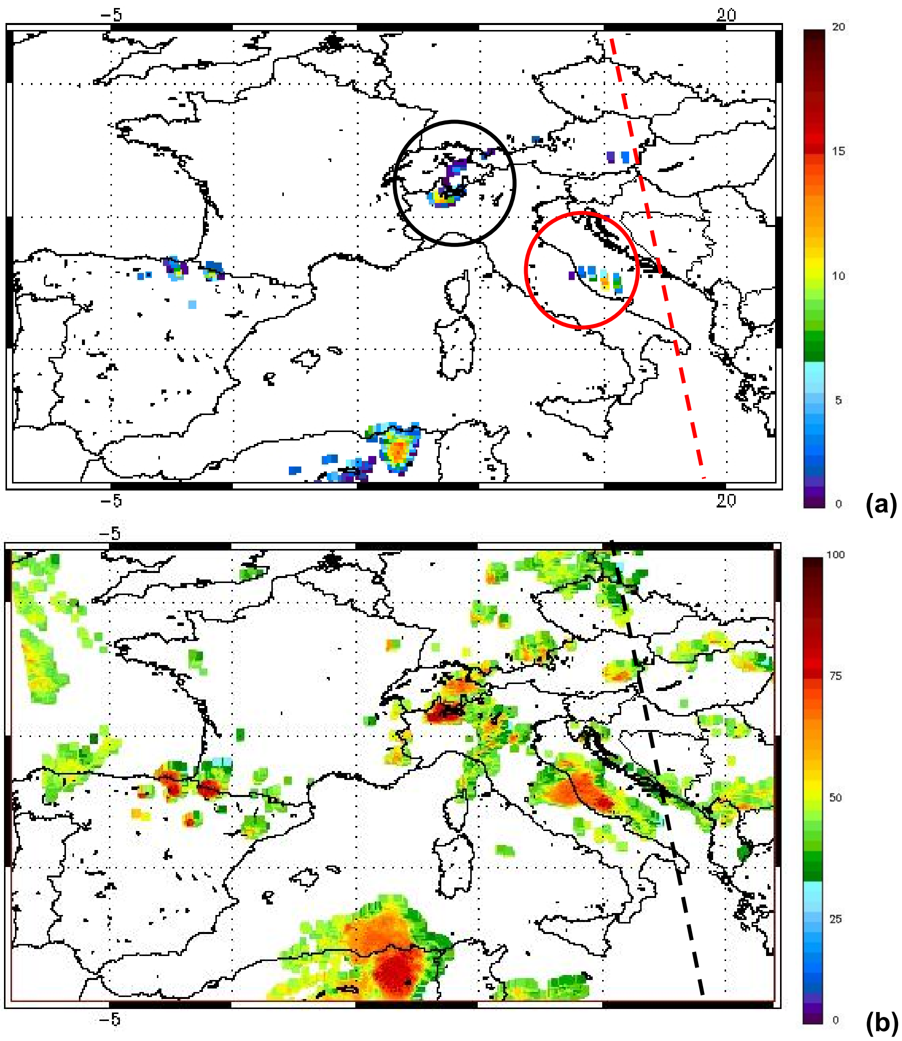

FIGURE.2. *12 June 2007, 2112 UTC: a) 183-WSL; b) MSG-PI. Dashed lines delimit the edge of the AMSU-B swath.*

In agreement with the weighting function distribution, our results show that only rainy clouds positioned above 2 km altitude interact with opaque frequencies at 183.31 GHz and the interaction will be always more intense as the cloud becomes thicker.

3. METHOD AND APPLICATIONS

In the following a method to discriminate and possibly classify precipitation type is presented. Our classification scheme is based on a series of thresholds suitable for removing water vapor contributions from the 183-WSL algorithm results and separate stratiform rain from convective.

As a comparison we have used the Bennartz et al. (2002) rain-intensity classes to check our classification and quantify the precipitation rates for each class.

Figure 2 and 4 depict two case studies related to a series of precipitating events affecting the Mediterranean area during June 2007. Note that the 183-WSL algorithm is successful in correctly discriminating precipitating from just scattering clouds.

Figure 2 shows three interesting aspects: 1) Mesoscale Convective System (MCS). In the lower part of the figure we can spot an MCS moving from the African coast towards the Mediterranean Sea. Needless to say that in this case the detection is rather easy

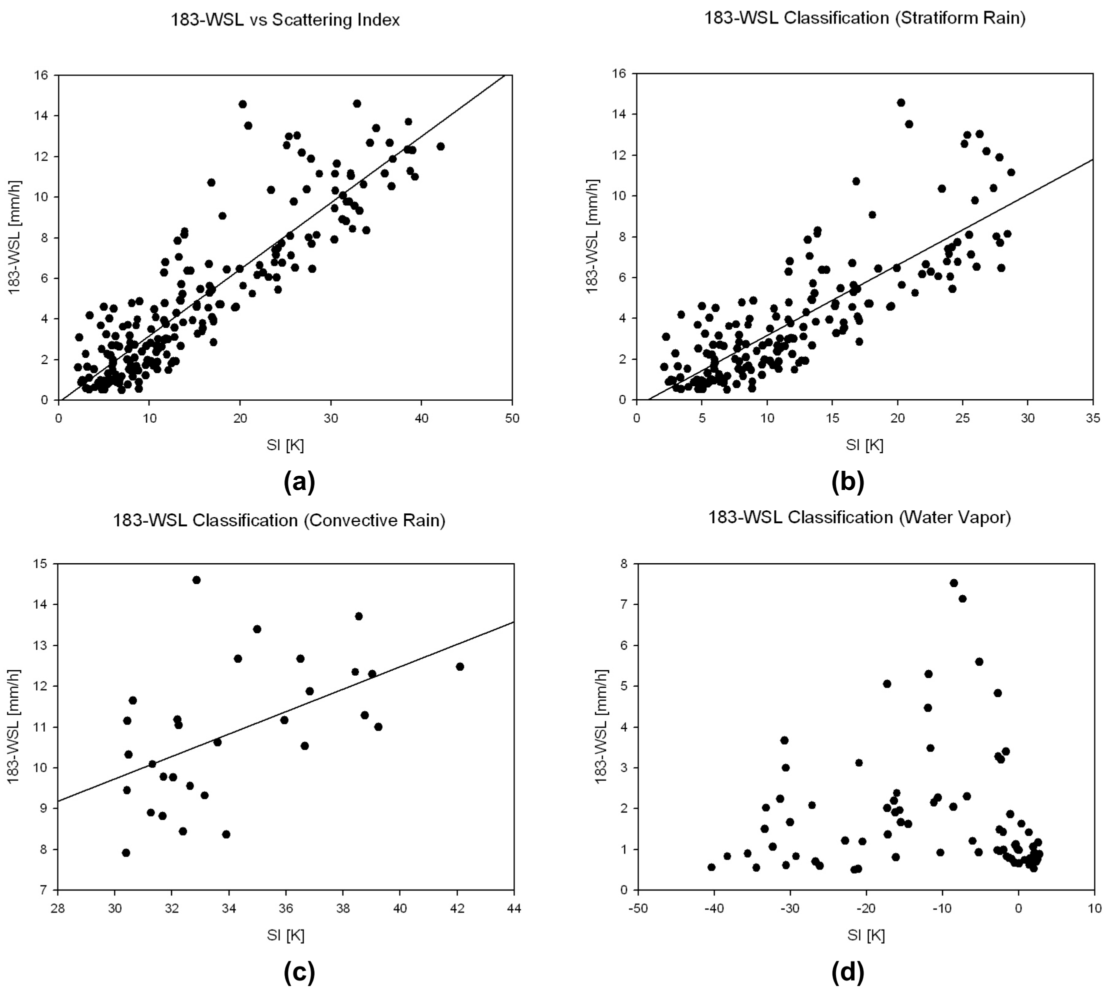

FIGURE 3. *12 of June 2007, 2112 UTC: a) scatter plot of 183-WSL vs SI; b) classification of stratiform rain compared to SI values; c) classification of convective rain compared to SI values; d) classification of water vapor values removed from the retrieval.*

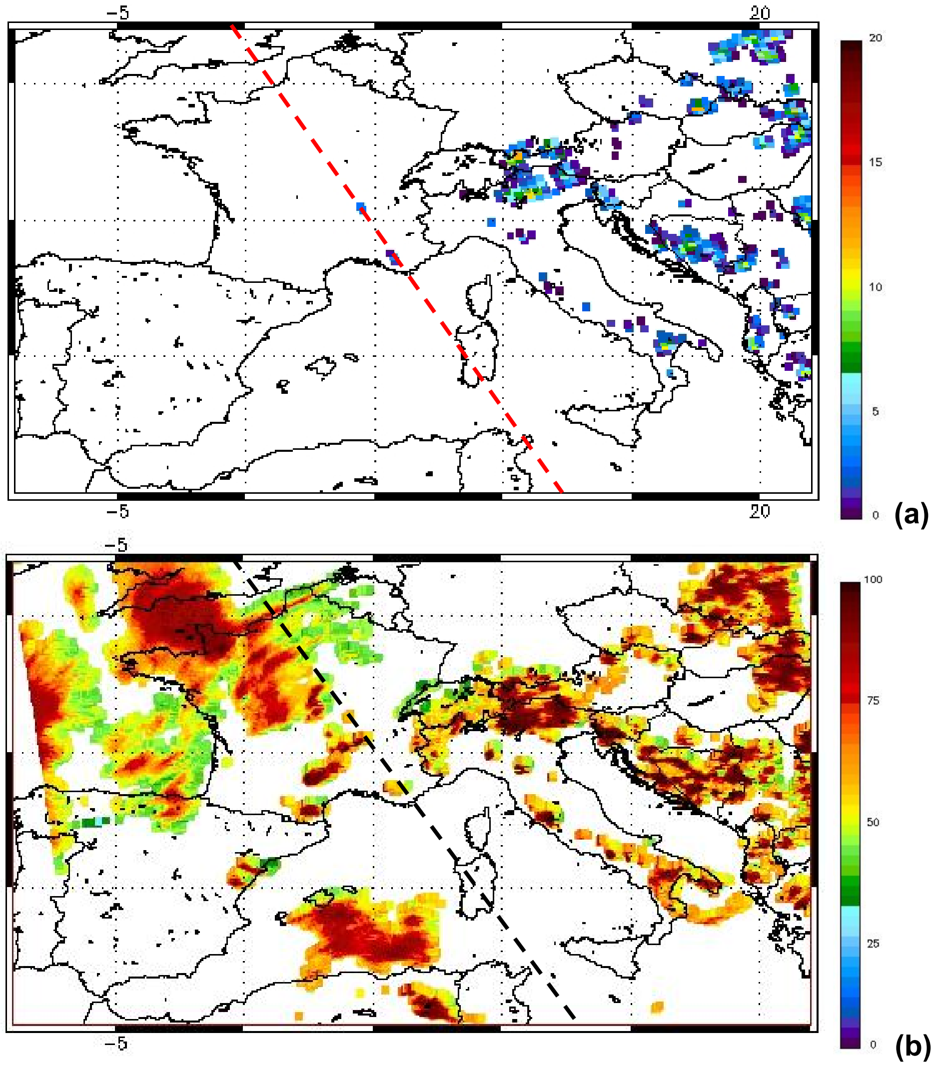

FIGURE 4. *Same as in Fig. 2 but for 12 June 2007, 2112 UTC.*

because during the formation of a deep convective system the greater amount of surrounding water vapor is condensed inside the cloud or strictly close to its border. Precipitation intensities associated to the different parts of the MSC can be distinguished moving from the convective core (red) to the cloud edge. Moreover, from the large rainy area detected in b) only higher scattering values (PI > 80) are flagged as precipitating by the 183-WSL.

2) Coastal system (red circle). This system is not characterized by heavy precipitation but the water vapor around the clouds has been filtered out using a threshold embedded into the retrieval scheme.

3) Orographic system (black circle). A small orographic cloud system close to the Alps is detected even if we did not evaluate the effects of snow cover and surface roughness on the AMSU-B channel 5.

Figure 3 shows a quantitative summary of the method's classification thresholds. The scattergrams describe how the high correlation between the 183-WSL and the SI (4-a) is mainly due to the stratiform rain (4-b) instead of the convective portion (4-c). Many pixels where precipitation intensities are up to 8 mm h^{-1} (4-d) have been flagged as water vapor and then removed from the retrieval.

Particularly interesting is the situation reported in Fig. 4 where only stratiform rain

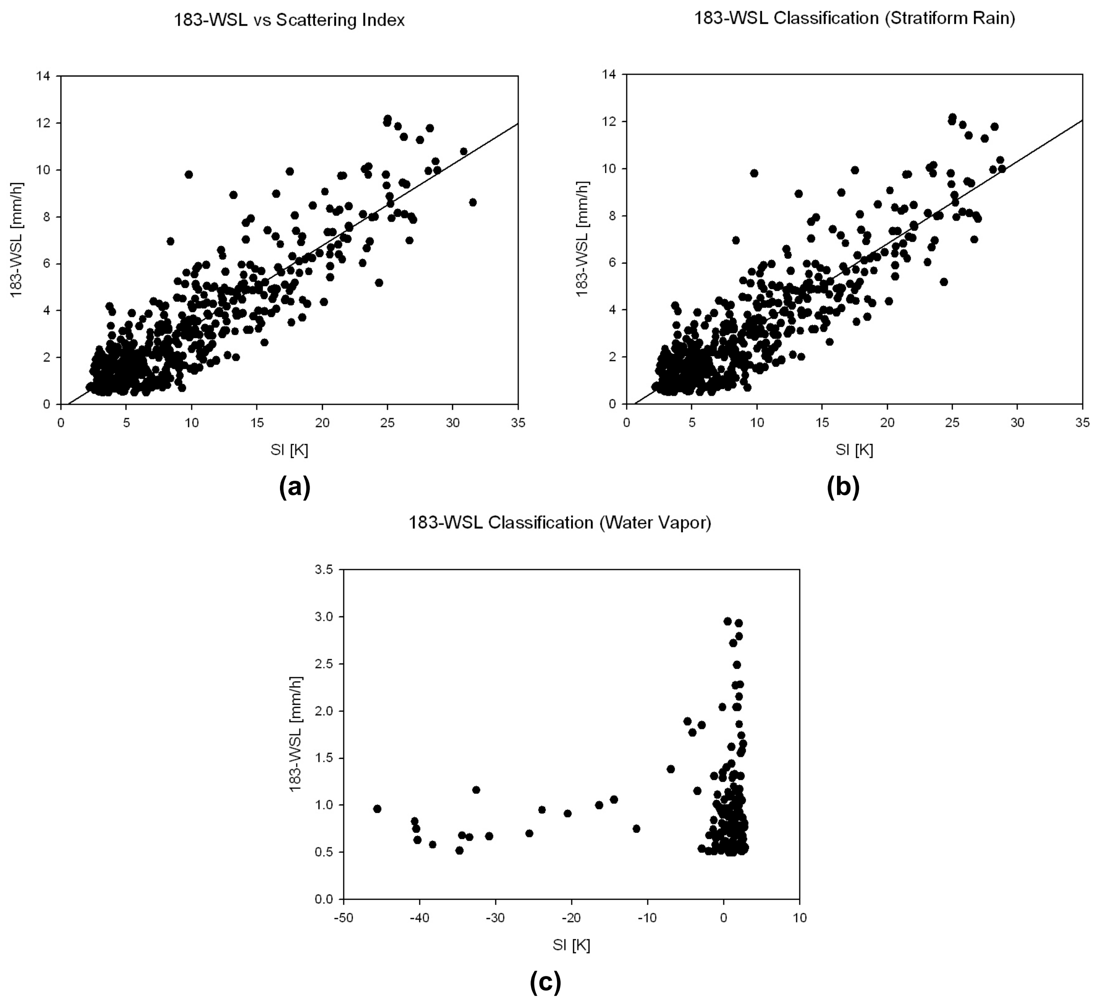

FIGURE 5. *12 of June 2007, 2112 UTC: a) scatter plot between 183-WSL vs SI; b) classification of stratiform rain compared to SI values; c) classification of water vapor values removed from the retrieval.*

classification were selected. A fast comparison with the SI Fig. 5 shows that all precipitating pixels are classified as stratiform and water vapor. Figure 5-b and 5-c in particular show that low and very low precipitation intensities (< 3 mm h^{-1}) would be associated to the stratiform rain class if the water vapor threshold were not removed from the computations.

4. CONCLUSIONS AND FUTURE WORK

Results of two new algorithms based on NOAA/AMSU-B 183.31 GHz absorption channels are presented. Although these frequencies are fully employed to retrieve the atmospheric water vapor, we develop two equations suited for calculating rain rates both over land and over water surfaces.

The drawback of these algorithms is their direct link with the atmospheric water vapor amount when condensation clusters are formed both in cloud free regions and in the surroundings of rainy clouds but not directly involved in the precipitation process. Our studies have shown that absorption due to the water vapor contaminates the algorithm estimations labeling as rainy some pixels in which only water vapor absorption was detected.

In order to prevent these incorrect rain-flags we calculate a series of thresholds to evaluate only water vapor contribution, to classify rain types and estimate precipitation intensities for each class. The results are encourage us to apply the method to precipitation events characterized by different features for a better understanding of the algorithm performances and an improvement of rain delineation in the winter season and at latitudes higher than 60 degrees.

BIBLIOGRAPHY

Bennartz, R., and A. Thoss, 2002: Precipitation analysis using the Advanced Sounding Unit in support of nowcasting applications. *Meteorol. Appl.*, **9**, 177-189.

Burns, B. A., X. Wu, and G. R. Diak, 1997: Effects of precipitation and clouds ice on brightness temperatures in AMSU moisture channels. *IEEE Trans. Geosci. Remote Sensing*, **35**, 1429-1437.

Evans, F., and G. F. Stephens, 1995a: Microwave radiative transfer through clouds composed of realistically shaped ice crystal. Part I: single scattering properties. *J. Atmos. Sci.*, **52**, 2041-2057.

Evans, F., and G. F. Stephens, 1995b: Microwave radiative transfer through clouds composed of realistically shaped ice crystal. Part II: single scattering properties. *J. Atmos. Sci.*, **52**, 2058-2072.

Ferraro, R. R., F. Weng, N. C. Grody, L. Zhao, H. Meng, C. Kongoli, P. Pellegrino, S. Qiu, and C. Dean, 2005: NOAA operational hydrological products derived from the Advanced Microwave Sounding Unit. *IEEE Trans. Geosci. Remote Sensing*, **43**, 1036-1049.

Greenwald, T. J., and S. A. Christopher S. A., 2002: Effect of cold clouds on satellite measurements near 183 GHz. *J. Geophys. Res.*, **107**, D13, AAC 3-1, AAC 3-6.

Grody, N. C., 1991: Classification of snow cover and precipitation using the Special Sensor Microwave/Imager. *J. Geophys. Res.*, **96**, 7423-7435.

Grody, N. C., F. Weng, and R. R. Ferraro R., 2000: Application of AMSU for obtaining hydrological parameters. In: *Microwave Radiometry and Remote Sensing of the Earth's Surface and Atmosphere*, P. Pampaloni and S. Paloscia, Eds.,USP Int. Science Publishers, Utrecht, 339-352.

Kakar, R. K., 1983: Retrieval of clear sky moisture profiles using the 183 GHz water vapor line. *J. Climate Appl. Meteor.*, **22**, 1282-1289.

Karstens, U., C. Simmer, and E. Ruprecht, 1994: Remote sensing of cloud liquid water. *Meteor. Atmos. Phys.*, **54**, 157-171.

Marshall, J. S., and W. McK. Palmer, 1948: The distribution of raindrops with size. *J. Meteor.*, **5**, 165-166.

Marshall, J. S., R. C. Langille, and W. McK. Palmer, 1947: Measurement of rainfall by radar. *J. Meteor*, **4**, 186-192.

Rosenkranz, P. W., 2001: Retrieval of temperature of moisture profiles from AMSU- and AMSU-B measurements. *IEEE Trans. Geosci. Remote Sensing*, **39**, 2429-2435.

Schmetz, J., P. Pili, S. Tjemkes, D. Just, J. Kerkmann, S. Rota, and A. Ratier, 2002: An introduction to Meteosat Second Generation (MSG). *Bull. Amer. Meteor. Soc.*, **83**, 977-992

Staelin, D. H., and F. W. Chen, 2000: Precipitation observations near 54 and 183 GHz using the NOAA-15 satellite. *Proc. 2000 IEEE Int. Geoscience and Remote Sensing Symp.*, 38, 5, 2322-2332.

Staelin, D. H., F. W. Chen, and A. Fuentes, 1999: Precipitation measurements using 183-GHz AMSU satellite observations. *Proc. 1999 IEEE Int. Geosci. and Remote Sensing Symp.,* 4, 2069-2071.

Thoss, A., A. Dybbroe, and R. Bennartz, 2001: The Nowcasting SAF precipitating clouds product. *Proc. 2001 EUMETSAT Satellite Data Users' Conf.*, Antalya, 1-5 Oct., 399-406.

Wang, J. R., T. T. Wilheit, and L. A. Chang, 1989: Retrieval of total precipitable water using radiometric measurements near 92 and 183 GHz. *J. Appl. Meteor.*, **28**, 146-154.

ACKNOWLEDGMENTS

Support from the Progetto Strategico della Regione Puglia “Nowcasting avanzato con l'uso di tecnologie GRIS e GIS” and from EUMETSAT's Satellite Application Facility in support to Hydrology and Operational Water Management are gratefully acknowledged. Discussions with F. J. Turk were very helpful.

THE RECENT FEATURES OF WATER VAPOR AND ITS TRANSPORT OVER EAST-CENTRAL REGION OF NORTHWEST CHINA

Li Zhaorong Chen Tianyu Chen Qian Pang Chaoyun
Gansu weather modification office, Lanzhou, 730020, China

1 INTRODUCTION

Northwest of China is far away from the sea, located at the combination area of Qinghai-Tibet Plateau, Inner Mongolian, Loess Highlands, with complex terrain. Precipitation is scarce and mainly occurs in the summer, relatively rich in some mountainous and plateau areas, and its distribution is quite unevenly. The precipitation is important water source supplies in this arid and half arid area. The water vapor supply and the terrain lifting are essential condition for forming cloud precipitation. The water vapor and its transfer over the unique geography topography in the Northwestern Region have their special features, especially in the important role of orographic effects on precipitation forming. The water vapor and its transfer fluxes features, the precipitation distribution effected by the terrain are analyzed based on 5-year sounding and DEM data in this paper.

2 DATA AND METHODOLOGY

The means of water vapor and the water-vapor transfer for entire level at two times (08:00, 20:00) daily are calculated over eastern region (89°E-112°E, 30°N-46°N) of Northwest based on 40 sounding stations day-to-day data during 2001-2005 year. The surface precipitation data from 2001 to 2005 at the 212 weather observation stations are used.

Water vapor content (V) is calculated by:

$$V = \int_{h_b}^{h_t} \rho_v \Delta s dh$$

where ρ_v is water vapor density, Δs is unit area, h_t top of Integral altitude, h_b bottom of Integral altitude.

Water-vapor transfer flux ($\vec{Q}$)calculated by:

$$\vec{Q} = \int_{h_{ground}}^{h_{100}} \vec{V} \cdot \rho_v \Delta s dh = \int_{h_{ground}}^{h_{100}} (u, v) \cdot \rho_v \Delta s dh$$

3 RESULTS

3.1 Distribution of water vapor content

The water vapor contents with very similar geographical distributions change obviously for different seasons, the largest one is in summer, the second large one in spring, smaller in autumn and the smallest in winter. The water vapor is abundant in south-eastern of GANSU, southern of SHANXI province and is particularly scarce in middle of the Qinghai-Tibet Plateau and the Badanjilin Desert.

The area of water vapor content large than 8mm expands gradually and extends toward north-west from spring to summer, so as to form a “wet tongue” along Qilian mountains, except that in winter.

3.2 Transfers of water vapor

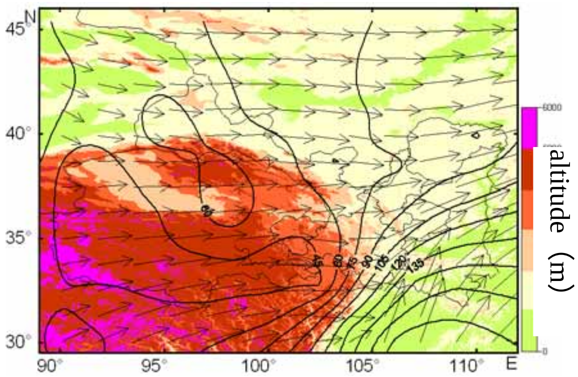

FIG.1. the contour of water vapor flux and transportation vector

It is an important factor the strong or the weak of water-vapor transfer to decide the effective precipitation formation, regarding to arid and half arid in Northwestern Region.

As show in Fig 1 and Fig 2, the water-vapor transfer in this region is mainly come from two directions, zonal transportation and meridional transportation. The zonal transportation primarily is in the west with the entire level water vapor flux less than 100Kg.cm^{-1}.s^{-1}. The more important path of water-vapor transfer is the meridional transportation in the southwest monsoon influence, from Bay of Bengal's southwest air current, with the water vapor flux more than 105Kg.cm^{-1}.s^{-1}.

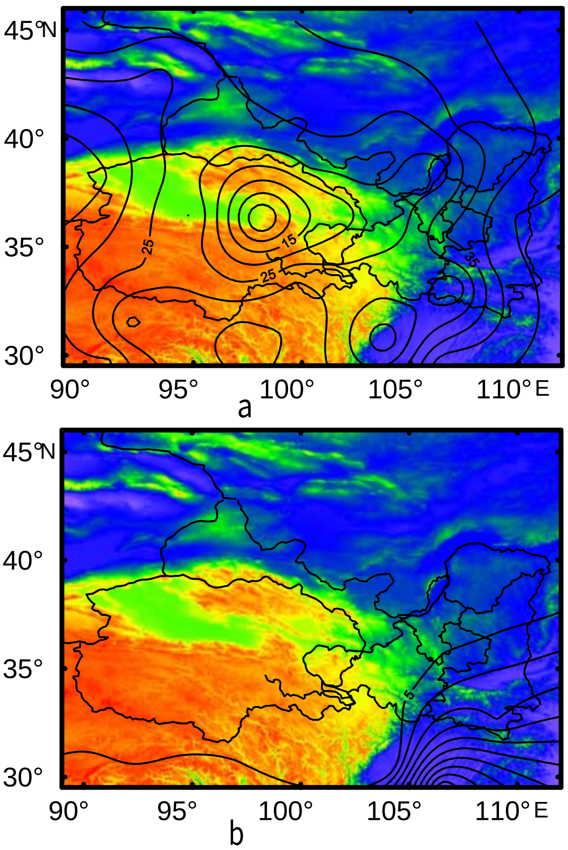

FIG.2. the mean water fluxes of zonal transportation (a) and radial transportation (b).

According to water-vapor transfer flux divergence equation:

$$\nabla \cdot \vec{Q} = \frac{1}{g}\int \nabla \cdot (\vec{V}q)dp = \frac{1}{g}\int \vec{V} \cdot \nabla q dp + \frac{1}{g}\int q \cdot (\nabla \cdot \vec{V})dp$$

the divergence of water-vapor transportation consists of water vapor advection (first part in right) and wind field divergence item (second part in right). The westerly wind average transportation is some of dry transportation because the water vapor content reduces gradually from west to east. It is not favorable to the formation of precipitation. It is well known that the effective precipitation is hardly formed if the water vapor flux does not converge. The water convergence is formed in some of region due to special landform and high mountains retarding and uplifting the incoming water vapor in west China. It finally results in precipitation formation. The positions of precipitation center and the water vapor convergence are very consistent in this area.

The water vapor transportations by zonal northwest airflow and the westerly wind airflow are the basic water vapor supply, and the powerful water vapor transported by southwest monsoon from Bay of Bengal, especially in summer, is advantageous in strengthening the precipitation intensity in this area. The zonal water vapor transportation, which the maximum value appears at 600 hPa, is the most important path in Qinghai-Tibet Plateau and its north. The meridional water transportation which concentrates below the height of 400 hPa only prevails in east Qinghai-Tibet Plain the edge and the east of the region.

4 CONCLUSIONS AND DISCUSSION

The regional water vapor and its transport features are analyzed in East-central Region of Northwest in China based on the data of recently five years. The results show that the water vapor contents from ground to upper atmosphere obviously vary with seasons and locations, and extend northwest like a “wet tongue” along Qilian mountains except that in winter. The vapor comes mainly from zonal transport guided by west wind and meridional transport dominated by southwest current. In Qinghai-Tibe plateau, the vapor transport are mainly from southwest current in south regions and from northwest current in north regions which vapor flux value is half as many as that in east Plateau, and upper vapor transport plays a more important role. The dry vapor transport led by northwest and west current is one of primary factors. It's clearly that precipitation and uneven distribution are greatly influenced by the terrain. In the summer, the zonal vapor transport in 600hPa is the strongest, and the longitudinal vapor transport in to the east of 103°E under 600hPa is stronger than other areas.

5 BIBLIOGRAPHIES

[1] Li Xinzhou, Ma Zhuguo,Liu Xiaodong. Inter-decadal Characteristics of Aridification over Northern China Associated with the Variation of Atmospheric Circulation During the Past 50 Years [J]. Chinese journal of atmospheric sciences,2006, 30 (2):277-284.

[2] Wang Keli, Jiao Hao, Zhao Hongyan. Atmospheric water vapor transport from westly and monsoon over the Northwest China[J].Advance in water science, 2005，16（3）：432－438.

[3] Zhou Changyan,Li Yueqing,Li Wei. Climatological Characteristics of Water Vapor Transport over Eastern Part of Qinghai-Xizang Plateau and Its Surroundings [J].Plateau meteorology, 2005,24(6): 880-888.

[4] Wang Baojian,Huang Yuxia,Tao Jianhong,et al. Regional features and variations of water vapor in northwest China[J].Journal of glaciology and geocryology, 2006，28(1):15-21.

[5] Jin Liya,Fu Jiaolan,Chen Fahu. Spatial and temporal distribution of water vapor and its relationship with precipitation over Northwest China[J].Journal of Lanzhou university (Natural science),2006，42（1）: 1-6.

[6] Cai Ying, Qian Zhen-an, Wu Tongwen, et al. Distribution,Changes of Atmospheric Precipitable Water over Qinghai－Xizang Plateau and Its Surroundings and Their Changeable Precipitation Climate [J]. Plateau meteorology, 2004,23 (1):1-10.

[7] Chen Tianyu,Li Zhaorong,Chen Qian,et al. The analysis of climate of characteristics of water vapor distribution over Northwest China with water vapor field retrieved from GMS5 satellite data. Chinese journal of atmospheric sciences, 2005，29（6）：864－871.

[8] Cui Yuqin.The transport of vapour and its sources in northwest China[J].Shuili xuebao, 1994，9：79－87.

[9] Wang Yongshen. Atmospheric Physics [M]. Beijing, China Meteorological Press, 1985, 18－19.

[10] Chen Yan,Ding Yihui,Xiao Ziniu. The Impact of Water Vapor Transport on the Summer Monsoon Onset and Abnormal Rainfall over Yunnan Province in May [J]. Chinese journal of atmospheric sciences, 2006，29（6）:864－871.

[11] Huang Ronghui,Zhang Zhenzhou, Huang Gang. Characteristics of the water vapor transport in East Asian monsoon region and its difference from that in south Asian monsoon region in summer [J]. Scientia atmospherica sinica, 1998, 22(4): 460-469.

[12] The reseach group of Qihai-Xizang Plateau meteorology. Research on low eddy shear of 500hPa in next half year over Qinghai－Xizang Plateau[M].Beijin. China Science Press, 1981，3－5，70－92.

VALIDATION OF THE PERFORMANCES OF THE EZ AEROSOL LIDAR AGAINST OTHER REMOTE OR IN-SITU SENSORS AND INSTRUMENT UNCERTAINTY ANALYSIS

S. Lolli[1], L. Sauvage[1], B. Guinot[1], M. Lardier[1]

[1]*Leosphere, 42 Rue de Clignancourt 75018 Paris, France(slolli@leosphere.fr)*

A compact and rugged eye safe UV lidar, the EZLIDAR™, was developed together by Laboratoire des Sciences du Climat et l'Environnement (LSCE) (CEA–CNRS) and LEOSPHERE (France) to study and investigate structural and optical properties of clouds and aerosols, thanks to the strong know-how of CEA and CNRS in the field of air quality measurements and cloud observation and analysis .

1. Introduction

EZLIDAR™ has been validated by different remote or in-situ instruments as MPL Type-4 lidar manufactured by NASA at ARM/SGP site or the LNA at Laboratoire de Metereologie Dynamique LMD(France) and in several intercomparison campaigns. Further EZLIDAR™ was deployed in different air quality and long distance aerosol transport research campaigns (LISAIR'05, AMMA Niger campaign in January 2006, ASTAR/IPY in April 2006, TIGERZ'08 together with NASA/AERONET).

2. EZLIDAR™ instrument

EZLIDAR™ Lidar uses a tripled pulse laser source ND:YAG at 355nm wavelength with an energy of 16mJ and pulse repetition frequency of 20 Hz. Both analog and photon counting detection is available. The lidar system provides a real time measurement with scanning capabilities of backscattering and extinction coefficients, Aerosol Optical Depth (AOD), automatic detection of the Planetary Boundary Layer (PBL) height and clouds base and top from 50m up to 20 km.

In table 1 are schematically reported the instrument characteristics

Range	**50m-20km**	**Environment**	**-20°C../+50°C**
Temporal Res	**1s(PBL)/30s**	**Humidity**	**0-100%**
Spatial Res	**1.5m/15m**	**Waterproofing**	**IP65**
Angular Res	**0.2°**	**Weight**	**~48 kg**
ScanningSpeed	**8°/s**	**Eye Safety**	**IEC60825-1 2001**

Table 1 EZLIDAR technical characteristics

3. Validation campaign at LMD

EZ Lidar was deployed at LMD in Palaiseu, France to validate the PBL height measurements with those retrieved by the algorithm STRAT[5] from large field LNA data of LMD. The 12-days measurement campaign of 5 min of PBL averaged height shows (Figure 1) a correlation between the instruments of 95%

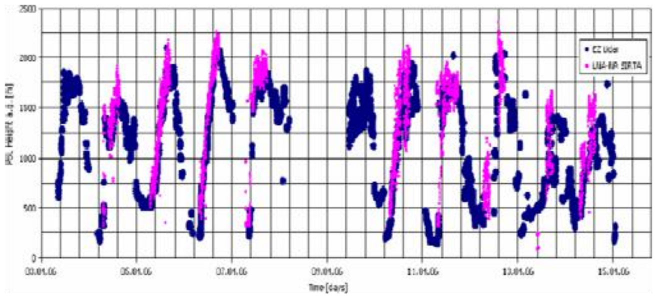

Figure 1 PBL Height retrieval from EZLIDAR (blue) and STRAT(fuchsia)

In addition, the EZ automatically retrieved Aerosol Optical Depth is compared in Figure 2 with the sunphotometer data (P.Goloub, AERONET, France). Around noon sunphotometer data were not available due to passing of subvisible clouds

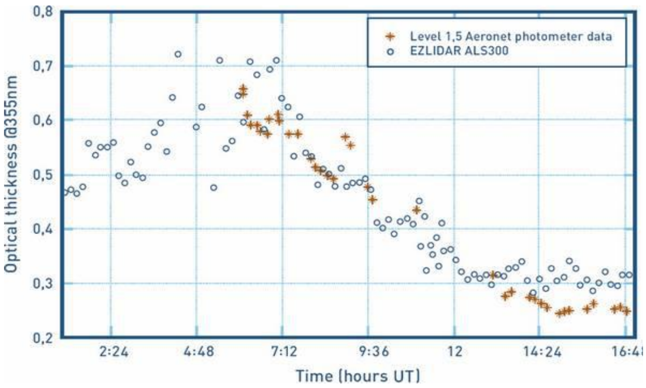

Figure 2 Level 1.5 Aeronet photometer data (red) AOD EZLIDAR retrieval (blue)

4. Validation campaign at ARM/SGP site

The intercomparison measurement campaign took place on 23rd and 24th October 2006 at Southern Great Plains, situated in Oklahoma, United States. SGP Central Facility coordinates are: N36° 37' W97° 30' with an altitude of 320 meters above sea level. Raman Lidar (RL) data measurements are available on 24th October

Raw data from MPL and EZLIDAR show for the first day clear atmosphere conditions, while on 24th October cirrus clouds between 10 and 12km, alto stratus and cumulus are present during the day.

In order to compare directly the instruments, the measurement time run from 5pm to 0am (UTC) on both days. Due to the different atmospheric conditions, it is possible to compare both systems in different features. The following plots show the range corrected signal [1] as function of the time for EZ, MPL and RL. on 24th Oct).

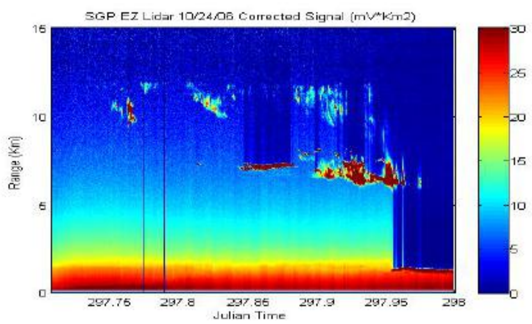

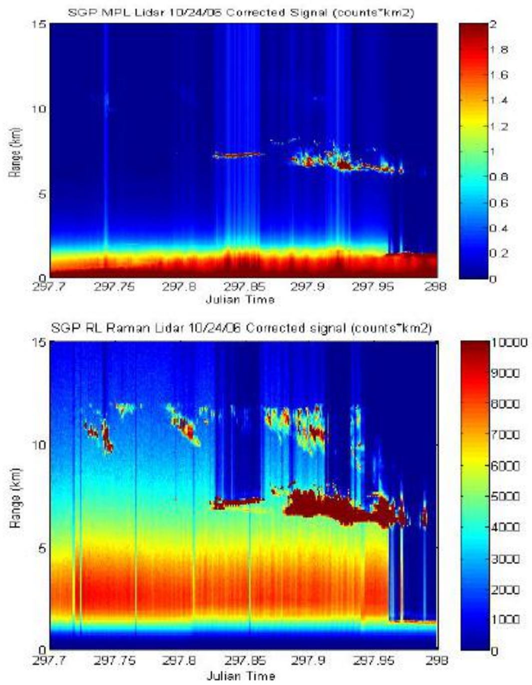

Figure 3 Range corrected signal for EZ lidar (top), MPL lidar (middle) and RL Raman Lidar (bottom) on 24th October 2006. Reference time is in UTC.

MPL data, not separated into polarized components, should be corrected with the recovered overlap function; also EZ data should be corrected by the overlap function. Both instrument overlap functions are plotted in Figure 4.

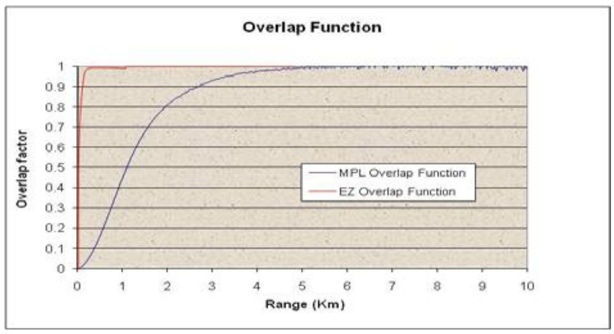

Figure 4 EZLIDAR(red) and MPL(blue) overlap function

It can be noticed that, due to the extremely narrow MPL Lidar field of view, complete overlap is reached around 5 km, while EZ lidar reaches it at 220 m (and 98% overlapping at 170m). A narrow field of view permits to reduce unwanted solar background and effects due to the multiple scattering, but presents less accuracy in the recovering region

The Signal-To-Noise Ratio (SNR) is a parameter to assess lidar performances. For a given lidar signal, being the received number of photons small enough to approximate the detected signal by a

Poisson distribution, SNR can be retrieved using the following equation [1]:

$$SNR\ (r) = \frac{NP\ (r)}{\sqrt{P(r)N\ +\ NP_{bkg}}} \qquad (1)$$

where N is the number of accumulated shots in 30s, P(r) is the received signal from range r and P_{bkg} is the received power due to the solar background.

It is now possible to compare SNR profiles for EZ, MPL and RL instruments, as plotted in figure 5.

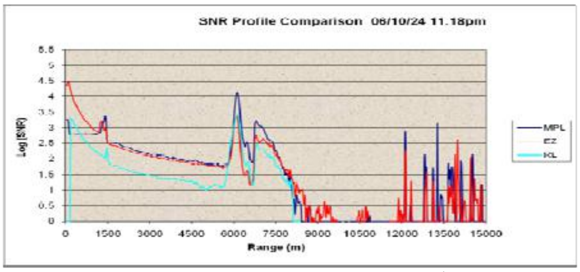

Figure 5 EZ, MPL, RL SNR profiles on 24th Oct, 11.18pm (UTC)

It is interesting to notice that EZ SNR is better in the first 1.5 km and it is comparable further. This is a consequence of a lower EZ full overlap, as showed in Figure 4. The results are schematically reported in Table 2, where the Lidar range is defined as the range at which SNR=1. Bias indicates the percentage divergence between the measured molecular signal and the normalized range corrected lidar signal

10/24/06 11.18pm	Lidar Range	SNR 10	Overlap	Bias @ 6km
EZ	~9000 m	~8500m	~320m	< 20 %
MPL	~8800 m	~8500 m	~5000m	< 15%
RL	~8000 m	~5000 m	n/a	<5%

Table 3 Comparison result for 24th Oct, 11.18pm (UTC)

5. Uncertainty analysis

The total and particle backscattering and extinction coefficients are directly retrieved processing the lidar signal returns as described in [3]. The total backscattering coefficient is given by:

$$\beta_{tot}(z) = \frac{\beta_m\, exp^{(S'(z)-S'_m)}}{1+2\beta_m L_R \int_{z_m}^{z} exp^{(S(z)-S'_m)} dz'} \qquad (2)$$

Where z_m is the reference altitude at which the inversion starts, β_m is the known molecular backscattering coefficient at z_m, S' is the normalized range corrected lidar signal return (NRB) and L_R the lidar ratio. The relative uncertainty in retrieving the total backscattering coefficient is given by:

$$\Delta\beta_{tot}(z) = \sqrt{\sum \left(\frac{\delta\beta_{tot}}{\delta X_j}\Delta X_j\right)^2} \qquad (3)$$

with β_{tot} function of the lidar ratio L_R, the molecular backscattering β_{mol} and the NRB. Each source error has been evaluated in a previous study[6], and from (3), it is possible to retrieve the backscattering coefficient with the relative uncertainty as plotted in Figure 6, for a measured profile at SGP

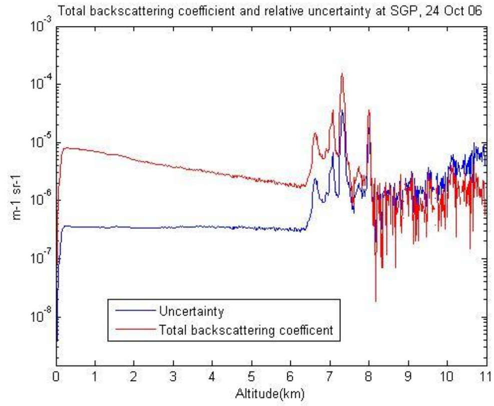

Figure 6 Total backscattering coefficient and relative uncertainty

The figure shows that the uncertainty on the backscattering coefficient retrieval is 100% at about 8000m. This is consistent with the lidar range calculated in table 3.

6. Conclusions

The EZLIDAR instrument has been validated in several intercomparison campaigns, with different remote o in-situ instruments. PBL height retrieval shows a correlation of 95% with STRAT retrieval algorithm at LMD.

The analysis of the obtained results at ARM/SGP campaign shows that EZ lidar data quality is comparable with MPL data during daytime and under multi layered cloud conditions, and present a better maximum range under clear sky conditions. In these calculations, MPL data are referred to parallel polarization, while EZ data contain both.

Outdoor and unattended use capabilities of the EZLIDAR™ added to its measurements performances define then this instrument as a good candidate for deployment into growing global aerosol and cloud monitoring networks and research measurement campaigns.

7. References

[1] J. R., Campbell, D. L. Hlavka, E. J. Welton, C. J. Flynn, D. D. Turner,J. D. Spinhirne, V. S. Scott, and I. H. Hwang, 2002: Full-time,eye-safe cloud and aerosol lidar observation at Atmospheric Radiation Measurement Program sites: Instrument and data processing. J. Atmos. Oceanic Technol., 19, 431–442.

[2] Ansman, A, M Riebesell, and C Weitkamp. 1990. “Measurements of atmospheric aerosol extinction profiles with Raman lidar.” Optics Letters 15:746-748.

[3] J. D. Klett, "Stable analytical inversion solution for processing lidar returns," Appl. Opt. 20, 211- (1981)

[4]Dave Turner et al. “Raman lidar measurements of the aerosol extinction-to-backscatter ratio over the Southern Great Plains” Journal of geophysical Research, Vol. 106, NO. D17, Pages 20,333–20,347, 2001

[5] Y.Morille, M.Haeffelin, P.Drobinsky, J.Pelon, *STRAT:* an automated algorithm to retrieve the vertical structure of the atmosphere from single channel lidar data, JAOT, Volume 24, Issue 5 (May 2007) pp. 761–775.

[6] S. Lolli Ez “Lidar Uncertainty Analysis in AOD retrievals.” LEOSPHERE internal communications, 2008

THE OBSERVATION OF WIRE ICING AND ITS WEATHER CONDITION IN GUIZHOU

LUO Ning[1] Wen Ji-fen[2] Ran Jia[3]
1: Guizhou Meteorological Bureau, Guiyang,550002,China
2:Guizhou Weather Modification Office, Guiyang,550002,China
3：Key Laboratory of Atmospheric Physics &Atmospheric Environment(LAPE), NUIST. Nanjing, 210044,China

1.INTRODUCTION

The emergence of the electric wire icing accumulated ice increased to build on stilts the perpendicular lotus of circuit to carry.Once over design standard, will take place ice to harm trouble, become disaster weather, bring national economy huge loss. Meteorological phenomena many years records the main body of a book according to Guizhou,the characteristic and oneself characteristic carry out analysis on electric wire icing meteorological phenomena , gets the parameter beneficial to harming an accident as well as electric wire icing occurrence temperature , wind speed , wind direction condition, ice happened. The temperature passed to once influence congelation process of cooling off the drop of water to influence the type of electric wire accumulated ice;The direction of wind, wind velocity passes the growth of the influence accumulated ice of the landings speed of changing the drop of water. May develop status according to accumulating the ice diameter and the thickness fluctuation , getting glaciation process's in glaciation process. As long as knowing ice density , glaciation diameter and glaciation weight hit the target, two parameters, are therefore likely to calculate out third parameters arbitrarily.

Atmosspheric ice accretion on wires is one of the major problems in planning and constructing power transmission lines and communications networks in regions where freezing temperatures occur frequently.Damage to structures by ice loads causes huge economic losses and operational difficulties in the power industry(GUIZHOU,2008).These estimates canbe obtained by collecting long time-series of observations on ice loads and quit extensive statistics have been obtained in this way for some location.

2. INVESTIGATED DATA

In order to reveal the law and mechanism of wire ice accretion in GUIZHOU plateau,micro-characteristics of fog and cloud were obseverved while investigating and collecting the macro-meteorological conditions in heavy ice accretion areas.

Accidents of wire ice accretion usually take place in heavy ice accretion areas . M ore fog is a typical climate characteristic of heavy ice accretion areas.Three heavy ice accretion areas og GUIZHOU Province were selected as field investigation areas in the project,they are MALUOQIN in the west LOUSHAN Mountain in north and YUNWU Mountain in the centre ,and their heights above sea level are 2128,1780 and 1659 meters respectively.The typical characteristic includes ice accretion data and routine meteological data: temperature,wind ,ice increasing and so on.

3. WEATHER CONDITION DURING ICE ACCRETION

During ice accretion, ice increasing has a direct bearing on temperature,wind velocity and wind direction.

3.1 THE AFFECT OF TEMPERATURE ON WIRE ICE ACCRETION

According to the meteological data of GUIZHOU Province over the past dacades, the temperature distribution scope is mainly 0℃ ～ -8℃ during ice accretion,selecting the temperature distribution of some meteological stations in east ,north and centre of GUIZHOU Province during heavy ice accretion year (1976,1984,1985,2008) and temperature distribution frequency of observtion spots in heavy ice accretion areas,table 1 obtained the height above sea level,the wider of the negative temperature areas.The temperature of MALUOQIN in 1976,1984 was calculated through linear regression with the temperature of SHUICHENG meteological station.The regression formula is T_m=1.03T_s-2.17.With 69 statistic samples.Coefficient of corretation r=0.89. Where: T_m the temperature of MALUOQIN, $T_s$the perature of SHUICHENG meteological station.

Tab1 Frequency of temperature distribution (%)

areas	place	Height (m)	temperature scope(℃)										year	Degree of ice accretion
			≥0	0～-1	-1～-2	-2～-3	-3～-4	-4～-5	-5～-6	-6～-7	-7～-8	<-8		
cities	Kaili	720	3	45	31	21							1976,1984,1985,2008	heavy
	Weining	2237	6	12	12	12	16	10	14	11	2	5		heavy
	Shuicheng	1811	5	26	19	15	14	17	4					heavy
	Zunyi	844		48	29	24								heavy
	Guiyang	1071		29	26	26	15	3						heavy
Moun-tain areas	Maluoqin	2128	2	2	3	27	18	15	14	17	2		1976,1984	heavy
		2128	11	9	10	40	21	6	3				1989	heavy
		2128		6	62	26	6						1991	light
	Loushan	1780		3	9	11	34	19	11	13			1990	heavy

2008,1984 and 1976 of GUIZHOU are especially heavy ice years.Some severe accidents such as poles collapsed and wires broken took place in many areas of GUIZHOU.Electric power accidents caused by ice took place in SHUICHENG,MALUOQIN in 1976,1984 and 1989. The damage of All GUIZHOU by ice took place in 2008.

In the light of analyse,the lowest temperature of longest last ice accretion of MALUOQIN in heavy and especially heavy years is -8℃,and the frequency between -2 ℃ ～ -5℃ is most offten,up to 60%,so is in LOUSHAN9(up to 64%).The minimal temperature of some cities whose heights above sealevel are below one km is -3℃ during heavy ice years.The heights above sea level of most mountain arears of GUIZHOU Province are between one km and two km.Their temperature is not below the temperature of SHUICHENG and MALUOQIN.One could infer:the temperature of most areas of GUIZHOU during ice accretion is between 0℃ and -5 ℃. Shown in fig1 and fig 2.

Temperature has a relationship with icing density ,when the temperature is blow 0℃ , the higher the temperature,the greater the icing density,and vice versa.the longer the ice accretion time,the more thickness the wires ice accretion. The thickness of ice accretion of wires shown fig 3.

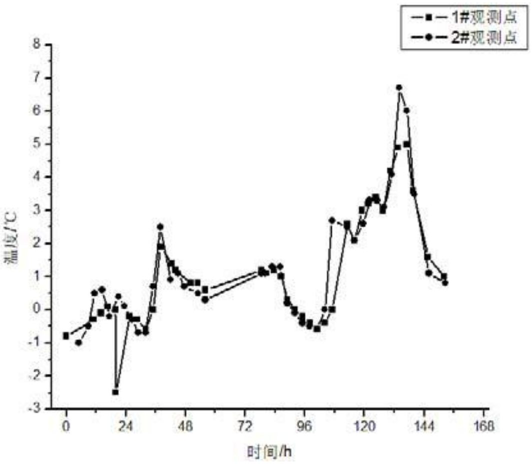

FIG.1. The Temperature change during ice accretion in 1990 in LOUSHAN

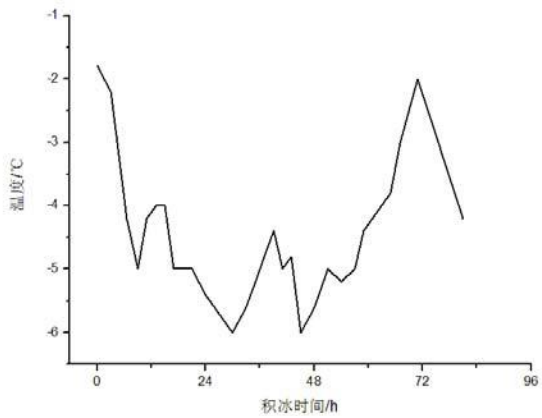

FIG.2. The Temperature change during ice accretion in 1994 in YUNWUSHAN

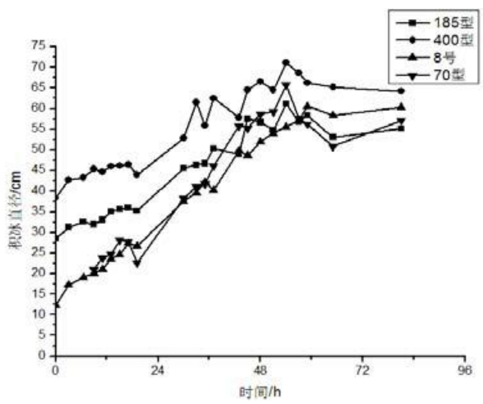

FIG.3. The change of thickness of wires ice accretion during ice accretion (sample93)

Three different kinds of temperature were given in Peksonne's wind tunnel experiment:T= -16℃,-5.4,-1.5℃,Under the same condition of equal LWC(liquid water content) and velocity,the icing density within 4hours is 0.32,0.54,0.89g/cm^3 respectirely. Compared with Peksonne's wind tunnel experiment,the ice accretion of GUIZHOU P rovice is one under relatiively high temperature.When temperatureis high,icing density is great,adhesive force of ice to wires is great,and ice is not easily dropped.It is main reason that calamity was easily caused by ice accretion in GUIZHOU Province. Four kinds of icing density between 0.79 and 0.89 g/cm^3 were observed in GUIZHOU Province in the study.

3.2THE AFFECT OF WIND ON WIRE ICE ACCRETION

Collection of cloud droplet of cylinder is related with wind velocity and wind direction.When wind direction is perpendicular to the cylinder,cloud droplet collection amount is maximal, and the speedof ice accretion is most fast.Wind direction is parallel to the cylinder,there no cloud droplet collection in theory. To show the effect of wind direction on ice loading in this paper,North—South direction is defined as 0° and West—East direction as 90° .If the angle between wind direction and North—South wires is greater than ∣45° ∣,the wind is to the east or to the west,and to the south or to the north on the contrary ice accretion long diameters of the North—South direction and West—East direction were observed for the simulation wires and expressed with D_s and D_e respectively. If $K_d= D_s / D_e$, K_d could be obtained for different wind direction and velocity and shown in table 2.Frequencey of wind distribution shown in fig 4.

Table 2 and Fig4 showns:wires ice accretion of North—South direction is more severe than that of West—East direction (except wind speed less than 2m/s).

Table 2 Average K_d of different wind

Velocity(m/s)	⊙ > 45°	samples	⊙ < 45°	samples
v < 2	2.27	6	0.17	6
2 < v < 4	4.50	4	3.2	4
4 < v < 5	2.86	8	2.57	8

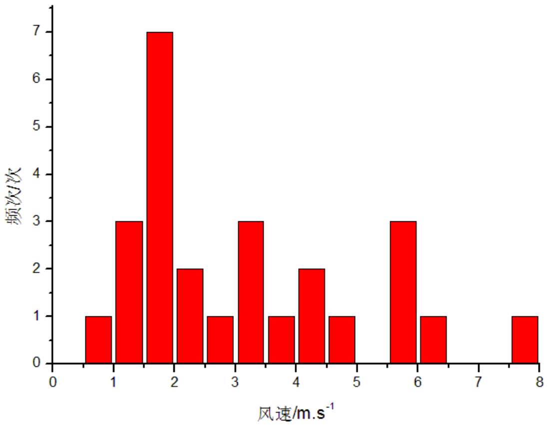

FIG.4. The Frequencey of wind distribution during ice accretion

That is related with the macro-weather and climatic characteristic of GUIZHOU cloud and fog.When the surface wind direstion is to the north ,cloud and fog is relatively thin,and LWC of cloud on mountain is little,which is not favourable to the ice accretion of West—East wires.However,when the surface wind is to the east under the stationary front weather,cloud and fog is relatively thick,and there are more big droplets,which is favourable to the ice accretion of North-South wires.The prevalent wind of GUOZHOU glaze and rime weather is all to the West—East.

4.CONCLUSIONS

The study of observation of wire icing and its weather condition indicates the following:

a. According to the investigation of historical data of GUIZHOU during heavy ice accretion years,the temperature distribution of GUIZHOU during ice accretion is between 0℃ ～ -8℃.The most concentrative temperature distribution is between 0℃ ～ -5℃ which contains the temperature distribution of cities and mountain areas.

b.The wire ice accretion of North—South direction is greater than that of West—East direction (excepl velocity less than 2m/s).The main reason is the existance of stationary front during ice accretion.When the surface wind direction is to the North—east,LWC is relatively great and sufficient liquid water is blow to the North—South wires.

c. Temperature has a relationship with icing density ,when the temperature is blow 0℃ , the higher the temperature,the greater the icing density,and vice versa.the longer the ice accretion time,the more thickness the wires ice accretion.

RADAR TRACKING METHOD FOR CLOUD SEEDING EXPERIMENTAL UNITS OVER CUBA

Sadiel Novo(1), Daniel Martínez(1), Carlos A. Pérez(1), Boris Koloskov(2) and Felix Gamboa(1)
(1) Institute of Meteorology, La Habana, Cuba. C.P. 11700
Tel-Fax: 537-881-3411 e-mail: sadiel.novo@insmet.cu
(2) Agency of Atmospheric Technologies (Agency ATTECH, ROSHYDROMET)
Novovagankovsky per. 8, Moscow, 123242, Russia.
Tel: +7(495)255-2372; Fax: +7(495)255-2134; e-mail: attech@mail.ru

1. INTRODUCTION

During October 2006 and August-October 2007, the second phase of the Randomized Convective Cold Cloud Seeding Experiment in Extense Areas (in Spanish, EXPerimento aleatorizado de siembra de nubes convectivas en AReas EXtensas, EXPAREX) was undertaken over Camaguey, in the eastern part of Cuba (Martinez et al, 2007). One of the main goals of this phase of the experiment was obtaining well defined experimental units for evaluating the seeding effect. In this respect, an experimental unit is defined as the clouds inside a circle of radius 25 km, centered at the location of initial seeding at the first instant, which moved along with the seeded system and inside which all the suitable clouds whose top regions were seeded (or not) with AgI ejectable flares are located. The tracking method used to follow the evolution of these experimental units, also known as floating targets, is the main objective of this paper.

2. DATA

Basic data consisted in MRL-5 (10 cm) automated radar products obtained with software Vesta (Pérez et al., 1999; Peña et al., 2000). Two-dimensional maps of maximum reflectivity, rainfall rate at 3 km height, maximum top height and height of maximum reflectivity within a circle of radius 180 km centered in radar, were ingested every 5 min by the tracking software with the aim of calculating the coordinates of the center of the experimental unit as well as its main characteristics. Resolution of maps was chosen to be 1.5 km. Besides that, coordinates of the initial treatment point were needed to initialize the tracking.

3. ALGORITHM

The tracking algorithm is based on the following hypothesis: the experimental unit will follow the average movement of the nearest surrounding storms. For each maximum reflectivity radar image, the method identifies as storms all the groups of pixels with reflectivity and area values greater than certain thresholds. The reflectivity threshold value (25 dBZ) is applied first, and consequently, connected components (up to second nearest neighbors) are labeled. Afterwards, the area threshold (7 km^2) is applied to discard the smaller echoes. Then, every echo region (storm) is associated with an ellipse, the normalized second order moments of which are equal to the ones of the echo region. This constraint leads to an eigenvalue problem allowing obtaining the parameters of the ellipse.

At the treatment instant, which is taken as initial time for tracking, all present storms are identified, and the corresponding ellipses are defined by the algorithm. The experimental unit boundary circumference is displayed, centered at the treatment point and extending to a radius of 25 km. In the next scan, every storm in the radar's field of vision is tracked by choosing the new center positions that are located at the minimum distances from the centers in the previous scan, provided a certain limit distance is not attained (typically 5 km for a time lag of 5 min between scans). After all the storms have been identified in the new step, their displacement vectors are obtained. An average displacement vector of the storms contained inside the experimental unit circle is then calculated. When there is no storm inside, the searching radius is set to higher values until finding storms to average. The average displacement vector thus obtained is assigned to the experimental unit. As output of the processing program, an image with the last maximum reflectivity map and the subsequent positions of the superimposed experimental unit circle is obtained (Figure1), and also a text file including date, time, coordinates of the center and the main parameters of the seeding circle for every instant, as well as for the total tracking time. The algorithm stops to follow an experimental unit when the elapsed time with total rainfall rate less than 2 mm/h inside the seeding circle reaches 30 min.

4. RESULTS

The tracking method was applied to the twenty experimental units obtained during the second phase of EXPAREX, in which experimental flights were carried out from October 3 to October 14 in 2006 and from August 24 to October 4 in 2007. Table1 shows some tracking parameters for all of them. Date-Time stands for the date (ddmmyy) and time (hh:mm) of first seeding, TT is the total tracking time, V the mean velocity and W is the total volume of precipitation (3 km height) accumulated in the floating target during its lifetime.

Table1: Tracking parameters for the experimental units.

#	Date-Time	TT (min)	V (km/h)	W (kT)
1	031006-14:20	225	30	55113
2	061006-15:20	415	17	14114
3	101006-13:50	45	14	15
4	101006-14:50	280	16	1358
5	111006-14:50	295	18	2729
6	121006-14:45	40	12	20
7	141006-15:15	523	20	25319
8	240807-14:05	535	24	10380
9	270807-13:35	235	28	11120
10	300807-14:00	245	14	4628
11	310807-13:15	275	17	2761
12	100907-14:05	220	27	3027
13	110907-13:30	525	24	12953
14	150907-13:40	320	18	7917
15	170907-14:15	530	12	12636
16	180907-14:30	230	15	1862
17	220907-13:55	355	20	3980
18	270907-13:15	845	20	34982
19	280907-13:45	340	15	5235
20	041007-13:25	515	15	10307

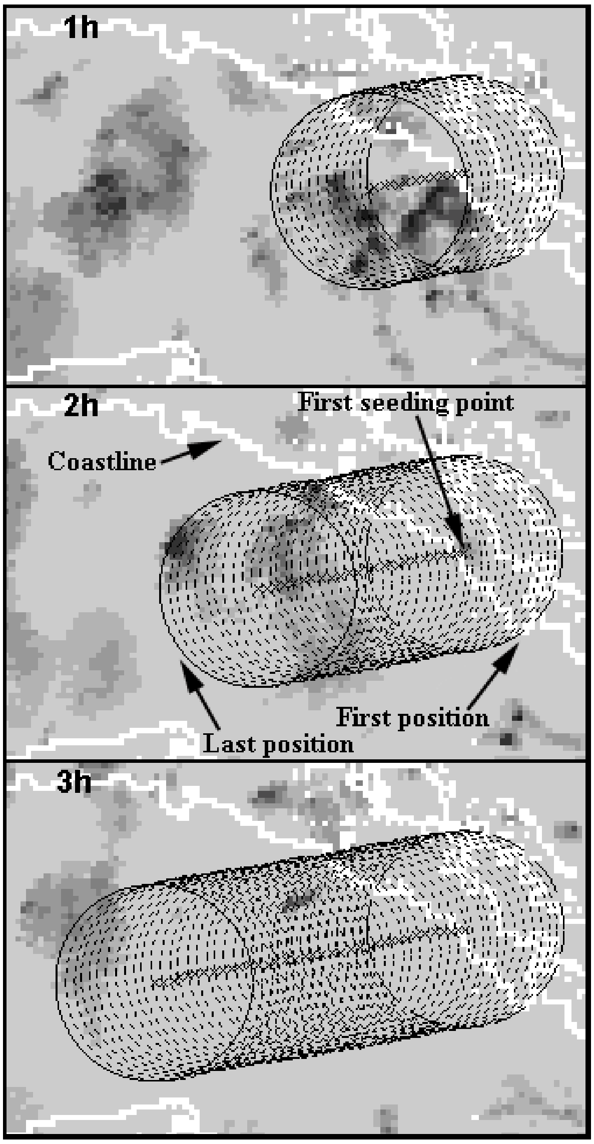

Figure1: Trajectory of first experimental unit for 1, 2 and 3 h of tracking until it was almost dissipated.

Figure1 shows the trajectory of the first experimental unit obtained on October 3, 2006 for 1, 2 and 3 h of tracking, until it was almost dissipated. This area moved fast (30 km/h in average) and maintained a course near to WSW.

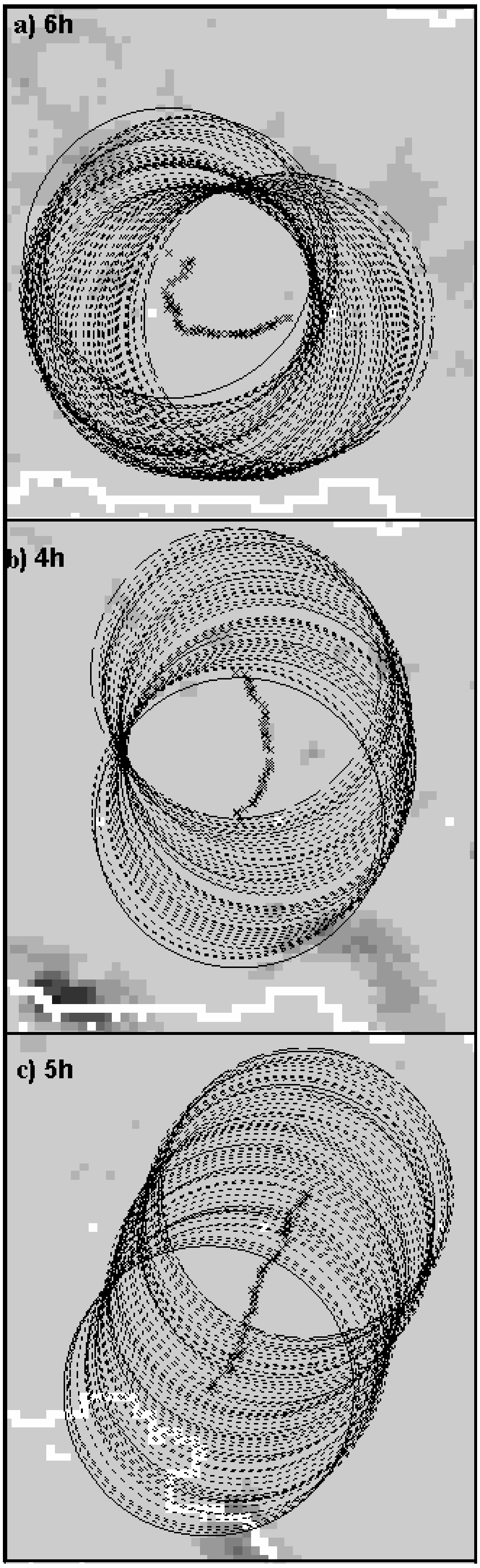

Figure2: Trajectories of experimental units 2 (a), 4 (b) and 5 (c) until almost dissipation. Tracking time is indicated.

For each trajectory, the broken line circle indicates the area occupied by the experimental unit at first instant (time for initial treatment), which center is the first seeding point inside the area. Circles limited by dotted lines indicate the intermediate positions of the tracking area and the continuous line circle marks the final one.

Figure2 shows the trajectories for experimental units 2, 4 and 5 (from 2006) until almost dissipation. Areas 3, 6 and 7 were not showed because they dissipated early or have a very long duration. A plot of Log(TT) versus Log(W) for the twenty 2006-2007 experimental units is shown in Figure3 with circles. Notice that we don’t know which ones of them were really seeded, because of the randomized and blind nature of the experiment.

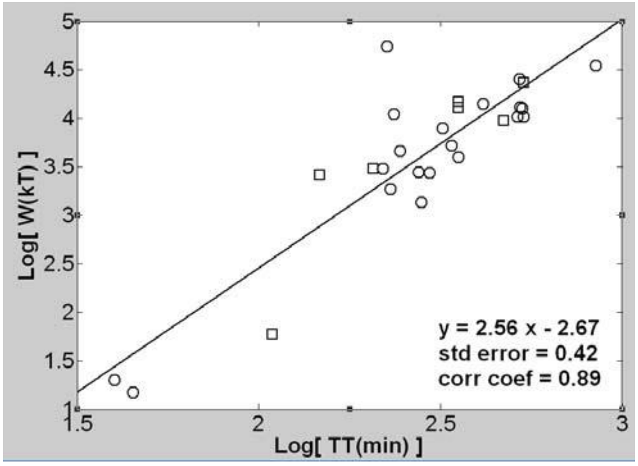

Figure3: Plot of TT versus Log(W) for all the experimental units in 2006 (circles) and 2005 (squares).

Table2: Tracking parameters for 2005 units.

#	Date-Time	TT (min)	V (km/h)	W (kT)
1	030905-15:01	354	9	12446
2	160905-14:50	121	30	60
3	170905-14:52	452	25	11611
4	210905-16:19	355	12	16571
5	220905-14:30	486	17	21550
6	230905-14:46	405	15	2481
7	270905-13:53	221	10	3033

Square marks in Figure3 belong to data from seven units more, all of them seeded, which were obtained during the first stage of EXPAREX (exploratory, non randomized experiment) in September 2005. Some tracking parameters for these 2005 experimental units appear in Table2. All the data in Figure3 were adjusted linearly and the corresponding equation and standard deviation were written on the plot. From the plot we can see that there is a gap without points between 1.8 and 3 in y axis. This seems to indicate that the three cases in the lower-left corner of the graph might belong to a different statistical ensemble in relation to the rest of the sample. The 2005 case is seeded, and the treatment of the two 2006 cases is not yet known. This may be an effect of the still limited size of the sample or may be caused by specific synoptic or mesoscale situation in these cases, or may be simply a problem of wrong experimental unit selection which has to be taken care of in the future, evaluating the possibility of considering these cases as outliers. As the randomized experiment goes on, the statistical properties of the ensemble of experimental cases will become clear.

5. CONCLUSIONS AND REMARKS

A method for tracking cloud seeding floating experimental units over Cuba has been developed. The algorithm uses maximum reflectivity maps to identify storms in the radar’s field of scanning. Looking for the nearest storm’s positions in the next scan, it follows the movement of each one. Then the average movement of nearest surrounding storms is assigned to the experimental area and its parameters calculated.

With data from 27 experimental units, it was found a linear relationship between the total precipitation volume accumulated at 3 km height and the total duration for each area. A gap without experimental units was found in the graph around 500 kT in rainfall volume. Points below this gap could indicate outliers, which should be clarified in subsequent analysis as the sample increases.

Radar-rain gauge calibration will give us the way to compare ground precipitation with the tracking parameters for a better evaluation.

6. REFERENCES

Martinez D., C.A. Perez, B.P. Koloskov, V.P. Korneev, V.V. Petrov, F. Gamboa and S. Novo, Randomized convective cold cloud seeding experiment in extended areas in Cuba (EXPAREX). *Proc. of 9th WMO Conf. on Wea. Mod.,* 22-24 October, Istanbul, Turkey, 2007.

Peña A., O. Rodriguez, M. Perez, R. Naranjo, L. Fernandez, A. Barreiras, A. Martinez and M.D. Rodriguez, Modernization of the Cuban weather radar network. *Phys. Chem. Earth (B)* 25, #10-12, 1169-1171, 2000.

Perez M., A. Peña and O. Rodriguez, Reengineering MRL-5 for the Cuban weather radar network. *29th Int. Conf. Rad. Met.*, Montreal, Quebec, Canada, 811-814, 1999.

Acknowledgements

The authors thank to the Cuban Government and particularly to the Institute for Civil Aeronautics for coordinating and financing EXPAREX.

UPGRADES TO THE FSSP-100 ELECTRONICS

Darren O'Connor, Brad Baker, R. Paul Lawson
SPEC Incorporated, Boulder, Colorado

1. INTRODUCTION

The forward scattering spectrometer probe (FSSP) was developed in the 1970's (Knollenberg 1981). The FSSP model 100 has been the subject of intensive instrument performance analysis (e.g., Dye and Baumgardner 1984; Cooper 1988; Brenguier 1989; Field et al. 2003) and upgrades (Cerni 1983; Brenguier et al. 1998). Brenguier et al. (1998) added the ability to record the arrival time of each particle and decreased the deadtime (time the probe was inactive while the electronics processed a particle event) from 6 μs to essentially 0 μs. Baker (1992) used particle interarrival times to investigate turbulent entrainment, mixing, and possible droplet clumping in cumulus clouds. Field et al. (2003) found that there were two fairly distinct peaks in particle arrival times when the probe was operated in the presence of large ice particles. One peak they attributed to closely spaced particles that resulted from ice shattering on the probe inlet, and a second, larger peak that was generated by particles passing unimpeded through the sample volume.

In this paper we describe upgrades to the FSSP-100 that result in:

1. Reduced offset errors associated with the AC coupling and baseline restoration circuitry.
2. Recording of signal and qualifier peak amplitudes of every particle, along with the particle transit time through the laser beam and the arrival time of the particle.
3. Sub-sampling (approximately 2%) of particle events that are digitized and recorded at a 40 MHz sample rate. The resulting time series of both the Signal and Qualifier waveforms may be viewed in post processing, (viewed as if a high-speed digital oscilloscope were probing the Signal and Qualifier channels in real time).
4. Data recorded at the probe on a flash disk. Data can also be recorded on an external computer via Ethernet connection. A field programmable gate array (FPGA) and onboard 400 Mhz Linux processor are completely programmable using an Ethernet connection, making field modifications easy to implement.

2. BASELINE RESTORATION CIRCUIT UPGRADE

The traditional FSSP100 baseline restoration circuit is shown in **Figure 1** and the newly implemented baseline restoration circuit is shown in **Figure 2.** In **Figure 1**, photodiode current into U1 is AC coupled through capacitor C4. This generates negative going pulses out U2 as particles pass through the FSSP 100 laser beam. C4 builds up a bias voltage as each particle event occurs, producing a baseline shift in the output of U2. During the pulse event, the previous baseline value is held at the output of U4, and is fed as an offset to U5. This removes the previously sampled baseline voltage from the final output of U5. When particles exit the beam, the DC bias due to C4 is fed to U3 as a positive voltage and forces its output to go high. Capacitor C3, is then charged until it matches he DC bias on C4. By feeding this voltage through the unity gain amplifier U4 and on to the input of U5, the baseline shift is subtracted off of U5's output.

Figure 3a is a simulation of the traditional baseline restoration circuit in the presence of several particle events. The large particle events are on the order of 500 μS, and are on the order of magnitude of the kind of signal durations that may occur during shattering events. The blue signal is the ideal output voltage and the green signal is the baseline restored output voltage. The baseline restoration circuit is not able to completely remove the baseline shift during the large transit time events, and by the 3rd one, centered at roughly 1.1 mS, the offset between the ideal and baseline restored outputs is 10 mV. When the pulse ends, the 10 mV offset remains. In the interval from 1.35 ms to 1.75 ms, the offset is seen to decay back to nearly zero volts.

Figure 4a shows a small particle event occurring immediately after the last of the large particles that were seen in **Figure 3**. At 1.355 mS, a pulse of ideal amplitude 25 mV occurs, but the baseline restore circuit outputs 35 mV due to the component of baseline shift that the baseline restoration circuit has not removed. 540 μs later, another particle event of the same amplitude occurs, shown in **Figure 4b**. At this time, the baseline restoration circuit is seen to have fully removed the baseline shift.

Photodiode current (represented by current source Ipd) in the newly implemented baseline restoration circuit, shown in **Figure 2**, is amplified through U1, then through U2 and U3. The signal is DC coupled throughout this series of amplifiers. When no particles are present, transistor Q1 is turned on, and any DC bias out of U3 is fed into U4. U4 integrates the DC bias, producing a negative accumulated output voltage. This negative voltage is fed back to U3, thus subtracting the DC bias from the output of U3, where the signal is then measured with DC bias removed. When particle events occur, the SFSSP logic turns off transistor Q1, and capacitor C6 serves to hold the accumulated DC bias correction voltage.

The output of U3 is fed to an analog-to-digital converter (ADC) that requires a 0.1 V offset for proper operation. This offset is achieved by feeding a 0.1 V reference into the positive terminal of U4. In the simulations (discussed next), this 0.1 V is subtracted off for clarity.

The main errors in this circuit are due to two sources:

1. When switch Q1 is off, or open circuit, the bias current of U4 flows through C6. At a typical value of 6 μA, it produces approximately a volt per second across C6, which is amplified by a gain of two through U3. Thus, during a 500 μs particle event, approximately 1 mV of baseline shift occurs at the output of U3. For typical transit times in flight of 2-3 μS, the offset is only on the order of 5 μV.
2. The input offset voltage of U4 is amplified by a gain of two through U3. This is a maximum of 550 μV (100 μV typical), producing approximately 1 mV of offset out of U3 after the gain is applied.

Figure 3b shows the new baseline restoration circuit response to the same particle events analyzed for the traditional circuit. Due to U4's offset voltage, a fixed offset of 1.2 mV exists on the baseline restored (green) signal. At the end of the last large particle event, again centered at 1.1 ms, the offset voltage is –3.2 mV, a change of 2 mV from nominal. Thus, compared to the traditional baseline restoration circuit, which drifted by 10 mV, the new baseline restoration circuit shows a five to one improvement.

Figure 4c shows a small particle event occurring immediately after the last of the large particles that were seen in **Figure 3**. At 1.355 mS, a pulse of ideal amplitude 25 mV occurs, but the new baseline restore circuit outputs 21.74 mV due to the component of baseline shift that the new baseline restoration circuit has not removed. This is roughly the same 3.2 mV offset seen at the peak of the previous particle. 540 μs later, another particle event of the same amplitude occurs, shown in **Figure 4b**. At this time, the baseline-restored output is at 23.04 mV, representing an 800 μV shift from the nominal fixed offset.

In summary, the new baseline restoration circuit allows the photodiode current to be DC coupled through the amplifier chain, using servo techniques to remove any DC biases from the signal. It further provides a 100 mV offset required by the SFSSP ADC. The new baseline restoration circuit kept simulated errors to within approximately 10%, while the traditional circuit produced errors as great as 40. In some cases of very large crystal break up, undesired offsets have been observed. These offsets were removed in real--time by an automatic algorithm that looks for particle events that last too long. The reset capability is a further feature of the new electronics, allowing the transistor Q1 to be forced on for brief periods, thus integrating off any spurious DC offsets.

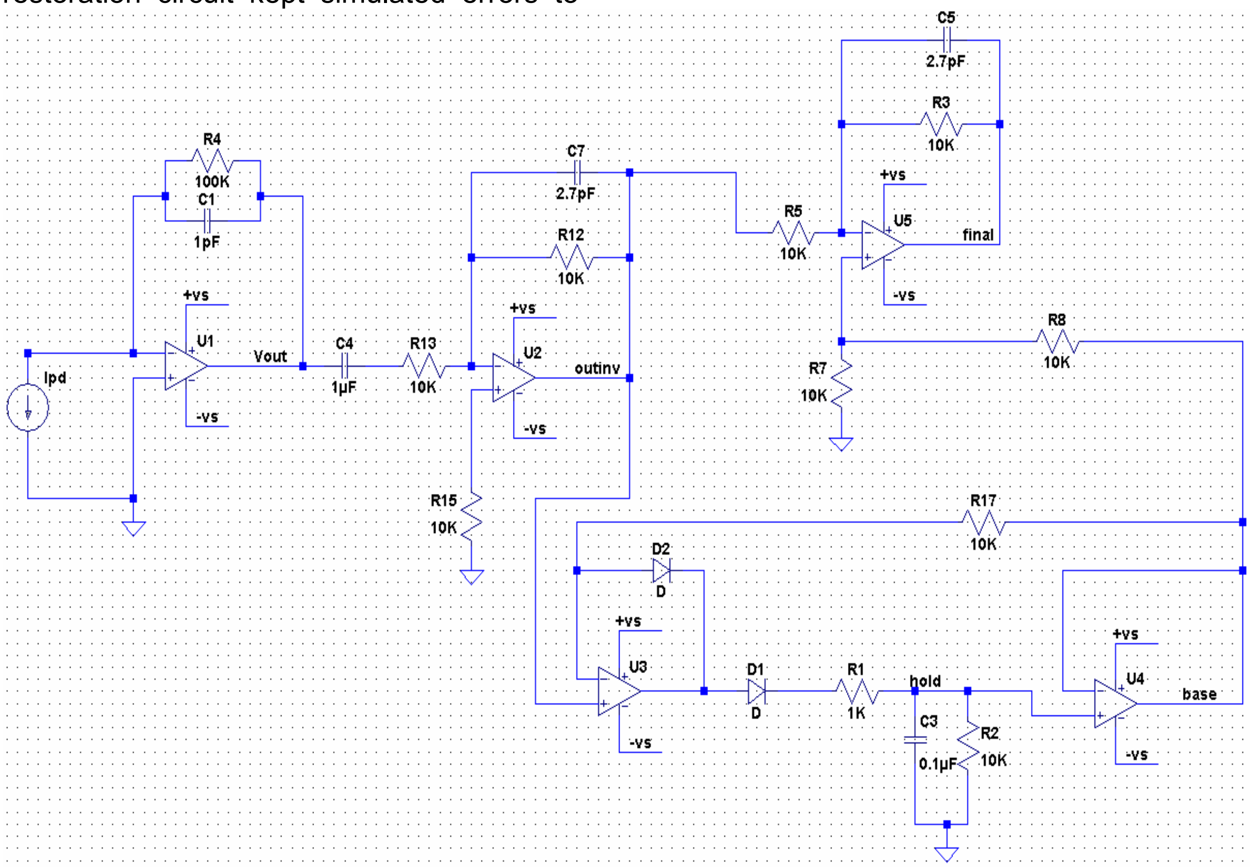

Figure 1. Traditional FSSP 100 front end amplifier (U1, U2) and baseline restoration (U3, U4, U5) circuitry. The Ipd current source models the photodiode behavior in the circuit.

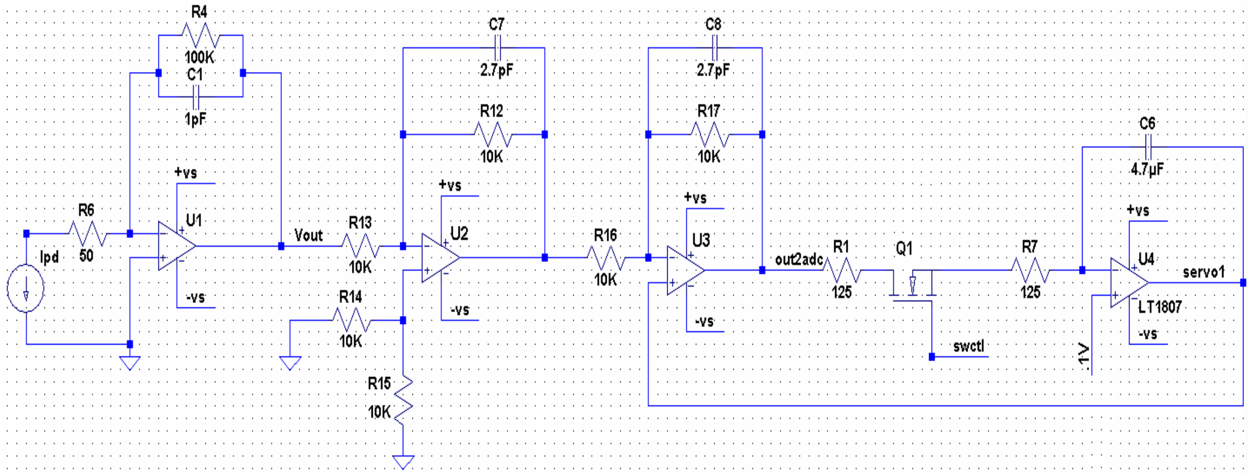

Figure 2. SPEC FSSP Upgrade front-end amplifiers (U1, U2 and U3) and new baseline restoration (U3, U4) circuitry. The Ipd current source models the photodiode behavior in the circuit.

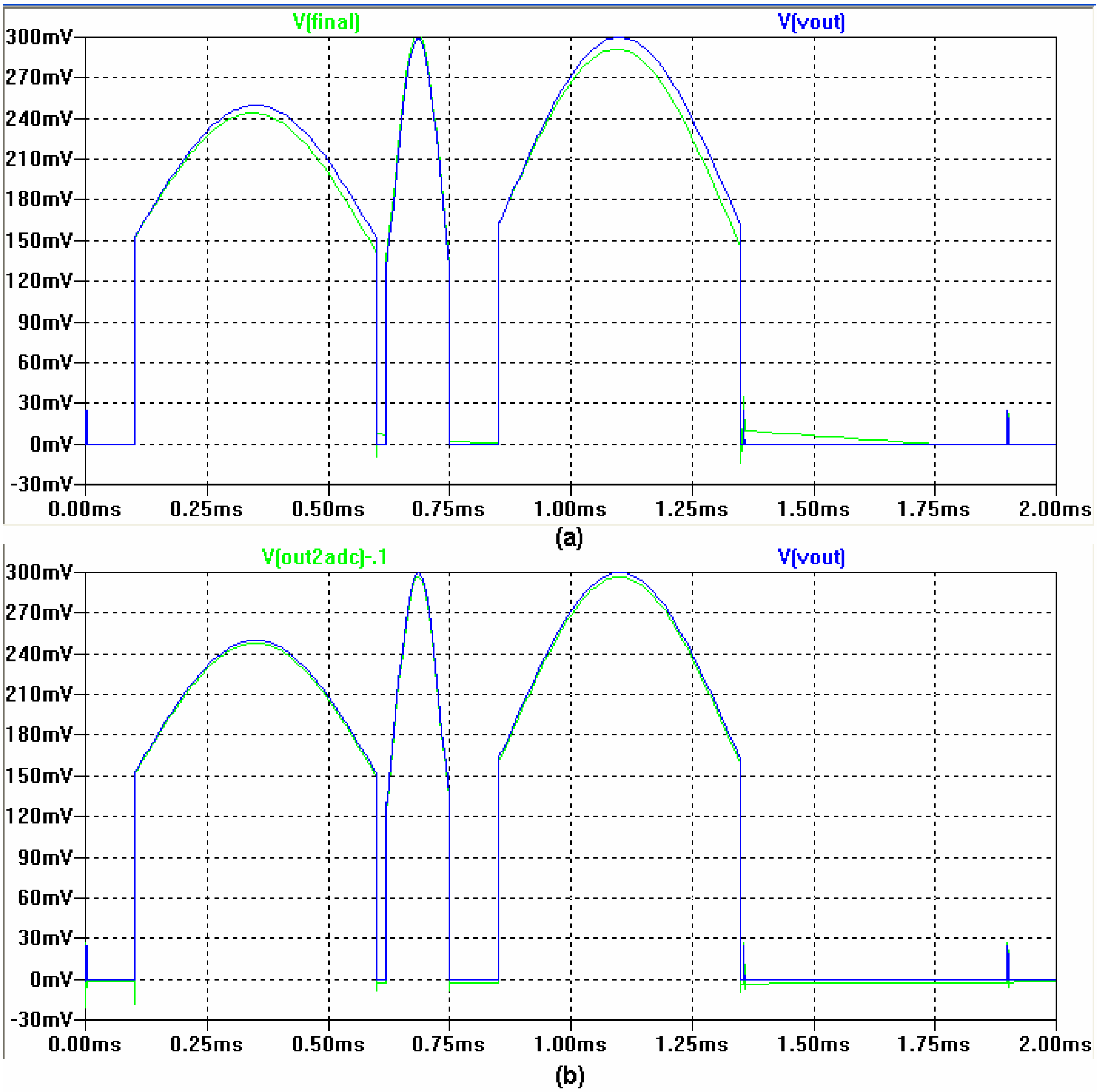

Figure 3. Ideal (blue) and baseline restored (green) signals for the traditional (a) and new (b) baseline restoration circuits. The large amplitude, long duration signals model shattering events.

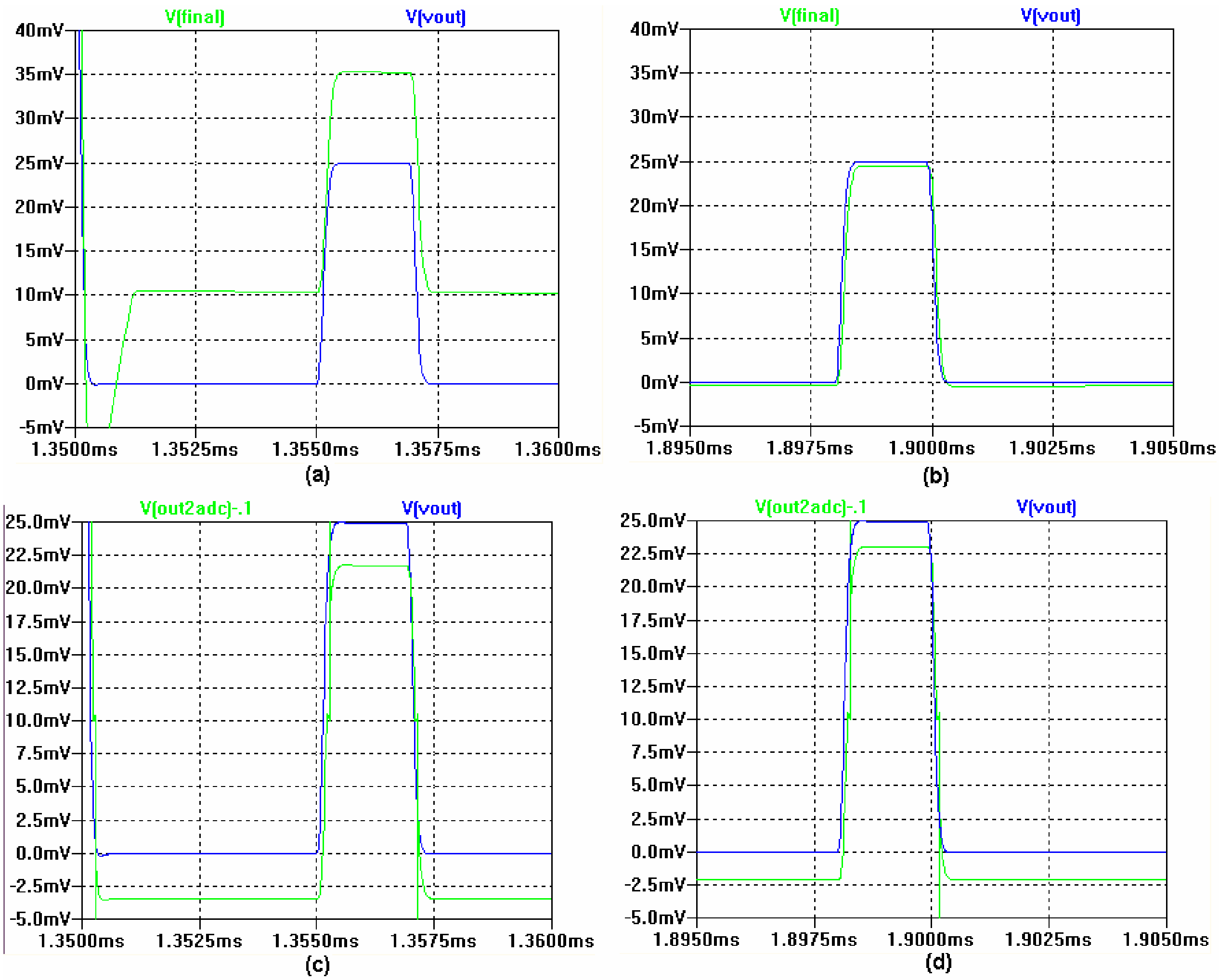

Figure 4. Ideal (blue) and baseline restored (green) signals for the traditional (a and b), and new (c and d) baseline restoration circuits. Plots (a) and (c) are for period immediately after the large signals in **Figure 3**. Plots (b) and (d) are 540 μs later.

3. SIGNAL AND QUALIFIER EVENT TIME SERIES CAPTURES

The SFSSP uses high-speed memory in the FPGA to not only capture particle-by-particle data, but also to capture entire particle events. A pair of examples is shown in **Figure 5**, where at concentrations on the order of 10^5 per liter (top panel), three coincident particle events were captured. The two marked with horizontal red arrows would normally be measured as good particles, since the transit time would exceed the running average used to define the beam diameter (Dye and Baumgardner 1984), and the maximum Signal peak exceeds the Qualifier peak. The effect of these accepted particles is to incorrectly bias the average transit time towards too large a value, and to produce measured peak values that are biased towards large particles. The latter effect is due to the probe only measuring the largest peak during the coincident event. The bottom panel in **Figure 5** shows a series of particle events that would be measured by the SFSSP as a single particle. This series was measured during a period of large ice, examined in detail in section 3.3.

The effects of coincidence on the FSSP have been analyzed in many studies, such as by Baumgardner et. al. (1985), Cooper (1988), Brenguier (1989), and Coelho et al. (2005). The SFSSP, which captures with full-particle events at known sub-sample rates (of total particle events) provides for an entirely new means of analyzing the FSSP 100. With these data, the techniques proposed for handling coincidence may be verified and fine-tuned.

A further potential use of particle event captures (PEC) is to correct particle sizes of individual particles, taking into account the time response of the analog amplifiers and the measured transit time of individual particles. Correction methods have been suggested by others (Korolev et. al., 1985; Cooper, 1988; Coelho, et. al. 2005, part I). A method based on the PEC capability of the SFSSP is discussed next.

3.1 TRANSIT TIME CORRECTIONS

The SFSSP measures real time particle events, allowing for unique analysis of the effects of the analog circuitry low-pass filtering on the waveform. The filter performs exponential smearing with a time constant τ. The value used in simulations to match a measured waveform was τ = 0.64 µs. **Figure 6** shows two simulations plotted against a measured (green) PEC. The simulation on top assumes the laser beam intensity is exactly Gaussian, corresponding to a $1/e^2$ beam width of 420 um, plotted in blue. The black signal is the simulated response of the filter to this signal. The simulation on the bottom is a modified Gaussian, using the same $1/e^2$ beam width, but modified by a gain and offset of 1.3 and –0.37, respectively. Negative values were then set to 0. This was done to attempt to match the resultant filtered waveform more closely to the measured response, as the HeNe laser is likely not a pure Gaussian in its intensity pattern

Using a 20 mV threshold for the minimum at which a particle is detected, the transit times of the simulated signals is measured and estimated in several ways. The filtered signal period between the 20 mV limits is measured; the area under the curve, divided by the voltage peak for the same limits (20 mV) is estimated; and the time from the first (leftmost) 20 mV crossing to the peak is measured, and this value multiplied by two. The results for the two simulated waveforms are shown in **Table 1**.

	Time, Real (us)	Time, Total (us)	% Error Total	Time, Area/Peak (us)	% Error Area/Peak	Time to peak x 2 (us)	% Error Time to Peak
Pure Gaussian	3.385	4.64	37	1.97	41.80	3.63	7.15
Modified Gaussian	2.45	4.67	96	1.85	24.5	3.11	27

Table 1. Estimates of transit time using measured time, area over peak, and time to peak (x2).

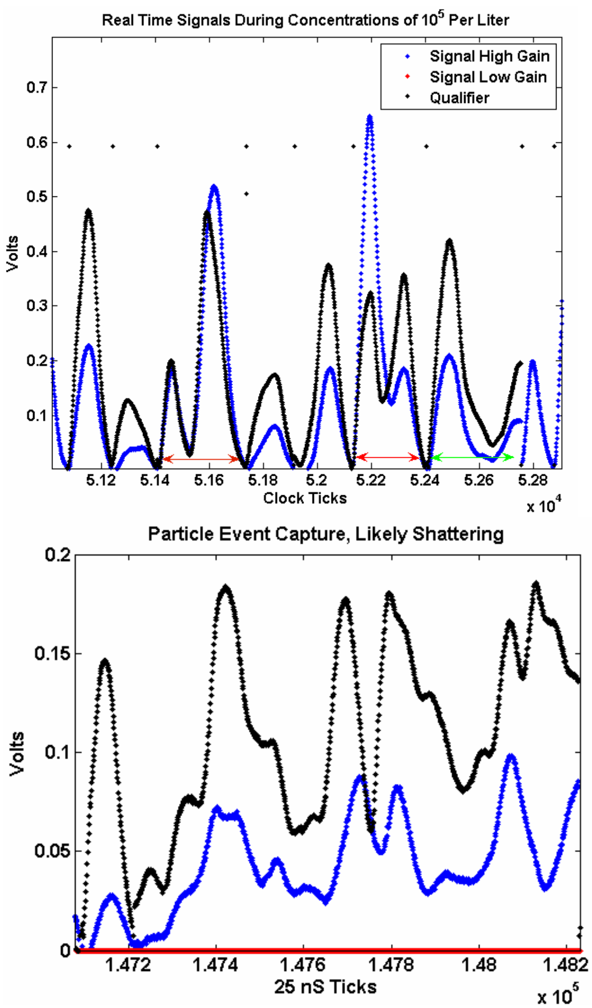

Figure 5. Total particle event captures by the SFSSP during concentrations of 10^5 per liter (top), and due to shattered ice particles (bottom).

The area divided by the peak, assuming a uniform distribution for the laser, results in a transit time estimate of:

$$t' = t / (1 - e^{-t/\tau})$$

Where

t' = estimated transit time
t = true transit time
τ = time constant of the filter.

If τ is 3 times greater, or more, than the actual transit time, the estimated transit time will be smaller by 5% or less than the actual transit time.

As the laser intensity becomes less uniform and approaches a Gaussian, this result becomes less and less applicable. This is illustrated in **Table 1**, where the pure Gaussian result for the area / peak technique underestimates by 42%, while the modified Gaussian estimate is only off by 24.5%. Returning to **Figure 6**, one may notice that the modified Gaussian is closer in shape to a uniform distribution than is the pure Gaussian.

Since the two techniques bound the real transit time above (time to peak method) and below (area over peak method), the average of the two may yield better results. For the true Gaussian, the resultant error is 17.3%; for the modified Gaussian, the resultant error is 1.3%.

Figure 7 shows the percentage error for a modified Gaussian distribution while varying the velocity from 100 to 200 ms^{-1}. Using the average of the two techniques produces a worst case error of 9%. All three techniques greatly improve upon the total measurement that would otherwise be used.

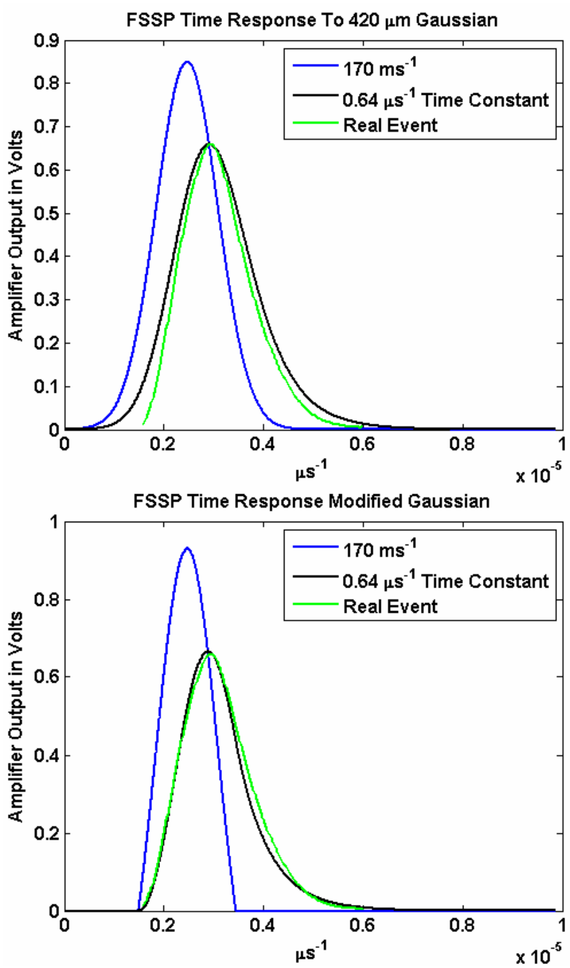

Figure 6. Simulated and measured FSSP waveforms. Blue is ideal (no exponential response smearing), black is with smearing (0.64 uS time constant), and green is a real measured event. Simulation done at 170 ms^{-1} to match assumed velocity of measurement. The top panel assumes the laser beam intensity is exactly Gaussian, corresponding to a $1/e^2$ beam width of 420 um. The bottom panel is a modified Gaussian, using the same $1/e^2$ beam width, but modified by a gain and offset of 1.3 and –0.37, respectively.

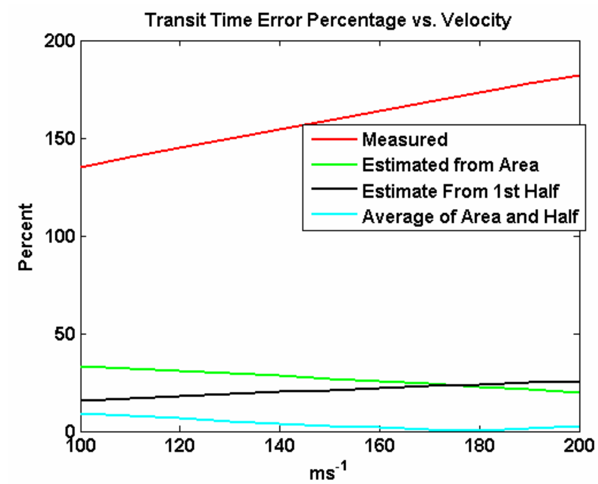

Figure 7. Absolute percentage error in estimating actual transit times across a 420 um $1/e^2$ Gaussian laser distribution. Errors are based on total measured transit time with no corrections (red); area under the voltage curve divided by the maximum voltage (green); transit time from the beginning to the peak times two (black); and average of the area / peak and peak times two methods (cyan).

3.2 PULSE HEIGHT CORRECTIONS

It is possible that with good transit time estimates, the decrease in the measured peak caused by the time response of the analog filter can be corrected. By simulating a range of particle sizes, as in **Figure 6**, the filtered peak (black in **Figure 6**) divided by the (assumed) real peak (blue in **Figure 6**) vs. transit time is seen to be a linearly decreasing value. This is seen in **Figure 8**, where the blue line is the ratio of measured to actual peak voltages vs. velocity of the simulated particle. The particle peak was 0.75 Volts. A least squares estimate of the blue curve, using the transit time estimated from the methods described above (average of area/peak and 1st half estimate) is also plotted in green.

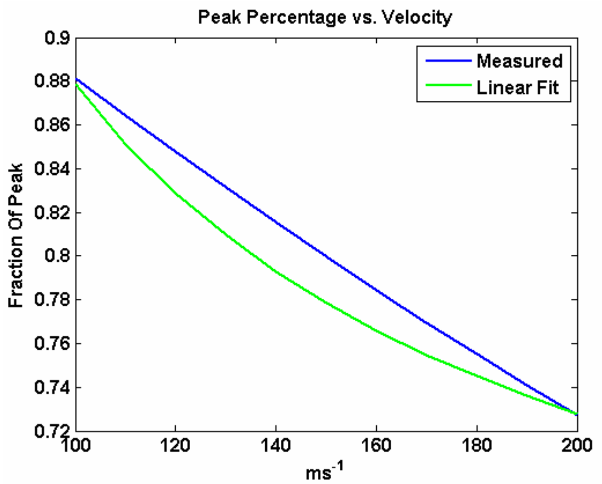

Figure 8. Ratio of measured peak to actual peak vs. velocity for 0.75 Volt signal .

The linear fit values from **Figure 8** are used to plot the peak voltages in **Figure 9**. The simulated peak voltage is plotted in blue, and the resultant peak voltages vs. velocity are plotted in red. The corrected values vs. velocity are plotted in green. The maximum error in the estimate is less than 3. The slope and offset values that generate the green line in **Figure8** work well for pulse heights ranging from 0.15 volts to 16 volts. At lower voltages, two other pairs of coefficients are used to cover the range of peaks from 20 mV to 150 mV, as the coefficients begin to change more rapidly in this pulse height region.

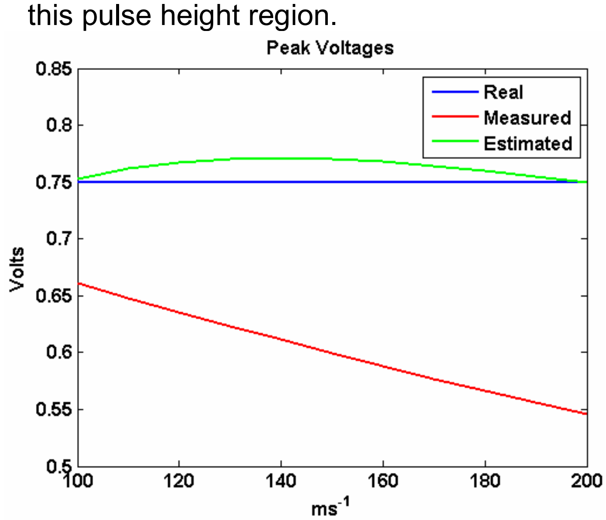

Figure 9. Real (blue), measured (red) and corrected estimate (green) peak values for a particle moving through the simulated FSSP at 100 to 200 meters per second.

Measured signals from the FSSP allow analysis of this correction. For example, to correct the measured (green) signal in the bottom panel of **Figure 6**, its transit time is first measured to be 2.13 uS. The pulse height of the simulated (blue) signal is then estimated from the following correction:

$$\text{Peak} = \text{measured peak} / (92{,}292 \bullet \text{transit time}_{\text{measured}} + 0.533)$$

Using the measured peak value of 0.659 volts and the measured transit time of 2.13 μs, the pulse height is estimated to be 0.90 volts. If one assumes the blue signal matches the original signal, before filtering, then the actual peak is close to its value: 0.85 volts. Without correction, the sizing error is –22.5%. After transit time correction, the error is 6.2%.

To further test the peak estimate two more particle events are shown in **Figures 10** and **11**. The measured PEC (green) signals in the two figures have peak values of 0.27 and 6.22, spanning a broad range of voltages due to large differences in particle sizes. The simulated peak values, without filtering, are 0.4 volts and 8.1 volts for the blue plots in **Figures 10** and **11**. The estimate of the peak for the signals in **Figure 10**, using the above transit time correction and the real, measured PEC, is 0.4 volts. This is an error of only 0.2%, compared to the original 33% underestimate . The estimate of the peak for the signal in **Figure 11** is 8.49 volts, a 4.9% overestimate, compared to the original 6.22 volt, 23% underestimate.

Although the corrected peak values are being compared to simulated waveforms (modified Gaussians), the results are still likely to represent an improvement in accuracy. Assuming the modified Gaussians are the correct signal, the errors for three different simulations were reduced from 22.5% to 6.2% (**Figure 6**), from 33% to

0.2% (**Figure 10**), and from 23% to 4.9% (**Figure 11**).

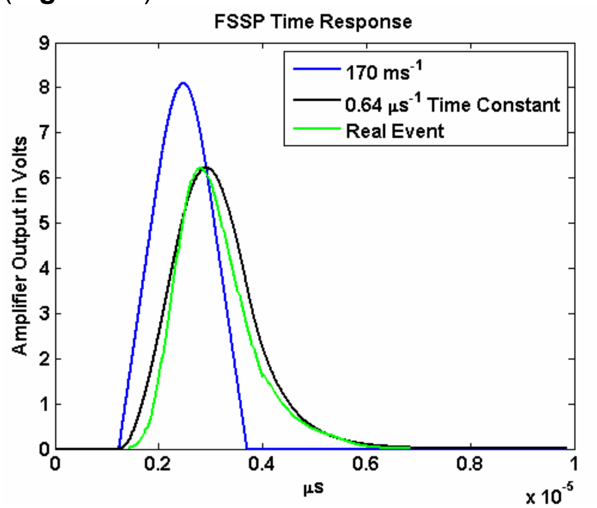

Figure 10. Measured signal (green) and simulated modified Gaussian without (blue) and with (black) filter effects. Actual Peak: 0.4, Measured Peak: 0.27 (33% low), Estimated Peak: 0.4 (0.2% over**)**

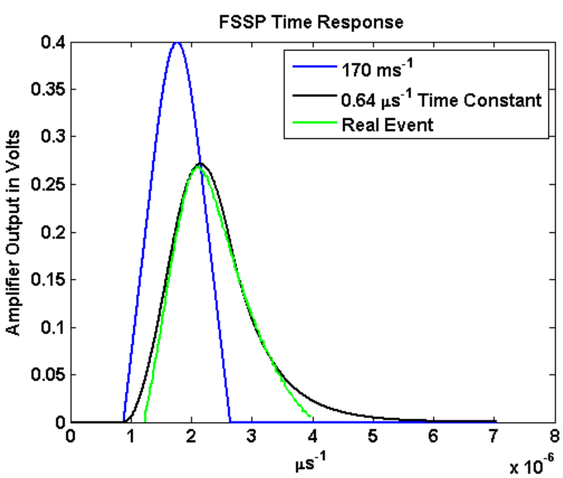

Figure 11. Measured signal (green) and simulated modified Gaussian without (blue) and with (black) filter effects. Actual Peak: 8.1, Measured Peak: 6.22 (23% low), Estimated Peak: 8.50 (4.9% high).

The SFSSP measures transit times three ways for particle by particle events:

1. Total transit time: the time it takes for a particle to rise above a minimum threshold of 10 mV, and to then fall below 5 mV. This method greatly overestimates transit times at aircraft speeds due to analog filter smearing of the signal during signal decay.
2. Time to peak: the time it takes for a particle to rise from the 10mV threshold to the peak. This method overestimates transit times, but by much less than the total transit time method.
3. Area / Peak Voltage: the area under the curve for the entire particle event is recorded. Dividing this value by the peak voltage yields an underestimate of the total transit time.

By using methods 2 and 3, and by determining the coefficients for transit time correction from the PEC data, a particle by particle correction to size may be implemented.

A more exhaustive method may be implemented using the techniques by which figures 6, 10 and 11 were generated. It involves estimating the original particle size by generating a modified Gaussian time series, simulating the low-pass filtering effect of the analog electronics on this series, and comparing the filtered output to the original PEC event. The peak of the modified Gaussian, before filtering, is the resultant estimate of the particle peak without the attenuating effect of the filter.

3.3 AN EXAMPLE OF ICE CRYSTAL SHATTERING

Here we examine an example of ice crystal shattering from the recent DOE Atmospheric Radiation Measurement (ARM) ISDAC field project staged from Fairbanks, Alaska in April 2008. ISDAC Research Flight #32, the 3rd of three flights on April 27th, 2008, included data collection by the Canadian NRC CV-580 research aircraft in cirrus clouds. As will be demonstrated**,** the cloud consisted of relatively few small ice particles (<200 μm). Shattering of larger crystals results in large over-estimates of the small ice concentration, in this situation, if shattering removal techniques (Field et al. 2003, Korolev and Isaac 2005) are not employed.

Figure 12 shows the size distributions from the 2D-S and the SFFSSP probes with and without removing shattering effects via inter-particle spacing information as described in Field et al. (2003) and Korolev and Isaac (2005) and suggested by Cooper (1977). In this situation of low natural concentrations, well over 90% of the standard measurements are actually effects of shattering.

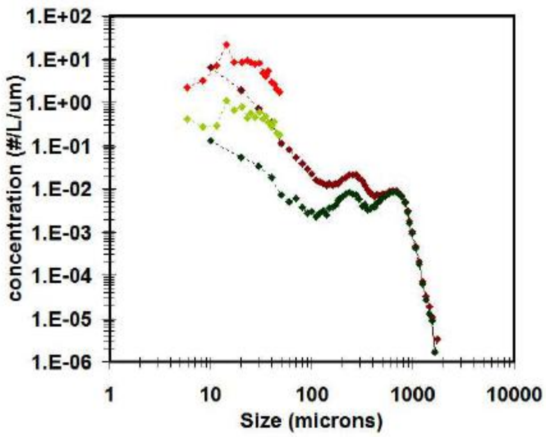

Figure 12: SFSSP PSDs via standard processing (light red) and with shattering removed (light green) averaged over a continuous 99-second period starting at 06:10:01 and 2D-S PSDs averaged over about the same period also with (dark green) and without shattering removed (dark red).

Since shattering removal algorithms are imperfect, estimates of the remaining natural small ice concentrations have uncertainties as large as the estimates themselves. However, this situation yields good estimates of the shattering effect and thus may be used to quantify that effect.

Figure 13 shows a scatter plot of the spurious small (<50 μm here) ice mass content measured by the SFSSP versus the precipitation ice content (all sizes) measured by the 2D-S. There is a good correlation as expected since one is a direct effect of the other. About 7% of the precipitation mass content is converted to spurious small ice mass content via shattering into the FSSP sample volume.

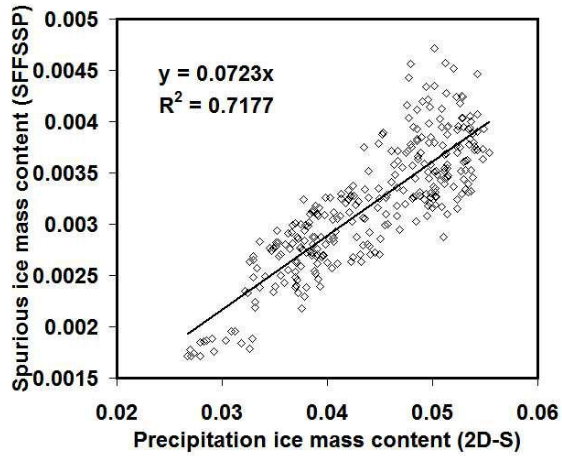

Figure 13: Scatter plot of the spurious SFFSSP ice mass content versus the precipitation ice mass content as measured by the 2D-S. Also shown are the linear regression and the square of the correlation coefficient.

4. SUMMARY

New electronics upgrades to the FSSP-100 are discussed. The new upgrades (i.e., the SFSSP probe) contain advanced technology enabling several improvements that make it possible to better understand instrument response.

Initial tests of an improved baseline restoration circuit show the new method works well. High concentrations are not expected to greatly alter the measured size distribution. Real time electronics monitors and resets the baseline when erroneous data occurs. The new baseline restoration circuit keeps simulated errors to within approximately 10%, while the traditional circuit produces errors as great as 40%.

The SFSSP has the unique ability to digitize and store both the signal and qualifier waveforms. By analyzing the time series from these waveforms, it is possible to correct transit time and pulse height measurements. The transit time is corrected for effects of the analog circuitry low-pass filtering on the waveform. Once the transit time is corrected, the decrease in measured peak voltage caused by the time response of the analog filter is corrected.

The SFSSP measures the arrival time of each individual particle. Using a technique similar to that described by Field et al. (2003), ice crystals that are suspected to have shattered on the probe inlet are removed by examination of their inter-arrival times. An example of shattered particle removal from the recent ISDAC field project is presented and discussed.

REFERENCES

Baker, B.A., 1992: Turbulent entrainment and mixing in clouds: A new observational approach, *J. Atmos. Sci.,* **49,** 387-404.

Baumgardner, D., Strapp, W., and Dye, J. E. 1985: Evaluation of the Forward Scattering Spectrometer Probe. Part II: Corrections for Coincidence and Dead—Time Losses. *J. Atmos. Oceanic Technol*., **2**, 626—632.

Brenguier, J. L., 1989: Coincidence and dead-time corrections for particle counter. Part II: High concentration measurements with an FSSP. *J. Atmos. Oceanic Technol.*, **6,** 585—598.

Brenguier, J-L., T. Bourrianne, A. de Araujo Coelho, J. Isbert, R. Peytavi, D. Trevarin, and P. Wechsler, 1998: Improvements of droplet size distribution measurements with the fast-FSSP. *J. Atmos. and Oceanic Tech*., **15**, 5, 1077-1090.

Cerni, T. A. 1983: Determination of the size and concentration of cloud drops with an FSSP. *J. Clim. & Appl. Meteorol*., **22**, 1346-1355.

Coelho, A., J-L. Brenguier, and Thierry Perrin: 2005: Droplet Spectra Measurements with the FSSP-100. Part I: Low Droplet Concentration Measurements. *J. Atmos. Oceanic Technol*. **22**, 1748—1755.

Coelho, A., J-L. Brenguier, and Thierry Perrin: 2005: Droplet Spectra Measurements with the FSSP-100. Part II: Coincidence Effects. *J. Atmos. Oceanic Technol.* **22**, 1756—1761.

Cooper, W. A., 1977: Cloud physics investigations by the University of Wyoming in HIPLEX 1977. *U.S. Bureau of Reclamation.*

Cooper, W. A., 1988: Effects of coincidence on measurements with a Forward Scattering Spectrometer Probe. *J. Atmos. Oceanic Technol*., **5**, 823—832.

Field, P., Wood, R., Brown, P. R. A., Kaye, P. H., Hirst, E., Greenway, R, and Smith, J. A., 2003: Ice Particle Interarrival Times Measured with a Fast FSSP. . *J. Atmos. Oceanic Technol*. **20**, 249—261.

Korolev, A. V., Makarov, Y. E., and Novikov, V. S., 1985: On the accuracy of photoelectric cloud droplet spectrometer FSSP—100., *Trans. Of Central Aerological Observatory (Trudi TsA0)*, 32—42.

Korolev A. V. and G. A. Isaac, 2005: Shattering during sampling by OAPs and HVPS. Part I: Snow particles. *J. Atmos. Oceanic Technol.* **22**, 528-542.

UPGRADES TO THE FSSP-100 ELECTRONICS

Darren O'Connor
SPEC Incorporated, Boulder, Colorado

1. INTRODUCTION

The forward scattering spectrometer probe (FSSP) was developed in the 1970's (Knollenberg 1981). The FSSP model 100 has been the subject of intensive instrument performance analysis (e.g., Dye and Baumgardner 1984; Cooper 1988; Brenguier 1989; Field et al. 2003) and upgrades (Cerni 1983; Brenguier et al. 1998). Brenguier et al. (1998) added the ability to record the arrival time of each particle and decreased the deadtime (time the probe was inactive while the electronics processed a particle event) from 6 μs to essentially 0 μs. Baker (1992) used particle interarrival times to investigate droplet clumping in cumulus clouds. Field et al. (2003) found that there were two fairly distinct peaks in particle arrival times when the probe was operated in the presence of large ice particles. One peak they attributed to closely spaced particles that resulted from ice shattering on the probe inlet, and a second, larger peak that was generated by particles passing unimpeded through the sample volume.

In this paper we describe upgrades to the FSSP-100 that result in:

1. Reduced offset errors associated with the AC coupling and baseline restoration circuitry.
2. Recording of signal and qualifier peak amplitudes of every particle, along with the particle transit time through the laser beam and the arrival time of the particle.
3. Sub-sampling (approximately 2%) of particle events that are digitized and recorded at a 40 MHz sample rate. The resulting time series of both the Signal and Qualifier waveforms may be viewed in post processing, (viewed as if a high-speed digital oscilloscope were probing the Signal and Qualifier channels in real time).
4. Data recorded at the probe on a flash disk. Data can also be recorded on an external computer via Ethernet connection. A field programmable gate array (FPGA) and onboard 400 Mhz Linux processor are completely programmable using an Ethernet connection, making field modifications easy to implement.

2. BASELINE RESTORATION CIRCUIT UPGRADE

The traditional FSSP100 baseline restoration circuit is shown in **Figure 1** and the newly implemented baseline restoration circuit is shown in **Figure 2.**. In **Figure 1**, photodiode current into U1 is AC coupled through capacitor C4. This generates negative going pulses out U2 as particles pass through the FSSP 100 laser beam. C4 builds up a bias voltage as each particle event occurs, producing a baseline shift in the output of U2. During the pulse event, the previous baseline value is held at the output of U4, and is fed as an offset to U5. This removes the previously sampled baseline voltage from the final output of U5. When particles exit the beam, the DC bias due to C4 is fed to U3 as a positive voltage and forces its output to go high. Capacitor C3, is then charged until it matches he DC bias on C4. By feeding this voltage through the unity gain amplifier U4 and on to the input of U5, the baseline shift is subtracted off of U5's output.

Figure 3a is a simulation of the traditional baseline restoration circuit in the presence of several particle events. The large particle events are on the order of 500 μS, and are on the order of magnitude of the kind of signal durations that may occur during shattering events. The blue signal is the ideal output voltage and the green signal is the baseline restored output voltage. The baseline restoration circuit is not able to completely remove the baseline shift during the large transit time events, and by the 3rd one, centered at roughly 1.1 mS, the offset between the ideal and baseline restored outputs is 10 mV. When the pulse ends, the 10 mV offset remains. In the interval from 1.35 ms to 1.75 ms, the offset is seen to decay back to nearly zero volts.

Figure 4a shows a small particle event occurring immediately after the last of the large particles that were seen in **Figure 3**. At 1.355 mS, a pulse of ideal amplitude 25 mV occurs, but the baseline restore circuit outputs 35 mV due to the component of baseline shift that the baseline restoration circuit has not removed. 540 μs later, another particle event of the same amplitude occurs, shown in **Figure 4b**. At this time, the baseline restoration circuit is seen to have fully removed the baseline shift.

Photodiode current (represented by current source Ipd) in the newly implemented baseline restoration circuit, shown in **Figure 2**, is amplified through U1, then through U2 and U3. The signal is DC coupled throughout this series of amplifiers. When no particles are present, transistor Q1 is turned on, and any DC bias out of U3 is fed into U4. U4 integrates the DC bias, producing a negative accumulated output voltage. This negative voltage is fed back to U3, thus subtracting the DC bias from the output of U3, where the signal is then measured with DC bias removed. When particle events occur, the SFSSP logic turns off transistor Q1, and capacitor C6 serves to hold the accumulated DC bias correction voltage.

The output of U3 is fed to an analog-to-digital converter (ADC) that requires a 0.1 V offset for proper operation. This offset is achieved by feeding a 0.1 V reference into the positive terminal of U4. In the simulations (discussed next), this 0.1 V is subtracted off for clarity.

The main errors in this circuit are due to two sources:

1. When switch Q1 is off, or open circuit, the bias current of U4 flows through C6. At a typical value of 6 μA, it produces approximately a volt per second across C6, which is amplified by a gain of two through U3. Thus, during a 500 μs particle event, approximately 1 mV of baseline shift occurs at the output of U3. For typical transit times in flight of 2-3 μS, the offset is only on the order of 5 μV.
2. The input offset voltage of U4 is amplified by a gain of two through U3. This is a maximum of 550 μV (100 μV typical), producing approximately 1 mV of offset out of U3 after the gain is applied.

Figure 3b shows the new baseline restoration circuit response to the same particle events analyzed for the traditional circuit. Due to U4's offset voltage, a fixed offset of 1.2 mV exists on the baseline restored (green) signal. At the end of the last large particle event, again centered at 1.1 ms, the offset voltage is –3.2 mV, a change of 2 mV from nominal.

Figure 4c shows a small particle event occurring immediately after the last of the large particles that were seen in **Figure 3**. At 1.355 mS, a pulse of ideal amplitude 25 mV occurs, but the new baseline restore circuit outputs 21.74 mV due to the component of baseline shift that the new baseline restoration circuit has not removed. This is roughly the same 3.2 mV offset seen at the peak of the previous particle. 540 μs later, another particle event of the same amplitude occurs, shown in **Figure 4b**. At this time, the baseline-restored output is at

23.04 mV, representing an 800 μV shift from the nominal fixed offset.

In summary, the new baseline restoration circuit allows the photodiode current to be DC coupled through the amplifier chain, using servo techniques to remove any DC biases from the signal. It further provides a 100 mV offset required by the SFSSP ADC. The new baseline restoration circuit kept simulated errors to within approximately 10%, while the traditional circuit produced errors as great as 40%. In some cases of very large crystal break up, undesired offsets have been observed. These offsets were removed in real--time by an automatic algorithm that looks for particle events that last too long. The reset capability is a further feature of the new electronics, allowing the transistor Q1 to be forced on for brief periods, thus integrating off any spurious DC offsets.

3. SIGNAL AND QUALIFIER EVENT TIME SERIES CAPTURES

The SFSSP uses high-speed memory in the FPGA to not only capture particle-by-particle data, but also to capture entire particle events. An example is shown in **Figure 5**, where at concentrations on the order of 10^5 per liter, three coincident particle events were captured. The two marked with horizontal red arrows would normally be measured as good particles, since the transit time would exceed the running average used to define the beam diameter (Dye and Baumgardner 1984), and the maximum Signal peak exceeds the Qualifier peak. The effect of these accepted particles is to incorrectly bias the average transit time towards too large a value, and to produce measured peak values that are biased towards large particles. The latter effect is due to the probe only measuring the largest peak during the coincident event. This is (currently) the case for the SFSSP when measuring particle-by-particle events, and is the case for the original FSSP as well.

The effects of coincidence on the FSSP have been analyzed in many studies, such as by Baumgardner et. al. (1985), Cooper (1988), Brenguier (1989), and Coelho et al. (2005). The SFSSP, which captures with full-particle events at known sub-sample rates (of total particle events) provides for an entirely new means of analyzing the FSSP 100. With these data the techniques proposed for handling coincidence may be verified and fine-tuned.

A further potential use of particle event captures (PEC) is to correct particle sizes of individual particles, taking into account the time response of the analog amplifiers and the measured transit time of individual particles. Correction methods have been suggested by others (Korolev et. al., 1985; Cooper, 1988; Coelho, et. al. 2005, part I). A method based on the PEC capability of the SFSSP is discussed next.

3.1 TRANSIT TIME CORRECTIONS

The SFSSP measures real time particle events, allowing for unique analysis of the effects of the analog circuitry low-pass filtering on the waveform. The filter performs exponential smearing with a time constant τ. The value used in simulations to match a measured waveform was $\tau = 0.64$ uS. **Figure 6** shows two simulations plotted against a measured (green) PEC. The simulation on top assumes the laser beam intensity is exactly Gaussian, corresponding to a $1/e^2$ beam width of 420 um, plotted in blue. The black signal is the simulated response of the filter to this signal. The simulation on the bottom is a modified Gaussian, using the same $1/e^2$ beam width, but modified by a gain and offset of 1.3 and –0.37, respectively. Negative values were then set to 0. This was done to attempt to match the resultant filtered waveform more closely to the measured response, as the HeNe laser is likely not a pure Gaussian in its intensity pattern

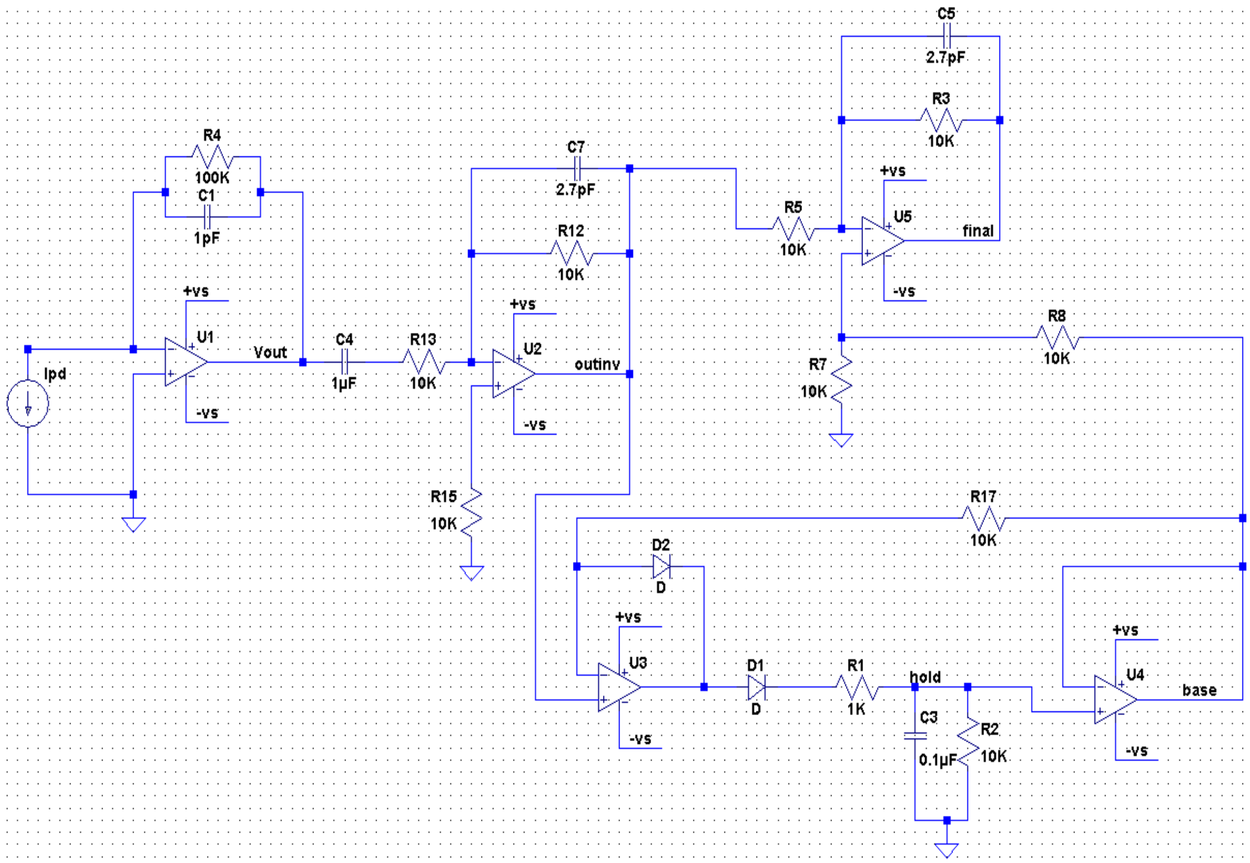

Figure 1. Traditional FSSP 100 front end amplifier (U1, U2) and baseline restoration (U3, U4, U5) circuitry. The Ipd current source models the photodiode behavior in the circuit.

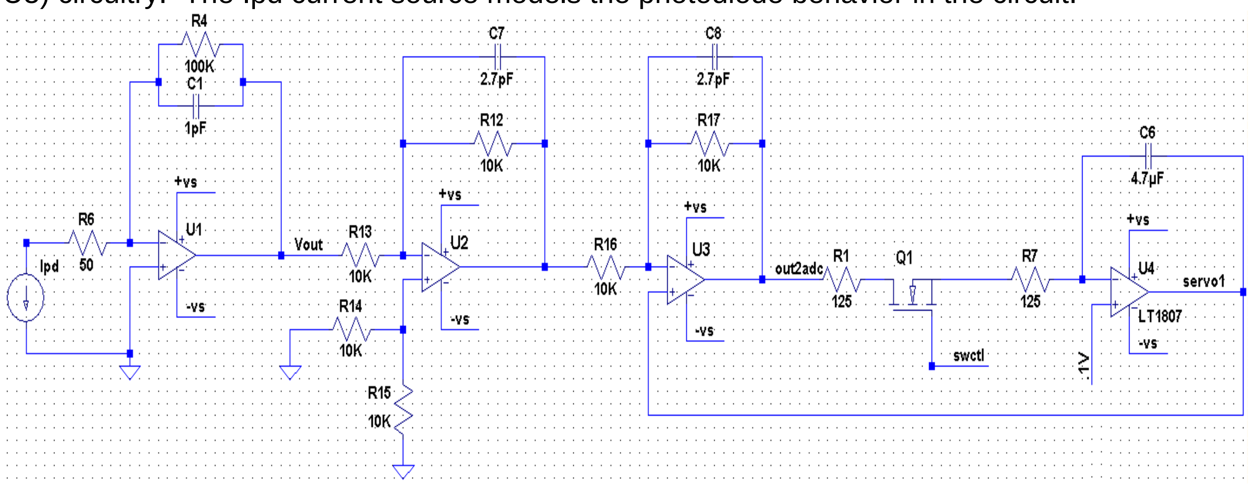

Figure 2. SPEC FSSP Upgrade front-end amplifiers (U1, U2 and U3) and new baseline restoration (U3, U4) circuitry. The Ipd current source models the photodiode behavior in the circuit.

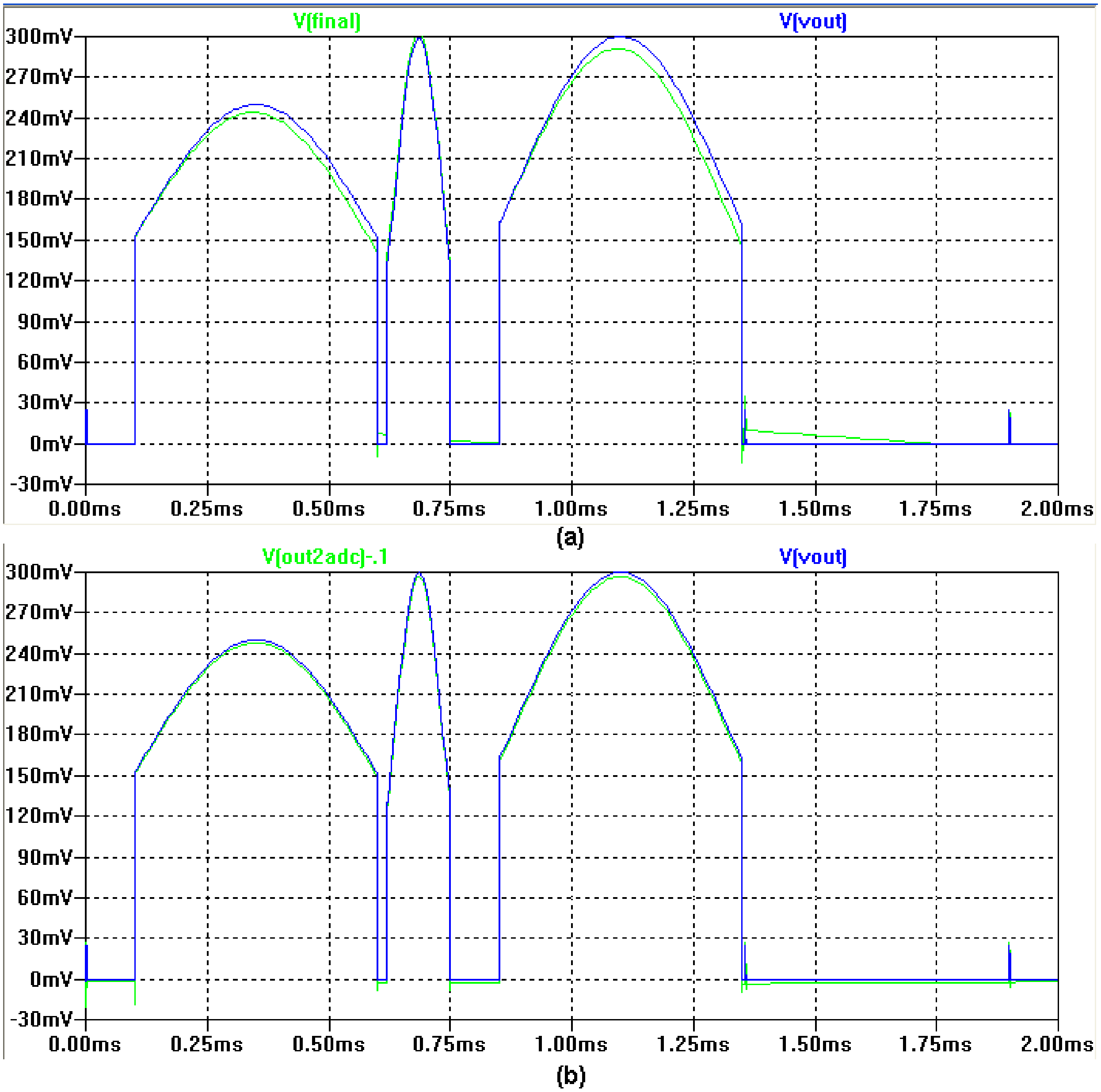

Figure 3. Ideal (blue) and baseline restored (green) signals for the traditional (a) and new (b) baseline restoration circuits. The large amplitude, long duration signals model shattering events.

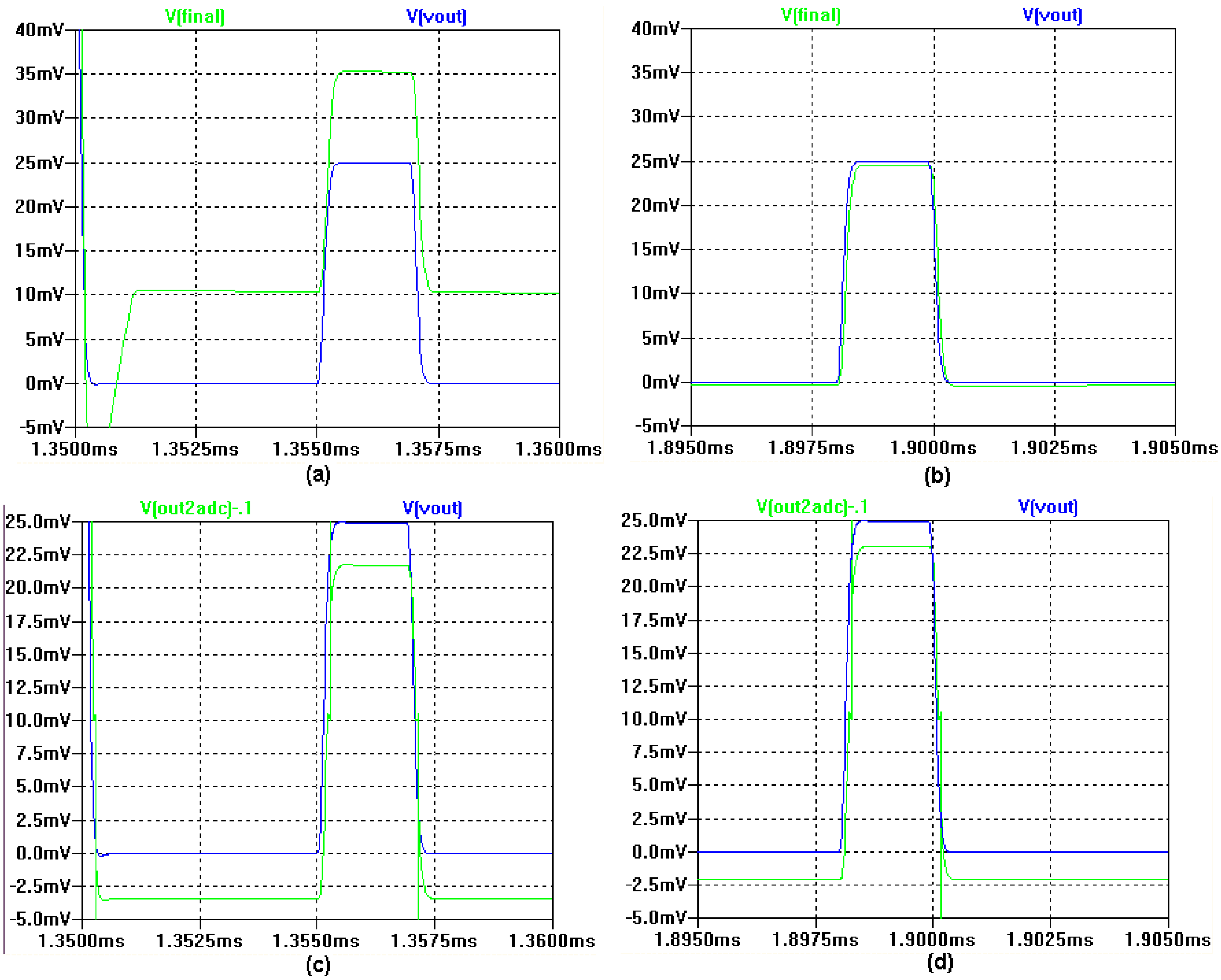

Figure 4. Ideal (blue) and baseline restored (green) signals for the traditional (a and b), and new (c and d) baseline restoration circuits. Plots (a) and (c) are for period immediately after the large signals in **Figure 3**. Plots (b) and (d) are 540 μs later.

Using a 20 mV threshold for the minimum at which a particle is detected, the transit times of the simulated signals is measured and estimated in several ways. The filtered signal period between the 20 mV limits is measured; the area under the curve, divided by the voltage peak for the same limits (20 mV) is estimated; and the time from the first (leftmost) 20 mV crossing to the peak is measured, and this value multiplied by two. The results for the two simulated waveforms are shown in **Table 1**.

Table 1. Estimates of transit time using measured time, area over peak, and time to peak (x2).

	Time, Real (us)	Time, Total (us)	% Error Total	Time, Area/Peak (us)	% Error Area/Peak	Time to peak x 2 (us)	% Error Time to Peak
Pure Gaussian	3.385	4.64	37	1.97	41.80	3.63	7.15
Modified Gaussian	2.45	4.67	96	1.85	24.5	3.11	27

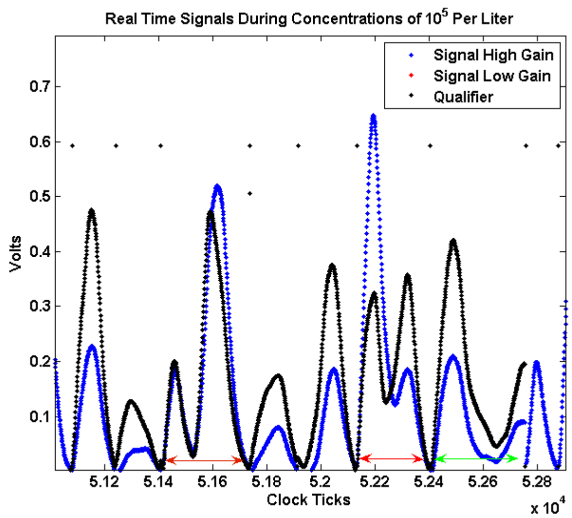

Figure 5. Total particle event captures by the SFSSP during concentrations of 10^5 per liter.

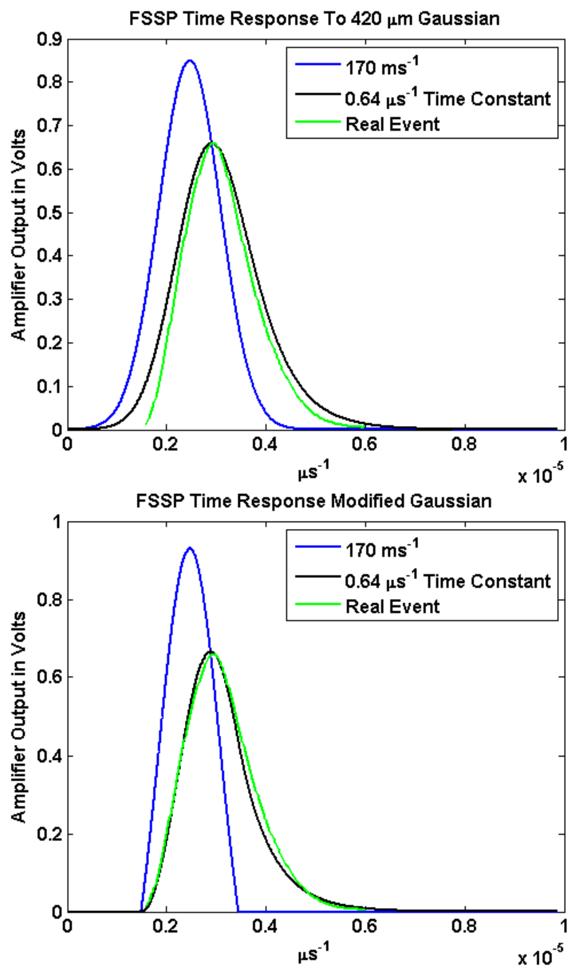

Figure 6. Simulated and measured FSSP waveforms. Blue is ideal (no exponential response smearing), black is with smearing (0.64 uS time constant), and green is a real measured event. Simulation done at 170 ms^{-1} to match assumed velocity of measurement. The top panel assumes the laser beam intensity is exactly Gaussian, corresponding to a $1/e^2$ beam width of 420 um. The bottom panel is a modified Gaussian, using the same $1/e^2$ beam width, but modified by a gain and offset of 1.3 and –0.37, respectively.

The area divided by the peak, assuming a uniform distribution for the laser, results in a transit time estimate of:

$$t' = t / (1 - e^{-t/\tau})$$

Where

t' = estimated transit time
t = true transit time
τ = time constant of the filter.

If τ is 3 times greater, or more, than the actual transit time, the estimated transit time will be smaller by 5% or less than the actual transit time.

As the laser intensity becomes less uniform and approaches a Gaussian, this result becomes less and less applicable. This is illustrated in **Table 1**, where the pure Gaussian result for the area / peak technique underestimates by 42%, while the modified Gaussian estimate is only off by 24.5%. Returning to **Figure 6**, one may notice that the modified Gaussian is closer in shape to a uniform distribution than is the pure Gaussian.

Since the two techniques bound the real transit time above (time to peak method) and below (area over peak method), the average of the two may yield better results. For the true Gaussian, the resultant error is 17.3%; for the modified Gaussian, the resultant error is 1.3%.

Figure 7 shows the percentage error for a modified Gaussian distribution while varying the velocity from 100 to 200 ms^{-1}. Using the average of the two techniques produces a worst case error of 9%. All three techniques greatly improve upon the total measurement that would otherwise be used.

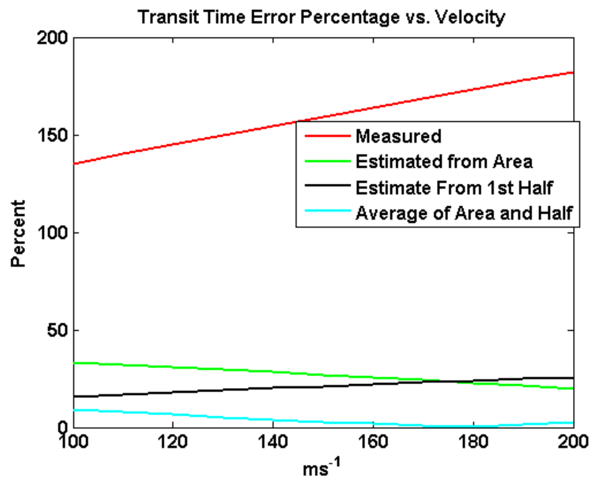

Figure 7. Absolute percentage error in estimating actual transit times across a 420 um $1/e^2$ Gaussian laser distribution. Errors are based on total measured transit time with no corrections (red); area under the voltage curve divided by the maximum voltage (green); transit time from the beginning to the peak times two (black); and average of the area / peak and peak times two methods (cyan).

3.2 PULSE HEIGHT CORRECTIONS

It is possible that with good transit time estimates, the decrease in the measured peak caused by the time response of the analog filter can be corrected. By simulating a range of particle sizes, as in **Figure 6**, the filtered peak (black in **Figure 6**) divided by the (assumed) real peak (blue in **Figure 6**) vs. transit time is seen to be a linearly decreasing value. This is seen in **Figure 8**, where the blue line is the ratio of measured to actual peak voltages vs. velocity of the simulated particle. The particle peak was 0.75 Volts. A least squares estimate of the blue curve, using the transit time estimated from the methods described above (average of area/peak and 1^{st} half estimate) is also plotted in green.

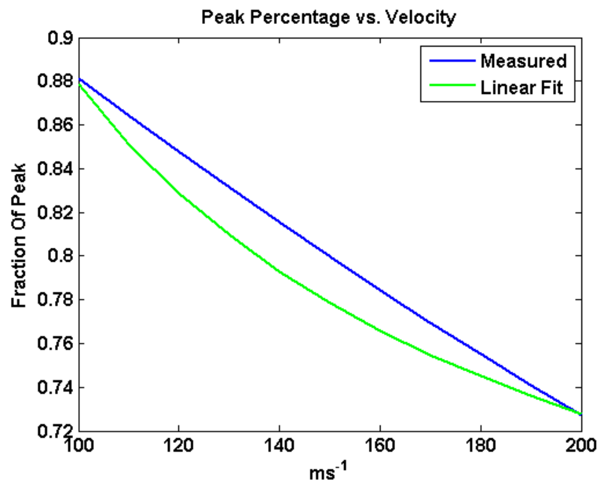

Figure 8. Ratio of measured peak to actual peak vs. velocity for 0.75 Volt signal.

Using the linear fit correction values from **Figure 8**, peak voltages are plotted in **Figure 9**. The actual peak voltage is plotted in blue, and the measured peak voltages vs. velocity are plotted in red. The corrected values vs. velocity are plotted in green. The maximum error in the estimate is less than 3%. Were one to perform a least squares fit for every simulation, this result would not be impressive or useful. However, the slope and offset values that generates the green line in **Figure8** works well for pulse heights ranging from 0.15 volts to 16 volts! At lower voltages, two other least squares fit values are used to cover the range of peaks from 20 mV to 150 mV, as the coefficients begin to change more rapidly in this pulse height region.

Measured signals from the FSSP allow analysis of this correction. For example, to correct the measured (green) signal on the right side of **Figure 6**, the transit time is first estimated to be 2.13 uS. This is different from the value in **Table 1**., because the simulated (black) signal was used to measure transit times in the table. Here, the real (green) signal is used and the pulse height of the simulated (blue) signal is then estimated from the following correction:

$$\text{Peak} = \text{measured peak} / (92292 \bullet \text{transit time}_{estimate} + 0.533)$$

Using the measured peak value of 0.659 volts and the estimated transit time of 2.13 us, the pulse height is estimated to be 0.90 volts. If one assumes the blue signal matches the original signal, before filtering, then the actual peak is close to its value: 0.85 volts. Without correction, the sizing error is –22.5%. After transit time correction, the error is 6.2%.

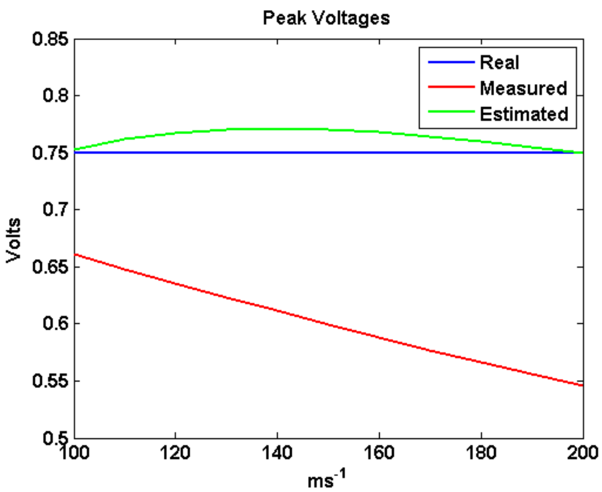

Figure 9. Real (blue), measured (red) and corrected estimate (green) peak values for a particle moving through the simulated FSSP at 100 to 200 meters per second.

To further test the peak estimate two more particle events are shown in **Figures 10** and **11**. The measured PEC (green) signals in the two figures have peak values of 0.27 and 6.22, spanning a broad range of voltages due to large differences in particle sizes. The simulated peak values, without filtering, are 0.4 volts and 8.1 volts for the blue plots in **Figures 10** and **11**. The estimate of the peak for the signals in **Figure 10**, using the transit time correction in EQ(1), is 0.4 volts. This is an error of only 0.2%, compared to the original 33% underestimate . The estimate of the peak for the signal in **Figure 11** is 8.49 volts, a 4.9% overestimate, compared to the original 6.22 volt, 23% underestimate.

Although the corrected peak values are being compared to simulated waveforms (modified Gaussians), the results are still likely to represent an improvement in accuracy. Assuming the modified Gaussians are the correct signal, the errors for three different simulations were reduced from 22.5% to 6.2% (**Figure 6**), from 33% to 0.2% (**Figure 10**), and from 23% to 4.9% (**Figure 11**).

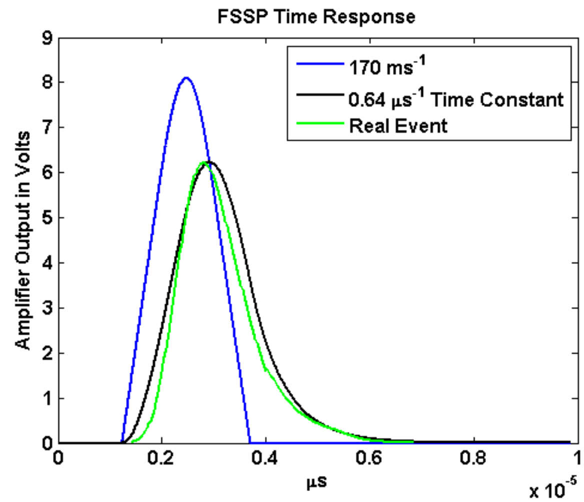

Figure 10. Measured signal (green) and simulated modified Gaussian without (blue) and with (black) filter effects. Actual Peak: 0.4, Measured Peak: 0.27 (33% low), Estimated Peak: 0.4 (0.2% over**)**

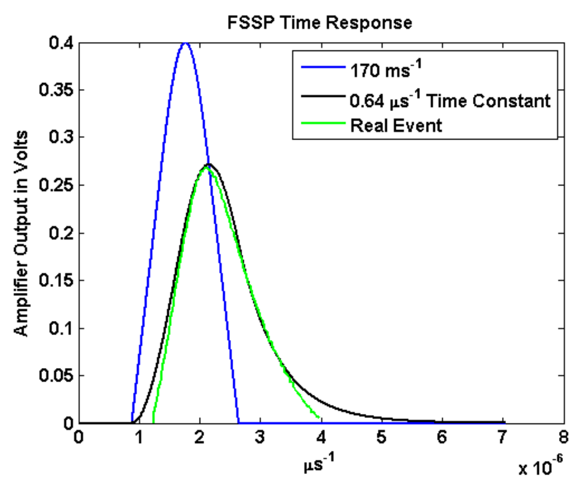

Figure 11. Measured signal (green) and simulated modified Gaussian without (blue) and with (black) filter effects. Actual Peak: 8.1, Measured Peak: 6.22 (23% low), Estimated Peak: 8.50 (4.9% high).

The SFSSP measures transit times three ways for particle by particle events:

1. Total transit time: the time it takes for a particle to rise above a minimum threshold of 10 mV, and to then fall below 5 mV. This method greatly overestimates transit times at aircraft speeds due to analog filter smearing of the signal during signal decay.
2. Time to peak: the time it takes for a particle to rise from the 10mV threshold to the peak. This method overestimates transit times, but by much less than the total transit time method.
3. Area / Peak Voltage: the area under the curve for the entire particle event is recorded. Dividing this value by the peak voltage yields an underestimate of the total transit time.

By using methods 2 and 3, and by determining the coefficients in EQ(1) from the PEC data, a particle by particle correction to size may be implemented.

A more exhaustive method may be implemented using the techniques by which figures 6, 10 and 11 were generated. It involves estimating the original particle size by generating a modified Gaussian time series, simulating the low-pass filtering effect of the analog electronics on this series, and comparing the filtered output to the original PEC event. The peak of the modified Gaussian, before filtering, is the resultant estimate of the particle peak without the attenuating effect of the filter.

3.3 AN EXAMPLE OF ICE CRYSTAL SHATTERING

Here we examine an example of ice crystal shattering from the recent DOE Atmospheric Radiation Measurement (ARM) ISDAC field project staged from Fairbanks, Alaska in April 2008. ISDAC Research Flight #32 included data collection by the Canadian NRC CV-580 research aircraft in cirrus clouds. **Figure 12**. shows the "wait time" (hereafter called w8 time) distribution from ISDAC flight #32. The ordinate is plotted as dN/dln(w8), where N is the number of particle events and a "tick" corresponds to one 25 ns clock period. The peak ending at approximately 30,000 w8 ticks indicates potential shattering events were prevalent at w8 times of this length and shorter (Field et. al. 2003). At the recorded aircraft speed of 138 ms^{-1}, this corresponds to an inter-arrival distance of 103.5 mm between particles. **Figures 13** and **14** are images captured by the SPEC CPI during this time period; **Figure 15** shows images captured by the SPEC 2D-S probe.

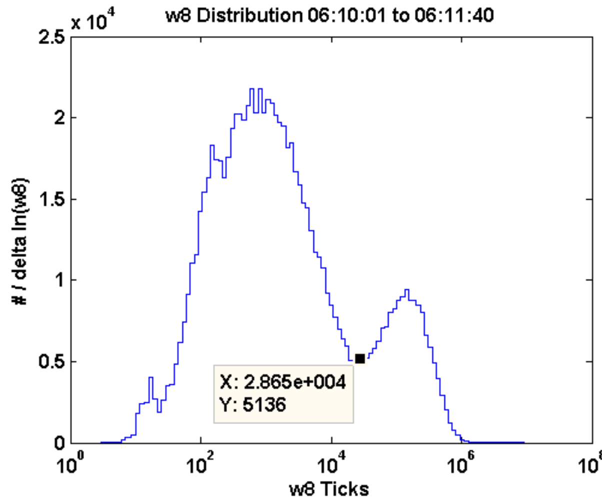

Figure 12. Inter-Arrival (w8) time / ln (w8 bin widths) distribution plotted vs. w8 ticks.

Figure 16 shows the particle size distribution for this period with all DOF and velocity average accepted particles (red), and without particles that have an inter-arrival time less than 30,000 clock periods (green). **Figure 17** shows the percentage of particles removed from the concentration distribution for each bin. The percent removed is relatively equal for all the bins, except for bins 2 and 3, corresponding to particle sizes between 1 and 5 μm. A possible explanation is that a real peak in the size distribution exists in these small sizes, and that most of the rest that were removed were due to shattering of larger particles. Both time periods in **Figure 17** show a clustering of particle events, which is to be expected in a period of shattering.

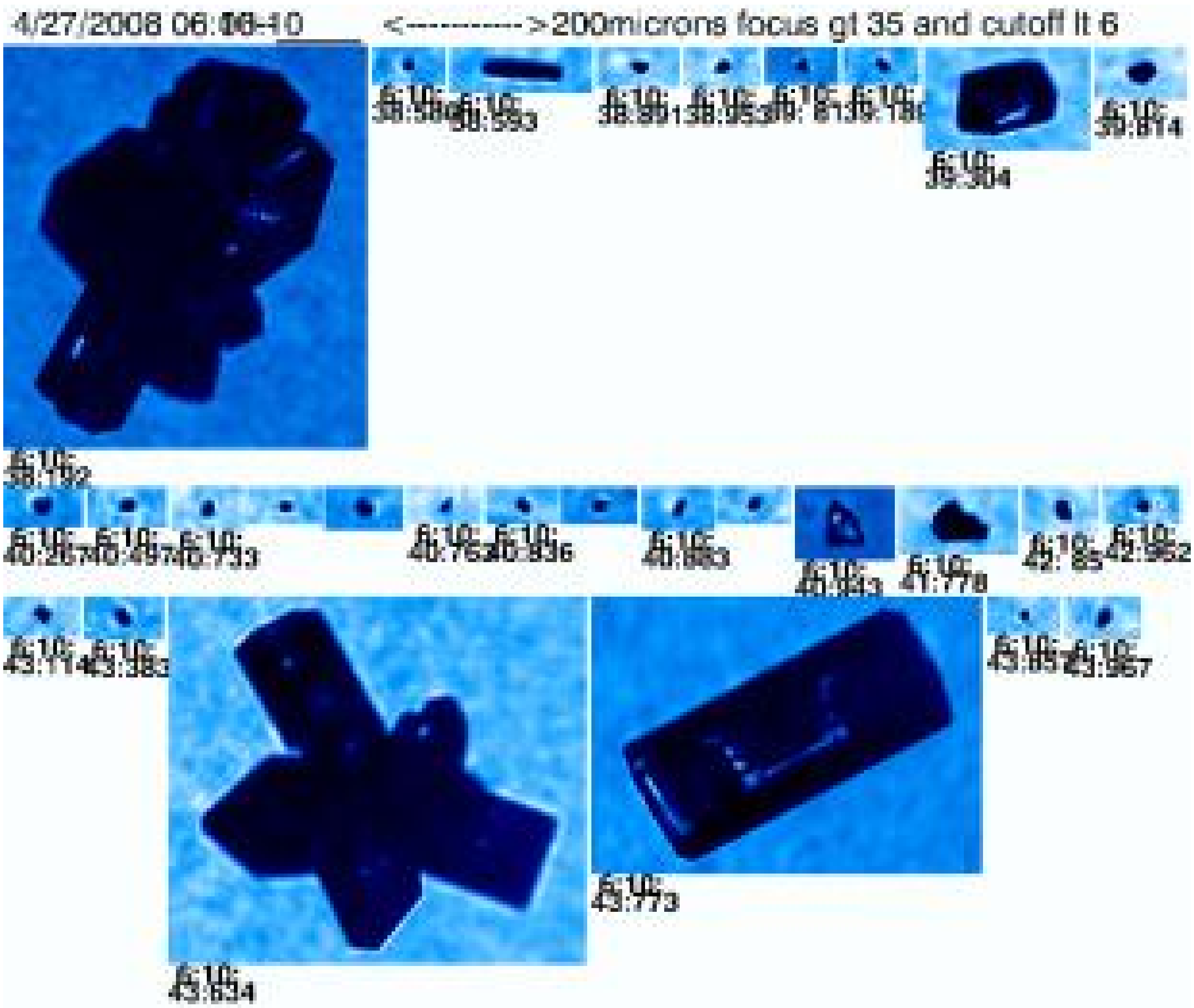

Figure 13. CPI images captured at approximately 06:10:44 during flight 32.

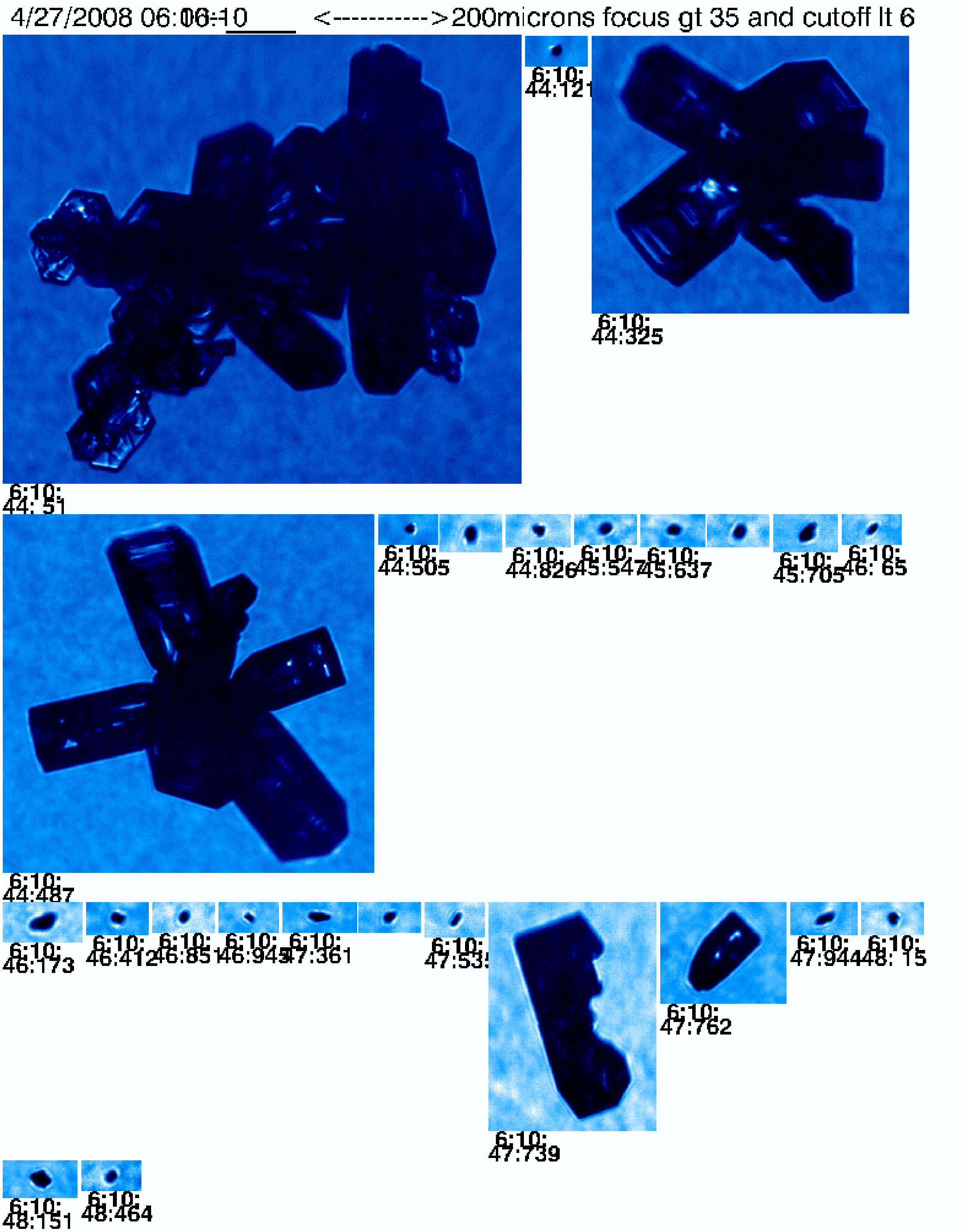

Figure 14. CPI images captured at approximately 06:10:48 during flight 32.

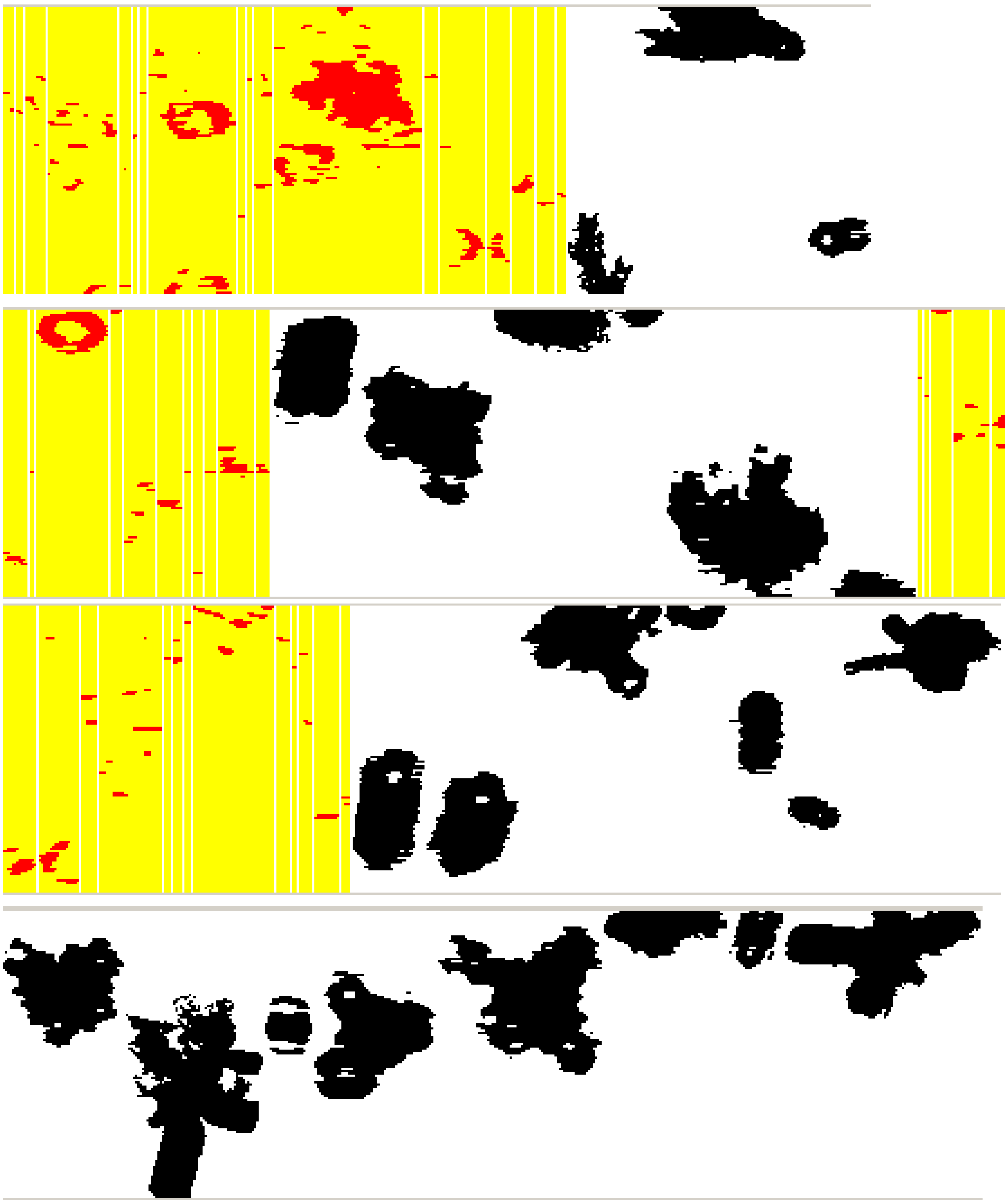

Figure 15. 2D-S images during period of interest. Heights of image strips are 1.28 mm. 2D-S shattering removal algorithms remove particles highlighted yellow.

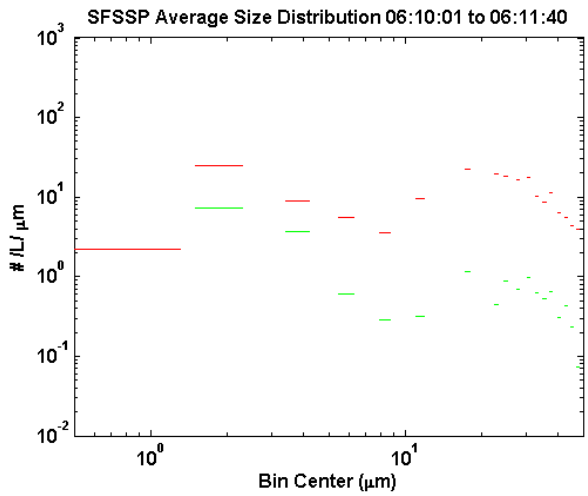

Figure 16. Average size distribution with velocity averaging accept and DOF accept limits (red), and with w8 time minimum of 30,000 ticks (green), or 103.5 mm.

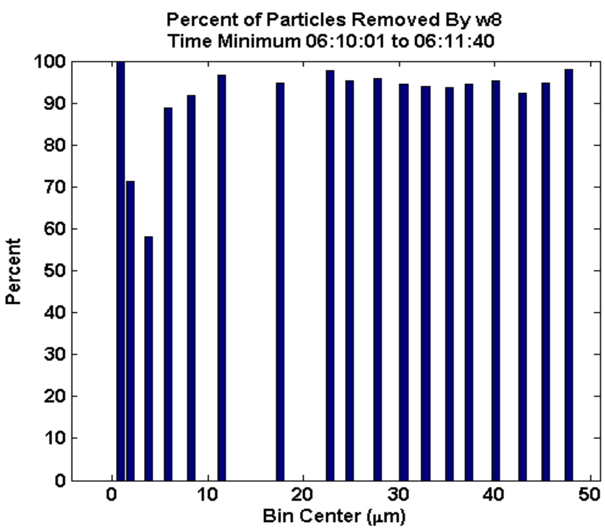

Figure 17. Percentage of concentration removed from each size bin by using the wait time minimum of 30,000 ticks = 103.5 mm.

Figures 18 and **19** show periods of particle event captures within the 100 second interval from which the average distributions in **Figure 16** were made. In **Figure18**, only one DOF accepted particle event is observed, with the signal channel voltage greater than the qualifier channel voltage. This one good particle would be sized in the 1 to 2.8 micron bin, where the peak in the distribution occurs in **Figure 1**. **Figure19** shows a very long PEC corresponding to a signal that goes high and stays high for much longer than the transit time of a single particle. The PEC in fact fails to record the entire event due to a limit on the amount of high speed memory devoted to capturing them. Clearly such a signal will bias the average transit time above the value that single particle transits would generate.

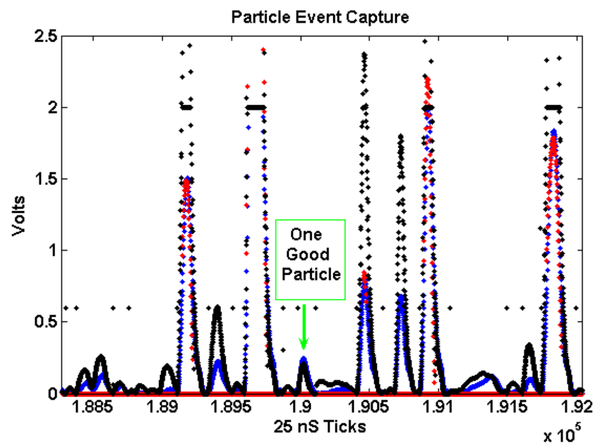

Figure 18. Real time signals (Signal channel in blue and red, Qualifier in black) within 06:10:01 to 06:11:40 period on flight 30.

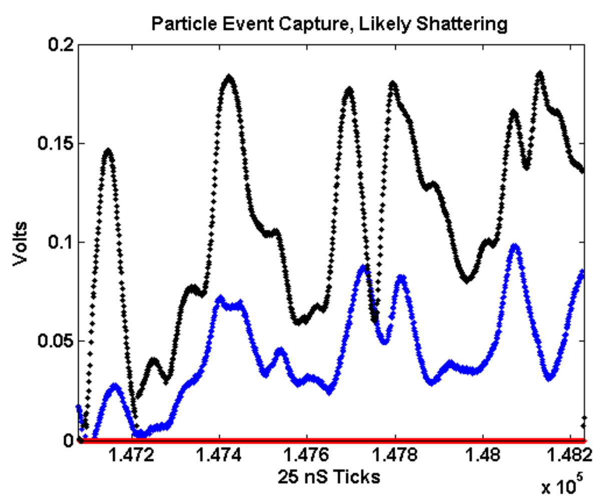

Figure 19. Real time signals (Signal channel in blue (high gain) and red(low gain), Qualifier in black) within 06:10:01 to 06:11:40 period on flight 32. Most of the time series is a single particle event.

4. SUMMARY

New electronics upgrades to the FSSP-100 are discussed. The new upgrades (i.e., the SFSSP probe) contain advanced technology enabling several improvements that make it possible to better understand instrument response.

Initial tests of an improved baseline restoration circuit show the new method works well. High concentrations are not expected to greatly alter the measured size distribution. Real time electronics monitors and resets the baseline when erroneous data occurs. The new baseline restoration circuit keeps simulated errors to within approximately 10%, while the traditional circuit produced errors as great as 40%.

The SFSSP has the unique ability to digitize and store both the signal and qualifier waveforms. By analyzing the time series from these waveforms, it is possible to correct transit time and pulse height measurements. The transit time is corrected for effects of the analog circuitry low-pass filtering on the waveform. Once the transit time is corrected, the decrease in measured peak voltage caused by the time response of the analog filter is corrected.

The SFSSP measures the arrival time of each individual particle. Using a technique similar to that described by Field et al. (2003), ice crystals that are suspected to have shattered on the probe inlet are removed by examination of their interarrival times. An example of shattered particle removal from the recent ISDAC field project is presented and discussed.

REFERENCES

Baker, B.A., 1992: Turbulent entrainment and mixing in clouds: A new observational approach, *J. Atmos. Sci.,* **49,** 387-404.

Baumgardner, D., Strapp, W., and Dye, J. E. 1985: Evaluation of the Forward Scattering Spectrometer Probe. Part II: Corrections for Coincidence and Dead—Time Losses. *J. Atmos. Oceanic Technol*., **2**, 626—632.

Brenguier, J. L., 1989: Coincidence and dead-time corrections for particle counter. Part II: High concentration measurements with an FSSP. *J. Atmos. Oceanic Technol.*, **6,** 585—598.

Brenguier, J-L., T. Bourrianne, A. de Araujo Coelho, J. Isbert, R. Peytavi, D. Trevarin, and P. Wechsler, 1998: Improvements of droplet size distribution measurements with the fast-FSSP. *J. Atmos. and Oceanic Tech*., **15**, 5, 1077-1090.

Cerni, T. A. 1983: Determination of the size and concentration of cloud drops with an FSSP. *J. Clim. & Appl. Meteorol*., **22**, 1346-1355.

Coelho, A., J-L. Brenguier, and Thierry Perrin: 2005: Droplet Spectra Measurements with the FSSP-100. Part I: Low Droplet Concentration Measurements. *J. Atmos. Oceanic Technol*. **22**, 1748—1755.

Coelho, A., J-L. Brenguier, and Thierry Perrin: 2005: Droplet Spectra Measurements with the FSSP-100. Part II: Coincidence Effects. *J. Atmos. Oceanic Technol*. **22**, 1756—1761.

Cooper, W. A., 1988: Effects of coincidence on measurements with a Forward Scattering Spectrometer Probe. *J. Atmos. Oceanic Technol*., **5**, 823—832.

Field, P., Wood, R., Brown, P. R. A., Kaye, P. H., Hirst, E., Greenway, R, and Smith, J. A., 2003: Ice Particle Interarrival Times Measured with a Fast FSSP. . *J. Atmos. Oceanic Technol*. **20**, 249—261.

Korolev, A. V., Makarov, Y. E., and Novikov, V. S., 1985: On the accuracy of photoelectric cloud droplet spectrometer FSSP—100., *Trans. Of Central Aerological Observatory (Trudi TsA0)*, 32—42.

RAIN DROPLET SCALE SPECTRUM & DROP SPEED DISTRIBUTION OBSERVATION AND ITS ANALYSIS WITH DIFFERENT PRECIPITATION

Pu Jiangping [1](1 Nanjing University of Information Science & Technology)
Jiang Aijun [2](2 Nanjing City Meteorological Bureaus)
Zheng Guoguang [3] (3 Chinese Academies of Meteorological Sciences)
Yao Zhanyu [3](3 Chinese Academies of Meteorological Sciences)
Kong Yi [4](4 Nanjing University of Science & Technology)
Yuan Dongmei [4](4 Nanjing University of Science & Technology)
Lu Jiong [4](4 Nanjing University of Science & Technology)
Lv Mei [4](4 Nanjing University of Science & Technology)

Precipitation is the result of the compositive effects of cloud microphysics process, dynamics process and various factors that influence the formation and development of precipitation[1]. The research of precipitation physics characteristic and precipitation formation mechanism requires considering both the macrophysics process and microphysics process. In the term of macroscopical characters, atmospheric circulation situation, weather system, radar echo and satellite image data can be used to analyze the precipitation process; as for microcosmic detecting, the data that collected directly by Particle Measurement System (PMS) that carried on a plane can be used in the farther research in the issues of microphysics parameters' temporal and spatial changing characters[1], like the cloud and rain droplet distribution spectra and LWC in precipitation, as well as the forming mechanism of precipitation. However, plane-born detecting can not get all of the microphysical information in cloud in every precipitation because of the influences from many factors. Because that ground raindrop spectra can be obtained easily without many limits, and also the ground raindrop spectra can show some microphysical characters in cloud, the ground raindrop spectra data is usually used to analysis the microphysical characters of precipitation.

This paper presents the study of using the optics particle spectra instrument-OTT PARSIVEL to continually detect the ground raindrop spectra in Nanjing, and doing some significant analysis of them. According to the satellite image, radar sounding data, spot cloud and weather observational data, we select raindrop spectra data from cumulus cloud and stratus cloud to discuss the characters of raindrop distribution spectra and microphysical parameters' evolving characteristic and regulation in precipitations of dissimilarity cloud.

The following charts show some particle spectra pictures that we observed in the station in Nanjing.

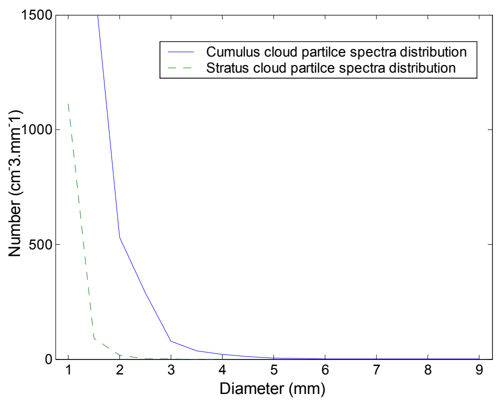

Fig1: two kind of particle spectra distribution

The particle spectra of stratus cloud precipitation is usually very narrow, and the max-diameter of the droplet is 3 mm, while the particle spectra of cumulus clouds precipitation is much broad, and the max-diameter of the droplet is 9.5 mm. The particle spectra curve of cumulus clouds precipitation is above the stratus cloud precipitation's, which means that the raindrop number density of different diameter in cumulus cloud precipitation is the largest, the stratus cloud precipitation the smallest.

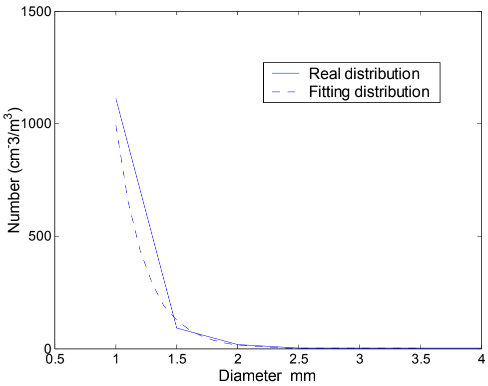

a

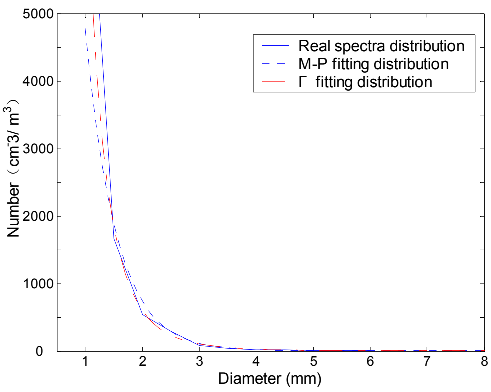

b

Fig2: particle spectra distribution fitting of stratus cloud precipitation(a) and cumulus cloud precipitation(b)

From the charts above we can find that the particle spectra of stratus cloud precipitation fit the M-P distribute, and the fitting-curve is very close to the real particle spectra curve when the raindrop diameter is larger than 1.6 mm. On the other hand, using *M-P* distribute[3] curve to fitting the particle spectra of cumulus clouds precipitation makes big deviation, while using *Γ* distribute[4] may obviously reduce the deviation.

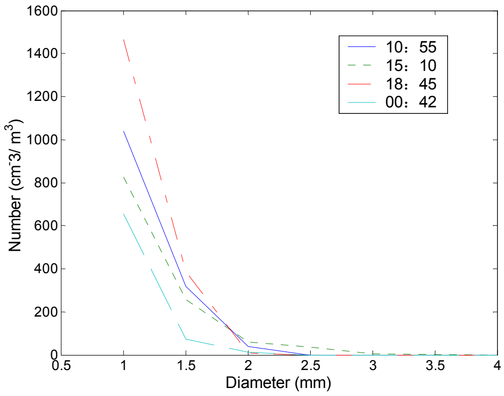

Fig3: particle spectra of different stage in one stratus cloud precipitation

Chart 3 shows some characters of precipitation at different stage in a stratus cloud precipitation. When it started to rain at 10:55, the total particle number is small, most of the droplets are little ones, the particle spectra are narrow, and the precipitation intensity is only 1.191 mm/h. When it lasted to 15:10, the intensity rose to 2.752 mm/h. There were much more large-droplet and less little ones. It might be the result of collision-coalescence between raindrops. Particle spectra became to be narrow again at 18:45, the number of little droplets increased rapidly which might because that the little ones no more depleted of collision-coalescence. As this precipitation came to over at 00:42, there is no more droplet that larger than 2 mm, the intensity was only 0.373 mm/h.

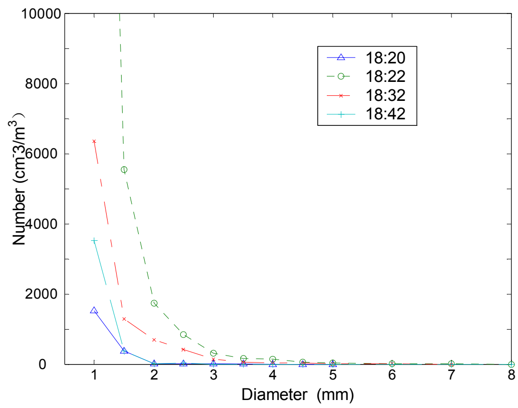

Fig4: particle spectra of different stage in one cumulus cloud precipitation

Fig4 chart shows some differences characters at different stage in a cumulus cloud precipitation. From the chart we find that at the beginning of this precipitation at 18:20, the particle number was small, about 1952/m^3 and the precipitation intensity was 3.229 mm/h. Two min later the particle number rose rapidly to 46628/m^3. The particle spectra broaden quickly, intensity rose rapidly also, and the precipitation intensity increased to 137.872 mm/h. Then the particle number decreased slowly, as well as the intensity. It was only 1.801 mm/h at 18.42 mm/h, and the precipitation finished soon.

Fig5 shows the precipitation intensity, droplet number and diameter change in by time. The intensity didn't change much, and the droplet diameter reached its max value followed by the intensity max. It is found that the particle number density, precipitation intensity and droplet mean diameter changes consistently.

From the chart below we find that the intensity of cumulus cloud precipitation changes a lot, it means that there were several precipitation centre in it, and the structure in cumulus cloud was not very uniform. When the largest-particle diameter appears the intensity also reaches its max. The instantaneous intensity max past over 162.647 mm/h, while the intensity min is only 0.013 mm/h, but the heavy instantaneous rain last a very short time. In this chart the max value of I or N value keeps consistent in the main and the max of mean diameter came out before them, that is cumulus cloud precipitation usually produce lager raindrop before the value of I or N rise.

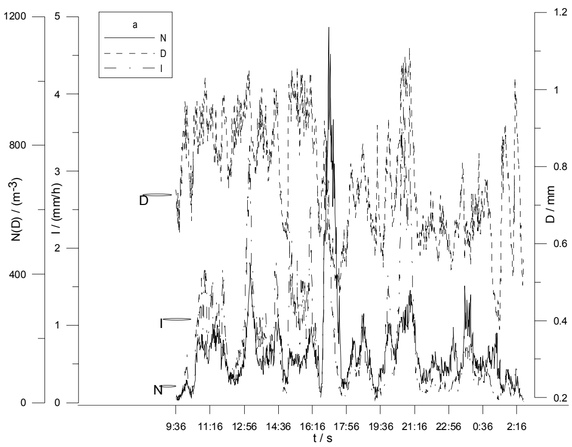

Fig5: precipitation intensity, droplet number and mean diameter in a stratus cloud precipitation change by time (N=droplet number, D=mean diameter, I=precipitation intensity)

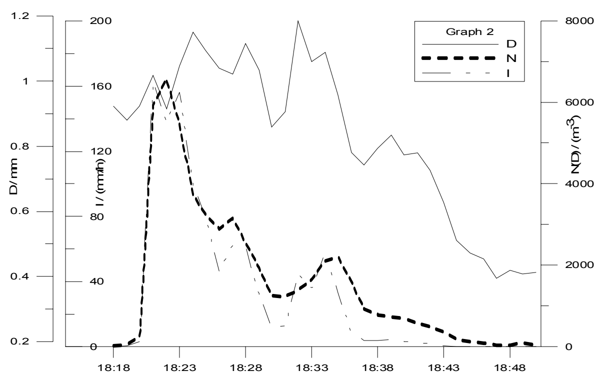

Fig6: precipitation intensity, droplet number and mean diameter in a cumulus cloud precipitation change by time (N=droplet number, D=mean diameter, I=precipitation intensity)

From the simple analysis, we may conclude that:

1、The mean raindrop spectra of these two precipitation clouds are simply different, the particle spectra of stratus cloud precipitation is usually very narrow and the other is usually broader. The particle spectra of stratus cloud precipitation fitting the *M-P* distribution well, and using *Γ* distribution can improve the precision of curve fitting from the particle spectra of cumulus cloud precipitation.

2、The magnitude of droplet number density in stratus cloud precipitation and cumulus cloud precipitation are 10^2、$10^3/cm^3$ separately. Microphysical parameters of stratus cloud precipitation change reposefully, and the period usually last for a long time. While in cumulus cloud precipitation the microphysical parameter changes a lot by time and the precipitation always last for a short time.

3、The particle number density, precipitation intensity and droplet mean diameter changes consistently, and it is found that super raindrops always appear before the enhancement or the increase precipitation intensity.

4、There are some internal relations between the changes of number density of small raindrops, collision-coalescence and broken mechanism of large raindrops.

These studies are important for the investigations of precipitation mechanism. It may help to the work of weather modification and result evaluation in some given place, and have constructive effect to quantitative measurement of rainfall intensity by radar and provide water resources index in weather modification.

References:

[1] Marshall J S, Palmer W McK. The distribution of raindrops with size. J Meteor., 1948, 5(4): 165-166.

[2] Liu weiguo, Su Zhengjun, Wang guanghe. Development and application of new generation airborne particle measuring system. J App. Meteor, 2003, 14, b03, 11-18.

[3] Joss J, Gori E G. Shapes of raindrop size distribution. J Appl. Meteor, 1978, 17(7):1054-1061.

[4] Zhang Chenchang, Zhen wenxian. Atmospheric Aerosol Tutorials. China Meteorological Press, 23-24.

AN OBSERVATIONAL STUDY OF CLOUD PARTICLE SPLASH/BREAKUP ARTIFACTS ON AIR SAMPLING FROM INLETS

David C. Rogers[1]
[1]NCAR, Boulder, Colorado USA

1. INTRODUCTION

Air inlets are used on research aircraft for sampling trace gases and aerosol particles. During passes through clouds, artifact particles can be generated when cloud drops or snow crystals collide with edges of the inlet. These artifact particles are passed to instruments downstream and will evaporate enroute. There can be some non-volatile residue that is measured by aerosol instruments, and this residue is an accidental contamination of the ambient aerosol.

The performance of "standard" inlet types for particle sampling is well understood in clear air. Processes leading to splash/breakup artifacts, however, are not. The goal of this investigation is to improve the understanding of these issues and work toward improved inlet designs.

This paper presents measurements of aerosol particles from recent projects and compares data from clear air and cloud passes. Future studies will attempt to identify the critical parameters that affect the generation of artifact particles.

2. FIELD PROJECTS

The U.S. National Science Foundation supports airborne research projects and the operation of instrumented aircraft for atmospheric research. For the present investigation, data were from the C-130 in two different projects.

Inlet geometries that were used in these projects include several types: forward-facing blunt and sharp-edged; aft-facing; and forward cone. Clouds in these studies include tropical strato-cumulus, super-cooled winter stratus, wave clouds that were mixed phase or ice, and cirrus. Air speeds ranged from ~100 to 150 m/s, and temperatures were +15 to -40℃. The aircraft were equipped with a variety of instruments to detect cloud particles, state parameters, kinematics, and aerosol size distributions.

3. INSTRUMENTATION

Primary measurements included thermodynamics, kinematics, position keeping, water and ice cloud particles. For the research described in this paper, the primary microphysics instruments are listed in Table 1. In all of these projects, there were additional instruments not listed here, that generated rich and diverse data sets. These included aerosol sensors for ice nuclei, size distributions ~10-1000 nm, trace gas sensors (O_3 and CO), and more.

project & aircraft	clouds	inlets	particle instruments
RICO C-130	marine Sc	forward-facing cone, aft-facing gooseneck	CN, CCN, RDMA, PCASP, FSSP, 260X, 2DC
ICE-L C-130	supercooled wave clouds	flow-through sharp edge diffuser with interior fwd-facing tube	CN, CCN, RDMA, UHSAS, CDP, 2DC

Table 1. Microphysics instrumentation

4. THEORY

The production of spray artifacts is a complicated process that depends on a number of variables. These include:

- particle phase (ice or liquid)
- particle size & shape
- inlet tip shape (blunt, sharp, rounded)
- surface properties of inlet tip (dry, wet)
- depth of flow boundary layer and distance from inlet tip to aircraft skin
- aircraft speed
- surface tension of water

Particles will impact the inlet or other aircraft structures upstream if they have sufficient inertia to cross the flow streamlines. Snow particles will break into fragments upon impact where the shear strength of ice is exceeded. For liquid particles, there are several possible results of impact. The drop can rebound, it can stick and flow as a surface layer, or it can be drawn into a thin sheet or filaments that break into smaller droplets.

The Weber number is used to predict the shape or breakup of liquid drops that are in motion relative to air -- free floating, not impacting on surfaces. It is the dimensionless ratio of particle kinetic energy to surface energy. For a spherical drop of unit density,

$$We = U^2 D / \sigma$$

where U is its velocity relative to the air, D is diameter, and σ is surface tension (Baron et al., 2001). Droplets with We > ~6-10 will deform and can break apart (Lefebvre, 1989). Note that it is not necessary for droplets to impact a surface in order to break up. They need only experience a significant acceleration. Break up may occur at We ~ 6 in turbulent flow.

Recent advances in high-speed video imaging and fluid dynamics modeling studies are improving the understanding of droplet impact and breakup. For example, Cossali et al. (1999) used high-speed CCD camera to study the impact of water drops on a liquid film. Over a range of We ~300-800, they characterized the shape and size of the splash "crown" from 3.8 mm diameter droplets. The number and size of secondary droplets depends on We and the Ohnesorge number,

$$Oh = \frac{\mu}{\sqrt{\rho \sigma L}}$$

where μ is liquid viscosity, ρ is liquid density, and L is a characteristic dimension (diameter). Shan et al. (2007) performed mathematical simulations of droplet breakup in two-particle collisions.

In earlier airborne studies, Hudson and Frisbie (1991) reported that measurements of CN concentrations were enhanced inside of warm marine Sc clouds, and they ascribed this to artifacts that were created by droplet impingement and breakup at the inlet tip. They estimated We >20 for all cloud drops (>1 µm), and asserted that all cloud droplets will breakup.

Weber (1998) analyzed observations from the NSF/NCAR C-130 and asserted that inlets with smaller openings will have higher concentrations of spray artifacts. This is because the fraction of artifacts entering the inlet hole scales with the ratio of volume to area. Their assertion was borne out by comparing artifact concentrations from the two different size inlets on the aircraft. Concentrations of in-cloud CN from the smaller inlet hole (1 mm dia) were 10-20X larger than out of cloud values. Artifact particles as small as ~3 nm were detected.

5. FIELD STUDIES

Examples are presented from two field projects. The first case from RICO shows consistent production of CN aerosol resulting from splash artifacts. The second case from ICE-L does not.

5.1 RICO – Marine Stratocumulus

The Rain In Cumulus over the Ocean experiment (RICO) occurred in Antigua-Barbuda December 2004-January 2005. The CN inlet was an aft-facing gooseneck tube, ~10 mm i.d. on the belly of the aircraft (Figure 1).

An example of data from the NSF/NCAR C-130 is in Figure 2. It shows that CN enhancement in clouds was ~10X greater than the out-of-cloud values. This enhancement does not seem to depend on the size of cloud drops, the presence of drizzle drops, or the amount of LWC. In addition to the leading edges of inlet probes, it is possible to generate drop splash artifacts when drops hitting the numerous surfaces on the belly of the aircraft. This spray of small particles will mix within the flow boundary layer and may be drawn into air sample inlets.

Figure 1. Belly of C-130 shows assortment of gooseneck inlets, antennas, and other instruments

5.2 ICE_L– supercooled wave clouds

The Ice in Clouds Experiment – Layer clouds (ICE-L) took place Nov-Dec 2007 in Colorado and Wyoming, USA and also used the NSF/NCAR C-130. In this project, the inlet was a sharp edge, forward-facing diffuser with interior pick-off tube – see Figure 3. The inlet tip was 6 mm i.d., and the inlet was mounted on the belly of the aircraft, 29 cm from the skin.

Figure 4 shows 21 minutes of data with three penetrations of a wave cloud at -25 to -32°C. The wave cloud had super-cooled liquid water (Rosemount icing probe). This case does not show enhancement of CN aerosol. There is considerable structure in the CN trace, but it is connected with crossing the air mass boundary that separates the upper dry layer (theta > 319 K) from the lower moist layer (CN > 100, theta < 319 K). Note the abrupt changes in CN and theta as the aircraft crosses cloud edges. In addition to the liquid water, these clouds also had many snow particles (2DC probe).

6. DISCUSSION

On-going studies are using similar data from several projects and different airplanes. These offer a wide variety of inlet types, particle instrumentation, cloud types, altitudes and airspeeds.

7. ACKNOWLEDGEMENTS

This research was supported by NSF grants ATM97-14177, NASA grant NASA NRA-01-OES-02 and by NCAR. The National Center for Atmospheric Research is operated by the University Corporation for Atmospheric Research under sponsorship of the National Science Foundation. Any opinions, findings, conclusions, or recommendations expressed in this publication are those of the author(s) and do not necessarily reflect the views of the National Science Foundation.

We are grateful for technical support from the Research Aviation Facility at NCAR and the University of Wyoming for helping install the instruments and conducting the flights.

Figure 3. Component view of iinlet used in ICE-L CN sampling. Airflow is left to right.

8. REFERENCES

Baron, P.A., M.K. Mazumder and Y-S. Cheng, 2001: chapter 17 in Aerosol Measurement Principles, Techniques, and Applications, Baron and Willeke (eds), Wiley-Interscience, New York, 1131p.

Cossali, G.E., G. Brunello, A. Coghe, M. Marengo, 1999: Impact of a single drop on a liquid film: experimental analysis and comparison with empirical models. Italian Congress of Thermofluid Dynamics UIT, Ferrara, 30 June-2 July.

Hudson, J.G., 1993: Cloud condensation nuclei near marine cumulus. J. Geophys. Res., 98, D2, 2693-2702.

Lefebvre, A.H., 1989: Atomization and Sprays. Taylor and Francis, Bristol, PA.

Shan, Y., T.W. Coyle, and J. Mostaghimi , 2007: Numerical simulation of droplet breakup and collision in the solution precursor plasma spraying. J. Thermal Spray Techn., 16, 698-704.

Weber, R.J., A.D. Clarke, M. Litchy, J. Li, G. Kok, R.D. Schillawski and P.H. McMurry, 1998: Spurious aerosol measurements when sampling from aircraft in the vicinity of clouds J. Geophys. Res., 103, D21, 28337-28346.

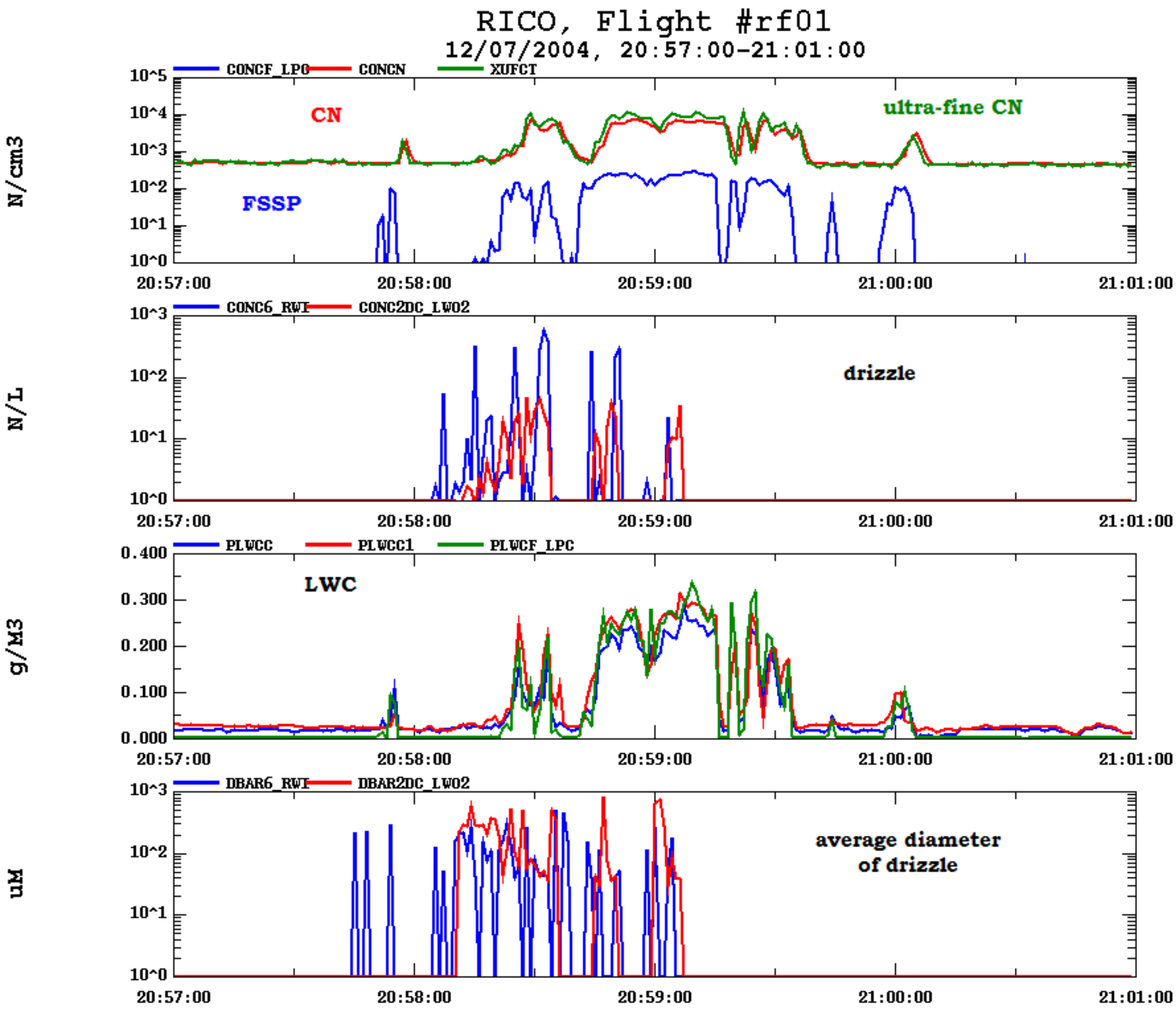

Figure 2. Four minutes of particle data during RICO project. CN concentrations enhanced during penetrations through marine strato-cumulus clouds. Altitude 800m MSL, airspeed 105 ms-1. The presence of drizzle-size drops did not affect the CN enhancement

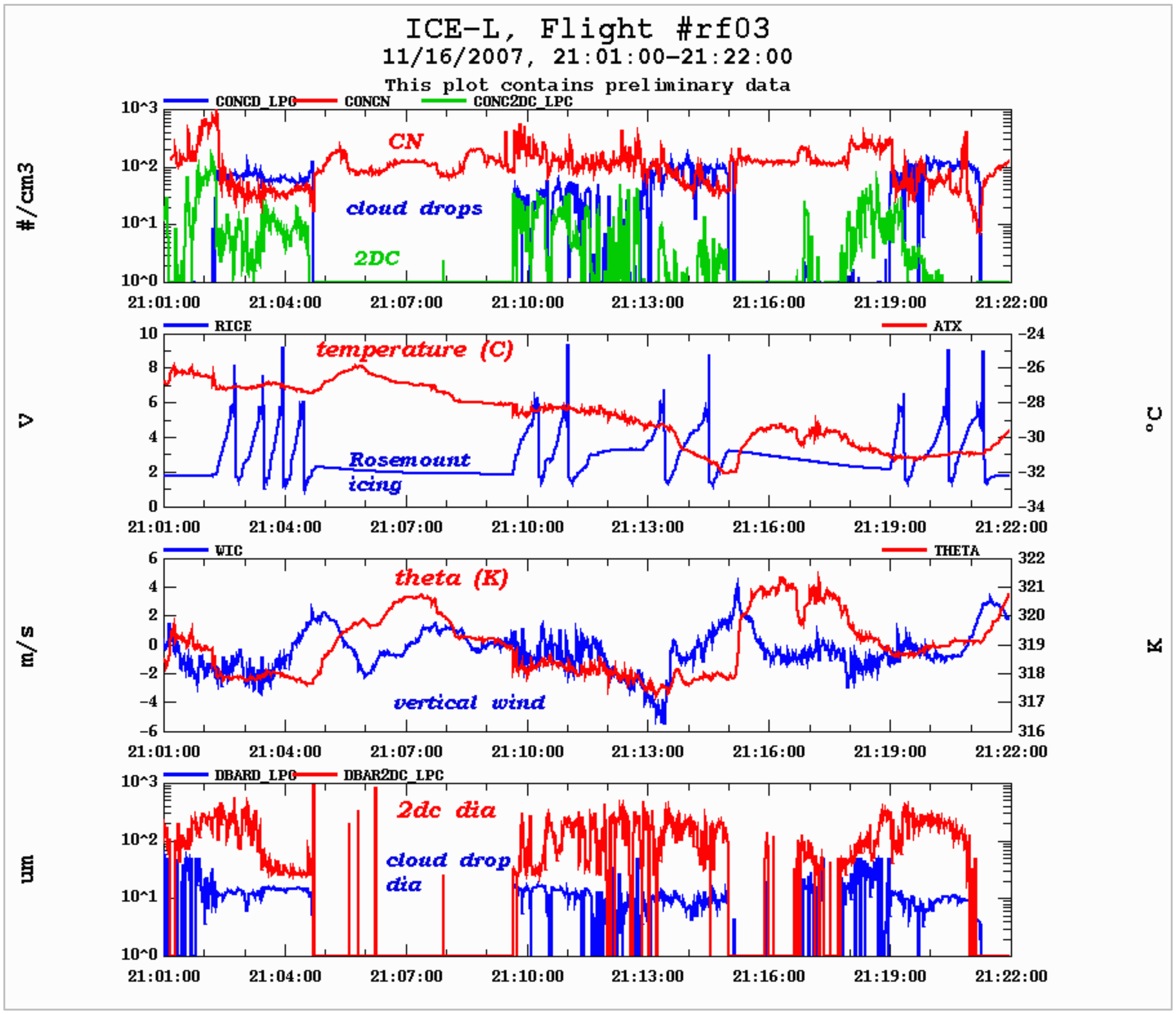

Figure 3. Three penetrations of a wave cloud (upwind/downwind) during 21 minutes, ICE-L project. CN concentrations were not enhanced. Altitude 800m MSL, airspeed 150 ms^{-1} in snow (2DC) and super-cooled liquid water (RICE and cloud drops).

INTERCOMPARISON OF WATER VAPOUR MEASUREMENT TECHNIQUES

H. Saathoff[1], V. Ebert[2], D. W. Fahey[3], R. S. Gao[3], O. Möhler[1], C. Schiller[4]
and the AquaVIT team

[1]Forschungszentrum Karlsruhe, Germany
[2]University of Heidelberg, Germany
[3]NOAA Boulder, CO, USA
[4]Forschungszentrum Jülich, Germany

1. INTRODUCTION

Accurate measurements of water vapour and total water concentrations are prerequisite for assessing and understanding upper tropospheric and stratospheric water and energy budgets, cirrus formation, fluxes of water, radiation, and atmospheric chemical processes. The discovery of unusually high supersaturations with respect to ice in upper tropospheric cloud-free air and inside cirrus clouds is one example that calls into question our understanding of the physics of ice cloud formation (Peter et al., 2006) or the accuracy of the humidity measurements.

At the core of understanding these processes is the requirement for accurate measurements of water vapour and total water concentrations in the atmosphere and in the laboratory. However, recent observations of unexpectedly high supersaturations using different kinds of instruments and also inconsistent results obtained with different instruments call for an intercomparison of currently applied and newly developed instruments for measuring water vapour.

The AQUAVIT campaign organised during October 8-26, 2007, offered a framework for a formal intercomparison of water vapour measurement techniques at the AIDA (Aerosol Interaction and Dynamics in the Atmosphere) facility of Forschungszentrum Karlsruhe. A number of 22 different instruments, both state-of-the-art and newly developed techniques, were provided by 17 groups from 7 countries, representing a large fraction of the atmospheric water measurement community (Table 1). All participants agreed on a data protocol which assured a careful and blind intercomparison of the data from the different instruments.

2. EXPERIMENTAL

Only a few instruments measured water vapour directly inside the large AIDA vessel with 84 m^3 volume (Figure 1). Most of the instruments were connected to the vessel by heated high-quality stainless steel tubes. A calibrated permeation source and a high-quality frost point mirror were also available for additional calibration runs of the different instruments.

In a first phase of the intercomparison measurements (see Table 2) the performance of the instruments was investigated for constant pressure and temperature conditions but with special focus on low water mixing ratios (e.g. 1-20 ppm).

In a second phase the intercomparison was done during dynamic changes of pressure, temperature, water concentration, and cloud density. Water vapour mixing ratios varied between 0.5 and 3800 ppm in the AIDA chamber depending on temperature ranging from 185 to 243 K and total pressure ranging from 50 to 500 hPa.

Not all instruments were able to measure under all these conditions. During the intercomparison no exchange of data among the participants was allowed and single blind experiments were performed. Three referees collected the data and did the intercomparison taking into account the characteristics of the individual instruments including sampling positions.

Table 1: List of the AquaVIT participants and instruments.

Participants	Institute	Instrument
Harald Saathoff	Forschungszentrum Karlsruhe (IMK-AAF)	AIDA TDL, MBW-373LX (FP)
Volker Ebert	University of Heidelberg	AIDA TDL
Cornelius Schiller	Forschunszentrum Jülich (ICG-1)	FISH-1 (Ly-α), FISH-2 (Ly-α), MBW-DP30 (FP)
Robert L. Herman, Robert F. Troy	JPL, Caltech	JPL-Laser-Hygrometer (TDL)
Holger Vömel	University of Colorado	CFH (FP)
Elliot Weinstock, Jessica Smith	Harvard University	Harvard Ly-α
Sergey Khaykin, Leonid Korshunov	Central Aerological Observatory	FLASH-A (Ly-α), FLASH-B (Ly-α)
Linnea Avallone, Sean Davis	University of Colorado	CLH (TDL)
Teresa Campos, Frank Flocke, Dennis Krämer	NCAR Boulder	NCAR OPLH (TDL)
Mark Zondlo	Southwest Science, Inc.	HIAPER VCSEL (TDL)
Martina Krämer	Forschunszentrum Jülich (ICG-1)	Ojster TDL
George Durry	University of Reims & INSU/CNRS	PicoSDLA (TDL)
Debbie O'Sullivan	UK Met Office	Met Office (Ly-α)
Theo Brauers, Rolf Häseler	Forschungszentrum Jülich (ICG-2)	Vaisala Sensor DM 500
Zoltán Bozóki, Arpad Mohacsi	University of Szeged	WaSul-Hygro (PA)
Andreas Zahn, Julia Keller, Christoff Dyroff	Forschungszentrum Karlsruhe (IMK-ASF)	CARIBIC (Buck FP, PA), Isotope TDL
Frank Wienhold, Ulrich Krieger, Martin Brabec	ETH Zürich	Snow-White (FP)
Ulrich Bundke	University of Frankfurt	PADDY (FP)
Peter Mackrodt	PTB Braunschweig	Water permeation source
Referees		
David Fahey, Ru-Shan Gao	NOAA, Boulder	
Ottmar Möhler	Forschungszentum Karlsruhe (IMK-AAF)	

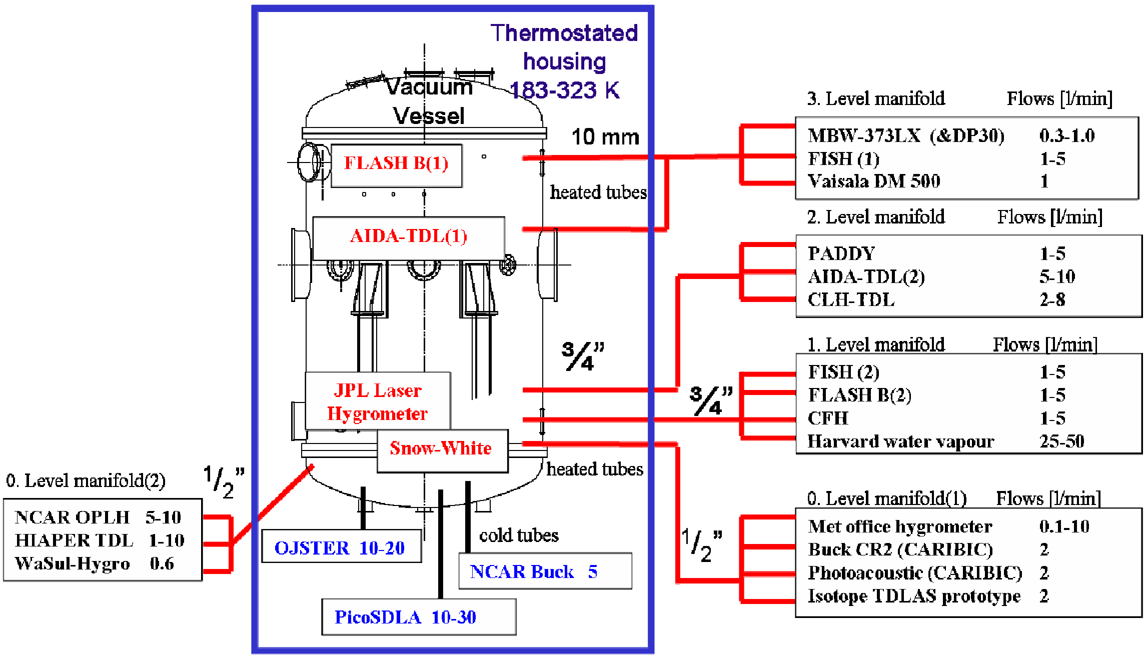

Fig.1: Schematic of the connection of the different instruments to the AIDA chamber during the Aqua-VIT campaign. The AIDA-TDL(1) is the in situ version APicT which will be used as a water vapour reference for the formal intercomparison. The AIDA-TDL(2) is a newly developed external TDL cell (APeT) taking a sample from the AIDA chamber and therefore measuring total water.

Table 2: List of the AquaVIT experiments and the conditions covered.

Exp. No.	Experiment type	T (K)	P (hPa)	H_2O (ppm)
3	Constant p,T	243	50-500-50	30 - 300
4, 5	Constant p,T	223	100-500-50	3 - 20
6	Constant p,T	213	100-300-50	3 - 20
7	Constant p,T	196	80-300-50	3 - 17
8	Constant p,T	185	80-500-50	0.5 - 3
9	Dynamic p,T	243	200 - 140	1800 - 3800
10	Dynamic p,T	223	200 - 140	190 - 400
11	Dynamic p,T	213	300 - 50	35 - 210
12	Dynamic p,T	200	300 - 50	5 - 30
13	Dynamic p,T	185	300 - 50	0.5 - 3

3. RESULTS

A result from the experiments with dynamic pressure and temperature changes in shown in Figure 2. The difference of total water, measured with a frost point mirror (MBW373), and water vapour, measured in situ by tunable diode laser absorption (AIDA-TDL) is in good agreement with the cloud (ice) water contend retrieved from in situ FTIR (Bruker IFS66v) measurement. This example demonstrates the quality of AIDA water measurements even in the presence of ice clouds.

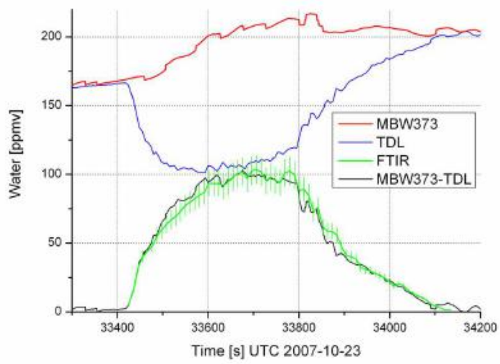

Fig. 2: Comparison of the ice water content in the AIDA chamber derived from FTIR extinction spectra and determined from the difference of the total water measurements with a chilled-mirror hygrometer (MBW373) and the water vapour measurements with the in situ AIDA TDL system APicT.

The results from the AquaVIT formal instrument comparison are not yet public and will be discussed among the participants during a wokshop on May 28 to 30, 2008, at the ETH Zurich, Switzerland.

First results will become available during June 2008 and will be presented and discussed on the poster.

ACKNOWLEDGEMENTS

Skilful on-the-spot support by the technical AIDA team is gratefully acknowledged. The authors thank the EU FP6 projects EUROCHAMP and SCOUT-O3, SPARC (a core project of the World Climate Research Program WCRP), ETH Zürich, Forschungszentrum Jülich, and Forschungszentrum Karlsruhe for financial support of the AquaVIT intercomparison activity.

BIBLIOGRAPHY

Peter, T., C. Marcolli, P. Spichtinger, T. Corti, M. B. Baker, T. Koop (2006). When Dry Air Is Too Humid. Science, 314, 1399-1402.

STUDY OF METHOD ON AUTOMATICAL ANALYSE SEEDING AREA BY USING THE DATA FROM NEW GENERATION RADAR NETWORK

Aili Shi[1] Yimei Huang [2]

[1] The centre of Weather Modification of CMA,

[1]Key Laboratory for Cloud Physics and Weather Modification of CMA, Chinese Academy of Meteorological Sciences, No.46, Nandajie, Zhongguancun, Haidian District, Beijing, 100081, shial@cams.cma.gov.cn，

[2] Weather Modification office of Henan Province, Zhengzhou，450003，huangyimei@sina.com

1. INTRODUCTION

It is very important to estimate and choose the seeding area in weather modification activities〔1-2〕. At present, the common method in commanding precipitation enhancement operation is combining the radar echo data and other data to roughly estimate the cloud seeding area〔3〕. However, this method is relatively simple and will influence the efficiency of precipitation enhancement. In this paper, we design a new method, which main idea is using the new generation radar net-work data and dealing with multi-relative data, applying the software technique to integratedly analyze the seeding area automatically.

2. THE METHOD OF USING KINDS OF DATA TO CHOOSE THE SEEDING AREA

According to the size of seeding area, the area is partitioned to bit matrix. The position of each value of multi-station radar volume-scan data need to be orientated and made it relative with some bit area. During processing, we only add up the numbers which below some fixed number like 6km.Because cloud seeding on airplane is always between 5-6km where the temperature below zero, if too high it will influence the proportion of the seeding point by adding up the areas that have no radar echo, and if too low, it will filter the seeding cloud's echo. We judge the seeding character by analyzing the proportion of the number which is included with the seeding index. This method can use several radars at the same time without graphic procession and overlap area procession. We can conclude the uncover areas from the areas around.

The product of numerical simulation, satellite retrieval, sounding and ground observation data should be processed separately according to different resolution. We judge the seeding character by analyzing the proportion of the number which resolution less than bit area resolution while inserting the dada that resolution larger than bit resolution. For the other data, we should set different weight coefficient and integratedly analyze the seeding area automatically.

The seeding areas can be organized as

a sparse matrix and saved by crossed linked list. We can find an unvisited node from all crossed linked list nodes firstly, insert it into a single linked list and mark it as “visited" at the same time. Then, beginning with this node, find out all unvisited nodes around it. Mark them as “visited” and insert into the end of single linked list. By the steps above mentioned, all the nodes of the single linked list were handled. Then the last single-linked list is a continuous seeding area. Repeat the operation above until crossed List all nodes have been visited, later all seeding areas can be found. According to adjacent distance between the discrete regions, we blend it properly. Then the final selection of the best seeding area can be found. Finally, we can make the automatically rainfall enhancement operations decision by aircraft come true by designing the airline according to seeding level wind speed operation, aircraft performance, operating disaster zone and so on.

3. APPLICATION OF THE METHOD

The case study was carried out with the radar data and sounding data of Henan province on 2 May, 2004. The seeding condition for radar data was that the echo intensity was larger than 20dBz, while for sounding data, the seeding condition was: -5℃<T<-15℃; T-Td<=2℃;e-Ei>=-0.1.

The area was divided into matrix of 34*34. The length of each bit side was 14. The resolving of pels was 1km. If the ratio of seeding dot account for the total pels of each bit is larger than 60%, the number of

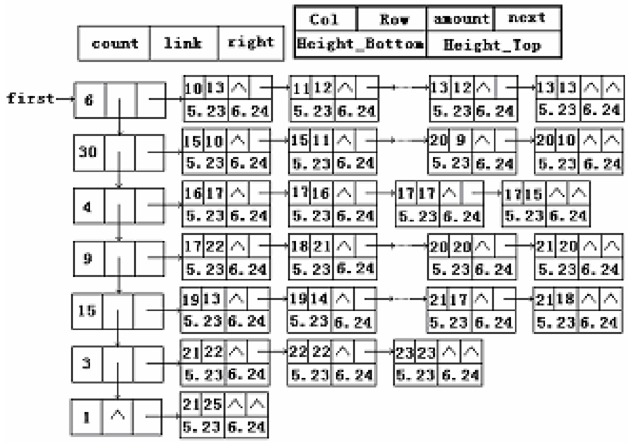

Fig.1 The seeding areas expressed with singly linked list

seeding bit was 68. Because there are only two sounding station of Henan province, we drew a beeline which was in the middle of the two stations and the slope was -1. If the bit was on the top of the beeline, the sounding data of Zhengzhou station was

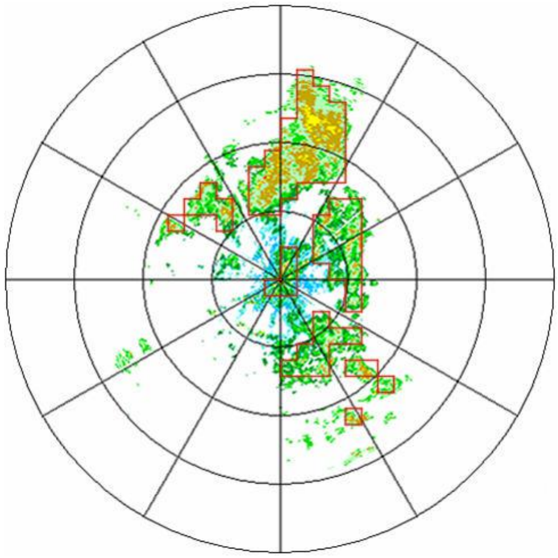
Fig.2 All the seeding areas

used, on the contrary, the sounding data of Nanyang station was used. Combining with the above mentioned seeding conditions of sounding data, the seeding height for the computed 68 seeding bit was between 5.23km and 6.45km. Building the matrix and using the above arithmetic, we can compute

7 seeding areas that were different size. The structure of the singly linked list and the seeding area border was expressed by the Figure. 1 and the Figure. 2, respectively.

4. BIBLIOGRAPHY

〔1〕Chengchang Zhang, Huanbin Xu, etc. Teaching Materials on Training the Weather Modification Professional Personnel. Beijing, Meteorological Press. 2003.7.

〔2〕Dashan Li, Chengchang Zhang, etc. The Status and Prospect on Weather Modification in China. Beijing, Meteorological Press. 2002.8.

〔3〕Cunzhang, Yuquan Zhou. Research on the Optimizing Technique of Weather Modification. Beijing, Meteorological Press. 2000.12.

Acknowledgements: This paper was supported by the National key project “Research on the WM key problems and facilities” (2006BAC12B06) funded by MOST during the 11th five year.

CALIBRATION OF ICE WATER CONTENT IN A WIND TUNNEL / ENGINE TEST CELL FACILITY

J. Walter Strapp[1], James MacLeod[2], and Lyle E. Lilie[3]

[1]Cloud Physics and Severe Weather Research Section, Environment Canada, Toronto, Canada
[2] Propulsions Group, Gas Turbine Laboratory, National Research Council of Canada, Ottawa, Canada
[3] Science Engineering Associates, Mansfield, CT, USA

1. INTRODUCTION

In recent years, aviation sector interest in the measurement of cloud ice particle total mass and mass distribution has grown due to an increasing number of in-service single and multiple jet engine power-loss events on commercial aircraft usually when flying in the vicinity of deep convection (Lawson et al. 1998, Mason et al. 2006, Pasztor, 2008). Pilot reports, flight data recorder data, and some industry flight test data strongly indicate that the events are probably related to the ingestion of high ice water content into the engines. Such events have obvious cost and safety implications to the industry and the public. Recently, the National Research Council of Canada (NRC) has been working to create an ice particle simulation facility for testing jet engine and/or engine components in high ice water content (IWC) conditions. Ice particles are created by shaving ice blocks, or by using a grinding mill. Environment Canada is collaborating with NRC on the calibration of the IWC quantities produced in the tunnel. By measuring the relative profile of IWC across the tunnel, and knowing the amount of ice delivered into the tunnel, it is possible to provide an absolute estimate of the tunnel IWC at any location across the tunnel.

The obvious application of this work to the cloud physics community is as a first step towards the 'absolute' calibration of in-situ airborne IWC sensors. Estimates of cloud ice water content (IWC) by airborne in-situ sensors have to date not been convincingly validated. Accuracy assessments have usually been attempted only through estimates of contributing errors, or through comparisons of instruments with different operating principles. In the case of cloud liquid water content measurements, absolute accuracy estimates of airborne sensors have been possible by comparison to icing cylinder and blade measurements in icing wind tunnels, where the errors in the latter measurements are relatively small and can be quantified (e.g. Strapp et al. 1982, King et al. 1985 , Strapp et al. 2002). No equivalent 'absolute' comparison standard has been available for IWC measurement systems. Airborne IWC instrument comparisons have tended to reveal relatively large discrepancies, and researchers have been reluctant to quote absolute accuracies.

This paper will describe an 'absolute' calibration of IWC in an engine test facility, where the emphasis has been on the creation of very high IWC conditions at relatively high velocities. The facility will ultimately also be used to evaluate current instrumentation and develop new instrumentation for the in-situ measurement of high IWC, to support future airborne cloud measurements planned in high IWC regions of deep tropical convection for engine power-loss studies.

2. THE TEST FACILITY AND TEST MATRIX

The National Research Council Gas Turbine Laboratory has several engine test cells used for testing of jet engines up to approximately 25,000 lbs thrust. The one used for this test is an open circuit tunnel that takes in air from outside the facility building into the test cell, and exhausts it outside the facility building. The disadvantage of this type of tunnel over a closed-loop tunnel is that it can only be operated when outside air temperatures are colder than about -10C in order to avoid melting and sticking of the ice particles in the delivery system. The very large advantage of the system however is that there is no recirculation of ice particles as has been observed in closed circuit tunnel. This is fundamentally important in the estimate of the absolute IWC by simply accounting for how much was shaved and into what volume it was injected. The NRC first developed this capability for ingesting ice particles into engines in the 1950s. The ice shaving device they developed consists of a rotating drum with teeth that rip at the surface of ice blocks that are pushed into the drum. Ice particles that are shaved off the block by this process fall into a chute and are blown into a duct towards the entrance of the tunnel by a 25 HP blower. The main chute divides into 4 smaller ducts that then eject the shaved ice into 4 quadrants at the inlet of the circular cross section that constricts to a 34.5 inch (87.6 cm) test section (Fig. 1). The maximum tunnel speed is approximately 160 ms^{-1}, depending on the amount of equipment in the test section.

Figure 1. Picture of entrance into the open circuit engine test cell/wind tunnel, with 4 ice-injection ducts (dark grey coloured) providing ice particles from the ice shaver, and water spray bars in behind (unused for this study). The diameter of the test section is ~88 cm.

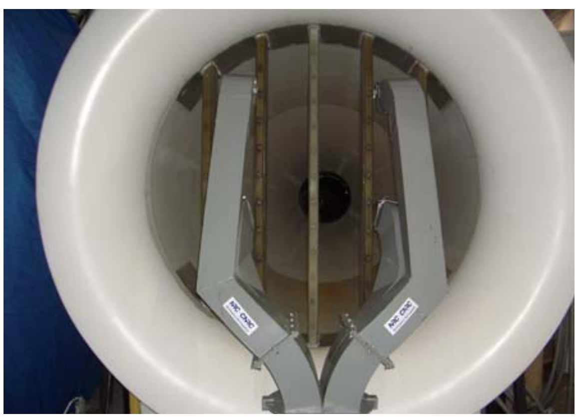

Shaver Rate (cm/min)	**Tunnel speed ms^{-1}**	**Fully Mixed IWC (gm^{-3})**	**Comments**
10.2	150	0.59	mapped
17.8	150	1.03	mapped
25.4	150	1.47	mapped
38.1	150	2.20	mapped
50.8	150	2.93	mapped
76.2	150	4.40	impractical to map
25.4	80	2.76	Comparison pt. to Cox & Co. tunnel, mapped

Table 1: IWC Test Matrix for NRC Test Cell Ice Simulation

Industry airborne studies in the 1950s measured IWC concentrations in deep tropical convection up to about 8.0 gm-3 (McNaughtan, 1959). Given that IWC values in deep adiabatic cores could at least in theory reach values in excess of 9 gm-3 (Mazzawy and Strapp, 2007), an industry-government working group concluded that 10 gm^{-3} would be a good preliminary design upper limit to adopt while implementing various parts of the technical plan addressing the engine power-loss issue. Therefore, a test matrix was developed that could be used to produce calibrated levels of IWC, with the hope of reaching 10 gm^{-3} at 150 ms^{-1} (Table 1). The actual test matrix spans the practical limits imposed by the ice shaver system. On the low IWC side, stable center-position IWC values could not be obtained. At the highest shaver rates, the time it takes to fully shave one ice block drops below 1.5 minutes, insufficient for stabilization and mapping of the tunnel. Therefore the practical lower and upper limits for the determination of the absolute calibration were for the 10.1 to 50.8 cm/min shaver rates, corresponding to 0.59 to 2.93 gm^{-3} if the ice were evenly distributed through the tunnel. Although this falls short of the initial target of 10 gm^{-3}, it was concluded that additional mass could be added in future years by adding an additional shaver or other ice producing device. Furthermore, it was expected that the IWC values of the 76.2 and

Shaver Rate (cm/min)	Fully mixed IWC	Est. Median Mass Dia (μm)
5.1	0.59	197
10.2		218
25.4	1.47	228
50.8	2.93	267

Table 2: Estimates of median mass diameter of ice particles from 2DCgrey images, taken at 80 ms^{-1}

106.7 cm/min points could be determined by extrapolation of the other lower shaver rate points, and used for special short experiments increasing the fully-mixed IWC values to about 6 gm^{-3}.

Ice slide and visual impressions of the plume of ice particles produced by the shaver suggests that the median mass diameter of the particles can be varied substantially by changing the drum rotation speed and 'wobble' of the cutting teeth. Due to lack of time, the size varying capabilities of the shaver have not been characterized. Rather, it was decided to always run the same rotation and wobble speeds so as to produce what was thought to be the smallest ice particles, to hopefully simulate the small particle sizes observed near cores of thunderstorms. A 15 micron resolution Particle Measuring Systems 2DC-grey cloud imaging particle spectrometer was used to

Figure 2: Sample 2DCgrey images from the 25.4 cm/min ice shaver run at 80 ms^{-1}. The images with green circumscribed boxes are accepted by the 2D analysis software. The height of the box is 960 μm

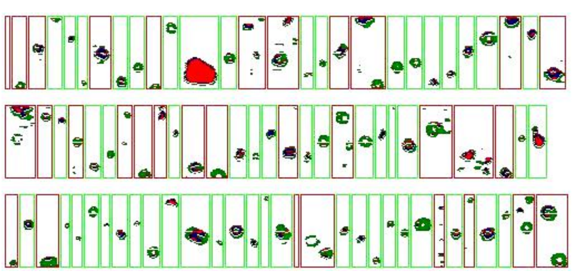

measure the particle spectra and estimate the median mass diameters (MMD) at the different shaver rates. It was necessary to perform these tests at 80 ms^{-1} rather than 150 ms^{-1} because the probe repeatedly failed at high airspeeds and high IWCs, possibly due to effects caused by the high electrostatic charging by the ice particle impacts on the probe. This type of failure has also been observed with similar particle spectrometer probes during industry flight testing in high IWC regions near thunderstorm cores. Results of the testing at shaver rates of 5.1, 10.2, 25.4, and 50.8 cm/min are shown in Table 2. Sample 2DC-grey images from the 25.4 cm/min run are given in Fig. 2, and a normalized mass distribution for the 25.4 cm/min run is shown in Fig. 3. Although these MMD results cannot be considered highly accurate because the measurements below 100 μm are known to have limited accuracy (e.g. Korolev et al. 1998, Strapp et al. 2001), they do provide a first approximation, and probably an upper limit to the median mass diameters of the ice particles in the tunnel for this shaver configuration. The estimated MMDs are found to increase from about 200 to 270 μm with increasing shaver rate (IWC). The values are similar to those reported for the Cox and Co. Icing Wind Tunnel for their shaved ice clouds (Emery et al. 2004).

Figure 3: Mass distribution for 25.4 cm/min ice shaver run at 80 ms^{-1}. Data are from a PMS 2DCgrey cloud particle spectrometer.

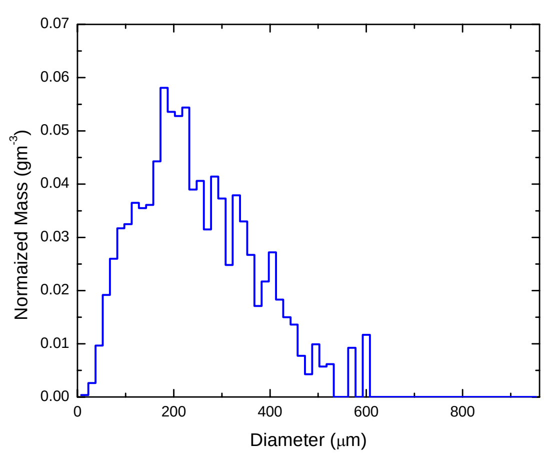

3. INSTRUMENTATION AND TEST METHOD

For a given shaver rate, assuming that conditions are reproducible to an acceptable level, the absolute IWC at any location in the tunnel can be determined by mapping the tunnel with a probe that measures IWC, producing isopleths of relative IWC across the tunnel, and then by scaling the isopleths of IWC so that they produce the known flux of ice that is being injected into the tunnel by the shaver. One necessary requirement is that the IWC probe must measure a constant fraction of IWC; it does not matter if the fraction is close to unity although that is of course preferable. An end result of a series of calibrations at different shaver rates is that the probe itself is calibrated, and its linearity with IWC is thereby determined. Another necessary condition is that all of the ice particles are deposited into the tunnel, and do not build up in the ducting or shaver. Normally, this did not occur as long as the outside air temperature was colder than -10 C, and the ducting was frequently inspected for confirmation. Finally, there must be no melting and evaporating of the ice by the shaving drum. A simple experiment was performed by catching all of the ice particle shaved by the rotating drum, and a comparison to the calculated mass based on the loss of volume of the shaved block revealed a loss of less than 3%.

The isopleths of relative IWC in the tunnel were determined by mapping the tunnel with vertical traverses with the IWC probe at 3 inch (7.62 cm) intervals with a vertical movement of about 50 cm/minute. Traverses at each horizontal map location were repeated three times to establish variability and to provide a more representative average.

Following experience on an industry test aircraft program (Strapp et al, 1999), it was recognized that there was probably no airborne total water content system that could perform adequately in the high-speed/high IWC environment. In response, a Science Engineering Associates (SEA) hot wire total

Figure 4. Picture of the early SEA TWC sensor design used in 2007 testing. This sensor was used successfully at 100 ms^{-1}. but was bent and damaged at 150 ms^{-1} in high IWC values. The sense element is a solid-wire, 2 mm deep half-cylinder

water content system was specially modified to provide sufficient power to measure the expected high IWC values. Furthermore, it was felt that the solid wire of the early version of the SEA sensor available at the time (a 2 mm deep half cylinder) would be more resistant to the destructive effects of the particle impacts at these higher speeds than other wound-wire alternatives. Although this early sensor has been used successfully in Environment Canada/NRC airborne studies on the NRC Convair 580 at 100 ms^{-1} for several years, the ice particle impacts in the tunnel at the higher airspeed did indeed eventually bend the sensor in the center of the sample tube and break the connection to the sample tube at the top of the sensor. A picture of the damage to the sensor head used in the winter of 2007 is shown in Fig. 2. In fact, when the higher IWC values were sampled, these sensors were damaged very rapidly, resulting in the early cancellation of the tunnel testing in 2007. It is data from this first season that will be provided in the next section, from a shaver rate that did not result in destruction of the sensor. It was however concluded that a newer more robust sensor would need to replace the standard sensor the following winter. The new sensor developed for the winter of 2008 by SEA is

Figure 5. Picture of new robust TWC sensor designed by Science Engineering Associates for high-speed/high IWC operation. This sensor was operated successfully in winter 2008 testing at 150 ms^{-1} and IWC estimated to be in excess of 8 gm^{-3}. The same sense element as in the 2007 model is used, but was imbedded in a leading edge.

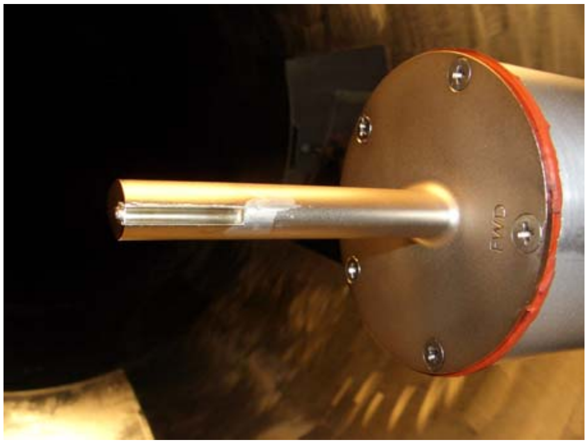

shown in Fig. 5. This sensor incorporates the same sold wire and catch geometry as the early SEA TWC sensor, but it is imbedded into the leading edge of a 12 mm wide strut. This sensor was successfully tested in December 2007, and performed without any discernible damage or measurement corruption throughout the mapping of the test matrix completed in January and February of 2008. It has been exposed to estimated IWC values in excess of 8 gm^{-3} at 150 ms^{-1} without any indication of damage or saturation.

4. 2007 RESULTS.

This section will describe the results of the 2007 calibration of the NRC engine test cell calibration for IWC for the 25.4 cm/minute shaver rate case, using an early version of the SEA TWC sensor shown in Fig.4.

The TWC sensor was mounted on a traversing arm that could be manually adjusted for horizontal position, and was motor-driven in the vertical position. The procedure to map the tunnel concentrations is best illustrated with an example (Fig. 6). The horizontal position of the probe was stepped at 7.6 cm intervals. At each interval the TWC instrument traversed vertically at about 50 cm/min. The points shown in small print on Fig. 6 represent the positions at which centered 10 s average TWC values were calculated. Next, data from three complete mappings as in Fig. 6 for the same setting were averaged to give a final smoothed

Figure 6: Illustration of raw data collection points during vertical traverses of tunnel, used to create isopleths of IWC for a given ice shaver setting

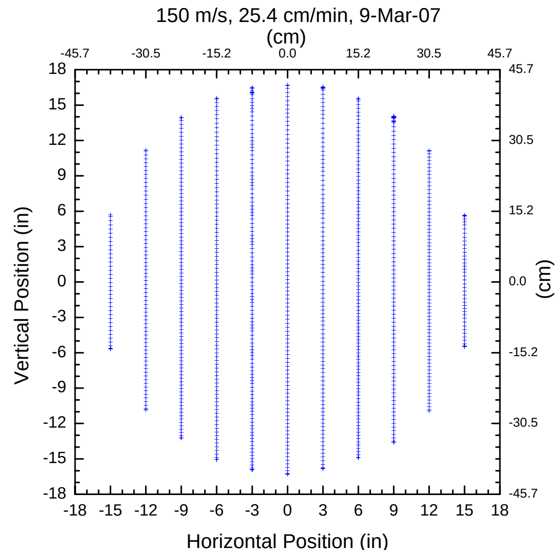

Figure. 7. Isopleths of IWC as measured by the early version of the SEA TWC sensor (Fig. 4).

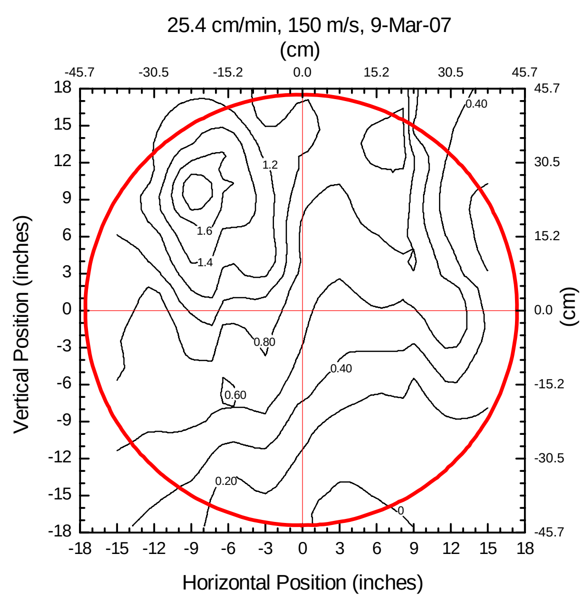

representation of the TWC distribution in the tunnel. The isopleths of IWC, as measured by the SEA sensor, are given in Fig. 7. Note that the measured IWC at the center of the tunnel, the prime measurement location, is approximately 0.65 gm^{-3}, but there is a concentrated maximum of in excess of 1.8 gm^{-3} in the top-left quadrant of the diagram. Fig. 7 shows the isopleths of IWC as viewed looking upstream in the tunnel, so when compared to the photograph looking down the tunnel in Fig. 1, the right and left quadrants must be flipped. The offset maximum is then easily explained. The bends in the ducting result in the top-right duct shown in Fig. 1 being the one with the most direct route for the ice particles. Centrifugal forces due to the bends direct the ice particles more favourably to this duct.

The final step in the calibration is the comparison of the estimated measured total mass flux down the tunnel to the estimated true mass flux. The true mass flux is estimated from the volume of ice shaved per unit time based on the shaver rate and the cross sectional area of the ice blocks, the density of the ice blocks, and the airspeed in the tunnel. The ice blocks used in these tests are commercially produced in such a way as to minimize the number of air bubbles, and are commonly used for ice sculptures. The density of the ice was estimated by the block weight and volume to be approximately 0.92 gcm^{-3}. At 25.4 cm/min, the 348 cm^2 blocks inject approximately 25.4x348x0.92 g of ice into the tunnel (8132 g) per minute, or 135.5 g/s. One of the intermediate products used to produce the isopleth diagram of Fig. 7 is an estimated 1 cm x 1 cm IWC matrix, which can be used to calculate the flux of ice through each 1 cm x 1 cm square by multiplying the IWC matrix value by the tunnel velocity. When these fluxes, based on the instrument response, are added up to give the total instrument-based flux through the tunnel cross-section, the value obtained for this setting is 68.2 g/s. Therefore, the efficiency of the sensor is 68.2/135.5, or approximately 0.50. The instrument reads approximately a factor of 2 low. These results are not unexpected, and qualitatively agree with past wind tunnel data collected at the Cox and Co. Icing Wind Tunnel, also using an ice shaver to create ice particle clouds. Emery et al. (2004) and Strapp et al. (2005) have provided evidence from high speed video records of ice particles being ejected from the capture area of hot-wire TWC sensors, and pooling of the Nevzorov TWC sensor in high IWC conditions. Although the results are confounded by ice particle recirculation, Strapp et al. (2005) also showed that the deepest sensor tested (16 mm) showed the least mass ejected from the capture volume, and its response of was at least a factor of 2 larger than the lowest reading shallow sensor (2 mm). Emery et al. (2004) also showed that a variety of hot wire devices responded within about 25% in liquid conditions at ~20 μm MVD, indicating that the difference in hot wire response in ice particle conditions was not due to electronics. Isaac et al. (2006) have also observed with high-speed video the breakup and ejection of some of the mass of natural dendrites striking the cone of the Nevzorov probe, indicating that underestimates of ice mass may also be expected in natural clouds.

5. 2008 RESULTS.

After limited measurements in 2007, measurements were resumed in the winter of 2008 with the newly designed robust hot-wire TWC probe (Fig. 5). A full set of mappings of the tunnel at all of the ice shaver settings listed in Table 1 was accomplished, with the exception of the highest setting that was deemed impractical to map due to short ice block shaving times (see section 2). The analysis of these results into tunnel profiles and absolute calibration points for the new robust sensor is ongoing, and could not be completed in time for this report.

In addition to the tunnel mapping, a series of runs were performed at the center of the tunnel to provide some data to support the linearity of the new robust probe's response with IWC. The geometry of the new sensor is very similar to the early sensor (Fig. 4), in that the sensing elements are 4 mm half-cylinders with a depth of 2 mm in each case. Since the response of the older probe was found to be linear with the rate of injection of ice into the tunnel (Strapp et al. 2005), it was hoped that the same would be true for the new probe. Fig. 8 displays the response of the new probe as a function of ice shaver rate for two locations in the tunnel, the center and near the 'hot-spot' (maximum) located in Fig. 7. Note that at both locations, the response of the probe is indeed linear with respect to the rate at which ice is delivered to the tunnel. The values in Fig. 8 are averages varying between about 1-3 minutes, the time decreasing with increasing shaver rate. The repeatability of the results is quite good, with the exception of the highest shaver rate, where the short averaging interval and the evidently reduced shaver stability result in noticeably higher variability. Note that the results of Fig. 8 are encouraging, since the absolute calibration method requires that the mapping device measure linearly with respect to IWC. The final verification of the method will be the probe efficiencies, determined as in the case of the tunnel mapping example summarized in section 4. If the efficiencies

Figure. 8: Response of the new robust hot-wire TWC sensor as a function of delivery rate of ice particles to tunnel. Results are shown for the center of the tunnel, and a location near the tunnel 'hot-spot'.

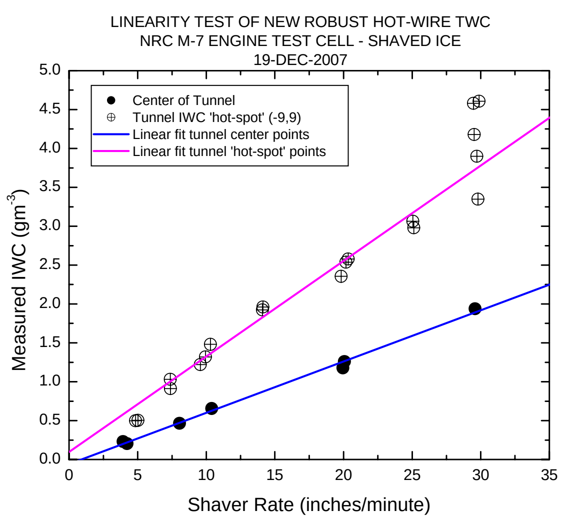

remain relatively constant with increasing IWC, this basic linearity requirement will be confirmed.

The similarity of the new sensor to the old sensor also suggests that the response of the sensors might be similar for the same shaver rate. The IWC at the center position of Fig. 7, estimated at about 0.65 gm^{-3} for the early sensor, compares very favourably to the new sensor. The best fit line for the center position in Fig. 8 indicates an IWC of ~0.60 gm^{-3}. This implies that the efficiency of the new probe may also be of the order of 50%.

6. SHAVED ICE VERSUS NATURAL ICE

The main focus of this work is to create a calibrated ice cloud simulation in the NRC M-7 test cell that can be used in the short-term for qualification of existing IWC and other airborne probes in the high speed, high IWC environment, for the development of new instrumentation, and for physical testing of engine components to help answer how ice particles cause ice accretion in a jet engine. Although there is no doubt that the shaved-ice simulation cannot duplicate natural ice crystal morphology, in particular the large complex and often delicate particles seen in nature, it is vital that existing resources be developed on a time scale of less than 2-3 years that can realistically meet the target IWC values thought to be required to induce engine power-loss events. Since the median mass diameter of the ice clouds that induce power-loss events is thought to be perhaps less than 200 μm or so, it is suggested that shaved ice may be a reasonable facsimile for the majority of the natural ice particle spectra, given that large particles are unlikely to remain intact any appreciable distance into the engine. The simulation of calibrated IWC mass concentrations is highly important in providing first-order confidence that heat-transfer conditions thought to be critical to engine icing are realistic.

Probes that are qualified and calibrated in the M-7 test cell will ultimately be used as part of an industry technical plan to characterize the high IWC environment in a focused field program. The instrument calibrations derived from the shaved ice simulations will somehow need to be tested in natural clouds. It is anticipated that this will be accomplished by comparison of the relationships between various IWC measurement probes in the tunnel versus in natural clouds. Other special airborne experiments, such as the further use of high speed video of probe sensing elements, may be also pursued. IWC measurement devices must be able to accurately operate in both simulated ice conditions and natural ice conditions. The calibration in simulated ice conditions moves us one step forward towards this goal.

7. FUTURE PLANS

The analysis of the 2008 calibration data for the 5 ice shaver rates shown in Table 1 will be completed shortly, in a manner similar to that described in section 4. This will provide a tunnel with estimated IWC at the center varying between approximately 0.5 and 3.6 gm^{-3}, and at a tunnel hot-spot for special experiments between approximately 1.5 and 11 gm^{-3}. This will also provide an 'absolute' calibration of the robust hot-wire TWC sensor within this IWC range. Once completed, a series of calibrations are planned for the DMT Counter Flow Virtual Impactor, the Nevzorov and possibly other hot-wire devices. A new isokinetic total water content measuring device targeting up to 10 gm^{-3} at 150 ms^{-1} is also being developed by NRC and EC for this project, and if successful its comparison to the tunnel values will help substantiate the calibrations using the robust sensor. A variety of further instrument testing experiments are planned to check the performance of pitots, temperature probes, and wind/gust measuring devices in the high IWC environment. The tunnel will also be used for experiments using model engine components to investigate the engine icing problem.

8. SUMMARY

An ice-cloud simulation in an open-circuit wind tunnel/engine test cell has been documented in an attempt to provide an absolute calibration of IWC. This work has been motivated by a growing number of jet engine power-loss events thought to occur in high IWC clouds. Absolute calibration of IWC at a velocity of 150 ms^{-1} has been accomplished by measuring the total amount of ice injected into the tunnel, mapping with a hot-wire probe the spatial distribution of the ice in the tunnel, and then performing a mass-closure calculation. A full example for one ice shaver rate was given, which provided a map of the estimated absolute IWC at all locations across the tunnel sample section. This calibration also revealed that the mapping probe measured about 50% of the true IWC. A full set of 5 ice shaver rates, expected to provide IWC values near the center of the tunnel between 0.5 and 3.6 gm^{-3}, and near a 'hot-spot' in the tunnel of between 1.5 and approximately 11 gm^{-3} have now been measured, and will be analysed over the next several months.

Measurement of the high IWC environment at high speed has been found here and by others to be very challenging. An early hot-wire probe used in 2007 for the tunnel mapping failed repeatedly at the higher IWC values due to the destructive nature of the particle impacts. A new robust version of the probe was developed in 2008, which performed without problems throughout the range of IWC values. A necessary condition for the absolute calibration method is that the probe used to map the spatial distributions has a linear response with respect to IWC. Data collected in 2008 do indeed suggest that the robust probe has a linear response to IWC.

9. REFERENCES

Emery, E., D. Miller, S. Plaskon, J.W. Strapp, and L.E. Lilie, 2004: Ice Particle Impact on Cloud Water Content Instrumentation, *42nd AIAA Aerospace Sciences Meeting and Exhibit*, Jan 2004, AIAA-2004-0731.

Isaac, G.A., A.V. Korolev, J.W. Strapp, S.G. Cober, F. Boudala, D. Marcotte, and V. Reich, 2006: Assessing the Collection Efficiency of Natural Cloud Particles Impacting the Nevzorov Total Water Content Probe, *44th AIAA Aerospace Sciences Meeting and Exhibit,* 9-12 Jan. 2006, Reno, NV, AIAA2006-1221.

King , W.D., J.E. Dye, J.W. Strapp, D. Baumgardner, and D. Huffman, 1985: Icing wind tunnel tests on the CSIRO liquid water probe. *J. Atmos. Oceanic Technol.*, 2, 340-352.

Korolev, A.V., J.W. Strapp, and G.A. Isaac, 1998: Evaluation of the accuracy of PMS optical array probes. *J. Atmos. Oceanic Technol.*, 15, 708-720

Lawson, R.P., L.J. Angus, and A.J. Heymsfield, 1998: Cloud Particle Measurements in Thunderstorm Anvils and Possible Weather Threat to Aviation. *J. Aircraft*, 35, 113-121.

Mason, J.G., J.W. Strapp, and P. Chow, 2006: The Ice Particle Threat to Engines in Flight. *44th AIAA Aerospace Sciences Meeting and Exhibit,* Reno, NV, Jan 9-12, 2006, AIAA 2006-206.

Mazzawy, R., and J.W. Strapp, 2008: Appendix D – An Interim Icing Envelope. *SAE 2007 Tranactions, J. Aerospace*, in print.

McNaughtan, I.I., 1959: The Analysis of Measurements of Free Ice and Ice/Water Concentrations in the Atmosphere of the Equatorial Zone, *R.A.E. Technical Note No. ME.283*, 17 pp

Pasztor, A., 2008: Airline Regulators Grapple with Engine-Shutdown Peril. *The Wall Street Journal Online WSJ.COM*, April 7, 2008.

Strapp, J.W., and R.S. Schemenauer, 1982: Calibrations of Johnson-Williams liquid water content meters in a high speed icing tunnel. *J. Appl. Meteor.*, 21, 98-108.

Strapp, J.W., Chow, P. Moltby, M. Beezer, A.D. Korolev, A.V. Stronberg, I. and Hallett, J. 1999: Cloud microphysical measurements in thunderstorm outflow regions during Allied/BAE 1997 flight trials. *AIAA 37th Aerospace Sci. Meeting and Exhibit*, Reno, Nevada, 11-14 January 1999, AIAA 99-0498, pp10.

Strapp, J.W., F. Albers, A. Reuter, A.V. Korolev, U. Maixner, E. Rashke, and Z. Vukovic, 2001: Laboratory Measurements of the Response of a PMS OAP-2DC*. J. Atmos. Oceanic Technol.*, 18,1150-1170.

Strapp, J.W., J. Oldenburg, R. Ide, L. Lilie, S. Bacic, Z. Vukovic, M. Oleskiw, D. Miller, E. Emery, and G. Leone, 2002: Wind Tunnel Measurements of the Response of Hot-Wire Liquid Water Content Instruments to Large Droplets, *J. Atmos. Oceanic Technol.*, 20, 791-806.

Strapp, J.W., Lilie, L.E., Emery, E. and D. Miller, 2005: Preliminary Comparison of Ice Water Content as Measured by Hot Wire Instruments of Varying Configuration. *43rd AIAA Aerospace Sciences Meeting,* Reno, NV, 11-13 January 2005**,** AIAA-2005-0860

Acknowledgements.

Funding for this work was provided by the National Research Council of Canada, Environment Canada, Science Engineering Associates, the FAA Technical Center, and Transport Canada. The authors would like to acknowledge the special efforts of the NRC technical staff in the operation of the test cell.

FIELD STUDIES OF DRIFTING AND BLOWING SNOW

Peter Taylor, Mark Gordon, Sergiy Savelyev, Sumita Biswas and Marna Albarran-Melzer

Centre for Research in Earth and Space Science, York University, Toronto, Canada

1. INTRODUCTION

There has been an ongoing debate about sublimation rates in drifting and blowing snow, and the impact on the water budget of snow covered areas. Models such as the Prairie Blowing Snow Model (PBSM) and PIEKTUK have computed distinctly different rates of snow cover loss through this process. These, and other models are strongly dependent on the assumptions made concerning source strengths and near surface particle concentrations and size distributions. In order to provide information for these models we have made a number of field studies using particle counters, camera systems, other instruments and snow bags at three locations in the Canadian north. These have included participation in the CASES (Canadian Arctic Shelf Exchange Study) 2003 - 04 expedition between mid January and early May 2004 on first-year ice in Franklin Bay, NWT, measurements near Churchill, Manitoba in winters 2005/6 and 2006/7 and near Iqaluit, Nunavut as part of the STAR (Storm Studies in the Arctic) project in winter 2007/8.

Results include threshold conditions on wind and other factors for drifting and blowing snow to occur, vertical profiles of wind and particle number density and the impacts of blowing snow on visibility. Analysis of the camera data provides size distributions of the blowing snow particles and, in conjunction with saltation models, estimates of the upward fluxes of snow particles from the surface and the height of the saltation layer. Lagrangian simulation has also been used to model these processes.

2. BLOWING SNOW MODELS

The Piektuk model was developed by Déry et al (1998). As with the PBSM (Pomeroy et al, 1993) the basic situation considered is of a strong wind blowing over a snow surface of limited fetch, picking up particles of snow, which are then advected along and diffused upwards, but which may also sublimate during the process. A distribution of particle sizes is considered and sublimation will modify this size distribution. Piektuk emphasises the fact that this sublimation will to some extent be a self-limiting process as the relative humidity will increase as water vapour is added to the

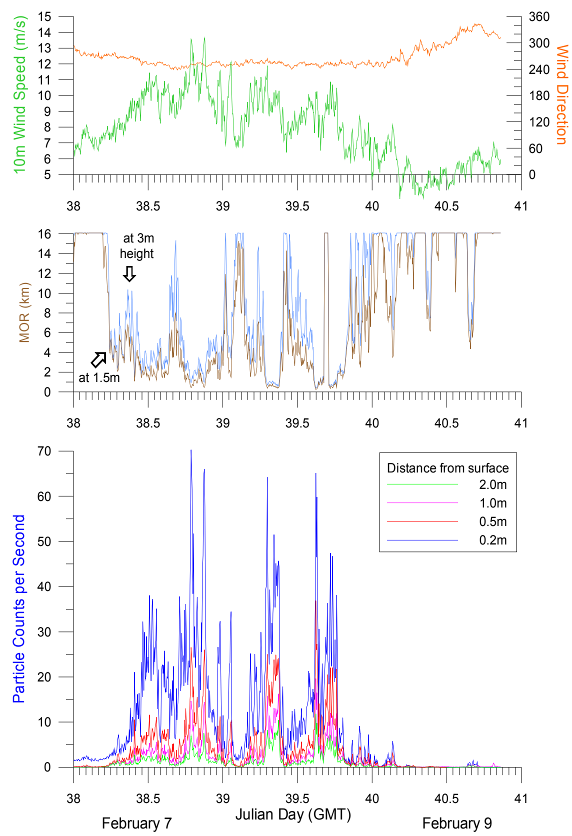

Figure 1. Data from a blowing snow event over Arctic Ocean ice during CASES. Feb 7-9, 2004. Note MOR is Meteorological Optical Range from a Sentry visibility sensor. Maximum range is 16 km.

air due to sublimation and the two models give rather different estimates of the overall loss of snow cover as a result of sublimation. The Piektuk model typically (U_{10} = 15 ms^{-1}, Initial RH_{ice} = 70%) estimates that the increased humidity effects reduce sublimation rates by a factor of 3 or 4 (see Déry et al, Fig 10) after a fetch of order 5-10 km.

A common limitation of both the PBSM and Piektuk is a reliance on limited amounts of data concerning the rates at which snow particles are lifted from the surface, and their size distributions. In order to address this we have conducted a number of field studies.

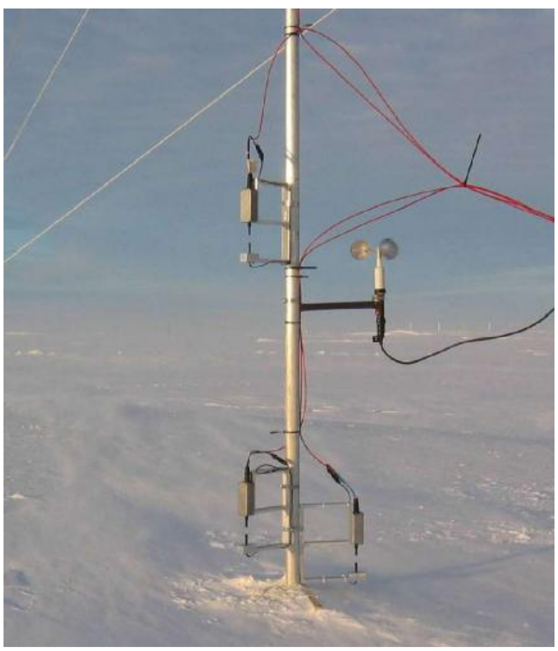

Figure 2. Particle counters deployed during CASES 03/04.

3. CASES 2003/4

Savelyev et al (2006) describes the blowing snow studies conducted in this Canadian Arctic Shelf Exchange Study, over first year ice in Franklin Bay, NWT. Instrumentation included particle counters mounted at several heights above the snow surface, wind profiles and visibility sensors. Figure 1 shows typical data from the study, clearly indicating a rapid decrease in the particle number flux with height.

The particle counters shown in Figure 2 are based on a design of Brown and Pomeroy (1989). An infra-red light beam is directed through a 2 cm long, 150μm diameter sample volume in front of a detector. Whenever the received light is reduced the electronics generate a pulse which is then counted by the data logger. Typical counts are of order 10-100 per second.

Huang et al (2008) have also established a strong correlation between particle number density and visibility as shown in Fig 3.

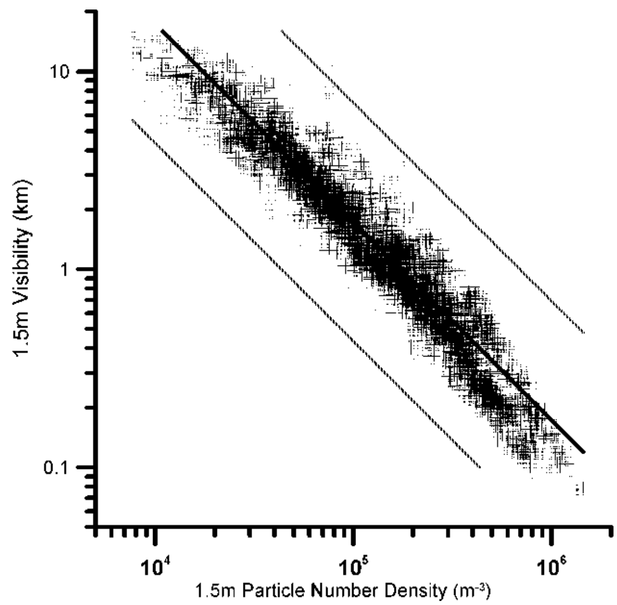

Figure 3. Relationship between particle number density and Meteorological Range. Data from CASES 03/04. Solid line corresponds to particles with an area-weighted mean radius, of 50 μm. Results with radii 25 μm and 100 μm are also shown.

4. Churchill studies

During our field studies in and around Churchill, Manitoba we made use of a camera system to determine particle size distributions. Details are presented in Gordon and Taylor (2008) and show that particle size distributions can generally be represented by a two parameter gamma distribution,

$$f(r) = \frac{N r^{\alpha-1} \exp(-r/\beta)}{\beta^{\alpha}\Gamma(\alpha)},$$

with α ranging from 1.5 to 2.5 and mean radii of order 100µm, and not varying significantly with height

5. STAR, 2007/8

As a part of a study of Storms in the Artic we deployed similar instrumentation to that used in CASES at the airport weather station at Iqaluit, Nunavut during winter 2007/8. The camera system and snow bags (Fig 4) were also deployed. In this case we were able to link the data logger at the tower to a PC at the weather station and post data to our web site for easy access from our home base in Toronto throughout the winter.

Figure 4 Snow bags and other equipment at Iqaluit airport site, February 2008

We were on site however throughout February 2008 (Fig 5). February is climatologically the winter month with most blowing snow. This year however was relatively calm, though not entirely so.

Detailed analysis of these data is ongoing but generally confirms our previous studies in terms of threshold wind speeds, particle densities and visibility reductions. Sample data are shown in Figure 6. Air temperature was about -35C that day with winds in excess of 15 ms^{-1} and much reduced visibility.

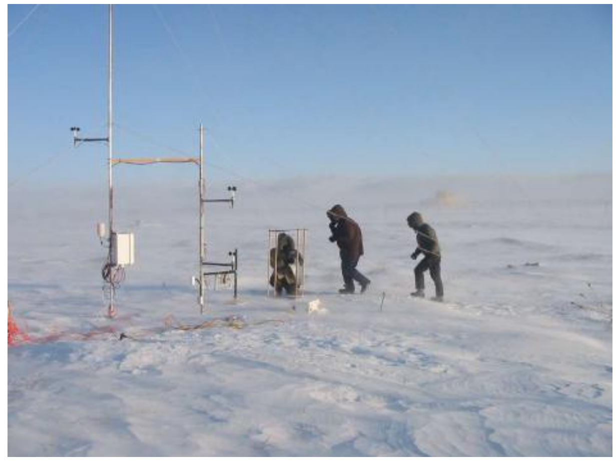

Fig 5 Graduate students enjoying field work at -30C and 10 ms^{-1} winds. One student is from Mexico, another from Bangladesh.

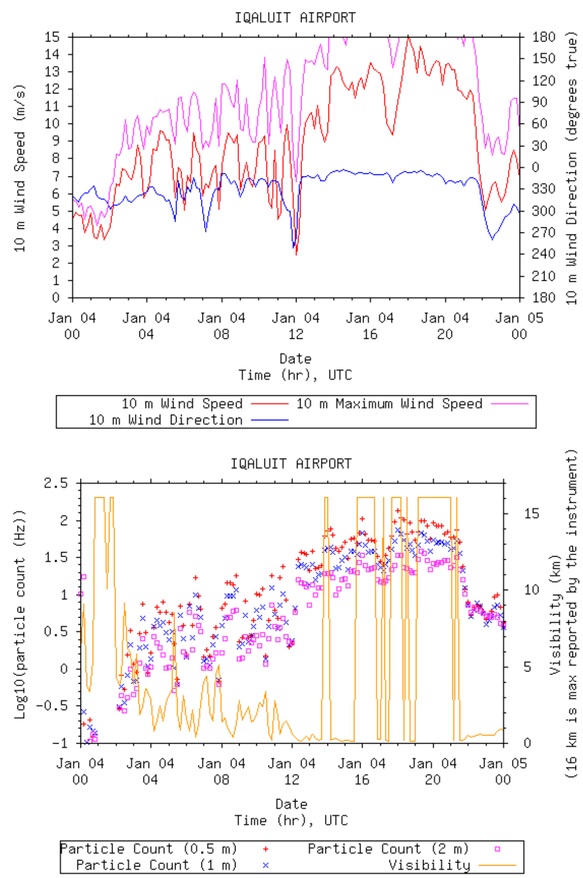

Figure 6 Wind speeds, particle counts and visibility during a blowing snow event: Iqaluit Airport, Jan 4 2008.

Acknowledgements

Most of our work on blowing snow has been funded by the Canadian Foundation for Climate and Atmospheric Sciences. Work during CASES was partially supported by ArcticNet. We thank the captain and crew of CCGS Amundsen for support during CASES, the Churchill Northern Studies Centre for accommodation and use of facilities in Churchill and Environment Canada for allowing us use of facilities at Iqaluit Airport weather station during the STAR field program.

REFERENCES

Brown, T. and Pomeroy, J.W., 1989: A blowing snow Particle Detector. Cold Regions Science and Technology, **16**, 167-174

Déry, S.J., Taylor, P.A. and Xiao, J., 1998, On the Thermodynamic Effects of Sublimating Blowing Snow in the Atmospheric Boundary Layer, Boundary-Layer Meteorology, 89, 251-283.

Gordon, M. and Taylor, P.A. 2007, Measurements of blowing snow, part I: particle size distribution, velocity, number and mass flux at Churchill, Manitoba, Canada. in press, Cold Regions Science and Technology.

Huang Q., Hanesiak J., Savelyev S., Papakyriakou T. and Taylor, P.A., 2008, Visibility During Blowing Snow Events Over Arctic Sea Ice, Internal Report, U of Manitoba

Pomeroy, J.W., Gray, D.M. and Landine, P.G., 1993, The Prairie Blowing Snow Model; Characteristics, Validation, Operation, J. Hydrol., 144, 165-192.

Savelyev, S., Gordon, M., Hanesiak, J., Papakyriakou, T and Taylor, P.A., 2006, Blowing Snow Studies in CASES (Canadian Arctic Shelf Exchange Study) 03-04, Hydrological Processes, 20, 817-827

Backscatter Color Ratios of Cirrus Clouds Measured by the Cloud Physics Lidar

M. A. Vaughan[1], M. J. McGill[2], Z. Liu[3], Y. Hu[1], and R. E. Kuehn[4], and S. D. Rodier[4]

NASA Langley Research Center, Hampton VA USA 23681-2199
NASA Goddard Space Flight Center, Greenbelt MD USA 20771
National Institute of Aerospace, Hampton VA USA 23666-6147
Science Systems and Applications, Inc., Hampton VA USA 23666

ABSTRACT

The Cloud Physics Lidar (CPL) is a three-wavelength, polarization-sensitive elastic backscatter lidar that flies aboard NASA's high-altitude ER2 research aircraft. This work presents spatial and optical analyses of the combined cirrus cloud measurements acquired by CPL during eight separate field campaigns occurring from 2002 to 2007. Particular attention is given to the retrieval and characterization of the backscatter color ratio, defined as the ratio of the particulate backscatter coefficients measured at 1064 nm and 532 nm. Recent space-based lidar missions rely on assumptions about the backscatter color ratio to calibrate their 1064 nm measurements. Because the signal-to-noise ratio of the CPL data is substantially higher than that of space-based systems, CPL can calibrate its 1064 nm channel using the well-established molecular normalization technique. Analysis of the CPL data sets can therefore provide the independent evaluation of cirrus cloud backscatter color ratios that is required to validate fundamental components of the calibration schemes employed by space-based lidars.

INTRODUCTION

Over the past decade, the Cloud Physics Lidar (CPL [1]) has made extensive measurements of cirrus clouds during numerous long-duration field campaigns. CPL typically flies aboard NASA's high-altitude ER2 research aircraft, and its three-wavelength (355 nm, 532 nm, 1064 nm), polarization-sensitive (at 1064 nm) configuration is especially well suited for assessing the spatial and optical properties of cirrus. In this work we present a comprehensive analysis of cirrus cloud measurements acquired during eight different field campaigns. These experiments took place between 2002 and 2007, spanning latitudes between 52° N and 4° N, and longitudes from Nova Scotia westward to the Hawaiian Islands, and thus should provide a reasonable representation of the scattering characteristics of northern hemisphere.

CPL has long been the lidar of choice for field campaigns that seek to investigate cirrus clouds using a fully coincident combination of remote sensing and in-situ measurement techniques. With the launch of the Cloud Aerosol Lidar and Infrared Pathfinder Satellite Observation (CALIPSO) mission [2] on April 28, 2006, CPL acquired a new and substantial role as one of the primary resources for validating CALIPSO measurements of cirrus clouds. Like CPL, the CALIPSO lidar is a multi-wavelength (532 nm and 1064 nm), polarization-sensitive (at 532 nm) elastic backscatter system. CALIPSO orbits the Earth ~15 times per day, making continuous measurements of attenuated backscatter profiles over a constant altitude range from ~40-km above mean sea level (MSL) to ~2-km below. Because the ER2 typically flies at an altitude of 20 km or above, CPL too can measure the entire vertical extent of the troposphere. Thus, in addition to sharing many basic design similarities, the two lidars also share similar down-looking measurement geometries and enjoy a considerable overlap in their vertical sampling ranges.

While CALIPSO and CPL are similar in many ways, there are also several significant differences between the two instruments. In particular, CPL enjoys a substantial advantage in signal-to-noise ratio (SNR). This difference manifests itself in the methods used to calibrate the two systems. At 532 nm, both lidars can use the traditional technique of normalizing their signals with respect to a molecular scattering model in a high altitude, aerosol-free region of the atmosphere. To obtain reliable calibration coefficients using this approach, the CALIPSO backscatter data must be averaged over many hundreds of kilometers [3]. At 1064 nm, the two lidars must use different calibration targets, as the molecular backscatter cross-section is a factor of ~16 lower at 1064 nm than at 532 nm. Due to its superior SNR, CPL is largely impervious to the diminished scattering efficiency at 1064 nm, and can therefore employ the molecular normalization approach at both wavelengths. CALIPSO cannot: the large reduction in backscatter magnitude, when combined with the relatively high dark noise generated by the avalanche photodiode detector, renders the molecular signal unsuitable for calibrating CALIPSO's 1064 nm data. For this reason, CALIPSO uses cirrus clouds as a calibration target, with the assumption that backscatter, like extinction, is spectrally independent at 532 nm and 1064 nm [4]. The identity of the extinction coefficients in the spectral region of the CALIPSO wavelengths is well established [5]. Previous work also suggests that a median value of the backscatter color ratio of $\chi = \beta_{1064}/\beta_{532} = 1$ would be appropriate, albeit with some caveats about the bimodal shape of the distribution [6]. However, as we show in the sections that follow, based on an analysis of over 400 hours of CPL measurements, a much more reasonable value is $\chi = 0.84 \pm 0.19$.

DATA SELECTION AND ANALYSIS

CPL data is publicly distributed via the CPL web site at http://cpl.gsfc.nasa.gov/. In Table 1 we summarize the dates and locations for all field measurements used in the current study. Both the normalized relative backscatter (NRB) files and the final optical properties (OP) files are used. The NRB files contain range-corrected, energy normalized profiles of altitude-resolved backscatter data, N(z), averaged to a temporal resolution of 1-second. Each 1-second average represents a distance of ~200 meters along the ER2 ground track. By applying the calibration coefficients obtained from a separate CPL-supplied calibration file, the NRB profiles are converted to attenuated backscatter coefficients,

$$\beta'(z) = \left(\beta_m(z) + \beta_p(z)\right) T_m^2(z)\, T_p^2(z)\,, \qquad (1)$$

where $\beta_k(z)$ is the volume backscatter coefficient for scattering species k, $T_k^2(z)$ is the two-way transmittance for scattering species k, and the subscripts m and p represent, respectively, contributions from molecules and particulates (e.g., cloud particles). Each NRB file also contains a profile of the local molecular number density, obtained from nearby rawinsonde measurements. The number density profiles are used to estimate and remove the molecular two way transmittance component of attenuated backscatter coefficients, yielding profiles of particulate-attenuated total backscatter, B(z), such that

$$B(z) = \frac{\beta'(z)}{T_m^2(z)} = \left(\beta_m(z) + \beta_p(z)\right) T_p^2(z)\,, \qquad (2)$$

Layer heights, optical depths (τ), and extinction-to-backscatter ratios (S, AKA lidar ratios) are retrieved from the OP files. The layer boundaries and the derived profiles of $B_{532}(z)$ and $B_{1064}(z)$ are then used to compute the layer integrated attenuated backscatters, γ'_{532} and γ'_{1064}, where

$$\gamma'_\lambda = \int_{z_{top}}^{z_{base}} \beta_{\lambda,p}(z)\, T_{\lambda,p}^2(z)\, dr \qquad (3)$$

Numerically, γ'_λ is computed as follows:

$$g_\lambda = \frac{1}{2}\sum_{j=top}^{base-1}\left(z_j - z_{j+1}\right)\left(B_\lambda\left(z_j\right) + B_\lambda\left(z_{j+1}\right)\right)$$

$$\Delta g_\lambda = \frac{1}{2}\left(z_{top} - z_{base}\right)\left(B_\lambda\left(z_{top}\right) + B_\lambda\left(z_{base}\right)\right) \quad (4)$$

$$\gamma'_\lambda = g_\lambda - \Delta g_\lambda$$

where $g_\lambda \approx \int_{z_{top}}^{z_{base}} \left(\beta_{\lambda,m}(z) + \beta_{\lambda,p}(z)\right) T^2_{\lambda,p}(z)\,dr$

and $\Delta g_\lambda \approx \int_{z_{top}}^{z_{base}} \beta_{\lambda,mp}(z)\, T^2_{\lambda,p}(z)\,dr$.

Assuming that $\chi = \beta_{1064,p}(z)/\beta_{532,p}(z)$ is constant throughout each cloud, robust estimates of χ can be derived from γ'_{532} and γ'_{1064} using

$$\chi' = \gamma'_{1064} \big/ \gamma'_{532}\,. \quad (6)$$

Table 1: CPL field campaigns used to derive spatial and optical statistics. Data was compiled from all flights during each campaign, excluding only those for which the measurements were compromised due to an instrument malfunction.

Mission	Date	Range
CRYSTAL-FACE	July 2002	14° N – 29° N
TX-2002	November – December, 2002	26° N – 38° N
THORPEX-Pacific	February – March, 2003	16° N – 40° N
GLAS Cal-Val	October 2003	33° N – 47° N
THORPEX-Atlantic	November – December, 2003	32° N – 53° N
CC-VEX	July – August, 2006	23° N – 40° N
CLASIC	June 2007	28° N – 40° N
TC4	July – August, 2007	3° N – 39° N

Only the uppermost layer in each profile is included in the analyses. The data was further restricted to those clouds for which $\gamma'_{532} \geq 0.015\,sr^{-1}$ and for which the 1064 nm layer integrated depolarization, δ_{1064}, was greater than 0.2. Imposing the γ'_{532} threshold value minimizes the effects of noise, while simultaneously ensuring that only strongly scattering clouds are selected. Similarly, requiring $\delta_{1064} \geq 0.2$ restricts the data set to cirrus clouds only.

RESULTS

The γ'_{532} distribution harvested from the CPL measurements is shown in Figure 1. The clouds analyzed are quite clearly cirrus: the mean cloud top for these data is 12.6 km ± 2.3 km, and the mean δ_{1064} value is 0.41 ± 0.09. The γ'_{532} distribution is seen to be highly asymmetric, with a mean of 0.022 sr^{-1} ± 0.007 sr^{-1}, and a median value of just under 0.020 sr^{-1}. For the most part, these clouds totally attenuate the lidar backscatter signal, so that no additional layers are detected below.

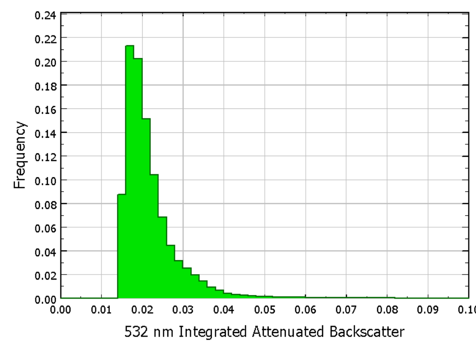

Figure 1: γ'_{532} distribution derived from 155,039 CPL measurements of cirrus cloud.

The relationship between backscatter (γ') and extinction (τ) is non-linear, and is modulated by both the cloud lidar ratio (S) and the layer effective multiple scattering (η). Assuming a mean lidar ratio of 25 sr for the CPL measurements [7], the single scattering optical depth (i.e., η = 1) for the median γ'_{532} value can be computed according to the formula derived by Platt [8]:

$$\tau = -\frac{1}{2\eta}\ln\left(1 - 2\eta S \gamma'\right) \quad (7)$$

The single scattering optical depth for the median value of $\gamma'_{532} = 0.01997\,sr^{-1}$ is 3.25, which is consistent with the maximum optical depth that can be measured by CPL

[1]. Obtaining the larger integrated backscatter values requires contributions to the signal from multiple scattering within the cloud (i.e., $0 < \eta < 1$).

The distribution of backscatter color ratios estimated using equation (6) is shown in Figure 2. The distribution is approximately symmetric about a mean of 0.84, with a standard deviation of 0.19. The difference between these measurements and the expectations of the space-based lidar community (i.e., $\chi = 1$) is thus seen to be quite large. The variability of the distribution is also substantially larger than expected [4].

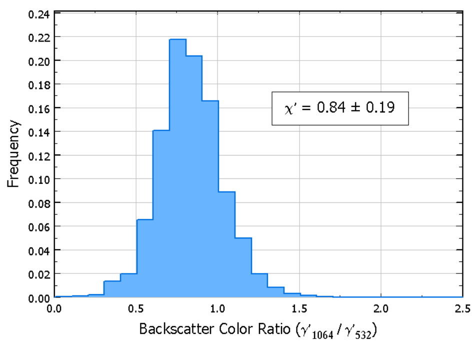

Figure 2: distribution of backscatter color ratios corresponding to the distribution of 532 nm integrated attenuated backscatter shown in Figure 1.

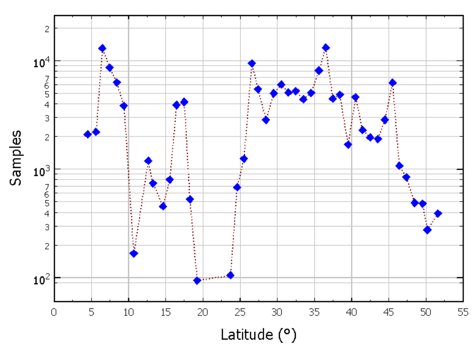

Figure 3: Samples acquired as a function of latitude for the high, dense cirrus measured by CPL

To begin investigating factors that may be contributing to the color ratio distribution, we look first at possible latitudinal changes. Unlike space lidar measurements, CPL data is acquired in limited geographic areas, dictated by the research objectives of the various field missions. Despite this limitation, CPL still provides reasonable coverage for a range of latitudes between ~52° N and ~4° N. The actual number of high, dense cirrus samples acquired for each 1° of latitude is shown in Figure 3.

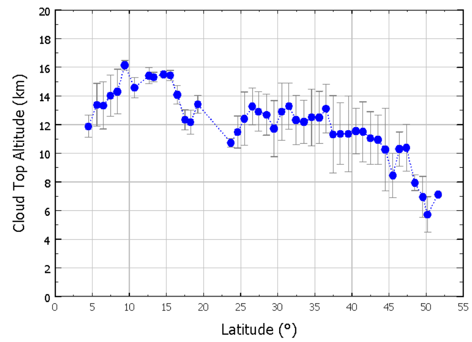

Figure 4: Cloud top as a function of latitude for the CPL data set

For the purposes of this study, dense cirrus is defined by the γ'_{532} threshold. To be identified as high cirrus, a cloud only need be the uppermost ice cloud detected in any profile. The latitudinal distribution of cloud tops used in this study is shown in Figure 4. As expected, the height of the cirrus is seen to rise from north to south, consistent with the change in mean tropopause height over the same latitude band.

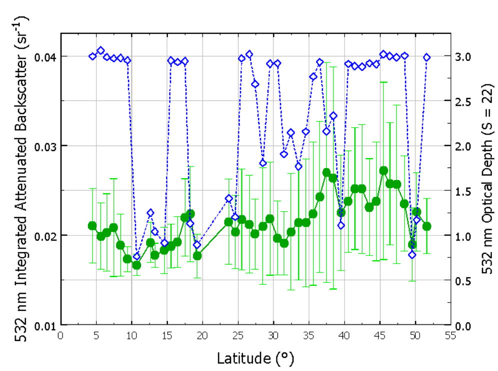

Figure 5: Latitudinal distribution of γ'_{532} (green circles, left Y-axis) and τ_{532} (blue diamonds, right Y-axis).

The latitudinal distributions of integrated backscatter and estimated cloud optical depth are shown in Figure 5. Below ~35° N, γ'_{532} appears to remain relatively constant, hovering around ~0.020 sr^{-1}. There appears to be a step increase in γ'_{532} northward of 35° N. The cause of this phenomenon is currently unknown. However, the measurements acquired south of ~30° N were acquired predominantly over water. Above 30° N, the fraction of measurements acquired over land rises significantly, and this difference in land vs. water data acquisition may contribute to the changes seen.

As seen in Figure 6, the latitudinal distribution of γ'_{532} is not reflected by the backscatter color ratios. Instead, a sharp discontinuity in χ' is observed at ~14° N, where the values increase from just under 0.8 to slightly above 1.0. As the region between 6° N and 10° N is well samples (see Figure 3), this would not appear to be a statistical aberration. At present, however, we are not prepared to suggest possible causal mechanism(s) for the change. A somewhat similar, but less dramatic, change occurs north of 48° degrees, but the sampling in this region is rather sparse.

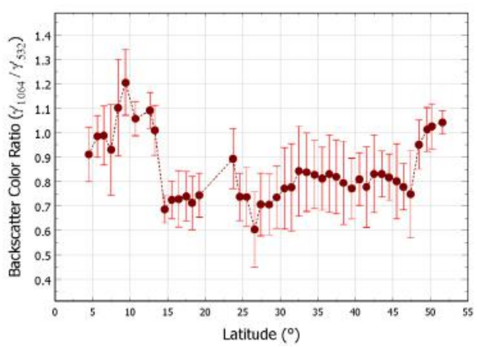

Figure 6: backscatter color ratio as a function of latitude for six years of CPL measurements

CONCLUSIONS

In this study we have analyzed dense cirrus clouds measured by the Cloud Physics Lidar during eight separate field campaigns that took place between July 2002 and August 2007. We find backscatter color ratios that are substantially lower than had been expected based on previous reports. We further find that the distribution of values is broader than had been anticipated by the space-based lidar community. Of particular interest, we also note that there appears to be some latitudinal variation in χ', perhaps suggesting microphysical differences in the composition of high altitude cirrus. These observations should have a significant impact on the 1064 nm calibration schemes implemented by space-based lidars, as the CPL-measured color ratio of χ' = 0.84 ± 0.19 varies considerably from the value of 1.0 typically assumed by these systems for calibration purposes.

REFERENCES

[1] McGill, M. J., D. L. Hlavka, W. D. Hart, V. S. Scott, J. D. Spinhirne, and B. Schmid, 2002: The Cloud Physics Lidar: Instrument description and initial measurement results, *Appl. Opt.*, **41**, 3725– 3734.

[2] Winker, D., M. Vaughan, and B. Hunt, 2006: The CALIPSO mission and initial results from CALIOP, *Proc. SPIE*, **6409**, doi:10.1117/12.698003.

[3] Hostetler, C. A., Z. Liu, J. A. Reagan, M. A. Vaughan, D. M. Winker, M. T. Osborn, W. H. Hunt, K. A. Powell, and C. R. Trepte, 2006: CALIPSO Algorithm Theoretical Basis Document: Calibration and Level 1 Data Products, PC-SCI-201, Release 1.0 (available at http://www-calipso.larc.nasa.gov/resources/project_documentation.php)

[4] Reagan, J. M., X. Wang, and M. T. Osborn, 2002: Spaceborne lidar calibration from cirrus and molecular backscatter returns, *IEEE Trans. Geosci. Remote Sens.*, **40**, 2285– 2290.

[5] Kent, G. S., D. M. Winker, M. T. Osborn, and K. M. Skeens, 1993: A Model for the Separation of Cloud and Aerosol in SAGE II Occultation Data, *J. Geophys. Res.*, **98** (D11), 20725–20735.

[6] Beyerle, G., M. R. Gross, D. A. Haner, N. T. Kjome, I. S. McDermid, T. J. McGee, J. M. Rosen, H.-J. Schäfer, and O. Schrems 2001: A lidar and backscatter sonde measurement campaign at Table Mountain during February–

March 1997: Observations of cirrus clouds, *J. Atmos. Sci.*, **58**, 1275–1287.

[7] Vaughan, M. R. Kuehn, S. Young, M. McGill, Z. Liu, and Y. Hu, 2008: Validating Cirrus Cloud Optical Properties Retrieved by CALIPSO, Proceedings of the 24th International Laser Radar Conference (ILRC), *in press*.

[8] Platt, C., D. Winker, M. Vaughan, and S. Miller, 1999: Backscatter to extinction ratios in the top layers of tropical mesoscale convective systems and in isolated cirrus from LITE observations, *J. App. Meteorol.*, **38**, 1330–1345.

ANALYSIS ON THE PRECIPITATION ENHANCEMENT POTENTIAL AREA OF CYCLONE

Yilin Wang

Shangdong Research Institute of meteorology , Jinan, P.R.China, 250031,
Email: qxwyl@sohu.com

Potential area is the main problem in precipitation enhancement operation. In foreign countries, various atmosphere-detecting apparatus are adopted to detect the precipitation enhancement potential area before it is operated. In China, the use of radar, particle measuring system (PMS), radiosonde, etc. plays a vital role in detecting the potential area and making commands before the precipitation enhancement operation. It is our contention that the ice crystal should primarily be at the state of ice-saturation ($e-E_{ice}>0$) and there must be sufficient supply of vapor to increase the condensation or deposition of the ice crystal, according to which potential areas are judged. Based on most statistic analyses, we believe that the precipitation enhancement potential area in cold clouds must have three conditions, namely, the ice-saturation area, the area in which vapor integral below 0℃ is greater than 9mm and vertical transportation of water vapor. Analyses on potential area of cyclone are conducted as follows.

1. SYNOPTIC SITUATION

From March 3 to March 4 in 2007, a cyclonic weather process influences Shandong Province. At 8:00(Beijing time) on March 3, the foreside of the cyclone influences the province and it starts to rain. At 2:00 on March 4, it advances to the Yellow Sea. After 8:00 on March 4, the raining area recedes out of Shandong Province and the raining process ends.

2. ANALYSIS ON THE POTENTIAL AREA

2.1 The Ice-saturation Area

According to the ice-water transformation theory, in order to get the ice crystal to grow, seeding with silver iodide requires that the cold cloud achieves the ice-saturation state. Therefore, the existence of the ice-saturation area is the first condition of the existence of the potential area. Adopting the MM5 model, forecasting figures of the ice-saturation area are drawn every 5℃ during the level of 0–-30℃. Figure 1 shows the changes of the ice-saturation area at the level of -10℃ from 5:00 on March 3, 2007 to 8:00 on March 4, 2007. It is seen from Figure 1 that at 5:00 on March 3, 2007 the ice-saturation area (shadow area in Figure 1) is located in the western periphery of Shandong Province and at 8:00 on March 3, 2007, it goes into its western area and expands to the eastern area, then it advances into its eastern area at 8:00. on March 4, 2007. From 8:00 on March 3, 2007 to 8:00 on March 4, 2007, the cloud at the level of -10℃ above Shandong Province is at the ice-saturation state from west to east, which is fit for the growth of ice crystal and fulfils the first condition of the precipitation enhancement potential area.

2.2 Vapor Integral below 0℃ (W)

It is pointed out in the numerical simulation that the introduction of ice crystal will convert some of the super ice-saturated vapor into rain. Vapor plays an important

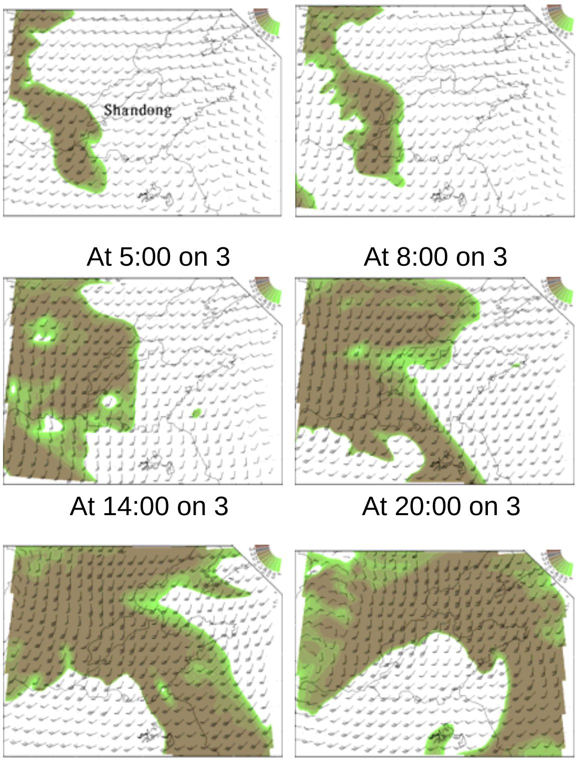

At 5:00 on 3 At 8:00 on 3

At 14:00 on 3 At 20:00 on 3

At 02:00 on 4 At 08:00 on 4

Fig.1 Distribution ice-saturation (shaded areas)on -10℃ from 5:00 on 3 to 8:00 on 4 March 2007

role in the Bergeron theory. The growth speed of the ice crystal in cold clouds is directly related to the amount of vapor in its environment. As a result, the amount of vapor in cold clouds, in a sense, reflects the enhancement potential of the clouds. Statistics show that in cold cloud raining, the vapor integral amount between 0–-30℃ (W) is closely related to rainfall on the ground. W increases rapidly before raining and decreases rapidly after it. When W attains 9mm, it is preferable for precipitation enhancement operation. Thus, that W is greater than 9mm becomes the second condition of the potential area. Figure 2 indicates the distribution of W at the level of -10℃ from 5:00 on March 3, 2007 to 8:00 on March 4, 2007. At 5:00 on March 3, 2007, the area where the W is 9mm (shadow area of the graph) is located in the west of Shandong Province and expands from west to east. At 8:00 on March 4, 2007, the area is located in the east of Shandong Province and recedes out of it thereafter (The figure is omitted.). From 5:00 on March 3, 2007 to 8:00 on March 4, 2007, the area of Shandong Province fulfils the second

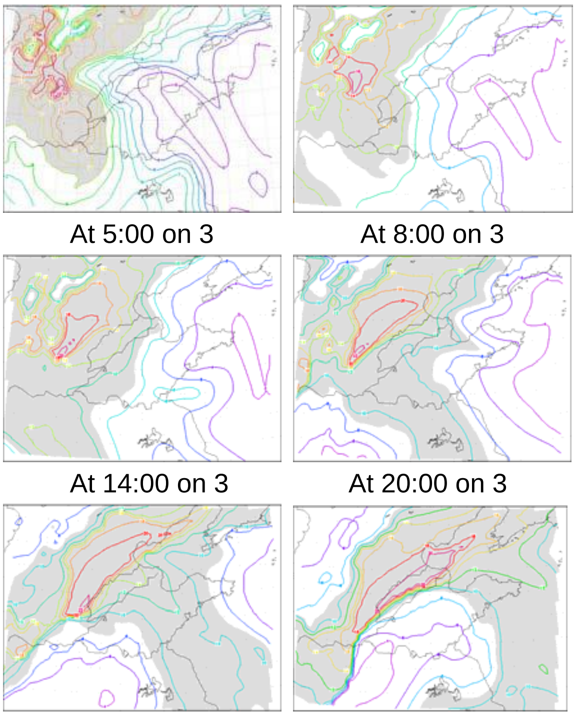

At 5:00 on 3 At 8:00 on 3

At 14:00 on 3 At 20:00 on 3

At 02:00 on 4 At 08:00 on 4

Fig.2 Distribution integral vapor value below 0℃ from 5:00 on 3 to 8:00 on 4 March 2007(vapor integral value in shaded areas is bigger than 9mm.)

condition of the precipitation enhancement potential area from west to east.

2.3 Vertical Transportation of Water Vapor

As is known to all, in every raining process, the amount of static vapor in the atmosphere is far lower than that of the rainfall and the raining process requires consecutive supplies of vapor. The transportation of vapor in the potential area will increase the density of vapor and fulfils the vapor condition for the growth of ice crystal and water drops through condensation and deposition. In order to get sufficient vapor in the potential area, a great amount of vapor should be transported upward through the level of 0℃ to make the ice crystal and water drops grow. In the mid-lower part of the atmosphere, vapor decreases from downside to upside. The vertical transportation of water vapor is indicated by the multiplication of relative humidity and ascending speed, which is the third condition of the potential area. Figure 3 is the distribution of the area of vertical transportation of water vapor from 5:00 on March 3, 2007 to 8:00 on March 4, 2007 at

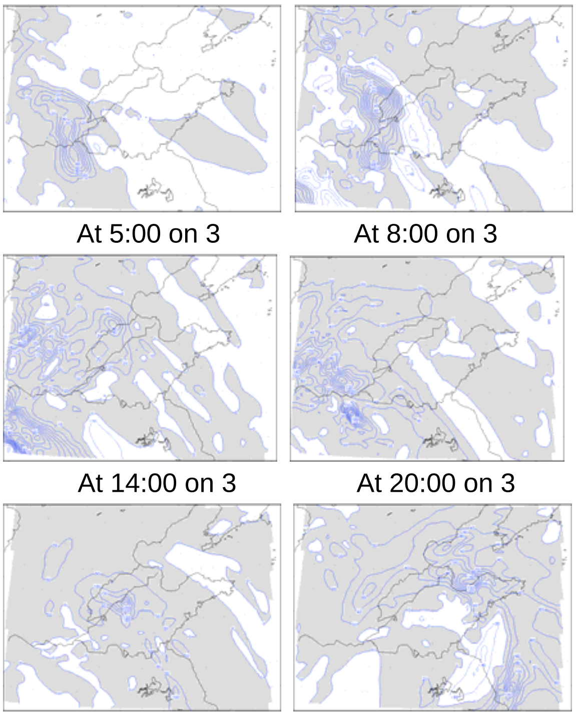

At 5:00 on 3 At 8:00 on 3

At 14:00 on 3 At 20:00 on 3

At 02:00 on 4 At 08:00 on 4

Fig.3 Distribution vertical water vapour transportation from 5:00 on 3 to 8:00 on 4 March 2007(water vapour in shades areas was transported upwards)

the level of -10℃(The shadow area indicates the area of vertical transportation of water vapor.). At 5:00 on March 3, 2007, the area advances into Shandong Province and expands from west to east. From 5:00 on March 3, 2007 to 8:00 on March 4, 2007, the area of Shandong Province fulfils the third condition of the precipitation enhancement potential area from west to east.

3. APPLICATION OF THE CONDITIONS

3.1 Area and Time of Precipitation Enhancement Operation

The area that fulfils the above three conditions is the preferable area for precipitation enhancement. As is seen from Figure 1 to Figure 3, from 5:00 on March 3, 2007 to 5:00 on March 4, 2007, the area of Shandong Province fulfils the conditions of the potential area from west to east. Therefore, in Shandong, precipitation enhancement should be operated in potential area from west to east.

3.2 Height of Precipitation Enhancement Operation

The area that fulfils the equation of T-Td<=2℃ is the quasi-saturation area. The vertical distribution of the quasi-saturation area helps to locate the vertical scope of the cloud area. Thick quasi-saturation areas provide a fine environment for the growth of rain particles, while lower height of the bottom of clouds decrease the evaporation of raindrops which drop out of clouds. Figure 4 is a vertical section graph of the quasi-saturation area and ice-saturation area at 17:00 on March 3 at 36º30´N. As is seen from figure 4(on the left), the quasi-saturation area extends to the ground. From the grounds of the western area of Shandong Province to level -15℃ is the quasi-saturation area, which provides a fine environment for the growth of rain particles. In choosing the height of the operation, it should be taken into consideration of the temperature at which the silver iodide forms nucleus and the height to which the apparatus is capable of conveying. As is seen from Figure 4(on the right), at 17:00 on

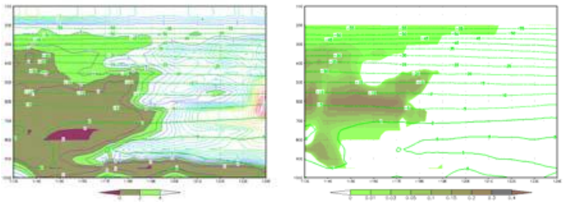

Fig.4 Cross-section along 36°30'N, quasi-saturation (shaded areas) (left) , ice-saturation (shaded areas)(right), at 17:00 on 3 March 2007

March 3, the west of Shandong Province at the level of 0–-15ºC is at the state of ice-saturation (Shandong Province is roughly located at 115—123ºE). There is a center of the ice-saturation area which exceeds 0.15pa at the level of -5–-10ºC. As is seen from Figure 1 to Figure 4, the best height of enhancement operation is at the level of -5ºC in the west of Shandong Province.

3.3 Cloud water and rain water

Super-cooled water is the main condition of the precipitation enhancement area. The amount of water contained in cold clouds directly reflects the potential of precipitation enhancement. Figure 5(on the left) demonstrates the vertical distribution of cloud water at 36º30´N at 17:00 on March 3.

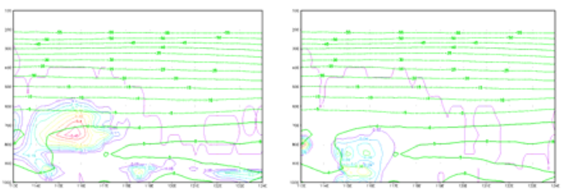

Fig.6 Cross-section along 36°30'N, cloud-water (left),rainfall-water (right) at 17:00 on 3 March 2007

It shows that the maximum area of cloud water lies above the west of Shandong Province and there is a center of cloud water at the 0–-10ºC level. Seen from the distribution of rainfall (Figure 5 on the right), the rain has reached the ground at 17:00, which means it is raining. Besides, the center is situated in the west of Shandong Province, which provides a good opportunity for precipitation enhancement.

4. OPERATION OF PRECIPITATION ENHANCEMENT

According to the distribution of the potential areas, 70 rockets and 18 Guns in 14 regions of Shandong Province conducted precipitation enhancement from 8:00 on March 3 to 5:00 on March 4, 2007 and fine results are achieved. It also proves that this cyclonic weather process has great potential of precipitation enhancement in Shandong Province.

5. CONCLUSIONS

(1) Under the synoptic situation which facilitate precipitation enhancement, it is preferable to conduct the process when the potential area fulfils the three conditions of the ice-saturation area, the area in which vapor integral below 0℃ is greater than 9mm and vertical transportation of water vapor.

(2) The height of operation should be chosen at the ice-saturation area, the area of vertical transportation of water vapor and the quasi-saturation area. It should be taken into consideration of the temperature at which the silver iodide forms nucleus and the height to which the apparatus is capable of conveying.

THE NEW INTEGRATED CLOUD OBSERVATION CAPABILITIES OF WYOMING KING AIR BY COMBINING RADAR, LIDAR, MICROWAVE RADIOMETER AND IN SITU MEASUREMENTS

Zhien Wang, Perry Wechsler, Jeff French, Alfred Rodi, Samuel Haimov, Gabor Vali, and Dave Leon
Department of Atmospheric Science, University of Wyoming, Laramie, WY 82071

Andrew L. Pazmany
Prosensing Inc.

1. INTRODUCTION

Clouds are a critical component of the coupled earth water and energy cycles. The poor understanding of cloud-radiation-dynamics feedbacks results in large uncertainties in forecasting human-induced climate changes (Stephens, 2005; IPCC, 2007). Our current understanding of rain formation processes continues to present many challenges for weather predictions (Fritsch and Carbone, 2004). One of the greatest challenges in advancing cloud physics and model parameterizations is to provide the links involving aerosols, water vapor, cloud, precipitation, and dynamics. Continually improving our understanding of cloud physics through observations is a critical step for improving physically-based cloud microphysics parameterizations for climate and weather models. Advanced airborne cloud observational capabilities are important to achieve this goal.

Airborne in situ cloud observations have played an important role in advancing our understanding of cloud microphysical and dynamic processes by providing detailed measurements at high temporal and spatial resolutions. However, these detailed measurements are only available along a line through the cloud at flight altitude. For many physical process studies, information on the vertical structure of the cloud properties is needed. Furthermore, for many studies, interpretation of measurements from in situ probes is quite limited due to their small sampling volumes. For example, in situ cloud probes only have sampling volumes from ~40 to ~10^4 cm^3/s. The small sampling volume is an issue when studying atmospheric and cloud properties in regions with strong spatial inhomogeneities or small concentrations (such as early formation of precipitation).
Airborne remote sensing overcomes the two weaknesses of in situ sampling, although the measurements may be not as detailed as the in situ sampling. Airborne vertical profiling capabilities are mainly provided by active sensors, such as lidar and radar. Airborne radars provide unique measurements of cloud, precipitation, and cloud scale dynamics (Hildebrand et al. 1996; Heymsfield et al. 1996a; Vali et al. 1998), and have provided many insights into convective cloud systems and hurricanes (Heymsfield et al. 1996b), marine Sc clouds (Vali et al. 1998; Stevens et al. 2003; Leon et. al. 2006), and cumulus clouds (Damiani et al. 2005). Lidars operate at much shorter wavelength than radars and can provide unique measurements of cloud beyond what can be provided through radar (McGill et al. 2002). Different remote sensors, such as lidars, radars, and radiometers, respond differently to cloud particle size, concentration, and phase. For example, lidars are more sensitive to small particles and radars are more sensitive to large particles. Therefore optimally combining multiple remote sensor measurements provides potentials to improve cloud microphysical property retrievals (Wang and Sassen 2001 and 2002).

The integration of airborne in situ sampling and remote sensing provides new observational capabilities for the study of atmospheric processes and clouds. For Two-dimensional cross-sections of cloud microphysical properties retrieved from remote sensor measurements provide a context to understand detailed in situ cloud measurements. The integration of in situ and remote sensing measurements can be achieved with one or more aircraft in a field campaign. The NASA Cirrus Regional Study of Tropical Anvils and Cirrus Layers-Florida Area Cirrus Experiment (CRYSTAL-FACE, http://www.espo.nasa.gov/crystalface/ index.html) in 2002 is a great example of how multiple-aircraft can be utilized effectively for interpreted integration. With two dedicated remote sensing aircraft, two in situ aircraft, and carefully coordinated flights, CRYSTAL-FACE provided a comprehensive dataset to study convectively generated anvil clouds. However, such multiple-aircraft field campaigns are very expensive to conduct. Integration of in situ and remote sensors on a single aircraft, such as reported herein, is important from an economic and logistical point of view.

Here we report on new integrated cloud observation capabilities developed for the University of Wyoming King Air (UWKA) by combining measurements from the Wyoming Cloud Lidar (WCL), a 183 GHz microwave radiometer, the Wyoming Cloud Radar (WCR) and in situ probes. The WCR has served the atmospheric community for more than 10 years and provides measures of radar reflectivity and Doppler velocity to be used to infer cloud structure and dynamics. The WCL is a newly developed compact elastic polarization lidar to provide cloud boundary as well as backscattering and depolarization ratio profiles. The radiometer provides total precipitable water vapor (PWV) and liquid water path (LWP) measurements. Combining these remote sensor measurements allows us to apply several remote sensing retrieval algorithms to better characterize the macrophysical and microphysical properties of ice, mixed-phase and water clouds. Combining in situ data and microphysical property profiles from these remote sensors provides an advanced capability to study clouds from a single aircraft. Examples are presented to illustrate this new capability.

2. INSTRUMENTATION

The UWKA is an NSF supported national, lower atmospheric observing facility and is well equipped for cloud, aerosol, and PBL studies (http://www.atmos.uwyo.edu/n2uw). The in situ and remote sensing instrumentation for cloud study is briefly discussed here.

2.1 Wyoming Cloud Radar (WCR)

The Wyoming Cloud Radar (WCR, http://www.atmos.uwyo.edu/wcr/), a 95 GHz, Doppler radar, has evolved during last 10 years. The current WCR specification is listed in Table1. It has four antennas for multiple radar beam operation (see Fig. 1). The multi-beam configuration can provide vertical and or horizontal profiles of reflectivity and Doppler velocity through clouds. The WCR has been installed in the UWKA and NCAR/NSF C-130 to study marine boundary-layer clouds, convective clouds and mixed-phase clouds.

Table 1: WCR Specifications

<table>
<tr><td>Transmit Frequency</td><td>94.92 GHz (λ=3.16 mm)</td></tr>
<tr><td>Peak Power / Max Duty Cycle</td><td>1.6 KW / 1 %</td></tr>
<tr><td>Pulse</td><td>100-500 ns</td></tr>
<tr><td>Pulse Repetition Frequency (prf)</td><td>1000 Hz – 20 KHz</td></tr>
<tr><td>Antennas:

▪ Side/Up (beam 1, use mirror for Up)
▪ Side-fore (beam 3, 36° forward)
▪ Down (beam 2, near nadir)
▪ Down-fore (beam 4, 26° forward)</td><td>4
aperture | beamwidth | polarization
0.31 m | 0.7° | H, V
0.31 m | 0.7° | single, linear
0.46 m | 0.5° | single, linear
0.38 m | 0.6° | single, linear</td></tr>
<tr><td>Antenna modes (typical):
▪ DPDD (dual-plane dual-Doppler)
▪ VPDD (vertical plane dual-Doppler)
▪ VPDD + up or side
▪ HBDD (horizontal beam dual-Doppler)
▪ HBDD+down
▪ Profiling (up+down or side+down)
▪ Profiling (up+down) + side-fore</td><td>Beams:
1,2,3,4
2,4
1,2,4
1,3
1,2,3
1,2
1,2,3</td></tr>
<tr><td>Receiver channels:
▪ receiver outputs:
▪ receiver dynamic range</td><td>2
mag: logarithmic; phase: linear
> 70 dB</td></tr>
<tr><td>Dwell time/ Along-track sampling</td><td>30 ms / 3 – 5 m (typical)</td></tr>
<tr><td>Min. detectable signal
(side-antenna , 1 StDev above mean noise)</td><td>-30 dBZ @ 1km, 250ns, 500 avrg</td></tr>
<tr><td>Resolution:
▪ range
▪ volume @ 1 km, 250 ns pulse</td><td>
15 – 75 m
37 x 12 x 15 m</td></tr>
<tr><td>Doppler velocity processor:
▪ pulse pair
▪ fft spectrum (single beam only)</td><td>
1st & 2nd moments
32 or 64 spectral lines</td></tr>
<tr><td>Max unambiguous Doppler</td><td>±15.8 m/s</td></tr>
</table>

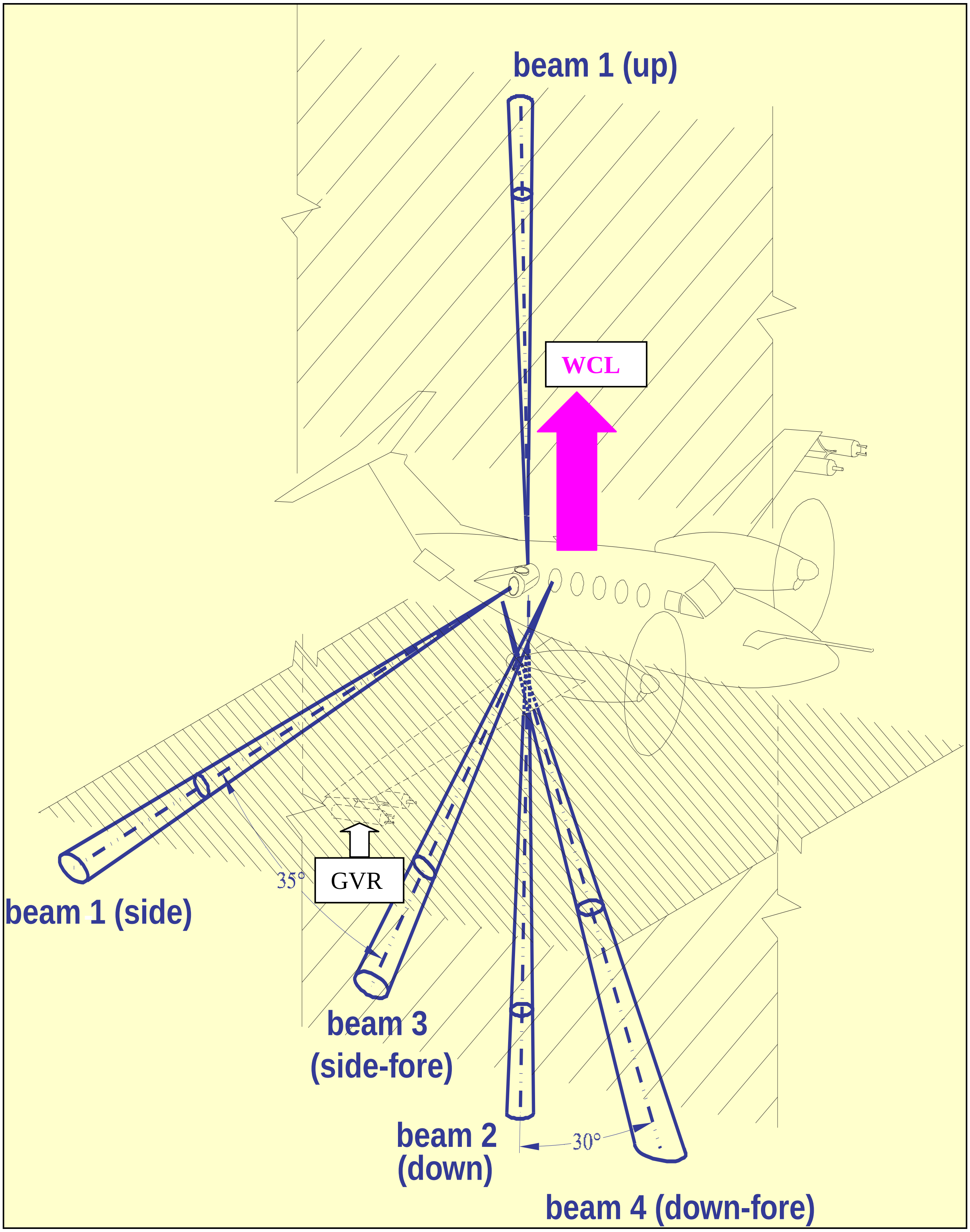

Figure 1: The beam configuration of the WCR and the installation of WCL and GVR on the Wyoming King Air.

2.2 Wyoming Cloud Lidar (WCL)

The WCL is a compact polarization lidar to provide cloud vertical structure as well as cloud particle phase information. The design goal of the WCL is to work together with the WCR to provide better cloud macrophysical and microphysical properties from UWKA or NCAR/NSF aircraft. Because of very limited space and power on the UWKA, it is not possible to simultaneously operate the WCR and a lidar with a large telescope. To use one of the existing small upward-looking ports to operate the lidar, the WCL uses a relatively high pulse-energy laser to provide the needed sensitivity. System specifications are summarized in Table 1. With the size, weight, pulse energy and eye safety of the laser in mind, the Ultra Pulsed Nd:YAG Laser from the Big Sky laser technique, Inc. is selected for the WCL. The laser provides 20 Hz 16 mJ outputs at 355 nm. The 355 nm wavelength not only provides a stronger molecular backscattering signal than other standard lidar wavelengths with the same laser energy (important for calibrating backscattering coefficients) but also eases limitations for achieving eye safe operation. The laser beam (3 mm in diameter at exit laser) is expanded 5 times before being emitted into atmosphere. This system is eye safe beyond a distance ~65 m. To improve lidar linear depolarization measurements, a ¼ λ wave plate is placed after the beam expander to work together with a cubic polarization beam splitter in the receiver path.

The laser head is integrated with transmitting and receiving optics into a compact package as the lidar head. This package is light enough to be attached to an upward-looking port on the aircraft with no additional structure. This compact design not only makes it easy to install the system on an aircraft, but also provides high mechanical stability to maintain optical alignment.

Table 2: The WCL Specification

Transmitter	
Laser Wavelength	355 nm Nd:YAG
Repetition Frequency	20 Hz
Pulse width	~8 ns
Pulse Energy	16 mJ
Receiver	
Diameter	~ 75 mm
Field of view	300 and 2000 μrad
Data System	
Number of Channels	Two
Detector	PMT
Range Resolution	3.75m, 7.5m, 15m, 30m (programmable)
Maximum Range	30 km
Data acquisition system	Combined analog and photon counting system from LICEL, GmbH

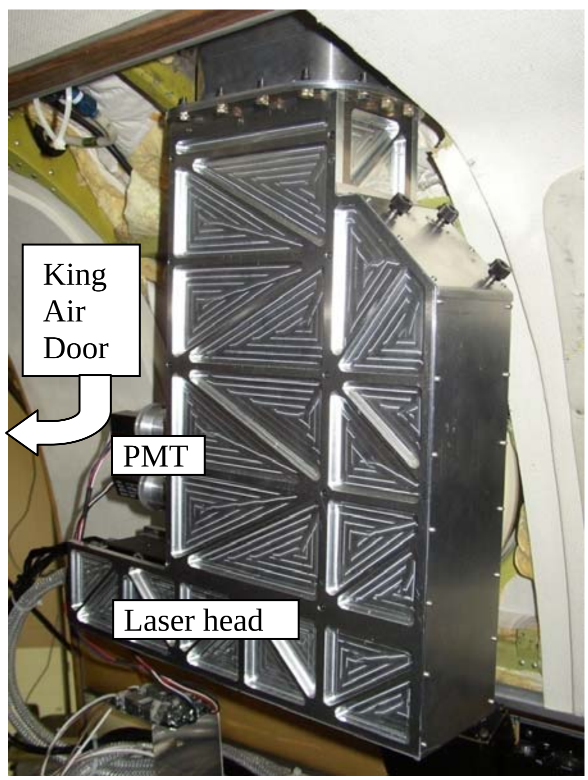

Figure 2. The WCL installation in the Wyoming King Air

2.3 Airborne 183 GHz microwave radiometer

ProSensing Inc. has developed a pod mounted G-band water Vapor Radiometer (GVR) that is mounted in a standard 2-D PMS probe canister (Pazmany 2007). Precipitable Water Vapor (PWV) and Liquid Water Path (LWP) are estimated from brightness temperatures measured in four double-sideband receiver channels, centered at 183.31 ± 1, ± 3 and ± 7, and ± 14 GHz. The airborne GVR has been installed on the CANADA NRC Convair-580 aircraft and the UWKA. The installation on UWKA is shown in Figure 3.

Because the 183 GHz water vapor absorption band is much stronger than the 23 GHz band, the GVR has better sensitivity for low PWV measurements. The 183 GHz also has stronger liquid water absorption than 31 GHz used in the traditional ground-based two-channel microwave radiometers. Thus, the GVR's high sensitivities to water vapor and liquid water make it a good microwave radiometer for airborne measurements of PWV and LWP. These column integrated quantities are important for understanding cloud system development and evolution.

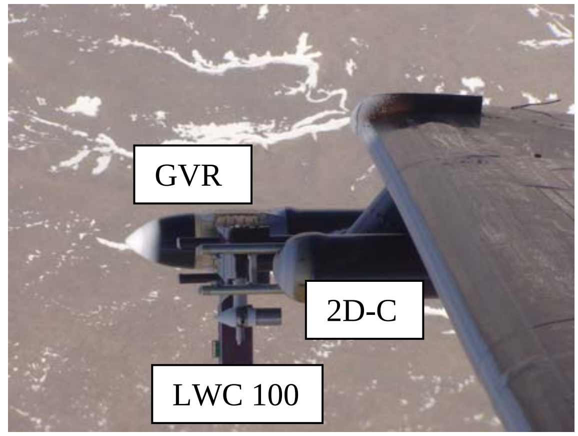

Figure 3. The GVR on the UWKA. The white cap on the GVR is the icing after penetrating a wave clouds.

2.4 In situ clouds probes

The UWKA can carry traditional in situ cloud probes (see Table 3) to provide liquid water content and hydrometer size distributions. Due to the shattering effect, the UWKA lacks capability to estimate size distributions of small ice crystals. Ice water contents (IWC) can be estimated from size distributions with factor of 2 uncertainties. Efforts are underway to upgrade the UWKA capabilities for in situ observations of ice particles.

Table 3. Current King Air in situ probes

Instrument	Measurements Available
Rosemount 871FA	Icing Rate
DMT LWC-100	Cloud Liquid Water
Gerber PVM-100	Cloud Liquid Water, Droplet Surface Area, Droplet Effective Radius
PMS FSSP-100	Cloud Particle Size Distribution (0.5 – 47μm; selectable), Total Concentration, Derived Liquid Water Content, Derived Droplet Effective Radius, Derived Droplet Surface Area, Derived Mean Volume Radius
PMS OAP-200X (1DC)	Cloud Particle Size Distribution (12.5 – 185.5 μm)
PMS OAP-2DC	Cloud Particle Images (>25 μm), Cloud Particle Size Distribution
PMS OAP-2DP	Precipitation Particle Images (>200 μm), Precipitation Particle Size Distribution

3. WYOMING AIRBORNE INTEGRATED CLOUD OBSERVATION (WAICO) EXPERIMENT

The WAICO-I experiment was conducted during February-March 2008 near Laramie, Wyoming and is supported by US National Science Foundation. The primary goal of the WAICO experiments is to develop new cloud microphysical observation capabilities by integrating the measurements of remote sensors and in situ probes.

To achieve this goal, the first task was to install the WCL, WCR, and GVR on the UWKA while carrying the full array of in situ probes. Initial challenges included staying within the allowable power budget on the UWKA. This was the first installation of the GVR on the UWKA and several technical challenges needed to be addressed before we were able to collect high quality data from this instrument. The WAICO-I successfully integrated the WCR, WCL, and GVR together with an FSSP, 2D-C and 2D-P for cloud observations. Aerosol information was provided by a Passive Cavity Aerosol Spectrometer Probe (PCASP) Model 100 and a model 3010 condensation particle counter (CPC). In addition, radiation measurements from upward- and downward-looking pyranometers (Eppley PSP, 0.285-2.8 μm), and pyrgeometers (Eppley PIR, 3.5-50 μm) were also available during the experiment.

The second task was to collect data for cloud retrieval algorithm development and validation. Based on ground-based measurements, we developed multi-sensor cloud retrieval algorithms to retrieve ice, water, and mixed-phase cloud microphysical properties (Wang and Sassen 2001 and 2002; Wang et al. 2004). The similar approaches can be applied to airborne measurements. However, the algorithms need to be modified for different combination of measurements and further validation is required. The WAICO flight patterns and target clouds were selected to collect data appropriate for both algorithm development and validation.

The third task was to collect data to study mixed-phase clouds. Compared to water and ice phase clouds, mixed-phase clouds are more complicated and are less well understood. Further, properly representing mixed-phase clouds in general circulation models (GCMs) is very important for climate simulation. Fowler et al. (1996) shows that the variation of glaciation temperatures from 0° to -40°C in a GCM simulation yields about 4 and -8 W m^{-2} differences in the top-of-atmosphere longwave and shortwave cloud radiative forcing, respectively. Other studies (Li and Le Treut 1992; Sun and Shine 1994; Gregory and Morris 1996) have shown that the treatment of mixed-phase clouds in GCMs affects either their climate sensitivity or their mean climate impact.

The integrated airborne observations developed during the WAICO provide the best observations to study mixed-phase clouds to date. The WCR is more sensitive to ice crystals than water droplets while the WCL signals are mainly dominated by water phase in the mixed-phase clouds. The LWP from GVR provide an important constraint of liquid water in the mixed-phase cloud layer. During the WAICO-I, we collected data in mixed-phase wave- and altocumulus clouds. Mixed-phase regions were also observed in deep nimbostratus clouds.

4. OBSERVATION EXAMPLES

Examples of observations from the WCR, WCL, GVR and in situ probes during the WAICO are presented in this section. The WCR provides cloud vertical structure above and below the aircraft. The WCL provides cloud structure above the aircraft. The WCL is capable of providing measurements of clouds beyond 10 m range, but the WCL signals are often saturated within 50 m. The yellow and red regions in WCL uncalibrated linear depolarization ratio indicate ice particles. The 2D-C measurements show ice crystal size distributions at flight altitude while FSSP measurements mainly show water phase properties (the red region). It is very clear that FSSP measurements are affected by large ice crystals due to the shattering effect. As illustrated in Fig. 4, LWP measurements are consistent with FSSP and lidar measurements and provide a vertical constrain on supercooled water in wave clouds above the aircraft.

4.1 wave clouds

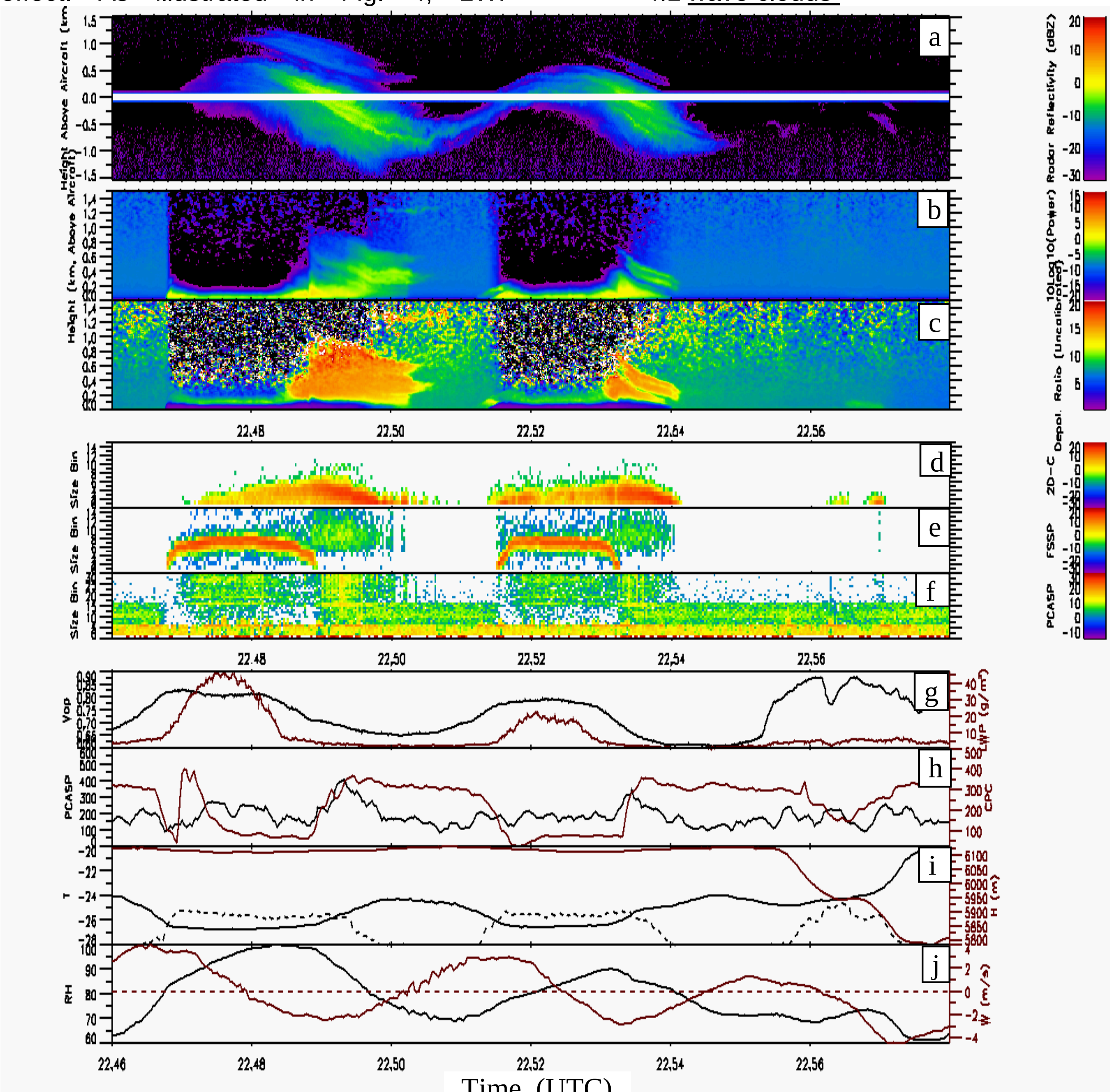

Figure 4. a) WCR radar reflectivity (the white gap indicates a zone near aircraft without measurements), b) WCL (upward pointing) returned power, c)WCL linear depolarization ratio (uncalibrated), d) 2D-C number concentration (N) for each bin (plotted as 10log(N)), e) FSSP number concentration (N) for each bin (plotted as 10log(N)), f) PCASP number concentration (N) for each bin (plotted as 10log(N)), g) Precipitable Water Vapor (Vap) and Liquid Water Path (LWP) derived from a G-band (183 GHz) water Vapor Radiometer (GVR) measurements, h) PCASP and CPC total number concentration, i) Temperature and aircraft altitude, j) RH and vertical velocity.

4.2 Optically thick ice clouds

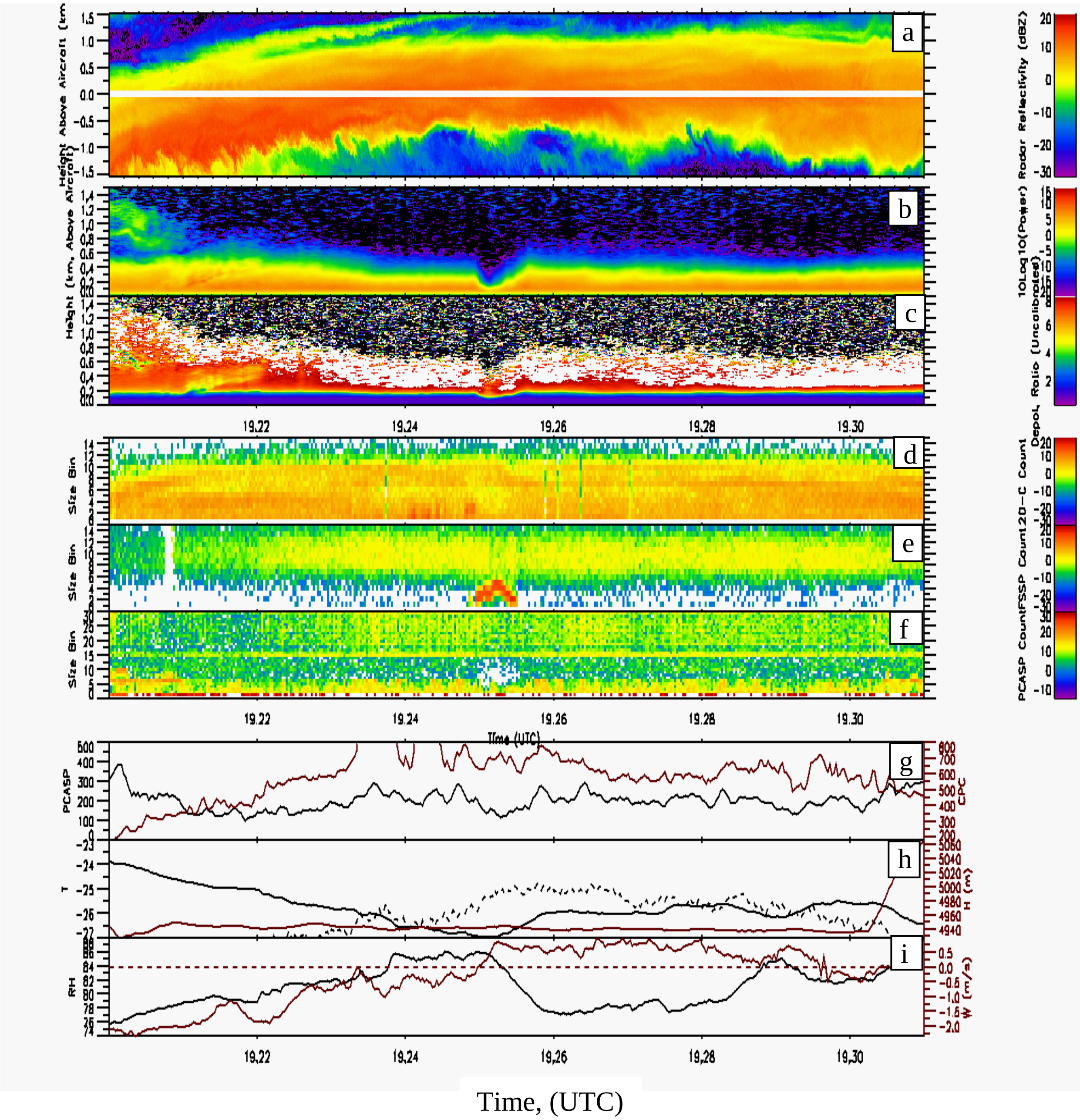

Figure 5. a) WCR radar reflectivity (the white gap indicates a zone near aircraft without measurements), b) WCL (upward pointing) returned power, c)WCL linear depolarization ratio (uncalibrated), d) 2D-C number concentration (N) for each bin (plotted as 10log(N)), e) FSSP number concentration (N) for each bin (plotted as 10log(N)), f) PCASP number concentration (N) for each bin (plotted as 10log(N)), g) PCASP and CPC total number concentration, h) Temperature and aircraft altitude, i) RH and vertical velocity.

4.3 Ice generating cell

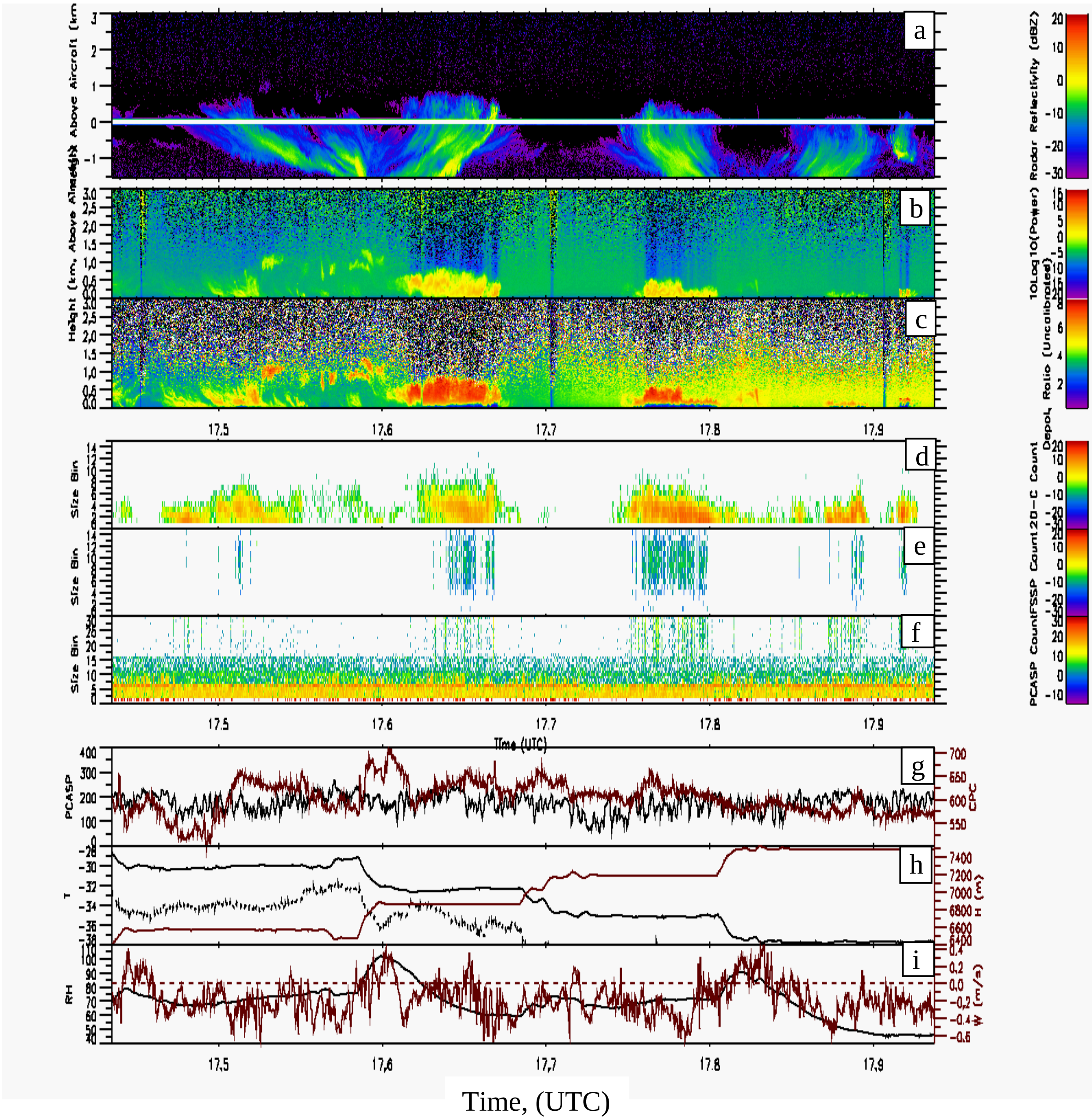

Figure 5. a) WCR radar reflectivity (the white gap indicates a zone near aircraft without measurements), b) WCL (upward pointing) returned power, c)WCL linear depolarization ratio (uncalibrated), d) 2D-C number concentration (N) for each bin (plotted as 10log(N)), e) FSSP number concentration (N) for each bin (plotted as 10log(N)), f) PCASP number concentration (N) for each bin (plotted as 10log(N)), g) PCASP and CPC total number concentration, h) Temperature and aircraft altitude, i) RH and vertical velocity.

5. CONCLUSION AND FUTURE WORK

We successfully integrated the WCR, WCL, and GVR together with a suite of in situ probes on the UWKA to observe ice and mixed-phase clouds. Combining multi-remote sensor measurements can provide cloud microphysical property vertical structures, which further provides an important context to study in situ measurements and to better understand cloud microphysical processes.

Developing algorithms to provide microphysical properties retrievals and further analysis of WAICO-I data is underway. We are planning to add a down-ward pointing lidar and test it as part of the WAICO-II campaign in spring, 2009.

With these and further planned instrumentation developments and integration and algorithm developments, we will enhance the UWKA capability to provide extended cloud microphysical and dynamic measurements for cloud study in the near future.

6. REFERENCES:

IPCC, 2007: Climate Change 2007: The Physical Science Basis. Contribution of Working Group I to the Fourth Assessment Report of the Intergovernmental Panel on Climate Change [Solomon, S., D. Qin, M. Manning, Z. Chen, M. Marquis, K.B. Averyt, M. Tignor and H.L. Miller (eds.)]. Cambridge University Press, Cambridge, United Kingdom and New York, NY, USA, 996 pp.

Damiani, R., G. Vali, and S. Haimov, 2006: The structure of thermals in cumulus from airborne dual-Doppler radar observations. *J Atmos Sci*, 1432-1450.

Fritsch, J. M., and R. E. Carbone, 2004: Improving quantitative precipitation forecasts in the warm season: A USWRP research and development strategy. *Bull. Amer. Meteor. Soc.*, **85**, 955-965.

Fowler, L. D. and D. A. Randall, 1996: Liquid and ice cloud microphysics in the CSU general circulation model .3. Sensitivity to modeling assumptions. *J Climate*, 561-586.

Gregory, D. and D. Morris, 1996: The sensitivity of climate simulations to the specification of mixed phase clouds. *Clim Dynam*, 641-651.

Heymsfield, G. M., I. J. Caylor, J. M. Shepherd, W. S. Olson, S. W. Bidwell, W. C. Boncyk, and S. Ameen, 1996a: Structure of Florida thunderstorms using high-altitude aircraft radiometer and radar observations. *J Appl Meteorol*, 1736-1762.

Heymsfield, G. M., S. W. Bidwell, I. J. Caylor, S. Ameen, S. Nicholson, W. Boncyk, L. Miller, D. Vandemark, P. E. Racette, and L. R. Dod, 1996b: The EDOP radar system on the high-altitude NASA ER-2 aircraft. *J Atmos Ocean Tech*, 795-809.

Hildebrand, P. H., W. C. Lee, C. A. Walther, C. Frush, M. Randall, E. Loew, R. Neitzel, R. Parsons, J. Testud, F. Baudin, and A. LeCornec, 1996: The ELDORA/ASTRAIA airborne Doppler Weather Radar: High-resolution observations from TOGA COARE. *B Am Meteorol Soc*, 213-232.

Li, Z. X. and H. Letreut, 1992: Cloud-Radiation feedbacks in a general circulation model and their dependence on cloud modeling assumptions. *Clim Dynam*, 133-139.

McGill, M., D. Hlavka, W. Hart, V. S. Scott, J. Spinhirne, and B. Schmid, 2002: Cloud Physics Lidar: instrument description and initial measurement results. *Appl Optics*, 3725-3734.

Pazmany, A., 2007: A Compact 183-GHz Radiometer for Water Vapor and Liquid Water Sensing. *Geoscience and Remote Sensing, IEEE Transactions on*, **45,** 2202 - 2206.

Stephens, G. L., 2005: Cloud Feedbacks in the Climate System: A Critical Review. *Journal of Climate*, **18**, 237-273.

Stevens, B., D. H. Lenschow, G. Vali, H. Gerber, A. R. Bandy, B. Blomquist, J. L.

Brenguier, C. S. Bretherton, F. Burnet, T. Campos, S. K. Chai, I. Faloona, D. Friesen, S. Haimov, K. Laursen, D. K. Lilly, S. M. Loehrer, S. P. Malinowski, B. M. Morley, M. D. Petters, D. C. Rogers, L. Russell, V. Savic-Jovac, J. R. Snider, D. Straub, M. J. Szumowski, H. Takagi, D. C. Thornton, M. Tschudi, C. Twohy, M. Wetzel, and M. C. van Zanten, 2003: Dynamics and chemistry of marine stratocumulus - Dycoms-II. *B Am Meteorol Soc*, 579-593.

Sun, Z. and K. P. Shine, 1994: Studies of the radiative properties of ice and mixed-phase clouds. *Q J R Meteorol Soc*, 111-137.

Vali, G., R. D. Kelly, J. R. French, S. Haimov, D. Leon, R. E. McIntosh, and A. Pazmany, 1998: Finescale structure and microphysics of coastal stratus. *J Atmos Sci*, 3540-3564.

Wang, Z. and K. Sassen, 2001: Cloud type and macrophysical property retrieval using multiple remote sensors. *J Appl Meteorol*, 1665-1682.

Wang, Z. and K. Sassen, 2002: Cirrus cloud microphysical property retrieval using lidar and radar measurements. Part II: Midlatitude cirrus microphysical and radiative properties. *J Atmos Sci*, 2291-2302.

Wang, Z., K. Sassen, D. Whiteman, and B. Demoz 2004: Studying altocumulus plus virga with ground-based active and passive remote sensors. *J. Appl. Meteor.,* **43**, 449-460.

Acknowledgements

This research is supported by NSF under award of ATM 0645644. The Wyoming King Air is supported by NSF award ATM 0334908. The authors would like to thank the UWKA facility team involved in the WAICO experiment.

OBSERVATIONS OF SUPERCOOLED CLOUDS USING AIRBORNE G-BAND RADIOMETER AND W-BAND RADAR

M. Wolde[1], A. L., Pazmany[2], D. Hudak[3], J. W. Strapp[3], A. Korelev[3] and H. Barker[3]

[1]Institute for Aerospace Research, NRC, Ottawa, Canada
[2]ProSensing Inc., Amherst, MA, USA
[3]Environment Canada, Toronto, Canada

1. INTRODUCTION

There are numerous research publications focused on the development of remote sensing systems and methodologies for retrievals of cloud properties. Ground and space-based remote sensing systems now routinely provide quantitative estimation of precipitation amount and types for operational and research applications. However, there is still a need to develop or improve existing retrieval techniques by combining new systems such as CloudSat and CALIPSO satellites. Often, validation of ground and space based remote sensing systems and model-based retrieval techniques require measurements of cloud microphysical properties and remote sensing data that are matched both spatially and temporally. Instrumented research aircraft equipped with highly sensitive radars and radiometers can provide these datasets. Aircraft measurements also have the advantage of targeting weak cloud systems that might be undetectable from ground or space based systems. For example, cloud microphysical properties such as effective radius, r_{eff} and concentration, N, of supercooled clouds are very important parameters necessary for characterizing liquid cloud properties. These parameters are needed to estimate the energy feedback mechanism between liquid clouds and the boundary layer or the severity of aircraft icing potential in supercooled liquid clouds, as few relevant examples. This paper highlights the use of aircraft based systems in the study of cloud structure by comparing airborne in-situ cloud microphysical data collected in a layered winter cloud system with retrieved cloud properties from a 94 GHz (W-band) cloud radar and a 183 GHz water vapour radiometer (G-band) installed on the National Research Council (NRC) of Canada Convair-580 research aircraft.

2. INSTRUMENTATION

The data used in this paper were collected during one of the flights of the Canadian CloudSat and CALPSO satellite Validation Project (C3VP) conducted between October 31, 2006 and March 01, 2007 over Ontario, Canada using the NRC Convair-580 research aircraft. The main objective of the C3VP campaign was to validate the CloudSat and CALIPSO satellite measurements using ground based as well as airborne systems. In addition, a number of weather related flights, similar to the case presented in this paper, were also conducted around Environment Canada's (EC) Center for Atmospheric Research Experiment (CARE) site located in Egbert, Ontario. This paper presents data collected using the airborne in-situ and remote sensing instruments, described below. Detailed descriptions of the C3VP campaign can be found in Hudak et al. (2006) and also on the project web site (www.c3vp.org).

Corresponding author address: Dr. Mengistu Wolde, Flight Research Laboratory, Institute for Aerospace Research, National Research Council, Ottawa, Ontario, K1A 0R6; email: mengistu.wolde@nrc-cnrc.gc.ca.

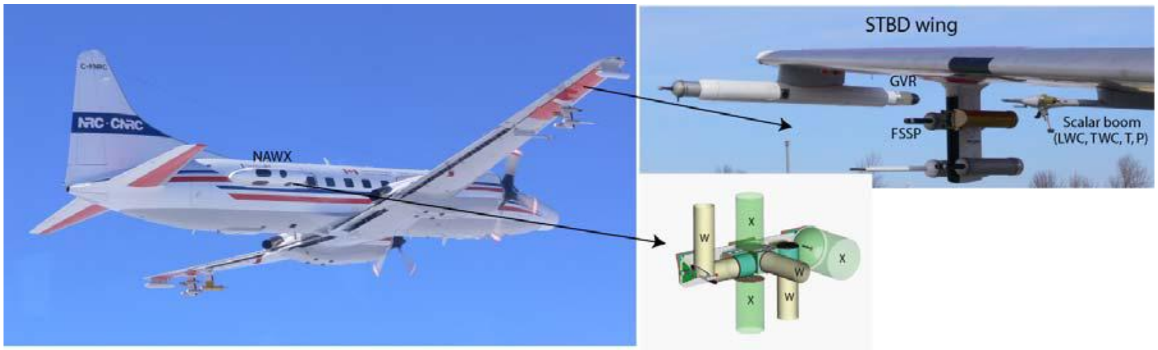

Fig. 1. During the C3VP field project, the NRC Convair-580 aircraft was equipped with an array of in-situ Cloud Physics instruments mounted in under-wing and wing-tip pylons. Schematics of the NAWX antenna configurations in the blister radome and the in-situ probes mounted on the starboard side of the aircraft including the GVR installation on the wingtip are shown in the picture.

During the C3VP field campaign, NRC and EC jointly instrumented the NRC Convair-580 with its standard suites of in-situ and remote sensing probes for atmospheric research (Fig.1). In addition, the NRC Airborne W and X-band radar system (NAWX) and a 183 GHz G-band water Vapor Radiometer (GVR), developed by ProSensing Inc. (Pazmany, 2007) were integrated on the aircraft for the first time.

The NAWX radar system (Wolde and Pazmany, 2005; www.nawx.nrc.gc.ca) has polarimetric and Doppler capabilities at both frequencies and can switch electronically between zenith, nadir and side looking antennas. Using a motorized reflector plate, the zenith W-band antenna is also capable of scanning -5° aft to +45° forward in the horizontal and vertical directions, to provide a dual-Doppler capability. The compact airborne GVR was installed on the NRC Convair-580 in a PMS-type wing-tip pod (Fig. 2). The key system parameters of the airborne GVR are summarized in Table 1. The Liquid Water Path (LWP) and Perceptible Water Vapour (PWV) were estimated from the up-looking GVR brightness temperature measurements using a neural network technique described by Pazmany (2007) and Cadeddu et al. (2007).

Fig. 2. Airborne GVR installed on the NRC Convair-580 aircraft (upper left), in a standard PMS probe canister (middle) and with the radome head removed, showing the fixed 90 degree metal mirror and the solenoid

The Convair in-situ cloud physics measurements were used when evaluating the radar and radiometer retrieval results. These include, liquid cloud particle concentrations and size measured by one of the Forward Scattering Spectrometer Probe

TABLE I
AIRBORNE GVR KEY PARAMETRERS

Frequency:	183.31 ±1, ±3, ±7 and ±14 GHz
Bandwidth:	0.5 (1), 1.0 (3), 1.4 (7) and 2.0 (14) GHz
Receiver Noise T:	1750 K (1), 1610 K (3), 1600 K (7) and 2170 K (14)
ΔT:	0.2 K @ 200 ms integration (5 Hz data rate)
Allan Deviation:	0.05 K @ 500 sec.
Measurement Rate:	up to 20 Hz with a 0.25 sec calibration gap once every 3 seconds
Antenna:	10 cm (4") Aperture, 90 deg Parabolic Metal Mirror, 1.7° BW
Radome:	Matched TPX (Polymethylpentene) Window
Weight (Probe)	10 kg (22 lb) without Canister
Power	28 W @ 115 VAC, 126 W @ 28 VDC
Data	RS422 Serial Data Stream, Notebook PC Recorder

(FSSP), Liquid Water Content (LWC) measured by King Probe, particle images measured by a PMS 2D-C Probe. For a detailed description of the NRC Convair-580 in-situ cloud physics measuring probes refer to Isaac et al. (2001).

3. RADAR/RADIOMETER RETRIEVAL TECHNIQUE

The effective radius, r_{eff} is defined in terms of the cloud drop size distribution, *n(r)* at some height, *h* as (Szczodrak et al., 2001):

$$N(h) = \int_0^\infty n(r,h)dr \text{ and}$$

$$r_{eff} = \int_0^\infty n(r,h)r^3 dr \Big/ \int_0^\infty n(r,h)r^2 dr .$$

The zenith pointed GVR measured LWP which is the height integrated Liquid Water Content (*LWC*), given by

$$LWC(h) = \frac{4\pi}{3}\int_0^\infty n(r,h)r^3 dr \quad \text{and}$$

$$LWP = \int_0^\infty LWC(h)dh .$$

In stratoform clouds, LWC may be estimated from the GVR retrieved LWP by flying the aircraft in a porpoise pattern or stepped ascent/descent through a liquid cloud depth. The zenith beam of the W-band radar samples a very similar cloud volume and for small cloud droplets, Z from the W-band can be approximated using Rayleigh scattering as the sixth moment of the drop size distribution:

$$Z(h) = 2^6 \int_0^\infty n(r,h)r^6 dr$$

From the third and sixth moment of the drop size distribution, a new, *Z*-based estimate of the characteristic cloud drop radius, r_Z may then be obtained according to:

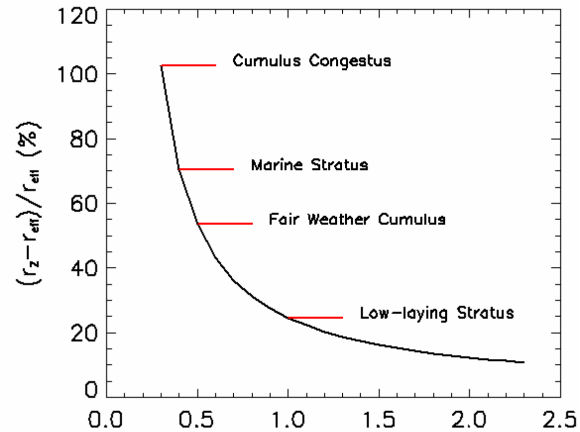

Fig. 3. Percent error between effective radius, r_{eff}, and the radar reflectivity based estimate of cloud drop size, r_Z, calculated based on the modified gamma drop-size distribution and cloud parameters tabulated in Ulaby et al. (1981) and the marine stratus distribution shape observed by Vali (1998).

$$r_Z = \sqrt[3]{\frac{\pi}{48}\frac{Z(h)}{w}} = \sqrt[3]{\int_0^\infty n(r,h)r^6 dr \Big/ \int_0^\infty n(r,h)r^3 dr}$$

The difference between r_{eff} and r_Z is primarily a function of the width of the drop size distribution and often can be estimated based on cloud type. This difference, expressed in terms of percent error in r_Z relative to r_{eff} is illustrated in Fig. 3, assuming a modified Gamma cloud drop-size distribution for a number of common cloud types. This figure can be used to estimate r_{eff} from r_Z and then to obtain the effective number density according to:

$$N_{eff}(h) = \frac{3}{4\pi}\frac{LWC(h)}{r_{eff}^3} .$$

4. DATA

On January 26, 2007 the NRC Convair 580 made repeated measurements in two different locations over Southeastern Ontario (Fig. 4). The Convair first sampled a deep cloud system around the EC CARE site and then headed north to near Georgian Bay to sample a lake-effect storm system detected by ground radars. The aircraft made the transit from the CARE

Fig. 4. The NRC Convair-580 flight track on Jan 26, 2007. The data used in this presentation were collected between 22:29 and 24:16 UTC around Midland, Ontario, highlighted by the blue arrow.

facility to the targeted region at an altitude of 2.5 km and then made a spiral ascent (23:29-23:39 UTC) when it reached the targeted cloud system. The vertical profiles of temperature and LWC and the W-band radar equivalent reflectivity (Z) obtained from the NAWX radar are shown in Fig 5. The figures show a marked inversion layer extending from the lowest level of the aircraft height to about 3 km with regions of supercooled cloud with LWC of up to 0.6 g m^{-3} at the top of the inversion layer. The LWP estimated from the GVR show a maximum value of 0.1 mm (Fig. 6) just before the aircraft was ascending through the supercooled cloud top with low reflectivity values of less than -20 dBZ (~23:30 UTC). As indicated from the in-situ data, the base of the upper cloud layer consisted mainly of irregular ice crystals with no liquid (Fig. 6). The GVR also show very low LWP (< 0.02 mm - close to the baseline) in the upper ice clouds layer suggesting that there was no liquid above the aircraft. As can be seen from the zenith looking W-band measurements as well as the in-situ data, the upper cloud layer extended from 4 km to 8 km and was fairly uniform during the spiral ascent. In contrast, the low cloud cell started to dissipate with significant intrusion of clear air separating the upper and lower cloud systems.

After the spiral, the aircraft made five transects along a south-north line. Each of these legs were 6-8 minutes long with the aircraft mainly porposing between 2.5-5 km. Figure 7 shows the vertical Z profiles along this S-N track. The radar as well as the in-situ data presented in Fig. 6 show a change in cloud composition and thickness during the 45 minutes of sampling. In the first S-N leg, the aircraft stayed in the glaciated system, so no temperature inversion was measured during the descent. The W-band vertical Z profile clearly shows the layered clouds, with clear air at around 3 km, extended from the southern edge to mid-way of the track. At the northern edge of the track (top Panel in Fig. 7), the cloud deck extended from the surface to 8 km. In the reverse N-S track (Leg-2 - Panel 2 of Fig. 7), the cloud structure remained similar, but the aircraft sampled the clear air and went through a temperature inversion and a supercooled cloud layer. Similar to the measurements during the spiral ascent, the GVR measurements of LWP in the

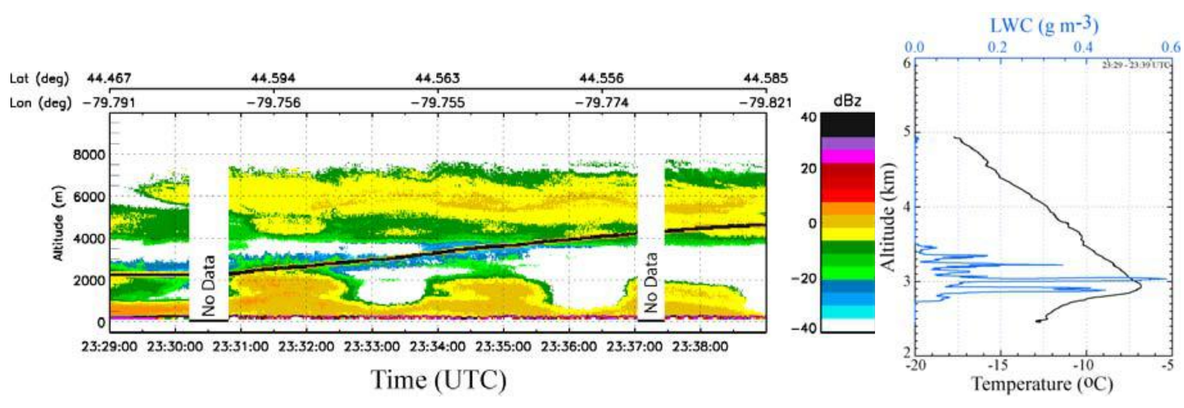

Fig. 5 Left: Vertical Profile of W-band Z measured by the NAWX zenith and nadir-looking antennas during the spiral ascent in a multi-layer cloud system. The aircraft altitude is shown by the black line. Right: vertical profiles of T (black) and LWC (blue) measured during the spiral ascent.

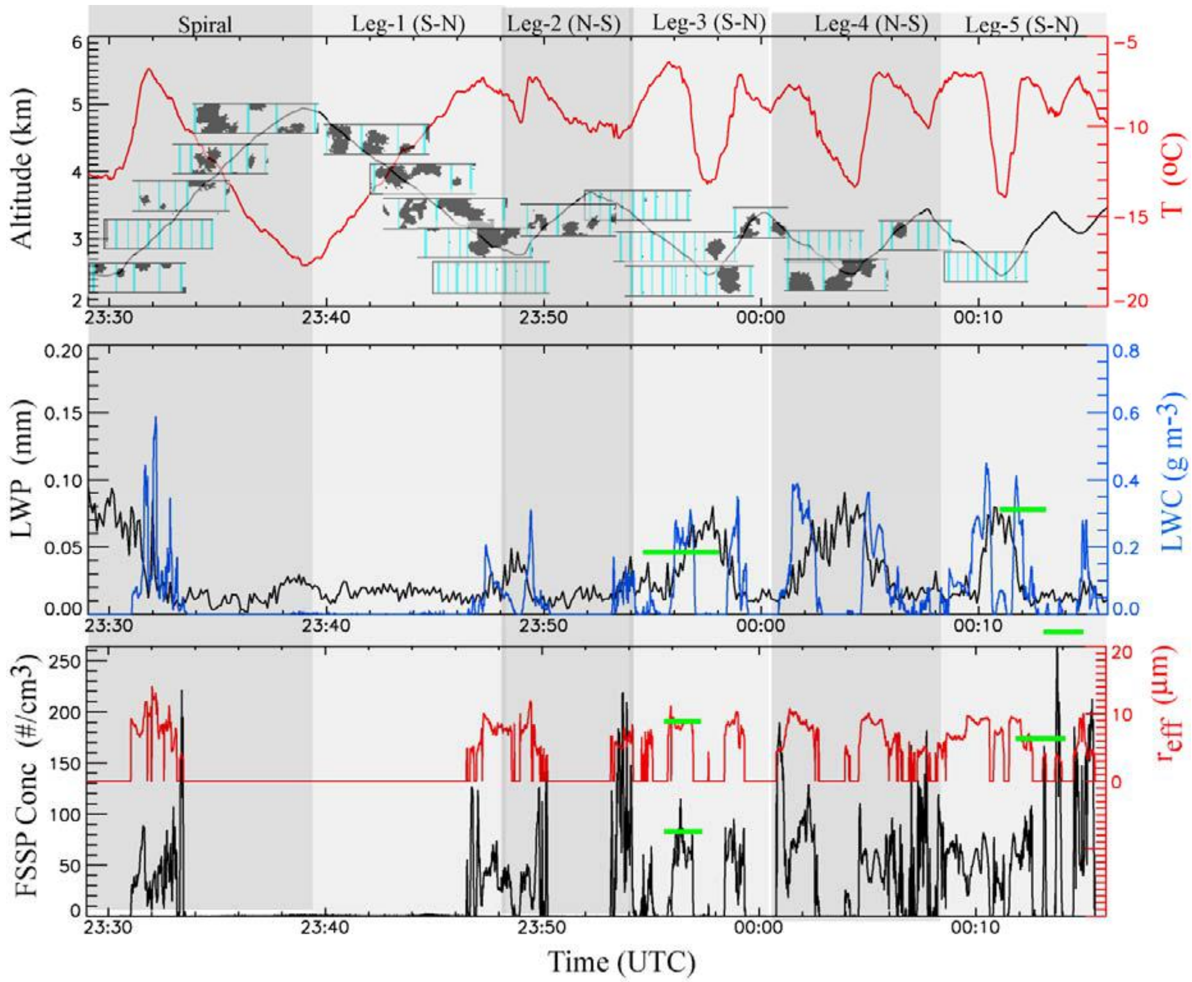

Fig. 6. Time series of in-situ and GVR measurements of the study area. Top panel: aircraft altitude (black), T (red) and examples of particle images measured by the PMS 2D-C probes (vertical scale ~ 800 μm). Middle panel: LWP estimated from GVR (black) and LWC (blue) measured by the King probe. Bottom panel: Liquid particle concentrations (black) and effective radius (red) measured by one of the FSSP probes (red). The green lines in the bottom and middle panels show retrieved values from GVR and NAWX radar data.

supercooled layer agrees very well with the in-situ data measurements (Fig. 6). The next three legs (23:50-00:16 in Fig. 6 and Panels 3-5 in Fig. 7) captured the progression of a formation/movement of a solid supercooled cloud deck at the top of the low cloud layer (~700 m thick) with LWC of up to 0.4 g m^{-3}. The GVR show a LWP of 0.08 mm at the base of the supercooled layer. The GVR LWP measurements during the porpoise maneuver in and out of the liquid layer also tells a consistent story with that of the in-situ LWC.

5. SUMMARY DISCUSSION

Examples of the cloud microphysical properties (LWC, r_{eff} and N) estimated from the GVR and NAWX radar as described in Section 3 are shown by the green horizontal line in Fig. 6 (23:57 UTC descent and 00:12 UTC ascent). The LWC values estimated from the GVR data (0.16 g/m3 in Leg-3 and 0.30 g/m^3 in Leg-5) compare well with the in situ probe measured values of 0.25 g m^{-3} and 0.4 g m^{-3}. Both the low Z values (<-20 dBZ) and the in-situ particle size data suggests the supercooled layer was dominated by small liquid drops (<100 μm in size), so the Rayleigh scattering approximation and the retrieval of particle size information and concentration outlined in Section 3 should be valid. The characteristic cloud drop radius, r_Z was

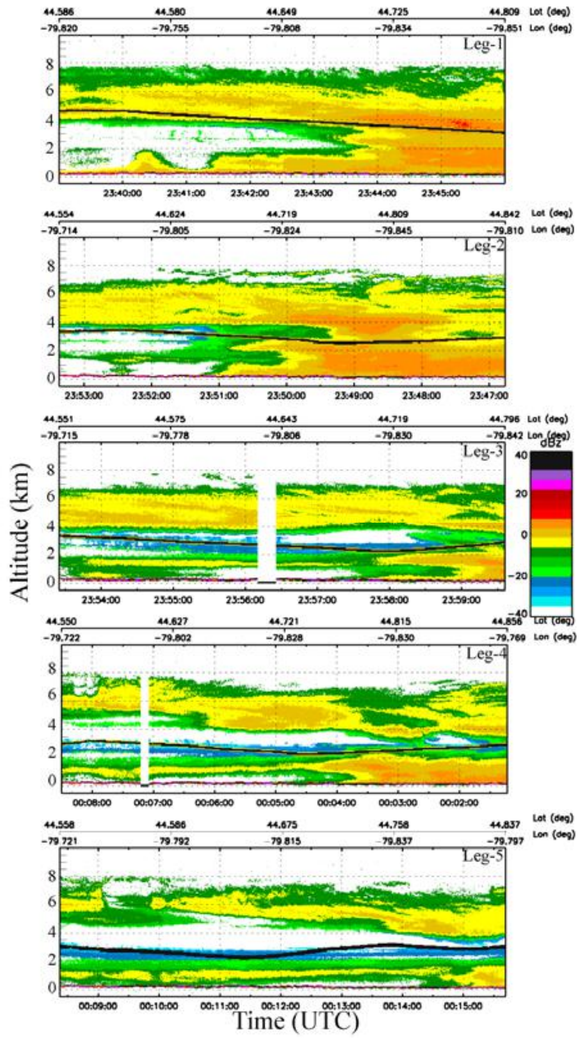

Fig. 7. Sequences of vertical profiles of Z measured by the zenith and nadir-looking W-band radar along a S-N track, while doing porpoise maneuver between 2.5 km and 4 km. The back line shows the aircraft altitude.

estimated using the measured LWC and Z values measured by the zenith-looking W-band radar data. After estimating r_Z, a 40% difference was applied to obtain r_{eff} by assuming a continental stratus cloud type, with a size distribution width between cumulus and low-lying stratus. The GVR derived r_{eff} values of 7.6 μm and 6.2 μm are within the 5-10 μm range measured by the FSSP. Finally, the effective number concentration was calculated from LWC and r_{eff}. The total particle concentrations estimate of 87 cm^{-3} in Leg-3 compares very well with the FSSP measured concentration of 80-100 cm^{-3}, while the concentration estimate of 300 cm^{-3} at Leg-5 is higher than the 100-250 cm^{-3} measured by the FSSP.

The airborne G-band radiometer and NAWX radar data presented in this paper are preliminary and more analysis will be done using a larger dataset to quantify the performance of the two instruments and to thoroughly test the retrieval algorithms described in this paper. However, the limited GVR and airborne W-band data presented in this paper are consistent with the in-situ measurements and also show promise for retrieval of liquid cloud microphysical properties from combined airborne G-band radiometer and W-band radar measurements.

ACKNOWLEDGMENTS

The Canadian Space Agency, NRC and EC funded the C3VP field project. Many technicians, engineers and scientists from the NRC, EC and ProSensing Inc. worked tirelessly during the instrument integration on the aircraft as well as the C3VP field project flights. We would like to acknowledge NRC for providing funding for the development of the NAWX radar system as well as the integration of GVR on the NRC Convair-580. Special thanks to Yizhe Shen from Carleton University, who processed the radar data that are used in this paper.

REFERENCES

Cadeddu, M. P., J. C. Liljegren and A. L. Pazmany: “Measurements and retrievals from a new 183-GHz water-vapor radiometer in the Arctic”. Trans. Geosci. and Remote Sensing, 45, 7, 2207-2215, 2007.

Hudak, D., H. Barker, P. Rodriguez, and D. Donovan: “The Canadian CloudSat Validation Project", paper presented at 4th European Conf. on Radar in Hydrology and Meteorology, Barcelona, Spain, 18-22 September, 2006.

Isaac, G.A, S. G. Cober, J. W. Strapp, A. V Korolev, A. Trembly, and D.L. Marcotte:, “Recent Canadian research on aircraft in-flight icing”. Canadian Aeronautics and Space Journal, Vol. 47, 213-221, 2001.

Pazmany, A. L. :“A compact 183-GHz radiometer for water vapor and liquid water sensing”. IEEE Trans. Geosci.. Remote Sens. Vol. 45, No. 7, pp. 2202-2206, July 2007.

Szczodrak, M., P. H. Austin, P. B. Krummel, “Variability of optical depth and effective radius in marine stratocumulus clouds” J. Atmos. Sci., Vol 58, pp. 2912-2926, 2001.

Ulaby, F. T., R. K. More and A. K. Fung: “Microwave Remote Sensing”, Vol. 1, *Addision-Wesley Publishing Co.,* 1981.

Wolde and Pazmany: “NRC Dual-frequency airborne radar for atmospheric research”, paper presented at the *32nd Conference Radar Meteorology, Albuquerque, NM, 24-29 October, 2005.*

Vali, G., R. D. Kelly, J. French, S. Haimov, D. Leon, R. E. McIntosh and A. L. Pazmany: “Finescale structure and microphysics of coastal stratus”, Vol. 55, No. 24, pp. 3540-3564, Dec. 1998.

CLOUD LIQUID WATER RETRIEVAL IN NON-PRECIPITATING CLOUD WITH SATELLITE MIVROWAVE DATA OVER HENAN REGION

Zhanyu YAO Liang PENG

Key Laboratory for Cloud Physics and Weather Modification of CMA,

Chinese Academy of Meteorological Sciences, Beijing 100081, P. R. China

Email:yaozy@cams.cma.gov.cn

1. Introduction

Cloud Liquid Water (CLW) is one of the most important uncertainty factors on the analysis of global climate change and local precipitation condition. The condition of CLW has the significant effect on the conversion process of hydrometer and the balance of radiation in troposphere. The data of CLW are the key parameter for improving simulating precipitation process. CLW is also one of the most important indices for cloud seeding of precipitation enhancement.

The data of CLW taking by aircraft are basic data for the study of rain process, but they are unwonted and very expensively. Multichannel microwave radiometer on the ground can get abundant information of CLW over a site by retrieval method without influence from the different surface emissivity, but it is very difficult to get the whole information of a cloud system with one immobility observation site. Satellite data, however, are very useful for retrieving different levels of CLW with particular spatial and temporal speciality. The advance of satellite technique will provide plenty of cloud information for the study of precipitation condition in future. The CLW sounding from TRMM Microwave Imager (TMI) can provide potential information to the precipitation condition and it is the key data source to verify the analysis result of CLW by various retrieval method.

2. Retrieval Method for CLW in Non-Precipitating Cloud

The radiis of cloud particle in non-precipitating cloud is less than the microwave length. According to the Rayleigh theory, the absorption section of cloud particle in non-precipitating cloud is bigger than the scatter section when assuming a horizontal and parallel atmosphere in a local thermal steady state.

The particulate scattering is related to the sector of cloud particle and the absorption is related to the bulk of cloud particle, so the atmospheric absorption is directly related to the total CLW in cloud particle and less effected by the distribution of cloud particles according to the Planck assumption.

Most incunabular retrieval tests for CLW in non-precipitating cloud with satellite microwave are limited on the clouds over oceans where the physical status is simple. The surface radiative character of land is much more complexity than that of sea surface. Firstly a strong radiance background exists because the surface emissivity is bigger than that of the sea surface. In addition, the microwave radiation over land is very complicated, and the surface emissivity varies with the substantial configuration, the thermal temperature, the geometry shape, the particle structure inside, the surface roughness, and the physical character of land. The intricacies of surface property make it difficult to retrieve CLW in non-precipitating cloud over land with satellite microwave data.

Grody et al.（1976）set a regression equation for CLW in the various kind of cloud by assuming that surface emissivity is uniformly distributed from 0.9 to 1.0 . But their results showed that the retrieval error is too large to reflect the true state of CLW. Jones et al.（1990）retrieved CLW using iterative method with a radiative transfer model and the data at 85.5GHz SSM/I. Greenwald et al.（1997） and Combs et al.（1998）retrieved CLW using polarization difference of brightness temperature. The method reduces the CLW retrieval error in lower cloud and decreases the influence from the vertical profile of CLW, but it can be only applied to the polar surface and the random error of CLW aggrandizes with the instrumental error.

The precision of retrieved CLW is limited when using surface emissivity from experiential result and calculation methods by Grody（1976）, Feddes and Liou（1978）, Liou and Duff（1978）. Jones et al (1990) are very complex to calculate surface emissivity using the infrared channel data. Zhao and Wang (1997) calculated surface temperature and surface emissivity by a method with the data of 2 channels or 3 channels. Deeter and Vivekanandan（2005）calculated CLW with the data of dual channels without surface emissivity assuming that the polarization difference of surface emissivity is not relate to frequency.

Using TRMM/TMI 85.5GHz vertical polarization brightness temperature data, surface emissivity is calculated by an iterative method with VDISORT from the cloudless data on 6 Mar. 2005. According to the analysis by Jones et al., surface emissivity has less change in 15 days. The amount of CLW over Henan region on 21 Mar. 2005 and its distribution were retrieved using NCEP data, the calculated surface emissivity on 6 Mar. 2005 and brightness temperature data. Compared with the infrared image of FY-2C Satellite, TRMM 2A12 products, and NCEP data, the method used in this paper was feasible in retrieving CLW in non-precipitating cloud.

3. Estimation of surface microwave emissivity

There are only 2 radiosonde sites in Henan region. We use temperature, air pressure, and humidity from NCEP 1°×1° data which have the coverage of Henan region. The surface emissivity in Henan region on 6 Mar. 2005 was calculated by the numerical step-by-step method with VDISORT based on the vertical polarization brightness temperature data from TRMM/TMI 85.5GHz channel. TRMM passed over Henan region three times on 6 Mar. 2005, which are 10:31:57 to 10:33:35, 12:09:22 to 12:11:16, and 13:46:41 to 13:48:58. Fig. 1 shows surface emissivity calculated by brightness temperature from TRMM data during 12:09:22-12:11:16 UTC on 6 Mar. 2005 over Henan region. The result from the calculation in Fig.1 is similar to the surface conditions image in cloudless from Google Earth on 8 April 2007 in Henan region.

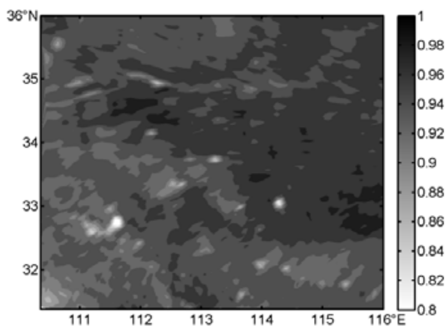

Fig. 1: The distribution of surface emissivity calculated by brightness temperature from the TRMM data during 12:09:22-12:11:16 UTC on 6 Mar. 2005 in Henan region.

4. Retrieval test of CLW in non-precipitating cloud over Henan region

Retrieval test of CLW in non-precipitating cloud over land in Henan region uses the vertical polarization brightness temperature data from TRMM 85.5GHz channel during 03:06:33 to 03:08:11 on 21 Mar. 2005. The surface emissivity calculated from TRMM/TMI data on 6 Mar. 2005 are interpolated to pixels on 21 Mar. 2005. The total CLW in non-precipitating cloud is then calculated using the retrieval method with VDISORT model, combined with the interpolated surface emissivity, vertical polarization brightness temperature data from TRMM 85.5GHz channel during 03:06:33 to 03:08:11, and the NCEP data at 02:00 UTC on 21 Mar. 2005. Fig.2 shows the result of CLW during 03:06:33 to 03:08:11 on 21 Mar. 2005 in non-precipitating cloud calculated by the retrieval method.

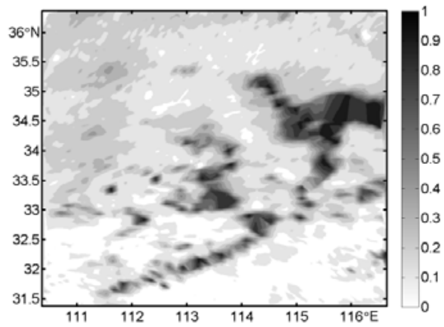

Fig.2: The total CLW during 03:06:33 to 03:08:11 on 21 Mar. 2005 in non-precipitating cloud calculated by the retrieval method

5. Contrast Analysis

5.1 Contrast of the retrieval result with FY-2C cloud image

Fig.3 is an infrared cloud image from FY-2C at 03:00 UTC on 21 Mar. 2005. The cloud distribution in the black box in Fig.2. is similar to the distribution of the total CLW in non-precipitating cloud calculated by using the retrieval method in Fig.1.

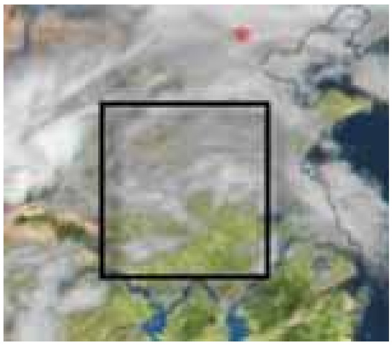

Fig. 3: The infrared cloud image from FY-2C at 03:00 UTC on 21 Mar. 2005.

5.2 Contrast of the retrieval result with TRMM 2A12 product

Fig.4 shows the total CLW from the TRMM 2A12 product during 03:06:33-03:08:11 on 21 Mar. 2005. It is similar to the total CLW in non-precipitating cloud calculated by the retrieval method. The coverage of the CLW observed from TRMM 2A12 is smaller than that from the retrieval method and the CLW value in Fig.4 is about half of the CLW value in Fig.2.

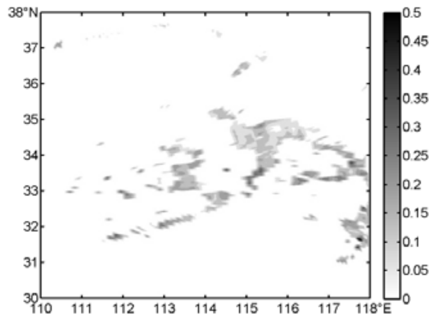

Fig.4 The total CLW from TRMM 2A12 product during 03:06:33-03:08:11 on 21 Mar. 2005.

5.3 Contrast of the retrieval result with the result from NCEP data

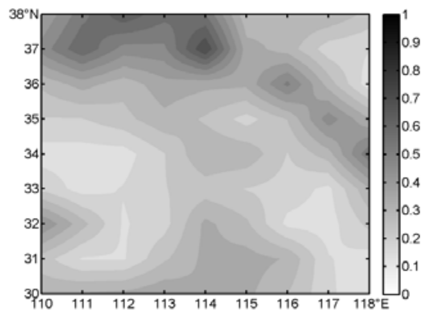

Fig.5 : The total CLW from NCEP at 02:00 UTC on 21 Mar. 2005.

Fig.5 is the total CLW from NCEP at 02:00 UTC on 21 Mar. 2005. Larger difference exists compared with the total CLW in non-precipitating cloud that calculated by the retrieval method (Fig 2).

6. Error Analysis

6.1 Error from the vertical profile of CLW in non-precipitating cloud

Fig.6 is the error effect that the simulation change of CLW at a 2 km depth cloud body with brightness temperature at 85.5GHz SSM/I by VDISORT model from the different cloud base height. The error of the brightness temperature accuracy by VDISORT model is increase with cloud base height uplifting.

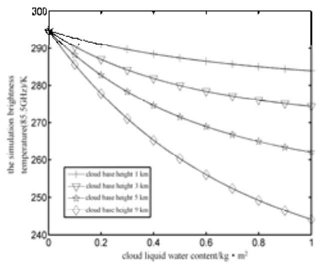

Fig.6: The effect that the simulation change of CLW at a 2 km depth cloud body with brightness temperature at 85.5GHz SSM/I by VDISORT model from the different cloud base height.

6.2 Error from the substitute of the NCEP data in VDISORT

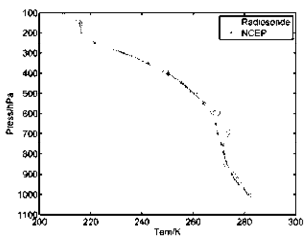

Fig.7: The contrast that the temperature profile from radiosonde data at 5:00 UTC to the corresponding temperature profile from NCEP data at 02:00 UTC on 21 Mar. 2005.

Fig.7 is contrast of the temperature profile from radiosonde data at 5:00 UTC with the corresponding temperature profile from NCEP data at 02:00 UTC on 21 Mar. 2005. The difference of the calculated brightness temperature is only 5K by VDISORT model and the error analysis result is 0.1 g/m^2 with substitute of the radiosonde data by the NCEP data.

7. Conclusions

7.1 It is feasible to estimate surface emissivity using step by step method and calculate total CLW in non-precipitating cloud with VDISORT model and the radiosonde data.

7.2 Compared with NCEP data and TRMM product of the total CLW, the total CLW in non-precipitating cloud calculated by our retrieval method provides the best result. The NCEP data fail to show the total CLW in non-precipitating cloud and the CLW coverage from TRMM 2A12 is smaller than our retrieval result.

7.3 The effect of the simulation brightness temperature by VDISORT model is decrease with cloud base height uplifting.

7.4 The error is 0.1 g/m2 with the substitute of the radiosonde data by the NCEP data. The error elimination should base on the acquisition of radiosonde data with the increase of the temporal resolution in field experiment.

7.5 The retrieval method is only the qualitative analysis for cloud liquid water in non-precipitating cloud with satellite microwave data. The quantitative analysis exist many difficulties to overcome with the help of plenty of observation data in future.

Acknowledgements

This work is supported by the Natural Science Foundation of China (40375001) and the National Key Research Project of Ministry of Science and Technology of China (2006BAC12B02).

CONSTRUCTION OF A GROUND SYNTHETIC SYSTEM FOR CLOUD ANALYSIS BASED ON WEBGIS

Jiping You, Yongji Feng
Weather Modification Office of Guangdong Province, Guangzhou, 510080

1. INTRODUCTION

Recently，the Ground Synthetic System for Cloud Analysis has been built in many provinces in China[1-4]. With the development of WebGIS technique, WebGIS has been applied in meteorological field[5-6]. ArcGIS is one kind of commercial software developed by a company of the United States named ESRI. It is a platform based on GIS, utilizing many important techniques in computer, such as GIS, Databank, Software engineering, artificial intelligence, etc. It is composed of three basic parts. They are Application Platform of ArcGIS Desktop, ArcSDE Platform of managing data-base and ArcIMS, which is based on Internet distributed data and GIS service. Our system is designed mainly on the basis of the ArcIMS part.

2. IDEA OF CONSTRUCTION

The ArcGIS software platform and the hardware platform of computer servers are used to construct a ground synthetic system for cloud analysis based on the WebGIS techniques. The system is built on three layers. The bottom layer is for the management of data, which are made up of three types. The first is the weather satellites and radar data. The second is the spatial geographical data of the whole Guangdong province and the network of airports. The third is the discrete data, which include automatic rain gauges, lightning, forest fires and flight track, which are all stored in real-time in the Oracle databank. The intermediate layer is for technological treatment, in which the ArcGIS is used to build a WebGIS-based software to support the system. The software is made up of ArcSDE (Space Data Engine) and ArcIMS (Internet Map Server). The part of ArcIMS is constructed based on Internet distributed data and GIS service. It is composed of the Client (or browser) and the Server. The part of Server uses Web server and the Client uses the ordinary browser of WWW for interactive processing, so that the ArcIMS can distribute maps, data or metadata via the Internet. For example, when the Client sends a request via IE browser to inquire for some kind of meteorological products, the Web server communicates with ArcIMS Server through the ArcXML (Extensible Markup Language). Then the ArcIMS receives the request and analyzes, then submits it to the ArcSDE. The ArcSDE is responsible for managing the information of data-base. It is used to supervise space utilization and provide its information, so that the system can read and write the geographical data of map correctly, which are stored in the databank, and execute those commands of searching space data or lodging the operation data, and send the data which meet the requests of the ArcIMS. Then the ArcIMS sends it to the browser of Client. In this way, the system can provide the services of display and searching space data in the mode of Web. Fig.1 shows System Architecture of ArcIMS.

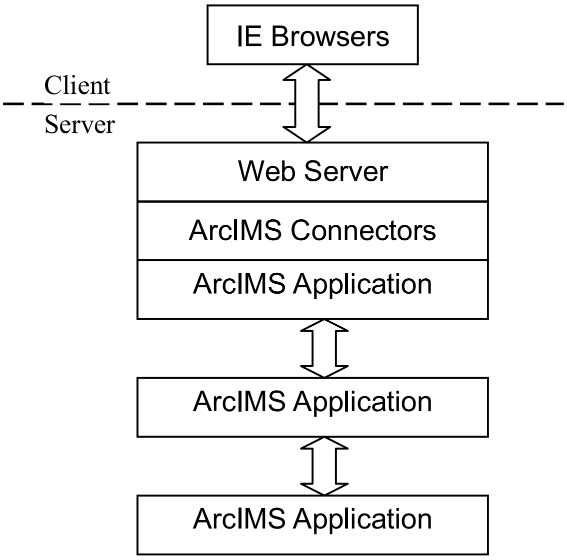

Fig.1 Sysetm Architecture of ArcIMS

The top layer is for application, which is also the layer being displayed in the terminal. It consists of weather analysis, radar echo prediction, cloud observations and numerical simulation etc. Fig.2 shows cloud and precipitation in real time mode platform.

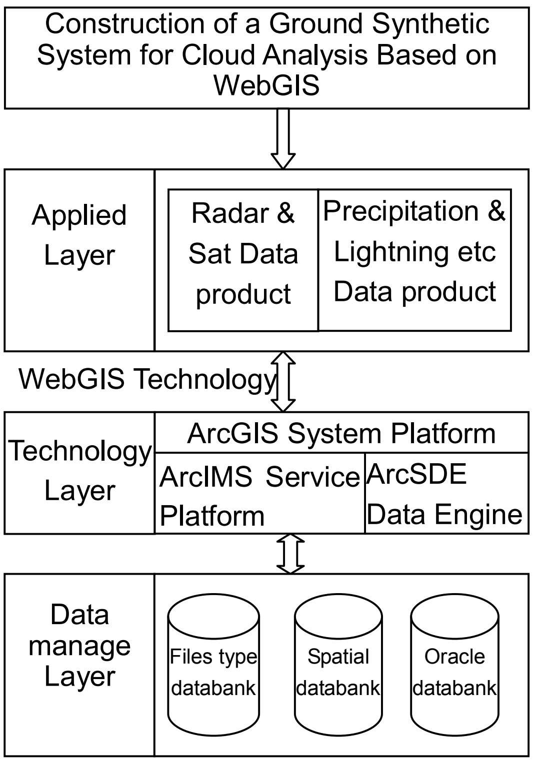

Fig 2:Cloud And Precipitation In Real Time Mode Platform

3. PIVOTAL TECHNIQUE

How to make full use of internet technique and meteorological information detected (such as data obtained by satellite and Doppler radar) to construct a display system, which can display weather events in real time (based on GIS) and can run automatically in operation, is the key point and a difficult task in constructing a system. We use image files (in the format of IMG) as one layer of pictures added to GIS and can display via the web. The format of IMG is one of the popular formats used in remote image files and corresponding software. We transfer the detected products to IMG format files at set time intervals in operation. Based on the data of precipitation and lightning, which are distributed on discrete points, we send them via a ftp server and write to the Oracle database. The flow chart of processed data of satellite, Doppler radar, precipitation and lightning is shown in fig3.

ArcIMS connector is used to connect Web server and ArcIMS application server. ArcIMS

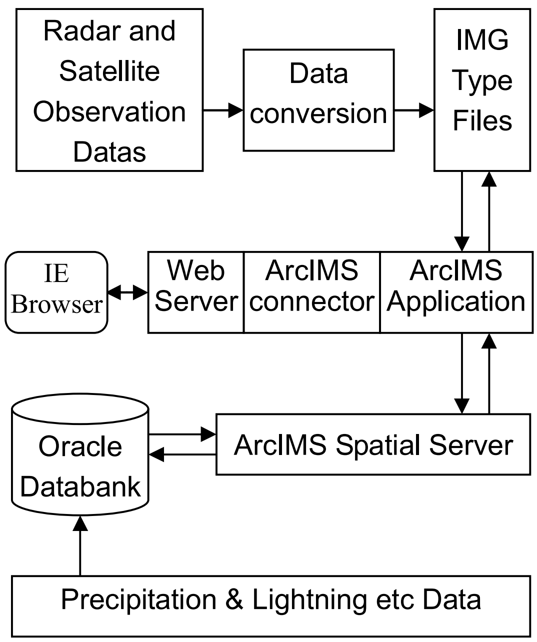

Fig3：Display of Data product and GIS

application server deals with requested load balance and assigns certain ArcIMS spatial server to run for task of map service. ArcIMG spatial server is the kernel of ArcIMS. It creates a dynamic map according to map data requests and relevant information. The map is sent to the IE browser of clients.

4. DISCUSSION AND CONCLUSION

This system provides a convenient tool for cloud and precipitation analysis. With the GIS and Internet techniques, it is also a command platform for rainfall enhancement operations. It is now possible to have access to the real situation of weather modification across the province from the Internet. With the availability, particularly, of real-time and dynamic monitoring from web browsers of flight track, operation vehicle, radar and satellite measurements and display of meteorological observations in any needed combination with GIS, terminal users are able to operate the commanding system right from computers connected with the Internet. It brings much convenience to the operators of weather modification and improves the efficiency of relevant decision-making. The successful construction of the system makes it easier to run weather modification and speeds up the operational development of weather modification in Guangdong province. Fig 4:Shows the flow chart of airplane and vehicle rain enhancement in real time mode.

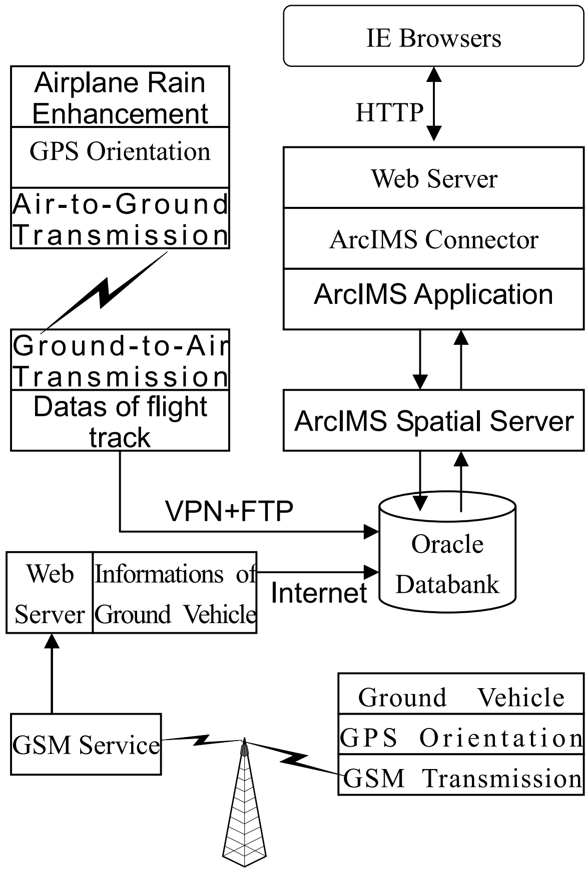

Fig 4:The Flow chart of Airplane and Vehicle Rain Enhancement In Real Time Mode

5. REFERENCES

[1] Jiping You and Yongji Feng. The Plan of Commanding System for Artificial Rain Enhancement on Guangdong Province. J. Guangdong Meteorology, 2006(1), 57-65. (in Chinese)

[2] Zhou Yuquan and Cun Zhang. The Design, Development and Application of New--Generation Operational System of Henan Province. Quarterly Journal of Applied Meteorlolgy,2001,12(3),173-184. (in Chinese)

[3] Huailiang Chen, Chunhui Zou and Yuquan Zhou. GIS Platform for the Decision and Command of Weather Modification. Journal of Nanjing Institute of Meteorology, 2002, 25(2), 265- 270. (in Chinese)

[4] Jingyan You, Ying Duan, and Laiguang You. Cloud & Precipitation Physics and Technique Research on weather modification. Beijing, China Meteorological Press, 1993, 295pp. (in Chinese)

[5] Guangyuan Liu, Qinghua Nie and Ming Zhao. Agricultural Environmental Information System Based on ArcIMS Developing WebGIS.

Geospatial Information, 2007, 5(1), 40-44. (in Chinese)
[6] Zhuang Liwei, Liu Gengshan and Wang Shili. Study On The Agrometeorological Infprmation Share And Delivery Technology Based On WebGIS. Quarterly Journal of Applied Meteorology, 2004, 15(06), 745-753. (in Chinese)
[7] Xia Hou and Guofu Liu. The Application Research of Statistical function in ArcGIS. Heilongjiang Science and Technology Information, 2007 (06), 56. (in Chinese)

Acknowledgements
The Paper Was Helped by Mr. Yin Duan and Mr. Lixin shi on Weather Modification Office of Hebei Province. The authors thank Mr. Chaoxiong Cao and Miss Yanyan Huang of Guangzhou Institute of Tropical and Marine Meteorology for their kind help in the work.

A 35-GHz RADAR FOR CLOUD AND PERCIPITATION STUDIES IN CHINA

Lingzhi Zhong[1, 2] Liping Liu [1] Lin Chen [3] Sheng Fen[4]

1.State Key Laboratory of Severe Weather，Chinese Academy of Meteorological Sciences

2. Nanjing University of Information Science &Technology

3. Institute of Atmospheric Physics, Chinese Academy of Sciences

4. Beijing institute of radio measurement

1. INTRODUCTION[1]

With the recent emphasis on understanding the role of clouds in the global radiation budget, cloud detection becomes more and more important. Although there are optical remote sensing techniques (e.g., satellite lidar, ceilometer, etc.) to measure cloud properties, optical signals cannot penetrate into thick cloud to observe the cloud's horizontal and vertical dimensions and its internal structure.

The scope of radar meteorology has expanded to include measurements of cloud properties and structure for radar's wavelength is close to cloud's diameter. Millimeter-wavelength radar is recognized as having the potential to provide a more sensitive probe of cloud particles ranging from a few micrometers in diameter to precipitation drops. Since the backscatter cross section of tiny drops (i.e., several tens of micrometers in diameter) increases in proportion to λ^{-4}, where λ is the radar wavelength, cloud drops are more easily detected by radars of millimeter rather than centimeter wavelengths. On the other hand, attenuation of millimeter waves is much stronger, and the λ^{-4} advantage gained using millimeter waves is offset by the strong attenuation these waves experience. The 10-cm-wavelength radar, used principally for storm warnings, can't detect weak and no precipitation clouds well, compared with the 8.6-mm-wavelength radar described in this paper. Because there are several strong absorption bands at millimeter wavelengths, observations are practical at few spectral windows (i.e., λ = 8.6, 3.2, 2.14, and 1.36mm). But, high-power millimeter wavelength radars are only affordable at λ = 8.6 and 3.2 mm.

Several 35-GHz research radars have been developed for the purpose of cloud observation (e.g., Pasqualucci 1983, 1984; Hobbs et al. 1985; Krofli 1994). Sekelsky and McIntosh(1996) and Mead et al.(1994) describe multiparameter radars for frofiling clouds. The radar is also used to measure drop-size distributions (e.g., Pasqualucci, 1975) and other physical parameters, such as cloud liquid water content and effective radius (Atlas, 1954; Sauvageot and Omar, 1987; Fox et al., 1997; Baedi, 2000). A radar operating at 35-GHz was designed and assembled primarily for observation of clouds and precipitation by 2007. This is the first millimeter-wavelength radar with polarization and Doppler capability used for

[1] *Corresponding author address:* Lingzhi. Zhong, Room 709-2, No.46, South Street, Village ZhongGuan, Haidian, Beijing, China.
Zip code: 100081
E-mail: zlingzhi007@gmail.com

clouds research in China.

The traditional application of radar in meteorology has focused on the detection and analysis of the structure and intensity of precipitation. These studies focused on classifying cloud types, establishing delectability limits, detecting cloud top and base heights, describing cloud morphology, and estimate cloud liquid water content. This paper is composed of several parts, including the radar system, data and signal processing techniques such as signal integrator and signal auto-covariance estimator, the minimum detectable signal and cloud detection, and the applications on cloud and precipitation. We will give the results of observations of a number of clouds and precipitation structures, including marine stratocumulus, cirrus, which shows the capability of this radar. Also presented are the liquid water content and the effective radius retrieved by radar.

2. RADAR SYSTEM

a. General description

The State Key Laboratory of Severe Weather (LaSW) of CAMS (Chinese Academy of Meteorological Sciences) has developed a new Doppler radar operating at 8.6 mm wavelength and incorporating a dual-polarization and Doppler capability. The radar is vertically pointing and operates at a frequency of 34.7GHz. The transmitter operates with a peak power of ~ 140kW at a pulse repetition frequency of 1000Hz. Radar system parameters are listed under below.

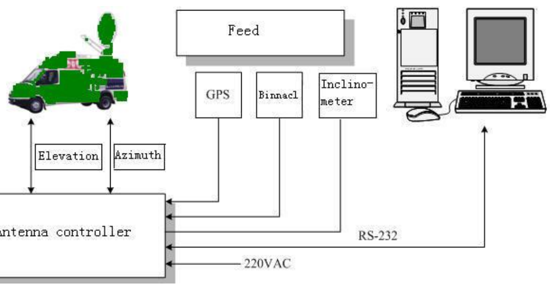

FIG.1 Equipment theory

TABLE1. Performance characteristics

Frequency, wavelength	35GHz, λ =8.6mm
Unambiguous range	30 km
Antenna type	1.5-m diameter
Antenna gain	50 dB
Beamwidth	$0.45°$
Polarization	Linear horizontal
Beam directions	0~$360°$ azimuth, $-2°\sim 90°$ elevation
Rotation rate	$36°$ s^{-1} azimuth, $6°$ s^{-1}elevation
Pulse repetition frequency	1 KHz ~ 3 KHz
Peak output power	> $600W$
Pulse width	$0.3\mu s$ $1.5\mu s$ $20\mu s$

b. Dopplerization and Polarization

The use of Dopplerization and polarization diversity in incoherent radars (McCormick and Hendry, 1975; Seliga and Bringi, 1976) has opened new horizons in the field of remote sensing of the microphysics of clouds and precipitation. Again, recent advances in microwave technology allow polarization techniques to be incorporated in millimeter-wavelength radars. The radar described in this paper has Dopplerization and linear-polarization capability.

c. Antenna

The antenna is equipped with a 2-m-diameter parabolic antenna with an antenna gain of 50dB and a 3-dB beamwidth of 0.3°, resulting in a spatial resolution in the measurements.

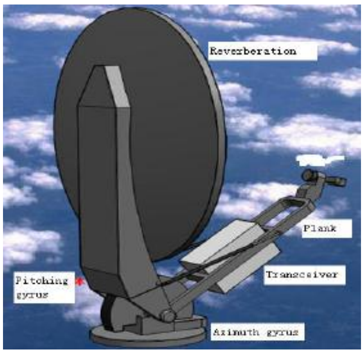

(a)

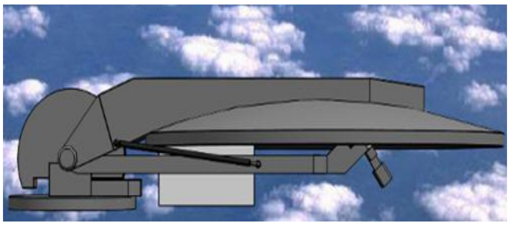

(b)

FIG.2 Antenna on (a) and off (b)

It scans according to a programmable sequence over 360° for full azimuthal coverage, or over azimuthal sectors, with elevation angles ranging from −2° to +90°. The maximum azimuth and elevation rotation rates are 36° s^{-1} and 6° s^{-1} for azimuth and elevation directions, respectively. Also, it will fold down when radar doesn't work. This can help the antenna to keep away from the dust (Fig.2 (b)).

d. Signal processing

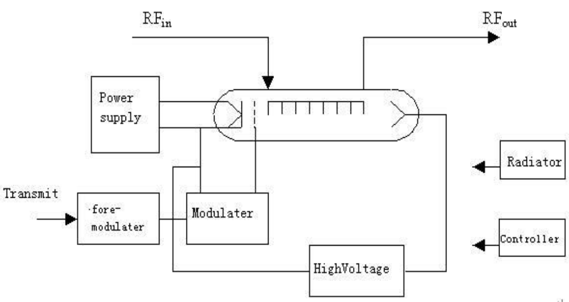

(a)

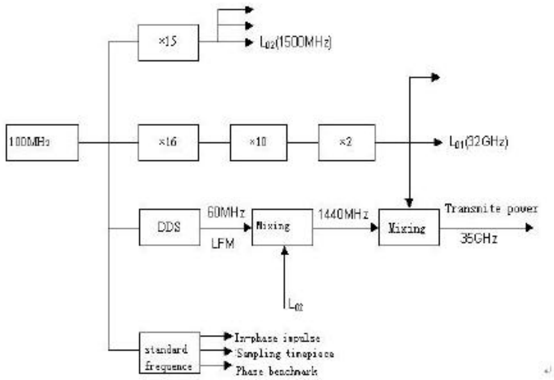

(b)

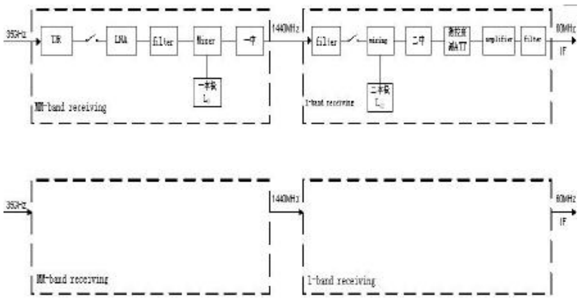

(c)

FIG.3 Transmitter system(a) and receiver system(c)(d).

Two intermediate frequency received by radar will be imported into the receiver to process with A/D 、 digital frequency conversion、creating horizontal IH,QH and vertical IV,QV digital signals. With using PPP or FFT technique to process the two signals, some parameters about radar reflectivity Z, mean velocity V, velocity spectrum width, and LDR can be output.

3. APPLICATIONS OF CLOUD AND PRECIPITATION

a. Radar base products of high clouds

This radar can detect four base parameters including radar reflectivity, Doppler velocity, Doppler spectrum width, and LDR.

Fig.4 shows a detection about high clouds in winter.

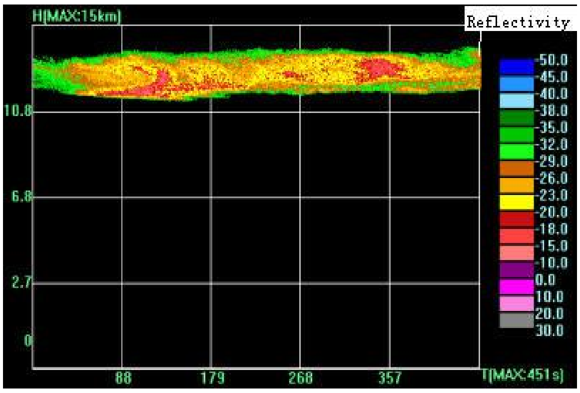

(a)

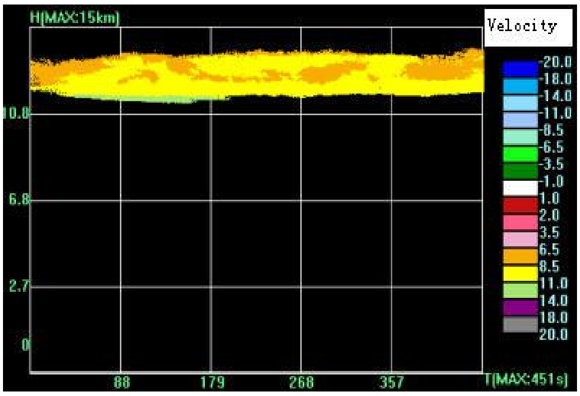

(b)

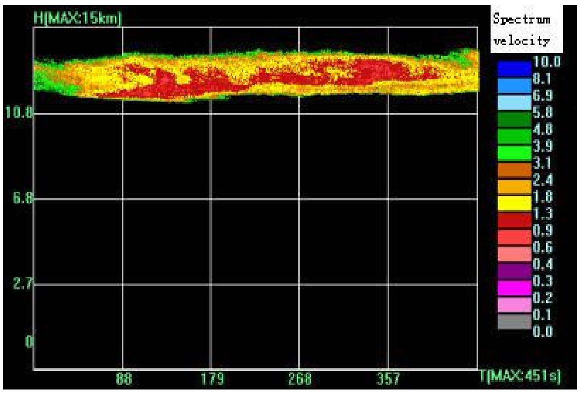

(c)

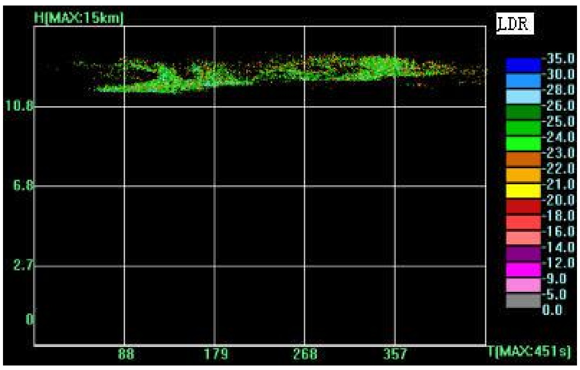

(d)

FIG. 4 Radar base products detected from high cloud: Reflectivity (a), Velocity (b), Doppler spectrum width(c), LDR (d).

b. Cloud top and base height

The radar was pointing vertically. For lower cloud, it's probably to retrieve top and base height using radar reflectivity.

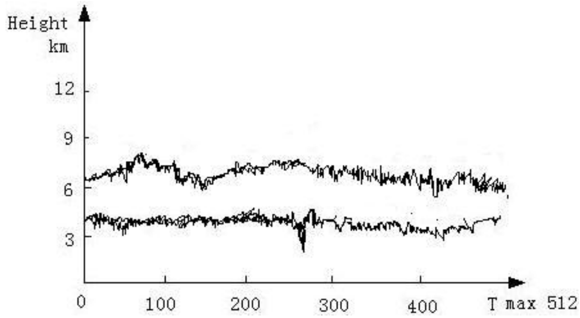

FIG. 5 Cloud top and base height

c. Clouds phase

Since particle size distribution, shape, and fall orientation are interrelated, droplet phase can be classified by radar's polarization capability (Sassen, 1991; Doviak and Zrnic, 1993; Sassen and Benson, 2001; Cao and Liu, 2005), such as one of the linear polarization measurements LDR, which is identified as:

$$L_{DR} = 10\lg(Z_{HV} / Z_{HH})$$

Z_{HV} is the radar reflectivity factor determined by transmitting a vertically polarized signal while measuring the horizontally polarized portion of the backscattered signal. Z_{HH} is the radar reflectivity factor determined by transmitting a horizontally polarized signal while measuring the horizontally polarzed portion of the backscattered signal.

Here, we use parameter V, Z, and L_{DR} to classify water and ice clouds.

d. LWC and r_e

In general there are several different ways to derive the liquid water content and the effective radius of water clouds from ground based remotely sensed data. For single radar technique, a quadratic relationship between reflectivity and liquid water content and effective radius has been established by the formers. (Atlas, 1954; Sauvageot and Omar, 1987; Baedi, 2000.) This relationship was derived by calculating reflectivities from in situ airborn droplet size measurements and relating them to the calculated liquid water content. In this study we retrieved the LWC and r_e for non and weak precipitating water cloud according to the classic relationship.

Classic relationship

Firstly, we assume a gamma distribution over a range of number concentrations N(D):

$$N(D) = AD^{\beta}\exp(-bD)$$

Where D is the droplet radius and A、β、b are the spectrum parameters. We have got a relation between radar reflectivity Z and the spectrum parameters like:

$$Z = A\frac{(\beta+6)!}{b^{(\beta+7)}}$$

also have we another relation between LWC and the parameters:

$$LWC = \frac{\pi\rho A}{6}\frac{(\beta+3)!}{b^{(\beta+4)}}$$

$$r_e = \frac{\beta+3}{b}$$

Then Z-LWC and Z-r_e is established easily.

$$Z = \frac{9}{2\pi^2 kN}\frac{(\beta+6)!}{(\beta+3)!(\beta+3)^3}\frac{LWC^2}{\rho^2}$$

$$LWC = \left(\frac{Z}{a}\right)^{1/b} \qquad r_e = \left(\frac{Z}{c}\right)^{1/d}$$

Table 2 gives a and b value in Z-LWC relationship got by the former scientists.

TABLE2. Classic value of a and b in Z-LWC

	a	b
Atlas(1954)	0.048	2.00
Sauvageot and Omar(1987)	0.030	1.31
Fox and Illingworth(1997)	0.031	1.56
Baedi et al. (2000)	57.544	5.17

4. SUMMARY

A dual-polarization pulse Doppler radar system has been described. The radar uses only one antenna for the transmitter and the receiver, and operates at 8.6mm wavelength with a transmitted peak power of 100kW. The receiver and the data acquisition and processing system allow dual-polarization measurements. Different scan modes can be selected to match the experimental requirements.

Reflectivities and extinction rates were calculated for a wide range of cloud conditions using observed liquid water contents and droplet diameters and assuming gamma distributions. These calculations indicate that the radar, with capability to detect reflectivities as low as -43dBz at a range of 1km, should give returns for nearly all boundary layer status and cumulus but may be unable to detect most altocumulus.

In this article, we Give results of radar base products, cloud top and base height, water and ice clouds, and liquid water content and droplet effective radius. Results of observations of a number cloud structures, including marine stratocumulus, cirrus, and stratus and cirrus are also described.

5. BIBLIOGRAPHY

[1] Atlas, D., 1954: The estimation of cloud parameters by radar. J. Meteor., 11, 309–317.

[2] Austin, R. T., and G. L. Stephens, 2001: Retrieval of stratus cloud microphysical parameters using millimeter-wave radar and visible optical depth in preparation for CloudSat. 1. Algorithm for mulation. J. Geophys. Res., 106, 28 233–28 242.

[3] Baedi et al., 2000 R.J.P. Baedi, J.J.M. de Wit, H.W.J. Russchenberg, J.E. Erkelens and J.P.V. Baptista, Estimating effective radius and liquid water content from radar and lidar based on the CLARE'98 data-set, *Phys. Chem. Earth, B* **25** (2000), pp. 1057–1062.

[4] Doviak R J , Zrnic D S. Doppler Radar and Weather Observations[M] . Academic Press ,1993 , 562

[5] Fox N I , Illingworth A J . The retrieval of stratocumulus cloud properties by ground2based cloud radar [J] . J . Appl. Meteor. 1997 , 36 : 485 - 492.

[6] Frisch, A. S., C. W. Fairall, and J. B. Snider, 1995a: Measurement of stratus cloud and drizzle parameters in ASTEX with aKa-band Doppler radar and a microwave radiometer. *J. Atmos. Sci.,* 52**,** 2788–2799.

[7]http://cloudsat.atmos.colostate.edu/overview

[8] Hobbs, P. V., N. T. Funk, R. R. Weiss, and J. D. Locatelli, 1985: Evaluation of a 35-GHz radar for cloud physics research. *J. Atmos. Oceanic Technol.,* **2,** 35–48.

[9] Junwu Cao, Liping Liu, Runsheng Ge. A study of fuzzy logic method in classification of hydrometeors based on polarimetric radar measurement. Chinese Journal of Atmospheric Sciences2005,29(5)：827~836.

[10] Kropfli, B. W. Bartram, and S. Y. Matrosov, 1990: The upgraded WPL dual-polarization 8-mm-wavelength Doppler radar for microphysical and climate research. Preprints, Conf. on Cloud Physics, San Francisco, CA, Amer. Meteor. Soc., 341–45.

[11] Liu H , Chandrasekar V. Classification of hydrometeor type based on polarimet ric radar measurements : Development of fuzzy logic and neuro2 fuzzy systems , and in situ verification [J] . J . Atmos. Oceanic Technol . , 2000 , 17 : 140 - 164.

[12]Matrosov, S. Y., 2004: Attenuation-Based Estimates of Rainfall Rates Aloft with Vertically Pointing K_a-Band Radars. J. Atmos. Oceanic Technol., 22,1, 43–54.

[13] McCormick, G.C., and A.Hendry, 1975: Principles for the radar determination of the polarization properties of precipitation. Radio Sci., 10, 421-434.

[14] Pasqualucci, F.,1984: Drop size distribution measurements in convective storms with a vertically pointing Doppler radar. Radio Sci.,19,177-183.

[15] Pasqualucci, F., B. W. Bartram, R. A. Kropfli, and W. R. Moninger, 1983: A millimeter-wavelength dual-polarization Doppler radar for cloud and precipitation studies. J. Climate Appl. Meteor.*,* **22,** 758–765.

[16] Sauvageot, H., and J. Omar, 1987: Radar reflectivity of cumulus clouds. J. Atmos. Oceanic Technol., 4, 264–272.

[17] Sassen K, Liao L. Estimation of cloud content by W2band radar [J] . J . Appl . Meteor . , 1996 , 35 : 932 - 938

[18] Sassen K. The polarization lidar technique : A review and current assessment [J] . Bull . Amer . Meteor . Soc. , 1991 , 72 : 1848 -1866.

[19] Sassen K, Benson S. A midlatitude cirrus cloud climatology from the Facility for Atmospheric Remote Sensing. Part II : Microphysical properties derived f rom lidar depolarization [J] . J . Atmos. Sci . , 2001 , 58 : 2103 - 2112.

[20] Sekelsky S M and R E McIntosh. Cloud observation with a polarimetric 33GHz and 95GHz radar. Meteor.Atmos.Phys. 1996,59:123-140.

[21] Seliga, T. A., and V.N.Bringi, 1976: Potential use of radar reflectivity measurements at orthogonal polarization for measuring precipitation. J. Appl. Meteor., 15,69-75.

Acknowledgements. Design and development of the radar was supported by the 23rd graduate school of the Second Academy of China Aerospace. The construction of the radar would not have been possible without the excellent skills of people working in Beijing institute of radio measurement. Chinese Academy of Meteorology and Sciences provided a very health and comfortable environment for our research. We would like to thank Prof. Runsheng Ge of the State Key Laboratory of Severe Weather for the whole work of radar hardware testing. Hongyan Wang and Zhiqiang Zhang contributed for displaying and processing the radar data. Our research is supported by National natural science foundation. We do thanks for the WMO, IUGG,IAMAS and ICCP to support us with financial aid to attend this conference.

RETRIEVAL METHOD OF PATH-INTEGRATED LWC FOR AIRBORNE UPWARD-LOOKING MICROWAVE RADIOMETER USING CLOUD MODEL

ZHOU Jun[1, 2], Lei Heng-Chi[1], WEI Chong[1], HU Zhao-Xia[1], YANG Jun[2], and JI Lei[2]

1 Institute of Atmospheric Physics, Chinese Academy of Sciences, Beijing 100029

2 Nanjing University of Information Science and Technology, Nanjing 210044

1. INTRODUCTION

Cloud liquid water content is always one of the most important quantities in many subjects and operations, particularly in modification weather. In order to detect the path-integrated cloud liquid water content (L), the Institute of Atmospheric Physics, Chinese Academy of Science develops the airborne up-looking microwave radiometer.

1.1 FORMER METHOD (METHOD 1) [1]

In lower and middle troposphere the relationship between bright temperature (Tb) and L is as follow:

$$L(h)=a_1(h)+a_2(h)\times(Tb(h)-a_0(h))+a_3(h)\times((Tb(h)-a_0(h))^2 \quad (1)$$

h is the height of the radiometer; $a_1(h)$, $a_2(h)$, $a_3(h)$ are the coefficients of the equation; $a_0(h)$ is the average value of Tb at the height h. The a_0, a_1, a_2, a_3 are obtained as the function of height.

$$a_j(h)=\sum_{i=0}^{5}a_{ji}(h-h_0)^i,(j=1,2,3) \quad (2)$$

$$a_0(h)=\sum_{i=0}^{3}a_{0i}(h-h_0)^i \quad (3)$$

h_0 is the average value of height and a_{ji}、a_{0i} are the fitting coefficients.

The coefficients of retrieval equation are obtained through statistic regression method. In the former method (method 1), the statistical samples (sample 1) are produced by historic radiosonde data which are employed to determine the vertical distribution of cloud liquid water content by testing for relative humidity above some threshold value. But such method has some shortages: ①As the dynamic and microphysical processes of stratiform cloud are not considered, the statistical samples are not consistent with the synoptic observations very well; ②As the background atmospheric conditions (i.e. the vertical distribution of vapor and oxygen) of the radiosonde data which are from many years have very large differences, the relationship between Tb and L is not quite accurate; ③ It’s not very convenient to pick up radiosonde data from many years for a certain place and a certain month especially during dry season.

1.2 NEW METHOD (METHOD 2 AND 3)

In order to solve the above-mentioned problems, we develop a new retrieval method (method 2) in this paper. The coefficients of retrieval equation are obtained through statistic regression method like former but the statistical samples (sample 2) are produced by the one-dimensional stratiform cloud model [2]. The input of the model include the radiosonde data which is most close to the time when the microwave radiometer works and the actual profile of vertical updraft velocity. The output is the temporal and spatial distributions of cloud liquid water content. As the actual profile of vertical updraft velocity is unknown, we assume several typical profiles [3] (fig. 1) to simulate the possible processes in the stratiform cloud.

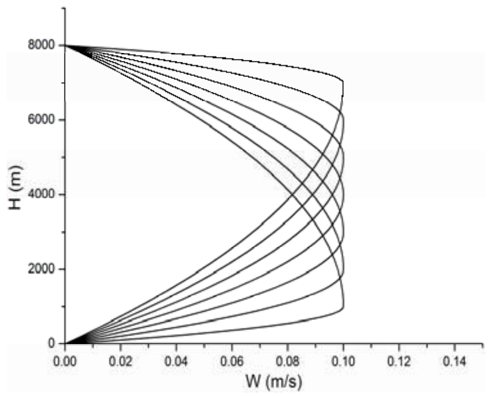

Fig. 1 Profiles of vertical updraft velocity *w* (every line represents a type of profile)

The factor analysis indicates that the errors caused by the uncertainty of the vertical distribution of cloud liquid water content can not be ignored when compared with the errors caused by the background and the instrument drift errors. In order to improve the retrieval accuracy, we use selected cloud samples (sample 3) which are supplied by cloud model to regress retrieval coefficients according to the synoptic observation (method 3).

2 THE CASE OF 8 JULY 2001 IN JILIN

The flight record and the radiosonde date at 8:00 (CST) that day showed that there were large area of Sc and As on the route and the top of the cloud was above 4km.

2.1 METHOD 2

The samples which have two-layer structure in sample 2 is 35.6% while in sample 1 is 12.5%; the samples whose top of cloud exceeding 4km in sample 2 is 100% while in sample 1 is 40.8%. It's obvious that sample 2 is consistent with synoptic observations much better than sample1.

The fig. 2 compares sample 2 and sample 1 at 0.239km (i.e. the altitude of the station) and 4.039km (i.e. the altitude of the flight). We can see that: ① When L is small sample 2 is concentrated in the middle of sample 1. That's because method 2 decreases the uncertainty of backgrounds of the samples. ② When L is large most of the samples in sample 2 are below sample 1 which makes the fitting line of method 2 migrating downward. That's because the tops of clouds in sample 2 are higher and the temperatures of the clouds are lower, so for the same value of L, the corresponding Tb is higher.

The fig. 3 and 4 show the numerical simulation tests [1] for the fitting coefficients obtained from method 1 and 2. The independent test result indicates that the retrieval accuracy of method 2 is better than method 1 at all altitudes and the statistical relative errors has decreased by 0.15%～7.28% .

The fig. 5 show retrieval results of the radiometric data. When we compare this figure with fig. 4 and correlated contents in literature [4], we can see that: ① The two retrieval results have a positive correlationship. ② The retrieval result is correlated with the PPI of radar qualitatively. ③ The improvement is meaningful when compared with the instrument drift errors.

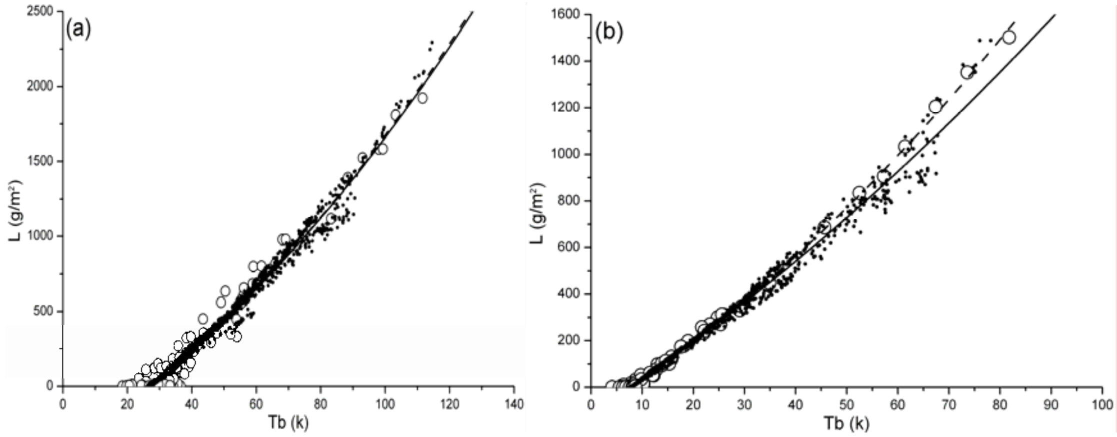

Fig. 2 The comparison of statistical samples at 0.239 km (a) and at 4.039 km (b) produced by method 1 and 2. Open points for fitting sample 1 and dashed line for its fitting line; solid points for fitting sample 2 and solid line for its fitting line

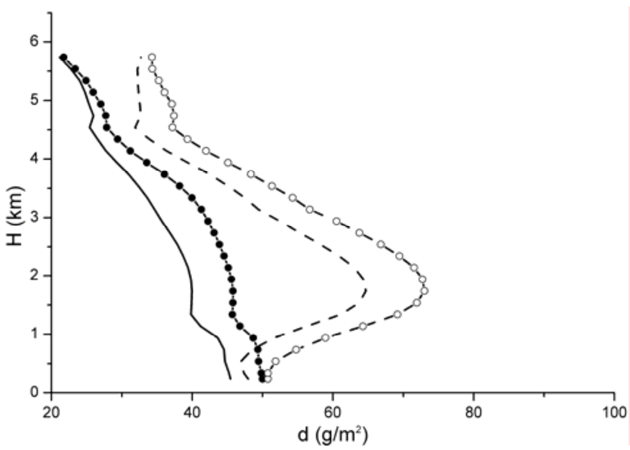

Fig. 3 RMS-errors of retrieved integrated liquid water content with its simulated 'true'
Solid line for self-test results of coefficient 2; dashed line for self-test results of coefficient 1. Solid points for independent test results of coefficient 2; open points for independent test results of coefficient 1

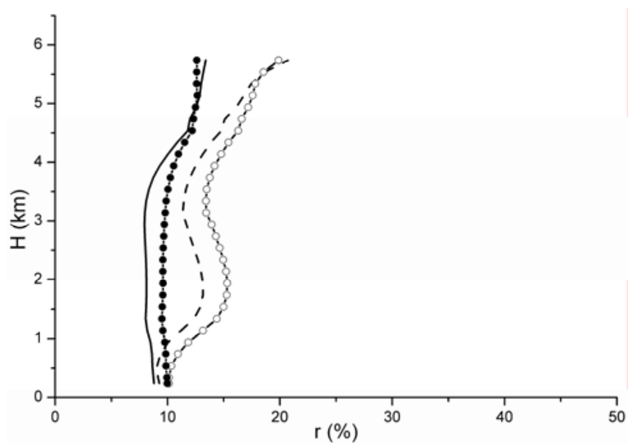

Fig. 4 The same as fig. 3, but for relative errors

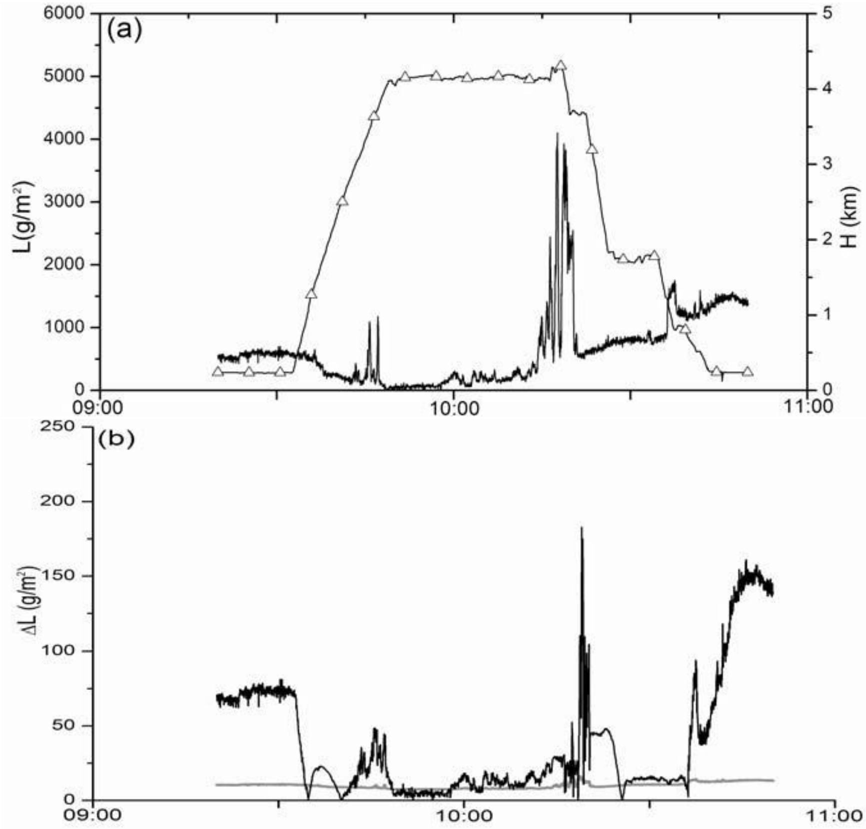

Fig. 5 Retrieval results of the radiometric data in 8 July 2001 with method 1 and 2: (a)Method 2, solid line for temporal series of L, open triangle for flight height measured by a GPS system; (b) Black line for absolute difference between retrieval results of method 1 and 2, gray line for maximum absolute errors caused by instrument drift errors

2.2 METHOD 3

In this method, we select the samples which have two-layer structure and whose tops of clouds exceeding 4km according to the synoptic observation.

The independent test results in fig. 6 and 7 indicate that RMS-errors and relative errors decrease at all altitudes and the relative errors decrease by 0.9%～15.9% when compared with method 1 and 0.5%～4.6% when compared with method 2. In conclusion, method 3 makes a further improvement of retrieval accuracy.

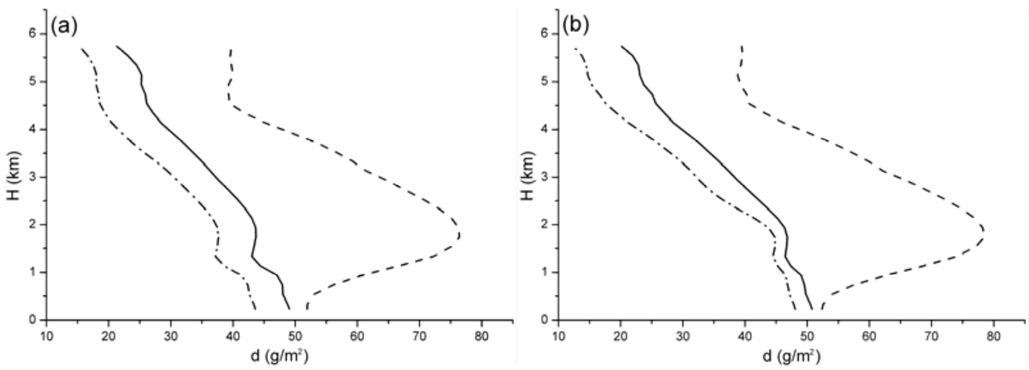

Fig. 6 RMS-errors of retrieved column liquid water content with its simulated 'true'

(a)Self-test; (b)Independent test

Dashed line for method 1; solid line for method 2; dot-dashed line for method 3

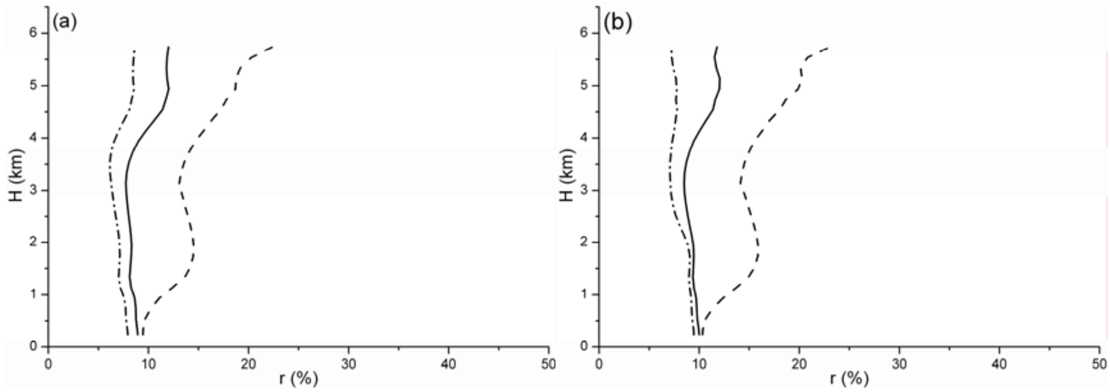

Fig. 7 The same as fig. 6 but for relative errors

3 CONCLUSIONS

Besides the case of 8 July 2001, we have made experiments on more cases, such as 9 July 2001 and 22 April 2002 in Jilin. They all show some similar results:

①The statistical samples of new method are consistent with the synoptic observations much better than the samples of former method.

②The uncertainty of the background field decreases obviously.

③The retrieval accuracy of method 3 increases by 0.9% ～ 37.2% when compared with method 1. This improvement is meaningful when compared with the instrument drift errors.

④The horizontal distributions of L are correlated with the distributions of PPI echo intensity of surface weather radar very well.

REFERENCES

[1] Jiang Fang, Wei Chong, Lei Hengchi et al. Measurement of column cloud liquid water content by airborne upward-looking microwave radiometer. (II): Retrieval method. Plateau Meteorology (in Chinese), 2003, **23**(1): 33~39

[2] Hong Yanchao. A Numerical model of mixed convective-stratiform cloud. Acta Meteorologica Sinica, 1997, **11**(4): 489~502

[3] Cui Zhehu. Space-borne microwave remote sensing of stratified precipitating cloud. Ph. D. dissertation (in Chinese). Institute of Atmospheric Physics, Chinese Academy of Sciences, 1999

[4] Lei Hengchi, Wei Chong, Shen Zhilai et al. Measurement of column cloud liquid water content by airborne upward-looking microwave radiometer. (I): Instrument and its calibration. Plateau Meteorology (in Chinese), 2003, **22**(6): 551~557

Acknowledgements

I am grateful to my teachers for their helpful suggestions and solicitudes. This research is funded by the National Natural Science Foundation under contract 40537034 and Chinese academy of Sciences Knowledge Innovation Program under contract KZCX3-SW-225.